

EBA13²⁰²⁰

13th Brazilian Meeting on Adsorption

DIGITAL

Diana Cristina Silva de Azevedo
Moisés Bastos-Neto
(Organizadores)



UNIVERSIDADE
FEDERAL DO CEARÁ
PRÓ-REITORIA DE
PESQUISA E PÓS-GRADUAÇÃO



FILIAÇÃO A





EBA13²⁰²⁰

13th Brazilian Meeting on Adsorption

DIGITAL

CONFERENCE E-BOOK



Fortaleza
2021



Presidente da República

Jair Messias Bolsonaro

Ministro da Educação

Milton Ribeiro



UNIVERSIDADE FEDERAL DO CEARÁ – UFC

Reitor

Prof. José Cândido Lustosa Bittencourt de Albuquerque

Vice-Reitor

Prof. José Glauco Lobo Filho

Pró-Reitor de Pesquisa e Pós-Graduação

Prof. Jorge Herbert Soares de Lira

Pró-Reitor de Planejamento e Administração

Prof. Almir Bittencourt da Silva



IMPRENSA UNIVERSITÁRIA

Diretor

Joaquim Melo de Albuquerque

Anais do 13th Brazillian Meeting on Adsorption

Copyright © 2021 by Diana Cristina Silva de Azevedo, Moisés Bastos-Neto.

Todos os direitos reservados

PUBLICADO NO BRASIL / PUBLISHED IN BRAZIL

Imprensa Universitária da Universidade Federal do Ceará (UFC)
Av. da Universidade, 2932, fundos – Benfica – Fortaleza – Ceará

Coordenação editorial

Ivanaldo Maciel de Lima

Capa

Valdiano Macedo

Dados Internacionais de Catalogação na Publicação
Bibliotecária Perpétua Socorro Tavares Guimarães CRB 3/801-98

13 th Brazilian Meeting on Adsorption (13. : 2020)

Anais (recurso digital) 13th Brazilian Meeting on Adsorption, November 25- December 3, 2020. Organized by Diana Cristina Silva de Azevedo, Moisés Bastos-Neto. - Fortaleza: Imprensa Universitária, 2021.

1101 p.

(Edição Digital)

ISBN: 978-65-88492-52-9

DOI: <http://doi.org/10.51996/9786588492529>

1. Adsorção- aplicações ambientais –Brasil I. Azevedo, Diana Cristina Silva de
II. Bastos-Neto, Moisés III. Título.

CDD: 660.284

PROCEEDINGS

ANAIS DO EVENTO

EBA13 2020
13th Brazilian Meeting on Adsorption
DIGITAL

13th BRAZILIAN MEETING ON ADSORPTION

FOREWORD

The Brazilian Meeting on Adsorption (acronym EBA, in Portuguese) has been held every two years since 1996 by different institutions across the country, alternating venues in the Northeast and South/Southeast regions. The main objective of the conference is to bring together the scientific, academic and industrial communities related to the Adsorption field in Brazil and abroad, seeking greater interaction between the R&D groups and national/international companies. In addition, the event disseminates the science of Adsorption in the academic and industrial environment, showcasing the latest progress in the area, fostering interaction and networking among researchers in this field.

The program comprised three main tracks: scientific, technical and educational. The technical-scientific contribution took place by the presentation of new findings by scientists and practitioners in the area of adsorption, encouraging the dissemination of research, the discussion of ideas and match-making among researchers from different locations. The educational aspect of the event was also present, through the Adsorption School, an opportunity for participants to attend tutorial lectures delivered by a balanced mix of senior and junior scientists, focusing on fundamentals and applications of adsorption.

Due to the Covid19 pandemic of year 2020, the 13th edition of the meeting exceptionally became 100% digital. The conference was chaired by Prof. Diana Azevedo and broadcasted live by a digital platform from Nov 30th to Dec 3rd 2020. All conference contents (lectures, discussions, poster and paper files) were available for viewing by the participants up to 30 days after the conference closure.

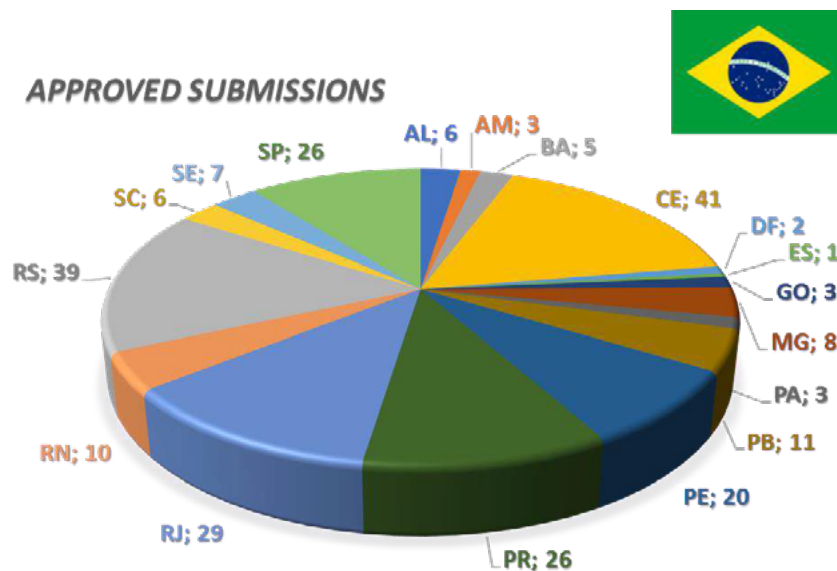
For the first time in the history of this conference series, English was adopted as the official written language. During the meeting, the Brazilian Adsorption Society was established. There were 4 keynote lectures, 6 plenary lectures and 20 invited talks presented by outstanding scientists from Brazil and from abroad. The technical sessions comprised 51 oral presentations and 131 poster presentations with intense discussion and interaction mediated by the digital platform made available by the event organizers.

Despite the innovative format of this digital event, EBA 13 attracted the registration of 230 attendees among academicians, scientists, (graduate and undergraduate) students and industrial practitioners from Chemistry, Chemical Engineering, Materials Engineering, Food Engineering, Environmental Engineering, Physics and related fields. This E-book brings the proceedings of the event, highlighting this historical landmark of a fully digital scientific meeting, 24 years after the 1st in-person edition, organized again by UFC.

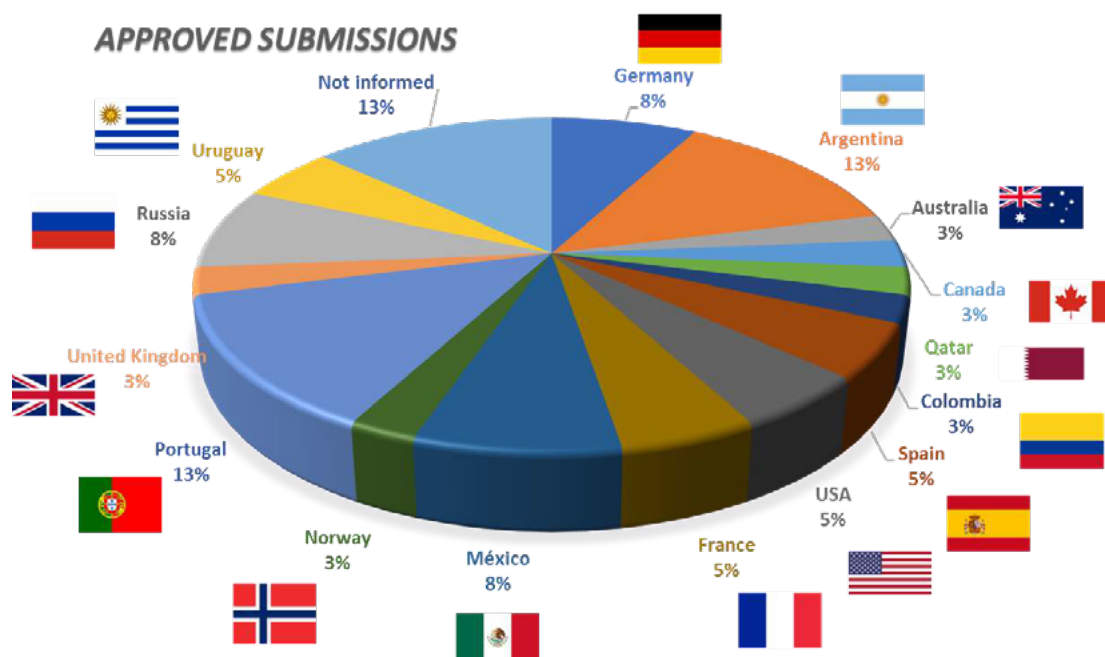


Fortaleza, March 2021
EBA13 Organizing Committee

The conference in numbers



TOTAL FROM BRAZIL: 246 (87%)



Organizing committee

Chair

Diana Cristina Silva de Azevedo

Andréa da Silva Pereira
Antônio Eurico Belo Torres
Célio Loureiro Cavalcante Júnior
Daniel Vasconcelos Gonçalves
Débora Aline Soares Maia
Enrique Vilarrasa-Garcia
Francisco Murilo Tavares de Luna
Hugo Leonardo de Brito Buarque
Ivanildo José da Silva Junior
José Carlos Alexandre de Oliveira
Juliana Amorim Coelho
Maria Cristiane Martins de Souza
Moisés Bastos-Neto
Pedro Felipe Gadelha Silvino
Rafaelle Gomes Santiago
Rodrigo Silveira Vieira
Sebastião Mardônio Pereira de Lucena

Scientific committee

Chair

Moises Bastos-Neto

Adonay Rodrigues Loyola
Adriano da Silva
Adriano Rodrigues Azzoni
Amaro Gomes Barreto Júnior
Andréa da Silva Pereira
Antônio Souza de Araújo
Celmy Maria Bezerra de Menezes Barbosa
Cesar Augusto Moraes de Abreu
Cesar Costapinto Santana
Daniel Vasconcelos Gonçalves
Dárley Carrijo de Melo
Débora Aline Soares Maia
Dilson Cardoso
Enrique Vilarrasa-Garcia
Everaldo Silvino
Flávio Luiz Honorato da Silva
Francisco Murilo Tavares de Luna
Francisco Wilton Miranda da Silva
Frederico Wanderley Tavares
Guilherme Luiz Dotto
Heloise Pastore
Hugo Leonardo de Brito Buarque
Igor Tadeu Lazzarotto Bresolin
Indianara Conceição Ostroski
Ivanildo José da Silva Junior
José Carlos Alexandre de Oliveira
Juliana Amorim Coelho
Jussara Lopes de Miranda
Liliana Amaral Feris
Lucas Meili
Lucienne Lobato Romanielo
Luís Antonio de Almeida Pinto
Marcelino Luiz Gimenes
Marcos Juliano Prauchner
Maria Cristiane Martins de Souza
Marisa Masumi Beppu
Maurício Alves da Motta Sobrinho
Meiry Gláucia Freire Rodrigues
Melissa Gurgel Adeodato Vieira
Meuris Gurgel Carlos da Silva
Nehemias Curvelo Pereira
Nina Paula Gonçalves Salau
Odelsia Leonor Sanchez de Alsina
Pedro Augusto Arroyo
Pedro Felipe Gadelha Silvino
Rafael Barbosa Rios
Rafaelle Gomes Santiago
Regina De Fátima Peralta Muniz Moreira
Rodrigo Silveira Vieira
Ronaldo Ferreira do Nascimento
Sebastião Mardônio P. Lucena
Selene Maria de Arruda Guelli Ulson de Souza
Sibele Berenice Castellã Pergher
Simone Monteiro e Silva
Sônia Maria Alves Bueno
Tirzhá Lins Porto Dantas

EBA13 2020 DIGITAL

13th Brazilian Meeting on Adsorption

November 25 - December 3,
2020

With the sponsorship and support of



Promoted by



Managed by



Featured by



UNIVERSIDADE
FEDERAL DO CEARÁ

Summary

1. Program

Day 01 – Nov 30th

Day 02 – Dec 01st

Day 03 – Dec 02nd

Day 04 – Dec 03rd

2. **Keynote lectures**

3. **Plenary lectures**

4. **Invited lectures**

5. Papers in oral sessions

FA: Fundamentals of Adsorption

SCAC: Synthesis and Characterization of Adsorbents and Catalysts

AMB: Environmental

MSPA: Molecular Modeling and Simulation of Adsorptive Processes

PG: Oil and Natural Gas

PA: Adsorption Processes

BIO: Biotechnology

6. Papers in poster sessions

FA: Fundamentals of Adsorption

SCAC: Synthesis and Characterization of Adsorbents and Catalysts

AMB: Environmental

MSPA: Molecular Modeling and Simulation of Adsorptive Processes

PG: Oil and Natural Gas

PA: Adsorption Processes

BIO: Biotechnology



Brazil Time (UTC-3)	Monday, Nov 30 th		
8:30 – 8:50	Opening Ceremony 13EBA		
9:00 – 9:45	Keynote 1 Paul Webley Temperature Swing Adsorption for CO ₂ Capture: A Perspective		
10:00 – 10:35	Plenary 1 Lev Sarkisov From Crystal to Column: multiscale strategies in the design of PSA processes for carbon capture		
10:45 – 11:10	Invited Speaker 1 Alexandre Ferreira Water harvesting by MOF based TSA processes	Invited Speaker 2 Dárley Carrijo Offshore Natural Gas Processing for Sustainable Oil & Gas Production	Invited Speaker 3 Everaldo dos Santos Expanded Bed Adsorption (EBA) – An important integrative technique in downstream processing
11:10 – 11:55	102 - Separation of ethylene from ethane with Metal-organic Frameworks	23 - Adsorption kinetics of asphaltenes in oil-water interfaces: effects of time, concentration, and heptol ratios	240 - Method for estimation the protein binding affinity using a robust Poisson-Boltzmann model for the adsorption of lysozyme in SBA-15
	182 - Optimization of Temperature Swing Adsorption Unit for Gas Dehydration	244 - Simulation of high-pressure sour natural gas adsorption on 13X zeolite	130 - Adsorption capacity evaluation of Beta zeolite as adsorbent for isoniazid.
	Q&A (PA)	289 - Adsorption of Polycyclic Aromatic Hydrocarbons from Heavy Naphthenic Oil: Evaluation of the Adsorbent Regenerability	Q&A (BIO)
11:55 – 12:10	Q&A (PG)		
14:00 – 14:15	Ametek do Brasil - Molecular Sieve Pilot Plants for Hydrocarbons Analysis Samuel Santos		
14:15 – 14:30	Networking Session with Acil & Weber Adsorption studies of porous and nonporous materials with various adsorptives in the entire temperature range from 77 K up to 323 K Mauro Weber		
14:30 – 14:55	Invited Speaker 4 Dilson Cardoso Synthesis of a zeolite for drying natural gas	Invited Speaker 5 Liliana Feris Adsorption of pharmaceutical compounds: challenges and perspectives	Invited Speaker 6 Dr Rodrigo Silveira Vieira Adsorption on bio-based materials
14:55 – 15:40	74 - CO ₂ adsorption on LTA zeolite with different particle dimensions	169 - Study of the effect of the HLD cations precursors on the removal of arsenic in aqueous solutions	127 - D-optimal experimental designs for adsorption isotherms
	223 - Application of In-situ X-ray Characterization Techniques in Zeolites: A Review	179 - Evaluation of dried <i>Salvinia auriculata</i> as a biosorbent in natura in lead removal in aqueous solutions	273 - Insights on the use of different gases at 77 K to assess the specific surface area of silica nanoporous materials
	302 - Synthesis of zeolites from hydrothermal solution reuse for CO ₂ capture	277 - Metals ions adsorption using synthesized 4A zeolite: effect of coal fly ash as silica and aluminum source	345 - Isotherm, kinetic and thermodynamic studies of Rhodamine B adsorption on coconut fiber-based adsorbents
15:40 – 15:55	Q&A (SCAC)	Q&A (AMB)	Q&A (Oral 6)
16:05 – 16:30	Posters 1 (PA & PG)		
16:30 – 17:15	Q&A Session (Posters PA)		Q&A Session (Posters PG)
17:15 – 17:50	Plenary 2 Fateme Rezaei Multicomponent Adsorptive Separation of CO ₂ , CO, CH ₄ , N ₂ , and H ₂ over Core-Shell Zeolite@MOF Composite Adsorbents		



Brazil Time (UTC-3)	Tuesday, Dec 1 st		
9:00 – 9:45	Keynote 2 Conchi Ania Combining gas adsorption and in situ XRD to describe unusual gas adsorption features of nanoporous materials		
10:00 – 10:35	Plenary 3 Tereza Bandosz Towards highly efficient gas desulfurization adsorbents: exploring porosity development in biosolid- based materials		
10:45 – 11:10	Invited Speaker 7 Lucas Meili Malachite Green adsorption onto Mytella falcata shells: preliminary studies	Invited Speaker 8 Nina Salau Computational intelligence applied to adsorption processes	Invited Speaker 9 E. Rodrigues-Castellón Assessing CO ₂ Adsorption on amino-functionalized mesocellular foams synthesized at different aging temperature
11:10 – 11:55	225 - Technological Bottlenecks in purification of monoclonal antibodies: prospective study and proposals for improved process design	108 - Optimization of an Aromatics Complex Including a Simulated Moving Bed for p-Xylene Production	72 - CO ₂ capture in carbon microfibers doped with nitrogen
	231 - Effect of temperature on oxidative degradation of bleached Hybrid (<i>E. guineensis</i> x <i>E. oleifera</i>) and Africanpalm oil (<i>Elaeis guineensis</i>)	124 - Critical review of batch adsorption kinetic models: simplifications derived from the infinite bath model	275 - Characterization of mesoporous region by the scanning of the hysteresis loop in adsorption-desorption isotherms
	247 - Adsorption of a synthetic red food-colorant by circulating percolation of the solution through a packed-bed of wheat bran	207 - Studies of interaction potentials effects in the DFT approach for confined fluids	353 - Importance of the Polarity on Nanostructured Silica Materials to Optimize the Hydrolytic Condensation of Molecules Related to CO ₂ Adsorption
11:55 – 12:10	Q&A (PA)	Q&A (MSPA)	Q&A (SCAC)
14:00 – 14:15	Pensalab - On-line Monitoring of Trace H₂O levels in Natural Gas at the Outlet of Molecular Sieve Dehydration Vessels Michael Downey		
14:30 – 14:55	Invited Speaker 10 Igor Bresolin Ultrapure monoclonal antibodies: hydrophobic interaction chromatography as polishing step in downstream processing	Invited Speaker 11 Sibele Pergher Molecular sieves: tunable porosity materials for adsorption and catalytic processes	Invited Speaker 12 César Abreu Simultaneous adsorption and desorption of CH ₄ -CO ₂ to improve the storage capacity of natural gas
14:55 – 15:40	66 - Antibiotic removal from water using MgFe/layered double hydroxide as adsorbent	21 - Amino-functionalized graphene oxide anchored in charcoal matrix as adsorbent of textile wastewater: characterization and adsorption properties	75 - Thermodynamics of adsorption systems based on nanoporous carbons for methane storage and transportation
	135 - Purification of rabbit polyclonal IgG using dye ligandaffinity chromatography	22 - Removal of the Drimaren Red from aqueous solutions by adsorption onto amino-Fe ₃ O ₄ -functionalized multilayer Graphene Oxide	268 - Characterization of sorption kinetics of CO ₂ from N ₂ -rich gas mixtures studied by breakthrough experiments on Zeolites
	148 - Elution conditions for purification of rabbit polyclonal antibodies using Protein A column	Q&A (SCAC)	286 - Carbon dioxide and water vapor adsorption on commercial and synthesized zeolites
15:40 – 15:55	Q&A (BIO)		Q&A (FA)
16:05 – 16:30	Posters 2 (BIO & SCAC)		
16:30 – 17:15	Q&A Session (Posters BIO)		Q&A Session (Posters SCAC)
17:15 – 17:50	Plenary 4: Guilherme Dotto Alternative adsorbents from wastes and its application for water decontamination		



Brazil Time (UTC-3)	Wednesday, Dec 2 nd	
9:00 – 9:45	Keynote 3 Mardônio Lucena New perspectives in carbon based materials characterization	
10:00 – 10:35	Plenary 5 Philip Llewellyn Using adsorption calorimetry to highlight the flexible behavior of Metal-Organic Frameworks	
10:45 – 11:10	Invited Speaker 13 Marcelo Castier Modeling Adsorption in Porous Solids with Equations of State for Confined Fluids	Invited Speaker 14 Marisa Beppu Influence of surface topography parameters on macromolecule deposition in LbL (layer-by-layer) processes
11:10 – 11:55	56 - Adsorption-induced deformation of porous solids. New approach for estimation of compressibility factor of microporous carbon adsorbents	47 - Organosolv lignin/Fe3O4 nanoparticles applied as textile dye adsorbent
	175 - Mesoporous metal-organic structure MIL-100 (Fe) as drug carrier	80 - Lipases Immobilization via Adsorption on Laboratory-Scale Synthesized Graphene Oxide Using Modified Hummers Method and Magnetic Nanoparticles
	288 - Assessment of Intracrystalline Diffusion for C8 Aromatics Isomers in Beta Zeolite using the ZLC Technique	209 - Evaluation of lipase A from Candida antarctica immobilization onto agroindustrial residue by Taguchi method
11:55 – 12:10	Q&A (FA)	Q&A (BIO)
14:00 – 14:15	Hidden Isochema - Measuring binary gas adsorption equilibria using the Integral Mass Balance (IMB) method Darren Broom	
14:30 – 14:55	Invited Speaker 15 Pedro Arroyo High Pressure H2S Adsorption from Natural Gas Streams Using Zeolite NaY	Invited Speaker 16 Amaro Barreto Jr. Challenges to connect the effects of fluid confinement to the engineering of adsorption systems
14:55 – 15:40	92 - Regeneration of granular activated carbon using thermal technique	156 - Modeling adsorption microcalorimetry to estimate intraparticle diffusion rate constants: Parameter sensitivity analysis.
	115 - Multiscale Design Of A Pressure Swing Adsorption Process For Natural Gas Purification	246 - Separation of Methane and Carbon Dioxide mixtures by Adsorption on Calcite Nanopores via Molecular Dynamics
	254 - Perspectives on the synthesis, characterization, and application of hydroxyapatite-based sorbents for gaseous mercury removal	279 - Importance of Molecular Simulation for Interpreting Gas Adsorption by Porous Materials: The Case of the Ethane/Ethylene Mixture
15:40 – 15:55	Q&A (PA)	Q&A (MSPA)
16:05 – 16:30	Posters 3 (FA & MSPA)	
16:30 – 17:15	Q&A Session (Posters FA)	Q&A Session (Posters MSPA)
17:15 – 17:50	GENERAL MEETING - BAS (Brazilian Adsorption Society) FOUNDATION	
17:50 – 18:00		



Brazil Time (UTC-3)	Thursday, Dec 3 rd	
9:00 – 9:45	Keynote 4 Carlos Grande Cost-Based approach to design biogas upgrading systems	
10:00 – 10:35	Plenary 6 Reiner Staudt Investigation of Mixed Gas Sorption in Lab-Scale Experiment and Evaluation	
10:45 – 11:10	Invited Speaker 17 Regina Moreira Application of geopolymers in carbon capture and sequestration	Invited Speaker 18 Adriano Azzoni Development and evaluation of adsorbents for plasmid DNA purification
11:10 – 11:55	68 - Concentration of anthocyanins from Pinot Noir grape skins in alginate beads through the adsorption operation	119 - Enzyme immobilization by adsorption: CALB lipase onto magnetic nanoparticles, a heterogeneous biocatalyst.
	191 - High-Pressure Bulk CO ₂ Gas Adsorption on a Fixed Bed of Zeolite NaY: upward and downward flow comparison	269 - Adsorption of paracetamol from aqueous solutions on activated carbons
11:55 – 12:10	Q&A (BIO)	
12:10 – 12:30	Q&A (PA)	
14:30 – 14:55	Invited Speaker 19 Marcos Prauchner The use of H ₃ PO ₄ activated carbons as support in catalysts intended for the production of biofuels through the hefa route	Invited Speaker 20 César Santana Adsorption in Oil/Water Interfaces: Aspects of Kinetics and Equilibrium in Systems Containing Asphalthenes
14:55 – 15:40	26 - Iron oxide nanoparticles: design of the reactor for synthesis and characterization	267 - Breakthrough Curves of Propane at Different Relative Humidities
	264 - Trimodal hierarchical zeolite LTA for adsorption: a preliminary characterization study	280 - H ₂ O sorption on nanoporous carbons
15:40 – 15:55	Q&A (SCAC)	Q&A (FA)
16:05 – 16:30	Posters 4 (AMB)	
16:30 – 17:15	Q&A Session (Posters AMB)	
17:15 – 17:50	Closing Ceremony	
17:50 – 18:00		



Keynote lectures

Keynote 1: Paul Webley

kn-01

Temperature Swing Adsorption for CO₂ Capture: A Perspective

Keynote 2: Conchi Ania

kn-02

Combining gas adsorption and in situ XRD to describe unusual gas adsorption features of nanoporous materials

Keynote 3: S. Mardônio P. de Lucena

kn-03

New perspectives in carbon based materials characterization

Keynote 4: Carlos Grande, Boguslaw Ziemniak

kn-04

Cost Based approach to design biogas upgrading systems



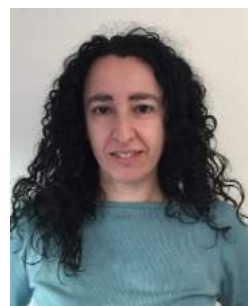
Speakers



Professor **Paul Webley** is currently a Professor of Chemical Engineering and Director of the Woodside Monash Energy Partnership at Monash University. He has a PhD in Chemical Engineering from MIT (1990). In his current role, he is responsible for driving the decarbonization transition for Woodside through innovative research and leadership in new energy, carbon technology, and business models. Prior to this role, Prof Webley was Professor and Director of the Clean Energy Laboratory at The University of Melbourne and Head of the Department of Chemical Engineering. The Laboratory has produced over 300 papers in scientific and engineering journals and books, which has attracted over 15,000 citations and received over \$10m in research funding. His interests are adsorption science and technology for CO₂ capture and conversion, application of thermodynamics to energy systems, and the development and use of advanced hydrogen technologies.

<https://orcid.org/0000-0003-3598-3767>

Conchi Ania received her PhD degree in Chemistry by the University of Oviedo (Spain) in 2003, and performed postdoctoral stays in USA (City College of New York), and France (CNRS). In 2007 she incorporated to Instituto Nacional del Carbón (Spain) belonging to Agencia Estatal CSIC where she is Investigador Científico (currently in leave of absence). In 2017 she also joined CNRS (France) as Directrice de Recherche at CEMHTI (Orléans), where she is the head of POR2E research group. Current research interests focus on the use of nanoporous solids for water treatment (photocatalytic, electroassisted processes), gas adsorption and separation, and solar energy conversion. As for scientific contributions, she has supervised 9 PhD theses and published over 155 papers in peer-reviewed scientific journals with an H-index of 43. She is also coinventor of two patents, one of them transferred to industry on the preparation of porous materials for gas separation.



<https://orcid.org/0000-0001-9517-8132>



Mardônio Lucena is associate professor at the Federal University of Ceará, Brazil. PhD in Chemical Engineering from the State University of Campinas. Research internship in the Prof. Snurr molecular simulation group at Northwestern University - USA. Research interest in molecular simulation with emphasis on adsorption and transport properties methods based on statistical mechanics (Monte Carlo and molecular dynamics) applied on new adsorbents for CO₂ capture, characterization of materials, energy storage and separations by adsorption.

<https://orcid.org/0000-0001-8379-2098>

Carlos A. Grande got a PhD degree at the University of Porto (Portugal) in 2005. His thesis was about adsorption processes for propane – propylene separation, supervised by Prof. Alirio Rodrigues. Since 2011, he works in SINTEF in Oslo, Norway where he is now Senior Research Scientist. In SINTEF he works in two topics: adsorption processes and process intensification by digitalization of the chemical industries. He coordinates different projects from industry, Norwegian Research Council and European.

<https://orcid.org/0000-0002-9558-5413>



Temperature Swing Adsorption for CO₂ Capture: A Perspective

Paul Webley

Department of Chemical Engineering, Faculty of Engineering, Monash University, Wellington Road, Clayton, VIC 3800, Australia

Abstract

CO₂ capture is conventionally done using a liquid solvent-based scrubber/stripper system. Although based on a mature motif, this system has undergone significant improvements in efficiency and scale over the past 20 years, promoted by the urgency of climate change and the promise of carbon capture and storage as a potential mitigation strategy. In contrast, capture of CO₂ using solid adsorbents is relatively, commercially, immature. A vast amount of adsorbent development work has been done focusing on both chemical and physical adsorbents and some pilot scale testing has demonstrated the concepts and highlighted engineering limitations but to date, there are no commercially operating large scale adsorbent based CO₂ capture systems. In this presentation, I will discuss the aspects of adsorption based temperature swing adsorption, which bear on its limitations, and highlight the fundamental and engineering obstacles which must be overcome in order for temperature swing adsorption to move from the laboratory or pilot plant to large scale application.

Keywords: gas separation; adsorption; TSA; CCS

Combining Gas Adsorption and In-Situ XRD to Describe Unusual Adsorption Features of Nanoporous Materials

Conchi Ania^{a,b,*}

^a CEMHTI (CNRS UPR 3079) 45071, Orléans, France

^b Instituto Nacional del Carbón (INCAR, CSIC) 33080 Oviedo, Spain

Abstract

The characterization of the nanoporous structure of materials from the analysis of experimental adsorption isotherms of various gases and temperatures is a valuable tool to comprehend the features of highly porous materials with tailor-made high surface areas and pore volumes in the full nanopore range. While the determination of surface areas and microporosity seems to be fairly understood, the assessment of the pore network structure for mesoporous materials (particularly for disordered ones) is still a challenge, and remains a widely investigated topic. In this regard, useful information can be obtained from a proper interpretation of hysteresis loops of the adsorption isotherms, in combination with advanced experimental procedures such as hysteresis scanning. In this work we have analyzed the gas adsorption features of ultrahigh pore volume materials showing unusual shapes in the gas adsorption isotherms. The analysis of the experimental data combining various probes (e.g. N₂, Ar, CO₂), temperatures, and scanning hysteresis and different models has revealed interesting information about the porosity of these materials and the connectivity of the porous network. Also, combining adsorption with in-situ synchrotron radiation XRD, we will discuss the insights on the mechanisms governing structural deformations during gas adsorption of various solids (i.e., ZIFs and zeolites) displaying unusual multi-stepped gas adsorption features and varied porosity and topology.

This work has been funded by the ERC through a Consolidator Grant (648161), the ESRF (MA 3691) and the Spanish MINECO (25-01-1057, 25-01-1001, 25-01-965, 25-01-888, 25-01-492 25-01-1006, 25-02-774).

Keywords: in-situ XRD; high resolution gas adsorption; scanning hysteresis; porosity.

New perspectives in carbon based material characterization

Sebastião Mardonio Pereira de Lucena^a

^a *Laboratório de Modelagem e Visualização 3D, GPSA, Dept. Chem. Engineering Universidade Federal do Ceará, Campus do Pici, Bl. 709, 60455-760, Fortaleza, CE, Brazil*

Abstract

Carbons are fascinating nanoporous materials useful in many separation process and catalysis. The lack of long range order makes advanced experimental techniques like neutron diffraction and HRTEM (high-resolution transmission electron microscopy), to extract only indirect data from structural elements. Thus modeling and simulation tasks become exceptionally challenging. Our group has sought procedures for the generation of less arbitrary model morphologies, particularly in the explicit heterogeneous structures associated with the oxidative process. A major advance in obtaining those realistic structures from oxidative process was achieved by applying reactive molecular dynamic in graphene-based models. The potentials of reactive molecular dynamic allow the study of large-scale chemical reactions with rigor similar to quantum methods. We use these potentials to generate graphene structures where no empirical precondition is established in the process, only the underlying chemical phenomena oriented by bond distance/bond order relations to enable formation and dissociation of bonds. The new heterogeneous models obtained presented improved performance compared to implicit models (DFT-density function theory) in the reproduction of reference experimental adsorption isotherms and heat from different carbons. The existence of such reliable explicit models, appropriated to kernels, allows extensive studies which were previously not possible. As an example of these studies, we present a new proposal for the design of heterogeneous multikernels that is based on: 1 our realistic models of activated carbon; 2- reproducibility of carbon energy diversity and 3 testing on virtual models. These new tools offer in-deep structural insights and open up new opportunities for structure property investigation.

Keywords: Reactive molecular dynamics; Adsorption; Carbon; Molecular simulation; Characterization.

Cost based approach to design biogas upgrading systems

Carlos A. Grande* and Boguslaw Ziemniak

** SINTEF AS, Forskningsveien 1, Oslo 0373, Norway*

Abstract

In biogas upgrading, the purity of the bio-methane is fixed (pipeline-grade) and in many countries, the level of emissions of methane is also limited (less than 1% in Scandinavia). The method to optimize a PSA unit is to find a configuration that gives maximum adsorbent productivity and reduced energy consumption. This is done by experience or by trial and error once that there is no theoretical method for optimizing a PSA unit. This methodology aims that the size of the unit will be the smallest possible (for that given material) and the amount of material will be reduced. Indeed, one of the accepted myths about pressure swing adsorption (PSA) is that its cost is dictated by the cost of the adsorbent. However, when the PSA is designed for processing few cubic meters per hour, the cost of the unit is given by multiple effects and the configuration with less material is not necessarily the cheapest one. In such a case, it is possible to establish a top-bottom approach by using the cost analysis for PSA optimization. For this purpose, the cost analysis will identify which are the costly parts of the unit restricting the options for optimization of the PSA unit. Our initial analysis demonstrated that the cost of the adsorbent can be around 5% of the total. This preliminary analysis demonstrates that materials with double cost, but double performance can be economically favourable.

Keywords: Pressure swing adsorption; biogas; optimization; cost analysis



Plenary lectures

Plenary 1: Lev Sarkisov, Amir H. Farmahini, Daniel Friedrich, Stefano Brandani

pl-01

From Crystal to Column: multiscale strategies in the design of PSA processes for carbon capture

Plenary 2: Qasim Al-Naddaf, Ali A. Rownaghi, Fateme Rezaei

pl-02

Multicomponent Adsorptive Separation of CO₂, CO, CH₄, N₂, and H₂ over Core Shell Zeolite@MOF Composite Adsorbents

Plenary 3: Marc Florent, Giacomo de Falco, Teresa J. Bandosz

pl-03

Towards highly efficient gas desulfurization adsorbents: exploring porosity development in biosolid based materials

Plenary 4: Guilherme Dotto

pl-04

Alternative adsorbents from wastes and its application for water decontamination

Plenary 5: Philip Llewellyn

pl-05

Using adsorption calorimetry to highlight the flexible behavior of Metal Organic Frameworks

Plenary 6: Reiner Staudt, A. Möller, R. Eschrich, C. Reichenbach, J. Möllmer

pl-06

Investigation of Mixed Gas Sorption in Lab Scale Experiment and Evaluation






Speakers




Dr. Lev Sarkisov
Professor of Chemical Engineering
Head of the Chemical Engineering and Analytical Science Department
The University of Manchester, UK
 <https://orcid.org/0000-0001-7637-7670>



Dr. Fateme Rezaei
Associate professor of Chemical and Biochemical Engineering
Missouri University of Science and Technology, USA
 <https://orcid.org/0000-0002-4214-4235>




Dr. Teresa Badosz
Full professor of Chemistry and Chemical Engineering
City College of New York, USA
 <https://orcid.org/0000-0003-2673-3782>




Dr. Guilherme Dotto
Professor
Chemical Engineering Department
Federal University of Santa Maria (UFSM), Brazil
 <https://orcid.org/0000-0002-4413-8138>



Dr. Philip Llewellyn
CCUS R&D Program Manager with TOTAL
Former 1st class Research Director with the CNRS and Aix-Marseille University, France
 <https://orcid.org/0000-0001-5124-7052>



Dr.-Ing. habil. Reiner Staudt
Professor of Thermodynamics and Chemical Engineering
University of Applied Sciences Offenburg, Germany
 <https://www.scopus.com/authid/detail.uri?authorId=57211464601>

From crystal to column: multiscale strategies in the design of PSA processes for carbon capture

Lev Sarkisov^{a,b,*}, Amir H. Farmahini^{a,b}, Daniel Friedrich^b, Stefano Brandani^b

^aDepartment of Chemical Engineering and Analytical Science, the University of Manchester, UK

^bSchool of Engineering, the University of Edinburgh, UK

Abstract

The discovery of new classes of porous adsorbents such as metal-organic frameworks (MOFs) has opened access to a very large number of porous structures with a wide range of functionalities, which can be potentially exploited in different separation applications. Experimental evaluation of all these materials for specific applications is not feasible, and as a result, this prompted the development of high throughput computational screening methods. So far, these screening methods have been predominantly based on certain adsorbent metrics, such as pore volume and surface area, and equilibrium and dynamic properties, such as adsorption isotherms, selectivity and diffusivity, obtained from molecular simulations. It is now becoming apparent that a more complete picture of the performance of porous materials in a PSA or VSA process should be obtained from the actual process simulation. In our presentation, we reflect on the development of the multiscale strategies that combine molecular simulations and pressure swing adsorption modelling and optimization to predict performance of the materials on the process scale. Several studies that employ these strategies have already emerged, ranking MOFs and other materials for post-combustion carbon capture. Here we specifically focus on the challenges associated with the interface between molecular and process levels of description and demonstrate that the emerging picture is quite complex.

Keywords: carbon capture, multiscale strategy, PSA, molecular simulations, process design.

Multicomponent Adsorptive Separation of CO₂, CO, CH₄, N₂, and H₂ over Core-Shell Zeolite-5A@MOF-74 Composite Adsorbents

Qasim Al-Naddaf, Ali A. Rownaghi, Fateme Rezaei*

^a Department of Chemical and Biochemical Engineering, Missouri University of Science and Technology, Rolla, Missouri 65409-1230, United States

Abstract

With the aim of developing more efficient H₂ purification adsorbents, we demonstrated the application of novel hybrid nanocomposites comprising of zeolite 5A and MOF-74 with core-shell structure in purification of H₂ from SMR off-gas streams, in the first part of this investigation. Through equilibrium adsorption measurements, it was shown that zeolite-5A@MOF-74 with weight ratio of 5:95 exhibited 20–30% increase in CO₂, CO, CH₄, and N₂ uptake than the bare MOF, as a result of its higher surface area and pore volume. In this work, dynamic adsorption performance of zeolite-5A@MOF-74 in H₂ purification process were evaluated through binary and multi-component breakthrough measurements at various pressures. Moreover, high pressure adsorption isotherms (up to 20 bar) were used to estimate the selectivity values for CO₂/H₂, CO/H₂, CH₄/H₂, and N₂/H₂. At 20 bar and room temperature, the composite exhibited equilibrium capacities of 13.8, 8.0, 7.7, and 6.7 mmol/g for CO₂, CO, CH₄, and H₂, respectively which were higher than those of parent adsorbents. Moreover, multicomponent breakthrough results showed that the selectivity for (CO₂ + CO + CH₄)/H₂ over the composite adsorbent is higher to that over the parent MOF-74 and zeolite 5A. The total mass transfer coefficients estimated from breakthrough simulations ranged from 6.22×10⁻², 4.73×10⁻², and 3.29×10⁻² s⁻¹ for H₂ to (9.23×10⁻⁵, 7.6×10⁻⁵, and 6.61×10⁻⁵ s⁻¹ for CO₂ at 1 bar for zeolite-5A@MOF-74, MOF-74, and zeolite 5A, respectively, with the coefficients slightly decreasing as total pressure increased to 15 bar.

Keywords: H₂ purification; Composite adsorbents; High-pressure isotherms, Multicomponent breakthrough; Selectivity

Towards highly efficient gas desulfurization adsorbents: exploring porosity development in biosolid- based materials

Marc Florent, Giacomo de Falco, Teresa J. Bandosz*

Department of Chemistry and Biochemistry, The City College of New York, 160 Convent Ave., New York, NY 10031, USA

Abstract

Dewatered sewage sludge, referred to as biosolid, is a municipal waste rich in catalytical metals and organic carbon. Its further utilization/recycling has been the subject of intensive research efforts. A well-known way of its conversion into value-in products is its high temperature pyrolysis, which leads to stable materials. They can be further used in separation process either from gas or liquid phase. Numerous papers have been published on the application of pyrolyzed sewage sludge, either as-received or activated, to remove hydrogen sulfide from gas streams. On its surface, hydrogen sulfide is oxidized to elemental sulfur or reacts with the active phase consisting of catalytic metals. Even though the catalytic activity of pyrolyzed sewage sludge towards H₂S removal/oxidation is greater than that of commercial activated carbon, when calculated per an available surface area, their limited pore volume makes these materials inferior to other porous carbonaceous adsorbents. In fact, a high surface area/porosity is needed to store the oxidation products and it is an important factor determining an efficient desulfurization process with a high amount of H₂S adsorbed per unit mass of the adsorbents or per its unit volume. To overcome this serious limitation, the strategies to develop the porosity in pyrolyzed biosolids are explored. In this particular effort we have mixed specific small-weight organic polymers with dewatered sludge before its pyrolysis. Then the mixture was pyrolyzed at 950 °C at various heating rates. Both, the addition of polymers and heating rates led to the porosity development. This, in turn, resulted in ~ 20 wt.% of hydrogen sulfide retained on the surface of our adsorbents. The main product was elemental sulfur stored in the developed pore volume (mesopores). These results show a promising path towards effective utilization of the catalytic phase of biosolids.

Keywords: biosolids; pyrolysis; desulfurization; porosity; catalytic oxidation.

Alternative adsorbents from wastes and its application for water decontamination

Guilherme Luiz Dotto*

Universidade Federal de Santa Maria, Roraima Avenue, 1000, Santa Maria, 97105-900, Brazil

Abstract

The contamination of waters and wastewaters by different molecules and ions is one of the most important topics of the environmental research. Dyes, heavy metals, pesticides, pharmaceuticals, hormones and personal care products are examples of water contaminants that are harmful for the environment and human health. In this sense, technologies to remove these contaminants from waters and wastewaters are welcome. Adsorption is an effective unit operation that can be used to uptake water contaminants, mainly when these compounds are present in concentrations of mg/L. One of the most advantages of adsorption is the use of alternative adsorbents from wastes. This practice can reduce the operational costs. In this plenary, several ways to obtain alternative adsorbents from various industrial and agricultural wastes are presented. The characteristics of these adsorbents and its potential to remove a series of contaminants are addressed. The advantages, limitations and challenges related with the preparation and use of alternative adsorbents will be also discussed.

Keywords: Agro-wastes; adsorption; development of alternative adsorbents; industrial wastes.

Using adsorption calorimetry to highlight the flexible behavior of Metal-Organic Frameworks

Philip Llewellyn ^{a,b}

^a TOTAL E&P, CSTJF, Pau (France)

^b MADIREL, Aix-Marseille Univ., CNRS, Marseille (France)

Abstract

Recently several groups have explored flexibility in ordered materials with a particular interest in Metal-Organic Frameworks. Our specific input into this research area has been to use, and develop when needed, methodologies based on calorimetry in order to directly follow the heat effects. Calorimetry can notably be of interest to follow the heat effects measured in compliant materials during (i) the compression / decompression on applying mechanical pressure and (ii) the adsorption of gases and vapors. Indeed, the former applies an external pressure whereas the latter can be perceived as applying an 'internal' pressure to the material.

Three particular materials will be discussed from this family of Metal-Organic Frameworks. The first of these is MIL-53 which has extensively been studied for applications at ambient temperatures. This sample was first synthesized in Versailles in the group of Gérard Férey. Depending on the nature of the gas or vapor, an increase in pressure will result in the material to undergo a 'breathing' type phenomena in which the initial 'open' form can be narrowed prior to reopening with an approximate 35% volume change. Each of these transitions gives rise to quite different energetic signatures and it can be difficult to deconvolute the signal to identify signals due to the 'adsorption' and to the 'structure transition'. In this particular case, it is possible to place the 'open' form of MIL-53 into a transmitter fluid and compress the system. Doing this inside a calorimeter can lead to a direct measurement of the 'heat' of the open ↔ narrow pore transition.

A second system of interest is CoBDP which was synthesized in the group of Jeff Long at Berkeley. Adsorption of nitrogen at 77 K gives a multistep structure from a closed form with a gradual opening via 5 different structure forms. Carrying out this experiment in a calorimeter leads to a signal for the adsorption in each structural form. Furthermore, the experiment developed in Marseille allows for a slow, but continuous introduction of gas giving a 'high resolution' signal in and it is possible to observe variations in the signal highlighting each transition. The CoBDP system is well known for its high methane storage working capacity at ambient temperature. This is due to the pores being 'closed' at the lower working pressure and fully open at the higher working pressure. Again, calorimetry can be used to estimate the heat effects and can confirm the conclusion concerning the interest of this material from a heat management point of view.

The final system that will be discussed is DUT-49 and its related family of compounds. This material was discovered in Dresden by Stefan Kaskel and co. On adsorption with increasing pressure, this material undergoes a sudden contraction with an expulsion of part of the gas which is already adsorbed. This phenomenon has been termed 'negative gas adsorption'. Our most recent work has studied this phenomenon using calorimetry showing highly unusual signals whether at room temperature or at 77 K.

Our work has opened a series of questions concerning why different gases show different phenomena, signal deconvolution and more recently to effects of stress/strain and crystal/domain size. These questions may well be the same as those posed for more complex disordered media and it may be of interest to discuss parallels

Keywords: Metal-organic framework, flexibility, adsorption

Investigation of Mixed Gas Sorption in Lab-Scale Experiment and Evaluation

R. Staudt^{a,*}

A. Möller^b, R. Eschrich^b, C. Reichenbach^b

J. Möllmer^c

^a University of Applied Sciences, Badstr. 24, 77652 Offenburg, Germany

^b 3P Instruments GmbH, Bitterfelder Str. 1, 04129 Leipzig, Germany

^c Institut für Nichtklassische Chemie e.V., Permoserstr. 15, 04318 Leipzig, Germany

Abstract

All gas cleaning and gas separation processes based on adsorption on porous materials are related to competitive adsorption phenomena. Usually thermodynamic models are used to predict such equilibria data from pure component isotherms. However due to numerous assumptions such predictions should be double-checked by experimental results. Some different experimental setups for the determination of mixture equilibria as well as the widely used models will be presented and discussed. As an example, the mixture of CO₂ and CH₄ was investigated on different adsorbent materials.

Keywords: Breakthrough Curves; Competitive Adsorption; Mixture Equilibria

1. Introduction

Adsorptive separation and purification processes are mainly based on the gas flow of a gas mixture through a fixed bed filled with adsorbents. One or more components are preferentially adsorbed until the adsorbent is saturated and their concentration increases over time at the outlet of the adsorber. According to that, such adsorbers are systems under unsteady conditions. The description of such processes is even more difficult by the presence of several components, whose sorption behavior has to be predicted by thermodynamic approaches to mixture sorption.

2. Experimental

The presentation will address which thermodynamic properties of the adsorbent, especially in the context of measuring and

prediction of competitive adsorption is useful. Some classical experimental setups will be discussed and an overview about the very common thermodynamic models will be given. The evaluation of mixture data from breakthrough curves will be analyzed in more detail.

3. Results

Some experimental data of CO₂ and CH₄ on different materials will be discussed with respect to their separation performance. Simple multicomponent models were applied on pure component data and compared to the experimental mixture equilibria. It can be shown, that under dry conditions zeolite 13X has the best thermodynamic selectivity for the investigated materials and therefore gave the best separation performance for that mixture.



Invited lectures

Invited Speaker 1: Márcia P. Silva, Ana M. Ribeiro, Idelfonso B. R. Nogueira, José M. Loureiro, Alírio E. Rodrigues, Alexandre Ferreira

is-01

Water harvesting by MOF based TSA processes

Invited Speaker 2: Dárley Carrijo de Melo

is-06

Offshore Natural Gas Processing for Sustainable Oil & Gas Production

Invited Speaker 3: Everaldo dos Santos

is-07

Expanded Bed Adsorption (EBA) – An important integrative technique in downstream processing

Invited Speaker 4: Dilson Cardoso

is-08

Synthesis of a zeolite for drying natural gas

Invited Speaker 5: Liliana Feris

is-09

Adsorption of pharmaceutical compounds: challenges and perspectives

Invited Speaker 6: Erika Patricia Chagas Gomes Luz, Fabia Karine Andrade, Rodrigo Silveira Vieira

is-10

Adsorption on bio-based materials

Invited Speaker 7: Daniel Uchoa Quintela, Daniely Carlos Henrique, Alessandra Honjo Ide, José Leandro da Silva Duarte, Carmem Lucia de Paiva e Silva Zanta, Lucas Meili

is-11

Malachite Green adsorption onto Mytella falcata shells: preliminary studies

Invited Speaker 8: Nina Salau

is-16

Computational intelligence applied to adsorption processes

Invited Speaker 9: J.A. Cecilia, E. Vilarrasa-García, P.A.S. Moura, C.L. Cavalcante Jr., D.C.S. Azevedo and Enrique Rodrigues-Castellón

is-17

Assessing CO₂ Adsorption on amino functionalized mesocellular foams synthesized at different aging temperature

Invited Speaker 10: Iara Rocha Antunes Pereira Bresolin, Igor Tadeu Lazzarotto Bresolin, Nico Lingg, Alois Jungbauer

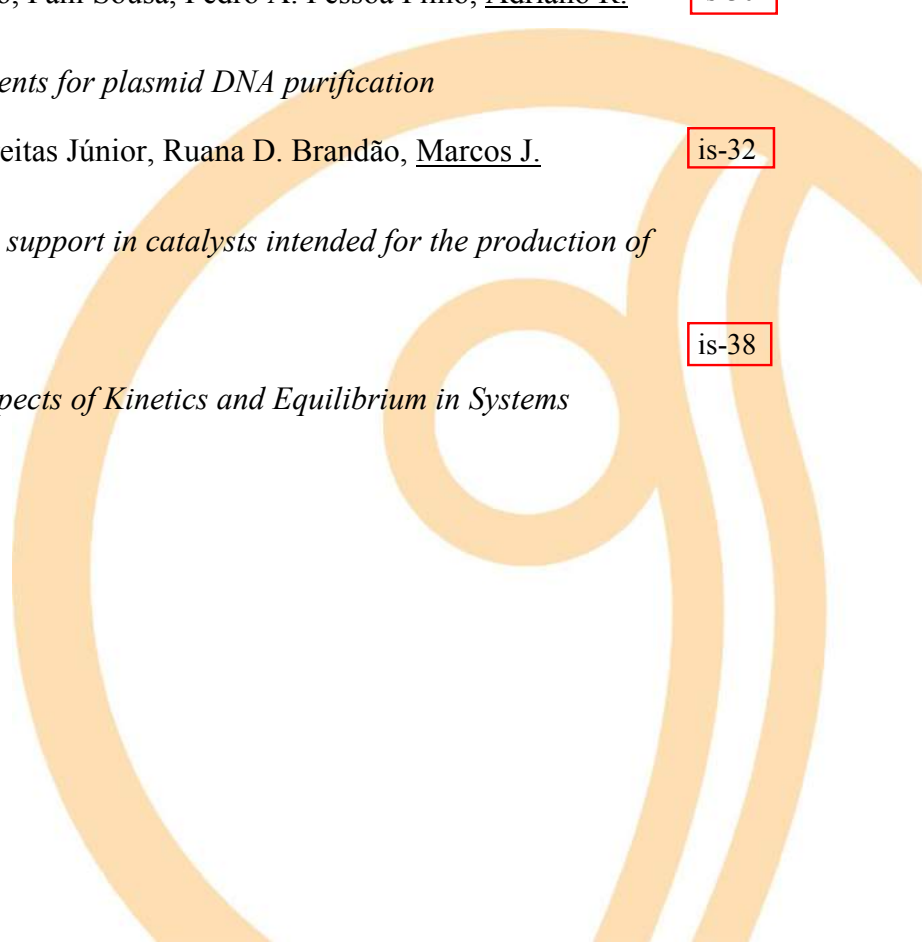
is-18

Ultrapure monoclonal antibodies: hydrophobic interaction chromatography as polishing step in downstream processing

Invited Speaker 11: Sibele Pergher

is-19

Molecular sieves: tunable porosity materials for adsorption and catalytic processes

- Invited Speaker 12:** Rodrigo G. Martins, Deivson C. S. Sales, Cesar A. M. Abreu is-20
Simultaneous adsorption and desorption of CH₄-CO₂ to improve the storage capacity of natural gas
- Invited Speaker 13:** Marcelo Castier is-25
Modeling Adsorption in Porous Solids with Equations of State for Confined Fluids
- Invited Speaker 14:** Gabriel A.T. da Silveira, Marisa M. Beppu, Hernandes Carvalho is-26
Influence of surface topography parameters on macromolecule deposition in LbL (layer by layer) processes
- Invited Speaker 15:** Leonardo Hadlich de Oliveira, Marcus Vinicius Pereira, Artur Lemes Moretti, Mateus Urias Cerdeira Braga, Pedro Augusto Arroyo is-27
High Pressure H₂S Adsorption from Natural Gas Streams Using Zeolite NaY
- Invited Speaker 16:** Amaro Barreto Jr. is-28
Challenges to connect the effects of fluid confinement to the engineering of adsorption systems
- Invited Speaker 17:** Alisson Lopes Freire, Humberto Jorge José, Regina de Fatima Peralta Muniz Moreira is-29
Application of geopolymers in carbon capture and sequestration
- Invited Speaker 18:** Sara I. B. Cardoso, Fani Sousa, Pedro A. Pessoa Filho, Adriano R. Azzoni is-30
Development and evaluation of adsorbents for plasmid DNA purification
- Invited Speaker 19:** Antônio M. de Freitas Júnior, Ruana D. Brandão, Marcos J. Prauchner is-32
The use of H₃PO₄ activated carbons as support in catalysts intended for the production of biofuels through the hefa route
- Invited Speaker 20:** César C. Santana is-38
Adsorption in Oil/Water Interfaces: Aspects of Kinetics and Equilibrium in Systems Containing Asphalthenes
- 

Speakers



Dr. Alexandre F. P. Ferreira
Full Faculty & Researcher
LA LSRE-LCM, Faculty of Engineering
University of Porto
[id https://orcid.org/0000-0002-6746-8973](https://orcid.org/0000-0002-6746-8973)



Dr. Everaldo Silvino dos Santos
Professor of Chemical Engineering
Federal University of Rio Grande do Norte
[id https://orcid.org/0000-0001-7384-1140](https://orcid.org/0000-0001-7384-1140)



Dr. Liliana Amaral Feris
Associate Professor
Federal University of Rio Grande do Sul
[id https://orcid.org/0000-0002-5900-4474](https://orcid.org/0000-0002-5900-4474)



Dr. Lucas Meili
Adjunct Professor of Petroleum Engineering
Federal University of Alagoas
[id https://orcid.org/0000-0002-0307-8204](https://orcid.org/0000-0002-0307-8204)



Dr. Enrique Rodriguez-Castellón
Full Professor of Inorganic Chemistry
University of Málaga
[id https://orcid.org/0000-0003-4751-1767](https://orcid.org/0000-0003-4751-1767)



Dr. Sibele B. Castellã Pergher
Professor of Chemistry
Federal University of Rio Grande do Norte
[id https://orcid.org/0000-0002-5825-958X](https://orcid.org/0000-0002-5825-958X)



Dr. Marcelo Castier
Professor of Industrial Engineering
Universidad Paraguayo Alemana
Texas A&M University at Qatar
[id https://orcid.org/0000-0003-1005-1517](https://orcid.org/0000-0003-1005-1517)



Dr. Pedro Augusto Arroyo
Associate Professor of Chemical Engineering
State University of Maringa
[id https://orcid.org/0000-0001-7350-0469](https://orcid.org/0000-0001-7350-0469)



Dr. Regina F. P. Muniz Moreira
Professor of Chemical and Food Engineering
Federal University of Santa Catarina
[id https://orcid.org/0000-0002-2863-7260](https://orcid.org/0000-0002-2863-7260)



Dr. Marcos Juliano Prauchner
Associate Professor
Brasilia University
[id https://orcid.org/0000-0003-4096-2071](https://orcid.org/0000-0003-4096-2071)

Dr. Dárley Carrijo de Melo
Researcher and Project Manager
PETROBRAS Research Center (CENPES)
[id https://orcid.org/0000-0002-8765-2321](https://orcid.org/0000-0002-8765-2321)



Dr. Dilson Cardoso
Senior Professor
Federal University of São Carlos
[id https://orcid.org/0000-0003-3504-4516](https://orcid.org/0000-0003-3504-4516)



Dr. Rodrigo Silveira Vieira
Associate Professor of Chemical
Engineering
Federal University of Ceara
<https://orcid.org/0000-0003-4569-9655>



Dr. Nina Paula G. Salau
Associate Professor of Chemical Engineering
Federal University of Santa Maria
[id https://orcid.org/0000-0002-6139-7369](https://orcid.org/0000-0002-6139-7369)



Dr. Igor T. L. Bresolin
Associate Professor of Chemical Engineering
Federal University of São Paulo
[id https://orcid.org/0000-0001-9868-7362](https://orcid.org/0000-0001-9868-7362)



Dr. César A. M. Abreu
Emeritus Professor
Chemical Reaction Engineering
Federal University of Pernambuco
[id https://orcid.org/0000-0002-8455-294X](https://orcid.org/0000-0002-8455-294X)



Dr. Marisa M. Beppu
Full Professor of Chemical Engineering
University of Campinas (UNICAMP)
[SC https://www.scopus.com/authid/detail.uri?authorId=7005082971](https://www.scopus.com/authid/detail.uri?authorId=7005082971)



Dr. Amaro Gomes Barreto Jr
Associate Professor of Chemical Engineering
Federal University of Rio de Janeiro
[id https://orcid.org/0000-0001-8238-2310](https://orcid.org/0000-0001-8238-2310)



Dr. Adriano Azzoni
Assistant Professor
University of São Paulo
[id https://orcid.org/0000-0003-0696-4663](https://orcid.org/0000-0003-0696-4663)



Dr. César Costapinto Santana
Full Professor
Universidade Tiradentes
[id https://orcid.org/0000-0002-8962-173X](https://orcid.org/0000-0002-8962-173X)



Water Harvesting by MOF based TSA processes

Márcia P. Silva^a, Ana M. Ribeiro^a, Idelfonso B. R. Nogueira^a, José M. Loureiro^a, Alírio E. Rodrigues^a, Alexandre Ferreira^a

^a *Laboratory of Separation and Reaction Engineering - Laboratory of Catalysis and Materials (LSRE-LCM), Associate Laboratory LSRE-LCM, Faculdade de Engenharia, Universidade do Porto, Rua Dr. Roberto Frias, 4200-465 Porto, Portugal*

Abstract

The water crisis is one of the main global risks based on its societal impact, particularly the access to safe drinking water in regions with a dry (arid) or mainly dry (semi-arid) climate. To cover the lack of potable water, several techniques are being developed. Seawater desalination is one of the solutions; yet, in non-coastal arid regions, this technique is not suitable to be applied. Therefore, in areas where no viable liquid water source is available, water in the atmospheric air can be considered as a possible water source. The moist from atmospheric air can be extracted by Atmospheric Water Vapor Processing (AWVP) technologies. AWVP technologies can be classified as surface cooling using heat pumps or radiative cooling (Type 1), water vapor concentration by desiccants (Type 2), or by convection induced/controlled in a structure (Type 3). Adsorption-based processes belong to Type 2 and can be employed to capture water. A cyclic adsorption process must include regeneration of the adsorbent step, which can be done by increasing the temperature, in a process termed temperature swing adsorption (TSA). In this study, the potential MOF adsorbents, for adsorption based atmospheric water extraction processes, will be explored, namely of Aluminum (Al)-based ones. The operating conditions of the proposed TSA cycles were optimized, and show that Metal-Organic Frameworks (MOFs) are promising material for water harvesting from atmosphere, with productivities between $22 \text{ l}\cdot\text{day}^{-1}\cdot\text{ton}^{-1}$ and $147 \text{ l}\cdot\text{day}^{-1}\cdot\text{ton}^{-1}$, depending on the material and regeneration conditions.

Keywords: water; air; adsorption; MOFs; TSA.

1. Introduction

The water crisis is one of the primary global risks based on its societal impact, particularly the access to safe drinking water in regions with a dry (arid) or mainly dry (semi-arid) climate [1]. More than 40% of the present world population has lack of water [2]. Over the past decades, the rate of demand for water is two times higher than the rate of population growth rate [3, 4]. About 66% of the world population (4 billion) faced water scarcity episode for at least one month a year [5]. Transportation of water from other places to arid regions, to mitigate this problem, can be a very expensive option [6]. Therefore, in areas where no viable liquid water source is available, such as arid regions, war zones, natural calamity areas, heavily chemically/biologically contaminated water supply areas), water in the atmospheric air can be considered as a possible water source. Indeed, on

Earth, while the surface fresh water sources (rivers and lakes) only sum up to 1200 km^3 , there are 14000 km^3 of water in air [7]. Atmospheric water generators (AWGs) can be an alternative to capture and deliver water in these problematic regions [8-10]. The AWVP technology can be classified as surface cooling using heat pumps or radiative cooling (Type 1), water vapor concentration by desiccants (Type 2) or by convection induced/controlled in a structure (Type 3) [11]. Water harvesting from air provides water with sufficient quality for drinking [12], doesn't have spatial limitations, and can be powered by renewable energies [13]. Recently, Metal-Organic Frameworks (MOFs) have generated interest in the scientific community. The Al-based MOF have been investigated and applied in different fields, such as sensing, catalysis, gas storage, gas purification, desalination, and water harvesting [14-19]. Their characteristics, such as high

hydrothermal stability, inexpensive, and non-toxic, make them potential water adsorbents [20-22]. In this study, the potential of the Al-MOF MIL-160 for water capture from air was assessed. Herein, adsorption equilibrium data of CO₂, O₂, N₂ and H₂O vapor were measured. Fixed bed experiments were carried out at 298 K in order to study the dynamic adsorption of H₂O vapor on the adsorbent. A mathematical model was developed to predict the adsorption dynamic behaviour of granulates MIL-160(Al). The optimal conditions of TSA process were obtained by optimization process in order to achieve the maximum water productivity.

2. Experimental

MIL-160(Al) was synthesized at the Korea Research Institute of Chemical Technology (KRICT) and the preparation was performed following the recipe described by Permyakova, et al. [23]. The adsorbent is a MOF material and is isostructural to CAU-10 [24]. This material was built up from inorganic aluminum helical chains which are connected by carboxylate groups [25] [25, 26]. The helical chains are created by the bridge between hydroxyl ions with the Al centers. The 3D framework presents square shape channels with pore size of 4 to 6 Å.

Adsorption equilibrium isotherms of H₂O vapor, CO₂, N₂, and O₂ were assessed in a Rubotherm magnetic suspension microbalance (precision of 0.01 mg), in batch mode. MIL-160(Al) samples were activated at 423 K during 12 h under vacuum.

Breakthrough experiments were performed in a bench-scale fixed bed unit at 298 K and 1 bar. The stainless-steel column was packed with MIL-160(Al) and both ends of column were capped with a layer of glass wool. Prior to breakthrough experiments, material was activated by heating up to 423 K under helium flow for 12 h. Single and binary breakthrough curves were performed.

MIL-160(Al) granules were characterized by scanning electron micrography (SEM), X-ray diffraction (XRD) pattern, N₂ and CO₂ adsorption equilibrium isotherms, particle crushing strength/hardness measurements, mercury (Hg) porosimetry and thermogravimetric (TG) analysis.

3. Process model

Material, momentum and energy balances were used to develop the mathematical model. The mathematical model describe the dynamic behavior of components in the cyclic adsorption process. The following assumptions were taking into consideration in order to select the essential conservation equations: (i) ideal gas behavior for the fluid phase; (ii) homogeneous temperature inside each particle; (iii) the film model describe external mass and heat transfer; (iv) mass, heat and velocity gradients in radial direction were neglected; (v) bidisperse porous nature of the adsorbent was considered and expressed by a bi-linear driving force (bi-LDF) with micro and macropores mass diffusion; (vi) the Ergun equation is valid locally; and (vii) constant void fraction within the column. More detailed information regarding to the mathematical model can be found in previous works [27-29].

3.1. Objective function - Definition

The definition of objective function in the optimization process is an important factor to achieve the optimal conditions. It is propose to apply an objective function with penalties, namely a constant penalty is applied to a solution that violate the initial defined constraints. Hence, the objective function is defined as:

$$\min(J) = \sum_k^{nk} \left(\frac{1}{Pr_k} \right) \quad (1)$$

4. Results

The H₂O vapor adsorption equilibrium isotherms at 303, 323, and 343 K were performed in the range pressures of 0.48 – 32.0 mbar (Fig. 1a)). The H₂O vapor adsorption equilibrium isotherms were fitted with the Cooperative Multimolecular Sorption (CMMS) model (Fig. 1b)). CMMS model was capable to describe the H₂O vapor adsorption behavior on MIL-160(Al). Adsorption equilibrium isotherms present a shape of type V isotherm, according with IUPAC classification, confirming the hydrophilic character of the adsorbent [23, 25, 30-32]. In all H₂O adsorption isotherms is not visible a hysteresis loop.

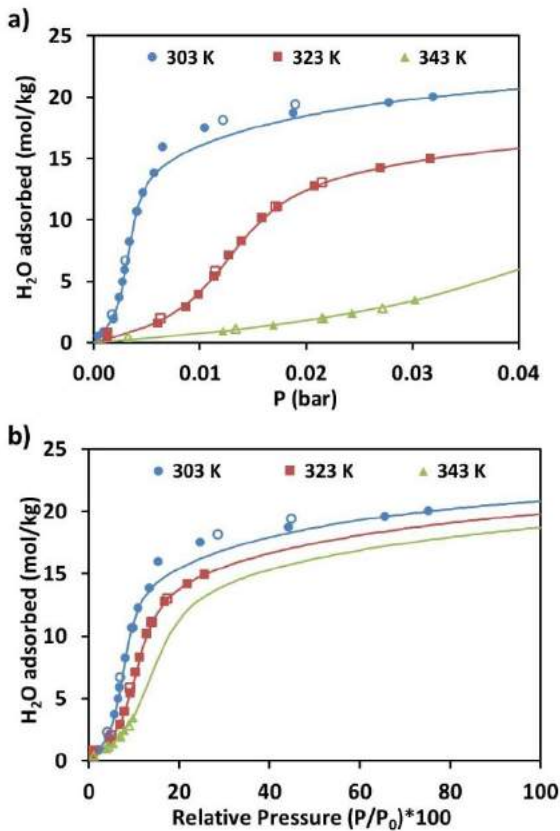


Fig. 1. Water vapor adsorption–desorption equilibrium isotherm on MIL-160(Al) at 303, 323, and 343 K in function of: (a) absolute pressure, and (b) relative pressure (filled symbol: adsorption, open symbol: desorption), and CMMS fitting lines.

Fig. 2 presents the breakthrough curve of H₂O vapor. Firstly, a dispersive front ($P/P_0 \leq 0.05$) followed by a compressive front ($0.05 < P/P_0 < 0.5$) is visible during the adsorption step. Similar behavior was observed during desorption step ($P/P_0 = 0.5$ to 0.14 – compressive; $P/P_0 = 0.14$ to 0 – dispersive). The observed behavior is in accordance with H₂O vapor adsorption equilibrium isotherm presented in Fig. 1. The mathematical model developed can predicted well the H₂O vapor breakthrough history on MIL-160(Al) (Fig. 2 – full line).

The unit to produce water harvesting from thin air by adsorption and its posterior condensation from the regeneration outlet stream was designed. The adsorption cyclic process followed two steps, feed and co-current purge. In the process design, a column with a volume of 1 m^3 (length = 1.25 m , diameter = 1 m) packed with 480 kg of MIL-160(Al) granules operating under adiabatic conditions was considered.

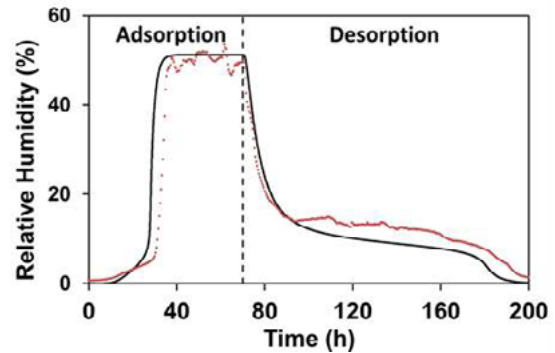


Fig. 2. Water vapor adsorption-desorption breakthrough curve obtained at 298 K (Red points represent experimental data, full line correspond to simulation results, dashed line represents the beginning of the regeneration step).

The operating conditions of the proposed TSA cycles were optimized (eq. 1), varying the duration each step, and the regeneration conditions (temperature, flow rate). Pressure and condensation temperature were considered to 1.01325 bar and 283 K , respectively. Fig. 3a) presents the maximum water productivity by optimizing the flow rate and fixing purge temperature (353 K), while in Fig. 3b) represents the inverse scenario, with a flow rate of $0.3 \text{ m}^3 \cdot \text{s}^{-1}$ and varying purge temperature.

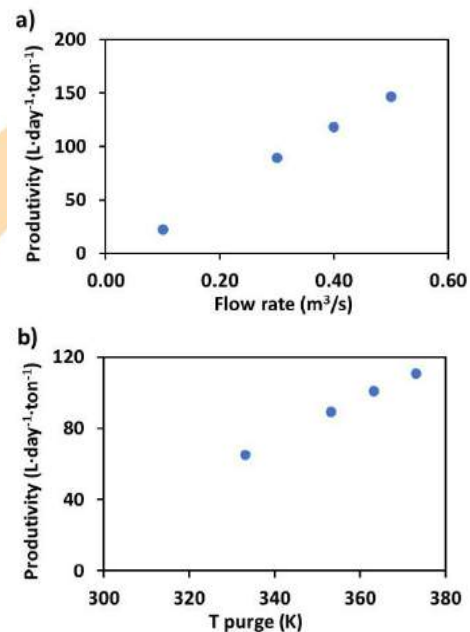


Fig. 3. Maximum water production by optimal unit performance parameters in terms of: a) flow rate and b) purge temperature.

The most promise scenario where obtained for purge temperature equal to 353 K and flow rate of $0.50 \text{ m}^3 \cdot \text{s}^{-1}$, with a highest H_2O productivity of $147 \text{ l} \cdot \text{day}^{-1} \cdot \text{ton}^{-1}$.

5. Conclusions

H_2O adsorption equilibrium isotherms present a shape of Type V isotherm, according with IUPAC, not being visible any hysteresis. Due to its high capacity and step increase at moderate relative pressures, makes it a good candidate for water harvesting semi-arid and arid environments. The breakthrough curve of water vapor, firstly a dispersive front at low P/P_0 is present, followed by a compressive front, as expected by the H_2O adsorption equilibrium isotherms.

TSA process proved the potential application of MIL-160(Al) as a material for water harvesting capable to produce $147 \text{ l} \cdot \text{day}^{-1} \cdot \text{ton}^{-1}$ of liquid water (purge temperature – 353 K, condensation temperature – 283 K, and flowrate – $0.50 \text{ m}^3 \cdot \text{s}^{-1}$).

Acknowledgements

This work was a result of project “AIProcMat@N2020 - Advanced Industrial Processes and Materials for a Sustainable Northern Region of Portugal 2020”, with the reference NORTE-01-0145-FEDER-000006, supported by Norte Portugal Regional Operational Programme (NORTE 2020), under the Portugal 2020 Partnership Agreement, through the European Regional Development Fund (ERDF); Associate Laboratory LSRE-LCM - UID/EQU/50020/2019 - funded by national funds through FCT/MCTES (PIDDAC).

References

- [1] Balon M, Dehnad F. Water crisis in arid and semi-arid regions- an international challenge. In: 12-13, September 2006. 2006; Tehran (Iran); 2006.
- [2] Pires V. Análise das secas em Portugal Continental. In., vol. I: Instituto de Meteorologia; 2008: 15.
- [3] Shiklomanov IA. World Water Resources: A new appraisal and assessment for the 21st century. In. United Nations Educational, Scientific and Cultural Organization (UNESCO), ; 1998.
- [4] Pazwash H. Urban Storm Water Management: CRC Press 2016.
- [5] Mekonnen MM, Hoekstra AY. Four billion people facing severe water scarcity. *Science Advances* 2016; 2(2).
- [6] Hamed AM, Aly AA, Zeidan EB. Application of Solar Energy for Recovery of Water from Atmospheric Air in Climatic Zones of Saudi Arabia *Natural Resources* 2011; 2(1): 8-17.
- [7] Obrezkova VE. Hydro-energy. In: *Energoatomezdat. Moscow*; 1988.
- [8] Kim H, Rao SR, Kapustin EA, Zhao L, Yang S, Yaghi OM, Wang EN. Adsorption-based atmospheric water harvesting device for arid climates. *Nature Communications* 2018; 9(1): 1191.
- [9] Wang JY, Wang RZ, Tu YD, Wang LW. Universal scalable sorption-based atmosphere water harvesting. *Energy* 2018; 165: 387-95.
- [10] Yaghi OM, Kalmutzki MJ, Diercks CS. Water Sorption Applications of MOFs. In: *Introduction to Reticular Chemistry*. edn.; 2019: 395-427.
- [11] Wahlgren RV. Atmospheric water vapour processor designs for potable water production: a review. *Water Research* 2001; 35(1): 1-22.
- [12] Fessehaye M, Abdul-Wahab SA, Savage MJ, Kohler T, Gherezghiher T, Hurni H. Fog-water collection for community use. *Renewable and Sustainable Energy Reviews* 2014; 29: 52-62.
- [13] Kogan B, Trahtman A. The moisture from the air as water resource in arid region: hopes, doubts and facts. *Journal of Arid Environments* 2003; 53(2): 231-40.
- [14] Weiss A, Reimer N, Stock N, Tiemann M, Wagner T. Surface-modified CAU-10 MOF materials as humidity sensors: impedance spectroscopic study on water uptake. *Physical Chemistry Chemical Physics* 2015; 17(33): 21634-42.
- [15] Borges DD, Normand P, Permiakova A, Babarao R, Heymans N, Galvao DS, Serre C, De Weireld G, Maurin G. Gas Adsorption and Separation by the Al-Based Metal-Organic Framework MIL-160. *The Journal of Physical Chemistry C* 2017; 121(48): 26822-32.
- [16] Elsayed E, Al-Dadah R, Mahmoud S, Anderson PA, Elsayed A, Youssef PG. CPO-27(Ni), aluminium fumarate and MIL-101(Cr) MOF materials for adsorption water desalination. *Desalination* 2017; 406: 25-36.
- [17] Kim H, Yang S, Rao SR, Narayanan S, Kapustin EA, Furukawa H, Umans AS, Yaghi OM, Wang EN. Water harvesting from air with metal-organic frameworks powered by natural sunlight. *Science* 2017; 356(6336): 430-34.
- [18] Hanikel N, Prévot MS, Fathieh F, Kapustin EA, Lyu H, Wang H, Diercks NJ, Glover TG, Yaghi OM. Rapid Cycling and Exceptional Yield in a Metal-Organic Framework Water Harvester. *ACS Central Science* 2019.
- [19] Elsayed E, Al-Dadah R, Mahmoud S, Elsayed A, Anderson PA. Aluminium fumarate and CPO-27(Ni)

- MOFs: Characterization and thermodynamic analysis for adsorption heat pump applications. *Applied Thermal Engineering* 2016; 99: 802-12.
- [20] Tannert N, Jansen C, Nießing S, Janiak C. Robust synthesis routes and porosity of the Al-based metal-organic frameworks Al-fumarate, CAU-10-H and MIL-160. *Dalton Transactions* 2019; 48(9): 2967-76.
- [21] Cadiou A, Lee JS, Damasceno Borges D, Fabry P, Devic T, Wharmby MT, Martineau C, Foucher D, Taulelle F, Jun CH, Hwang YK, Stock N, De Lange MF, Kapteijn F, Gascon J, Maurin G, Chang JS, Serre C. Design of hydrophilic metal organic framework water adsorbents for heat reallocation. *Adv Mater* 2015; 27(32): 4775-80.
- [22] Gaab M, Trukhan N, Maurer S, Gummaraju R, Müller U. The progression of Al-based metal-organic frameworks – From academic research to industrial production and applications. *Microporous and Mesoporous Materials* 2012; 157: 131-36.
- [23] Permyakova A, Skrylnyk O, Courbon E, Affram M, Wang S, Lee U-H, Valekar AH, Nouar F, Mouchaham G, Devic T, De Weireld G, Chang J-S, Steunou N, Frère M, Serre C. Synthesis Optimization, Shaping, and Heat Reallocation Evaluation of the Hydrophilic Metal-Organic Framework MIL-160(Al). *ChemSusChem* 2017; 10(7): 1419-26.
- [24] Reinsch H, van der Veen MA, Gil B, Marszalek B, Verbiest T, de Vos D, Stock N. Structures, Sorption Characteristics, and Nonlinear Optical Properties of a New Series of Highly Stable Aluminum MOFs. *Chemistry of Materials* 2013; 25(1): 17-26.
- [25] Cadiou A, Lee JS, Damasceno Borges D, Fabry P, Devic T, Wharmby MT, Martineau C, Foucher D, Taulelle F, Jun C-H, Hwang YK, Stock N, De Lange MF, Kapteijn F, Gascon J, Maurin G, Chang J-S, Serre C. Design of Hydrophilic Metal Organic Framework Water Adsorbents for Heat Reallocation. *Advanced Materials* 2015; 27(32): 4775-80.
- [26] Weiss A, Reimer N, Stock N, Tiemann M, Wagner T. Screening of mixed-linker CAU-10 MOF materials for humidity sensing by impedance spectroscopy. *Microporous and Mesoporous Materials* 2016; 220: 39-43.
- [27] Da Silva FA, Silva JA, Rodrigues AE. A General Package for the Simulation of Cyclic Adsorption Processes. *Adsorption* 1999; 5(3): 229-44.
- [28] Plaza MG, Ribeiro AM, Ferreira A, Santos JC, Lee UH, Chang J-S, Loureiro JM, Rodrigues AE. Propylene/propane separation by vacuum swing adsorption using Cu-BTC spheres. *Separation and Purification Technology* 2012; 90: 109-19.
- [29] Ribeiro AM, Campo MC, Narin G, Santos JC, Ferreira A, Chang J-S, Hwang YK, Seo Y-K, Lee UH, Loureiro JM, Rodrigues AE. Pressure swing adsorption process for the separation of nitrogen and propylene with a MOF adsorbent MIL-100(Fe). *Separation and Purification Technology* 2013; 110: 101-11.
- [30] Leclerc M, Gauvin R. Functional materials for energy, sustainable development and biomedical sciences; 2014.
- [31] Coelho JA, Ribeiro AM, Ferreira AFP, Lucena SMP, Rodrigues AE, De Azevedo DCS. Stability of an Al-Fumarate MOF and Its Potential for CO₂ Capture from Wet Stream. *Industrial and Engineering Chemistry Research* 2016; 55(7): 2134-43.
- [32] Ruthven DM. Principles of Adsorption and Adsorption Processes. New York: John Wiley and Sons; 1984.

Offshore Natural Gas Processing for Sustainable Oil & Gas Production

Dárley Carrijo de Melo

PETROBRAS/CENPES/PDDP/TPP, 21941-915, Rio de Janeiro – RJ – Brazil

Abstract

The discovery of the pre-salt brought great prospects for the increase in oil and gas production in Brazil. Giant hydrocarbon reserves, containing good quality oil and gas, with high rates of successful exploration and productivity, raise the quality of the pre-salt reserves to World Class reserves. However, several challenges have also emerged. A large and variable occurrence of CO₂ in these reservoirs brought the need to remodel the offshore gas processing, in order to separate CO₂ for reinjection into the reservoirs, while making the gas available for use in the national energy matrix. The benefits are diverse. By giving CO₂ an appropriate destination, it is possible to meet the commitment to develop oil and gas production in a sustainable manner, without venting the CO₂ found in the reserves into the atmosphere. In addition, the use of natural gas, the least polluting fossil source, thus very important for a low-carbon future matrix, is made viable and becomes a great support for renewable energy sources development, which will grow in importance.

Keywords: Natural gas; CO₂; energy; offshore gas

Expanded Bed Adsorption (EBA) – An important integrative technique in downstream processing

Everaldo Silvino dos Santos

Laboratory of Biochemical Engineering, Chemical Engineering Department, Federal University of Rio Grande do Norte (UFRN), Natal-RN and CEP: 59078 970, Brazil

Abstract

Expanded bed adsorption chromatography (EBAC) or simply expanded bed adsorption (EBA) allows for the direct purification of bioproducts from unclarified feedstocks where additional solid–liquid separation and concentration steps are not necessary prior to the purification process. EBA has emerged as a powerful technique during downstream processing mainly because it combines clarification, concentration and primary purification into a one step-operation. Additionally, it provides significant advantages compared to traditional chromatographic processes in terms of process robustness, flexibility, and economy. In this speech we are going to address important parameters of the technique as well as we are to revisit few of the main results obtaining for our research group using such technique.

Keywords: EBAC, EBA, bioproducts, chromatography, adsorption

Synthesis of Zeolite for Drying Natural Gas

Dilson Cardoso

*Laboratory of Applied Catalysis and Adsorption - LACap
Chemical Engineering Department
Federal University of São Carlos, SP, Brazil*

Abstract

Zeolites are crystalline aluminosilicates containing micropores (pore diameter less than 2 nm). They are widely used in adsorption, catalytic and ion exchange processes. Depending on their application, they may be employed in the form of powders, grains or membranes.

In this presentation we report general information about the synthesis of zeolites and, in particular, of zeolite 4A (LTA, according to IUPAC) in order to apply it in the drying of natural gas.

The results show that the zeolite 4A properties, especially the particle diameter, are very dependent on the synthesis conditions. Noteworthy is the synthesis of this zeolite in the presence of a surfactant, resulting in a material that allows nitrogen adsorption at its boiling point (-195o C), which does not occur in the usually synthesized material.

Keywords: zeolite; synthesis; natural gas; gas drying;

Adsorption of Pharmaceutical Compounds: Challenges and Perspectives

Liliana Amaral Féris^a

^a*Department of Chemical Engineering, Federal University of Rio Grande do Sul (UFRGS)
Rua Ramiro Barcelos, 2777. Postcode 90035-007 – Porto Alegre – RS – Brazil.*

**Corresponding author liliana.feris@gmail.com
Tel.: +55-51-3308 2148*

Abstract

Pharmaceutical compounds (PhCs) are detected in various environmental matrices. These compounds, whether not removed by treatment techniques, contribute to bacterial resistance and negative environmental impacts on water resource. Specifically, hospital wastewaters exhibit high concentrations of these compounds mainly by the excretion of patients. The interest in the presence of emerging pollutants in the environment has increased significantly because of their potential impact on the environment and possibly human health, even at trace concentrations. Furthermore, the analytical techniques improvement allows detecting traces of substances (ng.L^{-1} or less) in many environmental matrices. Most separation and purification processes, based on the adsorption technology are generally considered for wastewater treatment due to ease operation and simplicity in the process. Moreover, these processes can eliminate or reduce the different types of organic and inorganic pollutants in water or sewage, and therefore have wide application for pollution control. So, considering this picture what are the challenges and perspectives involved in the use of adsorption for pharmaceutical compounds removal? How to understand properly the different mechanisms involved between emerging micro-pollutants and the functional groups present in the adsorbents surface?? How to manage solid regeneration to minimize the environmental impact of adsorption process? Issues we need to discuss for a near future to follow the society needs and world legislation standards.

Keywords: Pharmaceutical compounds; adsorption; wastewater treatment

Adsorption on bio-based materials

Erika Patricia Chagas Gomes Luz, Fabia Karine Andrade, Rodrigo Silveira Vieira*

** Department of Chemical Engineering, Federal University of Ceara' (UFC), Bloco 709, Fortaleza, Ceará, 60455-760, Brazil*

Abstract

In the last years, bio-based materials such as cellulose, chitin-chitosan and algae have been extensively designed to be sorbent material. Bio-based polymers have low cost and the advantage of being physically or chemically modified to tailor the adsorbent performance. The work aims to describe some examples of natural polymers developed by our Group as adsorbents for environmental, food, and biological applications. Chitosan is a natural polymer mostly studied for heavy metal adsorption applications since its structure contains amino and hydroxyl groups. We have used chitosan membranes for copper, chromium, and mercury adsorption and investigated adsorption mechanisms by different analytical techniques like FTIR, XPS, and Raman spectroscopy. Chitosan was also used for food packaging as a film and as a support for inorganic adsorbents (zeolites) for ethylene adsorption (a hormone responsible for developing and ripening fruits and vegetables). Chitosan was also functionalized with histidine and described the chelation potential with Cu^{2+} , Fe^{3+} , and Zn^{2+} ions, for chelation therapy purposes. The amino acid, histidine, was used to mimic the $\text{A}\beta$ peptide and add new active sites. We have evaluated protein adsorption (BSA and fibrinogen) to tailor a surface with less interaction with these proteins, in some biological processes to develop anti-thrombogenic surfaces. A hybrid material of bacterial cellulose with strontium apatite was developed and investigated the strontium delivery to develop a biomaterial with osteoconductivity potential. The natural polymers have been successful as adsorbent, and their properties are modified in accordance with the application.

Keywords: natural polymers; chitosan; biomaterials.

Malachite green adsorption onto *Mytella falcata* shells: preliminary studies

Daniel Uchoa Quintela¹, Daniely Carlos Henrique¹, Alessandra Honjo Ide¹, José Leandro da Silva Duarte^{1,2}, Carmem Lucia de Paiva e Silva Zanta², Lucas Meili^{1,*}

¹Laboratório de Processos, Centro de Tecnologia, Universidade Federal de Alagoas, Maceió, Alagoas

²Laboratório de Eletroquímica Aplicada, Instituto de Química e Biotecnologia, Universidade Federal de Alagoas, Maceió, Alagoas

Abstract

Malachite green (MG) is a non-biodegradable target compound, widely used in aquaculture due to its antiprotozoal and antifungal activity and relatively low operating cost. MG also has other applications, such as dyeing cotton, silk, paper, leather and in the manufacture of paints and printing inks. In this preliminary work, *Mytella falcata* shells were successfully used as adsorbent for MG removal from aqueous solution. The material was characterized, thereafter, particle diameter and adsorbent dosage were investigated. Above 90% of MG removal was achieved for the lowest particle diameter ($0.212 < d_p < 0.300$ mm) and the lowest adsorbent dosage (1 g.L^{-1}). Kinetic study was conducted at MG initial concentration of 100 mg.L^{-1} . Equilibrium was reached after 120 min of contact, attaining almost 96.1 mg.g^{-1} of adsorption capacity. Pseudo-second order model best represented the kinetic data, indicating the rate limiting step was chemisorption. These findings suggest *Mytella falcata* shells as a suitable adsorbent for MG removal from water, requiring additional studies.

Keywords: Aquaculture biocide, removal, mollusk, water treatment, biosorbent

1. Introduction

The environmental consequences of economic development coupled with rapid population growth are one of today's major concerns. Although industries account for much of the economy, their wastewater is a huge source of water pollution [1]. Among the several classes of chemicals present in industrial effluents, synthetic dyes are extensively used in the textile, pharmaceutical, food, automotive, cosmetics and other industries [2]. Dyes are highly harmful to aquatic life and are carcinogenic and mutagenic, causing serious problems for humans [3-4].

Their chemical structures are usually complex making the removal from water very difficult [5]. Some physical, chemical and biological treatments are employed, such as coagulation/flocculation, membrane filtration, electrochemical destruction, ion exchange, advanced oxidative processes,

microbiological decomposition and adsorption [6]. Adsorption is considered a very effective and viable method for the treatment of effluents, such as the low cost and easy operation. Although adsorption processes are well-known, the use of waste as adsorbent materials is a subject of increasing interest [7].

Sururu (*Mytella falcata*, Fig. 1) is a mussel widely appreciated in Alagoas state (Brazil) gastronomy. Moreover, its extraction plays an important role to the local economy. On the other hand, the inappropriate disposal of the shells in the environment causes several problems, such as the proliferation of diseases and visual pollution [8].

In this context, the present work aimed to show the preliminary results achieved by using *Mytella falcata* shells to remove malachite green (MG, Fig. 2) from water. For such purpose, the material was washed, dried, sieved and the particles were standardized. The adsorbent was then characterized and used in the adsorption studies.



Fig. 1. *Mytella falcata* (a), shells (b) and irregular disposal in the environment (c).

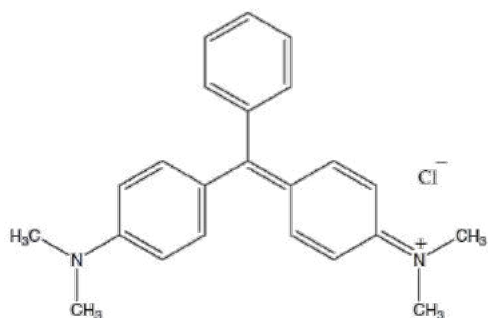


Fig. 2. Chemical structure of malachite green.

2. Experimental

1.1. Adsorbate

Malachite green, $C_{23}H_{25}ClN_2$, was used as adsorbate. A stock standard solution ($1000 \text{ mg}\cdot\text{L}^{-1}$) was prepared and appropriately diluted to obtain all other solutions used in this study. MG quantification was performed using a spectrophotometer Shimadzu MultiSpec-1501, with absorbance measurements at 617 nm. The analytical curve was plotted with concentrations ranging from 1.0 to $12.0 \text{ mg}\cdot\text{L}^{-1}$.

1.2. Adsorbent

Sururu shells (*Mytella falcata*) were obtained from Mundaú Lake, in Maceió city, Alagoas, Brazil. The shells were previously washed in current water in order to remove the residual organic matter and then dried in an oven at 60°C for 8 h. Subsequently, the material was crushed in an industrial blender and then classified by a Tyler series sieves to particle sizes of $0.212 < d_p < 0.300 \text{ mm}$, $0.300 < d_p < 0.425$ and $0.425 < d_p < 0.600 \text{ mm}$.

1.3. Adsorbent characterization

Scanning electron microscopy (SEM), infrared spectroscopy (FT-IR) and X-ray diffraction (XRD) were used to characterize the adsorbent material. The shells surface were analyzed by the SSX-500 Superscan, Shimadzu, after 6 min of gold metallization under 10 mA (Quick Coater SC-701, Sanyu Electron). The functional groups present in the material were identified by the IR-PRESTIGE-21 spectrophotometer, Shimadzu. The crystal structure was determined by the XRD-6000 diffractometer, Shimadzu.

1.4. Adsorption assays

The adsorption assays were performed in a finite bath, in triplicate. In a typical adsorption experiment, an exact amount of weighted adsorbent was added to 50 mL of the adsorbate solution in a 250 mL Erlenmeyer, which was kept under agitation at 140 rpm for a certain period of contact time. After that, the mixture was transferred to a 50 mL falcon tube and centrifuged at 2,000 rpm for 10 min. The final MG concentrations were measured in the supernatant. The adsorption capacity of the adsorbent material ($q_t, \text{ mg}\cdot\text{g}^{-1}$) was determined by Equation 1 and the removal percentage (%) was calculated by Equation 2.

$$q_t = \frac{(C_0 - C_t)}{W} * V \quad (1)$$

$$\% \text{ removal} = \frac{C_0 - C_t}{C_0} * 100 \quad (2)$$

where C_0 , C_e and C_t are the concentrations ($\text{mg}\cdot\text{L}^{-1}$) of the adsorbate solution at the beginning, at equilibrium and at time t , respectively. W is the mass (g) of adsorbent and V (L) is the volume of the solution.

In the preliminary adsorption studies, the influence of the particle diameter ($0.212 < d_p < 0.300$ mm, $0.300 < d_p < 0.425$ and $0.425 < d_p < 0.600$ mm.) and adsorbent dosage (1.0, 2.0, 4.0 and 5.0 g.L⁻¹) were evaluated, using initial MG concentration of 100 mg.L⁻¹ at 30°C.

The best conditions obtained in the preliminary adsorption assays were applied in the kinetic studies (MG initial concentration of 100 mg.L⁻¹ at 30°C). The final concentrations of MG remaining in the solution were measured in predetermined time intervals (5, 10, 15, 30, 60, 120, 180 e 240 min) and the kinetic data obtained were fitted to the pseudo-first order (Equation 3) and pseudo-second order models (Equation 4) [9-11].

$$q_t = q_e [1 - \exp(-k_1 * t)] \quad (3)$$

$$q_t = \frac{k_2 q_e^2 t}{1 + k_2 q_e t} \quad (4)$$

where k_1 (1.min⁻¹) and k_2 (g.mg⁻¹ min) are the constants of pseudo-first order and pseudo-second order, respectively, q_t (mg.g⁻¹) is amount adsorbed at time t and q_e (mg.g⁻¹) is the amount adsorbed at equilibrium.

3. Results and discussion

3.1 Adsorbent characterization

The images obtained from the SEM analysis (Fig. 3) show a very heterogeneous surface in relation to the particle size, showing small pores and lamellar structure, suggesting characteristics of a potential adsorbent material.

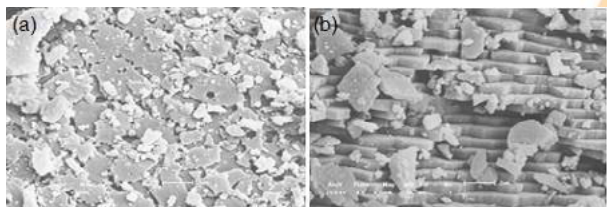


Fig. 3. SEM images from the *Mytella falcata* shells surface, 5000x magnification.

FT-IR analysis showed the functional groups found on the adsorbent surface (Table 1). MG, a cationic dye, interacts with the negative groups, such as OH⁻, HCO₃⁻ and CO₃²⁻, present on *Mytella falcata* shells [12-13].

The XRD analysis of the shells (data not shown) confirmed the carbonaceous nature of the material, showing peaks which are characteristics of aragonite and calcite, the main constituents of seashells [13].

Table 1. *Mytella falcata* functional groups identified by FT-IR analysis.

Wavenumber (cm ⁻¹)	Groups
3496	OH
2765	CH
2559	HCO ₃
1614	CO
1186	CO
944	CO ₃
775	OCO

3.2 Adsorption assays

Particle diameter and adsorbent dosage are important parameters in the adsorption process. Therefore, these variables were carefully evaluated in the MG adsorption onto *Mytella falcata* shells. According to the data obtained, the smallest particle size range ($0.212 < d_p < 0.300$ mm) provided the highest removal (Fig 4a). This result was expected, once reducing the particle size increases the surface area of the material, favoring the adsorption process. On the other hand, increasing the adsorbent dosage from 1.0 to 5.0 g.L⁻¹ did not substantially increase MG removal (Fig. 4b).

Thus, the kinetic study was performed using the lowest particle diameter and also lower adsorbent dosage (1.0 g.L⁻¹), with MG initial concentration of 100 mg.L⁻¹. From the results achieved (Fig. 5), equilibrium was reached after 120 min of contact, with maximum adsorption capacity of 96.1 mg.g⁻¹.

The experimental data were fitted to the pseudo-first order and pseudo-second order models and the kinetic parameters attained are shown in Table 2. From the results obtained, the adsorption

mechanism tends to the pseudo-second order model, suggesting a chemical sorption, due to the lower ARE values and higher R^2 . The chemisorption can be justified due to the interactions between the positive charges present in the MG structure and the negative functional groups of the adsorbent surface, as previously reported in the characterization section.

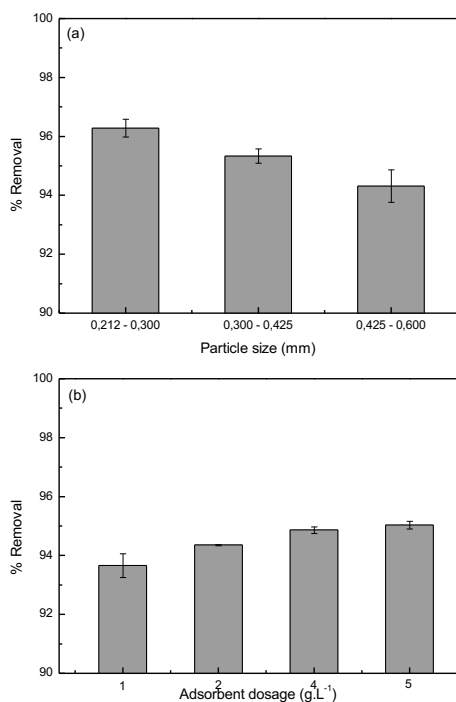


Fig. 4. Influence of particle diameter (a) and adsorbent dosage (b) in MG adsorption onto *Mytella falcata* shells.

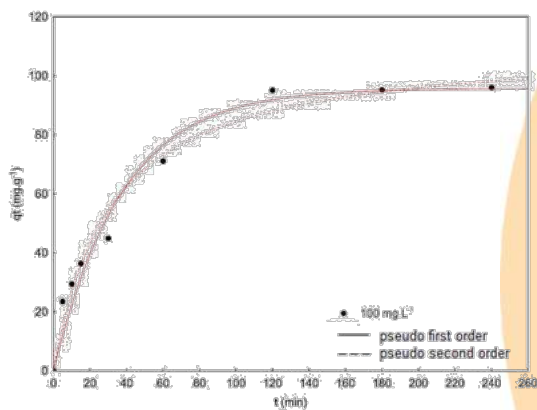


Fig. 5. MG adsorption kinetic curve onto *Mytella falcata* shells.

Table 2. Kinetics parameters obtained for MG adsorption onto *Mytella falcata* shells

Pseudo-first order	q_e (mg.g ⁻¹)	95.79
	k_1 (min ⁻¹)	0.026
	ARE	12.80
	R^2	0.970
Pseudo-second order	q_e (mg.g ⁻¹)	105.94
	k_2 (g.mg ⁻¹ .min ⁻¹)	0.003
	ARE	8.69
	R^2	0.978

4. Conclusion

In this work, *Mytella falcata* shells were successfully applied for malachite green dye removal from aqueous media. The characterization analyses confirmed the carbonaceous nature of the adsorbent material, revealing a lamellar structure on the shell surface. From the assays performed, 1g.L⁻¹ of adsorbent (0.212 < d_p < 0.300 mm) was able to remove over 90% of MG from water (100 mg.L⁻¹) in 120 min of contact, reaching the adsorptive capacity of 96.1 mg.g⁻¹.

In short, the preliminary results showed in the present contribution indicate that sururu shells can be used as alternative adsorbent for malachite green removal from water. In addition, the use of a large-scale waste produced in the state of Alagoas can contribute to reducing the environmental problems associated with its improper disposal.

Acknowledgements

The authors wish to thank Conselho Nacional de Desenvolvimento Científico e Tecnológico (CNPq/Brazil), Coordenação de Aperfeiçoamento de Pessoal de Nível Superior (CAPES/Brazil) and fundação de Amparo à Pesquisa do Estado de Alagoas (FAPEAL/Brazil).

References

- [1] Bharagava RN. Environmental Pollutants and their Bioremediation Approaches. CRC Press, 2017.

- [2] Demirbas A. Agricultural based activated carbons for the removal of dyes from aqueous solutions: a review. *J. Hazard. Mat.* 2009;167:1-9.
- [3] Mashkoo F, Nasar A. Preparation, characterization and adsorption studies of the chemically modified *Luffa aegyptica* peel as a potential adsorbent for the removal of malachite green from aqueous solution. *J. Molec. Liq.* 2019;274:315-27.
- [4] Salleh, MAM, Mahmoud DK, Karim WAWA, Idris A. Cationic and anionic dye adsorption by agricultural solid wastes: A comprehensive review. *Desalination* 2011;280:1-13.
- [5] El Haddad M, Regti A, Laamari MR, Slimani R, Mamouni R, Antri SE, Lazar S. Calcined mussel shells as a new and eco-friendly biosorbent to remove textile dyes from aqueous solutions. *J. Taiwan Inst. Chem. E.* 2014; 45(2):533-40.
- [6] Singh SN. *Microbial degradation of synthetic dyes in wastewaters.* Springer, 2014.
- [7] Cirini G, Lichtfouse, Wilson LD, Morin-Cirini N. Conventional and non-conventional adsorbents for wastewater treatment. *Environ. Chem. Let.* 2019;17:195-213.
- [8] Fransozo A, Negreiros-Fransozo, ML *Zoologia dos Invertebrados.* 1. ed. –(Reimpr), Rio de Janeiro: Roca, 2017.
- [9] Lagergren S. About the theory of so-called adsorption of soluble substances. *K Sven Vetenskapsakademiens* 1898;24:1-39.
- [10] Ho YS, McKay G. Sorption of dye from aqueous solution by peat. *Chem Eng J.* 1998;70:115–124.
- [11] Ho YS, McKay. Pseudo-second order model for sorption processes. *Process Biochem.* 1999;34:451–465.
- [12] Chowdhury S, Saha P. Sea shell powder as a new adsorbent to remove Basic Green 4 (Malachite Green) from aqueous solutions: Equilibrium, kinetic and thermodynamic studies. *Chem. Eng. J.* 2010;164:168-77.
- [13] Silva TS, Meili L, Carvalho SHV, Soletti JI, Dotto GL, Fonseca EJS. Kinetics, isotherm, and thermodynamic studies of methylene blue adsorption from water by *Mytella falcata* waste. *Environ Sci Pollut Res.* 2017.

Computational intelligence applied to adsorption processes

N. P. G. Salau

Universidade Federal de Santa Maria, Roraima Avenue, 1000, Santa Maria, 97105-900, Brazil

Abstract

Computational intelligence is a powerful tool and has recently made great progress in many applications including the development of models to accurately predict the performance of complex systems in various fields of science and engineering. Recently, two techniques based on computational intelligence have been mainly applied in complex adsorption systems: Artificial Neural Networks (ANN) and Adaptive Neuro-Fuzzy Inference System (ANFIS). Application of both techniques in adsorption systems have been widespread owing to two major factors: (i) the evaluation of adsorption behavior is not available for all operating conditions because of the high cost and time required to collect and analyze the experimental data and (ii) theoretical models (either first- principles or empirical) are not capable of predicting the complex behavior of multi-solute systems due to the probability of diverse adsorbent-solutes interactions as well as the nonlinear relationships between dependent and independent process variables. Models based on computational intelligence can predict the nonlinear relationships between input and output variables, without any prior assumptions about their nature. They also allow to include the characteristics of adsorption systems to predict the process performance at different scenarios, besides identifying the relevant parameters of the adsorption process. Such models can also be used alone or hybridized with theoretical models and different optimization algorithms to generalize the performance of any adsorption system. This mini-review summarizes the benefits, drawbacks and current trends of the use of computational intelligence in the field of adsorption.

Keywords: Adsorption modelling; Complex non-linear mechanisms; ANN; ANFIS; Optimization.

Assessing CO₂ Adsorption on amino-functionalized mesocellular foams synthesized at different aging temperature

J.A. Cecilia^a, E. Vilarrasa-García^b, P.A.S. Moura^b, C.L. Cavalcante Jr.^b,
D.C.S. Azevedo^b and E. Rodríguez-Castellón^{a*}

^aDepartment of Inorganic Chemistry, Crystallography and Mineralogy, Universidad de Málaga, Campus de Teatinos, 29071, Málaga, Spain

^b Department of Chemical Engineering, Grupo de Pesquisa em Separações por Adsorção, Universidade Federal do Ceará, Campus do Pici, 60455760, Fortaleza CE, Brazil

Abstract

Scientific community worldwide investigate different pathways to mitigate CO₂ emissions, by capturing them using alternative technologies to the current ones with technical and economic advantages. A wide variety of solid sorbents has been synthesized lately to be applied in CO₂ adsorption. Among them, mesoporous silicas deserve attention due to their ability to accommodate large concentrations of different chemicals as a consequence of their surface chemistry and tunable pore structure. Functionalized materials exhibit promising features for CO₂ adsorption at high temperatures and low CO₂ concentrations. This work aimed to assess the influence of the textural properties on the performance of CO₂ adsorption over functionalized mesoporous silica. With this goal, several mesoporous silica foams were synthesized by varying the aging temperature, obtaining materials with larger pore diameter. Thus, the synthesized materials were functionalized by grafting or impregnation with 3-aminopropyltriethoxysilane, polyethylenimine and tetraethylenepentamine as amine sources. The synthesized materials were characterized by Small-angle X-ray Scattering, N₂ adsorption-desorption isotherms at 77K, Transmission Electron Microscopy, Fourier Transform Infrared Spectroscopy and Elemental Chemical Analysis. Finally, the amino functionalized materials were assessed on CO₂ capture by means of CO₂ adsorption isotherms at 298, 318 and 338K up to 1 bar.

Keywords: silica, synthesis, amino groups, CO₂ adsorption

Ultrapure monoclonal antibodies: hydrophobic interaction chromatography as polishing step in downstream processing

Iara Rocha Antunes Pereira Bresolin^{a,b}, Igor Tadeu Lazzarotto Bresolin^{a,b,*}, Nico Lingg^{b,c},
Alois Jungbauer^{b,c}

^a Departamento de Engenharia Química, Universidade Federal de São Paulo, Diadema, SP, Brasil

^b Department of Biotechnology, University of Natural Resources and Life Sciences, Vienna, Austria

^c Austrian Centre of Industrial Biotechnology (ACIB), Vienna, Austria

* bresolin@unifesp.br

Abstract

Adalimumab is the first fully human therapeutic monoclonal antibody (mAb) available in market, being successfully used for the treatment of several diseases, such as ulcerative colitis, arthritis uveitis and Crohn's disease. To avoid side effects in patients, the mAb preparation must be as pure as possible. Thus, to be considered an ultrapure mAb, there must be a guarantee of removal of all kinds of impurities, like the process-related (such as host cell proteins – HCP – and DNA) and the product-related (such as aggregates, variants, and fragments). During the downstream processing, this can be achieved by several unit operations and by exploiting a combination of different chromatography techniques (anion or cation exchange, affinity or hydrophobic interaction). Hydrophobic interaction chromatography (HIC) explores the hydrophobicity characteristics of mAbs through the interaction between nonpolar regions present on their surface and hydrophobic ligands in presence of a kosmotropic salt. The mAbs hydrophobicity is comparatively high, which makes HIC a versatile tool applied in separation processes. In this study, we present a polishing procedure to obtain an ultrapure antitumor necrosis factor (TNF) alpha IgG1 using hydrophobic interaction chromatography in Toyopearl Phenyl 650 M. Adsorption isotherms, breakthrough curves and chromatographic runs were carried out. Eluted mAb was recovered with 99.9% purity when a linear gradient of ammonium sulphate was used. Process-related and product-related impurities (aggregates and HCP) were below the limit of detection of HPLC size exclusion chromatography (0.06%), and ELISA (1.1 ppm), respectively.

Keywords: hydrophobic interaction chromatography, adsorption, monoclonal antibodies, Adalimumab;

Molecular sieves: Tunable porosity materials for adsorption and catalytic processes

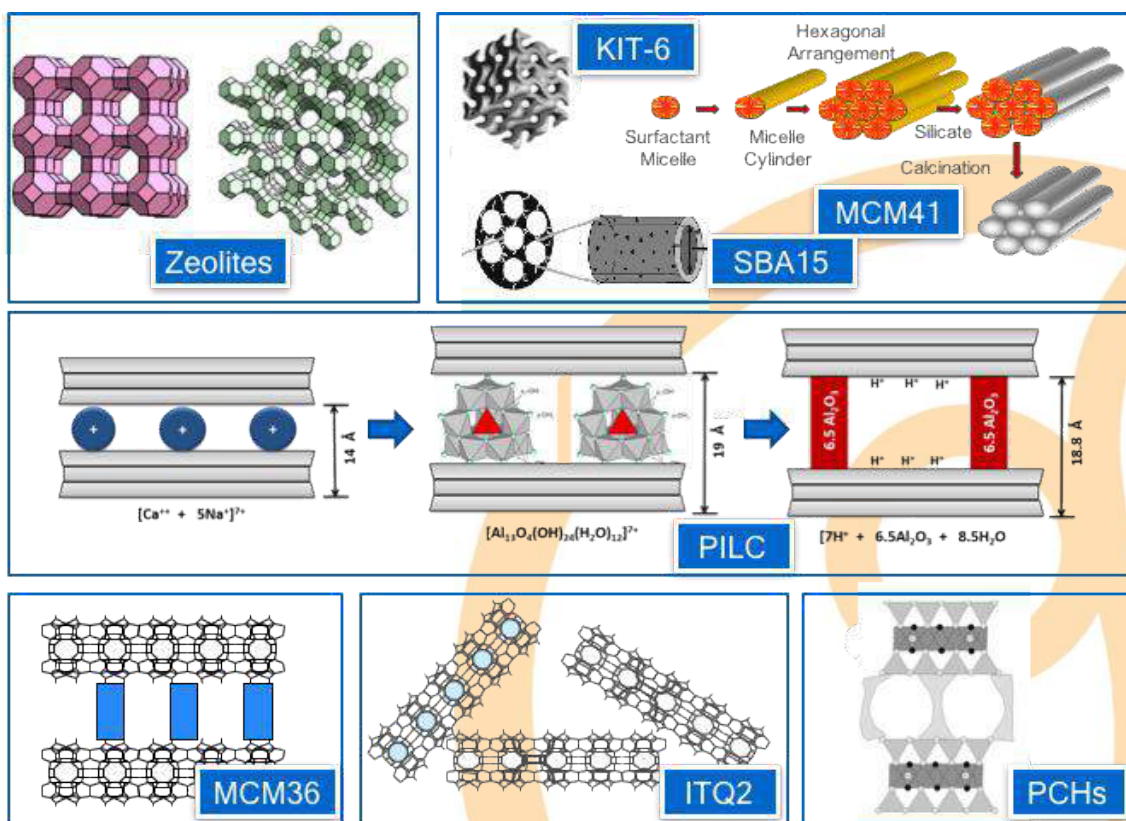
Sibele Pergher*

Laboratório de Peneiras Moleculares – LABPEMOL, Universidade Federal do Rio Grande do Norte – UFRN,
Av. Senador Salgado Filho, 3000 – CEP: 59078-970 - Natal – RN - Brazil

Abstract

Molecular Sieves are solids with defined porosity and with the capacity of differentiate molecules through their dimensions and geometries. They can be used as catalysts for several kinds of reactions, and also for separation and adsorption processes. In this talk, we describe different materials that can be obtained with different porosities for application in adsorption processes: We describe the advances using Zeolites, mesoporous materials, layer materials and hierarchical materials.

Keywords: Molecular Sieves; zeolites; mesoporous materials



Simultaneous adsorption and desorption of CH₄-CO₂ to improve the storage capacity of natural gas

Rodrigo G. Martins, Deivson C. S. Sales, Cesar A. M. Abreu

*Department of Chemical Engineering, Federal University of Pernambuco,
50.740-521 Recife, Pernambuco, Brazil*

Abstract

The expansion of the use of natural gas (NG) and the need to mitigate CO₂ emissions are factors that motivate developments related to the capture and storage of these gases. Thus, through the adsorbed gas technology, greater storage capacities are achieved under the same pressure or the same storage capacity is achieved under a lower pressure. The intensified storage operations were carried out using a coaxial system (two concentric cylinders) with equal loads of activated carbon, using the energetic combination of the effects of simultaneous adsorption and desorption. The evaluations were carried out according to the barometric technique, with pressures in the range of 10.0 bar to 40 bar for CO₂ and 10.0 bar to 61.7 bar for CH₄, operating with flow rates between $1.14 \times 10^3 \text{ m}^3 \text{ min}^{-1}$ and $9.09 \times 10^3 \text{ m}^3 \text{ min}^{-1}$. The behavior of the semi-continuous processes of simultaneous charge and discharge of CH₄ and CO₂ was described by a mathematical model, predicting changes in pressure and the amount adsorbed. The increases in mass of stored gas were quantified when compared with the traditional system in a single reservoir, providing in operations with flow rates of $9.09 \times 10^3 \text{ m}^3 \text{ min}^{-1}$ approximately 50 % additional for CH₄ at 60.0 bar and 70 % for CO₂ at 10.0 bar.

Keywords: gas storage, adsorption, methane, carbon dioxide, coaxial system.

1. Introduction

The expansion of the use of natural gas (NG) and the need to mitigate CO₂ emissions are factors that motivate developments related to the capture and storage of these gases. Thus, through the adsorbed gas technology (GNT), greater storage capacities are achieved under the same pressure, or the same storage capacity is obtained under a lower pressure.

Adsorption on porous solid has been used to improve the storage of natural gas in addition to the compression effect ([1], [2]). Stored NG to be supplied must be decompressed, and also desorbed. Heat released and maintained in the adsorber during the exothermic adsorption of NG onto activated carbon (AC) reduces the adsorbed amount of the gas toward a lower equilibrium content on the AC surface. On the other hand, heat absorbed from adsorber medium during endothermic desorption can promote retention of the gas diminishing the desorbed amount of NG ([4], [5]).

The supply of natural gas from different sources is operated with storage tanks connected to points of discharge of the domestic or industrial users. A natural gas network formed by a gas supply,

pipeline and discharge points can be identified as a dynamic storage system, where the conditions of supply and discharge are established and maintained [6].

Thus, in these systems, various events can occur that can require quick and increasing gas supply such as: the unstable conditions due to the events of peak demand (spiking), supplying by transported pressurized tanks.

The gas storage devices are presented as solutions ([7], [8]) to the supply during spiking, for the needs to transport higher amount of gas per storage unit, and for quick and complete releasing for industrial units.

In the present work, a NG storage process operating by compression and adsorption was developed through an improved way in a new storage device [9], which associates opposite heat transfer effects involving exothermic adsorption and endothermic desorption. The cylindrical coaxial system, containing activated carbon in annular and central reservoirs, was evaluated through operation steps of simultaneous charge and discharge, and storage equilibria. Applications were developed for methane-methane and methane-carbon dioxide systems.

2. Experimental

Compression and adsorption storage was performed with the gases: methane (99.5% vv), carbon dioxide (99.999% vv), and helium (99.9990% vv) supplied by White Martins, Brazil. The adsorption of gases was carried out on an activated carbon bed of the Nuchar NG type from Mead Westvaco, USA, produced from wood and chemically activated. The compression and adsorption evaluations were performed in a semi-pilot unit composed of a single reservoir (500 cm³, 304L-HDF4-1000, Swagelok, USA) and the co-axial cylinder system (2000 cm³, external, 304L-HDF4-1000, Parr; 500 cm³, internal, Swagelok, USA). A scheme of the co-axial system is represented in Figure 1.

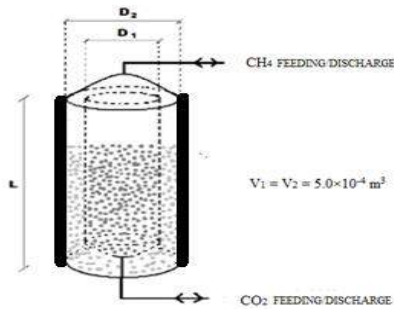


Figure 1. Co-axial gas storage system.

The co-axial storage system, thermally insulated on its external wall, consists of two concentric cylinders, each containing the same mass of activated carbon. The experimental evaluations of storage were carried out through simultaneous charge and discharge operations. The loading process consisted of alternately feeding methane or carbon dioxide into the storage cylinder under constant flow, up to a certain loading pressure. The discharge process consisted of releasing the gas stored in the cylinder, under constant flow until the gauge pressure of 0.1 bar. The effects of compression and adsorption and desorption of each gas were considered, in charge and discharge, respectively.

3. Mathematical modeling

With a view to predicting the behavior of the CH₄ and CO₂ storage operations in the co-axial system, a mathematical model (Equations 1, 2) was developed, applicable to the both co-axial sections (cylinder) of the reservoir. For each section with activated carbon bed it was considered: uniform pressure in the storage reservoir, instantaneous equilibrium, fixed feed flow, no internal convection effects.

Indications are given for the operation variables and the heat rates released by the adsorption process in the inner cylinder, and for the absorbed heat rates, associated with the desorption process in the outer cylinder.

$$\frac{dP_{gas}}{dt} = \left\{ \left(\frac{M_{gas} f_{gas}}{L} \right) + \left(\frac{M_{gas}}{R} \right) \frac{P_{gas}}{T_{int}^2} \frac{dT_{int}}{dt} \right\} \left(\frac{RT_{int}}{M_{gas}} \right) - \left\{ \frac{(1-\varepsilon)}{\varepsilon} \rho_c \frac{dq_{gas}}{dt} \right\} \quad (1)$$

$$\frac{dT_{int}}{dt} = \left\{ \left(\frac{M_{gas} f_{gas}}{L} \right) C_{p_{gas}} (T_{int} - T_{amb}) + \frac{(1-\varepsilon)}{\varepsilon} \rho_c \Delta H_{ads} \left(\frac{dq_{gas}}{dt} \right) \right\} / \left\{ \left(\frac{1-\varepsilon}{\varepsilon} \right) C_{pc} \rho_c \right\} + \left\{ \left(\frac{C_{p_{gas}} M_{gas}}{R} - 1 \right) \left(\frac{dP_{gas}}{dt} \right) + \frac{Q_{T_{ext}}}{V_{cilindro}} \right\} \quad (2)$$

$$\frac{dQ_{T_{int}}}{dt} = \left(\rho_{gas} C_{p_{gas}} V_{in_{gas}} + \left(\frac{1-\varepsilon}{\varepsilon} \right) m_c C_{pc} \right) \frac{dT_{int}}{dt} - \left(\frac{1-\varepsilon}{\varepsilon} \right) m_c \Delta H_{ads} \frac{dq_{gas}}{dt} - M_{gas} f_{gas} A_t C_{p_{gas}} (T_{int} - T_{amb}) \quad (3)$$

The initial conditions are written as:

$$P_{int}(0) = P_{int,Inicial}; T_{int}(0) = T_{int,Inicial};$$

$$q_{gas,Interno}(0) = q_{gas,Interno,Inicial}; Q_{T_{int}}(0) = Q_{T_{int,Inicial}}$$

where, T_{int} is the temperature of the activated carbon bed in the inner and outer cylinders, respectively, and T_p the temperature of the inner cylinder wall. V_{fed} and V_{rel} are the volumes of gas fed and released, and A_t the cross-sectional area of the cylinder. M_{gas} , f_{gas} and q_{gas} are the molar mass, the molar flow and the amount of gas adsorbed, respectively.

Adsorption is quantified by the LDF model as, $dq_{gas}/dt = k_{gas}(q_{gas}^* - q_{gas})$, and according Langmuir-Freundlich $q_{gas}^* = q_{gasSAT} P_{gas}^d / [1 + K_{gas} P_{gas}^d]$.

4. Results and discussion

The storage process was carried out by compression and adsorption in the axial storage device, using activated carbon beds and associating opposite heat transfer effects from exothermic adsorption and endothermic desorption. Figures 2 and 3 show the evolution of the pressure of methane and carbon dioxide for the charging and discharging cycles in the external and internal cylinders, respectively.

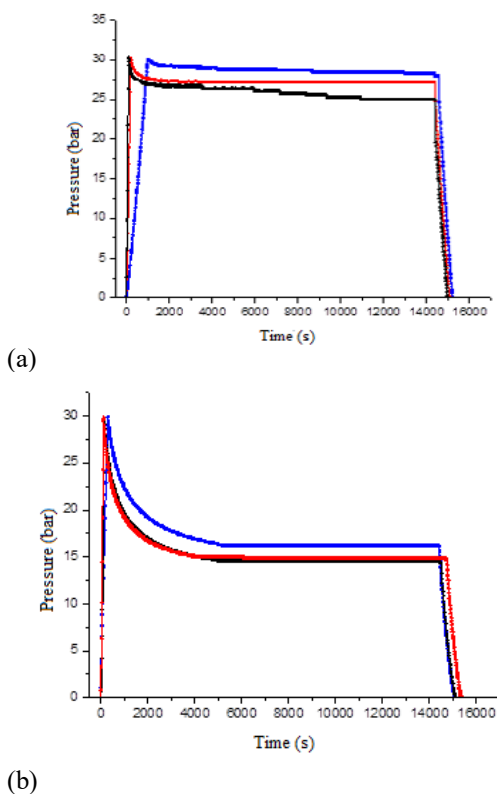


Figure 2. Evolution of methane and carbon dioxide pressure. Co-axial system: (a) CH₄, outer cylinder, (b) CO₂, inner cylinder. 30.0 bar, 30 °C, [1.14 – 9.09] x 10⁻³ m³ min⁻¹.

The pressure changes refer to the charge, equilibrium and discharge steps for methane in the outer cylinder (a) and carbon dioxide in the inner cylinder (b). In both cases the storage pressure was reached quickly and at a lower level in relation to the charging pressure (CH₄, 28.0 – 25.0 bar; CO₂, 17.0 – 15.0 bar) due to the exchange of energy between cylinders, providing a faster

adsorption and allowing a greater adsorption capacity.

Figure 3 shows the evolution of the pressure of carbon dioxide in the single and coaxial systems.

The comparison indicates that the CO₂ storage pressure in the co-axial system is reached quickly and at a lower level than that of the single system, considering that the storage is processed in a reservoir with lower temperatures.

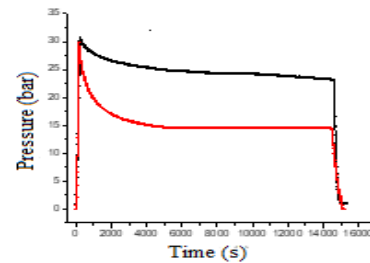


Figure 3. Evolution of carbon dioxide pressure. Co-axial system: (a) outer cylinder, (b) inner cylinder. 30.0 bar, 30 °C, [1.14 - 9.09] x 10⁻³ m³ min⁻¹.

The temperature variation in one of the beds of the coaxial system was measured when the charge or discharge of the adjacent bed was performed, observing effects according to the pressure applied. Measurements carried out at 60.0 bar with CH₄ reached the following values: in the load of the internal cylinder, the external bed increased by 5.4 °C; in the discharge of this cylinder, the external bed varied by 5.7 °C.

The predictive aspects of the evaluation of the coaxial storage system were obtained through solutions of the model equations that included the parameters of the adsorption isotherms (q_{gasSAT} , K_{gas}) evaluated in the experiments, with the following orders of magnitude: for CH₄ 1.84 × 10⁻¹ g g⁻¹, 8.19 × 10⁻² bar⁻¹, and for CO₂ 1.72 × 10⁻¹ g g⁻¹, 5.51 × 10⁻² bar⁻¹.

The thermal parameters and mass transfer coefficients are in the following order of magnitude: C_{pCH_4} 2.45 kJ kg⁻¹ K⁻¹, C_{pCO_2} 0.85 kJ kg⁻¹ K⁻¹, C_{pAC} 1.28 kJ kg⁻¹ K⁻¹; k_{CH_4} 6.95 × 10⁻¹ s⁻¹, k_{CO_2} 1.50 × 10⁻¹ s⁻¹

Figure 4 shows the solutions in Equations 1 and 2, in terms of the evolution of pressure and temperature for operations with CO₂.

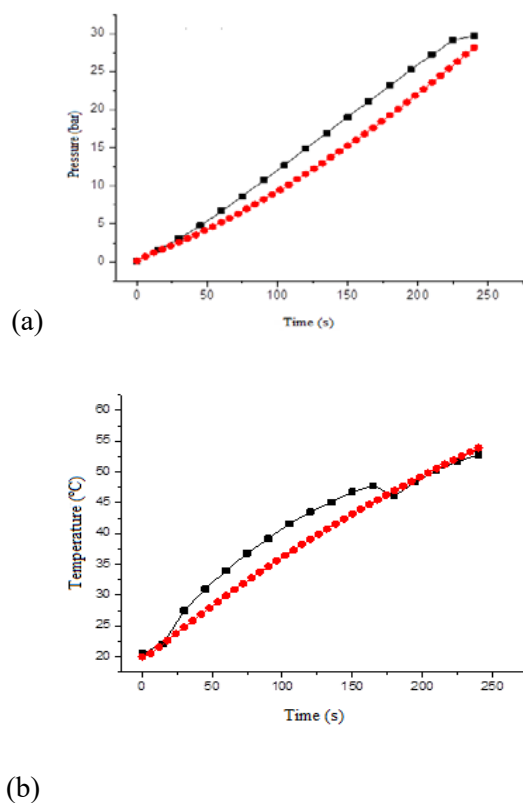


Figura 4. Evolution of pressure and temperature in CO₂ storage. Model (●) vs. experimental (■) (a) single system, (b) co-axial system. 30.0 bar, 5.13x10⁻³ m³ min⁻¹

The evaluation of the storage process via model and according to the pressure (P) and temperature (T) behavior, in the domains of up to 30.0 bar and 60 °C, occurred with average standard deviations, $\langle d_p \rangle = 0.24$; $\langle d_T \rangle = 0.14$, meaning adequate representation of the experimental results.

In Table 1, the performance of the co-axial system in relation to storage in the single system is quantified in terms of the amount adsorbed and the volume stored for methane and carbon dioxide.

Table 1. Storage performance. Conditions: 30.0 bar, 5.13x10⁻³ m³ min⁻¹.

gas	yield (% wt., kg kg ⁻¹)	yield (% vol., m ³ m ⁻³)	ratio (wt./vol.)
CH ₄	33.44	21.04	1.59
CO ₂	24.72	10.62	2.33

Under the operating conditions of the coaxial system (30.0 bar, 9.09x10⁻³ m³ min⁻¹), the storage performance related to the single system can be quantified using the ratio between the adsorbed quantity and the stored volume, estimated at 1.6 for CH₄ and 2.3 for CO₂. For both gases, storage performance was significant, with emphasis on the adsorption contribution, having meant an improvement of about 60 % and 130 %, respectively.

5. Conclusions

The operation of the coaxial storage device, with two contiguous reservoirs, filled with CH₄ and CO₂, respectively, occurred with the use of thermal transfer between them, ensuring small temperature variations below 6 °C.

The storage of gases in the reservoir sections (internal CO₂; external CH₄) allowed to obtain increases in relation to the traditional system of a single reservoir with activated carbon, expressed in terms of added adsorbed mass and volumetric capacity, as follows: 50% by weight and 28% by volume of CH₄ at 60.0 bar and 70% by weight and 45% by volume of CO₂ up to 10.0 bar, respectively.

Acknowledgments

Acknowledgments to CNPq, Brazil and ANP - Agencia Nacional do Petroleo, Brazil for the financial support given to this project.

References

- [1] Alhasan S, Carriveau R, Ting DSK. A review of adsorbed natural gas storage technologies. *Int. J. Environmental Studies* 2016; 1: 1–15.
- [2] Matthew B, Anne D. Adsorbed methane storage for vehicular applications. *Applied Energy* 2015; 149: 69–74.

- [3] Sahoo S, Ramgopal M. Theoretical performance of an adsorbed natural gas storage system subjected to variable charge–discharge conditions, *Int. J. Ambient Energy* 2014; DOI: 10.1080/01430750.2014.977495.
- [4] Yang XD, Zheng QR, Gu AZ, Lu XS. Experimental studies of the performance of adsorbed natural gas storage system during discharge. *Applied Thermal Engineering* 2005; 25: 591–601.
- [5] Pupier O, Goetz V, Fiscal R. Effect of cycling operations on an adsorbed natural gas storage. *Chemical Engineering and Processing* 2005; 44: 71–79.
- [6] Bilóé S, Goetz V, Mauran S. Dynamic discharge and performance of a new adsorbent for natural gas storage. *AIChE Journal* 2001; 47: 2819-2830.
- [7] Chang KJ, Talu O. Behavior and experimental performance of adsorptive natural gas storage cylinders during discharge. *Applied Thermal Engineering* 1996; 16:359-374.
- [8] Mota JPB. Impact of gas composition on natural gas storage by adsorption. *AIChE Journal* 1999; 45: 986-996.
- [9] Martins RG, Sales DCS, Lima Filho NM, Abreu CAM. Development of a system of natural gas storage governed by simultaneous processes of adsorption-desorption. *Adsorption* 2015; 21: 523 – 531. doi.org/10.1007/s10450-015-9691-7.

Modeling Adsorption in Porous Solids with Equations of State for Confined Fluids

Marcelo Castier

*Chemical Engineering Program
Texas A&M University at Qatar, Doha, Qatar*

Abstract

Mathematical models for adsorption equilibrium vary from empirical expressions, of little computational effort, to detailed molecular simulations, whose computational load prevents their regular use for chemical process design. This presentation will focus on models of intermediate complexity, which are based on equations of state (EoS) originally intended for process design, such as the Peng-Robinson and the SAFT-VR Mie EoS. It will be shown how to extend these models for adsorption by introducing terms to account for the interactions between the molecules of the fluid and the pore wall, which is modeled as a homogeneous surface. Models derived in this way are capable of correlating/predicting pore condensation, several types of adsorption isotherms and can be successfully used to infer the pore size distribution of various adsorbents, including that of novel materials such as zeolitic imidazolate frameworks. They can also be applied to predict the separation of components from mixtures of an arbitrary number of components with a computational load comparable to that of the models from which they are derived.

Keywords: modeling; EoS; adsorption; thermodynamics

Influence of surface topography parameters on macromolecule deposition in LbL (layer-by-layer) processes

Gabriel A.T. da Silveira^a, Marisa M. Beppu^{a*}, Hernandes Carvalho^b

^a School of Chemical Engineering, University of Campinas, Campinas SP 13083-852, Brazil

^b Biology Institute, University of Campinas, Campinas SP 13083-852, Brazil

Abstract

Surface properties play a key role in how biomaterials interact with the environment. In the context of biological phenomena, several studies report changes in cellular behavior promoted by changes on chemical and physical properties of surfaces. Biological events, such as adsorption of biomacromolecules and successive adhesion and cell growth, can be modulated by surface modifications. However, the complexity of the cell adhesion and the singularity of each type of cell make the construction of functional biomaterials even more challenging and impose difficulties to correlate specific cellular functions to a particular topography characteristic. This study explored topographic fractal analyses of different surfaces to understand how layer-by-layer (LbL) technique modifies surface morphology and how roughness can influence the adhesion of the prostatic tumor cell line PC3. Therefore, chemically similar substrates with different roughness profiles were produced and characterized by three different topography parameters such as the width of interface (σ^2), the lateral correlation length (ξ) and roughness exponent (α). These substrates were evaluated before and after LbL coating and cell adhesion assays on these materials were conducted to investigate the relative impact of each surface parameter on PC3 cell adhesion. Although the experimental noise, a strong correlation between the roughness exponent with the adhesion of PC3 cells was observed in PDMS samples. In this case, surfaces with a smoother local profile proved to be potentially better in applications that seek to promote cell adhesion. This information is useful to design applications such as in the development of biosensors.

Keywords: Fractal analysis; roughness; topography; cell adhesion; layer-by-layer.

High Pressure H₂S Adsorption from Natural Gas Streams Using Zeolite NaY

Leonardo Hadlich de Oliveira, Marcus Vinicius Pereira, Artur LemesMoretti, Mateus Urias Cerdeira Braga, Pedro Augusto Arroyo*

Laboratory of Adsorption and Ion Exchange (LATI), Department of Chemical Engineering (DEQ), State University of Maringá (UEM), 87020-900, Maringá, PR, Brazil

Abstract

Acid gases contaminants found in natural gas streams, such as H₂S, can damage processing equipment by corrosion, becoming necessary its removal. Several processes can be used to remove sulfur from natural gas, such as hydrodesulfurization, oxidation, absorption, and adsorption. Adsorption processes are considered an economic alternative due to the possibility of adsorbent reuse, simplicity of operation, high product recoveries and low energy costs. Therefore, this work aimed to evaluate the use of zeolite NaY in high-pressure H₂S adsorption, up to 40 bar total pressure, in equilibrium and fixed bed conditions. Equilibrium results indicate a strongly favorable isotherm with maximum uptake capacities above 6.0 mol H₂S kg⁻¹ at highest partial pressure (1.2 bar), also a desorption hysteresis was observed, which can be attributed to H₂S chemisorption. However, isotherm modeling suggests the predominance of H₂S physisorption on NaY. Fixed bed adsorption data showed breakthrough curves were nonsymmetrical, which indicated the presence of internal resistance mainly, probably due to the adsorbent microporosity. In accordance, MTZ did not vary significantly with different inlet flow rate. Effective intraparticle mass transfer coefficients obtained with LDF model increases as flow rate increases, due to higher availability of H₂S molecules at adsorbent surface, which increases the driven force necessary for intraparticle mass transfer. Further, accelerated deactivation tests for 15 adsorption/desorption cycles in fixed bed conditions showed the adsorbent regenerability, similar breakthrough behavior and times, after the first adsorption cycle. Thus, results indicate the potential of NaY application in modulated adsorption processes.

Keywords: Adsorbent regenerability; H₂S chemisorption; Tóth isotherm; breakthrough curves; LDF model

Challenges to connect the effects of fluid confinement to the engineering of adsorption systems

Amaro Gomes Barreto Junior

*Chemical and Biochemical Process Engineering (EPQB), School Of Chemistry (EQ),
Federal University of Rio de Janeiro (UFRJ), Rio de Janeiro, Brazil*

Abstract

Thermodynamic modeling of confined fluids and the study of adsorptive phenomena are essential for several current industrial systems, such as the separation process using porous adsorbents. For systems engineering purposes, the modeling of adsorptive phenomena is required to calculate the thermodynamic properties of the phases, such as the adsorbed and bulk. In many cases, simplistic thermodynamic models are enough. It can be seen when the process is designed to operate at low pressure combined with a macroporous adsorbent. However, when microporous adsorbent is required, the porous size becomes a state variable in the thermodynamic sense. So, the confinement effect plays a role in the adsorbed phase properties. Under this perspective, the modeling of confined fluids brings more thermodynamic consistency for the adsorbed phase behavior calculations if its basic concept is consistent with the bulk phase model. In literature, there are many confined fluid models available. Our group has worked on applying classical density functional theory (cDFT) for calculation adsorbed phase combined with PC-SAFT for bulk phase properties. In this work, we divided the approach into two parts. The first one is related to engineering for adsorption systems. In this part, the optimization of temperature swing adsorption for gas dehydration is the case studied. This methodology, focused on conceptual designs, was adapted to optimization, resulting in inequality equations or constraints. The objective was to propose the lowest cost design of a unit present on an oil platform. The second one is on modeling phases present in the scenarios regarding contaminant removal from natural gas. Predicting water content can be a challenging task in some conditions. It is the case when acid gases are present in natural gas mixtures. A slight error in calculating saturated water in natural gas can leave dehydration units undersized, hence the importance of reliable water content predictions. We make available a ready-to-use and straightforward alternative for many common industrial challenges by presenting this approach. We also present the PC-SAFT-QSDFT approach consistent with the PC-SAFT equation of state while treating the adsorbent explicitly. We used the estimated parameters to analyze the phase transition inside a mesopore with the same physical characteristics at higher pressures. The approach presented here is a reliable way to consider properties ranging from molecular and pore scales to process scales to better understand and predict phase transition events in adsorption systems..

Keywords: Fluid confined; thermodynamic phase properties, conceptual design; optimization

Application of geopolymers in carbon capture and sequestration

Alisson Lopes Freire, Humberto Jorge José, Regina de Fatima Peralta Muniz Moreira

Department of Chemical and Food Engineering, Federal University of Santa Catarina, Campus Universitário, Trindade, 88040-900 Florianópolis, SC, Brazil

Abstract

Several carbon capture and sequestration (CCS) technologies are being tested to reduce the amount of greenhouse gases released into the atmosphere in recent years. After CO₂ separation and capture, a promising technology is its injection into suitable geological formation, such as coal beds, aquifers, and depleted oil and gas reservoirs. One additional benefit of CCS is that the CO₂ injection into oil and gas reservoirs is an enhanced oil recovery strategy. However, the cement used as well lining or plugs may have undergone degradation due to the CO₂ exposure, increasing the risk of CO₂ gas leakage to the surface. Special modified cements and geopolymers are being developed to be applied in CCS sites. However, little work has been made on studying the interaction of CO₂ and adsorption capacity of geopolymeric materials to be used in CCS. This study reports the application of geopolymers produced with fly ash and rice husk ash as an adsorbent material for the capture of CO₂. Different geopolymer formulations were used to produce high mechanical resistance and CO₂ adsorption capacity materials. The quantification of the reactive oxides in the precursor materials was carried out to obtain a better degree of geopolymerization. The geopolymers were characterized by XRD, BET, SEM and compressive strength analysis. Calcined rice husk ash activated by NaOH was found to be the most suitable precursor material to produce a geopolymer for CO₂ adsorption, with a capacity 24.4% higher than the best geopolymer adsorbent reported in the literature to date.

Keywords: CO₂ adsorption; Geopolymers; Carbon capture and sequestration.

Development and evaluation of adsorbents for plasmid DNA purification

Sara I. B. Cardoso¹, Fani Sousa², Pedro A. Pessoa Filho¹, Adriano R. Azzoni^{1*}

¹*Departamento de Engenharia Química, Escola Politécnica, Universidade de São Paulo, CEP 05508-900, São Paulo, Brazil.*

²*CICS-UBI - Centro de Investigação de Ciências da Saúde, Universidade da Beira Interior, 6200-506, Covilhã, Portugal.*

Abstract

The use of plasmid DNA (pDNA) for advanced therapeutic applications has increased in recent years, particularly for the production of viral vectors used for gene and cell therapies. In this context, chromatography appears as the most common operation used to obtain highly purified pDNA. However, the chromatographic resins available today still present a series of limitations, namely the low binding capacity and specificity. For this reason, the search for more efficient ligands is necessary. In this study, we evaluated the adsorption of nucleic acids on agarose resins containing immobilized arginine as the ligand. Binding capacities for pDNA and RNA (a relevant process impurity) were investigated to compare and gather crucial information about adsorption mechanisms involved in this type of affinity system. Langmuir and Freundlich isotherm models were used to describe the adsorption equilibrium. The best fit for both nucleic acids was achieved using the Freundlich model. The arginine amino acid immobilized on agarose were also evaluated and compared for plasmid DNA purification from *Escherichia coli* lysate samples. Furthermore, the correct choice of pH showed to be important for controlling the efficacy of arginine-nucleic acid interaction and promote pDNA and RNA separation. In conclusion, the specificity of arginine peptides appears as a promising strategy for plasmid pDNA purification.

Keywords: Plasmid DNA, RNA, arginine-agarose, adsorption isotherms.

1. Introduction

Chromatography is the most common process operation used to obtain plasmid DNA with the high degree of purity required for therapeutic applications [1,2]. However, the development of chromatographic resins for this use still presents a series of challenges, namely in the search of specific ligands and matrices capable of accommodating this type of molecule. Several studies have shown the potential of amino acids to establish specific and preferential interactions with the pDNA [3]. On the other hand, conventional agarose resins still appear as interesting matrices due to their prompt availability and easy modification using validated protocols [3]. Here, the arginine amino acid was immobilized on activated agarose resin. In the first part of this

work, we investigated the adsorption equilibrium of plasmid DNA, as well as the interaction with its main impurity (RNA) on arginine-agarose supports in batch mode. Langmuir and Freundlich models were used to describe the adsorption equilibrium in order to compare and gather crucial information about adsorption mechanisms involved in this type of affinity system.

2. Material and Methods

2.1 Bacterial growth and plasmid DNA/RNA purification

Production of pre-purified plasmid DNA and RNA were performed by growing *Escherichia coli* DH10B carrying the pVAXGFP plasmid (3697 bp) in 1 L shake flasks containing 250 mL of terrific

broth medium according to the protocol described previously [1,2].

2.2. Adsorption isotherms and plasmid DNA purification using chromatography

Equilibrium batch studies were performed through pre-purified samples, using arginine-based ligands by varying the adsorption conditions at pH values of 6.0 and 7.0. Langmuir (Eq. 1) and Freundlich (Eq. 2) models were used to describe the adsorption equilibrium as shown elsewhere [3].

$$q = q_{max} K_A \frac{C}{1+K_A C} \quad (1)$$

$$q = K_f C^{\frac{1}{n}} \quad (2)$$

The maximum binding capacity (q_{max}), the association constant (K_A), and the Freundlich constants (K_f and n) were obtained from the best fit of the isotherms to the experimental data for each set of conditions tested.

3. Results and Discussion

Equilibrium batch studies were performed to evaluate pDNA and RNA adsorption onto the arginine-agarose resin, varying the adsorption conditions at pH 6.0 and 7.0. Langmuir and Freundlich isotherm models were used to describe the adsorption equilibrium. The best fit for both nucleic acids was achieved using the Freundlich model, which was more effective in describing some deviations from the ideality, indicated by the higher correlation factors along with smaller mean square weighted deviations (Table 1 and Fig. 1).

Table 1. Langmuir and Freundlich isotherm parameters of plasmid DNA and RNA adsorption obtained by nonlinear fitting.

Model	Parameters	pDNA pH 6.0	pDNA pH 7.0	RNA pH 6.0	RNA pH 7.0
Langmuir	q_{max} (mg/mL resina)	0.509 ± 0.047	0.519 ± 0.035	8.88 ± 1.12	9.50 ± 0.781
	K_A (mL/μg)	1.15 ± 1.44	6.23 ± 4.98	0.0240 ± 0.0075	0.0379 ± 0.0081
	R^2	0.924	0.836	0.959	0.982
	χ^2	1.03 × 10 ⁻²	8.83 × 10 ⁻¹	0.479	0.292
	K_f	0.356 ± 0.013	0.368 ± 0.019	0.861 ± 0.096	0.890 ± 0.098
Freundlich	n	11.3 ± 1.24	9.76 ± 1.40	2.42 ± 0.165	2.11 ± 0.120
	R^2	0.983	0.944	0.985	0.988
	χ^2	3.91 × 10 ⁻⁴	1.13 × 10 ⁻¹	9.18 × 10 ⁻²	0.134

Overall, the correct choice of pH showed to be important for controlling the efficacy of arginine-nucleic acid interaction, being highly related to the impact of this parameter on their structures (data not shown). This type of analysis is quite useful for improving the selectivity and binding capacities of the resins for plasmid DNA purification purposes.

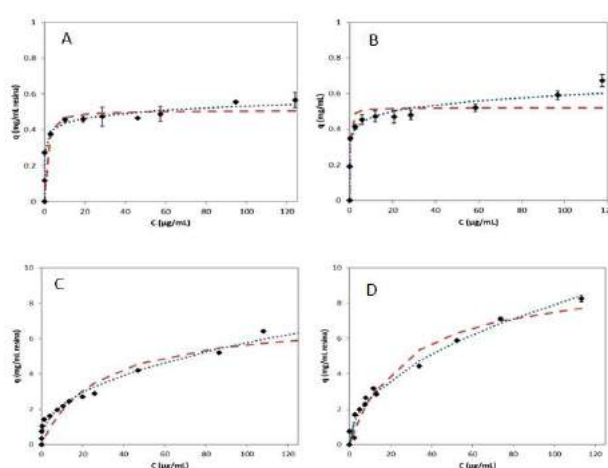


Fig. 1. Adsorption isotherms for the adsorption of pDNA and RNA onto arginine-agarose resin at different pH values, as described in Table 1. Legends: pDNA pH 6.0 (A), pDNA pH 7.0 (B), RNA pH 6.0 (C) and RNA pH 7.0 (D); Langmuir (- - -) and Freundlich (•••••) models.

Acknowledgments

This work was supported by FAPESP - Fundação de Amparo à Pesquisa do Estado de São Paulo (grant 2013/23780-1), and CNPq - Conselho Nacional de Desenvolvimento Científico e Tecnológico (grants 306184/2017-6 and 304125/2018-0). The authors also acknowledge the financial support of the Coordenação de Aperfeiçoamento de Pessoal de Nível Superior - Brazil (CAPES/PROEX) - Finance Code 001.

References

- [1] Cardoso, S., De Alcântara, P. F., Sousa, F., Azzoni, A. R. Arginine and di-arginine ligands for plasmid DNA purification using negative chromatography. *Separation and Purification Technology*, 2018, 202, 281-289.
- [2] Cardoso, S., Sousa, A., Queiroz, J. A., Azzoni, A. R., Sousa, F. Arginine homopeptides for plasmid DNA purification using monolithic supports. *Journal of Chromatography B.*, 2018, 1087-1088, 149-157.
- [3] Desenvolvimento e avaliação de adsorventes para purificação de DNA plasmidial por meio de cromatografia baseada em ligantes de arginina; PhD Thesis, Universidade de São Paulo, 2018.

THE USE OF H₃PO₄ ACTIVATED CARBONS AS SUPPORT IN CATALYSTS INTENDED FOR THE PRODUCTION OF BIOFUELS THROUGH THE HEFA ROUTE

Antônio M. de Freitas Júnior, Ruana D. Brandão, Marcos J. Prauchner*

*Instituto de Química, Universidade de Brasília, Campus Darcy Ribeiro, Brasília-DF, CEP: 70904 970, Brazil (*marcosjp@unb.br)*

Abstract

The present work concerns pioneer studies about the use of activated carbons (AC) as the support of molybdenum/nickel sulfide or platinum in catalysts intended for the production of hydrocarbonic biofuels through the HEFA route (hydroprocessing of esters and fatty acids). The starting AC was prepared by chemical activation with H₃PO₄. This activation methodology was chosen because it has shown to be the one that generates adsorbents that better conciliate a high specific surface area and the presence of pores with relatively large dimensions (mesopores). Such large pores are important to favor the access of the large fatty chains to the active catalyst sites. The AC was used as obtained or after additional treatment with HNO₃ (1 mol/L; 75°C) or H₂ (850 °C), which aimed to increase or reduce the content of surface acidic groups on the AC surface, respectively. The best conditions for preparing the catalysts were searched. The reaction tests were carried out in a batch system having as substrate lauric acid (a model compound) and coconut oil. The work rendered catalysts that promoted an efficient hydrodeoxygenation of the substrates. Remarkably, the results were even better than verified for catalysts consisting of similar active phases but traditional inorganic supports (Al₂O₃ and SAPO-11 zeolite). The reaction products were constituted basically by n-alkanes. The results were encouraging in terms of using H₃PO₄ ACs as support in catalysts employed in HEFA processes for the production of hydrocarbonic biofuels.

Keywords: activated carbons; catalyst; hydroprocessing; HEFA; biofuels.

1. Introduction

1.1. Hydrocarbonic biofuels

The development of biofuels have two main goals: (i) to provide alternative feedstocks to attend the ever-increasing demand for fuel in the transport sector; (ii) to make available fuels that are less harmful to the environment.

Currently, bioethanol and biodiesel (fatty acid esters) are by far the most worldwide employed biofuels. In spite of its lower energetic density if compared to gasoline, bioethanol has satisfactorily met the needs of internal combustion engines. In turn, biodiesel has been largely employed in diesel cycle engines. Nevertheless, biodiesel molecules have features that impair some fuel properties. Besides reducing the energetic density, the ester groups increase the hydrophilicity and the intermolecular forces. A higher hydrophilicity is undesirable because water promotes biological growth in storage tanks, therefore promoting the

formation of sludge and slime, which can block filters and lines.¹ In turn, stronger intermolecular forces increase viscosity and harm the fuel cold properties. In this respect, unsaturated molecules reduce viscosity and improve the fuel cold flow properties.² But, on the other hand, polyunsaturations pronouncedly reduce the oxidative stability, what can cause acidity and formation of insoluble gums and sediments.³ Finally, the presence of free fatty acids can also cause corrosion.

In face of what was sated above, it becomes clear the convenience that alternative fuels be also constituted by hydrocarbons. Therefore, these fuels can exhibit performance closer to that of petroleum-based fuels, can be used without engine modification, can utilize current supply infrastructure (tanks, pumps, pipelines, etc) and can be co-mingled with conventional fuel in any ratio, therefore attending to the drop-in concept. These issues become especially relevant in the aviation sector due to the inherent risks involved.



Nowadays, HEFA (Hydroprocessing of esters and fatty acids) is by far the route at the most advanced development stage that permits to synthesize hydrocarbonic biofuels.⁴ It comprises the thermal treatment of lipidic feedstocks at middle temperature ($\approx 300\text{--}400\text{ }^\circ\text{C}$) under elevated H_2 pressure ($\approx 20\text{--}100\text{ bar}$) in the presence of heterogeneous catalysts. The route has been used to produce fuel for jet turbines (the so-called HEFA-SPK - synthetic paraffinic kerosene) and diesel engines (the so-called renewable diesel, green diesel or HVO - hydrotreated vegetable oil).⁵⁻⁷

The catalysts usually employed in HEFA processes are sulfides of Mo (or W) promoted by Ni (or Co) deposited over oxide supports (mainly Al_2O_3). Alternatively, catalysts consisting of metals with hydrogenating/dehydrogenating properties (Pt, Pd, Ni) deposited over acidic supports (mainly zeolites and metal oxides) are also used.⁵

1.2. Activated carbons as catalyst support

Activated carbons (ACs) are a class of adsorbents characterized by remarkably high specific surface areas, which is the result of a well-developed structure of micropores and, to a lesser extent, mesopores. Thanks to that, ACs are extensively employed in a large range of applications such as purification of liquids and gases, gas separation, gas storage and catalysis.

In the present work, ACs are investigated as the support in catalysts employed in the synthesis of hydrocarbonic fuels through the HEFA route. The motivations for replacing traditional inorganic supports (e.g. alumina and zeolites) were that, besides their much higher surface areas, ACs: are thermally stable and resistant to chemical attack in both acidic and basic media; do not contain very strong acidic centers, which otherwise could provoke undesirable side reactions; can be obtained from cheap and abundant precursors (e.g. biomass residues and coal); permit to recover deposited metals from spent catalysts by burning the support. Further, the pore size distribution and surface chemistry of ACs can be tailored according to the application they are intended for.

2. Experimental

2.1. ACs preparation and modification

A starting AC sample was synthesized by chemical activation of dried coconut shell with H_3PO_4 using a previously described procedure.⁸ The

employed P/precursor ratio (in mass) was 0.54 (for this reason, the obtained sample was termed P54).

The AC P54 had its surface acidity increased or decreased by means of thermal treatments with a solution of HNO_3 (1 mol/L; 10 mL per g of P54; 75°C ; 1 h) or under a H_2 atmosphere (800°C ; 2 h; $5^\circ\text{C}/\text{min}$), respectively. The modified ACs were termed P54A and P54H. The goal of these modifications was to evaluate the influence of the surface acidic groups on the activity of the catalysts prepared in the sequence.

2.2. Catalysts preparation

The ACs P54, P54A and P54H were employed as supports for the preparation of two kind of catalysts: based on Mo sulfide or metallic Pt. In the first case, the presence of Ni as a promoting metal was evaluated. Different preparation conditions were tested in order to determine those that lead to the catalysts with the best performances.

Two impregnation methodologies were tested: wet impregnation and incipient impregnation.⁹ For the Mo-based catalysts, 7.8% of Mo or 6.0% of Mo plus 1.8% of Ni were deposited from $(\text{NH}_4)_6\text{Mo}_7\text{O}_2$ e NiNO_3 solutions. The metals were deposited simultaneously or one at a time. After impregnation, the material was calcined at 400 or 500°C (2 h; N_2) to render the respective metal oxides. For the Pt-based catalysts, 1.0% of Pt was deposited from a H_2PtCl_6 solution, which was or not additionally acidified with HCl. After impregnation, the material was reduced under H_2 at 400°C (2 h).

The obtained catalysts were labeled as it follows.

a) Firstly, the deposited metals were indicated. If Mo and Ni were deposited from a simple solution, they were listed together (MoNi); if they were deposited one at a time, they were listed in the sequence of deposition separated by the letter “d” in brackets (the letter “d” indicates that a drying step was carried out from one deposition to another).

b) In the sequence, the employed support is indicated after a slash.

c) Finally, in brackets: the term “ac.” indicate that HCl was added to the H_2PtCl_6 solution; the letters “w” or “i” indicate if wet or incipient impregnation was used; the calcination temperature is indicated in the case of the Mo-based catalysts.

Just as an example, the Ni(d)Mo/P54H(w,400) catalyst was prepared with the sequential wet impregnation of Ni and Mo onto the surface of the modified P54H support, with a drying step from one deposition to another, with a calcination temperature of 400°C .

2.3. ACs and Catalysts characterization

The ACs had the chemical composition determined by elemental analyses (Perkin Elmer EA 2400) and Boehm titration. Further, Thermal Programed Desorption (TPD) was performed in an automated system AMI-90R from Altamira Instruments (Ar; 10 °C min⁻¹), coupled to a quadrupole mass spectrometer model Dymaxion from Ametek.

Parameters of pore morphology were determined from N₂ adsorption isotherms acquired at -196 °C in a Quantachrome NovaWin 2200e system. The calculation methodologies were described elsewhere.¹⁰ XRDs (X-ray diffractograms) were obtained in a Rigaku instrument Miniflex 300 using a Ni-filtered Cu-K α radiation ($\lambda = 1.5406 \text{ \AA}$).

2.4. Hydroprocessing

The hydroprocessing tests were carried out in a cylindrical stainless steel reactor ($\approx 100 \text{ cm}^3$). The lipidic feedstock was coconut oil, which is constituted mainly by C₁₂ chains. Preliminary tests were carried out using lauric (dodecanoic) acid as a model compound. Prior to the HDO tests:

- Mo-based catalysts (0.5 g) were sulfided *in situ* with CS₂ (0.5 mL) at 400 °C (1 h) under H₂ (30 bar).
- Pt-based catalysts were rereduced *in situ* at 400 °C (1 h) under H₂ (30 bar).

After that, the system was cooled, purged with N₂ and 10 mL of feedstock were charged. Then, the reactor was pressurized with H₂ and heated at 340 °C for the desired period of time. The H₂ pressure was 30 bar and 20 bar for the tests with Mo-based and Pt-based catalysts, respectively.

Comparative tests were carried out with a sulfided NiMo/Al₂O₃ catalyst supplied by Petrobras Oil Company (Brazil) and a Pt/SAPO-11 catalyst prepared in a similar way as the Pt/P54(w) sample, but using the zeolite SAPO-11 as support.

The liquid hydroprocessing products had their acid indexes (AI) determined according to the AOCS method Cd-3d-63-O. The results were expressed in milligram of KOH per gram of oil. FTIR spectra were acquired in a Shimadzu IR Prestige-21 spectrometer. The products were qualitatively analyzed by GC-MS using a GC-17a gas chromatograph interfaced to a QP5050A mass spectrometer (Shimadzu). For quantitative analyses, GC-FID analyses were performed in a GC-2010 equipment (Shimadzu). A Rtx-5MS polydimethylsiloxane column (30 m, 25 mm) was used in both GC-MS and GC-FID analyzes.

3. Results and discussions

3.1. ACs and catalysts characterization

As previously described, the higher the proportion of H₃PO₄ employed in chemical activation, the higher the achieved porosity and volume of mesopores.¹⁰ Taking it into account, the AC used as starting material was prepared using the relatively high P/precursor ratio of 0.54. In this way, a material with a well developed mesopore structure was achieved (Table 1), which is important to reduce diffusional restrictions and increase the access of the substrates to the metallic active sites.

Nevertheless, it is valid to mention that both the treatment with HNO₃ and H₂ appreciably reduced the porosity and the surface area. In the case of the HNO₃, it can be attributed to the introduction of functional groups that can tighten the pores or block their entrances. Furthermore, the acid can attack pore walls and collapse them. In turn, the treatment with H₂ promoted a weight loss ($\approx 8\%$) because the employed temperature (800 °C) was much higher than that reached during the AC synthesis (450 °C). This weight loss provoked a material shrinkage, with consequent reduction of the pore volume (see the work of Prauchner et al.¹¹).

Table 1. Textural characterization of the ACs and some selected catalysts.

Catalyst	S _{BET} (m ² /g)	V _{mic} (cm ³ /g)	V _{mes} (cm ³ /g)
P54	1649	0.72	0.44
P54A	1129	0.51	0.17
P54H	1303	0.48	0.32
Mo(d)Ni/P54(w,400)	688	0.31	0.10
Mo(d)Ni/P54A(w,400)	363	0.17	0.03
Mo(d)Ni/P54H(w,400)	631	0.27	0.20
Pt/P54(ac.,w)	1627	0.70	0.41
Pt/P54A(ac.,w)	1005	0.46	0.14
Pt/P54H(ac.,w)	1324	0.58	0.32

¹Specific surface area; ²micropore volume; ³mesopore volume

As expected, the deposition of relatively large proportions of metals caused substantial reductions of porosity and specific surface area in the Mo-based catalysts. In turn, since the proportion of Pt deposited in the Pt-based catalysts was low, 1%, it did not significantly influence the pore morphology. (Table 1)

The AC P54 shows elevated oxygen content (Table 2). According to the TPD profiles of CO₂ and

CO (Figure 1) and the Boehm titration data (Table 3), this oxygen is mainly due to acidic functional groups such as carboxylic acids (strong and weak acids; SA and WA), anhydrides (An) and phenols (Ph), besides neutral or weakly basic groups such as ketones (Ke) and quinones (Qu).

Table 2. Elemental analysis of the ACs.

AC	C (%)	H (%)	N (%)	*O (%)
P54	67.4	3.4	0.6	27.4
P54A	58.1	3.0	1.3	37.5
P54H	77.7	1.5	0.4	19.1

*by difference taking on a dry ash-free basis.

Table 3. Results of Boehm titration for the ACs.

AC	Acidity (mmol/g)			Basicity (mmol/g)
	Strong acids	Intermediary acids	Weak acids	
P54	0.55	0.07	1.21	0.00
P54A	1.26	0.42	1.19	0.05
P54H	0.29	0.18	0.68	0.23

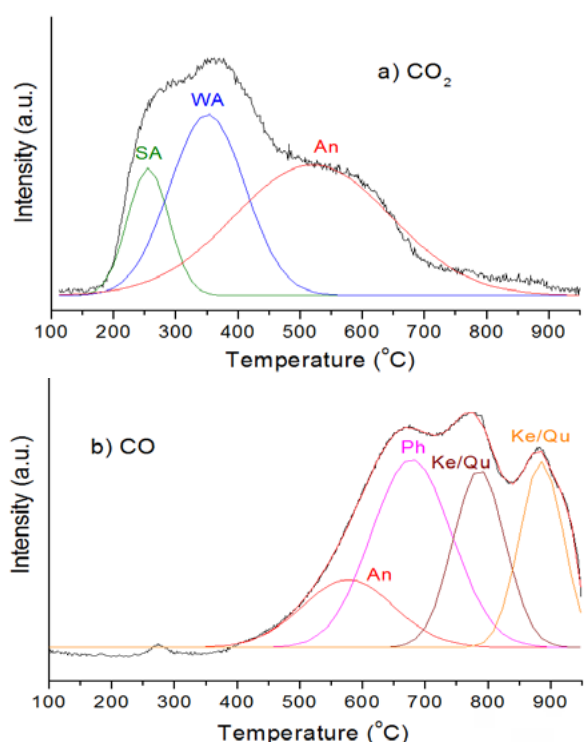


Fig. 1. Deconvolution of the (a) CO₂ and (b) CO TPD profiles for the AC P54.

As expected, the treatment with HNO₃ pronouncedly increased the content of acidic groups, remarkably carboxylic acids and lactones (Figure 2, Table 3). In turn, the treatment under H₂

atmosphere pronouncedly reduced the content of acidic groups. The most prominent events in the TPD profiles of the resulting AC concern a CO₂ and a CO evolution centered at around 840 °C, which supposedly result from an anhydride-like structure.

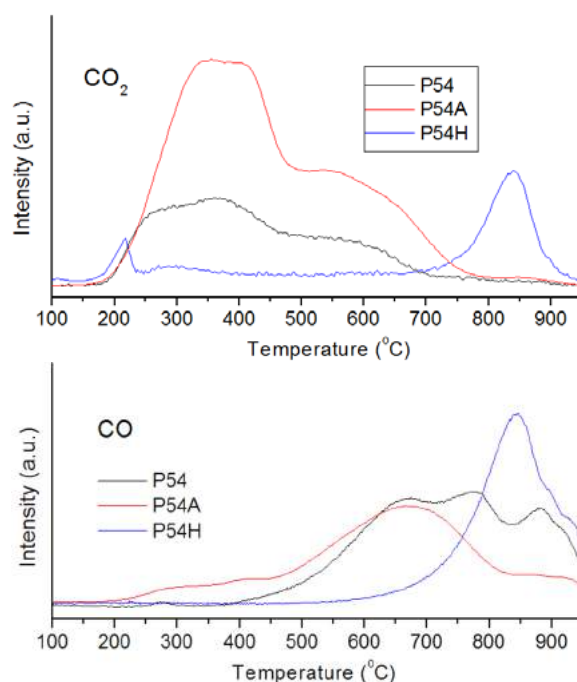


Fig. 2. (a) CO₂ and (b) CO TPD profiles.

3.3. Hydroprocessing tests

3.3.1. Hydroprocessing of lauric acid with the Mo-based catalysts

Initially, a blank test with lauric acid was carried out using the AC P54 instead of any of the prepared catalyst. The AI of the resulting product was high, 264.4 (Table 4), what reveals that the AC by itself has a low, if any, HDO activity.

Table 4. AIs for the products of the hydroprocessing of lauric acid with Mo-based catalysts for 3 h.

Entry	Catalyst	AI
1	P54	264.6
2	Mo/P54(i,400)	8.1
3	MoNi/P54(i,400)	8.6
4	Mo(d)Ni/P54(i,400)	2.0
5	Mo(d)Ni/P54(w,400)	0.5
6	Mo(d)Ni/P54(w,500)	0.8
7	Mo(d)Ni/P54A(w,400)	8.2
8	Mo(d)Ni/P54H(w,400)	1.1

The deposition of Mo onto the P54 support by incipient impregnation resulted in a catalyst active for HDO (Entry 2, Table 4). Furthermore, the insertion of Ni increased the catalyst activity if the depositions of Mo and Ni were proceeded one at a time (entry 4, Table 4).

The comparison of entries 5 and 4 in Table 4 reveals that even better results were achieved by employing the wet impregnation. Further, the comparison of entries 6 and 5 shows that an increase of the calcination temperature from 400 to 500 °C is not benefit to the catalyst activity.

The best conditions verified for the preparation of the Mo-based catalysts using as support the unmodified AC P54 were replicated to those catalysts prepared using the modified ACs P54A and P54H. The results showed that the activity of the catalysts prepared using the modified supports were somewhat lower than verified for the catalyst prepared from P54 (compare entries 7 and 8 with entry 5 in Table 4). This behavior seems to be related to the lower surface area and porosity of the catalysts prepared from the modified supports (compare the data in Table 1) rather than to the influence of surface groups on the dispersion of the metallic active phase. Nevertheless, deeper studies must be carried out on this matter in order to explain unequivocally this behavior.

3.3.2. Hydroprocessing of lauric acid with the Pt-based catalysts

The Pt-based catalysts were also active for HDO. Concerning the unmodified support P54, the best activity was achieved by using the wet impregnation without the addition of HCl to the H_2PtCl_6 solution (Figure 3).

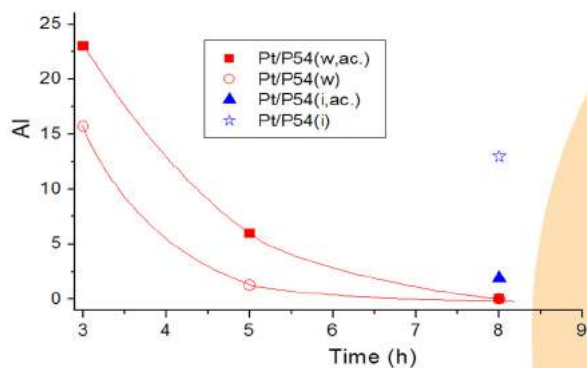


Fig. 3. AI vs. reaction time for the hydroprocessing of lauric acid with Pt-based catalysts.

The tests concerning the catalysts that were prepared with the support P54A showed that the

increase in the content of acidic groups pronouncedly harmed the activity of the resulting catalyst (compare entries 3 and 4 with entries 1 and 2 in Table 4). In turn, the removal of acidic groups from the support by means of the thermal treatment with H_2 resulted in a catalyst with higher activity if the impregnating H_2PtCl_6 solution was acidified with HCl (entry 6, Table 4), in spite of the lower porosity of the P54H support (Table 1).

Table 4. AIs for the products of the hydroprocessing of lauric acid with Pt-based catalysts for 5 h.

Entry	Catalyst	AI
1	Pt/P54(w)	1.2
2	Pt/P54(ac.,w)	7.0
3	Pt/P54A(w)	73.8
4	Pt/P54A(ac.,w)	81.0
5	Pt/P54H(w)	2.6
6	Pt/P54H(ac.,w)	0.4

These results are attributed mainly to the different degrees of Pt dispersion, as evidenced by XRD (Figure 4). Namely, four peaks characteristic of Pt can be identified at 36.7, 46.1, 67.5 and 81.1 in the diffractogram of the catalyst Pt/P54A(ac.,w), prepared with the acidified support. In turn, the diffractogram of the Pt/P54H(ac.,w) catalyst presents only two much broad diffraction peaks characteristics of amorphous carbons, what reveals that the Pt is so well dispersed throughout the support surface that no diffraction peak is generated.

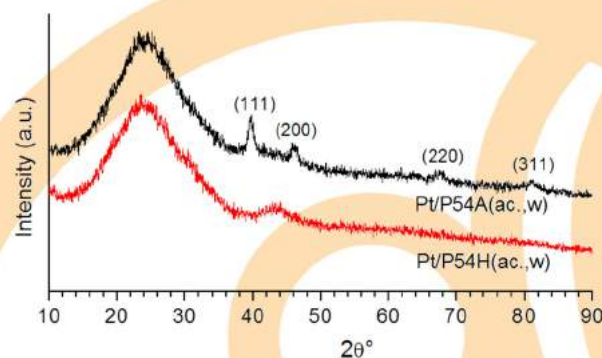


Fig. 4. XRD patterns of the Pt/P54H(ac.,w) and Pt/P54A(ac.,w) catalysts.

3.3.3. Hydroprocessing of coconut oil

Supposedly, the higher hydrophilicity of the acidified support P54A would favor the adsorption of water in detriment to the $[PtCl_6]^{2-}$ species, so that the Pt dispersion is hindered. In turn, the more basic surface of the P54H support would be in some

extent protonated, so that the adsorption and dispersion of the anionic $[PtCl_6]^{2-}$ species is favored. By the way, this effect would be able to explain why the catalysts prepared from the P54H support showed higher activity if HCl was added to the impregnating H_2PtCl_6 solution.

The Mo and Pt-based catalysts that presented the best results in the hydroprocessing of lauric acid were then tested with coconut oil. Although higher reaction times were needed (Table 5), it was possible to obtain mixtures constituted basically by linear alkanes in the range of C_{11} - C_{18} , as evidenced by GC/MS and FTIR.

Table 5. AIs for the products obtained from the hydroprocessing of coconut oil.

Catalyst	Reaction time (h)	AI
Mo(d)Ni/P54(w,400)	3	1.1
Mo(d)Ni/P54(w,400)	6	0.0
Sulfided NiMo/ Al_2O_3	3	6.3
Pt/P54H(ac.,w)	5	1.4
Pt/P54H(ac.,w)	7	1.1
Pt/SAPO-11	5	153.8

The best catalysts prepared in the present work showed HDO activity remarkably higher than those presented by catalysts consisting of similar active phases but traditional inorganic supports (Table 5). For example, while an AI of 1.1 was verified for the product of the hydroprocessing of coconut oil by 3 h with the catalyst Mo(d)Ni/P54(w,400), a sulfided NiMo/ Al_2O_3 catalyst used by Petrobras (Brazil) in its refineries rendered a product with IA 6.3. In turn, while an AI of 1.4 was verified for the product of the hydroprocessing of coconut oil by 5 h with the catalyst Pt/P54H(ac.,w), a Pt/SAPO-11 catalyst rendered a product with the quite high IA of 153.8.

4. Conclusions

The present work permitted to use ACs as the support of catalysts with high activity for HDO. Concerning the Mo-based catalysts, the highest activity was verified for the material prepared by wet impregnation of the unmodified AC, adding Ni as promoting metal, carrying out the deposition of Mo and Ni one at a time and using 400 °C as the calcination temperature. In turn, the highest activity for the Pt-based catalysts was obtained by carrying out the wet impregnation of the AC heat treated with H_2 , using a H_2PtCl_6 solution additionally acidified with HCl.

Remarkably, the performances of the best catalysts prepared with ACs were higher than those verified for catalysts consisting of similar active phases but traditional inorganic supports (Al_2O_3 and SAPO-11 zeolite). The possibility of molding the surface chemistry and the pore structure were decisive for that. These results are encouraging in terms of using H_3PO_4 ACs as support in catalysts employed in HEFA processes for the production of hydrocarbonic biofuels.

Acknowledgements

The authors thanks the Coordenação de Aperfeiçoamento de Pessoal de Nível Superior - Brasil (CAPES) by the financial support to this research (Finance Code 001).

References

- [1] Fregolente PBL, Maciel MRW, Oliveira LS. Removal of water content from biodiesel and diesel fuel using hydrogel adsorbents. *Braz J Chem Eng* 2015;32:895-901.
- [2] Dwivedi G, Sharma MP. Cold Flow Behaviour of Biodiesel - A Review. *Int J Renew Energ Res* 2013;3:827-36.
- [3] Ferrari RA, Oliveira VS, Scabio A. Oxidative stability of biodiesel from soybean oil fatty acid ethyl esters. *Sci Agric* 2005;62:291-95.
- [4] International Air Transport Association. Fact Sheet. *Alternative Fuels*. 2016.
- [5] Mohammad M et al. Overview on the production of paraffin based-biofuels via catalytic hydrodeoxygenation. *Renew Sust Energ Rev* 2013;22:121-132.
- [6] Hermida L, Abdullah AZ, Mohamed AR. Deoxygenation of fatty acid to produce diesel-like hydrocarbons: A review of process conditions, reaction kinetics and mechanism. *Renew Sust Energ Rev* 2015;42:1223-33.
- [7] Pattanaik BP, Misra RD. Effect of reaction pathway and operating parameters on the deoxygenation of vegetable oils to produce diesel range hydrocarbon fuels: a review. *Renew Sust Energ Rev* 2017;73:545-57.
- [8] Toso JP et al. Evaluation of a mixed geometry model for the characterization of activated carbons. *Adsorption* 2011;17:551-60.
- [9] Haber J, Block H, Damon B. Manual of Methods and Procedures for Catalyst Characterization. *Pure Appl Chem* 1995;67:1257-1306.
- [10] Prauchner MJ, Sapag K, Rodríguez-Reinoso F. Tailoring biomass-based activated carbon for CH_4 storage by combining chemical activation with H_3PO_4 or $ZnCl_2$ and physical activation with CO_2 . *Carbon* 2016;110:138-47.
- [11] Prauchner MJ, Rodríguez-Reinoso F. Chemical versus physical activation of coconut shell: A comparative study. *Micropor Mesopor Mat* 2012;152:163-71.

Adsorption in Oil/Water Interfaces: Aspects of Kinetics and Equilibrium in Systems Containing Asphaltenes

César Costapinto Santana ^a

^b Center for Studies in Colloidal Systems, Universidade Tiradentes (UNIT), Aracaju-SE, 49032-040, Brazil

Abstract

The technique of pendant drop tensiometry was used to investigate the interfacial properties of asphaltenes at toluene/water and heptol (heptane+toluene)/water interfaces. Proportions of the organic solvents 1:1 e 1,5:1 and asphaltenes concentration were varied. Through the application of Gibbs excess surface and Langmuir equations isotherms were determined for these systems. Rheological interfacial properties are also useful to understand the asphaltenes adsorption in liquid-liquid interfaces on a macroscopic level. The reduction of the asphaltenes molecules action is reflected in the experimental data for the dynamic interfacial tensiometry for toluene+asphaltene/water interface. These results can be explained by the strong affinity between the asphaltenes and toluene due to the high solubility. On the other hand, the interaction between asphaltenes and (heptol, 1: 1 and 1.5: 1)/water interface is weaker and causes the increase of the asphaltenes molecules activity at the interface. Kinetics models were applied to describe the diffusion processes at liquid-liquid interfaces.

Keywords: Asphaltenes; Interfaces; Equilibrium; Kinetics



Papers in oral sessions

FA: Fundamentals of Adsorption

- 056** - Adsorption-induced deformation of porous solids. New approach for estimation of compressibility factor of microporous carbon adsorbents op-001
A.V. Shkolin, A.A. Fomkin, I.E. Men'shchikov
- 075** - Thermodynamics of adsorption systems based on nanoporous carbons for methane storage and transportation op-004
I.E. Men'shchikov, A.V. Shkolin, A.A. Fomkin
- 127** - D-optimal experimental designs for adsorption isotherms op-009
Roger Kober, Elisa Barbosa-Coutinho,, Evandro Steffani, Marcio Schwaab
- 175** - Mesoporous metal-organic structure MIL-100 (Fe) as drug carrier op-015
Diony N. Gomes, Paulo G. M. Mileo, Nara A. L. Maranhão, Daniel V. Gonçalves, Sebastião M. P. Lucena
- 267** - Breakthrough Curves of Propane at Different Relative Humidities op-020
A. Möller, R. Eschrich, C. Reichenbach, A. Seidler, D. Klank, D. Forberg
- 268** - Characterization of sorption kinetics of CO₂ from N₂- rich gas mixtures studied by breakthrough experiments on Zeolites op-022
A. Möller, R. Eschrich, C. Reichenbach
- 273** - Insights on the use of different gases at 77 K to assess the specific surface area of silica nanoporous materials op-024
Jhonny Villarroel-Rocha, Deicy Barrera, José J. Arroyo-Gómez, Karim Sapag
- 280** - H₂O sorption on nanoporous carbons op-030
Diaz Cristian A., Villarroel-Rocha Jhonny, Sapag Karim
- 286** - Carbon dioxide and water vapor adsorption on commercial and synthesized zeolites op-036
Rafael Morales-Ospino, Ricardo A. Lima Jr, A. Eurico B. Torres, Enrique Vilarrasa-García, Moises Bastos-Neto, Celio L. Cavalcante Jr, Diana C. Silva de Azevedo, Carolina Resmini Melo Marques, Thiago Fernandes de Aquino, Lidia Baraky
- 288** - Assessment of Intracrystalline Diffusion for C8 Aromatics Isomers in Beta Zeolite using the ZLC Technique op-040
J. Wilson V. Lima Jr., F. Murilo T. de Luna and Célio L. Cavalcante Jr.
- 345** - Isotherm, kinetic and thermodynamic studies of Rhodamine B adsorption on coconut fiber-based adsorbents op-045
Rogério José Melo Nascimento, Kilton R. A. Pereira, Francisco Avelino



SCAC: Synthesis and Characterization of Adsorbents and Catalysts

- 021** - Amino-functionalized graphene oxide anchored in charcoal matrix as adsorbent of textile wastewater: characterization and adsorption properties op-051
Tiago J. M. Fraga, Letticia E. L. Ferreira, Bruna F. Nascimento, Maryne P. da Silva, Marcos G. Ghislandi, Eleonora M. P. de Luna Freire, Marilda N. Carvalho, Maurício A. da Motta Sobrinho
- 022** - Removal of the Drimaren Red from aqueous solutions by adsorption onto amino-Fe₃O₄-functionalized multilayer Graphene Oxide op-057
Tiago J. M. Fraga, Caroline M. B. de Araújo, Letticia E. L. Ferreira, Maryne P. da Silva, Marilda N. Carvalho, Eleonora M. P. Luna Freire, Jorge V. F. L. Cavalcanti, Marcos G. Ghislandi, Maurício A. da Motta Sobrinho
- 026** - Iron oxide nanoparticles: design of the reactor for synthesis and characterization op-063
Maria Teresa Garcia Badoch, Regina Maria Matos Jorge, Tirzhá Lins Porto Dantas
- 072** - CO₂ capture in carbon microfibers doped with nitrogen op-069
Reyna Ojeda-López, Guadapule Ramos-Sánchez, Diana C.S. de Azevedo, J. Marcos Esparza-Schulz, Armando Domínguez-Ortiz
- 074** - CO₂ adsorption on LTA zeolite with different particle dimensions op-074
Edilene D. S. Ferracine, Juliana A. Coelho, Kele T. G. Carvalho, Darley C. Melo, Dilson Cardoso
- 223** - Application of In-situ X-ray Characterization Techniques in Zeolites: A Review op-079
Khalil Kashefia, Darley C Melo, Frederico W Tavares, Amaro G Barreto Jr.
- 264** - Trimodal hierarchical zeolite LTA for adsorption: a preliminary characterization study op-085
Raquel de A Bessa, André L S Pereira, Morsyleide F Rosa, Michael W. Anderson, Adonay R Loiola
- 275** - Characterization of mesoporous region by the scanning of the hysteresis loop in adsorption-desorption isotherms op-088
C. Toncón-Leal, J. Villarroel-Rocha, M. T. P. Silva, T. P. Braga, K. Sapag
- 302** - Synthesis of zeolites from hydrothermal solution reuse for CO₂ capture op-093
Suelen Gislon, Vanessa Viola, Sabrina Estevam, Thiago Aquino, Carolina Marques, Lidia Vasconcelos
- 353** - Importance of the Polarity on Nanostructured Silica Materials to Optimize the Hydrolytic Condensation of Molecules Related to CO₂ Adsorption op-098
O. Medina-Juárez, R. Ojeda-López, F. Rojas-González

AMB: Environmental

169 - Study of the effect of the HLD cations precursors un the removal of arsenic in aqueous solutions op-104

Barroso Quiroga, María Martha; Iglesias Juncà, Mònica; Merino, Nora A.

179 - Evaluation of dried *Salvinia auriculata* as a biosorbent in natura in lead removal in aqueous solutions op-110

Adriano Cosme Pereira Lima, Tereza S. M. Santos , Tahise Neiva Campodonio

277 - Metals ions adsorption using synthesized 4A zeolite: effect of coal fly ash as silica and aluminum source op-115

Silva, L. T. V.; Vidal, C. B.; Freitas, A. D. L.; França, A. M. M.; Loiola, A. R.; Nascimento, R. F.

MSPA: Molecular Modeling and Simulation of Adsorptive Processes

108 - Optimization of an Aromatics Complex Including a Simulated Moving Bed for p-Xylene Production op-121

Jonathan C. Gonçalves, Alexandre F. P. Ferreira, Alírio E. Rodrigues

124 - Critical review of batch adsorption kinetic models: simplifications derived from the infinite bath model op-124

Vânia Queiroz da Silva, Daniel Souza de Almeida, Evandro Steffania, Elisa Barbosa-Coutinho, Marcio Schwaab

207 - Studies of interaction potentials effects in the DFT approach for confined fluids op-130

V. M. Sermoud, G.D. Barbosa, A. G. Barreto Jr, F. W. Tavares

156 - Modeling adsorption microcalorimetry to estimate intraparticle diffusion rate constants: Parameter sensitivity analysis op-136

K.F.S. Richard, A.E.B. Torres, D.A.S. Maia, D.C.S. Azevedo, M. Bastos-Neto

246 - Separation of Methane and Carbon Dioxide mixtures by Adsorption on Calcite Nanopores via Molecular Dynamics op-142

Yamara Matos Oliveira, Charlles Rubber de Almeida Abreu, Frederico Wanderley Tavares

279 - Importance of Molecular Simulation for Interpreting Gas Adsorption by Porous Materials: The Case of the Ethane/Ethylene Mixture op-147

José R. B. Gomes, Renjith S. Pillai, Germán Pérez-Sánchez, Christopher Campbell, Miguel Jorge, Moisés L. Pinto

PG: Oil and Natural Gas

- 023** - Adsorption kinetics of asphaltenes in oil-water interfaces: effects of time, concentration, and heptol ratios op-151
Walisson de Jesus Souza, Cláudio Dariva, Alexandre F. Santos, Gustavo R. Borges, Elton Franceschi, Cesar Costapinto Santana
- 244** - Simulation of high-pressure sour natural gas adsorption on 13X zeolite op-157
Pereira, M.V., de Oliveira, L. H., do Nascimento, J. F., Arroyo, P.A.
- 289** - Adsorption of Polycyclic Aromatic Hydrocarbons from Heavy Naphthenic Oil: Evaluation of the Adsorbent Regenerability op-163
F. Murilo T. de Luna and Célio L. Cavalcante Jr.


PA: Adsorption Processes

- 068** - Concentration of anthocyanins from Pinot Noir grape skins in alginate beads through the adsorption operation op-169
Cláudio P. Pinheiro, João O. Castro, Loreane M. K. Moreira, Stephany S. Alves, Tito R. S. C. Junior, Luiz A. A. Pinto
- 092** - Regeneration of granular activated carbon using thermal technique op-173
Leticia Weidlich Sfredo, Morgana Rosset, Liliana Amaral Féris
- 102** - Separation of ethylene from ethane with Metal-organic Frameworks op-178
João Pires, José R. B. Gomes, Germán Pérez-Sánchez, Farid Nouar, Christian Serre, Moisés L. Pinto
- 115** - Multiscale Design of a Pressure Swing Adsorption Process for Natural Gas Purification op-182
I. C. C. Quaranta, L. S. Pinheiro, D. V. Gonçalves, H. R. Peixoto, S. M. P. Lucena
- 182** - Optimization of Temperature Swing Adsorption Unit for Gas Dehydration op-187
Felipe Braun, Yuri Paiva, Caio Marcellos, Argimiro Secchi, Amaro G. Barreto Jr.
- 191** - High-Pressure Bulk CO₂ Gas Adsorption on a Fixed Bed of Zeolite NaY: upward and downward flow comparison op-193
Artur Lemes Moretti, Marcus Vinícius Pereira, Leonardo H. de Oliveira, Jailton F. do Nascimento, Pedro Augusto Arroyo
- 225** - Technological Bottlenecks in purification of monoclonal antibodies: prospective study and proposals for improved process design op-199
Gabriela Freire de Arruda, Marcia Soares Lima de Mello, Rafael Cavalcante dos Santos, Marlon de Souza Gama, Caio Felipe Curitiba Marcellos, Amaro Gomes Barreto Jr.

- 231** - Effect of temperature on oxidative degradation of bleached Hybrid (*E. guineensis* x *E. oleifera*) and African palm oil (*Elaeis guineensis*) op-205
Erislene S. Almeida, Ivanildo José da Silva Júnior, Simone Monteiro
- 247** - Adsorption of a synthetic red food-colorant by circulating percolation of the solution through a packed-bed of wheat bran op-211
Samuel Pratavieira de Oliveira, Fernanda Perpétua Casciatori
- 254** - Perspectives on the synthesis, characterization, and application of hydroxyapatite-based sorbents for gaseous mercury removal op-214
Carla L. M. Camargo, Amanda G. Oliveira, Neuman S. Resende, Vera M. M. Salim
- 354** - Competitive adsorption of pharmaceutical compounds onto nanoporous carbon fibres: effect of pH and ionic strength op-220
Ana Claudia Pina, Nestor Tancredi, Alejandro Amaya, Conchi Ania

BIO: Biotechnology

- 047** - Organosolv lignin/Fe₃O₄ nanoparticles applied as textile dye adsorbent op-224
Carlos Eduardo de Araújo Padilha, Cleitiane da Costa Nogueira, Everaldo Silvino dos Santos
- 066** - Antibiotic removal from water using MgFe/layered double hydroxide as adsorbent op-230
Douglas Phelipe de Lima, Mateus Ferreira da Silva, Anamália Ferreira da Silva, Alessandra Honjo Ide, Lucas Meili
- 080** - Lipases Immobilization via Adsorption on Laboratory-Scale Synthesized Graphene Oxide Using Modified Hummers Method and Magnetic Nanoparticles op-235
Alexandre Diório, Anna Clara Labes Gonçalves, Danielle Faxina de Lima, Rosângela Bergamasco, Marcelo Fernandes Vieira
- 119** - Enzyme immobilization by adsorption: CALB lipase onto magnetic nanoparticles, a heterogeneous biocatalyst op-241
João Brandão Júnior, Debora Cristina Ferreira, Francisco Silvio Maia, Gabrielly Ferreira Mota, Jean Gleison Andrade do Nascimento, Rodolpho Ramilton de Castro Monteiro, Aluísio Marques da Fonseca and Maria Cristiane Martins de Souza
- 130** - Adsorption capacity evaluation of Beta zeolite as adsorbent for isoniazid op-245
Iane M. S. Souza, C. Ignacio Sainz-Díaz, César Viseras, Sibebe B. C. Pergher
- 135** - Purification of rabbit polyclonal IgG using dye ligand affinity chromatography op-250
Tiago Severo Estrázulas, Natália Aragão Dias, Thais Ribeiro Nunes, Diego Romão Gondim, Mauricio Fraga van Tilburg, Ivanildo José da Silva Júnior

- 148** - Elution conditions for purification of rabbit polyclonal antibodies using Protein A column op-255
Natália Aragão Dias, Tiago Severo Estrázulas, Ivanildo José da Silva Júnior, Diego Romão Gondim
- 209** - Evaluation of lipase A from *Candida antarctica* immobilization onto agroindustrial residue by Taguchi method op-261
Paula Jéssyca Morais Lima, Bruna Bandeira Pinheiro, Rodolpho Ramilton de Castro Monteiro, Juliana de França Serpa, Maria Valdevez Ponte Rocha, Maria Cristiane Martins de Souza, Luciana Rocha Barros Gonçalves and José Cleiton Sousa dos Santos
- 240** - Method for estimation the protein binding affinity using a robust Poisson-Boltzmann model for the adsorption of lysozyme in SBA-15 op-265
Marlon de Souza Gama, Amaro Gomes Barreto Jr., Frederico Wanderley Tavares
- 269** - Adsorption of paracetamol from aqueous solutions on activated carbons op-271
Nayara Martins Conrado, Mayara Raquel de Sousa Cavalcante, Juli Emille Pereira de Melo, Ana Lorena de Brito Soares, Vitória Cibely Silveira Penha, Rafael Barbosa Rios, Francisco Wilton Miranda da Silva
- 

Adsorption-induced deformation of porous solids. New approach for estimation of compressibility factor of microporous carbon adsorbents

A.V. Shkolin^{a*}, A.A. Fomkin^a, I.E. Men'shchikov^a

^a *Frumkin Institute of Physical Chemistry and Electrochemistry, Russian Academy of Sciences, Moscow, 119071 Russia*

**e-mail: shkolin@phyche.ac.ru*

Abstract

A new approach for estimation of maximal values of adsorption-induced deformation of porous materials upon adsorption has been represented. An assumption, that the density of adsorbate inside micropores is equal to the density of bulk liquid and Guggenheim theory were set as basis for building the approach and determination of main parameters of adsorption systems, such as thermodynamic properties of adsorbate in pores. Experimental data of adsorption-induced deformation of SiC-based carbon adsorbent ACC upon adsorption of normal hydrocarbons n-C₇H₁₆, n-C₅H₁₀ and n-C₈H₁₈ was used for calculations of its compressibility at different temperatures. It was shown that the average compressibility of the ACC adsorbent ($\approx 6 \dots 8 \cdot 10^{-6} \text{ bar}^{-1}$) was close to constant value at different temperatures and slightly depended on the properties of the adsorbate. The described approach can be adopted for a preliminary assessment of the maximal adsorption-induced deformation of carbon adsorbents in different technological processes.

Keywords: adsorption-induced deformation; microporous solids; high-pressure; adsorption stress; carbon.

1. Introduction

The interaction of adsorbate molecules with a microporous solid during adsorption process leads to the deformation of the latter. Since the compressibility of solids is rather small, the adsorption deformation of porous materials such as activated carbons, which are relatively "hard" adsorbents, usually does not exceed one percent [1, 2].

Moreover, at pressures close to the saturated vapor pressure, adsorption deformation reaches its maximum value, which can lead to destruction of the adsorbent granules and to degradation of dynamic characteristics of adsorption. In addition, adsorption deformation at high pressures affects the behavior of the thermodynamic functions of adsorption [3, 4].

Due to the lack of clear understanding of the behavior of adsorbent deformation for a wide range of adsorption systems, development of theoretical approaches for assessment of adsorption-induced deformation values and its impact on industrial adsorption processes is of great scientific interest. At the same time, investigation of maximal values of adsorption-induced deformation at isothermal conditions seems to be the most useful and preferable for comparison of adsorbents in order to determine the most durable materials in a given technological process.

In this regard, in the work based on the approach presented in [5], the maximum values of the deformation and compressibility factors of carbon adsorbents during the adsorption of hydrocarbons were estimated.

2. Theoretical approach and calculations

To calculate the maximum values of adsorption deformation under isothermal conditions, the following assumption was used. At high adsorption fillings, molecular associates of high density, close to the density of the liquid, are formed in micropores. At reduced temperatures $T/T_{cr} > 0.8$, the average density of the adsorbate in micropores is close to the density of the liquid [6]. This property was used to determine the compressibility of the microporous adsorbent. The isothermal compressibility of the thermodynamic system [7] was determined by (1):

$$\gamma = (1/\nu) \cdot (d\nu/dP)T \quad (1)$$

where ν is the specific volume of system; P is the external pressure on the system; T is the temperature of the system.

The relative deformation of the adsorption system was determined by (2):

$$(\Delta V/V)_{T=const} = \gamma_a \cdot (\pi - P) \quad (2)$$

where γ_a is the compressibility of adsorption system; π is the internal pressure of adsorbate in micropores; P is the equilibrium pressure of the gas phase.

It was believed that the adsorbent deformation is isotropic, and on the saturation line $P = P_s$ the properties of the adsorbate are thermodynamically equivalent to the properties of a free liquid, that is, the internal pressure π is equal to the kinetic pressure in the liquid P_{kin} [7].

Thus, the relative linear adsorption strain determined in the experiment can be calculated for the case of limiting adsorption (deformation) on the saturated vapor pressure line according to (3):

$$\left(\frac{\Delta l}{l_0}\right)_{P=P_s} = \frac{\gamma_a}{3} \cdot (P_{kin} - P) = \frac{\gamma_a}{3} \cdot \left(T \left(\frac{dv}{dT} \right)_p \left(\frac{dv}{dP} \right)_T P \right) \quad (3)$$

where v is the specific volume of liquid; p is the external pressure.

The compressibility of the adsorption system was determined by (4):

$$\gamma_a = 3 \left(\frac{\Delta l}{l_0} \right)_{P=P_s} / (P_{kin} - P) \quad (4)$$

Using the experimental data $(\Delta l / l_0)_{P=P_s}$ for the adsorption deformation of ACC upon adsorption of n-octane $P = P_s$, its compressibility was calculated according to (4).

3. Results and discussion

Experimental data of adsorption-induced deformation of carbon adsorbent ACC (SiC-based) upon adsorption of normal hydrocarbons n-C₇H₁₆, n-C₅H₁₀ and n-C₈H₁₈ was used for calculations. Calculated compressibility values are presented in the Tables 1-2.

Table 1. Parameters of adsorption systems and compressibility of microporous carbon adsorbent ACC. Experimental data from [8-10].

System	ACC- n C ₈ H ₁₈	ACC- n C ₇ H ₁₆
T, K	273	293
T/T _{kp}	0,725	0,73
P _{kin} , bar	2710	2620
(Δl/l ₀) _{P=P_{exp}}	0,58	0,58
γ _a ·10 ⁶ , bar ⁻¹	6,8	6,9
γ _a / γ _m	2,3	2,3

Table 2. Parameters of adsorption systems and compressibility of microporous carbon adsorbent ACC. Experimental data from [8-10].

System	ACC- n C ₅ H ₁₂		
T, K	243	273,1	293
T/T _{kp}	0,52	0,58	0,62
P _{kin} , bar	2520	2350	2180
(Δl/l ₀) _{P=P_{exp}}	0,68	0,61	0,56
γ _a ·10 ⁶ , bar ⁻¹	8	7,8	7,8
γ _a / γ _m	2,7	2,6	2,6

Parameter γ_m in the tables is the compressibility of non-porous graphite equal to $3 \cdot 10^{-6} \text{ bar}^{-1}$ [11].

From the Tables 1 and 2 it follows that the average compressibility of the ACC adsorbent is close to constant value at different temperatures and does not depend on the properties of the adsorbate. If hydrocarbons n-C₅H₁₀ and n-C₇H₁₆ are considered, an average value of γ_a is equal to $7.7 \cdot 10^{-6} \pm 0.3 \cdot 10^{-6} \text{ bar}^{-1}$.

During the adsorption of n-C₈H₁₈, the ACC compressibility is slightly lower and lays in the range $6.8 \dots 6.9 \cdot 10^{-6} \text{ bar}^{-1}$. The difference can be explained as follows. The condition for equality of the density of the adsorbate inside narrow pores of ACC to the density of the liquid phase is better realized for lighter hydrocarbons than for heavy.

Compared with non-porous graphite, the compressibility of the ACC adsorbent is on average 2.5 times higher.

4. Conclusion

A new approach for estimation of maximal values of adsorption-induced deformation of porous materials upon adsorption has been represented. An assumption, that the density of adsorbate inside micropores is equal to the density of bulk liquid and Guggenheim theory were set as basis for building the approach and determination of main parameters of adsorption systems, such as thermodynamic properties of adsorbate in pores. Experimental data of adsorption-induced deformation of SiC-based carbon adsorbent ACC upon adsorption of normal hydrocarbons n-C₇H₁₆, n-C₅H₁₀ and n-C₈H₁₈ was used for calculations of its compressibility at different temperatures. It was shown that the average compressibility of the ACC adsorbent ($\approx 6 \dots 8 \cdot 10^{-6} \text{ bar}^{-1}$) was close to constant value at different temperatures and slightly depended on the properties of the adsorbate. The described approach can be adopted for a preliminary assessment of the maximal adsorption-induced deformation of carbon adsorbents in different technological processes.

Acknowledgements

The work was implemented in the frames of State Scientific Program of the Russian Federation N 0067-2019-0011, state registration number AAAA-A19-119111590053-4.

References

- [1] Balzer C, Cimino RT, Gor GY, Neimark AV, Reichenauer G Deformation of Microporous Carbons during N₂, Ar, and CO₂ Adsorption: Insight from the Density Functional Theory, *Langmuir* 32 (32), 8265-8274.
- [2] Gor GY, Huber P, Bernstein N Adsorption-induced deformation of nanoporous materials – A review, *Applied Physics Reviews* 4, 2017, 011303.
- [3] Shkolin AV, Fomkin AA, Potapov SV Thermodynamics of krypton adsorption on microporous carbon adsorbent at high pressures, *Russian Chemical Bulletin*. 2017. V. 66, No 4, P. 607-613.
- [4] Shkolin AV, Fomkin AA Thermodynamics of methane adsorption on the microporous carbon adsorbent ACC, *Russian Chemical Bulletin*, 2008. V. 57, No 9, P. 1799-1805.
- [5] Fomkin AA, Shkolin AV, Pulin AL, Men'shchikov IE, Khozina EV, *Colloid J*. 2018. V. 80. № 5. P.578.
- [6] Dubinin MM, Fomkin AA, Seliverstova II, Serpinsky VV *Proceedings of the 5-th International conference on zeolites*. Naples, Italy. 1980. P. 468.
- [7] Guggenheim EA, *Modern Thermodynamics by the Methods of Willard Gibbs*, Methuen, 1933.
- [8] Shkolin AV, Fomkin AA, Sinitsyn VA *Protection of Metals and Physical Chemistry of Surfaces*. 2011. V. 47. No5. P. 555.
- [9] Shkolin AV, Fomkin AA *Protection of Metals and Physical Chemistry of Surfaces*. 2013. T. 49. No4. P. 373.
- [10] Shkolin AV, Fomkin AA, Men'shchikov IE, Pulin AL, Yakovlev VY *Colloid journal*. 2019. V.81, No 5, P. 613-620.
- [11] Novikova SI *Thermal expansion of solids (translation from Russian – Teplovoe rasshirenie tverdykh tel)* Nauka; 1974:90.

Thermodynamics of adsorption systems based on nanoporous carbons for methane storage and transportation

I.E. Men'shchikov^{a*}, A.V. Shkolin^a, A.A. Fomkin^a

^a *Frumkin Institute of Physical Chemistry and Electrochemistry, Russian Academy of Sciences, Moscow, 119071 Russia*

**e-mail: i.menshchikov@phycbe.ac.ru*

Abstract

Thermodynamic properties of adsorption systems based on microporous carbon adsorbents of different origin and methane were calculated using methane adsorption experimental data in wide ranges of temperatures and pressures. Molecular dynamics (MD) approach was used for simulation of adsorbate state inside micropores of carbon adsorbents employing the model slit-like shape of pores. Major thermodynamic functions – isosteric heats of adsorption have been calculated using V. Bakaev approach, which takes into account non-ideality of equilibrium gas phase and non-inertness of adsorbent (adsorption-induced and thermal deformation). Other function such as entropies, enthalpies and heat capacities of adsorption systems were also calculated. It was shown that thermodynamic functions could provide important information concerning the state of adsorbate inside micropores at different levels of adsorption value. Obtained results were in good agreement with the data from MD simulation. Finally, integral heats of adsorption of the systems were estimated, which can be used for determination of the thermal properties of scaled adsorption systems during adsorption/desorption processes.

Keywords: thermodynamics of adsorption; nanoporous carbons; high-pressures; molecular dynamics; methane storage.

1. Introduction

Storage and transportation of natural gas methane in an adsorbed state (ANG) is an effective alternative to CNG and LNG. In this case, the most crucial task in the development of such systems is the selection of a special effective porous material. In a number of studies, it was shown that activated carbons of various origins are most effective for ANG systems [1, 2].

When selecting an adsorbent for an ANG system, its key indicator, which is taken as the basis in most works, is adsorption activity to methane [3, 4]. However, as is known, the processes of adsorption and desorption of gases are accompanied, respectively, by the release and absorption of heat. These thermal effects have a significant impact on the characteristics of the adsorption storage system. Thus, the study of the thermodynamic characteristics of adsorption systems “carbon adsorbent – methane” is an important and relevant scientific task.

An objective of current research is a study of adsorption and thermodynamic properties of carbon adsorbents, derived from various raw materials, from the point of view of natural gas methane storage in adsorbed state.

2. Experimental

2.1 Objects of study

Effective carbon adsorbents for methane storage based on raw materials of various origins (plant materials, peat, polymers) synthesized by different methods [1] were selected as objects of study.

For experimental measurements, methane of high purity (99.9%) was used.

2.2 Measurements of adsorption

Measurements of nitrogen adsorption at 77 K and pressures up to atmospheric were undertaken using Quantachrome *iQ* pore and surface analyzer. Obtained results were used for determination of structural and energy characteristics of the materials.

Methane adsorption equilibria in objects of study were measured in the range of temperatures 178 – 333 K and pressures 5 Pa – 30 MPa. For this purpose, customized original adsorption setups of volumetric and volume-gravimetric types [5-6] were employed.

Measurements of the adsorption-induced and thermal deformation of carbon adsorbents upon methane adsorption were carried out according to the method and using an installation described in [7].

2.3 Calculation of thermodynamic functions of adsorption systems

The isosteric heat of adsorption q_{st} is the most important thermodynamic function that characterizes the adsorption system from the point of view of the energy of the adsorption process. From a physical point of view, its value is equal to the difference between the enthalpy of the equilibrium gas phase h_g and the differential enthalpy of the adsorption system H_1 (2):

$$q_{st} = h_g - H_1 \quad (1)$$

In works [8-9], dedicated to study of thermodynamic functions of adsorption processes, it was shown, that most complete equation for calculating the differential molar isosteric heat of adsorption from the point of view of taking into account the properties of non-idealized systems is the Bakaev equation (2):

$$q_{st} = -R \cdot Z \cdot \left[\frac{\partial(\ln P)}{\partial(1/T)} \right]_a \cdot \left[1 - \left(\frac{\partial V_a}{\partial a} \right)_T / v_g \right] - \left(\frac{\partial P}{\partial a} \right)_T \cdot \left[V_a - T \cdot \left(\frac{\partial V_a}{\partial T} \right)_a \right] \quad (2)$$

where Z is the compressibility factor the equilibrium gas phase at pressure P , Pa and temperature T , K;

v_g is the specific volume of the gas phase, m³/kg;

R is the universal gas constant, J/(mol·K);

$V_a = V_0/m_0$ is the specific reduced volume of the adsorption system, cm³/g;

V_0 and m_0 are the volume and mass of the regenerated adsorbent, respectively.

The equation most fully takes into account the physical factors affecting the value of the differential isosteric heat of adsorption, such as:

1. deformation of adsorbent at constant temperature $(\partial V_a/\partial a)_T$ (isothermal deformation);
2. deformation of adsorbent at constant adsorption $(\partial V_a/\partial T)_a$ (isosteric deformation);
3. the slope of adsorption isotherms $(\partial P/\partial a)_T$ and isosteres $[\partial \ln P/\partial(1/T)]_a$;
4. the non-ideality of gas phase Z .

Using q_{st} data, other important thermodynamic functions, such as entropy, enthalpy, and heat capacity of the adsorption system over a wide range of pressures and temperatures were calculated.

2.5 Molecular dynamic simulations

The behavior of the thermodynamic functions of adsorption systems makes it possible to characterize the energy interactions “adsorbent-adsorbate” and “adsorbate-adsorbate” inside the pores of the adsorbent. At the same time, in order to interpret the energy properties of adsorption systems, it is important to understand the characteristic states of the adsorbate in the pores.

To this end, methane adsorption in the pores of the slit-like configuration was simulated using the molecular dynamics approach and model described in [10].

3. Results and discussion

2.5 Porous structure of materials

The Table 1 represent the structural and energy characteristics of carbon adsorbents, determined using the M.M. Dubinin Theory of volume filling of micropores (TVFM) [11] and BET theory [12].

Table 1. Structural and energy characteristics of carbon adsorbents [1].

Parameter	C-7	T-6	P-300
Micropore volume W_0 , cm ³ /g	0.40	0.60	0.95
BET surface area S_{BET} , m ² /g	790	1334	2015
Effective width of micropores X_0 , nm	1.00	1.26	1.78
Standard characteristic energy of benzene adsorption E_0 , kJ/mol	23.9	19.1	13.5
C – plant-based precursor	P – polymer precursor		
T – peat-based precursor			

From the Table 1 it follows that the adsorbents have significant differences in the parameters of the porous structure.

2.6 Methane adsorption

Figure 1 shows the isotherms of methane adsorption in the adsorbents, which implies, that the adsorbent P-300 has the highest adsorption activity to methane at moderate and high pressures due to the higher micropore volume compared to C-7 and T-6.

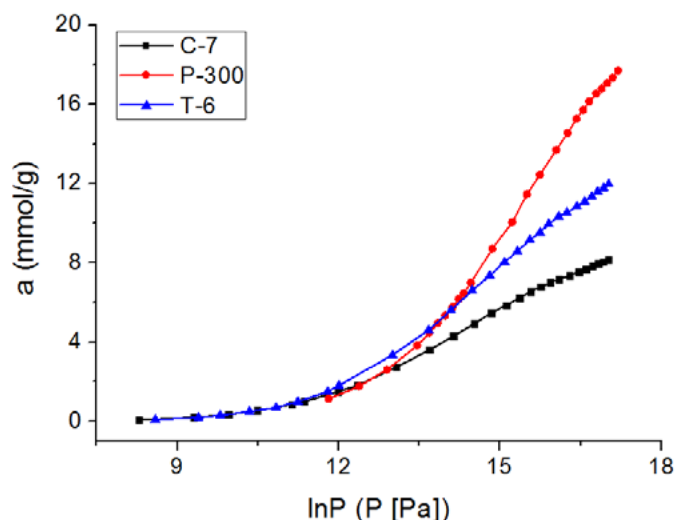


Figure 1. Methane adsorption isotherms in carbon microporous adsorbents at 300 K.

At the same time, adsorbents based on plant precursor and peat (C-7 and T-6 respectively) have higher E_0 , which provides higher adsorption at low pressures. Based on measured adsorption amounts, thermodynamic functions of adsorption systems were calculated.

2.6 Differential isosteric heat and entropy of adsorption system

Calculated thermodynamic functions can provide information about the state of adsorbate in pores within change of adsorption amount. As an example, Figure 2 represents the dependences of the isosteric heat of adsorption of methane on the amount of adsorption for a system based on T-6 at 178 and 300 K, calculated according to (2).

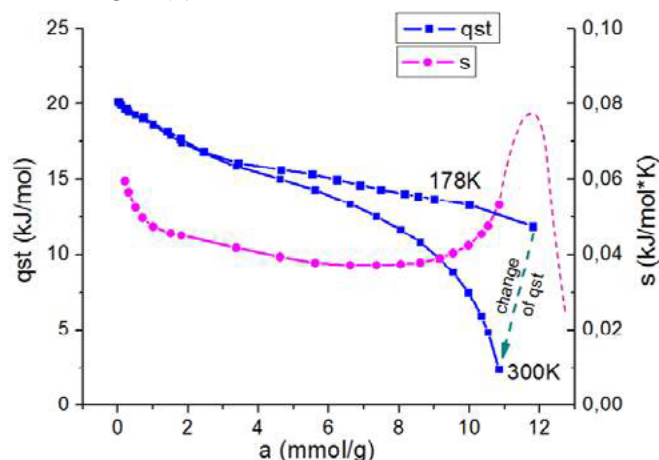


Figure 2. Isosteric heats of methane adsorption at 178 and 300 K (blue curves) and the entropy of the T-6-methane adsorption system at 300 K (purple curve) depending on adsorption.

From the Figure 2 it follows that as adsorption increases, the heat of adsorption decreases. In the region of initial fillings, the adsorption heat reaches its maximum values due to the interaction of methane molecules with high-energy adsorption centers on the surface of adsorbent.

Further decrease of q_{st} occurs as the pores of adsorbent are filled with methane molecules. The temperature dependence of the heat of adsorption, which decreases with increasing temperature, can be also observed.

Entropy of adsorption also characterizes the state of the adsorbate in the pores. In the region of initial fillings, a sharp drop of entropy occurs, due to the localization of methane molecules at the adsorption centers. Next, a gradual decrease of entropy can be observed with the gradual filling of the porous space with adsorbed molecules and an increase in the “adsorbate-adsorbate” interaction.

However, in the region of high fillings, a sharp rise of $s(a)$ is revealed. This is probably due to the fact, that at high adsorption, addition of new gas molecules into the pores of the adsorbent due to the work of external pressure leads to a change in the structure of the adsorbate in the pores. It was shown in [13] that, with an increase of adsorption up to maximal fillings, the function $s(a)$ reached its maximum and dropped sharply reaching the limit adsorption. A dashed line in the Figure 2 represents predicted behavior of the entropy at the region of maximal adsorption fillings.

The results obtained are in good agreement with the data obtained by modeling adsorption using the molecular dynamics method.

2.7 Molecular dynamics simulations

To understand the processes occurring in the micropores of the studied adsorbents upon methane adsorption, the molecular dynamics simulation of methane adsorption in model slit-like micropores was carried out using the TINKER software package [14]. The universal atom-atomic force field OPLSAA [15], which simulates the total interaction potential, was used to reduce computer solving time.

Modeling was carried out in a microcanonical (N, V, E) ensemble. For all systems, molecular dynamics tracks were studied with a time of 2×10^{-9} s. The elementary step of integrating the equation of motion was 10^{-15} s. The parameters of the system for processing the results of a numerical experiment were averaged every 10^{-12} s. The time to reach equilibrium states of the systems was estimated by the change in total energy over time (less 1×10^{-9} s).

A slit-like model of micropore formed by two square-shaped graphene layers with a side of about 1.5 nm was employed for simulation. The average size of graphenes forming a model micropore was chosen on the basis of data on the dimensions of carbon nanocrystallites in active carbons [16]. The distance between graphene layers varied according to the pore-width of real adsorbents determined from the TVFM taking into account dimensions of carbon atoms.

A different number of methane molecules from 20 to 400 was placed in the simulation cell. The temperature of the simulation system was set 293 K.

As a result of the simulation, the probability densities of the location of the methane molecules in the model pores of the studied carbon adsorbents were determined, as well as the probability of the formation of molecular associates in the pores of the adsorbents. The association of methane molecules was determined by the average distance between the molecules and the residence time of the molecules at the required distance from each other.

It was shown that appearance of methane molecular associates inside the micropores is peculiar for the region of high adsorption fillings (in the region of relatively high adsorption values).

2.8 Thermal properties of adsorption systems

Based on the obtained data on the isosteric heat of adsorption, the integral heats of adsorption were calculated as follows (3):

$$Q = \int_0^a q_{st} da \quad (3)$$

Values of Q for 300 K are presented in the Table 2.

Table 2. Integral heats of adsorption calculated for $T=300$ K.

Parameter	C-7	T-6	P-300
Q , kJ/kg	105.4	149.3	157.2

From the data in the Table 2, it follows that the largest value of Q is typical for a system based on P-300, and the minimum for C-7, due to the difference in adsorption. The data obtained can be used for determination of thermal properties of adsorption systems during the processes adsorption and desorption.

4. Conclusion

Using experimental data on methane adsorption in nanoporous carbons in wide ranges of temperatures and pressures thermodynamic functions of the systems were determined. Major thermodynamic functions isosteric heats of adsorption have been calculated using V. Bakaev approach, which takes into account non-ideality of equilibrium gas phase and non inertness of adsorbent (adsorption-induced and thermal deformation).

It has been shown that behavior of the functions can provide important information concerning understanding of adsorbate state inside nanopores upon adsorption process. Obtained results were in good agreement with the data from MD simulation of methane adsorption inside model slit-like pores. Finally, integral heats of adsorption of the systems were estimated, which can be used for determination of the thermal properties of scaled adsorption systems during adsorption/desorption processes.

Acknowledgements

The work was implemented in the frames of State Scientific Program of the Russian Federation.

References

- [1] Bastos-Neto, M., Canabrava, D.V., Torres, A.E.B. et al. Effects of textural and surface characteristics of microporous activated carbons on the methane adsorption capacity at high pressures, *Applied Surf. Sci.*, 253, 5721–5725 (2007).
- [2] Men'shchikov, I.E., Fomkin, A.A., Tsivadze, A.Y. et al. *Adsorption* 23, 327 (2017). doi.org/10.1007/s10450-016-9854-1
- [3] Bazan, R.E., Bastos-Neto, M., Staudt, R., Papp, H., Azevedo, D.C.S., Cavalcante Jr., C.L.: Adsorption equilibria of natural gas components on activated carbon: pure and mixed gas isotherms. *Adsorpt. Sci. Technol.* 26, 323–332 (2008).
- [4] Tsivadze A. Yu. et al. *Russ. Chem. Rev.* 87, 950 (2018). [10.1070/rcr4807](https://doi.org/10.1070/rcr4807)
- [5] Fomkin, A.A., Shkolin, A.V., Menshchikov, I.E., Pulin, A.L., Pribylov, A.A., Smirnov, I.A.: Measurement of adsorption of methane at high pressures for alternative energy systems. *Meas. Tech.* 58(12), 1387–1391 (2016). [10.1007/s11018-016-0904-6](https://doi.org/10.1007/s11018-016-0904-6)
- [6] Shkolin, A.V., Fomkin, A.A., Pulin, A.L., Yakovlev, V.Yu. A technique for measuring an adsorption-induced deformation. *Instruments and Experimental Techniques* 51(1), 150-155 (2008). doi.org/10.1134/S0020441208010211
- [7] Men'shchikov, I.E., Shkolin, A.V., Fomkin, A.A.: Measurements of Adsorption and Thermal Deformations of Microporous Carbon Adsorbents. *Meas. Tech.* 60(10), 1051–1057 (2018). doi.org/10.1007/s11018-018-1317-5
- [8] Shkolin, A.V., Fomkin, A.A.: Thermodynamics of methane adsorption on the microporous carbon adsorbent ACC. *Russ. Chem. Bull.* 57(9), 1799–1805 (2008). doi.org/10.1007/s11172-008-0242-1
- [9] Bakaev, V.A. *Russ Chem Bull* 20, 2516 (1971). doi.org/10.1007/BF00853614.
- [10] Shkolin, A.V., Fomkin, A.A., Tsivadze, A.Y. et al. *Prot Met Phys Chem Surf* (2016) 52: 955. doi.org/10.1134/S2070205116060186.
- [11] Dubinin, M.M., Astakhov, V.A. *Russ Chem Bull* 20, 3 (1971). doi.org/10.1007/BF00849307.

- [12] Brunauer, S.: The adsorption of gases and vapors, vol. I. Oxford University Press, Oxford (1943).
- [13] Fomkin, A.A. Adsorption 11, 425 (2005).
doi.org/10.1007/s10450-005-5636-x.
- [14] Rackers, J.A, Laury, M.L., Lu, C. et al. TINKER 8: A Modular Software Package for Molecular Design and Simulation (2017).
- [15] Jorgensen, W.L., Maxwell, D.S. Tirado-Rives, J. J. Am. Chem. Soc. (1996), 118, p.11225
- [16] Dubinin, M.M., Microporous structures of carbon adsorbents. Carbon 6, 183-192 (1968).

D-optimal experimental designs for adsorption isotherms

Roger Kober^a, Elisa Barbosa-Coutinho^b, Evandro Steffani^a, Marcio Schwaab^{a*}

^a Departamento de Engenharia Química, Escola de Engenharia, Universidade Federal do Rio Grande do Sul.
Rua Ramiro Barcelos, 2777 - Prédio 22202, Porto Alegre, RS, 90035-007, Brasil

^b Departamento de Físico-Química, Instituto de Química, Universidade Federal do Rio Grande do Sul.
Av. Bento Gonçalves, 9500, Porto Alegre, RS, 91501-970, Brasil

Abstract

D-optimal designs for Langmuir and Freundlich isotherms were obtained using two different approaches. The first consisted in defining the equilibrium concentration as the independent variable and the solid equilibrium concentration as the dependent variable, as usually done in literature. The second approach consisted in defining the equilibrium concentration as the dependent variable and a function of the initial solute concentration, solution volume and mass of adsorbent, which is closer to what occurs in actual adsorption experiments. By defining the equilibrium concentration as the independent variable, analytical solutions were obtained, showing that the model parameters with a linear relation to the dependent variable do not affect the optimal design results. In the case of the second approach, where the equilibrium concentration is the dependent variable of the system, it was possible to observe that, when the solution volume to adsorbent mass ratio is kept constant, the optimal experimental conditions depend on the value of all model parameters for each isotherm. Additionally, it was possible to observe that the analytical solutions obtained in the first approach are special cases of experimental designs computed when the solution volume to adsorbent mass ratio is constant and tends to infinity. Finally, it was also shown that experimental designs obtained by optimizing both the initial solute concentration and the solution volume to adsorbent mass ratio simultaneously lead to parameters with lower uncertainties.

Keywords: Design of experiments; Adsorption equilibrium; D-optimal designs

1. Introduction

The study of adsorption equilibrium is one of the most important steps when evaluating an adsorption process, since it provides information on how much material the adsorbent can accommodate under certain conditions [1]. For liquid-solid systems, this state of equilibrium is described by adsorption isotherms, which establish the mathematical relation between the amount of adsorbed material onto de solid, Q_e , and the equilibrium concentration of the fluid phase, C_e [2,3].

To analyze the adsorption equilibrium of a particular adsorbate-adsorbent system, researchers usually perform the estimation of model parameters of a number of different adsorption isotherms, identifying which best describes the available data [3,4]. In order to draw reliable conclusions from

such models, the parameter estimates must be obtained by using proper parameter estimation methods (usually non-linear) and optimal experimental conditions, as discussed by different authors in the literature [5,6,7].

Optimal experimental conditions are determined through the optimization of a certain experimental design criterion, which varies depending on the objective of the experimenter [8,9]. For estimation of parameters with lower uncertainties, different design criteria can be developed by evaluating how the experimental conditions affect the joint confidence region of parameter estimates [9,10]. One of such design criteria is D-optimality, which is the most used criterion amongst all design criteria available due to its invariance to the scale of the variables and parameter values [8].

D-optimal designs are obtained by minimizing the determinant of the posterior covariance matrix

of parameter estimates, computed by Eq. (1) for the design of an initial set of experiments and for a constant variance [10]. Matrix \mathbf{B} in Eq. (1) is the model sensitivity matrix and contains the derivatives of the model with respect to the model parameters in each experimental condition in the experimental design. By minimizing the determinant of Eq. (1), the volume of the joint confidence region of parameter estimates is also minimized, thus reducing the uncertainties of the model parameters [10].

$$\hat{\mathbf{V}}_0 = \sigma^2 [\mathbf{B}^T \mathbf{B}]^{-1} \quad (1)$$

D-optimal designs applied to adsorption models were first studied by Rodriguez-Aragón and López-Fidalgo [11]. In their work, designs for the BET and GAB models applied to the adsorption of water vapor onto food materials were computed, obtaining the optimal water activities values as function of the model parameters in each isotherm. Mannarswamy et al. [12], on the other hand, analyzed D-optimal designs for Langmuir, Freundlich and Redlich-Peterson isotherms. In this case, optimal values of C_e (independent variable) were computed as function of model parameters, resulting in designs with the number of experimental conditions equal to the number of parameters in the isotherm of interest. In both cases, the minimization of the determinant of matrix $[\mathbf{B}^T \mathbf{B}]^{-1}$ was carried out numerically,

In most adsorption equilibrium researches, the equilibrium concentration, C_e , is regarded as the independent variable, while Q_e is the dependent variable. However, adsorption experiments are usually carried out by either keeping the initial solute concentration, C_0 , constant while varying the ratio between the solution volume, V , and mass of adsorbent, M , or by varying C_0 while V/M is kept constant [6]. The equilibrium concentration, in this context, is a variable measured experimentally for each combination of C_0 , V and M , acting, in reality, as the dependent variable of the system. The quantity of adsorbed material onto the solid, Q_e , is not measured directly, but inferred from measurements of C_e through Eq. (2) [5]. Thus, experimental designs should be obtained with respect to C_0 and V/M , since these are the variables that are actually controlled by the experimenter.

$$Q_e = \frac{V}{M} (C_0 - C_e) \quad (2)$$

Based on these remarks the objective of the work is to evaluate D-optimal designs for Langmuir and Freundlich isotherms using C_e as function of C_0 , V and M . Firstly, analytical solutions for the D-optimal designs assuming Q_e and C_e are the dependent and independent variables, respectively, will be presented. Secondly, two examples of designs where C_e is a function of C_0 , V and M will be analyzed. In the first example, experimental designs for a constant V/M ratio were obtained for each isotherm, while in the second example, D-optimal designs for Langmuir isotherm were obtained by computing the optimal C_0 and V/M values.

2. Methodology

In all cases the D-optimal experimental designs were obtained by assuming that the variance of experimental measurements, σ^2 , was independent of the experimental conditions. Thus, D-optimality was achieved through the minimization of the determinant of matrix $[\mathbf{B}^T \mathbf{B}]^{-1}$. The minimization of this determinant was achieved numerically with the Particle Swarm Optimization (PSO) method, a global optimization method based on the social behavior of collections of animals [13], except for when C_e was taken as the independent variable.

Two main approaches were considered in the present work: (a) assuming that C_e is the independent variable; (b) assuming that C_e is a function of C_0 , V and M , as observed in real adsorption experiments. The models evaluated were Langmuir and Freundlich isotherms, which are given by Eq. (3) and (4). The description of these isotherms' behaviors and the meaning of each model parameter can be found elsewhere [7,14]

$$Q_e = \frac{Q_m K_L C_e}{1 + K_L C_e} \quad (3)$$

$$Q_e = K_F C_e^n \quad (4)$$

2.1. Q_e versus C_e

In this particular case, the optimal experimental conditions that minimize the determinant of $[\mathbf{B}^T \mathbf{B}]^{-1}$ were obtained analytically. The D-optimal designs were obtained for a dimensionless equilibrium concentration, c_e , given by Eq. (5), where $C_{e,max}$ is the maximum equilibrium concentration in the design space. Thus, the dimensionless equilibrium concentration ranges from zero to 1 ($C_e = C_{e,max}$).

$$c_e = \frac{C_e}{C_{e\max}} \quad (5)$$

In order to maintain the isotherms' consistency, adjustments on the model parameters were also performed. For the Langmuir isotherm, a dimensionless version of parameter K_L was defined as shown in Eq. (6). For the Freundlich isotherm, however, a dimensionless version of parameter K_F defined by Eq. (7) was used.

$$k_L = K_L C_{e\max} \quad (6)$$

$$k_F = K_F (C_{e\max})^n \quad (7)$$

2.2. C_e versus C_0, V and M

In this case, the dimensionless equilibrium concentration was defined as presented in Eq. (8). Modifications similar to the previous case were used for the model parameters, where $C_{e\max}$ was substituted by $C_{0\max}$, as defined in Eq. (10) and (11).

$$c_e = \frac{C_e}{C_{0\max}} \quad (8)$$

$$k_m = K_m C_{e\max} \quad (9)$$

$$k_F = K_F (C_{0\max})^n \quad (10)$$

The dimensionless equilibrium concentration, c_e , as function of C_0, V and M was computed by solving Eq. (11), where c_0 is the ratio between C_0 and $C_{0\max}$ and $f(C_e)$ represents the isotherm of interest. Eq. (11) was solved numerically using the Newton-Raphson method in each iteration of the computation of the D-optimal designs.

$$\frac{VC_{0\max}}{M} (c_0 - c_e) = f(c_e) \quad (11)$$

The D-optimal designs obtained using C_e as a function of C_0, M , and V were computed iteratively for different parameter values for Langmuir and Freundlich isotherms. These D-optimal designs were obtained either by finding the optimal values for C_0 (constant V/M) or by finding the optimal values for both C_0 and V/M . The first case was considered for Langmuir and Freundlich isotherms,

while the second was considered only for Langmuir isotherm.

3. Results and Discussion

The D-optimal designs obtained for all isotherms resulted in the selection of a number of different experimental conditions equal to the number of parameters in the selected model, with an equal distribution of experiments between them. As pointed out by Atkinson *et al.* [8], this result is often obtained for D-optimal designs for non-linear models with one experimental factor. The same behavior was obtained by Mannarswamy *et al.* [12], where Q_e was regarded as the dependent variable of the system and function of C_e (independent variable).

3.1. Q_e versus C_e approach

Taking this definition of dependent and independent variables, it was possible to apply the D-optimal design methodology and obtain analytical solutions that minimize the determinant of matrix $[\mathbf{B}^T \mathbf{B}]^{-1}$. As discussed previously, the number of experimental conditions obtained was equal to the number of parameters in each model. This means that the D-optimal designs for Langmuir and Freundlich isotherms consist of two c_e values, i.e., $c_{e,1}$ and $c_{e,2}$. The solutions for $c_{e,1}$ are given by Eq. (12) and (13), for Langmuir and Freundlich isotherms, respectively. Details on how these solutions can be obtained are described elsewhere [14]. It is possible to observe that, for Langmuir isotherm, $c_{e,1}$ will tend to 0.5 as k_L tends to 0, while it will tend to zero when k_L tends to infinity. Analyzing Eq. (13), it is possible to observe that $c_{e,1}$ will tend to zero when n tends to zero. When n tends to 1, which is the highest value allowed for n when Freundlich isotherm is given by Eq. (4) [5,7], it is possible to observe that $c_{e,1}$ will tend to e^{-1} .

$$c_{e,1} = \frac{1}{k_L + 2} \quad (12)$$

$$c_{e,1} = \exp\left(-\frac{1}{n}\right) \quad (13)$$

The behavior of Eq. (12) and (13) are the same as the results obtained numerically by Mannarswamy *et al.* [12], with the advantage of allowing the definition of the exact limits of the $c_{e,1}$ in the D-

optimal experimental designs for Langmuir and Freundlich isotherms. The second experimental condition, $c_{e,2}$, was equal to 1 (i.e. $C_e = C_{e,max}$) independently of the model parameters, as observed by Mannsarwamy et al. [12].

Although these results provide an insight on optimal experimental designs for Langmuir and Freundlich isotherms, it is important to note that the equilibrium concentration is not a variable that can actually be controlled during the execution of adsorption experiments. Therefore, these designs have limited practical meaning, since, in reality, C_e is the response variable of the system, obtained from selected values of C_0 , V and M .

3.2. C_e versus C_0 , V and M approach

The results obtained when C_e is a function of C_0 , V and M (V/M constant) for Langmuir isotherm are presented in Figures 1 and 2. Just as in the case where C_e was taken as the independent variable, the number of different experimental conditions in these D-optimal designs was always equal to the number of model parameters in each isotherm. In the approach evaluated here, the optimal conditions are defined by $c_{0,1}$ and $c_{0,2}$, with the resulting optimal value for the latter always equal to 1, that is, $C_{0,2} = C_{0,max}$.

Analyzing Figure 1, it is possible to observe that as a higher V/M ratio is used, more the optimal values of experimental condition $c_{0,1}$ are closer to the values that would be obtained for $c_{e,1}$ in Eq. (12). For lower V/M ratios, however, it is possible to observe that the optimal designs for c_0 are considerably different from those described by Eq. (12). From the results shown in this figure, $c_{0,1}$ seems to start from a value close to 0.5, decreasing as k_L increases for all V/M above 1 L/g.

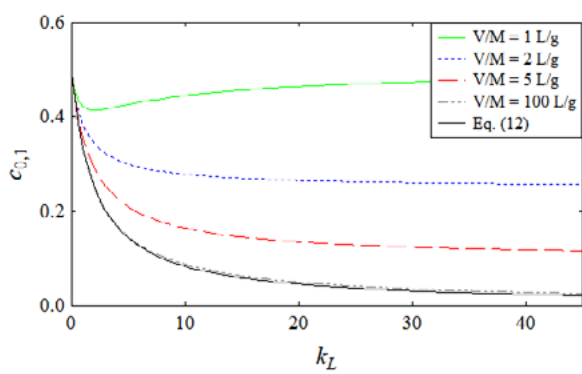


Fig. 1. Results for optimal $c_{0,1}$ as function of model parameter k_L ($Q_m/C_{0,max} = 0.5$ L/g) for Langmuir isotherm.

A similar behavior with respect to V/M was observed for Freundlich isotherm (Figure 2), that is, higher V/M values lead to results closer to Eq. (13), which is the optimal c_e for Freundlich equation when C_e is the independent variable. Differently from the results obtained for Langmuir isotherm, however, the optimal $c_{0,1}$ values for Freundlich isotherm increases as n goes from 0 to 1, except when V/M is equal to 1 L/g. Figure 2 also shows that in all cases the optimal experimental design will be composed of one experimental condition with $c_{0,1}$ equal to e^{-1} when n is equal to 1.

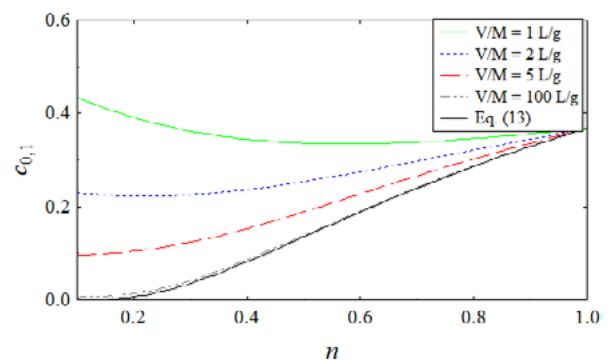


Fig. 2. Results for optimal $c_{0,1}$ as function of model parameter ($k_F/C_{0,max} = 0.5$ L/g) for Freundlich isotherm.

This change in the designs obtained for different fixed values of V/M can be explained by analyzing Eq. (14). This equation was obtained by substituting $f(C_e)$ in Eq. (11) by the Langmuir isotherm (Eq. 3), and dividing both sides by Q_m , resulting in a dimensionless equation. The right-hand side of Eq. (14) describes a straight line that represents the mass balance on the adsorbent, going from c_0 up to the value of c_e obtained after the system has reached equilibrium. It is possible to observe that the slope of this line is directly proportional to the value of V/M . Higher V/M values lead to higher slopes and vice-versa. As V/M increases, the values obtained for c_e approach the values of c_0 , since the slope mentioned above increases. For infinitely large values of V/M , c_e will be equal to c_0 and, in this situation, the experimental designs for both variables will have the same results. Thus, the experimental designs obtained in Eq (12) and (13) can be regarded as special cases of the accurate D-optimal designs obtained for C_0 , being strictly valid when V/M is constant and tends to infinity. A similar behavior is observed with respect to parameter Q_m , but in this case the slope of the right-hand side of Eq. (14) increases as Q_m decreases. Thus, the parameters of proportionality (Q_m for Langmuir

isotherm and K_F for Freundlich equation) also affect the optimal experimental design results.

$$\frac{V}{M} \frac{C_{0\max}}{Q_m} (c_0 - c_e) = \frac{k_L c_e}{1 + k_L c_e} \quad (15)$$

As discussed previously, different experimental measurements of C_e are usually obtained by either changing C_0 , while V/M is kept constant, or by changing V/M , while C_0 is a constant. Thus, it is important to evaluate optimal designs that optimize C_0 and V/M simultaneously.

Takin this observation into consideration, D-optimal designs for Langmuir isotherm were obtained with C_0 and V/M as variables to be optimized. Some results are presented in Table 1 for different values of $Q_m/C_{0\max}$ and k_L . As in the previous cases, the resulting D-optimal designs consisted on a number of different experimental conditions equal to the number of model parameters. For the optimization of C_0 and V/M , however, it is possible to observe that in both experimental conditions the optimal value of the dimensionless initial concentration is equal to 1, while the optimal values of V/M change with the parameter values. Thus, when both variables are optimized, D-optimal designs are obtained by keeping the initial concentration at its maximum value and using different values of V/M in order to obtain different measurements of C_e .

Table 1. D-optimal designs through the optimization of C_0 and V/M for Langmuir isotherm.

$Q_m/C_{0\max}$ (L/g)	k_L	$c_{0,1}$	$c_{0,2}$	V/M_1	V/M_2
0.5	5	1	1	0.835	0.293
0.5	10	1	1	0.837	0.357
0.5	25	1	1	0.793	0.419
0.5	50	1	1	0.750	0.450
1	5	1	1	1.671	0.586
1	10	1	1	1.674	0.714
1	25	1	1	1.587	0.839
1	50	1	1	1.500	0.899

In order to evaluate how these results compare to the D-optimal designs obtained when only C_0 is optimized, Table 2 present the determinants obtained in both cases for different parameter values. It is possible to observe that lower values for the determinant of $[\mathbf{B}^T \mathbf{B}]^{-1}$ were obtained for D-optimal designs where both C_0 and V/M are the variables to be optimized. Hence, joint confidence

regions of parameter estimates with lower volumes are obtained in this case, resulting in parameters with lower uncertainties.

Table 2. Determinants of $[\mathbf{B}^T \mathbf{B}]^{-1}$ for D-optimal designs obtained through the optimization of C_0 (Det_{C_0}) and C_0 and V/M ($Det_{C_0, V/M}$) for Langmuir isotherm.

$Q_m/C_{0\max}$ (L/g)	k_L	Det_{C_0}	$Det_{C_0, V/M}$
0.5	5	37	12
0.5	10	97	37
0.5	25	554	227
0.5	50	2719	1063
1	5	136	47
1	10	515	148
1	25	4216	906
1	50	24528	4251

The results presented in Table 1 and 2 show that, under the assumption of a constant variance, parameters with lower uncertainties are obtained for experimental designs where the initial concentration is kept at the maximum value allowed while different values of V/M are used, resulting in different C_e measurements. It is important to note that the variance of the experimental measurements of C_e might not be constant in the experimental region of interest, especially when the solution volume to adsorbent mass ratio is not kept constant [5,7]. Nevertheless, these results show that the correct definitions of dependent and independent variables in fact lead to different results and provide experimental designs that can more easily translated into real adsorption experiments, as discussed in mode details by Kober *et al.* [14, 15].

4. Conclusions

In this work, D-optimal designs for Langmuir and Freundlich isotherms were obtained by either defining C_e as the independent variable or by defining C_e as a function of C_0 , V and M , which are the actual independent variables in adsorption equilibrium experiments. In the first approach, analytical solutions were obtained, providing an exact description of how the experimental design depend on the model parameters. In the second approach, however, the D-optimal designs were obtained only by numerical methods. This approach was divided in two cases; the first where the solution volume to adsorbent mass was kept constant (optimization of C_0 only) and the second

where both C_0 and V/M were optimized simultaneously.

For all designs, the number of different experimental conditions was equal to the number of parameters of each isotherm. When C_e was taken as the independent variable and Q_e as the dependent one, the experimental design for both Langmuir and Freundlich isotherms was composed of the experimental conditions $c_{e,1}$ and $c_{e,2}$. It was possible to observe that $c_{e,2}$, for any parameter values, was always equal to 1, meaning that in $C_{e,2} = C_{\text{max}}$. For $c_{e,1}$, however, mathematical expressions that relate this experimental point with parameter k_L , for Langmuir isotherm, or parameter n , for Freundlich equation, were obtained. It was also observed that the parameters with a linear relation to the dependent variable, Q_e in this case, had no influence on the experimental design for both models.

Defining C_e as the dependent variable and C_0 , V and M as independent variables, it was shown that all model parameters have influence on the experimental designs results. When the V/M ration was kept constant, it was shown that the experimental designs resulted in the selection of two experimental points, $c_{0,1}$ and $c_{0,2}$, where $c_{0,2}$ was always equal to 1, while $c_{0,1}$ varied with the values attributed to the model parameters. As the values of V/M increased, it was possible to observe that the experimental design for C_0 approaches the results obtained when C_e is the independent variable. This shows that the D-optimal designs in this for C_e as independent variable are only a special case of the accurate experimental designs, where C_e is a dependent variable, valid only when V/M tends to infinity.

Finally, D-optimal designs were also obtained by optimizing C_0 and the V/M ratio simultaneously. In this case, it was observed that the optimal dimensionless initial concentration value in all experimental conditions was equal to 1, that is, the initial concentration was always equal to the maximum value allowed in the experimental range, while the optimal values of V/M depended on the model parameter values. Also, the results indicate that parameters with lower uncertainties are obtained by keeping the C_0 at its maximum value and using different values of V/M , in order to obtain different measurements of C_e . A more detailed discussion of D-optimal designs for C_e as function of C_0 , V and M , including for models with more than 2 parameters, can be found elsewhere [14, 15].

Acknowledgements

The authors thank CNPq/Brazil and CAPES/Brazil for supporting this research and providing scholarships.

References

- [1] Do D. Adsorption analysis: equilibria and kinetics. 1st ed. London: Imperial College Press; 1998.
- [2] Foo KY, Hameed, BH. Insights into the modelling of adsorption isotherm systems. Chem Eng J 2010; 156:2-10.
- [3] Osmari A, Gallon R, Schwaab M, Barbosa-Coutinho, E, Severo JB, Pinto JC. Statistical analysis of linear and non-linear regression for the estimation of adsorption isotherm parameters. Adsorpt Sci Technol 2013; 31:433-458.
- [4] Dabrowski A. Adsorption: from theory to practice. Adv Colloid Interface Sci 2007; 147:401-411.
- [5] Cassol GO, Gallon R, Schwaab M, Barbosa-Coutinho, E, Severo JB, Pinto JC. Statistical analysis of non-linear parameter estimation procedures for adsorption equilibrium models. Adsorpt Sci Technol 2014; 32:257-273.
- [6] Kumar KV, Sivanesan S. Equilibrium data, isotherm parameters and process design for partial and complete isotherm of Methylene blue onto activated carbon. J of Hazard Mater 2006; B134:237-244.
- [7] Tolazzi N, Steffani E, Barbosa-Coutinho E, Severo JB, Pinto JC, Schwaab M. Adsorption equilibrium models: computation of confidence regions of parameter estimates. Chem Eng Res Des 2018; 138:144-157.
- [8] Atkinson AC, Donev N, Tobias RD. Optimum Experimental Design, with SAS. 1st ed. New York: University Press; 2007.
- [9] Bard Y. Nonlinear Parameter Estimation. 1st ed. New York: Academic Press; 1974.
- [10] Schwaab M, Pinto JC. Análise de Dados Experimentais II: Planejamento de Experimentos. 1st ed. Rio de Janeiro: e-Papers; 2011.
- [11] Rodriguez-Aragón LJ, López-Fidalgo J. T-, d- and c- optimum designs for BET and GAB adsorption isotherms. Chemom Intell Lab Syst 2007; 89:36-44.
- [12] Mannarswamy A, McGee SHM, Steiner R, Andersen PK. D-optimal experimental designs for Freundlich and Langmuir adsorption isotherms. Chemom Intell Lab Syst 2009; 97:146-151.
- [13] Kennedy J, Eberhart R. Particle Swarm Optimization. In: Proceedings of the IEE International Conference on Neural Networks, Perth, Australia 1995; 4:1942-1948.
- [14] Kober R, Schwaab M, Steffani E, Barbosa-Coutinho E, Alberton AL, Pinto JC. D-optimal designs for parameter estimation of adsorption equilibrium models. Chemom Intell Lab Syst 2019; 192:103823.
- [15] Kober R, Schwaab M, Steffani E, Barbosa-Coutinho E, Alberton AL, Pinto JC. Effect of different optimizable variables in D-optimal designs for adsorption equilibrium models. Submitted for publication in Chemom Intell Lab Syst.

Mesoporous metal-organic structure MIL-100 (Fe) as drug carrier

Diony N. Gomes^a, Paulo G. M. Mileo^{a,b}, Nara A. L. Maranhão^a, Daniel V. Gonçalves^a,
Sebastião M. P. Lucena^{a,*}

^a Dept. Eng. Química, Laboratório de Modelagem e Simulação 3D – GPSA, Universidade Federal do Ceará, Campus do Pici, Bl. 709, 60455-760, Fortaleza, CE, Brazil

^b Institute for Molecular Chemistry and Material Sciences, University of Montpellier, Montpellier, France

Abstract

Bio-distribution of drugs in human metabolism has been widely studied in the pharmacological field. The main objectives of these trials are to transport the active agents as well as to control their release, causing a minor side effect. Among the various materials analyzed for controlled release, Metal-organic Framework (MOFs), clusters and organic binders with a large surface area have been tested for this purpose due to their high adsorption capacity and adaptation to different types of molecules. The benefits of these structures are their three-dimensional conformation, which allows for a particular porosity design. Molecular simulation using the Monte Carlo method in the canonical grand ensemble is suitable for investigating adsorption in MOF structures. In this work, the organic metal structure, MIL-100 (Fe) was investigated for its ability to retain the pharmaceutical interest molecules ibuprofen, caffeine, nicotine and fluorouracil. The model used was validated with experimental ibuprofen data. We observed that the affinity sequence of MIL-100 (Fe) is caffeine > ibuprofen > fluorouracil > nicotine. We have found record mass retention for the fluorouracil molecule. Adsorption sites and heat were also investigated.

Keywords: MOF, Adsorption, Drug, Molecular Simulation;

1. Introduction

Often therapeutic agents cannot be administered in natura due to their ineffective bio-distribution, toxicity or instability under temperature or pH conditions of human tissues. In response to this problem, several intelligent drug delivery platforms have been studied and set up in a promising branch in pharmacology with a greater emphasis on biomedical applications [1]. Several drug distribution strategies through organic compounds (eg polymers, dendrimers, liposomes) and inorganic solids (eg silicas and zeolites) have been extensively studied; however, they still have several limitations such as low adsorptive capacity, uncontrolled release and toxicity [1,2].

Metal-organic structures (MOFs) are nanoporous materials formed by the coordination of organic binders to metallic clusters. These structures generally have large surface areas and porous volumes and can be decorated with functional groups (e.g. -COOH and -NH₂). These

characteristics, as well as low toxicities, make them ideal candidates for biomedical applications [3].

Due to the multitude of already synthesized metal-organic structures and also the vast amount of drugs that are difficult to administer, experimental study of all possible drug-MOF pair configurations would be impractical. Molecular simulation is an effective tool for the elucidation of adsorption mechanisms and can be applied to drug-MOF systems and suggest strategies for the incorporation of new drugs. Among the various information provided through molecular simulation are the prediction of capacities, enthalpies and adsorption sites [4]. The Monte Carlo method applied to the canonical grand ensemble (GCMC) is often used to obtain the mentioned information.

In this work, we use GCMC simulations to analyze the adsorbed amount of different drugs in a biocompatible MOF suitable to support the transport of different drugs, the MIL-100 (Fe).

2. Methodology

2.1. MIL-100 (Fe) Model

The MIL-100 (Fe) is composed of Fe (III) trimers connected to the trimesate ligand [5], forming supertetrahedrons which, connected together, result in a macrostructure with 25 and 29 Å mesopores and 8.5 Å hexagonal windows, and 5 Å pentagonals [2]. In this work, we considered structures containing the F- and OH- counter-anions. The molecules used in this work - nicotine, ibuprofen, caffeine and fluorouracil - were chosen based on their relevance in the pharmaceutical field [2]. Due to the presence of impurities or incomplete synthesis of the MOF crystal, it is not uncommon to find defects and synthesis residues that restrict access to volumes of their original porosity. Thus, we analyzed the maximum drug adsorption capacity in MIL-100 (Fe) considering total and partial access to the MOF pores. A rigorous atomistic model for MIL-100 (Fe) was used, the unit cell has the coordinates of the atoms described according to their crystallographic positions. [5] The atoms of this primitive unit cell were then geometrically optimized by an energy minimization based on the UFF force field [7] using the Forcite module of the BIOVIA Materials Studio software package [6].

The potential energy of the solid was modeled by van der Waals and electrostatic interactions, using respectively the Lennard-Jones 12-6 (LJ) and Coulomb potentials. The LJ parameters assigned to atoms of inorganic clusters and organic ligands were respectively taken from the generic force fields UFF and DREIDING [7,8]. To obtain partial atomic charges, the MOF was subjected to a quantum calculation using the GGA / PBE-coupled Functional Density Functional Theory combined with double numerical base sets containing polarization functions (DNP) using the Dmol3 module of the software. Studio material. [6,9]

2.2. Drug Models

Caffeine (Figure 1), Ibuprofen (Figure 1), Nicotine (Figure 2) and Fluorouracil (Figure 2) molecules were modeled and geometrically optimized at the DFT level using functional B3LYP combined with dual numeric base sets containing polarization functions (DNP) as implemented in the Dmol3 module of Material Studio [6,10,11].

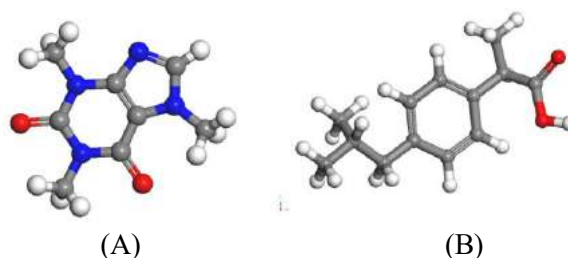


Fig.1. Caffeine (A) and ibuprofen (B) molecule. Identification of atoms: Carbon (gray), hydrogen (white), nitrogen (blue), oxygen (red).

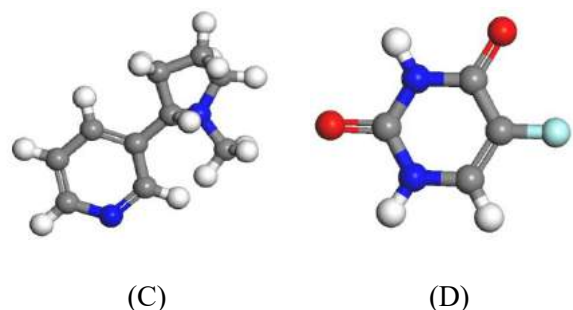


Fig. 2. Nicotine (C) and fluorouracil (D) molecule. Identification of atoms: Carbon (gray), hydrogen (white), nitrogen (blue), fluorine (light blue).

Because these drugs have a limited degree of freedom with respect to torsion harmonics, we assume that DFT-optimized molecule models are rigid in the calculations performed in this study. Potential LJ 12-6 parameters of these molecules were obtained from the OPLS-AA force field and partial atomic loads were derived from CM1A charges according to the LigParGen parameter generator [12,13,14].

2.3. Computational details.

Drug adsorption was performed by Monte Carlo simulations in the Grand Canonical ensemble (GCMC) at 310 K to emulate body temperature. The RASPA code was used for these calculations. Electrostatic interactions were calculated by summing Ewald using a tolerance of 10^{-6} . Dispersive interactions were considered up to a cutoff of 12 Å. To ensure that the system achieved thermodynamic equilibrium, 1×10^4 Monte Carlo equilibrium cycles and 8×10^4 production cycles were performed in sequence. Monte Carlo motions performed in each cycle are proportional to the number of molecules in the system [16].



3. Results and Discussions

3.1. Maximum capacity of adsorption.

According to molecular simulation a high adsorption capacity (above 700 mg/g) was observed for all studied components. The results reinforce the applicability of the material as a potential drug carrier.

Comparing the results obtained by simulation, taking into account the maximum adsorption capacity shown in table 1, fluorouracil showed a higher adsorption. We see an adsorption affinity sequence defined by fluorouracil > caffeine > nicotine > ibuprofen. The high adsorption rate of simulated drugs is favored by the polar groups (hydroxyls, carboxyls, amines, carbonyls) present in their structures, showing an affinity with the adsorbent metal site, promoting an interaction between the metal ion and the adsorbent surface.

Table 1. Simulated maximum adsorption capacity and experimental capacity of drugs in the MOF MIL-100 (Fe) and simulated adsorption heat at 10^{-7} Pa.

Drug	Simulated Maximum (mg/g)	Experimental [2] (mg/g)	Adsorption Heat (KJ/mol)
Fluorouracil	1209	-	-90.9648
Caffeine	920	242	-127.142
Nicotine	748	-	-143.276
Ibuprofen	703/503	330	-112.088

Part of the discrepancy between the simulated and experimental values may be related to the conditions of the experiment (adsorption in aqueous medium). The experimental results may not be optimized for maximum adsorption capacity, while molecular simulation represents the theoretical maximum adsorption capacity.

According to Table 1, the maximum adsorption capacity for the drug ibuprofen presents a significant difference (approximately 53%) between the experimental and simulated values, both performed with mesoporous structure MIL-100 (Fe). In addition to the differences arising from the experimental method, we also need consider the difference due to the accessibility of the molecule to the micropore region of the MIL-100 (Fe) that must

be kinetically impeded, causing diffusion and uptake problems.

Since molecular simulation considers all volume of micropores, the distribution of molecules occurs throughout the volume of the structure with equal probability. Therefore, it is expected that higher adsorption will occur than in the experiment.

In order to examine a possible kinetic problem, a new simulation was performed, where the 25 Å cavities were blocked, making IBU adsorption in these regions impossible. Figures 3 and 4 show the difference in adsorbed amounts before and after blocking.

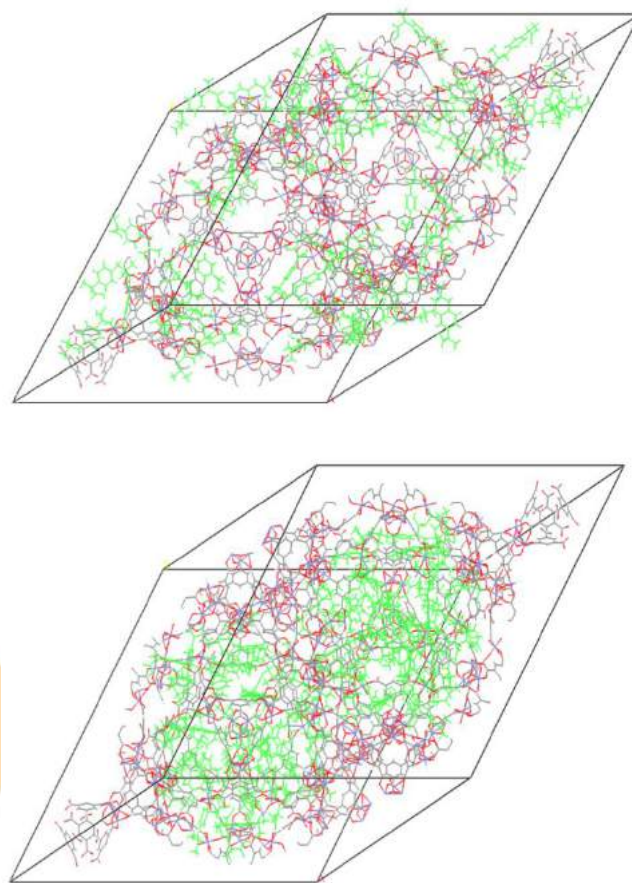


Fig.3. Snapshot of ibuprofen molecules adsorbed inside the MOF pores. No blocking (top) and blocked (bottom). Ibuprofen in green. MOF structure in red and gray.

In Figure 4, we clearly see that blocking the 25 Å cavities in the MIL100 (Fe) mesoporous structure causes a considerable reduction in the amount adsorbed. As the blocked value is closer to the

experimental value, it is possible that the lower experimental value is a result of the inability of ibuprofen molecules to access these cavities through their windows. This may also be the case for the caffeine molecule that has a much lower experimental value than simulated.

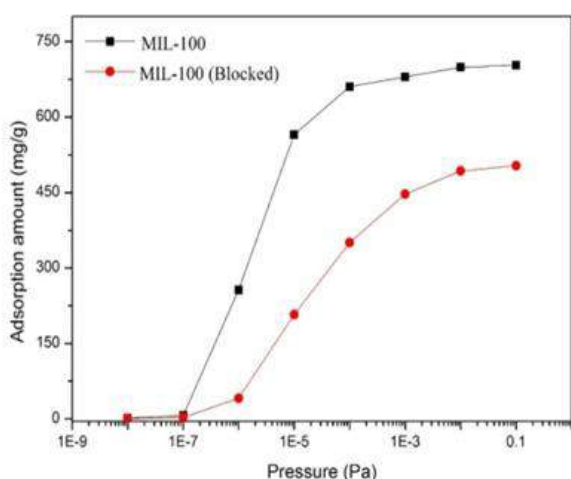


Fig. 4. Ibuprofen adsorption isotherms at 310 K. No blocking (black dots) and blocked (red dots).

Figure 5 shows a sequence of isotherms that were simulated, taking into account pressure and temperature conditions (310 K) and applying the OPLS-AA force field. Each curve relates to a characteristic drug that was adsorbed on the mesoporous structure, MIL-100 (Fe).

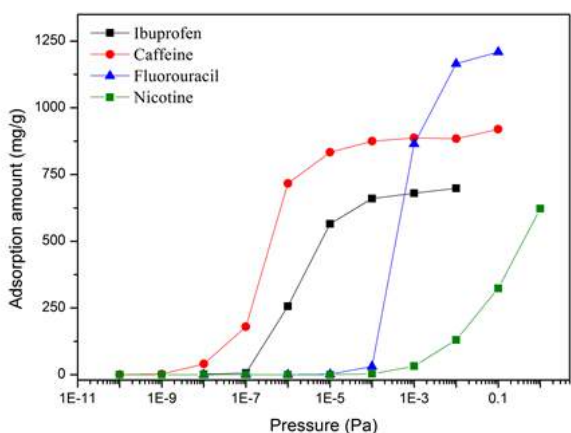


Fig. 5. Adsorption isotherms of ibuprofen, caffeine, fluorouracil and nicotine drugs on MIL-100 (Fe) at 310 K.

Analyzing the behavior of isotherms, caffeine has the highest affinity for MOF adsorbing at very low pressures compared to the others, this is due to a strong interaction between structure and molecule. As can be seen in table 1, the simulated adsorption heat of caffeine is higher than that of the other molecules analyzed.

Regarding the fluorouracil drug, he observed that the fluorouracil-fluorouracil interactions are dominant in the adsorption of this system, compared to the fluorouracil-MOF interactions. The high adsorption rate of fluorouracil is driven by the molecule-molecule interaction and the large volume availability in the MOF pores, as it is the smallest molecule among those tested.

Although the adsorptive capacity of molecules has varied, MOF MIL-100 (Fe) is promising for application in drug bio-distribution, because the order of magnitude of interactions acting on the system is moderate. Thus, drug release will tend to be satisfactory, since strong interactions make drug release impossible, as well as weak interactions provided rapid release.

3. Conclusion

We used GCMC simulation to study drug adsorption capacity in MIL100 (Fe). Based on the methodology employed, we obtained a prediction of the maximum adsorption capacities.

The mesoporous structure MIL-100 (Fe) has the following affinity sequence: fluorouracil > caffeine > nicotine > ibuprofen. The drugs showed high adsorption capacities, suggesting their use for drug delivery. Regarding the fluorouracil drug, we found a maximum load capacity related to the adsorbate-adsorbate interaction, that is more significant than the adsorbate-adsorbent interaction, associated to the large availability of adsorption volumes inside the MOF pores.

In addition, we tested the adsorption of ibuprofen molecules on MIL-100 (Fe), with the smaller cavities blocked, in order to verify the possible causes of the difference between the maximum simulated adsorption capacity and the experimental value. The result shows a reduction in the load soon after the block, but still far from the experimental one.

We hope that GCMC simulations will allow us to study the suitability of porous material as a potential drug carrier before performing any experiments. Since the experiments take time and financial

investment, the use of validated models would provide an optimization of the discovery process of appropriate drug carrier MOF. This strategy may facilitate the development of new drug delivery systems in future studies.

Acknowledgements

The authors wish to acknowledge financial support for this study from CNPq, CAPES and FUNCAP.

References

- [1] Chun-Yi Sun, ChaoQin, Xin-Long Wang & Zhong-Min Su (2013) Metal-organic frameworks as potential drug delivery systems, *Expert Opinion on Drug Delivery*, 10:1, 89-101
- [2] BERNINI, María C.; FAIREN-JIMENEZ, David; PASINETTI, Marcelo. Screening of bio-compatible metal-organic frameworks as potential drug carriers using Monte Carlo simulations. *J. Mater. Chem. B*, [s.l.], v. 2, n. 7, p.766-774, 2014. Royal Society of Chemistry (RSC). <http://dx.doi.org/10.1039/c3tb21328e>
- [3] Horcajada, P., Christian Serre, Maria Vallet-Regi, Muriel Sebban, Francis Taulelle, and Gerard Férey. Metal-Organic Frameworks as Efficient Materials for Drug Delivery. *Angew. Chem. Int. Ed.* 2006, 45, 5974–5978.
- [4] DUREN, T.; BAE, Y.S.; SNURR, R.Q. Using molecular simulation to characterize metalorganic frameworks for adsorption applications. *Chem. Soc. Rev.*, v. 38, p. 1237-1247, 2009.
- [5] Horcajada, P.; Surblé, S.; Serre, C.; Hong, D.-Y.; Seo, Y.-K.; Chang, J.-S.; Grenèche, J.-M.; Margiolaki, I.; Férey, G. Synthesis and Catalytic Properties of MIL-100(Fe), an Iron(III) Carboxylate with Large Pores. *Chem. Commun.* 2007, 100 (27), 2820–2822.
- [6] Dassault Systèmes BIOVIA. Materials Studio. San Diego 2017.
- [7] Rappé, A. K. K.; Casewit, C. J. J.; Colwell, K. S. S.; Goddard III, W. A.; Skiff, W. M. UFF, a Full Periodic Table Force Field for Molecular Mechanics and Molecular Dynamics Simulations. *J. Am. Chem. Soc.* 1992, 114 (25), 10024–10035.
- [8] Mayo, S. L.; Olafson, B. D.; Iii, W. a G.; Eb, E.; El, E. a E. T. DREIDING: A Generic Force Field for Molecular Simulations. *J. Phys. Chem.* 1990, 101 (Suite 540), 8897–8909.
- [9] Perdew, J. P.; Burke, K.; Ernzerhof, M. Generalized Gradient Approximation Made Simple. *Phys. Rev. Lett.* 1996, 77 (18), 3865–3868.
- [10] Stephens, P. J.; Devlin, F. J.; Chabalowski, C. F.; Frisch, M. J. Ab Initio Calculation of Vibrational Absorption and Circular Dichroism Spectra Using Density Functional Force Fields. *J. Phys. Chem.* 1994, 98 (45), 11623–11627.
- [11] Kim, K.; Jordan, K. D. Comparison of Density Functional and MP2 Calculations on the Water Monomer and Dimer. *J. Phys. Chem.* 1994, 98 (40), 10089–10094.
- [12] Jorgensen, W. L.; Maxwell, D. S.; Tirado-Rives, J. Development and Testing of the OPLS All-Atom Force Field on Conformational Energetics and Properties of Organic Liquids. *J. Am. Chem. Soc.* 1996, 118 (45), 11225–11236.
- [13] Dodda, L. S.; Vilseck, J. Z.; Tirado-Rives, J.; Jorgensen, W. L. 1.14*CM1A-LBCC: Localized Bond-Charge Corrected CM1A Charges for Condensed-Phase Simulations. *J. Phys. Chem. B* 2017, 121 (15), 3864–3870.
- [14] Dodda, L. S.; De Vaca, I. C.; Tirado-Rives, J.; Jorgensen, W. L. LigParGen Web Server: An Automatic OPLS-AA Parameter Generator for Organic Ligands. *Nucleic Acids Res.* 2017, 45 (W1), W331–W336.
- [15] Liédana, N., Galve, A., Rubio, C., Téllez, C. and Coronas, J. (2012) *ACS Appl. Mater. Interfaces.* 4, 5016.
- [16] D. Dubbeldam, S. Calero, D. E. Ellis and R. Q. Snurr, RASPA 1.0, Northwestern University, Evanston, IL, (2008).

Breakthrough Curves of Propane at Different Relative Humidities

A.Möller^{a,*}, R.Eschrich^a, C.Reichenbach^a, A.Seidler^a, D.Klank^a, D.Forberg^b

^a 3P Instruments GmbH, Bitterfelder Str. 1, 04129 Leipzig, Germany

^b helsatech GmbH, Bayreuther Str. 9-11, 95482 Gefrees, Germany

Abstract

In many applications organic compounds have to be removed from wet gas mixtures. To improve the efficiency of such applications, investigations of different materials under same conditions are necessary. However even for activated carbons, the preconditioning of the samples can result in opposite data if the humidity is directly dosed with the organic compound or if the sample was fully equilibrated before. Here we determined breakthrough curves of propane with already with water equilibrated activated carbon at different relative humidities. Vice versa a sample, equilibrated with propane before dosing water was under investigation. One can show a high uptake for propane on the samples with an amount of water below the capillary condensation. The sample preconditioned at higher relative humidities exhibits a very low uptake for propane, indicating a hindered accessibility of the surface by the liquid-like water in the mesopores of the sample.

Keywords: Breakthrough Curves; Competitive Adsorption; Water; Propane

1. Introduction

In many separation processes organic compounds have to be adsorbed in the presence of water vapor. Based on such conditions, the competitive adsorption of water vapor can have a considerable influence on the sorption capacity of the organic components. Applications with such conditions are waste air cleaning, odor elimination or respiratory protection.

2. Experimental

In this study a couple of breakthrough curves on an activated carbon (AC) with water and propane were determined with a commercial breakthrough analyzer mixSorb L. Different relative humidities were investigated to observe the influence of present water on the sorption capacity of propane. Furthermore, different preconditioning of the sample were performed. For this purpose the activated carbon was preconditioned at 30% RH and a propane breakthrough experiment was performed.

After that, the water concentration was further increased up to 85% RH.

In another run the precondition was at 85% RH before dosing propane. These preconditionings have large effects on the later results.

3. Results

The study shows that a preconditioning of the sample with water vapor at different concentrations will have a tremendous influence on the sorption capacity of propane. For relative humidities below the capillary condensation, the adsorption of propane is preferred on the activated carbon. Here sorption capacities similar to pure component data can be observed for propane. An explanation for that can be found in very strong interactions of the propane with the nonpolar surface of the activated carbon against water. This scenario is presented in figure 1. In this plot one can see a slight replacement of water by propane and high temperature peaks, due to the adsorption of propane.

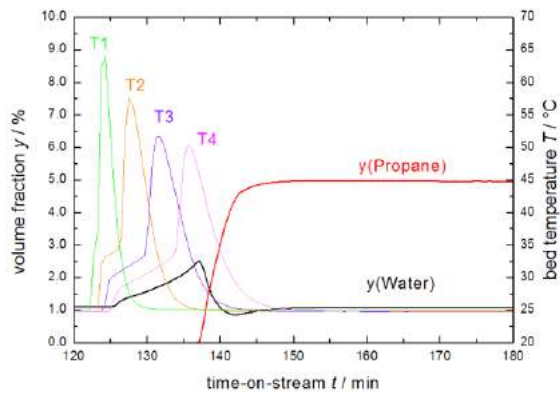


Fig. 1 breakthrough curve of propane on preconditioned AC at 30% RH

By further increasing of the water concentration up to 85% RH, only a small amount of propane was replaced. The whole process at such high water concentrations was very slow. The result of this part of the experiment is given in fig. 2

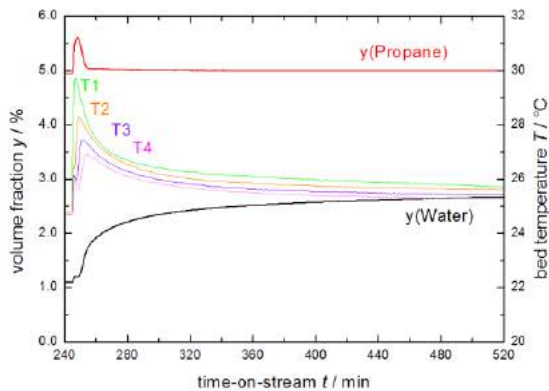


Fig. 2 breakthrough curve of water at 85% RH on AC, preadsorbed with propane and low water content

However, a sample preconditioned at high relative humidity shows the opposite behavior. The carbon can only adsorb small amounts of propane under these conditions, which indicates a limited access to the active adsorption sites. The surface of the activated carbon is completely blocked by the liquid-like water adsorbate in the filled pore system of the sample.

Characterization of sorption kinetics of CO₂ from N₂-rich gas mixtures studied by breakthrough experiments on Zeolites

A.Möller^{a,*}, R.Eschrich^a, C.Reichenbach^a

^a 3P Instruments GmbH, Bitterfelder Str. 1, 04129 Leipzig, Germany

Abstract

The removal of CO₂ from CO₂ containing gas mixtures is an important step in many gas cleaning and gas separation processes. For dry gas mixtures this aim can be realized by adsorption of CO₂ on zeolites. In this study different commercial available zeolites were measured with CO₂ containing N₂-rich gas mixtures with velocities between 0.4 m s⁻¹ and 1.4 m s⁻¹. The breakthrough of CO₂ on zeolite 3A results in a spontaneous breakthrough curve due too narrow pore size in this material and therefore by kinetic-steric exclusion of CO₂. All other zeolites exhibit high sorption capacities, attended by huge heat effects. The study will demonstrate that in all cases heat effects and the shape of the isotherms must be taken into account to get linear driving force constants from such breakthrough experiments.

Keywords: Breakthrough Curves; Kinetics; Linear Driving Force Constants

1. Introduction

The removal of CO₂ from CO₂-containing gas mixtures is essential in many purification processes. This purification step plays a major role for cleaning of natural gas, for upgrade of bio- or synthesis gas as well as for the purification of hydrogen after a steam reforming process and removal of CO₂ from air before cryogenic air separation [1,2,3]. For dry gas mixtures this purpose can be achieved by adsorption of CO₂ on zeolites. Along with the knowledge of isotherms the comprehension of the kinetic behavior of such materials is of high interest for an optimal process design.

2. Experimental

In this study we investigated the shape and steepness of breakthrough curves for CO₂ from mixtures with N₂ on zeolite 3A, 4A, 5A and 13X. All materials were purchased from the same supplier with same particle sizes of 1.6 mm to 2.5 mm. Superficial velocities up to 0.8 m s⁻¹ were investigated. Based on triples of pure component

isotherms for CO₂ and N₂, mixed equilibria were predicted with simple multi component approaches and compared to the experimental results. Afterwards mass- and energy balances were used to calculate breakthrough curves and to estimate Linear Driving Force constants by fitting the model on experimental breakthrough curves. Different approaches for the concentration dependency and temperature dependency of the breakthrough behavior were calculated and the resulted LDF constants were compared.

3. Results

The breakthrough of CO₂ on zeolite 3A results in a spontaneous breakthrough curve due too narrow pore size in this material and therefore by kinetic-steric exclusion of CO₂. All other zeolites exhibit considerable adsorption behavior with different shapes of the breakthrough curves and some differences in the corresponding temperature profiles in the adsorber bed. Zeolites 5A and 4A have similar breakthroughs in the initial part of the curves, therefore only 5A was considered further. Obviously, one can observe the steepest breakthrough curve for the zeolite 13X material. Although the pure component isotherm of CO₂ in

the pressure range of 50 mbar results in a higher sorption capacity for CO₂ on 5A zeolite, the initial breakthrough for CO₂ on 13X starts latest. The breakthrough curves at 1 bar, 0.12 m s⁻¹ and 5% CO₂ on 3A, 5A and 13X are summarized in fig. 1.

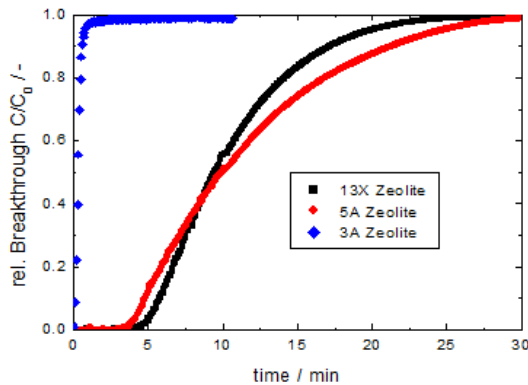


Fig. 1 breakthrough curves of 5% CO₂ from N₂ on different Zeolites at 1 bar, 20 °C and 0.12 m s⁻¹

The difference between the 13X and 5A zeolite can be explained either by the different pore size within the small crystals (micropore diffusion resistance) or by different transport pores within the binder (macropore diffusion resistance). Based on mercury intrusion and tests with different particle sizes both mechanisms may be distinguished, which is still under investigation.

The influence of non-isothermal effects on the resulted LDF constants during the dynamic process was investigated on 13X as an example. The concentration profiles can be described well with both, the isothermal as well the non-isothermal model. However the ratio between the resulted LDF constants is factor 5, which indicates that such non-isothermal effects cannot be neglected.

The adsorption part is much steeper as the desorption profile. This difference will show the influence of the strong curved Type I isotherm of CO₂ on the shape of the breakthrough curves for adsorption and desorption on 13X zeolite. The experimental, isothermal modeled as well as the non-isothermal calculated adsorption and desorption curve are summarized in fig. 2.

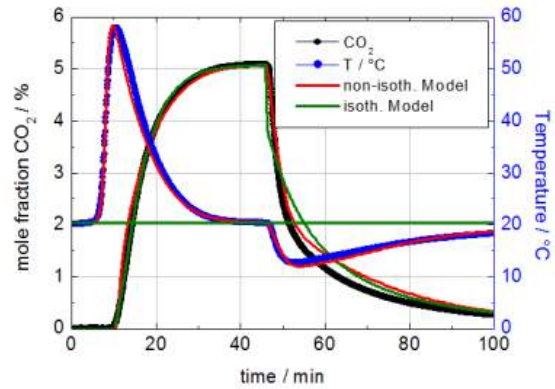


Fig. 2 Adsorption and desorption of 5% CO₂ from N₂ at 1 bar and 20 °C on 13X zeolite. Gas velocity was 0.417 m s⁻¹

References

- [1] S. Cavenati, C.A. Grande, A.E. Rodrigues, *Energy Fuels*, **20** (6), 2648–26591 (2006).
- [2] A. Möller, R. Eschrich, C. Reichenbach, J. Guderian, M. Lange, J. Möllmer, *Adsorption*, **23** (2-3), 197-209 (2017).
- [3] C.A. Grande, R. Blom, A. Möller, J. Möllmer, *Chem. Eng. Sci.*, **89**, 10-20 (2013).

Insights on the use of different gases at 77 K to assess the specific surface area of silica nanoporous materials

Jhonny Villarroel-Rocha^{a,*}, Deicy Barrera^a, José J. Arroyo-Gómez^a, Karim Sapag^a

^a *Laboratorio de Sólidos Porosos, Universidad Nacional de San Luis, Ejército de los Andes 950, San Luis 5700, Argentina*

Abstract

There is a well-known relationship between porous materials performance in several processes and their textural properties such as specific surface area, pore volume and pore size distribution. The most widely used experimental technique and adsorbate to determine the textural properties of porous materials are gas adsorption and N₂ at 77 K, respectively. Due to its quadrupole moment, the N₂ generates specific interactions with the surface groups as silanol ones present in ordered silica materials, causing a preferential orientation effect on the adsorbed N₂ molecule. Herein, alternative adsorptives as Ar, O₂ and CH₄ were evaluated and compared with N₂ to assess the specific surface area in ordered silica materials: MCM-41, MCM-48, SBA-15 and SBA-16. These adsorptives were chosen due to Ar and CH₄ molecules do not present quadrupole moment; and that of O₂ is four times less than N₂. Additionally, at 77 K the Ar and CH₄ are above their triple-point temperature, and N₂ and O₂ are in the same thermodynamic state (i.e., vapor). It was found that the variation of transversal area for the N₂ molecule on silica materials was between 0.133 and 0.149 nm², whereas in the case of O₂ molecule at same temperature this value was almost constant, with an average of 0.123 nm². These results showed that the quadrupole moment of the O₂ at 77 K is low enough to not interact with surface silanol groups present in the samples, making oxygen a potential and reliable adsorptive to determine the specific surface area of silica materials.

Keywords: Textural characterization; N₂, Ar, CH₄ and O₂ adsorption; BET method; ordered nanoporous materials

1. Introduction

Several industrial, environmental and energy applications involve adsorption processes where the adsorbent plays an important role and the best performance is given by those which porous structure with pore sizes from 1 to 100 nm (nanoporous). Among these materials, those with mesoporous structure (2–50 nm) allow a better diffusion of many molecules. Particularly, the ordered mesoporous materials (OMM), have been widely used in the above mentioned applications due to their high specific surface area and porosity [1]. Those materials are considered as model adsorbents, due to the symmetry presented at the mesoscopic level, making them suitable to match experimental data with theoretical models, in particular for textural characterization (e.g., measurement of the specific surface area and pore size distribution).

In most applications, mainly processes involving adsorption or heterogeneous catalysis, both efficiency and selectivity are in direct relationship with the textural properties of the used materials. This dependence has been demonstrated and studied by several researchers, in applications, such as the adsorption of: gases, vapors, organic and pharmaceutical compounds, proteins, heavy metals, and diverse catalytic applications, among others. The performance of the porous materials in the applications mentioned above are mainly related with the specific surface area, which, according to the IUPAC [2] is a “fingerprint” of the adsorbents.

N₂ adsorption-desorption at 77 K has been considered the standard technique to assess the textural properties of porous materials mainly for its availability as probe gas and cryogenic liquid [2]. Nonetheless, several researchers [3] and even the IUPAC, advice that the permanent quadrupole moment of N₂ molecule presents specific interactions with surface groups, e.g., the silanol surface groups present in the silica materials, which

cause an effect of preferential orientation in the adsorbed N_2 molecules. For this case, IUPAC recommends the use of Ar at 87 K, due to its null quadrupole moment. On the other hand, the use of adsorptives different than N_2 at different temperatures in adsorption-desorption studies can be useful to obtain complementary information regarding the texture and/or porous structure of the materials. Adsorption of different gases apart from N_2 has been reported to characterize OMM. All of them can be studied at 77 K, which is interesting because of the accessibility of liquid N_2 as cryogenic system. There are few reports with O_2 , CH_4 and CO , although the use of latter is not recommended for routinary characterization due to its high toxicity. Finally, it should be highlighted that at 77 K, those adsorbates might be in different thermodynamic states, which should be considered for the analysis.

Based on the aforementioned, in this work we used different adsorptives such as N_2 , Ar, O_2 , and CH_4 , with a different quadrupolar moment and thermodynamic properties, at 77 K to characterize silica OMM, such as SBA-15, SBA-16, MCM-41, and MCM-48.

2. Materials and methods

2.1. Synthesis of OMM

Silica ordered mesoporous materials were obtained based on different synthesis procedures. All of these materials were obtained under non-hydrothermal conditions, controlling the main steps as surfactant:silica ratio, stirring, aging temperature and time, washing and calcination. The studied materials were obtained under synthesis conditions previously reported: MCM-41 [4], MCM-48 [5], SBA-15 [4] and SBA-16 [6]

2.2. Gas adsorption

N_2 (99.999 %), Ar (99.999 %), O_2 (99.8 %) and CH_4 (99.995 %) adsorption-desorption isotherms at 77 K were measured in a manometric adsorption equipment Micromeritics ASAP-2000. Before each analysis, the samples were degasified at 150 °C for 12 h. The experiments were performed at the temperature of liquid nitrogen, which during the experiments was 76.8 K on average. Under this condition, the experimental average saturation pressures of the different adsorptives, p^o , were 712, 181, 142 and 8.8 torr, for N_2 , Ar, O_2 and CH_4 , respectively. In each case, the saturation pressure was measured during all experiments.

2.2.1. Thermodynamic conditions and properties of the adsorptives

The thermodynamic states and adsorptives properties are displayed in Tables 1 and 2.

Table 1. Thermodynamic properties of adsorptives at subatmospheric pressures.

Gas	T_c (K)	T_b (K)	T_{TP} (K)
N_2	162.2	77.35	63.15
Ar	150.7	87.30	83.80
O_2	154.6	90.20	54.34
CH_4	190.6	111.6	90.70

T_c : Critical temperature, T_b : Normal boiling point, T_{TP} : Triple point temperature

Table 2. Properties and thermodynamic state of adsorptives.

Gas	Thermodynamic state at 77 K and below p^o	Quadrupole Moment ($C \cdot m^2$)	Molecular size (nm)*
N_2	Subcritical state; gas-liquid interfase	$46.65 \cdot 10^{-41}$	0.36
Ar	Subcritical state; gas-solid interfase	0	0.34
O_2	Subcritical state; gas-liquid interfase	$11.43 \cdot 10^{-41}$	0.35
CH_4	Subcritical state; gas-solid interfase	0	0.38

* Kinetic diameter

Under experimental conditions (77 K), the adsorptives are in the thermodynamic state of subcritical gases ($T/T_c < 1$), and additionally CH_4 is in a temperature below its triple point, behaving as a subcooled liquid ($T/T_{TP} < 1$) (Table 1). The selection of the adsorptives was based on the molecular dimensions as well as their quadrupole moments as is shown in Table 2, in order to study the effect of these parameters on the textural analysis of the silica OMM. As is shown in Table 1, Ar and CH_4 have a quadrupole moment of zero whereas N_2 presents a quadrupole moment four times larger than O_2 .

2.2.2. Specific surface area

The specific surface area of the silica OMM materials, S_{BET} , was determined using the standard

BET method equation and taking into account the criteria suggested by the IUPAC [2] For the evaluation of the S_{BET} it is necessary to know the value of the transversal area of the adsorbed molecule on the surface, σ [3]. The corresponding values of σ at 77 K 0.162, 0.138, 0.141 and 0.156 nm² for N₂, Ar, O₂ and CH₄, respectively.

3. Results and discussion

3.1 N₂, Ar, O₂ and CH₄ adsorption-desorption at 77 K

In MCM-41 isotherms (Fig. 1) can be seen that after the capillary condensation in the primary mesopores, there is a plateau almost horizontal, suggesting no significant presence of secondary mesopores (mesoporosity related to disorder in the OMM). Another worth-mentioning aspect is that with all gases, except N₂, the materials present a slight hysteresis loop. The reversibility of the N₂ isotherm is due to the MCM-41 primary mesopore size, which is below the nitrogen capillary critical size (ca. 4 - 5 nm), at $p/p^0 \approx 0.42$. In the case of Ar and O₂, the critical size is ca. 2.5 - 3.0 nm, for this reason, these isotherms present a small hysteresis loop.

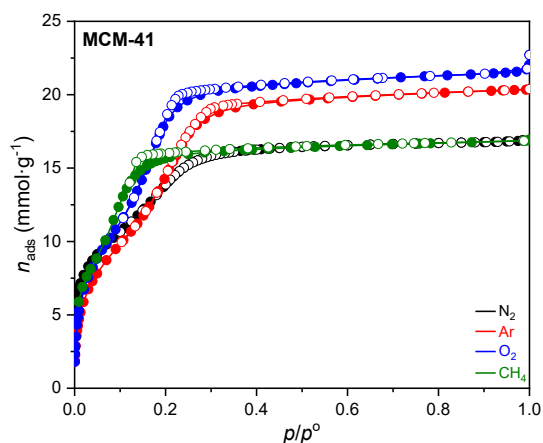


Fig. 1. N₂, Ar, O₂ and CH₄ adsorption-desorption isotherms at 77 K MCM-41.

Regarding CH₄, although there is no reported data for its capillary critical size from the results presented in Figure 1, it can be inferred that it must be lower than 4-5 nm, or a similar value to those of Ar and O₂ (i.e., this value should be between 2.5 and 4 nm).

In general, the begin of the capillary condensation is close to the mono-multilayer adsorption region; particularly for CH₄, the capillary condensation is

overlapped with the mono-multilayer adsorption, likely related to CH₄ low saturation pressure (8.8 torr).

Fig. 2 displays the N₂, Ar, O₂ and CH₄ adsorption-desorption isotherms at 77 K of MCM-48. Here, a well-defined stage of capillary condensation is also observed and the plateau after the ending of this stage indicates a low amount of secondary mesopores. The behavior of the hysteresis loops of the isotherms is similar to that in the MCM-41, where the N₂ isotherms are reversible in the capillary condensation / evaporation stage, and the presence of small hysteresis loops for the other gases. These results support the hypothesis that the capillary critical size of CH₄ at 77 K is between 2.5 and 4 nm.

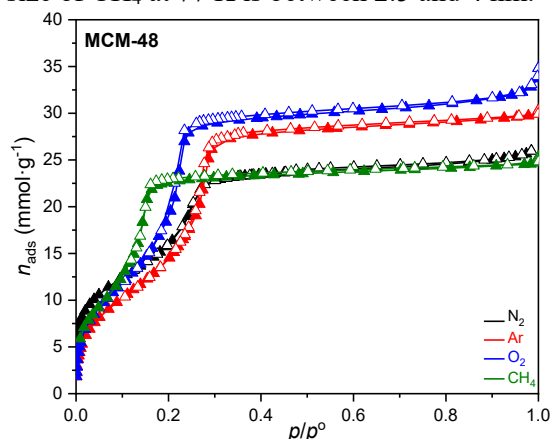


Fig. 2. N₂, Ar, O₂ and CH₄ adsorption-desorption isotherms at 77 K of MCM-48.

Fig. 3 shows the N₂, Ar, O₂ and CH₄ adsorption-desorption isotherms at 77 K for the SBA-15. N₂ and O₂ adsorption isotherms show an increase in the amount adsorbed at high relative pressures, indicating the presence of secondary mesopores greater than 40 nm, which cannot be seen by Ar at 77 K given that this adsorptive only can provide information of pore sizes below 15 nm, as reported previously [7]. Considering that CH₄ at 77 K and 1 bar have the same properties as Ar at the same conditions, i.e., both are below their triple point, it is probable that CH₄ also can measure pores sizes up to the same magnitude order (ca. 15 nm).

Figure 4 displays the experimental N₂, Ar, O₂ and CH₄ adsorption-desorption isotherms at 77 K of SBA-16 sample. This sample shows an important ordering degree (according to the isotherm shape).

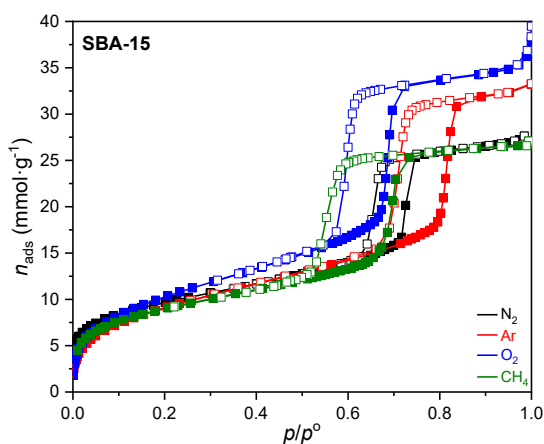


Fig. 3. N₂, Ar, O₂ and CH₄ adsorption-desorption isotherms at 77 K SBA-15.

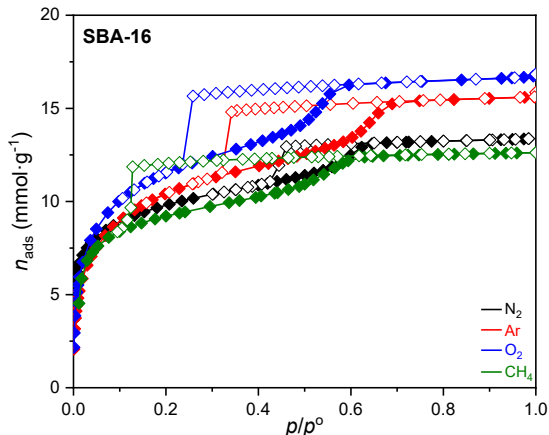


Fig. 4. N₂, Ar, O₂ and CH₄ adsorption-desorption isotherms at 77 K SBA-14.

This material (SBA-16) presents an H2(a) hysteresis loop, characteristic of materials with an important network effect in their pore structure, and where the desorption branch can be affected by cavitation or pore blocking phenomena [8]. Unlike pore blocking, cavitation does not depend on the adsorbent nature, nor its porous structure; it is an adsorptive characteristic. Each adsorbative has its own critical size (w_c) and its own critical relative pressure ($(p/p^0)_c$), therefore, if the pore neck size (w) is below w_c , cavitation will take place at $(p/p^0)_c$. Conversely, when $w > w_c$ the phenomenon present is the pore blocking, which occurs a pressure greater than the critical pressure. Based on the mentioned above, it is possible to state that:

- In the case of N₂ adsorption isotherms at 77 K of SBA-16 sample the hysteresis loops close abruptly at $p/p^0 = 0.42$, indicating the presence of cavitation phenomenon, therefore, their pore neck sizes are < 5 nm.

- The Ar, O₂ and CH₄ isotherms at 77 K of SBA-16 sample present hysteresis loops that close abruptly at 0.33, 0.23 and 0.10 for Ar, O₂ and CH₄ at 77 K, respectively, indicating that the cavitation is the only phenomenon present. Therefore, these values are the critical relative pressures of these adsorbatives. The obtained value for Ar at 77 K is in agreement with that reported by Kruk and Jaroniec (2003) [9].

- In the desorption branch of the N₂ isotherm at 77 K of SBA-16 sample, the amount adsorbed starts to decrease gradually at p/p^0 ca. 0.55 (like forming a knee), until the hysteresis loop closes at $p/p^0 = 0.42$, this would be indicating that is in the transition limit between the capillary evaporation and cavitation, which is limited to a critical size at 5 nm for N₂ at 77 K. This means that this sample presents a group of interconnected pores, with a size of ca. 5 nm.

- The Ar, O₂ and CH₄ isotherms at 77 K of SBA-16 present a hysteresis loop in which a first desorption step due to the capillary evaporation (with meniscus formation) is observed, due to the emptying of some pores (blocked and unblocked) with a certain size ($w > w_c$). Additionally, at a lower relative pressure (critical relative pressure) abrupt desorption is observed (due to cavitation, without the formation of meniscus) until the closing of the hysteresis loop, which is due to the emptying of pores with pore sizes smaller than w_c ($w < w_c$).

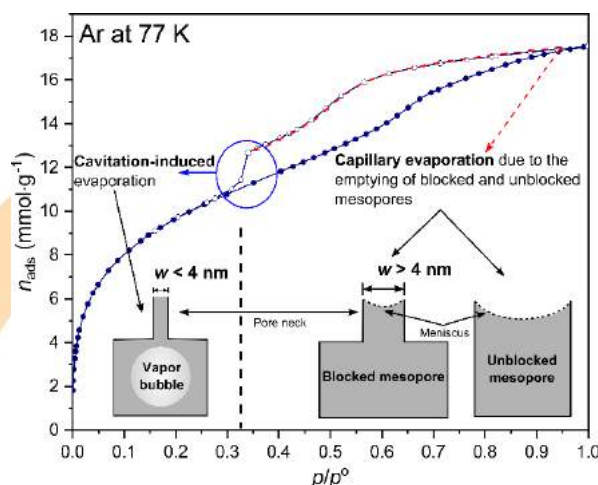


Fig. 5. Scheme of the cavitation and capillary evaporation phenomena in the Ar adsorption-desorption isotherm at 77 K of SBA-16. w : pore neck size, and w_c : critical size (4 nm for Ar at 77 K).

Therefore, it can be stated that in the desorption branches of the Ar, O₂ and CH₄ isotherms at 77 K two phenomena are present: capillary evaporation (of unblocked and blocked pores) and cavitation,

this fact was reported previously by Reichenbach et al. [10]. For a better understanding, in Figure 5 a schematic illustration of these phenomena in the Ar adsorption-desorption isotherm at 77 K is shown. Because this behavior was also observed with O₂ and CH₄ at 77 K, and knowing that the critical size for Ar at 77 K is 4 nm, it can be inferred that critical size for O₂ and CH₄ at 77 K is similar. This information is relevant because it can be inferred that besides N₂ at 77 K, another adsorptives (Ar, O₂ or CH₄ at 77 K) can give provide additional information regarding the interconnected pores of a given material.

3.2 Specific surface area analysis with different adsorptives

Table 3 presents the specific surface areas (S_{BET}) and parameter C from BET equation [2] of silica OMM obtained from N₂, Ar, O₂, and CH₄ adsorption data at 77 K. It can be seen from the values of parameter C , the order of adsorbate – adsorbent interaction energies for OMM with small mesopore sizes (i.e., MCM-41 and MCM-48) is: CH₄-silica > N₂-silica > O₂-silica ≈ Ar-silica. Whereas for the OMM with larger mesopore sizes (i.e., SBA-15 and SBA-16), the order is N₂-silica > CH₄-silica > O₂-silica ≈ Ar-silica.

Table 3. C values and S_{BET} of OMM determined with N₂, Ar, O₂, and CH₄ at 77 K.

Sample	MCM-41	MCM-48	SBA-15	SBA-16
C	65	72	148	195
N₂				
S_{BET} (m ² ·g ⁻¹)	1080	1230	780	755
C	35	28	54	63
Ar				
S_{BET} (m ² ·g ⁻¹)	935	1030	645	685
C	36	31	53	70
O₂				
S_{BET} (m ² ·g ⁻¹)	1080	1170	745	790
C	160	87	93	144
CH₄				
S_{BET} (m ² ·g ⁻¹)	875	1030	705	716

Comparing the S_{BET} values obtained with the different adsorptives, it can be observed that there is no agreement. Considering the S_{BET} value with Ar at 77 K as reference, we observe that: *i*) N₂

overestimates the S_{BET} between 8 and 22 %, *ii*) O₂ overestimates the S_{BET} between 13 and 16 %, and *iii*) CH₄ gives underestimates S_{BET} values up to 7 % or overestimates up to 9 %. Table 3 shows S_{BET} values of silica OMM using different adsorptives, presenting a variation among them. Using the S_{BET} values from Ar at 77 K as reference (S_{BET-Ar}), the variation percentages of S_{BET} for each adsorptive are 9-22 % for N₂, 13-17 % for O₂, and up to 9 % for CH₄, respectively.

In order to have a more representative amount of samples, two other materials with different surfactant:silica molar ratio were included for each silica OMM. Using the S_{BET} values from Ar at 77 K (Table 3) as reference, the variation percentages of S_{BET} for other adsorptives are: 9-22 % for N₂, 13-17 % for O₂, and up to 9 % for CH₄, respectively. Furthermore, in order to evaluate these variations, with each sample, we calculate the transversal areas (σ) of N₂, O₂ and CH₄ at 77 K to obtain the same S_{BET-Ar} value.

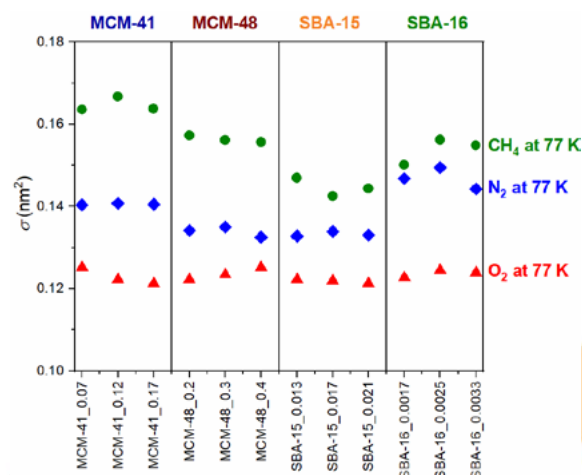


Fig. 6. σ values calculated for N₂, O₂ and CH₄ at 77 K.

The obtained σ values for N₂, O₂ and CH₄ at 77 K are displayed in Figure 6, which reflect the behavior of the results presented in Table 3. It can be observed in Figure 6 that both N₂ and CH₄ at 77 K are the adsorptives that present the highest variation of σ values. The results that can be highlighted from Figure 6 are:

This behavior is related with the fact that the N₂ at 77 K presents σ values between 0.133 and 0.149 nm², where the lower limit is close to the reported values of 0.13-0.135 nm² for the case of oxides (silica) using Ar at 77 K as reference [3], and for the case of amorphous silica using TEM measurements. This variation range (which is below

the usual value of 0.162 nm^2) is due to the N_2 molecule presents the highest permanent quadrupole moment among the studied adsorptives, producing specific interactions with surface silanol groups (Si-OH) of silica OMM; these interactions cause a preferential orientation of the N_2 molecule adsorbed on the surface of silica OMM. For instance, if N_2 molecules are capable of interacting vertically with the -OH groups of silica surface, the σ value of this configuration becomes 0.11 nm^2 [3] In this sense, depending on the number of surface silanol groups on the silica, there will be in adsorbed monolayer on surface a certain amount of N_2 molecules oriented vertically (with 0.11 nm^2), and others oriented horizontally (with 0.162 nm^2), with an average σ value below 0.162 nm^2 , which is in agreement with the results obtained. When the percentage of vertically oriented molecules is calculated, values between 25 and 56 % (corresponding to 0.149 and 0.133 nm^2 , respectively) are obtained.

- For CH_4 at 77 K, σ values between 0.143 and 0.167 nm^2 were found, and the value used initially (0.156 nm^2) was within this range. Methane does not present quadrupole moment (Table 2), therefore the variation found in the σ values is directly related to the errors in the determination of the amount adsorbed in the monolayer. Specifically, in MCM-41 and MCM-48 materials, which have small mesopores (3-4 nm), its well-defined capillary condensation stage is close (or superposed) to the mono-multilayer filling region, this makes difficult to find a suitable region to apply the BET equation, which considers only the mono-multilayer filling. In the case of O_2 at 77 K, the σ values (between 0.121 and 0.125 nm^2) are almost constant, with an average value of 0.123 nm^2 , which is lower than the usual value of 0.141 nm^2 . Although the size and shape of the O_2 molecule is very similar to N_2 , and both molecules, at 77 K, are in the same thermodynamic state (vapor), the only difference between them is that O_2 has a quadrupole moment four times lower than N_2 , indicating that this quadrupole moment is low enough to not interact with surface silanol groups present in OMM.

4. Conclusions

The O_2 at 77 K can be considered as an interesting adsorptive for the S_{BET} determination (using a σ value of 0.123 nm^2), complementing the reported by Jagiello and Kenvin (2019) [11] where they use O_2 at 77 K as a probe adsorptive to obtain the pore size distribution of different carbon materials. Also this

adsorptive has the advantage (with respect to Ar at 77 K) that the temperature of adsorption is above its triple-point temperature, which means that it does not behave like a subcooled liquid. Regarding to CH_4 adsorption at 77 K on the OMM with narrow mesopores between 3 and 4 nm, it did not present a clear “knee” formation (B point), this because the capillary condensation stage occurs along with the mono-multilayer adsorption (possibly due to its low saturation pressure, ca. 9 mm Hg).

References

- [1] Davis ME. Ordered porous materials for emerging applications. *Nature* 2002;417:813-821.
- [2] Thommes M, Kaneko K, Neimark AV, Olivier JP, Rodriguez-reinoso F, Rouquerol J, Sing KSW. Physisorption of gases, with special reference to the evaluation of surface area and pore size distribution. IUPAC Technical Report. *Pure Appl Chem* 2015;87: 1051-1069.
- [3] Rouquerol F, Rouquerol J, Sing, KSW, Llewellyng P, Maurin G. Adsorption by powders and porous solids: Principles, methodology and applications. Elsevier, Oxford. 2014.
- [4] Barrera D., Villarroel-Rocha J, Marenco L, Oliva MI, Sapag K. Non-hydrothermal synthesis of cylindrical mesoporous materials: Influence of the surfactant / silica molar ratio. *Ads Sci & Tech* 2011;29: 957-988.
- [5] Schumacher K, Ravikovitch PI, Chesne AD, Neimark AV, Unger KK. Characterization of MCM-48 Materials. *Langmuir*. 2000;16:4648-4654.
- [6] Stevens WJJ, Mertens M, Mullens S, Thijs I, Van Tendeloo G, Cool P, Vansant EF. Formation mechanism of SBA-16 spheres and control of their dimensions. *Micropor Mesopor Mater* 2006;93:119-124.
- [7] Thommes M, Köhn R, Fröba M. Sorption and pore condensation behavior of nitrogen, argon, and krypton in mesoporous MCM-48 silica materials. *J Phys Chem B* 2000;104:7932-7943.
- [8] Landers J, Gor GY, Neimark AV. Density functional theory methods for characterization of porous materials. *Colloids and Surfaces A: Physicochemical and Engineering Aspects* 2013;437:3-32.
- [9] Kruk M., Jaroniec M. Argon adsorption at 77 K as a useful tool for the elucidation of pore connectivity in ordered materials with large cage-like mesopores. *Chemistry of Materials* 2003;15:2942
- [10] Reichenbach C., Kalies G., Enke D., Klank D. Cavitation and pore blocking in nanoporous glasses. *Langmuir* 2011;27:10699-10704.
- [12] Jagiello J, Kenvin J. Consistency of carbon nanopore characteristics derived from adsorption of simple gases and 2D-NLDFT models. Advantages of using adsorption isotherms of oxygen (O_2) at 77 K. *J. Colloid Interface Sci* 2019;542:151-158.

H₂O sorption on nanoporous carbons

Diaz Cristian A.^a, Villarroel-Rocha Jhonny^a, Sapag Karim^{a*}

^a Laboratorio de Sólidos Porosos, INFAP (UNSL-CONICET), Ejercito de Los Andes 950, San Luis AR5700, Argentina

Abstract

The behavior of the H₂O sorption was studied on three porous carbon materials, an activated carbon and two mesoporous carbons, previously synthesized and characterized in the Laboratorio de Sólidos Porosos. A prior N₂ adsorption-desorption analysis at 77K was performed to the materials, from these data the textural properties of these materials were obtained. Then, H₂O adsorption-desorption isotherms at 298K were performed to the materials, and correlating these results with their textural properties. The results showed that the micropore volume obtained with H₂O is smaller than that obtained with N₂ and may be due to the hydrophobic character of carbons. In addition, a clear hysteresis on isotherms in the microporous region could be observed for the three materials, most evident being the case in activated charcoal, which is fundamentally microporous.

Keywords: Water sorption; carbon; nanoporous materials; textural characterization

1. Introduction

Porous materials have been a subject of extensive study within the scientific community, due to its multiple applications, among which are catalysis, gas storage, removal of contaminants, drug delivery, among others [1-4]. The interest on these materials is due to what is known as their textural properties; specific surface area, pore volume and pore size distribution.

Traditionally the study of these properties is done by means of the adsorption-desorption technique of N₂ to 77K, this is due to its abundance and because it is a molecule without dipolar interactions. However, molecules such as H₂O, which has a considerable electrical dipolar moment, can interact with polar surface functional groups in materials. In addition, due to the thermodynamics of H₂O, isotherms can be carried out at temperatures close to the environment. In addition to the electrical characteristics of the H₂O, its kinetic size is smaller than that of other absorbable (H₂O (0.27nm), N₂ (0.36nm), Ar (0.34nm) and CO₂ (0.33nm)) [5], allowing it to enter ultra-micropore regions.

This work proposes an analysis of the materials by means of a complementary technique, which is the adsorption-desorption of H₂O at 298K. This technique provides information that N₂ technique alone is not able to do [6], such as the hydrophilic/hydrophobic character of the materials,

this technique allows to provide information on the micropore scale, as well as information on surface functional groups [7]. Three materials are used in the study; a microporous activated carbon, and two micro mesoporous nanostructured carbons, in order to see the behavior of the technique along different textural properties of these carbon materials.

2. Synthesis of materials

2.1. Activated carbon

The activated charcoal material was synthesized at the Laboratorio de Sólidos Porosos (LabSoP) facility by Mg. Dimar Villarroel-Rocha. For the synthesis of this material was departed from peach pits, from the province of Mendoza, Argentina. The seed was removed from the pits (Figure 1), and after crushing and sifting it, particles of about 2mm in size were obtained. This material was washed with distilled water and dried at 110°C for 24h. Once the dry and dry material was obtained, an impregnation was performed with a chemical agent, in this case a water solution of ZnCl₂ was used. Then the material is charred at a temperature of 550°C by 3h in an atmosphere of N₂. Finally, the activated charcoal obtained was washed, to reach the final material, which is studied in this work.



Fig. 1. Example of starting material for CA-Zn synthesis.

2.2. Micro- meso-porous nanostructured carbons

Within the carbon materials, in addition to the microporous activated carbon material, a micro-mesoporous nanostructured material, type CMK-8, which is obtained by the nanocasting method [8] was studied. This method consists, in obtaining from silica material that serves as a template, a carbon material with a structure that is the reverse replica of the starting material, on Figure 2 a general scheme of the synthesis is shown. In this case the KIT-6 silica material was used as template, which after filling the pores with sucrose as a source of carbon, and a subsequent heat treatment, the coal present in the composite material, becomes a porous graphite structure. Finally, after the silica template is removed with an acid treatment, the material of interest, that is, the material CMK-8, which is, the reverse replica of the KIT-6 is obtained. Two variations of the CMK-8 type materials were studied, which are obtained with different ratios of KIT-6/sucrose. Taking as reference the synthesis reported in previous works [9], the so-called CMK-8_B2 was synthesized with the template/sucrose ratio equal to twice the standard, while the so-called CMK-8_B3 is synthesized with a template/sucrose ratio equal to the half of the standard.

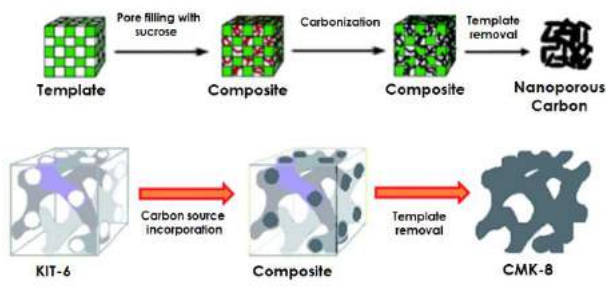


Fig. 2. CMK-8 synthesis scheme.

3. Textural characterization

5.1. N₂ adsorption-desorption isotherms at 77K on CA-Zn

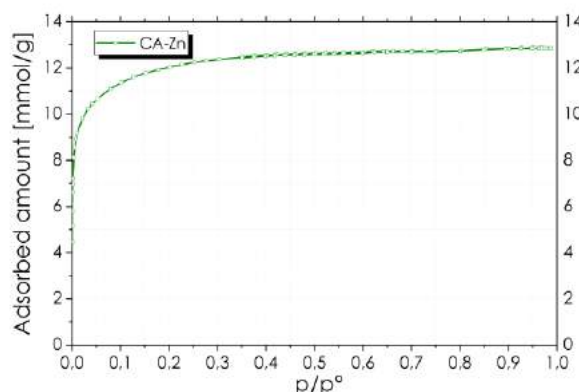


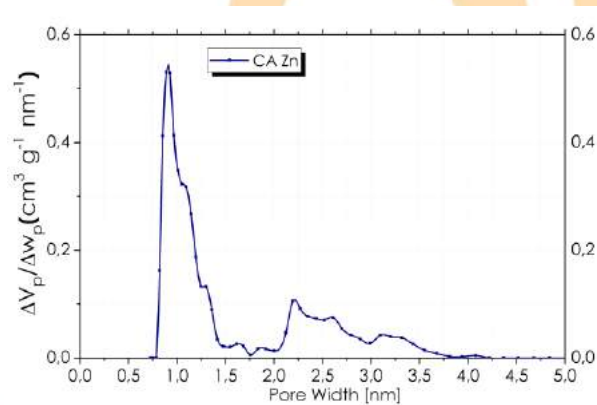
Fig. 3. N₂ adsorption-desorption isotherm at 77K on CA-Zn

N₂ adsorption-desorption analysis at 77K was performed on the activated charcoal sample, the results are shown in Figure 3. Isotherm is a Type I, according to the IUPAC classification [10], characteristic of microporous materials. From the experimental adsorption data of N₂ the textural properties of the CA were determined, which are presented in Table 1, it can be observed that this material presents high values of S_{BET} and V_{TP} .

Figure 4 presents the pore size distribution (PSD) of the AC, which was obtained from the N₂ desorption data, using DFT method (QSDFT: Quenched Solid Density Theory Functional), in particular the kernel, "N₂ at 77K on carbon, slit pore, equilibrium model", using ASiQwin v.4.0 software (Quantachrome Instruments).

The pore size distribution for this material mainly shows micropores less than 1.5nm, and a mesoporosity around 2.5nm, which confirms that it is a fundamentally microporous material.

Fig. 4. Pore size distribution of the CA-Zn sample



5.2. H₂O adsorption-desorption isotherms at 298K on CA-Zn

Figure 5 shows the H₂O adsorption-desorption isotherm at 298K on CA-Zn. In the adsorption isotherm it can be observed 3 regions: (i) at low relative pressures (< 0.35) the sample has a small adsorbed amount of H₂O which can be attributed to the presence of superficial functional groups, since for coal surfaces it is known to have a hydrophobic character; (ii) at a pressure of 0.4 p/p° an abrupt increase of adsorbed amount is evidenced, which is attributed to the filling of micropores of such material, and finally (iii) from 0.75 p/p° and up to 0.95 p/p° a plateau can be observed because the micropores of the material (fundamentally microporous) are completely filled. On the other hand, H₂O adsorption-desorption presents a clear hysteresis loop (at $p/p^\circ < 0.80$), and up to 0.35 of p/p° which is the point of the isotherm where the adsorption and desorption branches close.

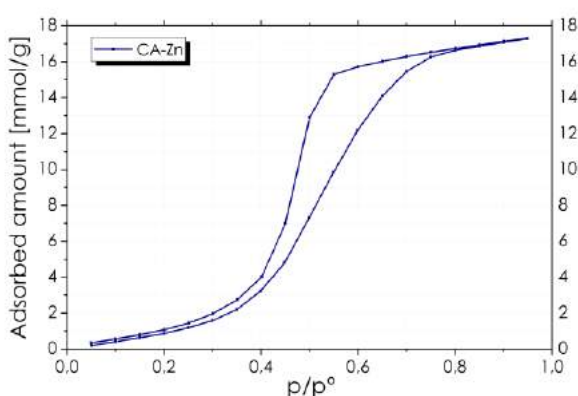


Fig. 5. H₂O adsorption-desorption isotherm at 298K on CA-Zn

It is important to note that, as observed from the analysis with N₂ adsorption-desorption at 77K, the analyzed material is fundamentally microporous, which shows us that hysteresis seen in the H₂O adsorption-desorption isotherm, is occurring in micropores. This fact shows an important difference on the H₂O adsorption-desorption isotherms behavior respect to N₂, as adsorptive, with the fist having hysteresis in the micropore region which is not the case with N₂ (when working with rigid porous structures). This behavior, i.e. the presence of hysteresis in the H₂O adsorption-desorption isotherms at 298K, in microporous materials, is already known and was reported in previous articles such as Velasco 2016 [11] and Dubinin 1980 [12].

Because hysteresis occurs due to different mechanisms for filling and emptying of the pores, this phenomenon can be very useful for the study of such mechanisms are in the micropores region of materials, and from this their structure.

Table 1. Textural properties of the CA-Zn

Material	S_{BET}	V_{TP}	$V_{\mu P-N_2}^1$	$V_{\mu P-N_2}^2$	$V_{\mu P-H_2O}^1$
	m ² /g	cm ³ /g	cm ³ /g	cm ³ /g	cm ³ /g
CA-Zn	1020	0.45	0.38	0.32	0.29

1- Calculated with α_s -plot method

2- Calculated with Dubinin-Radushkevich method

On the other hand, the fact that a plateau is reached in the adsorption branch (indicative of the micropores were filled), makes it possible to determine the volume of micropores using the s-plot method.

For the application of the t-plot method with H₂O a reference isotherm [13] was used with low adsorbate-adsorbent interaction ($C=5.2$), since, as mentioned, coal is known to has a hydrophobic character. The results obtained are shown in Table 1.

5.3. Adsorption-desorption isotherms of N₂ at 77K on CMK-8

N₂ adsorption-desorption isotherms at 77K on both CMK-8 (Figure 6 and 7) were performed using the ASAP 2000 sortometer (Micromeritics). A degassed at 200°C for 12h pre-treatment was performed to the materials.

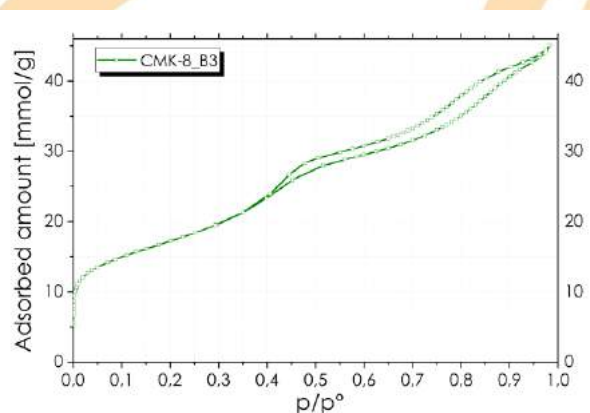


Fig. 6. N₂ adsorption-desorption isotherm at 77K on CMK-8_B3

Both materials have Type IV(a) isotherms according to the IUPAC classification, with

hysteresis loops typically of mesoporous materials. In addition, it should be noted that the CMK-8_B2 material has a significantly lower N₂ adsorption capacity than the CMK-8_B3, and an isotherm corresponding to a more ordered material, conversely the CMK-8_B3 has a high N₂ adsorption capacity, and a considerable adsorbed amount (between 0.7 and 0.95 of p/p°) on larger mesopores (secondary mesoporosity).

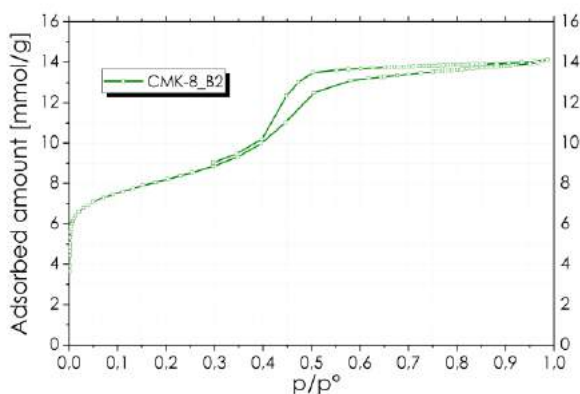


Fig. 7. N₂ adsorption-desorption isotherm at 77K on CMK-8_B2

The textural properties presented in Table 2 were calculated from the adsorption branch of these isotherms. It can be observed that, while both materials have similar V_{MP} , they have a considerable different S_{BET} and V_{TP} .

Table 2. Textural properties of CMK-8 materials

Material	S_{BET}	V_{TP}	$V_{MP-N_2}^1$	$V_{MP-N_2}^2$	$V_{MP-H_2O}^1$	$V_{MMP-H_2O}^1$
	m ² /g	cm ³ /g	cm ³ /g	cm ³ /g	cm ³ /g	cm ³ /g
CMK-8_B2	671	0.49	0.14	0.35	0.02	0.38
CMK-8_B3	1367	1.56	0.16	1.40	Non-determinable	

1- Calculated with α_S -plot

2- $V_{MP} = V_{TP} - V_{MP}$

PSDs of the carbon materials with N₂ adsorption data at 77K was obtained using ASiQwin, v.4.0 software (Quantachrome Instruments) by the QSDFT method with the Kernel for carbons with slit-cylindrical geometry.

In Figure 8 you can see the PSD for both CMK-8. We observe the presence of two primary porosities, a microporous region (~1nm), and a mesoporous region (~4.5nm). Besides both materials have pores of similar size, the CMK-8_B3 has a higher pore volume, in addition to the presence of a secondary mesopores higher than 6nm.

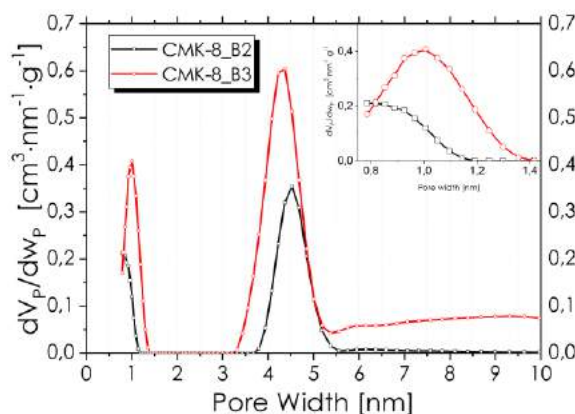


Fig. 8. Pore size distribution of the CMK-8 carbons

5.4. H₂O adsorption-desorption isotherms at 298K on CMK-8

H₂O adsorption-desorption isotherm at 298K on CMK-8_B2, is shown in Figure 9, which presents on the adsorption branch, three regions clearly distinguishable. From the data obtained with N₂ isotherms it could be associated with specific processes; (I) up to relative pressures less than 0.3 a small amount adsorbed occurs on the functional groups on the surface of the material, (II) a second region in the range of 0.3 to 0.78 of p/p° micropore filling would be occurring, it is observed that since a pseudo plateau is generated, the microporosity of the material is completely filled, and (III) a third region, for pressures greater than 0.78 of p/p° , in which the narrow mesopores filling occurs, which is also completed, which is observed by the shape of the isotherm at pressures ~0.98 p/p° (where reach a plateau).

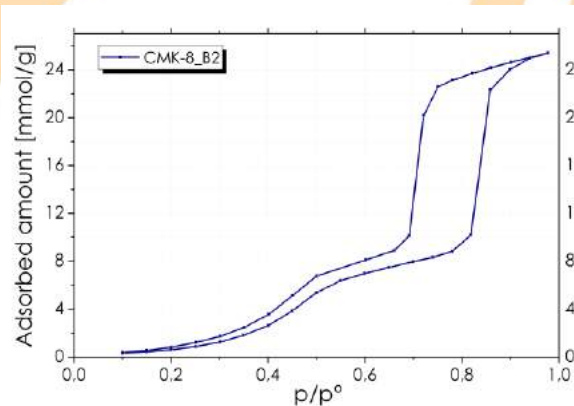


Fig. 9. H₂O adsorption-desorption isotherm at 298K on CMK-8_B2

In Figure 10, H₂O adsorption-desorption at 298K isotherm on CMK-8_B3, at the same with CMK-8_B2, is also observed three regions in the adsorption branch. However, in the third region not form a plateau, because the presence of larger mesopores amount, as was observed in the study with N₂, produces a H₂O isotherm associated with a more disordered material, which is evidenced by the adsorption/desorption branches are not parallel, unlike for CMK-8_B2.

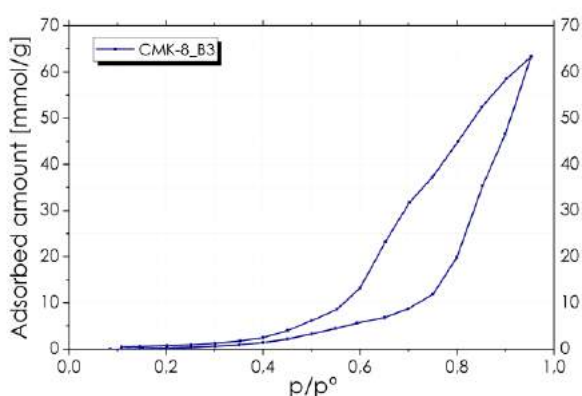


Fig.10 H₂O adsorption-desorption isotherm at 298K on CMK-8_B3

In this sense, since the isotherm does not form a plateau at pressures close to 0.98 p/p° , and correlating this result with the PSD obtained with N₂ adsorption data, it is concluded that, the filling of all mesoporosity, in particular the secondary, is not completed, which could be indicative that for this type of carbon materials the adsorption technique of H₂O at 298K would be seeing pores up to about 6nm.

From the H₂O adsorption isotherm, an analysis was performed using the t-plot technique to calculate the micro and mesopore volumes, for this purpose previously reported reference isotherms [13] were used. Table 2 shows the obtained values. From these values it can be seen that the V_{MP} observed with H₂O is smaller than that obtained with N₂, ($V_{\text{MP-H}_2\text{O}}=0.02 \text{ cm}^3/\text{g}$ and $V_{\text{MP-N}_2}=0.14 \text{ cm}^3/\text{g}$) despite the kinetic size of the H₂O molecule is smaller than that of N₂ [5], this is the same phenomenon which is observed in the CA-Zn case. It can be understood taking into account that carbons have a hydrophobic character, which makes the water not fully occupy the volume of the pores. In the case of mesoporosity the volumes determined by both adsorptive are similar ($V_{\text{MPP-H}_2\text{O}}=0.35 \text{ cm}^3/\text{g}$ and $V_{\text{MPP-N}_2}=0.38 \text{ cm}^3/\text{g}$). In the CMK-8_B3 material the t-plot method could not be applied using

H₂O, since as in the isotherm there are no well-defined regions where the filling of the different types of porosity is completed.

6. Conclusions

The carbons under study were characterized texturally, having a microporous activated carbon and two CMK-8 micro mesoporous carbons, in the latter an important difference in the ordering of the material was observed, being the CMK-8_B3 more disordered due to the presence of secondary mesoporosity. In the analysis with H₂O, it was possible to see a clear process of hysteresis in the microporous region of all the materials under study, being more noticeable in the CA-Zn which does not have a considerable mesoporosity. In addition, a difference was observed in the V_{MP} observed with both adsorptives, which is attributed to the carbon hydrophobic character. This hydrophobic character is also observed in the change of the overall shape of the isotherm, specifically in the region of low pressures when changing adsorptive.

Acknowledgements

This work was financially supported by UNSL, ANPCyT and CONICET (Argentina).

References

- [1]Kumar, K. V., Preuss, K., Titirici, M. M., & Rodríguez-Reinoso, F. (2017). Nanoporous Materials for the Onboard Storage of Natural Gas. *Chemical Reviews*, 117(3), 1796–1825.
- [2]Mohan, D., & Pittman, C. U. (2007). Arsenic removal from water/wastewater using adsorbents-A critical review. *Journal of Hazardous Materials*, 142(1–2), 1–53.
- [3]Frackowiak, E., & Béguin, F. (2001). Carbon materials for the electrochemical storage of energy in capacitors. *Carbon*.
- [4]Corma, A. (1997). From microporous to mesoporous molecular sieve materials and their use in catalysis. *Chemical Reviews*.
- [5]Sing, K. S. W., & Williams, R. T. (2004). The use of molecular probes for the characterization of nanoporous adsorbents. *Particle and Particle Systems Characterization*, 21(2), 71–79.
- [6]Thommes, M., Morell, J., Cychosz, K. A., & Frackowiak, M. (2013). Combining nitrogen, argon, and water adsorption for advanced characterization of ordered mesoporous carbons (CMKs) and periodic mesoporous organosilicas (PMOs). *Langmuir*, 29(48), 14893–14902.
- [7]Nguyen, V. T., Horikawa, T., Do, D. D., & Nicholson, D. (2014). Water as a potential molecular probe for functional groups on carbon surfaces. *Carbon*, 67, 72–78.

- [8] Lu, A. H., & Schoth, F. (2006). Nanocasting: A versatile strategy for creating nanostructured porous materials. *Advanced Materials*, 18(14), 1793–1805.
- [9] Kleitz, F., Hei Choi, S., & Ryoo, R. (2003). Cubic Ia3d large mesoporous silica: synthesis and replication to platinum nanowires, carbon nanorods and carbon nanotubes Electronic supplementary information (ESI) available: TEM images of mesoporous cubic silica and Pt networks, XRD patterns during forma. *Chemical Communications*, 9(17), 2136.
- [10] Thommes, M., Kaneko, K., Neimark, A. V., Olivier, J. P., Rodriguez-Reinoso, F., Rouquerol, J., & Sing, K. S. W. (2015). Physisorption of gases, with special reference to the evaluation of surface area and pore size distribution (IUPAC Technical Report). *Pure and Applied Chemistry*, 87(9–10), 1051–1069.
- [11] Velasco, L.F., Snoeck, D., Mignon, A., Misseuw, L., Conchi, O.A., Van Vlierberghe, S., Dubruel, P., de Belie, N., Lodewyckx, P. (2016). Role of the surface chemistry of the adsorbent on the initialization step of the water sorption process. *Carbon*, 106, 284–288.
- [12] Dubinin, M.M. (1980). Water vapor adsorption and the microporous structures of carbonaceous adsorbents. *Carbon*, 18(5), 355–364.
- [13] J. Hagymassy Jr., Stephen Brunauer, R. Sh Mikhail, "Pore structure analysis by water vapor adsorption: I. t-Curves for water vapor," *J. Colloid Interface Sci.*, vol. 29, no. 3, pp. 485–491, 1969.

Carbon dioxide and water vapor adsorption on commercial and synthesized zeolites

Rafael Morales Ospino^a, Ricardo A. Lima Jr^a, A. Eurico B. Torres^a, Enrique Vilarrasa García^a, Moises Bastos-Neto^a, Celio L. Cavalcante Jr^a, Diana C. Silva de Azevedo^a, Carolina Resmini Melo Marques^b, Thiago Fernandes de Aquino^b, Lidia Baraky^c

^a Universidade Federal do Ceará, Campus do Pici, Fortaleza CEP 60455-900, Brazil

^b Associação Beneficente da Indústria Carbonífera de Santa Catarina (SATC), Rua Pascoal Meller 73, Criciúma CEP 88805 380, Brazil

^c ENEVA, Empresarial Mourisco -Praia de Botafogo 501, Rio de Janeiro CEP 22250-040, Brazil

Abstract

CO₂ and water adsorption capacity were estimated in commercial (13X and 4A) and synthesized (Type X and type A) zeolites via adsorption isotherms. The isotherms were carried out by gravimetric method using a magnetic suspension balance. Pure gas CO₂ isotherms were obtained at 50, 70 and 90°C until 1bar and water adsorption isotherms at the same temperatures until the adsorbent saturation. Binary isotherms of water/CO₂ were also performed at 50°C using different initial water loading to assess the water impact on the CO₂ adsorption capacity. Preliminary results indicated that commercial zeolite 4A was more affected by the presence of water than commercial zeolite 13X.

Keywords: Zeolites; CO₂; water adsorption; fly ash.

1. Introduction

CO₂ is one of the main greenhouse effect gases. Its growing emissions to the atmosphere are believed to contribute to global warming. They have become a major environmental concern, which has driven governments and researchers to develop more efficient carbon capture processes from large releasing sources of CO₂ like coal-fired power plants [1-3]. Zeolites are considered promising materials for CO₂ capture due to their high uptake and selectivity, even at low pressures [4]. However, their CO₂ adsorption capacity might be impaired by the presence of water in the flue gas due to their hydrophilic character. CO₂ separation is considered the most expensive step (60-70% of total cost) in the Carbon Capture and Storage chain [5]. Consequently, in an attempt to decrease the cost in carbon capture, easily available low-cost precursors for zeolite synthesis like fly ashes have been considered to produce zeolites given their rich content in silicon and alumina [6, 7]. In this work, benchmark commercial zeolites (13X and 4A) and

Type X and A synthesized zeolites from fly ash have been evaluated on their CO₂ and water adsorption capacities. Additionally the impact of water presence in CO₂ uptake has been assessed by means of binary isotherms at 50 °C.

2. Materials and methods

2.1. Materials

- Commercial adsorbents: Zeolite type 13X (Zeo13X) from Shangai Hengye Chemical Industry and Zeolite type 4A (Zeo4A) from Zeochem.
- Synthesized adsorbents: The synthesized adsorbents were obtained from coal fly ash of two power plants in Brazil. Type X zeolite (XFF) was synthesized from fly ash of Paulo Lacerda Power plant (Capivari de Baixo, Brazil) and type A zeolite (PAF) was synthesized from fly ash of Pecém II Power plant (Pecém, Brazil). The synthesis of zeolites A and X was carried out following a procedure reported in the literature [8].

2.2. Methods

Pure CO₂ and water vapor adsorption experiments were performed using a magnetic suspension balance Rubotherm (Bochum, Germany). Since the aforementioned magnetic suspension balance was not originally manufactured for water vapor adsorption measurements, the balance was adapted to obtain water vapor adsorption isotherms as observed in Figure 1. The modifications included:

- an AISI 316 stainless steel cylinder to store the water,
- a micrometric valve for water dosing,
- a pressure transducer model P 10 (WIKA, Germany) ranging between de -1 and 2 bar gauge for a better accuracy and precision of the pressure measurement and,
- a heating system to produce the water vapor within the cylinder at a desired experiment temperature and to prevent water condensation in the pipes and valves along the water vapor pathway towards the adsorption measurement cell.

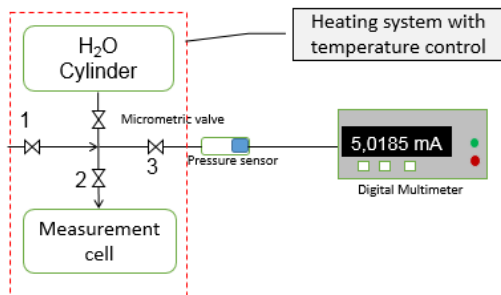


Figure 1. Water adsorption dosing system.

The pure CO₂ isotherms were obtained at 50, 70 and 90 °C up to 1bar and the water adsorption isotherms at the same temperatures up to adsorbent saturation. The binary water/CO₂ isotherms were performed at 50°C using different initial water loadings. After a given water loading, CO₂ isotherms were measured until 1 bar. This experimental sequence for binary isotherms was only possible once water loading is not affected by the coadsorption of CO₂ on zeolites, so that the loading of water vapor can be assumed constant for this study [9].

The Sips equilibrium model [10] was used to fit pure gas CO₂ experimental data (Eq. 1).

$$q_i = q_{m,i} \frac{(K_{eq,i}P)^{1/n_i}}{1 + (K_{eq,i}P)^{1/n_i}} \quad (1)$$

where q_i is the quantity of gas adsorbed per unit mass of adsorbent at a given T and P , $q_{m,i}$ is the maximum adsorbed concentration in mmol.g⁻¹. Parameter $K_{eq,i}$ (bar⁻¹) is related to the affinity between adsorbate and adsorbent (Langmuir constant) and n_i the heterogeneity parameter.

Considering that the choice of the temperature-dependence form of q_m can be arbitrarily chosen, the exponential function shown below was employed (Eq. 2):

$$q_{mi} = qm_{0i} + X_i \left(\frac{1}{T} - \frac{1}{T_0} \right) \quad (2)$$

where $q_{mi,0}$ is the value of q_m at a reference temperature T_0 and χ is an extra parameter in mmol.K g⁻¹. The dependence of the affinity constant and n_i parameter on temperature can be expressed respectively as follows:

$$K_{eqi} = k_{0i} \exp \left[\frac{Q_{0i}}{R} \left(\frac{1}{T} - \frac{1}{T_0} \right) \right] \quad (3)$$

$$n_i = a_i + b_i \times \frac{T}{T_0} \quad (4)$$

3. Results

The commercial samples exhibited a slightly superior performance than the synthesized zeolites on CO₂ adsorption for the 3 temperatures tested (50, 70 and 90 °C) in the pressure range from 0 to 1 bar as observed in Figure 2 and 3. Type X zeolites showed higher CO₂ adsorption capacity than the type A zeolites specially when the pressure is increased, as observed in Figure 2 and 3; however, type X zeolites seemed to be more affected by the temperature change than the type A zeolites. The

CO₂ adsorption capacity at post-combustion conditions (0.15 bar and 50°C) followed the sequence: Zeo13X (2.26 mmol.g⁻¹) > Zeo4A (2.16 mmol.g⁻¹) > XFF (1.87 mmol.g⁻¹) > PAF (1.82 mmol.g⁻¹).

Sips model fittings, for pure CO₂ for the three selected temperatures, showed good agreement with experimental data. The fitting parameters of Sips model for single adsorption isotherms of CO₂ for all the samples are shown in Table 1.

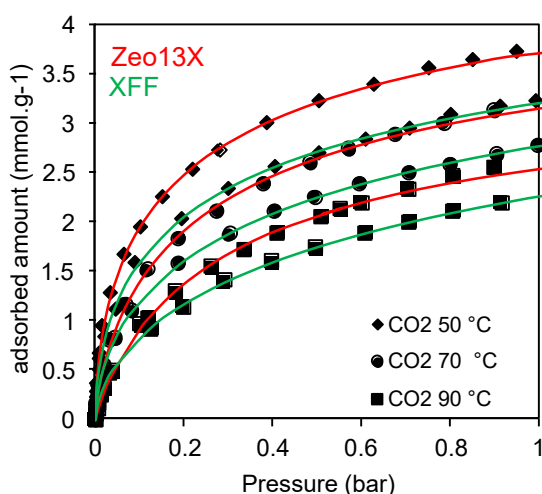


Figure 2. CO₂ adsorption isotherms at 50, 70 and 90 °C for Type X zeolites (Zeo13X and XFF). Symbols are experimental points and lines fitted data by Sips model.

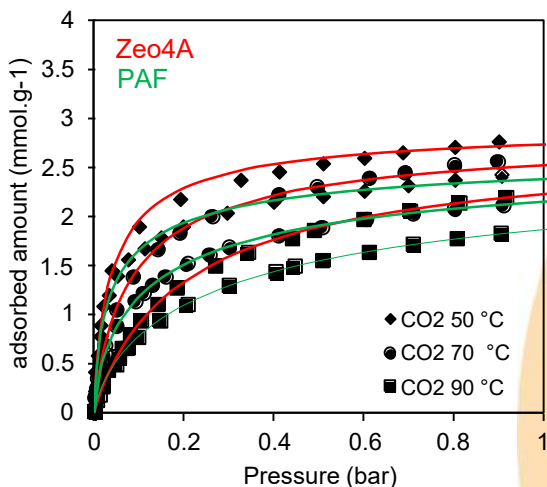


Figure 3. CO₂ adsorption isotherms at 50, 70 and 90 °C for Type A zeolites (Zeo4A and PAF). Symbols are experimental points and lines fitted data by Sips model.

Pure H₂O isotherms were obtained at 50, 70 and 90°C for 13X and 4A zeolites (Figure 4). The water adsorption capacity of 13X zeolite is slightly higher than 4A. Thus, 13X zeolite showed a saturation capacity of 12 mmol H₂O/g while 4A zeolite reached 11 mmol/g.

Table 1. Sips model parameters for CO₂ adsorption on commercial and synthesized zeolites.

Parameters	Zeo13X	XFF	Zeo4A	PAF
k_0 (bar ⁻¹)	3.75	2.5	24.27	19.78
Q_0 (J.mol ⁻¹)	5360.14	31077.5	39912.6	46600.5
qm_0 (mol.kg ⁻¹)	5.47	5.16	2.94	2.69
X	5622.48	75.07	506.73	6.75
a	5.95	2.76	2.47	2.51
b	-4.28	-0.99	-1.22	-1.02

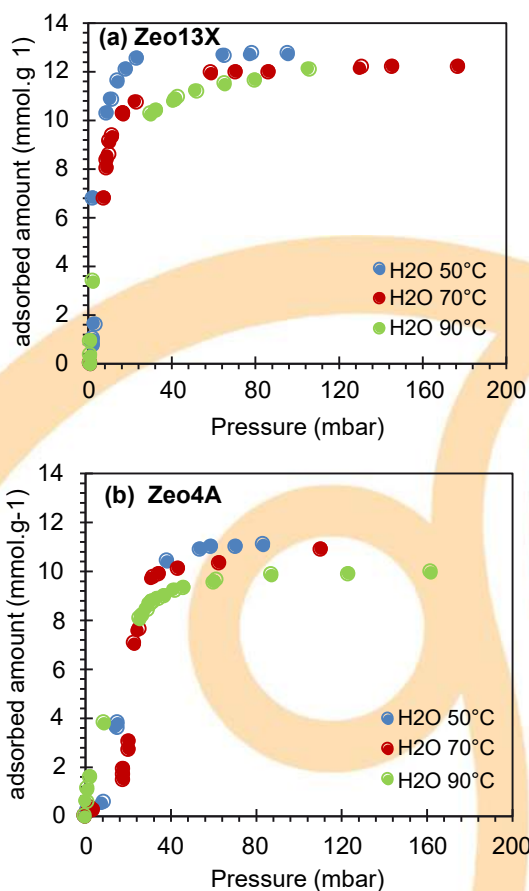


Figure 4. H₂O adsorption isotherms at 50, 70 and 90 °C for (a) zeolite 13X and (b) 4A

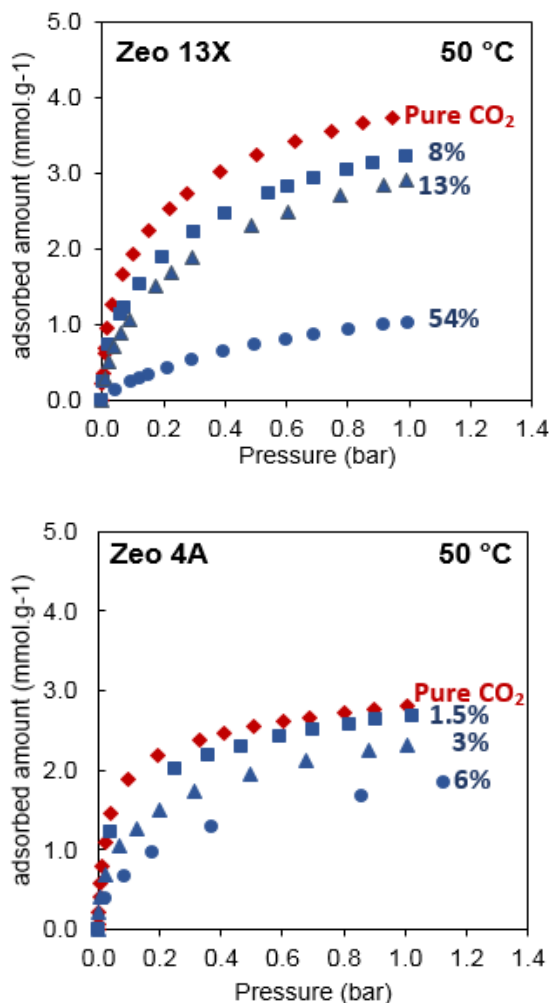


Figure 5. Adsorption isotherms at 50°C for 13X and 4A zeolites with and without coadsorbed water molecules. The percentages showed are the percentage of H₂O from saturation concentration.

To assess the influence of H₂O presence on the CO₂ adsorption capacity of the commercial zeolites, the materials were initially loaded with a water concentration lower than that of the saturation. The initial loadings represented a percentage of the water vapor saturation concentration as shown in Figure 5. The decrease of CO₂ adsorption capacity observed in both zeolites after H₂O loading implies that CO₂ and H₂O binding sites maybe overlap each other so that the CO₂ adsorption capacity is significantly reduced with the molecules competing for the same sites. This effect is more evident in 4A zeolite than 13X, where it is necessary to load a higher amount of H₂O to observe a significant CO₂ capacity decrease.

4. Conclusion

Type X zeolites exhibited a higher CO₂ adsorption capacity in comparison with type A zeolites in pressure levels between 0 and 1 bar. Both commercial zeolites (13X and 4A) displayed comparable water adsorption capacities; however, the CO₂ adsorption capacity for 4A zeolite was more affected by the presence of water.

Acknowledgements

The authors acknowledge financial support from ENEVA S.A. and CNPq (Conselho Nacional de Desenvolvimento Científico e Tecnológico)

References

- [1] Samanta, A., Zhao, A., Shimizu, G. K. H., Sarkar, P., and Gupta, R. Post-Combustion CO₂ Capture Using Solid Sorbents: A Review. *Industrial & Engineering Chemistry Research*, v. 51, n. 4, p. 1438-1463, 2011.
- [2] Liang, Z., Fu, K., Idem, R., and Tontiwachwuthikul, P. Review on current advances, future challenges and consideration issues for post-combustion CO₂ capture using amine-based absorbents. *Chinese Journal of Chemical Engineering*, v. 24, n. 2, p. 278-288, 2016.
- [3] Nie, L., Mu, Y., Jin, J., Chen, J., and Mi, J. Recent developments and consideration issues in solid adsorbents for CO₂ capture from flue gas. *Chinese Journal of Chemical Engineering*, v. 26, n. 11, p. 2303-2317, 2018.
- [4] Modak, A. and Jana, S. Advancement in porous adsorbents for post-combustion CO₂ capture. *Microporous and Mesoporous Materials*, v. 276, p. 107-132, 2019.
- [5] Bhowan, A. S. and Freeman, B. C. Analysis and status of post-combustion carbon dioxide capture technologies. *Environ Sci Technol*, v. 45, n. 20, p. 8624-32, 2011.
- [6] Querol, X., Moreno, N., Umaña, J. C., Alastuey, A., Hernández, E., López-Soler, A., and Plana, F. Synthesis of zeolites from coal fly ash: an overview. *International Journal of Coal Geology*, v. 50, n. 1, p. 413-423, 2002.
- [7] Henmi, T. Synthesis of Hydroxy-Sodalite ("Zeolite") from Waste Coal Ash. *Soil Science and Plant Nutrition*, v. 33, n. 3, p. 517-521, 1987.
- [8] Izidoro, J. d. C., Fungaro, D. A., Abbott, J. E., and Wang, S. Synthesis of zeolites X and A from fly ashes for cadmium and zinc removal from aqueous solutions in single and binary ion systems. *Fuel*, v. 103, p. 827-834, 2013.
- [9] Wang, Y. and Levan, M. D. Adsorption Equilibrium of Binary Mixtures of Carbon Dioxide and Water Vapor on Zeolites 5A and 13X. *Journal of Chemical & Engineering Data*, v. 55, n. 9, p. 3189-3195, 2010.
- [10] Sips, R. Combined form of Langmuir and Freundlich equations. *Chem. Phys.*, v. 16, p. 385-471, 1948.

Assessment of Intracrystalline Diffusion for C₈ Aromatics Isomers in Beta Zeolite using the ZLC Technique

J. Wilson V. Lima Jr., F. Murilo T. de Luna and Célio L. Cavalcante Jr.

Departamento de Engenharia Química – Universidade Federal do Ceará, Grupo de Pesquisa em Separações por Adsorção, Núcleo de Pesquisa em Lubrificantes, Campus do Pici, Bloco 1010, CEP: 60.455-900, Fortaleza – CE – Brasil.

Abstract

The separation of xylenes is an issue that has been investigated due the importance of these compounds and the difficulty of obtaining them in the pure form, from conventional separation processes. The diffusional kinetics is a factor that can be determinant in separation processes. Measurements for intracrystalline diffusivities, with strong adsorbed species, becomes more difficult since, as the strength of adsorption increases, resulting in difficult to eliminate the intrusion of heat and mass transfer resistances to bed diffusion. This diffusivity, particularly in zeolite crystals with hydrocarbons, can be assessed from the ZLC (Zero Column Length) technique, which uses a small amount of solid, in a very short column, eliminating these drawbacks. In this study, diffusivities are reported for xylene isomers in Beta zeolite (two dimensional pore systems). An Approach of long and short time analysis in spherical model for the Zero Length Column method was used. The range of temperature evaluated was between 80 and 120 °C and the values determined by both methods presented a small discrepancy. The diffusivity values for the components under study were close for the temperatures evaluated, in the order of $10^{-15} \text{ m}^2 \text{ s}^{-1}$.

Keywords: Xylene; Adsorption; Beta zeolite; Diffusion; ZLC.

1. Introduction

C₈ aromatics isomers are intermediates in several polymers manufacturing processes. Their separation by conventional processes is not feasible due to their very close boiling points. Adsorption processes have been applied in the last decades using molecular sieves, mainly faujasite type zeolites, for *p*-xylene separation.

More recently, Beta zeolite has also been investigated for this purpose. In usual adsorption applications, the diffusional kinetics behavior should be determined in order to assess possible drawbacks in real process operations. It is well known that measurements of intracrystalline diffusivities of strongly adsorbed compounds may be affected by possible intrusion of heat and external mass transfer resistances. In these cases, the Zero Length Column technique (ZLC) has been used since it employs a very small amount of adsorbent sample thus minimizing (or eliminating) those possible external resistances [1].

Studies of C₈ aromatic diffusivity in natural faujasite-type and NaX zeolites indicated similar diffusivities for xylenes isomers [2]. The evaluation of different sizes of crystals of these zeolites has confirmed the dominance of intracrystalline diffusion as controlling step. The diffusivity investigated in ion-exchanged faujasite type zeolite having cation Ba, by modeling and simulation, has shown that macropore diffusion is the controlling step in the process at temperatures between 80 °C and 180 °C for *p*-xylene and between 50 °C and 180 °C for *o*-xylene [3]. The diffusivity values for both isomers showed similar.

Formed from an intergrowth of two different polytypes (A and B), zeolite Beta is a three-dimensional 12-membered-ring array of channels material, very important for industrial processes [4,5,6]. It is a commodity catalytic material in petrochemical and fine chemical industries due to its characteristics, such as high thermal and hydrothermal stabilities with adjustable acidity [7]. Although this zeolite exhibits great

performance in various application, its high cost for synthesis is a drawback and limitation [8]. Source from natural aluminosilicate minerals and distinct via has been studied for synthesis of zeolite Beta in order to reduce the costs in production and to be more environmentally-benign [9,10].

In this study, the intracrystalline diffusion of C₈ aromatics isomers in Beta zeolite was evaluated at different temperatures using ZLC method with the long time (LT) and short time (ST) approaches.

2. Materials and methods

2.1. Materials

The xylene isomers, *o*-, *m*- and *p*-xylene, and ethylbenzene (Sigma-Aldrich, EUA) were used as adsorbates in the experiments. The sample of Beta zeolite (Si/Al = 25) were provided by Zeolyst Company (USA). The adsorbent, in column, was regenerated on the temperature of 150 °C for at least 15 hours, prior to be used in experiments.

2.2. Adsorbent characterization

The adsorbent used in this work was characterized using Autosorb-1 MP (Quantachrome, USA) to measure N₂ isotherms at 77 K for the determination of textural properties. The specific surface area was calculated using the BET method and micropore volume was determined using the Dubinin-Radushkevich (DR) equation. A Mastersizer (Malvern Instruments), model 2000, was used to estimate the average particle diameter. This was aided by the Hydro 2000MU dispersion unit (Malvern Instruments), using water as dispersing agent.

2.3. Zero Length Column method

The Zero Length Column technique has as principle use a short column, as the proper name suggests, putting the sorbent, in form of powder or pellet, between two sintered discs inside the column. The purpose of this method is use a small quantity of adsorbent in the column and a relative high flow of gas to avoid external mass and heat transfer resistances at the particles' surface and axial dispersion.

This method can be used for a wide range of hydrocarbons sorbates, due the exploit the high

sensibility of a flame ionization detector, but has proved especially useful for study of strongly adsorbed species such as the aromatic and polyaromatic hydrocarbons [11]. This technique has as basis, follow the desorption curve for a small sample of adsorbent previously saturated and equilibrated with the sorbate under controlled conditions.

The experimental setup (Figure 1) had a thermostatic bath and a Varian Gas Chromatograph (CP-3380). Their operational parameters are shown in Table 1. The column inside the gas chromatograph (GC) oven, instead of a traditional packed column, is a union of 1/8" tube. The extension of tubing, inside the chromatograph, was put to ensure that the temperature of sorbate get equilibrium with the oven before reach the column.

Table 1. Carrier gas, detector and bath conditions.

Bath temperatures	- 15 °C (OX) / - 19 °C (MX) 16 °C (PX) / - 20 °C (EB)
Carrier gas	He
Detector	FID / 300°C
(Type/Temperature)	

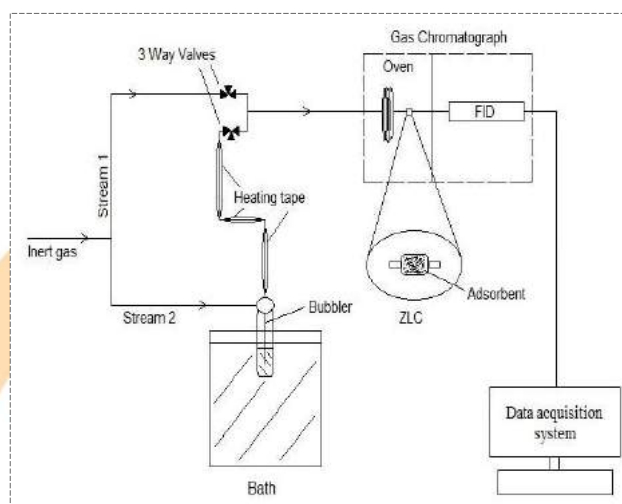


Figure 1. Schematic diagram of ZLC.

The sorbent was used in powder form, inside the column. The bath, which had a bubbler, where the liquid hydrocarbon, was used to control the temperature and pressure of the adsorbate. The concentration of the sorbate should be preferably within the Henry's Law region.

The line of transmission from the bath to chromatograph had a heating tape to eliminate condensation of the vapor in the tubing. The stream 2 of inert gas carried the adsorbate to saturate the adsorbent in the column. After reached the time to saturate the solid, the flow was changed by the stream 1, which had just inert gas to initiate the desorption. The variation of concentration, due to sorbate desorption, was measured by the detector (FID), and the data was monitored and saved by the computer. Since the sorbate is in low concentration from the zeolite layer after each experiment, several experiments could be performed without need for further regeneration of the sample. Prior to the experiments, the sample was regenerated at 150 °C overnight with the pure inert gas flow.

3. Results and discussion

3.1. Adsorbent properties

The textural properties were estimated from the physisorption of N₂ at 77 K. The particle diameter value was obtained from the particle size distribution. The values of these properties are presented in Table 2.

Table 2. Properties of the Beta zeolite.

BET surface area (m ² g ⁻¹)	440
Total pore volume (cm ³ g ⁻¹)	0.206
Micropore volume (cm ³ g ⁻¹)	0.170
Particle diameter (µm)	6

3.2. Validation of ZLC data

Prior to analysis with the adsorbent it is advisable to experiment with an empty column, free of solid (blank test), showed in Figure 2.

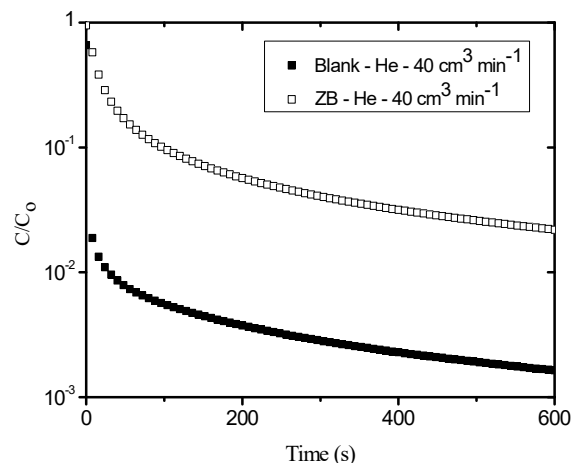


Figure 2. Desorption curves for MX at 80 °C.

This procedure allows evaluating the adsorption process is actually occurring from desorption curves. As can be seen in Figure 2, there is a significant difference between the curves for the experiments in the presence and absence of beta zeolite (ZB). The rapid decrease in the blank curve shows that there is no adsorption on the walls of the pipe and that the slower decrease of the c/c_0 signal in the curve with the zeolite is a function of the process of adsorption. This behavior was repeated for the tests with the other xylenes.

In order to ensure that the system is under equilibrium or kinetic control another test should be assessed, that include the c/c_0 vs Ft plot. A series of experiments with different flowrates should be carried out to evaluate the system. These experiments can be used to check if the ZLC desorption curves are consistent [12]. The plot of c/c_0 vs. Ft allows ensuring that equilibrium is being studied when the curves with different flowrates overlap. The same plot can be used to show that kinetic is controlling the system. The curves in Figure 3 show that curves at higher flowrates begin on a steeper descendent but after cross the curves at lower flowrates, which can indicate that the system is under kinetic control.

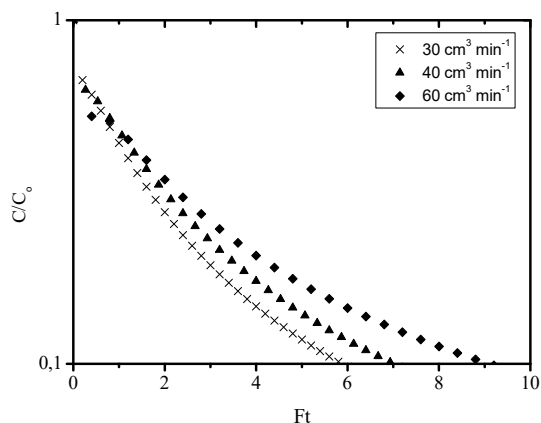


Figure 3. Experimental Ft vs C/C_0 plot for PX with distinct flowrates at 80 °C.

3.3. Short time analysis (ST)

In order to obtain the diffusional time constant (D/R_p^2) by the ST method, the spherical model [13] was used as a function of beta zeolite have two types of channels in a three-dimensional structure. Some results are shown in Table 3.

Table 3. Diffusional time constant by ST analysis

Sorbate	Temp. (°C)	D/R_p^2 (s ⁻¹) x 10 ⁴
OX	80	1.46
	120	2.91
MX	80	1.68
	120	3.12
PX	80	1.58
	120	2.79
EB	80	1.50
	120	3.39

The values calculated by the short time method presented a discrepancy from those obtained by the long time. This result may have occurred due to the high concentration of the sorbate, which could be outside the linear region (Henry). This condition is responsible for the presence of external resistance to the crystals, which significantly affects the analysis of the initial part of the desorption curve.

3.4. Long time analysis (LT)

The D/R_p^2 values calculated for the study components from LT are summarized in Table 4.

Table 4. Diffusional time constant by LT analysis

Sorbate	Temp. (°C)	D/R_p^2 (s ⁻¹) x 10 ⁴
OX	80	1.95
	120	2.66
MX	80	2.05
	120	2.59
PX	80	1.97
	120	2.56
EB	80	1.97
	120	3.00

The diffusivity values, which are obtained directly from the diffusional time constant, increased with raising of temperature, within the same order of magnitude. The estimated activation energies were within the range of 8-12 kJ.mol⁻¹. The values of the intracrystalline diffusivities, calculated using the crystal radius, were in the range of 10⁻¹⁵ m².s⁻¹ for all C₈ aromatics, which are about two orders of magnitude lower than the values for diffusivities of C₈ aromatics in faujasite type zeolites under similar conditions [3].

4. Conclusions

The evaluation of the intracrystalline diffusivity of the xylenes in the beta zeolite was performed using the zero-length column chromatography method (ZLC). This method uses a simple experimental apparatus that allows the determination of diffusivity, mainly, for hydrocarbons in porous materials.

The data obtained for the determination of the kinetic parameters of all components were validated from the experiments with different flow rates.

The values of the diffusional time constants obtained by long-time (LT) and short-time (ST) methodologies presented slight discrepancies. The calculation of these parameters from the short-time method is more reliable than that of LT, however they become imprecise since the concentration of adsorbate is high. The presence of external resistance, due to a high concentration of xylenes



(outside the Henry region), may have resulted in the observed discrepancy between the values.

Acknowledgements

The authors wish to thank financial support provided by CNPq (Conselho Nacional de Pesquisa e Desenvolvimento Científico) and FUNCAP (Fundação Cearense de Apoio ao Desenvolvimento Científico e Tecnológico).

References

- [1] Ruthven DM, Stapleton P. Measurement of Liquid Phase Counter-diffusion in Zeolite Crystals by the ZLC Method, *Chemical Engineering Science* 48, 89-98, 1993.
- [2] Goddard M, Ruthven DM. Sorption and diffusion of C₈ aromatic hydrocarbons in faujasite type zeolites. II. Sorption kinetics and intracrystalline diffusivities. *Zeolites*, v. 6, p. 283-289, 1986.
- [3] Minceva M, Rodrigues AE. Adsorption of Xylenes on Faujasite-Type Zeolite, Equilibrium and Kinetics in Batch Adsorber. *Chemical Engineering Research and Design*, v. 82, p. 667-681, 2004.
- [4] Higgins JB, LaPierre RB, Schlenker JL, Rohrman A C, Wood JD, Kerr GT, Rohrbaugh WJ. The framework topology of zeolite beta. *Zeolites*, v. 8, p. 446-452, 1988.
- [5] Treacy MMJ, Newsam JM. Two new three-dimensional twelve-ring zeolite frameworks of which zeolite beta is a disordered intergrowth. *Nature*, v. 332, p. 249-251, 1988.
- [6] Martínez-Iñesta MM, Peral I, Proffen T, Lobo RF. A pair distribution function analysis of zeolite beta. *Microporous and Mesoporous Materials*, v. 77, p. 55-66, 2005.
- [7] Ping L, Yue Y, Xingguang Z, Jun W. Rare Earth Metals Ion-exchanged β -Zeolites as Supports of Platinum Catalysts for Hydroisomerization of n-Heptane. *Chinese Journal of Chemical Engineering*, v. 19, p. 278-284, 2011.
- [8] Shen B, Wang P, Yi Z, Zhang W, Tong X, Liu Y, Guo Q, Gao J, Xu C. Synthesis of Zeolite β from Kaolin and Its Catalytic Performance For FCC Naphtha Aromatization. *Energy & Fuels*, v. 23, p. 60-64, 2008.
- [9] Xie B, Song J, Ren L, Ji Y, Li J, Xiao F. Organotemplate-Free and Fast Route for Synthesizing Beta Zeolite. *Chemistry of Materials*, v. 20, p. 4533-4535, 2008.
- [10] Yue Y, Liu H, Zhou Y, Bai Z, Bao X. Pure-phase zeolite beta synthesized from natural aluminosilicate minerals and its catalytic application for esterification. *Applied Clay Science*, v. 126, p. 1-6, 2016.
- [11] Eic M, Ruthven DM. A new experimental technique for measurement of intracrystalline diffusivity. *Zeolites*, v. 8, p. 40-45, 1988.
- [12] Brandani S. A Simple Graphical Check of Consistency for Zero Length Column Desorption Curves. *Chemical Engineering & Technology*, v. 39, p. 1194-1198, 2016.
- [13] Cavalcante Jr CL, Brandani S, Ruthven DM. Evaluation of the main diffusion path in zeolites from ZLC desorption curves. *Zeolites*, v. 18, p. 282-285, 1997.

Isotherm, kinetic and thermodynamic studies of Rhodamine B adsorption on coconut fiber-based adsorbents

Rogério José Melo Nascimento^a, Kilton R. A. Pereira^a, Francisco Avelino^{a*}

^aFederal Institute of Education, Science and Technology of Ceará, 63503-790, Iguatu, CE, Brazil

Abstract

In this work, the equilibrium, kinetic and thermodynamic mechanisms of Rhodamine B (Rh-B) adsorption process using crude and modified coconut fiber (CCF and MCF, respectively). CCF was chemically modified by formosolv process under mild conditions using 85 % wt. formic acid combined to 2.0 % v/v HCl as catalyst, yielding the MCF. The biosorbents were characterized using the following analyses: chemical composition, XRD and TGA. The adsorption assays were carried out in batch mode, in which the effects of adsorbent concentration, reaction time, initial concentration of Rh-B and temperature on adsorption capacity of RB in CF and TF were evaluated. The equilibrium experimental data were fitted to Langmuir and Freundlich isotherms, while the kinetic one were fitted to pseudo-first order, pseudo-second order, intraparticle diffusion and Elovich models. The experimental values of adsorption capacity at equilibrium of Rh-B using CCF and MCF showed a better fitting to the Freundlich isotherm under conditions at 298 K and 60 minutes. The pseudo-first and pseudo-second order models provided a better fitting for CCF and MCF, respectively, although it was also observed that the Rh-B adsorption in CCF and MCF can also occur by intraparticle diffusion. The thermodynamic parameters indicated that the adsorptive process of Rh-B on the biosorbents was spontaneous ($\Delta G^\circ < 0$), endothermic ($\Delta H^\circ > 0$), suggesting a chemical adsorption ($\Delta S^\circ > 0$) with a more spontaneous process for MCF. It can be concluded that a novel biosorbent can be produced from cheap and abundant agrowastes using a biorefinery process, showing a great potential for removing dyes from wastewater textiles.

Keywords: biomass valorization; formosolv; batch adsorption; adsorption mechanisms; modelling.

1. Introduction

Currently, the scientific community has investigated the features and potential of alternative adsorbents, such as lignocellulosic biomass residues [1,2] in the removal of toxic pollutants present in the wastewater. However, several chemical treatments are performed to obtain structural modifications on the lignocellulosic materials properties [1], in order to obtain better adsorptive performance.

Rhodamine B (Rh-B) is a basic organic dye, which is highly toxic and can be quite harmful to human health and aquatic organisms [3], being widely used by textile and foodstuff industries [4].

In this context, the aim of this work was to evaluate the isotherm, kinetic and thermodynamics parameters involved in the Rhodamine B adsorption using crude and modified coconut fiber as biosorbents.

2. Materials and methods

2.1. Adsorbent and adsorbate preparation

The crude coconut fiber was milled in a knife mill (Fritsch pulverisette 19) for size reduction using sieves with pores diameter (500 μm).

CCF was submitted to formosolv process for chemical modification. CCF (10 g) was added in a round-bottom flask, containing 100 mL of formic solution (85 % wt., Synth) and HCl (2 % v/v, Synth) as catalyst. The reaction was performed at 100 °C during 1 hour under reflux and atmospheric pressure.

UV-Vis spectrophotometer (Femto 700 Plus) was used to determine residual concentration of Rh-B ($\lambda_{\text{max}} = 479 \text{ nm}$) in the supernatant solution after adsorption assays. Figure 1 shows the calibration curve for synthetic solutions of Rh-B (5 at 100 ppm). The experiments were performed in triplicate.

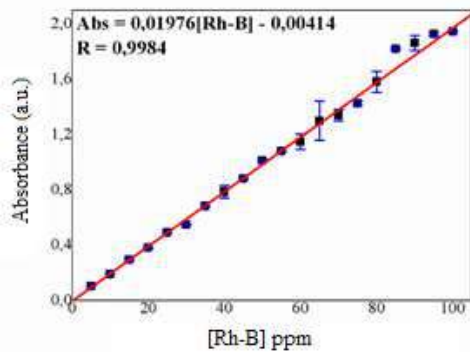


Figure 1 – Calibration curve of Rhodamine B.

2.2. Characterization of adsorbents materials

The methodology used for determining the chemical composition of CCF and MCF was carried out as reported by Nascimento et al. (2014) [5].

XRD analyses were performed in a X-ray diffractometer (PANanalytical X'pert PRO MPD), in the 2θ range from 5 to 50° using Co-K_α ray [5]. The crystallinity index (CI) was obtained from Equation 1:

$$\text{CI} = 1 - \frac{I_1}{I_2} \quad (1)$$

where I_1 I_2 are the minimum intensity related to the amorphous region ($2\theta = 21.5^\circ$) and maximum intensity related to the crystalline region ($2\theta = 26^\circ$), respectively.

2.3. Batch adsorption study

All batch adsorption experiments were performed under constant agitation (150 rpm), 25 mL of Rh-B for several initial concentrations (25, 50 and 75 ppm), adsorbent dosage (2, 3 and 4 g L⁻¹), reaction times (0 – 60 min) and temperatures (298, 308 and 318 K). For those experiments, a thermostatic shaker (Marconi MA-420) was used. The amount of Rhodamine B adsorbed on CCF and MCF at equilibrium time was calculated by using Equation 2 [6]:

$$q_{t,e} = \frac{(C_0 - C_{t,e})V}{M} \quad (2)$$

where C_0 and $C_{t,e}$ are the Rh-B concentrations, initial and at time t or equilibrium (mg L⁻¹), respectively; V (L) is the volume of Rh-B solution and M is the mass of biosorbent (g). The experiments were performed in triplicate.

2.4. Adsorption kinetic

For the kinetic study, four models were applied: pseudo-first order (PFO), pseudo-second order (PSO), intraparticle diffusion (ID) and Elovich, which were expressed at linear form according Equations 3, 4, 5 and 6, respectively [3,7].

$$\ln(q_e - q_t) = \ln q_e - K_1 \cdot t \quad (3)$$

$$\frac{t}{q_t} = \frac{1}{K_2 q_e^2} + \frac{1}{q_e} t \quad (4)$$

$$q_t = K_d t^{0.5} + C \quad (5)$$

$$q_t = \frac{1}{\beta} \ln(\alpha\beta) + \frac{1}{\beta} \ln(t) \quad (6)$$

where K_1 (min⁻¹) and K_2 (g mg⁻¹ min⁻¹) are the kinetic constants of PFO and PSO, respectively; K_d (mg g⁻¹ min^{-0.5}) is the intraparticle diffusion constant and C (mg g⁻¹) represents the diffusion resistance coefficient; α (mg g⁻¹ min⁻¹) is the initial adsorption rate, β (g mg⁻¹) is the constant related to the degree of coverage and the activation energy involved in the chemisorption process. The kinetic parameters were obtained from the slope and intercept of the plot for each model.

The evaluation and choice of the kinetic model that better describes the adsorption mechanism involved in the Rh-B adsorption was based on the correlation coefficient (R^2) and comparison of the calculated adsorptive capacity ($q_{e,calc}$) by the model and the experimental data ($q_{e,exp}$).

2.5. Equilibrium isotherms

Langmuir and Freundlich isotherms were applied for obtaining the equilibrium parameters. The linear Langmuir model is represented by Equation 7 [8]:

$$\frac{C_e}{q_e} = \frac{C_e}{q_m} + \frac{1}{K_L} \quad (7)$$

where q_m (mg g⁻¹) is the maximum adsorption capacity of Rh-B in CCF and MCF and K_L (L g⁻¹) is the Langmuir constant.

The linear form of the Freundlich model can be obtained according Equation 8 [4]:

$$\ln(q_e) = \frac{1}{n} \ln(C_e) + \ln(K_F) \quad (8)$$

where K_F and n are dimensionless constants related to the bonding energy and heterogeneity factor, respectively.



The values of adsorption isotherm constants were calculated from the slope and intercept of the plots and the choice of the isothermal model that best fitted the experimental data was based on the correlation coefficient (R^2). All graphs and modelling were performed using the software Excel.

2.6. Effect of temperature on adsorption

Different temperatures were investigated (298, 308 and 318 K) to determine the thermodynamic parameters (ΔH^0 , ΔS^0 and ΔG^0) involved in the Rh-B adsorption process using CCF and MCF. The thermodynamic parameters were calculated from Equations 9 and 10 [9]:

$$\ln\left(\frac{q_e}{C_e}\right) = -\frac{\Delta H^0}{RT} + \frac{\Delta S^0}{R} \quad (9)$$

$$\Delta G^0 = \Delta H^0 - \Delta S^0 T \quad (10)$$

where T (K) is the temperature; R is the gas constant ($8.314 \text{ J mol}^{-1} \text{ K}^{-1}$). The values of ΔH^0 and ΔS^0 were calculated from the slope and intercept values of $\ln(q_e/C_e)$ vs $1/T$ graph.

3. Results and discussion

3.1. Characterization of adsorbents

3.1.1. Chemical composition

Table 1 shows the chemical composition obtained for CCF and MCF.

Table 1. Chemical composition for samples fiber.

Component	CF (%)	TF (%)
Holocellulose	54.9 ± 2.2	55.1 ± 1.4
α -cellulose	23.3 ± 0.5	31.7 ± 0.2
hemicellulose	22.7 ± 0.8	14.3 ± 1.6
Insoluble lignin	27.41 ± 0.25	33.6 ± 0.9
Soluble lignin	0.03 ± 0.005	0.006 ± 0.002
Extractives	15.2 ± 0.48	1.04 ± 0.1
Ash	4.5 ± 0.1	1.2 ± 0.2

As can be seen in Table 1, the chemical treatment applied to the CCF by formosolv process promoted a reductions in its components content such as hemicellulose, lignin, ash and extractives, caused by the acid hydrolysis. The change caused in the chemical composition of the fiber led to modifications in its morphological, structural, thermal and textural properties, which can affect its

performance as an adsorbent material for removing dyes.

3.1.2. XRD analyses

Figure 2 shows XRD patterns obtained for CCF (a) and MCF (b). It was observed that both samples exhibited diffraction patterns typical of cellulose I [10], with peaks at 17.5° (plane 1 0 1) 18.9° (plane 1 0 $\bar{1}$), 26.1° (plane 0 0 2) and 40.6° (plane 0 4 0). The peaks observed (18.9° and 40.6°) for MCF (b) were more intense and defined in comparison of that to CCF(a). This indicates that the amorphous components present in the structure of lignocellulosic material were probably removed, corroborating with the values obtained for the CI values of 51.1% and 46.5% for CF and TF, respectively.

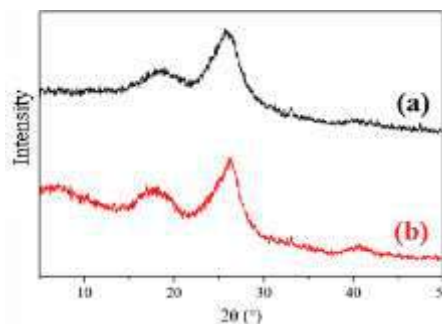


Figure 2 - X-Ray diffractograms: (a) CCF and (b) MCF.

3.2. Adsorption assays

Figures 3(a) and 3(b) show the behavior of adsorption capacity of Rh-B ($C_0 = 50 \text{ mg L}^{-1}$) onto CCF and MCF (4 g L^{-1}) at 25°C in time t and equilibrium, respectively. Figure 3(a) shows that MCF presented a high performance in the Rh-B adsorption when compared to CF, mainly between 20 and 60 minutes. It is also possible to observe that after this period there was no significant variations in the adsorption capacity values. The q_t values obtained at 60 min were 11.18 mg g^{-1} for MCF (at 90 min) and 4.61 mg g^{-1} for CCF (at 60 min).

The effects caused by increasing the initial concentration of Rh-B is shown in Figure 3(b). It can be noted that there was a significant increase in the q_e values from 6.41 mg g^{-1} in CCF to 17.00 mg g^{-1} in MCF. This demonstrates that the saturation of the material's surface did not occur and that there was an affinity of Rh-B molecules for lignocellulosic materials, especially for MCF. This

fact can be attributed to a higher exposure of binding sites (hydroxyl groups) present in its structure, causing a higher electrostatic interaction with the cationic dye [11].

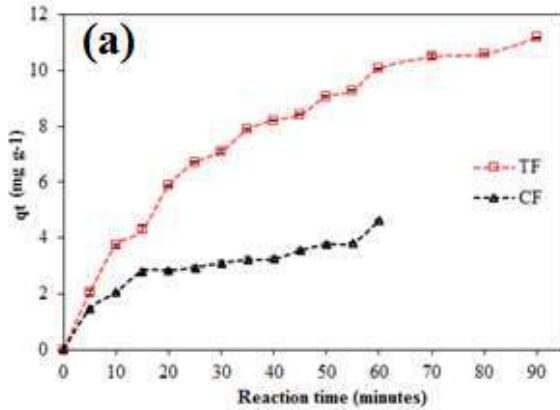


Figure 3 - Amount of Rh-B adsorbed per gram of CCF and MCF at (a) time t and (b) equilibrium.

3.3. Kinetic studies

Table 2 presents the kinetics parameters obtained from application of the models. It is observed that adjusted correlations were obtained in relation to the experimental data. However, the $q_{e,calc}$ values obtained by the models suggest that the PFO and PSO models describe the adsorption kinetics for MCF and CCF, respectively. Similar results have been observed in the adsorption of Rh-B in agro-industrial wastes [4] and modified coir pith [9]. It is also possible to verify the congruence of the data for the pseudo-first-order (PFO) and pseudo-second order (PSO) models to MCF and CCF, respectively, Figure 4.

Table 2. Kinetic parameters for Rh-B adsorption in CCF and MCF.

Model	Parameters	CCF	MCF
PFO	K_1	0.027	0.032
	$q_{e,calc}$	3.548	10.55
	R^2	0.934	0.941
PSO	K_2	0.022	0.003
	h	0.490	0.573
	$q_{e,calc}$	4.287	13.57
	R^2	0.965	0.935
ID	K_d	0.506	1.250
	C	0.324	-0.055
	R^2	0.951	0.983
Elovich	β	1.015	0.371
	α	0.998	1.836
	R^2	0.956	0.949

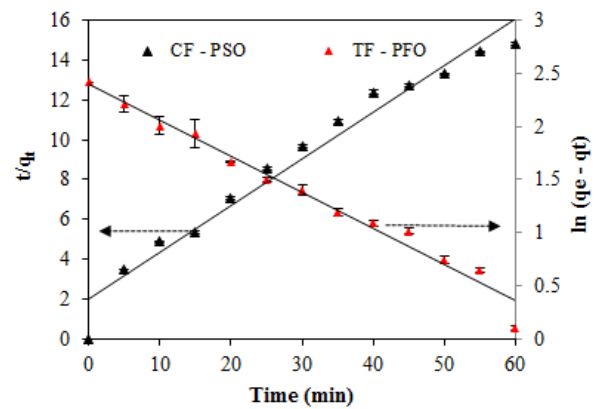
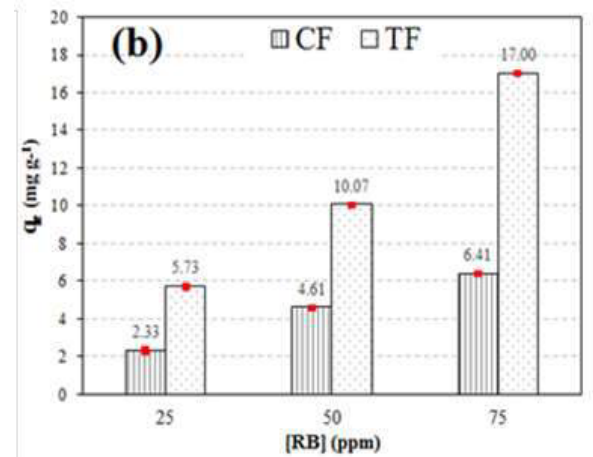


Figure 4 - Plots of the pseudo-second order kinetics for Rh-B adsorption in CCF and MCF.

These characteristics describe that the chemisorption controls the Rh-B adsorption process



by the lignocellulosic fibers [4], where interactions occur between hydroxyl groups of the fiber and cationic dye (Rh-B).

3.4. Equilibrium isotherms

Table 3 is presents the equilibrium parameters obtained from application of Langmuir and Freundlich models.

Table 3. Equilibrium parameters for Rh-B adsorption in CCF and MCF.

Model	Parameters	CCF	MCF
Langmuir	K_L	0.093	0.431
	q_{max}	5.16	17.48
	R^2	0.583	0.652
Freundlich	K_F	0.301	2.302
	n	1.41	1.10
	R^2	0.615	0.938

In Table 3, it is observed that the Freundlich isotherm presented the best fitting to the

experimental data for CCF and MCF, indicating that during the adsorption process the Rh-B molecules form multilayers, which are heterogeneous energetic distribution of active sites on the surface of the adsorbent material. K_F and n values were calculated from the slope and intercept of the plot of $\ln q_e$ vs $\ln C_e$.

The K_F value obtained for MCF (2.302) was much higher compared to that of CCF, demonstrating that there was a significant increase in the binding energy involved during the Rh-B adsorptive process. This fact may be associated with the presence of a greater number of active sites available in adsorbent. Figures 5(a) and 5(b) the plots of q_e vs C_e for the Rh-B adsorption onto CCF and MCF, respectively, based on the obtained equilibrium parameters.

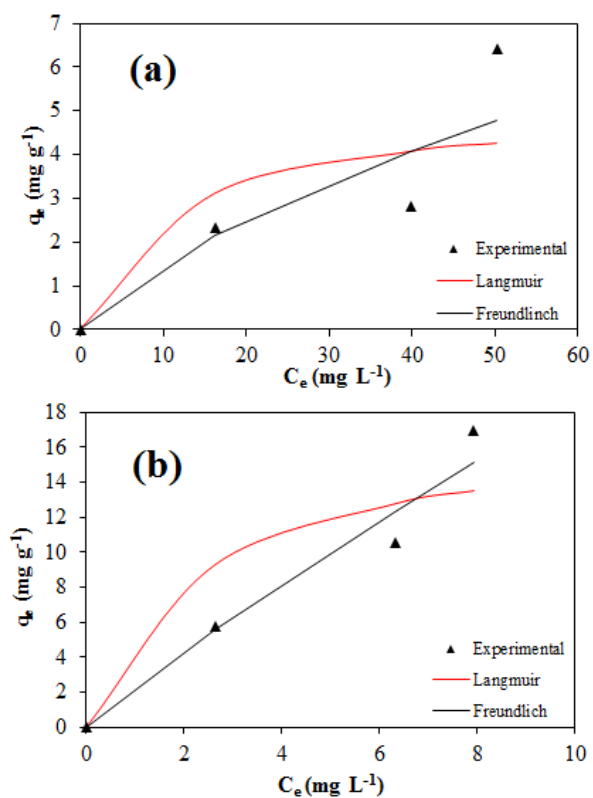


Figure 5 - Plots of q_e vs. C_e for Rh-B adsorption onto (a) CCF and (b) MCF.

3.5. Thermodynamic parameters

Table 4 show the thermodynamic parameters obtained in the Rh-B adsorption using CCF and MCF, while Figure 6 presents the plots of $\ln(q_e/C_e)$ vs $1/T$.

Table 4. Equilibrium parameters for Rh-B adsorption on CCF and MCF (initial [RB]: 50 mg/L, adsorbent dosage: 4 g L⁻¹).

Fiber	T (K)	ΔG^0 (kJ/mol)	ΔH^0 (kJ/mol)	ΔS^0 (J mol ⁻¹ K ⁻¹)
CF	298	-39.4	45.7	132.2
	308	-40.7		
	318	-42.0		
TF	298	-45.6	51.1	159.7
	308	-49.2		
	318	-50.7		

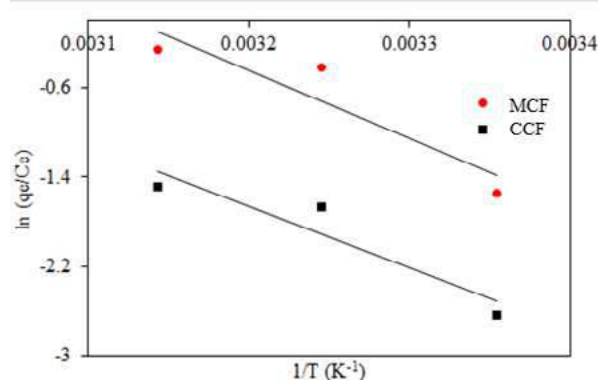


Figure 6 - Plots of $\ln(q_e/C_e)$ vs $1/T$ for Rh-B adsorption onto CCF and MCF.

From the results shown in Table 4, it can be observed that the Rh-B adsorption process on CCF and MCF occurs spontaneously ($\Delta G^0 < 0$) and is endothermic ($\Delta H^0 > 0$). The enthalpy values suggest that the process is driven by chemical adsorption ($\Delta H^0 > 40$ kJ / mol) [3]. In addition, for the analyzed temperature range, there was an increase in the adsorption capacity of the material, which is an indicative of positive entropy values, especially for MCF, corroborating with the results obtained for the equilibrium and kinetic experiments.

4. Conclusions

The formosolv process can be an alternative chemical treatment to modify the coconut fiber surface, improving its adsorptive features to remove Rh-B from aqueous solution.

The adsorption capacity of the MCF reached higher levels ($q_{e,max} = 17.00$ mg g⁻¹) compared to CCF ($q_{e,max} = 6.41$ mg g⁻¹), caused by the increase in number of hydroxyl groups (active sites).

The adsorption kinetics data showed good fitting for the pseudo-first order and pseudo-second order models for MCF and CCF, respectively. The Freundlich isotherms described the mechanism of

the adsorption process and the thermodynamic parameters indicated the occurrence of a chemisorption type process.

Acknowledgments

The authors acknowledge Brazilian agencies CNPq, CAPES and FUNCAP (DEP – 0164-00174.01.00/19) for the financial support, Laboratório de Raios X at UFC for XRD analyses, Dr. Niédja Fittipaldi for the assistance with XRD data and BSc. Luiz Carlos for the technical assistance in the adsorption assays.

References

- [1] P.F. Santos, J.B. Neris, F.H.M. Luzardo, F.G. Velasco, M.S. Tokumoto, R.S. Da Cruz, Chemical modification of four lignocellulosic materials to improve the Pb²⁺ and Ni²⁺ ions adsorption in aqueous solutions, *Journal of Environmental Chemical Engineering*. 7 (2019). <https://doi.org/10.1016/j.jece.2019.103363>.
- [2] N.B. Singh, G. Nagpal, S. Agrawal, Rachna, Water purification by using Adsorbents: A Review, *Environmental Technology and Innovation*. 11 (2018) 187–240. <https://doi.org/10.1016/j.eti.2018.05.006>.
- [3] T.A. Khan, S. Dahiya, I. Ali, Use of kaolinite as adsorbent: Equilibrium, dynamics and thermodynamic studies on the adsorption of Rhodamine B from aqueous solution, *Applied Clay Science*. 69 (2012) 58–66. <https://doi.org/10.1016/j.clay.2012.09.001>.
- [4] H. Parab, M. Sudersanan, N. Shenoy, T. Pathare, B. Vaze, Use of agro-industrial wastes for removal of basic dyes from aqueous solutions, *Clean - Soil, Air, Water*. 37 (2009) 963–969. <https://doi.org/10.1002/clen.200900158>.
- [5] D.M. Nascimento, J.S. Almeida, A.F. Dias, M.C.B. Figueirêdo, J.P.S. Morais, J.P.A. Feitosa, M.D.F. Rosa, A novel green approach for the preparation of cellulose nanowhiskers from white coir, *Carbohydrate Polymers*. 110 (2014) 456–463. <https://doi.org/10.1016/j.carbpol.2014.04.053>.
- [6] M.T. Yagub, T.K. Sen, M. Ang, Removal of cationic dye methylene blue (MB) from aqueous solution by ground raw and base modified pine cone powder, *Environmental Earth Sciences*. 71 (2014). <https://doi.org/10.1007/s12665-013-2555-0>.
- [7] F. Bagheban Shahri, A. Niazi, A. Akrami, Application of Full Factorial Design for Removal of Polycyclic Aromatic Dye from Aqueous Solution Using 4A Zeolite: Adsorption Isotherms, Thermodynamic and Kinetic Studies, *Polycyclic Aromatic Compounds*. 38 (2018) 141–156. <https://doi.org/10.1080/10406638.2016.1173074>.
- [8] G.D. Değermenci, N. Değermenci, V. Ayyaoğlu, E. Durmaz, D. Çakır, E. Akan, Adsorption of reactive dyes on lignocellulosic waste; characterization, equilibrium, kinetic and thermodynamic studies, *Journal of Cleaner Production*. 225 (2019) 1220–1229. <https://doi.org/10.1016/j.jclepro.2019.03.260>.
- [9] M. V. Sureshkumar, C. Namasivayam, Adsorption behavior of Direct Red 12B and Rhodamine B from water onto surfactant-modified coconut coir pith, *Colloids and Surfaces A: Physicochemical and Engineering Aspects*. 317 (2008) 277–283. <https://doi.org/10.1016/j.colsurfa.2007.10.026>.
- [10] J.T. Bonarski, W. Olek, Application of the crystalline volume fraction for characterizing the ultrastructural organization of wood, *Cellulose*. 18 (2011) 223–235. <https://doi.org/10.1007/s10570-010-9486-7>.
- [11] J.F. Duarte Neto, I.D.S. Pereira, V.C. Da Silva, H.C. Ferreira, D.G.A. Neves, R.R. Menezes, Study of equilibrium and kinetic adsorption of rhodamine B onto purified bentonite clays, *Ceramica*. 64 (2018) 598–607. <https://doi.org/10.1590/0366-69132018643722429>.

Amino-functionalized graphene oxide anchored in charcoal matrix as adsorbent of textile wastewater: characterization and adsorption properties

Tiago J. M. Fraga^a, Letticia E. L. Ferreira^{a,b}, Bruna F. Nascimento^a, Maryne P. da Silva^{a*}, Marcos G. Ghislandi^{a,c}, Eleonora M. P. de Luna Freire^a, Marilda N. Carvalho^a, Maurício A. da Motta Sobrinho^a

^a Department of Chemical Engineering, Federal University of Pernambuco (UFPE), 1235 Prof. Moraes Rego Av., Recife, Zip Code 50670-910, Brazil

^b Center of Bioscience, Federal University of Pernambuco (UFPE), Prof. Moraes Rego Av, W/N, Recife, Zip Code 50670-420, Brazil

^c Engineering Campus (UACSA), Federal Rural University of Pernambuco (UFRPE), 300 Cento e Sessenta e Três Av., Cabo de Santo Agostinho, Brazil

Abstract

Graphene and its derivatives play a prominent role nowadays in the development of catalysts and adsorbents due to their outstanding physic-chemical properties. In this sense, a novel amino-functionalized multilayer graphene oxide (mGO-NHR) was synthesized and anchored in charcoal obtained from gasification process with wood wastes. The nanocomposite was characterized by X-ray diffraction, infrared and Raman spectroscopies, dynamic light scattering and specific surface area. Characterization data evidenced that the mGO-NH was successfully grafted on wood charcoal surface, since infrared spectra showed characteristic bands of amine, amide and carboxyl groups. Moreover, Raman spectra exhibited the characteristic G and D band and an increase in I_D/I_G ratio from 1.05 to 1.31, after amino-functionalization, indicating an increase in disorder degree in sp^2 domain. Finally, adsorptive experiments with Methylene Blue showed that the charcoal monolayer adsorptive capacity increased from 45 to 54 $mg \cdot g^{-1}$ after the anchoring of mGO-NH over its surface and Langmuir isotherm was the one which best fitted the equilibrium data. Kinetic experiments showed that the equilibrium state was reached after 10 min, with experimental equilibrium adsorptive capacity 24.90 $mg \cdot g^{-1}$. Moreover, pseudo-first-order model best fitted the kinetic data.

Keywords: Graphene Oxide; functionalization; wood waste charcoal; nanosorbent; wastewater treatment

1. Introduction

In the last decade, the number of research involving the use of nanocomposites in different branches of Environmental Sciences and Technologies has grown greatly, due to the versatility of these materials. In this field, graphene nanosheets, a highly flexible material with excellent mechanical resistance, electrical and thermal conductivity, chemical selectivity, high specific surface area ($\sim 2630 \text{ m}^2 \cdot \text{g}^{-1}$), and other properties [1, 2] In order to increase the adsorption capacity of multilayer graphene oxide (mGO), several works reported in the literature have developed different functionalization routes in order to potentiate some of their properties [2]. Functionalization may occur covalently, where the

functional groups are bound to the surface and ends of the mGO by strong and high energy interactions, such as covalent bonds, which usually changes the sp^2 hybridization of their G networks, resulting in the formation of defects and changes of electronic properties. Non-covalent functionalization, on the other hand, can be obtained by employing functional groups that remain attached to the mGO plane by weak interactions, such as van der Waals forces, electrostatic interactions and π - π stacking interactions [2]. In this work, mGO was synthesized by modified Hummers method, functionalized with diethylenetriamine (DETA) [Fig. 1a] and concomitantly anchored in wood residue charcoal. The novel adsorbent was then employed in the adsorption of the cationic Methylene Blue (MB).

2. Experimental

2.1. Synthesis of mGO

Multilayer Graphene Oxide (mGO) was synthesized by the modified Hummers method [3]. 1.0 g of graphite powder (*Synth*, 99% A.P.) was added along with 25 ml of 99% H₂SO₄ (*Química Moderna*, 97% A.P.) in a flask, under agitation and temperature strictly controlled between 12–15°C. Thereafter, 3.0 g of KmNO₄ (*Dinâmica*, 99% A.P.) was slowly added and the temperature was adjusted to 32°C during 6 hours. Then, 35 mL of 30% v/v H₂O₂ was added to complete the oxidation. Then 200 ml of solution of HCl 25% was added and subsequently, the sample was successively washed with distilled water. After washing, the graphite oxide was exfoliated under sonication for 4h to obtain mGO nanomaterial.

2.2. Amino-functionalization of mGO and anchoring in wood charcoal

For amino-functionalization, an aliquot of 330.0 mL of go suspension (~ 0.0035 g·mL⁻¹) was separated and mixed with 250 mL of monoethylene glycol. In the sequence, it was added 1.0 g of wood residue charcoal, 3.0 g of sodium acetate and 30 ml of diethylenetriamine (DETA, *Sigma-Aldrich*, 99% A.P.) to the sample. The functionalization reaction occurred in batch mode in a 600 mL reflux reactor, with vigorous stirring for 6 hours and temperature controlled at 180°C. After the reaction, the mixture was cooled to room temperature (24°C). Subsequently, washed with 150 mL of ethanol and washed successively with distilled water. Finally the suspension was decanted and the supernatant was removed. Wood waste from school furniture in the city of João Pessoa/PB was used as the raw material of a fixed-bed gasifier (Fig. 1), having as its by-product the charcoal.

2.3. Characterization

The new adsorbent (mGO-NH-C) was characterized by X-Ray Diffraction (XRD), Fourier-Transform Infrared Spectroscopy (FTIR), Raman spectroscopy, Dynamic Light Scattering

(DLS) and Scanning Electron Microscopy (SEM) techniques.

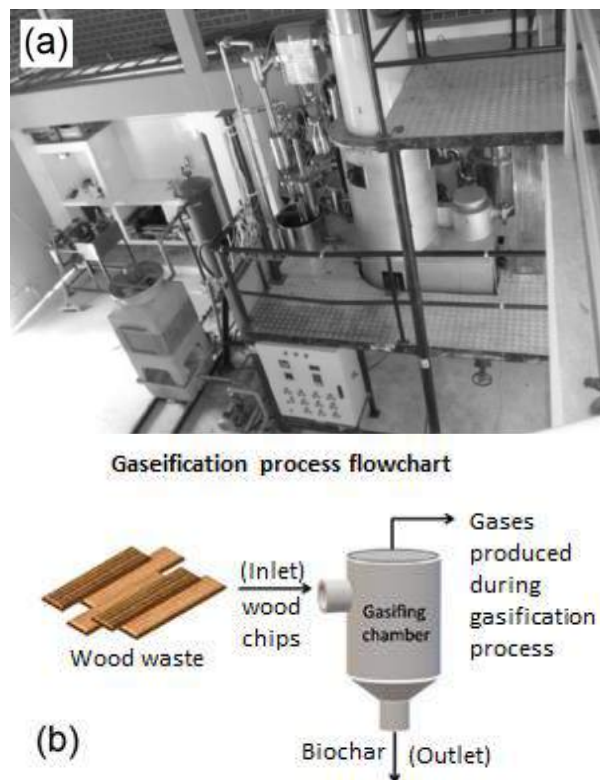


Fig. 1. a) photo of the gasifier installed in the Innovation Laboratory, DEM/UFPB; b) schematic illustration of the gasification process.

2.4. Adsorption experiments

Adsorption experiments were carried out in batch, with constant agitation and under the following conditions: environmental temperature and pH of the MB solution, 12.0. For that, 1.0 g of mGO-NH-C was added to aliquots of 25 mL of MB solution (with concentration determined according to the experiment performed), under stirring velocity of 300 rpm. For kinetic experiments, the contact time ranged from 1 to 120 min. For equilibrium experiments, the models of Langmuir (Eq. 2), Freundlich (Eq. 3), and Langmuir-Freundlich, L-F (Eq. 4) were fitted to experimental data. Moreover, for kinetic experiments, the models evaluated in this work were pseudo-first-order (PFO, Eq. 5), pseudo-second-order (PSO, Eq. 6) and the intraparticle diffusion (IPD, Eq. 7). Mathematical

modeling was performed by non-linear fit tool of in Origin™ 9.0 software.

The adsorption capacity (mg.g^{-1}) is given by the Eq. 1:

$$q = \frac{V(C_0 - C)}{m} \quad (1)$$

Where: q (mg.g^{-1}) is the adsorptive capacity; C and C_0 (mg.L^{-1}) are the final and initial concentration; V (L) is the volume of adsorbate; m (g) is the adsorbent dosage.

Equilibrium isotherms of Langmuir, Freundlich and L-F are respectively given by the following equations:

$$\frac{q}{q_m} = \frac{K_L C}{(1 + K_L C)} \quad (2)$$

$$q = K_f C^{1/n} \quad (3)$$

$$\frac{q}{q_m} = \frac{K_{LF} C^n}{(1 + K_{LF} C^n)} \quad (4)$$

Where q and q_m (mg.g^{-1}) are the adsorptive capacity by each concentration and in the monolayer, respectively; C (mg.L^{-1}) is the equilibrium concentration; K_L , K_f and K_{LF} are the adsorption equilibrium constant for Langmuir, Freundlich and L-F models; n is the heterogeneity factor.

Kinetic models are given by the following equations:

$$q_t = q_e(1 - e^{-k_f t}) \quad (5)$$

$$\frac{q}{q_m} = \frac{k_s q_e^2 t}{(1 + k_s q_e t)} \quad (6)$$

$$q_t = k_{ID} t^{1/2} + k_0 \quad (7)$$

Finally, the isoelectric point of the adsorbent was acquired by the 12 points assessment with salt solution (NaCl). mGO-NH-C samples were placed in flasks with 40 mL of solution and agitation for 24h. The pH was controlled with standard solutions of HCl and NaOH (6.0M and 0.1 M) and measured before and after the contact time.

3. Results and Discussion

3.1. Characterization

FTIR spectra (Fig. 2a) evidenced peaks at 1650 cm^{-1} , present in all samples, which are attributed to carbonyl (-C=O) stretching vibration. Moreover, peaks at 1570 cm^{-1} present in mGO-NH and mGO-NH-C spectra, attributed to amine groups. The presence of amine groups is evidenced too in narrowing of the band at 3500 cm^{-1} (-OH) after functionalization. Raman Spectroscopy (Fig. 2b) showed the disappearance of the peak at 2900 cm^{-1} after functionalization, which is referent of 2D band of the well-organized multi-layered structure of charcoal. Moreover, Raman spectra exhibited an increase of I_D/I_G ratio from 1.05 to 1.31 after mGO functionalization. According to reported works, increases in I_D/I_G ratio are indicatives of increases in disorder degree, associated to chiralities, defects and impurities [4,5]. The insertion of functional moieties between graphene layers and in their edges provokes a disorder in sp^2 domain, which results in increases in I_D/I_G ratio. Isoelectric point analysis showed that the pH_{PZC} was 8.1 (Fig. 2c). Finally, DLS specific surface area of mGO-NH-C was $0.30 \text{ m}^2 \cdot \text{g}^{-1}$.

X-ray diffractograms showed that peaks at 26.5° and 54.6° , diffraction planes (002) and (004), referring to the basal planes of the graphene, were observed in addition to the plane (101) in 44.5° , characteristic of 3D crystalline graphite. The plane (002) is quite narrow and intense. XRD patterns of the synthesized mGO and mGO-NH show the same behavior (Fig. 2c), and there is an indication of an amorphous band characteristic of non-crystalline materials. Amorphous traces of the peak related to plane (002) were shifted to 25.5° and suggest that the oxidation of graphite structure was not sufficient to oxidize 100% of the layers. For the charcoal, it is verified an amorphous characteristic, since there are no defined peaks from 2θ 0– 25° ; however, a certain degree of crystallization can be observed due to the appearance of the peak at 27° .

SEM images of charcoal, mGO and mGO-NH are depicted in Fig. 3a, b and c, respectively, and evidence the porous structure of wood waste charcoal. After amino-functionalization, the mGO morphology showed wrinkles and folds, characteristic of aggregation and re-stacking of successive mGO nanosheets.

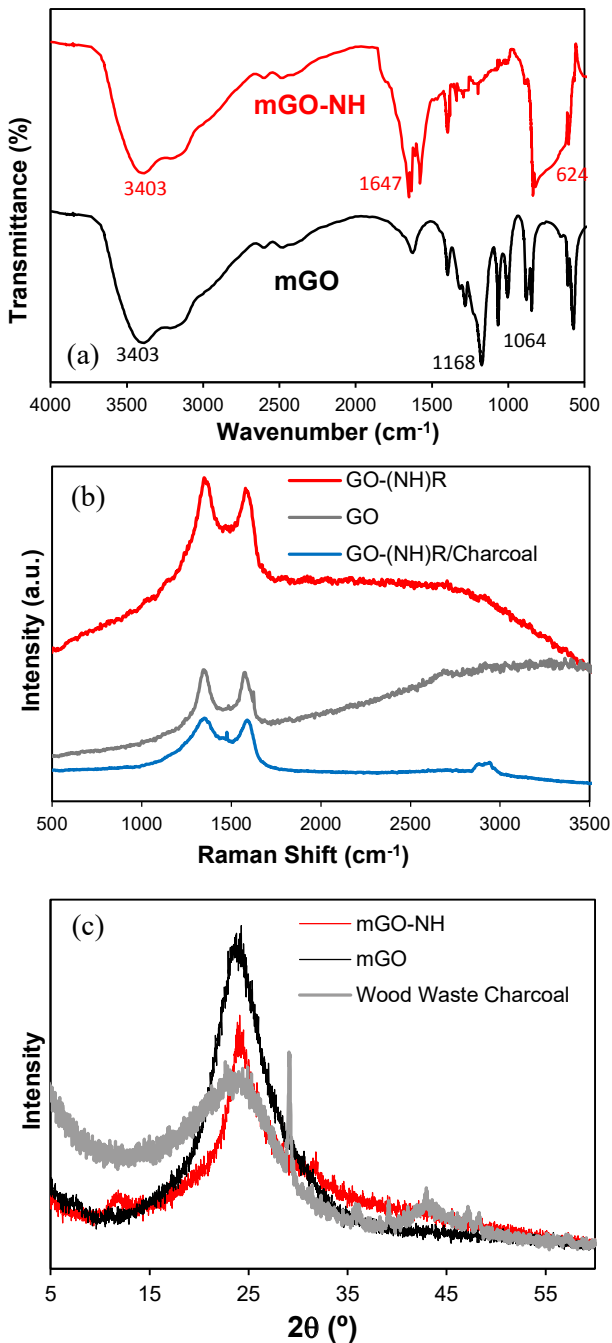


Fig. 2. a) FTIR spectra for mGO, mGO-NH and mGO-NH-C; b) Raman spectra for mGO, mGO-NH and mGO-NH-C; c) XRD patterns of mGO, mGO-NH and charcoal.

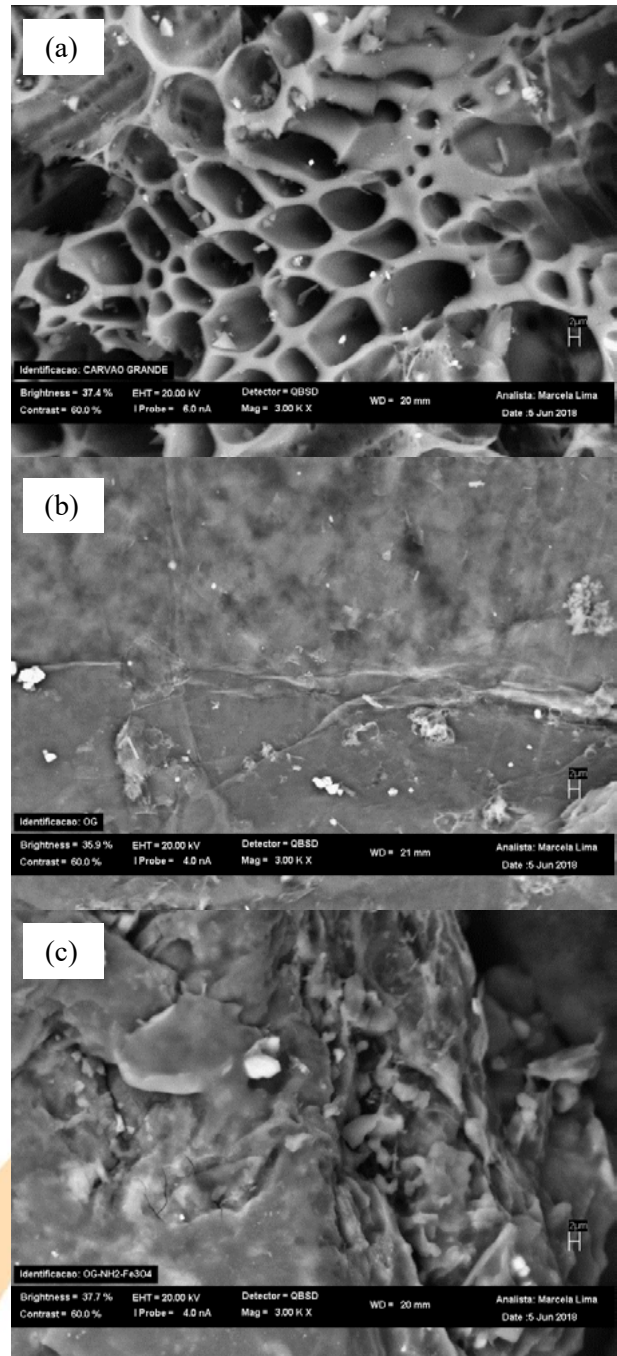


Fig. 3. SEM microscopy of: a) wood waste charcoal; b) mGO; c) mGO-NH. Magnification of 3000 x.

3.2. Adsorption of Methylene Blue

The isoelectric point (pH_{PZC}) for mGO-NH-C was 8.10 (Fig. 4a). Equilibrium experiments, carried out for MB removal, revealed that the mGO-NH-C saturated from 100 mg.L^{-1} , and showed a maximum experimental adsorptive capacity (q_m^{exp}) of nearly 54.0 mg.g^{-1} . Moreover, from the mathematical modeling, it is observed that Langmuir model was the one which best fitted the equilibrium data (Fig. 4b), with satisfactory coefficient of determination (R^2 0.971). Equilibrium parameters are described in Table 1. Kinetic experiment showed that the equilibrium state was reached within 10 min (Fig. 4c), with experimental equilibrium adsorption capacity (q_e^{exp}) of 24.90 mg.g^{-1} . The model of PFO best fitted the experimental data with coefficient of determination 0.999, thus the chi-square factor (χ^2) for this model was slightly lower than PSO (Table 2). Kinetic parameters are described in Table 2. PSO fitting leads to the conclusion that the adsorption mechanism is governed by bulk resistance to mass transfer, than the intrapore diffusion [6,7], since IPD model did not show a good fit (R^2 0.009).

Table 1. equilibrium parameters for the adsorption of MB by mGO-NH-C.

	Langmuir	Freundlich	L-F
q_m	52.98	K_f 17.59	q_m 50.07
K_L	0.76	n 4.52	K_{LF} 0.67
R_L	0.003		n 0.86
R^2	0.971	R^2 0.879	R^2 0.969
χ^2	14.33 6	χ^2 60.625	χ^2 15.540

Where q_m is given in (mg.g^{-1}), K_L and K_{LF} are given in (L.mg^{-1}) and K_f is given in (mg.L^{-1}).

Table 2. Kinetic parameters for MB adsorption

	PFO	PSO	IPD
q_e	24.67	q_e 24.82	k_0 16.194
k_f	4.32	k_s 1.969	k_{ID} 2.75
R^2	0.999	R^2 0.999	R^2 0.009
χ^2	0.001	χ^2 0.002	χ^2 79.112

Where q_e and k_0 are given in (mg.g^{-1}), k_f is given in (min^{-1}) and k_s is given in ($\text{g.mg}^{-1}.\text{min}^{-1}$)

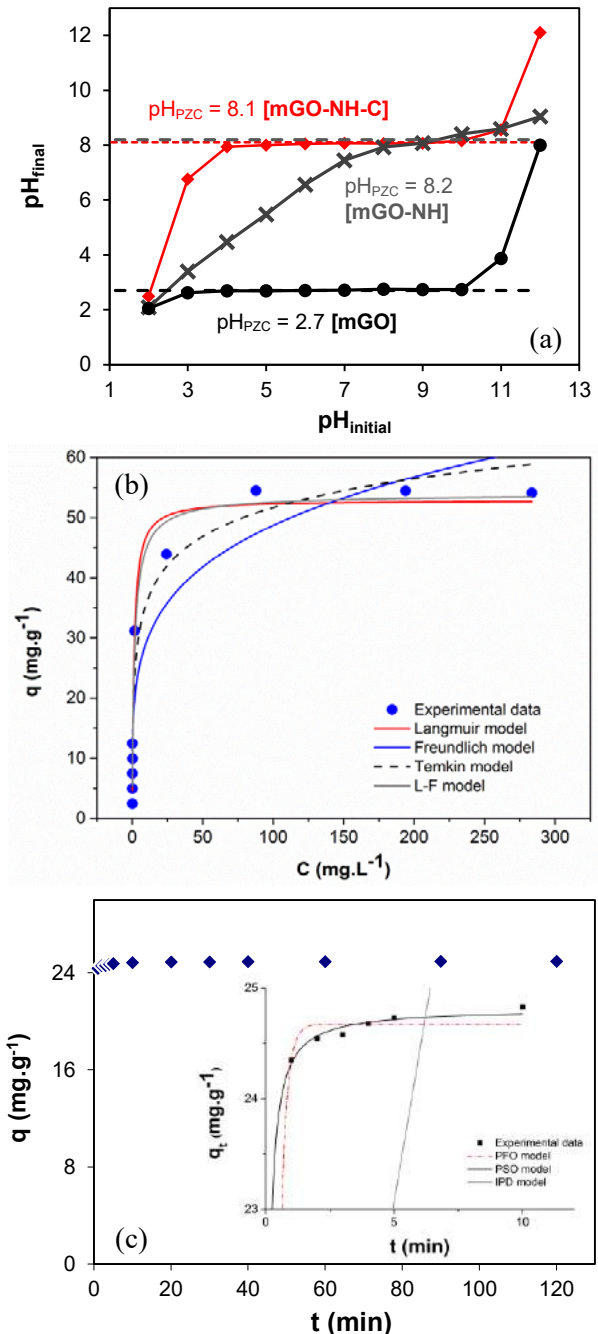


Fig. 4. a) isoelectric point of mGO-NH-C; b) equilibrium data and isotherms for the adsorption of MB; c) kinetic data for the adsorption of MB by mGO-NH-C.

4. Conclusions

Wood residues were benefited by gasification process and were employed as support for mGO-NH anchoring. Multilayer graphene oxide (mGO) was synthesized by the modified Hummers method and then submitted to covalent functionalization to insert nitrogen organic functional groups over mGO surface. Characterization data exhibited the presence of characteristic peaks in FTIR spectra, related to the presence of amines and amides in the sample. Raman spectra evidenced an increase in the disorder degree after amino-functionalization of the mGO. Finally, the novel adsorbent was then tested in the removal of the cationic MB dye with monolayer adsorptive capacity of 52.98 mg.g⁻¹ and the Langmuir model best fitted the experimental data. Kinetic experiments showed that the adsorption of MB took place quickly (within 10 min) and both PFO and PSO models showed satisfactory fit. These data evidence that mGO-NH-C can be applied as adsorbent of cationic dyes, with easy separation in comparison to hydrophilic mGO.

Acknowledgements

The authors acknowledge the financial support provided by the *Fundação de Apoio à Ciência e Tecnologia do Estado de Pernambuco* (FACEPE) and the *Conselho Nacional de Desenvolvimento Científico e Tecnológico* (CNPq). Moreover, the authors also acknowledge the technical support provided by the *Laboratório de Análises de Minerais, Solos e Água* of UFPE, the *Centro de Pesquisas Avançadas em Grafeno, Nanomateriais e Nanotecnologias* (MackGraphe)/Universidade Presbiteriana Mackenzie, São Paulo-SP, the *Centro de Tecnologias Estratégicas do Nordeste* (CETENE).

References

- [1] Park S, Ruoff SR. Chemical methods for the production of graphenes. *Nat. Nanotechnol.* 2009;5:217-224.
- [2] Eigler S, Hirsch A. Chemistry with graphene and graphene oxide – challenges for synthetic chemists, *Angew. Chem. Intl. Ed.* 2014;53:2–21.
- [3] Hummers WS, Offeman RE. Preparation of Graphitic Oxide. *J. Ame. Chem. Soc.* 1958;80(6):1339–1339.
- [4] Ferrari AC, Meyer JC, Scardaci V, Casiraghi C, Lazzeri M, Mauri F, Piscanec S, Jiang D, Novoselov KS, Roth S, Geim AK. Raman spectrum of graphene and graphene layers. *Phys. Rev. Lett.* 2006;97:1–4.
- [5] Englert JM, Dotzer C, Yang G, Schmid M, Papp C, Gottfried JM, Steinrück HP, Spiecker E, Hauke F, Hirsch A. Covalent bulk functionalization of graphene. *Nat. Chem.* 2011;3:279–286.
- [6] Fraga TJM, de Souza ZSB, Marques Fraga DMS, Carvalho MN, Luna Freire EMP, Ghislandi MG, da Motta Sobrinho MA. Comparative approach towards the adsorption of Reactive Black 5 and methylene blue by n-layer graphene oxide and its amino-functionalized derivative. *Adsorption* (in press) 2019. <https://doi.org/10.1007/s10450-019-00156-9>
- [7] Ganesan V, Louis C, Damodaran SP. Graphene oxide-wrapped magnetite nanoclusters: a recyclable functional hybrid for fast and highly efficient removal of organic dyes from wastewater. *J. Environ. Chem. Eng.* 2018;6(2):2176–2190.

Removal of the Drimaren Red from aqueous solutions by adsorption onto amino-Fe₃O₄-functionalized multilayer Graphene Oxide

Tiago J. M. Fraga^a, Caroline M. B. de Araújo^a, Letícia E. L. Ferreira^b, Maryne P. da Silva^{a*}, Marilda N. Carvalho^a, Eleonora M. P. Luna Freire^a, Jorge V. F. L. Cavalcanti^a, Marcos G. Ghislandi^{a,c}, Maurício A. da Motta Sobrinho^a

^a Department of Chemical Engineering, Federal University of Pernambuco (UFPE), 1235 Prof. Moraes Rego Av., Recife, Zip Code 50670-910, Brazil

^b Center of Bioscience, Federal University of Pernambuco (UFPE), Prof. Moraes Rego Av, W/N, Recife, Zip Code 50670-420, Brazil

^c Engineering Campus (UACSA), Federal Rural University of Pernambuco (UFRPE), 300 Cento e Sessenta e Três Av., Cabo de Santo Agostinho, Brazil

Abstract

Multilayer graphene oxide (mGO) has been produced from the oxidation of graphite and successive exfoliation according to modified Hummers method. Aiming to improve mGO adsorptive efficiency, the nanomaterial was submitted to amino-functionalization with diethylenetriamine and magnetite anchoring via solvothermal method, generating the novel amino-Fe₃O₄-functionalized multilayer graphene oxide (mGO-NH-Fe₃O₄). The nanocomposites were characterized by atomic force microscopy, infrared and Raman spectroscopies, X-ray diffraction and dynamic light scattering techniques. Furthermore, mGO-NH-Fe₃O₄ was employed as nanosorbent of the anionic dye Drimaren Red (DR) from aqueous media. Maximum monolayer adsorption capacity was 219.75 mg.g⁻¹ and the Brunauer-Emmett-Teller isotherm best fitted the experimental data. Kinetic experiments were carried out and the time in which the equilibrium was reached was 120 min, with experimental adsorptive capacity 172.00 mg.g⁻¹. This satisfactory results leads to excellent perspectives to employ mGO-NH-Fe₃O₄ as a profitable nanosorbent of textile wastewaters, once the techniques of production and scale-up is mastered.

Keywords: Multilayer Graphene Oxide; Reactive dye; Adsorption; nanomaterials; covalent functionalization

1. Introduction

The impact of textile dyes on the environment has been a matter of great concern to the governments of several countries and the scientific community, as these substances can cause the death of microorganisms responsible for photosynthesis and the degradation of water bodies, if are disposed of without proper treatment [1]. In this scenario, many methods for treating effluents from the textile industry have been proposed. Among a number of materials used in textile dye adsorption, carbon nanocomposites stand out, which has been the subject of several recent studies. Among these carbonaceous materials, graphene has attracted huge worldwide research interest due to its unique structural characteristics and high adsorption performance. It is worthy to mention some of the outstanding properties of graphene nanosheets:

high specific surface area (theoretical ~ 2632 m².g⁻¹), high mechanical and thermic resistances, flexibility, transparency, between others [2,3]. Therefore, there has been a growing interest among the scientific community in investigating different aspects, particularly surface modification, of graphene [1,4]. The functionalization of graphene nanosheets can take place via covalent routes, in which the functional groups stays linked to graphene basal plane through strong interactions of covalent nature; and by non-covalent routes, in which, the ligands are attached to graphene structure by weak interactions, such as van der Waals forces, electrostatic and π - π stacking interactions, London forces, etc. [1]. In the present work, the performance of amino-Fe₃O₄-functionalized multilayer graphene oxide (mGO-NH-Fe₃O₄) was evaluated as adsorbent of Drimaren Red (DR). The kinetic and adsorption equilibrium



models and parameters of DR adsorption were carefully evaluated.

2. Materials and Methods

2.1. Synthesis of mGO

Multilayer Graphene Oxide (mGO) was synthesized by the modified Hummers method [5]. 1.0 g of graphite powder (*Synth*, 99% A.P.) was added along with 25 ml of 99% H₂SO₄ (*Química Moderna*, 97% A.P.) in a flask, under agitation and temperature strictly controlled between 12–15°C. Thereafter, 3.0 g of KmNO₄ (*Dinâmica*, 99% A.P.) was slowly added and the temperature was adjusted to 32°C during 6 hours. Then, 35 mL of 30% v/v H₂O₂ was added to complete the oxidation. Then 200 ml of solution of HCl 25% was added and subsequently, the sample was successively washed with distilled water. After washing, the graphite oxide was exfoliated under sonication for 4h to obtain mGO nanomaterial.

2.2. Amino-functionalization of mGO and solvothermal method for Fe₃O₄ anchoring

For amino-functionalization, an aliquot of 330.0 mL of go suspension (~ 0.0035 g·mL⁻¹) was separated and mixed with 250 mL of monoethylene glycol. In the sequence, it was added 0.5 g of FeCl₃·6H₂O (*Dinâmica*, 99% A.P.), 3.0 g of sodium acetate (*Sigma-Aldrich*, 99% A.P.) and 30 ml of diethylenetriamine (DETA, *Sigma-Aldrich*, 99% A.P.) to the sample. The functionalization reaction occurred in batch mode in a 600 mL reflux reactor, with vigorous stirring for 6 hours and temperature controlled at 180°C. Both amino-functionalization and the non-covalent anchoring of Fe₃O₄ nanoparticles over mGO structure took place simultaneously. After the reaction, the mixture was cooled to room temperature (24°C). Subsequently, washed with 150 mL of ethanol and washed successively with distilled water. Finally the suspension was decanted and the supernatant was removed.

2.3. Characterization

The new adsorbent (mGO-NH-Fe₃O₄) was characterized by Fourier-Transform Infrared Spectroscopy (FTIR), Raman spectroscopy, X-Ray

Diffraction (XRD), Dynamic Light Scattering (DLS) and Atomic Force Microscopy (AFM) techniques.

2.4. Adsorption experiments

Adsorption experiments were carried out in batch, with constant agitation and under the following conditions: environmental temperature and pH of the DR solution, 12.0. For that, 1.0 g of mGO-NH-Fe₃O₄ was added to aliquots of 25 mL of DR solution (with concentration determined according to the experiment performed), under stirring velocity of 300 rpm. For kinetic experiments, the contact time ranged from 1 to 120 min. For equilibrium experiments, the following models were fitted to experimental data: Langmuir (Eq. 2), Freundlich (Eq. 3), and Temkin (Eq. 4) and BET adapted for liquid-solid interfaces (Eq. 5) [6]. Moreover, for kinetic experiments, the models evaluated in this work were pseudo-first-order (PFO, Eq. 6), pseudo-second-order (PSO, Eq. 7) and the intraparticle diffusion (IPD, Eq. 8). Mathematical modeling was performed by non-linear fit tool of in Origin™ 9.0 software.

The adsorption capacity (mg·g⁻¹) is given by the Eq. 1:

$$q = \frac{V(C_0 - C)}{m} \quad (1)$$

Where: q (mg·g⁻¹) is the adsorptive capacity; C and C₀ (mg·L⁻¹) are the final and initial concentration; V (L) is the volume of adsorbate; m (g) is the adsorbent dosage.

Equilibrium isotherms of Langmuir, Freundlich Temkin and BET are respectively given by the following equations:

$$\frac{q}{q_m} = \frac{K_L C}{(1 + K_L C)} \quad (2)$$

$$q = K_f C^{1/n} \quad (3)$$

$$q = \frac{RT}{bT} \ln(a_T C) \quad (4)$$

$$q = q_m \left[\frac{K_s C}{(1 + K_L C)(1 - K_L C - K_s C)} \right] \quad (5)$$

Where q and q_m ($\text{mg}\cdot\text{g}^{-1}$) are the adsorptive capacity by each concentration and in the monolayer, respectively; C ($\text{mg}\cdot\text{L}^{-1}$) is the equilibrium concentration; K_L ($\text{L}\cdot\text{g}^{-1}$) and K_f are the adsorption equilibrium constant for Langmuir and Freundlich models; n is the heterogeneity factor; a_T and b_T ($\text{kJ}\cdot\text{mol}^{-1}$) are Temkin constants; finally, K_1 , K_s are constants for BET model related to the coverage.

Kinetic models are given by the following equations:

$$q_t = q_e(1 - e^{-k_f t}) \quad (6)$$

$$\frac{q}{q_m} = \frac{k_s q_e^2 t}{(1 + k_s q_e t)} \quad (7)$$

$$q_t = k_{ID} t^{1/2} + k_0 \quad (8)$$

3. Results and Discussion

3.1. Characterization of mGO and mGO-NH-Fe₃O₄

FTIR spectra for mGO and mGO-NH-Fe₃O₄ are depicted in Fig. 1a and exhibited the characteristic peaks at 1632.5 cm^{-1} , attributed to the mGO carbonyl ($-\text{C}=\text{O}$) stretching vibration; a wide band appeared between at 3427 and 3250 cm^{-1} and is referent to the O-H stretching vibration of carboxylic groups of mGO [7], this band was also revealed at mGO-NH-Fe₃O₄ spectrum. However, bands with medium intensity between 3300 and 3500 cm^{-1} might be attributed to $-\text{NH}$ stretching vibration of amine groups on the sorbent surface. In the spectrum of mGO-NH-Fe₃O₄, the peak at 580 cm^{-1} is attributed to the Fe-O bond vibration of Fe₃O₄ nanoparticles in the sorbent [8]. N-H bond is represented by peaks at 1572.5 cm^{-1} and is caused by the stretching vibration and bending vibration; this is regarded to the presence of amino groups on the surface of the functionalized graphene [9]. Additionally, the intense peak at 1658.0 cm^{-1} might be attributed to amide groups, caused by parallel reactions during the functionalization synthesis.

Raman spectra of mGO, mGO-NH-Fe₃O₄ and graphite powder are compared in Fig. 1b. The spectra of all carbon systems have a set of characteristic bands; the main bands are the D band

($\sim 1360 \text{ cm}^{-1}$) and G band ($\sim 1560 \text{ cm}^{-1}$), as well as few other second order harmonics. Moreover, it is observed an increase in I_D/I_G rate from 1.22 to 2.80 after mGO functionalization (Fig. 1b). This is an evidence of a decrease in sp^2 carbon domain with the introduction of sp^3 defective sites, which are related to new Raman vibrational modes [10]. Moreover, increase in I_D/I_G ratio is an indicative of an extent of sp^3 disorder in bonded graphitic domain [2]. Morphologically, the intensity of I_D/I_G ratio can be used to describe disorder degree due to edges defects, chiralities, ripples, charged impurities, presence of domain boundaries, among others [10].

Graphite powder, mGO and mGO-NH-Fe₃O₄ were characterized by XRD (Fig. 1c) and compared to the standard of graphite (JCPDS 75-2078, $3,347 \text{ \AA}$). For graphite, the peaks equal to 26.5° and 54.6° , diffraction planes (002) and (004), referring to the basal planes of the graphene, were observed in addition to the plane (101) in 44.5° . All these peaks are characteristic of three-dimensional crystalline graphite [7,10]. The plane (002) is quite narrow and intense. The spectra of the synthesized mGO and mGO-NH-Fe₃O₄ show the same behavior (Fig. 1c), there is an indication of an amorphous band characteristic of non-crystalline materials, such as few layer graphene; however, it is possible to notice the presence of small peaks.

AFM analysis showed the presence of some flakes with thickness peaks smaller than 2.0 nm in mGO sample (Fig. 2a). Additionally, mGO average thickness was 5.79 nm and mean square roughness (RMS) 9.31 nm , data measured through 30 profiles. Differently, mGO-NH-Fe₃O₄ exhibited an average thickness of 8.43 nm , RMS 12.14 nm and the sample exhibited small agglomerated packs of nanoflakes, that reached 41.99 nm of maximum thickness (Fig. 2b). According to the international standard ISO TS 80004/2017, as a matter of nomenclature, graphene can be considered as nanosheets or nanoblocks with a maximum stacking of 10 nanolayers for electrical measurements [10,11]. It is important to note that most of mechanic exfoliation methods are not sufficient to fully exfoliate graphite oxide, since several monolayers of GO remain stacked one to others by interactions between their functional moieties.

Finally, the dynamic light scattering showed that the average particle size for mGO and mGO-NH-

Fe₃O₄ were 16.36 μm and 17.09 μm, respectively. The increase in particle size is another indicative of re-stacking of graphenic nanosheets due to the amino-functionalization. Furthermore, specific surface area measured by this technique was 0.367 m².g⁻¹ and 0.351 m².g⁻¹ for mGO and mGO-NH-Fe₃O₄, respectively. However, it must be carefully taken into account, since nanometric particles can influence the scattering of laser light, which might lead to false results, according to reported in the literature [12].

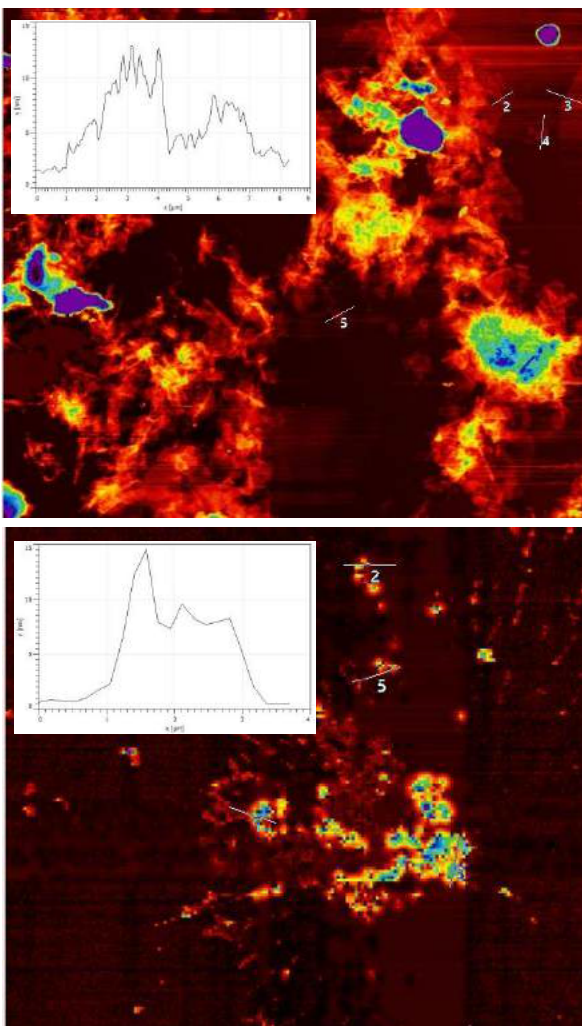


Fig. 1. AFM images for mGO (a) and mGO-NH-Fe₃O₄ (b), with their respective profiles assessment. Source: adapted from Fraga *et al.* (2019) [10], with permission from Springer-Nature, Copyright 2019.

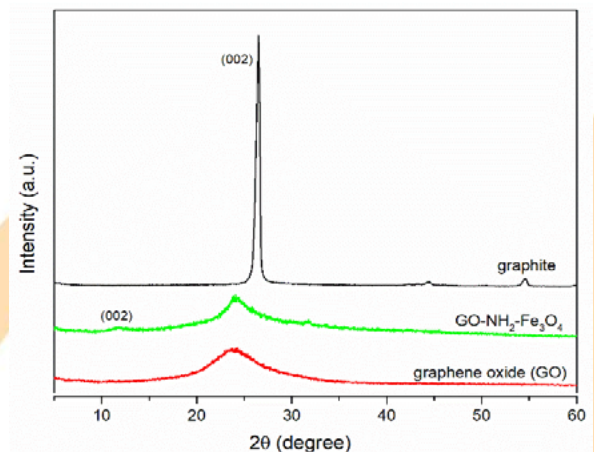
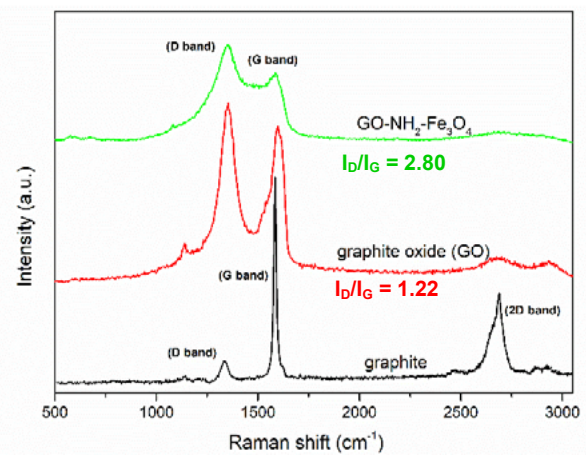
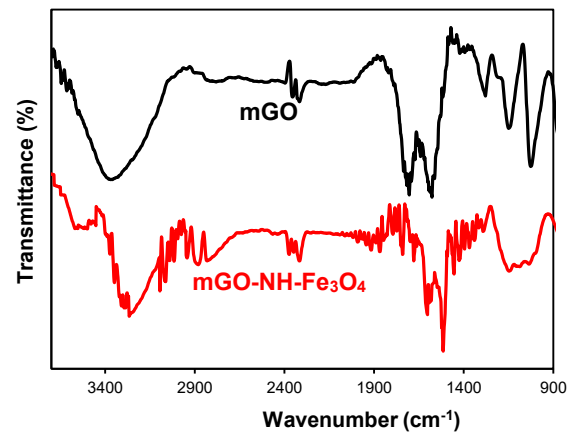


Fig. 2. a) FTIR spectra for mGO and mGO-NH-Fe₃O₄; b) Raman spectra of mGO and mGO-NH-Fe₃O₄ adapted from Fraga *et al.* (2018) [7], with permission from Springer-Nature, Copyright 2019; c) XRD patterns of graphite powder, mGO-NH-Fe₃O₄ and mGO, reproduced from Fraga *et al.* (2018) [7], with permission from Springer-Nature, Copyright 2019.

3.2. Adsorption of DR by mGO-NH-Fe₃O₄

The chemical structure of DR is depicted in Fig. 3, as well as its properties summarized in the caption.

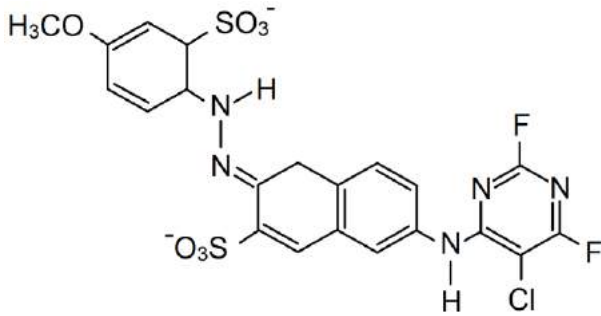


Fig. 3. molecular structure of the reactive Drimaren Red, molecular weight 584.93 g·mol⁻¹; maximum wavelength (λ_{\max}) 540 nm; supplier: Clariant do Brasil S/A.

As it can be seen, equilibrium data was poorly adjusted to Langmuir, Freundlich and Temkin isotherms. This is verified in the correlation coefficients (R^2) were all below 0.87 (Table 1), and the χ^2 values were also very high, ranging from 10,000 to 45,150. A satisfactory adjustment, however, was observed for the BET model, which followed experimental data (Fig. 4d). In this situation, the R^2 value was near 0.95, and χ^2 was at least less than a half compared to those from other models. Kinetics experiments showed that the adsorption of DR by mGO-NH-Fe₃O₄ reached the equilibrium state within 25 min. PSO model better fitted the experimental kinetic data (Fig. 5) in comparison to the other two models evaluated (R^2 0.982), with k_s 0.02 g·mg⁻¹·L⁻¹ and equilibrium sorption capacity (q_e) 172.00 mg·g⁻¹.

Table 1. equilibrium parameters acquired from the modeling for DR adsorption by mGO-NH-Fe₃O₄

Langmuir		Freundlich		Temkin		BET	
Param.	Value	Param.	Value	Param.	Value	Param.	Value
q_m	1.76	n	1.04	a_T	210.08	q_m	219.75
(mg/g)	$\square 10^4$	K_F		(L/mol)		(mg/g)	
K_L	1.9 \square	(mg/g)	3.79	b_T	54.30	K_1	2.7 $\square 10^3$
(L/g)	10^{-4}	(L/mg) ⁿ				K_s	36.32
R^2	0.86	R^2	0.86	R^2	0.49	R^2	0.95
χ^2	11.99	χ^2	11.86	χ^2	45.15	χ^2	5.22
(10 ³)		(10 ³)		(10 ³)		(10 ³)	

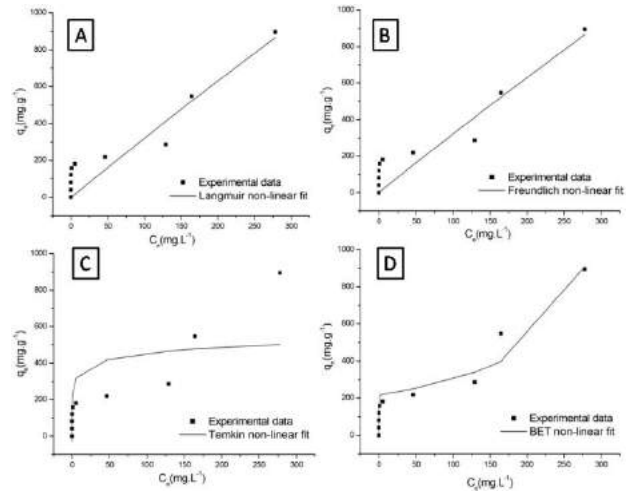


Fig. 4. adsorption isotherms applied for equilibrium data. Models: Langmuir, Freundlich, Temkin and BET adapted for L-S interfaces. Experiments performed with DR solution, pH 6.0, 300 rpm, time of contact 20 min, sorbent dosage: 1.0 mL (6.2 mg·mL⁻¹); mathematical modeling carried out by “non-linear fit” tool of Origin™ 9.0.

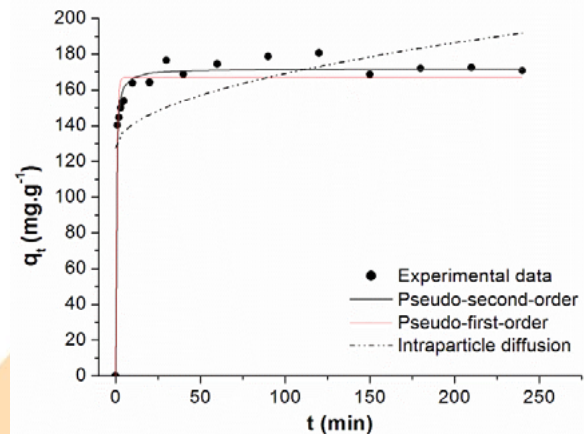


Fig. 5. Kinetic experimental data and model fitting for the adsorption of DR by mGO-NH-Fe₃O₄. Experiments performed under 298 K, 25 mL of DR solution with initial concentration 20 mg·L⁻¹, pH 6.0, stirring velocity 300 rpm, mGO-NH-Fe₃O₄ suspension dosage: 1.0 mL (6.2 mg·mL⁻¹); mathematical modeling performed through non-linear fitting tool of Origin™ 9.0.

4. Conclusions

Textile effluents are considered as one of the most toxic and harmful pollutants to environment and human health. Over the past decades, several researches have been conducted in order to develop profitable adsorbents to remove textile dyes from wastewaters. In this work, graphene oxide has been successfully functionalized with amine and Fe_3O_4 nanoparticles to enhance its adsorption capacity towards the toxic Drimaren Red dye. Characterization analyses were performed to unravel the new mGO-NH- Fe_3O_4 nanosorbent properties. In FTIR spectra it was observed the presence of characteristic bands referring to amide and amine groups, present on mGO-NH- Fe_3O_4 structure. Through XRD patterns, it was noticed the diminishing of the peak at 2θ 25° which is an indicative that graphite was not entirely oxidized. AFM images and profiles exhibited morphological changes on graphene oxide structures after the functionalization; its thickness increase confirms aggregation effects of mGO-NH- Fe_3O_4 . Kinetic and equilibrium experiments showed that mGO-NH- Fe_3O_4 reached the equilibrium within 25 min, and pseudo-second-order better fitted the experimental data; mGO-NH- Fe_3O_4 has also shown outstanding maximum adsorption capacity of DR 219.75 $\text{mg}\cdot\text{g}^{-1}$, with BET model, applied for liquids, better adjusted to equilibrium data. This excellent performance shows the great potential that mGO-NH- Fe_3O_4 has to be applied as a dye adsorbent, even on a larger scale.

Acknowledgements

The authors acknowledge the financial support provided by the *Fundação de Apoio à Ciência e Tecnologia do Estado de Pernambuco* (FACEPE) and the *Conselho Nacional de Desenvolvimento Científico e Tecnológico* (CNPq). Moreover, the authors also acknowledge the technical support provided by the *Laboratório de Análises de Minerais, Solos e Água* of UFPE, the *Centro de Pesquisas Avançadas em Grafeno, Nanomateriais e Nanotecnologias* (MackGraphe)/Universidade Presbiteriana Mackenzie, São Paulo-SP, the *Centro de Tecnologias Estratégicas do Nordeste* (CETENE).

References

- [1] Georgakilas V, Tiwari JN, Kemp KC, Perman JA, Bourlinos AB, Kim KS. Noncovalent functionalization of graphene and graphene oxide for energy materials, biosensing, catalytic, and biomedical applications. *Chem. Rev.* 2016;116(9):5464–5519.
- [2] Zhu Y, Murali S, Cai W, Li X, Suk JW, Potts JR, Ruoff RS. Graphene and Graphene Oxide: Synthesis, Properties, and Applications. *Adv. Mater.* 2010;22:3906–3924.
- [3] Park S, Ruoff RS. Chemical methods for the production of graphenes. *Nat. Nanotechnol.* 2009;4:217–224.
- [4] Kuila T, Bose S, Mishra AK, Khanra P, Kim NH, Lee JH. Chemical functionalization of graphene and its applications. *Prog. Mater. Sci.* 2012;57:1061–1105.
- [5] Hummers WS, Offeman RE. Preparation of Graphitic Oxide. *J. Ame. Chem. Soc.* 1958;80(6):1339–1339.
- [6] Ebadi A, Mohammadzadeh JSS, Khudiev A. What is the correct form of BET isotherm for modeling liquid phase adsorption? *Adsorption*, 2009;15:65–73.
- [7] Fraga TJM, Lima LEM, de Souza ZSB, Carvalho MN, Luna Freire EMP, Ghislandi MG, da Motta MA. Amino- Fe_3O_4 -functionalized graphene oxide as a novel adsorbent of Methylene Blue: kinetics, equilibrium, and recyclability aspects. *Environ. Sci. Pollut. Res.* (in press) 2018. <https://doi.org/10.1007/s11356-018-3139-z>
- [8] Guo LQ, Ye PR, Wang J, Fu FF, Wu ZJ. Three-dimensional Fe_3O_4 -graphene macroscopic composites for arsenic and arsenate removal. *J. Hazard. Mater.* 2015;298:28–35.
- [9] Zhao D, Gao X, Wu C, Xie R, Feng S, Chen C. Facile preparation of amino functionalized graphene oxide decorated with Fe_3O_4 nanoparticles for the adsorption of Cr(VI). *Appl. Surf. Sci.* 2016;384:1–9.
- [10] Fraga TJM, de Souza ZSB, Marques Fraga DMS, Carvalho MN, Luna Freire EMP, Ghislandi MG, da Motta Sobrinho MA. Comparative approach towards the adsorption of Reactive Black 5 and methylene blue by n-layer graphene oxide and its amino-functionalized derivative. *Adsorption* (in press) 2019. <https://doi.org/10.1007/s10450-019-00156-9>
- [11] International Organization for Standardization. ISO TS 80004/2017: Nanotechnologies – Vocabulary – Part 13: Graphene and related two-dimensional (2D) materials. *Organisation Internationale de Normalisation* (ISO), Geneve, 2017. <https://www.iso.org/obp/ui/#iso:std:iso:ts:80004:-13:ed-1:v1:en>
- [12] Richardson JF, Harker JH, Backhurst JR. Coulson & Richardson's Chemical Engineering, v. 2, Particle technology and Separation Processes, 5th Ed. London, Butterworth Heinmann, 2002.

Iron oxide nanoparticles: design of the reactor for synthesis and characterization.

Maria Teresa Garcia Badoch^a, Regina Maria Matos Jorge^b, Tirzhá Lins Porto Dantas^{b,*}

^aAcademic Department of Chemistry and Biology, Federal Technological University of Paraná, Curitiba, Brazil

^bChemical Engineering Department, Federal University of Paraná, Curitiba 80035-210, Brazil

Abstract

The use of nanoscale particles finds promising applications in many sciences due, in small sizes, particles tend to have their specific surface area and hence the amount of available sites increased. This work aims to design a reactor and synthesize maghemite by hydrothermal method from inorganic precursor: ferric chloride ($\text{FeCl}_3 \cdot 6\text{H}_2\text{O}$), sodium hydrogen phosphate ($\text{NaH}_2\text{PO}_4 \cdot \text{H}_2\text{O}$) and sodium sulphate (Na_2SO_4). The synthesis reactor was designed to guarantee a closed system under pressure and was made of 304 stainless steel. An aqueous solution of the salts was treated at 220°C for 48h to synthesize hematite ($\alpha\text{-Fe}_2\text{O}_3$). Hematite particles were subjected to a heat treatment at 360°C in an oxygen-free atmosphere for 5h to be reduced to the magnetite (Fe_3O_4). The magnetite particles were exposed to air at 240°C for 2h to be obtained the Maghemite, $\gamma\text{-Fe}_2\text{O}_3$. The synthesized particles were characterized by measurements of liquid nitrogen sorption isotherms, X-ray Photoelectron Spectroscopy (XPS) and Scanning Electron Microscopy (SEM). These characterization analyzes showed that the particles have a specific area of $20.23 \text{ m}^2 \cdot \text{g}^{-1}$ and dimensions around 200 nm.

Keywords: maghemite; hydrothermal synthesis, iron oxide, nanoparticles.

1. Introduction

Iron is the most abundant transition metal on earth and much of the iron element in the earth's crust is in the form of Fe^{2+} , however it can be rapidly oxidized to Fe^{3+} . According to Cornell & Schwertmann [1], there are 16 (sixteen) types of iron ores – including oxides, hydroxides and oxyhydroxides – found in nature. Natural and synthetic iron oxides, depending on their crystal structure and oxidation state, come in various forms. Most iron oxides, hydroxides and oxyhydroxides have crystal structure. However, the degree of structural ordering and crystal size vary according to the conditions under which the crystals were obtained [1]. The main naturally occurring iron ores are hematite, goethite and magnetite. These ores have 70%, 63% and 72%, respectively, in iron mass [2], besides having remarkable diversity of properties and a very interesting chemistry [3].

Due to their wide distribution in nature, many sciences are interested in their properties and make use of these compounds. Among the various fields, the application stands out as adsorbents and

catalysts. This is due to its textural and reductive characteristics [1]

Among the industrial processes in which iron oxides act as catalysts we can highlight [1,3]: Haber-Bosh process; Fischer-Tropsch process; Conversion of carbon monoxide to carbon dioxide at elevated temperatures; Dehydrogenation of ethylbenzene to styrene; Production of acrylonitrile from propene (Amoxidation), Oxidative dehydrogenation from butene to butadiene.

Among the applications in fine chemistry and other new applications of technological appeal can also be highlighted: oxidation of monoterpenic alkenes to obtain epoxides, replacement of the current catalysts used in the Merox Process - disulfide thiols oxidation widely used in the Oil Refining industry to thiols removal - and photocatalytic cleavage of water to produce hydrogen [3]. Iron oxides have also excelled in environmental chemistry applications such as adsorbents of undesirable ions and metals and as catalysts for oxidation reactions [1].

The adsorptive capacity of iron oxides is well known. Because they have a relatively high specific surface area, they often control concentrations of organic matter and free metals in

soil or water through adsorptive mechanisms [4]. However, most of these iron oxides are available only in fine powder form or are generated in aqueous suspension in the form of iron hydroxide flakes or gel. In this form, these oxides retain their adsorptive properties, but their practical applications are limited [4]. Iron oxide coating techniques on solid supports could overcome these difficulties. Sand, activated carbon and polymeric supports have been reported as suitable supports for iron oxides [5,6,7].

Nanoparticles have high area / volume ratios and structure and properties may differ from larger particles. So reducing the size of the iron oxide particles could increase the surface reactivity.

Some synthesis procedures aiming to obtain nanoparticulate iron oxides are reported in the literature [1,8,9,10,11,12,13]. Teja and Koh present several obtaining methods and divide them into gas phase, liquid phase, two phases, sol-gel and hydrothermal with high pressure [14]. Mahmoudi and collaborators indicate that iron oxides with specific properties – or SPIONs (Superparamagnetic Iron Oxide Nanoparticles) – can be prepared by physical, chemical and biological methods [15].

The objectives of this work were: (1) to design a reactor for the synthesis of iron oxide particles, (2) to synthesize iron oxide nanoparticles by hydrothermal method using ferric chloride as precursor and (3) to characterize as the use of iron oxide iron.

2. Experimental Section.

2.1. Reactor design

The reactor was designed based on the general reaction parameters: temperature of 250 °C and pressure of 4.0 MPa. Under these conditions, overheated steam will be present inside the reactor.

Thus, the reactor was built of 304 stainless steel and internally coated with polytetrafluoroethylene (PTFE). It was proposed a reactor with an internal volume of 150 mL and a flanged closure system sealed with a brass-PTFE ring (Figure 1).

2.2. Synthesis of iron oxides nanoparticles

The synthesis of iron oxide nanoparticles was performed em 3 (threes) steps: (1) Initially there is the formation of hematite ($\alpha\text{-Fe}_2\text{O}_3$) from ferric chloride; (2) then reduction of of hematite to magnetite ($\text{FeO}\cdot\text{Fe}_2\text{O}_3$) and (3) finally oxidation to

maghemite ($\gamma\text{-Fe}_2\text{O}_3$). The reactions are presented in Equations (1) to (3) [1].

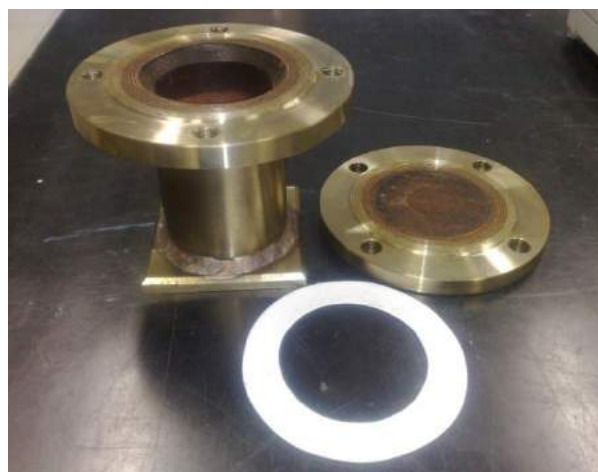
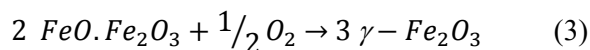
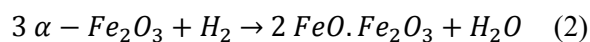
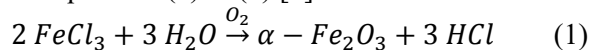


Fig. 1. The stainless steel reactor and the brass-PTFE ring.

To ensure reproducibility between the batches of synthesis, two stock solutions were prepared:

1. Solution A: 4.0×10^{-2} mol.L⁻¹ Ferric chloride ($\text{FeCl}_3 \cdot 6\text{H}_2\text{O}$) solution;
2. Solution B: Mixed solution of a 3.6×10^{-4} mol.L⁻¹ sodium dihydrogen phosphate (NaH_2PO_4) solution and a 1.1×10^{-3} mol.L⁻¹ sodium sulfate (Na_2SO_4) solution.

The hematite ($\alpha\text{-Fe}_2\text{O}_3$) was synthesized by adding 60 mL of solution A and 60 mL of solution B to the reactor. The reactor was then brought to a muffle maintained at 220 °C for 48h.

After this step, the material was centrifuged and the particles washed 3 (three) times with deionized water and 2 (two) times with absolute ethanol using a vortex mixer to ensure suspension. After each wash, the particles were separated by centrifugation at 3000 rpm for 2 min. The particles were then dried in a digital oven at 80 °C for 2 hours. Magnetite (Fe_3O_4) was prepared by a high temperature reduction process. The hematite particles were taken to a vacuum oven for 5 hours with a controlled atmosphere of hydrogen and argon at 360 °C. After the reaction time, it was allowed to cool down in the same reduction atmosphere.

After magnetite cooling, the maghemite ($\gamma\text{-Fe}_2\text{O}_3$) was prepared by oxidation with heating and

exposure to air. The furnace containing the magnetite was opened to ensure atmosphere exchange and closed again. The temperature was set to 240 °C and held for 2 hours.

2.2. Analyzes of Catalysts Characterization.

The synthesized maghemite particles were characterized by nitrogen adsorption-desorption isotherm measurements at -196.15 °C, that is, at the normal boiling point of nitrogen. The isotherms were performed on an AUTOSORB-1 automated gas sorption analyzer (Quantachrome Instruments, USA).

The synthesized iron oxide particles were also characterized by X-ray photoelectron spectroscopy (XPS) and Scanning Electron Microscopy (SEM).

Analysis of the relative concentrations of surface elements was obtained by X-ray Photoelectron Spectroscopy (XPS) performed on a MULTILAB ESCA3000 spectrometer (VG Microtech, UK). The energy used in the analyzer was 58.7 eV to obtain high resolution spectra. The relative concentrations of adsorbent surface elements were calculated by measuring the peak areas in the generated high resolution spectrum.

Particle morphological analyzes using Scanning Electron Microscope (SEM) were performed on EVO MA 15 equipment (Carl Zeiss, Germany) with continuous magnification of 7 to 10⁶ times and secondary electron detectors - EDS Oxford X-Max 20 mm² with resolution 125 eV (resolution from 3 nm to 30 kV). The analysis was performed at 20 kV with gold particle coating.

The BET specific surface area analysis and pore size and volume distribution werw performed by Quantachrome Instruments - Quantachrome Autosorb Automated Gas.

3. Results

The adsorption-desorption isotherm of liquid nitrogen on synthesized iron oxide is shown in Figure 2.

According to IUPAC - International Union of Pure and Applied Chemistry - the obtained isotherm is classified as type II. In type II isotherms, the adsorbent is allowed the ability to continuously advance from a layer to multilayer adsorption. Thus, the BET thermodynamic model is easily adjustable [16]. This isotherm, without hysteresis, is typical of macroporous or nonporous solids [17,18]. Cornell & Schwertmann [1] mention

that maghemite obtained from magnetite is considered non-porous.

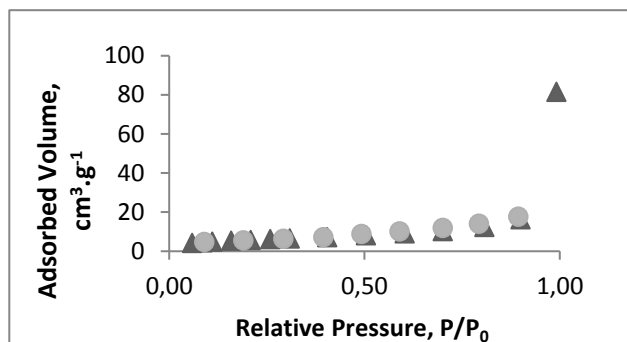


Fig. 2. Adsorption-desorption isotherm.

Table 1 presents the textural characterization of iron oxide. Specific surface area was obtained by the BET equation [19]. The textural characterization of the particles shows that the specific surface area of the analyzed sample was 20.2 m².g⁻¹. According to Cornell & Schwetmann [1] the specific surface area of maghemite is between 8 to 130 m².g⁻¹, depending on synthesis method. These authors also mention that when maghemite is obtained from magnetite oxidation, the area may vary between 5.8 and 98 m².g⁻¹, showing that the value obtained at is within the predicted value. Also, the average pore diameter - 24.9 nm - characterizes the particles as mesoporous.

Table 1. Textural Characterization of particles.

BET specific surface area, m ² /g	20.2
Total pore volume with diameter less than 219.4 nm at P/P ₀ = 0.991, cm ³ /g	0.13
Average pore diameter, nm	24.99

The high resolution spectra with the iron and oxygen peaks are shown in Figures 3 and 4, respectively.

It is observed that for the Iron element a peak was found - represented by the letter "A" in Figure 3 - with the maximum binding energy at 711.36 eV. According to Tan and coauthors [20] the peak at 711.4 eV corresponds to FeOOH. Brainard & Wheeler [21] state that this value is typical of Fe₂O₃. But McIntyre and Zetarunk [22] affirms that the values for FeOOH, α-Fe₂O₃ and γ-Fe₂O₃ oxides are very close. The synthesized particles has magnetic characteristics. Thus, it is believed that in fact the material is γ-Fe₂O₃ (maghemite).

In the high resolution spectrum of the oxygen element, there are two peaks (Figure 4). In the case of this element the maximum binding energies found were 531.16 eV - peak A - and 528.22 eV - peak B. These values are quite consistent with those found by Haber and colleagues [23]. For these authors, the oxygen binding energy values in oxides are 531.5 eV for $\text{Fe}(\text{OH})_3$, 531.8 eV for FeOOH and 532.1 eV for Fe_2O_3 . Elemental analysis was performed by measuring the peak areas in the high resolution spectrum and provided an iron concentration of 18,861% and an oxygen concentration of 81,139%. One of the explanations for the existence of two oxygen peaks could be the presence of water molecules in the material that would justify the ratio between the elements Fe and O. However, this hypothesis cannot be proven, since the maximum energy values of The oxygen binding of the water molecule appears with binding energy between 532.80 eV and 538.00 eV, ie values greater than the highest value presented by the spectrum in question, 528.22 eV. Thus, it is possible that the material analyzed is a mixture of iron oxides including oxides from the intermediate steps of synthesis.

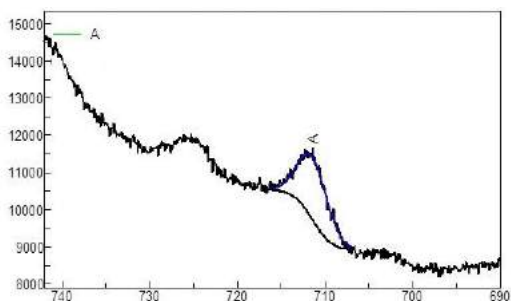


Fig. 3. Detail of high resolution spectrum with iron peak.

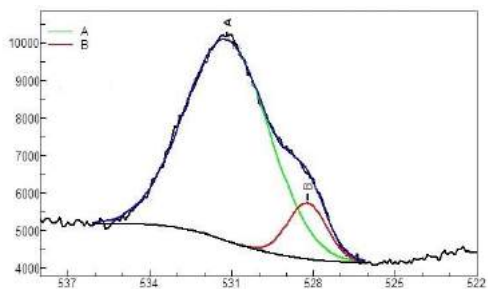


Fig. 4. Detail of high resolution spectrum with oxygen peak.

The Scanning electron microscopy showed that the synthesized particles have a similar format to that presented by Jia and coauthors. Figure 5 shows a comparison image between the particles obtained in this work and by Jia and coauthors. What can be seen from the image on the left, in Figure 5, is that the particles obtained in this work are agglomerated and have larger dimensions. Jia and coauthors report a range of 150 to 170 nm in external diameter and 80 to 120 nm in height. The particles obtained in this work had dimensions between 180 and 265 nm for the external diameter and 141 and 174 nm for the height, as can be observed in Figures 6 and 7 respectively.

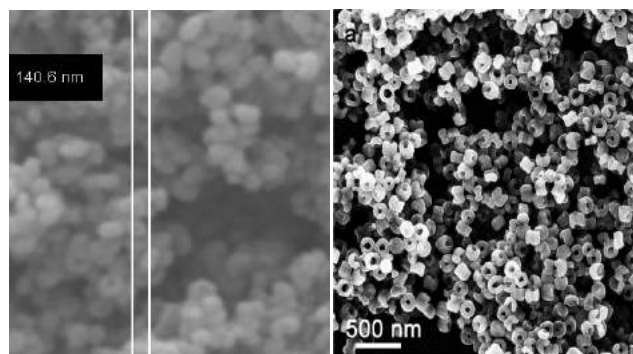


Fig. 5 – Comparative of particles obtained (a) at this work and (b) by Jia and coauthors.

Conclusions

The reactor that was designed to suport high pressures and temperatures in the presence of superheated steam shows efficient for iron oxide synthesis which was confirmed by the presence of high yield maghemite. The characterization of the particles showed that they were mostly composed of ring-shaped iron oxides with dimensions around 200 nm. The specific surface area obtained was in agreement with what was found in the literature when obtaining maghemite from the magnetite oxidation. From the average pore diameter, 25.0 nm, it can be concluded that the particles have mesopores.

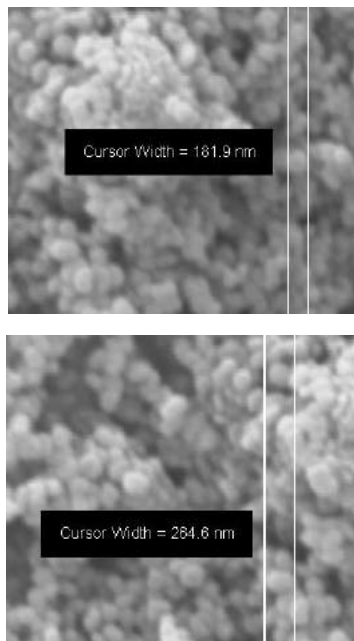


Fig. 6 – Measures of the external diameter of the particles.

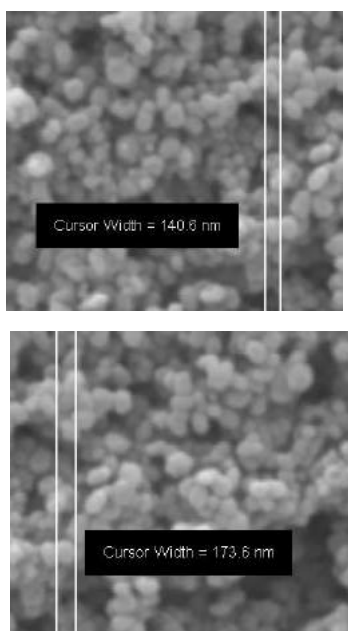


Fig. 7 – Measures of the height of the particles.

Acknowledgements.

The authors are grateful to the Auracária Foundation - Foundation for Supporting Scientific and Technological Development of Paraná, Brazil.

References

- [1] Cornel RM., Schwertmann U. The Iron Oxides. 3rd. ed.: Wiley-BCH GmbH & Co., 2003.
- [2] Guimarães IR, Oliveira LCA, Queiroz PF, Ramalho TC, Pereira M, Fabris JD, Ardisson, JD. Modified goethites as catalyst for oxidation of quinoline: Evidence of heterogeneous Fenton process. Applied Catalysis: A, 2008, 89-93.
- [3] Oliveira LCA, Fabris JD.; Pererira MC. Óxidos de Ferro e suas Aplicações em Processos Catalíticos: Uma Revisão. Química Nova 2013, 123-130.
- [4] LAI CH, CHEN CY. Removal of metal ions and humic acid from water by iron-coated filter media. Chemosphere. 2011, 1177-1184.
- [5] Benjamin MM, Sletten RS, Bailey RP. Bennett T. Sorption and filtration of metals using iron-oxide-coated sand. Water Research, 1996, 2609-2620.
- [6] Oliveira LCA, Rios RVRA, Fabris JD, Garg V, Sapagb K. Lago RLM. Activated carbon/iron oxide magnetic composites for the adsorption of contaminants in water. Carbon, 2002, 2177-2183.
- [7] Katsoyiannis IA, Zouboulis AI. Removal of arsenic from contaminated water sources by sorption onto iron-oxide-coated polymeric materials. Water Research, 2002, 5141-5155.
- [8] Cheng FY, Su CH, Yang YS, Yeh CS, Tsai CY, Wu MT, Shieh D-B. Characterization of aqueous dispersions of Fe₃O₄ nanoparticles and their biomedical applications. Biomaterials, 2005, 729-738.
- [9] Deshpande K, Nersesyan M, Mukasyan A, Varna A. Novel Ferrimagnetic iron oxide nanopowders. Industrial and Engineering Chemical Research, 2006, 6196-6199.
- [10] Giri S, Samanta S, Maji A, Ganguli S, Bhaumi A. Magnetic properties of α -Fe₂O₃ nanoparticle synthesized by a new hydrothermal method. Journal of Magnetism and Magnetic Materials, 2005, 296-302.
- [11] Hyeon T, Lee SS, Park J, Chung Y, Na HB. Synthesis of Highly Crystalline and Monodisperse Maghemite Nanocrystallites without a Size-Selection Process. Journal of American Chemical Society, 2001, 12798-12801.
- [12] Reynolds CH, Annan N, Beshah K, Huber JH, Shaber SH, Lenkiski RE, Wortman JA. Gadolinium-Loaded Nanoparticles: New Contrast Agents for

CO₂ capture in carbon microfibers doped with nitrogen

Reyna Ojeda-López^{a,b,*}, Guadapule Ramos-Sánchez^b, Diana C.S. de Azevedo^a,
J. Marcos Esparza-Schulz^b, Armando Domínguez-Ortiz^{b,*}

^aDepartamento de Engenharia Química, Universidade Federal do Ceará, 60455-760, Fortaleza, CE Brasil.

^bDepartamento de Química, Universidad Autónoma Metropolitana, 09340, CDMX, México.
e mail: imdrol87@gmail.com (ROL), doar@xanum.uam.mx (ADO).

Abstract

The interest in carbon microfibers (CMF) as an adsorbent material for CO₂ and CH₄ capture has increased in the last few years. The gas adsorption capacity depends on the chemical and morphological structure of CMF. The CMF physicochemical properties change according to the stabilization protocol and carbonization temperatures. In this work, carbonization of polyacrylonitrile microfibers (PANMF) is performed at five different temperatures: 600, 700, 800, 900, and 1000 °C, maintaining a constant temperature of 280 °C for the stabilization process. As a result, the CMF chemical composition directly affects the CO₂ adsorption capacity, specifically due to the presence of basic sites from nitrogen groups. Thus, the variety in chemical composition may be useful to develop carbon microfibers with a high adsorption capacity and selectivity despite a low specific surface area. CO₂ adsorbed concentration at 25 °C and 1.0 bar ranges between 2.0 and 2.6 mmol/g adsorbent, depending on the calcination procedure; these values are comparable to other greenhouse gases adsorbents.

Keywords: Carbon microfibers; carbonization temperature; CO₂ capture.

1. Introduction

In the last few years, carbon dioxide (CO₂) and methane (CH₄) have become the most important greenhouse gases (GHGs) with emissions having the largest impact on climate change [1]. As a result, several researchers have focused on the development of efficient materials for CO₂ and CH₄ capture. A viable methodology for GHG capture is adsorption at mild conditions because adsorbent materials are easily tunable, reusable, and require relatively low energy for cyclic use [2–4]. Some materials have been tested as adsorbents for greenhouse gases, for example, zeolites, alumina, mesoporous silica, and porous carbons (graphite, carbon nanotubes, and carbon nanofibers). Particularly, ideal CO₂ adsorbents should comply with the following characteristics: a high specific surface area, homogeneous micro- and mesoporous structure, and many active sites on the surfaces, such as amine functional groups and basic metal oxide [5]. Within the materials that satisfy those requirements are the carbon microfibers (CMF), due to their adequate physical and chemical properties such as large specific surface area, high electronic conductivity, active nitrogen sites, and remarkable mechanical and thermal resistances.

In order to improve the adsorption efficiency of CMF, it is necessary to determine which physicochemical properties are the most important to achieve this goal, and how the heat treatments in the synthesis influence them. Usually, carbon microfibers are synthesized by electrospinning because of its simplicity, low-cost and industrial scalability. The electrospinning process consists of the use of polymer solutions subjected to a high voltage difference to force the generation of polymer fibers. The most used polymer for this process is polyacrylonitrile (PAN), mainly due to its high thermal deformation resistance and carbon yield. After the formation of PAN microfibers (PANMF), a thermal process is necessary to obtain CMF, which involves two heat sequential treatments: i) stabilization at temperatures between 250 to 300 °C in an oxidizing atmosphere (air) and ii) carbonization at temperatures above 600 °C in an inert atmosphere (nitrogen) [6].

The first heat treatment (stabilization) involves structural stretching and chemical reactions: cyclization, dehydrogenation, aromatization, oxidation, among others; resulting in the formation

of a structure in the form of a ladder. In general, the linear molecules of polymer precursors (PAN) are cyclized. The use of air in the process produces the oxidation and the dehydrogenation of polymeric microfibers, possibly due to the activation of cyclization centers by oxygen and the promotion of the dehydrogenation process. During the cyclization process, the nitrile groups have their triple bond structure converted to a double bond structure ($C\equiv N \rightarrow C=N$), producing pyridine rings [6–8].

In the second treatment (carbonization), dehydrogenation and denitrogenation take place. Hence, adjacent polymer chains are bound by C–C bonds due to the aromatization process, resulting in broader carbon sheets. Under nitrogen atmosphere, temperatures higher than 3000 °C allow obtaining pure carbon structure. At temperatures lower than 3000 °C, some nitrogen functional groups remain, such as pyridine N (N-6), pyrrolic N (N-5), pyridone (N-P), quaternary-N or graphitic-N (N-Q), and pyridinic-N-oxide (N-X) [8]. The control of the content of the nitrogen groups during the carbonization of microfibers provides a material with specific structural and electrocatalytic properties.

2. Materials and methodology

The polymer precursor, polyacrylonitrile (PAN) was supplied by Sigma Aldrich, with an average molar mass of 150,000 uma and it was used as received without additional purification. The solvent N,N dimethylformamide (DMF) anhydrous grade (99.8%) was also acquired from Sigma-Aldrich.

PANMF were synthesized using 10 % (w/w) PAN, the electrospinning apparatus was set at a flow rate of 1.0 mL/h, voltage of 15 kV and 10 cm distance between the tip of the syringe and the collector. All fibers were stabilized at 280 °C (in air) and carbonized at five different temperatures, 600, 700, 800, 900, and 1000 °C (nitrogen atmosphere).

3. Results

The morphology of synthesized carbon microfibers can be observed in Figure 1. Note that the fibrous structure is preserved when the material is carbonized at 900 °C. The diameter of these fibers oscillate between 300 and 500 nm.

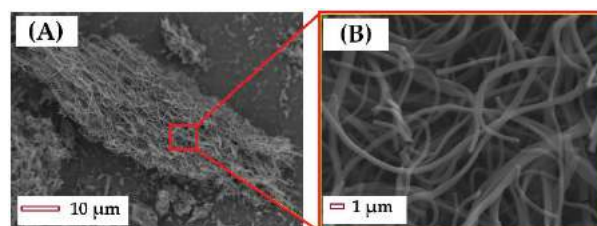


Figure 1. SEM images of PANMF stabilized at 280 °C and carbonized at 900 °C.

The modification in the morphological structure of the carbon microfibers is mainly affected by a variation in the stabilization temperature whereas the modification in the chemical composition is primarily due to the variation in the carbonization temperature. The specific surface area rises as the carbonization temperature increases, from a BET area of 296 m²/g for SC-600 sample to 822 m²/g for SC-1000 sample (Figure 2 and Table 2).

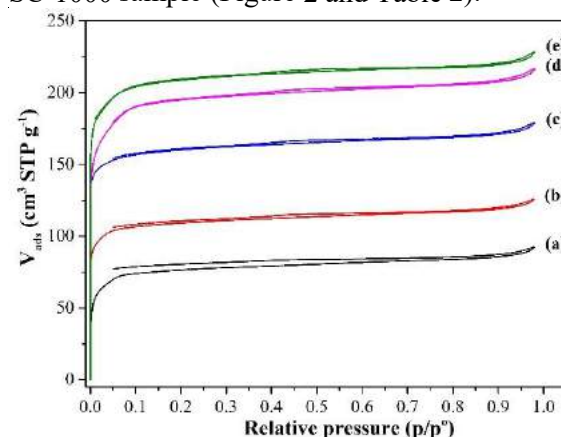


Figure 2. N₂ isotherms of PANMF carbonized at (a) 600 °C, (b) 700 °C, (c) 800 °C, (d) 900 °C, and (e) 1000 °C.

To obtain information from micropores, CO₂ adsorption isotherms were measured. Because of kinetic restrictions at the cryogenic temperature of nitrogen (-196 °C), these isotherms have limited value for the characterization of very narrow micropores. One way of addressing this problem is to use CO₂ (kinetic dimension 0.33 nm) as the adsorbate at 0 °C, where the saturation vapor pressure of CO₂ is very high (~35 bar) and hence the pressures required for micropore size analysis are in a moderate range (~0.001 to 1.000) bar. Because of these relatively high temperatures and pressures, diffusion is much faster and pores as small as 0.4 nm can be accessed [9]. The pore size distribution (PSD) obtained by CO₂ adsorption isotherms at 0 °C in Figure 3, it shows that all materials have a preferential pore diameter 0.40 and 0.60 nm, which is consistent with the distance between plates calculated using TEM micrographs.

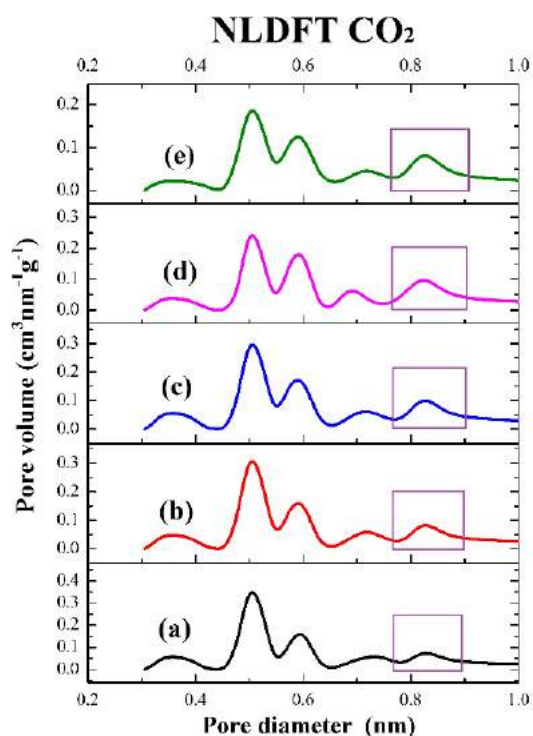


Figure 3. NLDFT of PANMF stabilized at 280 °C and carbonized at (a) 600 °C, (b) 700 °C, (c) 800 °C, (d) 900 °C, and (e) 1000 °C.

The elemental surface composition of CMF and PAN was investigated using XPS. The XPS survey scan of CNM and PAN revealed the presence of carbon, nitrogen, and oxygen (Figure 4). The composition of C, O, and N (wt. %) were calculated from the corresponding peak areas of the XPS spectra (Table 1).

When the material is carbonized at higher temperatures, O 1s has a small variation; C 1s shows a gradual increase from 73 to 91 %, and N 1s decreases from 25 to 5 %. Note that the signal of N 1s for PAN presents the highest value with respect to all carbonized materials; this behavior is related to the lack of thermal treatment, as it is taken as a reference to compare changes in nitrogen concentration.

The general XPS spectra allow identifying the surface composition of the samples. To obtain a more specific study on some of elements, it is necessary to carry out a high-resolution analysis. In this way, the different nitrogen species present in the carbon nanofibers are determined. Figure 5 shows high-resolution spectra for N 1s region.

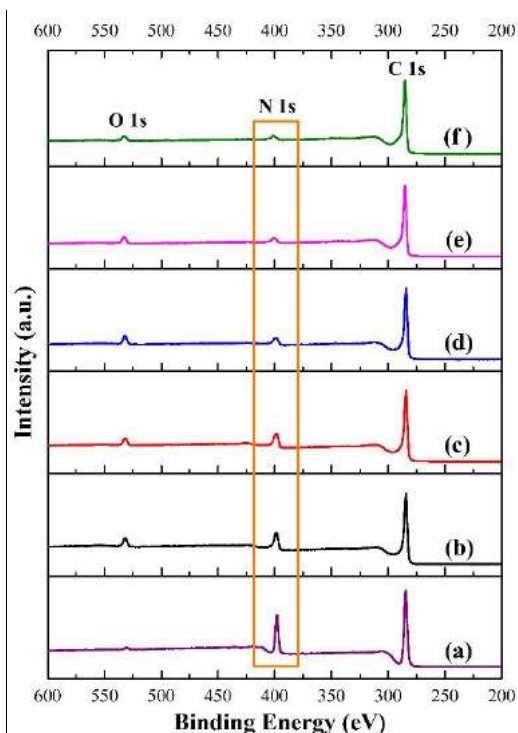


Figure 4. XPS survey spectrum. (a) PAN polymer precursor. PANMF carbonized at (b) 600 °C, (c) 700 °C, (d) 800 °C, (e) 900 °C, and (f) 1000 °C.

Table 1. Surface composition of PAN and CNF derived of from the XPS spectra (wt. %).

Sample	C 1s	N 1s	O 1s
PAN	73	25	2
SC-600	78	16	6
SC 700	82	13	5
SC 800	85	9	6
SC 900	90	5	5
SC-1000	91	5	4

For the purpose of quantification, the deconvolution of the spectra shown in Figure 5 was performed. Seven binding regions can be assigned to the different nitrogen groups (peaks), these peaks could be assigned to: i) residual PAN (397.8 eV); ii) pyridine-N (398.8 eV); iii) cyanide functional group, C≡N (399.5 eV); iv) pyrrolic-N/pyridone (400.5 eV); v) quaternary-N or graphitic-N (401.8 eV); vi) pyridine-N-oxide (403.1 eV); vii) chemisorbed nitrogen oxide species/ $\pi \rightarrow \pi^*$ transitions (405.12 eV). Pels *et al.* mentioned that the chemical environment of the nitrogen atom in pyridone is similar to pyrrolic-N: in both, the nitrogen atom contributes with two pi electrons to the system, while the hydrogen atom is bound in the plane of the ring; therefore, within the accuracy of XPS measurements, pyridone cannot be distinguished from pyrrolic-N [10].

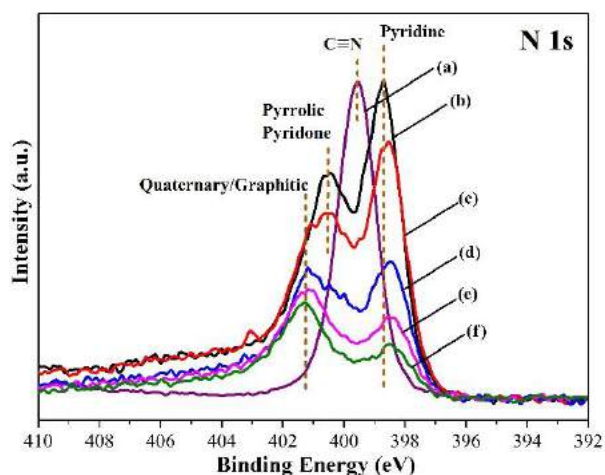


Figure 5. High resolution XPS of N 1s. (a) PAN polymer precursor. PANMF carbonized at (b) 600 °C, (c) 700 °C, (d) 800 °C, (e) 900 °C, and (f) 1000 °C.

Figure 6 shows the contribution of nitrogen species for all materials, calculated from the deconvolution of the high-resolution XPS spectra for N1s, considering the total amount of nitrogen in each material, using the values of the surface composition presented in Table 1. Three main species predominate in CMF. The first of these are pyridine nitrogen, which originally comes from the precursor used and decreases with rising carbonization temperatures. Pyrrolic and pyridone nitrogen are abundant at temperatures below 800 °C. Finally, quaternary/graphitic nitrogen remains practically constant with the change in carbonization temperature. The number and types of nitrogen species are determinant in the application for CNF, for example, as catalysts for the oxygen reduction reactions (ORR) and CO₂ capture.

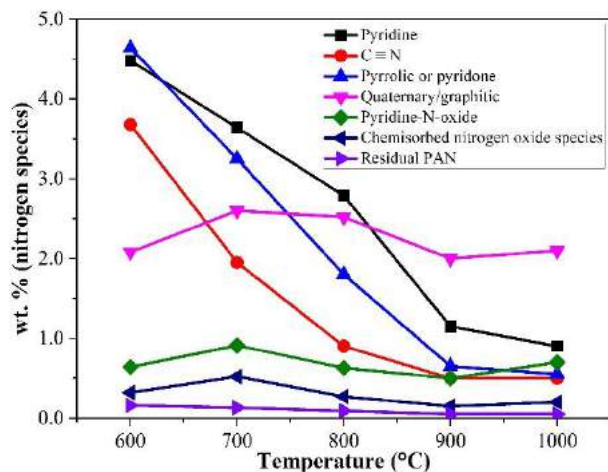


Figure 6. Nitrogen functional groups obtained through high resolution XPS spectra for N 1s.

The CO₂ adsorption isotherms at 25 °C of PANMF samples stabilized a 280 °C and carbonized at 600, 700, 800, 900, and 1000 °C are shown in Figure 7. In general, the increase in carbonization temperature produces an increase in CO₂ uptake. However, for sample SC-1000, despite the larger area, there is a decrease in adsorbed CO₂ with respect to samples SC 800 and SC 900, *viz* Table 2. This means that the increase in carbonization temperature resulted in the loss of chemical groups able to interact with CO₂. Therefore, the CO₂ adsorption capacity does not increase proportionally to the surface area. In this way, the CO₂ adsorption capacity in carbon microfibers can be determined by the presence of basic sites from nitrogen groups. Samples SC-800 and SC-900 exhibit the highest CO₂ adsorption and presents the highest N and oxygen percentage (Table 1), it may be that the positive effect is due to pyridine and pyrrolic groups. These groups decrease at 1000 °C and sample SC-1000 reduces its adsorption capacity (Figure 6).

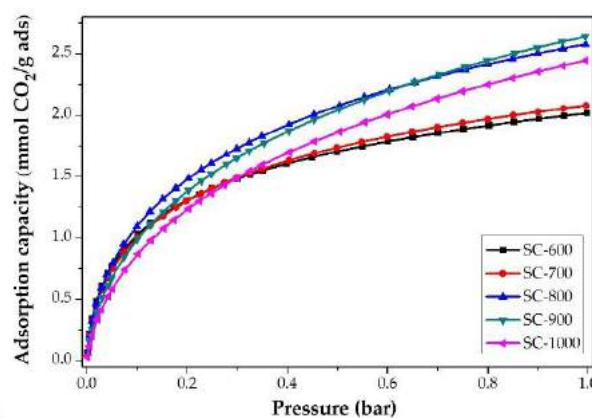


Figure 7. CO₂ adsorption isotherms at 25 °C of PANMF carbonized.

Table 2. BET areas and CO₂ adsorption capacity (1 bar, 25 °C) in carbonized materials.

Sample	S _{BET} m ² /g	mmol CO ₂ /g	mg CO ₂ /g
SC-600	296	2.0	88.7
SC-700	431	2.1	92.4
SC 800	635	2.6	114.4
SC 900	710	2.6	114.4
SC-1000	822	2.4	105.6

To evaluate the reusability of CMF, a collection of CO₂ adsorption isotherms at 0 °C are shown in Figure 8. After ten adsorption/desorption runs, CMF preserves their adsorption capacity. For the first experiment, the CMF were degassed at 200 °C

by 8 h, and then the CO₂ adsorption analysis was performed at 0 °C. For the second analysis, the same sample was degassed at 200 °C by 2 h and again analyzed. The following analyses followed this procedure. This allows us to conclude that the synthesized materials can be used more than ten times maintaining their adsorptive capacity.

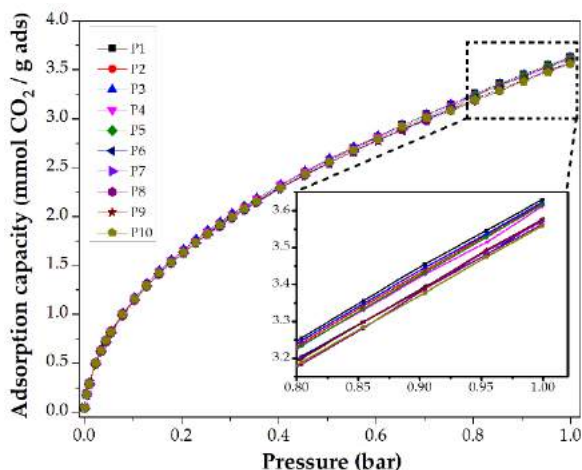


Figure 8. CO₂ adsorption isotherms at 0 °C of PANMF stabilized a 280 °C and carbonized at 900 °C: evaluation of reusability.

4. Conclusions

Carbonization temperature of PAN carbon fibers changed the area and the chemical composition and the latter feature has a direct impact on CO₂ adsorption. The results corroborate that the specific surface area is important, but not the only determining factor for CO₂ adsorption in these materials. Thus, it is very important to take into account the chemical structure, especially for the enhancement of the interaction between CO₂ and nitrogen groups, particularly the pyridinic and pyrrolic groups. The total content of quaternary/graphitic species remains constant with the calcination temperature. Furthermore, the amount adsorbed is similar and even higher than that of other materials such as zeolites, mesoporous silicas and activated carbon, ranging between 2.0 and 2.6 mmol CO₂/g, depending on the carbonization temperature.

Acknowledgements

This research was funded by the Consejo Nacional de Ciencia y Tecnología (CONACyT) and the project SECITI/080/2017. To the network SEP-PROMEP “Diseño Nanoscópico y Textural de Materiales Avanzados”, with the Project “Síntesis y Fisicoquímica de Materiales Mesoporosos” (UAM-I CA-31 Fisicoquímica de Superficies). ROL acknowledgement to Isaac J. Pérez Hermosillo and Carlos Juárez Yescas by academic support.

References

- [1] Zhang XB, Xu J. Optimal policies for climate change: A joint consideration of CO₂ and methane. *Appl Energy* 2018;211:1021-9.
- [2] Meng L-Y, Park S-J. Superhydrophobic carbon-based materials: a review of synthesis, structure, and applications. *Carbon Lett* 2014;15:89-104.
- [3] Lee SY, Park SJ. A review on solid adsorbents for carbon dioxide capture. *J Ind Eng Chem* 2015;23:1-11.
- [4] Chaffee AL, Knowles GP, Liang Z, Zhang J, Xiao P, Webley PA. CO₂ capture by adsorption: Materials and process development. *Int J Greenh Gas Control* 2007;1:11-8.
- [5] Meng LY, Park SJ. Effect of heat treatment on CO₂ adsorption of KOH-activated graphite nanofibers. *J Colloid Interface Sci* 2010;352:498-503.
- [6] Rahaman MS a, Ismail a. F, Mustafa a. A review of heat treatment on polyacrylonitrile fiber. *Polym Degrad Stab* 2007;92:1421-32.
- [7] Ojeda López R, Pérez Hermosillo IJ, Esparza Schulz JM, Ramos-Sánchez G, Domínguez-Ortiz A. Controlling Structural and Electrochemical Properties of CNF through Calcination. In: Maryann C. Wythers, editor. *Adv. Mater. Sci. Res.*, New York: Nova Science Publishers; 2019, p. 79-118.
- [8] Schierholz R, Kröger D, Weinrich H, Gehring M, Tempel H, Kungl H, et al. The carbonization of polyacrylonitrile-derived electrospun carbon nanofibers studied by: In situ transmission electron microscopy. *RSC Adv* 2019;9:6267-77.
- [9] Thommes M, Kaneko K, Neimark A V., Olivier JP, Rodriguez-Reinoso F, Rouquerol J, et al. Physisorption of gases, with special reference to the evaluation of surface area and pore size distribution (IUPAC Technical Report). *Pure Appl Chem* 2015;87:1051-69.
- [10] Pels JR, Kapteijn F, Moulijn JA, Zhu Q, Thomas KM. Evolution of nitrogen functionalities in carbonaceous materials during pyrolysis. *Carbon NY* 1995;33:1641-53.

CO₂ adsorption on LTA zeolite with different particle dimensions

Edilene D. S. Ferracine¹, Juliana A. Coelho¹, Kele T. G. Carvalho¹, Darley C. Melo², Dilson Cardoso^{1*}

¹Laboratório de Catálise e Adsorção Aplicadas-LACAp, Universidade Federal de São Carlos, São Carlos, Brasil.

²Petrobras/Cenpes-Tecnologia de Processamento Primário. Rio de Janeiro, Brasil.

*E-mail: dilson@ufscar.br

Abstract

Natural gas extracted from pre-salt reservoirs in Brazil contains significant amounts of carbon dioxide (15-20% or up to 60% based on oil and gas production in 2018) and water (about 1000 ppm) which, if not reduced or removed, can cause obstruction in pipelines due to hydrocarbon hydrate formation and compromise safety of the system due to corrosion. This difficulty has been one of the most serious problems facing the offshore natural gas industry. Thus, reduction of undesirable components is a very important operation in offshore gas processing and the use of molecular sieves as adsorbents is one of the most robust technology for natural gas purification. For the purpose of improving the adsorption technology through the application of solids with enhanced properties, the main objective of this study was to synthesize zeolite A with mean particle size smaller than 250 nm and to compare its adsorptive properties with commercial LTA zeolite with average particle size of 2.0 μm . LTA zeolites were extruded to have their CO₂ adsorption capacities evaluated.

Keywords: natural gas, LTA zeolite, adsorption capacity

1. Introduction

Zeolites with LTA structure (3A, 4A and 5A) are adsorbents to most small molecules due to the high adsorption capacity by physical interactions. Therefore, these materials are mainly used in hydrocarbon storage processes [1], purification or separation of CO₂, H₂O, N₂, H₂S from natural and/or industrial gas [1-3]. A common destination for natural gas containing these contaminants is to be reinjected to avoid environmental contamination and to maintain oil reservoir pressure under operating conditions. Among the recommended specifications for gas reinjection, there is the maximum moisture content, which should be around 1 ppm. Because of some characteristics like well depth reservoir pressure, the pressure in the injection pipeline is high, and if the gas is humid, hydrocarbon hydrates will form and consequently clog the flow area.

The use of adsorbents capable of reducing the mass transfer zone length (MTZ) within the columns seems to be a good strategy to improve the efficiency of adsorption water removal processes and thereby decrease the weight of the processing towers.

In this sense, the reduction in the size of the zeolitic particles and the creation of mesoporosity in

the particles could shorten the length of the diffusion path and, consequently, reduce the mass transfer resistances, increasing the utilization of the adsorption bed.

In order to produce reduced particle size adsorbents to be commercially viable, it is essential to develop a method of synthesis with reduction of synthesis time and without organic directing agent, as its use increases the costs of production.

The synthesis of materials with nanometric dimensions has considerable advantage in this regard. In previous works by our group [4], modifications were made to the synthesis parameters, such as: addition of the aging stage and alteration of the basicity of the reaction medium. In addition, studies were performed on the time and temperature of aging and crystallization. Zeolites with LTA structure were obtained with different characteristics from that obtained following the procedure described in the Verified Syntheses of Zeolitic Materials [5], mainly regarding particle sizes, which originally had micrometer dimensions.

Thus, the objective of this work was to prepare and evaluate the adsorption properties of extrudates containing nanometer particles of LTA zeolite. These adsorbents were evaluated using CO₂ as a probe molecule. CO₂ adsorption equilibrium isotherms were obtained up to 1 bar and

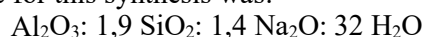
breakthrough curves of CO₂ (diluted in He) at partial pressures of 0.2 and 1.0 bar and 35 °C.

2. MATERIALS AND METHODS

2.1. Synthesis of “LTA small”

Nanometric LTA zeolite was synthesized by the method of a single isothermal step [4].

The precursor sources of silicon and aluminum were sodium silicate solution (SiO₂ = 28,7%, Na₂O = 9,12%, H₂O = 62,18%, Cenpes/Petrobras) and sodium aluminate (Sigma-Aldrich), respectively. The composition of the reaction mixture for this synthesis was:



Initially the sources of silicon and aluminum were dissolved separately in water and then mixed until homogenized for approximately 15 min. The resulting mixture (~ 240 g) was transferred to a PARR® stainless steel reactor and crystallized at 50 °C for 20 h. After this time the obtained solid was washed with distilled water until reaching pH 8.0 and dried at 80 °C and named as LTA-small.

2.2. Granulation of the adsorbent

The adsorbent obtained in powder form was granulated to perform the fixed bed CO₂ adsorption tests.

Firstly, a physical mixture of LTA zeolite and binder was performed, in a mass ratio of 3:1, respectively. The binder used was montmorillonite hydrophilic clay (Sigma Aldrich), whose molecular formula is Al₂O₃: 2SiO₂: H₂O.

After homogenization of the mixture, an amount of water close to 40 wt.% of the dry mixture was added to give a paste.

Then, the paste was accommodated in a screw-type mini-extruder with a transverse die and holes with a diameter of 3.8 mm.

The wet cylindrical extrudates were dried at 30 °C for 3 h and cut to approximately 5 mm in length.

The extruded material was named Pellet-LTA-small. A commercial Sigma Aldrich (SA) LTA zeolite with an average particle size around 2 μm was used, and the extrudate obtained under the conditions mentioned above was named Pellet-LTA-large.

The pellets were annealed at 400 °C for 30 min, using a heating rate of 2 °C·min⁻¹.

2.3. Adsorbents characterization

The adsorbents in powder and cylindrical extruded form were characterized by X-ray diffraction (XRD) using a Rigaku Miniflex diffractometer with Cu Kα radiation (λ = 0.1542 nm), at 2θ from 5 to 50°, in continuous scan mode with a step width of 0.02° and a scan speed of 10° min⁻¹. Scanning electron microscopy (SEM) was used to determine the morphology and particle size distribution and to analyze the surface of the adsorbents. The microscope used was the Magellan / FEI. CO₂ physisorption analyzes at 0 °C were performed on ASAP 2020 equipment (Micromeritics) to characterize LTA zeolite microporosity. Micropore volume was determined by the Dubinin-Radushkevich (DR) method [6]. The samples were pretreated at 350 °C under vacuum for 8 h. Nitrogen physisorption isotherms at -196 °C were obtained using a Micromeritics ASAP 2020 equipment. The total pore volume of the extrudates was calculated at P/P₀ = 0.85.

2.4. Breakthrough curves of CO₂

In order to evaluate the mass transfer in these materials, breakthrough curves of 2% and 10% CO₂ diluted in He were obtained at 35 °C, 10 bar and total flow of 1.0 SLPM, using a column of 9.0 cm in length and 0.85 cm in diameter. The adsorbents were pretreated at 300 °C under He flow (30 mL·min⁻¹) for 7 h. Mass after pretreatment was estimated by mass loss obtained from thermogravimetric analyzes.

2.5. CO₂ adsorption equilibrium isotherms

To assist in the interpretation of breakthrough curves, CO₂ adsorption equilibrium isotherms were performed at 35 °C and pressures up to 1.0 bar using an ASAP 2020 volumetric adsorption system (Micromeritics). The adsorption capacity obtained in this experiment was compared with that obtained in the experiment of section 2.4. The samples were pretreated at 300 °C under vacuum for 7 h.

3. RESULTS AND DISCUSSION

As shown in Figure 1, the powder and extruded samples exhibited XRD patterns with the crystalline plane diffraction peaks (2 0 0) (2 2 0) (2 2 2) (4 2 0) (4 4 2) (6 2 2) (6 4 2) (8 2 2) (6 6 4) corresponding to the LTA crystal structure.

Some peaks attributed to montmorillonite, used as binder, were also observed in the cylindrical extrudates.

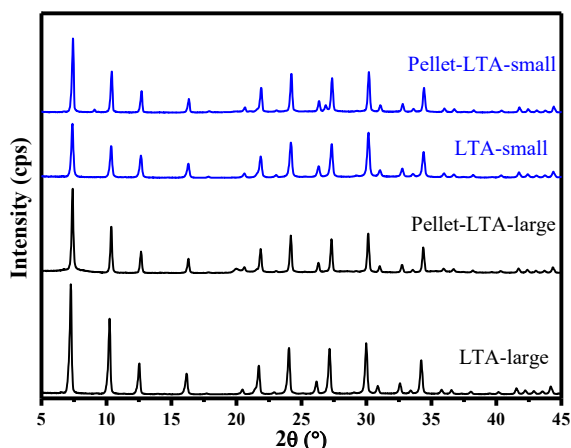


Fig. 1. X-ray diffractograms of LTA zeolites in powder and extruded form.

Figure 2 shows the SEM images of LTA zeolites in powder form. Synthesized LTA zeolite (*LTA-small*) exhibited greater uniformity in particle size (average particle size around 250 nm) than the commercial LTA zeolite (*LTA-large*). It is also noted that *LTA-large* zeolite has cubic crystalline habit, whereas *LTA-small* zeolite presents spherical particles.

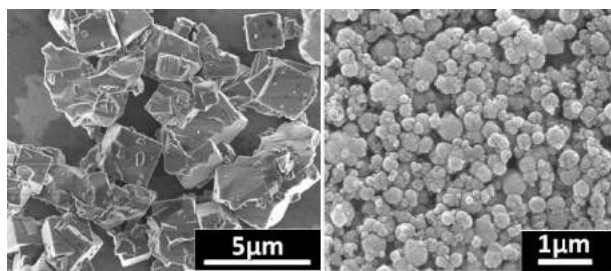


Fig. 2. SEM of zeolites (a) *LTA-large* and (b) *LTA-small*.

The micropore volume of the extruded and powder LTA zeolites (Table 1) was estimated by the CO_2 adsorption isotherms at 0°C (Figure 3).

The micropore volumes of the *LTA-large* and *LTA-small* zeolites in powder form are similar. For extruded zeolites, micropore volume decreased about 16% in comparison to the micropore volume value of the powder material. This decrease was due to the composition of the extruded grain, in which

the non-porous binder material represents about 25% of the total mass.

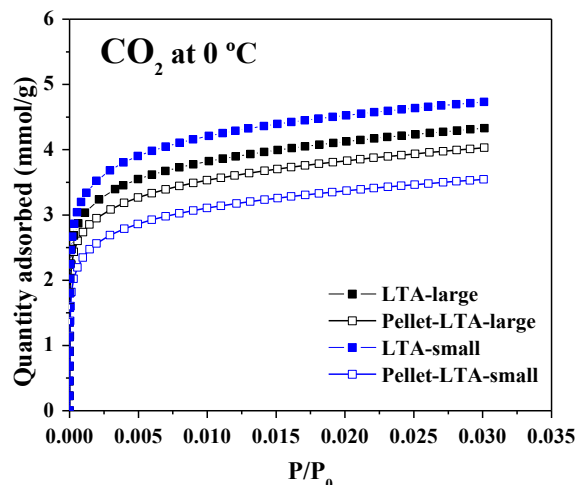


Fig. 3. CO_2 adsorption isotherm at 0°C of powder materials (closed symbols) and extruded materials (open symbols).

Table 1. Textural properties of powder and extruded zeolites.

Adsorbent	$^aV_{\text{micro}}$ ($\text{cm}^3 \cdot \text{g}^{-1}$)	$^bV_{\text{Total}}$ ($\text{cm}^3 \cdot \text{g}^{-1}$)
<i>LTA-large</i>	0.19	-
Pellet- <i>LTA-large</i>	0.16	0.016
<i>LTA-small</i>	0.21	-
Pellet- <i>LTA-small</i>	0.16	0.029

^aMicropore volume estimated by DR CO_2 adsorption

^bTotal pore volume estimated by N_2 adsorption (it does not include micropore volume).

Figure 4 shows the N_2 physisorption isotherms at -196°C of the extruded materials. The NaA zeolite isotherm does not show N_2 adsorption at low relative pressures ($P/P_0 < 0.02$), indicating that N_2 molecules cannot easily diffuse into LTA zeolite micropores [7]. This fact is attributed to the small micropore opening (0.42 nm) of NaA zeolite, since the kinetic diameter of N_2 molecules is 0.44 nm [8]. Thus, the isotherms presented indicate the porosity of the pellet formed in the granulation process.

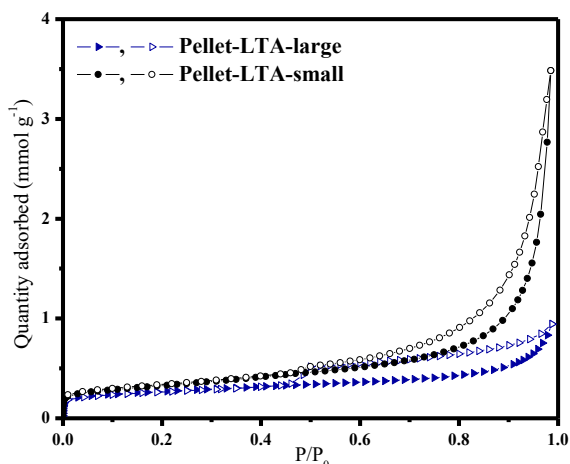


Fig. 4. N₂ adsorption-desorption isotherms at -196 °C of the extruded LTA zeolites.

According to IUPAC, the Pellet-LTA-small sample presented type II isotherm, typical of non-porous materials, but with hysteresis from the interparticular mesopores generated in the grain extrusion process. This type of isotherm represents a solid with wide pore size distribution.

The SEM images (Figure 5) show the surface of the extruded cylinders in the longitudinal direction of the grain. From the images with higher magnification, it is observed that the particles of the samples are similar, as observed in powder form (Figure 2), suggesting that the granulation process does not cause any significant morphological changes in these materials.

The micrographs show that the surface of the Pellet-LTA-small has as many defects as the surface of the Pellet-LTA-large sample, indicating that the extrusion system was similar for both samples.

Figure 6 shows the CO₂ adsorption isotherms at 35 °C. As expected, the CO₂ adsorption capacity of pellets is lower than that of powder materials, since for each gram of grain there is approximately 0.75 g of zeolite, which indeed adsorbs.

In this figure, it is also observed that for the powder adsorbents, the CO₂ adsorption capacity of both zeolites was similar, with a difference of approximately 5%, which is within the error range of the technique. However, for grain-shaped materials, Pellet-LTA-small adsorbent showed a greater reduction in adsorption capacity than Pellet-LTA-large. This reduction in CO₂ adsorption capacity is also observed by comparing the breakthrough curves performed at 1.0 SLPM shown in Figure 7. The rupture time for the Pellet-LTA-small sample was shorter than that of the Pellet-LTA-large. Although it is not possible to observe a

considerable difference in the shape of the curves, the Pellet-LTA-small has a breakthrough curve flatter than that of the Pellet-LTA-large, indicating a better mass transfer. It is intended to perform experiments with lower gas flow and/or partial pressure to better observe the phenomenon of mass transfer.

To assessment if this improvement in the mass transfer generates a reduction in adsorption capacity, it is also interesting to perform experiments under conditions as an industrial process to find out whether the zeolites with nanometer particles have an advantage over zeolites with micrometer particles..

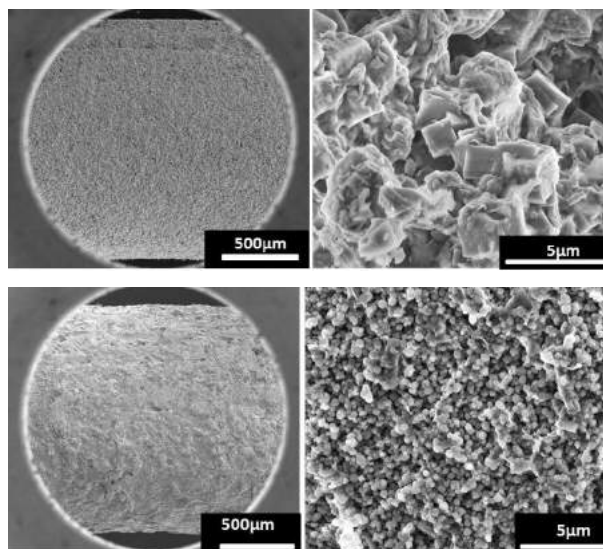


Fig. 5. Micrograph of the extruded: (A) Pellet-large and (B) Pellet-LTA-small.

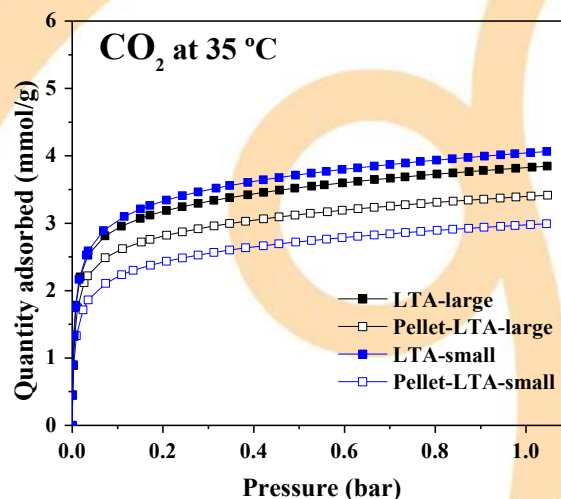


Fig. 6. CO₂ adsorption isotherms at 35 °C of powder materials (closed symbols) and extruded materials (open symbols).

Comparing the packing of the extruded materials, it is observed that the packing bed density (defined as the ratio of adsorbent mass to column volume) formed by Pellet-LTA-small is slightly lower (~10%) than that formed by Pellet-LTA-large. These data are presented in Table 2.

Table 2. Packing Bed Density

Adsorbent	Adsorbent mass (g)	Packing Bed Density (g·cm ⁻³)
Pellet-LTA-large	2.07	0.41
Pellet-LTA-small	1.90	0.37

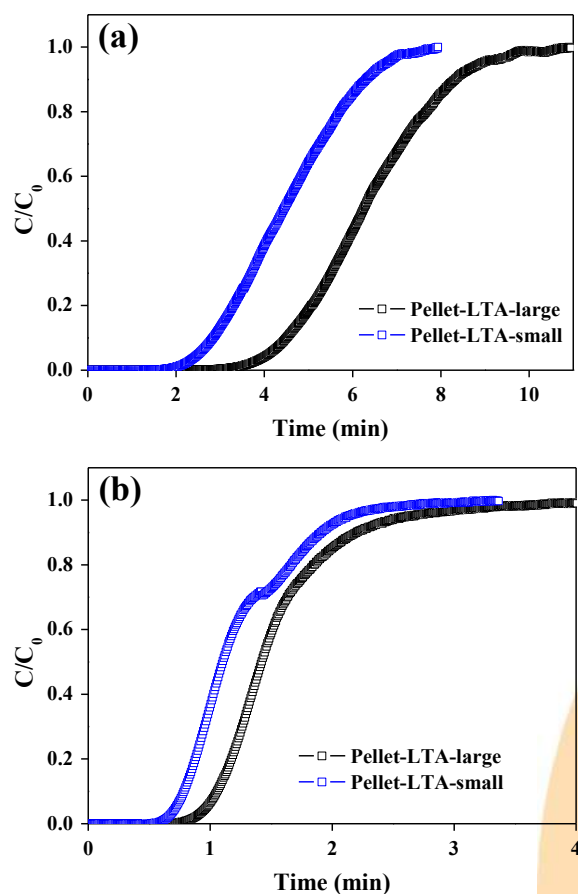


Fig. 7. Breaking curves of experiments with: (a) 2% of CO₂ and (b) 10% of CO₂ diluted in He at 35 °C and 10 bar.

3. Conclusions

The synthesis results showed that, using 20 h of synthesis and low temperature of hydrothermal treatment, it is possible to obtain LTA zeolite with particles with nanometer dimensions, with size around 250 nm. Thus, this synthesis is more attractive compared to that performed with long aging times of the reaction mixture.

CO₂ adsorption isotherms showed a tendency for a small reduction in adsorption capacity with decreasing average zeolite particle size. This effect is probably due to structural defects caused by the reduction in the average particle size. However, although this reduction occurs, the faster diffusion of gases into nanometric materials could make them promise for use in cyclic adsorption processes: Pressure Swing Adsorption or Temperature Swing Adsorption.

Acknowledgements

The authors are grateful for the financial support provided by Petrobras and the UFSCar Structural Characterization Laboratory (LCE) for the microscopy analysis.

References

- [1] Meier, W.M. Molecular Sieves, Soc. Chem. Ind., London, 1968.
- [2] Ruthven, D. M. Microporous and Mesoporous Materials. v. 162. p.69-79, 2012.
- [3] Ahmad, J.; Hägg, M. J. Membrane Science. v.427. p.73-84, 2013.
- [4] E. D. S. Ferracine et al., 20º Congresso Brasileiro de Catálise, 2019.
- [5] H. Robson; K. P. Lillerud, Verified syntheses of zeolitic materials., Elsevier Science, 2001, vol 2.
- [6] Rouquerol, F. et al. Adsorption by Powders and Porous Solids Adsorption by Powders and Porous Solids. 2nd ed. Elsevier (2014).
- [7] Breck, D.W. - Zeolite Molecular Sieves - Wiley and Sons, New York (1974).
- [8] Hirschfelder, J.O., Curtiss C.F., Bird R.B. - Molecular Theory of Gases and Liquids - John Wiley & Sons, New York (1964).

Application of In-situ X-ray Characterization Techniques in Zeolites: A Review

Khalil Kashefi^a, Darley C Melo^b, Frederico W Tavares^c, Amaro G Barreto Jr^{a,*}

^aPrograma de Pós Graduação em Engenharia de Processos Químicos e Bioquímicos, EQ-UFRJ, and ^bCENPES, PETROBRAS S.A., and ^cPrograma de Engenharia Química, COPPE, UFRJ, Rio de Janeiro, Brazil

Abstract

Zeolites have wide range of application. The mechanisms involved (in adsorption and desorption) are affected by parameters such as the porous media structure on the surface and bulk, affinity to the adsorbate, and also the interactions between solid-fluid and fluid-fluid. Therefore, using various types of characterization techniques is inevitable to explore the mechanisms and the effect of the mentioned parameters, in particular at real condition (temperature, pressure and presence of the fluids). In this review, in-situ characterization of zeolites using X-ray based techniques is discussed. Some popular techniques such as XRD, IR, Raman, NMR, XPS, SEM/EDS and CT are briefly introduced and some recent research works on the application of zeolites are mentioned. The combination of the techniques such as XRD or microscopy with other spectroscopic methods is reported to be able to provide complementary information. It is shown that with the aid of newly available characterization techniques, synchrotron facilities and experimental cells, it is possible to carry out experiments in the scale of micro to meter, uncovering new findings to improve the present separation and dehydration processes.

Keywords: Zeolite, X-ray characterization, In-situ techniques

1. Introduction

Zeolites are usually based on silicate frameworks that some of the Si are displaced with Al leads to a negative charge on the framework, with cations (usually Na, Ca, Mg or other alkalin) within the pore structure. These are porous crystalline framework materials with pores of molecular size. They are available in nature and can be synthesized in laboratory. The first synthetic zeolite was made from Na, Si, and Al named zeolite A, which is capable of adsorbing water as a drying agent and also n-paraffins [1]. By 2007, about 176 known structures of zeolites were reported [2] with application in chemical reactions (as catalysts) and selective adsorbents.

In designing a new catalyst/adsorbent or in optimizing the performance of an existing one, the knowledge of activity, selectivity, and durability is needed. The zeolites of Al/Si frameworks are negatively charged materials that are balanced by cations. The cations are located on a set of zeolite sites that leads to a stable structure. The localization of the cations is affected by temperature and presence of H₂O, CO₂ or other species. It is therefore not possible to know the

structural details by extrapolating from room temperature structural information [3]. This means that to fully understand the physical properties of the material, both the framework structure and the cation positions need to be determined under actual working conditions using in situ time-resolved situation to improve the understanding of the mechanisms [4].

Due to the large penetration depth of X-rays, the interaction of X-rays with matter has been applied extensively as popular characterization techniques [5]. During the last decade, in situ spectroscopic methods have provided an unprecedented level of detail of the underlying molecular mechanisms and their kinetics and they have emerged as principal tools for the in situ observation of crystallization. Spectroscopic methods are especially informative when used in conjunction with other techniques such as in situ X-ray diffraction (XRD) [6], which is a common tool used to investigate cation distributions, the interaction between cations and guest molecules and the structure [4]. FTIR and NMR spectroscopy are universally used methods for the investigation of catalytically active sites in solid catalysts and the reactants interacting with these sites [7]. X-ray microscopy and computed tomography (CT) can be combined with various X-ray analytical techniques, yielding elemental,

structural, and chemical contrast [3]. CT can truly provide 3D measurement as an in situ technique [8]. Synchrotron X-rays are generated by large particle accelerators where high-speed electrons (approaching the speed of light) are accelerated in magnetic lattices such as bending magnets and insertion devices that can provide more information about material via higher penetration and brilliance [9]. Most of the above mentioned techniques can be performed in a beamline with better resolution in an in situ situation.

With the aim to review different application, capabilities and possibilities of using X-ray characterization techniques with focus on in-situ conditions, some of the research works reported in literature on zeolite molecular sieve under different adsorption and desorption conditions (temperature, pressure, adsorbate and so on) are discussed in this communication.

Table 1 summarizes all the mentioned research works reported in the following sections.

2. X-ray Diffraction

X-ray diffraction (XRD) is an essential and useful tool in the identification and characterization of zeolites at various stages in their syntheses, modifications, and different applications. XRD allows us to examine the long-range atomic structure of crystalline materials. For zeolites this includes the framework topology and the positions of extra-framework cations and/or adsorbed molecules. This method, first of all, discriminates between amorphous and crystalline samples. For crystalline materials, it allows for the determination of the component phases. Furthermore, it allows for the determination of particle size and other characteristics of the component crystallites. In most cases, it also allows for the determination of the atomic arrangement of the atoms in the crystallographic unit cell [1], [3]. The in situ setups include different parts such as X-ray sources, flow control, product analysis, in situ cells and detectors. A large portion of recent in situ X-ray measurements have taken place at synchrotron sources because of their high intensity [3].

Two types of zeolites, 13X [10] and 4A [11] with the application in adsorption (H_2O , CO_2 , CH_4 , H_2S and COS) were investigated using different techniques, including XRD. The intensity and broadening of the XRD peaks showed that the synthesized zeolites 13X and 4A samples have considerable crystallinity. The XRD pattern of the

mentioned synthesized zeolites compare well with the dehydrated zeolites data reported by IZA [2].

In another study [12], by in situ synchrotron high-resolution X-ray powder diffraction (XRPD) and in situ Fourier transform infrared (FTIR) spectroscopy, host-guest and guest-guest interactions, cation distribution, probing physisorbed / chemisorbed, formation of other compounds in adsorption and effect of temperature / pressure on the process of CO_2 adsorption/desorption in two nanosized FAU zeolite samples (with different Si/Al ratios) were investigated. For XRPD measurement, the following procedure was taken: After sample activation (heating at $250^\circ C$ and 5×10^{-6} bar) the diffraction patterns were recorded. Data collections were performed at RT, at $250^\circ C$, at RT after dehydration, after CO_2 loading, and at RT after evacuation. The presence of physisorbed or chemisorbed CO_2 and the form of chemisorbed species were detected by XRPD.

Structure of zeolite FAU (Ba-Y) frameworks with presence of H_2O or NO_2 molecules were investigated [4] using an in situ time-resolved X-ray diffraction (synchrotron-based). In the hydrated structure, water molecules form four double rings of hexagonal icelike clusters $[(H_2O)_6]$ in the 12 ring openings of the supercage. These water rings interact with the cations and the zeolite framework through four cation/water clusters centered over the four six-membered rings of the supercage (site II). Interpenetrating tetrahedral water clusters $[(H_2O)_4]$ and tetrahedral Ba cation clusters are observed in the sodalite cage.

An in situ X-ray diffraction cell and a methodology were developed [13] to study structural modifications induced by the dehydration of SrRbX zeolite at $250^\circ C$. In situ dehydration process was characterized by an increase of the cell parameters, variation of diffracted intensities and modification of the cationic distribution. The results obtained by Rietveld refinement showed that the dehydration process led to a decrease of the total number of cations per unit cell located in the supercage and a displacement of Sr^{+2} and Rb^+ cations.

Thermal dehydration of zeolite bikitaite at temperature up to $800^\circ C$ was studied [14] using an in situ XRD. A high stability was observed during the process regardless of low Si/Al ratio. This stability was referred to the presence of columns of 5-membered tetrahedral rings.

Some selected studies on in-situ XRD application were mentioned in this section. As it can be seen, there is a high potential to deepen the



knowledge on zeolite structure, stability and adsorption/desorption mechanisms under severe operational conditions and presence of different adsorbate with using this technique.

3. Infrared and Raman Spectroscopy

Infrared spectroscopy (IR) has been used to almost all aspects of zeolite chemistry, formation, framework vibrations, surface property, adsorption and catalysis. In general, near-IR spectroscopy provides information on adsorbed species such as water, organic molecules and small gas molecules, etc. in zeolite cavities or channels. Raman spectroscopy gives vibrational information that is complementary to IR. Raman is preferred for studying host-guest interactions in zeolites via monitoring the guest molecules due to the very weak Raman scattering nature of the “normal” zeolite framework [1].

As mentioned in XRD section, in-situ FT-Raman was used to analyze the surface of the two zeolites and to identify any reactions that may occur during the adsorption process [10], [11]. The zeolite samples were pretreated in the environmental chamber at 200°C for 48 h under vacuum to remove any contaminants before exposure to the pure components at 25°C. Raman spectra were recorded under application of CO₂, H₂S and CH₄ (pressure up to 13.8 bar and ambient temperature) and the related bonds were recognized successfully. In addition, in-situ CO₂ adsorption using FT-IR was used [11] to investigate zeolite 4A under CO₂ presence and physisorption of CO₂ and possibility of chemisorption of carbonate and/or impurities within the CO₂ was detected.

As mentioned earlier, both in-situ FTIR and XRD spectroscopies were performed on two zeolite samples [12]. The in-situ FTIR measurements were carried out in these steps: samples activation under vacuum and high temperature (up to 250°C), under CO₂ presence, under high vacuum desorption at RT and also desorption at 250°C. Using this technique, physically adsorbed, chemisorbed and non-adsorbed (in gas phase, due to the broadening of the feature) CO₂ were determined. The detected chemisorbed CO₂ corresponds to different types of carbonates because of the participation of framework oxygen atoms. Upon subjecting the samples to high vacuum desorption at RT, the band corresponding to physisorbed CO₂ (and CO₂ in the gas phase) diminished drastically, whereas those

corresponding to the chemisorbed CO₂ remained unchanged. An interesting observation lies on the existence of bidentate carbonate in zeolite with lower ratio of Si/Al. The lower Si/Al ratio of the sample induces a closer proximity of Al within the framework and then of Na cations, and thus higher possibilities for the formation of bidentate species exist.

In-situ IR spectroscopy was successfully employed [15] to study the surface species formed during adsorption of NO, NO+O₂ and NO₂ on zeolites type Y (Na and Br) and also sorption sites at temperature range up to 450°C.

The studies that were mentioned above showed that in-situ IR and Raman spectroscopies can enhance our knowledge on adsorbate-adsorbent interaction.

4. Solid-State NMR Spectroscopy

In-situ NMR experiments are performed in solid state MAS mode, in a rotor spinning at high frequency to gain detailed information concerning the atomic environments of framework building elements in the solid [6]. Solid-state NMR spectroscopy allows the investigation of the local structure of nuclei in the solids under study. The specific behavior of zeolites often depends on local effects, such as framework defects, the substitution of framework atoms, guest compounds etc. Therefore, solid-state NMR spectroscopy is a widely applied analytical method for delivering structure data, which are complementary to those of diffraction methods suitable for investigating the long-range order [1]. A recent review considered the NMR studies of CO₂ adsorption [16] and it is mentioned that there is a wide array of NMR methods that are suitable to study molecular and mesoscopic aspects of physi- or chemisorbed CO₂ and the method has mainly been used to characterize CO₂ sorbents.

Solid-state NMR experiments has now matured to the stage where characterization of the structure, disorder and dynamics of microporous materials is possible [17].

5. X-ray Photoelectron Spectroscopy

In XPS, an X-ray photon impinges on a sample, a photoelectron is emitted, and its kinetic energy is measured. The kinetic energy of the photo-emitted electron is a sensitive measure of both the element from which the electron was emitted and the chemical surroundings of that element. The



technique of X-ray photoelectron spectroscopy (XPS) is among the most used techniques to measure the composition and chemical state of adsorbent at high-vacuum condition [3].

Different characterization techniques including XPS was employed [18] to study CO₂ adsorption on zeolite 13X (treated with amino groups). The surface atomic concentrations of elements nitrogen were obtained by XPS measurements. In addition, the binding energy values for C 1s and N 1s could reveal the types of bonds available.

The investigation on the adsorption of carbon dioxide and water on a nanoporous zeolitic imidazolate frameworks film was performed [19] using XPS (for surface) and TPD (for bulk) at 90 K. By using this combination, authors were able to distinguish between a molecule (H₂O) that adsorbs to the outer nanoparticle surfaces and a molecule (CO₂) which diffuses into the pores.

XPS test needs to be done at ultra high vacuum, so only temperature can be manipulated as an in-situ technique, however it is reported [3] that recently a modern form of XPS that can be used at gas pressures up to about 7 mbar known as ambient pressure X-ray photoelectron spectroscopy (AP-XPS) is developed.

6. Microscopy and EDS

Primary zeolite particles can be relatively large, ~1µm, thus, secondary electron imaging (SEI) in the scanning electron microscope (SEM) provides very useful information about the general microstructure. The zeolite unit cell, however, is significantly smaller, typically ~1–3 nm, so is better characterized by transmission electron microscopy (TEM). Secondary electrons are, by definition, low energy electrons, so they are generated from the top few nanometers of the material's surface, making a relatively straightforward, intuitive interpretation. In the case of zeolites, the general crystal morphology is typically characterized in the SEM using the SEI [1]. Energy-dispersive X-ray spectroscopy (EDS) as an elemental analysis is frequently useful in both SEM- and TEM-based studies. EDS is based on the collection of X-rays generated as incident electrons impinge upon specimens in both the SEM and TEM [1].

The crystal morphology and Si/Al ratio of the previously mentioned zeolites, 13X [10] and 4A [11], were subjected to be determined using SEM and EDS microanalysis. The SEM images of zeolites 13X and 4A (chamfered-edges cubes)

clearly present that the samples are an agglomerated crystalline material. EDS at multiple points shows that the Si/Al mole ratios of the product were found to be 1.8 and 1.14 for zeolite 13X and 4A, respectively.

In other work, in addition to study of high-pressure adsorption of methane, carbon dioxide, and nitrogen on zeolite 13X, the average crystal size of the sample was obtained by scanning electron microscopy (SEM) [20]. In a similar study, the images obtained by TEM related to the previously mentioned sample (FAUs) [12] show the high crystallinity with octahedral morphology and uniform particles with average sizes of 20 nm (Si/Al of 1.24) and 150 nm (Si/Al of 2.54).

7. Computed Tomography

X-ray computed tomography (CT) allows one to probe the adsorption process in three dimensions, in-situ condition, in bench/lab scale setup, with instruments able to cover a wide range of resolutions and system sizes from the micrometer (crystal size) to the meter (reactor size).

Spatially resolved adsorption isotherms of 3 fixed-bed column were measured with CT [8]. Experiments have been carried out in a column bed (length of 11cm, inner diameter of 5 cm) with a multilayered fixed-bed consisting of glass beads, zeolite 13X pellets, and activated carbon rods at 25 °C and pressure up to 30 bar using CO₂. The results of this work comprise a set of 4D data in the form of three-dimensional scans of a layered bed at different partial pressures of CO₂. It was shown the ability to couple conventional subcritical gas adsorption experiments and interpretation with X-ray CT imaging for 3D characterization of porous systems at resolutions spanning multiple length scales from the micrometer to the meter useful for the systematic design of formulation processes and scale up of nanoporous solids into shaped structures, such as pellets, monoliths, or foams. This work was continued by reporting the results of a first in-depth study [21], where measurements of space-resolved adsorption isotherms (3D mapping of gas physisorption) are combined with machine learning to provide a three dimensional characterization of an adsorbent bed.

8. Conclusions

In-situ X-ray characterization techniques can provide important theoretical and practical



knowledge on zeolite as molecular sieve at the micro and nano scale. The capability of the in-situ approaches to develop a realistic view on zeolite in operation condition is demonstrated by reviewing some available works. This review shows the complexity of an adsorption/desorption process regarding many factors, such as effect of temperature, pressure, zeolite stability and structure and the possibility of physi/chemisorption, that are involved in this mechanism. It is reported also that the characterization methods can be combined to complete their range of application. Some popular combinations are mentioned as XDR or microscopic method coupled with spectroscopic techniques.

The in-situ X-ray characterization techniques are making progress both in quality of the information due to high technology implemented in synchrotron beamlines and in delivering data in the range of high temperature/pressure and in monitoring the chemical/zeolite interactions involved in the process. Therefore, there are much more valuable scientific investigations that can be performed in this area.

Acknowledgements

The authors wish to thank CENPES/Petrobras for supporting this research.

References

- [1] A. W. Chester and E. G. Derouane, Zeolite characterization and catalysis. 2009.
- [2] "International Zeolite Association (IZA)." [Online]. Available: <http://www.iza-online.org/>.
- [3] In-Situ Characterization of Heterogeneous Catalysts, vol. 2013, no. 12. 2013.
- [4] X. Wang, J. C. Hanson, J. H. Kwak, J. Szanyi, and C. H. F. Peden, "Cation Movements during Dehydration and NO₂ Desorption in a Ba-Y,FAU Zeolite: An in Situ Time-Resolved X-ray Diffraction Study," *J. Phys. Chem. C*, vol. 117, no. 8, pp. 3915–3922, Feb. 2013.
- [5] J. Singh, C. Lamberti, and J. A. van Bokhoven, "Advanced X-ray absorption and emission spectroscopy: in situ catalytic studies," *Chem. Soc. Rev.*, vol. 39, no. 12, p. 4754, 2010.
- [6] A. Aerts, C. E. A. Kirschhock, and J. A. Martens, "Methods for in situ spectroscopic probing of the synthesis of a zeolite," *Chem. Soc. Rev.*, vol. 39, no. 12, p. 4626, 2010.
- [7] M. Hunger, "Applications of in situ spectroscopy in zeolite catalysis," *Microporous Mesoporous Mater.*, vol. 82, no. 3, pp. 241–255, Aug. 2005.
- [8] L. Joss and R. Pini, "Digital Adsorption: 3D Imaging of Gas Adsorption Isotherms by X-ray Computed Tomography," *J. Phys. Chem. C*, vol. 121, no. 48, pp. 26903–26915, 2017.
- [9] B. T. W. Lo, L. Ye, and S. C. E. Tsang, "The Contribution of Synchrotron X-Ray Powder Diffraction to Modern Zeolite Applications: A Mini-review and Prospects," *Chem*, vol. 4, no. 8, pp. 1778–1808, Aug. 2018.
- [10] K. G. Wynnyk, B. Hojjati, and R. A. Marriott, "High-Pressure Sour Gas and Water Adsorption on Zeolite 13X," *Ind. Eng. Chem. Res.*, vol. 57, no. 45, pp. 15357–15365, 2018.
- [11] K. G. Wynnyk, B. Hojjati, P. Pirzadeh, and R. A. Marriott, "High-pressure sour gas adsorption on zeolite 4A," *Adsorption*, vol. 23, no. 1, pp. 149–162, 2017.
- [12] M. Polisi et al., "CO₂ Adsorption/Desorption in FAU Zeolite Nanocrystals: In Situ Synchrotron X-ray Powder Diffraction and in Situ Fourier Transform Infrared Spectroscopic Study," *J. Phys. Chem. C*, vol. 123, no. 4, pp. 2361–2369, Jan. 2019.
- [13] C. Pichon, H. Palancher, B. Rebours, J. Lynch, J. F. Béar, and J. L. Hodeau, "In situ characterisation by anomalous X-ray diffraction of the cationic distribution of dehydrated SrRbX zeolite," 2004, pp. 1641–1648.
- [14] O. Ferro et al., "Dehydration dynamics of bikitaite: Part I. In situ synchrotron powder X-ray diffraction study," *Am. Mineral.*, vol. 89, no. 1, pp. 94–101, Jan. 2004.
- [15] C. Sedlmair, B. Gil, K. Seshan, A. Jentys, and J. A. Lercher, "An in situ IR study of the NO_x adsorption/reduction mechanism on modified Y zeolites," *Phys. Chem. Chem. Phys.*, vol. 5, no. 9, pp. 1897–1905, Apr. 2003.
- [16] D. Bernin and N. Hedin, "Perspectives on NMR studies of CO₂ adsorption," *Curr. Opin. Colloid Interface Sci.*, vol. 33, pp. 53–62, Jan. 2018.
- [17] S. E. Ashbrook, D. M. Dawson, and V. R. Seymour, "Recent developments in solid-state NMR spectroscopy of crystalline microporous materials," *Phys. Chem. Chem. Phys.*, vol. 16, no. 18, pp. 8223–8242, 2014.
- [18] D. P. Bezerra et al., "CO₂ adsorption in amine-grafted zeolite 13X," *Appl. Surf. Sci.*, vol. 314, pp. 314–321, Sep. 2014.
- [19] F. Tian et al., "In Situ Measurement of CO₂ and H₂O Adsorption by ZIF-8 Films," *J. Phys. Chem. C*, vol. 119, no. 27, pp. 15248–15253, Jul. 2015.
- [20] S. Cavenati, C. A. Grande, and A. E. Rodrigues, "Adsorption Equilibrium of Methane, Carbon Dioxide, and Nitrogen on Zeolite 13X at High Pressures," *J. Chem. Eng. Data*, vol. 49, no. 4, pp. 1095–1101, 2004.
- [21] L. Joss and R. Pini, "3D mapping of gas physisorption for the spatial characterisation of nanoporous materials," *ChemPhysChem*, p. cphc.201801148, Dec. 2018.

Table 1. Summary of the reviewed research works.

Ref.	Techniques
X-ray Diffraction (XRD)	
[10]	① Zeolite 13X, ② Adsorption: H ₂ O, CO ₂ , CH ₄ , H ₂ S, COS, ③ Ambient T and P, ④ Crystallinity of zeolites
[11]	① Zeolite 4A, ② Adsorption: CO ₂ , CH ₄ , H ₂ S, COS, ③ Ambient T and P, ④ Crystallinity zeolites
[12]	① Zeolite FAU (different Si/Al ratios), ② Adsorption: CO ₂ , ③ i) In situ XRD Synchrotron, ii) T up to 250°C, iii) P, high vacuum to 1.85 bar, ④ i) Average structure, ii) Probing the CO ₂ adsorption/desorption, iii) Detecting physisorbed and/or chemisorbed CO ₂ in zeolites, iv) Detecting bidentate bicarbonate groups
[13]	① Zeolites SrRbX and NaX, ② Dehydration, ③ i) In situ XRD Synchrotron, ii) T up to 250°C, ④ Using Rietveld refinement, it was observed: i) Dehydration process led to a decrease of the total number of cations per unit cell located in the supercage, ii) Displacement of Sr ²⁺ and Rb ⁻ cations
[14]	① Zeolite bikitaite, ② Thermal dehydration stability, ③ i) In situ XRD, ii) T up to 800°C, ④ High stability was observed
[4]	① FAU (Ba-Y), ② Catalyst study, ③ i) In situ XRD Synchrotron, ii) Time resolved, iii) T up to 350°C, ④ Provide information about the migration of the Ba ²⁺ cations in the zeolite framework during dehydration and during NO ₂ adsorption/desorption
Infrared (IR) and Raman Spectroscopy	
[10]	① Zeolite 13X, ② Adsorption: H ₂ O, CO ₂ , CH ₄ , H ₂ S, COS, ③ In situ CH ₄ , CO ₂ , and H ₂ S adsorption using FT-Raman (P up to 13.85 bar T at 25 °C), ④ i) In situ FT-Raman: Symmetric and asymmetric T–O–T stretching modes were detected, ii) CO ₂ , H ₂ S and CH ₄ were identified via their bonds
[11]	① Zeolite 4A, ② Adsorption: CO ₂ , CH ₄ , H ₂ S, COS, ③ i) In-situ CO ₂ adsorption using FTIR (P up to 12.53 bar and T at 25 °C), ii) In situ CH ₄ , CO ₂ and H ₂ S adsorption using FT-Raman (P up to 13.85 bar T at 25 °C), ④ i) In situ FTIR: determination of physisorbed CO ₂ on the zeolite 4A and possibility of chemisorbed CO ₂ (as carbonate and/or impurities), ii) In situ FT-Raman: Symmetric and asymmetric T–O–T stretching modes were detected. Also CO ₂ , H ₂ S and CH ₄ were identified via their bonds
[12]	① Zeolite FAU (different Si/Al ratios of 1.24 and 2.54), ② Adsorption: CO ₂ , ③ i) In situ FTIR, ii) T up to 250 °C, iii) P from high vacuum to 1.85 bar, ④ i) Probing the CO ₂ adsorption/desorption, ii) Detecting physisorbed and chemisorbed CO ₂ in zeolites, iii) Detecting bidentate bicarbonate groups and comparison the presence possibility between two zeolite types
[15]	① Zeolite Y (Na and Br), ② Adsorption: NO _x , ③ i) In situ IR, ii) T up to 450°C, ④ i) Surface species formed during adsorption of NO _x , ii) Identifying sorption sites
Solid-State NMR Spectroscopy	
[1], [6], [16], [17]	② Mostly in synthesizing the adsorbents, ④ There is a high potential in using solid-state NMR experiments to characterize the structure, disorder and dynamics of many microporous materials due to development in different aspects of this technique (experimental and theory)
X-ray Photoelectron Spectroscopy (XPS)	
[18]	① Zeolite 13X (treated with amino groups), ② Adsorption: CO ₂ , ③ Ambient T and ultra high vacuum, ④ i) Elemental analysis, ii) Binding energy
[19]	① Zeolitic imidazolate frameworks (ZIF), ② Adsorption: CO ₂ , H ₂ O, ③ Ultra high vacuum and T 90 K, ④ Adsorption information from the surface
Microscopy and EDS	
[10]	① Zeolite 13X, ② Adsorption: H ₂ O, CO ₂ , CH ₄ , H ₂ S, COS, ③ Ambient T and P, ④ i) Crystal shape of the synthesized zeolites (SEM), ii) Si/Al ratio (EDS)
[11]	① Zeolite 4A, ② Adsorption: CO ₂ , CH ₄ , H ₂ S, COS, ③ Ambient T and P, ④ i) Crystal shape of the synthesized zeolites (SEM), ii) Si/Al ratio (EDS)
[20]	① Zeolite 13X, ② Adsorption: CO ₂ , CH ₄ , N ₂ , ③ i) SEM, ii) Ambient T and P, ④ Crystal size distribution
[12]	① Zeolite FAU (different Si/Al ratios of 1.24 and 2.54), ② Adsorption: CO ₂ , ③ Ambient T and P, ④ Average particle size and morphology
Computed Tomography (CT)	
[8]	① i) Activated carbon, ii) Zeolite 13X, iii) Glass beads, ② Adsorption: CO ₂ , ③ i) T at 25°C, ii) P up to 30 bar, ④ Demonstrated the capability of combining conventional gas adsorption experiments X-ray CT imaging for 3D characterization of porous systems

① Adsorbent type, ② Objectives, ③ Conditions, ④ Outcome

Trimodal hierarchical zeolite LTA for adsorption: a preliminary characterization study

Raquel de A Bessa^a, André L S Pereira^b, Morsyleide F Rosa^b, Michael W. Anderson^c,
Adonay R Loiola^{a,*}

^a Department of Organic and Inorganic Chemistry - Federal University of Ceará, Pici Campus, Fortaleza 60440-900, CE, Brazil.

^b Brazilian Agricultural Research Corporation, R Dra Sara Mesquita 2270, Fortaleza 60511-110, CE, Brazil.

^c Centre for Nanoporous Materials, The University of Manchester, Manchester M13 9PL, UK.

Abstract

In order to overcome issues related to compaction and mass transfer blockages in liquid and gas adsorption systems, hierarchical structures have been widely studied and developed in the last two decades. This work evaluates cartridges formed with the 3 pore types (micro-, meso- and macropores). Characterization by XRD demonstrates that zeolite A (LTA) is formed as a single phase with high crystallinity, even using a bifunctional surfactant during the synthesis and SEM micrographs show the cubic shape of the crystals that are formed by nanoparticles surrounding the mesopores. When added to bacterial cellulose, the crystals of zeolite A seem to interact well with the cellulose, while being spread throughout the sheets with only a minor percentage of agglomerated particles observed. The N₂ adsorption/desorption isotherms show the meso- and macroporosity for those materials with improved surface area when compared with conventional zeolite A, whilst ionic exchange experiments present slight decrease in the ion removal rate.

Keywords: zeolite LTA; hierarchical pore systems; bacterial cellulose; TPOAC.

1. Introduction

In the last 10 years, there was ~200% increase in Hierarchization-related publications. Among the materials with a great impact to this characteristic, zeolites can be highlighted. This is due to the big industrial interest to exploit their chemical and physical properties, such as ionic exchange capacity, molecular sieving characteristic and acid sites for catalysis that are hindered by separation processes in a post-application step or even for problems related to mass transfer in single bed experiments. [1, 2]

Many approaches can be used to obtain zeolites with a similar structure and in a bottom-up method, where surfactants introduce the mesoporosity in addition to the zeolite micropores. The use of two directing agents in the gel usually results with a reaction mixture containing amorphous phases. The bifunctional surfactants, on the other hand, can be used for a variety of zeolite structures to produce pure phases containing both types of pore systems to a good extent. [3]

Several works deal with this type of materials especially in catalytic processes and the advantages related to them are remarkable and very promising

for other applications where zeolites have importance and great use, as in adsorption systems. [4]

The aim of this work is to evaluate preliminarily the synthesis of a novel material containing bacterial cellulose to introduce macroporosity and work as a support to a hierarchical zeolite A (LTA) prepared using a bottom-up approach with a bifunctional surfactant.

2. Methods

Hierarchical zeolite A was synthesized by adopting a strategy based on the use of the bifunctional surfactant [(3-trimetoxyethyl)propyl] octadecyldimethyl-ammonium chloride-TPOAC, (42 wt.%, Sigma-Aldrich), which forms micelles in due to its long carbon chain and thus, directs the formation of mesopores, whilst its hydrophilic part interacts with the aluminosilicate species present in the gel giving rise to micropores.



The oxides ratio used was 100 SiO₂/333 Na₂O/67.0 Al₂O₃/20000 H₂O/8 TPOAC, as suggested by Cho *et al.*, 2009 [5], where Al₂O₃ source was NaAlO₂; SiO₂, Na₂SiO₃; Na₂O, NaOH. TPOAC was added to the silicate portion of the gel prior the addition to the aluminate portion. The gel was aged for 1 day at room temperature and then crystallized for 4 h in a pre-heated oven. The products were washed by filtration with distilled water, dried and calcined in an oven at 550 °C/ 6h.

Bacterial cellulose (BC) suspensions were obtained from pellicles produced after 10 days of cultivation and fermentation, followed by purification, disintegration and oxidation, homogenized into a 0.5 wt.% suspension.

Composite BC/zeolite cartridges were prepared by mixing 1.0 wt.% of zeolite to this BC suspension, using an ultrasonic bath for 5 minutes and then freezing with liquid N₂. The cartridges obtained after the freeze-drying were composed 2/3 of zeolite, in mass.

The formed materials were characterized using X-ray powder diffraction (XRD), scanning electron microscopy (SEM), N₂ adsorption/desorption and ionic exchange experiments (10 mg of material + 25 mL of Ca²⁺ 100ppm solution; 30 minutes; magnetic stirring). A cartridge containing just cellulose and a zeolite A powder produced by the conventional method [6] were used to compare the measured properties for the hierarchical sample.

3. Results and discussion

The XRD results are presented in Figure 1, where the peak position analysis indicates zeolite A as main pure phase, presenting a good crystallinity and thus, the aluminosilicate gel in presence of TPOAC

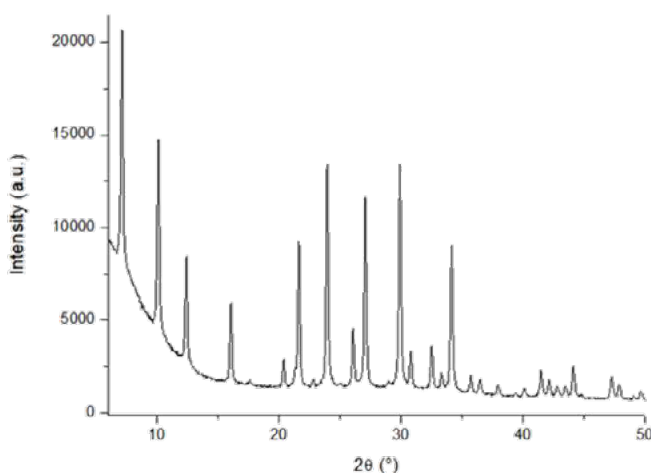


Figure 1. XRD pattern for bifunctional zeolite A.

can be used for hierarchical zeolite synthesis using a bottom-up approach.

As shown in SEM micrographs, the zeolite A crystals present morphology compatible to zeolite A, with cubic habit having ca. 2 μm diameter. The most prominent characteristic is that the particles are composed of numerous domains of interconnected nanocrystals. It is also noticed that the particle outline is more rounded than a conventional zeolite A. These characteristics are desirable towards the next step of cartridge formation as the presence of those defects on the structure promotes a better interaction with the cellulosic matrix, as presented in Figure 2.

In the composite cartridges, the zeolite crystals are mostly dispersed throughout cellulose sheets, which are formed by nanofibrils with big voids among them. The images show that these spaces are interconnected, forming a hierarchical material,

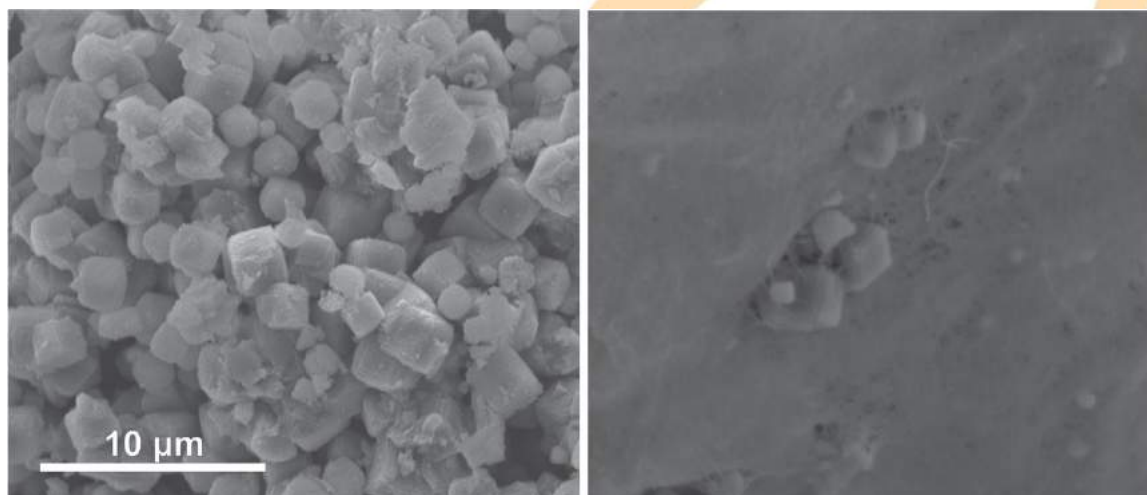


Figure 2. SEM micrographs of zeolite A bifunctional (left) and its composite, dispersed in cellulose fibrils (right).

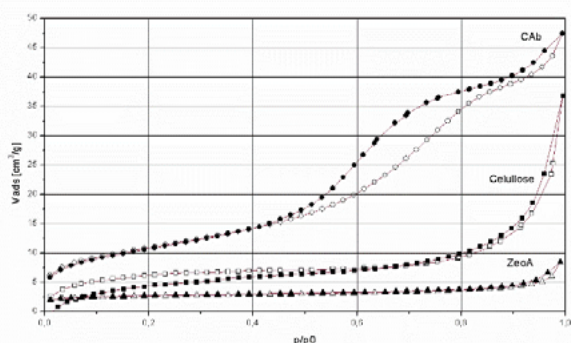


Figure 3. N₂ adsorption/desorption isotherms of conventional zeolite A, cellulose and bifunctional zeolite A

with 3 types of pore systems that, most importantly, are interconnected.

Although some agglomeration can be seen, it appears as a minor effect, as can be evidenced in the N₂ adsorption/desorption experiments. Also, the agglomeration is not causing compaction or other problems related to the mass transfer, and this can be improved in the future work.

The N₂ adsorption/desorption characterization of cellulose, zeolite A and the composite with the hierarchical zeolite A are presented in Figure 3. These characterizations were performed using a degas program at 90 °C/12 h to avoid damage of the cellulose structure.

Both zeolite A and cellulose have low surface area (8 and 20 m² g⁻¹, respectively, as expected for the used conditions). When the bimodal zeolite is added to the BC, A bigger surface area is observed, ~ 38 m² g⁻¹, and a hysteresis type IVa in the isotherm, characteristic of meso+macroporous materials. Thus, we have evidence of the good interaction between the zeolite A and the bacterial cellulose, even with some agglomeration points, and the formation of the hierarchy desired with the 3 pore types.

The ionic exchange experiments were carried out to evaluate whether the pore structure underwent any damages due to the zeolite A formation in the presence of the surfactant. After the batch experiments, they were removed from solution by filtration and characterized using ICP. The results are presented as molar composition in Figure 4.

It is observed that for zeolite A almost all Ca²⁺ ions were removed, exchanged by the Na⁺ ions, while the bifunctional sample presents a lower exchange rate, since this is not related to the surface area, but to charges on structure, and to the presence of the surfactant in the synthesis gel, which promotes molecular bonds with the aluminosilicate

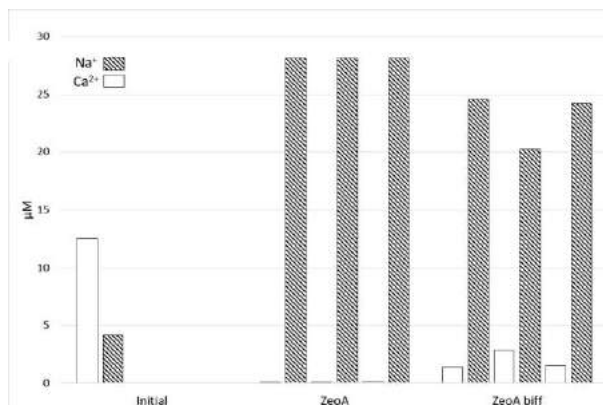


Figure 4. Ionic exchange data for conventional and bifunctional zeolite A

precursor in addition to ion-ion interactions, decreasing the amount of sodium in the structure in comparison with the conventional zeolite A. Even though, around 80% removal is observed. Experiments using the specific amounts for complete exchange and characterization of other active sites are planned to be done in the next steps of this work.

4. Conclusions

In summary, hierarchical zeolite A was successfully obtained via a bottom-up approach, using TPOAC as a surfactant and the product presented a cubic aspect formed by nanocrystals that are connected in the structure. When added to the cellulose, a 3 pore system is formed, with interconnected spaces, being like this, a hierarchical porous material.

Acknowledgements

This study was financed in part by the Coordenação de Aperfeiçoamento de Pessoal de Nível Superior - Brasil (CAPES) - Finance Code 001.

References

- [1] Cychosz KA, Guillet-Nicolas R, Garcia-Martinez J, Thommes M. *Chem Soc Rev* 2017; 46, 389.
- [2] Wei Y, Parmentier TE, de Jong KP, Zecevic J. *Chem Soc Rev* 2015; 44, 7234.
- [3] Verboekend D, Nuttens N, Locus R, Van Allstate J, Verolme P, Groen, Perez-Ramirez J, Selsa BF. *Chem Soc Rev* 2016; 45, 3331.
- [4] Hartmann M, Machoke AG, Schwiager W. *Chem Soc Rev* 2016; 45 3313
- [5] Cho K, Cho HS, de Menorval L-C, Ryoo R. *Chem Mater* 2009; 21, 5664.
- [6] Mintova S, Barrier N. *Verified Syntheses of Zeolitic Materials* 2016; p 255.



Characterization of mesoporous region by the scanning of the hysteresis loop in adsorption-desorption isotherms.

C. Toncón-Leal^a, J. Villarroel-Rocha^{a*}, M. T. P. Silva^b, T. P. Braga^b, K. Sapag^a

^a Laboratorio de Sólidos Porosos – Instituto de Física Aplicada – Universidad Nacional de San Luis, Ejército de los Andes, 950 – San Luis – CP: 5700, Argentina.

^b Laboratorio de Peneiras Moleculares – Instituto de Química – Universidad Federal do Rio Grande do Norte, Av. Sen. Selgado Filho 3000 – Natal – CP: 58078-970, Brasil.

Abstract

Scanning hysteresis loop provide information about the correlation of the pore network with regards to connectivity and pore size distribution, which cannot be revealed from the complete isotherm. To analyze this effect for ordered mesoporous materials such as SBA-15 and SBA-15 modified with iron and cobalt oxides, it was performed the N₂ and Ar adsorption-desorption isotherms and the corresponding scanning of the hysteresis loops. Two mathematical models based on the independent domains theory, Uncorrelated Model and Partial Correlated Model, were applied to adjust the desorption branches in the hysteresis loops associating these results to the connectivity in the porous network and the presence of pore blocking effects.

Keywords: Capillary condensation; Scanning hysteresis loop; ordered mesoporous materials.

1. Introduction

There are mesoporous materials that have an ordered porous structure and narrow pore sizes. These materials usually have a high specific surface area and a large pore volume, providing a high adsorption capacity, which is an interesting characteristic to be used in industrial applications as catalytic processes [1].

The capillary condensation phenomenon of fluids in mesoporous materials is used to understand effects such as: confinement of fluids, diffusion of fluids and even the tortuosity or interconnected porous network [2]. This phenomenon is usually an irreversible process in which a hysteresis loop is formed during adsorption/desorption experiments [3-4]. Hysteresis loops can be observed in materials with unconnected and interconnected pores, caused by the transition vapor-liquid-vapor, where the adsorption process occurs under a metastable equilibrium and the desorption from thermodynamic equilibrium. The presence of interconnected pores can be associated to constrictions inside the pores or "bottlenecks pores" among others which causes a delay in the desorption process compared to adsorption [5-6].

Therefore, understand the behavior of hysteresis loops would allow characterize the porous network of materials. It is known that the hysteresis shape contains information about the porous structure, and through the scanning of the hysteresis loop it is possible obtain information about of the porous network, connectivity or interconnection and pore size distribution and the adsorption/desorption mechanisms in the mesoporous region [7-8]. Hence, the detailed study of these aspects may contribute to the characterization and understanding of the porous network and the adsorption/desorption mechanisms.

Cimino et al. proposed a Uncorrelated (*UM*) and a Partially Correlated Models (*PCM*), which can be used to determine if exist or not correlation in the mesoporous structure by adjusting the desorption branch in the hysteresis loops of the isotherms. These models can be used to study isotherm of N₂ at 77 K as well as Ar at 87 K.

In this work, it was used the Cimino et. al models to analyze the hysteresis loops in ordered mesoporous materials like SBA-15 and the same impregnated with iron and cobalt [9]. The isotherms and the corresponding scanning analysis of the hysteresis loop for SBA-15 was carried out by Nitrogen isotherms at 77 K while for the modified SBA-15 sample, by Argon at 87K.



2. Materials and Methods

2.1 Reagents

The used reagent in the mesoporous support and the catalyst synthesis were triblock co-polymer (EO20-PO70-E20) Pluronic 123 (P123) (Sigma Aldrich), tetraethyl ortosilicate (TEOS) 98 % (Merck), HCl 37 % wt. (Merck), EtOH absolute (Merck), $\text{Fe}(\text{NO}_3)_3 \cdot 9\text{H}_2\text{O}$ (Anedra), $\text{Co}(\text{NO}_3)_2 \cdot 6\text{H}_2\text{O}$ (Anedra) and distilled water.

2.2 Mesoporous support synthesis

Pluronic-123 was used as structure driver, TEOS as Si source and HCl as catalysts. The process consisted of dissolving P-123 in 37 wt.% $\text{HCl}_{(\text{ac})}$ and kept under stirring for 3 h at 35 °C, TEOS was later added and the stirring was kept for 24 h at the same temperature. Afterwards, the mixture was treated in an autoclave at 100 °C for 24 h. The resulting solid was washed with distilled water and filtered. The material was finally calcined at 600 °C for 6 h using a heating rate of $2^\circ\text{C} \cdot \text{min}^{-1}$.

2.3 Incorporation of the Fe and Co

Cobalt nitrate (II) and iron nitrate (III) were dissolved in distilled water. Afterward, both solutions were mixed. The impregnation was made by adding this solution to the SBA-15 support. Later, the samples were thermally treated for 2 h at 700 °C. The amount of salt was adjusted to obtain the desired percentage of metal in the resulting material, where the active phase percentages were 13 wt.% Fe/3 wt.% Co.

2.4 Characterization

The hysteresis loop scanning as well as the complete isotherms by N_2 and Ar adsorption-desorption isotherms at 77 K and 87 K, respectively, were made in a manometric adsorption equipment Autosorb iQ (Quantachrome Instruments); where the samples were previously degassed at 475 K for 12 h.

2.5 Models

The more adopted adsorption-desorption models to study the mesoporous region using capillary theory are according to *independent pore theory* to adjust experimental results. This theory was proposed by Everett which says that each pore of

the material is an adsorption-desorption domain that does not interact with other domains [10]. More recently, based in the behavior of the hysteresis loops, Cimino et al. proposed a Uncorrelated (*UM*) and a Partially Correlated Models (*PCM*).

2.5.1 Uncorrelated Model (*UM*)

This model make the assumption that condensation and desorption pressures in pores are not correlated. This model is based on experimental observations that in the absence of interconnection effects the shape of the cycling resembles the shape of the main isotherm

$$Q_-(X, X_a) = Q_+(X_a) - (1 - Q_+(X_a))Q_-(X) \quad (1)$$

The *UM* model is described by equation 1, where Q refers to the fraction of unfilled pores and the subscripts + and - are of the adsorption and desorption branch respectively. X is the relative pressure and the subscript a is the value corresponding to the relative pressure where begin the hysteresis loop in the adsorption branch.

2.5.2 Partial Correlation Model (*PCM*)

. This model implies that desorption cycles are a linear function of the unfilled pore fraction.

$$Q_-(X, X_a) = Q_+(X_a) - (Q_-(X_a) - Q_+(X_a))(Q_-(X)/Q_-(X_a)) \quad (2)$$

Equation 2 describes the *PCM* model, where the variables have the same meaning as those mentioned in the previous model and the subscript d is the value corresponding to the relative pressure where begin the hysteresis loop in the desorption branch.

3. Results and Discussion

Figure 1 show N_2 adsorption-desorption isotherm at 77 K (gray with filled symbols) and scanning desorption of the hysteresis loop (black with open symbols) for pure SBA-15 material (without Fe and Co). The hysteresis loop corresponds to a type H1 that is characteristic of materials with a well-defined mesoporous structure, which have a narrow pore size distribution.

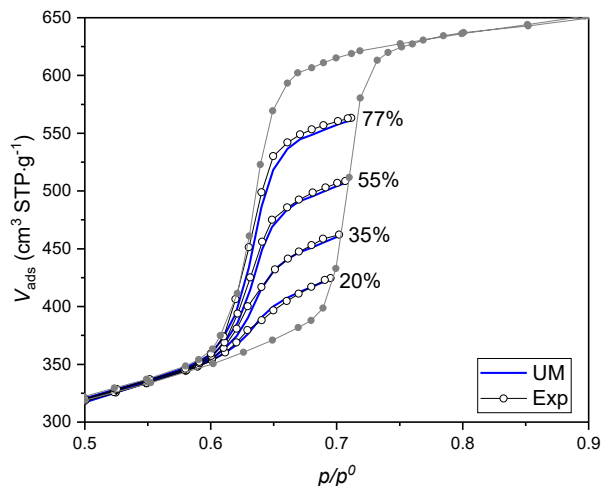


Fig. 1. N₂ at 77 K scanning desorption of the hysteresis loop for SBA-15 material. (○) experimental data, (—) *UM* model.

UM model was applied to scanning desorption branches, which fits with the experimental data. Therefore, the mesopores can be considered as independent domains, i.e. there are no interconnection or pore blocking effects.

Figure 2 shows Ar adsorption-desorption isotherm at 87 K and scanning desorption branches for SBA-15/FeCo material. After iron-cobalt incorporation, the shape of the hysteresis loop of SBA-15/FeCo isotherm changed to type H5, related to the presence of both open and partially blocked mesopores.

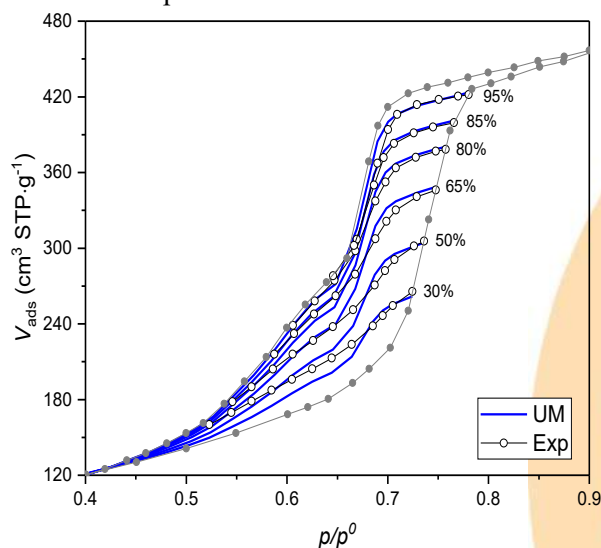


Fig. 2. Ar at 87 K scanning desorption of the hysteresis loop for SBA-15/FeCo. (○) experimental data, (—) *UM* model.

The hysteresis loop present two desorption stages: the first (between 0.7 and 0.65 of p/p^0) is given by the emptying of open mesopores and the second, which is less pronounced, (between 0.65 and 0.5 of p/p^0) is associated by the emptying of blocked mesopores (necks), which contribute to the formation of interconnected pores.

Applying the *UM* model to scanning desorption branches (Figure 2), it is observed that the model adjust those desorption points where emptying of the open mesopores occurs. However, the model does not fit the stage where the blocked mesopores are emptied (at relative pressures less than 0.65), overestimating the desorbed volume. If the model does not fit the experimental data, it indicates the presence of interconnection or pore blocking effects that make desorption a cooperative process.

A bimodal distribution centered on 6.5 and 8 nm is observed in the PSD (Figure 3), which is consistent with the two desorption stages mentioned above. These mesopores sizes are the contribution of the interconnection (bottleneck) and the size of the open mesopores.

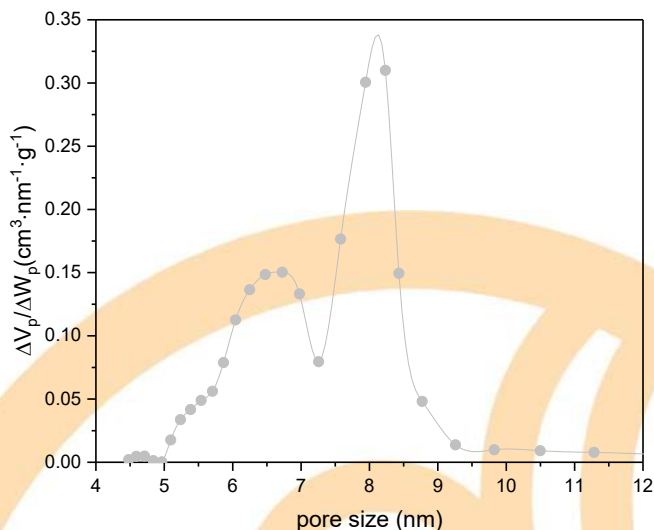


Fig. 3. Pore size distribution of SBA-15/FeCo

Due to the aforementioned interconnection effects, additional to *UM* model it was also used the *PCM* model to adjust the hysteresis loops (Figure 4). In this Figure it is observed that the experimental data at relative pressures between 0.65 and 0.8 (emptying region of the open mesopores) fits with the *UM* model. However, *PCM* model, unlike the *UM* model, fits the data between 0.5-0.65 of relative pressure (emptying region of the blocked pores).

As observed in Figure 2 the UM model adjust to desorption points where emptying of the open mesopores occurs. However, this model does not fit the stage where the blocked mesopores are emptied (at relative pressures less than 0.65),

overestimating the desorbed volume. Then, we can conclude that in the region where the UM model it is not adequate can be associated with the presence of interconnection or pore blocking effects.

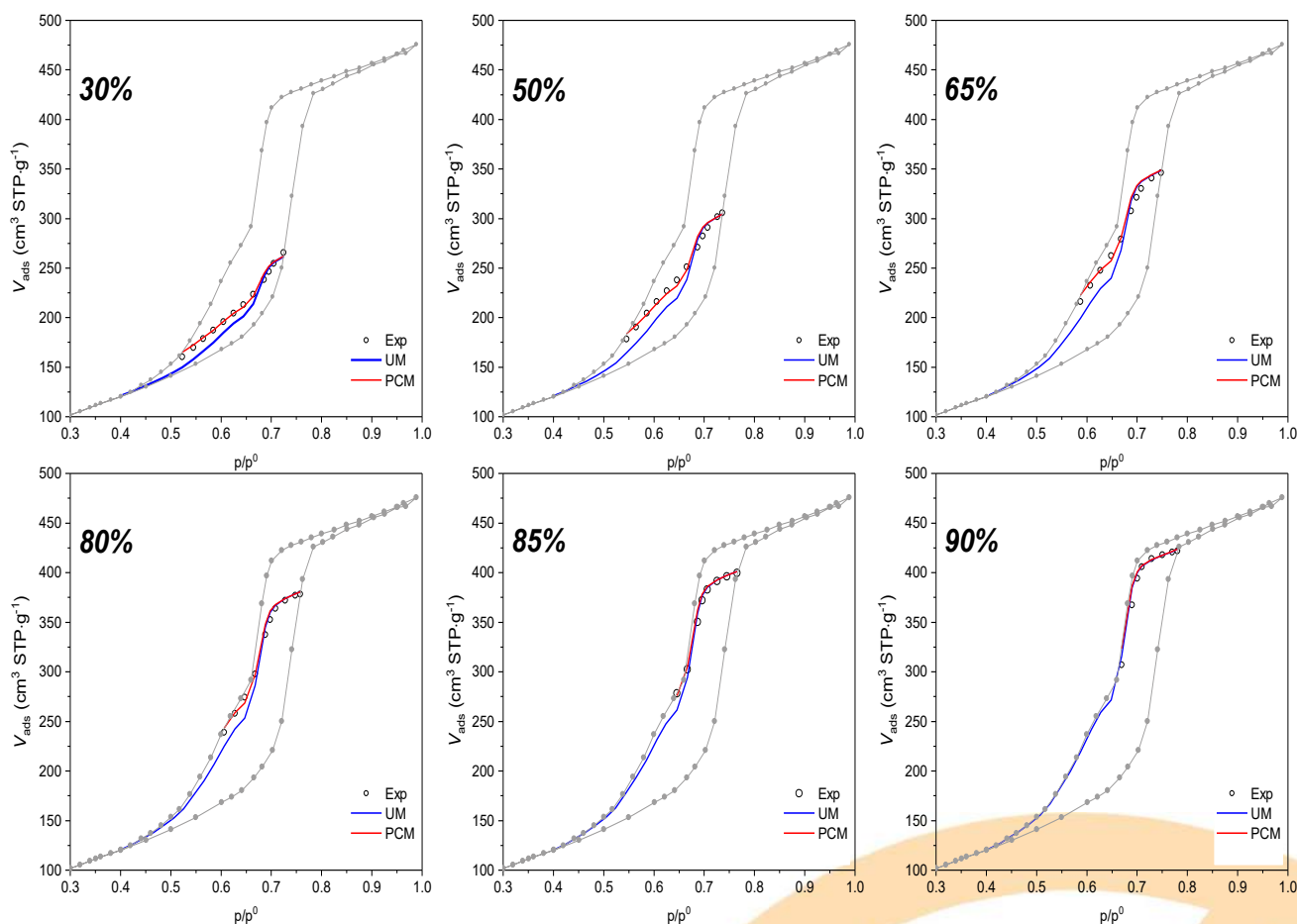


Fig. 4. Scanning of the hysteresis loop desorption of Ar at 87 K on SBA-15/FeCo. *UM* models (red), *PCM* (blue)

Adjusting the *PCM* model with the experimental data, meaning that there is no presence of network effects in the porous structure of the SBA-15/FeCo material. Hence, the open mesopores and the blocked mesopores by the metal oxide particles inside the pores, are independent of each other.

Iron and cobalt can be stabilized as oxides inside or outside the porosity of the SBA-15 or a combination of both. If iron and cobalt particles are located inside the mesopores, it can be expected that those nanoparticles generate pore blocking or interconnections between mesopores with different sizes, as schematized in Figure 5.

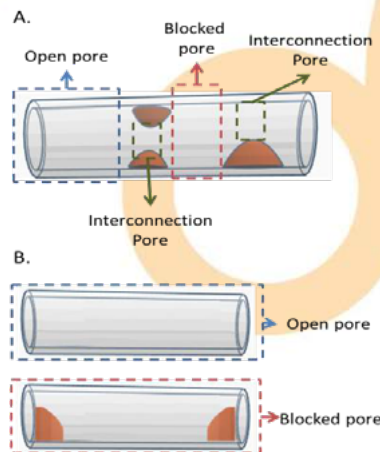


Fig. 5. Schematic representation of: open pores, blocked pores and interconnections between cylindrical geometry pores.

Acknowledgements

The authors want to thank UNSL, UFRN, ANPCyT and CONICET for the financial support of this work.

References

- [1] Medeiros-Costa I, Laroche C, Pérez-Pellitero J, Coasne B. Characterization of hierarchical zeolites: Combining adsorption/intrusion, electron microscopy, diffraction and spectroscopic technique. *Micropor Mesopor Mat* 2019;287:167-176.
- [2] Bruschi L, Mistura G, Liu L, Lee W, Gösele U, Coasne B. Capillary Condensation and Evaporation in Alumina Nanopores with Controlled Modulations. *Langmuir* 2010;26(14):11894-11898.
- [3] Gelb LD, Gubbins KE, Radhakrishnan R, Sliwinska-Bartkowiak M. Phase separation in condensed systems. *Rep Prog Phys* 1999; 62: 1573-1659.
- [4] Bruschi L, Mistura G. Adsorption within and on regularly patterned substrates. *J Low Temp Phys* 2009;157:206-220.
- [5] Cohan L. Sorption Hysteresis and the Vapor Pressure of Concave Surfaces. *J Am Chem Soc.* 1983;60(2):433-435
- [6] Everett DH. In *The Structure and Properties of Porous Materials*. Butterworths: London; 1958.
- [7] Rouquerol J, Avnir D, Fairbridge CW, Everett DH, Haynes JM, Pernicone N, Ramsay JDF, Sing KSW, Unger KK. Recommendations for the characterization of porous solids. *IUPAC Recomm* 1994;66:1739-1758
- [8] Lowell JSS, Shields JE, Thomas MA, Thommes M. *Surface Area, Porosity and Density*. The Netherlands: Kluwer Academic Publishers; 2004.
- [9] Cimino R, Cychosz KA, Thommes M, Neimark AV. Experimental and theoretical studies of scanning adsorption-desorption isotherms. *Colloids Surf A* 2013;437:76-89.
- [10] Everett DH. Adsorption hysteresis. In: E.A. Flood (Ed.). *The Solid-Gas Interface*. Decker: New York; 1967.

Synthesis of zeolites from hydrothermal solution reuse for CO₂ capture

Suelen Gislon^a, Vanessa Viola^a, Sabrina Estevam^a, Thiago Aquino^a, Carolina Marques^a,
Lídia Vasconcelos^b

^a Beneficent Association of the Santa Catarina Coal Industry (SATC), Pascoal Meller St. 73, Criciúma - 88805-380, Brazil

^b ENEVA S.A., Praia de Botafogo 501, Rio de Janeiro - 22250-040, Brazil

Abstract

Synthetic zeolites have several industrial applications due to their excellent physicochemical properties and have been widely obtained from wastes such as coal ashes. Most of the obtaining processes involve methods that use hydrothermal solutions that are discarded after the synthesis procedure, with few studies on the reuse of the generated effluents. Thus, considering the minimization of environmental risks and optimization of the synthesis process of NaX zeolite from coal fly ash, the possibility of reusing the residual solution from the hydrothermal reaction step in the synthesis of new zeolites was studied. From this reuse, there is the possibility of a large reduction in the use of NaOH and clean water used in the process. In this same context, it was also verified the influence of use water from the regional supply network to replace the distilled water used during laboratory experiments. The mineralogical composition (XRD) and CO₂ adsorption capacity (TGA) analyzes were performed to evaluate the products. The results showed the possibility of a reduction of around 33 % in the amount of NaOH added in the fusion step and the possibility of reusing 40 % of the residual solution without losses in the CO₂ adsorption capacity. In addition, the possibility of using the water from the supply network was also proven, where a slight increasing of the adsorption capacity was obtained in comparison with distilled water (from 2.15 to 2.51 mmol/g).

Keywords: Zeolite synthesis. Coal ash. Hydrothermal solution reuse. CO₂ adsorption.

1. Introduction

Synthetic zeolites have been indicated as potential adsorbents to CO₂ adsorption process because of their good properties, such as: high adsorption capacity, high specific surface area and pore volume, chemical and thermal stability and others [1]. The synthesis of zeolites from industrial wastes, such as coal ashes, has been widely studied and products with commercial quality have already been cited in the literature [2,3,4].

Most of the synthesis processes involve methods that use hydrothermal solutions, which are discarded after the procedures. Therefore, there are few studies on the reuse of the generated effluents, mainly for the hydrothermal reaction method preceded by previous fusion [2,4]. In this synthesis method, the main waste produced is the hydrothermal solution, an effluent that contains high concentrations of sodium, silicon and aluminum. Thus, their disposal

requires proper treatment to minimize the risk of environmental contamination and increases the added value of synthesized zeolites [5]. As the chemical elements found in the residual hydrothermal solution are consistent with the composition of the synthesized zeolites, the present work aimed to reuse the hydrothermal solution and reduce the amount of reactants used in the synthesis. In addition, the application of water from the supply network in the synthesis of zeolites as well its reuse was also evaluated.

2. Materials and Methods

The fly ash sample used in this study was collected at Jorge Lacerda power plant in the city of Capivari de Baixo (Santa Catarina state, Brazil). All the reactants were analytical grade. To compare the results of CO₂ adsorption capacity, it was used a

powder commercial zeolite NaX from Shanghai Hengye Chemical Industry.

2.1 Synthesis method of the initial zeolites

In the present study, zeolites type NaX were synthesized based on previous studies, where the parameters of the processes have been already optimized [2,4,6]. The syntheses were carried out by a two-step process consisting of prior fusion of the ash with sodium hydroxide (NaOH) and subsequent hydrothermal reaction. The flowchart in Figure 1 shows the synthesis steps.

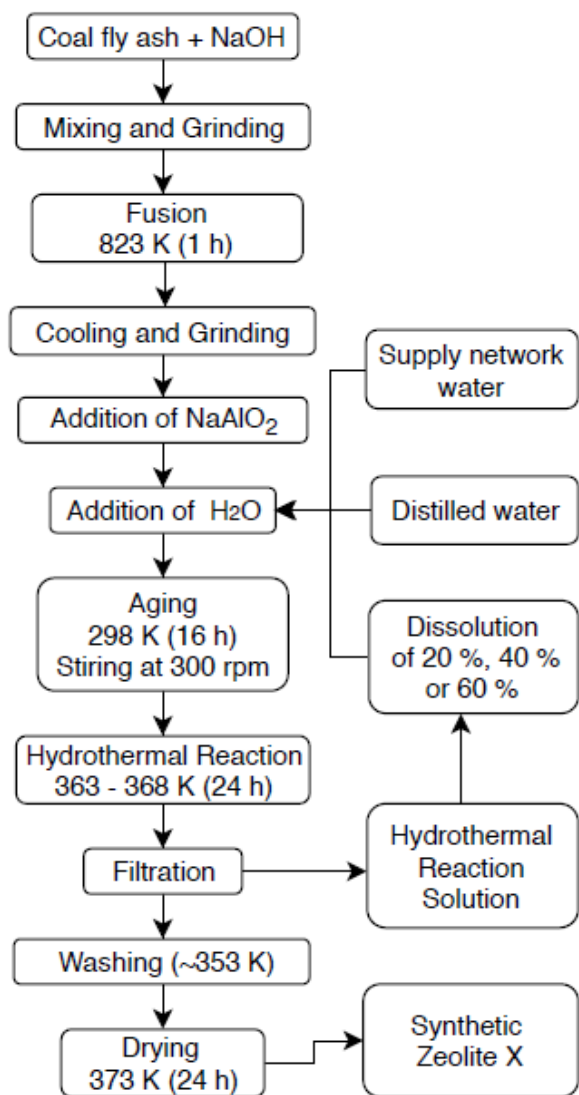


Fig.1. Synthesis step flowchart.

The ratio of NaOH/ash mixture was previously defined in order to obtain the desired zeolite considering the chemical characterization of the ash

(in terms of major elements) and the quantification of phases performed by XRD (mineralogical composition). For the adjustment of the molar ratios, the amorphous percentage of silicon and aluminum was considered.

After the fusion step, the samples were cooled and grinded, and NaAlO_2 and H_2O were added. Their value was set according to the desired Si/Al and Na/Si ratio. The sample was homogenized by agitation at 300 rpm at room temperature for 16 h. After the solubilization step, the hydrothermal reactions were performed in a static PTFE reactor with controlled temperature between 363 and 368 K during 24 h.

Once the hydrothermal reaction was completed, the solution was filtered and the zeolite sample was dried at 373 K for 24 h. Initially, two samples were synthesized and the molar ratios of their main components are presented in Table 1. The reduction of NaOH/ash ratio in the sample 2 had as main objective verify the possibility of reducing the amount of NaOH added in the fusion step without loss the product quality, since the addition of residual water will provide an extra amount of Na in the mixture. The difference between NaOH used in sample 1 to sample 2 is 33.33 %.

It is important to emphasize that the addition of NaOH needs to be enough to break the crystalline structures of the ash (quartz and mullite) in the fusion but cannot be high enough to modify the type of zeolite formed [2]. The ratio of 0.8 was fixed based on previous studies of the fusion step.

Table 1. Molar ratios of the main components used in the synthesis with distilled water.

Sample	1	2
$\text{SiO}_2/\text{Al}_2\text{O}_3$	3.50	3.50
$\text{Na}_2\text{O}/\text{SiO}_2$	2.05	1.42
NaOH/Ash	1.20	0.80
$\text{H}_2\text{O}/\text{Na}_2\text{O}$	51	51

2.2 Hydrothermal reaction solution reuse

To study the reuse of the wastewater from the hydrothermal reaction, the solution produced from the Sample 1 was used and the ratios between the main oxides were kept the same as in Sample 2. The use of the solution was varied from 100 % to 40 %, together with distilled water as showed in Table 2. The Na, Si and Al concentrations of the solution were determined by inductively coupled plasma optical emission spectrometry (ICP-OES).

Table 2. Tests performed for the use of residual solution.

Sample	3	4	5	6
Distilled Water (%)	0	20	40	60
Hydrothermal reaction solution (%)	100	80	60	40

2.3 Synthesis using water from supply network

Based on the good results obtained in the previous step and considering the use of industrial scale zeolite synthesis method, one synthesis was carried out using water from the supply network (Sample 7) with the same ratios used for the synthesis of Sample 1. Then, the best reuse condition previously verified (supply network water = 60 % and hydrothermal reaction solution = 40 %) was applied for the synthesis of Sample 8.

2.4 Zeolite characterization

All samples were characterized by X-ray diffraction (XRD) technique (Shimadzu, XRD-6100), using the powder method, to verify the formation of the zeolite of interest (NaX zeolite). The determination of the CO₂ adsorption capacity was also performed for all samples through a thermogravimetric analyzer (TGA) (TA Instruments, SDT 650). For the adsorption, the samples were previously activated for 30 min at 723 K under N₂ flow and then cooled at 303 K. For the adsorption step, the N₂ flow was switched to a 7 % CO₂/N₂ mixture flow and kept for 20 min. The use of this CO₂ concentration intended to simulate the composition of exhaust gases generated in the combustion of coal power plants.

3. Results and Discussion

3.1 Initial synthetic zeolites

The XRD patterns for Sample 1 and Sample 2 are shown in Figure 2. Both samples show good NaX zeolite formation, which can be observed by the low background and high intensity, with few impurities from other zeolites present. For Sample 2, it can be observed that a smaller amount of NaOH used was already enough to break the crystal structure of the ash and form a good quality zeolite. Thus, it was possible to define the NaOH/ash ratio of 0.8 for the next tests, ensuring that the use of the Na-rich residual solution did not cause an excessive sodium

concentration in the solution, which could lead to the formation of other zeolite structures.

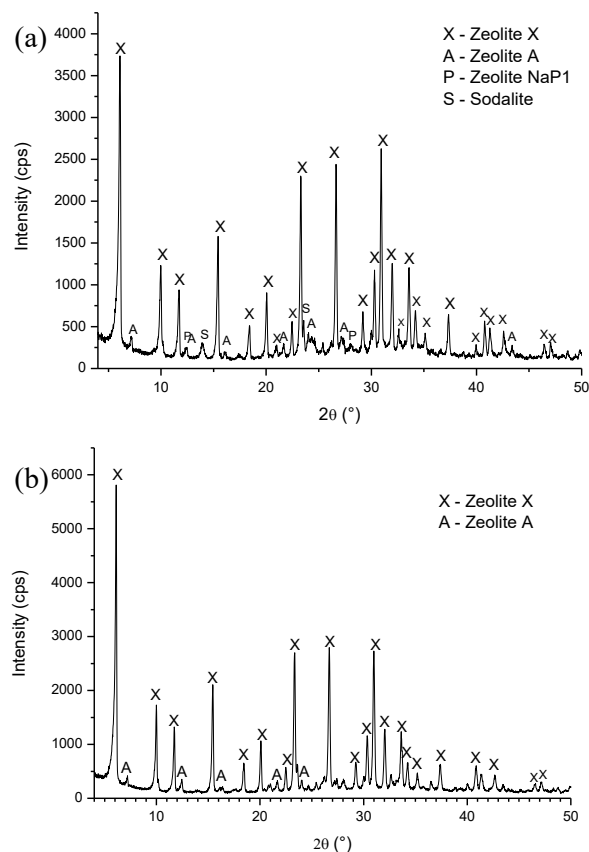


Fig.2. XRD patterns of the samples obtained with distilled water: (a) sample 1 e (b) sample 2.

3.2 Synthetic zeolite with hydrothermal reaction solution reuse

The residual solution used in the synthesis presented high concentrations of Na (58.400 mg/L), Al (450 mg/L) and Si (2.163 mg/L), as expected, since the concentration of NaOH used in the synthesis is high, and the precursor ashes of the zeolitic material have high concentrations of Al and Si [7,8,9].

All synthesized samples presented the formation of zeolite type NaX, but the samples that used 100 % and 80 % of the residual solution presented lower crystalline intensities and higher formation of other zeolitic structures, such as zeolite A, NaP1 and sodalite, a fact probably related to the excessive presence of Na⁺ ions in the reaction step [2,10,11]. Figure 3 presents the XRD patterns of the Sample 5 and Sample 6. Considering the tests performed with the NaOH/ ash ratio of 0.8 and H₂O/Na₂O of 51, on a laboratory scale, an average of 40 % of water in

the process is lost through evaporation. Therefore, for use of the residual solution, a minimum dilution of 40 % (60 % residual solution) would be required. However, considering an industrial process, this loss may be higher, so in order to ensure a minimum residual solution stock for use in the reaction step, the condition of Sample 6 (40 % residual solution) is indicated as an optimal condition for application in larger scale processes.

3.3 Synthetic zeolites obtained from water of supply network

The XRD pattern of the zeolite synthesized using the water from supply network (Sample 7) is shown in Figure 4. The result shows high intensity peaks of NaX zeolite with little impurities and the background indicates its good quality.

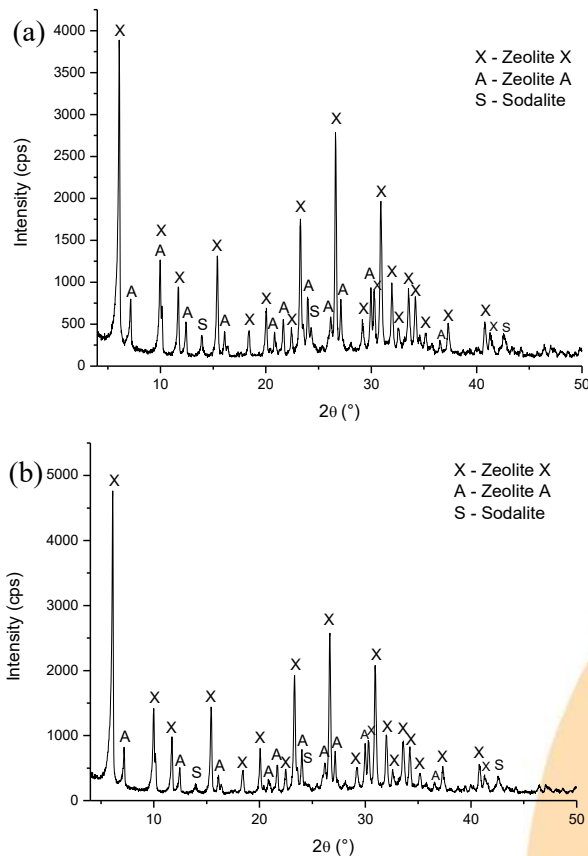


Fig.3. XRD patterns of the samples obtained with the hydrothermal reaction solution.: (a) Sample 5 (60 %) e (b) Sample 6 (40 %).

It also shows that the use of non-distilled water does not harm the quality of the obtained zeolite. Figure 5 shows the XRD pattern of the zeolite

obtained from the water supply system and 40 % reuse of synthesis water (Sample 8). This sample has a higher amount of impurities formed, but still has intense peaks of zeolite type X and low background, indicating a good quality. Considering only the structure of the samples, it is verified that the use of water from the supply network in conjunction with the reuse of the residual solution can be employed in the synthesis of NaX zeolite, without loss of quality in the products.

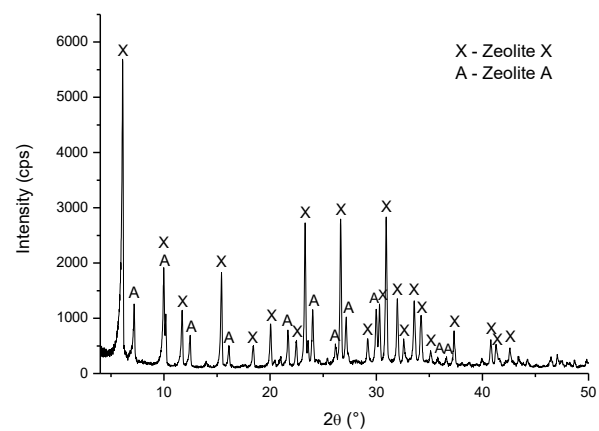


Fig.4. XRD pattern of the sample obtained with the supply network water.

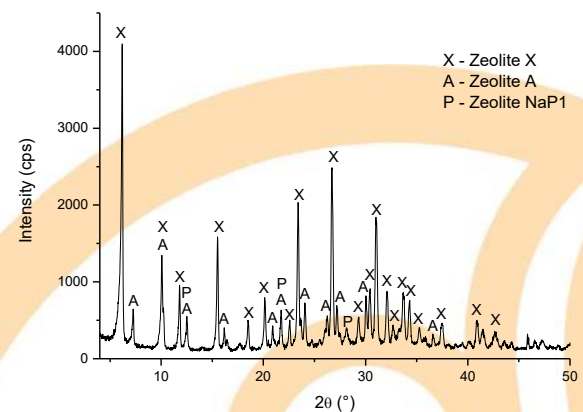


Fig.5. XRD pattern of the sample obtained with the supply network water and 40 % hydrothermal reaction solution.

3.4 Adsorption Capacity

Table 3 shows the adsorption capacity of some samples. Sample 1 that was synthesized with pure distilled water have similar capacity value with the commercial zeolite (CZ), indicating the possibility of application to CO₂ separation processes. Considering that Sample 6 refers to the sample

synthesized with 40 % residual solution reuse (result previously indicated for larger scale applications) the adsorption capacity is excellent. Sample 7, synthesized with water from the supply network, also shows a very satisfactory result, proving the possibility of using a common supply water, with possible presence of halogens (Cl and F), for a synthesis process without loss of the adsorption property. The reuse test, Sample 8, shows a larger decrease in adsorption capacity (1.78 mmol/g), confirming the need for further studies to optimize the use of the water from the supply network as diluent.

Table 3. CO₂ adsorption capacity.

Samples	CZ	1	6	7	8
Adsorption Capacity (mmol/g)	2.4	2.15	2.22	2.51	1.78

4. Conclusions

From the results obtained, it is possible to confirm the possibility of reducing the NaOH content (33.33 % reduction) in the fusion step and also reuse the waste water of type X zeolite synthesis in new synthesis processes. With the use of 40 % of the solution it is possible to maintain a minimum storage for constant reuse of the solution and, above all, decrease the water consumption in the process, which can also be reflected in the reduction of wastewater treatment costs for larger scale synthesis plants. In addition, studies have also shown the possibility of using and reusing water directly from the supply network, despite the need for further study to optimize its reuse while maintaining the desired zeolite quality.

Acknowledgements

The authors are grateful to the ENEVA S.A. and FAPESC (Research Support Foundation of Santa Catarina State) for the funding provided.

References

- [1] Wilcox J. Carbon Capture. 1 st ed. New York: Springer; 2012.
- [2] Aquino TF. Synthesis of type X zeolites from mineral coal fly and bottom ashes for CO₂ capture. Thesis, Doctorate in Chemical Engineering, UFSC. Brazil (Santa Catarina); 2018. p.170. Portuguese.
- [3] Costa BM, Ferrarini SF, Pires MN, Callil CF, Aquino TF, Estevam ST, Melo CR, Melo AR, Marcello RR,

- Riella HG. Influence of Pre-treatment of Brazilian Coal Ash on The Hydrothermal Synthesis of Zeolites. International Zeolite conference; 2016. Rio de Janeiro, 2016.
- [4] Izidoro CI, Fungaro DA, Abbott JE, Wang S. Synthesis of zeolites X and A from fly ashes for cadmium and zinc removal from aqueous solution in single and binary ion systems. *Fuel*. 2012;103:827-34.
- [5] Wu D; Zhang HB; Yan L; Kong H; Wang X. Effect of Some Additives on Synthesis of Zeolite from Coal Fly Ash. *International Journal of Mineral Processing*. 2006;80:266-72.
- [6] Aquino TF, Estevam ST, Corrêa GR, Marques CRM, Melo AR, Marcello RR, Pires MN, Hammerschmitt M, Riella HG. Synthesis of Type X Zeolites from Coal Fly and Bottom ash. *Brazilian Mineral Coal Congress*; 2017. Criciúma; 2017.
- [7] Cardoso AM, Horn MB, Ferret L, Azevedo CMN, Pires M. Integrated synthesis of zeolite 4A and Na-P1 using coal fly ash for application in the formulation of detergents and swine wastewater treatment. *Journal of Hazardous Materials*. 2015;287:69-77.
- [8] Melo CR. Synthesis of zeolite type 5A from kaolin to the adsorption of heavy metals from aqueous solutions. Thesis, Master in Chemical Engineering, UFSC. Brazil (Santa Catarina); 2009. p. 89. Portuguese.
- [9] Bortollato LB. Synthesis and characterization of Y zeolite with alternative sources of silicon and aluminium. Thesis, Master in Chemical Engineering, UFSC. Brazil (Santa Catarina); 2014. p. 100. Portuguese.
- [10] Querol X, Moreno N, Umaa JC, Alastuey A, Hernández E, López-Soler A, Plana F. Synthesis of zeolites from coal fly ash: an overview. *International Journal of Coal Geology*. 2002;50:413-23.
- [11] Shigemoto N, Hayashi H, Miyaura K. Selective formation of Na-X zeolite from coal fly ash by fusion with sodium hydroxide prior to hydrothermal reaction. *Journal of Materials Science*. 1993;28:4781-86.

Importance of the Polarity on Nanostructured Silica Materials to Optimize the Hydrolytic Condensation of Molecules Related to CO₂ Adsorption

O. Medina-Juárez^{a,*}, R. Ojeda-López^{a,b}, F. Rojas-González^{a,*}

^aDepartamento de Química, Universidad Autónoma Metropolitana Iztapalapa, CDMX, 09340, México.

^bDepartamento de Engenharia Química, Universidade Federal do Ceará, Fortaleza, CE, 60455 760, Brazil.

e mail: mjuryu@gmail.com (OMJ), fernando@xanum.uam.mx (FRG)

Abstract

CO₂ capture on nanoparticles adsorbents is of great interest, due to this gas is one of the major contributors of the greenhouse effect; this phenomenon is nowadays one of the most important ecological problems. This work shows evidence of the textural changes inflicted on KIT-6 and SBA-15 by thermal and chemical treatments. We have two aim: 1) increase the number of surface silanol groups (*i.e.* -Si-OH) and 2) improve CO₂ adsorption for their storage and eventual regeneration for practical use. For the first goal, the polarity is a key for an effective hydrolytic condensation with amine species, these molecules are of a basic nature, which is convenient for fixing the slightly acidic CO₂ molecule on the silica surface. Therefore, the mesoporous silica adsorbents were subjected to thermo-alkaline treatments (NaOH 0.025 M and 313 K), and then, the materials were chemically modified by the attachment of N'- (3-trimethoxysilylpropyl)diethylenetriamine (NAEPTES). The textural and chemical properties were determinate by: X-Ray Diffraction (XRD), Pyridine Desorption by Infrared Spectroscopy with Fourier Transform (FTIR-Py), Nuclear Magnetic Resonance (NMR), and Nitrogen Adsorption. Finally, the CO₂ adsorption capacity of the amine-functionalized SiO₂ substrates were determined experimentally and the Isosteric Heat of Adsorption was calculated from the corresponding CO₂ adsorption isotherms evaluated at 263-303 K.

Keywords: silica adsorbents; alkaline hydroxylation; hydrolytic condensation; CO₂ enhanced capture.

1. Introduction

Sorption researches as alternatives to Carbon Capture and Storage (CCS) are diverse, and in particular the adsorption processes involve the use of structures such as zeolites [1], hydrotalcites [2], activated carbon [3], carbon fibers [4], oxides porous [5], functionalized nanoporous materials [6] and recently ordered organometallic structures (MOFs) [7]. Other publications use mesostructured materials such as MCM-41 [8] and SBA-15 [9] mainly, these materials are superficially modified with amine molecules for CCS and form bonds that can be stabilized within or on the surfaces of homogeneous ordering study. This strategy reduces the oxidation problems caused by using amine species in the aqueous phase for these purposes.

There are several reports on the CO₂ capture and they usually go after: 1) understand the impact of a porous medium for adsorption purposes, 2) visualize the adsorbent-adsorbate interaction of different nature, 3) monitor the CO₂ capture efficiency and 4) observe the effects of thermal stability. However, there are few reports interested in increasing the

number of anchor sites (*e.g.* for Si-OH silica materials) responsible for binding molecules related to CO₂ adsorption. Ojeda-López *et al* 2015 [10] and Medina-Juárez *et al* 2016 [11] proposed alternatives to favor conventional SBA-15 materials with more silanol (Si-OH) species to generate more anchoring sites with alkoxyamines and promote CO₂ adsorption. Furthermore, the method called alkaline hydroxylation improves the selectivity of adsorbents between CO₂ and CH₄. In this sense, modulating the polarity of the adsorbents favors or decreases the affinity of certain adsorbents and even has various applications.

This work uses the treatment of alkaline hydroxylation to modify the textural and chemical properties. First, the textural changes caused on the solid SBA-15 and KIT-6 models are useful to see the structural stability by supports and in turn explore the effects of curvature for hydrolytic condensation between the study supports and NAEPTES alkoxyamine. The contrast of the nature of amine species is also studied. One additional experiment was performed for SBA-15 subjected to the functionalized with aminopropyltriethoxysilane (APTES) 3) the performances of all these materials.

2. Experimental section

2.1 Synthesis of Precursor SBA 15 Solids

The following molar ratio sequence was employed to prepare SBA-15 silica: TEOS: 197H₂O: 6.2HCl: 0.017P123. The synthesis was performed according to the method devised by Zhao *et al* 1998. [9]. The ensuing material was washed, filtered, put in contact with ethyl alcohol under stirring, and dried for 14 h at 373 K. Finally, the solid was calcined at 723 K for 6 h, while employing a heating ramp of 1 °C·min⁻¹.

2.2 Synthesis of Precursor KIT-6 Solids

This synthesis was carried out using the cooperative self-assembly partition method proposed by (Wang *et al.* 2014) [12] under the following molar ratio: 1TEOS: 0.017P123: 1.93 HCl: 195 H₂O: 1.31 CH₃ (CH₂)₃OH. The resulting solid was filtered and immersed in ethyl alcohol with gentle stirring overnight. Finally, this material was calcined at 723 K for 6 h using a ramp of 1 K·min⁻¹.

2.3 Soft Thermo-Alkaline Treatment Performed over SBA-15 and KIT-6 Precursor Materials

250 mg sample of each silica adsorbents (S15 or K6 denoted) was subjected to a desilication (*i.e.*, hydroxylation) process was performed by adding a 0.025 M NaOH solution at 313K (2h). The resultant solid was washed with deionized water, filtered, and dried at 373 K for 2 h. The ensuing substrate were labeled as S15H or K6H.

2.4 Chemical Anchoring of N' (3 trimethoxysilylpropyl)diethylenetriamine (NAPTES) on the Surface of SiO₂ Mesoporous Solids.

Before NAEP TES surface deposition, the precursor SiO₂ solids were treated at 473 K under vacuum for 2 h in order to remove organic impurities and to promote the activation of the silanol (SiOH) groups already residing on the surface. The molar ratio involved in this functionalization reaction corresponded to 3SiO₂:2NAEP TES and this procedure was carried out at 353 K under a N₂ atmosphere and continuous magnetic stirring of a reflux system during 20 h, while employing toluene as the NAEP TES dispersion medium. The final solids were separated by filtration and dried at 373 K for 2 h. These

materials were labeled as S15N, K6N, S15HN and K6HN. The additional experiment to carry out the hydrolytic condensation of the S15H solid with AP TES was carried out in the same molar ratios and experimental conditions described here and is label S15HA.

2.5 CO₂ Sorption Experiments at Different Temperatures

Before CO₂ sorption experiments, each sample was outgassed at 373 K under high vacuum for 6h. The adsorption temperature interval utilized for these experiments was chosen between 273 and 303 K instep intervals of 10 K. Finally, the adsorption capacity of the amine-functionalized SiO₂ substrates was determined experimentally, in an automatic adsorption instrument (Quantachrome Autosorb 1LC, Quantachrome Instruments, Boston Beach, FL, USA). Additional textural and thermal (isosteric heat of adsorption, -ΔH_{ads}) properties were, calculated from the corresponding CO₂ adsorption isotherms evaluated at the different temperatures.

3. Characterization techniques

X ray diffraction (XRD): The parameters of the network were measured from a Bruker D8 Advance instrument (Bruker AXS, Madison, WI, USA) employing a Cu-Kα radiation wavelength of 1.54 Å in the low angle (0.6° to 5.0° in the 2θ scale).

N₂ Sorption: The textural properties of the silica adsorbents were determined from an ASAP 2020 automatic instrument (Micromeritics Instrument Corp., Norcross, GA, USA), employing N₂ at its boiling point (76 K at Mexico City's altitude). The materials were previously outgassed at 373 K for 12 h. under a turbo molecular vacuum of 10⁻⁶ mbar. The surface area was determined from either the BET or t-methods, while the pore size distribution was obtained through the Non-Localized Functional Theory (NLDFT) approach. The kernel employed for this calculation was that corresponding to the filling of cylindrical pores along the boundary N₂ adsorption curve at 76 K.

Acidity quantification by pyridine desorption by Infrared Spectroscopy with Fourier Transform (FTIR-Py): These experiments were performed on a Nicilet 17SX spectrophotometer. Each material subjected to this test was pressed to obtain a transparent tablet, which was placed in a glass cell equipped with CaF₂ windows and a vacuum (0.001 Torr) was applied. Under these conditions, it was heated with a ramp of 5 K·min⁻¹ starting from room temperature until reaching 653 K for 30 min in order

to clean the tablet. Then it could cool again to room temperature, then the vacuum was suspended, and the pyridine was introduced into the cell to reach the adsorption equilibrium. Excess pyridine is evacuated at the same temperature by applying the vacuum again. Subsequently, the evolution of pyridine desorption as a function of temperature was monitored through the FTIR spectra taken from room temperature to 423 K with the same heating ramp mentioned above, the spectra were collected at temperature intervals of 323 K.

Nuclear Magnetic Resonance (NMR): experiments were run on a Bruker Advance II300 spectrometer (Bruker BioSpin, The Woodlands, TX, USA), operating at 59.62 MHz for ^{29}Si and ^{13}C . The magic angle spinning technique was altogether employed with the NMR use reference of tetramethylsilane (TMS).

CO_2 adsorption: different temperatures were performed on a Quantachrome Autosorb 1LC instrument; for this task, the samples were previously outgassed at 373 K for 6 h. CO_2 adsorption isotherms were obtained from 263 to 303 K in order to obtain the CO_2 enthalpy of adsorption at pressures from 0.001 to 1bar.

4. Results and Discussions

4.1 XRD

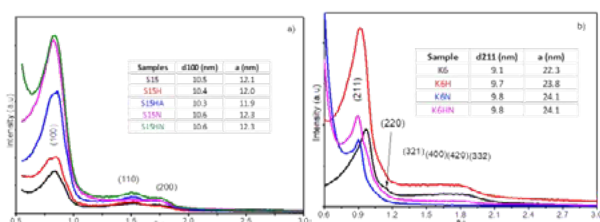


Fig. 1. X-ray Diffraction of the mesoporous silica: a) SBA-15 and b) KIT-6.

The diffractograms reported in Figure 1a) present the planes (100), (110) and (200) typical of cylindrical arrangements packed in a hexagonal shape ($p6mm$). As can be seen, the anchoring mechanism between the APTES and NAEPTES molecules on the S15H support is different, which is attributed to the difference in the magnitudes of the alkoxyamine molecules. However, for all cases, all the characteristic signs of this type of material are appreciated, assuming therefore that the surface modifications were carried out homogeneously within the porous cavities.

The analogous study for the KIT-6 materials functionalized with NAEPTES can be seen in Figure 1b) the symmetry planes assigned to cylinders

interpenetrated with $Ia3d$ symmetry, with the main plane of diffraction (211). These results show that the K6N solid presents an appreciable deformation reflected in the intensity of the interplanar distance d_{211} and even, at this scale, the other planes of symmetry assigned to this structure are not appreciated, and this phenomenon was also observed for the K6HN solid but to a lesser extent. This reflects that the alkaline hydroxylation treatment generated a better distribution of NAEPTES molecules on the KIT 6 surface than the non-hydroxylated precursor solid. Note also that the porous geometry of KIT-6 is not trivial and that NAEPTES molecules possibly generate agglomerates that deform pore arrays.

4.2 N_2 adsorption at 76 K

The textural parameters reported for both materials are consistent with the reports described in detail in the previous study [11]. Table 1 shows the following trends due to alkaline hydroxylation treatments: 1) decrease in the magnitudes of A_{BET} and A_{mic} , 2) increase in pore size and 3) greater coverage of alkoxyamine species with respect to conventional solids that were not hydroxylated, this is reflected when comparing the decrease in total area (A_{BET} and A_{mic}) for solids modified by the presence of amine species (e.g K6N vs K6HN).

Table 1. Textural properties obtained from N_2 sorption at 76 K.

Sample	A_{BET} ($\text{m}^2 \cdot \text{g}^{-1}$)	A_{mic} ($\text{m}^2 \cdot \text{g}^{-1}$)	D (nm)
S15	817.9	238.9	7.6
S15H	448.0	29.2	8.2
S15HA	280.1	0.0	7.0
S15N	209.2	0.0	6.3
S15HN	226.6	0.0	6.8
K6	669.8	313.8	7.3
K6H	492.6	155.8	7.6
K6N	170.3	0.0	6.1
K6HN	166.3	0.0	6.3

A_{BET} is the Brunauer-Emmett-Tell surface area, A_{mic} is the micropore surface area and D is the pore diameter arising from NLDFT approach by employing a kernel that utilizes the boundary desorption isotherm relative to N_2 at 76 K in cylindrical pores.

Nitrogen isotherms are shown in Figure 2. On base to IUPAC they are characteristic Type IV (A) isotherms with H1 hysteresis cycle assigned for homogeneously ordered cylindrical mesoporous structures [13]. Therefore, the thermo alkaline treatment generates a homogeneous increase in the pore diameter and that the presence of NAEPTES generates a slight deformation of the porous arrangement. In the graph at the top left of Figure 2,

it is possible to see a greater occlusion of the pores in the interval between 2.0 and 5.0 nm, due to the presence of NAEPTES for the K6HN solid compared to the K6N solid.

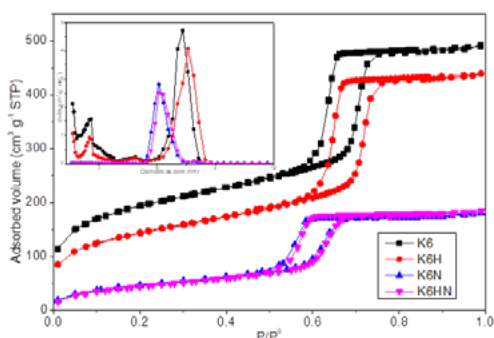


Fig. 2. N₂ sorption isotherms at 76 K and pore size distribution curves (figure inset) of KIT-6 substrates.

4.3. FTIR-Py

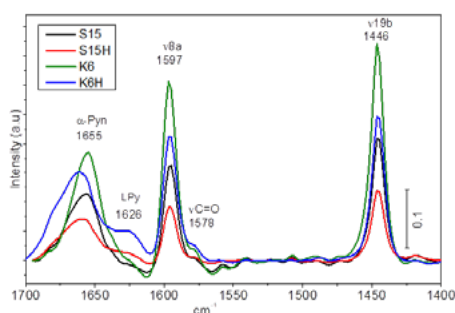


Fig. 3. Pyridine Infrared spectra (FTIR-Py) on solids SBA15 precursor (S15), SBA15 hydroxylated (S15H), KIT-6 precursor (K6) and KIT-6 hydroxylated (K6H) in vacuum at 323 K.

The spectra reported in Figure 3 expose the weak interactions that exist between Py and the SiO₂ matrices through: the vibrational modes ν_{8a} (1597 cm⁻¹) and ν_{19b} (1446 cm⁻¹) attributed to Lewis acid sites (LPy) and the coordination between pyridine and the superficial Si-OH acid sites on the S15 and S15H materials in question (HPy) [14]. Furthermore, the absence of Bronsted acid sites (BPy) is confirmed, which would be reported around 1540 cm⁻¹ [14]. A pronounced band corresponding to the formation of νC=O bonds with pyridine and the α pyridone species (α Pyn) reported in the 1680-1650 cm⁻¹ region is also observed. Additionally, around 1626 cm⁻¹ an assigned signal is observed for surfaces that have strong Lewis acid sites (LPy) which are not susceptible to oxidation at temperatures around 300 K [14].

These results indicate: 1) the superficial SiOH groups act as Lewis acids of different nature (strong and weak) in the presence of Py and 2) the lateral and remaining SiOH groups act as nucleophiles exclusively on the LPy sites reported at low frequencies (1446 cm⁻¹) to generate the α-pyridone species and therefore [14], evidencing that the SiO₂ matrices have an acid base character.

Finally, Figure 3 shows that the materials exposed to the alkaline hydroxylation treatment (S15H and K6H) generate a higher intensity in the signal assigned for strong LPy sites (1626 cm⁻¹) compared to the precursor solids (S15 and K6). This evidence is highly relevant because it indicates that the thermo-alkaline treatment generates solids more susceptible to nucleophilic attack by alkoxyamine species compared to materials that were not exposed to this treatment.

4.4. NMR (²⁹Si and ¹³C)

The deconvolution of the ²⁹Si NMR spectra was performed using the HPDEC spectra and the results are shown in Table 2, where it is confirmed that the thermo-alkaline treatment: 1) generates less condensed solids and more abundant silanol Q³ groups compared to the non-hydroxylated precursor materials, 2) the formation of the bonds is favored using three superficial SiOH groups to anchor a NAEPTES molecule, therefore, their union is more stable, and 3) the formation of T² type bonds between the functionalized alkoxy and the hydroxylated SiO₂ surfaces is inhibited.

Table 2. % area of signal deconvolution of ²⁹Si HPDEC spectra by SBA 15 and KIT 6 type mesostructured solids functionalized with NAEPTES.

Bond	²⁹ Si (ppm)	S15N	S15HN	K6HN
Q ⁴	-112.3	71.0	59.6	66.2
Q ³	-102.5	13.1	16.6	18.3
Q ²	-93.8	0.7	9.7	0.7
T ³	-70.6	1.7	4.8	4.3
T ²	-66.6	4.6	1.0	0.0
T ¹	59.4	9.0	8.3	10.6

Figure 4 reports the ¹³C CP-MAS-NMR spectra with chemical shifts of 47, 39, 20, and 9 ppm assigned to the aliphatic carbons of NAEPTES anchored to the porous matrices under study [15]. Additionally, a well defined signal at 164 ppm is seen, attributed to the presence of carbamate species formed by the reaction between CO₂ with the amino

groups anchored to the SiO₂ matrices and the signal at 160 ppm belongs to the formation of carbamic acid formed by the reaction between one amine species and CO₂ without any subsequent reaction with another amine species [16]. In the graph inserted into Figure 4, it is clearly observed that the S15N material shows a signal at 160 ppm, this indicates that the porous cavities are saturated with CO₂, but that there are no attached amines to stabilize the carbamic acid to carbamate. This same signal is suggested for the K6HN solid, but it is practically comparable in intensity to spectral noise, and on the contrary it is not appreciated for the S15HN solid. This implies that the S15HN and K6HN species present dense amine species capable of forming the carbamate bond in the presence of CO₂ present in the environment.

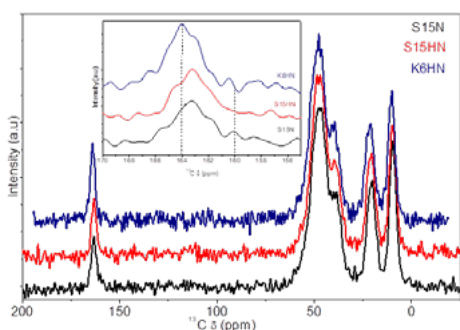


Fig. 4. ¹³C CPMAS NMR spectrum of solids modified by the presence of NAEPTES: S15N, S15HN and K6HN.

4.5. CO₂ adsorption

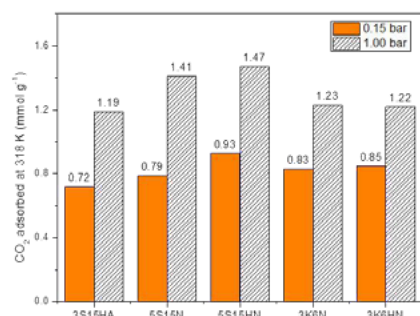


Fig. 5. CO₂ adsorbed at 0.15 and 1.00 bar at 318 K on the study adsorbates.

The difference between the APTES and NAEPTES molecules is that the former is a molecule that has a primary amine as a terminal species, while the NAEPTES molecule contains a pair of intermediate secondary amines and additionally a terminal primary amine. NAEPTES has more nitrogen species capable of coordinating with CO₂ per anchored molecule compared to APTES. For this

reason, S15N and S15HN solids adsorb more CO₂ than S15HA solid. Additionally, this report shows the impossibility of the nature of the porous order for the anchorage of amine species. Note that there is no significant difference in CO₂ adsorption between K6N and K6HN solids.

The amount of CO₂ capture is important, but also the strength with which the CO₂ is adsorbed on the study substrate is important, because it is related to the effectiveness of the anchorage of the amine molecules. The profiles of adsorption isosteric enthalpies on the functionalized solids in question are shown below (Figure 6).

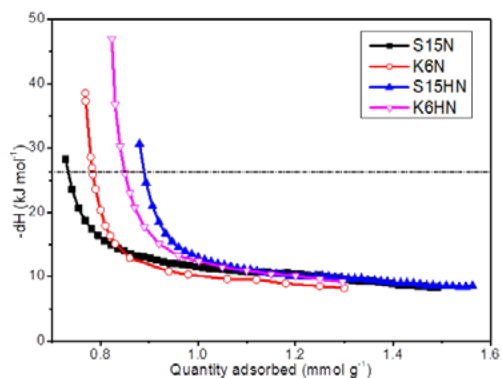


Fig. 6. Isothermic enthalpies of adsorption of solids: SBA-15 and KIT 6 precursors and hydroxylated with NaOH 0.025 M at 313 K and modified with NAEPTES.

The CO₂ capture of the S15HN and K6HN materials are more energy-related to adsorb this gas compared to the S15N and K6N solids (see Figure 6). However, the trend reported in Figure 6 is general where energy heterogeneity predominates and at low pressures the adsorbate-adsorbent forces dominate, but at higher coverage the weak adsorbate-adsorbent forces dominate. In addition, an ordered amine species anchorage produces an efficient and stable cooperative adsorption effect that is further favored by the increase in the polarity of the starting matrices due to the hydroxylation treatment.

5. Conclusions

The thermoalkali treatment used generates the presence of strong Lewis acid sites susceptible to the nucleophilic addition of alkoxyamines capable of stabilizing CO₂ in carbamate. Furthermore, an orderly anchorage of amine species produces a cooperative effect of efficient and stable adsorption of CO₂, which is further favored by the increase in the polarity of the precursor matrices when subjected to thermo alkaline treatment.



Acknowledgements

This research was funded by the Consejo Nacional de Ciencia y Tecnología (CONACyT). To the network SEP-PROMEP “Diseño Nanoscópico y Textural de Materiales Avanzados”, with the Project “Síntesis y Fisicoquímica de Materiales Mesoporosos” (UAM I CA 31 Fisicoquímica de Superficies).

References

- [1] Hernández Huesca R, Aguilar Armenta G, Domínguez G. Isothermic Heats of Adsorption of N₂O and NO on Natural Zeolites. *J Mex Chem Soc.* 2010;54:111-116.
- [2] León M, Díaz E, Bennici S, Vega A, Ordoñez S, Auroux A. Adsorption of CO₂ on Hydrotalcite-Derived Mixed Oxides: Sorption Mechanisms and Consequences for Adsorption Irreversibility. *Ind Eng Chem Res.* 2010;49:3663-3671.
- [3] Songolzadeh M, Ravanchi MT, Soleimani M. Carbon Dioxide Capture and Storage: A General Review on Adsorbents. *World Acad Sci Eng Technol.* 2012;6:10-24.
- [4] Lu C, Bai H, Wu B, Su F, Hwang JF. Comparative Study of CO₂ Capture by Carbon Nanotubes, Activated Carbons, and Zeolites. *Energy Fuels.* 2008;22: 3050-3056.
- [5] Kumar S, Saxena SK. A comparative study of CO₂ sorption properties for different oxides. *Mater Renew Sustain Energy.* 2014;3:1-15.
- [6] Sanz-Pérez ES, Fernández A, Arencibi A, Calleja G, Sanz R. Hybrid amine silica materials: Determination of N content by ²⁹Si NMR and application to direct CO₂ capture from air. *Chem Engin Journ.* 2019;373:1286-1294.
- [7] Oschatz M, Antonietti M. A search for selectivity to enable CO₂ capture with porous adsorbents. *Energy Environ Sci.* 2018;11:57-70.
- [8] Janicke MT, Landry CC, Christiansen SC, Birtalan S, Stucky GD, Chmelka BF. Low Silica MCM 41 Composites and Mesoporous Solids. *Chem Mater.* 1999;11:1342-1351.
- [9] Zhao D, Feng J, Huo Q, Melosh N, Fredrickson GH, Chmelka BF, Stucky GD. Triblock copolymer syntheses of mesoporous silica with periodic 50 to 300 angstrom pores. *Science.* 1998;279:548-552.
- [10] Ojeda López R, Pérez Hermosillo IJ, Esparza Schulz JM, Cervantes-Urbe A, Domínguez-Ortiz A. SBA-15 materials: Calcination temperature influence on textural properties and total silanol ratio. *Adsorp.* 2015;21:659-669.
- [11] Medina-Juárez O, García-Sánchez MÁ, Arellano-Sánchez U, Kornhauser-Straus I, Rojas-González F. Optimal Surface Amino-Functionalization Following Thermo-Alkaline Treatment of Nanostructured Silica Adsorbents for Enhanced CO₂ Adsorption. *Materials.* 2016;9:898-922.
- [12] Wang W, Qi R, Shan W, Wang X, Jia Q, Zhao J, Zhang C, Ru H. Synthesis of KIT-6 type mesoporous silica tunable pore, wall thickness and particle sizes via the partition cooperative self assembly process. *Microp and Mesop Mater.* 2014;194: 167-173.
- [13] Thommes, K. Kaneko, A. V. Neimark, J.P. Olivier, F. Rodriguez Reinoso, J. Rouquerol, K.S.W. Sing, Physisorption of gases, with special reference to the evaluation of surface area and pore size distribution (IUPAC Technical Report), *Pure Appl. Chem.* 87 (2015) 1051-1069.
- [14] Zaki MI, Hasan MA, Al-Sagheer FA, Pasupulety L. In situ FTIR Spectra of pyridine adsorbed on SiO₂-Al₂O₃, TiO₂, ZrO₂ and CeO₂: general considerations for the identification of acid sites on surfaces of finely divided metal oxides. *Colloids and Surfaces.* 2001;190:261-274.
- [15] Zakharova MV, Masoumifard N, Hu Y, Han J, Kleitz F, Frédéric-Georges F. Designed Synthesis of Mesoporous Solid-Supported Lewis Acid-Base Pairs and Their CO₂ Adsorption Behaviors. *ACS Appl Mater Interfaces.* 2018;10:13199-13210.
- [16] Pinto ML, Mafra L, Guil M.J, Pires J, Rocha J. Adsorption and Activation of CO₂ by Amine-Modified Nanoporous Materials Studied by Solid State NMR and CO₂ adsorption. *Chemistry of Materials.* 2011;23:1387-1395.

Study of the effect of the HDL cations precursors in the removal of arsenic in aqueous solution

Barroso Quiroga, María Martha^a; Iglesias Juncà, Mònica^b; Merino, Nora A.^{c,*}

^aDepartamento de Minería, FCFMyN (UNSL). Chacabuco y Pedernera – CP: 5700 – San Luis – Argentina.

^bDepartamento de Química, Universidad de Girona, Campus de Montilivi – CP: 17071 Girona – España.

^cINTEQUI (CONICET) – FICA (UNSL). Campus Universitario. Ruta Prov. N° 55 (Ex 148) Extremo Norte - CP: 5730 - Villa Mercedes - San Luis - Argentina. noraandreamerino@gmail.com

Abstract

Layered double hydroxides (LDH) are anionic clays, used as adsorbents, ion exchange material and catalysts. Generally, they present high specific surface areas, alkaline character, high metallic dispersion and high thermal stability. If they contain a transitional element in their structure, it is possible that the solid presents redox properties. LDH were synthesized with the following combinations: MgAl, MgFe, and ZnMgFe, aiming to determinate the effect of cationic nature in the structure and the functionality of the synthesized clay as adsorbents in polluted aqueous effluents. The textural properties were determined by nitrogen adsorption isotherms. Crystalline structure was studied by XRD and the presence of the anions of the interlayer was determined by FTIR spectroscopy. From the results that were obtained from the studies of removal of As(III) and As(V) from aqueous solutions, using the LDH, it is possible to observe that at 24 h the solids had a high percentage of removal. ZnMgFe solid removed both species of arsenic with values of 95 % for As(III) and 98 %, for As(V). The MgFe and MgAl solids showed selectivities to the uptake of As(V) and As(III), respectively. This selective behavior can be beneficial in studies of arsenic speciation.

Keywords: layered double hydroxides; MgAl; MgFe; As(III); As(V)

1. Introduction

Arsenic (As) is a highly toxic, mutagenic and carcinogenic element. The continuous ingestion of polluted waters with it could cause skin, lung, bladder, and kidney cancer as well as pigmentation changes, skin thickening (hyperkeratosis) neurological disorders, muscular weakness, loss of appetite and nausea [1-2].

Among the available technologies for As removal adsorption presents many advantages, such as (i) high efficiency, (ii) it is a low-cost process, (iii) it usually does not need a large adsorbent volume and additional chemicals, (iv) it is easy to operate (v) it does not produce harmful by-products [3].

Within the clay family, hydrotalcites (HTs) are anionic clays that have been widely used as adsorbents for the removal of inorganic materials from aqueous media [4-6]. HTs are lamellar solids with a structure similar to brucite, $M(OH)_2$, where M is a bivalent cation, octahedrally coordinated with

six oxydryl groups. When M^{2+} ions are replaced by M^{3+} cations, a positive charge arises that is neutralized by interleaved anions in the interlamellar regions. It is possible to produce hydrotalcite type materials with different divalent cations (Mg^{2+} , Cu^{2+} , Co^{2+} , Ni^{2+} , Zn^{2+}) and trivalent (Al^{3+} , Ni^{3+} , Co^{3+} , Fe^{3+} , Cr^{3+}), as well as different anions (CO_3^{2-} , NO_3^- , SO_4^{2-} , WO_4^{2-} , CrO_4^{2-}) [6]. The calcination of HTs results in different phases of simple, dimethyl or trimetallic oxides, depending on the calcination temperature and the metal components of the structure [7]. The most interesting properties of these oxides are: high surface area, synergistic effects between the elements and memory effect [8]. These properties added to its low cost and versatility, allow the use of oxides derived from hydrotalcites in multiple applications [6].

The aim of this work is to evaluate the behavior of two layered double hydroxides (LDH) with different trivalent cations, as adsorbents of arsenical species present in aqueous solution and to study the effect of the modification of the cation in its application. The effect of factors such as initial pH and initial As concentrations were tested.

2. Materials and Methods

1.1. Hydrotalcite-like compound synthesis

Layered double hydroxides of Mg, Fe and Al, with a molar ratio of $\text{Me}^{2+}/\text{Me}^{3+} = 3/1$, were synthesized by the coprecipitation method. Two solutions were mixed, the first one was a mixture of the salts of the metal precursors, that was dropwise mixing with the second one, alkaline mixture of KOH and K_2CO_3 in distilled water, with a vigorous mechanical agitation, using a constant pH of 9.5- 10 and at 70 °C. The salt solution mixed consisted of $\text{Mg}(\text{NO}_3)_2 \times 6\text{H}_2\text{O}$ (Biopack), $\text{Zn}(\text{NO}_3)_2 \times 6\text{H}_2\text{O}$ (Riedel-de Haen), $\text{Al}(\text{NO}_3)_3 \times 9\text{H}_2\text{O}$ (Merck) and $\text{Fe}(\text{NO}_3)_2 \times 9\text{H}_2\text{O}$ (Anedra). The suspension was aged at room temperature for 24 hours. The precipitate was washed until a pH of 7 was reached and then dried, in a SE33T model (San Jor) oven, at 110 °C for 24 hours. An aliquot of dried solid was calcined, in a 134 model (Indef) electric furnace, at 500 °C, keeping it at this temperature for 1 hour. From now on solids obtained will be called MgAl110, MgFe110 and ZnMgFe110 (dried) and MgAl500, MgFe500 and ZnMgFe500 (calcined).

1.2. Analytical methods

The temperatures of phase changes and the choice of calcination temperature were observed by the thermograms analysis using a TGA-50 Shimadzu thermobalance. In the TGA-DTA essays approximately 30 mg of sample were used, in a nitrogen atmosphere with a flow of 20 mL min^{-1} , with a heating rate of 5 °/min, from room temperature up to 900 °C, keeping at this temperature for 30 minutes. BET specific surface areas of samples were calculated by the BET method. A Gemini V from Micromeritics apparatus was used. Samples were degassed at 250 °C during 1 h and the nitrogen adsorption isotherms measured at -196 °C. The diffraction patterns were obtained by using a Rigaku Ultima IV Type 2 diffractometer operated at 30 kV and 20 mA by Cu $K\alpha$ Nickel filtered radiation ($\lambda = 1.5406 \text{ \AA}$). The spectra were collected at 2θ ranges of 5°–70°, at a scanning speed of 3° min^{-1} ; the crystalline phases were identified by reference to powder diffraction data. The presence of the anions was studied by infrared spectroscopy with Fourier transform (FTIR) using a Perkin-Elmer Spectrum RX1 equipment. The solids were diluted

with KBr. The redox behavior of metals and precursor anions, in synthesized solids, was analyzed by the programmed temperature reduction technique (RTP). It was performed in a quartz U type tubular reactor using a TCD detector and 100 mg and 200 mg samples were used. The reducing gas was a mixture of 10% v/v H_2/N_2 at a total flow of 30 mL min^{-1} and the temperature was increased at a rate of 10 °C/min from room temperature to 600 °C and maintained at this temperature 1 hour. The samples were pretreated at 200 °C, in a nitrogen atmosphere.

1.3. Arsenic removal

The removal capacity of As (III) and As (V) ions was evaluated by preparing suspensions with a 0.4 $\text{g}_{\text{LDH}}/\text{L}$ solution of NaAsO_2 (Fluka) and $\text{Na}_2\text{HAsO}_4 \cdot 7\text{H}_2\text{O}$ (Merck) using MiliQ water, with initial concentrations of 0.5 ppm and 1.5 ppm, at pH 6 and 8. In the case of evaluating the difference in pH, the arsenic solutions were adjusted to the pH 6 or 8 by the addition of HCl or NaOH solution using the glass pH electrode. The suspensions were kept stirred for 24 h at room temperature on a Labinco model (Dinko Instruments) centrifuge tube rotator shaker, at 40 rpm. The tests were performed in duplicate. The suspension was centrifuged, and then filtered with a 0.1 μm cellulose acetate membrane filter. 4% of ethanol 96 %v/v was added to improve sensitivity to the filtrate, and it was analyzed for residual As(V) or As(III) concentration using ICP-OES.

3. Results and Discussion

The anionic clays were synthesized by the coprecipitation method, using an acid solution with the precursors, the nitrates of the constituent metals of its structure, and a solution with KOH and K_2CO_3 , used as precipitating agent and to maintain the pH constant. The dried and calcined solids were physicochemically characterized to study the influence of the trivalent cation in the structure of the laminar clay and in the oxides obtained from their calcination. The thermograms of the dried samples showed a loss of endothermic mass at temperatures up to 200 °C, which occurs at lower temperatures with the replacement of aluminum by iron. The two subsequent mass losses are exothermic processes, the first occurs between 180

and 300 °C, and the third stabilizes approximately between 550 and 600 °C. The first decomposition is attributed to interlaminar water removal while the remaining ones to the reactions of dehydroxylation and decomposition of the interlaminar anions [9]. The calcination temperature was chosen because at 500 °C simple oxides are present, but in an unstable way, so the hydrotalcite structure can be obtained again, since its property of memory effect.

Table 1 shows the textural properties of synthesized, dried and calcined solids, obtained from fisorption tests with nitrogen. It is possible to observe a different behavior of solids according to the trivalent cation present in the structure.

Table 1. Textural properties of the dried bimetallic solids.

LDH	Specific Surface Area S_{BET} (m^2/g)	Pore Volume V_p (cm^3/g)	Pore diameter D_p (Å)
MgAl110	103	0.632	176.2
MgAl500	128	0.796	192.3
MgFe110	63	0.376	181.9
MgFe500	39	0.262	181.9

Solids with aluminum show an increase in specific surface area with calcination, as reported in the literature [10], since calcination leads to a destruction of the laminar structure, which causes the formation of low crystallinity phases. (oxides of the constituent metals). On the other hand, solids with iron, after calcination, suffer an appreciable loss of their BET area. All synthesized, dried and calcined solids have a pore size distribution in the mesoporous region (pore size between 20 and 500 Å), according to the IUPAC classification [11]. The tendency in the growth of the diameter and volume of the pores are inverse. With aluminum the pore volume increases and the pore diameter decreases after calcination, while when the aluminum is partially or completely replaced by iron, the pore volume decreases and the pore diameter increases after calcination. Hydrotalcite has a mesoporous structure due to the size and shape of the particles and their interconnection pattern. It can be inferred from the results obtained that the morphology of these solids is modified by the initial synthesis conditions (different nature of the ions present in the synthesis medium, different concentrations of the precursor solutions, etc.) [9].

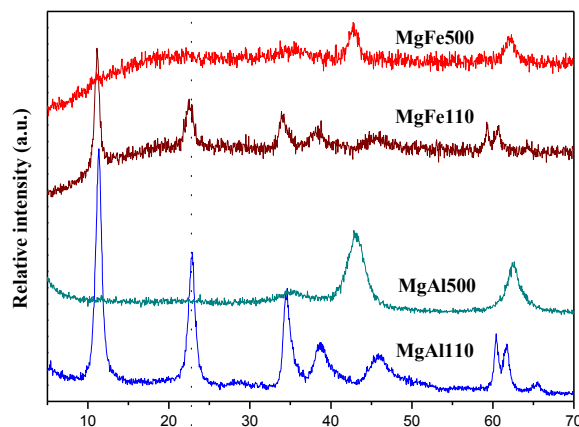


Fig. 1. Diffractograms of the dried and calcined bimetallic solids.

The diffraction lines of all the solids studied are presented in Figure 1. The diffractograms of the solids dried at 110 °C and containing Al have the laminar structure of the corresponding hydrotalcite, although they have impurities of simple and mixed spinel type oxides. The calcination stage leads to the formation of the simple oxides of the metals present or the mixed phases, depending on the nature of the metals. In addition, the elimination of oxhydryl groups and intercalated anions occurs. [11].

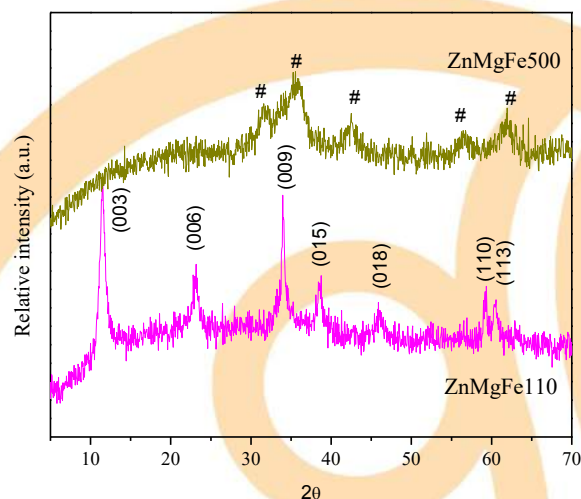


Fig. 2. Diffractograms of the dried and calcined trimetallic solid. # $MgFe_2O_4$ (PDF 88-1943) or $ZnFe_2O_4$ (PDF 82-1042)

The diffraction lines of MgAl110 show a shift towards lower diffraction angles when compared with those corresponding to a hydrotalcite structure

at $2\theta = 11.66^\circ; 23.44^\circ; 34.91^\circ$ (PDF 089-0460). In addition, it is possible to observe peaks attributable to spinel phases, $2\theta = 38.82^\circ; 65.76^\circ$ (PDF 002-1086) and $2\theta = 54.31^\circ$ (PDF 087-0343). This calcined solid only has the MgO phase (PDF 089-7746). The alumina phase (Al_2O_3), which may be present, cannot be identified as being amorphous. Al^{3+} cations are forming this phase or crystalline phases of low concentration, highly dispersed. The XRD patterns of ZnMgFe110 and its calcined sample ZnMgFe500 are shown in Fig. 3. All the characteristic peaks including (003), (006), (009), (015), (018), (110) and (113) corresponding to the trimetallic LDH could be found. After calcination, the characteristic peaks of MgFe_2O_4 (PDF 88-1943) or ZnFe_2O_4 (PDF 82-1042) [12] were observed. The d spaces decreased after calcination, indicating a partial interlayer molecules and ions were removed during thermal treatment, which could improve the adsorption capacity by ion intercalation during the layer reconstruction process [13-14].

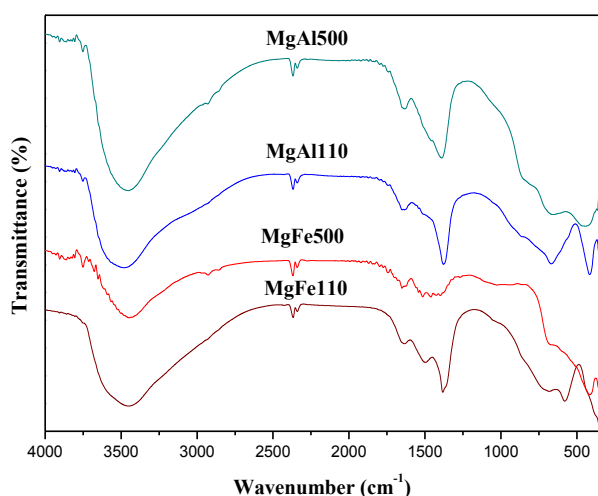


Fig. 3. FTIR spectra of the dried and calcined bimetallic solids.

The three HDL showed the same behavior when the initial concentration of As(V) is 0.5 ppm, as the adsorbed amount of As(V) has similar values, and at higher pH it has a slightly better performance in adsorption. For the higher initial concentration of As(V), 1.5 ppm, the adsorption capacity is much higher than the lower initial concentration, and greater amounts of As(V) are adsorbed at pH 6 than at pH 8. This could be explained due to the pH_{pzc} of the HDL. The pH_{pzc} is an important parameter, it corresponds to the pH value of the liquid surrounding particles when the sum of surface

positive charges balance the negative charges. The pH_{pzc} values reported in literature for this kind of materials are around 10 [15]. So, when the solution pH is higher than this pH_{pzc} , the surface of the HDL is negatively charged. Therefore, the arsenate anionic species have been repelled by the HDL surface. When the solution pH is lower than the pH_{pzc} of the HDL, the surface of LDHs is positively charged, which is beneficial for the adsorption of the negatively charged anionic species [15-16].

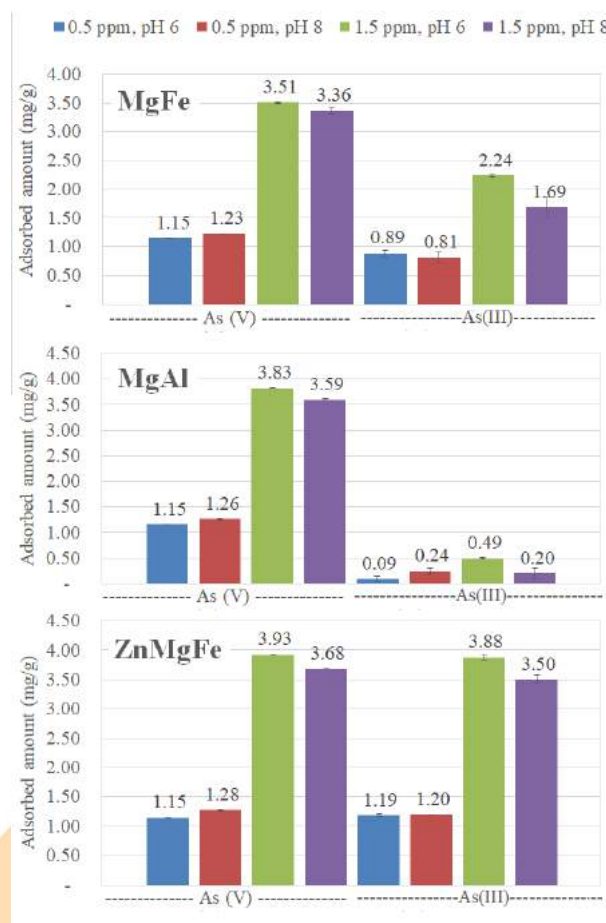


Fig. 4. As(III) and As(V) adsorbed amount for the solids

Results of the adsorption essays are shown in Figure 4. The effect of the pH of the initial solution on the adsorption of As(III) is similar to As(V), it does not have influence when the initial concentration is 0.5 ppm, but at 1.5 ppm, when the pH is higher, the adsorption capacity lowers. The decrease in sorption of As(III) with increasing pH could be attributed to the increasing concentrations of hydroxyl ions which have a high affinity for HDL surfaces [16].

Bimetallic solids does not have a great affinity with As(III), and MgAl has a much lower adsorption capacity than MgFe. Several authors claim that the difference in the total amounts sorbed of As(III) and As(V) on the bimetallic adsorbents may be related to the different species found in solution for these two forms of As with different oxidation states, such as H_2AsO_4^- and HAsO_4^{2-} versus H_3AsO_3 . [16-17]

On the other hand, ZnMgFe had almost the same adsorption performance for both As(III) and As(V). The presence of Zn on the trimetallic solid apparently enhances the performance of the adsorption. The difference on the behavior of the MgAl solid and the ZnMgFe for the adsorption of different species of As(III) and As(V) could be used to separate this species one from the other.

Although the adsorption capacity is lower than others reported in literature for this kind of materials [18], the adsorption capacity is in concordance with the adsorbent dosage used on this study.

4. Conclusions

The laminar structure evidenced by both DRX and RTP was obtained. Both cations have different electronic configurations and sizes of ionic radii, so their electrostatic interactions are different. Hydrotalcite has a mesoporous structure due to the size and shape of the particles and their interconnection pattern. The morphology differs according to the trivalent cation, since the chemical behavior of metals is remarkably different.

The studies of the removal of As (III) and As (V) from aqueous solutions showed that, at 24 h, all the three solids had a good performance in adsorption for As(V). The MgAl mostly removed As(V), and ZnMgAl had an excellent performance for both arsenic species, As(III) and As(V). This selective behavior could be beneficial in studies of arsenic speciation.

Acknowledgements

The authors gratefully acknowledge Universidad Nacional de San Luis and CONICET for supporting our work. Also to Fundación Carolina for the grant to Dra. Barroso-Quiroga, and Universitat de Girona where the adsorption experiments were accomplished.

References

- [1] Mohan, D., Pittman Jr., C.U. Arsenic removal from water/wastewater using adsorbents-a critical review. *J. Hazard. Mater.* 2007; 142 (1-2): 1-53.
- [2] Guidelines for drinking water quality. Recommendations. 3rd Ed. WHO, Geneva, Switzerland.
- [3] Singh, R., Singh, S., Parihar, P., Singh, V.P., Prasad, S.M. Arsenic contamination, consequences and remediation techniques: a review. *Ecotoxicol. Environ. Saf.* 2015; 112:247-270.
- [4] M. Sánchez-Cantú, J. A. Galicia-Aguilar, D. Santamaría-Juárez, L. E. Hernández-Moreno. Evaluation of the mixed oxides produced from hydrotalcite-like compound's thermal treatment in arsenic uptake. *Appl. Clay Sci.* 2016, 121-122, 146-147.
- [5] K. S. Triantafyllidis, E. N. Peleka, V. G. Komvokis, P. P. Mavros. Iron-modified hydrotalcite-like materials as highly efficient phosphate sorbents. *J. Colloid Interface. Sci.* 2010, 342, 427-436.
- [6] M. Jabłonska, L. Chmielarz, A. Węgrzyn, K. Guzik, Z. Piwowarska, S. Witkowski, R. I. Walton, P. W. Dunne, F. Kovanda. Thermal transformations of Cu-Mg (Zn)-Al(Fe) hydrotalcite-like materials into metal oxide systems and their catalytic activity in selective oxidation of ammonia to dinitrogen. *J. Therm Anal. Calorim.* 2013, 114-2;731-747
- [7] Cavani, F.; Trifirò, F.; Vaccari, A. Hydrotalcite-type anionic clays: Preparation, properties and applications. *Catal. Today* 1991, 11;173-301.
- [8] A. Vaccari. Preparation and Catalytic Properties of Cationic and Anionic Clays. *Catal. Today* 1998, 41;53-71.
- [9] G. Carja, R. Nakamura, H. Niyama. Copper and iron substituted hydrotalcites: Properties and catalyst precursors for methylamines synthesis. *Appl. Catal. A: General* 2002, 236, 91-102.
- [10] D. Carriazo, M. del Arco, E. García-López, G. Marci, C. Martín, L. Palmisano, V. Rives. Zn,Al hydrotalcites calcined at different temperatures: Preparation, characterization and photocatalytic activity in gas-solid regime. *J. Mol. Catal. A: Chemical* 2011, 342-343;83-90.
- [11] Li. Hui, H. Jia. L. Wei, W. Ping. Phase transformations behaviors of aluminium hydroxides to alpha alumina in air and molten sal. *J. Mater. Sci.* 2005, 40;3259-3261.
- [12] D. Wang, J. Wu, D. Bai, R. Wang, F. Yao, S. Xu. Mesoporous spinel ferrite composite derived from a ternary MgZnFe-layered double hydroxide precursor for lithium storage. *J. Alloy. Comp.* 2017, 726;306-314.
- [13] Kang, X. Yu, S. Tong, M. Ge, J. Zuo, C. Cao, W. Song. Performance and mechanism of Mg/Fe layered double hydroxides for fluoride and arsenate removal from aqueous solution. *Chem. Eng. J.* 2013, 228;731-740.
- [14] Liu, J., Wu, P., Li, S., Chen, M., Cai, W., Zou, D., & Dang, Z. Synergistic deep removal of As (III) and Cd (II) by a calcined multifunctional MgZnFe-CO₃ layered double hydroxide: Photooxidation, precipitation and adsorption. *Chemosphere* 2019, 225;115-125.



- [15] Y. Guo et al. Adsorption of arsenate on Cu/Mg/Fe/La layered double hydroxide from aqueous solutions. *J. Hazard. Mater.* 2012, 239–240;279–288.
- [16] A.G. Caporale, M. Pigna, S.M.G.G. Azam, A. Sommella, M.A. Rao, A. Violante. Effect of competing ligands on the sorption/desorption of arsenite on/from Mg-Fe layered double hydroxides (Mg-Fe-LDH). *Chem. Eng. J.* 2013, 225;704–709.
- [17] L. Yang, Z. Shahrivari, P.K.T. Liu, M. Sahimi, T.T. Tsotsis, Removal of trace levels of arsenic and selenium from aqueous solutions by calcined and uncalcined layered double hydroxides (LDHs), *Ind. Eng. Chem. Res.* 2005, 44;6804–6815.
- [18] Mukarram Zubaira, Muhammad Daudb,c, Gordon McKayd, Farrukh Shehzadb, Mamdouh A. Al-Harthib. Recent progress in layered double hydroxides (LDH)-containing hybrids as adsorbents for water remediation. *Appl. Clay Sci.* 2017, 143;279–292.

Evaluation of dried *Salvinia auriculata* as a biosorbent in natura in lead removal in aqueous solutions

Adriano Cosme Pereira Lima, Tereza S. M. Santos, Tahise Neiva Campodonio

Universidade Estadual de Feira de Santana (UEFS), Programa de Pós-graduação Engenharia Civil e Ambiental (PPGCEA). Av. Transnordestina, s/n, Novo Horizonte, 44036-900 Feira de Santana, Bahia, Brazil.

Abstract

Lead contaminated *Salvinia auriculata* were collected from the Marimbus Pantanal, Chapada Diamantina, -BA and tested as biosorbents in the removal of the same metal in aqueous solutions. The samples were dried and characterized by thermogravimetric analysis. The leaching capacity of macrophyte lead was evaluated at different pH values. Equilibrium data were obtained in batch equilibrium experiments at 25 ° C, with 0.30 g of adsorbent in 30 mL of Pb solution, varying the initial concentration in the range of 0.1 and 6 mg L⁻¹. The macrophyte mass by combustion reduced by 81%, and by pyrolysis 68.8%. After leaching tests, it was observed that the metal is leached to the solution at any pH value, reaching the highest concentrations in most basic solutions, pH > 8. The adsorption equilibrium data best fit the Langmuir isotherm, $q_m = 0.245 \text{ mg g}^{-1}$. Considering the adjustment by Freundlich the value of parameter $n > 1$ indicates that even dehydrated macrophyte *Salvinia auriculata* in a lead contaminated environment still preserves its chemical affinity. The results of FTIR analysis show the presence of functional groups characteristic of biomass and after lead adsorption specific bands were modified indicating interaction with the metal.

Keywords: *Salvinia auriculata* ; bioadsorbents, lead;

1. Introduction

Aquatic environments have been receptors of organic and inorganic pollutants from various anthropogenic activities in recent years. This heterogeneity of effluents that are discharged into untreated water bodies is highly toxic, causing a negative effect on the environment which has contributed to the degradation of water quality and availability affecting the health of all living organisms [1-3]. The discharge of large volumes of industrial effluents containing various metals, including lead, in concentrations above the limit allowed by current legislation, can be seen as one of the main environmental impacts on rivers, wetlands, marshes, lakes and lagoons [4,5]. Effluents with high concentrations of Pb require proper treatment before discharge into aquatic environments, however, records show that this is not occurring properly and this metal has been concentrated in the environment because of its bioaccumulation property [5]. Several biological and physicochemical techniques have been used for

the removal and treatment of contaminated environments such as phytoremediation, absorption, precipitation, reduction, artificial membranes and ion exchange [6,7]. Aquatic macrophytes have been used to treat effluents and as a natural metal remover due to their large scale production in water sources. However, it has generated other environmental problems including the final destination of these plants when they are removed from the contaminated environment [8-10]. The objective of this work was to evaluate the leaching capacity of Pb containing macrophytes and their adsorption capacity when used as a biosorbent in wastewater treatment.

2. Methodology

2.1. Macrophyte collection and biosorbent synthesis

The aquatic macrophytes of the species *Salvinia auriculata* were collected from the Marimbus Pantanal, in Chapada Diamantina, Bahia, Brazil. These species belong to the group of pteridophytes

and have the only genus *Salvinia*. This aquatic macrophyte has no roots, and it organizes itself into long mats on water surfaces. It inhabits lentic environments such as lakes, ponds, marshes, wetlands and marshlands (Figure 01).

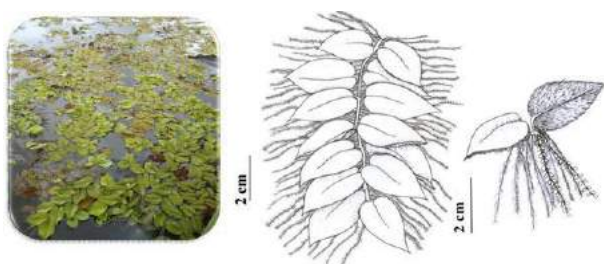


Fig. 1: Morphology of *Salvinia auriculata*
Photo: Lima, A.; Illustration: Pimenta, K. (2016)

Samples were collected manually and packed in perforated plastic bags for the water to runoff and to prevent anaerobic decomposition of the material. In the laboratory the samples were initially washed in running water to eliminate debris and organic matter. After washing, they were dried in a natural environment. They were then put in an oven at 65°C air circulation for 48 hours. After this, all the material was ground in an IKA type mill and the biosorbent was named SALV. Adsorption tests were performed with 200 mesh granulometry for the *in natura* adsorbent.

2.2. Biosorbent characterization

The macrophytes were characterized by TGDTA (Shimadzu DTG-H60), from 25 to 1000°C, with heating rate of 10°C min⁻¹ and 50 mL min⁻¹ air flow of synthetic air, and nitrogen flow. The characterization to identify the functional groups present on the adsorbent surface was performed by infrared absorption spectroscopy. For spectroscopic characterization the Perkin Elmer equipment was used, with spectrum between 4000 and 400 nm⁻¹, 2 cm⁻¹ resolution, 20 scans, with samples prepared in KBr pellets.

2.3. Adsorption Studies

Adsorption experiments were performed in triplicate and the suspensions were separated by vacuum filtration on a 0.45 µm cellulose acetate membrane. The determination of lead concentration was determined by flame atomic absorption spectrometry (FAAS) on Avanta GBC

model HG-3000 equipment with an air-acetylene flame and Pb hollow cathode lamp at a wavelength of 217 nm. To study the effect of pH on adsorption, samples of 0.5g of *Salvinia auriculata* were added to erlenmeyers containing pH solutions ranging from 2 to 10, then stirred for 24 hours at room temperature and the final pH was measured with a potentiometer, Quimis brand and a glass electrode. The pH of the solutions was adjusted by the addition of 0.1 mol L⁻¹ NaOH or 0.1 mol L⁻¹ HCl.

The batch equilibrium experiments were performed at 25°C, with 0.30 g of adsorbent in 30 mL of Pb solution, for 24 hours, varying the initial concentration in the range of 0.1 and 6 mg L⁻¹. The general methodology of adsorption studies was adapted from Modenes *et al.* [7]. The data obtained were fitted for Langmuir and Freundlich, adsorption isotherm models [11]. The equations that describe the models are presented in Table 1:

Table 1: Isotherm models Langmuir and Freundlich.

Isotherm	Equation	Results
Langmuir	$q_e = q_m K_L \frac{C_e}{1 + K_L C_e}$	C _e equilibrium concentration (mg L ⁻¹) q _m and q _e adsorption capacity (mg.g ⁻¹) K _L (mg g ⁻¹) Langmuir constant
Freundlich	$q_e = K_F C_e^{\frac{1}{n}}$	n e K _F (mg g ⁻¹) Freundlich constants

3. Results and Discussion

Lead levels in water with macrophyte *Salvinia auriculata* were determined by Avanta GBC Flame Atomic Absorption Spectrometry (FAAS), model HG – 3000, flame air-acetylene, at the Department of Technology Sanitation Laboratory (UEFS- BA), as presented in the work of Lima and colleagues. Our results showed that the *Salvinia* samples contain lead at concentrations below the tolerance limits for plant tissues, prompting us to investigate the potential of this biomass in the preparation of biosorbents. [3].

The decomposition of the macrophyte with increasing temperature was studied in two different atmospheres: inert (N₂) and oxidant (O₂/N₂). Fig. 02 shows these variations of mass fractions.

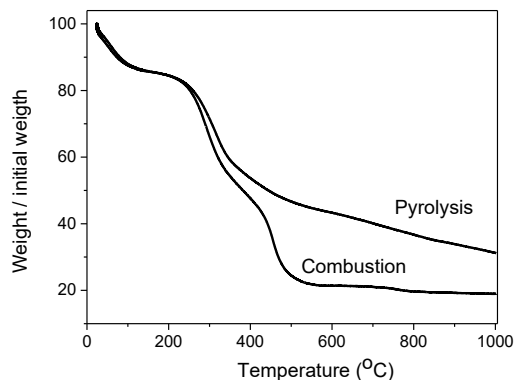


Fig. 2: Thermal analyses of SALV. Conditions: 20 mg, in air flow (combustion) or in N₂ flow (Pyrolysis), 50 mL min⁻¹, and heating rate 10°C min⁻¹

Considering both pyrolysis and combustion, macrophyte decomposition can be observed at the beginning of heating, a similar behavior to other species. The behaviors start to differ at around 230°C. From this temperature on the combustion process leads to a more pronounced decrease, while pyrolysis mass loss is more attenuated. The macrophyte mass reduced by 81% by combustion and by pyrolysis 68.8%. From the technical point of view of preparing biosorbents materials, the pyrolysis activated carbon production may be the most suitable for this biomass considering the residual content of the carbon content.

Lead leaching present in the SALV samples was evaluated as a function of the pH of aqueous solutions without the presence of the metal. The results are shown in Fig. 3.

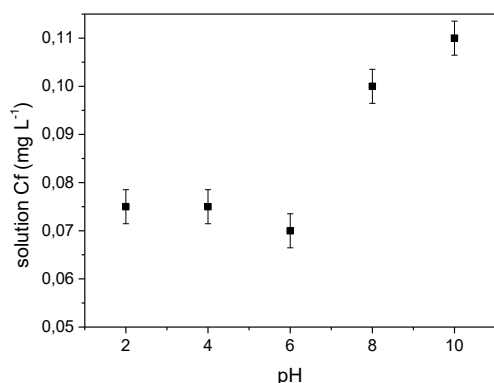


Fig. 3: Effect of pH on lead leach present in dry macrophyte

Fig. 3 shows the final lead concentration in the solution after 24 hours of stirring, and the results indicate that the metal is leached into solution at any pH value, reaching the highest concentrations in most basic solutions, pH > 8. This is a concern due to the environmental risks associated with lead contamination in aquatic environments. The Ministry of the Environment establishes as a limit levels of contamination of 0.01 mg L⁻¹ Pb in freshwater in Resolution CONAMA430/2011 [12]. This means that the macrophytes used in a remediation process have to be properly disposed of after they are removed from their habitats.

From perspective of using this material in the preparation of biosorbents, the adsorption capacity of the SALV samples was tested in lead solutions, at concentrations ranging from 0.1 to 6 mg L⁻¹, and the results are presented as an adsorption isotherm, Fig. 4. In order to establish the most appropriate adsorption equilibrium correlation, the experimental data were modelled using different mathematical correlations and are shown in Fig. 4 and Table 2.

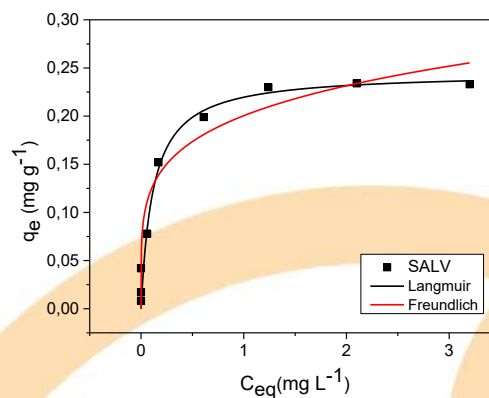


Fig. 4: Langmuir and Freundlich, adsorption isotherms of Pb on SALV adsorbent

Table 2: Isotherms models Langmuir and Freundlich.

Isotherm	Parameters	Results
Langmuir	q_m (mg g ⁻¹)	0,245
	K_L (L mg ⁻¹)	8,536
	R^2	0,965
Freundlich	K_F (mg g ⁻¹)	0,200
	n	4,808
	R^2	0,928

The SALV biosorbent completely removed lead in solutions of concentrations up to 0.5 mg L^{-1} , as observed in Fig. 4. After this, the percentage of removal begins to decrease, and at concentrations above 9.0 mg L^{-1} the equilibrium changes and the predominant process is desorption.

The data presented in Table 2 indicates that the equilibrium data fit both models well, and the adjustment to the Langmuir isotherm ($R^2 = 0.965$) was slightly better. The maximum adsorbed amount (q_m) estimated by this was 0.245 mg g^{-1} . Considering the adjustment by Freundlich ($R^2 = 0.928$), the value of parameter $n > 1$ indicates that even dehydrated macrophyte *Salvinia auriculata* in a lead contaminated environment still preserves its chemical affinity[13].

The FTIR spectra of SALV and SALV-Pb (biosorbent after lead adsorption) are shown in Fig. 5.

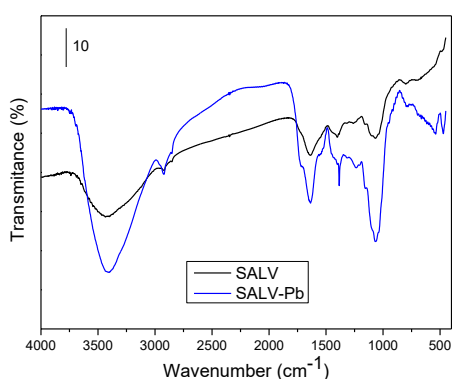


Fig. 5: FTIR spectra of SALV and SALV-Pb.

The results of the FTIR analysis show the presence of functional groups characteristic of biomass. The bands at 3300 cm^{-1} are related to hydroxyl groups ($-\text{OH}$), and the bands at 2920 and 2850 cm^{-1} are associated with C-H, aliphatic mixtures associated with the glycid part of lipids. They range from 1639 to 1540 cm^{-1} , which is commonly related to vibrations of amine groups (NH_2 -) that form part of the amino acid molecules in proteins. After lead adsorption, some vibrations appear more pronounced or shoulders that were previously imperceptible become more visible. In particular, we can mention the 2919 cm^{-1} band referring to the C-H stretch, the 1724 cm^{-1} shoulder more accentuated after the incorporation of Pb which represents the lipid-related C = O bond in the region from 1650 to 1060 cm^{-1} referring to the protein structures and nucleic acids of biological systems, all were modified after Pb adsorption. [14,15].

4. Conclusion

Salvinia auriculata macrophyte in natura found in lentic aquatic environments is able to adsorb lead present in the medium. Therefore, it can be used in the phytoremediation process. However, when it is collected after use it must be disposed of properly because the leaching of lead retained in the plant occurs in a contamination-free aqueous medium in any pH range. This macrophyte can potentially be used as a precursor material for biosorbent synthesis, even when it contains a lead content within the limit of its cellular resistance. It can be used to remove lead up to a concentration of 6 mg L^{-1} from contaminated aquatic environments.

References

- [1] Barakat MA. New trends in removing heavy metals from industrial wastewater. *Arabian J Chem* 2011; 4:361-377.
- [2] Bhuyana MS, Abu Bakar M, Akhtara A, Hossain MB, Alid MM, Islam MS. Heavy metal contamination in surface water and sediment of the Meghna River, Bangladesh. *Environ Nanotechnol Monit Manag* 2017; 8:273-279.
- [3] Lima ACP, França F, Jesus TB. Avaliação dos níveis de metais pesados no pantanal dos Marimbus, Bahia, Brasil. *Eng Sanit Ambient* 2018; 23:591-598.
- [4] Rai PK. Seasonal monitoring of heavy metals and physico-chemical characteristics in a lentic ecosystem of subtropical industrial region, India. *Environ Monit Assess* 2010; 165: 407-433.
- [5] Trindade WM, Horn AH, Ribeiro EV. Concentrações de metais pesados em sedimentos do rio São Francisco entre Três Marias e Pirapora-Mg: geoquímica e classificação de risco ambiental. *Geonomos* 2012; 20: 64-75.
- [6] Zewail TM, Yousef NS. Kinetic study of heavy metal ions removal by ion exchange in batch conical air spouted bed. *Alex Eng J* 2015; 54:83-90.
- [7] Modenes AN, Espinoza-Quinones FR, Santos GHF, Borba CE, Rizzuto MA. Assessment of metal sorption mechanisms by aquatic macrophytes using PIXE analysis; *Journal of Hazardous Materials* 2013; 261:148-154.
- [8] Ali H.; Khan E, Sajad MA. Phytoremediation of heavy metals – Concepts and applications. *Chemosphere* 2013; 91:869-881.
- [9] De Jesus TB, Souza SS, Santos LTS, De Aguiar WM. Avaliação da Potencialidade de Utilização de Espécies de Macrófitas como Acumuladoras de Metais Pesados. *Rev. Virtual Quim.* 2015; 7:1102-111.
- [10] Yang ZH, Xiong S, Wang B, Li Q, Yang WC, Cr(III) adsorption by sugarcane pulp residue and biochar; *J. Cent. South Univ.* 2013; 2:1319-1325.
- [11] Foo KY; Hameed BH. Insights into the modeling of adsorption isotherm systems. *Chem. Engineer. J.* 2010; 156:2-10.

[12] BRASIL, 2011, Resolução CONAMA n°. 430, de 16 de maio 2011. Dispõe sobre as condições e padrões de lançamento de efluentes, complementa e altera a Resolução n° 357, de 17 de março de 2005, do Conselho Nacional do Meio Ambiente-CONAMA. Diário Oficial da União Brasília, 16 de maio de 2011.

[13] Liliç Z., Atakal O., Aras S., Cansaran-Duman D., Çelikkol P., Emregul E. Evaluation of different isotherm models, kinetic, thermodynamic, and copper biosorption efficiency of *Lobaria pulmonaria* (L.) Hoffm. Journal of the Air & Waste Management Association 2014; 64:115-123.

[14] Módenes AN, de Oliveira, AP, Espinoza-Quiñones FR, Trigueros DGE, Kroumov AD, Bergamasco R. Study of the involved sorption mechanisms of Cr(VI) and Cr(III) species onto dried *Salvinia auriculata* biomass. Chemosphere 2017; 172:373-383.

[15] Fourest E, Volesky B. Contribution of Sulfonate Groups and Alginate to Heavy Metal Biosorption by the Dry Biomass of *Sargassum fluitans*. Environ. Sci. Technol. 1996, 30:277-282.

Metals ions adsorption using synthesized 4A zeolite: effect of coal fly ash as silica and aluminum source

Silva, L. T. V.^a; Vidal, C. B.^a; Freitas, A. D. L.^b; França, A. M. M.^a; Loiola, A. R.^b; Nascimento, R. F.¹

^a Federal University of Ceará, Department of Analytical Chemistry and Physical Chemistry, Fortaleza CEP 60.020-18, CE, Brasil

^b Federal University of Ceará, Department of Organic Chemistry and Inorganic, Fortaleza CEP 60.020-18, CE, Brasil

Abstract

Metal ions are of particular concern because they are produced and consumed by various industrial sectors, which generate a large volume of toxic wastewater [1]. Several techniques are used for removing these metals from wastewater including chemical precipitation, ion exchange, and adsorption, the latter being the most promising technique [2]. Thus, this work focuses on removal of Cu^{2+} , Cd^{2+} , Pb^{2+} and Zn^{2+} ions from aqueous solutions using zeolite 4A. The adsorbents were synthesized using both coal fly ash and standard chemical reagents as silica and aluminum source. The samples are referred to as ZA and ZA-P, respectively. Both materials were characterized using different techniques. Batch adsorption tests were carried out with 100 mg L^{-1} of metal ions aqueous solution at constant stirring of 200 rpm. The effect of adsorbent dosage (0.10, 0.09, 0.07, 0.05, 0.03, 0.01 g) and contact time were evaluated and isothermal equilibrium studies were conducted to further understand the adsorption mechanism. It was used Flame Atomic Absorption Spectroscopy (FAAS) for initial and final metals quantification. The characterization results showed that both materials presented mainly the crystalline phase corresponding to zeolite 4A. From the adsorption test, it was revealed that when 0.10 g of mass adsorbent was used in the process for both ZA-P and ZA, the efficiency removal increased. ZA material reached equilibrium time in 10 minutes, while ZA-P took longer (50 min). Therefore, results indicated coal fly ash as a promising alternative silica and aluminum source for synthesis of zeolites, leading to a higher efficiency adsorbent for metal ions removal.

Keywords: Metals Adsorption; Coal Fly Ash; Zeolite.

1. Introduction

Improper disposal of effluents containing metals and other pollutants can lead to serious consequences for many ecosystems. Industries such as battery building, electroplating, paper, tanning, textiles, pesticides and dyeing discharge effluents containing heavy metals into aquatic ecosystems [3]. These metals in aqueous medium have non-biodegradable, bioaccumulative and recalcitrant behavior, causing serious diseases [4]. In addition, ingestion of toxic metals creates imminent problems to human health, such as vomiting, nausea, anemia, central nervous system disorders, stomach cramps, skin irritation, seizures, cancer, etc. [5]. Thus, among the various technologies developed for the removal of metallic pollutants, the most efficient

methods for wastewater treatment are based on adsorption processes [6, 7].

Adsorption is defined as a mass transfer operation, in which certain solids have the ability to concentrate certain amounts of substances (ions or molecules) in liquid or gaseous fluids on their surfaces, allowing the separation of these components from the fluids [8]. Such solids are known as adsorbents, and have a high surface area to favor the adsorption process. In this sense, generally the materials used as adsorbents are solid with cavities or pores [9]. Among the main adsorbents applied in the adsorption process, zeolites stand out because they have interesting properties for adsorption applications [10].

Zeolites are microporous structures of hydrated crystalline aluminosilicates with three-dimensional tetrahedron corner-sharing networks $[\text{TO}_4]$, where T generally represents silicon (Si) or aluminum (Al)



that are interconnected with each other through oxygen atoms. The structure composed of purely $[\text{SiO}_4]$ units is neutral. However, when Al with 3+ charged is an isomorphic substitute for Si with 4+ charged, the structure becomes negatively charged, which is electronically compensated by extra structural cations (Na^+ , K^+ or Ca^{2+}), leading to its ability to exchange cations [11]. Zeolites can be synthesized by different methods, including hydrothermal synthesis consisting of the addition of Si and Al-based precursors to a mineralizing agent, usually alkali metal hydroxides [12].

Thus, among the sources of Si and Al for the synthesis of zeolite, coal fly ash is a great alternative because it has high levels of silica and alumina [13]. Recycling fly ash is very important as large amounts of this waste are disposed of in ponds and landfills, making this by-product an agent of water and soil pollution, disturbing ecological cycles and causing environmental hazards [14].

Therefore, this work aims to study the application of zeolite 4A as adsorbent for the process of adsorption of metallic cations in aqueous solution (Cu^{2+} , Cd^{2+} , Pb^{2+} and Zn^{2+}). In addition, to verify the use of zeolite 4A from fly ash from steel industries as a precursor source for the synthesis of this material, aiming at the recycling of this waste, and to compare with the efficiency of standard zeolite, based on standard reagents.

2. Material and Methods

2.1 Reagents and solutions

The ENEVA group (Energia Pécem, Ceará, Brazil) supplied the fly ash from coal used for the synthesis of zeolite 4A. Inorganic reagents were supplied by Dynamics as analytical grade reagents. The metallic ions studied were Pb (II), Cu (II), Zn (II) and Cd (II). A synthetic copper, cadmium, lead and zinc solution was prepared using their respective nitrate salts, $\text{Cu}(\text{NO}_3)_2 \cdot 3\text{H}_2\text{O}$, $\text{Cd}(\text{NO}_3)_2 \cdot 4\text{H}_2\text{O}$, $\text{Pb}(\text{NO}_3)_2$ and $\text{Zn}(\text{NO}_3)_2 \cdot 6\text{H}_2\text{O}$ in solution. $\text{CH}_3\text{COOH}/\text{CH}_3\text{COONa}$ buffer (pH = 5.0).

2.2 Zeolite Synthesis

Zeolite 4A was synthesized using two different precursor sources for comparison purposes, one from standard reagents (ZA-P) and the other from coal fly ash (ZA).

In the first case, the synthesis of ZA-P was performed by dissolving 13.5 g of sodium

metasilicate (Na_2SiO_3) in 35 mL of 4.35 mol L^{-1} sodium hydroxide (NaOH) solution. Subsequently, 7.22 g of sodium aluminate (NaAlO_2) was dissolved in 35 mL of 4.35 mol L^{-1} NaOH. Then the sodium metasilicate solution was added to the sodium aluminate solution, leading to the formation of a white colored mixture. Soon after, this mixture was placed in an autoclave made of stainless steel with internal Teflon coating and transferred to an oven at 95 ° C for 4h in order to obtain the crystallization of zeolite 4A. The system was subsequently cooled and the resulting synthesis material was washed successively with deionized water through the centrifugation process. Finally, the material was brought back to the oven at 80 ° C for 12h for drying.

In the second case, for the synthesis of ZA, fly ash went through a pre-treatment process, in order to remove salts that could interfere with the silica and alumina extraction process, in which the portions that separated make up the fly ash. The NMF (Non Magnetic Fraction) portion of the magnetization process was used in the synthesis. A portion of approximately 10 g of ash (NMF) was extracted with 65.5 mL of sodium hydroxide (NaOH) 4.35 mol L^{-1} , to solubilize the required Si and Al components for one hour at 90 ° C and stirring in a glycerin bath. After this procedure, the resulting solution was centrifuged to separate the supernatant from the precipitate. To the supernatant was added 1.34 g of sodium aluminate (NaAlO_2) and NaOH 4.35 mol L^{-1} for volume adjustment of 65.5 mL. After this step the hydrothermal route applied to ZA-P was the same one used to obtain ZA.

2.3 Characterization

X-ray Diffraction (XRD), Scanning Electron Microscopy (SEM), Fourier Transform Infrared spectroscopy (FTIR) and Cation Exchange Capacity (CTC) techniques, characterized the synthesized materials.

2.4 Batch Adsorption Study

The effect of dosing was verified using a 100 mg L^{-1} multielemental solution of Cu^{2+} , Cd^{2+} , Pb^{2+} and Zn^{2+} ions at pH 5.0. In this study, 25 mL of this solution was added to each Erlenmeyer containing different masses of adsorbent materials (0.01, 0.03, 0.05, 0.07, 0.09 and 0.1 g), in which they were kept under stirring at 200 rpm for 120 min. Then, the material was filtered and the residual solutions were

analyzed to determine the percentage of metal ion removal using the flame atomic absorption spectrometry (FAAS) technique, with the air-acetylene flame type and wavelengths Cu^{2+} (324.7nm), Cd^{2+} (228.8nm), Pb^{2+} (217.0nm), Zn^{2+} (213.9nm). In order to obtain the adsorption capacity, the amount of adsorbed ions by the adsorbent mass and the percentage of removal, these parameters were evaluated using Equation 1 and 2, respectively.

$$Q_e = \frac{C_o - C_e}{m} \times V \quad (1)$$

$$\%R = \frac{C_o - C_e}{C_o} \times 100 \quad (2)$$

Where Q_e is the adsorption capacity (mg g^{-1}), m is the adsorbent mass used (g), V is the solution volume (L) and C_o and C_e are the metal ion concentrations (mg L^{-1}) in the initial solution and equilibrium respectively and $\%R$ is the percentage of removal.

The contact time were studied using a fixed mass of 0.1 g ZA- P and ZA in batch and duplicate method. The material was contacted with 25 mL of 100 mg L^{-1} multi-element (Cu^{2+} , Cd^{2+} , Pb^{2+} and Zn^{2+}) in buffer solution (pH 5.0) while stirring at 200 rpm. At predetermined intervals (0.5, 1, 3, 5, 7, 10, 20, 30, 50, 60 min) aliquots were filtered off and analyzed by Flame Atomic Absorption Spectrometry (FAAS) and using the Equation 2 the percentage of metal removal by the adsorbent materials was calculated.

3. Results and Discussions

3.1 Characterization

X-ray diffractograms of standard zeolite 4A (ZA-P), zeolite 4A from coal fly ash (ZA) and commercial zeolite 4A were arranged together in Figure 1.

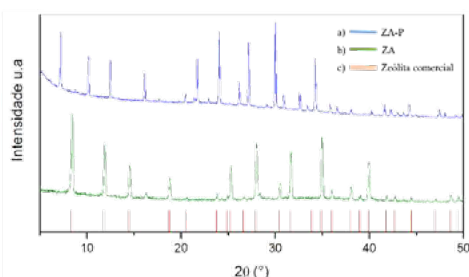


Fig. 1. Difratoograma de raios-X para a) ZA-P, b) ZA e c) padrão da zeólita 4A

According to the diffractograms, we can infer that the synthesized materials are 4A zeolite, since the peaks relative to ZA-P and ZA are in agreement with the peaks of the zeolite pattern. Zeolites were identified as a single crystalline phase free of impurities as shown by peak identification using ICDD database 00-043-0142.

Figure 2 shows the Scanning Electron Micrographs (SEM) of ZA-P and ZA.

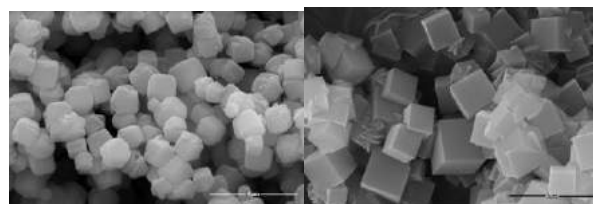


Fig. 2. Scanning Electron Micrograph for ZA-P and ZA.

The micrographs, Figure 7, show that the materials consist of small particle agglomerates of uniform size in the order of $1 \mu\text{m}$, presenting symmetry of cubic crystals, as well as morphology as well-defined edges characteristic of zeolite 4A phase.

Figure 3 shows the Fourier Transform Infrared spectroscopy (FTIR) for both materials.

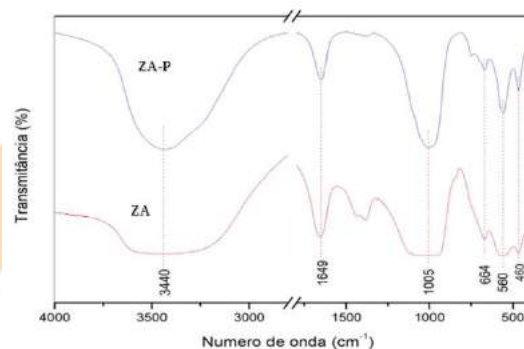


Fig. 3. ZA-P and ZA KBr Tablet Infrared Spectrum.

According to the spectrum, Figure 3, the absorption bands 3440 and 1649 cm^{-1} refer to symmetrical stretching $\nu_{(\text{O-H})}$ and angular deformation $\delta_{(\text{O-H})}$ of the water molecule $-\text{OH}$ bond adhered to the surface of materials due to medium humidity [15].

The band present around 1000 cm^{-1} is related to internal vibrations of the asymmetric stretching of the T-O bonds (T = Si or Al), whereas the bands present in the regions between $400\text{-}700\text{ cm}^{-1}$ are associated with typical vibrations of the T-O bonds. Secondary building units of nanostructured material, known as the fingerprint of each zeolite [16]. The 461 , 560 and 664 cm^{-1} bands are related to the deformation vibration of the T-O external bonds, deformation vibrations on the D4-R rings and the symmetrical T-O stretching vibrations of the internal zeolite tetrahedra, respectively [16].

The Cation Exchange Capacity (CTC) is an important parameter that must be evaluated for the choice of material used in the metal adsorption process, since the removal efficiency is directly related to the amount of exchange cations, i.e. the number of available negative loads of material [17]. In this sense, it was observed that parts of sodium ions (Na^+) present in the mass of 1g of the materials were replaced by ammonium ions (NH_4^+). This incorporation being 23 mg for ZA-P and 39 mg for ZA of NH_4^+ , which are equivalent to 127 meq 100 g^{-1} ZA-P and 214 meq 100 g^{-1} ZA.

3.2 Batch Adsorption Study

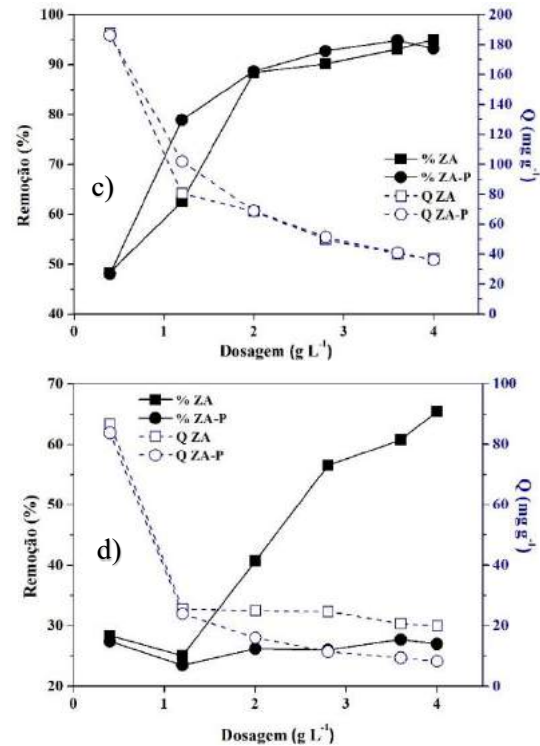
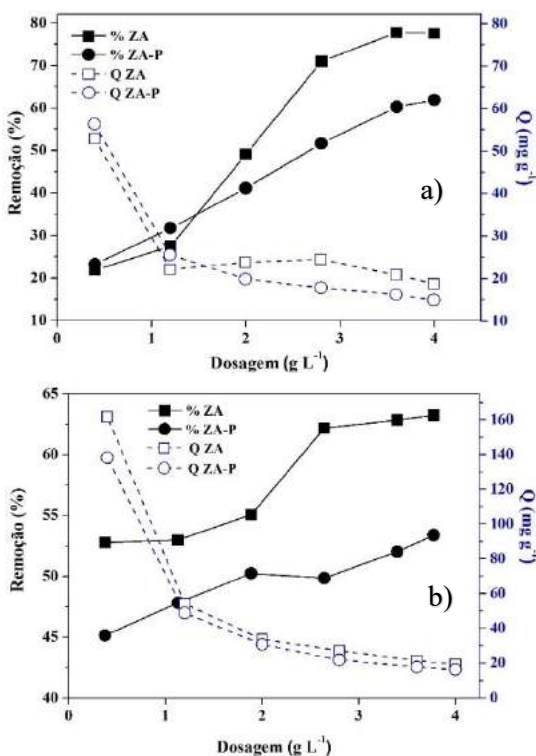


Fig. 4. Effect of ZA and ZA-P zeolite dosage on adsorption capacity and cation removal a) Cd^{2+} , b) Cu^{2+} , c) Pb^{2+} and d) Zn^{2+} (T, $\pm 28\text{ }^\circ\text{C}$; stirring speed, 200 rpm; V, 25 mL; metal solution 100 mg L^{-1} ; time 120 min.).

The adsorption results of metals by zeolitic materials, ZA and ZA-P, with different dosages are shown in Figure 4. The initial concentration of each metal was 100 mg L^{-1} . The behavior for the adsorption capacity was observed similar for both materials, with the increase of the material dosage. adsorbent active sites, so higher removal percentages can be established. However, a fraction of these sites remain unsaturated, decreasing the adsorption capacity. As increased removal contributes to the lack of ions in solution with respect to the high number of active sites capable of adsorption [18]. In addition, the decrease in surface area caused by the agglomeration of adsorbent particles at high dosages, in which some active sites overlap, makes it difficult for some ions to access it, contributing to a decrease in adsorption capacity [18].

zeolite ZA had better results for the removal of all metals when compared to ZA-P, being zinc (Zn^{2+}), Figure 4 (d), cation as the largest removal difference between materials, about 38.5%. The selective behavior by lead cation (Pb^{2+}), Figure 4 (c), was observed for both materials, with removal values close to 95% for ZA and 93% for ZA-P, when the mass used was 0.1 g (4 g L^{-1}). The least adsorbed cation by the materials was copper (Cu^{2+}), figure 4 (b), for ZA and zinc (Zn^{2+}), figure 4 (d), for ZA-P, obtaining removal values close to 63% and 27%, respectively. Cadmium (Cd^{2+}), Figure 4 (a), was the second most adsorbed cation for both materials, achieving removals for ZA and ZA-P of approximately 77% and 62%, respectively. It is possible from the results of this test to infer that the dosage of 4 g L^{-1} (0.1g) was the amount of material with the best results for the metal ion adsorption for both materials. Therefore, this dosage was chose to proceed with the other adsorption tests.

200 rpm; V 25 mL; metal solution 100 mg L^{-1} ; dosage 4 g L^{-1}).

Contact time is an important parameter to be evaluated as it may reflect the adsorption kinetics of an adsorbent for a given concentration of adsorbate [19].

Figure 5 shows the metal removal profiles (Cu^{2+} , Cd^{2+} , Pb^{2+} and Zn^{2+}) for a 100 mg L^{-1} multi-element solution as a function of contact time with each material.

According to Figures 5a and 5b, we can see that the adhesion of metal ions to both materials occurs very quickly (between 1 and 5 minutes), yet the adsorption equilibrium is not yet reached.

Analyzing Figure 5a for the adsorption of metal ions by zeolite ZA, it can be seen that the Cd^{2+} ion reached 90.1% removal values with only 7 minutes of contact with the material, not varying over time, reaching values of 91.74% and 90.66%, for the times of 20 and 60 minutes, respectively.

For the Zn^{2+} ion, high removal values (76.8%) were reached within 10 minutes of contact, reaching a maximum value of 81.15% within 30 minutes.

The metallic ions Pb^{2+} and Cu^{2+} had similar behavior for ZA, reaching removal values of 61% and 59.4%, respectively, in the first 10 minutes and maintaining a removal range during the remaining 50 minutes, reaching until the end of 60 minutes of this test the removal values of 57% and 54%, respectively.

According to figure 5b, we can understand the time – removal profile of metal ions for zeolite ZA-P. Thus, we can see that the Pb^{2+} and Cd^{2+} ions had the particular behavior where at the beginning of the process Pb^{2+} reaches higher and higher values than the removal Cd^{2+} , reaching 80% with only 1 minute of contact, but Pb^{2+} removal decreases. and that of Cd^{2+} increases until reaching removal values close to 57.12% and 55.4%, respectively, with 10 minutes of removal, and from that point on, ZA-P has a preference for Cd^{2+} and it begins to reach higher removal values in relation to Pb^{2+} , reaching at the end of 60 minutes 72% and 61% for Cd^{2+} and Pb^{2+} , respectively. This behavior can be explained by the fact that the Cd^{2+} ion has a smaller ionic radius and a consequent hydration ionic radius than those related to the Pb^{2+} ion, which make the initial adsorption kinetics of Cd^{2+} slow, as it has to spend more energy to release water molecules, making them less removed at the beginning and increasing over time because of the metal's affinity with the surface of the material.

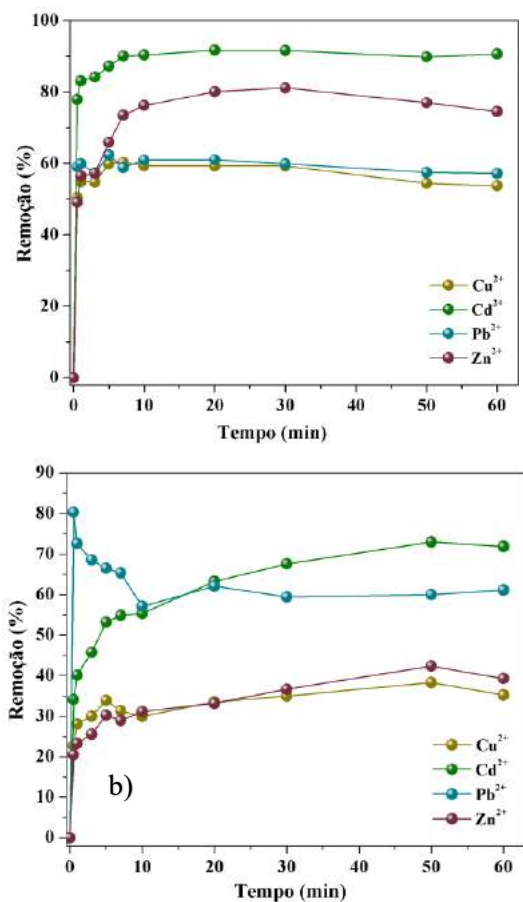


Fig. 5. Effect of contact time on the removal of metal ions a) ZA b) ZA-P (T, $\pm 28^\circ\text{C}$; stirring speed

The same behavior was observed between the metals Zn^{2+} and Cu^{2+} , in the first minutes Cu^{2+} has removal values higher than Zn^{2+} , reaching 33% with 5 minutes of contact, while Zn^{2+} reached 30% for the same time. This behavior changed after 20 minutes of contact, in which Zn^{2+} and Cu^{2+} reached approximately equal removal values, 33.2% and 33.5%, respectively. After this time the removal profile of Zn^{2+} was higher than that of Cu^{2+} , reaching final removal values with 60 minutes of contact of 39% and 35%, respectively. The same explanation used for the behavior between Pb^{2+} and Cd^{2+} can be used for the case between Zn^{2+} and Cu^{2+} , although although Zn^{2+} has a slightly larger ionic radius than for Cu^{2+} , it has a larger hydration radius, which makes so that the initial adsorption velocity is lower and thus decreasing the removal at the beginning. Moreover, it was observed that ZA reaches equilibrium with 10 minutes, being faster than ZA-P that reached this behavior with 50 minutes.

Therefore, from the results obtained the time of 60 minutes was chose as the time used for the subsequent tests, since in this time all metals for both metals reached equilibrium. In this sense, it was noted that the materials have different preferences for the materials studied, being this ordered as $Cd^{2+} > Zn^{2+} > Pb^{2+} > Cu^{2+}$ and $Cd^{2+} > Pb^{2+} > Zn^{2+} > Cu^{2+}$ for ZA and ZA-P, respectively. The metal with higher (Cd^{2+}) and lower (Cu^{2+}) removal was the same for both materials, and ZA (90.66% and 54%) had better results when compared to ZA-P (72% and 35%).

Acknowledgements

CNPq, CAPES and UFC

References

- [1] S.H. Lin, R.S. Juang. *Journal of Hazardous Materials B* 92., 315–326 (2002).
- [2] G.D.Vukovic, A.D. Marinkovic, S.D. Skapin, M.D.Ristic, R. Aleksic, A.A.Peric-Grujic, P.S.Uskokovic, *Chemical Engg. J.* 173., 855–865 (2011).
- [3] N.Oyaro, O. Juddy, E.N.M Murago, E. Gitonga, *Int. J. Food.Agri.Env.* 5 (2007)119-121.
- [4] VISA, M. Synthesis and characterization of new zeolite materials obtained from fly ash for heavy metals removal in advanced wastewater treatment. *Powder Technology*, 2016.
- [5] SRIVASTAVA, N. K.; MAJUMDER, C. B. Novel biofiltration methods for the treatment of heavy metals from industrial wastewater *ournal of Hazardous Materials*, 2008.
- [6] CHOI, H. J.; YU, S. W.; KIM, K. H. Efficient use of Mg-modified zeolite in the treatment of aqueous solution contaminated with heavy metal toxic ions. *Journal of the Taiwan Institute of Chemical Engineers*, 2016.
- [7] FANG, L. et al. A novel method for the sequential removal and separation of multiple heavy metals from wastewater. *Journal of Hazardous Materials*, v. 342, p. 617–624, 15 jan. 2018.
- [8] KAST, W. Principles of adsorption and adsorption processes. *Chemical Engineering and Processing: Process Intensification*, 1985.
- [9] ROUND, C. I. et al. The crystal morphology of zeolite A. The effects of the source of the reagents. *Microporous Materials*, 1997.
- [10] BANDURA, L. et al. Synthetic zeolites from fly ash for an effective trapping of BTX in gas stream. *Microporous and Mesoporous Materials*, 2016.
- [11] YUNA, Z. Review of the natural, modified, and synthetic zeolites for heavy metals removal from wastewater *Environmental Engineering Science*, 2016.
- [12] FEIJEN, E. J. P.; MARTENS, J. A.; JACOBS, P. A. Zeolites and their Mechanism of Synthesis. *Studies in Surface Science and Catalysis*, 1994.
- [13] ALQADAMI, A. A. et al. Efficient removal of toxic metal ions from wastewater using a recyclable nanocomposite: A study of adsorption parameters and interaction mechanism. *Journal of Cleaner Production*, 2017.
- [14] TEMUJIN, J. et al. Processing and uses of fly ash addressing radioactivity (critical review) *Chemosphere*, 2019.
- [15] TOMBÁČZ, E. Ph-dependent surface charging of metal oxides. *Periodica Polytechnica Chemical Engineering*, 2009.
- [16] AMEH, A. E. et al. Influence of aluminium source on the crystal structure and framework coordination of Al and Si in fly ash-based zeolite NaA. *Powder Technology*, 2017.
- [17] MINAMISAWA, H. et al. Preconcentration and determination of cadmium by GFAAS after solid-phase extraction with synthetic zeolite. *Analytical Sciences*, 2006.
- [18] ZHANG, Y. et al. Zeolite synthesized from coal fly ash produced by a gasification process for Ni^{2+} removal fromwater. *Minerals*, 2018.
- [19] WANG, S. G. et al. Removal of lead(II) from aqueous solution by adsorption onto manganese oxide-coated carbon nanotubes. *Separation and Purification Technology*, 2007.

Optimization of an Aromatics Complex Including a Simulated Moving Bed for *p*-Xylene Production

Jonathan C. Gonçalves*, Alexandre F. P. Ferreira, Alírio E. Rodrigues

Laboratory of Separation and Reaction Engineering - Laboratory of Catalysis and Materials (LSRE-LCM), Department of Chemical Engineering, University of Porto, Rua Dr. Roberto Frias, s/n, 4200-465 Porto, Portugal.

Abstract

An aromatics complex, also called BTX complex, is a chemical plant including several processes for the production of benzene, toluene, and xylenes. After benzene, *p*-xylene is the aromatic compound with more applications as polymer precursor. Due to the thermodynamic equilibrium and similar properties of the xylene isomers, the production of *p*-xylene is conducted through an energy-intensive cycle loop. Many efforts are devoted to reduce the energy consumption within the process units; however, studies involving the optimization of the whole complex are very scarce. Based on the aforementioned, an aromatics complex consisting of a simulated moving bed for *p*-xylene separation combined with other units such as crystallization was optimized taking into account the operating costs of the other units including distillation columns, isomerization unit, among others. Simplified models were used for the other units while a rigorous model was applied for the simulated moving bed. The results showed that longer switching times and more columns in zones 1 and 4 are more advantageous for the simulated moving bed, while a propylene refrigeration system is more economical for the crystallization unit despite of the lower recovery ratio.

Keywords: Xylene; Adsorption; Simulated Moving Bed; Crystallization; Optimization

1. Introduction

p-Xylene is the main precursor for polyethylene terephthalate, which is used in the production of fibers, films, and bottles. The demand for *p*-xylene has exhibited a steady increase over the last years, especially from China.

The most common source for aromatics is reformed naphtha, also called reformat, which contains benzene, toluene, xylene, heavy aromatics, and naphthenes. In a typical aromatics complex, the reformat is fed to a fractionation column where benzene and toluene are obtained in the top and sent to an aromatics extraction unit (ArEx). Benzene and toluene are obtained as final products although toluene is often converted to additional benzene and xylenes. The bottom of the fractionation column is sent to the xylene loop where *p*-xylene and *o*-xylene can be obtained as final products. The loop consist of a splitter that separates part of *o*-xylene through the bottom, taking advantage of the 5-degree boiling point difference with *m*-xylene, and heavy aromatics; *o*-xylene is then separated in a dedicated

column. The top of the splitter, consisting of *p*-, *m*-, *o*-xylene, ethylbenzene, and a fraction of naphthenes, is sent to a *p*-xylene separation unit where *p*-xylene is obtained as final product. The other compounds are sent to an isomerization unit (Isom) to produce more *p*-xylene, by reestablishing the thermodynamic equilibrium, and to crack and separate the naphthenes to prevent them from building up in the loop. Since *p*-xylene is not favored by the thermodynamic equilibrium, a significant amount of energy is required within the loop to produce the desired isomer.

The separation of *p*-xylene can be conducted through adsorption, crystallization, or a combination of both. The most employed process is selective adsorption through the simulated moving bed (SMB) technology. In this work, an SMB unit was optimized considering the operating costs of an aromatic complex including a crystallization unit (Crys) to further purify the *p*-xylene from the SMB as presented in Fig.1. Two cases were considered: Case A, where crystallization operates at lower temperature and the mother liquor is sent to the isomerization unit, and Case B, where the

crystallization operates at higher temperature and the mother liquor is sent back to the SMB.

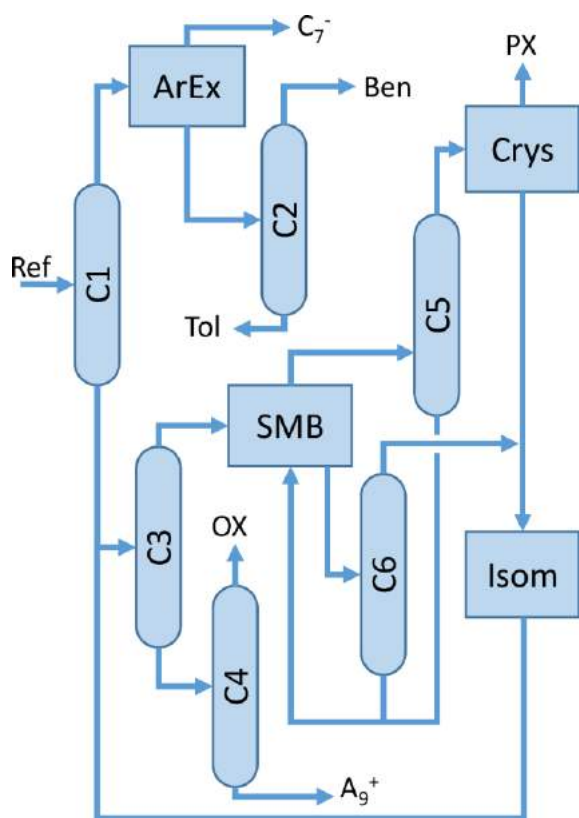


Fig. 1. Aromatics Complex – Case A. ArEx: Aromatics Extraction; Ben: Benzene; C1: Reformate Fractionation; C2: Benzene Column; C3: Xylene Splitter; C4: *o*-Xylene Column; C5: Extract Column; C6: Raffinate Column; Crys: Crystallization Unit; Isom: Isomerization Unit; Ref: Reformate; SMB: Simulated Moving Bed Unit.

2. Methodology

The objective function to be maximized was the products sells minus the operating costs of each unit keeping the reformate fixed for each case. The cost of the reformate and the utilities required in the fractionation (C1) were not considered. The cost of chemicals and utilities were obtained from Turton et al. [1] and are presented in Table 1. The decision variables included column arrangement, switching time, and flow rates of the SMB unit. The required purity of the final product and the maximum pressure drop of the unit constituted the constraints. The models used for each unit, validated against reported data, are described herein after.

Table 1. Chemicals and utilities costs

Benzene	\$1140/ton
Toluene	\$1033/ton
<i>p</i> -Xylene	\$1488/ton
<i>o</i> -Xylene	\$1235/ton
Fuel oil	\$14.2/GJ
Cooling Water	\$0.354/GJ
Electric power	\$16.8/GJ
Refrigerant at 239 K	\$10.165/GJ
Refrigerant at 213 K	\$15.105/GJ

2.1 Distillation columns

The mole fraction of the key compounds was set to 0.001 assuming no distribution for the rest of the species. For the xylene splitter, the mole fraction of *o*-xylene in the bottom was set to obtain 1.1 ton/h of *o*-xylene as final product. The minimum reflux was calculated through the Underwood equation using the equation of state from Peng and Robinson to determine the relative volatility of each compound. The pressure of the top of the column and the pressure drop were set to 138 kPa and 69 kPa, respectively. Condenser and reboiler duties were calculated using a reflux ratio of 1.3 times the minimum reflux and the enthalpy of vaporization calculated at the corresponding temperatures.

2.2 Aromatics extraction

The operating costs of the aromatics extraction unit were estimated from a Sulfolane unit with a capacity of 11.8 t/h of benzene from Stoodt and Negiz [2].

2.3 Isomerization

The industrial unit described by Gonçalves and Rodrigues [3] was used. The duty required by the deheptanizer column was calculated as described in Section 2.1; a heptane fraction 0.02 wt% was assumed. The heat exchanged between the feed and the reactor outlet was calculated following a minimum temperature approach of 25 K. The main utilities of this unit are the fuel oil, cooling water, and electric power for the recycle compressor.

2.4 Crystallization

The solid-liquid equilibrium was used to calculate the concentration of *p*-xylene in the

mother liquor at the operating temperature, which was kept above the eutectic point as in previous work [4]. The efficiency of the centrifuge and washing units was not taken into account. In this unit, the major utility is the compressor for the refrigeration system. For simplicity, the relationship developed by Turton et al. [1] was applied to determine the energy required at two temperatures (see Table 1). Warmer temperatures lead to an above-equilibrium concentration of *p*-xylene in the mother liquor and the stream must be sent back to the SMB unit.

2.5 Simulated moving bed

The unit was modeled by the true moving bed strategy with 24 columns ($d \times h = 4.12 \times 1.14$ m) distributed in four zones. The assumptions were the following:

- Isothermal conditions.
- Axial dispersed plug flow for the fluid phase.
- Plug flow for the solid phase.
- Varying flow rate in each zone.
- Mass transfer described by the linear driving force.
- Pressure drop calculated as fixed bed.
- Danckwerts boundary conditions.

The adsorption data, at 450 K and 900 kPa, was taken from Silva et al. [5]. The desorbent was *p*-diethylbenzene.

3. Results and conclusions

The optimizations were conducted in the commercial software gPROMS using the control vector parameterization algorithm via single shooting; the results for both cases are presented in Table 2. In both cases the revenue from the products is the same since the amount of reformat was constant and the same amount of benzene, toluene, *p*-, and *o*-xylene was obtained as final products.

Comparing to the industrial SMB normally used for *p*-xylene separation, larger number of columns in zones 1 and 4 and longer switching times were obtained. Those operating conditions led to lower desorbent flow rate and higher *p*-xylene recovery, which contribute to the reduction of the energy consumption within the cycle loop.

The major difference between the two cases is the energy consumed in crystallization. The higher recovery at lower temperatures does not compensate

the energy cost. The higher amount of *p*-xylene fed to the SMB does increase the energy consumed by the extract column (C5); however, the overall energy consumption, including the isomerization unit, was lower in Case B.

Table 2. Optimization results

	Case A	Case B
Sells (\$/kg)	38482	38482
Operating costs (\$/h)	1864	1826
ArEx (%)	19.0	19.4
Crys (%)	5.2	3.3
Isom (%)	19.2	19.4
C2 (%)	7.7	7.8
C3 (%)	15.9	16.2
C4 (%)	3.3	3.4
C5 (%)	6.4	6.6
C6 (%)	23.4	23.9
SMB		
Column arrangement	10-5-3-6	10-5-3-6
Switching time (s)	180	180
Recovery (%)	99.96	99.99
Crys		
Recovery (%)	99.35	97.98

Acknowledgements

This work was financially supported by: Associate Laboratory LSRE-LCM - UID/EQU/50020/2019 - funded by national funds through FCT/MCTES (PIDDAC).

References

- [1] Turton R, Bailie RC, Whiting WB, Shaeiwitz JA, Bhattacharyya D. Analysis, Synthesis, and Design of Chemical Processes. 4th ed. New Jersey: Prentice Hall; 2012.
- [2] Stoodt TJ, Negiz A. UOP Sulfolane Process. In: Meyers RA, editor. Handbook of Petroleum Refining Processes. New York: McGraw-Hill; 2003. P. 2.13
- [3] Gonçalves JC, Rodrigues AE. Industrial xylene/ethylbenzene isomerization unit using a radial-flow reactor and euo-type zeolite. Chem Eng Technol 2013; 36:1658-64.
- [4] Gonçalves JC, Rodrigues AE. Revamping an Existing Aromatics Complex with Simulated Moving Bed Reactor for *p*-Xylene Production. Chem Eng Technol 2015; 38:2340-4.
- [5] Silva MSP, Mota JPB, Rodrigues AE. Adsorption Equilibrium and Kinetics of the Parex' Feed and Desorbent Streams from Batch Experiments. Chem Eng Technol 2014;37:1541-51.

Critical review of batch adsorption kinetic models: simplifications derived from the infinite bath model

Vânia Queiroz da Silva^a, Daniel Souza de Almeida^a, Evandro Steffani^a, Elisa Barbosa-Coutinho^b, Marcio Schwaab^{a*}

^a Departamento de Engenharia Química, Escola de Engenharia, Universidade Federal do Rio Grande do Sul, R. Ramiro Barcelos, 2777. Sala 253, Prédio 22202, Porto Alegre, RS 90040-040, Brasil

^b Departamento de Físico-Química, Instituto de Química, Universidade Federal do Rio Grande do Sul, Av. Bento Gonçalves, 9500, Porto Alegre, RS, 91501-970, Brasil

Abstract

Adsorption is a technique widely used in effluent treatment processes. Evaluating the kinetics of this phenomenon is fundamental to obtain information on the mechanisms that occur during mass transfer and to evaluate the performance of a given adsorbent. Several mathematical models have been developed to describe the processes that occur in the adsorption; however, these models are often used to adjust the kinetic data in an erroneous or inadequate manner. This is mainly because the boundary and/or initial conditions of the models are not adequate for the process being evaluated. For this reason, the main objective of this study is to review some kinetic models of adsorption derived from the infinite bath model, such as the Boyd/Reichenberg, the Weber-Moris and the Vermeulen models, emphasizing the assumptions made for their formulations as well as the initial and boundary conditions used.

Keywords: Adsorption kinetics; diffusion models; mass transfer modeling.

1. Introduction

Adsorption is a technique widely used in effluent treatment processes. The adsorbents commonly used are activated carbon, zeolites, silica and ion exchange resins. [1, 2]. Understanding its kinetics is fundamental to evaluate the performance of a given adsorbent and to obtain information about the mechanisms that occur during the adsorption. From the kinetic analysis it is obtained information about the adsorbate-adsorbent behavior and the efficiency of the adsorption process, besides predicting the necessary time for the process to go into equilibrium.

Several models were developed to describe the processes that occur in adsorption. These models are usually classified as reaction and diffusion models. The diffusion models comprise a sequence of steps. Initially, (i) the mass is transferred from within the fluid to the external surface of the solid through the boundary layer. Then, (ii) the diffusion of the solute occurs in the liquid contained inside the adsorbent pores and along the pore walls. Step (iii) consists of the kinetics of mass transfer from the liquid phase to the solid surface inside the pores. Models founded

on mass transfer are based on intraparticle diffusive mass transport and/or convective mass transport. Usually, these models consider that the adsorption kinetics is instantaneous. The reaction models, unlike the diffusive ones, do not consider these steps [3, 4].

Several of these models are often used to adjust kinetic data in an erroneous or inappropriate manner. This is mainly because the boundary and/or initial conditions of the models are not suitable for the process being evaluated. For this reason, the objective of this study is to review some kinetic models of adsorption such as the Boyd/Reichenberg, the Weber-Moris and the Vermeulen models, emphasizing the hypotheses assumed for their formulations as well as the initial and boundary conditions used. It is believed that this critical review is significant for improving the research involving the processes that use adsorption and model its kinetics.

2. Theoretical background

The mass transfer within a porous solid particle is mathematically described by a partial differential equation, Eq. (1), obtained from a mass balance at

the adsorbent particle and determines how the solute concentration varies as a function of time t and space r . In Eq. (1), C_p is the fluid phase concentration within the particle pores, S defines the particle geometry, being equal to 0 for infinite plate, 1 for infinite cylinder and 2 for sphere [5]. Thus, r is the radius for cylindrical and spherical particles and the distance from the center for flat particles. Time and space were used in the dimensionless form according to Eqs. (2) e (3).

$$\frac{\partial C_p}{\partial \tau} = \frac{\partial^2 C_p}{\partial \eta^2} + \frac{S}{\eta} \frac{\partial C_p}{\partial \eta} \quad (1)$$

$$\eta = \frac{r}{R} \quad (2)$$

$$\tau = \frac{D_{app} t}{R^2} \quad (3)$$

D_{app} is the apparent diffusivity, defined in Eq (4), and is function of the diffusivities in the fluid phase within the pore, D_p , and on the solid surface, D_s , solid porosity, ε , particle density, ρ_p and the derivative of the adsorption isotherm, $[dq/dC]$.

$$D_{app} = \frac{\varepsilon D_p + \rho_p [dq/dC] D_s}{\varepsilon + \rho_p [dq/dC]} \quad (4)$$

To solve Eq. (1), one initial condition and two contour conditions are required. As usually the solid adsorbent used is initially free of any solute (or adsorbate), the initial condition can be defined according to Eq. (5). Considering that the particle is symmetrical, at r (or η) equal to zero, we have the relation as established by Eq. (6) [5].

$$C_p|_{\tau=0} = 0 \quad (5)$$

$$\left. \frac{\partial C_p}{\partial \eta} \right|_{\eta=0} = 0 \quad (6)$$

The second boundary condition is defined on the outer surface of the particle and you usually have two options. The first one neglects any external resistance to mass transfer and the concentration on the surface is equal to that of the solution, C_B , defined according to Eq. (7). The second one takes

into account the external resistance to mass transfer, as presented in Eq. (8), where Bi_m is the dimensionless mass Biot number and is a function of k_m , the convective mass transfer coefficient, and of the diffusion coefficients.

$$C_p|_{\eta=1} = C_B \quad (7)$$

$$-\left. \frac{\partial C_p}{\partial \eta} \right|_{\eta=1} = Bi_m (C_p|_{\eta=1} - C_B) \quad (8)$$

$$Bi_m = \frac{k_m R}{\varepsilon D_p + \rho_p [dq/dC] D_s} \quad (9)$$

It should be noted that the D_{app} is function of the derivative of the adsorption isotherm and is usually a function of the concentration, so that Bi_m is not constant and τ could not be used as dimensionless time. For the analytical solutions to be reached, the hypothesis made is that the isotherm is linear (Henry's Law) and, in this case, the derivative is equal to the constant K .

It is important to note that so far, two important hypotheses have been made in developing the model. The first one is that the kinetics of adsorption itself is instantaneous, that is, the speed of the process is limited by the mass transfer steps. The second hypothesis is that the adsorption isotherm is linear.

Adding to these two hypotheses, a third one that is usually made is considering the bath as infinite, so that the concentration of the solution, C_B , can be assumed to be constant over time. In this case, Eq. (1) has analytical solution as presented in Eqs (10) and (11), respectively for the boundary conditions of Eqs. (7) e (8).

$$\bar{q} = KC_B \left(1 - 2(S+1) \sum_{n=1}^{\infty} \frac{1}{\gamma_n^2} \exp(-\gamma_n^2 \tau) \right) \quad (10)$$

$$\bar{q} = KC_B \left(1 - 2(S+1) \sum_{n=1}^{\infty} \frac{1}{\gamma_n^2} \frac{Bi_m^2 \exp(-\gamma_n^2 \tau)}{\gamma_n^2 + Bi_m^2 + (1-S)Bi_m} \right) \quad (11)$$

These equations show how the average concentration within the solid phase changes over time. It should be noted that in typical adsorption experiments, considering that the solution concentration remains constant is not reasonable,

since it is precisely the decrease in the solution concentration that is monitored over time for evaluating adsorption kinetics.

On the other hand, Eq. (1) can be solved by the Laplace method [5] and solutions for the geometries of flat plate, cylinder and sphere are, respectively, in Eqs. (12), (13) and (14), always considering the case in which the external resistance to mass transfer is neglected, that is, the boundary condition defined in Eq. (7) [6].

$$\bar{q} = KC_B 2\sqrt{\tau} \left\{ \frac{1}{\sqrt{\pi}} + 2 \sum_{n=1}^{\infty} (-1)^n \operatorname{ierfc} \left(\frac{n}{\sqrt{\tau}} \right) \right\} \quad (12)$$

$$\bar{q} = KC_B 4 \left(\frac{\sqrt{\tau}}{\sqrt{\pi}} - \frac{\tau}{4} - \frac{1}{12\sqrt{\pi}} \sqrt{\tau^3} + \dots \right) \quad (13)$$

$$\bar{q} = KC_B 6 \left\{ \sqrt{\tau} \left[\frac{1}{\sqrt{\pi}} + 2 \sum_{n=1}^{\infty} (-1)^n \operatorname{ierfc} \left(\frac{n}{\sqrt{\tau}} \right) \right] - \frac{\tau}{2} \right\} \quad (14)$$

The solution of the intraparticle diffusion model can also be obtained for semi-infinite particles. In this case, only flat plates can be considered, since it is assumed that diffusion occurs across an infinite distance without variation in the area. The solutions found by the Laplace transforms method for the cases when the external resistance to mass transfer can be neglected, Eq. (15), and when it is significant Eq. (16) [5].

$$\bar{q} = KC_B \sqrt{\frac{4\tau}{\pi}} \quad (15)$$

$$\bar{q} = KC_B \left[\sqrt{\frac{4\tau}{\pi}} - \frac{1 - \exp(Bi_m^2 \tau) \operatorname{erfc}(Bi_m \sqrt{\tau})}{Bi_m} \right] \quad (16)$$

The solutions obtained in the previous section are the basis for several derived models, although the hypotheses considered in obtaining these solutions are not always valid, in particular considering linear isotherm and infinite bath (constant solution concentration).

2.1. Weber-Morris Model

The solutions presented in the Eqs. (12) to (14) proposed by Crank [6] were obtained through the Laplace transform method, and are valid for all time

values, although their convergence is very slow for higher time values. On the other hand, since these solutions converge very quickly to short time values, the Eqs. (10) to (12) can be simplified considering only the term of the equation with the square root of time, leading to Eq. (17) [5].

$$\bar{q} = KC_B (S+1) \sqrt{\frac{4\tau}{\pi}} \quad (17)$$

The use of the relationship between the amount adsorbed and the square root of time is routinely used to evaluate intraparticle diffusion. This relationship is referred to as "the Weber and Morris intraparticle diffusion model". Usually, this correlation is represented by Eq. (18), where the adsorbed quantity, q_t , varies linearly as a function of the square root of time, where K_{id} is the intraparticle diffusion rate constant and C is a constant that, according to some studies, would represent the thickness of the boundary layer [7].

$$q_t = K_{id} \sqrt{t} + C \quad (18)$$

2.2. Boyd/Reichenberg Model

Another model derived from mass transfer equations was proposed by Boyd *et al.* [8] to describe the kinetics of ion exchange process; Reichenberg [9], in turn, presented simplifications for this model.

The model by Boyd *et al.* [8] starts from the solution of Eq. (1) for the case in which the external resistance to mass transfer is neglected, assuming spherical particles ($S = 2$) and infinite bath. The solution is presented in Eq. (19) and is identical to Eq. (10), since the roots of the characteristic equation are $\gamma_n = n\pi$ and the maximum adsorption value q_{∞} is equal to KC_B . F is the adsorbed fraction relative to q_{∞} .

$$F = \frac{q}{q_{\infty}} = 1 - \frac{6}{\pi^2} \sum_{n=1}^{\infty} \frac{1}{n^2} \exp \left(-\frac{D_{app} \pi^2 n^2 t}{R^2} \right) \quad (19)$$

Reichenberg [9] proposed approximations for Eq. (19) in which at sufficiently high values of F , only one term of the series is used. Therefore, Eq. (19) is reduced to Eq. (20). For small values of F , Eq. (21) was obtained. Note that this form consists

in the solution presented in Eq. (14) considering the term proportional to the square root and the linear term of time, *i.e.*, one term more than the Weber-Morris model, Eq. (17).

$$F = 1 - \frac{6}{\pi^2} \exp(-Bt) = 1 - \frac{6}{\pi^2} \exp(-n^2 \pi^2 \tau) \quad (20)$$

$$F = \frac{6}{\pi^{3/2}} \sqrt{Bt} - \frac{3}{\pi^2} (Bt) = \frac{6}{\sqrt{\pi}} \sqrt{\tau} - 3\tau \quad (21)$$

In the Eqs. (20) and (21) B is a parameter defined by Eq. (22).

$$B = \frac{D_{app} \pi^2 n^2}{R^2} \quad (22)$$

2.3. Vermeulen Model

In his work Vermeulen [10] studied an empirical approach to the infinite series obtained by the resolution of the intraparticle diffusion model as proposed by Boyd *et al.* [8] and Crank [6] in Eq. (10). According to Vermeulen [10], Eq. (20) indicates that F is a function only of t and can be replaced by Eq. (23) as an empirical approximation.

$$F = (1 - \exp(-Bt))^{1/2} \quad (23)$$

Starting from the solution presented in Eq. (20), note that term $6/\pi^2$ was omitted and the right side was squared.

3. Materials and methods

The solutions obtained from the different models presented were compared to clarify the validity of the infinite bath approach and the simplifications proposed in the literature. The solid radius R (radius for cylinder and sphere and half of thickness for flat plate) was considered equal to 0.1 cm and an apparent diffusivity equal to $10^{-6} \text{ cm}^2 \cdot \text{s}^{-1}$.

4. Results and Discussion

From the hypotheses considered to obtain the analytical solutions, the greatest incoherence made is considering the solution an infinite bath, that is, to assume that the bulk phase concentration remains constant, since, usually, it is precisely the decrease

in this concentration that is used as a measure of the amount adsorbed. Some studies justify the use of these models in initial times, considering that the decrease in the concentration of the bulk phase is small, but many studies in the literature use these approximations for wide ranges of time and variation in the adsorbed amount, violating this hypothesis.

The second hypothesis commonly violated is considering the isotherma as linear. Some works wrongly even argue that assuming the linear isotherm in initial times is valid, but in fact, the use of the linear isotherm is only correct at low concentrations, when the Henry's law is applicable. However, considering the adsorption kinetics as instantaneous is actually a reasonable hypothesis, since the diffusive processes are generally very slow and are the limiting step of the whole process. Some other simplifications are discussed in more detail below.

4.1. Weber-Morris Model

These models are derived from the semi-infinite solid hypothesis, Eq. (15), or only considering the term with lowest exponent from the solution obtained through the Laplace transform, according to Eq. (17). This solution is valid just for the initial instants, because, besides being based on the infinite bath hypothesis, the discarded terms are only small at initial instants, even if the infinite bath hypothesis was valid. Figure 1 shows the comparison between the infinite bath solution and the approximate solution, Eq. (17), for the three geometries.

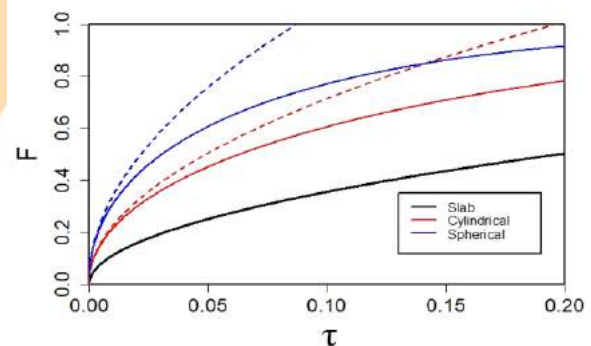


Fig. 1. Comparison between the solutions for the 3 geometries using the Square Root (dashed line) and Infinite Bath (full line) models.

In Figure 1, it is evidenced the error resulting from the neglected terms of the complete solution,

Eqs. (12-14). Figure 1 shows that the similarity between the two models is lost in Fourier values greater than 0.057 for spherical particles, considering a deviation of up to 1%. The same was observed for cylindrical particles, with a limit of 0.099, while for flat plates the approaches remained similar until Fo is of approximately 0.5. This greater difference between the solutions for cylinders and spheres can be understood through the analysis of the Eqs. (12-12). It is observed that in Eq. (12), relative to the infinite flat plate, the terms of the sum of the ierfc function are discarded. However, in Eq. (13) relative to the cylinder, proportional terms τ , $\tau^{3/2}$, ... are discarded; in Eq. (14) relative to the sphere, the terms of the sum of the ierfc function and a term proportional to τ . For short times, the terms of the sum of the ierfc function can actually be discarded, but counting out the proportional terms leads to greater inaccuracies, which may be linked to the fact that the decrease of the area in the direction perpendicular to the transfer of mass to the cylinder and sphere leading to this greater difference between the solutions.

It is also important to emphasize that these solutions do not consider the external resistance to mass transfer. Many studies argue that when the external resistance to mass transfer is significant, the straight line of q vs \sqrt{t} does not pass through the origin. Although this statement is approximately correct, justifying the use of constant C in Eq. (18), this constant should always be negative, because there is no way to add a resistance to mass transfer which would accelerate the process so that the constant C is positive, as can be observed in the experimental data in the works of McKay *et al.* [15] and Zhu *et al.* [16]. The error that is made here is to use experimental data for adjusting straight lines at higher times [17, 18, 19 and 20], when the hypotheses used in the development of this model no longer are valid.

Still linked to this misconception is using multiple lines to describe the adsorption process by assigning a step for the mass transfer process. If this model is valid only for initial times, because it is based on infinite bath and on the discard of solution terms that are small only when the time is close to zero, there is not the slightest logic in using this kind of procedure.

4.2. Boyd/ Reichenberg Model

The simplification proposed by Reichenberg [10] takes into account two models, for small and for large values of F , the value for the exchange between Eqs. (20) and (21) is 0.85 for sphere. Thus, Eq. (21) is used for values of F between 0 and 0.85 and Eq. (20) from 0.86 to 1. These calculations were remade in this study and an optimal F value equal to 0.87 was found, next to the one obtained by Reichenberg.

It is interesting to observe that Equation (21) proposed by Reichenberg [10] can be derived from the complete solution presented in Eq. (14), considering, besides the term with the square root of τ , the linear term of τ , so that the quality of the approximation for the initial part is up to a value of F equal to 0.87, while the Weber-Morris model that takes into account only the term with the square root of τ is valid until values of F are around 0.3.

We could still perform a similar analysis for particles with flat plate or cylindrical geometry. But it is important to note that the solution proposed by Boyd *et al.* [9] and later simplified by Reichenberg [10] has a series of considerations made that should be valid for its correct application. Once again, the most inadequate hypothesis is the consideration of infinite bath, that is, constant bulk phase concentration, besides considering that the isotherm is linear. Despite this, these simplified models are widely used in the literature [2, 11].

4.3. Vermeulen Model

The model proposed by Vermeulen [10] is very close to the solution obtained for the infinite bath model, as shown in Figure 2.

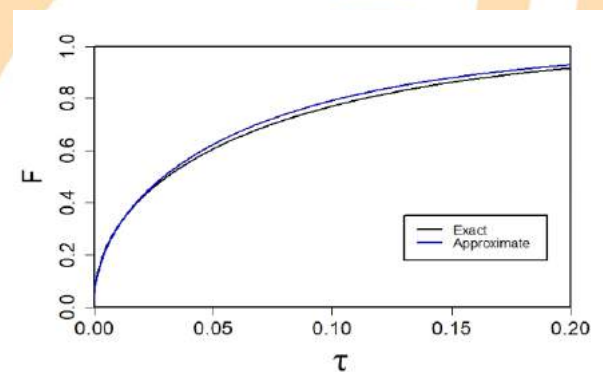


Fig. 2. The solution of Infinity Bath model (full line) and the Vermeulen approach (dashed line).

However, although it has good similarity with the complete solution, this similarity is with a model that considers infinite bath and linear isotherm, very rough approximations of typical batch adsorption experiments, where the concentration of the liquid phase changes greatly over time and relatively high concentrations are used.

5. Conclusion

In general, the models presented here fail mainly by considering the bulk phase concentration as constant, *i.e.*, the infinite bath model, and by considering the linear isotherm. Among the simplified models, no matter how close they are to the exact models, they are usually rough simplifications of the typical conditions under which the batch adsorption experiments are performed, where the liquid phase concentration changes significantly over time and high concentrations are used. Thus, the use of finite-bath and isothermal models suitable for each system should be encouraged, even if this involves the numerical resolution of systems of ordinary and partial differential equations, a fact that should not be seen as a major difficulty nowadays, considering the availability of numerical-computational routines capable of solving these problems with great efficiency.

Acknowledgements

This work was financed in part by Conselho Nacional de Desenvolvimento Científico e Tecnológico – Brasil (CNPq) and by Coordenação de Aperfeiçoamento de Pessoal de Nível Superior – Brasil (CAPES).

References

- [1] Kaur S, Rani S, Mahajan RK, Asif M, Gupta VK. Synthesis and adsorption properties of mesoporous material for the removal of dye safranin: Kinetics, equilibrium, and thermodynamics. *J. Ind. Eng. Chem.* 2015;22:19-27.
- [2] Yao C, Chen T. A film-diffusion-based adsorption kinetic equation and its application. *Chem. Eng. Res. Des.* 2017;119:87-92.
- [3] Qiu H, Lv L, Pan B, Zhang Q, Zhang W, Zhang Q. Critical review in adsorption kinetic models. *J. Zhejiang Univ. A* 2009;10:716-724.
- [4] LeVan MD, Carta G, Yon CM. Adsorption and ion exchange. In: Perry RH, Green DW, Maloney JO, editors. *Perry's Chemical Engineers' Handbook*. 7th ed. New York: McGraw- Hill Inc; 1997. p. 16.1-.66.
- [5] Schwaab M, Steffani E, Barbosa-Coutinho E, Severo JB. Critical analysis of adsorption/diffusion modelling as a function of time square root. *Chem. Eng. Sci.* 2017;173:179-186.
- [6] Crank J. *The mathematics of diffusion*. Oxford, 1975.
- [7] Weber WJ, Morris JC. Kinetics of adsorption on carbon from solution. *J. Sanit. Eng. Div.* 1963;89:31-59.
- [8] Boyd GE, Adamson AW, Myers LS. The Exchange Adsorption of Ions from Aqueous Solutions by Organic Zeolites. II. Kinetics. *J. Am. Chem. Soc.* 1947;69:2836-2848.
- [9] Reichenberg D. Properties of Ion-Exchange Resins in Relation to their Structure. III. Kinetics of Exchange. *J. Am. Chem. Soc.* 1953;75:589-597.
- [10] Vermeulen T. Theory for Irreversible and Constant-Pattern Solid Diffusion. *Ind. Eng. Chem.* 1953;45:1664-1670.
- [11] Gupta VK, Ali I. Removal of DDD and DDE from wastewater using bagasse fly ash, a sugar industry waste. *Water Res.* 2001;35:33-40.
- [12] Glueckauf E. Theory of chromatography. Part 10.- Formulæ for diffusion into spheres and their application to chromatography. *Trans. Faraday Soc.* 1955;51:1540-1551.
- [13] Rodrigues AE, Silva CM. What's wrong with Lagergreen pseudo first order model for adsorption kinetics? *Chem. Eng. J.* 2016;306:1138-1142.
- [14] Edeskuty Fred J, Amundson NR. Effect of Intra article Diffusion Agitated Nonflow Adsorption Systems. *Ind. Eng. Chem.* 1952;44:1698-1703.
- [15] Mckay G, Poots VJP. Kinetics and Diffusion Processes in Colour Removal from Effluent Using Wood as an Adsorbent. *J. Chem. Technol. Biotechnol.* 1980;30:279-292.
- [16] Zhu Q, Moggridge GD, Agostino CD. Adsorption of pyridine from aqueous solutions by polymeric adsorbents MN 200 and MN 500. Part 2: Kinetics and diffusion analysis. *Chem. Eng. J.* 2016;306:1223-1233.
- [17] Ahmad MA, Rahman NK. Equilibrium, kinetics and thermodynamic of Remazol Brilliant Orange 3R dye adsorption on coffee husk-based activated carbon. *Chem. Eng. J.* 2011;170:154-161.
- [18] Mahamoud DK, Sallleh MAM, Karim WAWA, Idris A, Abidin ZZ. Batch adsorption of basic dye using acid treated kenaf fibre char: Equilibrium, kinetic and thermodynamic studies. *Chem. Eng. J.* 2012;182:449-457.
- [19] Shi Q, Zhang J, Zhang C, Nie W, Zhang B, Zhang H. Adsorption of Basic Violet 14 in aqueous solutions using KMnO₄-modified activated carbon. *J. Colloid Interface Sci.* 2010;343:188-193.
- [20] Srivastava VC, Swamy MM, Mall ID, Prasad B, Mishra IM. Adsorptive removal of phenol by bagasse fly ash and activated carbon: Equilibrium, kinetics and thermodynamics. *Colloids Surf. A.* 2006;272:89-104.

Studies of interaction potentials effects in the DFT approach for confined fluids

V. M. Sermoud^{a*}, G.D. Barbosa^a, A. G. Barreto Jr.^b, F. W. Tavares^{a,b}

^a Chemical Engineering Program (PEQ/COPPE), Federal University of Rio de Janeiro (UFRJ), Rio de Janeiro, Brazil

^b Chemical Engineering Department (DEQ), Federal University of Rio de Janeiro (UFRJ), Rio de Janeiro, Brazil

Abstract

The challenges of density functional theory (DFT) lie in bringing the acuity observed in molecular simulation to the phenomena generally recognized on a mesoscopic scale. DFT models appear as tools by the modeling of the adsorption phenomenon in nanoconfinement environments. Among the nanoconfinement modeling strategies, we can describe two distinct approaches, the most common form of classical DFT, the Non-Local Density Functional Theory (NLDFE), and the Quenched Solid Density Functional Theory (QSDFT). In NLDFE models, we approach the adsorbent by a continuous potential, while on QSDFT, we describe the solid molecules explicitly. We do not only distinguish DFT models by how we describe the adsorbent, but also how we describe the interaction between confined fluid molecules. Here, we present a study about the effects of the interaction potential on the NLDFE and QSDFT models for confined fluids, and consecutively on the production of sorption isotherms. This study presents the difference in fluid-structure prediction of confined fluids by applying two dispersion terms and two different rigid sphere terms.

Keywords: Inhomogeneous fluids, NLDFE, QSDFT, porous material.

1. Introduction

We find porous materials in various sectors of the petrochemical and chemical industry, either in the form of adsorbents and catalysts or even as oil reservoir rocks. Therefore, there is a great interest in model fluid behavior within the cavities of these solids.

One of the complexities in studying these materials is the difficulty in the measurement of fluid properties within a single pore. Therefore, we obtain these properties indirectly. Considering processes in which the system achieves the thermodynamic equilibrium, we use adsorption isotherms to correlate the amount present in a pore of a material, given a volumetric condition of temperature and relative pressure.

In this context, we can apply the tools of the density functional theory (DFT), which brings the acuity observed in molecular simulation assays, with a lower computational cost. The formulation of DFT is mainly based on the grand canonical ensemble, whose natural variables are chemical potential, volume, and temperature. Therefore, given these quantities the adsorption process in a

porous media can be carried out by a minimizing process.

Particularly, among the known approaches for simulation of adsorbed fluids in nanopores, IUPAC recommends the application of the DFT with a non-local approximation (NLDFE). In this approximation, we describe the induction of adsorbent walls over a fluid by an induction field. This methodology was successful in representing sorption hysteresis in addition to capillary condensation, especially for solids with a high degree of crystallinity[1].

Here we study the effects of different functional forms on the fluid distribution inside a pore media.

2. DFT formulation

On the classical DFT approach the local density is achieved by solving the non-linear set of equations (Equation 1).

$$\rho(\vec{r}) = \Lambda^{-3} \exp \left(\frac{1}{k_B T} \left(\frac{\delta F_{exc}[\rho(\vec{r})]}{\delta \rho(\vec{r})} - (\mu - V(\vec{r})) \right) \right) \quad (1)$$

$$F_{exc}[\rho(\vec{r})] = F_{HS}[\rho(\vec{r})] + F_{att}[\rho(\vec{r})]$$

Where F_{att} and F_{HS} are the terms of excess free energy, adding the contributions of the dispersion and rigid sphere interactions of fluid molecules. Also, $V(r)$ is the interaction potential, inducing the structure of the adsorbate.

To represent the adsorption in solids with a more amorphous character, Neimark et al., [2] developed QSDFT (Equation 2), which presents the solid explicitly, assuming a roughness factor. This tool allowed us to obtain sorption curves that better represented this material class.

$$\rho(\bar{r}) = \Lambda^{-3} \exp \left(\frac{1}{k_B T} \left(\frac{\delta F_{exc}[\rho(\bar{r}); \rho_s(\bar{r})]}{\delta \rho(\bar{r})} - \mu \right) \right) \quad (2)$$

$$F_{exc} = F_{HS} + F_{att}$$

In which, $\rho_s(\bar{r})$ is the local density distribution of the solid.

We applied two approaches for modeling the dispersive forces, and also the contribution of rigid spheres. We describe these methodologies below.

2.1. Dispersive forces

We approximate the contribution of dispersion forces by the mean-field theory. For the NLDFT model, free energy is a functional dependent only on the contribution of fluid phase components. (Equation 3)

$$F_{att}^{NLDFT}[\rho(\bar{r})] = \frac{1}{2} \iint \rho(\bar{r}) \rho(\bar{r}') \phi_{att}(|\bar{r} - \bar{r}'|) d\bar{r} d\bar{r}' \quad (3)$$

In which ϕ_{att} is the dispersive potential considering the interaction between two molecules.

In the QSDFT model, the dispersion term also accounts for the induction effect of the pore walls.

$$F_{att}^{QSDFT}[\rho(\bar{r})] = \frac{1}{2} \iint \rho(\bar{r}) \rho(\bar{r}') \phi_{att}^{ff}(|\bar{r} - \bar{r}'|) d\bar{r} d\bar{r}' \quad (4)$$

$$\iint \rho_s(\bar{r}) \rho(\bar{r}') \phi_{att}^{sf}(|\bar{r} - \bar{r}'|) d\bar{r} d\bar{r}'$$

$$\frac{1}{2} \iint \rho_s(\bar{r}) \rho_s(\bar{r}') \phi_{att}^{ss}(|\bar{r} - \bar{r}'|) d\bar{r} d\bar{r}'$$

For the calculation of free energy terms for both NLDFT and QSDFT, one must choose how to describe the interaction potential between molecules. For this, we used two different approaches found in the literature.

The first approach to model Φ_{disp} was to approximate the dispersive contribution by the attractive term of Lennard-Jones potential for distances greater than the molecular diameter (Equation 5).

$$\phi_{VSD}(|\bar{r}|) = \begin{cases} -4\epsilon \left(\frac{d}{|\bar{r}|} \right)^6 & \text{se } |\bar{r}| > d \\ 0 & \text{se } |\bar{r}| \leq d \end{cases} \quad (3)$$

This approach was previously applied by Vanderlick et al., (1988) [3], in which they considered that the whole repulsive term would be due to the rigid sphere terms. In this paper, we will call this potential VSD (Vanderlick - Scriven - Davis) because it is the initials of the authors of the article.

The second approach considered in this study was the application of the potential of Weeks-Chandler-Andersen (Equation 5).

$$\phi_{WCA}(|\bar{r}|) = \begin{cases} 0 & \text{se } |\bar{r}| > 5d \\ -4\epsilon \left[\left(\frac{d}{|\bar{r}|} \right)^{12} - \left(\frac{d}{|\bar{r}|} \right)^6 \right] & \text{se } 2^{1/6}d < |\bar{r}| \leq 5d \\ -\epsilon & \text{se } |\bar{r}| < 2^{1/6}d \end{cases} \quad (4)$$

This potential has been used by Ravikovitch [4], [5] to simulate the contribution of the London forces on DFT models.

2.2. Hard-sphere terms

Rosenfeld (1989) [5-7] modeled the contribution of hard-sphere, developing the Fundamental Measurement Theory (FMT). This approach consists of convolving density distribution by geometry functions of rigid spheres. Thus, we can describe the contribution of hard-sphere by the Equation 6.

$$F_{HS}^{QSDFT}[\rho(\bar{r})] = k_B T \int \phi_{HS}[n_\alpha(\bar{r})] d\bar{r} \quad (5)$$

In which, is an energy density term, consistent with an equation of state for the bulk phase. In this study, we applied two methods to describe this potential. However, n_α 's (r) formulation is the same for both approaches [7].

In this study we used the functional FMT-Percus-Yevick and FMT-Carnahan-Starling. For further details on these models, it is recommended to read Roth's review [8].

What mathematically differentiates this methodology from the previous one is how to describe Φ_{HS} as a function of n_α 's.

2.3. Wall potential

In the case of QSDFT, the interactions between the adsorbent and adsorbate molecules will be described by the terms of rigid spheres and the dispersion term. However, in NLDFT, the induction of the solid will be approximated by a force field.

In this study, we approximate the cavities by a set of semi-infinite coverslips. To represent the induction of a graphite pore, we use Steele's potential (10-4-3) (Equation 7).

$$\phi_{st} = \epsilon_w \left(\frac{2}{5} \left(\frac{\sigma_{sf}}{z} \right)^{10} - \left(\frac{\sigma_{sf}}{z} \right)^4 - \frac{\sigma_{sf}}{3\Delta(z + \alpha\Delta)^3} \right) \quad (6)$$

In which Δ represents the distance between lamellae. α , σ_{sf} and ϵ_w are specific parameters for each adsorbent-adsorbate pair.

Additionally, the interaction potential must take into account both pore walls (Equation 8).

$$V(z) = \phi_{st}(z) + \phi_{st}(H - z) \quad (7)$$

In which, H is the distance between the walls.

The parameters used can be found in the works of Ravikovitch et al. (2001), [4] for the NLDFT model. The QSDFT parameters, also the local density distribution used to describe the adsorbent, can be found in the work of Landers et al., (2013) [9].

2. Simulation result

In the adsorption literature, it is common for the production of isotherms in relation to the relative pressure of the volume phase. Therefore, the sorption isotherms described in this section will be described by the relative pressure of the argon in the volume phase, considering a temperature of 87.4 K, rather than being described by the chemical potential, which is the natural variable of the canonical grand ensemble.

In the grand canonical ensemble, when we set the temperature, volume, and chemical potential, it is possible to obtain all the thermodynamic properties of the system. In this study, the DFT model brings the local density distribution of fluid components within the cavity. To transform this information into an adsorbed quantity, we must integrate the density distribution into the cavity space.

Figures 1, 3, 5 and 7 show the ability of DFT models to represent typical mesoporous solids isotherms. In these graphs, it is possible to observe sorption hysteresis in addition to capillary condensation.

Figure 1 shows the sorption isotherms considering the NLDFT model, with a WCA potential dispersion term, in which the blue triangles represent the points of the adsorption isotherm, while the red circles represent the desorption. The adsorption curve ends in capillary condensation, in which saturation occurs at a relative pressure lower than the saturation pressure, identified by the first-order transition to a relative pressure of 0.77.

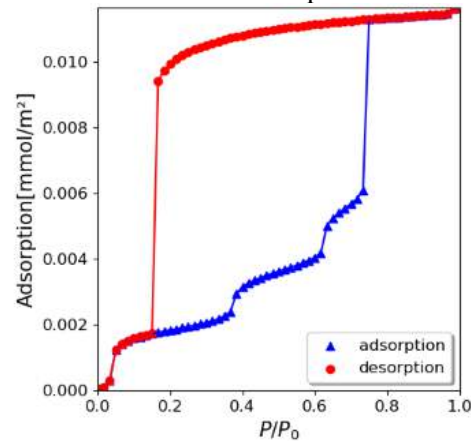


Figure 1 - Adsorption (red circles) and desorption (blue triangles) isotherms, considering the NLDFT model with WCA approximation for the dispersive term and Hard sphere term consistent with the PY equation of state. Argon on graphite at 87.4 K.

This approach predicts the presence of steps in the adsorption curve. To understand the meaning of this behavior, Figure 2 (a and b) show the local density distribution profile of the confined fluid within the adsorbent cavity. In these graphs, the adsorbent walls are on the left and right ends.

In Figure 2 (a), considering a relative pressure of 0.00021 (purple curve), the density profile has a single peak near each wall. With the increment on the P/P_0 , it is possible to observe the consecutive formation of multiple peaks until the pore saturation occurs (blue curve). Thus, we can explain the multiple steps in the sorption isotherm by the formation of multiple adsorbed layers, identified by each peak of the local density distribution.

In Figure 2 (b), for the relative pressure points belonging to the hysteresis zone, local density curves support the observed saturation profile, justifying the shape of the hysteresis.

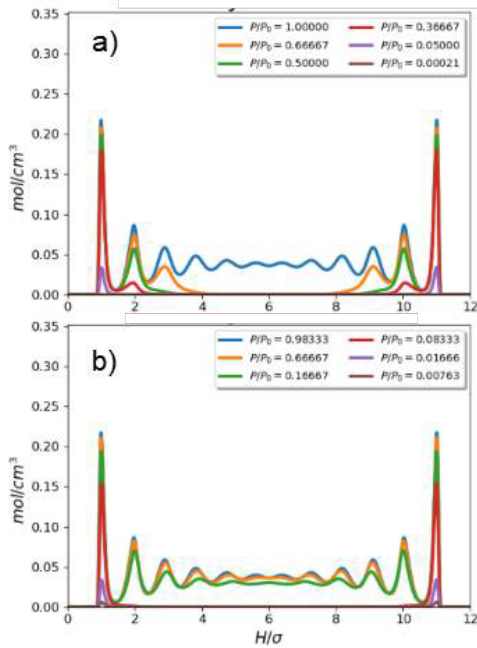


Figure 2 - Density distribution curves of the (a) adsorption and desorption (b) isotherm, calculated by the NLDFT model, for the argon on graphite. Dispersive forces modeled by WCA approximation, and hard-sphere contribution calculated by FMT approximation, consistent with the PY equation of state.

Figure 3 shows the sorption curve for the model with the VSD dispersion term. When compared to the previous case, it is possible to identify the three steps and the sorption hysteresis. However, we can observe a higher adsorbed amount, after the saturation.

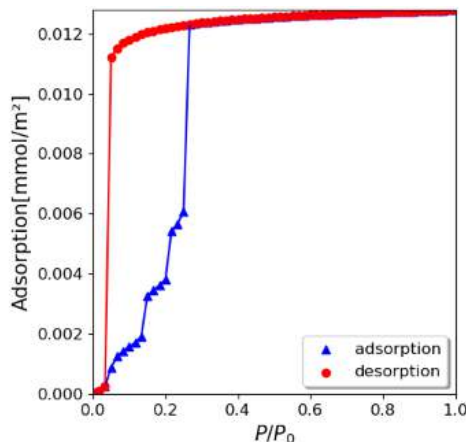


Figure 3 - Adsorption (red circles) and desorption (blue triangles) isotherms, considering the NLDFT model with VSD approximation for the dispersive

term and Hard sphere term consistent with the CS equation of state. Argon on graphite at 87.4 K.

The peaks in the local density distribution curves for the VSD potential model (Figure 4 a and b) are much more pronounced, indicating a higher structure factor, almost as if the fluid had crystallized inside the cavity. This potential reflects a much strong attraction between fluid molecules when compared to the WCA potential.

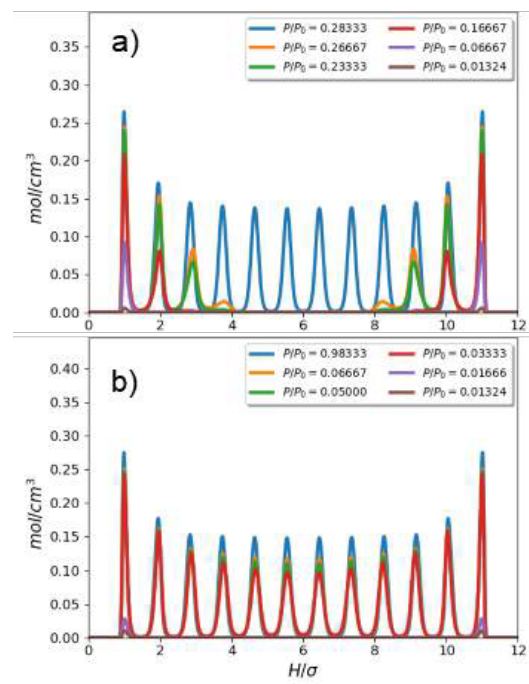


Figure 4 - Density distribution curves of the (a) adsorption and desorption (b) isotherm, calculated by the NLDFT model, for the argon on graphite. Dispersive forces modeled by VSD approximation, and hard-sphere contribution calculated by FMT approximation, consistent with the CS equation of state.

The presence of steps on the adsorption isotherms is a characteristic of crystalline solids. To be able to model the adsorption in adsorbents with a more amorphous character, Neimark *et al.*, (2009) [2] developed the QSDFT, which allows considering the surface roughness of the adsorbents, thus obtaining smoother curves.

Figure 5 shows the sorption isotherms for black carbon argon adsorption, at 87.4 K when we use a dispersion term with the potential of WCA and rigid sphere terms, consistent with the PY equation of state. When compared to NLDFT models, it is possible to see that the adsorption curve (blue

triangles) has a single step, which culminates in capillary condensation at a P / P_0 of 0.42.

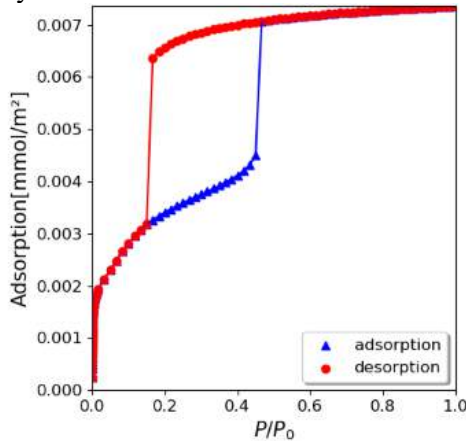


Figure 5 - Adsorption (blue triangle) and desorption (red circles) isotherms, considering the QSDFT model with WCA approximation for the dispersive forces and Hard sphere term consistent with the PY equation of state. Argon on black carbon at 87.4 K.

Figure 6 (a and b) show the local density distributions of the QSDFT solutions for the sorption isotherm. The gray curve, in both charts, refers to the solid molecules. To simulate black carbons, Neimark et al., (2009)[2] considered a roughness factor, for the adsorbent structure. We can observe this surface heterogeneity by the slope of the density distribution between 2 and 4 H/σ .

In desorption solutions, it is possible to identify the maintenance of a saturation structure at a relative pressure lower than that of capillary condensation.

When we replaced the scattering potential with the VSD potential, we identified similar changes to those observed in the results of the NLDFT models. Capillary condensation was anticipated to lower relative pressure. Also, the adsorption capacity was lower when compared to the other QSDFT approach.

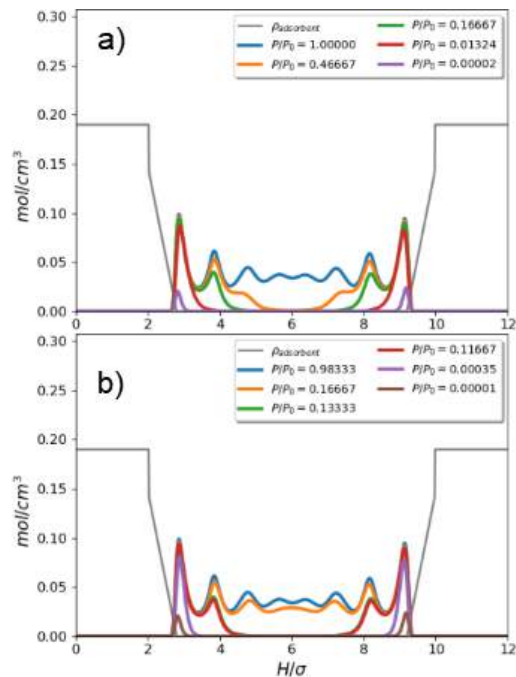


Figure 6 - Density distribution curves of the (a) adsorption and (b) desorption isotherm, calculated by the QSDFT model, for the argon on black carbon. Dispersive forces modeled by WCA approximation, and hard-sphere contribution calculated by FMT approximation, consistent with the PY equation of state.

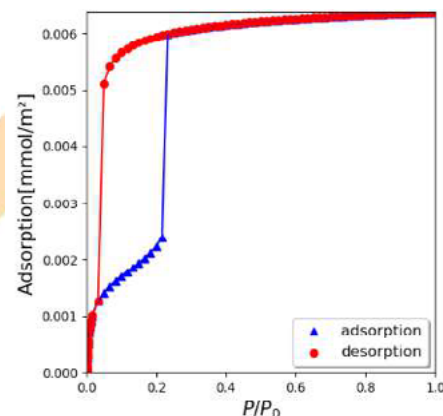


Figure 7 - Adsorption (red circle) and desorption (blue triangle) isotherms, considering the QSDFT model with the VSD approximation for the dispersive forces and Hard sphere term consistent with CS equation of state. Argon on black carbon at 87.4 K.

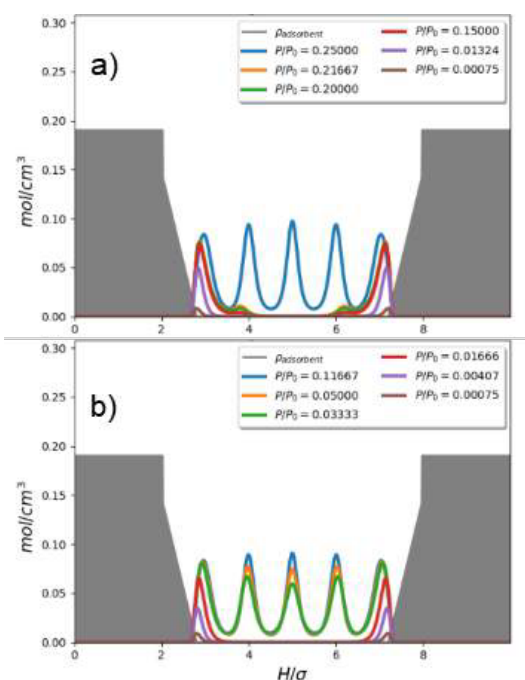


Figure 8 - Density distribution curves of the (a) adsorption and (b) desorption isotherm, calculated by the QSDFT model, for the argon on black carbon. Dispersive forces modeled by VSD approximation, and hard-sphere contribution calculated by FMT approximation, consistent with the PY equation of state.

The saturation profiles of both graphs (Figure 8 - a and b) have a downward concavity due to the strong repulsion that the roughness term induced on the fluid.

Conclusion

In this work, two approaches for the simulation of confined fluid adsorption (NLDFE and QSDFT) were presented, with two different ways of describing both the potential of rigid spheres and the dispersion term. The local density profiles obtained, when we use the WCA potential, describe a smoother structural effect, compared with the solutions of the VSD potential. The degree of fluid structuring affected not only the pressure in which the capillary condensation occurred but also at the value of the adsorption capacity of the adsorbent modeled.

Acknowledgements

This study was financed in part by the Coordenação de Aperfeiçoamento de Pessoal de

Nível Superior - Brasil (CAPES) - Finance Code 001.

References

- [1] M. Thommes and K. A. Cychoz, "Physical adsorption characterization of nanoporous materials: Progress and challenges," *Adsorption*, vol. 20, no. 2–3, pp. 233–250, 2014.
- [2] A. V. Neimark, Y. Lin, P. I. Ravikovitch, and M. Thommes, "Quenched solid density functional theory and pore size analysis of micro-mesoporous carbons," *Carbon N. Y.*, vol. 47, no. 7, pp. 1617–1628, 2009.
- [3] T. K. Vanderlick, L. E. Scriven, and H. T. Davis, "Molecular theories of confined fluids," *J. Chem. Phys.*, vol. 90, no. 4, p. 2422, 1989.
- [4] P. I. Ravikovitch, A. Vishnyakov, and A. V. Neimark, "Density functional theories and molecular simulations of adsorption and phase transitions in nanopores," *Phys. Rev. E - Stat. Nonlinear, Soft Matter Phys.*, vol. 64, no. 1, pp. 1–20, 2001.
- [5] P. I. Ravikovitch and A. V. Neimark, "Characterization of nanoporous materials from adsorption and desorption isotherms," *Colloids Surfaces A Physicochem. Eng. Asp.*, vol. 187–188, pp. 11–21, 2001.
- [6] Y. Rosenfeld, "Free-energy model for the inhomogeneous hard-sphere fluid mixture and density-functional theory of freezing," *Phys. Rev. Lett.*, vol. 63, no. 9, pp. 980–983, 1989.
- [7] Y. Rosenfeld, "Free energy model for inhomogeneous fluid mixtures: Yukawa-charged hard spheres, general interactions, and plasmas," *J. Chem. Phys.*, vol. 98, no. 10, p. 8126, 1993.
- [8] R. Roth, "Fundamental measure theory for hard-sphere mixtures: A review," *J. Phys. Condens. Matter*, vol. 22, no. 6, 2010.
- [9] J. Landers, G. Y. Gor, and A. V. Neimark, "Density functional theory methods for characterization of porous materials," *Colloids Surfaces A Physicochem. Eng. Asp.*, vol. 437, no. 2010, pp. 3–32, 2013.

Modeling adsorption microcalorimetry to estimate intraparticle diffusion rate constants: Parameter sensitivity analysis.

K.F.S Richard , A.E.B Torres , D.A.S Maia , D.C.S Azevedo , M. Bastos-Neto

LPACO2/GPSA Department of Chemical Engineering – Federal University of Ceará, Campus do Pici Bloco 731, Fortaleza-CE, 60440-900, Brazil

Abstract

A microcalorimetry experiment measures energy-related properties by reporting the heat transferred through the calorimetric cell in function of time. The rate of generation of energy by adsorption can be expressed as a function of the sorption kinetics, so, in theory, a microcalorimeter would be able to determine intraparticle mass transfer coefficients. A model is derived to describe the microcalorimetric experiments performed on a calorimeter model C80 (Setaram, France) coupled with a manometric setup for gas adsorption [7]. A theoretical analysis was done based on the similar single-step temperature response method proposed by Grenier[9] and by the evaluation of the piezometric method by Brandani[10]. The analysis is done by checking the influence of many parameters on the evaluation of diffusion coefficients, experimental sensibilities and constraints. The results show that the microcalorimetric could be, indeed, used to determine kinetics parameters under the proper conditions revealed by the model.

Keywords: Adsorption ; Microcalorimetry; Diffusion; Modeling; Simulation

1. Introduction

The determination of kinetic parameters of adsorption is an important task required in the design of many industrial adsorption processes. Proper evaluation of intraparticle mass transfer is necessary to size fixed bed adsorbers because ongoing rates of diffusion affect the bed length directly [1]. It is also important for the choice of cycle times of periodic processes, like PSA or TSA [2].

Adsorption microcalorimetry has been ordinarily used to determine heat-related properties of porous solids, such as the Enthalpy of Adsorption and adsorption isotherms [3, 4]. The technique provides a possible advantage over the existing ones, such as Zero Length Column (ZLC) [5] and uptake rate Methods [6], as it takes into account the adsorption and heat equilibrium properties and kinetic measurements in a single experiment.

The objective of this work is to use a simulation-based rationale to assess the accuracy and feasibility of this method.

2. Materials and methods

2.1 Experimental setup

The simulation analysis is based on experiments that may be carried out in a setup consisting of a C80 (Setaram, France) microcalorimeter coupled with a manometric device. This arrangement provides a simultaneous evaluation of sorption isotherms through measurement of equilibrium pressures, and differential sorption enthalpies [7]. Figure 1 shows the scheme of the experiment apparatus.

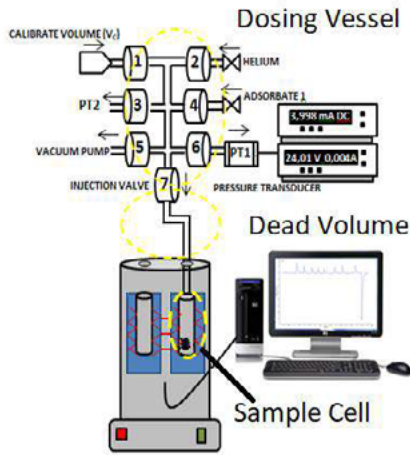


Fig. 1. Microcalorimetry experimental setup.

A regular experiment starts by dosing the sorbate gas in the dosing vessel until a set pressure is reached. Then, valve seven is opened, the gas flows into the microcalorimetric cell and adsorption takes place. The response curve of the experiment is a microcalorimetric peak, Figure 2, which plots the heat rate through the thermocouples as a function of time, the peak reports positive values for adsorption and negative for desorption.

A desorption experiment follows the same principle of the previously described experiment. The difference is that the sorbent is initially saturated with sorbate and the dosing vessel is maintained at a lower pressure, so when valve seven opens, the flow is in the inverse direction, leaving the sample cell and thus reducing the cell pressure.

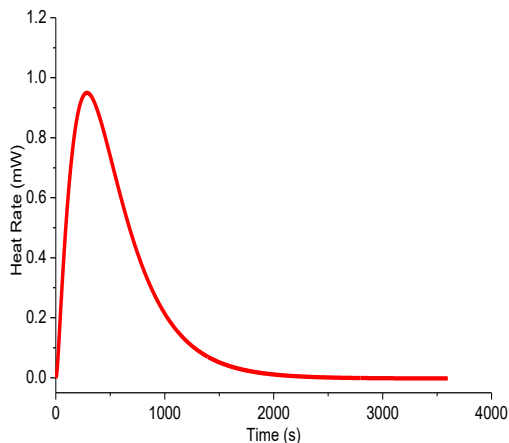


Fig. 2. Microcalorimetric Peak

The diffusion coefficients would be determined by reproducing the response curve with a convenient mathematical model, using mass transfer constants as the fitting parameters.

2.2 Model

This model for the estimation of diffusion coefficients was written to describe a desorption experiment. The control volumes considered in the model are illustrated in figure 3: the calorimetric cell and the dead volume.

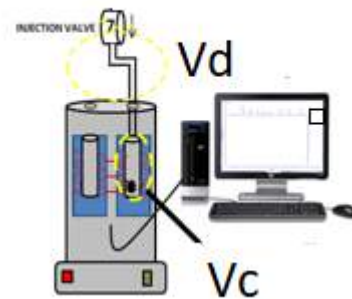


Fig. 3. Domain division of the model

The mass and energy balances for the two control volumes are described by equations 1 to 4.

$$\frac{dC_c}{dt} V_c = -n_{out} - m_s \frac{dq}{dt} \quad (1)$$

$$\frac{dC_d}{dt} V_d = n_{out} - n_{in} \quad (2)$$

$$C_c c_p \frac{dT_c}{dt} V_c + m_s c_{ps} \frac{dT_c}{dt} + m_s c_p q \frac{dT_c}{dt} = V_c \frac{dP_c}{dt} - h_c A_c (T_c - T_w) + m_s (-\Delta H_{ads}) \frac{dq}{dt} \quad (3)$$

$$C_d c_p \frac{dT_d}{dt} V_d = V_d \frac{dP_d}{dt} - h_d A_d (T_d - T_a) \quad (4)$$

The experiments are performed at low pressures, so the equation of state used was of the ideal gas law, equation 5. It is assumed that the pressure of the cell is the same as the pressure of the dead volume, equation 6. The cell pressure behavior follows an exponential decay, equation 7.

$$P_c = C_c R_g T_c \quad (5)$$

$$P_d = P_c \quad (6)$$

$$P_c = P_E + (P_0 - P_E)e^{(-\alpha t)} \quad (7)$$

The model for intraparticle mass transfer is the intracrystalline diffusional control, equation 8. The equilibrium isotherm equation used was of Sips model[8]. Equation 9.

$$\frac{\partial q}{\partial t} = \frac{D_c}{R_c^2} \left(\frac{\partial^2 q}{\partial r_a^2} + \frac{2}{r_a} \frac{\partial q}{\partial r_a} \right) \quad (8)$$

$$q_e = \frac{q_m b P^n}{(1 + b P^n)} \quad (9)$$

The output of estimation method is the diffusional time constant represented by the term D_c/R^2 in equation 8. The input parameters used for the simulation are listed in table 1.

Table 1. Input parameters used in the simulations

Parameter	Model values (SI units)
C_p	37.6 J/mol.K
C_{ps}	915 J/kg.K
m_s	1.79E-4 kg
V_c	8.88E-6 m ³
V_d	10.8E-6 m ³
q_m	2.70 mol/kg
b	7E-4 Pa ⁻¹
n	0.66
R_g	8.314 J/mol.K
h_c	0.165 W/m ² .K
A_c	0.00305 m ²
$h_d A_d$	0.01 W/K
ΔH_{ads}	-35.73E3 kJ/mol
T_w	298.15 K
T_a	294.15 K
P_0	94556 Pa
P_E	90515 Pa

3 Results and discussion

The rationale underlying the analysis of the results is based on the work of Grenier [9]. The mentioned paper proposes a method called single-

step temperature response, which induces a pressure change into a sorbate-sorbent system and monitors the temperature response, which is an analogous response as that of the calorimeter experiment.

Another used reference is the evaluation of the piezometric method by Brandani[10]. As a larger classification, the presented calorimetric method fits into a piezometric method that measures heat instead of pressure. The key concepts of these papers is to analyze the influence of secondary mass and heat transfer resistances, that could impact on the estimation of diffusion rate constants.

For a proper evaluation of intraparticle mass transfer, it is essential to make sure that this is the controlling step of the overall mass and heat transfer phenomena. If diffusion is too fast compared to other resistances, it is not possible to accurately assess this property. Thus, the response curve of the calorimetric peak must be sensitive to the diffusion parameters.

The response curve is a record of heat rate leaving the cell as a function of time, so the equation that describes this curve is represented by the convection term of equation 3, shown by equation 10 below.

$$Q = h_c A_c (T_c - T_w) \quad (10)$$

3.1 Valve effects

Following the references of Brandani and Schumacher [10,11] the valve restriction in the experiment acts as an extra mass transfer resistance, so its effect in the system must be properly taken into account. On the derived model, the valve restriction is represented by parameter α of the pressure decrease equation; the higher the value of this parameter, the lower the valve restriction.

Starting with an ideal condition, with a very low valve restriction, represented by $\alpha = 1000$, figure 4 shows the results of the response curve for different diffusional time constants values.

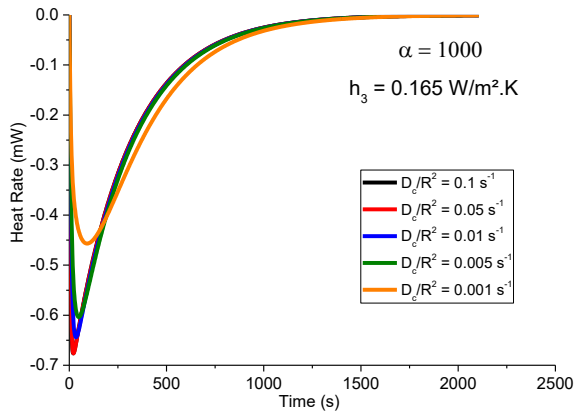


Fig. 4. Sensitivity of the model for different diffusional time constants at low valve restrictions

A seemingly relevant sensibility arises for a value $D_c/R_c^2 = 0.005 \text{ s}^{-1}$ or lower, but if the graph is changed to a short time scale, the sensibility threshold of this parameter becomes clear, figure 5.

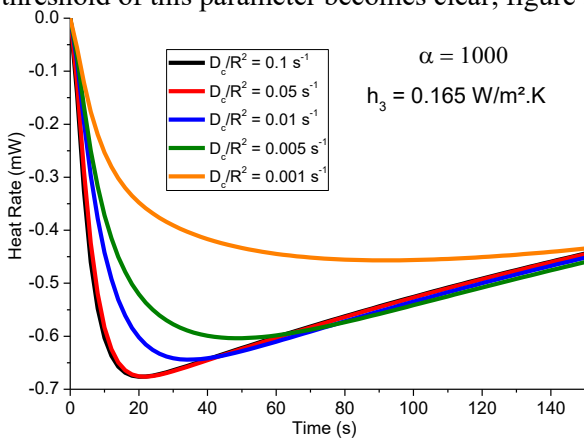


Fig. 5. Short time Sensitivity of the model for different diffusional time constants at low valve restrictions

The plot shows that the actual sensitivity starts at values at the order of $D_c/R_c^2 = 0.01 \text{ s}^{-1}$. Another important conclusion of the comparison (figure 4) is that, for larger values of the diffusion coefficients, the long-time range of the curves, represented by the thermal relaxation, are controlled by convection. Hence, parameter h_c can be estimated from the peak if the intraparticle mass transfer is fast enough.

Changing the conditions to a moderate valve restriction, $\alpha = 30$, figure 6 shows that the sensibility threshold becomes lower, starting now at $D_c/R_c^2 = 0.005 \text{ s}^{-1}$.

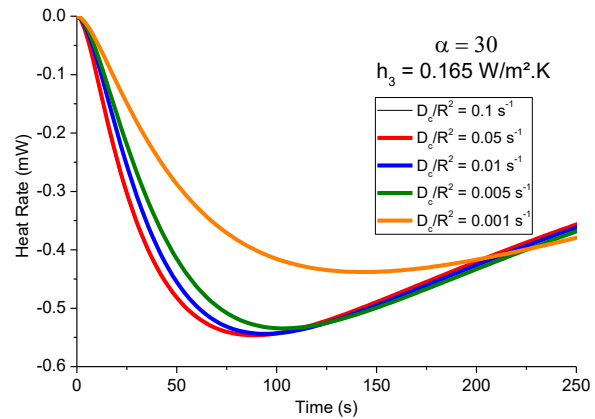


Fig. 6. Short time Sensitivity of the model for different diffusional time constants at moderate valve restrictions

Lastly, analyzing a large valve restriction, $\alpha = 2$, the sensitivity threshold is reduced even further, starting at around $D_c/R_c^2 = 0.001 \text{ s}^{-1}$, as illustrated in Figure 7. This result is consistent with the cited references; as the valve restriction grows larger, the mass transfer resistance imposed on flow into the cell becomes larger and starts controlling the overall process, regardless high intraparticle diffusion.

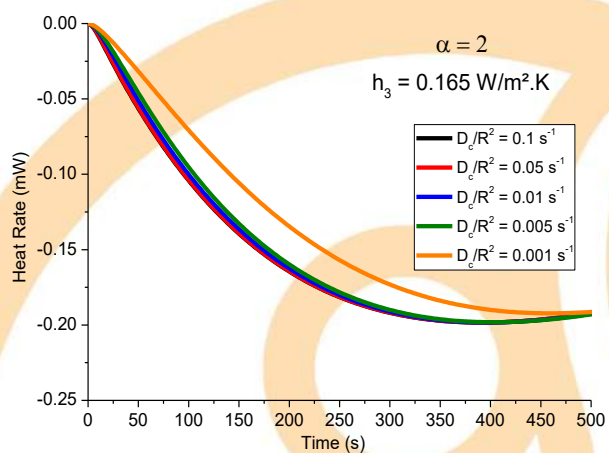


Fig. 7. Short time Sensitivity of the model for different diffusional time constants at large valve restrictions

3.2 Convection heat transfer effects

Another important effect to be evaluated is the influence of the convection heat transfer resistance on the response curve, represented by parameter h_c . As noted in previous figures, convection controls the response curve stabilization (long-time range) for fast diffusing species, which is consistent with the findings of Grenier[9].

Figure 8 shows the impact of the heat transfer coefficient on the response curve, suggesting unlimited influence on the heat rate, as all values tested deform the curve, even at orders of magnitude apart. This results contrasts with the results of Grenier[9,12]. In the cited paper, the peak temperature response always has a period where convection is not relevant for the process.

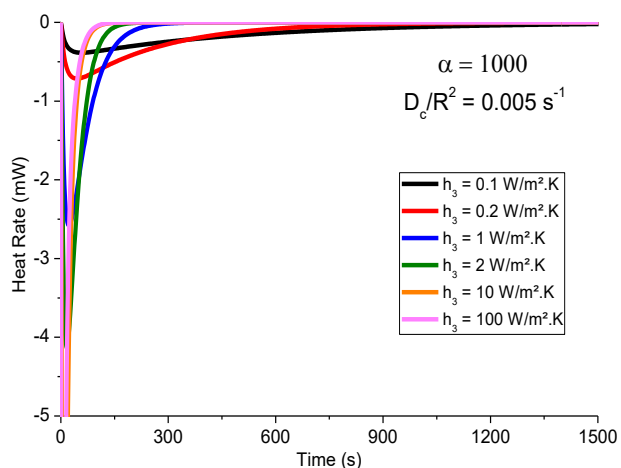


Fig. 8. Effect of heat transfer coefficient on the response curve

4 Conclusions

The simulations show that desorption calorimetric peaks are indeed sensitive to changes in the diffusional properties of gas species and the technique may be applied for estimation purposes. However, caution should be exercised when designing experiments in order to avoid those other ongoing mass transfer phenomena (e.g. through valves) become the governing resistance as compared to the intraparticle diffusion.

Future work will include experimental data and model validation for adsorbate-adsorbent systems reported in the literature.

Acknowledgements

The authors would like to acknowledge Petrobras and CAPES.

References

- [1] Ruthven, D.M. Principles of Adsorption and Adsorption processes. John Wiley & Sons, 1984.
- [2] Ruthven, D. M.; Farooq, S.; Knaebel, K. S. Pressure Swing Adsorption. Wiley-VCH, 1994.
- [3] F. Rouquerol, J. Rouquerol, and D. H. Everett, "Gas-solid interactions. General derivation of reaction enthalpies from the data of isothermal microcalorimetry," *Thermochim. Acta*, vol.41, pp. 311–322, 1980.
- [4] F. Rouquerol, J. Rouquerol, and K. S. W. Sing, *Adsorption by Powders and Porous Solids*. San Diego: Academic Press, 1999.
- [5] Ruthven, D. M., & Eic, M. (1988). Intracrystalline Diffusion in Zeolites. *Perspectives in Molecular Sieve Science*, 362–375
- [6] Ruthven, D. M., & Lee, L.-K. (1981). Kinetics of nonisothermal sorption: Systems with bed diffusion control. *AIChE Journal*, 27(4), 654–663.
- [7] Maia DAS, Alexandre de Oliveira JC, Nazzarro MS, Sapag KM, López RH, Lucena SMP, de Azevedo DCS (2018) CO2 gas-adsorption calorimetry applied to the study of chemically activated carbons. *Chem. Eng. Res. Des.* 136: 753–760.
- [8] Kärger, J., Ruthven, D.M., Theodorou, D.N. *Diffusion in nanoporous materials vol 1*. Wiley-VCH, Germany, 2011
- [9] Grenier, Meunier, F., Gray, P. G., Kärger, J., Xu, Z., & Ruthven, D. M. (1994). Diffusion of methanol in NaX crystals: Comparison of i.r., ZLC, and PFG-n.m.r. measurements. *Zeolites*, 14(4), 242–249.
- [10] Brandani, S. (1998). Analysis of the Piezometric Method for the Study of Diffusion in Microporous Solids: Isothermal Case. *Adsorption*, 4(1), 17–24.
- [11] Schumacher, R., Ehrhardt, K., & Karge, H. G. (1999). Determination of Diffusion Coefficients from Sorption Kinetic Measurements Considering the Influence of Nonideal Gas Expansion. *Langmuir*, 15(11), 3965–3971.
- [12] Grenier, P., Bourdin, V., Sun, L. M., & Meunier, F. (1995). Single-step thermal method to measure intracrystalline mass diffusion in adsorbents. *AIChE Journal*, 41(9), 2047–2057

Notations

α – Pressure decrease exponential parameter

A_c – Area of the microcalorimetric cell (m²)

A_d – Area of the dead volume (m²)

b – Affinity parameter of sips equation (Pa⁻¹)

C_c – Gas concentration at microcalorimetric cell (mol/m³)

C_d – Gas concentration at dead volume (mol/m³)

c_p – Gas molar heat capacity (J/mol.K)

c_{ps} – Adsorbent heat capacity (J/kg.K)

$\frac{D_c}{R_c^2}$ – Diffusional time constant (s⁻¹)

h_c – Convection heat transfer coefficient between gas and cell wall (W/m².K)

h_d – Convection heat transfer coefficient between gas and dead volume wall (W/m².K)

m_s – Adsorbent mass (kg)

n – Exponent parameter of Sips model.

n_{in} – Molar flowrate leaving the dead volume (mol/s)

n_{out} – Molar flowrate leaving the microcalorimetric cell. (mol/s)

P – Partial pressure of gas (Pa).

P_c – Gas pressure at microcalorimetric cell(Pa).

P_d – Gas pressure at dead volume(Pa).

P_E – Equilibrium pressure (Pa).

P_0 – Initial Pressure (Pa).

Q – Heat rate, response curve (W)

q – Adsorbed quantity (mol/kg).

q_e – Equilibrium Adsorbed quantity (mol/kg).

q_m – Maximum adsorbed quantity, Sips model (mol/kg).

r_a – Dimensionless radius.

R_g – Gas constant (J/mol.K).

T_a – Ambient temperature (K)

T_c – Gas temperature at microcalorimetric cell (K).

T_d – Gas temperature at dead volume (K).

T_w – Microcalorimeter Cell wall temperature (K).

V_c – Cell volume (m³).

V_c – Dead volume (m³).

Notations

grand canonical ensemble matching the chemical potential of the confined fluid with its chemical potential in the bulk phase. To perform the MC simulation we use the software Cassandra [5].

Table 1. Force-field parameters for methane, carbon dioxide [2], [3].

Pseudo-atom	σ \AA	ϵ kJ/mol	q e
CH ₄	3.730	1.231	0.0
C (in CO ₂)	2.800	0.234	+0.651
O (in CO ₂)	3.028	0.668	-0.326

Table 2. Force-field parameters for methane, carbon dioxide [2], [3].

Pseudo-atom	k_{bond} $\text{kJ/mol}\text{\AA}^2$	r_o \AA	k_{angle} kJ/molrad^2	θ $^\circ$
CH ₄	-	-	-	-
C (in CO ₂)	8443	1.162	451.9	180°
O (in CO ₂)	-	-	-	-

We used the GERG [6] equation of state available in the REFPROP [7] software to get the chemical potentials. For pure methane the chemical potential was -7.65 KJ/mol. In the 1 to 1 mass fraction mixture, methane was -5.81 KJ/mol and carbon dioxide was -17.93 KJ/mol. As response, we obtained the adjusted densities of a methane-filled calcite pore, with 656 molecules and a methane and carbon dioxide-filled pore, with 556 and 111 molecules of methane and carbon dioxide respectively. The systems were simulated by 10 million Monte Carlo steps and the properties computed at each 10,000 steps.

These densities were used to assemble the new simulation box. Molecular dynamics (MD) simulations of slit-shaped nanopores of containing CO₂, CH₄ and its mixtures were carried out to analyze the effects of the solid wall on the adsorption of each compound. All of the MD simulations were performed using the Large-scale

Atomic/Molecular Massively Parallel Simulator (LAMMPS) package [8]. The NVT ensemble was considered so as to keep the pore volume constant. The atoms of solid matrix were kept immobile. A time step of 1.0 fs was used, and the equations of motion for a system under the influence of a Nosé-Hoover chain thermostats [9] were integrated with the reversible algorithm described by Martyna [10]. Coulombic and van der Waals contributions represent the nonbonded energies, and the stretch and bend terms represent the intramolecular energies – harmonic potential for both angle and bond were used as in Cygan's work [3]. Standard Lorentz–Bertholet mixing rules were used to evaluate unlike atom interactions. The force-field used in this work for methane was TraPPE [2] For carbon dioxide, the non-bonded interactions parameters were also taken from Cygan's force-field [3]. The force fields used for calcite was the model proposed by Xiao [11]. CH₄ was represented as a single-site molecule, CO₂ as a fully flexible three-site model and, finally, the solid were represented as rigid and immobile structure. Initial velocities were assigned using a Gaussian random number generator with standard deviation compatible with the specified temperature according the Maxwell-Boltzmann distribution. A particle-particle-particle mesh (PPPM) solver was used with a desired relative error in forces of 1×10^{-4} to calculate the long-range Coulombic interactions. Standard long-range corrections to the energy was also included, and conventional periodic boundary conditions were applied.

The structures of solids were constructed from unit cells from Avogadro software [12]. The $x \times y$ dimensions of the simulation box were set equal to $29.95 \times 43.23 \text{ \AA}^2$. Pore widths were specified by following the studies by Santos and specified as 20.0 \AA for calcite [13]. The confined fluids are studied in terms of density profile inside the pore because of the anisotropic behavior of the pressure tensor in the pore. Given an initial configuration of the fluid molecules, during equilibration, asymmetries between the density profiles in the fluid–solid interfaces at the bottom and at the top of the simulation box are expected to arise. That is the reason why it is important to rise up the temperature, equilibrate the system, and, then, slowly decrease the temperature down to the desired value. This procedure is used so that molecules do not stagnate

in a local minimum. After equilibrating the system for 2 ns, the ensemble average was studied.

Table 3. Force-field parameters for barite, and calcite [11], [14]

<i>Pseudo-atom</i>	σ <i>Å</i>	ϵ <i>kJ/mol</i>	q <i>e</i>
Ca in CaCO ₃	2.370	2.000	+1.668
C in CaCO ₃	2.604	3.690	+0.999
O in CaCO ₃	3.091	0.582	-0.889

The production time was 5 ns, during which the positions were recorded every 0.1 ps so that the density profile could be calculated by splitting the simulation box into parallel slabs and calculating the density average in each one. The force field parameters for both solid and fluids are summarized in Tables 1, 2 and 3.

3. Results

The main goal of this work was to study mixtures of CO₂ + CH₄ inside calcite nanopore and compare their behaviors to those of the respective pure substances. By this procedure, we intended to observe the impact of one component on the adsorption of the other one on the pore wall list of references and vice versa. The methodology was based on the work of Santos [13]. The difference is that, here, we apply a flexible force field for CO₂ as suggested in the work of Cygan [3] for more accurate results.

Figures 1 and 2 show snapshots from the end of the simulation of the calcite pore filled only with methane and of the calcite pore filled with methane and carbon dioxide. Their corresponding density profiles inside the pore are also shown. Although it cannot be assumed that the behavior of the snapshot is always similar to the graphic, there are times that is possible to observe that the displacement of the molecules is visible and corroborates the behavior illustrated in the graphs.

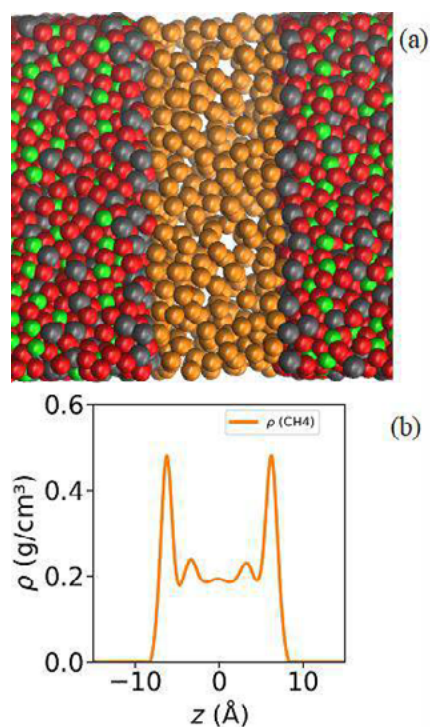


Fig. 1. Snapshot from the end of the simulation (a) and density profiles (b) of calcite nanopore filled with methane (orange).

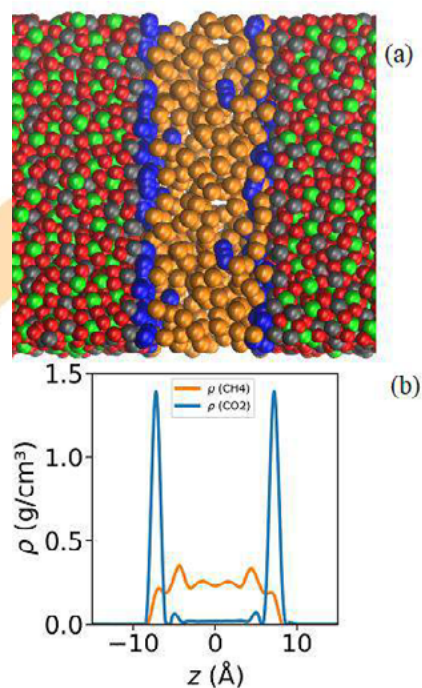


Fig. 2. Snapshot from the end the simulation (a) and density profiles (b) of calcite nanopore filled with methane (orange) and carbon dioxide (blue).

The methane density near the wall reaches 0.5 g/cm^3 when pure and drops to 0.3 g/cm^3 when in mixture with a first layer of carbon dioxide.

The high affinity of the calcite surface's for CO_2 , when compared to methane, is attributed to the stronger polarity of CO_2 . The results obtained here support the idea that CO_2 reinjection into calcite rich reservoirs might enhance gas recovery. These results we generated fixing the density inside the pore in 166 kg/m^3 for the pure methane and 322 kg/m^3 for the mixture of methane and carbon dioxide, inserted in equal mass.

We are now working on adjusting the global density inside the pores by running a Monte Carlo simulation so we can present more realistic results. The first result we have is for the mixture and is given by Figure 3.

We can observe that the carbon dioxide's profile remained similar to the previous results, but there was a major change to methane's profile. This is due to the fact that a much larger number of molecules were placed than in the previous case because of Monte Carlo's simulation results. The behavior close to the walls remains repulsive, however methane also has a density peak there that was not happening before. We can also observe a behavior of layers throughout the pore.

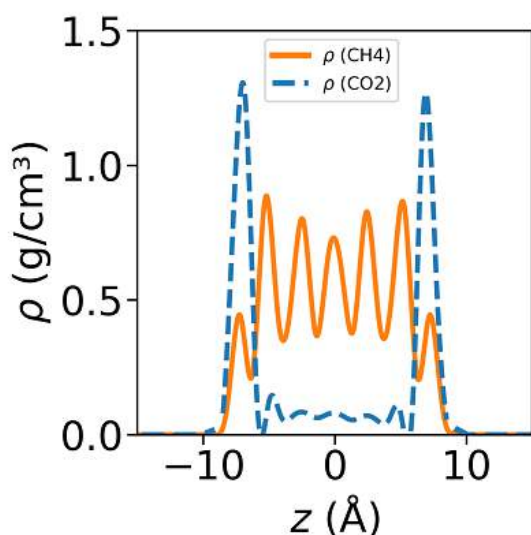


Fig. 3. Density profiles of calcite nanopore filled with methane (orange) and carbon dioxide (blue).

4. Conclusion

In this work, a series of molecular dynamics simulations was carried out in order to predict the effect of CO_2 on the adsorption of methane inside a calcite nanopore. The results obtained here support the idea that CO_2 reinjection into reservoirs might enhance gas recovery. It was concluded that for a better result the density adjustment is necessary so more realistic results are presented. So, we are now working on that.

Acknowledgements

Y.M.O thanks the Federal University of Rio de Janeiro and the ATOMS laboratory, of which she is a member. The authors thank CAPES and as well as the staff of supercomputer Lobo Carneiro for the technical support.

References

- [1] M. E. Tuckerman, *Statistical Mechanics: Theory and Molecular Simulations*, 1st ed. new york: Oxford University Press, 2010.
- [2] G. M. Martin and J. I. Siepmann, "Transferable Potentials for Phase Equilibria. 1. United-Atom Description of n-Alkanes," *J. Phys. Chem. B*, vol. 102, no. 25, pp. 2569–2577, 1998.
- [3] R. T. Cygan, V. N. Romanov, and E. M. Myshakin, "Molecular simulation of carbon dioxide capture by montmorillonite using an accurate and flexible force field," *J. Phys. Chem. C*, vol. 116, no. 24, pp. 13079–13091, 2012.
- [4] C. R. A. Abreu, "Playmol." 2018.
- [5] J. K. Shah *et al.*, "Cassandra: An open source Monte Carlo package for molecular simulation," *J. Comput. Chem.*, pp. 1727–1739, 2017.
- [6] O. Kunz and W. Wagner, "The GERG-2008 Wide-Range Equation of State for Natural Gases and Other Mixtures: An Expansion of GERG-2004," *J. Chem. Eng. Data*, vol. 57, pp. 3032–3091, 2012.
- [7] Lemmon, E.W., I. H. Bell, M. L. Huber, and M. O. McLinden, "NIST Standard Reference Database 23: Reference Fluid Thermodynamic and Transport Properties-REFPROP." National Institute of Standards and Technology, Standard Reference Data Program, Gaithersburg, 2018.
- [8] Steve Plimton, "Fast Parallel Algorithms

- for Short-Range Molecular Dynamics,” *J. Comput. Phys.*, vol. 117, no. 1, pp. 1–19, 1995.
- [9] William G. Hoover, “Canonical dynamics: Equilibrium phase-space distributions William,” *Phys. Rev. A*, vol. 31, no. 4, pp. 1695–1697, 1985.
- [10] G. J. Martyna, M. E. Tuckerman, D. J. Tobias, and M. L. Klein, “Explicit reversible integrators for extended systems dynamics,” *Mol. Phys.*, vol. 87, no. 5, pp. 1117–1157, 1996.
- [11] Y. H. Jang *et al.*, “The MSXX force field for the barium sulfate-water interface,” *J. Phys. Chem. B*, vol. 106, no. 38, pp. 9951–9966, 2002.
- [12] M. D. Hanwell, D. E. Curtis, D. C. Lonie, T. Vandermeersch, E. Zurek, and G. R. Hutchison, “Avogadro: An advanced semantic chemical editor, visualization, and analysis platform,” *J. Cheminform.*, vol. 4, no. 8, 2012.
- [13] M. S. Santos, L. F. M. Franco, M. Castier, and I. G. Economou, “Molecular Dynamics Simulation of n-Alkanes and CO₂ Confined by Calcite Nanopores,” *Energy and Fuels*, vol. 32, no. 2, pp. 1934–1941, 2018.
- [14] S. Xiao, S. A. Edwards, and F. Gräter, “A new transferable forcefield for simulating the mechanics of CaCO₃ crystals,” *J. Phys. Chem. C*, vol. 115, no. 41, pp. 20067–20075, 2011.

Importance of Molecular Simulation for Interpreting Gas Adsorption by Porous Materials: The Case of the Ethane/Ethylene Mixture

José R. B. Gomes^{a*}, Renjith S. Pillai^a, Germán Pérez-Sánchez^a, Christopher Campbell^b, Miguel Jorge^b, Moisés L. Pinto^c

^aCICECO - Aveiro Institute of Materials, Department of Chemistry, University of Aveiro, Campus Universitário de Santiago, 3810-193 Aveiro, Portugal

^bDepartment of Chemical and Process Engineering, University of Strathclyde, 75 Montrose Street, Glasgow, Scotland G1 1XJ, United Kingdom

^cCERENA, Instituto Superior Técnico, Universidade de Lisboa, Av. Rovisco Pais, n° 1, 1049-001 Lisboa, Portugal

Abstract

The separation of small gas molecules has always been a technological challenge to obtain high-purity/high-value gases for the chemical and petrochemical industry. A paradigmatic example is the separation of olefins from paraffins (e.g. propylene from propane or ethylene from ethane), which is normally carried out by cryogenic distillation. Other less energy intensive processes are needed. One alternative are the adsorption-based processes but they require selective adsorbent materials. Metal organic frameworks have been proposed for such applications but some of their intrinsic characteristics are still insufficient for realistic applications. Despite possessing massive porous volumes and surface areas, their stabilities and selectivities are low and further advances are needed. From collaborative experimental and computational work, we have been analyzing with atomistic detail some MOF features that are important for improving the potential of MOFs for gas adsorption / separation applications.

Keywords: Density functional theory; grand canonical Monte Carlo; Periodic and cluster models.

1. Introduction

The separation of mixtures of olefins and paraffins, such as ethane/ethylene, constitutes one of most challenging problems in the chemical industry.[1] Adsorption-based processes, like pressure swing adsorption (PSA) or simulated moving bed (SMB), have been suggested as replacements for the more energy and cost intensive distillation process. However, adsorption processes strongly rely on an adequate choice of the adsorbent material.

Metal-organic framework (MOF) materials, a class of porous solid materials that appeared in the late 1990s, are quite promising candidates for adsorption based olefin/paraffin separations. The synthesis, characterization and application of MOFs in the fields of gas adsorption and gas separation was triggered essentially by their intrinsic hybrid organic-inorganic structures. In fact, MOFs are based on two types of structural building units

(SBUs), namely, single metals or polynuclear metal based clusters and organic moieties. The former are intermediated with the latter to produce nanometer-scale crystalline structures with porous channels and cavities. MOFs present not only exceptionally high surface areas and pore volumes, but may have some intrinsic characteristics that have been found to be important in gas separation processes, such as controllable framework flexibility (e.g., “breathing”), structure interpenetration and coordinatively unsaturated metal sites (a.k.a. open metal sites).[2]

In the past five years, in close collaboration with experimental adsorption measurements, we have been employing diverse computational strategies, namely, density functional theory (DFT) calculations, and grand canonical Monte Carlo (GCMC) simulations, to obtain an atomistic understanding of gas adsorption / gas separation by MOFs adsorbents displaying different structural topologies (e.g. nature and size of cages), with or

without the presence of structure interpenetration or coordinatively unsaturated sites.[3-5] The present communication will highlight the most striking results from the simulations and how they can be used to rationalize adsorption experimental data.

2. Computational details

2.1 Density functional theory calculations

Two different structural model approximations were considered for the DFT studies, namely, the cluster and the periodic model approaches.[6] The former relies on a finite number of atoms, centred at an interesting region of the crystalline structure, with dangling bonds being saturated by hydrogen atoms. The periodic cell approach is based on a repetition of a suitable unit cell in the three spatial dimensions. The problems caused by the finite size of the system associated with the cluster model approach are absent in the latter approach. However, since most of the quantum-mechanical studies employing periodically repeated cells consider plane-wave basis sets, the selection of the unit cell is very critical when dealing with MOFs, since the empty space in the very large pores is also included in the calculations.

The DFT calculations [3] employing the cluster models were performed with the Gaussian 09 code, using all-electron Gaussian basis sets. Core-electrons of metal atoms were treated with effective core potentials. The M06-L (a meta-GGA) exchange-correlation functional was considered. The periodic model calculations [5] were performed with the VASP code, using plane-waves for valence and projected-augmented wave potentials for the core electrons. The PBE-D3 or the vdW-DF2 functionals were employed. These codes were employed to obtain the sets of atomic charges used in the GCMC simulations and to optimize the positions of the hydrogen atoms which are not defined well in the experimental crystallographic structures.

2.2 Grand canonical Monte Carlo simulations

The pure component adsorption isotherms for ethane and ethylene, the adsorption selectivity of the binary ethane/ethylene mixture, and the isothermal-isobaric xy diagrams of the ethane/ethylene mixture were obtained from GCMC simulations using the MUSIC [3] or the RASPA [5] codes. The chemical potential, temperature, and

volume were fixed in the simulations. The simulations consisted of equilibration and production stages, with different number of steps, depending on the code used. The Lennard-Jones (LJ) potential was cut with a cutoff distance of 12.8 Å. The MOF structures were considered rigid in the GCMC simulations. As in previous studies, the LJ parameters of the all framework atoms were taken from the DREIDING and/or UFF force fields. The ethane and ethylene molecules used the LJ parameters from the united atom TraPPE model. Charges were derived from the DFT wavefunctions using the REPEAT or the DDEC methods.[3,5]

3. Results and discussion

The relevance of computer simulations for the understanding of gas adsorption and gas separation processes is presented for MOFs presenting different structural specificities that may affect the interpretation of experimental data, namely, the presence of different topologies, of interpenetration and of open metal sites.

3.1 Interpenetration

Pires et al. [7] reported an experimental study on the adsorption of ethane and ethylene by IRMOF-8 ($Zn_4O(ndc)_3$, ndc = naphthalene-2,6-dicarboxylate, Figure 1). Contrary to what usually happens with MOFs, IRMOF-8 exhibited greater adsorption capacity for ethane than for ethylene at low pressure.

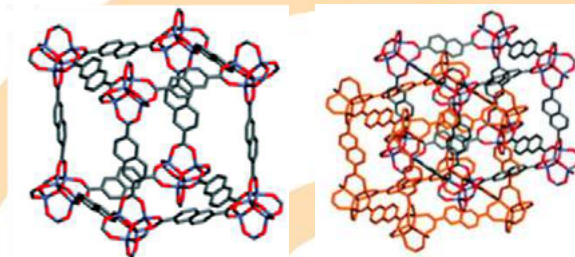


Fig 1. Structure of IRMOF-8 without (left) and with (right) interpenetration.

Interestingly, IRMOF-1 ($Zn_4O(bdc)_3$, bdc = benzene-2,6-dicarboxylate), which has a structure identical to that of IRMOF-8 but with the organic spacer having a single benzenic ring, shows the expected behavior, i.e., it adsorbs more ethylene than ethane. DFT calculations with the M06-2X functional and with molecular models based on small fragments of the periodic structure of IRMOF-8 were used to obtain the geometry and energy of the

interaction of ethane and ethylene with different regions of the framework, namely, i) the organic region, ii) the interface between the organic part and iii) the inorganic part and the inorganic region (Figure 1). The calculated data were not conclusive because the adsorption energies calculated were identical for both gases.[7]

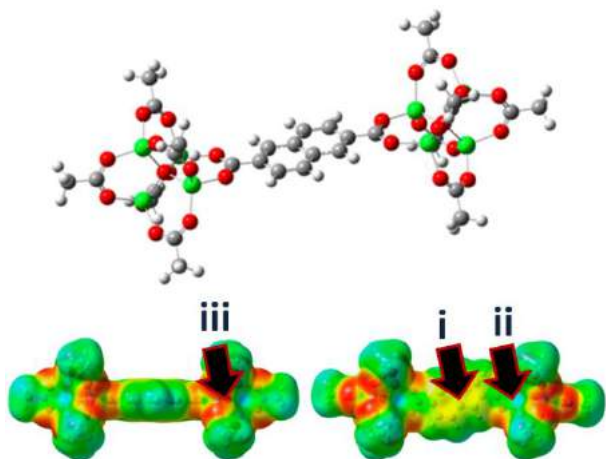


Fig 2. Cluster used to model IRMOF-8 (i-iii labels denote adsorption sites studied, see text). Color code for spheres: White, H; Grey, C; Red, O; Green, Zn.

In a following study, GCMC simulations with periodic models were performed for obtaining adsorption isotherms that were compared directly with the experimental ones.[3] Very satisfactory agreement between calculated and experimental adsorption was obtained for IRMOF-1 while for IRMOF-8 there were significant deviations. Because of the similar structures of these MOFs, the results prompted us to recalculate the ethane and ethylene adsorption isotherms using another molecular model for IRMOF-8 with structural interpenetration. Significant improvements were found for the estimated isotherms. Additionally, it was demonstrated that structural interpenetration originates interactions of the van der Waals type, between the organic ligands of the two interpenetrated structures and the adsorbate molecules, which are more favorable for ethane than for ethylene. Thus, although the interpenetration phenomenon is generally avoided when MOFs are synthesized for gas adsorption, because it causes the reduction of the porous volume, the computational studies clearly showed that MOFs with interpenetrated structures can be quite promising for gas separation processes.

3.2 Coordinatively unsaturated sites

Some classes of MOFs develop unsaturated metal centers upon the activation step prior to adsorption. This happens when inorganic moieties of the MOFs include metal sites that are not fully coordinated to organic linkers but rather to a guest molecule (e.g. a molecule from the solvent). Upon removal of the guest molecule, the metal is left with a free unsaturated site, which were found to display selective and strong adsorption for gases as carbon dioxide or ethylene. The enhanced selectivity was thought to have the potential for practical olefin/paraffin separations.

The first computational studies failed (adsorption was underestimated) in the description of the correct adsorption behavior of adsorbates as ethylene in MOFs having open metal sites, while reasonable descriptions were made for adsorbates as ethane. This was due to the failure of standard force fields to account for complex orbital interactions, but to deal solely with van der Waals forces. Therefore, it was clear that the force fields had to be improved, which was done upon a combination of classical Monte Carlo simulations and DFT calculations, using new parameters to match adsorption energies of ethylene on a MOF with open metal sites, namely, HKUST-1. The interaction potential was improved through the addition of a new interaction site at the center of the olefin double bond, together with a cutoff scheme that prevents the metal site from interacting with more than one adsorbate molecule at the same time.[4]

3.3 Topology

MOFs built from Zr-based inorganic moieties were found to be hydrolytically and thermally very robust, with UiO-66 and MIL-140 families being important examples. UiOs are based on discrete Zr_6 oxoclusters within a three-dimensional (3D) pore system, while MIL-140s exhibit infinite metal oxide rods as building units with 1D triangular channels. Besides the different topology, as it happens with other families, these MOFs may display different aromaticity depending on the organic moieties linking the inorganic nodes. For example, the UiO-66 and UiO-NDC materials are composed of tetrahedral cages of about 7.5 and 10 Å, respectively, and octahedral cages of about 10 and 13 Å, respectively, while the MIL-140A and MIL-140B hybrid materials have 1D triangular channels with diameters of about 3.2 and 4 Å, respectively (Figure 3). Due to the slightly bigger size of the

ethane molecule, it is expected that this species will interact more with the pore walls by nonspecific dispersion forces than ethylene (i.e., as a consequence of the higher polarizability of ethane than that of ethylene).

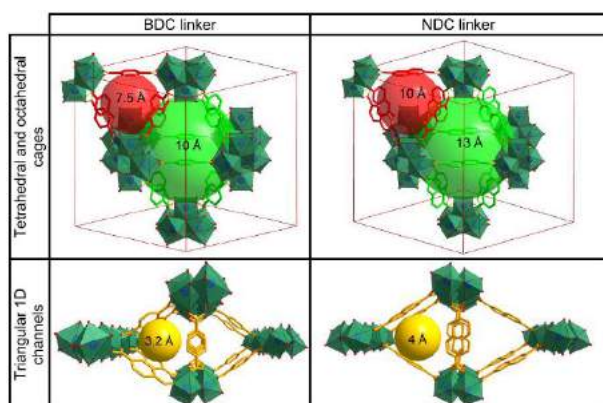


Fig 3. Schematic representation of the pores of the Zr-based MOFs with benzene (BDC) and naphthalene (NDC) linkers.

Pires et al. investigated the adsorption of ethane and ethylene with these MOFs.[5] The adsorption experiments revealed that the size and type of pores have a more pronounced effect on the selectivity than the aromaticity of the linker. The increase in pore size when changing from benzene to naphthalene dicarboxylate ligand makes UiO-NDC less selective (1.3–1.4) than UiO-66 (1.75–1.9) within the pressure range (100–1000 kPa), while the 3D pores of the UiOs favor the adsorption of ethane due to the interactions between ethane with more spacers than in the case of the 1D channels of MIL-140s. Additional experimental studies with UiO-66 functionalized with two perfluoro groups in the aromatic rings (UiO-66-2CF₃) showed a noticeable increase of selectivity (up to 2.5).

UiO-66-2CF₃ revealed a unique combination of selectivity and working capacity at high pressures. Computer simulations showed that this is due to a complex adsorption mechanism involving a different distribution of the guest molecules in the different cages associated with changes in the ligand/perfluoro orientation when the pressure increases, favoring the ethane adsorption at high pressures.

4. Conclusions

Using a combination of experimental and computational approaches it has been possible to understand important structural characteristics of porous hybrid organic-inorganic materials that can be tuned for improving their potential as adsorbents.

Acknowledgements

This work was developed in the scope of the Projects UID/CTM/50011/2019 (CICECO), and UID/ECI/04028/2019 (CERENA), financed by national funds through the FCT/MEC and cofinanced by FEDER under the PT2020 Partnership Agreement.

References

- 1- P. F. Bryan, Removal of propylene from fuel-grade propane. *Sep. Pur. Rev.* 33 (2004) 157.
- 2- M. A. O. Lourenço, J. R. B. Gomes, P. Ferreira, "Gas-organic and gas-inorganic interfacial effects in gas-adsorbent interactions: The case of CO₂/CH₄ separation, in Hybrid organic-inorganic interfaces: Towards advanced functional materials, Eds. M. -H. Delville and A. Taubert, Wiley-VCH, January 2018.
- 3- R. S. Pillai, M. L. Pinto, J. Pires, M. Jorge, José R. B. Gomes, Understanding Gas Adsorption Selectivity in IRMOF-8 Using Molecular Simulation, *ACS Appl. Mater. Inter.*, 7 (2015) 624.
- 4- C. Campbell, C. Ferreira-Rangel, M. Fischer, J. R. B. Gomes, M. Jorge, A Transferable Model for Adsorption in MOFs with Unsaturated Metal Sites, *J. Phys. Chem. C* 121 (2017) 441.
- 5- J. Pires, J. Fernandes, K. Dedecker, J. R. B. Gomes, G. Pérez-Sánchez, F. Nouar, C. Serre, M. L. Pinto, Enhancement of the ethane selectivity in ethane-ethylene mixtures with the bulky perfluoro groups in Zr carboxylate-based Metal-Organic Frameworks, *ACS Appl. Mater. Interfaces*, 11 (2019) 27410.
- 6- M. Fischer, J. R. B. Gomes, M. Jorge, Computational approaches to study adsorption in MOFs with unsaturated metal sites, *Mol. Simul.*, 40 (2014) 537.
- 7- J. Pires, M. L. Pinto, V. K. Saini, Ethane selective IRMOF-8 and its significance in ethane-ethylene separation by adsorption. *ACS Appl. Mater. Interfaces*, 6 (2014) 12093

Adsorption kinetics of asphaltenes in oil-water interfaces: effects of time, concentration, and heptol ratios

Walisson de Jesus Souza^a, Cláudio Dariva^b, Alexandre F. Santos^c, Gustavo R. Borges^b, Elton Franceschi^b, Cesar Costapinto Santana^{b*}

^aFaculdade Pio Décimo, Aracaju-SE, 49075-010, Brazil.

^bState University of Campinas (Unicamp) and Center for Studies in Colloidal Systems, Universidade Tiradentes, Campinas, SP 13083-055 and Aracaju-SE, 49032-040, Brazil

^cDepartment of Chemical Engineering, Federal University of Paraná, Curitiba-PR 81531-990, Brazil

Abstract

The use of interfaces involving simple organic compounds and water as a model for asphaltenes adsorption enables an alternative way of seizing the main features of the phenomena. The generation of liquid-liquid interfaces of this kind is largely found during the formation of emulsions and flooding operations in the petroleum industry. This study aims to analyze the adsorption kinetics taking into account the effect of asphaltenes obtained by extraction through the precipitation of different Brazilian oils using n-heptane as the precipitant agent in toluene-water interfaces and heptol (n-heptane + toluene) – water solutions. The pendant drop tensiometry technique and dynamical interfacial tensions (DIFTs) measurements are used to investigate the effect of different asphaltene concentrations and several heptol proportions to explain experimental data of interfacial tension as a function of time using an empirical model, a dynamic adsorption model, and an exponential decay model. The reduction of the interfacial action of the asphaltene molecules is reflected on the DIFT experimental data for toluene+asphaltene/water interfaces. This can be explained by the strong affinity between asphaltene molecules and the solvent, due to a high solubility between them. Otherwise, the interaction between the asphaltene and solvent molecules is weaker in lower solubility solvents (heptol, 1: 1 and 1.5: 1) and as a result, it increases the interfacial activity of asphaltene molecules. Results indicate that the kinetic process of asphaltene molecules not only depends on the diffusion step, but also on self-aggregation of the molecules.

Keywords: Asphaltene; Liquid-liquid interfaces; Interfacial properties; Interfacial activity; crude oil emulsions; Interfacial tension;

1. Introduction

Crude oil includes a variety of different types containing mainly hydrocarbons with a wide range of molar mass and structures. The complexity of this chemical system contributes to the formation and stability of emulsions especially due to the hydrophilic and hydrophobic characteristics of the molecules which confer polar and non-polar regions to the mixture [1, 2]. However, the stability of emulsions depends of several factors, such as the presence of natural emulsifying agents that reduce the probability of coalescence among droplets.

Dynamic interfacial tension (DIFT) is the interfacial tension of the system prior to reaching an equilibrium condition. In the generation process of a new surface in a surfactant solution, the initial surface composition is identical to that of the

liquid, and the interfacial tension is close to that of the major component of the solution. However, surfactant molecules tend to accumulate on the surface, inducing a decrease in the surface tension mixture. This process is time-dependent, and occurs during the spread of a surfactant mixture. Fan et al. [3] studied interfacial film properties of asphaltene in the oil/water interface, with emphasis on the concentration of the asphaltene as well as in the solvent type and found a clear time-dependence for surface/interface tension.

Rane et al. [4-5] presented studies with asphaltene in the adsorption kinetics of oil-water interfaces using a pendant drop tensiometry technique. The authors investigated the solvent type and the concentration of asphaltene on interfacial properties, and proposed a short-time asphaltene adsorption kinetics mechanism.

The use of interfaces involving simple organic compounds and water as a model for asphaltene



adsorption, enable an alternative way to investigate the main aspects of the mass transfer phenomena. The aim of this present study is to explore the adsorption kinetics of asphaltenes from two different types of Brazilian oil, in toluene-water and heptol (n-heptane + toluene) – water interfaces. The pendant drop tensiometer technique was applied with Dynamic interfacial tension (DIFT), using proportions of organic solvents in ratios of 1:1 and 1.5:1 at several asphaltene concentrations. In addition, DIFT data are modeled using three models mentioned in the literature [6].

Both short and long-time adsorption dynamic approaches are used to estimate the diffusion coefficients of asphaltene molecules in each concentration within the systems studied. The exponential decay model describes a very rapid diffusion and the reorganization of the molecules of the asphalt fraction on the oil/water interfaces. There is also an empirical model which is used to determine four regions for the behavior of the kinetics process in the liquid-liquid interface. These regions were previously pointed out [7] and named (as the systems) in four regions: (I) inducing region, (II) rapid drop region, (III) meso-equilibrium, adsorption time and (IV) equilibrium region.

2. Interfacial Tension Dynamic Models

2.1. Adsorption Dynamic Models

When a solution of surfactants (hydrocarbon phase or oil crude) is placed in contact with an aqueous phase, it is necessary that the time tends to a high value and so the surfactants may spread and migrate to the oil/water interface until the system is balanced. The adsorption dynamics is controlled by two main processes involving the transfer of molecules from both the surface layer and the subsurface layer, and further, the exchange of molecules between the subsurface and the bulk solution. The classical forms of diffusion-controlled adsorption models had already been derived and are presented below.

2.2. Short-term controlled-diffusion approach

The mathematical formulation is formulated by considering that at the beginning of the adsorption process where the subsurface concentration is low and the following formula can be used to represent the interface tension of surfactants,

$$\gamma_t - \gamma_0 = -2RTC \sqrt{\frac{3Dt}{7\pi}} \quad (1)$$

In Eq. (1) γ_t is the interfacial tension over time, γ_0 is the interfacial tension of the pure solvent, R is the universal gas constant, T is temperature, t is time, D is the diffusion coefficient of the surfactant, C is the concentration of the surfactant, and π is the surface pressure referred to as the difference between the pure solvent interfacial tension and the mixture interfacial tension.

2.3. Long-time controlled-diffusion approach

This step occurs when the adsorption process approaches the equilibrium and the following expression is given to this situation:

$$\gamma_t = \gamma_e + \frac{R\Gamma^2}{C_0} \sqrt{\frac{7\pi}{12Dt}} \quad (2)$$

In Eq. (2), γ_e is the interfacial tension at equilibrium. This equation also shows that a linear relation is expected for the variables γ and $t^{-\frac{1}{2}}$, after a long period of time and that if the diffusivity is known, then the surface excess concentration Γ expressed in the unit mol/m² can be calculated from the slope of this line. In general this equation is only valid in the analysis of dilute solutions because of the assumption of a monolayer formation. After determining the surface excess concentration, it is then possible to obtain diffusivity of the surfactants using Eq. (2).

2.4. Empirical Model

The empirical approach describe the liquid – liquid interface as containing the five regions mentioned before for the adsorption kinetics and uses a plot of γ_t versus $\log((\gamma_0 - \gamma_t)/(\gamma_t - \gamma_e))$ as a try to fit the following equation (5) with t and n as parameters:

$$\frac{(\gamma_0 - \gamma_t)}{(\gamma_t - \gamma_e)} = \left(\frac{t}{t^*}\right)^n \quad (3)$$

3. Materials and Methods

Asphaltene extraction was performed through the precipitation of different types of Brazilian oil using n-heptane as the precipitant agent in a volumetric proportion of 40 to 1 in relation to the oil. The aqueous phase was deionized Milli-Q grade, with a conductivity of approximately 0.05 $\mu\text{S}/\text{cm}$. Filtration was done to quantify precipitates, adapted on ASTM 6560-00. The solids present in the filter are mainly composed by asphaltenes plus some resins. The advantage of the methodology adopted is that it represents a possible reproduction of a real system while the drawbacks are the presence of different unknown impurities as long-chain paraffins as well as other impurities.

3.1. Oil Phase Preparation

Two designated Brazilian oils (A and B) were studied. The oily phase was formed from toluene plus asphaltenes and by n-heptane plus toluene (known as heptol), with ratios varying from 1:1 to 1.5:1 v/v. These heptol ratios were combined with asphaltenes at concentrations of 0, 25, 100, 200, 300, and 500 ppm. The samples were initially prepared using manual stirring for 30s followed by sonication at a constant room temperature (27 °C) for 20 min, in a USC (1880A) sonicator.

3.2. Pendant drop experiments

Pendant drop tensiometer (Tracker, TECLIS-IT Concept (Fig.1) was used for the analysis of the interfacial tension of the systems studied in this work, from the shape of a pendant drop using the axisymmetric drop shape analysis technique. Before each experiment, the system was evaluated by measuring pure water obtaining an average value within 72.8 ± 1 mN/m. All experiments were duplicated and the values for DIFTs of the toluene/water and n-heptane/water systems were 35.79 and 51.08 mN/m, respectively. The ascending mode for the operation of the tensiometer was used to insert the oil phase through a syringe with a needle. The oil drop was formed with the syringe immersed in a bucket containing the aqueous phase to create an oil/water interface. Due to its amphiphilic nature, the asphaltic fraction present in the oily phase tended to migrate to the interface and form an interfacial film.

DIFTs are heavily dependent of the surfactant action in the system, and they were obtained by scanning the oil drop profile using a CCD camera.

The Young-Laplace equation of capillarity was fit to the drop profile shape. The equipment was placed in an acclimatized, anti-vibration room with a gas piston table to absorb the vertical and horizontal vibrations. The DIFTs of the oily phase (i.e., asphaltene in toluene, heptol 1:1 and heptol 1.5:1) plus MilliQ water were then measured for the different concentrations of asphaltene.

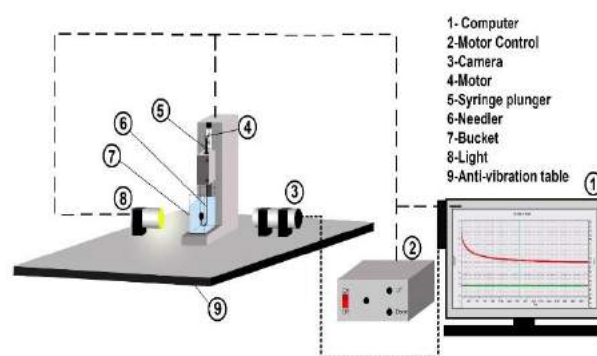


Figure 1- Main parts of IT Concept pendant drop tensiometer

4. Results and Discussion

Results for DIFTs of the systems composed by asphaltene in toluene, heptol 1:1, and heptol 1.5:1/water for concentrations of asphaltenes at 0, 25, 100, 200, 300, and 500 ppm extracted from oil A are shown in Fig. 2 while in Fig. 3, the results exhibited are for analogous systems containing asphaltenes extracted from oil B. The solubility of asphaltenes was then studied for different ratios of heptane/toluene. The asphaltene samples were soluble in toluene and insoluble in heptane. When a good solvent such as toluene is used, the high solubility enables a reduction of the interfacial activity of asphaltene molecules because of the strong attraction to the solvent molecules. This effect can be easily observed in Fig. 2-a and Fig. 3-a. On the other hand, when the asphaltene and solvent molecules interact in the presence of a poor solvent (i.e. heptol, 1:1 and 1.5:1), a weak interaction between them and this fact, induces an increase of the interfacial activity of the asphaltene molecules (Fig. 2-b, Fig. 2-c, Fig. 3-b, and Fig. 3-c).

An attempt to fit the experimental data of DIFTs as a function of time is made for the three models described by Equations (1), (2) and (3) to understand the mechanisms involved in the kinetics of adsorption of asphaltene molecules into

different interfaces, were selected from the literature. The assumption of a dilute solution is reasonable in the short-time approximation because the measured interfacial tension is close to that of the pure solvent. At this limit, the linear isotherm described by Henry's law can be applied, and the diffusion coefficient can be obtained from Eq. (1).

reaches equilibrium. To check the time of equilibrium, an empirical model was used.

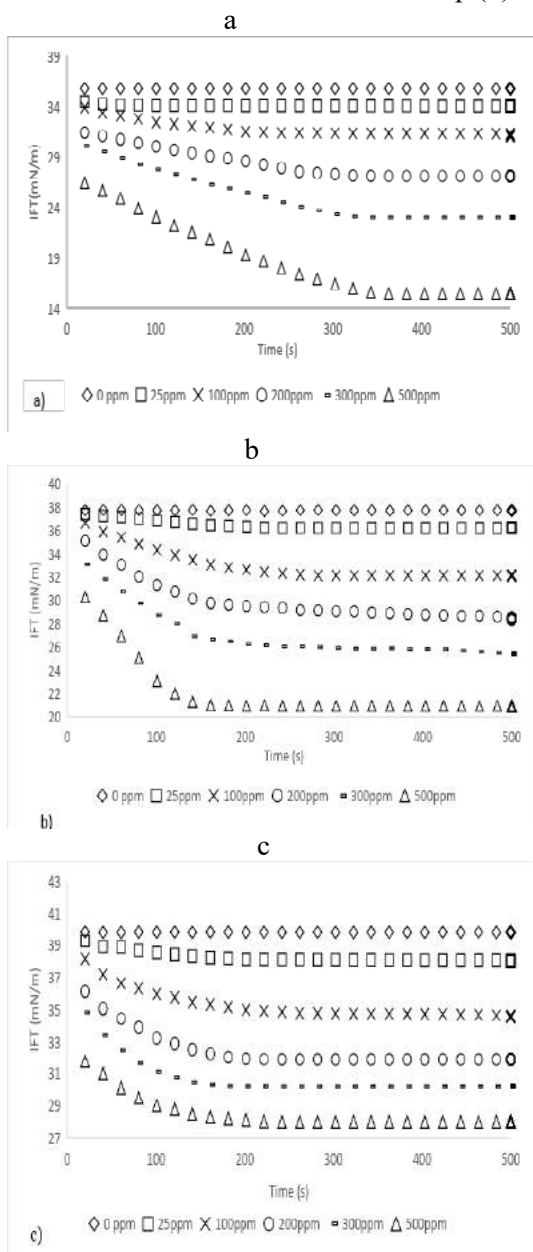


Figure 2- DIFTs from model systems of oil/water to oil A for different concentrations of asphaltene in interfaces: a) toluene/water; b) heptol 1:1/water; c) heptol 1.5:1/water.

All kinetic curves of DIFTs in the toluene/water systems and heptol-water were obtained in a minimum of 500 seconds and when the system

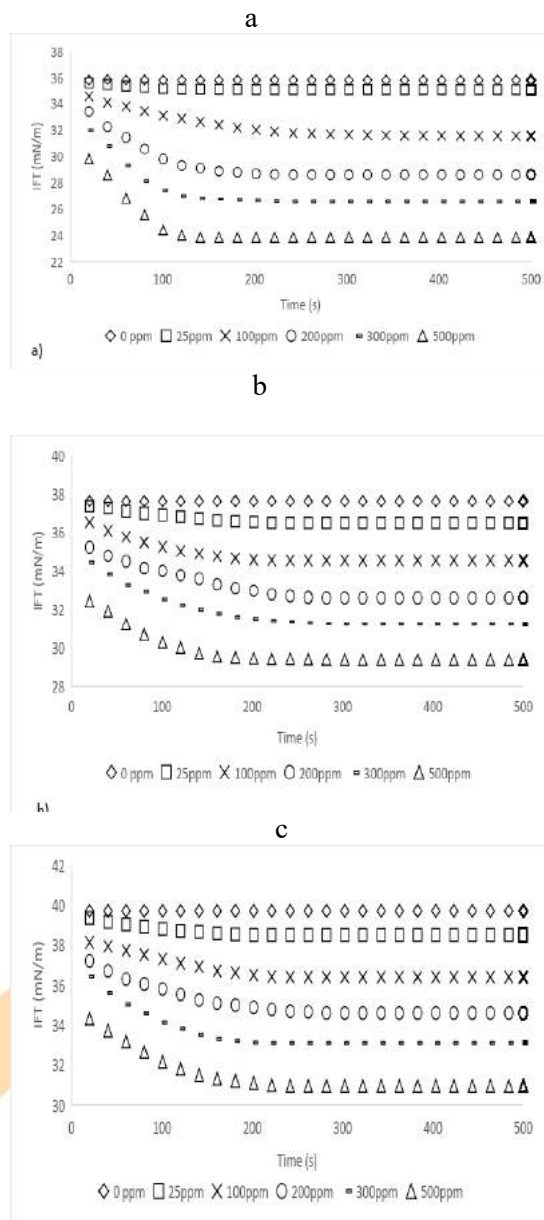


Figure 3- DIFTs from model systems of oil/water to oil B for different concentrations of asphaltene in interfaces: a) toluene/water; b) heptol 1:1/water; c) heptol 1.5:1/water.

A detailed analysis of the results indicates that the presence of asphaltene causes a considerable variation in interfacial tension even in the system containing only toluene as the oil phase. This effect occurs mainly with high concentrations of asphaltene. With 500 ppm of asphaltene, as example, the IFT change from 27 to 15 mN/m (~44% variation) in the toluene-asphaltene/water system, the IFT change from 30 to 21 mN/m (~30%

variation) in the heptol 1:1-asphaltene/water system and the IFT change from 32 to 28 mN/m (only ~13% variation) in the heptol 1.5:1-asphaltene/water system.

The fit of the short-time and long-time controlled-diffusion approach to the IFT experimental data is shown in Fig. 4, and from this match, it is possible to estimate the diffusion coefficient in the oil-water interface using the Equations (1) and (2). The good behavior of the short time model points out that this model be used to describe the region of diffusive process of surfactants for oil/water interfaces. On the other hand, the reorganization of the surfactant at the interface until equilibrium is best described by the long-time controlled-diffusion approach.

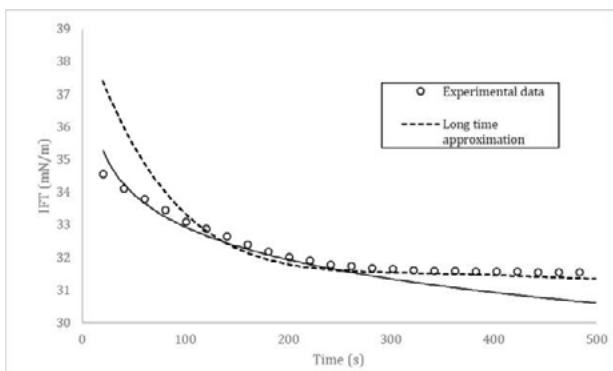


Figure 4 - Dynamic adsorption models for systems containing toluene/water at a concentration of 100 ppm of asphaltenes extracted from oil B.

An example in the use of the empirical model is shown in Figs. 5a and 5b for systems containing toluene, heptol 1:1, and heptol 1.5:1 at a concentration of 500 ppm for asphaltenes precipitated from oil A and oil B. From this attempt, it is possible to try to characterize the systems in three regions relatively well defined induction, rapid fall, and equilibrium as shown in Fig. 5. The region of meso-equilibrium is too short to be fully depicted in this same graph.

Equilibrium times were determined in these systems, and they are defined as is the amount of time taken for the asphaltene molecules adsorb the oil/water interfaces and fill all available sites.

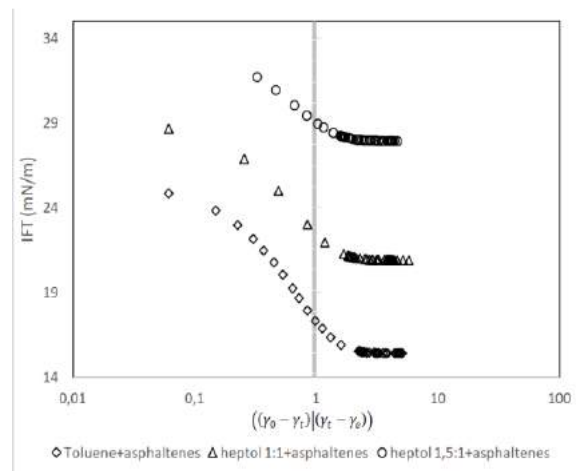


Figure 5a. DIFT of toluene+asphaltenes, heptol 1:1+asphaltenes and heptol 1.5:1+asphaltenes/water for Oil A.

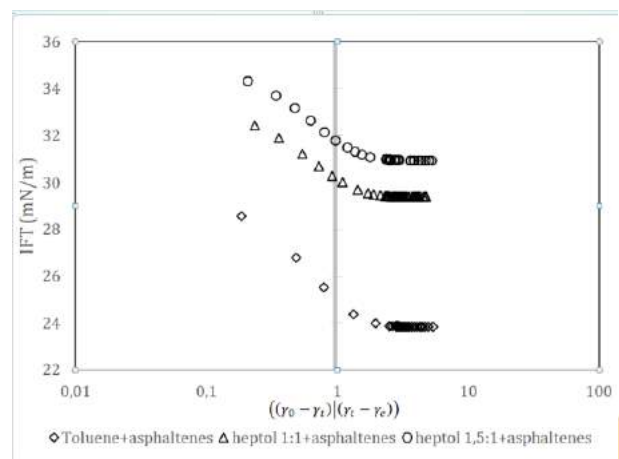


Figure 5b. DIFT of toluene+asphaltenes, heptol 1:1+asphaltenes and heptol 1.5:1+asphaltenes/water for Oil B

An example of DIFT of toluene+asphaltenes/water interface behavior at a concentration of 500 ppm versus $((\gamma_0 - \gamma_t) / (\gamma_t - \gamma_e))$ is shown in Fig. 6.

This plot is based on the empirical equation for extracted asphaltenes from oil A. The equilibrium time estimated was approximately 343 s.

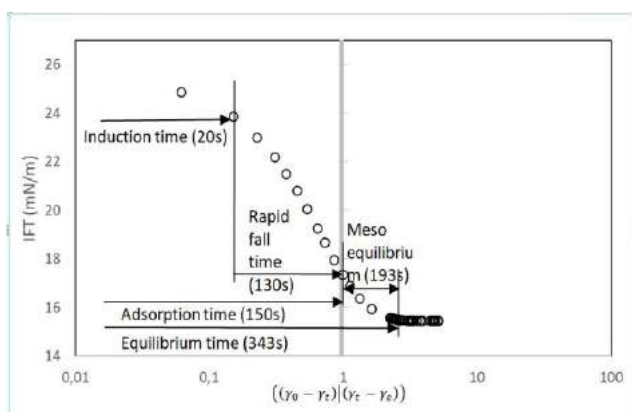


Figure 6. DIFT of toluene+asphaltenes/water interface behavior at a concentration of 500 ppm versus $((\gamma_0 - \gamma_t)/(\gamma_t - \gamma_e))$ based on empirical equation for extracted asphaltenes from oil A.

The first step involved induction time, and it was characterized by the onset of asphaltene adsorption process for the interfaces; in all cases, the induction time was approximately 20 s.

5. Conclusions

The approach adopted in this study is strongly based on the behavioral description of asphaltene adsorption kinetics using dynamic interfacial tension models employing experimental data of DIFTs for two Brazilian oils obtained using a pendant drop tensiometer at different oil-water interfaces. Model systems which enable a better comprehension of the interfacial phenomena in simpler interfaces were built employing different interfaces containing toluene, heptol (heptane / toluene, with ratios of 1:1 and 1.5:1) and MilliQ water with asphaltene concentrations of 0, 25, 100, 200, 300, and 500 ppm.

The reduction of the interfacial action of the asphaltene molecules is reflected on the DIFT experimental data for toluene+asphaltenes/water interfaces. This can be explained by the strong affinity between asphaltene molecules and the solvent, due to the high solubility between them. Otherwise, the interaction between the asphaltene and solvent molecules is weaker for lower solubility solvents (heptol, 1: 1 and 1.5: 1), thus producing an increase in the interfacial activity of asphaltene molecules. To better understand the experimental data of IFTs over time, an empirical model was applied and succeeded in showing the

four regions for the behavior of the kinetics process in the liquid-liquid interface.

Acknowledgments

The authors wish to thank ANP/PETROBRAS, FAPITEC/SE, CAPES, and CNPq for their financial support and scholarships.

References

- [1] Souza, W. J.; Santos, K.M.C.; Cruz, A.A.; Franceschi, E.; Dariva, C.; Santos, A.F.; Santana, C.C., Effect of water content, temperature and average droplet size on the settling velocity of water-in-oil emulsions. *Brazilian Journal Chemical Engineering*; 2015, 455-464.
- [2] Arditty, S.; Schmitt, V.; Kahn, J. G.; Leal-Calderon, F., Materials based on solid- stabilized emulsions. *Journal of Dispersion and Interface Science*; 2004, 275, 659-664.
- [3] Fan, Y.; Simon, S.; Sjöblom, J. (2010). Interfacial shear rheology of asphaltenes at oil–water interface and its relation to emulsion stability: Influence of concentration, solvent aromaticity and nonionic surfactant, *Colloids and Surfaces A*; 2010, 366, 120-128.
- [4] Rane, J.P.; Harbottle, D.; Pauchard, V.; Couzis, A.; Banerjee, S., Adsorption kinetics of asphaltenes at the oil-water interface and nanoaggregation in the bulk *Langmuir*; 2012, 28, 9986–9995.
- [5] Rane, J. P.; Pauchard, V.; Couzis, A.; Banerjee, S., Interfacial Rheology of asphaltenes at oil–water interfaces and interpretation of the equation of state *Langmuir*; 2013, 29, 4750 - 4759.
- [6] Lashkarbolooki, M.; Ayatollahi, S.; Riazi, M., Mechanistic study on the dynamic tension crude oil+water systems: Experimental and modeling approaches, *Journal of Industrial and Engineering Chemical*; 2016, 35, 408-416.
- [7] Iglauer, Stefan and Wu, Yongfu and Shuler, Patrick and Tang, Yongchun and Goddard III, William A., Alkyl polyglycoside surfactant-alcohol cosolvent formulations for improved oil recovery, *Colloids and Surfaces A: Physicochemical and Engineering Aspects*; 2009, 339, 48-52.

Simulation of high-pressure sour natural gas adsorption on 13X zeolite

Pereira, M.V.^a, de Oliveira, L. H.^a, do Nascimento, J. F.^b, Arroyo, P.A.^{a,*}

^aLaboratory of Adsorption and Ion Exchange, Department of Chemical Engineering, State University of Maringá, Maringá, Paraná, Brazil.

^bPETROBRAS/CENPES/PDDP/TPP, Rio de Janeiro, Rio de Janeiro, Brazil.

Abstract

Natural gas sweetening usually relies on expensive unit processes and adsorption is a viable alternative. Therefore, the usage of adsorption for natural gas sweetening commit on adsorbent potentiality. Thus, in this work, the potential usage of 13X zeolite for natural gas sweetening at high-pressure (4 MPa and 298 K) were investigated by simulations using a validated MPTA-DRA model. The model validation showed low deviation for CO₂ (< 5%) simulation and good agreement with N₂ experimental data. Monocomponent experimental data shows favorable isotherms for all components and correlation using MPTA-DRA model are in good agreement with experimental data and deviation were low (< 7.6 %). Multicomponent sour natural gas adsorption simulation indicates that almost none CH₄ and N₂ are adsorbed in these conditions and CO₂ and H₂S competes for adsorption sites. Separation factor of H₂S increased 18.90 to 43.30 with decrease of CO₂ molar fraction in bulk phase. The selectivity of H₂S over CO₂ followed a different trend, decreasing from 27.16 to 20.14. Thus, simulations indicate that 13X zeolite is a potential adsorbent for natural gas sweetening at 4 MPa and 298 K

Keywords: Sour-gas adsorption; high-pressure adsorption; multicomponent gas adsorption simulation;

1. Introduction

Natural gas, a fossil fuel composed of mostly methane, is one of the cleanest burning alternative fuels and was responsible for approximately 23 % of the world's energy consumption in 2018 [1]. With the increase of natural gas usage and production, the search for better technologies for its contaminants removal, mainly removal of sour gases, *e.g.* hydrogen sulfide (H₂S) and carbon dioxide (CO₂).

Among the processes for gas sweetening, adsorption shows great potential due to, *i.e.*, its relative low-cost, capability of purification of bulk separation and possibility of adsorbent regeneration [2]. The potential for use of adsorption relies mainly on the adsorbent properties, such as high adsorption capacity, mechanical and thermal resistance, low-cost and others [3]. Many adsorbents for natural gas sweetening were investigated in literature, such as activated carbon and NaY Zeolite [4,5]. Zeolite material possesses good advantages such as thermal

stability, high H₂S and CO₂ affinity and selectivity. Another commonly investigated zeolite is the 13X [6,7].

The potential use of adsorbents are commonly measured using mono- and multicomponent adsorption isotherms and since the experimental determination of adsorption capacity in adsorption of multicomponent gas mixtures are uneconomical, due to the many conditions of pressure, temperature and composition, the prediction using monocomponent data are commonly used [8,9]. Among the models found in literature, the models based on the Potential Theory of Adsorption (PTA) shows good agreement with experimental data in non-ideal systems and high-pressure [10].

Literature review shows no experimental or simulated data of multicomponent gas adsorption of natural gas containing N₂, CO₂ and H₂S on 13X zeolite. Thus, in this work, the potential usage of 13X zeolite for sweetening of natural gas containing N₂, CO₂ and H₂S at high pressure were investigated

by simulations using the multicomponent potential theory of adsorption (MPTA).

2. Materials and Methods

2.1 Multicomponent Potential Theory of Adsorption

In the MPTA theory, the adsorbate inside the pores is considered a real fluid subjected to an external adsorption potential (ε_i) of attractive nature emitted from the adsorbent surface and decreases as the distance from the surface (z) increases. The criterium for equilibrium between the bulk phase and a respective position in the adsorbed region is given by:

$$f_{ad,i}(x_{z,i}, P_z) = f_{bulk,i}(y_i, P) \exp\left(\frac{\varepsilon_{z,i}}{RT}\right) \quad (1)$$

Where: $f_{bulk,i}$ and $f_{ad,i}$ are the bulk and adsorbed phase fugacity (Pa) of component i , respectively, $x_{z,i}$ is the molar fraction of component i in the z position in the adsorbed region, P_z is the pressure in the z position in the adsorbed region (Pa), y_i is the molar fraction of component i in the bulk phase, P is the system pressure (Pa), $\varepsilon_{z,i}$ is the adsorption potential at z position in the adsorbed region (J), R is the universal gas constant ($8.314 J mol^{-1} K^{-1}$) and T is the absolute temperature (K). Eq. 1 $i \in 1 \dots N_c$ (number of components).

The adsorption potential can be obtained by different equations [11,12] such as the *Dubinin-Radushkevich-Atakhov* (DRA):

$$\varepsilon_z = \varepsilon_0 \ln\left(\frac{z_0}{z}\right)^{1/\beta} \quad (2)$$

Where ε_0 is the characteristic adsorption energy ($J mol^{-1}$), z_0 can be interpreted as the adsorbent porous volume ($cm^3 g^{-1}$) and β is the heterogeneity parameter.

In this work, a system of equations derived from Equation 1 and presented by Shapiro and Stenby (1998) were solved using the consecutive substitution method, proposed by the original authors [14], and Brent's method and the DRA potential. Thermodynamic properties (ϕ, ρ) were calculated by a volume translated Peng-Robinson Equation of State [15,16] with binary interaction parameters set to zero. The model was named MPTA-DRA.

2.2 Monocomponent adsorption isotherms

Monocomponent adsorption data of CO_2 , CH_4 , H_2S and N_2 on zeolite 13X (Z13Xa) at 298 K were obtained from literature and are summarized in Table 1.

Table 1. Monocomponent adsorption isotherm data.

Gas	Temperature (K)	Pressure range (MPa)	Ref.
CO_2	≈ 298	0.92 – 4.57	[17]
CH_4		0.55 - 10	
H_2S		0.01 – 0.88	
N_2		0.27 - 11.2	

2.3 Sour natural gas adsorption simulation

Multicomponent sour gas adsorption on Z13Xa were simulated using MPTA-DRA at 4 MPa and 298 K. H_2S and N_2 molar fraction were kept constant at 0.02 and 0.05, respectively, CO_2 ranged from 0.05 to 0.9 and balance were made with CH_4 , as summarized in Table 2.

Table 2. Gas molar fraction used in simulation.

Gas	Molar fraction (y)
CO_2	0.05-0.9
CH_4	balance
H_2S	0.02
N_2	0.05

Results from simulation were evaluated through its adsorbed molar fraction (x), its partition coefficients (K), which indicates the distribution of a given species between equilibrium phases, and the adsorbent selectivity of H_2S over CO_2 given by Eqs. 3 and 4, respectively

$$K_i = x_i/y_i \quad (3)$$

$$S_{H_2S} = K_{H_2S}/K_{CO_2} \quad (4)$$

2.4 Model validation and deviation

Monocomponent isotherm correlation and multicomponent prediction was evaluated using the percentage absolute relative deviation (σ):

$$\sigma_i = \frac{100}{N_{p,i}} \sum_{i=1}^{N_{p,i}} \left| \frac{n_{exp,i}^{ex} - n_{calc,i}^{ex}}{n_{exp,i}^{ex}} \right| \quad (5)$$

Where N_p is the total number of points of component i , $n_{exp,i}^{ex}$ and $n_{calc,i}^{ex}$ are the experimental and calculated excess adsorbed amount, respectively.

Since, to the authors knowledge, no CO₂, CH₄, H₂S and N₂ high pressure quaternary adsorption data are available in literature, the MPTA-DRA model was validated using CO₂ and N₂ adsorption data Hefti et al. (2015) on Z13Xb at 303.15 K and pressure up to 1 MPa.

3. Results and discussion

3.1 Model validation

Monocomponent adsorption isotherms of CO₂ and N₂ on Z13Xb at 303.15 K are shown in Figure 1.

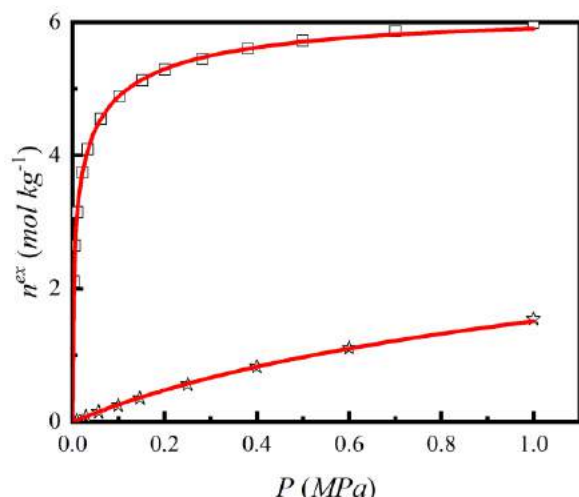


Figure 1. Monocomponent isotherms of CO₂ (□) and N₂ (☆) correlated by the MPTA-DRA model (—) on Z13Xb. Experimental data from [19].

From Figure 1 is possible to observe the higher adsorption capacity of CO₂ with Z13Xb than N₂ at 303.15 K. This correlates with the polarizability of both gases and, also, their respective kinetic diameter. The MPTA-DRA were able to successfully represent the experimental data and the obtained parameters are presented in Table 3.

Table 3. MPTA-DRA parameters for Z13Xb at 303.15 K.

Gas	ϵ_0 (J mol ⁻¹)	z_0 (cm ³ g ⁻¹)	β	σ (%)
CO ₂	20520	0.2081	2.804	0.37
N ₂	8618			2.10

From Table 3 is possible to confirm the higher affinity of CO₂ with the zeolite surface through its characteristic energy, being twice higher than the obtained for N₂. Also, pore volume obtained are close to those obtained in characterization (~0.27 cm³ g⁻¹). With the parameters shown in Table 3, binary data were simulated for CO₂-N₂ mixtures with feed percent composition of 75-25, 50-50, and 25-75 mol% at 303.15 K and are shown in Figure 2.

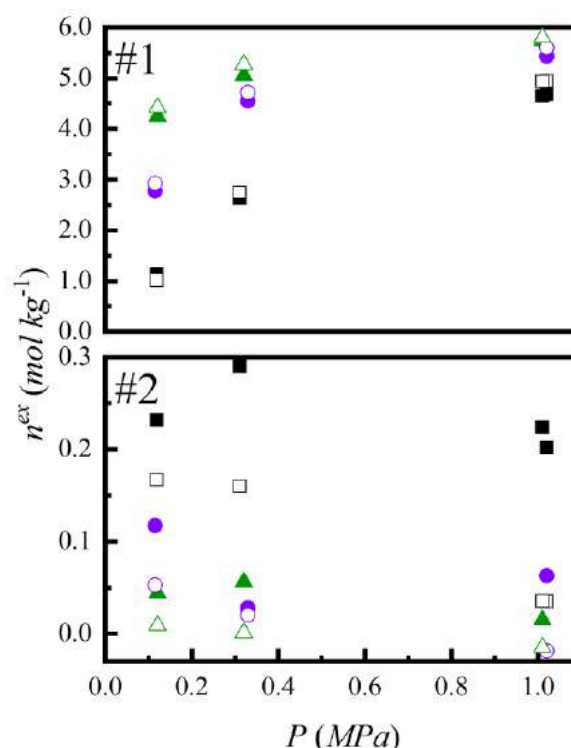


Figure. 2. Multicomponent experimental (closed symbols) and simulated (open symbols) CO₂ (#1) and N₂ (#2) binary adsorption isotherms on Z13Xb with feed percent composition of 75-25 (triangle), 50-50 (circle) and 25-75 (square) at 303.15 K. Experimental data from [19].

Since the simulation of multicomponent isotherms depends on the equilibrium gas composition, it is not possible to predict a full isotherm and, thus, simulation need to be carried out *point-by-point*. In Figure 2, is possible to observe the simulation capability of CO₂-N₂ binary adsorption data using MPTA-DRA method. Excess adsorbed quantity simulation σ_{CO_2} ranged from 6.49 % at 25 mol% in feed to 3.10% at 75 mol% in feed. On the other hand, σ_{N_2} were above 59 % for all cases, therefore, simulated data are in the same order of magnitude of experimental data.

With simulation capability of the MPTA-DRA model validated, monocomponent H₂S, CO₂, CH₄ and N₂ isotherms on Z13Xa shown in section 2.1 were correlated and a sour natural gas mixture adsorption were simulated using conditions presented in section 2.3.

3.2 Monocomponent correlation

Monocomponent adsorption isotherms of CO₂, CH₄, H₂S and N₂ on Z13Xa at 298 K are shown in Figure 3.

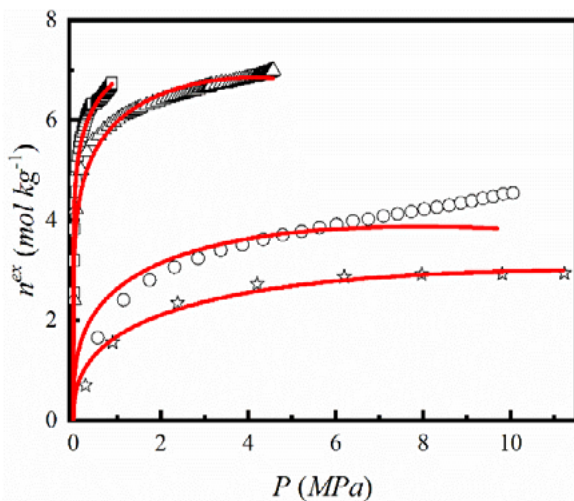


Figure 3. Monocomponent isotherms of CO₂ (Δ), H₂S (\square), CH₄ (\circ), N₂ (\star) correlated by the MPTA-DRA model (—) on Z13Xa at 298 K.

From Figure 3 it can be verified favorable isotherms for all components and, for H₂S and CO₂ higher adsorption capacity, this can be explained by many reasons, such as smaller kinetic diameter, higher polarizability [3]. The MPTA-DRA model was able to represent adsorbed data for all isotherms with just N_c+2 adjusted parameters. Correlated parameters and data deviation are shown in Table 4.

Table 4. MPTA-DRA parameters for Z13Xa.

Gas	ϵ_0 ($J mol^{-1}$)	Z_0 ($cm^3 g^{-1}$)	β	σ (%)
CO ₂	14518			1.808
CH ₄	7351	0.275	0.965	6.977
H ₂ S	19026			2.623
N ₂	5502			7.600

In Table 4, it can be verified the higher adsorbate-adsorbent affinity of H₂S followed by CO₂, CH₄ and N₂, respectively. Adsorbent pore

volume correlated is in agreement with experimental values [17,18]. MPTA-DRA model σ increased in the following order: CO₂ < H₂S < CH₄ < N₂.

3.3 Sour natural gas adsorption simulation

Multicomponent sour natural gas adsorption on Z13Xa was simulated with conditions presented in Section 2.3 using the parameters shown in Table 4. The results are presented in Figures 4-6.

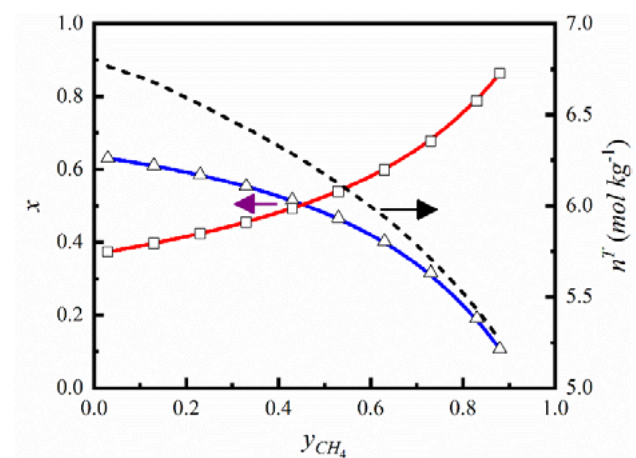


Figure 4. Total excess adsorbed amount (dashed line) and adsorbed molar fraction of CO₂ (triangle) and H₂S (square) as function of methane molar fraction on equilibrium bulk phase on Z13Xa at 298 K and 4 MPa.

In Figure 4 is possible to observe the adsorbed region CO₂ and H₂S molar fraction (x) in function of y_{CH_4} in equilibrium bulk phase. Summation of x_{CO_2} and x_{H_2S} are approximately or equal to 1, indicating that none or almost none CH₄ and N₂ are adsorbed in these conditions, also, with the decrease of y_{CH_4} , CO₂ strongly competes with H₂S for adsorption sites, and, thus, x_{H_2S} decreases with y_{CO_2} increase. With data presented in Figure 4, K separation factors (Equation 4) were calculated for CO₂ and H₂S and are shown in Figure 5.

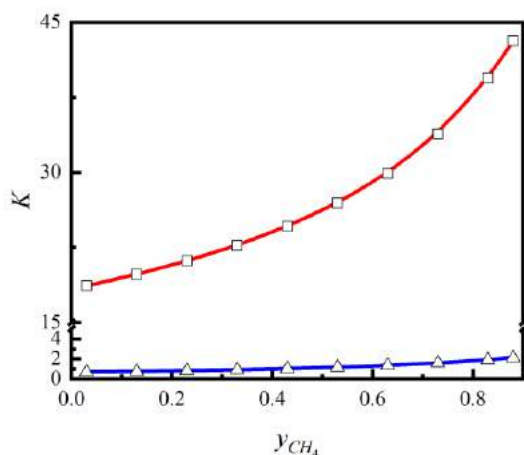


Figure 5. Separation factors for CO₂ (triangle) and H₂S (square) as function of CH₄ molar fraction on equilibrium bulk phase on Z13Xa at 298 K and 4 MPa.

Simulated K_{H_2S} , shown in Figure 5, ranged from 18.90 to 43.30 with increase of y_{CH_4} . On the other hand, K_{CO_2} ranged from 0.69 to 2.15 with increase of y_{CH_4} . The decrease of K_{CO_2} with increase of y_{CO_2} indicates a decrease of CO₂ removal capability of Z13Xa when H₂S is present at 4 MPa and 298 K which is in agreement with selectivity of H₂S over CO₂, calculated from Equation 5, presented in Figure 6.

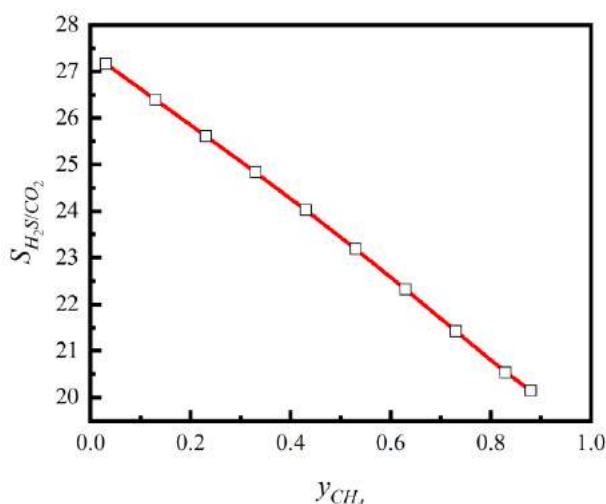


Figure 6. Selectivity for H₂S over CO₂ as function of y_{CH_4} on equilibrium bulk phase on Z13Xa at 298 K and 4 MPa.

The decrease of H₂S selectivity over CO₂ with the increase of y_{CH_4} , shown in Figure 5, suggests the best configuration for H₂S removal using Z13Xa is with less y_{CO_2} in feed composition, since both gases competes for adsorption sites.

The above results indicate the Z13Xa as a potential adsorbent for sour gas removal from natural gas streams at 4 MPa and 298 K.

4. Conclusions

In this work, a MPTA-DRA model was implemented, and its correlation and simulation capability were validated using CO₂ and N₂ monocomponent and binary adsorption data. The model showed low deviation for CO₂ (< 5%) simulation and good agreement with N₂ experimental data.

The validated model was used to correlate high-pressure H₂S, CO₂, CH₄ and N₂ monocomponent adsorption isotherms and simulate a multicomponent sour natural gas mixture adsorption on 13X zeolite at 298 K and 4 MPa.

Monocomponent experimental data shows favorable isotherms for all components and correlation using MPTA-DRA model are in good agreement with experimental data and deviation were low (< 7.6 %).

Multicomponent sour natural gas adsorption simulation indicates that almost none CH₄ and N₂ are adsorbed under these conditions and CO₂ and H₂S competes for adsorption sites. Separation factor of H₂S increased from 18.90 to 43.30 with decrease of CO₂ molar fraction in bulk phase. The selectivity of H₂S over CO₂ followed a different trend, decreasing from 27.16 to 20.14, suggesting higher selectivity when a lower CO₂ molar gas fraction is present.

The simulations indicate that 13X zeolite is a potential adsorbent for natural gas sweetening at 4 MPa and 298 K.

Acknowledgements

Authors would like to thank Petrobras for the financial support (Cooperation Number 5850.0102576.16.9).

References

- [1] BPSTATS. BP Statistical Review of World Energy Statistical Review of World, 68th edition. *Ed BP Stat Rev World Energy* 2019: 1–69.
- [2] Alcheikhhamdon, Y., Hoorfar, M. Natural gas quality enhancement: A



- review of the conventional treatment processes, and the industrial challenges facing emerging technologies. *J Nat Gas Sci Eng* 2016; **34**: 689–701.
- [3] Yang,RT. *Adsorbents : Fundamentals and Applications*. John Wiley & Sons, Inc.; 2003.
- [4] de Oliveira,LH., Meneguim,JG., Pereira,MV., da Silva,EA., Grava,WM., do Nascimento,JF., Arroyo,PA. H2S adsorption on NaY zeolite. *Microporous Mesoporous Mater* 2019; **284**(December 2016): 247–257.
- [5] de Oliveira,LH., Meneguim,JG., Pereira,M V., do Nascimento,JF., Arroyo,PA. Adsorption of hydrogen sulfide, carbon dioxide, methane, and their mixtures on activated carbon. *Chem Eng Commun* 2019; **206**(11): 1544–1564.
- [6] Beutekamp,S., Harting,P. Experimental determination and analysis of high pressure adsorption data of pure gases and gas mixtures. *Adsorption* 2002; **8**(4): 255–269.
- [7] Cavenati,S., Grande,CA., Rodrigues,AE. Adsorption equilibrium of carbon dioxide, methane and nitrogen onto mordenite at high pressures. *J Chem Eng Data* 2004; **49**: 1095–1101.
- [8] Suzuki,M. *Adsorption engineering*. 1991.
- [9] Keller,J., Staudt,R. *Gas Adsorption Equilibria - Experimental Methods and Adsorptive Isotherms*. Springer; 2005.
- [10] Bartholdy,S., Bjørner,MG., Solbraa,E., Shapiro,A., Kontogeorgis,GM. Capabilities and limitations of predictive engineering theories for multicomponent adsorption. *Ind Eng Chem Res* 2013; **52**(33): 11552–11563.
- [11] Nesterov,I., Shapiro,A., Kontogeorgis,GM. Multicomponent adsorption model for polar and associating mixtures. *Ind Eng Chem Res* 2015; **54**(11): 3039–3050.
- [12] Bjørner,MG., Shapiro,AA., Kontogeorgis,GM. Potential theory of adsorption for associating mixtures: Possibilities and limitations. *Ind Eng Chem Res* 2013; **52**(7): 2672–2684.
- [13] Shapiro,AA., Stenby,EH. Potential Theory of Multicomponent Adsorption. *J Colloid Interface Sci* 1998; **201**(2): 146–157.
- [14] Shapiro,AA., Stenby,EH. High pressure multicomponent adsorption in porous media. *Fluid Phase Equilib* 1999; **158160**: 565–573.
- [15] Abudour,AM., Mohammad,SA., Robinson,RL., Gasem,KAM. Volume-translated Peng-Robinson equation of state for saturated and single-phase liquid densities. *Fluid Phase Equilib* 2012; **335**: 74–87.
- [16] Abudour,AM., Mohammad,SA., Robinson,RL., Gasem,KAM. Volume-translated Peng-Robinson equation of state for liquid densities of diverse binary mixtures. *Fluid Phase Equilib* 2013; **349**: 37–55.
- [17] Wynnyk,KG., Hojjati,B., Marriott,RA. High-Pressure Sour Gas and Water Adsorption on Zeolite 13X. *Ind Eng Chem Res* 2018; **57**(45): 15357–15365.
- [18] Wang,Y., Helvensteijn,B., Nizamidin,N., Erion,AM., Steiner,LA., Mulloth,LM., Luna,B., Levan,MD. High pressure excess isotherms for adsorption of oxygen and nitrogen in zeolites. *Langmuir* 2011; **27**(17): 10648–10656.
- [19] Hefti,M., Marx,D., Joss,L., Mazzotti,M. Adsorption equilibrium of binary mixtures of carbon dioxide and nitrogen on zeolites ZSM-5 and 13X. *Microporous Mesoporous Mater* 2015; **215**: 215–226.

Adsorption of Polycyclic Aromatic Hydrocarbons from Heavy Naphthenic Oil: Evaluation of the Adsorbent Regenerability

F. Murilo T. de Luna and Célio L. Cavalcante Jr.

Departamento de Engenharia Química – Universidade Federal do Ceará, Grupo de Pesquisa em Separações por Adsorção, Núcleo de Pesquisa em Lubrificantes, Campus do Pici, Bloco 1010, CEP: 60.455-900, Fortaleza – CE – Brasil.

Abstract

In this study, successive column experiments were carried out to evaluate the reduction in capacity along continuous cycles and optimal operational conditions. A column simulation model, using the particle parameters obtained in the previous study, was applied to predict breakthrough curves for adsorption and desorption runs. Adsorption and desorption of polycyclic aromatic hydrocarbons (PAHs) from heavy naphthenic oils (HNO) were performed using commercial activated carbon on fixed bed experiments. After several cycles, using solvent or inert gas, only a slight decrease in PAH adsorption capacity was observed. Selectivities for PAH adsorption in relation to aromatics adsorption were also estimated from the adsorption breakthrough curves data. A conceptual continuous process was simulated using the proposed model and evaluated based on productivity in terms of volume of treated oil per mass of adsorbent per time, showing a maximum value of $0.53 \text{ m}^3/(\text{kg ads.})\cdot\text{h}$ at space velocity of *ca.* 4 h^{-1} .

Keywords: adsorption; PAH; heavy naphthenic oil; activated carbons; fixed bed column.

1. Introduction

The behavior of activated carbons and acid clays for total aromatics removal from light mineral naphthenic oil (MNO) was investigated by Luna *et al.* [1], with activated carbons being more adequate for aromatics removal in that system. However, the removal of polycyclic aromatic hydrocarbons (PAH) from complex oil mixtures has been scarcely reported in the open literature.

Studies focusing on removal of PAH from hot gas emissions and contaminated soils have been performed using adsorption procedures. Several materials have been reported for PAH removal in different systems, such as plant residues, [2,3] mesoporous organosilica,[4] mesoporous materials [5] and commercial activated carbons.[1,6,7] Adsorption appears as a promising process because of its low-energy demand, possibility of adsorbent regeneration and broad availability of adsorbents.

Luna *et al.* [6] reported equilibrium and kinetic data for the batch adsorption of polycyclic aromatic hydrocarbons (PAH) from heavy naphthenic oil (HNO) using commercial activated carbons. In this study, samples of heavy naphthenic oils (HNO) were treated for PAHs removal in continuous mode using adsorption onto

granular commercial activated carbons in a fixed bed experimental setup. HNO is a vacuum industrial distillate with viscosities varying between 380 and 420 cSt (at 40°C), obtained from different types of Brazilian crude petroleum and mainly applied to formulation of special waxes and lubricants. Without proper treatment, HNO presents high PAHs concentration. Hence, it is important to reduce its concentration, to encompass regulatory requisitions for commercial applications. Oils with PAH contents lower than 3 % wt. are classified as non-carcinogenic.[8]

A column simulation model, including a dual-resistance (pore and surface) particle diffusion model, was applied to interpret and validate the experimental results. Parameters such as adsorption capacity in adsorption and desorption breakthrough steps, adsorbent regenerability after up to 10 adsorption/desorption cycles, and selectivities for PAH adsorption in relation to other aromatics were used to evaluate the dynamics behavior of the adsorption column. A productivity in terms of volume of treated HNO (≤ 3 % wt. of PAH) per mass of adsorbent per time, in a conceptual continuous process, was also proposed and evaluated against the space velocity in the column.

2. Experimental and Modeling

2.1. Materials

The Heavy Naphthenic Oil (HNO) sample was provided by PETROBRAS (Brazil). Dimethyl sulfoxide - DMSO (> 99 % wt., JT Baker, USA), spectrophotometric grade cyclohexane (Merck, USA), sodium chloride (JT Baker, USA) and deionized water obtained by the Milli-Q system (Millipore, USA) were used in procedures of polycyclic aromatic extractions. *n*-Hexane (> 99 % wt., JT Baker, USA) was used as solvent in the column experiments. Commercial Nitrogen (> 90% wt.) was provided by White Martins-Praxair, Brazil.

A granular activated carbon, provided by Norit (Netherlands), was used in this study (GAC830W). Prior to use in the experiments, the activated carbon was washed with deionized water and thermally treated using an electrical oven, initially at 40 °C for 1 h, and then heated slowly at 30 °C/h up to 120 °C.

2.2. Column experiments

Adsorption and desorption curves of HNO through a fixed bed system (Figure 1) were obtained at different conditions. An adsorption column containing the adsorbent was connected to a HPLC pumping system (Varian ProStar 210, USA). Initially, the pumping system delivered pure solvent (*n*-hexane) in order to establish the flow rates through the column. The total aromatic and PAHs concentrations were obtained using FTIR methods, as previously reported in Luna *et al.* [9].

The adsorption capacity was calculated using the breakthrough curve for each experiment. The area above the curve corresponds to the integral which appears in the column mass-balance (Eq. 1) to calculate the amount adsorbed in equilibrium (q_0) with initial concentration (C_0).

$$q_0 = \frac{C_0}{M_B} \left[Q \int_0^t \left(1 - \frac{C}{C_0} \right) dt - V_C \varepsilon \right] \quad (1)$$

For the desorption step, the area under the curve provides a confirmation of the aromatics or PAHs amounts retained in the column during the adsorption step.

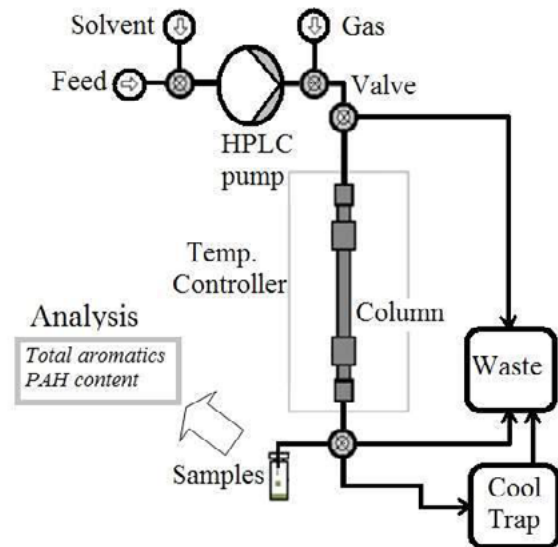


Fig. 1. Experimental setup used for adsorption/desorption column experiments.

The regenerability of the bed after multiple cycles was evaluated using two different procedures: initially using only solvent at the same operational conditions; and afterward using inert gas (N_2) at different temperatures (120-150 °C).

2.3. Modeling of the adsorption/desorption process

A general rate model, using pore and surface diffusion resistances in the particle [10-12] was applied to predict the breakthrough curves and validate the experimental data (Eqs. 2-8):

Differential mass balance in liquid phase:

$$\varepsilon \frac{\partial C}{\partial t} + u \frac{\partial C}{\partial z} = \varepsilon D_L \frac{\partial^2 C}{\partial z^2} - (1 - \varepsilon) \frac{3k_f}{R} \left(C - C_p \Big|_{r=R_p} \right) \quad (2)$$

Initial conditions:

$$t = 0, C(z, 0) = 0; C_p(z, 0) = 0; q(z, 0) = 0 \quad (3)$$

Boundary 1:

$$z = 0, \quad \left[uC - D_L \frac{\partial C}{\partial z} \right] = uC_0 \quad (4)$$

Boundary 2:

$$z = L, \quad \frac{\partial C}{\partial z} = 0 \quad (5)$$



Differential mass balance in solid phase:

$$\varepsilon_p \frac{\partial C_p}{\partial t} + (1 - \varepsilon_p) \frac{\partial q}{\partial t} \rho_{ap} = D_p \frac{1}{r^2} \frac{\partial}{\partial r} \left(r^2 \frac{\partial C_p}{\partial r} \right) + D_s \frac{\rho_{ap}}{r^2} \frac{\partial}{\partial r} \left(r^2 \frac{\partial q}{\partial r} \right) \quad (6)$$

Boundary 1:

$$r = 0, \quad \frac{\partial C_p}{\partial r} = 0 \quad (7)$$

Boundary 2:

$$r = R_p, D_p \frac{\partial C_p}{\partial r} + D_s \frac{\partial q}{\partial r} \rho_{ap} = k_f (C - C_p) \quad (8)$$

Instantaneous equilibrium is assumed between the concentration in the fluid phase within the particles (C_p) and the concentration in the solid adsorbent (q), for any particle radius (r), Eq. 9.

$$q = f(C_p) \quad (9)$$

The axial dispersion coefficients were estimated using Eq. 10.

$$\varepsilon \frac{D_L}{u \cdot 2R_p} = 0.2 + 0.011 \text{Re}^{0.48} \quad (10)$$

The external mass transfer coefficient was calculated from the following correlation proposed by Wakao and Funazkri:

$$Sh \equiv \frac{2 \cdot R_p \cdot k_f}{D_m} = 2 + 1.1 (Sc)^{1/3} (\text{Re})^{0.6} \quad (11)$$

The molecular diffusivity (D_m), in cm^2/min , of PAHs was estimated based on the Wilke and Chang correlation:

$$D_m = 4.44 \cdot 10^{-6} \frac{(\phi MM)^{1/2} T}{\eta V_b^{0.6}} \quad (12)$$

The value of V_b ($213.8 \text{ cm}^3/\text{mol}$) was obtained by LeBas volumes, using pyrene as a model molecule, and ϕ is an association coefficient, assumed to be 1.0 for aromatics.

The pore diffusion coefficient was estimated from the molecular diffusivity (Eq. 13), using tortuosity factor of 5.0, as usually found for this type of system.

$$D_p = \frac{D_m \varepsilon_p}{\tau} \quad (13)$$

The surface diffusion coefficient (D_s) was obtained from the particle adsorption studies previously reported [6].

For the desorption simulations, the same mass balances are used, with the following initial and boundary conditions for the column balance:

Initial conditions:

$$t = 0, \quad C(z, 0) = C_0 \quad (14)$$

$$t = 0, \quad C_p(z, 0) = C_0; \quad q(z, 0) = f(C_p), \quad \forall r \quad (15)$$

Boundary in liquid phase:

$$z = 0, \quad \left[uC - D_L \frac{\partial C}{\partial z} \right] = 0 \quad (16)$$

The system of algebraic and partial differential equations, with the respective initial and boundary conditions, was implemented according to the standard gPROMS syntax. The axial and radial domains are discretized using a third order orthogonal collocation method in finite elements (OCFEM) with 6 sections and 3 placing spots per section.

3. Results and discussion

The experimental data of the HNO adsorption experiments with GAC at 30°C are shown in Figure 2. A remarkable agreement may be observed, especially because this simulation was performed using solely the data obtained from the batch experiments (Luna *et al.* [6]), operational conditions, and column and oil properties.

Adsorption and desorption cycles were carried out to assess operation conditions of using activated carbon to remove PAHs from HNO in a continuous column process. The regenerability of the bed after each cycle was evaluated initially by using only solvent at the same operational conditions and later using inert gas at high temperatures.

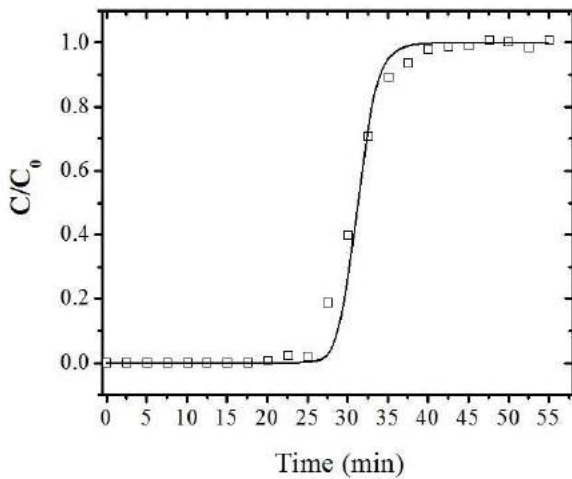


Fig. 2. Breakthrough curve in terms of PAH ($C_0 = 73 \text{ mg/g}$) of HNO samples over GAC at $30 \text{ }^\circ\text{C}$. $Q = 0.20 \text{ mL/min}$. (\square) Experimental data; Full line is the model representation.

According to the areas above the breakthrough curves, the adsorption capacities after consecutive cycles were calculated (see Table 1). It may be observed that the GAC showed initially adsorption capacities of 218.0 and 184.8 mg/g assessed in terms of total aromatics (TA) and PAHs, respectively. These values are in good agreement with the values obtained for the same activated carbon sample in the particle batch experiments previously reported. Changes in adsorption capacities after two and three cycles may also be seen in Table 1, showing slight reduction in both total aromatics and PAHs capacities with the number of cycles. However selectivity values between polyaromatics (PAH) and single aromatics (A), estimated using Eq. 17, increase with the number of cycles from 11.0 at the first cycle to around 16 after the second and third cycles.

Table 1. Adsorption capacities and equilibrium selectivities for three successive cycles.

Cycles	Adsorption capacity (mg/g of ads.)		$\alpha_{PAH/A}$
	TA	PAH	
1 st	218.0	184.8	10.9
2 nd	199.1	178.2	16.8
3 rd	197.3	175.8	16.1

$$\alpha_{PAH/A} = \frac{q_{PAH} / (q_{TA} - q_{PAH})}{C_{PAH} / (C_{TA} - C_{PAH})} \quad (17)$$

Adsorption/desorption cycles were performed to assess the regeneration of the adsorbent in a continuous process. The experimental data of the first desorption step with solvent at the same temperature of $30 \text{ }^\circ\text{C}$, in which the adsorption was previously assessed, are shown in Figure 3. An adsorption capacity of 180.7 mg/g can be estimated from this first desorption run, which is slightly lower than the previously estimated value in the first adsorption step (see Table 2).

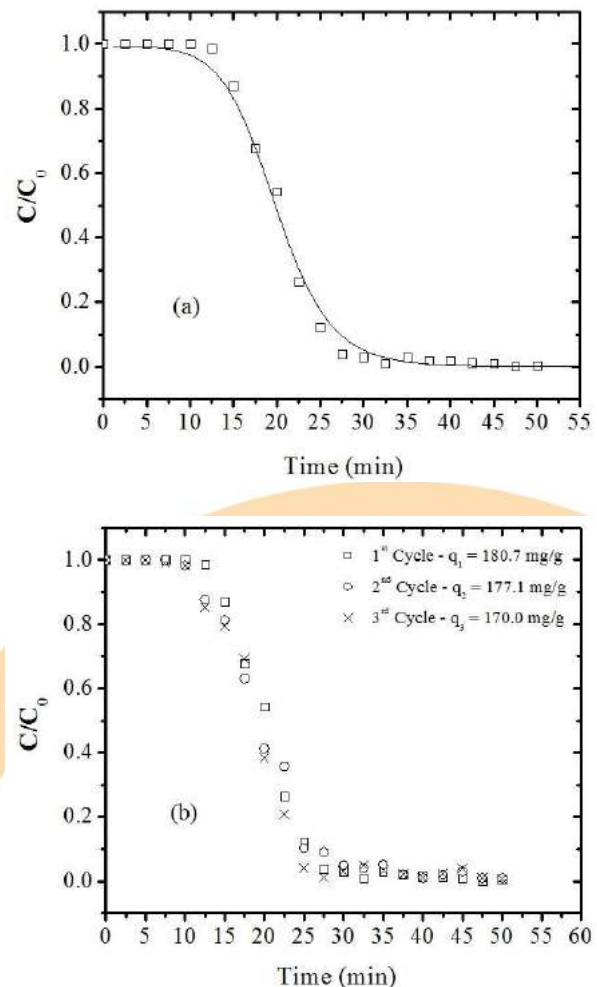


Fig. 3. Desorption curves for HNO over GAC at $30 \text{ }^\circ\text{C}$ using solvent at same adsorption conditions ($\epsilon = 0.39$; $Q = 0.20 \text{ mL/min}$). (a) 1st cycle and model simulation results; (b) Data for three successive adsorption/desorption cycles and respective adsorbent capacities.

The same simulation model, with proper modifications in initial and boundary conditions (Eqs. 14-16), was evaluated with the data of the desorption step. It may be observed that, using again only the data obtained from the batch experiments, operational conditions, and column and oil properties, there is a remarkable good representation of the experimental desorption curve (Figure 3a).

The experimental data of three adsorption/desorption cycles using n-hexane as solvent at the same temperature and flow rate are shown in Figure 3b. A slight decrease (*ca.* 6%) in adsorbent capacity with the number of cycles may be observed (180.7 mg/g for the 1st cycle to 170.0 mg/g for the 3rd cycle) from this data.

Since the adsorption capacity of the adsorbent in the bed decreases slightly with the number of cycles, suggesting that some compounds may be retained in the adsorbent even after the liquid solvent elution, further experiments were planned to more fully desorb the PAHs from the column, by raising the bed temperature under a flow of inert gas. For this purpose, additional adsorption/desorption cycles, starting again with fresh adsorbent in the column, were performed to evaluate the trend in adsorbent capacity reduction with respect to the duration and temperature of the desorption step with inert gas. After the bed saturation, the temperature of the system was raised, as shown in Table 2, for 10 consecutive cycles, with a gas flow of N₂ of 40 NmL/min at the column inlet.

Following the modeling of the phenomena involved in a column adsorption process of PAHs in activated carbons, a possible industrial continuous process is proposed schematically in Figure 4. Two columns with adsorbent may be operated simultaneously in adsorption/desorption cycles. While column A is adsorbing the PAHs from a HNO feed (7.3 % wt. PAHs) at 30 °C at a given space velocity (*v*), column B is being regenerated, using inert gas at high temperature, desorbing the material adsorbed in the previous step.

The adsorption step is run through column A until a product of treated HNO with 3 % wt. of PAHs is obtained in the tank. At this point of time (*t_s*), the feed is switched to column B, and desorption starts from column A.

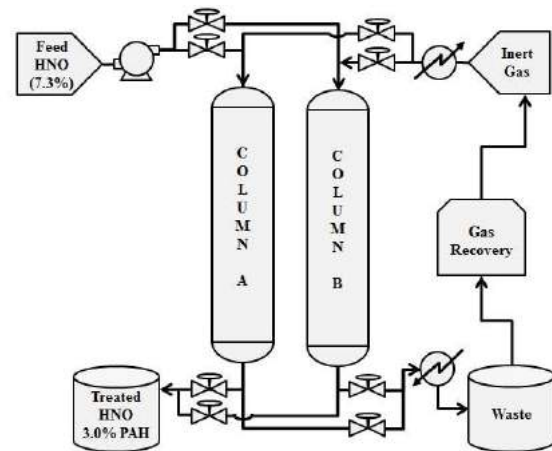


Fig. 4. Conceptual continuous process using two columns operated simultaneously in adsorption/desorption cycles.

Simulations were performed at different space velocities in the adsorption step, calculating the switching time necessary to reach the desired purity of treated HNO in the product tank, and thus estimating a productivity in terms of volume of treated oil per mass of adsorbent per time (Eq. 18).

$$productivity = \frac{F \cdot (1 - C_r) \cdot \int_0^{t_s} (1 - C) dt}{M_B (1 - C_o) t_s} \quad (18)$$

The productivity increases with increasing space velocity up to values of *v* of *ca.* 4.0 h⁻¹ (0.53 m³/(kg ads.)h) For higher values of space velocity, the mass transfer resistances hinder adsorption of PAH within the particle and the productivity decreases with increasing space velocities.

Table 2. Experimental conditions of 10 adsorption/desorption cycles using hot inert gas in the desorption steps.

Run	Desorption Time	Temp.	Adsorption cap. (mg/g)
1	60 min	120°C	182.7
2			180.5
3			176.2
4			173.4
5	120 min	120°C	171.3
6			170.9
7			170.2
8	180 min	150°C	169.4
9			169.5
10			169.4



4. Conclusion

The adsorption capacity of 185 mg/g, assessed in terms of PAHs, was obtained for the fresh activated carbon sample. A slight decrease (*ca.* 6%) in adsorbent capacity was observed after three adsorption/desorption cycles using n-hexane as solvent in the desorption step.

For desorption with inert gas at high temperatures, the capacity was kept essentially constant after the 5th cycle, an interesting characteristic for a continuous operation process. Finally, a continuous process was evaluated for a proposed setup with two columns operated simultaneously in adsorption/desorption cycles. Productivity values, expressed in terms of volume of treated HNO (≤ 3 % wt. of PAH) per mass of adsorbent per time, increased with increasing space velocity up to values of *ca.* 4.0 h⁻¹.

Symbols

C - concentration in bulk phase (mg/g);
 C_0 - feed concentration (mg/g);
 C_p - intra-particle liquid phase conc. (mg/g);
 C_{tr} - concentration of treated oil (3.0 % wt.);
 C_{PAH} - concentration of PAHs;
 C_{TA} - concentration of Total Aromatics;
 D_L - axial dispersion coefficient (cm²/min);
 D_p - pore diffusion coefficient (cm²/min);
 D_S - surface diffusion coefficient (cm²/min);
 F - feed flow rate (cm³/min);
 k_f - mass transfer coef. on the film (cm/min);
 M_B - bed mass (g);
 MM - molar mass of HNO (g/mol);
 M_B - adsorbent mass (g);
 q_0 - solid phase conc. (mg/g of adsorbent);
 q_{PAH} - conc. of PAHs in the solid phase;
 q_{TA} - conc. of Total Aromatics in the solid phase;
 R_p - average particle radius (cm);
 r - radial coordinate (cm);
 t - time (min);
 T is the temperature (°C);
 u - superficial velocity (cm/min);
 V_b - molar volume (cm³/mol);
 V_C - column volume (cm³);
 z - spatial coordinate (cm).

Greek symbols

$\alpha_{PAH/A}$ - selectivity of PAH with respect to single aromatics compounds;

ε - bed porosity;
 η - oil viscosity (cP);
 ϕ - association coefficient, assumed to be 1.0 for aromatics.

Acknowledgements

The authors wish to thank financial and logistic support provided by PETROBRAS (Petróleo Brasileiro S.A.) and CNPq (Conselho Nacional de Pesquisa e Desenvolvimento Científico). The authors are also grateful to NORIT Activated Carbon (Netherlands) for providing activated carbon samples.

References

- [1] Luna FMT, Pontes-Filho AA, Trindade ED, Silva IJ, Azevedo DCS, Cavalcante Jr. CL. Ind Eng Chem Res, 2008; 47:3207.
- [2] Chen B, Yuan M, Liu H. J Hazard Mater, 2011 188:436.
- [3] Xi Z, Chen B. J Environ Sci, 2014; 26:737.
- [4] Vidal CB, Barros AL, Moura CP, Lima AC, Dias FS, Vasconcellos LC, Nascimento RF. J Colloid Interf Sci, 2011; 357:466.
- [5] Araújo RS, Azevedo DCS, Cavalcante Jr. CL, Jiménez-López A, Rodríguez-Castellón E. Micropor Mesopor Mat, 2008; 108:213.
- [6] Luna FMT, Oliveira Filho AN, Araújo CCB, Azevedo DCS, Cavalcante Jr. CL, Ind Eng Chem Res, 2016; 55: 29.
- [7] Luna FMT, Araújo CCB, Veloso CB, Silva Jr. IJ, Azevedo DCS, Cavalcante Jr. CL, Adsorption 2011; 17:937.
- [8] Commission Regulation, Official Journal of the European Union, N. 552, 2009.
- [9] Luna FMT, Pontes Filho AA, Trindade ED, Cavalcante Jr. CL. Environ Monit Assess, 2016; 188:215.
- [10] Guiochon G. J Chromatogr A, 2002; 965: 129.
- [11] Do DD, Rice RG. Chem Eng Sci, 1987; 42: 2269.
- [12] Hu X, Do DD, Rao GN. Chem Eng Sci 1994; 49:2145.

Concentration of anthocyanins from Pinot Noir grape skins in alginate beads through the adsorption operation

Cláudio P. Pinheiro^a, João O. Castro^a, Loreane M. K. Moreira^a, Stephany S. Alves^a, Tito R. S. C. Junior^a, Luiz A. A. Pinto^a

^a Escola de Química e Alimentos, Universidade Federal do Rio Grande (FURG), Rio Grande and 96203-900, Brazil

Abstract

Anthocyanins were extracted from Pinot Noir grape skins with water. Beads of sodium alginate were prepared and used for anthocyanins discontinuous adsorption. The equilibrium adsorption was determined for different pH (3, 4, 5, 6, 7 and 8), and adsorption isotherms were performed at pH 4 and temperatures of 298, 308 and 318 K. Adsorption equilibrium was achieved in 24 h, with the values of adsorption maximum capacity of 73.25 ± 1.22 mg g⁻¹ and 70.94 ± 1.12 mg g⁻¹ at pH 3 and 4, respectively. However, it was not possible to verify adsorption at pH 7 and 8 because the sodium alginate beads dissolve. The pH decrease favored the adsorption capacity, probably due to the formation of flavylium cation, and the temperature increase favored adsorption capacity. Freundlich and Langmuir isotherms presented good fitting to the experimental data. TGA before and after adsorption demonstrated different behaviors.

Keywords: Grape; Equilibrium isotherms; Extraction; TGA

1. Introduction

Anthocyanins are a group consisting of over 500 compounds that are present in most vegetables and fruits. Anthocyanins are glycosylated derivatives of flavylium cation. The enormous variety of anthocyanins is due to the glycosidic bond that joins a carbohydrate molecule to another group. In addition, organic acids can acylate carbohydrates, increasing the number of possible molecular structures [1]. Anthocyanins present in grapes accumulate mainly in the skin, and only the varieties known as teinturier grapes accumulating anthocyanins within the pulp. Genetic factors are known to be the major determinants of grape color, thus influencing the anthocyanins pattern. Thus, the relative content of anthocyanins is almost constant and independent of environmental conditions [2]. Pinot Noir is among the best-known red wines in the world, and it has only 5 types of anthocyanins, all of which are monoglycosides and have no acylated groups. Among Pinot Noir anthocyanidins, malvidin is predominantly followed by peonidin [2, 3].

The use of biodegradable polymeric carriers (alginate) for the drug delivery systems has gained a wide interest, mainly for their biocompatibility. The preparation usually consists of dissolved the drug in an aqueous solution containing the soluble polymer and addition or dripped on a coagulant solution, in the case of carboxylate polymers (alginate) is used Ca²⁺ or Al³⁺ as coagulant solution, the hydrophilic colloids interact with metal ions to form crosslinked insoluble complexes, that precipitate incorporating the drug [4]. Adsorption is an alternative method for the formation of this complex, having the advantage to achieve high concentrations of drug, since adsorption proceeds until it achieves equilibrium.

Adsorbents such as chitosan can adsorb anthocyanin [5]. However, the reduction in pH tends to decrease the adsorption capacity of chitosan, because, there is repulsion of the protonated groups of the chitosan and the flavylium cation of the anthocyanins [5]. However, sodium alginate is insoluble in an acid medium and may interact with the flavylium cation. Thus, the aim of this work was to preparation sodium alginate beads for

anthocyanins discontinuous adsorption from Pinot Noir grape skins.

2. Methods

2.1. Extraction of anthocyanin from Pinot Noir grape skins

Grape pomace was obtained from wineries located in Rio Grande City/RS/Brazil. First, the seeds and other impurities were separated from grape skins and the moisture content was determined [6]. Extraction was performed using distilled water, with mass:solvent ratio was of 1:5 and temperature of 50 °C for 100 min. After extraction, the solution was centrifuged (5000 × g). These conditions were used based on previous extraction studies, that showing extraction yields close to other solvents tested. Eq. 1 was used to determine the anthocyanins concentration [5], $[An]$ (mg mL⁻¹), where Abs_{550} is the absorbance for the wavelength 550 nm.

$$[An] = 3,9455Abs_{550} \quad (1)$$

2.2. Adsorbent beads

Sodium alginate beads were prepared by a solution of 2 g of sodium alginate in 50 mL of distilled water under stirring (600 rpm) for 2 h, at room temperature (25 ± 2 °C). Then, it was dripped on a coagulant solution CaCl₂ (10%, m v⁻¹) through a burette (50 mL) positioned 1.5 cm from the solution surface, and remained in for 4 h. Afterward, the beads were filtered and washed with 0.85% NaCl (m v⁻¹). The moisture content and the average diameter (D_m) were determined. Thermogravimetric analyses (TGA) of the beads before and after adsorption were performed on a thermal weigher (PG Instruments, SDT Q600, ING), with a heating rate of 10 °C min⁻¹ in modified atmosphere (100 mL min⁻¹).

2.3. Equilibrium adsorption experiments

Equilibrium adsorption experiments were carried out at pH 3, 4, 5, 6, 7 and 8, with McIlvaine buffer (10% v v⁻¹) totaling 200 mL, under stirring (50 rpm) at 298.15 K. In each experiment have been used 150 mg of beads (dry basis). The anthocyanins concentrations were determined before and after (24h and 48h) of the adsorption, where the

adsorption capacity at equilibrium, q_e (mg g⁻¹), was calculated by Eq. 2, and removal percentage, $R(\%)$, was calculated by Eq. 3. In which, C_0 and C_e are the initial and equilibrium concentrations in the liquid phase (mg L⁻¹), respectively. m is the adsorbent mass (g) and V is the volume of the solution (L).

$$q_e = \frac{(C_0 - C_e)}{m} V \quad (2)$$

$$R\% = \frac{C_e}{C_0} 100 \quad (3)$$

2.4. Equilibrium isotherms

Equilibrium isotherms were obtained experimentally using different temperatures (298 K, 308 K and 318 K) in pH 4, with McIlvaine buffer (10% v v⁻¹) totaling 200 mL of solution, under the stirring of 50 rpm. The anthocyanins concentrations were determined before and after (24h) adsorption, the anthocyanins concentrations varied from 50 to 300 mg L⁻¹. 150 mg of beads (d. b.) were used in each experiment. The results were evaluated by fitting the isotherms models of Henry, Langmuir, Freundlich, according to Eqs. 4, 5 and 6 respectively; where k_H is the Henry equilibrium constant, q_m is the maximum adsorption capacity in the monolayer (mg g⁻¹) and k_L is the Langmuir constant (L mg⁻¹). k_F Freundlich's constant ((mg g⁻¹) (L mg⁻¹)^{1/n}) and n^{-1} the heterogeneity factor.

$$q_e = k_H C_e \quad (4)$$

$$q_e = \frac{q_m k_L C_e}{1 + k_L C_e} \quad (5)$$

$$q_e = k_F C_e^{1/n} \quad (6)$$

3. Results

The moisture content obtained from grape skins was of 83.9 ± 0.6%. The concentration of anthocyanin extracted was of 231.5 ± 0.6 mg L⁻¹. The literature shows that there are only 5 types of anthocyanins in the Pinot Noir grape skins, and that it does not have acylated anthocyanins [6]. Cortell et al. [3] extracted anthocyanins from Pinot Noir grape skins with 40% ethanol and 100 mg L⁻¹ of SO₂, obtained concentrations from 162 to 210 mg L⁻¹, depending on the cultivar type.

The moisture content of the beads was of 92.0 ± 1%. The average diameter of the beads was 3.09 ±

0.08 mm. The adsorption capacities for 24h e 48h showed no significant differences ($p > 0.05$). The adsorption capacity of anthocyanins increased with decreasing pH (Table 1). The alginate can interact with various divalent cations (Ca^{2+} , Mg^{2+}) due to the carboxylate groups. The pH reduction leads to the increase of the flavylium cation concentration, which is actually the sole chemical species in fairly acidic aqueous solution ($\text{pH} < 2$) [67]. Flavylium cation may compete for carboxylate groups; in addition, under acidic conditions, the carbonyl group becomes protonated because of the excess of H^+ all around, and the flavylium ion in the excited state is a strong acid; thus, is allowed nucleophilic acyl substitution [8]. There was no statistically significant difference ($p > 0.05$) between the adsorption capacity at pH 3 and 4. However, the beads dissolved at pH 7 and 8 due to the alginate carboxyl groups, because at higher pH levels the anthocyanins have an anionic base. Removal percentage increased with pH reduction, reaching 40.3% for pH 3.

Table 1. Effect of pH on the removal percentage and adsorption capacity.

pH	* q_e (mg g ⁻¹)	*R(%)
3	117.25±1.22 ^a	40.3±0.3 ^a
4	113.84±2.12 ^a	38.9±0.2 ^b
5	88.39±1.13 ^b	30.3±0.3 ^c
6	79.90±0.90 ^c	27.3±0.4 ^d
7	-	-
8	-	-

*Mean ± standard deviation (n = 3). Different letters in same column indicate significant differences ($p < 0.05$).

The thermal decomposition, in general, includes the desorption of physically absorbed water, the dehydration, follows the rupture of C-O and C-C bonds generating CO, CO₂ and H₂O, and the formation of polynuclear aromatic and graphitic carbon structures [9]. In Fig. 1, the loss of water molecules for alginate beads occurred at temperature range between 40 °C and 200 °C, however, the weight loss of beads with anthocyanins was constant until to 350 °C. The residue left was 36% and 25% for alginate and alginate plus anthocyanins, respectively. The greatest loss of mass of beads with anthocyanin was probably due to the presence of anthocyanins, which are more sensitive to thermal degradation.

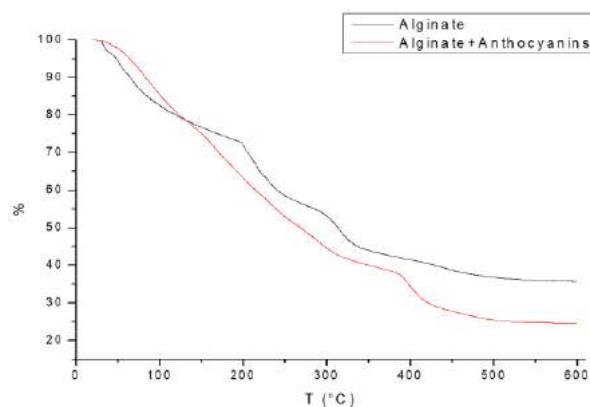


Fig. 1. TGA of alginate beads before and after adsorption.

Experimental data were adjusted to the Henry, Langmuir and Freundlich models to describe the anthocyanins adsorption behavior in alginate beads. The coefficient of determination and the mean relative error were evaluated to choose the most suitable model, and they are presented in Table 2.

Table 2. Parameters of adsorption isotherm models

T (K)	Henry			
	k_H^*	R ²	MRE(%)	
298	0.513±0.004	0.610	6.5	
308	0.533±0.006	0.561	3.7	
318	0.558±0.005	0.521	1.7	
T (K)	Langmuir			
	k_L^*	q_m^*	R ²	MRE(%)
298	0.0326±0.0001	129.2±0.6	0.995	2.4
308	0.0350±0.0002	132.9±0.5	0.996	2.0
318	0.0366±0.0003	138.3±1	0.995	1.4
T (K)	Freundlich			
	k_F^*	n^*	R ²	MRE(%)
298	36.74±0.2	4.8±0.3	0.999	2.4
308	40.29±0.3	5.0±0.4	0.999	2.4
318	43.60±0.5	5.2±0.3	0.999	2.6

*Mean ± standard deviation (n = 3). R²: coefficient of determination; MRE: mean relative error.

Freundlich and Langmuir isotherms models were the best fit to experimental data. Freundlich model showed $n > 1$, and this value may be due to any factor that caused a decrease in adsorbent-adsorbate interaction with increasing surface density. One of the major disadvantages of the Freundlich equation is that it does not predict a maximum adsorption capacity. Langmuir isotherm showed a maximum adsorption capacity, q_m , on average 17% higher than the experimental value obtained for adsorption with the highest concentration of anthocyanins. Fig. 2 shows a good Langmuir and Freundlich model fitting.

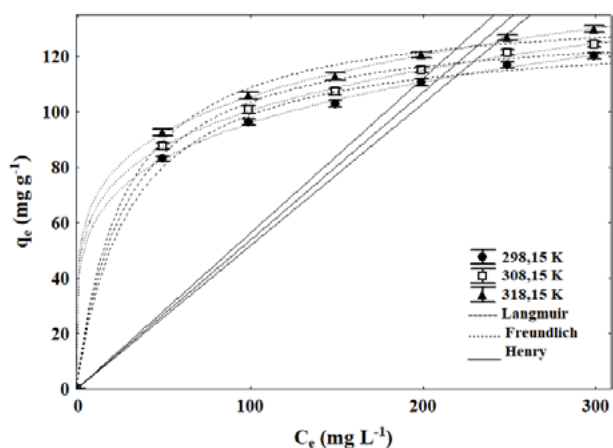


Fig. 2. Henry, Langmuir and Freundlich models their fitting.

4. Conclusion

The adsorption capacities of the anthocyanins from Pinot Noir grape skins onto the sodium alginate beads, in discontinuous adsorption, for 24 h and 48 h showed no significant difference ($p > 0.05$). The best adsorption capacities were obtained at pH 3 and 4. Freundlich and Langmuir adsorption isotherms were suitable for fitting to experimental data. Thermogravimetric analysis showed that beads after adsorption display a greater degradation.

Acknowledgements

The authors would like to thank CAPES (Coordination for the Improvement of Higher Education Personnel), Finance Code: 001, and

CNPq (National Council for Scientific and Technological Development).

References

- [1] Durst RW, Wrolstad RE. Separation and characterization of anthocyanins by HPLC. *Curr Protoc Food Anal Chem* 2001;00:F1.3.1-F1.3.13
- [2] Dimitrovska M, Bocevska M, Dimitrovski D, Murkovic M. Anthocyanin composition of vranec, cabernet sauvignon, merlot and pinot noir grapes as indicator of their varietal differentiation. *Eur Food Res Technol* 2011;232:591–600.
- [3] Cortell JM, Halbleib M, Gallagher AV, Righetti TL, Kennedy JA. Influence of vine vigor on grape (*Vitis vinifera* L. Cv. Pinot Noir) anthocyanins. 1. Anthocyanin concentration and composition in fruit. *J Agric Food Chem* 2007;55:6585-6595.
- [4] González-Rodríguez ML, Holgado MA, Sánchez-Lafuente C, Rabasco AM, Fini A. Alginate/chitosan particulate systems for sodium diclofenac release. *Int J Pharm* 2002;232:225-234.
- [5] Carvalho VL, Gonçalves JO, Silva A. T.R. Cadaval TR, Pinto LAA, Lopes TJ. Separation of anthocyanins extracted from red cabbage by adsorption onto chitosan films. *Int J Biol Macromol* 2019;131:905-911.
- [6] Beneytez EG, Cabello FL, Revilla E. Analysis of grape and wine anthocyanins by HPLC-MS. *J Agric Food Chem* 2003;51:5622-5629.
- [7] Müller-Maatsch J, Gurtner K, Carle R, Steingass CB. Investigation into the removal of glucosinolates and volatiles from anthocyanin-rich extracts of red cabbage. *Food Chem* 2019;278:406-414.
- [8] Dangles O, Fenger JÁ. The chemical reactivity of anthocyanins and its consequences in food science and nutrition. *Molecules* 2018;23:online
- [9] Adzmi F, Meon S, Musa MH, Yusuf NA. Preparation, characterisation and viability of encapsulated *Trichoderma harzianum* UPM40 in alginate-montmorillonite clay. *J Microencapsul* 2012;29:205-10



Regeneration of granular activated carbon using thermal technique

Letícia Weidlich Sfreddo^a, Morgana Rosset^{a,*}, Liliana Amaral Féris^a

^a Federal University of Rio Grande do Sul (UFRGS), Rua Ramiro Barcelos, 2777, Porto Alegre 90040-040 RS Brazil
morganar@enq.ufrgs.br*

Abstract

Conventional treatment processes are not able to remove emerging compounds as drug diclofenac in wastewater. Adsorption has been widely used to remove pollutants. Together with the adsorption, the regeneration of solid adsorbents can be carried out. The present work aims to evaluate the best conditions for the removal of diclofenac and the performance of cycles of adsorption/regeneration using the regenerative thermal technique. The main adsorption parameters were natural pH, solid sorbent dosage of 20 g L⁻¹ and contact time of 60 min. Analyzing the behavior of the cycles, it was possible to observe regeneration of 100% that persisted for six cycles. The final regeneration percentage obtained in the eighth and last cycle was 75%. The thermal technique was shown to be effective in adsorption/regeneration cycles with granular activated carbon in the removal of diclofenac. This work aims at the removal of sodium diclofenac from an aqueous synthetic solution through the batch adsorption process using activated charcoal as a sorbent solid.

Keywords: Adsorption parameters; Diclofenac; Contact time; Cycle.

1. Introduction

Chemicals present in many organic commercial compounds such as human and veterinary drugs, personal care products (PCP), steroids and hormones, pesticides, surfactants and industrial additives are considered emerging contaminants (EC) [1,2]. They are introduced via excretion or disposal to conventional wastewater plants, which are not designed to effectively remove them[3]. Pharmaceuticals as emerging pollutants have become a major concern because of their low biodegradability, high persistence, and facile bioaccumulation [4]. The presence of trace pharmaceuticals in drinking water has a toxic effect on human and animal health [5]. Emerging pollutants have become one of the most important issues in wastewater treatment.

Diclofenac appears to be one of the most concerning compounds because it has been extensively used as a non-steroidal anti-inflammatory drug (NSAID) and commonly found in influents and effluents of wastewater treatment plants as well as drinking water [6,7]. Consequently, NSAID is among the most detected drugs in the aquatic environment at concentrations up to $\mu\text{g L}^{-1}$ [8], due to their properties of hydrophilicity and stability in the aqueous phase [4].

Several treatment technologies to remove emerging compounds have been proposed and

investigated. Among these technologies, can be highlighted the adsorption [9-11], which is a simple, cheap, and versatile technique for holding these pollutants without the generation of harmful byproducts. From the high variety of available adsorbents, activated carbon is, by far, the most widely used in the removal of nonsteroidal anti-inflammatory compounds [12]. Activated carbon as adsorbent has been effectively utilized to remove pharmaceutical pollutants from wastewaters [10,13].

According to the literature, activated carbon is a well-known conventional adsorbent with many applications due to its hydrophobicity, surface functionality, pore structure, surface area and high adsorptive capacity [14,15]. Furthermore, activated carbon is a versatile adsorbent material that has been employed in many industrial processes, including technologies, is suitable for the removal of hazardous contaminants from water and effluents (e.g., aromatic compounds, drugs, and pesticides) [16]. In addition, there is the possibility of reuse and regeneration of versatile adsorbents for the removal of emerging micro-pollutants.

Depending on its adsorption capacity, the activated carbon saturates after some time. When activated carbons reach their saturation limit, they fail to adsorb the targeted pollutants [16]. Thus, the spent carbon should be regenerated for wider application of carbon adsorption processes and to prevent environmental contaminations. It is desirable to regenerate the spent adsorbents and



simultaneously decompose the organic adsorbates, especially the regenerated adsorbents that have the same sorption capacity as the original ones [17].

Several methods are being proposed in the literature for application in the regeneration of saturated solids. Among them, we can mention thermal decomposition; solvent extraction; ultrasound; microwave and chemical or electrochemical regeneration [16,18,19]. The most attractive option is the one that gathers the best compromise among the cost, the regeneration efficiency and the number of adsorption-regeneration cycles that allows the recovery of a considerable degree of carbon's porosity.

This work aims at the removal of sodium diclofenac from an aqueous synthetic solution through the batch adsorption process using activated charcoal as a sorbent solid. As well as, to study the capacity of regeneration of the carbon saturated by the thermal decomposition.

2. Experimental

2.1. Materials

In this present work, it was used as solid adsorbent a commercial activated carbon from Synth with granulometry of 14 mesh-Tyler (diameter between 2.0 and 1.88 mm). The textural result of the activated carbon was $S_{BET} = 641 \text{ m}^2 \text{ g}^{-1}$. For the sorbate the drug diclofenac sodium from Sigma-Aldrich presenting purity > 99% was used. A solution of 1000 mg L^{-1} of diclofenac was prepared and all the solutions were obtained from dilutions in distilled water.

2.2. Adsorption assays

The adsorption tests were performed in batch mode using 250 mL Schott flasks, 50 mL of a synthetic solution 10 mg L^{-1} of diclofenac were placed in the flasks and left under stirring on a Wagner Shaker (Marconi brand, model MA160BP) at 30 rpm and room temperature. All experiments were evaluated in duplicate and the standard deviation was calculated. The initials and finals concentrations were analyzed by the spectrophotometry method, measured at the wavelength of highest absorbance, in the case of diclofenac of 276 nm. After adsorption tests, the removal capacity (Rc) is obtained through Equation 1:

$$Rc (\%) = \left(\frac{C_0 - C}{C_0} \right) * 100 \quad (1)$$

where C_0 : initial concentration of DCF (mg L^{-1}) and C : final concentration of DCF (mg L^{-1}).

During the pH tests, it was used as an acid and as a basic solution, respectively, hydrochloric acid (1M) and sodium hydroxide (1M). The pH effect study was performed by varying the initial pH of the solution to pH 2, 4, 6, 8, and 10, remaining at 60 minutes of the contact time and using 10 g L^{-1} adsorbent in solution. After determining the best adsorption pH, the adsorbent solids concentrations of 4, 6, 8, 10, 15, 20, 25, and 30 g L^{-1} were analyzed, keeping the contact time of 60 minutes constant. Then, after obtaining the ideal pH and solid concentration for the sorption process, the influence of the contact time of the sorbent solid in solution was analyzed. Tests were performed at 5, 10, 20, 30, 40, 60, 90, 120, and 150 minutes. The obtained pH and solid concentration obtained in the previous experiments were kept constant.

2.3. Adsorption/regeneration cycles

Starting from the results obtained on the adsorption experiments, the regeneration cycle tests began. The experimental conditions were maintained in Schott flasks with 50 mL of a diclofenac solution of 10 mg L^{-1} and placed on a Wagner shaker. The regeneration was realized by thermal treatment in a muffle for 2 hours at $400 \text{ }^\circ\text{C}$ [19]. The quantification of regeneration efficiency, RE (%) (Eq.2), of each regeneration cycle was defined as:

$$Re (\%) = (q_i/q_0). 100 \quad (2)$$

where q_i is the adsorption capacity of regenerated activated carbon in a given reuse cycle, and q_0 is the adsorption capacity of fresh activated carbon.

Results and Discussion

2.4. Adsorption assays

Figure 1 shows the results of the removal of diclofenac sodium obtained at different pH values of the solutions. As can be seen the removal increases as the pH decreases. The best pH for the adsorption of diclofenac sodium was 2, this result indicated a pH lower than the pKa of this drug (pKa = 4.20) since the DCF is present in its neutral form and its solubility decreases [20]. However, at

pH 2, diclofenac precipitates in solution. Thus, it was not possible to estimate its actual removal by the adsorption process under this condition. An increase in pH above 4.0 ($\text{pH} > \text{pK}_a$) shows a decreasing tendency in adsorption due to an increase in the solubility of DCF in water [21]. The reduction of the percentage of DCF removal with increasing pH of the solution is also observed by other authors with activated carbon [9,22]. Therefore, it was decided to use its natural pH around 5.5 (DCF plus carbon solution).

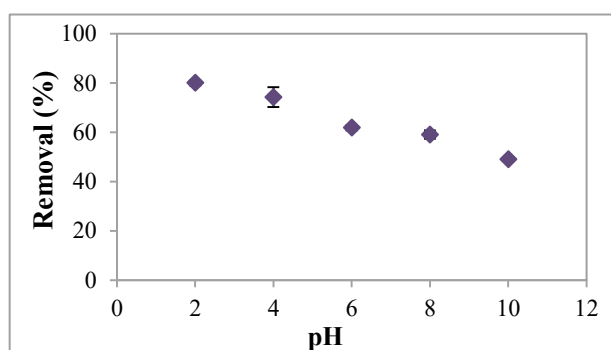


Fig. 1. pH tests, solid concentration of 10 g L^{-1} , 60 min of contact time and a synthetic solution 10 mg L^{-1} of diclofenac.

The effect of activated carbon dosage on diclofenac sodium removal was studied using a 4– 30 g L^{-1} adsorbent dosage. Observing Figure 2 it is possible to see that as we increase the solid sorbent dosage, the removal efficiency of diclofenac also increases. This behavior happens until a certain point, where it is achieved removal of 72%, and after that, the values remain constant. It is readily understood that the number of available adsorption sites increases by increasing the adsorption dose and it, therefore, results in the increase of removal efficiency. The decrease in adsorption density with an increase in the adsorbent dose is mainly due to the unsaturation of adsorption sites through the adsorption reaction [23]. The dosage choice to follow the tests was 20 g L^{-1} with a removal of 75%.

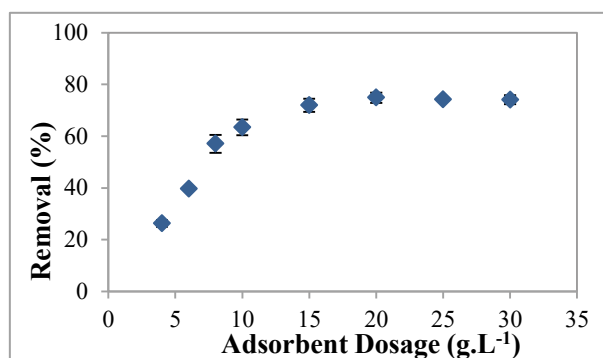


Fig. 2. Adsorbent dosage test with natural pH, 60 min of contact time and synthetic solution 10 mg L^{-1} of diclofenac.

The effect of contact time on the removal of diclofenac sodium is shown in Figure 3, maintaining the previous parameters (pH, adsorbent dosage, initial concentration). The adsorbed amount of diclofenac increased with the increase of contact time and the chemical equilibrium is reached after 60 min. In the first hour, the adsorption capacity showed rapid growth in the amount of adsorption, removing 70% of diclofenac. This fast adsorption capacity at the initial stage by activated carbon indicated a higher driving force that made the fast transfer of DCF to the surface of activated carbon particles [20,21]. Therefore, an equilibrium time of 60 min was assumed for all further experiments.

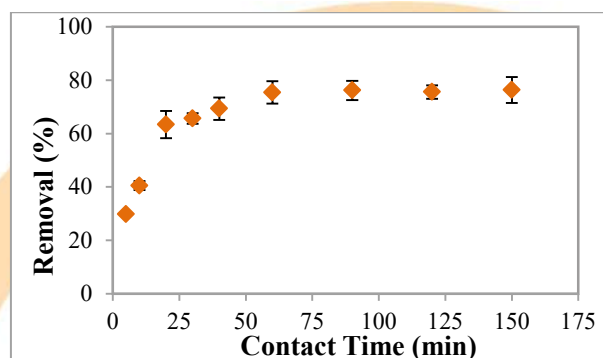


Fig. 3. Contact time test with natural pH, adsorbent dosage of 20 g L^{-1} and synthetic solution 10 mg L^{-1} of diclofenac.

For Figure 4, what is called “Cycle 0” is simply the first adsorption performed. The subsequent regeneration values will be based on this first removal value to analyze the regeneration for each subsequent cycle. During the cycles, no adjustment of the activated carbon’s mass was made, regardless of the loss of mass.

The adsorption/regeneration thermal cycles are presented in Figure 4. As it can be observed, the regeneration capacity remained almost constant in 100% until the sixth cycle. The subsequent cycles lose their capacity for regeneration. Even reducing its capacity, the technical presented in the last cycle a regeneration of 75%. The reduction on the final may be due to the loss of solid mass, since a considerable decrease was observed, approximately 70%, in the course of the cycles. In the Marques *et al.*[16] study, they report that activated carbon adsorbents can be reused at least twice, maintaining adsorption capacities above 50%. The granular carbon nanotubes can be regenerated by heating at 400 °C under air atmosphere to decompose the adsorbed pollutants, this adsorbent was stable and little loss of sorption capacity was observed in ten cycles reuse[17].

The diclofenac removal also remained stable until the sixth cycle. It is possible to observe that from Cycle 0 to Cycle 1 the removal percentual increased from 79% to 87%. The explanation for this event is perhaps that, in the first regeneration, possible impurities found in the activated carbon were removed, so that their removal power was increased as soon as they were eliminated.

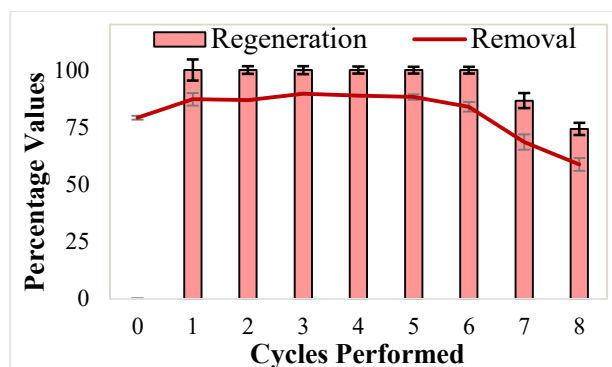


Fig. 4. Cycles performed with thermal regeneration with the removal and regeneration percentages found in each of the cycles.

3. Conclusions

The adsorption tests showed that granular activated carbon could efficiently remove sodium diclofenac. Removal values were obtained in the range of 80% with the parameters of pH (5.5), contact time (60 min) and adsorbent dosage (20 g L⁻¹). It was possible to perform 8 adsorption/regeneration cycles. This technique presented the value of 100% of regeneration persisting for six cycles. The use of thermal

regeneration was proved to be a highly feasible technique to provide the decomposition of diclofenac.

Acknowledgements

The authors thank the National Counsel of Technological and Scientific Development (CNPq) and the Coordination for the Improvement of Higher Education Personnel (CAPES) of the Brazilian Government for the financial support granted to carry out this work.

References

- [1] Haro NK, Vecchio P Del, Marcilio NR, F LA. Removal of atenolol by adsorption - Study of kinetics and equilibrium. *J Clean Prod* 2017;154:214–9.
- [2] Leone VO, Pereira MC, Aquino SF, Oliveira LCA, Correa S, Ramalho TC, et al. Adsorption of diclofenac on a magnetic adsorbent based on maghemite: experimental and theoretical studies †. *New J Chem* 2017;42:437–49.
- [3] Landry KA, Boyer TH. Diclofenac removal in urine using strong-base anion exchange polymer resins. *Water Res* 2013;47:6432–44.
- [4] Ahmed MJ, Hameed BH. Removal of emerging pharmaceutical contaminants by adsorption in a fixed-bed column: A review. *Ecotoxicol Environ Saf* 2018;149:257–66.
- [5] Rad LR, Irani M, Barzegar R. Adsorptive removal of acetaminophen and diclofenac using NaX nanozeolites synthesized by microwave method. *Korean J Chem Eng* 2015;32:1606–12.
- [6] Jauris IM, Matos CF, Saucier C, Lima EC, Zarbin AJG, Fagan SB, et al. Adsorption of sodium diclofenac on graphene: a combined experimental and theoretical study. *Phys Chem Chem Phys* 2015;18:1526–36.
- [7] Lin K-YA, Yang H, Lee W-D. Enhanced removal of diclofenac from water using a zeolitic imidazole framework functionalized with cetyltrimethylammonium bromide (CTAB). *RSC Adv* 2015;5:81330–40.
- [8] Graouer-Bacart M, Sayen S, Guillon E. Adsorption and co-adsorption of diclofenac and Cu (II) on calcareous soils. *Ecotoxicol Environ Saf* 2016;124:386–92.
- [9] Baccar R, Sarrà M, Bouzid J, Feki M, Blánquez P. Removal of pharmaceutical compounds by activated carbon prepared from agricultural by-product. *Chem Eng J* 2012;211–212:310–7.

- [10]Franco AM De, Carvalho CB De, Bonetto MM, Soares RDP, Féris LA. Diclofenac removal from water by adsorption using activated carbon in batch mode and fixed-bed column: Isotherms, thermodynamic study and breakthrough curves modeling. *J Clean Prod* 2018;181:145–54.
- [11]Rosset M, Sfredo LW, Hidalgo GEN, Perez-Lopez OW, Féris LA. Adsorbents derived from hydrotalcites for the removal of diclofenac in wastewater. *Appl Clay Sci* 2019;175:150–8.
- [12]Álvarez-Torrellas S, Munoz M, Zazo AJ, Casa AJ, García J. Synthesis of high surface area carbon adsorbents prepared from pine sawdust- *Onopordum acanthium* L. for nonsteroidal anti-inflammatory drugs adsorption. *J Environ Manage* 2016;183:294–305.
- [13]Sotelo JL, Ovejero G, Rodríguez A, Álvarez S, Galán J, García J. Competitive adsorption studies of caffeine and diclofenac aqueous solutions by activated carbon. *Chem Eng J* 2014;240:443–53.
- [14]Torrellas SÁ, García Lovera R, Escalona N, Sepúlveda C, Sotelo JL, García J. Chemical-activated carbons from peach stones for the adsorption of emerging contaminants in aqueous solutions. *Chem Eng J* 2015;279:788–98.
- [15]Ahmed MJ. Adsorption of non-steroidal anti-inflammatory drugs from aqueous solution using activated carbons: Review. *J Environ Manage* 2017;190:274–82.
- [16]Marques SCR, Marcuzzo JM, Baldan MR, Mestre AS, Carvalho AP. Pharmaceuticals removal by activated carbons: Role of morphology on cyclic thermal regeneration. *Chem Eng J* 2017;321:233–44.
- [17]Wei H, Deng S, Huang Q, Nie Y, Wang B. Regenerable granular carbon nanotubes/alumina hybrid adsorbents for diclofenac sodium and carbamazepine removal from aqueous solution. *Water Res* 2013;47:4139–47.
- [18]Guo D, Shi Q, He B, Yuan X. Different solvents for the regeneration of the exhausted activated carbon used in the treatment of coking wastewater. *J Hazard Mater* 2011;186:1788–93.
- [19]Xin-hui D, Srinivasakannan C, Qu WW, Xin W, Jin-hui P, Li-bo Z. Regeneration of microwave assisted spent activated carbon: Process optimization, adsorption isotherms and kinetics. *Chem Eng Process Process Intensif* 2012;53:53–62.
- [20]Jodeh S, Abdelwahab F, Jaradat N, Warad I, Jodeh W. Adsorption of diclofenac from aqueous solution using *Cyclamen persicum* tubers based activated carbon (CTAC). *J Assoc Arab Univ Basic Appl Sci* 2016;20:32–8.
- [21]Larous S, Meniai AH. Adsorption of Diclofenac from aqueous solution using activated carbon prepared from olive stones. *Int J Hydrogen Energy* 2016;41:10380–90.
- [22]Bhadra BN, Seo PW, Jung SH. Adsorption of diclofenac sodium from water using oxidized activated carbon. *Chem Eng J* 2016;301:27–34.
- [23]Shukla A, Zhang Y-H, Dubey P, Margrave JL, Shukla SS. The role of sawdust in the removal of unwanted materials from water. *J Hazard Mater* 2002;B95:137–52.

Separation of ethylene from ethane with Metal-organic Frameworks

João Pires^a, José R. B. Gomes^b, Germán Pérez-Sánchez^b, Farid Nouar^c, Christian Serre^c,
Moisés L. Pinto^{d*}

^aCentro de Química e Bioquímica and CQE, Faculdade de Ciências, Universidade de Lisboa, 1749-016 Lisboa, Portugal

^bCICECO - Aveiro Institute of Materials, Department of Chemistry, University of Aveiro, Campus Universitário de Santiago, 3810-193 Aveiro, Portugal

^cInstitut des Matériaux Poreux de Paris (IMAP), UMR CNRS 8004, Ecole Normale Supérieure de Paris, Ecole Supérieure de Physique et de Chimie Industrielles de Paris, PSL University, 75005 Paris, France.

^dCERENA, Instituto Superior Técnico, Universidade de Lisboa, Av. Rovisco Pais, n° 1, 1049-001 Lisboa, Portugal

Abstract

The separation of ethylene from ethane could be alternatively made by an adsorption process if the adsorbent would preferentially adsorb ethane over ethylene. Materials that exhibit this feature are scarce. Here we present our studies of metal-organic frameworks, IRMOF-8 and a series of zirconium-dicarboxylate based MOFs of the UiO-66 (tetrahedral and octahedral cages) or MIL-140 (triangular channels), for which the adsorption isotherms of ethane and ethylene were measured at 298 and 318 K up to pressures of 1000 kPa. Van der Waals interactions seem to be enhanced in the interpenetrated structure of IRMOF-8, favoring ethane adsorption in a wide pressure range. Results indicate that the 3D pores of the UiOs favor the adsorption of ethane due to the interactions between ethane with more spacers than in the case of the 1D channels of MIL-140s. The impact of the functionalization on the UiO-66 type revealed a very interesting increase of selectivity when two perfluoro groups are present on the aromatic ring (UiO-66-2CF₃) (value of 2.5 up to 1000 kPa). Indeed, UiO-66-2CF₃ revealed a unique combination of selectivity and working capacity at high pressures.

Keywords: Metal-organic framework; ethane; ethylene; gas separation.

1. Introduction

Ethylene is an important basic raw material for the synthesis of several products (world production capacity will reach 200 million tons in 2020), [1,2] Its main purification operation is its separation from ethane. The cyclic adsorption separation process can be an alternative to the cryogenic distillation, currently used in the industry with high energy consumption, if the adsorbent material used presents more adsorption affinity to ethane than to ethylene. Several adsorbents reported in literature, for long time, show high adsorbed amounts and high selectivity for this separation. Nevertheless, cryogenic separation remains the technique of choice, even though columns with more than 100 plates and very high reflux rates need to be used, [3] mainly because the majority of reported adsorbents

(zeolites and clay based materials for instance) show higher affinity to adsorb ethylene over ethane. [4] So, although the selectivity can be high, they are not attractive for this industrial application because the adsorbent selectivity will occur at the cost of ethylene being the more adsorbed species, with a concomitant low purity of ethylene in the stream that is obtained in the blow down step (desorption) of the cyclic separation.

Metal-organic frameworks (MOFs) are presently a well-known recent class of ordered porous hybrid materials, which display a large variety of structures and chemical compositions. [5–7] This makes MOFs highly interesting to the design of porous materials with new properties and opens the possibility to investigate how the selectivity of the materials can be tuned for the desired order, *i.e.* selective for ethane rather than for ethylene. When strong local charges are present in the MOF structure, like

coordinatively unsaturated metal sites as it happens for instance in the activated HKUST-1 (copper benzene-1,3,5-tricarboxylate)[8–10] and in $\text{Fe}_2(\text{dobdc})$,[11] ethylene interacts strongly with these sites and is preferentially adsorbed over ethane, thus not presenting any advantage over the classic adsorbents, like zeolites, for example. Therefore, the absence of strong local charges at the structure of the materials arises as a necessary requisite for obtaining structures that preferentially interact with ethane.

In recent years our team has been investigating MOF structures that can have an enhanced selective interaction with ethane to allow the application of these materials for ethane/ethylene separations. In a previous work, we have found that IRMOF-8, a Zn based MOF, presents selectivity for ethane [12] and that this is enhanced in the interpenetrated form of the material.[13] More recently, we explored the more robust family of Zr MOFs with UiO-66 or MIL-140 type structures, and the effect of the type of linker and substitutions on the desired ethane adsorption selectivity.[14] In this communication, we will discuss the results of our recent studies.

2. Experimental

2.1 Synthesis of materials

The synthesis of the zirconium MOFs was carried out under solvothermal conditions in dimethylformamide (DMF) using ZrCl_4 (for MIL-140A, MIL-140B, UiO-66, UiO-66-Br, UiO-66-2CF₃ and UiO-NDC) or ZrOCl_2 (for UiO-Fum) as the zirconium source and the correspondent carboxylic acid according to the procedures previously reported.[14]

For the synthesis of IRMOF-8 zinc nitrate hexahydrate $\text{Zn}(\text{NO}_3)_2 \cdot 6\text{H}_2\text{O}$ and naphthalene-2,6-di-carboxylic acid were used in DMF. The synthesis procedure was adapted from a previous study.[15]

2.2 Characterization of materials

All synthesised materials were characterized with the powder X-ray diffraction (PXRD), thermogravimetric analyses (TGA) and low temperature nitrogen adsorption, to ascertain the phase structure and purity.

2.3 High-pressure adsorption of ethane and ethylene

Pure gas isotherms with ethane (Air Liquide, 99.995%) and ethylene (Gasin, 99.99%) were measured on each material. A conventional stainless-steel volumetric apparatus was used to carry out adsorption experiments up to 1000 kPa. The apparatus was equipped with a pressure transducer (Pfeiffer Vacuum, APR 266), connected to a vacuum system, which could maintain a vacuum better than 10^{-2} Pa. The adsorption temperatures of 25 or 45 °C were maintained with a stirred thermostatic water bath (Grant Instrument, GD-120). Before experiments, each sample was degassed for 2.5 h at 150 °C. In the calculation of the adsorbed amounts, the non-ideality of the gas phase was considered by using the second virial coefficients. Excess adsorbed amounts determined experimentally were converted to absolute amounts using the gas density and porous volumes of the samples. The isotherm data was fitted with a Virial equation of the form

$$p = n^{\text{ads}}/K \exp(C_1 n^{\text{ads}} + C_2 n^{\text{ads}2} + C_3 n^{\text{ads}3}) \quad (1)$$

where p is the pressure, n^{ads} is the adsorbed amount, K is the Henry's constant and C_1 , C_2 and C_3 are the Virial coefficients. The selectivity and phase diagrams of binary $\text{C}_2\text{H}_6/\text{C}_2\text{H}_4$ mixtures were estimated by a method based on the Ideal Adsorbed Solution Theory (IAST), which was described in detail in previous works.[16,17]

3. Results and discussion

High pressure adsorption of ethane and ethylene on the eight different MOF structures was performed up to 1000 kPa (Fig. 1). The analysis of the data was carried with the IAST to obtain selectivity and phase diagrams that were helpful to rationalize the influence of the type of structure, pore size and ligand functionalization on the adsorption behavior.

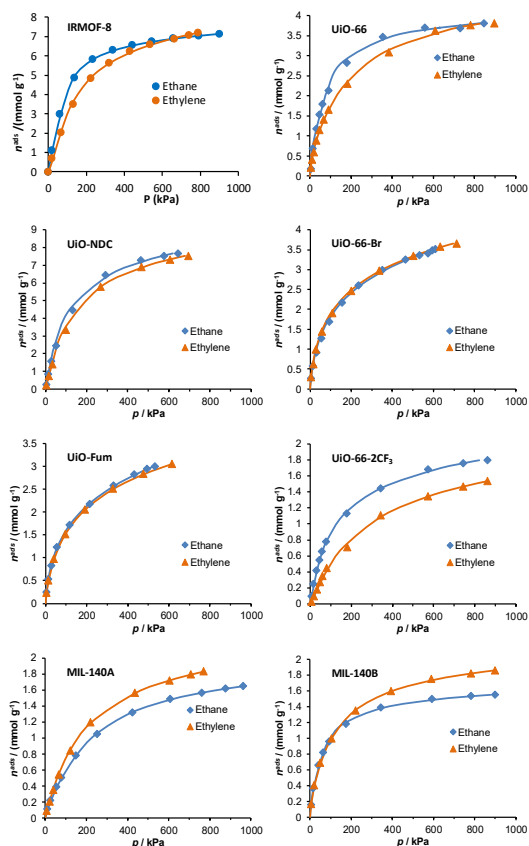


Fig 1. Ethane and ethylene adsorption isotherms, at 25 °C. Lines represent the virial isotherm fits to the experimental data.

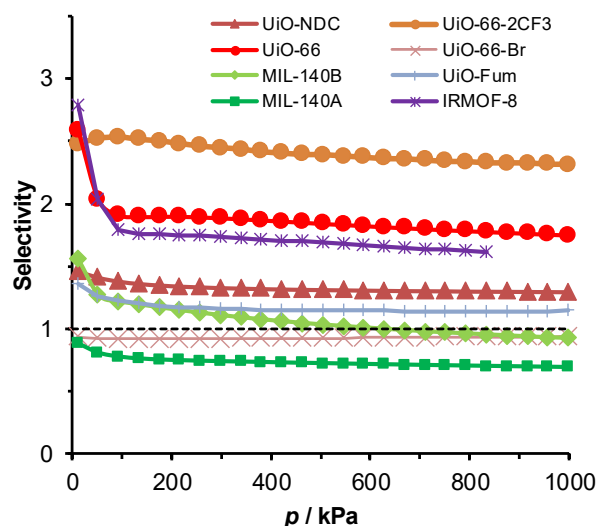


Fig. 2. Selectivity of adsorption of the binary mixture ethane/ethylene, with pressure, at 25 °C.

Regarding the selectivity for ethane (selectivity values higher than 1), several of the MOFs studied

presented this capacity (Fig. 2), although the most interesting ones are the IRMOF-8, UiO-66 and UiO-66-2CF₃.

Our results have shown that the IRMOF-8 presents higher adsorbed amounts of ethane than of ethylene in a wide range of pressures, near ambient temperature. This was one of the first reported cases where preferential adsorption of ethane over ethylene is reported and the selectivity values range between 3.4 and 1.6 depending on the temperature and pressure. Separation of mixtures was achieved in flow experiments, giving the desired higher retention for ethane, allowing ethylene to be obtained first out of the column.

Molecular insight on the preferential ethane adsorption over ethylene, obtained by Monte Carlo simulations, indicated that van der Waals interactions are the cornerstone to the desired selectivity and that the interpenetrated structure of IRMOF-8 is the reason for the observed ethane selectivity.

Regarding the Zr MOFs with two possible topologies, with three dimensional tetrahedral and octahedral pore arrangements (UiO-66 type) and with one dimensional triangular pore channels (MIL-140 type), results demonstrate that the three-dimensional pores of the UiO type structure are better to give the desired ethane selectivity. The increase in the pore size of the UiO type structure, when the naphthalene dicarboxylate and the benzene dicarboxylate linkers are compared, the effect of the aromaticity increase in the former linker is not effective at high pressures. Thus, UiO-66 turns to have a better selectivity than UiO-NDC.

The best strategy to enhance the ethane selectivity is to introduce two perfluoro groups on the aromatic ring (UiO-66-2CF₃ MOF), with a concomitant improvement of the selectivity over a wide pressure range, with selectivity values close to 2.5. The UiO-66-2CF₃ has a unique combination of selectivity and working capacity (about 1 mmol g⁻¹ between 100 and 1000 kPa) that makes it very interesting for cyclic separations with pressure swing.

Acknowledgements

The work was financed by Fundação para a Ciência e a Tecnologia (FCT) through project IF/00993/2012/CP0172/CT0013. This work was developed in the scope of the Projects POCI-01-0145-FEDER-007679 | UID/CTM/50011/2019 (CICECO), UID/MULTI/00612/2019 (CQB), UID/ECI/04028/2019 (CERENA) and Programa Investigador FCT, financed by national funds



through the FCT/MEC and cofinanced by FEDER under the PT2020 Partnership Agreement.

References

- [1] Eramo M. Ethylene Forum. Ethyl Mark Outlook 2013.
- [2] Steve Lewandowski. Ethylene - Global. Asia Chem. Conf., IHS Markit; 2016.
- [3] Eldridge RB. Olefin/paraffin separation technology: a review. *Ind Eng Chem Res* 1993;32:2208–12. doi:10.1021/ie00022a002.
- [4] Ruthven DM, Reyes SC. Adsorptive separation of light olefins from paraffins. *Microporous Mesoporous Mater* 2007;104:59–66. doi:10.1016/j.micromeso.2007.01.005.
- [5] Zhou H-CJ, Kitagawa S. Metal–Organic Frameworks (MOFs). *Chem Soc Rev* 2014;43:5415–8. doi:10.1039/C4CS90059F.
- [6] Maurin G, Serre C, Cooper A, Férey G. The new age of MOFs and of their porous-related solids. *Chem Soc Rev* 2017;46:3104–7. doi:10.1039/C7CS90049J.
- [7] Metal-Organic Frameworks special issue. *Chem Rev* 2012;112:673–1268.
- [8] Jorge M, Fischer M, Gomes JRB, Siquet C, Santos JC, Rodrigues AE. Accurate Model for Predicting Adsorption of Olefins and Paraffins on MOFs with Open Metal Sites. *Ind Eng Chem Res* 2014;53:15475–87. doi:10.1021/ie500310c.
- [9] Fischer M, Gomes JRB, Jorge M. Computational approaches to study adsorption in MOFs with unsaturated metal sites. *Mol Simul* 2014;40:537–56. doi:10.1080/08927022.2013.829228.
- [10] Campbell C, Gomes JRB, Fischer M, Jorge M. New Model for Predicting Adsorption of Polar Molecules in Metal–Organic Frameworks with Unsaturated Metal Sites. *J Phys Chem Lett* 2018;9:3544–53. doi:10.1021/acs.jpcclett.8b00967.
- [11] Bloch ED, Queen WL, Krishna R, Zdrozny JM, Brown CM, Long JR. Hydrocarbon separations in a metal-organic framework with open iron(II) coordination sites. *Science* 2012;335:1606–10. doi:10.1126/science.1217544.
- [12] Pires J, Pinto ML, Saini V. Ethane Selective IRMOF-8 and its Significance in Ethane–Ethylene Separation by Adsorption. *ACS Appl Mater Interfaces* 2014;6:12093–9. doi:10.1021/am502686g.
- [13] Pillai RS, Pinto ML, Pires J, Jorge M, Gomes JRB. Understanding Gas Adsorption Selectivity in IRMOF-8 Using Molecular Simulation. *ACS Appl Mater Interfaces* 2015;7:624–37. doi:10.1021/am506793b.
- [14] Pires J, Fernandes J, Dedecker K, Gomes JRB, Pérez-Sánchez G, Nouar F, et al. Enhancement of Ethane Selectivity in Ethane–Ethylene Mixtures by Perfluoro Groups in Zr-Based Metal–Organic Frameworks. *ACS Appl Mater Interfaces* 2019;11:27410–21. doi:10.1021/acsami.9b07115.
- [15] Orefuwa SA, Yang H, Goudy AJ. Rapid solvothermal synthesis of an isoreticular metal–organic framework with permanent porosity for hydrogen storage. *Microporous Mesoporous Mater* 2012;153:88–93. doi:10.1016/j.micromeso.2011.12.036.
- [16] Pinto ML, Pires J, Rocha J. Porous Materials Prepared from Clays for the Upgrade of Landfill Gas. *J Phys Chem C* 2008;112:14394–402. doi:10.1021/jp803015d.
- [17] Pires J, Saini VK, Pinto ML. Studies on Selective Adsorption of Biogas Components on Pillared Clays: Approach for Biogas Improvement. *Environ Sci Technol* 2008;42:8727–32. doi:10.1021/es8014666.

MULTISCALE DESIGN OF A PRESSURE SWING ADSORPTION PROCESS FOR NATURAL GAS PURIFICATION

I. C. C. Quaranta^a, L. S. Pinheiro^a, D. V. Gonçalves^a, H. R. Peixoto^a, S. M. P. Lucena^{a*}

^a Grupo de Pesquisa em Separações por Adsorção – GPSA, Departamento de Engenharia Química, Universidade Federal do Ceará, Campus do Pici, Bl. 709,60455-760 Fortaleza, CE, Brazil

Abstract

Adsorption processes with activated carbons can be used to remove hydrocarbons with carbon chain longer than ethane from a natural gas flow, specially, considering a Pressure Swing Adsorption. To analyze this process, a simulation in Aspen Adsorption® was made. The adsorption isotherms for the involved components were obtained from molecular simulation, using a nitrogen isotherm at 77 K, for three different carbons: WV-1050, Norit R1 e Maxsorb. The geometry of the bed was set to suit the minimum fluidization velocity, with a L/D ratio of 5. The process considers adsorption at 15 bar and regeneration at ambient pressure. The times from each step was obtained from the breakthrough curves and a sensitivity analysis from the process. Adsorbents performance in the bed were evaluated with three indicators: productivity, purity and recovery of the product. The preliminary design of a PSA unit indicated that the carbon Maxsorb was the best choice with high productivity and recovery, also higher product purity.

Keywords: PSA; Natural Gas; Skarstrom; Aspen; Activated Carbon;

1. Introduction

Technology associated to natural gas (NG) for vehicular use has been object of study for several researchers. Despite being a non-renewable fuel, NG has a great amount of reserves, which suggest a better global supply. Also, it has a clean combustion, being able to burn in ways to minimize oxides as CO, NO_x e SO_x [1]. Along these lines, its usage as an alternative for gasoline and diesel, for example, has great economic and environmental significance. Moreover, it has favorable characteristics such as great energetic potential and a relatively low cost [2]. Although, its utilization as vehicular fuel is limited by the required geometry for its transportation [3].

Compressed Natural Gas (CNG) is stored under high pressures, circa 20 MPa, for transportation and operation, mainly due its low volumetric energy density under ambient temperature conditions. [2,3]. Therefore, it must be carried by vessels with set geometry and weight, leading to high storage costs.

Storage pressure can be easily reduced by adsorption in a porous medium [2,4]. Adsorbed

Natural Gas (ANG) allows the internal pressure to be reduced to 3,5 to 4 MPa, providing lower vessel construction costs and higher safety. [2,5]. However, this technology is limited by adsorbent deactivation along the operation cycles [5].

Deactivation of the adsorbent is a consequence of the composition of the NG, which causes an accumulation of heavier hydrocarbons, with carbon chains longer than ethane, that are not removed during desorption [4]. After several charge and discharge cycles, less sites are available for light fractions to be adsorbed, as the pores are loaded with heavier components that did not desorb during regeneration [5]. Guard-beds in the storage tanks has been proposed as a possible solution, however we argue that the removal of heavier hydrocarbon fractions in the NG processing unit, before storing CNG, is a better solution.

A clean CNG composition could be reached through a better specification of traditional NG processing methods, as refrigerated lean oil absorption and cryogenic expander process, or with adsorption, using, for example Pressure Swing Adsorption (PSA) [6,7]. The PSA advantage is that

it can operate as a polishing unit, processing a percentage of all NG produced, with strict specifications for very low C3 and C4 concentrations, for a fraction of the cost of reparameterize a whole traditional unit.

As a first evaluation of the idea, a PSA process was numerically designed to obtain the desired ANG composition. Molecular simulation was incorporate in the methodology to generate monocomponent isotherms of each carbon species eliminating costly laboratory tests.

2. Models and Methods

Processed Natural Gas is distributed in a standardized composition, with essentially methane. It also contains fractions of ethane, propane, butane and minor amounts of higher hydrocarbon chains, besides N₂ and CO₂.

Therefore, the composition of the gas can be reduced to its main components, such as methane, ethane, propane and butane, being fed as showed in Table 1.

Table 1. Natural gas feed composition.

Component	Molar Fraction
Methane	0.884
Ethane	0.1
Propane	0.009
Butane	0.007

Simulations were performed using the commercial software Aspen Adsorption, considering Skarstrom cycle for PSA operation.

2.1. Skarstrom Cycle

The process consists of two identical beds operating in opposite stages in a 4 steps cycle. Each stage is ruled by opening or closing valves, in order starting with (i) pressurization, (ii) adsorption, (iii) countercurrent blowdown and (iv) countercurrent purge. Steps (i) and (iii) are simultaneous in opposite beds, as well steps (ii) and (iv).

Pressurization is performed with the feed flow and a fraction of the product obtained is used in purge step [7].

2.2. Design Step

The first step to design a PSA is to set a geometry. In other words, to obtain the length (L) and the diameter (D) of the bed. Initially, from feed flow

rate, the diameter is calculated for a surface velocity. With the calculated diameter value, length size is calculated by a ratio L/D of 5.

Three types of activated carbons were evaluated for the process, being studied WV 1050, Maxsorb and Norit.

Breakthrough curves for each material were simulated at 15 bar. Through these simulations, a first estimate for the operational process of PSA for each adsorbent was obtained.

Times of adsorption step, and consequently purge, were defined as smaller than the breakthrough for the main adsorbed component, represented by propane and butane in this work. Pressurization and blowdown were selected with a sensitivity analysis of process performance.

2.3. PSA Modeling

In the development of the model, the following simplifications were adopted:

- Ideal gas phase through the column.
- Vertically oriented bed
- Negligible thermal effects
- Plug flow with negligible axial dispersion
- Pressure drop in the bed modeled with Ergun equation
- Instantaneous mass transfer
- No chemical reaction

Isothermal process was considered to simplify the proposed model, aiming to obtain a quick solution to determine an operational profile.

2.3.1. Mass Balance for the gas phase

Mass balance represented by Equation 1 considers convection, gas phase accumulation and mass transfer rate to solid surface.

$$\frac{\partial(v_g c_i)}{\partial z} + \epsilon_T \cdot \frac{\partial c_i}{\partial t} + \rho_B \cdot \frac{\partial w_i}{\partial t} = 0 \quad (1)$$

In which, v_g (m s⁻¹) is the superficial velocity of the gas phase, z and t are axial and time coordinates, ρ_B (kg m⁻³) is the bulk adsorbent density, w_i (kmol kg⁻¹) is the adsorb mass of component i and c_i (kmol m⁻³) is the molar concentration of i component in the fluid phase. It is noteworthy that $\epsilon_T = \epsilon_B + \epsilon_P(1 - \epsilon_B)$, where ϵ_P is the porosity of the adsorbent particle and ϵ_B is the bed void fraction.

2.3.2. Momentum Balance

Momentum balance is described using Ergun equation [8], given by equation 3, being applied to laminar and turbulent flow.

$$\frac{\partial P}{\partial z} = - \left(\frac{1,5 \cdot 10^{-3} (1 - \epsilon_B)^2}{(2 r_p \psi)^2 \epsilon_B^3} \mu v_g + 1,75 \cdot 10^{-5} M \rho_g \frac{(1 - \epsilon_B)}{2 r_p \psi \epsilon_B^3} v_g^2 \right) \quad (3)$$

P (bar) is the pressure thought axial axis, r_p (m) is the radius and ψ the sphericity of the particle, M is the molar mass of the gas mixture and ρ_g (kmol m^{-3}) is gas phase molar density.

Considering ideal behavior for the gas phase, ideal gas law can be applied. R is the universal ideal gas constant (bar m^3 kmol $^{-1}$ K $^{-1}$) and T_g the gas phase temperature.

$$P = R T_g \rho_g \quad (4)$$

2.3.3. Multicomponent Adsorption Equilibrium

Adsorption equilibria was chosen in order to consider the competitiveness between the molecules for the adsorption sites available for of the adsorbates. Extended Multicomponent Langmuir Isotherm was used considering the negligible effects from the temperature variations in the absorbed mass [9].

The model also adjusts the parameters ($IP_{1,i}$ e $IP_{2,j}$) using mono-component isotherms, as well as considering the partial pressure of each species (P_i e P_j) and not its concentration.

$$w_i^* = \frac{IP_{1,i} P_i}{1 + \sum_j (IP_{2,j} P_j)} \quad (4)$$

2.4. Resolution Method

Aspen Adsorption uses a set of differential and algebraic equations to describe adsorption process. Additionally, it considers initial values and boundary conditions. Therefore, an adequate mathematical method needs to be chosen for this type of solution.

Among the available methods in the software, *Upwind Differencing Scheme 1* (UDS1) was used. It establishes as a first order Taylor expansion with 100 nodes. It provides a reduced calculation time, a more stable solution and an acceptable precision for similar simulations [10,11].

3. Results and Discussion

3.1. Adsorption Equilibrium

Equilibrium data for the adsorption of the main components of natural gas was calculated through molecular simulation. Experimental nitrogen isotherms at 77 K were used for each adsorbent. The adopted methodology is described in another paper from our research group [12]. Table 2 shows the tuning parameters of the equilibrium data for Langmuir equation of each component in every activated carbon at 298 K.

Table 2. Equilibrium parameters (Langmuir).

Component	IP_1 (kmol kg $^{-1}$ bar $^{-1}$)	IP_2 (bar $^{-1}$)
WV-1050		
C1	0.00367	0.02481
C2	0.00228	0.22741
C3	0.00876	0.98746
C4	0.05537	8.72597
NORIT R1		
C1	0.00051	0.02481
C2	0.00228	0.80297
C3	0.03736	7.21752
C4	1.05482	323.668
MAXSORB		
C1	0.00066	0.02986
C2	0.00428	0.26601
C3	0.01581	1.03801
C4	0.10182	9.18025

3.2. Bed specifications

Feed flow rate is 300 Nm 3 /h, therefore, for the superficial velocity be of 80% of the minimum fluidization velocity, the column diameter is 0.42 m. Accordingly, the length of the bed is 2.1 m.

Table 3. Properties of the adsorbents.

Parameter	Value		
	WV-1050	NORIT R1	MAXSORB
ϵ_p	0.731	0.592	0.798
ϵ_B	0.4	0.4	0.4
ρ_b (kg m $^{-3}$)	385	583	289
r_p (m)	4.0E-4	4.0E-4	4.0E-4

Table 3 gives the properties of the bed for each adsorbent. The calculations were done considering

same bed porosity and same particle radius (r_p) for all three materials. The porosity of the particle and the bed and the density of the bed were estimated from specific volumes calculated from molecular simulation [12].

3.3. Breakthrough curves

Breakthrough curves were obtained for the previously described conditions, 298 K and 15 bar (Figure 1). Comparing all three materials, it is expected that NORIT R1 can provide a better separation of the light from the heavy components.

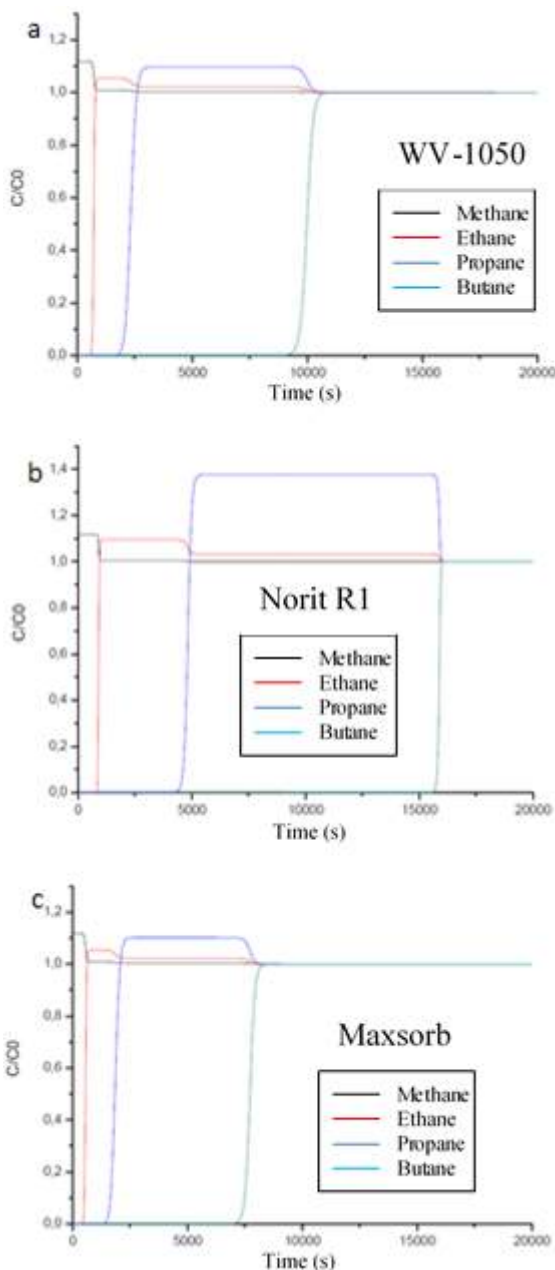


Fig. 1. Breakthrough curves at 298 K and 15 bar.

WV-1050 and MAXSORB shows similar behavior, although, as the first has a lower density, the column takes longer to saturate

3.4. PSA design and performance

PSA process run between two pressure levels. High pressure is at 15 bar, and the low pressure (of regeneration) was chosen as 1 bar. Figure 2 shows pressure history for one analyzed cycle of the activated carbon NORIT R1. Different total cycle times were tested. Best results were obtained at 1500 seconds. Longer times, overall, contaminate feed product with heavy hydrocarbons, which is not interesting. Shorter times, on the other hand, generally, show low productivity.

To analyze the times for each step, a sensitivity analysis was performed, shifting the time ratio of pressurization and adsorption between 0.05 and 0.20. The superficial velocity of the gas phase was not taken in consideration during pressurization and depressurization steps.

Table 4 brings the parametric analysis performed. Product purity, recovery and productivity (methane + ethane) were calculated. Only MAXSORB was able to remove all heavy hydrocarbons, providing a 100% pure product. Time ratio of 0.05 maximizes productivity ($78.4 \text{ mol kg}^{-1}\text{h}^{-1}$) and recovery (71.8%) of the product for this adsorbent, being the most viable operational condition.

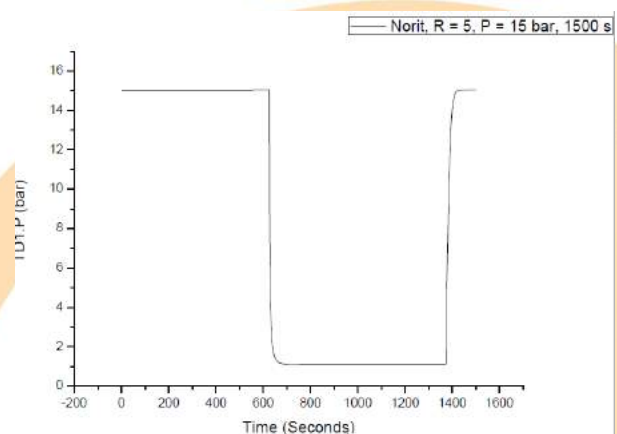


Fig. 2. Pressure history of a Skarstrom cycle.

It is worth to mention that the adsorbent NORIT R1 provides the best recovery rates, but, as a result of its high density, it shows a lower productivity.

Table 4. Parametric analysis of a PSA performance

$t_{\text{ads}}/t_{\text{press}} = 0.20$	Pur. (%)	Rec. (%)	Prod. ($\text{mol kg}^{-1} \text{h}^{-1}$)
WV- 1050	99.99	72.8	51.7

	Pur. (%)	Rec. (%)	Prod. (mol kg ⁻¹ h ⁻¹)
NORIT R1	99.88	76.5	34.8
MAXSORB	100.0	69.6	68.34
$t_{ads}/t_{press} = 0.15$			
WV- 1050	99.99	73.4	53.9
NORIT R1	99.84	77.4	36.2
MAXSORB	100.0	70.4	71.2
$t_{ads}/t_{press} = 0.10$			
WV- 1050	99.99	74.1	56.5
NORIT R1	99.8	78.3	37.96
MAXSORB	100	71.1	74.6
$t_{ads}/t_{press} = 0.05$			
WV- 1050	99.99	74.8	59.4
NORIT R1	99.74	79.4	39.98
MAXSORB	100	71.8	78.4

- [5] Rios BR, Bastos-Neto M, Amora Jr MR, Torres EB, Azevedo DCS, Cavalcante Jr CL. Experimental analysis of the efficiency on charge/discharge cycles in natural gas storage by adsorption. *Fuel Adsorption* 2010;90:113–119.
- [6] Sircar S. Basic Research Needs for Design of Adsorptive Gas Separation Processes. *Ind. Eng. Chem.* 2006;45:5435–5448.
- [7] Ruthven DM, Farooq S, Knaebel KS. *Pressure Swing Adsorption*. New York: VCH-Wiley; 1994.
- [8] Bird RB, Stewart WE, Lightfoot EN. *Transport Phenomena*. New York: Wiley International; 2006.
- [9] Ruthven DM, *Principles of Adsorption and Adsorption Processes*. New York: Wiley-Interscience; 1984.
- [10] ASPEN ADSIM. *Adsorption Reference Guide 2004.1* Cambridge: Aspen Technology, 2005.
- [11] Peixoto HR. Modelagem da separação de CO₂ em processos de pós-combustão por PSA. Ms Dissertation – Federal University of Ceará, Brazil 2015.
- [12] Lucena, S. M. P.; Gomes, V. A. Gomes, Gonçalves, D. V., Mileo, P. G. M.; Silvino, P. F. G., *Carbon*, 2013, **61**, 624-632.

4. Conclusion

From atomistic calculations, using as experimental data only the nitrogen isotherm at 77 K, it was possible to generate monocomponent isotherms and used then to design a PSA unit for deep natural gas purification, selecting the ideal carbon adsorbent among an unlimited number of samples. A preliminary design and optimization of a PSA unit indicated that the carbon Maxsorb is the best choice with high productivity (78.4 mol kg⁻¹h⁻¹) and recovery (71.8%). We hope that this methodology can help enable ANG technology.

Acknowledgements

The authors thank financial support provided by PETROBRAS/CAPES.

References

- [1] Bastos-Neto M, Torres AEB, Azevedo DCS, Cavalcante Jr CL. A theoretical and experimental study of charge and discharge cycles in a storage vessel for adsorbed natural gas. *Adsorption* 2005;11:147–57.
- [2] Talu O. An Overview of Adsorptive Storage of Natural Gas. *Studies in Surface Science and Catalysis* 1993;80:655-662.
- [3] Menon VC, Komarneni S. Porous adsorbents for vehicular natural gas storage: a review. *J Porous Mater* 1998;5:43–58.
- [4] Mota JPB. Impact of Gas Composition on Natural Gas Storage by Adsorption. *AIChE Journal* 1999;45:986-996.

Optimization of Temperature Swing Adsorption Unit for Gas Dehydration

Felipe Braun^b, Yuri Paiva^a, Caio Marcellos^a, Argimiro Secchi^c, Amaro G. Barreto Jr.^{a*}

^aDepartment of Chemical Engineering, Centre of Technology, Federal University of Rio de Janeiro, 21941-909, RJ, Brazil

^bPetróleo Brasileiro S.A. (Petrobras), Rio de Janeiro, 21941-909, RJ, Brazil

^cDepartment of Chemical Engineering, Centre of Technology, COPPE - Federal University of Rio de Janeiro, 21941-914, RJ, Brazil

Abstract

The optimization of Temperature Swing Adsorption for gas dehydration in solid bed is addressed. The proposed optimization has comprised two approaches, the first based on empirical design rules established by practice over the years and synthesized in 'Gas Conditioning and Processing' by Campbell (2004). This methodology, focused on conceptual designs, was adapted to optimization, resulting in inequality equations or constraints. The results from this first approach were used as input for a second one, more accurate, based on phenomenological simulation. Part of the constraints used in the first approach was replaced by differential equations that represent mass balance, energy, adsorbent capture rate, etc. The objective of this work was to propose the lowest cost design of a unit present in an oil platform. With this purpose, an objective function was proposed based on CAPEX and OPEX. The optimization problem was implemented in Matlab software, applying the finite difference method to discretize the spatial domain of the partial differential equations. The comparative analysis between the two approaches pointed to more process understanding and gain in accuracy when carrying out the project through the use of phenomenological modeling and optimization.

Keywords: optimization; adsorption; temperature swing adsorption; simulation; zeolite.

1. Introduction

Dehydration of natural gas is an essential process in the treatment of gas produced in stationary production units, as the presence of water in gas can lead to problems such as hydrate formation or corrosion, especially in the presence of contaminants such as CO₂ and H₂S. In certain situations such as production fields with high gas flow, this unit has a high cost, high thermal demand, high operating expense, among other difficulties.

Among the available dehydration techniques, solid bed adsorption has been widely employed due to its high contaminant retention capacity, removing virtually all water present in the gas. In this process, the component to be separated migrates from a fluid to the surface of a solid (adsorbent). At the end of the process, the fluid has its water content reduced or even eliminated, while the adsorbent solid becomes rich in water on its surface and must be regenerated to be used again in the adsorption step. Therefore, the dehydration process has a continuous cyclic operation, so that at least two vessels in parallel must be used for a

continuous operation, alternating between the adsorption and regeneration steps.

Suitable mathematical models are required to predict the performance of an adsorption separation. With an appropriate model, it is possible to act on the optimization of sizing and operation [1]. A complete mathematical model capable of describing the dynamic behavior of a fixed bed adsorption system is based on a set of partial algebraic-differential equations, which represent conservation of mass, energy and momentum, as well as transport rate equations and equilibrium isotherms [2].

In this work, we studied the optimization of TSA (Temperature Swing Adsorption) dehydration units considering installation (CAPEX) and operation cost (OPEX). We have compared a heuristic based approach of Campbell (2004)[3] with the optimization using prediction from the theoretical model with the partial differential equations of conservation. The adsorption and regeneration steps compete with each other in the optimization process, so reducing the cost of one can lead to increased cost of the other.

2. Methodology

Choosing the optimal operating conditions of a system is a complex optimization problem because the effect of all process variables (cycle time, bed length, adsorption and desorption temperatures, purge gas velocity) are coupled,[4] and also causes indirect impacts on other units of the platform. The main parameters to be determined are: configuration (number of adsorbing and desorbing beds), adsorption time, regeneration time for bed heating (desorption), regeneration time for bed cooling (preparation for adsorption), diameter of vessels, bed height, percentage of treated gas destined for the regeneration step, waiting time (intended for adsorption preparation, valve maneuvers and operational intervention), regeneration gas temperature, choice of adsorbent solid and particle size, for instance.

The bed volume determines a maximum adsorption time, which can be extracted from the rupture curve. From that instant, the treated gas would leave the product specification. Although bed volume is the main determinant of maximum adsorption time, other factors are also relevant, such as the gas flow in a bed, determined by the number of beds, the percentage of treated gas destined for regeneration, etc.

All of these factors together determine a maximum adsorption time. The adsorption time (design variable) should be less than the calculated maximum, preferably close, so as not to waste unused part of the bed. Similarly, the bed volume in conjunction with the other system parameters determines a minimum desorption time for water to be properly removed from the bed. That is, the time required for bed heating should be sufficient to regenerate. This time can be extracted from the breaking curves. Likewise, the time spent on cooling the regenerating bed should be sufficient to cool the bed properly.

The three time constraints mentioned above must be met, one of maximum time and two of minimum time. Determining the adsorption time also determines the regeneration time due to constraint imposed by the cyclic operation to result in a global continuous unit [5].

We used the flexible polyhedra optimization method developed by Nelder and Mead (1965)[6], which was applied in two models, the first based on empirical design rules established by operational practice and synthesized in Campbell (2004) and the second in rigorous phenomenological modeling. Campbell (2004) has been adapted to optimization, resulting in design inequalities or constraints. An objective function

was proposed based on CAPEX and OPEX, using the methods described in the textbook of Seider (2003)[7] and Towler and Sinnott (2013)[8].

The finite difference method was used to solve the numerical problem. All equations were entered in the Matlab program. The results of optimization with the empirical model served as input to the optimization with the phenomenological model. Part of the criteria used in the first optimization were replaced by differential equations that represent the balance of mass, energy, adsorbent capture rate, etc.

Optimization involves two types of variables: fixed variables (such as temperature, inlet gas water content, etc.), which should have their values determined before starting the project, and free variables (such as bed diameter and height, number of vessels, etc.), which should be adjusted to generate the lowest cost or highest return, meeting all design constraints. The free variables are depicted in Table 2.

Table 2. Free variables in the optimization.

Description	Variable
Number of beds adsorbing	x1
Adsorption time	x2
% for regeneration	x3
Internal diameter	x4
Bed height	x5
% of regeneration time for heating	x6
Stand-by time	x7
Regeneration temperature	x8

The empirical model does not represent the adsorption phenomenon accurately, as it is based on average adsorbent and gas properties. On the other hand, this sizing approach has yielded reliable and consistent results with sizing made by manufacturers, provided its simplicity and the addition of rule of thumbs from engineering experience.

The phenomenological mathematical model used to describe the adsorption dynamics considers a favorable nonlinear adsorption isotherm with high affinity for water vapor adsorption, axial plug flow and the approximate global mass transfer rate by Linear Driving Force (LDF), suitable for the optimization problem and sufficiently accurate for project proposals. Mass and energy balance were incorporated into the equation. The model representation takes into account the following assumptions: an adiabatic vessel, negligible radial dispersion, negligible changes in fluid velocity, homogeneous adsorbent particles in size, density and fractional spherical constant voids. The design

constraints for the empirical model and for the phenomenological model are depicted in Appendix A.

CAPEX computation approaches were compared [7]–[9]. It was concluded that SEIDER et al. (2003) presented relative results closer to the average, except for the column cost. We chose to follow the methodologies employed in Seider et al. (2003), but with column acquisition cost calculated by Towler and Sinnott (2013).

Total capital investment can be calculated as (SEIDER et al., 2003):

$$C_{TI} = 1,18 (C_{TBM} + C_{site} + C_{buildings} + C_{offsite}) \quad (1)$$

where C_{TI} is the total investment cost, C_{TBM} is the sum of all bare module cost, which represents the total cost of purchase, materials, personnel, and all indirect costs involved in installing an equipment; C_{site} , $C_{buildings}$ and $C_{offsite}$ are costs related to installation and auxiliary requirements. The total cost of a dehydration unit installed on an oil rig can be estimated by summing the CAPEX cost with the OPEX, which is a summation of adsorbent replacement and utilities. The final value of the obtained cost is not accurate, since it is based on preliminary studies, however the comparison of cost between configurations is a good approach for process optimization [8].

3. Results and Discussions

The assumptions and recommendations of Campbell (2004) were strictly following in a preliminary test. However, based on operational parameters and better optimal solution, the solid adsorption capacity was adjusted to 0.14 kg H₂O/kg adsorbent and we relaxed the length to diameter recommendation to values between 1.5 and 6.0, the result can be seen in Table 3.

Note that the configurations with 2, 3 and 4 beds presented slightly similar results. From an engineering point of view, the results do not differ significantly, presenting theoretical coherence. From a sensibility evaluation, we noted that the characteristics of the adsorbent has a strong influence on the result, favoring either solution depending on the parameter that was changed. It is also possible to conclude that an adsorbent with superior properties and internal vessel insulation generates a large cost reduction compared to a lower adsorbent with the same cost and uninsulated vessel.

Table 3.

VARIABLE	Optimal		
Number of beds adsorbing	2	3	4
Adsorption time [h]	8.6	7.5	8.7
% for regeneration	8.2	10.7	12
Internal diameter [m]	2.61	2.16	1.88
Bed height [m]	3.47	2.9	3.34
% of regeneration time for heating	69.6	70	70
Standby[h]	1	1	1
Objective function [10 ⁶ U\$S]	59.7	55.8	57.7

The optimization using the phenomenological model also considered the desorption temperature, being limited to a range of 220 and 340 °C. The results when using the phenomenological model is presented in Table 4. For single bed configuration, the constraint related to the pressured drop by bed length is a limiting factor, which causes a higher regeneration flow rate. A further consequence is that the single bed configuration is the only with regeneration temperature smaller than the maximum constraint due to the elevated regeneration flow-rate.

For the multi-bed configurations, Table 4 shows a tendency of increasing the percentage of gas for regeneration when the number of bed is increased. Additionally, the 3 and 4 bed configuration were not constrained by the minimal bed size, which is obtained from the maximum pressure drop by bed length constrain. For 3 beds the minimal bed length is 2.86 m and for 4 beds is 2.61 m. Higher bed lengths results in increased maximum adsorption time constraint, but also causes a increase in the minimum regeneration time constraint.

A further inspection of the results of the 3 and 4 bed configuration was made to verify if the minimum is in the direction of the obtained answers. The size of the bed was fixed 1 m higher and then reduced by 1 m in height. The results are presented in Table 5. The alternative with 3 m of bed height, close to the minimum (2.86m) actually presented higher cost, as the alternative with 5m of bed. With less percentage gas intended for regeneration, the diameter can be slightly reduced as the total flow rate is slightly smaller. In the case of the 3-bed configuration, the reduction of the bed to the minimum imposed by restrictions and the consequent reduction of the adsorption time as well as the time available for regeneration (causing

Table 4. Comparison of optimal solution using the phenomenological model.

VARIABLE	Optimal			
Number of beds adsorbing	1	2	3	4
Adsorption time [h]	5.8	5.2	6.1	7.9
% for regeneration	12.0	8.7	11.4	12.2
Internal diameter [m]	3.76	2.63	2.19	2.0
Bed height [m]	4.91	3.44	4.00	4.51
% of regeneration time for heating	70.0	67.9	68.9	70.0
Regeneration temperature [°C]	300	340	340	340
Objective function [10 ⁶ US\$]	94.5	60.5	63.7	68.6

Table 5. Optimization results for phenomenological model varying the bed length by 1 m.

Beds Number	Tads [h]	Gas for reg.[%]	Diameter [m]	height[m]	% treg for heat	Temp. Reg. [°C]	Obj. Function [10 ⁶ US\$]
3	6,1	11,4	2,19	4	68,9	340	63,7
3	7,7	9,1	2,16	5	68,5	340	65,4
3	4,9	18,5	2,24	3	73	340	69,4
4	7,85	12,3	2	4,51	70	340	68,65
4	9,69	9,3	2	5,51	68	340	69,5
4	5,98	22,8	2	3,51	73	340	76,15

Table 6. Optimal solutions for the phenomenological approach with 1/8 particle diameter.

Beds Number	Tads [h]	Gas for reg.[%]	Diameter [m]	height[m]	% treg for heat	Temp. Reg. [°C]	Obj. Function [10 ⁶ US\$]
2	4,9	9,9	2,33	4,5	70	340	61
2	4,8	10,7	2,5	3,9	70	340	64
3	6,2	11,8	1,93	5,5	70	340	64,2
3	6,2	11,5	2,2	4,2	70,3	340	66
3	5,4	15,2	2,2	3,7	72,5	340	68,5

an increase in the percentage of gas for regeneration) was no longer advantageous than the opposite way, increased height. The same effect is observed for 4 beds.

As the pressure drop by length was a relevant factor, it is necessary to verify the particle influence, which in the previous results was spherical of 1/16 in. Both extruded and spherical 1/8 in particles are also common. The 1/16 in extruded particle has the largest drop in length and the smallest in spherical 1/8. Particles with greater pressure drop by length imply increased bed diameter. For this reason, it is interesting to test the option for 2, 3 and 4 bed configurations with 1/8 spherical particles.

The results can be seen in Table 6, which presents the optimal result for 2 and 3 beds, as well as an alternative solution. Note that, although the bed diameter has decreased compared to the 1/16 case, the total cost are close to and slightly higher than the optimal values obtained with the spherical 1/16 particle (Table 4). For 2 beds, unlike the 1/16 in particle, the bed was not restricted to the “minimum bed”, indicating difficulties in the

regeneration stage. That is, the cost reduction due to the diameter reduction was offset by the greater difficulty of regeneration. Particle diameter has a great influence on mass and energy transfer phenomena. It is also noted that the percentage destined for regeneration also increased, again indicating the greater difficulty of regeneration.

The alternative solution presented in Table 6 explore solutions considering a similar bed volume, but with a slightly larger diameter and slightly smaller height, which generated higher costs, showing that the optimal is at the minimum diameter.

4. Conclusion

It is not possible to compare exactly the results of the optimization with the empirical model with the phenomenological model, because the empirical model starts from an average adsorption capacity while in the phenomenological model this capacity is variable. When approaching the empirical and phenomenological models and solid properties were verified an approximation of the

results. However, only the phenomenological model can accurately predict the results and is recommended for basic projects. It should also be emphasized that the suitability of a unit to a specific solid should only be done with the phenomenological model, since only in the phenomenological model are the intrinsic characteristics of the product explored, which can have a great influence on the dimensioning, as for example, the micropore diffusion resistance, given by the micropore diffusivity and its radius. It should also be noted that the phenomenological model can be used for operational monitoring, with data adjusted for each unit.

Optimization with the phenomenological model tended to adopt more “severe” conditions, such as maximizing regeneration temperature, loss of load per length and adoption of fast cycles. However, the acceptable severity depends on how well the zeolite withstands such conditions. That is, the cost is strongly influenced by the product used. The challenge is to develop a solid that at the same time has high resistance to high gas flow and high temperatures, without losing life, without fragmentation or deterioration, with high mechanical resistance and especially with high capacity, i.e. high porosity, diffusivity and adsorption, and some of these characteristics of interest compete with each other, such as high porosity and high mechanical resistance.

The restrictions imposed have a great influence on the cost, and for each configuration adopted the limiting restrictions were different. Constraints need to be criticized when they have limiting factors, as some of them are practical and historical recommendations, and may not be relevant as processes/products evolve. For the base case studied, the configurations with 2/3 adsorbing and 1 regenerating bed were the ones that best fit the constraints, with the lowest cost. However, it is not possible to establish a general rule to be adopted, and each case must be optimized and analyzed individually.

Acknowledgements

CAPES, CNPQ and Petrobras.

References

[1] M. S. Shafeeyan, W. M. A. Wan Daud, and A. Shamiri, “A review of mathematical modeling of fixed-bed columns for carbon dioxide adsorption,” *Chem. Eng. Res. Des.*, vol. 92, no. 5, pp. 961–988, May 2014.

- [2] K. S. Hwang, J. H. Jun, and W. K. Lee, “Fixed-bed adsorption for bulk component system. Non-equilibrium, non-isothermal and non-adiabatic model,” *Chem. Eng. Sci.*, vol. 50, no. 5, pp. 813–825, Mar. 1995.
- [3] “Campbell, J. 1992 Gas Conditioning And Processing: The Basic Principles: Free Download, Borrow, and Streaming: Internet Archive.” [Online]. Available: <https://archive.org/details/CampbellJ.1992GasConditioningAndProcessingTheBasicPrinciples>. [Accessed: 27-Nov-2019].
- [4] D. M. Ruthven, *Principles of adsorption and adsorption processes*. John Wiley & Sons, 1984.
- [5] F. E. Braun, “Modelagem e otimização de projeto de unidades de desidratação de gás natural por adsorção,” p. 130.
- [6] J. A. Nelder and R. Mead, “A simplex method for function minimization,” *Comput. J.*, vol. 7, no. 4, pp. 308–313, 1965.
- [7] W. D. Seider, J. D. Seader, and D. R. Lewin, *PRODUCT & PROCESS DESIGN PRINCIPLES: SYNTHESIS, ANALYSIS AND EVALUATION*, (With CD). John Wiley & Sons, 2009.
- [8] G. Towler and R. Sinnott, *Chemical engineering design: principles, practice and economics of plant and process design*. Elsevier, 2012.
- [9] M. S. Peters, K. D. Timmerhaus, and R. E. W. E. Professor, *Plant Design and Economics for Chemical Engineers*, Edição: 5. New York: McGraw-Hill Education, 2002.

Appendix

Table A.1. Restrictions used in the optimization. For more details, see [5].

Restriction	
$\frac{L}{D} < 6,0$	$\frac{1,15x_5}{x_4} - 6,0$
$\frac{L}{D} > 1,5$	$1,5 - \frac{1,15x_5}{x_4}$
$\frac{\Delta P}{L} > 10$	$C_2 \frac{x_3}{x_1 x_4^2} + C_3 \left(\frac{x_3}{x_1 x_4^2} \right)^2 - 10$
$\frac{\Delta P}{L} > 5$	$5 - C_2 \frac{x_3}{x_1 x_4^2} - C_3 \left(\frac{x_3}{x_1 x_4^2} \right)^2$
$\frac{\Delta P_{min}}{L} > 0,23$	$0,23 - C_{25} \frac{x_3 - 1}{x_4^2} - C_{26} \left(\frac{x_3 - 1}{x_4^2} \right)^2$
$\frac{t_{ads}}{Bed\ s} - t_{standby} > 0$	$\frac{-x_2}{x_1} + x_7$
$V_{beds} > V_{ads, required}$	$-\pi \frac{x_4 x_5}{4} + C_4 \frac{x_2 x_3}{x_1}$
$Q_{req} > Q_{heat, required}$	$-100C_{18}(x_3 - 1) + \frac{C_{15} \frac{x_2 x_3}{x_1} + C_{16} x_5 x_4^2 + C_{17} x_4^3}{\frac{x_6}{100} \left(\frac{x_2}{x_1} - x_7 \right)}$
$Q_{req} > Q_{cool, required}$	$-100C_{18}(x_3 - 1) + \frac{C_{24} \frac{x_2 x_3}{x_1} + C_{22} x_5 x_4^2 + C_{23} x_4^3}{\frac{100 - x_6}{100} \left(\frac{x_2}{x_1} - x_7 \right)}$
Gas specification	$t_{ads} - t_{ads, max}$
Gas regeneration	$t_{reg, min} - t_{reg, heat}$

High-Pressure Bulk CO₂ Gas Adsorption on a Fixed Bed of Zeolite NaY: upward and downward flow comparison

Artur Lemes Moretti^a, Marcus Vinícius Pereira^a, Leonardo H. de Oliveira^a, Jaílton F. do Nascimento^b, Pedro Augusto Arroyo^{a*}

^a Laboratory of Adsorption and Ion Exchange, State University of Maringá, Colombo Avenue, 5.790, Maringá, 87020-900, Brazil

^b PETROBRAS/CENPES/PDDP/TPP, Fundação Island, Rio de Janeiro, Brazil

Abstract

Adsorption is an appealing technology for the removal of CO₂ in natural gas because it can handle high CO₂ concentration at high pressure. The determination of monocomponent breakthrough curves provides heat and mass transfer parameters that can be used to assess separation effectiveness in a real separation process. However, in lab-scale fixed-bed adsorption, it may be difficult to perform this assessment because low flow conditions are usually employed, affecting the flow regime, relying on the operation conditions. For this purpose, adsorption runs on a fixed bed of a binderless zeolite NaY were performed on a homemade high-pressure lab-scale apparatus. It was used beads of mean diameter of 0,7250 mm and a 10,5 cm high bed on a tubular column of 2,00 cm internal diameter. Upward and downward flow were conducted under 528.82± 4.59 NmL min⁻¹ initial mass flow rate, 51 bar and 30 °C. Residence time distribution (RTD) approach was performed to verify flow regime and mass transfer zone length (MTZ) were estimated. It was observed that downward flow conditions promote higher concentration spread than upward flow. RTD approach showed that downward flow is dominated by laminar convection while upward flow is dominated by dispersion. MTZ length increase from 0,64 cm in upward flow to 5,81 cm in downward flow. Therefore, assessing fluid density is an additional care that should be taken when dealing in lab-scale fixed-bed adsorption under high pressure because density changes can severely affect flow regime and, consequently, separation effectiveness assessment.

Keywords: Natural gas; CO₂ removal; Bulk gas adsorption; Flow direction; Residence time distribution.

1. Introduction

Natural gas consumption is increasing worldwide due to the low cost compared to other fuels and the increase in global gas availability [1]. However, in the Brazilian energy market, natural gas is not a fuel available at a competitive price, mainly due to high exploration costs [2].

Pre-salt polygon oil wells can contain up to 250 Nm³ of gas per m³ of oil and up to 40% (mol/mol) CO₂ [3]. However, commercial natural gas can contain up to 3% mol/mol of CO₂ [4]. Thus, the removal of this contaminant is essential.

Technologies that are available for CO₂ removal from natural gas are membrane separation and adsorption processes [5]. Adsorption is a mature technology for pre-combustion CO₂ capture [6] and emerging technology for natural gas purification [7].

PSA and TSA adsorption/desorption cycles are the technologies available for bulk gas separation [8].

The study of the separation process by adsorption is often performed through the analysis of breakthrough curves of mono and bicomponent gas adsorption [9]. The shape of this curve is vital in the design of adsorption beds and cyclic separation processes since it is related to the type of adsorption isotherm and the mass and heat transfer phenomena that occur along with the adsorption [10].

According to [11], the breakthrough curve would be a replica of the input, with a time delay, related to the retention time in the column when the following conditions are observed: favorable adsorption isotherm, no mass transfer resistance, no temperature variation, and plug flow. In practice, the response is always dispersive due to heat and mass transfer resistances and by axial and radial dispersion [12].

The flow regime in an adsorption fixed bed is usually assumed to be a plug flow or a dispersed plug flow [13]. These models are usually applied to predict the behavior of adsorption/desorption cycles, even though flow direction may change according to the step [7].

Bench-scale high-pressure adsorption setups operate under low flow regime. Although the dispersed plug flow model is used under these conditions, the agreement with experimental data becomes poor when pressure increases [14]. Thus, the correct assessment of the flow regime that is observed can help to provide realistic predictions of the fixed bed dynamics.

The residence time distribution (RTD) approach to nonideal flow is a tool that is extensively used in catalysis [15] and can provide a better understanding of the flow regime in packed beds, reactors, and more complex systems.

Therefore, the objective of this work is to apply the RTD approach to provide a better understanding of the flow regime configuration in the adsorption of CO₂ in a fixed bed of zeolite NaY at 51 bar and 30 °C under upward and downward flow conditions.

2. Materials and Methods

2.1. Adsorbent

The adsorbent used was NaY zeolite, kindly donated by PETROBRAS. The solid was previously pelletized, crushed, and sieved. Particles trapped between the 20-28 mesh sieves were collected, causing the mean particle diameter to be $d_p = 0.7250$ mm. The material was previously characterized in [16]

2.2. Fixed bed adsorption module

A homemade high-pressure gas adsorption module located at the Laboratory of Adsorption and Ion Exchange (LATI/UEM) was used. As shown in Figure 1, the module consists of a Teledyne ISCO® syringe pump (SP); an inlet needle valve (NV1); the adsorption bed, which consists of a 2.00 cm internal diameter stainless steel cylinder; a K-type 6 points thermocouple; an aluminum heat exchanger that allows heating by electrical resistance and heating/cooling by water flow; a thermostatic bath; two pressure transducers, one at the bed inlet and another at the bed outlet; an outlet needle valve (NV2); a six-way automatic Valco® valve (V8) and a vacuum pump (VP). This configuration allows for *in situ* thermal treatment with vacuum before or

after adsorption experiments. In addition, a MATLAB® based application has been developed for monitoring and acquisition of pressure and temperature data.

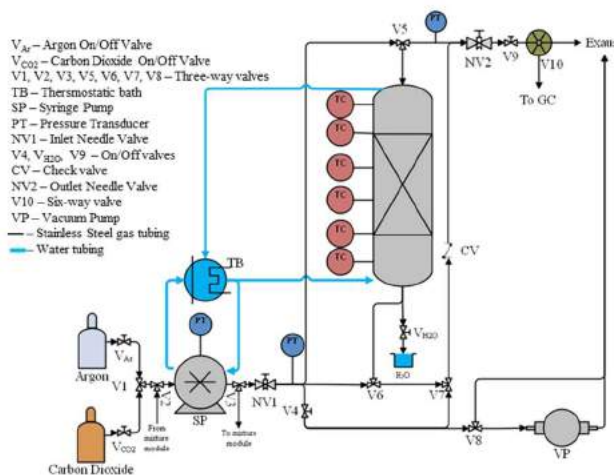


Figure 1 – Experimental high-pressure fixed bed adsorption setup located at LATI/UEM.

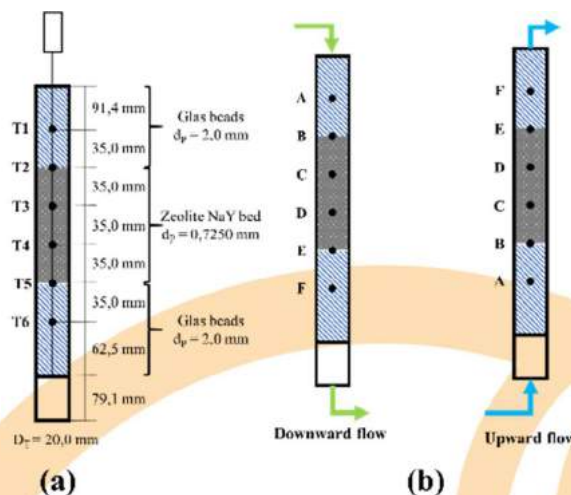


Figure 2 – Adsorption bed configuration and thermocouple positioning in (a). Thermocouple nomenclature in downward and upward flow in (b).

As shown in Figure 2a, NaY zeolite beads were placed between glass beads of mean diameter of 2.0 mm. Quartz wool was placed at the beginning and at the end of the bed. In total 15,8083 g of zeolite and 114,3719 g of glass beads were used. Both glass beads and quartz wool are assumed to have negligible adsorption capacity of CO₂. Therefore, all heat effects are caused by adsorption on the zeolite NaY.

Figure 2b shows thermocouple nomenclature for representation purposes. The change in nomenclature is important because temperature profiles can be compared at the same position relative to the bed inlet.

The experiments were conducted with the following steps: activation, inert pressurization, adsorption and reactivation steps, as described below.

Activation: This step began by the flowing of Argon (Messer, 99.999%) at atmospheric pressure with a flow rate of 50 ml / min, controlled by NV1. At the same time, the bed was heated to 300 °C with a heating ramp of 10 °C/min, removing adsorbed water. When temperature reached the desired value, vacuum was performed, and activation lasted for 6h at 300 °C. This step was performed just once, prior the first adsorption run.

Pressurization step: After activation, the bed was pressurized with Argon at 51 bara. The syringe pump was first loaded with Argon at this pressure and the NV1 valve was partially opened. Water heating was then turned on, allowing the bed to reach the adsorption temperature.

Adsorption step: In this step, the gas line before the adsorption bed was depressurized and cleaned with the adsorbate. The syringe pump was filled with CO₂ at 50 bar pressure and 30 °C and kept at constant pressure mode. The temperature was kept constant at the pump cylinder and at the fixed bed by the thermostatic bed. Upward adsorption experiments began by opening V6 and NV2 valves at the same time, while downward flow adsorption experiments began by opening V5 and NV2 at the same time. It is assumed that a step input at the bed inlet was obtained by this procedure.

Adsorbent reactivation step: Finally, the bed was depressurized by the opening of NV2 valve. When the pressure reached 1 bar, a vacuum was performed on the system and temperature was raised to 150 °C at 10°C/min for 60 minutes. This step was performed after every adsorption run.

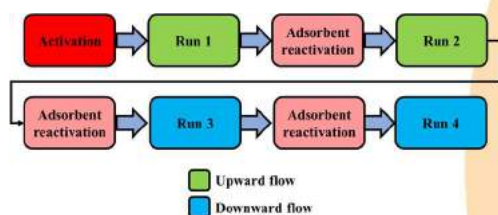


Figure 3 – Sequence of the experimental procedure.

Activation step took place before the first run, while the reactivation step took place between the following adsorption runs, as shown in Figure 3. Runs 1 and 2 were performed by an upward flow of CO₂, while downward flow was performed on runs 3 and 4. All experiments were conducted at 30 °C and 51 bara. The initial mass flow was measured by the syringe pump and was 528.82± 4.59 NmL min⁻¹.

2.3. Breakthrough curves determination

Breakthrough curves were determined by periodic injection of gas samples in a Shimadzu GC-2014 gas chromatogram (GC). The six-way valve was activated every 64 seconds, allowing enough time for proper peak separation. The sample loop was 100 μL in volume and were kept at 50 °C. A capillary SH-Rt®-Q_Bond column (30 m, 1/8 in x 20 μm) was kept at 50 °C. A Thermal Conductivity Detector (TCD) kept at 50 °C was utilized. CO₂ and Ar molar fraction were determined by the method described by [17]. Finally, CO₂ initial concentration, C₀, was then calculated through the Peng-Robinson equation of state [18].

2.4. Residence time distribution curves

Age distribution (E_{θ}) curves were obtained through Equation 1. These curves were then compared to the models presented in [15] to identify the proper flow model.

$$E_{\theta} = \frac{\int_0^t C dt}{C_0} \quad (1)$$

E_{θ} curves were plotted against nondimensional time, related to the mean retention time, as shown in the following equation.

$$\theta = \frac{t}{\bar{t}} \quad (2)$$

2.5. Mass transfer zone analysis

The length of the mass transfer zone (MTZ) was estimated through equations 3 to 5. The breakthrough time, t_b , was assumed to be the time where $y_{CO_2}=0,015$, while the saturation time, t_s , was assumed to be the time where $y_{CO_2} = 0,98$. H_T is the total length of adsorption bed, equal to 10,5 cm.

$$MTZ = \left(1 - \frac{t_u}{t_t}\right) H_T \quad (3)$$

$$t_u = \int_0^{t_b} \left(1 - \frac{C}{C_0}\right) dt \quad (4)$$

$$t_t = \int_0^{t_s} \left(1 - \frac{C}{C_0}\right) dt \quad (5)$$

3. Results and discussion

Figure 4 displays the breakthrough curves obtained. Downward flow spreading was much higher than upward flow. Upward flow breakthrough curves are almost a replica of a step input, indicating low mass transfer resistance, while downward flow breakthrough curves spread indicates a high mass transfer resistance process. However, when the age distribution curves are compared, E_θ curves for runs 1 and 2 have maximum values closer to $\theta = 1.0$ and present uniform distribution. This behavior is typical for flows dominated by effective diffusion [19]. Runs 3 and 4, on the other hand, have E_θ curves present the maximum closer to $\theta = 0.5$ and a long tail distribution curve. This behavior is common in flows dominated by laminar convection [15]. The change in behavior can be attributed to the density difference of the gas stream. Feeding heavier gas on the top promotes a parabolic concentration profile with maximum velocity at the center that is twice the mean velocity [20], explaining why first adsorbate fractions are observed at half the mean retention time.

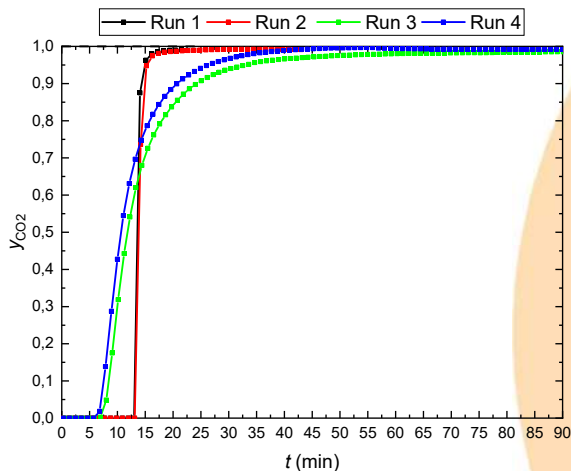


Figure 4 – Breakthrough curves for upward flow, runs 1 and 2, and for downward flow, runs 3 and 4.

Mass transfer zone lengths are shown in Table 1. Mass transfer zone estimation can be heavily affected by the change in the flow direction. Mean mass transfer length (MTZ_{mean}) for upward flow is about 10 times lower than downward MTZ_{mean} . The spread observed in downward flows could lead to a misinterpretation of the adsorption process. If no considerations in the flow regime are made, runs 1 and 2 could be attributed to a very efficient adsorption process with small mass transfer resistances, while runs 3 and 4 would be interpreted as an adsorption process that may need adjustments in operating conditions to improve the length of the used bed.

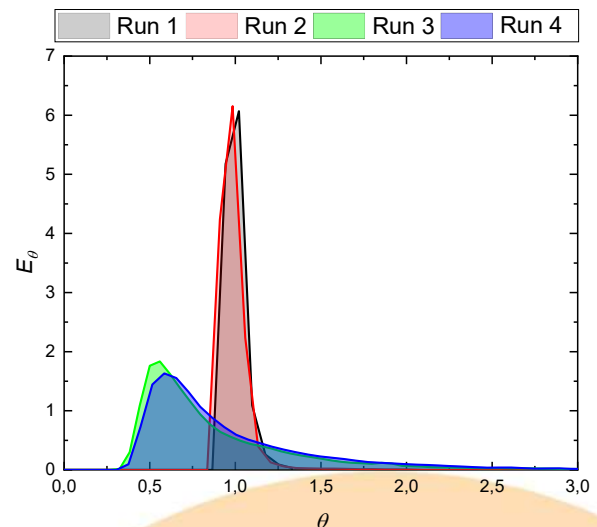


Figure 5 – Age distribution of fluid for upward flow, runs 1 and 2, and for downward flow, runs 3 and 4.

Table 1. Mass transfer zone length.

Run	Flow direction	MTZ (cm)	MTZ_{mean} (cm)
1	Upward	0,56	0,64
2		0,73	
3	Downward	5,94	5,81
4		5,67	

Heat effects also change when flow direction is changed. In Figure 4, temperature profiles from the multipoint thermocouple are aligned with the bed inlet. In both cases, temperature only starts to increase in the first thermocouple that is in contact with the adsorption bed. This means that: (i) the assumption of negligible heat effects in the glass beads are verified, and (ii) no appreciable heat transfer by conduction can be detected before bed

inlet. The thermal front travels along the bed with temperature maximum indicated in Table 1. Upward flow has (i) delayed and (ii) higher temperature maximum, when compared to downward flow. *E* curves analysis showed that downward flow is more dispersed than upward flow. The less dispersed concentration front has higher heat production in a more localized place, while the dispersed concentration front has dispersed heat generation along the adsorption bed.

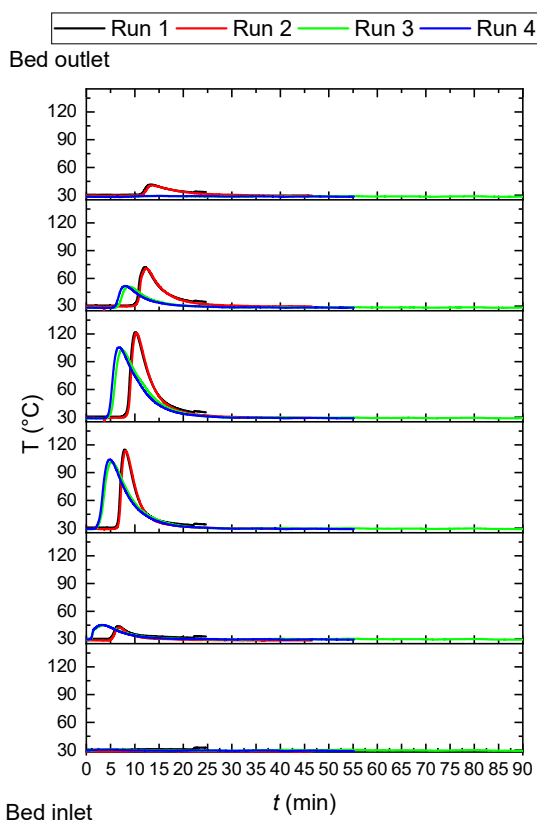


Figure 4 – Temperature profiles at the same position for upward flow, runs 1 and 2, and for downward flow, run 3 and 4.

4. Conclusions

Breakthrough curves of the adsorption of CO₂ on a fixed bed of zeolite NaY at 30 °C and 51 bar were measured under upward and downward flow conditions. The DTR analysis suggests that the downward flow presents typical characteristics of laminar convection dominated flow, while the upward flow presents a typical behavior of dispersion dominated flow. When flow regime is not considered, mass transfer zone length estimates show that flow direction can profoundly affect the

analysis of the adsorption bed, leading to erroneous conclusions about the adsorbent effectiveness on the separation process. Finally, heat effects are also affected by changing the flow direction. Higher temperatures can be achieved in upward flows, with more localized heat than that observed in downward flows.

Acknowledgments

Financial support from CAPES and PETROBRAS is gratefully acknowledged.

References

- [1] BP. BP Statistical Review of World Energy 2017. Br Pet 2017;1–52.
- [2] PETROBRAS. Pré-Sal: Produção de Petróleo e Gás Natural | Petrobras 2018.
- [3] Araújo O de QF, Reis A de C, de Medeiros JL, Nascimento JF do, Grava WM, Musse APS. Comparative analysis of separation technologies for processing carbon dioxide rich natural gas in ultra-deepwater oil fields. J Clean Prod 2017;155:12–22.
- [4] AGÊNCIA NACIONAL DO PETRÓLEO GNEB. RESOLUÇÃO ANP N° 16, DE 17.6.2008 - DOU 18.6.2008 O. 2008.
- [5] Kidnay A, Parrish W. Fundamentals of Natural Gas Processing 2006:1–440.
- [6] Bonalumi D, Lillia S, Manzolini G, Grande C. Innovative Process Cycle with Zeolite (MS13X) for Post Combustion Adsorption. Energy Procedia, 2017.
- [7] Grande C a. Advances in Pressure Swing Adsorption for Gas Separation. ISRN Chem Eng 2012;2012:1–13.
- [8] Doong S-J, Yang RT. Bulk separation of multicomponent gas mixtures by pressure swing adsorption: Pore/surface diffusion and equilibrium models. AIChE J 1986;32:397–410.
- [9] Ruthven D, Farooq S, Knaebel K. Pressure Swing Adsorption 1993:352.
- [10] Yang R. Gas Separation by Adsorption Processes. vol. 2. 1988.
- [11] Ruthven DM. Principles of adsorption and adsorption processes. John Wiley & Sons; 1984.
- [12] Gutiérrez Ortiz FJ, Barragán Rodríguez M, Yang RT. Modeling of fixed-bed columns for gas physical adsorption. Chem Eng J 2019;378:121985.

- [13]Shafeeyan MS, Wan Daud WMA, Shamiri A. A review of mathematical modeling of fixed-bed columns for carbon dioxide adsorption. *Chem Eng Res Des* 2014;92:961–88.
- [14]Grande CA, Blom R, Möller A, Möllmer J. High-pressure separation of CH₄/CO₂ using activated carbon. *Chem Eng Sci* 2013;89:10–20.
- [15]Wiley J, Hepburn K, Levenspiel O. *Chemical Reaction Engineering*. vol. 19. 1964.
- [16]de Oliveira LH, Meneguim JG, Pereira MV, da Silva EA, Grava WM, do Nascimento JF, et al. H₂S adsorption on NaY zeolite. *Microporous Mesoporous Mater* 2019;284:247–57.
- [17]W. A. Dietz. Response factors for gas chromatographic analyses. *J Chromatogr Sci* 1967;5:68–71.
- [18]Peng D-Y, Robinson DB. A New Two-Constant Equation of State. *Ind Eng Chem Fundam* 1976;15:59–64. h
- [19]Levenspiel O. *Tracer Technology*. vol. 53. 2019.
- [20]Ananthakrishnan V, Gill WN, Barduhn AJ. Laminar dispersion in capillaries: Part I. Mathematical analysis. *AIChE J* 1965;11:1063–72.

Technological Bottlenecks in purification of monoclonal antibodies: prospective study and proposals for improved process design

Gabriela Freire de Arruda^a, Marcia Soares Lima de Mello^a, Rafael Cavalcante dos Santos^a,
Marlon de Souza Gama^b, Caio Felipe Curitiba Marcellos^a, Amaro Gomes Barreto Jr.^{a,*}

^a School of Chemistry, Federal University of Rio de Janeiro (UFRJ)- Technology Center, Block E, Cidade Universitária, 21941-909, RJ, Brazil.

^b Chemical Engineering Program/COPPE, Federal University of Rio de Janeiro (UFRJ)- Technology Center, Block G, Cidade Universitária, 21941-914, RJ, Brazil.

Abstract

Monoclonal antibodies (mAbs) are high-cost biological drugs of increasingly strategic importance to public health in Brazil. Efforts have been employed towards a national production of mAbs by both public and private pharmaceutical laboratories in order to decrease the dependence from foreigner markets and attend an increasing demand for this type of drugs. However, the purification steps on industrial process present itself as a major technological issue affecting the final cost of mAbs, and thus, its availability for the most of population. Beyond that, the lack of technical data related to mAbs physicochemical properties and relevant process variables difficult the development, optimization and absorption of current fabrication technologies. Conventionally, affinity chromatography, anion and cation exchange chromatography are employed to purify mAbs from other protein-based impurities. Well-designed chromatographic processes need to consider the effects of buffer pH, ionic strength, mAb concentration, aggregation and adsorptive behavior on definition of operational conditions. Process simulation softwares allow the integration of complex physicochemical and biological models in order to generate and analyze the system's response for different inputs. When combined with friendly user interfaces it is possible to expand the usability of the software to many technical professionals. In this work, we present a prospective study about the bottlenecks related to mAbs productions focusing on issues related to purification process steps. We present some models and results related to purification of trastuzumab and bevacizumab in cation exchange columns, as well as, a prototype of graphical software for ease simulation and evaluation of this chromatographic operation

Keywords: Monoclonal Antibodies; bevacizumab; trastuzumab; prospective study; chromatography.

1. Introduction

Monoclonal antibodies (mAbs) are a class of proteins with high specific targeting, produced by engineered mammalian cells. Its successful employment for therapeutic purposes (infiximab, trastuzumab, bevacizumab and rituximab are some examples) treating diseases such as different types of cancer, multiple sclerosis and immunological disorders such as rheumatoid arthritis, Crohn's disease, ulcerative colitis and organ transplantation motivated a worldwide expanding demand in the last 20 years. [1, 2].

The overall mAbs drug prices are heavily influenced by Cost-of-Goods, expensive downstream and clinical trials. [3]. The treatments

are costly but necessary for the survival of many patients around the world. MAb sales are expected to cross \$125 billion by 2020 and more than 50 mAbs have been approved. [2]

The large-scale mAbs manufacturing technology has been updated alongside several innovations. [3]. However, there are still limiting factors at DSP as the high operation expense narrows the availability of enough data for optimization research and the fact that the drug quality is usually assured by QbD (Quality by Design) practices within the companies, the current state-of-art and DSP information is barely shared on conferences and not published. [3] Simulation of biotechnological products are considered more challenge, since, in a great

extent, the production is in batches and the time-dependency and sequencing of events are of primary relevance [4].

1.1 Bottlenecks for biopharmaceuticals production and market: Brazilian scene

The Brazilian government considers 16 therapeutic mAbs essential for pharmaceutical assistance and spends around de R\$ 4 billion in biopharmaceuticals every year. [5]

Owing to high costs and issues associated with DSP process and low competition in private biopharmaceutical market, the Brazilian government ensures the availability of high-priced medicines by means of private-public partnership, establishing maximum prices for several pharmaceuticals or importing them from foreigner suppliers. [5]

There are few private companies that produce biopharmaceuticals in Brazil, most of those products are imported to supply the inner demand, even though about 56% of the twenty top-selling drugs are monoclonal antibodies. [6]

1.2 Technological bottlenecks

There have been exceptional advances in the Upstream Process in the last 10 years. However, the Downstream Purification (DSP) remains a major restriction and represents over 60% of the total manufacturing drug cost. The DSP must be customized for each protein based on intrinsic aspects and impurities and also the capture step is critical for determining the overall process effectiveness and efficiency. [1, 2]

Although chromatography simulation units can be used for virtual experiments of alternative processes, debottlenecking, throughput analysis, optimization and equipment sizing and cost, there is a dependence on entrance variables from the molecules and process.

There is a lack of available data from mAbs' DSP such as physicochemical properties, electrostatic characteristics, impurities and relevant process variables. The research advances on optimization is limited by protected information and inviable experiment trials due to mAbs high price.

1.3 MAb purification process

Purification of mAbs demands three different chromatographic operations beyond virus inactivation or removal, which increase process costs and complexity. [7] The conventional protocols apply affinity chromatography to recover mAbs from culture media as the first chromatographic operation, after its production. Adsorbents for affinity chromatography are functionalized with PtnA. [8]

Adsorbed mAbs and contaminants are desorbed from affinity chromatography and fed to the second chromatography column, where an anion exchange adsorbent retains contaminants that exhibit negative charge under certain pH and ionic force conditions. [7]

The unretained target mAb leaves the anion exchange column and can be separated from aggregated proteins, other undesired immunoglobulins and even from potentially infectious agents as virus capsids using a cation exchange column. [7, 9] High-grade of purity can be attained at this step, by tuning the pH or ionic force values (salt concentration) of the eluent buffer leading to fine separation and polishing of the desired mAb.

1.5 Structure of this research

The purpose of this work is to enlighten the scientific community about the bottlenecks for mAbs purification. Here we make an analysis of the application of a non-linear Poisson-Boltzmann linked with a chromatography column model for mAb separation. This model is reported in the previous work.[10] The adsorption affinity parameter is then applied on a column model for a monoclonal antibody solution that contain several different variants, being similar to each other in the textural properties and distinct by a few aminoacid groups, in the same condition as described by Guélat *et al.* (2012)[11].

Here we will focus on showing how a perturbation in the salt gradient input can influence the elution of mAbs, highlighting the critical necessity for a good control in the purification step.

In addition, we propose the development of a friendly simulation tools that can be useful to find the critical conditions for general separation of mAbs in ion-exchanger chromatographic separation.

2. Modeling Approach and Methodology

2.1 Column Chromatography model

We applied a mathematical model for the chromatography column that requires a dispersion equilibrium parameter. [12] The dimensionless equation is describe as follow:

$$\frac{\partial C_i}{\partial \tau} + \frac{1-\varepsilon'}{\varepsilon'} \frac{\partial q_i}{\partial \tau} + \frac{\partial C_i}{\partial z} = \frac{1}{Pe} \frac{\partial^2 C_i}{\partial z^2} \quad (01)$$

where C_i is the dimensionless concentration of the component i in the mobile phase, q_i is the saturation capacity for each component, ε' is the total porosity, z is proportional to the column length ($0 \leq z \leq 1$), $\tau = \frac{t \cdot u}{L}$, for t being the time, u is the phase mobile velocity and L is the total column length.

We calculated the Peclet number using:

$$Pe = \frac{L \cdot u}{D_{ax}} \quad (02)$$

where D_{ax} is the axial dispersion coefficient.

Initial conditions:

$$\tau = 0, C_i(z,0) = 1, q_i(z,0) = \frac{q_{i_0}}{C_{i_0}} \quad (03)$$

Boundary condition 1:

$$z = 0, -\frac{1}{Pe} \frac{\partial C_i}{\partial z} \Big|_{z=0} + C_i \Big|_{z=0} = C_f(\tau) \quad (04)$$

Boundary condition 2:

$$z = 1, \frac{\partial C_i}{\partial z} \Big|_{z=1} = 0 \quad (05)$$

For the differential partial equation resolution, we used a parabolic approximation in finite elements with the equation discretized in the spatial variable.

For the isotherm model, we used a

competitive multi-component Langmuir [11]:

$$q_i^{eq} = \frac{K_i^*(pH, I) \cdot C_i^*}{1 + \sum_{j=1}^n (K_j^*(pH, I) \cdot C_j^*) / q_j^{sat}} \quad (06)$$

where q_i^{eq} is the solid phase concentration (mg/mL) in equilibrium with the composition of the component i in the liquid phase concentration (C_i^* , mg/mL), q_j^{sat} is the saturation capacity (mg/mL solid).

The parameter K^* is the dimensionless Henry constant:

$$K_i^* = \frac{K_i(pH, I) \cdot A_s}{(1 - \varepsilon')} \quad (07)$$

where A_s is the accessible surface area per unit packed bed volume (set as $4.2 \cdot 10^{-7} \text{ m}^2/\text{m}^3$ for all mAbs variants). K is the dimensional Henry constant obtained as reported by Gama *et al.*, (2018).

2.2 Separation of mAbs in a column chromatography model

We used the same experimental conditions reported by Guélat *et al.* (2012) that described the separation of five mAb variants. The variant P is classified as the most abundant and the variants W1, W2 and W3 are the weakly and S1 the strongly, in respect to the adsorption retention.

A salt gradient is applied using a medium concentration of 2.8 g L^{-1} . For reproduce the effect of a variation in the input, a senoidal perturbation is applied using the range of $\pm 0.3 \text{ g L}^{-1}$.

Table 1 contains the charge density parameters, used to obtain the total charge of the monoclonal antibodies. We calculated these parameters by the ratio of a fitted ionizable number of groups with a mAb sphere radius of 5 nm. [11]

Table 1. Charge density parameters for each aminoacid group (mol m⁻²) for all mAb variants: $\sigma_{NH_3^+}$, σ_{His^+} and σ_{COO^-} are the density of amino, histidine and carboxyl groups.

mAb variant	$\sigma_{NH_3^+}$	σ_{His^+}	σ_{COO^-}
W1	$7.152 \cdot 10^{-7}$	$8.193 \cdot 10^{-8}$	$6.919 \cdot 10^{-7}$
W2	$7.152 \cdot 10^{-7}$	$8.193 \cdot 10^{-8}$	$6.856 \cdot 10^{-7}$
W3	$7.152 \cdot 10^{-7}$	$8.193 \cdot 10^{-8}$	$6.840 \cdot 10^{-7}$
P	$7.152 \cdot 10^{-7}$	$8.193 \cdot 10^{-8}$	$6.798 \cdot 10^{-7}$
S1	$7.289 \cdot 10^{-7}$	$8.193 \cdot 10^{-8}$	$6.798 \cdot 10^{-7}$

The chromatography column model were performed with 0.5 cm of internal diameter, 8.5 cm of height, flow rates of 0.5 mL min⁻¹, a column

Figure 01 shows the input vs output difference between the salt concentrations inside the column. As we can see, the concentration calculated in the output shows a variation of ± 0.05 g L⁻¹ due the balance of the diffusive and convective parameters and the presence of multicomponent.

Besides the small variation, the perturbation of the salt concentration makes a high impact in the mAbs behavior. Figure 02 shows the simulation of the multicomponent separation of a single mAb and its 4 variants using this salt perturbation.

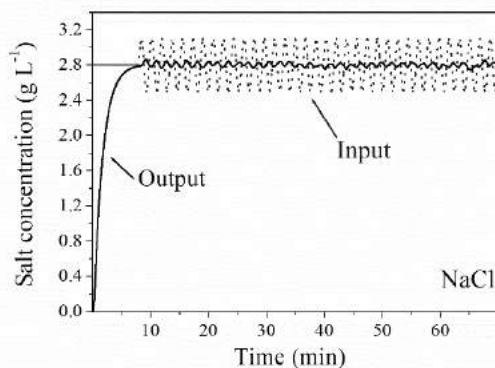


Figure 01: Salt behavior in a chromatogram of mAb variants using NaCl at operation conditions of 25 °C and pH 5.4.

porosity of 0.53 and a Peclet number of 1700 for the mAb and its variants.

2.3 Software Design

The proposed software integrates algorithms developed in Fortran, Python and C++, that compute the model's response from input values.

Adsorption column model, as well as the affinity constant model for mAbs, are both solved algebraically or from numeric PDE integration.

A graphical interface was developed for fast tuning of input variables and data visualization of simulated chromatographic profiles, intended to be operated by the final user.

3. Results and Discussion

3.1 Separation of mAbs using a salt perturbation input gradient

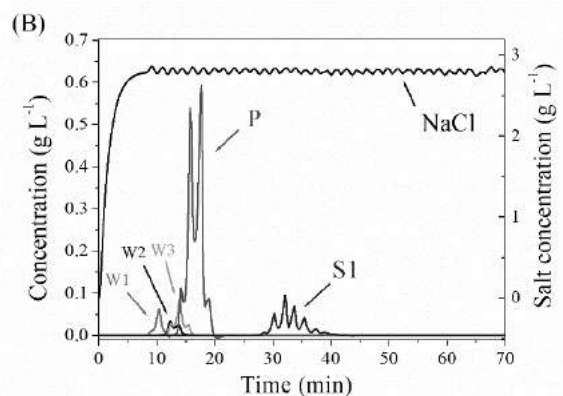
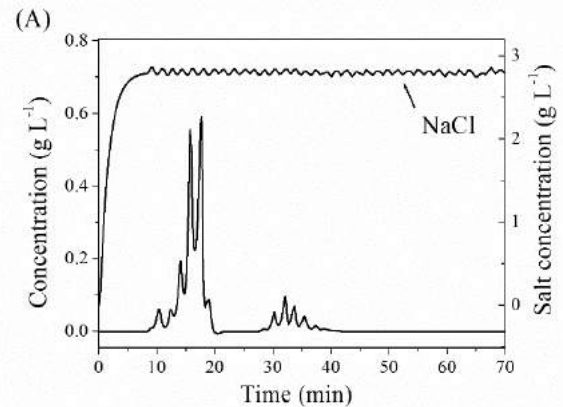


Figure 02: Chromatogram of mAb variants with a concentration of 15 g L⁻¹ using NaCl at operation conditions of 25 °C and pH 5.4. (A)

represents the sum of all the components and (B) the separated concentrations.

Figure 02 (A) shows the sum of all the concentration in the end of the simulation run. The perturbation interference was able to create a chaotic behavior for the elution. A single component, as S1, have 4 peaks in the range of 30-40 min. The principal mAb component (P) shows 2 main peaks between 15-20 min. In Figure 2 (B) we can see the components in a separated way, pointing out that in fact the peaks refer to the same component.

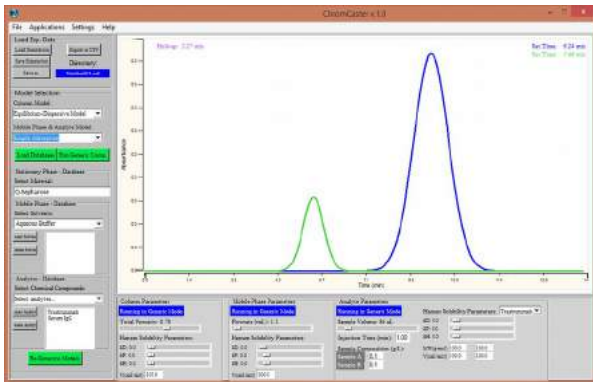


Figure 03: Prototype for a user interface for adsorption separation processes.

Figure 03 presents a prototype for a user interface of adsorption processes. The user can define the underlying model, stationary and mobile phases, configure components properties from a database and others operational conditions. In the current software version, the model parameters, such as porosity and isotherm coefficients, can be modified and the analyte elution curves are automatically computed and shown. This setup allows a user-friendly sensitivity analyses of the main parameters.

4. Conclusions

In this work, a simulation of the mAb separation process with a cation exchange column was addressed. Disturbs in the operational condition can have negative effects in the separation. We have shown that small variations in the NaCl setpoint can have pronounce impact in the elution profiles and can be a hindrance in the separation. Hence, an efficient monitoring and control of the process is necessary.

Process simulators are recognized as an important tool in the development, monitoring and

optimization of biotechnological downstream processing. We developed a prototype of a user interface for compound purification by adsorption. There are fully-fledged commercial simulators for biotechnological separation available with many features, such as a wide variety of unit operation, definition of batch processing protocols, flowchart for stream connections and a robust components database. However, the operation involved are often not accessible for an advanced user to customize for a certain application. Hence, in future works, our goal is to develop computational packages for biotechnological separation processes in which the mathematical models can be exposed for better customization of more advanced users.

References

- [1] M. DiLeo, A. Ley, A. E. Nixon, and J. Chen, "Choices of capture chromatography technology in antibody manufacturing processes," *J. Chromatogr. B*, vol. 1068–1069, pp. 136–148, Nov. 2017.
- [2] A. A. Shukla, L. S. Wolfe, S. S. Mostafa, and C. Norman, "Evolving trends in mAb production processes," *Bioeng. Transl. Med.*, vol. 2, no. 1, pp. 58–69, 2017.
- [3] B. Kelley, "Industrialization of mAb production technology: the bioprocessing industry at a crossroads," in *MAbs*, 2009, vol. 1, pp. 443–452.
- [4] R. G. Harrison, P. Todd, S. R. Rudge, and D. P. Petrides, *Bioseparations science and engineering*. Oxford University Press, USA, 2015.
- [5] L. Hasenclever, *Economia industrial de empresas farmacêuticas*. Editora E-papers, 2010.
- [6] M. S. Salerno, C. Matsumoto, and I. Ferraz, "Biofármacos no Brasil: características, importância e delineamento de políticas públicas para seu desenvolvimento," 2018.
- [7] E. Boschetti and A. Jungbauer, *Separation of antibodies by liquid chromatography*. Academic Press, San Diego, CA, 2000.
- [8] N. Eswar et al., "Current protocols in protein science," *Curr. Protoc. Protein Sci.*, vol. 50, p. 2.9, 2007.
- [9] J. Bonnerjea and A. Preneta, *Antibody purification by protein a and ion exchange chromatography*. Google Patents, 2011.
- [10] M. de Souza Gama, M. S. Santos, E. R. de Almeida Lima, F. W. Tavares, and A. G. B. Barreto Jr, "A modified Poisson-Boltzmann equation applied to protein adsorption," *J. Chromatogr. A*, vol. 1531, pp. 74–82, 2018.
- [11] B. Guélat, G. Ströhlein, M. Lattuada, L. Delegrange, P. Valax, and M. Morbidelli, "Simulation model for overloaded monoclonal antibody variants separations in ion-exchange chromatography," *J.*



Chromatogr. A, vol. 1253, pp. 32–43, Aug. 2012.

[12] J. SEVERO JR, “Avaliação de técnicas de planejamento de experimentos no reconhecimento do equilíbrio de adsorção em sistemas cromatográficos,” Tese de Doutorado, COPPE/UFRJ, Rio de Janeiro, 2011.

Effect of temperature on oxidative degradation of bleached Hybrid (*E. guineensis* x *E. oleifera*) and African palm oil (*Elaeis guineensis*)

Erislene S. Almeida^a, Ivanildo José da Silva Júnior^b, Simone Monteiro^{a,*}

^a University of Brasília, Campus Universitário Darcy Ribeiro, Brasília, Brasil

^b University of Ceará, Campus do Pici, Fortaleza, Brazil

Abstract

This work aimed to study the effect of bleaching and heating on carotene concentration and oxidation in palm oil. Hybrid palm oil and African palm oils were bleached with different adsorbents. Then, bleached and crude palm oils were submitted to heating. When comparing crude and bleached oil samples heated to 210 °C, the strong influence of temperature on the formation of dienes and trienes, secondary oxidation products, was observed. Considering the different types of studied bleaching earth, there was a noticeable difference in the formation of dienes and trienes. Finally, the higher the carotene thermal degradation and the higher carotene removal by adsorption, the greater the oxidation observed in the oil.

Keywords: oxidation; vegetable oils; refining; carotene.

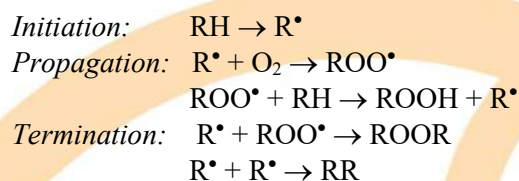
1. Introduction

In everyday and industrial use, vegetable oils are submitted to high temperatures in various situations. The thermal stress accelerates oxidative reactions, leading to the formation of primary and secondary oxidation products, as partial acylglycerols such as mono and diacylglycerols [1]. In industrial refining, the oil is submitted to processes that require high temperatures to remove some undesirable compounds [2]. For instance, crude palm oil (CPO), before it is ready for human consumption, undergoes a refining process that aims at removing compounds such as phospholipids, free fatty acids, oxidation products, pigments, metals and other undesirable components. CPO refining consists of bleaching (at temperatures higher than 100 °C) and deacidification/deodorization (at temperatures ranging from 150°C to 260 °C and pressure lower than 5 mmHg) [2].

The primary purpose of the bleaching process is to remove, by adsorption, metals that catalyze the oxidation process. Furthermore, bleaching removes pigments that would derail the vegetable oils color [3]. The combination of unsaturated fatty acid and high temperatures of the deacidification process can lead to the thermal degradation of CPO, and metals would make this reaction even more critical. On the

other hand, oxidation may be postponed by the presence of antioxidants in vegetable oil, such as carotenes and tocopherols.

Lipid oxidation involves a complex set of reactions between unsaturated fatty acids and oxygen, and those reactions may be divided into three different steps, as follows: [4]



The atmospheric oxygen attacks the double bonds leading to the formation of primary oxidation products, the hydroperoxides. Primary oxidation products are then decomposed in aldehydes, alcohols, lactones, ketones, epoxides and acids [5]. The rate of oxidation reactions will be influenced by the number of double bonds presented in the molecule. Oxidation reactions form conjugated double bonds, forming dienes and trienes, which strongly absorb at 232 and 268 nm, respectively [4].

It is well established that oxidation products lower the quality of the oil, as they are in part cytotoxic and genotoxic. Moreover, the type of bleaching clays affects oil oxidation stability. In this

sense, this work aims to evaluate oil oxidation and carotene degradation in oils bleached by different bleaching clays [3].

2 Material and Methods

Commercial crude oils obtained from two different oil palm – *Elaeis guineensis* and the interspecific hybridization of *Elaeis guineensis* × *Elaeis oleifera*, here so-called African (APO) and Hybrid palm oil (HPO), respectively – were kindly supplied by Denpasa (Santa Bárbara do Pará, PA, Brazil). The adsorption experiments were performed using two types of commercial bleaching earth widely used in the vegetable oil industry: the acid-activated adsorbent (ABE) Tonsil OPT 210 FF, manufactured by acid activation of calcium bentonite, which was kindly provided by Clariant (Germany); the neutral adsorbent (NBE) Pure Flo B 80, composed by bentonite, that was kindly provided by Oil Dri (USA). Moreover, it was tested three adsorbents synthesized by our research group, being LDH (Layered Double Hydroxide), PCH (Porous clay heterostructures) and Sepiolite.

Thermal degradation was evaluated by the formation of conjugated dienes and trienes and by the degradation of total carotenes and their isomers α - and β -carotene.

2.1. Analysis of conjugated dienes and trienes (oxidation)

The oil samples were diluted in iso-octane and its absorbance measured from 230 to 270 nm (Official method - Ch 5 - 91 AOCS, 2003). Conjugated dienes and trienes were determined at 232 and 268 nm, respectively [4].

2.2. Determination of total carotenes

Total carotene, expressed as β -carotene, was determined by UV-vis spectrometry (Varian - Cary 5000) [6]. β -carotene solutions (Sigma Aldrich) were used as the standard to construct the calibration curve. Quantification was performed by linear fitting ($R^2 > 0.99$). Degraded carotene was determined by difference: carotene concentration in CPO minus carotenes concentration after treatment.

2.3. Determination of α - and β -carotenes

Chromatographic analyses were performed by an HPLC (Shimadzu - Prominence) equipped with a quaternary pump system (LC - 20AD), UV - Vis DAD detector (SPD - M20A), autosampler (SIL - 20A) and oven (CTO - 20A). The oven temperature was adjusted to 40 °C and the chromatograms analyzed at 450 nm. Oil fractions were analyzed on C30 column (Develosil, 250 x 4.6 mm and 5 μ m particle size). Solvent A was acetonitrile; Solvent B was methanol/triethylamine (0.05 %), Solvent C was THF. Solvents were delivered in a total flow rate of 1.2 mL/min in a gradient elution as follows: Solvent C was maintained at 5 % all over the run; 0-10 min linear gradient from 0 to 30 % Solvent B; 10-20 min linear gradient to 40 % Solvent B; 20-60 min isocratic gradient 55 % Solvent A, 40 % Solvent B and 5 % Solvent C; 60.01 min 65 % Solvent A, 30 % Solvent B and 5 % Solvent C; 61-65 min linear gradient from 30 to 0 % Solvent B. The injection volume in all assays was 10 μ L. The calibration curve was performed using commercial standards of α - and β -carotenes.

2.4. Batch adsorption (bleaching)

Conditions similar to industrial bleaching were simulated in lab-scale to understand the effect of different types of bleaching earths on oxidation product formation and carotenes removal. Oil samples were bleached using the methodology proposed by Silva et al. [7], using 3% (w/w) of adsorbent at different temperatures. Bleached oils were analyzed regarding oxidation, total carotenes and α - and β - carotenes.

2.5. Thermal stability

In each test, 50 g of crude palm oil was placed into 100 mL Erlenmeyer flasks. Then, the following steps were performed: addition of 0.09 % m/m of citric acid (to chelate metals), as a 30 % w/w aqueous solution; high shear mixing at 20,000 rpm during 1 min to allow contact between aqueous and oil phases (mixer, Turratec, Tecnal, Brazil). Then, Erlenmeyer was closed with a cotton swab, through which nitrogen was purged into the oil for approximately 5 minutes.

The methodology for the study of oil thermal degradation kinetics for Hybrid palm and African oils was adapted from the literature [8]. This system was placed over a heating plate for approximately

225 minutes with a continuous nitrogen purge. The oil temperature was also monitored, and the experiment lasted until oil temperature reached 210 °C. Throughout the experiment, oil fractions (approximately 1 g) were collected at 150, 165, 180, 190, 200 and 210 °C. Samples were analyzed regarding conjugated dienes and trienes, total carotenes, α - and β -carotenes.

3 Results and Discussion

3.1. Oxidation during adsorption

Figure 1 shows a comparison of the spectra of bleached oils with commercial adsorbents (ABE and NBE) at temperatures of 90, 105 and 120 °C. Considering the commercial adsorbents, ABE and NBE, both showed a good ability to remove carotenes for both APO and HPO. Considering the formation of dienes and trienes, there was a direct relation of peaks intensity at 232 and 268 nm and temperature. The formation of dienes and trienes, as a product of oil oxidation, is potentiated by heating.

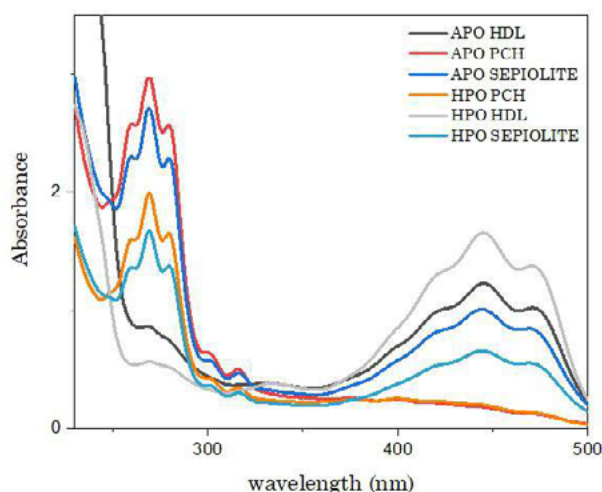


Figure 1: Comparison between APO and HPO spectra after the adsorption process with commercial adsorbents

Regarding the HPO, the observations regarding the temperature of the experiments and peak intensity in the region of 230 to 270 nm are also applied. When comparing the APO and HPO (highlighted in Figure 1), there is a considerable difference between the absorbance values obtained for the two oils. Higher absorbance values at 232

and 268 nm indicate higher peroxide content and oxidation by-products, i.e., higher peroxide content. The HPO presented lower absorbances, possibly due to the higher concentration of carotenes (antioxidants).

Figure 2 presents the spectra of HPO and APO bleached with LDH, PCH and Sepiolite, adsorbents synthesized in this work. Firstly, as those adsorbents are not traditionally used for bleaching, the region between 400 to 500 nm was studied to evaluate carotene removal. The PCH showed a performance comparable to commercial adsorbents to remove carotenes, i.e., signal extinction due to considerable carotene adsorption.

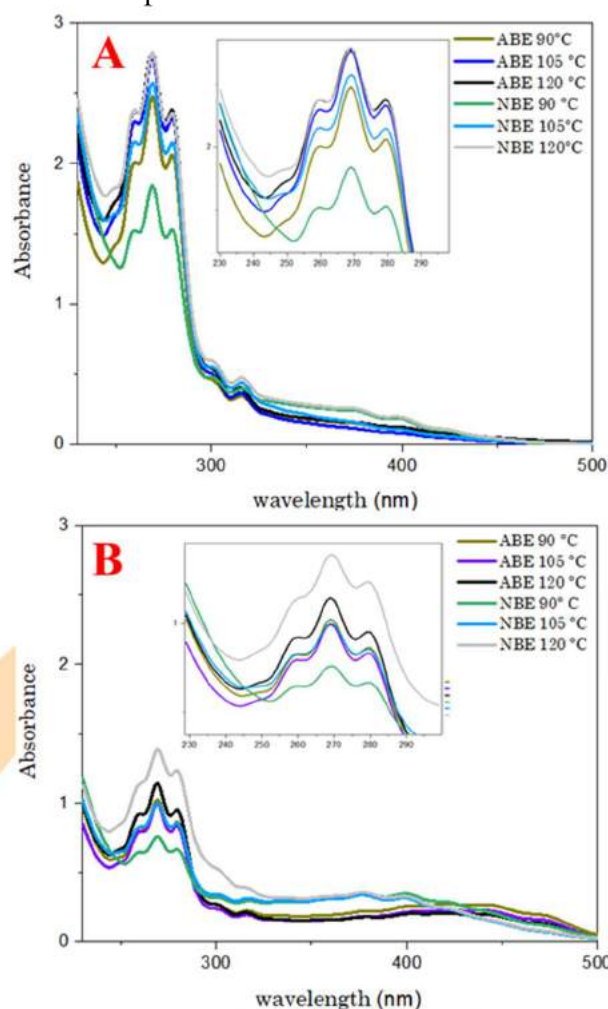


Figure 2: APO (A) and HPO (B) UV-vis spectra after carotene adsorption onto LDH, PCH, and Sepiolite.

Oil bleached with LDH adsorbent showed lower carotene removal, with the maintenance of carotene typical spectra of maximum absorption at 450 nm



and shoulders at 425 and 477 nm. Sepiolite presented a performance that can be said as intermediate between LDH and PCH.

Almeida et al. extensively studied carotenes adsorption by ABE and NBE. The authors observed a higher carotenes adsorption by ABE and attributed this to the larger pore size. The works of Aguiar et al. [9] and Gondim et al. [10] determined the structural properties of PCH and LDH synthesized using the same methodology used in this work. The PCH present pore volume almost twice higher than LDH. Thus, those results corroborate those found in the literature correlating adsorbent pore size with carotene adsorption.

Regarding oxidation products, it was observed an inverse correlation of the intensity of peaks in the region from 230 to 270 nm and carotene removal. The PCH, which present better carotene removal, also presented a stronger peak at the oxidation products region. On the other hand, LDH that presented a poor carotene removal, did not present a signal in this region. Similarly, sepiolite presented intermediate behavior between PCH and LDH. Carotenes are potent antioxidants, and those results suggest that their presence is vital to avoid oxidation reactions during bleaching.

Moreover, as previously explained, a low carotene removal may not mean poor adsorbent performance, because if good phosphorus and iron removal occurs without oxidation reactions, the carotenes may be further degraded in the subsequent process, the deacidification. This phenomenon is industrially known as heat bleaching [11].

Thus, the results show that further testing would be necessary to determine the performance of LDH adsorbent on the removal of other compounds and to be able to evaluate its capacity as adsorbent not only for LDH, but also for PCH and Sepiolite.

3.2. Carotenes removal by adsorption

Table 1 illustrates what was discussed above about carotenes removal. Total carotene content was 431 and 954 mg/kg for crude APO and HPO, respectively. After process with adsorbents synthesized in this work (LDH, PCH and Sepiolite), it can be observed for both APO and HPO, that the carotenes adsorbed was less than 5 %, but there was little alteration in the region indicating the presence of dienes and trienes compared to crude oils.

Sepiolite adsorbed between 20 and 50% of carotenes. Sabah et al. [12], using acid-activated sepiolite, removed about 95% of canola oil of β -carotene under optimized bleaching conditions. PCH adsorbed more than 85 % of carotenes from both palm oils. No experimental data were found in the literature using PCH for vegetable oil purification processes. The fewer carotenes left in the bleached oil, the higher the intensity of the peaks in the dienes and trienes region, confirming the action of carotenes as an antioxidant agent of oil [3]. The temperature influenced the formation of oxidation products, and it was also observed that the HPO had a lower formation of oxidation products, possibly due to the higher presence of carotenes. Regarding the influence of the type of adsorbents on the formation of dienes and trienes, it was necessary to perform new tests with different concentrations of adsorbents, as they may also act as pro-oxidants under some conditions.

Table 1: Total and adsorbed carotene content considering different adsorbent types and temperatures worked.

Adsorbent	Total (mg/kg)	% Adsorbed	
		APO	HPO
Crude	451.33	-	-
LDH	434.15	0.56	2.08
PCH	62.42	85.70	88.08
Sepiolite	346.50	20.64	54.45
ABE 90 °C	12.83	97.06	78.25
ABE 105°C	7.29	98.33	81.78
ABE 120 °C	18.05	95.87	84.20
NBE 90 °C	11.45	97.38	84.15
NBE 105°C	10.09	97.69	89.12
NBE 120 °C	15.29	96.50	88.42

3.3. Oxidation during heating treatment

Figure 3 shows the UV-vis absorption spectra of the oils subjected to heating. A difference was observed in the dienes and trienes region (230 to 270 nm). The APO formed a different-peak profile peak, with only the peak in the 268 (triene) steeper region and the 'shoulders' formed before and after this were less evident. This fact was not observed in the bleached APO (Figure 2). A possible explanation would be the presence of some compound in the African crude oil that was not present in the bleached oil because it was removed by adsorption. It was also possible to observe the

higher signal intensity in the region between 230 and 270 nm for the APO compared to the HPO, as was observed in the bleached oil. These differences were not observed for the HPO.

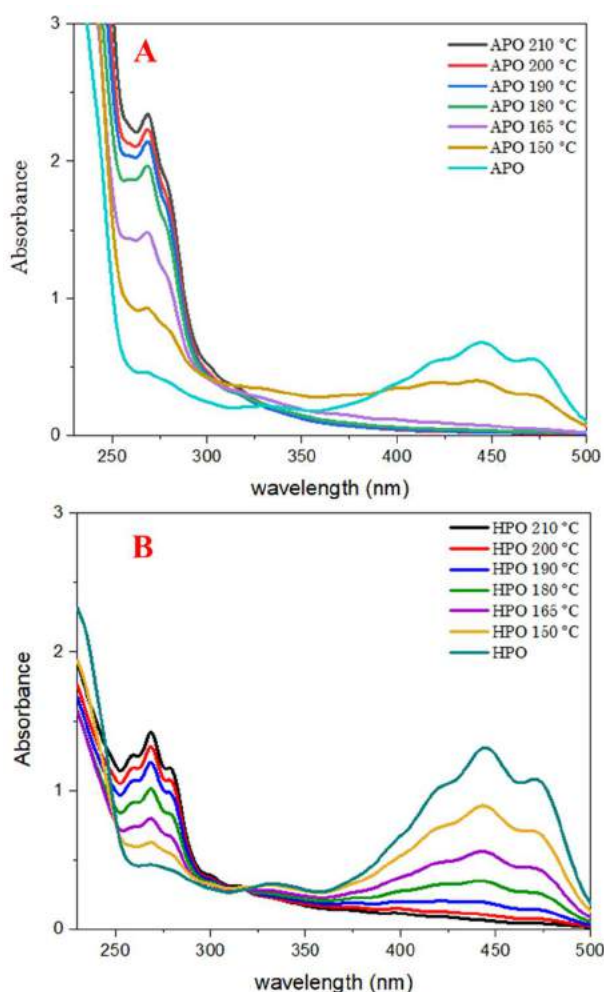


Figure 3: Heated oils. Comparison between APO (A) and HPO (B) in relation to the total carotene content remaining in the oil and formation of dienes and trienes

4. Conclusion

From the five tested adsorbents, four were capable of removing carotenes from crude palm oil. The only exception was LDH. A correlation was observed between the formation of oxidation products and the concentration of carotenes in the liquid phase after the adsorption process, showing the importance of these compounds to protect the oil from oxidation during the bleaching temperatures. It is fundamental to perform further experiments for metal removals to thoroughly evaluate the efficiency of adsorbents as bleaching earth.

Acknowledgments

The authors acknowledge CNPq (421852/2018-6; 429873/2018-2), FAPDF (224/2019) and FAPESP (2014/21252-0) for financial support.

5. References

- [1] Mahboubifar, M., et al., *Prediction of the acid value, peroxide value and the percentage of some fatty acids in edible oils during long heating time by chemometrics analysis of FTIR-ATR spectra*. Journal of the Iranian Chemical Society, 2016. **13**(12): p. 2291-2299.
- [2] Gibon, V., W. De Greyt, and M. Kellens, *Palm Oil Refining*. European Journal of Lipid Science and Technology, 2007. **109**: p. 315-335.
- [3] Taylor, D.R., *Bleaching*, in *Bailey's Industrial Oil and Fat Products*, F. Shahidi, Editor. 2005, John Wiley & Son: New York.
- [4] Schaich, K.M., *Lipid Oxidation: Theoretical Aspects*, in *Bailey's Industrial Oil and Fat Products*, F. Shahidi, Editor. 2005, John Wiley & Son: New York.
- [5] Liang, P., et al., *Application of Fourier Transform Infrared Spectroscopy for the Oxidation and Peroxide Value Evaluation in Virgin Walnut Oil*. Journal of Spectroscopy, 2013. **2013**: p. 5.
- [6] PORIM, *PORIM test methods: Carotene content*. 1990, Palm Oil Research Institute of Malaysia: Kuala Lumpur.
- [7] Silva, S.M., et al., *Adsorption of carotenes and phosphorus from palm oil onto acid activated bleaching earth: Equilibrium, kinetics and thermodynamics*. Journal of Food Engineering, 2013. **118**(4): p. 341-349.
- [8] Sampaio, K.A., et al., *Thermal Degradation Kinetics of Carotenoids in Palm Oil*. Journal of the American Oil Chemists' Society, 2013. **90**(2): p. 191-198.
- [9] Aguiar, J.E., et al., *Adsorption of Anionic and Cationic Dyes from Aqueous Solution on Non-Calcined Mg-Al Layered Double Hydroxide: Experimental and Theoretical Study*. Separation Science and Technology, 2013. **48**(15): p. 2307-2316.
- [10] Gondim, D.R., et al., *Influence of buffer solutions in the adsorption of human serum proteins onto layered double hydroxide*. International Journal of Biological Macromolecules, 2018. **106**: p. 396-409.



- [11] Ribeiro, J.A.A., et al., *Identification of carotenoid isomers in crude and bleached palm oils by mass spectrometry*. LWT - Food Science and Technology, 2018. **89**: p. 631-637.
- [12] Sabah, E., M. Çinar, and M.S. Çelik, *Decolorization of vegetable oils: Adsorption mechanism of β -carotene on acid-activated sepiolite*. Food Chemistry, 2007. **100**(4): p. 1661-1668.

Adsorption of a synthetic red food-colorant by circulating percolation of the solution through a packed-bed of wheat bran

Samuel Pratavieira de Oliveira^a, Fernanda Perpétua Casciotori^{a,*}

^a Federal University of São Carlos (UFSCar), Rod. Washington Luiz km 235, São Carlos 13565-905, Brazil

*Corresponding author: fernanda.casciotori@ufscar.br

Abstract

It has been assessed the suitability of an apparatus built as packed-bed (PB) to be used for adsorption processes by circulating percolation. Case-study was the adsorption of Allura or Red-40 synthetic food-colorant from a liquid solution by the low-cost adsorbent wheat bran, an abundant agro-industrial by-product. The apparatus consisted of a set of three stainless-steel modules: an entrance section (conical and packed with glass-beads); an exit section (conical and empty); and an adsorption section (packed with the adsorbent). The adsorbent was percolated for 3 hours by the liquid solution of the colorant (initial concentration 35 mg L⁻¹), circulated with a submerged pump. Solids load was 450 g per 4.5 L of solution (1:10 w/v). Absorbances at 523 nm were measured for samples taken along the circulation. Adsorption capacity of 0.2 mg colorant per gram of wheat bran and efficiency of 52 % of colorant removal were achieved, and equilibrium seemed to be reached in 100 minutes. Kinetic model of pseudo-first order fitted well to experimental data. Adsorption process conditions must be further optimized and the apparatus shall still be more extensively evaluated and improved, but it showed to be suitable for removing food colorants from wastewater percolating a bed of adsorbent.

Keywords: wastewater treatment; food and beverages; packed-beds; agroindustrial by-products.

1. Introduction

Effluents from beverage industries can become important sources of pollution due to their color, associated with the use of colorants, extensively applied in juices and soft drinks formulations. The artificial dye Red 40 or Allura is used in beverages to give them an intense red color. Once soft drink industries prepares concentrated syrups that are further diluted, high concentrations of Allura dye are expected to be found in discharge and wash water from tanks. Hence, there is a concern on the removal of this colorant from effluent of beverage industries.

Adsorption is a unit operation in which a chemical species (adsorbate) present in liquid phase is attached to the surface of a solid (adsorbent) [1]. Such low-cost and effective operation has found great application for the removal of artificial dyes from wastewater of many industries. Moreover, the adsorption of dyes by biological materials from agro-industrial waste, such as fruit peels, sugarcane bagasse, corn straw and cereal bran, has been investigated as feasible alternative.

Besides of choosing a suitable adsorbent, studies on the kinetics and on the development of apparatus for adsorption are also required. On the above, the objective of the current paper was to study the adsorption operation, using wheat bran as adsorbent, for the removal of the colorant red Allura from a synthetic aqueous solution that has been forced to circulate and percolate through a packed-bed of the agricultural residue. Concentration of the colorant in the solution were evaluated along 3 h of circulation. Adsorption efficiency was calculated and a kinetic model was fitted to experimental data.

2. Materials and Methods

As solid adsorbent, wheat bran (dry) was chosen. Adsorbate was red Allura, a synthetic food-colorant.

The column for adsorption by circulating percolation in a packed-bed of adsorbent consisted of a set of three stainless-steel modules: an entrance section (conical and packed with 3-mm glass-beads,

used to define the flow of the liquid); an exit section (conical and empty, a grid avoided adsorbent drag); and an adsorption section (fully packed with the adsorbent, contained in between two grids). Each module had diameter and length 10 cm. The apparatus is shown on Fig. 1.



Fig. 1. Apparatus for adsorption by circulating percolation; wheat bran packed at central module.

Adsorption tests were carried out with 450 g of wheat bran, packed into the intermediate module, that was percolated by 4.5 L of a solution of colorant concentration with initial concentration 35 mg L⁻¹ and pH adjusted to 4. A submerged pump was used to make the solution to circulate and percolate the packed-bed during 3 h. Samples were taken every 10, 20 and 30 minutes up to the first, the second and the third hour, respectively.

The absorbances of the liquid samples were read at 523 nm and the values were converted into concentrations by a standard curve.

2.1. Calculations

The adsorption capacity, that gives the amount of adsorbate retained per gram of adsorbent (q , mg g⁻¹) was calculated by Equation 1 [2]:

$$q = \frac{(C_0 - C)V}{m} \quad (1)$$

where C_0 and C are, respectively, the initial and current concentrations of the colorant in the solution (mg L⁻¹); V is the volume of solution (L); m is the amount of dry adsorbent (g).

The adsorption efficiency (E , %) was given by Equation 2 [2]:

$$E (\%) = \frac{(C_0 - C) 100}{C_0} \quad (2)$$

2.2. Kinetic model

To the experimental data along time, linear form of kinetic model of pseudo-first order has been fitted [2]. Correlation coefficient was analyzed and the kinetic parameters of Equation 3 were determined:

$$\ln(q_e - q) = \ln(q_e) - k_1 t \quad (3)$$

where t is time; q_e is amount adsorbed at equilibrium and k_1 is the rate constant.

3. Results and Discussion

Results of the experiment of adsorption are shown on Table 1. The kinetic curve decay of the concentration of colorant in the solution is shown on Fig. 2.

Table 1. Results of the adsorption experiment.

Time (min)	[colorant] (mg/L)	q (mg/g)	Efficiency of removal (%)
0	35.0	0.000	0.0
10	32.6	0.024	6.8
20	29.4	0.056	15.9
30	25.9	0.091	26.0
40	26.1	0.088	25.2
50	23.7	0.112	32.1
60	23.9	0.111	31.8
80	19.8	0.152	43.3
100	17.4	0.176	50.3
120	17.0	0.180	51.5
150	17.2	0.177	50.7
180	16.7	0.182	52.1

Equilibrium of adsorption has been reached after around 100 h of circulating percolation of the liquid through the packed-bed of wheat bran, with around 50 % of removal of the colorant from the solution. Once an agricultural waste in its raw form, with no pre-treatment, has been applied in the current runs for assessing the potential of the proposed apparatus on wastewater treatment by adsorption, the result can be considered good and promising. Gaspardi [3] studied adsorption of same colorant in wheat bran after acidic pre-treatment. In shaken flasks, the author achieved around 90 % adsorption efficiency.

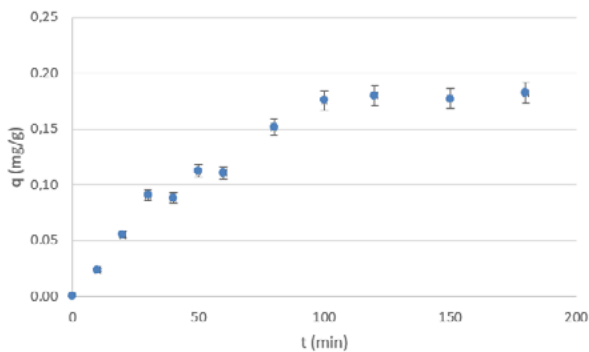


Fig. 2. Experimental curve of adsorption of Allura Red from the solution by wheat bran along time.

Fig. 3 present the fit of the linear form of the pseudo first-order kinetic model (Equation 3) to the experimental data, assuming $q_e = 0.18 \text{ mg/g}$ as amount adsorbed at equilibrium, based on Fig. 2. The constant rate of adsorption $k_1 = 0.023 \pm 0.002 \text{ h}^{-1}$, $R^2 = 0.93$, and predicted $q_e = 0.19 \text{ mg/g}$.

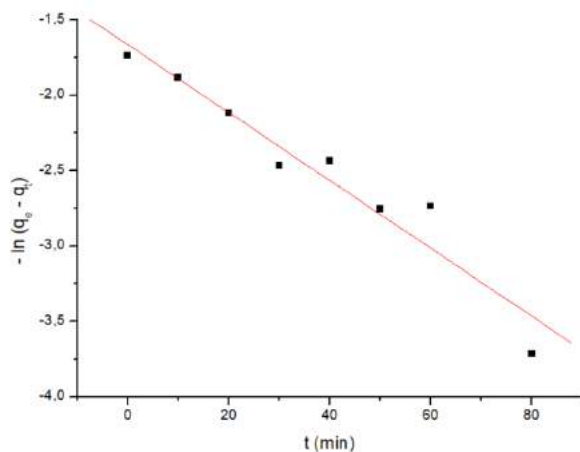


Fig. 3. Fit of kinetic first-order model.

Fig. 4 shows the aspect of the wheat bran at the end of 3 h of circulating percolation by Allura Red solution with initial concentration 35 mg L^{-1} .

Acknowledgements

Authors gratefully acknowledge to São Paulo Research Foundation (FAPESP) for financial support and scholarships (grant numbers 2018/00996-2 and 2018/26097-4).



(a)



(b)

Fig. 4. Wheat bran (a) packed into the bed (b) withdrawn from the bed, at the end of 3 h of percolation by Allura Red solution 35 mg L^{-1} .

References

- [1] Doran PM. Bioprocess engineering principles. 2nd. ed. Oxford: Elsevier; 2013.
- [2] Sá FP. Adsorção e Fotodegradação de Corantes, Amarelo Crepúsculo e Azul Brillhante, para tratamento de Indústrias Alimentícias. Tese de Doutorado. Goiânia: Universidade Federal de Goiás, 2013.
- [3] Gaspari I. Resíduos agroindustriais como adsorventes para remoção de corante vermelho Allura utilizado na indústria de alimentos e bebidas. Trabalho de Conclusão de Curso. São Carlos: Universidade Federal de São Carlos, 2018.

Perspectives on the synthesis, characterization, and application of hydroxyapatite-based sorbents for gaseous mercury removal

Carla L. M. Camargo^{a,b,*}, Amanda G. Oliveira^b, Neuman S. Resende^b, Vera M. M. Salim^b

^a Escola de Química, Universidade Federal do Rio de Janeiro, Centro de Tecnologia, Cidade Universitária, Rio de Janeiro, 21941-909, RJ, Brazil

^b Programa de Engenharia Química, PEQ/COPPE, Universidade Federal do Rio de Janeiro, Centro de Tecnologia, Cidade Universitária, Rio de Janeiro, 21941-914, RJ, Brazil

Abstract

Mercury contamination is a relevant issue concerning the natural gas processing industry, especially due to corrosion and embrittlement of aluminum equipment. In the search for solutions among different conventional methods, several regenerable and non-regenerable sorbents have been developed, revealing the fixed-bed sorption process ensures the general requirements for safe mercury removal. In this work, we aim to provide an overview of an extensive study addressing the development and improvement of hydroxyapatite-based adsorbents for gaseous mercury (Hg^0) removal. Results of the physicochemical characterization of adsorbents, as well as their performance in static adsorption studies, were according to the hypotheses of the previously proposed mathematical model. The mesoporous adsorbent presented well-dispersed Cu_xS_y active sites in the calcium-deficient hydroxyapatite matrix. Batch adsorption experiments confirmed that its mercury removal capacity was proportional to the copper content. The dynamic adsorption behavior in the presence of moisture was very similar to that in dry methane. Indeed, just a small difference ($>10\%$) was observed between the total mercury contents in the two used-adsorbents. These results ensured moisture has no detrimental effect on the performance of the synthesized HAp-based adsorbents. In short, results proved the development of an efficient adsorbent for the removal and stabilization of mercury from gaseous streams as well as the design and manufacture of pelletizing equipment, which allows thinking in the scale-up process.

Keywords: mercury removal; hydroxyapatite; adsorption; stabilization

1. Introduction

Due to its high toxicity and bioaccumulation capacity in the food chain, mercury is associated with serious risks to human health and is considered as one of the "priority hazardous substances" by the Food Safety Agency Toxic Substances and Disease Registry [1]. Nowadays, the development of new technologies for mercury emission control has been increasingly encouraged as environmental agencies are more deeply addressing the issue of mercury as a global pollutant [2,3]. Coal combustion has been identified as an important source of mercury emissions due to the high concentrations of mercury in this type of fuel [4]. Additionally, the presence of mercury in natural gas leads to additional concerns about accidents caused by mercury corrosion of aluminum equipment in cryogenic gas processing plants [5,6]. Here, we summarize a long-term R&D project [7-10] carried

out at LABEFIT at COPPE/UFRJ in collaboration with Petrobras. In this work, we present new results of static adsorption and stabilization studies, as well physicochemical characterization results for adsorbent and used adsorbent. The dynamic adsorption behavior in presence of moisture is also evaluated.

2. Background simulation model

Phenomenological models were proposed using different conceptual models for describing adsorbent particles and fixed-bed configuration [7-9]. We use dimensionless mathematical models in order to reduce both the number of parameters and the computational effort. Initial simulations were carried out at software Matlab, in which the partial differential equations were discretized using finite difference method and integrated using an implicit Runge-Kutta method [7]. A hybrid optimization algorithm combining the Particle Swarm Optimization (PSO) and a Newton-like method



was used in the parameter estimation. In a second step, partial differential equations of a more sophisticated model were reduced to a set of ordinary differential equations by the polynomial approximation in finite-element method. Simulations were carried out in the Environment for Modelling, Simulation and Optimization (EMSO) dynamic simulator and the DASSLC algorithm was used in the numerical integration. The flexible polyhedron optimization method was used in the parameter estimation [8]. In a subsequent step, the previous phenomenological models were revisited [9] and physicochemical characterization results along with molecular simulation insights [10] were used to propose a more realistic conceptual model. Based on the experimental observation and physicochemical characterization results, the dynamic adsorption system can be represented as shown in Fig. 1.

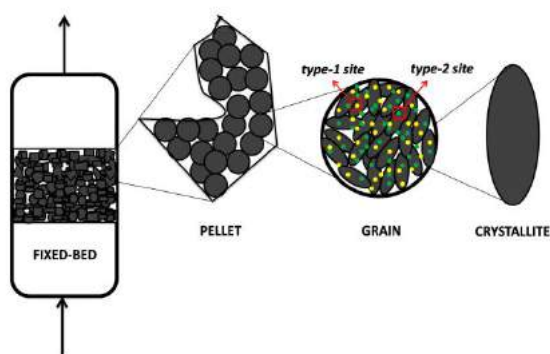


Fig. 1. Representation of the dynamic adsorption system using HAp-based adsorbent [9].

We consider the presence of two types of active sites located on crystallite surface in a new phenomenological model named Two-Sites Adsorption Model. Active sites are differentiated from one another by chemical nature leading to velocities of chemisorption specific for each one. A detailed description of the phenomenological model is described elsewhere [9].

3. Materials and Methods

3.1 Adsorbent preparation

Hydroxyapatite - $\text{Ca}_{10}(\text{PO}_4)_6(\text{OH})_2$ - was synthesized by the precipitation method using phosphate of ammonium and calcium nitrate solutions, at both constant pH and temperature. The resultant precipitate was consecutively washed, dried, and calcined under controlled

conditions of flow rate and temperature. After that, a copper nitrate solution was used to incorporate into its crystalline matrix a copper content up to 7%wt by ion-exchange method under constant magnetic stirring. The obtained precipitate was also dried and calcined at controlled conditions. In order to activate the mercury removal sites, the copper-modified hydroxyapatite samples were exposed to a containing H_2S stream immediately before the adsorption runs. Complete description of adsorbent preparation method is described elsewhere [9].

3.2 Physicochemical characterization

Physicochemical properties of the adsorbent (were determined by N_2 adsorption at 77 K (Micrometrics® ASAP 2000), X-ray fluorescence (XRF) (Rigaku RIX 3100), scanning electron microscopy (FEG-SEM) (FEI Company Quanta 400) with energy-dispersive X-ray spectroscopy (EDX), Raman Spectroscopy (LabRam HR-UV800 Jobin-Yvo), and X-ray diffraction (XRD) (Rigaku DMax 2200). The diffraction patterns were refined using the Rietveld method [11].

3.3 Static adsorption study

Allowing quick response times, the static adsorption system (Fig. 2) is made up of a sealed glass container with a mercury bed kept under stirring (IKA RTC Basic).



Fig. 2. Static system used in the batch adsorption studies.

A glass holder allows simultaneous exposure of up to six adsorbent samples to Hg^0 saturated vapor at room temperature. Hg content in solid sat the end of the adsorption tests was determined using atomic absorption spectrometer with Zeeman correction (RA-915+, Lumex) coupled to the Pyro device.

Before the analysis, the samples were diluted 100 times with hydroxyapatite to comply with the detection limit of the equipment. Each analysis was repeated five times and the error was calculated using Student's t-distribution (95% confidence level, normal distribution of fluctuations).

3.4 Dynamic adsorption study

The adsorbent performance for mercury removal in presence of moisture was evaluated in a dynamic system (Fig. 3 and Fig. 4).



Fig. 3. Experimental set-up used in the dynamic adsorption studies. (a) Mercury saturator, (b) fixed-bed reactor, and (c) mercury analyzer.

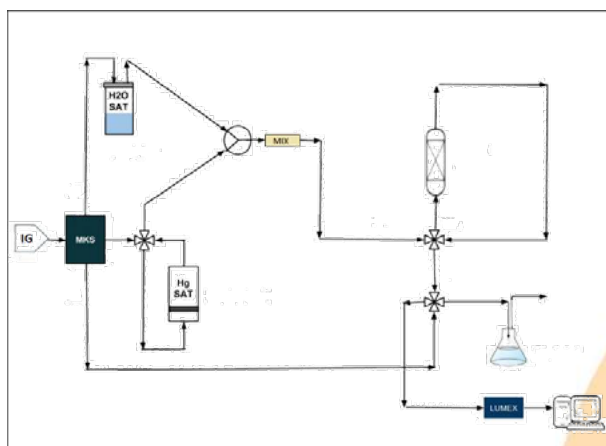


Fig. 4. Schematic representation of the dynamic adsorption system.

As represented in Fig. 4, the carrier gas passes through the mercury and water saturators at constant temperature. The two streams are mixed and the gas stream containing Hg and moisture is sent to the fixed-bed filled by the adsorbent (28°C). Lauda cooling baths and MKS mass flow controllers were used to keep the moisture and

mercury contents at required values. Mercury concentration in the inlet and outlet of the bed was monitored by a mercury analyzer (RA-915+ Lumex). A hydrochloric acid solution was used to capture mercury remaining in the effluent gas. Experimental conditions of dynamic adsorption runs are summarized in Table 1.

Table 1. Experimental conditions for column runs

Adsorbent	HAp-Cu _x S _y
Copper content	6.7%
Fixed-bed temperature (°C)	28
Carrier gas	CH ₄
Total gas flow (mL.min ⁻¹)	30
Bed diameter (cm)	1
Bed length (cm)	0.5
Adsorbent mass (g)	0.25
Hg ⁰ initial concentration (ng.m ⁻³)	11
Moisture content (µg.m ⁻³)	4.75

3.5 Stabilization tests

Thermal stability of samples from static tests was determined by monitoring the percolation of a fixed bed containing the spent adsorbent by an inert gas stream at different temperatures. The amount of mercury released at each temperature level (28 °C, 40 °C, 60 °C and 80 °C, heating rate of 10 °C/min) was monitored (Lumex RA-915 + analyzer).

4. Results and discussion

4.1 Physicochemical properties of the adsorbent

The adsorbent precursor was characterized as a calcium-deficient hydroxyapatite (HAp) (Ca/P ratio less than 1.67). Replacement of calcium by copper in the hydroxyapatite crystalline structure observed in the Rietveld refinement results (increase on Ca/P after chemical modification). Nitrogen isotherm for the HAp is of type IV, which are typical of mesoporous materials with pore average diameter about 30 nm. The same format of copper-modified hydroxyapatite isotherms indicates that the textural properties are maintained after the copper incorporation. EDX results (Fig. 5) confirm that the sulfur is well dispersed in the adsorbent structure.

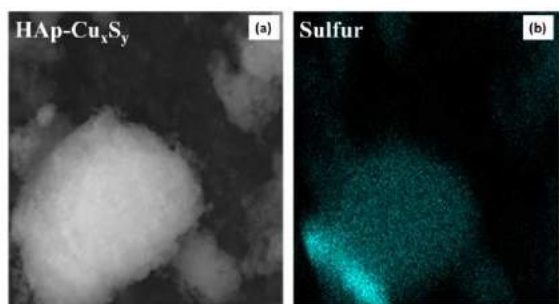


Fig. 5. (a) FEG-SEM image with (b) EDX analysis of the sulfided adsorbent (HAp-Cu_xS_y).

4.2 Adsorption capacity of the adsorbents

As can be seen in Table 2, the study in batch experiments (BE-1 and BE-2) reveals that the mercury removal capacity is proportional to copper content of the adsorbents.

Table 2. Results of batch adsorption experiments

Batch	Duration (days)	Material	Removal capacity (mg/g)
BE-1	21	HAp	0.003
		3,18% CuHAp	40.28
BE-2	54	HAp	0.014
		1,17% CuHAp	25.92

4.3 Dynamic behavior in the presence of moisture

As can be seen in Fig 6, the breakthrough curve in the presence of moisture is very similar to the analogous curve without moisture. This small difference is corroborated by comparing the total mercury content in the adsorbents used (Table 3).

Table 3. Mercury content in the used adsorbent

	Removal capacity (mg/g)
Without moisture	49.87±2.83
With moisture	44.84±1.70

These results show that moisture has no detrimental effect on the performance of the HAp-based adsorbent synthesized here. This behavior is correlated with the ability of hydroxyapatite to disperse the active phase. Another determining factor was the adjustment of the adsorbent textural properties, since the mesoporosity minimizes the effects of capillary condensation.

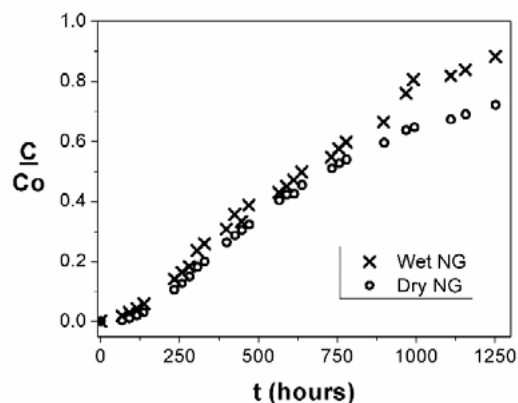


Fig. 6. Breakthrough curves in the presence (Wet NG) and absence of moisture (Dry NG).

4.3 Results for the used adsorbent

No alteration was observed in the morphology of samples when we compared FEG-SEM images for the sulfided (HAp-Cu_xS_y) and used adsorbent (Fig. 7).

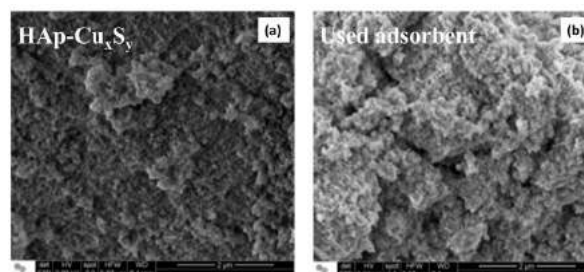


Fig. 7. FEG-SEM images of the (a) sulfided and (b) used adsorbent.

However, a new stable phase of HgS (metacinnabar) in the adsorbent used was identified in experimental XRD patterns (Fig. 8). This observation was made possible by the Rietveld refinement of XRD data, once amount of HgS produced was small (about 7% wt).

The metacinnabar phase was also identified in the Raman spectrum of the used adsorbent (Fig. 9), with the band at 270 cm⁻¹. In the presence of moisture, this phase can be oxidized to HgSO₄ which can also be identified in Raman spectrum (bands at 75, 590 and 1021 cm⁻¹). The characteristic band of HgSO₄ located at 971 cm⁻¹ is not noticed due to de overlap to the characteristic band of HAp (961 cm⁻¹).

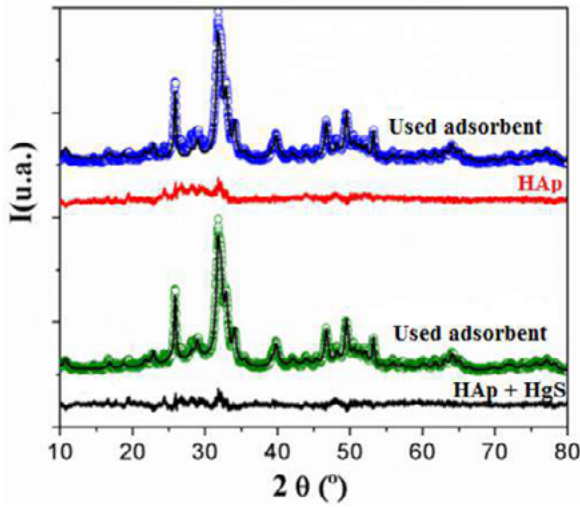


Fig. 8. XRD pattern of the adsorbent using HAp and HAp+HgS in the Rietveld Refinement.

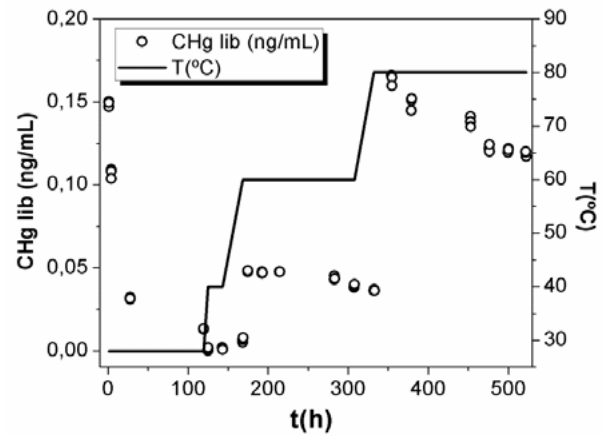


Fig. 9. Thermal stability results. Mercury liberation at different temperatures.

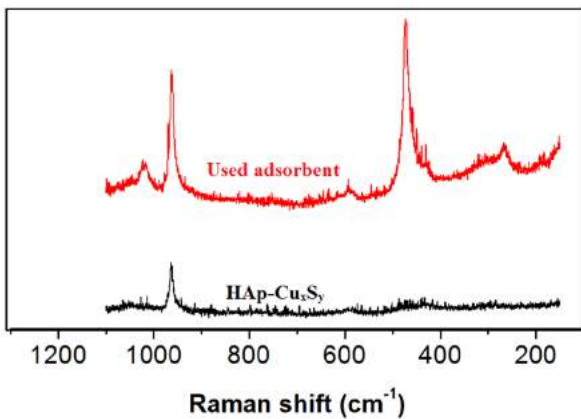


Fig. 9. Raman spectra of the adsorbent and used adsorbent.

At the end of the dynamic runs, the used adsorbent was submitted to the thermal stability test. Figure 10 shows the concentration of Hg observed at the outlet of the bed at different temperatures (28, 40, 60, and 80 °C). It is observed a rapid release of Hg at 28°C. According to the phenomenological model, this amount refers to the non-reacted Hg⁰ present in both gaseous and the porous particle. From Figure 10 and Table 3, it can be seen that negligible amounts of Hg were released at the following temperature thresholds. Results of Table 3 confirm the high stability of Hg in used adsorbent, as there is no significant difference between the solid Hg contents before and after the thermal desorption.

Table 3. Results of batch adsorption experiments

Temperature (°C)	Total time (h)	Hg liberated (ng)	Hg liberated (%wt)
28	119	11.37	0.38
40	24	0.09	0.04
60	165	18.10	0.75
80	216	69.37	2.89
TOTAL	522	98.93	4.00

3.6 Pelletizing

It is also worth noting that the high adsorption/stabilization capacity of HAp-based adsorbents for mercury removal justifies the scale-up of the process related here. In order to enable the scale-up of the process, we have designed and manufactured a pelletizing equipment that allows the production of pellets of similar size to commercial adsorbents used in industrial mercury removal units (MRU).

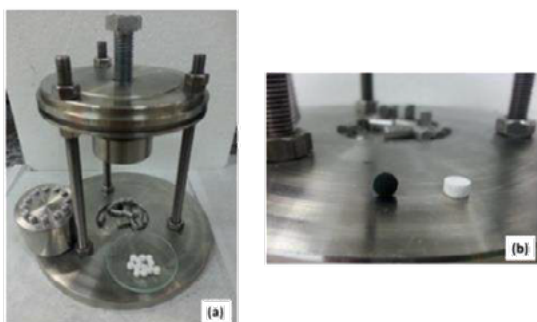


Fig. 10. (a) Pelletizer and (b) produced pellet (cylindrical white particle) in comparison with a commercial adsorbent (spherical black particle).

4. Conclusions

First, the mesoporous and non-stoichiometric HAp-based adsorbent allows the incorporation of Cu_xS_y active sites, which are well-dispersed in the hydroxyapatite matrix. The mercury removal is proportional to copper content, but not-affected by the presence of moisture in the gas stream. The mercury, in the used-adsorbent, is stabilized by the formation of HgS , which can be oxidized to $HgSO_4$ in the presence of moisture. We highlight the development of an efficient adsorbent for mercury removal and stabilization from gaseous streams. Finally, the pelletizing of the material enables the scale-up of the process as well as the execution of comparative pilot plant runs with commercial adsorbents.

Acknowledgements

The authors would like to thank Petrobras, CNPq, CAPES, and FAPERJ foundations by the financial support of this work.

References

- [1] Toxicological Profile for Mercury. Agency for Toxic Substances and Disease Registry (ATSDR). Atlanta, GA: U.S. Department of Health and Human Services, Public Health Service; 1999.
- [2] Global Mercury Assessment. Sources, Emissions, Releases and Environmental Transport. United Nations Environment Programme. UNEP-Chemicals, Geneva, Switzerland; 2013.
- [3] Driscoll CT, Mason RP, Chan HM, Jacob DJ, Pirrone N. Mercury as a global pollutant: sources, pathways, and effects. *Environ Sci Technol* 2013; 47:4967–83.
- [4] Liu H, Chang L, Liu W, Xiong Z, Zhao Y, Zhang J. Advances in mercury removal from coal-fired flue gas by mineral adsorbents, *Chem Eng J* 2020; 379: 122263.
- [5] Harfoushian JH. Quantification of low levels of mercury in gas reservoirs using advanced sampling and analysis techniques. In: SPE Annu Tech Conf Exhib. Society of Petroleum Engineers; 2013.
- [6] Wilhelm SM. Risk analysis for operation of aluminum heat exchangers contaminated by mercury. *Process Saf Prog* 2009; 28:259–66.
- [7] Camargo CLM, De Resende NS, De Oliveira AG, Salim VMM, Tavares FW. Investigation of adsorption-enhanced reaction process of mercury removal from simulated natural gas by mathematical modeling. *Fuel* 2014;129:129–37.
- [8] Camargo C, Oliveira A, Resende N, Biscaia E, Secchi A, Tavares F, Salim VMM. Modelling of Hg^0 removal from gaseous streams and its fixation in hydroxyapatite-based adsorbents modified with copper sulphide. *Adsorpt Sci Technol* 2015; 33(2):175-90.
- [9] Camargo CLM, Salim VMM, Tavares FW, Resende, NS. Phenomenological modeling for elemental mercury capture on hydroxyapatite-based adsorbents: An experimental validation. *Fuel* 2018, 225:509-18.
- [10] Camargo CLM, Resende NS, Perez CAC, Abreu CRA, Salim VMM, Tavares FW. Molecular dynamics simulation and experimental validation by X-ray data of hydroxyapatite crystalline structures. *J Fluid Phase Equilib* 2018;470:60-7.
- [11] Young RA, Robert A. The Rietveld method. International Union of Crystallography;1993.

Competitive adsorption of pharmaceutical compounds onto nanoporous carbon fibres: effect of pH and ionic strength

Ana Claudia Pina^{a,b,*}, Nestor Tancredi^a, Alejandro Amaya^a, Conchi Ania^b

^a Facultad de Química, Udelar, Gral. Flores 2124, Montevideo 11800, Uruguay

^b CEMHTI CNRS (UPR 3079), University of Orléans, 1D Avenue de la Recherche Scientifique CS 90055, Orléans 45071, France

Abstract

This work studies the single component and competitive adsorption of metronidazole (MNZ) and sulfamethoxazole (SMZ), two common antibacterial pharmaceuticals present in wastewaters. Nanoporous carbon fibres prepared upon physical activation of natural wool wastes were used as adsorbents for the adsorption experiments. Single component solutions and several binary mixtures with different molar ratios were prepared in order to investigate the uptake of both components and to assess the kinetic and adsorption models, as well as the influence of the solution pH and ionic strength on the overall adsorption capacity of both pollutants. Data showed that the equilibrium adsorption capacity recorded from single component solutions for MNZ was higher than that recorded from binary solutions, regardless the composition of the mixtures. In contrast, SMZ showed an opposite trend: the uptake of this compound from a binary solution in the presence of MNZ was almost completely suppressed at low concentrations of the pollutant indicating a clear preferential adsorption of MNZ over SMZ. A concentration threshold was needed to trigger the competitive adsorption of SMZ in the binary solutions. Regarding the effect of pH and ionic strength, the former decreased the uptake of SMZ and had no effect on MNZ adsorption, while the increase in the ionic strength decreased the uptake of MNZ, indicating a salting-out effect.

Keywords: competitive adsorption; activated carbon fibres; metronidazole; sulfamethoxazole; ionic strength.

1. Introduction

Pharmaceutically active compounds (PAC's) are emerging contaminants that have become a risk to the environment and to human health in recent years. Sulfamethoxazole (SMZ) and metronidazole (MNZ) are widely consumed prescribed antibiotics, which presence is regularly detected in watercourse ecosystems because of the ineffectiveness of conventional processes (i.e., biological treatment) to treat polluted waters, and because of their often very slow natural biodegradation [1]. Therefore, it is imperative to find more efficient technologies that allow the complete removal of such contaminants from treated effluents, before they are discharged to watercourses. Adsorption onto activated carbons is a well-known technology typically used as tertiary treatment in water and wastewater effluents processing. Its effectiveness to remove water pollution depends on several factors such as solution pH [2], ionic strength [3, 4], presence of various

pollutants, temperature, as well as the physicochemical characteristics of the carbon adsorbent. In this regard, the simultaneous adsorption of various pollutants is a scarcely investigated issue; despite it may affect the overall uptake of the pollutants due to the competition for the adsorption sites on the adsorbent. Hence, establishing the extent of this interdependence is of paramount importance for a successful adsorption.

In order to assess the adsorption behavior of two or more pollutants, several adsorption models can be found; the Langmuir Multicomponent (LM) model is among most widely used ones [5]. This model supposes that the competence among the different compounds is correlated to their respective equilibrium concentrations, and the parameters of the individual adsorption isotherms (1).

$$q_i = \frac{q_{m,i} K_i C_i}{1 + \sum_{j=i}^i K_j C_j} \quad (1)$$

where K_i and $q_{m,i}$ are the Langmuir model parameters of the individual adsorption isotherms of each component in the binary solution.

In this context, the main objective of this work was to investigate the competitive adsorption of two pharmaceutical compounds on nanoporous carbon fibers, to establish the removal efficiencies from equilibrium adsorption tests on single component solutions and binary mixtures, taking into account the effects of pH and ionic strength.

2. Experimental

2.1 Materials

Sulfamethoxazole and metronidazole were purchased from Sigma-Aldrich (reagent purity). All solutions were prepared from Milli-Q water purification Systems. Nanoporous carbon fibers (NCF) were synthesized by physical activation of wool fibre wastes. Briefly, the as-received wool fibres were carbonized under inert atmosphere and the obtained char was subsequently activated under CO_2 (ca. $950\text{ }^\circ\text{C}$, 200 mL min^{-1}) for 30 min, in a horizontal oven (Carbolite Furnaces).

2.2 Batch equilibrium adsorption tests

About 50 mL of unbuffered solutions of MNZ and/or SMZ were put in contact with ca. 25 mg of NCF and left under stirring (400 rpm) at room temperature until equilibrium was reached. Afterwards, the solutions were filtered and the concentration of each pollutant was measured by UV-vis spectrophotometry at their corresponding wavelengths (Shimadzu 2700 UV-Vis). Adsorption essays were carried out by duplicate. Solutions were also prepared adjusting the pH between 5-10 using 0.1M NaOH and HCl, and the ionic strength with 0.01 and 0.1M NaCl.

2.3 Characterization of the carbon adsorbent

The porosity of the NCF was characterized by gas N_2 and CO_2 adsorption isotherms at -196 and $0\text{ }^\circ\text{C}$ respectively in volumetric analyzers. Before the experiments, the samples were outgassed under vacuum (ca. 10^{-3} Torr) at $120\text{ }^\circ\text{C}$ overnight. Apparent specific surface area (S_{BET}), total pore volume (V_{T}), and micro-/mesopore volumes were determined from the gas adsorption data.

3. Results and discussion

Nanoporous carbon fibers prepared upon activation of wool wastes were used as carbon adsorbents for the removal of the targeted pharmaceutical compounds from aqueous solutions. The textural characterization of the prepared NCF showed that the materials displayed a type I nitrogen adsorption isotherm, characteristic of microporous adsorbents (Figure 1), with a specific surface area of ca. $700\text{ m}^2\text{ g}^{-1}$ and a total pore volume of $0.300\text{ cm}^3\text{ g}^{-1}$ -accounting for a large fraction of micropores (ca. 70 %). Such textural characteristics make this material an adequate one for the retention of small organic molecules (such as the selected pharmaceutical compounds).

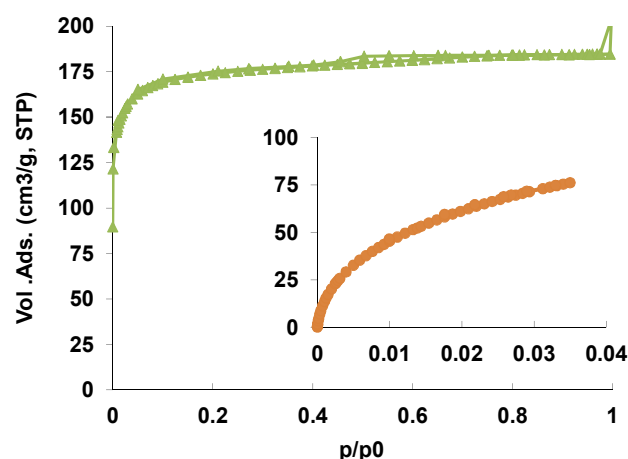


Fig. 1. N_2 and CO_2 (inset) adsorption-desorption isotherms at -196 and $0\text{ }^\circ\text{C}$, respectively, of the prepared nanoporous carbon fibers.

Initially, kinetic studies for the adsorption of SMZ and MNZ were carried out. Data showed that equilibrium was obtained after 48 hours for SMZ, while the uptake was much faster (ca. 2.5 hours) for MNZ. In both cases, a good fitting of the experimental kinetic data was obtained upon application of a pseudo second order kinetic model.

The equilibrium adsorption isotherms from single component solutions were measured for both compounds (Figure 2). The uptakes are in line with those reported in the literature for activated carbons with similar porous features [6]. As seen, the uptake of MNZ is higher than that of SMZ, indicating a higher affinity of the former for the adsorption sites on the carbon adsorbent. Data was fitted to the classical Langmuir and Freundlich models; in both cases, better fittings were obtained upon application

of the Langmuir model, indicating to similar adsorption sites on the carbon adsorbent. The main parameters from Langmuir fitting are compiled in (Table 1).

Table 1. Adsorption parameters obtained for the fitting of the experimental equilibrium data corresponding to single component solutions to Langmuir model.

	q_m (mmol g ⁻¹)	K (L mmol ⁻¹)	R^2
MNZ	0.28	96	0.98
SMZ	0.15	73	0.97

The uptake of both compounds was also assessed at different pH and ionic strength conditions. It can be observed that while the adsorption capacity of MNZ remained rather unmodified upon the effect of pH, the uptake of SMZ strongly decreased as the pH increased. On the other hand, the ionic strength decreased the adsorption capacities of the compounds (Figure 2).

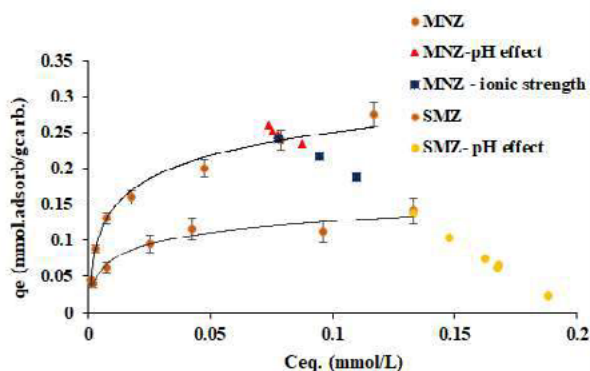


Fig. 2. Equilibrium adsorption isotherms of single component unbuffered solutions of MNZ and SMZ. The adsorption operating lines (blue squares and light orange circles) correspond to the uptake for a selected concentration upon modification of pH and ionic strength.

Several binary solutions were tested varying the molar ratio of the components (SMZ-MNZ) as follows: 1-1, 1-1.5, 1.5-1, 1-2 2-1, 1-10, 10-1, 100-1, and 1-100. The adsorption capacities of both compounds decreased compared to the overall uptake from single component solutions, being the effect much more pronounced in the case of SMZ. This seems reasonable since the single component solutions had already pointed out the higher affinity

of MNZ for the carbon adsorbent (Table 1, Figure 2).

When both components were simultaneously present in the solution, the adsorption kinetics remained unmodified, with a good fitting to a pseudo second order model. The equilibrium data corresponding to the uptake from the binary mixtures was fitted the Langmuir multicomponent model (Figure 3). Data showed a large deviation of the experimental adsorption data from the predictions upon application of the Langmuir multicomponent model (e.g., deviation for the bisectrix line in Figure 3), indicating strong competitive effects for these compounds.

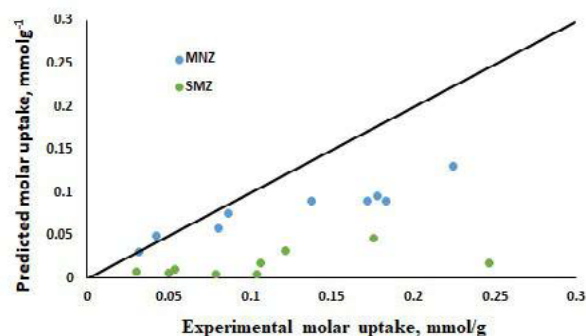


Fig. 3. Comparison between the experimental predicted molar uptake and the predicted uptake by the Langmuir multicomponent model for the adsorption of MNZ and SMZ from binary solutions at various molar ratios.

For low equilibrium concentrations, the adsorption of MNZ would seem to be independent of the presence of SMZ, as the adsorption carries out as if the compound were in a single component solution. In contrast, the retention of SMZ seems to be completely suppressed. Above an equilibrium concentration threshold, the uptake of both compounds is strongly affected by the competitive effects, suggesting that SMZ is able to displace MNZ from the adsorption sites only at high molar ratios.

4. Conclusions

The prepared nanoporous carbon fiber upon physical activation of wool fibers showed good adsorption capacities for the removal of both studied



drugs from aqueous solutions, with capacities similar to those obtained with commercial activated carbons. In addition, the solution pH and ionic strength affect the uptake of the compounds, particularly in the case of SMZ (ca. 23 % decrease in the amount adsorbed by increasing the pH). A strong competitive effect was found for the retention of MZN and SMZ in binary solutions, indicating that these compounds are adsorbed in the same sites of the carbon adsorbent. The uptake of MNZ was barely modified in the presence of small amounts of SMZ -while the uptake of SMZ is completely suppressed-, due to its higher affinity towards the carbon adsorbent. Above a SMZ concentration threshold, the uptake of MNZ starts to lower, indicating the displacement of the compound by SMZ when the latter is present at relatively large concentrations than the former.

Acknowledgements

This work was funded by ANII through a scholarship fund for national postgraduates (POS_NAC_2016_1_130887, PEDECIBA), and Region Centre Val de Loire (APR-IA, MOSAIK project).

References

- [1] Grenni P, Ancona V, Barra Caracciolo A. (2018) Ecological effects of antibiotics on natural ecosystems: A review, *Micochemical Journal*, 136, 25-39.
- [2] Kyriakopoulos G, Doulia, D. (2006) Effect of ionic strength and pH on the adsorption of selected herbicides on Amberlite. *International Journal of Environmental Analytical Chemistry*, 86, 3-4, 207-214.
- [3] Endo S, Pfennigsdorff A. (2012) Salting-out effect in aqueous NaCl solutions: trends with size and polarity of solute molecules. *Environmental Science and Technology*, 46, 1496 – 1503.
- [4] Mansouri H, Carmona R. (2015) Competitive adsorption of ibuprofen and amoxicillin mixtures from aqueous solution on activated carbons. *Journal of Colloid and Interface Science*, 449, 252 – 260.
- [5] Leyva-Ramos R, Bernal-Jerome L. (2001) Competitive adsorption of Cd(II) and Zn(II) from aqueous solution onto activated carbon. *Separation Science and Technology*, 36 (16), 3673 – 3687.
- [6] Ahmed M, Theydan S. (2013) Microporous activated carbon from *Siris* seed pods by microwave-induced KOH activation for metronidazole adsorption. *Journal of Analytical and Applied Pyrolysis*, 99, 101 – 109.

Organosolv lignin/Fe₃O₄ nanoparticles applied as textile dye adsorbent

Carlos Eduardo de Araújo Padilha^a, Cleitiane da Costa Nogueira^a, Everaldo Silvino dos Santos^{a,*}

^a *Laboratory of Biochemical Engineering, Chemical Engineering Department, Federal University of Rio Grande do Norte (UFRN), Natal-RN and CEP: 59078 970, Brazil.*

Abstract

The use of lignin is a path to the economic viability of biofuel production schemes from agro-industrial wastes. Then, the organosolv pretreatment black liquor from green coconut fiber (GCF) was used in the synthesis of lignin/Fe₃O₄ nanoparticles. The coating of Fe₃O₄ nanoparticles was evaluated by X-ray and dynamic light scattering analysis. In biosorption experiments, lignin/Fe₃O₄ nanoparticles exhibited low equilibration time and high adsorption capacity of Methylene blue (203.66 mg/g), Cibacron blue (112.36 mg/g) and Remazol red (96.46 mg/g) dyes. After four cycles, the adsorption of the Methylene blue dye on lignin/Fe₃O₄ nanoparticles reduced 43.68% using 0.1 M HCl as eluent. In summary, lignin-based nanostructured particles have been successful as magnetic-responsive biosorbent and their application should be encouraged to solve other engineering problems.

Keywords: Biomass, biorefinery, recycling, enzymatic hydrolysis

1. Introduction

Lignin is one of the main constituents of plant biomass, together with carbohydrates cellulose and hemicellulose, being the most prominent natural source of aromatic compounds [1]. In plants, this biopolymer is responsible for imparting rigidity and hydrophobicity to cell walls [2]. Since it is associated with the poor performance of the pulp and paper industries, lignin removal procedures are often recommended in these schemes without any conception of their recovery. However, recent literature highlights its potential as a by-product with potential for income generation [3].

Lignin incineration is a common practice in industrial plants as it meets the needs of heat and electricity but cannot handle the amount extracted from the biopolymer [1]. The structural complexity of lignin is a challenge for its use as a block molecule, so noble applications can be achieved by seeing it as a “building block” [4]. Lignin is

appointed as a polymeric matrix for the new generation of functional nanoparticles, replacing petroleum and inorganic materials [5]. Recently, there has been an intense search for nanostructured materials such as nanoparticles, nanotubes and biosorption nanocomposites. Nanostructured materials offer greater surface area, better coating and lower mass transfer resistance than conventional adsorbents [6].

In this context, the present study proposes the valorization of black liquor from pretreatment of green coconut fiber aiming to obtain functional lignin-based nanoparticles. The lignin/Fe₃O₄ nanocomposite was used as adsorbents for the removal of textile dyes in aqueous solutions.

2. Materials and methods

2.1. Chemicals

Citric acid, dibasic potassium phosphate, glycerol, hydrochloric acid (HCl), iron (III) chloride hexahydrate, iron (II) sulfate heptahydrate,

methylene blue dye, monobasic potassium phosphate, polyethylene glycol 400 (PEG 400), sodium azide, sodium citrate tribasic dihydrate, sodium hydroxide (NaOH), sulfuric acid and Tris were purchased from Synth (São Paulo, Brazil). The reactive dyes Cibacron blue 3R-P and Red Remazol RB 133% were kindly provided by the Department of Textile Engineering of the Federal University of Rio Grande do Norte.

2.2. Extraction of organosolv lignin from green coconut fiber

Green coconut shells were collected in urban areas of Natal (Rio Grande do Norte/Brazil). The material was cut with a machete, washed with tap water and dried in an air circulation oven at 50 °C for 72 h. Then pieces of the green coconut shell were ground in a knife mill (model TE-680, TECNAL, Brazil) to 20 mesh and stored in plastic bags.

Organosolv lignin was extracted via glycerol-based pretreatment of green coconut fiber (GCF), according to Padilha et al. [7]. Firstly, 20 g GCF (dry basis) and 400 g aqueous glycerol solution (80% w/w glycerol, 19% w/w deionized water and 1% w/w sulfuric acid) were added in 500 mL-Erlenmeyers and then kept at 121 °C (autoclave) for 120 min. After incubation time, the lignin-rich liquid fraction (also called black liquor) was recovered by cloth filtration and stored in refrigerator at -20 °C. The pretreated GCF was washed until neutral pH of the washing water and dried with air circulation oven at 50 °C for 48 h.

2.3. Synthesis of Fe₃O₄ and organosolv lignin/Fe₃O₄ nanoparticles

Fe₃O₄ nanoparticles were prepared by coprecipitation method in alkaline environment, as reported by Li et al. (2018b). Thus, 200 mL of iron salt solution (0.02 M Fe³⁺, 0.01 M Fe²⁺ and 0.1 M PEG 400) was placed in a three-necked flask, purged with N₂ gas and heated to 80 °C under stirring. Then 25 mL of 3 M NaOH solution was dripped to maintain the ambient pH above 10 and the reaction was kept under stirring for 60 min. The black product was cooled to room temperature for 60 min and washed five times with deionized water and once with anhydrous ethanol using a neodymium magnet for liquid phase separation.

Lignin/Fe₃O₄ nanoparticles were prepared by antisolvent precipitation. In summary, 10 mg of Fe₃O₄, 2.5 g of black liquor, 20 g of glycerol were placed in 250 mL-beaker under stirring at room temperature. Deionized water was added by dripping using a TE-BP-01 peristaltic pump (TECNAL, Brazil) to the final water content of 90% (w/w) and the suspension was stirred for 15 min. Then, the nanoparticles were washed with deionized water and resuspended to the final concentration of 1.0 mg/mL. The hydrodynamic size and zeta potential (ζ) of aqueous Fe₃O₄ and lignin/Fe₃O₄ suspensions were determined by 90Plus/Bi-MAS ZetaPlus (Brookhaven Inst. Co., USA) after ultrasonification.

2.4. Biosorption of textile dye

Lignin/Fe₃O₄ nanoparticles were also evaluated as adsorbents for the removal of Methylene blue (MB), Cibacron blue (CB) and Remazol red (RR) textile dyes. In the kinetic experiments, dye concentration of 10.0 µg/mL and lignin/Fe₃O₄ nanoparticles at 40, 100 and 200 µg/mL were added in 2.0 mL-centrifuge tubes and maintained under 30 °C and 150 rpm. The pH values of the suspensions were adjusted using 20.0 mM Tris-HCl buffer (pH 9.0) for MB dye and 20.0 mM sodium citrate buffer (pH 4.0) for CB and RR dyes. After incubation, the nanoparticles were separated by neodymium magnet and dye concentrations were analyzed by spectrophotometer (ThermoSpectronic Genesys 10 UV/Vis, USA) at 660 nm for MB dye, 622 nm for CB dye and 512 nm for RR dye. Similar to the previous procedure, equilibrium data were obtained after incubation of different dye concentrations using 100.0 µg/mL lignin/Fe₃O₄ nanoparticles for 240 min under 30 °C and 150 rpm.

The reuse of lignin/Fe₃O₄ nanoparticles as adsorbent was also investigated. After the adsorption step using 10 µg/mL MB dye and 100 µg/mL lignin/Fe₃O₄ nanoparticles, the supernatant was discarded via magnetic separation and 2 mL of 0.1 M HCl was used in the desorption step. Then the nanoparticles were washed with 2 mL of 50.0 mM citrate buffer (pH 4.0) and separated by centrifugation for a new adsorption step using 10 µg/mL MB dye solution.

The dye adsorption capacity (q) was calculated by Eq. 1, while the Langmuir isotherm model was used to adjust to equilibrium data and was expressed by Eq. 2.

$$q = \frac{(C_0 - C) \times V}{m} \quad (1)$$

$$q = \frac{q_{max}C}{k_d + C} \quad (2)$$

In Eq. 1, m is the mass of lignin/Fe₃O₄ nanoparticles, V is the volume of the liquid phase, C_0 and C are the initial dye concentration and the residual dye concentration, respectively. In Eq. 2, q_{max} is the maximum dye adsorption capacity, k_d is the dissociation constant. The parameters were determined from experiments performed at 25 °C and the determination coefficient (R^2) was used as a measure of goodness of fit to the experimental data.

3. Results and discussions

Physicochemical properties of organosolv lignin used in this study were previously reported in Padilha et al. (2019). This lignin has the following composition: 93.10% (w/w) Klason lignin, 3.73% (w/w) acid soluble lignin and 2.47% (w/w) polysaccharide residues. The concentration of organosolv lignin in black liquor was approximately 14 g/L and showed good solubility in organic solvents such as ethanol, acetone and tetrahydrofuran. In terms of reactivity, organosolv lignin had a higher concentration of phenolic hydroxyls (1.04 mmol/g) than some technical lignins, indicating its potential as a natural binder [8,9].

Figure 1 shows the size distributions of Fe₃O₄ and lignin/Fe₃O₄ nanoparticles obtained by dynamic light scattering (DLS) analysis. Obviously, lignin self-assembly promoted an increase in mean size and polydispersity compared to uncoated magnetic nanoparticles. Fe₃O₄ and lignin/Fe₃O₄ nanoparticles had an average size of 101.3 and 662.3 nm, respectively. Li et al. [10] reported that the thickness of lignin coating on lignin/Fe₃O₄ nanoparticles is a function of biopolymer concentration. DLS results also indicated negative surface charge for both magnetic nanoparticles at pH 5.0, with potential values of -10.1 and -28.2 mV for Fe₃O₄ and lignin/Fe₃O₄ nanoparticles, respectively. According to Sipponen et al. [11], zeta potential values greater than 20 mV (either positive or negative) prevent aggregation of lignin nanoparticles. However, lignin/Fe₃O₄ nanoparticles settle within a few hours, which can be attributed to the action of intermolecular forces (hydrogen bonding, pi-pi stacking and Van der Waals strength) or

composite size/density, as reported by Larsson et al. [12].

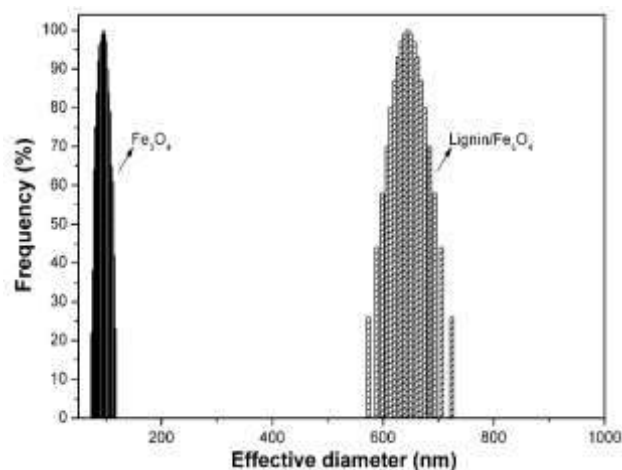


Figure 1. Hydrodynamic size of Fe₃O₄ and lignin/Fe₃O₄ nanoparticles measured by DLS

Adsorption-based processes are often chosen for wastewater treatment because of their simplicity, efficiency and scalability. Agitated tanks or fixed bed columns are employed in industrial scale to remove large volumes of pollutants including antibiotics, heavy metals and dyes [13]. Particularly, much attention has been paid to the disposal of textile dyes due to their stability in aqueous media and their possible mutagenic and carcinogenic effects on living organisms (Azari et al., 2019). Recent literature has shown advances in the use of lignin-based materials as a textile dye adsorbent in place of commercial activated carbon. Such adsorbents may comprise lignocellulosic residues such as peels, pomace, stems and fibers or composites that use lignin as a polymeric matrix [10, 15].

Thus, experiments were conducted to investigate the removal of MB, CB and RR textile dyes by adsorption on lignin/Fe₃O₄ nanoparticles, whose kinetic profiles are shown in Figure 2. All processes quickly reached the adsorption equilibrium (< 30 min). which can be attributed to the high surface area of this adsorbent and the absence of steric hindrance, as reported by Li et al. [10]. MB dye showed higher affinity for lignin Fe₃O₄ nanoparticles compared to other dyes. Using 40 µg/L nanoparticles, it was possible to remove 87.22% of the initial MB dye content from the liquid medium. On the other hand, kinetic studies showed removal

of only 66.78% for CB dye and 38.03% for RR dye using the maximum adsorbent dosage.

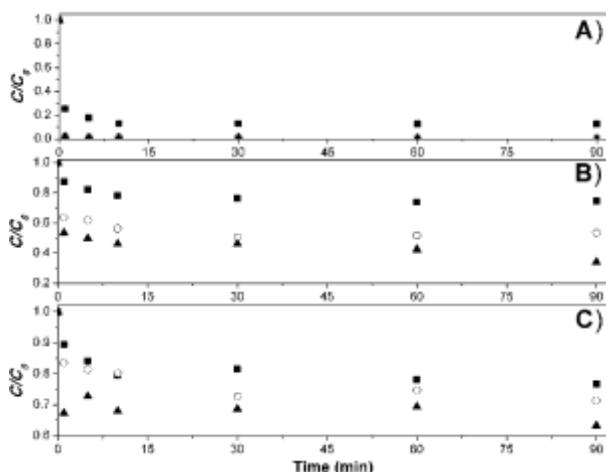


Figure 2. Adsorption kinetics of MB (A), CB (B), RR (C) dyes using 40 (■), 100 (○) and 200 µg/mL (▲) lignin/Fe₃O₄ nanoparticles. The following experimental conditions were: initial dye concentration of 10 µg/mL, pH 9.0 for MB dye experiments, pH 4.0 for CB and RR dye experiments, 30 °C and stirring of 150 rpm.

Adsorption equilibrium experiments and Langmuir isotherm were also performed to investigate the textile dyes affinity to adsorbent. They provide information on the maximum retention as well as the magnitude of adsorbate-adsorbent interactions [16]. In Figure 3, it can be seen that the Langmuir model fitted appropriately to the experimental data involving MB ($R^2 = 0.96$), CB ($R^2 = 0.99$) and RR ($R^2 = 0.99$) dyes. The maximum adsorption capacity (q_{max}) estimated for MB dye was 203.66 mg/g, being 81.26% (112.36 mg/g) and 111.14% (96.46 mg/g) higher than CB and RR dyes, respectively. The dissociation coefficients were 0.22, 12.84 and 16.28 µg/mL for MB, CB and RR dyes, respectively. Under alkaline conditions, the surface of the lignin acquires a negative electric charge and establishes electrostatic interactions with cationic molecules, which justifies the higher retention of MB dye [17].

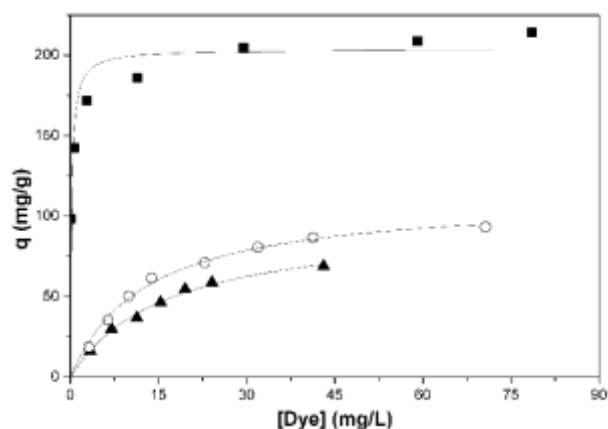


Figure 3. Adsorption equilibrium of MB (■), CB (○) and RR (▲) dyes using lignin/Fe₃O₄ nanoparticles as adsorbent and Langmuir (—) isotherm. The following experimental conditions were: pH 9.0 for MB dye experiments, pH 4.0 for CB and RR dye experiments, 60 min of incubation, 30 °C and stirring of 150 rpm.

The regenerative capacity of an adsorbent is critical in the development of economically viable processes [18]. In the present study, MB dye-impregnated lignin/Fe₃O₄ nanoparticles were eluted with 0.1 M HCl and promptly reused in a new adsorption step. After the first regeneration, the adsorbent adsorption capacity reached 97.70 mg/g, which represented a loss of only 1.54% of the initial retention potential (See Figure 4). The efficiency of this eluent is justified by the competition between the H⁺ ions and the dye molecules by the active site of lignin and by avoiding the ionizable change in the adsorbent state [19]. However, the dye adsorption capacity has reduced severely with the number of recycles. These results suggest that irreversible dye adsorption occurs on the lignin surface, as observed in Li et al. [10]. Nevertheless, further studies can be performed to improve the performance of this adsorbent in the treatment of contaminated waters, either by the use of other lignin source or by grafting electrically charged functional groups.

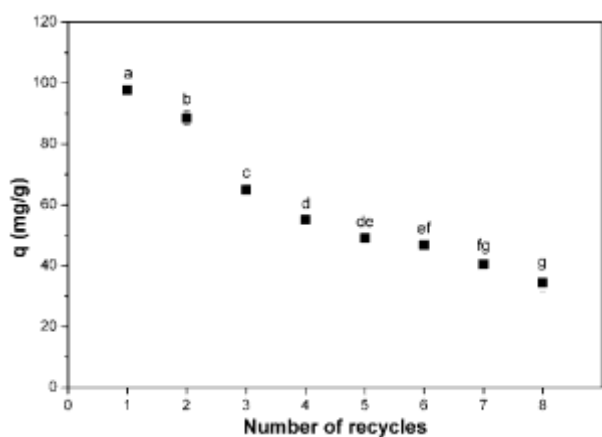


Figure 4. Impact of the number of recycles on MB dye removal using lignin/Fe₃O₄ nanoparticles as adsorbent. The following experimental conditions were: initial dye concentration of 10 µg/mL, pH 9.0 for MB dye experiments, 0.1 M HCl in desorption step, 30 °C and stirring of 150 rpm. Lowercase letters a, b, c, d, e, f and g were used for comparison of dye adsorption capacity. Values with the same letter are not statistically different between them using 95% confidence level ($p > 0.05$).

4. Conclusions

The anti-solvent precipitation method allowed the lignin self-assembly from organosolv black liquor on Fe₃O₄ nuclei and consequently the synthesis of nanoparticles for semi-stable suspensions. Due to their unique properties, lignin/Fe₃O₄ nanoparticles showed high adsorption capacity of textile dyes and low equilibrium time compared to other biosorbents. Thus, the proposed methodology proved successful in valuing lignins extracted from lignocellulosic residues.

Acknowledgement

The authors thank Coordination for the Improvement of Higher Education Personnel (CAPES) and Brazilian National Council of Research (CNPq) for the financial support (Grant number: 141275/2017-0).

References

- [1] Wyman, C. E., Ragauskas, A. J. Lignin Bioproducts to Enable Biofuels. *Biofuels, Bioproducts & Biorefining*, 2015: 9: 447-449.
- [2] Isikgor, F. H.; Becer, C. R. Lignocellulosic biomass: a sustainable platform for the production of bio-based chemicals and polymers. *Polymer Chemistry* 2015: 6: 4497-4559.
- [3] Graichen, F. H. M., Grigsby, W. J., Hill, S. J., Raymond, L. G., Sanglard, M., Smith, D. A., Thorlby, G. J., Torr, K. M., Warnes, J. M. Yes, we can make money out of lignin and other bio-based resources. *Industrial Crops and Products* 2017: 106: 74-85.
- [4] Chen, L., Zhou, X., Shi, Y., Gao, B. Wu, J., Kirk, T. B., Xu, J. Xue, W. Green synthesis of lignin nanoparticle in aqueous hydrotropic solution toward broadening the window for its processing and application. *Chemical Engineering Journal* 2018: 346: 217-225.
- [5] Tian, D., Hu, J., Bao, J., Chandra, R. P., Saddler, J. N., Lu, C. Lignin valorization: lignin nanoparticles as high-value bio-additive for multifunctional nanocomposites. *Biotechnology for biofuels* 2017: 10: 192-203.
- [6] Ahmad, R., Sardar, M. Enzyme immobilization: An Overview on Nanoparticles as Immobilization Matrix. *Biochemistry & Analytical Biochemistry* 2015: 4: 1-8.
- [7] Padilha, C. E. A., Nogueira, C. C., Souza, D. F. S., Oliveira, J. A., Santos, E. S. Valorization of green coconut fibre: Use of the black liquor of organosolv pretreatment for ethanol production and washing water for production of rhamnolipids from *Pseudomonas aeruginosa* ATCC 27583. *Industrial Crops and Products* 2019: 140: 111604.
- [8] Haz, A., Strizincova, P., Majova, V., Sskulcova, A., Surina, I., Jablonsky, M. Content of phenolic hydroxyl groups in lignin: Characterisation of 23 isolated non-wood lignin with various acid. *International Journal of Recent Scientific Research* 2016: 7: 11547-11551.
- [9] Wang, H., Liu, W., Huang, J., Yang, D., Qiu, X. 2018. Bioinspired Engineering towards Tailoring Advanced Lignin/Rubber Elastomers. *Polymers* 2018: 10: 1033-1047.
- [10] Li, X., He, Y., Sui, H., He, L. One-Step Fabrication of Dual Responsive Lignin Coated Fe₃O₄ Nanoparticles for Efficient Removal of Cationic and Anionic Dyes. *Nanomaterials* 2018: 8: 162-177.
- [11] Sipponen, M. K., Smyth, M., Leskinen, T., Johansson, L. S., Österberg, M. All-lignin approach to prepare cationic colloidal lignin particles: stabilization of durable Pickering emulsions. *Green Chemistry* 2017:19: 5831-5840.

[12] Larsson, M., Hill, A., Duffy, J. Suspension Stability; Why Particle Size, Zeta Potential and Rheology are Important. Annual Transactions of the Nordic Rheology Society 2012: 20: 209-214.

[13] Kyzas, G. Z., Kostoglou, M. Green Adsorbents for Wastewaters: A Critical Review. Materials (Basel) 2014: 7: 333-364.

[14] Azari, A., Noorisepehr, M., Dehganifard, E., Karimyan, K., Hashemi, S. Y., Kalhori, E. M., Norouzi, R., Agarwal, S., Gupta, V. K. Experimental design, modeling and mechanism of cationic dyes biosorption on to magnetic chitosan-lutaraldehyde composite. International Journal of Biological Macromolecules 2019: 131: 633-645.

[15] Castro, K. C., Cossolin, A. S., Reis, H. C. O., Morais, E. B. Biosorption of anionic textile dyes from aqueous solution by yeast slurry from brewery. Brazilian Archives of Biology and Technology 2017: 60: 1-13.

[16] Boudechiche, N., Mokaddem, H., Sadaoui, Z., Trari, M. Biosorption of cationic dye from aqueous solutions onto lignocellulosic biomass (*Luffa cylindrica*): characterization, equilibrium, kinetic and thermodynamic studies. International Journal of Industrial Chemistry 2016: 7: 167-180.

[17] Li, J., Li, H., Yuan, Z., Fang, J., Chang, L., Zhang, H., Li, C. Role of sulfonation in lignin-based material for adsorption removal of cationic dyes. International Journal of Biological Macromolecules 2019: 135: 1171-1181.

[18] Kumar, A. S. K., Jiang, S. J. Synthesis of magnetically separable and recyclable magnetic nanoparticles decorated with β -cyclodextrin functionalized graphene oxide an excellent adsorption of As (V)/(III). Journal of Molecular Liquids 2017: 237: 387-401.

[19] Azimvand, J., Didehban, K., Mirshokraie, S. A., Safrain-O removal from aqueous solutions using lignin nanoparticle-g-polyacrylic acid adsorbent: Synthesis, properties, and application. Adsorption Science & Technology 2018: 36: 1422-1440.

Antibiotic removal from water using MgFe/layered double hydroxide as adsorbent

Douglas Phelipe de Lima, Mateus Ferreira da Silva, Anamália Ferreira da Silva, Alessandra Honjo Ide, Lucas Meili*

Laboratório de Processos, Centro de Tecnologia, Universidade Federal de Alagoas, Maceió, 57072-970, Alagoas

Abstract

Layered double hydroxides (LDHs) are anionic clays of great interest due to their interesting properties, such as low cost, thermal stability, two-dimensional structure, high surface area, memory effect and high anion-exchange capacities, as well as the versatility of applications. In this context, an alternative adsorbent, MgFe/layered double hydroxide, is proposed for amoxicillin removal from water. The material was successfully synthesized via the co-precipitation method at constant pH, by using Mg and Fe as cations, intercalated with chloride anions. After characterization through X-ray diffraction and N₂ adsorption/desorption analysis, the material was evaluated in batch assays. From the preliminary results obtained, MgFe/LDH provided amoxicillin removal over 90% within 3 h of contact, reaching the adsorptive capacity of 9.11 mg.g⁻¹. Kinetic studies showed that pseudo-second order model better explained the experimental data, indicating the predominance of chemisorption. In brief, the data achieved suggested that the material under study can be a potential adsorbent for the antibiotic removal, requiring more investigation.

Keywords: Adsorption; LDH; hydrotalcite; emerging contaminants; amoxicillin

1. Introduction

Layered double hydroxides (LDHs) consists of piles of positively charged metal hydroxide layers with the presence of interlayer anions which maintain the charge neutrality in the structure (Fig. 1). The general formula is $[M^{+2}_{1-x}M^{+3}_x(OH)_2]^{+x}A^{-n}_{x/n} \cdot mH_2O$, where M⁺² is a divalent metal, M⁺³ is a trivalent metal, m is the number of molecules of water and A⁻ⁿ is an anion n valent. Commonly, the ratio between M⁺²/M⁺³ is 0.1 ≤ x ≤ 0.5 molecules [1].

LDHs have received attention due to the potential application in several areas, such as catalysis [3-4], adsorption [5-6] and anion exchange [7]. Moreover, they present interesting properties, i.e, low cost, thermal stability, two-dimensional structure, high surface area and memory effect. Although it can be found in nature in small quantities, their synthesis in the laboratory is considered simple and inexpensive. [8].

Thus, LDHs can be a promising adsorbent for water treatment. One of the biggest issues currently involving water and wastewater treatment is regarding the efficient removal of pharmaceutical products. Due to the intense use of these compounds in human and veterinary medicine and high complexity of the chemical structures, they are not always completely removed from water after conventional treatment systems [9].

Antibiotics are an important class of pharmaceuticals and the major problem related to their presence in the environment is the emergence of antibiotic-resistant bacteria [10]. Therefore, the use of processes that allow efficient removal of these compounds is of great importance.

In this context, the present contribution aimed to show the preliminary results achieved by using MgFe/LDH to remove amoxicillin (Fig. 2) from water. For such purpose, the adsorbent material was synthesized using the co-precipitation method at constant pH, characterized and then applied for the antibiotic adsorption under batch assays.

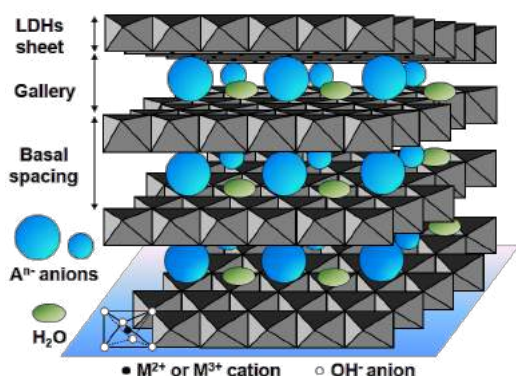


Fig. 1. General structure of a LDH [2].

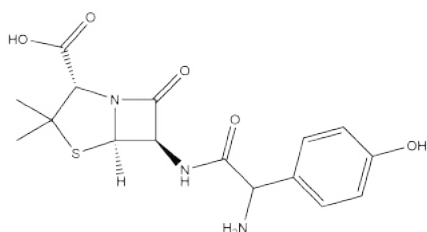


Fig. 2. Chemical structure of amoxicillin.

2. Experimental

1.1. Adsorbate

Amoxicillin was used as adsorbate. A stock standard solution ($1000 \text{ mg}\cdot\text{L}^{-1}$) was prepared and appropriately diluted to obtain all other solutions used in this study. Amoxicillin quantification was performed using a spectrophotometer Shimadzu MultiSpec-1501, with absorbance measurements at 226 nm. The analytical curve was plotted with concentrations ranging from 1.0 to $10.0 \text{ mg}\cdot\text{L}^{-1}$.

1.2. Adsorbent

MgFe/LDH was synthesized by the coprecipitation method at constant pH, based on Seida et al. methodology [11]. 24.007 g, of sodium hydroxide (NaOH, Synth), were dissolved in 200 mL of deionized water to prepare a $3 \text{ mol}\cdot\text{L}^{-1}$ solution. 30.6350 g of magnesium chloride ($\text{MgCl}_2\cdot 6\text{H}_2\text{O}$, Synth) and 20.964 g of iron chloride ($\text{FeCl}_3\cdot 6\text{H}_2\text{O}$, Synth) were weighed and added to 200 mL of deionized water, leaving under agitation

for 30 min to total dissolution of the solids. Subsequently, 165 mL of the NaOH solution were added and the pH was measured after 10 min. The final pH value was adjusted to 13.0 by adding few drops of the same NaOH solution. The mixture was kept under vigorous agitation at room temperature for 4 h. The precipitate was washed with deionized water and centrifuged for 5 min at 2,000 rpm, discarding the supernatant. This procedure was repeated until the supernatant reached the pH value 7.0. The material was transferred to Petri dishes and dried at 65°C for 24 h. After the synthesis, the MgFe/LDH was crushed and sifted to standardize the particle diameters (d_p), $d_p < 0.212 \text{ mm}$ and $0.212 \text{ mm} < d_p < 0.300 \text{ mm}$.

1.3. Adsorbent characterization

Specific surface area measurements and X-ray diffraction (XRD) were used to characterize the adsorbent material. The crystal structure was determined by the XRD-6000 diffractometer, Shimadzu. A scan rate of $5^\circ\cdot\text{min}^{-1}$ was applied in the range of 2° to 70° (2θ), the copper (Cu) radiation was the X-ray source, which corresponds to the wavelength of 0.15406 \AA , with voltage of 30 kV and current of 30 mA. The textural characteristics were determined by the N_2 adsorption/desorption technique by Brunauer, Emmet and Teller (BET) method using the equipment Quantachrome NOVA 2200e. The sample was left at 350°C for 12 h in order to eliminate possible contaminants physically adsorbed in the surface, obstructing the pores. Then, a nitrogen gas flow was applied at -196°C .

1.4. Adsorption assays

The adsorption assays were performed in a finite bath, in triplicate. In a typical adsorption experiment, an exact amount of weighted adsorbent was added to 10 mL of the adsorbate solution in a 30 mL amber flask, which was kept under agitation at 140 rpm for a certain period of contact time. After that, the mixture was transferred to a 50 mL falcon tube and centrifuged at 2,000 rpm for 10 min. The final amoxicillin concentrations were measured in the supernatant. The adsorption capacity of the adsorbent material (q_t , $\text{mg}\cdot\text{g}^{-1}$) was determined by Equation 1 and the removal percentage (%) was calculated by Equation 2.

$$q_t = \frac{(C_0 - C_t)}{w} * V \quad (1)$$

$$\% \text{ removal} = \frac{C_0 - C_t}{C_0} * 100 \quad (2)$$

where C_0 , C_e and C_t are the concentrations (mg.L^{-1}) of the adsorbate solution at the beginning, at equilibrium and at time t , respectively. W is the mass (g) of adsorbent and V (L) is the volume of the solution.

Kinetic studies were performed with amoxicillin initial concentration of 50 mg.L^{-1} at 30°C . The final concentration of amoxicillin remaining in the solution was measured in predetermined time intervals (0, 5, 10, 15, 30, 60, 120 and 180 min) and the kinetic data obtained were fitted to the pseudo-first order (Equation 3) and pseudo-second order models (Equation 4) [12-14]

$$q_t = q_e [1 - \exp(-k_1 * t)] \quad (3)$$

$$q_t = \frac{k_2 q_e^2 t}{1 + k_2 q_e t} \quad (4)$$

where k_1 ($1.\text{min}^{-1}$) and k_2 ($\text{g.mg}^{-1} \text{ min}$) are the constants of pseudo-first order and pseudo-second order, respectively, q_t (mg.g^{-1}) is amount adsorbed at time t and q_e (mg.g^{-1}) is the amount adsorbed at equilibrium.

3. Results and discussion

3.1 Adsorbent characterization

XRD analysis was performed in order to verify the MgFe/LDH formation. The diffractogram obtained (Fig. 3) revealed characteristic reflections of LDH materials, as reported in the literature [15], based on the reflections of the peaks (003), (006) and (009) in 2θ values of 11.14° , 22.28° and 34.08° respectively, showing that the adsorbent material was successfully synthesized.

Basal spacing (the sum of lamella thickness, constituted by metals, with the thickness of interlamellar zone) was calculated using the peak of higher intensity (003) and applying Bragg Law and the value obtained, 0.79 nm , is in agreement with data from the literature [16].

BET measurements provided superficial area of $136.4 \text{ m}^2.\text{g}^{-1}$, pore volume of $0.47 \text{ cm}^3.\text{g}^{-1}$ and pore size of 10.88 nm , values that are consistent with hydrotalcite-type materials [17].

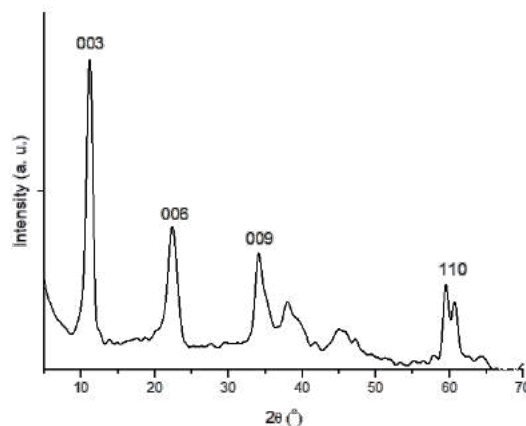


Fig. 3. XRD pattern of MgFe/LDH.

3.2 Adsorption assays

The kinetic study was performed with amoxicillin initial concentration of 50 mg.L^{-1} at 30°C . From the results achieved (Fig. 4), equilibrium was reached after 180 min of contact, with maximum adsorption capacity of 9.11 mg.g^{-1} .

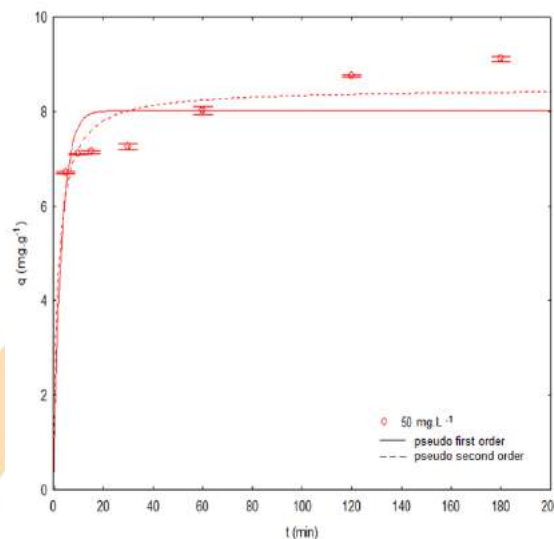


Fig. 4. Amoxicillin adsorption kinetics onto MgFe/LDH.

The kinetic models of pseudo-first order and pseudo-second order were fitted to the experimental data in order to better understand the adsorption process involved. The kinetic parameters obtained are shown in Table 1. From the results achieved, the adsorption mechanism tends to the pseudo-second order model, suggesting a chemical sorption, due to

the higher R^2 values and proximity of theoretical q_e with the experimental one.

Table 1. Kinetic parameters obtained for amoxicillin adsorption onto MgFe/LDH.

Pseudo-first order	q_e ($\text{mg}\cdot\text{g}^{-1}$)	8.02
	k_1 (min^{-1})	0.32
	R^2	0.941
Pseudo-second order	q_e ($\text{mg}\cdot\text{g}^{-1}$)	8.49
	k_2 ($\text{g}\cdot\text{mg}^{-1}\cdot\text{min}^{-1}$)	0.07
	R^2	0.971

4. Conclusion

In this work, MgFe/LDH was successfully synthesized by the co-precipitation method at constant pH and applied for amoxicillin removal from aqueous media. The characterization analyses confirmed the formation of the adsorbent material, revealing characteristic peaks of lamellar structures and satisfactory surface area. From the assays performed, 5.0 $\text{g}\cdot\text{L}^{-1}$ of adsorbent ($d_p < 0.212$ mm) was able to remove over 90% of amoxicillin from water (50.0 $\text{mg}\cdot\text{L}^{-1}$) in 180 min of contact, reaching the adsorptive capacity of 9.11 $\text{mg}\cdot\text{g}^{-1}$.

In brief, the preliminary results suggested that MgFe/LDH is a potential adsorbent for amoxicillin removal from water, requiring more studies. In addition, the synthesis of the material is simple, easy and present low cost, emphasizing its characteristics of a promising adsorbent.

Acknowledgements

The authors wish to thank Conselho Nacional de Desenvolvimento Científico e Tecnológico (CNPq/Brazil), Coordenação de Aperfeiçoamento de Pessoal de Nível Superior (CAPES/Brazil) and

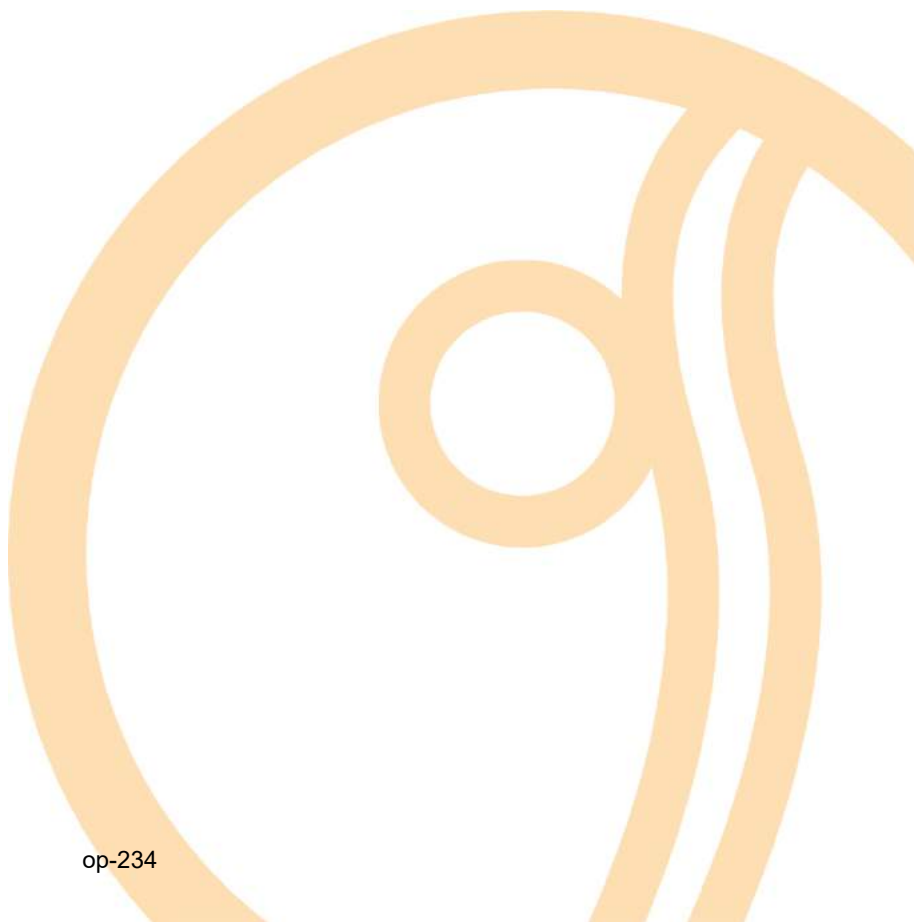
Fundação de Amparo à Pesquisa do Estado de Alagoas (FAPEAL/Brazil).

References

- [1] Crepaldi, EL, Valim JB., Hidróxidos duplo lamelares: síntese, estrutura, propriedades e aplicações. *Qui. Nova* 1998;21(3):300-11.
- [2] Bi X, Zhang H, Dou L. Layered Double Hydroxide-Based Nanocarriers for Drug Delivery. *Pharmaceutics* 2014;6(2):298-332.
- [3] Xu ZP, Zhang J, Adebajo MO, Zhang H, Zhou C. Catalytic applications of layered double hydroxides and derivatives. *Appl. Clay Sci.* 2011;53(2):139-50
- [4] Xu M, Wei, M. Layered Double Hydroxide-Based Catalysts: Recent Advances in Preparation, Structure, and Applications. *Adv. Funct. Mater.* 2018;28(47).
- [5] Cornejo J, Celis R, Pavlovic I, Ulibarri MA. Interactions of pesticides with clays and layered double hydroxides: a review. *Clay Mat.* 2008;43(2):155-75.
- [6] Liang X, Zang Y, Xu Y, Tan X, Hou W, Wang L, Sun Y. Sorption of metal cations on layered double hydroxides. *Colloid Surface A* 2013;433(20): 122-131.
- [7] Goh K, Lim T, Dong Z. Application of layered double hydroxides for removal of oxyanions: A review. *Water Res.* 2007;42(6-7):1343-68.
- [8] Crepaldi EL, Pavan PC, Valim JB. Comparative Study of the Coprecipitation Methods for the Preparation of Layered Double Hydroxides. *J. Braz. Chem. Soc.* 2000;11(1):64-70.
- [9] Verlicchi P, Al Alkidy M, Zambello E. Occurrence of pharmaceutical compounds in urban wastewater: Removal, mass load and environmental risk after a secondary treatment-A review. *Sci. Total Environ.* 2012;429(1):123-55.
- [10] Xu J, Xu Y, Wang H, Guo C, Qiu H, He Y, Occurrence of antibiotics and antibiotic resistance genes in a sewage treatment plant and its effluent-receiving river. *Chemosphere* 2015;119:1379-85.
- [11] Seida Y, Nakano Y, Nakamura Y. Rapid removal of dilute lead from water by Pyroaurite-like compound. *Water Res.* 2001;35:2341-46.
- [12] Lagergren S. About the theory of so-called adsorption of soluble substances. *K. Sven Vetenskapsakademiens* 1898;24:1-39.
- [13] Ho YS, McKay G. Sorption of dye from aqueous solution by peat. *Chem Eng J.* 1998;70:115-124.
- [14] Ho YS, McKay. Pseudo-second order model for sorption processes. *Process Biochem.* 1999;34:451-465.
- [15] Ahmed IM, Gasser MS. Adsorption study of anionic reactive dye from aqueous solution to Mg-Fe-CO₃



- layered double hydroxide (LDH). *Appl. Surf. Sci.* 2012;259:650-6.
- [16] Halajnia A, Oustan S, Najafi N. The adsorption characteristics of nitrate on Mg-Fe and Mg-Al layered double hydroxides in a simulated soil solution. *Appl Clay Sci.* 2012;70:28–36.
- [17] Bezerra DM, Rodrigues JEFS, Assaf EM. Structural, vibrational and morphological properties of layered double hydroxides containing Ni^{2+} , Zn^{2+} , Al^{3+} and Zr^{4+} cations. *Mater. Charact.* 2017;125:29–36.



Lipases Immobilization via Adsorption on Laboratory-Scale Synthesized Graphene Oxide Using Modified Hummers Method and Magnetic Nanoparticles

Alexandre Diório^{a,*}, Anna Clara Labes Gonçalves^a, Danielle Faxina de Lima^a, Rosângela Bergamasco^a, Marcelo Fernandes Vieira^a

^a Department of Chemical Engineer, State University of Maringá, Colombo avenue, 5790, Maringá-PR, 87020-900, Brazil
*Corresponding author e-mail: diorio.alexandre@gmail.com

Abstract

The global annual market of lipases in 2017 was estimated in 400.6 million USD with a share growth of 6.8% until 2023. For enhanced industrial process production, these lipases, as well as other enzymes, should be immobilized in an appropriate support for greater stability, ease in purification steps and reusability of this expensive biocatalyst. Therefore, the aim of this study was to immobilize five different types of lipases, via adsorption, on the graphene oxide synthesized by a laboratory-scale modified Hummers method and with magnetic properties due to nanoparticles of iron oxide for future application of this material as a biocatalyst for biotechnology processes. The highest protein immobilization concentration was achieved using lipase from *Candida sp* ($8.4 \text{ mg}_{\text{protein}} \text{ g}_{\text{support}}^{-1}$) but the specific activity achieved was low ($182 \text{ U mg}_{\text{protein}}^{-1}$) indicating denaturation of the adsorbed proteins or that the catalytic sites were not available for the hydrolysis reaction. Therefore, lipase from *Thermomyces lanuginosus* was considered the best enzyme immobilized ($5.1 \text{ mg}_{\text{protein}} \text{ g}_{\text{support}}^{-1}$ and $697 \text{ U mg}_{\text{protein}}^{-1}$). In conclusion, lipase from *Thermomyces lanuginosus* presented to be the best lipase, from the ones studied, to manufacture a biocatalyst using graphene oxide with magnetic properties as support for application in biotechnology processes.

Keywords: Lipase; Graphene oxide; Immobilization; Adsorption; Biocatalyst

1. Introduction

Enzymes have been used in many industrial process such as the textile industries, biofuel production, wastewater treatment plants, pharmaceutical companies, fine chemical industries and many other [3]. Unfortunately, these large-scale applications are limited due to enzymes costs, low chemical-mechanical-thermal stabilities and the difficult in separate and recovery of the free enzymes from the reaction media for reuse [2].

These drawbacks can be overcome with the use of an appropriate support where the enzymes will attach and, hence, improve stabilities, ease separation and purification steps and provide other advantages as well [1, 3, 11]. The choice of support is a crucial step in view of the immobilization

advantages. The support should increase the enzyme catalytic activity as well as decrease diffusional resistances [2]. Porous materials are preferable due to the high loading of protein they can support and their high surface area for the enzyme to immobilize and interaction to occur [9] and, also, enhance the enzymatic stabilities [5], immobilization yield, reaction selectivity and specificity [2].

In this sense, lipases unite adequately to hydrophobic supports via adsorption with their catalytic site still available for the chemical reaction due to the fact that the hydrophobic interactions occurs in the vicinities of the catalytic site and the support [6, 16].

Therefore, the aim of this study was to immobilize five different types of lipases via adsorption on a graphene oxide synthesized by a

laboratory-scale modified Hummers method and with magnetic properties due to nanoparticles of iron oxide for future application of this material as a biocatalyst for biotechnology processes.

2. Materials and Methods

2.1. Materials

Graphite flakes (Sigma), sulfuric acid (95-98%, Fischer), potassium permanganate (97-100%, Anachemia), hydrochloric acid (36%, Fisher), phosphorous pentoxide (99%, JT Baker), hydrogen peroxide solution (30%, EMD) and potassium persulfate (99-100%, Anachemia) were used as acquired, *i.e.*, with no further purification, or diluted as described in following protocols. The following lipases were acquired from Sigma-Aldrich: Amano Lipase M from *Mucor javanicus* (LMJ); Lipolase® from *Thermomyces lanuginosus* (TLL); Lipase from *Rhizopus niveus* (LRN); Lipase from *Candida sp* (CALA) and lipase from porcine pancreas (LPP).

2.2. Methods

2.2.1. Graphene oxide (GO) synthesis

The graphene oxide was synthesized according to the Hummers method [7] modified for lab-scale production as follow. Initially, 100 g of graphite flakes were placed in a three neck round bottom flask, through the central neck an agitation shaft was placed, a thermometer in the second neck and the third was sealed in a way to allow de addition of 360 mL of sulfuric acid. The system was maintained under agitation during all the reaction time. Slowly, 50 g of P₂O₅ were added and the system was heated until 80 °C with subsequent add of 50 g of potassium persulfate and kept reacting for 5 h. The pre-oxidized graphite were abundantly washed and dried at 50 °C for 12 h.

In sequence, 20 g of the pre-oxidized graphite were soaked with 360 mL of sulfuric acid and kept under agitation. 60 g of KMnO₄ was very slowly added due to the exothermic and explosive reaction formed. The system temperature was maintained under 40 °C and kept so for 2 h. Then, under an ice bath, the suspension was slowly diluted with 920 mL of distilled water and, then, transferred to a Becker with 2800 mL of distilled water. 50 mL of hydrogen peroxide was added under the ice bath and agitation. After 30 min, the reaction volume was completed until 5000 mL with an HCl 10%

solution. The suspension was left to sediment overnight, the supernatant was discharged and the volume was completed with 5000 mL of distilled water. This process was repeated several times until graphene oxide was detected in the supernatant under a scanning in a Thermo Fisher Scientific spectrophotometer model Genesys 10-S. Finally, after decantation, the system was dried in an oven at 50 °C and the resulting material was called graphene oxide (this was also confirmed through a series of analysis on the solid particles – data not shown).

2.2.2. Superparamagnetic nanoparticles (SPIONs) synthesis and GO modification

The superparamagnetic nanoparticles were synthesized according to the sol-gel protocol described by Silva et al. [13].

The deposition of superparamagnetic nanoparticles on the surface of the GO particles and between its carbon sheets was realized in a single-step emulsion method according to Silva et al. [13] and modifications due to the lab-scale production. Briefly, graphene oxide was sonicated in distilled water until dissolution was attained. Then, SPION particles were added in the proportion 2:1 GO-SPION and sonicate for 30 min. Then, the formed suspension was placed in a Petri dish to form a thin layer and dried in an oven at 50 °C. The membrane of GO:SPION was ground using a mixer Versatile (Mondial, 200 W) for 20 s with an intermediate mixture for homogenization. Finally, a neodymium magnet was used to separate the magnetic and non-magnetic modified GO.

2.2.3. Protein determination

The protein determination of free and immobilized proteins were realized according to the Bradford method [4]. Briefly, the *Coomassie Brilliant Blue G-250* binds itself to the proteins dyeing it blue and, thus, being possible to detect it by spectrophotometer absorbance at wavelength of 595 nm. The absorbance interpretation by means of concentration was realized performing a standard curve using bovine serum albumin (BSA) solutions with concentrations from 0.01 to 0.10 mg mL⁻¹. The blank used followed the same protocol but using distilled water instead of the protein solution.

2.2.4. Lipases immobilization via adsorption

The enzymatic immobilization of lipases via adsorption was performed suspending 1 g of support (GO modified with SPION) in 10 mL of sodium phosphate buffer solution (5 mmol L⁻¹ pH7.0). The suspension was kept under stirring in a water bath

Dubnoff shaker (Quimis®) with controlled temperature (25 °C). After thermic equilibrium, different lipases solutions were added to achieve 10 mg_{protein} g_{sup}⁻¹ for each experiment. Agitation was kept at 120 rpm during 1 h. The adsorption process was monitored sampling 100 µL of supernatant by placing the flask over a neodymium magnetic for residual protein concentration and catalytic activity (olive oil emulsion method) determinations. When null or constant values were achieved, the immobilization was ceased by washing the particles with 3 volumes of 10 mL sodium phosphate buffer solution (100 mmol L⁻¹ pH7.0) and, also, determining protein residual concentration and catalytic activity in each washing water. The biocatalyst prepared was, finally, dried overnight in a desiccator and stored in a refrigerator at 4 °C until used.

2.2.5. Determination of the immobilization parameter

The immobilized protein concentration at equilibrium (q_e - mg mL⁻¹) was determined according to Equation 1.

$$q_e = \frac{V \times (C_0 - C_e)}{m} \quad (1)$$

where V is the volume of lipase solution (mL). C_0 , C_e and C_w represents the initial, residual and washes protein concentrations (mg mL⁻¹), respectively, and m is the mass of support used (g).

The catalytic activity of immobilized lipases and residual from the supernatants were determined according to the olive oil emulsion method [2]. The emulsion was prepared with 1.25 g of olive oil, 87.5 mg of Arabic Gum, 2 mL of sodium phosphate buffer solution (100 mmol L⁻¹ pH7.0) and 1.25 mL of distilled water. The emulsion was incubated in a Shaker at 25 °C under stirring (120 rpm). The hydrolysis reaction of the olive oil started by adding 100 mg of the biocatalyst or 100 µL of solution sample. After 5 min of hydrolysis, the reaction was stopped adding 5 mL of anhydrous ethanol. Then, 2 drops of alcoholic phenolphthalein (99%) was added and, also, 10 or 20 mL of distilled water for ease turning point reading during the titration with KOH 0.02 M. One international unit (U) of activity was defined as the mass of immobilized or free protein able to release 1 µmol of fatty acids per minute of olive oil hydrolysis.

Specific activity (SA - U mg_{protein}⁻¹) was calculated according to Equation 2.

$$SA = \frac{A_{\text{immobilized}}}{q_e} \quad (2)$$

where $A_{\text{immobilized}}$ is the hydrolytic activity of the biocatalyst of the supernatant samples and q_e is the immobilized protein concentration at equilibrium (mg_{protein} g_{support}⁻¹).

The immobilized yield (IY - %) and the recovered activity (RA - %) were determined according to Equation 3 and 4, respectively, both in terms of proteins and catalytic activity.

$$IY (\%) = \frac{A_{\text{Theoretical Immobilized}}}{A_{\text{offered}}} \times 100\% \quad (3)$$

$$RA (\%) = \frac{A_{\text{immobilized}}}{A_{\text{Theoretical Immobilized}}} \times 100\% \quad (4)$$

where A_{offered} is the catalytic activity of the initial enzymatic solution (U g_{support}⁻¹ or mg_{protein} g_{support}⁻¹), $A_{\text{immobilized}}$ is the catalytic activity of the biocatalyst (U g_{support}⁻¹ or mg_{protein} g_{support}⁻¹), $A_{\text{Theoretical Immobilized}}$ is the catalytic activity of initial enzymatic solution minus the catalytic activity from the washes and the latest supernatant (at equilibrium conditions) (U g_{support}⁻¹ or mg_{protein} g_{support}⁻¹).

3. Results and Discussion

3.1. Graphene oxide synthesis

The spectrophotometer analysis of the supernatant washing water is shown in Figure 1.

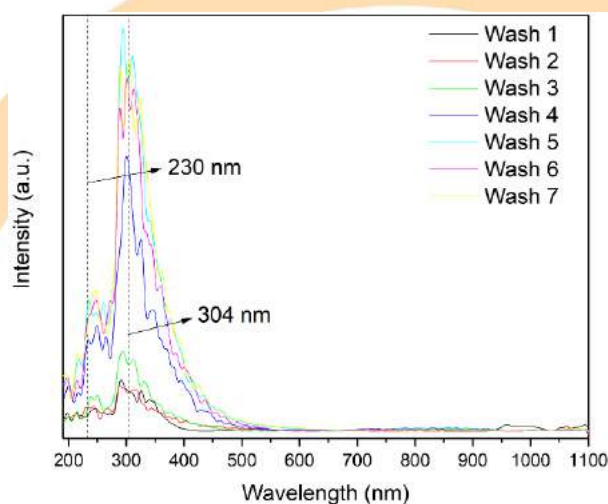


Figure 1. Spectrophotometer analysis of supernatant washing water during GO synthesis.

The laboratory-scale synthesis of graphene oxide employs high volume of washing water. Many

published protocols monitor the pH of the supernatant water and stops the washing process when pH reaches a neutral value, which is the distilled water pH [14], but this seems inconvenient for GO synthesis since GO particles naturally dissolves in distilled water due to the presence of oxygen-containing functional groups [15] which can alter the pH. As seen in Figure 1, between the washes 3 and 4 there is a difference in the peak intensity of graphene oxide detected in the supernatant, 230 nm for the aromatic C-C bond and 304 for the C=O bond [8]. In addition, pH determination of the supernatant water varied from 2.2 in the first wash due to the high HCl

concentration and increased until stable at 5.5 in the seventh wash, which is not the neutral pH of the distilled water.

3.2. Adsorption immobilization parameters

Five different types of lipase were immobilized via adsorption on the surface of graphene oxide synthesized through a laboratory-scale modified Hummers method and with magnetic properties due to the presence of superparamagnetic nanoparticles. The adsorption immobilization results for the five different lipases are shown in Figure 2.

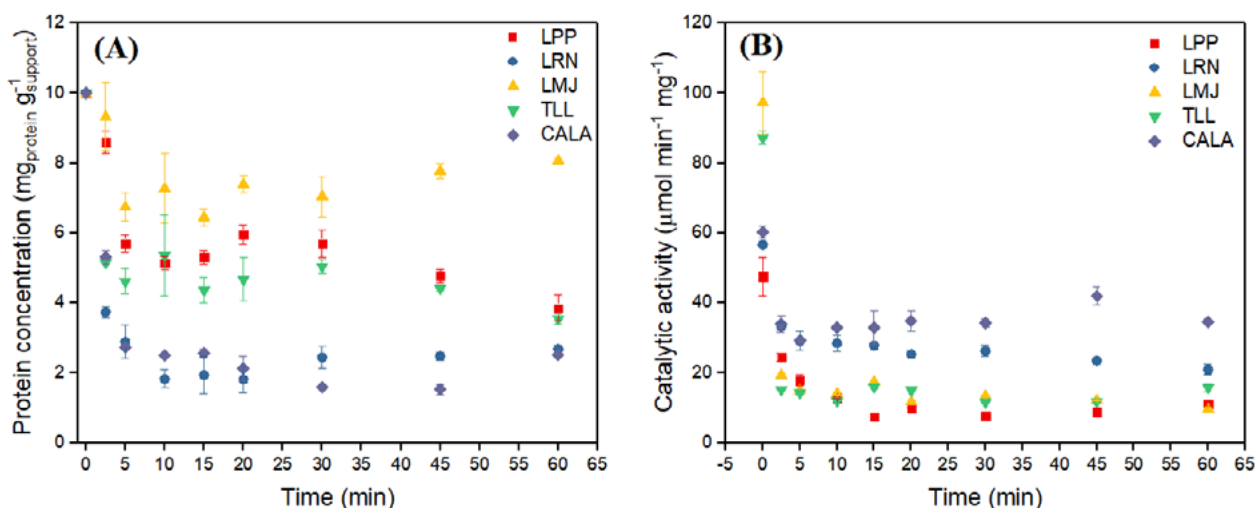


Figure 2. Adsorption of five lipases on graphene oxide modified with magnetic nanoparticles (A) in terms of protein concentration and (B) of catalytic activity.

The analysis of Figure 2-A confirmed that some, but not all, of the proteins present in the acquired lipases were immobilized on the GO:SPION particles since the residual protein concentration did not reach zero. Therefore, the initial protein loading (10 mg g⁻¹) and the immobilization time were enough to complete saturate the available adsorption sites of the support. The CALA was the lipase with the highest protein load immobilized due to the lowest residual protein concentration at equilibrium (less than 2 mg_{protein} g_{support}⁻¹). However, it is worth to note that this value is the residual protein concentration in the supernatant at equilibrium conditions (60 min). The posterior washing of the particles with buffer solution of high ionic strength removed some of the poorly adsorbed enzymes [2]. In addition, when analyzing the Figure 2-B, one can see that, for example, the CALA's catalytic activity was the lowest of all five

immobilized lipases. Therefore, although the protein concentration immobilized was high for CALA, the biocatalyst did not presented a significant catalytic activity, possible due to protein denaturation [10].

For LPP, Figure 2-A shows that for immobilization time longer than 20 min, there was a decrease in residual protein concentration. This may be due to the fact that longer immobilization times favors the formation of more interactions between the enzymes and the support [12]. However, since Figure 2-B shows no decrease in the catalytic activity of the supernatant, then one can assume that the proteins being immobilized for t>20min are not hydrolytic proteins.

The immobilization parameters, in terms of proteins and catalytic activity, are displayed in Table 1.

Table 1. Lipases immobilization parameters via adsorption on GO:SPION.

Parameter of immobilization	LPP	LRN	LMJ	TLL	CALA
<i>In terms of proteins*</i>					
C_0 (mg _{protein} g _{support} ⁻¹)	10.0 ± 0.0	10.0 ± 0.0	10.0 ± 0.0	10.0 ± 0.0	10.0 ± 0.0
C_e (mg _{protein} g _{support} ⁻¹)	3.15 ± 0.70	2.28 ± 0.40	7.93 ± 0.13	4.65 ± 1.11	1.50 ± 1.01
C_w (mg _{protein} g _{support} ⁻¹)	0.08 ± 0.07	0.05 ± 0.05	0.04 ± 0.03	0.28 ± 0.28	0.08 ± 0.08
q_e (mg _{protein} g _{support} ⁻¹)	6.78 ± 0.63	7.67 ± 0.35	2.03 ± 0.10	5.07 ± 1.39	8.42 ± 0.93
IY (%)	67.75 ± 6.26	76.69 ± 3.47	20.31 ± 0.97	50.65 ± 13.91	84.16 ± 9.30
<i>In terms of catalytic activity*</i>					
$A_{offered}$ (U g _{support} ⁻¹)	4517 ± 234	5925 ± 260	9242 ± 409	9072 ± 353	7084 ± 1064
A_e (U g _{support} ⁻¹)	1077 ± 16	2267 ± 174	1099 ± 132	1606 ± 25	2445 ± 1016
A_w (U g _{support} ⁻¹)	369 ± 90	705 ± 492	936 ± 834	230 ± 33	1730 ± 1469
$A_{Theoretical\ Immobilized}$ (U g _{support} ⁻¹)	3070 ± 309	2953 ± 406	7207 ± 1447	7237 ± 362	2910 ± 611
IY (%)	67.80 ± 3.32	50.24 ± 9.06	77.38 ± 11.63	79.73 ± 0.89	40.70 ± 2.52
$A_{immobilized}$ (U g _{support} ⁻¹)	1440 ± 80	1360 ± 120	1350 ± 350	3474 ± 766	1540 ± 260
RA (%)	47.12 ± 2.14	46.37 ± 2.31	20.53 ± 8.98	48.66 ± 13.02	53.40 ± 2.28
SA (U mg _{protein} ⁻¹)	215 ± 31	178 ± 24	658 ± 141	697 ± 40	182 ± 11

* mean value ± standard deviation. IY: immobilization yield; RA: recovered activity; SA: specific activity

From Table 1, the lowest immobilization yield was achieved when using the lipase from *Mucor javanicus*, but the specific activity was the second highest revealing that, even not much of the initial proteins offered were immobilized, the ones binded to the support presented high catalytic activity. The highest specific activity (697 U mg_{protein}⁻¹) was achieved for the adsorption of TLL and the lowest (178 U mg_{protein}⁻¹) for LRN. Available data, [2], revealed much lower specific activity (12.2 U mg_{protein}⁻¹) for TLL immobilized on mesoporous and hydrophobic resin, but the maximum immobilized protein concentration was much higher (134 mg g⁻¹) than found in this study. TLL was also immobilized in ion-exchange supports [3] with reported values of q_e , C_e and HA closer to the ones found here, but the SA varied from 27.5 to 213.3 U mg⁻¹, corroborating the results when compared with LPP, LRN and CALA, but being lower when compared with TLL and LMJ from this immobilization study.

4. Conclusion

This research investigated the immobilization, via adsorption, of five different types of lipase on the graphene oxide synthesized by a laboratory-scale modified Hummers method and with magnetic properties due to nanoparticles of iron oxide for future application of this material as a biocatalyst for biotechnology processes. The adsorption of lipase from *Thermomyces lanuginosus* presented the best immobilization parameters in comparison with the other lipases used: $q_e = 5.1$ mg_{protein} g_{support}⁻¹

¹, IY = 50.7% in terms of proteins or IY = 79.7% in terms of catalytic activity), RA = 48.7% and SA = 697 U mg_{protein}⁻¹. Therefore, lipase from *Thermomyces lanuginosus* presented to be the best lipase, from the ones studied, to manufacture a biocatalyst using graphene oxide with magnetic properties as support for application in biotechnology.

Acknowledgements

The authors are grateful for financial support and fellowship provided by CNPq.

References

- [1] Adlercreutz P. Immobilization and application of lipases in organic media. *Chemical Society Reviews* 2013; 42; 6406-6436.
- [2] Alves MD, Aracri FM, Cren É, Mendes AA. Isotherm, kinetic, mechanism and thermodynamic studies of adsorption of a microbial lipase on a mesoporous and hydrophobic resin. *Chemical Engineering Journal* 2017; 311; 1-12.
- [3] Bolina ICA, Salviano AB, Tardioli PW, Cren ÉC, Mendes AA. Preparation of ion-exchange supports via activation of epoxy-SiO₂ with glycine to immobilize microbial lipase – Use of biocatalysts in hydrolysis and esterification reactions. *International Journal of Biological Macromolecules* 2018; 120; 2354-2365.
- [4] Bradford MM. A rapid and sensitive method for the quantification of microgram quantities of protein utilizing the principle of protein-dye binding. *Analytical Biochemistry* 1976, 72, 248-254.
- [5] Brena BM, Batista-Vieira F. Immobilization of enzymes: a literature survey. In: J.M. Guisán (Ed.),



- Immobilization of Enzymes and Cells. Totowa Humana Press Inc; 2006. p. 15–30.
- [6] Kang Y, He J, Guo X, Guo X, Song Z. Influence of pore diameters on the immobilization of lipase in SBA-15. *Ind Eng Chem Res*; 2007; 46: 4474–4479.
- [7] Kovtyukhova NI, Ollivier PJ, Martin B R, Mallouk TE, Chizhik SA, Buzaneva EV, Gorchinskiy AD. Layer-by-layer assembly of ultrathin composite films from micron-sized graphite oxide sheets and polycations. *Chemistry of Materials* 1999; 11: 771–778.
- [8] Lai Q, Zhu S, Luo X, Zou M, Huang S. Ultraviolet-visible spectroscopy of graphene oxides. *AIP Advances* 2012; 2: 1-5.
- [9] Li Y, Gao F, Wei W, Qu JB, Ma GH, Zhou WQ. Pore size of macroporous polystyrene microspheres affects lipase immobilization, *Journal of Molecular Catalysis B: Enzymatic* 2010; 66: 182–189.
- [10] Mateo C, Palomo JM, Fuentes M, et al. Glyoxyl agarose: a fully inert and hydrophilic support for immobilization and high stabilization of proteins. *Enzyme and Microbial Technology* 2006; 39: 274–280.
- [11] Mohamed NR, Marzuki NHC, Buang NA, Huyop F, Wahab RA. An overview of technologies for immobilization of enzymes and surface analysis techniques for immobilized enzymes. *Biotechnology & Biotechnological Equipment* 2015; 29: 205-220.
- [12] Pinheiro BB, Rios NS, Aguado ER, Fernandez-Lafuente R, Freire TM, Fecine PBA, Santos JCS, Gonçalves LRB. Chitosan activated with divinyl sulfone: a new heterofunctional support for enzyme immobilization. Application in the immobilization of lipase B from *Candida antarctica*. *International Journal of Biological Macromolecules* 2019; 130: 798-809.
- [13] Silva MF, Hechenleitner AAW, Oliveira DMF, Agüeros M, Peñalva R, Irache JM, Pineda EAG. Optimization of maghemite-loaded PLGA nanospheres for biomedical applications. *European Journal of Pharmaceutical Sciences* 2013; 49: 343–351.
- [14] Smith AT, LaChance AM, Zeng S, Liu B, Sun L. Synthesis properties, and applications of graphene oxide/reduced graphene oxide and their nanocomposites. *Nano Materials Science* 2019; 1: 31–47.
- [15] Zhang H, Zhang N, Fang F. Fabrication of high-performance nickel/graphene oxide composite coatings using ultrasonic-assisted electrodeposition. *Ultrasonics sonochemistry* 2019; In Press.
- [16] Zheng MM, Lu Y, Dong L, Guo PM, Deng QC, Li WL, Feng YQ, Huang FH. Immobilization of *Candida rugosa* lipase on hydrophobic/strong cation-exchange functional silica particles for biocatalytic synthesis of phytosterol esters. *Bioresource Technology* 2012; 115: 141-146.

Enzyme immobilization by adsorption: CALB lipase onto magnetic nanoparticles, a heterogeneous biocatalyst

João Brandão Júnior^a, Debora Cristina Ferreira^a, Francisco Silvio Maia^a, Gabrielly Ferreira Mota^a, Jean Gleison Andrade do Nascimento^a, Rodolpho Ramilton de Castro Monteiro^b, Aluísio Marques da Fonseca^a and Maria Cristiane Martins de Souza^{a*}

^a Universidade da Integração Internacional da Lusofonia Afro-Brasileira -UNILAB- R. José Franco de Oliveira, s/n - Zona Rural, Redenção - CE, Brasil. Cep: 62790-970. *e-mail: mariacristiane@unilab.edu.br

^b Universidade Federal do Ceará- Departamento de Engenharia Química. Campus do Pici, BL. 709, Av. Mister Hull, s/n - Pici, Fortaleza - CE, 60455-760.

Abstract

Iron magnetic nanoparticles (Fe₃O₄) were evaluated as adsorption preparative heterofunctional support for the immobilization of lipase B from *Candida antarctica* (CALB). Heterogeneous magnetic catalysts are easy to recover by magnetic field, which may optimize operational cost and enhance the purity of the products. The nanoparticles were produced by the co-precipitation method. Modifications were carried out on the nanoparticles' surfaces with aminopropyltriethoxysilane (APTS). The adsorption was evaluated for 3.0 mg protein/g of support in the presence of 5mM sodium phosphate buffer, pH 7.0, at 25 °C and 0.5h of immobilization. In a solvent free medium, under 37 °C, the biocatalyst prepared has shown an activity of 2.2 U/g for the esterification of oleic acid after 0.5h, 37 kHz and 300 W. The results obtained with CALB adsorbed onto magnetic iron nanoparticles were compared with those of lipase B from *Candida antarctica* adsorbed onto acrylic resin (Novozym® 435). In this regard, under same reactional conditions, Novozym® 435 has presented an activity of 2.9 U/g.

Keywords: Immobilization; Lipase (CALB); Adsorption; Magnetic Nanoparticle.

1. Introduction

Enzymatic ester production has been widely studied by several authors, mainly using lipase B from *Candida antarctica* immobilized onto acrylic resin, commercially available as Novozym® 435. The main applications of such lipases are in high value-added products [1].

Esterification is a method used for the elimination of free fatty acids, under the action of acid catalysts, usually associated with low added value materials, such as acid sludge, and waste oil frying in biodiesel production. This step usually precedes the transesterification process in which oils and fats are transformed into fatty esters by generally basic catalysts. The model reagent, chosen to represent the carboxylic acids present in vegetable oils, was oleic acid. The alcohol used was ethanol (EtOH) [1].

The esterification of oleic acid (OIAc) can represent biodiesel production, since it is present in most of oil crops. With EtOH, ethyl oleate (OleOEt) is produced and water is the by-product,

according to the following equation:

$$C_8H_{17}CH=CH(CH_2)_7COOH + CH_3CH_2OH \rightleftharpoons C_8H_{17}CH=CH(CH_2)_7COOC_2H_5 + H_2O [2].$$

The industrial esterification processes carried out with strong Brønsted acid catalysts are not environmentally benign [3], since they require special treatments as neutralization involving costly catalyst separation steps from the homogeneous reaction mixtures [4]. Heterogeneous catalysts could be easier separated, they show high activity and stability and could be reused offering milder operating conditions.

The selection of an immobilization strategy is based on effectiveness of enzyme utilization, cost of the immobilization procedure, toxicity of immobilization reagents and the desired final properties of the immobilized biocatalyst [2].

Adsorption is the union between the enzyme molecule and an inert support. Adsorption supports may be organic and inorganic. Physical adsorption (ADS) is one of the simplest methods to immobilize enzymes and does not easily alter their active site. Physical forces involve only weak



interactions such as hydrogen bonding, hydrophobic bonding and van der Waals bonding [5].

The molar ratio of oleic acid/ethanol was 1:5 using an ultrasonic bath (37 kHz and 300 W) at a temperature of 37 °C for a period of 0.5 h. Anyhow, the biological nature of ethanol, which slightly increases the heat content and the esters cetane number, make ethyl esters (EEs) more interesting than methyl esters (MEs); moreover, EtOH is nontoxic and has better solvent properties than methanol for oil solubility and EEs have pour points lower than those of methyl esters [6].

2. Materials and methods

2.1 Materials

Iron magnetic nanoparticles (Fe_3O_4) were produced by the co-precipitation method [7]. Lipase B from *Candida antarctica* (CALB) was purchased from Codexis (Redwood, USA). Lipase B from *Candida antarctica* immobilized onto acrylic resin (Novozym® 435), γ -aminopropyltriethoxysilane (APTS) were purchased from. All other reagents (analytical grade) were purchased from Synth (São Paulo, Brazil) and Vetec (São Paulo, Brazil).

2.2. Synthesis of (Fe_3O_4)

Iron magnetic nanoparticles (Fe_3O_4), particle size of 11.0 nm, were produced by the co-precipitation method [7].

2.3. Treatment of the support with γ -aminopropyltriethoxysilane (APTS).

Iron magnetic nanoparticles were modified with γ -aminopropyltriethoxysilane (APTS). The reaction was initiated with the addition of a solution of APTS (2.0 % v/v) to the support in a liquid-solid ratio 0.2 (mL . mg^{-1} of support). The solution was heated at 100 °C for 10 hours under nitrogen atmosphere. The modified nanoparticles were washed with 100 mL of methanol and 100 mL of ethanol, separated by magnetism. After, dried at 30 °C for 24 hours [8].

2.4. CALB Immobilization

The immobilization of CALB in the previously functionalized support was performed in a batch at 25 °C. 2.54 mL of enzyme (0.51 mg) in sodium phosphate buffer (5 mM, pH = 7.0) was added. 0.1 g of APTS nanoparticles were added. Agitation speed of 90 rpm. Contact time 0.5h. CALB adsorption immobilized, called CALB-ADNs, was removed by magnetic separation and washed with sodium phosphate buffer (5 mM, pH = 7.0) [9,10].

2.5. Ethyl oleate synthesis

The esterification experiments were carried out in plastics tubes (2.0 mL) containing 0.6 g of oleic acid and 151 μ L of ethanol (molar ratio 1:1), as well as 0.023 g of biocatalyst CALB-ADNs (1.7 % of reaction mass). The reaction was conducted under orbital stirring (150 rpm), at 37°C. The acid index was evaluated by the Ca 5-40 AOCs method [11].

3.6. Enzymatic activity

Enzyme activity was calculated according to Equation 1.

$$A = \frac{(V_a - V_b) \times 1000 \times M \times V_{final}}{t \times V \times m}$$

where A is the esterification activity U/g; V_a is the volume NaOH spent on titration of sample taken at time zero (mL); V_b is the volume of NaOH spent on titration of sample taken after time t (mL); M is the molarity of the solution of NaOH (mmol/mL); V_{final} is the final volume of reaction medium (mL); m is the enzyme mass immobilized used in the reaction (g); V is the volume of the reaction medium aliquot taken to titration (mL) and t is time (min).

3. Results and Discussions

3.1. CALB Immobilization

The enzyme load may be explained from the analysis of interactions between the enzyme and the support. The increase in enzyme load allows more protein-protein interaction, thus an optimum amount of enzyme is sought. Increasing

the enzyme load also leads to the diffusional limitations, a barrier to products and substrates diffusion, and steric hindrance, which can also explain a greater difficulty in adsorption processes when related to processes involving covalent bonding, thus the same enzymatic charge of the commercial biocatalyst was used for the adsorption process.

The contact time was investigated as short as possible, 0.5h, due to rapid protein adsorption to the support, unlike for covalently bonded supports. This condition is necessary because the adsorption immobilization conditions favor the desorption of enzymes, a milder condition when the reaction medium with higher affinity for lipases, such as fatty acids, is used.

The objective of this work is to obtain the conversion rate of the oleic acid esterification reaction with ethanol using the heterogeneous CALB immobilized catalyst in magnetic nanoparticles.

3.2. Catalytic esterification

Oleic acid was esterified. In a solvent free medium, under 37 °C, the biocatalyst prepared has shown an activity of 2.2 U/g for the esterification of oleic acid after 0.5h, 37 kHz and 300 W. The results obtained with CALB adsorbed onto magnetic iron nanoparticles were compared with those of lipase B from *Candida antarctica* (covalent immobilization) onto acrylic resin (Novozym® 435). In this regard, under same reactional conditions, Novozym® 435 has presented an activity of 2.9 U/g.

The type of agitation was analyzed in which the interference of agitation can be directly related to the shear rate, which initially promotes more interactions between enzyme and support [12]. The ultrasonic bath allowed a higher substrate enzyme interaction in a shorter reaction time, 0.5h for both catalysts, Novozym® 435 and CALB-ADNs. The precipitate was baked at 30 ° C until complete drying. This process was completed after 32h and repeated two more times.

The results of our study are in agreement with those obtained for covalent commercial support. Enzyme stability is maximized through the use of nanoscale supports, modulating catalytic specificity, low resistance to mass transfer, thereby

improving diffusion and reducing operating cost [12].

The adsorption conditions of ethanol at the step of oleic acid reactions contributes to the reduction of the steric energy [13], where the reaction medium was ultrasonically bathed at a temperature of 37 °C and for a period of 0.5h.

Differentiating esterification and transesterification reactions in obtaining esters, it may be understood that the use of catalysts in these reactions yields a change in the catalytic medium [13]. By comparing the samples, it can be analyzed that the reaction occurred and there was ester production [14].

Temperature is one of the factors that can influence the speed of reaction catalyzed by two mechanisms: the chemical mechanism, in which the temperature increase and the consequent increase of the kinetic energy of the reagents result in the process acceleration, and the enzyme denaturation mechanism by the increase of temperature [12]. Thus, the temperature of 37 °C, as shown in the Souza et. al. works is ideal for performing esterification reactions [8].

The effect of pH on the adsorption of enzymatic activity has immobilization efficiency at pH 7.0 for this reaction [14].

The conversion rate for biodiesel production attracts considerable attention because of its profitability, degradability, low toxicity, high safety and renewability, are obtained through esterification and catalytic transesterification of free fatty acids. The chemically catalyzed transesterification process for biodiesel production, chemical catalysts are used. Enzymatic immobilization in materials as heterogeneous catalysts for esterification are used with complementary environment contributions [13].

4. Conclusion

The selection of an immobilization strategy is based on the efficiency of the enzyme use, the cost of the immobilization procedure, the toxicity of the immobilization reagents and the desired final properties of the immobilized biocatalyst. The temperature, the use of ultrasonic bath, besides the enzymatic extract, were indispensable factors to obtain the comparative value with a covalent commercial support. It is noteworthy that the enzymatic adsorption process



compared to other processes used for immobilization has potential with a preparative immobilization, thus the high enzymatic load can be used in a short time and stabilized after a second immobilization from covalent connections (heterofunctional biocatalysts). The utilization and conversion are efficient for the studied reaction medium. Finally, it was found that the esterification of oleic acid with ethyl alcohol and enzymatic combination of the enzyme CALB immobilized onto magnetic nanoparticles by adsorption achieved a favorable conversion rate and acceptable stoichiometry and may even serve as a parameter for prospecting new catalyst combinations.

Acknowledgments

We gratefully recognize the financial support from CNPq project: 409058/2016-5/Universal 01/2016, FUNCAP, CAPES and UNILAB.

References

- [1] C. Cannilla, G. Bonura, F. Costa, and F. Frusteri, "Biofuels production by esterification of oleic acid with ethanol using a membrane assisted reactor in vapour permeation configuration," *Appl. Catal. A Gen.*, vol. 566, pp. 121–129, Sep. 2018.
- [2] F. A. P. Voll *et al.*, "Thermodynamic analysis of fatty acid esterification for fatty acid alkyl esters production," *Biomass and Bioenergy*, vol. 35, no. 2, pp. 781–788, Feb. 2011.
- [3] M. Chai, Q. Tu, M. Lu, and Y. J. Yang, "Esterification pretreatment of free fatty acid in biodiesel production, from laboratory to industry," *Fuel Process. Technol.*, vol. 125, pp. 106–113, 2014.
- [4] M. S. Zanuttini, M. L. Pisarello, and C. A. Querini, "Butia Yatay coconut oil: Process development for biodiesel production and kinetics of esterification with ethanol," *Energy Convers. Manag.*, vol. 85, pp. 407–416, 2014.
- [5] N. B. Carvalho, Á. S. Lima, and C. M. F. Soares, "USO DE SÍLICAS MODIFICADAS PARA IMOBILIZAÇÃO DE LIPASES."
- [6] J. M. Encinar, J. F. González, and A. Rodríguez-Reinares, "Ethanolysis of used frying oil. Biodiesel preparation and characterization," *Fuel Process. Technol.*, vol. 88, no. 5, pp. 513–522, May 2007.
- [7] A. C. H. Barreto *et al.*, "Novel ferrofluids coated with a renewable material obtained from cashew nut shell liquid," *Microfluid. Nanofluidics*, vol. 12, no. 5, pp. 677–686, Mar. 2012.
- [8] C. G. C. M. Netto, L. H. Andrade, and H. E. Toma, "Enantioselective transesterification catalysis by *Candida antarctica* lipase immobilized on superparamagnetic nanoparticles," *Tetrahedron Asymmetry*, vol. 20, no. 19, pp. 2299–2304, Oct. 2009.
- [9] M. C. M. de Souza, "Imobilização de lipase de *Candida antarctica* do tipo B em nanopartículas magnéticas visando a aplicação na síntese de ésteres," Universidade Federal do Ceará, 2012.
- [10] C. Ortiz *et al.*, "Catalysis Science & Technology MINI REVIEW Novozym 435: the 'perfect' lipase immobilized biocatalyst?," *Cite this Catal. Sci. Technol.*, vol. 9, p. 2380, 2019.
- [11] J. Mossoba, M.; Kramer, J.; Delmont, P.; Yurawecz, M.; Rader, "Official methods for the determination of trans fat. [S.1.]," *AOCS Pres Champaign*, 2003.
- [12] M. C. M. de Souza, K. P. Dos Santos, R. M. Freire, A. C. H. Barreto, P. B. A. Fechine, and L. R. B. Gonçalves, "Production of flavor esters catalyzed by Lipase B from *Candida antarctica* immobilized on magnetic nanoparticles," *Brazilian J. Chem. Eng.*, vol. 34, no. 3, pp. 681–690, Jul. 2017.
- [13] J. Pang, G. Zhou, R. Liu, and T. Li, "Esterification of oleic acid with methanol by immobilized lipase on wrinkled silica nanoparticles with highly ordered, radially oriented mesochannels," *Mater. Sci. Eng. C*, vol. 59, pp. 35–42, Feb. 2016.
- [14] M. Cea, M. E. González, M. Abarzúa, and R. Navia, "Enzymatic esterification of oleic acid by *Candida rugosa* lipase immobilized onto biochar," *J. Environ. Manage.*, vol. 242, pp. 171–177, Jul. 2019.

Adsorption capacity evaluation of Beta zeolite as adsorbent for isoniazid

Iane M. S. Souza^a, C. Ignacio Sainz-Díaz^b, César Viseras^{b,c}, Sibeles B. C. Pergher^{a*}

^a Laboratório de Peneiras Moleculares, Universidade Federal do Rio Grande do Norte, 59078-970, Natal, Brazil.

^b Andalusian Institute of Earth Sciences (CSIC-University of Granada), Av. de las Palmeras 4, 18100, Armilla, Granada, Spain.

^c Department of Pharmacy and Pharmaceutical Technology, Faculty of Pharmacy, University of Granada, Campus Cartuja s/n, 18071, Granada, Spain.

Abstract

The zeolites can be classified as aluminosilicates that, due to their higher porosity, present the propriety to adsorb and protect different kind of organic molecules. Because of that, the adsorption on the Beta zeolite channels of isoniazid (INH), a class III drug according the Biopharmaceutics Classification System, has been studied. For that, kinetics at different pH's (3, 2 and 6) were performed to know the conditions that had better favor isoniazid adsorption. Also that, a hybrid material was formulated and characterized by some techniques such as XRD, TGA/DSC and FTIR. The results showed that beta zeolite have capacity to adsorb isoniazid with a pseudo-second order kinetic profile with fast initial adsorption and the pH 6 as the better condition. The solid characterization indicate that all the isoniazid was adsorbed inside the zeolite channels and the hybrid material get a better drug resistance on INH thermal degradation. The results obtained with isoniazid enable future studies in the development of more effective formulations for the treatment of tuberculosis.

Keywords: Adsorption; Zeolite, Isoniazid, Carrier, Drug delivery.

1. Introduction

The tuberculosis is the first cause of death from an infectious agent in the worldwide and its treatment is based on the administration of several tuberculostatic drugs, where the isoniazid (INH) is the most widely used during all the treatment [1]. The isoniazid present a higher aqueous solubility, low permeability, short plasma half-life and only low levels can access to plasma via oral route [2]. Because of that, the development of carries capable to improve the INH permeability is necessary.

New technological drugs formulation able to resolve the problems associated with drug degradation, toxicity and low bioavailability are widely studied [3]. Currently, studies apply clay minerals, such as smectites and kaolin, as excipients in the formulation of drugs in order to provide greater stability, solubility, improve pharmaceutical characteristics, among other properties [4]

The zeolites can be defined as materials that present a structure of bonded tetrahedral that contains channel and box-shaped cavities

commonly occupied by water molecules and cations [5]. Due to the zeolite characteristics of high pore volume, cation exchange capacity, acid stability and inertness, make them widely use in various industrial processes, such as catalyst support and adsorbents of pollutants from water [6, 7].

These properties of zeolite materials drove their investigation on medicine application, gained prominence as excipients in the formulation of modified drug delivery systems for same treatments as stomach and anti-inflammatory problems [8-10].

Therefore, the ability of beta zeolite to adsorb isoniazid was studied in order to promote hybrid materials capable of being used as advanced excipients in pharmaceutical dosage forms.

2. Material and Methods

2.1. Adsorption kinetics

Seven different contact times in separated batches (0.5, 1, 2, 4, 6, 10 and 24 h) between the beta zeolite and the isoniazid solution with three



different pH's (2, 3 and 6), buffered with HCl solution (1 mol.L^{-1}) were studied. For each experiment, 12 mg of zeolite was dispersed in 10 mL of isoniazid aqueous solution (100 mol.L^{-1}) and maintain in agitation in a thermostatic bath at $25 \text{ }^\circ\text{C}$. After each contact time, dispersions were centrifuged, the supernatant filtered and measured in Uv-vis (Uv-vis spectrophotometer Lambda 25, Perking Elmer, S) at a wavelength of 262 nm for the solution with pH 6 and 265 for the solutions with pH's 2 and 3, reported wavelength in the literature and corresponding for the quantification of isoniazid [11]. All assays were performed in triplicate. The quantification of the adsorbed isoniazid (q_t) was estimated considering the initial concentration of the drug solution and the final concentration of the measured supernatant, following models previously proposed [12, 13].

2.2. Preparation of hybrid materials

For the preparation of hybrid materials, 0.06 g of the zeolite was dispersed in 50 mL of isoniazid aqueous solution (2200 mg L^{-1}) at pH around 6 and maintain under stirring for 24 h at $25 \text{ }^\circ\text{C}$. After the contact time, the mixture was centrifuged, the solid separated from the supernatant and dried at $30 \text{ }^\circ\text{C}$ until all the liquid evaporated. The hybrid material was named HBINH.

2.3. Material characterization

Before and after the adsorption tests, the materials and the drug were characterized by a powder X-Ray diffraction (PXRD) by using a Philips®X-Pert diffractometer with Cu $K\alpha$ wavelength radiation, 45 kV, 40 mA, $4 - 70^\circ 2\theta$, a high-speed solid-state X'Celerator detector and rotating sample holder. The diffraction data were analyzed using the HighScore Plus® software.

Analysis of Infrared Spectroscopy by Attenuated Total Reflectance (ATR) were performed using a JASCO 6200 spectrophotometer with pure powder samples working in the medium infrared zone ($4000\text{-}400 \text{ cm}^{-1}$) with a resolution of up to 0.25 cm^{-1} .

Thermogravimetric analyzes were performed using a Libra TG209F1 analyzer, NETZSCH, with

air at a flow rate of 20 mL min^{-1} , from 30 to $1000 \text{ }^\circ\text{C}$ at a heating rate of $10 \text{ }^\circ\text{C.min}^{-1}$.

3. Results and discussions

3.1. Adsorption results

The kinetics results (Fig. 1) show profile for each pH studied. It is observed that at pH 6 and 3 obtained a similar and higher retention ability of isoniazid than at pH 2, that could be associated to the fact that at pH 6 and 3 the isoniazid molecule is neutral and exists on its cationic form in the aqueous medium [17]. In addition, a fast isoniazid adsorption, between 35 and 45 mg.g^{-1} , was observed in the first 30 minutes, increasing the adsorption up to 10 h of contact. Afterwards, a horizontal profile was observed with a minimum variation of the quantity adsorbed between 10 and 24 h.

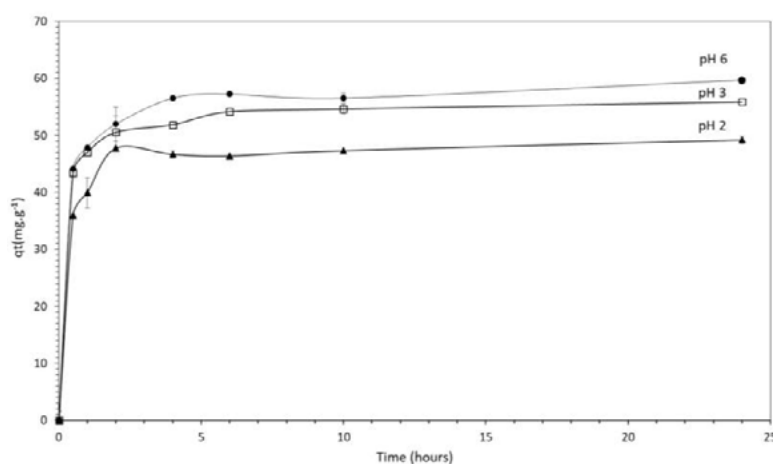


Figure. 1. Kinetics profile of isoniazid adsorption at pH 6, 3 and 2.

The kinetics of the adsorption was modeled considering the equations of Langergren [14] and the Pseudo-second order equation [15], the kinetics parameters calculated is presented in Table 1. According the values of R^2 , the pseudo second order linearization is the one that better describes the adsorption process in the three pH's conditions. The second order linearization affirms that the adsorption occurs at specific superficial sites of the adsorbent and that the adsorption energy does not depend on the formation of a layer on the adsorbent surface [15]. Also that, the amount of adsorbed compound to the adsorbent at equilibrium (q_e)

calculated show that at pH 6 is the higher amount adsorbed than at pH's 2 and 3.

Table 1: Kinetic parameters of the adsorption of isoniazid by beta zeolite in different pH's.

Sample	^a Pseudo-1 ^o			^a Pseudo-2 ^o		
	R ²	^b K ₁	^c q _e	R ²	^d K ₂	^c q _e
pH 6	0.937	0.216	27.350	0.998	0.020	69.930
pH 3	0.944	0.532	14.144	0.999	0.075	56.180
pH 2	0.829	0.506	11.430	0.999	0.080	49.505

^a Pseudo-first: Langergren linear equation [14], Pseudo-second: second order equation [15],

^b K₁, constant for the first-order adsorption process (min⁻¹).

^c q_e, amount of adsorbed compound to the adsorbent at equilibrium (mg g⁻¹).

^d K₂, constant of pseudo-second order adsorption rate (g mg⁻¹min⁻¹).

3.2. Characterization of hybrid materials

Uv-vis results for the hybrid material preparation, appoint that the beta zeolite adsorbed 158mg of isoniazid per gram of zeolite at the conditions proposed.

The X-ray diffraction patterns of isoniazid, the Beta zeolite and the hybrid materials formulates HBINH, are presented in Fig. 2. The isoniazid diffraction pattern presents typical reflections of its crystal lattice at 12°, 14°, 16° and 20° (2θ units) [11;16]. For the hybrid material is observed the main reflections from the zeolite in 2θ equal to 7.9, 22.6, 25.5, and 27.2, the absence of isoniazid reflection could indicate that all de drug adsorbed are inside the zeolite pore.

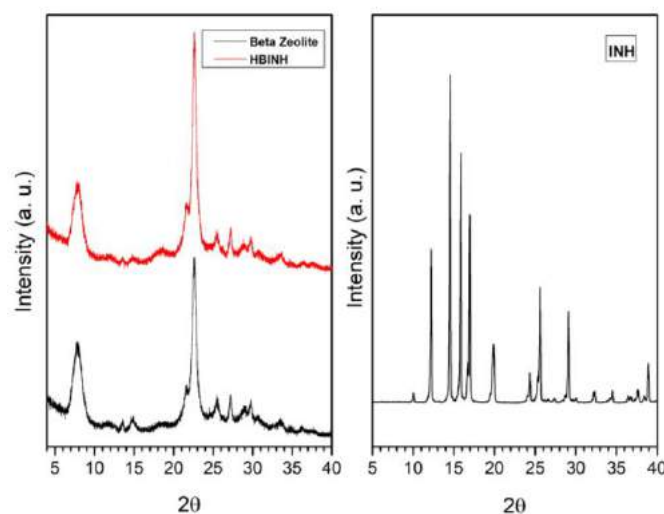


Figure. 2. X-ray diffraction patterns of isoniazid (INH), Beta Zeolite and the hybrid material (HBINH)

FTIR analysis (Figure 3) shows that for hybrid material, HBINH, bands appear in 849.16, 769.15, 669.23 and 492.28 associated with isoniazid, along with all beta zeolite groups. This result indicates the existence of the drug on the zeolite surface or cavities.

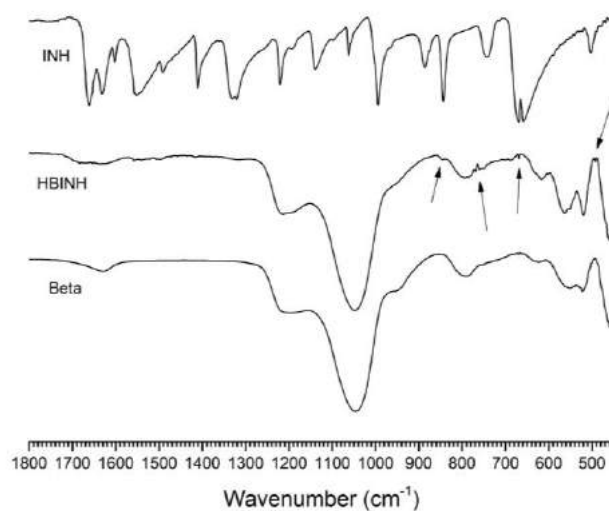


Figure 3: FTIR of Isoniazid (INH), Beta zeolite (Beta) and the hybrid material (HBINH).

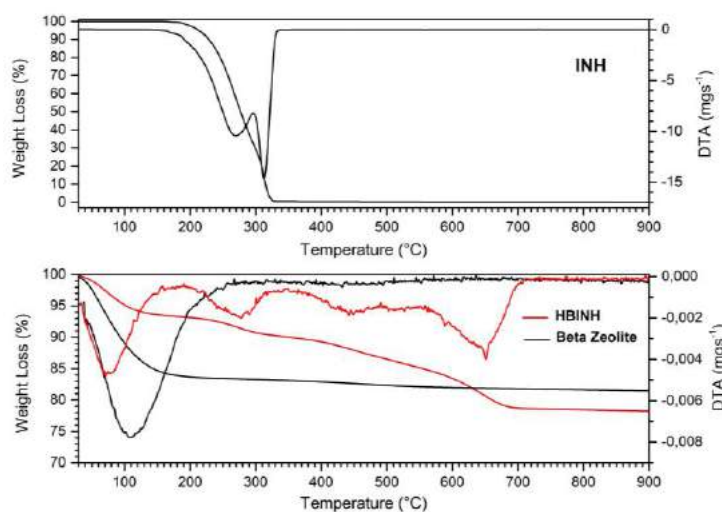


Figure 4: TGA and DTA of Isoniazid (INH), Beta Zeolite (Beta) and the hybrid (HBINH).

The TGA/DTA analysis results (Figure 4) show that the hybrid material (HBINH) has three stages of mass loss, a first around 150 ° C, associated with the loss of weakly adsorbed water, and another three at 250 ° C, 450 ° C and 650 ° C, corresponding to the degradation of isoniazid. Table 2 presents the variations in mass loss for each case. It is observed that at 150 ° C isoniazid is completely degraded, while for hybrid material it is completely degraded only after 700 ° C, indicating that Zeolite has a thermal protection capability to the drug, and these three stages of mass loss can confirm that adsorption occurs in different mechanisms. Another factor observed is that with the drug adsorbed, the zeolite beta has a smaller amount of water retained, 6.34%, compared to 15% alone.

Table 2: Stages of mass loss for isoniazid (INH), Beta zeolite (Beta) and the hybrid material (HBINH)

Sample	Temperature		
	150°C	150°C –350°C	>350°C
INH	-	100%	-
Beta	15%	1.4%	1.6%
HBINH	6.3%	3.8%	11.6%

4. Conclusions

The beta zeolite studied presented a favorable characteristic to work as adsorbent to isoniazid in the conditions proposed where at pH 3 is observed the higher quantity of INH retained. Besides the XDR analysis indicate that all drug was adsorbed inside the beta channels due to the not identification of INH reflections on hybrid material. Also that, the TGA/DTA analysis show that this zeolite can actuated as a protection for isoniazid degradation. This work is an initial study to the development of new and efficient carriers for the antituberculosis isoniazid.

Acknowledgements

This research was financed by Coordenação de Aperfeiçoamento de Pessoal de Nível Superior (CAPES), the Spanish Projects FIS-2016-77692-C2-2-P and, the Andalusian Project RNM-1897. Thanks to the Instituto Andaluz de Ciencias de la Tierra (IACT), to the pharmacy PhD program from University of Granada, Spain and to the materials science and engineering PhD program from Universidade Federal do Rio Grande do Norte (UFRN), Brazil.

References

- [1] WHO, Global Tuberculosis Report; 2018.
- [2] Esperanza Carazo, Giuseppina Sandri, Pilar Cerezo, Cristina Lanni, Franca Ferrari, Cristina Bonferoni, Cesar Viseras, Carola Aguzzi. Halloysite nanotubes as tools to improve the actual challenge of fixed doses combinations in tuberculosis treatment. *Journal of Biomedical Materials Research: Part a*, 2019, vol 107.
- [3] A.M. Ginsberg, M. Spigelman, Challenges in tuberculosis drug research and development, *Nat. Med.* 13 (2007) 290–294.
- [4] BORIN, M. F.; ARAUJO, A. C. F. Influência de Excipientes farmacêuticos em reações adversas a medicamentos. *Brasília Med*, v. 49(4), p. 267-278.
- [5] Giovanna Vezzalini, Simona Quartieri, Ermanno Galli, Alberto Alberti, Giuseppe Cruciani, Ake Kvik. Crystal structure of the zeolite mutinaite, the natural analog of ZSM-5, *Zeolites*, v. 9, p. 323-325, 1997.
- [6] A. Corma, H. Garcia, Supramolecular host-guest systems in zeolites prepared by ship-in-a-

bottle synthesis, *Eur. J. Inorg. Chem.* (2004) 1143–1164.

[7] J.P. Hee, M.L. Hyung, Antimicrobial properties of Ag-exchanged natural and synthetic zeolites: a short review, *Current Green Chemistry* 2 (2015) 354–361.

[8] PIÑEIRA, T. F. *Materiales Compuestos Zeolita-Surfactante-Fármaco com Uso Potencial em la Industria Farmacéutica*. 2010. 126f. Tese (Doutorado em Ciências Químicas) – Universidad de La Habana, Ciudad de La Habana.

[9] A. Datt, N. Ndiege, S.C. Larsen. Development of porous nanomaterials for applications in drug delivery and imaging, *ACS Symp. Ser.* 1119 (2012) 239–258.

[10] M. Grce, K. Pavelić, Antiviral properties of clinoptilolite, *Microporous Mesoporous Mater.* 79 (2005) 165–169.

[11] G.A. Brewer, K. Florey (Ed.), *Analytical Profiles of Drug Substances (Isoniazid)*, 6 Academic Press, 9780122608063, 1977, pp. 183–258.

[12] D.N.R. de Sousa, S. Insa, A.A. Mozeto, M. Petrovic, T.F. Chaves, P.S. Fadini, Equilibrium and kinetic studies of the adsorption of antibiotics from aqueous solutions onto powdered zeolites, *Chemosphere* 205 (2018) 137–146.

[13] L.N.M. Ribeiro, A.C.S. Alcântara, M. Darder, P. Aranda, F.M. Araújo-Moreira, E. Ruiz-Hitzky, Pectin-coated chitosan-LDH bionanocomposite beads as potential systems for colon-targeted drug delivery, *Int. J. Pharm.* 463 (2014) 1–9.

[14] S. Lagergren, Zur theorie der sogenannten adsorption gelöster stoffe, *Kungliga Svenska Vetenskapsakademiens, K. Sven. Vetenskapsakademiens.* 24 (1898) 1–39.

[15] Y.S. Ho, G. McKay, A kinetic study of dye sorption by biosorbent waste product pith, *Resour. Conserv. Recycl.* 25 (1999) 171–193.

[16] S.C. Angadi, L.S. Manjeshwar, T.M. Aminabhavi, Interpenetrating polymer network blend microspheres of chitosan and hydroxyethyl cellulose for controlled release of isoniazid, *Int. J. Biol. Macromol.* 47 (2010) 171–179.

[17] 38. C. Becker, J.B. Dressman, G.L. Amidon, H.E. Junginger, S. Kopp, K.K. Midha, V.P. Shah, S. Stavchansky, D.M. Barends, *Biowaiver Monographs For Immediate Release Solid Oral*

Dosage Forms: Isoniazid. Journal Of Pharmaceutical Sciences, 2017, 96.

Purification of rabbit polyclonal IgG using dye ligand affinity chromatography

Tiago Severo Estrázulas^a, Natália Aragão Dias^a, Thais Ribeiro Nunes^a, Diego Romão Gondim^b, Mauricio Fraga van Tilburg^c, Ivanildo José da Silva Júnior^a

^a Universidade Federal do Ceará (Campus universitário do Pici, Bloco 709, Fortaleza – CE, CEP 60455-760, Brazil)

^b Universidade Estadual Vale do Acaraú (Centro de Ciências Exatas e Tecnologia, Curso de Química, Campus Betânia, Sobral – CE, CEP 62040-370, Brazil)

^c Universidade Federal Rural do Semi-Árido (Departamento de Ciências Animal, Programa de Pós-Graduação em Ciência Animal, Mossoró, Rio Grande do Sul, CEP: 59.625-900, Brazil)

Abstract

Pharmaceutical industry uses the monoclonal antibody class for the diagnostic of several diseases. However, the use of these molecules is hindered due their production high costs, the downstream process (using Protein A resins) and also their hindering multiple antigen recognition. Therefore, the purification of the polyclonal antibodies employing pseudo-bio-specific ligand (e.g. dyes) may be an useful alternative to specific affinity chromatography (AC). Thus, the aim of this work was to investigate the better elution conditions for the purification of rabbit polyclonal IgG using commercial column Hitrap Blue HP. The experiments were performed with sodium phosphate and glycine-HCl buffers in elution step. Sequential analyses of SDS-PAGE were used in order to identify rabbit polyclonal IgG in the collected fractions. The highest retention of rabbit polyclonal IgG was observed with glycine-HCl buffer, resulting in a recovery of 61.23% of proteins with 0.1 M, pH 2.8. Thus, the use of glycine in the elution favored the elution of IgG with 7 high degree of purity. In the other hand, the elution step, with 0.1 mol.L⁻¹ of sodium phosphate buffer pH 7.0, also showed a good selectivity towards with the target-protein and albumin, once the co-elution of IgG and RSA were observed. The results demonstrate the potential application of Hitrap Blue HP for purify rabbit albumin serum. This work confirmed the feasibility of the elution conditions for the purification of rabbit polyclonal IgG, providing informations for the application of semi-continuous chromatography for a scale-up production of purify polyclonal antibodies.

Keywords: affinity chromatography; polyclonal antibodies; dye ligands; elution conditions;

1. Introduction

The production of antibodies has been applied in the pharmaceutical industry to develop new drugs and diagnoses of autoimmune diseases (i.e. cancer), especially in patients with metastasis or terminally illness [1,2]. Antibodies are selected due their high affinity and specificity for target molecules. Therefore, their use as an efficient immunotherapeutic agent make them important molecules for medicinal applications[2]. Antibodies can be characterized as monoclonal or polyclonal. The monoclonal types are those originated from cloning B lymphocyte, and they only can bind itself to a specific epitope in a single way. Polyclonal antibodies are generated by the cloning of different B lymphocytes and they will recognize several epitopes on the antigen [3].

The field of therapeutic antibodies is one of the fastest growing segments in the pharmaceutical industry. In that case, one of the mostly used antibodies are the monoclonal types, whose applications range from diagnostics to detect diseases i.e. pharyngitis and rheumatic fever [4,5] and in the treatment of some cancers [6].

However, this class of antibodies is less accessible due to their high production cost, including the difficulties associated with polyclonal antibody fractionation and production in culture medium, as well as the hindering recognition of multiple antigen in an infection, once these molecules are not suitable to bind to multiple epitopes of a same disease, having a reduced range of epitopes [2].

Among the antibodies, the most used in the drug industry is the G-type immunoglobulin (IgG). IgG is applied to infections defense and arises in the acute



phase of diseases, protecting the immune system from future infections. The IgG represent around of 80% of the body's immunoglobulins and are the most efficient antibody for the identification of the target molecules, being decisive in secondary immune response [7]. However, the studied with polyclonal IgG from human serum is difficult due to the high costs and the bureaucratic process related to its obtaining. On this hand, to facilitate the development of studies, polyclonal IgG purification present in mammalian serum, for example, may be useful, due their lower cost and is easier to access. Purified IgG can be used in the clinical diagnosis against hepatitis and allergic diseases and therapeutic treatment for viral infection, for example [4,5].

Most antibodies approved for clinical applications are obtained from mice. However, these animals have a small spleen, which offers a smaller diversity of immune response when compared to the rabbit organism [8]. Rabbit serum antibodies have a faster reproductive cycle, produce fifty times more antibodies compared to mice serum, and can recognize multiple epitopes which do not elicit an immune response in mice or other animals [9].

Affinity chromatography (AC) is a chromatography method extensively used for IgG purification. This technique is based on specific biological interactions. This method offers a significant advantage for the purification of antibodies and antibody fragments for several protein sources, providing a high selectivity and a high capacity for target protein [10].

The ligand used in AC can be bio-specific or pseudo-bio-specific. Bio-specifics have high affinity for the target biomolecule; however, they are expensive and, generally, require a drastic condition to elution, as the case of Protein A. In contrast, pseudo-bio-specific ligands are related to the purification of dyes, amino acids and metal ions, which usually have medium affinity for typical serum proteins. These ligands are less expansive than protein A and also have been used for purification of human albumin and immunoglobulin [11,12].

The aims of this work were to investigate the better elution conditions using Hitrap Blue HP, for rabbit polyclonal IgG purification. Initial tests were performed with sodium phosphate (0.1 mol L⁻¹ pH 7.0) elution buffer with NaCl addition. After, the elution with glycine-HCl buffer was performed to improve the conditions used in the elution step. Purification of rabbit serum polyclonal IgG occurred using glycine-HCl (0.1 mol L⁻¹, pH 2.7) and the

analyses of SDS-PAGE were performed to identify the rabbit polyclonal IgG in the samples deriving from the chromatographic experiments.

2. Materials and Methods

2.1. Materials

Hitrap Blue HP column, Coomassie Brilliant Blue, tetramethylenedia (TEMED), ammonium persulfate and Trizma-base (TRIS) were obtained from Sigma Aldrich (USA). The 30% Acrylamide/bis solution was obtained from Bio Rad. Bovine Serum Albumin (BSA) was obtained from Inlab. The high molecular weight standard (HMW) was purchased from GE Healthcare (USA). The other reagents used are of analytical grade. All solutions were made with Mili-Q ultrapure water.

2.2. Methods

2.2.1 Chromatographic Assays:

Two chromatographic experiments were performed using Hitrap Blue HP with dye ligand, Cibacron Blue F3G-A. Rabbit serum samples were injected using 1 mL pulse with 1.0 mg mL⁻¹ of the protein solution with a flow rate of 1 ml min⁻¹. For the binding buffer experiments were used 0.025 mol L⁻¹ of sodium phosphate buffer (pH 7.0). The column was washed with the same binding buffer for 10 min. For the elution step the mixture of 0.1 mol L⁻¹ sodium phosphate buffer (pH 7.0) with 1.0 mol L⁻¹ NaCl was used for the first chromatography experiment, with a gradient of 25 min and an increase of the NaCl concentration from 0.0 to 1.0 mol L⁻¹ NaCl. In the second chromatography experiment the elution step was performed with 0.1 mol L⁻¹ glycine-HCl buffer (pH 2.8). All experiments were performed in a Contichrom® Lab 10 apparatus (Knauer, Germany). During the experiments, samples were collected at 1 minute intervals for posterior analyses of SDS-PAGE and total protein quantification.

2.2.2 Total protein:

The total protein concentration of the samples collected from the culture medium was determined according to the Bradford method [13], using bovine serum albumin (BSA) as the standard for build the curve of calibration. The absorbance was measured

at 595 nm using a UV-Vis spectrophotometer (Thermo Scientific, USA).

2.2.3 SDS-PAGE Electrophoresis:

SDS-PAGE analyses were performed in a Mini Protean III device (BioRad, USA) using polyacrylamide gel (30% acrylamide and 2.7% bis-acrylamide), according to Laemmli [14] with a concentration of 10%. The chromatographic fractions from each stage were heated to 95 °C for 4 min and aliquots of 10 to 20 µL were inserted in the gel wells. A high molecular weight (HMW) protein standard and a buffer without β-mercaptoethanol were used. The runs were carried out at 150 V in the 7.5% separation gel and with a 4% stacking gel. Protein bands were revealed by Coomassie Blue (Sigma-Aldrich, USA).

3. Results and Discussion

3.1. Chromatography Assays with Hitrap Blue HP

Figure 1 shows the chromatographic run for rabbit serum in the Hitrap Blue HP with binding buffer sodium phosphate buffer 0.025 mol.L⁻¹ (pH 7.0) and 1 mg.ml⁻¹ of rabbit serum.

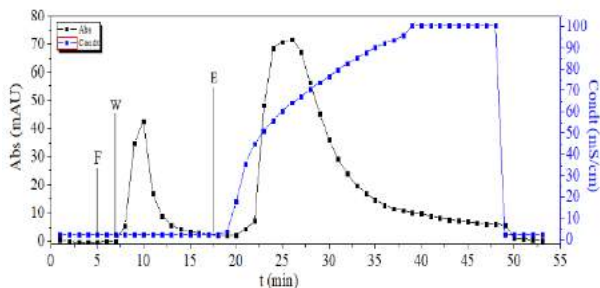


Figure 1 - The experiment conditions were: (W) Washing (Sodium phosphate buffer 0.025 mol L⁻¹ pH 7.0); (E) Elution (Sodium phosphate buffer 0.1 mol L⁻¹ pH 7.0 with NaCl 1.0 mol L⁻¹); flow rate = 1ml min⁻¹; F = Feed – rabbit serum with 1 mg mL⁻¹; W = Start of the washing stage; E = start of the elution stage. Linear

In Fig. 1, the peak obtained in the elution step (E) dominates the profile and was greater than that observed in the washing (W) step. According to the mass balance present in Table 1, around 81% of total proteins were retained by Hitrap Blue HP.

Table 1. Mass balance per step for AC Hitrap Blue HP. Feed - rabbit serum with 1 mg mL⁻¹. F diluted in Binding Buffer, Washing (Sodium phosphate buffer 0.025 mol L⁻¹ pH 7.0), Elution (Sodium phosphate buffer 0.1 mol L⁻¹ pH 7.0 with NaCl 1.0 mol L⁻¹).

Step	Mass (mg)	(%)
Feed	1.00	100.00
Loading	0.00	0.00
Washing	0.19	18.95
Elution	0.81	81.05
CIP	0.00	0.00
Total	1.00	100.00

Fig. 2 shows the electrophoresis of the collected fractions where rabbit polyclonal IgG was identified.

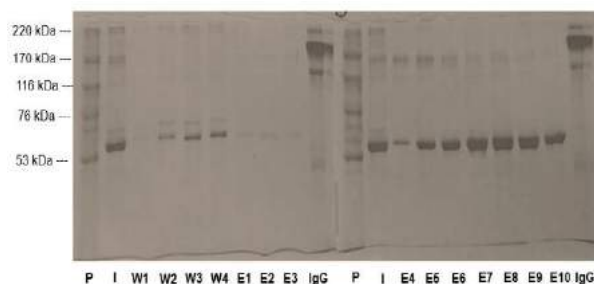


Figure 2. SDS-PAGE- chromatograph profile from Rabbit IgG purification using Hitrap Blue HP. P: High molecular weight standard; I: Initial Sample; Samples: W1-W4 (Washing) E1-E8 (Elution); IgG: Protein of reference (Human IgG).

In Elution step was observed that the most of the adsorbed proteins (IgG and rabbit serum albumin - RSA) was recovered at this step (E). Thus, during the elution with the linear gradient, was possible to evaluated that 81% of proteins were recovered with a low concentration of NaCl (around 0.0 to 250 mM NaCl).

The Blue HP is a group of specific adsorbents with an affinity for a large variety of biomolecules. The dye ligand, Cibacron Blue F3G-A, is covalently attached to the matrix via the triazine part of the dye molecule. Some proteins interact bio-specifically with the dye (e.g. albumin) [15].

A favored co-elution of IgG and RSA as observed in samples E4-E8 in the elution step (Figure 2). This can be attributed to the ligand characteristics, which can be used in serum albumin depletion. That occurred, once the use of the elution buffer (with 0.1 mol L⁻¹ sodium phosphate buffer)

together with the increasing of the saline gradient (with NaCl concentration), allow the bio-specifically interaction between the proteins present in the serum with the dye (due to their similarity with nucleotide cofactors). Thus, the higher albumin adsorption can be observed when compared to IgG adsorption.

In order to purify the polyclonal IgG from rabbit serum is necessary optimize the elution conditions to avoid the co-adsorption of albumin and IgG.

3.2. Elution condition using Glycine-HCl with Hitrap Blue HP

Figure 3 shows the chromatogram of Hitrap Blue HP and 1 mg.ml⁻¹ of rabbit serum using glycine-HCl as buffer in the elution step with the decrease of the pH. In this case, loading and washing steps were the same used in the previous experiments.

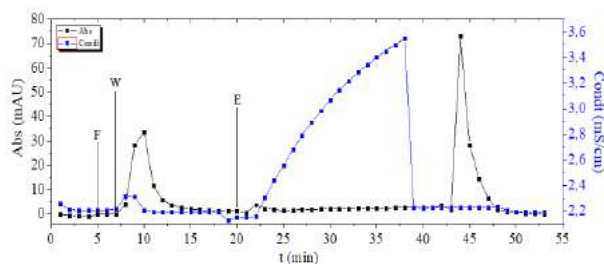


Figure 3 - Experimental conditions were: Linear elution gradient for 25 min. (W) Washing (Sodium phosphate buffer 0.025 mol L⁻¹ pH 7.0), (E) Elution (glycine-HCl buffer 0.1 mol L⁻¹ pH 2.8). Flow rate = 1ml min⁻¹, F = Feed - rabbit serum with 1 mg mL⁻¹, W = Start of the washing stage; E = start of the elution stage.

In Fig. 3, a prominent peak in the elution step was observed, indicating that the most concentration of proteins present in the initial sample were retained (Table 2).

Table 2. Mass balance per steps for AC Hitrap Blue HP using glycine-HCl 0.1 mol L⁻¹ with elution buffer. Feed - rabbit serum with 1 mg mL⁻¹ diluted in Binding Buffer, Washing (Sodium phosphate buffer 0.025 mol L⁻¹ pH 7.0), Elution (glycine-HCl buffer 0.1 mol L⁻¹ pH 2.8).

Step	Mass (mg)	(%)
Feed	1.00	100.00
Loading	0.00	0.00
Washing	0.21	20.91
Elution	0.61	61.23
CIP	0.15	16.91
Total	0.97	97.05

Fig. 4 shows the electrophoresis of fractions collected during the chromatographic experiment. The eluted samples were concentrated in 5 kDa Vivaspin® tube for better gel visualization.

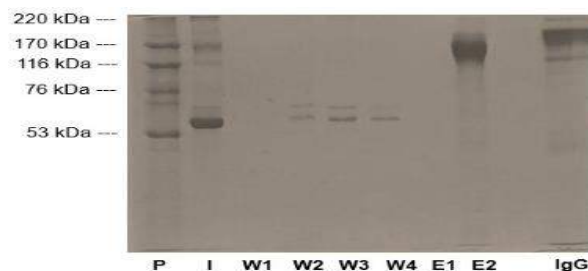


Figure 4. SDS-PAGE - chromatograph profile from Rabbit IgG purification using Hitrap Blue HP. P: High molecular weight standard; I: Initial Sample; Samples: W1-W3 (Washing), E1-E2 (Elution); IgG: Protein of reference (Human IgG).

In the Figure 4 is possible to verify that the sample related to the peak obtained in the elution presented a higher concentration of IgG compared to albumin. This result indicate that the use of glycine favored the elution of IgG with a high degree of purity. The specific affinity between the dye and the proteins noticed may is possibly due to the structural characteristics of the former. Hitrap Blue HP is classified as affinity binder due its interaction with the active sites of proteins, mimicking the structure of the substrates, cofactors or binding agents for these molecules [17,18].

It is also possible to verify a better resolution for the elution peak when compared to the elution experiment with NaCl-sodium phosphate buffer. This occurred due the decrease of the pH, which favored the preferential elution of the protein. In the previous assay the resolution was influenced by the presence of IgG and albumin co-adsorption.

The results obtained in the elution conditions using the pseudo-bio-specific ligand Hitrap Blue HP, provides a valuable route for an unrefined separation of polyclonal IgG from a rabbit serum. For more refined applications, where complete IgG purification is required, approaches as an optimization of the crucial process parameters (pH, ionic strength, temperature, flow rate, etc.) by design of experiments, were required.

The applications of these results are promising, once the elucidation of the better elution conditions can be potentially used in semi-continuous chromatography process, for the scale-up production of purified polyclonal antibodies, and applied for the development autoimmune disease

diagnostic kits, for example. In the order hand, the application of pseudo-bio-specific is required for reduce the operation costs in downstream processes.

4. Conclusion

In this work, different elution conditions in affinity chromatography were employed to assess the purification of the polyclonal IgG. A high retention of the target protein was observed using glycine-HCl as elution buffer in Hitrap Blue HP. Additionally, the IgG could be successfully separated from the initial sample proteins, with exception to RSA. The application of sodium phosphate buffer with NaCl-added showed a good selectivity for the target protein, demonstrating the potential application of this binder as a less costly alternative for purify rabbit albumin serum. However, future works for the parameter optimization are required of purification of IgG in higher levels. Finally, this work brings a markable information about the elution conditions in semi-continuous chromatography process for the purification of polyclonal antibodies from rabbit serum.

Acknowledgements

The authors are grateful to Funcap for providing financial support for this research.

References

- [1] Cordeiro ML da S, Silva NLF da, Vaz MRF, Nóbrega FF de F. Anticorpos Monoclonais: Implicações Terapêuticas No Câncer. *Rev Saúde Ciência Online* 2014;3:252–62.
- [2] Shimizu H, Nakagawa M, Todaka N, Imaizumi K, Kurosawa Y, Maruyama T, et al. Improving the quality of a recombinant rabbit monoclonal antibody against PLXDC2 by optimizing transient expression conditions and purification method. *Protein Expr Purif* 2018;146:27–33.
- [3] Lipman NS, Jackson LR, Trudel LJ, Weis-Garcia F. Monoclonal Versus Polyclonal Antibodies: Distinguishing Characteristics, Applications, and Information Resources. *ILAR J* 2005;46:258–68.
- [4] Ma Q, Song TY, Yuan P, Wang C, Su XG. QDs-labeled microspheres for the adsorption of rabbit immunoglobulin G and fluoroimmunoassay. *Colloids Surfaces B Biointerfaces* 2008;64:248–54.
- [5] Mariam SHS, Ooi CW, Tan WS, Janna OA, Arbakariya A, Tey BT. Purification of rabbit polyclonal immunoglobulin G with ammonium sulphate precipitation and mixed-mode chromatography. *Sep Purif Technol* 2015;144:133–8.
- [6] Díaz-Zaragoza M, Hernández-Ávila R, Govezensky T, Mendoza L, Meneses-Ruiz DM, Ostoa-Saloma P. Comparison patterns of 4 T1 antigens recognized by humoral immune response mediated by IgG and IgM antibodies in female and male mice with breast cancer using 2D-immunoblots. *Immunobiology* 2015;220:1050–8.
- [7] Guo W, Tang F, Qin K, Zhou M, Le Z, Huang W. Glycoengineering and glycosite-specific labeling of serum IgGs from various species. *Carbohydr Res* 2017;446:32–9.
- [8] Yu Y, Lee P, Ke Y, Zhang Y, Yu Q, Lee J, et al. A humanized anti-VEGF rabbit monoclonal antibody inhibits angiogenesis and blocks tumor growth in xenograft models. *PLoS One* 2010;5.
- [9] Weber J, Peng H, Rader C. From rabbit antibody repertoires to rabbit monoclonal antibodies. *Exp Mol Med* 2017:309.
- [10] Ayyar BV, Arora S, Murphy C, O’Kennedy R. Affinity chromatography as a tool for antibody purification. *Methods* 2012:116–29.
- [11] Vijayalakshmi MA. Pseudobiospecific ligand affinity chromatography. *Trends Biotechnol* 1989;7:71–6.
- [12] Arora S, Saxena V, Ayyar BV. Affinity chromatography: A versatile technique for antibody purification. *Methods* 2017:84–94.
- [13] Bradford MM. A rapid and sensitive method for the quantitation of microgram quantities of protein utilizing the principle of protein-dye binding. *Anal Biochem* 1976;72:248–54. [https://doi.org/10.1016/0003-2697\(76\)90527-3](https://doi.org/10.1016/0003-2697(76)90527-3).
- [14] Laemmli UK. Cleavage of structural proteins during the assembly of the head of bacteriophage T4. *Nature* 1970;227:280–5.
- [15] Jahanshahi M, Najafpour G. Advanced Downstream Processing in Biotechnology. *Biochem. Eng. Biotechnol.*, 2007, p. 390–415.
- [16] Thermo Scientific P. Antibody Production and Purification Technical Handbook. *Antib Handb* 2010:1–77.
- [17] Hermans P, Adams H, Detmers F. Purification of antibodies and antibody fragments using capture select™ affinity resins. *Methods Mol Biol* 2014;1131:297–314.
- [18] Vijayalakshmi MA. Pseudobiospecific ligand affinity chromatography. *Trends Biotechnol* 1989;7:71–6.

Elution conditions for purification of rabbit polyclonal antibodies using Protein A column

Natália Aragão Dias^a, Tiago Severo Estrázulas^a, Ivanildo José da Silva Júnior^a, Diego Romão Gondim^b

^a Universidade Federal do Ceará (Campus universitário do Pici, Bloco 709, Fortaleza – CE, CEP 60455-760, Brazil)

^a Universidade Estadual Vale do Acaraú (Centro de Ciências Exatas e Tecnologia, Curso de Química, Campus Betânia, Sobral – CE, CEP 62040-370, Brazil)

Abstract

This work aims to study the best elution conditions to purify polyclonal antibodies from rabbit serum using affinity chromatography technology in Protein A column. Through literature research, it was possible to establish initial conditions to operate the chromatographic runs. The sample concentration in the initial tests was 2.5 mg mL⁻¹. The buffer chosen in Loading, Wash and Regeneration steps was Phosphate buffer 25 mM pH 7.0. Chromatographic runs were performed using Sodium Citrate buffer 100 mM pH 3.3 and Glycine-HCl buffer 100 mM pH 2.8. Both had satisfactory results, but Glycine-HCl showed a narrowest peak in the elution step, showing a higher specificity to the protein. SDS-PAGE Electrophoresis was performed to identify the proteins in the collected samples. Rabbit serum albumin and rabbit IgG were obtained separately, in wash and elution step, respectively. The following tests carried out using different sample concentrations: 1.0 mg mL⁻¹ and 5.0 mg L⁻¹. The results showed that a higher or lower concentration did not have influence in the percentage of retained protein from the initial sample. Chromatographic runs with different buffer molarities were also performed. The best results were collected from the run which elution step consisted of Glycine-HCl buffer 100 mM pH 2.8 with 2.5 mg mL⁻¹ of sample loading. Around 20% of the loading protein was retained in the Protein A column. SDS-PAGE electrophoresis showed that the last sample collected from the Wash step consisted of Rabbit serum albumin and the elution samples were consisted of rabbit IgG.

Keywords: polyclonal antibodies; purification; affinity chromatography.

1. Introduction

The mammalian sera provide several applications for the pharmaceutical industry, including therapeutical proteins to develop treatment for immune diseases, diagnosis and research-based applications. The antibodies present in the serum are essential to protect the organism against foreign bodies, so they have a high specificity regarding antigen identification [1].

Several species have developed mechanisms with new genetic and structures, which provides a

wider antibody variety. However, most researches are carried out isolating it from human and rodent sources. Due to their high-value therapeutic, much innovation has resulted in new techniques to isolate new antibodies, which can be also obtained from different sources, such as cell cultivation. [2].

Rabbit antibodies have been used extensively in research and diagnostics due to their high antigen specificity and affinity, what makes them suitable for therapeutic applications [3]. These mammals can develop a different mechanism from mice and humans in the production of different kinds of

antibodies. In this way, they provide a strong immunological response against foreign organisms. When compared to mice, rabbits have a bigger spleen, which generates a higher number of antibodies with high affinity and specificity. Also, mice usually are inbred, which offers a less diversity of immune responses [4,5].

The antibodies can be classified in monoclonal and polyclonal antibodies. Polyclonal antibodies are considered more effective than monoclonal antibodies due to their ability to bind to multiple epitopes on the same antigen [1].

In biochemical research, polyclonal antibodies have been used as ligands for the production of affinity columns [6]. Also, they are used for determination of molecules in several assays, such as ELISA, Radial Immuno Diffusion, Western blot, RIA[7,8,9].

Rabbit polyclonal antibodies were able to be purified using different chromatographic techniques, such as mixed-mode chromatography [1], dye-ligand affinity chromatography [10] and ion exchange chromatography [11].

Affinity Chromatography is widely used as a tool for protein purification due to its high specificity to antibodies. Protein A affinity chromatography is one of the first discovered immunoglobulin binding molecules that has been extensively studied for decades. Immunoglobulin (Ig) provided by animals' immune system is a class of antibodies which responses to foreign organisms such as viruses, bacteria or cancer cells. Immunoglobulins of isotype G (IgGs) are the most abundant antibodies found in the body of animals (around 80%) [12].

The chromatographic process should be carefully studied. Antibody purification processes involves expensive materials. Washing and elution conditions should be optimized for maximum process optimization. Protein A columns may be the most expensive item compared to other materials required for the antibody purification process. In addition, they can cost up to 15 times more than many ion exchange columns [13]. Research through literature showed that one of the most used binding buffers is Sodium Phosphate buffer at neutral pH, used in chromatographic columns to adsorb antibodies [13, 14, 15, 16, 17, 18]. The binding buffer should have a pH above pI values from polyclonal antibodies such as Immunoglobulin G, pI ranging from 5.3 to 7.1 [19] and Rabbit Serum Albumin, pI = 5.7 [20]. On the other hand, some authors chose elution buffers with low pH when working with protein

purification, such as glycine-hcl and sodium citrate [13,14, 21].

In this work, different elution buffers were studied to purify rabbit polyclonal antibodies from rabbit plasma collected from rabbit blood, using a Protein A chromatographic column.

2. Materials and Methods

2.1 Materials

Rabbit blood was donated from Zootechnics Department from Federal University of Ceará (Fortaleza, Brazil). The rabbit serum was extracted from the blood by centrifugation at 6000 rpm for 10 minutes (refrigerated microcentrifuge Cientec CT-15000R, USA). All chromatographic runs were performed in ÄKTA Start Protein Purification System (GE Life Sciences, USA). HiTrap® Protein A column was used in all analysis (GE Healthcare, USA). Citric acid, sodium citrate, glycine, hydrochloric acid, ethanol, sodium phosphate monobasic and sodium phosphate dibasic were purchased from Sigma Aldrich (USA). Ultrapure water (Milli-Q System, Millipore, USA) was used to prepare all buffers and other solutions.

2.2 Methods

2.2.1 ÄKTA

A method was created in ÄKTA System using HiTrap® Protein A column features provided by UNICORN Start 1.0. The software has predefined steps for several techniques, including affinity chromatography using this specific column.

All solutions used in the chromatographic system were filtered using a 2 stages vacuum pump (Mastercool, USA) and degassed using a ultrasonic cleaner (Prolab, Brazil). The tubes in the equipment are kept in Ethanol 20%. After washing it extensively with Ultrapure water (filtered and degassed), the procedure started. Therefore, the chromatographic run consisted in Prime and Equilibration (15 minutes), Sample Application (3 minutes), Wash (10 minutes), Elution (10 minutes), Prime and Equilibration (3 minutes). For the initial runs, the rabbit serum was diluted in sodium phosphate buffer 25 mM pH 7.0, so the sample concentration would be 2.5 mg.mL⁻¹.

Several tests were performed to optimize the time of each step in the chromatographic run. Sodium citrate 100 mM pH 3.3 and Glycine-HCl

100 mM pH 2.8 were the buffers used in the elution phase and sodium phosphate buffer 25 mM pH 7.0 used in the other steps. 50 μ L of Tris-HCl 100 mM pH 9.0 were added to the samples collected in the elution step on the runs with Glycine-HCl 100 mM pH 2.8, so the proteins could remain stable. Other tests were carried out varying the sample concentration and the elution buffer ionic strength. This way, it would be possible to establish the best conditions to purify antibodies from the rabbit serum. All experiments were performed in triplicate. After finishing the procedures of the day, the equipment was washed extensively with ultrapure water and then 20% ethanol. Figure 1 shows the ÄKTA System with HiTrap® Protein A ready for use:



Fig. 1. ÄKTA Start Protein Purification System

The results from ÄKTA System show the area of each absorbance peak of the chromatographic run. Since the total injected protein is the sum of all areas, it is possible to know how much of the protein was bound to the Protein A column, since it comes from the elution peak.

$$P_{total} = P_{retained} + P_{loading} + P_{washing} \quad (1)$$

$$P_{total} = \frac{P_{elution}}{P_{total}} \quad (2)$$

P_{total} is the total protein loaded in the chromatographic system; $P_{loading}$ is the total protein which leaves the chromatographic column after the serum sample is loaded, represented by the first UV absorbance peak and $P_{retained}$ is the total protein that leaves the chromatographic column in the elution step, represented by the second UV absorbance peak.

2.2.2 Electrophoresis analysis

Electrophoresis SDS-PAGE of samples from the chromatographic runs were performed using 7.5 % polyacrylamide gels under denaturing reducing conditions [22] using a Mini-Protean III System (Bio-Rad, USA). The procedures were performed at 180 V in 7.5 % separation gels with a 4 % stacking gel. Protein bands were formed using Coomassie Blue dye with Methanol.

3. Results and Discussion

The initial chromatographic runs using Glycine-HCl 100 mM pH 2.8 as the elution buffer showed a narrowest peak and a higher absorbance when compared to the experiments using Sodium Citrate 100 mM pH 3.3, which indicates a greater selectivity regarding the adsorbed molecules.

Initially, the loaded protein is diluted in a neutral pH. That pH is higher than pI and the proteins are negatively charged. When the elution buffer with pH lower than pI passed through the column, the proteins became positively charged and left the column.

The elution step requires a buffer with very low pH. Sodium citrate and glycine-HCl are biological buffers which can reach such an extreme condition, differently from other buffers such as Tris-HCl and Sodium Acetate, etc.

Some conditions may have supported the best results using Glycine-HCl as elution buffer: Sodium citrate (Figure 2) has a big molecular structure full of free electrons, which demands a higher amount of H^+ ions to stabilize it in solution. These ions would be less available to interact with the protein molecules in the chromatographic column. Furthermore, The Glycine-HCl molecule is smaller in size, which is great for electrostatic interaction with other molecules, because there is less steric hindrance. In addition, it can achieve a lower pH than Sodium Citrate Buffer, making elution more efficient.

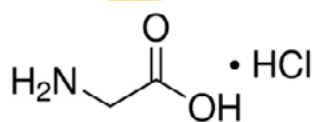


Fig. 2. Glycine-HCl molecular structure

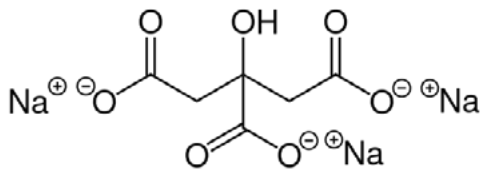


Fig. 3. Sodium Citrate molecular structure

Figure 4 shows the chromatograms obtained in ÄKTA System using the conditions explained in the Figure subtitle:

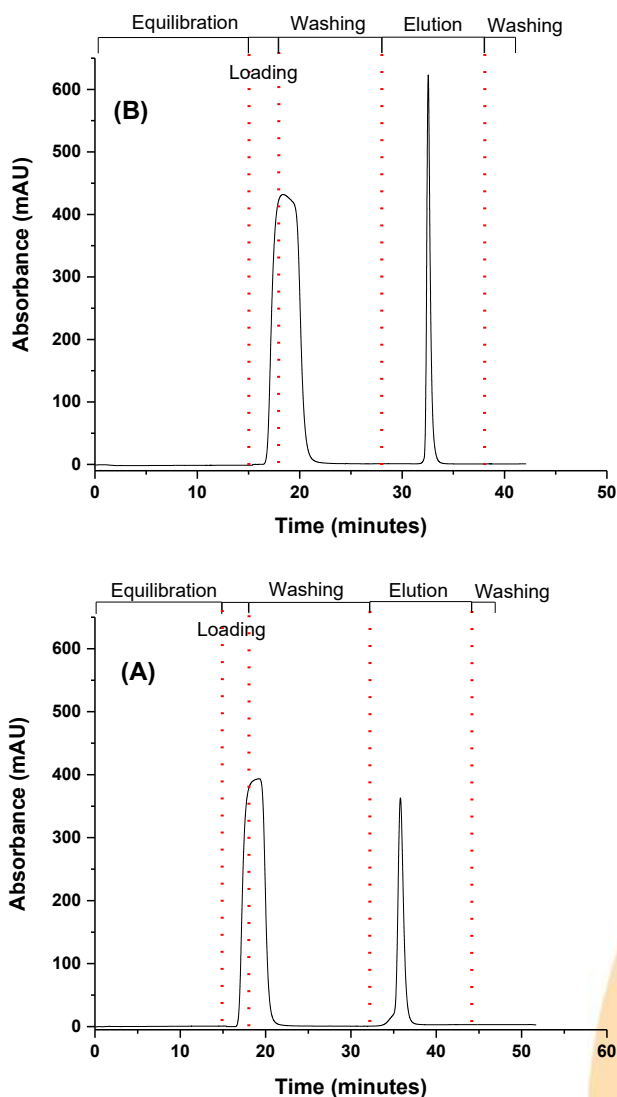


Fig. 4. (A) Sample: Rabbit serum, concentration = 2.5 mg mL^{-1} . Washing buffer: Sodium Phosphate 25 mM pH 7.0. Elution buffer: Sodium Citrate 100 mM pH 3.3 (B) Sample: Rabbit serum, concentration = 2.5 mg mL^{-1} . Washing buffer: Sodium Phosphate 25 mM pH 7.0. Elution buffer: Glycine-HCl 100 mM pH 2.8.

The peak areas were measured in UNICORN Start 1.0. The total retained protein is the protein which left the column after the elution buffer passed through it. The percentage of the total protein loading that was retained by HiTrap® Protein A column was: 20.0% using Glycine-HCl 100 mM pH 2.8 as elution buffer and 21.3% using Sodium Phosphate 25 mM pH 7.0

In order to investigate which proteins are present in which step, the Electrophoresis analysis were carried out, as Figure 5 shows:

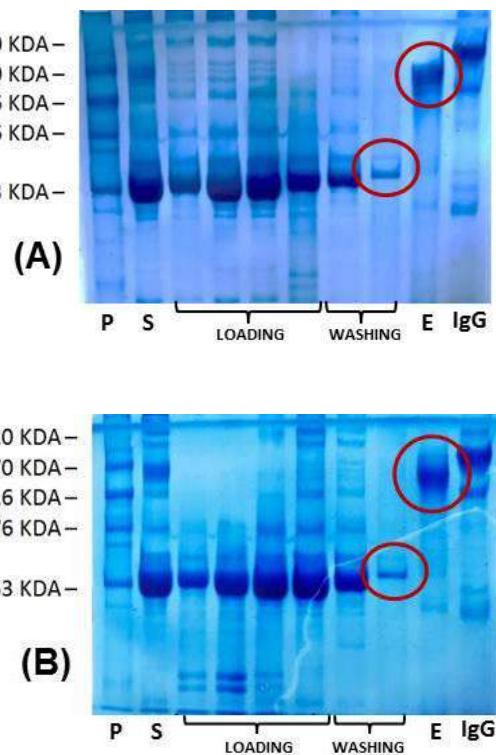


Fig. 5. (A) Electrophoresis from the initial chromatographic runs. Elution buffer: Glycine-HCl 100 mM pH 2.8.. Concentration of the loaded sample: 1.0 mg mL^{-1} (B) Electrophoresis from the initial chromatographic runs. Elution buffer:.. Concentration of the loaded sample: 1.0 mg mL^{-1} . P is the protein pattern, S is the sample loaded, E is the sample from elution. Washing buffer: Sodium Phosphate 25 mM pH 7.0.

Both Chromatographic runs had the total adsorbed protein around 20% of the total loaded protein. Also, a visible band of Rabbit IgG protein has shown up practically isolated, more pure than the standard sample of IgG, as well as Rabbit Albumin in the last sample of Washing step.



Since the experiments with Glycine-HCl 100 mM pH 2.8 as Elution Buffer showed a greater selectivity due to their narrowest peak and the total protein retained values were practically the same, the following tests were carried out with Glycine-HCl pH 2.8 for the Elution step.

The IgG pattern used in electrophoresis is human IgG, which presents a light migration difference because of their different subclasses, not present in the rabbit IgG.

The second phase of experiments consisted in varying the initial protein concentration loaded in the column. The experiments were carried out with diluted rabbit serum in sodium phosphate buffer 25 mM pH 7.0 at concentrations of 1.0 mg mL⁻¹ and 5.0 mg mL⁻¹. The UV Absorbance profiles were similar to Figure 2A.

Table 1. Retained protein: comparison among different rabbit serum concentrations in the samples. Washing buffer: Sodium Phosphate 25 mM pH 7.0. Elution buffer: Glycine-HCl 100 mM pH 2.8.

Rabbit Serum Conc. (mg mL ⁻¹)	Retained Protein
1,0	22,0%
2,5	20,0%
5,0	18,7%

All percentages of retained protein were around 20%, which indicates that the concentration of loaded protein does not have severe influence in the adsorption process. The following tests were performed with the mean concentration (2.0 mg mL⁻¹). The third phase of experiments consisted in investigating the influence of the ionic strength of the elution buffer on the adsorption process. Glycine-HCl pH 2.8 was prepared in 4 more different concentrations:

Table 2. Total Retained Protein from each chromatographic run varying the concentration of the Elution buffer Glycine-HCl pH 2.8.

Buffer Conc. (mM)	1	2	3	SD	Average
50	16.7%	16.9%	17.2%	0.3%	16.9%
100	19.9%	16.3%	17.4%	1.87%	17.9%
200	17.0%	17.3%	17.0%	0.2%	17.0%
500	16.1%	14.8%	16.1%	0.8%	15.7%
1000	15.9%	14.8%	14.1%	0.9%	14.9%

Table 3 shows that the buffer concentration does not have a significant influence in the elution step. The conditions of the initial runs ended up being the best ones to the protein purification.

The electrophoresis of the third phase chromatographic runs showed a similar pattern to the previous experiments, fulfilling the objective of purifying the target molecules, immunoglobulin G and rabbit albumin.

Overall, all chromatographic runs under all conditions tested showed satisfactory purification of rabbit Immunoglobulin G, as the electrophoresis bands were less contaminated than the commercial Immunoglobulin standard itself.

4. Conclusion

The Protein A column was able to purify rabbit immunoglobulin G and serum albumin using Glycine-HCl 100 mM pH 2.8 and Sodium Citrate 100 mM pH 3.3 as elution buffers. Glycine-HCl buffer showed a narrowest peak at the elution step, which represents a greater selectivity of the target molecules. Electrophoresis analysis showed purified Rabbit albumin and rabbit IgG with both buffers at washing and elution steps, respectively. The total retained protein had a satisfactory percentage, since the concentration of rabbit IgG in rabbit serum is around 21%, showing that most of it was purified using the Protein A chromatographic column. In that way, the buffer conditions used were suitable to purify rabbit polyclonal antibodies from rabbit serum.

Acknowledgements

The authors are grateful to CNPq and CAPES for providing financial support for this research. The authors also thank Prof. DSc. Denise Cavalcante Hissa (Federal University of Ceará, Department of Biology) for the availability of the equipments and tools used in this work.

References

- [1] Mariam SHS, Ooi CW, W.S. Tan WS, Janna OA, Arbakariya A, B.T. Tey BT. Purification of rabbit polyclonal immunoglobulin G with ammonium sulphate precipitation and mixed-mode chromatography. *Sep. Purif. Technol.* 144 (2015) 133–138.
- [2] Conroy PJ, Law RHP, Caradoc-Davies TT, Whisstock JC. *Antibodies: From novel repertoires to*

defining and refining the structure of biologically important targets. *Methods* 116 (2017) 12-22.

- [3] Yu Y, Lee P, Ke Y, Zhang Y, Yu Q, Lee J, et al. A Humanized Anti-VEGF Rabbit Monoclonal Antibody Inhibits Angiogenesis and Blocks Tumor Growth in Xenograft Models. *PLoS ONE* 5 (2010).
- [4] Bystryń JC, Jacobsen JS, Liu P, Heaney-Kieras J. Comparison of cell-surface human melanoma-associated antigens identified by rabbit and murine antibodies. *Hybridoma* 1 (1982) 465-472.
- [5] Raybould TJ, Takahashi M. Production of stable rabbit-mouse hybridomas that secrete rabbit mAb of defined specificity. *Science* 24 (1988)1788-1790.
- [6] Shin K, Hayasawa H, Lonnerdal B. Purification and quantification of lactoperoxidase in human milk with use of immunosorbants with antibodies against recombinant lactoperoxidase. *Am J Clin Nutr* (2001) 73 984-989.
- [7] Calabozo B, Duffort O, Carpizo JA, Barber D and Polo F. Monoclonal antibodies against the major allergen of *Plantago lanceolata* pollen, Pla 1 1: affinity chromatography purification of the allergen and development of an ELISA method for Pla 1 1 measurement. *Allergy* 56 (2001) 429-435.
- [8] Cheung HY, Chan KM, Ng TB and Cheng CH. Production of a polyclonal antibody against recombinant goldfish prolactin and demonstration of its usefulness in a non-competitive antigen-capture ELISA. *Comp Biochem Physiol B Biochem Mol Biol* 131 (2002) 37-46.
- [9] Verdoliva A, Basile G, Fassina G. Affinity purification of immunoglobulins from chicken egg yolk using a new synthetic ligand. *J Chromatogr B* 749(2000) 233-242.
- [10] Wongchuphan R, Tey BT, Tan WS, Taip FS, Kamal SMM, Ling TC. Application of dye-ligands affinity adsorbent in capturing of rabbit immunoglobulin G, *Biochem Eng J* 45 (2009) 232-238.
- [11] Wongchuphan R, Tey BT, Tan WS, Subramanian SK, Taip FS, Ling TC. Purification of rabbit polyclonal immunoglobulin G using anion exchangers. *Process Biochem* 46 (2011) 101-107.
- [12] Burnouf T, Radosevich M. Affinity chromatography in the industrial purification of plasma proteins for therapeutic use. *J Biochem Biophys Meth* 49 (2001) 575-586.
- [13] Rudolf J, Führer M, Galler B, Ansari P, Hasenhindl C, Baumgartner S. Differences in usability of rabbit IgG and chicken IgY after clean-up and impact on gold labelling properties. *J Immunol Methods* 350 (2009) 79-88.
- [14] Luo H, Lee N, Wang X, Li Y, Schmelzer A, Hunter AK, Pabst T, Wang WK. Liquid-liquid phase separation causes high turbidity and pressure during low pH elution process in Protein A chromatography. *J Chromatogr A* 1488 (2017) 57-67.
- [15] Forrer N, A. Butté A, Morbidelli M. Chromatographic behavior of a polyclonal antibody mixture on a strong cation exchanger column. Part I: Adsorption characterization. *J Chromatogr A* 1214 (2008) 59-70.
- [16] Guélat B, Ströhlein G, Lattuada M, Morbidelli M. Electrostatic model for protein adsorption in ion-exchange chromatography and application to monoclonal antibodies, lysozyme and chymotrypsinogen A. *J Chromatogr A* 1217 (2010) 5610-5621.
- [17] Guélat B, Delegrange L, Valax P, Morbidelli M. Model-based prediction of monoclonal antibody retention in ion-exchange chromatography. *J Chromatogr A* 1298 (2013) p. 17-25.
- [18] Angelo JM, Lenhoff AM. Determinants of protein elution rates from preparative ion-exchange adsorbents. *J Chromatogr A* 1440 (2016) 94-104.
- [19] Clauss MA¹, Jain RK. Interstitial transport of rabbit and sheep antibodies in normal and neoplastic tissues. *Cancer Res* 50 (1990) 3487-3492.
- [20] _____. Albumin (ALB) Protein. Available in: <<https://www.antibodies-online.com/protein/458626/Albumin+ALB+protein/>>. Access in: 05 nov. 2019.
- [21] Tsumoto K, Ejima D, Senczuk AM, Kita Y, Arakawa T. Effects of salts on protein-surface interactions: applications for column chromatography. *J Pharm Sci* 96 (2007)1677-1690.
- [22] LAEMMLI, U. K. Cleavage of structural proteins during assembly of head of bacteriophage-T4. *Nature* 227 (1970) 680-685.

Evaluation of lipase A from *Candida antarctica* immobilization onto agroindustrial residue by Taguchi method

Paula Jéssyca Morais Lima^a, Bruna Bandeira Pinheiro^a, Rodolpho Ramilton de Castro Monteiro^a, Juliana de França Serpa^a, Maria Valderéz Ponte Rocha^a, Maria Cristiane Martins de Souza^{b*}, Luciana Rocha Barros Gonçalves^a and José Cleiton Sousa dos Santos^b

^a Universidade Federal do Ceará- Departamento de Engenharia Química. Campus do Pici, BL. 709, Av. Mister Hull, s/n - Pici, Fortaleza - CE, 60455-760.

^b Universidade da Integração Internacional da Lusofonia Afro-Brasileira -UNILAB- R. José Franco de Oliveira, s/n - Zona Rural, Redenção – CE, Brasil. Cep: 62790-970. *e-mail: jcs@unilab.edu.br

Abstract

An agroindustrial residue, cashew apple bagasse, was used as a support for the immobilization of lipase A from *Candida antarctica* (CALA). Cashew bagasse, besides having very low cost and reducing environmental impacts, has good physical and mechanical properties favorable to enzymatic immobilization. Therefore, this work proposes the use of *in natura* cashew apple bagasse, aiming to minimize costs related to the pretreatments generally employed to use such residue as support. Among the immobilization techniques generally used, adsorption allows the interaction between the support and the enzyme, resulting in a better enzymatic stabilization. In this study, divinyl sulfone (DVS) was used to activate the support and thus to test its effect on enzyme-support interactions. An advanced experimental design by the Taguchi method was performed, with a standard orthogonal matrix L16 ('L' and '16' represent the Latin square and the number of experiments, respectively) to enhance derivative activity. Under optimized conditions (DVS concentration: 4.5 M, buffer molarity: 5 mM, pH: 3; temperature: 30 °C and activation time: 12 hours), the experimental activity of the derivative was 6.8 U/g, while the theoretical activity of the derivative was 6.5 U/g. The thermal and pH stability of the free and immobilized enzyme were determined, promoting an increase in thermal stability at 70 °C at pH 5, 7 and 9.

Keywords: Enzymatic immobilization; Lipase A from *Candida antarctica*; Agroindustrial residue; Taguchi method.

1. Introduction

Lipases are the most commonly used enzymes in biocatalysis due to their high stability, high substrate specificity, high regio, chemo and stereoselectivity [1]. Lipase A from *Candida antarctica* (CALA) is a very attractive biocatalyst due to high thermostability and selectivity for trans fatty acids; the stability in the acid pH range, in addition, it presents high selectivity regarding to amine groups [2]. However, lipases generally require improvements to be used as biocatalysts because they exhibit some undesirable properties when in their soluble form, such as water solubility, which makes isolation difficult and expensive [3].

The disadvantages of free enzymes are mitigated by immobilization, improving their catalytic properties and their application at the industrial level. Among the immobilization techniques generally used, adsorption, which is a simple and widely used method, allows the interaction between the support and the enzyme, resulting in a better enzymatic stabilization [4]. The covalent bonds formed between the lipases and the support also show improved enzymatic stability as well as stiffness in the bonds [5]. In order to minimize the costs related to pretreatments commonly used for cashew bagasse as support and to test the divinylsulfone (DVS) effect in enzyme-support interactions, an advanced experimental design by the Taguchi method was used, in order to determine the optimal conditions



for cashew apple bagasse preparation (DVS and buffer concentration, pH, temperature and time), aiming at the production of a new biocatalyst. Taguchi method is a very important tool for improving the productivity of many processes ([6], [8], [9]) and significantly improving product quality, in a short time at low cost [10].

2. Materials and methods

2.1 Materials

Lipase A from *Candida antarctica* (CALA) (20.88 mg of protein per mL) was supplied by Novozymes (Alcobendas, Spain). Cashew bagasse (*Anacardium occidentale* L.) was donated by Jandaia Juice Processing industry (Ceará, Brazil). All other chemical reagents used were of analytical grade.

2.2 Methodology

2.2.1 Preparation of the Support

The preparation of the cashew bagasse (BAG) was carried out following a previously described methodology [11]. The collected BAG was washed three times with distilled water, dried at 60 °C for 24h and milled in a hammer mill to obtain an average particle size of less than 0.177mm, then used as a carrier.

2.2.2 Experimental design and statistical analysis

The support treatment (1.0g) was performed in tubes (20 mL) with sodium bicarbonate solution, varying the concentration (5, 25, 100 and 350 mM) and pH (3, 5, 7 and 12.5) of the solution, under constant agitation in orbital shaker incubators. The activating agent used was DVS, varying the amount added in four levels (1, 3, 5 and 7.5 mL). Activation occurred during 0.5, 3, 12 and 24 h and at 4, 15, 25 and 30 °C. After the specific activation time for each assay, the activated support was used for the immobilization of CALA, determining the derivative activity for each sample. The experiments were performed in triplicate and the results are reported as the mean values obtained and the standard deviation kept below 10%.

2.2.3 Enzyme Immobilization

A mass of 1.0 mg enzyme per g support to immobilize CALA was used in the presence of 0.01% Triton-X and 5 mM sodium phosphate buffer pH 7.0 for 24 h at 25 °C under continuous agitation [12]. After immobilization, the biocatalysts were incubated in 100 mM bicarbonate buffer at pH 10.0 (1:10 w / v) at 25 °C for 24 h; then in 1 M EDA at pH 10.0 also for 24 h at 4 °C. Finally, the biocatalysts were washed with 25 mM sodium phosphate buffer pH 7.0, vacuum dried and stored at 4 °C.

2.2.4 Determination of enzyme activity

The hydrolytic activity of soluble and immobilized CALA was performed following the previously methodology described [14]. *p*-Nitrophenyl butyrate (50mM *p*-NPB in acetonitrile) was used as a substrate solution. To this, 50 µL of *p*-NPB solution were added to 2.5 mL of 25 mM sodium phosphate buffer at pH 7.0 and 25 °C and 50 µL of enzymatic solution or 30 mg of immobilized enzyme, under stirring. The reaction product, *p*-nitrophenol, was quantified spectrophotometrically at 348 nm ($\epsilon = 5.236 \text{ mol}^{-1} \text{ cm}^{-1}$, under these conditions). One unit of activity (U) was defined as the amount of enzyme that hydrolyzes 1 µmol of *p*-NPB per minute under the previously described conditions. The protein concentration was determined using the method described by Bradford [13] and bovine serum albumin was used as reference.

2.2.5 Immobilization Parameters

The immobilization parameters were determined according to the previously methodology presented [14]. The immobilization yield (IY) is calculated by the difference between the initial activity and the final activity of the supernatant divided by the initial activity. The theoretical activity (AtT) of lipase immobilized to the support was calculated using an amount of enzyme offered per g of support and the

immobilization yield. The recovery activity is a percentage of enzymatic activity that is measured in the immobilized enzyme *versus* a theoretical immobilized activity.

2.2.6 Thermal and pH Inactivation

The biocatalyst was incubated in sodium acetate buffer (5 mM; pH 5.0), sodium phosphate buffer (5 mM; pH 7.0) or sodium carbonate buffer (5 mM; pH 9.0) at 70 °C. The activity was measured periodically using *p*-NPB and the residual activity was expressed as percentage of initial activity (hydrolytic activity before thermal incubation). Half-lives were calculated from enzyme deactivation according to the Sadana and Henley's model [14].

3. Results and Discussions

There are different pretreatments that aim the hydrolysis of lignocellulosic biomass [15]. Therefore, in order to optimize the bagasse preparation process together with its activation step, an advanced experimental design by the Taguchi method was used, with a standard orthogonal matrix L16 ('L' and '16' represent the Latin square and number of experiments, respectively), in which five factors at four levels were analyzed (DVS concentration: 1, 3, 5 and 7.5; buffer concentration: 5, 25, 100 and 350 mM; pH: 3, 5, 7 and 12.5; temperature: 4, 15, 25 and 30 °C; activation time: 0.5, 3, 12, and 24 hours) in order to maximize the derived activity.

Completed the experimental design, the ideal conditions were found to be: DVS concentration: 4.5 M, buffer molarity: 5 mM, pH: 3; temperature: 30 °C and activation time: 12 hours, obtaining a derivative activity of 6.8 U/g. The other immobilization parameters are presented in Table 1. The biocatalyst showed immobilization yield of 24.1%, theoretical activity of 5.14 ± 0.1 and recovery activity of 130.0%, after incubation in alkaline buffer and in EDA.

Table 1. Results of the immobilization of the biocatalyst, conducted in 5 mM sodium phosphate buffer at pH 7.0 for 24 h at room temperature.

Biocatalyst	IY (%)	At _T (U/g)	At _{Df} (U/g)	At _R (%)
BAG-	24,1	5,14	6,83	130,0
DVS-	±	±	±	±
CALA	0,5	0,1	0,55	12,2

It is important to note that the ideal pH determined as optimal condition was very acidic. According to the literature [15], acid pretreatment may hydrolyze and reduce cellulose crystallinity and weaken lignin structure, increasing the bagasse surface area and pore volume, which facilitates immobilization.

On the other hand, vinyl sulfone groups present higher reactivity at more basic pHs, as presented by Pinheiro et al. (2019).

This biocatalyst showed higher value of derivative activity than that obtained by literature work, [14], which used DVS as an activating agent to immobilize CALB in chitosan (0.2 mg protein/g support) at pH 10, yielding 68.1%, derivative activity of 1.73 U/g and recovered activity of 35.62%.

Furthermore, thermal and pH stability of the free and immobilized CALA were determined. According to [16], CALA is able to maintain its hydrolytic activity at high temperatures (90 °C) and over a broader pH range (5-9). The immobilization of CALA in BAG provided a significant increase in thermal stability at 70 °C at pHs 5, 7 and 9. Thus, the biocatalyst produced is promising for lipase immobilization, in addition to improving its stability.

4. Conclusion

The results showed that the immobilization of CALA in cashew apple bagasse is promising. The immobilization performed at pH 7.0 presented a considerable activity value of the derivative of 6.83 ± 0.55 (U/g); besides, it was quite stable at different pHs. Thus, this strategy to obtain a new biocatalyst of such agroindustrial residue may be considered environmentally benign, aiming its use in reactions of industrial interest.

References

- [1] Lima, G.V.; da Silva, M.R.; de Sousa Fonseca, T.; de Lima, L.B.; de Oliveira, M. da C.F.; de Lemos, T.L.G.; Zampieri, D.; dos Santos, J.C.S.; Rios, N.S.; Gonçalves, L.R.B.; et al. Chemoenzymatic synthesis of (S)-Pindolol using lipases. *Appl. Catal. A Gen.* 2017, 546, 7–14.
- [2] Ondul, E.; Dizge, N.; Albayrak, N. Immobilization of *Candida antarctica* A and *Thermomyces lanuginosus* lipases on cotton terry cloth fibrils using polyethyleneimine. *Colloids Surfaces B Biointerfaces* 2012, 95, 109–114.
- [3] Gupta, S.; Bhattacharya, A.; Murthy, C.N. Tune to immobilize lipases on polymer membranes: Techniques, factors and prospects. *Biocatal. Agric. Biotechnol.* 2013, 2, 171–190.
- [4] Jesionowski, T.; Zdarta, J.; Krajewska, B. Enzyme immobilization by adsorption: A review. *Adsorption* 2014, 20, 801–821.
- [5] Dos Santos, J.C.S.; Rueda, N.; Barbosa, O.; Fernández-Sánchez, J.F.; Medina-Castillo, A.L.; Ramón-Márquez, T.; Arias-Martos, M.C.; Millán-Linares, M.C.; Pedroche, J.; Yust, M.D.M.; et al. Characterization of supports activated with divinyl sulfone as a tool to immobilize and stabilize enzymes via multipoint covalent attachment. Application to chymotrypsin. *RSC Adv.* 2015, 5, 20639–20649.
- [6] Balaram Naik, A.; Chennakeshava Reddy, A. Optimization of tensile strength in TIG welding using the Taguchi method and analysis of variance (ANOVA). *Therm. Sci. Eng. Prog.* 2018, 8, 327–339.
- [7] Kaytakoğlu, S.; Akyalçın, L. Optimization of parametric performance of a PEMFC. *Int. J. Hydrogen Energy* 2007, 32, 4418–4423.
- [8] Brar, L.S.; Elsayed, K. Analysis and optimization of multi-inlet gas cyclones using large eddy simulation and artificial neural network. *Powder Technol.* 2017, 311, 465–483.
- [9] Ouyang, K.; Wu, H.W.; Huang, S.C.; Wu, S.J. Optimum parameter design for performance of methanol steam reformer combining Taguchi method with artificial neural network and genetic algorithm. *Energy* 2017, 138, 446–458.
- [10] Li, Y.; Zhu, L. Optimization of user experience in mobile application design by using a fuzzy analytic-network-process-based Taguchi method. *Appl. Soft Comput. J.* 2019, 79, 268–282.
- [11] De Souza, T.C.; De Fonseca, T.S.; Da Costa, J.A.; Rocha, M.V.P.; De Mattos, M.C.; Fernandez-Lafuente, R.; Gonçalves, L.R.B.; Dos Santos, J.C.S. Cashew apple bagasse as a support for the immobilization of lipase B from *Candida antarctica*: Application to the chemoenzymatic production of (R)-Indanol. *J. Mol. Catal. B Enzym.* 2016, 130, 58–69.
- [12] Pinheiro, B.B.; Rios, N.S.; Rodríguez Aguado, E.; Fernandez-Lafuente, R.; Freire, T.M.; Fehine, P.B.A.; dos Santos, J.C.S.; Gonçalves, L.R.B. Chitosan activated with divinyl sulfone: a new heterofunctional support for enzyme immobilization. Application in the immobilization of lipase B from *Candida antarctica*. *Int. J. Biol. Macromol.* 2019, 130, 798–809.
- [13] M. M. Bradford A rapid and sensitive method for the quantitation of microgram quantities of protein utilizing the principle of protein-dye binding. *Anal. Biochem.* 1976, 72, 248–254.
- [14] Pinheiro, M.P.; Monteiro, R.R.C.; Silva, F.F.M.; Lemos, T.L.G.; Fernandez-Lafuente, R.; Gonçalves, L.R.B.; dos Santos, J.C.S. Modulation of Lecitase properties via immobilization on differently activated Immobead-350: stabilization and inversion of enantiospecificity. *Process Biochem.* 2019.
- [15] de Albuquerque, T.L.; Gomes, S.D.L.; Marques, J.E.; Silva, I.J. da; Rocha, M.V.P. Xylitol production from cashew apple bagasse by *Kluyveromyces marxianus* CCA510. *Catal. Today* 2015, 255, 33–40.
- [16] Ericsson, D.J.; Kasrayan, A.; Johansson, P.; Bergfors, T.; Sandström, A.G.; Bäckvall, J.E.; Mowbray, S.L. X-ray Structure of *Candida antarctica* Lipase A Shows a Novel Lid Structure and a Likely Mode of Interfacial Activation. *J. Mol. Biol.* 2008, 376, 109–119.

Method for estimation the protein binding affinity using a robust Poisson-Boltzmann model for the adsorption of lysozyme in SBA-15

Marlon de Souza Gama^a, Amaro Gomes Barreto Jr.^b, Frederico Wanderley Tavares^{a,b,*}

^a Programa de Engenharia Química - PEQ/COPPE, Universidade Federal do Rio de Janeiro, Rio de Janeiro, RJ, Brasil

^b Escola de Química, Universidade Federal do Rio de Janeiro, Rio de Janeiro, RJ, Brasil

* Corresponding author: tavares@eq.ufrj.br

Abstract

A modified Poisson-Boltzmann model can be successful used for determinate the binding affinity, as a Henry constant, for the interaction of proteins in ion-exchanger columns. For isothermal protocols, usually is necessary a set of parameters estimation for a single isotherm. Here, we show that the binding affinity parameter can be calculated using a mesoscopic model and the maximum capacity adsorption can be estimated using this information. In this work, before the parameter estimation for the maximum capacity adsorption (q_{sat}), we first use the information of binding affinity of lysozyme and ion-exchange chromatography to estimate the parameters of density groups: $1,11 \cdot 10^{-6}$, $1,15 \cdot 10^{-7}$ e $4,45 \cdot 10^{-7}$ mol m⁻² for the amino, histidine and carboxylic groups, respectively. This set of parameters gives a pI value of 10.9, closed to the pI reported for the protein. Using the estimated parameters as the main contribution for the surface charge, q_{sat} was estimated using isothermal data found in the literature for pH 10.5 at 25 °C and buffer ionic strength (25 mM). The value of q_{sat} is 699.86 mg g⁻¹, in a good agreement with the isothermal data. The results show that the protocol applied can be used to reduce the parameters fitting in a Langmuir like-model.

Keywords: Poisson-Boltzmann, Parameter estimation, Lysozyme, SBA-15;

1. Introduction

The purification/separation of proteins using adsorption process is a common unit operation applied in the biopharmaceutics industries. There are different forms to select the best adsorbent, including the analysis of textural properties as porous diameters, surface area and pore volume. Another form to compare the potential application of one adsorbent is the kinetic and isothermal assays.

While the kinetic gives information about how long an adsorbent will saturate (time to reach the equilibrium), for the isotherm it is necessary a step of parameter estimation for obtaining a critical data: the maximum capacity of adsorption [1], [2]. Here we will focus in the isothermal assay.

The practical of parameter estimation for the Langmuir equation is a common protocol applied when a single or different isotherms are analyzed. For complex interactions as mixed-mode, a single variations in pH or ion strength will change the

constant of affinity and the maximum capacity if both are estimated simultaneously, as reported for *human serum albumin* (HAS) using MabDirect MM [3].

A similar effect is observed by the adsorption of *bovine serum albumin* (BSA) and lysozyme in the presence of salt for the interaction of protein and silica [4].

1.1. The binding affinity parameter based on electrostatic interactions

The application of the modified model of the Poisson-Boltzmann equation in bispherical coordinates was predictive for the calculation of the interaction between monoclonal antibodies in ion exchange resins [5]. Thus, it was necessary to identify the charge density present on the surface of the adsorbent and the antibodies. Therefore, based on the algorithm for predicting the retention constant, we can associate this parameter with the Langmuir constant.

The objective of this work is to reduce the number of parameters to be estimated in the isotherm step. For a case study of the adsorption of lysozyme in an ordered mesoporous silica like SBA-15, we intent to predict the binding interaction using the robust modified Poisson-Boltzmann equation. In the isothermal, the only parameter to be estimated will be the maximum capacity of adsorption.

2. Methodology and modeling approach

2.1. Obtaining the binding affinity parameter using the potential of mean force based on electrostatic interaction

The use of bispherical coordinates appears as a promising alternative in the discretization of nonlinear models [6].

The hypothesis applied are: a macromolecule geometry is spherical, the aminoacid groups are distributed homogeneously on the surface, the amino, histidine and carboxylic groups are the principal groups that contributed with the macroscopic charge while the silanol groups are used to set the silica charge surface.

We define the Poisson-Boltzmann equation in bispherical coordinates (η, θ) as follows:

$$\nabla^2 \psi = \frac{(\cosh \eta - \cos \theta)}{a^2 \sin \theta} \left[\frac{\partial}{\partial \theta} \left(\frac{\sin \theta}{\cosh \eta - \cos \theta} \frac{\partial \psi}{\partial \theta} \right) + \sin \theta \frac{\partial}{\partial \eta} \left(\frac{1}{\cosh \eta - \cos \theta} \frac{\partial \psi}{\partial \eta} \right) \right] \quad (01)$$

where ψ is the dimensionless electrostatic potential $(e\phi/\kappa_B T)$, e is the elemental electron charge, κ_B is the Boltzmann constant and T is the temperature; $a = k_D h \sinh(\eta_0)$, with k_D being the inverse of the Debye length, h is the distance between the surfaces of the macromolecule and the adsorbent and η_0 is related with the initial sphere surface.

The aminoacids groups are influenced by the pH, salt concentration and its properties. Therefore, we use the following equation for calculating the protein charge:

$$\sigma(pH, I) = \sigma_{NH_3^+} + \sigma_{His^+} + \sigma_{COO^-} \quad (02)$$

where $\sigma_{NH_3^+}$ is the contribution of the density of amina groups, σ_{His^+} for the histidine groups, σ_{COO^-} for the carboxylic groups and I is the ionic strength. Those parameters are estimated as reported in the section 2.2. For silica, section 2.3 resume the methodology applied for the charge density calculation.

The force (Equation 03) and electrostatic energy (Equation 04) between the mAbs-resin surfaces are calculated according:

$$\frac{W^{PB}(k_D h)}{\kappa_B T} = -\epsilon \epsilon_0 \left(\frac{\kappa_B T}{e^2} \right)^{k_D h} \int_{\infty}^h f(h) d(h) \quad (03)$$

The Henry constant is calculated as a function of the potential of mean force (W), as suggested by [7]:

$$K = \frac{q(pH, I)}{c_0} = \int_0^{\infty} \left[\exp\left(-\frac{W(I, pH, h)}{\kappa_B T}\right) - 1 \right] dh \quad (05)$$

where K is the dimensional Henry constant (m), q is the excess surface concentration for a given pH and ionic strength, c_0 is the bulk colloid concentration.

The parameter W represents the total sum of the potential of mean force contribution. Besides the W^{PB} , calculated as show in Equation 03, a non-Coulombic potential known as Hamaker dispersion needs to be include to provide the ionic specificity to the model:

$$W^{Ham} = \begin{cases} -\frac{H}{6} \left(\frac{r_p}{r_p + r_H} \right) & \text{for } h \leq r_p + r_H \\ -\frac{2H}{9} \left(\frac{r_p}{h} \right)^3 & \text{for } h > r_p + r_H \end{cases} \quad (06)$$

$$f(\eta) = 2\pi \int_0^\pi \left\{ \left[\frac{a^2 (\cosh \psi - 1)}{(\cosh \eta - \cos \theta)^2} + \frac{1}{2} \left(\left(\frac{\partial \psi}{\partial \theta} \right)^2 - \left(\frac{\partial \psi}{\partial \eta} \right)^2 \right) \times (1 - \cosh \eta \cdot \cos \theta) \right] + \frac{\partial \psi}{\partial \theta} \frac{\partial \psi}{\partial \eta} \sinh \eta \cdot \sin \theta \right\} \frac{\sin \theta}{\cosh \eta - \cos \theta} \cdot d\theta \quad (04)$$

where W^{Ham} is the Hamaker potential, r_p represents the hydrodynamic protein radius (5 nm), r_H is the hydration-layer thickness (1.5 Å for proteins) and H is set as $2k_{BT}$ for the interaction between the protein and the silica wall.

A mathematical discussion, the hypotheses applied and a sensitivity analysis for different salts are reported at the previous work [5] for the case study of mAbs in ion-exchange chromatography.

2.2. Charge density estimation

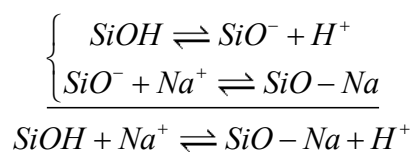
Group density values are scarce for lysozyme. Therefore, it is intended to estimate the protein charge density using the literature data [7].

The parameters $\sigma_{NH_3^+}$, σ_{His^+} and σ_{COO^-} will be estimated for the lysozyme retention in an ion exchange column containing Fractogel EMD SE HiCap as a stationary phase. We use a stochastic optimization method (PSO - Particle Swarm Method), implemented in Fortran.

These data will be used as an input for model the protein affinity for the silane groups, as observed in SBA-15 surface characteristics.

2.3. Charge density for the silane groups

The density values for the silane groups are reported by $1,60 \cdot 10^{-6}$ mol m⁻² [8]. The following association and dissociation reactions for the silane groups on the SBA-15 surface are considered:



Where the acid-base dissociation constant of SiOH is pKd = 2.5 [9] (mean value between germinal and vicinal groups - Fig. 2). The effective association constant of the SiO-Na group is given by pKa = -0.3.

Figure 2 shows the main silane groups. We used in this step, only the germinal and vicinal groups.

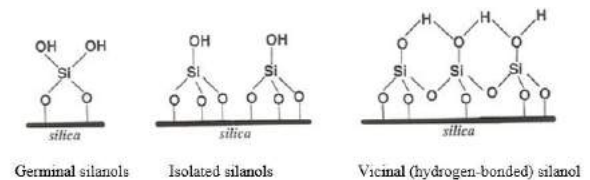


Fig. 2: Types of silane groups on the silica surface [9].

2.4. Maximum adsorption capacity estimation

Equation 5 shows a dimensional Henry constant unit by its definition between the volume and accessible area (m³/m²). As reported by Guélat and coworkers [2], a dimensionalization can be given by:

$$K^* = \frac{A_s}{1 - \varepsilon} K \quad (07)$$

where K^* is the adimensional Henry constant [-], A_s is the accessible surface area of the adsorbent and ε is the porosity of the adsorbent. The porosity of the SBA-15 is set as 0.65.

The A_s parameter ($3.69 \cdot 10^8$ m²/m³) was calculated based on the values of surface area (609 m² g⁻¹) and total pore volume (1.65 cm³ g⁻¹) [10].

The K^* parameter is applied in the Langmuir model as the following format:

$$q = \frac{K^* C_{eq}}{1 + \frac{K^* C_{eq}}{q_{sat}}} \quad (08)$$

were C_{eq} is the protein concentration in the bulk phase at the equilibrium and q_{sat} is the maximum adsorption capacity, estimated in this work for the isothermal data adsorption of lysozyme in SBA-15 reported by [10].

3. Results and Discussion

Figure 3 shows the result of density groups estimation using the particle swarm. All profiles at different pHs were used for estimation. The density of the amino, histidine and carboxylic groups are respectively: $1,11 \cdot 10^{-6}$, $1,15 \cdot 10^{-7}$ e $4,45 \cdot 10^{-7}$ mol m^{-2} .

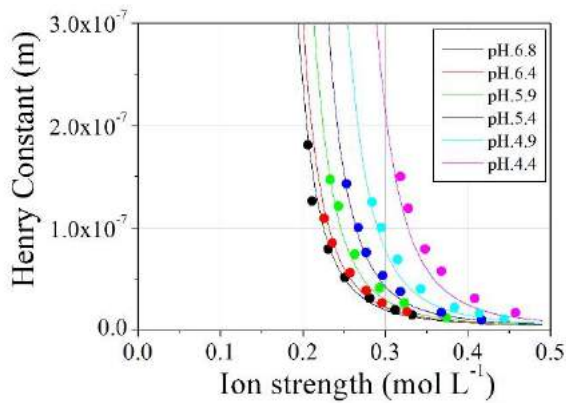


Fig. 3: Behavior for the Henry constant profile for the lysozyme adsorption on an ion-exchange column using Fractogel EMD SE Hi-Cap as adsorbent (10 μ m). The line represent the model (Eq. 05) and the circles are experimental data reported in the bibliography [7].

To make sure these estimated parameters have any physical significance, we calculated the charge density profile as a function of pH (Figure 4). As observed by the value of σ_p , the total density charge is zero at pH 10.9, which is close to the reported value of the lysozyme isoelectric point ($pI = 11$).

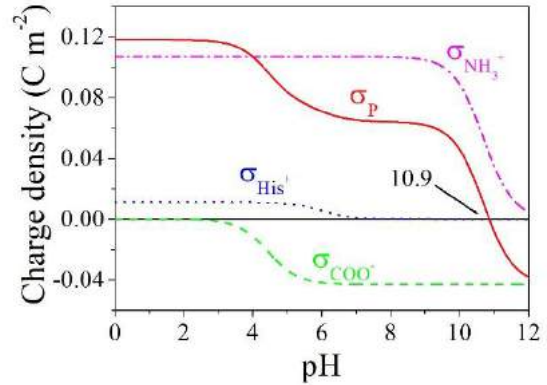


Fig. 4: Charge density values as a function of pH using the estimated parameters. The σ_p represent the sum of all densities without addition of salt.

Figure 5 shows the same charge density profile as above for different salt concentrations. This information is fed into the model, assisting in a better prediction of values.

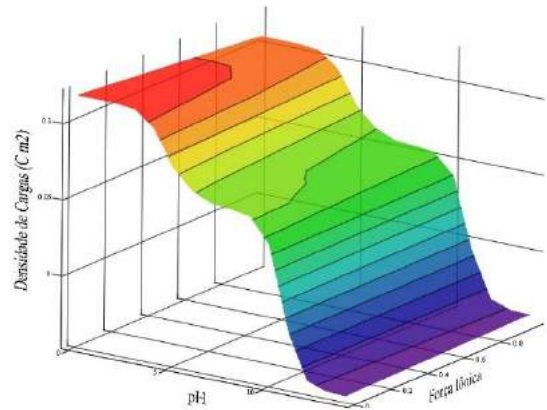


Fig. 5: Total charge density (σ_p) as a function of pH and ionic strength.

The estimated charge group densities and silane group density were used as inputs to the modified Poisson-Boltzmann model to obtain the mean field potential between lysozyme and silica surface. The value obtained from the potential of mean force is omitted in this work. Figure 5 shows the Henry constant profile as a function of ionic strength for the pH value used in the isotherm step (pH 10.5).

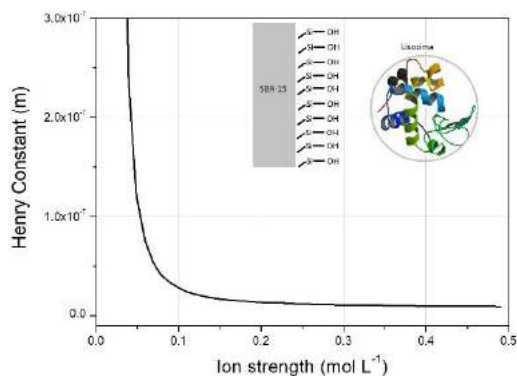


Fig. 6: Estimative for the Henry constant profile for the lysozyme adsorption on the silica wall. The conditions are pH 10.5 at 25 °C.

Figure 6 shows an electrostatic binding for the interaction between the protein and the silica wall with increasing ionic strength. For a salt concentration above 0.1 M, the electrostatic contribution may be neglected. It is reported a lysozyme adsorption in silica at concentrations above 0.1 M [4]. Thus, this suggests that other forces become representative in this range for the adsorption process.

In order to use the model in the system where the electrostatic interaction is valid, we chose to calculate the Henry constant considering only the buffer ionic strength (25 mM). For this case, Henry's constant has a value of $1.94 \cdot 10^{-6}$ m.

Figure 7 presents the result of the maximum capacity estimation. The value of q_{sat} , in mg g^{-1} , is 699.86 for a R^2 of 0.8537.

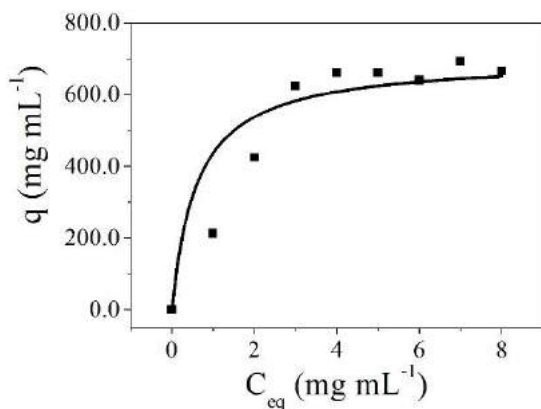


Fig. 7: Isothermal Adsorption of lysozyme in SBA-15. The q_{sat} (Eq. 8) was estimated using the

information of K given by the Henry constant calculated using a robust modified Poisson-Boltzmann equation. The line represent the Langmuir model and the point the experimental data [10] for pH 10.5 at 25 °C and buffer ionic strength (25 mM).

4. Conclusion

We applied a non-linear Poisson-Boltzmann model in bispherical coordinates for obtain a Henry constant for the adsorption of lysozyme on a silica wall, related to a SBA-15 surface. The methodology allowed an explicit dependence of the ionic strength and pH by the Henry constant. The charge density for the lysozyme was estimated using the information of the binding with an ion-exchanger chromatography resin. The parameters obtained are used for understand the behavior for the protein surface as a function of pH and ion strength. Thus, we estimated in the isotherm only the maximum adsorption capacity. This value is in the same order of magnitude as the maximum capacity of lysozyme in silica reported by the literature. This result showed that knowledge of the nature of protein-adsorbent interaction was able to reduce one of the parameters that is normally estimated in the adsorption process.

Acknowledgements

We gratefully acknowledge the support of the CNPq and the ATOMS group.

References

- [1] N. Ayawei, A. N. Ebelegi, and D. Wankasi, "Modelling and Interpretation of Adsorption Isotherms," *J. Chem.*, vol. 2017, pp. 1–11, 2017.
- [2] M. E. Mahmoud, M. F. Amira, S. M. Seleim, and A. K. Mohamed, "Adsorption Isotherm Models, Kinetics Study, and Thermodynamic Parameters of Ni(II) and Zn(II) Removal from Water Using the LbL Technique," *J. Chem. Eng. Data*, vol. 62, no. 2, pp. 839–850, Feb. 2017.
- [3] P. F. Gomes, J. M. Loureiro, and A. E. Rodrigues, "Adsorption of Human Serum Albumin (HSA) on a mixed-mode adsorbent: equilibrium and kinetics," *Adsorption*, vol. 23, no. 4, pp. 491–505, May 2017.
- [4] K. A. B. Nogueira, "Study of biomolecules adsorption (Serum Albumin Bovine and Lysozyme) in mesoporous materials," Universidade Federal do Ceará, 2016.
- [5] M. de S. Gama, M. S. Santos, E. R. de A. Lima, F. W. Tavares, and A. G. B. Barreto, "A modified

Adsorption of paracetamol from aqueous solutions on activated carbons

Nayara Martins Conrado^a, Mayara Raquel de Sousa Cavalcante^a, Juli Emille Pereira de Melo^a, Ana Lorena de Brito Soares^b, Vitória Cibely Silveira Penha^a, Rafael Barbosa Rios^a, Francisco Wilton Miranda da Silva^a

^a Grupo de Estudos em Termodinâmica, Adsorção e Bioprocessos – GETAB, Departamento de Engenharia e Tecnologia, Universidade Federal Rural do Semi-Árido, 59625-900, Mossoró, RN, Brazil

^b Grupo de Pesquisa em Separações por Adsorção – GPSA, Departamento de Engenharia Química, Universidade Federal do Ceará, Campus do Pici, Bl. 709, 60455-760 Fortaleza, CE, Brazil

Abstract

Samples of commercial activated carbon (WV1050) and synthesized activated carbon (A10a Xp = 0.9) from peach stone were evaluated as adsorbents for paracetamol removal from aqueous solution. The adsorbents were characterized based to the textural properties and the zero charge point (pH_{pzc}), which was pH_{pzc} = 6.43 for commercial carbon and pH_{pzc} = 7.17 for synthesized carbon. The pH was studied in order to identify in which situation (ideal pH) the drug adsorption is favored. Consecutively, the adsorption kinetics experiments were performed at pH 2 (ideal) and at pH 6.42 (pH_{pzc}) for the commercial adsorbent. For the synthesized adsorbent, kinetics was made at pH 7.17 (pH_{pzc}) and pH 2 (ideal). In all the samples, the adsorbed quantities were very similar, regardless solution pH, showing pH has a little influence on adsorption, especially for synthesized activated carbon. Adsorption equilibrium was determined at different pHs and Langmuir and Freundlich models fitted well to the experimental data. A higher adsorption capacity was obtained for the commercial sample, probably due to higher microporosity.

Keywords: : adsorption; paracetamol; solution pH; activated carbon.

1. Introduction

Pharmaceuticals use has grown more and more as a result from medicine development and the growth of pharmaceutical industries. Due to this, a large amount of these products have been improperly discarded, causing pollution especially in surface and wastewaters. Even in small concentrations, drugs are continuously introduced into environment, which can affect water quality and potentially impact drinking water supply, the ecosystem and human health [1, 2].

Several studies have pointed out that pharmaceutical origin substances are not completely eliminated during wastewater treatment and also are not biodegraded in the environment, thus constituting a persistent emerging contaminant [4-6]. Moreover, it is known these compounds, even at low concentrations can disrupt the endocrine system of animals, interfere and modify the physiological organism functions due to structural similarity with hormones and antibiotics, and also they may lead to bacterial resistance [7].

Drugs removal from water is only safe if advanced technologies are used, such as advanced oxidative processes, reverse osmosis, adsorption and membrane filtration [3]. Adsorption on activated carbon is one of the treatment processes that has been widely studied and shown to be a good alternative for recalcitrant compounds removal [8]. Activated carbons are known to be very effective adsorbents due to the unique combination of highly developed porous network, coupled with their ability to react with other heteroatoms, what creates a variety of functionalities on their surface and structural framework [9,10].

Paracetamol is one of the most studied pharmaceuticals in adsorption removal. This medicine it's widely used to combat pain and fever and is sold without need prescription, therefore one of the most widely released drugs in the environment [11].

In this context, this work aims to evaluate adsorption capacity of paracetamol from aqueous solution using activated carbons, one commercial (CAC) and one synthesized (CAS), evaluating the effect of solution's pH on the removal.

2. Materials and Methods

2.1 Materials

2.1.1 Adsorbent

For the experiments, was used a Commercial Activated Carbon (CAC) WV1050 sample from Mead-Westvaco (USA). For comparison purposes, a synthesized activated carbon (SAC) A10a Xp = 0.9 sample was used, prepared by chemical activation with peach seed phosphoric acid [12]. The *Universidade Federal do Ceará* kindly provided all samples of activated carbon.

2.1.2 Adsorbate

The adsorbate used was paracetamol in powdered form with a nominal purity of 100%, provided by the FAGRON. Aqueous solutions were prepared with Milli-Q water at desired pH and concentrations.

2.2 Methods

2.2.1 Characterization of activated carbons

The adsorbent was characterized according to its Point of Zero Charge (pHpzc) and its textural properties.

The pHpzc is the pH at which positive and negative charges are equal, i.e., the charge is neutral. When the surface charge is positive it indicates that the pH is less than pHpzc, when the charge is negative, the pH is higher than the pHpzc [13].

The importance of this variable in adsorption is that adsorbate and adsorbent charges must be opposite so that there is a greater electrostatic interaction between both, because if the charges are equal, the adsorption process will be harmed because there will be electrostatic repulsion [14].

To perform this experiment, firstly, water was prepared under different initial pH's (2, 3, 4, 5, 6, 7, 8, 9, 10, 11 and 12), adjusted with 1 mol/L HCl or NaOH solution. Then 0.01 g of adsorbent was placed in contact with 20 mL of 0.01 mol/L aqueous NaCl solution at initial pH's at 30 °C with 160 rpm agitation, and the pH was determined after 24 h of equilibration. After this procedure, an initial pH versus final pH curve was plotted for pHpzc analysis, where this is the midpoint in which the final pH remains constant.

Textural properties were determined by N₂ adsorption and desorption isotherms at 77 K in a textural properties analyzer, Autosorb-1 MP (Quantachrome, USA). Specific surface and micropore volume were calculated by Brunauer-Emmett-Teller (BET) method and Dubinin-Radushkevich equation (DR method), respectively [15]. The total pore volume was calculated as the adsorbed volume at $P/P^0 \approx 1$, assuming that the pores are totally filled with liquid adsorbate.

2.2.2 Study of pH of the solution

The pH test was performed to determine which medium would have the highest paracetamol adsorption after a 24 h period (ideal pH). Firstly, the adsorbent sample was heated to 120°C in a drying stove for a period of 12 h. Analyzed pHs (2, 5, pHpzc, 8, 11) were prepared using 0.1 mol/L NaOH (0.1 Mol L⁻¹) and HCl (0.005 Mol L⁻¹) solutions using a pH Meter (Tec-3MP model of TECNAL brand). Subsequently, aqueous solutions of paracetamol at a concentration of 100 mg/L were prepared using water at the studied pH.

The experiments was carried out by placing 20 mL of the solution in contact with 0.01 g of the adsorbent (activated carbon) in a 50 mL erlenmeyer, followed by a controlled temperature of 30°C and stirring of 160 rpm. After a period of 24 h, the final concentration was finally measured and the amount of paracetamol removed from each sample was calculated. All assays are done in duplicate.

2.2.3 Adsorption kinetics

In this experiment, samples of 0.01 g of adsorbent were weighed and then placed in contact with 20 mL of the aqueous solution of paracetamol at an initial concentration of 100 mg/L adjusted to the analyzed pH's (ideal pH and pHpzc). After this procedure, the samples were placed on an orbital shaker (SHAKER SL 222 of SOLAB brand) with a speed of 160 rpm at 30 °C. The concentration of the solution was measured at the time intervals of: 5, 30, 60, 120, 180, 300, 480, 720, 1080, 1440, 1800, 2160, 2520 and 2880 minutes. The final absorbance reading of paracetamol in the solution was performed on a spectrophotometer (Model UY/Vis-34G from GENAKA). The wavelengths used were 243 nm for all pH's. All tests were performed in duplicates.

The amount of paracetamol removed as a function of time was calculated by the following equation:

$$Q_{ads} = \frac{(C_0 - C_t) \cdot V}{m} \quad (1)$$

where, Q_{ads} is the adsorbed amount of paracetamol per unit mass of activated carbon at time t (mg g^{-1}); C_0 is the initial concentration of the paracetamol solution (mg L^{-1}); C_t is the concentration of paracetamol solution at time t (mg L^{-1}); V is the volume of the paracetamol solution used in the experiment (L); and m is the mass of the activated carbon sample used (g).

2.2.4 Adsorption isotherm

The equilibrium adsorption experiments were performed in duplicates with variation of the initial concentration of solution. Samples of 0.01 g of adsorbent were placed in contact with 20 mL of the paracetamol solution in different concentrations (20, 30, 40, 50, 75, 100, 125 and 150 mg/L) adjusted to the ideal pH and pH_{pcz}. Then, the samples were placed on the orbital shaker under constant rotation at 160 rpm at 30 °C. The initial absorbance was measured before the samples went to the shaker, and the final, after the contact hours determined using the spectrophotometer (Model UV/Vis-34G of GENAKA mark) at the particular wavelength.

3. Results and discussion

3.1 Characterization of the adsorbents

Table 1 presents the results obtained for the textural properties from adsorption and desorption of nitrogen at 77 K. It is observed that the samples present high surface areas, characterized as porous materials.

N_2 nitrogen adsorption/desorption isotherms (Fig. 1) can be classified as Type I, which are characterized by microporous solids, such as activated carbon [15]. The nitrogen adsorption isotherm of carbon SAC is characterized by a wide knee at low relative pressures, as well as a gradually upward increase at relative pressures above 0.1, as opposed to the nearly horizontal plateau shown by sample CAC. This is indicative of the presence of a developed mesoporosity in SAC, along with a large microporosity.

Table 1. Textural properties of ACs [12, 16].

Properties	CAC ^[16]	SAC ^[12]
BET surface area ($\text{m}^2 \text{g}^{-1}$)	1674	1922
Total Pore Volume ($\text{cm}^3 \text{g}^{-1}$)	1.10	1.31
Micropore Volume ($\text{cm}^3 \text{g}^{-1}$)	0.59	0.55
Microporosity (%)	54	42

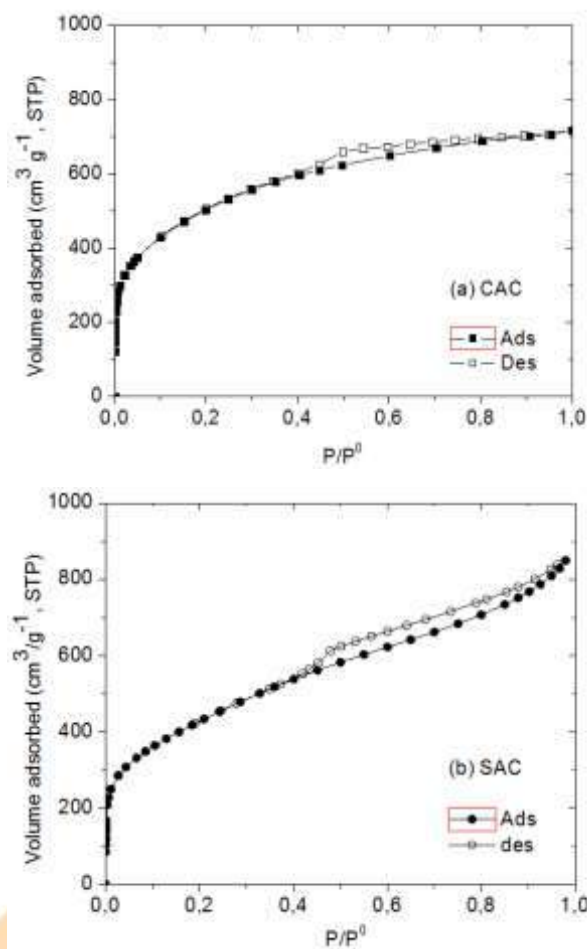


Fig.1 N_2 adsorption and desorption isotherms at 77 K: (a) Commercial Activated Carbon, CAC (WV1050); (b) synthesized activated carbon, SAC, (A10a, $X_p = 0,9$).

Regarding the determination of the pH at the point of zero charge (pH_{pcz}), the values estimated were 6.43 (CAC) and for 7.17 (SAC). The point zero charge is an important parameter for analogy with the pH of the solution in contact with the adsorbent. For example, cation adsorption is favored when the adsorbent surface charge is negative (whereas pH_{pcz} < solution pH).

3.2 Determination of optimum solution pH

The amounts of adsorbed paracetamol in relation to the pHs studied are presented in Table 2. Paracetamol removal efficiency was similar for pHs evaluated. For the commercial sample (CAC) pH 2 was ideal, whereas for the synthesized (SAC) a higher adsorption capacity was obtained at pH 7.17.

Table 2. Amount of adsorbed paracetamol (Q_{ads}) in relation to the solution pH.

pH	Q_{ads} (mg/g)	
	CAC	CAS
2,0	85,29	73,58
5,0	77,79	70,84
pH _{pzc}	74,90	74,38
8,0	75,30	68,53
11,0	42,50	60,61

Ferreira et al. (2015) also analyzed the effect of solution pH on paracetamol adsorption on the activated carbon from dende coconut mesocarp [17]. The authors also found that the amount adsorbed was independent of pH, except at pH 11. This result was explained by the molecular form of paracetamol. The neutral molecule occurs in the pH range between 2.0 and 10.0. At pH 11, paracetamol molecule appears in anionic form due to the presence of the negative charge in the phenolic groups and, therefore, repulsion with the phenolic groups present on the surface of the adsorbent. In this work, the lowest capacity was also obtained at pH 11.

3.3 Kinetic adsorption

This study was carried out with control of solution pH at 30 °C. The choice of pHs were according to the results obtained in the pH test and pH_{pzc} (pH 2,0 and pH_{pzc} for both samples). Kinetic results are displayed in Fig. 2.

For the commercial sample (CAC), adsorption rate increases rapidly up to 300 min, and from this time the adsorbed amount increases gradually until reaching the equilibrium time of 720 min. For the synthesized sample (SAC) it was assumed that system reached equilibrium at 600 min. It is proved that pH has little influence on adsorption, as mentioned previously in the pH test, since the adsorbed amounts were very similar, regardless of pH, especially for carbon synthesized from peach stone.

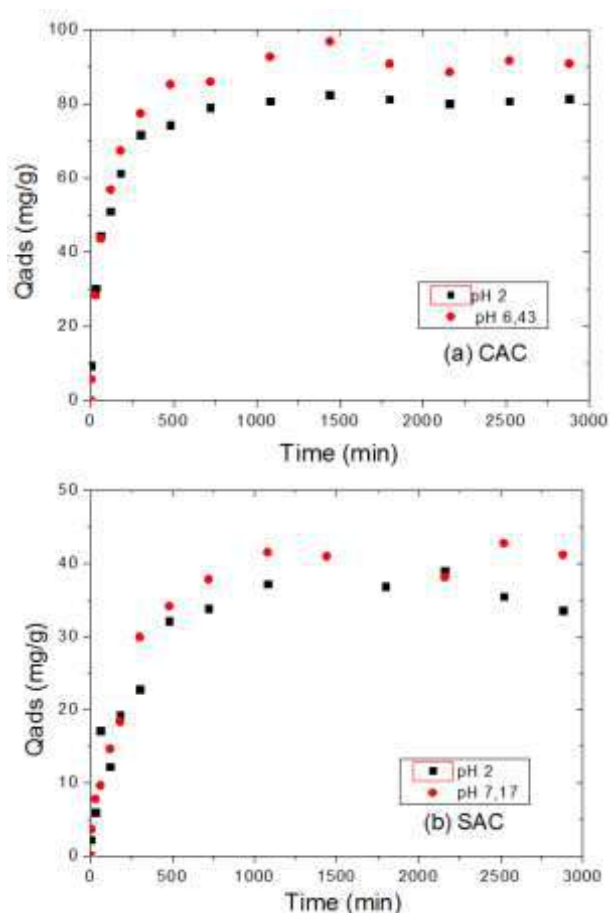


Fig. 2. Kinetics results of paracetamol adsorption at 30 °C: (a) CAC; (b) SAC.

3.4 Equilibrium adsorption

The aim of this work to investigate the effect of solution pH on the removal of paracetamol by activated carbons. The experimental adsorption isotherms for paracetamol are illustrated in Fig. 3. Measurements were made at 30 °C and equilibrium time of 720 min.

For the commercial sample, the adsorption isotherms are very similar, which shows again that the solution pH has no influence on paracetamol adsorption. The synthesized sample adsorbed less paracetamol compared to commercial. At the equilibrium concentration of 60 mg L⁻¹, the adsorbed amount of paracetamol was 94 and 53 mg g⁻¹ for CAC (at pH 2) and SAC samples, respectively. The pharmaceuticals amount adsorbed on activated carbon is usually directly proportional to the micropore volume [17-19]. Therefore, the higher adsorption capacity for the commercial sample, can be due to higher

microporosity. For a more reasoned analysis are needed other characterization data, such as analysis of surface groups.

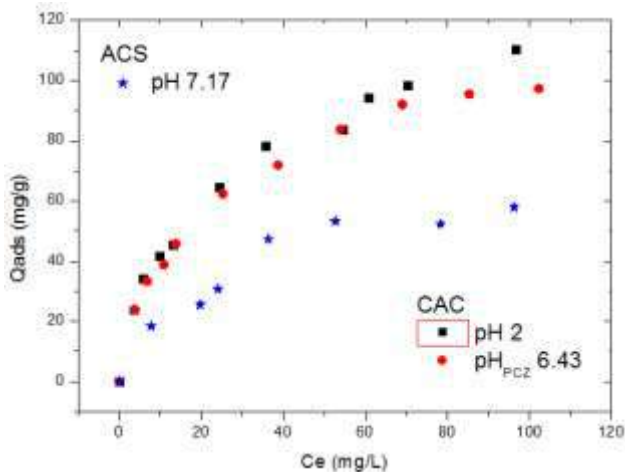


Fig. 3. Equilibrium adsorption isotherms at 30 °C.

Finally, the curves that represent the fitting obtained by Langmuir and Freundlich models are presented in Fig. 4. The model constants are listed in Table 4. Both models fit well to the experimental data, obtaining high correlation coefficient values, R^2 , greater than 0.93. Parameter n , calculated for the Freundlich model, indicates how the active sites are distributed on the adsorbent surface. According to Giles et al. (1960), for the values of $n > 1$, the adsorption process is favorable, and this was found for all experiments performed [20].

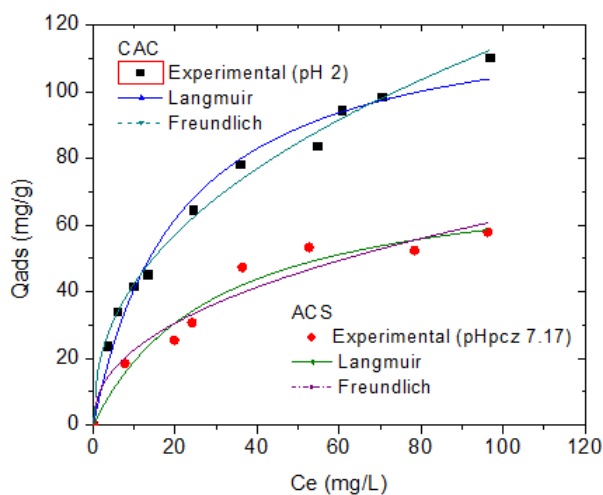


Fig.4 Experimental adsorption isotherms at 30 °C and fitting to the Langmuir and Freundlich models.

Table 4. Fitting parameters of the isotherms to the Langmuir and Freundlich models.

Sample	Model	
	Langmuir	Freundlich
CAC	$q_{max} \text{ (mg g}^{-1}\text{)} = 126,24$ $K_L \text{ (L mg}^{-1}\text{)} = 0,0479$ $R^2 = 0,98109$	$n = 2,33366$ $K_F \text{ (L g}^{-1}\text{)} = 15,8434$ $R^2 = 0,99344$
SAC	$q_{max} \text{ (mg g}^{-1}\text{)} = 76,89$ $K_L \text{ (L mg}^{-1}\text{)} = 0,03314$ $R^2 = 0,95948$	$n = 2,37247$ $K_F \text{ (L g}^{-1}\text{)} = 8,3072$ $R^2 = 0,93895$

4. Conclusions

Removal of paracetamol on activated carbon was investigated. It was possible to verify with the experiments that solution pH has no influence on paracetamol adsorption. Evaluating the adsorption kinetics was possible to verify that the contact time necessary to reach the equilibrium was 720 min (12 h) for both adsorbents. In the investigation of adsorption equilibrium, the commercial sample had higher removal capacity, probably due to its higher microporosity (micropore fraction of 54% and 42% for CAC and SAC, respectively). For the isotherms, the Langmuir and Freundlich models fit well with the experimental data. Considering the experimental data obtained in this study, it was concluded that the pH of the solution does not influence the adsorption capacity and that the CAC is the most promising.

Acknowledgements

The authors thank to the *Grupo de Pesquisa em Separações por Adsorção (GPSA)* from *Universidade Federal do Ceará (UFC)* for kindly provide us with the activated carbon samples and Milli-Q water.

References

- [1] Kolpin DW et al. Pharmaceuticals, hormones, and other organic wastewater contaminants in U.S. streams, 1999–2000: a national reconnaissance. *Environ. Sci. Technol.* 36, p. 1202–1211, 2002.
- [2] Yuan F, Hu C, Hu X, Qu J, Yang M. Degradation of selected pharmaceuticals in aqueous solution with UV and UV/H₂O₂. *Water Res.* 43, p. 1766–1774, 2009.



- [3] Rivera-Utrilla J et al. Pharmaceuticals as emerging contaminants and their removal from water: A review. *Chemosphere*, v. 93, n. 7, p. 1268-1287, 2013.
- [4] Bila DM, Dezotti M. Fármacos no meio ambiente. *Química Nova*. p. 523-530, 2003.
- [5] Hernandez F et al. Antibiotic residue determination in environmental waters by LC-MS. *Trends in Analytical Chemistry*, p. 466-485, 2006.
- [6] Tundisi JG. Água no século XXI: enfrentando a escassez. São Carlos: Rima, 2005: 248. USEPA-United States Environmental Protection Agency. Pharmaceuticals and Personal Care Products (PPCPs) in Water, 2013.
- [7] Pagsuyoin SA et al. Predicting edc concentrations in a river mixing zone. *Chemosphere*, v. 87, n. 10, p. 1111-1118, 2012.
- [8] BOUND JP, Voulvoulis N. Predicted and measured concentrations for selected pharmaceuticals in UK rivers: Implications for risk assessment. *Water Research*, v. 40, n. 15, p. 2885-2892, 2006.
- [9] Bandoz TJ, Ania CO. Surface chemistry of activated carbons and its characterization, in: Bandoz TJ (Ed.), *Activated Carbon Surfaces in Environmental Remediation, Interface Science and Technology*, vol. 7, Elsevier, New York, p. 159-229, 2006.
- [10] Marsh H, Rodriguez-Reinoso F, *Activated Carbon*, Elsevier Science, Oxford, UK, 2006.
- [11] Bernal V et al. Effect of solution pH on the adsorption of paracetamol on chemically modified activated carbons. *Molecules*, v. 22, n. 7, p. 1032, 2017.
- [12] Maia DAS et al, CO₂ gas-adsorption calorimetry applied to the study of chemically activated carbons. *Chemical Engineering Research and Design*, v. 136, p. 753-760, 2018.
- [13] Pinto RLS et al. Determination of the zero point of charge of the northeast of Pará bauxite. p. 465-467, 2012.
- [14] Toledo BI et al. Bisphenol a removal from water by activated carbon, Effects of carbon characteristics and solution chemistry. *Environmental Science Technology*, v. 39, p. 6246-6250, 2005.
- [15] Rouquerol F, Rouquerol J, Sing K. *Adsorption by Powders and Porous Solids*. Academic Press, San Diego (1999).
- [16] Rios RB. Avaliação da separação de CO₂-N₂ para fins de captura através de medidas em leito fixo e de simulações. Thesis, Universidade Federal do Ceará, 2015.
- [17] Ferreira RC, Couto Junior OM, Carvalho KQ, Arroyo PA, Barros MASD. Effect of Solution pH on the Removal of Paracetamol by Activated Carbon of Dende Coconut Mesocarp. *Chem. Biochem. Eng. Q.* 2015; 29 (1): 47-53.
- [18] Cabrita I, Ruiz B, Mestre AS, Fonseca IM, Carvalho AP, Ania CO. Removal of an analgesic using activated carbons prepared from urban and industrial residues. *Chemical Engineering Journal* 2010; 163: 249-255.
- [19] Hoppen MI, Carvalho KQ, Ferreira RC, Passig FH, Pereira IC, Rizzo-Domingues RCP, Lenzi MK, Bottini RCR. Adsorption and desorption of acetylsalicylic acid onto activated carbon of babassu coconut mesocarp. *J of Environmental Chemical Engineering* 2019; 7: 102862.
- [20] Giles, CH, Macewan, TH, Nakhwa SN, Smith D. Studies in adsorption: part XI. A system of classification of solution adsorption isotherms, and its use in diagnosis of adsorption mechanism and in measurement of specific surface areas of solids. *J. Chem. Soc.* 1960; 111: 3973-3993.



Papers in poster sessions

FA: Fundamentals of Adsorption

- 071** - Capillary Condensation in Elliptical Pores: A Study of the Effect of the Variable Curvature During the Course of Adsorption by Means of the Brockhoff and De Boer Approach pp-001
Aguilar-Huerta Ma. Erendira, Rojas-González Fernando, Cordero-Sánchez Salomón
- 132** - Assessment of Zeolites Hydrothermal Aging by Adsorption Microcalorimetry pp-004
Thalita M. Azevedo, Vitória N. S. Oliveira, Wagner A. Sousa, Débora A. S. Maia, Dárley C. Melo, Moises Bastos-Neto, Diana C. S. Azevedo
- 138** - H₂S Adsorption on KOH-Modified Commercial Activated Carbon pp-010
Luiza C. Carvalho, Jorge L. B. de Oliveira, Raífelle G. Santiago, Juliana A. Coelho, Diana C.S. de Azevedo e Moisés Bastos-Neto
- 290** - Evaluation of C8 Aromatics Adsorption in Porous Clay Heterostructures Using the Headspace Technique pp-015
João Victor S. Cardoso, José Wilson V. Lima Jr., Rosana M. A. Saboya, F. Murilo T. de Luna, Célio L. Cavalcante Jr.
- 300** - Novel Application for Palygorskite Clay Mineral: A Kinetic and Thermodynamic Assessment of Diesel Fuel Desulfurization pp-019
Anne B. F. Câmara, Rafael V. Sales, Enrique Rodríguez-Castellón, Luciene S. de Carvalho
- 348** - Statistical Analysis of Parameters and Adsorption Isotherms Models pp-025
Felipe Rocha Pinto, Carla Manske Camargo, Amaro Gomes Barreto

SCAC: Synthesis and Characterization of Adsorbents and Catalysts

- 019** - Synthesis of Faujasite and β -zeolite for Cadmium Removal in Aqueous Solution pp-031
Djanyna V. C. Schmidt, Gabriela R. Ribeiro, Marcela T. U. Rocha, Fabiana S. dos Santos, Mendelssolm K. de Pietre
- 030** - Evaluation of Tetracycline Adsorption Capacity in Aqueous Solution Using Conventional Adsorbent and CuSO₄ Functionalized Solid pp-037
Letícia Reggiane de Carvalho Costa, Líliliana Amaral Féris
- 043** - Evaluation of Red Bezaktiv Dye Adsorption on the LaCoO₃ Material pp-043
Iasmin A. Ribeiro, Juli E. Couto, Jéssica A.S. Lemos, Marcelo J. B. Souza, Anne M. Garrido Pedrosa
- 044** - Heterogenized Complexes of Ni/KIT-6 and Ni/ SBA-15: a Comparative Application for Ethylene Oligomerization pp-048
Adriano Martinez Basso, Bruna Pes Nicola, Katia Bernardo-Gusmão, Sibebe B. C. Pergher

- 057** - Evaluation of LaNiO_3 Type Materials Prepared by Different Routes as Adsorbent for Dyes Removal pp-053
Júlia B. R. Fernandes, Andreza A. Souza, Iasmin A. Ribeiro, Marcelo J. B. Souza, Anne M. Garrido Pedrosa
- 059** - Study of the Influence of Perovskite Structure Site A Metals on the Adsorptive Properties in Liquid Medium pp-059
Jéssica A. S. Lemos, Vitória M. S. C. Souza, Iasmin A. Ribeiro, Marcelo J. B. Souza, Anne M. Garrido Pedrosa
- 065** - Synthesis of LaFeO_3 Material for Application in Congo Red Dye Removal by Adsorption pp-064
Juli E. N. Couto, Iasmin A. Ribeiro, A. M. Garrido Pedrosa, Marcelo J. B. Souza
- 088** - Synthesis and Characterization of Polyacrylamide-Chitosan Cryogels for Adsorption of Biomolecules pp-070
H. S. D. R. Hamacek, S. M. A. Bueno
- 091** - Diclofenac and Paracetamol Removal from Contaminated Water by Adsorption onto MgAl-Hydroxalcite pp-074
Morgana Rosset, Leticia W. Sfreddo, Oscar W. Perez-Lopez, Liliana Amaral Féris
- 106** - Synthesis and Characterization of Zn-Al-LDH for Application in Adsorption of 2-nitrophenol from Aqueous Solution pp-080
Fabiola Balzan Dalla Nora, Sabrina Frantz Lütke, Lucas Meili, Guilherme Luiz Dotto
- 117** - Synthesis and Characterization of Clay-based Catalysts Prepared from Natural Clays pp-086
A. Santos Silva, Jose L. Diaz de Tuesta, H. T. Gomes, Juliana G. Sgorlon
- 137** - Evaluation of the Influence of H_2S in the Deactivation of Mesoporous Silicas Functionalized with Amino Groups for CO_2 Capture pp-092
Jaryson A. R. de Sousa, Jorge L. B. de Oliveira, Karine O. Moura, Juan A. Cecilia, Enrique Vilarrasa-Garcia, Moisés Bastos-Neto, Diana C.S. de Azevedo
- 142** - Influence of Microwave Radiation on Characteristics of Carbon Composites Based on Resorcinol-Formaldehyde Resin Chars Filled with Carbon Nanotubes pp-098
Mariia Galaburda, Viktor M. Bogatyrov, Anna Deryło-Marczewska, M. Nazarkovsky
- 145** - In situ Synthesis of Zeolite LTA in Glass Fibers $\text{Al}_2\text{O}_3\text{-SiO}_2$ pp-101
Antonia M. M. França, Marco V. M. do Nascimento, Raquel de A. Bessa, Edipo S. de Oliveira, Adonay R. Loiola, Ronaldo F. do Nascimento
- 178** - Synthesis of a New Adsorbent, from Sugarcane Bagasse, for Removal of As(V) from Aqueous Solution: Using an Agricultural Waste to Water Treatment pp-106
L. C. Maia, M. M. C. E. Carvalho, L. C. Soares, L. V. A. Gurgel

- 214** - Ciprofloxacin Removal by Biochar Produced from Banana Pseudostem: Kinetics, Equilibrium and Thermodynamics pp-112
Fabiano Bisinella Schefe, Júnior Staudt, Caroline Ribeiro, Carlos Eduardo Borba, Aparecido Nivaldo Módenes, Alice B. Koerich, Felipe E. Bueno Silva, Helton J. Alves
- 218** - Characterization of Fresh and Aged Zeolites Using Different X-ray and Adsorption/Desorption Isotherm Techniques pp-118
Khalil Kashef, Darley C Melo, Frederico W Tavares, Amaro G Barreto Jr.
- 228** - Comparative Study on the Properties of NaOH Activated Carbons Produced from Passion Fruit Seed and Tamarind Seed pp-124
Fernanda dos Santos Aguilari Leite, Deiviti Filipe Impossetto, Rúbia Michele Szuki, Maria Carolina Sergi Gomes, Juliana Guerra Sgorlon, Caroline Casagrande Sipoli
- 263** - Synthesis of Amino Silica Gel Derivative: Crystal Violet Adsorption pp-129
Rayane Carvalho Pinto, Aparecido Junior de Menezes, Kenia da Silva Freitas, Robson Valentim Pereira
- 315** - The LaMnO₃ as Adsorbent: Kinetic Studies and of the Regeneration and Reuse of Adsorbent pp-132
É. V. Nascimento, A. M. Garrido Pedrosa, M. J. B. Souza
- 332** - Study of Catalytic Pyrolysis of Low-Density Polyethylene (LDPE) on HY Zeolite Containing Niobium pp-138
A. V. Anjos, A. M. Garrido Pedrosa, A. O. S. Silva, M. J. B. Souza
- 335** - Synthesis and Characterization of an Unprecedented Sugarcane Bagasse Cellulose Ester: Investigation of its Environmental Applicability to Remove Cd(II) and Pb(II) by Adsorption pp-144
Megg Madonyk Cota Elias Carvalho, Mariana Viviane Lima Dias, Luisa Cardoso Maia, Liliane Catone Soares, Leandro Vinicius Alves Gurgel
- 339** - Synthesis and Characterization of Adsorbents from Lignocellulosic Residues in the Removal of Different Contaminants pp-150
Lizeth Vanessa Amado Jurado, Ana Carolina da Silva, Eliana Zaroni Megale, Gabriela Machado Chemp, Brunno Almeida de Carvalho e Silva, Matheus Santos Parente Carneiro, Izadora da Silva Santos, Lindoval Domiciano Fernandes, Marcos Antonio da Silva Costa, Francisco Eduardo Aragão Catunda Júnior, Marisa Fernandes Mendes
- 346** - Influence of Residence Time and Temperature of Pyrolysis on the Production of Biochar from Sewage Sludge pp-156
Victória Regina Celso Monteiro, Carlos Eduardo Barquilla, Maria Cristina Borba Braga
- 347** - Synthesis and Characterization of SAPO-18 and MeAPSO-18 Molecular Sieves: Effect of the Chemical Composition on the Acidity pp-162
Guilherme Raymundo Sá, Izadora da Silva Santos, Bianca Pedroso Silva Santos, Núbia Caroline de Almeida, Lindoval Domiciano Fernandes

351 - Adsorption Calorimetry as a Tool for the Characterization of Catalysts Used in CO₂ Conversion pp-168

Rafaelle Gomes Santiago, Aline Estevam Carvalho, Wagner Alves de Sousa, Juliana Amorim Coelho, Diana Cristina Silva de Azevedo and Moises Bastos-Neto

352 - Synthesis and Characterization of the Modified HZSM-5 Zeolite by Alkaline Treatment pp-173

Isadora da Silva Santos, Bianca Pedroso Silva Santos, Núbia Caroline de Almeida, Lindoval Domiciano Fernandes

359 - Efficient Adsorbents of Pollutants Based on Inorganic-Organic Sepiolite Systems pp-178

Hugo Baldan Junior, Evane da Silva, Michelle Saltarelli, Denise Crispim, Eduardo J. Nassar, Raquel Trujillano, Vicente Rives, Miguel A. Vicente, Antonio Gil, Sophia A. Korili, Emerson H. de Faria, Katia J. Ciuffi

AMB: Environmental

027 - Catalytic Decomposition of Hydrogen Peroxide in an Iron Oxide Nanoparticle pp-180

Maria Teresa Garcia Badoch, Regina Maria Matos Jorge, Tirzhá Lins Porto Dantas

031 - Adsorption and Peroxymonosulfate Catalytic Oxidation of Anti-Hypertensive Pharmaceutical Using Porous Structure with Embedded N, S-Codoped Core-Shell Co@C Nanoparticles pp-185

Júlia Resende de Andrade, Wenjie Tian, Meuris Gurgel Carlos da Silva, Melissa Gurgel Adeodato Vieira, Shaobin Wang

032 - Application of Different Regeneration Techniques to Exhausted Adsorbent with Tetracycline Antibiotic by the Adsorption Process pp-191

Leticia Reggiane de Carvalho Costa, Luana de Moraes Ribeiro, Liliana Amaral Féris

039 - Removal of the Emerging Pollutant Metronidazole by Adsorption pp-196

Cassandra Bonfante de Carvalho, Keila Guerra Pacheco Nunes, Ivan Reis Rosa, Liliana Amaral Féris

051 - Evaluation of different adsorbents and pre-treatments for boron removal from water pp-200

J. C. V. Azevedo, S. A. Valverde, P. L. Mesquita

087 - Evaluation of Acid Activation and Ultrasound Effect on the Adsorption Dye Potential of an Agro-Industrial Waste pp-206

Matias Schadeck Netto, Evandro Stoffels Mallmann, Raíssa da Cunha Bevilacqua, Isadora Argenta Preigschadt, Nathália Favarin da Silva, Guilherme Luiz Dotto

097 - Study of Adsorption Capacity of Sodium Diclofenac and Ibuprofen Drugs Using Cellulose Biopolymer pp-212

Mariele Dalmolin da Silva, Matheus Londero da Costa, William Leonardo da Silva,

- 107** - Adsorption of 2-chlorophenol Using ZnCl₂ Activated Biochar from Brewing Industry Solid Waste pp-219
Lauren Marcilene Maciel Machado, Sabrina Frantz Lütke, Julia Zanuzo Kuntz, Gabriela Carvalho Collazzo, Daniele Perondi, Guilherme Luiz Dotto
- 110** - Removal of Crystal Violet Dye from Solutions Using Lychee Bark and Seed as Adsorbents pp-225
Nathália Favarin da Silva, Matias Schadeck Netto, Isadora Argenta Preigschadt, Raíssa da Cunha Bevilacqua, Evandro Stoffels Mallmann, Guilherme Luiz Dotto
- 133** - Cu²⁺ Adsorption Equilibrium and Kinetic Study Using Activated Carbon Prepared from Corn Cob as Adsorbent pp-231
Natalia Ferreira Campos, Giovanna Amaral Jorge Correia Guedes, Brígida Maria Villar da Gama, Leticia de Paula Silva Oliveira, Beatriz Galdino Ribeiro, Alex Leandro Andrade de Lucena, Marta Maria Menezes Bezerra Duarte
- 134** - Activated Charcoal Material Prepared from Fish Scales as Biosorbent to an Application for Rhodamine B Dye Adsorption pp-236
Daniel Moro Druzian, Vitória de Mello Figueiredo, Luiz Fernando Rodrigues Junior, Joana Bratz Lourenço, William Leonardo da Silva
- 139** - Study of the Removal Capacity of Potassium Diclofenac Drug Using the Rice Husk as a Biosorbent Alternative pp-242
Leandro Rodrigues Oviedo, Carolina Denardi Merlugo, Aline Marques da Silva, William Leonardo da Silva
- 161** - Kinetics, Equilibrium and Thermodynamics of the Adsorption Process of Oxytetracycline in Rice Husk Ash pp-247
Christhell A. Andrade, Nelson S. Oliveira, Judite S. Vieira, Luís Angel Zambrano-Intriago, Hipatia Delgado-Demera, Joan Manuel Rodriguez-Díaz
- 165** - Mathematical Modeling of Paracetamol Adsorption on Activated Carbon pp-255
Aline Estevam Carvalho, Juli Emille Pereira de Melo, Wendy de Oliveira Nunes, Kleide Dayana Oliveira Mendes, Francisco Victor Marinho Fernandes, Rafael Magalhães Siqueira, Francisco Wilton Miranda da Silva, Rafael Barbosa Rios
- 170** - Green Synthesis of Metallic Nanoparticles Impregnated on Carbon Nanotubes for Glyphosate Removal from Aqueous Matrix pp-260
Júlia Cristina Diel, Hercules Abie Pereira, Dison S. P Franco, Isaac dos Santos Nunes, Matias Schadeck Netto, Edson L. Foletto, Guilherme Luiz Dotto
- 197** - Pecan Nutshell Activated Hydrochar for Methylene Blue Adsorption pp-266
Rogério S. Maniezzo, Hugo H. C. de Lima, Maria Eugênia G. Llop, Vicente L. Kupfer, Pedro A. Arroyo, Emerson M. Giroto, Marcos R. Guilherme, Andrelson W. Rinaldi

- 261 - Adsorption Kinetics of Amaranth Dye on Organonano clay** pp-272
Gleiciely Lima Domingos, Thaís Mayra Israel de Oliveira Lima, Pedro Henrique dos Santos Morais, Júlia Oliveira Gurgel, Lenemeire Teixeira Araújo, Leonardo Levy da Silva França, Yasmin de Sousa Lima, Hugo Leonardo de Brito Buarque
- 270 - Sururu Shells as a Potential Biosorbent to Remove Rifampicin from Water** pp-277
Daniely Carlos Henrique, Daniel Uchoa Quintela, José Leandro da Silva Duarte, Alessandra Honjo Ide, Carmem Lucia de Paiva, Silva Zanta, Lucas Meili
- 276 - Ceramic Monoliths Composed with Natural Zeolite for the Removal of Contaminants in Aqueous Media** pp-284
C. Garcia-Carvajal, V. C. de Souza, J. Villarroel-Rocha, M. M. Barroso-Quiroga, K. Sapag
- 285 - Adsorption of Thiamethoxam in Water and Sugarcane Juice by Magnetic Nanommodified Activated Carbon and Determination by HPLC-DAD** pp-290
Driêlle Aparecida de Freitas, Roberta Ferreira Nocelli, Geórgia Labuto, Elma Neide Vasconcelos Martins Carrilho
- 323 - Fixed-bed Adsorption of Linear Alkylbenzene Sulfonate (LAS) by Granular Activated Carbon** pp-296
Henrique Baldi Faccenda, Thaís Strieder Machado, Gabriel Damini, Lucas Kayser da Silva, Jeferson Steffanello Piccin
- 343 - Adsorption of Caffeine Using Steel Wastes Composed of Magnetite** pp-301
Iara Jennifer Moura Duarte, Thaís Mayra Israel de Oliveira Lima, Hugo Leonardo de Brito Buarque, Ronaldo Ferreira do Nascimento
- 349 - Influence of Temperature of Pyrolysis and Activation Conditions on the Adsorption of Ammonia Nitrogen onto Orange Peel Biochar** pp-307
Larissa Firmino de Lima, Carlos Eduardo Rodrigues Barquilha, Maria Cristina Borba Braga
- MSPA: Molecular Modeling and Simulation of Adsorptive Processes**
- 18 - Modeling the Nickel Adsorption Equilibrium on Low-Cost Adsorbents and Activated Carbon Using Artificial Neural Network** pp-312
P.S. Pauletto, G.L. Dotto, N.P.G. Salau
- 35 - Modeling and Simulation of the Process of Biosorption of Real Textile Effluent in Sugarcane Bagasse Through Artificial Neural Networks** pp-318
Vitória Brocardo de Leon, Claiton Zanini Brusamarello, Gustavo Petroli, Fernanda Batista de Souza
- 49 - Mathematical Modeling and Simulation of Fixed-Bed Adsorption Column with Axial Particle Diameter Profile for Removal of Dilute Solutions** pp-324
Cristiane G. Ferrarezzi, Reginaldo Guirardello

- 58** - Analytical Solution for Pore Volume and Surface Diffusion Model in Batch Adsorption Systems pp-330
Gabriel Miglioranza, Marcio Schwaab
- 95** - Application of Artificial Neural Network Modeling to Fit the Isotherm Parameters of Aqueous-Phase Adsorption Systems pp-336
J. L. S. Fagundes, N. P. G. Salau
- 96** - Insensitivity in the Characterization of Ultra-Microporous Carbon Materials by CO₂ Adsorption pp-342
V. Cornette, J. Villarroel Rocha, K. Sapag, R. Delagdo Mons, J. P. Toso, R. H. López
- 126** - Evaluation of Estimation Procedures of Mass Transfer Coefficients from Batch Adsorption Kinetic Data pp-350
Daniel Souza de Almeida, Vânia Queiroz da Silva, Evandro Steffani, Elisa Barbosa-Coutinho, Marcio Schwaab
- 136** - Analysis of Phenol Removal Capacity from Water by Adsorption on Activated Carbon pp-356
Ana Luisa M. Galdino, José C. A. Oliveira, Madson L. Magalhães, Sebastião M. P. Lucena
- 149** - Performance of CO₂ AA and UA Models in γ -Alumina Adsorption Isotherms pp-361
Andréa S. Pereira, Rafael V. Gonçalves, Lucas Philipovsky, Daniel V. Gonçalves, Sebastião M. P. Lucena
- 152** - PSA Scheduling and Modeling for CH₄/CO₂ Separation pp-366
Rafael M. Siqueira, Klaus F. R. Soares, A. Eurico B. Torres, Alexandre F. P. Ferreira, Alirio E. Rodrigues, Diana C. S. Azevedo, Moises Bastos-Neto
- 158** - Evaluation of Single and Binary Adsorption Equilibrium of Cobalt Ions and Methylene Blue in Aqueous Systems onto Ultrasonic Modified Chitin pp-372
P.S. Pauletto, G.L. Dotto, N.P.G. Salau
- 213** - Mathematical Modeling of Low-Pressure Biogas H₂S Removal by Granular Activated Carbon in Fixed Bed Column pp-378
Fabiano Bisinella Scheufele, Helton José Alves, Rodrigo Sequinel, Bárbara Bulhões Cazula, Eliane Soares da Silva, Laressa Caciano, Carlos Eduardo Borba, Thiago Fernando Magrini Lopez, Alessandra Freddo, Giovani Silvero Patuzzo
- 215** - Neural Network Modeling of Successive Ni²⁺-Zn²⁺ Adsorption Cycles by Sargassum Filipendula in Fixed Bed Column pp-384
Paulo H. N. Ferreira, Araceli A. Seolatto, Eneida S. Cossich, Célia R. G. Tavares, Edson A. da Silva, Tiago D. Martins
- 242** - Experimental Design for Adsorption Isotherms Discrimination pp-390
Diego Del Fabro Kunzler, Roger Kober, Marcio Schwaab, Evandro Staffani, Elisa Barbosa-Coutinho

250 - A Framework to Estimate the Thermodynamic Parameters on Adsorption Equilibria Using Particle Swarm Optimization pp-396

M. Maraschin, P.L. Limberger, N.P.G. Salau

256 - Experimental and Computational Analysis of CO₂, N₂, and CO Adsorption on Hydroxyapatite pp-401

Gabriel D. Barbosa, Carla L. M. Camargo, Frederico W. Tavares, Neuman S. Resende, Vera M. M. Salim

258 - Estimation of the Transfer Free Energy of POE Tails and Application for a Spherocylindrical Structure Prediction for a Mixture of P123 and F127 Surfactants pp-407

Marlon S. Gama, Gabriel D. Barbosa, Carla L. M. Camargo, Frederico W. Tavares

265 - Molecular Dynamics of LTA Zeolite: Checking Force Fields Using X-Ray Diffraction Patterns pp-411

Jéssica C. da S. L. Maciel, Carla L. M. Camargo, Amaro G. Barreto Jr., Frederico W. Tavares

299 - Assessing Interactions in Diesel Fuel Adsorptive Desulfurization over Ag/MCM-41 by Computational and Experimental Studies pp-415

Rafael V. Sales, Enrique Rodríguez-Castellón, Anne B. F. Câmara, Heloíse O. M. A. Moura, Sergio R. B. Silva, Miguel A. F. de Souza, Leila M. A. Campos, Luciene S. de Carvalho

337 - Phenomenological and Neural Network Modeling of Successive Ni²⁺ Desorption Cycles with Eluent Recycle pp-421

Lucas P. de Carvalho, Araceli A. Seolatto, Edson A. da Silva, Eneida S. Cossich, Célia R. G. Tavares, Tiago D. Martins

PG: Oil and Natural Gas

045 - Effect of Ultrasound on Sulfur Adsorption in Activated Carbon Using Synthetic and Commercial Diesel pp-427

Thaís Becker, Cassio G. Dal Molin, Fernanda S. Maia, João L. Uller, Carlos I. Yamamoto, Myriam Lorena M. N. Cerutti

143 - Adsorbents Based on Metal-Organic Porous Structures for Small-Scale Energy-Saturated Adsorption Systems pp-433

M. K. Knyazeva, O.V. Solovtsova, A.A. Fomkin, A.V. Shkolin, I.E. Men'shchikov, E.V. Khozina, A.L. Pulin

174 - Optimization of Adsorption Process in the Removal of Basic Nitrogenous Compounds from Petroleum Using Activated Carbon pp-438

M. A. F. Carvalho, L. A. de Andrade, B. G. Vaz, I. C. Ostroski

- 189** - Adsorption of CO₂ and CH₄ on MIL-101: Mixture Prediction Utilizing Tóth and IAST pp-443
Guilherme Magon Martins, Marcus Vinicius Pereira, Leonardo Hadlich de Oliveira, Jailton Ferreira do Nascimento, Gisella Maria Zanin, Pedro Augusto Arroyo
- 224** - Pilot Plant for H₂S and CO₂ Separation from Humid Mixtures with CH₄ through Swing Adsorption Processes: Concept and Operation pp-449
Leonardo Hadlich de Oliveira, Marcus Vinicius Pereira, Rafael Luan Sehn Canevesi, Marcelo da Costa Amaral, Jailton Ferreira do Nascimento, Pedro Augusto Arroyo
- 230** - Adsorption of a Natural Surfactant Obtained from Crude Glycerin in Sandstone Reservoirs pp-453
Panazzolo, Guilherme F.T., Prates, Viviane R., Camargo, Carla M., Nicolini, João Victor, Nele, Márcio, Ferraz, Helen C.
- 272** - Deoxygenation of Oleic Acid as a Model Compound to Produce Diesel-Range Hydrocarbons over Ni₂P/H-ZSM-5 pp-458
Mariana de Oliveira Camargo, Celso Hissao Maeda, João Lourenço C. W. Pimenta, Pedro Augusto Arroyo
- 293** - Adsorption of Carbon Dioxide on CHA Molecular Sieve – a Model to Account for Thermal Degradation pp-464
Geovani Rocha de Freitas, Rafaele Gomes Santiago, Darley Carrijo de Melo, Diana Cristina Silva de Azevedo, Moisés Bastos-Neto
- 338** - Kinetic and Equilibrium Studies of Ni-OEP Adsorption on Coconut Shell Activated Carbon pp-470
Gabriela Costa Caetano, Indianara Conceição Ostroski
- 341** - Experimental Design and Optimization of Ni-OEP Adsorption and Desorption Processes on Coconut Shell Activated Carbon pp-475
Gabriela Costa Caetano, Laiane Alves de Andrade, Indianara Conceição Ostroski

PA: Adsorption Processes

- 020** - Evaluation of Sericin and Alginate Particles Chemically Crosslinked by Polyvinyl Alcohol for Rare-Earth Metals Removal from Aqueous Solutions pp-481
Talles Barcelos da Costa, Meuris Gurgel Carlos da Silva, Melissa Gurgel Adeodato Vieira
- 024** - Adsorption of The Antibiotic Ofloxacin in Calcined Verde-Lodo Clay: Experimental Design pp-487
Raissa Antonelli, Geoffroy Roger Pointer Malpass, Meuris Gurgel Carlos da Silva, Melissa Gurgel Adeodato Vieira
- 025** - Response Surface Methodology Approach for Optimization of Dysprosium Adsorption onto Expanded Vermiculite pp-492
Giani de Vargas Brião, Meuris Gurgel Carlos da Silva, Melissa Gurgel Adeodato Vieira

- 028** - CO₂ Adsorption in 13X Zeolites Modified by Cation Exchange with Alkaline Earth Metals pp-498
Vanessa R. C. Moura Barbalho, Mariana M. V. M. Souza
- 036** – Ionic Flocculation Obtained from Sunflower Oil for the Removal Methylene Blue pp-503
Teixeira, Y.N., Melo, R.P.F., Carmo, S.K.S., Evangelista, M.N.D.
- 037** - Effluent treatment contaminated by Malachite Green through ionic flocculation pp-509
Teixeira, Y.N., Melo, R.P.F., Fernandes, M.R., Carmo, S.K.S.
- 046** - Kinetic Study of Adsorption and Ionic-Exchange of Cd²⁺ Ions in Expanded Vermiculite and Sodium-Treated Vermiculite pp-515
Henrique S. de C. Neves, Meuris G. C da Silva, Reginaldo Guirardello, Melissa G. A. Vieira
- 053** - Morphological Characterization and Biosorption Thermodynamics of Reafix Yellow B8G Dye onto Malt Bagasse pp-521
Emanuele Sansana Delgobo, Juliana Martins Teixeira de Abreu Pietrobelli, Bruna Cassia da Silva, Deborah Cristina Crominski da Silva Medeiros, Joelma Correa
- 069** - Concentration of Betalains from Beetroot in Alginate Beads through the Adsorption Operation pp-526
Cláudio P. Pinheiro, João O. Castro, Loreane M. K. Moreira, Stephany S. Alves, Tito R. S. C. Junior, Luiz A. A. Pinto
- 098** - Calcined Sludge from a Water Treatment Plant as Adsorbent for Fluoride Removal pp-530
Renata Segatto Pigatto, Nátalie De Paula, Manoel Maraschin, Ezequiel Andrei Somavilla, Sérgio Luiz Jahn, Elvis Carissimi, Guilherme Luiz Dotto
- 109** - Lecithin Removal of Vegetable Oils by Sucrose Adsorption pp-534
Ana Amélia de Lurdes Coelho Rodrigues, Valter Luís Zuliani Stroppa, Sandra Bizarria Lopes Villanueva, Igor Tadeu Lazzarotto Bresolin
- 120** - Bovine Immunoglobulin G Adsorption onto Monolithic Cryogel of Polyacrylamide/Alginate Derivatized with IDA pp-538
Igor F. Fioravante, Camila Marcuz, and Sônia M. A. Bueno
- 125** - Adsorption of 2-nitrophenol by Calcium and nickel hidrotalcites pp-542
Keterli Dalmagro, Bianca S. Marques, Matias S. Netto, Sérgio L. Jahn, Guilherme L. Dotto
- 128** - Liquid Phase Adsorption of Siloxane D4 on White and Blue Silica Gel pp-548
E.N. Silva, D.A.S. Maia, K.O. Moura, M.C. Castrillon, W. M. Barcellos, M. Bastos-Neto, D.C.S. Azevedo

- 159** - Evaluation of Binary Adsorption of Bright Blue and Tartrazine Dyes under Dynamic Conditions Using Rice Husk pp-554
Kevin Jhon Fernández-Andrade, María Cristina González-Vargas, Ricardo José Baquerizo-Crespo, Enrique Ruiz-Reyes, Luis Santiago Quiroz-Fernández, Joan Manuel Rodríguez-Díaz
- 166** - A comparison of Numerical Methods for the Dynamic Simulation of Temperature Swing Adsorption pp-560
Caio Curitiba Marcellos, Felipe Rocha Pinto, Yuri Paiva, Carla Manske Camargo, Amaro Gomes Barreto
- 168** - Application of an Important Brazilian Agricultural Residue to Water Decontamination: Using Modified Sugarcane Bagasse to Remove Cd(II) and Pb(II) from Monometal Spiked Aqueous Solution pp-566
Megg Madonyk Cota Elias Carvalho, Mariana Viviane Lima Dias, Luisa Cardoso Maia, Liliane Catone Soares, Leandro Vinícius Alves Gurgel
- 172** - Adsorptive Processes for Dye Removal Using Adsorbents Obtained from Alginate and Chitosan Doped with Cu²⁺ Ions pp-572
Francisco Mateus Gomes do Nascimento, Francisco Renan Lima Amorim, Guilherme Augusto Magalhães Júnior, Mayara de Sousa Oliveira
- 173** - CO₂ Capture by Biochars Produced from “Açaí” Stones pp-578
Júnior Staudt, Rafael Luan Sehn Canevesi, Helton José Alves, Lázaro José Gasparrini, Fabiano Bisinella Scheffele and Carlos Eduardo Borba
- 181** - Evaluation of the Fruit *Terminalia catappa* Linn as Adsorbent of Dyes Present in Aqueous Effluents pp-584
Lizeth Vanessa Amado Jurado, Gabriela Machado Chemp, Marisa Fernandes Mendes
- 192** - Study of Addition of Zeolites A, X and Y in Polyaspartic Coating to Remove Moisture pp-588
Machado, M. P. M., Gomes, E. L., Bresolin, I. T. L.
- 198** - Technical Evaluation of Activated Carbon from Ginger (*Zingiber Officinale Roscoe*) Residues as Adsorbent of Methyl Orange Dye pp-594
Ana Carolina da Silva, Marisa Fernandes Mendes
- 199** - Application of Southwell Plot Method for Determining Equilibrium Time in Adsorption Processes pp-599
Máira Luane S. de Almeida, Tamille A. Souza, Daniel S. Costa Neto, Koji de J. Nagahama, Alexilda O. Souza, Tereza S. M. Santos
- 200** - Adsorption of Estradiol Hormone in Bone Activated Carbon pp-605
Mara Heloisa Neves Olsen Scaliante, Ramiro Picoli Nippes, Fernando Henrique da Silva, Gabriela Nascimento da Silva, Thaisa Frossard Coslop

- 202** - pH Effect and Kinetics of Diclofenac Sodium (DCF) Adsorption in Solution Using Activated Carbon from the Tucuma (*Astrocaryum aculeatum*) Endocarp pp-610
W.J.P. Costa, R.L.T. Costa, R.C.S. Araújo, R.A. Nascimento, R.L. Santos, E.M.P. Sousa, L.J.G. Faria
- 203** - Adsorption of Remazol Black B Dye Using Biochar Produced from Gasification Residues pp-616
Bruna F. do Nascimento, Adjane D. de Oliveira, Rafaella de Moura Medeiros, Alisson C. do Nascimento, Caroline Maria B. de Araujo, Maryne Patrícia da Silva, Ronald K. da Silva Santo, Maurício A. da Motta Sobrinho
- 208** - Furfural Adsorption Using a Biochar Obtained from the Gasification of Acai Endocarp pp-622
Bruna F. do Nascimento, Alisson C. do Nascimento, Caroline Maria B. de Araujo, Riann de Queiroz Nóbrega, Francisco Everton T. de Luna, Flávio Luiz H. da Silva, Jorge Vinícius F. Lima Cavalcanti, Maurício A. da Motta Sobrinho
- 219** - Phosphorus Adsorption in Aqueous Medium Using Biocarbon from Cassava Agricultural Residue (*Manihot esculenta*) pp-627
Carlos Augusto de Sousa Araújo Neto, Walber José Pereira Costa, Yan Nunes Dias, Marcelo Costa Santos, Erika Milene Pinto de Sousa, Edna Santos de Souza
- 226** - Relations Between Ni^{2+} , Cu^{2+} , and Cr^{3+} During Adsorption in Multielementary Solutions Using Activated Carbon from Passion Fruit Peel pp-632
Bianca de Paula Ramos, Isadora Dias Perez, Rosane Freire Boina
- 237** - Furfural's Adsorption Using Activated Carbon from Sisal (*Agave Sisalana*) pp-635
Ysrael Simões Lins de Oliveira, Flávio Luiz Honorato da Silva, Ellen Alves dos Santos, Josevan da Silva, Leanderson Marques Túlio Lemos, Odelsia Leonor Sánchez de Alsina, Acácia Lima Silva, Joan Manuel Rodríguez Díaz
- 245** - CO₂ Capture Using High Surface Area Activated Carbon pp-641
Simone F. Santos, José L.C. Cordeiro, Raildo A. Fiuza-Jr.
- 259** - Rhodamine 6G Adsorption from Aqueous Solution Using as a Biosorbent the NaOH-Activated Acai Stalk pp-646
R. C. S. Araújo, C. A. Azevedo, R. L. T. Costa, W. J. P. Costa, R. L. Santos, C. A. Azevedo, L. J. G. Faria.
- 262** - Multivariate Optimization of Textile Wastewater Treatment by Adsorption Using Blast Furnace Dust pp-652
Larissa Granjeiro Lucena, Antonia Mayza de Moraes França, Nayara Oliveira Lima, Ronaldo Ferreira do Nascimento
- 271** - Diffusion Model on Solid Applied to Kinetics of Dye Adsorption on Different Activated Carbons pp-658
Celso Hissao Maeda, Artur Lemes Moretti, Mariana de Oliveira Camargo, Dayane Samara de Carvalho Coltre, Caroline Apoloni Cionek, Pedro Augusto Arroyo

- 274** - Effect of pH on Cephalexin Adsorption Using Mesoporous Silica pp-664
Kiara Montiel-Centeno, Deicy Barrera, Leslie Aragón, Elbio Saidman, Karim Sapag
- 281** - Temperature Influence in the Deactivation of LTA Commercial Zeolites pp-670
Beatriz O. Nascimento, Bianca F. dos Santos, Débora A. S. Maia, Darley C. Melo, Enrique Vilarrasa-García, Moisés Bastos-Neto, Diana C. S. de Azevedo
- 283** - Biobased Phenolic Resin: an Alternative Material for Micropollutant Removal pp-676
Wardleison Martins Moreira, Paula Valéria Viotti, Mara Heloisa Neves Olsen Scaliante, Cristina Maria Gaudencio Baptista, Marcelino Luiz. Gimenes
- 314** - Investigation of Natural Clinoptilolite Over the Adsorption Process of Psychotropic Drug pp-680
Tháisa Frossard Coslop, Ramiro Picoli Nippes, Gabriela Nascimento da Silva, Rosângela Bergamasco, Mara Heloisa Neves Olsen Scaliante, Marcelino Luiz Gimenes
- 334** - Development of a Biosorbent from Coconut Fiber Biorefinery for Removing Rhodamine B from Textile Wastewater pp-685
Rogério José Melo Nascimento, Kilton R. A. Pereira, Francisco Avelino
- 340** - Kinetic Modeling of the Adsorption Process Using Different Biomass pp-691
Ana Carolina da Silva, Lizeth Vanessa Amado Jurado, Eliana Zaroni Megale, Gabriela Machado Chemp, Brunno Almeida de Carvalho e Silva, Matheus Santos Parente Carneiro, Francisco Eduardo Aragão Catunda Júnior, Marisa Fernandes Mendes
- 342** - Synthesis of Molecularly Imprinted Polymer for Recovery of 5-Hydroxymethyl-2-Furfuraldehyde in Hemicellulosic Hydrolysate pp-697
N.R.M. Tanure, B.E.L. Baeta, L.C. Soares, L.V.A. Gurgel
- 344** - Adsorption of Ethidium Bromide from Aqueous and Whey Solutions by Activated Carbon and Natural Pumice Stone pp-702
Paola Giambiaggi, Silvia Bentancur, Andres Cuña, Mirian Casco
- 350** - Ammonium Removal from Aqueous Solution by Activated Orange Peel Biochar: Kinetic, Isotherm and Thermodynamic Analysis pp-708
Larissa Firmino de Lima, Carlos Eduardo Rodrigues Barquilha, Maria Cristina Borba Braga
- 355** - Uranium Biosorption by Hydroxyapatite and Bone Meal pp-714
Tamires Watanabe, Sabine Neusatz Guilhen, Júlio Takehiro Marumo, Leandro Goulart de Araujo
- 183** - H₂ storage in modified natural clinoptilolite pp-719
V. C. de Souza, J. Villarroel-Rocha, M. K. Sapag, S. B. C. Pergher



BIO: Biotechnology

029 - Equilibrium Studies of Europium Biosorption by Dead Fungal Biomass

pp-723

Ana Carolina Sales Pereira de Souza, Nice Vasconcelos Coimbra, Ellen Cristine Giese

141 Evaluation of different adsorbents for the purification of anthocyanins from *Syzygium cumini* L.

pp-727

Luiz Bruno de Sousa Sabino, Edy Sousa de Brito, Ivanildo José da Silva Júnior

257 - Protease Immobilization onto Grapheme Oxide via Adsorption: A Preliminary Study

pp-732

Paula Valéria Viotti, Wardleison Martins Moreira, Paulo Waldir Tardioli, Marcelo Fernandes Vieira



Capillary Condensation in Elliptical Pores: a study of the Effect of the Variable Curvature during the course of Adsorption by means of the Broekhoff and de Boer approach

Aguilar-Huerta Ma. Erendira^a, Rojas-González Fernando^a, Cordero-Sánchez Salomón^a

^a Universidad Autónoma Metropolitana-Iztapalapa, Departamento de Química, México City, CP 09340, México

Abstract

In this paper we numerically study the effect of the curvature of the condensed layer in ellipsoidal mesopores during the course of adsorption of Nitrogen at 77.35 K, by using the Broekhoff and de Boer approach [1] and using a Lennard Jones potential (12 – 6) for the fluid – fluid and the solid – fluid pair interactions [2] and by defining the curvature of the liquid – vapor interface at each point of the interface surface [3]. The pore geometry was examined for two cases of elliptical pores: oblate and prolate. The stability conditions of the liquid – vapor interface were established and therefore the conditions for the development of capillary condensation. It was observed that the pore size and the eccentricity determine the development of capillary condensation, taking place in accordance to the adsorption conditions, a multilayer or a continuous adsorption. Also, it was verified that the distribution of the thickness of the condensed layer during capillary condensation is modified when the eccentricity increases or decreases. The instability of the liquid – vapor interface that originates capillary condensation takes place in the regions with the greater value of curvature of each pore type.

Keywords: Elliptical pore; curvature; adsorption

1. Introduction

The progress in the synthesis of porous solids allows the synthesis of materials with different properties that comply with determined requirements, such as arrangement, size and shape pore [4]. In this regard, new porous materials with elliptical shapes have been developed, for example, elliptical pores from zeolites (extra-large-pore, UTD-1) with 0.75 x 1.00 nm and 0.66 x 0.39 nm of pore size [5, 6]. Also, the trapping of porphyrins inside solid networks (xerogels) has made possible the synthesis of pores endowed with this geometry (semi-axes ranging from 1.6 to 10 nm) [7]. It is known that geometry, size and chemical composition of pores determine the development of adsorption [8]. Taking into account the above, the aim of this work is to explain the development of adsorption verified in elliptical mesopores. To this end, a model that incorporates gas – solid interactions (adsorbent forces) and the contribution of variable curvature of the liquid – vapor interface was used using the framework provided by the Broekhoff and de Boer approach (BdB). Due to the latter it was

possible to characterize the conditions under which occurs capillary condensation in elliptical pores with Nitrogen at 77.35 K.

2. Model

We incorporated the adsorption potential between gas and solid molecules and the contribution of variable curvature of the liquid – vapor interface under the BdB approach. The interaction of the gas – solid potential was represented by means of the Lennard Jones (LJ) potential. Then, the position of the gas atom relative to the i th atom within the solid was mathematically developed to approximate the whole attraction and repulsion forces verified in the total volume of the pore with an ellipsoidal shape. The curvature of the liquid – vapor interface was incorporated through the two principal radii of curvature on the interface. The condensed layer was considered as having a thickness (t) that is a function of the two semi-axes that describe the pore. Other variables taken into account were the azimuthal angle (θ) and the pressure (p) at a given temperature (T). The

interaction parameters used for the N_2 adsorption at 77.35 were [9]: $\varepsilon_{sf}/\kappa_B=147.3$ K, $\varepsilon_{ff}/\kappa_B=94.45$ K, $\sigma_{ff}=0.357$ nm, $\sigma_{sf}=0.317$ nm. The interfacial tension and the molar volume at the given conditions were 8.88 mN/m and 34.66 cm³/mol, respectively.

3. Results

The adsorption potential and the interface curvature were evaluated in different pore regions with constant values of the angle θ . It was found that the instability of the liquid-vapor meniscus that causes capillary condensation is localized in different pore regions for each elliptical pore (the derivatives of the adsorption potential and the curvature meet at different values of pressure, figure 1; however, capillary condensation initiates when two curves meet at the lowest value of pressure). In the oblate it occurs at $\pi/2$ and in the prolate at the values 0 and π (Fig. 1.). However, when the pore size was small enough or the eccentricity was high enough, none of the curves intersected over the whole range of values of θ . This last situation could indicate an adsorption mechanism of continuous filling of the pore.

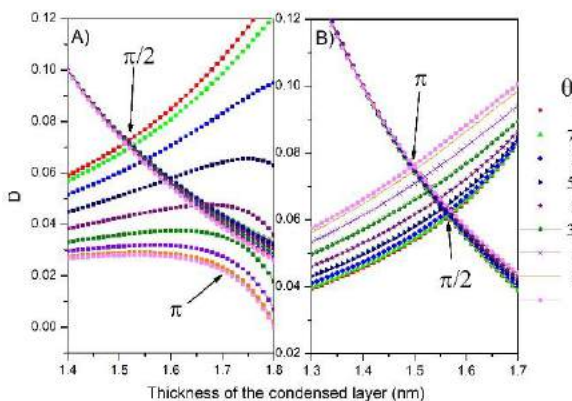


Fig. 1. Curves of the derivatives of the adsorption potential (circles) and curvature of the liquid - vapor interface (square) vs the thickness of the condensed layer for different values of θ . A) Oblate and B) Prolate with an eccentricity of 0.417.

The distribution of the thickness of the condensed layer was evaluated for the whole range of values of θ (Fig. 2.). There, it is shown that the absolute maximum of the thickness is localized in the pore regions with the values of θ referred to in the previous paragraph ($\theta=\pi/2$,

oblates; $\theta=0,\pi$, prolates). The effect of the eccentricity is also shown in this last figure. An increment in the eccentricity causes the apparition of local maxima of the thickness of the condensed layer. The value of these local maxima increases as $\xi \rightarrow 1$.

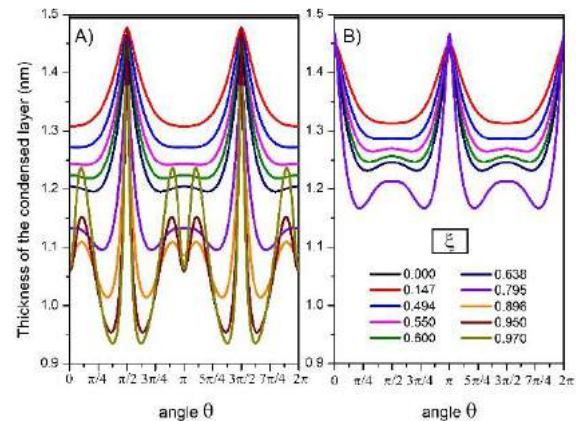


Fig. 2. Distribution of the thickness of the condensed layer at capillary condensation pressure for different values of eccentricity (ξ : 0, 0.147, 0.494, 0.550, 0.600, 0.638, 0.795, 0.896, 0.950, 0.970). A) Oblate and B) Prolate.

In addition to the eccentricity, the pore size determines also the appearance of local maxima of the thickness of the condensed layer on the pore surface. This is shown in figure 3 where it is compared two pore sizes with the same value of eccentricity ($\xi=0.795$). The decrease of the ellipsoidal semi-axis size causes the apparition of local maxima in the distribution of the thickness. The pore size effect is also observed over the N_2 isotherms shapes (Fig. 4.). When the pore size is small enough (Fig. 4A.), the adsorbed volume is greater at low pressures. The increase of the semi-axis size causes the total adsorbed volume to lower.

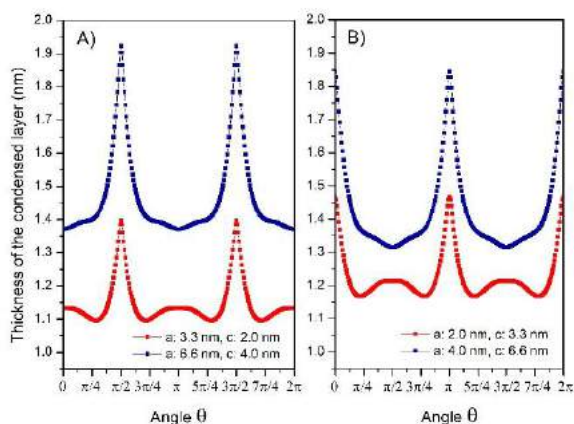


Fig. 3. The distribution of the condensed layer thickness for eccentricity equal to 0.795. A)Oblate and B)prolate.

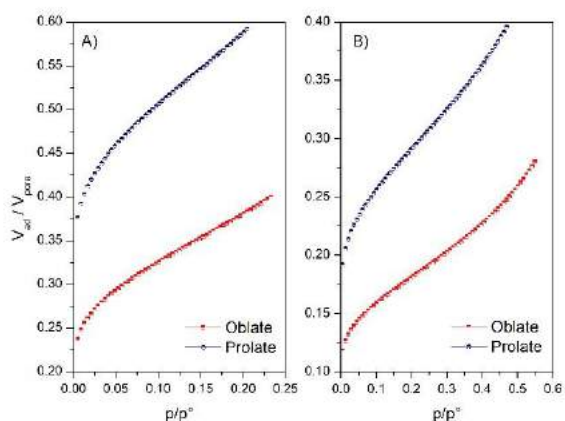


Fig. 4. Nitrogen isotherms for eccentricity equal to 0.795. A) Oblate (a:3.3 nm c:2.0 nm) and prolate (a:2.0 nm c:3.3 nm) and B) Oblate (a:6.6 nm c:4.0 nm) and prolate (a:4.0 nm c:6.6 nm).

4. Conclusions

The thickness of the condensed layer changes as a function of the curvature of the liquid – vapor interface. The limit of stability that indicates the onset of capillary condensation results different for oblates and prolates ($\theta = \pi/2$ and $\theta = 0, \pi$, respectively). Pore size and eccentricity determine the distribution of the values of the thickness of the condensed layer during the course of adsorption and the pressure values at which initiates capillary condensation. The decrease of the eccentricity causes two absolute maxima in the thickness of the condensed film, while the increase causes the apparition of local maxima.

Acknowledgements

We thank CONACyT for scholarship 738057.

References

- [1] Broekhoff JC, De Boer JH. Studies on pore systems in catalysts: IX. Calculation of pore distributions from the adsorption branch of nitrogen sorption isotherms in the case of open cylindrical pores A. *Fundamental equations. Journal of Catalysis.* 1967;9:8-14.
- [2] Steele WA. The physical interaction of gases with crystalline solids: I. Gas-solid energies and properties of isolated adsorbed atoms. *Surface Science.* 1973;36:317-52.
- [3] Tolman RC. The effect of droplet size on surface tension. *The journal of chemical physics.* 1949;17:333-7.
- [4] Davis ME. Ordered porous materials for emerging applications. *Nature.* 2002;417:813.
- [5] Freyhardt CC, Tsapatsis M, Lobo RF, Balkus Jr KJ, Davis ME. A high-silica zeolite with a 14-tetrahedral-atom pore opening. *Nature.* 1996;381:295.
- [6] Kuznicki SM, Bell VA, Nair S, Hillhouse HW, Jacobinas RM, Braunbarth CM, Toby BH, Tsapatsis M. A titanosilicate molecular sieve with adjustable pores for size-selective adsorption of molecules. *Nature.* 2001;412:720.
- [7] García-Sánchez MA, Rojas-González F, Menchaca-Campos EC, Tello-Solís SR, Quiroz-Segoviano R, Diaz-Alejo LA, Salas-Bañales E, Campero A. Crossed and linked histories of tetrapyrrolic macrocycles and their use for engineering pores within sol-gel matrices. *Molecules.* 2013;18:588-653.
- [8] Bohlen H, Schoen M. Effect of fluid-substrate attraction and pore geometry on fluid adsorption. *The Journal of chemical physics.* 2005;123:124714.
- [9] Ravikovitch PI, Vishnyakov A, Neimark AV. Density functional theories and molecular simulations of adsorption and phase transitions in nanopores. *Physical Review E.* 2001;64:011602.

Assessment of zeolites hydrothermal aging by adsorption microcalorimetry

Thalita M. Azevedo^a, Vitória N. S. Oliveira^a, Wagner A. Sousa^a, Débora A. S. Maia^{a*},
Dárley C. Melo^b, Moises Bastos-Neto^a, Diana C. S. Azevedo^a

^a Laboratório de Pesquisas em Adsorção e Captura de CO₂/GPSA - Departamento de Engenharia Química – Universidade Federal do Ceará. Campus do Pici, Bloco 731 – Fortaleza, CE – Brasil.

^b PETROBRAS/CENPES, Rio de Janeiro, Brazil *Email: debora.maia@gpsa.ufc.com

Abstract

A Tian-Calvet microcalorimeter coupled to a manometric setup was used to evaluate CO₂ adsorption isotherms and enthalpies of fresh and aged commercial zeolites commonly used in the petroleum and petrochemical industry. The experimental setup was designed for controlling gas dosing to allow simultaneous measurements of isotherm and heats of CO₂ adsorption at 298 K. Additionally, the technique was used to assess intraparticle mass transfer by fitting microcalorimetric peaks to a deterministic mathematical model. The results showed that the microcalorimeter output data (isotherms and microcalorimetric peaks) are sensitive to the hydrothermal degradation the zeolites underwent. The mathematical model based on differential mass and energy balances allowed for the estimation of intraparticle mass transfer parameters.

Keywords: Adsorption microcalorimetry; Zeolites; Mass transfer; hydrothermal degradation.

1. Introduction

Calorimetric methods are especially used to characterize the chemical nature of surfaces, providing direct and reliable data that are necessary for a complete understanding of surface phenomena [1]. Adsorption Microcalorimetry is proposed as a high sensitivity technique capable of providing very accurate adsorption enthalpy data. [2]

To showing how precise this technique could be, zeolites were used as the adsorbent due their great CO₂ adsorption capacity [3]. They are hydrated crystalline aluminosilicates, generally containing alkali or alkaline earth metals as counter ions. Zeolite structure is formed by a tridimensional network of interconnected tetrahedra, containing sites of molecular dimensions [4].

Zeolites also have a well-defined pore distribution. Because of that, those molecular sieves facilitate the observation in the change of its structure even small ones. Previous work has used this knowledge to add specific functional groups, such as amines, in mesoporous silica and use adsorption microcalorimetry for a characterization. [5].

In this study, a Tian-Calvet microcalorimeter coupled to a manometric setup was used to evaluate the adsorption enthalpy of commercial zeolites in fresh and hydrothermally aged forms. The

experimental system was designed for controlled gas dosing to measure simultaneously CO₂ isotherm and heats of adsorption at 298 K. Additionally, a mathematical model - based on mass and energy balances - was used to calculate intraparticle mass transfer coefficients using the experimental microcalorimetric peaks.

Notation Section

A_c	Internal Lateral Surface Area of the microcalorimetric cell (m ²)
A_{c0}	External Lateral Surface Area of the microcalorimetric cell (m ²)
C	Gas concentration inside the microcalorimetric cell (mol/m ³)
c_i	Heat Capacity of the i component (J/(Kg.K))
c_p	Heat Capacity of the gas (J/(mol.K))
c_{ps}	Heat Capacity of the adsorbent particles (J/(kg.K))
C_v	Gas concentration in the dosing vessel (mol/m ³)
C_{vm}	Gas concentration in the transfer line (mol/m ³)
h_c	Heat transfer coefficient between the gas and the microcalorimetric cell wall (W/(m ² .K))
$h_v A_v$	Heat transfer coefficient times the lateral dosing cell tubing area (W/K)
$h_{vm} A_{vm}$	Heat transfer coefficient times the lateral transfer line tubing area (W/K)

K_i	Thermal Conductivity of the i component (W/m.K)
m_s	Adsorbent particles mass (kg)
n_e	Number of moles entering the microcalorimetric cell (mol)
n_s	Number of moles leaving the dosing vessel (mol)
q	Average adsorbed quantity per unit of mass (mol/kg)
q_{eq}	Average equilibrium adsorbed quantity per unit of mass (mol/kg)
R	Radial Coordinate of the calorimetric model (m)
R_1	Radius of the inner wall of the microcalorimetric cell (m)
R_2	Radius of the outer wall of the microcalorimetric cell (m)
R_3	Radius of the alumina lining (m)
R_g	Gas constant (J/(mol.K))
r	Radial Coordinate of adsorbent particle (m)
T_c	Radial temperature of the microcalorimetric cell wall and alumina lining (K)
ΔH_{ads}	Heat of adsorption (J/mol)
ρ_i	Component i density (kg/m ³)
ρ_p	Adsorbent particle density (kg/m ³)

2. Materials and Methods

2.1 - Materials

Four samples were used in this work: fresh commercial pellet zeolites CHA (UOP, EUA), LTA (Sigma Aldrich, Brazil), and the same samples aged using a lab protocol reported elsewhere [6]. They were labeled as CHAD and LTAD.

Briefly, the fresh samples were aged using an accelerated aging protocol as described by Santiago, R. G., et al. [6]. The sample, with controlled temperature and pressure, undergoes alternating heating and cooling cycles, in the presence of humidity, CO₂ and CH₄. The temperature shift can lead to a slow and irreversible degradation of the zeolite crystal structure, decreasing adsorbent uptake of target adsorbents.

2.2 - Methods

2.2.1 Experimental

The samples were previously outgassed in the microcalorimetric setup at 300°C for 8 hours. The setup comprises a microcalorimeter coupled to a manometric device, together with data acquisition system, as shown in Figure 1.

The Tian-Calvet microcalorimeter (Setaram model C80 France) is a high sensitivity open system. It is

composed by two cells: one in which the sample is placed a reference cell. The cells are surrounded by thermopiles and thermocouples, which in turn are enclosed by a thermostat with high thermal inertia. This allows the system to maintain a stable temperature.

The manometric device is composed by seven control valves and two pressure transducers, which provide information needed to measure the adsorption isotherm, plus a high vacuum pump (Pfeiffer Vacuum, USA) to apply vacuum to the system during the experiments.

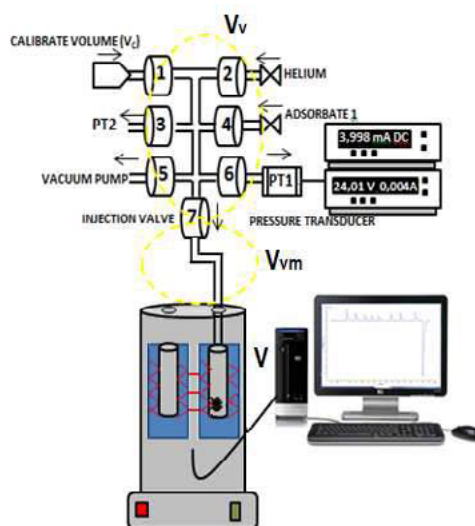


Fig. 1. Adsorption microcalorimetric setup

This system is based on the concept of material balance over PVT measurements, using Equations of State to calculate the amount of adsorbed gas. A calibrated volume is used as a standard to calibrate the dosing volume [7]. The dosing volume is defined as the central part of the connecting pipes between the valves and one of the pressure transducers. The dead volume, represented by V_{vm} , includes the volume below the injection valve, except the volume occupied by the sample, as shown in Figure 1.

After the manometric system has been calibrated, the adsorption isotherms can be measured. After regeneration, when a stable microcalorimetric baseline is obtained, the adsorbate is dosed stepwise, gradually increasing the pressure upon each gas injection. The pressure and the temperature of each dose should be measured and then the injection valve is opened, allowing the gas to flow into the adsorption cell. Once in equilibrium, the amount of adsorbed gas can be calculated. [7]

The contact of each gas dose with the adsorbent produces a thermal effect and this effect results in a peak in the heat curve over time. Each peak represents a point on the isotherm and the differential adsorption enthalpy can be calculated by integrating the peaks generated during the experiment [7], as in equation (1):

$$\frac{dQ_{rev}}{dn^\sigma} + V_c \left(\frac{dp}{dn^\sigma} \right)_{T,A} = \Delta H_{ads} \quad (1)$$

Where dQ_{rev} is the heat measured by the calorimeter, dn^σ is the amount adsorbed for a given increase in pressure dp and V_c is the dead cell volume in contact with the thermopiles [7].

2.2.2 Modeling

In order to investigate whether hydrothermal aging can affect the adsorption kinetics of CO₂ on the zeolites, the heat flow curve (microcalorimetric peak) experimentally obtained was described by a mathematical model that includes a mass balance for the adsorbent, mass and energy balances for the calorimetric cell and an energy balance for the wall. Mass transfer during adsorption can be described by a Linear Driving Force (LDF) approximation, leading to a model that depends on a single fitting parameter: the LDF constant (K_{LDF}).

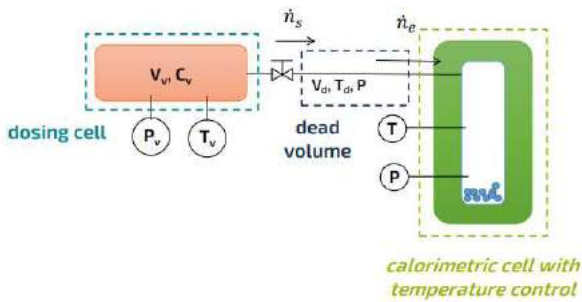


Fig. 2. Schematic modeling system

Mass and energy balances for the three control volumes described in Fig 2 were written under the following assumptions:

- The dosing cell and the dead volume are under isothermal operation
- The pressure in the dead volume is the same of the calorimetric cell
- Pressure in the transfer line is equal to that in the dosing cell at any time;
- The temperature of the adsorbent and the adsorbed phase are the same as the temperature of the gas in the dosing cell at any time;

- Equation of state for CO₂ was the ideal gas law under the pressure and temperature ranges of the experiments.
- Film and macropore resistances were assumed as negligible.

The final equations for all control volumes are the following.

Mass and energy balances for the dosing cell:

$$\frac{dC_v}{dt} = \frac{\dot{n}_s}{V_v} \quad (2)$$

$$c_v c_p \frac{d(T_v)}{dt} V_v - \frac{dP_v}{dt} V_v = h_v A_v (T_{01} - T_v) \quad (3)$$

Mass and energy balances for the transfer line

$$\frac{dC_{vm}}{dt} V_{vm} = \dot{n}_s - \dot{n}_e \quad (4)$$

$$c_{vm} c_p \frac{d(T_{vm})}{dt} V_{vm} - \frac{dP_{vm}}{dt} V_{vm} = \dot{n}_s c_p (T_v - T_{vm}) - h_{vm} A_{vm} (T_{vm} - T_{01}) \quad (5)$$

Mass and energy balances for the microcalorimetric (sample) cell:

$$\frac{dC}{dt} V = \dot{n}_e - m_s \frac{d\bar{q}}{dt} \quad (6)$$

$$C c_p \frac{dT}{dt} V - \frac{dP}{dt} V + m_s c_{ps} \frac{dT}{dt} + m_s \frac{d\bar{q}}{dt} (-\Delta H_{ads}) + m_s c_p \bar{q} \frac{dT}{dt} = \dot{n}_e c_p (T_{vm} - T) - h_c A_c (T - T_c(R_1)) \quad (7)$$

$$P = f(t) \quad (8)$$

The equation for energy balances for the cell wall and external lining (composite cylindrical wall) takes the form:

$$\rho_i c_i \frac{dT_i}{dt} = \frac{1}{R} K_i \left(\frac{\partial}{\partial R} \left(R \frac{\partial T_i}{\partial R} \right) \right) \quad (9)$$

for $R_1 < R < R_2$ (i represents cell wall) and for $R_2 < R < R_3$ (i represents alumina lining)

To solve those equations the Dirichlet and Robin Boundary conditions was applied such as the initial conditions. In the initial time, the dossing cell and the dead volume have the same and known temperature (T_{01}); in the microcalorimetric cell, (T_{02}).

The heat flux out of the cell is given by

$$\dot{Q}_1 = K_c A_{c0} \frac{\partial T_c(R_2)}{\partial R} \quad (10)$$

Adsorption isotherm (Equilibrium model) was model by the equation SIPS and the intraparticle mass transfer rate (Adsorption kinetics) was described by Linear Driving Force (LDF) with the adsorbed amount being a function of radius and time

$$\frac{d\bar{q}}{dt} = K_{LDF} (q_{eq} - \bar{q}) \quad (11)$$

The experimental procedure includes blank experiments (without sample) to determine the parameters of the model ($h_c A_v$, $h_c A_{vm}$ and R_3). The equations for this situation are the same as above with $m_s = 0$. For a given experimental microcalorimetric curve, the total evolved heat (area under the experimental peak) is set equal to the amount Q_{total} of the model, in order to obtain the heat of adsorption. The calculated heat of adsorption and the other parameters obtained from the blank experiments are then used as the model input data. The kinetic parameter is then fitted to adjust the experimental peak to the corresponding simulated curve (Q_1 versus t).

3. Results and discussion

The specific surface area and total pore volume of the samples were calculated using N_2 adsorption and desorption isotherms at 77 K measured in an Autosorb-iQ3 analyzer (Quantachrome, USA). To calculate the specific surface area from the experimental data, the Brunauer – Emmett – Teller (BET) equation was used. The application of this mathematical model to isotherms of microporous solids is questionable, but it continues to be the most widely used equation for any adsorbent surface area in spite of the weakness of its theoretical foundations [8]. Additionally, it is known that the adsorption of N_2 at 77 K on the commercial LTA has kinect problems because of its very narrow micropores. However, as the samples are in pellet

form, this analysis gives important comparative results. To calculate the total pore volume the Gurvich rule at relative pressures of 0.985 was applied [7], and the micropore volumes were estimated using the Dubinin-Radushkevich (DR) equation.[7,9]

Table 1: Textural characterization of the samples

Samples	A_{BET} ($m^2.g^{-1}$)	V_{poros} ($cm^3.g^{-1}$)	V_{micro} ($cm^3.g^{-1}$)
CHA	398	0.28	0.160
CHAD	300	0.23	0.100
LTA	39	0.10	0.010
LTAD	25	0.09	0.006

Table 1 summarizes the textural characterization data. There is a moderate reduction in the textural properties of both zeolites after hydrothermal aging, which suggests partial blocking of pores due to binder or crystal degradation or coke formation caused by the heating/cooling cycles.

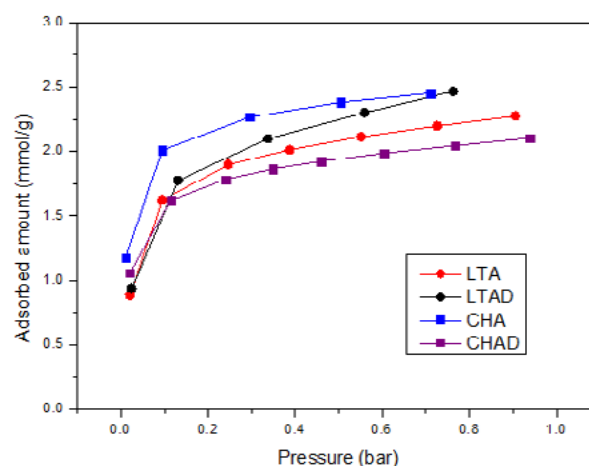


Fig. 3 – CO_2 adsorption isotherms at 298 K.

Figure 3 describes the CO_2 adsorption isotherms for the four samples studied in this work. CHA adsorbs more CO_2 than CHAD, showing that the sample lost adsorption capacity with the aged protocol. This also happened to LTA and LTAD samples.

Figure 4 describes the CO_2 adsorption enthalpy of the four samples under study. The plot shows a decreasing enthalpy with the increase in sorbate loading. Which suggests that the materials have a heterogenous surface according to the classification

proposed by Llwellyn [10]. When comparing both fresh samples with respect to the aged counterparts, it is noteworthy that CHAD and LTAD enthalpy decreases more steeply, which indicates that the aged samples do not have the same surface characteristics as the fresh ones.

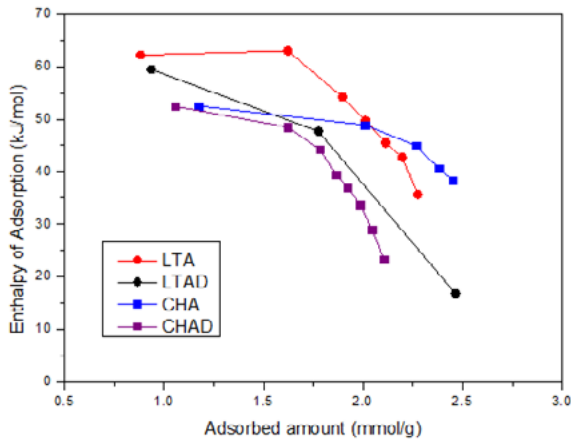


Fig. 4 – CO₂ adsorption enthalpy curves at 298 K

Besides affecting the adsorption capacity in the equilibrium isotherms, the aging process also causes a change in the CO₂ adsorption kinetics of these samples. For the same amount of gas injected on the experimental system, the microcalorimetric peaks of CHA and CHAD are shown in Figure 5 (a). It seems to be no appreciable kinetic difference between fresh and aged samples. On the other hand, the aged sample has less interaction with CO₂ than the fresh CHA for the same amount of injected gas. The microcalorimetric peak was also obtained for LTA and LTAD, shown in Figure 5 (b). The LTAD peak takes longer than the LTA peak to return to the baseline.

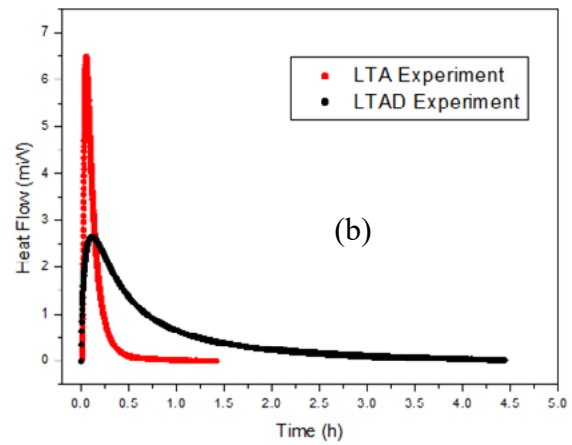
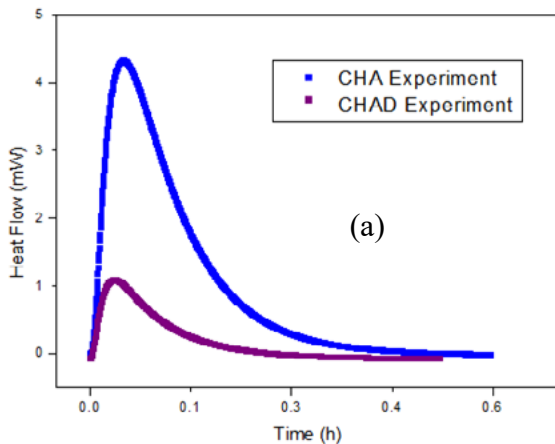


Fig. 5. Microcalorimetric peaks of the samples for the same injection pressure.

They have similar enthalpy value (62.17 and 59.44 kJ/mol, respectively) which means that the final peak area and amount adsorbed is almost the same, but the kinetics process is very different.

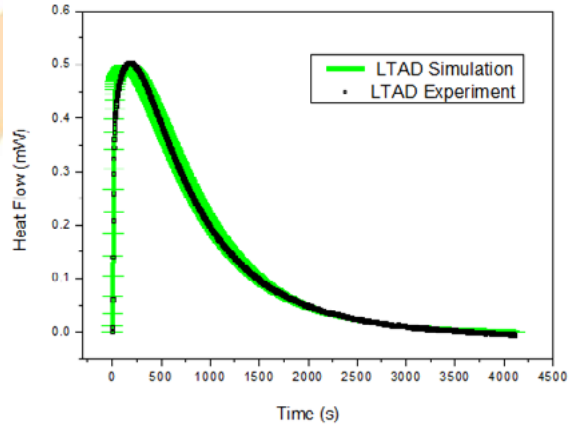
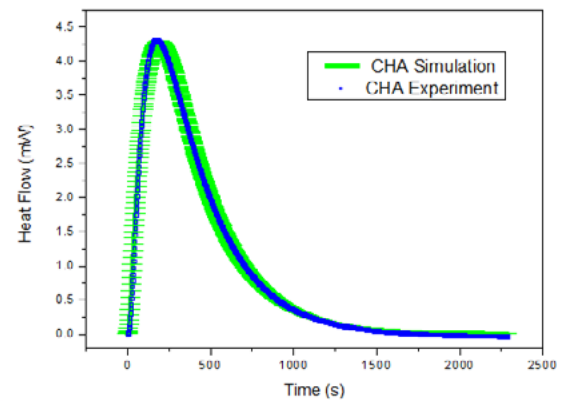


Fig. 6. Comparison between experimental and simulated peaks

The peaks in Figure 5 are a direct result from the microcalorimetric system. The experimental results are compared to simulated ones according to the

modeling equations described in the section 2.2.2 (see Figure 6). An excellent agreement was observed for both the fresh and aged sample.

Table 2 shows the average K_{LDF} parameter estimated for all experimental peaks obtained for CHA, CHAD, LTA and LTAD samples. Confirming what was shown in the experimental peaks on the Figure 5(a), the average K_{LDF} for the two samples is almost the same, suggesting that there is no significant change in CO_2 intraparticle diffusion for CHA zeolite after the aging process. On the other hand, LTA and LTAD have a K_{LDF} difference of two orders of magnitude as expected from the experimental peaks (Fig. 5b).

Table 2. Average of mass transfer constant K_{LDF} estimated

Sample	K_{LDF} (s^{-1})
CHA	0.044
CHAD	0.043
LTA	0.025
LTAD	0.0006

The K_{LDF} constant found by microcalorimetry is comparable to the range reported in the literature for both samples [11,12].

4. Conclusion

Microcalorimetric adsorption peaks have shown high sensitivity to obtain energetic and kinetic data with potential to be a reliable method to characterize adsorbent aging. In this work, two commercial zeolite samples with small pores were tested, each in fresh form and after being hydrothermally aged. Aging led to a decrease in textural properties in both cases. Furthermore, changes in CO_2 intraparticle diffusivity and CO_2 interaction with the surface were observed for LTA and CHA, respectively. For a deeper understanding of the aging mechanisms in each case, additional chemical and structural analysis (e.g. elemental analysis, XRD, RMN) would be required.

5. Acknowledgement

The authors would like to thank the CENPES/PETROBRAS and Conselho Nacional de Desenvolvimento Científico e Tecnológico – CNPq for the financial support of this research.

6. References

- [1] Maia DAS, Alexandre de Oliveira JC, Nazzarro MS, Sapag KM, López RH, Lucena SMP, de Azevedo DCS, CO_2 gas-adsorption calorimetry applied to the study of chemically activated carbons. *Chem. Eng. Res. Des.* 136: 753–760, 2018
- [2] Sanchez-Zambrano, K. et al. CO_2 Capture with Mesoporous Silicas Modified with Amines by Double Functionalization: Assessment of Adsorption/Desorption Cycles. *Materials* 11, n. 6, 25, 2018.
- [3] Silva JAC, Schumann, K; Rodrigues, AE. Sorption and kinetics of CO_2 and CH_4 in binderless beads of 13X zeolite. *Microporous And Mesoporous Materials* 158, p.219-228, 2012.
- [4] Shriver, DF. et al. *Química Inorgânica*. 4. ed. Porto Alegre: Bookman, 2008. Tradução de: Roberto de Barros Faria.
- [5] Sanchez-Zambrano, K.S. et al. Adsorption microcalorimetry as a tool in the characterization of amine-grafted mesoporous silicas for CO_2 capture. *Adsorption* p.1-2, 2019.
- [6] Santiago, RG et al. Investigation of premature aging of zeolites used in the drying of gas streams. *Chemical Engineering Communications* 206, n. 11, p.1378-1385, 2018.
- [7] Rouquerol F, Rouquerol J, Sing KSW, Llewellyn PL, Maurin G. *Adsorption by Powder & Porous Solids – Principles Methodology and Applications*, Academic Press, London, 2014
- [8] Thommes, M., Kaneko, K., Neimark, A., et al. Physisorption of gases, with special reference to the evaluation of surface area and pore size distribution (IUPAC Technical Report). *Pure and Applied Chemistry*. 87, 1051-1069, 2015.
- [9] Dubinin, M. Adsorption in micropores. *J. Colloid InterfaceSci.* 23, 487–499, 1967.
- [10] Llewellyn, P.: Characterization of microporous materials by adsorption microcalorimetry, *Recent Adv. Gas Sep. Microporous Ceram. Membr.* 6, 213–230, 2000.
- [11] Velte, A.; Fuldner, G.; Laurenz, E.; Schnabel, L. Advanced Measurement and Simulation Procedure for the Identification of Heat and Mass Transfer Parameters in Dynamic Adsorption Experiments. 2017.
- [12] Seabra, R., Ribeiroa, A.M., Gleichmannb, K., Ferreira, A.F.P., Rodrigues, A.E. Adsorption equilibrium and kinetics of carbon dioxide, methane and nitrogen on binderless zeolite 4A adsorbents. *Microporous and Mesoporous Materials* 277, 105–114, 2019.

H₂S adsorption on KOH-modified commercial activated carbon

Luiza C. Carvalho, Jorge L. B. de Oliveira, Rafaelle G. Santiago, Juliana A. Coelho,
Diana C.S. de Azevedo e Moisés Bastos-Neto*

^a Grupo de Pesquisa em Separações por Adsorção (GPSA), Chemical Engineering Department, Campus do Pici, bl. 731, Universidade Federal do Ceará, Fortaleza - CE, 60760-400, Brazil

**Corresponding author:
E-mail address: mbn@ufc.br*

Abstract

Among the technologies used in the removal of hydrogen sulfide (H₂S), toxic and corrosive gas, in the biogas production is the adsorption on activated carbons. In this work, adsorption data of H₂S was obtained for a commercial activated carbon, referred to as WV-1050, further impregnated with potassium hydroxide (KOH), in order to evaluate the effect of chemical impregnation. The tests were performed using a fixed bed unit and subjected to different temperatures in order to evaluate the main adsorption mechanism. X-ray fluorescence (XRF) and N₂ adsorption/desorption isotherms at 77 K were applied for chemical and textural characterization, respectively. XRF confirmed the presence of the K-impregnated specie in the modified sample. Textural characterization revealed high surface area in the unmodified sample. Fixed bed experiments revealed a great influence of the chemisorption, increasing up to 17 times the retained amount of H₂S for the potassium-impregnated sample (from 1.21 to 21.21 mg g⁻¹).

Keywords: H₂S; biogas; fixed bed; activated carbon; impregnation.

1. Introduction

Biogas is a gas mixture with potential to replace the fossil fuels as an energy source due to its relevant calorific value. However, in order to go through that application, the biogas needs to be cleansed of its contaminants that decrease its calorific value and pose a threat to the environment [1]. One of the main contaminants of this gas mixture is the H₂S, a toxic and corrosive gas that must be removed from biogas prior any applications [2].

Adsorption in porous solids is one of the most effective methods to achieve this removal and activated carbon has been commonly used as adsorbent due to its unique characteristics, such a large porous structure and a tunable surface chemistry [3]. In addition to that, activated carbon from waste materials has an easy availability and it is relatively cheap.

Regarding the surface chemistry, activated carbons impregnated with caustics, such as NaOH or KOH, are extensively studied and used due to their high efficiency, since these alkaline compounds create a basic environment on the

carbon surface, which facilitates the H₂S dissociation and acid-base reaction [4].

Therefore, this work aimed to impregnate a commercial activated carbon using KOH as the caustic compound and evaluate the H₂S retention capacity in a fixed-bed unit. The tests were subjected to different temperatures to evaluate the main adsorption mechanism.

2. Experimental Methods

2.1 Materials

One commercial activated carbon was evaluated in this work: sample WV-1050, produced and supplied by MeadWestvaco, USA. The carbon was crushed and sieved down to 18×30 mesh to minimize packing issues in the fixed bed. It was further impregnated with potassium hydroxide (KOH) (Dinâmica Química Contemporânea Ltda., Brazil) and referred to as WV-1050-K. The gases used in the adsorption tests were hydrogen sulfide (diluted in helium at 200 ppm) and helium (99.999%). Carbon dioxide (99.8%) and nitrogen (99.999%) were used to determine the textural



properties of the samples. All gases were supplied by White Martins Praxair Inc. (Brazil).

2.2 Impregnation process of activated carbon

Impregnation process was realized according to procedure previously described by Bagreev and Badosz [5], with some modifications. A sample of 20 g of carbon was washed with 20 mL of a 50% (v/v) solution of ethanol in water to create a hydrophilic environment on the surface of the carbon. Then, the sample was subjected to three consecutive washes with 22 mL of distilled water (for each wash). Finally, the sample was brought into contact with 20 mL of an alkaline solution of potassium hydroxide (KOH) (10% wt) and put to stir for 30 min at room temperature. After this period, the carbon was placed in an oven at 373 K to dry for 24 h.

2.3 Adsorbent characterization

Chemical characterization was determined by X-ray fluorescence (XRF) semiquantitative analysis using a Rigaku ZSX-Mini. Textural properties were evaluated from N₂ and CO₂ isotherms at 77 and 273 K, respectively, using an Autosorb-IQ₃ (Quantachrome Instruments, EUA). The samples were outgassed at 423 K under vacuum (10⁻⁶ bar) for 6 h prior the experiments. Specific surface area (A_{BET}) was calculated using Brunauer-Emmett-Teller (BET) equation, total pore volume (V_p), micropore volume (V_{DR}), and microporosity (V_{DR}/V_p) were obtained by Dubinin-Radushkevich (DR) model.

2.4 H₂S Retention Capacity

The dynamic H₂S adsorption tests were based on breakthrough curves. These were obtained using a fixed bed column (4.6 mm internal diameter and 50 mm of length) containing approximately 0.5 g of sample, installed inside a gas chromatograph oven (Varian CP-3800). A Pulsed Flame Photometric Detector (PFPD) is coupled to the equipment and was used to monitor H₂S at the outlet of the column. The column temperature and the detector signal were both controlled using a computer.

The packed column was subjected to a regeneration process in order to remove any impurities the adsorbents may contain. The process

was carried out under helium flow (15 mL min⁻¹) for 12 h at 423 K.

After that, the GC oven was set to the desired temperature and the fixed bed was fed with 100 mLmin⁻¹ of a H₂S solution (diluted in He at 200 ppm).

The breakthrough curves generated by the computer are used to determine the H₂S retention capacity of the material; however, it was not possible to measure the complete breakthrough curves due to the upper detection limit of the PFPD detector (about 6 ppm of H₂S). Then the criterion used to compare the adsorption capacities of the samples was based on the “breakpoint” time, where is defined as the point at which a given fraction of the feed concentration was reached (5 or 10%). For diluted systems, the breakpoint time is not expected to be significantly different from the stoichiometric time and, consequently, the curve should have a step function shape [6,7].

The H₂S retention capacities (mg g⁻¹) were calculated according to Equation 1, which was adapted from Choo et al. [8].

$$q_{bt} = \frac{C_o \times t_b \times Q \times MM_{H_2S}}{MM_{ads}} \quad (1)$$

where C_o is the feed concentration (mmol.mL⁻¹); t_b is the breakpoint time (min); Q is the volumetric feed flow (mL.min⁻¹); M_{ads} is the adsorbent mass after regeneration (g), MM_{H₂S} is the molar mass of H₂S (g.mol⁻¹) and q_{bt} is the H₂S retention capacity by the breakpoint column (mg.g⁻¹).

3. Results and Discussion

3.1. Activated carbons characterization

3.1.1. Surface chemistry

Table 1 presents the main chemical elements in the samples that were obtained by the XRF semiquantitative analysis. As it can be seen, the sample WV 1050 presented calcium (Ca), that is known for presenting a catalytic effect similar to that proposed for impregnated carbons where KOH or NaOH reacts with H₂S, promoting its dissociation [9].

Table 1. Proportion of metals detectable by XRF in the activated carbon samples.

Element (wt %)	WV 1050	WV-1050-K
Ca	16.81	-
K	-	94.82

Furthermore, chemical impregnation on the sample was evidenced by the presence of potassium (K) as it can be seen in Table 1, which is absent in the unmodified sample. Then, it can be expected that the adsorption capacity increases in the impregnated sample by means of chemisorption.

3.1.2. Textural characterization

According to N₂ isotherms at 77 K (Figure 1), all samples presented a behavior of microporous materials, being Type 1 isotherms. It can be seen that at low relative pressures, a significant retention of N₂ was observed, which indicates the filling of narrow micropores.

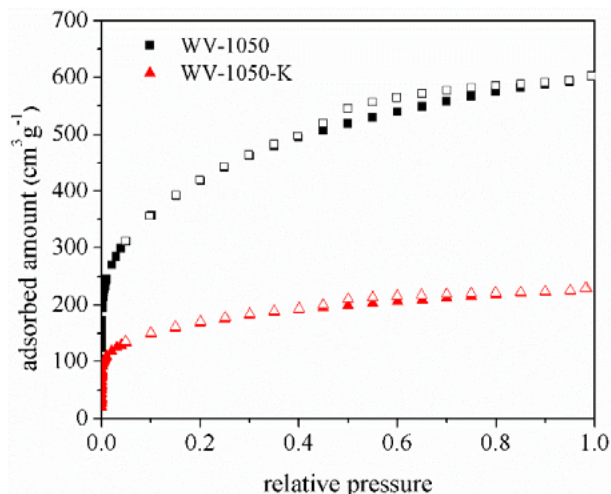


Fig 1. N₂ adsorption (filled symbols)/desorption (empty symbols) isotherms at 77 K of the samples.

Table 2 summarizes all textural characteristics obtained by N₂ adsorption/desorption isotherms illustrated in Figure 1. Sample WV-1050 presented a high value of surface area compared to the impregnated sample, which is interesting for the adsorption of gases. As for the modified sample, the low surface area can be attributed to the chemical impregnation that may have led to a pore occlusion and, consequently, decreased the available pore volume.

Table 2. Textural properties obtained by N₂ adsorption/desorption isotherms at 77 K.

Sample	A _{BET} m ² g ⁻¹	V _P cm ³ g ⁻¹	V _{DR} cm ³ g ⁻¹	V _{DR} /V _P %
WV-1050	1506	0.93	0.53	56.34
WV-1050-K	575	0.35	0.23	64.06

3.2. Breakthrough curves

Figures 2 and 3 show the breakthrough curves of WV-1050 and WV-1050-K, respectively, at different temperatures. Table 3 resumes the retention capacities under the studied conditions.

At 298 K and 1 bar, it was observed that impregnation with KOH considerably increased the breakpoint time and retained amount of H₂S. Despite presenting a low surface area, which reduces its ability of adsorbing physically, the impregnated material presented an average increase of 17 times in its retention capacity, which can be attributed to the presence of the impregnated specie potassium that strengthens the acid-base bonds with H₂S [10]. Consequently, chemical adsorption, as the main adsorption mechanism in WV-1050-K, increases the retained amount of H₂S not only at 298 K, but also at 348 and 423 K, as evidenced by the increase of breakpoint time with temperature.

As for the unmodified sample, when comparing its retained amount of H₂S to the impregnated one at 298 K, it is interesting to point out that it is likely possible that Ca, that was detected by XRF, did not improve the H₂S retention by chemisorption due to the low reactivity of its oxides at room temperature and dry conditions [9]. Thus, at 298 K, physical adsorption should prevail in this sample due to its high surface area. As temperature is increased, chemisorption takes place and the retained amount of H₂S increases.

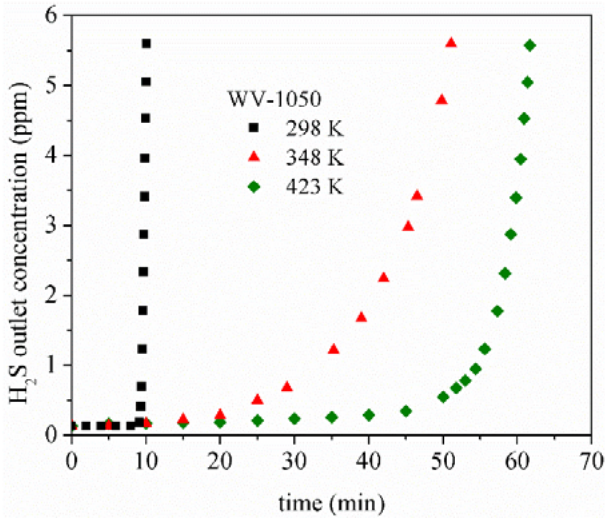


Fig. 2. Breakthrough curves of H₂S in He (200 ppm) for WV-1050.

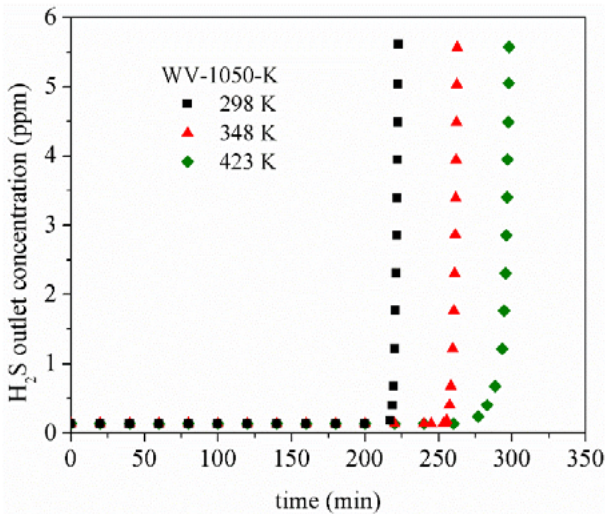


Fig.3. Breakthrough curves of H₂S in He (200 ppm) for WV-1050-K.

Table 3. H₂S retention capacities of the samples at breakpoint at different temperatures.

Sample	q _{bt} (mg g ⁻¹)		
	298 K	348 K	423 K
WV-1050	1.21	3.66	6.55
WV-1050-K	21.22	24.67	27.86

4. Conclusions

Breakthrough data of H₂S have shown that the retained amount of H₂S increased in the activated carbon WV-1050 after impregnation with KOH. It was observed an increase in adsorption capacity up to 17 times (1.21 to 21.22 mg g⁻¹) at 298 K and 1 bar after impregnation. Dynamic H₂S adsorption tests at different temperatures revealed that chemical adsorption was the main adsorption mechanism on both unmodified and modified samples.

Acknowledgements

LCC thanks Universidade Federal do Ceará for the scholarship granted in the *Programa Institucional de Bolsas de Iniciação Científica* (PIBIC/UFC, Ministry of Education, Brazil). The authors acknowledge financial support from CNPq (Conselho Nacional de Desenvolvimento Científico e Tecnológico) and CAPES (Coordenação de Aperfeiçoamento de Pessoal de Nível Superior).

References

- [1] I. Ullah Khan et al., "Biogas as a renewable energy fuel – A review of biogas upgrading, utilisation and storage," *Energy Convers. Manag.*, vol. 150, no. August, pp. 277–294, 2017.
- [2] Y. Zeng et al., "Biogas desulfurization under anoxic conditions using synthetic wastewater and biogas slurry," *Int. Biodeterior. Biodegrad.*, vol. 133, no. March, pp. 247–255, 2018.
- [3] E. M. Calvo-Muñoz, F. J. García-Mateos, J. M. Rosas, J. Rodríguez-Mirasol, and T. Cordero, "Biomass waste carbon materials as adsorbents for CO₂ capture under post-combustion conditions," *Front. Mater.*, vol. 3, no. May, pp. 1–14, 2016.
- [4] R. Sithikhankaew, D. Chadwick, S. Assabumrungrat, and N. Laosiripojana, "Effects of humidity, O₂, and CO₂ on H₂S adsorption onto upgraded and KOH impregnated activated carbons," *Fuel Process. Technol.*, vol. 124, pp. 249–257, 2014.
- [5] A. Bagreev and T. J. Bandoz, "A role of sodium hydroxide in the process of hydrogen sulfide adsorption/oxidation on caustic-impregnated activated carbons," *Ind. Eng. Chem. Res.*, vol. 41, no. 4, pp. 672–679, 2002.
- [6] Z. Aksu and F. Gönen, "Binary biosorption of phenol and chromium(VI) onto immobilized activated sludge in a packed bed: Prediction of kinetic parameters and breakthrough curves," *Sep. Purif. Technol.*, vol. 49, no. 3, pp. 205–216, 2006.
- [7] D. M. Ruthven, "Fundamentals of adsorption equilibrium and kinetics in microporous solids," *Mol. Sieves - Sci. Technol.*, vol. 7, no. January 2006, pp. 1–43, 2008.
- [8] H. S. Choo, L. C. Lau, A. R. Mohamed, and K. T. Lee, "Hydrogen sulfide adsorption by alkaline impregnated coconut shell activated carbon," *J. Eng. Sci. Technol.*,

- vol. 8, no. 6, pp. 741–753, 2013.
- [9] A. Bagreev and T. J. Bandosz, “On the mechanism of hydrogen sulfide removal from moist air on catalytic carbonaceous adsorbents,” *Ind. Eng. Chem. Res.*, vol. 44, no. 3, pp. 530–538, 2005.
- [10] W. Feng, S. Kwon, E. Borguet, and R. Vidic, “Adsorption of hydrogen sulfide onto activated carbon fibers: Effect of pore structure and surface chemistry,” *Environ. Sci. Technol.*, vol. 39, no. 24, pp. 9744–9749, 2005.

Evaluation of C₈ Aromatics Adsorption in Porous Clay Heterostructures using the Headspace Technique

João Victor S. Cardoso, José Wilson V. Lima Jr., Rosana M. A. Saboya,
F. Murilo T. de Luna and Célio L. Cavalcante Jr.

*Universidade Federal do Ceará, Grupo de Pesquisa em Separações por Adsorção,
Núcleo de Pesquisa em Lubrificantes, Campus do Pici, Bloco 1010, CEP: 60.455-900, Fortaleza – CE – Brasil.*

Abstract

The C₈ aromatics fraction in a petrochemical industry consists of four isomers: *o*-xylene (OX), *m*-xylene (MX), *p*-xylene (PX) and ethylbenzene (EB). They are the raw material for plastics, dyes, synthetic fibers and other products. The separation of xylenes has become one of the most important applications of liquid phase adsorption separation processes. In this study, the selective separation of xylene isomers in porous clay heterostructures (PCH) was investigated. Samples of PCH with Zr, Ti and Si (PCH-Zr, PCH-Ti and PCH-Si) were evaluated. A headspace technique was applied to acquire equilibrium data for adsorption of xylenes using small samples. Meta-xylene selectivity in relation to all the other C₈ aromatics was observed for the PCH samples. For PCH-Si, meta-xylene/ethylbenzene selectivity of 4.3 was obtained.

Keywords: xylenes; adsorption; headspace; selectivity; porous clay heterostructures.

1. Introduction

The BTEX compounds (benzenes, toluene, ethylbenzene and isomers of xylene) have a high market value, being therefore of interest their separation and purification. Highlighting ethylbenzene (EB) and isomers of xylenes, *o*-xylene (OX), *p*-xylene (PX) and *m*-xylene (MX), have the same number of carbons (C₈) and have boiling points very close, what makes difficult to separate them by fractional distillation. An alternative is the separation by liquid phase adsorption in porous materials/molecular sieves.

The chromatography with headspace sampler may be used to study the selectivity of molecular sieves in multicomponent systems [1,2]. For this, the determination of liquid phase adsorption selectivity depends directly on the relationships between the molar fractions of the adsorbed, liquid and vapor phase of the system. The point at which saturation of adsorbent pores occurs is also the same in which adsorption selectivity to a given adsorbate is determined by the adsorbent [2]. This technique has been demonstrated in determination

of BaY zeolite para-selectivity in a mixture of *o*-xylene and *p*-xylene [1,2].

A group of porous materials that appear as promising in the liquid phase separation is the porous clay heterostructures (PCH). Studies indicate that the PCH present selective adsorption capacities of mixtures of volatile organic compounds, showing benzene/*n*-hexane, toluene/*n*-hexane and *p*-xylene/benzene selectivity [3]. Hydrophobic PCH with benzene in this composition presents affinity to volatile organic compounds [4] and PCH with decylamin shows affinity to methane, ethanol and methyl ethyl ketone [5]. The PCH samples have more affinity to adsorption of aliphatic compounds such acetone in relation to aromatic compounds such as toluene, because the aliphatic compounds has high occupied molecular orbitals with lower energy than the aromatics [6].

In this study, the selectivity of porous clay heterostructures (PCH) with Si (PCH-Si), Zr (PCH-Zr) and Ti (PCH-Ti) for separation of xylene isomers and ethylbenzene was investigated using the headspace technique.

2. Materials and methods

2.1. Materials

The xylene isomers, *o*-, *m*- and *p*-xylene, and ethylbenzene (Sigma-Aldrich, EUA) were used as adsorbates in the experiments. The adsorbent studied was three porous clay heterostructures (PCH) with Si, Zr and Ti pillars.

2.2. Headspace Chromatography Technique

The gas chromatograph was the Varian 450-GC model (Figure 1). For all experiments a DB-Wax column (60m x 0.32mm x 0.25 μ m) with 60°C oven program was used. A Varian headspace system composed of an incubator (40°C) and a shaker (250 rpm), with a headspace syringe was used. A FID detector was used with the gases H₂ (30mL/min), N₂ (30mL/min) and Air (300mL/min) at 250°C. N₂ was used as carrier gas with 2 mL/min. The time analysis was 16 min.

The samples were prepared following the adsorbate/adsorbent mass ratio (g/g): 0.05, 0.075, 0.1, 0.15 and 0.20. These adsorbate/adsorbent ratio values (g/g) were calculated by setting the mass value of the adsorbent to 0.05 g and varying the added mass values of the equimolar mixture of xylenes.

The adsorption selectivity was calculated at the point of saturation of the adsorbent pores. That is, at the point where there is the largest difference

between the molar fraction values of the vapor phase between two adsorbates in the mixture.

The calculation considers the analyzed system as ideal and in thermodynamic equilibrium between the adsorbed, liquid and gas phase. For this, Raoult's Law is used (Eq.1):

$$\frac{x_A}{x_B} = \frac{P_B^{sat} y_A}{P_A^{sat} y_B} \quad (1)$$

The molar fractions of the substances A and B in the vapor phase (y_A and y_B) are calculated with the data obtained in the headspace analysis. The Antoine Equation [7] determines the vapor pressures at saturation point (P_A^{sat} and P_B^{sat}).

The selectivity (α) between a pair of components (A and B) was calculated using Eq. 2:

$$\alpha_{A/B} = \frac{z_A}{z_B} \frac{x_A}{x_B} \quad (2)$$

where the values of z_A and z_B are the mole fractions of substances A and B in the adsorbed phase and have the same values as the mixture prepared at saturation point.

For this experiment, the z values of each component are 0.25, since the mixture is composed of 4 isomers in an approximately equimolar amount. Using the z and P° values of each isomer, it was possible to calculate the x_A/x_B ratio values and, consequently, the selectivity ($\alpha_{A/B}$).

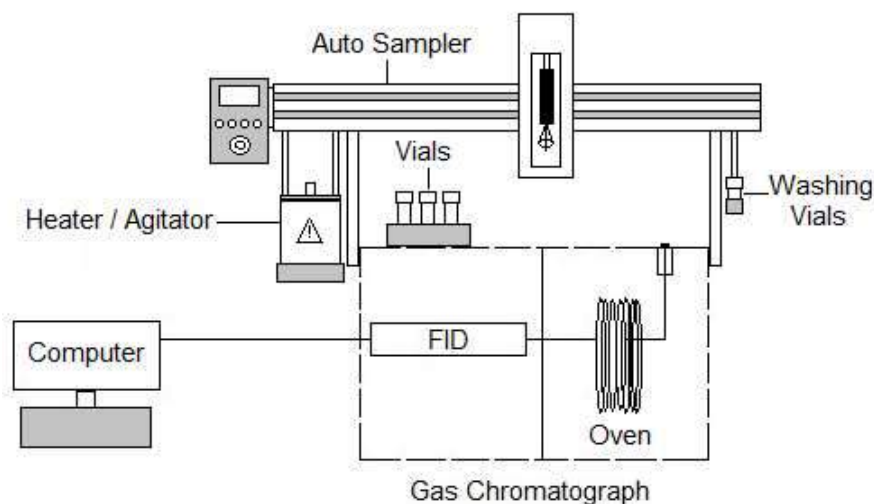


Fig. 1. Experimental setup of headspace technique.

3. Results and discussion

The adsorption data of xylene isomers on PCH with Zr, Ti and Si, using equimolar mixtures are presented in Figures 2, 3 and 4, respectively. According to Luna et al. [2] the maximum and minimum in these plots represent the concentrations at which the pores have just become saturated with the sorbates. At this point, one can calculate the adsorption selectivity at saturation conditions using Eq. 2.

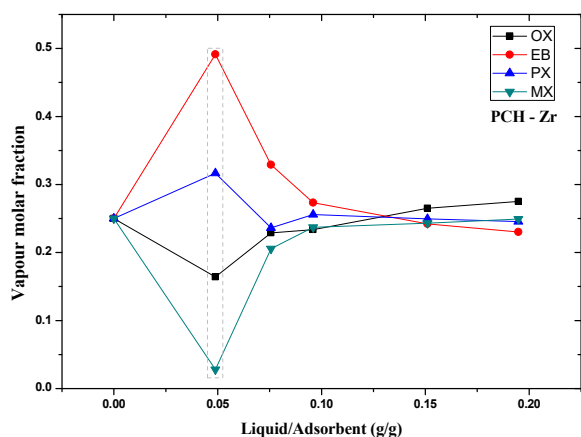


Fig. 2. Quaternary experimental run: p-xylene (PX), m-xylene (MX), o-xylene (OX) and ethylbenzene (EB) equimolar mixture on PCH-Zr at 40 °C.

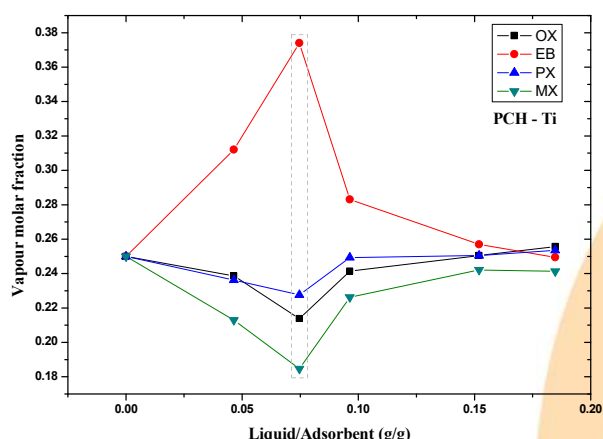


Fig. 3. Quaternary experimental run: p-xylene (PX), m-xylene (MX), o-xylene (OX) and ethylbenzene (EB) equimolar mixture on PCH-Ti at 40 °C.

The PCH exhibited a selectivity of *m*-xylene in relation to others compounds. The selectivity to *m*-

xylene was higher with respect to ethylbenzene in all three adsorbents, since the molar fraction of the vapor phase of the latter is the largest of all the isomers, indicating relatively low adsorption of ethyl benzene in all adsorbents samples.

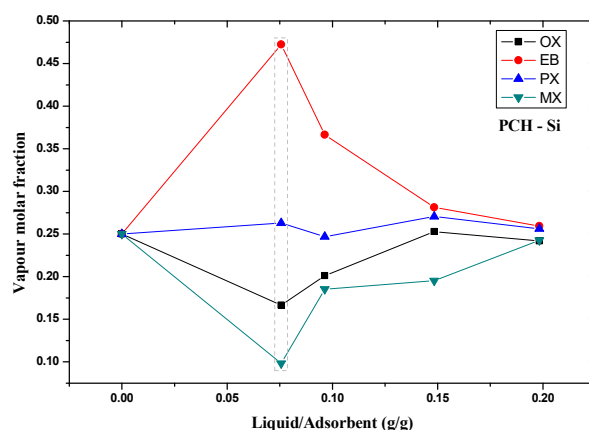


Fig. 4. Quaternary experimental run: p-xylene (PX), m-xylene (MX), o-xylene (OX) and ethylbenzene (EB) equimolar mixture on PCH-Si at 40 °C.

The adsorption selectivity values to MX/EB, MX/PX and MX/OX for PCH-Zr, PCH-Ti and PCH-Si at saturation point of each adsorbent are shown in the Figure 5.

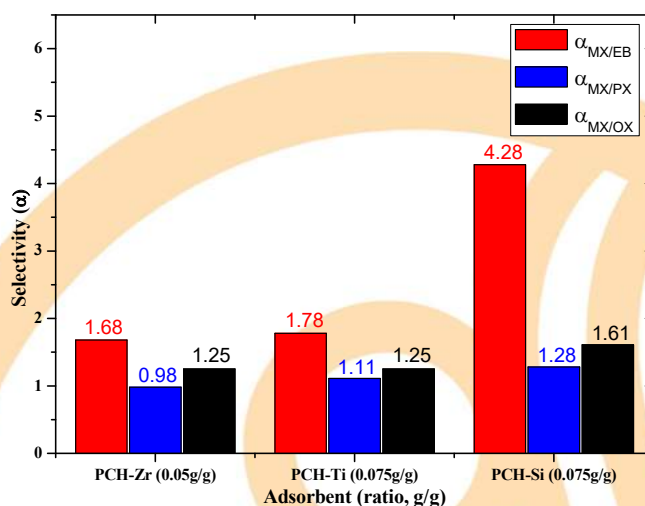


Fig. 5. Values of $\alpha_{MX/EB}$, $\alpha_{MX/PX}$ and $\alpha_{MX/OX}$ for PCH-Zr, PCH-Ti and PCH-Si at saturation point.

For PCH-Si, in the adsorbate/adsorbent mass ratio of 0.075, the $\alpha_{MX/EB}$ value was 4.28, indicating a strong affinity of such clay to the *m*-xylene. The adsorbents PCH-Zr and PCH-Ti presented the same value of $\alpha_{MX/OX}$ (~1.7), but in



different mass ratios adsorbate/adsorbent. All three adsorbents show an increasing trend in adsorption that follows the order: $\alpha_{MX/PX} < \alpha_{MX/OX} < \alpha_{MX/EB}$.

4. Conclusion

The headspace technique provides a simple and useful method for measuring multi-component equilibrium data at full loading in liquid phase. This approach can be very useful for screening potential adsorbents as well as for investigating the variation in selectivity in relation to composition.

The porous clay heterostructures are presented as possible adsorbents for the separation of xylene isomers in an equimolar mixture. The selectivity of *m*-xylene/ethylbenzene was observed for all samples. The PCH with Si presented the highest selectivity value (> 4.0), presenting as the most effective material for selective separation of *m*-xylene/ethylbenzene.

Acknowledgements

The authors wish to thank financial support provided by CNPq (Conselho Nacional de Pesquisa e Desenvolvimento Científico) and FUNCAP (Fundação Cearense de Apoio ao Desenvolvimento Científico e Tecnológico).

References

- [1]Torres AEB, Neves SB, Abreu JCN, Cavalcante Jr. CL, Ruthven, DM. Single-and multi-component liquid phase adsorption measurements by headspace chromatography. *Braz J Chem Eng*, 2001; 18: 121-125.
- [2]Luna FMT, Coelho JA, Otoni JCF, Guimarães AP, Azevedo DCS, Cavalcante Jr. CL. Studies of C8 aromatics adsorption in BaY and mordenite molecular sieves using the headspace technique, *Adsorption*, 2010; 16:525-530.
- [3]Pinto ML, Pires J. Porous and hybrid clay based materials for separation of hydrocarbons. *Micropor Mesopor Mat*, 2012; 151:403-410.
- [4]Ferreira P, Nunes CD, Pires J, Carvalho AP, Brandão P, Rocha J. Hydrophobic porous benzene-silica clay heterostructures and its application in the adsorption of volatile organic compounds. *Mater Sci Forum*, 2016; 514: 470-474.
- [5]Pires J. Porous materials from clays by the gallery template approach: synthesis, characterization and adsorption properties. *Micropor Mesopor Mat*, 2004; 73:175-180.
- [6]Qu F, Zhu L, Yang K. Adsorption behaviors of volatile organic compounds (VOCs) on porous clay heterostructures (PCH). *J Hazard Mater*, 2009; 170: 7-12.
- [7]Poling BE, Prausnitz JM, O'connell JP. *The Properties of Gases and Liquids*. 5^a ed. New York: McGraw-Hill, 2001.

NOVEL APPLICATION FOR PALYGORSKITE CLAY MINERAL: A KINETIC AND THERMODYNAMIC ASSESSMENT OF DIESEL FUEL DESULFURIZATION

Anne B. F. Câmara^a, Rafael V. Sales^a, Enrique Rodríguez-Castellón^b Luciene S. de Carvalho^{a*}

^a Energetic Technologies Laboratory (LTEN), Institute of Chemistry, Federal University of Rio Grande do Norte, Energetic Technologies Research Group, 59078 900, Natal, Brazil.

^b Dpto. de Química Inorgánica, Cristalografía y Mineralogía, Facultad de Ciencias, Universidad de Málaga, 29071, Málaga, Spain

*E mail: luciene_car@hotmail.com

Abstract

Palygorskite (Pal) is a low-cost clay mineral material and was investigated in this study as a novel material for adsorptive desulfurization of petroleum refining fractions from the Clara Camarão Potiguar Refinery (RPCC) in Brazil. This clay mineral was characterized by X ray fluorescence (XRF), X ray photoelectron spectroscopy (XPS), X ray diffraction (XRD), and N₂ adsorption/desorption isotherm analyses. Palygorskite textural properties (specific surface area 156 m².g⁻¹, total pore volume 0.36 cm³.g⁻¹) and specific surface chemistry activity with several metals were crucial to efficient adsorption, proposing that an interaction between adsorbate/adsorbent involves π -complexation mainly with Fe species. This material was used in raw and thermally activated forms to evaluate the adsorption capacity. The pseudo-second order kinetic model for the studied adsorbent showed a high fitting ($R^2 > 0.99$), suggesting a chemisorption process as the determining step. Maximum adsorption capacity calculated from the Langmuir isotherm ($R^2 > 0.97$) was 6.25 mg.g⁻¹ for raw Pal at 318 K. The adsorption thermodynamic assessment of S compounds indicated an endothermic process, and there was consequently an increase in spontaneity at higher temperatures. The adsorbent raw-Pal displayed good potential in the adsorption of sulfur compounds in real diesel fuel. Palygorskite stands out for being an abundant clay mineral in nature, environmentally safe, and with high possibility of its applications in adsorption and catalysis processes.

Keywords: Palygorskite clay mineral; Adsorptive desulfurization; Thermodynamics; Kinetic; Equilibrium.

1. Introduction

Palygorskite (Pal) is a hydrated magnesium aluminum silicate present in nature with a fibrous morphology [1], which presents a unique structure and specific surface properties such as low surface charge, high porosity, ion exchange capability, active surface groups and high specific surface area (SSA), conferring important adsorptive properties to pal [2].

Sulfur compounds are the most undesirable and notorious contaminants present in fossil fuels, mainly in petroleum, and a large portion of these compounds are aggregated to diesel oil during the refining process [3]. The conventional method used by oil refineries for sulfur removal is hydrodesulfurization (HDS), which reduces S-compounds to hydrogen sulfide (H₂S) using hydrogen gas and hard conditions (> 300 °C; >4 MPa) of pressure and temperature in the presence of Ni/Mo or Co/Mo catalyst, resulting in an increase in the process operation costs [4]. However, this method has shown some limitations regarding the treatment of alkylated aromatic sulfur

compounds such as benzothiophene and their derivatives [5].

This work proposes an investigation of sulfur compounds removal using a cheap raw material, which enables reducing industrial costs when associated with the HDS process. Among the use of this clay mineral for several applications, its use in sulfur adsorption in diesel fuel is a novel approach and has not been reported earlier. This work was performed with kinetic, thermodynamic and equilibrium adsorption studies for studying the applicability of readily available clay mineral to remove this contaminant which causes industrial and environmental damage. Furthermore, the study of palygorskite with a thermal treatment demonstrates that excellent adsorptive performance could be achieved, even without any purification or physical/chemical treatment.

2. Experimental

2.1 Palygorskite clay mineral preparation

Palygorskite samples were obtained from deposits located in Guadalupe in the state of Piauí, Brazil, and provided by the Mineral Technology

Center (CETEM/RJ). The clay mineral was submitted to wet granulometric classification using 45 μm and 20 μm sieves prior to use. A fraction with less than 20 μm was submitted to magnetic separation in BOXMAG RAPID equipment with a high intensity field of approximately 15 kGauss. The non-magnetic and the magnetic fraction were filtered at 6 bar and dried in an oven (Quimis, Q316m) at 60 °C. Fractions with less than 20 μm were disaggregated in a Retsch RS 200 brand mill for 2 minutes and 800 rpm. The sample was then subjected to a heat treatment for its activation in a muffle furnace (MAGNUS, 2006) at temperatures of 400 °C, 500 °C and 600 °C for 24 hours, and a heating rate of 10 °C.min⁻¹ in ambient atmosphere. After activation, the samples were named Raw-Pal, Pal-400, Pal-500 and Pal-600.

2.2 Adsorbent characterization

The X-ray diffraction (XRD) patterns were obtained with a Bruker D2 Phaser with CuK α radiation ($\lambda=1.5406 \text{ \AA}$), 30 kV filament, 10 mA current, Ni filter and a LYNXEYE detector. Textural parameters were determined by N₂ adsorption-desorption isotherms at 77 K using a Micrometrics ASAP 2420 apparatus. The pore size distribution was calculated by the Barrett-Joyner-Halenda (BJH) method.

X-ray photoelectron spectra (XPS) was performed by a Physical Electronics PHI 5700 spectrometer with non-monochromatic Al K α radiation (95.2 W, 15 kV, and 1486.6 eV) and a multi-channel detector. Binding energy (BE) was calibrated to the C1s line (284.8 eV). Multipack software version 9.6.0.15 was used for data analysis.

2.3 Adsorption tests

The adsorption experiments were performed by the finite bath method at ambient temperature and pressure. 0.3 g of adsorbent and 8.0 mL of diluted real diesel prepared by a solution of the high (1234.9 ppm) and low-sulfur (5.1 ppm) samples donated by Clara Camarão Potiguar Refinery (RPCC), were placed in erlenmeyer flasks under constant stirring (100 rpm) in a stirring table (Solab, SL 180/DT) for 3 h for evaluating the sulfur adsorption equilibrium over Pal surface.

Sulfur adsorption capacity per gram of adsorbent at equilibrium (q_e) was calculated using the following equation:

$$q_e = \frac{V(C_i - C_e)}{M_{\text{adsorbent}}} \quad (1)$$

where V is the diesel solution volume (L), $M_{\text{adsorbent}}$ is the adsorbent mass (g) and C_i and C_e are the initial sulfur content in the fuel (mg/L) and at equilibrium, respectively.

The effect of temperature in S-compound adsorption was studied by varying temperature from 298 to 308 and 318 K in the equilibrium studies. The changes in standard free energy (ΔG°), standard enthalpy (ΔH°) and standard entropy (ΔS°) were determined by the following equations [5]:

$$K_C = \frac{C_A}{C_e} \quad (2)$$

$$\Delta G^\circ = -RT \ln K_C \quad (3)$$

$$\ln K_C = \frac{\Delta S^\circ}{R} - \frac{\Delta H^\circ}{RT} \quad (4)$$

Where K_C is the equilibrium constant, C_A is the solid phase concentration at equilibrium (mg.L⁻¹) and C_e is the equilibrium concentration in solution (mg.L⁻¹). The ΔH° and ΔS° values were obtained from the slope and intercept of linear Van't Hoff plot, respectively.

A solution of model diesel with 500 ppm of dibenzothiophene (DBT) diluted in decane was used for kinetic tests. The supernatant fluid was collected at different time intervals.

The solids were separated by centrifugation and the residual sulfur contents in the liquid phase were collected for quantification by a total sulfur analyzer via ultraviolet fluorescence (UVF) spectrometry (Antek Multitek, PAC, L.P) in triplicate, following ASTM D5453 methodology.

3. Results and Discussion

3.1 Characterizations

The X-ray fluorescence (XRF) results allows to infer the chemical composition of the major oxides present in the raw-Pal (Table 1). These results indicated that the samples are mainly constituted by MgO, Al₂O₃, Fe₂O₃ and SiO₂.

Table 1. XRF from raw-Pal

Component	Weight (%)
MgO	5.4
Al ₂ O ₃	13.5
SiO ₂	53.5
K ₂ O	1.9
CaO	0.23
TiO ₂	0.55
MnO	0.13
Fe ₂ O ₃	7.0
*LOI	17.8

*LOI lost on ignition

The results from XPS, XRD and N₂ adsorption-desorption isotherms are depicted in Fig. 1. X-ray photoelectron spectroscopy (XPS) was a very important technique to provide information about the surface chemical composition and the species identifications of the adsorbents. The binding energies measured by XPS are depicted in Fig. 1a. The XPS of raw-Pal indicated the presence of O, Si, Mg, Fe and Al elements and their valence state.

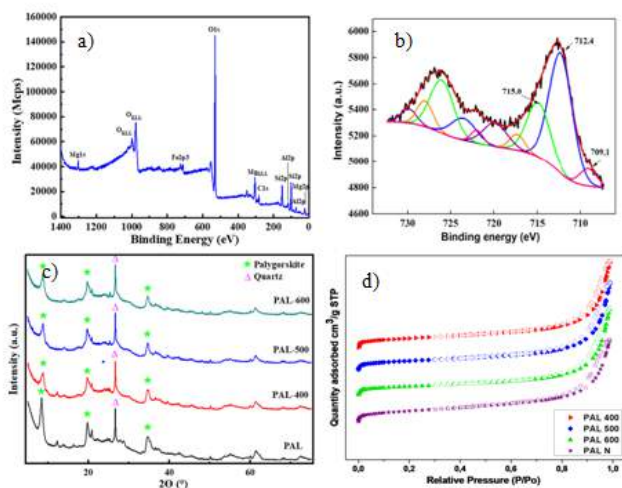


Fig. 1. (a) Raw-PAL XPS spectrum; (b) Fe species deconvolution; (c) XRD diffractogram and (d) N₂ adsorption-desorption isotherms from the studied clay minerals.

Iron (Fe) species stands out from other metals in this clay mineral for desulfurization since the Fe³⁺ ions (1s²2s²2p⁶3s²3p⁶3d⁵4s⁰) and the thiophenic aromatic rings could generate a strong interaction denominated π -complexation. The Fe XPS deconvolution (Fig. 1b) shows the presence of Fe(0), Fe(III) and FeOOH in 709.1 eV, 712.4 eV

and 715 eV, respectively, in the 2p^{3/2} peak, and its satellite at 2p^{1/2}. The FeOOH peak is referent to the binding between Fe²⁺ ions and the OH⁻ present in silanol groups in the adsorbent structure.

The X-ray diffraction patterns from natural and thermally activated palygorskite are depicted in Fig. 1 (c). The intense Pal reflection at 8.42° 2 θ corresponds to the crystalline (110) plane, with basal value of 10.50 Å, as obtained by the Braggs equation. The reflections in the planes (200) and (400) were also identified at angles 13.84° (3.19 Å) and 27.92° (6.40 Å) 2 θ , respectively. The presence of quartz was implied by the reflection at 26.61° 2 θ . It is possible to notice a decrease in the intensity of the (110) plane with the increased temperature in the thermally activated samples. This can be related with the dehydration of palygorskite structure due to the partial losses of coordinating and adsorbed water molecules in the channels of the material. The increase in temperature causes a decrease in the reflection (110) that tends to be displaced and may disappear [2].

The N₂ adsorption-desorption isotherms of the sorbents corresponded to Type-II according to IUPAC classification with a H3-type hysteresis loop, representing unrestricted monolayer-multilayer adsorption [6]. Table 2 summarized the textural parameters from the adsorbents.

Table 2. Textural properties of the adsorbents.

Sample	S _{BET} (m ² /g) ^a	V _p (cm ³ /g) ^b	Maximum pore diameter (Å)
MCM-41	722	0.79	23.48
Ag/MCM-41	656	0.74	24.82

As can be seen in Table 2, the specific surface areas (S_{BET}) of Pal greatly decreased after the thermal activation because some pores might have been blocked by the dehydration of the palygorskite structure [8].

3.2 Adsorption kinetics

Five kinetic models were selected in this study to test the experimental data in order to evaluate the controlling mechanism of the sorption process: pseudo-first order, pseudo-second order, Elovich, intraparticle diffusion and Boyd film-diffusion models. Table 3 summarized the estimated

parameters and the determination coefficients (R^2) of the models.

Table 3. Parameters for the fitting to pseudo-first order, pseudo-second order, intraparticle diffusion and Elovich models of model diesel adsorption on raw-Pal.

Parameters	raw-Pal
q _{max} exp	1.94
Pseudo-first order model:	
q _e (mg g ⁻¹)	0.56
k ₁	0.16
R ²	0.87
Pseudo-second order model:	
q _e (mg g ⁻¹)	1.95
k ₂	0.12
H	0.02
R ²	0.99
Intraparticle diffusion	
K _{id}	0.04
C	1.43
C/q _{max}	0.7
R ²	0.95
Boyd	
k _{id}	0.03
R ²	0.98
Elovich	
α	1.13x106
β	0.11
R ²	0.86

The results for recalcitrant sulfur adsorption over Pal surface were better fit to the pseudo-second order, with higher determination coefficient ($R^2 > 0.99$) and similar calculated (1.95 mg g⁻¹) and experimental (1.94 mg g⁻¹) q_e values. The good fit to pseudo-second order model suggest that the rate determining step is chemisorption, involving valence forces through sharing or exchange of electrons between adsorbent and adsorbate [9].

The data of adsorbed DBT in model diesel on Pal were also significantly fitted to intraparticle diffusion model, with R^2 equal to 0.95. The positive C value suggests rapid adsorption and suggest that the mechanism should occur in two stages, where the first one represents external surface adsorption and the second one corresponds to a final equilibrium step, with the solutes moving from larger pores to micropores [9,10].

Boyd's film diffusion was applied in order to obtain more information about the diffusion parameters. The fitting to this model suggests that the pore-diffusion is not the mechanism rate controlling step and indicated the existence of a resistance step to mass transfer in the external film [11].

3.3 Adsorption equilibrium

The S compound adsorptions are more fitted to Langmuir ($R^2 = 0.972$), which suggests a monolayer adsorption onto the adsorbent's surface with a finite number of adsorption sites, assuming there is no transference of the adsorbate onto the surface plane and that uniform energies exist on the surface. The $0 < R_L < 1$ obtained for these compounds indicates a favorable adsorption process [12]. The Langmuir monolayer adsorption capacity (Q_m) increased from 1.63 to 6.25 mg.g⁻¹ as temperature increased from 198 K to 318 K, indicating that the adsorption is endothermic.

The Freundlich isotherm models indicate a favorable adsorption process in heterogeneous systems or multilayer adsorption. This model presents a fit to Pal, with $R^2 > 0.915$. The values in the range of $n < 1$ highlight that the adsorption of S-compounds was a chemical process and indicated the favorability of this adsorption [12].

3.4 Adsorption thermodynamics

Raw Pal thermodynamic assessment in the temperature range of 298 to 318 K are shown in Table 4. The values of ΔH° and ΔS° can be calculated from the slope and intercept, respectively, from the Van't Hoff plot (Fig. 2).

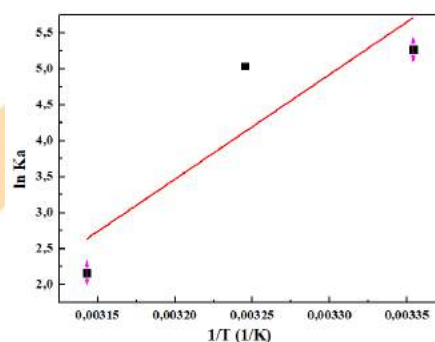


Fig. 2. Linear Van't Hoff plot of $\ln K_c$ versus $1/T$.

Table 4. Thermodynamic parameters for raw-Pal.

Adsorbent	T (K)	ΔG° (kJ mol ⁻¹)	ΔH° (kJ mol ⁻¹)	ΔS° (J K ⁻¹ mol ⁻¹)
raw-Pal	298	-5.36	-43.14	14.56
	308	-12.90		
	318	-13.93		

The negative value for ΔH° indicates an exothermic process. The positive value for ΔS° indicated that a random increase in the solid/solution interface system occurs during the adsorption process [13,14]. The negative ΔG° values confirm the spontaneity of the adsorption process and the decreasing in these values shows adsorption being favored at higher temperature [6].

3.5 Proposed adsorption mechanism

S-compound adsorption onto the Pal surface was evaluated to determine the adsorption mechanism between the adsorbent-adsorbate interactions. Fig. 3 shows several coordination configurations that could be formed between S compounds and Pal structure.

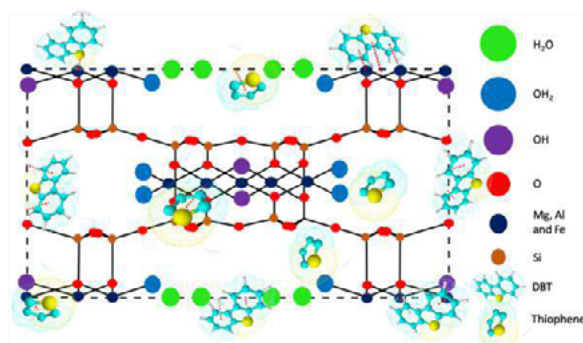


Fig. 3. Proposed mechanism for S-compounds adsorption onto Pal surface.

Active sites such as Lewis acids, electronic defect centers and van der Waals interactions can participate in the adsorptive process [9]. In addition, the presence of Fe species in the clay mineral structure could form a bond with the aromatic rings of DBT. This result indicated that the interaction between adsorbate/adsorbent involves π -complexation.

Furthermore, equilibrium studies have shown that S-compounds followed the Langmuir isotherm, indicating a monolayer adsorption onto the adsorbent's surface with a finite number of adsorption sites. Adsorption kinetics followed a pseudo second order model involving the formation of valence forces through sharing or exchanging electrons between adsorbent and adsorbate. Thermodynamic parameters showed an influence of physisorption as the temperature increased. Based on this, the proposed adsorption mechanism in this study suggest the occurrence of

combination processes (chemical and physical process), with the domination of chemisorption involving the formation of strong chemical bonds based on π -complexation of S-compounds onto the Pal surface

4. Conclusions

Raw palygorskite appears in this work as a promising adsorbent in diesel fuel desulfurization due to its specific characteristics such as the chemical composition and textural properties, which was proven by different characterizations. Kinetic and equilibrium models were used to evaluate sulphur compounds' adsorption with palygorskite, which were able to evaluate these types of data. The adsorption data was fitted to the pseudo-second order kinetic and the Langmuir isotherm model, describing that the adsorption of S-compounds in diesel fuel onto the adsorbent layer is determined by a chemisorption process. Pal is a low-cost material that exhibited some advantages, since it is environmentally friendly and abundant in nature. Furthermore, palygorskite presented better adsorptive capacity of sulfur compounds than other clays studied in the literature, and could be used as a complementary technique to the one used in industry (HDS process), thus permitting a reduction in the operational costs and decreasing polluting emissions into the environment.

Acknowledgements

The authors acknowledge the support provided by the Post-Graduate Chemistry Program PPGQ/UFRN, the Energetic Technologies Research Group, the Analytical Central (IQ/UFRN) and the Coordination for the Improvement of Higher Education Personnel (CAPES - Brazil) - Finance Code 001.

References

- [1] Rusmin R, Sarkar B, Biswas B, Churchman J, Liu Y, Naidu R. Structural, electrokinetic and surface properties of activated palygorskite for environmental application. *Appl Clay Sci* 2016;134:95-102.
- [2] Xavier KCM, Santos MSF, Osajima JA, Luz AB, Fonseca MG, Silva Filho EC. Thermally activated palygorskite as agents to clarify soybean oil. *Appl Clay Sci* 2016;119:338-47.



- [3] Choi AES, Roces S, Dugos N, Arcega A, Wei Wan M. Adsorptive removal of dibenzothiophene sulfone from fuel oil using Clay material adsorbents. *J Clean Prod* 2017;161:267-76.
- [4] Bordoloi NK, Rai SK, Chaudhuri MK, Mukherjee AK. Deep-desulfurization of dibenzothiophene and its derivatives present in diesel oil by a newly isolated bacterium *Achrompacter* sp. to reduce the environmental pollution from fossil fuel combustion. *Fuel Process Technol* 2014;119:236-44.
- [5] Duarte FA, Mello PA, Bizzi CA, Nunes MAG, Moreira EM, Alencar MS, Motta HN, Dressler VL, Flores EMM. Sulfur removal from hydrotreated petroleum fractions using ultrasound-assisted oxidative desulfurization process. *Fuel* 2011;90:2158-64.
- [6] Guan Y, Wang S, Wang X, Sun C, Wang Y, Hu L. Preparation of mesoporous Al-MCM-41 from natural palygorskite and its adsorption performance for hazardous aniline dye-basic fuchsin. *Microporous Mesoporous Mater* 2018;266:266-74.
- [7] Wang W, Tian G, Zhang Z, Wang A. A simple hydrothermal approach to modify palygorskite for high-efficient adsorption of Methylene blue and Cu(II) ions. *Chem Eng J* 2-15:265:228-38.
- [8] Zhang X, Cheng L, Wu X, Tang Y, Wu Y. Activated carbon coated palygorskite as adsorbent by activation and its adsorption for methylene blue. *J Environ Sci* 2015;33:97-105.
- [9] Habibi A, Belaroui LS, Bengueddach A, Galindo AL, Díaz CIS, Peña A. Adsorption of metronidazole and spiramycin by an Algerian palygorskite. Effect of modification with tin. *Microporous Mesoporous Mater* 2018;268:293-302.
- [10] Wu FC, Tseng RL, Juang RS. Initial behavior of intraparticle diffusion model used in the description of adsorption kinetics. *Chem Eng J* 2009;153:1-8.
- [11] Oliveira MF, da Silva MGC, Vieira MGA. Equilibrium and kinetic studies of caffeine adsorption from aqueous solutions on thermally modified Verde-lodo bentonite. *Appl Clay Scien* 2019;168:366-73.
- [12] Saleh TA, Sulaiman KO, AL-Hammadi SA, Dafalla H, Danmaliki GI. Adsorptive desulfurization of thiophene, benzothiophene and dibenzothiophene over activated carbon manganese oxide nanocomposite: with column system evaluation. *J Clean Prod* 2017;154:401-12.
- [13] Ben-Ali S, Jaouali I, Souissi-Najar S, Ouederni A. Characterization and adsorption capacity of raw pomegranate peel biosorbent for cooper removal. *J Clean Prod* 2017;142:3809-21.
- [14] Khan Rao RA, Khatoon A. Aluminate treated *Casuarina equisetifolia* leaves as potential adsorbent for sequestering Cu(II), Pb(II) and Ni(II) from aqueous solution. *J Clean Prod* 2017;165:1280-95.

Statistical analysis of parameters and adsorption isotherms models

Felipe Rocha Pinto^a, Carla Manske Camargo^a, Amaro Gomes Barreto^{a*}

^aPrograma em Engenharia de Processos Químicos e Bioquímicos, Escola de Química, Universidade Federal do Rio de Janeiro

Abstract

The present work seeks to contribute to the discussion of parameter estimation and statistical analysis in the field of adsorption. The Langmuir and Toth isotherm models are compared for a set of carbon dioxide adsorption data on 13X zeolite at different temperatures: 30, 50, 100 and 150°C. Parameter estimation was performed by associating the Particle Swarm Optimization (PSO) with the Gauss Newton method. Statistical analyzes of the parameters were performed by regions of confidence in terms of elliptical approximation and likelihood region. The results showed the importance of knowing precisely the experimental errors and how differences in experimental fluctuation (SD) affects the minimum value of the objective function. In this context, Langmuir's model was rejected by the chi square test for a SD of 5%, but accepted for 10%. On the other hand, Toth's model was accepted with SD of 5% and considered overestimated for 10%. It was also observed that the elliptical and likelihood approaches lead to similar results for Toth's model, but not much for Langmuir's model. Finally, correlation matrices show that Toth's equation returned less correlated parameters (0.92) than the Langmuir's (0.98), despite having an extra parameter. The importance of obtaining poorly correlated parameters and non-over-parameterized models is in the use of these models in operational conditions optimization procedures of separation units taking into account the parametric uncertainties.

Keywords: adsorption equilibrium, parameter estimation, confidence regions, experimental errors.

1. Introduction

An important information for describing the adsorption phenomenon is the equilibrium adsorption isotherms, that directly relate the amount adsorbed on the solid phase with the partial pressure or concentration of the adsorbing component. Over the years, numerous models were presented in the literature, some of them having a thermodynamic basis, while others are semi-empirical equations [3].

In general, adsorption at low concentrations of adsorbate returns isotherms very close to linearity and the observed relationship can be expressed by Henry's Law, in which the amount adsorbed on the solid phase can be calculated with just one parameter H , an equilibrium constant also known as Henry's constant. Henry's Law (Equation 1) is no longer applicable with increasing concentration, since there will be a saturation in the adsorbed phase.

$$q^* = H P \quad (1)$$

Therefore, non-linear models are necessary for a better description of other adsorption processes. The model of Langmuir is certainly the most well-known theoretical model, developed on the premise

that each active site can only adsorb one molecule of adsorbate. The classical form of monocomponent Langmuir model is presented as Equation 2. In this model, q^* represents the concentration of the adsorbate in the solid phase in equilibrium with the fluid phase at a pressure P , k is an equilibrium constant, and q_{sat} is the amount adsorbed on saturation.

$$q^* = q_{sat} \frac{k P}{1+k P} \quad (2)$$

The model developed by Toth (Equation 3) brings a modification in relation to Langmuir by the addition of a parameter n , characterized as the measure of the heterogeneity of the solid [1]. Such parameter n can vary from 0 to 1, where in the case equal to 1, the Toth isotherm becomes identical to Langmuir.

$$q^* = q_{sat} \frac{k P}{(1+(k P)^n)^{1/n}} \quad (3)$$

In addition, the equilibrium constant k can be modified in order to take into account the effect of the temperature. In this sense, Eq.4 presents Van't Hoff's law:

$$\frac{d \ln k}{dT} = \frac{\Delta H_{ads}}{RT} \quad (4)$$

Considering that ΔH_{ads} does not vary with temperature, the equilibrium constant k can be written as follows:

$$k = k_0 \exp\left(\frac{-\Delta H_{ads}}{RT}\right) \quad (5)$$

With this definition, for modeling purposes, the Langmuir model now has 3 parameters (q_{sat} , k_0 and ΔH_{ads}) and the Toth model has 4 parameters ($q_{sat,n}$, k_0 and ΔH_{ads}).

These mathematical models are capable of describing the equilibrium adsorption behavior of different systems, having the amount adsorbed on the solid phase as a dependent variable and the concentration or partial pressure of the fluid phase as the independent variable [4].

A very common procedure is to estimate the unknown parameters of the adsorption isotherm models using the equilibrium experimental data for a specific system. It is important to note that as important as observing the fit of the model to the experimental data is to determine the statistical quality of the parameters [4].

Based on the previous remarks, the objective of present work is to estimate and statistically analyze the unknown parameter values for Langmuir and Toth models using the equilibrium experimental data from Dantas [1]. In addition, we evaluate the influence of experimental errors in the parameters uncertainties and the model choice.

2. Methodology

The present work was carried out with carbon dioxide adsorption equilibrium data in Zeolite 13X at different temperatures: 30, 50, 100 and 150 °C. The experimental results were originally published by Dantas [1], which are obtained in the pressure range of 0 to 5 bar by *Rubotherm's* gravimetric instrument.

Parameter estimation was performed using the maximum likelihood estimation (MLE), which allows a more rigorous analysis in relation to least square method. Using the MLE method we suppose that some assumptions are true: the distributions of experimental errors follow normal distribution and the model is perfect and all the

experiment are valid [2]. In this sense, Equation 6 shows the objective function for this estimation problem:

$$F_{obj} = \sum_{i=1}^{NE} \sum_{j=1}^{NY} \frac{(y_{ij}^e - y_{ij}^m)^2}{\sigma_{ij}^2} \quad (6)$$

In which: NE and NY are the number of experiments and experimental variables, y^e is the variable experimental value, y^m is the variable value calculated by the model and σ_{ij}^2 is the variance for each data.

The estimation was performed by using the Particle Swarm Optimization (PSO), a heuristic algorithm implemented in Python through PySwarms' package [3]. The PSO routine generates a large number of parameter sets which are used in the build of the parameters confidence region. The PSO results are used as an initial estimative to a subsequent refining of estimated parameters using a Gauss-Newton method. This deterministic method uses an approximation for the Hessian matrix present in the Newton method and has a great advantage in reducing computational cost [2].

After the estimation procedure of parameters for Langmuir and Toth models, a statistical interpretation of the results is required. Since the maximum likelihood hypothesis has been used, the statistical evaluation of the model can be performed using chi-square test.

Analysis of parameters are necessary in order to evaluate the accuracy of the estimates. This kind of analysis is usually obtained through confidence regions by an elliptical approximation or likelihood method. Both methods arise from Taylor series approximation of the objective function around the optimum parameters [4].

Equation 7 expresses the elliptical confidence region, where: α is the column vector of parameters; $\hat{\alpha}$ is the column vector with optimal parameters values; \mathbf{V}_{α}^{-1} is the inverse of covariance matrix and \mathbf{F} is the value of Fisher statistic for a γ confidence interval.

$$(\alpha - \hat{\alpha})^T \mathbf{V}_{\alpha}^{-1} (\alpha - \hat{\alpha}) \leq F_{obj}(\hat{\alpha}) * \left(\frac{NP}{NE-NP}\right) * F_{NP,NE-NP}^{\gamma} \quad (7)$$

However, due to the non-linearity of the adsorption models, the regions of confidence may deviate from the elliptical shape [2]. Thus, a statistical evaluation is employed by restricting the

maximum value of objective function accepted by Fisher's test at a certain degree of confidence. In this scenario, the several values of objective function obtained by PSO method were tested using the restriction imposed by Eq. 8. In general, a set of parameters are accepted if the resulting objective function is less than the value found on the right side of the equation.

$$Fobj(\alpha) \leq Fobj(\hat{\alpha}) * \left(1 - \frac{NP}{NEXP-NP} * F_{NP,N-NP}^Y\right) \quad (8)$$

All analyzes were performed with 95% confidence interval.

3. Results and Discussion

3.1. Estimation of parameters

As mentioned, the parameter estimation was performed using a hybrid PSO + Gauss-Newton optimization method. Table 2 shows the estimation results for each model.

Figure 1 shows the curves generated by the Langmuir and Toth models, as well as the experimental equilibrium data for carbon dioxide in 13X zeolite at a temperature of 30 ° C. As shown, both models return good estimates in the region of low partial pressures. However, after the beginning of CO₂ saturation, the Toth model presents a better fit in the higher-pressure range.

Table 2. Parameters estimation results

	<i>Langmuir</i>	<i>Toth</i>
<i>qsat</i>	4.02	4.58
<i>k₀</i>	3.35*10 ⁻⁵	4.71*10 ⁻⁵
ΔH_{ads}	-31280.47	-32384.22
<i>n</i>	-	0.60

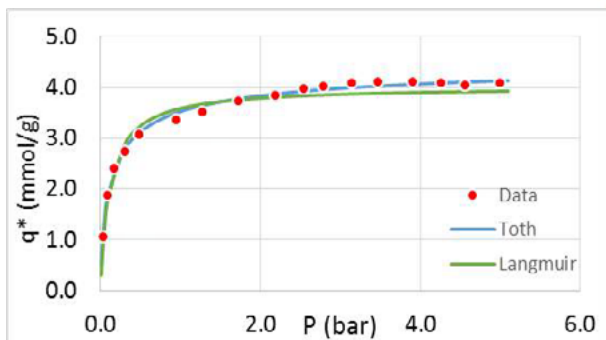


Figure 1: Calculated and experimental adsorption isotherm results. Experimental data are indicated by points.

3.2. Statistical analysis of models

In the statistical analysis of this work, two standard deviation values for experimental fluctuation of variable “q*” were considered in the data set taken from Dantas [1]. This strategy was used to evaluate the sensitivity of the parameter estimation and the model discrimination procedures.

First, an analysis was performed with the standard deviation (SD) equal to 5% in the variable measured experimentally (*q**) and then, the same procedure was repeated for a standard deviation equal to 10%.

According to the previously mentioned hypotheses of the maximum likelihood estimation, the experimental errors must present a normal distribution. Thus, the model can represent the experimental data satisfactorily if the result of the calculated objective function is between the maximum and minimum values of the chi-square statistic with a degree of freedom (*v*) equal to $v = NE - NP$ [2], where *NP* is the number of parameters. The results of the statistical test for both models are presented in Table 3.

Table 3. Chi-square test for SD5%

	<i>v</i>	χ_{min}	χ_{max}	<i>Fobj</i>
<i>Langmuir</i>	67	46.26	91.52	271.51
<i>Toth</i>	66	45.43	90.35	66.21

It is notable that Toth's model is in the range between the test values, which indicates the model is acceptable along with the estimated parameters to a standard deviation of 5% in the experimental data. On the other hand, the Langmuir model presented an objective function value above the upper limit of the chi-square statistic. This result indicates that the model is not able to explain the experimental errors, thus the prediction errors can be greater than the experimental errors [2].

In order to analyze the importance of experimental errors in statistical tests, the procedure was performed with a standard deviation equal to 10% of the measured variable and the results are shown in Table 4.

Table 4. Chi-square test for SD=10%

	<i>v</i>	χ_{min}	χ_{max}	<i>Fobj</i>
<i>Langmuir</i>	67	46.26	91.52	67.88
<i>Toth</i>	66	45.43	90.35	16.52

One can observe that an increase in the standard deviation of the experimental error of q^* from 5% to 10% resulted in a decrease in the objective function for both models.

Consequently, the Langmuir model falls within the acceptance range of the chi-square test, while the Toth model has an objective function lower than the minimum value of the statistic test. This result indicates a possibility of over-parametrization in the model. Therefore, knowledge of the experimental data with replicates enough to obtain its confidence interval is fundamental in choosing the most statistically reliable model.

3.3. Statistical analysis of parameters

As in the previous item, analyzes were performed for standard deviation equal to 5% and 10% of the measured variable. For this procedure, it is extremely important to calculate the covariance matrix of the parameters and the correlation matrix of the parameters. The first is part of elliptical approximation presented in Equation 7, while the second measure the true need for the parameters present in each model and how they affect each other.

Table 5 shows the parameter correlation matrix obtained for the Toth model with a standard deviation of 5%, where the highest correlations are for the parameters k_0 and ΔH_{ads} (0.92), $qsat$ and n (-0.87). Usually, when the correlation has an absolute value greater than 0.9, there is an indication that the parameters in question are much related [2]. Additionally, increasing the standard deviation to 10% provides small changes (third decimal place) for the correlation matrix values.

Table 5. Parameters correlation matrix for Toth model

	$qsat$	k_0	n	ΔH_{ads}
$qsat$	1.0	0.33	-0.87	0.16
k_0	0.33	1.0	-0.26	0.92
n	-0.87	-0.26	1.0	0.04
ΔH_{ads}	0.16	0.92	0.04	1.0

Table 6 shows the parameters correlation matrix obtained for the Langmuir model with a standard deviation of 10%, where the greatest correlation is between the parameters k_0 and ΔH_{ads} (0.98). As in the previous case, reducing the standard deviation to 5% barely changes the matrix. The values

observed in both matrices are interesting since the model with fewer parameters, showed a greater correlation for the parameters k_0 and ΔH_{ads} . For this data set, these parametric correlation values show that the presence of parameter n to the Toth model is important for reducing the correlation between k_0 and ΔH_{ads} and consequently, one can find a better fit.

Table 6. Parameter correlation matrix for Langmuir model

	$qsat$	k_0	ΔH_{ads}
$qsat$	1.0	0.05	0.20
k_0	0.05	1.0	0.98
ΔH_{ads}	0.20	0.98	1.0

Obtaining confidence regions is also an important step during evaluation of the model's parameters. Thus, the present work will present the confidence regions obtained for the most related parameter pairs in both models. The classic procedure for building the elliptical confidence region is given by Eq. VII, while Eq. VIII provides the plot of the likelihood region.

The confidence region of the estimated parameters can be defined as the region in which the values of the parameters preserve the model fit statistical significance. For linear models, the confidence region is well represented by an ellipse, however the same is not valid for non-linear models [4]. Therefore, a concomitant evaluation of the confidence region based on statistical tests is important.

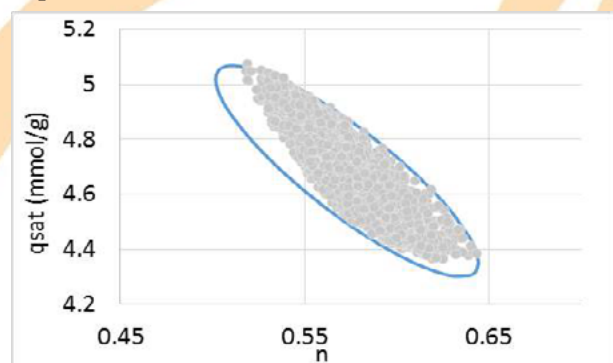


Figure 2. Confidence region of parameters $qsat$ and n for the Toth model using a standard deviation of 5%.

Figures 2 and 3 show the regions found for the Toth model when using a standard deviation of 5%, where the line represents the elliptical region and the dots form the likelihood region. The

likelihood region was obtained by filtering the results of the PSO with an acceptance limit for the objective function. One can also note the likelihood region is not restricted only to the interior of the ellipse, which can be explained by the non-linearity of the model.

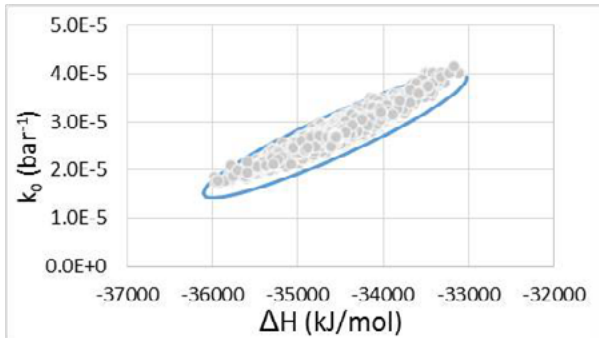


Figure 3. Confidence region of parameters k_0 and ΔH for the Toth model using a standard deviation of 5%.

Figures 4 and 5 show the regions found for the Toth model when using a standard deviation of 10%. One can observe the increase in the standard deviation barely changed the elliptical region, but caused a small enlargement in the likelihood region. As result, there is greater similarity with the ellipse for this case than 5% SD.

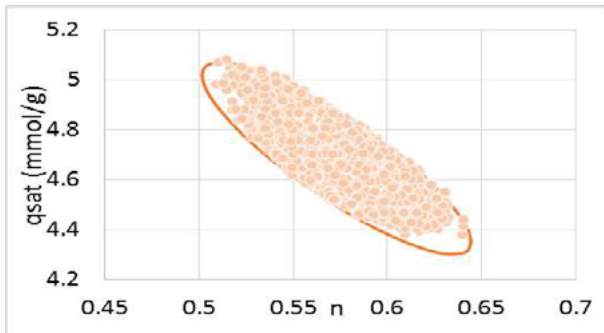


Figure 4. Confidence region of parameters q_{sat} and n for the Toth model using a standard deviation of 10%.

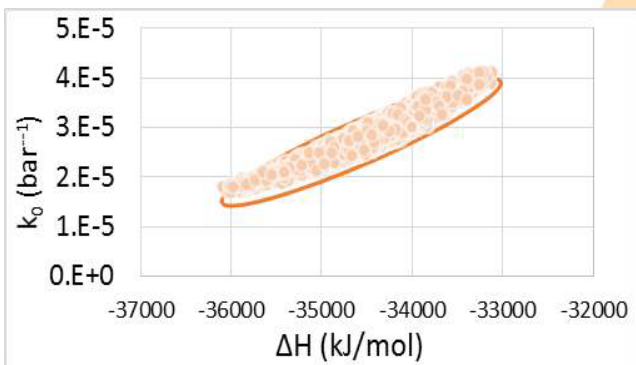


Figure 5. Confidence region of parameters k_0 and ΔH for the Toth model using a standard deviation of 10%.

Figures 6 and 7 show the regions found for the Langmuir model when using standard deviations of 5% and 10% respectively. Both graphs show that the likelihood regions have a concave shape and many pairs of parameters accepted by Fisher's statistic outside the elliptical region.

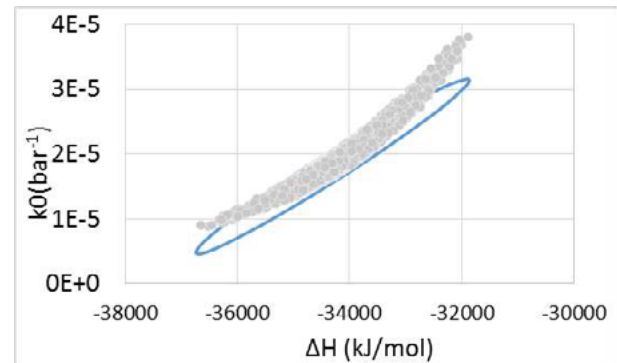


Figure 6. Confidence region of parameters q_{sat} and n for the Langmuir model using a standard deviation of 5%.

In comparison with the Toth model, one can notice that the ellipses are narrower. Such flattening is directly related to the high correlation between the parameters k_0 and ΔH_{ads} (0.98), that is, the greater the correlation, the narrower the ellipse. The regions of Figures 6 and 7 showed little difference between them, the enlargement of the likelihood region is not as observable as in the case of Toth.

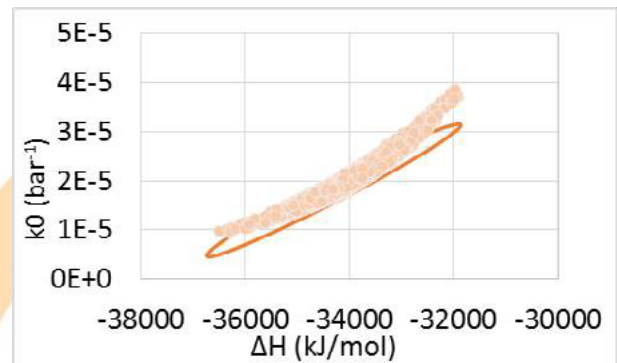


Figure 7. Confidence region of parameters q_{sat} and n for the Toth model using a standard deviation of 10%.

4. Conclusions

In the present work, the unknown parameters of Toth and Langmuir models were estimated for a study case of the literature: carbon dioxide adsorption in 13X zeolite at four different temperatures (30, 50, 100 e 150°C). In a first analysis, Toth's isotherm seems to describe better

the experimental points. However, both isotherm models were also evaluated by the statistical methodologies including the chi-square test. The main conclusion was that the choice of the model depends on the experimental error, since Toth model is accepted with smaller experimental errors (SD=5%) while the Langmuir model is preferred with higher experimental errors (SD=10%). Such results confirm the importance of knowing the errors inherent to the experiment, since variations can cause the model to be statistically accepted or rejected.

In the analysis of the parameters, the Langmuir model showed a high correlation (0.98) for the pair k_0 and ΔH_{ads} . This result is not desirable, since a strong relationship between two parameters reduces the ability to fit the experimental data. The analysis of the confidence regions for these parameters generated a narrow ellipse and a likelihood region with a concave shape for both cases of standard deviation. This concave shape shows that there are many pairs of parameters statistically accepted outside the elliptical region.

Finally, one can observe that the parameter n of the Toth's model has an important role for the best adjustment to the experimental data. This characteristic is observed by the lower value of the correlation between the pair of parameters k_0 and ΔH_{ads} . Analyzes of the confidence regions were made for two pairs of parameters: k_0 and ΔH_{ads} ; q_{sat} and n . The first pair had a concave shape similar to that observed for Langmuir, however a smaller number of points showed a distance from the elliptical region. For the second pair of parameters, the elliptical approximation had good agreement with the likelihood region.

References

- [1] Dantas, Tirzhá Lins Porto. Separação de dióxido de carbono por adsorção a partir de misturas sintéticas do tipo gás de exaustão (Tese de Doutorado). Universidade Federal de Santa Catarina, Centro Tecnológico. Programa de Pós-Graduação em Engenharia Química, 2009.
- [2] Schwaab, Marcio; Pinto, José Carlos. Análise de dados experimentais, I: fundamentos de estatística e estimação de parâmetros. Rio de Janeiro: E-Papers, 2007.
- [3] Rouquerol, J.; Rouquerol, L.; Sing, K.S. Adsorption by Powders and Porous Solids Principles: Methodology and Applications, Academic Press, San Diego, 1999.
- [4] Tolazzi, Natália; Steffani, Evandro; Barbosa-Coutinho, Elisa; Severo Junior, João B.; Pinto, José Carlos; Schwaab, Marcio. Adsorption equilibrium models: computation of confidence regions of parameter estimates. Chemical Engineering Research and Design, 2018.
- [5] Miranda L.J., PySwarms: a research toolkit for Particle Swarm Optimization in Python. Journal of Open Source Software, 3(21), 433, 2018.

Synthesis of Faujasite and β -zeolite for cadmium removal in aqueous solution

Djanyna V. C. Schmidt^a, Gabriela R. Ribeiro^a, Marcela T. U. Rocha^a, Fabiana S. dos Santos^b, Mendelssolm K. de Pietre^{a*}.

^a Fluminense Federal University, Department of Chemistry-ICEx, Rua Des Ellis Hermydio Figueira, 783, Volta Redonda – RJ, Brazil, *mkpietre@yahoo.com.br

^b Fluminense Federal University, Avenida dos Trabalhadores, 420, Volta Redonda – RJ, Brazil.

Abstract

The adsorption behavior of Faujasite and β -zeolite prepared from hydrothermal treatment and the effect of their chemical and textural properties on the cadmium ions removal from aqueous solutions are studied in this work. The samples were characterized by N_2 physisorption, X-ray diffraction, X-ray fluorescence, scanning electron microscopy and solid-state ^{27}Al nuclear magnetic resonance spectroscopy. The better performance of faujasite could be due to a higher density of Al-related sites, which is responsible for the ion-exchange process and its improved textural characteristics, with larger surface area and pore volume when compared to β -zeolite. Kinetic studies followed the pseudo-second order model, while the adsorption isotherms were well described by the Langmuir model, suggesting that the adsorption process took place by ion exchange on the zeolite monolayer surface.

Keywords: isotherms, adsorption, ion exchange, heavy metal.

1. Introduction

In recent years, problems caused by heavy metal contamination (including lead, copper, zinc and others) have become a worldwide challenge due to the rapid development of industries involved with metal plating and the production of textiles, fertilizers and pesticides, among others [1].

To avoid these problems, many technologies have been employed in order to minimize the presence of heavy metals in the environment. Studies have shown that, among several remediation techniques zeolites have been shown to exhibit high efficiency for heavy metal uptake, since these materials present a porous network with large availability of active sites that can be accessed by several adsorbates [2].

Zeolites have been extensively used in both catalysis and adsorption processes due to some particular characteristics, such as: high specific surface area and adsorption capacity; structure and composition that allow the creation of active sites, specially ion exchange sites; and a complex network of channels and cavities compatible with the size of molecules present in substances used in many industrial processes [3-4].

The control of relative amounts of Si^{4+} and Al^{3+} ions in the structure gives rise to a negative charge in the framework, which must be balanced by cations (usually exchangeable Na^+ ions from

reactants). Furthermore, controlled synthesis can provide wider pore structures, which are potentially promising for processes involving bulk molecules such as isomerization, dewaxing, environmental applications and petrochemical processes [5]. Thus, structures with both high Al content and large pore sizes are potentially desirable for ion exchange operations.

Among several zeolites, β -zeolite (also known as Beta or BEA) displays superior performance in different segments because it has a 3D network comprised by large pores when compared to other microporous solids, besides exhibiting high Al insertion capacity. This structure comprises the arrangement of two types of 12-membered ring pores, with pore diameters of 0.76 and 0.64 nm, in the a and b axis directions, respectively, and 0.55 and 0.55 nm in the channel parallel to the c axis.

The faujasite family (zeolites X and Y) is among the zeolites with the highest adsorptive capacity due to its high surface area, pore volume and diameter (≈ 0.74 nm), as well as the high Al content in its crystal structure.

The objective of this study was to synthesize and evaluates the zeolites (β -zeolite and Faujasite) with different structural and textural properties on the removal of cadmium ions from aqueous solutions.



2. Experimental

2.1. Synthesis

The synthesis procedure for β -zeolite (Si/Al=40) in the gel was recently reported by our group [6]. Briefly, 0.19 g of NaOH and 0.60 of NaAlO_2 were added into 32.50 g of TEAOH aqueous solution. Afterwards, 32.50 g of tetraethylorthosilicate were added. The mixture was kept under stirring for 4 h at room temperature before being transferred to a stainless steel autoclave lined with teflon and maintained at 140 °C for 48 h. The solid was washed, filtered and dried before calcination at 580 °C at 3 °C.min⁻¹ in air atmosphere for 5 h.

Regarding the faujasite synthesis (Si/Al=18), two systems were prepared; System A consists of 3g of NaOH, 12.25 g of sodium silicate and 24 g of distilled water. The gel was aged for 24h under constant magnetic stirring. Gel B was obtained by dissolving 0.13 g NaOH and 9.39 g sodium aluminate in 160 g of distilled water. Subsequently, 12.25 g of gel A was added to gel B. The resulting mixture was aged for 24h under mechanical agitation before hydrothermal treatment at 100 °C for 5 h. The solid was washed, filtered and dried overnight at desiccator.

2.2. Characterization

The adsorbents were characterized by X-ray diffraction (XRD) using a Shimadzu XRD-6000 powder diffractometer (CuK α radiation, 40 kW, 40 mA), scanned from 5 to 50° (2 θ) at 2° min⁻¹. The porosity of the samples was investigated by N₂ physisorption at -96 °C using an Autosorb 1 (from Quantachrome) instrument. The semi-quantitative elemental analysis was performed by X-ray fluorescence spectrometry (XRF) using a Bruker S8/Tiger instrument. Scanning electron microscopy (SEM) images were obtained in a Shimadzu S5X-550 microscope, equipped with an accessory for energy dispersive X-ray spectroscopy (EDS) analysis. The local chemical environment was investigated by solid-state ²⁷Al magic angle spinning (MAS) nuclear magnetic resonance (NMR) experiments. The experiments were performed using a Varian/Agilent VNMR 400 MHz spectrometer operating at a magnetic field of 9.4 T (²⁷Al NMR frequency of 104.16 MHz). Single pulse excitation experiments were conducted with duration of 1.0 μ s, a recycle delay of 1.0 s and a MAS rate of 14 kHz (accumulation

of 200 transients). The frequency shifts were externally referenced to Al(NO₃)₃.

2.3. Adsorption Experiments

In a typical batch experiments 0.05 g of the solids were suspended in 120 mL of single metal solution. The parameters investigated were: initial pH, concentration and contact time. After the uptake of Cd²⁺ on the synthetic zeolites, aliquots were withdrawn in duplicate and quantified by atomic absorption spectrometry (Varian, 55B SpectrAA). The removal efficiency (RE%) of the cadmium ions adsorbed at equilibrium and the adsorption capacity (q_e in mg.g⁻¹) were determined according to equations (1) and (2), respectively.

$$RE\% = \frac{C_0 - C_e}{C_0} \times 100, \quad (1)$$

$$q_e = \frac{C_0 - C_e}{m} \times V \quad (2)$$

where, where C_0 and C_e are the initial and the equilibrium concentrations (mg.L⁻¹) of the metal ions, respectively, V is the solution volume (L) and m is the adsorbent mass (g).

The kinetic data were investigated according to the pseudo-first order, pseudo-second order and intra-particle diffusion (Morris-Weber) models and their corresponding linear equations, expressed below (equations 3-5) [6].

$$\ln(q_e - q_t) = \ln q_e - K_1 \times t. \quad (3)$$

$$\frac{t}{q_t} = \frac{1}{K_2 q_e^2} + \frac{1}{q_e} \times t. \quad (4)$$

$$q_t = K_{ipd} \times t^{0.5}. \quad (5)$$

q_t and q_e (mg.g⁻¹) are the amounts of ions adsorbed on zeolite at any time t (min) and at equilibrium, respectively; K_1 (min⁻¹) and K_2 (g.mg⁻¹.min⁻¹) are the pseudo-first-order and pseudo-second-order rates constants of adsorption, respectively; and K_{ipd} is the rate constant of intra-particle diffusion.

Regarding the adsorption isotherms studies, Langmuir and Freundlich models, in their linear expressions, (equations 6-7) were tested, respectively [6-7].

$$\frac{C_e}{q_e} = \frac{1}{K_L \cdot q_m} + \frac{C_e}{q_m}, \quad (6)$$

$$\ln q_e = \ln K_F + \frac{1}{n} \cdot \ln C_e, \quad (7)$$

where q_m is the maximum adsorption capacity ($\text{mg} \cdot \text{g}^{-1}$), K_L ($\text{L} \cdot \text{mg}^{-1}$) is the Langmuir equilibrium constant, K_F ($\text{mg} \cdot \text{g}^{-1}$) is the Freundlich constant (related to the adsorption capacity of the adsorbent) and $1/n$ is the empirical constant associated with surface heterogeneity [6-8].

From equation 6, the dimensionless Langmuir parameter R_L can be defined, according to:

$$R_L = \frac{1}{1 + K_L \cdot C_0}, \quad (8)$$

where, for $0 < R_L < 1$, the adsorption process is considered favorable and for $R_L > 1$, the adsorption process is considered unfavorable (Malamis and Katsou, 2013; Pandey et al. 2015).

3. Results and Discussion

3.1. Characterization

According to the diffractograms patterns displayed in Figure 1, crystalline phases were satisfactorily obtained without any impurities for both β -zeolite and faujasite, respectively. In addition, the broad peaks observed in the XRD patterns shown in Fig. 1 suggest the presence of nanocrystals in both samples. According to the Scherrer equation, the values of average crystallite sizes found were 15 and 27 nm for faujasite and β -zeolite, respectively, evidencing the nanocrystalline nature of these structures.

SEM images (Fig. 2) revealed that the crystal morphology of β -structure consists of spherical-like aggregates with regular sizes (Fig. 2A), while the faujasite zeolite (Fig. 2B) presents both octahedral/cubic morphologies characteristics of the faujasite structure. EDS studies performed in the regions shown in Fig. 2 (not shown) indicated that both samples contain only Si, Al, O and Na in their composition.

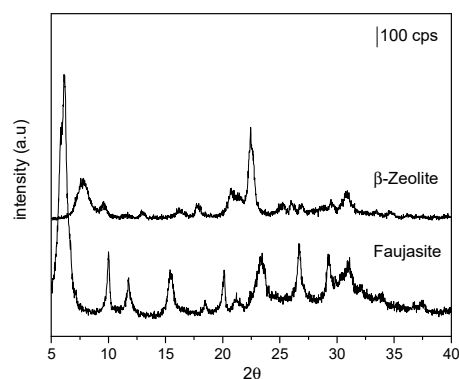


Fig. 1. XRD patterns of β -zeolite and faujasite, respectively.

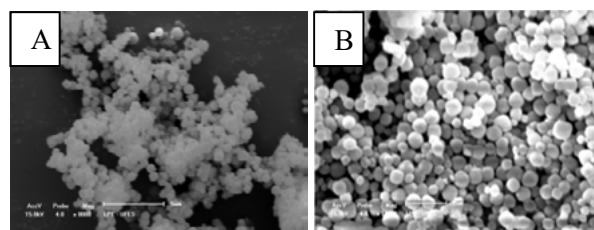


Fig. 2. SEM images of (A) β -zeolite and (B) Faujasite.

The XRF results presented in Table 1 show that the Si/Al molar ratio found in the solids is lower when compared to synthetic gels and suggests that most of Al atoms are preferably introduced into the zeolite structure, while considerable amount of Si remains dissolved in supernatant during the hydrothermal synthesis, due to the greater solubility of Si species in the alkaline medium [9].

The isotherm observed for β -zeolite (Fig. 3) is typical of microporous solids (type I), where an initial intense N_2 uptake takes place when the monolayer is formed at low relative pressures. Also, a H4 hysteresis loop is observed, characteristic of solids consisting of non-rigid aggregates of nanoparticles [6].

Regarding the isotherm of faujasite, a gradual increase in N_2 uptake with pressure was detected. Similar behavior was also observed by Chaves et al [9], which was ascribed to the adsorption of nitrogen in void spaces formed by aggregation of nanocrystals. The high surface area (S_{BET}) value found for both solids is typical of nanoparticle formation.

On the other hand, the higher surface area value obtained by the faujasite could be related to the smaller crystallite sizes, obtained by the Scherrer equation.

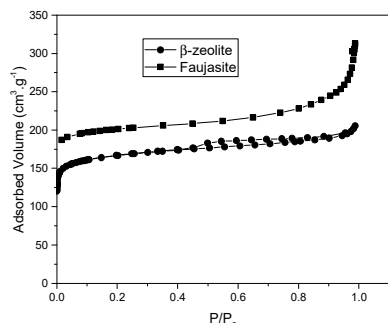


Fig. 3. N₂ Physisorption isotherms of the solids synthesized.

Table 1. Textural and Chemical properties of the solids.

Parameters/Zeolite	β-zeolite	Faujasite
(Si/Al) _{gel}	40	17.6
(Si/Al) _{solid}	6.3	1.5
S _{BET} (m ² g ⁻¹)	536	668
S _{EXT} (m ² g ⁻¹)	90	90
V _{Total} (cm ³ g ⁻¹)	0.213	0.259

S_{BET} = surface area, S_{EXT} = external surface area, V_{Total} = total pore volume.

The local environment of Al sites was investigated by ²⁷Al MAS NMR (Fig. 4). The intense signal centered at 56 ppm (faujasite) and 60 ppm (β-zeolite) is attributed to tetra-coordinated Al in the zeolitic framework, responsible for the negative charge in the network and, therefore, is important for ion exchange processes [3]. The small signal observed at 0 ppm for β-zeolite is due to octahedral Al, associated with an extra-phase formed during the zeolite synthesis or as a consequence of the easy access of water molecules to tetrahedral aluminum ions [3]. Thus, it can be concluded that nearly all Al atoms are inserted into the structures, ensuring maximum efficiency on metallic ions uptake.

Based on this set of characterization results, it should be reasonable to expect higher heavy metal ions removal onto faujasite than β-zeolite, since the former sample exhibits higher aluminum content and considerably larger surface area and pore volume, providing a solid with high density of accessible ion exchange sites.

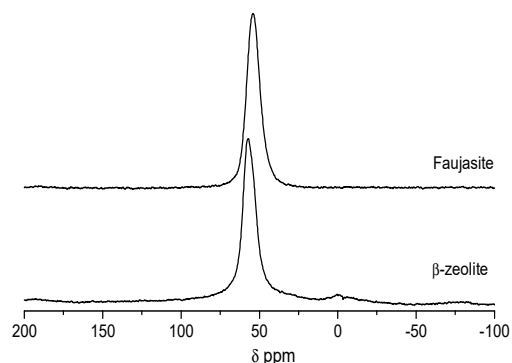


Fig. 4. ²⁷Al NMR spectra of the solids.

3.2. Adsorption experiments

Fig. 5 displays the Cd²⁺ adsorption on the zeolites as function of initial metal concentration. As expected, faujasite zeolite showed better performance than β-zeolite, since faujasite presents higher aluminum content and larger total/external surface area, which may provide more available active sites. The maximum of metal removal on faujasite was obtained at ≈ 42 mg.L⁻¹ whereas for β-zeolite the highest efficiency of cadmium ion removal occurred at ≈ 10 mg.L⁻¹. It is important to mention here that in preliminary studies (not shown), the optimum pH value at which the maximum metal uptake could be achieved was 5.2.

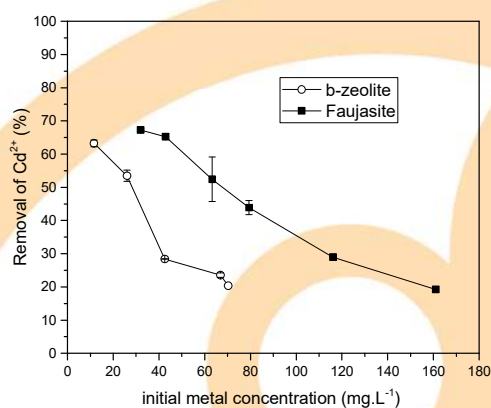


Fig. 5. Effect of initial Cd²⁺ concentration. Conditions: t=30 min; V=120mL and pH=5.2.

The maximum removal efficiency was obtained at the lowest metal concentration, which means that these interaction basically derive from the variations in the diffusion rates (driving forces to overcome the mass transfer resistance) of Cd^{2+} towards the adsorbent active sites under diluted solution. However, at more concentrated solutions, a decrease in the uptake efficiency (%) was observed. In such case, a further increase in metal concentration leads to the saturation of adsorption sites.

As observed in Fig. 6, faujasite presented higher adsorption capacity than β -zeolite. This effect can be attributed to the higher total surface area, besides the larger total pore volume observed for faujasite sample when compared to β -zeolite. In addition, the higher Al content found in faujasite also influences the higher metal removal by this solid. In other words, the better performance displayed by faujasite could be attributed to: (i) a higher density of Al-related sites, which is responsible for the ion-exchange process and (ii) its improved textural characteristics, with larger surface area and pore volume when compared to β -zeolite [6].

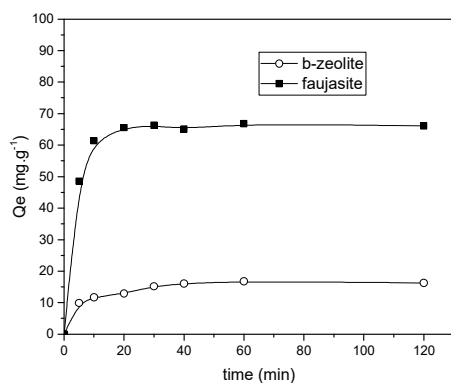


Fig. 6. Effect contact time on Cd^{2+} removal. Conditions: $[\text{Cd}^{2+}] = 44 \text{ mg.L}^{-1}$ for faujasite and 10 mg.L^{-1} for β -zeolite; $V = 120 \text{ mL}$ and $\text{pH} = 5.2$.

The knowledge about the kinetics of heavy metal ions adsorption is important because, from these data, the optimum operational conditions for full-scale metal removal processes may be achieved. Table 2 summarizes the kinetic data obtained from pseudo-first order, pseudo-second order and intra-particle diffusion models.

The q_e values determined using the pseudo-first order model were significantly different from the experimental ones ($q_{e,\text{exp}}$) and the corresponding coefficients of determination were relatively small. This means that the experimental data did not fit well to the pseudo-first order model and, thus, the adsorption processes were not diffusion controlled.

On the other hand, the q_e values calculated by the pseudo-second order model showed good agreement with the $q_{e,\text{exp}}$ values and the corresponding R^2 values were found to be ≥ 0.995 for both samples. Therefore, these kinetic data strongly suggest that the adsorption of Cd^{2+} ions onto the zeolites prepared in this study follows the pseudo-second order model, where the rate limiting step is controlled by the ion exchange between the metal ions and the zeolite surface.

Regarding the intra-particle diffusion fit for the adsorption of Cd^{2+} onto zeolites, the plots exhibited a first steep linear increase of qt followed by an almost horizontal line (not shown). The linear segment, with higher slope, can be attributed to the external surface adsorption. Deviation of the straight lines from the origin gives an idea about the thickness of the boundary layer and probably could be due to the difference in the rate of boundary layer diffusion in the initial stage of adsorption [6-9].

Table 2. Kinetic data for the adsorption of Cd^{2+} on zeolites.

sample	$q_{e(\text{exp})_1}$ mg.g ⁻¹	Pseudo first-order $q_e \text{ mg.g}^{-1}$ (R^2)	Pseudo second-order $q_e \text{ mg.g}^{-1}$ (R^2)	intra-particle diffusion $K_{\text{ipd}} \text{ min}^{-0.5}$ (R^2)
β -zeolite	16.4	4.60 (0.921)	17.0 (0.997)	0.42 (0.683)
faujasite	64.0	7.9 (0.561)	64.9 (0.999)	1.33 (0.345)

The second segment of the lines (almost horizontal lines) reflects a gradual adsorption stage, related to intra-particle diffusion, as the final equilibrium stage is reached and the adsorption rate becomes very slow, with the observation of the maximum amount of adsorbed material. Based on these results, it can be verified that the layer diffusion, observed at the first stage, is faster and also more important than the intra-particle diffusion, which occurs at the second stage.

This means that the intra-particle diffusion is not the only rate-limiting step, with the adsorption rate being associated with some other processes.

With respect to the adsorption isotherms, the Langmuir model gave the best fit ($R^2 > 0.992$) for all zeolites studied (Table 3).

The investigation of adsorption isotherms is crucial for the understanding about the adsorption capacity of a given adsorbent, i.e., information on equilibrium adsorption data gives fundamental physicochemical parameters to design a practical operating procedure.

Table 3. Isotherms parameters for the adsorption of Cd^{2+} onto zeolites.

Model	Parameters	β -zeolite	Faujasite
Langmuir	q_m ($\text{mg}\cdot\text{g}^{-1}$)	29.5	51.3
	K_L ($\text{L}\cdot\text{mg}^{-1}$)	0.12	1.56
	R_L	(0.104-0.416)	(0.043-0.108)
	R^2	0.993	0.996
Freundlich	K_F ($\text{mg}\cdot\text{g}^{-1}$)	16.8	38.0
	$1/n$	0.143	0.19
	R^2	0.801	0.726

The dimensionless Langmuir parameter R_L found in Table 3 varies between 0 and 1, which means a favorable process of adsorption of the Cd^{2+} on zeolites surfaces. The value of the maximum adsorption capacity (q_m) is related to the total capacity of the monolayer coverage for a given metal ion. According to the values of the q_m parameter, the monolayer capacity follows the order: faujasite > β -zeolite. As stated above, the chemical composition (Si/Al molar ratio) and improved textural characteristics of faujasite play important role on metal uptake.

Regarding the Freundlich parameters, $1/n$ is less than 1, evidencing a favorable adsorption process in all cases. In addition, K_F represents the adsorption capacity on a heterogeneous surface and the values found indicate high affinity for the zeolites.

4. Conclusions

Faujasite and β -zeolite with distinct chemical and textural properties were synthesized and efficiently applied on cadmium removal from aqueous solution. Faujasite sample presented better performance on heavy metal ions removal due to its higher amount of framework Al content, which

is responsible for ion exchange sites generation as well as higher surface area and pore volume. Kinetic studies and adsorption isotherms have shown that metal ions adsorption on zeolites follows pseudo-second order and Langmuir models, which means that the limiting step is probably controlled by the ion exchange process on the monolayer surface.

Acknowledgements

The authors acknowledge the FAPERJ for financial support to this work. The support from CAPES is also gratefully acknowledged. The authors are thankful to UFES and to Instituto Nacional de Tecnologia for the samples characterization.

References

- [1] Shinzato MC, Montanheiro TJ, Janasi VA, Andrade S, Yamamoto JK. Removal of Pb^{2+} from aqueous solutions using two Brazilian rocks containing zeolites. *Environ Earth Sci* 2013; 66:363–370.
- [2] Misaelides P. Application on natural zeolites in environmental remediation: A short review. *Micropor Mesopor Mat* 2011; 144:15-18.
- [3] Pietre MK, Bonk FA, Rettori C, Garcia FA, Pastore HO. Delaminated vanadoaluminosilicate with [V,Al]-ITQ-18 structure. *Micropor Mesopor Mat* 2012; 156:244-256.
- [4] Ramos FSO, Pietre MK, Pastore HO. Lamellar zeolites: an oxymoron? *RSC adv* 2013; 3:2084-2111.
- [5] Cundy CS, Cox PA. The hydrothermal synthesis of zeolites: Precursors, intermediates and reaction mechanism. *Micropor Mesopor Mater* 2005; 82: 1–78.
- [6] Pratti LM, Reis GM, Gonçalves GR, Freitas JCC, Santos FS, Pietre MK. Effects of textural and chemical properties of β -zeolites on their performance as adsorbents for heavy metals removal. *Environ Earth Sci* 2019, 78:553-567.
- [7] Cantuaria ML, Neto AFA, Nascimento ES, Vieira MGA. Adsorption of silver from aqueous solution onto pre-treated bentonite clay: complete batch system evaluation. *J Cleaner Prod* 2016; 112:1112-1121.
- [8] Malamis S, Katsou E A review on zinc and nickel adsorption on natural and modified zeolite, bentonite and vermiculite: Examination of process parameters, kinetics and isotherms. *J Hazard Mater* 2013; 252(253):428-461.
- [9] Chaves TF, Pastore HO, Hammer P, Cardoso D. As-synthesized TEA-BEA zeolite: Effect of Si/Al ratio on the Knoevenagel condensation. *Micropor Mesopor Mater* 2015; 202:198–207.

Evaluation of tetracycline adsorption capacity in aqueous solution using conventional adsorbent and CuSO₄ functionalized solid

Letícia Reggiane de Carvalho Costa^{a,*}, Liliana Amaral Féris^a

Separation Laboratory and Unit Operations (LASOP). Federal University of Rio Grande do Sul, Department of Chemical Engineering, Ramiro Barcelos Street, 2777, Postcode: 90035-007, Porto Alegre – RS, Brazil.

**leticiaREGICAR@hotmail.com*

Abstract

Residual drugs are often found in aqueous matrices. Tetracycline presents a huge hidden danger to human health due to its high persistence and ease of bioaccumulation. The functionalization of adsorbent solids introduces material specific characteristics in order to enhance the removal capacity of certain pollutants. In this context, the present study investigated the application of copper sulfate impregnated activated carbon adsorbent solid in the tetracycline removal by adsorption, making a direct comparison with the conventional solid. The results showed that the time required for the system to reach equilibrium for both solids was 120 min, according to a kinetics described by the pseudo first and pseudo second order models. The maximum adsorption capacity was 41.5 mg.g⁻¹ for the impregnated solid and 23.0 mg.g⁻¹ for the fresh solid, following the Langmuir isotherm model for both. In addition, impregnation of the solid provided a decrease in the adsorbent concentration used by approximately 85% (from 30 g.L⁻¹ to 5 g.L⁻¹). Thus, the application of this CuSO₄ derived composite as adsorbent solid is technically feasible and most suitable for the removal of tetracycline in wastewater treatment.

Keywords: copper sulfate; adsorption; tetracycline; impregnated solid.

1. Introduction

Drugs are often found in aqueous matrices [1]. Due to low biodegradability, high persistence and ease of bioaccumulation, these compounds are highly resistant to conventional treatment processes and are difficult to remove by them [2].

Tetracycline (TC) represents a class of broad spectrum antibiotics [3]. After ingestion, about 20 to 40% is excreted by the body without change and in the form of metabolites. Zhang et al. [4] revealed that tetracycline may be present in the environment at concentrations up to 110 µg.L⁻¹. The product has also been found in some foods such as eggs, milk and fish [5]. In addition, they have been found in soil and sediment matrices [6].

Low contamination levels and complexity of environmental matrices require the use of alternative methods that have high sensitivity and selectivity [7,8].

The adsorption is still considered one of the most promising means for the elimination of contaminants from the aquatic environment due to its advantages of simple operation, low investment

cost [9]. Additionally, the solids used in this type of process can be functionalized, introducing characteristics to the material in order to enhance the adsorption capacity in the removal of certain pollutants.

The presence of metal ions in the adsorbent is known to promote mainly the adsorption removal of antibiotics through the formation of cationic bonding bridges [10]. In studying the adsorption of tetracycline by immobilized alginate with Cu, Zhang et al. [11] obtained a maximum adsorption capacity of 53.26 mg.g⁻¹ of this compound at pH 3 and initial TC concentration of 90 mg.L⁻¹.

In this context, the present study investigated the application of copper sulfate impregnated adsorbent solid in the tetracycline removal by adsorption, making a direct comparison with the conventional solid.

2. Experimental procedure

2.1 Adsorbent solid impregnation

Copper sulfate 2% w/v aqueous solution was prepared by dissolving copper sulfate pentahydrate ($\text{CuSO}_4 \cdot 5\text{H}_2\text{O}$). Two grams of activated carbon (Scientific Exodus), with particle size between 1.40 and 1.00 mm, were added to 100 mL of the pre-formulated solution and stirred at 150 rpm for 24 hours at 25 °C. Finally, the CA-Cu particles were washed with deionized water to remove excess SO_4 and oven dried for 4-6 hours at 100 °C.

2.2 Characterization of adsorbents

Adsorbent materials were characterized prior to adsorption using Fourier transform infrared (FTIR, Nicolet 6700) and X-ray diffraction (XRD, Bruker). In addition, N_2 adsorption/desorption physical assays were also performed, where specific surface area and porosity were calculated using the Brunauer – Emmett – Teller (BET) methods and using the Barrett-Joyner-Halenda (BJH) equation.

2.3 Tetracycline adsorption study

Tetracycline was acquired from Sigma-Aldrich, purity $\geq 98.0\%$. Adsorption tests were performed in batch using 100 mL volumes of solution. To evaluate tetracycline adsorption as a function of pH, measurements were made over a pH range ranging from 2 to 10 for 30 min and a mass of 1 g of each adsorbent solid. At the same adsorbent dosage, the adsorption kinetics measurements were performed over a period of time ranging from 5 to 300 min under the best pH conditions found for the solids. After contact time was defined, the effect of solid dosage on tetracycline adsorption was evaluated from experiments performed with different solids concentrations (0.5-75 $\text{g}\cdot\text{L}^{-1}$).

With the best conditions obtained in the previous tests, adsorption isotherms were constructed by varying the initial TC concentration. The experiments were performed on a refrigerated bench stirrer at a constant temperature of 25 °C and agitation of 150 rpm. In order to establish the most appropriate correlation for equilibrium curves, three isotherm models were used: Langmuir (Eq. 1), Freundlich (Eq. 2) and Redlich-Peterson (Eq. 3), where q_e and C_e , respectively, are the adsorbed amount ($\text{mg}\cdot\text{g}^{-1}$) and equilibrium solute concentration ($\text{mg}\cdot\text{L}^{-1}$).

$$q_e = \frac{Q_m \cdot K_L \cdot C_e}{1 + K_L \cdot C_e} \quad (1)$$

where Q_m is the maximum adsorption capacity in the monolayer ($\text{mg}\cdot\text{g}^{-1}$), K_L is the Langmuir constant for adsorption energy ($\text{L}\cdot\text{mg}^{-1}$).

$$q_e = K_F \cdot C_e^{1/n} \quad (2)$$

where K_F is the Freundlich constant which measures the adsorption capacity ($(\text{mg}\cdot\text{g}^{-1}) \cdot (\text{L}\cdot\text{mg}^{-1})^n$), n is the Freundlich constant which estimates the adsorption intensity.

$$q_e = \frac{K_R \cdot C_e}{1 + a_R \cdot C_e^\beta} \quad (3)$$

where K_R ($\text{L}\cdot\text{mg}^{-1}$) and a_R ($\text{L}\cdot\text{mg}^{-1}$) $^\beta$ are the constants of Redlich-Peterson and β is the exponent of the equation.

All assays were performed in duplicate and the standard deviation was calculated to evaluate the dispersion of the experimental points. At the end of each experiment, the supernatant liquid was filtered and analyzed using a Thermo Scientific spectrophotometer, Genesys 10S UV-Vis, at the 357 nm TC detection wavelength. Error correction caused by TC retained in the filter was performed by reading the solution before and after filtration.

3. Results and discussion

3.1 Characterization of adsorbents

Specific surface area and pore distribution of materials were determined by N_2 adsorption/desorption. The solids of this study had a BET area of 508.03 and 533.5 $\text{m}^2\cdot\text{g}^{-1}$ for CA and CA-Cu, respectively. It can be observed that impregnation of a high amount of copper causes an increase in specific surface area, which suggests a better adsorption behavior. These results corroborate what was obtained by Nero [12]. The conventional solid had a total pore volume of 0.103 $\text{cm}^3\cdot\text{g}^{-1}$ while for CA-Cu it was 0.122 $\text{cm}^3\cdot\text{g}^{-1}$. The pore diameters of the samples indicate that the solids were mainly microporous.

The vibrational spectra of solids are shown in Figure 1.

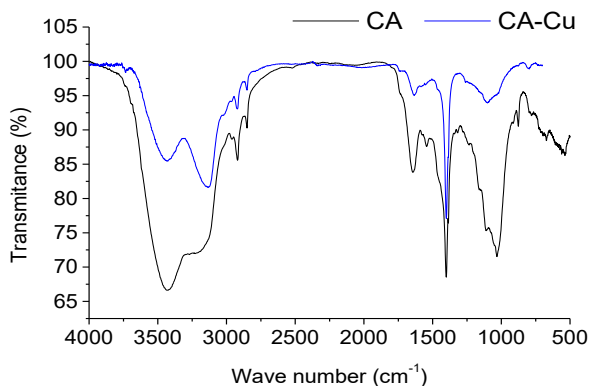


Fig. 1. FTIR spectra of solids before and after impregnation.

The presence of a broad and strong band at 3402 cm^{-1} , which may be attributed to the vibrational elongation of the hydroxyl (O-H) bond; the 2920 cm^{-1} region indicates a vibrational elongation of the bond (C-H). Peaks at 1740 , 1421 , and 1151 cm^{-1} refer to the vibrational elongation of carbonyl (C-O) bonding [13]. CA-Cu band intensities were weaker, which may suggest that the impregnating solution interact or overlap with the CA surface groups. In addition, peak changes indicate that the surface chemical status of the corresponding groups changes after the impregnation process.

The XRD profiles of solids before and after CuSO_4 impregnation are illustrated in Figure 2. Two graphite carbon diffraction peaks can be verified between the adsorbents at reflections at 2θ angles near 25° and 45° , indicating that a amorphous phase is formed and activated carbons are ordered by stacking micrographs [14].

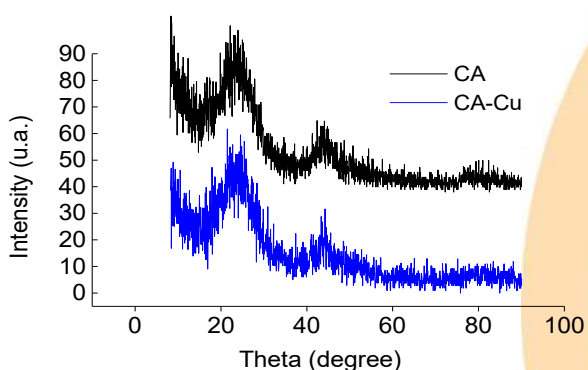


Fig. 2. Diffractograms of solids before and after impregnation.

3.2 Effect of pH solution

According to the distribution of TC chemical species, their solutions are very stable at neutral or weakly acidic pH values [15]. Therefore, adsorption is considered to be favorable at pH in this range. Figure 3 shows the effect of pH on the adsorption assay performed on both solids from tetracycline synthetic solution.

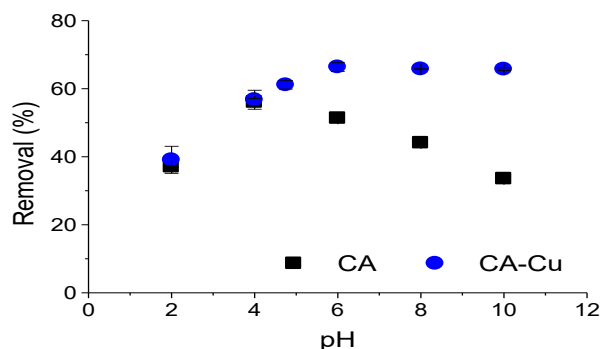


Fig. 3. Effect of pH on tetracycline adsorption assay using adsorbent solids. Conditions: solid dosage 10 g.L^{-1} , time 30 min, 20 mg.L^{-1} de TC in 100 mL solution.

The pH chosen as the most suitable for the conventional solid was pH 4, which presented a higher percentage of TC removal compared to the others (54%).

It was observed that for CA there was an increase in TC adsorption capacity with the increase of acid degree of the solution. This behavior may be due to the cationic character of TC at lower pH. As the pH increases, the negative charge density of activated carbon increases and electrostatic repulsion plays a major role between activated charcoal surface charges and the anionic character of TC, causing a decrease in adsorption capacity. A similar trend was found for TC removal by adsorption on corn husk-derived biochar [16].

Surface impregnation with copper introduces more acidic functional groups into activated carbon and can provide more surface active sites for adsorption and therefore increase this adsorption capacity. Thus, for CA-Cu composite, TC adsorption is higher than CA (66%). In addition, as mentioned in item 3.1, this composite had a higher surface area and volume of micropores. For CA-Cu pH 4.75 (without adjustment) was considered as

optimal pH for continuity of the study.

3.3 Effect of adsorbent dosage

By analyzing the effect of adsorbent dosage, it can be seen from Figure 4 (a and b) that increasing the specific amount of sorbent leads to an increase in tetracycline removal efficiency of 20 to 90%. It is also observed that, from a given concentration, the removal percentage was approximately constant, caused by the saturation of the materials.

The adsorbent dosage of 5 g.L⁻¹ was selected as ideal for CA-Cu, culminating in a removal percentage around 75.2%. For CA, the percentage of removal stabilized with a adsorbent solid concentration of 30 g.L⁻¹ reaching a maximum value of 92.7% with a residual TC concentration of 1.45 mg.L⁻¹.

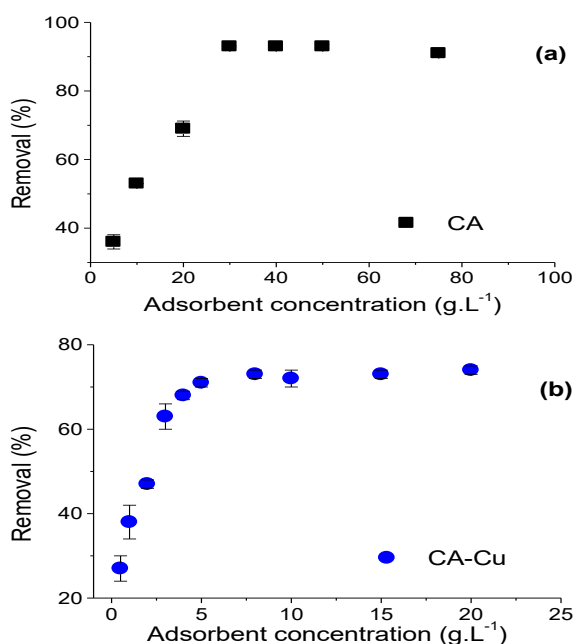


Fig. 4. Adsorption capacity according to the dosage of the adsorbent solid: (a) CA and (b) CA-Cu. Conditions: pH 4.0 for CA, natural pH for CA-Cu, time 120 min, 20 mg.L⁻¹ TC in 100 mL solution.

Comparatively, CA-Cu showed the highest tetracycline uptake, despite the smaller surface area compared to CA, providing an 85% reduction in adsorbent mass for tetracycline adsorption. This large difference suggests that tetracycline removal depends on the nature of the sites rather than the amount of sites available. In addition, it has been

reported in the literature that this compound could synergistically improve the absorption and removal of tetracycline from aqueous solutions [17].

3.4 Time effect and adsorption kinetics

It is observed in Figure 5 that for both solids, the adsorption equilibrium begins to be reached from 120 minutes, with no significant variations observed later. It is also noted that there is a difference in the rate of removal of the two adsorbents since for CA there was a slower initial kinetics compared to CA-Cu.

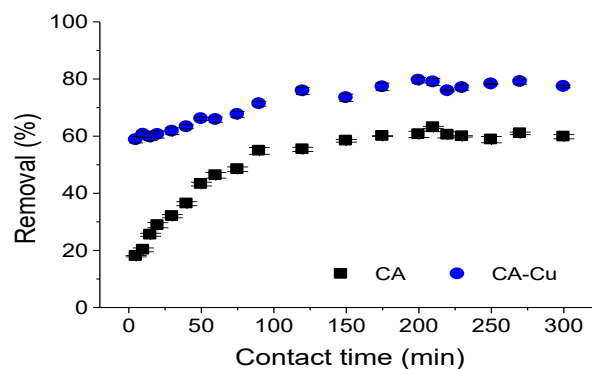


Fig. 5. Adsorption capacity according to contact time. Conditions: pH 4.0 for CA, natural pH for CA-Cu, 10 g.L⁻¹ solid dosage, 20 mg.L⁻¹ TC in 100 mL solution.

According to Wang et al. [18], tetracycline can be bonded to metal ions to form an antibiotic-metal complex and can also form antibiotic-metal-adsorbent complexes. Additionally, the empty orbitals present in the Cu electronic structure can accept electrons in the tetracycline molecule. Thus, rapid drug adsorption on the surface of the impregnated solid indicates a higher affinity between adsorbent-adsorbent, showing that interactions may be superficial.

For a better understanding of this mechanism, pseudo first and pseudo second order models were applied to the experimental data. The values found for each model are shown in Table 1.

Comparing the results for the two proposed models, it is observed that both satisfactorily describe the adsorption kinetics, since they presented linear correlation coefficient (R²) higher than 0.99 for both solids.

These results demonstrated that the sorption of TC in CA and CA-Cu is controlled by the chemoreaction mechanism, involving valence

forces through electron sharing or exchange between adsorbent and adsorbate [19], as well as by the physisorption mechanism.

Table 1. Kinetic parameters of pseudo 1st and pseudo 2nd order models adjusted to experimental data for CA and CA-Cu at 25 °C.

Model	Parameters	Adsorbents	
		CA	CA-Cu
Pseudo 1st order	Qe*	1.24	1.38
	K ₁ * ¹	0.03	0.29
	R ²	0.981	0.992
Pseudo 2nd order	Qe*	1.40	1.41
	K ₂ * ²	0.11	2.06
	R ²	0.997	0.993

*(mg.g⁻¹); *¹ (min⁻¹); *² (g.mg⁻¹.min⁻¹);

3.5 Adsorption Isotherm

In order to observe the equilibrium relationship between the amount of adsorbed material and the concentration in the liquid phase, the adsorption isotherm at 25 °C was studied for both solids with different initial TC concentrations, using the optimal operating conditions found in item 2.3 (pH and solid dosage). The experimental equilibrium results are shown in Figure 6.

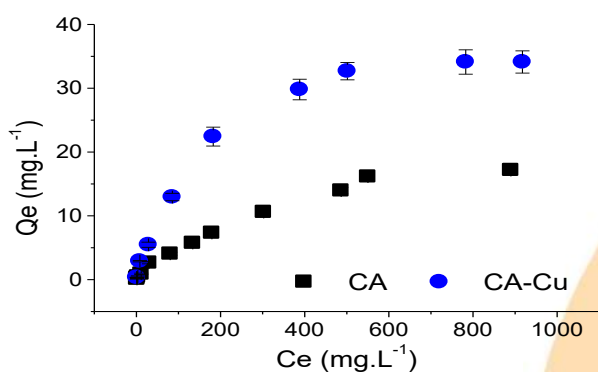


Fig. 6. Experimental isotherm at 25 °C for CA and CA-Cu. Conditions: pH 4.0 for CA, natural pH for CA-Cu, 5 and 30 g.L⁻¹ solid dosage for CA and CA-Cu respectively, time 24 h.

Higher efficiency was observed for the copper sulfate functionalized solid (41.5 mg.g⁻¹), with twice the adsorption capacity than the in conventional solid (23.0 mg.g⁻¹).

As in the kinetic study, to establish the most

appropriate correlation for equilibrium curves and to estimate isotherm parameters, experimental data were modeled for Langmuir, Freundlich and Redlich-Peterson isotherms. Table 2 presents the constants and correlation coefficients for each type of model.

Analyzing the data, the Langmuir and Redlich-Peterson models presented the best prediction of the experimental data at the evaluated temperature (25 °C), with R² above 0.99. However, the Langmuir model was selected as the best isotherm model, since Redlich-Peterson is the combination of the Langmuir and Freundlich equations, resulting in a hybrid sorption mechanism, in which at low adsorption concentrations the Redlich-Peterson isotherm approaches the Langmuir equation and on highs, Freundlich equations. Moreover, the analysis of the parameter β shows that at the three temperatures studied it approaches 1, indicating the model's validity and the tendency to approach the Langmuir model [20].

Table 2. Parameters of isotherm models adjusted to experimental data at 25 °C.

Model	Parameters	Adsorbents	
		CA	CA-Cu
Freundlich	K _F * ²	0.66	1.72
	N	2.12	2.20
	R ²	0.959	0.967
Langmuir	Qm*	22.89	41.47
	K _L * ¹	0.003	0.006
	R ²	0.988	0.997
Redlich-Peterson	K _r * ¹	0.05	0.22
	A _r * ³	0.0001	0.0024
	B	1.37	1.11
	R ²	0.994	0.998

*(mg.g⁻¹); *¹(L.mg⁻¹); *²(mg.g⁻¹).(L.mg⁻¹)^{1/n}; *³(L.mg⁻¹)^β

3. Conclusion

In the present study, the efficiency of tetracycline removal was evaluated by CuSO₄ functionalized adsorbent solid and in conventional solid during the adsorption process. In general, the two adsorbents studied were efficient in removing the emerging pollutant. Among them, the best result was obtained with CA-Cu solid, presenting a

removal above 75%, with a contact time of 120 min and a solid dosage 84% lower than that used for the in conventional solid (5 g.L^{-1}), confirming a better affinity between adsorbent-adsorbent. The pseudo first and pseudo second order models satisfactorily fit the experimental data for both adsorbents, presenting physical and chemical sorption characteristics. Furthermore, it was found that the Langmuir isotherm model was more suitable for the process, being able to model the gradual and subtle increasing behavior presented due to the electrostatic charges of the tetracycline molecule. For both solids there is the possibility of their regeneration and reuse, based on effective regeneration techniques for TC removal.

Acknowledgements

To the Federal University of Rio Grande do Sul (UFRGS) and the Coordination for the Improvement of Higher Education Personnel (CAPES) for the support received.

References

- [1] Zhang, S.; Dong, Y.; Yang, Z.; Yang, W.; Wu, J.; Dong, C. Adsorption of pharmaceuticals on chitosan-based magnetic composite particles with core-brush topology. *Chem. Eng. J.* **2016**, *304*, 325–334.
- [2] Bisognin, R.P.; Wolff, D.B.; Carissimi, E. Revisão sobre fármacos no ambiente. *Rev. DAE* **2018**, *66*(210), 78–95.
- [3] Dagherir, R.; Drogui, P. Tetracycline antibiotics in the environment: A review. *Environ. Chem. Lett.* **2013**, *11*(3), 209–227.
- [4] Luo, Y.; Guo, W.; Hao, H.; Duc, L.; Ibney, F.; Zhang, J.; Liang, S.; Wang, X.C. A review on the occurrence of micropollutants in the aquatic environment and their fate and removal during wastewater treatment. *Sci. Total Environ.* **2014**, *473–474*, 619–641.
- [5] Silva, B. Resíduos de antibióticos e antiparasitários em alimentos de origem animal. *Aleph* **2015**, 0–38.
- [6] Regitano, J.B.; Leal, R.M.P. Comportamento e impacto ambiental de antibióticos usados na produção animal Brasileira. *Rev. Bras. Cienc. do Solo* **2010**, *34*(3), 601–616.
- [7] Ginebreda, A.; Muñoz, I.; Alda, M.L. de; Brix, R.; López-Doval, J.; Barceló, D. Environmental risk assessment of pharmaceuticals in rivers: Relationships between hazard indexes and aquatic macroinvertebrate diversity indexes in the Llobregat River (NE Spain). *Environ. Int.* **2010**, *36*(2), 153–162.
- [8] Valcárcel, Y.; Alonso, S.G.; Rodríguez-Gil, J.L.; Maroto, R.R.; Gil, A.; Catalá, M. Analysis of the presence of cardiovascular and analgesic/anti-inflammatory/antipyretic pharmaceuticals in river- and drinking-water of the Madrid Region in Spain. *Chemosphere* **2011**, *82*(7), 1062–1071.
- [9] Ahmed, M.J. Adsorption of quinolone, tetracycline, and penicillin antibiotics from aqueous solution using activated carbons: Review. *Environ. Toxicol. Pharmacol.* **2017**, *50*, 1–10.
- [10] Ji, L.; Chen, W.; Duan, L.; Zhu, D. Mechanisms for strong adsorption of tetracycline to carbon nanotubes: A comparative study using activated carbon and graphite as adsorbents. *Environ. Sci. Technol.* **2009**, *43*(7), 2322–2327.
- [11] Zhang, X.; Lin, X.; He, Y.; Chen, Y.; Luo, X.; Shang, R. Study on adsorption of tetracycline by Cu-immobilized alginate adsorbent from water environment. *Int. J. Biol. Macromol.* **2019**, *124*, 418–428.
- [12] Nero, G. Uso de excremento de cupim como precursor na fabricação de carvão ativado magnetizado para adsorção de amoxiciclina. *J. Chem. Inf. Model.* **2019**, *53*(9), 1689–1699.
- [13] Diana L. Vullo. Interacción En Beneficio Del Medio Ambiente. *Química Viva* **2003**, *2*(3), 93–104.
- [14] Beltrame, F.A. Valorização De Resíduos Sólidos Orgânicos Para Grandes Geradores: Avaliação da viabilidade técnica de equipamentos compactos. 2018. 93 f. Dissertação (Mestrado), Universidade de São Paulo, São Paulo - SP, **2018**.
- [15] Jekel, M. Partition and Adsorption of Organic Contaminants in Environmental Systems Refractory Organic Substances in the Environment. Berlin, Germany: John Wiley & Sons; **2006**.
- [16] Saygili, H.; Güzel, F. Effective removal of tetracycline from aqueous solution using activated carbon prepared from tomato (*Lycopersicon esculentum* Mill.) industrial processing waste. *Ecotoxicol. Environ. Saf.* **2016**, *131*, 22–29.
- [17] Qin, Q.; Wu, X.; Chen, L.; Jiang, Z.; Xu, Y. Simultaneous removal of tetracycline and Cu(II) by adsorption and coadsorption using oxidized activated carbon. *RSC Adv.* **2018**, *8*(4), 1744–1752.
- [18] Wang, Y.U.J.; Jia, D.E.A.N.; Rui-Juan, S.U.N.; Hao-Wen, Z.H.U.; Zhou, D.M. Adsorption and cosorption of tetracycline and copper(II) on montmorillonite as affected by solution pH. *Environ. Sci. Technol.* **2008**, *42*(9), 3254–3259.
- [19] Ho, Y.S.; Mckay, G. Sorption of copper (II) from aqueous solution by peat. *Water. Air. Soil Pollut.* **2004**, *158*(Ii), 77–97.
- [20] Pezoti, O.; Cazetta, A.L.; Bedin, K.C.; Souza, L.S.; Souza, R.P.; Melo, S.R.; Almeida, V.C. Percolation as new method of preparation of modified biosorbents for pollutants removal. *Chem. Eng. J.* **2016**, *283*, 1305–1314.

Evaluation of red bezaktiv dye adsorption on the LaCoO_3 material

Iasmin A. Ribeiro^{a*}, Juli E. Couto^b, Jéssica A.S. Lemos^a, Marcelo J. B. Souza^b, Anne M. Garrido Pedrosa^a

^aGraduate Program in Chemistry, Federal University of Sergipe, Av. Marechal Rondon, Rosa Elze, São Cristóvão-SE, 49100-000, Brazil

^bGraduate Program in Chemical Engineering, Federal University of Sergipe, Av. Marechal Rondon, Rosa Elze, São Cristóvão-SE, 49100-000, Brazil

Abstract

The LaCoO_3 material with perovskite structure has been synthesized by the modified proteic method using cobalt and lanthanum nitrates as the starting material and gelatin protein as complex agent, subsequently calcined to 900°C. The material obtained was characterized by XRD, SEM, PCZ, and SSA. It was applied in the adsorption of the red bezaktiv dye. In the XRD patterns profile it is observed that the material LaCoO_3 was formed, identified by perovskites phases (ICSD 247225) and secondary phases related to the La_2O_3 (ICSD 56771). The adsorbent obtained has a surface area of 32 m² g⁻¹ and PCZ equal to 7.26. The lanthanum cobaltite obtained adsorbs the dye at pH = 5 with 97% dye removal efficiency.

Keywords: Perovskite structure; LaCoO_3 ; Modified proteic method; Dye; Adsorption.

1. Introduction

Perovskites are ceramic materials with a general formula ABO_3 [1], where in position A can be a rare earth, alkaline or alkaline earth metal, while in position B they can be transition metal ions (3d, 4d and 5d) [2].

These materials have several applications such as catalysts, the Mg-substituted $\text{K/La}_{0.8}\text{Ce}_{0.2}\text{CoO}_3$ has proven catalytic activity in the removal of diesel soot [3], in the removal of dyes such as $\text{La}_{0.8}\text{Ba}_{0.2}\text{TiO}_{3.5-8}$ in the degradation of the Congo red dye [4], LaCoO_3 in the degradation of the rhodamine B (RB) dye [5], MgTiO_3 in the degradation of the synthetic solution blue reactive (QR-19) dye [2] among others.

The synthesis method employed to obtain these materials influences their properties, such as the oxidative co-precipitation method, in which it is possible to obtain very fine solids and high areas. In the amorphous citrate method, more uniform structures are obtained [6] and in the Pechini method, high purity powders with homogeneous composition are obtained [7].

Dyes from effluents, has become a problem about water pollution. These compounds, mainly from dyeing industries, have become threats to aquatic ecosystems due to their toxicity and its stability,

making it difficult to remove it from aquatic systems [8].

The adsorption process is a viable means for the decontamination of textile and dyeing effluents [8]. Perovskites have gained attention in pollution reduction and environmental remediation processes due to their properties such as ion exchange, adsorption, catalytic potential, good thermal stability and redox properties [4].

According to what has been described, obtaining materials with beneficial properties to the environment, as regards the adsorption of dyes in aqueous medium, becomes indispensable for application against environmental pollution. Thus, perovskites with proven adsorption activity were synthesized using the modified protein method to test their efficiency on the adsorption of the Red Bezaktiv dye.

2. Experimental

2.1. Synthesis of the perovskite

LaCoO_3 perovskite-type oxide was synthesized by the modified proteic method [1] using cobalt and lanthanum nitrates as the starting material and gelatin protein as complex agent. The synthesis procedure consisted in the dissolution of cobalt and



lanthanum nitrates in distilled water under magnetic stirring. After the solution was heated to 70 °C, and gelatin protein was added, resulting in a viscous system which was heat treated at 350 °C for 2 hours, with a heating rate of 10 °C min⁻¹. A precursor powder was obtained (LC3-G) after heat treatment and calcined at 900 °C for 2 h at a rate of 10 °C min⁻¹ (LC9-G).

2.2. Characterization of the perovskite

FTIR analyses were recorded from 4000 to 400 cm⁻¹ in a Varian 640-IR FT-IR spectrophotometer, using the KBr pellet method.

X-ray diffraction was performed using a D8 Advance Bruker diffractometer, operated with CuK α ($\lambda = 1.5418 \text{ \AA}$) and 2θ in the range of 10–60° and scan step of 0.020°min⁻¹. Phase identification was performed by comparison with data from ICSD (Inorganic Crystal Structure Database).

The LC9-G sample was submitted to nitrogen adsorption at 77 K for the determination of the specific surface area by the BET method.

The material porosity was analyzed using the HITACHI Scanning Electron Microscopy (SEM), model TM 3000.

The determination of the point of zero charge was obtained by adapted methodology of the reference [12].

2.3. Adsorption from liquid phase tests

Prior to the dye removal studies an analytical curve was obtained from the mean absorbance at the maximum wavelength of the bezaktiv red dye aqueous solutions with pH measured to pH5 at the respective concentrations 10; 20; 30; 40 and 50 mg L⁻¹ (triplicate). From these data the actual concentrations of the solutions used in the tests were estimated.

For the adsorption tests, 250 mL of dye solution with a concentration of 30 mg L⁻¹ was prepared and analyzed using Shimadzu UV-1800 spectrophotometer, 3.5 mL quartz cell with a 1.0 cm optical path and applying a scan in the range from 200 to 700 nm. The obtained curve was used as reference and maximum absorption wavelength of the dyes is at 427 nm. Before adsorption tests, the pH of the dye solution was adjusted for 5 and the system dye + adsorbent was maintained under agitation by 1 hour. After this, the system was submitted to filtration and obtained the spectrum in the same conditions of the reference solution. The effect of the mass of adsorbent used also was

studied using 10, 20 and 30 mg of LaCoO₃ as adsorbent.

3. Results and discussion

The Figure 1 shows FTIR spectra of the samples calcined at 900°C (LC9-G) and heat treated at 300°C (LC3-G) and for the gelatin protein. Gelatin protein is formed by amino acids which are joined together by peptide bonds. The spectrum shows protein characteristic bands at 1665 cm⁻¹ relative to overlapping bands related to asymmetric N-H and COO- bond stretches. The 1475 cm⁻¹ band for asymmetric angular deformation of the N-H bond for primary amine and the 1387 cm⁻¹ band for symmetric COO- stretch [9].

In the LC3-G sample it is still possible to observe the gelatin protein-related bands at lower wavelengths. Overlap of the asymmetric stretch bands of the N-H and COO bonds by 1641 cm⁻¹, the asymmetric angular deformation of the N-H bond to primary amine at 1468 cm⁻¹ and the symmetrical COO stretch at 1384 cm⁻¹ [9]. The bands at 665 cm⁻¹ and 581 cm⁻¹ refer to the M-O bond probably from the perovskite structure [10].

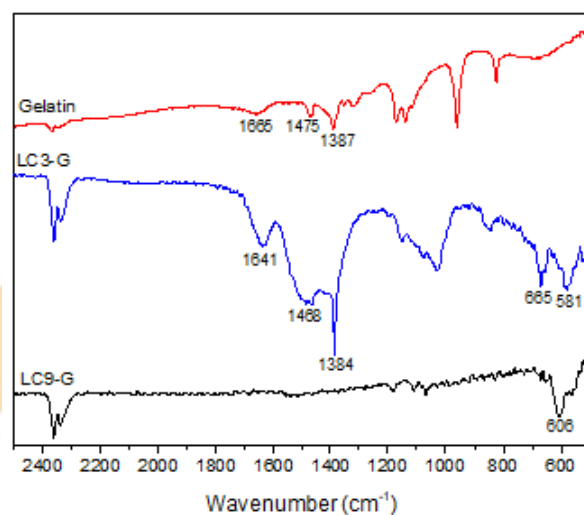


Fig. 1. FTIR spectra for gelatin protein, LC3-G and LC9-G.

In the spectrum of material LC9-G, it is observed that the gelatin protein bands are absent, which is expected due to the calcination temperature of 900 °C that decomposes the organic matter. As the 606 cm⁻¹ band is attributed to the elongation of the M-O

bond, important evidence of the formation of an oxide phase may be perovskite [10].

Figure 2 shows the XRD patterns of the LC9-G sample, in which the diffractogram showed the presence of peaks referring to the perovskite phase with 2θ in 23.23° , 32.91° , 33.24° , 40.66° , 41.34° , 47.50° , 53.26° , 53.84° and 58.96° with monoclinic geometry and space group $I12/a1$, according to ICSD chart no. 247225. In addition to the formation of perovskite, there was the formation of secondary phase corresponding to lanthanum (La_2O_3) according to ICSD chart No. 56771 with low intensity 2θ peaks at 28.55° , 28.88° , 29.83° and 50.15° with trigonal geometry and P-3m1 space group. Based on the literature, the characteristic peaks of LaCoO_3 perovskite phase are observed in the synthesized compound, corroborating the elucidation performed in the diffractogram obtained [11].

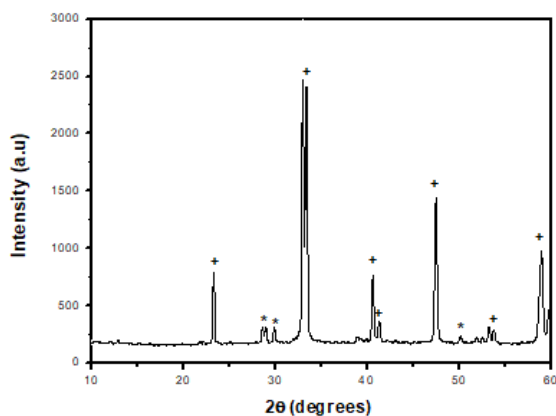


Fig. 2. X ray diffraction patterns of the LaCoO_3 material (LC9-G): LaCoO_3 (+) and La_2O_3 (*).

The zero load point (PCZ) for the calcined sample at 900°C was determined based on the methodology adapted from the literature [12]. Based on this method, when the surface hydroxyl groups remain undissociated in aqueous solutions, the oxide surface is said to be at its isoelectric point (pH_{pzc}) and will have a net surface charge of zero. If the pH is less than the isoelectric point, the surface will acquire a positive charge, If the pH is greater than the isoelectric point, the surface will acquire a negative charge [13]. The PCZ of LaCoO_3 perovskite is 7.26, so we can infer that the adsorption above this value is with cationic dyes and below with anionic dyes.

According to the scanning electron microscopy image, (Figure 3) it appears that the obtained powder is porous, and it is possible to observe that

is without agglomerations of the particles. The porous material is important in adsorption.

Perovskites have generally low surface areas, smaller than $10\text{ m}^2\text{ g}^{-1}$, and the larger the surface area generally, the greater the efficiency of dye removal, although this is not the only factor that influences the process when using mixed oxides. The relationship between crystallite size and surface area is essential to determine an efficient more adsorption, because the smaller the crystallite size, the larger the surface area [5]. The LaCoO_3 material obtained has a surface area of $32\text{ m}^2\text{ g}^{-1}$ and a crystalline size of 45 nm.

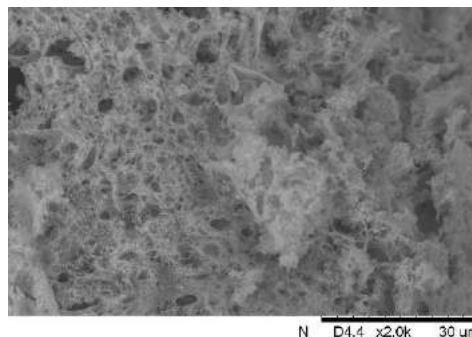


Fig. 3. SEM image of LaCoO_3 material.

The UV-Vis spectrum for the red bezaktiv indicated that the region of highest absorption for dye is in 427 nm. According to the tests, a marked removal of the dye is occurring when is used the LaCoO_3 as adsorbent as can see in the spectra showed in the Figure 4.

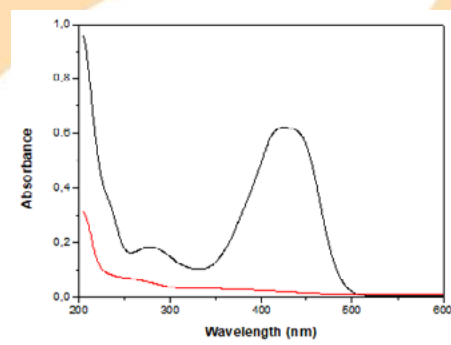


Fig. 4. UV-Vis spectra of the dye solution (in black) and the dye solution spectra after adsorption tests (in red).

Figure 5 shows data obtained for dye removal efficiency, E (%), and the amount (q) of dye removed from the medium in the adsorbent mass study using 10 mg, 20 mg and 30 mg at a fixed time of 1 hour and with system pH adjusted to pH5. The results indicated the LaCoO_3 material with the perovskite structure can be applied as adsorbent.

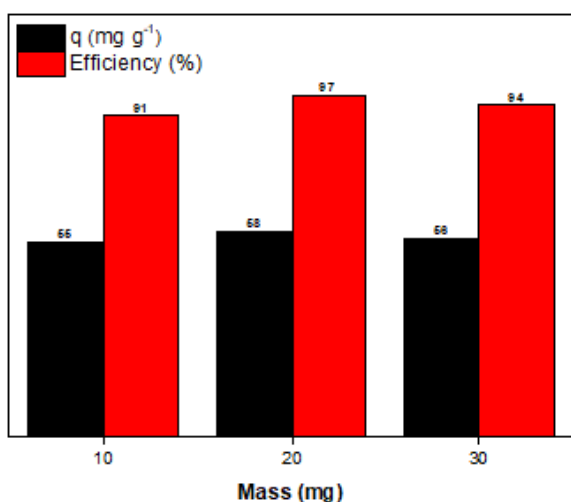


Fig. 5. Dye removal efficiency, E (%), and the amount (q) of dye removed using LaCoO_3 material.

From the results obtained, it can infer that for larger adsorbent masses, the removal efficiency happens more efficiently. We can observe that the efficiency values for the tests using the 20 and 30 mg masses occur similarly, since the difference between the adsorbent masses is 10 mg. The fact that larger masses provide greater removal efficiency can be explained by the greater amount of adsorbent material in contact with the dye, enabling greater contact between the active sites responsible for the removal of bezaktiv red dye.

4. Conclusion

LaCoO_3 perovskite showed high removal efficiency of bezaktiv red dye, with removal efficiency up to 97%. This is due to the properties in which the material presents, with the predominance of the porous perovskite phase, adequate crystallite size and surface area for dye removal. This makes it possible to apply mixed perovskite oxides for the dye adsorption in aqueous medium.

Acknowledgements

The authors acknowledge to PPGQ/UFS, CNPq and CAPES for its financial support. This study was financed in part by the Coordenação de Aperfeiçoamento de Pessoal de Nível Superior - Brasil (CAPES) -Finance Code 001.

References

- [1] Santos, A. G.; Leite, J. O.; Souza, M. J. B.; Gimenez, I. F.; Pedrosa, A. M. G. Effect of the Metal Type in Perovskites Prepared by Modified Proteic Method in Dye Adsorption from Aqueous Medium. *Ceram. Int.*, **2018**, *44* (5), 5743–5750. <https://doi.org/10.1016/j.ceramint.2017.12.232>.
- [2] Giuriatti, G.; Marques, R. G.; Pereira, C. A. A. Estudo Dos Pós Cerâmicos MgTiO_3 Na Degradação Fotocatalítica de Corantes Têxteis. *Fórum Ambient. da Alta Paul.*, **2015**, *11* (8), 129–138.
- [3] Wang, L.; Fang, S.; Feng, N.; Wan, H.; Guan, G. Efficient Catalytic Removal of Diesel Soot over Mg Substituted $\text{K/La}_{0.8}\text{Ce}_{0.2}\text{CoO}_3$ Perovskites with Large Surface Areas. *Chem. Eng. J.*, **2016**, *293*, 68–74. <https://doi.org/10.1016/j.cej.2016.02.038>.
- [4] Bradha, M.; Vijayaraghavan, T.; Suriyaraj, S. P.; Selvakumar, R.; Ashok, A. M. Synthesis of Photocatalytic $\text{La}_{(1-x)}\text{A}_x\text{TiO}_{3.5-\delta}$ (A=Ba, Sr, Ca) Nano Perovskites and Their Application for Photocatalytic Oxidation of Congo Red Dye in Aqueous Solution. *J. Rare Earths*, **2015**, *33* (2), 160–167. [https://doi.org/10.1016/S1002-0721\(14\)60397-5](https://doi.org/10.1016/S1002-0721(14)60397-5).
- [5] Lin, K. Y. A.; Chen, Y. C.; Lin, Y. F. LaMO_3 Perovskites (M=Co, Cu, Fe and Ni) as Heterogeneous Catalysts for Activating Peroxymonosulfate in Water. *Chem. Eng. Sci.*, **2017**, *160*, 96–105. <https://doi.org/10.1016/j.ces.2016.11.017>.



- [6] Santos, H.; De Silva, L. P. C.; Passos, F. B. Aplicação de Óxidos Mistos Do Tipo Perovskita Para Obtenção de Gás de Síntese a Partir Da Conversão Do Metano. *Rev. Virtual Quim.*, **2015**, *7* (4), 1441–1468. <https://doi.org/10.5935/1984-6835.20150079>.
- [7] Zarei, M.; Borhani Zarandi, M.; Alizadeh, M. Preparation of CuO/CeO₂ Composites by the Pechini Method and Investigation of Their Structural and Electrical Properties. *Ceram. Int.*, **2019**, *45*, 1991–1997. <https://doi.org/10.1016/j.ceramint.2018.10.096>.
- [8] Saha, T. K. Adsorption of Methyl Orange onto Chitosan from Aqueous Solution. *J. Water Resour. Prot.*, **2010**, *02* (10), 898–906. <https://doi.org/10.4236/jwarp.2010.210107>.
- [9] Pavia, D. L.; Lampman, G. M.; Georg S. Kriz. *Pavia - Introduction to Spectroscopy*, third edit.; Thomson Learning: United States of America, 2001.
- [10] Mahmoudi, F.; Farhadi, S.; Machek, P.; Jarosova, M. Phosphotungstic Acid Supported on Silica-Coated LaCoO₃: Synthesis, Characterization and Application as a Novel and Efficient Adsorbent for the Removal of Organic Pollutants. *Polyhedron*, **2019**, *158*, 423–431. <https://doi.org/10.1016/j.poly.2018.11.012>.
- [11] Akbari-Fakhrabadi, A.; Rodríguez, O.; Rojas, R.; Meruane, V.; Pishahang, M. H. Ferroelastic Behavior of LaCoO₃: A Comparison of Impression and Compression Techniques. *J. Eur. Ceram. Soc.*, **2019**, *39*, 1569–1576. <https://doi.org/10.1016/j.jeurceramso.2018.11.008>.
- [12] Smičiklas, I. D.; Milonjić, S. K.; Pfindt, P.; Raičević, S. The Point of Zero Charge and Sorption of Cadmium (II) and Strontium (II) Ions on Synthetic Hydroxyapatite. *Sep. Purif. Technol.*, **2000**, *18*, 185–194. [https://doi.org/10.1016/S1383-5866\(99\)00066-0](https://doi.org/10.1016/S1383-5866(99)00066-0).
- [13] McCafferty, E. Relationship between the Isoelectric Point (PH_{pzc}) and the Potential of Zero Charge (E_{pzc}) for Passive Metals. *Electrochim. Acta*, **2010**, *55*, 1630–1637. <https://doi.org/10.1016/j.electacta.2009.10.040>.

Heterogenized complexes of Ni/KIT-6 and Ni/ SBA-15: a comparative application for ethylene oligomerization

Adriano Martinez Basso^{1*}, Bruna Pes Nicola², Katia Bernardo-Gusmão², Sibeles B. C. Pergher¹

^a Federal University of Rio Grande do Norte (UFRN), Av. Senador Salgado Filho, 3000, Lagoa Nova, Natal, 59078-970 Brazil

^b Federal University of Rio Grande do Sul (UFRGS), Av. Paulo Gama, 110, Farroupilha, Porto Alegre, 90040-060, Brazil

Abstract

The mesoporous materials SBA-15 and KIT-6 were complexed with nickel synthesizing two different heterogenized catalytic precursors. This methodology starts reacting the ligand 2-(phenyl)amine-4-(phenyl)imine-2-pentene with (3-chloropropyl) trimethoxysilane (CPTMS), which is the silane source. The product obtained was anchored to mesoporous SBA-15 and KIT-6 supports through condensation of the silanols from silica matrix, hereafter the nickel was complexed on this anchored product. These materials were tested as a catalysts precursors for ethylene oligomerization processes. They were characterized using diverse techniques such as ¹H and ²⁹Si NMR, small angle XRD, thermogravimetric analysis, N₂ sorption, elemental analysis and flame atomic absorption spectroscopy. The heterogenized complexes were less active and more selective for ethylene oligomerization compared with the homogeneous media. The Ni-β-diimine /KIT-6 (KIT-L) complex displayed an activity of 7.0×10³ h⁻¹ for the ethylene oligomerization with 93% selectivity to C₄ products and 94% to α-C₄. Closed results were acquired from the Ni-β-diimine/SBA-15 (SBA-L) complex exhibiting an activity of 8.0×10³ h⁻¹ for the ethylene oligomerization with 98% selectivity to C₄ products and 93% to α-C₄. This results demonstrate that, both SBA-15 and KIT-6, exhibit similar properties in terms of catalysis.

Keywords: KIT-6; SBA-15; heterogenized complexes; β-diimines; oligomerization.

1. Introduction

Transform the successful homogeneous catalyst into a heterogeneous catalytic system is a general trend in catalysis. The use of heterogeneous solid catalysts has an obvious advantage in terms of easy separation and eventually its reuse, although it requires dedicated synthesis effort. In order to compensate this synthetic effort is by producing a solid catalyst that is durable and reusable for many runs, exhibiting a total productivity that compensates for all this effort [1].

The oligomerization of olefins is an attractive method for producing longer chain olefins which have several applications, especially in the petrochemical's products [2]. The effects of the ligand structure of transition metal complexes on their catalytic properties in oligo/polymerization reactions have been devoted for studying [3].

The mesoporous materials have unique properties such as high surface area, controllable pore structures, chemical stability, functionalizable surface and favorable morphologies [4]. Nanostructured materials have been extensively studied for several applications, especially on heterogeneous catalysis.

The nanostructured SBA-15 is a well-ordered hexagonal mesoporous silica structure with tunable large uniform pore sizes (up to 30 nm), with a highly ordered two-dimensional (2D) hexagonally (*p6mm* symmetry) mesostructured and thick uniform silica walls (3.1 to 6.4 nm) [5]. The large mesoporous silica KIT-6 with cubic *1a3d* symmetry are a molecular sieve prepared with the same reactants used on SBA-15, adding butan-1-ol like a swelling agent. This material has typically surface area of 800 m² g⁻¹, high pore volume reaching 1.05 cm³ g⁻¹ and average pore size of 8.5 nm [6].

In this work, the mesoporous materials SBA-15 and KIT-6 were synthesized, covalently

functionalized with a β -diimine ligand and heterogeneized with nickel to test in ethylene oligomerization, for comparing the silica's influence on catalytic activities and selectivities.

2. Experimental

The mesoporous support was first synthesized by typical routes [5,6]. The KIT-6's and SBA-15's synthesis gel had, respectively, the molar composition 1 TEOS: 0.017 P₁₂₃: 1.83 HCl: 195 H₂O: 1.31 Butanol and 1 TEOS: 0.017 P₁₂₃: 5.9 HCl: 194 H₂O. After that, they were calcinated at 600°C for 5 h. The ligand 2-(phenyl)amine-4-(phenyl)imine-2-pentene was synthesized by reacting acetylacetone and aniline (molar proportion 1:2) in the presence of HCl as the catalyst at room temperature [7]. The mesoporous materials were covalently functionalized with the ligand combined with the reactant (3-chloropropyl) trimethoxysilane (CPTMS). The hybrid products were ordered via interactions with the silanols of the silicas matrices and complexed with nickel by reacting with Ni(CH₃CN)₂Br₂ at room temperature for five days.

These materials were characterized using ¹H, and ²⁹Si NMR, small angle XRD, thermogravimetric analysis, elemental analysis, N₂ sorption, MET, and F-AAS. The oligomerizations reactions were monitored and characterized with gas chromatography.

3. Results and Discussion

The ligand 2-(phenyl)amine-4-(phenyl)imine-2-pentene was characterized by ¹H-NMR spectrum, shown in the Figure 1. The typical signal and its assignments are indicated in the Table 1.

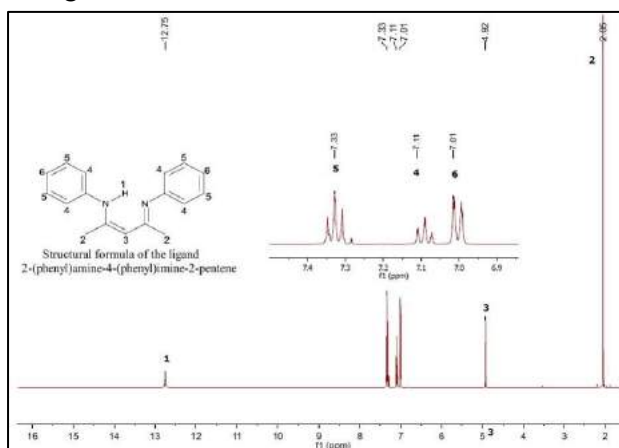


Figure 1. ¹H-NMR spectrum of the ligand.

According to the Figure and Table 1, the ¹H NMR spectrum clearly shows the ligand was produced in an acceptable pureness. The 12.75 ppm chemical shift is a strong indicative the presence of the H less shield, that is covalently bonded in a N atom.

Table 1. ¹H-NMR dates of the β -diimine ligand.

Sample	Assignment	δ (ppm)
Ligand (C ₁₇ H ₁₈ N ₂)	s, 1H, H-N	12.75
	t, 4H, <i>m</i> -ArH	7.33
	t, 2H, <i>p</i> -ArH	7.11
	t, 4H, <i>o</i> -ArH	7.01
	s, 1H, β -CH	4.92
	s, 6H, α -CH ₃	2.05

The calcinated mesoporous materials were characterized by small angle XRD presented in the Figure 2.

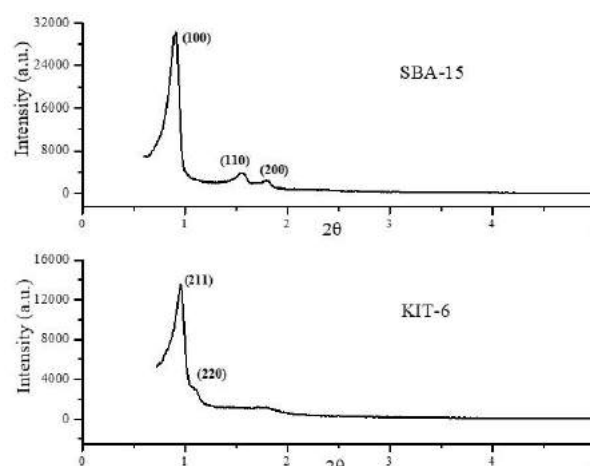


Fig. 2. XRD patterns of SBA-15 and KIT-6 calcinated.

The low-angle reflection peaks indexable as (100), (110), (200) diffractions associated with *p6mm* hexagonal symmetry can be observed, confirming the formation of SBA-15-type mesoporous silicas [5]. In the same way, the peaks indexable as (211), (220) associated with *Ia3d* cubic symmetry can confirm the formation of KIT-6 [6].

The N₂ sorption measurements for the SBA-15 and KIT-6 calcinated with and without the ligand anchored are shown in Figures 3 and 4, respectively. The Table 2 brings the textural properties of this materials.

Table 2. Some textural properties of the materials.

Sample	A_{BET} (m^2g^{-1})	V_T (cm^3g^{-1})	V_{Me} (cm^3g^{-1})	P_w (nm)
SBA	840	1.23	1.21	8.0
SBA-L	196	0.29	0.01	6.6
KIT	615	0.66	0.63	6.8
KIT-L	270	0.32	0.32	6.2

A_{BET} is the total specific area obtained from BET method. V_T is the total pore volume obtained with a relative pressure p/p^0 of 0.98. V_{Me} is the mesopore volume obtained using α -plots methodology. P_w is the pore width obtained through the BJH method corrected by the VBS method.

All samples show type-IV(a) isotherms with H1 hysteresis loops [8]. The SBA-15 calcinated has $840 m^2g^{-1}$ of BET area, $1.23 cm^3g^{-1}$ of total volume, $1.21 cm^3g^{-1}$ of mesopore volume and 8.0 nm of pore width. The same properties to the SBA-15 change drastically after anchoring the ligand (SBA-L). The new BET area was $196 m^2g^{-1}$, the total volume decreased to $0.29 cm^3g^{-1}$, the mesopore volume practically disappeared ($0.01 cm^3g^{-1}$) and the pore width was diminished to 6.6 nm.

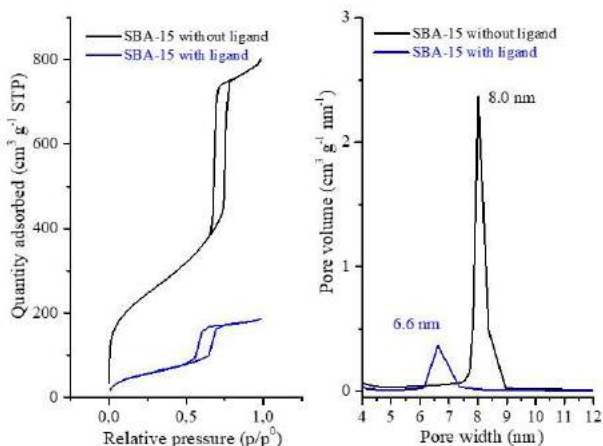


Fig. 3. N_2 adsorption-desorption isotherms and pore size distributions of SBA-15 calcinated with and without the ligand anchored.

The same behavior was observed to the KIT-6 calcinated and with the ligand anchoring (KIT-L), but not too discrepant. The BET area decreased (615 to $270 m^2g^{-1}$), the total pore volume and the mesopore volume had the diminished values almost in 50% (0.66 to $0.32 cm^3g^{-1}$ and 0.63 to $0.32 cm^3g^{-1}$, respectively). Only the pore width stayed almost unaltered (6.8 to 6.2 nm). All these dates confirm the presence of the ligand on the surface of the mesoporous.

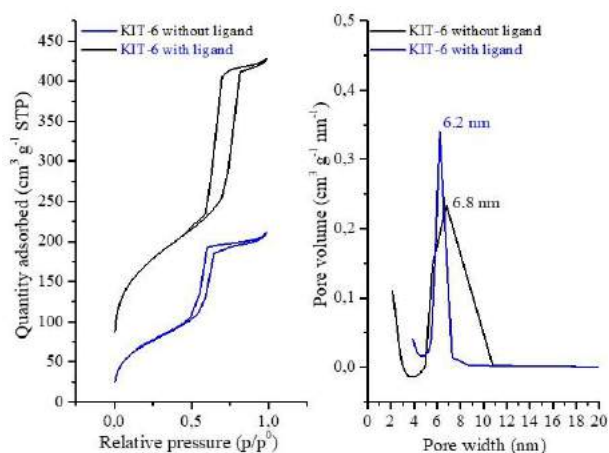


Fig. 4. N_2 adsorption-desorption isotherms and pore size distributions of KIT-6 calcinated with and without the ligand anchored.

Although the sorption isotherm suggest clearly the presence of the ligand on the mesoporous structure, the samples were analyzed using solid state $^{29}Si\{^1H\}$ cross-polarization-magic angle spinning (CP-MAS) nuclear magnetic resonance (NMR) to confirm the covalent bond between the ligand and the silanols from the molecular sieves. The results are shown in the Figure 5.

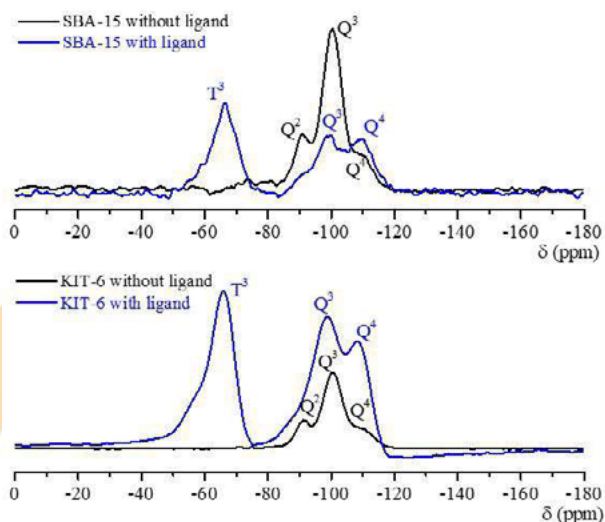


Figure 5. ^{29}Si NMR spectrum of calcinated SBA-15 with and without ligand (above) and calcinated KIT-6 with and without ligand (below).

According to the literature [9], three distinct resonance peaks corresponding to Q^n are observed to materials like SBA-15 and KIT-6, representing their silica sites. The NMR signal closed to -90 ppm referring to Q^2 , germinal silanol $(SiO)_2Si(OH)_2$, closed to -100 ppm assigned to Q^3 , single silanol

(SiO)₃Si(OH) and near to the – 110 ppm report to siloxane (SiO)₄Si.

The ²⁹Si CP-MAS-NMR analyses indicate that the ligand β-diimine was successfully anchored covalently to the both silicas support through the chemical Si–O–C bonds. The appearance of T³ signal (closed to -70 ppm) indicates the C–Si(OSi)₃ covalent bond formation. At the same time, the disappearance of Q² signal and the increase of the Q⁴ signal indicate the consumption of silanols, like Si(OH)₂. The ligand and nickel incorporations percentages attributed to the SBA-L and KIT-L can be seen in the Table 3.

Table 3. Elemental analysis and flame atomic absorption data for the heterogenized materials.

Sample	C (%)	H (%)	N (%)	Ligand content (μmol/g) ^a	Nickel content (μmol/g) ^b
SBA-L	9.41	2.31	0.45	160.70	56.22
KIT-L	8.48	2.05	0.28	100.0	39.18

^a Ligand incorporation calculated from the %N obtained from the elemental analysis.

^b Nickel content of complexes obtained from FAAS.

Both ligand and nickel contents were higher in the complexes of SBA-15 than KIT-6, respectively, 160.7 against 100.0 μmol/g for ligand content and 56.22 against 39.18 μmol/g for nickel purport. This result is explained by the SBA-15's major textural properties presented by Table 2, like the total specific area, the total pore volume, the mesopore volume and the pore width.

The nickel catalytic precursors anchored to the SBA-15 and to the KIT-6 were used as catalysts with ethylaluminumsesquichloride (EASC) for ethylene oligomerization. This result was compared with that for homogeneous media and it is exhibit in the Table 4. All the reactions were done in duplicated. The reaction conditions utilized on the heterogeneous media like temperature, pressure, solvent, reaction time, co-catalyst, Al/Ni ratio were previously studied [10].

Table 4. Results of ethylene reactions with the heterogeneous nickel complexes compared to homogeneous.

Sample	TOF ^a (10 ³ h ⁻¹)	S _{C4} (%)	S _{α-C4} (%)	S _{C6} (%)	S _{C8+} (%)
Homo	72	86	49	9	-
SBA-L	8	98	93	1	1
KIT-L	7	93	94	2	4

^a TOF: ml of ethylene oligomerized/(mol Ni×hours)
nNi = 15 μmol, Al/Ni ratio = 200, T = 10 °C, time = 0.5 h, Pressure = 15 bar of ethylene, Solvent = toluene (60 mL), Cocatalyst = EASC

The lower catalytic activity of the heterogenized complex (SBA-L and KIT-L) compared with the homogeneous complex (Homo) is attributed to two factors. The first one is that the complex anchored is less disponible that the homogeneous one. The second one is the fewer active species, which is related to the larger fact that part of EASC is consumed by the hydroxyl groups present in the mesoporous matrix. This decrease the quantity of active species formed. [2]. Nevertheless, the heterogenized complexes exhibited best selectivities for the C₄ and for α-C₄ fractions when compared to the homogeneous nickel complexes. This results are consistent with the literature [10].

Comparing to SBA-15 and KIT-6, both have the same behavior in terms catalytic, with narrow differences in values to the selectivity and to the catalytic activity.

4. Conclusion

The mesoporous KIT-6 is a good alternative to produce the catalytic precursor to be used in heterogenized catalysis. The KIT-6's results, comparing with the homogeneous media, is similar with the SBA-15, like decrease in catalytic activity and increase in α-C₄ selectivity. Despite the biggest goal of the heterogeneous catalytic system is the recycle reaction, it shall be performed to the KIT-6 soon and the results shall be presented in next works.

Acknowledgements

All the Authors are kindly thanked for supporting from LABPEMOL and LRC Brazilian laboratories groups, situated, respectively, in the cities Natal/RN and Porto Alegre/RS. This study was financed by the CAPES – Finance Code 001.

References

- [1] Corma A, Garcia H. Silica-Bound Homogenous Catalysts as Recoverable and Reusable Catalysts in Organic Synthesis. *Adv Synth Catal* 2006;348:1391-1412.
- [2] Rossetto E, Caovilla M, Thiele D, de Souza RF, Bernardo-Gusmão K. Ethylene oligomerization using nickel- β -diimine hybrid xerogels produced by the sol-gel process. *Appl Catal A Gen* 2013;454:152-159.
- [3] Bianchini C, Giambastiani G, Luconi L, Meli, A. Olefin oligomerization, homopolymerization and copolymerization by late transition metals supported by (imino)pyridine ligands. *Coord Chem Rev* 2010;254:431-455.
- [4] Dinari M, Mohammadnezhad G, Nabiyan A. Preparation and characterization of nanocomposite materials based on polyamide-6 and modified ordered mesoporous silica KIT-6. *J Appl Polym Sci* 2016;133:43098-43104.
- [5] Zhao D, Feng J, Huo Q, Melosh N., Fredrickson GH, Chmelka BF, Stucky GD. *Science* 1998;279:548-552.
- [6] Kleitz F, Choi SH, Ryoo R. Cubic Ia3d large mesoporous silica: synthesis and replication to platinum nanowires, carbon nanorods and carbon nanotubes. *Chem Comm* 2003;7:2136-2137.
- [7] Tang LM, Duan YQ, Li XF, Li YS. Syntheses, structure and ethylene polymerization behaviour of β -diiminato titanium complexes. *J Organomet Chem* 2006;691:2023-2030.
- [8] Thommes M, Kaneko K, Neimark AV, Olivier JP, Reinoso FR, Rouquerol J, Sing KSW. Physisorption of gases, with special reference to the evaluation of surface area and pore size distribution (IUPAC Technical Report) *Pure Appl Chem* 2015; aop.
- [9] Serrano DP, Aguado J, Vargas C A comparison of methods for the heterogenization of the chiral Jacobsen catalyst on mesostructured SBA-15 supports. *Appl Catal A Gen* 2008;335:172-179.
- [10] Rossetto E, Nicola BP, De Souza RF, Bernardo-Gusmão K, Pergher SBC. Heterogeneous complexes of nickel MCM-41 with β -diimine ligands: Applications in olefin oligomerization. *J Catal* 2015;323:43-54.

Evaluation of LaNiO_3 type materials prepared by different routes as adsorbent for dyes removal

Júlia B. R. Fernandes^a, Andreza A. Souza^b, Iasmin A. Ribeiro^b, Marcelo J. B. Souza^c, Anne M. Garrido Pedrosa^{a,b}

^aDepartament of Chemistry, Federal University of Sergipe, Av. Marechal Rondon, Rosa Elze, São Cristóvão-SE, 49100-000, Brazil

^bGraduate Program in Chemistry, Federal University of Sergipe, Av. Marechal Rondon, Rosa Elze, São Cristóvão-SE, 49100-000, Brazil

^cDepartament of Chemical Engineering, Federal University of Sergipe, Av. Marechal Rondon, Rosa Elze, São Cristóvão-SE, 49100-000, Brazil

Abstract

Mixed oxides with perovskite structure have shown great prominence in the last years for being materials that present high stability and diverse properties interesting to the industrial sector, as applications in catalysis and adsorption. The synthesis method used may influence in properties of the material obtained, such as particle size, surface area, structure and number of phases present. The synthesis methods studied in this work were: protein modified, mechanosynthesis and plate combustion. The synthesized materials were calcined at 900 °C. The samples were characterized by X-ray diffraction patterns, zero charge point and specific surface area. The materials were studied through adsorption tests with Congo red dye at different times of contact with the adsorbent. LaNiO_3 perovskite oxides presented satisfactory removal efficiency, especially the materials synthesized by the modified protein method.

Keywords: LaNiO_3 ; adsorption; dyes; Congo red.

1. Introduction

Dyes in general have great importance in the industrial sectors such as industry food, textiles among others [1], but can become contaminants and cause risks for the aquatic environment. During tissue dyeing processes, about 20% of the dye used is lost in the medium [2], this becomes problematic due to the presence of azo groups present in the dye structure [3].

Perovskite is a ceramic material derived from calcium titanate (CaTiO_3) [4] and is classified as a mixed oxide that combines metallic and non-metallic materials of formula ABX_3 . Site A is occupied by large metal cations such as lanthanides, Site B is occupied by smaller metal cations as transition metals of block d and X is occupied by oxygen anions [5-7]. It is important that there is electroneutrality, in which the sum of the charges of A and B must be equivalent to the charge of the anions of X [8-9]. The material has predominantly ionic bonds [8] and also has several structural forms

such as orthorhombic, rhombohedral, tetragonal and triclinic, being ideal the cubic [10-11].

Mixed oxides with perovskite structure have been the subject of constant studies in the last decades for its ease of obtaining and for presenting numerous properties that drive many researches. Its application involves industrial, environmental and technological sectors and its properties stand out as adsorptive, catalytic, electrical, optical, magnetic, ferroelectric, superconductivity, thermoelectric batteries, fuel cells, electronic devices and generally have good thermal stability. These properties depend on the composition, oxide structure, and synthesis method [4-6,10,12-17].

The synthesis method can influence the material characteristics and properties [4-6, 9, 12] such as particle size, surface area, structure and number of secondary phases. For this reason, there is an interest in studying and testing different routes of synthesizing this material.

The LaNiO_3 type perovskite in particular is applied as an electrode in electronic devices, is generally rhombohedral in shape [13] and has proven adsorptive power in dye solutions [5-6].



In the present work mixed oxides of type perovskite were synthesized by different synthesis routes, calcined and characterized by physicochemical techniques. Application as adsorbent material was tested with Congo red dye solutions using a batch system.

2. Experimental

2.1. Synthesis of $LaNiO_3$ material

The materials were synthesized by the modified protein method [5-7, 9] mechano-synthesis [5, 14] and plate combustion [9]. After obtaining the materials by the three different methods they were calcined at 900 °C at rate of 10 °C min⁻¹.

For the preparation of the material by the modified protein method, industrial soybean with nickel nitrate/soybean ratio of 1.0/0.5 was used. The procedure begins by dissolving the stoichiometric mass of $Ni(NO_3)_2 \cdot 6H_2O$ in 100 mL of stirring water for 30 minutes at room temperature. Then the stoichiometric mass of $La(NO_3)_3 \cdot 6H_2O$ is added and stirred under the same time and temperature conditions. Then the temperature is raised to 70 °C and the soybean is added under constant stirring. The mixture is allowed to stir for 1 hour while remaining at 70 °C. After this time, the solution is pre-calcined at 350°C for 2 hours at 10 °C min⁻¹.

Mechano-synthesis is a method in which stoichiometrically adding nickel and lanthanum oxides to a grinding vessel in a ball mill under the effects of rotation and time. For synthesis of the material by this method La_2O_3 and Ni_2O_3 were used as reagents in stoichiometric quantities. The Retsch PM 100 ball mill was used. Three balls composed of tungsten carbide were used and the system was rotated at 400 rpm for 6 hours with a break of 3 minutes every 1.5 hours.

The plate combustion method is similar to the modified proteic method, however there is no addition of chelating agent but of a oxidizing agent (urea). First, a stoichiometric mass of urea (CH_4N_2O) was solubilized in 20 mL of water under stirring for 3 minutes. The solution is then added to the nickel and lanthanum nitrates aqueous system and transferred to a porcelain dish and brought to a plate (300-350 °C) for the combustion reaction to occur.

2.2. Characterization of synthesized materials

The samples calcined at 900 °C were characterized by X-ray diffraction patterns (XRD),

specific surface area (SSA), zero charge point (PCZ). The surface area was determined from the N_2 adsorption isotherm at 77 K and by using the BET method.

2.3. Adsorption tests

To verify the efficiency of materials prepared as adsorbents, adsorption assays with Congo red dye were performed in triplicate and by using the calcined samples obtained by the three different synthesis methods.

To determine the amount of dye adsorbed in the tests, the UV-Vis spectrophotometer of the Shimadzu brand and model UV-1800 was used, using 3.5 mL quartz cuvettes with 1.0 cm optical path and applying a sweep in the range of wavelength between 400 and 700 nm.

Removal assays of the dye from the medium were performed in batch using 150 mL of a 30 ppm Congo red dye aqueous solution and 0.1 g of the adsorbent sample (perovskite). At time intervals aliquots were taken, subjected to filtration and analyzed on the UV-Vis spectrophotometer in the range of 400 to 700 nm.

To obtain quantitative values of dye removal efficiency and evaluation of the amount of mass of adsorbed dye from the medium, equations 1 and 2 were used.

$$E\% = \left(\frac{C_0 - C}{C_0} \right) \times 100 \quad (1)$$

E = Removal Efficiency (%)

C = is the average concentration of the solution over a given time in mg L⁻¹

C₀ = the initial concentration of the solution in mg L⁻¹.

$$q = \frac{(C_0 - C)V}{m} \quad (2)$$

q = amount of adsorbed dye (mg g⁻¹)

m = is the mass of adsorbent in g

V = is the volume of the solution in L

3. Results and discussion

Figure 1 shows the X-ray diffraction patterns for materials obtained by the three different synthesis methods.

For the LN9-GP sample, derived from the modified protein method, the result indicates the presence of peaks with values close to the standard chart number 330711, with maximum perovskite peak at $2\theta = 32.71^\circ$. The other peaks also attributed to the LaNiO_3 phase presented 2θ values at 23.16° , 40.52° , 47.17° , 53.43° and 58.45° . One also notices a NiO phase-related peak at 43.26° and one two La_2O_3 related peaks at 28.70° and 52.35° .

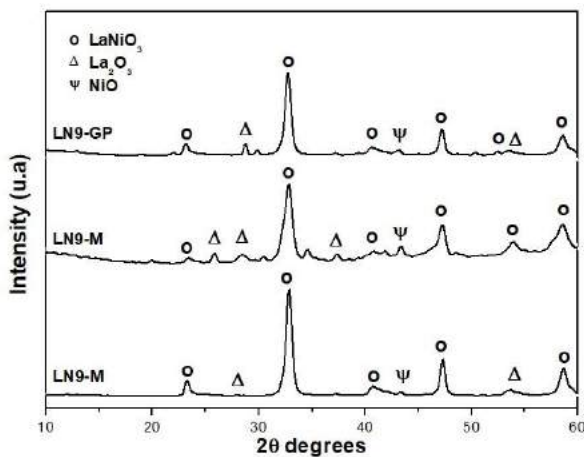


Fig 1. X-ray diffractogram of materials obtained by the three different synthesis methods.

The results for the calcined sample LN9-M, obtained by the mechanosynthesis method, indicate the presence of peaks close to the standard chart number 330711, with a maximum peak at $2\theta = 32.79^\circ$ related to the perovskite phase. The other peaks attributed to the phase presented 2θ values in 23.48° , 40.61° , 47.36° , 53.89° and 58.62° . It is also noticed a NiO phase-related peak at 43.43° and three La_2O_3 -related peaks at 25.71° , 28.42° and 37.35° .

The LN9-CP calcined sample, synthesized by the plate combustion method, indicated the presence of peaks very close to the standard chart number 330711, with a maximum peak at $2\theta = 32.71^\circ$ related to the perovskite phase. The other peaks attributed to perovskite presented 2θ values at 23.16° , 40.52° , 47.52° and 58.62° . Two peaks related to the La_2O_3 phase are also noted at 37.24° and 53.43° . For the NiO phase a peak at 43.26° was visualized.

The three calcined samples showed peaks related to the perovskite phase, especially the material synthesized by the combustion method (LN9-CP). The sample synthesized by the mechanosynthesis method revealed the presence of many secondary phases, this may be related to the synthesis method.

The sample from the modified protein method showed peaks related to the perovskite phase but also secondary phases related to the synthesis method.

Figure 2 shows the zero charge point (PCZ) results for materials synthesized by the three synthesis routes. To determine the zero charge point, the method by system equilibrium fixed in agitation was used [18]. The PCZ results indicated that LaNiO_3 synthesized perovskites are around $\text{pH} = 7$.

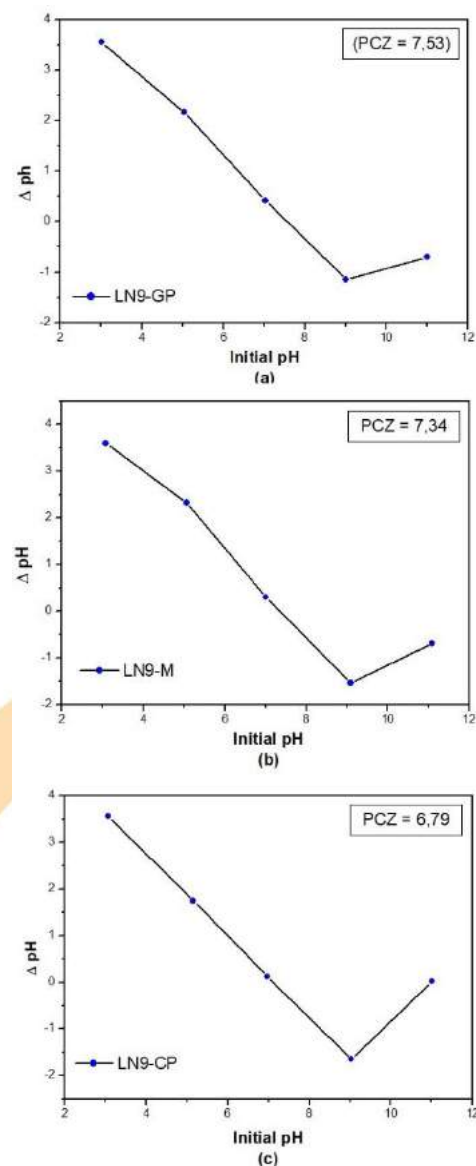


Fig 2. PCZ determination for LN9-GP (a), LN9-M (b) and LN9-CP (c) materials.

Specific surface area values of mixed oxides are generally relatively low due to the processes of

synthesis and calcination, which involve high temperatures [5-6,8-9]. For the material synthesized by the modified protein method (LN9-GP) and plate combustion (LN9-CP) the area values were 26 and 28 m² g⁻¹ respectively, and the values are higher compared to the sample area synthesized by the mechanosynthesis method (LN9-M) of 21 m² g⁻¹.

Dye removal efficiency results using the three prepared materials can be seen in Table 1. From the data it can be noted that the longer the contact time of the dye with the sample, the greater the adsorption efficiency, ie the greater the amount of dye removed from the medium. The three samples from the three synthesis methods enable the dye to be adsorbed effectively. The efficiency values are shown in Table 1.

Table 1. Dye removal efficiency using different materials.

Time (min)	Removal Efficiency (%)		
	LN9-GP	LN9-M	LN9-CP
0	0	0	0
10	63	48	53
20	62	48	50
30	63	48	52
40	63	50	56
50	64	51	59
60	66	51	62

The most efficient material for dye removal was the obtained by the modified protein method (LN9-GP) which had 66% efficiency in 60 minutes of testing, ie the material removed the largest amount of dye and has the greatest potential for use as an adsorbent. Next, the 62% plate combustion method and the lowest efficiency was the material obtained by mechanosynthesis method with 51% dye removal efficiency in 60 minutes of assay. This material presented the smallest surface area. Adsorption studies with the same dye using other adsorbent materials show similar values of the amount of dye removed and removal efficiency (keeping the conditions of the experiment) [5-6].

The kinetic study was applied using the pseudo first order (PFO) and pseudo second order (PSO) models using equations from the literature [5]. Figure 3 presents the results of adsorption kinetics by applying the PFO and PSO models.

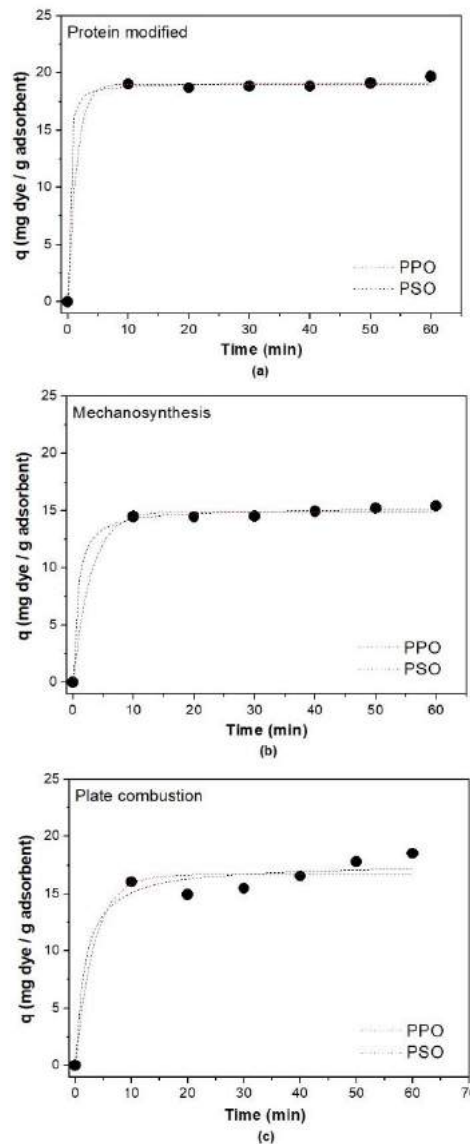


Fig 3. Adsorption kinetics of Congo red dye using materials prepared by different methods.

Table 2 shows the amount of adsorbed dye, the velocity constant and the correction factor of the two models.

Both kinetic models presented high values of linear coefficients, indicating the effectiveness of applying the models to study the tests. Despite this, the pseudo second order model was the best fit to the experimental values since the R² values were the closest to 1. For the other hand, when observing the velocity constants of the two models for all materials, it can be noted that for all materials had

higher k_1 velocity constants when applied PFO model.

Table 2. Parameters obtained using PFO and PSO models.

PFO			
Adsorbents	$k_1(\text{min}^{-1})$	$q_1(\text{mg g}^{-1})$	R^2
LN9-GP	0.71711	19.03411	0.99805
LC9-M	0.34227	14.91542	0.99618
LN9-CP	0.29827	16.69267	0.96302
PSO			
Adsorbents	$k_2(\text{g mg}^{-1}\text{min}^{-1})$	$q_2(\text{mg g}^{-1})$	R^2
LN9-GP	0.28138	19.17516	0.99823
LC9-M	0.09351	15.25062	0.99769
LN9-CP	0.03317	17.66183	0.97256

Although the predicted k values for the two models (PFO and PSO) were different, the predicted q values for the two models are very close when comparing the sample produced by each synthesis method.

4. Conclusion

Based on the obtained results, it is possible to prepare mixed oxides with LaNiO_3 type perovskite structure by the modified protein method, mechanosynthesis and plate combustion, followed by calcination at 900°C . The plate combustion method resulted in a smaller number of secondary phases, which indicates to be a more efficient method to obtain the LaNiO_3 perovskite.

From the adsorption tests it was observed that the calcined materials of the three methods obtained satisfactory results as adsorbent materials, in particular the sample synthesized by the modified protein gel method, which had better behavior in the adsorption of the Congo red dye, with efficiency of 66% removal after 60 minutes of assay.

Acknowledgements

The authors acknowledge to CNPq and CAPES for its financial support.

References

- [1] Debrassi, A. et al. Adsorption of Congo Red dye by hydrophobically modified O-Carboxymethyl chitosan derivatives, *Quim. Nova*. Vol 34. N° 5 (2011) 764-770.
- [2] Dallago, R. M e Smaniotto, A. Tannery Solid Residues as adsorbents for the removal of dyes in aqueous media, *Quim. Nova*. Vol 28. N° 3 (2005) 433-437.
- [3] Rodrigues, K. et al. Dye removal using *Aspergillus Niger* An400 in a sequential batch reactor, *Quim. Nova*. Vol 34. N° 7 (2011) 1119-1123.
- [4] Wanderley, J. B. M et al. Synthesis and microstructural study of perovskite type $\text{La}_{0.8}\text{Ca}_{0.2}\text{MO}_3$ (M = Co or Mn) with gelatin as an organic precursor for application in automotive catalysis, *Cerâmica* 59 (2013) 156-159.
- [5] A.G. Santos, J.O. Leite, M.J.B. Souza, I.F. Gimenez, A.M.G. Pedrosa, Effect of the metal type in perovskites prepared by modified protein method in dye adsorption from aqueous medium, *Ceram. Int.* 44 (2018) 5743-5750.
- [6] A.G. Santos, J.O. Leite, I.F. Gimenez, M.J.B. Souza, A.M.G. Pedrosa, Effect of the B-site cation from LaBO_3 and $\text{LaBO}_3/\text{TiO}_2$ (B = Mn or Ni) perovskites prepared by mechanosynthesis in adsorption of Congo red dye from aqueous medium. *Materials Research Express*, 6 (2019) 105065.
- [7] J.C. Santos, M.J.B. Souza, J.A.C. Ruiz, D.M.A. Melo, M.E. Mesquita, A.M.G. Pedrosa, Synthesis of LaNiO_3 perovskite by the modified protein gel method and study of catalytic properties in the syngas production, *J. Braz. Chem. Soc.* 23 (2012) 1858-1862.
- [8] D. M. H. Martinelli, D. M. A. Melo, A. M. G. Pedroza, A. E. Martinelli, M. A. F. Melo, R. C. Bitencourt. Use of Perovskite-Type Lanthanum Nickelate Synthesized by the Polymeric Precursor Method in the Steam Reforming Reaction of Methane. *Materials Sciences and Applications* 03 (2012) 363-368.
- [9] E.O. Moraes Júnior, J.O. Leite, A.G. Santos, M.J.B. Souza, A.M.G. Pedrosa, Nickel-based perovskite catalysts: synthesis and catalytic tests in the production of syngas, *Cerâmica*. 64 (2018) 436-442.
- [10] Silva, P. R. N. Use of Perovskite Oxides in the Oxidations of Propane and CO, *Quim. Nova*. Vol 27. N° 1 (2004) 35-41.
- [11] Soares, A. B. et al Study of Total Ethanol Oxidation Using Type Oxides Perovskita LaBO_3 (B= Mn, Ni, Fe), *Quim Nova*. Vol 30. N° 5 (2007) 1061-1066.

Study of the influence of perovskite structure site A metals on the adsorptive properties in liquid medium

Jéssica A. S. Lemos^a, Vitória M. S. C. Souza^b, Iasmin A. Ribeiro^a, Marcelo J. B. Souza^c, Anne M. Garrido Pedrosa^{a,b}

^aGraduate Program in Chemistry, Federal University of Sergipe, Av. Marechal Rondon, Rosa Elze, São Cristóvão-SE, 49100-000, Brazil

^bDepartament of Chemistry, Federal University of Sergipe, Av. Marechal Rondon, Rosa Elze, São Cristóvão-SE, 49100-000, Brazil

^cGraduate Program in Chemical Engineering, Federal University of Sergipe, Av. Marechal Rondon, Rosa Elze, São Cristóvão-SE, 49100-000, Brazil

Abstract

Perovskites are crystalline materials classified as mixed oxides that have several applications due to their magnetic, electrical, catalytic and optical properties. In addition, they have recently excelled in environmental applications for contaminant removal due to adsorptive characteristics. In this work the influence of the site A metals of the perovskite structure LaNiO_3 and $\text{La}_{0.5}\text{Ca}_{0.5}\text{NiO}_3$ synthesized by the mechanochemical synthesis method was studied. The obtained materials were calcined at 900 °C for two hours, subjected to characterization by X-ray powder diffractometry (XRD), which indicated the formation of the perovskite phase in all calcined materials as well as the presence of secondary phases. By scanning electron microscopy (SEM) and N_2 adsorption at 77 K, and using BET method, which showed porosity in both materials. The adsorption tests of the turquoise dye with the LaNiO_3 and $\text{La}_{0.5}\text{Ca}_{0.5}\text{NiO}_3$ perovskites showed removal of 96 and 89%, respectively. Kinetic studies showed that the pseudo first order and pseudo second order models presented high values of linear coefficients, indicating the effectiveness of applying the models to the test studies.

Keywords: Perovskite; Mechanochemical synthesis; Adsorption

1. Introduction

The progressive population increase has exposed the environment to various forms of contamination. Among them, the most worrying concerns the water bodies, where the indiscriminate use of water by the population, the neglect and unpreparedness of the chemical residues present in it have made it increasingly scarce and inadequate for human consumption [1].

Textile effluents are currently classified among substances considered harmful to the environment [2]. Characterized by being highly colored due to the presence of dyes, the effluent when reaching rivers causes a reduction in sunlight penetration, which ultimately decreases photosynthetic activity, dissolved oxygen concentration and water quality [3].

Textile dyes are organic compounds that have complex aromatic structures usually consisting of a chromophore group responsible for color and auxiliary groups responsible for fixation. These

include the class of azo dyes, such as the turquoise dye (Fig. 1), used in this work [4].

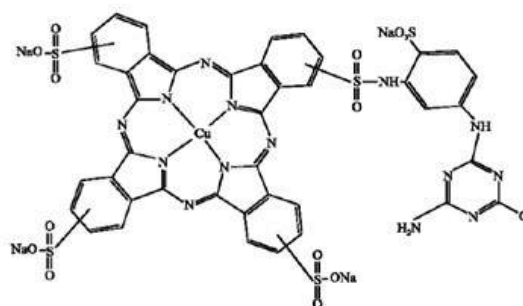


Fig. 1. Chemical structure of turquoise dye.

Removal by conventional physical, chemical and biological treatments has been increasingly hampered by the thermal and chemical stability of the dyes [2,5]. Therefore, the application of the adsorption technique and the use of new materials have been studied in order to minimize or eliminate these contaminants from water bodies [6].

Perovskites are crystalline materials that have the general formula ABX_3 , where position A is

occupied by metal ions that have large atomic rays such as alkaline metals, alkaline earth and rare earth, position B is occupied by ions of the smaller metals such as the outer transition metals and X is most often O^{2-} [7].

Studies focusing on the use of perovskites with adsorptive properties for dye removal are still scarce in the literature, but there are good results using as adsorbent in the removal of Congo red dye [8]. Therefore, the present work describes the study of the influence of the metals that occupy the site A of the perovskite structure on the adsorptive properties in liquid medium.

2. Materials and methods

2.1. Synthesis of the perovskites

To obtain $LaNiO_3$ oxide, the procedure consisted of adding stoichiometric quantities of the masses of lanthanum (III) and nickel (III) oxides in the grinding vessel, having a powder/sphere mass ratio of 1:20. The vessel/beads/powder system was rotated at 400 rpm for 6 hours, so that every 1.5 hours of milling there was a 3 minute break and then reversal of direction. At the end of 6 hours, a precursor powder was obtained and separated into two parts: the first was calcined at 900 °C for 2 hours at a rate of 10 °C min^{-1} and the remainder was stored for further analysis.

The same procedure described above was used for the synthesis of $La_{0.5}Ca_{0.5}NiO_3$ perovskite oxide structure, but with the addition of stoichiometric amounts of CaO at site A.

The samples calcined at 900 °C were named: LN-M9 for $LaNiO_3$ and LCN-M9 for $La_{0.5}Ca_{0.5}NiO_3$.

2.2. Characterization of the perovskites

X-ray diffraction was performed using a D8 Advance Bruker diffractometer, operated with $CuK\alpha$ ($\lambda = 1.5418 \text{ \AA}$) and 2θ in the range of 10–60° and scan step of 0.020° min^{-1} . Phase identification was performed by comparison with data from ICSD (Inorganic Crystal Structure Database).

The material porosity was analyzed using the HITACHI Scanning Electron Microscopy (SEM), model TM 3000. The surface area was determined from the N_2 adsorption isotherm at 77 K and by using the BET method.

2.3. Adsorption tests in liquid phase

After obtaining the dye absorption spectrum and analytical curve, studies were performed to evaluate dye removal. For the adsorption tests 250 mL of the 30 $mg L^{-1}$ turquoise dye solution was prepared, acidified and then 0.05 g perovskite was added. This system was kept under stirring and for fixed time intervals of 5, 15, 30, 60 and 90 min, aliquots were collected and filtered to separate the perovskite from the solution. For each aliquot, the filtrate was analyzed by UV-visible absorption spectrophotometry at 628 nm wavelength.

Adsorption efficiency ($E\%$) and amount of adsorbed dye (q) values in milligrams per gram of adsorbent were calculated based on equations 1 and 2 [9], respectively.

$$E\% = \left(\frac{C_0 - C}{C_0} \right) \times 100 \quad (1)$$

$$q = \frac{(C_0 - C)V}{m} \quad (2)$$

Where:

C_0 is the initial concentration solution in $mg L^{-1}$;
 C is the concentration solution at time t in $mg L^{-1}$;
 V is the volume of the solution in L;
 m is the mass of the adsorbent, in g.

The pseudo first order (PFO) and pseudo second order (PSO) kinetic models are classic models and were used for the adsorption kinetic study, as shown in equations 3 and 4, respectively [10].

$$q(t) = q_e [1 - e^{(-k_1 t)}] \quad (3)$$

$$\frac{t}{q(t)} = \frac{t}{q_e} + \frac{1}{k_2 q_e^2} \quad (4)$$

Where:

$q(t)$ is the amount of adsorbed solute;
 q_e is the amount of equilibrium adsorbed solute;
 t is the time;
 k_1 is the pseudo first order velocity constant;
 k_2 is the pseudo second order velocity constant.

3. Results and discussion

Figure 2 shown X-ray diffraction patterns for the adsorbents synthesized. For the LN-M9 sample, the perovskite structure was characterized by a high intensity peak at $2\theta = 32.71^\circ$ and other, less intense peaks observed at 2θ equal to 23.10° , 40.48° , 47.19° , 53.46° and 58.41° with trigonal structure (ICSD n° 43-4014). However, there are peaks at 2θ at 28.51° and 29.80° , which are attributed to La_2O_3 (ICSD n°

25-7585) and peaks at 2θ at 37.14° and 43.20° , associated with Ni_2O_3 (ICSD n° 25-9699).

For the LCN-M9 sample, the perovskite structure was characterized by a high intensity peak at $2\theta = 33.17^\circ$, but other peaks were also observed at 2θ equal to 47.62° and 58.43° , which confirm the formation of mixed oxide (ICSD n° 43-4014). In addition, the diffractograms showed a high intensity peak at $2\theta = 31.78^\circ$ and others less intense at 2θ at 24.30° , 28.32° and 44.20° for the La_2NiO_4 spinel phase (23-0389) [11].

Low intensity peaks for other secondary phases are also observed with 2θ values at 37.15° and 43.20° for Ni_2O_3 (JCPDS n° 25-9699), while the 2θ peak at 37.15° may also be related to CaO (JCPDS n° 26-1847).

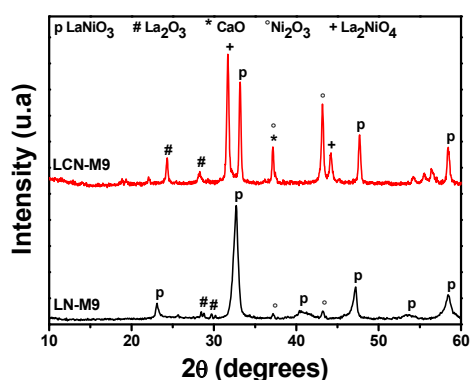


Fig. 2. XRD patterns for LN-M9 and LCN-M9.

Analyzing Fig. 2, it can be observed that in the calcium-free sample, the perovskite structure prevails, presenting peaks with very low intensities related to the secondary phases of La_2O_3 and Ni_2O_3 . However, in the sample with partial calcium doping, the diffraction lines for the La_2NiO_4 spinel phase are observed along with the perovskite structure, in addition to the secondary phases of La_2O_3 , Ni_2O_3 and CaO [4, 12].

The micrographs of LN-M9 and LCN-M9 samples synthesized by the mechanochemical method as observed in Fig. 3, showed uniformly distributed morphology with porosity and little agglomeration, and the LCN-M9 sample appears to have a system slightly larger porous than the sample LN-M9. This fact may be associated with partial doping of site A [4].

The surface area values for the LN-M9 and LCN-M9 materials were 29 and $32 \text{ m}^2 \text{ g}^{-1}$, respectively. Typically, the perovskites oxides type has low surface areas, smaller than $10 \text{ m}^2 \text{ g}^{-1}$, and the larger the surface area can be obtained by modifications in the synthesis procedure and/or the composition the structure [4]. Data from the literature indicated that in the dye adsorption that is not the only factor that influences the process when using mixed oxides [13,14].

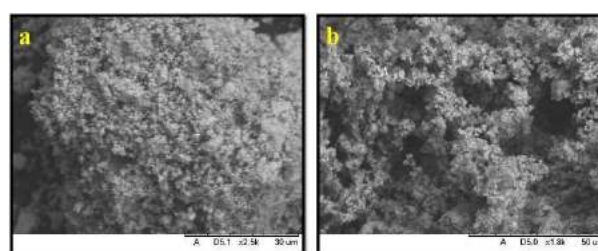


Fig. 3. SEM image for (a) LN-M9 and (b) LCN-M9.

Fig. 4 shows the results of adsorption efficiency and the amount of adsorbed dye using the perovskites LN-M9 and LCN-M9, respectively, and calculated according to Eq. 1 and 2, respectively. Within 90 minutes, the adsorption efficiencies were 96% and 89% for systems containing 30 mg L^{-1} Turquoise Blue dye. And the amounts of adsorbed dye were 143 mg g^{-1} for sample LN-M9 and 134 mg g^{-1} for sample LCN-M9. These data indicate that over time, the dye concentration in the solution decreases and consequently the adsorption efficiency ($E\%$) values and the amount of dye adsorbed in milligrams per gram of adsorbent (q_e) increase [13, 14].

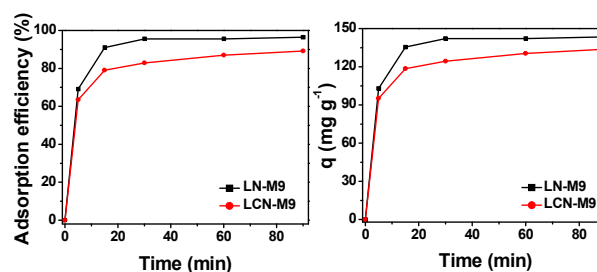


Fig.4. Adsorption efficiency and amount of dye adsorbed at different times for LN-M9 and LCN-M9 samples.



It is known that in chemical adsorption, adsorbate molecules generally break apart losing their original structure, dividing into radicals which are attached to the adsorbent surface. One can then consider a possible coordination between cations of the sites A and/or B from the perovskite with electron density donor groups present in the turquoise blue structure such as (SO_3^-) , whose coordination points are oxygen, in addition to the groups (NH_2) and $(N=N)$, where the coordinating points are nitrogen atoms [13,14].

It is noted that Ca^{2+} ion insertion in the material caused a subtle decrease in the adsorbent activity, indicating that by partially replacing site A ions with other lower valence cations, such as the substitution of La^{3+} with Ca^{2+} , the interaction between the cations of the sites A and/or B from the perovskite with electron density donor groups present in the dye are affected.

The kinetic study was performed for all calcined materials that were submitted to the adsorption tests, applying the pseudo first order (PFO) and pseudo second order (PSO) models. Table 1 shows the amount of adsorbed dye, velocity constants, and correction factors for the two models to verify which model is best applied to the experimental data.

Table 1. Parameters obtained using PFO and PSO models.

Pseudo First Order (PFO)			
Samples	$k_1(\text{min}^{-1})$	$q_1(\text{mg g}^{-1})$	R^2
LN-M9	0.255 ± 0.0105	141.738 ± 1.0073	0.9991
LCN-M9	0.265 ± 0.0328	127.691 ± 2.6712	0.9920
Pseudo Second Order (PSO)			
Samples	$k_2(\text{g mg}^{-1}\text{min}^{-1})$	$q_2(\text{mg g}^{-1})$	R^2
LN-M9	0.003 ± 0.0004	149.357 ± 2.2928	0.9974
LCN-M9	0.003 ± 0.0002	135.254 ± 0.9434	0.9995

Both kinetic models presented high values of linear coefficients, indicating the effectiveness of applying the models for the study of the tests.

For the LN-M9 material the highest correlation factor was for the pseudo first order kinetic model, while for the LCN-M9 material the pseudo second order kinetic model. By analyzing the amounts of adsorbed dye it is again noted that the pseudo first order model was the best for the perovskite LN-M9 and the pseudo second order model was the best for the perovskite LCN-M9, as they are closer of experimental values [15,16].

In addition to the amount of adsorbed dye and the linear coefficients, the models allowed the determination of the velocity constants k_1 for pseudo first order and k_2 for pseudo second order. It is possible to observe that k_1 is greater than k_2 for both models and materials, this means that the velocity constant is higher for the pseudo first order kinetic model, ie the reaction speeds are faster for this model.

The results indicated that when used the LN-M9 adsorbent the adsorption mechanism is mainly controlled by intraparticle diffusion, while when used the LNC-M9 adsorbent the adsorption mechanism is mainly controlled by boundary layer effect and the adsorption involves sharing and electron exchange.

4. Conclusions

Perovskites $LaNiO_3$ and $La_{0.5}Ca_{0.5}NiO_3$ can be prepared by the mechanochemical synthesis method. Obtaining the desired materials was confirmed for all samples, even with the appearance of some secondary phases. The very porous structure of the adsorbents could be confirmed by scanning electron microscopy. Regarding the application of perovskites as adsorbents, it was found that the sample LN-M9 and LCN-M9 showed removal efficiency of 96 and 89%, respectively, for the removal of Turquoise Dye in aqueous solution. Thus, LN-M9 doped material showed better adsorption efficiency compared to calcium-doped at site A (LCN-M9). The pseudo first order and pseudo second order kinetic models presented high values of linear coefficients, indicating the effectiveness of applying the models for the study of the tests.

Acknowledgements

The authors acknowledge to PPGQ/UFS, CNPq and CAPES for its financial support. This study was financed in part by the Coordenação de Aperfeiçoamento de Pessoal de Nível Superior - Brasil (CAPES) -Finance Code 001.

References

- [1] Starling MCVM., Leão MMD, Amorim CC. Occurrence, control and fate of contaminants of emerging concern in environmental compartments in Brazil, *J. Hazard. Mater.* 2019, 372, 17-36.
- [2] López MJ, Guisado G, Vargas-García MC, Suárez-Estrella F, Moreno J. Decolorization of industrial



- dyes by ligninolytic microorganisms isolated from composting environment. *Enzyme Microb Technol.* 2006, 40(1), 42-45.
- [3] Li J, Smith AE, Kwong KS, Powell C, Sleight AW, Subramanian MA. Lattice crossover and mixed valency in the $\text{LaCo}_{1-x}\text{Rh}_x\text{O}_3$ solid solution, *J Solid State Chem.* 2010, 183, 1388-1393.
- [4] Moure C, Peña O. Recent advances in perovskites: Processing and properties. *Prog Solid State Chem.* 2015, 43, 123-148.
- [5] Imanieh MH, Rad MH, Nadarajah A, González-Platas J, Rivera-López F, Martín IR. Novel perovskite ceramics for chemical looping combustion application, *J CO₂ Util.* 2016, 13, 95-104.
- [6] Tunç O, Tanaci H, Aksu Z. Potential use of cotton plant wastes for the removal of Remazol Black B reactive dye, *J. Hazard. Mater.* 2009, 163(1), 187-198.
- [7] Kunz A, Peralta-Zamora P, De Moraes SG, Durán N. Novas tendências no tratamento de efluentes têxteis. *Quim Nova.* 2002, 25(1), 78-82.
- [8] Holkar CR, Jadhav AJ, Pinjari D V., Mahamuni NM, Pandit AB. A critical review on textile wastewater treatments: Possible approaches, *J Environ Manage.* 2016, 182, 351-366.
- [9] Guo, J.; Khan, S.; Cho, S.; Kim, J. Preparation and immobilization of zinc sulfide (ZnS) nanoparticles on polyvinylidene fluoride pellets for photocatalytic degradation of methyleneblue in wastewater. *Applied Surface Science* 2019, 473, 425-432.
- [10] Simonin, J. On the comparison of pseudo-first order and pseudo-second order rate laws in the modeling of adsorption kinetics. *Chemical Engineering Journal* 2016, 300, 254-263.
- [11] Lima, S. M.; Peñab, M. A.; Fierrob, J. L. G.; Assafa, J. M. Perovskites as catalyst precursors: partial oxidation of methane on $\text{La}_{1-x}\text{Ca}_x\text{NiO}_3$, *Elsevier B. V.* 2007, 481-486.
- [12] Anderson M. T.; Vaughey, J. T.; Poeppelmeier, K. R. Structural similarities among oxygen-deficient perovskites, *Chem. of Mater.* 1993, 5, 151.
- [13] A.G. Santos, J.O. Leite, M.J.B. Souza, I.F. Gimenez, A.M.G. Pedrosa, Effect of the metal type in perovskites prepared by modified protein method in dye adsorption from aqueous medium, *Ceram. Int.* 44 (2018) 5743-5750.
- [14] Bradha, M.; Vijayaraghavan, T.; Suriyaraj, S. P.; Selvakumar, R.; Ashok, A. M. Synthesis of photocatalytic $\text{La}_{(1-x)}\text{A}_x\text{TiO}_{3.5-\delta}$ (A=Ba, Sr, Ca) nano perovskites and their application for photocatalytic oxidation of congo red dye in aqueous solution, *Journal of Rare Earths.* 2015, 33, 160-167.
- [15] Esquedo, V. M.; Silva, J. B.; Quintana, T. M.; Dotto, G. L.; Pinto, L. A. A. Cinética de adsorção do corante amarelo Tartrazina por uma esponja megaporosa de quitosana. In X Encontro Brasileiro sobre adsorção, 2014, São Paulo.
- [16] Alfredo, A. P. C.; Gonçalves, G. C.; Lobo, V. S.; Montanher, S. F. Adsorção de azul de Metileno em casca de batata utilizando sistemas em batelada e coluna de leito fixo. *Revista Virtual de Química* 2015, 7, 1909-1920.

Synthesis of LaFeO_3 material for application in Congo red dye removal by adsorption

Juli E. N. Couto^a, Iasmin A. Ribeiro^b, A. M. Garrido Pedrosa^b, Marcelo. J. B. Souza^a

^aGraduate Program in Chemical Engineering, Federal University of Sergipe, Av. Marechal Rondon, Rosa Elze, São Cristovão-SE, 49100-000, Brazil

^bGraduate Program in Chemistry, Federal University of Sergipe, Av. Marechal Rondon, Rosa Elze, São Cristovão-SE, 49100-000, Brazil

Abstract

The environmental impacts caused by the emission of colored effluents to water bodies have attracted attention due to the toxicity and difficulty to treat dyeing wastewaters. Dyes are organic compounds of natural or synthetic origin with high thermal and optical stability. Among the techniques employed in the treatment of dyeing wastewaters, adsorption technology is one of the most efficient to remove dyes from aqueous solution. Many materials have been used as adsorbents, but studies with materials with perovskite structure, that is a highly versatile mixed oxide that has been tested as adsorbent with the proposal of easy obtaining and simple recovery against classic adsorbents. This study aims to synthesize LaFeO_3 material and apply to remove Congo red dye from aqueous media. The adsorbent was synthesized by the modified protein method and the characterizations of XDR, SSA and PZC were performed. The removal efficiency of adsorbent was measured over the time. Kinetic studies were applied using the Lagergren models of pseudo-first and pseudo-second order. Lastly, the adsorption equilibrium of the adsorbent was determined using classic models of Langmuir and Freundlich. Recovery and reuse tests were done.

Keywords: Synthesis of adsorbent; LaFeO_3 ; dye removal; Congo red dye.

1. Introduction

Dyes are generally aromatic organic compounds with complex structure formed by several functional groups whose main objective is to give color to a material [1-2]. Over 10,000 types of dyes and pigments being used by industries and approximately 0.7 million tons of these compounds are synthesized every year [3]. Dyes may be of natural or synthetic origin and may be classified into acid, basic, azo dyes as well as dyes belonging to the class of metal complexes [4,5].

Congo red (benzidine diazobis-1-naphthylamino-4-sulfonic acid sodium salt) corresponds to a type of synthetic dye belonging to the azo group. Synthetic dyes, of which Congo red is part, are dyes that are difficult to biodegrade due to their complex aromatic structures, which give

them physical, chemical, thermal and optical stability [6,7].

Several industries use dyes in their processes and produce high color concentration residues such as the food, pharmaceutical and textile industries [8]. The textile industry is especially regarded as one of the most polluting because of its strong color, high organic load, and toxic compounds [9].

In order to treat wastewater dyeing, a wide range of physical, chemical and biological techniques are introduced among the years [10]. Chemical coagulation [11], chemical and electrochemical oxidation [12], ozonation [13], surface ultrafiltration [14] and adsorption [15,16,17] can be applied as example. However, adsorption has been highly regarded and shown to be superior to other treatment routes due to simplicity of operation, satisfactory cost and high removal efficiency of unwanted residues [16,17].



Many materials have been used as adsorbents to remove dyes, as example, activated carbon [18], zeolites [19], chitosan [20] and metallic oxides [7,16]. Among these adsorbents, activated carbon is the most used in dye removal processes due to its high efficiency [18]. However, this material has some disadvantages such as high cost, difficult disposal and regeneration. In addition, there are cases where activated carbon has the limitation of being selective to some dyes [21]. In order to overcome these limitations, the search for new materials has been developed to replace conventional adsorbents.

Recently, studies using mixed-oxides like perovskites as adsorbents have been shown a promising alternative to remove dyes from aqueous media. The literature brings recent developments showing the use of perovskites based on iron [7], manganese [15], cobalt [22] to remove Congo red dye from water achieving good results. Therefore, the use of perovskite is a suitable route due to the low cost of synthesis, good efficiency and regeneration.

This paper describes a study about the synthesis of perovskite LaFeO_3 to be applied as adsorbent in the removal of Congo red dye by the liquid phase adsorption method.

2. Materials and methods

2.1 Synthesis of the adsorbent

Analytical grade reagents, lanthanum nitrate ($\text{La}(\text{NO}_3)_3 \cdot 6\text{H}_2\text{O}$), iron nitrate ($\text{Fe}(\text{NO}_3)_3 \cdot 9\text{H}_2\text{O}$), collagen were used in the synthesis of LaFeO_3 adsorbent.

The synthesis of the LaFeO_3 perovskite was performed by the modified protein method. The chosen synthesis route was adapted based on other works in the literature that used this methodology [23]. A stoichiometric amount of iron nitrate in 200 mL of distilled water at 30°C was added. This solution was subjected to a stirring system for 30 minutes until complete dissolution. Then solid lanthanum nitrate was added to the stirred system at 30°C for a further 30 minutes. After this time, the system temperature is raised to 70°C and then the solid collagen mass is added. The system was kept at 70°C under stirring for 1 hour. Then, a viscous gel was obtained and heat treated in the muffle furnace at 350°C for 2 hours with a heating rate of $10^\circ\text{C min}^{-1}$. The material obtained after this stage

was macerated and calcined at 900°C for 2 hours to eliminate organic matter and obtain perovskite.

In the present work a nomenclature was adopted for the adsorbent LaFeO_3 , it will be called as LFO.

2.2 Characterization of adsorbent

The identification of the crystalline phases present was made by X-ray diffractograms (XRD) by the powder method obtained from a Rigaku DMAX100 diffractometer, using $\text{CuK}\alpha$ radiation ($\lambda = 1.5406$) and 2θ in the range of 10 to 60° , with a step of 0.020 . The identification was performed by comparison with the data from the JCPDS - International Center of Diffraction Data.

The nitrogen adsorption at 77 K was used to determine the specific surface area (SSA) of the adsorbent. The analysis was performed on the Quantachrome NOVA equipment and using the method developed by Brunauer, Emmett and Teller (BET).

The determination of the point of zero charge was obtained by adapted methodology of the reference [24]. Sodium chloride solutions with 0.1 mol L^{-1} under 5 different initial pH values (3, 5, 7, 11) were prepared. The pH of each solution was adjusted as necessary with hydrochloric acid or sodium hydroxide solutions of 0.1 mol L^{-1} concentration. After adjusting the pH of the solutions, 20 ml of each solution were added and 20 mg of the adsorbent added in a beaker. The system was kept under stirring at room temperature for 90 minutes. After this period, the solutions were filtered and the final pH values determined with the help of benchtop pH meter.

2.3 Adsorption tests on liquid phase and adsorbents recovery process

For the adsorption tests, Congo red dye solution was prepared at concentration of 30 ppm. That solution were analyzed using a Shimadzu UV-1800 spectrophotometer with a 3.5 mL quartz cell with a 1.0 cm optical path and scanning in the range 400 to 700 nm. The analytical curve was used as a reference and the maximum absorption wavelength of the dye was obtained at 493 nm.

Adsorption tests were carried out in a batch tests at room temperature using 20 mL of the dye reference solutions and 0.020 g of the adsorbent material. These system was kept under stirring and fixed time intervals (10, 20, 30, 40, 50, 60, 70, 80, 90 minutes), an aliquot was collected and placed

under a centrifuge at 3500 rpm for 5 minutes. Finally, the supernatant was analyzed by UV-visible absorption spectrophotometry, applying the same conditions used in the analysis of the reference solution. The tests were run out in triplicate.

For the adsorption equilibrium tests, Congo red solution also was prepared with concentrations of 10 and 50 ppm and analyzed in similar conditions to kinetic studies, but only in the equilibrium time. The models of the Freundlich and Langmuir isotherms were used.

The kinetics studies were performed applied pseudo-first order model (Equation 1):

$$q_t = q_e \left(1 - e^{-k_1 t}\right) \quad (1)$$

where q_t is the adsorption capacity at time t in mg g^{-1} ; q_e is the theoretical value of adsorption capacity at equilibrium in mg g^{-1} and k_1 is the pseudo-first order adsorption rate constant in min^{-1} and t is the time in minutes.

And pseudo-second order model (Equation 2):

$$q_t = \frac{t}{\left(\frac{1}{K_2 q_e^2}\right) + \left(\frac{t}{q_e}\right)} \quad (2)$$

where k_2 is the pseudo-second order adsorption rate constant in $\text{g mg}^{-1} \text{min}^{-1}$.

After adsorption tests, the material used was recuperated, calcined and evaluated the re use at equilibrium time (90 minutes) and the aliquot was analyzed similarly to that described above.

3. Results and Discussion

Fig. 1 shows the XRD patterns for the and LFO perovskite obtained by the modified protein method. All perovskite phase peaks for LaFeO_3 are labeled on the Figure 1 by the Miller index.

The XDR pattern for LFO sample displays the perovskite phase in crystalline form of LaFeO_3 at peaks 2θ equal to $22,64^\circ$, $32,33^\circ$, $39,65^\circ$, $46,16^\circ$, $57,50^\circ$ where was confirmed by the diffraction pattern JCPDS n° 37-1493 and JCPDS de n° 88-0641. This material shows the dominance of crystalline structure of perovskite orthorhombic [25]. Also, there are peaks of lower intensity characterized by secondary phases with formation of Fe_2O_3 at $2\theta = 47,70^\circ$, $52,03^\circ$, $53,48^\circ$ comparing pattern JCPDS de n° 65-3107 and La_2O_3 at 2θ equals to $28,82^\circ$ e $29,86^\circ$.

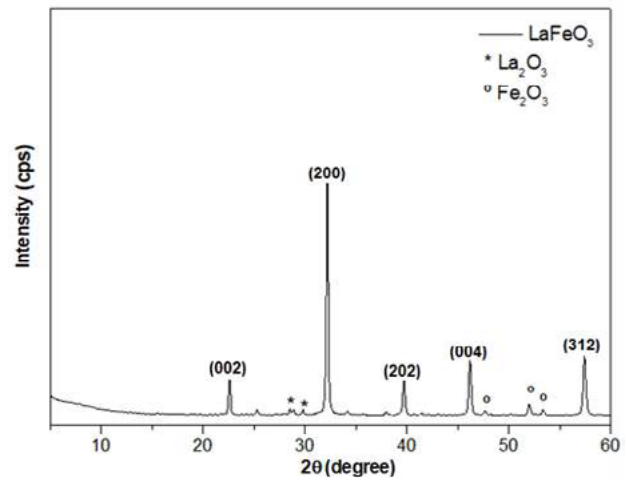


Figure 1. XRD patterns for LFO sample

Table 1 shows the specific surface area (SSA) data for the adsorbent. The results showed SSA of $25 \text{ m}^2/\text{g}$. The area value found is lower when comparing with activated carbon ($<100 \text{ m}^2/\text{g}$) [18]. But it is close to other studies of perovskites using the same synthesis route [23,26]. The literature shows that the specific surface area obtained for perovskite oxides is strongly related to the synthesis method employed [15]. Perovskites are porous materials with a small specific surface area, which can be improved by using doping in its synthesis [16].

Table 1. Specific surface area (SSA) and point of zero charge of adsorbent.

Adsorbent	SSA (m^2g^{-1})	PCZ
LFO	25	6.6

The point of zero charge (pH_{PCZ}) is defined as the pH at which the adsorbent surface has a neutral charge. Their knowledge allows to predict the ionization of surface functional groups and their interaction with the chemical structure of the dye [27].

Table 1 displays the PCZ for the adsorbent. The point of zero charge was obtained at $\text{pH} = 6.6$ (showed on Table 1). This result expose the proper pH to run the adsorption tests. In this study, it was used the Congo red that it is an anionic dye where adsorption is favored when the adsorbent contacts a liquid solution with a pH lower than PCZ [28].

At lower pH than the measured in point of zero charge enable strong electrostatic attraction between the positive ions from the metals of perovskite structure and the negatively charged

sulfonic group of CR dye [17-27]. In our case, adsorption of Congo red dye occurs at pH around 5 to 6. Therefore, pH adjustment is not necessary since the pH of the dye is lower than PCZ and adsorption is favored.

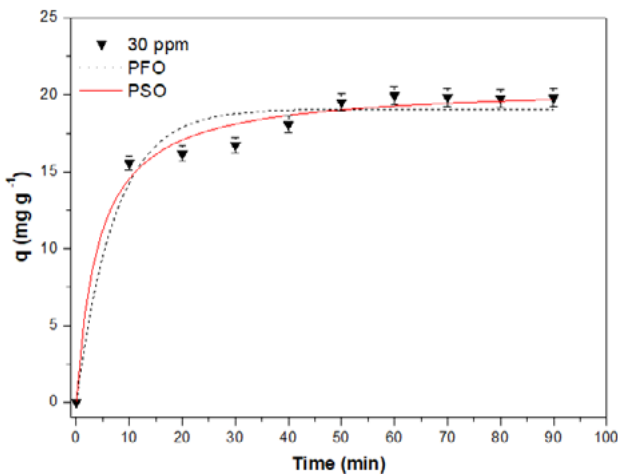


Figure 2. Removal efficiency for CR dye on LFO adsorbent.

Figure 2 shows the effect of contact time on the removal efficiency of the dye. Adsorption time and dye removal efficiency are important factors that should be considered for wastewater treatment. The adsorbent sample showed a relatively fast adsorption time, about one hour until the probably equilibrium stage.

The maximum removal efficiency of dye in the system at 30 ppm concentration was 67%. The result is quite distant when comparing with conventional adsorbents such as activated carbon that has efficiency over 90% [18]. However this material like explained before has some limitations

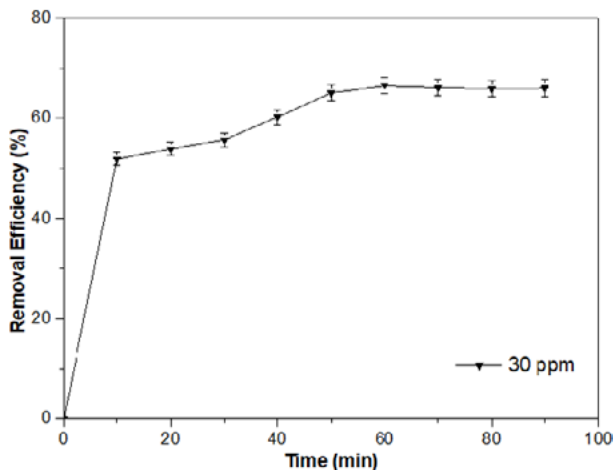


Figure 3. Kinetic adsorption studies using pseudo-first order and pseudo-second order models and LFO adsorbent.

like disposal and regeneration, which allows the application of perovskite materials to be considered, although these adsorbents have inferior performance.

By the other hand, studies with mixed oxides show close removal efficiency using the same synthesis method, which shows consistency in the results [15,23].

The kinetic studies were carried based on Lagergren models of pseudo-first order and pseudo-second order. Equations used to calculate the kinetic parameters were showed on Equations (1) and (2) previously exposed.

Figure 3 shows both models being applied. It is possible to see that the pseudo-second order model fits the system better. The kinetic parameters exposed on Table 2 confirm the graphical conclusion. The correlation coefficient is higher in the PSO model where it was R^2 is closest to 1.

Table 2. Pseudo-first order (PFO) and pseudo-second order (PSO) kinetic parameters.

Model	Parameters	
PFO	$k_1(\text{min}^{-1})$	0.13858
	$q_{e1}(\text{mg g}^{-1})$	19.0691
	R^2	0.96264
PSO	$k_2(\text{g mg}^{-1}\text{min}^{-1})$	0.01166
	$q_{e2}(\text{mg g}^{-1})$	20.60717
	R^2	0.9847

When comparing the calculated amount dye absorbed, q_{e2} and q_{e1} (Table 2) with experimental q equals to 20.07 mg g^{-1} (data not showed) it is seen that adsorption capacity gets closer to the pseudo second order. This indicates that the pseudo-second order model was adequate to evaluate the adsorption velocity, suggesting that the reaction velocity depends on the adsorbate concentration [29].

The maximum adsorption capacity (q_{max}) of others conventional adsorbents as zeolite/chitosan composite is about 199 mg g^{-1} [31], activated carbon 230 mg g^{-1} [32] and natural clays, 77 mg g^{-1} [33]. These results from literature show that the adsorbent in study has lowest adsorption capacity. However, the simplicity of the synthesis, low cost and possibility of regeneration makes LFO an adsorbent to be considered in the process of removing the Congo red dye.

Table 3 shows the parameters obtained from the linearization of Langmuir and Freundlich isotherm models.

The classical models of the Freundlich and Langmuir isotherms were used to describe the equilibrium system. The Langmuir model is an isotherm model that assumes monolayer coverage on the surface of the adsorbent, ie this isotherm admits that the structure of the adsorbent is homogeneous, where all sorption sites are energetically identical [29,30]. Meantime, Freundlich isotherm is used to describe the adsorption process on heterogeneous and multilayer surfaces and non-ideal systems. This model considers a relationship between the amount of adsorbed material and the concentration of material in solution in a model with empirical characteristics. [30,31].

Table 3. Parameters obtained for the Freundlich and Langmuir isotherms.

Models	Parameters	
Langmuir	$1/k_A q_{AS}$	0.3653
	$1/q_{AS}$	0.0162
	R^2	0.9905
Freundlich	$\log K_F$	0.75
	$1/n$	1.163
	R^2	0.9903

The results suggest that the Langmuir's model was better suited than Freundlich's isotherm. Therefore, it is possible to suggest that for LFO material the adsorption process occurs on monolayer coverage at the surface of perovskite by CR dye molecules [30].

After dye adsorption, the perovskite/adsorbate system has been calcinated and the adsorbent was recovery. A comparative analysis was made relating the dye removal efficiency (E) and adsorption capacity (q) for the adsorbents before and after reuse. The efficiency and capacity of adsorption remained close.

Adsorption efficiency remained almost the same with a maximum variation of 2%. Similar results have been achieved in other study using perovskites [7] where the dye removal efficiency remained similar after recovery and reuse in five adsorption cycles.

4. Conclusion

The $LaFeO_3$ perovskite were successfully synthesized by the modified proteic method. The characterizations of the adsorbent showed XRD

patterns with formation of crystalline structures of the perovskites $LaFeO_3$ with orthorombic geometry. The specific surface area of the LFO material indicated an area of $25 \text{ m}^2\text{g}^{-1}$. The point of zero charge (PCZ) was evaluated in order to ensure the proper pH that adsorbents should operate well, obtaining the pH_{PZC} at 6.6. The $LaFeO_3$ material was applied to remove Congo red dye by adsorption from aqueous media at concentration of 30 ppm. The maximum removal efficiency occurred at time of 60 minutes achieving an efficiency of 67%. Among the kinetic models studied, the pseudo-second order was better fitted to adsorbent. Adsorption equilibrium showed that Langmuir model suited better for LFO material. The $LaFeO_3$ material with perovskite structure can be recovery and re use in new adsorption cycles.

Acknowledgements

The authors acknowledge to PEQ/UFS, and CAPES for its financial support. This study was financed in part by the Coordenação de Aperfeiçoamento de Pessoal de Nível Superior - Brazil (CAPES) -Finance Code 001.

References

- [1] Asku, Z. Application of biosorption for the removal of organic pollutants: a review. *Proc. Biochem.* 2005; 40: 997-1026.
- [2] Bhatnagar, A. and Jain, A.K. A Comparative Adsorption Study with Different Industrial Wastes as Adsorbents for the Removal of Cationic Dyes from Water. *J. Col. and Int. Sci.* 2005; 281: 49-55.
- [3] Ogugbue, C.J., Sawidis, T., 2011. Bioremediation and detoxification of synthetic wastewater containing Triarylmethane dyes by aeromonas hydrophila isolated from industrial effluent. *Biotechnol. Res. Int.* 2011; 1-11.
- [4] V. Khandegar, A.K. Saroha, Electrocoagulation for the treatment of textile industry effluent - a review, *J. Environ. Manag.* 128 (2013) 949–963. E. Brillas, C.A. Martínez-Huitle, Decontamination of wastewaters containing synthetic organic dyes by electrochemical methods. An updated review, *Appl. Catal. B.* 2015; 166–167: 603–643.
- [6] S. Chatterjee, M.W. Lee, S.H. Wooa, Adsorption of Congo red by chitosan hydro- gel beads impregnated with carbon nanotubes, *Bioresour. Technol.* 2009; 100: 3862–3868.
- [7] Wang, L.; Li, J.; Wang, Y.; Zhao, L. Preparation of nanocrystalline $Fe_{3-x}La_xO_4$ ferrite and their adsorption

capability for Congo red. *J. Haz. Mat.* 2011; 196:342–349.

[8] H. Jalife-Jacobo, R. Feria-Reyes, O. Serrano-Torres, S. Gutiérrez-Granados, J.M. Peralta-Hernández, Diazo dye congo red degradation using a boron-doped diamond anode: an experimental study on the effect of supporting electrolytes, *J. Haz. Mater.* 2016; 319:78–83.

[9] Arslan-Alaton, I.; Gursoy, B. H.; Schmidt, J. E. Advanced oxidation of acid and reactive dyes: Effect of Fenton treatment on aerobic, anoxic and anaerobic processes. *Dyes and Pig.*, 2008; 78: 117-130.

[10] Kunz, A.; Zamora, P. P.; Moraes, S.G.; Duran, N. Novas tendências no tratamento de efluentes têxteis. *Quím Nov.* 2002; 1:78-82.

[11] T.-H. Kim, C. Park, J. Yang, S. Kim, Comparison of disperse and reactive dye removals by chemical coagulation and Fenton oxidation, *J. Hazard. Mater.* 2004; 112(1-2) 95.

[12] L. Szpyrkowicz, C. Juzzolino, S.N. Kaul, A Comparative study on oxidation of disperse dyes by electrochemical process, ozone, hypochlorite and fenton reagent, *W. Res.* 2009; 35(9) 2129.

[13] N.M. Mahmoodi, Photocatalytic ozonation of dyes using copper ferrite nanoparticle prepared by coprecipitation method, *Desal.* 2011; 279(1).

[14] A. Ahmad, S. Puasa, M. Zulkali, Micellar-enhanced ultrafiltration for removal of reactive dyes from an aqueous solution, *Desal.* 2006, 191(1-3) 153.

[15] Santos, A. G.; Leite J.O.; Souza M.J.B.; Gimenez I.F, Garrido P. A.M. Effect of the metal type in perovskites prepared by modified proteic method in dye adsorption from aqueous medium. *Ceram. Int.*, 2018; 44: 5743–5750.

[16] S.M. Seyed Arabi, R.S. Lalehloo, M.R.T.B. Olyai, G.A.M. Ali, H. Sadegh, Removal of congo red azo dye from aqueous solution by ZnO nanoparticles loaded on multiwall carbon nanotubes, *Phys. E: Low-dim. Sys. Nan.* 2018.

[17] Shu, J.; Wang, Z.; Huang, Y.; Huang, N.; Ren, C.; Zhang, W. Adsorption removal of Congo red from aqueous solution by polyhedral Cu₂O nanoparticles: Kinetics, isotherms, thermodynamics and mechanism analysis. *Jour. Alloys and Comp.*, 2015; 633: 338-346.

[18] M.K. Purkait, A. Maiti, S. Dasgupta, S. De, Removal of Congo red using activated carbon and its regeneration, *J. Hazard. Mater.* 2007; 145(1-2):287-295.

[19] A new route to fabricate high-efficient porous silicate adsorbents by simultaneous inorganic-organic functionalization of low-grade palygorskite clay for removal of Congo red. *Micr. and Meso. Mat.* 2019; 277:267-276.

[20] Kloster G.A., Mosiewicki M.A., Marcovich N.E. Chitosan/iron oxide nanocomposite films: Effect of the composition and preparation methods on the adsorption

of Congo red. *Carbo. Polym.* 2019; 221: 186-194.

[21] Deniz, F; Kepekci, R.A. Dye biosorption onto pistachio by-product: a green environmental engineering approach. *J. Molec. Liq.* 2016; 219:194-200.

[22] Z.Ding, W.Wang, Y.Zhang, F.Li, J.Ping Liu. Synthesis, characterization and adsorption capability for Congo red of CoFe₂O₄ ferrite nanoparticles. *J. Alloys and Comp.* 2015; 640: 362-370.

[23] Santos, J. C. Dissertação de Mestrado: Desenvolvimento de catalisadores a base de níquel com estrutura perovskita para a utilização na produção de gás de síntese. Programa de Pós-Graduação em Química. UFS. 2011.

[24] Fagnani, H.M.C; Deolin M. E.; Barros, M.A.S.; Arroyo P. A. Identificação dos mecanismos de sorção em zeólita NaY e sílica gel. *Ver. Mat.*, 2017; 3-22.

[25] Hiromishi. A, Musashi. T., Y. Sadaoka. Conventional synthesis method for fine polymetallic LaFeO₃ using ethylene glycol solvent addition. *J. Cer. Soc.* 2009; 117:1048.

[26] Toniolo, F.S.; Magalhães, R.N.S.H. ; Perez, C.A.C.; Schmal, M. Structural investigation of LaCoO₃ and LaCoCuO₃ perovskite-type oxides and the effect of Cu on coke deposition in the partial oxidation of methane. *Applied Catal. B* 2012; 117- 118:156-166.

[27] Kragovic M.; Stojmenovic M.Petrovic J.; et al. Influence of Alginate encapsulation on point of zero charge (pH_{PZC}) and thermodynamics properties of the natural and Fe(III)-modified zeolite. *Proc. Man.* 2019; 32:286-293.

[28] Ribeiro, G. A. C.; Santana, S. A. A.; Bezerra, C. W. B.; Silva, H. A. S.; Vieira, A. P. Casca de arroz in natura e tratada com ácido nítrico como adsorventes para remoção do corante têxtil violeta brilhante remazol. In: 51, Congresso Brasileiro de Quim. São Luís., 2011.

[29] Schmal, M. *Catálise Heterogênea; Synerg.*, Rio de Janeiro, RJ, 2011.

[30] Yagub, M. T.; Sen, T. K.; Afroze, S.; Ang, H. M. Dye and its removal from aqueous solution by adsorption: A review. *Adv. in Col. and Interf. Sci.* 2014; 209:172-184.

[31] Khanday, W.A.Asif M.,Hameed B.H. Cross linked beads of activated oil palm ash zeolite/ chitosan composit as bio-adsorbent for the removal of methylene blue and acid blue. *Int J. Biol. Macr.* 2017; 95:895-902.

[32] Chenhao T., Chenghong F., Mingzhi W. Yuehan W. Enhanced adsorption of anionic toxic contaminant Congo red by activated carbon with electropositive amine modification. *Chem.* 2018; 208:476-483.

[33] Chaari, IFakhfakh, E., Medhioub M., Jamoussi F. Comparative study on adsorption of cationic and anionic dyes by smectite rich natural clays. *J. Molec. Struct.* 2019; 1179:672-677.

Synthesis and characterization of polyacrylamide-chitosan cryogels for adsorption of biomolecules

H. S. D. R. Hamacek^a, S. M. A. Bueno^a

^a School of Chemical Engineering, University of Campinas
Av. Albert Einstein, 500 – CEP: 13083-852 – Campinas, SP, Brazil

Abstract

The development of new materials and techniques for biomolecules purification is a current requirement in the biopharmaceutical industry. Thereby, in this work, a monolithic stationary phase was synthesized from the cryogelation of acrylamide and chitosan to be used as the solid matrix in affinity chromatography for the adsorption of biomolecules. The produced material was characterized for its morphology, flow resistance, and swelling capacities. The obtained material is spongy, macroporous, homogeneous, and it has a high interconnectivity between their pores as analyzed by scanning electron microscopy (SEM). Besides, its polymer chains are expected to produce a semi-interpenetrating and intertwined network. The porosity of the material was estimated to be $78.0 \pm 0.9\%$. The swelling capacity obtained was 2.02 ± 0.46 g H₂O/g dry gel. Moreover, studies regarding its flow permeability showed that the cryogel is permeable to flow rates even higher than 5 mL min^{-1} . All the determined properties of the synthesized material guarantee the cryogel important characteristics for the efficient application in adsorption and purification of biomolecules.

Keywords: cryogel; monolith; synthesis; adsorbent; characterization

1. Introduction

Advancements in technology related to genetic engineering and recombinant DNA generated a significant increase in demand for pure proteins. Although, unit operations employed in production of these biomolecules are costly. Thereby, there is interest in the development of new cost-effective and simple procedures and materials, which could help minimize costs and increase availability of different biomolecules to the population [1,2]

Chromatographic techniques are one of the most applied methods in biomolecules purification [3]. Membranes, particles, and monoliths are generally the adsorbents used as the stationary phase of the liquid chromatography [4,5]. Regarding the monoliths, studies have shown that these structures enable chromatographic procedures to have improved mass transfer, smaller diffusion paths, lower pressure drops, and reduced presence of preferential paths than membranes and particles [6].

Cryogels are materials which can be synthesized as monoliths and applied in various types of chromatography for biomolecules purification,

including the separation and purification of DNA, plasmids, and immunoglobulins from human or bovine plasma [7,8]. They differ from other gels because of their elastic and spongy structure [9].

By cryogenically treating a system, which can form a gel, it is possible to synthesize cryogels. A polymeric cryogel is produced by cooling a monomer mixture to temperatures of $-5\text{ }^{\circ}\text{C}$ to $-20\text{ }^{\circ}\text{C}$, in which the solvent is found to be mostly crystallized. Simultaneously, the monomers concentrate in regions around of the solvent crystals called liquid microphases [10] where the polymerization occurs. When the reaction is completed, the system is thawed, originating a high interconnected and macroporous structure due to the solvent crystals acting as porogen [11].

Diverse formulations of cryogel precursors could be employed to synthesize a monolithic material. Cryogels produced from synthetic polymers, such as polyacrylamide, have already been applied as stationary phase in affinity chromatography for the purification of proteins [12]. Similarly, cryogels could also be synthesized from natural polymers, like polysaccharides [7].

Chitosan is a natural polymer produced from the deacetylation of chitin, which can be obtained from



cell walls of fungi and from the exoskeleton of crustaceans, insects, and arachnids [13]. Structurally, it is constituted of D-glucosamine and N-acetyl-D-glucosamine. Additionally, it is a polymer with a consolidated use in medicine, with various applications in wound treatment, tissue engineering, and drug delivery. Furthermore, it is non-toxic with fast biodegradability [14,15].

Monolithic chitosan cryogels made solely from chitosan were described as fragile [16], thereby their use as the stationary phase in chromatography is limited. In order to avoid this poor mechanical resistance, copolymers with chitosan and other polymers, particularly polyacrylamide [17], poly(N-isopropylacrylamide) [18], polypyrrole [19], and hyaluronic acid [20] started to be developed.

The cryogel composed by polyacrylamide and chitosan was applied in cell cultivation studies and it was described to have large pores (10 to 100 μm), low flow resistance and high biocompatibility [21].

Notably, in acidic pH values, chitosan's structure is positively charged owing to the protonation of the amine groups on the chitosan molecule [22]. This characteristic facilitates the adsorption of negatively charged amino acid residues or electron dense heteroatoms and groups exposed on the surface of the protein in solution [23]. Concomitantly, the chitosan structure is easily activatable to enable the immobilization of affinity ligands due to the presence of the amine and hydroxyl groups.

In this study, the synthesis and characterization of a polyacrylamide-chitosan cryogel was performed to verify its applicability as the stationary phase of chromatography for the purification of proteins and other biomolecules from complex biological fluids.

2. Materials and Methods

2.1. Materials

Chitosan (shrimp, $\geq 75\%$ deacetylated) and ammonium persulfate (APS) were obtained from Sigma-Aldrich (USA). N,N,N',N'-tetramethylethane-1,2-diamine (TEMED) was acquired from GE Healthcare (USA). Acrylamide (AAm), N,N'-methylenebisacrylamide (MBAm) was obtained from Bio-Rad (USA). Glacial acetic acid was acquired from Chemco (Brazil). Ultrapure Milli-Q water from Millipore (USA) was used on the procedures.

2.2. Methods

2.2.1. Preparation of chitosan solution: 1.0 g of chitosan was dissolved in 100 mL of acetic acid solution (0.1 mol L⁻¹) and solubilized with mechanical agitation (QUIMIS 0250M2, Brazil) for 1 hour. The solution was left to rest at room temperature for 24 hours to promote the deposit of the insoluble particles. Finally, the mixture was filtered in a sintered-glass filter for clarification.

2.2.2. Synthesis of the polyacrylamide-chitosan (PAAm-CS) cryogel: 0.474 g of AAm and 0.126 g of MBAm were mixed and dissolved in 4 mL of ultrapure water and 5 mL of chitosan solution (1% w/v) was added to the monomer mixture (6% w/v final monomer concentration and 0.5% w/v final chitosan concentration). The resulted solution was degasified in an ultrasound bath (Branson 3510, Branson Ultrasonics, USA) for 20 minutes. The solution was cooled in the refrigerator until it reached the temperature of 4 °C. Then, 20 mg of APS was dissolved in 600 μL of acetic acid 0.1 mol L⁻¹ and added to the monomer mixture. Lastly, 20 μL of TEMED was dissolved in 380 μL of acetic acid and added to the mixture under magnetic agitation. Quickly, the reaction mixture was transferred into 3 mL plastic syringes (0.5 cm diameter) or glass columns (1 cm diameter) submerged in cold ethanol bath. The system was transferred to a freezer where it stayed for 16 hours at -20 °C. After the time had elapsed, the cryogel was thawed at room temperature and washed with ultrapure water to eliminate unreacted monomers.

2.2.3. Determination of the swelling capacity: The synthesized cryogel was stored in a recipient with ultrapure water for 24 hours. After that, the water inside the cryogel was removed using a sintered glass filter and a vacuum pump (TE-058 Tecnal, Brazil), the cryogel was weighted to determine its wet mass (m_w). Subsequently, the material was oven dried at 60 °C until its weighted mass was constant (m_d). The swelling capacity ($S_{w/w}$) was calculated using the equation 1. The result is the mean of three measurements.

$$S_{w/w} = \frac{m_w - m_d}{m_d} \quad (1)$$



2.2.4. Determination of the estimated porosity: The cryogel was saturated with ultrapure water and its volume was determined through the water displacement when the cryogel was submerged in a recipient. Herein, the volume of the saturated cryogel (V) was calculated by the difference initial and final volumes obtained. The saturated cryogel was weighted and its saturated mass (m_{sat}) was attained. Then, the water was removed from the material through compression. The cryogel was weighted again and its mass after compression (m_c) was determined. Afterwards, the estimated porosity (ϕ) was calculated through the application of equation 2, where ρ_{water} is the specific mass of water at the temperature of the experiment. The result was taken as mean of three measurements.

$$\phi = \frac{m_{sat} - m_c}{\rho_{water} \times V} \quad (2)$$

2.2.5. Morphology characterization: The surface morphology of the cryogel was obtained through the scanning electron microscopy (SEM) method, performed at the Laboratório de Caracterização de Biomassa, Recursos Analíticos e de Calibração (LRAC), at UNICAMP. The cryogel was lyophilized and its surface and cross sections cuts were done, then, the fragments were covered in 20 nm of gold (Sputter Coater - EMITECH K450, UK). The samples were visualized and analyzed by the electronic microscope LEO (Electron Microscopy, England).

2.2.6. Determination of permeability: The permeability of the cryogel was evaluated in glass columns (model C10/10, 1 cm ID, GE Healthcare, USA) on a low-pressure chromatograph (Biologic LP System, Bio-Rad, USA). Using ultrapure water, flow-rates of 1.0 to 5.0 mL min⁻¹ were evaluated for 10 minutes each. The procedure was stopped if the water flow was obstructed and that flow would be the maximum permeability of the cryogel.

3. Results and Discussion

The cryogels were successfully produced with the conditions mentioned previously. They were characterized as homogeneous and white,

squeezable, spongy, flexible, and not brittle. When dried or compressed, they rapidly return to their original conformation in contact with water. Fig. 1. presents the produced cryogel.



Fig. 1. Digital photograph of the polyacrylamide and chitosan cryogel synthesized.

The swelling capacity determined for the PAAm-CS cryogel was 2.02 ± 0.46 g H₂O/ g dry gel and the estimation of the porosity was calculated to be approximately $78.0 \pm 0.9\%$. This high porosity is mainly in consequence of the ice crystals acting as porogen and the small concentration of precursors used in the synthesis. Also, these results are comparable to the values from other authors that synthesized cryogels with polyacrylamide-chitosan with different compositions for application as scaffold in a perfusion bioreactor [21].

SEM photographs of the surface and cross section of the cryogel are shown in Fig. 2a and 2b, respectively, with 250x magnification. It is possible to observe macropores with different dimensions varying from 15 to 150 μ m and the presence of a continuous and interconnected structure, which was created because of the elevated amount of ice crystals formed during freezing.

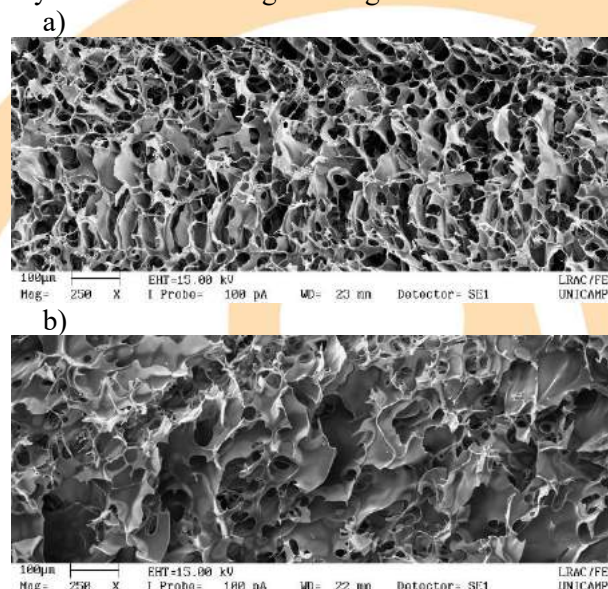


Fig. 2. SEM photographs of the a) surface and b) cross section of the continuous PAAm-CS cryogel. Magnification of 250x.

The maximum flow-rate the cryogel supported was determined and the results show that the material was permeable to flow-rates even higher than 5.0 mL min⁻¹. Usually, chromatographic procedures operate with flow-rates of 1.0 to 2.0 mL min⁻¹, which are inferior to the maximum flow-rate determined with this procedure.

4. Conclusion

The cryogel composed by chitosan and polyacrylamide chains exhibited adequate features for the application as a stationary phase in affinity chromatography, as shown in the results obtained for the synthesis and characterization of this material. This potential is due to its high permeability, high porosity, and its large and interconnected pores. Also, chitosan is a biopolymer with functional groups that are easily activatable for the immobilization of affinity ligands. Therefore, studies related to biomolecule adsorption capabilities of this matrix are going to be performed to elucidate its efficiency as a stationary phase in chromatography.

Acknowledgements

The authors acknowledge financial support from Coordenação de Aperfeiçoamento de Pessoal de Nível Superior, CAPES/PROEX, finance code 001, Brazil. And, Conselho Nacional de Desenvolvimento Científico e Tecnológico, Brazil (CNPq).

References

- [1] Roque A, Lowe C, Taipa M. Antibodies and genetically engineered related molecules: production and purification. *J. Chromatogr. A*; 2007;1160:44-55.
- [2] Singh NK, Dsouza RN, Grasselli M, Fernández-Lahore M. High capacity cryogel-type adsorbents for protein purification. *J. Chromatogr. A*; 2014; 1355:143-8.
- [3] Fang YM, Lin DQ, Yao SJ. Review on biomimetic affinity chromatography with short peptide ligands and its application to protein purification. *J. Chromatogr. A*; 2018;1571:1-15.
- [4] Bueno SMA, Miranda EA. Membranas adsorptivas. In: Pessoa Jr. A, Kilikian BV, editors. *Purificação de produtos biotecnológicos*, E-Manole, 2005.
- [5] Arora S, Saxena V, Ayyar V. Affinity chromatography: a versatile technique for antibody purification. *Methods*; 2017;116:84-94.
- [6] Çorman M. Poly-l-lysine modified cryogels for efficient bilirubin removal from human plasma. *Colloid Surf. B*; 2018;167:291-8.
- [7] Barroso T, Hussain A, Roque ACA, Aguiar-Ricardo A. Functional monolithic platforms: chromatographic tools for antibody purification. *Biotechnol. J.*; 2013;8:671-681.
- [8] Bakhshpour M, Idil N, Perçin I, Denizli A. Biomedical applications of polymeric cryogels. *Appl. Sci.*; 2019;9:553.
- [9] Gagnon P. Technology trends in antibody purification. *J. Chromatogr. A*; 2012;1221:57-70.
- [10] Lozinsky VI. Cryogels on the basis of natural and synthetic polymers: preparation, properties and applications. *Russ. Chem. Rev.*; 2002;71:489-511.
- [11] Hixon KR, Lu T, Sell SAA. A comprehensive review of cryogels and their roles in tissue engineering applications. *Acta Biomater.*; 2017;62:29-41.
- [12] Lozinsky VI, Galaev IY, Plieva FM, Savina IN, Jungvid H, Mattiasson B. Polymeric cryogels as promising materials of biotechnological interest. *Trend. Biotechnol.*; 2003;21:877-902.
- [13] Merzendorfer H. The cellular basis of chitin synthesis in fungi and insects: common principles and differences. *Eur. J. Cell Biol.*; 2011;90:759-769.
- [14] Khor E, Lim LY. Implantable applications of chitin and chitosan. *Biomater.*; 2003; 24:2339-2349.
- [15] Ono K, Saito Y, Yura H, Ishikawa K, Kurita A, Akaike T, Ishihara M. Photocrosslinkable chitosan as a biological adhesive. *J. Biomed. Mater. Res.*; 2000;49:289-295.
- [16] Jain E, Damania A, Shakia AK, Kumar A, Sarin SK, Kumar A. Fabrication of macroporous cryogels as potential hepatocyte carriers for bioartificial liver support. *Colloid Surf. B*; 2015;136:761-771.
- [17] Jain E, Karande AA, Kumar A. Supermacroporous polymer-based cryogel bioreactor for monoclonal antibody production in continuous culture using hybridoma cells. *Biotechnol. Prog.*; 2011;27:170-180.
- [18] Yang X, Debeli DK, Shan G, Pan P. Selective adsorption and high recovery of La³⁺ using graphene oxide/poly(N-isopropyl acrylamide-maleic acid) cryogel. *Chem. Eng. J.*; 2020;379:122335.
- [19] Makkliang F, Kanatharana P, Tharavangkul P, Thammakhet-Buranachai C. A polypyrrole-chitosan cryogel stir-bead micro-solid phase extractor for the determination of phthalate esters in contact lenses storage solutions and in artificial saliva in contact with baby teethers. *Anal. Chim. Acta*; 2017; 985:69-78.
- [20] Kutlusoy T, Oktay B, Apohan NK, Süleymanoglu M, Kuruca SE. Chitosan-co-hyaluronic acid porous cryogels and their application in tissue engineering. *Int. J. Biol. Macromol.*; 2017;103:366-378.
- [21] Jain E, Kumar A. Designing supermacroporous cryogels based on polyacrylonitrile and a polyacrylamide-chitosan semi-interpenetrating network. *J. Biomater. Sci. Polym. Ed.*; 2009;20:877-902.
- [22] Ma J, Sahai Y. Chitosan biopolymer for fuel cell applications. *Carbohydr. Polym.*; 2013;92:955-975.
- [23] Zeng X, Ruckenstein E. Membrane chromatography: preparation and applications to protein separation. *Biotechnol. Prog.*; 1999;15:1003-1019.

Diclofenac and Paracetamol Removal from contaminated water by adsorption onto MgAl-hydrotalcite

Morgana Rosset^{a,*}, Letícia W. Sfreddo^a, Oscar W. Perez-Lopez^a, Liliana Amaral Féris^a

^a Federal University of Rio Grande do Sul (UFRGS), Rua Ramiro Barcelos, 2777, Porto Alegre – 90040-040 – RS – Brazil
morganar@enq.ufrgs.br*

Abstract

The presence of pharmaceuticals in aquatic environments poses potential risks to the ecology and human health. This study investigated the removal of two widely detected and abundant compounds, namely, diclofenac and paracetamol from aqueous systems using the adsorbent MgAl hydrotalcite (HT Mg) synthesized by the coprecipitation method. The synthesized adsorbent was characterized by specific surface area (BET), powder X-ray diffraction and Fourier transform-infrared spectroscopy. The effect of adsorbent concentration and contact time were studied in a batch system. The kinetic data were analyzed using pseudo first order and pseudo second order. The pseudo first order kinetic model fitted the equilibrium data best for diclofenac and the maximum sorption capacity obtained was 3.768 mg g⁻¹. The opposite was observed for paracetamol, the pseudo-second-order kinetic model fitted the equilibrium data best and the sorption capacity of paracetamol was 0.688 mg g⁻¹, which was lower than diclofenac. In general, the adsorbent presented better performance for diclofenac removal, this may be due to the affinity of the adsorbent with the adsorbent. Moreover, this study provides a promising adsorbent with higher efficiency for adsorption of pharmaceutical compounds.

Keywords: Adsorption; Diclofenac; Paracetamol; Hydrotalcite.

1. Introduction

Residues of pharmaceutical products are considered to be emerging compounds (EC), which are not completely regulated [1]. Since they usually are polar molecules and soluble in water, pharmaceutically active compounds are not completely metabolized by organisms [2]. They have become a major concern because of their low biodegradability, high persistence, and facile bioaccumulation and are often detected in trace concentrations in the µg L⁻¹ or ng L⁻¹ range in the aquatic environment [3].

Most of the pharmaceutical residues found in wastewater are composed of non-steroidal anti-inflammatory drugs (NSAID), which constitute a group of pharmaceuticals with analgesic, antipyretic and anti-inflammatory properties[4]. These drugs are widely used without prescription and, consequently, have a high annual consumption reaching hundreds of tons worldwide [5]. Diclofenac and Paracetamol are some of the most commonly used NSAID to treat fever and pain, these drugs have often been detected in wastewater.

Some studies have indicated that the conventional processes usually applied in

wastewater treatment plants do not completely remove emerging contaminants. Adsorption is one of the most pertinent and promising methods, due to its advantages. It is simple to operate, has a low investment cost, and there is the possibility of reuse and regeneration of versatile adsorbents for the removal of emerging micro-pollutants [6].

Different adsorbent materials have been widely used to remove emerging contaminants from wastewater [1,3,7]. Hydrotalcites are widely applied as remarkable adsorbents due to their major properties: large interlayer spaces (high porosity), a great number of exchangeable anions between the positively charged layers, and water-resistant structure [8]. Thus, the removal of a variety of organic and inorganic pollutants has been reported through the use of hydrotalcites as adsorbents such as pesticides, heavy metals, such as hexavalent chromium, cadmium, lead and chromium, and dyes [9 12]. However, to date, little attention has been given to the removal of drugs using hydrotalcites [13].

The aim of the present work is to study the removal of sodium diclofenac and paracetamol in contaminated water solutions by the adsorption technique using a mixed oxide composed of



magnesium-aluminum derived from hydrotalcite as adsorbent.

2. Experimental

2.1. Synthesis of the adsorbent

HT-Mg hydrotalcite adsorbent was synthesized by the conventional coprecipitation method [14]. In summary, two aqueous solutions were added simultaneously into a stirred reactor (CSTR): a solution containing the magnesium and aluminum nitrate salts (molar ratio 2:1) and the other solution composed of sodium carbonate and hydroxide. The synthesis was conducted under pH = 9 (± 0.1) and a temperature of 50 °C. The obtained solid was heat-treated in a muffle furnace at 400 °C for a period of 12h to obtain the mixed oxide and then was denominated C-Mg. The particle size of the sorbent solid used was less than <60 mesh (0.355 mm).

2.2. Characterization of the adsorbent

The specific surface area of C-Mg was estimated in 120 m² g⁻¹ by the BET method, pore volume 0.29 cm³ g⁻¹ and pore diameter 6.4 nm were calculated by the BJH method, and the point of zero charges of pHZPC = 10.5.

Powder X-ray diffraction (XRD) was used to obtain information on the structure and crystalline phases of the material. The diffractograms were obtained using Bruker D2-Phaser diffractometer with Cu- α radiation ($\lambda = 1.54 \text{ \AA}$), 0.05° step, at 30 kV, and 10 mA.

Fourier transform-infrared spectroscopy (FTIR) was used to provide information on the presence of functional groups present in the structure of substances. The data was obtained using a PerkinElmer FTIR/NIR Frontier spectrophotometer in the wavelength range on of 4000–600 cm⁻¹ at room temperature.

2.3. Adsorption experiments

Sodium diclofenac (DCF) and paracetamol (PARA) (purity $\geq 99\%$) from Sigma-Aldrich were used to prepare synthetic solutions in different concentrations. The molecule diameter of each drug was calculated using the Avogadro® Program and assumed the largest distance between the extreme atoms, thus obtaining 0.962 nm for the sodium diclofenac and 0.829 nm for the paracetamol.

Adsorption assays were performed in batch using 50 ml Schott vials of a 10 mg L⁻¹ synthetic drug solution under 30 rpm agitation on a Wagner shaker, room temperature, and pH natural of 10. The concentrations of both drug solutions were obtained through a calibration curve developed from the linearization of experimental data. The initial and final concentrations of the samples were analyzed by the UV-vis spectrophotometry (Shimadzu Corporation UV-2550) measured at the highest absorbance wavelength, DCF-276 nm, and PARA-243 nm. All experiments were performed at natural pH, which is the pH resulting from the mixture of the adsorbent solid with the drug solution. The adsorption experiments were performed to evaluate the effect of the parameters, adsorbent concentration and contact time.

2.4. Adsorbent concentration experiments

The effects of the adsorbent solid concentration, C-Mg, experiments were 0.5, 1, 2, 6, 10, and 15 g L⁻¹ for the sodium diclofenac (10 mg L⁻¹) and 1, 2, 6, 10, 14, and 20 g L⁻¹ for the paracetamol (10 mg L⁻¹), and then maintaining the contact time in 60 min.

2.5. Adsorbent contact time (Kinetics models)

Influence of contact time was conducted varying the time in 5, 10, 20, 30, 60, 90, 120, 240, and 360 min, using the best adsorbent concentration obtained previously. The adsorption capacity of DCF and PARA on the C-Mg (q_t) was determined by mass balance Equation (1):

$$q_t = ((C_0 - C_t) \cdot V) / W \quad (1)$$

where q_t (mg g⁻¹) is the amount of drug adsorbed in at any time, C_0 (mg L⁻¹) is the initial drug concentrations, C_t (mg L⁻¹) is the drug concentrations at any time, V (L) is the volume of the solution, and W (g) is the amount of adsorbent.

The study of kinetics provides more information about the main mechanism governing the kinetics of an adsorption process. In this work, it was studied pseudo-first-order (PFO) (Equation 2) and pseudo-second-order (PSO) (Equation 3) models:

$$q_t = q_1(1 - e^{-k_1 \cdot t}) \quad (2)$$

$$q_t = t / ((1 / (k_2 \cdot q_2^2)) + (t / q_2)) \quad (3)$$

where q_1 and q_2 (mg g⁻¹) are the amounts adsorbed at equilibrium the PFO and the PSO, respectively

qt (mg g^{-1}) is amount adsorbed at time t , t (min) is the time, k_1 (min^{-1}) and k_2 ($\text{g.mg}^{-1} \text{min}^{-1}$) rates constant the PFO and the PSO, respectively.

3. Results and discussion

Fig. 1 shows the results concerning the influence of C-Mg concentration on diclofenac and paracetamol removal with adsorption. It is seen that the efficiency of DCF and PARA removal increases gradually with the increasing concentration adsorbent in the system. This behavior can be explained by the increase of active sites available in the solid for pollutant adsorption, with the increase of the mass of the sorbent in the solution.

In addition, there can be a very significant difference for drug removal. The removal capacity for DCF was higher at low values of adsorbent concentration, with equilibrium reached at 2 g L^{-1} . On the other hand, acetaminophen removal reaches its highest value with an adsorbent concentration of 20 g L^{-1} . The concentration of 3 g L^{-1} was adopted for DCF since the additional amount of C-Mg does not cause improvement in the process. For paracetamol, however, the concentration of 10 g L^{-1} was adopted. This choice was based on the cost associated with the synthesis for this type of material, making it interesting to select the lowest possible dosage as the ideal operating point. The C-Mg adsorbent for paracetamol removal needs more mass to saturate and the others saturate because it has low exchange affinity.

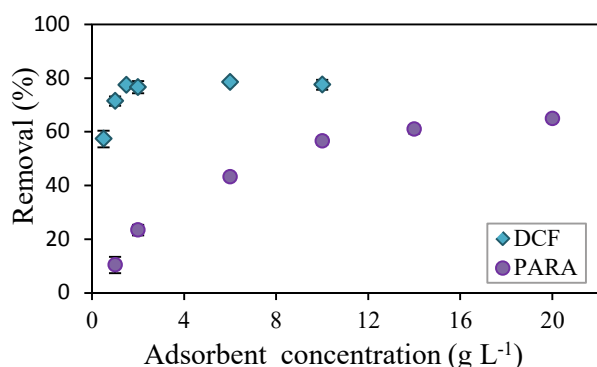


Fig. 1. Adsorption capacity by varying the sorbent solid concentration.

Fig. 2 shows the contact time influence on the percentage of sodium diclofenac and paracetamol removal from the solution. Applying the C-Mg adsorbent for diclofenac adsorption, it was possible

to observe that the removal increased rapidly in the first 60 min and then stabilized. The rapid adsorption of diclofenac onto the solid surface of the material indicated a higher affinity of these solid toward the diclofenac. It is possible to notice that C-Mg adsorbent showed slightly different kinetics with slower initial adsorption for paracetamol, reaching equilibrium after 180 min. The time required for adsorption of molecules is related to adsorbent-adsorbate interactions, that is, the forces involved between the pollutant and the solid, causing the compound adsorption on the surface or active centers of the adsorbent. Removal of 78% and 67% were achieved for DCF and PARA respectively.

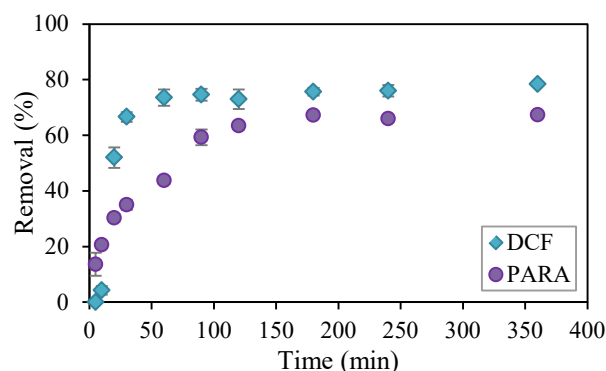


Fig. 2. Adsorption capacity according to contact time.

Table 1 summarizes the parameter estimation data for the kinetic model of pseudo-first-order and pseudo-second-order and the determination coefficient (R^2). It was observed that in DCF the model that best fits the experimental data was the PFO. However, literature reports still state that the pseudo-second-order model is the most suitable for describing DCF adsorption kinetics [15–17]. On the other hand, the model that best described the data for the PARA was PSO. Similarly, PARA adsorption in other adsorbents evaluated in the literature [18,19] followed the behavior of the PSO model over the PPO model. Therefore, the adsorption kinetics of diclofenac is better represented by the PSO equation, suggesting that the adsorption rate-controlling step corresponds to the chemisorption [17].

Table 1. Kinetic parameters and coefficient of pseudo-first-order and pseudo-second-order models.

Model	Parameter	DCF	PARA
Experimental	qt	3.7173	0.6884
PFO	q1	3.7685	0.6719
	k1	0.0385	0.0260
	R ²	0.9403	0.9790
PSO	q2	4.414	0.7661
	k2	0.0093	0.0432
	R ²	0.9052	0.9834

Fig. 3 shows X-ray diffractograms of uncalcined (HT Mg) and calcined (C Mg) samples before and after the adsorption of diclofenac (C-Mg-DCF) and paracetamol (C-Mg-PARA). HT-Mg exhibited reflections at angles 11.6°, 23°, 35°, 39°, 46.8°, 60°, and 62°, which are characteristic of the hydrotalcite-like compounds with a high degree of crystallinity [9]. The absence of the characteristic peaks of the hydrotalcite was noted for C-Mg. In addition, it showed two reflections at angles 42.7° and 62° typical to the MgO like phase, which indicates that the thermal treatment at 400 °C promoted the decomposition of the hydroxyls and intercalated carbonate, and amorphous oxides were formed after calcination [20,21].

The XRD patterns of C-Mg-DCF and C-Mg-PARA shows that the samples return to their hydrotalcite structure after the adsorption of both drugs. The reconstruction of hydrotalcite is due to the memory effect property of this type of material [22]. This effect happens when some hydrotalcite samples, previously calcined, are put in water or an aqueous solution of some anions. The mixed oxide obtained by calcination is rehydrated, recovering the pristine structure and the anions present in the solution must be intercalated to balance the positively charged layers [23].

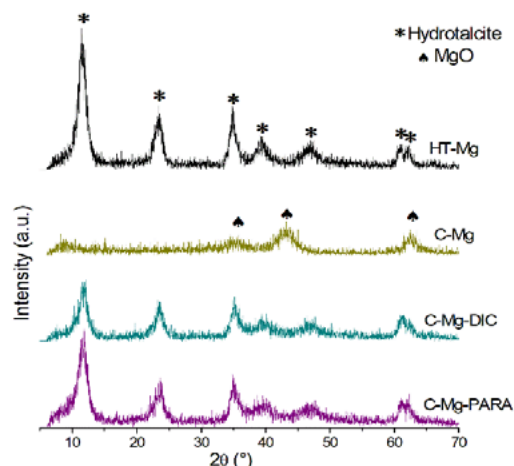


Fig. 3. Diffractogram of the solid before and after the calcination and after the adsorption of diclofenac and paracetamol.

The FTIR spectra of the HT-Mg sample (Fig. 4) showed broadband in the range of 3400–3500 cm⁻¹, which corresponds to the O-H stretching vibration of surface and interlayer water molecules [24]. Also, it was observed the sharp band at 1357 cm⁻¹ that reveals the presence of the CO₃²⁻ anion [25]. After calcination of hydrotalcite, a significant decrease in the intensity of bands related to water and carbonate occurred due to the removal of CO₂ and water vapors.

The FTIR spectra of C-Mg samples at 400 °C revealed the formation of oxides of MgO, due to dehydration, dehydroxylation, and decarbonation [26]. The C-Mg-DCF and C-Mg-PARA samples exhibit similar behavior, returning to the hydrotalcite structure after diclofenac and paracetamol. These results are in agreement with the XRD pattern of these samples (Fig. 3). Rives et al. [27] indicated that the hydrotalcite type compounds, when calcined at moderate temperature (< 500 °C), formed mixed oxides that have the ability to reconstruct the layered structure when they are exposed to solutions that contain anions.

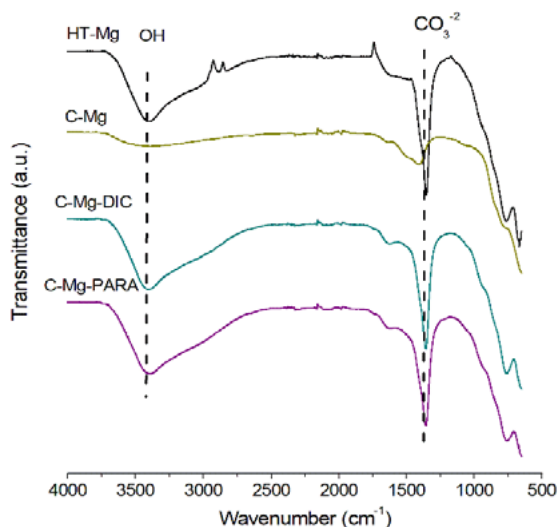


Fig. 4. FTIR spectra of the solid before and after the calcination and after the adsorption of diclofenac and paracetamol.

4. Conclusions

The performance of C-Mg (calcined) for adsorption of DCF and PARA was investigated. The effect of residence time on adsorption of DCF and PARA using Mg-hydrotalcite indicated that the obtained equilibrium times were 1h and 3h, respectively. The kinetic data of DCF and PARA adsorption using C-Mg were well described using PFO and PSO kinetic models, respectively. The results indicated that the adsorption efficiencies followed an order: DCF > PARA. Through XRD and FTIR results it can be verified that both drugs allowed the lamellar reconstruction of the adsorbent.

Acknowledgements

The authors acknowledge the Coordination for the Improvement of Higher Education Personnel (CAPES) of the Brazilian Government for the financial support granted to carry out this work.

References

[1] Carmalin SA, Lima EC. Removal of emerging contaminants from the environment by adsorption. *Ecotoxicol Environ Saf* 2018;150:1–17.
 [2] Kummerer K. The presence of pharmaceuticals in the environment due to human use – present knowledge and future challenges. *J Environ Manage* 2009;90:2354–66.
 [3] Ahmed MJ, Hameed BH. Removal of emerging

pharmaceutical contaminants by adsorption in a fixed-bed column: A review. *Ecotoxicol Environ Saf* 2018;149:257–66.

[4] Ziyilan A, Ince NH. The occurrence and fate of anti-inflammatory and analgesic pharmaceuticals in sewage and fresh water: Treatability by conventional and non-conventional processes. *J Hazard Mater* 2011;187:24–36.
 [5] Tewari S, Jindal R, Kho YL, Eo S, Choi K. Major pharmaceutical residues in wastewater treatment plants and receiving waters in Bangkok, Thailand, and associated ecological risks. *Chemosphere* 2013;91:697–704.
 [6] Vona A, Martino F di, Garcia-Ivars J, Picó Y, Mendoza-Roca JA, Iborra-Clar MI. Comparison of different removal techniques for selected pharmaceuticals. *J Water Process Eng* 2015;5:48–57.
 [7] Grassi M, Kaykioglu G, Belgiorno V. Removal of Emerging Contaminants from Water and Wastewater by Adsorption Process. *Briefs Green Chem Sustain* 2012;45:15–37.
 [8] Saha S, Ray S, Acharya R, Chatterjee TK, Chakraborty J. Magnesium, zinc and calcium aluminium layered double hydroxide-drug nanohybrids: A comprehensive study. *Appl Clay Sci* 2017;135:493–509.
 [9] Khitous M, Salem Z, Halliche D. Effect of interlayer anions on chromium removal using Mg – Al layered double hydroxides: Kinetic, equilibrium and thermodynamic studies. *Chinese J Chem Eng* 2016;24:433–45.
 [10] Chaara D, Pavlovic I, Bruna F, Ulibarri MA, Draoui K, Barriga C. Removal of nitrophenol pesticides from aqueous solutions by layered double hydroxides and their calcined products. *Appl Clay Sci* 2010;50:292–8.
 [11] Mishra G, Dash B, Pandey S. Layered double hydroxides: A brief review from fundamentals to application as evolving biomaterials. *Appl Clay Sci* 2018;152:172–186.
 [12] Pérez A, Otero R, Esquinas AR, Jiménez JR, Fernández JM. Potential use of modified hydrotalcites as adsorbent of Bentazon and Metazachlor. *Appl Clay Sci* 2017;141:300–7.
 [13] Kameda T, Kondo E, Yoshioka T. Kinetics of Cr(VI) removal by Mg-Al layered double hydroxide doped with Fe²⁺. *J Water Process Eng* 2014;4:134–6.
 [14] Rosset M, Sfredo LW, Hidalgo GEN, Perez-Lopez OW, Féris LA. Adsorbents derived from hydrotalcites for the removal of diclofenac in wastewater. *Appl Clay Sci* 2019;175:150–8.

- [15]Baccar R, Sarrà M, Bouzid J, Feki M, Blánquez P. Removal of pharmaceutical compounds by activated carbon prepared from agricultural by-product. *Chem Eng J* 2012;211–212:310–7.
- [16]Torrellas SÁ, García Lovera R, Escalona N, Sepúlveda C, Sotelo JL, García J. Chemical-activated carbons from peach stones for the adsorption of emerging contaminants in aqueous solutions. *Chem Eng J* 2015;279:788–98.
- [17]Larous S, Meniai AH. Adsorption of Diclofenac from aqueous solution using activated carbon prepared from olive stones. *Int J Hydrogen Energy* 2016;41:10380–90.
- [18]Mphahlele K, Onyango MS, Mhlanga SD. Adsorption of aspirin and paracetamol from aqueous solution using Fe/N-CNT/ β -cyclodextrin nanocomposites synthesized via a benign microwave assisted method. *J Environ Chem Eng* 2015;3:2619–30.
- [19]Rad LR, Irani M, Barzegar R. Adsorptive removal of acetaminophen and diclofenac using NaX nanozeolites synthesized by microwave method. *Korean J Chem Eng* 2015;32:1606–12.
- [20]Constantino VRL, Pinnavaia TJ. Basic Properties of Mg^{2+} i - j Al₃ + x Layered Double Hydroxides Intercalated by Carbonate, Hydroxide, Chloride, and Sulfate Anions. *Inorg Chem* 1995;34:883–92.
- [21]Carvalho DL, De Avillez RR, Rodrigues MT, Borges LEP, Appel LG. Mg and Al mixed oxides and the synthesis of n-butanol from ethanol. *Appl Catal A Gen* 2012;415–416:96–100.
- [22]Cavani F, Trifirò F, Vaccari A. Hydrotalcite-type anionic clays: Preparation, properties and applications. *Catal Today* 1991;11:173–301.
- [23]Extremera R, Pavlovic I, Pérez MR, Barriga C. Removal of acid orange 10 by calcined Mg/Al layered double hydroxides from water and recovery of the adsorbed dye. *Chem Eng J* 2012;213:392–400.
- [24]Feng Y, Li D, Wang Y, Evans DG, Duan X. Synthesis and characterization of a UV absorbent-intercalated Zn-Al layered double hydroxide. *Polym Degrad Stab* 2006;91:789–94.
- [25]Gu Z, Thomas AC, Xu ZP, Campbell JH, Qing G, Lu M. In Vitro Sustained Release of LMWH from MgAl-layered Double Hydroxide Nanohybrids. *Chem Mater* 2008;20:3715–22.
- [26]Zeng H, Feng Z, Deng X, Li Y. Activation of Mg – Al hydrotalcite catalysts for transesterification of rape oil. *Fuel* 2008;87:3071–6.
- [27]Rives V, del Arco M, Martín C. Intercalation of drugs in layered double hydroxides and their controlled release: A review. *Appl Clay Sci* 2014;88–89:239–69.

Synthesis and characterization of Zn–Al–LDH for application in adsorption of 2–nitrophenol from aqueous solution

Fabiola Balzan Dalla Nora^a, Sabrina Frantz Lütke^a, Lucas Meili^b, Guilherme Luiz Dotto^a

^a Chemical Engineering Department, Federal University of Santa Maria – UFSM, Roraima Avenue, 1000 – 97105–900 – Santa Maria – RS – Brazil

^b Center of Technology, Federal University of Alagoas – UFAL, Lourival Melo Mota Avenue, 57072–900 – Maceió – AL – Brazil

Abstract

In this work, an Zn–Al–LDH was produced, characterized and applied as adsorbent for the removal of 2–nitrophenol from aqueous solution. The synthesis was realized by coprecipitation method. XRD, FTIR, SEM and N₂ adsorption/desorption curves were used to characterize the Zn–Al–LDH. The characterization indicated a high degree of crystallinity and a well organized and lamellar structure, confirming the efficiency of the Zn–Al–LDH synthesis. The specific surface area was 104.1 m² g⁻¹, total pore volume was 0.216 cm³ g⁻¹ and an average pore size was 25.06 nm. The adsorption kinetics was investigated at different initial 2–nitrophenol concentrations (40 to 150 mg L⁻¹). At the initial 2–nitrophenol concentration of 150 mg L⁻¹ the adsorption capacity was 174.56 mg g⁻¹. The Elovich model was the more suitable to describe the kinetic adsorption experimental data. These results demonstrate that the Zn–Al–LDH is a promising adsorbent that can be used to treat 2–nitrophenol containing wastewaters.

Keywords: Zn–Al–LDH; adsorption; kinetic; 2–nitrophenol

1. Introduction

Phenols are contaminants of high priority concerns because of their toxicity and possible accumulation in the environment [1]. Phenolic compounds are found in effluents of pharmaceutical, insecticides and herbicides industries, and also, petroleum refineries [2,3]. Due to the high toxicity and difficult to biological degradation, rigid limits have been set for the acceptable level of phenols in the environment [4]. The World Health Organization (WHO) recommends the threshold concentration of phenol in drinking water should fall below 1.0 µg L⁻¹ [2]. Among the phenolic compounds, nitrophenols are highlighted due to their high toxicity [5]. Different technologies for remove phenolic pollutants from wastewaters can be used, as catalytic reduction [6], photocatalytic degradation [7], Fenton catalysts [8] and adsorption [3]. When compared to these other methods, adsorption has advantages such as ease of implementation and operation, high efficiency, low cost and regeneration capacity [9].

Layered double hydroxides (LDH), also known as anionic clays, are bi–dimensional solids that have general formula $[M^{2+}_{(1-x)}M^{3+}_x(OH)_2](A^{n-})_x/n \cdot zH_2O$, where M is a metallic cation and Aⁿ⁻ is

an interlayer anion. LDH layers have excess positive charge and thus are able to incorporate anions between the layers. These anions, along with water molecules, promote stacking of double hydroxide layers [10]. The simplest and most commonly used method for LDH synthesis is coprecipitation. This method has been used extensively for the one–pot direct synthesis of LDHs containing a variety of layer cations and interlayer anions [11].

Layered double hydroxides have been widely studied for their potential use in important areas. Due to its features of mechanical and chemical stability, high specific surface area, high exchange capacity, layered double hydroxides can be used for contaminant removal from aqueous solutions through adsorption [12]. Zn–Al–LDH synthesis and its application as adsorbent for removal of various contaminants have already been reported in the literature [13–15]. However, there are no studies regarding the Zn–Al–LDH synthesis and its application as an adsorbent for removing 2–nitrophenol from aqueous solution.

In this context, the aim of this work was to evaluate the potential of an Zn–Al–LDH adsorbent to remove 2–nitrophenol from aqueous solution through adsorption. First, the Zn–Al–LDH adsorbent was prepared by coprecipitation method

and characterized. Then, adsorption kinetics was investigated in different initial 2-nitrophenol concentrations. Pseudo-first order, pseudo-second order and Elovich models were used to evaluate the kinetic curves obtained.

2. Material and Methods

2.1. Synthesis of Zn-Al-LDH adsorbent

Zn-Al-LDH adsorbent was synthesized by the coprecipitation method. For this, 21.72 g of $\text{AlCl}_3 \cdot 6\text{H}_2\text{O}$ and 36.78 g of ZnCl_2 (ratio Zn:Al of 3:1) were added in 100 mL of deionized water. The mixture was kept under constant stirring for effective dissolution for 30 min and the pH of solution was adjusted to 10 by addition of sodium hydroxide solution (2 mol L^{-1}). Then, the system was stirred for further 24 h at constant temperature. The obtained product was washed several times with deionized water and, between each wash, was centrifuged for 5 min at 3000 rpm (Petrotest, Petrocen 6-15H). After washing, the material was oven-dried for 24 h at $80 \text{ }^\circ\text{C}$ (Fanem, Orion 515). Finally, the material was ground and sieved through a $250 \mu\text{m}$ sieve to obtain uniform particle size [16,17].

2.2. Zn-Al-LDH characterization

Zn-Al-LDH adsorbent was characterized in relation to the crystallinity by X-Ray diffraction (XRD) (Rigaku, Miniflex 300, Japan), with Ni-filtered Cu K α radiation ($\lambda = 1.54051 \text{ \AA}$, 30 kV, 10 mA), using $2\theta = 0-100^\circ$. The information about the functional groups were investigated by Fourier transform infrared (FTIR) spectroscopy (Shimadzu 01722, IR Prestige, Japan). The analyses were realized by direct transmittance technique, using KBr tablets. The spectra were obtained with a resolution of 2 cm^{-1} over the range of $400-4500 \text{ cm}^{-1}$, performing 44 scans. The surface morphology was obtained by Scanning Electron Microscopy (SEM) (Jeol, JSM-6010LV, Japan). The textural properties (specific surface area, total pore volume and average pore size) were determined based on nitrogen adsorption/desorption isotherms at 77 K, using an automated gas sorption analyzer (Micromeritics, ASAP 2020, USA). The specific surface area was obtained from the Brunauer-Emmett-Teller (BET) method and the pore size distribution was obtained from the Barrett-Joyner-Halenda (BJH) method through nonlinear regression using the Quasi-

2.3. Adsorption kinetic experiments

The adsorption kinetic experiments were carried out in a thermostatic shaker (Solab, SL 222, Brazil) at $25 \text{ }^\circ\text{C}$ and stirring rate of 150 rpm. The studies were performed using initial 2-nitrophenol concentrations of 40, 60, 80, 100 and 150 mg L^{-1} . The adsorbent dosage was 0.5 g L^{-1} and the pH of the solution was 3.0. Aliquots were removed at set time intervals (0-180 min). After the experiments, the solution and solid phase were separated by centrifugation at 3500 rpm for 5 min in a table-top centrifuge (LGI-DLC-802B). The remaining 2-nitrophenol concentration in the liquid phase was measured by UV-VIS spectrometer (Shimadzu, UVmini-1240, Japan) at 279 nm. The assays were performed in replicate ($n=3$) and blank tests were realized. The adsorption capacity at time t (q_t , mg g^{-1}) was determined by Eq. (1).

$$q_t = \left(\frac{C_0 - C_t}{m} \right) V \quad (1)$$

where C_0 is the initial 2-nitrophenol concentration in liquid phase (mg L^{-1}), C_t is the 2-nitrophenol concentration at time t (mg L^{-1}), m is amount of adsorbent (g), and V is the volume of solution (L).

2.4. Kinetic models and statistical analysis

The kinetic data were evaluated by pseudo-first order (Eq. 2), pseudo-second order (Eq. 3) and Elovich (Eq. 4) models [18]:

$$q_t = q_1(1 - \exp(-k_1 t)) \quad (2)$$

$$q_t = \frac{t}{(1/k_2 q_2^2) + (t/q_2)} \quad (3)$$

$$q_t = \frac{1}{b} \ln(1 + abt) \quad (4)$$

where k_1 and k_2 are the rate constants of pseudo-first order (min^{-1}) and pseudo-second order ($\text{g mg}^{-1} \text{ min}^{-1}$) models, respectively, q_1 and q_2 are the theoretical values for adsorption capacity (mg g^{-1}), a is the initial sorption rate due to dq/dt with $qt = 0$ ($\text{mg g}^{-1} \text{ min}^{-1}$) and b is the desorption constant of the Elovich model (g mg^{-1}).

The models were fitted to experimental data Newton method by the Statistic 7.0 software

(StatSoft, USA). The fit quality was obtained through determination coefficient (R^2), adjusted determination coefficient (R^2_{adj}), average relative error (ARE) and Akaike information criterion (AIC).

3. Results and Discussion

3.1. Zn–Al–LDH characteristics

The XRD pattern in the range of 0–100° of the Zn–Al–LDH adsorbent is shown in Fig. 1. The diffractogram indicates a high degree of crystallinity. It is suggested that the peak 23° refers to Al cations and the peak at approximately 34° refers to Zn [19,20]. The peaks corresponding to 11°, 23° and 62° are characteristic of clay minerals having layered structure [21].

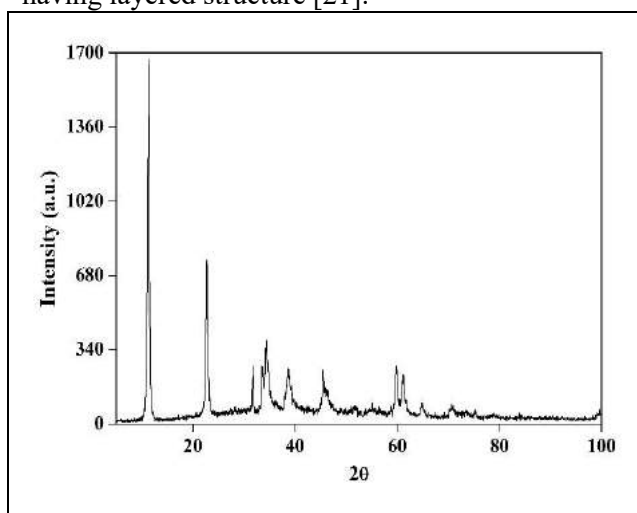


Fig. 1. XRD pattern of the Zn–Al–LDH.

Fourier transform infrared spectroscopy was able to identify the main absorption bands of the adsorbent, and the spectrum is shown in Fig. 2. The bands at 3450 and 1630 cm^{-1} represents the OH stretching vibrations of the hydroxyl groups of the adsorbent and interlamellar water [22]. The bands around 500–100 cm^{-1} are related to the M–O or M–O–M [13]. The presence of these absorption bands confirms the efficiency of Zn–Al–LDH synthesis.

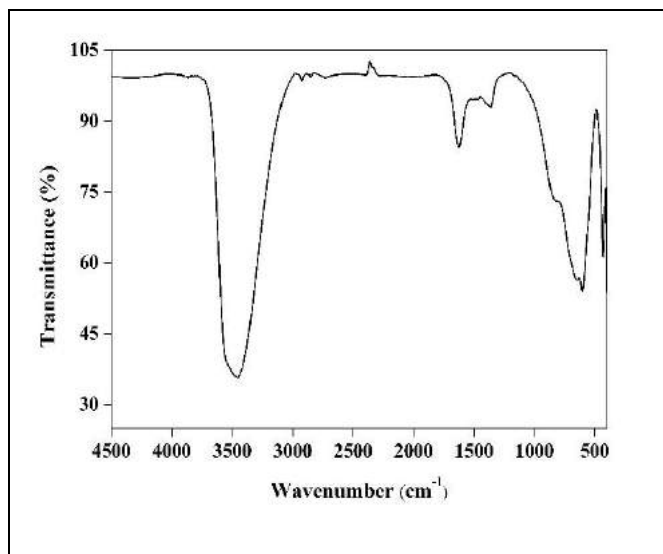


Fig. 2. FTIR spectrum of the Zn–Al–LDH.

SEM image of Zn–Al–LDH is shown in Fig. 3. It is possible to observe a typical well organized and lamellar structure.

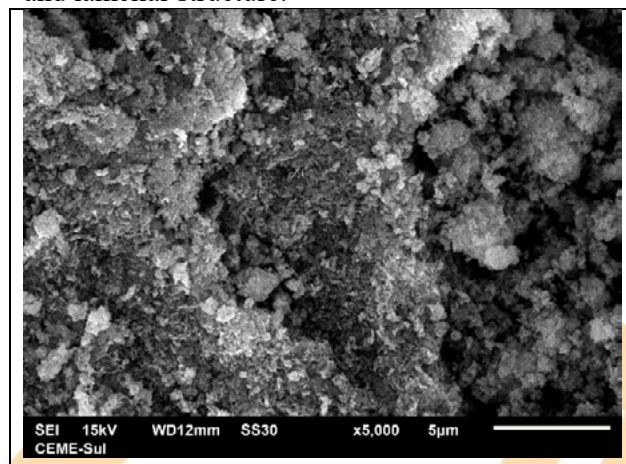


Fig. 3. SEM image ($\times 5.000$) of the Zn–Al–LDH.

In Fig. 4 are shown the N_2 adsorption–desorption isotherm and the BJH desorption pore size distribution of Zn–Al–LDH. According to international union of pure and applied chemistry (IUPAC) classification of adsorption isotherms [23], the isotherms recorded for the Zn–Al–LDH showed a mixture of Type II and Type IV isotherms, where Type II isotherm represents a typical characteristic of microporous materials and Type IV isotherm represents a typical characteristic of mesoporous materials [23]. Also, there is an adsorption hysteresis present in the adsorption–desorption isotherms, which is classified according to IUPAC. The adsorption hysteresis exhibited by Zn–Al–LDH can be

classified as Type H3, which implies that the material does not have well-defined mesoporous structure and is characteristic of plate-like particles (e.g., certain clays) [23]. The Zn–Al–LDH presented specific surface area of $104.1 \text{ m}^2 \text{ g}^{-1}$, total pore volume of $0.216 \text{ cm}^3 \text{ g}^{-1}$ and an average pore size of 25.06 nm .

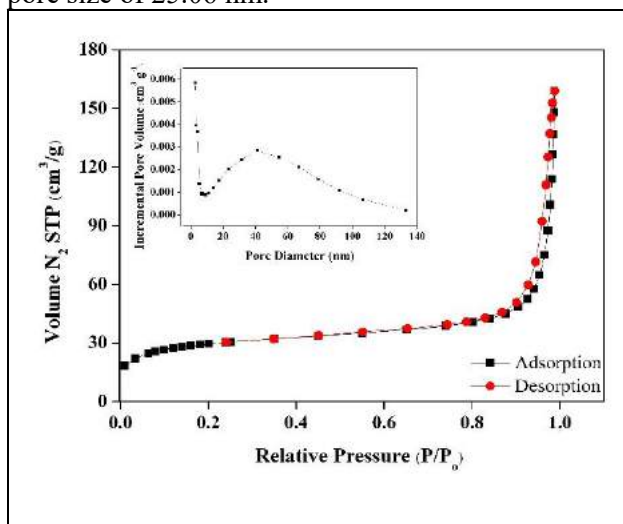


Fig. 4. Nitrogen adsorption-desorption isotherms and BJH desorption pore size distribution of the Zn–Al–LDH adsorbent.

3.2. Kinetic studies

The adsorption kinetic curves were obtained at initial 2-nitrophenol concentrations of 40 to 150 mg L^{-1} . Fig. 5 shows the kinetic curves obtained.

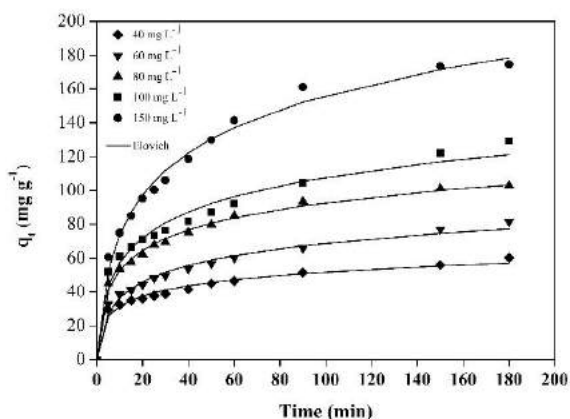


Fig. 5. Kinetic curves for adsorption of 2-nitrophenol onto Zn–Al–LDH adsorbent.

It was possible to observe that the adsorption was fast in the first 30 min. Later, the adsorption rate gradually decreased and the curves tended to

the equilibrium. It was also observed that the increase in the initial concentration provided an increase of 60.21 to 174.56 mg g^{-1} in the adsorption capacity.

The kinetic curves were also investigated using the pseudo-first order (PFO), pseudo-second order (PSO) and Elovich models. Table 1 shows the kinetic parameters for 2-nitrophenol adsorption onto Zn–Al–LDH. Considering the higher values of determination coefficient and adjusted determination coefficient and the lower values of average relative error and Akaike information criterion (AIC), the Elovich model was the more adequate to represent the adsorption kinetic of 2-nitrophenol onto Zn–Al–LDH. Elovich model is adequate when the adsorption rate decreases with time due to the saturation of the adsorption sites in the adsorbent surface.

4. Conclusions

Zn–Al–LDH was successfully synthesized through coprecipitation method. The high degree of crystallinity, the presence of M–O or M–O–M vibration bands and the observed organized and lamellar structure confirmed the efficiency of the Zn–Al–LDH synthesis. The material presented specific surface area of $104.1 \text{ m}^2 \text{ g}^{-1}$, total pore volume of $0.216 \text{ cm}^3 \text{ g}^{-1}$ and an average pore size of 25.06 nm . 2-nitrophenol adsorption kinetic curves were faster within the first 30 min, but the equilibrium was not reached in 180 min. The increase in the initial concentration provided an increase of 60.21 to 174.56 mg g^{-1} in the adsorption capacity. The Elovich model was the more suitable to describe the kinetic adsorption experimental data. Overall, Zn–Al–LDH can be used as a potential adsorbent material to remove 2-nitrophenol from aqueous solution.

Acknowledgements

The authors would like to thank CAPES (Brazilian Agency for Improvement of Graduate Personnel) and CNPq (National Council of Science and Technological Development) for the financial support. Furthermore, the authors would like to thank CEME-SUL/FURG (Electron Microscopy Center of South/Federal University of Rio Grande/RS/Brazil) due to the scanning electron microscopy images.

Table 1. Kinetic parameters for adsorption of 2-nitrophenol onto Zn-Al-LDH adsorbent.

Model	Initial 2-nitrophenol concentration (mg L ⁻¹)				
	40	60	80	100	150
Pseudo-first order					
q_1 (mg g ⁻¹)	49.48	69.09	91.51	108.41	163.73
k_1 (min ⁻¹)	0.0823	0.0537	0.0639	0.0530	0.0413
R^2	0.8163	0.8476	0.8854	0.8202	0.9249
R^2_{adj}	0.7996	0.8338	0.8750	0.8038	0.9180
ARE (%)	12.49	13.05	10.96	14.26	11.20
AIC	52.41	58.60	61.98	72.52	71.77
Pseudo-second order					
q_2 (mg g ⁻¹)	55.47	78.40	102.74	122.95	187.99
k_2 (g mg ⁻¹ min ⁻¹)	0.00210	0.00093	0.00088	0.00059	0.00028
R^2	0.9176	0.9303	0.9577	0.9126	0.9684
R^2_{adj}	0.9102	0.9240	0.9553	0.9047	0.9656
ARE (%)	8.31	8.68	6.78	9.92	7.02
AIC	41.99	48.42	49.01	63.14	60.49
Elovich					
a (mg g ⁻¹ min ⁻¹)	0.1122	0.0688	0.0562	0.0439	0.0262
b (g mg ⁻¹)	29.5743	16.431	32.5799	25.6971	22.5069
R^2	0.9839	0.9855	0.9953	0.9772	0.9909
R^2_{adj}	0.9825	0.9842	0.9949	0.9752	0.9900
ARE (%)	3.62	4.12	2.30	5.00	3.51
AIC	20.75	28.02	20.48	45.66	44.39
q_e (exp) (mg g ⁻¹)	60.21	81.54	102.87	129.08	174.56

References

- [1] Lin SH, Juang RS. Adsorption of phenol and its derivatives from water using synthetic resins and low-cost natural adsorbents: A review. *J. Environ. Manage.* 2009;90:1336–1349.
- [2] Álvarez-Torrellas S, Martín-Martínez M, Gomes HT, Ovejero G, García J. Enhancement of p-nitrophenol adsorption capacity through N₂-thermal-based treatment of activated carbons. *Appl. Surf. Sci.* 2017; 414:424–434.
- [3] Gu X, Kang H, Li H, Liu X, Dong F, Fu M, Chen, J. Adsorption removal of various nitrophenols in aqueous solution by aminopropyl-modified mesoporous MCM-48. *J. Chem. Eng. Data.* 2018;63:3606–3614.
- [4] Srivastava VC, Swamy MM, Mall ID, Prasad B, Mishra IM. Adsorptive removal of phenol by bagasse fly ash and activated carbon: Equilibrium, kinetics and thermodynamics. *Colloids Surfaces A Physicochem. Eng. Asp.* 2005;272:89–104.
- [5] Chen J, Sun X, Lin L, Dong X, He Y. Adsorption removal of o-nitrophenol and p-nitrophenol from wastewater by metal-organic framework Cr-BDC. *Chin. J. Chem. Eng.* 2017;25:775–781.
- [6] Aamir M, Farooq M, Ambreen J, Ahmad N, Iqbal M, Haleem A, Saeed S, Shah A, Siddiq M. Synthesis and characterization of gum arabic microgels stabilizing metal based nanocatalysts for ultrafast catalytic reduction of 4-nitrophenol at ambient conditions. *J. Environ. Chem. Eng.* 2019;7:103280.
- [7] Bekena FT, Abdullah H, Kuo DH, Zeleke MA. Photocatalytic reduction of 4-nitrophenol using effective hole scavenger over novel Mg-doped Zn(O,S) nanoparticles. *J. Ind. Eng. Chem.* 2019;78:116–124.
- [8] ElShafei GMS, Al-Sabagh AM, Yehia FZ, Philip CA, Moussa NA, Eshaq G, ElMetwally AE. Metal oxochlorides as robust heterogeneous Fenton catalysts for the sonophotocatalytic degradation of 2-nitrophenol. *Appl. Catal. B Environ.* 2018; 224:681–691.
- [9] Lütke SF, Igansi AV, Pegoraro L, Dotto GL, Pinto LAA, Cadaval Jr TRS. Preparation of activated carbon from black wattle bark waste and its application for phenol adsorption. *J. Environ. Chem. Eng.* 2019;7:103396.



- [10] Goh KH, Lim TT, Dong Z. Application of layered double hydroxides for removal of oxyanions: A review. *Water Res.* 2008;42:1343–1368.
- [11] He J, Wei M, Li B, Kang Y, Evans DG, Duan X. Preparation of Layered Double Hydroxides. In: Duan X, Evans DG. *Layered Double Hydroxides. Structure and Bonding*, vol 119. Springer, Berlin, Heidelberg.
- [12] Bakr AA, Sayed NA, Salam TM, Ali IO, Abdel Gayed RR, Negm NA. Kinetics and thermodynamics of Mn(II) removal from aqueous solutions onto Mg–Zn–Al LDH/montmorillonite nanocomposite. *Egypt. J. Pet.* 2018;27:1215–1220.
- [13] Barnabas MJ, Surendran P, Mathew A, Park SS, Vinu A, Ha, CS. Highly efficient and selective adsorption of In³⁺ on pristine Zn/Al layered double hydroxide (Zn/Al–LDH) from aqueous solutions. *J. Solid State Chem.* 2016;233:133–142.
- [14] Srilakshmi C, Thirunavukkarasu T. Enhanced adsorption of Congo red on microwave synthesized layered Zn–Al double hydroxides and its adsorption behavior using mixture of dyes from aqueous solution. *Inorg. Chem. Commun.* 2019;100:107–117.
- [15] Hatami H, Fotovat A, Halajnia A. Comparison of adsorption and desorption of phosphate on synthesized Zn–Al LDH by two methods in a simulated soil solution. *Appl. Clay Sci.* 2018;152:333–341.
- [16] Menezes J, Silva T, Santos J, Catari E, Meneghetti M, Matta C, Alexandre–Moreira M, Santos–Magalhães N, Grillo L, Dornelas C. Layered double hydroxides (LDHs) as carrier of antimony aimed for improving leishmaniasis chemotherapy. *Appl. Clay Sci.* 2014;91–92:127–134.
- [17] Abderrazek K, Najoua FS, Srasra E. Applied Clay Science Synthesis and characterization of [Zn–Al] LDH: Study of the effect of calcination on the photocatalytic activity. *Appl. Clay Sci.* 2016;119: 229–235.
- [18] Ho YS, McKay G. A Comparison of chemisorption kinetic models applied to pollutant removal on various sorbents. *Process Saf. Environ. Prot.* 1998;76:332–430.
- [19] Zhao D, Sheng G, Hu J, Chen C, Wang X. The adsorption of Pb(II) on Mg₂Al layered double hydroxide. *Chem. Eng. J.* 2011;171:167–174.
- [20] Benalioua B, Mansour M, Bentouami A, Boury B, Elandaloussi EH. The layered double hydroxide route to Bi–Zn co–doped TiO₂ with high photocatalytic activity under visible light. *J. Hazard. Mater.* 2015;288:158–167.
- [21] Islam M, Patel R. Nitrate sorption by thermally activated Mg/Al chloride hydrotalcite–like compound. *J. Hazard. Mater.* 2009;169:524–531.
- [22] Meili L, Lins PV, Zanta CLPS, Soletti JI, Ribeiro LMO, Dornelas CB, Silva TL, Vieira MGA. MgAl–LDH/Biochar composites for methylene blue removal by adsorption. *Appl. Clay Sci.* 2018;168:11–20.
- [23] Thommes M, Kaneko K, Neimark AV, Olivier JP, Rodriguez–Reinoso F, Rouquerol J, Sing KSW. *Physisorption of gases , with special reference to the evaluation of surface area and pore size distribution (IUPAC Technical Report)*. Pure Appl. Chem. 2015.

Synthesis and characterization of clay-based catalysts prepared from natural clays

A. Santos Silva^{a,b,c}, Jose L. Diaz de Tuesta^{b,c}, H. T. Gomes^{b,c}, Juliana G. Sgorlon^{a*}

^a Federal University of Technology - Paraná, R. Marcílio Dias, 635 – Jardim Paraíso, Apucarana, 86812600, Brazil

^b Centro de Investigação de Montanha (CIMO), Instituto Politécnico de Bragança, Campus Santa Apolónia, Bragança, 5300252, Portugal

^c Laboratory of Separation and Reaction Engineering-Laboratory of Catalysis and Materials (LSRE-LCM), R. Dr. Roberto Frias, Porto, 4200465, Portugal

Abstract

This work deals with the synthesis and characterization of clay-based catalysts. The catalysts prepared in this work were clays activated through acid treatment and clays pillared with Co and Fe. For the preparation, natural clays from four different regions of Kazakhstan were used: Akzhar, Asa, Karatau and Kokshetau. The FTIR analysis showed that the pillared clays have an amount of iron in its structure. The N₂ adsorption isotherms obtained were classified as Type II, according to IUPAC classification, typical of macroporous materials. The S_{BET} calculated with the N₂ adsorption isotherms for the activated clays showed to be higher than the S_{BET} results for natural clays. XRD patterns helped to gather information about crystalline phases of the clay, allows classifying the type of clay used in the work. The acid characterization showed that the procedures used for the preparation of the acid activated clays and pillared clays caused structural modifications, which is another result that suggests the success of both methods.

Keywords: low-cost materials; pillared clays; activated clays; synthesis and characterization

1. Introduction

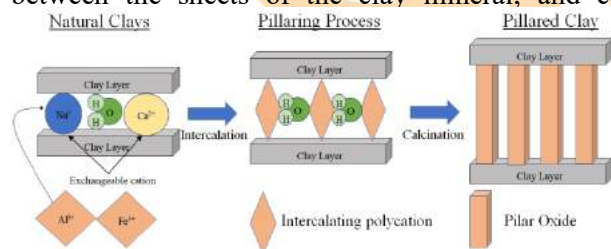
In addition to cost, catalytic properties and availability are important criteria for choosing a good catalyst. This has encouraged the scientific community to search for materials that are both efficient and cheap. There are in the literature several reports of different low-cost materials that can be used as catalysts, such as chitosan hydrogel, lignin and modified clays [1].

Modified clays have been explored for several applications as low-cost materials, showing interesting catalytic and adsorptive properties[2,3]. In the last years, studies about layered aluminosilicate (clays) report its high activity in the Fenton-like process used in the oxidation of organic pollutants. Furthermore, such materials are also a good option for the removal of pollutants by adsorption.

Among modified clays, the pillared clays have been frequently studied for different applications. Pillared clays (PILCs) are porous materials resulting from the process of pillaring lamellar clays. The preparation of pillared clays is one approach to the rational design of porous solids with a pore size

distribution on a molecular length scale. Pillared clays are a special class of intercalated materials in which the intercalant gallery is sufficiently large to allow access to the intracrystal surfaces of the layered structure [4]. Their surface area and permanent porosity allow them to be very attractive solids for adsorption and catalysis purposes.

PILCs can be obtained from smectite clay minerals, which is a phyllosilicate class of minerals with TOT structure, through a procedure that can be divided into three fundamental steps: a) preparation of the pillaring solution that contains the pillaring cations (as for example Al³⁺, Ga³⁺, Ti⁴⁺, Zr⁴⁺, Fe³⁺ and Cr³⁺); b) intercalation of these cations into the interlayer space of the clays, which involves the natural substitution of exchangeable cations present between the sheets of the clay mineral; and c)





during 72 h and then the material was filtered and washed several times until the rinsing waters reach the natural pH. For the last step of the preparation of the pillared clay, the filtered material was dried in an air atmosphere oven at 60 °C overnight and then calcined at 600 °C for 5 h in an air atmosphere muffle. This procedure resulted in the AKP, ASP, KAP and KOP pillared clays from the AKN, ASN, KAN and KON, respectively.

2.2 Characterization

2.2.1 Fourier transformed Infra-red spectroscopy (FTIR)

The FTIR spectra of the 16 different samples were recorded on a Perkin Elmer FT-IR spectrophotometer UATR Two infrared spectrophotometer, with a resolution of 4 cm⁻¹. The range of wavenumber used in the analysis was from 450 to 4000 cm⁻¹. All the measurements were done from the solid samples at room temperature.

2.2.2 Surface and pore analyzer

The textural properties of the materials were determined from N₂ adsorption-desorption isotherms at 77 K, obtained in a Quantachrome instrument NOVA TOUCH LX⁴ using long cells with a bulb and an outer diameter of 9 mm. The specific surface area (S_{BET}) was calculated by the BET method using the software Quantachrome TouchWin, in the range of p/p_0 0.05 – 0.35.

2.2.3 X-ray diffraction (XRD)

The measurements of powder X-ray diffraction (XRD) were obtained by depositing the material in the glass sample holder and analyzing on a diffractometer DRON 3. For the interpretation of the results, the software HighScore Demo was used, from PANalytical.

2.2.4 Acid characterization

One of the tests that can be done for the acid characterization of the clays is the pH of the point of zero charge (pH_{PZC}). For this determination, 0.09 g of clay was added in 6 different erlenmeyers and then 15 mL of 0.01 M NaCl with distinct initial pH values (pH_0) adjusted to different values (2, 4, 6, 8, 10 and 12) by means of 0.02 M NaOH and 0.02 M HCl solutions. The erlenmeyers were placed in an orbital shaker IKA KS 130 Basic and agitated for 24

h at 400 rpm. After the agitation, the suspension was filtered and the pH of the filtrate was measured (pH_F). The pH of the point of zero charge was found in the interception between the curve $pH_0 \times pH_F$ and the identity curve.

The second test used in this work for acid characterization is the acidity and basicity determination. In order to determine the acidity and basicity in the different samples, 0.2 g of catalyst was added in 2 different erlenmeyers. One of the erlenmeyers contained 25 mL of a 0.02 M HCl solution for basicity determination, and the other 25 mL of a 0.02 M NaOH solution for acidity determination. The resulting suspensions in the erlenmeyers were placed in an orbital shaker IKA KS 130 Basic and agitated during 48 h at 400 rpm. After the agitation, the suspension of each erlenmeyer was filtered to remove the solid material, and 20 mL was used for the determination of the concentration by titration. Knowing the concentration of the resulting solution it is possible to obtain the number of moles that react with the acidic or basic centers of the clay, and then, to calculate the acidity and basicity for each sample. Phenolphthalein was used as an indicator in both titrations.

3. Results

3.1. Fourier transformed infra-red spectroscopy (FTIR)

The FTIR spectra obtained by analysis of the different prepared clays are depicted in Fig.3.

In the Kokshetau spectra given in Figure 3(A), it is possible to observe a band appearing at 3,692 cm⁻¹ for the natural clay. This band is due to the –OH stretching vibration for water adsorbed at the interlayer, the reason why this signal is absent in the samples subjected to a calcination treatment [7]. Observing the spectra of Akzhar, Asa, and Karatau clays, it is possible to realize that the natural clays have a band in the range of 1,440 – 1,455 cm⁻¹. This band is due to the presence of calcite in the materials, and its disappearance is a consequence of the exchange between calcium and the pillaring metals, indicating the success of the pillarization [8]. That band was found to be absent in the FTIR spectra of the pillared clays and of the activated clays, explained by the fact that the acid treatment and the pillaring process causes a structural modification.

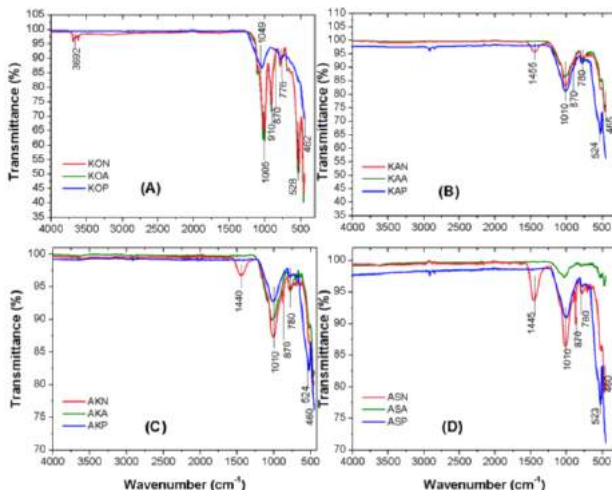


Fig.3. FTIR spectra of the A) Kokshetau clays, B) Karatau clays, C) Akzhar clays and D) Asa clays.

The band in the range of 1,005 to 1,010 cm^{-1} is present in the spectra of all samples and represents the stretching vibrations of the Si–O bond group. The band at 870 cm^{-1} for natural samples can be ascribed to the Al-Mg-OH bending vibrations [7]. The absence of transmittance in this band in the spectra of the pillared samples also could mean that the cation Mg^{2+} was exchanged in the pillaring procedure by the pillaring cations used. In the range of wavenumber from 776 to 780 cm^{-1} , there is a signal of transmittance attributed to the presence of quartz impurity.

The last band, which is present in the range of 460 to 465 cm^{-1} , represents important information deserving special attention. This band is related to the presence of bending vibrations of Si–O–Fe bonds, which is present in all of the samples since the natural clays also contain an amount of these bonds in its structure [9]. The signal of the transmittance in this band is present in AKP, ASP, KAP, and KOP pillared clays, which suggests the successful incorporation of Fe by the pillaring process in the structure of the clay.

3.2. Surface and pore analysis

The adsorption isotherms of N_2 at 77 K on prepared samples are depicted in Fig. 4. As can be observed, the acid activated materials show the highest adsorption capacity. The higher adsorption for the activated sample is less visible for the KOA sample, and this occurs because the acid treatment was not able to significantly increase the surface area of this material. Besides that, the same tendency can be observed in Akzhar, Asa, and Karatau samples, with higher adsorption being

obtained in the activated sample followed by the natural and pillared samples. According to the IUPAC classification, it is possible to conclude that the physisorption isotherms obtained in this work fit in Type II. This classification is attributed to nonporous or macroporous adsorbents, for which the shape of the isotherm is a result of unrestricted monolayer-multilayer adsorption up to high p/p^0 [10].

The results of S_{BET} obtained from the adsorption isotherms are shown in Table 1. The S_{BET} values confirm that the materials with the highest BET surface area are the acid activated clays, which represents a good result since the main goal of this kind of treatment is to increase the surface area of the material. The pillared clays presented a lower surface area than that of the natural clays. This effect occurred by the fact that the calcination treatment done as the last step of the pillaring procedure may have caused the collapse of the pillars. This supposition is valid taking into consideration some works reporting that above 400 °C the pillars collapse in some samples, and this can be the case in this work. Another explanation for the result obtained could be the blockage of the pores of the material with the particles of iron and cobalt, as a consequence of the high concentration of these metals in the pillaring solution.

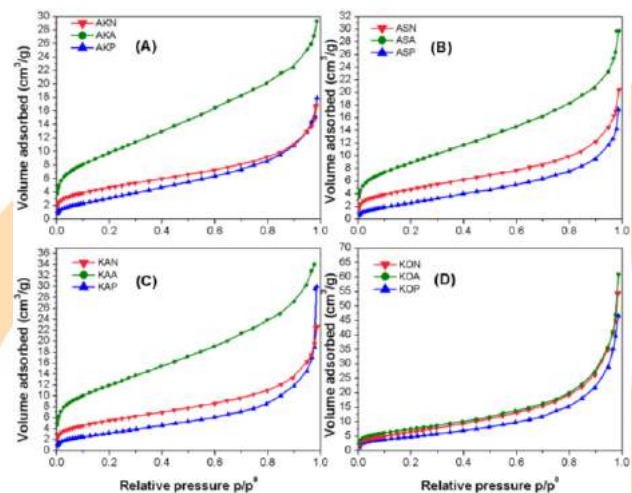


Fig. 4. Adsorption isotherms of N_2 at 77 K of the A) Akzhar clays, B) Asa clays, C) Karatau clays and D) Kokshetau clays.

Table 1- S_{BET} from the materials.

Material	$S_{\text{BET}}(\text{m}^2/\text{g})$	Material	$S_{\text{BET}}(\text{m}^2/\text{g})$
AKN	17	KAN	20

AKA	35	KAA	43
AKP	13	KAP	13
ASN	17	KON	26
ASA	32	KOA	28
ASP	11	KOP	19

3.3. X- Ray diffraction (XRD)

For this analysis, Karatau and Kokshetau clays were chosen, since they showed the highest surface areas among the clays. Fig. 5 gathers the XRD diffractograms of the analysed samples. Observing the XRD patterns obtained, it is possible to realize that both clays present the typical reflection of montmorillonite [11]. In KAN it is also possible to find traces of saponite, kaolinite, and muscovite [13,14]. In KON, in addition to the already mentioned montmorillonite, there is also the correspondence for the presence of kaolinite [12]. Therefore, both clays can be classified as bentonite, which is the denomination given to the clays composed by a mixture of different clay minerals, with a majority composition of montmorillonite [14].

All the samples present a peak at 26.7° related to the presence of quartz (SiO₂ impurities). The analysis of the diffractograms also allowed the identification of calcite for the Karatau sample and the absence of calcite for Kokshetau samples, which corroborates with FTIR results.

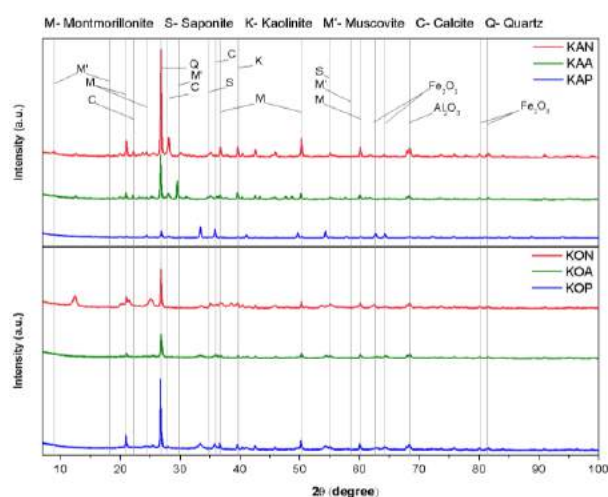


Fig. 5. XRD diffractograms of the A) Karatau samples and B) Kokshetau samples.

It is possible to observe that the signal for SiO₂ and metal oxides such as aluminum oxide and iron oxide [15] decreased in the diffractograms of the

Karatau and Kokshetau samples after the acid treatment. This can be explained by the fact that the acid treatment washed the impurities of SiO₂ from the clay structure, also leaching a small amount of iron metals. For the pillared sample KAP, it is possible to observe that the signal for the SiO₂ impurities decreased and that the signal for the iron oxide increased significantly, putting in evidence the incorporation of iron in the material. In fact, the signal attributed to iron oxide in this sample was higher than in the others.

Finally, in the diffractogram of KOP, the signal for iron oxide was significantly higher than in that observed for the natural sample KON, also confirming the successful incorporation of iron in the clay structure. Besides all the differences between the signals in both diffractograms of the Karatau and Kokshetau samples, it is interesting to observe that the signal for montmorillonite, kaolinite, saponite, and muscovite were not significantly changed in the different samples. This suggests that the structure of the clay is stable, although passing through some structural changes the main structure remained [16].

3.4. X- Acid characterization

The results obtained for both analysis is exposed in Table 2.

Table 2. Results for the acid characterization.

Samples	Acidity (μmol/g)	Basicity (μmol/g)	pH _{PZC}
AKP	812	538	7.15
ASP	475	372	7.55
KAP	687	627	7.42
KOP	950	652	7.37
KOA	987	614	7.24
KON	350	245	7.77

The results obtained for acidity and basicity show that this feature is weak for the samples. As can be observed, all pillared clays have a similar result for the pH_{PZC}, with a difference in the decimal case. An interesting comparison can be done between the samples KOA, KON, and KOP. According to specific studies of pH_{PZC} of pillared clays is expected that the result for the pillared clay is lower than the result obtained with the natural sample. For this work, even than small, it is possible to observe that there is a difference between the pH_{PZC} of the KON and the pH_{PZC} of the KOP, showing that

structural modification has occurred in the clay. Not only the KOP but also the KOA present a different result for pH_{PZC} , which suggests that structural modifications also occurred with the acid treatment [17].

4. Conclusion

The acid activated clays and pillared clays were successfully prepared in this work. The characterization techniques allowed ensuring that structural modification occurred in the clay and that these modifications are related to the formation of the desired materials. In FTIR analysis, for example, the disappearance of the calcite band after the pillaring procedure is the strongest clue of the formation of pillared clays. N_2 adsorption isotherms allowed the calculation of S_{BET} areas, and showed the increase in the area for the acid activated clays, suggesting that the acid activation was successful. XRD analysis reinforced the presence of calcite in natural samples and its absence in pillared samples, which corroborates with FTIR results. At last, the acid characterization results supported the idea that structural modifications occurred in the clay after the acid activation and pillaring procedure.

Acknowledgements

This work is a result of the Project “AIProcMat@N2020 - Advanced Industrial Processes and Materials for a Sustainable Northern Region of Portugal 2020”, with the reference NORTE-01-0145-FEDER-000006, supported by ERDF; the CIMO - UID/AGR/00690/2019 – funded by FCT and FEDER under Programme PT2020 and the Associate Laboratory LSRE-LCM - UID/EQU/50020/2019 - funded by national funds through FCT/MCTES (PIDDAC).

References

- [1] S. T. Khankhasaeva, E. T. Dashinamzhiylova, and D. V. Dambueva, “Oxidative degradation of sulfanilamide catalyzed by Fe/Cu/Al-pillared clays,” *Appl. Clay Sci.*, vol. 146, pp. 92–99, Sep. 2017.
- [2] S. Jain and M. Datta, “Montmorillonite-alginate microspheres as a delivery vehicle for oral extended release of Venlafaxine hydrochloride,” *J. Drug Deliv. Sci. Technol.*, vol. 33, pp. 149–156, 2016.
- [3] W. Yu *et al.*, “Acid-activated and WO_x -loaded montmorillonite catalysts and their catalytic behaviors in glycerol dehydration,” *Chinese J. Catal.*, vol. 38, no. 6, pp. 1087–1100, Jun. 2017.
- [4] H. Shi, T. Lan, and T. J. Pinnavaia, “Interfacial Effects on the Reinforcement Properties of Polymer–Organoclay Nanocomposites,” *Chem. Mater.*, vol. 8, no. 8, pp. 1584–1587, Jan. 1996.
- [5] A. Gil, S. A. Korili, M. A. Vicente, and R. Trujillano, *Pillared Clays and Related Catalysis*. 1994.
- [6] C. N. Rhodes, M. Franks, G. M. B. Parkes, and D. R. Brown, “The effect of acid treatment on the activity of clay supports for $ZnCl_2$ alkylation catalysts,” *J. Chem. Soc. Chem. Commun.*, no. 12, pp. 804–807, 1991.
- [7] T. Li *et al.*, “Design and preparation acid-activated montmorillonite sustained-release drug delivery system for dexibuprofen in vitro and in vivo evaluations,” *Appl. Clay Sci.*, vol. 163, pp. 178–185, Oct. 2018.
- [8] V. J. Bruckman and K. Wriessnig, “Improved soil carbonate determination by FT-IR and X-ray analysis,” *Environ. Chem. Lett.*, vol. 11, no. 1, pp. 65–70, 2013.
- [9] S. Wang, Y. Dong, M. He, L. Chen, and X. Yu, “Characterization of GMZ bentonite and its application in the adsorption of Pb(II) from aqueous solutions,” *Appl. Clay Sci.*, vol. 43, no. 2, pp. 164–171, 2009.
- [10] M. Thommes *et al.*, “Physisorption of gases, with special reference to the evaluation of surface area and pore size distribution (IUPAC Technical Report),” *Pure Appl. Chem.*, vol. 87, no. 9–10, pp. 1051–1069, 2015.
- [11] P. Trigueiro *et al.*, “When anthraquinone dyes meet pillared montmorillonite: Stability or fading upon exposure to light?,” *Dye. Pigment.*, vol. 159, no. June, pp. 384–394, 2018.
- [12] M. Sprynskyy *et al.*, “Preparation of AgNPs/saponite nanocomposites without reduction agents and study of its antibacterial activity,” *Colloids Surfaces B Biointerfaces*, vol. 180, no. April, pp. 457–465, 2019.
- [13] B. L. Zhu *et al.*, “Synthesis, characterization and acid-base properties of kaolinite and metal (Fe, Mn, Co) doped kaolinite,” *Appl. Clay Sci.*, vol. 179, no. April, p. 105138, 2019.
- [14] R. R. Widjaya, A. L. Juwono, and N. Rinaldi, “Bentonite modification with pillarization method using metal stannum,” in *AIP Conference Proceedings*, 2017, pp. 1–7.
- [15] E. Howard and E. Tatge, “Patterns, Chapter 2,” in *Circular of the Bureau of Standards: Standard X-ray diffractions powder patterns*, 1966, pp. 3–84.
- [16] J. Matusik *et al.*, “[Ti,Zr]-pillared montmorillonite – A new quality with respect to Ti- and Zr-pillared clays,” *Microporous Mesoporous Mater.*, vol. 202, pp. 155–164, 2014.
- [17] S. Mnasri, N. Hamdi, N. Frini-Srasra, and E. Srasra, “Acid–base properties of pillared interlayered clays with single and mixed Zr–Al oxide pillars prepared from Tunisian-interstratified illite–smectite,” *Arab. J. Chem.*, vol. 10, no. 8, pp. 1175–1183, 2017.

Evaluation of the influence of H₂S in the deactivation of mesoporous silicas functionalized with amino groups for CO₂ capture

Jaryson A.R. de Sousa^a, Jorge L.B. de Oliveira^a, Karine O. Moura^b, Juan A. Cecilia^c, Enrique Vilarrasa-Garcia, Moisés Bastos-Neto e Diana C.S. de Azevedo^{*}

^a GPSA, Departamento de Engenharia Química – Universidade Federal do Ceará, Campus do Pici, bl. 731 – 60760-400, Fortaleza, Ceará, Brasil. Telefone: (85) 3366-9240 – Email: diana@gpsa.ufc.br

^b IFCE, Instituto Federal do Piauí, Campus Paulistana, Rodovia Br 407, Km 5, s/n – 64750-000, Lagoa dos Canudos, Paulistana, Piauí, Brasil.

^c Departamento de Química Inorgánica, Cristalografía y Mineralogía. Facultad de Ciencias – Universidad de Málaga, Campus Teatinos, – 29071, Málaga, España.

Abstract

Hollow microspheres of silica were synthesized and functionalized with amino groups in order to enhance carbon dioxide adsorption, since CO₂ interacts with the amine groups by an acid- base interaction. The CO₂ adsorption isotherms shape of functionalized silica revealed that this material shows a coexistence of chemical and physical adsorption sites, which means that can occur adsorption on micropores and also through the interaction with the amino groups. In addition, the materials were saturated with H₂S (200 ppm in Helium) to test their efficiency in the purification of natural gas/ biogas in pre-combustion scenarios, since H₂S is also an acid gas and can interact with amine groups, which ended up reducing the CO₂ adsorption capacity. The adsorption isotherms showed that the most promising adsorbent was synthesized with ammonium fluoride and trimethylbenzene and functionalized post synthesis with 20% (v/v) of aminopropyltriethoxysilane, showing a higher CO₂ adsorption capacity under the studied conditions.

Keywords: mesoporous silica; functionalization; CO₂; H₂S; purification.

1. Introduction

The increase in CO₂ emissions has been pointed as the main factor for the increase of global warming and the strengthening of the greenhouse effect [1]. Industrial gases containing a considerable fraction of CO₂ have been studied in recent decades, considering the problem of the presence of CO₂ in both flue gases and biogas [2]. The presence of CO₂ as biogas impurity causes a reduction in its calorific value [3]. As biogas has been presented as an important alternative for the diversification of the world energy matrix, along with the possibility of being used as a partial substitute for petroleum fuels, the interest in developing methods for its purification has increased [4].

Mesoporous silica-based materials [5-7] have been gaining ground in the context of biogas purification in pre-combustion scenarios due to the need for a porous support with high mechanical and thermal stability under those conditions. Chemical and physical characterization of the adsorbents is performed in this work [8] to evaluate these materials before and after their contact with H₂S, providing an understanding of the

mechanisms involved in the deactivation of amines in conditions closer to reality.

2. Experimental Methods

2.1 Synthesis and functionalization of the porous materials

The synthesis of hollow silica microspheres (HMS) was carried out following the hydrothermal routes described by Araújo *et al.* (2009) [9] with some minor modifications, as the incorporation of swelling agents, such as trimethylbenzene (TMB) and NH₄F (F) to increase the pore size.

The synthesized samples were grafted with 20% (v/v) of 3-aminopropyltriethoxysilane (APTES) according to the methodology described by Hiyoshi *et al.* (2005) [10].

2.2 Characterization of samples

HMS-F-TMB and HMS-F-TMB 20% APTES samples were characterized using Fourier transform infrared spectroscopy (FTIR) to analyze the presence of functional groups. The samples were diluted in KBr (10 wt.%) to obtain the

absorption spectra and to assess the functionalization by the presence of bands that indicates the occurrence of amino groups. A FT-IR VERTEX 70V (Bruker, UK) equipment was used under vacuum at room temperature.

Thermogravimetric analysis (TGA) coupled with mass spectrometer was used to evaluate the thermal stability of the studied materials. The analysis was performed using the TGA-QMS equipment, customized, model STA 409 CD/403/5/G SKIMMER (Netzsch, Germany).

In order to evaluate the textural properties of the samples, N₂ adsorption/desorption isotherms were performed at 77 K, using an IQ₃ equipment (Quantachrome instruments, USA).

2.3 Adsorption measurements

Experiments with the CO₂ and CH₄ pure gases and the CO₂/CH₄ (30/70 v/v) binary mixture were performed using a magnetic suspension balance equipped with a gas dosing unit (Rubotherm, Germany).

The binary isotherms were obtained under dynamic conditions to ensure that the gas mixture composition was held constant until equilibrium was reached.

The samples were outgassed prior the experiment at 393 K for 4 h (heating ramp of 1 K min⁻¹). The isotherms were obtained at 323 and 348 K, in the pressure range of 0-12 bar.

2.4 Breakthrough curves

H₂S retention experiments were based on breakthrough curves, which represent the adsorption behavior in a fixed bed column over time, considering dispersion and mass transfer effects.

The breakthrough curves were obtained using a fixed bed column (4.6 mm internal diameter and 50 mm length) containing approximately 0.6 g of sample, placed inside a gas chromatograph (Varian CP-3800). A Pulsed Flame Photometric Detector (PFPD) is coupled to the equipment and was used to monitor H₂S at the outlet of the column. The breakthrough curves are used to determine the H₂S retention capacity of the material, where in this work was measured at the breakpoint time. That was defined as the point at which a given fraction of the feed concentration is reached. The tests for each sample were performed according to a procedure previously described by Menezes *et*

al.(2018) [11]. The gas inlet was 200 ppm H₂S in He (total pressure 1 bar and 298K).

3. Results and discussion

3.1 Characterization of the porous silicas

The FTIR spectra of the porous silica are compiled in Fig. 1. All spectra display a main band between 1000 and 1200 cm⁻¹, which can be deconvoluted in Si-O-Si longitudinal asymmetric stretching, with a maximum about 1100 cm⁻¹ [12]. The band located about 970 cm⁻¹ is attributed to stretching vibrations of Si-O in plane. In addition, all spectra exhibited a wide band between 3800 and 2700 cm⁻¹, assigned to the presence of stretching mode of the hydrogen of surface silanol bonded to molecular water (SiO-O· · ·H₂O) besides of the existence of stretching bands from hydrogen-bonded water molecules (H-O-H) [12].

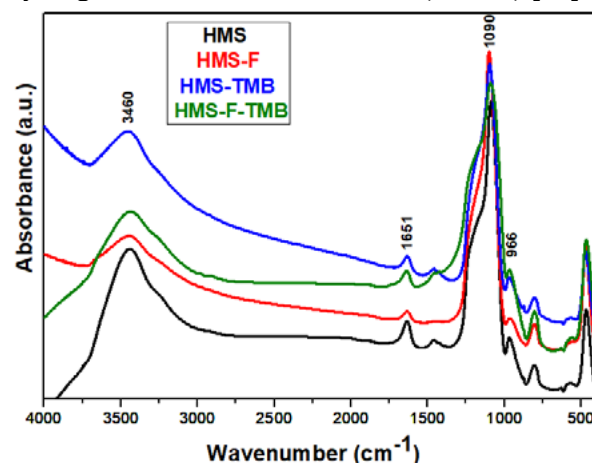


Fig. 1. FTIR spectra of raw supports.

The FTIR spectra of the hollow silica microspheres functionalized with 20% (v/v) APTES, Fig. 2, displayed the presence of two bands located at 1565 and 1485 cm⁻¹, that are ascribed to the presence of asymmetric and symmetric bending of N-H primary amines. Another band attributed to amine species was located about 690 cm⁻¹, attributed to N-H wag.

After saturation with H₂S, the bands related to the presence of amino groups located at 1565 and 1485 cm⁻¹ were not detected (Fig 2). It was expected that the presence of H₂S bonded on the silica surface exerted an influence on the deactivation of the amine active sites [12,13].

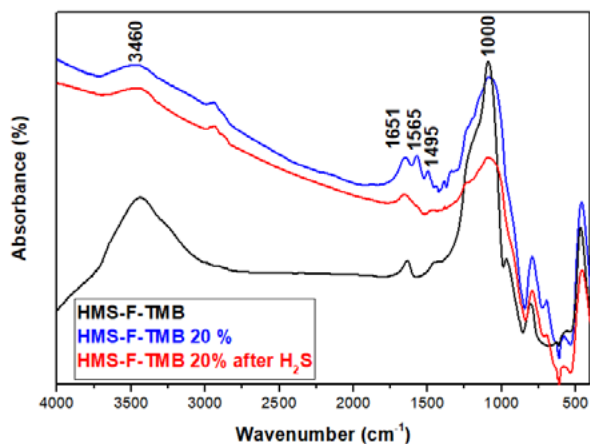


Fig. 2. FTIR spectra of HMS-F-TMB, HMS-F-TMB functionalized with 20% (v/v) APTES before and after H₂S saturation.

According to the thermogravimetric analysis, shown in Fig. 3, it was observed that HMS-F-TMB sample displayed only one mass loss, corresponding to the water physically adsorbed. In the functionalized sample, in addition to water loss, it was also observed a second mass loss related to amine groups, equivalent to 2.5 mmol of nitrogen/g.

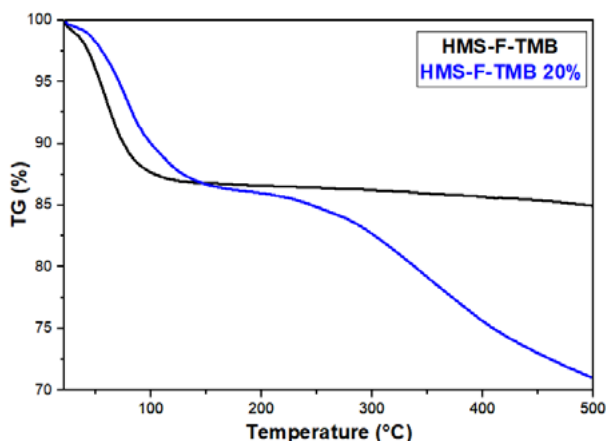


Fig. 3. TGA of samples before (black line) and after functionalization (blue line).

The results of the thermogravimetric analysis coupled with mass spectrometry (shown in Fig. 4), for the support, displayed the signal corresponding to m/z ratio of 17, 18 and 44, attributed to the release of OH, H₂O and CO₂, respectively.

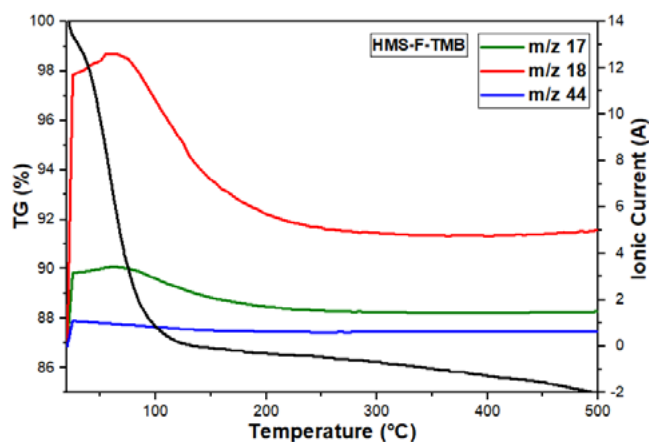


Fig. 4. Mass spectroscopy curves of samples before functionalization with 20% APTES.

After the functionalization, the m/z ratio of 16 was also observed (Fig. 5). This m/z corresponds to release of NH₂, proving that the functionalization was successful [14].

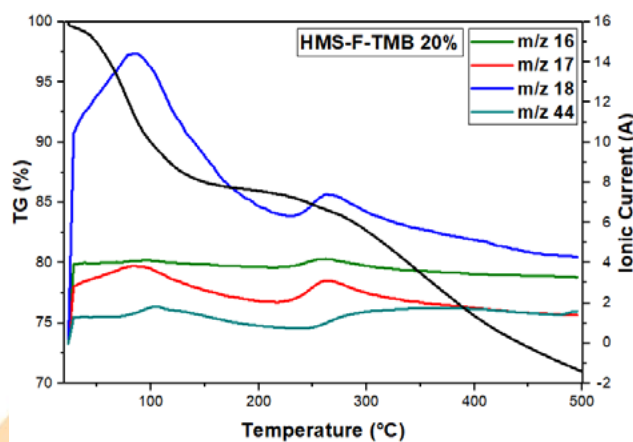


Fig. 5. Mass spectroscopy curves of samples after functionalization with 20% APTES.

The textural properties of the porous silicas were evaluated by N₂ adsorption/desorption isotherms at 77 K (Fig. 6). All supports presented Type IV isotherms, characteristic of mesoporous materials. It should be noted that the HMS and HMS-TMB materials presented Type IV (b) isotherms, completely reversible, characteristics of mesoporous materials with a narrow pore ordering, with cylindrical pores less than 4 nm. While the HMS-F and HMS-F-TMB materials presented isotherms Type IV (a), characteristic of materials with pore width higher than 4 nm [15].

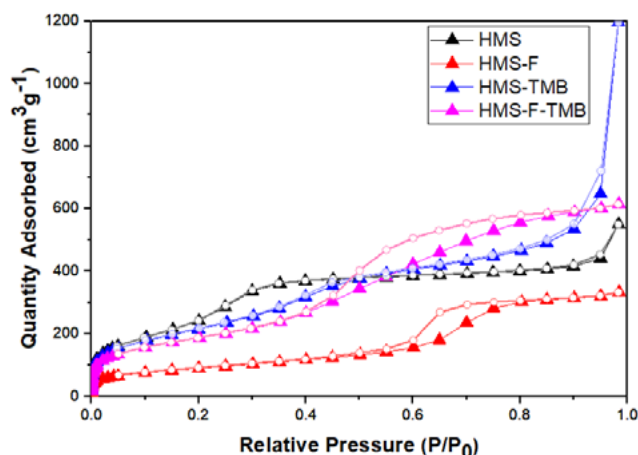


Fig. 6. N₂ adsorption/desorption isotherms at 77K for HMS, HMS-F, HMS-TMB and HMS-F-TMB materials

The textural properties of pure and functionalized samples are summarized in Table 1. It was possible to observe that there was a reduction in pore volume and surface area in the functionalized sample, as expected.

Table 1. Textural parameters of the hollow silica microspheres.

Sample	S_{BET} (m ² g ⁻¹)	V_p (cm ³ g ⁻¹)	V_{MIC} (cm ³ g ⁻¹)
HMS-F-TMB	673	0.952	0.249
HMS-F-TMB 20% APTES	550	0.502	-

The pore size distribution, estimated by DFT model (Fig. 7), showed that the materials have pores in the mesoporous region (2-50 nm). It was possible to observe the displacement to a larger pore diameter as the pore expanders are added. The material chosen for analysis was the HMS-F-TMB, considering that this material presents an intermediate distribution of pores, regarding the supports under analysis. This material provides a better surface area/pore volume ratio to improve the grafting yield of amine groups [12].

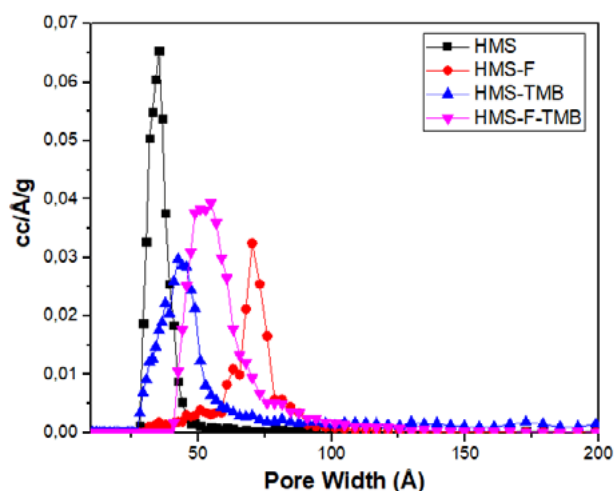


Fig. 7. Pore size distribution estimated by DFT method

3.2 Adsorption Measurements

The breakthrough curve (not shown) of the HMS-F-TMB 20% APTES after its being put into contact with H₂S presented a retention time of 62 min H₂S (3.6 mg g⁻¹) under the studied conditions (H₂S diluted in helium at 200 ppm and total pressure of 1 bar and 298 K). Subsequently, the sample was subjected to a regeneration process and brought into contact with CO₂. The results showed that HMS-F-TMB 20% APTES presented a lower CO₂ adsorption capacity, which could be due to the deactivation of some of the amine sites promoted by the acid-base interaction with H₂S, compromising the chemical adsorption of CO₂.

The CO₂ adsorption isotherms at 323 and 348 K for HMS-F-TMB 20% APTES, before and after saturation with H₂S, are shown in the Fig 8 and 9. At both temperatures, the reduction in the CO₂ adsorption after H₂S contact is noticeable. This is related to the fact that acid gases cause a probably deactivation of the amino groups. In addition, when comparing the isotherms of these figures, one can see a slight increase in the adsorption capacity with increasing temperature, may be related to the existence of chemisorption

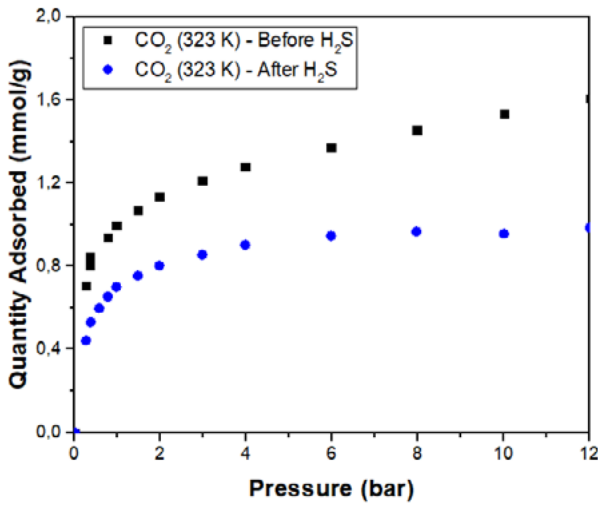


Fig. 8. CO₂ adsorption isotherms at 323 K for HMS-F-TMB 20% APTES

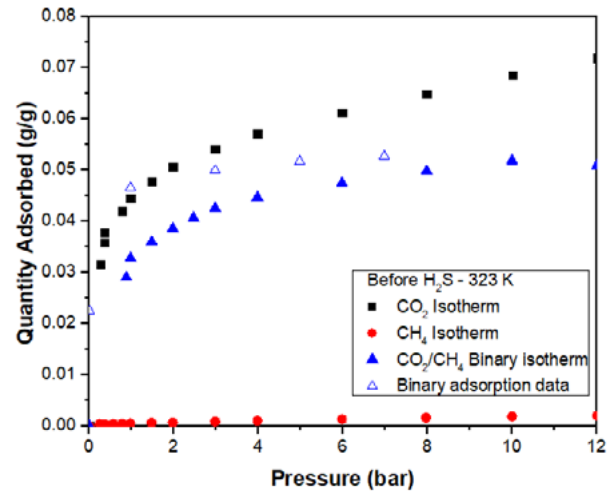


Fig. 10. Pure CO₂, CH₄ and CO₂/CH₄ (30/70 v/v) adsorption binary isotherms at 323K before H₂S

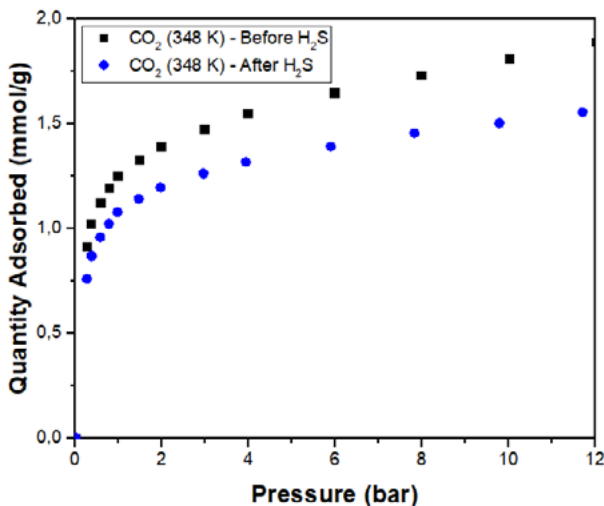


Fig 9. CO₂ adsorption isotherms at 348 K for HMS-F-TMB 20% APTES

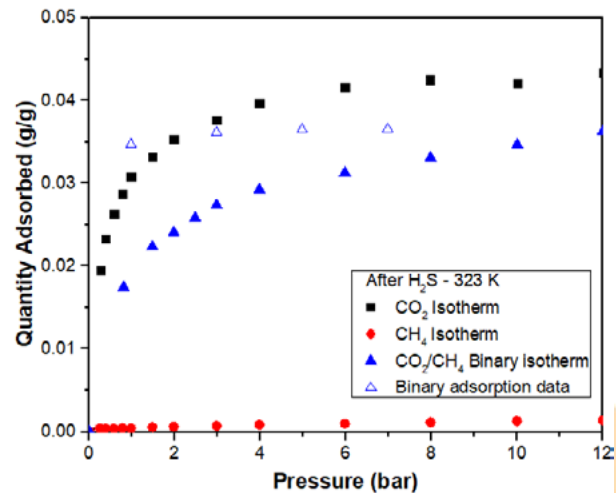


Fig. 11. Pure CO₂, CH₄ and CO₂/CH₄ (30/70 v/v) adsorption binary isotherms at 323K after H₂S

The CO₂/CH₄ (30/70 v/v) binary isotherms at 323 K, before and after saturation with H₂S, are shown in Fig. 11 and Fig. 12, respectively. It can be observed the higher CO₂/CH₄ selectivity for functionalized materials when analyzing both figures, namely binary isotherm is closer to CO₂ pure isotherm, emphasizing the fact that the sample is more selective to CO₂. Furthermore, there was a reduction in the adsorption capacity after H₂S-saturation, reinforcing the fact that H₂S promotes a deactivation of amino groups. Moreover, it is observed that the sample after H₂S-saturation, shows a greater hysteresis loop.

Kinetic measurements for CO₂ adsorption were performed for functionalized HMS-F-TMB before and after H₂S contact. By fixing CO₂ pressure (0.2 bar) and temperature (323 K), the sample mass gain was registered as a function of time until equilibrium mass was reached. The kinetic curves in Fig. 12 show that sample saturated with H₂S reaches adsorption equilibrium slower (90 % of the equilibrium adsorbed concentration is reached in 130 and 70 min for saturated and unsaturated sample, respectively). The acid-base reactions between the amines and H₂S are irreversible under the regeneration conditions studied, forming products that hinder CO₂ diffusion.

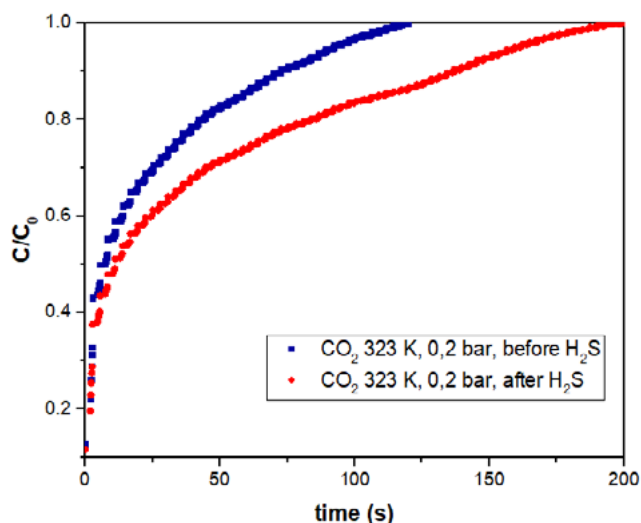


Fig. 12. Uptake data of CO₂ at 0.2 bar and 323K for amino grafted silicas before and after H₂S (200 ppm in He) saturation.

Conclusions

Mesoporous silicas functionalized with amine groups present a good performance on CO₂ capture at high temperatures and low pressures. However, the presence of acid gases in gaseous currents, such as H₂S, generates competitiveness between the gases, leading to a loss of CO₂ capacity. Thus, the adsorbed amount of CO₂ decreased drastically after the saturation of materials with H₂S. After H₂S adsorption, the samples were degassed but did not recover the initial CO₂ capacity, which is an indicative that some amino groups reacted irreversibly with H₂S. The H₂S adsorption mechanism on amino functionalized materials could be described by the following steps: (i) H₂S molecules diffusion from bulk gas phase to external surface of adsorbent, (ii) H₂S molecules diffuse from external surface of adsorbent to the inside of pores, (iii) chemical reaction between H₂S molecules and amino groups with formation of a sulfur containing organic compound and (iv) complete deactivation the amino groups. This S-organic compound is not fully outgassed at 393K as observed by the decreasing on the CO₂ capacity on the regenerated sample after H₂S contact. The use of functionalized materials for CO₂ removal on biogas purification, may not be indicated without the presence of a previous adsorption bed, where the selective adsorption of H₂S takes place.

Acknowledgements

JARS thanks the Federal University of Ceará for the scholarship granted in the *Programa Institucional de Bolsas de Iniciação Científica* (PIBIC/UFC, Ministry of Education, Brazil). We also thank to *Conselho Nacional de Desenvolvimento Científico e Tecnológico* (CNPq, Ministry of Science and Technology, Brazil) and *Coordenação de Aperfeiçoamento de Pessoal de Nível de Superior* (CAPES, Ministry of Education, Brazil) for financial support.

References

- [1] Yu, C.H., Huang, C.H., Tan, C.S., *Aerosol Air Qual. Res.* 2012;12;745–769.
- [2] Kargari, A., Revanchi, M.T.: Carbon Dioxide: Capturing and utilization. In: *Greenhouse Gases-capturing. Utilization and reduction*. In tech. Croatia, 2012.
- [3] Finsy, V., L. MA, L. Alaerts, D.E. De Vos, G.V. Baron, J.F.M. Denayer, Elsevier 2009;120;221-227.
- [4] Ferreira, A.F.P., Ribeiro, A.M., Kulaç, S., Rodrigues, A.E., *Chem. Eng. Sci.* 2014;124;
- [5] Sanz, R. Calleja, G., Arencibia, A., Sanz-Perez, E.S., *Microporos and Mesoporous Materials* 2012;158;309-317.
- [6] Sanz-Pérez, E.S., Olivares-Marín, M., Arencibia, A., Sanz, R., Calleja, G., Maroto-Valer, M.M., *International Journal of Greenhouse Gas Control*, 2013; 17; 366-375.
- [7] Vilarrasa-García, E., Cecilia, J.A., Santos, S.M.L., Cavalcante Jr., C.L., Jiménez-Jiménez, J., Azevedo, D.C.S., Rodríguez-Castellón, E., *Microporous and Mesoporous Materials*, 2014;187;125-134.
- [8] Vilarrasa-García, E., Cecilia, J.A., Ortigosa-Moya, E., Cavalcante Jr., C.L., Azevedo, D.S.C, Rodríguez-Castellón, E., *Materials*, 2015;8(5);2495-2513;
- [9] Araujo, R.S., Azevedo, D.C.S., Rodríguez-Castellón, E., Cavalcante Jr., C.L., Jiménez-López, A. *Appl. Surf. Sci.* 2009;255;6205-6290.
- [10] N. Hiyoshi, K. Yogo, T. Yashima, *Microporous and Mesoporous Materials* 2005;84;357-365.
- [11] Menezes, R.L.C.B, Moura, K.O., Lucena, S.M.P., Azevedo, D.C.S, Bastos-Neto, M. *Ind. Eng. Chem. Res.*, 2018; 57; 2248-2257.
- [12] Cecilia, J.A., Vilarrasa-García, E., García-Sancho, C., Saboya, R.M.A. Azevedo, D.C.S., Cavalcante Jr., C.L., Rodríguez-Castellón, E. *International Journal of Greenhouse Gas Control*, 2016;52;344-356.
- [13] Ji, Chen-hui, Li, Jum-jie, Hou, Chang-jun, Huo, Dan-gun, Yang, Mei, Zhang, Liang, Elsevier 2017;240;718-725.
- [14] Sanchez-Zambrano, K.S., Vilarrasa-García, E., Maia, D.A.S., Bastos-Neto, M., Rodríguez-Castellón, E., Azevedo, D.C.S. *Adsorption* 2019, In press.
- [15] Thommes, M., Kaneko, K., Neimark, A.V., Olivier, J. P., Rodríguez-Reinoso, F., Rouquerol J., Sing, K. S. W. (IUPAC Technical Report). *Pure and Applied Chemistry*, 2015;87;1051-1069

Influence of microwave radiation on characteristics of carbon composites based on resorcinol-formaldehyde resin chars filled with carbon nanotubes

Mariia Galaburda^a, Viktor M. Bogatyrov^a, Anna Deryło-Marczewska^b, M. Nazarkovsky^{c*}

^a Chuiko Institute of Surface Chemistry, 17 General Naumov Street, Kiev 03164, Ukraine

^b Faculty of Chemistry, Maria Curie-Skłodowska University, Maria Curie Skłodowska Sq 3, 20-031 Lublin, Poland

^c Chemistry Department, Pontifical Catholic University of Rio de Janeiro, 225 Marquês de São Vicente Str., 22435-900 Rio de Janeiro, RJ, Brazil.

Abstract

The polymer-nanocarbon composites containing carbon nanotubes were prepared using resorcinol-formaldehyde resin with further carbonization in an argon atmosphere at 800 °C and formation of carbon-based nanomaterials. The resultant materials were analyzed in respect to their textural and morphological characteristics by means of scanning electron microscopy (SEM), Raman spectroscopy, and low-temperature nitrogen adsorption-desorption (BET method). The effect of microwave treatment conditions during the synthesis upon the morphological and textural characteristics of the carbon nanocomposites was investigated and generalized.

Keywords: Resorcinol-formaldehyde resin; multi-walled carbon nanotubes; nanocomposites; carbonization; sorbents.

1. Main text

Porous carbonaceous materials are among the most effective adsorbents, carriers, polymer fillers, and additives used in industry, medicine, and biotechnology. This is due to both outstanding textural characteristics (great pore volume and specific surface area) and surface structure features (morphology). These properties can be easily varied while synthesizing of polymers, their carbonization, and activation of chars or can be modified upon additional treatment or chemical modification of the materials. In the present work, the microwave radiation (MWR) was involved for processing of chars as an energy efficient, rapid heating, low operating cost approach to control the texture, grain size, and other characteristics of the final carbon composites.

The polymer composites were prepared by dissolving resorcinol in formalin (37% of formaldehyde) in the presence of the set amount of Na₂CO₃, which in turn, serves as a catalyst. The reaction mixture was stirred. After a weighed portion of multi-walled carbon nanotubes

(MWCNT, Chuiko Institute of Surface Chemistry, Kyiv) had been introduced, the blend was sonicated to obtain a homogeneous suspension (MW oven “Saturn”, 2.45 GHz - S band, 700 W, 30 sec.). The weight ratio of resorcinol to formalin (37%) was 1:2. The suspension placed in a closed container was heated at 85 °C for 20 h undergoing the sol-gel process and resulting in solid structures of brown color. The reference resorcinol-formaldehyde sample (RFR) without filler was synthesized according to the method described in detail elsewhere [1]. All samples were pyrolyzed in a quartz tubular reactor at 800 °C under the inert atmosphere (Ar) and the reference sample was labeled as RFC1 after pyrolysis.

The textural characteristics of chars depend on the ratio of resorcinol to water, as well as on the presence of fillers and catalysts [2]. To study these factors, two samples were prepared using different resorcinol/water ratios: 5 g or 3.5 g of 0.02 M aqueous solution of Na₂CO₃ per gram of resorcinol at the same content of MWCNT and were labeled as RFC2 and RFC3, respectively, after carbonization.

The treatment with microwave radiation was carried out utilizing 1.5 g of char particles at the sizes of 0.25-0.5 mm and placed in a closed quartz dish. Four MWR treatment cycles of 30 sec. each sample were undertaken within the 3 min interval (the samples became red upon this heating). Optionally, the respective samples after MWR treatment were labelled with “mw”, e.g. RFC1→ RFC1mw.

The phase composition was established with the instrumentality of a DRON-4-07 (Burevestnik) spectrometer (Cu K α , $\lambda = 0.154178$ nm) equipped with a Ni filter with the $2\theta = 10 - 80^\circ$ range at the set step $2\theta = 0.1^\circ$.

A JSM 6700F microscope (JEOL) was exploited for scanning the morphology of the subject samples.

Textural properties related to the porosity of the nanocomposites were determined using low-temperature nitrogen adsorption-desorption isotherms technique utilizing a ASAP 2405N facility. The total pore volume was calculated at the maximal adsorption point ($p/p_0 \approx 0.98-0.99$). The pore size distribution, in turn, was established through the method described in [3]. The method was upgraded by comprising interparticle space as a pore shape model. In other words, this space can be represented as voids among the spherical particles inside of composite materials [4].

SEM images (Fig. 1) show significant changes in the surface morphology of chars affected by both MWR and the presence of fillers. Unmodified RFC1 composite demonstrates mainly smooth surfaces typical for nonporous or nanoporous carbons, while RFC2 has rough surfaces, because own structures of the fillers (Fig a, b). The surface roughness becomes greater after MWR treatment of filled RFC3 chars (Fig 1 c,d). An amorphous component attributed to disordered carbons formed from a RFR fraction can be removed more easily upon MWR treatment than the fragments of MWCNT. Therefore, the tube-like filler fragments are better observed at the surfaces of composite chars after MWR treatment (Fig. 1).

According to the Raman spectra (Fig. 2), the peak of the G band (sp^2 C atoms in relatively large polyaromatic graphene structures) is more intensive than that of the D band (disordered structures with sp^3 C atoms out of planes in small carbon structures). For chars, the I_{D1}/I_{G1} ratio varies in such a sequence: 0.88

(MWCNT), 2.4 (RFC1), and 2.6 (RFC1mw), 2.3 (RFC2), and 2.5 (RFC2mw), 2.7 (RFC3). The RFC3mw sample was measured three times and all spectra are characterized by significant difference among each another. However, the I_{D1}/I_{G1} ratio is higher in the sample before the microwave treatment. This indicates an increase in the nanotubes content in the surface layer and the heterogeneity of the surface structures confirmed also with SEM.

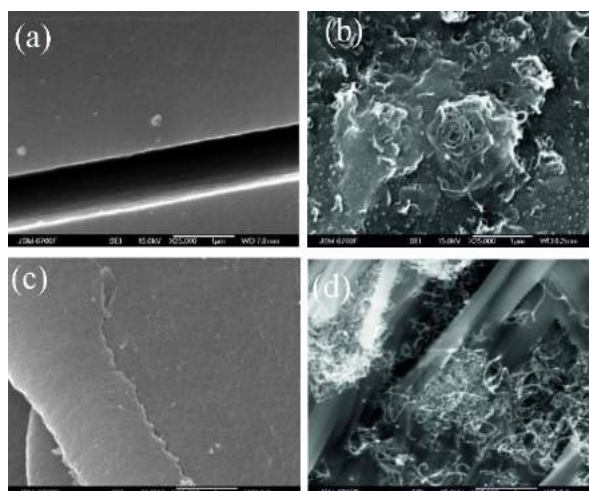


Figure 1. SEM images of RFC1 (a), RFC2 (b), RFC3 (c), and RFC3mw (d) chars.

The Raman spectra show that there is no correlation between the water content in the reaction medium, affecting the RFC morphology. This is due to several factors: the cross-linking, degree affecting ordering of structures in the polymers and the chars, different contributions of pores of different types affecting sheet-sheet interactions— as in non-filled chars, as well as in MWCNT-filled ones.

The chars are nano/mesoporous at the average pore radius $R < 5$ nm, pore volume of 0.1-0.3 cm^3/g , and specific surface area 200-460 m^2/g (Fig.3).

Specific surface area of the reference sample augments up to 250 m^2/g after microwave processing. This kind of crucial changes may be caused by blocked micropores. These pores occur in the structure though, they are not accessible to nitrogen while adsorption.

It can be concluded that the MWR processing leads to a certain increase in the values of V_p and S_{BET} , surface roughness, and contributions of sp^2 -C atoms. In other words, the MWR treatment enhances removal of amorphous

fragments with sp^3 -C atoms than with sp^2 -C atoms.

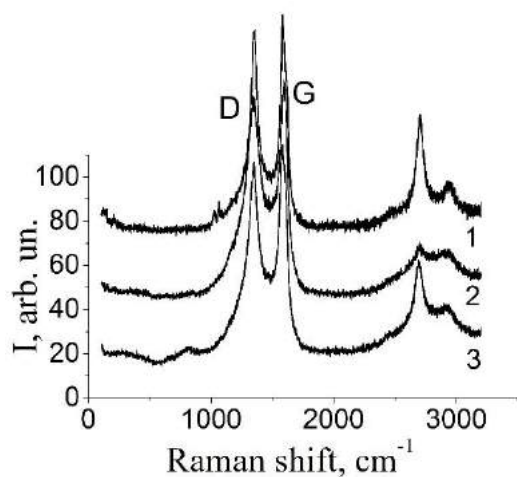


Figure 2. Raman spectra of chars of RFC3mw composite (different surface regions) at $I_{D1}/I_{G1}=1.14$ (1), 1.96 (2) and 0.95 (3).

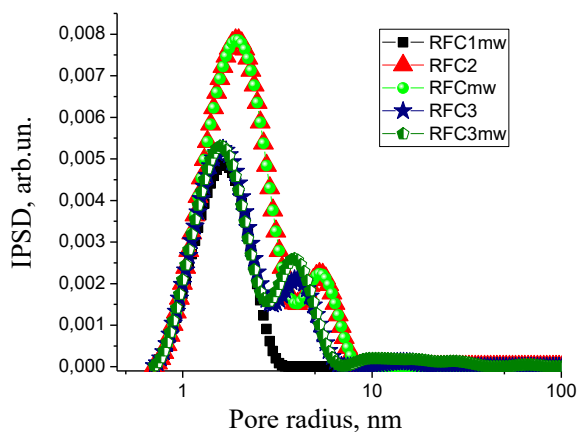


Figure 3. SCV/SCR PSD for RFC1mw, RFC2, RFC2mw, RFC3, and RFC3mw composites.

Acknowledgements

M.V.G. gratefully acknowledges the financial support provided by the International Visegrad Fund (Scholarship No. 51910536).

References

- [1] Pekala RW. Organic aerogels from the polycondensation of resorcinol with formaldehyde. *J Mater Sci* 1989;24(11):3221-7.
- [2] Galaburda M.V., Bogatyrov V.M., Oranska O.I., Skubiszewska Zięba J., Gun'ko V.M., Sternik D. Magneto-Sensitive Ni/C Adsorbents: Synthesis, Properties and Applications. *Adsorpt. Sci. Technol.* 2015;33(6-8): 523-530.
- [3] Nguyen C., Do D.D. A new method for the characterization of porous materials. *Langmuir* 1999; 15: 3608-3615.
- [4] Gun'ko V.M., Turov V.V., Leboda R., Zarko V.I., Skubiszewska-Zięba J., Charmas B. Adsorption, NMR and thermally stimulated depolarization current methods for comparative analysis of heterogeneous solid and soft materials. *Langmuir* 2007; 23: 3184-3192.

In situ synthesis of zeolite LTA in glass fibers $\text{Al}_2\text{O}_3\text{-SiO}_2$

Antonia M. M. França^a, Marco V. M. do Nascimento^a, Raquel de A. Bessa^b,
Edipo S. de Oliveira^b, Adonay R. Loiola^b, Ronaldo F. do Nascimento^a.

^a Department of Analytical Chemistry and Physical Chemistry - Federal University of Ceará, Pici Campus, Fortaleza 60440-900, CE, Brazil.

^b Department of Organic and Inorganic Chemistry - Federal University of Ceará, Pici Campus, Fortaleza 60440-900, CE, Brazil.

Abstract

The glass fibers reacted to a NaOH solution at 110 °C at different reaction times. After some time, with increasing Si and Al concentrations in the solution by the dissolution of the glass fibers, crystallization of zeolite LTA occurs on the fiber surface. In situ coating of zeolite LTA crystals on glass fibers $\text{Al}_2\text{O}_3\text{-SiO}_2$ has been investigated by several characterization techniques. With X-ray diffraction measurements, zeolite LTA was observed as a single crystalline phase with no impurities, for samples F4B and F6B. In addition, the infrared spectra for them presents the characteristic bands for zeolite LTA at 464, 558 and 665 cm^{-1} . According to the SEM, the uniform formation of zeolite LTA on the glass fibers was observed only for F4B, since F6B presented higher solubility for some fibers due to longer reaction times and zeolite pickling on surface. Therefore, F4B was the material applied in the Cu^{2+} , Pb^{2+} and Cd^{2+} ion adsorption tests, in which the following adsorptive sequence was verified: $\text{Pb}^{2+} > \text{Cu}^{2+} > \text{Cd}^{2+}$.

Keywords: Zeolites; Hierarchical; Fiber Glass; Adsorption; Metal.

1. Introduction

Zeolites are crystalline microporous materials with substantial technological interest in chemical process industries. Their applications cover a wide range of areas such as adsorption/separation, catalysis, ion exchange, sensing and chromatography [1] [2] [3]. The zeolites production usually occurs as very fine powders, with tens of nanometers or micrometers in diameter, however, for some applications, this characteristic is not very effective. Therefore, they are usually used as pellets, tablets or other shapes suitable for practical use using binders, presenting also disadvantages. The use of binders dilutes the effectiveness of zeolites and reduces mass transfer [4]. As pellets and tablets, the disadvantage is related to the access hindrance to the zeolites active sites, decreasing their performance [5] [2]. Thus, the importance on zeolite hierarchization is emphasized. An example of hierarchical material associated with the zeolite distribution on an appropriate support (non-zeolitic), which improves mechanical strength and

mass transfer rates, as well as it helps the access of analytes to the adsorption pores [2] [6] [7].

Several types of supports can be used for this purpose where the fiber glass can be highlighted since the zeolite crystals can be inserted by surface coating using a precursor gel mixed with the fibers and heated in hydrothermal conditions forming the grains surrounding the fibers or through the in situ coating where the zeolite grains are preferably deposited on the fiber surface after their partial dissolution by the reactive solution. In the latter case, glass fibers $\text{Al}_2\text{O}_3\text{-SiO}_2$ present specific starting composition that may be useful for the in situ by surface coating zeolite, especially the LTA type, which has hydrophilic properties and high water vapor adsorption capacity [6] [8] [9].

In situ coating is more viable economically than coating with a precursor gel and the bonds strength between the zeolite crystals and the fibers was considered as one of the advantages for this process [10].

Thereby, the aim of the present study was to evaluate in situ surface coating of zeolite LTA on a glass fiber $\text{Al}_2\text{O}_3\text{-SiO}_2$ as well as the adsorptive capacity of this material for toxic metals.

2. Experimental

2.1 Synthesis

Commercial fiberglass $\text{Al}_2\text{O}_3\text{-SiO}_2$ was used as starting material for the synthesis with a chemical composition of and 68.77 % SiO_2 e 29.69 % Al_2O_3 and a Si/Al ration of 2.28, suitable for the production of zeolite 4A on its surface.

Crystallization of zeolite on the fiber occurred by treatment with 4 mol L^{-1} NaOH solution at different reaction times (2, 4 and 6 h), F4B2, F4B4 and F4B6, respectively. This was performed in teflon crucibles coupled to stainless steel autoclaves (closed system) at 110 °C. Thereafter, the system was slowly cooled and the resulting material was washed successively with distilled water to neutrality.

2.2 Characterization

The materials were characterized aiming to obtain information on their physicochemical properties and structural, such as: crystallinity and phase identification using the X-ray diffraction diffraction technique and determine characteristic vibrations of the material present bonds by the infrared spectroscopy technique and verification of morphology by scanning electron microscopy.

- *X-ray Diffraction*

XRD experiments were performed using a Panalytical (X-Pert Pro MPD) x-ray powder diffractometer. The powder patterns were collected in the continuous mode with 2 θ scan speed of 0.5° min^{-1} . Co-K α radiation was used, obtained with the tube operating at 40 kV and 40 mA. The measurements were performed at the Laboratory of the UFC Physics Department. The identification of crystalline phases was performed using the software X-Pert HighScore Plus (Panalytical).

- *Infrared vibrational spectroscopy*

Absorption spectra in the infrared region of the fiber before and after treatment with NaOH solution, were obtained using the spectrometer of Shimadzu IRTracer-100. The analyzes were performed in the region 400-4000 cm^{-1} using shares dispersed in KBr (3 mass %). The measurements were performed at the analytical center of the Graduate Program in Chemistry of UFC.

- *Scanning Electron Microscopy (SEM)*

Information on the morphology of zeolite LTA in fiber glass was obtained by scanning electron microscopy (SEM) using a Quanta 200-FEI microscope with magnifications of up to 800 x using tungsten filament electron beam and acceleration of 5.0 to 8.0 kV and secondary electron detector. Samples were prepared on aluminum supports using double-sided carbon tape and metallized with approximately 10 nm platinum layer metallizer located at The University of Manchester, School of Materials.

2.3 Adsorption Tests

In order to verify the adsorptive efficiency of zeolite LTA on fiber glass $\text{Al}_2\text{O}_3\text{-SiO}_2$, an initial adsorption test was performed. For this study, 25 mL of a 100 mg L^{-1} multicomponent solution of Cd^{2+} , Cu^{2+} and Pb^{2+} at pH 5,0 was added to a 125 mL Erlenmeyer flask containing 0.3 g of fiber-supported zeolite and stirred for 24 h at 200 rpm. Subsequently, the material was filtered and the supernatant analyzed by Flame Atomic Absorption Spectroscopy (FAAS) for quantification of metals not removed by the adsorbent.

3. Results and discussion

3.1 Characterization

- *X-ray Diffraction*

Figure 1 shows the glass fiber $\text{Al}_2\text{O}_3\text{-SiO}_2$ diffractograms before (FB-AS) and after (F2B, F4B and F6B) treatment with NaOH solution.

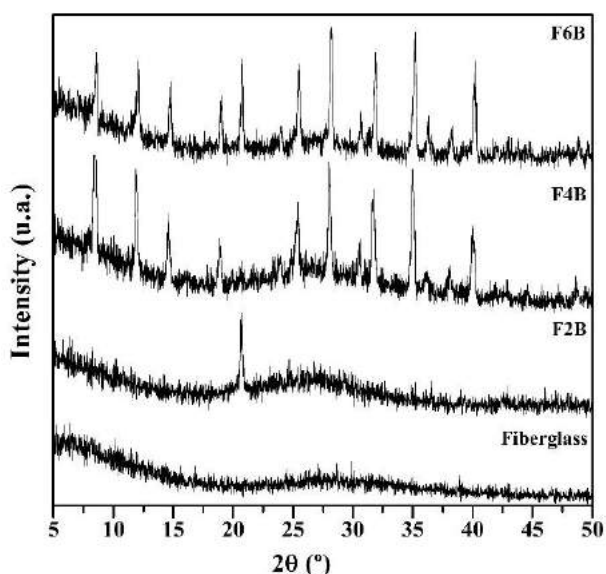


Fig. 1. Comparison of fiberglass X-ray diffractograms before and after reaction with NaOH solution.

For FB-AS, the fiber before the reaction, it was not observed the presence of crystalline phases, since the fiber presents amorphous characteristics. For F2B, it is noticed that a crystalline phase starts to be observed on the fiber, and as observed for F4B and F6B, fibers after 4 and 6h respectively, zeolite LTA can be identified as single phase [11] [12].

- *Infrared vibrational spectroscopy*

The infrared spectra for fiber glass $\text{Al}_2\text{O}_3\text{-SiO}_2$ before (FB-AS) and after reaction with NaOH at different times (F2B, F4B and F6B) are shown in figure 2.

In samples F4B and F6B, a characteristic zeolite LTA band was observed, at 464 cm^{-1} attributed to the internal vibration of deformation of the T-O (T = Si or Al) bond, which makes up a four-membered double ring (D4-R), at 558 cm^{-1} , a band referring to the external vibrations of the D4-R was also verified and at 665 cm^{-1} it is attributed to the internal symmetrical stretching vibrations of the T-O bonds. At 1005 cm^{-1} , the internal vibrations of the asymmetrical stretching of T-O bonds is observed and at 1656 cm^{-1} the band is related to the angular deflection of hydroxyl group for water. The bands described above are observed for both F6B and F4B [13] [14].

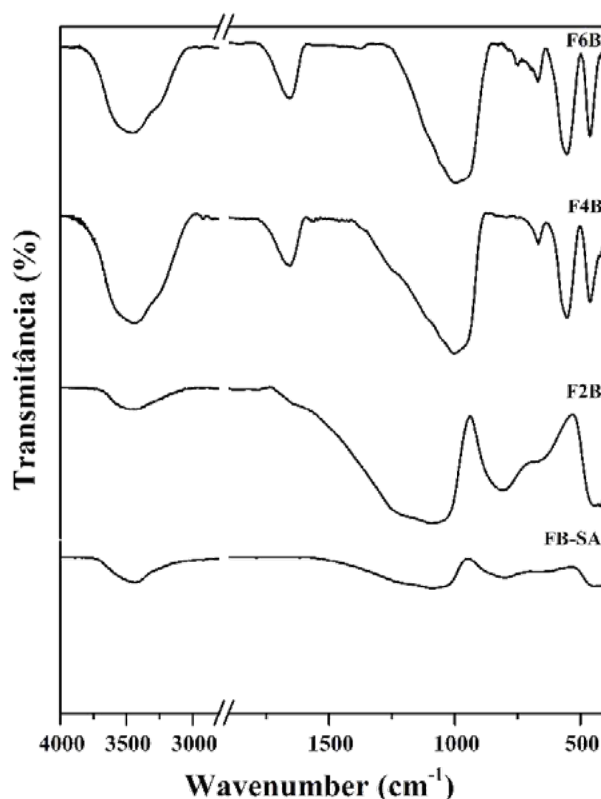


Fig. 2. Fiberglass infrared spectra before and after reaction with NaOH solution.

For F2B however, undefined bands were identified, indicating partial dissolution of the fiber for the zeolite crystals formation on its surface. This fact can be evidenced by the slight disagreement in the position of the bands when comparing them with samples F4B and F6B.

Finally, for FB-SA, these bands are not verified, showing the absence of zeolitic materials in the starting fiber.

- *Scanning Electron Microscopy (SEM)*

Figure 3 shows the fiber glass $\text{Al}_2\text{O}_3\text{-SiO}_2$ micrographs before and after the crystallization process.

Figure 3a shows that the fiber, prior to reaction with the NaOH solution, has a uniform morphology in which it has a smooth appearance on the surface. Figure 3b, after 2 h of reaction with NaOH, shows roughness on the surface, indicating only the start of fiber dissolution. The uniform formation of zeolite LTA on the glass fibers $\text{Al}_2\text{O}_3\text{-SiO}_2$ was observed in 4 h (figure 3c) of reaction with NaOH, this fact is due to the dissolution rate of Si and Al components and its crystallization on the surface [9]. At 6 h (figure 3d), the presence of this

zeolite was also found, however, due to the longer reaction time, it was noticed that some fibers suffered greater alkaline attack than others and that part of the zeolite formed on its surface detached, due to the pickling phenomenon.

Thus, F4B was the material selected for the initial adsorption tests, indicating favorable conditions for zeolite LTA formation.

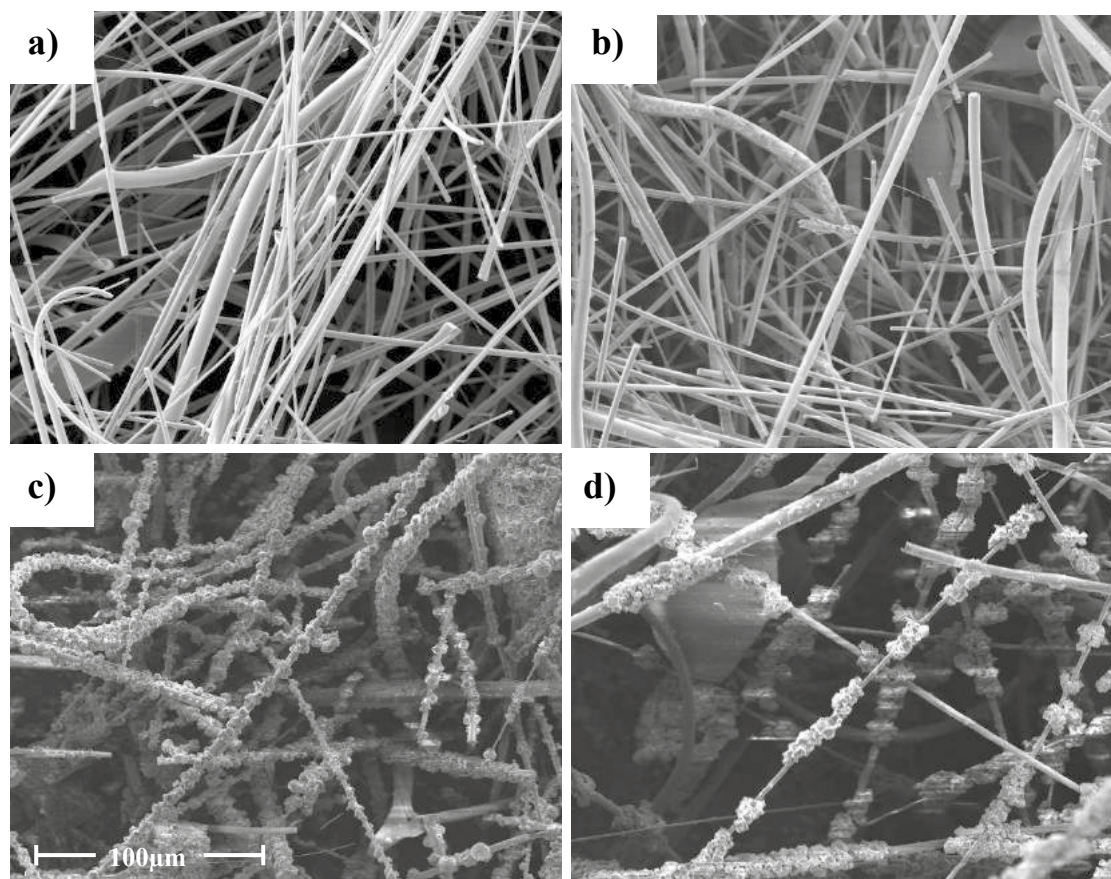


Fig. 3. Micrographs for FB-SA (a), F2B (b), F4B (c) e F6B (d).

3.2 Adsorption test

According to the results, it was found that the material in study (F4B) is efficient for adsorption of Cu^{2+} , Pb^{2+} and Cd^{2+} ions, which have the following adsorption capacities 3.63 mg g^{-1} , 5.64 mg g^{-1} and 2.76 mg g^{-1} , respectively. In addition, there was a higher adsorption preference for Pb^{2+} and lower adsorption for Cd^{2+} , verifying the following adsorption sequence: $\text{Pb}^{2+} > \text{Cu}^{2+} > \text{Cd}^{2+}$. Given the results, it is suggested that this material can be applied in both batch and fixed bed adsorption studies, since it is a fibrous material that highlights problems related to column compaction.

4. Conclusions

In summary, zeolite LTA was able to be obtained by in situ synthesis on fiber glass with NaOH and in absence of a precursor gel, having the best assembly for 4h treatment.

For the adsorption studies, the zeolite LTA supported on fiber glass can be readily used as adsorbents for Cu^{2+} , Pb^{2+} and Cd^{2+} ions, presenting the adsorptive sequence: $\text{Pb}^{2+} > \text{Cu}^{2+} > \text{Cd}^{2+}$. Moreover, it is suggested that this material can be used both in batch and fixed bed adsorption studies.



Acknowledgements

The authors thank UFC for all support, the CAPES, FUNCAP and CNPQ for their financial support.

References

- [1] WECKHUYSSEN, B. M.; YU, J. Recent advances in zeolite chemistry and catalysis. **Chemical Society Reviews**, v. 44, n. 20, p. 7022-7024, 2015.
- [2] YANG, X. *et al.* Solvent-free preparation of hierarchical 4A zeolite monoliths: Role of experimental conditions. **Journal of Crystal Growth**, v. 528, p. 125286, 2019.
- [3] GAO, X. *et al.* Fabrication of stainless steel hollow fiber supported NaA zeolite membrane by self-assembly of submicron seeds. **Separation and Purification Technology**, v. 234, p. 116121, 2020.
- [4] VASILIEV, P. *et al.* Strong hierarchically porous monoliths by pulsed current processing of zeolite powder assemblies. **ACS applied materials & interfaces**, v. 2, n. 3, p. 732-737, 2010.
- [5] WEI, Y. *et al.* Tailoring and visualizing the pore architecture of hierarchical zeolites. **Chemical Society Reviews**, v. 44, n. 20, p. 7234-7261, 2015.
- [6] LARLUS, O. *et al.* Preparation of silicalite-1/glass fiber composites by one-and two-step hydrothermal syntheses. **Microporous and mesoporous materials**, v. 56, n. 2, p. 175-184, 2002.
- [7] YANG, X.-Y. *et al.* Hierarchically porous materials: synthesis strategies and structure design. **Chemical Society Reviews**, v. 46, n. 2, p. 481-558, 2017.
- [8] YAMAZAKI, S.; TSUTSUMI, K. Synthesis of an A-type zeolite membrane on silicon oxide film-silicon, quartz plate and quartz fiber filter. **Microporous Materials**, v. 4, n. 2-3, p. 205-212, 1995.
- [9] OKADA, K. *et al.* In-situ coating of zeolite Na-A on Al₂O₃-SiO₂ glass fibers. **Journal of Porous Materials**, v. 5, n. 2, p. 163-168, 1998.
- [10] OKADA, K. *et al.* In situ zeolite Na-X coating on glass fibers by soft solution process. **Microporous and mesoporous materials**, v. 37, n. 1-2, p. 99-105, 2000.
- [11] SHEN, X. *et al.* Multiple copper adsorption and regeneration by zeolite 4A synthesized from bauxite tailings. **Environmental Science and Pollution Research**, v. 24, n. 27, p. 21829-21835, September 01 2017.
- [12] SEABRA, R. *et al.* Adsorption equilibrium and kinetics of carbon dioxide, methane and nitrogen on binderless zeolite 4A adsorbents. **Microporous and Mesoporous Materials**, v. 277, p. 105-114, 2019.
- [13] ANBIA, M.; KOOHSARYAN, E.; BORHANI, A. Novel hydrothermal synthesis of hierarchically-structured zeolite LTA microspheres. **Materials Chemistry and Physics**, v. 193, p. 380-390, 2017.
- [14] WANG, P. *et al.* Synthesis of Zeolite 4A from Kaolin and Its Adsorption Equilibrium of Carbon Dioxide. **Materials**, v. 12, n. 9, p. 1536, 2019.

Synthesis of a new adsorbent, from sugarcane bagasse, for removal of As(V) from aqueous solution: using an agricultural waste to water treatment

L. C. Maia^{a*}, M. M. C. E. Carvalho^a, L. C. Soares^a, L. V. A. Gurgel^a

^a Grupo de Físico-Química Orgânica, Instituto de Ciências Exatas e Biológicas, Campus Universitário Morro do Cruzeiro, s/nº, Universidade Federal de Ouro Preto, Ouro Preto 35400-000, Brazil.

*Corresponding author. Tel.: +55 31 3559-1725; fax: +55 31 3559-1725; E-mail address: luisa.maia@aluno.edu.br (L.C. Maia).

Abstract

Arsenic contamination of drinking and groundwater is a public health problem in many parts of the world. Several arsenic removal techniques have been studied, emphasizing the adsorption as one of the most efficient techniques to remove toxic elements. Sugarcane bagasse is a promising material to be used as an adsorbent because it comes from renewable sources and it has a low cost. In addition, it is feasible its structural modification to improve adsorption capacity. In this study, a new adsorbent from chemically modified sugarcane bagasse for adsorption of arsenic oxyanions was developed and evaluated. The chemical modification of sugarcane bagasse was performed using epichlorohydrin, with subsequent reaction with trimethylamine (TEA) for introducing amino groups in the solid support, producing a quaternary function of ammonium (BTEA). For this, a multivariate optimization was employed for determining the optimum condition of synthesis by Doehlert Experimental Design (DED). BTEA was characterized by percent weight gain (*pwg*), FTIR, point of zero charge (pH_{PCZ}), elemental analysis, and surface area (BET). The optimized condition of synthesis was: 6.4 mL of epichlorohydrin and 11.0 mL of TEA at 100°C, obtained a *pwg* of the modified SB of 27±2%. BTEA presented a pH_{PCZ} of 7.3, indicating the best range of pH for adsorption of As(V). The carbon, hydrogen, nitrogen, and chloride contents for BTEA were 45.3±0.6%, 6.9±0.1%, 1.54±0.07%, and 4.11±0.08%, respectively. The adsorbent surface area and the average half pore width were 2.022 m² g⁻¹ and 22.44 Å, presenting a density of 1.330 ±0.003 g cm⁻³. The adsorbent was used to remove As(V) from aqueous solution in monocomponent batch system. It presented an As(V) adsorption capacity of 0.365±0.002 mmol g⁻¹, which indicates the potential of the material as a biosorbent for effluent and water treatment.

Keywords: bioadsorption; multivariate optimization; triethylamine; water decontamination; toxic elements.

1. Introduction

The intensification of industrial activities associated with the naturally occurring high concentrations of toxic elements has caused the contamination of water bodies by elements of notorious toxicity such as arsenic. Exposure to arsenic contributes to the onset of diseases such as dermatitis, heart problems, cancer, and poisoning [1].

About 70 countries present environmental problems of groundwater contamination from natural arsenic sources affecting more than 140 million people [2]. This problem affects many

countries with severe episodes of arsenic exposure worldwide.

Various techniques can be used to remove arsenic from water, especially adsorption, which has proven efficiency and operational flexibility, producing a high quality treated effluent [3, 4].

Conventional adsorbents exhibit non-selective behavior for the oxyanions removal and are ineffective for arsenic removing from water [5, 6]. New adsorbents have been developed for the removal of toxic elements.

Sugarcane bagasse is an agricultural waste that can be used in the adsorption process as biosorbent because it has low-cost, is renewable and available on a large scale [7, 8]. Chemical modification is employed to improve the physical and chemical

properties of lignocellulosic materials by introducing suitable functional groups on its surface, which can improve the adsorption capacity of toxic elements [8, 9].

In this sense, this study aimed to develop a new adsorbent from trimethylamine (TEA) chemically modified bagasse sugarcane (BTEA) to remove As(V) from aqueous solutions in monocomponent batch adsorption systems.

2. Material and Methods

2.1. Material

The sugarcane bagasse (SB) used in this study was obtained at Ouro Preto, Minas Gerais, Brazil. Before use, SB was milled in a Wiley mill (DeLeo Brazil) and sifted on an electromagnetic stirrer (Bertel, Brazil) using a sieve system composed of 30 (0.595 mm), 45 (0.354 mm), 60 (0.250 mm), and 100 (0.149 mm) mesh. The 100 mesh fraction was collected and washed with distilled water under stirring at 70°C for 1 h and dried at 90°C, removing water-soluble compounds. After this, SB was washed in Soxhlet apparatus using a 1:1 n-hexane/ethanol mixture for 4 h to remove the SB extractives, and then oven-dried at 90°C.

Epichlorohydrin and trimethylamine (TEA) were purchased from Sigma-Aldrich (Brazil). TEA was refluxed with NaOH and distilled before use. Diethyl ether, and N, N-dimethylformamide (DMF) were purchased from Synth (Brazil). DMF was treated with molecular sieves (3 Å). CaCl₂, ethanol (EtOH), hexane, HCl, Na₃AsO₄·7H₂O, and NaOH were purchased from Neon (Brazil). Quantitative filter paper (black ribbon, JP-41) was purchased from Jprolab (Brazil).

2.2. SB modification with trimethylamine (BTEA)

The synthesis route of the BTEA was based on the literature [10, 11, 12]. Firstly, the epichlorohydrin introduction and the bagasse fibers amination were performed by univariate experiments, defining the factors and levels for multivariate optimization. A multivariate optimization using Doehlert Experiment Design (DED) was employed to define the optimum condition of synthesis of the biosorbent.

DED allowed reaction limiting factors (volume of epichlorohydrin and TEA) to be evaluated in more detail. One of the advantages of DED is a thorough study of the variables that have the most significant effect on the system.

Synthesis optimization was performed in two stages. In the first optimization, the epichlorohydrin volume (*EPI*, mL) and reaction temperature (*T1*, °C) were evaluated. It was adopted 10% molar excess of TEA to ensure that all epichlorohydrin was consumed in this step. In the second optimization, the TEA volume (*TEA*, mL) and the reaction temperature (*T2*, °C) were evaluated, determining the optimum condition of synthesis. The unselected factors were fixed in all experiments.

For the synthesis of the BTEA, a double neck round-bottom flask connected to a reflux condenser followed by CaCl₂ bulb (drying tube) was used. In the other neck, an addition funnel was attached. The flask was heated in an oil bath at different temperatures (Table 1) on a heating plate (Corning®, model PC 420D).

0.5 f of dried SB, 10 mL of DMF, and different volumes of epichlorohydrin (Table 1) were added to the flask. The suspension was stirred at 400 rpm for 1h at different temperatures (Table 1). The epichlorohydrin volumes and reaction temperatures were defined by the first step of optimization. After this, different volumes of TEA were added to the flask using the addition funnel, maintaining the suspension under constant stirring for 2 h. The TEA volumes and reaction temperatures were defined by the second stage of optimization. Then, the suspension was filtered using a Büchner glass funnel (porosity 2) and the solid was washed with distilled water, HCl solution (0.1 mol L⁻¹), distilled water, EtOH 95%, and diethyl ether. The obtained biosorbent was dried in a vacuum oven at 35° for 24 h before use.

Dependent variables used as response in the optimization were percent weight gain (*pwg*, %), adsorption capacities (*q_{As(V)}*, mmol g⁻¹) and nitrogen content (*N*, %). In the models, only the main quadratic and linear effects were considered.

Triplicate at center point were used for error estimation. The models were evaluated by analysis of variance (ANOVA) using a confidence level of 95% (*p* < 0.05). All statistical analyses were performed using Statistica® routines (StatSoft, Inc., version 10.0).

2.3. Characterization of BTEA

The *pwg* of modified material was calculated using Eq. (1).

$$pwg / (\%) = \frac{w_{BTEA} - w_{SB}}{w_{SB}} \times 100 \quad (1)$$

where w_{BTEA} and w_{SB} (g) are the masses of BTEA and SB, respectively.

SB and BTEA were analyzed by Fourier Transform Infrared (FTIR) spectroscopy at a resolution of 4 cm^{-1} and 32 scans per sample on an ABB Bomem MB 3000 FTIR spectrometer equipped with ZnSe optics and a deuterated triglycine sulfate (DTGS) detector. For this, 2.0 mg of sample (SB and BTEA) was mixed to 100 mg of spectroscopy grade KBr, both dried at 90°C for 1 h before use. The mixture was pressed in a hydraulic press (Pike CrushIR, model 181-1110) at 6 tons to prepare KBr pellets.

The point of zero charge (pH_{PZC}) was determined by the solid addition method [13]. The pH value where the curve crosses the abscissa corresponds to a pH_{PZC} .

Elemental analysis was used to determine the carbon (C), hydrogen (H), and nitrogen (N) contents in SB and BTEA using a Perkin Elmer 2400 Series II CHN elemental analyzer. The chlorine content (Cl) of BTEA was determined by volumetric analysis.

The adsorbent surface area and pore size were determined by the method of Brunauer, Emmett, and Teller (BET) [14] and the DR method, respectively. For this propose, measurements were performed on a surface area analyzer (Quantachrome, Nova 1200e®) using adsorption/desorption isotherms of N_2 at 77.35 K. The SB and BTEA samples were degassed for 4 h at 70°C and 25°C , respectively.

Adsorption experiments to determine As(V) adsorption capacity were performed in batch mode. Aliquot of 100 mL of As(V) solution (0.27 mmol L^{-1}), at pH 6.0, was added to pre-thermostated Erlenmeyer flasks at 25°C in an orbital shaker incubator (Marconi, model MA- 830) for 1 h. BTEA ($0.0200 \pm 0.0001\text{ g}$) was weighed in cylindrical glasses (1.8 mm height and 2.2 mm diameter), added to the Erlenmeyer flasks and stirred at 200 rpm for 15 h. After this time, the solution was filtered using filter paper by a single filtration. The arsenic concentration was determined by inductively coupled plasma optical emission spectrometry (ICP-OES). Adsorption capacity (q_x) of biosorbent was determined by Eq. (2).

$$q_x / (\text{mmol g}^{-1}) = \frac{(C_i - C_x) \times V}{w_{BTEA}} \quad (2)$$

where q_x is the adsorption capacity of As(V) on biosorbent at time ($x = t$) or equilibrium ($x = e$); C_i and C_x are the concentrations (mol L^{-1}) initially and at time t ($x = t$) or equilibrium ($x = e$), respectively; V (L) is the As(V) solution volume, and w_{BTEA} is the mass of the BTEA adsorbent.

3. Results and Discussion

3.1. Synthesis of BTEA

The experimental matrix for optimizing the introduction of epichlorohydrin into the sugarcane bagasse is shown in Table 1. Experiment 2 was responsible for obtaining higher values of pwg and, consequently, As(V) adsorption capacity and nitrogen content, obtaining 21.95%, 0.39 mmol g^{-1} and 1.55%, respectively. For this, the following experimental condition was used: 6.25 mL of EPI at 100°C .

Table 1. Doehlert experimental design for optimization of the epichlorohydrin introduction.

Run	EPI (mL)	T (°C)	pwg (%)	$q_{e, As(V)}$ (mmol g ⁻¹)	N (%)
BTEA1	8.00	70	15.19	0.271	1.12
BTEA2	6.25	100	21.95	0.386	1.55
BTEA3	1.00	70	4.38	0.093	0.58
BTEA4	2.75	40	0.04	0.027	0.38
BTEA5	6.25	40	0.48	0.036	0.43
BTEA6	2.75	100	18.02	0.336	1.35
BTEA7	4.50	70	13.76	0.214	1.00
BTEA8	4.50	70	18.31	0.271	0.98
BTEA9	4.50	70	15.84	0.240	1.05

For pwg , ANOVA indicated that the quadratic model generated by DED presented a significant regression ($p = 0.004$) and a non-significant lack of fit ($p = 0.5$). The model also presented a high value of R-square (0.9621). The same condition was verified in the quadratic model for As(V) adsorption capacity, presenting a significant regression ($p = 0.003$), a non-significant lack of fit ($p = 0.4$), and an R-square of 0.9663. For nitrogen content, the quadratic model also presented a significant regression ($p = 0.0009$) and a non-significant lack of fit ($p = 0.1$), with an R-square of 0.9828. The desirability function was used to optimize multiple responses simultaneously. The desirability profiles are shown in Fig. 1.

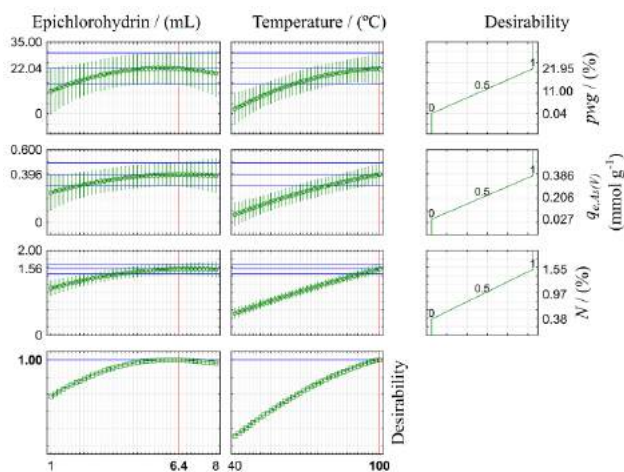


Fig. 1. Profiles for predicted values of desirability for (a) epichlorohydrin volume and (b) temperature, respectively.

The optimization of multiple responses provided by the critical point for each response variable, which estimated a maximum value of pwg (22.04%), $q_{e, As(V)}$ (0.39 mmol g^{-1}), and N (1.56%). Therefore, the optimum condition of synthesis was obtained using 6.4 mL of epichlorohydrin at 100°C. The optimum synthesis condition based on the desirability function was reproduced, and then, the model was validated (Table 2).

Table 2. Validation of the optimization model for introducing of epichlorohydrin into the SB.

Response variables	Predict value	Observed value
pwg (%)	22.04	18 ± 2
$q_{e, As(V)}$ (mmol g^{-1})	0.395	0.294 ± 0.003
N (%)	1.56	1.40 ± 0.01

These results indicate that the SB was successfully modified, observing an increase of nitrogen content of SB, which has a nitrogen content of $0.19 \pm 0.03\%$.

After the optimization of the epichlorohydrin introduction, the design of experiments was performed for optimizing the material amination. For this, the optimum condition of the first step was fixed in all experiments.

The experimental matrix for optimizing the SB amination is shown in Table 3. As can be seen, the highest values of pwg (15.61%), $q_{e, As(V)}$ (0.301 mmol g^{-1}), and N (1.63%) were obtained in experiment 15, which was used 20.0 mL of TEA at 105°C. The results indicated that the reactivity limit was reached, and then, the increase of amine did not favor the reaction.

Table 3. Doehlert experimental design for optimization of the bagasse fibers amination.

Run	TEA (mL)	T (°C)	pwg (%)	$q_{e, As(V)}$ (mmol g^{-1})	N (%)
BTEA10	29.0	85	7.15	0.232	1.43
BTEA11	24.5	105	14.49	0.305	1.47
BTEA12	11.0	85	12.11	0.232	1.35
BTEA13	15.5	65	5.34	0.109	0.92
BTEA14	24.5	65	1.09	0.102	0.90
BTEA15	15.5	105	15.61	0.301	1.63
BTEA16	20.0	85	8.25	0.221	1.33
BTEA17	20.0	85	5.84	0.238	1.38
BTEA18	20.0	85	7.32	0.243	1.38

The evaluation of the quadratic models was carried out through ANOVA. The pwg model presented a statistically significant regression ($p = 0.003$) and a non-significant lack of fit ($p = 0.5$), with high value of R-square (0.9689). For $q_{e, As(V)}$, the model had a significant regression ($p = 0.0002$) and did not present a lack of fit ($p = 0.9$). The N model also had a significant regression ($p = 0.004$), and lack of fit was not significant ($p = 0.09$). The R-square (0.9624) indicate that the model can well explain the data.

Desirability function determined the optimum condition of the synthesis second step as 11 mL of TEA at 105°C. The optimum condition of the synthesis second step was determined by desirability function, predicting the values of 19.47%, 0.302 mmol g^{-1} , and 1.57% for pwg , $q_{e, As(V)}$ and N , respectively (Fig. 2). The following condition was predicted: 11 mL of TEA at 105°C.

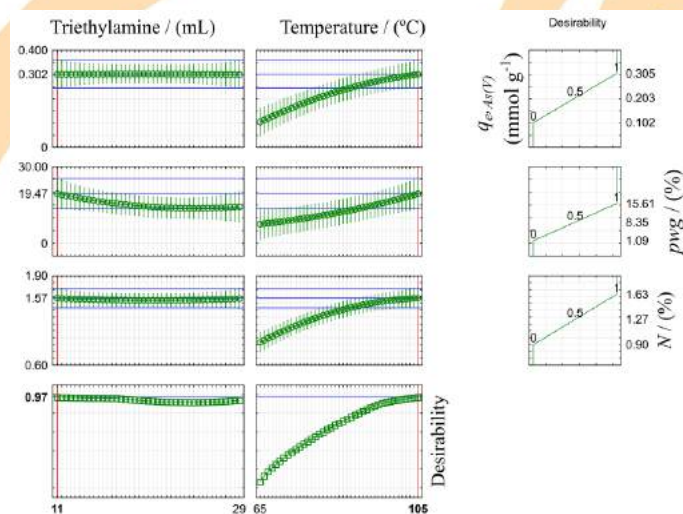


Fig. 2. Profiles for predicted values of desirability for TEA volume and temperature.

This condition defined by the desirability function was reproduced and the model has been successfully validated (Table 4).

In addition, chlorine content analyses were also performed to evaluate the chemical modification of the samples obtained by the optimum condition. The results are showed in Table 5, demonstrating the effectiveness of the epichlorohydrin introduction in the SB. The highest *Cl* (%) values demonstrate that the limiting reactant was the nucleophile (tertiary amine) employed for the modification.

The final material was prepared based on the optimum condition determined by the design of experimental. Thus, the synthesis was performed using 6.4 mL of epichlorohydrin and 11.0 mL of TEA, adopting a temperature of 100°C for both reactions.

Table 4. Validation of the optimization model for optimization of the bagasse fibers amination.

Response variables	Predict value	Observed value
<i>pwg</i> (%)	19.47	19 ± 2
$q_{e, As(V)}$ (mmol g ⁻¹)	0.302	0.33400 ± 0.00009
<i>N</i> (%)	1.57	1.41 ± 0.05

Table 5. Chlorine content of the BTEA samples from optimizations.

Material	<i>Cl</i> / (%)
BTEA-EPI	3.3 ± 0.1
BTEA-TEA	3.50 ± 0.05

BTEA-EPI = material from validation of the first step of the optimization.

BTEA-TEA = material from validation of the second step of the optimization.

3.1. Characterization of BTEA

BTEA was prepared on a large scale, obtaining a *pwg* of 27±2%, corroborating to the industrial application of this material.

Fig. 3 shows the FTIR spectra for SB and BTEA. Modification is suggested by the appearance of the band at 1325 cm⁻¹ in the BTEA spectra, which corresponds to the stretching vibration of C–N in the amine groups, and bands at 3020 and 1424 cm⁻¹ corresponding to the ammonium quaternary groups [10, 13].

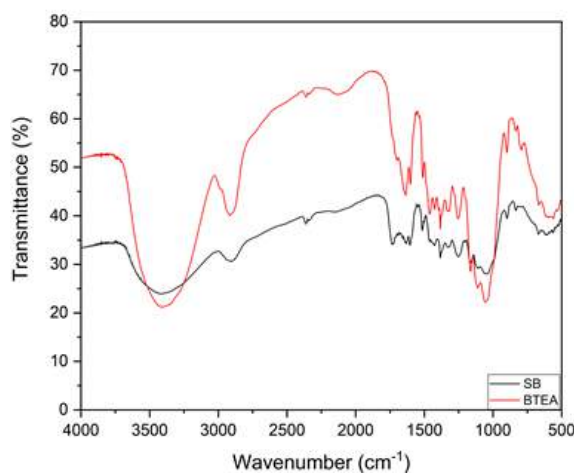


Fig. 3. FTIR spectra of SB and BTEA.

The pH_{PCZ} values of BTEA and SB are 7.30 and 6.0, respectively. For pH values lower than 7.30, the material has a positive net surface charge, presenting adsorption sites for As(V) adsorption.

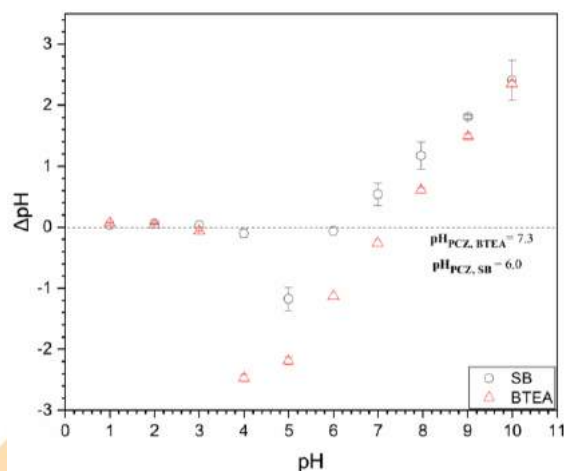


Fig. 4. FTIR spectra of SB and BTEA.

The carbon, hydrogen, nitrogen and chloride contents for BTEA were 45.3±0.6%, 6.9±0.1%, 1.54±0.07%, and 4.11±0.08%, respectively. These results indicate that the introduction of epichlorohydrin into the bagasse was successful, and then, the reaction limiting agent was TEA, a weak nucleophile.

SB and BTEA presented a surface area of 1.564 and 2.022 m² g⁻¹, respectively. The surface area and porosity (Table 6) of the modified material increased, favoring the adsorption process. BTEA is classified as a mesoporous material (pores with diameter between 20 and 500 Å) [15].

Table 6. Determination of surface area and pore size distribution.

Parameters	SB	BTEA
Density / (g cm^{-3})	1.52 ± 0.01	1.33 ± 0.003
Surface area / ($\text{m}^2 \text{g}^{-1}$)	1.564	2.022
Average Half pore width / (Å)	14.079	22.445
Micropore volume / (cm^3/g)	0.0011	0.0008

The As(V) adsorption capacity of the BTEA was increased on a large scale ($0.365 \pm 0.002 \text{ mmol g}^{-1}$), which improves the economic feasibility of material.

4. Conclusions

The proposed synthesis route for chemical modification of sugarcane bagasse was successful, producing a quaternary ammonium function in the SB surface. This is corroborated by the characterization of the BTEA, which showed a significant increase in adsorption capacity due to the introduction of adequate functional groups on the surface of the SB. This indicates a potential industrial application of the material for effluent and water treatment for As(V) removal.

Acknowledgements

The authors are grateful to Universidade Federal de Ouro Preto and Fundação de Amparo à Pesquisa do Estado de Minas Gerais for funding this research. The authors are also grateful to Coordenação de Aperfeiçoamento de Pessoal de Nível Superior [Finance Code 001].

References

- [1] Fagundes T, Bachmann AWL, Tomaz HSO, Rodrigues CA. Adsorção de arsênio(V) pela quitosana ferro-III reticulada. *Química Nova* 2008; 31 (6): 1305-1309.
- [2] Unicef - The United Nations Children's Fund. Arsenic contamination in Groundwater. Current Issues 2. New York: 2013.
- [3] Fu F, Wang Q. Removal of heavy metal ions from wastewaters: A review. *Journal of Environmental Management* 2011; 92: 407-418.
- [4] Kyzas GZ, Bikiaris DN. Recent modifications of chitosan for adsorption applications: a critical and systematic review. *Marine Drugs* 2015; 13:312-337.
- [5] Kanematsu M, Young TM, Fukushi K, Sverjensky DA, Green P G. Quantification of the Effects of Organic and Carbonate Buffers on Arsenate and Phosphate Adsorption on a Goethite-Based Granular Porous Adsorbent. *Environmental Science & Technology* 2011; 45:561-568.
- [6] Fakour H, Pan YF, Lin TF. Effect of humic acid on arsenic adsorption and pore blockage on iron-based adsorbent. *Water, Air, & Soil Pollution* 2015; 226:1-16.
- [7] Karnitz Júnior O, Gurgel LVA, Gil LF. Removal of Ca(II) and Mg(II) from aqueous single metal solutions by mercerized cellulose and mercerized sugarcane bagasse grafted with EDTA dianhydride (EDTAD). *Carbohydrate Polymers* 2010; 79:184-191.
- [8] Rangabhashiyam S, Anu N, Selvaraju N. Sequestration of dye from textile industry wastewater using agricultural waste products as adsorbents. *Journal of Environmental Chemical Engineering* 2013; 1: 629-641.
- [9] Melo D de Q, Neto V de OS, Barros FC de F, Raulino GSC, Vidal CB, Nascimento R F de. Chemical modifications of lignocellulosic materials and their application for removal of cations and anions from aqueous solutions. *J. Appl. Polym. Sci.* 2016; 133 (15): n/a- n/a.
- [10] Xu X, Gao B, Tang X, Yue Q, Zhong Q, Li Q. Characteristics of cellulosic amine-crosslinked copolymer and its sorption properties for Cr(VI) from aqueous solutions. *J. Haz. Mat.* 2010; 189: 420-426.
- [11] Yu J, Wang L, Chi R, Zhang Y, Xu Z, Guo J. Adsorption of Pb^{2+} , Cd^{2+} , Cu^{2+} , and Zn^{2+} from aqueous solution by modified sugarcane bagasse. *Res. Chem. Intermed.* 2015; 41: 1525-1541.
- [12] Yu J, Xiong W, Zhu J, Chi R. Separation of Cu^{2+} and Pb^{2+} by tetraethylenepentamine-modified sugarcane bagasse fixed-bed column: selective adsorption and kinetics. *Int. J. Environ. Sci. Technol.* 2016; 13: 1933-1940.
- [12] Colthup NB, Daly LH, Wiberley SE. Introduction to Infrared and Raman Spectroscopy. Elsevier, 1990.
- [13] Balistrieri LS., Murray JW. *Am. J. Sci.* 1981; 28:788-806.
- [14] Brunauer S, Emmett PH., Teller E. Adsorption of Gases in Multimolecular Layers. *Journal of the American Chemical Society* 1938; 60: 309-319.
- [15] Thommes M, Kaneko K, Neimark AV, Olivier JP, Rodriguez-Reinoso F, Rouquerol J, Sing KS. Physisorption of gases, with special reference to the evaluation of surface area and pore size distribution (IUPAC Technical Report). *Pure and Applied Chemistry* 2015; 87:1051-1069.

Ciprofloxacin removal by biochar produced from banana pseudostem: kinetics, equilibrium and thermodynamics

Fabiano Bisinella Schefe^{a,*}, Júnior Staudt^b, Caroline Ribeiro^b, Carlos Eduardo Borba^b, Aparecido Nivaldo Módenes^b, Alice B. Koerich^c, Felipe E. Bueno Silva^c, Helton J. Alves^c

^a Federal Technological University of Paraná (UTFPR), Cristo Rei St., 19, Toledo, 85902-490, Brazil

^b West Parana State University (UNIOESTE), Faculdade St., 645, Toledo, 85903-000, Brazil

^c Federal University of Paraná (UFPR), Pioneiro St., 2153, Palotina 85950-000, Brazil

Abstract

Pharmaceutical compounds are emerging pollutants that represent challenges for the water treatment plants, since the conventional methods are not always efficient. Adsorption stands out as a simple and efficient process, but is commonly limited by the high costs of commercial adsorbents. The present work aims to assess the removal of the antibiotic Ciprofloxacin by a biochar produced from banana pseudostem. For this, adsorption kinetic tests were performed at different initial concentrations and different temperatures, also allowing the study on equilibrium and thermodynamics of the process. The biochar was characterized by N₂ physisorption, Scanning Electron Microscopy and point of zero-charge. The main results indicated that the produced biochar is mainly mesoporous ($d_p > 2.0$) with some associated micropores and presents a slightly acid its surface. The process was endothermic, with change of enthalpy of 123.5 kJ/mol, whereas the highest adsorption capacity was achieved at 50 °C ($q = 95 \text{ mg}_{\text{CIP}} \text{ g}^{-1} \text{ biochar}$). The Langmuir isotherm model showed a good agreement with the experimental data at 50 °C ($r^2 = 0.9864$), with parameters estimated of $b = 1.04 \times 10^{-1} \text{ mg L}^{-1}$ and $q_{\text{max}} = 96.26 \text{ mg g}^{-1}$ for Langmuir affinity constant and maximum adsorption capacity, respectively. Adsorption kinetics was also extremely favorable and well described by Elovich model at 50 °C ($r^2 = 0.9850$), indicating a chemical adsorption. Overall, it can be said that the biochar produced from banana pseudostem presented potential of removing CIP from water and therefore could be applied in further tests in continuous systems.

Keywords: emerging pollutants, adsorption, synthesis, residual biomass, modeling.

1. Introduction

The consume of pharmaceutical compounds has been recently expressively growing, which in turn leads to higher generation of effluents [1]. Since there are yet several drawbacks on the treatment of emergent pollutants such as the antibiotics, their presence in receiving water such rivers and lakes can be easily confirmed by several studies [2,3].

Alternative techniques have been largely assessed to substitute the conventional treatments, which are based in physico-chemical processes such as sedimentation, filtration, coagulation and flocculation [4]. Among the promising processes for the removal of pollutants such as the pharmaceutical compounds, separation processes like adsorption and ion exchange can highlighted

due to their capacity of capturing organic compounds even they are in trace level in the liquid phase [5]. Advanced oxidative processes could also be mentioned as potential alternatives for the treatment of emerging pollutants, although these processes present the drawback of the possible formation of harmful by-products [6].

Although the adsorption process is widely employed for the transference of undesirable components (adsorbate) from a fluid phase (liquid or gas) to a solid phase (adsorbent), the choice of the adsorbent is an essential point to allow the efficiency and especially to avoid elevating the costs of the process. Reports on the literature show that commercial materials like polymeric resins, zeolites, and carbon molecular sieves were successfully used for the removal not only of pharmaceutical compounds but also of components



such as heavy metals and dyes, that also hardly efficiently treated by conventional processes [7].

On other hand, commercial adsorbents commonly represent high costs for the design of an industrial-level equipment, so that residual biomasses have been recently tested to remove different kinds of pollutants from water. Some residual biomasses that were reported as efficient adsorbents are fish scales [8], sugarcane [9] and cassava root husks [10]. This study aims thus to assess the removal of the antibiotic Ciprofloxacin from water by a biochar produced from banana pseudostem. In addition, a comprehensive study on important operating conditions such as pH and temperature is provided.

2. Materials and methods

All chemical reagents used in this work were of analytical grade. The solution of CIP were prepared in distilled water by the dissolution of ciprofloxacin hydrochloride (CIP (HCl) – $C_{17}H_{18}FN_3O_3$). The solution pH was adjusted by adding aliquots of sodium hydroxide (NaOH 0.1 mol L⁻¹) or hydrochloric acid (HCl 0.1 mol L⁻¹). In addition, the biochar was dried in oven at 105 °C prior to any test.

2.1. Synthesis of the biochar

The precursor material used to produce the biochar was the banana pseudostem (BPS - *Musa paradisiaca L.*), which were kindly donated by local producers from Cascavel, Paraná. The BPS were cut into pieces, dried in oven at 105 °C, and stored up to the production of the biochar, which took place following two steps:

- BPS was chemically activated by using zinc chloride (ZnCl₂), by impregnating 5 g (dry basis) of the material with the activating agent at the ratio of 1:4 ($m_{\text{precursor}}/V_{\text{activating agent}}$) for 6 h.
- Pyrolysis of the previously activated biomass in a pyrolysis furnace (FIVE PQ 10P – EDG) at controlled atmosphere with N₂ flow of 100 mL min⁻¹ for 1 h at 800 °C (10 °C min⁻¹ of heating rate). The material was then washed into a hydrochloric acid solution (HCl – 1.0 mol L⁻¹) for 6 h, whit constant agitation (150 rpm) at room temperature, in order to remove the excess of activating agent and unblocking the pores generated on the biochar.

It is worth mentioning that these pyrolysis conditions, namely concentration of the activating agent, temperature of activation, and heating rate, are results of a Box-Behnken experimental design that was carried out in a previous study and reported elsewhere [11].

2.2. Characterization of the biochar

Aiming to assess the BPS' textural properties, N₂ physisorption isotherms were measured in the relative pressure range from 10⁻⁶ to 1, at 77 K (NOVA 200e, Quantachrome), whit prior outgassing of the samples at 250 °C for 12 h. The surface area was determined by the BET multipoint technique [12], whereas area and volume of micropores (A_m and V_m) were achieved by Dubinin-Radushkevich method (DR) [13]. In addition, total pore volume (V_p) and the mean pore diameter (d_p) were obtained by the single point method at P/P₀=0.99 and by Barrett-Joyner-Halenda method [14], respectively.

Furthermore, BPS samples were submitted to Scanning Electron Microscopy (SEM) to analyze the morphology aspect of the produced biochar. For that, the samples were coated with a thin layer of gold and fixed in a sample holder by a carbon tape. SEM images were taken from the surface of the material at magnifications from 500× to 50,000× (Vega 3, Tescan).

The point of zero-charge (pH_{pzc}) of the biochar was determined by the “drift method” as follows: 50 mg of BPS were subsequently added to NaCl aqueous solutions (50 mL, 0.01 mol L⁻¹) with pH ranges from 2 to 12. The biomass was kept in contact with the solutions for 24 h under controlled agitation and temperature (150 rpm, 30 °C) in a bath (MATOLI 170M012). The final pH values were then were measured with pH-meter (MS TECNOPON model mPA - 210).

2.3. CIP-adsorption experiments

The experiments of CIP-adsorption were carried out in closed-batch system by adding known amounts of dried biochar into Erlenmeyer flasks containing 50 mL of CIP-solutions, which were kept under controlled conditions of agitation (150 rpm) and temperature in a thermostatic bath (MATOLI 170M012) for 24 h. At predetermined times, samples were collected and the concentration of CIP in solution was determined at the maximum light absorbance, which was achieved at the wavelength of 272 nm, by UV-Vis

molecular absorption spectrophotometry (Thermo – Genesys 10UV).

2.3.1. Preliminary tests – effect of pH

In order to determine the pH range that would favor the CIP-adsorption onto the BPS-biochar, preliminary tests with different initial pH of the solutions (3, 4, 5, 7, 9, 11) were performed. To this end, the procedure described in section 2.3 was followed, using an initial CIP-concentration in solution of 100 mg L⁻¹ and 0.05 g of BPS-biochar for all pH ranges.

2.3.2. CIP-adsorption kinetics

To evaluate the kinetic behavior of the CIP-adsorption onto the BPS-biochar, several initial concentrations of CIP in liquid phase were tested (from 50 to 200 mg L⁻¹), whereas the amount of adsorbent was fixed at 0.05 g (dry basis). Moreover, in order to get some information on the thermodynamics of the process, the tests were conducted at three different temperatures (30 °C, 40 °C, and 50 °C). Samples were collected at predetermined time intervals (5 min to 24 h), and the amount of CIP removed from the liquid phase by the BPS-biochar could be calculated by Eq. (1).

$$q(t) = \frac{V(C_0 - C(t))}{m_{BPS}} \quad (1)$$

where q is the amount of CIP on the adsorbent at time t (mg g⁻¹); V the volume of solution (L); C_0 and C the initial and final concentrations of CIP in solution, respectively (mg L⁻¹); and m_{BPS} the mass of adsorbent (g).

To describe the kinetic experimental data, the mathematical of Elovich [15] was applied.

2.4. CIP-adsorption equilibrium

The adsorption equilibrium data were obtained from the experimental kinetic data, several concentrations were tested and the samples were collected up to the point in which there was no mass transfer between phases (i.e. adsorption equilibrium). Therefore, the concentration at the equilibrium for each initial concentration could be obtained by Eq. 2, and thus adsorption isotherms could be built.

$$q_{eq} = \frac{V(C_0 - C_{eq})}{m_{BPS}} \quad (2)$$

where q_{eq} and C_{eq} are the amounts of CIP on the solid (mg g⁻¹) and in the liquid phase (mg L⁻¹) at equilibrium, respectively.

To describe the equilibrium data, the well-known Langmuir model [16] was used.

3. Results and discussion

3.1. Characterization of the biochar

The results of the textural properties of the produced adsorbent are presented in Table 1, wherein one may notice that it presented characteristic of a mesoporous material ($d_p > 2.0$) according to the IUPAC classification. On other hand, there is an expressive presence of micropores (A_m and V_m).

Table 1. Textural properties of the biochar produced from banana pseudostem, obtained by N₂-physisorption.

Textural property	Value
Surface area	67.1 (m ² g ⁻¹)
Micropores' area	84.8 (m ² g ⁻¹)
Total pore volume	0.0945 (c ³ g ⁻¹)
Micropores' volume	0.0301 (c ³ g ⁻¹)
Mean pore diameter	2.81 (nm)

The surface area can be considered relatively low in comparison with some microporous materials, which may present areas of up to 1500 m² g⁻¹ [17]. On other hand, it should be noted that the applicability of an adsorbent is associated with the specificity of the adsorbate due to the diameter of accessible pores. Organic molecules such as CIP molecules, for instance, may present some steric hindrances due their great molecular dimensions [18].

The presence of micropores could be also suggested from the micrographs at the magnitude of 30,000 times (Fig. 1c), in which small cracks, probably generated by activation with ZnCl₂, can be observed on the material's surface. By the analysis of lower magnifications presented in Fig. 1a and Fig1b, it is possible to identify besides the fibrous appearance related to the lignocellulose complex of the precursor material (banana pseudostem), a great heterogeneity in the shape and size of the particles.

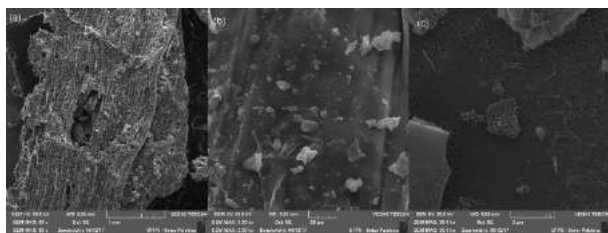


Figure 1. Micrographs of the BPS-biochar. (a) Mag. of 80x; (b) Mag. 2,000x; and (c) Mag. 15,000x.

Moreover, the point of zero-charge (pH_{pzc}) of the BPS particles is 5.0 ± 0.1 , presenting a relatively neutral charge in the pH range between 4 and 9. If the pH of the solution is lower than the pH_{pzc} , the adsorbent's surface will have a positive charge. In contrast, for pH values higher than the pH_{pzc} , the adsorbent will have a negative character on its surface.

3.2. Preliminary tests

The best pH condition for the CIP-adsorption within the tested range was $pH=4$, which may be explained by the fact the CIP molecules are mainly positively charged (CIP^+) at pH values below $pH=6$, presenting more than 99% of CIP^+ species at $pH=4$ [18], whereas the surface of the adsorbent is neutral. In the case that the BPS surface is also acid, repulsive forces will act between adsorbent and adsorbate instead of attractive ones, due to their equally positive character. This is the reason why the CIP-adsorption is not that favored at $pH=3$ as it is at $pH=4$. In other words, the BPS particles will only have affinity with the CIP^+ species its surface presents mainly neutral or negative charges.

3.3. CIP-adsorption kinetics

The kinetic behavior of the CIP-adsorption onto the BPS-biochar was evaluated at different initial concentrations of CIP in solution and different temperatures at the best pH condition achieved in the preliminary tests ($pH=4$). It could be noted that the adsorption equilibrium was achieved after 20 h except for the lowest initial concentration (50 mg L^{-1}), due to the lower availability of CIP molecules in the liquid phase (see Fig. 2).

As expected, on other hand, the adsorption capacity increased with the increase of the initial concentration of the pharmaceutical compound in solution, since there is a greater driving force for

the mass transfer produced by the higher concentration gradient between phases.

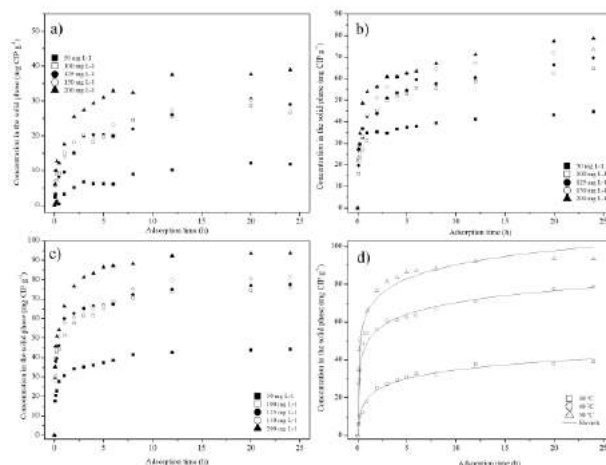


Figure 2. Experimental and model CIP-adsorption kinetics onto the BPS-biochar. (a) 30 °C; (b) 40 °C, (c) 50 °C, and (d) Elovich model fitting for initial concentration of 200 mg L^{-1} . (Experimental conditions: $m_{BPS} = 50 \text{ mg}$, $V = 50 \text{ mL}$, $pH=4$).

It has to pointed out that despite the relative long equilibrium times observed for the highest CIP-initial concentrations in liquid phase, a favorable kinetic behavior can be noted by analyzing the curves' slopes at the first stage of the mass transfer. As an example, for the initial concentration of $C_0 = 200 \text{ mg L}^{-1}$ at 30 °C (Fig. 2a), the adsorption capacity after 1 h was already $q(t=1 \text{ h}) = 18 \text{ mg g}^{-1}$, confirming the high initial adsorption rates.

Moreover, it should be highlighted that the adsorption kinetics is favored by the temperature, so that the initial adsorption rate is even greater at higher temperatures (e.g. $q(t=1 \text{ h}, T=50^\circ\text{C}, C_0=200 \text{ mg L}^{-1}) = 67 \text{ mg g}^{-1}$). In addition, the influence of the temperature that can be evidenced by comparing Figs. 2(a)-(c), indicating the endothermic characteristic of the CIP-adsorption onto the BPS-biochar, which is in accordance with the calculated thermodynamic parameters (see section 3.5).

The kinetic model of Elovich showed the best agreement with the experimental data compared to the other tested models, as can be observed (see Fig. 2d), which makes sense considering the heterogeneous surface of the adsorbent. Furthermore, this fact might indicate that a chemical adsorption took place.

Table 2. Kinetic parameters estimated by Elovich model.

T (°C)	α ($\text{mg g}^{-1} \text{h}^{-1}$)	β (g mg^{-1})	r^2
30	120.24	0.1502	0.9853
40	2126.70	0.1105	0.9862
50	4602.83	0.0926	0.9850

3.4. CIP-adsorption equilibrium

By the analysis of the equilibrium data of the CIP-adsorption onto the BPS-biochar (Fig. 5), it can be observed the tendency of a sigmoidal behavior for all tested temperature conditions, which is characteristic of monolayer adsorption followed by multilayer adsorption.

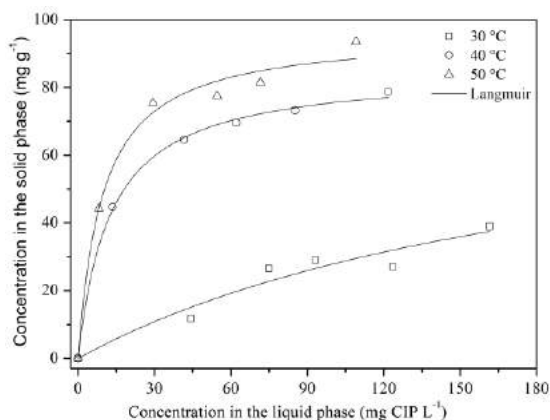


Figure 3. Experimental equilibrium data and Langmuir isotherm model fitting for CIP-adsorption at 30 °C, 40 °C, and 50 °C.

Overall, according to the qualitative results presented in Fig. 3 and to the parameters presented in Table 3, the Langmuir equilibrium model could describe adequately the experimental data at all temperatures tested, evidencing elevated values of adsorption capacity and adsorbate-adsorbent affinity, especially at higher temperatures.

Table 3. Equilibrium parameters estimated by Langmuir model.

T (°C)	b (L mg^{-1})	q_{max} (mg g^{-1})	r^2
30	4.90×10^{-3}	85.2214	0.9260
40	8.90×10^{-2}	85.0413	0.9984
50	1.04×10^{-1}	96.2633	0.9864

3.5. CIP-adsorption thermodynamics

Based on the equilibrium data, thermodynamic parameters were obtained. The value found for the adsorption enthalpy was 123.5 kJ/mol, confirming the endothermic character observed by analyzing the kinetic and equilibrium behavior of the adsorption process of CIP onto the BPS-biochar. Moreover, considering that this value is higher than 40 kJ/mol, the process can be characterized as chemisorption [19], which is in accordance with the Elovich model assumptions.

This fact could be explained by admitting that the chemisorption process might be associated with molecular interactions such as hydrogen bonds and electrostatic interactions between the active sites and the adsorbate molecules, which depending on the operational conditions (e.g. temperature, pH) can be more or less intense.

4. Conclusions

Overall, the banana pseudostem biochar produced by ZnCl_2 chemical activation showed chemical and textural desirable features. Therefore, based on the characterization results, along with equilibrium, kinetics and thermodynamics experiments, the BPS-biochar showed favorable equilibrium behavior, affinity and elevated adsorption capacity of ciprofloxacin as well as favorable kinetics and thermodynamics. Therefore, the BPS-biochar presents potential considering the adsorbent observed properties as well as its residual and renewable characteristics.

Acknowledgements

The authors thank the National Council for Scientific and Technological Development (CNPq) for the financial support (Process n° 404420/2016-8).

References

- [1] F.H. Borba, A. Schmitz, L. Pellenz, F. Bueno, N. Kasper, B.M. Wenzel, S. Baroni, I.C. Dall'Oglio, A.N. Módenes, Genotoxicity and by-products assessment in degradation and mineralization of Ciprofloxacin by UV/H₂O₂ process, *Journal of Environmental Chemical Engineering*. 6 (2018) 6979–6988.
- [2] E. D'Angelo, D. Starnes, Desorption kinetics of ciprofloxacin in municipal biosolids determined by diffusion gradient in thin films,

- Chemosphere. (2016).
- [3] P.E. Stackelberg, J. Gibs, E.T. Furlong, M.T. Meyer, S.D. Zaugg, R.L. Lippincott, Efficiency of conventional drinking-water-treatment processes in removal of pharmaceuticals and other organic compounds, *Science of the Total Environment*. (2007).
- [4] P.E. Stackelberg, E.T. Furlong, M.T. Meyer, S.D. Zaugg, A.K. Henderson, D.B. Reissman, Persistence of pharmaceutical compounds and other organic wastewater contaminants in a conventional drinking-water-treatment plant, *Science of the Total Environment*. (2004).
- [5] T. Wang, Y. Zheng, X. Wang, Q. Wang, C. Ke, D.E. Austin, X. Han, Z. Zhang, Abnormal adsorption and desorption behavior of pharmaceutical drugs on polystyrene microspheres, *RSC Advances*. (2017).
- [6] M.G. Sausen, F.B. Scheufele, H.J. Alves, M.G.A. Vieira, M.G.C. da Silva, F.H. Borba, C.E. Borba, Efficiency maximization of fixed-bed adsorption by applying hybrid statistical-phenomenological modeling, *Separation and Purification Technology*. 207 (2018).
- [7] J. Staudt, F. Bisinella Scheufele, C. Ribeiro, T. Yudi Sato, R. Canevesi, C. Eduardo Borba, Ciprofloxacin desorption from gel type ion exchange resin: desorption modeling in batch system and fixed bed column, *Separation and Purification Technology*. (2019).
- [8] C. Ribeiro, F.B. Scheufele, F.R. Espinoza-Quiñones, A.N. Módenes, M.G.C. da Silva, M.G.A. Vieira, C.E. Borba, Characterization of *Oreochromis niloticus* fish scales and assessment of their potential on the adsorption of reactive blue 5G dye, *Colloids and Surfaces A: Physicochemical and Engineering Aspects*. (2015).
- [9] F.B. Scheufele, A.N. Módenes, C.E. Borba, C. Ribeiro, F.R. Espinoza-Quiñones, R. Bergamasco, N.C. Pereira, Monolayer-multilayer adsorption phenomenological model: Kinetics, equilibrium and thermodynamics, *Chemical Engineering Journal*. (2016).
- [10] A.O. Jorgetto, R.I. V Silva, M.J. Saeki, R.C. Barbosa, M.A.U. Martines, S.M.A. Jorge, A.C.P. Silva, J.F. Schneider, G.R. Castro, Applied Surface Science Cassava root husks powder as green adsorbent for the removal of Cu (II) from natural river water, *Applied Surface Science*. 288 (2014) 356–362.
- [11] B.F. Santos, P. G., Koerich, A. B., Puttkammer, D. L., Scheufele, Produção de carvões ativados a partir do pseudocaule da bananeira visando a adsorção de ciprofloxacina, 6° Simpósio de Biotecnologia Na Agroindústria . 08 e 09 Junho de 2017 , UFPR - Setor Palotina. (2017) 3157.
- [12] S. Brunauer, P.H. Emmett, E. Teller, Adsorption of Gases in Multimolecular Layers, *Journal of the American Chemical Society*. 60 (1938) 309–319.
- [13] M.M. Dubinin, Theory of the physical adsorption of gases and vapors and adsorption properties of adsorbents of various natures and porous structures, *Bulletin of the Academy of Sciences of the USSR Division of Chemical Science*. (1960).
- [14] E.P. Barrett, L.G. Joyner, P.P. Halenda, The Determination of Pore Volume and Area Distributions in Porous Substances. I. Computations from Nitrogen Isotherms, *Journal of the American Chemical Society*. 73 (1951) 373–380.
- [15] M.J.D. Low, Kinetics of Chemisorption of Gases on Solids., *Chemical Reviews*. 60 (1960) 267–312.
- [16] I. Langmuir, The Adsorption of Gases on Plane Surfaces of Glass, Mica and Platinum, *Journal of the American Chemical Society*. 40 (1918) 1361–1403.
- [17] V.K. Gupta, Suhas, Application of low-cost adsorbents for dye removal - A review, *Journal of Environmental Management*. (2009).
- [18] M.E. Roca Jalil, M. Baschini, K. Sapag, Influence of pH and antibiotic solubility on the removal of ciprofloxacin from aqueous media using montmorillonite, *Applied Clay Science*. 114 (2015) 69–76.
- [19] A. Çelekli, G. Ilgün, H. Bozkurt, Sorption equilibrium, kinetic, thermodynamic, and desorption studies of Reactive Red 120 on *Chara contraria*, *Chemical Engineering Journal*. 191 (2012) 228–235.

Characterization of Fresh and Aged Zeolites Using Different X-ray and Adsorption/Desorption Isotherm Techniques

Khalil Kashefi^a, Darley C Melo^b, Frederico W Tavares^c, Amaro G Barreto Jr.^{a,*}

^aPrograma de Pós Graduação em Engenharia de Processos Químicos e Bioquímicos, EQ-UFRJ, and ^bCENPES, PETROBRAS S.A., and ^cPrograma de Engenharia Química, COPPE, UFRJ, Rio de Janeiro, Brazil

Abstract

Characterization of zeolites provides useful information to select the correct porous media for different applications such as desiccant, separator or catalyst. Properties such as activity, selectivity, durability, structure and acceptable reaction rate are the most important parameters to design or optimize a zeolite. In this work, a commercial zeolite, in two states of fresh and aged, is considered for investigation. The aged sample was obtained from an industrial natural gas dehydration plant. The effect of aging process on the structure and the capability of the sample to perform adsorption/desorption process were assessed using different characterization methods. Techniques such as XRF, XPS and EDS/SEM were utilized for elemental and bonding analysis and also to recognize the type of carbon deposition. XRD was used to verify any structural changes during aging process, and N₂ adsorption/desorption were employed to measure the specific surface and volume of the samples. It was observed that the aging after abundant adsorption/desorption cycles for gas dehydration process, mostly affected the activation of zeolite by hydrocarbon deposition. Some minor changes in the structures, such as size and migration of cations, were detected.

Keywords: Zeolite; Aging; Characterization; Dehydration

1. Introduction

Zeolites and zeolite-like materials do not comprise an easily definable family of crystalline solids [1] and are part of the larger class of materials called molecular sieves, which allow mixtures of molecules of differing structures to be separated. These are porous crystalline framework materials containing pores of molecular size. Conventional zeolites are based on silicate frameworks in which substitution of some of the Si with Al (or other metals) leads to a negative charge on the framework, with cations (usually Na or other alkaline) within the pore structure. The T atoms (T=Si, Al, etc.) linked by oxygen ions [2].

Activity, selectivity, durability, structure and acceptable rate are the most important considerations to design or optimize an adsorbent [3]. On the other hand, zeolites are among the most sophisticated inorganic solids with crystallographic unit cells often counting hundreds of atoms with complex structures and still poorly understood [4], so the application of various types of characterization techniques is inevitable. There are numerous well-studied zeolite characterization techniques, such as calorimetry, FTIR and NMR

spectroscopies, TGA, TPD, XRD [5], N₂ adsorption/desorption, EDS coupled with SEM, each with different contributions to explore the zeolite structure.

Some of these techniques are based on type of excitation (photons, electrons, neutrons, ions, electromagnetic field, heat, etc.) to which the surface responds. For example, X-ray diffraction (XRD), X-ray absorption spectroscopy (XAS), and X-ray photoelectron spectroscopy (XPS) all use photons for probing the sample and are among the most frequently employed techniques for catalyst characterization. XRD occurs in the elastic scattering of X-ray photons by atoms in a periodic lattice and can be used to obtain structural information. In contrast, irradiating a catalyst with X-ray photons can induce excitation of electrons from occupied core levels to empty valence levels (XAS) or generate photoelectrons (XPS), yielding information about the composition of the sample and the electronic properties of the elements present [3]. Other techniques such as N₂ adsorption/desorption and TPD are based on the performance of the adsorbent during adsorption/desorption cycles. The techniques employed in this work are mentioned in the

following paragraphs and a short description is presented on each method:

X-ray fluorescence (XRF) is reported to be a non-destructive, fast with minimal preparation and cost-effective elemental analysis method. The method depends on fundamental principles that are common to several other instrumental methods involving interactions between electron beams and X-rays with samples (such as X-ray spectroscopy and X-ray diffraction) [6]. The method only provides information for the elements heavier than fluorine (F), so the elements such as oxygen, carbon and hydrogen cannot be detected using this technique.

X-ray diffraction (XRD) is mainly used to define the structure and phase of the samples. In this method, the X-ray diffraction intensity is measured from a powder sample as a function of scattering (diffraction) angle by using a diffractometer, which is a precision instrument with two axes (ω and 2θ) of independent rotation. Bragg's law under the condition of X-rays of known wavelength is applied in this method [7].

EDS coupled with SEM has become commonplace technique and is getting attraction in characterization. By this combination, in addition to imaging, high spatial resolution elemental analysis is possible [2].

X-ray photoelectron spectroscopy (XPS) is employed to verify chemical composition and bonds in the samples. Using this method, it is possible to measure the whole range of chemicals including carbon and oxygen contents which is not possible in XRF and EDS.

N₂ adsorption/desorption experiment is used in this work to measure the surface area. This is one of the most important properties for the characterization of microporous materials, such as zeolites. Most experimental results of surface areas are reported as either the Langmuir surface area or the BET surface area derived from nitrogen adsorption isotherms at 77 K. The choice between these two surface areas depends on whether the pore sizes support multilayer (BET) or only monolayer (Langmuir) adsorption [8].

In this communication, a commercial zeolite, in two states of fresh and aged, is considered to be investigated. The two fresh and aged samples were analyzed using above mentioned methods. The effect of aging process on the structure and the capability of the sample to perform the adsorption/desorption process were investigated by comparing the characterization results of two samples.

2. Experiments

2.1. Materials

The zeolite samples of Z1 (fresh and aged) are commercial zeolite. The aging process of the adsorbent (CHA zeolite) was performed during a natural gas dehydration process using an adsorption-desorption column (40-230 °C) in an industrial unit.

2.2. Characterization techniques

In this section, the characterization techniques along with the equipment that are employed in this study are reported.

The X-ray fluorescence experiments were performed using XRF instrument on a model S8 TIGER—Bruker (Tokyo, Japan). The samples were analyzed in He with an X-ray source of Pd operating at 50 kV. The results of chemical analysis by this technique were used to define the structure of the samples in XRD method. A bench top XRD equipment (D2 PHASER, Bruker) was employed and to define the crystals, EVA and Jade were used. EDS/SEM was used to measure the chemical composition of the samples using energy dispersive X-ray spectroscopy (EDS) (Bruker, Quantax 70) on a scanning electron microscope (SEM) (Hitachi, TM3030 plus) to visualize the location of the atoms. This test is a qualitative experiment. Using this method, it is possible to have a general view of the microstructure. Firstly, the sample (in pellet form) was put on a carbon tape to fix it in a stable location. To obtain internal view, we cut (break) the pellet, so we could have both lateral and internal views. In order to make the surface of samples conductive (ready for the test), “carbon sputtering” was performed. So we cannot quantify carbon in our samples. XPS technique was employed to measure chemical composition and also to obtain some details about the chemical bonds in the samples. The XPS spectra were obtain for fresh and aged samples (Thermo Scientific™ ESCALAB™) and the data were gathered and analyzed by Thermo Scientific Advantage® Data System. This software uses a combination of Lorentzian and Gaussian functions to generate the fitting curve for XPS data. The N₂ adsorption and desorption isotherms were measured (Micromeritics, ASAP 2020) and the data were used to perform BET, Langmuir and BJH analysis. About 0.2 g sample in pellet form was used for each test.

It is worth mentioning that for XPS, XRD and XRF methods, powder form, and for EDS/SEM and N₂ adsorption/desorption, the pellet were used to perform the tests.

3. Results and discussion

3.1. X-ray fluorescence (XRF)

The elemental composition was measured with XRF for chemicals heavier than Fluorine (F). As it can be seen in Table 1, the main cation in this sample is sodium (Na⁺) with a minor change after aging. Other cations, Mg⁺² and Ca⁺² are present in low content, but decreased after aging process. The increase in Na⁺ and K⁺ can be ignored, since this is probably due to reduction in Al and Si and it is not a real change. The ratio of Si/Al is decreased slightly, which is a sign of minor change in the structure of the sample after aging. Due to the presence of sulfur species in the natural gas under dehydration process, sulfur deposition was observed in the aged sample. The data obtained in this test, used to identify the structures using XRD.

Table 1. Chemical compositions of the samples (powder) using XRF

Elements	Z1-Fresh w/w %	Z1-Aged w/w %	Change %
Na	11.979	12.439	+4
Mg	2.194	1.973	-10
Al	19.822	18.371	-7
Si	51.405	49.668	-3
S	1.985	5.15	+159
Cl	0.846	0.687	-23
K	2.152	2.522	+17
Ca	1.2667	0.974	-23
Ti	0.59	0.663	+12
Fe	7.209	7.1	-2
Si/Al	2.59	2.70	+4

3.2. X-ray diffraction (XRD)

The spectra of the samples were obtained in 2θ ranging from 7-90 degree. Using EVA and Jade software, in zeolite sample Z1, in fresh (Z1-F) and aged (Z1-Aged) states, different types of Chabazite (Na, Ca, K and Mg) were identified. The XRD patterns of the two samples are illustrated Fig. 1 (a, b and c). In this graph (a), only the spectra ranging from 2θ: 7-35 are shown since the higher degree did not provide informative spectra. Other graphs

in this figure (b: 7-24 and c: 24-35) are demonstrated the magnified version of the spectra for better view of the peaks. As it can be seen, generally the structure remained intact after aging process. There can be seen a forward shift in spectra which can be due to a small contraction in the size of zeolite unit cell [9]. Also some of the peaks were missed in the aged sample as in 2θ of about 21.5, 23.8, 27, 27.9 and 34.

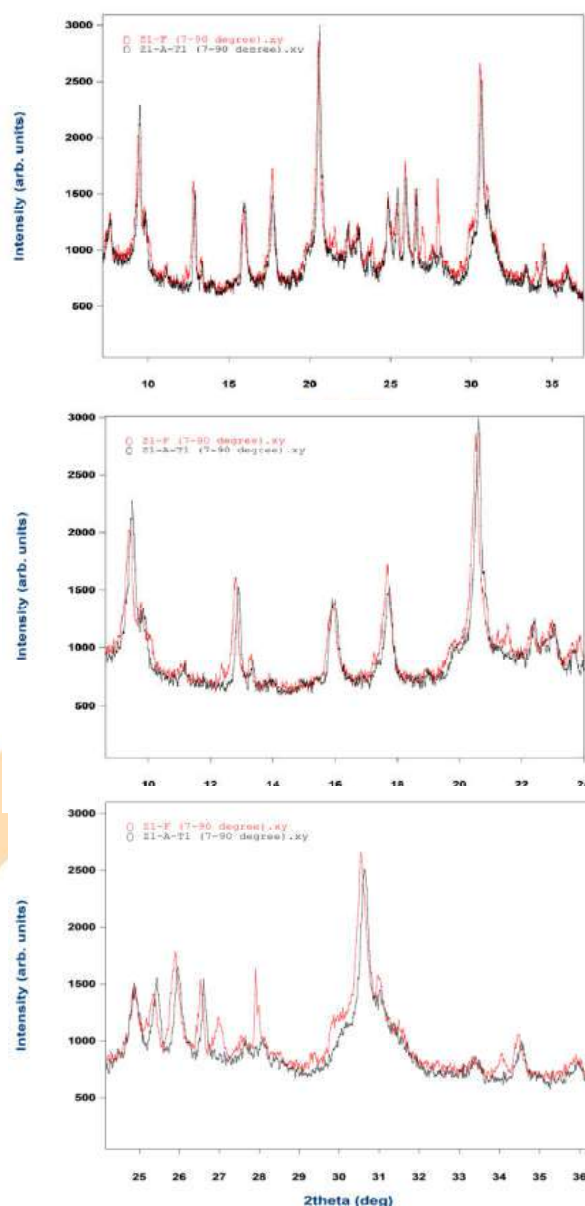


Fig. 1. XRD spectra of fresh (F) and aged(A) zeolite samples (WinPlotr-2006).

3.3. Energy dispersive X-ray spectroscopy (EDS) coupled with scanning electron microscopy (SEM)

EDS/SEM provided information related to the surface of the sample (zeolite pellet). The data obtained from inner view was not reliable, since it was not a good (smooth) cut and it was made by breaking the pellet. So here only the data related to the lateral view are discussed. Table 2 summarizes and compares the chemical compositions of the zeolites samples, in fresh and aged states, using EDS/SEM. Since this technique provides chemical composition with oxygen, the contents of elements are different from the results of XRF (Table 1). Also this technique provides information from surface, but the XRF gives the bulk information.

By comparing the two Tables (1 and 2), it can be seen that the amount of Al and Si reduced in the bulk after aging process, but there is an increase in the surface, however the ratio of Si/Al increased slightly after aging in both bulk and surface. Cations, Na and Mg, did not change drastically, but Ca dropped by almost 50% by aging process which is also visible in Fig. 2 as an agglomeration of calcium. Other elements did not show drastic difference in microscopy analysis. These figures show the elemental mapping of the zeolite pellets from the lateral views for the samples.

3.4. X-ray photoelectron spectroscopy (XPS)

The XPS experiments were performed on the mentioned fresh and aged samples in powder form, so the results represent the bulk properties. The survey spectra along with the content of each element in each zeolite are presented in Fig. 3. With this method it could be possible to track carbon as well as other elements in both samples. In addition, the XPS data were analyzed to calculate the binding energies assigned to each elements along with the percentages of each assignments. Table 3 summarizes this information [10], [11]. As it can be seen in the survey graph, carbon is almost doubled after aging process. This is mostly due to deposition of hydrocarbon (C bond) as it is detailed in Table 3. This shows a coking process as it was expected. Other bonds with C are with H and O (single and double) that did not change drastically after aging. Three assignments as Al, Si and H₂O, were found for O and all were remained almost constant after aging. For Si, two bonds were found with O, one at about 102 eV (with any possible Si bond) and the other at about 104 which is a silicate

Table 2. Chemical compositions of the samples (pellet, lateral view) using EDS/SEM

Elements	Z1-Fresh w/w %	Z1-Aged w/w %	Change %
O	51.5	46.1	-10
Na	5.5	5.2	-4
Mg	0.79	0.77	-3
Al	10.7	11.9	+12
Si	23.9	28.7	+20
S	2.0	2.4	+18
K	0.6	0.7	+11
Ca	3.2	1.6	-49
Fe	1.9	2.6	+42
Si/Al	2.2	2.4	+7

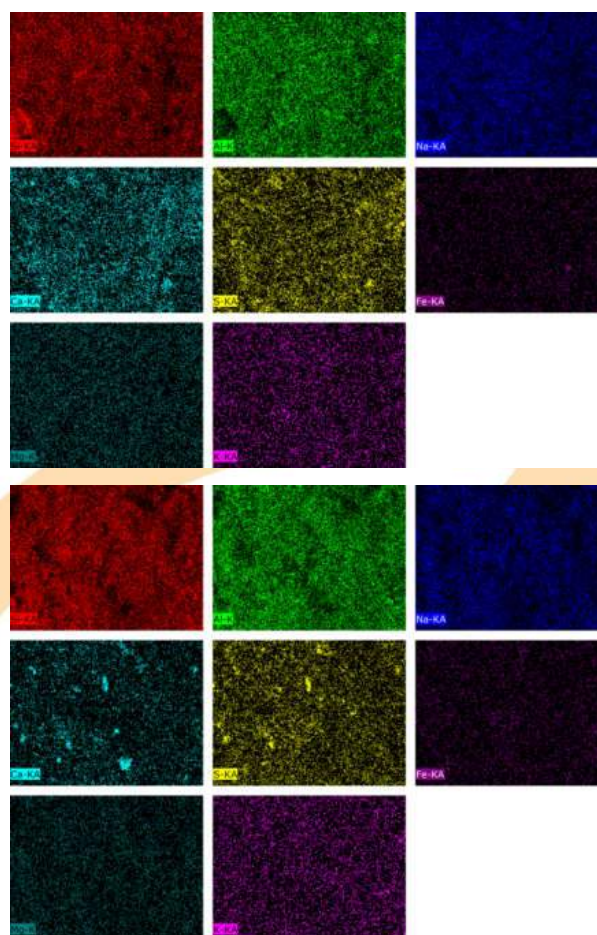


Fig.2. Elemental mapping by EDS/SEM method from the lateral view of the zeolite pellet (top photos: fresh sample of Z1-F, below photos: aged sample of Z1-A,)

bond. In Al, also two bonds at about 74 and 76 eV were identified that can be assigned to Al₂O₃ (as the higher content) and probably a double bond (AlO(OH)), respectively. Na bond is recognized as molecular sieve bonding without any change in fresh and aged samples. This observation is in agreement with XRD, since the structure did not change due to aging. Not much sulfur was detected, that is probably related to the point (beam incident point) that instrument was receiving information.

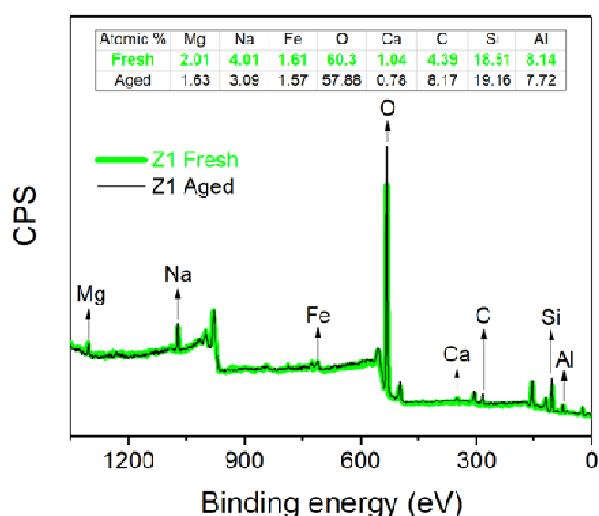


Fig 3. XPS survey spectra of Z1 fresh and aged samples along with the atomic content of each element according to the survey.

Table 3. Binding energy (BE), assignments (Asg.) and content percentage (Ct.%) of each element in fresh and aged zeolite [10], [11].

Z1-Fresh			Z1-Aged			
BE	Asg.	Ct.%	BE	Asg.	Ct.%	
531.7	Al	83	531.7	Al	88	
O	533.5	Si	13	533.4	Si	12
	534.7	H ₂ O	4	-	-	
Si	102.4	O	82	102.3	O	89
	104.6	O	18	104.1	O	11
Al	74.3	O	83	74.2	O	91
	76.6	O	17	76.1	O	9
Na	1072	Mol-Siev.	84	1072	Mol-Siev.	88
	284.3	C	48	284.3	C	63
C	285.6	H	22	285.7	H	19
	286.9	- O	18	286.9	- O	11
	289.1	= O	12	288.9	= O	7

3.5. N₂ adsorption/desorption

The results of N₂ adsorption/desorption experiments are summarized in Table 4. It can be seen that the reduction of the specific surface (and volume) for Z1 fresh and aged is between 13-28% using different method. This reduction may be related to loss of some cations or migration of some elements, or deposition of carbon. Usually carbon deposition can be in the form of carbonate and coking, but as discussed in XPS section, here the coking process is more responsible for carbon bond presence. Due to the results of XRD, the main reason of specific surface reduction cannot be the loss of structure, since it was observed a minor change in structure size. In this table, also it can be seen that pore size width was increased after aging. This can also confirm the loss of elements or changing the structure size. The Nitrogen isotherm plot in both adsorption and desorption paths on zeolite samples are depicted Fig. 4. A reduction of about 25% in quantity of the adsorbed gas is measured due to aging.

Table 4. Specific surface/volume and pore size of the fresh and aged sample using N₂ isotherms.

Parameters	Z1-F	Z1-A	Δ%
Specific Surface Area (m²/g)			
Surf. area at P/Po = 0.21	324.2	242.7	-25
BET Surface Area	312.8	234.2	-25
Langmuir Surface Area	420.1	314.9	-25
t-Plot micropore Area	255.3	183.5	-28
t-Plot External Surface Area	57.5	50.8	-12
BJH Ads. cumul. surf. area of pores	46.3	39.6	-14
BJH Des. cumul. surf. area of pores	59.5	51.2	-13
Specific Pore Volume (m³/g)			
Single point ads. total pore vol.	0.299037	0.2614	-13
t-Plot micropore volume	0.120674	0.0870	-28
BJH Ads. cumul. volume of pores	0.190414	0.1875	-2
BJH Des. cumul. volume of pores	0.217544	0.2141	-2
Pore Size (Å)			
BET Ads. avg. pore width	38.2355	44.649	+17
BJH Ads. avg. pore diameter	164.487	189.46	+15
BJH Des. avg. pore diameter	146.364	167.44	+14

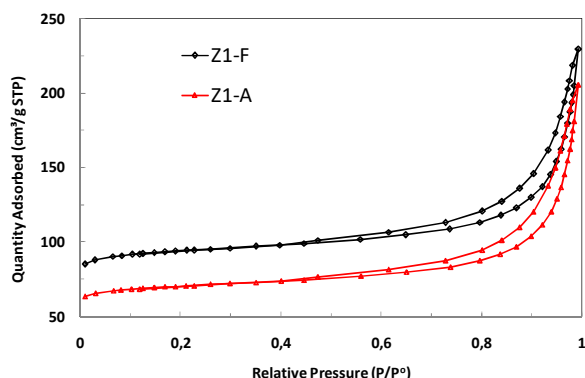


Fig.4. Nitrogen isotherm in both adsorption and desorption paths for fresh and aged samples at -195.7°C ($P^0 \approx 770$ mmHg).

4. Conclusions

A zeolite which is available commercially, in two states of fresh and aged, was used to study the effect of aging on the structure and efficiency of the adsorbent. The aging process was performed under the condition of an industrial natural gas dehydration plant. Different characterization methods based on X-ray such as XRF, XRD, XPS, EDS/SEM for structural, elemental and bonding analysis and a method based on N_2 adsorption and desorption isotherms to measure the specific surface and volume of the samples were employed. The aging after several adsorption/desorption cycles in gas dehydration process, mostly affected the activation of zeolite by hydrocarbon deposition (coking). This was seen by analyzing the XPS spectra since the only major change was in C-C binding not in other elements binding energy. This observation was confirmed with XRD. Some minor changes in the structures, such as size and migration of cations, were detected by XRD and EDS/SEM techniques. Reduction in capability of adsorption/desorption and also specific surface values were detected using N_2 adsorption and desorption isotherms. These techniques provided informative knowledge to the nature of the two porous materials in fresh and aged states.

Acknowledgements

The authors wish to thank CENPES/ Petrobras for supporting this research.

References

- [1] L. B. McCusker, D. H. Olson, and C. Baerlocher, "Atlas of Zeolite Framework Types," 2007.
- [2] A. W. Chester and E. G. Derouane, Zeolite characterization and catalysis. 2009.
- [3] In-Situ Characterization of Heterogeneous Catalysts, vol. 2013, no. 12. 2013.
- [4] A. Aerts, C. E. A. Kirschhock, and J. A. Martens, "Methods for in situ spectroscopic probing of the synthesis of a zeolite," Chem. Soc. Rev., vol. 39, no. 12, p. 4626, 2010.
- [5] B. T. W. Lo, L. Ye, and S. C. E. Tsang, "The Contribution of Synchrotron X-Ray Powder Diffraction to Modern Zeolite Applications: A Mini-review and Prospects," Chem, vol. 4, no. 8, pp. 1778–1808, Aug. 2018.
- [6] M. S. Shackley, "An Introduction to X-Ray Fluorescence (XRF) Analysis in Archaeology," in X-Ray Fluorescence Spectrometry (XRF) in Geoarchaeology, New York, NY: Springer New York, 2011, pp. 7–44.
- [7] Y. Waseda, E. Matsumura, and K. Shinoda, X-Ray Diffraction Crystallography. Berlin, Heidelberg: Springer Berlin Heidelberg, 2011.
- [8] Y.-S. Bae, A. O. Yazaydin, and R. Q. Snurr, "Evaluation of the BET Method for Determining Surface Areas of MOFs and Zeolites that Contain Ultra-Micropores," Langmuir, vol. 26, no. 8, pp. 5475–5483, Apr. 2010.
- [9] C. A. C. Perez, N. S. de Resende, V. M. M. Salim, and M. Schmal, "Water Interaction in Faujasite Probed by in Situ X-ray Powder Diffraction," J. Phys. Chem. C, vol. 121, no. 5, pp. 2755–2761, Feb. 2017.
- [10] "NIST X-ray Photoelectron Spectroscopy Database." [Online]. Available: https://srdata.nist.gov/xps/main_search_menu.aspx.
- [11] "X-ray Photoelectron Spectroscopy (XPS) Reference Pages." [Online]. Available: <http://www.xpsfitting.com/>.

Comparative Study on the Properties of NaOH Activated Carbons produced From Passion Fruit Seed And Tamarind Seed

Fernanda dos Santos Aguilari Leite^a, Deiviti Filipe Impossetto^a, Rúbia Michele Szuki^a,
Maria Carolina Sergi Gomes^a, Juliana Guerra Sgorlon^a, Caroline Casagrande Sipoli^a

^a *Technological University Federal of Paraná - Campus Apucarana, Marcílio Dias Street, 635, Apucarana, 86812-460, Brazil*

Abstract

The culture of consum tropical fruits grows every day and consequently generates an increase of residues. With this, a search for methods to reuse these generated residues is being developed, being one of these methods activated carbon production. Thus, the purpose of this work is to compare two adsorbent materials produced using the passion fruit seeds and tamarind seeds as precursor by chemical activation with sodium hydroxide (3: 1 m / m). This comparative study was based on the characterizations: MBI, NI, CZP, SEM, FTIR and Boehm Method. The AC-PS and AC-TS presented values for pH at charge zero point 7.10 and 6.87, NI 1064.10 ± 12.32 and 989.64 ± 22.78 mg g⁻¹ and MBI 488.45 ± 0.73 and 286.20 ± 3.99 mg g⁻¹, through the MBI we can estimate the specific area 942.70 ± 1.41 m² g⁻¹ and 552.36 ± 7.70 m² g⁻¹ respectively. From the FTIR it was possible to determine the functional groups present in the AC's and, with Boehm's method it was possible to confirm that the surfaces of the AC's have basic characteristics. In addition, the adsorbents compared indicated a higher microporosity and although undergoing the same type of activation and showing up to be very similar, AC-PS showed better results.

Keywords: Adsorption; Residue; Chemical Activation.

1. Introduction

The consumption culture of tropical fruits grows every day generating the increase of residues such as peels and seeds, which represent a large part of the weight of the fruits. In the productive development from these fruits for the production of food, medicine, among others, there is a large generation of waste generally discarded.

Thus, adding value to these by-products is of economic, scientific and technological interest [1]. One of the alternatives is the reuse in the production of low cost adsorbents, such as activated carbon (CA) that can be used in environmental decontamination processes, for example [2]. Therefore, passion fruit and tamarind seeds can be considered good precursors for this purpose because they are cheap and renewable products, and in the literature, there are few studies reporting the use of these residues as precursors of CAs. According to Fernandes [3], in the CA production process, the raw material is submitted to the carbonization and activation steps. The activation aims to increase the

specific area of carbon by increasing its porosity and consequently helps to control the characteristics of the material such as pore distribution, specific area, mechanical strength, etc. Basic activation has the characteristic to producing highly porous adsorbent materials. In this type of process, sodium hydroxide has been widely used as a chemical activating in the production of CA [5].

Several parameters can be used to describe the adsorptive capacity of AC, including iodine number (IN) and methylene blue index (MBI)[6]. IN is a relative indicator of the porosity of a AC, where it requires pores 1 nm to are expected to adsorb, on the other hand the MBI determines the adsorptive capacity of medium molecules similar to methylene blue (MB) dye. In this context, the present study aimed to compare activated carbons from different precursors, passion fruit and tamarind seeds through chemical activation using NaOH.

2. Methodology

The passion fruit seed activated carbon (AC-PS) and the tamarind seed activated carbon (AC-TS)



compared in this study, were produced in the Technological University Federal of Paraná - Campus Apucarana. Initially, the carbonization of the precursor materials was carried out, which were placed in a stainless steel reactor with holes for the entry and exit of gases. The reactor was heated in a muffle furnace (model Zezimaq FHMP), at $10^{\circ}\text{C min}^{-1}$ from room temperature to 400°C , and under a flow of N_2 (100 mL min^{-1}), which was maintained for 2 hours, resulting in a carbonized material (CM). The subsequent activation step was carried out using a 3: 1 (m/m) impregnation ratio of NaOH:CM . For each fraction of NaOH:CM , 10,0 mL of distilled water was added under mechanical stirring for 2 hours and then placed in the oven at 130°C for 12 hours. The dry sample was taken to the muffle at $10^{\circ}\text{C min}^{-1}$ from room temperature to 750°C , under N_2 flow ($100 \text{ cm}^3 \text{ min}^{-1}$) for 1,5 hours. After cooling, the AC-PS and the AC-TS resulting were washed with HCl (0.1 mol L^{-1}) followed by distilled water, until $\text{pH}=6,5$, to remove the residues of the activating agent and, in then dried in the oven for 4 hours at 100°C . For the characterization of the materials obtained, we used the methods Methylene Blue Index (MBI), the Iodine Number (IN), Charge Zero Point (CZP), Scanning Electron Microscopy (SEM), Fourier Transform Infrared Spectroscopy (FTIR) and Boehm's method.

2.1 Methylene Blue Index

The MBI obtained based on methodologies Mocelin [7] and Brown et al. [8]. The specific area of the ACs (SAM) was estimated from the adsorption of methylene blue and was obtained from equation 1:

$$SAM(\%) = SAM^{\circ} \times b \quad (1)$$

On what SAM° is the specific area AM ($1.93 \text{ m}^2\text{mg}^{-1}$) and b is the maximum adsorption capacity of the AM AC.

2.2 Iodine Number

The IN AC's was obtained according to ABNT MB-3410 [9].

2.3 Charge Zero Point

The CZP was determined according to the methods proposed by Regalbuto and Robles [10]. After the test, the final pH of the solution was measured [11] [12] and the final pH chart versus initial pH was plotted. CZP is assigned to the point where $\Delta\text{pH} = 0$.

2.4 Scanning Electron Microscopy

The SEM was obtained by equipment Quanta 250 (FEI Company) and was used for was to investigate the physical morphology of the obtained carbon's surfaces.

2.5 Fourier Transform Infrared Spectroscopy

The FTIR was obtained using a Boehm MB-100 spectrophotometer. About 0.2 mg of sample was mixed with KBr and pressed into tablet. FTIR spectra were recorded between 4000 and 667 cm^{-1} in resolution of 4 cm^{-1} . The analyzes were performed for both the seeds and for the AC's.

2.6 Boehm's Method

To confirm the functional groups adsorbent material evidenced in the FTIR was made Boehm titration method [13].

3. Results and discussions

According to Moreno et al. [8] the cross section of the methylene blue molecule is approximately 0.8 nm, and this is why it is more accessible to the mesoporous region. Thus, MBI can be used to estimate the mesoporosity of a ACs and based on the methodologies Mocelin [7] and Brown et al. [8] we can estimate approximate values of the specific area of the ACs. IN, according to Di Bernardo et al., [6] is related to the adsorption of molecules small weight molecular, being used as a representative index of the amount of micropores present in the AC sample [14]. Table 1 shows the results of the MBI, IN and SAM of the AC's produced.

Table 1. Surface Characterization Tests

Parameter	AC-PS	AC-TS
MBI (mg g ⁻¹)	488,45±0,73	286,20 ± 3,99
IN (mg g ⁻¹)	942,70±1,41	552,36 ± 7,70
SAM (m ² g ⁻¹)	1064,10±12,32	989,64 ± 22,78

AC-PS and AC-TS showed higher adsorptive capacities of methylene blue dye and higher estimates of specific areas compared to commercial coal found by Brum et al. [4], respectively being 232.6 mg g⁻¹ and 933.0 m² g⁻¹. Regarding the IN, both values were higher than the minimum required for marketed coals, 600 mg g⁻¹, according to the EB-2133 standard [15].

It can be observed that the adsorbents analyzed tend to be microporous, since the two ACs showed a lower MBI value and the methylene blue dye molecules are accessible to macropores. The AC-PS and AC-TS have this characteristic because according to Andas and Satar [16] in the two-stage process, which begins with carbonization, there is a great elimination of volatile material, which favors the formation of a very stable structure and the improvement of the pores when in contact with the product chemical on activation. According to them, the results are satisfactory when compared to the one-step process, as there is greater degradation of the precursor material and less elimination of volatile matter. It is worth mentioning that, although both materials have favorable characteristics as precursors of CA, a more porous material was obtained from the passion fruit seed in relation to the tamarind seed. This fact can be indicated by the high content of crude fiber in passion fruit [17], found in tamarind with low content, however, other comparative factors still need to be analyzed.

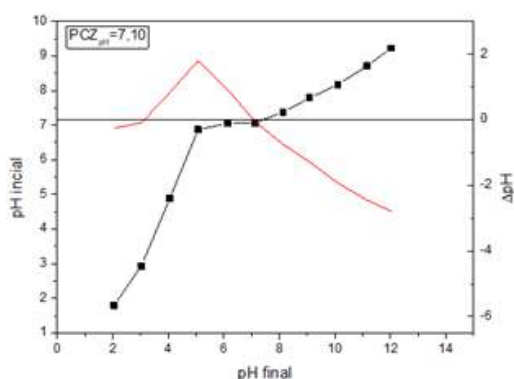


Fig. 1. CZP AC-PS.

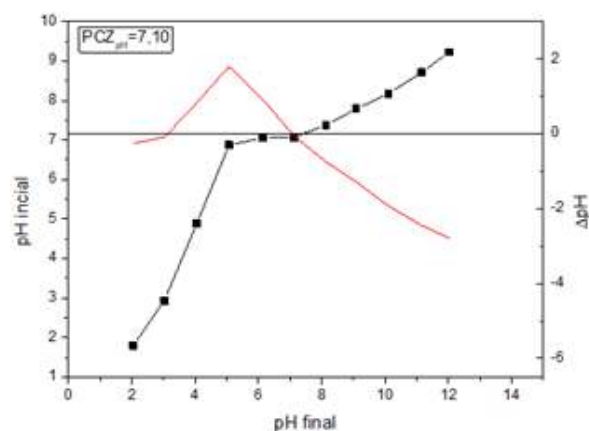


Fig. 2. CZP AC-TS.

The CZP was obtained to define the best adsorption pH, presented in Figures 1 and 2. According to the results, the value found for CA-PS is 7.10 and for AC-TS is 6.87 that values very close and similar to those found by Pezoti et al. [18] in the study of removal of amoxicillin with microporous activated carbon produced from guava seeds activated with NaOH (3:1), being 6.74.

The FTIR analysis of precursors and AC's provided qualitative information of the functional groups distributed on the surface of the adsorbent material. Thus, in both precursors we have stretches 1746cm⁻¹ (Figure 3) shown in Figure 4 as 1748cm⁻¹, assigned to C = O of carboxylic acid. Already in ACs, we have in common the 950 cm⁻¹ stretches (Figure 3) representing the 979 cm⁻¹ stretch in Figure 4, both corresponding to C-O which may be phenol, alcohol or carboxylic acid.

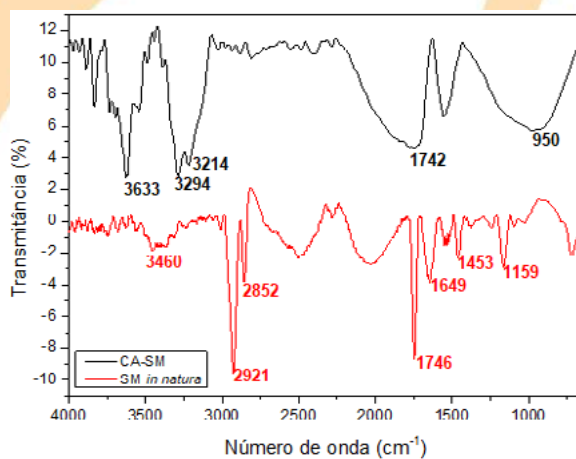


Fig. 3. FTIR PS *in nature* e AC-PS.

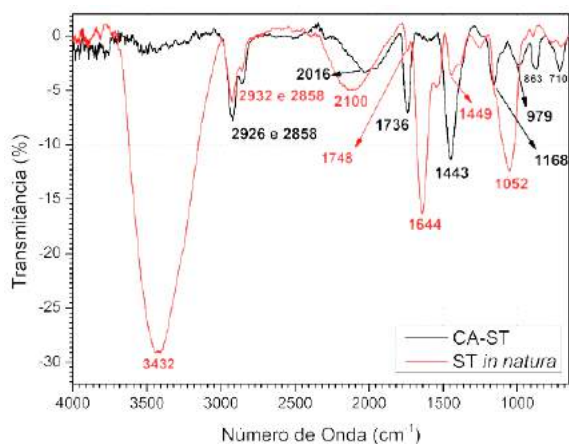


Fig. 4. FTIR TS *in natura* e AC-TS.

Through the Boehm method it was possible to confirm the basic characteristics of the surfaces of the adsorbent materials, being for AC-PS 55.65% and for AC-TS 86.73% and the presence of carboxylic acids in their structures 43.29% and 9.47%, respectively.

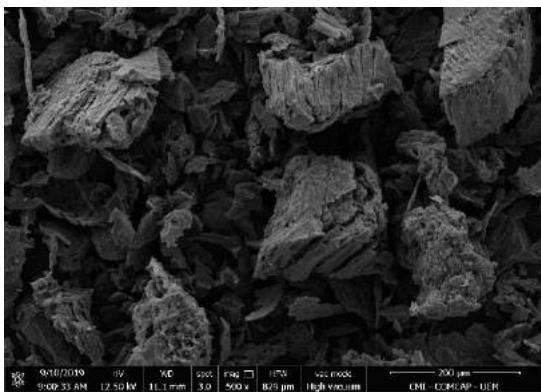


Fig. 5. SEM AC-PS.

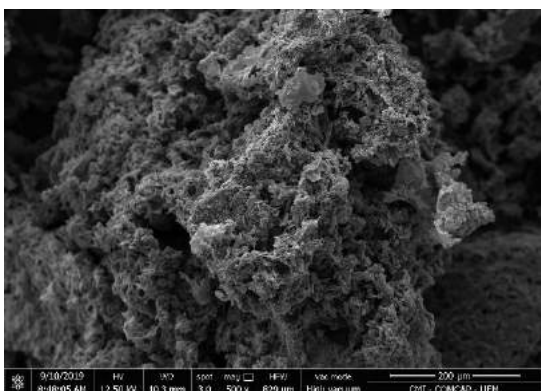


Fig. 6. SEM AC-TS.

In contrast, from Figures 5 and 6, it is possible to visualize the influence of the precursor on the pore formation of the carbonaceous material. As much as the same carbonization and activation process have been done and the same basic and functional groups characteristics have been found in the FTIR and Boehm's method, we can see equally microporous materials, which corroborates with that found in the IN, however with irregular and different surfaces due to their different precursors.

4. Conclusion

The analyzes showed that both materials have high adsorptive capacities and predominant microporous characteristics. However, AC-PS is more porous material in relation to TS, and this may be due to the high content of crude fiber found in its precursor, but more comparative studies need to be done for this to be stated. In addition, both obtained an IN higher than the minimum required for commercialization and SAMs were higher than the value found for commercial coal. With the SEM it was possible to see that, although the precursors have some similar characteristics on their surfaces (evidenced in the FTIR and confirmed by Boehm's method), the AC's from the PS and TS resulted in irregular and different surfaces with respect to each other with regard the distribution of their pores.

Acknowledgements

We appreciate the support of CAPES, UTFPR, and the advisor Prof^a Dr. Rúbia M. Suzuki for the development of the research.

References

- [1] FERRARI, Roseli Aparecida; COLUSSI, Francieli; AYUB, Ricardo Antonio. Caracterização de subprodutos da industrialização do maracujá- aproveitamento das sementes. Revista Brasileira de fruticultura, v. 26, n. 1, p. 101-102, 2004.
- [2] DE SALES, P. F.; BERTOLI, A. C.; PINTO, F. M.; MAGRIOTIS, Z. M. Produção, caracterização e aplicação do carvão ativado obtido a partir do sabugo de milho: a busca pelo reaproveitamento de um resíduo agroindustrial. Revista Virtual de Química, v. 7, n. 4, p. 1174-1188, 2015.
- [3] FERNANDES, Kendra D'Abreu Neto. Uso de carvão ativado de endocarpo de coco no tratamento de água. Pontifícia Universidade Católica do Rio Grande do Sul. Programa de Pós-Graduação em Engenharia Química,

2010. Disponível em: <http://www.pucrs.com.br>> Acesso em: 19 de março de 2018.
- [4] BRUM, Sarah Silva et al. Preparação e caracterização de carvão ativado produzido a partir de resíduos do beneficiamento do café. *Química Nova*, v. 31, n. 5, p. 1048-1052, 2008.
- [5] CUBAS, Karina Guedes. Avaliação do desempenho de carvões ativos usados na remoção de composto orgânicos de água naturais proveniente de cianobactérias e suas toxinas. Universidade Federal do Paraná. Curitiba-PR. 2010. Disponível em: <http://www.rbciamb.com.br>> Acesso em: 19 de março de 2018.
- [6] DI BERNARDO, Luiz; DANTAS, Angela di B. Métodos e técnicas de tratamento de águas. 2.ed.São Carlos:RiMa,2005.
- [7] MOCELIN, C.; Pirólise de lodo de esgoto sanitário: produção de adsorvente e óleos combustíveis. 2007. 113f. Dissertação (Mestrado em engenharia) - Departamento de pesquisa e pós-graduação, Programa de pós-graduação em engenharia mecânica e de materiais, Universidade Tecnológica Federal do Paraná, Curitiba.
- [8] MORENO, R. M.; JUNIOR, E.C. A.; FRANCO, T. T. Predição da porosidade e capacidade de adsorção em carvões ativados utilizando iodo e azul de metileno. In: VI CONGRESSO BRASILEIRO DE ENGENHARIA QUÍMICA EM INICIAÇÃO CIENTÍFICA. 2005, São Paulo.
- [9] ASSOCIAÇÃO BRASILEIRA DE NORMAS TÉCNICAS – ABNT, Carvão ativado pulverizado – Determinação do número de iodo – MB-3410. Rio de Janeiro, 1991B
- [10] REGALBUTO, J. R.; ROBLES, J. The engineering of Pt/carbon catalyst preparation. University of Illinois, Chicago, 2004.
- [11] GUILARDUCI, V. V. DA S. et al. Adsorção de fenol sobre carvão ativado em meio alcalino. *Química Nova*, v. 29, n. 6, p. 1226–1232, 2006.
- [12] MIMURA, A. M. S.; VIEIRA, T. V. A.; MARTELLI, P. B.; GORGULHO, H. F. Aplicação da casca de arroz na adsorção dos íons Cu^{2+} , Al^{3+} , Ni^{2+} e Zn^{2+} . *Química Nova*, v. 33, n. 6, p. 1279–1284, 2010.
- [13] BOEHM, H. P. Some aspects of the surface chemistry of carbon blacks and other carbons. *Carbon*, v. 32, n. 5, p. 759-769, 1994.
- [14] BRANDÃO, C.C.S.; SILVA, A.S. Remoção de cianotoxinas por adsorção em carvão ativado. In: PÁDUA, V.L. (Org.). Contribuição ao estudo da remoção de cianobactérias e microcontaminantes orgânicos por meio de técnicas de tratamento de água para consumo humano. Rio de Janeiro: ABES, 2006. p. 415-465.
- [15] ASSOCIAÇÃO BRASILEIRA DE NORMAS TÉCNICAS – ABNT, Carvão ativado pulverizado para tratamento de água – especificações: EB – 2133. Rio de Janeiro, 1991.
- [16] ANDAS, J.; SATAR, N. A. A. Synthesis and characterization of tamarind seed activated carbon using different types of activating agents: a comparison study. *Materials Today: Proceedings*, v. 5, n. 9, p. 17611-17617, 2018.
- [17] TOCCHINI, R. P. III Processamento: produtos, Caracterização e Utilização. In: Maracujá: cultura, matéria-prima e aspectos econômicos. 2. ed. Revista e ampliada. Campinas: Ital, 1994. p. 161-175.
- [18] PEZOTI, O.; CAZETTA, A. L.; BEDIN, K. C.; SOUZA, L. S.; MARTINS, A. C.; SILVA, T. L.; JÚNIOR, O. O. S.; VISENTAINER, J. V. ALMEIDA, V. C. NaOH-activated carbon of high surface area produced from guava seeds as a high-efficiency adsorbent for amoxicillin removal: kinetic, isotherm and thermodynamic studies. *Chemical Engineering Journal*, v. 288, p. 778-788, 2016.

Synthesis of Amino Silica Gel Derivative: Crystal Violet Adsorption

Rayane Carvalho Pinto^a, Aparecido Junior de Menezes^b, Kenia da Silva Freitas^a, Robson Valentim Pereira^{a,*}

^a Grupo de Eletroquímica e Polímeros Naturais – GEPN, Universidade Federal do Rio de Janeiro, campus de Macaé, Brasil

^b Universidade Federal de São Carlos, Campus Sorocaba, Sorocaba Brasil

Abstract

In this work amino silica gel was functionalized with ethoxymethylene-malononitrile. Fourier transform infrared spectroscopy confirms the introduction of cyano groups with a stretching at 2230 cm^{-1} . Elemental analysis showed that the best experimental condition to modification is 1 mmol of amino silica gel to 2 mmol malononitrile reagent (1:2) and 3 h of reaction. The adsorption capacity and remove percentage of product was evaluated to crystal violet. The maximum adsorption capacity was found at pH 9 to an initial dye concentration of 0.1 mM and a remove percentage reached about 90% at 2 g.L^{-1} of adsorbent. The amount of crystal violet adsorbed decrease with an increase of amino silica gel derivative dosage due to decrease the adsorbate to adsorbent ratio. Also, adsorption capacity and remove percentage decrease to acid solutions, probably due to the nitrogen protonation bound to vinylic group, that decrease the electron delocalization to cyano groups, decreasing the interaction to cationic dye.

Keywords: Amino silica gel; crystal violet; malononitrile

1. Introduction

Silica gels are greatly employed in chromatography techniques. Besides that, these materials have interesting characteristics for adsorption studies, such as large surface area, high chemical and thermal stability, reuse, and selectivity [1]. In last years, many silica gels have been functionalized to increase their binding capacity: monoamine modified silica particles (MAMS), silica gel Schiff base [2], silica with immobilized phosphinic acid [3], silica gel supported amidoxime [4]. Many of these materials have been used in environmental applications: dyes and heavy metals remove in aqueous systems. In this work, amino silica gel was functionalized with malononitrile group (Figure 1) and the material was employed to adsorption of crystal violet, an important textile effluent.

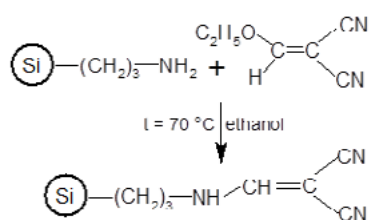


Figure 1. Chemical reaction of amino silica gel with ethoxymethylene-malononitrile.

2. Material and Methods

3-aminopropyl silica gel (200-400 Mesh) and ethoxymethylene-malononitrile (purity 98%) were purchase from Sigma Aldrich. Crystal violet (98%), NaH_2PO_4 , Na_2HPO_4 , methanol, propanone were purchase from Vetec (Brazil). All solvents and reagents were used without further purification. Dye solutions used in the adsorption studies were 0.05 and 0.1 mmol.L^{-1} . The buffer solutions were $0.05\text{M NaH}_2\text{PO}_4/\text{Na}_2\text{HPO}_4$ (from pH 5 to 9). The amino silica gel derivative was synthesized by dispersing 0.5 g of 3-aminopropyl silica gel (0.5 mmol/g of amino group) in ethanol (30 mL) at $70\text{ }^\circ\text{C}$. After that, an appropriate quantity of malonitrile reagent was added and allowed to react at different times (Table 1). The product was washed with ethanol, methanol, acetone and water in a sintered Buchner glass funnel (porosity 4), and dried at $25\text{ }^\circ\text{C}$ in a desiccator under vacuum previous use. Elemental analysis was analyzed on at CHN Perkin Elmer Series II equipment. Fourier transform infrared spectroscopy (FTIR) analysis were performed in a Shimadzu, model IR-408. For this, 1 mg of silica gel derivative was mixed with 100 mg of spectroscopy grade KBr.

Adsorption experiments were performed using Erlenmeyers flasks containing 50 mL of buffered solution. The flasks were stirred at 130 rpm and 25 °C for 24 h. The adsorption experiments were studied as a function of adsorbent dosage (5, 10, 20, 30, 50, 70, 100 mg) keeping dye concentration at 0.1 mM, initial dye concentration (0.05, and 0.1 mM) keeping adsorbent dosage at 50 mg, and solution pH (5, 7, 8, 9) keeping adsorbent dosage at 50 mg. Adsorption capacity and dye removal percentage (R%) were calculated using equations 1 and 2, respectively.

$$q_e / \text{mmol g}^{-1} = \frac{(C_i - C_e)V}{W} \quad (1)$$

$$R\% = \left(\frac{C_0 - C_e}{C_0} \right) \times 100 \quad (2)$$

Where q_e (mmol g^{-1}) is the adsorption capacity of dye on the amino silica gel derivative at equilibrium and C_i and C_e (mmol L^{-1}) are the dye solution concentrations initially and equilibrium respectively.

2. Results and Discussion

The optimization of the experimental conditions for amino silica gel functionalized was presented in table 1.

Table 1. Elemental analysis of amino silica gel functionalized as a function of malonitrile quantity and reaction time.

t (h)	Molar ratio	C(%)	H(%)	N(%)	C/N (%)
3	1:1	7.59	2.12	2.79	2.72
6	1:1	7.11	2.12	2.71	2.62
3	1:2	7.89	2.04	3.17	2.49
6	1:2	7.90	1.86	3.11	2.54

The functionalized amino silica gel shows an increase in carbon and nitrogen percentage as compared with amino silica gel (5.18% C, 2.10 % H, 1.48% N, C/N = 3.50). The best experimental condition observed in this study was 3 h of time reaction and 2 mmol of malonitrile group. In this case the experimental condition come close C/N theoretical (C/N = 2.30).

Infrared spectroscopy confirms the success of the reaction, showing a sharp peak appears at 2230 cm^{-1} (Figure 2b), corresponding to the stretching of the CN bond. The amino silica gel does not have this transition (Figure 2a), showing only characteristic bands of silica, such as stretching vibrations at 794, 1070, and 1217 cm^{-1} attributed to Si-O-Si bands. The band at 1647 cm^{-1} is assigned to the binding vibration of water molecules adsorbed on the surface of silica.

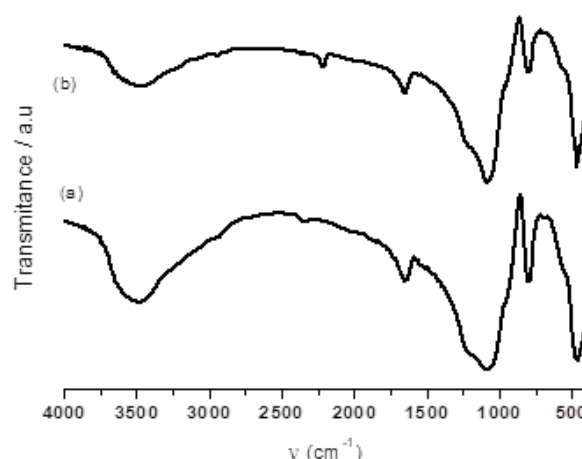


Figure 2. FTIR spectra of amino silica gel (a) and amino silica gel derivative (b).

The behavior of the crystal violet adsorption as a function of the adsorbent is showed in Figure 3.

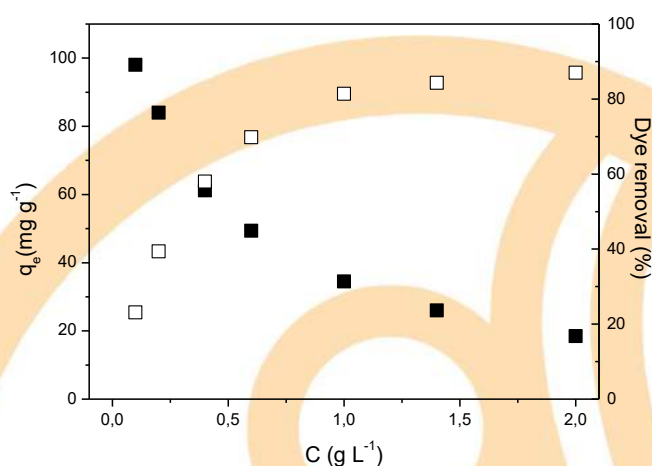


Figure 3. Effect of amino silica gel derivative dosage on dye adsorption capacity (■) and removal percentage (□). (pH 9, 0.1 mM of crystal violet, 25 °C and 130 rpm for 24 h).

The amount of crystal violet decrease with the increase of adsorbent concentration due to decrease in the adsorbate to adsorbent ratio [5]. On the other hand, the remove percentage of the dye increase reaching about 90%.



The adsorption capacity as a function of pH demonstrated a decrease in adsorption and removal percentage of dye with a decreased pH (Figure 4).

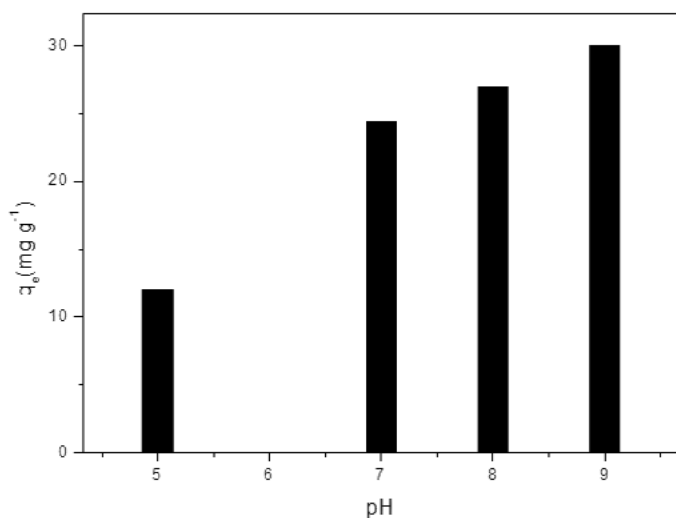


Figure 4. Effect of pH on dye adsorption capacity. ($C= 1\text{g/L}$ of adsorbent, 0.1 mM of crystal violet, $25\text{ }^\circ\text{C}$ and 130 rpm for 24 h).

The adsorption in pH values smaller than 7 decrease because the nitrogen bound to vinylic group is protonated, decreasing the delocalization of electrons to cyano group, and then reducing the electron density charge on these groups.

3. Conclusions

Amino silica gel was functionalized with vinylic groups in diferentes experimental conditions. The better condition was 1 mmol of amino silica gel to 2 mmol of ethoxymethylene-malononitrile in 3 h . The product shows adsorption capacity and removal percentage of crystal violet specially in pH 9.

Acknowledgements

The authors are grateful to Universidade Federal do Rio de Janeiro.

5. References

[1] Da'na E. Adsorption of heavy metals on funcionalized-mesoporous sílica: A review. *Microporous and medoporous materials* 2017; 247:145 – 157.

- [2] Kursunlu A N, Guler E, Dumrul H, Kocyigit O, Gubbuk I H. Chemical modification of sílica gel with synthesized new schiff base derivatives and sorption studies of cobalto (II) and nickel (II). *Applide surface Science* 2009; 255: 8798 – 8803.
- [3] Budnyak TM, Strizhak AV, Płaska AG, Dariusz S, Komarov IV, Kolody'nska D, Majdan M, Tertykh VA. Silica with immobilized phosphinic acid-derivative for uranium extraction. *Journal of Hazardous Materials* 2016; 314: 326–340.
- [4] Chen J, Qu R, Zhang Y, Sun C, Wang C, Ji C, Yin P, Chen H, Niu Y. Preparation of sílica gel supported amidoxime adsorbents for selective adsorption of Hg (II) from aqueous solution 2012; 209: 235 – 244.
- [5] Ferreira BCS, Teodoro FS, Mageste AB, Gil LF, de Freitas RP, Gurgel LVA. Application of a new carboxylate-functionalized sugarcane bagasse for adsorptive removal of crystal violet from aqueous solution: kinetic, equilibrium and thermodynamic studies. *Ind. Crop. Prod.* 65C 2015. p. 521–534.



The LaMnO₃ as adsorbent: kinetic studies and of the regeneration and reuse of adsorbent

É. V. Nascimento^a, A. M. Garrido Pedrosa^b, M. J. B. Souza^a

^aGraduate program at Chemical Engineering/PEQ/UFS, Marechal Rondon Avenue, w/n, São Cirstóvão/SE – CEP: 49100-000, Brasil.

^bChemistry Department/UFS, Marechal Rondon Avenue, w/n, São Cirstóvão/SE – CEP: 49100-000, Brasil.

Abstract

The viability of the adsorption process is often dependent on the possibility of reuse the adsorbent employed. Therefore, research should be done in order to obtain adsorbents that are regenerable and that do not lose their adsorptive capacity throughout the adsorption-regeneration cycles. In this work, LaMnO₃ mixed oxide was synthesized through the modified proteic method, using collagen as a chelating agent and a calcination process at 700°C/2h. This oxide was used as an adsorbent in the removal of *Bezaktiv Blue S-Matrix* dye in batch process. Previous studies have shown that LaMnO₃ has zero charge point around neutrality. The oxide was characterized using XRD and FTIR techniques. A material with a perovskite structure and an average crystallite size of 26 nm was obtained. The FTIR indicated that the adsorption process is not destructive to the structure of the adsorbent. The kinetic study performed indicated a kinetics following the pseudo second order model (PSO). The adsorption process occurs through electrostatic interactions between the adsorbate and the adsorbent. LaMnO₃ loaded with dye was thermally regenerated and reused five more times, without losing its adsorptive capacity.

Keywords: LaMnO₃; adsorbent; regeneration; reuse.

1. Introduction

The discharges of industrial wastewater containing dyes cause serious environmental problems because of its high toxicity and possible accumulation in the environment. The presence of dyes in water, even very low concentrations, reduces light penetration through the water surface, precluding photosynthesis of the aqueous flora. Therefore, their removal from wastewater is environmentally important [1].

The adsorption technique is a viable alternative, because it presents low initial cost, simplicity of design, easy operation and non-toxicity of the adsorbents used [2]. However, the process viability depends on the possibility of reuse the adsorbent employed. Therefore, research should be done in order to obtain adsorbents that are regenerable and do not lose their adsorptive capacity throughout the adsorption-regeneration cycles.

Mixed oxides with perovskite structure are a class of materials with diverse properties and considerable multifunctionality. The most numerous and interesting compounds of this type of material have the general formula ABO₃, where

A-site is usually occupied by a rare earth metal and B-site by a metal from the external transition block [3]. In recent years, a new potentiality has been studied for these oxides, their adsorptive capacity in the liquid phase. Due to their structure, these materials are expected to interact electronically with the dye molecules. In addition, its cohesive crystalline structure allows the application of high temperatures in thermal regeneration without damage to its structure.

Therefore, the objective of this work is to synthesize LaMnO₃ oxide with perovskite structure through the modified proteic method, characterize it using the techniques of X-ray Diffractometry (XRD) and Fourier Transform Infrared Spectroscopy (FTIR) and, then, evaluate its adsorptive potential in the removal of *Bezaktiv Blue S-Matrix* dye. Finally, the regeneration of the adsorbent and its effect on the adsorptive capacity in several reuse cycles was studied.

2. Materials and Methods

2.1. Synthesis of LaMnO_3 (adsorbent)

The LaMnO_3 was synthesized through the modified proteic method. Initially, manganese nitrate ($\text{Mn}(\text{NO}_3)_2 \cdot 4\text{H}_2\text{O}$ – Neon (98.8%)) was dissolved in 200 ml of distilled water at 25°C, under stirring, for five minutes. Then, lanthanum nitrate was added ($\text{La}(\text{NO}_3)_3 \cdot 6\text{H}_2\text{O}$ – Dinâmica (95%)) to the system and left it stirring for another five minutes. Soon afterwards, the system temperature was raised to 70°C to then add, slowly, the collagen (structure complexing agent). This done, the system was kept under agitation for another thirty minutes. The solution obtained was then concentrated in an oven at 120°C for two hours and then pre-calcined in a muffle furnace, under the following heating schedule: from 30°C to 120°C, remaining thirty minutes; from 120°C to 250°C, remaining thirty minutes; from 250°C to 350°C, remaining for one hour. This procedure was performed under a heating rate of 5°C/min. A material with a brittle consistency was obtained, which was crushed and then calcined at 700°C for two hours, under a heating rate of 10°C/min. A fine powder with dark coloring was obtained.

2.2. Characterization of LaMnO_3

X-ray diffractogram (XRD) was performed under radiation $\text{Cu-K}\alpha$ ($\lambda = 0.15406$ nm), with scanning step of 0.026° and scanning angle between 20° and 60°. The crystallite size was calculated using the Scherrer Equation, taking the average value obtained for the three highest intensity peaks. FTIR analyses were obtained in the wave number range between 4000-400 cm^{-1} , using the KBr pellet method.

2.3. Adsorption tests

The adsorption tests were carried out in batch mode, single stage, in which the kinetics of removal of the dye dissolved in distilled water with an initial concentration of 10 ppm (mg/L) was evaluated. Before the experiments, the adsorbent was dried in an oven at 80°C for thirty minutes. In erlenmeyer flasks, 20 mg of the adsorbent were contacted with 20 ml of the dye solution, under stirring and at room temperature (23°C). Dye removal was evaluated at the following times: 10, 20, 30, 40, 50, 60, 70, 80 and 90 minutes.

At the end of each time, the adsorbents loaded with dye were removed by filtration. The solution was analyzed and its absorbance was measured using a UV-visible spectrophotometer at a wavelength $\lambda = 601$ nm, referring to the maximum absorbance of the dye.

Previous studies have shown that the best results are obtained at acidic pH. Therefore, the experiments were carried out in triplicate with the solution at an initial pH adjusted to 3.

The solution concentration was calculated using Equation (1). The *amount of dye adsorbed by the adsorbent* was calculated using Equation (2). The *removal efficiency* was calculated using Equation (3).

$$C = C_0 \left(\frac{A}{A_0} \right) \quad (1)$$

$$q = \frac{(C_0 - C)V}{m} \quad (2)$$

$$E(\%) = \left(\frac{C_0 - C}{C_0} \right) \times 100\% \quad (3)$$

Where “C” represents the *dye concentration in the solution* (mg/L), “A” the *absorbance*, “V” the *solution volume* (L), “m” the *adsorbent mass* (g) and “q” the *amount of dye adsorbed by the adsorbent* (mg/g). The sub-index zero represents the values for zero time, in the absence of the adsorbent.

Preliminary studies were carried out to obtain the analytical curve, to determine the most suitable pH for the adsorption studies and to verify whether the aqueous solution of the dye with pH adjustable to the best pH is photostable during the time and conditions of the experiment. In addition, the zero charge point of the adsorbent was determined.

2.4. Regeneration and reuse study

After the adsorption tests, the adsorbent loaded with the dye was regenerated by heating to 700°C (under the same calcination condition used in the adsorbent synthesis) in order to decompose the adsorbed dye and recover the adsorbent.

Then, the regenerated adsorbent was reused five times, using consecutive masses of 100, 80, 60, 40 and 20 mg. The reuses were carried out under the same conditions as the adsorption tests, but only for the time of 90 minutes.

3. Results and discussion

3.1. Preliminary studies

Preliminary studies have shown that the adsorbent zero charge point of the adsorbent is equal to 7.5, around the neutrality. These studies indicated that the best removal percentages are obtained at acidic pH (pH = 3), suggesting that the dye is anionic. In addition, it was found that the dye solution is photostable during the experiment time and conditions.

3.2. Structural characterization

The X-ray diffractogram of calcined LaMnO_3 is exposed in Figure 1. The confirmation of obtaining the LaMnO_3 phase with a perovskite structure was made by comparing the XRD obtained with the standard crystallographic chart ICSD n° 82226 and with the diffractograms presented in the works in the Table 1, except for [4].

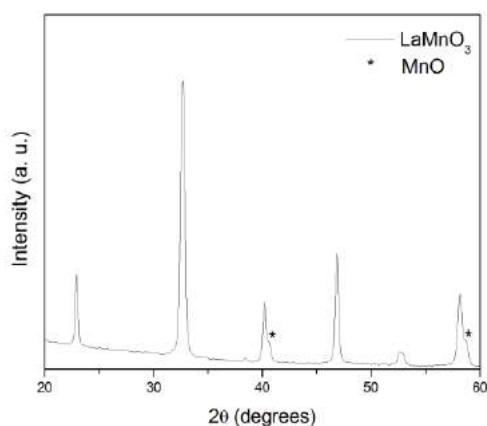


Fig. 1. X-ray diffractogram of LaMnO_3 .

In addition to the perovskite phase, a small relative amount of manganese oxide II (ICSD n° 643195) was also obtained as a secondary phase. This oxide was probably generated by the excess of the manganese reagent which, at high calcination temperature and in contact with oxygen in the common atmosphere, was converted to manganese oxide II.

Table 1 shows a comparative between the crystallographic data of this work and other works that synthesized the same material. The most common structures are orthorhombic and rhombohedral, as seen in the other work present in the table. Regarding the crystallite size, the obtained value is in agreement with the other

studies and classifies the synthesized material as nanometric. Although they are materials that usually has few pores and have a low specific surface area and performance dependent on electron exchanges and/or surface interactions [11], smaller crystallite sizes are expected to increase the specific surface area and improve the material adsorptive capacity.

Comparing the synthesis methods, it is evaluated that the method employed in this work is effective, as it produces nanocrystalline perovskites with relatively small crystal size through milder calcination conditions (lower temperature and/or time) and employing a cheaper chelating agent, collagen.

Table 1. Characteristics of LaMnO_3 material and conditions for obtaining it for some works.

Synthesis method	Calc. condition	Structure	Crystal size (nm)	Ref.
MP	700°C/2h	O	26.0	This work
MP	700°C/2h	O	-	[4]
CSG	750°C/3h	O	25.6	[5]
CSG	700°C/5h	R	23.4	[6]
CSG	650°C/9h	R	28.0	[7]
CSG	700°C/5h	R	23.4	[8]
SSR	800°C/2h	R	29.0	[9]
AC	600°C/5h	O	30.0	[10]

Orthorhombic - O; Rhombohedral- R; Modified proteic - MP; Citrate sol-gel - CSG; Solid state reaction - SSR; Auto combustion - AC

Figure 2 shows the FTIR spectra for the dye (A), the adsorbent before adsorption (B) and after adsorption (C). Not much information is available in the literature about the structure of the *Bezaktiv Blue S-Matrix* dye. Rodrigues [12] studied the removal of this same dye on chitosan and characterized it using the techniques of XRD, XRF and FTIR. For the FTIR, the author assigned three bands: the first around 3447 cm^{-1} , related to the stretching of the O-H bond, probably present due to the physically adsorbed water, the second between 1551 cm^{-1} and 1508 cm^{-1} , referring to the symmetrical stretching of the C=N bond and the third around 1394 cm^{-1} , referring to the symmetrical stretching of the C=N group present in the aromatic ring.

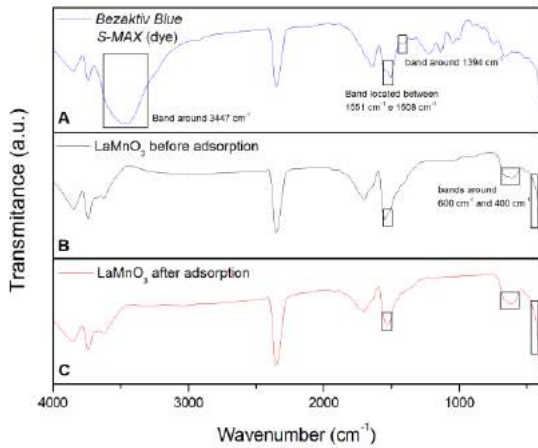


Fig. 2. FTIR of dye (A), LaMnO₃ before adsorption (B) and LaMnO₃ after adsorption (C).

The spectra of LaMnO₃ oxide before and after adsorption (B and C, respectively) show bands around 600 cm⁻¹ and 400 cm⁻¹, characteristics of the metal-oxygen bonds present in the perovskite structure [10, 13]. In addition, these bands maintained their position and intensity, indicating that the oxide maintained its structure after the adsorption process. This fact also suggests that the adsorption did not occur through strong interactions, but through weak interactions. Therefore, it is implied that a regeneration process that can remove/decompose the adsorbate without destroying the adsorbent structure will maintain the adsorptive capacity of perovskite.

The only evidence that the adsorbent is loaded with dye is in the slight elongation of the band located between 1551 cm⁻¹ and 1508 cm⁻¹. The probable explanation for the absence of the characteristic bands of the dye in the spectrum of the adsorbent loaded with it is due to the low concentration of the dye solution employed, resulting in a small absolute amount of adsorbed dye.

3.3. Adsorption tests

With the adsorption tests, the adsorption kinetic curves were obtained. Typically, the adsorption process occurs in three stages. In the first, there is the external mass transfer of the adsorbate present in the bulk solution to the external surface of the adsorbent, followed by the internal diffusion of the adsorbate to the adsorptive sites and finally the adsorption on the sites. Some kinetic models are based on the fact that adsorption is the limiting

step of the process, while others assume that diffusion is the rate limiting step [14].

The mixed oxide with perovskite structure generally does not have pores in their structure and have a low specific surface area due to the high temperatures applied in the synthesis processes. Therefore, these oxides have a better catalytic behavior in reactions or processes that involve the electrons transfer and/or surface interactions [11]. An analogy can be made to their behavior as an adsorbent.

In this work, the kinetic data were evaluated according to the kinetic models of pseudo-first order (PFO) [15] and pseudo-second order (PSO) [16]. The respective model equations are shown in Equations (4) and (5).

$$q = q_e (1 - e^{-k_1 t}) \quad (4)$$

$$q = \frac{t}{\frac{1}{k_2 q_e^2} + \frac{t}{q_e}} \quad (5)$$

Where q (mg/g) and q_e (mg/g) are the *adsorption capacities* (or *concentration in the adsorbent*) at a time “ t ” in equilibrium, respectively, and k_1 (min⁻¹) and k_2 (g/mg.min) are the *adsorption rate constants of pseudo-first and pseudo-second order*, respectively. Figure 3 shows the nonlinear regression curves obtained and in Table 2 are the estimated values for the parameters.

The LaMnO₃ oxide with perovskite structure showed excellent behavior in the process, as it reached equilibrium quickly (from 10 minutes onwards, the percentage increases are very small), and removed 92% of the dye. Evaluating the values of the *correlation coefficients squared* (R^2) and *Person's qhi-square* (χ^2), it is concluded that the PSO model is the one that best describes the process kinetics. However, the PPO model also provides reliable results.

Table 2. Estimated parameters in non-linear adjustment.

PFO	PSO
$q_e = 8.9527 \pm 0.0416$ mg/g	$q_e = 9.0457 \pm 0.0487$ mg/g
$k_1 = 0.3625 \pm 0.0521$ min ⁻¹	$k_2 = 0.2554 \pm 0.0820$ mg.s ⁻¹ .min ⁻¹
$R^2 = 0.9985$	$R^2 = 0.9990$
$\chi^2 = 0.0136$	$\chi^2 = 0.0085$

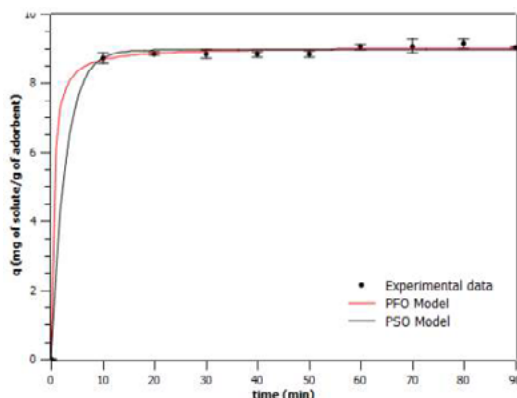


Fig. 3. Non-linear adjustment of experimental data to PFO and PSO models.

The PSO model was formulated considering that the limiting step of the process is an adsorption mechanism [17], which may be a chemisorption, in which electron exchange or sharing occurs between the adsorbent and the adsorbate [16]. Therefore the result is physically based, after all, the process involving oxides with perovskites structure occur through electron transfer and/or surface interactions [11], with the electrostatic attraction between the dye molecules and the adsorbent surface being the predominant mechanism [18].

Table 3. Comparative use of LaMnO_3 as adsorbent.

Synthesis method	Dye	Initial conc.	Eq. time	E(%)	Ref.
MP	BB	10 ppm	90 min	92%	This work
MP	CR	50 ppm	120 min	63%	[4]
AC	MB	25 ppm	240 min	43%	[10]
AC	MO	25 ppm	240 min	9%	[10]

BB - Bezaktiv Blue; CR - Congo Red; MB - Methylene Blue; MO – Methyl orange; Modified proteic - MP; Auto combustion - AC

Table 3 shows a comparative table between the studies that used LaMnO_3 as an adsorbent. The adsorbent synthesized in this work showed a higher removal efficiency percentage in a shorter batch time. However, it is emphasized that the concentration employed is lower, which limits the comparison. In addition, since they are different dyes, the adsorbate-adsorbent interaction must be favorable to the BB dye. A better comparison between the adsorbents would be possible with the parameter of the *maximum adsorption capacity* (q_{\max}), obtained through the adsorption equilibrium

study. Even so, the chosen synthesis method proved to be effective because it produced a material with high adsorptive capacity under mild synthesis conditions and with a cheaper chelating agent.

Figure 4 shows the removal percentages for each of the five adsorption-regeneration cycles. The results indicate that the regeneration method employed was successful. The increase in removal percentages along the reuses is due to the presence of more adsorptive sites in contact with the dye (greater mass of adsorbent).

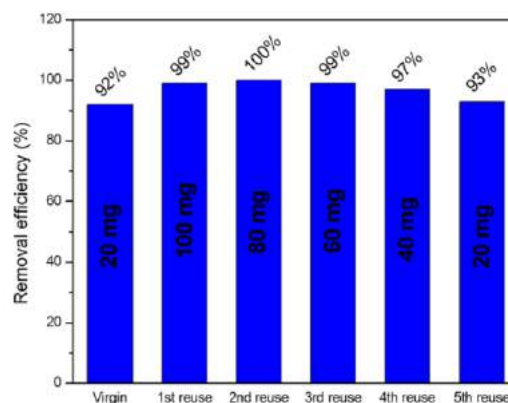


Fig. 4. Removal efficiency for each reuse of adsorbent LaMnO_3 .

Comparing the use of virgin adsorbent with the fifth reuse, both employing the same mass, it is noticed that there was practically no change in the adsorptive capacity, indicating that the adsorbent was regenerated and, mainly, maintained its adsorptive capacity throughout the cycles.

Occasionally, the regeneration process may have recrystallized the perovskite structure, after all, it is the same calcination temperature. However, the results shown that this fact, if it happened, did not change the adsorptive capacity and practically maintained the original matrix of the oxide structure.

Hashemian e Foroghmoqhadam [19] regenerated and reused the ilmenite oxides (not perovskite) CoTiO_3 and CuTiO_3 loaded with CR by the same method of this work, but at $300^\circ\text{C}/1\text{h}$. The oxides practically maintained their adsorptive capacity for five cycles, with a low decrease until the eighth cycle, the last one.

4. Conclusions

The results show that the synthesis was successful, indicating the obtaining of a LaMnO_3 nanocrystalline material with perovskite structure and with an average crystallite size of 26 nm. The comparison with other works that synthesized the same material shows that the method achieves excellent results using a cheaper chelating agent and a condition of softer synthesis. FTIR spectra showed that the adsorption process does not damage the adsorbent structure. The zero charge point of the adsorbent is around the neutrality.

The kinetic study of adsorption indicates that the PSO model is the one that best represents the process, indicating that the adsorption step on the sites is the slowest. The process occurs through electrostatic interactions between the adsorbent and the adsorbate. The adsorbent removed 92% of the dye in ninety minutes of contact, proving to be as effective as other oxides used as adsorbents. The regeneration process was able to eliminate the adsorbate and not decrease the adsorptive capacity of adsorbent over five cycles of adsorption-regeneration.

Acknowledgements

The authors are grateful at Conselho Nacional de Desenvolvimento Científico e Tecnológico (CNPq). This study was financed in part by the Coordenação de Aperfeiçoamento de Pessoal de Nível Superior - Brasil (CAPES) – Finance Code 001.

References

- [1] Konicki W, Sibera, D, Mijowska, E, Lenzion-Bielun Z, Narkiewicz U. Equilibrium and kinetic studies on acid dye Acid Red 88 adsorption by magnetic ZnFe_2O_4 spinel ferrite nanoparticles. *J. Colloid Interface Sci.* 2013; 398;152-160.
- [2] Ghaedi M, Sadeghian B, AmiriPebdaniA, Sahraei R, DaneshfarA, Duran C. Kinetics, thermodynamics and equilibrium evaluation of direct yellow 12 removal by adsorption onto silver nanoparticles loaded activated carbon. *Chem. Eng. J.* 2012; 187;133-141.
- [3] Tanaka H, Misono M. Advances in designing perovskite catalysts. *Curr. Opin. SolidState Mat. Sci.* 2001;5;381-7.
- [4] Santos AG, Leite JO, Souza MJB, Gimenez IF, Garrido Pedrosa AM. Effect of the metal type in perovskites prepared by modified proteic method in dye adsorption from aqueous medium. *Ceram. Int.* 2018;44;5743-50.
- [5] Ran R, Wu X, Weng D, Fan J. Oxygen storage capacity and structural properties of Ni-doped LaMnO_3 perovskites. *J. Alloy. Compd.* 2013;577;288-94.
- [6] Chen J, Shen M, Wang X, Qi G, Wang J, Li W. The influence of nonstoichiometry on LaMnO_3 perovskite for catalytic NO oxidation. *Appl. Catal. B-Environ.* 2013;134-135;251-7
- [7] Sanaeishoar T, Tavakkoli H, Mohave F. A facile and eco-friendly synthesis of imidazo[1,2-a]pyridines using nano-sized LaMnO_3 perovskite-type oxide as an efficient catalyst under solvent-free conditions. *Appl. Catal. A-Gen.* 2014;470;56-62.
- [8] Shen M, Zhao Z, Chen J, Su Y, Wang J, Wang X. Effects of calcium substitute in LaMnO_3 perovskites for NO catalytic oxidation. *J. Rare Earths.* 2013;31(2);119-23.
- [9] Wenwei W, Jinchao C, Xuehang W, Sen L, Kaituo W, Lin T. Nanocrystalline LaMnO_3 preparation and kinetics of crystallization process. *Adv. Powder Technol.* 2013;24;154-9.
- [10] Farhadi S, Mahmoudi F, Amini MM, Dusek M, Jarosova M. Synthesis and characterization of a series of novel perovskite-type LaMnO_3 /Keggin-type polyoxometalate hybrid nanomaterials for fast and selective removal of cationic dyes from aqueous solution. *Dalton Trans.* 2017;46;3252-64.
- [11] Zhu J, Li H, Zhong L, Xiao P, Xu X, Yang X, Zhao Z, Li J. Perovskite oxides: Preparation, characterization and applications in heterogeneous catalysis. *ACS Catal.* 2014;4;2917-40.
- [12] Rodrigues PAS. Quitosana como adsorvente para remoção de cor em solução aquosa de corante reativo.85 p. Dissertação (Mestrado em Ciência e Engenharia de Materiais) – Programa de Pós-Graduação em Ciência e Engenharia de Materiais – UFRN. 2016.
- [13] Nakamoto K. Infrared and Raman spectra of Inorganic and coordination compounds. 3rd ed. NewYork: Jonh Wiley and sons; 1977.
- [14] Largitte L, Pasquier R. A review of the kinetics adsorption models and their application to the adsorption of lead by an activated carbon. *Chem. Eng. Res. Des.* 2016;109;495-504.
- [15] Febrianto J, Kosasih AN, Sunarso J, Ju Y, Indraswati N, Ismadji S. Equilibrium and kinetic studies in adsorption of heavy metals using biosorbent: A summary of recent studies. *J. Hazard. Mater.* 2009;162;616-45.
- [16] Ho YS, Mckay G. Pseudo-second order model for sorption processes. *Process Biochem.* 1999;34;451-65.
- [17] Aksu Z, Tezer S. Equilibrium and kinetic modeling of biosorption of Remazol Black B by *Rhizopusarrhizus* in a batch system: effect of temperature. *Process Biochem.* 2000;36;431-9.
- [18] Al-Degs YS, El-Barghouthi MI, El-Sheikh AH, Walker GM. Effect of solution pH, ionic strength, and temperature on adsorption behavior of reactive dyes on activated carbon. *Dyes Pigment.* 2008;77;16-23.
- [19] Hashemian S, Foroghmoqhadam A. Effect of copper doping on CoTiO_3 ilmenite type nanoparticles for removal of congo red from aqueous solution. *Chem. Eng. J.* 2014;235;299-306.



Study of catalytic pyrolysis of low-density polyethylene (LDPE) on HY zeolite containing niobium

A. V. Anjos^a, A. M. Garrido Pedrosa^b, A. O. S. Silva^c, M. J. B. Souza^a

^a Graduate Program in Chemical Engineering, Federal University of Sergipe, São Cristóvão, 49.100 000, Sergipe, Brazil

^b Department of Chemistry, Federal University of Sergipe, São Cristóvão, 49.100 000, Sergipe, Brazil

^c Department of Chemical Engineering, Federal University of Alagoas, Maceió, 57.072 970, Alagoas, Brazil

Abstract

Plastic waste has been a major problem for humanity over the years. Once used, plastics are transformed into waste causing serious environmental problems. In order to avoid an amplification of the problem, catalytic pyrolysis has become a very attractive process in relation to the chemical treatment of these types of materials, thus promoting processes that demand lower energy costs and with greater selectivity in products with high added value, as well as, in reducing the operational limitations of thermal pyrolysis. Thus, in this research work heterogeneous microporous acid catalysts impregnated with different ratios of calcined niobium oxide (10% Nb₂O₅/HY and 20% Nb₂O₅/HY) were developed. The obtained catalysts were characterized by X-ray diffraction (XRD). Through this characterization technique, we aim to develop a series of catalysts with characteristics suitable for pyrolysis application. The thermal and catalytic pyrolysis reactions were carried out at different heating rates (5, 10 and 20°C min⁻¹), using low density polyethylene (LDPE), where an evaluation and analysis of the conversion curves were carried out. For the polymer degradation process, the initial and final degradation temperatures, respectively, were 311 and 476 for the heating rate of 5°C min⁻¹, 338 and 487 for the heating rate of 10°C min⁻¹, and 373 and 513 for the heating rate of 20°C min⁻¹.

Keywords: Pyrolysis; Zeolite HY; Nb₂O₅; Low Density Polyethylene (LDPE).

1. Introduction

Plastics have replaced or acted in conjunction with glass, metals, rubber, wood and inorganic substances, and thus make fundamental contributions to our society. They are widely used in everyday applications, such as packaging, containers, toy industry, electronics industry, among others. Its cost-benefit ratio and ease of applicability increased its consumption, and consequently, the amount of waste, which is a serious concern for the environment [1].

There are different types of plastics, they have a variety of characteristics and properties, which assists in countless applications of these materials. Approximately half of the global plastic production is composed of polyolefins, including 40% polyethylene (PE) (subdivided into linear low density polyethylene - LLDPE, low-density polyethylene - LDPE and high-density polyethylene - HDPE), followed by polypropylene (PP) responsible for 20% of global plastics production and consumption, followed by poly(vinyl chloride) (PVC) with 13%. Engineering thermoplastics and mixtures represent 9% [2].

Landfills are the most common method of processing solid urban waste. However, plastic waste does not decompose like organic waste,

remaining in landfills for hundreds of years. Incineration has been used as a substitute for the landfill for the disposal of plastic waste, where burning is carried out in a controlled environment to extract chemical energy in the form of heat and then use it to generate electricity. However, in addition to the high cost of building a facility, the generation of harmful pollutants during the incineration process is still the main limitation of this method [3]. The chemical recovery of polyolefins, using methods such as pyrolysis, is a potentially interesting alternative to deal with these plastic residues [4]. In addition to providing a solution to a disposal problem, this process also preserves valuable petroleum resources by recycling carbon materials that have been placed in the polymers.

Pyrolysis is the process of cracking polymers at high temperatures in an inert medium and under vacuum, using reducing and oxidizing agents, with or without the aid of a catalyst. During the breaking process, polymer chains break and new molecules are produced [5]. As most of these generated molecules have characteristics of free radicals, they are transformed into gaseous, liquid and solid products, undergoing a series of reactions among themselves. During the pyrolysis of PE waste, for example, at 480°C, the total production of gas and



liquid reaches 65% [6]. HDPE waste plastics can produce 52% gas and 35% liquid product at 500°C [7]. Another study of LDPE catalytic pyrolysis reported that pyrolysis can produce about 70% gas at 350°C [8]. Several studies have demonstrated the feasibility of using this process in the main plastic waste recycling industries [9,10].

Polyethylene can be converted into hydrocarbons by thermal or catalytic degradation for use as a raw material for the chemical industry or as fuels. However, comparing thermal degradation, in the absence of a catalyst, with a catalytic one, we will notice that the thermal process occurs at relatively high reaction temperatures [11]. On the other hand, catalytic degradation allows the plastic cracks to proceed at much lower temperatures, thus reducing energy consumption, which can also lead to better control of yield and product distribution [12,13]. With this reaction, several catalysts were tried and different studies on the subject have been published, showing that, among the various catalysts, the selectivity of the products differs greatly in terms of temperature and reaction time of the process [14,15].

Therefore, this work has as main objective to study the efficiency of microporous acid catalysts (zeolite HY) containing niobium oxide (Nb_2O_5) for the catalytic pyrolysis of LDPE.

2. Experimental Section

2.1. Synthesis of HY zeolite

The zeolite Y used in the work was obtained from its sodium form (commercial NaY, Sigma Aldrich). The HY zeolite was synthesized by the ion exchange method [16].

2.2. Incorporation of Nb_2O_5 in HY zeolite

Nb_2O_5 was obtained from hydrated commercial niobium oxide (CBMM - Companhia Brasileira de Metalurgia e Mineração), and underwent a calcination process at 300°C in a Mufla oven (Quimis®) with a heating rate of 10°C min⁻¹ for 2 hours, obtaining the material $\text{Nb}_2\text{O}_5\text{-C}$ (calcined). $\text{Nb}_2\text{O}_5\text{-C}$ was incorporated into HY zeolite through the mechanosynthesis process [17]. Multifunctional catalysts 10% $\text{Nb}_2\text{O}_5\text{/HY}$ and 20% $\text{Nb}_2\text{O}_5\text{/HY}$ were also obtained via

mechanosynthesis, starting from the individual materials previously prepared (HY and $\text{Nb}_2\text{O}_5\text{-C}$), with uniform homogenization for 5 minutes. The working materials obtained (HY, $\text{Nb}_2\text{O}_5\text{-C}$, 10% $\text{Nb}_2\text{O}_5\text{/HY}$ and 20% $\text{Nb}_2\text{O}_5\text{/HY}$) were subjected to characterization test and catalytic pyrolysis tests.

2.3. Characterization of catalysts

The XRD analysis of the HY, $\text{Nb}_2\text{O}_5\text{-C}$ and $\text{Nb}_2\text{O}_5\text{/HY}$ catalysts in the different proportions were obtained by the powder method in a PANalytical Empyrean TCU 1000N diffractometer with $\text{Cu K}\alpha$ (1.5418 Å) radiation source, voltage 40 kV, current 40 mA, step 0.026° and scanning speed of 2° min⁻¹. For the catalysts, an angular range of (2 θ) was used from 5 to 55°. The diffractograms obtained were used for identification of the crystalline structure of the materials and identify the presence of contaminant phases by comparison with literature data [18].

2.4. LDPE thermal and catalysis

The LDPE thermal and catalytic pyrolysis tests were performed on a thermal analysis equipment TG/DTG from Shimadzu model DTG-60H, under an inert and dynamic N_2 atmosphere, with a flow of 50 mL min⁻¹, at heating rates of 5, 10 and 20°C min⁻¹. The LDPE sample used in this work was obtained commercially from Sigma Aldrich in powder form. The thermogravimetric curves were obtained by heating the pure LDPE (thermal pyrolysis) and the LDPE mixed with the catalysts (HY, $\text{Nb}_2\text{O}_5\text{-C}$, 10% $\text{Nb}_2\text{O}_5\text{/HY}$ and 20% $\text{Nb}_2\text{O}_5\text{/HY}$, catalytic pyrolysis) via the mechanosynthesis process, in a weights ratio of 80% of the polymer and 20% of the catalysts. The studies were carried out in the temperature range of 30 to 900°C, using approximately 10 mg of sample for each test.

3. Results and discussion

3.1. Characterization of catalysts

Fig. 1 shows the X-ray diffractogram for the HY zeolite obtained in the present study. The structure shown in the diffractogram is similar to zeolite taken as a comparison standard [18]. Well-defined and narrow peaks are observed indicating

that zeolite is characterized by high crystallinity and purity. Comparing all reflections of the diffractogram of the HY zeolite with a standard 73-2310 file from the database of the Joint Committee for Powder Diffraction Studies - International Center for Diffraction Data (JCPDS - ICDD), and with data from the literature [17,19], it can be seen that the sample is formed by a material with a faujasite type structure. This diffractogram shows intense diffraction peaks at angles $2\theta = 6.23; 10.15; 11.91; 15.67; 18.69; 20.38; 22.82; 23.67; 25.82; 27.08; 29.66; 30.79; 31.42; 32.48; 34.13$ and 37.97° , indexed to their respective crystallographic plans in relation to the Faujasite structure [18].

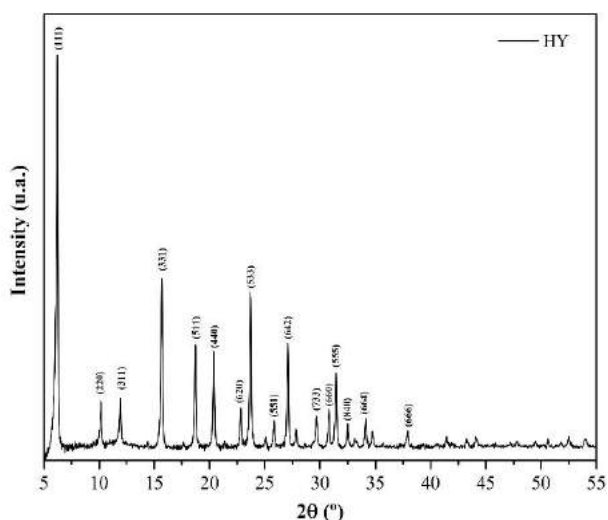


Fig. 1. X-ray diffractogram of HY zeolite.

Fig. 2 shows the diffractograms of calcined Nb_2O_5 and $\text{Nb}_2\text{O}_5/\text{HY}$ catalysts in both proportions (10% $\text{Nb}_2\text{O}_5/\text{HY}$ and 20% $\text{Nb}_2\text{O}_5/\text{HY}$). It is observed that no crystalline peak was formed in the diffractogram of the Nb_2O_5 calcined at 300°C , showing a totally amorphous structure, as reported in the literature [20].

The diffractograms of the 10% $\text{Nb}_2\text{O}_5/\text{HY}$ and 20% $\text{Nb}_2\text{O}_5/\text{HY}$ catalysts showed diffraction peaks characteristic of the HY zeolite (Fig. 1), thus confirming that after the mechanosynthesis process, the zeolite structure in the catalyst was maintained. In parallel, no XRD pattern related to any Nb_2O_5 species was observed for the current $\text{Nb}_2\text{O}_5/\text{HY}$ catalysts, suggesting a high dispersion of this oxide over the zeolite structure, regardless of the niobium oxide load [21].

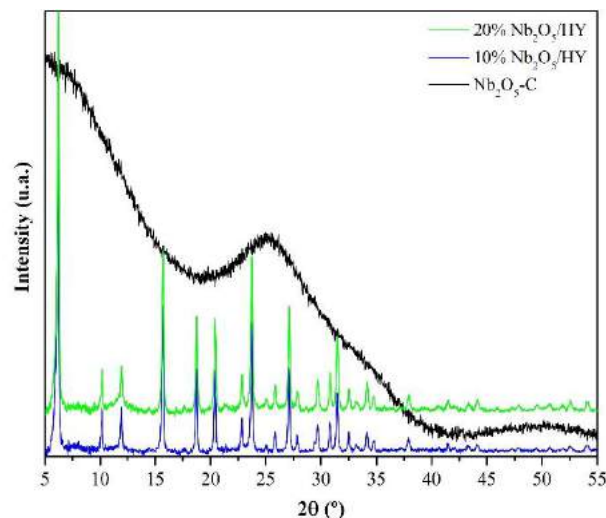
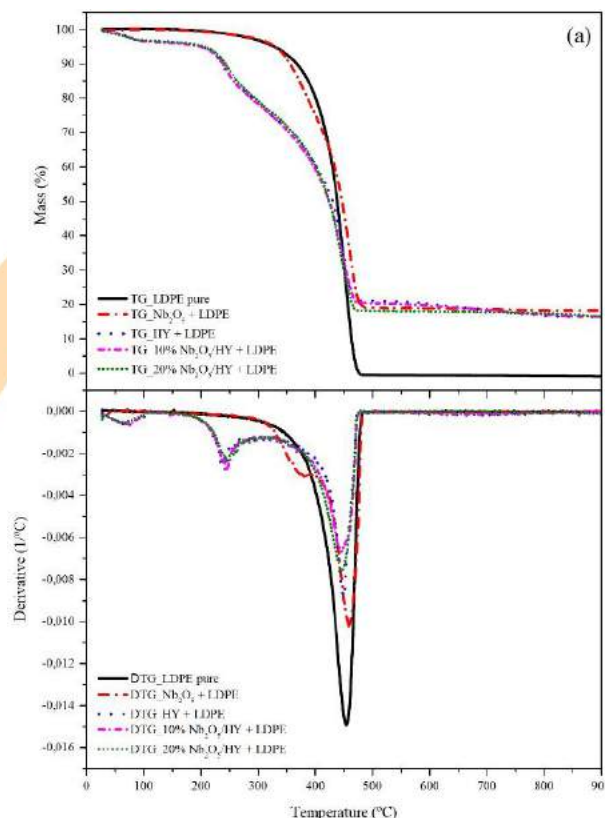


Fig. 2. X-ray diffractogram of samples synthesized from calcined Nb_2O_5 and $\text{Nb}_2\text{O}_5/\text{HY}$ in different proportions.

3.2. LDPE thermal and catalytic pyrolysis

Figure 3 shows the TG/DTG curves for the thermal degradation of pure LDPE and catalytic pyrolysis using the synthesized samples, with heating rates of (a) 5, (b) 10 and (c) $20^\circ\text{C min}^{-1}$, respectively.



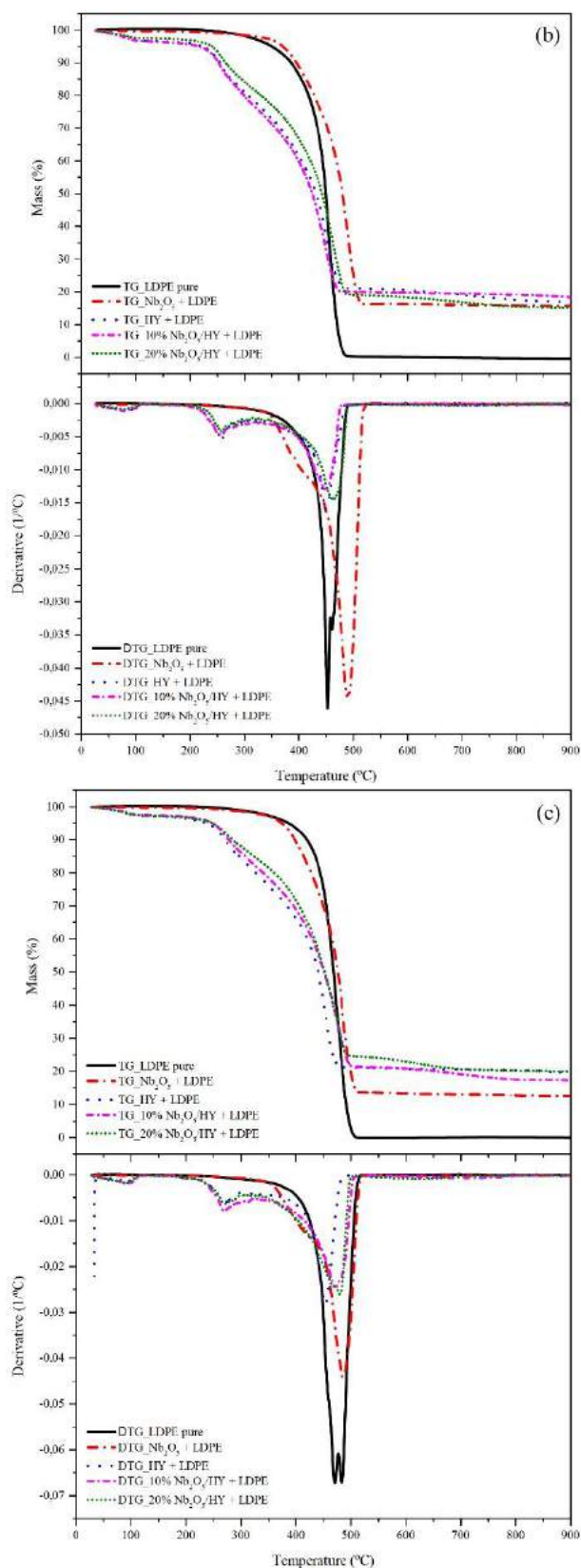


Fig. 3. TG/DTG curves of pure LDPE; Nb₂O₅-C+LDPE; HY+LDPE and Nb₂O₅/HY+LDPE in the proportions of 10 and 20%, in the heating rates of (a) 5, (b) 10 and (c) 20°C min⁻¹.

For the thermal degradation of pure LDPE, the curves showed only one decomposition event. It is noted that the variation of the heating ratio causes significant differences in the initial, final and maximum peak degradation temperatures in the DTG curves and in the percentage of residual mass. It appears that the samples undergo a complete degradation in the range of 476 to 513°C, for the different heating rates. Therefore, it is concluded that there is no presence of polymeric residues at the end of the tests.

The curves for the catalytic pyrolysis tests showed one to three mass loss events. For the first event, there is about 2 to 5% of loss of mass between 30 and 107°C, attributed to the evaporation of physically adsorbed water. The second event, in the range of 173 to 327°C, begins the reduction of the molecular weight of fission-living and chem-living molecules, with about 7 to 11% reduction in mass. And finally, the third event, with about 80% loss of mass in the temperature range between 292 to 517°C, referring to the dominant process of depolymerization of LDPE over catalysts [22]. For all tests using catalysts at different heating rates, at the end of the process, the percentage of mass remaining in the sample crucible was in the range of 13 to 24%, with a residual average of 19.8%. All values for temperatures and relative mass losses of the main degradation events are shown in Table 1.

Table 1. Values of temperatures and relative mass losses of the main events of thermal and catalytic degradation of LDPE, at different heating rates.

Sample	β (°C min ⁻¹)	Event II			
		Temperature Range (°C)	T _{onset} (°C)	T _{peak} (°C)	Mass T _{peak} (%)
Pure LDPE	5	-	-	-	-
	10	-	-	-	-
	20	-	-	-	-
Nb ₂ O ₅ -C	5	-	-	-	-
	10	-	-	-	-
	20	-	-	-	-
HY	5	173-270	173	239	10,8
	10	197-282	197	259	11,5
	20	226-294	226	271	10,3
10% Nb ₂ O ₅ /HY	5	179-274	179	244	11,7
	10	185-327	185	258	11,7
	20	215-323	215	269	8,4
20% Nb ₂ O ₅ /HY	5	190-267	190	245	10,8
	10	206-313	206	257	8,3
	20	217-298	217	270	7,8

Sample	β (°C min ⁻¹)	Event III					
		Temperature Range (°C)	T _{onset} (°C)	T _{peak} (°C)	Mass I _{peak} (%)	Residue I _{peak} (%)	Residue (%)
Pure LDPE	5	311-476	311	454	75,4	24,6	-
	10	338-487	338	458	69,1	30,9	-
	20	373-513	373	477	65,9	34,1	-
Nb ₂ O ₅ -C	5	292-480	292	459	63,2	36,8	19,2
	10	330-517	330	490	63,2	36,8	16,3
	20	350-516	350	485	64,0	36,0	13,6
HY	5	316-470	316	449	65,1	34,9	21,4
	10	319-482	319	450	63,2	36,8	21,3
	20	359-482	369	453	62,1	37,9	21,4
10% Nb ₂ O ₅ /HY	5	337-471	337	445	64,0	36,0	20,7
	10	327-474	327	449	66,5	33,5	20,4
	20	323-503	323	471	62,5	37,5	21,4
20% Nb ₂ O ₅ /HY	5	322-470	322	445	65,9	34,1	18,4
	10	345-488	345	463	65,8	34,2	19,2
	20	340-498	340	480	68,2	31,8	24,7

4. Conclusions

For XRD analyzes, the structure of the HY zeolite showed similarities with the zeolite taken as a comparison standard (faujasita type), with well-defined and narrow peaks. In the calcined Nb₂O₅ diffractogram, no crystalline peak was formed showing a totally amorphous structure. For the Nb₂O₅/HY catalysts (10% Nb₂O₅/HY and 20% Nb₂O₅/HY), the diffractograms showed diffraction peaks characteristic of the HY zeolite, maintaining the structure of the zeolite in the catalyst.

The catalytic potential of all synthesized materials was studied by thermal and catalytic degradation of LDPE via TG/DTG thermal analysis. For the polymer degradation process, the initial and final degradation temperatures, respectively, were 311 and 476 for the heating rate of 5°C min⁻¹, 338 and 487 for the heating rate of 10°C min⁻¹, and 373 and 513 for the heating rate of 20°C min⁻¹. For catalytic pyrolysis, all catalytic curves showed lower temperature ranges than pure LDPE. These results demonstrate that the catalysts are promising for industrial applications.

Acknowledgements

The authors acknowledge Graduate Program in Chemical Engineering (PEQ/UFS), Synthesis Laboratory of Catalysts (LSCAT/UFAL) and Laboratory of Catalysis (LABCAT/UFES) for the support in the experimental analysis of this work. This study was financed in part by the National Council of Technological and Scientific Development (CNPq) and Coordenação de

Aperfeiçoamento de Pessoal de Nível Superior - Brasil (CAPES) – Finance Code 001.

References

- [1] Abbas-Abadi MS, Haghghi MN, Yeganeh H. The effect of temperature, catalyst, different carrier gases and stirrer on the produced transportation hydrocarbons of LLDPE degradation in a stirred reactor. *J. Anal. Appl. Pyrolysis* 2012;95:198–204.
- [2] Kassargy C, Awad S, Burnens G, Kahine K, Tazerout M. Gasoline and diesel-like fuel production by continuous catalytic pyrolysis of waste polyethylene and polypropylene mixtures over USY zeolite. *Fuel* 2018;224:764–773.
- [3] Innocent AJ, Chamhuri S, Md AHB. Incineration and its implications: the need for a sustainable waste management system in Malaysia. *Int J Environ Sci.* 2013;4:367–378.
- [4] Silva EA, Moita Neto JM. Possibilidades de melhorias ambientais no processo de reciclagem do polietileno. *Polímeros* 2016;26:49-54.
- [5] Sharuddin SDA, Abnisa F, Daud WMAW, Aroua K. A review on pyrolysis of plastic wastes. *Energy Conversion and Management* 2016;115:308–326.
- [6] Lopez A, Marco I, Caballero BM, Laresgoiti MF, Adrados A, Torres A. Pyrolysis of municipal plastic wastes II: influence of raw material composition under catalytic conditions. *Waste Manag.* 2011;31:1973-1983.
- [7] Olazar M, Lopez G, Amutio M, Elordi G, Aguado R, Bilbao J. Influence of FCC catalyst steaming on HDPE pyrolysis product distribution. *J. Anal. Appl. Pyrol.* 2009;85:359-365.
- [8] Shah J, Jan RM, Hussain Z. Catalytic pyrolysis of low-density polyethylene with lead sulfide into fuel oil *Polym. Degrad. Stabil.* 2005;87:329-333.
- [9] Aydemir B, Sezgi NA. Pyrolysis of polyethylene over aluminum-incorporated MCM-41 catalyst. *Chem Eng Commun.* 2016;203:635–641.
- [10] Kunwar B, Moser BR, Chandrasekaran SR, Rajagopalan N, Sharma BK. Catalytic and thermal depolymerization of low value post-consumer high-density polyethylene plastic. *Energy* 2016;111:884–892.
- [11] Aguado J, Serrano DP, Miguel GS, Escola JM, Rodríguez JM. Catalytic activity of zeolitic and mesostructured catalysts in the cracking of pure and waste polyolefins. *Journal of Analytical and Applied Pyrolysis* 2007;78(1):153-161.
- [12] Silva AOS, Souza MJB, Graciliano EC, Pedrosa AMG, Coriolano ACF, Fernandes Jr VJ, Araujo AS. Development of HZSM-12 zeolite for catalytic degradation of high-density polyethylene. *Microporous and Mesoporous Materials* 2017;244:1-6.



- [13] Souza MJB, Silva THA, Ribeiro TRS, Silva AOS, Pedrosa AMG. Thermal and catalytic pyrolysis of polyvinyl chloride using micro/ mesoporous ZSM-35/MCM-41 catalysts. *Journal of Thermal Analysis and Calorimetry* 2020;140:167-175.
- [14] Santana JC, Machado SWM, Souza MJB, Pedrosa AMG. Desenvolvimento de materiais híbridos micro-mesoporosos do tipo ZSM-12/MCM-41. *Química Nova* 2015;38(3):321-327.
- [15] Lima Sobrinho RA, Andrade GRS, Costa LP, Souza MJB, Souza AMGP, Gimenez IF. Ordered micro-mesoporous carbon from palm oil cooking waste via nanocasting in HZSM-5/SBA-15 composite: preparation and adsorption studies. *Journal of Hazardous Materials* 2019;362:59-61.
- [16] Machado SWM. Desenvolvimento de materiais híbridos micro-mesoporosos contendo terras raras para utilização no craqueamento de frações de petróleo. M.Sc. Thesis, Federal University of Sergipe, São Cristóvão, Brazil, 2015.
- [17] Lima Sobrinho RA, Andrade GRS, Costa LP, Souza MJB, Souza AMGP, Gimenez IF. Ordered micro-mesoporous carbon from palm oil cooking waste via nanocasting in HZSM-5/SBA-15 composite: preparation and adsorption studies. *Journal of Hazardous Materials* 2019;362:59-61.
- [18] Treacy MMJ, Higgins JB. Collection of simulated XRD powder patterns for zeolites. 5rd ed. Amsterdam: Elsevier Science; 2007, 742p.
- [19] Pedrosa, AMG.; Souza, M.J.B.; Melo, D.M.A.; Araújo, A.S. Cobalt and nickel supported on HY zeolite: Synthesis, characterization and catalytic properties. *Mater. Res. Bull.* 2006;41(6):1105-1111.
- [20] Braga VS, Dias JA, Dias SCL, De Macedo JL. Catalyst materials based on Nb₂O₅ supported on SiO₂-Al₂O₃: Preparation and structural characterization. *Chemistry of Materials* 2005;17(3):690-695.
- [21] Ferreira C, Araujo A, Calvino-Casilda V, Cutrufello MG, Rombi E, Fonseca AM, Bañares MA, Neves IC. Y zeolite-supported niobium pentoxide catalysts for the glycerol acetalization reaction. *Microporous and Mesoporous Materials* 2018;271:243-251.
- [22] Bezerra FA. Estudo comparativo entre a pirólise de polietileno de baixa densidade, utilizando vermiculita modificada e SBA-15. 2014. 98 f. Dissertação, Universidade Federal do Rio Grande do Norte, Natal, 2014.

Synthesis and characterization of an unprecedented sugarcane bagasse cellulose ester: investigation of its environmental applicability to remove Cd(II) and Pb(II) by adsorption

Megg Madonyk Cota Elias Carvalho^a, Mariana Viviane Lima Dias^a, Luisa Cardoso Maia^a, Liliane Catone Soares^a, Leandro Vinícius Alves Gurgel^{a,*}

^aGrupo de Físico-Química Orgânica, Departamento de Química, Universidade Federal de Ouro Preto, Campus Universitário Morro do Cruzeiro, s/n°, Bauxita, 35400-000 Ouro Preto, Minas Gerais, Brazil, *legurgel@ufop.edu.br

Abstract

Agricultural lignocellulosic wastes are a promising source of potential bioadsorbent materials due to their high availability and low cost. Sugarcane bagasse (SB) has been widely investigated because of its energy potential, high availability and its physical and chemical properties. Therefore, it is possible to give it a noble destination and add value to it. SB can be used as bioadsorbent in natura and after chemical reactions that increase its adsorptive properties. The present work report the production of an unpublished adsorbent material synthesized from a chemical modification of SB with 1,2,3,4-butanotetracarboxylic acid dianhydride (BTCA) in a only step reaction. The carboxylate groups inserted in the structure are mainly responsible for the removal of positively charged species, such as toxic metal ions as Pb(II) and Cd(II). The synthesis was evaluated by a multivariate planning (Doehlert) where the independent variables were reaction time, temperature and amount of dianhydride. The response variables were the Cd(II) and Pb(II) adsorption capacities obtained by exploratory adsorption studies. Characterization analyses such as FTIR, ¹³C NMR and pH_{PCZ} suggested that the synthesis was successful. An exploratory adsorption study based on one-component aqueous solutions synthetically contaminated with Cd(II) and Pb(II) obtained adsorption capacities of 0.76 mmolg⁻¹ and 0.51 mmolg⁻¹ for Pb(II) and Cd(II), respectively.

Keywords: biosorbent; esterification; lignocellulosic materials; waste recovery; only step synthesis.

1. Introduction

Brazil is one of the largest producers of sugarcane in the world, therefore, among some important agro-industrial residues, sugarcane is very prominent [1]. During its processing, a large amount of sugarcane bagasse (SB) is produced which is used in the industry itself for the energy cogeneration by burning boilers. Nevertheless, 20% of the SB volume is still considered surplus and it is stored in the industry yards [2]. In addition, a new demand for the use of SB is increasing, which is its use for the production of second-generation ethanol [3] and/or adding value to the SB, providing these nobler applications, as a precursor material for the production of adsorbents used for water and industrial effluent treatment [4, 5].

The rapid industrial development and the overexploitation of natural resources has caused serious environmental and human health damage, so it is essential to find alternative and less costly ways to solve such ecological problems [6]. When widely

available bioadsorbents such as lignocellulosic matrix agricultural residues are used, adsorption is an effective and inexpensive method for removing contaminants from gas and aqueous phases [7]. Lignocellulosic material is mainly constituted by lignin and cellulose, and other components but to a lesser extent as hemicelluloses, extractives, lipids, proteins, simple sugars, starch, water, hydrocarbons and ashes [1].

Currently, several studies report the use of SB after chemical modification as an advantageous option to remove inorganic contaminants, such as toxic metals from effluents [8].

Several metallic cations of environmental concern have been studied. Among them, Pb(II) and Cd(II) are of extreme concern. Pb is suspected to be carcinogenic, it can cause loss of appetite, anemia, muscle and joint pain [9]. Cd is carcinogenic, can cause pulmonary fibrosis and weight loss [10].

In this context, this work proposes to use an important agro-industrial residue, the SB, as a starting material in an esterification reaction using 1,2,3,4-



butanotetracarboxylic acid dianhydride (BTCA) to produce an unprecedented bio adsorbent material. In addition, to study its application to remove Pb(II) and Cd(II) from aqueous solutions by adsorption.

2. Material and methods

2.1. Material

The Jatiboca mill, Urucânia, Minas Gerais, Brazil provided the sugarcane bagasse (SB) used in the synthesis. Acetone, pyridine, hexane, ethanol, acetic anhydride, sodium acetate trihydrate, HCl and HNO₃ were purchased from Synth (Brazil). Pb(NO₃)₂ PA, NaCl PA and NaOH PA were purchased from Vetec (Brazil). N,N-dimethylacetamide (DMAc) was purchased from Neon. 1,2,3,4-butanotetracarboxylic acid (BTCA) (98%) was purchased from Alfa Aesar. Cd(NO₃)₂·4H₂O PA was purchased from Dynamics. Glacial acetic acid PA was purchased from Alphatec. Black Belt Quantitative Filter Paper (JP-41) was purchased from Jprolab, Brazil. Deionized water was produced by a Millipore ultrapurifier, Milli-Q Simplicity® model.

2.2. Methods

2.2.1. Synthesis of dianhydride of the 1,2,3,4-butanotetracarboxylic acid (DBTCA)

The methodology to prepare dianhydride BTCA (DBTCA) was adapted from Blackwell (1993)[11]. In a round bottom flask with Schlenk line, BTCA and acetic anhydride 1:3 (m v⁻¹) were added. The balloon was sealed with a rubber septum. An inert atmosphere was made inside the reaction flask to remove all air. The flask was immersed in a canola oil bath at 110°C for 2 h. After this period, the heating was suspended and the system was stirred for 24 h at 25°C at 300 rpm. The contents of the flask were filtered and the white solid obtained was washed with hexane and oven dried under reduced pressure at 25°C.

2.2.2. Synthesis of modified sugarcane bagasse (MSB)

SB was pretreated as described by Elias et. al (2019) [12]. Soxhlet extraction was performed using ethanol and cyclohexane (1:1 v v⁻¹). The SB was filtered under reduced pressure and oven dried at 85°C for 1 h. 1.000 g of SB and an amount of DBTCA (Table 1) was added in a 50 mL round bottom flask followed by of pyridine (7.5 mL) and DMAc (7.5 mL). The flask was connected to a ball condenser and immersed

in a canola oil bath at a desired temperature using a stirring and warming plate (Corning®, model PC 420 D), and for the time determined (Table 1), under agitation of 300 rpm. After the reaction time, the contents of the flask were filtered and the retained solid was washed with ethanol, distilled water, 0.01 mol L⁻¹ NaOH, distilled water, 0.01 mol L⁻¹ HCl solution, distilled water, ethanol and acetone. MSB was collected and oven dried at 90°C for 2h. Masses (g) of DBTCA as well as reaction temperature (T) and time (t) were varied according to a Doehlert multivariate experimental design with triplicate at the center point built using the Statistica 12.0 software (StatSoft Inc. 2010, USA) to investigate the influence of independent variables on the system. The response variables were the adsorption capacities of Pb(II) ($q_{e,Pb}$), Cd(II) ($q_{e,Cd}$) (obtained from an exploratory adsorption study) and $q_{e,tot}$ ($q_{e,Cd} + q_{e,Pb}$).

2.2.3. Batch adsorption exploratory studies

100.0 mL of the buffered metal solution (pH = 5, 1.93 mmol L⁻¹) was added in 250 mL Erlenmeyer flasks, thermostated at 25°C in an incubator (Tecnal, model TE-424, Piracicaba, São Paulo) with orbital shaking for 1h. Amounts of 0.0500±0.0001 g of the MSB bioadsorbent were weighed into cylindrical glasses (1.8 mm height × 2.2 mm diameter), added to the Erlenmeyer flasks and stirred at 130 rpm and 25°C for 4h. After this time, the samples were filtered and Cd and Pb contents in filtrates were quantified using a flame absorption spectrophotometer (Varian, model SpectrAA 50B). All adsorption studies were performed in triplicate and the buffer solution used was 0.05 mol L⁻¹ acetic acid/sodium acetate. The adsorption capacity is calculated by Eq. (1).

$$q_e = \frac{(C_i - C_t) \cdot V}{m_{MSB}} \quad (1)$$

where q_e is the adsorption capacity; C_i and C_t are the initial and the after contact time concentrations (mmol L⁻¹), respectively, m_{MSB} is the bio sorbent mass (g) and V (L) is the solution volume.

2.2.4. Characterization of BTCA, BTCAD, SB and MSB

Amounts of 2.0 mg of SB, MSB, BTCA and DBTCA were weighed, macerated and homogenized with 100 mg of spectroscopic grade KBr in an agate grade. Then, the sample was pressed in a hydraulic press (Pike, model 181-1110) with 8 tons of pressure for 1 min, obtaining a 13 mm diameter tablet. The FTIR



spectra were recorded with a resolution of 4 cm^{-1} from 400 to 4000 cm^{-1} and 32 scans per sample, using a deuterated triglycine sulfate detector (DTGS) (ABB Bomen MB 3000 FTIR spectrometer, Quebec, Canada).

Solid State ^{13}C NMR experiments were performed for the SB and MSB samples using a Bruker Avance 400 spectrometer equipped with a 4 mm Bruker dual resonance MAS probe, the ^{13}C frequency used was 100.5 MHz .

The points of zero charge (pH_{PZC}) of SB and MSB were determined by the solid addition method [13]. The pH values ($\Delta\text{pH} = \text{pH}_i - \text{pH}_e$) were calculated and the graph ΔpH versus pH_i was plotted. The pH value where the curve crosses the abscissa ($\Delta\text{pH} = 0$) corresponds to a pH_{PZC} .

The specific surface areas of SB and MSB materials were measured in a pore and surface analyzer (Quantachrome, model Nova 1200E) using N_2 adsorption/desorption isotherms at 77.35 K . The sample was degassed at 30°C for 24h at 0.016 mmHg before measurement. The specific surface area was determined by the Brunauer, Emmett and Teller (BET) method [14].

3. Results and Discussion

3.1 Synthesis

The model was validated using analysis of variance (ANOVA) and evaluating the regression and lack of model fit to a significance level of 0.05 (95% confidence). A matrix with 13 distinct synthesis conditions was generated. One of them corresponds to the central point condition which was made in triplicate, totaling 15 syntheses. The results are shown in Table 1. ANOVA showed that the regression was not significant for $q_{e,\text{Pb}}$, and the lack of fit was significant. For $q_{e,\text{Cd}}$ and $q_{e,\text{tot}}$, the regression was significant and the lack of fit was not significant. Therefore, these last two variables were chosen to evaluate the optimization of the synthesis conditions. For $q_{e,\text{Cd}}$, the amount of BTCAD is significant with positive effect as well as the interaction between BTCAD and temperature (both in linear terms). For the variable $q_{e,\text{tot}}$, the temperature (quadratic term), the reaction time (quadratic term) and the amount of BTCAD (linear term) were significant and with positive effects. These results indicate that, in order to obtain the best answers, the independent variables must be at their maximum levels. The generated desirability profile (Figure 1) suggested 4 g of

BTCAD, 22h of reaction and 100°C as optimal condition by analyzing $q_{e,\text{Cd}}$ and $q_{e,\text{tot}}$.

Table 1. Doehlert planning matrix for optimizing conditions for MSB synthesis.

Test	Independent variables			Dependent variables		
	T °C	t h	m_{DBTCA} g	$q_{e,\text{Cd}}$ mmol/g	$q_{e,\text{Pb}}$ mmol/g	$q_{e,\text{tot}}$ mmol/g
1	75.0	11.5	4.0	0.68	0.73	1.41
2	75.0	22.0	3.2	0.59	0.63	1.22
3	100.0	15.0	3.2	0.68	0.96	1.64
4	75.0	11.5	0.8	0.20	0.28	0.48
5	75.0	1.0	1.6	0.33	0.64	0.97
6	50.0	8.0	1.6	0.42	0.72	1.14
7	75.0	22.0	3.2	0.57	0.59	1.16
8	50.0	18.5	3.2	0.44	0.72	1.16
9	100.0	15.0	1.6	0.41	0.77	1.18
10	50.0	18.5	2.4	0.42	0.75	1.17
11	100.0	15.0	1.6	0.43	0.79	1.22
12	100.0	4.5	2.4	0.42	0.76	1.18
13(C)	75.0	11.5	2.4	0.40	0.32	0.72
14(C)	75.0	11.5	2.4	0.44	0.36	0.80
15(C)	75.0	11.5	2.4	0.46	0.37	0.83

Analyzing the data from an economic point of view, these conditions were considered infeasible due to the high energy and operational cost and an extremely long reaction time. Because of this, a milder condition was used and the conditions were chosen based on the data from Table 1 and initial investigative tests (data not shown), with conditions equal to 4 g of DBTCA for 1 g of SB, 1h reaction and temperature at 70°C . The material obtained under these conditions was used in an exploratory adsorption test and found the values of 0.76, 0.51 and 1.27 mmol g^{-1} for $q_{e,\text{Pb}}$, $q_{e,\text{Cd}}$ and $q_{e,\text{tot}}$, respectively. These values are similar to the values obtained in tests 2 and 11 and slightly lower than those obtained in tests 1 and 3. However, in these tests, the reaction times were much longer and some of them used a higher temperature (Table 2). Therefore, we opted for a more economical synthesis to produce a cheaper bioadsorbent and with good adsorptive capacity for Cd(II) and Pb(II).

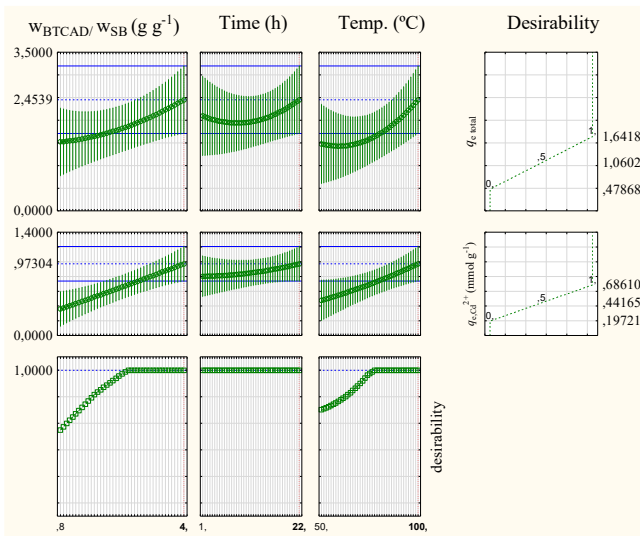


Fig. 1. Profiles for predicted values of desirability for conditions to MSB synthesis.

3.2. Characterization analyses

DBTCA was successfully obtained according to the proposed methodology. The FTIR spectra (Fig. 2) shows bands at 1793 and 1859 cm^{-1} of the carbonyl group bond stretching, which are characteristic of carboxylic acid anhydrides (normal frequencies for anhydrides are 1760 and 1810 cm^{-1}). The broad band of the O-H stretching involved in hydrogen bonds in the region of 3000 cm^{-1} is no longer observed (which is observed in the BTCA spectrum). The smallest thin band at 3608 cm^{-1} in the DBTCA spectrum is related to the O-H stretching that is not involved in hydrogen bonding [15].

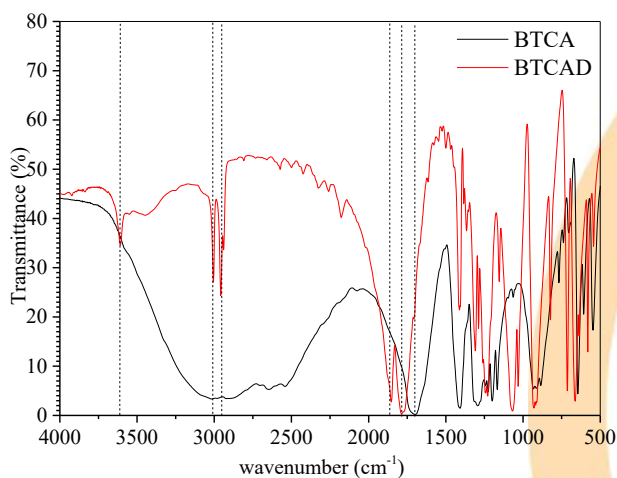


Fig. 2. FTIR spectrum of 1,2,3,4-butanetetracarboxylic acid (BTCA) and dianhydride from BTCA (DBTCA).

In order to prove the insertion of acid functions on the SB surface, SB and MSB were analyzed by FTIR (Fig. 3). SB has been characterized by FTIR by several studies [12]. The main changes observed were the appearance of a strong band at 1726 cm^{-1} related to the ester carbonyl group (C=O) stretching (the normal basic frequency of esters is 1735 cm^{-1}) and a band at 1258 cm^{-1} related to the carboxylic acid ester stretching [15].

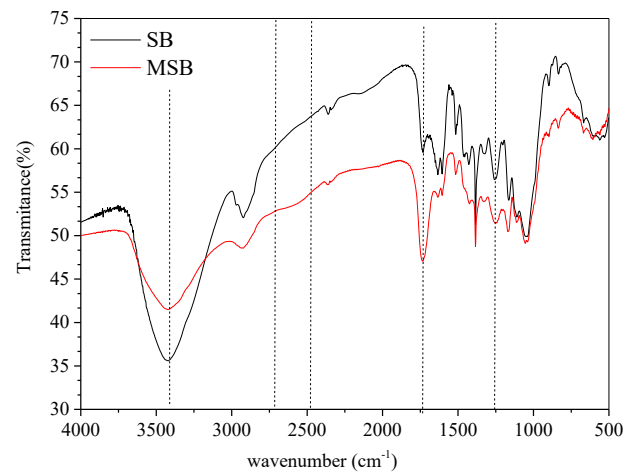


Fig. 3. FTIR spectrum for unmodified sugarcane bagasse (SB) and for sugarcane bagasse modified with dianhydride from 1,2,3,4-butane tetracarboxylic acid (MSB).

Fig. 4 shows the ^{13}C NMR spectra of SB and MSB. The 17 signals numbered in the spectrum are shown in different colors to highlight the chemical displacements of carbon from cellulose, hemicelluloses and lignin. The 10 signal refers to cellulose anomeric carbon (C1), 7 and 8 signals refer to C4, 5 and 6 signals refer to C2, C3 and C5, and 3 and 4 signals refer to C6 [16]. According to Rezende et al. (2011) [17], the 3 and 7 signals are predominantly due to amorphous cellulose carbons, while 4 and 8 signals are related to crystalline cellulose carbons. The carbon signals present in lignin are mainly concentrated between 110 and 160 ppm. They are relatively broader due to the complexity of the structure of this macromolecule, in addition to the carbon signal of the methoxy group (-O-CH₃) of aromatic portions present in the lignin structure. 1, 9, 16 and 17 signals are assigned only to hemicelluloses carbons. The differences between SB and MSB spectra are concentrated in two regions: region 1, between 35 and 55 ppm, showing the appearance of bands related to aliphatic methylene

carbons (-CH₂-CH-) present in the BTCA unit added to the bagasse matrix. The region 2 shows a significant increase of the 16 and 17 signals indicating an increase in carboxylic acid functions in the modified material, which in addition to being present in the hemicelluloses and lignin of SB, are also present in a BTCA unit. Integration calculations revealed that for each cellobiose unit, 0.3 BTCA unit was entered.

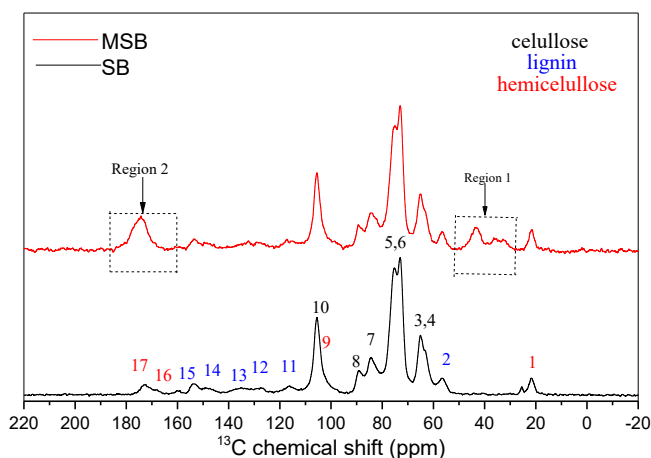


Fig. 4. ¹³C Multi-CP solid-state nuclear magnetic resonance spectra of SB and MSB.

The pH_{PCZ} values of SB and MSB were 6.11 and 4.01, respectively (Fig. 5). The pH_{PCZ} value of SB was lower than the pH_{PCZ} of MSB because of the chemical modification which expands the pH range for application to remove cationic species from aqueous solutions. The adsorption of Cd(II) and Pb(II) is favored at pH values higher than pH_{PCZ} because the material has a negative net charge.

Table 2 shows the results of surface analysis for SB and MSB. Both are mesoporous materials (pores with diameter between 20 and 500 Å [18]). There is also a significant decrease in the specific surface area of the MSB in relation to SB. It is related to the larger inserted groups in the cellulose fibers of the SB promoted by the chemical modification.

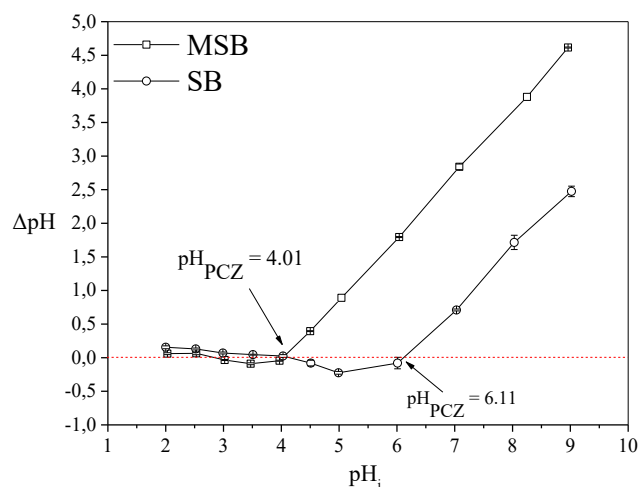


Fig. 5. Curves for pH_{PCZ} determination of SB and MSB materials.

Table 2. Results of surface characterization of SB and MSB

Material	SB	MSB
Surface area (m ² g ⁻¹)	14.2	3.3
Average pore sizes (Å)	39.6	34.2
Total pore volume (cm ³ g ⁻¹)	0.015	0.006

The MSB synthesized on a larger scale showed adsorption capacities equal to 0.76 and 0.51 mmol g⁻¹ for Pb(II) and Cd(II), respectively. Therefore, an efficient and low cost versatile adsorbent was produced.

4. Conclusions

This work contemplates the synthesis and characterization of a new adsorbent based on agricultural waste. Another work will address batch studies as a function of pH, contact time and initial concentration, in addition to desorption studies for the Pb(II) and Cd(II) ions. MSB bioadsorbent was successfully produced and FTIR and ¹³C NMR techniques proved the chemical modification. MSB material proved to be viable for adsorption of Cd(II) and Pb(II).

Acknowledgements

The authors are grateful to the Federal University of Ouro Preto (UFOP), Rede Mineira de Química (RQ-MG) and the funding agencies Conselho Nacional de Desenvolvimento Científico e Tecnológico (CNPQ), Fundação de Amparo à Pesquisa do Estado de Minas Gerais (FAPEMIG) and Coordenação de

Aperfeiçoamento de Pessoal de Nível Superior (CAPES) [Finance Code 001].

References

- [1] Mendes F. Efeito da umidade nas propriedades físicas e estruturais do bagaço de cana. *Blucher Chemical Engineering Proceedings* 2015;1:6401.
- [2] UNIÃO DIDC-D. AÇÚCAR (UNICA). O MERCADO INTERNACIONAL DO ETANOL São Paulo 2013.
- [3] de Araujo GJF, Santos BAS. O etanol de segunda geração e sua importância estratégica ante o cenário energético internacional contemporâneo. *Periódico Eletrônico Fórum Ambiental da Alta Paulista* 2013;9.
- [4] do Carmo Ramos SN, Xavier ALP, Teodoro FS, Elias MMC, Gonçalves FJ, Gil LF, et al. Modeling mono- and multi-component adsorption of cobalt (II), copper (II), and nickel (II) metal ions from aqueous solution onto a new carboxylated sugarcane bagasse. Part I: Batch adsorption study. *Industrial Crops and Products* 2015;74:357.
- [5] Ferreira BCS, Teodoro FS, Mageste AB, Gil LF, de Freitas RP, Gurgel LVA. Application of a new carboxylate-functionalized sugarcane bagasse for adsorptive removal of crystal violet from aqueous solution: kinetic, equilibrium and thermodynamic studies. *Industrial Crops and Products* 2015;65:521.
- [6] Dai Y, Sun Q, Wang W, Lu L, Liu M, Li J, et al. Utilizations of agricultural waste as adsorbent for the removal of contaminants: A review. *Chemosphere* 2018;211:235.
- [7] Sud D, Mahajan G, Kaur M. Agricultural waste material as potential adsorbent for sequestering heavy metal ions from aqueous solutions—A review. *Bioresource technology* 2008;99:6017.
- [8] Bailey SE, Olin TJ, Bricka RM, Adrian DD. A review of potentially low-cost sorbents for heavy metals. *Water research* 1999;33:2469.
- [9] Flora G, Gupta D, Tiwari A. Toxicity of lead: a review with recent updates. *Interdisciplinary toxicology* 2012;5:47.
- [10] Flora S, Pachauri V, Saxena G. Arsenic, cadmium and lead. *Reproductive and developmental toxicology*. London: Academic Press; 2011.
- [11] Blackwell GB. Dental/medical composition and use. *Google Patents*; 1993.
- [12] Elias MMC, Ferreira GMD, de Almeida FTR, Rosa NCM, Silva IA, Filgueiras JG, et al. Synthesis and application of sugarcane bagasse cellulose mixed esters. Part I: Removal of Co^{2+} and Ni^{2+} from single spiked aqueous solutions in batch mode using sugarcane bagasse cellulose succinate phthalate. *Journal of colloid and interface science* 2019;533:678.
- [13] Balistrieri L, Murray JW. The surface chemistry of goethite ($\alpha\text{-FeOOH}$) in major ion seawater. *American Journal of Science* 1981;281:788.
- [14] Brunauer S, Emmett PH, Teller E. Adsorption of gases in multimolecular layers. *J Am Chem Soc* 1938;60:309.
- [15] Pavia DL, Lampman GM, Kriz GS, Vyvyan JA. *Introduction to spectroscopy*: Cengage Learning; 2014.
- [16] de Melo JC, da Silva Filho EC, Santana SA, Airoidi C. Maleic anhydride incorporated onto cellulose and thermodynamics of cation-exchange process at the solid/liquid interface. *Colloids and Surfaces A: Physicochemical and Engineering Aspects* 2009;346:138.
- [17] Rezende CA, de Lima MA, Maziero P, Ribeiro de Azevedo E, Garcia W, Polikarpov I. Chemical and morphological characterization of sugarcane bagasse submitted to a delignification process for enhanced enzymatic digestibility. *Biotechnology for Biofuels* 2011;4:54.
- [18] do Nascimento RF, de Lima ACA, Vidal CB, de Quadros Melo D, Raulino GSC. *Adsorção: aspectos teóricos e aplicações ambientais*. Biblioteca de Ciências e Tecnologia 2014.

Synthesis and characterization of adsorbents from lignocellulosic residues in the removal of different contaminants

Lizeth Vanessa Amado Jurado, Ana Carolina da Silva, Eliana Zaroni Megale, Gabriela Machado Chemp, Brunno Almeida de Carvalho e Silva, Matheus Santos Parente Carneiro, Izadora da Silva Santos, Lindoval Domiciano Fernandes, Marcos Antonio da Silva Costa^a, Francisco Eduardo Aragão Catunda Júnior^b, Marisa Fernandes Mendes

^a*Institute of Chemistry, Universidade Estadual do Rio de Janeiro, St. São Francisco Xavier 524, Rio de Janeiro, CEP 20550-900, Brazil.*

^b*Center for Exact, Natural and Technological Sciences, Universidade Estadual da Região Tocantina do Maranhão, Imperatriz, Maranhão, CEP 65900-000, Brazil.*

Department of Chemical Engineering, Universidade Federal Rural do Rio de Janeiro, Rod BR 465 Km 7, Seropédica, CEP 23897-000, Brazil

Abstract

The use of agricultural residues to produce carbonaceous adsorbents can be considered a solution for the high cost of treating industrial effluents, and the large waste of biomass from food. To reduce these costs, this study was carried out to evaluate the efficiency of biomass as adsorbents in the removal of contaminants, such as residues of ginger, almond and rubber tree. Each biomass has undergone a thermal and chemical activation process. For the structural analysis, the techniques of scanning electron microscopy (SEM), infrared spectroscopy with Fourier transform (FTIR), and specific area by the BET method were used. After the characterization, the potential to remove the adsorbents for two different contaminants was evaluated, with glycerol being tested for the rhizomes of ginger and the methyl orange for the endocarp of the almond tree and rubber seed shell. It was observed that the biomasses presented similar structural characteristics for all types of treatment, being constituted of irregular and heterogeneous surfaces. The FTIR spectra showed absorption bands characteristic of lignocellulosic materials for the adsorbents in nature, whereas for the activated ones, the presence of characteristic bands of carbonaceous materials was observed. The results suggested a good affinity between the adsorbents and the adsorbates, which can be corroborated by the characterization analyzes. Based on the results presented, it can be said that the use of biomass in the future is promising and can be applied in different treatment processes to remove contaminants.

Keywords: ginger; almond; rubber tree; activated carbon; adsorption.

1. Introduction

One of the most popular and widely used adsorbents in various types of adsorption processes are carbonaceous adsorbents, such as activated carbon (AC). The production of them is done by a pyrolysis process of the raw materials to create an intermediate carbonized material, followed by the activation step to increase its porous structure [1].

There are many researches committed to acquire low-cost ACs from agricultural residuals, such as rice husk [2], hazelnut and walnut shell [3], apple pulp [4], and coconut shell [5]. In addition, these materials are relatively cost effective compared to

other organic adsorbent such as commercially available activated carbon [3].

The adsorption property of adsorbent is basically affected by physical characteristics, such as specific surface area, pore size distribution and pore volume. In general, large specific area means excellent adsorption capacity on account of providing more active sites [6]. N-containing functional groups can increase the polarity of carbon surface and facilitate interactions between carbon surfaces and target molecules [7].

In this way, this work has the motivation to use rhizomes of ginger, endocarp of almond and rubber seed shell as precursors for the preparation of an AC, that will be applied for the removal of different

contaminants. For this purpose, the biomass and the AC's characterization studies were carried out determining their chemical and surface properties through FTIR, BET and SEM analysis. After characterization, the potential to remove the adsorbents for two different contaminants were evaluated, with glycerol being tested for the rhizomes of ginger and methyl orange dye (MO) for the endocarp of almond fruit and rubber seed shell.

2. Materials and methods

2.1. Preparation and synthesis of the adsorbents

Ginger: Ginger rhizomes were bought in a local market in Seropédica-RJ. They were washed to remove all impurities, and dried at ambient temperature. After that, the material was pressed in a manual and hydraulic press to obtain ginger residues, which were dried at 60 °C for 12 h in an oven. Then, they were milled, and it was done a granulometric analysis. The sample retained between the 20-80 mesh particle size was passed through a calcination process at 350 °C for 180 min. The calcined material was washed with distilled water for the removal of ash and other impurities, and then was dried again at 60 °C for 12 h.

Chemical activation was performed based on the methodology applied by [8]. A solution of phosphoric acid was used in a mass fraction of acid for aqueous solution of 0.1. Then, the adsorbent was added in a feed/solution ratio of 0.5, being kept in an oven at 100 °C for 150 min and, subsequently, at room temperature until 24 h. The material was washed with distilled water until reaching neutral pH, and dried in an oven at 100 °C for 15 h.

Thus, three adsorbents were obtained: ginger in nature (IN-G), thermally treated ginger (TTG) and chemically treated ginger (QTG).

Rubber seed shell: The seed samples were collected in Maranhão, a state of the northeast region of Brazil. The rubber seed shells were washed and dried in an oven at 80 °C for 12 h. Then, the rubber seed shells were milled, and the samples were separated using the mesh sieves of the Tyler series. The particles retained between 24 and 80 mesh were selected for the analyses. Part of the sample was reserved, and the other part was treated.

The material was calcined in a muffle furnace (Vulcan model 3-550) at 400 °C for 90 min. After the calcination, the material was washed with distilled water, and dried in an oven at 100 °C for 12 h. Part of the material was reserved, and the other part was treated with nitric acid.

The chemical activation was performed based on a methodology [9], adding nitric acid 25% in a ratio of 1:2, and putting it in a muffle furnace at 500 °C for 20 min. After this process, the material was washed to remove the residue of nitric acid, and dried again in an oven at 105 °C for 12 h.

Thus, three adsorbents were obtained from the rubber seed shells, the in nature adsorbent (IN-RSS), the thermally activated adsorbent (TRSS), and the chemically activated adsorbent (QRSS).

Almond: The fruit samples were collected in the Universidade Rural do Rio de Janeiro, Seropédica, Brazil. The fruit was peeled for endocarp separation, washed, and dried in an oven at 373.15 K for 24 h. The biomass was grounded, and the sample retained between 80-150 mesh sieves were used. Part of this material was reserved in nature for the experiments and the other part was treated.

The thermal activation was performed using a muffle furnace, at 400 °C for 2 h, with a heating rate of 10 °C.min⁻¹. After calcination, the material was washed with distilled water for ashes removal, and dried in an oven at 100 °C for 24 h.

Chemical activation of the biomass was performed using $m_{\text{endocarp}}/m_{\text{H}_3\text{PO}_4}$ ratio of 1:1, followed by the addition of distilled water (250 mL). The biomass/H₃PO₄ mixture was allowed to heat stand within 4 h under light agitation. After that, it washed and dried at 100 °C, over 36 h. Then, in a muffle furnace, the material was heated at the rate of 10 °C.min⁻¹ from room temperature to 350 °C, and remained at this temperature for 2 h. The material was then washed with distilled water until pH characteristic of water. Three adsorbents were obtained from the endocarp of almond fruit, the in nature adsorbent (IN-A), the thermally activated adsorbent (TA), and the chemically activated adsorbent (QA).

2.2. Characterization of the adsorbent

The physical, structural, and chemical properties of the biomass and the activated carbons were evaluated using several analytical methods. Fourier transform infrared (FTIR) spectroscopy was carried out using a JASCO FT/IR-4100 FTIR spectrometer

between 4000 and 400 cm^{-1} with a resolution of 2 cm^{-1} using KBr discs. The surface morphology analyses of the activated carbons were performed by scanning electron microscopy (SEM) using a Shimadzu SS 550 SEM microscope. Brunauer–Emmett–Teller (BET) and Barrette Joynere Halenda (BJH) methods were utilized to calculate the specific surface area, and the pore size distribution by N_2 adsorption/desorption isotherm on a micromeritics BET model ASAP 2020.

2.3. Batch adsorption procedure

Adsorption experiments were conducted in a batch mode, using Erlenmeyer flasks with 25 mL of solutions, 298 K, maintaining the agitation at 180 rpm until the equilibrium time and with fixed mass being 0.05 g for ginger, and 0.15 g for almond fruit and rubber seed shell.

For ginger, the contaminant studied was glycerol with concentration of 30 mg/L, whereas for rubber seed shell and almond fruit it was MO. For the rubber seed shell adsorbents, the initial concentration was 25 mg/L and 100 mg/L for almond. The adsorption of contaminants on activated carbon was evaluated in terms of removal percentage, calculated by Eq. (1) (%R) with C_0 as the initial concentration of solution and C_e as concentration at equilibrium.

$$\%R = (C_o - C_e) \left(\frac{100}{C_o} \right) \quad (1)$$

3. Results and discussion

3.1. SEM

The scanning electron microscopy analysis were carried on for all adsorbents. Figure 1 illustrates the micrographs obtained for the materials in the nature form.

It was possible to observe an irregular, uneven, heterogeneous surface with agglomerates, and the absence of pores on the surface of both materials, almond and rubber seed shells. Similar structures were observed in the morphology of the macadamia endocarp [10]. In case of ginger, these agglomerates indicated the presence of starch grains, similar to the ones observed in ginger samples in previous works [11, 12].

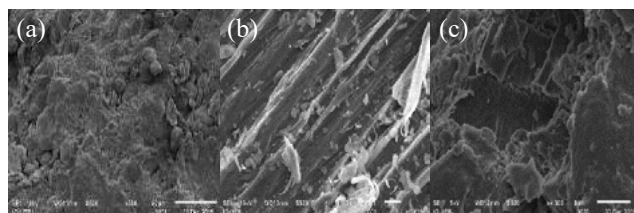


Fig. 1. SEM of in nature adsorbents: IN-G (a), IN-RSS (b) and IN-A (c)

Figure 2 illustrates the micrographs obtained with the thermally activated materials. It was possible to notice the effect of pyrolysis process, in which is evident the degradation of cellulosic material and the presence of small cavities. This is due to the evaporation of volatile components, present in cellulosic cracks in all lignocellulosic adsorbents in this study. In addition, for ginger, starch degradation was also observed as a consequence of this process, according to this discussed in other studies [11].

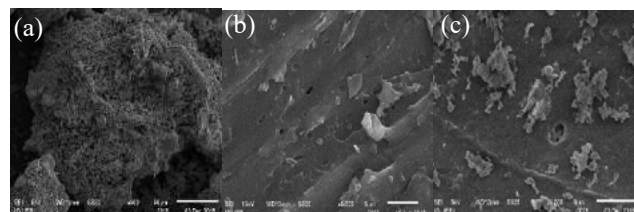


Fig. 2. SEM of thermally activated materials: TTG (a), TRSS (b) and TA (c)

It was also possible to observe crystal particles on the TA surface, probably formed by condensed ash with low melting point released during burning. This presence was also observed in the production of activated charcoal from corn stalks [12].

Figure 3 illustrates the micrographs obtained with the adsorbents chemically activated.

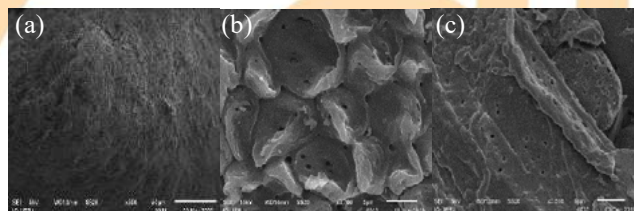


Fig. 3. SEM of chemically activated adsorbents: QTG (a), QRSS (b) and QA (c)

After chemical activation, it was observed a higher volume of pores in the adsorbents from rubber seed shells and almond. This effect was also shown by activated carbon from orange peel [14]

and banana peel [15] after acid treatment, which was responsible for the release of pores.

However, the chemical treatment did not provide significant structural changes in ginger after this process, in comparison to thermal treatment. Similar result was obtained after chemical treatment of *Jatropha* shell [8].

3.2. BET

Table 1 shows the BET data for the adsorbents studied. As can be noticed, the activation process led an increase in surface area; since there was a release of the pores present in the material caused by the loss of organic material.

Table 1. BET of the adsorbents.

Adsorbent	Surface area (m ² .g ⁻¹)	Pore Diameter (nm)	Pore volume (cm ³ .g ⁻¹)
TG	13.18	12.50	0.017
TRSS	141.03	-	-
QRSS	381.30	0.09	0.93
IN-A	0.02	2.06	0.0001
TA	13.18	12.50	0.03
QA	698.75	2.17	0.34

In relation of the N₂ adsorption/desorption process, the RSS and IN-G samples did not occur. Because of that the BET analysis could not be performed, indicating a low adsorption capacity of the material. This behavior seemed to agree according to the low porosity visualized through the analysis of SEM. This analysis was not applied for QTG due to the lack of material available to it.

The largest surface areas were obtained through acid treatment of the almond endocarp and of the rubber seed shell, 698.75 m².g⁻¹ and 381.30 m².g⁻¹, respectively.

Despite the low surface area of QTG in comparison to the other adsorbents, its adsorbent capacity was satisfactory because a larger surface area does not imply that is entirely available for adsorption, since factors such as steric impediment and non-specific site for adsorbate can limit the use of the adsorbent.

3.3. FTIR

FTIR spectrum of adsorbents in nature is presented in Figure. 4. In general, the adsorbents in nature presented the characteristic band around 3330 cm⁻¹, which is associated with the O-H stretching vibration of the hydroxyl group present in lignin, cellulose and hemicellulose [16]; the band around 2900 cm⁻¹ corresponds to the symmetrical and asymmetric stretching of C-H of methoxy groups present in cellulose, hemicellulose, lignin and aliphatic acids [17]. The band around 1700 cm⁻¹ was also observed, which is attributed to the C=O bond of carboxylic acid, commonly found in fibrous materials containing pectin [18, 19]. bands located around in 1240 and 1030 cm⁻¹ are attributed to the presence of aliphatic acids and the stretching of the bonds C=C-OH and C-O-C, present in esters and ethers [19].

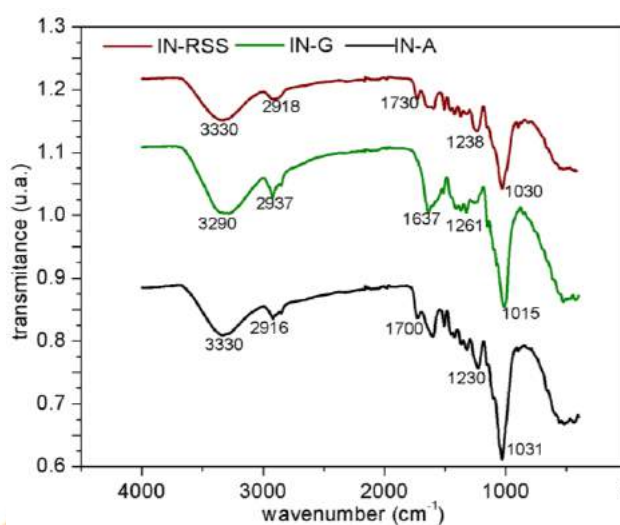


Fig. 4. FTIR spectrum of adsorbents in nature.

FTIR spectrum of adsorbents after thermal activated is presented in Figure 5. It was also possible to observe a band at 1578 cm⁻¹ in TRSS and TA, attributed to the stretching of the C=C bond that composes aromatic benzene molecules or lignin rings, typical of carbonaceous materials [21].

For ginger, two peaks at 1662 cm⁻¹ and 1404 cm⁻¹ were attributed to stretching aldehydes, ketones, acids and for bending alkyl, aliphatic groups, respectively [3].

In addition, it was also noticed the flattening of the band close to 3330 cm⁻¹ and the disappearance of the 2900 cm⁻¹ band, indicating the decomposition of the lignocellulosic components of these adsorbents. For rubber seed shell, the disappearance

of the 1031 cm^{-1} band and appearance of 1182 cm^{-1} band were observed. However, for the other adsorbents only this flattening was observed.

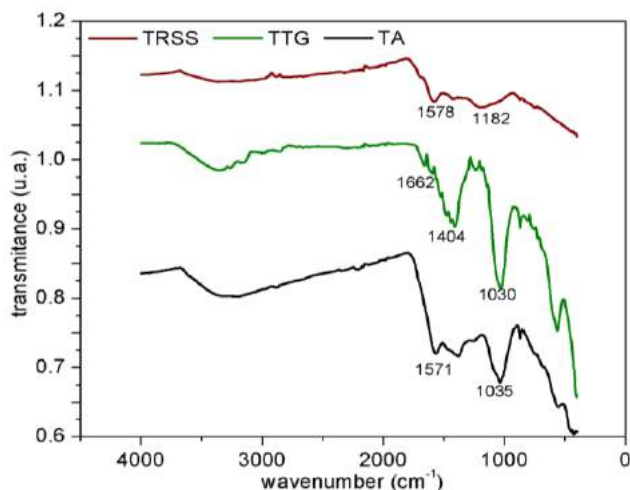


Fig. 5. FTIR spectrum of adsorbents after thermal activated

FTIR spectrum of the adsorbents after chemical activated is presented in Figure. 6. As can be noticed, there was not significant change in the material bands after thermal and chemical treatment. Although the band in 1575 cm^{-1} still remained in all adsorbents, there was a flattening of the 1030 and 1058 cm^{-1} band present in ginger and almond fruit.

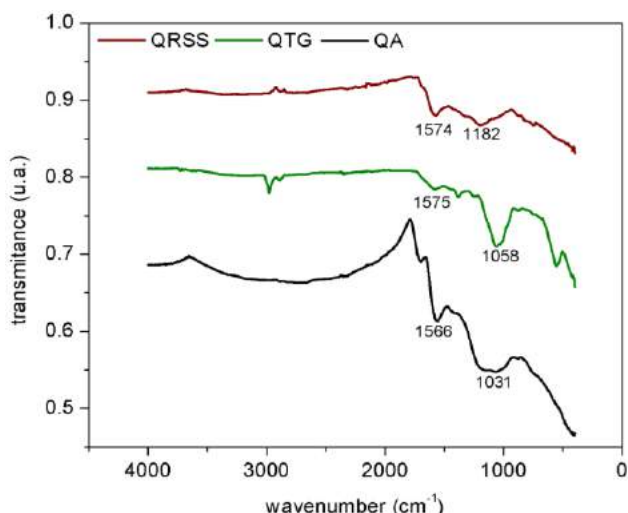


Fig. 6. FTIR spectrum of the adsorbents after chemical activated

3.4. Batch adsorption

Figure 7 shows the percentage of removal of contaminants and the equilibration time for each of adsorbents studied. Adsorption experiments were not conducted with IN-G due to color release showed by ginger. As ginger presents in its composition some natural dyes, it would generate some errors. For IN-RSS adsorbent, there was not removal of the MO even after a prolonged contact time.

Through the analysis of the adsorption process, was possible to notice an increase of the adsorption rate associated with the thermal and chemical treatments of the rubber seed shell and almond adsorbents. The removal percentage increased from 60.29% for QRSS to 100% for QA.

In the case of ginger, chemical treatment caused the loss of functional groups that was responsible for the interactions with adsorbate. As a result, in comparison with thermal treatment, the removal percentage was lower, reaching 56%.

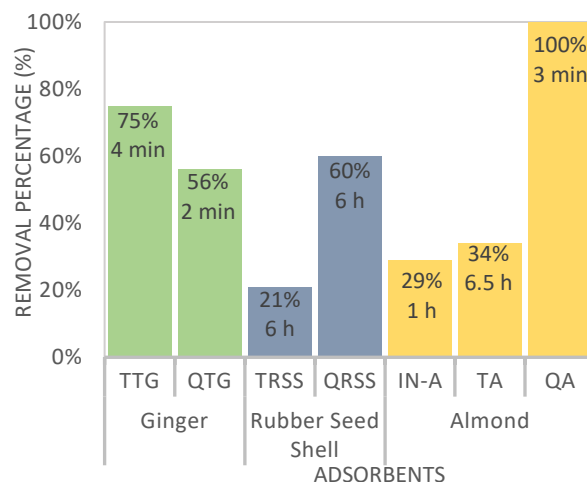


Fig. 7. Removal percentage and equilibrium time obtained for removing glycerol for ginger and MO for rubber seed shell and almond fruit.

4. Conclusion

The byproducts originated from agricultural wastes demonstrated to be effective in the removal of the contaminants. The degradation of the cellulosic material was confirmed by the FTIR analysis. The use of activation of these materials, both thermal and chemical, provided an increase in the surface area and porosity, as it was corroborated by the analysis of BET and SEM.

Despite of that, in the case of ginger, chemical activation did not cause significant structural changes in comparison with the thermal treatment.

Based on the results, it was concluded that the use of biomass in the future is promising and can be applied in different treatment processes in the removal of contaminants.

Acknowledgements

The authors would like to thank FAPERJ and CNPq / PIBIC for their financial support. The Analytical Center of the Chemistry Institute (Univerdade Federal Rural do Rio de Janeiro) for FTIR analysis. This work was carried out with the support of the Higher Education Personnel Improvement Coordination - Brazil (CAPES) - Financing Code 001”.

References

- [1] Mochidzuki K, Sato N, Sakoda, A. Production and characterization of carbonaceous adsorbents from biomass wastes by aqueous phase carbonization. *Adsorption* 2005; 11:669-673.
- [2] Jian X, Zhuang X, Li B, Xu X, Wei Z, Song Y, Jiang E. Comparison of characterization and adsorption of biochars produced from hydrothermal carbonization and pyrolysis. *Environ Technol Innov* 2018; 10:27-35.
- [3] Kaya N, Arslan F, Uzun Z. Production and characterization of carbon-based adsorbents from waste lignocellulosic biomass: their effectiveness in heavy metal removal. *Fullerenes, Nanotub Carbon Nanostructures* 2020; 1-12.
- [4] Cagnon B, Py X, Guillot A, Stoeckli F, Chambat G. Contributions of hemicellulose, cellulose and lignin to the mass and the porous properties of chars and steam activated carbons from various lignocellulosic precursors. *Bioresour Technol* 2009; 100:292-298.
- [5] Aljeboree A, Alshirifi A, Alkaim A. Kinetics and equilibrium study for the adsorption of textile dyes on coconut shell activated carbon. *Arab J Chem* 2017; 10:S3381-S3393.
- [6] Zhang Y, Liu W, Zhang J, Zhu W, Ma Q, Zong X, Xu C. Influence of micro-alloying with Cd on growth pattern, mechanical properties and microstructure of as-cast Mg₉₄ Y_{2.5} Zn_{2.5} Mn₁ alloy containing LPSO structure. *Mater Sci Eng A* 2019; 748:294-300.
- [7] Ma X, Li L, Zeng Z, Chen R, Wang C, Zhou K, Li H. Synthesis of nitrogen-rich nanoporous carbon materials with C3N-type from ZIF-8 for methanol adsorption. *Chem Eng J* 2019; 363:49-56.
- [8] Habaki, H.; Hayashi, T.; Sinthupinyo, P.; Egashira, R. Purification of glycerol from transesterification using activated carbon prepared from *Jatropha* Shell for biodiesel production. *J Environ Chem Eng* 2019; 7: 103303.
- [9] Rattanapan S, Srikrum J, Kongsune P. Adsorption of methyl orange on coffee grounds activated carbon. *Energy Procedia* 2017; 138:949-954.
- [10] Junior, SS. Carvão ativado produzido a partir do endocarpo de coco da baía (*Coccoloba nucifera*) aplicado no tratamento de efluente têxtil. Dissertação – Departamento de Engenharia Civil e Ambiental, UFPPB, João Pessoa, 2014.
- [11] Moreschi, S. R. M.; Leal, J. C.; Braga, M. E. M.; Meireles, M. A. A. Ginger and turmeric starches hydrolysis using subcritical water + CO₂: The effect of the SFE pre-treatment. *Braz J Chem Eng* 2006; 23:235-242.
- [12] Supardan, M. D.; Fuadi, A.; Alam, P. N.; Arpi, N. Solvent Extraction of Ginger Oleoresin using Ultrasound. *MAKARA Sci Ser* 2011; 15:163-167.
- [13] Lin B, Zhou J, Qin Q, Song X, Luo Z. Thermal behavior and gas evolution characteristics during co-pyrolysis of lignocellulosic biomass and coal: A TG-FTIR investigation. *J Anal Appl Pyrolysis* 2019; 144:104718.
- [14] Guediri A, Bouguettoucha A, Chebli D, Chafai N, Amrane A. Molecular dynamic simulation and DFT computational studies on the adsorption performances of methylene blue in aqueous solutions by orange peel-modified phosphoric acid. *J Mol Struct* 2019; 127290.
- [15] Zhou N, Chen H, Feng Q, Yao D, Chen H, Wang H, Lu X. Effect of phosphoric acid on the surface properties and Pb (II) adsorption mechanisms of hydrochars prepared from fresh banana peels. *J Clean Prod* 2017; 165:221-230.
- [16] Stavrinou A, Aggelopoulos CA, Tsakiroglou CD. Exploring the adsorption mechanisms of cationic and anionic dyes onto agricultural waste peels of banana, cucumber and potato: adsorption kinetics and equilibrium isotherms as a tool. *J Environ Chem Eng* 2018, 6:6958-6970.
- [17] Chen H, Zhao J, Wu J, Dai G. Isotherm, thermodynamic, kinetics and adsorption mechanism studies of methyl orange by surfactant modified silkworm exuviae. *J Hazard Mater* 2011; 192:246-254.
- [18] Luis-Zarate VH, Rodriguez-Hernandez MC, Alariste-Mondragon F, Chazaro-Ruiz LF, Rangel-Mendez JR. Coconut endocarp and mesocarp as both biosorbents of dissolved hydrocarbons in fuel spills and as a power source when exhausted. *J Environ Manage* 2018; 211:103-111.
- [19] Li X, Wang Z, Ning J, Gao M, Jiang W, Zhou Z, Li G. Preparation and characterization of a novel polyethyleneimine cation-dye modified persimmon tannin bioadsorbent for anionic dye adsorption. *J Environ Manage* 2018; 217:305-314.
- [20] Garg U, Kaur MP, Jawa GK, Sud D, Garg VK. Removal of cadmium (II) from aqueous solutions by adsorption on agricultural waste biomass. *J Hazard Mater* 2008; 154:1149-1157.

Influence of Residence Time and Temperature of Pyrolysis on the Production of Biochar from Sewage Sludge

Victória Regina Celso Monteiro^a, Carlos Eduardo Barquilla^a, Maria Cristina Borba Braga^a

^a Federal University of Paraná - UFPR, Coronel Francisco Heráclito dos Santos, 350. Block 5 – DHS – Centro Politécnico – Jardim das Américas, Curitiba, 81.531-900, Brazil

Abstract

The amount of sewage sludge generated in sewage treatment plants due to urbanization and the improvement of sanitation in larger cities, has raised concerns on adequate and more sustainable alternatives for the treatment, disposal and reuse of sludge. Pyrolysis is an alternative for the reuse of sludge because it produces, among other advantages, biochar, a multifunctional material. However, many parameters can influence the characteristics of the biochar produced by pyrolysis. The objective of this research was to investigate the influence of residence time and temperature of pyrolysis in the characteristics of the biochar produced from sewage sludge of aerobic and anaerobic treatment plants. The sludges were collected from two sewage treatment plants, dried and pyrolyzed with temperatures of 450°C, 650°C, and 850°C and residence times of 60, 90 and 120 minutes. The parameters pH, pyrolysis yield, surface area, pore volume and pore size were analyzed and used as responses for an experimental design. Ten types of biochar were obtained with yields varying from 34.9% to 56.2%, surface area from 3.7 m².g⁻¹ to 114.0 m².g⁻¹ and pore size from 16.6 Å to 52.2 Å. The pH varied in the range of 4.6 to 9.9, and the pore volume between 0.001 cm³.g⁻¹ and 0.105 cm³.g⁻¹. Based on the calculated effects of the experimental design, both variables exerted influence on the characteristics of the biochar. Nevertheless, the more expressive effects were related to the temperature of pyrolysis. Biochars 4 and 8, produced at 850°C, presented the best characteristics to be used as adsorbents.

Keywords: thermal treatment; circular economy; biochar; experimental design, adsorption.

1. Introduction

Sewage sludge is a biosolid produced in sewage treatment plants, and the amount generated is closely related to the extension of collection and the process used in the treatment facility. As the urban population grows and, in particular, the universalization of sanitation actions become of major importance, in countries such as Brazil, the amount of sewage sludge produced is directly related to the amount of sewage collected and treated. Thus, there is a need to develop alternatives for the treatment and adequate disposal of this biosolid.

Data on amounts of sewage sludge produced in Brazil are scarce, however, the production can be estimated by information on both the extension of the collection system and the efficiency of the treatment plant. Considering that approximately 87 million inhabitants are connected to the sewage collection network, it can be estimated that from 9 thousand to 13 thousand tons of dewatered sewage sludge per day is produced [1].

Nevertheless, in order to an alternative of sewage sludge treatment or final disposal to be adequately applied, each one of them depends on an accurate evaluation of potentialities and possibilities for each region or city.

According to data collected by the 2008 National Basic Sanitation Survey [2], the disposal of sludge in sanitary landfills has been the most common alternative used in Brazilian cities. However, this action tends to progressively decrease, since the disposal of sludge in landfills conflicts with the 2010 National Solid Waste Policy. This law determines that no waste that still can be reused, is allowed to be disposed of in landfills. It also establishes that the amount of residues disposed of in a landfill should be reduced, reused and recycled [3,4].

Among all alternatives of treatment and final disposal of sewage sludge, agricultural recycling, landfill disposal, incineration, composting and recovery of degraded areas [5], the thermal treatment by pyrolysis can be considered as an alternative for the treatment and recycling of sewage sludge. This technology is in accordance with the concept of circular economy; a model in which

recirculation of resources and energy, resource minimization and resource recovery are advocated [6].

Pyrolysis, a thermal treatment technique, has been developed over the last decade, and due to recovery of minerals and a more effective energy recovery if compared with incineration, can be considered a sustainable method for sludge treatment [7]. This is due to the multifunctional characteristics of the biochar, such as carbon sequestration, contaminant immobilization, greenhouse gas reduction, soil fertilization and, water and effluent treatment [8]. In addition, the pyrolysis promotes sludge mass reduction to be disposed of and elimination of microorganisms present in the sludge, which is related to a safer product to be reused.

Usually, biochar is produced by the carbonization of materials by pyrolysis or thermal decomposition at high temperatures, between 400°C and 900°C, in the absence of oxygen. In this process, many parameters can be varied, such as residence time, pyrolysis temperature, pressure, heating rate and method, drying of feedstock, chemical activation, crushing, and sieving, which changes physical and chemical characteristics of the biochar [9, 10].

According to Agrafioti et al. [10], the optimal pyrolysis temperature depends on the intended application. High temperatures can improve the porosity of the biochar produced, which could increase the efficiency of pollutant adsorption.

Thus, the main goal of this research was to investigate the influence of residence time and the temperature of pyrolysis on the characteristics of biochar produced using sludge from aerobic and anaerobic sewage treatment plants, with a view to its use as an adsorbent.

2. Methodology

2.1. Sludge collection and pyrolysis

To perform the biochar production tests, sewage sludge was collected from an aerobic and an anaerobic treatment plant, located in Curitiba, Paraná. Samples of sludge from both facilities were collected after dewatering and before lime application. A 30-litre aliquot of sludge was collected, taken to the laboratory and dried in laboratory oven (Lucadema) at 100°C, for approximately 72 hours. After drying, the sludge samples were stored in plastic bags, closed and kept at room temperature until use.

The design of experiments was applied to optimize the pyrolysis conditions to be tested. This was carried out by two-level-two factors (2²) experimental design with a central point, using the methodology described by Barros Neto et al. [11].

The selected variables were residence time and temperature of pyrolysis, to be studied at two levels, the low represented by (-), the high by (+) and the central point, represented by (0), as presented in Table 1. The same design was used for aerobic and anaerobic sludges.

Starting from the definition of variables and levels an organized 5-condition sequence was specified, as presented in Table 1.

Table 1. Experimental design for biochar production using aerobic and anaerobic sludges

Variables	Levels		
	Low (-)	Central Point (0)	High (+)
Time (t) (min)	60	90	120
Temperature (T) (°C)	450	650	850
Conditions	Variables		
	t	T	t x T
1	-	-	+
2	+	-	-
3	-	+	-
4	+	+	+
5	0	0	0

For the pyrolysis, samples of dried sludges were taken and ground in grit with a pistil, transferred to covered porcelain crucibles, weighed, sprayed with nitrogen gas for 2 minutes, in accordance with the procedure described by Prado [12]. Aiming at reducing the contact with oxygen, the crucibles were wrapped in aluminum foil.

The crucibles were taken to the muffle-furnace (Fornitec, F3-DM/T - three phase), where they were also sprayed with nitrogen gas through the door hole, for 2 minutes.

Five pyrolysis test sets were carried out, with medium heating rate of 14°C min⁻¹. The temperatures were 450°C, 650°C and 850°C with residence times of 60 min, 90 min and 120 min.

After the muffle-furnace had cooled down, biochars were removed, weighed, ground to powder in grit with a pistil, passed through a 425-µm sieve and stored in sterilized plastic bottles.

2.2. Initial characterization of biochar

- pH

pH values were determined using 4 g of biochar in 10 mL of distilled water, mixed in falcon tubes for 60 seconds and let to rest for 1 hour. After this time,

the samples were lightly shaken and the pH was measured with a stand pHmeter (QX 1500 Plus – Qualxtron) [13].

- **Pyrolysis Yield**

The pyrolysis yield was determined as the ratio of the weight of the produced biochar to the dry weight of the sewage sludge before pyrolysis [10].

- **Surface Area, Pore Size and Pore Volume**

In order to determine the surface area, the pore size and the pore volume, a Quantachrome NovaWin – Nova Instrument was used to obtain the N₂ gas adsorption and desorption isotherms. Before the analyses the samples were outgassing for 4 hours in 120°C. These procedures were performed in the Mineralogy of Soils Laboratory, at the Department Soil and Agricultural, of Paraná Federal University.

3. Results and Discussion

After pyrolysis, ten types of biochar were obtained changing temperatures and residence times. The biochars are referred to as shown in Table 2.

Table 2. Denomination of produced biochars according to the characteristics.

Biochar	Type of Sludge	Residence Time	Temperature of Pyrolysis
Bio 1	Aerobic	60 min	450°C
Bio 2	Aerobic	120 min	450°C
Bio 3	Aerobic	60 min	850°C
Bio 4	Aerobic	120 min	850°C
Bio 5	Aerobic	90 min	650°C
Bio 6	Anaerobic	60 min	450°C
Bio 7	Anaerobic	120 min	450°C
Bio 8	Anaerobic	60 min	850°C
Bio 9	Anaerobic	120 min	850°C
Bio 10	Anaerobic	90 min	650°C

The pyrolysis yield, pH, surface area, pore volume and pore size of the produced biochars are presented in the Table 3. As it can be observed, the pyrolysis yield slightly decreased with the increase of the residence time. It can be stressed that for the time of pyrolysis of 60 min used to treat Bio 1, the pyrolysis yield was 45.9%, whereas Bio 2 with residence time of 120 minutes presented a yield of 43.9%, a variation of 2 percentile points. The same behavior can be observed between the biochars 3-4, 6-7 and 8-9.

Table 3. Pyrolysis yield, pH, surface area (SA), pore volume (PV) and pore size (PZ) of the produced biochars

Biochar	Yield (%)	pH	SA (m ² .g ⁻¹)	PV (cm ³ .g ⁻¹)	PS (Å)
Bio 1	45.9	7.4	3.7	0.001	52.2
Bio 2	43.9	8.6	9.1	0.015	32.4
Bio 3	35.6	8.1	99.7	0.083	16.6
Bio 4	34.9	8.2	114.4	0.098	17.1
Bio 5	38.2	9.9	26.7	0.029	21.7
Bio 6	56.2	7.6	16.7	0.022	26.4
Bio 7	54.3	7.7	17.6	0.023	25.7
Bio 8	45.3	5.0	104.2	0.105	20.2
Bio 9	45.6	4.6	95.6	0.095	19.9
Bio 10	51.4	9.3	24.2	0.024	19.5

However, the yield decreased considerably with the increase in the temperature of pyrolysis. For instance, it has been observed that for Bio 6, treated at 450°C, for 60 min, the yield was 56.2%, whereas for Bio 8, treated at 850°C, for 60 min, the yield was 45.3%. These results represent a decrease of 10 percentile points. Biochars 2 and 3, as well as 7 and 9 presented the same behavior.

Influence of pyrolysis temperature on the production of biochar from sewage sludge was also observed by other authors [10,14,15]. Biochars produced on the basis of central point of experimental design, which considered intermediate values of temperature (650°C) and time (90 min), presented intermediate yield of 38.2% and 51.4% for the biochars 5 and 10, respectively. The results showed that the biochars produced from anaerobic sludge presented higher yields, approximately 10 percentile points above the value produced by those from aerobic sludge, under all temperatures and residence times tested.

Values of pH varied from 4.6, for Bio 9 to 9.9, for the Bio 5. According to Ok et al., most of the biochars are slightly basic, and the temperature of pyrolysis affects the resulting pH values of biochars. Therefore, there is a tendency of increasing pH values with increasing temperature of pyrolysis. On the other hand, lower temperatures can produce more acidic biochars [9].

Regarding the effect of temperature, it was observed that biochars produced from aerobic sludge, at 850°C, presented pH values of approximately 8.0. However, among the biochars

produced from aerobic sludge, Bio 5, treated at 650°C, showed the highest pH value of all aerobic biochars, i.e., 9.9.

On the other hand, biochars produced at 850°C from anaerobic sludge presented decreasing values of pH with increasing temperature. As an example of this characteristic, Bio 8 and Bio 9 presented pH values of 5.0 and 4.6, respectively. Nevertheless, Bio 10, treated at 650°C, followed the same tendency as that of aerobic biochars, with a pH value of 9.3, higher than that of Bio 6 and Bio 7, both treated at 450°C.

Méndez et al. [16] produced 10 biochars, 5 from aerobic sludge, and 5 from anaerobic sludge from different treatment plants in Madrid. In this study the temperature of pyrolysis was 450°C and the residence time was 1 hour. These authors observed that pH values varied from 7.1 to 8.1. This range can be compared to that of biochars 1, 3, 4, 6, and 7, which varied from 7.4 to 8.2. On the other hand, Figueredo et al. [17], produced biochars at 350°C and 500°C, with resulting pH values of 4.5 and 5.2, respectively. These values were close to those observed for Bio 8 and Bio 9.

Regarding the results on the surface area, it was observed that there was a considerable increase as the temperature of pyrolysis increased, as shown in Table 4. It can be observed that the surface area of biochars produced from aerobic sludge increased from 3.7 m².g⁻¹ to 99.7 m².g⁻¹, and from 9.1 m².g⁻¹ to 114.4 m².g⁻¹, under temperatures of 450° and 850°C, respectively. Similar behavior was observed for biochars produced from anaerobic sludge. The surface area increased from 16.7 m².g⁻¹ to 104.2 m².g⁻¹, and from 17.5 m².g⁻¹ to 95.6 m².g⁻¹ at the same temperature of pyrolysis, respectively.

Alterations in the surface area of biochars are intrinsically related to the temperature of pyrolysis. The resulting alterations can be attributed to changes in the chemical structure of the original matrix submitted to thermal treatment. As the temperature of pyrolysis increases, the aromaticity in the structure of the biochar also increases. The same response is observed when it comes to micro and mesopores as they are related to higher specific area [10]. In addition, the surface area is an important characteristic associated with the adsorption capacity of contaminants. It also provides habitat for the development of biofilm and retention of water and nutrients, in case the biochars are applied in soils [8].

Pore volume varied from 0.001 cm³.g⁻¹ to 0.105 cm³.g⁻¹, and a small variation was observed as a function of the residence time. In relation to pore

size, according to the IUPAC classification, micropores are those smaller than 20 Å, whereas, mesopores are between 20 Å and 500 Å and macropores are bigger than 500 Å [18]. Thus, the pore sizes of biochars 1, 2, 5, 6, and 7 can be classified as mesopores, whereas, biochars 3, 4, 9, and 10 as micropores. Bio 8 presented a pore size of 20.2 Å and, therefore, close to the smallest value of the micropore classification.

Based on the parameters evaluated, it can be pointed out that Bio 4 and Bio 8 present higher surface area, pore volumes, and pore sizes, which classifies both as micropores. Hence, with the potential for being used in further studies involving the adsorption process.

Results presented in Table 4 are those produced from the association among signals from the experimental design and the obtained parameters (yield, pH, surface area, pore volume and pore size).

Table 4. Effects of residence time, pyrolysis temperature and combined effects

Effects of Experimental Design			
Parameters	t	T	t × T
Yield (%)			
Aerobic Biochar	-1.3	-9.6	0.6
Anaerobic Biochar	-0.8	-9.8	1.1
pH			
Aerobic Biochar	0.6	0.1	-0.6
Anaerobic Biochar	0.1	-3.1	0.0
Surface Area			
Aerobic Biochar	10.1	100.7	4.7
Anaerobic Biochar	-3.9	82.8	-4.8
Pore Volume			
Aerobic Biochar	0.015	0.083	0.001
Anaerobic Biochar	-0.005	0.078	-0.006
Pore Size			
Aerobic Biochar	-9.7	-25.5	10.2
Anaerobic Biochar	-0.5	-6.0	0.2

Notes: t: residence time, T: pyrolysis temperature

The positive (implicit) signals indicate an increase in the values of the parameters, whereas the negative values indicate a decrease.

As presented in Table 4, residence time (t) and temperature of pyrolysis (T) were associated with negative effects on the yield and the size of pores of aerobic and anaerobic biochars, promoting a decrease in the yield and pore size values. However, the effect of 'T' is more expressive than 't' (-1.3 and -9.6 for "t" and "T", respectively, for the aerobic biochars yield, for example). This evaluation agrees with the 10 percentile points of decrease observed in yield with the increasing of the temperature of pyrolysis (T), while only 2 percentile points of

decrease was observed with the increasing of the residence time (t).

Nevertheless, the pH value of biochars produced from aerobic sludge showed a different correlation. In this case, the residence time (t) presented a stronger effect than that of the temperature of pyrolysis (T), whereas the combined effect ($t \times T$) was negative, implying that both parameters acting together can cause a decrease in pH.

The surface area, pore volumes, and pore sizes of both aerobic and anaerobic biochars were more affected by the temperature of pyrolysis (T) than by the residence time (t). In any circumstances, the combined effect ($t \times T$) was higher than that of the temperature of pyrolysis, with regard to all parameters evaluated.

The negative effect of the residence time on the surface area confirms the slight decrease of the value of this parameter, in particular when the residence time increased from 60 min to 120 min, as it was observed for Bio 8 and Bio 9 ($104.2 \text{ m}^2 \cdot \text{g}^{-1}$ to $95.6 \text{ m}^2 \cdot \text{g}^{-1}$).

Three-dimensional images (Figure 1) relate the temperature of pyrolysis and residence time with the surface area of aerobic and anaerobic biochars.

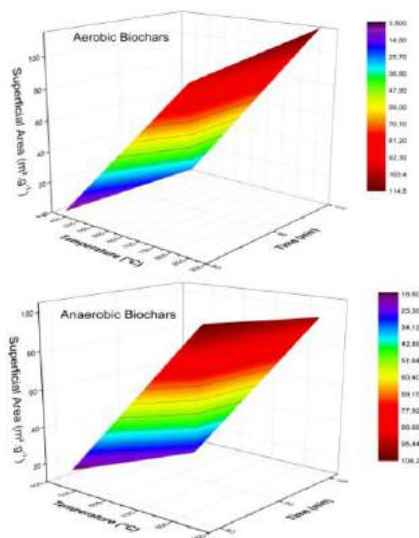


Fig 1. Superficial area related to time and temperature of pyrolysis of aerobic and anaerobic biochars

Three-dimensional images relating the temperature of pyrolysis and residence time with pore volume and pore size, respectively, for aerobic and anaerobic biochars are presented in Figures 2 and 3.

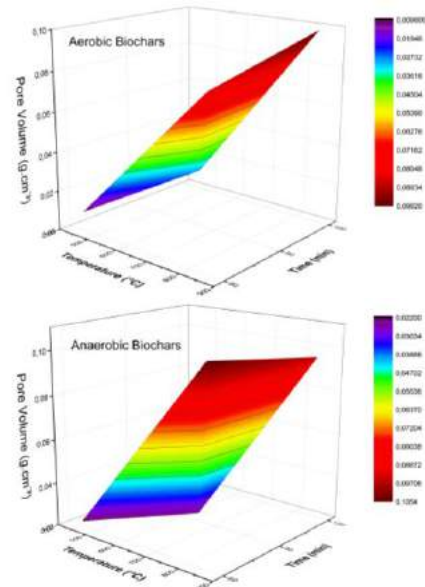


Fig 2. Pore volume related with time of pyrolysis and temperature of aerobic and anaerobic biochars

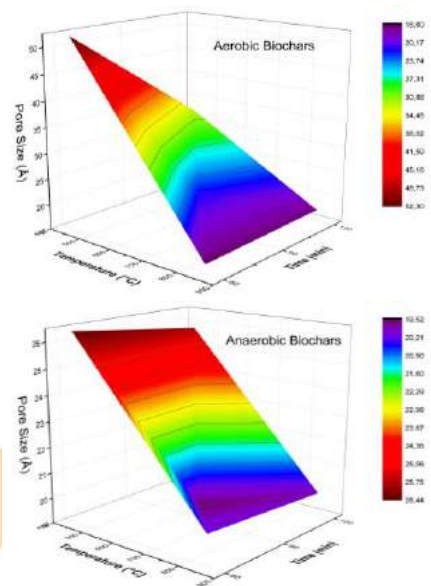


Fig 3. Pore size related with time and temperature of pyrolysis of aerobic and anaerobic biochars

Regarding biochar produced from aerobic sludge, as it can be observed in Figures 1, 2, and 3, the largest surface area and pore volumes were obtained in association with the highest temperature (850°C) and residence time (120 min). On the other hand, the biggest pore size was obtained at the lowest temperature and residence time.

Results for the biochars produced from anaerobic sludge presented the highest surface area and pore volume at the highest temperature of pyrolysis and at the lowest residence time (60 min), which disagree with those of aerobic biochars. The smallest pore size was related to the intermediate temperature and residence time (650°C and 90 min).

Therefore, it can be pointed out that temperature and residence time exert a great deal of influence on the thermal treatment by pyrolysis. This is due to the direct effect on the surface area, the pore volume, and the pore size of biochars. Based on these results, these parameters could be adjusted and manipulated to find the best condition to prepare the biochars.

4. Final Considerations

The experimental design has proven to be an adequate tool for planning the phases of pyrolysis, since it helped to organize and optimize the preparation of biochars. Furthermore, the adopted approach has facilitated the calculations of the effects caused by both temperature of pyrolysis and residence time in the evaluated parameters.

Biochars produced from aerobic and anaerobic sludges, presented similar characteristics. However, regarding biochar production, the anaerobic sludge was related to a higher yield for all tested conditions, and also generate acidic biochars that were prepared in high temperatures. These results indicated that the pH was not only influenced by the two variables studied by also by the inherent characteristics of the sludge.

In general, it was observed that both variables residence time and temperature of pyrolysis affected the evaluated parameters. Nevertheless, a major impact on the characteristics of the biochar seemed to be caused by the temperature of pyrolysis.

Finally, it can be stressed that the biochars 4 and 8 were the best produced. This is due to having presented the largest surface areas, pore volumes and micropores, which can indicate an adequate potential for adsorption application.

Acknowledgements

The authors acknowledge the Water Resources and Environmental Engineering Post-Graduate Programme, Paraná Federal University (PPGERHA- UFPR) for funding and CAPES-DS for the scholarship granted.

References

[1] Andreoli C V., Sperling M Von, Fernandes F (2014) Lodo de esgotos: tratamento e disposição final, 2a Edição. Editora Universidade Federal de Minas Gerais, Belo Horizonte-MG
[2] Instituto Brasileiro de Geografia e Estatística - IBGE (2010) Pesquisa Nacional De Saneamento Básico - 2008. Rio de Janeiro - RJ

[3] Brasil (2010) Lei 12.305 - Institui a Política Nacional de Resíduos Sólidos; altera a Lei no 9.605, de 12 de fevereiro de 1998; e dá outras providências
[4] Bringhenti JR, Boscov MEG, Piveli RP, Günther WMR (2018) Codisposição de lodos de tratamento de esgotos em aterros sanitários brasileiros: aspectos técnicos e critérios mínimos de aplicação. Eng Sanit e Ambient 23:891–899.
[5] Von Sperling M (2005) Introdução á Qualidade das Aguas e ao Tratamento de Esgotos, 3a. Departamento de Engenharia Sanitária e Ambiental, Universidade Federal de Minas Gerais, Belo Horizonte
[6] Prieto-sandoval V, Jaca C, Ormazabal M (2018) Towards a consensus on the circular economy. J Clean Prod 179:605–615.
[7] Stunda-Zujeva A, Kreicbergs I, Medne O (2018) Sustainable utilization of sewage sludge: Review of technologies. Key Eng Mater 762:121–125.
[8] Ok YS, Uchimiya SM, Chang SX, Bolan N (2016) Biochar Production, Characterization and Applications. Taylor & Francis Group, Nova Iorque
[9] Lehmann J, Stephen Joseph (2009) Biochar for Environmental Management: Science and Tecnology. Earthscan, London, UK
[10] Agrafioti E, Bouras G, Kalderis D, Diamadopoulos E (2013) Biochar production by sewage sludge pyrolysis. J Anal Appl Pyrolysis 101:72–78.
[11] BARROS NETO B., SCARMINIO IS., BRUNS RE (2001) Como fazer experimentos: Pesquisa e desenvolvimento na ciência e na indústria, 2a. Editora Unicamp, Campinas-SP
[12] Prado LL do (2018) Utilização de lodo de esgoto pirolisado como adsorvente de amônio de lixiviado de aterro sanitário. Dissertação (mestrado). Universidade Federal do Paraná
[13] EMBRAPA (2017) Manual De Métodos de Análise de Solo, 3o Edição. Embrapa Solos, Brasília- DF
[14] Zielínska A, Oleszczuk P (2015) Evaluation of sewage sludge and slow pyrolyzed sewage sludge-derived biochar for adsorption of phenanthrene and pyrene. Bioresour Technol 192:618–626.
[15] Chen H, Zhai Y, Xu B, et al (2015) Characterization of bio-oil and biochar from high-temperature pyrolysis of sewage sludge. Environ Technol (United Kingdom) 36:470–478.
[16] Méndez A, Gascó G, Freitas MMA, et al (2005) Preparation of carbon-based adsorbents from pyrolysis and air activation of sewage sludges. Chem Eng J 108:169–177.
[17] Figueredo NA, da Costa LM, Melo LCA, et al (2017) Characterization of biochars from different sources and evaluation of release of nutrients and contaminants. Rev Cienc Agron 48:395–403.
[18] Rouquerol J, Avnir D, Fairbridge CW, et al (1994) Recommendations for the Characterization of Porous Solids. Great Britain



Synthesis and Characterization of SAPO-18 and MeAPSO-18 Molecular Sieves: Effect of the Chemical Composition on the Acidity

Guilherme Raymundo Sá^a, Izadora da Silva Santos^a, Bianca Pedroso Silva Santos^a, Núbia Caroline de Almeida^a, Lindoval Domiciano Fernandes^a

^a Department of Chemical Engineering, Universidade Federal Rural do Rio de Janeiro, Rod BR 465 Km 7, Seropédica, CEP 23897-000, Brazil

Abstract

Samples of SAPO-18 with SiO₂/Al₂O₃ molar ratio (SAR) values equal to 0.1, 0.2 and 0.4 were prepared using a standard literature procedure. Additionally, samples of MeAPSO-18 were also prepared using the Co²⁺ and Fe³⁺ transition metal cations, with Me/Al₂O₃ molar ratio equals to 0.01, 0.02, 0.03 or 0.04. The synthesized samples were characterized by X-ray diffraction, nitrogen adsorption, ³¹P, ²⁹Si and ²⁷Al solid-state NMR spectroscopy, scanning electron microscopy and temperature programmed desorption of ammonia. It was observed samples of pure SAPO-18 (AEI type phase) having good crystallinity have been obtained from SAPO-18 and MeAPSO-18 synthesis gels. This observation was confirmed by the values of the micropore volume determined from their nitrogen adsorption isotherms. As for total acidity, a maximum at a SiO₂/Al₂O₃ molar ratio of 0.2 was noted increasing framework silicon content. This indicated that silicon atoms were inserted as isolated sites for lower SAR values and as silicon islands at higher SAR values. For the CoAPSO-18 samples, it was observed Co content does not influence acidity significantly. However, Fe presence in the FeAPSO-18 samples resulted to a large increase in the total acidity.

Keywords: silicoaluminophosphates; SAR; acidity; catalysis; low pore size molecular sieves

1. Introduction

Microporous crystalline aluminophosphates (called AlPO₄-n) formed of AlO₄ and PO₄ tetrahedral connected by their vertices, form a family of molecular sieves with adsorption capacity similar to that presented by zeolites [1,2]. However, its application in heterogeneous catalysis is limited by the fact its structure is electrically neutral and, therefore, does not present active centers. However, isomorphic substitution of phosphorous for silicon atoms results in a negatively charged structure, requiring the presence of extra lattice cations to compensate these charges. When the compensation cation is a proton, we have a material presenting Bronsted acidity, which may be active in acid catalysis. The isomorphic substitution of aluminum for transition metal cations (Fe³⁺, Ni²⁺, Co²⁺, Mn²⁺, and so on) gives materials having different acidic properties called MeAPSO-n [3-11].

Recently, silicoaluminophosphates and derivatives presenting small pores have been investigated as selective catalysts for the conversion of methanol into light olefins [12-34]. These materials exhibit selectivity for the formation of low

molecular weight olefins due the porous structure, which has not enough space for the growth of the carbon chain beyond C₃. Aluminophosphates and silicoaluminophosphates having AEI type structure present orthorhombic C₂cm symmetry, with the following unit cell parameters: a = 13.7 Å, b = 12.6 and c = 18.5 Å. They have a tridimensional pore system, consisting of 8-membered ring pore channels with diameter apertures about 3.8 Å. Martinez-Franco et al. [5] related Si distribution in SAPO-18 samples depended strongly on the organic structure directing agent (OSDA) used. They noted using N,N-diisopropylethylamine as OSDA results in SAPO-18 samples having about 50% of the Si species agglomerated under different Si environments, i.e. as Si (3Al), Si (2Al), Si (1Al) and S (0Al). They also observed for lower Si content, the proportion of isolated Si atoms notoriously increased. Using N,N-dimethyl-3,5-dimethylpiperidinium as OSDA, they noted the formation of SAPO-18 samples presenting almost all Si atoms in the Si (4Al) environment, i.e. as isolated sites. Chen *et al.* [5] observed the formation of SAPO-18 samples presenting agglomerated Si species using N,N-diisopropylethylamine as OSDA.

In a previous work, we have presented a study about the synthesis and characterization of SAPO-34 and MeAPSOs-34 [35]. In that work, results pointed the incorporation of a very small amount of a transition metal into the SAPO-34 structure caused a deep modification on acidity of the resulting sample. As a continuation of that work, a study about the influence of silicon and/or transition metal content over the physical-chemical properties of a silicoaluminophosphate having another crystalline structure (SAPO-18) was made.

2. Experimental Section

2.1. Samples Preparation

SAPO-18 and MeAPSO-18 samples were synthesized using a standard literature procedure [5]. For the SAPO-18 samples synthesis, it was prepared gels having the following molar composition: 1.0 Al₂O₃:0.95 P₂O₅:x SiO₂:1.8 R:50

H₂O, where R is the organic template, the N,N-diisopropylethylamine and x is the SiO₂/Al₂O₃ molar ratio value and was varied in the 0.1-0.4 range. In this preparation, 33.09 g of aluminum hydroxide (76.5% Al₂O₃, Vetec) were added over a solution containing 57.25 g of phosphoric acid (H₃PO₄ 85%, Vetec) in 251.91 g of deionized water. Over this suspension, were added 57.75 g of N,N-diisopropylethylamine (Sigma-Aldrich) and pyrolyzed amorphous silica (Aerosil 200, Degussa-Evonik) in an amount calculated to result in the SiO₂/Al₂O₃ molar ratio desired. After stirring for 15 min, the resulting mixture was placed in Teflon and steel autoclaves and heated at 160 °C for 15 days. The solid obtained was recovered by centrifugation, washed, dried and calcined at 600 °C for 8 h, heating being carried out in a ramp of 0.2 °C/min. These samples were named S_x, where x is the SiO₂/Al₂O₃ molar ratio. For the MeAPSO-18 samples synthesis, it was prepared gels having the following molar composition: 1.0 Al₂O₃:0.95 P₂O₅:0.2 SiO₂:y MeO:1.8 R:50 H₂O, where R is the organic template, the N,N-diisopropylethylamine, and y is the Me/Al₂O₃ molar ratio value which were 0.01, 0.02, 0.03 or 0.04. It was done a similar procedure to that of SAPO-18 synthesis, except for the addition of Co (NO₃)₂ or Fe(NO₃)₃ salts. After stirring for 15 min, the resulting mixture was placed in Teflon and steel autoclaves and heated at 160 °C for 15 days. The solid obtained was recovered by centrifugation, washed, dried and calcined at 600 °C for 8 h, heating being carried out in a ramp of 0.2

°C/min. These samples were named S_xMe-y, where x is the SiO₂/Al₂O₃ molar ratio, Me is the transition metal symbol and y is the Me/Al₂O₃ molar ratio. All samples gels composition are summarized in Table 1.

Table 1. Synthesis gel molar composition.

Sample	Al ₂ O ₃	P ₂ O ₅	SiO ₂	Co	Fe
S0.1	1.0	0.95	0.1	0.0	0.0
S0.2	1.0	0.95	0.2	0.0	0.0
S0.4	1.0	0.95	0.4	0.0	0.0
S0.2Co-y	1.0	0.95	0.2	y	0.0
S0.2Fe-y	1.0	0.95	0.2	0.0	y

2.2 Samples Characterization

Powder X-ray diffraction (XRD) patterns were recorded on a Rigaku Miniflex diffractometer using CuK radiation and operating at 30 kV and 15 A. Typically, the XRD data were collected from 4.0 to 50° (2θ) with 0.05° step size and 2 s step time. The nitrogen adsorption and desorption isotherms at 77 K were measured using a Micrometrics ASAP2020 system. Before the measurements, the samples were outgassed at 300 °C during 12 hours in the degas port of the adsorption analyzer. From these isotherms, the surface area was calculated by BET method, while pore volume and pore size distribution were determined by t and BJH methods, respectively. For determining pore size distribution, the adsorption branch of the isotherms was used.

The acidity of the samples was determined by a homemade multipurpose chemisorption unit, coupled to a quadrupole mass spectrometer Pfeiffer PrismaPlus QMG220, using the dynamic method. Before analysis, the samples were pre-treated at 600 °C for 60 minutes in a 30 cm³/min helium gas flow. The heating rate was 0.5 °C/min with two ramps of 30 minutes each at 150 °C and 350 °C. The chemisorption of ammonia was carried out from a mixture of ammonia in helium (5.0% ammonia, molar based) at a temperature of 100 °C. For such, a 30 cm³/min ammonia/helium mixture gas flow was passed over the sample until its saturation. Then, a 30 cm³/min pure helium gas flow was passed to remove the weakly adsorbed ammonia. This procedure of adsorption and desorption of the weakly adsorbed ammonia was performed twice, and the sample total acidity was calculated from the difference between the two absorption peaks areas. After this stage, a temperature programmed desorption was carried out from 100 °C to 600 °C

under a 30 cm³/min helium gas flow, with a heating ramp of 10°C/min. The micrographs were obtained in a scanning electronic microscope with energy dispersive spectroscopy of X-ray, Leo Model 440i, operating with acceleration voltage of 15 kV and beam current of 50 pA. ³¹P, ²⁹Si and ²⁷Al solid-state NMR spectra were collected on a Bruker Advance II spectrometer with magnetic field strength of 400 MHz. The ²⁹Si MAS NMR spectra were obtained at 79.49 MHz, with 2.70 s pulse delay and at a spinning rate of 8 kHz. The ²⁷Al MAS NMR spectra were collected at 104.26 MHz, with a 3.40 s pulse delay and at a spinning rate of 8 kHz. The ³¹P spectra were collected at 161.97 MHz, with a 3.20 μs pulse delay and at a spinning rate of 8 kHz.

3. Results and Discussion

For the SAPO-18 samples, initially was performed a study varying synthesis time at 160 °C from 5 to 18 days. XRD analysis indicates the obtaining high crystalline SAPO-18 samples from 15 days of hydrothermal synthesis time. For low silicon content samples obtained at shorter synthesis time, it was noted the appearance of diffraction peaks associated to a AFI type contaminant phase. X-ray diffraction patterns of the SAPO-18 samples presenting different SiO₂/Al₂O₃ molar ratios were shown in the Figure 1 and indicated they presented good crystallinity and no contaminant phases.

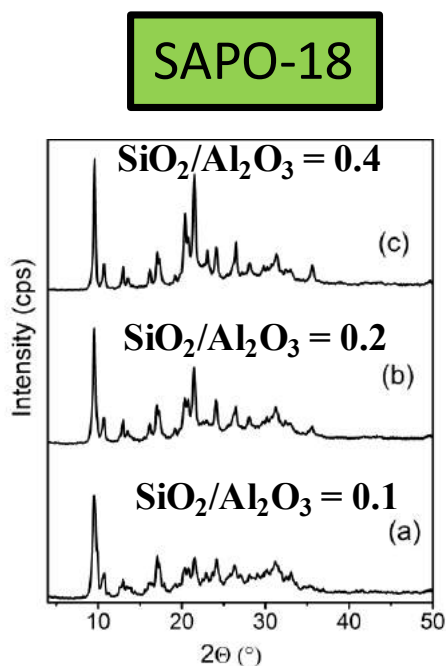


Fig. 1. XRD patterns of SAPO-18

Figure 2 shows the X-ray diffraction patterns of the CoAPSO-18 samples presenting different values of the metal content. From this figure, it can be inferred all CoAPSO-18 samples have good crystallinity and does not showed the presence of contaminant phases. X-ray diffraction patterns of the FeAPSO-18 samples presenting different Fe content, shown in the Figure 3, indicated they presented good crystallinity and no contaminant phases.

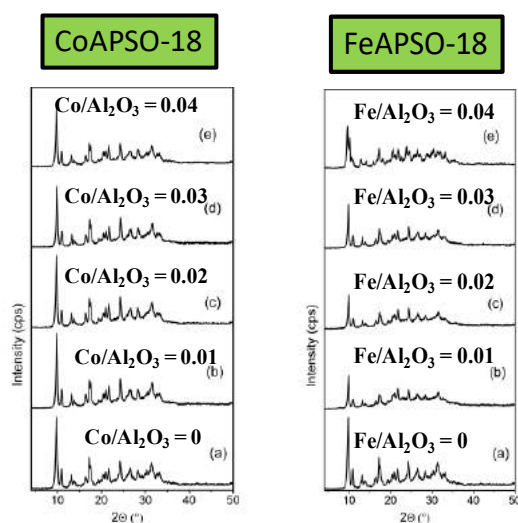


Fig. 2. and Fig.3 XRD patterns of CoAPSO-18 and FeAPSO-18.

²⁷Al MAS NMR spectra presented only one peak, located at about 55 ppm, for all SAPO-18 samples that showed good crystallinity by XRD analysis. This indicated Al atoms were present exclusively in the tetrahedral sites into the SAPO-18 structure. ³¹P MAS NMR spectra presented only one peak at about -20 ppm, corresponding to P(4Al) environments. Figure 4 presents the ²⁹Si MAS NMR spectra of the SAPO-18 samples presenting different SiO₂/Al₂O₃ molar ratio values. It can be observed the NMR spectra of samples with lower Si content (0.1 and 0.2) showed no peaks or only very low peaks. From the spectrum of the sample with SiO₂/Al₂O₃ molar ratio equal to 0.4 a broad peak is observed at about -90 ppm, with shoulders at -95, -100, -105 and -110 ppm, corresponding to the various environments around the Si atoms, i.e., Si (4Al), Si (3Al), Si (2Al), Si (1Al) and Si (0Al), respectively [8]. The distribution of the silicon atoms between the various possible environments indicated the presence of silicon islands. This observation was in agreement with the literature data for SAPO-18 samples prepared using N,N-diisopropylethylamine as OSDA [5-33]. Due to the

small content of the silicon atoms into the SAPO-18 samples, the ^{29}Si MAS NMR spectra presented low signal to noise ratio and it was not possible to quantify the individual peaks assigned to Si(nAl) environments.

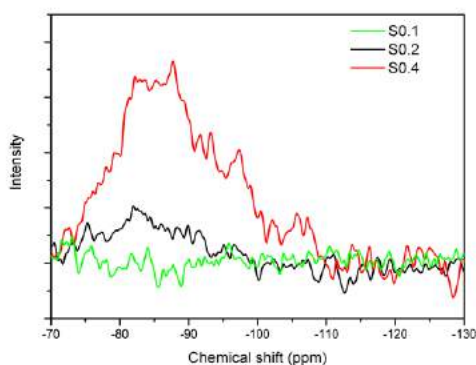


Fig. 4. ^{29}Si MAS NMR spectra of the SAPO-18 samples presenting different values of the $\text{SiO}_2/\text{Al}_2\text{O}_3$ molar ratio.

Table 2 presents the textural properties of the SAPO-18 and MeAPSO-18 synthesized samples, determined from nitrogen adsorption isotherms. These values of micropores volume found in this work are in the range usually reported in the literature for high crystalline SAPO-18 samples.

Table 2. Textural properties measured from nitrogen adsorption isotherms for the SAPO-18 and MeAPSO-18 samples.

Sample	Surface area (m^2g^{-1})		Pore volume (cm^3g^{-1})	
	BET	External	Micropore	Mesopore
S0.1	474	22	0.213	0.093
S0.2	452	32	0.198	0.149
S0.4	440	24	0.194	0.063
S0.2Co-0.01	606	24	0.274	0.05
S0.2Co-0.02	550	15	0.251	0.04
S0.2Co-0.03	578	18	0.263	0.04
S0.2Fe-0.01	321	26	0.171	0.134
S0.2Fe-0.02	381	19	0.170	0.06
S0.2Fe-0.03	439	20	0.197	0.06
S0.2Fe-0.04	644	48	0.280	0.254

It could also be noted all SAPO-18 samples showed high values for external surface area and for the volume of mesopores. This indicates they are formed by very small particles. Scanning electron micrographs of these samples confirmed this observation (Figure 5). From these figures, it can be seen the samples having $\text{SiO}_2/\text{Al}_2\text{O}_3$ molar ratio values of 0.1, 0.2 and 0.4, that was obtained for 15

days of hydrothermal synthesis time at $160\text{ }^\circ\text{C}$ were mainly made up of particles having sizes smaller than 100 nm . Thus, the volume of mesopores should be caused by inter-particle spaces. From these figures, it could be observed some particles having cubelike shape that would be expected for SAPO-18 samples. The S0.2 micrograph showed this sample was formed by smaller particles than S0.1 and S0.4 samples. Really, this sample presented the highest value of mesopore volume.

CoAPSO-18 samples presented values of micropore volume compatible with high crystalline AEI type phase. They presented low values of mesopore volume, indicating they were formed by greater particles. FeAPSO-18 samples presented values of micropore volume slightly smaller of the CoAPSO-18 and SAPO-18 samples, conforming the XRD analysis that indicated smaller crystallinity degree.

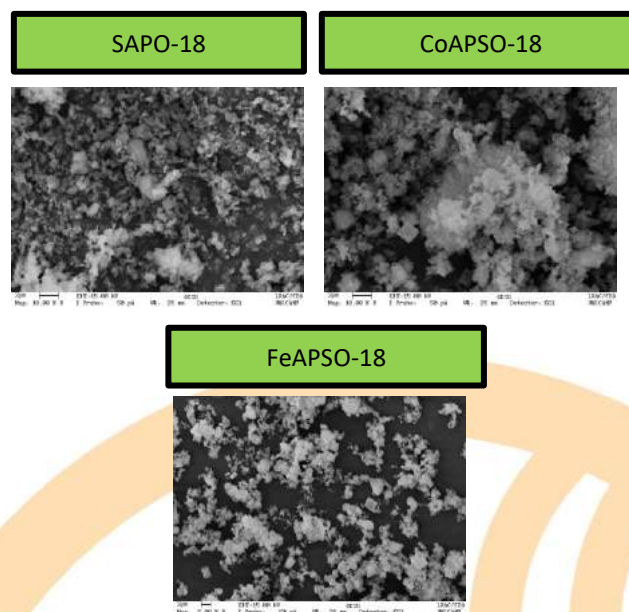


Fig.5. Scanning electron micrographs of the SAPO-18, CoAPSO-18 and FeAPSO-18 samples presenting $\text{SiO}_2/\text{Al}_2\text{O}_3$ molar ratio equals to 0.1, 0.2 and 0.4, respectively.

Table 3 presents the results of total acidity measured by temperature programmed desorption of ammonia (TPD/ NH_3). Among the SAPO-18 series, it was observed a maximum at $\text{SiO}_2/\text{Al}_2\text{O}_3$ molar ratio value of 0.2. Probably at low SAR values, silicon atoms should be occupying isolated sites into the SAPO-18 framework and, thus, each silicon atom corresponded to an acid site.

The samples having $\text{SiO}_2/\text{Al}_2\text{O}_3$ molar ratios equal to 0.1 and 0.2 presented approximately equal values for the total acidity and silicon content. This indicated that, for these samples, each silicon atom generated an acid site. On the other hand, the samples having $\text{SiO}_2/\text{Al}_2\text{O}_3$ molar ratio equal to 0.4 presented values of the total acidity value approximately equal to 50% of the silicon content. This behavior indicated not at all the silicon atoms generated acid sites, probably producing silicon islands, forming acid sites only on its edges [5-33]. The Co content in the CoAPSO-18 series of samples did not influence total acidity significantly. However, Fe content in the FeAPSO-18 series caused a larger increase in the total acidity. These acidity increases were much higher than the metal content, indicating Fe affects silicon atoms dispersion into the FeAPSO-18 structure.

Table 3. SAPO-18 and MeAPSO-18 samples acidity measured by NH_3 -TPD.

Samples	Total acidity ($\mu\text{mol}_{\text{NH}_3}\text{g}^{-1}$)
S0.1	481
S0.2	796
S0.4	677
S0.2Co-0.0	970
S0.2Co-0.01	1084
S0.2Co-0.02	1041
S0.2Co-0.03	1023
S0.2Co-0.04	1479
S0.2Fe-0.01	1767
S0.2Fe-0.02	1433
S0.2Fe-0.03	796

Figure 6 shows the ammonia temperature programmed desorption curves for the set of the SAPO-18 samples. This Figure reveals the area under the curve has a maximum for $\text{SiO}_2/\text{Al}_2\text{O}_3$ molar ratio equals to 0.2. This confirms the observed behavior for the total acidity calculated from the adsorption of ammonia (Table 3). In addition, all samples have acid strength distribution with similar profiles, presenting two types of sites, wherein the weak ones were predominant. This Figure also revealed the presence of two types of acid sites, and incorporation of the Co atoms apparently caused the increase of the proportion of the strongest acid sites until $\text{Co}/\text{Al}_2\text{O}_3$ equals to 0.02. For the highest Co content sample (S0.2Co-

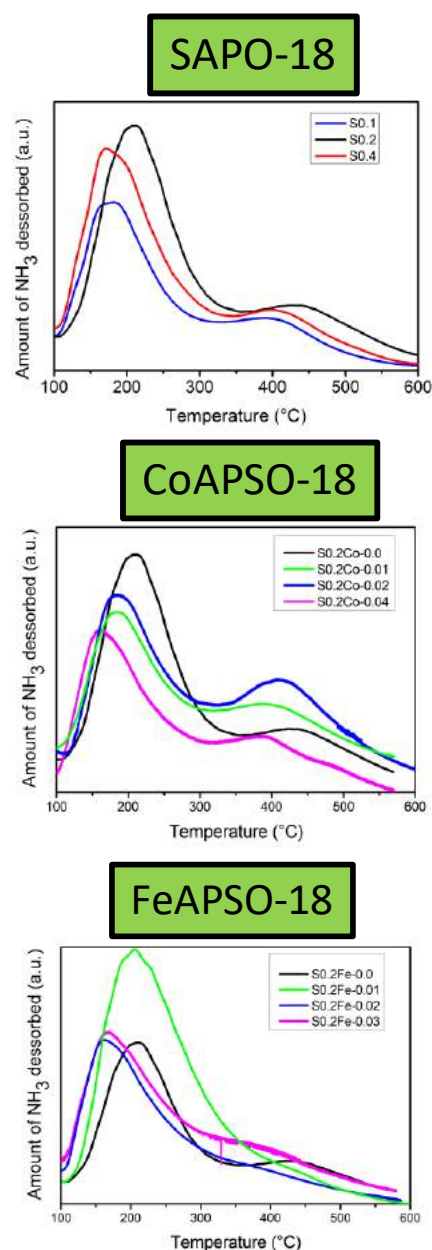


Fig.6. NH_3 -TPD curves of the SAPO-18, CoAPSO-18 and FeAPSO-18 samples having different values of the $\text{SiO}_2/\text{Al}_2\text{O}_3$ molar ratio obtained after 15 days of hydrothermal synthesis at 160 samples, respectively.

0.04), it was observed a decrease in the proportion of the strongest acid site. Already, the incorporation of Fe atoms in the structure of SAPO-18 caused a sharp change in the ammonia desorption profile, and in FeAPSO-18 samples is not observed the presence of the peak associated with strong acidity. Thus, the incorporation of Fe atoms in the crystal lattice of SAPO-18 resulted in an increase of acid sites total number, but a decrease in strong acidity.

4 Conclusions

Through the synthesis procedures used in this work, it was possible to prepare SAPO-18, CoAPSO-18 and FeAPSO-18 samples having good crystallinity and presenting different silica and the transition metal contents. It was observed total acidity of the SAPO-18 samples had a maximum with increasing framework silica content. This indicates for lower concentrations of silica, silicon atoms were inserted into the structure as isolated sites, while for the highest levels, they were inserted as silicon islands forming acid sites only on its edges.

Co and Fe atoms' incorporation into the SAPO-18 structure caused different behaviors. While CoAPSO-18 samples showed only small differences in both total acidity and acid sites strength distribution, Fe atoms' incorporation caused an increase in the total acidity and reduction of the stronger acid sites proportion.

Acknowledgements

We thank Petrobras S/A for financial support and FEQ/UNICAMP for the scanning electron micrographs.

References

1. B.M. Lok, C.A. Messina, R.L. Patton, R.T. Gajek, T.R. Cannan, E.M. Flanigen. Crystalline silicoaluminophosphates. U. S. Pat. 4440871 (1984)
2. B. Lok, C. Messina, R. Pation, R. Gajek, T. Cannan, E. Flanigen, J. Am. Chem. Soc. 106, 6092 (1984)
3. A.M. Prakash, S. Unnikrishnan, J. Chem. Soc. Faraday Trans. 90(15), 2291 (1994)
4. A.M. Prakash, M. Hatmann, L. Kevan, Chem. Mater. 10(3), 932 (1998)
5. J. Chen, P.A. Wright, J.M. Thomas, S. Natarajan, L. Marchese, S.M. Bradley, G. Sankar, C.R.A. Catlow, P.L. Gai-Boyes, R.P. Townsend, C.M. Lok, J. Phys. Chem. 98(40), 10216 (1994)
6. S.T. Wilson, B.M. Lok, E.M. Flanigen. Crystalline metallophosphate compositions. US. Pat. 4310440 (1982)
7. S. Wilson, P. Barger, Microp. Mesop. Mater. 29, 117 (1999)
8. L. Wang, C. Guo, S. Yan, X. Huang, Q. Li, Microp. Mesop. Mater. 64, 63 (2003)
9. P. Wang, A. Lv, J. Hu, J. Xu, G. Lu, Microp. Mesop. Mater. 152, 178 (2012)
10. W. Shen, X. Li, Y. Wei, P. Tian, F. Deng, X. Han, X. Bao, Microp. Mesop. Mater. 158, 19 (2012)
11. T. Fjermestad, S. Svelle, O. Swang, J. Phys. Chem C 119, 2086 (2015)
12. D. Dubois, D. Obrzut, J. Liu, J. Thundimadathil, P. Adekkanattu, J. Guin, A. Punnoose, M. Seehra, Fuel Processing Technology 83, 203 (2003)
13. D. Chen, K. Moljord, T. Fuglerud, A. Holmen, Microp. Mesop. Mater. 29, 191 (1999)
14. D. Chen, H.P. Rebo, A. Grønsvold, K. Moljord, A. Holmen, Microp. Mesop. Mater. 35-36, 121 (2000)
15. I.M. Dahl, S. Kolboe, J. Catal. 149, 458 (1994)
16. I.M. Dahl, H. Mostad, D. Akporiaye, R. Wendelbo, Microporous Mesoporous Mater. 29, 185 (1999)
17. W.J.H. Dehertog, G.F. Froment, Appl. Catal. 71, 153 (1991)
18. M.A. Djieugoue, A.M. Prakash, L. Kevan, J. Phys. Chem. B 104, 6452 (2000)
19. G.J. Hutchings, R. Hunter, Catalysis Today 6, 276 (1990)
20. M. Inoue, P. Dhupatemiya, S. Phatanasri, T. Inui, Microp. Mesop. Mater. 28, 19 (1999)
21. T. Inui, M. Kang, Appl. Catal. A. Gen. 164, 211 (1997)
22. M. Kang, Journal of Molecular Catalysis A: Chemical 160, 437 (2000)
23. W.W. Kaeding, S.A. Butter, J. Catal. 61, 155 (1980)
24. M.J.V. Niekerk, J.C.Q. Fletcher, C.T. O'Connor, Appl. Catal. A. Gen. 138, 135 (1996)
25. M. Stocker, Microp. Mesop. Mater. 29, 3 (1999)
26. J.M. Thomas, Y. Xu, C.R.A. Catlow, J.W. Couves, Chem. Mater 3(4), 667 (1991)
27. T. Tsoncheva, R. Dimitrova, Appl. Catal. A. Gen. 225, 101 (2002)
28. R. Wendelbo, D. Akporiaye, A. Andersen, I.M. Dahl, H.B. Mostad, Appl. Catal. A. Gen. 142, L197 (1996)
29. T. Alvaro Muñoz, C. M. Arques-Alvarez, E. Sastre, Catalysis Today 213, 219 (2013)
30. Journal of Natural Gas Science and Engineering 22, 245 (2015)
31. J. Chen, J. Li, Y. Wei, C. Yuan, B. Li, S. Xu, Y. Zhou, J. Wang, M. Zhang, Z. Liu, Catal. Commun. 46, 36 (2014)
32. Y. Zhou, L. Qi, Y. Wei, C. Yuan, M. Zhang, Z. Liu, Chin. J. Catal. 37, 1496 (2016)
33. R. Martinez-Franco, Z. Li, J. Martinez-Triguero, M. Moliner, A. Corma, Catal. Sci. Technol. 6, 2796 (2016)
34. T. Alvaro Muñoz, C. M. Arques-Alvarez, E. Sastre, Top. Catal. 59, 278 (2016)
35. F. Sena, B. de Souza, N. de Almeida, J. Cardoso, L. Fernandes, Appl. Catal. A. Gen. 406(1), 59 (2011)
36. C. Blackwell, R. Patton, J. Phys. Chem. 88(25), 6135 (1984)

Adsorption Calorimetry as a Tool for the Characterization of Catalysts Used in CO₂ Conversion

Rafaelle Gomes Santiago, Aline Estevam Carvalho, Wagner Alves de Sousa, Juliana Amorim Coelho, Diana Cristina Silva de Azevedo and Moises Bastos-Neto

*^a Laboratório de Pesquisa em Adsorção e Captura de CO₂ - Grupo de Pesquisa em Separações por Adsorção – Departamento de Engenharia Química – Universidade Federal do Ceará, Campus do Pici, Fortaleza, CEP: 60455760, Brazil
Email: rafaelle.santiago@gpsa.ufc.br*

Abstract

Recent technologies and studies for carbon dioxide conversion have been evaluated as a strategy to mitigate the greenhouse effect by converting it in renewable fuels such as dimethyl ether (DME). The catalytic properties are the key factors to enable this process and to promote its reactions. For a better understanding about how the catalysts behave and interact with the carbon dioxide, the microcalorimetric technique was applied for catalysts characterization. The CuO/Al₂O₃ and CuO-ZnO/Al₂O₃ with 1:1, 2:1 and 4:1 proportions of copper-zinc catalysts were also characterized by X-ray diffraction (XRD), and nitrogen adsorption-desorption isotherms. The CO₂ interaction with the catalysts was evaluated by the adsorption heats of CO₂ measured by calorimetry. The results demonstrated that higher adsorption heats were achieved for higher zinc proportions, besides the lower values for specific area and porosity showed by textural properties. These outcomes pointed to the promoter zinc effect in the interaction between CO₂ and the catalyst.

Keywords: microcalorimetry; CO₂ conversion; catalysts

1. Introduction

Carbon dioxide has been explored as a potential source of carbon alternative to conventional fossil fuels. Some studies also point out that converting CO₂ into useful chemicals could be more attractive than its geological storage for post capture purposes [1-2]

The main challenge in converting CO₂ into other chemicals is due to its relatively low reactivity, which requires the use of high temperatures and/or pressures. Fortunately, recent advances in heterogeneous catalysis make it possible for these reactions to occur under milder conditions using specific catalysts.

Among the chemicals obtained from CO₂, the dimethyl ether (DME) has been increasingly gaining attention as a potential alternative fuel due to its good self-ignition characteristic with a low emission of NO_x, SO_x and particulates [3-6]. The synthesis of DME from CO₂ occurs in two reactions: (i) methanol production from CO₂ hydrogenation and (ii) methanol dehydration to DME.

The main challenge of the direct DME synthesis is to develop an efficient multifunctional catalyst

that has not only metallic function for the synthesis of methanol but also acid function for the dehydration of methanol to DME. Copper based catalysts have been reported as a material with the best catalytic performance for CO₂ hydrogenation to methanol compared to other metals [7] and zinc oxide shows a significant promotional effect for methanol synthesis [8-10]. In addition, aluminum oxide in Cu-Zn-based catalyst has been reported as a stable catalyst for methanol synthesis [11-13]. For the reaction of methanol dehydration to DME, the most studied catalyst is γ -Al₂O₃ due to its low cost, high surface area, good thermal and mechanical resistance [12,14]. γ -Al₂O₃ is an amorphous oxide of high specific surface area that constitute the support of many metallic catalysts and presents suitable acidity playing a role as a bifunctional catalyst in direct conversion of CO₂ to DME [15].

The catalytic activity of a material is related to its structural, textural, morphological, and chemical characteristics. Several characterization techniques can be used to better understand the catalytic performance.

Thermal methods are applied as a tool to study materials for several applications in the field of

adsorption and catalysis. Among these methods, calorimetry has been extensively applied to characterize both the solid material and the gas-solid interactions [16-19].

The main goal of the present study is to characterize a series of bimetallic catalysts supported on alumina to be used in catalysis reaction CO₂ conversion by means of calorimetry. The series of catalysts are based on copper, zinc, and aluminum oxides (CZA catalysts) prepared by wetness impregnation with different zinc compositions. The influence of zinc composition in the material has been evaluated according to the point of view of the heat of adsorption to assess the interaction with CO₂.

2. Materials and Methods

2.1. Materials

CuO-ZnO/Al₂O₃ catalysts were prepared by wet impregnation from commercial CuO/Al₂O₃ 13% CuO on alumina (Sigma-Aldrich) with aqueous solution of zinc acetate at the desired ratio. This method was described by Badmaev et al. and Semelsberger et al. [20-21]. The solid was dried in a rotary evaporator at 80 °C for 1.5 h and 42 rpm, after it was dried at 80 °C for 24 h in an oven and calcined at 300 °C for 2 h at 5 °C min⁻¹. This procedure was conducted using different amounts of zinc acetate solution to obtain catalysts with mass compositions of 1:1, 2:1 and 4:1 of Cu:Zn. It is worth mentioning that the zinc solution is added to form ZnO in calcination step, based on CuO composition of the commercial material.

2.2. Techniques

X-rays diffraction measurements were obtained by a Bruker D8 Advance diffractometer operating at 40 kV and 40 mA with the Cu K α radiation in the 2 θ range 5-80°. This technique was applied to identify crystalline phases of samples catalysts. The phase identification was carried out based on the JCPDS data (Joint Committee on Powder Diffraction Standards, Swarthmore, USA).

Textural properties, such as specific surface area, pore and micropore volume, were obtained by nitrogen physical adsorption method at -196 °C using an Autosorb-iQ3 (Quantachrome Instruments, USA). Prior to the measurements, the catalysts were degassed at 200 °C for 6 h. The surface area was determined by fitting the Brunauer-Emmett-Teller (BET) equation in the P/P₀ range from 0.05 to 0.2

[22]. The total pore volume was obtained from the volume adsorbed at P/P₀ ~ 1, considering that liquid adsorbate fills all the pores.

Experimental heat peaks of CO₂ adsorption were obtained using a Tian-Calvet type microcalorimeter (C80 Setaram, France) coupled to a manometric system assembled in stainless steel as illustrated in Figure 1. Increasing doses of gas were injected into the sample cell, which was placed in the calorimeter. By measuring pressure differences (initial and equilibrium), as well as the calorimetric peak associated with each gas dose, it was possible to calculate the adsorbed concentration and energy release per mol adsorbed. Prior to each experiment, the adsorbent was outgassed under 10⁻⁶ bar at 200 °C for 6 h. These experiments were carried out at 25 °C at pressures up 1 bar. The correction for the heat evolved in the gas compression associated to the gas entrance in the cell was determined by previous blank experiments with helium.

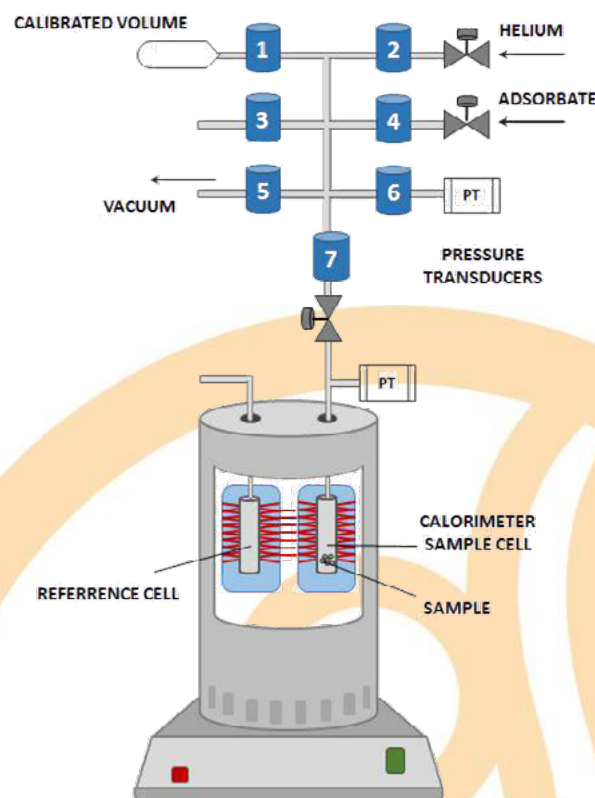


Fig. 1. Schematic representation of the calorimeter coupled to the manometric system.

3. Results

Figure 2 shows the XRD diffractograms for the catalysts prepared by wet impregnation (CZA) from commercial catalyst CuO/Al₂O₃. The impregnation of ZnO did not alter the structure of commercial catalyst, since the patterns are similar for all samples. These patterns exhibit the typical γ -phase alumina by the peak at 2θ of 36.8° and 67.2° (PDF-00-046-1131). The peaks corresponding to CuO and ZnO metallic phases cannot be observed probably due to a high dispersion of these phases or due to their low content in the catalyst. Similar results have been reported in the literature [13,23].

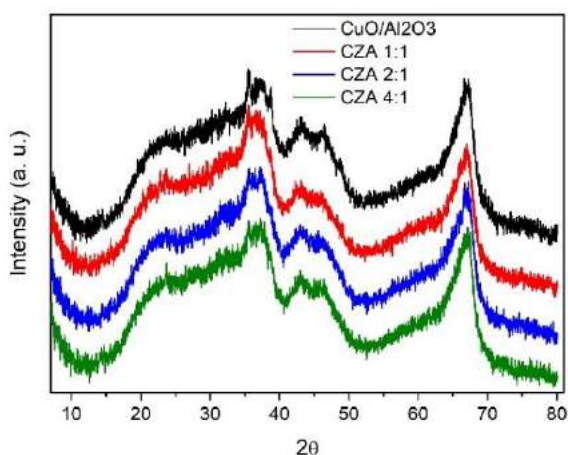


Fig. 2. XRD diffractograms for CZA catalysts.

N₂ adsorption isotherms are shown in Figure 3. All isotherms are of type IV with hysteresis, which are typical for mesoporous materials [24]. Although the shape of the isotherms is quite similar, it is possible to observe that the adsorbed amount of nitrogen decreases as the zinc composition increases.

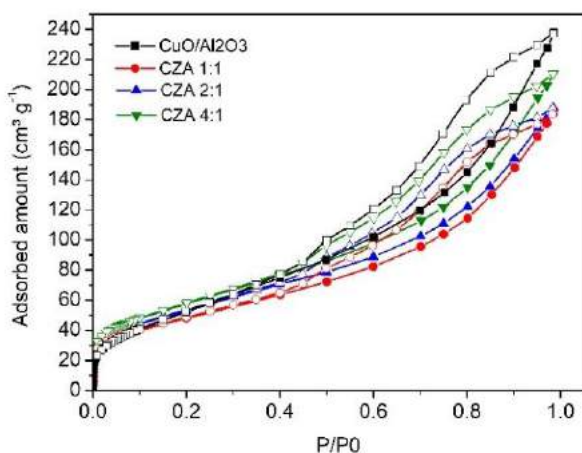


Fig. 3. N₂ adsorption isotherms for the studied samples. Filled symbols represent the adsorption branch and empty symbols the desorption branch.

The textural properties of the samples obtained from the isotherms (Figure 3), are shown in Table 1.

Table 1. Textural properties of the catalysts

Samples	S _{BET} (m ² /g)	V _P (cm ³ /g)
CuO/Al ₂ O ₃	227	0.32
CZA 1:1	147	0.26
CZA 2:1	178	0.27
CZA 4:1	200	0.30

For the catalysts prepared by wet impregnation method, both surface area and porosity decrease progressively due to the filling of γ -alumina pores by zinc solution that occurs during impregnation. Similar behavior is reported for supported catalysts by Bonura et al (2017) and Gentzen et al (2018) [3,25].

The differential heat adsorption curves for CO₂ at 25 °C are shown in Figure 4.

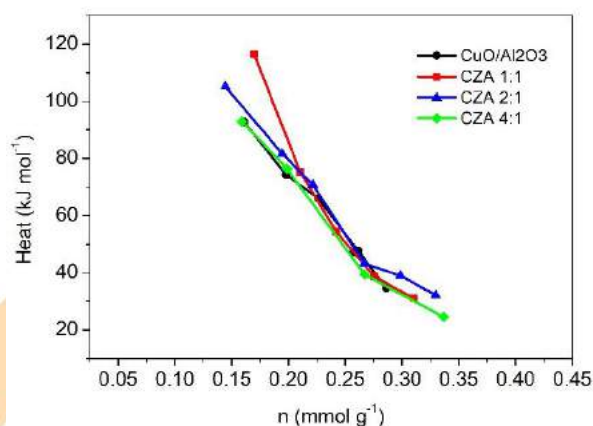


Fig. 4. Differential heat of CO₂ adsorption at 25 °C.

The heat measured by the microcalorimeter includes the energy related to the CO₂ physisorption in the pores and the energy associated to the interactions of CO₂ molecules with the chemical groups on the material's surface. The highest adsorption heats are obtained at low coverage and decreases progressively with increasing pressure, reaching values of about 20 kJ mol⁻¹.

According to the results presented in Figure 4, it is possible to note that commercial and CZA 4:1 samples have similar heat profiles. In contrast, the CZA 1:1 sample presents highest zero cover heat.

Since the only difference between samples is the amount of zinc, these results show that zinc improves the interaction between CO₂ and catalyst as presented by several works [26-28].

4. Conclusions

The adsorption heats measured by calorimetric technique made it possible evaluate the zinc influence on the catalyst regarding interactions with CO₂. It was possible notice that the material with zinc presents higher adsorption heat and these values increase as zinc amount.

The results also indicate that calorimetry can be applied to a better understanding of the interaction mechanisms between CO₂ and the catalyst and its importance to improve the superficial interactions.

The evaluation of the performance of these catalysts and its relation to the adsorption heats shall be the object of a future work.

Acknowledgements

The authors acknowledge financial support from PETROBRAS.

References

- [1] Al-Mamoori, A.; Krishnamurthy, A.; Rownaghi, A. A.; Rezaei, F. Carbon Capture and Utilization Update Energy Technol, 2017; 5: p. 834-849.
- [2] Alvarez, A.; Bansode, A.; Urakawa, A.; Bavykina, A. V.; Wezendonk, T. A.; Makkee, M.; Gascon, J.; Kapteijn, F. Challenges in the Greener Production of Formates/Formic Acid, Methanol, and DME by Heterogeneously Catalyzed CO₂ Hydrogenation Processes. Chem Rev, 2017; 117: p. 9804-9838.
- [3] Bonura, G.; Cannilla, C.; Frusteri, L.; Mezzapica, A.; Frusteri, F. DME production by CO₂ hydrogenation: Key factors affecting the behaviour of CuZnZr/ferrierite catalysts. Catal Today, 2017;281: p. 337-344.
- [4] Arcoumanis, C.; Bae, C.; Crookes, R.; Kinoshita, E. The potential of di-methyl ether (DME) as an alternative fuel for compression-ignition engines: A review. Fuel, 2008. 87(7): p. 1014-1030.
- [5] Ateka, A.; Ereña, J.; Sánchez-Contador, M.; Perez-Urriarte, P.; Bilbao, J.; Aguayo, A. Capability of the Direct Dimethyl Ether Synthesis Process for the Conversion of Carbon Dioxide. Appl Sci, 2018. 8(5): p. 677.
- [6] Kim, M. Y.; Yoon, S. H.; Ryu, B. W.; Lee, C. S. Combustion and emission characteristics of DME as an alternative fuel for compression ignition engines with a high pressure injection system. Fuel, 2008. 87(12): p. 2779-2786
- [7] Catizzone, E.; Bonura, G.; Migliori, M.; Frusteri, F.; Giordano, G. CO(2) Recycling to Dimethyl Ether: State-of-the-Art and Perspectives. Molecules, 2017. 23(1): p. 1-28.
- [8] Chinchén, G. C.; Waugh, K. C.; Whan, D. A. The Activity and State of the Copper Surface in Methanol Synthesis Catalysts. Appl Catal, 1986. 25: p. 101-107.
- [9] Ma, Y.; Sun, Q.; Wu, D.; Fan, W.-H.; Zhang, Y.-L.; Deng, J.-F. A practical approach for the preparation of high activity Cu/ZnO/ZrO₂ catalyst for methanol synthesis from CO₂ hydrogenation. Appl Catal A-Gen, 1998. 171: p. 45-55.
- [10] Nakamura, J.; Nakamura, I.; Uchijima, T. Methanol synthesis over a Zn-deposited copper model catalyst. Catal Lett, 1995. 31: p. 325-331.
- [11] Naik, S. P.; Ryu, T.; Bui, V.; Miller, J. D.; Drinnan, N. B.; Zmierzak, W. Synthesis of DME from CO₂/H₂ gas mixture. Chem Eng J, 2011. 167(1): p. 362-368.
- [12] Aguayo, A. T.; Ereña, J.; Mier, D.; Arandes, J. M.; Olazar, M.; Bilbao, J. Kinetic Modeling of Dimethyl Ether Synthesis in a Single Step on a CuO-ZnO-Al₂O₃/γ-Al₂O₃ Catalyst. Ind Eng Chem Res, 2007. 46: p. 5522-5530.
- [13] Ereña, J.; Vicente, J.; Aguayo, A. T.; Olazar, M.; Bilbao, J.; Gayubo, A. G. Kinetic behaviour of catalysts with different CuO-ZnO-Al₂O₃ metallic function compositions in DME steam reforming in a fluidized bed. Appl Catal B-Environ, 2013. 142-143: p. 315-322.
- [14] Aboul-Fotouh, S. M. K. Production of dimethylether (DME) as a clean fuel using sonochemically prepared CuO and/or ZnO-modified γ-alumina catalysts. J Fuel Chem Technol, 2014. 42(3): p. 350-356.
- [15] Manchado, M. C.; Guil, J. M.; Masiá, A. P.; Paniego, A. R.; Menayo, J. M. T. Adsorption of H₂, O₂, CO, and CO₂ on a 7-Alumina: Volumetric and Calorimetric Studies. Langmuir, 1994. 10: p. 685-691.
- [16] Haines, P. J.; Reading, M.; Wilburn, F. W. Differential thermal analysis and differential scanning calorimetry. In: Handbook of Thermal Analysis and Calorimetry. Vol. 1: Principles and Practice, 1998.
- [17] James, T. E.; Hemmingson, S. L.; Sellers, J. R. V.; Campbell, C. T. Calorimetric measurement of adsorption and adhesion energies of Cu on Pt(111). Surf Sci, 2017. 657: p. 58-62.
- [18] Lin, J.; Li, L.; Huang, Y.; Zhang, W.; Wang, X.; Wang, A.; Zhang, T. In Situ Calorimetric Study: Structural Effects on Adsorption and Catalytic Performances for CO Oxidation over Ir-in-CeO₂ and Ir-on-CeO₂ Catalysts, 2011. 15: p. 16509-16517.
- [19] Auroux, A (Ed). Calorimetry and Thermal Methods in Catalysis. Springer Series in Material Science v. 154. Springer, Heidelberg, 2013.
- [20] Badmaev, S. D.; Pechenkin, A. A.; Belyaev, V. D.; Sobyanin, V. A. Hydrogen production by steam reforming of dimethoxymethane over bifunctional CuO-ZnO/γ-Al₂O₃ catalyst. Int J Hydrogen Energ, 2015. 40: p. 14052-14057.
- [21] Semelsberger, T. A.; Ott, K. C.; Borup, R. L.; Greene, H. L. Generating hydrogen-rich fuel-cell feeds from dimethyl ether (DME) using Cu/Zn supported on various solid-acid substrates. Appl. Catal A-Gen, 2006. 309 (2): p. 210-223.

- [22] Brunauer, S.; Emmett, P. H.; Teller, E. Adsorption of Gases in Multimolecular Layers. *J Am Chem Soc*, 1938, 60(2): p. 309-319.
- [23] Huang, C.; Chen, S.; Fei, X.; Liu, D.; Zhang, Y. Catalytic Hydrogenation of CO₂ to Methanol: study of synergistic effect on adsorption properties of CO₂ and H₂ in CuO/ZnO/ZrO₂ system. *Catalysts*, 2015. 5(4): p. 1846-1861.
- [24] Thommes, M.; Kaneko, K.; Neimark, A. V.; Olivier, J.P.; Rodriguez-Reinoso, F.; Rouquerol, J.; Sing, K.S.W. Physisorption of gases, with special reference to the evaluation of surface area and pore size distribution (IUPAC Technical Report). *Pure Appl. Chem*, 2015. 87: p. 1051-1069.
- [25] Gentzen, M.; Doronkin, D. E.; Sheppard, T. L.; Grunwaldt, J. D.; Sauer, J.; Behrens, S. Bifunctional catalysts based on colloidal Cu/Zn nanoparticles for the direct conversion of synthesis gas to dimethyl ether and hydrocarbons. *Appl Catal A-Gen*, 2018. 557: p. 99-107.
- [26] Tseng, H.; Lin, H.; Kuo, Y.; Su, Y. Synthesis, characterization, and promoter effect of Cu-Zn/ γ -Al₂O₃ catalysts on NO reduction with CO. *Chem Eng J*, 2010. 160 (1): p. 13-19.
- [27] Shishido, T.; Yamamoto, Y.; Morioka, H.; Takehira, K. Production of hydrogen from methanol over Cu/ZnO and Cu/ZnO/Al₂O₃ catalysts prepared by homogeneous precipitation: steam reforming and oxidative steam reforming. *J Mol Catal*, 2007. 268 (1-2): p. 185-194.
- [28] Lee, W. J.; Bordoloi, A.; Patel, J.; Bhatelia, T. The effect of metal additives in Cu/Zn/Al₂O₃ as a catalyst for low-pressure methanol synthesis in an oil-cooled annulus reactor. *Catal Today*, 2020. 343: p. 183-190.

Synthesis and characterization of the modified HZSM-5 zeolite by alkaline treatment

Izadora da Silva Santos^a, Bianca Pedroso Silva Santos^a, Núbia Caroline de Almeida^a,
Lindoal Domiciano Fernandes^a

^a *Departament of Chemical Engineering, Universidade Federal Rural do Rio de Janeiro, Rod BR 465 Km 7, Seropédica, CEP 23897-000, Brazil*

Abstract

Zeolites are microporous aluminosilicates that have a high surface area, chemical, and thermal stability. As the pore size is a key factor to obtain good activity and selectivity. Thus, post-synthesis treatments such as desilication, which is the removal of silicon from the network through basic solutions, is an alternative for the creation of extra-porosity. In this work, samples of ZSM-5 with post-synthesis treatment were synthesized using solutions of 0.5 and 0.7 mol / L of NaCO₃ and NaOH in the presence or not of CTABr (cationic surfactant). The techniques used to characterize the samples were X-ray diffraction (XRD), nitrogen adsorption and desorption, and infrared absorption spectroscopy (FTIR). The diffraction profile contains peaks characteristic of the ZSM-5 zeolite for all samples. There was an increase in crystallinity when comparing the pattern with the others. Using the N₂ adsorption and desorption technique, it is possible to observe the presence of an H4 type hysteresis loop, associated with mesopores that coexist with the micropores. The bands, as a result of the IR analysis, generally present the same intensity profile for all samples. The 550 cm⁻¹ band is characteristic of the five-membered double ring, confirming the structure of the ZSM-5 zeolite. The best results obtained were for samples without surfactant, as this caused a reduction in the surface area that may be due to the high amount used. The method adopted for generating mesopores was effective since there was an increase in the volume of mesopores compared to the standard sample.

Keywords: Zeolite ZSM-5, mesoporosity, alkaline treatment, surfactant.

1. Introduction

Zeolites are crystalline and microporous materials that consist of tetrahedral units of SiO₄ and AlO₄ linked by oxygen atoms that offer several advantages. These solids are environmentally harmless, non-corrosive, chemically stable, have a high versatility, and exhibit high thermal stability, which is necessary to regenerate the catalyst by burning coke deposits [1,2]. ZSM-5 zeolite is a microporous aluminosilicate with an orthorhombic structure, which is known as a solid acid catalyst for the efficient conversion of fossil and biomass resources to fuels and chemicals [1]. The controlled formation of mesopores in zeolites can be carried out through the formation of hierarchical structures such as desilication: extraction of silicon from the structure by treatment in basic solutions [3]. Some of the strategies for the development of micro / mesoporous compounds through alkaline treatment were presented by [1,4-7] that showed that the

selective removal of silicon from the zeolite structure occurs without changes in the structure.

The objective of this work is to investigate the mechanism of mesoporous formation and the effects of the treatment with alkali on the structural and catalytic properties of ZSM-5, using low concentrations of NaOH and Na₂CO₃ solution with the addition of CTABr as a treatment medium. The physical and textural properties were determined through the analysis of XRD, N₂ adsorption / desorption and FTIR.

2. Materials and Methods

2.1. Synthesis of ZSM-5 Zeolite

ZSM-5 zeolite was synthesized as described previously by [8] and the molar composition of synthesis gel was 3.25 Na₂O: 1.0 Al₂O₃: 30 SiO₂: 958 H₂O. The seeding gel preparation started with dissolving 13.80 g sodium hydroxide pellets in 710.3 g of deionized water and the resulting mixture was stirred until completely dissolved. Over this



solution, 117.0 g of TPA-OH (20%) was added under continuous stirring for 10 min. After this step, 158.9 g of SiO₂ and 0.5 H₂O were added gradually and mixed for 1 h at room temperature. Then, the seed gel was placed in a Teflon-lined stainless steel autoclave and it was heated at 100 °C for 16 hours. At the end, the gel was removed from the containers and reserved.

To prepare the synthesis gel, 8.8 g of sodium hydroxide was dissolved in 884.77 g of deionized water. Over this solution, 96.14 g of SiO₂ was gradually added and stirred for 1 hour at room temperature. Finally, 50 g of the seed gel prepared previously, was added and stirred again for 1 hour at room temperature. After that time, the gel was placed in a Teflon lined stainless steel autoclave and heated at 180 °C for 72 h for nucleation and crystal growth. The last step was the solids were recovered through vacuum filtration and dried at 100 °C for 24 h and finally calcined at 550 °C for 12 h in order to free the pores.

2.2. Post-Synthesis treatment

In post-synthesis treatment of desilication was employed types of alkaline solutions, NaOH and Na₂CO₃. Some samples was added cetyltrimethylammonium bromide (CTABr) cationic surfactant, as shown in Table 1.

Table 1. Nomenclature of the samples and their respective concentrations of alkaline solutions and the surfactant.

Sample code	Concentration of alkaline solution	CTABr (g)
ZSM-5	without treatment	-
Z1-0.5	0.5 mol/L NaCO ₃	-
ZC1-0.5	0.5 mol/L NaCO ₃	2.5
Z1-0.7	0.7 mol/L NaCO ₃	-
ZC1-0.7	0.7 mol/L NaCO ₃	2.5
Z2-0.5	0.5 mol/L NaOH	-
ZC2-0.5	0.5 mol/L NaOH	2.5
Z2-0.7	0.7 mol/L NaOH	-
ZC2-0.7	0.7 mol/L NaOH	2.5

2.3. Ion Exchange

All samples that underwent an alkaline treatment were subjected to ion exchange to replace Na⁺ cations with ammonium (NH₄⁺). For this, 5% solids were placed in contact with an aqueous solution of ammonium acetate with a molar ratio NH₄⁺/Al = 10. This suspension was stirred for 2.5 h at 100 °C under reflux. Then the solids were recovered by

vacuum filtration, followed by washing with the same solution (2nd ion exchange) and then they were washed with deionized water until neutral pH and dried at 100 °C for 24 h. Finally, the samples were calcined. All samples were subjected to calcination to remove the surfactant and thus release the pores. The calcination was carried out at 550 °C for 12 hours at a heating rate of 0.2 °C/min.

2.4. Sample Characterization

The physical-chemical characterization of the catalysts allows to elucidate the important relationship between structure, property and performance. The results of the techniques used in this work, including X-ray diffraction (XRD), Nitrogen adsorption/desorption, Infrared absorption spectrometry (FTIR), are crucial for the evaluation and development of more efficient catalysts.

The crystallinity of the materials was investigated by X-ray diffraction (XRD). The measurements were performed using a Rigaku Miniflex II diffractometer using Cu-K α radiation ($\lambda = 1.54 \text{ \AA}$) equipped with a Ni filter, operating at 30 kV and 15 mA. The scanning was performed from 1 to 50° (2 θ) at intervals of 0.02° and 2 s of acquisition time.

N₂ adsorption/desorption of nitrogen at 77.3 K was performed in a physical nitrogen adsorption analyzer ASAP2020 from Micromeritics, to determine the surface area and pore volume of the samples. For each analysis, approximately 0.12 g of sample were used, which underwent a pre-treatment under vacuum at 300 °C for 12 h. The surface area of the samples was determined by the Brunauer-Emmet-Teller (BET) method, which consists of obtaining the capacity of the manocamada from the adsorption isotherms. The mesoporous volume and the pore size distribution were determined by the method of Barrett, Joyner and Halenda (BJH). In addition, the microporous volume and external surface area were determined by t-plot method.

Fourier-transform infrared (FTIR) spectra were recorded using a Nicolet 6700 Alum spectrometer at room temperature in the range of 400–4000 cm⁻¹ with resolution 4 cm⁻¹. Initially, the samples were dried in an oven at 100 °C for 2 h and homogenized with KBr in about 1%(m/m) of the sample.

3. Results and Discussion

X-ray diffraction was performed to confirm the structure of the synthesized zeolites and to

investigate possible structural changes after desiccation treatment. Figure 1 shows the X-ray diffractograms of the samples treated with NaOH and Na₂CO₃ and the untreated HZSM-5 sample. All samples showed typical XRD patterns of the MFI structure and no additional phase or amorphous silica was observed. [4] also did not observe changes in the samples treated with Na₂CO₃ that presented crystallinity values varying between 98% and 100%. The intensity of the diffraction peaks in the ranges of 7 to 9 ° and 22.5 to 25.0 ° increased in the samples treated with alkaline solutions compared to the sample of H-ZSM-5 without treatment. This proves that even with Si removal from the structure, the network was preserved, as well as the ordering of the crystals. [3] observed that the structure of zeolites was not altered at low concentrations of NaOH. The addition of the surfactant CTABr did not cause significant changes in the crystallinity of the samples.

Table 2 shows the textural properties obtained by the adsorption/desorption of N₂.

Tabela 2. Textural properties measured from nitrogen adsorption isotherms for the ZSM-5 samples and samples treated with alkali.

Sample	Surface		Pore Volume	
	Área (m ² /g)		(cm ³ /g)	
	S _{BET} ^a	S _{ext} ^b	V _{micro} ^c	V _{meso} ^d
ZSM-5	263	39	0.104	0.044
Z1-0.5	317	76	0.112	0.077
ZC1-0.5	313	74	0.111	0.075
Z1-0.7	427	99	0.153	0.105
ZC1-0.7	311	75	0.110	0.075
Z2-0.5	297	76	0.103	0.098
ZC2-0.5	315	79	0.110	0.099
Z2-0.7	325	89	0.110	0.130
ZC2-0.7	295	82	0.099	0.111

^a Derived from the BET equation. ^b External surface area (S_{ext}) was derived from the t-plot method. ^c Micropore volume (V_{micro}) was evaluated by the t-plot method. ^d Mesopore volume (V_{meso}) was calculated by BJH method.

The values of BET and micropore volume did not show significant differences, except for the sample Z1-0.7, which was treated with Na₂CO₃, since a higher concentration of CO₃⁻ can cause hydrolysis of these species, generating OH⁻ ions that are capable of removing silicon avoiding precipitation and blocking pores, as observed by [1].

After the alkaline treatment, there was an increase in the volume of mesopores, with more expressive values in the samples treated with NaOH. The external surface area of the sample after alkaline treatment has changed considerably. This behavior can be explained by the formation of mesopores at the expense of micropores [3]. The addition of CTABr caused a low decrease in the BET area.

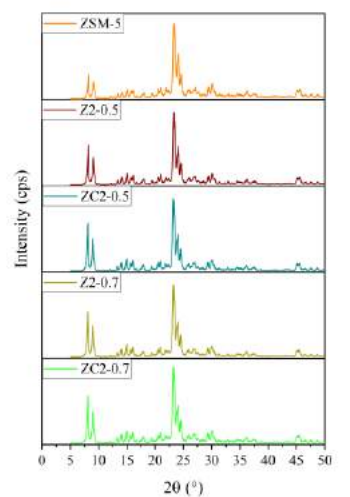
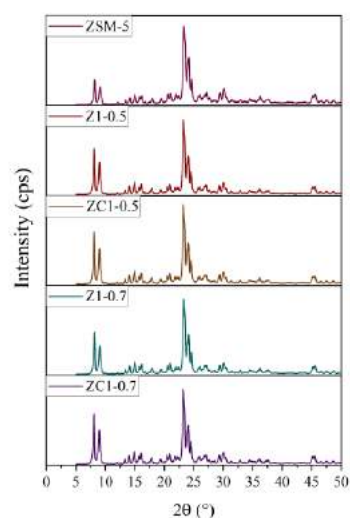


Figure 1 – (a) X-ray diffraction of ZSM-5 samples with desilication treatment using Na₂CO₃. (b) X-ray diffraction of ZSM-5 samples with desilication treatment using NaOH.

Figure 2 shows the adsorption isotherms of all synthesized samples. It is possible to observe a combination of isotherms of types I and IV with an H3 hysteresis loop in P/P_0 of 0.45-0.99 and an increase in adsorption at intermediate pressures caused by capillary condensation [8]. A lower concentration of alkaline solution caused a reduction in the amount of N_2 adsorbed. At higher relative pressure, the amount of adsorbed N_2 increases in the treated samples. This phenomenon is more visible in higher concentrations of alkali.

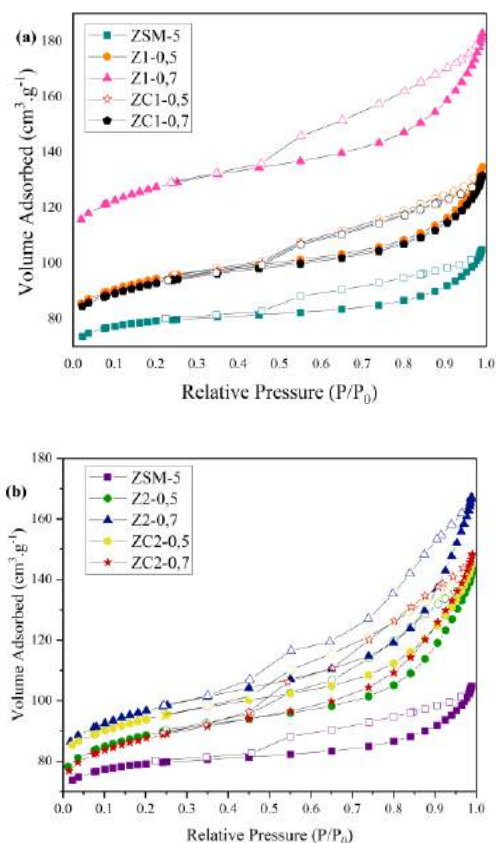


Figure 2. Adsorption isotherms from ZSM-5 samples. (a) untreated sample and treated samples Na_2CO_3 . (b) untreated sample and samples treated with NaOH.

FTIR analysis was performed in the structural region, between 400 and 1200 cm^{-1} shown in Figure 3. The bands around 550 and 450 cm^{-1} are characteristic of the crystal structure ZSM-5 [10] in that the 450 cm^{-1} band is attributed to the T-O vibration of the SiO_4 and AlO_4 tetrahedral units. The bands that appear approximately and 550 cm^{-1} are characteristic of the double rings of five members.

The absorbances at 800 cm^{-1} and 1100 cm^{-1} are attributed to the external symmetrical stretching vibration of the internal asymmetric stretching of the Si-O-T bond (where T was Si or Al), respectively.

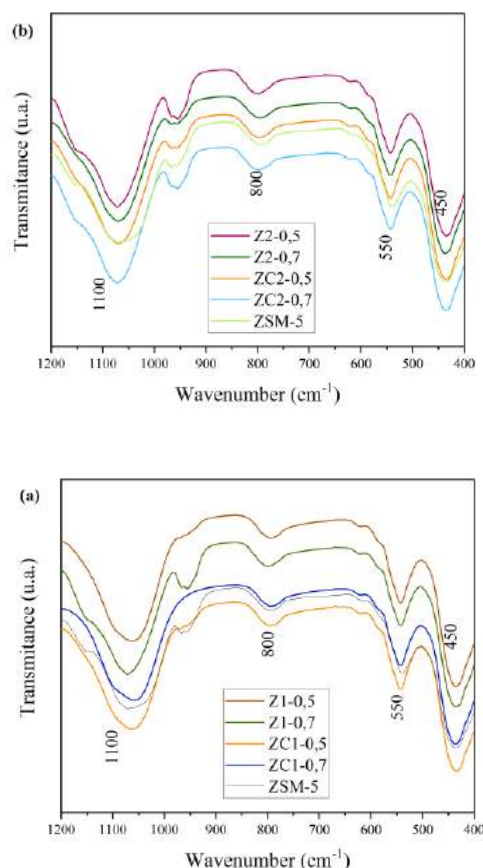


Figure 3. FT-IR spectra of ZSM-5: (a) Treated with Na_2CO_3 H-ZN-30, (b) Treated with NaOH.

4. Conclusion

Analyses of N_2 adsorption showed that the alkaline treatment in the ZSM-5 zeolite leads to a combination of porous material with increased mesoporosity and preserved microporosity. The formation of mesopores is a result of the dissolution of Si from the zeolite structure. XRD analysis shows the permanence of the crystalline structure, even after the treatment of desilication. The best results obtained were for samples without surfactant, as this may have caused a reduction in the surface area due to the high amount used. The method adopted for generating mesopores was effective, since there was



an increase in the volume of mesopores compared to the standard sample, also confirmed by the high crystallinity of the treated samples that can, in this way, improve the diffusion and adsorption properties reducing the formation of coke, increasing catalytic activity and yield.

Acknowledgements

The Analytical Center of the Chemistry Institute (Univerdade Federal Rural do Rio de Janeiro) for FTIR analysis. This work was carried out with the support of the Higher Education Personnel Improvement Coordination - Brazil (CAPES) - Financing Code 001.

References

- [1] Lago, C. D., Decolatti, H. P., Tonutti, Lucas G., Dalla Costa, B. O. Querini, C. A.. Gas phase glycerol dehydration over H-ZSM-5 zeolite modified by alkaline treatment with Na₂CO₃. *J. Catal.*, v. 366, p. 16–27, 2018.
- [2] Neves, T. M., Fernandes, J., Oliveira L., Morais, L., Silva, D., Rosa, E., Mortola, C., Bongalhardo. V., Glycerol dehydration over micro- and mesoporous ZSM-5 synthesized from a one-step method. *Microp. Mesop. Mater.*, v. 275, p. 244–252, 2019.
- [3] Gil, B.; Mokrzycki, Ł., Sulikowski, B. Olejniczak, Z. Walas, S. Desilication of ZSM-5 and ZSM-12 zeolites: Impact on textural, acidic and catalytic properties. *Catal Today*, v. 152, n. 1–4, p. 24–32, 2010.
- [4] Barakov, R., Shcherban, N., Yaremov, P., Bezverkhyy, I. Baranchikov, A., Trachevskii, V. Tsyryna, V. Ilyin, V. Synthesis of micro-mesoporous aluminosilicates on the basis of ZSM-5 zeolite using dual-functional templates at presence of micellar and molecular templates. *Microp. Mesop. Mater.*, v. 237, p. 90–107, 2017.
- [5] Groen, J. C. Groen, J. C. Peffer, L. A. A. Moulijn, J. A. Pérez-Ramírez, J.. Mesoporosity development in ZSM-5 zeolite upon optimized desilication conditions in alkaline medium. *Colloids Surf, A Physicochem Eng Asp.* v. 241, n. 1–3, p. 53–58, 2004.
- [6] Sachse, A. Linares, N., Serrano, A., Grau-Atienza, E., Jardim, A., Silvestre-Albero, E., Cordeiro, J., Fauth, M., Beobide, F., Garikoitz, C., García-Martínez, J., Development of Intracrystalline Mesoporosity in Zeolites through Surfactant-Templating. *Cryst Growth Des*, v. 17, n. 8, p. 4289–4305, 2017.
- [7] Wang, X. Chen, H., Meng, F., Gao, F., Sun, C., Sun, L., Wang, S., Wang, L., Wang, Y., CTAB resulted direct synthesis and properties of hierarchical ZSM-11/5 composite zeolite in the absence of template. *Microp. Mesop. Mater.*, v. 243, p. 271–280, 2017.
- [8] Kleinwort, R., Kessler, H., Perego, G., Carati, A., Gomaro, U., Fatore, V., Grobet, P. J., Meyer, A. MFI High-Al ZSM-5. v. 24, n. 93, p. 7–8, 2019.
- [9] Chen, H., Wang, Y., Sun, C., Wang, X. Wang, C. Synthesis of hierarchical ZSM-5 zeolites with CTAB-containing seed silicalite-1 and its catalytic performance in methanol to propylene. *Catal. Commun.*, v. 112, n. April, p. 10–14, 2018.
- [10] Yaripour, F. Shariatinia, Z., Sahebdehfar, S., Irandoukht, A. *J. Nat. Gas Sci. Eng.* 22 (2015) 260–269

Efficient adsorbents of pollutants based on inorganic-organic sepiolite systems

Hugo Baldan Junior^a, Evane da Silva^a, Michelle Saltarelli^a, Denise Crispim^a, Eduardo J. Nassar^a, Raquel Trujillano^b, Vicente Rives^b, Miguel A. Vicente^b, Antonio Gil^c, Sophia A. Korili^c, Emerson H. de Faria^a, Katia J. Ciuffi^a

^a Universidade de Franca, Av. Dr. Armando Salles Oliveira, 201 - Pq. Universitário, 14404-600 Franca, SP, Brazil.

^b GIR-QUESCAT, Departamento de Química Inorgánica, Facultad de Ciencias Químicas, Universidad de Salamanca, 37008 Salamanca, Spain.

^c INAMAT²-Departamento de Ciencias, Edificio de los Acebos, Universidad Pública de Navarra, Campus Arrosadía, 31006 Pamplona, Spain.

Abstract

Sepiolite clay mineral was functionalized with (3-chloropropyl)triethoxysilane (CIPTES) or 3-[tri(ethoxy/methoxy)silyl]propylurea (TEMSPU) alkoxides and tested as adsorbent for herbicide glyphosate and also of caffeine, two pollutants with very different chemical composition. The materials obtained were characterized by X-ray diffractometry, infrared spectroscopy, thermal analyses, scanning electron microscopy and nitrogen adsorption at -196 °C, and submitted to toxicity and desorption tests. Silane functional groups blocked sepiolite active positions, and adsorption occurred within the zeolitic channels and on the surface of the functionalized solids. Caffeine and glyphosate effectively interacted with urea groups from grafted alkoxide, which could lower the mobility of the adsorbed contaminants. Glyphosate adsorbed on functionalized sepiolite derivatives showed low toxicity.

Keywords: Sepiolite; glyphosate; caffeine; organically modified sepiolite; herbicide.

1. Introduction

Environmental remediation requires new materials consisting of solid matrixes that can act as active, selective and recyclable adsorbents or heterogeneous catalysts for emerging contaminants (ECs) removal, such as pesticides, fertilizers, pharmaceuticals, disinfectants, and natural and synthetic hormones. Nanocomposite materials can help to overcome the pollution problems related to ECs. Sepiolite, $Mg_8Si_{12}O_{30}(OH)_4(H_2O)_4 \cdot 8H_2O$, is a fibrous, hydrated magnesium silicate. It resembles porous structures such as zeolites and mesoporous silicas, with a high specific surface area, and excellent adsorption properties. Currently, its industrial applications are diverse and are based on its ab/adsorptive properties. For instance, sepiolite can absorb 2.5 times its mass in water, which underlies the great plasticity of the clay/water system. Functionalization by alkoxides increases the

number of active sites for chemical bonding, enhancing its adsorptive capacity.

In this work, a sepiolite clay was functionalized with CIPTES or TEMSPU. The prepared materials were characterized by powder X-ray diffraction (PXRD), Infrared absorption spectroscopy (FT-IR), Thermal analyses (TGA), Scanning Electron Microscopy (SEM) and nitrogen adsorption/desorption at -196 °C, and submitted to toxicity and desorption tests. The materials were then applied as adsorbents of two pollutants with chemical structures very different, namely caffeine, considered as a probe molecule, and the widely used herbicide glyphosate (N-(phosphonomethyl)glycine).

2. Results

Sepiolite was successfully functionalized with CIPTES or TEMSPU alkoxides (see Figure 1). The obtained solids, Sep-CIPTES and Sep-TMSPU, efficiently adsorbed glyphosate (the amount

adsorbed decreasing in the order Sep > Sep-CIPTES > Sep-TMSPU) and caffeine (Sep > Sep-TMSPU) (see Figure 2). Adsorption results evidenced that functional groups blocked the active sites of the adsorbents and suggested that glyphosate and caffeine adsorbed within the zeolitic channels and on the surface of the clay minerals. The differences between chloropropyl and urea groups suggested a steric hindrance promoted by the grafting of the silanes on the surface of the sepiolite fibers. The desorption experiments proved an effective interaction via hydrogen bonds between caffeine and glyphosate with urea groups from grafted alkoxide; the adsorbates showed a higher stability on the grafted solids, the effective interactions could lead to lower mobility of the contaminants in the solids. Cytotoxicity results evidenced that glyphosate adsorbed on functionalized sepiolite derivatives showed low toxicity.

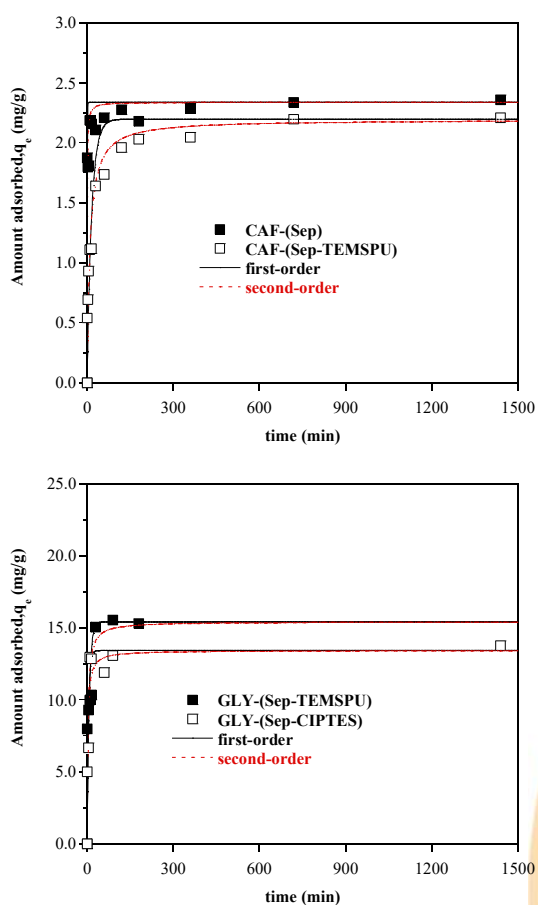


Fig. 2. Kinetic adsorption data for caffeine (CAF) and glyphosate (GLY) adsorption on the modified sepiolites.

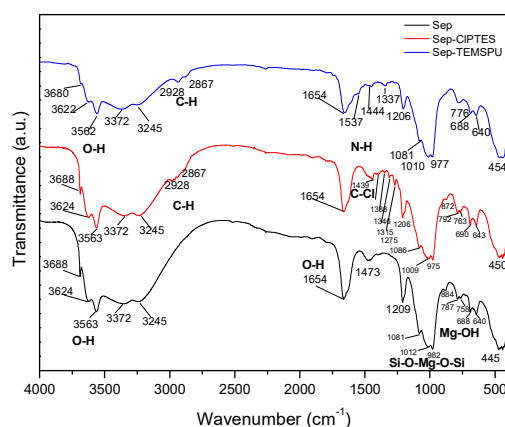


Fig. 1. Infrared spectra of Sep, Sep-CIPTES and Sep-TEMSPU solids.

Acknowledgements

The authors thank a Cooperation Grant jointly financed by Universidad de Salamanca (Spain) and FAPESP (Brazil), reference 2016/50322-2. The Spanish group acknowledges the support from MINECO and ERDF (MAT2016-78863-C2-R), and AG also thanks Santander Bank for funding via the Research Intensification Program. Thanks are given to Dr. R Furtado for support in biological assays. Brazilian group acknowledges the support from research funding agencies Fundação de Amparo à Pesquisa do Estado de São Paulo, FAPESP (2013/19523-3, 2018/26569-3 and 2017/15482-1), and Coordenação de Aperfeiçoamento de Pessoal de Nível Superior (CAPES) and Conselho Nacional de Desenvolvimento Científico e Tecnológico, CNPq (311767/2015-0 and 303135/2018-2). The equipment of Brazilian group has been financed by FAPESP (1998/11022-3, 2005/00720-7, 2011/03335-8, 2012/11673-3 and 2016/01501-1).

References

- [1] Marçal L, de Faria EH, Nassar EJ, Trujillano R, Martín N, Vicente MA, Rives V, Gil A, Korili SA, Ciuffi KJ. Organically modified saponites: SAXS study of swelling and application in caffeine removal. *ACS Appl Mater Interf* 2015; 7; 10853-62.
- [2] Moreira MA, Ciuffi KJ, Rives V, Vicente MA, Trujillano R, Gil A, Korili SA, de Faria EH. Effect of chemical modification of palygorskite and sepiolite by 3-aminopropyltriethoxysilane on adsorption of cationic and anionic dyes. *Appl Clay Sci* 2017; 135: 394-404.
- [3] Junior HB, da Silva E, Saltarelli M, Crispim D, Nassar EJ, Trujillano R, Rives V, Vicente MA, Gil A, Korili SA, de Faria EH, Ciuffi KJ. Inorganic-organic hybrids based on sepiolite as efficient adsorbents of caffeine and glyphosate pollutants. *Appl Surf Sci Adv* 2020; 1; 100025.

Catalytic decomposition of hydrogen peroxide in an iron oxide nanoparticle

Maria Teresa Garcia Badoch^a, Regina Maria Matos Jorge^b, Tirzhá Lins Porto Dantas^{b,*}

^aAcademic Department of Chemistry and Biology, Federal Technological University of Paraná, Curitiba, Brazil

^bChemical Engineering Department, Federal University of Paraná, Curitiba 80035 210, Brazil

Abstract

The use of nanoscale particles finds promising applications in many sciences because, in small sizes, particles tend to have their surface area and hence the amount of available sites increased. Iron oxides are used as catalysts for various reactions; in the area of wastewater treatment, they can be used as catalysts in the decomposition of hydrogen peroxide, forming free radicals with high oxidizing power. The objective of this work was to verify the catalytic capacity of previously synthesized ferrous oxide particles – Maghemite, $\gamma\text{-Fe}_2\text{O}_3$. At pH around 3.0, was obtained a catalytic decomposition of hydrogen peroxide close to 30% with an Fe/H₂O₂ ratio of approximately 70. The hydrogen peroxide decomposition kinetics was described according to the Langmuir-Hinshelwood mechanism.

Keywords: iron oxide, nanoparticles, catalytic decomposition.

1. Introduction

Iron is the most abundant transition metal on earth and much of the iron element in the earth's crust is in the form of Fe²⁺; however it can be rapidly oxidized to Fe³⁺. According to Cornell & Schwertmann there are 16 (sixteen) types of iron ores - including oxides, hydroxides and oxyhydroxides - found in nature [1]. Natural and synthetic iron oxides, depending on their crystal structure and oxidation state, come in various forms. Most iron oxides, hydroxides and oxyhydroxides have crystal structure. However, the degree of structural ordering and crystal size vary according to the conditions under which the crystals were obtained[1]. The main naturally occurring iron ores are hematite, goethite and magnetite. These ores have 70%, 63% and 72%, respectively, in iron mass [2], besides having remarkable diversity of properties and a very interesting chemistry [3].

Due to their wide distribution in nature, many sciences are interested in their properties and make use of these compounds. Among the various fields, the application stands out as adsorbents and catalysts. This is due to its textural and reductive characteristics [1]

The development of systems in which the iron catalyst is in non-soluble form - heterogeneous systems - has emerged as an alternative to counteract the problems arising from the use of soluble iron. Iron may be supported on a solid matrix - for example, activated carbon - or hematite, goethite, and ferrhydrite iron oxides may be [4,5]. Iron oxides, in some of their forms, have magnetic properties and this facilitates their separation from the liquid medium [6]. It is also possible to reuse these oxides, although their activity presents reduction with the number of uses [8,9,10,11].

Heterogeneous catalytic processes promoted by iron oxides are strongly affected by iron morphology, particle size and specific area [3]. Chiou and coworkers mention that metal nanoparticles have a higher Fermi potential and that this property is useful in catalysis of electron transfer reactions [12]. This represents an advantage in radical formation reactions. Fermi's potential or energy is "the most energetic electron energy in the ground state of a n-density free electron gas (Fermi gas)" [13]. Therefore this energy influences the electron exchange capacity. This property is also characteristic of semiconductors, a category in which iron oxides fall [1,3].

The objective of this work is to evaluate the catalytic activity of iron oxide (maghemite)

nanoparticles through hydrogen peroxide decomposition and to evaluate the kinetic model for hydrogen peroxide decomposition.

2. Experimental Section.

2.1. Analysis of Hydrogen Peroxide and Iron Concentration.

The true concentration of hydrogen peroxide solution (INTEROX® 50-10) was determined by the permanganate titration method [14]. This method is suitable for assessing concentrations of aqueous H₂O₂ solutions between 0.25 to 70 m / m.

Residual H₂O₂ analyzes were performed using the colorimetric ammonium vanadate method [15]. This method is suitable for measuring concentrations up to 400 mg.L⁻¹ and presented less variability than the iodometric titration method.

Total iron, iron II and iron III analyzes were performed by the potassium thiocyanate colorimetric method [14].

All colorimetric readings were performed on a photocolorimeter (visible spectrophotometer).

2.2. Decomposition of Hydrogen Peroxide on iron oxides nanoparticles

The synthesis of iron oxide nanoparticles was performed in 3 (three) steps: (1) initially there is the formation of hematite (α -Fe₂O₃) from ferric chloride; (2) then reduction of hematite to magnetite (FeO.Fe₂O₃) and (3) finally oxidation to maghemite (γ -Fe₂O₃). All the particles synthesis and characterization were reported in a previous work. The nanoparticles BET specific surface area was 20.23 m².g⁻¹.

The catalytic activity of the synthesized iron oxide particles was evaluated by the hydrogen peroxide decomposition reaction. Hydrogen peroxide decomposition reactions were carried out in 500 mL stirring batch reactors (Jar Test type) maintained at room temperature. The tests were performed with agitation speed of 200 rpm.

A suitable volume of distilled water was adjusted to pH by addition of 10% H₂SO₄ solution or 30% NaOH solution. After pH adjustment, an appropriate amount of 48.33% hydrogen peroxide was added to obtain a solution at the desired concentration. 100 mL of solution was measured and then transferred to the stirred reactors and then to each reactor was added the appropriate catalyst mass.

A sample was regularly collected to verify peroxide decomposition. That is, the variable analyzed was the concentration of H₂O₂ in the solution to calculate the decomposition percentage.

In parallel the analysis of the concentration of ferric and ferrous ions in solution was performed. The objective was to verify if there was iron leaching and, if hydrogen peroxide decomposition was performed in solid phase or by iron in solution.

Prior to analysis, samples were filtered on vinyl acetate membrane (pore size 0.22 μ m). Filtration is necessary to stop the degradation of H₂O₂ by iron oxide and because the iron analysis method uses reagents that solubilize the iron present in the oxide

2.3. Design of Experiments and Statistical treatment

The pH value was set and a two-variable design with three levels was proposed. The pH was set at 3.0 and the catalyst concentration and peroxide concentration varied by 3 (three) levels (Table 1).

Table 1. Variables and levels

Variables Level	Catalyst concentration, g/L	H ₂ O ₂ concentration, g/L
-1	0.0	0.02
0	1.0	0.06
+1	2.0	0.10

For statistical analysis we used the design of factorial experiments. For this model the number of experiments is calculated by Equation (1).

$$N_T = F^n \quad (1)$$

where N_T is the total number of experiments, F is the number of levels and n the number of variables.

Using the conditions presented in Table 1, nine experiments were outlined (3²) and, to confirm the data obtained, two repetitions of the central point (A10 and A11) were performed according to the conditions presented in Table 2.

The experiments were followed up to 240 min and the hydrogen peroxide concentration to determine the decomposition percentage was obtained by the colorimetric method.

The design of experiments is used to verify which experimental condition brings the best decomposition of hydrogen peroxide. For the statistical treatment of the results and to obtain the optimal condition, the best technique to be used is

the response surface (RSM) based on least squares modeling.

To avoid statistical distortion the experiments were performed in random order (second column of Table 2). Randomization helps to prevent undesirable factors from affecting the effects of interest to the study. Data obtained from experiments A1 to A11 were analyzed using the free statistical software programR.

Table 2. Experiments for Verification of catalytic activity.

Experiment	Order	Level of Catalyst	Level of H ₂ O ₂	Fe/ H ₂ O ₂
A1	5	-1	-1	0.00
A2	3	-1	0	0.00
A3	11	-1	1	0.00
A4	8	0	-1	34.98
A5	1	0	0	11.66
A6	6	0	1	6.99
A7	9	+1	-1	69.94
A8	4	+1	0	23.23
A9	10	+1	+1	13.99
A10	7	0	0	11.66
A11	2	0	0	11.66

3. Results

Table 3 presents the results of the experiment design presented in Table 2. It can be observed that the results of the central points are very close and that, in the absence of the iron catalyst, the hydrogen peroxide decomposition is negligible. Iron concentration in the liquid phase was measured and the results showed that less than 1.0% of iron was leached.

Figure 1 shows the percentage of hydrogen peroxide decomposition as a function of its concentration and different catalyst masses. The results show that there is a tendency to decrease decomposition with decreasing Fe/(H₂O₂) ratio. This results are in accordance with previously results published [16,17].

Table 4 shows the results of the statistical treatment. The probability column data from Table 4 shows that the hydrogen peroxide concentration range is significant at 5% (0.014370), but the catalyst concentration range is greater than 10% (0.153793). Despite the low significance relative to catalyst concentration, the interaction between the two variables has significance below 10% (0.084853), which means that there is interaction between the two variables. Another data that proves

the validity of the data is the value of R² which is 0.8124.

Table 3. Hydrogen Peroxide Decomposition percentage.

Experiment	Fe/ H ₂ O ₂	% H ₂ O ₂ decomposition
A1	0.00	3.7
A2	0.00	10.7
A3	0.00	0.0
A4	34.98	21.4
A5	11.66	14.7
A6	6.99	2.4
A7	69.94	28.6
A8	23.23	8.0
A9	13.99	0.8
A10	11.66	14.3
A11	11.66	14.7

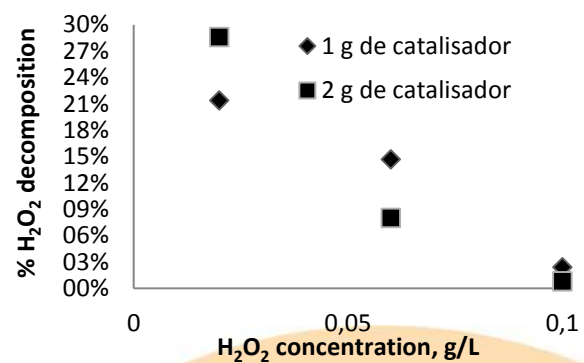


Fig. 1 – Percentage of hydrogen peroxide decomposition versus concentration of hydrogen peroxide.

Table 4. Statistical Parameters

Second Order Estimate	Error	T value	Probability (> t)
x_1 - [catalys]	0.0287321	4.0364	0.009958**
x_2 - [H ₂ O ₂]	0.0228657	1.6800	0.153793
$x_1 : x_2$	-0.0228657	-3.6749	0.014370*
$x_1 : x_2$	0.0280046	-2.1443	0.084853•
x_1^2	0.0351895	-0.8013	0.459327
x_2^2	0.0351895	-0.0623	0.962729

Significance Codes: 0.001 ‘***’ 0.01 ‘*’ 0.05 ‘•’ 0.1

Figures 4 and 5 shows the response surface and contour lines generated by the model. The response surface and the level curve shown were generated

using the mathematical model presented in Equation 2.

$$\hat{y} = 0,115975 + 0,038414x_1 - 0,084029x_2 - 0,028197x_1^2 - 0,002193x_2^2 - 0,060051x_1x_2 \quad (2)$$

where x_1 is the catalyst concentration and x_2 is the hydrogen peroxide concentration

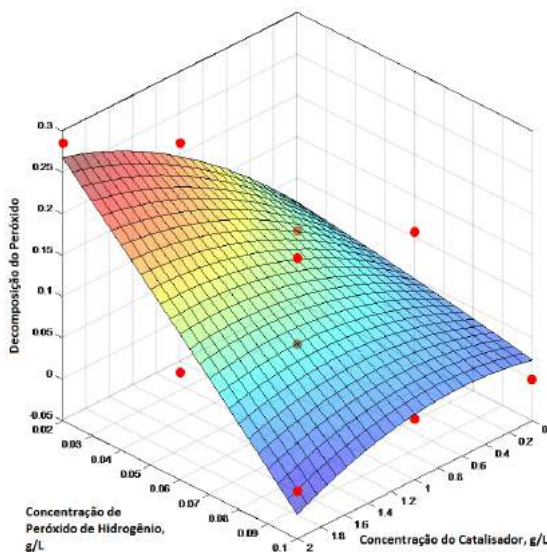


Fig. 4 – Response surface or the model

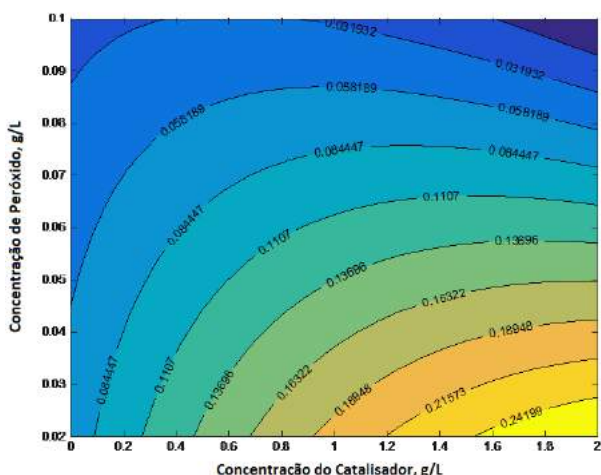


Fig. 5 – Level Curves

The mathematical model presented in Equation 2 is characteristic of a surface with saddle geometry. The visual inspection of Figure 4 also supports the mathematical analysis of the format. It can be observed from the direct inspection of Figure 4 that

the maximum point, in the domain of the experimented variables, occurs for the condition of maximum catalyst concentration, corresponding to 2.0 g.L⁻¹, and minimum peroxide concentration, which corresponds to at 0.02 g.L⁻¹. The decomposition value predicted by the model at this point is 26.8%, whose value has a deviation of -6.7% compared to the experimentally found 28.6%.

However, a decomposition of approximately 30% of the peroxide, for a Fe/(H₂O₂) ratio of approximately 70, may be considered low. The literature presents higher decomposition values using maghemite and lower Fe/(H₂O₂) ratios [7,17,18]. The low decomposition found in this work may be due to the particle being formed by ferric ions, when it is the ferrous ions that catalyze the formation of the hydroxyl radical. Another possibility is the need for radiation activation, since maghemite is a semiconductor.

Conclusions.

Using the synthesized particles as a catalyst, it was possible to decompose approximately 30% hydrogen peroxide with a Fe/(H₂O₂) ratio of approximately 70 and pH close to 3.

Considering that iron oxide has semiconductor characteristics it is possible that it can be photoactivated, thus improving the decomposition rate.

The experimental design and its statistical treatment proved that the maximum decomposition of hydrogen peroxide occurs, in the domain of the variables tested, for the condition of maximum catalyst concentration (2.0 g.L⁻¹) and minimum peroxide concentration (0,02 g.L⁻¹), with a deviation of -6.7% relative to experimentally verified decomposition.

Acknowledgements.

The authors are grateful to the Auracária Foundation - Foundation for Supporting Scientific and Technological Development of Paraná, Brazil.

References

- [1] Cornel RM., Schwertmann U. The Iron Oxides. 3rd. ed.: Wiley-BCH GmbH & Co., 2003.
- [2] Guimarães IR, Oliveira LCA, Queiroz PF, Ramalho TC, Pereira M, Fabris JD, Ardisson, JD. Modified goethites as catalyst for oxidation of quinoline: Evidence

of heterogeneous Fenton process. *Applied Catalysis: A*, 2008, 89-93.

[3] Oliveira LCA, Fabris JD.; Pererira MC. Óxidos de Ferro e suas Aplicações em Processos Catalíticos: Uma Revisão. *Química Nova* 2013, 123-130.

[4] Dantas TLP. Decomposição de Peróxido de Hidrogênio em um Catalisador Híbrido e Oxidação Avançada de Efluente Têxtil por Reagente Fenton Modificado. Dissertação (Mestrado em Engenharia Química) Centro Tecnológico, Universidade Federal de Santa Catarina, Florianópolis, 2005.

[5] Kwan WP, Voelker BM. Rates of Hydroxyl Radical Generation and Organic Compound Oxidation in Mineral-Catalyzed Fenton-like Systems. *Environmental Science Technology*. USA, 2003, 1150-1158.

[6] Jia C, Sun L, Luo F, Han X, Heyderman L, Yan C, Na Z, Zheng K, Zhang Z, Takano M, hayasgi N, Eltschka M, Klaui M, Rudige U, Kasama T, Cervera-Gontard L. Large-Scale Synthesis of Single-Crystalline Iron Oxide Magnetic Nanorings. *Journal of American Chemical Society*, 2008, 16968-16977.

[7] Ferroudj N, Nzimoto J, Davidson A, Talbot D, Briot E, Dupuis V, Bée A, Medjram MS, Abramson S. Maghemite Nanoparticles and Maghemite/Silica Nanocomposite Microspheres as Magnetic Fenton Catalysts for the Removal of Water Pollutants. *Applied Catalysis B: Environmental*. Elsevier: USA, 2013, 9-18.

[8] Gui, M, Smulec V, Ormsbee LE, Sedlak DB. Iron Oxide Synthesis in Aqueous and Membrane Systems for Oxidative Degradation of Trichloroethylene from Water. *Journal of Nanoparticle Research*, Springer International, 2012, 861.- 8667.

[9] Karthikeyan S, Boopathy R, Gupta VK, Sekaran G. G. Preparation, Characterizations and Its Applications of Heterogeneous Fenton Catalyst for the Treatment of Synthetic Phenol Solution. *Journal of Molecular Liquids*, Elsevier: USA, 2013, 402-408

[10] Nogueira RFP, Trovó AG, Silva MRA, Villa RD. Fundamentos e Aplicações Ambientais dos Processos fenton e Foto-Fenton. *Química Nova*, Rio de Janeiro, 2007, 400-408.

[11] Weng C., Lin Y, Chang C, Liu N. Decolourization of Direct Blue 15 by Fenton/Ultrasonic Process using a Zer-Valent Iron Aggregate Catalyst. *Ultrasonics Sonochemistry*. USA, 2013, 970-977.

[12] Chiou J, Lai B, Hsu K, Chen D. One-Pot Green Synthesis of Silver/Iron Oxide Composite Nanoparticles for 4-Nitrophenol Reduction. *Journal of Hazardous Material*. USA, 2013, 394-400.

[13] Rodrigues J, Murteira M. Energia de Fermi. Instituto Superior Técnico, 2011. Disponível em: <https://fenix.tecnico.ulisboa.pt/downloadFile/3779576924823/energiadefermi_prata.pdf>.

[14] APHA, AWWA, WPCF. Standard Methods for the Examination of Water and Wastewater. American Public Health Association, Washington DC, 19th edition.

[15] Nogueira RFP, Oliveira MC, Paterlini, WC. Simple and fast spectrophotometric determination of H₂O₂ in photo-Fenton reactions using metavanadate. USA, 2005. 86-91.

[16] Bach A, Shemer H, Semiat R. Kinetics of Phenol Mineralization by Fenton-Like Oxidation. *Desalination: USA*, 2010, 188-192.

[17] Cui Z, Chen Z, Cao C, Jiang L, Song, WA. Yolk-Shell Structured Fe₂O₃ Mesoporous SiO₂ Nanoreactor for Enhanced Activity as a Fenton Catalyst in Total Oxidation of Dyes. *Chemical Communication*. UK, 2013, 2332-2334

[18] Shahwan T, Sirriah SA, Nairat M, Boyaci E, Eroglu AE, Scott TB, Hallam KR. Green Synthesis of Iron Nanoparticles and their Application as Fenton-Like Catalyst for the Degradation of Aqueous Cationic and Anionic Dyes. *Chemical Engineering Journal*, 2011, Elsevier, 258-266.

Adsorption and peroxymonosulfate catalytic oxidation of anti-hypertensive pharmaceutical using porous structure with embedded N, S-codoped core-shell Co@C nanoparticles

Júlia Resende de Andrade^a, Wenjie Tian^{b,c}, Meuris Gurgel Carlos da Silva^{a,*},
Melissa Gurgel Adeodato Vieira^a, Shaobin Wang^{b,c}

^aUniversity of Campinas, School of Chemical Engineering, Albert Einstein Avenue 500, Campinas 13083-852, Brazil

^bCurtin University, Department of Chemical Engineering, GPO Box U1987, Perth WA 6845, Australia

^cThe University of Adelaide, School of Chemical Engineering, Adelaide SA 5005, Australia

Abstract

Pharmaceuticals are emerging contaminants, which widespread presence in the environment raises increasing concerns. State-of-the-art technologies, such as advanced oxidation processes (AOPs), have been researched aiming at the effective removal of pharmaceutical emerging contaminants from water and/or wastewater. Advanced carbon-based catalysts have been pursued for improved performance in peroxymonosulfate (PMS) activation for enhanced generation of reactive species. In the present work, a hierarchically porous carbon with embedded Co core@N, S codoped C-shell nanoparticles (Co@N,S-PC) was employed in PMS activation for oxidative decomposition of losartan potassium as model pharmaceutical pollutant. Co@N,S-PC presented adsorptive ability inferior to 6% for losartan, but high catalytic behavior in PMS activation with 100% degradation of losartan within 45 min reaction time. The kinetics followed pseudo-first-order pattern and the reaction rate constant was appraised as 0.183 min^{-1} . Losartan removal efficiencies were compared to those previously reported in the literature and functional groups of Co@N,S-PC were characterized by Fourier-transform infrared spectroscopy (FTIR).

Keywords: adsorption; advanced oxidation process; porous carbon; emerging pharmaceutical contaminant; losartan potassium.

1. Introduction

Water pollution is one of the most critical global challenges and pharmaceuticals emerge as contaminants of increasing concern. Despite the fact that pharmaceuticals are usually traced in the environment at levels below therapeutic dosages (ng/L- $\mu\text{g/L}$ range), the permanent and accumulative exposure can cause negative consequences on non-target aquatic organisms, such as reproductive alterations in fishes and development of bacterial pathogen resistance [1].

The worldwide detection of pharmaceuticals in surface waters demonstrates that conventional approaches of water and wastewater treatments are not adequate to remove such kind of micropollutants [2]. Consequently, it is urgent to

research versatile technologies for environmental remediation of pharmaceuticals, such as adsorption [3] and advanced oxidation processes (AOPs) [4].

AOPs have been shown high effectiveness for total degradation and mineralization of organic contaminants [5]. AOPs are typically based on the generation of strong oxidizing species, such as hydroxyl ($\bullet\text{OH}$) and sulfate ($\text{SO}_4^{\bullet-}$) radicals. Comparatively to $\bullet\text{OH}$, $\text{SO}_4^{\bullet-}$ presents higher redox potential and longer life span [6].

The radicals $\bullet\text{OH}$ and $\text{SO}_4^{\bullet-}$ can be simultaneously generated from activated peroxymonosulfate (HSO_5^- , PMS). PMS can be activated via diverse transition metal ions, including cobalt (Co^{2+}). Although homogeneous Co^{2+} /PMS system depicts high performance, metal leaching cannot be completely prevented, which may severely affect public health due to potential



toxicity of Co^{2+} [7]. Alternatively, heterogeneous catalytic activation of PMS has been exploited owing to high productivity, low energy requirements and reduced propensity of metal leaching [8,9]. In heterogeneous catalytic systems, besides oxidation itself, adsorption concurrently occurs on the surface of the catalyst [10,11].

Amidst catalysts, there is great interest in carbon-based materials due to environmental benignity, affordable costs, large surface area and unique physicochemical and electronic properties. However, pristine carbons suffer from low stability and catalytic efficiency, thus advanced carbon materials with tailored properties have been searched [12-14]. The doping with heteroatoms, such as N, S, B and P, has been researched for the synthesis of functional carbon catalysts [15]. While single N doping and single S doping can induce tuned electronic properties and improved chemical reactivity, respectively, dual N-S doping can prompt superior catalytic performance due to synergistic effects [5].

The recent paper of Tian et al. [10] described the homogeneous assembly of Co core@N-S codoped C-shell nanoparticles into hierarchically porous structures (Co@N,S-PCs). A bread-making inspired strategy was employed with wheat flour as carbon source, sodium bicarbonate as porogen, cysteine as source of N and S atoms, and cobalt nitrate as cobalt precursor. After drying and carbonization under different temperatures, Co@C nanoparticles were *in-situ* generated in the pores of the carbon structure, forming the Co@N,S-PCs. The synthesized materials presented highly efficient catalytic activity in PMS activation for complete degradation of *p*-hydroxybenzoic acid (HBA) and phenol.

Considering the ubiquity of pharmaceuticals in the environment and the difficulty for their complete remediation, the present study aims to employ Co@N,S-PC in activation of PMS for oxidative decomposition of losartan potassium as model emerging pharmaceutical contaminant. Losartan potassium has been traced in surface waters, drinking water, industrial wastewater and effluents from wastewater treatment plants [16]. The oxidative degradation of losartan potassium has been recently examined using N single-doped metal-free porous carbon (N-PC) [17]; however, the co-doping and embedded Co@C nanoparticles of Co@N,S-PC are believed to promote enhanced catalytic performance.

The main objective of this work is to examine the losartan potassium oxidation by PMS catalytic

activation using Co@N,S-PC. The following parameters were assessed for degradation efficiency: total removal percentage, reaction time and reaction rate constant. Losartan potassium removal achieved by adsorption onto Co@N,S-PC was measured without the introduction of PMS.

2. Material and methods

2.1. Catalyst synthesis

The Co@N,S-PC used in this work had its synthesis detailed by Tian et al. [10]. Briefly, 50 mL wheat flour solution (40 g/L) was mixed with 80 mL solution containing sodium bicarbonate (37.5 g/L) and cysteine (3.75 g/L). Cobalt nitrate solution (15 g/L) was dripped into the prepared solution, which was dried at 80 °C under constant stirring. The obtained homogeneous mixture was pyrolyzed at 700 °C for 2 h, using a tube furnace with N_2 flow and 5 °C/min heating rate. The carbonized material was grounded, washed with water and ethanol, and dried in oven at 60 °C.

Three distinct pyrolysis temperatures, 700, 800 and 850 °C, were previously tested and it was verified that 700 °C was the most adequate to prepare Co@N,S-PC aiming large-scale applications with comparable catalytic efficiency for HBA and phenol removal [10].

2.2. Pharmaceutical solution

Losartan potassium (100%), referred here as losartan, was purchased from Sigma-Aldrich and the pharmaceutical solutions were prepared using ultra-pure water.

The losartan concentration in solution was assessed by ultra-high performance liquid chromatography system with UV-Vis detector (UHPLC) (UltiMate 300, Thermo Fisher Scientific). The instrument was furnished with Acclaim® Organic Acid column (150 mm×4 mm i.d., 5 µm, Thermo Fisher Scientific). The mobile phase employed was 0.1% solution of phosphoric acid and acetonitrile at 60:40 volume ratio. Additional conditions were: flow rate 1.0 mL/min, column temperature 35 °C, injection volume 10 µL, detection wavelength 254 nm.

2.3. Adsorption study

To distinguish losartan removal achieved by adsorption, a test was performed without PMS

superoxide. A water bath equipment was used at 25 °C. The dosage of Co@N,S-PCs was 0.026 g/L, as adopted by De Andrade et al. [17]. The solid was dispersed in 150 mL of losartan solution at initial concentration of 0.04 mmol/L. Aliquots of 1 mL were collected at pre-defined time intervals and filtered with 0.22 µm filters. The residual concentration of losartan was determined by UHPLC.

The removal efficiency of losartan was computed by Equation 1:

$$EF = (C_i - C_f) / C_i \times 100 \quad (1)$$

In which: *EF* (%) is the oxidation efficiency, and *C_i* and *C_f* (mmol/L) represent the initial and final concentration of losartan, respectively.

2.4. Oxidation study

The oxidation assay was also conducted 25 °C in water bath apparatus, using the same Co@N,S-PC dosage of adsorption test. PMS is stabilized in the triple potassium salt, 2KHSO₅·KHSO₄·K₂SO₄, commercially named Oxone[®]. Oxone[®] (100%) was purchased from Sigma-Aldrich. Co@N,S-PC (0.026 g/L) and PMS (3.5 mmol/L) were simultaneously added into 150 mL losartan solution (0.04 mmol/L) to initiate the reaction. Periodically, 1 mL aliquots were withdrawn, filtered with 0.22 µm membrane, and straightway mixed with 0.5 mL of methanol to stop reaction prior quantification by UHPLC.

The degradation efficiency in Co@N,S-PC/PMS system was calculated by Equation 1.

The model of pseudo-first order was been extensively employed in literature to describe catalytic reaction patterns [18-21]. The linear correlation of pseudo-first order rate law is presented in Equation 2:

$$\ln C / C_i = -k_1 \times t \quad (2)$$

In which: *C* (mmol/L) is the concentration of losartan at certain time *t* (min) and *k₁* (min⁻¹) stands for the pseudo-first order rate constant.

2.5. Fourier-transform infrared spectroscopy FTIR

Functional groups and molecular interactions of Co@N,S-PC were characterized by FTIR (Thermo Scientific/Nicolet 6700, Madison, USA) in transmittance mode (scan 64, 4000–400 cm⁻¹

range, 4 cm⁻¹ resolution). The samples were prepared with KBr and pressed into pellets.

3. Results and discussion

3.1. Identification of functional groups and molecular interactions - FTIR

The functionalities of the as-prepared Co@N,S-PC were examined by FTIR, which baseline-corrected spectrum is shown in Figure 1. The material presents dominant peaks at 3423, 1577, 1184, 1108 and 618 cm⁻¹.

The broad absorption band at 3423 cm⁻¹ corresponds to stretching vibrations of OH groups. The band at 1577 cm⁻¹ refers to C=C stretching vibration. C–O bonds are observed at 1184 cm⁻¹. The band at 1108 cm⁻¹ can be attributed to C–O/C–N. Finally, symmetrical stretching of C–S can be identified at 618 cm⁻¹ [22,23].

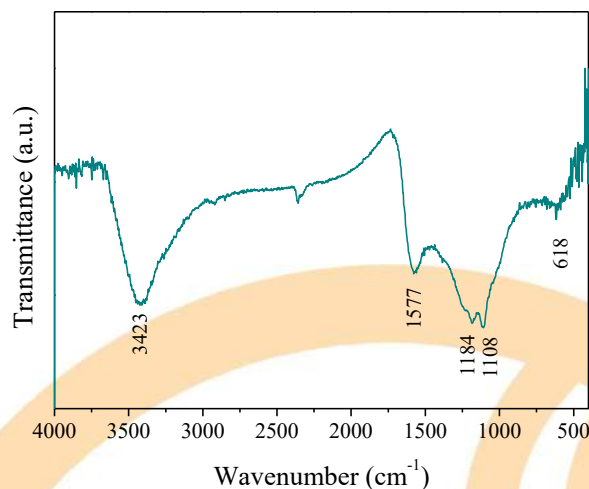


Fig. 1. FTIR baseline-corrected spectrum of the as-synthesized Co@N,S-PC

3.2. Losartan adsorption

Figure 2 depicts the removal of losartan achieved using Co@N,S-PC and Table 1 summarizes the results from the present study and those from [17], which also evaluated losartan removal (adsorption and AOP) but using an N single-doped carbo-catalyst (N-PC).

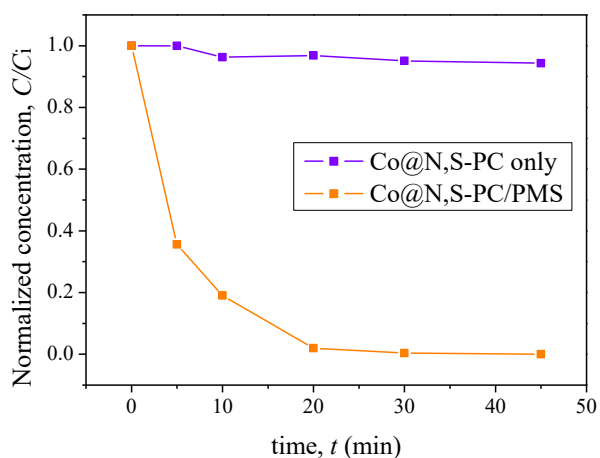


Fig. 2. Losartan removal by adsorption over Co@N,S-PC and oxidation by Co@N,S-PC/PMS system (temperature: 25 °C, adsorbent/catalyst: 0.026 g/L, PMS: 3.5 mmol/L, losartan: 0.04 mmol/L).

Table 1. Comparative losartan removal efficiency and pseudo-first order degradation constant using PMS only and N-PC or Co@N,S-PC as adsorbents and catalysts.

System	EF (%)	k_1 (min ⁻¹)	Reference
N-PC only	52	--	[17]
Co@N,S-PC only	5.6	--	This work
PMS only	36	--	[17]
N-PC/PMS	100	0.021	[17]
Co@N,S-PC/PMS	100	0.183	This work

It was observed that the adsorptive removal of losartan over Co@N,S-PC was about 6%. Previously, less than 10% of HBA or phenol were adsorbed using the same material, but at higher adsorbent loading of 0.066 g/L [10]. Of note, the adsorbent N-PC alone was formerly verified to remove more than 50% of losartan at the same experimental conditions of the present work [17]. It is tenable to associate the superior adsorption performance of N-PC to its huger specific surface area (SSA). The assed SSA of N-PC is 1791 m²/g [17], while the SSA of Co@N,S-PC is 505 m²/g [10].

3.3. Catalytic oxidation of losartan

PMS alone has strong redox potential (1.82 V) [4] and was verified to selectively degrade sulfonamide antibiotics with high efficiency (95%) without any external activation method [24].

Nevertheless, PMS self-oxidation showed minor performance for removing other pharmaceuticals, such as paracetamol (< 5%) [18] and ciprofloxacin (< 10%) [25]. In the case of losartan, PMS only (3.5 mmol/L) was verified to promote 36% degradation rate of losartan. The introduction of carbo-catalyst N-PC expressively enhanced PMS activation and losartan was 100% removed after 240 min reaction time [17]. This may be ascribable to the increased generation of reactive species, including the radicals $\bullet\text{OH}$ and $\text{SO}_4^{\bullet-}$.

The effect of Co@N,S-PC on catalytic oxidation of losartan using PMS is shown in Figure 2. Remarkably, 45 min were enough to ensure the complete removal of the pharmaceutical. The faster degradation rate obtained using Co@N,S-PC compared to N-PC indicates that, despite higher adsorption ability, the latter carbocatalyst has inferior catalytic performance.

Figure 3 presents the satisfactory linear fitting of pseudo-first order rate law for kinetic data with high correlation coefficient of $R^2 > 0.99$. The apparent reaction rate constant in Co@N,S-PC/PMS system was evaluated to be 0.183 min⁻¹, which is about 9 times higher than that on N-PC (0.021 min⁻¹, $R^2 > 0.95$) for losartan degradation.

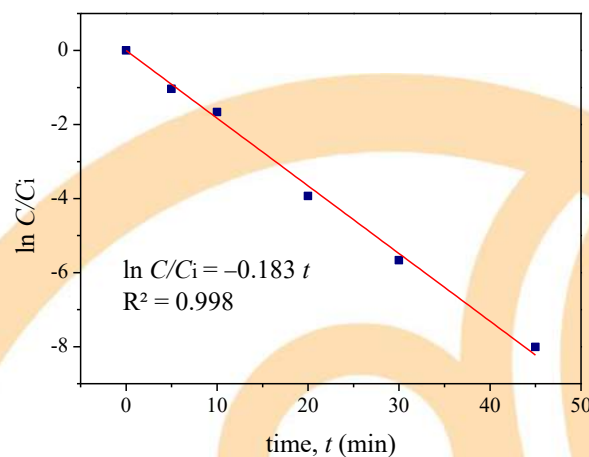


Fig. 3. Adjustment of pseudo-first order model for the reaction kinetics of losartan by Co@N,S-PC/PMS system.

According to Tian et al. [10], the high catalytic performance of Co@N,S-PC can be contributed to N and S dual doping, as well as to Co cores in Co@C nanoparticles. The substitution of C atoms in the carbon matrix by doped N atoms creates more catalytically active centers due to charge

transference between doped N and adjacent C atoms [26]. In turn, S atoms are large and so S doping can form defects in the carbon structure, which leads to increased edge-active sites [27]. Finally, encapsulated Co nanoparticles modifies the electron densities of C in the external carbon shells, since Co can promote increased ratio of more ordered sp^2 -hybridized carbon, which is more effective for PMS activation than inactive sp^3 -C [28]. Thus, Co-C interaction improves catalytic reactivity of functionalized C atoms [10].

4. Conclusions and future perspectives

The present work verified the superb catalytic performance of the porous structure with embedded N, S-codoped core-shell Co@C nanoparticles (Co@N,S-PC) for PMS activation aiming the degradation of losartan potassium from aqueous solution. The catalyst alone led to removal efficiency lower than 6%, thus adsorption effect could be ignored. Losartan was rapid decomposed in Co@N,S-PC/PMS system and total removal was achieved within 45 min reaction time. Losartan degradation well obeyed pseudo-first order kinetic model ($R^2 > 0.99$) and the apparent rate constant was determined as 0.183 min^{-1} . The catalytic activity of Co@N,S-PC for PMS activation was verified to be superior to that of N-doped porous carbon previously reported in the literature. The improved performance was associated to the synergistic effects of Co-C interactions and N, S dual doping, which further yield catalytic active sites and ameliorate chemical reactivity.

The results from this work encourages deeper examinations for the stability and reusability of Co@N,S-PC in consecutive cycles for losartan decomposition. Moreover, the process should be examined for the effects of background species, such as inorganic ions and natural organic matters. Further efforts should also be made to clarify the mechanisms of PMS activation for losartan degradation.

Acknowledgements

This study was financed in part by the Coordenação de Aperfeiçoamento de Pessoal de Nível Superior - Brasil (CAPES) - Finance Code 001 [Proc. 88882.329686/2018-01; 88881.188856/2018-01, 88881.310551/2018-01], Conselho Nacional de Desenvolvimento Científico e Tecnológico (CNPq) [Proc. 406193/2018-5] and

Fundação de Amparo à Pesquisa do Estado de São Paulo (FAPESP).

References

- [1] Sekulic MT, Boskovic N, Milanovic M, Grujic Letic N, Gligoric E, Pap S. An insight into the adsorption of three emerging pharmaceutical contaminants on multifunctional carbonous adsorbent: Mechanisms, modelling and metal coadsorption. *J Mol Liq* 2019;284:372-382.
- [2] Larsson DGJ, de Pedro C, Paxeus N. Effluent from drug manufactures contains extremely high levels of pharmaceuticals. *J Hazard Mater* 2007;148:751-755.
- [3] de Andrade JR, Oliveira MF, da Silva MGC, Vieira MGA. Adsorption of Pharmaceuticals from Water and Wastewater Using Nonconventional Low-Cost Materials: A Review. *Ind Eng Chem Res* 2018;57:3103-3127.
- [4] Wang J, Wang S. Activation of persulfate (PS) and peroxymonosulfate (PMS) and application for the degradation of emerging contaminants. *Chem Eng J* 2018;334:1502-1517.
- [5] Tian W, Zhang H, Duan X, Sun H, Tade MO, Ang HM, Wang S. Nitrogen- and Sulfur-Codoped Hierarchically Porous Carbon for Adsorptive and Oxidative Removal of Pharmaceutical Contaminants. *ACS Appl Mater Interfaces* 2016;8:7184-7193.
- [6] Duan X, Sun H, Shao Z, Wang S. Nonradical reactions in environmental remediation processes: Uncertainty and challenges. *Appl Catal, B* 2018;224:973-982.
- [7] Hu P, Long M, Bai X, Wang C, Cai C, Fu J, Zhou B, Zhou Y. Monolithic cobalt-doped carbon aerogel for efficient catalytic activation of peroxymonosulfate in water. *J Hazard Mater* 2017;332:195-204.
- [8] Ghanbari F, Moradi M. Application of peroxymonosulfate and its activation methods for degradation of environmental organic pollutants: Review. *Chem Eng J* 2017;310:41-62.
- [9] Shukla P, Wang S, Singh K, Ang HM, Tade MO. Cobalt exchanged zeolites for heterogeneous catalytic oxidation of phenol in the presence of peroxymonosulphate. *Appl Catal, B* 2010;99:163-169.
- [10] Tian W, Zhang H, Qian Z, Ouyang T, Sun H, Qin J, Tade MO, Wang S. Bread-making synthesis of hierarchically Co@C nanoarchitecture in heteroatom doped porous carbons for oxidative degradation of emerging contaminants. *Appl Catal, B* 2018;225:76-83.
- [11] Kang J, Zhang H, Duan X, Sun H, Tan X, Liu S, Wang S. Magnetic Ni-Co alloy encapsulated N-doped carbon nanotubes for catalytic membrane degradation of emerging contaminants. *Chem Eng J* 2019;362:251-261.
- [12] Peng G, Zhang M, Deng S, Shan D, He Q, Yu G. Adsorption and catalytic oxidation of pharmaceuticals by nitrogen-doped reduced graphene oxide/Fe₃O₄ nanocomposite. *Chem Eng J* 2018;341:361-370.
- [13] Ahamad T, Naushad M, Ruksana, Alhabarah AN, Alshehri SM. N/S doped highly porous magnetic carbon aerogel derived from sugarcane bagasse

- cellulose for the removal of bisphenol-A. *Int J Biol Macromol* 2019;132:1031-1038.
- [14] Wang Q, Li L, Luo L, Yang Y, Yang Z, Li H, Zhou Y. Activation of persulfate with dual-doped reduced graphene oxide for degradation of alkylphenols. *Chem Eng J* 2019.
- [15] Liang J, Jiao Y, Jaroniec M, Qiao SZ. Sulfur and Nitrogen Dual-Doped Mesoporous Graphene Electrocatalyst for Oxygen Reduction with Synergistically Enhanced Performance. *Angew Chem Int Ed* 2012;51:11496-11500.
- [16] Godoy AA, Kummrow F, Pamplin PAZ. Ecotoxicological evaluation of propranolol hydrochloride and losartan potassium to Lemna minor L. (1753) individually and in binary mixtures. *Ecotoxicology* 2015;24:1112-1123.
- [17] de Andrade JR, Vieira MGA, da Silva MGC, Wang S. Oxidative degradation of pharmaceutical losartan potassium with N-doped hierarchical porous carbon and peroxymonosulfate. *Chem Eng J* 2019. DOI: 10.1016/j.cej.2019.122971.
- [18] Tan C, Gao N, Fu D, Deng J, Deng L. Efficient degradation of paracetamol with nanoscaled magnetic CoFe₂O₄ and MnFe₂O₄ as a heterogeneous catalyst of peroxymonosulfate. *Sep Purif Technol* 2017;175:47-57.
- [19] Lin K-YA, Lin J-T, Jochems AP. Oxidation of amaranth dye by persulfate and peroxymonosulfate activated by ferrocene. *J Chem Technol Biotechnol* 2017;92:163-172.
- [20] Tan C, Gao N, Deng Y, Deng J, Zhou S, Li J, Xin X. Radical induced degradation of acetaminophen with Fe₃O₄ magnetic nanoparticles as heterogeneous activator of peroxymonosulfate. *J Hazard Mater* 2014;276:452-460.
- [21] Tian W, Zhang H, Sun H, Tadé MO, Wang S. One-step synthesis of flour-derived functional nanocarbons with hierarchical pores for versatile environmental applications. *Chem Eng J* 2018;347:432-439.
- [22] Jin Z-e, Wang J-l, Zhao R-j, Guan T-t, Zhang D-d, Li K-x. Synthesis of S, N co-doped porous carbons from polybenzoxazine for CO₂ capture. *New Carbon Mater* 2018;33:392-401.
- [23] Țucureanu V, Matei A, Avram AM. FTIR Spectroscopy for Carbon Family Study. *Critical Reviews in Analytical Chemistry* 2016;46:502-520.
- [24] Yin R, Guo W, Wang H, Du J, Zhou X, Wu Q, Zheng H, Chang J, Ren N. Selective degradation of sulfonamide antibiotics by peroxymonosulfate alone: Direct oxidation and nonradical mechanisms. *Chem Eng J* 2018;334:2539-2546.
- [25] Nekouei F, Nekouei S, Kargarzadeh H. Enhanced adsorption and catalytic oxidation of ciprofloxacin on hierarchical CuS hollow nanospheres@N-doped cellulose nanocrystals hybrid composites: Kinetic and radical generation mechanism studies. *Chem Eng J* 2018;335:567-578.
- [26] Sheng J, Wang L, Deng L, Zhang M, He H, Zeng K, Tang F, Liu Y-N. MOF-Templated Fabrication of Hollow Co₄N@N-Doped Carbon Porous Nanocages with Superior Catalytic Activity. *ACS Appl Mater Interfaces* 2018;10:7191-7200.
- [27] Guo Y, Zeng Z, Zhu Y, Huang Z, Cui Y, Yang J. Catalytic oxidation of aqueous organic contaminants by persulfate activated with sulfur-doped hierarchically porous carbon derived from thiophene. *Appl Catal, B* 2018;220:635-644.
- [28] Sun H, Liu S, Zhou G, Ang HM, Tadé MO, Wang S. Reduced Graphene Oxide for Catalytic Oxidation of Aqueous Organic Pollutants. *ACS Appl Mater Interfaces* 2012;4:5466-5471.

Application of different regeneration techniques to exhausted adsorbent with tetracycline antibiotic by the adsorption process

Letícia Reggiane de Carvalho Costa^{a,*}, Luana de Moraes Ribeiro^a, Liliana Amaral Féris^a

Separation Laboratory and Unit Operations (LASOP), Federal University of Rio Grande do Sul, Department of Chemical Engineering, Ramiro Barcelos Street, 2777, Postcode: 90035-007, Porto Alegre – RS, Brazil.

**leticiaREGICAR@hotmail.com*

Abstract

Tetracycline is a licit drug widely used in the pharmaceutical field, being part of the composition of various medicines, foods and beverages. Considered an indicator of anthropogenic contamination, it is of great interest to study effective techniques for its removal. The adsorption process can be considered as a complementary treatment to conventional water and wastewater treatment. However, after some time, the adsorbent solids used in the adsorption become saturated. In this context, the objective of this study was to evaluate the performance of regeneration techniques applied to the adsorbent solid saturated with the emerging pollutant tetracycline. For this, tests were performed using two regenerative methods - chemical and ultrasonic, where through them were analyzed the influence of solvent type and sonification time, respectively. Virgin, saturated and regenerated solids were characterized according to their physical structure. Both techniques employed were effective in regenerating the compound. The morphological analyzes of the adsorbent solid showed that there was a significant removal of the TC deposited on the surface of the material after the solid was reused within eight cycles for 5 minutes ultrasonic treatment and five cycles for heated water treatment.

Keywords: adsorption/desorption; regeneration techniques; tetracycline; saturated solid.

1. Introduction

The presence of chemical substances characteristic of anthropogenic action in the environment, particularly in aqueous matrices, has been recognized as an important environmental problem. Among these pollutants are drugs, hormones, pesticides, among others [1].

Given the wide variety of drugs available, tetracycline (TC) is one of the most widely used licit drugs, and is very present in food, beverages and medicines [2]. Its molecular structure is based on a four linear ring system and has multiple functional groups with acid-base properties [3]. This compound has high solubility in alcohols such as methanol and ethanol and a moderate solubility in organic solvents such as acetone and acetonitrile [4]. It also has three different pKa ranges: 3.3; 7.8 and 9.6 [5], with isoelectric point at pH 4.0 and 6.0.

According to Verlicchi [6], adsorption processes have shown great potential in the removal of pharmaceutical compounds. However, the surface pores of the solids used in this process are filled after some time, making them saturated. Depending on the

process speed, there may be a higher demand for replacement of these materials, resulting in a large amount of solid waste. Thus, there is a need to develop methods to regenerate and reuse the adsorbent solid.

There are several studies in the literature that report adsorbent solids regeneration techniques [7–11]. Among them, chemical regeneration is pointed as a simple technique with low energy cost [7]. Moreover, it can be done relatively quickly in situ and offers low material wear or pore structure degradation [12]. Similarly, ultrasonic regeneration is considered a process with low equipment cost, minimal carbon loss, low water consumption and high economic potential [13].

Thus, the performance of chemical and ultrasonic techniques was evaluated by comparative study of regeneration of adsorbed solid saturated by TC.

2. Experimental procedure

Adsorption and desorption experiments were conducted on commercial activated carbon (Scientific Exodus), with particle size between 1.40 and 1.00 mm. As adsorbate was used tetracycline (Sigma Aldrich) with purity greater than 98%.

2.1. Characterization methods

In order to evaluate surface characteristics and possible morphological, structural and textural changes, virgin, saturated and regenerated solids were characterized according to N₂ physical adsorption/desorption isotherms and scanning electron microscopy (SEM) analyzes.

2.2. Saturation of adsorbent solid

Prior to the adsorbent solid regeneration tests, 3 g of dry activated charcoal were added to 250 mL Schott vials, each filled with 100 mL of tetracycline aqueous solution with an initial concentration of 20 mg.L⁻¹, in the best condition. pH verified on adsorption, obtained from initial tests. All flasks were shaken on a temperature controlled shaker (New Lab, NL 161-04) at 150 rpm and 25 °C until equilibration time was reached. After filtration, the absorbance of the 357 nm TC solution was measured by UV-Vis spectrophotometer (Thermo Scientific, Genesys 10S UV-Vis) and the retained solid was stored for further regeneration assays. The amount of solid phase TC (mg.g⁻¹) was determined by Equation 1.

$$Q_{TC} = \frac{(C_0 - C_e) \cdot V}{m} \quad (1)$$

where, C₀ and C_e is the initial and equilibrium TC concentration (mg.L⁻¹) respectively, V represents the solution volume (L) and m is the adsorbent mass (g).

Error correction caused by TC trapped in the filter was performed by reading the solution before and after filtration.

2.3. Regeneration study

At this stage of the work, the activated carbon particles saturated with TC and separated in the previous stage were submitted to different types of regenerative treatments to evaluate the most efficient method.

Chemical treatment with 100% methanol solution (M1), 100% deionized water with heating at 60 °C (A2) and ultrasonic treatment at 5 (U5) and 20 (U20) minutes were tested.

In all methods 100 ml of the regenerating solution was used, a mass of 3 g of the saturated adsorbent solid and, in the case of chemical treatment, a desorption time of 1 hour. After the process is

performed, the adsorbent material goes through the saturation step (2.2) again.

From the best regeneration efficiency results, adsorption/desorption cycles were performed to evaluate the regenerative capacity of the saturated solid under study. This procedure is subdivided into four stages: saturation of the adsorbent solid (item 2.2), solid-liquid separation where the solid is retained after filtration and the remaining TC concentration is read in a spectrophotometer, drying the solid in an oven 105 °C for 24 hours and desorption experiments using the regenerative techniques mentioned above.

The adsorption capacity of the solid in each cycle was obtained from Eq. 1 and the regeneration efficiency (ER) was calculated according to the following equation (Eq. 2):

$$ER(\%) = \frac{Q_{de}}{Q_{ad}} \cdot 100 \quad (2)$$

where, Q_{de} is the amount of adsorbed desorbed adsorbent (mg.g⁻¹) and Q_{ad} is the amount of adsorbed solid phase retained (mg.g⁻¹).

3. Results and discussion

3.1. Initial characterization of adsorbent before and after adsorption

N₂ physical adsorption/desorption tests were performed to determine the specific surface area, calculated by the BET method, and the pore volume and diameter, calculated by the BJH method. Virgin (CA) and saturated (CA-TC) coals had a surface area of 508.12 and 439.84 m².g⁻¹, respectively. As expected, the impregnation of tetracycline to charcoal pores during the adsorption process caused a decrease in this surface area. The same was observed in the surface area and volume of mesopores where, from 285.06 to 234.25 m².g⁻¹ and 0.103 to 0.086 cm³.g⁻¹, respectively.

During the characterization of the coals prepared for the removal of sulfur and nitrogen compounds from petroleum derivatives, Pereira [14] reported that the previously visible pores were filled with copper and palladium salts after treatment, which resulted in a decrease in both area surface area and pore volume.

Figure 1 (a and b) shows the surface morphological structures of the adsorbent solid before and after adsorption.

It is noted that the surface of CA (a) showed well developed porosity while for CA-TC (b) there is a formation of a closed pore structure probably caused by the presence of tetracycline, without the relevant presence of fissures and micropores.

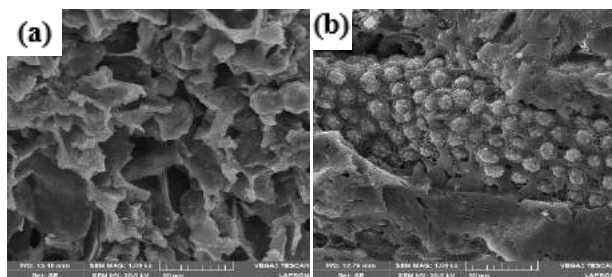


Fig. 1. SEM 1000x images of (a) CA and (b) CA-TC.

3.2. Regeneration efficiency

Figure 2 shows the efficiency comparison of different treatment processes applied to tetracycline-saturated activated charcoal regeneration. The obtained results showed values above 93% of regenerative potential.

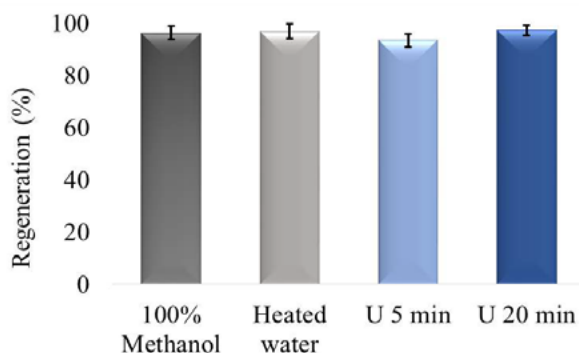


Fig. 2. Regeneration efficiency comparative analysis between different techniques employed.

Among the chemical treatments used, it is noted that the two regenerating solutions chosen showed a regeneration efficiency around 96%. That could be explained by the behavior of organic solvents with different polarities, which can compete with tetracycline to occupy activated carbon adsorption sites. Thus, a high affinity of the drug with the regenerating solution and the temperature effect may explain these results, as both techniques facilitate solubility/removal of the carbon compound used, probably caused by the polarity difference between them and also by molecular size.

Żóltowska-Aksamitowska et al. [15] tested water, methanol and ethanol for regeneration of ibuprofen and paracetamol from a chitin and lignin biosorbent. Desorption of ibuprofen and acetaminophen was favorable in ethanol (82%) and methanol (80%), respectively.

Concerning the ultrasonic technique, the influence of the regeneration time was evaluated. It can be observed that the best result was obtained within 20 minutes, achieving a regeneration efficiency of 97%. However, no significant difference was observed when results were compared to 5 minutes (93%). Thus, considering the operational issue, even for energy consumption, it is believed to be preferable to perform regeneration in shorter times. Furthermore, this process can accelerate the destruction of contaminants in the liquid phase [16], due to the collapse of cavitation bubbles and formation of strong non-selective oxidants from organic pollutants present in effluents [13].

3.3. Regeneration capacity analysis: cycles (adsorption/desorption)

Adsorption efficiency and adsorbent mass loss were determined to evaluate the reuse capacity of the solid. Adsorption/desorption cycles were performed with a regeneration capacity limit set at 60% at the end of the cycles for both chemical treatments with 100% deionized water with 60 °C heating and ultrasonic treatment within 5 minutes in order to compare them. Results are shown in Figure 3 (a and b).

Considering cycle 1 as the first step of solid contact with the pollutant, it is noted that the ultrasonic treatment achieved a decrease in the gradual regeneration capacity until the eighth regeneration cycle, reaching a regenerative percentage of around 55%. Comparatively, the chemical treatment with heated water was not totally favorable, since in the fifth cycle already presented the same regenerative percentage (55%).

The effect of tetracycline removal was more severe as there was a sharp decrease in this percentage as the number of cycles increased. This behavior can be attributed to the deposition of both adsorbed and unregenerate pollutant and impurities on the surface of the adsorbent solid [17]. Thus, there is a progressive blockage of the active pores of the material, preventing an efficiency in the new adsorption.

Kyzas et al. [18] noting the adsorptive capacity decrease of the adsorbent as the adsorption and

desorption cycles of the Red Remazol 3BS dye increased, they attributed to the irreversibility of the reaction and changes in the surface characteristics of the adsorbent.

Adsorbent mass loss over cycles is also a factor to be considered. During the analyzes, there was a general loss of adsorbent and this may influence the optimal conditions proposed for the adsorption to be complete. Additionally, there was a decrease in the surface area of the solid at the end of the cycles, showing values of 367.88 and 304.13 $\text{m}^2.\text{g}^{-1}$ for 5 minutes ultrasonic treatment and heated water chemical treatment, respectively. Compared to virgin solid, there was a decrease in area between 27.6 - 40.8%.

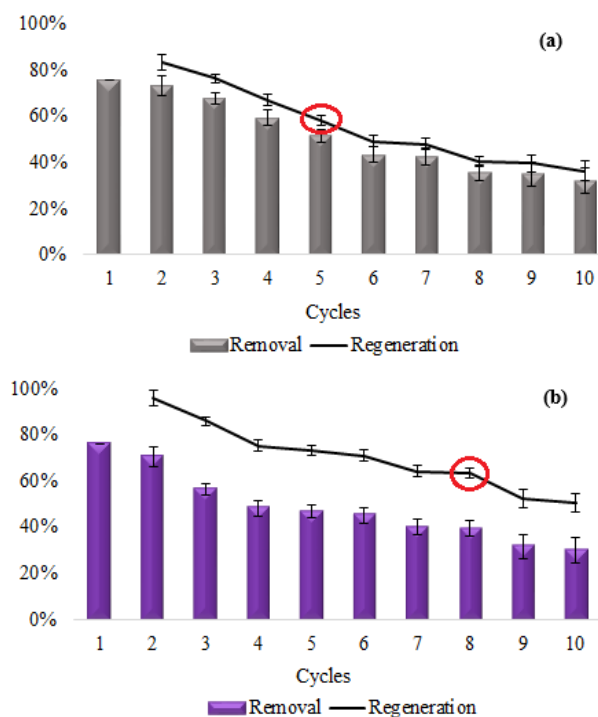


Fig. 3. Adsorption/desorption cycles for (a) 100% deionized water with 60 °C heating and (b) ultrasonic treatment 5 min.

Similar results were found by Machado [19] who studied the regeneration with NaOH in saturated activated carbon used in the treatment of oil refinery effluents. At the end of the experiments, saturated charcoal had a smaller surface area of all 488 $\text{m}^2.\text{g}^{-1}$ coals, followed by regenerated coal at 0.5% NaOH at 597 $\text{m}^2.\text{g}^{-1}$.

In addition, regenerative methods may have changed the surface characteristics of the adsorbent. Deprotonation of important functional groups to the sorption process may have occurred due to

modification of the surface charge of the material. After regeneration, the carbon surfaces corroded to varying degrees and showed an apparent difference in structure (Fig. 4a and b). In the ultrasonic assay (Fig. 4b), the erosion effect of cavitation is sometimes significant [20].

In general, in all regeneration techniques evaluated, it was observed that the adsorbent pores were clean after the regeneration, reconstituting the porosity of the material. Although some adsorption sites are not fully recovered, which may be associated with the accumulation of substances in carbon during application, these images indicated a significant removal of TC deposited on the material surface (Fig. 1b).

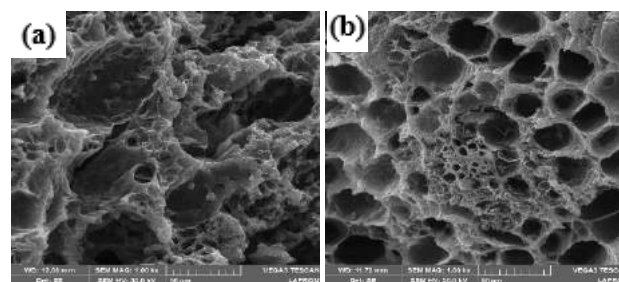


Fig. 4. SEM 1000x images for (a) 100% deionized water with 60 °C heating and (b) ultrasonic treatment 5 min at the end of the cycles.

4. Conclusion

In this work the efficiency and regeneration capacity of TC saturated activated carbon through chemical and ultrasonic regeneration was investigated. Considering the operational issue, it was preferable to perform regeneration both in shorter times and with simpler regenerating solutions. In the evaluation of regenerative capacity, there was a decrease in the desorption and removal percentages as the number of cycles increased. Even so, morphological analyzes of the adsorbent solid showed that after the regeneration cycles the pores were cleaned and there was a significant removal of the TC deposited on the surface of the material after the solid was reused within 8 cycles for 5 minutes and 5 minutes ultrasonic treatment cycles for treatment with heated water.

Acknowledgements

To the Federal University of Rio Grande do Sul (UFRGS) and the Coordination for the Improvement

of Higher Education Personnel (CAPES) for the support received.

References

- [1] Luo, Y.; Guo, W.; Hao, H.; Duc, L.; Ibney, F.; Zhang, J.; Liang, S.; Wang, X.C. A review on the occurrence of micropollutants in the aquatic environment and their fate and removal during wastewater treatment. *Sci. Total Environ.* **2014**, *473–474*, 619–641.
- [2] Daghrir, R.; Drogui, P. Tetracycline antibiotics in the environment: A review. *Environ. Chem. Lett.* **2013**, *11*(3), 209–227.
- [3] Couto, C.M.C.M.; Conceição, M.; Montenegro, B.S.M.; Reis, S. Complexação da tetraciclina, da oxitetraciclina e da clortetraciclina com o catião cobre (II). estudo potenciométrico. **2000**, *23*(II), 457–460.
- [4] Anderson, C.R.; Rupp, H.S.; Wu, W.H. Complexities in tetracycline analysis - Chemistry, matrix extraction, cleanup, and liquid chromatography. *J. Chromatogr. A* **2005**, *1075*(1–2), 23–32.
- [5] Pamreddy, A.; Hidalgo, M.; Havel, J.; Salvadó, V. Determination of antibiotics (tetracyclines and sulfonamides) in biosolids by pressurized liquid extraction and liquid chromatography-tandem mass spectrometry. *J. Chromatogr. A* **2013**, *1298*, 68–75.
- [6] Verlicchi, P.; Aukidy, M. Al; Zambello, E. What have we learned from worldwide experiences on the management and treatment of hospital effluent? - An overview and a discussion on perspectives. *Sci. Total Environ.* **2015**, *514*, 467–491.
- [7] Guo, D.; Shi, Q.; He, B.; Yuan, X. Different solvents for the regeneration of the exhausted activated carbon used in the treatment of coking wastewater. *J. Hazard. Mater.* **2011**, *186*(2–3), 1788–1793.
- [8] Zanella, O. Produção de carvão ativado a partir do engaço da uva e estudo da regeneração eletroquímica do mesmo em um reator desenvolvido em escala laboratorial. **2015**.
- [9] Cazetta, A.L.; Junior, O.P.; Vargas, A.M.M.; Silva, A.P. Da; Zou, X.; Asefa, T.; Almeida, V.C. Thermal regeneration study of high surface area activated carbon obtained from coconut shell: Characterization and application of response surface methodology. *J. Anal. Appl. Pyrolysis* **2013**, *101*, 53–60.
- [10] Marques, S.C.R.; Marcuzzo, J.M.; Baldan, M.R.; Mestre, A.S.; Carvalho, A.P. Pharmaceuticals removal by activated carbons: Role of morphology on cyclic thermal regeneration. *Chem. Eng. J.* **2017**, *321*, 233–244.
- [11] Lim, J.L.; Okada, M. Regeneration of granular activated carbon using ultrasound. *Ultrason. Sonochem.* **2005**, *12*(4), 277–282.
- [12] Cooney, D.O.; Nagerl, A.; Hines, A.L. Solvent regeneration of activated carbon. *Water Res.* **1983**, *17*(4), 403–410.
- [13] Garbellini, G.S.; Salazar-banda, G.R.; Avaca, L. a; Química, I. De; Carlos, D.S.; Paulo, U.D.S.; Sp, S.C. Aplicação Do Ultra-Som Em Sistemas Eletroquímicos: Considerações Teóricas E Experimentais. *Quim. Nova* **2008**, *31*(1), 123–133.
- [14] Pereira, F.A.V. Desenvolvimento e aplicação de adsorventes para a remoção de compostos de enxofre e nitrogênio de derivados do petróleo. 2015. 230 f. Tese (Doutorado), Universidade Federal de Santa Catarina, Florianópolis - SC, **2015**.
- [15] Żóltowska-Aksamitowska, S.; Bartczak, P.; Zembrzaska, J.; Jesionowski, T. Removal of hazardous non-steroidal anti-inflammatory drugs from aqueous solutions by biosorbent based on chitin and lignin. *Sci. Total Environ.* **2018**, *612*, 1223–1233.
- [16] Adewuyi, Y.G.; Appaw, C. Sonochemical oxidation of carbon disulfide in aqueous solutions: Reaction kinetics and pathways. *Ind. Eng. Chem. Res.* **2002**, *41*(20), 4957–4964.
- [17] Kyzas, G.Z.; Deliyanni, E.A. Modified activated carbons from potato peels as green environmental-friendly adsorbents for the treatment of pharmaceutical effluents. *Chem. Eng. Res. Des.* **2015**, *97*(September), 135–144.
- [18] Kyzas, G.Z.; Lazaridis, N.K.; Kostoglou, M. Adsorption/desorption of a dye by a chitosan derivative: Experiments and phenomenological modeling. *Chem. Eng. J.* **2014**, *248*, 327–336.
- [19] Machado, L.M. de O. Estudo da regeneração com NaOH em carvão ativado saturado no tratamento de efluentes de refinaria de petróleo. **2013**.
- [20] Saoudi, F.; Hamdaoui, O. Innovative technique for 4-chlorophenol desorption from granular activated carbon by low frequency ultrasound: Influence of operational parameters. *Microporous Mesoporous Mater.* **2011**, *141*(1–3), 69–76.

Removal of the emerging pollutant metronidazole by adsorption

Cassandra Bonfante de Carvalho^a, Keila Guerra Pacheco Nunes^a, Ivan Reis Rosa^a, Liliana Amaral Féris^{a*}

^aDepartment of Chemical Engineering, Federal University of Rio Grande do Sul (UFRGS)
Rua Ramiro Barcelos, 2777. Postcode 90035-007 – Porto Alegre – RS – Brazil.

*Corresponding author liliana.feris@gmail.com
Tel.: +55-51-3308 2148

Abstract

Pharmaceutical products are one of the most frequent emerging pollutants. As conventional treatment does not always completely remove these pollutants, other alternative technologies such as adsorption have been studied. Activated carbon is the most commonly used adsorbent due to its high removal capacity. This work aimed to study the removal of metronidazole from an aqueous solution by adsorption on activated carbon. The adsorbent material had surface area and pore size defined by N₂ adsorption. Tests were performed to verify the influence of pH (2, 4, 6, 8, 10), contact time (5, 10, 15, 20, 30, 40, 50, 75, 90, 120, 150 and 180 minutes), and concentration of adsorbent (2.5; 5; 7.5; 10; 12.5 g L⁻¹). The results showed that the ideal conditions for metronidazole removal were natural pH (6), contact time of 120 minutes and concentration of adsorbent solid of 12.5 g L⁻¹. The proposed kinetic study demonstrated that the pseudo-second order kinetics is the model that best describes the behavior of the adsorption process under the established conditions.

Keywords: activated carbon, metronidazole, adsorption

1. Introduction

The growth of the world population and the increased life expectancy caused the raise in production of pharmaceutical drugs. Allied to this, uncontrolled consumption and lack of concern with the disposal of these drugs are among the main causes of contamination of water resources [1,2].

Emerging pollutants, such as pharmaceutical drugs, are not completely removed by conventional water treatments as they have persistent chemical properties, high potential for bioaccumulation and low biodegradability. Therefore, residual amounts remain in the treated water and accumulate in surface water, being found in the range of ng L⁻¹ to µg L⁻¹ [3]. Thus, there is a need to study alternative technologies for the removal of these compounds [4].

Due to their chemical structure, emerging contaminants are easily transported through the water cycle presenting a potential risk to environmental ecosystems and human health [5]. Metronidazole is an antibiotic from nitroimidazole class that is widely used for treating infections caused by anaerobic bacteria and protozoans. It is non-biodegradable with high solubility in water, can be toxic to aquatic system and has potential carcinogenic [6].

In this context, the adsorption technique appears as an advantageous alternative, economically and technically viable. Physicochemical properties of adsorbents such as hydrophobicity, surface functional groups, pore size, external surface area and chemical composition determine the removal efficiency along with other experimental parameters such as pH and temperature [7].

Among the adsorbent materials, activated carbon stands out for its high surface area, abundance of porous structures and strong surface interaction, thus demonstrating high adsorption capacity. Adsorption on powder activated carbon has been the most adopted alternative by water treatment stations, including Brazilian ones. In general, it has the advantage of not requiring adaptation and construction of new facilities [8].

The aim of this work was to evaluate the best operational conditions for metronidazole removal using commercial activated carbon as adsorbent material in a batch scale adsorption system.

2. Materials and methods

2.1. Materials

Metronidazole was purchased from Sigma-Aldrich. The commercial activated carbon (CAC) was supplied by the Êxodo Científica with particle size fraction between 1.4 and 2.36 mm. The CAC was characterized by N₂ adsorption techniques to

evaluate the surface area, pore diameter, and the point of zero charge (pH_{PCZ}). The pH_{PCZ} is defined as the pH at which the adsorbent surface has a neutral charge and was determined by solid addition method [9].

2.2. Batch adsorption

Adsorption tests were performed in 250 mL Erlenmeyer, using 100 mL of 20 mgL^{-1} metronidazole solution, in refrigerated orbital incubator shaker (New Lab 161-4). This concentration was chosen to allow the determination by spectrophotometry. The influence of pH, contact time and CAC concentration was studied.

After each experiment, the solutions were filtered and the metronidazole concentration, before and after the adsorption process, was determined by a UV/VIS spectrophotometer at wavelength of 320 nm. The pH of each experiment was maintained in the analysis and quartz cuvettes were used.

2.3. Effect of pH

For the experiments of pH influence, metronidazole solutions were adjusted with NaOH and HCl solutions in different values (2, 4, 6, 8 and 10). The concentration of CAC was 10 $g.L^{-1}$ and the contact time was 30 minutes.

2.4. Effect of contact time – kinetic study

The tests to evaluate the contact time influence were performed at 5, 10, 15, 20, 30, 40, 50, 60, 75, 90, 120, 150 and 180 minutes. The concentration of CAC was 10 $g.L^{-1}$ and the pH was the one evaluated in the tests described in 2.3. Results obtained using natural pH (5.8) were also considered in the pH study.

In the kinetic tests, the experimental data were analyzed using the kinetic models of pseudo-first order (equation 1) and pseudo-second order (equation 2).

$$q_t = (1 - e^{-k_1 t}) \quad (1)$$

$$q_t = \frac{q_e^2 k_2 t}{1 + q_e k_2 t} \quad (2)$$

where:

q_e is the amount of solute adsorbed ($mg\ g^{-1}$) at equilibrium,

q_t is the amount of solute adsorbed ($mg\ g^{-1}$) at time,

k_1 is pseudo-first rate constant (min^{-1}),

k_2 is pseudo-second order rate constant ($g\ mg^{-1}\ min^{-1}$).

2.5. Effect of adsorbent concentration

In the tests to evaluate the concentration of CAC, concentrations of 2.5; 5; 7.5; 10 and 12 $g.L^{-1}$ were studied. Contact time and pH were those established in previous experiments.

3. Results and discussion

3.1. CAC characterization

The results of N_2 adsorption determination showed a surface area of 444.2 m^2g^{-1} and pore diameter of 19.2 Å. This value agrees with other studies found in the literature, such as Franco [10] who used activated coal for diclofenac removal.

Figure 1 shows the CAC point of zero charge.

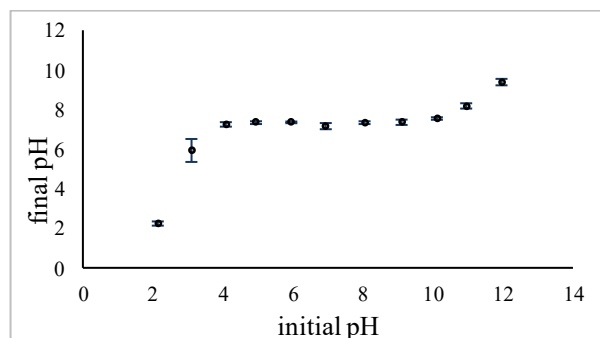


Figure 1: CAC point of zero charge (pH_{PCZ}).

According to Figure 1 the final pH remains constant between the initial pH values of 4 and 9. The point of zero charge (pH_{PCZ}) is 6.5. Below this value the surface charge is positive, and the adsorption of anions is favored; above this value the surface charge is negative and the adsorption of cations is enhanced [11].

3.2. Effect of pH

Figure 2 presents the effect of pH on the adsorption of metronidazole by CAC.

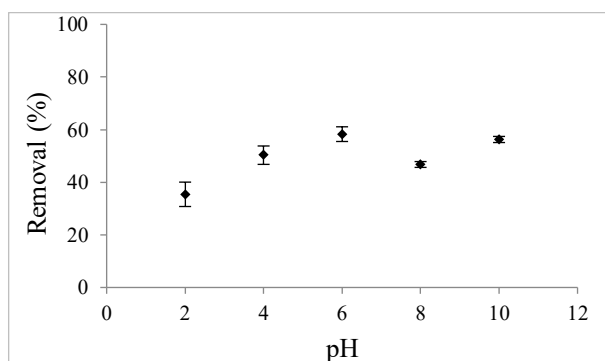


Figure 2: Effect of pH on the adsorption of metronidazole by CAC ($C_0 = 20 \text{ mg L}^{-1}$; $C_{CAC} = 10 \text{ g L}^{-1}$; $T = 20^\circ\text{C}$; for 30 minutes).

Figure 2 shows that the best removal was at pH 6, in which was possible obtain a removal of 58%. Metronidazole is a weak base with one of its pKa equal to 2.38, so it has a positive charge at acidic pH (less than 5) and is protonated, favoring interactions with countercharge compounds [12]. To avoid pH adjustments and reagent consumption, it was decided to perform the other tests at metronidazole solutions at natural pH (pH 5.8).

3.3. Effect of contact time – kinetic study

The effect of contact time on the adsorption of metronidazole by CAC is shown in Figure 3.

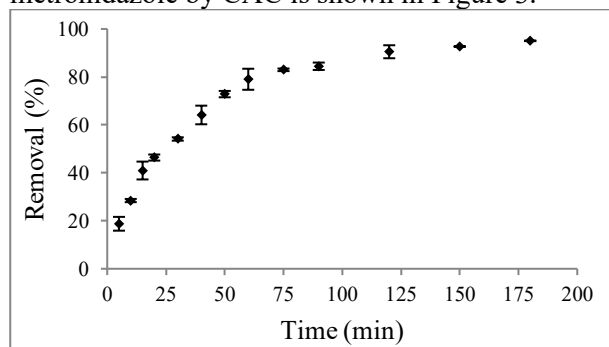


Figure 3: Effect of contact time on the adsorption of metronidazole by CAC ($C_0 = 20 \text{ mg.L}^{-1}$; natural pH; $C_{CAC} = 10 \text{ g.L}^{-1}$; $T = 20^\circ\text{C}$).

It is possible to identify in Figure 3 that after 120 minutes the removal was almost constant. Then submitting these data to a statistical analysis (ANOVA, with 5% significance level) it was found that, between 120, 150 and 180 minutes, there was no significant difference ($p=0.133$) in the removal.

The adjustment of kinetic models to experimental data can be seen in Figure 4.

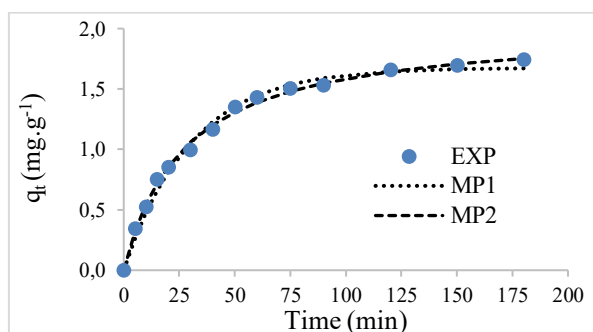


Figure 4: Comparison of kinetic models of pseudo-first and pseudo-second order and experimental data of metronidazole adsorption on CAC (EXP = experimental data; MP1 = model of pseudo-first and order and MP2 = model of pseudo-second order).

The model that best fits experimental data is the pseudo-second order (MP2) model, with $R^2=0.9996$. In this model, the rate-controlling step involves chemisorption. Experimental value of the amount of metronidazole adsorbed (q_e) at the equilibrium was 1.66 mg g^{-1} .

3.4. Effect of adsorbent concentration

Figure 5 shows the effect of adsorbent concentration on metronidazole removal.

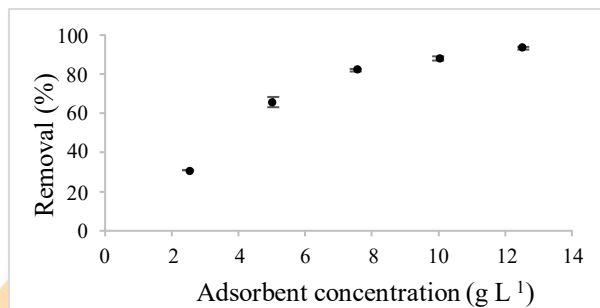


Figure 5: the effect of adsorbent concentration on metronidazole removal by CAC ($C_0 = 20 \text{ mg.L}^{-1}$; natural pH; $T = 20^\circ\text{C}$; for 120 minutes).

According Figure 5, with $12,5 \text{ g.L}^{-1}$ of CAC concentration was obtained approximately 95% of metronidazole removal within 120 minutes of contact.

4. Conclusion

The present work aimed to evaluate the potential of activated carbon in the removal of metronidazole by adsorption using a synthetic solution. The

influence of pH, contact time, equilibrium kinetics and contact time was studied.

The most appropriate value for pH, considering the percentage of removal and economic factors, was the natural one, which presented approx. 60% of metronidazole removal. The best contact time found was 120 min, corresponding to a 90.5% removal. The concentration of adsorbent that obtained the highest removal (93%) was 12.5 g.L⁻¹.

In kinetic studies, the model that best fits the experimental data was the pseudo-second order with a coefficient of determination close to unit ($R^2 = 0.9996$) indicating that the adsorption process studied is mostly controlled by chemical interactions.

Acknowledgements

The authors thank the National Council of Technological and Scientific Development (CNPq) of the Brazilian Government for the financial support granted to carry out this work.

References

- [1] Zapparoli, I., Camara, M. D., Beck, C. Medidas mitigadoras para a indústria de fármacos comarca de Londrina-PR, Brasil: impacto ambiental do despejo de resíduos em corpos hídricos. In: 3rd International Workshop Advances in Cleaner Production, 2011.
- [2] La Farre, M., Pérez, S., Kantiani, L., Barceló, D. Fate and toxicity of emerging pollutants, their metabolites and transformation products in the aquatic environment. *TrAC Trends in Analytical Chemistry*, 2008, 27 (11), 991–1007.
- [3] Starling, M. C. V., Amorim, C. C., Leão, M. M. D. Occurrence, control and fate of contaminants of emerging concern in environmental compartments in Brazil. *Journal of hazardous materials*, 2018.
- [4] Pinto, G. M. F., Sampaio, S. I., Pereira, R. F. A. B., Silva, K. R. Estudo do descarte residencial de medicamentos vencidos na região de Paulínia-SP. *Engenharia Sanitária e Ambiental*, 2014, 19 (3).
- [5] Rodriguez-Narvaez, O. M., Peralta-Hernandez, J. M., Goonetilleke, A., Bandala, E. R. Treatment technologies for emerging contaminants in water: A review. *Chemical Engineering Journal*, 2017, 323, 361–380.
- [6] Aboudalle, A.; Djelal, H.; Fourcade, F.; Domergue, L.; Assadi, A. A.; Lendormi, T.; Taha, S.; Amrane, A. Metronidazole removal by means of a combined system coupling an electro-Fenton process and a conventional biological treatment: By-products monitoring and performance enhancement. *Journal of Hazardous Materials*, 2018, 359, 85-95.
- [7] Lonnapan, L.; Brar, S. K.; Das, R. K.; Verma, M.; Surampalli, R. Y. Diclofenac and its transformation products: Environmental occurrence and toxicity - A review. *Environmental International*, 96, 2016, 127 - 138.
- [8] Muller, C. C.; Raya-Rodriguez, M. T.; Cybis, L. F. Adsorção em carvão ativado em pó para remoção de microcistina de água de abastecimento público. *Engenharia Sanitária e Ambiental*, 2009, 14, 29-38.
- [9] Sadaf, S., Bhatti, H.N., 2014. Batch and fixed bed column studies for the removal of Indosol Yellow BG dye by peanut husk. *J. Taiwan Inst. Chem. Eng.* 45 (2), 541e553
- [10] Franco, A. M. De, Carvalho, C. B. De, Bonetto, M. M., Soares, R. D. P., Féris, L. A. Diclofenac removal from water by adsorption using activated carbon in batch mode and fixed-bed column: Isotherms, thermodynamic study and breakthrough curves modeling. *J. Clean. Prod.*, 2018, 181, 145–154.
- [11] Nascimento, R. F.; De Lima, A. C. A.; Vidal, C. B.; Melo, D. Q.; Raulino, G. S. C. Adsorção: Aspectos teóricos e aplicações ambientais. Fortaleza, CE. Editora UFC, 2014.
- [12] Habibi, A.; Belaroui, L. S.; Bengueddach, A.; Galindo, A. L.; Díaz, C. I. S.; Peña, A. Adsorption of metronidazol and spiramycin by an Algerian palygorskite. Effect of modification with tin. Microporous and mesoporous materials, 2018, 268, 293 – 302.
- [13] Malakootian, M.; Karthik, K.; Gharaghani, M. A.; Dehdarirad, A.; Nasiri, A.; Shahamat, Y. D.; Mahdizadeh, H. Removal of metronidazole from wastewater by Fe/charcoal micro electrolysis fluidized bed reactor. *Journal of Environmental Chemical Engineering*. 2019.
- [14] Nasseh, N.; Barikbin, B.; Taghavi, L.; Nasserri, M. A. Adsorption of metronidazol antibiotic using a new magnetic nanocomposite from simulated wastewater (isotherm, kinetic and thermodynamic studies). *Composites part B*, 2019, 159, 146 – 156.
- [15] Manjunath, S. V.; Kumar, M. Evaluation of single-component and multi-component adsorption of metronidazole, phosphate and nitrate on activated carbon from *Prosopis juliflora*. *Chemical Engineering Journal*, 2018, 346, 525 – 534.

Evaluation of different adsorbents and pre-treatments for boron removal from water

J. C. V. Azevedo^a, S. A. Valverde^a, P. L. Mesquita^a

^a Department of Chemical Engineering - Universidade Federal de Sao Joao del Rei,
Campus Alto Paraopeba - Rodovia MG 443, Km 07, Fazenda do Cadete, Ouro Branco 36400 000, MG, Brasil

Abstract

Boron contamination in water bodies has increased significantly in the last years and its (difficult) removal from aqueous systems is getting attention worldwide. In this context, this study aimed at investigating boron removal from synthetic effluent by the adsorption process, applying different adsorbents (bovine bone char, coconut shell charcoal, conventional activated carbon, waste tire rubber and *Luffa cylindrica*) as well as to evaluate different pre-treatments for bone char (curcumin, turmeric powder, xylitol and oxalic acid) for the removal of the contaminant. The adsorption experiments were conducted in batch mode, solid/liquid ratio of 59.95 g of adsorbent/kg of effluent in a shaker at 25.0 ± 0.1 °C and 180 ± 1 rpm for 24 hours. Among the adsorbents tested, higher boron removal ($R=39 \pm 3\%$) and adsorptive capacity ($q_e=0.12 \pm 0.01$ mg.g⁻¹) were achieved while applying bovine bone char, a material made from residue of food industry and tannery. Lower initial concentration ($C_0=8.0 \pm 0.1$ mg.L⁻¹) favored boron percentage removal by bone char, as well, achieving $64 \pm 3\%$ of boron percentage removal, as less resistance to mass transfer was present. Concerning the pre-treatments, none was effective to enhance performance and a higher boron removal was observed while applying non-treated new bovine bone char.

Keywords: adsorption; boron; bovine bone char; pre-treatment, water

1. Introduction

Boron is an element that can be found in rocks, soil and water. Although it is widely distributed in nature, boron is always found as other element compounds in lower concentrations [1]. However, in last years, the significant increase of boron concentration in surface water was observed, mainly due to industrial activities. Indeed, boric acid and boron salts are largely used in many industrial processes, i.e., for the manufacture of fuels, soft drinks, catalysts, glasses, cosmetics, steel mills and others [2].

According to Wang *et al.* [3], one of the potential techniques to be applied for boron removal is adsorption, as the process requirements are simple and it can be used even in scenarios of low boron concentrations. Several adsorbents have been tested and used for boron removal in aqueous solutions, like composites from carbon and iron oxide [4], zirconium chitosan hydrogel spheres [5], activated carbon impregnated with curcumin [6] and natural minerals [7]. However, these materials present limitations for real applications due to their

relatively expensive cost and low performance for boron removal [3]. Thus, adsorbents produced from waste from other activities, such as bovine bone char [8, 9, 10], tire rubber residue [11], coconut shell charcoal [12, 13, 14] and *Luffa cylindrica* [15, 16, 17], are attracting interest for contaminated water treatments, due to their lower cost, excess and renewable resource.

Bovine bone char, produced from waste of the food industry and the tanneries, is an adsorbent used for decontamination of water due to its superficial area and porosity [10]. *Luffa cylindrica* is a natural low cost, non-toxic, biodegradable and abundant material. According to Arana *et al.* [15], it is made of cellulose and lignin, structures that have functional groups and offer the possibility to create bonds that support adsorption. Coconut shell charcoal, biomass material and promptly available, has high mechanical resistance, good abrasion resistance and an inherent granular structure, besides high superficial area and pore volume [12]. Nevertheless, although such adsorbents have been reported by literature for other contaminants removal, none was applied for boron removal specifically, what motivated this study. In addition,

several researchers have demonstrated that boron adsorption onto activated carbon might be improved by impregnation with various compounds as curcumin, xylitol and tartaric acid [6, 18, 19].

Thus, the purpose of this work was to accomplish a study of the efficiency in the use of bovine bone char, coconut shell charcoal, conventional activated carbon, *Luffa cylindrica* and waste tire rubber as adsorbents for the boron removal from synthetic effluent with typical concentrations found in industrial sectors, for example, in wastewater due to the steel rolling. Furthermore, the bovine bone char was also pre-treated chemically for the evaluation of the efficiency to remove boron from water.

2. Materials and methods

2.1. Reagents and adsorbents

Boric acid used in the standard solution prepared was manufactured by Êxodo Científica. Carminic acid was manufactured by Merck. Oxalic acid and the hydrochloric acid were manufactured by Cromoline. Deoxidizing ROLLITEZ 505 used to prepare the synthetic effluent was manufactured by Budenheim México S.A. Bovine bone char was provided by Bonechar Carvão Ativado Ltda. Coconut shell charcoal was manufactured by Tobasa Bioindustrial. Granular activated carbon was manufactured by Dinâmica. Xylitol and turmeric powder were purchased from Real Food, in Conselheiro Lafaiete-MG, Brazil. Curcumin was manufactured by Florien. Waste tire rubber was provided by Tonella Pneus, in Conselheiro Lafaiete-MG, Brazil. *Luffa cylindrica*, was acquired from a small plantation in a rural area of Conselheiro Lafaiete-MG, Brazil.

2.2. Preparation of materials and samples for the adsorption tests

Bovine bone char, coconut shell charcoal and activated carbon were quartered according to Brazilian technical standards for reducing field samples to laboratory testing size [20]. A particle size analysis was performed using a vibrating sieving system (Bertel Indústria Metalúrgica - Ltda.), for 15 min at 5 rpm and particles of 12-32 mesh (0.5 to 1.4 mm) were taken for the adsorption tests [8]. The adsorbent was washed 4 times with distilled water for the removal of tiny particles that might be adhered to the material

surface and it was dried in an oven (Sterilifer SX1.1 DTME) at 120 °C for 2 hours [8, 21].

Aiming at removing impregnated grime from *Luffa cylindrica* and waste tire rubber surfaces, these materials have undergone a cleaning process. Based on Bastos *et al.* [22], *Luffa cylindrica* was cut into 3 cm - long pieces, approximately, and it was divided in 2 halves. The portions were immersed in a beaker with distilled water for 24 hours. After the washing phase, the material was dried in an oven for 24 hours at 60 °C. The waste tire rubber was washed with distilled water in a mechanical stirrer for 3 hours and then dried in an oven for 5 hours at 60 °C [11].

After the drying process, the materials were used as “*in natura*” adsorbents. Waste tire rubber and *Luffa cylindrica* were processed for size reduction in a multiprocessor (Philco). These materials underwent the same size analysis used for the other adsorbents, in vibrating sieving system, for 15 minutes at 5 rpm, and particles of 12-32 mesh (0.5 to 1.4 mm) were taken for the adsorption tests.

2.3. Pre-treatment of bovine bone char

Xylitol, curcumin, oxalic acid and turmeric powder were used as pre-treatment reagents for bovine bone char and coconut shell charcoal modification. The impregnation tests were performed at 25.0±0.1 °C and took place in a shaker (Nova Técnica-712) at 180±1 rpm for 24 hours, solid/liquid ratio of 100 g of bone char/kg of impregnated solution. The modifiers xylitol and oxalic acid concentration were 152 g.L⁻¹ and 90 g.L⁻¹, respectively [18], while the curcumin and turmeric powder solution concentration was 5 g.L⁻¹ [6]. The resulting modifiers adsorbents were filtered, washed with water (up to constant pH) and dried at 60 °C for 24 hours.

2.4. Batch mode adsorption tests using bone char

In the adsorption tests to assess different adsorbents and pretreatments, the masses were measured in analytical balance (Shimadzu - AY220) and added to 100 ml of synthetic effluent in erlenmeyers of 250 mL, solid/liquid ratio of 59.95 g of adsorbent/Kg of effluent. Previously to boron quantification, the samples were filtered through quantitative filter paper (8µm) in order to eliminate suspended solids bigger than this size and only boron in solution was quantified.

All of the batch adsorption tests were performed at 25.0 ± 0.1 °C, in a shaker (Nova Técnica-712) at 180 ± 1 rpm for 24 hours. Initial effluent concentration was 8.0 ± 0.1 mg.L⁻¹ of boron for the tests to ascertain the efficiency of the modification in the bone char surface. For the tests that evaluated different adsorbents for boron removal, an initial concentration of 18.0 ± 0.2 mg.L⁻¹ of boron was applied. Solution pH (Digimed – 22 pHmeter) was corrected in all the tests to 7.7 ± 0.1 , using nitric acid solution 0.1 mol. L⁻¹.

2.5. Boron quantification

Boron quantification was performed according to the Carmine Method (4500-B) [24]. The absorbance was analyzed in spectrophotometer (Drawell-DU 8200) at wavelength of 585 nm.

The efficiency for boron removal and the adsorptive capacity were estimated using Equations 1 and 2, respectively.

$$R(\%) = \frac{C_0 - C}{C_0} \times 100 \quad (1)$$

$$q = \frac{C_0 - C}{m} \times V \quad (2)$$

Where: R (%) is the percentage removal[%], C₀ e C are the initial and final boron concentrations in the effluent [mg.L⁻¹], respectively, q is the adsorptive capacity [mg.g⁻¹], V is the effluent volume [L] and m is the adsorbent mass [g].

3. Results and discussion

3.1. Evaluation of the adsorbents for boron removal

Figure 1 presents the percentages for boron removal attained while using the five adsorbents investigated.

The highest boron removal ((R= $39 \pm 3\%$) and adsorptive capacity ($q_e = 0.12 \pm 0.01$ mg.g⁻¹) were achieved applying bovine bone char as adsorbent. This can be explained by distinguished composition of bone char, compared to the other charcoals. Around 70 to 75% of bone char is calcium phosphate as hydroxyapatite. Yoshikawa *et al.* [25] reported promising results in the boron removal by the formation reaction of hydroxyapatite. The authors noticed that when Ca(OH)₂ reacted with (NH₄)₂HPO₄ to create

hydroxyapatite in a synthetic effluent with 17.5 mg.L⁻¹ of boron at room temperature, the residual concentration of boron was reduced to levels inferior to 0.1 mg.L⁻¹.

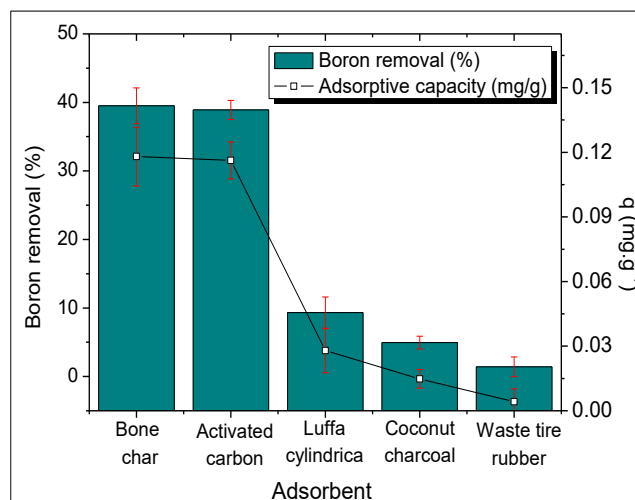


Fig. 1. Comparison of boron removal for different adsorbents materials (pH= 7.7 ± 0.1 , 25.0 ± 0.1 °C, 180 ± 1 rpm, $C_0 = 18.0 \pm 0.2$ mg. L⁻¹, 59.95 g of adsorbent/kg of effluent).

Activated carbon performance was 1.5% and 4.2% inferior, compared to bone char, for percentage removal and adsorption capacity, respectively. Kluczcka *et al.* [18] studied different types of commercial activated carbons to adsorb boron, applying solid/liquid ratio of 40 g of charcoal/kg of effluent. The authors noticed 23%, 31% and 51% of the boron removal using the granular activated charcoal WG 12, Aquasorb and Fitsorb 400, respectively. However, the activated carbons present some limitations due to their expensive cost [3]. Therefore, bovine bone char might be more attractive to be applied for boron removal, due to its low cost, abundance and initial renewable resource [8].

For other adsorbents, adsorption performance was inferior to bone char and activated carbon. The percentage boron removal and the adsorptive capacity for *Luffa cylindrica*, for example, was $9 \pm 2\%$ and 0.03 ± 0.01 mg.g⁻¹. The small percentage of boron removal and the low adsorptive capacity might be related to the use of the materials *in natura*. Indeed, literature reinforces that the production of bio activated charcoals may improve adsorption and makes the process more selective by surface modification, superficial area maximization, especially by broadening the porous

network of the adsorbent. Indeed, this was noticed by Liatsou *et al.* [16], who reported favorable results in their studies of removal of Cu (II) using *Luffa cylindrica* bio charcoal as adsorbent.

Comparing boron removal percentage using bovine bone char, activated carbon and coconut shell charcoal, this last one presented the smallest percentage for boron removal ($5.0 \pm 0.9\%$) and very low adsorptive capacity ($0.02 \pm 0.01 \text{ mg} \cdot \text{g}^{-1}$). However, the small boron removal may be attributed to the adsorbent nature and the activation method.

Waste tire rubber *in natura* showed boron removal of only $2 \pm 1\%$, what was not expected, once Babiker *et al.* [11] reported a removal of 74%, applying particle sizes of 0.125 to 0.250 mm of the same adsorbent. Comparing these results, particle size of waste tire rubber used in this study was 80% bigger compared to the cited work. According to Aisien *et al.* [26], the negative correlation between the adsorptive capacity and the particle size of the adsorbent occurs because the smaller the particles sizes, the bigger will be the superficial area, the adsorbents porous volume and hence, more active sites will be available for the adsorption process. Moreover, for adsorbents with greater particle size, the ratio diffusion resistance and mass transference will be superior, therefore, a large portion of the adsorbent inner surface may not be totally explored for the adsorption process to occur and, thereafter, the amount of boron adsorbed will be minor [26].

3.2. Pre-treatment of bovine bone char

As bone char presented the highest percentage for boron removal among the adsorbents tested, pre-treatments of this material with the impregnation of curcumin, turmeric powder, xylitol and oxalic acid, which have the capacity to form complex with boron [3], were tried to evaluate possible enhancing of adsorption performance. Figure 2 presents the percentage for boron removal and the adsorptive capacity obtained from the different pre-treatments used.

Boron adsorption was superior using new bovine bone char, compared to all other pretreatments applied, achieving percentage removal and adsorptive capacity of $64 \pm 3\%$ and $0.09 \pm 0.01 \text{ mg} \cdot \text{g}^{-1}$, respectively, for $C_0 = 8.0 \pm 0.1 \text{ mg} \cdot \text{L}^{-1}$. Bone char impregnated with curcumin presented a little inferior boron removal and the almost the same adsorptive capacity ($60 \pm 1\%$ e $0.09 \pm 0.01 \text{ mg} \cdot \text{g}^{-1}$, respectively). Halim *et al.* [6] explored boron

removal using activated carbon impregnated with curcumin and they reported an improvement of 88% for adsorptive capacity. However, bone char has a distinct chemical composition, therefore, the impregnation might not have been effective. It was also tested the impregnation of bone char with turmeric powder, due to its low cost, regarding the curcumin, once the curcumin is a reagent extracted from turmeric powder. The impregnation with turmeric powder resulted in a percentage for boron removal of $54 \pm 4\%$ and an adsorptive capacity of $0.08 \pm 0.01 \text{ mg} \cdot \text{g}^{-1}$. Thus, neither curcumin nor turmeric powder could improve the capacity of bone char to adsorb boron, as it was reported in the literature for activated carbon.

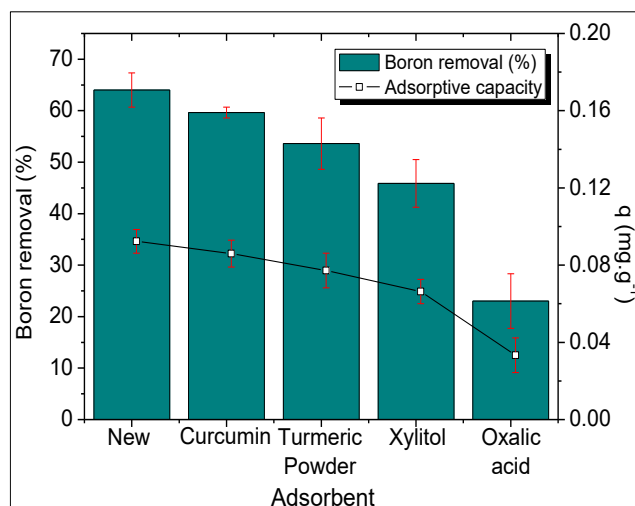


Fig. 2. Comparison among different pre-treatments for bovine bone char for boron removal (pH=7.7±0.1, 25.0±0.1 °C, 180±1 rpm, C₀=8.0±0.1 mg.L⁻¹, 59.95 g of adsorbent/kg of effluent).

The percentage of boron removal using bone char impregnated with xylitol was 28% inferior, compared to new bone char, contradicting the observation of Kluczka *et al.* [18]. These authors report an improvement of 44% in boron removal using the impregnation of activated carbon Fitsorb 400 with xylitol in their study, attributed to a selective functional group for boron.

Bone char impregnated with oxalic acid presented a percentage of boron removal and an adsorptive capacity of $23 \pm 7\%$ and $0.03 \pm 0.01 \text{ mg} \cdot \text{g}^{-1}$ respectively. Kluczka *et al.* [19] used various impregnation onto the activated carbon to adsorb boron from aqueous solutions. According to the



authors, the best adsorbent was the activated carbon impregnated with tartaric acid, presenting an increase in the adsorptive capacity of 78%, compared to new carbon. The lower percentage of removal found in this study, $23\pm 7\%$, may be explained due to the fact that tartaric acid creates more stable complexes with boron, compared to oxalic acid, as the first has two hydroxyl groups while the oxalic acid molecule has only one hydroxyl group [19].

Therefore, the idea to increase selectivity of bone char regarding boron removal, applying reagents capable to complex with boron, was not effective. This might be associated with the different chemical nature of bone char, comparatively to the activated carbon used for the cited authors. Bone char presents only 10% of carbon mass, and majorly is constituted of calcium phosphate as hydroxyapatite [8, 9, 10].

It is worth mentioning that in all impregnations, the bovine bone char was washed several times with distilled water, up to constant washing solution pH, in order to prevent curcumin, turmeric powder, xylitol and oxalic acid from being eluted from the bone char and not polluting the solution. However, at the end of the adsorption process, the pH of the treated effluents was around 8.8 ± 0.1 , while the pH of the effluent that was treated with bone char impregnated with oxalic acid was 5.9 ± 0.1 . Thus, boron adsorption was closely related to the pH of the solution, since in a more acidic medium the percentage of boron removal and the adsorptive capacity was lower compared to the other solutions that presented basic pH. Indeed, according to Bursali *et al.* [27], boron adsorption depends on which boron species are dominant in the solution. Boron removal at acidic pH is low, because of the lack of charge of non-ionized boric acid and its small size. On the other hand, at alkaline pH, where there is a predominance of borate ion, in addition to being more hydrated, boron is removed due to its large radius and the presence of its negative charge [28].

In addition, Oladipo *et al.* [29] suggest that boron removal in acidic solutions is inferior compared to alkaline solutions due to the lack of electrostatic attraction. The small size of boric acid, on the other hand, hinders adsorption in the mesoporous structure of bovine bone coal due to steric effect [28]. The Figure 3 compares the size of boric acid with some species in aqueous solution.

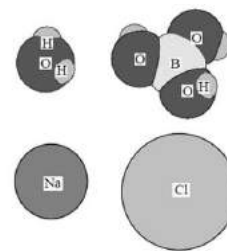


Fig. 3. Size comparison between boron acid and some other species in aqueous solution [28].

Another important point to ponder was the relevant interference of initial concentration on adsorption performance. For boron initial concentration of $8.0\pm 0.1 \text{ mg.L}^{-1}$, the percentage removal was 38% superior, compared to the one obtained for the initial concentration of $18.0\pm 0.2 \text{ mg.L}^{-1}$. Thus, bone char was able to remove $64\pm 3\%$ of boron from water, when C_0 was $8.0\pm 0.1 \text{ mg.L}^{-1}$. Indeed, as Freitas *et al.* [30] state, when there is low initial concentration, there is less mass transfer resistance and, consequently, more adsorbate removal [30]. Furthermore, in scenarios with higher initial concentrations, the greatest driving force, coming from the concentration gradient, supports the diffusion stage, causing more adsorbate to be promptly available in the adsorbent surface, favoring the fast saturation of the available active sites.

4. Conclusion

Boron removal from water is a possible, but also difficult, process and bovine bone char, a material produced from the residue of the food industry and tannery, may be an adsorbent material for its removal, even partial, from water. Comparatively to activated carbon, coconut charcoal, *Luffa cylindrica* and waste tire rubber, bone char was the most efficient adsorbent for boron removal, achieving $64\pm 3\%$ of boron percentage removal, at $C_0=8.0\pm 0.1 \text{ mg.L}^{-1}$. The pre-treatments with curcumin, turmeric powder, xylitol and oxalic acid, reagents capable to complex with boron, did not support the adsorptive process and boron adsorption performance was superior when using non-treated new bovine bone char. Lower boron initial concentration favored its removal, as it offered a scenario with less mass transference resistance.

Acknowledgements

The authors would like to acknowledge UFSJ, PIBIC/UFSJ and CAPES for the financial support,

as well as Bonechar Carvão Ativado do Brazil, for providing the bone char.

References

- [1] Wolska J, Bryjak M. Methods for Boron Removal from Aqueous Solutions- A Review. *Desalin* 2013; 310:18-24.
- [2] Bodzek M. The removal of boron from the aquatic environment-state of the art. *Desalin. Water Treat* 2015; 57:1107-1131.
- [3] Wang B, Guo X, Bai P. Removal technology of boron dissolved in aqueous solutions-a review. *Colloid. Surf. A Physicochem. Eng. Asp* 2014; 444:338-344.
- [4] Affam AC, Wong CC, Seyam MAB, Frederick Matt, CAA, Sumbai, JLA, & Evuti, AM. Study of Granular Activated Carbon/Iron oxide composite for the Removal of Boron and Organics from Wastewater. *E3S Web of Conferences* 2018; 34:02006.
- [5] Kluczka J, Gnus M, Kazek-Kęsik A, & Dudek G. Zirconium-chitosan hydrogel beads for removal of boron from aqueous solutions. *Polymer* 2018; 150:109-118.
- [6] Halim AA. Roslan, NA. Yaacub NS. Latif T. Boron removal from aqueous solution using curcumin-impregnated activated carbon. *Sains Malays.* 2013; 42:1293-1300.
- [7] Jalali M, Rajabi F, Ranjbar F. The removal of boron from aqueous solutions using natural and chemically modified sorbents *Desalin. Water Treat* 2016; 383:29-37.
- [8] Mesquita PL, Cruz MAP, Souza CR, Santos NTG, Nucci ER, Rocha SDF. Removal of refractory organics from saline concentrate produced by electro dialysis petroleum industry using bone char. *Adsorption* 2017; 23: 983-997.
- [9] Cruz MAP, Guimarães LCM, Da Costa Júnior EF, Rocha SDF, Mesquita, PL. Adsorption of crystal violet from aqueous solution in continuous flow system using bone char. *Chemical Engineering Communications* 2019, 1-10.
- [10] Nigri EM, Bhatnagar A, Rocha SDF. Thermal regeneration process of bone charused in the fluoride removal from aqueous solution. *J. Clean. Prod.* 2017; 142:3558-3570.
- [11] Babiker E, Al-Ghouthi MA, Zouari N, Mckay G. Removal of boron from water using adsorbents derived from waste tire rubber. *Journal of Env. Chem. Engineering* 2019; 7: 102948.
- [12] Hao Z, Wang C, Yan Z, Jiang H, Xu H. Chemosphere Magnetic particles modification of coconut shell-derived activated carbon and biochar for effective removal of phenol from water. *Chemosphere* 2018; 21:962-969.
- [13] Godda AA, Patidar R, Rebary B. An adsorption study of Sr 2 + from saline sources by coconut shell charcoal. 2018; 38:162-1167.
- [14] Tirtayasa SA, Selatan L. The effect of reduction time and size distribution of mixed iron ore with coconut shell charcoal on the percentage of metallization by using a rotary kiln Soesaptri Oediyani, Willyand. 1, Suharto 2016; 2:366-373.
- [15] Arana J, Gonzalez S, Navarrete L, Caicedo O. *Luffa cylindrica* as a natural adsorbent of cyanide ion in aqueous medium. *Dyna rev.fac.nac.minas* 2017; 84:210-215.
- [16] Liatsou I, Pashalidis I, Dosche C. Cu (II) adsorption on 2-thiouracil-modified *Luffa cylindrica* biochar fibres from artificial and real samples, and competition reactions with U (VI). 383:
- [17] Demir H, Arzu M. Comparison of Ultrasound and Conventional Technique for Removal of Methyl Orange by *Luffa cylindrica* Fibers. *Arabian Journal for Science and Engineering* 2018; 43:5881-5889.
- [18] Kluczka J, Pudło W, Krukiewicz K. Boron adsorption removal by commercial and modified activated carbons. *Chemical Engineering Research and Design* 2019; 147:30-42.
- [19] Kluczka J, Ciba J, Trojanowska J, Zolotajkin M, Turek M, Dydo P. Removal of boron dissolved in water. *Environ.Prog* 2007. 26:71-77.
- [20] ABNT - Associação Brasileira de Normas Técnicas. ABNT NBR NM 27:2001 -Agregados - Redução da amostra de campo para ensaios de laboratório. 2001.
- [21] Ribeiro MV. Use of bovine bone coal to defluoride water for use in public supply. Dissertation (Master) - Federal University of Minas Gerais. Graduate Program in Metallurgical Engineering. Belo Horizonte, MG, 2011.
- [22] Bastos PC, Rocha SDF. Characterization of *Luffa cylindrica* biosorbent in natura and functionalized and its use in the removal of etherine from aqueous solutions. Dissertation (Master) - Federal University of Minas Gerais. Graduate Program in Metallurgical Engineering. Belo Horizonte, MG, 2018.
- [23] Brandão PC. Evaluation of the use of sugarcane bagasse as adsorbent for the removal of contaminants, petroleum derivatives, from effluents. Dissertation (Master). Federal University of Uberlândia, Postgraduate program in Chemical Engineering. Uberlandia, 2006.
- [24] APHA. Standard Methods for Examination of Water and Wastewater. Washington: American Public Health Association, 2017.
- [25] Yoshikawa E, Sasaki A, Endo M. Removal of boron from wastewater by the hydroxyapatite formation reaction using acceleration effect of ammonia. *J. Hazard. Mater.*, 237-238 277-282, 2012.
- [26] Aisien FA, Amenaghawon NA, Akhidenor SA. Adsorption of ethylbenzene from aqueous solution using recycled rubber from scrap tyre *J. Sci. Res. Rep.* 2013; 2:497-512.
- [27] Bursali EA, Seki Y, Seyhan S, Delener M, Yurdakoç M. Synthesis of chitosan beads as boron sorbents. *J Appl Polym* 2011; 122: 657-665.
- [28] Kabay N, Bryjak M, Hilal N. Boron Separation Processes. 1rd ed. Amsterdam: Elsevier; 2015.
- [29] Oladipo AA, Gazi M. Efficient boron abstraction using honeycomb-like porous magnetic hybrids: Assessment of techno-economic recovery of boric acid. *J Env. Manag.*, 2016b; 183: 917-924.
- [30] Freitas ED, Vieira MGA. Competitive adsorption of silver and copper ions in bentonite clay. Dissertation (Master). Federal University of Campinas, Faculty of Chemical Engineering. Campinas, 2016.

Evaluation of acid activation and ultrasound effect on the adsorption dye potential of an agro-industrial waste

Matias Schadeck Netto*, Evandro Stoffels Mallmann, Raíssa da Cunha Bevilacqua, Isadora Argenta Preigschadt, Nathália Favarin da Silva, Guilherme Luiz Dotto**

Departamento de Engenharia Química, Universidade Federal de Santa Maria, Av. Roraima, 1000, 97105900, Camobi, Santa Maria, RS.

Abstract

In the present work, it was proposed the modification of an agro-industrial waste (avocado seed) through acid activation and simultaneous ultrasound utilization to improve the efficiency as dye adsorbent. FTIR results showed that there was no significant change in the spectra using acids at long ultrasound times. The XRD results showed an increase in the material crystallinity and an increase in the structural modification of the materials with the increase of the ultrasound time. The Sips model best described adsorption isotherms of fuchsin, regardless the adsorbent material. The best condition to improve the avocado seed performance was using HCl with sonication of 3h. In this condition, the maximum adsorption capacity was 121.0 mg g⁻¹. The raw avocado seed, in turn, presented maximum adsorption capacity of 56.5 mg g⁻¹. Thus, the use of acid treatment with ultrasound assistance can be efficiently used for the modification of agroindustrial wastes for use as dye adsorbents in aqueous solution.

Keywords: Acid activation; Avocado seed; Fuchsin; Sonication.

1. Introduction

In the last years, due to the large increase of industrial activities in a wide variety of sectors, effluent treatment methods are required to ensure water resources preservation. Dyes are compounds used in several industries to vest color to their substrates, and, because of their complex structures and toxicity, they must be removed from industrial effluents [1,2].

Adsorption is an efficient technique for wastewater treatment, since it is simple to operate low cost and does not require large physical spaces [3]. Agroindustrial wastes can be used as adsorbents as they are very low-cost materials as well as highly available. However, due to their structural properties such as surface area, porosity and thermochemical stability, these materials generally have low adsorption capacity, presenting, therefore, limited industrial application [4].

Chemical activations such as acid attacks can be used to improve morphological properties of adsorbents in order to increase their adsorption capacity [5]. The acid agent promotes a modification by penetration in the material structure, with partial dissolution of the biomass,

increasing both, its surface area and porosity [6]. The use of ultrasound in adsorbent synthesis also has a positive effect on the adsorption capacity of materials. The cavitation generated by ultrasound results in more developed heat and mass transfer, besides eroding the particles, increasing the surface area of the adsorbents, which benefits the adsorption [7].

In the present work, chemical activation process was evaluated with two different acids (hydrochloric and sulfuric acid) in synergy with 3 ultrasound times (10 min, 1 h and 3 h) to improve the adsorption performance of an agro-industrial waste (avocado seed) in relation to fuchsin dye.

2. Materials and methods

2.1. Materials, chemicals and dye

Fortuna avocado cultivar (*Persea Americana mill*) was purchased at a local market; basic fuchsin (molar mass: 337.86 g mol⁻¹, CAS number: 8075-08-9) was purchased from Chemical Exodus; sulfuric acid 95% and hydrochloric acid 35% were supplied by Sigma-Aldrich. Deionized water was used in the solutions preparation.

2.2. Adsorbent modification

The avocado seed was initially grinded in a knife mill with output sieve of 0.5 mm, washed with deionized water to remove impurities and then dried at 60 °C for 48 h. In total, six different adsorbents were synthesized from raw avocado seed. The modifications of the adsorbent consisted of adding 5 g of seed in 100 mL of 0.5 mol L⁻¹ solutions of each acid (sulfuric and hydrochloric acid), then placing this mixture under the influence of ultrasound in a titanium sonotrode (UP 200S, Hielscher, Germany) with frequency of 300 kHz, amplitude of 80% and maximum operating temperature of 80 °C for 10 min, 1 h or 3 h.

2.3. Adsorbent characterization

Fourier Transform Infrared Spectroscopy (FTIR) was used to determine the presence of functional groups in each material and to evaluate the influence of chemical and ultrasound treatments. A Shimadzu spectrophotometer, IR Prestige 21 model, with KBr pellet method and reading range of 4500 and 450 cm⁻¹ was used for the analyses. X-ray diffraction was used to determine the crystallinity of the modified materials in a Rigaku diffractometer, model Miniflex 300, under the conditions of radiation analysis. Cu K α ($\lambda = 1.54051 \text{ \AA}$) with step size of 0.03 ° and a count time of 0.5 seconds per step. The specific surface area of materials was measured by the Brunauer–Emmett–Teller (BET) method using a Micrometrics brand equipment, model ASAP 2020.

2.4. Adsorption experiments

Adsorption experiments were conducted on a thermostated stirrer Dubnoff SL – 157 model. A stock solution of fuchsin was prepared at a concentration of 1000 mg L⁻¹ and then diluted to the desired concentrations. All tests were conducted under stirring rate of 150 rpm, temperature at 25 °C and using 50 mL of dye solution. The mass of each synthesized adsorbent and the pH at which the adsorption experiments were performed were determined by preliminary tests. The mass used was 0.5 g L⁻¹ and the pH was set at 9. All tests were done in triplicate.

The influence of ultrasound time and acid type were estimated by equilibrium isotherms made with each of the adsorbent material and with the raw avocado seed. Equilibrium isotherms were

performed with initial fuchsin concentrations of 25, 50, 100, 150 and 200 mg L⁻¹. After 150 min of contact between adsorbents and dye solutions, the solid was separated by centrifugation and the residual concentration of fuchsin in the liquid phase was determined by spectrometry.

The models used to describe equilibrium isotherms were Langmuir [8] (Eq. 1), Freundlich [9] (Eq. 2) and Sips [10] (Eq. 3).

$$q_e = \frac{q_m k_l c_e}{1 + (k_l c_e)} \quad (1)$$

$$q_e = k_f (c_e)^{\frac{1}{n_f}} \quad (2)$$

$$q_e = \frac{q_m (k_s c_e)^{1/n_s}}{1 + (k_s c_e)^{1/n_s}} \quad (3)$$

where q_m (mg g⁻¹) represents the maximum adsorption capacity of the Langmuir or Sips model, k_l (L mg⁻¹) represents the Langmuir model constant, k_f (mg g⁻¹ (mg L⁻¹)^{-1/n_f}) is the Freundlich model constant, c_e (mg L⁻¹) is the equilibrium concentration, n_s represents the degree of system heterogeneity and k_s (L mg⁻¹) is the Sips model constant.

3. RESULTS AND DISCUSSION

3.1. Adsorbent characterization

Figure 1 (a) shows the FTIR of raw avocado seed. In the untreated material spectrum, characteristic bands of lignocellulosic materials are observed. The band at 3400 cm⁻¹ is associated with the O-H bonds. The band at 2920 cm⁻¹ is associated with the elongation of the C-H bond present in lignin [4]. The band at 1740 cm⁻¹ refers to the stretching of bonds in ester groups. The bands at 1530 cm⁻¹ and 1440 cm⁻¹ are associated with aromatic ring bond vibrations [11]. The band at 1160 cm⁻¹ corresponds to the asymmetrical elongation of the C-O-C bonds of cellulose and hemicellulose. The band at 1018 cm⁻¹ is associated with the elongation of C-O binding in cellulose [12]. As it can be seen from figures 2 (b) and 2 (c) representing the FTIR of the materials modified by sulfuric acid and hydrochloric acid respectively, for each treatment at different ultrasound times, there were no significant changes in the structure of the adsorbents since the spectra are similar, showing the presence of lignin, cellulose and hemicellulose.

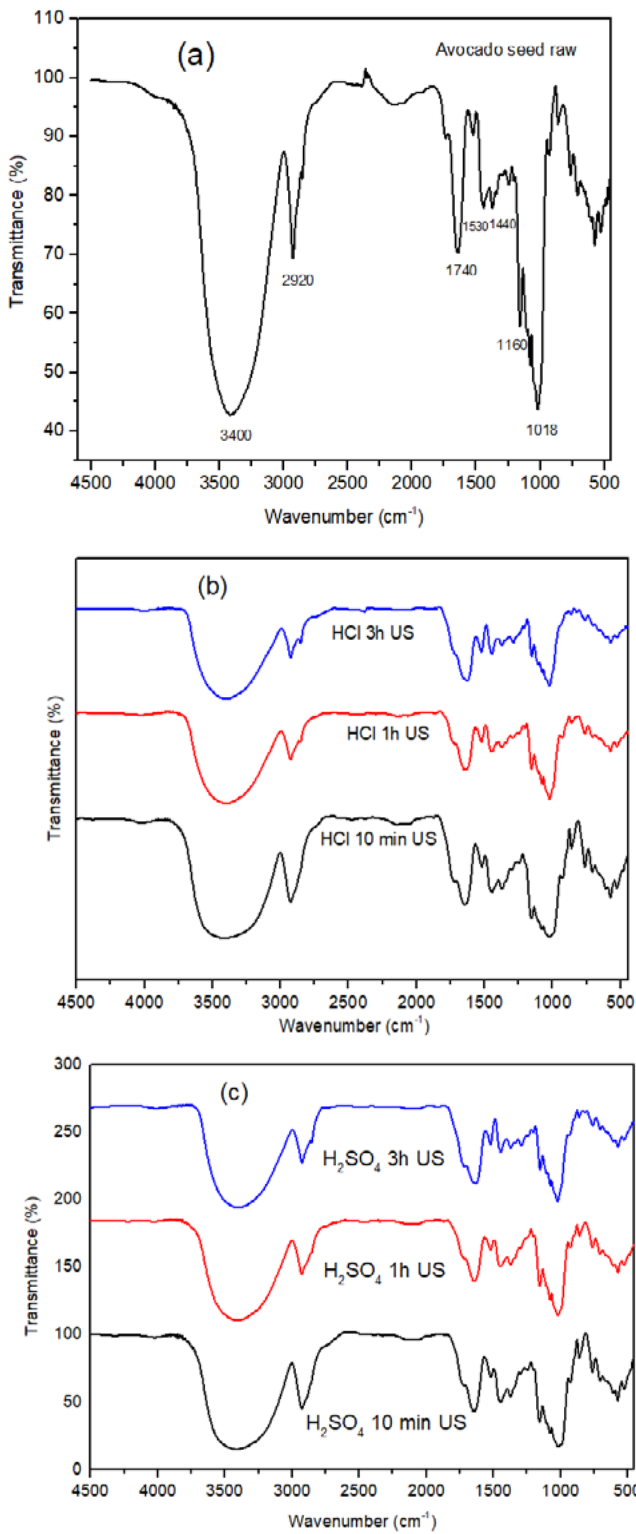


Fig. 1. FT-IR spectra of avocado seed raw (a), treatment with HCl (b) and H₂SO₄ (c)

The XRD analysis is shown in Figure 2. It shows the amorphous character of the raw avocado seed (Fig. 2 (a)), between 10° and 40°.

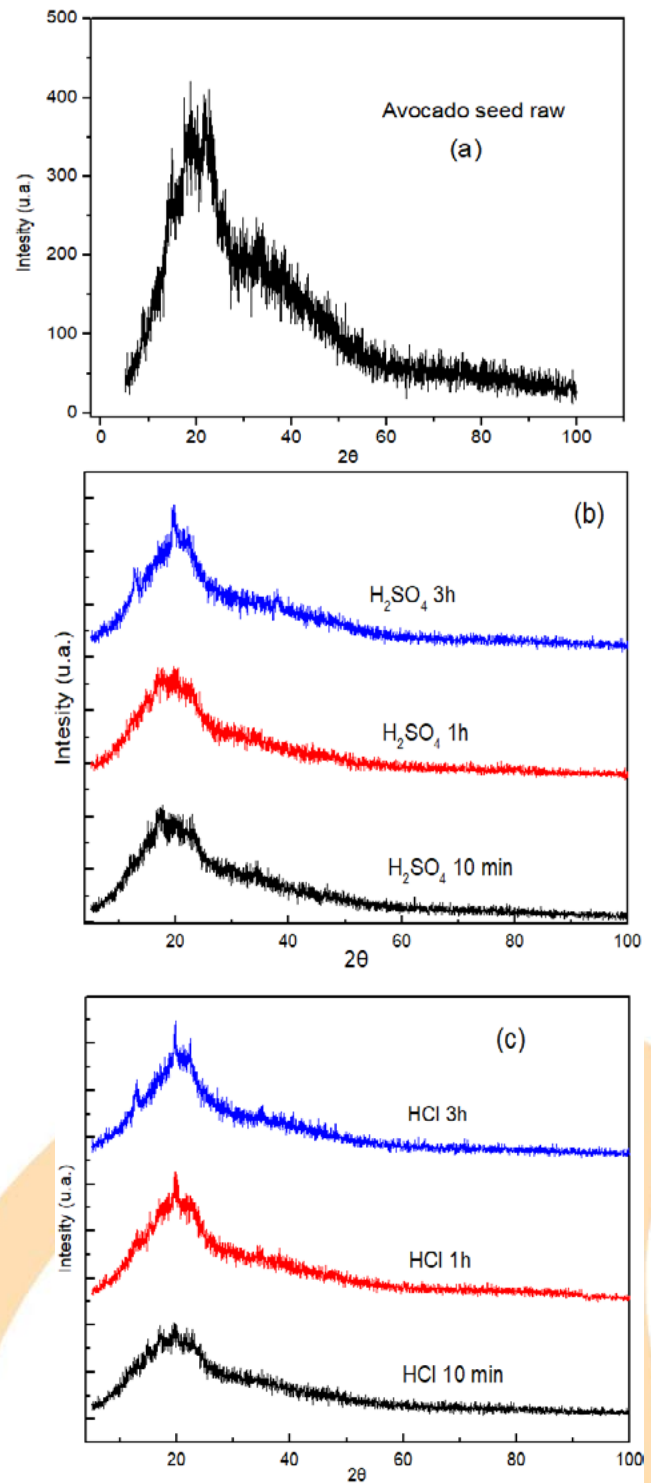


Fig. 2. XRD spectra of avocado seed raw (a), treatment with H₂SO₄ (b) and HCl (c)

As the acid attack time increases in the presence of ultrasound, some crystalline peaks can be seen, as shown in Figures 2 (b) and 2 (c). This behavior may

occur due to the partial removal of hemicellulose and the modification and condensation of lignin on the biomass surface, since acid chemical pre-treatments are widely used for hemicellulose removal, modification and reallocation of lignin in biomasses in order to increase cellulose accessibility to enzymatic hydrolysis in bioprocesses. This generates an increase in material crystallinity by partially removing hemicellulose and lignin. Similar results were found by Zhao et al using a 0.4M sulfuric acid concentration [13]. It is also noteworthy here that treatment with hydrochloric acid resulted in better removal of hemicellulose and lignin modification, leading to greater exposure of cellulose crystallinity, as peaks are more evident than in sulfuric acid treatment.

The surface areas of each of the modified materials and raw avocado seed are shown in table 1.

Table 1 – Surface area of adsorbents

Material	Surface area (m ² g ⁻¹)
Avocado seed raw	2.16
H ₂ SO ₄ 10 min	3.22
HCl 10 min	3.88
H ₂ SO ₄ 1h	7.74
HCl 1h	9.82
H ₂ SO ₄ 3h	13.21
HCl 3h	15.56

It is possible to observe that as the ultrasound treatment time increases, the surface area of the material increases as well, and when the comparison between types of acid used is made, hydrochloric acid promoted a better change in the structure of the material than the treatment using sulfuric acid.

3.2. Adsorption Isotherms

The equilibrium data of fuchsin adsorption by ultrasound-modified avocado seed with different types of acid attack are shown in Figure 3 and Tables 2 and 3.

Compared to the raw seed isotherm, all adsorbents that were modified showed an improvement in their adsorption capacity. This happens by modifying the structure of the adsorbent. From the values of the coefficient of determination (R^2), adjusted coefficient of determination (R^2_{adj}) and average relative error ($ARE\%$), it is concluded that the model that best

described the equilibrium isotherms was the Sips model, where the highest theoretical capacity for fuchsin adsorption by avocado seed was 120.96 mg g⁻¹ for the HCl 3h US arrangement. It is also concluded that the longer the adsorbent is left in the ultrasound, the greater the adsorption capacity of the material. In terms of the influence of acids, at all ultrasound times, hydrochloric acid caused a more significant change in the structure of the adsorbent, leading to a better adsorption capacity.

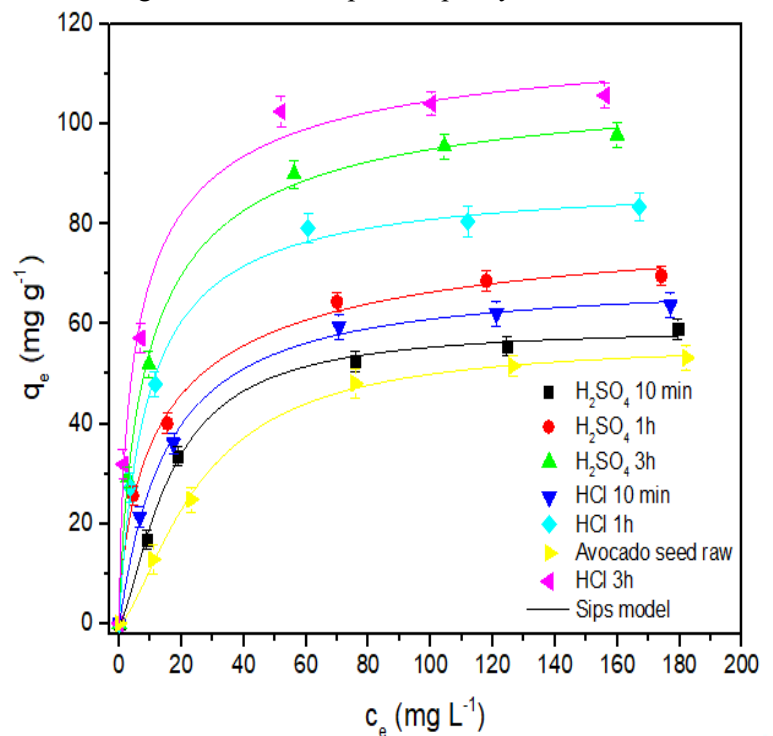


Fig. 3. Adsorption isotherms for fuchsin adsorption on avocado seeds.

Regarding the influence of acids, it can be concluded that a stronger acid, such as hydrochloric acid, caused more significant change in the structure of avocado seed. The acidity constant K_a is used to define the strength of an acid. The higher the K_a value, the stronger the acid. According to Simões et al. hydrochloric acid has a K_a of 10^7 , while sulfuric acid has a K_a 10^3 [14]. This may explain the difference in chemical activation between the two acids, resulting in better treatment by hydrochloric acid. Hydrochloric acid can also lead to an improvement in chemical activation, as it is much smaller than sulfuric acid, so it can penetrate the adsorbent particles more efficiently.

Table 1. Isotherm parameters for fuchsin adsorption on avocado seeds (H₂SO₄ treated).

Model	Avocado seed			
	Raw	H ₂ SO ₄ 10min	H ₂ SO ₄ 1h	H ₂ SO ₄ 3h
<i>Langmuir</i>				
q_m (mg g ⁻¹)	66,7	66,0	73,8	102,6
k_l (L mg ⁻¹)	0,027	0,047	0,990	0,123
R^2	0,991	0,994	0,992	0,996
R^2_{adj}	0,989	0,993	0,99	0,995
ARE (%)	5,01	4,59	4,37	3,74
<i>Freundlich</i>				
n_f	2,45	3,06	3,91	3,88
k_f (mg g ⁻¹ (mg L ⁻¹) ^{-1/nf})	6,97	11,49	19,82	28,4
R^2	0,955	0,966	0,983	0,975
R^2_{adj}	0,944	0,957	0,979	0,969
ARE (%)	11,95	11,13	5,15	7,71
<i>Sips</i>				
q_m (mg g ⁻¹)	56,5	59,4	84,0	110,2
k_s (L mg ⁻¹) ^{1/n}	0,038	0,061	0,065	0,099
n_s	1,497	1,440	0,710	0,797
R^2	0,999	0,998	0,997	0,998
R^2_{adj}	0,998	0,997	0,995	0,997
ARE (%)	2,19	2,07	2,54	2,01

Table 2. Isotherm parameters for fuchsin adsorption (HCl treated).

Model	Avocado seed		
	HCl 10 min	HCl 1h	HCl 3h
<i>Langmuir</i>			
q_m (mg g ⁻¹)	70,8	88,0	109,2
k_l (L mg ⁻¹)	0,075	0,114	0,207
R^2	0,996	0,997	0,986
R^2_{adj}	0,995	0,997	0,983
ARE (%)	3,19	2,46	7,17
<i>Freundlich</i>			
n_f	3,61	4,03	4,48
k_f (mg g ⁻¹ (mg L ⁻¹) ^{-1/nf})	16,7	25,0	37,0
R^2	0,971	0,968	0,970
R^2_{adj}	0,964	0,960	0,962
ARE (%)	9,51	8,33	7,45
<i>Sips</i>			
q_m (mg g ⁻¹)	67,5	89,5	121,0
	(continue)		

Model	Avocado seed			
	Raw	H ₂ SO ₄ 10min	H ₂ SO ₄ 1h	H ₂ SO ₄ 3h
k_s (L mg ⁻¹) ^{1/n}	0,084	0,109	0,150	
n_s	1,210	0,938	0,687	
R^2	0,997	0,998	0,994	
R^2_{adj}	0,995	0,997	0,99	
ARE (%)	2,21	2,05	3,78	

4. Conclusion

In this work, raw avocado seed was modified with different acid types and ultrasound times, in order to obtain the best condition for maximum dye removal and adsorption capacity for basic fuchsin dye. The adsorption isotherms of the raw material and under the influence of acids were adjusted and it was concluded that the model that best described the equilibrium isotherms was the Sips model. Considering the isotherm performed with raw seeds, all modifications were efficient for the improvement of adsorption capacity. Hydrochloric acid activation was more efficient than sulfuric acid activation. The best modification condition was using HCl with 3h of sonication. Using the adsorbent modified in this condition, the maximum adsorption capacity was 121,0 mg g⁻¹. This value is around two times higher in relation to the adsorption capacity found using the raw avocado seeds. Thus, due to the significant increase in avocado seed adsorption capacity, the treatment with hydrochloric acid in the presence of ultrasound can be used efficiently in the treatment of lignocellulosic wastes in order to improve the adsorptive capacity of these materials for the removal of organic contaminants in aqueous effluents.

5. References

- [1] Salleh MAM, Mahmoud DK, Karim WAWA, Idris A. Cationic and anionic dye adsorption by agricultural solid wastes: A comprehensive review. *Desalination*, 2011; 280(1-3): 1-13.
- [2] Šafaříková M, Ptáčková L, Kibrikova I, Šafařík I. Biosorption of water-soluble dyes on magnetically modified *Saccharomyces cerevisiae* subsp. *uvarum* cells. *Chemosphere*. 2005; 59(6): 831-835.
- [3] Alouani, MEL, Alehyen, S, Achouri, MEL, Taibi M. Removal of cationic dye – methylene blue – from

aqueous solution by adsorption on fly ash-based geopolymer. *J Mater Environ Sci*, 2018, 9(1), 32-46.

[4] Netto MS, da Silva N F, Mallmann ES, Dotto GL, Foletto EL. Effect of Salinity on the Adsorption Behavior of Methylene Blue onto Comminuted Raw Avocado Residue: CCD-RSM Design. *Water Air Soil Poll.* 2019; 230(8): 187.

[5] Karagöz S, Tay T, Ucar S, Erdem M. Activated carbons from waste biomass by sulfuric acid activation and their use on methylene blue adsorption. *Bioresour Technol.* 2008; 99(14): 6214-6222.

[6] Liu QS, Zheng T, Wang P, Guo L. Preparation and characterization of activated carbon from bamboo by microwave-induced phosphoric acid activation. *Ind Crop Prod.* 2010; 31(2): 233-238.

[7] Jafari K, Heidari M, Rahmanian O. Wastewater treatment for Amoxicillin removal using magnetic adsorbent synthesized by ultrasound process. *Ultrason Sonochem.* 2018; 45:248-256.

[8] Langmuir I. The adsorption of gases on plane surfaces of glass, mica and platinum. *J. Am. Chem. Soc.* 1918; 40: 1361-1403.

[9] Freundlich H. Over the adsorption in solution. *Z. Phys. Chem.* 1906; 57: 358-471.

[10] Sips R. On the structure of a catalyst surface. *J. Chem. Phys.* 1948; 16: 490-495.

[11] Hospodarova V, Singovszka E, Stevulova N. Characterization of cellulosic fibers by FTIR spectroscopy for their further implementation to building materials. *Am J Analyt Chem.* 2018; 9(06): 303.

[12] Xu F, Yu J, Tesso T, Dowell F, Wang D. Qualitative and quantitative analysis of lignocellulosic biomass using infrared techniques: a mini-review. *Appl energy.* 2013; 104:801-809.

[13] Zhao H, Kwak JH, Zhang ZC, Brown HM, Arey BW, Holladay JE. Studying cellulose fiber structure by SEM, XRD, NMR and acid hydrolysis. *Carbohydrate polymers.* 2007; 68(2): 235-241.

[14] Simões TS, Queirós MA, Simões MO, *Química em Contexto – Livro de Atividades.* Porto: Porto editora; 2004.

Study of adsorption capacity of sodium diclofenac and ibuprofen drugs using cellulose biopolymer

Mariele Dalmolin da Silva^{a*}, Matheus Londero da Costa^a, William Leonardo da Silva^{a,b}

^aChemical Engineering Course, Franciscan University, Santa Maria-RS, 97010-491, Brazil

^b Postgraduate Program in Nanosciences, Franciscan University, Santa Maria-RS, 97010-491, Brazil

Abstract

The presence of drugs in water bodies has received attention for the incomplete removal through conventional wastewater treatment processes. Therefore, the present work aims to evaluate the removal capacity organic pollutants (sodium diclofenac and ibuprofen drugs) using the cellulose in nature (CN) biopolymer and modified cellulose (FC) through kinetic study and adsorption isotherms. Moreover, the cellulose was chemically modified with FeCl₃, and were characterized by N₂ porosimetry, X-ray diffraction (XRD), Fourier Transform Infrared Spectroscopy (FT-IR) and zeta potential (ZP) in order to evaluate its textural and structural properties. The adsorption tests were in batch reactor, with drugs (60 mg L⁻¹) with 0.7 g L⁻¹ of the biosorbent, evaluating the kinetic and equilibrium parameters. Biosorbents have characteristics of mesoporous materials, with considerable specific area (205.9 m² g⁻¹ and 304.2 m² g⁻¹ to CN and CF, respectively), negative surface charge, presence of amorphous and crystalline phases, and characteristic functional groups of cellulose and hemicellulose. Adsorption kinetics was well represented by the pseudo-second order model, and Freundlich model was the best to represent the equilibrium. Results showed that alternative cellulose materials can be used as adsorbents to treat drug effluents.

Keywords: Biopolymer; Removal; Biosorption.

1. Introduction

Nowadays, it is well known that environmental legislation is becoming more stringent, establishing specific parameters in order to control environmental liabilities. Thus, one of the most common causes of contamination are drugs, such as high consumption by the population, mainly from self-medication. In addition, most drugs have a stable and difficult to break down structure, often are not absorbed into the body and, together with incorrect disposal of drugs that are not consumed [1].

In addition, many drugs are not biodegradable and do not allow them to be total removal in traditional wastewater treatments [2] compromising

water quality and causing a major environmental impact [3].

For example, non-steroidal anti-inflammatory drugs (NSAIDs), such as diclofenac and ibuprofen, which do not need a prescription for purchase, have high use by the population being in the group of medicines most commonly found in wastewater [4]. Thus, the detected concentrations range from less than 1 µg L⁻¹ to 40,000 µg L⁻¹ [5].

At the same time, the most of polymeric materials are produced from non-renewable raw materials, not being biodegradable and therefore making its disposal also become a major problem because the structure. The polymeric molecule has covalent bonds that interact in countless ways with the polymer itself and the environment, causing its slow degradation [6].

Therefore, there is a strong demand for the replacement of conventional polymers by



biopolymers, which can be produced from renewable sources and biodegradable, such as cellulose [7]. Among the techniques that have been used for water treatment adsorption emerges as an alternative treatment [8], since which provides the most economically viable and most accurate output environmentally friendly as it makes use of waste that would no longer be used (alternative biosorbents), besides having advantages such as simplicity of operation and cost [9].

In this context, the present work aims to evaluate the capacity of removal of sodium diclofenac (SD) and ibuprofen (Ibu) drugs using cellulose in nature (CN) biopolymer and functionalized (CF) with FeCl_3 , evaluating the effect of biosorbent concentration and correlating with its textural and structural properties.

2. Materials and Methods

2.1 Extraction and functionalization of the cellulose biopolymer

The cellulose biopolymer was extracted according to the methodology adaptation [10], where initially 50 g of the bleached leaf were hydrated in 1000 mL of distilled water for 24 hours, followed by trituration of the material with water. Thus, the obtained cellulignin was delignified with a 1% (w/v) solution of sodium hydroxide (NaOH) for 12 hours, obtaining the crude pulp. Finally, it was dried in a greenhouse (DeLeo, Model: A53E) at 50°C for 12 hours for 5 days. The extracted fresh cellulose sample was called CN.

In order to provide a greater compatibility of charges between biosorbent and drug, the functionalization of cellulose extracted with FeCl_3 (Vetec, PA) was performed, as adapted from the literature [11] in the proportion of 25% w/w, followed by magnetic stirring for 90 minutes and calcination (450 °C for 4 hours). The functionalized cellulose sample was called CF.

2.2 Biosorbent characterization techniques

For characterization of biosorbent crystallinity, X-ray diffraction (XRD), after extraction, was performed in an X-ray diffractometer (Bruker Optics, D2 Advance, United States) with copper tube ($K\alpha\text{-Cu} = 1, 5418 \text{ \AA}$), in a range of 2θ from 10° to 70°, acceleration voltage and applied current of 30 kV and 30 mA, respectively.

N_2 porosimetry was used to determine the specific area and porosity (diameter and pore

volume) of the biopolymer, where previously the samples were degassed at a pressure of 10-2 mbar with a temperature of 120 °C for 12 h, in a Gemini 2375 equipment from Micromeritics®. Specific areas (S_{BET}) were determined by the Brunauer-Emmett-Teller Equation (BET Method), in the range of $P/P_0 = 0.05$ to 0.35, while pore diameters and volumes by the Barret-Joyner-Equation. Halenda (BJH Method).

Surface charge was determined via zeta potential (PZ) in a Malvern-Zetasizer® nanoZS brand (ZEN3600, United Kingdom) with cell (DTS 1060) (Malvern Instruments, United Kingdom) using a 4 mW He-Ne laser (633 nm).

Fourier transform infrared spectroscopy (FT-IR) was used to obtain the structural information of the samples concerning the groups Functions in Varian 640-IR Fourier Transform Infrared Spectroscopy, in transmittance mode in the region from 450 to 4000 cm^{-1} , with 32 scans and 4 cm^{-1} to resolution.

2.3 Adsorption Tests

Adsorption tests were performed in batch. So the solution the drugs chosen for the test was ibuprofen (Multilab®) and sodium diclofenac (Multilab®), with a concentration of 60 mg L^{-1} and 0.7 g L^{-1} of the biopolymers (CN and CF). Thus, 100 mL of the solution were kept in contact with the biopolymer under magnetic stirring (150 rpm) for 180 minutes. During the stirring, samples were collected (4 mL) and placed in Eppendorfs® in predetermined times (0, 5, 15, 30, 45, 60, 90, 120, 150 and 180 minutes) for 0.7 g L^{-1} to CN and CF, and filtered (0.22 μm filter, millex GP), **according to literature [12]**. Finally, the variation of the SD and Ibu concentration over time was determined by reading the absorbance in the characteristic wavelength of the 276 nm (SD) and 222 nm (Ibu). To determine the absorbance was used two quartz cuvettes, one filled with distilled water and deionized (reference cuvette) and the other filled with the sample to be analyzed (sample cuvette). Equation (1) and (2) presents the drugs calibration curve sodium diclofenac and ibuprofen, respectively [11].

$$Abs = 0.0519 \cdot C(\text{mgL}^{-1}) \quad (1)$$

$$Abs = 0.0284 \cdot C(\text{mgL}^{-1}) \quad (2)$$

Drugs removal percentage (R%) and adsorption capacity of the biopolymers (q) were determined by Equation (3) and (4), respectively.

$$R(\%) = \frac{C_0 - C_t}{C_0} \cdot 100 \quad (3)$$

$$q = \frac{(C_0 - C_t) \cdot V}{m} \quad (4)$$

where C_0 is the initial concentration (mg L^{-1}); C_t is the drug concentration at the time (mg L^{-1}); V represents the solution (L); m the mass of biosorbent used (g).

2.4. Kinetic and equilibrium studies

Adsorption kinetic and equilibrium data were analyzed using the models presented in the Equations (5-8), according to literature [13-16].

$$q_t = q_1(1 - \exp(-k_1 t)) \quad (5)$$

$$q_t = \frac{t}{(1/k_2 q_2^2) + (t/q_2)} \quad (6)$$

$$q_e = \frac{q_m k_L C_e}{1 + k_L C_e} \quad (7)$$

$$q_e = k_F C_e^{1/n} \quad (8)$$

where: k_1 : rate constant of pseudo-first order (min^{-1}); q_1 : theoretical value of adsorption capacity (mg g^{-1}); k_2 : rate constant of pseudo-second order ($\text{g mg}^{-1} \text{min}^{-1}$); q_2 : theoretical value of adsorption capacity (mg g^{-1}); q_m : maximum adsorption capacity (mg g^{-1}); k_L : Langmuir constant (L mg^{-1}); k_F : Freundlich constant ($\text{mg g}^{-1}(\text{mg L}^{-1})^{-1/n}$) and $1/n$: heterogeneity factor.

3. Results and Discussion

3.1. Biopolymer characterization

Table 1 shows the results of surface area, pore volume and pore diameter of the CN and CF, where it was possible to verify that the functionalization with FeCl_3 provided a 48% increase in the surface area (from 205.9 to 304.2 $\text{m}^2 \text{g}^{-1}$), indicating a greater amount of active sites for adsorption, favoring drug removal. In addition. Moreover, the CN and CF samples had a negative charge.

Table 1. Surface area (S_{BET}), pore volume (V_p), pore diameter (D_p) and zeta potential (ZP) of the biosorbents (CN and CF).

Sample	S_{BET} ($\text{m}^2 \text{g}^{-1}$)	V_p ($\text{cm}^3 \text{g}^{-1}$)	D_p (nm)	ZP (mV)
CN	205.9	0.92	22.5	-8.29 ± 3.23
CF	304.2	0.02	2.87	-30.2 ± 1.90

Figure 1 shows the adsorption/desorption isotherms, indicating a type III isotherm, characterizing a mesoporous material, which consists of pore filling, increasing the adsorption value to high P/P_0^{-1} values, confirmed by pore diameter ($2 < D_p < 50 \text{ nm}$) according to IUPAC [17]. While, Figure 2 shows the infrared vibrational spectrum of the CN and CF samples, Thus, it was possible to identify characteristic peaks, such as [18-19]: (1) a broad and wide band between 3,600 and 3,400 cm^{-1} attributed to the O-H ($\nu_{\text{O-H}}$) OH) stretch frequency. cellulose / adsorbed water; (2) in the region of 2,895 cm^{-1} the asymmetric stretch of the C-H bond present in cellulose and hemicellulose; (3) at 1,636 cm^{-1} the angular deformation of the OH group of the cellulose/absorbed water; (4) for 1,428 cm^{-1} symmetrical angular deformation of the CH_2 group and angular deformation of the C-O and C-H bond present in polysaccharides; (5) at 1316 cm^{-1} the flexural vibration of the C-H and C-O bonds in the aromatic polysaccharide rings and, (6) at 612 cm^{-1} the Fe-O bond stretch for FeCl_3 functionalization.

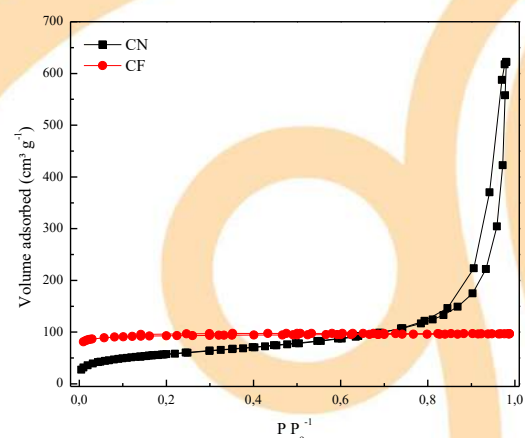


Figure 1. N_2 adsorption-desorption isotherms of CN and CF samples.

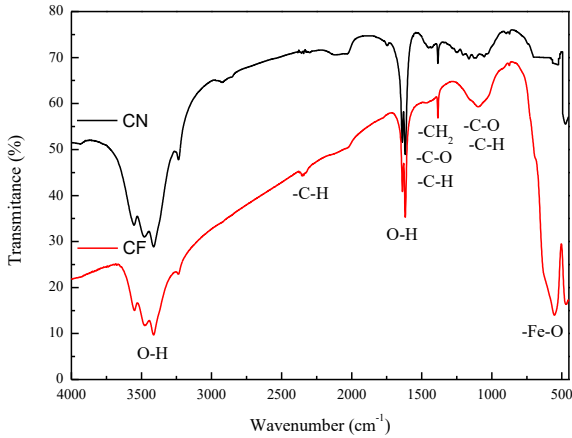


Figure 2. FTIR spectra of the CN and CF samples.

Figure 3 shows the diffractograms of the CN and CF samples. Thus, in the CN sample it is possible to identify an amorphous phase (16°) and characteristic crystalline peaks of commercial crystalline cellulose ($22-23^\circ$) [20]. The CF sample presented crystalline characteristics with the identification of Fe_2O_3 oxide peaks at 33.2° , 35.6° , 40.9° , 54.1° , 64.1° (Joint Committee for Powder Diffraction Standards - n° 01-1053), from the process of functionalization.

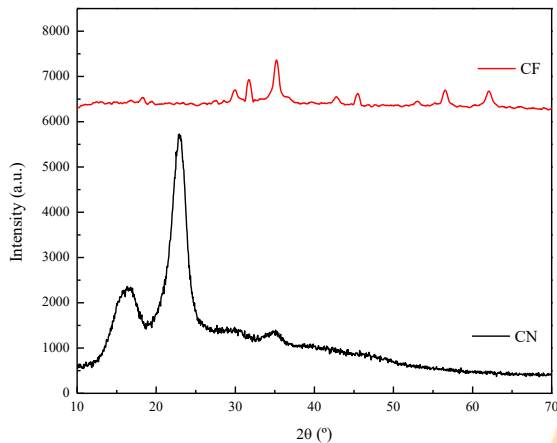


Figure 3. XRD patterns of the CN and CF samples.

3.2 Adsorption kinetics

The adsorption kinetic curves of SD and Ibu on CN and CF are shown in Figs. 4(a) and 4(b), respectively. The adsorption occurred fast within the first 15 min and the rate gradually decreased until equilibrium. This is due to the reduction of unoccupied adsorption sites and decrease of concentration gradient. The adsorption capacities

for all initial concentrations remained nearly constant after 30 min.

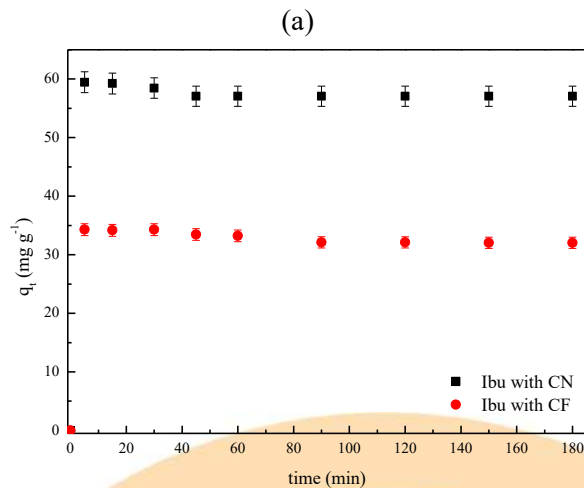
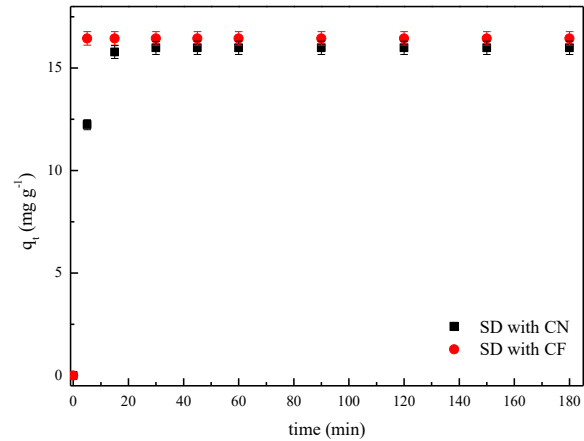


Figure 4. Kinetic curves for SD (a) and Ibu (b) adsorption on CN and CF ($T = 25^\circ\text{C}$; drug concentration = 60 mg L^{-1} ; natural pH and biosorbent concentration = 0.7 g L^{-1}).

Kinetic curves were fitted with the pseudo-first order (Eq. (5)) and pseudo-second order (Eq. (6)) models, according to Table 2. The more adequate model was selected by the evaluation of determination coefficient (R^2), adjusted determination coefficient (R^2_{adj}) and average relative error (ARE). Thus, the greater R^2 and R^2_{adj} values were found for the pseudo-second order model, with the lower values of ARE were verified for this model. These indications revealed that this model was suitable to represent the adsorption of SD and Ibu on CN and CF. The q_2 values were higher using the CF sample, showing that

adsorption capacity was favored due to its textural and structural characteristics. The k_2 parameter presented little variation, showing that, the adsorption rate was similar during the entire period. Furthermore, it can be stated that ibuprofen adsorption was faster than sodium diclofenac, as the higher adsorption capacities, can be attributed to the different molecular characteristics.

Table 2. Kinetic parameters for the SD and Ibu adsorption onto CN and CF.

	Sodium diclofenac		Ibuprofen	
	CN	CF	CN	CF
Pseudo-first order				
q_1 (mg g ⁻¹)	15.98	16.44	17.02	20.32
k_1 (min ⁻¹)	0.39	0.35	0.42	0.52
R^2	0.873	0.942	0.912	0.923
R^2_{adj}	0.865	0.934	0.902	0.912
ARE	2.72	3.02	2.72	3.05
Pseudo-second order				
q_2 (mg g ⁻¹)	25.15	27.52	28.93	32.45
k_2 (g mg ⁻¹ min ⁻¹)	0.12	0.14	0.15	0.11
R^2	0.986	0.997	0.993	0.998
R^2_{adj}	0.982	0.992	0.991	0.993
ARE	0.92	1.2	1.5	1.7

According to Table 2, pseudo-second order model showed the better adjustment for the adsorption of the both drugs using CN and CF, such as biosorbents. Moreover, this model describes well the chemical adsorption process, involving the exchange or the donation of electrical between adsorbed and adsorbent, such as covalent and ionic exchanges [14]. In addition, the adsorption capacity, for both drugs, was higher for CF in relation to CN, mainly due to the larger specific surface area (larger number of active sites), as well as a greater zeta potential,

leading to greater interaction between biosorbent and drugs.

3.3 Adsorption isotherms

The equilibrium isotherms for SD and Ibu onto CN e CF were obtained at temperature 298 K, natural pH (≈ 8.5), stirring rate of 150 rpm and adsorbent concentration of 0.7 g L⁻¹. The estimated equilibrium parameters are presented in Table 3, according Eq. (7) and Eq. (8).

Table 3. Isotherm parameters for SD and Ibu adsorption on CN and CF.

	Sodium diclofenac		Ibuprofen	
	CN	CF	CN	CF
Langmuir				
q_m (mg g ⁻¹)	22.21	23.25	32.21	35.67
k_L (L mg ⁻¹)	0.012	0.015	0.016	0.014
R^2	0.995	0.938	0.992	0.937
R^2_{adj}	0.987	0.916	0.9934	0.923
ARE	1.2	2.15	0.65	1.54
Freundlichr				
k_F (mg g ⁻¹)(mg L ⁻¹) ^{-1/n}	7.19	6.56	7.52	4.03
n	1.43	1.72	2.43	2.65
R^2	0.998	0.997	0.993	0.983
R^2_{adj}	0.967	0.992	0.991	0.982
ARE	0.57	1.34	2.34	2.19

According to Table 3, the Freudlich model showed higher values of coefficient of determination (R^2), adjusted coefficient of determination (R^2_{adj}) and lower values of average relative error (ARE), may be considered more adequate to represent the SD and Ibu adsorption on CN and CF. The maximum adsorption capacity were 23.25 and 35.67 mg g⁻¹ for SD and Ibu, respectively using CF. The value can be considered



satisfactory in comparison with the literature [21-22], indicating a high applicability of cellulose biopolymer for drug adsorption.

In addition, the parameter determines the intensity of adsorption, and since it is between 0 and 10, it suggests favorable adsorption [23]. Moreover, Langmuir isotherm is based on the movement of adsorbed molecules on the surface, providing a uniform distribution (monolayer and homogeneous), with adsorption occurring in the statistics and no interaction between variables [22].

Conclusion

In this work, cellulose (in nature and functionalized) was used to evaluate its adsorption capacity in the removal of diclofenac sodium and ibuprofen drugs from aqueous solutions. The adsorption kinetics followed the pseudo-second order model and the Freundlich model was the best to represent the adsorption equilibrium. The CN and CF showed specific area of 205.9 m² g⁻¹ and 304.2 m² g⁻¹, pore volume of 0.92 and 0.02 cm³ g⁻¹ and pore diameter of 22.5 nm and 2.87 nm, respectively. Therefore, cellulose biopolymer materials have potential to treat drugs wastewater.

Acknowledgements

The authors would like to thank the Unit Operations Laboratory (109) from the Franciscan University (UFN) for their support and assistance in present work. Moreover, this work received financial support from the Foundation for Research of the State of Rio Grande do Sul (FAPERGS – 19/), so all thanks.

References

[1] Villaescusa, I, et al. Mechanism of paracetamol removal by vegetable wastes: the contribution of π - π interactions, hydrogen bonding and hydrophobic effect. *Desalination*, v. 270, n. 1-3, p. 135-142, 2011.

[2] Jones, O.A.H. et al. Questioning the excessive use of advanced treatment to remove organic micropollutants from wastewater. *Environmental Science & Technology*, v. 41, n. 14, p. 5085-5089, 2007.

[3] Stackelberg, P.E. et al. Persistence of pharmaceutical compounds and other organic wastewater contaminants in a conventional

drinking-water-treatment plant. *Science of the Total Environment*, v. 329, n. 1-3, p. 99-113, 2004.

[4] Pacheco, I.S. Removal of emerging contaminants diclofenac and ibuprofen by adsorption in anionic clays: batch process. 2019. (Engineering Course), Federal University of Uberlândia, Uberlândia, Minas Gerais, 2019.

[5] Stelato, E.S. et al. Assessment of the presence of non-inflammatory anti-inflammatory residues municipality of Presidente prudent (sp), Brazil. *Brazilian Journal of Environmental Sciences (Online)*, n. 39, p. 97-113, 2016.

[6] Róz, A.L ; Giesse, R.O. The future of plastics: biodegradable and photodegradable. *Polymers: Science and Technology*, v. 13, no. 4, p. E4-E5, 2003.

[7] Brito, G.F. et al. Biopolymers, biodegradable polymers and green polymers. *Electronic Journal of Materials and Processes*, v. 6, n. 2, p. 127-139, 2011.

[8] Crini, G. Recent developments in polysaccharide-based materials used as adsorbents in wastewater treatment. *Progress in Polymer Science*, v. 30, p. 38-70, 2005.

[9] Bhatnagar, A.; Jain, A. K. A. Comparative adsorption study with different industrial wastes as adsorbents for the removal of cationic dyes from water. *Journal of Colloid Interface Science*, v. 281, p. 49-55, 2005.

[10] Casey, J.P. *Pulp and Paper. Chemistry and Chemical Technology*. Vol I. 3.ed. Wiley Interscience, New York, 1980.

[11] Da Silva, W.L. et al. Photocatalytic degradation of rhodamine B, paracetamol and diclofenac sodium by supported titania-based catalysts from petrochemical residue: effect of doping with magnesium. *Water Science and Technology*, v. 74, n. 10, p. 2370-2383, 2016

[12] Stefano, T.S. et al. The usage of cellulose biopolymer for the application in the adsorption of dyes in aqueous medium. *Disciplinarum Scientia*, v. 20, n. 1, p. 71-84, 2019.

[13] Lagergren S. About the theory of so-called adsorption of soluble substances. *Kung Svenska Vetenskap* 1898; 24:1-39.

[14] Ho YS, Mckay G. Kinetic models for the sorption of dye from aqueous solution by wood. *Proc Safety Environ Protect* 1998;76:183-91.

[15] Langmuir I. The adsorption of gases on plane surfaces of glass, mica and platinum. *J Amer Chem Soc* 1918; 40:1361-403.

[16] Freundlich H. Over the adsorption in solution. *Z Physic Chem* 1906; A57:358-471.



- [17] International Union of Pure and Applied Chemistry - IUPAC - Recommendations. Pure and Applied Chemistry, v. 57, n. 4, p. 603-619, 1985.
- [18] Benvenuti, E.V. et al. Silica-based hybrid materials obtained by the sol-gel method. New Chemistry, v. 32, p. 1926-1933, 2009.
- [19] Lu, H. et al. Preparation of $\text{CoFe}_2\text{O}_4@$ vacancy@mSiO₂ core-shell composites for removal of organic pollutant in aqueous solution. Journal of Saudi Chemical Society. In Press, 2018.
- [20] Rosa, M.F. et al. Cellulose nanowhiskers from coconut husk fibers: Effect of preparation conditions on their thermal and morphological behavior. Carbohydrate Polymers, v. 81, p. 83-92, 2010.
- [21] Mezzari, I.A. Use of adsorbent coals for the treatment of effluents containing pesticides. 2002. 117 p. Dissertation (Master in Chemical and Food Engineering) - Federal University of Santa Catarina, Florianópolis, Santa Catarina, 2002.
- [22] Chen, H.; Wang, A.Q. Kinetic and isothermal studies of lead ion adsorption onto palygorskite clay. Journal of Colloid and Interface Science, v. 307, p. 309-316, 2007.
- [23] Do Nascimento, R.F. et al. Adsorption: Theoretical aspects and environmental applications. Fortaleza: University Press, p. 256, 2014.

Adsorption of 2-chlorophenol using ZnCl₂ activated biochar from brewing industry solid waste

Lauren Marcilene Maciel Machado^a, Sabrina Frantz Lütke^a, Julia Zanuzo Kuntz^a, Gabriela Carvalho Collazzo^a, Daniele Perondi^b, Guilheme Luiz Dotto^a

^a Chemical Engineering Department, Federal University of Santa Maria – UFSM, Roraima Avenue, 1000 – 97105-900 – Santa Maria – RS – Brazil

^b Postgraduate Program in Chemical Engineering, University of Caxias do Sul – UCS, Francisco Getúlio Vargas Street, 1130 – 95070-560 – Caxias do Sul – RS – Brazil

Abstract

Barely malt bagasse is the main solid waste generated in the brewing processing. Due to the high amounts generated, alternatives have been investigated to provide an appropriate destination for barely malt bagasse. In this work, an activated biochar was produced from barely malt bagasse, characterized and applied as adsorbent for the removal of 2-chlorophenol from aqueous solution. The material was prepared by chemical activation using zinc chloride. N₂ adsorption/desorption curves, SEM and FTIR were used to characterize the activated biochar. The results indicated that the activated biochar presented a micro/mesoporous structure, with specific surface area of 545.05 m² g⁻¹ and total pore volume of 0.109 cm³ g⁻¹. The pH effect was investigated and the results showed that the adsorption of 2-chlorophenol was favored under acid conditions (pH 2-6). The adsorption kinetics was investigated at different initial 2-chlorophenol concentrations (25 to 200 mg L⁻¹) and, at all initial concentrations, the equilibrium was reached in 80 min. The adsorption capacity was 65.56 mg g⁻¹. The pseudo-second order model was the more suitable to describe the kinetic adsorption data. These results demonstrate that the activated biochar produced is a promising adsorbent which can be used to treat 2-chlorophenol containing wastewaters.

Keywords: biochar; malt bagasse; adsorption; 2-chlorophenol.

1. Introduction

Brewing processing generates a considerable amount of solid wastes. Barely malt bagasse is the first solid waste generated in the brewing processing and represents 85% of the total solid wastes. It is estimated that to 100 L of beer, 20 kg of dry barely malt bagasse are generated [1]. This waste is widely used for animal feed. However, due to the high amount generated, other alternatives may be explored [2].

Barely malt bagasse is a lignocellulosic waste, that is, mainly composed of lignin, cellulose and hemicellulose. Besides that, barely malt bagasse is available in high amounts at all times of the year. Thus, this waste is a good candidate to be used as precursor material for biochar production [3,4]. Biochar can be produced through pyrolysis under inert atmosphere. An activation process can be used in order to improve the specific surface area and total pore volume of the biochar. This activation can be performed by physical, chemical

or physicochemical methods, and the final product can be named activated biochar [5]. ZnCl₂ has been widely used as an activating agent in the activated biochar production. Many studies have shown that ZnCl₂ can induce the production of a high surface area and high total pore volume activated biochar [6-8]. Due to these surface characteristics, activated biochar is a good material to be used for the treatment of industrial wastewaters through adsorption operations [9].

The disposal and treatment of organic wastewaters have received worldwide attention, since the discharging amount is increasing rapidly as the industrial production continuously rise [10]. In this scenario, chlorophenols have been extensively used by many industries, as petroleum and petrochemical, pesticides, plastic and coal conversion [11]. Chlorophenols have carcinogenic and mutagenic effects. Besides that, they are persistent in many environments, because of inappropriate conditions for biodegradation [12]. Due to their adverse effects on humans and environment, chlorophenols are classified as toxic

and hazardous pollutants and are on the list of priority organic pollutants proposed by the United States Environmental Protection Agency (US EPA) [13]. Therefore, chlorophenols must be removed from wastewaters before disposing in the environment

In this context, the aim of this work was to evaluate the potential of an activated biochar obtained from barely malt bagasse to remove 2-chlorophenol from aqueous solution through adsorption. First, the biochar was prepared by chemical activation using ZnCl_2 and characterized. Then, 2-chlorophenol adsorption was investigated in relation to the pH and kinetics. Kinetics investigation was performed under different initial 2-chlorophenol concentrations using the pseudo-first order, pseudo-second order and Avrami models.

2. Material and Methods

2.1. Material

Barley malt bagasse, used as precursor material, was supplied by a beer industry located in Santa Catarina, Brazil. The material was sun dried for 2 days, and then was oven dried at 50 °C for 6 h, ground in a knife mill and sieved. The fraction with diameter of particles smaller than 0.5 mm was used in the preparation of the activated biochar. 2-chlorophenol ($128.56 \text{ g mol}^{-1}$, purity $\geq 99\%$) was obtained from Sigma-Aldrich (Brazil).

2.2. Biochar preparation

The activated biochar was prepared by chemical activation using zinc chloride as activating agent. The procedure was adapted from [14] as follows: 40 g of barley malt bagasse, 40 g of inorganic components (80% ZnCl_2 + 20% CaO) and deionized water were stirred at room temperature for 1 h to produce a homogeneous paste. The homogeneous paste (ratio of material precursor: inorganic components of 1:1) was then oven dried at 50 °C for 12 h. For the pyrolysis process, 40 g of the paste was placed in a quartz reactor. The atmosphere inside the quartz reactor was regulated at 150 mL min^{-1} of nitrogen gas (N_2). The temperature was increased at a rate of 5 °C min^{-1} until 900 °C, being held at 900 °C for 50 min. The resultant material was washed with $\text{HCl } 6 \text{ mol L}^{-1}$ for 24 h in an orbital shaker, to remove Zn^{2+} , and

subsequently washed several times with deionized water until the solution pH 6. Finally, the material was oven dried at 50 °C for 12 h.

2.3. Biochar characterization

The textural properties of the activated biochar (specific surface area, total pore volume and average pore size) were determined based on nitrogen adsorption/desorption isotherms at 77 K, using an automated gas sorption analyzer (Quantachrome Instruments, 1200e, USA). Before the analysis, the degassing process was conducted under vacuum, at 380 °C for 20 h. The specific surface area was obtained from the Brunauer-Emmett-Teller (BET) method and the pore size distribution was obtained from the Barrett-Joyner-Halenda (BJH) method. The surface morphology of the malt bagasse and activated biochar was obtained by scanning electron microscopy (SEM) (Tescan, Mira3, Japan). The information about the functional groups of the malt bagasse and activated biochar were investigated by Fourier transform infrared (FTIR) spectroscopy (Shimadzu 01722, IR Prestige, Japan). The analyses were realized by direct transmittance technique, using KBr tablets. The spectra were obtained with a resolution of 2 cm^{-1} over the range of $400\text{--}4500 \text{ cm}^{-1}$, performing 44 scans.

2.4. Adsorption experiments

The adsorption experiments were carried out in a thermostatic shaker (Solab, SL 222, Brazil) at 25 °C and stirring rate of 150 rpm. The pH effect on adsorption of 2-chlorophenol was first evaluated. The studied pH was from 2 to 12, being the values adjusted by the addition of HCl or NaOH . Initial 2-chlorophenol concentration was 50 mg L^{-1} and adsorbent dosage was 0.5 g L^{-1} . The contact time was 2 h. Kinetic assays were carried out with initial 2-chlorophenol concentrations from 25 to 200 mg L^{-1} and adsorbent dosage of 0.5 g L^{-1} . Aliquots were removed at set time intervals (2-120 min). Afterward, the solutions were filtered, and the remaining 2-chlorophenol concentration in the liquid phase was measured by UV-VIS spectrometer (Shimadzu, UVmini-1240, Japan) at 273 nm. The assays were performed in replicate ($n=3$) and blank tests were realized. The adsorption capacity (q) was determined by Eq. (1).

$$q = \left(\frac{C_0 - C_f}{m} \right) V \quad (1)$$

where C_0 is the initial 2-chlorophenol concentration in liquid phase (mg L^{-1}), C_f is the 2-chlorophenol concentration in liquid phase after the adsorption (mg L^{-1}), m is amount of adsorbent (g), and V is the volume of solution (L).

2.5. Kinetic models and statistical analysis

The kinetic data were evaluated by pseudo-first order (Eq. 2), pseudo-second order (Eq. 3) and Avrami (Eq. 4) models [15]:

$$q_t = q_1(1 - \exp(-k_1 t)) \quad (2)$$

$$q_t = \frac{t}{(1/k_2 q_2^2) + (t/q_2)} \quad (3)$$

$$q_t = q_{av}(1 - \exp(-k_{av} t)^{n_{av}}) \quad (4)$$

where q_t is the 2-chlorophenol adsorption capacity at time t (mg g^{-1}), k_1 and k_2 are the rate constants of pseudo-first order (min^{-1}) and pseudo-second order ($\text{g mg}^{-1} \text{min}^{-1}$) models, respectively, q_1 and q_2 are the theoretical values for adsorption capacity (mg g^{-1}), k_{av} is the Avrami fractional order constant rate (min^{-1}) and n_{av} is a fractional kinetic order (Avrami), which is related to the adsorption mechanism.

The models were fitted to experimental data through nonlinear regression using the Quasi-Newton method by the Statistic 7.0 software (StatSoft, USA). The fit quality was obtained through determination coefficient (R^2), adjusted determination coefficient (R^2_{adj}) and average relative error (ARE).

3. Results and Discussion

3.1. Characterization

Fig. 1 shows the N_2 adsorption-desorption isotherms and the BJH desorption pore size distribution of the activated biochar. According to IUPAC classification of adsorption isotherms [16], the adsorption isotherm for the activated biochar showed a mixture of Type I and Type IV isotherms. Type I isotherm is a typical

characteristic of microporous materials, while Type IV isotherm is a typical characteristic of mesoporous materials [16]. Furthermore, an adsorption hysteresis is present in adsorption-desorption isotherms. The adsorption hysteresis exhibited by the activated biochar can be classified as Type H4, which is characteristic of micro/mesoporous carbonaceous materials [16]. The activated biochar presented a high BET surface area ($545.05 \text{ m}^2 \text{ g}^{-1}$), high total pore volume ($0.109 \text{ cm}^3 \text{ g}^{-1}$) and an average pore size of 1.69 nm.

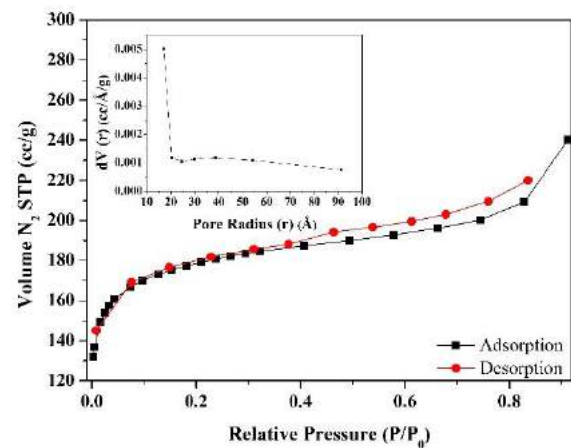


Fig. 1. Nitrogen adsorption-desorption isotherms and BJH desorption pore size distribution of the activated biochar.

Fig. 2 shows SEM images of malt bagasse (Fig. 2a) and activated biochar (Fig. 2b).

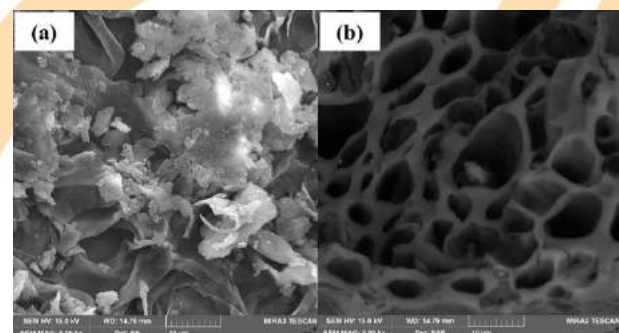


Fig. 2. SEM images ($\times 5.000$): (a) malt bagasse and (b) activated biochar.

It is possible to observe irregularities on the surface of the malt bagasse, forming a kind of overlapping of the fibers. After the activation process, changes occurred on the surface of the

material. It can be observed that the surface of the activated biochar is full of cavities. The development of the cavities was caused by the effect of $ZnCl_2$ and the release of the volatile material during the activation process. Of course that this developed structure of cavities is favorable for adsorption processes.

Fig. 3 shows the FTIR spectra of the malt bagasse and activated biochar.

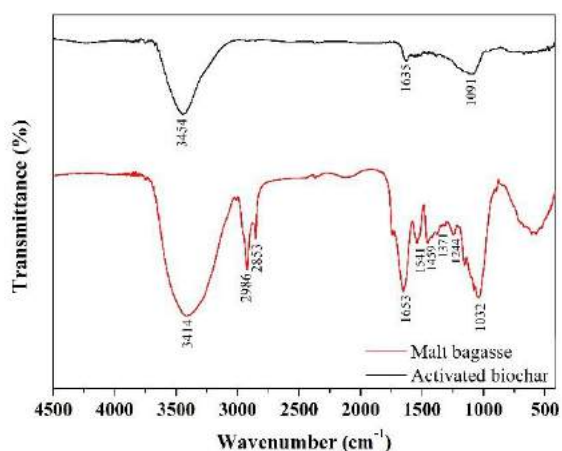


Fig. 3. FTIR spectra of malt bagasse and activated biochar.

In the FTIR spectrum of malt bagasse, it is possible to observe the characteristic bands of hemicellulose, cellulose and lignin. Changes can be verified in the FTIR spectrum of the activated carbon. The spectrum presented a lower number of bands when compared to the spectrum obtained for the malt bagasse. This result is due to the removal of volatile matter in pyrolysis. Only bands at 3454, 1635 and 1091 cm^{-1} remained, nevertheless to a lesser extent. The band at 3454 cm^{-1} is relative to the stretching of O-H bonds of hydroxyls present as functional groups on the surface of the activated biochar. The band at 1635 cm^{-1} can be attributed to the stretching of the C=C bond of the aromatic rings resulting from the dehydration and cyclization of carbohydrates during pyrolysis. Finally, the band at 1091 cm^{-1} can be attributed to the C-O stretch of hydroxyl groups.

3.2. pH effect on 2-chlorophenol adsorption

The adsorption of 2-chlorophenol was investigated from pH 2 to 12 and the results are

shown in Fig. 4.

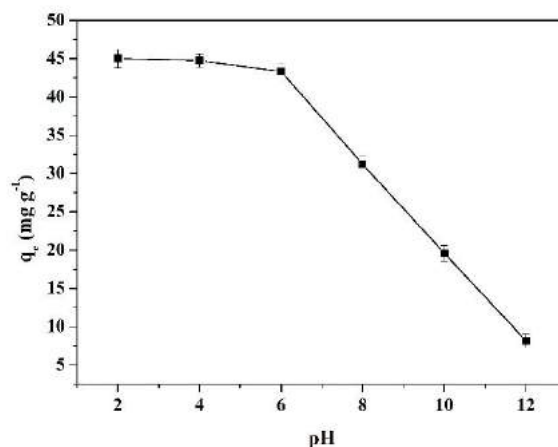


Fig. 4. Effect of pH on the adsorption capacity of 2-chlorophenol onto the activated biochar.

It was observed that the adsorption of 2-chlorophenol increased with the pH decrease. High adsorption capacity was obtained for pH 2-6 and, in basic pH values, a pronounced decrease was observed. The pH of the solution influences the surface charge of the adsorbent and in the degree of ionization of 2-chlorophenol. 2-chlorophenol is a weak acid ($pK_a=8.85$) and exists as a neutral molecule in acid pH [11]. In relation to the activated biochar, under acid conditions its surface becomes positively charged. In this way, electrostatic attraction can occur between the 2-chlorophenol molecules and the positively charged activated biochar surface [17]. As the pH of the solution increases, 2-chlorophenol starts to undergo to an anionic form. In the same way, activated carbon surface becomes negatively charged. Thus, an electrostatic repulsion interaction can take place between the adsorbate and the adsorbent. In addition, the competitive adsorption of OH^- ions can also result in a decrease in the adsorption capacity [17].

3.3. Kinetic studies

The adsorption kinetic curves were obtained at pH 6 and initial 2-chlorophenol concentrations of 25 to 200 $mg L^{-1}$. Fig. 5 shows the kinetic curves obtained.

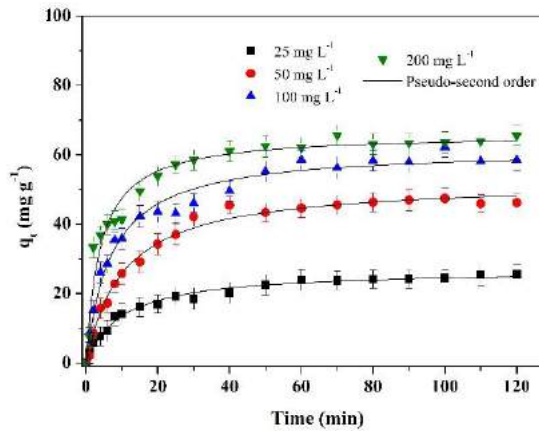


Fig. 5. Kinetic curves for adsorption of 2-chlorophenol onto the activated biochar.

It was possible to observe that the adsorption was fast in the first few minutes. Later, the adsorption rate gradually decreased. It was found that the adsorption rate tended to increase with the

increase in the initial concentration. Besides that, the increase in the initial concentration provided an increase of 25.56 to 65.56 mg g⁻¹ in the adsorption capacity. For all initial concentrations, the equilibrium was reached within 80 min.

To better understand the kinetic profile, pseudo-first order, pseudo-second order and Avrami models were fitted to the experimental data. The results are presented in Table 1. Based on the higher values of determination coefficient and adjusted determination coefficient and the lower values of average relative error, it can be concluded that the pseudo-second order model was the more suitable to represent the 2-chlorophenol adsorption onto the activated biochar. For all initial concentrations, q_2 values were closed to the experimental value. This confirms the good fit of the pseudo-second order model. Besides that, as expected, q_2 values increased with the increase of 2-chlorophenol initial concentration, indicating that adsorption capacity was higher at 200 mg L⁻¹.

Table 1. Kinetic parameters for adsorption of 2-chlorophenol onto activated biochar.

Model	Initial 2-chlorophenol concentration (mg L ⁻¹)			
	25	50	100	200
Pseudo-first order				
q_1 (mg g ⁻¹)	23.62	46.34	54.56	60.42
k_1 (min ⁻¹)	0.0834	0.0747	0.1156	0.1734
R^2	0.9612	0.9909	0.9382	0.9018
R^2_{adj}	0.9582	0.9898	0.9338	0.8920
ARE (%)	11.38	10.32	11.51	13.77
Pseudo-second order				
q_2 (mg g ⁻¹)	26.97	52.31	61.90	66.15
k_2 (g mg ⁻¹ min ⁻¹)	0.0037	0.0019	0.0023	0.0039
R^2	0.9878	0.9835	0.9793	0.9529
R^2_{adj}	0.9867	0.9814	0.9778	0.9482
ARE (%)	6.45	16.96	5.70	13.55
Avrami				
q_{av} (mg g ⁻¹)	23.62	46.34	54.56	60.42
k_{av} (min ⁻¹)	0.1540	0.1851	0.0823	0.2330
n_{av}	0.542	0.403	1.403	0.744
R^2	0.9612	0.9909	0.9382	0.9018
R^2_{adj}	0.9582	0.9898	0.9338	0.8920
ARE (%)	11.38	10.32	11.51	13.77
q_e (exp) (mg g ⁻¹)	25.56	46.21	58.50	65.56

4. Conclusions

Barley malt bagasse was used as precursor material to produce an activated biochar through chemical activation with zinc chloride. The activated biochar presented a micro/mesoporous structure, with specific surface area of $545.05 \text{ m}^2 \text{ g}^{-1}$ and total pore volume of $0.109 \text{ cm}^3 \text{ g}^{-1}$. It was observed that the activation process leads to the development of cavities in the surface of the material. The surface chemistry of the activated biochar is composed by hydroxyl groups. Adsorption was favored under acid conditions (pH 2-6). For all initial 2-chlorophenol concentrations, the equilibrium was reached in 80 min. The increase in the initial concentration provided an increase of 25.56 to 65.56 mg g^{-1} in the adsorption capacity. The pseudo-second order model was the more suitable to describe the kinetic data. Overall, barley malt bagasse can be used as a potential alternative precursor material to produce activated biochar.

Acknowledgements

The authors would like to thank CAPES (Brazilian Agency for Improvement of Graduate Personnel) and CNPq (National Council of Science and Technological Development) for the financial support.

References

- [1] Franciski MA, Peres EC, Godinho M, Perondi D, Foletto EL, Collazzo GC, Dotto GL. Development of CO_2 activated biochar from solid wastes of a beer industry and its application for methylene blue adsorption. *Waste Manage.* 2018;78:630-638.
- [2] Vanreppelen K, Vanderheyden S, Kuppens T, Yperman J, Carleer R. Activated carbon from pyrolysis of brewer's spent grain: Production and adsorption properties. *Waste Manage. Res.* 2014;32:634-645.
- [3] Balogun AO, Sotoudehniakarani F, McDonald AG. Thermo-kinetic, spectroscopic study of brewer's spent grains and characterisation of their pyrolysis products, *J. Anal. Appl. Pyrolysis.* 2017;127:8-16.
- [4] Mussatto S, Dragone G, Roberto I. Brewer's spent grain: Generation, characteristics and potential applications. *J. Cereal Sci.* 2006;43:1-14.
- [5] Lee Y, Park J, Ryu C, Gang KS, Yang W, Park YK, Jung J, Hyun S. Comparison of biochar properties from biomass residues produced by slow pyrolysis at $500 \text{ }^\circ\text{C}$, *Bioresour. Technol.* 2013;148:196-201.
- [6] Miao Q, Tang Y, Xu J, Liu X, Xiao L, Chen Q. Activated carbon prepared from soybean straw for phenol adsorption. *J. Taiwan Inst. Chem. Eng.* 2013;44:458-465.
- [7] Boonamnuayvitaya V, Sae-Ung S, Tanthapanichakoon W. Preparation of activated carbons from coffee residue for the adsorption of formaldehyde. *Sep. Pur. Technol.* 2005;42:159-168.
- [8] Namasivayam C, Sangeetha D. Recycling of agricultural solid waste, coir pith: removal of anions, heavy metals, organics and dyes from water by adsorption onto ZnCl_2 activated coir pith carbon. *J. Hazard. Mater.* 2006;135:449-52.
- [9] Bhatnagar A, Hogland W, Marques M, Sillanpää M. An overview of the modification methods of activated carbon for its water treatment applications. *Chem. Eng. J.* 2013;219:499-511.
- [10] Zhang Z, Sun D, Li G, Zhang B, Zhang B, Qiu S, Li Y, Wu T. Calcined products of Mg-Al layered double hydroxides/single-walled carbon nanotubes nanocomposites for expeditious removal of phenol and 4-chlorophenol from aqueous solutions. *Colloids Surf., A.* 2019;565:143-153.
- [11] Soltani T, Lee BK. Mechanism of highly efficient adsorption of 2-chlorophenol onto ultrasonic graphene materials: Comparison and equilibrium. *J. Colloid Interface Sci.* 2016;168-180.
- [12] Eslami A, Mehralian M, Moheb A. A study of 4-chlorophenol continuous adsorption on nano graphene oxide column: model comparison and breakthrough behaviors. *J Water Reuse Desal.* 2017;7:272-279.
- [13] WHO (World Health Organization), 1989. *Environmental Health Criteria 93. Chlorophenols Other than Pentachlorophenol.* Geneva.
- [14] Streit AFM, Côrtes LN, Druzian SP, Godinho M, Collazzo GC, Perondi D, Dotto GL. Development of high quality activated carbon from biological sludge and its application for dyes removal from aqueous solutions. *Sci. Total Environ.* 2019;660:277-287.
- [15] Thue PS, Adebayo MA, Lima EC, Sieliechi JM, Machado FM, Dotto GL, Vagheti JCP, Dias SLP. Preparation, characterization and application of microwave-assisted activated carbons from wood chips for removal of phenol from aqueous solution. *J. Mol. Liq.* 2016;223:1067-1080.
- [16] Thommes M, Kaneko K, Neimark AV, Olivier JP, Rodriguez-Reinoso F, Rouquerol J, Sing KSW. *Physisorption of gases, with special reference to the evaluation of surface area and pore size distribution (IUPAC Technical Report)*, 2015.
- [17] Zhang A, Zhang B, Wu T, Sun S, Lia Y. Adsorption behavior and mechanism of chlorophenols onto organoclays in aqueous solution. *Colloids Surf., A.* 2015;484:118-129.

Removal of crystal violet dye from solutions using lychee bark and seed as adsorbents

Nathália Favarin da Silva^a, Matias Schadeck Netto^a, Isadora Argenta Preigschadt^a, Raíssa da Cunha Bevilacqua^a, Evandro Stoffels Mallmann^a, Guilherme Luiz Dotto^a.

^a Universidade Federal de Santa Maria, Av. Roraima n° 1000, Santa Maria – 97105–900, Brazil

Abstract

Dyes are substances with high application potential in several areas, been used to color industrial end products such as textiles. An effective process for effluent treatment is adsorption, that uses biosorbents in order to reduce costs. The present work aims to investigate the adsorption capacity of lychee bark and seed in the removal of crystal violet dye. Adsorption–initiated assays were carried out from an experimental design of the central rotational composite type 2², where the influence of adsorbent dosage and solution pH were analyzed. For both materials, the best adsorbent dosage was 0.295 g L⁻¹, while the solution pH did not present significant influence. The Langmuir model was the most suitable to reproduce the experimental data of equilibrium isotherms. The maximum adsorption capacities were 197.4 mg g⁻¹ for bark and 151.8 mg g⁻¹ for seed. These are interesting values and show that lychee bark and seed can be explored regarding other aspects of an adsorbent.

Keywords: adsorption; effluent; dye.

1. Introduction

Dyes contribute in the pollution of water resources, hindering the penetration of sunlight, impairing the photosynthetic metabolism of some species; furthermore, they are compounds recalcitrant and potentially carcinogenic [1]. If dye containing effluents are not properly treated before disposal, dyes can cause serious damage to the ecosystem and population health [2].

Conventional methods for colored water decontaminating, in the textile industry, are economically unfavorable and/or technically complex [3]. Adsorption is preferred due to some characteristics, including easy operation, low energetic requirements, and high efficiency [4]. Development in biosorbents utilization can be considered an alternative or complement to conventional wastewater treatment processes. The use of biosorbents can reduce the adsorption costs being an attractive option [5].

In the present work, fresh lychee bark and seed were used to evaluate the process of crystal violet dye adsorption in aqueous solutions. The development of the adsorption study was carried out through experimental design and equilibrium isotherms to determine the best condition for maximum removal and adsorption capacity of both materials.

2. Materials and methods

2.1. Preparation of adsorbents

Lychee bark and seeds were collected in the north area of Rio Grande do Sul State. After collecting, the residues were washed with distilled water and dried in an oven for 48 h at 60 °C. Then they were comminuted in a shoe mill and sieved by separating the 0.5 mm particle size.

2.2. Adsorbent characterization

The bark and seed were characterized by the following methods: Fourier Transform Infrared Spectroscopy (FTIR), used to determine the presence of functional groups in each material. To later be performed on a Shimadzu spectrophotometer, IR Prestige 21 model, with KBr pellet method and reading range of 4500 and 450 cm⁻¹; the zero point of charge (pH_{ZPC}) was determined by adding 20 mg of the adsorbent in 20 mL of 0.1 mol L⁻¹ aqueous NaCl solution under 9 different initial pH conditions (2.0 to 10.0). After 24 h of agitation in a thermostatic bath under 100 rpm at 25 °C, the solutions had the final pH determined; and X–ray diffraction (XRD), used to determine the crystallinity of the materials, was performed on a Rigaku diffractometer, model Miniflex 300, under the conditions of radiation

analysis. Cu K α ($\lambda = 1.54051 \text{ \AA}$) and 10 mA, with step size of 0.03° and a count time of 0.5 seconds per step.

2.3. Dye

In this work, crystal violet cationic dye (empirical formula $C_{25}H_{30}ClN_3$, molar mass: $407.99 \text{ g mol}^{-1}$, CAS number: 548–62–9), purchased from Chemical Exodus, used in the textile industry.

2.4. Adsorption experiments

Adsorption experiments were performed on a controlled temperature shaker (Dubnoff SL – 157 model) at 150 rpm. The stock solution of crystal violet was prepared at a concentration of 1000 mg L^{-1} and then diluted to the desired concentration. Firstly, from a central composite rotational design (CCRD), the effect of pH and adsorbent dosage was investigated (see levels and factors in Table 1). Adsorbents were placed in contact with 50 mL of a 50 mg L^{-1} dye solution at room temperature (25°C) for 2 h. Thus, in order to know the adsorbent efficiency, the adsorption isotherms for the bark and seed were determined. The isotherms were obtained at 25°C , contact time of 3 h and at initial concentrations of 25, 50, 100, 150, 200 and 300 mg L^{-1} . The adsorbent dosage was 0.015 g and the pH used was the previously determined by the experimental design (CCRD). Finally, the absorbance reading was performed with the aid of the spectrophotometer (Biospectro SP – 22, Brazil), using the dye wavelength ($\lambda = 590 \text{ nm}$). The equilibrium adsorption capacity (q_e) was obtained by equation 1:

$$q_e = \frac{(c_0 - c_e)V}{m} \quad (1)$$

Where c_0 (mg L^{-1}) is the initial dye concentration, c_e (mg L^{-1}) is the equilibrium concentration, m (g) is the adsorbent mass and V (L) is the volume of solution.

2.5. Adsorption models

To evaluate the dye adsorption isotherms, the Freundlich [6] and Langmuir [7] models, described by equations 2 and 3, respectively, were used:

$$q_e = k_F c_e^{1/n_F} \quad (2)$$

Where k_F ($(\text{mg}^{1-n_F} \text{L}^n \text{g}^{-1})$, where n_F is a Freundlich constant, and $1/n_F$ the heterogeneity factor.

$$q_e = \frac{q_m k_L c_e}{1 + k_L c_e} \quad (3)$$

Where q_m (mg g^{-1}) is the maximum adsorption capacity and k_L (L mg^{-1}) is the Langmuir constant.

2.5. Adjustment assessment

The equilibrium parameters values were determined by fitting the models to the experimental data using nonlinear regression, using the Quasi-Newton method in the 9.1 statistical software (Statsoft, USA). The quality of the model was measured by the determination coefficient (R^2), the adjusted coefficient of determination (R^2) and the average relative error (ARE) [8].

3. RESULTS AND DISCUSSION

3.1. Characteristics of lychee bark and seed

The FT-IR analysis allowed the evaluation of the lignocellulosic composition and existing bonds in the fresh lychee bark and seed. The infrared vibrational spectra of these materials are shown in the range $4500\text{--}500 \text{ cm}^{-1}$. According to Figure 1, the 3448 and 3415 cm^{-1} bands are O–H axial stretches [9]; The band at 2923 cm^{-1} and the band at 2854 cm^{-1} are due to the asymmetrical elongation vibration of CH_2 and the symmetrical elongation vibration of $-\text{CH}_3$, respectively [10]. The band observed between 1734 and 1721 cm^{-1} are indicative of C=O bond elongation [10]. Bands in the region of wavelength numbers smaller than 700 cm^{-1} could be assigned to bioligants containing N. Specifically, for the bark, the bands from 1526 to 1444 cm^{-1} aromatic ring bonds; the band at 1378 cm^{-1} of axial deformation of $-\text{CN}$ of amino and amide groups; the bands at 1060 and 1031 cm^{-1} of C–N and C–O groups [9]. The band at 1248 cm^{-1} is due to the C–O elongation vibration of ketones, aldehydes or carboxyl groups [12]. The band at 1318 cm^{-1} was assigned to the C–N groups on the biomass surface. Absorption band around 1153 cm^{-1} is indicative of PO elongation vibrations. At 825 cm^{-1} glycosidic bond in hemicellulose can be observed [13].

Specifically, for the seed, the 1080 cm^{-1} band is due to the elongation of the C–O bond of the primary lignin alcohol, while the 1019 cm^{-1} band is associated with the elongation of the C–O bond in the cellulose. The bands at 929 and 860 cm^{-1} correspond to the glycosidic bonds in cellulose and hemicellulose, respectively [13].

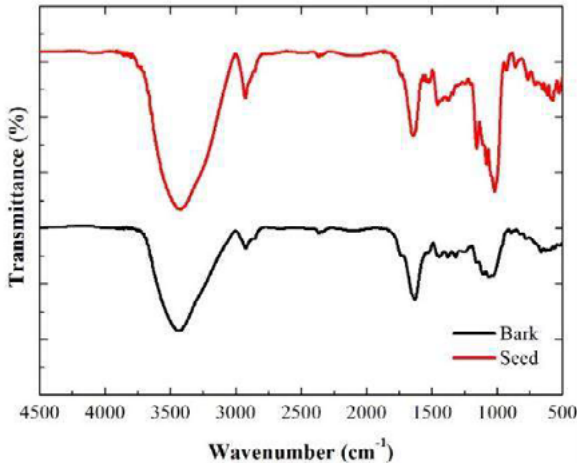


Fig. 1. FT-IR spectra of lychee bark and seed.

It can be concluded that the bark spectrum was similar to the seed spectrum. It is clear that both are characteristic of lignocellulosic materials. The largest differences occur in shorter wavelengths. All these groups can be responsible for dye adsorption.

The XRD patterns, showed in Figure 2, revealed that the adsorbent materials presented amorphous characteristics. The amorphous phase is characterized by the wide reflection range from 10° to 30° and can be attributed to the lignin content. The presence of small peaks at 15° and 25° of crystalline characteristic can be attributed to the cellulose content [13].

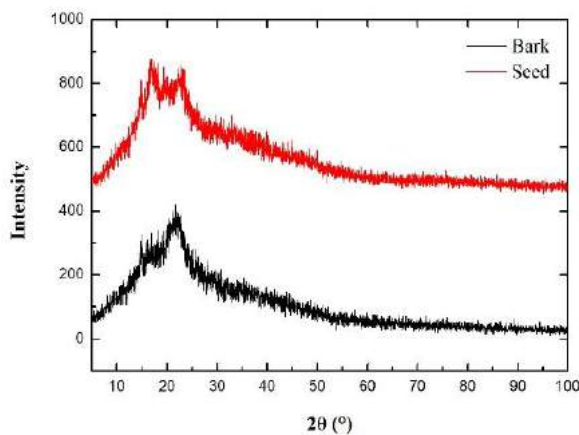


Fig.2. DRX spectra of lychee bark and seed.

The pH_{ZPC} values of lychee bark and seed were 6.9 and 7.3, respectively. When the pH of the solution is higher than the pH_{ZPC} of the solid material, the surface will be negatively charged. So, it can be concluded that bark is more attractive than seed to remove cations, since its surface is negatively charge in a larger pH range.

3.2. Response surface methodology

A 2^2 central composite rotational design was used to determine the best adsorbent dosage (Da) and pH to maximize dye removal (R) and adsorption capacity (q_e) of lychee bark and seed.

The actual and coded levels of the variables used in the design, and also the responses dye removal and adsorption capacity are shown in Table 1 and 2, for bark and seed, respectively.

Table 1. Variables and responses for the crystal violet adsorption on bark.

	pH	Da (g)	R (%)	q_e (mg g ⁻¹)
1	9 (1)	0,075 (1)	90,1	30,6
2	5 (-1)	0,075 (1)	94,6	32,1
3	9 (1)	0,025 (-1)	84,6	86,3
4	5 (-1)	0,025 (-1)	78,8	80,4
5	9,82 (1,41)	0,05 (0)	95,8	48,9
6	4,2 (-1,41)	0,05 (0)	91,7	46,7
7	7 (0)	0,085 (1,41)	97,4	29,2
8	7 (0)	0,015 (-1,41)	69,8	118,8
9	7 (0)	0,05 (0)	96,5	49,2
10	7 (0)	0,05 (0)	96,5	49,2
11	7 (0)	0,05 (0)	96,5	49,2

Table 2. Variables and responses for the crystal violet adsorption on seed.

	pH	Da (g)	R (%)	q_e (mg g ⁻¹)
1	9 (1)	0,075 (1)	94,6	34,0
2	5 (-1)	0,075 (1)	93,5	33,6
3	9 (1)	0,025 (-1)	81,3	87,3
4	5 (-1)	0,025 (-1)	72,5	78,3
5	9,82 (1,41)	0,05 (0)	94,4	51,0
6	4,2 (-1,41)	0,05 (0)	82,3	44,4
7	7 (0)	0,085 (1,41)	93,7	29,7
8	7 (0)	0,015 (-1,41)	118,8	68,0
9	7 (0)	0,05 (0)	49,2	93,6
10	7 (0)	0,05 (0)	49,2	94,7
11	7 (0)	0,05 (0)	49,2	94,1

For both adsorbents, bark and seed, only the linear and quadratic adsorbent dosage variables were found to be significant in a confidence interval of 95% ($p > 0.05$) in both responses, removal (R) and adsorption capacity (q_e). Thus, it is possible to obtain the model equations for the responses R and q_e as a function of their independent variables. For bark, the equations are 4 and 5. For seed, the equations are 6 and 7.

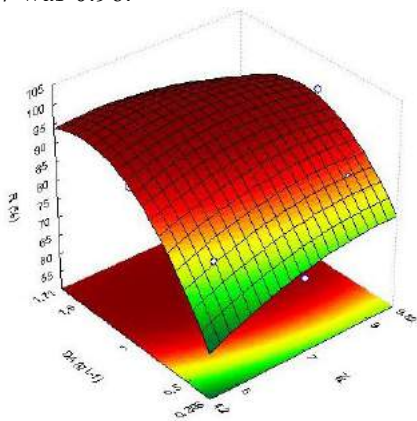
$$R(\%) = 96.55 + 7.55 x_2 - 6.78 x_2^2 \quad (4)$$

$$q_e = 49.2 - 28.86 x_2 + 11.55 x_2^2 \quad (5)$$

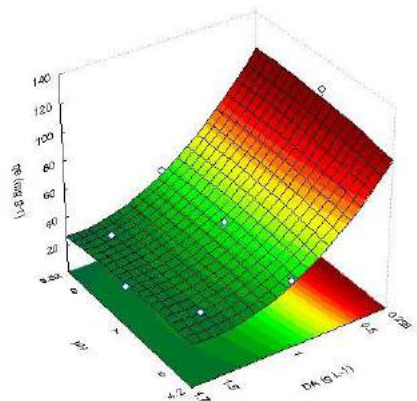
$$R(\%) = 94.20 + 8.82 x_2 - 6.46 x_2^2 \quad (6)$$

$$q_e = 50.88 - 28.75 x_2 + 11.82 x_2^2 \quad (7)$$

Where x_2 represents the adsorbent dosage. The coefficient of determination of equation 4 was 0.88 and for equation 5 was 0.97, both indicating a good fit to the model. In the same way, the coefficient of determination of equation 6 was 0.98 and for equation 7 was 0.96.



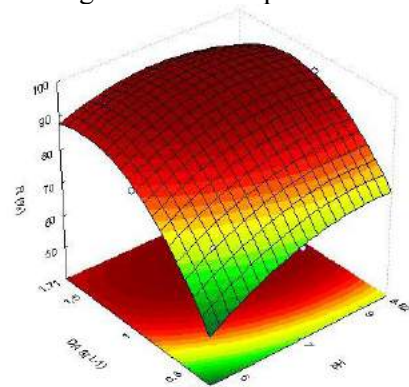
(a)



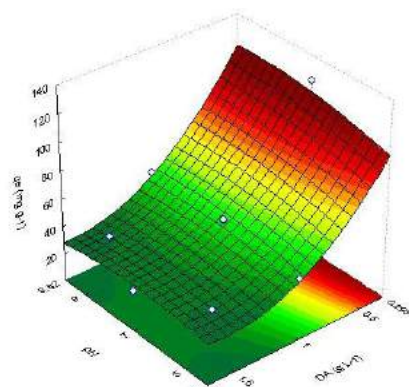
(b)

Fig. 3. Response surfaces for R (%) (a) and q_e (b) in the crystal violet adsorption on bark.

In order to generate the surface curves of each of the responses, the prediction model was evaluated by the Fischer test. For the bark adsorbent, the tabulated F value was 5.05 for both equations while the calculated F value was 17.63 and 86.61 for the removal equation (R%) and adsorption capacity (q_e), respectively. As the values of $F_{calc} > F_{tab}$, and good R^2 values were obtained, it was possible to generate the response surfaces. For the seed adsorbent, the tabulated F value was 5.05 for both equations while the calculated F value was 215.87 and 48.73 for the removal equation (R%) and adsorption capacity (q_e), respectively. As the values of $F_{calc} > F_{tab}$, it was also possible to generate the response surfaces.



(a)



(b)

Fig. 4. Response surfaces for R (%) (a) and q_e (b) in the crystal violet adsorption on seed.

In Figure 3 (a), the removal is enhanced in larger dosages of the bark material, around 0.05 and 0.085 g. As for figure 3 (b) the maximum adsorption capacity is in the region of lower adsorbent dosages, around of 0.025 and 0.015 g.

With this, the adsorbent dosage of 0.015 g and pH of the solution were chosen as optimal points to follow up the experiments, aiming to have a maximum adsorption capacity (q_e).

It can be observed that for both surfaces, the maximum removal (R%) and adsorption capacity (q_e) occurs in the whole pH range. However, the optimum adsorbent dosage applies to different value ranges for each surface.

In Figure 4 (a), the removal is enhanced in larger dosages of the material, around 0.05 and 0.085 g and for Figure 4 (b) the maximum adsorption capacity is in the region of lower adsorbent dosages, around of 0.025 and 0.015 g. With this, the adsorbent dosage of 0.015 g and pH of the solution were chosen as optimal points to follow up the experiments, aiming to have a maximum adsorption capacity (q_e).

3.3. Adsorption Isotherms

The equilibrium data of adsorption of crystal violet in bark and seed are presented in Figure 8 and table 3.

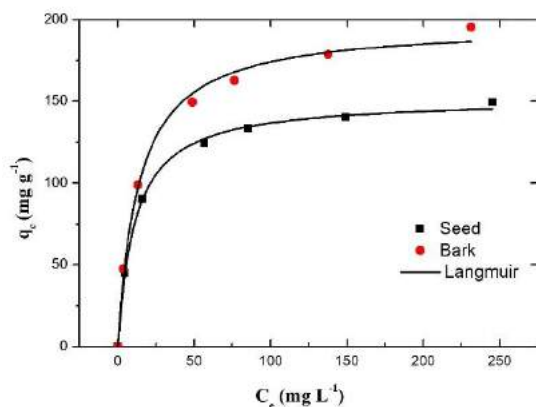


Fig. 8. Adsorption isotherms for crystal violet adsorption.

In Figure 8, the increase in adsorption capacity with concentration is probably due to a high driving force for mass transfer. In fact, the high concentration in solution implies high dye molecules attached to the surface of the adsorbent [14]. The highest adsorption capacity was found for the bark, at 197.45 mg g⁻¹. Under the same conditions, for the seed the maximum capacity was 151.82 mg g⁻¹. Langmuir model presented better fit to the data for both adsorbents, showing higher values of determination coefficients ($R^2 > 0.99$) and lower values of mean relative error

(ARE) compared to Freundlich model. This result suggests that the dyes are adsorbed homogeneously on a monolayer surface of the adsorbent.

Table 3. Isotherm parameters for crystal violet adsorption

Isotherm model	Temperature 25 °C	
	Bark	Seed
<i>Langmuir</i>		
q_m (mg g ⁻¹)	197,448	151,821
k_l (L mg ⁻¹)	0,074	0,091
R^2	0,997	0,999
R^2 adj	0,995	0,998
ARE (%)	3,631	1,467
<i>Freundlich</i>		
$1/n_f$	0,269	0,233
k_f [mg g ⁻¹ (mg L ⁻¹) ^{-1/nf}]	47,691	44,023
R^2	0,987	0,983
R^2 adj	0,975	0,965
ARE (%)	9,432	9,989

4. Conclusion

In this work were used the bark and the seed for crystal violet dye adsorption, with the objective of comparing the efficiency of both adsorbents and the best condition for the maximum dye removal and adsorption capacity in solution using an experimental design. The results showed that both materials presented a satisfactory removal performance and maximum adsorption capacity of the crystal violet dye, using 0.015 g of adsorbent and pH of the solution. Through the Freundlich and Langmuir equilibrium isotherms, it was found that the Langmuir model best described both adsorbents, presenting higher R^2 and smaller ARE values. The highest adsorption capacity was found for lychee bark, at 197.45 mg g⁻¹ compared to seed, at 151.82 mg g⁻¹. In this way, fresh litchi peel and seed can be used efficiently in wastewater treatment to improve dye removal capacity.

5. References

[1] Freire FB, Freitas SL. Avaliação da remoção de cor de um efluente têxtil sintético. Revista Engenharia Sanitária Ambiental., 2010: 7(3).

- [2] Aravind P, Subramanyan V, Ferro S, et al. Eco friendly and facile integrated biological–cum–photo assisted electrooxidation process for degradation of textile wastewater. *Water Research*, 2016; 93: 230–241.
- [3] Cardoso NF, Lima EC, Pinto IS, et al. Application of cupuassu shell as biosorbent for the removal of textile dyes from aqueous solution. *Journal of Environmental Management*. 2011; 92:1237–1247.
- [4] Franco DSP, Tanabe EH, Dotto GL. Continuous Adsorption of a Cationic Dye on Surface Modified Rice Husk: Statistical Optimization and Dynamic Models, *Chem. Eng. Commun.* 2017; 204, 625–634.
- [5] Pereira NA, Bretz JS, Magalhães FS, Mansur MB, Rocha SDF. Alternativas para o tratamento de efluentes da indústria galvânica. *Revista Engenharia Sanitária Ambiental*. 2008; 13, 263–270.
- [6] Freundlich H. Over the adsorption in solution. *Z. Phys. Chem.* 1906; 57: 358–471.
- [7] Langmuir I. The adsorption of gases on plane surfaces of glass, mica and platinum. *J. Am. Chem. Soc.* 1918; 40: 1361–1403.
- [8] Dotto GL, Costa JAV, Pinto LAA. Kinetic Studies on the Biosorption of Phenol by Nanoparticles from *Spirulina* sp. LEB 18, *J. Environ. Chem. Eng.* 2013; 4, 1137–1143.
- [9] Sousa FW, et al. Single and multielementary isotherms of toxic metals in aqueous solution using treated coconut shell powder. *Desalination and Water Treatment*. 2011; 36, 289–296.
- [10] Li H, Yang FT, Zhao Y, Xu R. Novel modified pectin for heavy metal adsorption. *Chin Chem Lett*. 2007; 18, 325–328.
- [11] Ibarra JV, Moliner R. Caracterização de carvão usando pirólise–FTIR. *Appl Anal Pyrol.* 1991; 20, 171 – 184.
- [12] Sills DL, Gossett JM. Using FTIR to predict saccharification from enzymatic hydrolysis of alkali pretreated biomasses. *Biotechnol Bioeng.* 2012; 109, 353–62.
- [13] Maneerung T, Tokura S, Rujiravanit R. Impregnation of silver nanoparticles into bacterial cellulose for antimicrobial wound dressing. *Carbohydrate Polymers*. 2008; 72 43–51.
- [14] Barka N, Abdennouri M, Makhfouk ELM. Remoção de azul de metileno e negro de eriocromo T de soluções aquosas por biossorção em *Scolymus hispanicus* L.: cinética, equilíbrio e termodinâmica J *Taiwan Inst Chem Eng.* 2011; 42, 320 – 326.

Cu²⁺ adsorption equilibrium and kinetic study using activated carbon prepared from corn cob as adsorbent

Natalia Ferreira Campos^a, Giovanna Amaral Jorge Correia Guedes^b, Brígida Maria Villar da Gama^b, Leticia de Paula Silva Oliveira^b, Beatriz Galdino Ribeiro^b, Alex Leandro Andrade de Lucena^b, Marta Maria Menezes Bezerra Duarte^b

^a Federal Rural University of Pernambuco, Department of Chemical, Rua. Dom Manuel de Medeiros, s/n, Recife, 52171-900, Brazil

^b Federal University of Pernambuco, Department of Chemical Engineering, Av. Artur de Sá, s/n, Recife, 50740-520, Brazil

Abstract

The objective of this work was to prepare activated carbon from corn cob to remove Cu²⁺ in aqueous solution. Activated carbon was prepared from biomass using H₃PO₄ as activating agent. The pH at the point of zero charge (pH_{PZC}) was determined before and after activation. A study of the initial pH effect on the Cu²⁺ solution, kinetic and adsorption equilibrium studies were performed. Activation causes a decrease in pH_{PZC} (from 4.7 to 3.0), which favored Cu²⁺ adsorption. The initial pH of the solution equal to 4 presented the best result. Kinetic evolution was rapid, with most adsorption around 100 min and after 240 minutes the system reached equilibrium. The Elovich model was the best fit to the experimental data indicating that heterogeneous diffusion occurs in the process. The adsorption isotherm showed a favorable behavior and the Sips model was the best fit to the experimental data with maximum adsorptive capacity of 0.47 mmol·g⁻¹. Activated carbon from corn cob showed technical potential to remove Cu²⁺ in aqueous solution.

Keywords: Activated carbon; Biomass; Copper; Waste.

1. Introduction

The copper is a heavy metal commonly present in wastewaters from automotive, paper and marine industries. The improper disposal of industrial effluents into rivers and streams contaminates soil, subsoil and groundwater. When water containing this metal is ingested by humans it can cause gastrointestinal, respiratory and kidney problems [1,2].

According to CONAMA Resolution n° 430 of May 13, 2011, which provides for effluents discharge standards and conditions, the maximum value of dissolved copper allowed to be discharged into the receiving body is 1.0 mg·L⁻¹. Failure to comply with resolutions, rules and laws may result in fines and other sanctions provided for in Law n° 9,605 of 12 of February of 1998 [3].

In order to remove copper ions (Cu²⁺) present in wastewater, a viable, simple and effective alternative is adsorption. Evaluation of factors such as adsorbent and adsorbate properties in the adsorptive process is essential, so a study is necessary to choose the appropriate adsorbent [4].

In order to verify alternative and low-cost sources for the preparation of activated carbon,

researchers proposed the use of agroindustrial waste as precursors in order to reduce production costs and also to make these residues useful by reinserting them into the production chain [5]. As an example, there are studies of the preparation of activated carbon from materials such as peanut husk [6], corn stalk [7], grape pomace [8] and corn cob [9].

The corn cob, having no commercial value, ends up being burned in open spaces, causing environmental pollution due to the lack of disposal or use [10]. Therefore, it is an alternative for the production of activated carbon, since it comes from available renewable sources and has low acquisition cost [11].

In view of this, this study aimed to evaluate the use of activated carbon prepared from corn cob to remove Cu²⁺ in aqueous solutions.

2. Methodology

A Cu²⁺ ion stock solution of 10 mmol·L⁻¹ concentration was prepared from Cu(NO₃)₂·3H₂O salt (Vetec, 99%) and the working solutions were obtained by dilution of the stock solution. The metal contents were quantified on the Flame Atomic Absorption Spectrometer (VARIAN brand,



AA 240 FS - *Fast Sequential Atomic Absorption Spectrometer*) at a wavelength of 218.2 nm, on an analytical curve with a linear range of 0.010 to 1.250 mmol·L⁻¹. The adsorptive capacity (q) was calculated from Equation 1:

$$q = \frac{(c_0 - c_f)V}{M} \quad (1)$$

being, C_0 and C_f , the initial and final concentration of the metal (mmol·L⁻¹), respectively; V , the volume of the solution (L) e and M , the mass of adsorbent (g).

2.1. Activated Carbon Preparation

The corn cob was washed in running water, cut into pieces, dried at 105°C in a drying oven (Splabor), ground, washed in distilled water and dried again in an oven for 1 hour at 60°C. This material was chemically activated using phosphoric acid (H₃PO₄ 85%, Vetec) at a ratio of 5: 3 (m/v) at 110°C for 16 h. Carbonization then occurred under muffled oxygen (Quimis[®]) at 500°C for 1 h, adapted from Patnukao and Pavasant [12] and Brito et al. [13].

The activate carbon was washed with a 1% sodium bicarbonate solution (NaHCO₃, Fmaia) and distilled water to remove residual acid and then dried in an oven for 1 hour at 60°C. The prepared activated carbon was classified in a series of Tyler sieves in the size of 0.2-1.0 mm.

2.2. pH at the point of zero charge

The pH at the point of zero charge (pH_{PZC}) of the corn cob and the activated carbon were estimated through measuring the solution pH before and after contact with the solids. In the assays, 0.1 g of the material was used for 25 mL of water, varying the pH between 2 and 10. The pH of the solutions was adjusted employing pH meter (Quimis, Q400AS) using either HNO₃ or NaOH (0.1 mol·L⁻¹). The solutions were stirred at 300 rpm for 24 hours and then filtered to measure the pH_{final}.

The ΔpH (pH_{final} - pH_{inicial}) versus pH_{inicial} plot was constructed, and the value of pH_{PZC} was estimated through this plot as according to Pezoti et al. [14].

2.3. Initial pH of the solution – effect study

The chemical equilibrium diagrams for the Cu²⁺ ion were obtained with the aid of HYDRA software, that was developed by Puigdomenech [15]. Thus, the range used in the study of the initial pH of the solution was determined, where 0.1 g of activated carbon remained in contact with 50 mL of Cu²⁺ solution at a concentration of 1.00 mmol·L⁻¹ while stirring at 300 rpm for 3h at 303K.

2.4. Kinetic Study

The kinetic assays were performed using 0.1g of activate carbon in contact with 50 mL of Cu²⁺ solution at a concentration of 1.00 mmol·L⁻¹ while stirring at 300 rpm in the time range of 3 to 480 min at 303K. To represent the kinetic behavior, the pseudo-first order (Equation 2), pseudo-second order (Equation 3) and Elovich (Equation 3) models were used. These models were adjusted to the experimental data using the nonlinear regression method with the aid of Origin 8.0 software.

$$\frac{dq_t}{dt} = k_1(q_e - q_t) \quad (2)$$

$$\frac{dq_t}{dt} = k_2(q_e - q_t)^2 \quad (3)$$

$$q_t = \frac{1}{b} \ln(1 + a \cdot b \cdot t) \quad (4)$$

being, q_e and q_t the adsorptive capacities (mmol·g⁻¹) at equilibrium and time t (min), respectively, k_1 is the pseudo-first order adsorption rate constant (min⁻¹), k_2 is the adsorption rate constant of pseudo-second order (g·mmol⁻¹·min⁻¹), a is the initial adsorption rate (g·mmol⁻¹·min⁻¹) and b is the constant related to the degree of coverage and activation energy involved in the chemisorption process (mmol·g⁻¹).

2.5. Adsorption Equilibrium

The adsorption equilibrium study was performed using 0.1 g of activated carbon in contact with 50 mL of Cu²⁺ solution at concentrations of 0.10; 0.25; 0.50; 0.75; 1.00; 1.25; 1.50 and 2.00 mmol·L⁻¹ while stirring at 300 rpm for 16 h at 303K. The samples were quantified on the Flame Atomic Absorption Spectrometer. The experimental results were applied to the Langmuir (Equation 5),

Freundlich (Equation 6) and Sips (Equation 7) models. The adjustments were performed using Origin 8.0 software to determine the process equilibrium data:

$$q_e = \frac{q_{max}K_L C_e}{1 + K_L C_e} \quad (5)$$

$$q_e = K_F C_e^{1/n_F} \quad (6)$$

$$q_e = \frac{q_{max}(K_S C_e)^{1/n_S}}{1 + (K_S C_e)^{1/n_S}} \quad (7)$$

in which C_e it's the liquid phase concentration at equilibrium ($\text{mmol}\cdot\text{L}^{-1}$), q_{max} is the maximum coverage capacity of the monolayer ($\text{mmol}\cdot\text{g}^{-1}$), K_L is the adsorption equilibrium Langmuir constant ($\text{L}\cdot\text{mmol}^{-1}$), K_F is the constant indicating the extent of adsorption ($\text{mmol}\cdot\text{g}^{-1}\cdot(\text{mmol}\cdot\text{L}^{-1})^{-1/n_F}$), n_F is the Freundlich intensity parameter, K_S is the Sips equilibrium constant ($\text{L}\cdot\text{mmol}^{-1}$) and n_S is the heterogeneity index.

3. Results

3.1. pH at the point of zero charge

The pH at the point of zero charge (pH_{PZC}) can be defined as the pH in which the net charge on the surface of the material is zero. Thus, the bioadsorbent surface will be positively charged when the pH of the solution $< \text{pH}_{\text{PZC}}$ and negatively charged when the $\text{pH} > \text{pH}_{\text{PZC}}$ according to Goswami and Phukan [16].

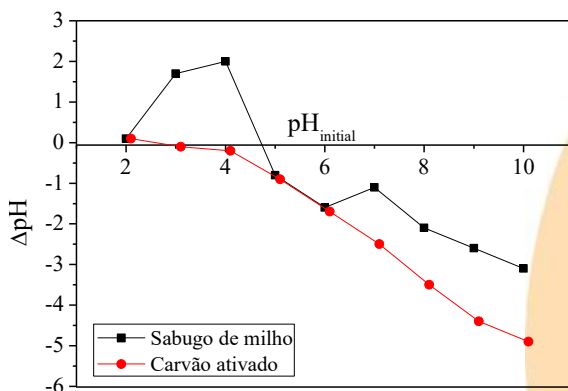


Fig. 1. pH at the point of zero charge for the corn cob and activated carbon.

The pH_{PZC} were 4.7 and 3.0 for the corn cob and activated carbon, respectively, showing that the value of pH_{PZC} decreases after activation with H_3PO_4 (Fig. 1). This effect may be related to the increase of negatively charged functional groups on the activated carbon surface, which favors the interaction with the Cu^{2+} .

3.2. Study of the effect of the initial pH of the solution

Solution pH may play an important role during the adsorption process, as it affects the adsorbate shape and adsorbent surface property (such as functional group dissociation and surface charge) according to Dong et al. [17]. Fig. 2 shows the concentrations for the tests with and without adsorbent for each pH studied.

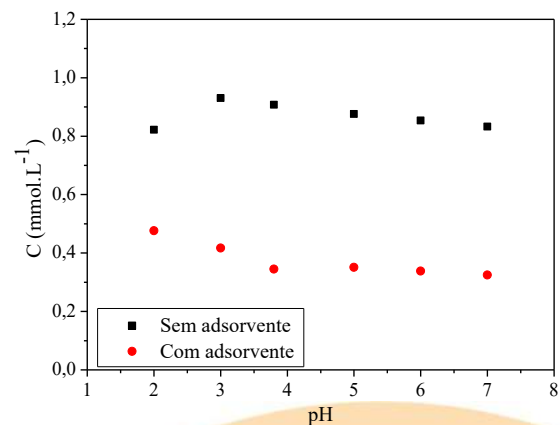


Fig. 2. Study of the initial pH of the Cu^{2+} .

According to the results presents in Fig. 2, it is observed that, in the studied interval, there was no significant occurrence of Cu^{2+} chemical precipitation. The pH value that presented the greatest difference between the concentrations with and without adsorbent was pH 4, which was selected for further studies. At this pH, the activated carbon surface is negatively charged ($\text{pH} > \text{pH}_{\text{PZC}}$) which favor Cu^{2+} adsorption.

3.3. Kinetic Study

The results of the kinetics as well as the fit to the pseudo-first order, pseudo-second order and Elovich models are presented in Fig. 3.

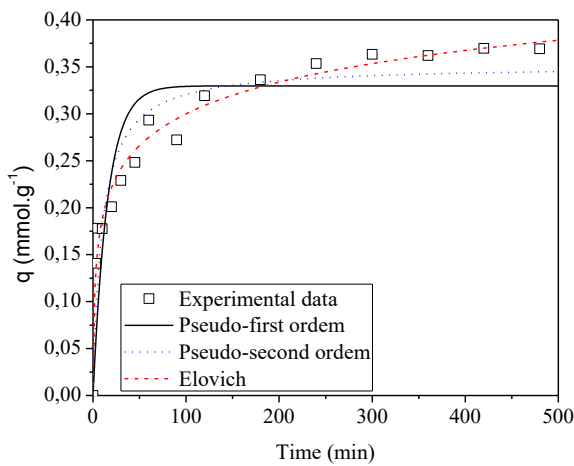


Fig. 3. Adsorption kinetics and adjustment to the studied kinetic models.

It was observed that Cu^{2+} adsorption in activated carbon was rapid in the first minutes, with most removal occurring up to 100 minutes. System equilibrium was reached after 240 minutes to $0.37 \text{ mmol} \cdot \text{g}^{-1}$. The parameters for the calculated kinetic models are presented in Table 1.

Table 1. Kinetic parameters of the pseudo-first order, pseudo-second order, and Elovich models.

Models	Parameters	Results
Pseudo-first order	q_e ($\text{mmol} \cdot \text{g}^{-1}$)	0.33 ± 0.02
	k_1 (min^{-1})	0.06 ± 0.02
	Sr^2	0.0332
Pseudo-second order	r	0.7828
	q_e ($\text{mmol} \cdot \text{g}^{-1}$)	0.35 ± 0.01
	k_2 ($\text{g} \cdot \text{mmol}^{-1} \cdot \text{min}^{-1}$)	0.29 ± 0.08
	Sr^2	0.0156
Elovich	r	0.8978
	a ($\text{mmol} \cdot \text{g}^{-1} \cdot \text{min}^{-1}$)	0.23 ± 0.06
	b ($\text{g} \cdot \text{mmol}^{-1}$)	20 ± 1
Elovich	Sr^2	0.0027
	R^2	0.9823

Based on Table 1, the model that best fitted the experimental data was the Elovich model, suggesting that heterogeneous diffusion occurred during adsorption. Similar result was obtained by Hu *et al.* [18] in Cu^{2+} adsorption in enhanced alginate-based microsphere with pore-forming agent.

3.4. Adsorption Equilibrium

The adsorption isotherm as well as the adjustment to the evaluated models for Cu^{2+} removal using activated carbon as adsorbent is presented in Fig. 4.

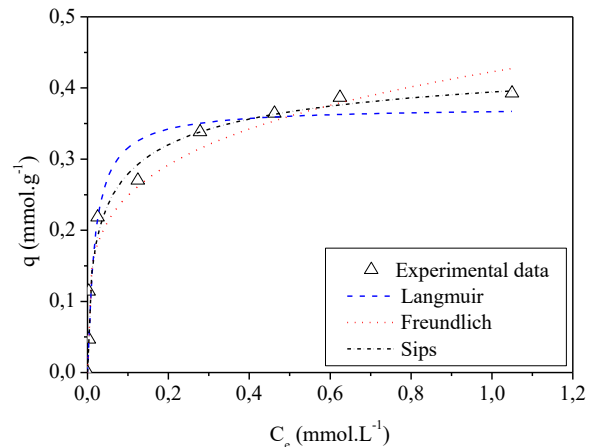


Fig. 4. Adjustment of the adsorption equilibrium models to experimental data.

The experimental parameters of Langmuir, Freundlich and Sips isotherms are presented in Table 2.

Table 2. Parameters of the isothermal models of the evaluated models.

Models	Parameters	Results
Langmuir	q_{max} ($\text{mmol} \cdot \text{g}^{-1}$)	0.37 ± 0.02
	K_L ($\text{L} \cdot \text{mol}^{-1}$)	54 ± 18
	Sr^2	0.0085
	r	0.9465
Freundlich	K_F ($\text{mmol} \cdot \text{g}^{-1} \cdot (\text{mmol} \cdot \text{L}^{-1})^{-1/n_F}$)	0.42 ± 0.02
	n_F	4.3 ± 0.6
	Sr^2	0.0083
Sips	r	0.9481
	q_{max} ($\text{mmol} \cdot \text{g}^{-1}$)	0.47 ± 0.09
	K_S ($\text{L} \cdot \text{mmol}^{-1}$)	5 ± 4
	n_S	1.8 ± 0.5
	Sr^2	0.0043
	R^2	0.9684

Through the results presented in Fig. 4 and Table 2, it can be observed that the model with the highest R^2 value (0.9684), accompanied by the smallest error ($\text{Sr}^2 = 0.0043$), was the Sips model. Its greater efficiency in representing experimental

data suggests that activated carbon has a heterogeneous surface with a heterogeneity factor (n_s) of 1.8.

These results agree with those reported in the literature by Fernández-López et al. [19] in the removal of Pb(II), Cu(II) and Cd(II) from aqueous solutions using agroindustrial waste biomass from globe artichoke.

4. Conclusion

It can be concluded that during the adsorption, the diffusion of Cu^{2+} ions occurs heterogeneously as described by the adjustment to the Elovich model. In addition, the best fit to the adsorption equilibrium data was from the Sips model, with q_{max} equal to $0.47 \text{ mmol} \cdot \text{g}^{-1}$.

The studies carried out show that the use of chemically activated carbon from corn cob as adsorbent was satisfactory for the removal of Cu^{2+} in aqueous solution. It is noteworthy that the adsorbent precursor is an abundant residue with no commercial value.

Acknowledgements

The authors would like to thank the CAPES, FADE/UFPE and NUQAAPE/FACEPE.

References

- [1] Vardhan KH, Kumar OS, Panda RC. A review on heavy metal pollution, toxicity and remedial measures: current trends and future perspectives. *J Mol Liq* 2019;290:111197.
- [2] Nascimento JM, Oliveira JD, Leite SGF. Chemical characterization of biomass flour of the babassu coconut mesocarp (*Orbignya speciosa*) during biosorption process of copper ions. *Environ Technol* 2019;16:1-12.
- [3] BRASIL. Ministério do Meio Ambiente. Resolução nº 430, de 13 de maio de 2011. Conselho Nacional do Meio Ambiente (CONAMA), Brasília, DF, 2011.
- [4] Ratan JK, Kaur M, Adiraju B. Synthesis of activated carbon from agricultural waste using a simple method: characterization, parametric and isotherms study. *Mater Today-Proc* 2018;5:3334-45.
- [5] Nascimento RF, Lima ACA, Vidal CB, Melo DQ, Raulino GSC. Adsorção – aspectos teóricos e aplicações ambientais. 1rd ed. Fortaleza: Imprensa Universitária; 2014.
- [6] Garg D, Kumar S, Sharma K, Majumder CB. Application of waste peanut shells to form activated carbon and its utilization for the removal of acid yellow 36 from wastewater. *Groundwater Sustainable Dev* 2019;8:512-9.
- [7] Cao Y, Keliang W, Xiaomin W, Zhengrong G, Ambrico T, Gibbons W, Qihua F, Talukderd AA. Preparation of active carbons from corn stalks for butanol vapor adsorption. *J Energy Chem* 2017;26:35-41.
- [8] Demiral H, Gungor C. Adsorption of copper (II) from aqueous solutions on activated carbon prepared from grape bagasse. *J Clean Prod* 2016;124:103-13.
- [9] Wang F, Dang Y-q, Tian X, Harrington S, Ma Y-q. Fabrication of magnetic activated carbons from corn cobs using pickle liquor from the surface treatment of iron and steel. *New Carbon Mater* 2018;33:303-9.
- [10] Shim J, Velmurugan P, Oh B-T. Extraction and physical characterization of amorphous silica made from corn cob ash at variable pH conditions via sol gel processing. *J Ind Eng Chem* 2015;28:110-6.
- [11] Rovani S, Rodrigues AG, Medeiros LF, Cataluña R, Lima EC, Fernandes AN. Synthesis and characterisation of activated carbon from agroindustrial waste – Preliminary study of 17 β -estradiol removal from aqueous solution. *J Environ Chem Eng* 2016;4:2128-37.
- [12] Patnukao P, Pavasant P. Activated carbon from Eucalyptus camaldulensis Dehn bark using phosphoric acid activation. *Bioresour Technol* 2008;99:8540-43.
- [13] Brito MJPB, Veloso CM, Santos LS, Bonomo, RCF, Fontan, RCI. Adsorption of the textile dye Dianix® royal blue CC onto carbons obtained from yellow mombin fruit stones and activated with KOH and H_3PO_4 : kinetics, adsorption equilibrium and thermodynamic studies. *Powder Technol* 2018;339:334-43.
- [14] Pezoti O, Cazetta AL, Bedin KC, Souza LS, Souza RP, Melo SR, Almeida VC. Percolation as new method of preparation of modified biosorbents for pollutants removal. *Chem Eng J* 2016;283:1305-14, 2016.
- [15] Puigdomenech I. HYDRA: Hydrochemical equilibrium-constant database. *Inorganic Chemistry Software*: Royal Institute of Technology, Estocolmo, 2004.
- [16] Goswami M, Phukan P. Enhanced adsorption of cationic dyes using sulfonic acid modified activated carbon. *J Environ Chem Eng* 2017;5:3508-17.
- [17] Dong J, Du Y, Duyu R, Shang Y, Zhang S, Han R. Adsorption of copper ion from solution by polyethylenimine modified wheat straw. *Bioresour Technol Rep* 2019;6:96-102.
- [18] Hu X, Long L, Gong T, Zhang J, Yan J, Xue Y. Enhanced alginate-based microsphere with the pore-forming agent for efficient removal of Cu(II). *Chemosphere* 2020; 240. <https://doi.org/10.1016/j.chemosphere.2019.124860>.
- [19] Fernández-López JA, Angosto JM, Roca MJ, Doval Miñarro M. Taguchi design-based enhancement of heavy metals bioremoval by agroindustrial waste biomass from artichoke. *Sci Total Environ* 2019;653:55-63.

Activated charcoal material prepared from fish scales as biosorbent to an application for Rhodamine B dye adsorption

Daniel Moro Druzian^{a*}, Vitória de Mello Figueiredo^b, Luiz Fernando Rodrigues Junior^c,
Joana Bratz Lourenço^b, William Leonardo da Silva^{a,b}

^aPostgraduate Program in Nanosciences, Franciscan University, Santa Maria-RS, 97010-491, Brazil

^bChemical Engineering Course, Franciscan University, Santa Maria-RS, 97010-491, Brazil

^cBiomedical Engineering Course, Franciscan University, Santa Maria-RS, 97010-491, Brazil

Abstract

The problem of dyes wastewater is a matter of environmental concern, since traditional methods are not able to remove these contaminants, requiring new technologies such as adsorption. Thus, the present work aims to evaluate the adsorption capacity of fish scales waste (in nature and as activated charcoal), as biosorbents, in the removal of Rhodamine B (RhB) dye in aqueous solution. The fish scales (FS) was used as precursor material to activated charcoal, where was washed (distilled water), dried (120 °C for 24 hours) and ground (ball mill - 15 minutes). For synthesis of activated charcoal (AC-FS), the methodology of chemical activation/carbonization was used with ZnCl₂ (1:2 w/w) and carbonization, (10 °C min⁻¹ to 600 °C for 240 minutes). The samples were characterized by X-ray diffraction (XRD), Fourier transform infrared spectroscopy (FT-IR), N₂ porosimetry (BET/BJH methods) and zeta potential (ZP) in order to evaluate its textural and structural properties. The adsorption tests were in batch reactor with RhB dye (60 mg L⁻¹) with 0.7 g L⁻¹ of the biosorbents, evaluating the kinetic (pseudo-first and second order) and equilibrium parameters (Langmuir and Freundlich isotherms). Adsorption kinetics was well represented by the pseudo-second order model (indicating the chemical adsorption), and **the Freundlich isotherm presented the better performance in relation to Langmuir isotherm, for FS and AC-FS, with an adsorption capacity of 56.12 mg g⁻¹**. Therefore, the results showed that alternative fish scales materials could be used as a new device for treating wastewater with dyes.

Keywords: activated charcoal; adsorption; fish scales; rhodamine B.

1. Introduction

Currently, the generation of anthropogenic and industrial waste and byproducts is notorious, creating a great environmental impact caused by inadequate wastewater treatment [1]. Moreover, industrial wastewater is mainly characterized by its diversity in chemical composition, from inorganic to organic compounds containing toxic and resistant pollutants [2], which can reach ecosystems, sewage treatment plants and water supply, becoming an environmental liability [3].

One of the main pollutants in the aquatic environment comes from industries that use dyes in their production processes, such as textiles, leather, paper, and plastics, consuming

a large volume of water and generating a significant amount of colored wastewater [4]. Thus, most dyes cause changes in the environment, visual pollution and modification of biological cycles, affecting aquatic beings and impairing photosynthesis processes [5]. Thus, the application of appropriate technology for wastewater treatment becomes necessary to minimize environmental impact and pollution, preserving the environment and comply with standards and legislation. One of the options is the use of absorption treatments, characterized by high efficiency, reduced use of synthetic products and the possibility of using the product in nature, such as lignocellulosic wastes, without any prior treatment [6]. However, the final cost for adsorbents production makes the large-scale application expensive or even infeasible [7].

Activated charcoal is the most used adsorbent in the industry due to its high surface area, highly porous structure, and significant functional groups on the surface, allowing its use to remove different molecules. However, its use in waste treatment is still limited due to its high cost [8]. A good alternative to adsorbents precursor materials are residues, such as lignocellulosic, fish scales, and several others [9], which can be used to remove dyes presented in wastewater. Activated carbon can be synthesized from agro-industrial waste, becoming a source of study as strategic raw materials to promote higher value-added manufacturing, reducing its production costs and encouraging the use of a cleaner and more sustainable production [10].

The use of fish scales in nature is already reported in literature to remove Rhodamine B, showing remarkable adsorption capacities due to the great adsorbent-adsorbate affinity [11]. In order to aggregate value for the fish scales agro-industrial waste, this work aims to evaluate the adsorption capacity of fish scales in nature and compare to a prepared activated charcoal, using Rhodamine B (RhB) as a dye, contributing for the treatment of waters and wastewaters containing dye molecules.

2. Materials and Methods

2.1 Preparation of fish scales waste

Fish scales (FS) collected from local producer, located in the city of Santa Maria-RS (Brazil), and used as precursor material to synthesize activated charcoal. Then, the FS precursor was washed several times with distilled water and oven dried (120 °C for 24 hours). After, it was ground in a ball mill (CT-241 Mill) by contacting the alumina balls (Al₂O₃) for 15 minutes without adding temperature to obtain particles lower than 2 nm.

2.2 Synthesis of the activated charcoal

The synthesis of activated charcoal was based on the literature adaptation [12], where for chemical activation, the activating reagent ZnCl₂ (Synth, P.A.) was used, in the ratio of 1:2 w/w, being dissolved in 50 mL of distilled water, followed by magnetic stirring for 30 minutes. For the carbonization, a heating rate of

10 °C min⁻¹ to 600 °C for 240 minutes was used. Thereafter, cooling to room temperature occurred at the natural rate of the furnace off, followed by ethanol (Synth, P.A.) washes to pH around 7 (simple filtration) to remove the chloride ions and surface ash. The material obtained from the activation/carbonization was labeled AC-FS, and the yield values of activated charcoal (R_{AC-FS}%) was calculated according to Eq. (1):

$$R_{AC-FS}(\%) = [(m_{AC-FS}) / m_{FS}] \cdot 100 \quad (1)$$

where:

m_{AC-FS}: mass of the activated charcoal obtained from fish scales (g)

m_{FS}: mass of fish scales (g).

2.2 Characterization of FS and AC-FS

FS and AC-FS were characterized by X-ray diffraction (XRD), N₂ porosimetry, zeta potential (PZ) and Fourier transform infrared spectroscopy (FT-IR). The samples crystallinity was verified by X-ray diffraction (XRD) using X-ray diffractometer (Bruker Optics, D2 Advance, United States) with copper tube (K α -Cu = 1,5418 Å), in a range of 2 θ from 10° to 70°, acceleration voltage and applied current of 30 kV and 30 mA, respectively. N₂ porosimetry was used to determine the specific area and porosity (pore volume and pore diameter) of the samples, where previously the samples were degassed at a pressure of 10⁻² mbar with a temperature of 120 °C for 12 h, in a Gemini 2375 equipment from Micromeritics®. Specific areas (SBET) were determined by the Brunauer-Emmett-Teller Equation (BET Method), in the range of P/P₀ = 0.05 to 0.35, while pore diameters and volumes by the Barret-Joyner-Equation. Halenda (BJH Method). Surface charge was determined via zeta potential (PZ) in a Malvern-Zetasizer® nanoZS brand (ZEN3600, United Kingdom) with cell (DTS 1060) (Malvern Instruments, United Kingdom) using a 4 mW He-Ne laser (633 nm). Fourier transform infrared spectroscopy (FT-IR) was used to obtain the functional groups in Varian 640-IR Fourier Transform Infrared Spectroscopy, in transmittance mode in the region from 450 to 4000 cm⁻¹, with 32 scans and 4 cm⁻¹ to resolution.

2.3 Adsorption tests

Adsorption tests were carried out in batch operating using magnetic attiring with RhB dye (60 mg L^{-1}), such as adsorbate, and FS and AC-FS (1.5 g L^{-1}), such as adsorbents, according to the literature [13]. Thus, 100 mL of the RhB solution were kept in contact with FS and AC-FS under magnetic stirring (150 rpm) for 180 minutes. During the stirring, samples were collected (4 mL) and placed in Eppendorfs® in predetermined times (0, 5, 15, 30, 45, 60, 90, 120, 150 and 180 minutes), and filtered (0.22 μm filter, millex GP). Finally, the variation of the RhB concentration over time was determined by reading the absorbance in the characteristic wavelength of the 553 nm. RhB removal percentage (R%) and adsorption capacity of the FS and AC-FS (q) were determined by Eq. (2) and (3), respectively.

$$R(\%) = \frac{C_0 - C_t}{C_0} \cdot 100 \quad (2)$$

$$q = \frac{(C_0 - C_t) \cdot V}{m} \quad (3)$$

where

C_0 : initial concentration (mg L^{-1});
 C_t : RhB concentration at the time (mg L^{-1});
 V : RhB solution (L);
 m : mass of adsorbent used (g).

2.4 Kinetic and equilibrium studies

Adsorption kinetic and equilibrium data were analyzed using the models presented in the Equations (4-7), according to literature [14-17].

$$q_t = q_1(1 - \exp(-k_1 t)) \quad (4)$$

$$q_t = \frac{t}{(1/k_2 q_2^2) + (t/q_2)} \quad (5)$$

$$q_e = \frac{q_m k_L C_e}{1 + k_L C_e} \quad (6)$$

$$q_e = k_F C_e^{1/n} \quad (7)$$

where:

k_1 : rate constant of pseudo-first order (min^{-1});

q_1 : theoretical value of adsorption capacity (mg g^{-1});

k_2 : rate constant of pseudo-second order ($\text{g mg}^{-1} \text{ min}^{-1}$);

q_2 : theoretical value of adsorption capacity (mg g^{-1});

q_m : maximum adsorption capacity (mg g^{-1});

k_L : Langmuir constant (L mg^{-1});

k_F : Freundlich constant ($\text{mg g}^{-1})(\text{mg L}^{-1})^{-1/n}$;

$1/n$: heterogeneity factor.

3. Results and Discussion

3.1 Yield of AC-FS

The yield of the chemical activation/carbonization process to the synthesis of the AC-FS was determined according to the Eq. (1). Thus, the yield value of AC-FS was 60.5%, which is in agreement with de values of the literature [18]. Highlighting that the chemical activation process is relatively large and can exceed that of the physical activation by up to 30%, besides generating a structure with considerable porosity [19,20].

3.2 Characterization of FS and AC-FS

FS and AC-FS were characterized by XRD, FT-IR, zeta potential (ZP) and N_2 porosimetry. The information about the crystallographic structure of FS and AC-FS were obtained by XRD measurements, according to Fig. 1.

Figure 1. XRD patterns of FS and AC-FS.

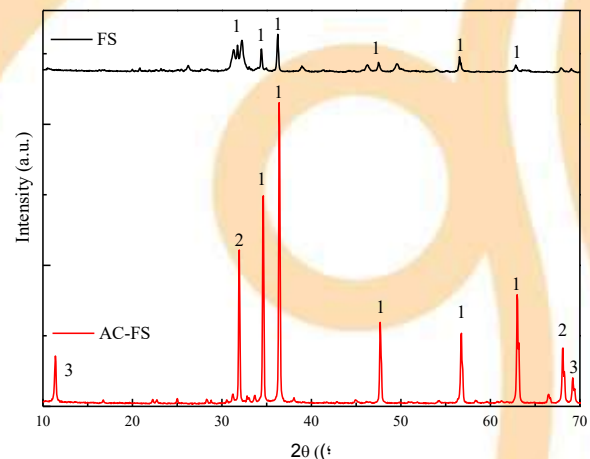


Figure 1. XRD patterns of FS and AC-FS.

According to Figure 1, the crystallinity of the FS is characteristic of the phase $\text{Ca}_4\text{Na}_6(\text{SO}_4)_6\text{F}_2$ - Calcium Sulphate Fluorine Sodium (PDF 029-1189 – number 1), while AC-FS showed a phase $\text{Ca}_{9.97}(\text{PO}_4)_6\text{C}_{11.94}$ - Chlorinated Apatite (PDF 088-2170 – number 2) and zinc hydroxide $\text{Zn}(\text{OH})_2$ (PDF 070-8070 – number 3), in addition to being more crystalline providing greater adsorption it can adsorb RhB in effluents. In addition, the average size of the crystallites showed an increase of 19.26 nm (calcium sulphate fluorine sodium) (FS) to 39.15 nm (zinc hydroxide) and 20.18 nm to Chlorinated Apatite (AC-FS), indicating a greater crystalline organization providing an increase in surface area and thus a greater number of active sites available for RhB adsorption.

The main functional group of FS and AC-FS can be visualized in Figure 2.

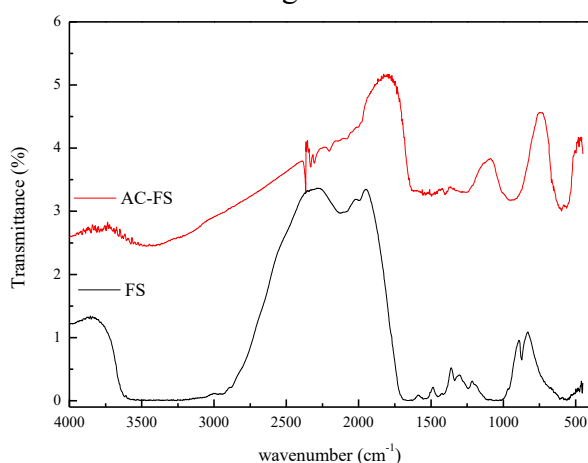


Figure 2. FT-IR spectra of FS and AC-FS.

According to Figure 2, it possible to identify characteristic peaks, such as [23,24]: (1) a broad and wide band between 3,600 and 3,400 cm^{-1} attributed to the O-H ($\nu_{\text{O-H}}$) OH) stretching that the -OH of hydroxyapatite remained after carbonization and (2) the bands at 1,027 cm^{-1} , 600 cm^{-1} and 578 cm^{-1} are assigned to vibration of $-\text{PO}_4^{3-}$ groups. Then, the FT-IR spectra data reflected that both materials are similar, and the functional groups of hydroxyapatite were unchanged even after the chemical activation/carbonization process.

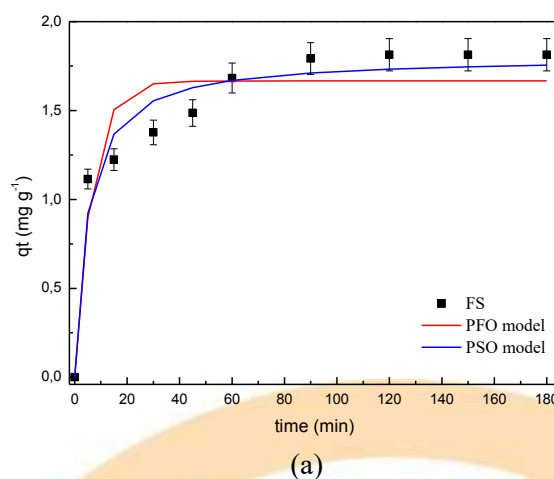
Table 1 shows the results of zeta potential of the FS and AC-FS, where it was possible to verify negative charge, indicating a charge compatibility between the biosorbent surface and the RhB charge, which is characterized by its cationic nature [21,22].

Table 1. Zeta potential (ZP) of the FS and AC-FS.

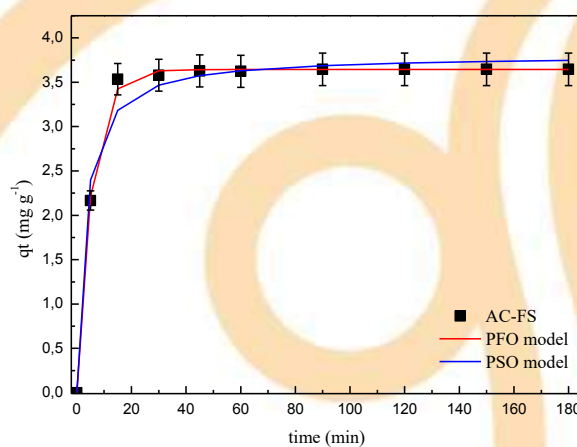
Sample	ZP (mV)
FS	-0.807 ± 1.76
AC-FS	-8.71 ± 1.57

3.2 Kinetic evaluation

The kinetic curves of RhB adsorption onto FS and AC-FS are showed in Fig. 3(a) and 3(b), respectively, which were obtained at temperature 298 K, natural pH (≈ 4.5), stirring rate of 150 rpm and adsorbent concentration of 1.5 g L^{-1} , according to Eqs. (4) and (5). The more adequate model (PFO or PSO) was selected by the evaluation of determination coefficient (R^2), adjusted determination coefficient (R^2_{adj}) and average relative error (ARE).



(a)



(b)

Figure 3. Kinetic curves for RhB adsorption onto FS (a) and AC-FS (b) ($T = 298 \text{ K}$; $[\text{RhB}] = 60 \text{ mg L}^{-1}$; $\text{pH} = 4.5$ and biosorbent concentration = 1.5 g L^{-1}).



According to Figure 3, it was possible to observe a progressive increase in the adsorption capacity along the time. Moreover, a fast adsorption was verified until 30 min and 90 min to AC-FS and FS, respectively, and the rate gradually decreased until equilibrium. This is due to the reduction of unoccupied adsorption sites and decrease of concentration gradient [23]. Table 2 shows the kinetic parameters obtained by pseudo-first order and pseudo- second order models.

Table 2. Kinetic parameters for the RhB dye onto CN and CF.

Pseudo-first order	FS	AC-FS
q_1 (mg g ⁻¹)	1.66	3.64
k_1 (min ⁻¹)	0.15	0.19
R^2	0.889	0.989
R^2_{adj}	0.876	0.992
ARE (%)	2.51	2.12
Pseudo-second order	FS	AC-FS
q_2 (mg g ⁻¹)	1.22	2.79
k_2 (g mg ⁻¹ min ⁻¹)	1.81	3.81
R^2	0.934	0.998
R^2_{adj}	0.925	0.992
ARE (%)	1.52	1.21

According to Table 2, the two models used presented a good values of R^2 , R^2_{adj} and ARE, with ARE values were always lower than 2.5% and the greater R^2 and R^2_{adj} values were found for the pseudo-second order model. These indications revealed that this model was suitable to represent the adsorption of RhB on FS and AC-FS, confirming that the control of the velocity mechanism is chemical adsorption (chemical reaction) [24].

3.3 Equilibrium isotherms

The equilibrium isotherms for RhB adsorption on FS and AC-FS were obtained at temperature of 298 K, pH of 4.5, stirring rate of 150 rpm and adsorbent concentration of 1.5 g L⁻¹, according to Eqs. (6) and (7), and the isotherm parameters are shown in Table 3.

Table 3. Isotherm parameters for RhB on FS and AC-FS.

	FS	AC-FS
Langmuir		
q_m (mg g ⁻¹)	56.12	115.82
k_L (L mg ⁻¹)	0.063	0,173
R^2	0.991	0.996
R^2_{adj}	0.989	0.992
ARE	0.54	2.52
Freundlich		
k_F (mg g ⁻¹)(mg L ⁻¹) ^{-1/n}	35.48	42.07
n	6.14	4.31
R^2	0.995	0.998
R^2_{adj}	0.994	0.997
ARE	1.47	1.24

According to Table 3, the Freundlich model showed higher values of coefficient of determination (R^2), adjusted coefficient of determination (R^2_{adj}) and lower values of average relative error (ARE), may be considered more adequate to represent the RhB on FS and AC-FS. The maximum adsorption capacity were 56.12 and 115.82 mg g⁻¹ for FS and AC-FS, respectively The values can be considered satisfactory in comparison with the literature [25], indicating a high applicability of fish scales for RhB adsorption.

Conclusion

In this work, fish scales (in nature and activated charcoal) were used to evaluate its adsorption capacity in the removal of RhB dye from aqueous solutions. The adsorption kinetics followed the pseudo-second order model and the Freundlich model was the best to represent the adsorption equilibrium.

Acknowledgements

The authors would like to thank the Unit Operations Laboratory (109) from the Franciscan University (UFN) for their support and assistance in present work. Moreover, this work received financial support from the Foundation for Research of the State of Rio Grande do Sul (FAPERGS – 19/2551-0001362-0), so all thanks.

References

- [1] Chen O., Fangyng J, Tingvi L, Peng Y, Wei G, Xuan X et al. Synergistic effect of bifunctional Co–TiO₂ catalyst on degradation of Rhodamine B: Fenton-photo hybrid process. *Chem Eng J* 2013; 229:57–65.
- [2] Ferreira-Leitão V, Gottschalk LMF, Ferrara MA, Nepomuceno AL, Molinari HBC, Bom EPS. Biomass Residues in Brazil: availability and potential uses. *Waste Biomass* 2010; 1:65-76.
- [3] Silveira MAK, Caldas SS, Guilherme JR, Costa, FP, Guimarães BS, Cerqueira, MBR, Soares. BM, Primel, EG. Quantification of pharmaceuticals and personal care product residues in surface and drinking water samples by SPE and LC-ESI-MS/MS. *J. Brazil. Chem. Soc.* 2013; 24:1385-1395.
- [4] Rafatullah M, Sulaiman O, Hashim R, Ahmad A. Adsorption of methylene blue on low-cost adsorbents: A review. *J. Hazard. Mater.* 2010; 177: 70-80.
- [5] Zanoni MVB, Carneiro PA. O descarte dos corantes têxteis. *Ciência Hoje* 2001; 174:61-71.
- [6] Crini, G. Recent developments in polysaccharide-based materials used as adsorbents in wastewater treatment. *Progress in Polymer Science*, v. 30, p. 38-70, 2005.
- [7] Wang L. Application of activated carbon derived from waste bamboo culms for the adsorption of azo disperse dye: Kinetic, equilibrium and thermodynamic studies. *J. Env. Manage.* 2012; 102:79-88.
- [8] Chen PY, Sokes AG, Mckittrick, J. Comparison of the structure and mechanical properties of bovine femur bone and antler of the North American (*Cervus elaphus canadensis*). *Acta Bio* 2008; 5: 693-706.
- [9] Brito MJP, Veloso CM, Bonomo RCF, Fontan RCI, Santos LS, Monteiro KA. Activated carbons preparation from yellow mombin fruit stones for lipase immobilization. *Fuel Proc. Technol.* 2017; 156: 421–428.
- [10] Prahas D, Kartika Y, Indraswati, N, Ismadji S. Activated carbon from jackfruit peel waste by H₃PO₄ chemical activation: pore structure and surface chemistry characterization. *Chem. Eng. J.* 2008; 140: 32–42.
- [11] Neves CV, Scheufel FB, Nardino AP, Vieira MGA, Silva MGC, Módenes AN, Borba CE. Phenomenological modeling of reactive dye adsorption onto fish scales surface in the presence of electrolyte and surfactant mixtures. *Environ. Technol.* 2018; 39: 2467-2483.
- [12] Schultz J. Obtenção de carvão ativado a partir de biomassa residual para a adsorção de poluentes. Tese (Doutorado em Química) – Programa de Pós-Graduação em Química, Setor de Ciências Exatas, Universidade Federal do Paraná. Paraná, p. 139, 2016.
- [13] Oliveira F.M. Síntese de nanopartículas anisotrópicas de ouro e sua avaliação como catalisadores na redução química do p-nitrofenol. 2017. p. 70. (Dissertação (Mestrado em Ciências) - Programa de Pós-Graduação em Química e Biotecnologia, Universidade Federal de Alagoas, Maceió, Alagoas, 2017.
- [14] Lagergren S. About the theory of so-called adsorption of soluble substances. *Kung Svenska Vetenskap* 1898; 24:1–39.
- [15] Ho YS, McKay G. Kinetic models for the sorption of dye from aqueous solution by wood. *Proc Safety Environ Protect* 1998;76:183–91.
- [16] Langmuir I. The adsorption of gases on plane surfaces of glass, mica and platinum. *J Amer Chem Soc* 1918; 40:1361–403.
- [17] Freundlich H. Over the adsorption in solution. *Z Physic Chem* 1906; A57:358–471.
- [18] Coelho ST, Gregotur C, Taccini MM, Sales BB, Dalmolin KPP, Figueiredo NJV, Barbosa RM, Grisoli RPS. Carvão vegetal aspectos Técnicos, Sociais, Ambientais e Econômicos. CEMBio. Programa de Pós-Graduação em Energia (PPGE) da Universidade de São Paulo (USP). 2008.
- [19] Lu, H. Preparation of CoFe₂O₄@vacancy@mSiO₂ core-shell composites for removal of organic pollutant in aqueous solution. *J. Saudi Chem. Soc.* In Press, 2018.
- [20] Debrassi, A. Removal of cationic dye from aqueous solution using N-benzyl-O-carboxymethylchitosan magnetic nanoparticles. *Chem. Eng. J.* 2011; 183: 284-293.
- [21] Salleh MAM. Cationic and anionic dye adsorption by agricultural and solid wastes: A comprehensive review. *Desalination* 2011; 280: 1-13.
- [22] Peres EC. Treatment of containing cobalt by adsorption on *Spirulina sp.* and activated charcoal. *J. Environ. Chem. Eng.* 2018; 6: 677-685.
- [23] Spinelli VA., Laranjeira MCM, Fávere VT. Kinetics and Equilibrium of Adsorption of oxyanions Cr (VI), Mo (VI) and Se(VI) by quaternary ammonium chitosan salt. *Polímeros: Ciência e Tecnologia* 2005; 15:218-223.
- [24] Machado A, Da Rosa AL, Carissimi E. Adsorção de Rodamina B em carvão ativado comercial. *Revista Ciatec-UPF* 2019; 11:100-107.
- [25] Alcântara RR. Síntese, caracterização de nanomaterial zeolítico de cinzas de carvão organomodificado e aplicação como adsorvente na remediação de água contaminada por Rodamina B e azul direto 71. 2016. 179 f. Dissertação (Mestrado em Ciências) – Programa de Pós-Graduação em Materiais, Instituto de Pesquisa Energéticas e Nucleares, São Paulo,

Study of the removal capacity of potassium diclofenac drug using the rice husk as a biosorbent alternative

Leandro Rodrigues Oviedo^{a*}, Carolina Denardi Merlugo^b, Aline Marques da Silva^b,
William Leonardo da Silva^{a,b}

^a *Postgraduate Program in Nanosciences, Franciscan University, Santa Maria-RS, 97010-491, Brazil*

^b *Chemical Engineering Course, Franciscan University, Santa Maria-RS, 97010-491, Brazil*

Abstract

Agriculture is the principle contribution of country's economy and about 71% correspond to rice production. However, the rice production generates solid wastes, mainly rice husk, which is either used as an energy source or discharged inadequately on soil. A solution to minimize adverse environmental impact is the valorization of this byproduct, using it as raw material in wastewater treatment. Wastewaters containing drugs is a current problem of paramount concern once the conventional methods do not remove them efficiently so that, new water purification technologies is required. The usage of rice husk as an adsorbent seems to be a good alternative to fix the problem. In this view, the present work aims to activation of rice husk with phosphoric acid, dimethylsulfoxide and dimethylformamide in order to obtain an activated carbon for removal of potassium diclofenac from aqueous solution. Natural and activated rice husk were characterized by nitrogen porosimetry (BET/BJH methods), zeta potential (ZP) and Fourier transformed Infrared spectroscopy (FT-IR) for the evaluation of the textural and structural properties. Moreover, the adsorption tests and equilibrium parameters (Langmuir and Freundlich isotherms) were obtained in batch operating. Therefore, the rice husk with phosphoric acid showed the best capacity of adsorption (42.73 mg g^{-1}) in relation to the others adsorbents, after 180 minutes of contact, due to the better charge surface compatibility with diclofenac potassium, specific area ($157.65 \text{ m}^2 \text{ g}^{-1}$) and pore volume ($0.93 \text{ cm}^3 \text{ g}^{-1}$). Therefore, the results showed that alternative rice husk could be used as a new device for treating wastewater with drugs.

Keywords: Biosorption; agroindustrial waste; sustainability; rice husk.

1. Introduction

Agriculture is the main contributor to country's development and represents a significant portion of economic questions when it is associated with urbanization [1]. Cereal, legumes, oilseed and grains production, especially rice and soya, are the main agricultural activities worldwide [2]. In this scenario, it is important to mention that the rice farming has increased 315% for over a period of 41 years due to exportation, consume and average yield [3].

Among Brazilian states, Rio Grande do Sul is considered the **largest** rice producer, **accounting for** about 71% of the national rice production [4]. However, rice production is generally associated to high waste generation levels. **Part of the** generated waste has been used in burning processes for energy

purposes. Other alternative to **using this** waste is based on **its** valorization: synthesis of biosorbents and oil remediation [5].

At the same time, wastewaters containing drugs is an environmental problem of great concern and is related to drug over uptake by most part of population [6]. This is the case of potassium diclofenac, one of the most consumed drugs around the world [7]. Its usage is explained by the ease of access **to** this drug and because it need **no** prescription [8]. In fact, these drugs are persistent and does not be removed by means of conventional wastewater treatments. Then, new purification of water technologies is required. Advanced Oxidation Processes (AOPs), membrane separation, Fenton's process and adsorption are outstanding technologies used to remove drugs **from** wastewater [9-11]. The latter **one** is considered the most feasible due to its

relative low cost, ease of operation and possibility of usage of adsorbent materials **produced** from different kinds of biomass [12].

In this context, this work aims to evaluate the adsorptive capacity of natural and activated rice husk in the removal of potassium diclofenac from wastewater.

2. Materials and Methods

2.1 Materials

Sodium acetate, dimethylsulfoxide (DMSO), and dimethylformamide (DMFA) were obtained from Synth. **Phosphoric acid (Neon, 85% v/v), lead nitrate (Merck, P.A.), urea (Nuclear, P.A.) and potassium diclofenac (Nuclear, P.A.) were used in the preparation of biosorbents.** All reagents were of analytical grade. Rice husk was obtained from local producer, located in the city of Santa Maria-RS (Brazil)

2.2 Preparation of biosorbent

Initially, natural rice husk (RH) was crushed in a household mixer and then activated according to the literature [13,14], into three different routes.

- First route: 15 g of rice husk were treated by 100 mL of phosphoric acid 85% v/v at ambient conditions during 24 hours under stirring. after, the result material was filtered and washed with ultrapure water until neutral pH was reached. It is important to mention that the water used must not contain phosphate ion into it. Then, the sample was labeled as RH-H₃PO₄.

- Second route: 10 g of rice husk were brought into contact with 1.0 mL of phosphoric acid, 100g of urea and 200 mL of DMFA at 70 °C during 1 h. Then the obtained powder was filtered, washed and dried in a stove at 80 °C for 1 h. Then, the sample was labeled as RH-DMFA.

- Third route: 10 g of rice husk were added to a solution containing 1.0 mL of phosphoric acid, 100 g of urea and 200 mL of DMSO. After, this solution was stirred at 80 °C during 1 h. Then, the resulted powder was filtered, washed and dried in a stove at 80 °C for 1 h. Then, the sample was labeled as RH-DMSO.

Finally, the rice husk obtained were submitted to ground (Tecnal, Willye TE-650, Brazil) and sieving to 0,425 mm (ABNT, TYLER 35#).

2.3 Characterization methods

To analyze the presence of functional groups the Fourier Transform infrared spectroscopy (FT-IR) was performed in an infrared spectrometer (Shimadzu, 8300, Japan) in transmittance mode in the region from 450 to 4000 cm⁻¹, with 32 scans and 4 cm⁻¹ to resolution. To verify the charge compatibility between adsorbate and adsorbent, the surface charge was analyzed by zeta potential (Malvern Zetasizer® nanoZS ZEN3600, United Kingdom) with cell (DTS 1060) (Malvern Instruments, United Kingdom) using a 4 mW He-Ne laser (633 nm). To evaluate the specific surface area, pore diameter and pore volume was used the N₂ porosimetry (Micromeritics, Gemini-2375) using Brunauer-Emmet-Teller Method (BET method), in the range of P/P₀ = 0.05 to 0.35, while diameters and volumes pore by the Barret-Joyner-Equation. Halenda (BJH Method).

2.4 Adsorption tests

Adsorption tests were performed batch process (duplicates), **according to the literature [15]**. Initially, 100 mL of 60 mg·L⁻¹ potassium diclofenac solution were brought into contact with 0.7 g·L⁻¹ of rice husk-based biosorbent at ambient conditions and contact time of 180 min. Aliquot samples were collected at predetermined time (0, 5, 15, 30, 45, 75, 90, 120 and 180 minutes) in order to measure the residual concentration of the drug in solution. Additionally, drug removal efficiency (%R) and adsorptive capacity of biosorbent were evaluated, according Equations (1) and (2), respectively.

$$R(\%) = \frac{C_0 - C_t}{C_0} \cdot 100 \quad (1)$$

$$q = \frac{(C_0 - C_t) \cdot V}{m} \quad (2)$$

where C₀: initial concentration of adsorbate (mg L⁻¹); C_t: concentration of adsorbate at the time (mg L⁻¹); V: solution of the potassium diclofenac (L); m: mass of adsorbent used (g) and q: adsorption capacity (mg g⁻¹).

The drug concentration was determined by a direct correlation **with** absorbance **from** a standard calibration curve (Equation 3) generated in a UV-vis spectrophotometer (Cary 100 Scan, USA).

$$Abs = 0.0929 C_t \quad (3)$$

2.5 Equilibrium studies

To understand the mechanism of adsorption, the Langmuir and Freundlich models were evaluated. These models are used for fitting of experimental data and can be expressed by Equations (4) and (5).

$$q_e = \frac{q_m k_L C_e}{1 + k_L C_e} \quad (4)$$

$$q_e = k_F C_e^{1/n} \quad (5)$$

where: q_m : maximum adsorption capacity (mg g^{-1}); k_L : Langmuir constant (L mg^{-1}); k_F Freundlich constant ($\text{mg g}^{-1}(\text{mg L}^{-1})^{-1/n}$) and $1/n$: heterogeneity factor.

3. Results and Discussion

3.1 Characterization of the biosorbents

The Table 1 shows the zeta potential values (ZP), specific surface area (S_{BET}), pore volume (V_p) and diameter pore (D_p) of natural and activated rice husk.

Table 1. Zeta potential (ZP), surface area (S_{BET}), pore volume (V_p) and diameter pore (D_p) of the biosorbents.

Sample	ZP (mV)	S_{BET} ($\text{m}^2 \cdot \text{g}^{-1}$)	D_p (nm)	V_p ($\text{cm}^3 \text{g}^{-1}$)
RH	21.1 ± 0.50	2.5	11.5	0.003
RH-DMFA	17.7 ± 0.50	138.4	4.89	0.0045
RH-DMSO	-18.0 ± 3.96	17.8	0.32	0.0011
RH- H_3PO_4	-7.32 ± 1.62	157.6	22.63	0.93

According to the Table 1, it was possible to **verify** that the surface area of activated rice husks increased in relation of the RH. Moreover, the RH- H_3PO_4 had the greatest values of surface area, volume and pore size. RH-DMSO had the lowest one. This was related to the activation agent effectiveness in providing a significant number of active sites in the biosorbent surface. Actually, when DMFA and H_3PO_4 were used, the resulting material contains a mesoporous structure. otherwise, when DMSO was used as an activation

agent. **Therefore**, these obtained structures explain the higher values of surface area, pore volume and pore diameter of biosorbents treated with H_3PO_4 . In relation to **ZP**, the higher values (least negative) correspond to better adsorption capacity for potassium diclofenac, whose surface charge is negative [16,17]. In this way, the lowest value of negative charge of the biosorbent prepared from H_3PO_4 favors the adsorption of potassium diclofenac due to better affinity between the adsorbate molecules and the surface of the solid material.

To identify the functional groups present on solid surface of biosorbent, a FT-IR was performed (Figure 1.)

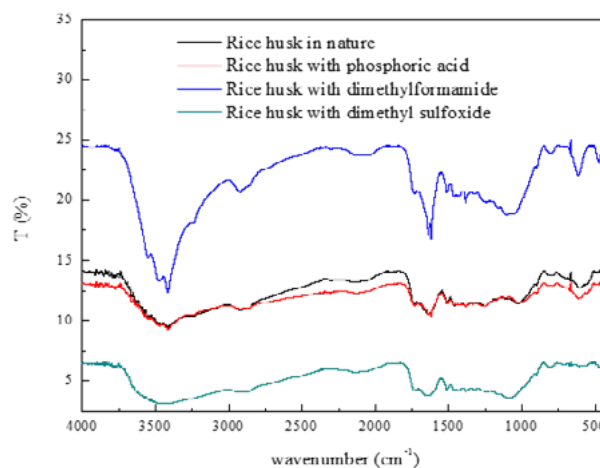


Figure 1. FT-IR spectra of natural and modified rice husk.

According to Figure 1, it was clear that the high content of fibers and starch was found in the rice husk. The peaks in the range of 3000 to 3750 cm^{-1} correspond to hydroxyl groups (-OH). In the 3000 to 2760 cm^{-1} range, C-H bonds related to lignocellulosic structures were found. Moreover, the peaks found from 1630 to 1660 cm^{-1} range correspond to C-O and C-OH bonds of ketones and aldehyde groups, mainly. Additionally, the peak near to the 1050 cm^{-1} band was found and was characteristic of silane groups (Si-O-Si) [18]. Therefore, the characteristic peaks around 600 cm^{-1} value correspond to amorphous structure of Si=O double bond [19]. In this way, one could observe the groups of both biosorbents (natural and modified) were the same, meaning that the natural structure of rice husk was preserved after activation.

3.2 Adsorptive capacity and removal efficiency

The Figure 2 shows the capacity adsorption versus time.

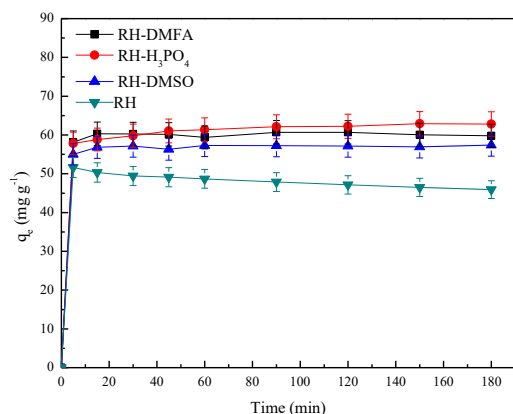


Figure 2. Potassium diclofenac adsorption profile. (Contact time = 180 min; drug initial concentration = 60 mg L⁻¹; adsorbent dosage = 0.7 g L⁻¹).

According to Figure 2, the best drug removal efficiency was obtained with RH-H₃PO₄. In fact, the rice husk modified with H₃PO₄ showed higher values of surface area, pore volume and pore diameter. In addition, this prepared material presented higher surface charge compatibility with diclofenac, compared to others.

3.3 Adsorption isotherms

To determine the mechanism of adsorption process performed, two isotherms were evaluated Langmuir and Freundlich models. Thus, the Langmuir model assumes formation of a monolayer of adsorption and no interaction between one adsorbate molecule and the surrounding one. Unlike this model, the Freundlich model consist in a heterogeneous behavior of adsorption, where there could be interaction among adsorbate molecules adjacent to one another [20]. In this case, the formation of multilayers is possible and the active sites of the solid surface are not equally energetic. Tables 3 and 4 shows the parameters obtained by models evaluated for the batch adsorption process.

Table 3. Evaluation of Langmuir isotherm model parameters

Biosorbent	Langmuir Model		
	K _L	Q _{max} (mg·g ⁻¹)	R ²
RH	0.089	51.33	0.726
RH-DMFA	0.178	59.62	0.781
RH-DMSO	0.14	54.17	0.799
RH-H ₃ PO ₄	0.19	60.45	0.795

Table 4. Evaluation of Freundlich isotherm model parameters.

Biosorbent	Freundlich Model		
	n	K _F	R ²
RH	1.31	557.56	0.998
RH-DMFA	2.26	215.13	0.999
RH-DMSO	1.91	275.04	0.999
RH-H ₃ PO ₄	2.40	199.48	0.998

According to Table 3 and 4, it was noticeable that the Freundlich model was the best fit of all experimental data (greater R² parameter). This assumes that the adsorption of potassium diclofenac shows an heterogeneous behavior, forming multilayers on the surface of rice husk. Regarding the reasons afore mentioned, the rice husk modified with H₃PO₄ led to the best adsorptive capacity and higher removal of potassium diclofenac.

Conclusion

In the **present** work, the evaluation of adsorptive capacity of rice husk as a biosorbent for removal of potassium diclofenac from water was **carried out**. **About** kinetics studies, the mechanism of adsorption was better understood using Langmuir and Freundlich models. In fact, between these models, is possible to say that the Freundlich model represented the best fit of all experimental data, suggesting heterogeneous adsorption. In respect to activation of the biosorbent, those activated by phosphoric acid has presented the best efficiency in the removal of potassium diclofenac from aqueous solution. It is directly related to the greater volume of pores, surface area and surface charge. Therefore, the usage of alternatives activation agents (strong acids and bases) are required in order to achieve improved adsorptive capacities for the drug tested.

Acknowledgements

The authors would like to thank the Unit Operations Laboratory (109) from the Franciscan University (UFN) for their support and assistance in present work. Moreover, this work received financial support from the Foundation for Research of the State of Rio Grande do Sul (FAPERGS – 19/2551-0001362-0), so all thanks.

References

- [1] Empresa Brasileira de Pesquisa Agropecuária - EMBRAPA. Visão 2030: o futuro da agricultura brasileira. Brasil: Embrapa, 2018.
- [2] Fuglie KO, Wang SL, BALL VE. Productivity growth in agriculture: an international perspective. Washington: CAB International, 2012.
- [3] Instituto Brasileiro de Geografia e Estatística. Produção agrícola por regiões. Disponível em: <<http://www.brasil.gov.br/economia-e-emprego/2014/08/ibge.npg/view>>. Acesso em> 02 abr. 2018.
- [4] Schneider LT. Casca de arroz como agente adsorvente no tratamento de óleo residual. 2017. 96 p. Dissertação (Mestrado em Energia na Agricultura) - Programa de Pós-Graduação em Engenharia de Energia na Agricultura, Universidade Estadual do Oeste do Paraná, Cascavel, 2017.
- [5] Mezzelani M, Gorbi S, Regoli F. Pharmaceuticals in the aquatic environments: Evidence of emerged threat and future challenges for marine organisms. *Mar Environ Res*:2018:140,41–60.
- [6] Goodman LS.; Gilman A. As bases farmacológicas da terapêutica: 11. ed. Rio de Janeiro: Amgh Editora. 2006.
- [7] De Souza BP. Avaliação da remoção de sulfametoxazol, diclofenaco e 17βestradiol em água por meio de processo oxidativo com cloro. 2014. 97 p. Dissertação (Mestrado em Engenharia Civil) - Programa de Pós-Graduação em Engenharia Civil, Universidade Estadual Paulista “Júlio de Mesquita Filho”, Ilha Solteira, 2014.
- [8] Ziylan A., Ince NH. The occurrence and fate of anti-inflammatory and analgesic pharmaceuticals in sewage and fresh water: Treatability by conventional and nonconventional processes. *J Hazard Mater*:2011:187,24-36.
- [9] Chen XM, Da Silva DR, Martínez-Huitle CA. Application of advanced oxidation processes for removing salicylic acid from synthetic wastewater. *Chin Chem Lett* 2010:21,101–104.
- [10] Minella MA, De Bellis NA, Gallo AB, Giagnorio MB, Minero CA, Bertinetti SA, Sethi RB, Tiraferri ABM, Vione D. Coupling of Nanofiltration and Thermal Fenton Reaction for the Abatement of Carbamazepine in Wastewater. *ACS Omega* 2018:3,9407-9418.
- [11] Zyła, R, Milala R, Kaminska r., Kudzin M, Gmurek M, Ledakowicz S.. Impact of Advanced Oxidation Products on Nanofiltration Efficiency. *Water* 2019:11,541-558.
- [12] Bhadra BN, Seo PW, Jung SH. Adsorption of diclofenac sodium from water using oxidized activated carbon. *Chem Eng J* 2016;301:27–34.
- [13] Zhang Y, Zhen R, Zhao J, Ma F, Zhang Y, Menq Q. Characterization of H3PO4-Treated Rice Husk Adsorbent and Adsorption of Copper(II) from Aqueous Solution. *Biomed Res Int* 2014:2014,1-8.
- [14] Oshima T, Kondo K, Ohto K, Inoue K, Baba Y.. Preparation of phosphorylated bacterial cellulose as an adsorbent for metal ions. *React Funct Polym* 2008:68,376-383.
- [15] Stefanelo TS, Da Silva AM, Da Silva WL. Utilização do biopolímero de celulose para a aplicação na adsorção de corantes em meio aquoso. *Disciplinarum Scientia. Série: Naturais e Tecnológicas* 2019:20, 71-84.
- [16] Toledo IB, Garcia FMA, Utrilla RJ, Moreno CC, Fernández VFJ. Bisphenol a removal from water by activated carbon: Effects of carbon characteristics and solution chemistry. *Environ Sci Technol* 2005:39, 6246–6250.
- [17] Cunha RR. Desenvolvimento de métodos rápidos para determinação de Codeína, Diclofenaco e seus contra-íons por eletroforese capilar em detecção condutométrica sem contato (CE-C4D). 2013. 96 p. Dissertação (Mestrado em Química) - Programa de Pós-Graduação do Instituto de Química. Universidade Federal de Uberlândia, Uberlândia, 2013.
- [18] Penha RS, Santos CC, Cardoso JJF, Silva HAS, Santana SAA, Bezerra CWB. Casca de Arroz Quimicamente Tratada como Adsorvente de Baixo Custo para a Remoção de Íons Metálicos (Co²⁺ and Ni²⁺). *Rev. Virtual de Quím.* 2016;8:588-604.
- [19] Chaves TF, Zilvanir FQ, Souza NR, Girao JHS, Rodrigues EA. Uso da cinza da casca do arroz (CCA) obtida da geração de energia térmica como adsorvente de Zn(II) em soluções aquosas. *Quím. Nova* 2009:32,1378-1383.
- [20] Geankoplis CJ. Transport processes and separation process principles. 5th ed. New York: Pearson; 2018.

Kinetics, equilibrium and thermodynamics of the adsorption process of oxytetracycline in rice husk ash

Christhell A. Andrade^{a,b,c,*}, Nelson S. Oliveira^b, Judite S. Vieira^b, Luís Angel Zambrano-Intriago^a, Hipatia Delgado-Demera^d, Joan Manuel Rodríguez-Díaz^{a,e,f*}

^a Laboratorio de Análisis Químicos y Biotecnológicos. Universidad Técnica de Manabí, Portoviejo 130105, Ecuador.

^b Laboratory of Separation and Reaction Engineering-Laboratory of Catalysis and Materials (LSRE-LCM), School of Technology and Management (ESTG), Polytechnic Institute of Leiria, 2411-901 Leiria, Portugal

^c Facultad de Ciencias Zootécnicas. Universidad Técnica de Manabí, Chone 130101, Ecuador

^d Facultad de Ciencias Veterinarias. Universidad Técnica de Manabí, Portoviejo 130105, Ecuador

^e Facultad de Ciencias Matemáticas, Físicas y Químicas. Universidad Técnica de Manabí, Portoviejo 130105, Ecuador

^f Programa de Pós-graduação em Engenharia Química. Universidade Federal da Paraíba. João Pessoa - 58051-900, Brasil

Abstract

The rice husk ash (RHA) is an agricultural biomass that has aroused as a potential alternative adsorbent for the removal of organic compounds. This study aims to investigate the feasibility of using RHA for the adsorption of OTC from aqueous solution. Batch studies were performed to assess the influence of various parameters as adsorbent dose, initial concentration, contact time, temperature and initial pH on the removal of OTC by RHA. RHA was characterized finding heterogeneous fibrous and porous particles, constituted predominantly by silica. It was found that OTC removal is dependent of pH, being favored at acid pH values. The RHA capacity of adsorption is related to initial OTC concentration and contact time. OTC concentration decreased sharply in the first 150 minutes, reaching the equilibrium at 420 min for lower concentrations and 360 min for higher concentrations. Kinetic data followed the Bangham model indicating pore diffusion, which was not the only rate controlling step as found by the multilinearity shown in the Weber Morris plot. The equilibrium isotherms were analyzed for 298, 318 and 328 K. The maximum adsorption capacity at 298 K was 2.76 mg.g⁻¹, however, this value could increase when the temperature increases. The Sips and Redlich-Petterson isotherms were the models that better represented the data for OTC adsorption on RHA. The process was found to be endothermic with the change of enthalpy (ΔH°) and entropy (ΔS°) being 20.55 kJ.mol⁻¹ and 185.90 J.mol⁻¹ respectively. The value of change in Gibbs free energy (ΔG°) was negative and decreased with temperature, indicating a feasible and spontaneous process.

Keywords: Oxytetracycline; Rice husk ash; Adsorption

1. Introduction

Antibiotics are widely used in human and veterinary medicine, but also as a feed supplement to promote growth in livestock and aquaculture industry. Oxytetracycline (OTC) is among the most used antibiotics worldwide [1]. It has been reported that 50-80% of OTC cannot be adsorbed and is

discharged unmetabolized via feces and urine [2-4]. The continuous input of OTC into water inhibits its self-depuration, moreover, it results in antibiotic-resistance and may be toxic for animals and humans, causing allergies and intoxications.

Oxytetracycline is difficult to remove from water due to its high solubility, its ability to form complexes with other species and its ionic state pH dependence [5]. Various methods have been used

for OTC removal, including ozonation, electrochemical processes, membrane technologies, and advanced oxidation processes [6]. Although these methods may be efficient, are usually expensive and could produce intermediate products that are even more toxic than the original compound [7, 8]. Adsorption has aroused as an attractive option for emerging pollutants removal because its high removal efficiency, low initial costs and simplicity [6, 9]. There is a global need for the development of low cost and easy accessibility adsorbent materials, therefore, agricultural biomasses are being studied for the removal of pollutants at different operating conditions.

Rice is the third biggest crop worldwide [10]. Approximately 20 % of the net weight of rice corresponds to its husk, which is considered a residue and its disposal constitutes an environmental problem.

The rice husks are composed of cellulose, hemicellulose, lignin and mineral ash (20%), which has a high content of silica (96.34%) [11]. This composition has positioned this biomass and its ashes as a potential low cost adsorbent. The aim of this study is to assess the behavior and feasibility of the adsorption of OTC in aqueous matrices onto raw rice husk ash (RHA) and investigate the influences of different conditions such as pH, contact time, initial concentration and temperature on the adsorption efficiency.

2. Materials and Methods

2.1 Materials and reagents

Oxytetracycline hydrochloride (OTC) used for the experiments was of an analytical grade and was obtained from Sigma Aldrich (USA). The chemical structure and pKa values of oxytetracycline are shown in Fig. 1. Solvents, including methanol, acetonitrile and formic acid, were of an HPLC grade (Merck). The NaOH and HCl used were of an analytical grade (Merck). The ultrapure water was obtained using Thermo Scientific Barnstead EasyPure II equipment. The rice husk ash (RHA) used in this study, was obtained from the “Charapotó” rice mill in Manabí, Ecuador and was collected at particular time intervals throughout the rice season.

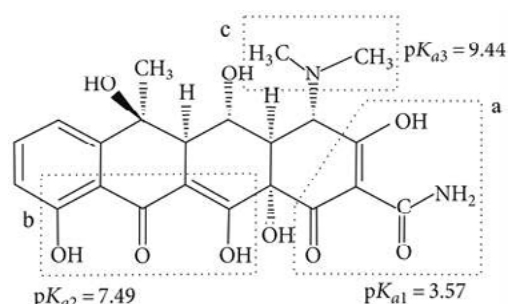


Fig. 1. Chemical structure of oxytetracycline and pKa values [3]

2.2 Analytical method

The quantification of OTC was carried out by High Performance Liquid Chromatography (HPLC), using a Thermo Accela chromatograph equipped with an automatic injector, a quaternary pump and a UV-VIS photodiode array detector (PDA). The analyses were performed with a C18 column, model 25005-104630 (5 μ m, 100 mm x 4.6 mm), with an injection volume of 10 μ L, at 25°C. A binary mobile phase composed by a mixture of acetonitrile and acidified water (pH 2, Formic Acid) (80:20, v:v) was used, at a constant flow rate of 0.900 ml min⁻¹. The detection was carried out at 350 nm. The retention time was 2.18 min.

2.3 Adsorbent characterization

The particle size of the RHA was determined by granulometry using a sieve column (Humboldt Standard) with sieve standard sizes of 12, 16, 20, 30, 40, 50, 100 and 200. Morphological characteristics of RHA were determined through scanning electron microscopy coupled with energy-dispersive X-ray spectroscopy SEM/EDX (Quanta 400FEG ESEM/EDAX Genesis X4M). The surface functional groups before and after adsorption were identified by the attenuated total reflectance (ATR) technique, in the wavelength range from 4000 to 400 cm⁻¹, using a Thermo Nicolet FT-IR. The RHA surface was characterized by the point of zero charge (pH_{pzc}), which is the pH at which the sorbent surface charge has zero value. The pH_{pzc} was determined by shaking 0.1 g of RHA in contact with modified pH distilled water at 300 rpm [12]. After 24 hours the solution was filtered with paper filter and pH was measured to plot the variation of pH (pH_{final} - pH_{initial}) vs pH_{initial}, where the intersection point with the x axis determines the point of zero charge pH_{pzc}. The pH was measured using a Fisher Scientific Accumet AB150 pHmeter.

2.4 Adsorption tests

Batch adsorption experiments were carried out to assess the effects of time, adsorbent dose, solution pH, initial concentration (20 – 160 mg.L⁻¹) and temperature. All the experiments were carried out by shaking 100 ml of OTC solution of the required concentration with a dose of RHA in a 250 ml Erlenmeyer flask wrapped up in aluminum foil to prevent photodegradation, using an orbital shaker (Thomas Scientific) at a speed of 300 rpm. After the predetermined contact time, the supernatant was filtered through 0.45 µm of polyvinylidene fluoride (PVDF) syringe filter and analyzed by HPLC. The amount of OTC adsorbed onto the RHA was determined using the following expressions:

$$q = \frac{(C_0 - C_t)V}{w} \quad (1)$$

$$\%R = \frac{(C_0 - C_t)}{C_0} \times 100 \quad (2)$$

where q (mg.g⁻¹) is the adsorption capacity of the system, C_0 (mg.L⁻¹) is the initial adsorbate concentration, C_t (mg.L⁻¹) is the adsorbate concentration at time t (min), V (ml) is the volume of solution and w (mg) is the mass of adsorbent. R is the percentage of removal.

2.5 Adsorption kinetics and equilibrium

The experimental data obtained were adjusted to non-linear models of adsorption kinetics and equilibrium using the Statistica 10.0 software. The kinetic models studied were pseudo-first order (PFO), pseudo-second order (PSO), Elovich, Bangham and Weber-Morris. The isotherms studied on the equilibrium tests were Langmuir, Freundlich, Toth, Redlich-Peterson and Sips.

2.6 Adsorption thermodynamics

The thermodynamic parameters, change of enthalpy (ΔH°), change of entropy (ΔS°) and Gibbs free energy (ΔG°), were calculated following the equations 3 and 4.

$$\Delta G^\circ = -RT \ln K_c \quad (3)$$

$$\ln K_c = -\frac{\Delta G^\circ}{RT} = \frac{\Delta S^\circ}{R} - \frac{\Delta H^\circ}{RT} \quad (4)$$

The K_c constant was obtained by multiplying the equilibrium constant by the molecular weight of

OTC and by 55.5 and 1000, as stated in Tran, et al. [13].

3. Results and Discussion

3.1 RHA characterization

Approximately 53% of the RHA consists of particles from 0.150 to 0.430 mm. The pH_{pzc} value of RHA was found to be 8. The microstructure of the RHA particles (Fig.1a) show a rectangular structure, curved inwards, with corrugated and spiky cuticles on the external surface. The internal surface of the particles has a heterogeneous fibrous and porous structure. The EDX spectrum (Fig.1b) shows that RHA is mainly composed of silica and oxygen, which are concentrated in the form of SiO₂ in the domed protuberances. The BET adsorption/desorption isotherms are classified as type IV, typical of mesoporous materials [14].

The infrared spectra of the RHA before and after OTC adsorption are shown in Fig.1c. Before the adsorption, the most prominent peaks correspond to the Si-O-Si (1051.26 cm⁻¹), Si-H (793.56 cm⁻¹) and Si-O (557.87 cm⁻¹) groups, which can be attributed to the high content of SiO₂ in the ashes, which is also evidenced by the EDX spectrum (Fig.1b). After the adsorption process new peaks corresponding to the groups -Si-OH, -OH, -CO- and -C-H appear. The displacement and increase in the peak at 3360.69 cm⁻¹ can be attributed to the stretching of the OH bond of the silanol group (Si-OH) and the water adsorbed on the surface of the RHA. The peak observed at 1621.86 cm⁻¹ may be caused by a stretching in the groups -C=O and -COH in aldehydes and ketones, related to electrostatic interactions [15]. The polar groups on the surface of the RHA confers the capacity of ionic adsorption and electrostatic interactions, and its stretching after adsorption indicates its participation in the process.

3.2 Adsorbent dose effect

The increase in the adsorbent dose improves the percentage of OTC removal. This can be attributed to the increase in the number of adsorption sites due to a greater mass which results in the increase of the RHA surface area. From 1.6 g, the percentage of removal is virtually constant, therefore, this was chosen as the optimal dose.

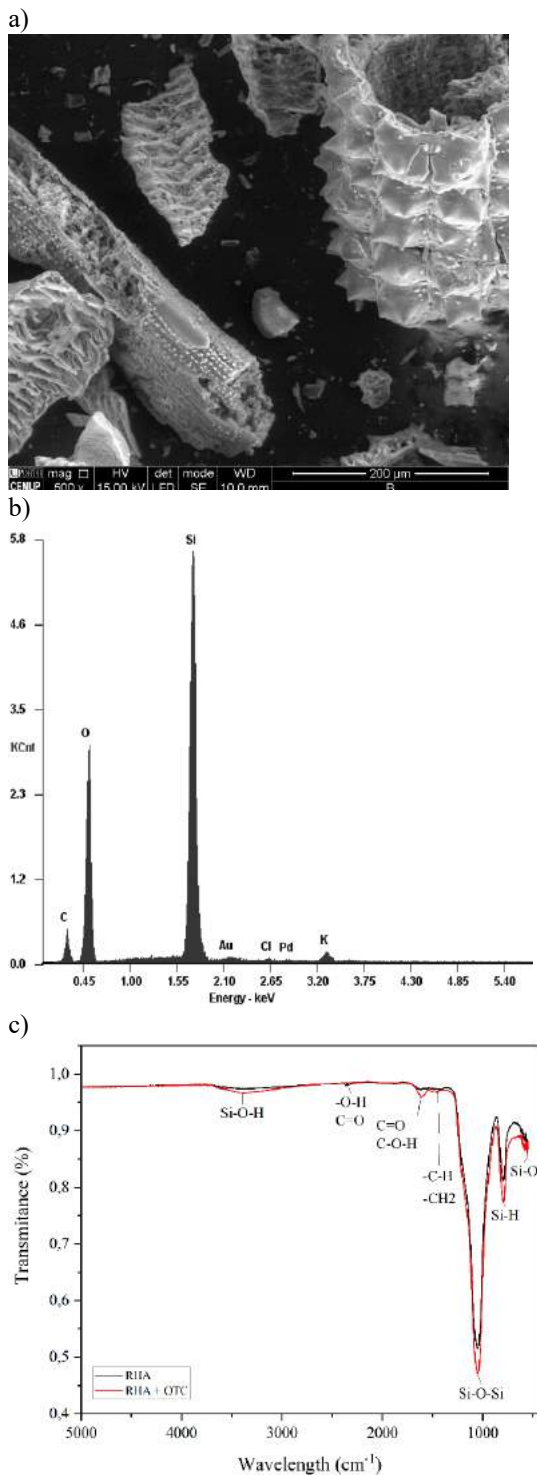


Fig. 2. Characterization of the adsorbent RHA (a) SEM of the RHA before adsorption; (b) Z1 point EDX spectrum; (c) FTIR spectroscopy of RHA before and after the OTC adsorption process

3.3 pH solution effect

The highest adsorption capacity was observed for acidic pH, attaining the highest efficiency at pH 6 and 4 (pKa₂). An increase in pH up to 8 and 10 (pKa₃) causes a significant decrease in the adsorption capacity.

When the OTC is at a pH lower than its pKa₁ (pH < 3.5), there is a predominance of positive charges (OTCH⁺). In the case of a solution pH < pH_{pzc}, the surface of the adsorbent is positively charged. Since the pH_{pzc} of the RHA is 8, and for OTC solution pH < 3.5, both OTC and the RHA are positively charged. Potential electrostatic attractions are depleted between the surface of the OTC and the RHA, giving rise to a possible cation exchange mechanism. For pH 4 and 6, values between pKa₁ and pKa₂, OTC is in the form of zwitterion, with a predominantly neutral charge (OTC[±]). At these values, the pH < pH_{pzc} of the RHA (predominance of positive charges in the adsorbent) may lead to the existence of electrostatic attractions, this being the possible majority mechanism. For pH values (8 and 10) greater than pKa₂ (7.49), OTC has a predominance of negative charges (OTC[±] and OTC⁻), being the pH_{pzc} (RHA) < pH (OTC), signifying that the surface charge of the adsorbent would, therefore, be mostly negative.

The presence of negative charges in both the adsorbent and in the adsorbate favors the electrostatic repulsion, thus disfavoring the adsorption process, which explains the decrease in the adsorption capacity of RHA. In addition, the presence of hydroxyl ions generates a competition with the OTC anion for the adsorption sites, which prevents the access of the OTC [6].

Since the original pH of OTC solutions is near the optimum pH, all the subsequent experiments were performed without modifying the pH values.

3.4 Contact time effect

The OTC concentration decreases rapidly during the first 150 minutes, followed by a gradual decrease, until reaching equilibrium at 420 minutes for lower concentrations (40 – 80 mg.L⁻¹) and 360 minutes for higher concentrations (100 – 160 mg.L⁻¹).

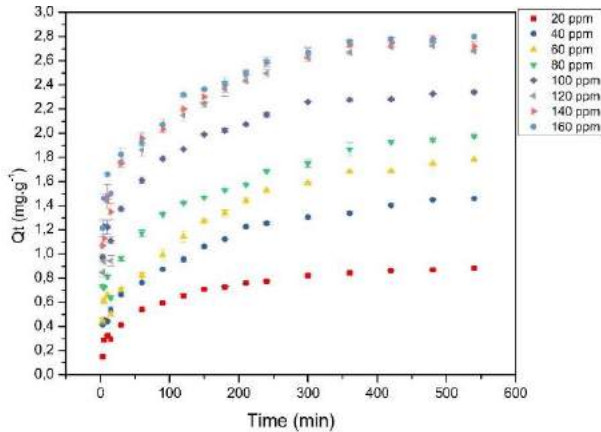


Fig. 3. Adsorption capacity of OTC onto RHA for different concentrations and contact times ($w = 1.6$ g, $V = 100$ ml, $T = 298$ K).

3.5 Adsorption kinetics

The experimental data was well fitted by the Bangham and Elovich models (Fig.3), with a high determination coefficient (R^2) (0.9565-0.9851) and a low chi-square (χ^2) (0.0357-0.4822) values. The Bangham rate constant (k_B) increases with the concentration, while the intensity of the adsorption (α) decreases. This behavior can be observed by the fact that shorter equilibrium times were obtained for higher concentrations, due to a higher rate of the process. The good fit observed with the Bangham model indicates that the adsorption process occurs by means of a pore diffusion mechanism. The adjustment to the Elovich model is related to the energy heterogeneity of the surface of the RHA [16]. The graphs of the Weber-Morris model for all the concentrations studied (Fig.4) indicate multilinearity (linearity in the three stages), besides, none of these stages projection passed through the origin. This experimental evidence indicates that intraparticle diffusion is not the only mechanism that controls the process, but that there are other mechanisms that occur simultaneously.

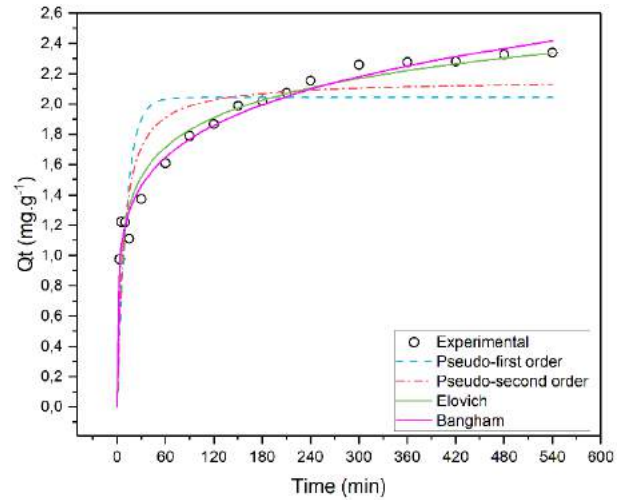


Fig. 4. Kinetic models fitted to experimental data PFO, PSO, Bangham and Elovich models ($C_0 = 100$ mg.L⁻¹, $w = 1.6$ g, $V = 100$ mL, $T = 298$ K)

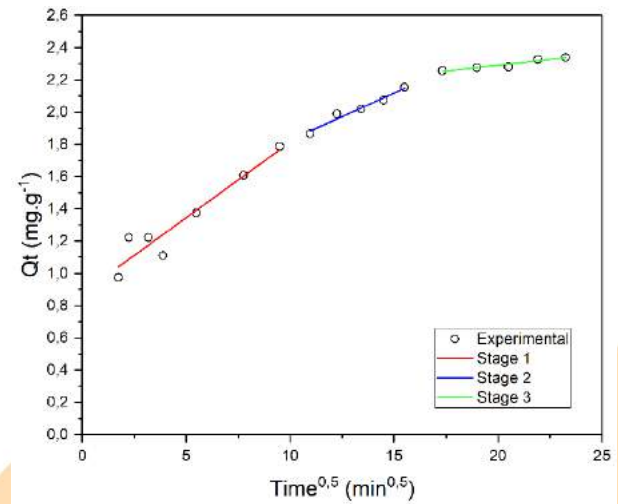


Fig. 5. Weber-Morris model. ($C_0 = 100$ mg.L⁻¹, $w = 1.6$ g, $V = 100$ ml, $T = 298$ K)

3.6 Adsorption isotherms

All the equilibrium models applied were adequately adjusted to the data for the three temperatures studied (Fig. 5).

The models that better represented the experimental data were the Sips and Redlich-Petterson (R-P) models, which had the highest R^2 and the lowest χ^2 . The adsorption equilibrium models proposed by the R-P and Sips models represent a hybrid isotherm between the Langmuir and Freundlich models. The K_{RP} adsorption

constant of the R-P model increases with temperature, suggesting the presence of an endothermic process, evidenced by the increase in the adsorption capacity of the process with temperature. The equilibrium parameters and the adjustment to the Sips isotherm (Fig. 5) have the same trend as the R-P model, in which the constant K_s increases with the temperature, indicating that the process is favored by a greater supply of energy.

The maximum adsorption capacity obtained at 298 K, 318 K and 328 K were 2.76, 2.99 and 4.67 $\text{mg}\cdot\text{g}^{-1}$ respectively. The Table 1 shows the adsorption capacity obtained for the removal of oxytetracycline using different adsorbents.

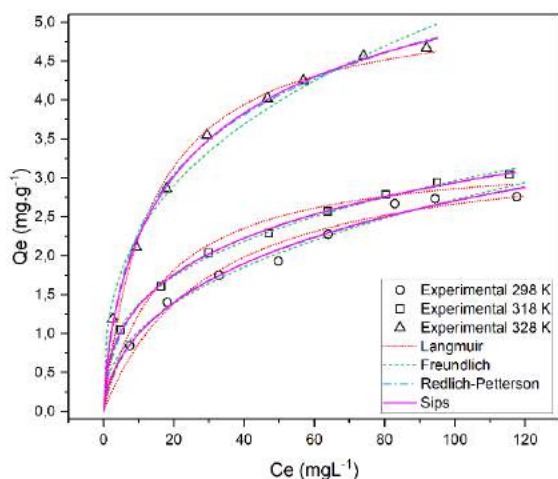


Fig.6. Temperature effect and isotherms fit

3.7 Adsorption thermodynamics

The ΔH° was $20.55 \text{ kJ}\cdot\text{mol}^{-1}$, which indicates an endothermic physical process ($\Delta H^\circ < 40 \text{ kJ}\cdot\text{mol}^{-1}$) [13]. A greater supply of energy can break the adsorbate-solvent bonds, thus decreasing the viscosity of the film surrounding the adsorbent and promoting the diffusion of the adsorbate to the adsorbent. As mentioned above, the temperature can dilate the pores of the RHA, allowing large molecules of OTC to enter in them. The positive values of ΔS° reflect the increase in the randomness in the solid liquid interface in the adsorption process with the increase in the temperature. This gives the species a greater degree of freedom and makes the process more stable, thus making it more irreversible. Negative values of ΔG° were obtained, and these decrease with the increase in temperature, which indicates a feasible and spontaneous process that improves with the supply of energy.

Table 1. Comparison of RHA adsorption capacity with other adsorbents

Adsorbent	[OTC] ₀ ($\text{mg}\cdot\text{L}^{-1}$)	q_e ($\text{mg}\cdot\text{g}^{-1}$)	References
Rice Husk Ash	160	2.76	This work
<i>Phaeodactylum tricornutum</i> microalga Living mass (Lm) and dead mass (Dm)	15	29.18 (Lm); 4.54 (Dm)	[17]
Willow residues roots (R) and desugared roots (DR)	10	0.464 (R) 1.175 (DR)	[18]
Powdered activated carbon (PAC)	5	0.247	[19]
Carbon from cotton linter fibers (CLAC)	530	738.5	[20]

Conclusions

Oxytetracycline can be removed from aqueous solutions using an agricultural residue such as rice husk ash. The adsorption process is endothermic and is favored at acid pH values. The maximum adsorption capacity for the removal of OTC using RHA is $2.76 \text{ mg}\cdot\text{g}^{-1}$ at 298 K but it can increase to $4.67 \text{ mg}\cdot\text{g}^{-1}$ if the temperature increases to 328 K. The process is well described by the Bangham model which evidences a pore adsorption mechanism that may occur due to ion exchange or electrostatic interactions between the OTC and the RHA surface, which is mainly composed of silica.

Acknowledgements

The authors would like to acknowledge the Secretaría Nacional de Educación Superior, Ciencia y Tecnología del Ecuador (SENESCYT) and Universidad Técnica de Manabí for the financial support granted for this work.

References

- [1] N. Ratasuk, M. Boonsaner, and D. W. Hawker, "Effect of temperature, pH and illumination on abiotic degradation of oxytetracycline in sterilized swine manure," *Journal of Environmental Science and Health, Part A*, vol. 47, pp. 1687-1694, 2012.
- [2] Y. Zhao, X. Gu, S. Li, R. Han, and G. Wang, "Insights into tetracycline adsorption onto kaolinite and montmorillonite: experiments and modeling," *Environmental Science and Pollution Research*, vol. 22, pp. 17031-17040, 2015/11/01 2015.
- [3] D.-H. Cheng, S.-K. Yang, Y. Zhao, and J. Chen, "Adsorption Behaviors of Oxytetracycline onto Sediment in the Weihe River, Shaanxi, China," *Journal of Chemistry*, vol. 2013, 2013.
- [4] W. Kong, C. Li, J. M. Dolhi, S. Li, J. He, and M. Qiao, "Characteristics of oxytetracycline sorption and potential bioavailability in soils with various physical-chemical properties," *Chemosphere*, vol. 87, pp. 542-548, 2012/04/01/ 2012.
- [5] M. J. Ahmed, "Adsorption of quinolone, tetracycline, and penicillin antibiotics from aqueous solution using activated carbons: Review," *Environmental Toxicology and Pharmacology*, vol. 50, pp. 1-10, 2017/03/01/ 2017.
- [6] M. Malakootian, S. Bahraini, and M. Zarrabi, "Removal of tetracycline antibiotic from aqueous solutions using modified pumice with magnesium chloride," *Jentashapir J. Health Res.*, p. e37583, 2016.
- [7] M. B. Ahmed, J. L. Zhou, H. H. Ngo, and W. Guo, "Adsorptive removal of antibiotics from water and wastewater: Progress and challenges," *Science of The Total Environment*, vol. 532, pp. 112-126, 2015/11/01/ 2015.
- [8] R. Li, Y. Jia, J. Wu, and Q. Zhen, "Photocatalytic degradation and pathway of oxytetracycline in aqueous solution by Fe₂O₃-TiO₂ nanopowder," *Rsc Advances*, vol. 5, pp. 40764-40771, 2015.
- [9] S. Priya and K. Radha, "Equilibrium, isotherm, kinetic and thermodynamic adsorption studies of tetracycline hydrochloride onto commercial grade granular activated carbon," *Int. J. Pharm. Pharm. Sci*, vol. 7, pp. 42-51, 2015.
- [10] K. Y. Foo and B. H. Hameed, "Utilization of rice husk ash as novel adsorbent: a judicious recycling of the colloidal agricultural waste," *Adv Colloid Interface Sci*, vol. 152, pp. 39-47, Nov 30 2009.
- [11] M. Ahmaruzzaman and V. K. Gupta, "Rice husk and its ash as low-cost adsorbents in water and wastewater treatment," *Industrial & Engineering Chemistry Research*, vol. 50, pp. 13589-13613, 2011.
- [12] E. Cristiano, Y.-J. Hu, M. Siegfried, D. Kaplan, and H. Nitsche, "A comparison of point of zero charge measurement methodology," *Clays and Clay Minerals*, vol. 59, pp. 107-115, 2011.
- [13] H. N. Tran, S.-J. You, and H.-P. Chao, "Thermodynamic parameters of cadmium adsorption onto orange peel calculated from various methods: A comparison study," *Journal of Environmental Chemical Engineering*, vol. 4, pp. 2671-2682, 2016/09/01/ 2016.
- [14] S. Brunauer, L. S. Deming, W. E. Deming, and E. Teller, "On a Theory of the van der Waals Adsorption of Gases," *Journal of the American Chemical Society*, vol. 62, pp. 1723-1732, 1940/07/06 1940.
- [15] V. C. Srivastava, I. D. Mall, and I. M. Mishra, "Characterization of mesoporous rice husk ash (RHA) and adsorption kinetics of metal ions from aqueous solution onto RHA," *Journal of Hazardous Materials*, vol. 134, pp. 257-267, 2006/06/30/ 2006.
- [16] Z. Yaneva, B. Koumanova, and S. Allen, "Applicability comparison of different kinetic/diffusion models for 4-nitrophenol sorption on *Rhizopus oryzae* dead biomass," *Bulgarian Chemical Communications*, vol. 45, pp. 161-168, 2013.
- [17] S. Santaefemia, E. Torres, R. Mera, and J. Abalde, "Bioremediation of oxytetracycline in seawater by living and dead biomass of the microalga *Phaeodactylum tricornutum*,"

- Journal of hazardous materials*, vol. 320, pp. 315-325, 2016.
- [18] D. Wang, H. Xu, S. Yang, W. Wang, and Y. Wang, "Adsorption Property and Mechanism of Oxytetracycline onto Willow Residues," *International Journal of Environmental Research and Public Health*, vol. 15, p. 8, 2018.
- [19] X. Zhang, W. Guo, H. H. Ngo, H. Wen, N. Li, and W. Wu, "Performance evaluation of powdered activated carbon for removing 28 types of antibiotics from water," *Journal of Environmental Management*, vol. 172, pp. 193-200, 2016/05/01/ 2016.
- [20] Y. Sun, Q. Yue, B. Gao, Q. Li, L. Huang, F. Yao, *et al.*, "Preparation of activated carbon derived from cotton linter fibers by fused NaOH activation and its application for oxytetracycline (OTC) adsorption," *Journal of Colloid and Interface Science*, vol. 368, pp. 521-527, 2012/02/15/ 2012.

Mathematical modeling of paracetamol adsorption on activated carbon

Aline Estevam Carvalho^a, Juli Emille Pereira de Melo^b, Wendy de Oliveira Nunes^b, Kleide Dayana Oliveira Mendes^b, Francisco Victor Marinho Fernandes^b, Rafael Magalhães Siqueira^a, Francisco Wilton Miranda da Silva^b, Rafael Barbosa Rios^b

^a Grupo de Pesquisa em Separações por Adsorção – GPSA, Departamento de Engenharia Química, Universidade Federal do Ceará, Campus do Pici, Bl. 709, 60455-760 Fortaleza, CE, Brazil

^b Grupo de Estudos em Termodinâmica, Adsorção e Bioprocessos – GETAB, Departamento de Engenharia e Tecnologia, Universidade Federal Rural do Semi-Árido, 59625-900, Mossoró, RN, Brazil

Abstract

The removal of paracetamol from concentrated aqueous solution (0.1 kg/m³) has been studied in fixed-bed column using as adsorbent a commercial activated carbon WV1050. Langmuir model has been used to describe the adsorption isotherm, considering its fit and the pH solution. To evaluate the mass transfer phenomena involved in the adsorptive process, a simulated breakthrough curve was predicted according to the suggested pseudo-homogeneous and one-dimensional mathematical model, which was implemented in gProms®. The model takes into account the dispersive and convective effects. Also, the micropore resistance into the particle was considered and it was mathematically described by the Linear Drive Force (LDF) model. To validate the model, an experimental breakthrough curve was obtained and compared with the simulated one. The results show that the mathematical model fits to the system. The breakpoint occurred in less than one minute, with a shape breakthrough curve suggesting a significant mass transfer zone and a high saturation time.

Keywords: acetaminophen; adsorption; mathematical model; LDF model.

1. Introduction

Paracetamol or acetaminophen is a common drug used in a diversity of pharmaceutical procedures as an analgesic and antipyretic [1]. As a lot of other pharmaceutical compounds (PC's), this one has been daily discarded directly in the environment, causing wastewater contamination as this contaminant is biologically active [2-5].

In the conventional wastewater treatment plants, the paracetamol it is not completely removed from water. Consequently, the presence of this drug in the reuse water can cause serious health problems due to its activity, requiring new treatment technologies for water decontamination before its reutilization [1,3].

In this scenario, the adsorption with activated carbon (AC) is a promising technique mainly carried out in fixed bed columns [6] to remove pharmaceutical contaminants from water [3], [7-9]. Considering this, the present work aims to

implement a suitable mathematical model and validate it from experimental data that accurately describe the adsorption dynamics of paracetamol removal using a commercial activated carbon.

2. Fixed Bed Adsorption Experimental Measurements

The adsorption of paracetamol on activated carbon WV1050 (MeadWestvaco, USA) was studied in a continuous fixed bed column. Activated carbon used has a specific surface area of 1615 m² g⁻¹, a micropore volume of 0.59 cm³ g⁻¹ and a total volume of 1.10 cm³ g⁻¹ [10]. The specific volume of the adsorbent, measured in the magnetic suspension balance, is 0.573 cm³ [10].

The model C 16/20 glass column (GE Healthcare, USA) used in the experiment has an inner diameter of 0.016 m, an outer diameter of 0.020 m and a total length of 0.20 m. The AC WV1050 was sieved and selected from 10 to 18 mesh sieves. The column was filled with 1.90x10⁻³

kg of these activated carbon regenerated, which led to a bed length of 0.04 m. In addition to the filters at the ends of the column, cotton was placed to prevent smaller particles of sample from leaving the column through the filter mesh. The pump used for pumping the solution was of the BP-200D dosing type and provided a flow rate of $1.67 \times 10^{-7} \text{ m}^3/\text{s}$.

Paracetamol solution was prepared at pH 2.0 and at a concentration of 0.1 kg/m^3 . This pH value was adopted based on previous work [11], where it was observed that such condition would be the most favorable for paracetamol adsorption on AC WV1050.

The fixed bed system, including the feed solution, was maintained at a temperature of 303.15 K from a SL-222 shaker incubator. The column bed, containing the activated carbon previously regenerated at 393.15 K, was washed for 20 min with Milli-Q water, before the paracetamol solution was injected. After feeding the drug solution into the column, aliquots of this solution collected at the column outlet were analyzed on a UV-340G spectrophotometer (Gehaka, Brazil), and the respective collection times of these aliquots were recorded. The experiment was conducted until to reach bed saturation, observed when the outlet concentration was equal to the inlet concentration.

3. Breakthrough Curves Simulation

Mathematical simulation models are used to estimate and describe the behavior of adsorption processes in a fixed bed reactor. These models can predict the breakthrough curves and provide information about the transport phenomena and effects of various process parameters.

3.1. Model assumptions

A model that considers axial dispersion, uniform fluid concentration and constant axial velocity has been used in this work. The fixed bed was operated under isothermal conditions and the radial dependence of the adsorbate concentration was neglected. The particles are considered spherical and homogenous.

Based on these assumptions, the model was described by a set of differential equations which involves the transient, convective, dispersive and adsorptive effects.

3.2. Mass balance for the fluid phase

The mass balance for the fluid phase is given by Eq. (1) in function of time t (s) and bed length z (m) [12]:

$$\epsilon_b \frac{\partial C}{\partial t} + v_0 \frac{\partial C}{\partial z} - D_{ax} \frac{\partial^2 C}{\partial z^2} + \rho_b \frac{\partial q}{\partial t} = 0 \quad (1)$$

In Eq (1), D_{ax} represents the axial dispersion coefficient (m^2/s), v_0 is the axial velocity (m/s), C is the bulk concentration (mol/m^3), ρ_b and ϵ_b are the density (kg/m^3) and the porosity of the bed, respectively, and q is the average adsorbed concentration per unit mass of solid (mol/kg).

3.2.1. Mass balance for the solid

The last term in Eq (1) is the average amount of paracetamol adsorbed due to the mass transfer between the bulk and the solid particles. The mass balance for the solid particles is given by *Linear Drive Force (LDF)* model [13], according to Eq (2):

$$\frac{\partial q}{\partial t} = K_{LDF} \cdot (q_{eq} - q) \quad (2)$$

where K_{LDF} is the LDF coefficient and q_{eq} is the adsorbed concentration in equilibrium (mol/kg).

3.3. Boundary and initial conditions

The following boundary and initial conditions were considered [14]:

For $z = 0$,

$$C_e = C_{(0,t)} - \left(\frac{D_{ax}}{v_0} \cdot \frac{\partial C}{\partial z} \right) \quad (2)$$

For $z = L$,

$$\frac{\partial C}{\partial z} = 0 \quad (3)$$

and

$$C(z, 0) = 0; \quad (0 < z < L) \quad (4)$$

$$q(z) = 0; \quad (0 \leq z \leq L) \quad (5)$$

3.4. Adsorption Equilibrium

The Langmuir model, Eq (9), was adopted to describe the data of the paracetamol solution adsorption isotherm at 303.15 K and pH 2.0 on the AC WV1050, obtained in a previous work [11], since it is a simple model and generally has good results.

$$q_{eq} = \frac{(q_m \cdot K_{eq} \cdot C)}{(1 + K_{eq} \cdot C)} \quad (6)$$

where q_m is the maximum adsorbate capacity ($\text{mol} \cdot \text{kg}^{-1}$) and K_{eq} is the equilibrium constant ($\text{m}^3 \cdot \text{kg}^{-1}$).

3.5. Parameters

The K_{LDF} was estimated adjusting the breakthrough simulated curve with the experimental data. The axial dispersion coefficient D_{ax} was calculated according to Eq (10) [12]:

$$D_{ax} = \frac{v_0 \cdot d_p}{(0.2 + 0.011 \text{Re}^{0.48})} \quad (7)$$

where d_p represents the particle diameter and Re is the Reynolds number.

4. Results and Discussion

4.1. Adsorption Isotherm Parameters

The Langmuir model was fitted to the adsorption isotherm data, where a good fit was observed. The paracetamol adsorption isotherm at 303.15 K and its Langmuir fit is show in Figure 1.

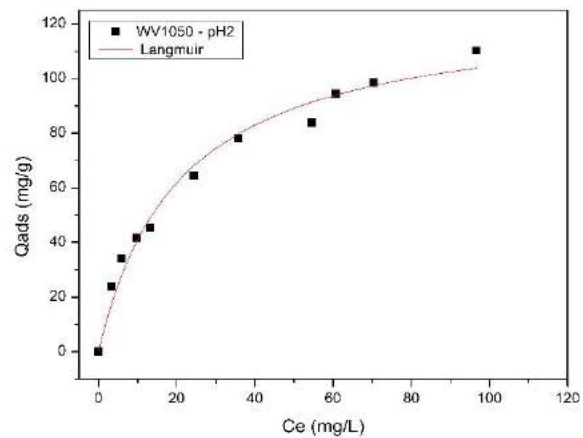


Fig 1. Paracetamol adsorption isotherm at 303.15 K and its Langmuir fit.

The parameters of the Langmuir isotherm model are presented in Table 1.

Table 1. Isotherm parameters.

q_m ($\text{mol} \cdot \text{kg}^{-1}$)	K_{eq} ($\text{m}^3 \cdot \text{kg}^{-1}$)	R^2
0.8315	7.2437	0.98109

4.2. Model Parameters

The parameter K_{LDF} was obtained according to the simulated curve adjustment from the experimental data. Since it was not possible to measure it experimentally, the parameter was estimated by simulation on software gProms® using a maximum likelihood objective function. Table 2 shows all the parameters obtained and considered for simulation.

Table 2. Model parameters.

K_{LDF}	D_{ax} m^2/s	ϵ_b
7.4238×10^{-5}	2.85×10^{-6}	0.61

4.3. Breakthrough curves

To evaluate the continuous adsorption of paracetamol in fixed bed column, the results of an experimental and simulated breakthrough curve were plotted as shown in Figure 2 in order to validate the mathematical model used.

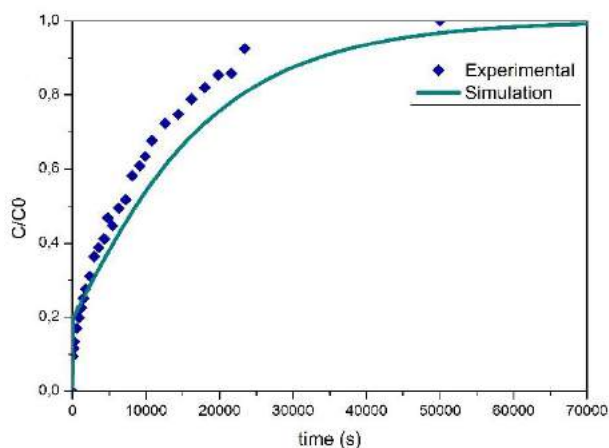


Fig. 2. Experimental and simulated breakthrough curves for paracetamol adsorption on activated carbon WV1050.

The curve has a dispersed shape, which is a characteristic of a higher mass transfer resistance. The shape of the curve resembles another work in literature [15] under similar conditions.

The almost instantaneous breakpoint can be justified by the short residence time of paracetamol molecules within the fixed bed column. This is explained by the short bed length associated with high feed flow and high resistance to mass transfer, which control the permanence of the drug within the column. Consequently, paracetamol does not have enough time to diffuse into the pores of the adsorbent, leaving the column earlier [12]. It is noteworthy that the inlet concentration will basically influence the stoichiometric time.

Column saturation time occurred at approximately 60×10^3 seconds. Comparing to other drugs, such as atenolol and ampicillin, paracetamol had higher affinity and adsorption capacity with activated carbons, which leads to a longer column saturation time [16]. This behavior can be noticed in similar studies of paracetamol adsorption on granular activated carbon, with saturation times about 10^5 seconds [7] at operating conditions similar to this work.

It may also be noticed that the mathematical model reproduced quite well the experimental data. The estimated K_{LDF} is in the same order of magnitude as shown in literature for AC, considering the temperature range of 288.15 K–308.15 K [6]. The discrepancy between the simulated and experimental curves could be justified by the equipment limitation, since it was necessary to collect several aliquots to have enough quantity for analysis in the spectrophotometer.

5. Conclusion

Removal of paracetamol from aqueous solution using a commercial activated carbon has been studied using an experimental and simulated continuous flow column adsorption. The suggested mathematical model using the concept of linear drive force shows that it can be obtained a reasonable predict of the fixed bed behavior.

Based on the operating conditions, the breakthrough curves demonstrate the influence of the mass transfer resistance in the adsorptive process and give information about process parameters, like saturation time of the column and breakpoint time.

Acknowledgements

We gratefully thank Petrobras and Centro de Pesquisas e Desenvolvimento Leopoldo Américo Miguez de Mello (Cenpes) for financial support.

References

- [1] V. Bernal, A. Erto, L. Giraldo, and J. C. Moreno-Piraján, "Effect of solution pH on the adsorption of paracetamol on chemically modified activated carbons," *Molecules*, vol. 22, no. 7, pp. 1–14, 2017.
- [2] M. Beretta, V. Britto, T. M. Tavares, S. Maria, and A. L. Pletsch, "Occurrence of pharmaceutical and personal care products (PPCPs) in marine sediments in the Todos os Santos Bay and the north coast of Salvador, Bahia, Brazil," pp. 1278–1286, 2014.
- [3] I. Cabrita, B. Ruiz, A. S. Mestre, I. M. Fonseca, A. P. Carvalho, and C. O. Ania, "Removal of an analgesic using activated carbons prepared from urban and industrial residues," *Chem. Eng. J.*, vol. 163, no. 3, pp. 249–255, 2010.
- [4] S. K. Behera, H. W. Kim, J. Oh, and H. Park, "Occurrence and removal of antibiotics, hormones and several other pharmaceuticals in wastewater treatment plants of the largest industrial city of Korea," *Sci. Total Environ.*, vol. 409, no. 20, pp. 4351–4360, 2011.
- [5] M. Saif *et al.*, "Chemosphere Global risk of pharmaceutical contamination from highly populated developing countries," *Chemosphere*, 2013.
- [6] F. J. García-Mateos, R. Ruiz-Rosas, M. D. Marqués, L. M. Cotoruelo, J. Rodríguez-Mirasol, and T. Cordero, "Removal of paracetamol on biomass-derived activated carbon: Modeling the



- fixed bed breakthrough curves using batch adsorption experiments,” *Chem. Eng. J.*, vol. 279, pp. 18–30, 2015.
- [7] L. Yanyan *et al.*, “Removal of acetaminophen from synthetic wastewater in a fixed-bed column adsorption using low-cost coconut shell waste pretreated with NaOH, HNO₃, ozone, and/or chitosan,” *J. Environ. Manage.*, vol. 226, no. August, pp. 365–376, 2018.
- [8] A. Macías-García, J. García-Sanz-Calcedo, J. P. Carrasco-Amador, and R. Segura-Cruz, “Adsorption of paracetamol in hospital wastewater through activated carbon filters,” *Sustain.*, vol. 11, no. 9, pp. 1–11, 2019.
- [9] E. E. Chang, J. C. Wan, H. Kim, C. H. Liang, Y. D. Dai, and P. C. Chiang, “Adsorption of selected pharmaceutical compounds onto activated carbon in dilute aqueous solutions exemplified by acetaminophen, diclofenac, and sulfamethoxazole,” *Sci. World J.*, vol. 2015, 2015.
- [10] R. B. Rios *et al.*, “Evaluation of carbon dioxide–nitrogen separation through fixed bed measurements and simulations,” *Adsorption*, vol. 20, no. 8, pp. 945–957, 2014.
- [11] N. M. Conrado, M. R. de S. Cavalcante, and F. W. M. da Silva, “Remoção de paracetamol de solução aquosa em carbono ativado.” pp. 1–11, 2019.
- [12] M. J. Quina, L. M. Gando-ferreira, and A. L. Arim, “Experimental and mathematical modelling of Cr (III) sorption in fixed-bed column using modified pine bark,” vol. 183, pp. 272–281, 2018.
- [13] J. I. Glueckauf, E. Coates, “Theory of Chromatography. Part 10 - Formulae for diffusion into spheres and their application to chromatography,” *J. Chem. Soc.*, pp. 1315–1321, 1955.
- [14] A. Hethnawi, N. N. Nassar, A. D. Manasrah, and G. Vitale, “Polyethylenimine-functionalized pyroxene nanoparticles embedded on Diatomite for adsorptive removal of dye from textile wastewater in a fixed-bed column,” *Chem. Eng. J.*, vol. 320, pp. 389–404, 2017.
- [15] M. O. W. Rheinheimer, “Remoção de paracetamol por adsorção em carvão ativado: Processo em Batelada e Coluna de Leito Fixo,” 2016.
- [16] N. K. Haro, “Remoção dos fármacos Atenolol, Paracetamol e Ampicilina por adsorção em carvão ativado,” p. 131, 2017.

Green synthesis of metallic nanoparticles impregnated on carbon nanotubes for glyphosate removal from aqueous matrix

Júlia Cristina Diel^a, Hercules Abie Pereira^a, Dison S. P Franco^a, Isaac dos Santos Nunes^a, Matias Schadeck Netto^a, Edson L. Foletto^a, Guilherme Luiz Dotto^{a*}

^aFederal University of Santa Maria, Roraima Avenue n° 1000, Santa Maria, 97105-900, Brazil

Abstract

The agricultural defensives based on glyphosate, a pesticide applied for the control of weeds, are the most used in Brazil and around the world. The large and uncontrolled application of glyphosate, as well its residues, is one of greatest environmental problems. In the present work, it was investigated the glyphosate removal from aqueous matrix, using functionalized carbon nanotubes (CNTs) impregnated with metallic nanoparticles. The CNTs were modified via green synthesis for the impregnation of metallic nanoparticles, using the reducing agents pomegranate leaf (*Punica granatum*), eucalyptus leaf (*eucalyptus*) and nutshell (*Carya illinoensis*), in the presence of copper and iron salts. The adsorbents characterization indicated that the CNT structure was maintained after the green synthesis. All the materials presented similar FT-IR trends, with the exception of the CNT with nutshell extract with iron (CNT-COOH3). Last, the adsorbents have been tested with success in the glyphosate removal. The CNT-COOH3 was the best adsorbent, presenting an adsorption capacity of 21.17 mg g⁻¹ with glyphosate removal of 84.08%.

Keywords: Glyphosate, adsorption, green synthesis

1. Introduction

A recent estimative indicated that 4.31 kg of agricultural defensives are used per hectare in Brazil [1], which is one of the world's leading agricultural produces. The Rio Grande do Sul state, in turn, is responsible for this estimative, since produce 12.4% of the crops in Brazil [2]. The agricultural defensives based on glyphosate are among the most commercialized and highly applied in the world, representing 35.51% of total sold on Brazil (195 thousand tons) [3]. Glyphosate is a non-selective pesticide and, when pulverized, penetrates into the plant cuticle by diffusion, being rapidly transported throughout the tissue [4]. The generalized use of glyphosate on the agricultural production leads to the contamination of the soils and hydric resources. This effect occurs due to

agricultural land runoff from the applied areas, and indiscriminate discharge of industrial wastewaters [5].

In Brazil, two normative establish the maximum glyphosate concentration on water samples. The first one is the CONAMA 325/2005 [6] that stipule maximum concentration of 0.065 mg L⁻¹ for Class 1 surface freshwater and 0.28 mg L⁻¹ for Class 2. Furthermore, the Ministry of Health rules [7] (n° 2914/2011) determinate the maximum glyphosate concentration on the water supply and drinking water as 0.5 mg L⁻¹. Taking into consideration the rigorous legislation and high consumption of glyphosate to ensure agricultural production on a large scale, the scientific community is working in viable and reliable methods for purifying the hydric resources. In this context, adsorption is highlighted as promisor technique, characterized by its flexibility, project simplicity, ease operation



and high efficiency [8]. In addition, the absence of secondary pollution and possibility of employing different materials is attractive [9].

A class of advanced materials for adsorption is the carbon nanotubes (CNTs), which are cylindrical structures with nanometer dimensions, obtained from graphene sheet winding [10]. CNTs present a high selectivity and adsorption capacity when adding different functional groups to its surface [11]. The impregnation of the metallic nanoparticle in the CNTs surface is one possibility; it can be achieved using green synthesis an environmental friendly methods. This method consists of a chemical reduction of metallic species along the CNTs surface, using extracts of different plants, polysaccharides and microorganisms [12, 13]. Plant-synthesized nanoparticles proved to be the best options because of their greater stability and viability of large-scale applications and the availability of materials. Different parts of plants such as leaves, roots, latex, seeds, bark, and stem can be used [14].

This work aimed the production of metallic nanoparticles impregnated on carbon nanotubes for glyphosate removal from aqueous matrix, using green synthesis with different plant extracts. Six adsorbents were developed, varying the type of CNTs, the vegetal extract and the metal type (Table 1). The materials were characterized and used for glyphosate removal from aqueous matrix.

2. Materials and Methods

2.1 Materials and chemicals

The multi-walled carbon nanotubes functionalized with OH and COOH were obtained from Nanostructured and Amorphous Materials. The glyphosate ($C_3H_8NO_5P$, CAS 1071-83-6, $\geq 98\%$), sodium molybdate ($MoNa_2O_4$, CAS 7631-95-0), and ninhydrin ($C_9H_6O_4$, CAS 485-47-2), all analytical grade reagents were acquired from Sigma Aldrich. Copper sulfate ($CuSO_4 \cdot 5H_2O$, CAS 7758-99-8, Alphatec, 98%) and iron sulfate ($FeSO_4 \cdot 7H_2O$, CAS 7782-63-0, Neon, 99.99%) were used for the metallic impregnation. All experiments were conducted using deionized water.

Pomegranate leaves (*Punica granatum*), eucalyptus leaves (*eucalyptus*) and nutshells (*Carya illinoensis*) were selected to be natural reducers. They were acquired in the region of Rio Grande do Sul state.

2.2 Green synthesis

The green synthesis was adapted from [15,16]. First, 60 g of the reducing agent was added to 1 L of deionized water at 80 °C. The mixture was agitated for 1 h using a magnetic agitator (Fisatom, 712, Brazil). After that, the solution was cooled at room temperature and vacuum filtered for separation of the solid material from the aqueous vegetal extract. Extract solutions were stored.

The metallic solutions were prepared using 1.5% in relation to the mass of each salt. These solutions were made using deionized water. Then the CNT functionalized with OH and COOH groups were added to the vegetal extract and to the metallic solutions of copper and iron, 2:1 proportions (40 mL of extract to 20 mL of metallic solutions). The mixtures were prepared using deionized water and agitated using shaker incubator with controlled temperature (Solar, SL-222, Brazil) at 25 °C and 160 rpm for 24 h. Last the solid material was separated through filtration and dried (Solar, SL-101, Brazil) at 50 °C for 24 h. The materials were stored for further use. The names and compositions of each adsorbent are presented in Table 1.

Table 1. Samples of adsorbents prepared from CNT metal impregnation.

Modified CNT	Vegetal extract	Metallic impregnation
CNT-OH1	pomegranate	Cu^{2+}
CNT-OH2	eucalyptus	Fe^{2+}
CNT-OH3	nutshell	Fe^{2+}
CNT-COOH1	pomegranate	Cu^{2+}
CNT-COOH2	eucalyptus	Fe^{2+}
CNT-COOH3	nutshell	Fe^{2+}

2.3 Adsorbent characterization

The CNTs were analyzed before and after the metallic impregnation by the following techniques: X-ray powder diffractometry (XRD) using a Rigaku model Miniflex 300 (Japan) operating with radiation of $Cu K\alpha$ ($\lambda = 1.54184 \text{ \AA}$) and energy source of 30 kV and 10 mA, for determinate the crystallinity phase of the materials; Fourier transformed infrared spectroscopy (FT-IR) was conducted for identifying the functional groups, for this was used a Shimadzu spectrum model Prestige 21 (Japan), operating using KBr tablets. For each sample 45 scans with a resolution of 2 cm^{-1} in the regions of 400 to 4500 cm^{-1} were performed.

2.4 Calibration curve and quantification

The glyphosate quantification followed the colorimetric methodology [17], consisting of the reaction of the ninhydrin and sodium molybdate. A stock solution of 50 mg L⁻¹ of glyphosate was diluted to 1, 5, 10, 15, 20, 25, 30, 35, 40 and 45 mg L⁻¹, and further added to 1 mL of ninhydrin (5% m/V) and 1 mL of sodium molybdate (5% m/V). After that, the test tubes were sealed and the mixtures were heated in a water bath at a temperature of 85 to 95 °C until a purple staining complex formed. Then, the samples were cooled at room temperature and further measured (λ_{\max} = 570 nm) using a spectrophotometer from Shimadzu, model UV-2600 (Japan). The blank test was also prepared with ninhydrin and sodium molybdate to ensure reproducibility.

2.5 Preliminary adsorption tests.

Adsorption tests were made to verify what adsorbent among the CNTs was the more adequate for glyphosate removal. 0.03 g of adsorbent was added to 20 mL of glyphosate solution, at natural pH (approximately 4), with initial concentration of 35 mg L⁻¹. The assays were conducted using shaker incubator (Solab, SL-222, Brazil) at 160 rpm for 2 h at 25 °C. Samples were collected and the liquid phase was separated through simple filtration from the solids. The determination followed the methodology previously described in section 2.4. The adsorbent evaluation was made through adsorption capacity (q_t) and efficiency of glyphosate removal (η %), here presented in Equation 1 and 2:

$$q_t = \frac{V(C_0 - C_t)}{m} \quad (1)$$

$$\eta = \frac{(C_0 - C_t)}{C_0} 100\% \quad (2)$$

where V is the solution volume (L), C₀ is the initial glyphosate concentration (mg L⁻¹), C_t is the glyphosate concentration measured in time (mg L⁻¹) and m is the adsorbent mass (g).

3. Results and Discussion

3.1 Characterization results

The XRD diffractogram for the CNTs before and after the green synthesis are presented in Fig. 1.

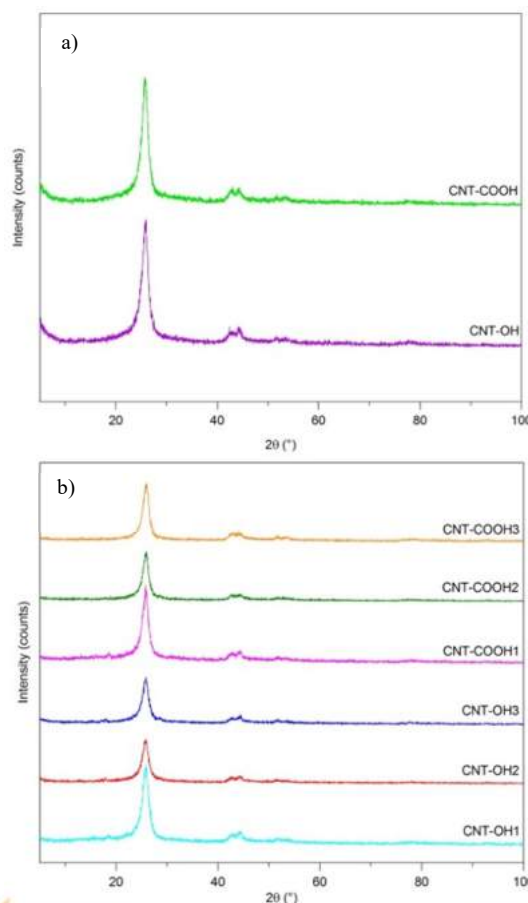


Fig. 1. Diffractogram for the (a) CNT functionalized with COOH and OH, and (b) CNT modified through the green synthesis.

From Fig. 1 (a) and (b) it is possible to observe the presence of diffraction peaks at 26 ° which are equivalent to the (0 0 2) graphite plane, characteristic of the amorphous carbon. The diffraction peak at 44 and 57 ° are correspondent to the graphite net (1 0 0) and (0 0 4), respectively [18]. When made the comparison of the diffractogram before and after the green synthesis, it is possible to observe that the peaks were not affected, indicating similar arrangements. This indicates that the structure of the material remains and no degradation was promoted.

The FTIR spectrum for the CNTs before and after the green synthesis is presented in Fig. 2.

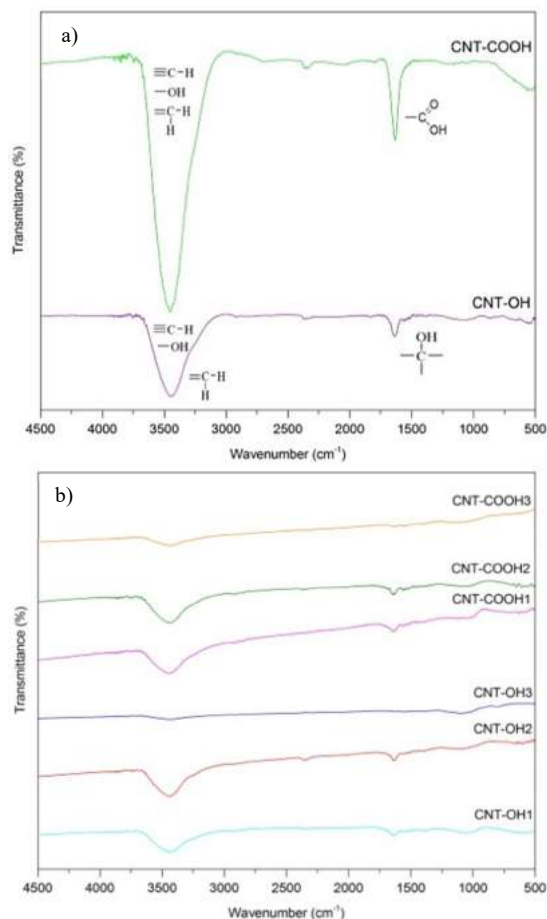


Fig. 2. FTIR spectra for the (a) CNT functionalized with COOH and OH, and (b) CNT modified through the green synthesis.

Fig. 2 (a) exhibits the spectra for the original commercial CNTs, functionalized with OH and COOH groups. In both cases it is possible to identify the following vibrations: $\equiv\text{C-H}$, $-\text{OH}$, $=\text{CH}_2$, with close vibrations. The difference between the COOH and OH bands can be related to the COOH repulsions, that tend to vibrate with higher frequency. Nevertheless, for both cases it was possible to identify the OH and COOH functional groups.

Fig. 2 (b) shows the modified CNT via green synthesis. From the comparison between the original CNTs and the modified ones (CNT-OH1, CNT-OH2, CNT-COOH1 e CNT-COOH2), it is possible to conclude that the material preserved its respective groups. However, less intensity was observed in the vibrations. On the other hand, for the CNT-OH3 and CNT-COOH3, obtained from a nutshell (*Carya illinoensis*) extract and iron

solution, it is possible to find out that the green synthesis caused a modification, probably breaking the $\text{C}\equiv\text{C}$ and $\text{C}=\text{C}$ bonds.

3.2 Preliminary adsorption assays

The adsorption capacity and efficiency of glyphosate removal for the modified CNTs are presented in Fig. 3.

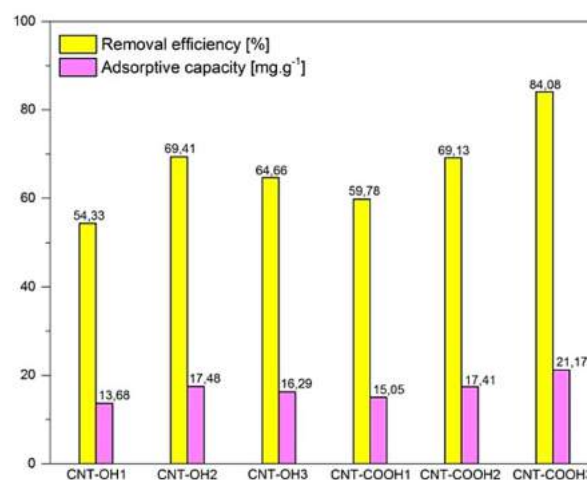


Fig. 3. Adsorption capacity and efficiency removal for the modified CNTs.

The results presented in Fig. 3 indicate that all the conditions of the green synthesis were favorable for the adsorption of glyphosate present in the liquid phase. The efficiency removal ranged from 54.33 to 84.04% and the adsorption capacity from 13.68 a 21.17 $\text{mg}\cdot\text{g}^{-1}$. The materials composed of iron were more efficient ($\eta > 60\%$) for glyphosate adsorption in comparison with the copper based materials. In addition, the CNT-COOH3 achieved an efficiency of 84.08% and adsorption capacity of 21.17 $\text{mg}\cdot\text{g}^{-1}$ in 120 min. In this context, the CNT-COOH3 was identified as the most efficient for the adsorption glyphosate removal and was chosen for further studies.

Table 2 presents different materials reported in the literature for the adsorption of glyphosate. From the comparison, the rice husk biochar and graphene oxide presented higher adsorption capacities [20,21]. On the other hand, the CNT-COOH3 presented the better efficiency of removal.

In this sense, the preliminary tests indicate that the modified CNTs via green synthesis can emerge as excellent adsorbents for the glyphosate removal.

This can lead to better results when optimized in relation to its operating condition.

Table 2. Comparison among the adsorbent reported in the literature for the glyphosate adsorption.

Adsorbent	q_{\max} [mg g ⁻¹]	η [%]	Reference
CNT-COOH3	21.17	84.08	This work
Tanning sludge	6.034	26.18	[19]
Graphene oxide	39	33	[20]
Rice husk biochar	31.6	82	[21]

4. Conclusions

In this work, the potential of the modified CNTs via green synthesis with the impregnation of metallic nanoparticles was tested on the removal of glyphosate from water. The XRD of the adsorbent indicates that the synthesis process did not affect the original structure of the CNTs, preserving its original peaks. From the FT-IR it was found the original CNTs presented OH and COOH functional groups. After the green synthesis, it was observed that most of the materials remain with original groups. In exception, the materials (CNT-OH3 and CNT-COOH3) made with a nutshell (*Carya illinoensis*) extract and the iron solution presented the break of the C≡C and C=C bonds. Last, the prelaminal adsorption tests indicate the modified CNT were efficient on the glyphosate removal. The best CNT was the CNT-COOH3, achieving an efficiency of removal of 84.08% and an adsorption capacity of 21.17 mg g⁻¹. Conclusively, Fe²⁺ and Cu²⁺ impregnation in CNT via green synthesis is a promising and efficient alternative for glyphosate removal in aqueous matrix.

Acknowledgments

The authors would like to thank CAPES for their financial assistance.

References

- [1] FAO. Food and Agriculture Organization of the United Nations. **Pesticides**. Available in: <>. Access in: November 5, 2019.
- [2] IBGE. Instituto Brasileiro de Geografia e Estatística. **Censo Agropecuário 2017: Resultados Preliminares**. Rio de Janeiro: IBGE, 2018.
- [3] IBAMA. Instituto Brasileiro do Meio Ambiente e dos Recursos Naturais Renováveis. 2016. **Relatórios de comercialização de agrotóxicos**. Available in: <https://www.ibama.gov.br/index.php?option=com_content&view=article&id=594&Itemid=54>. Access in: November 5, 2019.
- [4] FIORILLI, S.; *et al.* Iron oxide inside SBA-15 modified with amino groups as reusable adsorbent for highly efficient removal of glyphosate from water. **Applied Surface Science**, n. 411, p. 457–465, 2017.
- [5] ARIAS-ESTÉVEZ, M.; *et al.* Themobility and degradation of pesticides in soils and the pollution of ground water resources. **Agric.Ecosyst.Envirôn.**, v. 123, p. 247–260, 2008.
- [6] CONAMA. Conselho Nacional do Meio Ambiente. **Resolução 357 de 17/03/2015**. Available in: <<http://www2.mma.gov.br/port/conama/legiabre.cfm?codlegi=459>>. Access in: November 18, 2019.
- [7] MINISTÉRIO DA SAÚDE. **Portaria nº 2.914 de 12/12/2011**. Available in: <http://www.saude.mg.gov.br/images/documentos/POR_TARIA%20No-%202.914,%20DE%2012%20DE%20DEZEMBRO%20DE%202011.pdf>. Access in: November 18, 2019.
- [8] SALMAN, J. M.; ABID, F. M.. Preparation of mesoporous activated carbon from palm-date pits: optimization study on removal of bentazon, carbofuran, and 2,4-D using response surface methodology. **Water Science & Technology**, v. 68, p. 1503-1512, 2013.
- [9] ZHOU, C. R.; *et al.* Study on behavior of alkaline fiber FFA-1 adsorbing glyphosate from production wastewater of glyphosate. **Fluid Phase Equilibria**, n. 362, p. 69-73, 2014.
- [10] FERREIRA, F. V.; *et al.* Chapter one: Synthesis, Characterization, and Applications of Carbon Nanotubes. **Carbon-Based Nanofillers and their Rubber Nanocomposites**, p. 1-45, 2019.
- [11] FIYADH, S. S.; *et al.* Review on heavy metal adsorption processes by carbon nanotubes. **Journal of Cleaner Production**, v. 230, p. 783-793, 2019.
- [12] KARUPPIAH, M.; RAJMOHAN, R. Green synthesis of silver nanoparticles using *Ixora coccinea* leaves extract. **Materials Letters**, v. 97, p. 141–143, 2013.
- [13] HOLADE, Y.; *et al.* Recent Advances in Carbon Supported Metal Nanoparticles Preparation for Oxygen Reduction Reaction in Low Temperature Fuel Cells. **Catalysts**, v. 5, p. 310-348, 2015.
- [14] KHARISSOVA, O.V.; *et al.* The greener synthesis of nanoparticles. **Trends in Biotechnology**, v. 31, p. 240-248, 2013.
- [15] PETERNELA, J.; *et al.* Synthesis and Impregnation of Copper Oxide Nanoparticles on Activated Carbon through Green Synthesis for Water Pollutant Removal. **Materials Research**, v. 21, p. 1, 2018.

Pecan nutshell activated hydrochar for methylene blue adsorption

Rogério S. Maniezzo^{a†}, Hugo H. C. de Lima^a, Maria Eugênia G. Llop^a, Vicente L. Kupfer^a, Pedro A. Arroyo^a, Emerson M. Giroto^a, Marcos R. Guilherme^{a,b}, Andrelson W. Rinaldi^{a*}

^a Rinaldi Research Group - State University of Maringá - UEM, Av. Colombo, 5790, Maringá – 87020-900, Paraná

^b Cesumar Institute of Science, Technology and Innovation - ICETI, Av. Guedner, 1610, Maringá – 87900-130, Paraná

†rsmaniezzo@gmail.com *awrinaldi@uem.br

Abstract

Pecan nutshell was used to produce activated hydrochar with a large specific area. For activation, KOH was used and obtained activated hydrochar (HPN-ATV) was used for methylene blue (MB) adsorption. HPN-ATV has high BET area values (S_{BET}) 2342 m² g⁻¹. FTIR spectra and Boehm titration shows that the surface is rich in basic and acid functional groups and because these characteristics HPN-ATV is favorable for the adsorption of cationic molecules. For adsorption assay, the kinetic experimental data better correlated with the pseudo-second-order kinetic and Elovich equations, and the Langmuir model showed a better fit for the data of MB adsorption with a monolayer of 1190.62 mg g⁻¹ are much larger than other adsorbents. Thermodynamic parameters show that the adsorption process is spontaneous.

Keywords: methylene blue; pecan shell; adsorption; activated hydrochar; HTC

1. Introduction

Several industrial sectors, such as textiles, plastics, clothing, as well as the pharmaceutical industry, food use around 100,000 types of dyes and pigments. This reflects the late encounter of these dyes in wastewater from industrial processes. These residues can migrate to nature, from erroneous disposal to a poorly done or ineffective treatment process [1].

For the treatment of these residues, there are currently some effective ways, such as photodegradation [2], filtration [3], flocculation [4], biological treatments [5].

One process that has proven to be advantageous because it has high efficiency, easy operation, environmentally friendly, low cost compared to other methods of the adsorption [6-7]. Within this area, activated carbon is efficient for use in adsorption processes due to its porous structure and high specific area [8].

One of the techniques for converting the precursors to carbon is hydrothermal carbonization (HTC) where moderate temperatures (453 – 623 K) are used in the presence of pressurized water for several hours [9-10]. Hydrochar is a hydrophilic material with high carbon content, small aromatic

structure and high functional groups containing oxygen, such as hydroxyls, phenolics, carbonyls and carboxylyls on its surface.

Due the high number of functional groups containing oxygen, the hydrochars are appropriate for chemical activation where this activation will form pore and increase the surface area that facilitating the adsorption process [11].

The present work aims to synthesize pecan nutshell (PN) activated hydrochar using HTC process with temperature of 463 K for 48 hours and subsequently chemical activation with KOH for removal of methylene blue.

2. Materials and methods

2.1 – Materials

Hydrochloric acid (HCl), methylene blue (C₁₆H₁₈N₃S.2H₂O), sodium bicarbonate (NaHCO₃), sodium carbonate (Na₂CO₃), potassium hydrogen (KOH) and sodium hydrogen (NaOH) were used by Anidrol and use as purchased.

2.2 – Synthesis and chemical activation of hydrochars

Pecan nutshells (PN) were collected from a Brazilian company. After collection, the shells were ground and dried at 373 K for 12 hours. For produce hydrochars (HPN) sample, 5.00 grams of PN and 37 mL of deionized water were added to a Teflon® tube and stainless-steel autoclave (no model/supplier) at a temperature of 463 K for 48 hours. After the hydrocarbonization hydrochars were oven dried at 343 K for 12 hours and were named HPN.

Chemical activation was performed with an impregnation ratio of 1:5 (m/m) (HPN: KOH). Briefly, 3.00 g of HPN was mixed with 15.00 g of KOH and 50 mL of deionized water in a reactor under mechanical stirring for 20 min. After homogenization, the solvent was evaporated and the reactor was muffled and heated to 1073 K with a 298 K min⁻¹ heating ramp and maintained for 45 minutes under an Ar₂ flow rate of 250 mL min⁻¹. After the activation time, the flow was switched off and the sample was placed at room temperature. The formed product was washed with 0.1 M HCl and deionized water to pH 6.5. The powder (HPN-ATV) was dried at 373 K for 12 h.

2.3- Characterization of HPN-ATV

The textural properties were characterized by N₂ physisorption to 77K using an area analyzer. Specific area (S_{BET}) was determined by the Brunauer-Emmett-Teller equation (BET) and total pore volume (V_T) was defined by the maximum amount of N₂ adsorbed volume at relative pressure near p / p₀ = 0.99. Micropore volume (V_{micro}) was determined using the t-plot method and mesoporous volume (V_{meso}) was calculated by the difference of V_T and V_{micro}. The FTIR-ATR spectra were acquired in the range of 4000–400 cm⁻¹ with 2 cm⁻¹ resolution and acquisition of 128 scans. Micrographs were obtained using a scanning electron microscope (FEI-250). Raman spectra were obtained using a Micro Raman spectroscope (Bruker Senterra) employing a 532 nm laser. The surface chemistry characteristics of HPN and HPNATV were evaluated by performing Boehm titration [12] and the pH of zero loading point (pHPCZ) [13].

2.4 – Adsorption Studies

Adsorption assays were performed using 50 mL glass vials. For the assays, 0.005 g of HPN-ATV and 20 mL of methylene blue (MB) solution with concentration variation according to each assay were used. The temperature in each test was 298 K and agitation at 70 rpm using a Dubnoff. At the end of each test, the samples were centrifuged and an aliquot collected for quantitation by UV_Vis spectroscopy (Ocean Optics USB 4000) at λ_{max} at 660 nm. The adsorbed amount of each test was calculated using the mass balance, according to Equation 1.

$$q_t = q_e = \frac{(C_0 - C_f)v}{w} \quad (1)$$

Where q_t is the amount adsorbed at time t in mg g⁻¹, q_e is the amount adsorbed on equilibrium in mg g⁻¹, C₀ and C_f are the initial and final concentrations of MB in mg L⁻¹, v is the volume of the solution in L and w is the mass of adsorbent in g.

2.4.1– Effect of pH

The effect of the pH on the maximum amount adsorbed was evaluated from the tests performed with pH variations between 3.0 and 11.0, using solutions of NaOH or HCl, 0.1 M in 550 mg L⁻¹ MB during a period of 24 hours. H. The adsorbed amount of each experiment was calculated by the mass balance represented by Eq (1).

2.4.2 – Adsorption kinetics and isotherm

The adsorption kinetics were analyzed at time intervals from 0 to 1220 minutes at 150 rpm, 298 K, with 650 mg L⁻¹ MB solution at pH 11. The experimental data were correlated with kinetic models of pseudo-first order, pseudo-second order and Elovich.

The adsorption isotherms were obtained from solutions with MB concentrations of 100 to 550 mg L⁻¹ at pH 11, with temperatures of 308 K, 318 K and 328K, where they were shaken for 8h with the adsorbents. The experimental results are correlated with the Langmuir, Freundlich, Dubinin-Radushkevich and Redlich-Peterson isothermal models.

2.4.3– Adsorption thermodynamics

The thermodynamic parameters of the MBN-ATV MB adsorption process, such as Gibbs free energy (ΔG_{ads}), Enthalpy (ΔH_{ads}) and Entropy (ΔS_{ads}) were determined using the solute distribution coefficient between liquid and solid phase in equilibrium (K_d) at different temperatures using the following equations (3),(4) and (5):

$$K_d = \frac{q_e}{C_e} \quad (3)$$

$$\Delta G_{ads} = -RT \ln K_d \quad (4)$$

$$\ln K_d = -\frac{\Delta G_{ads}}{RT} = \frac{\Delta S_{ads}}{R} - \frac{\Delta H_{ads}}{RT} \quad (5)$$

Where T is the absolute system temperature (K) and R is the universal gas constant ($8.3145 \text{ J mol}^{-1} \text{ K}^{-1}$).

3. Results and discussions

3.1 – HPN-ATV characterization

The N_2 physisorption isotherm of HPN-ATV is shown in Fig. 1. According to the IUPAC (International Union of Pure and Applied Chemistry) classification, the HPN-ATV sample shows type I isothermal characteristics i.e., the sample shows a larger pore size distribution with wide micropores and narrow mesopores (Fig. 2), which is in agreement with the high $V_{\text{micro}}/V_{\text{meso}}$ ratio [14]. Table 1 shows the textural characterization values of HPN-ATV. HPN-ATV shows a SBET of $2342 \text{ m}^2 \text{ g}^{-1}$ and approximately 58.78% of micropores with a mean pore diameter of 2.24 nm, which is large enough for the adsorption of MB molecules.

Table 1. Textural characterization of HPN-ATV

Sample	HPN-ATV
$S_{\text{BET}} (\text{m}^2\text{g}^{-1})$	2342
$V_{\text{T}} (\text{cm}^3\text{g}^{-1})$	1.31
$V_{\text{micro}} (\text{cm}^3\text{g}^{-1})$	0.77
$V_{\text{meso}} (\text{cm}^3\text{g}^{-1})$	0.54
$V_{\text{micro}}/V_{\text{meso}}$	2.24
$A_{\text{p}} (\text{nm})$	2.24

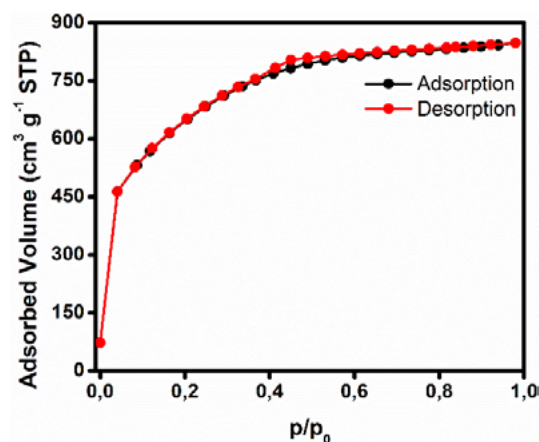


Fig. 1 - N_2 Physisorption of HPN-ATV

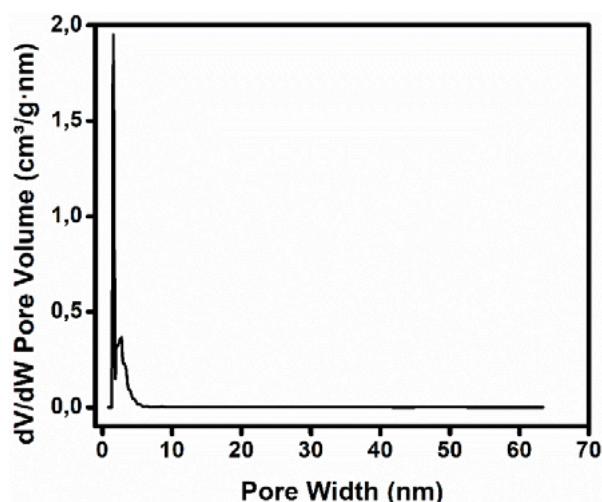


Fig. 2. Pore size distribution by DFT method.

Figure 3 and 4 shows the FTIR-ATR spectra e Raman, respectively. It is possible to observe in Figure 3 in the FTIR-ATR spectra the characteristic vibration bands of carbonaceous materials. The HPN has vibration bands in the region of 3700 to 3600 cm^{-1} , typical of hydroxyl elongation vibrations, referring to groups of carboxylic acids, phenols and alcohols. Approximately 3000 cm^{-1} are attributed the elongation vibrations of the C = O bonds, characteristic of functional groups such as ketones, aldehydes and carboxylic acids, near 1530 cm^{-1} the observed band is associated with elongation vibrations of the C = C bonds, at 1130 cm^{-1} referring to the elongation of the C-O vibrations and finally, in the region of 700 cm^{-1} , the flexion of the aromatic ring C-H bonds can be attributed.

The HPN-ATV spectra have the same bands of HPN, but to a lesser extent and a new band in the 1310 cm^{-1} region that can be attributed to aromatic vibrations of C-O functional groups.

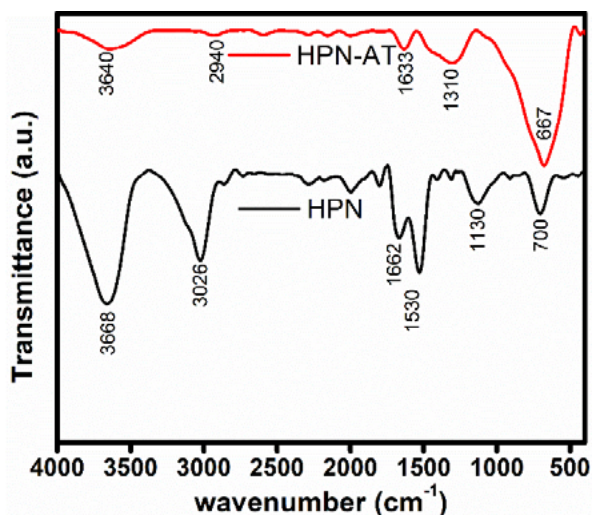


Fig. 3. - FTIR spectra for HPN-ATV

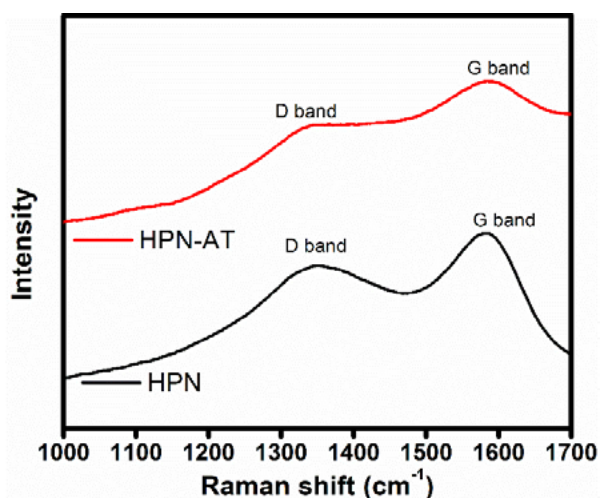


Fig. 4 - Raman spectroscopy for HPN-ATV

In Figure 4, the Raman spectrum of the HPN and HPN-ATV samples can be seen, where they have two characteristic bands at 1350 and 158 cm^{-1} , which are associated with band D and band G, respectively. The intensity ratio of these two bands (I_D / I_G) can be calculated and shows the surface disorder of the hydrochars. For HPN the ratio is 0.87 and HPN-ATV the ratio is 1.11, which indicates that both adsorbents have disordered coals on their surface.

Table 2 lists the amounts of acidic (carboxylic, phenolic and lactonic) and basic functional groups obtained by Boehm titration. It can be observed that HPN-TV has a higher number of basic groups ($14.66 \text{ mmol g}^{-1}$) and acid carboxylic functional groups is the acid group in HPN-ATV. The HPN-ATV zero charge point (pH_{pcz}) was 6.85.

Table 2. Boehm Titration Values

Number of Functional Groups (mmol g^{-1})				
Acid Functional Groups				
Carboxylic	Phenolic	Lactone	Total	Basics
9.97	0.0	0.0	9.97	14.66

3.2 – Adsorption Studies

Initially, the influence of solution pH on adsorption was studied. In acid medium, the activated hydrochar showed low efficiency in relation to the solution in basic medium (pH 11). The adsorbed maximum value was $1158.53 \text{ mg g}^{-1}$. This is easily explained because the hydrochar surface is rich in carboxylic groups and the deprotonation of these groups can create an electrostatic interaction between the positively charged dye molecules and the negatively charged surface of the adsorbent. Therefore, the other test (kinetics, isotherm and adsorption thermodynamics) were evaluated using solution with a pH 11.

As can be seen in Figure 5, the adsorption kinetics reaches its equilibrium in 600 minutes. Table 3 shows the kinetic models of pseudo first order, pseudo second order and Elovich.

From Table 3 we can see that the pseudo-second order and Elovich models correlated better with the experimental data, because they presented values of R^2 close to one. In addition, in the pseudo-second order model the values of q_e were close to the values of $q_{e,\text{exp}}$. Regarding the initial adsorption rate (h_0) was higher for the pseudo-second order model, indicating that the PNH-ATV presents higher speed in the adsorption process.

From these results we can infer that chemisorption can be the predominant process in adsorption. Moreover, according to the Elovich model, the α constant, which indicates the initial adsorption rate, is quite high ($1.44 \times 10^4 \text{ g mg}^{-1} \text{ min}^{-2}$), while β , which refers to the desorption constant, is low (0.007 mg g^{-1}), indicating the high affinity between the MB cationic molecules and the HPN-ATV adsorbed.

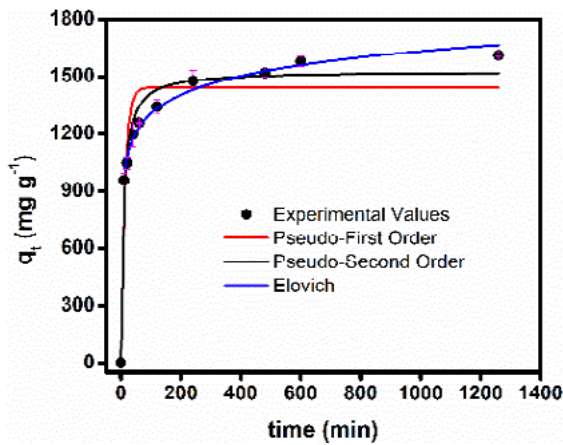


Fig. 5 - HPN-ATV MB adsorption kinetics

Table 3: Adsorption kinetic parameters

Kinetic parameter			
Pseudo-First Order			
$q_e=1441.37$	$k_1=0.08$	$h_0=115.30$	$R^2=0.9085$
Pseudo Second Order			
$q_e=1529.18$	$k_2=8,0 \times 10^{-5}$	$h_0=184.73$	$R^2=0.9728$
Elovich			
$\alpha= 1.44 \cdot 10^4$	$\beta=0.007$	$R^2=0.9954$	
q_e (mg g ⁻¹); k_1 = min ⁻¹ ; h_0 = mg g ⁻¹ min ⁻¹ ; k_2 = g mg ⁻¹ min ⁻¹ ; α = g mg ⁻¹ min ⁻² ; β = mg g ⁻¹ min ⁻¹			

The adsorption isotherms are shown in Figure 6, where it can be observed that with increasing the equilibrium concentration, the maximum adsorbed amount increases. Experimental data were adjusted to different adsorption isotherm models, including Langmuir, Freundlich, Dubini-Radushkevich and Redlich-Peterson models and these results are listed in Table 4.

Table 4. Parameters of MB adsorption isotherms in HPN-ATV.

Langmuir	Freundlich	DR
$q_{e,exp}=1178.88$	$k_F= 593.71$	$q_m=1151.2$
$q_{max}=1190.62$	$1/n = 7.35$	$k_{DR}=6.0 \times 10^{-6}$
$k_L = 0.28$		$E = 333.34$
$R^2=0.9615$	$R^2 = 0.9184$	$R^2 = 0.8151$

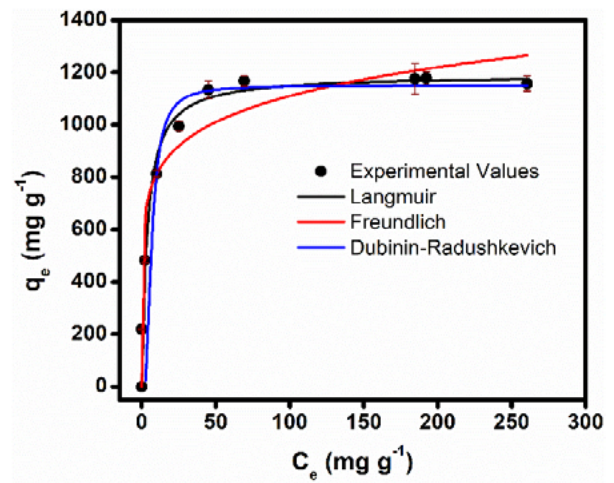


Fig. 6: HPN-ATV MB adsorption isotherm

The Langmuir model best presented a correlation of experimental data on MB adsorption on HPN-ATV. This shows that adsorption occurs in monolayer and the predominant process is chemisorption.

The effect of temperature on MB adsorption process was studied, taking it to temperatures of 298,308,318 and 328 K, as can be observed in Figure 7. It is possible to observe that with increasing temperature, the amount adsorbed MB increases. From these results we calculated the thermodynamic parameters using equation (3),(4) and (5). the values of ΔH and ΔS were calculated by linear regression of the van Hoff equation ($\ln k_d \times 1 / T$) according to Equation (5) and the values can be observed in Table 5.

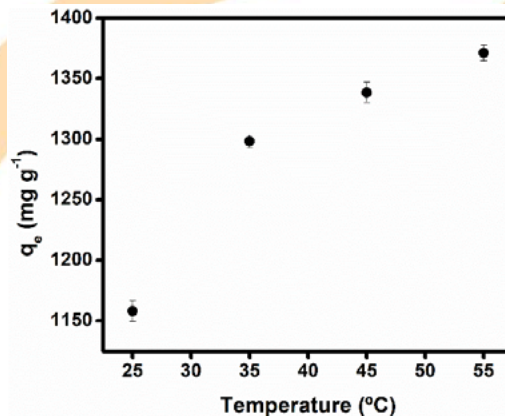


Fig. 7: HPN-ATV MB adsorption kinetics

From Table 5 it can be observed that there is an increase in the negative values of ΔG with the increase in temperature, indicating that the process of adsorption of MB in HPN-ATV is viable and

spontaneous. The positive value of ΔH suggests that the adsorption process is endothermic in nature and the positive value of ΔS for the adsorption of MB in HPN-ATV indicates that there is an increase in the number of species at the solid-liquid interface, which leads to an increase in the disorder of the solid-liquid interface, indicating the chemical affinity between the MB and the surface of HPN-ATV in the adsorption process.

Table 5: HPN-ATV MB adsorption thermodynamic parameters

Sample	ΔG				ΔH	ΔS
HPN-	298	308	318	328	17.84	72.56
ATV	-3.70	-4.69	-5.13	-5.29		

ΔG° (kJ mol⁻¹), ΔH° (kJ mol⁻¹) ΔS° (J mol⁻¹) and temperatura (K)

4. Conclusion

KOH-activated hydrocarbon produced from pecan shell (HPN-ATV) was effective in the adsorption of methylene blue (MB) in aqueous medium. According to the results presented, activated hydrocarbon was considered as a high efficiency adsorbent in MB removal, with a great potential for the application of organic compounds removal.

Acknowledgements

The authors thank the COMCAP-UEM for the SEM, the Brazilian Agencies for CNPq fellowship (Process: 577527/2008-8, 310820/2011-1, and 113881/2018-5), and Fundação Araucária/PR (Process: 830/2013) and CAPES for the financial support.

References

[1] Z. Jia, Z. Li, S. Li, Y. Li, R. Zhu, Adsorption performance and mechanism of methylene blue on chemically activated carbon spheres derived from hydrothermally-prepared poly(vinyl alcohol) microspheres, *J. Mol. Liq.* 220 (2016) 56–62. doi:10.1016/j.molliq.2016.04.063.

[2] A. A. Mir, A. A. Amooey, S. Ghasemi, Adsorption of direct yellow 12 from aqueous solutions by an iron oxide-gelatin nanoadsorbent; kinetic, isotherm and mechanism analysis, *J. Clean. Prod.* 170 (2018) 570–580. doi:10.1016/j.jclepro.2017.09.101.

[3] M. Soniya, G. Muthuraman, Comparative study between liquid-liquid extraction and bulk liquid membrane for the removal and recovery of methylene blue from wastewater, *J. Ind. Eng. Chem.* 30 (2015) 266–273. doi:10.1016/j.jiec.2015.05.032.

[4] S. Sadri Moghaddam, M.R. Alavi Moghaddam, M. Arami, Coagulation/flocculation process for dye removal using sludge from water treatment plant: Optimization through response surface methodology, *J. Hazard. Mater.* 175 (2010) 651–657. doi:10.1016/j.jhazmat.2009.10.058.

[5] B. E. L. Baêta, D. R. S. Lima, S. Q. Silva, S. F. Aquino, Evaluation of soluble microbial products and aromatic amines accumulation during a combined anaerobic/aerobic treatment of a model azo dye, *Chem. Eng. J.* 259 (2015) 936–944. doi:10.1016/j.cej.2014.08.050.

[6] D. W. Cho, B. H. Jeon, C. M. Chon, F. W. Schwartz, Y. Jeong, H. Song, Magnetic chitosan composite for adsorption of cationic and anionic dyes in aqueous solution, *J. Ind. Eng. Chem.* 28 (2015) 60–66. doi:10.1016/j.jiec.2015.01.023.

[7] H. Wang, R. Xie, J. Zhang, J. Zhao, Preparation and characterization of distillers' grain based activated carbon as low cost methylene blue adsorbent: Mass transfer and equilibrium modeling, *Adv. Powder Technol.* 29 (2018) 27–35. doi:10.1016/j.apt.2017.09.027.

[8] S. Cheng, L. Zhang, A. Ma, H. Xia, J. Peng, C. Li, J. Shu, Comparison of activated carbon and iron/cerium modified activated carbon to remove methylene blue from wastewater, *J. Environ. Sci. (China)*. 65 (2018) 92–102. doi:10.1016/j.jes.2016.12.027.

[9] M. A. Islam, M. J. Ahmed, W. A. Khanday, M. Asif, B.H. Hameed, Mesoporous activated coconut shell-derived hydrochar prepared via hydrothermal carbonization-NaOH activation for methylene blue adsorption, *J. Environ. Manage.* 203 (2017) 237–244. doi:10.1016/j.jenvman.2017.07.029.

[10] M. Hernández Rodríguez, J. Yperman, R. Carleer, J. Maggen, D. Daddi, G. Gryglewicz, B. Van der Bruggen, J. Falcón Hernández, A. Otero Calvis, Adsorption of Ni(II) on spent coffee and coffee husk based activated carbon, *J. Environ. Chem. Eng.* 6 (2018) 1161–1170. doi:10.1016/j.jece.2017.12.045.

[11] A. Kumar, H.M. Jena, Adsorption of Cr(VI) from aqueous solution by prepared high surface area activated carbon from Fox nutshell by chemical activation with H₃PO₄, *J. Environ. Chem. Eng.* 5 (2017) 2032–2041. doi:10.1016/j.jece.2017.03.035

[12] H.P. Boehm, SOME ASPECTS OF THE SURFACE CHEMISTRY, *Carbon N. Y.* 32 (1994) 759–769. [https://doi.org/10.1016/0008-6223\(94\)90031-0](https://doi.org/10.1016/0008-6223(94)90031-0)

[13] J. Park, J. R. Regalbuto, A simple, accurate determination of oxide PZC and the strong buffering effect of oxide surfaces at incipient, *J. Colloid Interface Sci.* 175 (1995) 239–252. <https://doi.org/10.1006/jcis.1995.1452>.

[14] M. Thommes, K. Kaneko, A. V. Neimark, J. P. Olivier, F. Rodriguez-Reinoso, J. Rouquerol, K.S.W. Sing, Physisorption of gases, with special reference to the evaluation of surface area and pore size distribution (IUPAC Technical Report), *Pure Appl. Chem.* 87 (2015) 1051–1069. doi:10.1515/pac-2014-1117.

Adsorption kinetics of amaranth dye on organonano clay

Gleiciely Lima Domingos, Thaís Mayra Israel de Oliveira Lima, Pedro Henrique dos Santos Moraes, Júlia Oliveira Gurgel, Lenemeire Teixeira Araújo, Leonardo Levy da Silva França, Yasmin de Sousa Lima, Hugo Leonardo de Brito Buarque*

*Instituto Federal do Ceará, campus Fortaleza., Av. Treze de Maio, 2081 - Benfica, Fortaleza - CE, 60040-531, Brazil

Abstract

The goal of this paper was to evaluate the possible use of an organonano clay modified with 3 aminopropyltriethoxysilane and octadecylamine for the removal of anionic azo dyes, widely used in the food industry. For this, kinetic data of adsorption of amaranth dye from aqueous solution using commercial nano clay modified with organic functional groups were obtained in this study. PZC curve was determined for the adsorbent and kinetic curve at room conditions was obtained and modeled with simple kinetic equations and intra-particle diffusion model. PCZ of the modified nano clay was 7.5 and the pseudo-second order model was the best fitted to data. Also, bulk diffusion, intra-particle diffusion and equilibrium step are the mechanisms involved in the adsorption of amaranth on nano clay evaluated.

Keywords: azo dye; modified nano clay; aqueous phase adsorption; industrial food effluents.

1. Introduction

In recent decades, the utilization of food coloring for industrial purposes spreads extensively, because it improves not only the appearance of processed foods, but also their shelf life. However, researches have revealed that these dyes can cause problems in human beings [1,2].

The effluents from these industries, in addition to their strong acid or basic character, have elevated concentration of suspended organic solids, high organic load and biochemical oxygen demand, strong coloration and poor biodegradability [3]. Dyes present in effluents are known to be very difficult to remove as their recalcitrant molecules are resistant to aerobic digestion and stable to oxidizing agents [3].

In Brazil, under current legislation, through ANVISA Resolutions Nr. 382 to 388 of August 9, 1999, only 11 artificial colors are allowed for use: Amaranth, Eritrosin Red, Red 40, Ponceau 4R, Dusk Yellow, Tartrazine Yellow, Indigotine Blue, Brilliant Blue, Azorubine, Rapid Green and V-Patent Blue [3].

The Amaranth is an azo dye widely used by industries. Azo dyes comprise various compounds having usually an aryl ring attached to a second aryl ring by an azo bond ($N=N$). These rings may contain one, two or three sulfonic groups. These

compounds represent the most important and used class of synthetic food additives [1].

Numerous treatment technologies have been developed and applied worldwide for dye removal [4]. Adsorption is an advantageous process widely used for this purpose due to its flexibility, low cost and low energy consumption.

In this context, nano clay has been investigated as adsorbent for the removal of synthetic dyes, because it is widely available, and it presents strong sorption ability [5]. Its particular characteristics, such as high surface area, chemical and mechanical stability, play an important role in the concentration of dye molecules on their surfaces [6,7].

The aim of this paper is to determinate the kinetic data of adsorption of an azo dye (amaranth) from aqueous solution using a commercial organonano clay as adsorbent. Also, intra-particle, pseudo-first order and pseudo-second order kinetic models were fitted to data. Additionally, some characteristics of the adsorbent have been obtained and discussed.

2. Methodology

2.1 Reagents and solutions

All solutions used in this study were prepared with analytical grade reagents and bidistilled water.

The amaranth dye (CAS 915-67-3, C.I. 16.185) used was purchased from Sigma-Aldrich, USA. The molecular structure of this colorant is depicted in Figure 1.

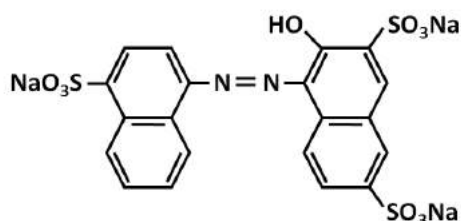


Figure 1. Molecular structure of the amaranth.

The adsorbent used was commercial nanoclay, surface modified with 15-35 wt. % octadecylamine and 0.5-5 wt. % aminopropyltriethoxysilane, purchased from Sigma Aldrich (Ref. 682632).

Functional groups present on the surface of this adsorbent were identified from the FTIR spectra obtained by Duarte et al. [8]. The FTIR spectra of the organonanoclay is given in Figure 2.

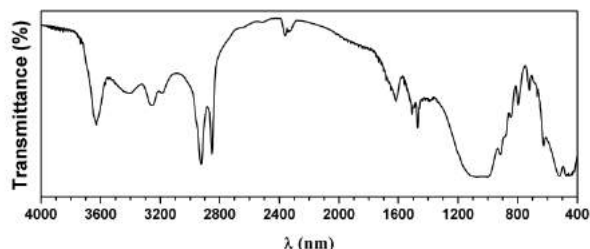


Figure 2. FTIR spectra for the modified nanoclay.

Duarte et al. [8] explains that the peculiar bands to montmorillonite are observed in the region at $1000\text{-}1100\text{ cm}^{-1}$ (typical of Si-O-Si groups) and the bands at 917 , 797 and 525 cm^{-1} were attributed to octahedrals of the aluminosilicates present in the molecular structure. A band near 3626 cm^{-1} is due to the stretching vibrations of the hydroxyl structural group typical of this kind of clay. The absorption bands at $3400\text{-}3465\text{ cm}^{-1}$ correspond to the O-H stretching frequency of water. Also, the additional peaks at 2850 and 2920 cm^{-1} , inherent to the symmetric and asymmetric vibration modes of the group CH_2 , are well highlighted, suggesting greater number of organophilic groups in the modified clay used in this study. The bands in the $1470\text{-}1500\text{ cm}^{-1}$ region indicate the presence of

vibrations C-N in tertiary amines, corroborating the superficial modification of the organonanoclay.

Those authors [8] also determined a specific superficial area of $326\text{ m}^2\text{ g}^{-1}$ for the adsorbent, using the spot test method with methylene blue.

The spectrophotometric determination of the concentration of amaranth dye in aqueous solution was done on a Shimadzu UV-1601PC spectrophotometer with 1.0 cm optical path quartz cuvette following Lessa et al. [3].

2.3 Influence of pH

The pH is an important controlling parameter in the adsorption process from aqueous media. The effect of pH on amaranth adsorption could be explained on the basis of chemical characteristics of the adsorbent and dye in solution.

Amaranth is an anionic dye. Thus, as the surface of modified nanoclay acquires positive charge by decreasing pH, it is expected a significantly high electrostatic attraction between this surface and the anionic dye molecules, leading to higher dye adsorption. Conversely, as the pH of the system increases, the number of negatively charged sites increases while the number of positively charged sites decreases, prejudicing the adsorption of dye anions due to electrostatic repulsion.

Thus, in order to obtain information about the influence of pH on the surface charge of the adsorbent, the point of zero charge (PZC) was determined by eleven point method: modified nanoclay (0.03 g) was added to flasks containing 30 mL of aqueous solution of HCl or NaOH adjusted at certain initial pH (1, 2, 3, 4, 5, 6, 8, 9, 10, 11, 12); afterward, the solutions were shaken on an orbital shaker at 140 rpm for 24 h at room temperature and light protected. The final pH of each solution was measured thereafter using a calibrated pH meter.

The PZC value obtained was used to choose initial pH in kinetic tests.

2.4 Kinetic study

The kinetic experiments were performed in batch and duplicate following Lessa [9] as methodological reference. Thus, each kinetic point used 0.05 g of modified nanoclay, which was placed in an erlenmeyer flask with 50 mL of bidistilled water and kept under stirring for 12 hours. After this period, 50 mL of a 40 mg L^{-1} amaranth dye solution was added to the flasks

resulting in 100 mL of adsorptive solutions with initial concentration of 20 mg L⁻¹ of dye. The initial values of pH of these solutions were adjusted with 0.1 mol L⁻¹ sodium hydroxide or hydrochloric acid solutions.

After the preset intervals of time, the residual concentrations of amaranth in the flasks were determined following Lessa et al. [3]. All tests were performed at room temperature (25°C ± 2°C).

The adsorption capacity of the dye on the adsorbents (*q* in mg g⁻¹) was calculated according to the equation:

$$q = \frac{V(C_o - C_f)}{m_{ads}} \quad (1)$$

where *V* (L), *C_o* (mg L⁻¹) and *C_f* (mg L⁻¹) are, respectively, the volume and the initial and final concentrations of the dye solution during contact time and *m_{ads}* (g) is the mass of nanoclay.

The adsorption efficiency (or removal) was calculated using the equation:

$$R = 100\% \frac{(C_o - C_f)}{C_o} \quad (2)$$

where *R* is the adsorption efficiency; *C_o* (mg L⁻¹) is the initial concentration of dye; *C_f* (mg L⁻¹) is the final dye concentration at time *t* (in min).

In this study, two reaction models (pseudo-first order and pseudo-second order) and one diffusion model (Weber-Morris intraparticle diffusion) were fitted to experimental data. The pseudo-first order and pseudo-second order models are presented in Equations (3) and (4), respectively and the intraparticle diffusion model is presented in Equation (5).

$$q_t = q_e - q_e \exp(-k_1 t) \quad (3)$$

$$q_t = \frac{q_e^2 k_2 t}{1 + q_e k_2 t} \quad (4)$$

$$q_t = k_{id} t^{0.5} - C \quad (5)$$

where *q_t* and *q_e* represent the amounts of adsorbed dye at time *t* (min) and at equilibrium, respectively; *k₁* (min⁻¹), *k₂* (g mg⁻¹ min⁻¹) and *k_{id}* (mg g⁻¹ min^{-0.5}) are the rate constants of pseudo-first order, pseudo-second order and intra-particle diffusion models, respectively; and *C* (mg g⁻¹) is a constant related to the thickness of the boundary layer.

The kinetic parameters (obtained by non-linear regression) and the fit quality statistics were found using the software Origin 9.1 (Originlab, USA).

3. Results and Discussions

3.1 Influence of pH

The plot of the final pH versus initial pH of the solutions is shown in Figure 3. It can be seen that PZC of modified nanoclay evaluated corresponds to a pH value around 7.5. This means that, at pH values below 7.5, the adsorbent surface has a net positive charge. Hence, the acidic pH facilitates the adsorption of anionic azo dyes onto modified nanoclay.

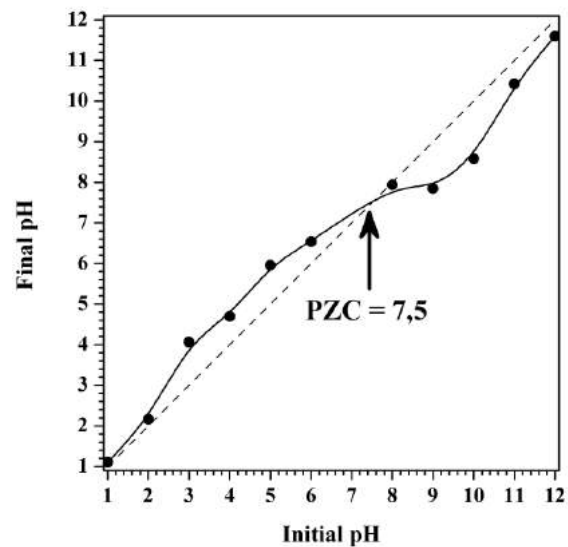


Figure 3. PZC curve for the modified nanoclay.

3.2 Adsorption mechanism and kinetics

The concentration plot of adsorbed amaranth versus contact time is shown in Figure 4. The reaction kinetic model (pseudo-second order) that was best fitted to the experimental data is also shown with the confidence and prediction bands in Figure 4. The kinetic parameters and the fit quality statistics for both reaction models evaluated are presented in Table 1. The adsorption of amaranth on modified nanoclay increased with time and equilibrium was attained within 720 min. The process showed removal efficiency of 78%. Rapid removal of adsorbate and reaching equilibrium in a short period of time are indications that the adsorbent is efficient.

Also, in order to find out the mechanism and potential rate-controlling, steps involved in the process of adsorption, an intra-particle diffusion model were made to fit the data. The obtained

parameters in the diffusion model fittings are also shown in Table 1. The intra-particle diffusion plot is presented in Figure 5.

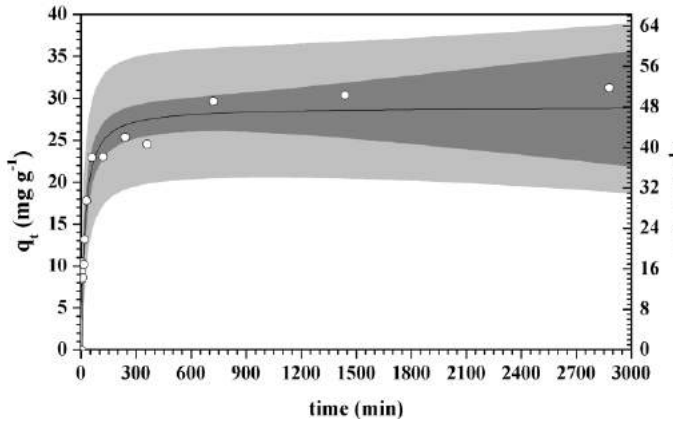


Figure 4. Kinetic curve of adsorption in aqueous phase of amaranth dye in organonano clay under the conditions tested.

Table 1 - Kinetics parameters and fit quality statistics for adsorption of amaranth onto modified nanoclay at 25°C and pH 7.0.

Model	Parameters	Values	t-value
PFO	q_e (mg g ⁻¹)	27.24 ± 3.54	16.6
	k_1 (min ⁻¹)	0.037 ± 0.019	4.3
	R^2_{adj}	0.8289	
	F-test	178	
	p-value	<0.0001	
PSO	q_e (mg g ⁻¹)	28.95 ± 3.54	17.7
	k_2 (g mg ⁻¹ min ⁻¹)	0.018 ± 0.001	3.3
	R^2_{adj}	0.8737	
	F-test	243	
	p-value	<0.0001	
IPD	K_{id-1} (g mg ⁻¹ min ^{-0.5})	2.45 ± 0.89	6.48
	C_1 (mg g ⁻¹)	3.18 ± 3.56	2.11
	R^2_{adj}	0.8368	
	F-test	42	
	p-value	0.0003	
	K_{id-2} (g mg ⁻¹ min ^{-0.5})	0.347 ± 0.25	4.50
	C_2 (mg g ⁻¹)	19.5 ± 4.3	14.6
	R^2_{adj}	0.8280	
	F-test	20	
	p-value	0.0205	
	K_{id-3} (g mg ⁻¹ min ^{-0.5})	0.060 ± 0.26	28.8
	C_3 (mg g ⁻¹)	28.1 ± 1.1	331
	R^2_{adj}	0.9976	
	F-test	831	
	p-value	0.0221	

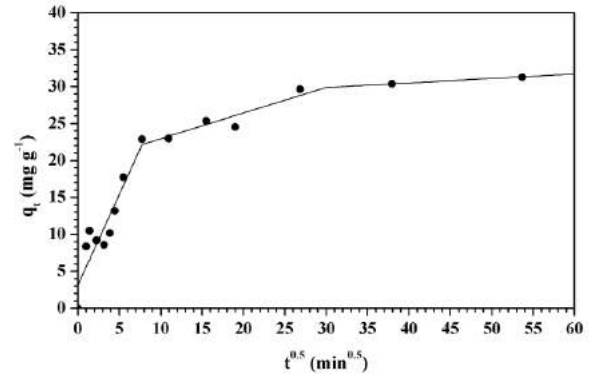


Figure 5. Intra-particle diffusion plot for the adsorption of amaranth onto organonano clay under conditions tested.

The non-zero C value indicated that the mechanism intraparticle diffusion is not the speed determining step in the process of mass transfer, other mechanisms must act simultaneously in the control of the adsorption process. In the conditions of experiments, the rate parameters for the diffusion in the three regions can be attributed to film or external diffusion, intra-particle diffusion and plateau portion represents the equilibrium.

4. Conclusions

The nanoclay modified with octadecylamine and 3-aminopropyltriethoxysilane was found to have adsorption efficiency of about of 75%.

The kinetic study indicated that the adsorption equilibrium under the study conditions (room temperature and pH 7) was reached in 720 minutes.

In the experimental conditions there are three adsorption rate determining steps: bulk diffusion, intra-particle and equilibrium.

The aim of this paper was to explore the possible use of commercial modified nanoclay as an adsorbent for the removal of amaranth dye from water.

References

- [1] Prado MA, Godoy, HT. Corantes artificiais em alimentos. *Alim e Nutr* 2003; 14(2) 237-250.
- [2] Anastácio LB, Oliveira DA, Delmaschio CR, Antunes LMG, Chequer FMD. Corantes alimentícios amarantho, eritrosina B e tartrazina, e seus possíveis efeitos maléficis à saúde humana. *JAPHAC* 2009; 2(3); 16-30.
- [3] Lessa RSF, Buarque HLB, Norberto JN, Mota PAL, Stefanutti R. Validação de método para determinação de corantes em efluentes. *Revista DAE* 2018; 66; 67-77.
- [4] Gupta VK, Agarwal S, Olgun A., Demir Hİ, Yola, ML., Atar N. (2016). Adsorptive properties of molasses modified boron enrichment waste based nanoclay for removal of basic dyes. *J Ind Eng Chem* 2016; 34; 244-249.
- [5] Adeyemo AA, Adeoye IO, Bello OS. Adsorption of dyes using different types of clay: a review. *Appl Water Sci* 2017; 7(2); 543-568.
- [6] Vanamudan A, Pamidimukkala P. Chitosan, nanoclay and chitosan–nanoclay composite as adsorbents for Rhodamine-6G and the resulting optical properties. *Int. J. Biol. Macromol* 2015; 74; 127-135.
- [7] Shirzad-Siboni M, Khataee A, Hassani A, Karaca S. Preparation, characterization and application of a CTAB-modified nanoclay for the adsorption of an herbicide from aqueous solutions: kinetic and equilibrium studies. *Comptes Rendus Chimie* 2015; 18(2); 204-214.
- [8] Duarte, I. J. M., Soares, A. J. R., Carvalho, J. R., & Buarque, H. L. D. B. (2019). Avaliação do uso de argilas montmorilonitas modificadas na adsorção de nitrato em meio aquoso. *Eng. sanit. ambient*, 21-31.
- [9] Lessa RSF. Removal of anionic azos dyes by silica gel adsorption functionalized with 3-aminopropyltriethoxysilane. *Fortress. (Doctorate in Civil Engineering) - Federal University of Ceará*, 2018.
- [10] Bertolini, T. C., & Fungaro, D. A. (2011). Balance studies and kinetic modeling of the adsorption of the crystal violet dye on light and heavy coal ash zeolites. In *3rd International Workshop Advances in Cleaner Production*, São Paulo.

Sururu shells as a potential biosorbent to remove rifampicin from water

Daniely Carlos Henrique¹, Daniel Uchoa Quintela¹, José Leandro da Silva Duarte^{1,2},
Alessandra Honjo Ide¹, Carmem Lucia de Paiva e Silva Zanta², Lucas Meili^{1,*}

¹Laboratório de Processos, Centro de Tecnologia, Universidade Federal de Alagoas, Maceió, Alagoas

²Laboratório de Eletroquímica Aplicada, Instituto de Química e Biotecnologia, Universidade Federal de Alagoas, Maceió, Alagoas

Abstract

Sururu (*Mytella falcata*) is a bivalve mollusk considered a symbol of cultural identity in Alagoas state, Brazil. However, its extraction generates a large amount of shells which are inappropriately disposed in the environment. In this context, the present contribution suggests the use of sururu shells as biosorbent to remove pollutants from water. For such purpose, rifampicin, an antibiotic, was chosen as model compound. The mussel shells were washed, dried and subjected to different thermal treatments: part of them remained *in natura*, a second part was pyrolysed and the third one was calcined. Adsorption batch assays showed that 10 g.L⁻¹ of the calcined sururu shells was able to remove over 90% of the adsorbate (50-100 mg.L⁻¹) in only 30 min of contact. Scanning electron microscopy (SEM), X ray diffraction (XRD) and X ray dispersive energy spectroscopy (EDS) are used for characterization of the selected adsorbent. They showed the presence of residual CaCO₃, mainly in the form of aragonite and calcite, and a porous structure with heterogeneous surface characterized by rounded particles. From The kinetic studies, the experimental data presented the best fit with pseudo-first order model and the adsorptive capacity achieved was 3.05, 4.58 and 7.00 mg.g⁻¹ (rifampicin initial concentrations of 50, 100 and 200 mg.L⁻¹, respectively). In short, these preliminary results indicated that sururu shells can be a potential biosorbent to remove rifampicin from water.

Keywords: Mollusk, biosorbent, antibiotic removal, adsorption, water treatment

1. Introduction

Sururu (*Mytella falcata*, Fig. 1) is a very popular bivalve mollusk in Alagoas gastronomy and its extraction moves the local economy. However, the shells are discarded in the environment with no final destination, causing health problems and visual pollution [1].



Fig. 1. Sururu shells.

In this context, it is relevant to search for alternatives for this waste utilization. Some studies can be found in the literature aiming the use of mussel shells as adsorbent for the removal of pollutants from water [2-4].

Biosorption or bio-adsorption is the phenomenon that occurs when a biological material attracts an adsorbate to its surface by physicochemical processes [5]. Biosorbents are potential materials for the removal of chemical substances from water due to their effectiveness and abundance. Moreover, these materials are harmless to nature and present advantages over conventional processes, such as simplicity of design, low cost and availability [6].

Emerging pollutants are chemical compounds that have been detected in the environment and have potential to cause adverse ecological and/or human health effects, but are not included in the current legislation [7]. Pharmaceuticals, pesticides, industrial chemicals, surfactants, and personal care products are some of the classes of these contaminants and most of them are not removed through conventional processes in water and wastewater treatment plants [8].

Thus, the present work aimed to show the potential of sururu shells as an adsorbent material to remove rifampicin (RIF, Fig. 2), an antibiotic widely used in the treatment of tuberculosis, from water. For such purpose, the material was washed, dried and subjected to different thermal treatments and evaluated through batch adsorption assays. Kinetic studies were also performed.

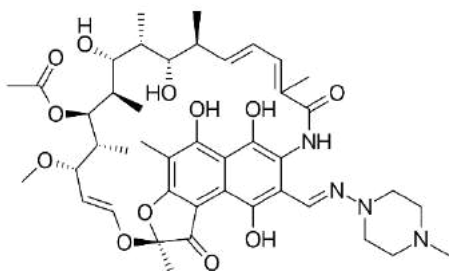


Fig. 2. Chemical structure of rifampicin.

2. Experimental

1.1. Adsorbate

Rifampicin was used as adsorbate. A stock standard solution ($1000 \text{ mg}\cdot\text{L}^{-1}$) was prepared and appropriately diluted to obtain all other solutions used in this study. RIF quantification was performed using a spectrophotometer Shimadzu MultiSpec-1501, with absorbance measurements at 474 nm.

The analytical curve was plotted with concentrations ranging from 5.0 to $45.0 \text{ mg}\cdot\text{L}^{-1}$.

1.2. Adsorbent

Sururu shells (*Mytella falcata*) were obtained from Mundaú Lake, in Maceió city, Alagoas, Brazil. The shells were previously washed in current water in order to remove the residual organic matter and then dried in an oven at 60°C for 8 h. The shells were separated into three parts: the first one remained *in natura* (Fig 3a), the second one was pyrolysed (Fig 3b) and the third fraction was calcined (Fig 3c). Pyrolysis was performed for 2 h at 700°C in a tubular furnace (Jung LT6 2010) and calcination (EDG F3000), for 5 h at the same temperature.



Fig. 3. Adsorbent materials produced: *in natura* (a), after pyrolysis (b) and after calcination (c).

1.3. Adsorbent characterization

The shells surface were analyzed by scanning electron microscopy (SEM) using the SSX-500 Superscan, Shimadzu, after 6 min of gold metallization under 10 mA (Quick Coater SC-701, Sanyu Electron).

1.4. Adsorption assays

The adsorption assays were performed in a finite bath, in triplicate. In a typical adsorption experiment, an exact amount of weighted adsorbent was added to 20 mL of the adsorbate solution in a 30 mL amber flask, which was kept under agitation at 140 rpm for a certain period of contact time. After that, the mixture was transferred to a 50 mL falcon tube and centrifuged at 2,000 rpm for 10 min. The final RIF concentrations were measured in the supernatant. The adsorption capacity of the adsorbent material ($qt, \text{ mg}\cdot\text{g}^{-1}$) was determined by Equation 1 and the removal percentage (%) was calculated by Equation 2.

$$q_t = \frac{(C_0 - C_t)}{W} * V \quad (1)$$

$$\% \text{ removal} = \frac{C_0 - C_t}{C_0} * 100 \quad (2)$$

where C_0 , C_e and C_t are the concentrations (mg.L^{-1}) of the adsorbate solution at the beginning, at equilibrium and at time t , respectively. W is the mass (g) of adsorbent and V (L) is the volume of the solution.

In the preliminary adsorption studies, the type of adsorbent material (*in natura*, pyrolysed and calcined shells), adsorbent dosage (1.0, 2.0 and 3.0 g.L^{-1}) and sample pH were evaluated, using initial RIF concentrations of 50 mg.L^{-1} at 30°C.

The best conditions obtained in the preliminary adsorption assays were applied in the kinetic studies (RIF initial concentration of 50 mg.L^{-1} at 30°C). The final concentrations of RIF remaining in the solution were measured in predetermined time intervals (5, 10, 30, 45, 60, 90 and 120 min) and the kinetic data obtained were fitted to the pseudo-first order (Equation 3) and pseudo-second order models (Equation 4) [9-11].

$$q_t = q_e [1 - \exp(-k_1 * t)] \quad (3)$$

$$q_t = \frac{k_2 q_e^2 t}{1 + k_2 q_e t} \quad (4)$$

where k_1 (L.min^{-1}) and k_2 ($\text{g.mg}^{-1} \text{min}$) are the constants of pseudo-first order and pseudo-second order, respectively, q_t (mg.g^{-1}) is amount adsorbed at time t and q_e (mg.g^{-1}) is the amount adsorbed at equilibrium.

3. Results and discussion

3.1. Adsorbent characterization

The images from the calcined sururu shells obtained from the SEM analysis (Fig. 3) show a very porous material, exhibiting rounded particles, as previously reported [12].

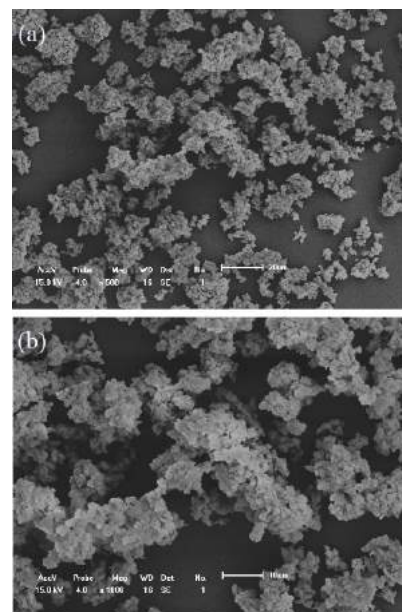


Fig. 3. SEM micrographs from the calcined shells surface, 500x (a) and 1000x (b) magnification.

The elemental composition of the bark of *Mytella falcata*, in a quantitative way, was determined from the X-ray dispersive energy spectroscopy (EDX), as shown in Table 1.

The Figure 4 shows the X-ray diffractogram for the shell of *Mytella falcata* and shows the presence of crystalline forms of calcium carbonate (CaCO_3) in the calcined shell. Aragonite (peaks A, B, C and F) and calcite (peaks D, E and G) were found mainly, which represent the composition of *Mytella falcata* shells and may vary according to the location and type of mollusk evaluated [13].

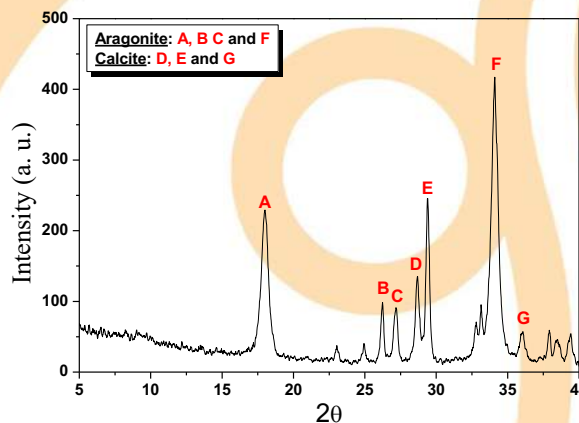


Fig. 4. Thermogravimetric analysis. B - X-ray diffraction (XRD).

Silva et al. [4] presented X-ray analysis of *Mytella falcata* without treatment. It is observed that the peaks found in this work are also found in the calcined shell, however, they are larger and narrower, demonstrating the greater crystallinity of the raw material.

The Figure 5 shows the infrared absorption spectrum (FTIR) for the calcined *Mytella falcata* shells.

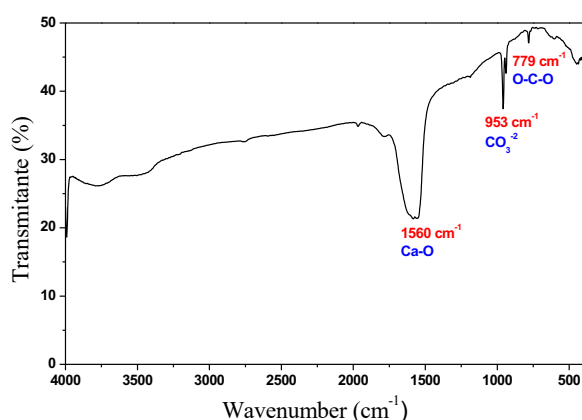


Fig. 4. Thermogravimetric analysis. B - X-ray diffraction (XRD).

Absorption band around 1560 cm^{-1} corresponds to Ca-O stretch vibration, corroborating the presence of CaO phase in the material structure. The bands around 779 cm^{-1} and 953 cm^{-1} attest the presence of carbonate groups. However, at 779 cm^{-1} the peak is related to the angular deformations outside the plane (CO_3). These bands were also found in oyster shells [5,6,13–15].

The elemental composition of the bark of *Mytella falcata*, in a quantitative way, was determined from the X-ray dispersive energy spectroscopy (EDX), as shown in Table 1.

Table 1. X-ray Dispersive Energy Spectroscopy of calc *Mytella falcata* shells

Compositi on	Percentage (%)
Ca	98.492
Sr	0.619
K	0.298
Si	0.271
S	0.119
Ni	0.077
Fe	0.049
Cu	0.044
Cr	0.030

3.2. Adsorption assays

The material has a high concentration of calcium (Ca) and much lower proportions of compounds such as Mr, K and Si. Comparing this result with that obtained by Silva et al. [4] for raw *Mytella falcata* shells from Maceió / AL (Brazil), it is observed that calcination favors the presence of Ca in the structure, probably in the form of CaO. There is an increase in the proportion of this element from 91.8% in the work cited to 98.492% in this work. El Haddad et al. [6], with calcined *Edulis Mytilus* also obtained a significant amount of Ca and smaller amounts of Si and Sr.

Since three different adsorbent materials were produced (*in natura*, pyrolysed and calcined shells), the first adsorption assay was performed in order to select the adsorbent with the best affinity for the adsorbate. From the results obtained (Fig. 6a), calcined shells provided the best antibiotic removal, reaching $78.0 \pm 0.2\%$. Therefore, this material was chosen for further studies.

Subsequently, adsorbent dosage was also evaluated, once it is a very important parameter in the adsorption process. Higher dosages were studied trying to increase adsorption. Results achieved (Fig 6b) showed an increment in RIF removal by doubling the amount of adsorbent but thereafter remained constant (around 91%). Thus, 0.2 g of calcined shells were used in the subsequent assays.

Sample pH was also analyzed (3.0, 7.0 and 13.0) and the data obtained (Fig. 6c) did not indicate relevant differences between neutral and basic pH. Therefore, pH 13.0 was used in the next studies, once this was the matrix pH after adding the adsorbent to the adsorbate solution.

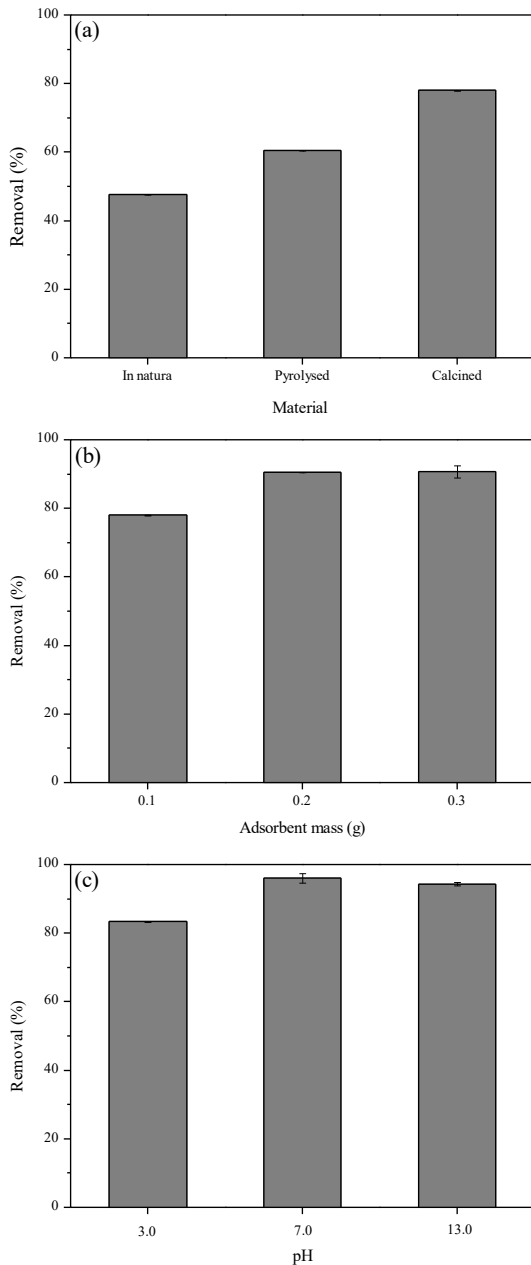


Fig. 6. Effect of type of adsorbent (a), adsorbent dosage (b) and matrix pH (c) in rifampicin adsorption onto sururu shells.

Kinetic study was performed using the best conditions achieved in the preliminary assays: 0.2 g of calcined shells in 20.0 mL of adsorbate solution without pH adjustment. Three different concentrations were evaluated (50, 100 and 200 mg.L⁻¹ of RIF) in time intervals from 5 to 120 min. From the results achieved (Fig. 7), equilibrium was

reached after 30 min of contact for 50-100 mg.L⁻¹ and 45 min for RIF initial concentration of 200 mg.L⁻¹.

The experimental data were fitted to the pseudo-first order and pseudo-second order models and the kinetic parameters attained are shown in Table 2. From the results obtained, the adsorption mechanism tends to the pseudo-first order model, suggesting a physical sorption.

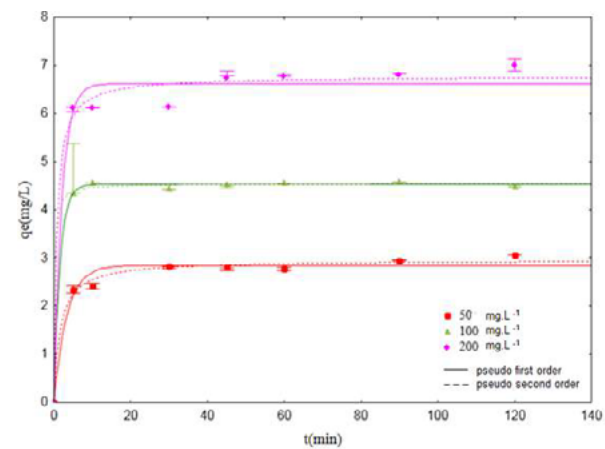


Fig. 7. Rifampicin adsorption kinetic curve onto calcined sururu shells.

Table 2. Kinetics parameters obtained for rifampicin adsorption onto calcined sururu shells

		50 mg.L ⁻¹	100 mg.L ⁻¹	200 mg.L ⁻¹
Pseudo-first order	q _e (mg.g ⁻¹)	2.846	4.526	6.614
	k ₁ (min ⁻¹)	0.301	0.639	0.488
	ARE	0.203	0.805	3.912
	R ²	0.989	0.999	0.983
Pseudo-second order	q _e (mg.g ⁻¹)	2.954	4.546	6.768
	k ₂ (g.mg ⁻¹ .min ⁻¹)	0.216	1.141	0.211
	ARE	2.546	0.950	2.644
	R ²	0.991	0.998	0.990

4. Conclusion

In the present contribution, calcined sururu shells were successfully applied for rifampicin removal from water. From the assays performed, 10 g.L⁻¹ of adsorbent was able to remove over 90% of rifampicin from water (50–100 mg.L⁻¹) in 30 min of contact, reaching the adsorptive capacity of 3.05, 4.58 and 7.00 mg.g⁻¹ (rifampicin initial concentrations of 50, 100 and 200 mg.L⁻¹, respectively).

According to the characterization analysis (XRD and FTIR) it was possible to confirm the residual presence of calcium carbonate (CaCO₃) in the crystalline structure of calcined shells, mainly as calcite and aragonite forms. The elemental composition of the bark of *Mytella falcata* (EDX), the material has a high concentration of calcium (Ca) and much lower proportions of compounds such as Mg, K and Si. SEM analysis showed a porous material with heterogeneous surface characterized by rounded particles.

The results indicated that sururu shells can be used as alternative adsorbent for rifampicin removal from aqueous matrices, although more studies are necessary. Moreover, by using a waste which is produced in large amounts in the region can contribute to reduce the environmental problems associated with its irregular disposal.

Acknowledgements

The authors wish to thank Conselho Nacional de Desenvolvimento Científico e Tecnológico (CNPq/Brazil), Coordenação de Aperfeiçoamento de Pessoal de Nível Superior (CAPES/Brazil) and Fundação de Amparo à Pesquisa do Estado de Alagoas (FAPEAL/Brazil).

References

- [1] Coutinho MK, Assad LT, Normande ACL, Brandão TBCB. A cada lata – A extração do sururu na Lagoa Mundaú – Alagoas. Editora IABS, Brasília-DF, Brasil, 2014.
- [2] Chowdhury S, Saha P. Sea shell powder as a new adsorbent to remove Basic Green 4 (Malachite Green) from aqueous solutions: Equilibrium, kinetic and thermodynamic studies. *Chem Eng J.* 2010;164: 168-177.
- [3] Peña-Rodríguez S, Fernández-Calviño D, Nóvoa-Muñoz JC, Arias-Estévez M, Núñez-Delgado A, Fernández-Sanjurjo MJ, Álvarez-Rodríguez E. Kinetics of Hg(II) adsorption and desorption in calcined mussel shells. *J Hazard Mater* 2010;180: 622–627.
- [4] Silva TS, Meili L, Carvalho SHV, Soletti JI, Dotto GL, Fonseca EJS. Kinetics, isotherm, and thermodynamic studies of methylene blue adsorption from water by *Mytella falcata* waste. *Environ Sci Pollut Res.* 2017.
- [5] Cirini G, Lichtfouse, Wilson LD, Morin-Cirini N. Conventional and non-conventional adsorbents for wastewater treatment. *Environ Chem Lett* 2019;17:195-213.
- [6] El Haddad M, Regti A, Laamari MR, Slimani R, Mamouni R, Antri SE, Lazar S. El Haddad, M., Regti, A., Laamari, M. R., Slimani, R., Mamouni, R., Antri, S. E., & Lazar, S. Calcined mussel shells as a new and eco-friendly biosorbent to remove textile dyes from aqueous solutions. *J Taiwan Inst Chem E* 2013;45(2): 533–540.
- [7] Rosenfeld PE, Feng LGH. 16 Emerging contaminants. *Risk of Hazardous Wastes* 2011:215-222.
- [8] Verlicchi P, Al Alkidy M, Zambello E. Occurrence of pharmaceutical compounds in urban wastewater: Removal, mass load and environmental risk after a secondary treatment-A review. *Sci. Total Environ.* 2012;429(1):123-55.
- [9] Lagergren S. About the theory of so-called adsorption of soluble substances. *K Sven Vetenskapsakademiens* 1898;24:1–39.
- [10] Ho YS, McKay G. Sorption of dye from aqueous solution by peat. *Chem Eng J.* 1998;70:115–124.
- [11] Ho YS, McKay. Pseudo-second order model for sorption processes. *Process Biochem.* 1999;34:451–465.
- [12] Ballester P, Mármol I, Morales J, Sánchez L. Use of limestone obtained from waste of the mussel cannery industry for the production of mortars. *Cement Concrete Res* 2007;37(4):559–564.
- [13] D. Silva, N.A. Debacher, A.B.C. Junior, F. Rohers, A.B. De Castilhos, F. Rohers, A.B.C. Junior, F. Rohers, Physical chemistry and micro structural characterization of shells of bivalve mollusks from sea farmer around the Santa Catarina island, *Quim. Nova.* 33 (2010) 1053–1058. doi:10.1590/S0100-40422010000500009.
- [14] H.-Y. Li, Y.-Q. Tan, L. Zhang, Y.-X. Zhang, Y.-H. Song, Y. Ye, M. S. Xia, Bio filler from waste shellfish shell: Preparation, characterization, and its effect on the mechanical properties on polypropylene composites, *J. Hazard. Mater.* 217–218 (2012)256–262. doi:10.1016/j.jhazmat.2012.03.028.
- [15] N. Mohammadian, B. Akhlaghinia, Magnetic

calcined oyster shell functionalized with taurine immobilized on β -cyclodextrin ($\text{Fe}_3\text{O}_4/\text{COS}@ \beta\text{-CD-SO}_3\text{H}$ NPs) as green and magnetically reusable nanocatalyst for efficient and rapid synthesis of spirooxindoles, *Res. Chem. Intermed.* 45 (2019) 4737–4756. doi:10.1007/s11164-019-03860-x.

Ceramic monoliths composed with natural zeolite for the removal of contaminants in aqueous media

C. García-Carvajal^{a*}, V. C. de Souza^a, J. Villarroel-Rocha^a, M. M. Barroso-Quiroga^b,
K. Sapag^a

^aLaboratorio de Sólidos Porosos - INFAP-CONICET - Universidad Nacional de San Luis
Avenida Ejército de los Andes 950 – CP: 5700 – San Luis – Argentina
Teléfono: (0266) 4520329 – Email: celene.garciac@gmail.com

^bDepartamento de Minería, FCFMyN, Universidad Nacional de San Luis / INTEQUI-CONICET, Chacabuco y Pedernera – CP: 5700 – San Luis – Argentina

Abstract

Organic pollutants are an outstanding problem due to their high toxicity and difficulty in removing them, among the dyes assiduously dumped by the textile industry stand out, being methylene blue one of the most frequent. For its removal, a variety of techniques have been studied, where adsorption process is one of the most used. A wide variety of adsorbents have been experienced, where those from natural materials have shown great efficiency, in addition to being low cost. The problem arises when using these adsorbents in powder form since it generates difficulties in its handling and extraction from the medium. In this work we propose the use of adsorbent materials arranged in a ceramic matrix like monoliths with honey comb structure, synthesized from zeolites and natural clays. These materials were studied in the removal of methylene blue finding an average value of removal capacity of 10 mg MB per gram of adsorbent.

Keywords: Natural zeolite; clay; formed ceramic materials; adsorption in solution; methylene blue.

1. Main text

The pollution of the environment is a phenomenon that severely affects the world population, being necessary to reduce the contamination in vital systems for health, such as air and water. This fact has generated concern in many communities, particularly in the scientific one, where important contributions can be made to solve it.

Water purification is one of the main concerns, because it is currently a large part of the population lacks the amount of drinking water necessary to meet their needs.

There are different pollutants discharged into aqueous systems during industrial processes such as organic compounds among them dyes, which are mainly issued by the textile industry. Methylene blue (MB) is an example of this type of contaminant, therefore is commonly used as a test molecule in removal studies [1].

Various treatments have been studied and proposed for the removal of contaminants from water, where chemical precipitation/co-precipitation, membrane filtration, and adsorption are the most conventional [2-4]. Each of these

methods has advantages, disadvantages and limitations in the application. For example, when the contaminant is present in high concentrations, try to concentrate and remove it from the medium. However, when the concentration is low (of the order of mg L⁻¹, as is the case with organic pollutants present in water) the adsorption processes begin to play a very important role. This last process is very effective when the adsorbent used has the ability to combine specific removal mechanisms, as ion exchange with the less specific ones, as physical adsorption or molecular sieving. For this reason, adsorption is a widely studied process, obtaining very good results where the use of natural materials making this process a feasible and economical technology [3,4].

Although the use of natural materials (clays, zeolites and other natural minerals) as adsorbents for methylene blue [5,6] presents an outstanding economic advantage, the main disadvantage is using it in powder form hindering its manipulation.

An alternative to solve this problem is to use conformed adsorbents, in suitable structural forms such as monoliths with ceramic structures, with high mechanical resistance, a fairly uniform porosity,

low pressure drop and therefore high resistance to effluent plugging [7].

In the present work ceramic materials formed by the extrusion technique from natural clays and zeolites were synthesized and tested in the removal of methylene blue from aqueous medium.

2. Materials and methods

2.1. Synthesis of natural zeolite ceramic monoliths (NZCM).

For the synthesis of ceramic materials formed from natural zeolite from Chile, the following steps were carried out:

- Dry mixing of raw materials: A 50% proportion of natural zeolite was used as adsorbent material, 30% bentonite clay as adsorbent and plasticizer, 15% alumina to grant the ceramic body and 5% starch as binder; These materials were placed in a horizontal mixer at 60 rpm for 10 mi to ensure the homogeneity of the solids.
- Obtaining ceramic paste: in order to obtain the appropriate plasticity and rheology to be able to be extruded correctly, water was added in a proportion of ~38%.
- Extrusion: at this stage the ceramic paste is added to the feed hopper of the extruder, which, using an endless screw, moves the paste and passes it through a honeycomb geometry nozzle, where finally monoliths of 20 cm long, 2,7 cm wide, 2 cm x 2 cm cells and 0,9 cm thick walls were obtained.
- Drying: for controlled drying of the monoliths obtained by extrusion, they are taken to a vacuum chamber for 24 h at room temperature and then placed in plaster molds for 48 h exposed to the environment, to finish the drying stage.
- Heat treatment: in order to confer the mechanical properties granted by ceramic materials, the monoliths were taken to an oven in which the heat treatment is carried out with a heating ramp of 3 °C min⁻¹ from room temperature up to 120 °C for 1 h to remove hydration water from the material, and a second heating of 3 °C min⁻¹ until reaching 575 °C for 1 h.

The materials obtained for this work can be seen in Figure 1.

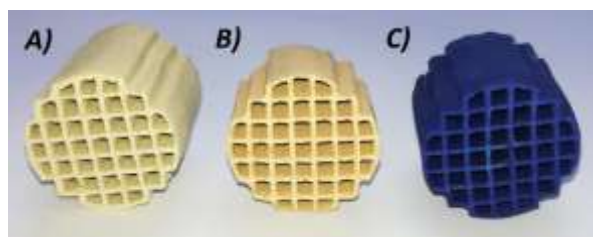


Fig. 1. Natural Zeolite Ceramic Monolith's, A) NZCM in green (before heat treatment) B) NZCM calcined at 575 ° C, C) NZCM after MB removal tests.

2.2. Characterization of materials

The thermogravimetric analysis was performed on a TGA Q600 SDT analyzer (TA Instruments) with 100 mL min⁻¹ flow in an oxidizing atmosphere with a heating rate 10 °C min⁻¹ from room temperature to 900 °C.

N₂ adsorption/desorption analysis at 77 K was performed on an Autosorb-1MP manometric adsorption instrument (Quantachrome Instruments). CO₂ adsorption at 273 K (up to 1000 kPa) was carried out on ASAP-2050 (Micromeritics). The sample was previously degassed at 353 K for 48 h. From N₂ adsorption data, specific surface area (S_{BET}) was calculated by Brunauer, Emmet, and Teller method using the IUPAC recommendations [8], the micropore volume was obtained using α_s plot method, the total pore volume was calculated with the Gurvich's rule at 0,985 of relative pressure and the pore size distribution was calculated with a NLDFIT method using the kernel "N₂ a 77K on silice (cylindrical pore, equilibrium model)". From the CO₂ adsorption, the micropore volume was obtained using the Dubinin Radushkevich (DR) method [9], and the micropore size distribution was obtained using the Horvath and Kawazoe (HK) method [10].

Mercury intrusion extrusion porosimetry was measurement on porosimeter analyzer, AUTOPORE III (Micromeritics) from 0.002 up to 150 MPa. The samples previously were degassed to a residual pressure of 30 μ m Hg. From mercury intrusion data, specific surface area (S_{Hg}), total pore volume (V_{TP}), porosity, and pore size distribution were obtained.

To evaluate the resistance to acidic and basic lixiviation we used 4 g of NZCM in 25 mL of water with pH 3 and with pH 12 in agitation (160 rpm) by 7 days. After, the samples were dried at 100 °C for 24 h and the percentage of lixiviation mass loss was calculated.

2.3. Methylene blue adsorption

For the calibration curve the concentrations of 2, 4, 6, 8 and 10 ppm of methylene blue were used and determined by uV-vis.

For adsorption kinetics we used methylene blue 675 mL at 100 ppm and NZCM 8,1 g under 160 rpm agitation. Aliquots were removed ($t=0, 5, 30, 120, 180, 360, 720, 1440, 1800, 2880$ and 7474 min) analyzed by uV-vis and the concentration determined by the equation obtained with the calibration curve.

For adsorption isotherm we used the initial concentrations of 10, 25, 50, 75, 100, 125, 150, 175 and 200 ppm of methylene blue (25 mL) and NZCM $\sim 0,3$ g under 160 rpm agitation by 24 h. The final concentrations were obtained by uV-vis.

To calculate the initial and final concentrations, the absorbance of the solutions at 665 nm in the uV-vis spectronic 20 spectrophotometer (Bausch and Lomb) was used.

3. Results and discussion

3.1. XRD

The raw material and the synthesized monoliths were characterized by x-ray diffraction, in Fig. 2 the diffractograms corresponding to the majority phases are presented, where it was confirmed that the material synthesized after the heat treatment continues to maintain the structure of the natural zeolite, and presents peaks of montmorillonite and corundum present as major phases of bentonite and alumina.

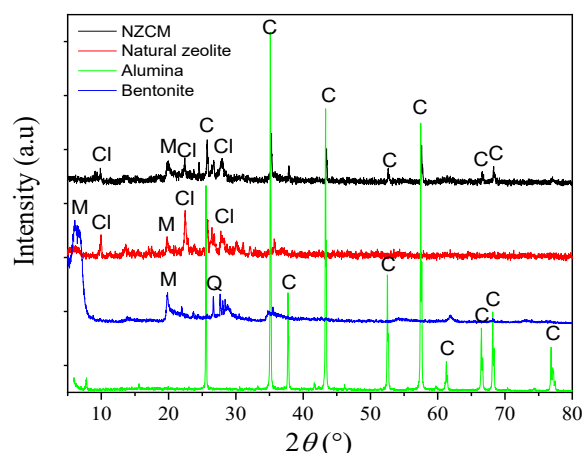


Fig.2. X-ray diffraction pattern of the NZCM and raw materials. *M*: Montmorillonite, *Cl*: Clinoptilolite, *C*: Corundum, *Q*: Quartz.

3.2. Textural analysis

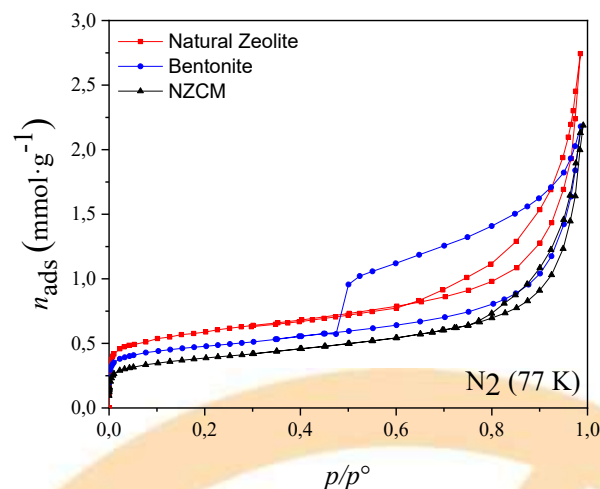


Fig. 3. N_2 adsorption-desorption isotherm at 77 K of the NZCM and raw materials.

Fig. 3 shows the N_2 adsorption/desorption isotherms. For natural zeolite and bentonite, we can see adsorption at low relative pressure and a quickly increase of the amount adsorbed at relative pressure near to 1, characteristic of interparticle pores or pores of the aggregates present in these raw materials. In Table 1 can be seen that the textural properties of NZCM decrease slightly, respect to natural zeolite.

The Fig 4 show the pore size distribution to NZCM and raw materials, where the bentonite and natural zeolite both have micropores less than 1 nm. In addition, the natural zeolite exhibits other micropores of 1,5 nm of modal size and mesopores with a wide pore size distribution. The NZCM has characteristic porosity of raw materials.

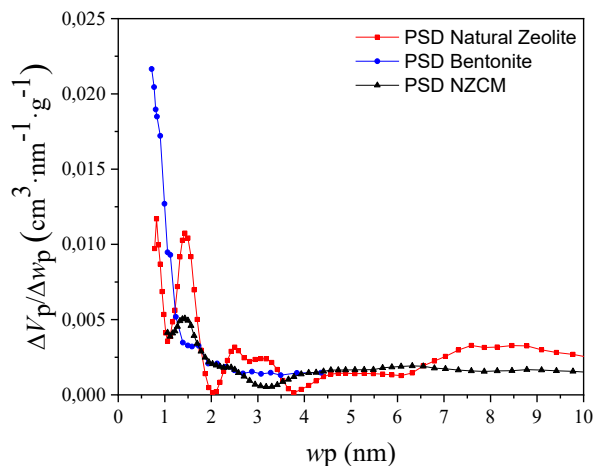


Fig. 4. Pore size distribution for the NZCM and raw materials using NLDFT.

In CO₂ adsorption isotherms (Fig. 5), which permits analyze the narrow micropores, can be seen that the natural zeolite show the larger CO₂ amount adsorbed than NZCM. That happens because the microporosity in the NZCM is supplied from natural zeolite that is 50% of the raw material used to obtain the NZCM. In Table 1 we can see that the natural zeolite presents the higher narrow micropore volume (0,07 cm³/g) than NZMC (0,03 cm³/g) but the modal micropore size (Fig. 6) is the same for both (0,44 nm).

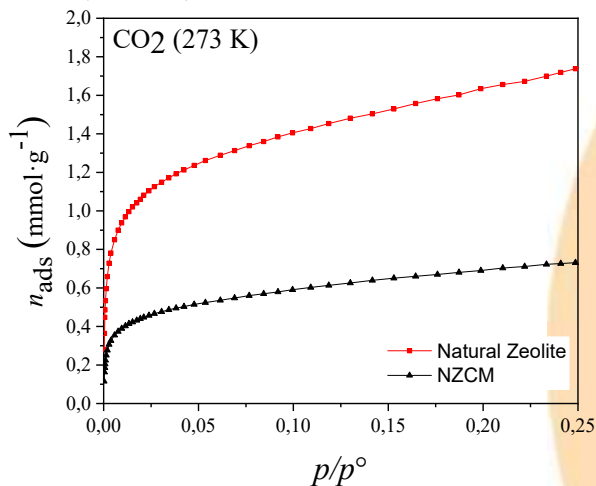


Fig. 5. CO₂ adsorption isotherm at 273 K of the NZCM and natural zeolite.

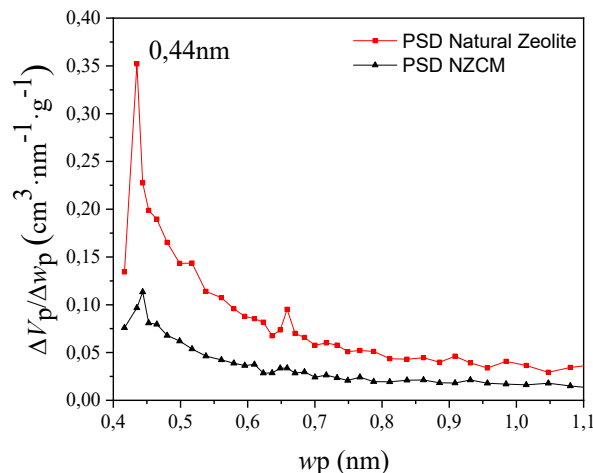


Fig. 6. Pore size distribution for the NZCM and natural zeolite using the HK method.

Table 1. Textural properties of the micro and mesopores of NZCM and raw materials.

Samples	S _{BET} [m ² /g]	V _{TP} [cm ³ /g]	V _{μP} [cm ³ /g]	V _{μP-CO₂} [cm ³ /g]	*w _p [nm]
Zeolite	47	0,10	0,01	0,07	0,44
Bentonite	40	0,07	0,01	-	-
Alumina	1	0,01	0,00	-	-
NZCM	31	0,07	0,00	0,03	0,43

*modal micropore size

The presence of large mesopores and/or macroporosity in materials under study were characterized by Hg porosimetry, thus mercury intrusion-extrusion curves can be seen in Fig. 7.

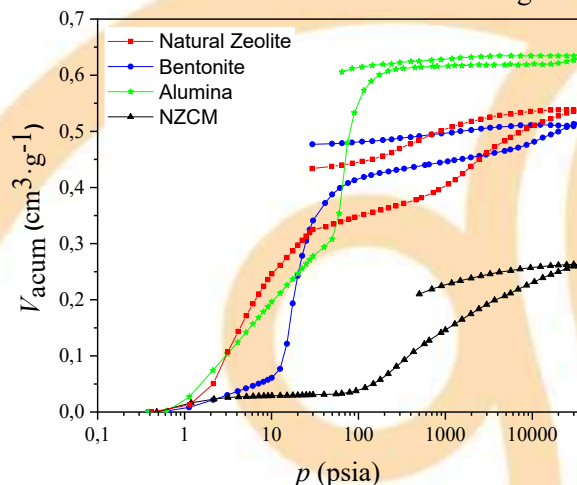


Fig. 7. Hg intrusion-extrusion curve for the NZCM and raw materials.

In mercury intrusion-extrusion curves, it can be seen that alumina and bentonite have an important growth at a pressure between 10-100 psia, which indicates that they have a narrow pore size

distribution, unlike the curves obtained for natural zeolite and NZCM, which show a gradual accumulated volume growth, which indicates that they have a wide distribution of pore size. It should be noted that in the curve obtained for the synthesized monolith it does not show an accumulated volume growth at low pressures (up to 100 psia), which indicates that the material does not have large macropores ($> 1 \mu\text{m}$).

This can be seen in Fig. 8. where the pore size distributions are shown from the mercury intrusion data of the NZCM and raw materials.

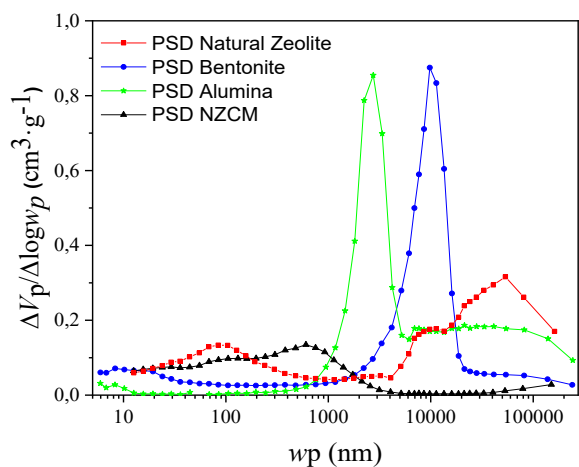


Fig. 8. Pore size distribution for the NZCM and raw materials obtained from Hg intrusion data.

The textural properties found from mercury porosimetry data are shown in Table 2.

Table 2. Textural properties of the meso and macro pores of NZCM and raw materials.

Samples	A_{TP} [m ² /g]	V_{TP-Hg} [cm ³ /g]	Porosity [%]	ρ_{bulk} [g/cm ³]	$\rho_{esqueleto}$ [g/cm ³]
Bentonite	18,5	0,51	57,6	1,12	2,64
Alumina	4,60	0,63	70,4	1,12	3,80
MCZN	21,3	0,26	38,6	1,47	2,39

3.3. Acidic and basic pH resistance

After 7 days immersed in water at pH 3, the sample NZCM didn't show weight loss, therefore, the material is resistance to acidic pH solutions. When in contact with water at pH 12, the sample NZCM showed 0,83% weight loss.

3.4. Methylene blue (MB) adsorption

Some visible results of the methylene blue removal tests at different concentrations are shown in Fig. 9.



Fig. 9. Adsorption tests of methylene blue at different concentrations.

In Fig. 10 we can see that the methylene blue adsorption kinetics in the NZCM sample is slow, with q_{ads} reach a value of 9.8 mg g^{-1} at a time of 7474 min. This slow adsorption probably occurs because of the slow diffusion of methylene blue within the narrow microporosity of the zeolite (0.44 nm) resulting in slow adsorption kinetics.

In short times, low adsorption can be attributed to the hydroxyl edge sites of the montmorillonite present in the bentonite clay, since it detects the active sites affected before being adsorbed on the micropores of the monolith.

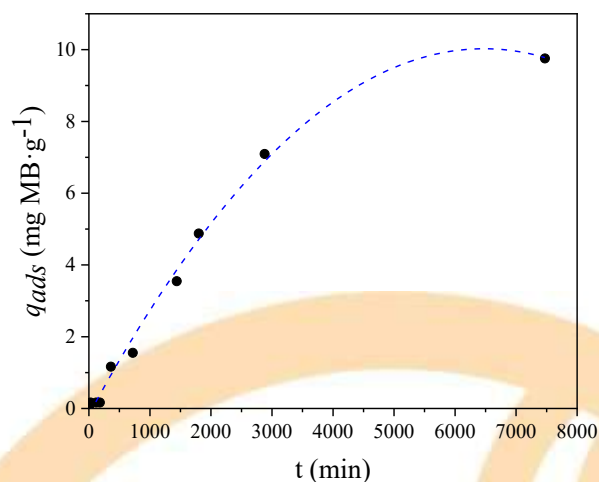


Fig. 10. MB adsorption kinetic on NZCM.

Conclusions

Ceramic materials of zeolite, bentonite and alumina synthesized at $575 \text{ }^\circ\text{C}$ were obtained for application in the removal of methylene blue in aqueous medium.

The microporosity of the material is mainly given by zeolite (main adsorption sites), meso and macropores mainly by bentonite and alumina as well as mechanical resistance in aqueous medium.

Although a high capacity for removal of MB with the ceramic monolith was not obtained, in the



present work the advantages of using the NZCM in effluents were evidenced.

Acknowledgment

This work was financially supported by UNSL and CONICET (Argentina).

References

- [1] El Mouzdahir Y, Elmchaouri A, Mahboub R, Gil A, Korili S. A. Equilibrium modeling for the adsorption of methylene blue from aqueous solutions on activated clay minerals. *Desalination*, 2010: 250(1), 335–338.
- [2] EPA (Org). *Arsenic Treatment Technologies for Soil, Waste, and Water*. EPA-542-R-02-004. United States; 2002.
- [3] Rafatullah M, Sulaiman O, Hashim R, Ahmad A. Adsorption of methylene blue on low-cost adsorbents: A review. *Journal of Hazardous Materials*, 2010: 177(1-3), 70–80.
- [4] Mohanty D. Conventional as well as Emerging Arsenic Removal Technologies—a Critical Review. *Water, Air, & Soil Pollution*, 2017: 228(10).
- [5] Rida K, Bouraoui S, Hadnine S. Adsorption of methylene blue from aqueous solution by kaolin and zeolite. *Applied Clay Science*, 2013: 83-84, 99–105.
- [6] Sarma GK, SenGupta S, Bhattacharyya KG. Methylene Blue Adsorption on Natural and Modified Clays. *Separation Science and Technology*, 2011: 46(10), 1602–1614.
- [7] Ávila P, Montes M, Miró E. Monolithic reactors for environmental applications: A review on preparation Technologies, *Chem. Eng. J.*, 2005: 109, 11–36.
- [8] Thommes M, Kaneko K, Neimark AV, Olivier JP, Rodriguez-Reinoso F, Rouquerol J, Sing KSW. Physisorption of gases, with special reference to the evaluation of surface area and pore size distribution (IUPAC Technical Report). *Pure and Applied Chemistry*, 2015: 87(9-10).
- [9] Dubinin MM. The Potential Theory of Adsorption of Gases and Vapors for Adsorbents with Energetically Nonuniform Surfaces. *Chem. Rev*, 1960: 60, 235.
- [10] Horváth, G.; Kawazoe, K. Method for the calculation of effective pore size distribution in molecular sieve carbon. *J. Chem. Eng. Jpn.* 1983: 16, 470–475.

Adsorption of thiamethoxam in water and sugarcane juice by magnetic nanomodified activated carbon and determination by HPLC-DAD

Driëlle Aparecida de Freitas^a, Roberta Ferreira Nocelli^a, Geórgia Labuto^b; Elma Neide Vasconcelos Martins Carrilho^a

^a Universidade Federal de São Carlos – Rodovia Anhanguera, km 174 – CEP: 13604-900 Araras – SP – Brazil

^b Universidade Federal de São Paulo – Rua São Nicolau, 210, Centro – CEP: 09913-030 Diadema – SP – Brazil.

Abstract

In Brazil, the cultivation of sugarcane (*Saccharum officinarum*) is of greater importance for the sugar-alcohol sector due to its high levels of sucrose. However, in order to guarantee high productivity, high levels of pesticides are applied in this crop, including the neonicotinoid and systemic thiamethoxam (TMX). By considering the sugarcane juice a food matrix and the risks that TMX residues can offer, the aim of this work was to develop a chromatographic method for its quantification, and to evaluate its removal from water and sugarcane juice matrices by magnetic nanomodified activated carbon (AC-MNP). This adsorbent was synthesized and characterized by FTIR, XDR, and SEM. TMX quantification was performed by High Performance Liquid Chromatography coupled to a diode array detector (HPLC-DAD) at 254 nm, acetonitrile:water (30:70) as mobile phase at 1.0 mL/min, using a C18 column, and 20 μ L sample volume. The nanomodification process was satisfactory and the characterization of AC-MNP allowed to observe the effective impregnation of the magnetite in AC. The TMX adsorption kinetics in sugarcane juice was a pseudo-second order type, with r^2 0.9999, indicating a chemical adsorption process. The experimental sorption capacity (SC) for both TMX (standard) and TMX-I (formulated product) were 13.3 and 65.7 mg/g, respectively, and Freundlich and SIPS best fit TMX data ($r^2 = 0.9740$ and 0.9716), while TMX-I data were adjusted to Langmuir and SIPS ($r^2 = 0.9941$ and 0.9943). Therefore, the chromatographic method was highly satisfactory and the efficiency of AC-MNP in the sorption of TMX was confirmed by the excellent values of SC and its kinetics.

Keywords: biosorption; sugarcane juice; magnetic nanoparticles; pesticide; insecticide

1. Introduction

The cultivation of sugarcane (*Saccharum spp*) is considered as one of the oldest and most important of human civilization. Brazil has become the largest producer of sugarcane, followed by India and China, and São Paulo State is responsible for almost 54% of all national production [1,2]. Sugarcane juice can be obtained by grinding the stalks of the plant and is a drink widely consumed in the countries where this cultivar is found. However, due to the wide variety of pesticides used in sugarcane crops to ensure productivity and minimize pest damage, products obtained from sugarcane are not free of these contaminants. The insecticide thiametoxam (TMX) is a systemic neonicotinoid used in the cultivation of sugarcane to control insects [3,4]. Its chemical structure is depicted in Figure 1.

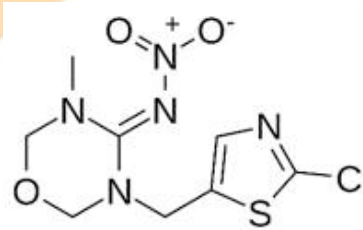


Fig. 1. Chemical structure of the insecticide thiametoxam (TMX), 3- [(2-cloro-1,3-tiazol-5-il) metil]-5-metil-N-nitro-1,3,5-oxadiazinan-4-imina.

The use of adsorbents as alternatives for pesticides removal in aqueous medium has been emphasized, and activated carbon has been efficiently used in the removal and quantification of analytes in complex samples [5, 6, 7, 8, 9, 10]. High performance liquid chromatography (HPLC)



with diode array detection (DAD) is a technique commonly used in the analysis of possible presence of pesticides in food matrices [11, 12, 13]. It is a very precise and efficiency technique for separation of toxicological species [14,15]. Therefore, the removal of TMX in aqueous medium and sugarcane juice (*Saccharum spp*) by magnetic nanomodified activated carbon (AC-MNP) and the residual determination of this insecticide by HPLC-DAD is proposed.

2. Material and Methods

2.1 Materials

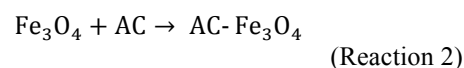
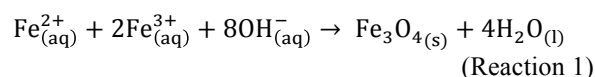
Purified water from a Direct-Q® 3 System (Merck Millipore – Germany) was used to prepare all solutions. Mesoporous activated carbon, FeCl₃·6H₂O, FeSO₄·7H₂O, HCl, and NH₄OH (Labsynth, São Paulo, Brazil) were used to synthesize the magnetic materials. Thiametoxam (TMX) (Sigma-Aldrich, 98%) was used as a reference standard and the Syngenta pesticide 250 WG® (TMX-I) was employed in the sorption studies. Acetonitrile (ACN) (HPLC grade, Honeywell, USA) was employed in the composition of the mobile phase, 30:70 (v/v) ACN:H₂O. All reagents and samples were filtered (0.45 µm Millex®) prior the HPLC analysis.

The mobile phase (MP) was filtered in PTFE 0.45 µm membrane (Unifil, São Paulo, Brazil) supported on a porous plate glass funnel (1.0-1.6 µm), coupled to a vacuum pump (Millipore®, model WP6111560, Billerica, USA). After filtration, the MP was sonicated in ultrasonic bath (Unique USC 2800 model, São Paulo, Brazil) for 30 min for degassing before chromatographic analysis.

2.2. Preparation of the adsorbent nanomodified activated carbon (AC-MNP)

The synthesis process of magnetite (Fe₃O₄) and adsorbent nanomodified activated carbon (AC-MNP) was performed by using the coprecipitation method [6] under acidic conditions. The approach employed 1:2 Fe(II) and Fe(III) salts in HCl 1.0 mol/L medium. To this solution, 0.7 mol/L NH₄OH was slowly added under constant stirring for 30 min. After the synthesis of magnetic nanoparticles,

this material was used to prepare the magnetic nanocomposite (AC-MNP) by adding AC to the suspension containing magnetite, Fe₂O₃ (MNP) in 5:1 ratio, under constant stirring and heating. The synthesis of MNP and AC-MNP are demonstrated in by reactions 1 and 2.



2.3. Adsorbent characterization

Nanomodified activated carbon (AC-MNP) was characterized by Fourier Transformed Infrared Spectroscopy – FTIR (Vertex Model, Bruker, Germany), Scanning Electron Microscopy (ZEISS LEO 440 with OXFORD detector 7060 model), and X-Ray Diffraction (XRD, Rigaku MiniFlex 600 Model).

2.4. Kinetic studies

Initially, the pH of sugarcane juice samples was measured to verify the need its adjustment according to the pH at point of zero charge (pH_{PZC}) of NAP [10] and to select times for the analyzes (5, 10, 30, 60, and 120 min).

Sugarcane juice was fortified from a 500 mg/L TMX stock solution to a final concentration of 10 mg/L TMX. In three Falcon tubes containing 100 mg AC-MNP, 40 ml of this solution was added and the assay started at room temperature (24 °C) under constant stirring at 120 rpm. Aliquots of 2 mL of each sample solution were diluted in mobile phase (1:1), filtered (Millex® 0.45 µm) into the injected vials. All TMX quantification was performed by High Performance Liquid Chromatography, coupled to a diode array detector (HPLC-DAD) at 254 nm. The chromatographic operating conditions were: mobile phase acetonitrile:water (30:70) at 1.0 mL/min, flow rate, C18 column, sample injection volume 20 µL, and 6-min analysis time.

Thiametoxan determination was carried out by High Performance Liquid Chromatography, using an UHPLC Ultimate 3000 (Thermo Fisher Scientific, USA), equipped with LPG-3400SD



pump and a DAD detector operating at 210 nm. A C18 (5 μm , 3.5 x 150 mm) column (Waters, USA) was used for TMX separation and acetonitrile (Sigma-Aldrich, USA) was used as mobile phase at 0.7 mL/min flow rate. The temperature of the column compartment was around 30 °C.

2.5. Nanomodified activated carbon sorption capacity for TMX and TMX-I

Initially, the pH of the juice was measured to verify the need to adjust its value according to the pH_{PZC} [10]. Then, TMX spikes in this sample were performed, in triplicates, to achieve final concentrations of 10, 20, 40, 60, 80, 100, 150, and 200 mg/L. Then, in 15 mL Falcon tubes containing 50 mg AC-MNP, 10 mL of each concentration was kept at room temperature (25 °C) and under constant agitation for 15 minutes on a shaker at 120 rpm.

Based on the favorable profile of TMX adsorption isotherm in sugarcane juice by AC-MNP [19], the sorption capacity test of the formulated pesticide (TMX-I) in sugarcane juice by AC-MNP was performed. The pH of the juice was measured to verify the need to adjust its value according to pH_{PZC} . Solutions containing 15, 35, 70, 120, 300, 730, 1300, and 2500 mg/L TMX-I in sugarcane juice, were prepared. Then, 10 mL of each solution was mixed with 50 mg AC-MNP, in Falcon tubes, kept under constant stirring, at room temperature (25 °C) for 15 minutes at 120 rpm.

3. Results and Discussion

3.1. Chromatographic profile of TMX

The residual determination of TMX-I in a sugarcane juice matrix after AC-MNP sorption allowed to analyze the chromatographic profile of the sample. Figure 2 illustrates the chromatogram profiles of 13 and 0.45 mg/L TMX-I in sugarcane juice, prior and after sorption by AC-MNP.

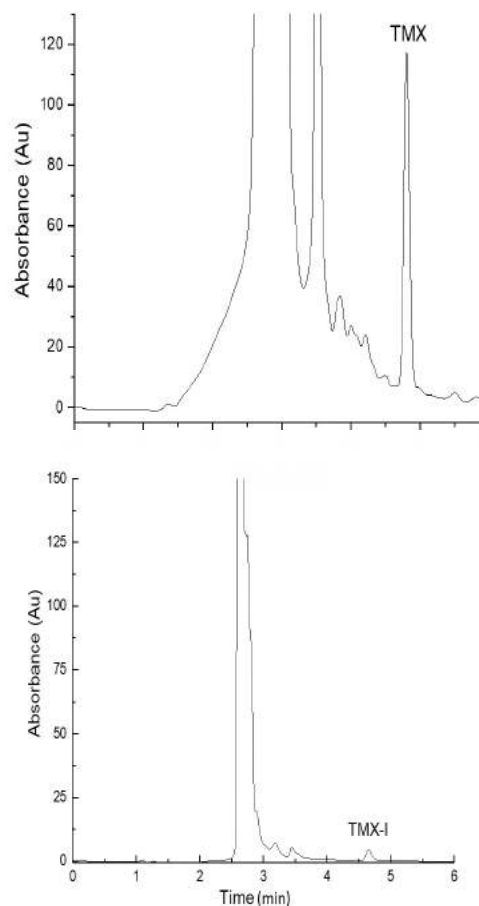


Fig. 2. Chromatogram profiles of TMX-I at (A) 13 mg/L and (B) 0.45 mg/L in sugarcane juice after sorption by 50 mg AC-MNP, at 254 nm.

3.2. Sorption pH and kinetics

Initially, the pH of sugarcane juice samples was measured to verify the need of its adjustment according to the pH at point of zero charge (pH_{PZC}) of AC-MNP [10] and to select times for the analyzes (5; 10; 30; 60 and 120 min).

The pH of fresh and fortified (11.8 mg/L TMX) sugarcane juice was 5.5 and 5.3, respectively, values below pH_{PZC} of AC-MNP. Therefore, no adjustment of pH was needed. After TMX adsorption, the pH for both matrices was observed to be 5.3.

Figure 3 shows the profile graph of adsorption kinetics as a function of contact time of TMX in sugarcane juice and AC-MNP. It is possible to verify that sorption occurs in the first 10 min, when

around 95% of TMX was adsorbed, indicating high sorption efficiency of this material.

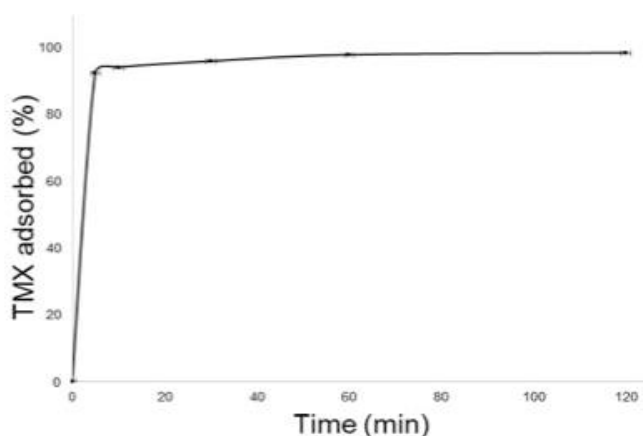


Fig. 3. Kinetics of 11.8 mg/L TMX sorption in 40 mL sugarcane juice, using 10 mg of AC-MNP.

Pseudo-first (Langergren equation) and pseudo-second order kinetic models [20] were applied to the experimental data to determine the type of TMX adsorption profile. These models describe the sorption profile of substances by solids. The adjustment equations for this study and the parameters r^2 (correlation coefficient), k_1 and k_2 (first and second order constants) indicate the affinity between adsorbate and adsorbent. It can be concluded that by the values of r^2 both the pseudo-first and pseudo-second equations provided good experimental adjustments. However, as a function of the Q_{max} values of the models, according to Ho and Mackay (2000) [16] and Ho (2006) [17], the pseudo-second order model describes the chemical adsorption process well, involving the exchange or donation of electrons between the adsorbate and the adsorbent as covalent and ion exchange forces.

The pH of fresh sugarcane juice and TMX-fortified samples, which resulted in concentrations 13.8, 19.1, 37.2, 58.7, 82.1, 98.5, 144.4, and 193.5 mg/L, it was 5.5. As this value is below the pH_{PZC} (6.4) [10] for AC-MNP, there was no need to adjust the adsorption pH, which remained at 5.3 after TMX sorption.

Juice alone and samples fortified with TMX-I at final concentrations 14.6, 35.9, 72.2, 122.2, 301.4, 730.7, 1298, and 2429 mg/L, at pH 5.5 (below the pH_{PCZ} of AC-MNP), were used to assess the sorption capacity. There was no need to adjust the

pH of the samples, which after sorption, remained at 5.3.

Four isotherm theoretical models were used to adjust the experimental data of TMX and TMX-I adsorption by AC-MNP, respectively, Langmuir, Freundlich, SIPS, and Dubinin Radushkevich (D-R). These adjustments are shown in Figure 4.

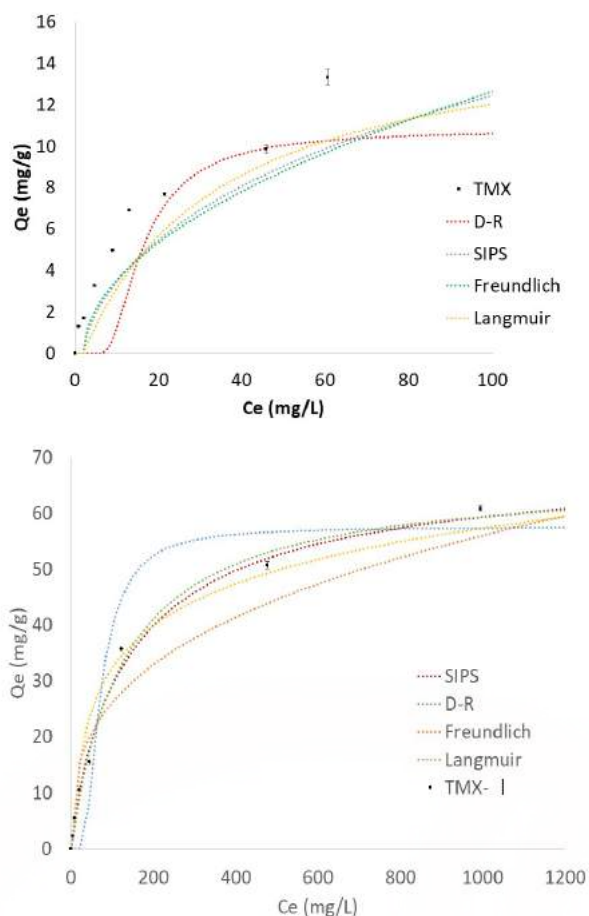


Fig. 4. Experimental curves and Langmuir, Freundlich, Sips, and Dubinin-Radushkevich (D-R) isotherm models fitting for TMX and TMX-I adsorption by AC-MNP.

It is observed that the maximum sorption capacity of TMX by AC-MNP was not reached without distinguishing an adsorption plateau and denoting that the adsorbent was not saturated. As for TMX-I, a defined level was observed for the experimental adsorption isotherms. Due to the acceptable values of r^2 or the Langmuir and SIPS models, the χ^2 values are not acceptable, denoting a considerable error in the adjustment of this

model. However, the EP values for the parameters provided for both models were low, which allows to suggest that the adsorption phenomenon of the active principle present in the pesticide TMX-PF is due to a process with a sorption characteristic involving energy of chemical bonds with the possibility of contribution of electrostatic attraction between adsorbent and adsorbate

3.2. Characterization of AC and AC-MNP

The FTIR analysis allowed to identify the functional groups in AC and AC-MNP by observing the main absorption bands in the spectra depicted in Figure 5. AC bands at 3550 and 1603 cm^{-1} are characteristic of vibrational stretching of O-H and C=C, respectively, and are typical groups in its structure [18]. The FTIR of AC-MNP shows the predominant bands of AC and from Fe-O stretch of the magnetite at 610 – 570 cm^{-1} , indicating that this material was efficiently synthesized and presents characteristics of its precursors.

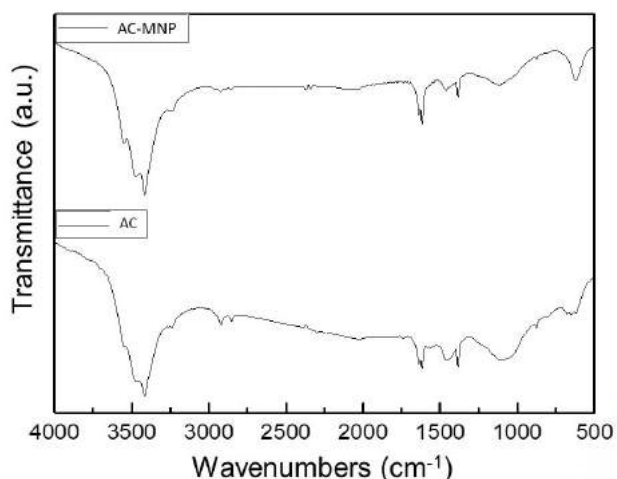


Fig. 5. FTIR spectra of activated carbon (AC) and synthesized nanomodified activated carbon (AC-MNP).

The diffractograms in Figure 6 show the crystalline structure of AC-MNP, which depicts the peaks presenting the main crystalline planes found in the structure of this composite: 30.09° (220), 3.42° (311), 43.05° (400), 53.39° (422), 56.94° (511), and 62.51°

(440). As for AC, a wide peak typical of an amorphous structure is observed. Therefore, it can be inferred that AC-MNP was efficiently synthesized, which is also indicated by the crystalline phases in the AC-MNP diffractogram.

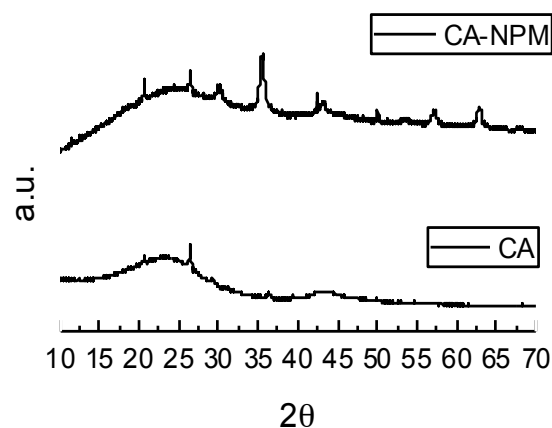


Fig. 6. X-ray diffractograms of activated carbon (AC) and synthesized nanomodified activated carbon (AC-MNP).

Conclusions

The chromatographic method was selective for TMX and showed no matrix effect, with the analytical curves r^2 around 0.9958-0.9985. Recovery tests showed results between 91-103% and coefficient of variation between 1.9-4.3%. It was also possible to conclude that the nanomodification of the activated carbon with magnetite was efficient by the crystalline peaks in the XRD analysis. The adsorption kinetics of TMX in sugarcane juice by AC-MNP was well adjusted to the pseudo-second order type, with r^2 0.9999, indicating a chemical adsorption process. Sorption capacity (SC) assays for both TMX (standard) and TMX-I (insecticide) showed experimental values of 13.3 and 65.7 mg/g, respectively and the best adjustments for the data obtained were Langmuir and SIPS isothermal models for TMX sorption, and Langmuir ($r^2 = 0.9944$) and SIPS ($r^2 = 0.9941$) for TMX-I. It was concluded that the chromatographic method for the quantification of TMX and TMX-I in aqueous and sugarcane juice matrices was highly satisfactory. The efficiency of AC-MNP in the sorption of this analyte was indicated by the excellent values of CS and

kinetics, indicating its favorable use in TMX removal from complex matrices.

Acknowledgements

The authors gratefully acknowledge the financial support by Fundação de Amparo à Pesquisa do Estado de São Paulo (FAPESP 2016/06271-4) and Coordenação de Aperfeiçoamento de Pessoal de Nível Superior (CAPES) for the scholarship provided.

References

- [1] CONAB – Companhia Nacional de Abastecimento. Cana-de-açúcar. safra 2017/2018. Primeiro levantamento. maio 2018. Disponível em: <<https://www.conab.gov.br/info-agro/safras/cana/boletim-da-safra-de-cana-de-acucar>> Acesso em: 10/08/2018.
- [2] Nova Cana. Cana-de-açúcar – Tudo sobre essa versátil planta. 2019 – Disponível em <<https://www.novacana.com/cana-de-acucar>> Acesso em: 11 março 2019.
- [3] Gallo, D.; Nakano, O.; Silveira Neto, S.; Carvalho, R.P.L.; Baptista, G.C.; Parra, J.R.P.; Zucchi, R.A.; Alves, S.B.; Vendramim, J.D.; Marchini, L.C.; Lopes, J.R.S.; Omoto, C. Entomologia Agrícola. FEALQ. São Paulo. Ceres. 2002. 920p.
- [4] Garcia, J.F. Manual de identificação de pragas da cana. Campinas – SP. Editora FMC. 2013.
- [5] El-Sheikh, A.H.; Sweileh, J.; Al-Degs, Y.S.; Insisi, A.A.; Al-Rabady, N. Critical evaluation and comparison of enrichment efficiency of multi-walled carbon nanotubes. C18 silica and activated carbon towards some pesticides from environmental waters. Talanta. 74, 1675-1680, 2007.
- [6] Salman. Jm; Njoku. Vo; Hameed. B. H. Adsorção de pesticidas a partir de solução aquosa sobre carvão ativado de haste de bananeira. Rev. Eng. Qui. 174(1), 41-48, 2011.
- [7] Coelho, E.R.C.; Vazzoler, H.; Leal, W.P. Emprego do carvão ativado para remoção de atrazina em água de abastecimento público. Eng. Saint Ambient. 17(4), 2012.
- [8] Barbosa, J.; Labuto, G.; Carrilho, E.N.V.M. Magnetic nanomodified activated carbon: characterization and use for organic acids sorption in aqueous medium. Chem. Engineer. Comm. 206(11), 1-14, 2020.
- [9] Barbosa, J.A.; Labuto, G.; Carrilho, E.N.V.M. Nanocompósito de Carvão Ativado e Magnetita: Caracterização, extração em fase sólida (SPE), e estudo isotérmico da sorção dos ácidos aconítico e cítrico. In: XXIV Jornada de Jovens Investigadores AUGM, 2018, Mendoza. Libro de resúmenes XXIV Jornada de Jovens Investigadores AUGM, 2018. v. 24. p. 357.
- [10] Barbosa, J.A. Nanocompósito de carvão ativado e magnetita (Fe₃O₄) como alternativa à pré-concentração de ácidos orgânicos para determinação por cromatografia líquida de alta eficiência. Trabalho de conclusão de curso. Licenciatura em Química. Universidade Federal de São Carlos, Araras, 2018.
- [11] Seccia, S.; Fidente, P.; Montesano, D.; Morrica, P. Determination of neonicotinoid insecticides residues in bovine milk samples by solid-phase extraction clean-up and liquid chromatography with diode-array detection. J. Chromatogr. 1214, 115–120. 2008.
- [12] Sampaio, M.R.F.; Tomasini, D.; Cardoso, L.V.; Caldas, S.S.; Primel, E.G. Determination of pesticide residues in sugarcane honey by QuEChER, and liquid chromatography. J. Braz. Chem. Soc. 23(2), 197-205, 2012.
- [13] Abd-Alrahman, S.H. Residue and dissipation kinetics of thiamethoxam in a vegetable-field ecosystem using QuEChERS methodology combined with HPLC–DAD. Food Chem. 159, 1-4, 2014.
- [14] Collins, C. H.; Braga, G.L.; Bonato, P.S. Fundamentos de Cromatografia. Campinas-SP. Editora da Unicamp. 2006. 453p.
- [15] Caldas, S.S.; Gonçalves, M.L.; Primel, E.G.; Prestes, O.D.; Martins, M.L.; Zanella, R. Principais técnicas de preparo de amostra para a determinação de resíduos de agrotóxicos em água por cromatografia líquida com detecção por arranjo de diodos e por espectrometria de massas. Quim. Nova. 34(9), 1604-1617. 2011.
- [16] Ho, Y.S.; Mckay, G. The kinetics of sorption of divalent metal ions onto sphagnum moss peat. Water Res. 34(3), 735-42. 2000.
- [17] Ho, Y.S. Review of second-order models for adsorption systems. J. Hazard. Mat. 136, 681–689, 2006.
- [18] Silverstein RM, Webster FX, Kiemle DJ Spectrometric identification of organic compounds. 8th ed., Wiley. New Jersey. 2012.

Fixed-bed adsorption of Linear Alkylbenzene Sulfonate (LAS) by granular activated carbon

Henrique Baldi Faccenda^a, Thaís Strieder Machado^a, Gabriel Damini^b, Lucas Kayser da Silva^b, Jeferson Steffanello Piccin^{a,b,*}

^a Post-graduate Program in Civil and Environmental Engineering, University of Passo Fundo, Passo Fundo, PC. 99050-900, Brazil.

^b Chemical Engineering Department, University of Passo Fundo, Passo Fundo, PC. 99050-900, Brazil.

*Corresponding author: jefersonpiccin@upf.br

Abstract

Adsorption has been pointed out as an attractive alternative to remove emerging contaminants from liquid phase. Researches have been done with greywater treatment, as it is denominated the domestic wastewater from bathing and washing. Personal care and hygiene products use is widespread and one of their main compounds are anionic surfactants, as Linear Alkylbenzene Sulfonate (LAS). Industries also have considerable discharges of anionic detergents containing LAS. The usual water and wastewater anaerobic treatment has shown insufficient removal of LAS. Therefore, this work applied commercial granular activated carbon (GAC) adsorption as treatment to anionic surfactant LAS in different operational designs, varying pH, column length and flow rate. Surface tension behavior of outflow was analyzed. Thomas Model was applied to estimate rupture curves and Mass Transfer Zone (Z_m) parameter. Estimated adsorption capacity (q_e) ranged from 11.1 mg g⁻¹ to 21.8 mg g⁻¹, and the best results were set in acid pH of 2.5, 4 cm bed length and 5 mL min⁻¹ flow rate. Z_m varied from 3.6 cm to 10.6 cm, which the shorter value correlated with the best estimated adsorption capacity. Effluent surface tension measures were close to regular water values before the breakthrough time, when it starts to decrease.

Keywords: Linear Alkylbenzene Sulfonate; Thomas Model; Greywater; Breakthrough time; Rupture curve.

1. Introduction

Anionic surfactants are common compounds in cleaning and personal care products, such as detergents and soaps. They represent more than half of the globally traded surfactants and the most produced is Linear Alkylbenzene Sulfonate (LAS), reaching the amount of [1].

LAS is commonly discharged in liquid effluents. In industry, the processes of cleaning and sanitization of production line requires high demand of these products, although in domestic background it is increasingly been used in typical and new personal care products [2].

This anionic surfactant is biodegradable under aerobic condition [3]. However, it tends to persevere in anaerobic environment, such as the individual wastewater treatment facilities adopted by Brazilian regulations in more than 50% of dwellings [4].

The potential toxicity of LAS has been observed in aquatic and terrestrial environment. Concentrations of 1.0 mg L⁻¹ damaged fish fertility and gills, swimming patterns of mussels, crustacean shells, and algae inhibition [3]. Anaerobic process rate decrease in the presence of anionic surfactant, negatively affecting wastewater treatment by suppressing bacterial activities [5]. Nonetheless, some plant species as oat, sunflower, tomato and potato were found to be underdeveloped when applied sludge with LAS concentrations as low as 0.1 mg L⁻¹ [6]. Brazilian federal drinkable water regulation requires maximum values of surfactants of 0.5 mg L⁻¹ [7]. The State of Rio Grande do Sul requires maximum of 2.0 mg LAS L⁻¹ for discharges in water bodies [8].

Some techniques have been explored to remove anionic surfactants from greywater (domestics wastewater from bath and washing), such as electrocoagulation, ultrafiltration and adsorption [6,9,10]. This last technique has shown economical

and operational advantages [6]. The adsorption consists in transferring pollutant particles from gas or liquid phase into a solid bulk, generally powdered or granulated. Activated carbon is one of the most popular adsorbents, it is usually made from biomass or solid waste, and it is widely used in water treatment process [11,12].

Granular Activated Carbon (GAC) has been used to remove heavy metals, dyes, pharmaceuticals, among others. In domestic waste, GAC have been tested as adsorbent to segregated greywater and laundry rinsing waters. GAC has shown capacities ranging from 20 to 600 mg g⁻¹ of LAS removal in batch experiments [13,14].

Fixed-bed adsorption systems have better dynamics behavior to real application than batch adsorption when considered operational factors, and it has been used in industrial scale. Adsorption capacity of fixed-bed is usually predicted by Thomas Model, however it can also be experimentally determined by the area above a rupture curve [13].

This work aimed to apply fixed-bed adsorption with Granulated Activated Carbon media to remove Linear Alkylbenzene Sulfonate (LAS) from aqueous solution, varying operational parameters and inspecting mass transfer zone and surface tension behavior.

2. Experimental

1.1. Materials and reagents

GAC #10 to #18 mesh and 35% porosity was kindly provided from BBI Filtration (Garibaldi, Brazil). Anionic surfactant LAS was obtained from Sigma-Aldrich (sodium dodecylbenzenesulfonate 80%). Its concentration was obtained through UV spectrophotometry at 223 nm wavelength (Tecnal Spec UV-5100) [14]. Surface tension was analyzed using Du-Nouy's ring method in a dynamic surface tensiometer (Sigma, model 702).

1.2. Adsorption experiments

A polyvinyl chloride (PVC) column was built from commercial pipes and connections. Chosen internal diameter was 32 mm. Inflow temperature was controlled by water bath with thermostat (Tecnal, TE-2005) and an infusion pump (Infusomat Compact) adjusted the flow rate.

The fixed-bed GAC adsorptions was operated in ascendant flux using a LAS inflow with concentration of 150 mg L⁻¹ at 25 °C. The effect of fixed-bed length (*h*, 2 cm, 4 cm and 8 cm, mass of GAC of 7 g, 14 g and 28 g, respectively), flow rate (*Q*, 5 mL min⁻¹; 10 mL min⁻¹ and 15 mL min⁻¹) and initial pH of LAS solutions (3.5, 6.5 and 8.5) were investigated. LAS concentration and surface tension were measured at preselected intervals in the column outlet effluent.

The rupture curves were analyzed by Thomas Model simplified form, according to Equation 1 [15,16]:

$$\frac{C}{C_0} = \frac{1}{1 + \exp\left(\frac{k_{Th}q_0m}{Q} - k_{Th}C_0t\right)} \quad (1)$$

where *C*₀ and *C* is inflow and outflow concentrations (mg L⁻¹), *k*_{Th} is the Thomas kinetic constant (L (mg min)⁻¹), *q*₀ is the stoichiometric capacity of the bed (mg g⁻¹), *m* is mass of adsorbent (g), *Q* is the operating flow rate (L min⁻¹) and *t* is time (min).

Mass transfer zone (*Z*_m, in cm) was calculated for the obtained results using Thomas Model, considering as breakthrough time (*t*_b) the legislation recommendation of 2.0 mg/L [8] and the exhaustion time (*t*_e) equal to 95% of outlet concentration [13]. The Equation 2 shows the mass transfer zone estimation used, considering *h* as the column height (or length). The surface tension analysis was applied to effluent of the higher observed results of breakthrough time.

$$Z_m = h \left(1 - \frac{t_b}{t_e}\right) \quad (2)$$

3. Results

The first run investigated the effect of fixed-bed length. Fig. 1 shows Thomas Model estimated rupture curves of three observed experiments in different column lengths, setting inflow rate to 15 mL min⁻¹ and pH to 6.5.

The 2 cm column was the first to achieve saturation, followed by the 4 cm and 8 cm column, respectively. The 2 cm column had initial outflow concentration of 20 mg L⁻¹, while 4 and 8 cm

columns started near 0 mg L^{-1} , pointing out the presence of mass transfer zone inside the column limits.

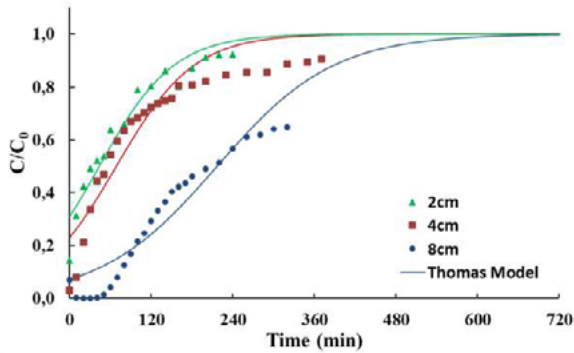


Fig. 1. Effect of column length on the LAS adsorption by GAC ($Q = 15 \text{ mL min}^{-1}$ and $\text{pH} = 6.5$).

The following runs evaluated the pH influence in adsorption. Fig. 2 demonstrates results of pH variation on a 4 cm length column with 5 mL min^{-1} inflow rate.

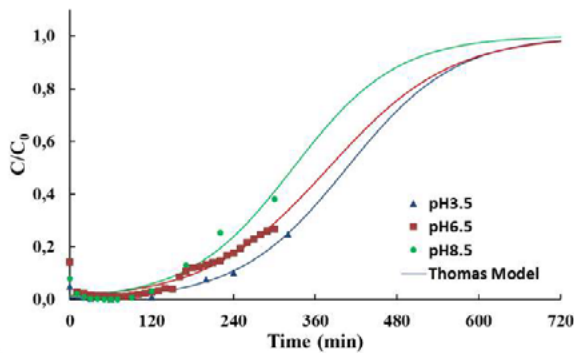


Fig. 2. Effect of pH on the LAS adsorption by GAC ($Q = 5 \text{ mL min}^{-1}$ and $h = 4 \text{ cm}$).

As it is shown on Fig. 2, LAS adsorption in GAC performed slightly better result on acid pH of 3.5. The saturation rate varied from 0.21 in acid income to 0.38 in basic income, for the 300 minutes assisted experiments.

The last experiment investigated the effect of flow rate. The Fig. 3 presents the results of three different flow rates in the 4 cm length column and pH 6.5. The same results are expressed in terms of volume in Fig. 4 to better measure the fixed-bed behavior to the same amounts of LAS inflow.

It can be seen in Fig. 4 that for the two highest flow rate, outflow LAS concentration initiate above 2.0 mg L^{-1} ($C/C_0 > 0,013$). This breakthrough point

happens after 450 mL income for 5 mL L^{-1} flow rate operation. It means that slower the ascendant speed, greater the adsorption capacity.

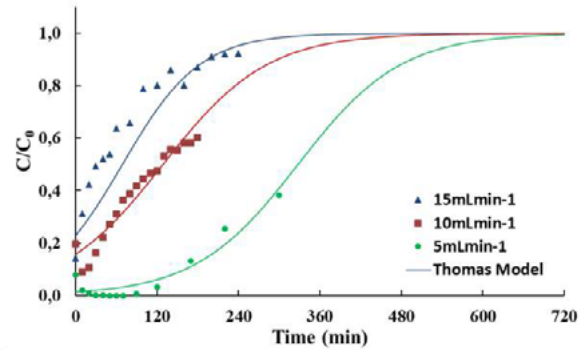


Fig. 3. Effect of flow rate on the LAS adsorption by GAC (column length of 8 cm and pH of 6.5) in terms of time.

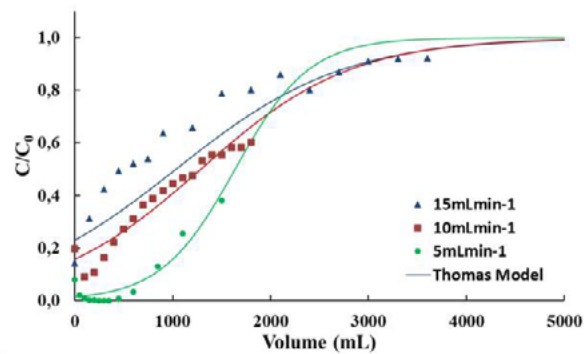


Fig. 4. Effect of flow rate on the adsorption of LAS in terms of volume ($h = 4 \text{ cm}$ and $\text{pH} = 6.5$) in terms of volume.

The adsorption capacity estimated by Thomas Model (Equation 1) of all experiments are summarized in Table 1. The columns Mass Transfer Zone were also calculated using Thomas Model data.

Surface tension was investigated for the outflow solution from the column. Fig. 5 shows surface tension outflow compared with LAS concentration outflow.

It is possible to see that surface tension initially oscillated from around 60 to 70 mN m^{-1} , reaching close to regular water values [17], while column outflow was near to zero LAS concentration. As soon as the breakthrough point is reached, rising the concentration curve, surface tension decreases to 50 mN m^{-1} , indicating the surfactant influence in water surface tension properties.

Table 1. Summary of observed and Thomas Model results for adsorption of LAS by GAC in fixed-bed column.

Q (mL min ⁻¹)	h (cm)	pH	k _{Th} (L (mg min) ⁻¹)	q _e (mg g ⁻¹)	t _{b,Th} (min)	t _{b,o} (min)	Z _m (cm)
Effect of column length (h)							
15.0	2.0	3.5	0.122	14.061	-190.0	no	3.8
15.0	4.0	6.5	0.117	11.083	-170.0	no	6.8
15.0	8.0	6.5	0.078	17.437	-150.0	50.0	10.6
Effect of pH							
5.0	4.0	3.5	0.084	21.783	70.0	150.0	3.6
5.0	4.0	6.5	0.075	20.360	0.0	90.0	4.0
5.0	4.0	8.5	0.088	17.559	20.0	100.0	3.9
Effect of flow rate (Q)							
5.0	8.0	6.5	0.048	19.507	130.0	270.0	7.1
10.0	8.0	6.5	0.081	19.372	-120.0	110.0	10.0
15.0	8.0	6.5	0.078	17.437	-150.0	50.0	10.6

no: not observed; k_{Th}: Thomas kinetic constant; q_e: adsorption capacity; t_{b,Th}: breakthrough time estimated by Thomas model; t_{b,o}: observed breakthrough time; Z_m: length of mass transfer zone

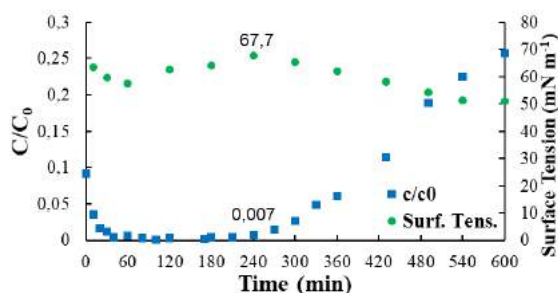


Fig. 5. Outflow surface tension and LAS concentration of LAS adsorption by GAC (Q = 5 mL min⁻¹; pH = 6.5 and h = 8 cm).

According with Thomas Model, the adsorption capacity of LAS in GAC fixed-bed in these runs were up to 21.78 mg g⁻¹, for the acid pH run, with the lowest flow rate and in a 4 cm length column. Despite this is nearly the lowest value considered by literature of LAS batch adsorption [3], it is still a reasonable capacity and feasible of replication in industrial and commercial scenario, once it achieves legislation requirements until its breakthrough point [7,8].

Breakthrough time was more notable and longer from observed experiments than Thomas Model estimations. The higher adsorption capacity experiment presented the lower Mass Transfer Zone estimated by Thomas Model. Z_m length is directly related to flow rate, as these experiments related. The shortest the Z_m value, closer the column is to an ideal system and a higher efficiency is expected [13].

4. Conclusions

GAC removed anionic surfactant LAS from aqueous solution. Adsorption capacity ranged from approximately 11.1 to 21.8 mg g⁻¹. The best operational result was observed to a 4 cm column, feed with a flow rate of 300 mL min⁻¹, in acid pH of 3.5.

Variations between acid and basic pH did not present great differences, as the column height of 4 cm and 8 cm also showed similar results. Flow rate above 10 mL min⁻¹ consistently reduced the fixed-bed capacity, elevating Z_m values.

Acknowledgements

To the University of Passo Fundo (UPF), the Coordination of Improvement of Higher Education Personnel (CAPES – Finance code 001) and to National Council for Scientific and Technological Development (CNPQ - Proc. 405311/2016–8) for the financial support to the research. Thanks to BBI Filtração for providing the Granular Activated Carbon.

References

- [1] Bain & Company. Potential diversification of Brazilian chemical industry. Report 4 – Surfactants (In Portuguese). BNDES, 2014.

- [2] Calvo-Flores FG, Isac-García J, Dobado JÁ. Emerging pollutants: origin, structure, and properties. Wiley-VCH Verlag, 2018.
- [3] Mungray AK, Kumar P. Fate of linear alkylbenzene sulfonates in the environment: a review. *International Biodeterioration & Biodegradation*; 2009. p. 981-987.
- [4] National Information System of Sanitation. Water and wastewater diagnostic service – 2016 (In Portuguese).. Brasília: SNSA/MCIDADES, 2018.
- [5] Jurado E, Fernández-Serrano M, Núñez-Olea J. Ecotoxicity of anionic surfactants. *Transactions on ecology and the environment*, 2011; 144; 497-505.
- [6] Tripathi SK, Tyagi R, Nandi BK. Removal of residual surfactants from laundry wastewater: a review. *Journal of dispersion science and technology*. 2013; 34; 1526-1534.
- [7] Health Ministry. Attachment XX of Consolidation Ordinance N° 5 (In Portuguese). 2017.
- [8] State of Rio Grande do Sul Council. Resolution CONSEMA n° 355. Criteria about liquid effluent. (In Portuguese). 2017.
- [9] Barişçi S, Turkay O. Domestic greywater treatment by electrocoagulation using hybrid electrode combinations. *Journal of Water Process Engineering*. 2016, 10, 56-66.
- [10] Bani-Melhem K, Smith E. Grey water treatment by a continuous process of an electrocoagulation unit and a submerged membrane bioreactor system. *Chemical Engineering Journal*. 2012, 199, 201-210.
- [11] Cooney DO, Adsorption design for wastewater treatment. New York: CRC Press LCC, 1998.
- [12] Piccin JS, Cadaval JTRS, Pinto LAA, Dotto GL. Adsorption isotherms in liquid phase: experimental, modelling and interpretations. in: *Adsorption processes for water treatment and purification*. Gewerbestrasse: Springer, 2017.
- [13] Bonilla-Petriciole A, Mendoza-Castillo DI, Reynel-Avila HE. In: *Adsorption processes for water treatment and purification*. Gewerbestrasse: Springer, 2017.
- [14] Schouten N, Ham LGV, Euverink GJ, Haan, AB. Selection and evaluation of adsorbents for the removal of anionic surfactants from laundry rinsing water. *Water research*. 2007; 41; p. 4233-4241.
- [15] Thomas HC. Heterogeneous ion exchange in a flowing system. *J Am Chem Soc*. 1944.
- [16] Tien C. *Adsorption calculations and modelling*. Boston: Butterworth-Heinemann, 1994.
- [17] Anguelova MD, Huq P. Effects of Salinity on Surface Lifetime of Large Individual Bubbles. *Journal of Marine Science and Engineering*. 2017.

Adsorption of caffeine using steel wastes composed of magnetite

Iara Jennifer Moura Duarte^a, Thaís Mayra Israel de Oliveira Lima^b, Hugo Leonardo de Brito Buarque^b, Ronaldo Ferreira do Nascimento^a

^a Universidade Federal do Ceará, Campus do Pici, R. Cinco, 100 - Pres. Kennedy, Fortaleza - CE, 60355-636, Brazil

^b Instituto Federal do Ceará, campus Fortaleza., Av. Treze de Maio, 2081 - Benfica, Fortaleza - CE, 60040-531, Brazil

Abstract

Caffeine is one of the most widespread pharmaceutical products in the world, generally proposed as a tracker of human pollution. This study preliminarily evaluated the caffeine adsorption capacity (CAF) using steel wastes (I, II, III, IV, V and VI), in an aqueous solution. The wastes used were pre-treated and later characterized as to their structure and surface morphology. The effects of parameters such as best adsorbent, adsorbent mass and pH of the solution were studied. The selected waste was IV with removal of around 48%. The study of the influence of pH on the adsorption capacity revealed better results working with acid pH solutions, while the evaluation of the effect of the VI mass on the adsorption capacity showed a greater adsorption capacity using smaller masses of adsorbent.

Keywords: Emerging contaminant; caffeine; steel wastes; adsorption.

1. Introduction

A considerable variety of emerging pollutants (EPs) originating from point and diffuse pollution is present in the aquatic environment. These are chemicals that are not normally monitored, but have the potential to enter the environment and can affect ecological balance and human health [1,2]. Among the emerging pollutants, contamination by medicines has attracted a lot of attention, due to highly adverse effects on living organisms [3] and represents a real scientific challenge in terms of ecotoxicity, public health, soil pollution and drinking water and effluent management strategies [4].

Caffeine is a psychoactive drug and despite its possible negative health effects is classified as “Generally Recognized as Safe” (GRAS) by the Federal Drug Administration (FDA) [5]. This compound is used as a cardiac, brain and respiratory stimulant and can also be used as an additive in medications to increase the analgesic effect [6]. In addition, caffeine is widely consumed in food and beverages (for example, chocolate, coffee, cocoa, tea, dairy desserts, soft drinks).

Based on this, caffeine has been considered the most representative pollutant of the pharmaceutically active compound (PhAC), based on its high abundance in the environment and the property indicating anthropogenic inputs of PhACs to water bodies [7], that is, it is an indication of the presence of other contaminants, which were not monitored, but may present risks to the environment [5]. Being proposed as a tracker of human pollution, since it can be almost entirely human [8]. According to [9], caffeine, when ingested, is metabolized by the human body, however, about 1 to 10% is excreted in the urine. The excreted caffeine would subsequently reach wastewater treatment plants (WWTPs) and enter the water cycle [10].

The effects of caffeine are related to the doses administered. In small doses, it has a stimulating effect on the nervous system. In large doses, it causes depletion of nerve cells and, in very large doses, it can cause death. A potentially toxic dose is considered to be greater than 10 mg kg⁻¹ [5]. Still on its effects, in the aquatic environment, some studies have indicated the distribution of caffeine in tissues of aquatic organisms, including fish, clams, macroalgae and other aquatic plants, suggesting bioaccumulation of caffeine in organisms [7].



Caffeine is generally accepted to show excellent removal efficiency during wastewater treatment [11]. However, the presence of caffeine residues has often been reported in drinking water sources worldwide, indicating that the amount of this popular PhAC introduced into the water body is greater than degradation [12].

In view of this problem, adsorption can be one of the most effective methods for purifying polluted water by dissolved substances and drugs [13]. The advantage of this method is the possibility of selectively adsorbing target substances from multicomponent mixtures, as well as achieving a high degree of purification, especially of wastewater with low concentrations of pollutants [14]. Various synthetic and natural porous materials (eg activated carbon, zeolites, ash, peat etc.) are used as adsorbents and the adsorption / removal efficiency can reach 80-95% [3,15,16].

The exploitation of efficient, economical and ecological adsorbents plays a vital role in removing antibiotics from wastewater [17]. In view of this, the steel waste composed mainly of iron oxides (magnetite / hematite), will allow adsorbing and removing the pharmaceutical compound from the water in a low cost adsorption process. Magnetite has a high pore structure and adsorption capacity, mainly related to the distribution of pore size, surface area and pore volume [18]. After the adsorption process, the saturated magnetite can be removed from the solution using a simple magnetic separation. This property can be a facilitator in the separation of the adsorbent from the treated water.

Several studies have proven the efficiency of magnetite in the adsorption of drugs [18–20]. The differential of this study is the use of steel waste composed mainly of magnetite (iron oxide) in the adsorption of caffeine, which will be done as a preliminary test, aiming in the future the adsorption of other pharmaceutical compounds. The selection of caffeine was based on the fact that caffeine is considered the most representative pollutant of (PhAC), its high abundance in the environment and the property indicating anthropogenic inputs of PhACs to water bodies.

2. Materials and Methods

2.1 Reactants

Caffeine was purchased from Sigma-Aldrich, with analytical purity (> 99.99%) and used directly in the experiments. Caffeine solutions were

prepared by diluting the stock solutions to the required concentrations. The molecular structure of caffeine is depicted in Fig.1. For pH adjustment, NaOH 1M and HCl 1M solutions were used, both P.A reagents (NaOH and HCl).

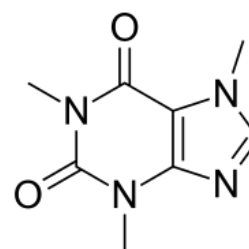


Fig. 1. Molecular structure of the caffeine.

2.2 Preparation of steel wastes

For the preliminary adsorption tests, 6 steel wastes obtained in the iron preparation stages were used, classified in I, II, III, IV, V and VI. Described below:

- Electrostatic Precipitated Powder (I);
- Carepa Placa (II);
- Powder Converter L.D (III);
- High Oven Collector Powder (IV);
- Dusting dust from Casa Corrida Alto Forno (V).
- KR powder (ACIARIA) (VI);

Before starting the tests, the wastes were pre-treated in order to remove some impurities present. The pre-treatment consists of washing the materials followed by filtration and centrifugation. Finally, the materials were dried in a vacuum oven for 24h at 90 ° C. Afterwards the wastes they were separated by size, where the fraction of particles ranging from 60 μm to 150 μm was used for the adsorption experiments.

2.3 Characterization

The morphology of each sample was analyzed using Scanning Electron Microscopy (SEM), where the samples were previously prepared on double-sided carbon tape on aluminum supports, metallized with gold in an argon atmosphere under low pressure, in Quorum equipment, model Q15DT ES and analyzed in FEG equipment, model Quanta 450, voltage 20kV. The chemical composition and Fe

ratios of the studied materials were estimated using X-Ray Fluorescence measurements with the aid of the ZSXMini - II Rigaku equipment.

2.4 Preliminary batch adsorption study

Preliminary adsorption studies were performed with 25 mL of CFN solutions with an initial concentration of 20 mg L⁻¹ and 100 mg of the respective steel wastes (I, II, III, IV, V, VI), placed in Erlenmeyers and stirred thermal incubator at 200 rpm. The remaining concentrations of CFN were determined (after removing the wastes by vacuum filtration with Millipore membrane -0.45 µm) from a calibration curve, using an Shimadzu UV-1800 spectrophotometer at the maximum wavelength (Xmax) of 273 nm. All studies were performed in triplicate.

After selecting the best adsorbent, new tests were performed considering the parameters such as adsorbent mass and pH influence on caffeine adsorption. The effect of the adsorbent dosage was carried out by varying the mass of the selected waste from 2 to 8 g / L, in 24 h tests, without adjusting the pH. The influence of pH on adsorption was also evaluated, whose pH values were adjusted to 3.0, 6.0 and 9.0, using solutions of HCl and NaOH (1.0 mol L⁻¹). The experiments were stirred 24 h, without temperature control.

The amount of CAF adsorbed at time t was evaluated using the Eq. (1).

$$qt = \frac{(C_i - C_t)V}{m} \quad (1)$$

where C_i (mg/L) is the initial CAF concentration in the solution, C_t (mg/L) is the final CAF concentrations in solution at time t, V (L) is the solution volume and m (g) is the dry weight of the adsorbent.

The efficiency of CFN removal was also calculated according to Eq. (2). R (%) represents a caffeine removal efficiency. C₀ is an initial AMX concentration and C_t is an AMX concentration at time t.

$$R(\%) = \frac{(C_0 - C_t)100}{C_0} \quad (2)$$

3. Results and discussion

3.1 Characterization of steel wastes

According to the results for FRX, verified in table 1 that the samples are formed mainly by Iron, followed by Calcium. As it is a steel waste, iron is the element present in greater quantity, about 70.29%, 96.82%, 77.82% and 95.64% by weight, for the samples (I, II, III, V) respectively. Sample IV showed levels of iron (33.43%) practically equivalent to those of calcium (37.23%). Only sample VI showed higher concentrations for calcium (59.05%), followed by iron (33.43%).

Table 1. Analysis X-ray fluorescence (FRX) of steel wastes.

Element quimic	I	II	III	IV	V	VI
	(%)					
Al	0,77	0,89	1,21	-	0,36	-
Si	1,89	1,54	3,26	1,21	1,13	0,42
P	0,11	-	-	0,17	0,11	-
S	2,55	-	1,08	0,52	0,34	0,58
Cl	4,88	-	2,48	1,88	0,06	0,02
K	8,35	0,04	5,42	1,05	0,67	0,43
Ca	9,59	0,35	6,73	37,23	0,87	59,05
Mn	0,24	0,35	0,32	2,57	0,27	0,20
Fe	70,29	96,82	77,37	33,43	95,64	38,92
Zn	0,07	-	1,41	21,21	0,53	0,21
Br	0,19	-	-	0,06	-	-
Pb	0,95	-	0,31	0,67	-	-
Cu	0,11	-	-	-	-	-
Ti	-	-	0,28	-	-	-
Rb	-	-	0,13	-	-	-
Co	-	-	-	-	-	0,10
Sr	-	-	-	-	-	0,08

The SEM images of iron wastes showed the particle morphology and distribution in the evaluated wastes, shown in Fig.2. Irregular spherical particles that are not different from chemically synthesized iron oxides nanoparticles [21]. Were observed for wastes III (Fig.2c), V (Fig.2e), and VI (Fig.2f). For wastes I (Fig.2a), II (Fig.2b) and IV (Fig.2d) the micrograph obtained by SEM shows that the morphology of the particles has a heterogeneous distribution of irregular shapes and particle sizes. The particle diameters of the

nanoscale wastes were in the range of 1.072 μm to 989.8 nm.

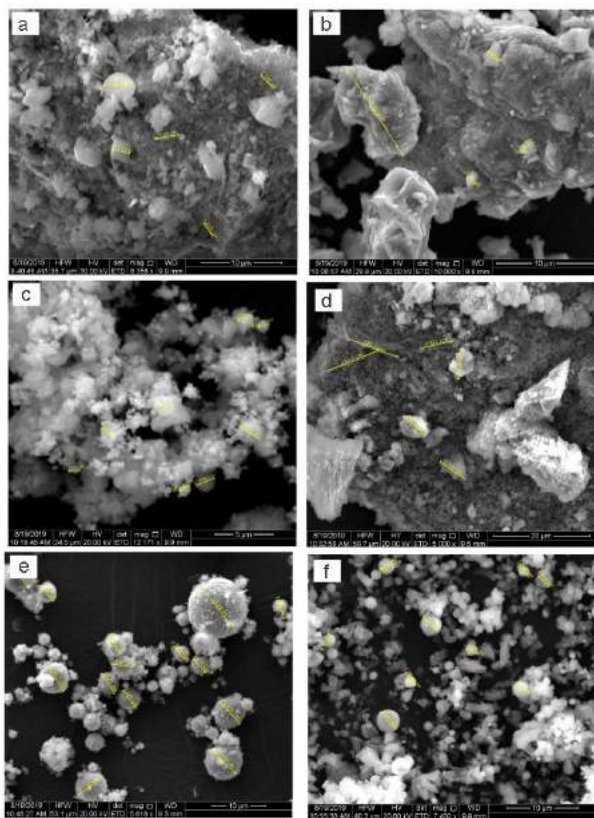


Fig. 2. SEM images for a) waste I, b) waste II, c) waste III, d) waste IV, e) waste V f) waste VI.

3.2 Batch adsorption studies

The preliminary adsorption test aims to initially assess which steel wastes could be potential adsorbents for the removal of caffeine in aqueous solution, based on the choice of the best adsorbent, further tests will be carried out. Among the wastes evaluated, the best in terms of removal potential ($R\%$) and q_e was the VI adsorbent obtaining 49% and 2.38 mg g^{-1} respectively, the other wastes did not obtain percentages higher than this, as can be seen in Fig.3.

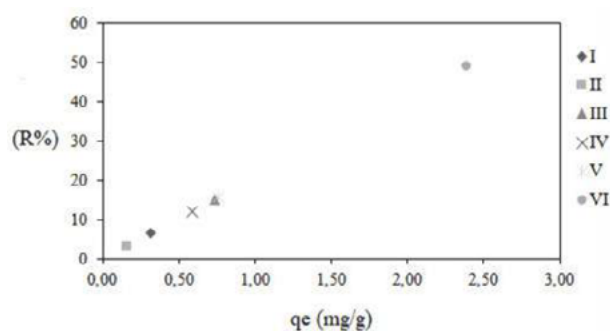


Fig. 3. Adsorption of caffeine using steel wastes I, II, III, IV, V, VI.

3.3 Adsorbent dosage

When analyzing Figure 4, it is possible to observe that the adsorption capacities were, respectively, about 2,32 mg g^{-1} , 1.89 mg g^{-1} , 1.36 mg g^{-1} , 1.20 mg g^{-1} for the mass of 2 g/L^{-1} , 4 g/L^{-1} , 6 g/L^{-1} , 8 g/L^{-1} of adsorbent (VI), respectively. It can be observed that, as the mass VI increased, the values of caffeine adsorption capacity (q_e) decreased, even with the constant initial concentration of the contaminant. This characteristic is mainly due to a greater availability of binding sites for adsorption [22]. The increase in mass from 2 g/L^{-1} to 4 g/L^{-1} , in percentage terms there was an increase of about 20% in the adsorption capacity. Although the use of 2 g/L^{-1} has obtained more satisfactory results in terms of adsorption capacity, for this study 4 g/L^{-1} of mass was adopted for caffeine adsorption.

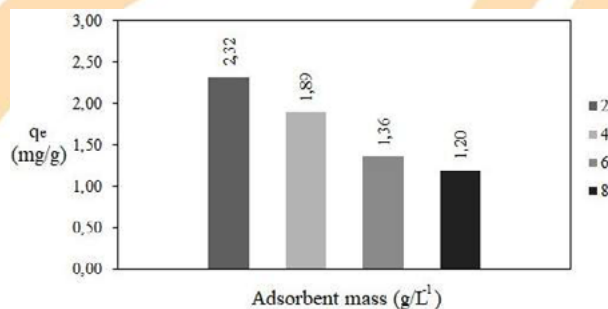


Fig. 4. Influence of adsorbent mass on caffeine adsorption.

3.4 Effect of pH on caffeine adsorption

The effect of the pH value of the solution on the adsorption of CAF by steel wastes was investigated between pH 3.0, 6.0 and 9.0 at a fixed concentration

of contaminant and room temperature in 24 h tests, is shown in Fig.5. The effect of the solution pH on adsorption processes is an important parameter to understand the interaction between adsorbents and adsorbates, once the pH variation can promote changes on the surface charges of adsorbents, and influence in the protonation of functional groups present on the surface of materials [10].

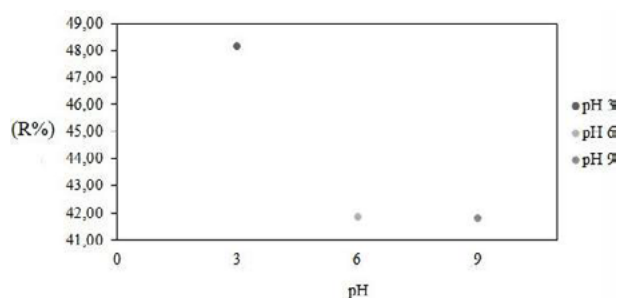


Fig. 5. Influence of pH on caffeine adsorption.

Fig.5 shows the adsorption as a function of the pH of the CFN solution using steel wastes. According to the results, the highest values of adsorption capacity (q_e) were found at pH 3.0 and decreased at pH values of 6.0 and 9.0. Therefore, it is noted that the initial pH of the solution affected the adsorption capacities of the CAF, since the increase in the pH of the solution promoted a decrease in the values of q_e , which can be attributed to the increase in the species of CFN^- in solution, suggesting that there is a repulsion between the CFN molecules and the surface of the steel waste. This is an indication that the availability of adsorption sites for contaminant molecules is reduced as the pH increases.

The best adsorption capacity obtained was for adsorbent VI occurred at pH 3.0, corresponding to 2.37 mg g^{-1} . Compared to pH 6.0 and 7.0, it is a 10% increase in caffeine adsorption at pH 3.0. This behavior corroborates with results found by [16,22,23], where caffeine was removed more efficiently by adsorption in an acid medium. Thus, the pH value of the CFN solution of 3.0 was selected for subsequent adsorption studies, as it is in the range of the highest q_e values.

4. Conclusions

According to the results obtained in this study, the steel waste VI obtained the best values of q_e and removal among those evaluated. PH 3 was ideal for

caffeine adsorption within the conditions evaluated in this study. The concentration of the chosen adsorbent was 4 mg / L^{-1} . In these conditions, 48% was removed. Fundamental studies (e.g. contact time, kinetics, isotherm) must be carried out later. The objective of this study was to carry out a preliminary selection of the best steel waste, with potential for the adsorption of caffeine.

Acknowledgements

The authors are grateful for the financial support provided by CAPES. To the support provided by the laboratories: LANAGUA (Federal University of Ceará); LQA (Federal Institute of Science and Technology Education of Ceará); LRX (Federal University of Ceará).

References

- [1] Elessawy NA, Elnouby M, Gouda MH, Hamad HA, Taha NA, Gouda M, et al. Ciprofloxacin removal using magnetic fullerene nanocomposite obtained from sustainable PET bottle wastes: Adsorption process optimization, kinetics, isotherm, regeneration and recycling studies. *Chemosphere* 2020;239:124728.
- [2] Geissen V, Mol H, Klumpp E, Umlauf G, Nadal M, van der Ploeg M, et al. Emerging pollutants in the environment: A challenge for water resource management. *Int Soil Water Conserv Res.* 2015;3(1):57–65.
- [3] Danalıoğlu ST, Bayazit ŞŞ, Kerkez Ö, Alhogbi BG, Abdel Salam M. Removal of ciprofloxacin from aqueous solution using humic acid- and levulinic acid- coated Fe_3O_4 nanoparticles. *Chem Eng Res Des.* 2017;123:259–67.
- [4] Bizi M, El Bachra FE. Evaluation of the ciprofloxacin adsorption capacity of common industrial minerals and application to tap water treatment. *Powder Technol* [Internet]. 2020;362:323–33.
- [5] Anastopoulos I, Pashalidis I, Orfanos AG, Manariotis ID, Tatarchuk T, Sellaoui L, et al. Removal of caffeine, nicotine and amoxicillin from (waste) waters by various adsorbents. A review. *J Environ Manage.* 2020;261.
- [6] Sotelo JL, Rodríguez A, Álvarez S, García J. Removal of caffeine and diclofenac on activated carbon in fixed bed column. *Chem Eng Res Des.* 2012;90(7):967–74.
- [7] Li S, He B, Wang J, Liu J, Hu X. Risks of caffeine residues in the environment: Necessity for a targeted ecopharmacovigilance program. *Chemosphere.* 2020;243:125343.
- [8] Álvarez S, Ribeiro RS, Gomes HT, Sotelo JL, García J. Synthesis of carbon xerogels and their application in adsorption studies of caffeine and diclofenac as emerging contaminants. *Chem Eng*



- Res Des. 2015;95:229–38.
- [9] Thorn CF, Aklillu E, McDonagh EM, Klein TE, Altman RB. Caffeine pathway. *Pharmacogenet Genomic.* 2012;22(5):389–95.
- [10] Beltrame KK, Cazetta AL, de Souza PSC, Spessato L, Silva TL, Almeida VC. Adsorption of caffeine on mesoporous activated carbon fibers prepared from pineapple plant leaves. *Ecotoxicol Environ Saf.* 2018;147(April 2017):64–71.
- [11] Kosma CI, Lambropoulou DA, Albanis TA. Investigation of PPCPs in wastewater treatment plants in Greece: Occurrence, removal and environmental risk assessment. *Sci Total Environ.* 2014;466–467:421–38.
- [12] Zhu S, Chen H, Li J. Sources, distribution and potential risks of pharmaceuticals and personal care products in Qingshan Lake basin, Eastern China. *Ecotoxicol Environ Saf.* 2013;96:154–9.
- [13] Sophia A. C, Lima EC. Removal of emerging contaminants from the environment by adsorption. *Ecotoxicol Environ Saf.* 2018;150(December 2017):1–17.
- [14] Mironyuk IF, Gun'ko VM, Vasylyeva H V., Goncharuk O V., Tatarchuk TR, Mandzyuk VI, et al. Effects of enhanced clusterization of water at a surface of partially silylated nanosilica on adsorption of cations and anions from aqueous media. *Microporous Mesoporous Mater.* 2019;277(August 2018):95–104.
- [15] Li S, Zhang X, Huang Y. Zeolitic imidazolate framework-8 derived nanoporous carbon as an effective and recyclable adsorbent for removal of ciprofloxacin antibiotics from water. *J Hazard Mater.* 2017;321:711–9.
- [16] Anastopoulos I, Katsouromalli A, Pashalidis I. Oxidized biochar obtained from pine needles as a novel adsorbent to remove caffeine from aqueous solutions. *J Mol Liq.* 2020;304:112661.
- [17] Fan H, Ma Y, Wan J, Wang Y, Li Z, Chen Y. Adsorption properties and mechanisms of novel biomaterials from banyan aerial roots via simple modification for ciprofloxacin removal. *Sci Total Environ.* 2020;708:134630.
- [18] Maichin F, Freitas LC, Ortiz N. The use of converter slag (Magnetite) and bentonite clay for amoxicillin adsorption from polluted water. *Orbital Electron J Chem.* 2013;5(3):1–5.
- [19] Silva GF, Freitas LC, Ortiz N. Steel magnetic residue used as substrate to treat and adsorb amoxicillin- kinetic studies. 2013;(1993):2001.
- [20] Lin CC, Lee CY. Adsorption of ciprofloxacin in water using Fe₃O₄ nanoparticles formed at low temperature and high reactant concentrations in a rotating packed bed with co-precipitation. *Mater Chem Phys.* 2020;240(February 2019):122049.
- [21] Aksu Demirezen D, Yıldız YŞ, Demirezen Yılmaz D. Amoxicillin degradation using green synthesized iron oxide nanoparticles: Kinetics and mechanism analysis. *Environ Nanotechnology, Monit Manag.* 2019;11(February).
- [22] Carolina A, Guerra S, Andrade MB De, Araujo LA. Estudo da capacidade de adsorção de caféina do meio aquoso por óxido de grafeno. *UniCesumar*, 2019.
- [23] Portinho R, Zanella O, Féris LA. Grape stalk application for caffeine removal through adsorption. *J Environ Manage.* 2017;202:178–87.

Influence of temperature of pyrolysis and activation conditions on the adsorption of ammonia nitrogen onto orange peel biochar

Larissa Firmino de Lima^{a,*}, Carlos Eduardo Rodrigues Barquilha^a, Maria Cristina Borba Braga^a

^a Department of Hydraulic and Sanitation, Federal University of Parana, 100 Cel. F. H. dos Santos Ave., Curitiba 81531-990, Brazil

Abstract

Effluents from anthropogenic activities may increase the availability of ammonia nitrogen (N-NH₄⁺) in water and lead to adverse effects on aquatic ecosystems. To remove N-NH₄⁺ from wastewater, biochar can be used as an alternative adsorbent. Biochar is a porous and carbon-rich material that is produced by pyrolysis from various feedstocks, including orange peels. This study evaluated the effect of temperature of pyrolysis and activation conditions on the adsorption capacity of N-NH₄⁺ onto orange peel biochar. Biochars were pyrolyzed at 400 °C (BC400) and 600 °C (BC600) for 1 h. BC400 and BC600 were chemically activated with HCl and KOH (1, 3, 5 and 7 M) at different ratios (1:3, 1:5 and 1:7). The yields of BC400 and BC600 were measured. The surface functional groups of orange peel and biochars were analyzed by FTIR spectroscopy. Batch adsorption experiments were carried out to identify the most promising production conditions. Pyrolysis yields of BC400 and BC600 were 33% and 28%, respectively. FTIR spectra of samples showed more significant changes in the surface functional groups due to the temperature of pyrolysis than to activation. The highest N-NH₄⁺ uptake, 8.49 mg g⁻¹, was obtained by the biochar produced at 400 °C and activated with KOH (3 M; 1:5). Results indicated that the temperature of pyrolysis and activation conditions play an important role in the adsorption performance of orange peel biochar. It can be concluded that biochar made from orange peels might be used as a cost-effective and eco-friendly adsorbent for N-NH₄⁺ adsorption from wastewaters.

Keywords: Ammonia nitrogen; adsorption; orange peel; biochar; FTIR analysis

1. Introduction

The discharge of agricultural, municipal and industrial wastewater into freshwater may cause an adverse ecological impact due to the increased availability of ammonia nitrogen (N-NH₄⁺). Although nitrogen is a macronutrient for some organisms, high abundance of ammonia nitrogen can be toxic to aquatic life and it is quite related to eutrophication of waterbodies [1]. According to Brazilian CONAMA Resolution n° 430/2011 [2], the N-NH₄⁺ maximum concentration for effluent discharges in waterbodies is 20 mg L⁻¹.

Therefore, to comply with the guideline values specified by this resolution and preserve the aquatic environment, several technologies have been used for the removal of ammonium ions. Among them, adsorption is considered an effective and easy-to-operate method. Among a wide range of adsorbents available, biochar has gained significant attention

due to its efficiency, sustainable approach, and low cost [3,4].

Biochar is a carbonaceous material produced by pyrolysis, which is a thermochemical conversion of biomass under limited oxygen conditions and controlled temperature [4]. Many feedstocks are suitable for biochar production, including agro-industrial waste, such as orange peels. In the production of orange juice, approximately 50% of the weight of the fruits utilized is turned into waste. As a result, this raw material is abundant and inexpensive, particularly in Brazil, the largest orange producer in the world [4,5].

It is worth mentioning that the choice of the feedstock may affect the properties of the resulting biochar. Additionally, the conditions of the biochar production, such as different pyrolysis temperatures and chemical treatments, can also play an important role. Higher pyrolytic temperatures can increase the specific surface area, enhance the carbon content, and be detrimental to the surface functional groups



on the biochar. On the other hand, lower temperatures of pyrolysis may improve the yield and preserve the adsorption sites of biochar. Chemical activation with acidic or alkaline solutions can increase the porosity, the specific surface area, and the abundance of oxygenated functional groups on the surface of the biochar. Furthermore, these parameters can alter the adsorption capacity of biochar [6,7].

Thus, this study investigated the influence of two temperatures of pyrolysis (400 °C and 600 °C) and different chemical activation conditions on the adsorption capacity of N-NH₄⁺ onto orange peel biochar. This research also highlights the use of agro-industrial waste as an alternative adsorbent for ammonium removal from wastewater.

2. Materials and methods

2.1. Feedstock

The orange peel waste used in this study was derived from orange juice production and obtained from a local fruit market near Curitiba, Brazil. Residual pulp, membranes and seeds were removed from the orange peels. Particles with average dimensions of 8 mm were produced by cutting the peels with a vegetable cube cutter and were subsequently washed with distilled water to remove residual impurities. Finally, the material was dried in an oven at 105 °C for 24 h.

2.2. Biochar production

The dried material was placed in porcelain crucibles, covered with fitting lids, and wrapped with aluminum foil to prevent atmospheric oxygen entrance. The crucibles were then pyrolyzed in a muffle-furnace (Coel, GMP-2) at an average heating rate of 10 °C min⁻¹. After reaching the specified temperatures of pyrolysis of 400 °C or 600 °C, the peak temperature was maintained for 1 h.

The resulting biochars, namely BC400 and BC600, were cooled to room temperature in a desiccator. The yield of each biochar was determined by Equation 1 [8]:

$$\text{Yield (\%)} = (W_{BC}/W_{OP}) \times 100 \quad (1)$$

Where: W_{BC} is the dry mass (g) of biochar and W_{OP} is the dry mass (g) of orange peels prior to pyrolysis.

Biochar samples were washed three times with deionized water and oven-dried at 105 °C for 24 h.

Finally, the granulometry of the biochar produced was measured using sieves, from 9.51 to 1.19 mm, with mechanical agitation.

2.3. Chemical activation

Samples of the produced biochars were subjected to chemical activation with HCl 1M or KOH 1M for 16 h, using the ratio of 1 g of biochar to 5 mL of solution. Subsequently, the samples were washed with deionized water, neutralized with 0.1 M KOH or 0.1 M HCl, and dried at 105°C for 24 h. The biochars from the acid treatment were labeled BC400A and BC600A, whereas those from the alkali treatment were labeled BC400B and BC600B.

2.4. N-NH₄⁺ adsorption

Batch adsorption tests were performed to evaluate the impact of the conditions of production on N-NH₄⁺ adsorption capacity of biochars (BC400, BC400A, BC400B, BC600, BC600A and BC600B). A fraction of 1 g of each biochar and 50 mL of NH₄Cl solution (500 mg L⁻¹) were added to Erlenmeyer flasks (125 mL). The flasks were sealed and shaken using an orbital shaking incubator (Tecnal, TE-420) at 100 rpm and 25 °C for 24 h. After agitation, the mixtures were filtered through a qualitative filter paper. The remaining N-NH₄⁺ concentrations in solution were determined using an ammonia gas-sensing electrode (OAKTON, 35802-00). The adsorption capacity of biochars was calculated by Equation 2 [4]:

$$q = [(C_0 - C_f)V]/m_d \quad (2)$$

Where: q is the amount of adsorbed N-NH₄⁺ on biochar (mg g⁻¹), C_0 is the initial N-NH₄⁺ concentration in solution (mg L⁻¹), C_f is the final N-NH₄⁺ concentration (mg L⁻¹), V is the volume of solution (L), and m_d is the dry mass of biochar (g).

The biochar with the highest uptake capacity was selected to be reevaluated under the same conditions, except by the concentration of the activation solution. The concentration of the acidic or alkaline solution was increased up to 3 M, 5 M, and 7 M. Finally, the solution concentration with the highest uptake capacity was investigated with the impregnation ratio varying from 1:3 to 1:7 (w/v).

2.5. FTIR spectroscopy

Samples of orange peels, BC400, BC600 and the activated biochar with the highest N-NH₄⁺

adsorption capacity were dried overnight at 105 °C and ground until powder with a pestle.

The surface functional groups of the samples were determined by Fourier transform infrared (FTIR) spectroscopy (BRUKER, VERTEX 70). All FTIR spectra were obtained from 4000 cm^{-1} to 400 cm^{-1} with 64 scans and using 4 cm^{-1} resolution.

3. Results and discussion

3.1. Yield and granulometry

The yields of BC400 and BC600 were 33% and 28%, respectively. The yield decreased due to the loss of water and volatile organic matter content related to the increase in pyrolysis temperature. The results were similar to those reported in previous studies with orange peel biochar produced at 400 °C and 600 °C [4,9]. The average particle size of biochars was 5.02 mm.

3.2. Temperature of pyrolysis and 1 M activation

The N-NH_4^+ adsorption capacities of the six biochars initially produced are presented in Fig. 1. Among them, the highest and the lowest N-NH_4^+ uptake were achieved by BC400B ($q = 5.47 \text{ mg g}^{-1}$) and BC600A ($q = 1.53 \text{ mg g}^{-1}$), respectively. The lower pyrolysis temperature may have preserved a larger number of functional groups on the surface of the biochar, favoring the adsorption process [4]. In addition, the alkaline treatment probably enhanced the porosity and the surface area of the biochar, and have also produced adsorption sites more favorable to N-NH_4^+ adsorption [7].

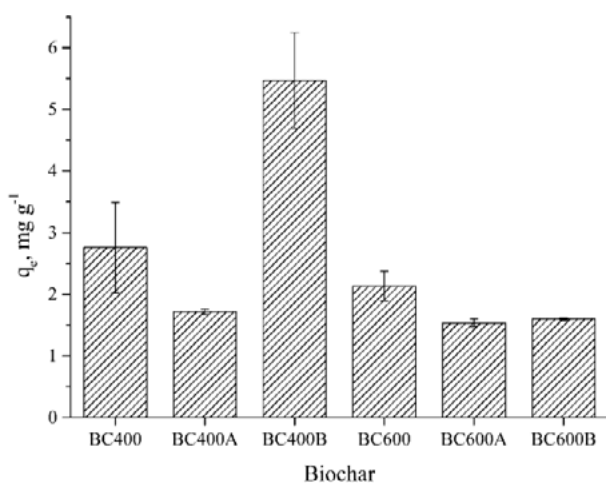


Fig. 1. N-NH_4^+ adsorption capacity of orange peel biochar at different conditions.

These results indicated that the adsorption of ammonium onto orange peel biochar is more effective at low temperature of pyrolysis and alkaline activation. Hence, the concentration of KOH solution was increased to 3 M, 5 M and 7 M.

3.3. Concentration of alkaline activation solution

The effect of alkaline concentrations on the adsorption of N-NH_4^+ is shown in Fig. 2. As it can be observed, increasing the KOH concentration from 1 M ($q = 5.47 \text{ mg g}^{-1}$) to 3 M ($q = 8.49 \text{ mg g}^{-1}$) promoted a higher adsorption capacity by biochar. The stronger activation condition may have increased the surface area and thus enhanced the adsorption sites of biochar [7]. However, further increases in KOH concentration of 3 M to 5 M ($q = 8.29 \text{ mg g}^{-1}$) and to 7 M ($q = 8.22 \text{ mg g}^{-1}$) seemed to have slightly decreased the N-NH_4^+ adsorption. These concentrations may have been strong enough to damage the surface structure of the biochar [10]. Consequently, BC400B chemically activated with KOH 3 M (BC400B-3M) was selected for the adsorption experiment with different impregnation ratios (1:3 and 1:7).

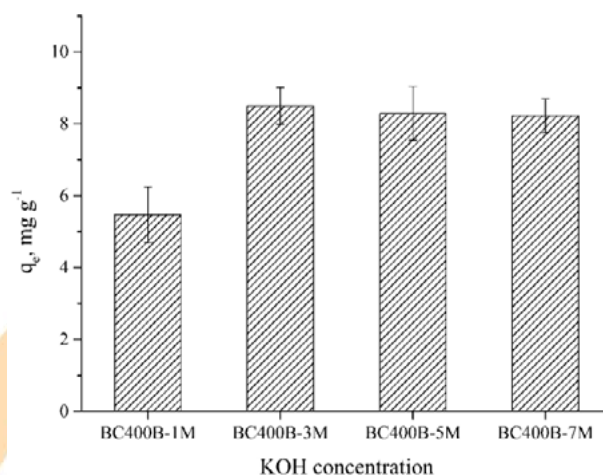


Fig. 2. Effect of different KOH concentration on N-NH_4^+ adsorption capacity of orange peel biochar.

3.4. Different impregnation ratios of alkaline activation solution

The impact of different impregnation ratios of biochar and 3 M KOH solution (weight/volume) on N-NH_4^+ adsorption is presented in Fig. 3. It can be observed that when the ratio was altered from 1:5 to 1:3 the adsorption capacity decreased from 8.49 mg g^{-1} to 7.29 mg g^{-1} , and to 7.24 mg g^{-1} when the ratio

was 1:7. The results were similar to previous research [10]. Therefore, BC400B treated with KOH 3 M at 1:5 impregnation ratio (BC400B-3M) was selected as the best biochar.

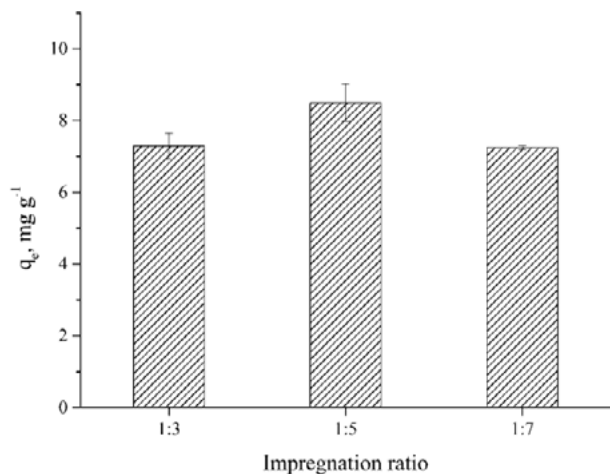


Fig. 3. Effect of different impregnation ratios on the adsorption capacity of N-NH₄⁺ by orange peel biochar.

3.5. FTIR analysis

The FTIR spectra of orange peel (OP), BC400, BC400B-3M and BC600 are shown in Fig. 4. It can be observed that various functional groups were eliminated or had the intensity of their bands decreased as the temperature of pyrolysis increased from 400 °C to 600 °C. This result allows to point out that lower temperature of pyrolysis can preserve a larger number of functional groups on the surface of the biochar. The 3 M KOH activation did not cause abrupt changes in the FTIR spectra. Thus, a higher N-NH₄⁺ adsorption capacity of BC400-3M is probably attributed to the opening of partially blocked pores, an increase in surface area, and a greater exposure of the existing adsorption sites. The identified peaks suggest the presence of the following functional groups: hydrogen-bonded hydroxyl (O-H), carboxyl (COOH), carbonyl (C=O), amine groups (N-H), ether (C-O-C), aliphatic compounds (C-H_x), and aromatic rings (C=C). The results were consistent with those by other authors [4,7,8,11].

4. Conclusion

This study demonstrated that both the temperature of pyrolysis and the activation conditions can influence the removal of N-NH₄⁺ by

orange peel biochar. The biochar produced at 400 °C and activated with 3 M KOH solution at 1:5 impregnation ratio (BC400B-3M) exhibited the highest N-NH₄⁺ adsorption capacity, with $q = 8.49$ mg g⁻¹.

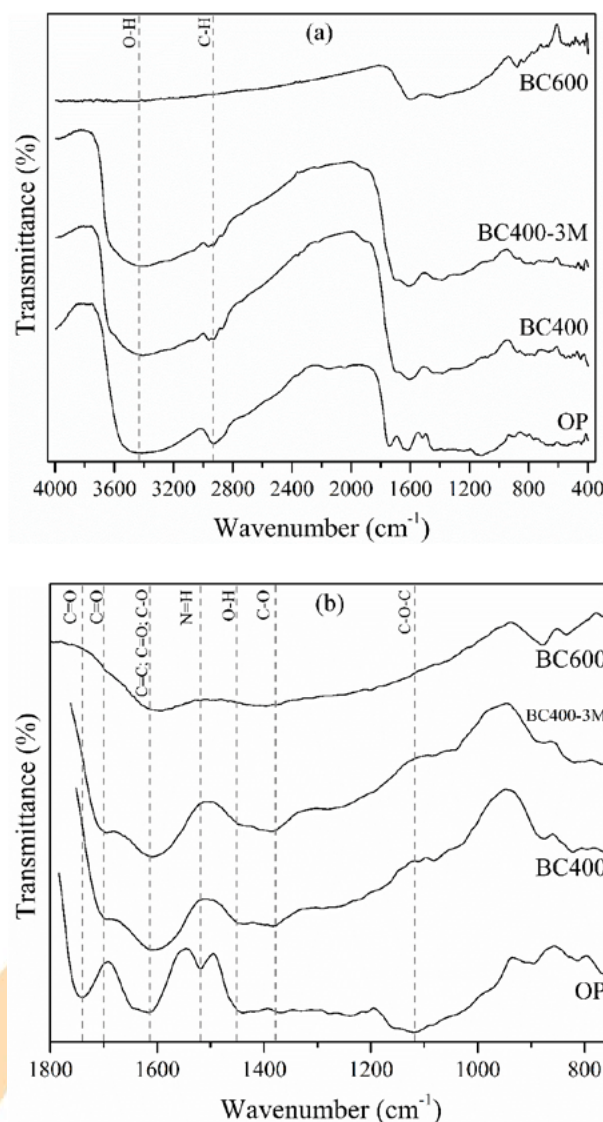


Fig. 4. FTIR spectra of OP, BC400, BC400B-3M and BC600 at (a) full and (b) fingerprint scale.

The results from this research suggest that lower temperatures of pyrolysis and alkaline treatment can enhance the availability of functional groups and may increase the surface area of biochar. Thus, it can be concluded that the biochar produced from a widely available feedstock, such as orange peels, can be used as a cost-effective and environmentally friendly adsorbent to remove N-NH₄⁺ from aqueous solutions, such as wastewaters rich in nitrogen.

Acknowledgements

This study was supported by the Brazilian research funding agency CAPES and the Postgraduate Program in Water Resources and Environmental Engineering – PPGERHA/UFPR.

References

- [1] Constable M, Charlton M, Jensen F, McDonald K, Craig G, Taylor KW. An ecological risk assessment of ammonia in the aquatic environment. *Human and Ecological Risk Assessment*. 2003;9(2):527-48.
- [2] Brazil, 2011. National Council of the Environment - CONAMA Resolution N° 430 of May 13, 2011. Official Diary of the Union. Available from: <http://www.mma.gov.br/port/conama/legiabre.cfm?codlegi=646>. (In Portuguese).
- [3] Gao F, Xue Y, Deng P, Cheng X, Yang K. Removal of aqueous ammonium by biochars derived from agricultural residuals at different pyrolysis temperatures. *Chemical Speciation & Bioavailability*. 2015;27(2):92-7.
- [4] Hu X, Zhang X, Ngo HH, Guo W, Wen H, Li C, Zhang Y, Ma C. Comparison study on the ammonium adsorption of the biochars derived from different kinds of fruit peel. *Science of the Total Environment*. 2020;707:135544.
- [5] Cypriano DZ, da Silva LL, Tasic L. High value-added products from the orange juice industry waste. *Waste Management*. 2018;79:71-8.
- [6] Tan X, Liu Y, Zeng G, Wang X, Hu X, Gu Y, Yang Z. Application of biochar for the removal of pollutants from aqueous solutions. *Chemosphere*. 2015;125:70-85.
- [7] Sizmur T, Fresno T, Akgül G, Frost H, Moreno-Jiménez E. Biochar modification to enhance sorption of inorganics from water. *Bioresource Technology*. 2017;246:34-47.
- [8] Mireles S, Parsons J, Trad T, Cheng CL, Kang J. Lead removal from aqueous solutions using biochars derived from corn stover, orange peel, and pistachio shell. *International Journal of Environmental Science and Technology*. 2019;16(10):5817-26.
- [9] Tran HN, You SJ, Chao HP. Effect of pyrolysis temperatures and times on the adsorption of cadmium onto orange peel derived biochar. *Waste Management & Research*. 2016;34(2):129-38.
- [10] Vu TM, Doan DP, Van HT, Nguyen TV, Vigneswaran S, Ngo HH. Removing ammonium from water using modified corncob-biochar. *Science of the Total Environment*. 2017;579:612-9.
- [11] Chen B, Chen Z. Sorption of naphthalene and 1-naphthol by biochars of orange peels with different pyrolytic temperatures. *Chemosphere*. 2009;76(1):127-33.

Modeling the nickel adsorption equilibrium on low-cost adsorbents and activated carbon using artificial neural network

P.S. Pauletto*, G.L. Dotto, N.P.G. Salau

Universidade Federal de Santa Maria, Roraima Avenue, 1000, Santa Maria, 97105-900, Brazil

Abstract

In this research, nickel adsorption equilibrium was compared among low-cost adsorbents and commercial activated carbon (AC). The low-cost adsorbents are from agricultural wastes such as sugarcane bagasse (SB), orange peel (OP), passion fruit waste (PW) and pineapple peel (PP). Experimental results revealed higher adsorption capacity for SB and OP that have a negatively charged surface ideal for removing cations; low adsorption capacity was found for PW and PP due to their low surface areas. A predictive artificial neural network (ANN) was implemented for modeling the Ni(II) equilibrium adsorption capacity as function of initial adsorbate concentration, solution temperature, point of zero charge and surface area of each adsorbent. The network was trained with the Levenberg–Marquardt back-propagation optimization, and according to the high correlation coefficient ($R = 0.9989$) and low root mean square error ($RMSE = 0.0109$) the best topology was found to be 4–5–1. Compared with Langmuir model, ANN proved to be a more efficient model because, unlike the conventional model that requires numerous parameter-fitting procedures, a single trained network was able to interpret the whole dataset. In addition, ANN proved to be more effective in predicting Ni(II) equilibrium adsorption capacity, as the R values were closer to unity for the majority of the systems.

Keywords: Nickel; agro-wastes; adsorption; artificial neural network.

1. Introduction

The presence of excess heavy metal ions such as nickel is becoming a serious problem for the environment and living organisms as it is reported to be non-biodegradable, toxic and carcinogenic [1]. Among various chemical, physical and biological remediation techniques, adsorption is the most widespread in heavy metal removal due to its economic viability, simplicity of design, low power supply and high efficiency [2]. Activated carbon (AC) is widely used as an adsorbent, but its cost is high in large industrial applications; therefore, a low-cost alternative to remove Ni(II) from aqueous effluents is through the use of agricultural residues such as sugarcane bagasse (SB), orange peel (OP), passion fruit waste (PW) and pineapple peel (PP) [3].

Lately, artificial neural networks (ANN) have been implemented successfully in simulation and prediction of the performance of the adsorption process in the liquid phase [4–7]. ANN approach is based on an advanced computational model capable to identifying and estimating nonlinear relationships between independent and dependent variables from an experimental dataset. In addition, the ANN

model can coordinate complex multidimensional problems with large datasets without any prior assumptions about the physical or chemical nature of the system [8].

In this work, the equilibrium adsorption of Ni(II) on low-cost adsorbents (SB, OP, PW and PP) was evaluated and compared with commercial activated carbon (AC). The novelty of this research study relies on developing a predictive ANN to establish the relationship among the equilibrium adsorption capacity of Ni(II) and four quantitative inputs variables: initial adsorbate concentration, solution temperature, point of zero charge and surface area of each adsorbent. Finally, the ANN was compared with Langmuir model using statistical metrics.

2. Materials and methods

2.1. Adsorbate

Ni(II) solutions were prepared with $\text{NiSO}_4 \cdot 6\text{H}_2\text{O}$ (Sigma-Aldrich) and distilled water to a concentration range from 50 to 300 mg/L. All other reagents were of analytical grade.

2.2. Adsorbents

The low-cost adsorbents (SB, OP, PW and PP) were obtained from national food industries and conserved at 269K until use. During the preparation, the agro-wastes were washed with deionized water until neutral pH, oven dried at 313K for 48 h, ground (Wiley Mill Standard, 03, USA) and sieved until the discrete particle size ranges from 250 to 500 μm . For comparison purposes, AC (Vetec, Brazil) was sieved until the same discrete particle size.

Details regarding the characterization of these adsorbents were presented in a previous study [3]. Table 1 summarizes the main results, indicating that the Ni(II) adsorption capacity was directly affected by the point of zero charge (pH_{ZPC}) and the surface area of each adsorbent.

Table 1. Adsorbent characteristics.

Adsorbent	pH_{ZPC}	Surface area (m^2/g)
SB	4.6	1.85
OP	4.9	1.73
PW	4.6	0.87
PP	6.0	0.75
AC	5.6	65.20

2.3. Equilibrium experiments

Batch adsorption experiments were performed with adsorbent dosage of 0.100 g in contact with 50 mL of Ni(II) solution at different initial concentrations (50, 100, 150, 200, 250 and 300 mg/L) at pH 6. The samples were agitated in a thermostatic agitator (Marconi, MA 093, Brazil) at 100 rpm and different temperatures (298, 308, 318 and 328 K). After 6 h, the solid phase was filtered (Whatman grade 40) and the remaining Ni(II) concentration in liquid phase was measured by atomic absorption spectrometry with flame (Agilent, 240 FS AA, USA). All experiments have been replicated. The equilibrium adsorption capacity (q_e) was determined by Eq. (1):

$$q_e = \frac{C_0 - C_e}{m} V \quad (1)$$

where, m is the adsorbent dosage (g), V is the volume of solution (L), C_0 and C_e are initial and

equilibrium concentrations of Ni(II) (mg/L), respectively.

2.4. Isotherm model

The adsorption equilibrium is usually interpreted by isotherms models, which relate the equilibrium adsorption capacity and the adsorbate equilibrium concentration at constant temperature. Langmuir model (Eq. (2)) is the most used since assumed that each site contain only one adsorbate molecule and adsorption occurs in a monolayer [9]:

$$q_e = \frac{q_{mL} K_L C_e}{1 + K_L C_e} \quad (2)$$

where, q_{mL} is the maximum adsorption capacity (mg/g) and K_L is the Langmuir constant (L/mg).

The isotherm parameters were estimated by minimization of the non-linear least square function between the experimental and predicted model data, using the function *lsqnonlin* based on Trust-Region-Reflective algorithm [10].

2.5. ANN model

The ANN structure is based on the biological neural network, composed of neurons that are organized and interconnected into input layer, hidden layer and output layer [11]. The number of neurons in the input and output layers are respectively the same as the input and output variables. However, the number of hidden neurons should be determined by trial and error methodology to achieve results with best accuracy [12].

The network was developed in MatLab software using the Levenberg-Marquardt back-propagation optimization (*trainlm*) for training, tan-sigmoid transfer function (*tansig*) at hidden layer and a linear transfer function (*purelin*) at output layer [6]. The ANN performance evaluation was measured through the correlation coefficient (R) and the root mean square error ($RMSE$):

$$R = \sqrt{1 - \frac{\sum_{i=1}^N (\hat{y}_i - y_i)^2}{\sum_{i=1}^N (\hat{y}_i - \bar{y})^2}} \quad (3)$$

$$RMSE = \sqrt{\frac{\sum_{i=1}^N (\hat{y}_i - y_i)^2}{N}} \quad (4)$$

where y_i is experimental data, \hat{y}_i is the predicted value, \bar{y}_i is the mean value of y_i and N is the number of experimental points.

After settling the correlation between the experimental inputs and output variable, the trained ANN were simulated with the entire set of experimental inputs variable to predict the output variable. Then, the predicted output variable were compared with the experimental output variable to evaluate the trained ANN performance.

3. Results and discussion

3.1. ANN performance

The equilibrium adsorption capacity of Ni(II) (output variable) was related with four input variables, including initial adsorbate concentration (50 to 300 mg/L), solution temperature (298 to 328K), pH_{ZPC} (4.6 to 6.0) and surface area (0.75 to 65.20 m²/g) of each adsorbent. The entire experimental database (140 set points) was randomly divided into train (98 set points), validation (21 set points) and test (21 set points) for ANN implementation.

The best ANN topology was investigated by varying the number of neurons at the hidden layer. Table 2 compares the different network topologies based on the values of statistical metrics. The closest R of the unit and the lowest value of $RMSE = 0.0109$ indicate the best topology with 5 hidden neurons. Hence, the topology 4–5–1 was selected according to Fig. 1.

Table 2. ANN performance in different topologies.

Hidden neurons	R	$RMSE$
1	0.9590	0.0927
2	0.9793	0.0458
3	0.9900	0.0345
4	0.9935	0.0282
5	0.9989	0.0109
6	0.9948	0.0253
7	0.9946	0.0258
8	0.9937	0.0249
9	0.9937	0.0251
10	0.9943	0.0261

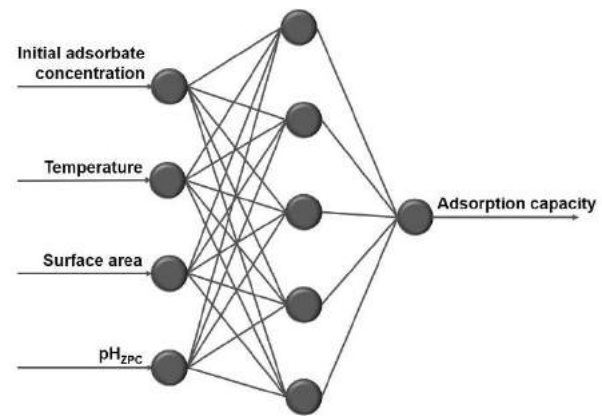


Fig. 1. ANN topology.

The normalized experimental data versus the ANN predicted data for equilibrium adsorption capacity are presented in Fig. 2. The results show same tendency between the test and training data, which indicates that, the network capture the experimental variability, and corroborates with the applicability of the trained network.

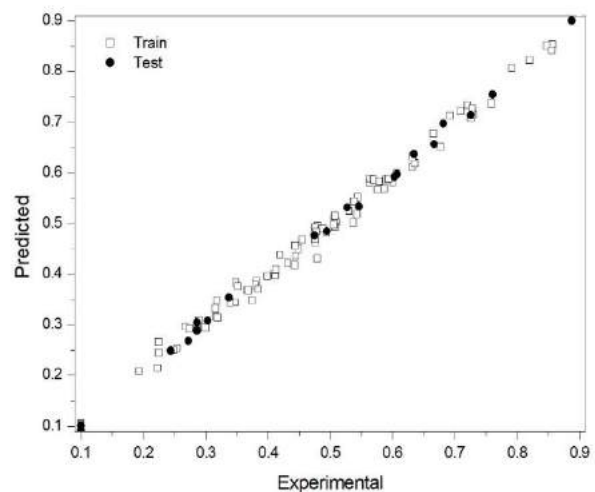


Fig. 2. Comparison of the normalized experimental data with ANN predicted.

3.2. Equilibrium isotherm

The equilibrium results are fundamental for comparing and evaluating the efficiency of different adsorbents. Fig. 3 presents the experimental equilibrium curves for all adsorbents at different temperatures. The adsorption isotherm curves can be classified as type “L2” [13], where the inclined portion characterizes the affinity among Ni(II) and

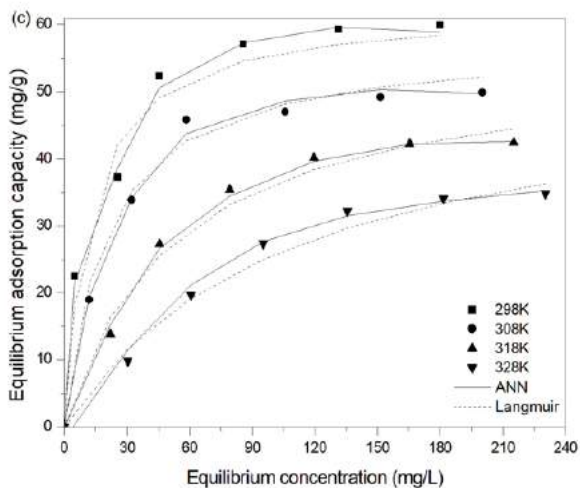
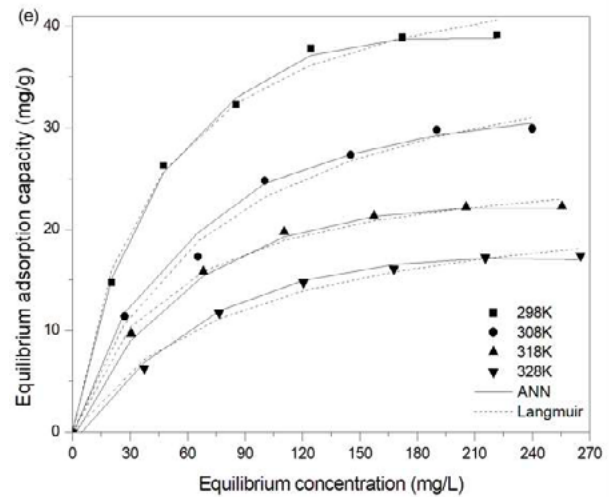
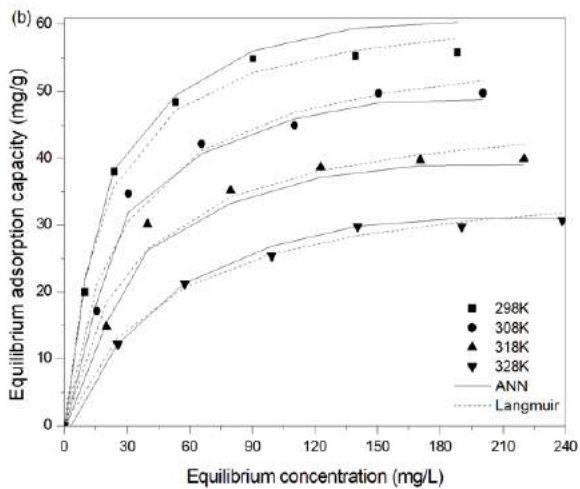
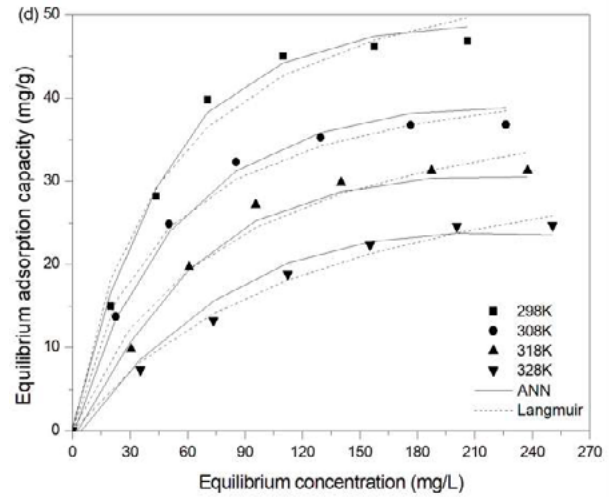
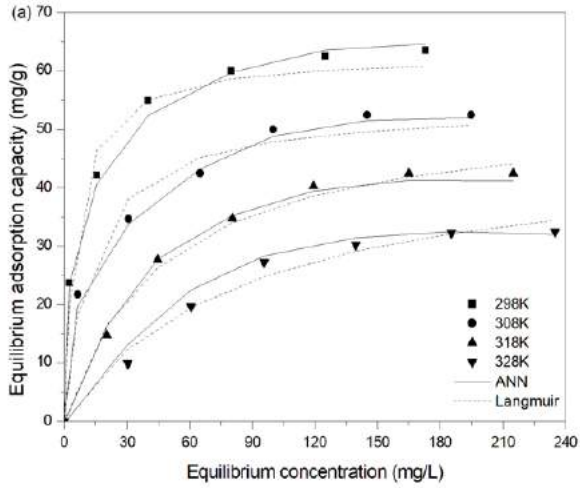


Fig. 3. Ni(II) equilibrium isotherms on (a) SB, (b) OP, (c) AC, (d) PW and (e) PP.

the adsorbents, and the plateau represents the maximum adsorption capacity. The Langmuir model generally fits the L-type isotherm through Eq. (2), and the estimated parameters are presented in Table 3.

The results of Table 3 indicate that SB, OP and AC are more capable adsorbents to remove Ni(II) than PW and PP, since the isotherms of SB, OP and AC were more inclined and the plateau presents higher values of q_{mL} . This can be explained due the fact that SB, OP and PW have negative surface charge ($pH_{ZPC} < pH$) that allows cation adsorption. However, PW even with low pH_{ZPC} showed poor removal performance, which can be attributed to its low surface area (53% minor than SB). Although,

AC presented good adsorption capacity, which can be attributed to their much higher surface area than low cost adsorbents (Table 1). In relation to temperature, for all the adsorbents, the adsorption capacity was favored by decreasing the temperature, indicating an exothermic adsorption process.

3.3. Model comparison

The graphical comparison between experimental data and those predicted by the Langmuir model is illustrated in Fig. 3 and indicates a suitable fit. However, the isotherm model requires a parameter estimation for each temperature and type of adsorbent, and in this study, for instance 20 different parameter-fitting procedures were required to estimate 40 parameters, since Langmuir model has two indeterminate parameters for each isotherm curve.

Table 3. Langmuir isotherm parameters.

Adsorbent	298 K	308 K	318 K	328 K
SB				
q_{mL} (mg/g)	62.66	54.03	53.63	46.96
K_L (L/mg)	0.182	0.079	0.022	0.012
OP				
q_{mL} (mg/g)	63.60	58.85	48.45	38.39
K_L (L/mg)	0.054	0.036	0.030	0.020
AC				
q_{mL} (mg/g)	62.40	57.45	55.56	53.25
K_L (L/mg)	0.082	0.050	0.019	0.009
PW				
q_{mL} (mg/g)	60.99	46.08	44.55	39.58
K_L (L/mg)	0.021	0.022	0.013	0.008
PP				
q_{mL} (mg/g)	48.17	40.97	27.49	24.16
K_L (L/mg)	0.024	0.013	0.020	0.011

The ANN emerges as a more efficient tool, in which a single trained network is able to predict the equilibrium adsorption capacity for all adsorbents and temperatures. The training process uses 98 data points to estimate 31 parameters (25 weights and 6 bias). The simulation results of the trained ANN with 4–5–1 topology are added in Fig. 3. Although ANN is an empirical model, i. e. it is not based on first principles, most of the values predicted by the network present results with physical meaning, since the graphical comparison indicates a better agreement between experimental data and those simulated by ANN.

In addition, Table 4 compares the correlation coefficient (R) between Langmuir and ANN models for all systems. It corroborates that ANN model has a superior prediction of equilibrium adsorption capacity.

Table 4. Statistical comparison.

Adsorbent	Correlation coefficient (R)	
	Langmuir	ANN
SB		
298 K	0.9936	0.9983
308 K	0.9902	0.9989
318 K	0.9966	0.9986
328 K	0.9912	0.9929
OP		
298 K	0.9962	0.9980
308 K	0.9908	0.9972
318 K	0.9884	0.9964
328 K	0.9972	0.9985
AC		
298 K	0.9912	0.9989
308 K	0.9949	0.9981
318 K	0.9933	0.9990
328 K	0.9926	0.9961
PW		
298 K	0.9912	0.9977
308 K	0.9952	0.9977
318 K	0.9884	0.9976
328 K	0.9955	0.9888
PP		
298 K	0.9975	0.9995
308 K	0.9953	0.9962
318 K	0.9977	0.9999
328 K	0.9955	0.9974

4. Conclusion

The equilibrium adsorption of nickel was compared among four low-cost adsorbents, SB, OP, PW and PP, and activated carbon (AC). Experimental results indicated that the adsorption process was exothermic for all systems. In addition, SB, OP and AC present higher adsorption capacity than PW and PP, this behavior can be explain by the low surface area of PW and PP; also, by the facility of capture of nickel ions due to the negatively charged surface ($pH_{ZPC} < pH$) of SB and OP.

ANN approach was used to predict the Ni(II) equilibrium adsorption capacity, using as input variables: initial Ni(II) concentration, solution temperature, pH_{ZPC} and surface area of each adsorbent. The number of hidden neurons were determined by the trial and error methodology, and the best ANN topology was established with five hidden neurons ($R = 0.9961$ and $RMSE = 0.0160$).

The conventional technique, using the Langmuir isotherm, required 20 parameter fitting procedure to satisfactory interpreted the equilibrium of all systems, whereas a single trained ANN was able to predict the entire experimental dataset with higher correlation coefficient. Therefore, ANN stands out as an efficient technique to predict the adsorption equilibrium capacity of Ni(II).

Acknowledgements

The authors are grateful for the financial support received from CAPES – Brazilian Federal Agency for Support and Evaluation of Graduate Education within the Ministry of Education of Brazil.

References

- [1] Aji MP, Wiguna PA, Karunawan J, Sulhadi. Removal of Heavy Metal Nickel-Ions from Wastewaters Using Carbon Nanodots from Frying Oil. *Procedia Eng* 2017;170:36–40.
- [2] Xu M, Liu J, Hu K, Xu C, Fang Y. Nickel(II) removal from water using silica-based hybrid adsorbents: Fabrication and adsorption kinetics. *Chin J Chem Eng* 2016;24:1353–1359.
- [3] Dotto GL, Meili L, Abud AKS, Tanabe EH, Bertuol DA, Foletto EL. Comparison between Brazilian agro-wastes and activated carbon as adsorbents to remove Ni(II) from aqueous solutions. *Water Sci Technol* 2016;73(11):2713–2721.
- [4] Khandanlou R. Enhancement of heavy metals sorption via nanocomposites of rice straw and Fe_3O_4 nanoparticles using artificial neural network (ANN). *Ecol Eng* 2016;91:249–256.
- [5] Moreno-Pérez J, Bonilla-Petriciolet A, Mendoza-Castillo DI, Reynel-Ávila HE, Verde-Gómez Y, Trejo-Valencia R. Artificial neural network-based surrogate modeling of multi-component dynamic adsorption of heavy metals with a biochar. *J Environ Chem Eng* 2018;6:5389–5400.
- [6] Souza PR, Dotto GL, Salau NPG. Artificial neural network (ANN) and adaptive neuro-fuzzy interference system (ANFIS) modelling for nickel adsorption onto agro-wastes and commercial activated carbon. *J Environ Chem Eng* 2018;6:7152–7160.
- [7] Sadeghizadeh A, Ebrahimi F, Heydari M, Tahmasebikohyani M, Ebrahimi F, Sadeghizadeh A. Adsorptive removal of Pb (II) by means of hydroxyapatite/chitosan nanocomposite hybrid nanoadsorbent: ANFIS modeling and experimental study. *J Environ Manage*, 2019;232:342–353.
- [8] Gadekar MR, Ahamed MM. Modelling dye removal by adsorption onto water treatment residuals using combined response surface methodology-artificial neural network approach. *J Environ Manage*, 2019;231:241–248.
- [9] Langmuir I. The adsorption of gases on plane surfaces of glass, mica and platinum. *J Am Chem Soc* 1918;40:1361–1403.
- [10] Coleman TF, Li Y. On the Convergence of Reflective Newton Methods for Large-Scale Non-linear Minimization Subject to Bounds. *Math Program* 1994;67(2):189–224.
- [11] Mendoza-Castillo DI, Villalobos-Ortega N, Bonilla-Petriciolet A, Tapia-Picazo JC. Neural network modeling of heavy metal sorption on lignocellulosic biomasses: effect of metallic ion properties and sorbent characteristics. *Ind Eng Chem Res* 2015;54:443–453.
- [12] Ghaedi AM, Vafaei A. Applications of artificial neural networks for adsorption removal of dyes from aqueous solution: A review. *Adv Colloid Interface Sci* 2017;245:20–39.
- [13] Giles CH, Smith D, Huitson A. A general treatment and classification of the solute adsorption isotherm. *J. Colloid Interface Sci* 1974;47:755–765.

Modeling and simulation of the process of biosorption of real textile effluent in sugarcane bagasse through artificial neural networks

Vitória Brocardo de Leon^{a,*}, Claiton Zanini Brusamarello^b, Gustavo Petrolí^b, Fernanda Batista de Souza^b

^a *Postgraduate Program in Environmental Engineering: Analysis and Environmental Technology (Programa de Pós-graduação em Engenharia Ambiental: Análise e Tecnologia Ambiental), Federal Technological University of Paraná (UTFPR), Linha Santa Bárbara s/n, Francisco Beltrão, 85601-970, PR, Brazil*

^b *Academic Department of Engineering (Departamento Acadêmico de Engenharia Química), Federal Technological University of Paraná (UTFPR), Linha Santa Bárbara s/n, Francisco Beltrão, CEP 85601-970, PR, Brazil*

Abstract

The present work evaluates the use of artificial neural networks for the modeling and simulation of the biosorption process, predicting the percentage of color removal of real textile effluent using chemically modified sugarcane bagasse as biosorbent material (BCM). Among the literature, there are few studies focused on the prediction of color removal of industrial effluent using artificial neural networks (RNA), dealing with works for the true color removal of textile effluent using sugarcane as biosorbent and prediction in RNA the literature is nonexistent. Data related to studies of the effect of effluent pH, particle size, amount of adsorbent, mixing time and color concentration of the effluent on the adsorption process were included in the RNA. The architecture adopted for RNA was multilayer perceptron (MLP) and the algorithm used was Levenberg-Marquardt. It was found that the RNA structure that best suited the experimental data was composed of 8 hidden layer neurons, with an MSE equivalent to 0.013. It was found that the RNA predicted results for color removal fit the data, experimental values with an $R = 0.928$ was found it. Finally, it can be said that besides BCM is a promising material for the biosorption process, RNA is a powerful tool, which combined with an adsorption system can work with a virtual sensor for effluent treatment.

Keywords: Artificial intelligence; Adsorption equilibrium and kinetics; Textile effluent; Colour; Biosorbent.

1. Introduction

With the increase in the demand for material goods and the consequent growth of industrial activity, new environmental problems arose, mainly related to solid waste disposal of solid waste and the launching of liquid effluents from the production stages.

According to Raman et al. (2016) it is estimated that approximately 3,000,000 L of wastewater is generated with daily production of 20,000 kg of tissues, and effluent characteristics will vary according to the quality of the fabric being processed, and the properties physical and chemical properties of the dye used, as well as equipment used (DASGUPTA et al., 2015).

The dyes that make up the textile effluent can be toxic, carcinogenic and mutagenic, causing problems for human health, besides modifying the transparency of water, affecting the photosynthetic activity of the aquatic environment (LIM; CHU; PHANG, 2010; MARTÍNEZ-HUITLE et al. ., 2012). Different treatment alternatives for the removal of dyes from textile effluent have been studied, and the biosorption for the removal of dyes is already a mature technology because over the years different types of biosorbent were being discovered and tested (VIJAYARAGHAVAN; BALASUBRAMANIAN, 2015).

However, the application of biosorption is very restricted to the laboratory, since most studies are based on the removal of dyes from synthetic effluents, which are elaborated only with the dilution of dyes in water.



Actual effluents contain other pollutants, which may interact with the dyes, modifying the efficiency of the adsorption process. In addition, other variables such as contact time between adsorbent and adsorbate, particle size and pollutant concentration can also interfere with the adsorption of the dye. Therefore, the modeling of this process using conventional statistical models is complicated, given that the relationship between variables is often nonlinear (GHAEDI; VAFAEI, 2017).

For this purpose, artificial neural networks (RNAs) have been presented as a powerful tool to predict the adsorption process, without the need to perform practical experiments at all times. RNA's are based on the functioning of the human brain, as the mathematical digits acquire knowledge through experiments with input data, so it is possible to perform revisions to the response data (COSTA et al., 2016; FAGUNDES-Klen et al., 2011).

Dye adsorption modeling has already been simulated using RNA's, as is the case of a recent study published by (IGWEGBE et al., 2019), where the network predicted the removal of 71.17% of the Blue Methylene dye using Ho-CaWO_4 with an R^2 of 0.99. In addition, other studies for dye removal using different materials such as activated sludge (Agarwal et al., 2016), activated charcoal (Dutta, Ghosh and Basu, 2012), polyaniline (Tanzifi et al., 2017), potato husk (Maleki et al., 2013) were also published, however, RNA applications for the removal of color from the real textile effluent are still scarce.

From these facts, the present work aims to perform the modeling and simulation in artificial neural networks of the removal of the true color of an industrial textile effluent through the process of biosorption with sugarcane bagasse.

2. Methods

2.1. RNA development

The experimental data used to feed the RNA, referring to the color removal of the industrial textile effluent, were taken from the work of Leon (2019). The input variables for the RNA of this study were the results from the effects of pH, particle size, biosorbent amount, adsorption time and effluent color concentration. The software used was Matlab 2016.

The architectural adopted was a multi-layered perceptron (MLP), breakthrough, with a hidden layer. Different numbers of neurons were tested to test which structure would be best to fit the data. The

developed RNA has an output layer composed of a neuron, which corresponds to the final true color of the effluent in PtCo. L^{-1} . Table 1 shows the predefined parameters for network creation and leaves a line clear before each heading.

Table 1. Parameters preestablished for RNA.

Parameter	Definitions
Number of input parameters	5
Number of neurons in the hidden layer	8
Number of neurons in the output layer	1
Hidden-layer activation function	Sigmoid tangent
Activation function for output layer	Purelin
Algorithm	<i>Levenberg-Marquardt</i>
Stopping criterion	Epoch number and error measure
Error measurement	Mean square error (MSE)

The training (stopping criterion) was interrupted when the mean square error (MSE) was within the required tolerance or when the maximum number of the epoch was obtained. The sum of the mean square errors demonstrates the performance of the network, so that the lower the value for the MSE for the training group, the better the training (FIORIN et al., 2011; GHAEDI; VAFAEI, 2017).

The correlation coefficient (R) also demonstrates network unemployment, which is a measure of linear association between experimentally obtained data and those predicted by RNA. When rises the value of the squared correlation coefficient, the coefficient of determination (R^2) is generated (FIORIN et al., 2011; GHAEDI; VAFAEI, 2017; PINHEIRO; RÜTHER; LOVATO, 2017).

3. Results and discussion

During the training stage, different numbers of neurons were tested for the hidden layer (Fig. 1). The structure with 8 neurons presented the best performance since it obtained the smallest square error (MSE), equivalent to 0.01314, therefore, this was the network chosen to simulate the predicted data.

The correlation coefficient (R) of the 6 structures are found in Table 2, where, it is noted that the R for

the structure with 8 neurons is close to 1, this value is considered as optimal, since it indicates that the data expected are very close to the real.

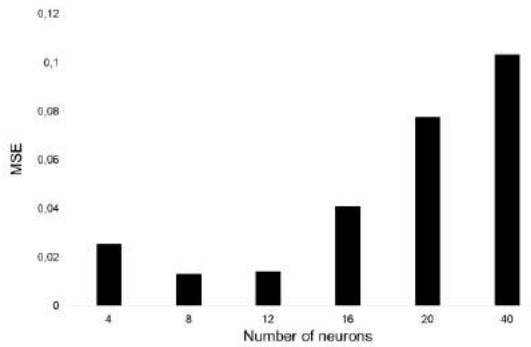


Fig. 1. Number of hidden layer neurons for RNA structure

Fig. 2 presents the R obtained for the training, validation and test group data, as well as for all experimental data together, using the configuration with 5 input variables, 8 hidden layer neurons and one response variable (5-8-1). The x-axis values represent those obtained experimentally and the y-axis values are predicted by RNA.

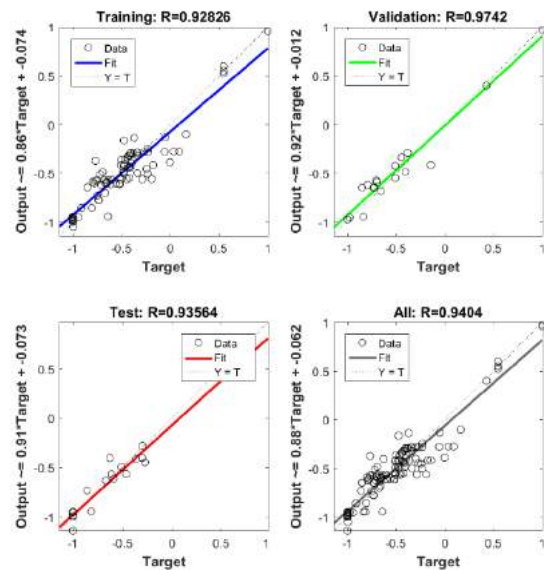


Fig. 2. Adjustments for the data present in the training, testing, validation and all experimental data sets together

Table 2. Optimum points for color removal presented by RNA (MSE ranged from 0,013 a 0,103).

Topology	Correlation (R)			
	Training	Validation	Test	All Experimental Points
5- 4 -1	0.9312	0.903	0.928	0.928
5-8-1	0.928	0.974	0.936	0.940
5- 12 -1	0.938	0.955	0.924	0.933
5-16-1	0.962	0.861	0.882	0.943
5-20-1	0.954	0.890	0.842	0.914
5-40-1	0.951	0.712	0.843	0.896

3.1. Comparison of actual data with predicted RNA

Data from the study of the effect of solution pH on the effluent true color removal were compared with those obtained by RNA, which are shown in Fig. 3. For the experiment, a dosage of 0.6 g of adsorbent, particle size of 0.5 mm, 24 h of adsorption and a pH range of 2-10 were used. It is noteworthy that the color of the initial actual effluent varied according to the day the duplicate was made, where the initial color of the effluent for the first duplicate was 619.93 PtCo.L⁻¹ and the initial color for the second duplicate was 802.05 PtCo.L⁻¹.

It is noted with the aid of Fig. 3 that the experimental data approximates that predicted by RNA, so that under conditions where the pH was more basic the predictions fit the experimental data better, this may have occurred because under these conditions (pH above 7) all experiments showed 0% true color removal, strengthening network learning and facilitating the prediction of color removal from these points.

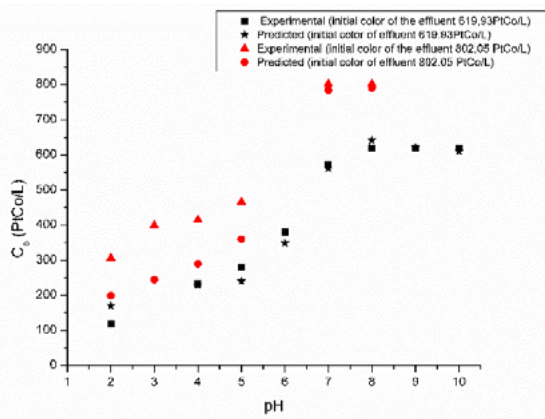


Fig. 3. Experimental data predicted by RNA for data from the pH effect. Particle size: 0.5 mm, amount of adsorbent: 0.6 g, time: 24 h

With the pH effect test, it can be observed that the maximum color removal occurred with pH 2 and 3, where the removals were equivalent to 71.31% and 62%, respectively. This justification may be given by the fact that the pH of the solution has a potential to change the load present on the surface of the adsorbent material, so that with the decrease of the pH below the zero load point ($pH_{pzc} = 2.6$) The amount of H^+ ions increases, leaving the surface of the material loaded with positive loads.

Fig. 4 shows the comparison between the experimental data obtained from the study of the effect of the amount of adsorbent on the true color removal of the effluent and those predicted by RNA. During the experiments, it was used a particle size of 0.5 mm, 24 h adsorption, pH of the solution adjusted to 2, initial effluent color for first duplicate of 775.20 PtCo.L⁻¹, initial color for second duplicate of 863.92 PtCo. L⁻¹ and the amount of adsorbent ranged from 0.4 to 0.7 g. From Fig. 4 it is possible to see that the experimental data are well fitted to those predicted by the network ($R = 0.928$). Note that using 0.6 g BCM gave the best percentage of true color removal, where experimentally it was found the value of 85.7% color removal.

The experimental and predicted data for the adsorbent size variable are expressed in Fig. 5, the experimental conditions used were: 0.6 g of material, 24 h of adsorption, pH 2, initial effluent color for the first duplicate of 867 PtCo.L⁻¹, initial color for second duplicate 1044 PtCo.L⁻¹ and particle size ranging from 0.3 to 1 mm. The experimental and predicted data by RNA are well adjusted ($R = 0.928$), and the net also predicted a particle size equivalent to 0.7 mm to promote the best true color removal. Experimentally, with a

particle size of 0.7 mm, A mean removal of 78.70% of true color was obtained.

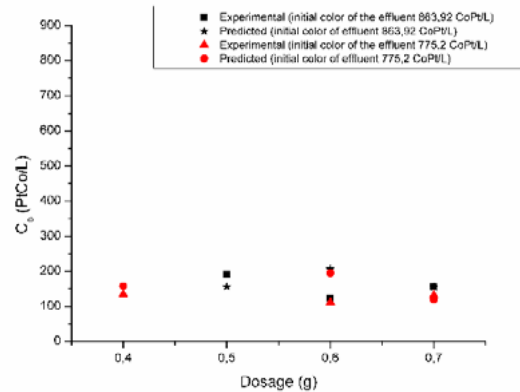


Fig. 4. Experimental data predicted by RNA for data from the material dosing effect. Particle size: 0.5 mm, amount of adsorbent: 0.6 g, pH: 2, time: 24 h

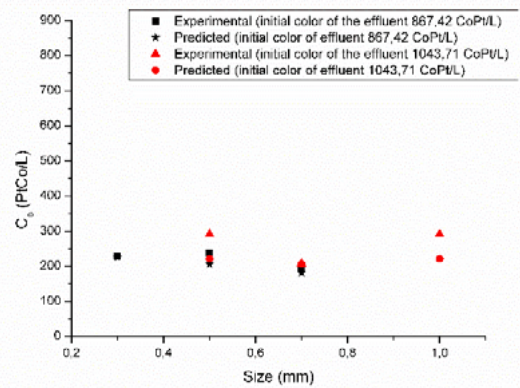


Fig. 5. Experimental data predicted by RNA for data derived from the particle size effect. Adsorbent amount: 0.6 g, pH: 2, time: 24 h

For the time variable, the experimental conditions were: material quantity 0.6 g, particle size 0.7 mm, pH 2, initial effluent color for first duplicate 1006 PtCo.L⁻¹, initial color for second duplicate 1007 PtCo.L⁻¹ and time ranging from 2 min to 1440 min. It should be noted that after 180 min of adsorption there was no significant alteration in the adsorption, this was presented by the experimental and predicted data, which can be observed in Fig. 6. The experimental and predicted data are also well adjusted.

To analyze the effect of the initial variation of the effluent color in the percentage of true color removal, 0.6 g of material, granulometry of 0.7 mm, pH 2 and 180 min of time were used. With Fig. 7, it

is observed that the RNA showed good predictions when the effluent had low colors, but with the increase in color, the predicted values were disparate, therefore, it is recommended to use the forecasts for an initial effluent color lower than 900 PtCo.L⁻¹.

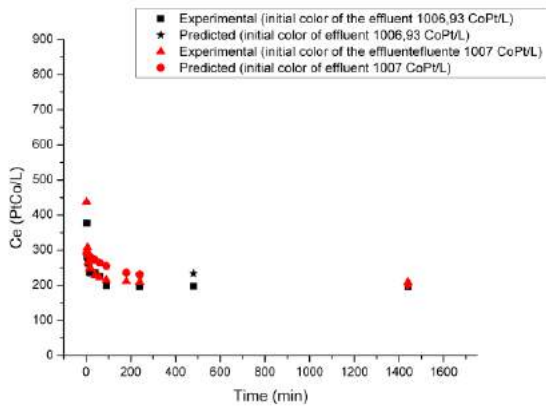


Fig. 6. Experimental data predicted by RNA for time effect data. Adsorbent amount: 0.6 g, particle size: 0.7 mm, pH: 2, time: 3 h

Even following the qualitative behavior adequately, the lack of precision in cases where the initial color concentration is high can be explained due to an insufficient amount of patterns used in learning (ASSIS, 2001), i.e. lack Experiments with high concentration of initial color , a situation that cannot be controlled when using the real effluent.

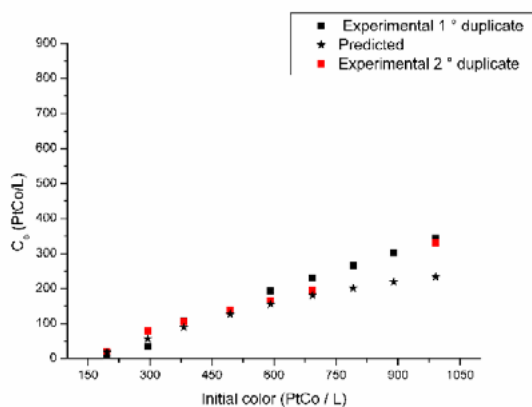


Fig. 7. Real and predicted RNA data for data from the effluent initial color effect. Adsorbent amount: 0.6 g, particle size: 0.7 mm, pH: 2, time: 3 h

The optimum adsorption point predicted by RNA, taking into account the initial effluent color, q_e and the percentage of color removal was the experiment performed at pH 2, with particle size of 0.7 mm, using 0.6 g of adsorbent and for a time of 24 hours, which showed a color removal, both experimental and predicted equivalent to 80%, q_e experimental and predicted 70 PtCo.g⁻¹ for initial coloration of 1043.71 PtCo.L⁻¹.

4. Conclusion

In the present study, an artificial neural network (RNA) with multilayer perceptron architecture (MLP) and the Levenberg-Marquardt algorithm were made to forecast color removal of real textile effluent using sugarcane bagasse as biosorbent. The effect of five variables on the adsorption process for true color removal was inserted into the RNA, namely: solution pH, particle size, adsorbent concentration, mixing time and initial effluent color concentration. The RNA structure that best suited the experimental data was composed of 8 hidden layer neurons, with an MSE equivalent to 0.013. With the structure composed of 8 neurons in the hidden layer it was possible to obtain an optimal fit ($R = 0.928$) for the experimental data to those calculated by the RNA model, proving that the RNA can be used to estimate the adsorption process under different experimental conditions. The best pH obtained in the studies was pH 2 with 71% true color removal and the particle size that presented the best color removal percentages (79%) was 0.7 mm and the amount of adsorbent that showed the best color removal was 0.6 g (86% removal). These conditions were also the best points for RNA.

Acknowledgements

We gratefully acknowledge the Research Support Program of the Federal Technological University of Paraná (UTFPR) - Campus Francisco Beltrão.

References

- [1] C.D. Raman, S. Kanmani, Textile dye degradation using nano zero valent iron: A review, *J. Environ. Manage.* 177 (2016) 341–355. doi:10.1016/j.jenvman.2016.04.034.
- [2] J. Dasgupta, J. Sikder, S. Chakraborty, S. Curcio, E. Drioli, Remediation of textile effluents by membrane

- based treatment techniques: A state of the art review, *J. Environ. Manage.* 147 (2015) 55–72. doi:10.1016/j.jenvman.2014.08.008.
- [3] C.A. Martínez-Huitl, E.V. Dos Santos, D.M. De Araújo, M. Panizza, Applicability of diamond electrode/anode to the electrochemical treatment of a real textile effluent, *J. Electroanal. Chem.* 674 (2012) 103–107. doi:10.1016/j.jelechem.2012.02.005.
- [4] S.L. Lim, W.L. Chu, S.M. Phang, Use of *Chlorella vulgaris* for bioremediation of textile wastewater, *Bioresour. Technol.* 101 (2010) 7314–7322. doi:10.1016/j.biortech.2010.04.092.
- [5] K. Vijayaraghavan, R. Balasubramanian, Is biosorption suitable for decontamination of metal-bearing wastewaters? A critical review on the state-of-the-art of biosorption processes and future directions, *J. Environ. Manage.* 160 (2015) 283–296. doi:10.1016/j.jenvman.2015.06.030.
- [6] A.M. Ghaedi, A. Vafaei, Applications of artificial neural networks for adsorption removal of dyes from aqueous solution: A review, *Adv. Colloid Interface Sci.* 245 (2017) 20–39. doi:10.1016/j.cis.2017.04.015.
- [7] E.M.F. Costa, M.A. Santos, A. Balieiro, O.L. Sanchez, C.M.F. Soares, M.S. Leite, Modelagem em um Processo de Adsorção da Lactose, *An. 2016 18a Sem. Pesqui. Da Univ. Tiradentes.* (2016) 1–4.
- [8] M.R. Fagundes-Klen, M.T. Veit, E.A. Da Silva, R. Bergamasco, T.D. Martins, R.L.S. Canevesi, Modelagem do efeito do pH na biossorção de metais pela alga marinha *Sargassum filipendula*, *Acta Sci. Technol.* 33 (2011) 439–446. doi:10.4025/actascitechnol.v33i4.7605.
- [9] C.A. Igwegbe, L. Mohmmadi, S. Ahmadi, A. Rahdar, D. Khadkhodaiy, R. Dehghani, S. Rahdar, Modeling of adsorption of Methylene Blue dye on Ho-CaWO_4 nanoparticles using Response Surface Methodology (RSM) and Artificial Neural Network (ANN) techniques, *MethodsX.* 6 (2019) 1779–1797. doi:10.1016/j.mex.2019.07.016.
- [10] S. Agarwal, I. Tyagi, V.K. Gupta, M. Ghaedi, M. Masoomzade, A.M. Ghaedi, B. Mirtamizdoust, Kinetics and thermodynamics of methyl orange adsorption from aqueous solutions - Artificial neural network-particle swarm optimization modeling, *J. Mol. Liq.* 218 (2016) 354–362. doi:10.1016/j.molliq.2016.02.048.
- [11] M. Dutta, P. Ghosh, J.K. Basu, Prediction of adsorption capacity of microwave assisted activated carbon for the decolorization of direct blue 86 by using artificial neural network, *Asian J. Appl. Sci.* 5 (2012) 414–422. doi:10.3923/ajaps.2012.414.422.
- [12] A. Maleki, H. Daraei, F. Khodaei, K. Bayazid-, Investigation of potato peel-based bio-sorbent efficiency in reactive dye removal: Artificial neural network modeling and genetic algorithms optimization, 1 (2013) 21–28.
- [13] V.B. DE LEON, REMOÇÃO DE COR VERDADEIRA DE EFLUENTE TÊXTIL REAL POR BISSORÇÃO: APLICAÇÃO E MODELAGEM POR REDES NEURAIAS ARTIFICIAIS, 2019.
- [14] D.V. Fiorin, F.R. Martins, N.J. Schuch, E.B. Pereira, Forecast of solar energy resource by using neural network methods, *Rev. Bras. Ensino Fis.* 33 (2011). doi:10.1590/S1806-1172011000100009.
- [15] E. Pinheiro, R. Rüter, A. Lovato, APLICABILIDADE DO ALGORITMO DE LEVENBERG-MARQUARDT PARA ANÁLISE DE GERAÇÃO DE ENERGIA ELÉTRICA DE UM SISTEMA FOTOVOLTAICO, *Rev. Produção Online.* 17 (2017) 1204–1217.
- [16] A.J. DE ASSIS, Identificação e controle de processos não lineares utilizando redes neurais artificiais, UNIVERSIDADE ESTADUAL DE CAMPINAS FACULDADE DE ENGENHARIA QUÍMICA, 2001.

Mathematical modeling and simulation of fixed-bed adsorption column with axial particle diameter profile for removal of dilute solutions

Cristiane G. Ferrarezzi^{a,*}, Reginaldo Guirardello^b

^{a,b}School of Chemical Engineering, State University of Campinas, Av. Albert Einstein 500, 13083-852, Campinas-SP, Brazil

Abstract

This study developed a mathematical model of a fixed-bed adsorption process that allows variations in particle diameter along the bed. The mathematical model assumes that the bed is formed by small spherical particles, that the feed solution is dilute (with Henry's linear approximation being applicable) and that the external resistance to mass transfer is negligible when compared to the resistance within the particle. The mass balance for solute concentration in the spheres is analytically solved and the mass balance for solute concentration in the mobile phase is numerically solved by trapezoidal rule, with subsequent adoption of the Thomas algorithm to solve the system of equations formed. The two solutions are joined together with Duhamel's theorem. Studies adopting a variable profile of particle diameter along the bed showed that the ascending and descending profiles presented equivalent breakthrough curves. It was also possible to conclude that studies adopting a variable diameter profile along the bed presented a breakpoint time lower than the bed with a single and intermediate particle diameter, as well as a breakthrough curve shape farther from the ideal profile of a step.

Keywords: Adsorption; Fixed-bed; Mathematical Modeling; Simulation; Henry's Law

Nomenclature

A	cross-sectional total area of the bed [cm ²];	Q	volumetric flow rate of the liquid phase [cm ³ /min];
c	concentration of the solute in the mobile phase inside the particle [mmol/L];	r	radial position [cm];
C	solute concentration in the mobile phase in the empty portions of the bed [mmol/L];	R _c	column radius [cm];
D _p	effective diffusion coefficient [cm ² /min];	t	time [min or h];
dp	particle diameter [μm];	t _s	saturation time [min];
dp _n	particle diameter corresponding to the n th portion of the bed [μm];	v _i	interstitial velocity [cm/min];
E _b	coefficient of axial dispersion along the bed [cm ² /min];	v _s	superficial velocity [cm/min];
k _f	external fluid film mass transfer coefficient [cm/min];	x	axial position [dimensionless];
K _L	Langmuir constant [L/mmol];	z	axial position [cm];
k _p	linear adsorption equilibrium constant [dimensionless];	ε _b	bed porosity [dimensionless];
L	bed length [cm];	ε _p	particle porosity [dimensionless];
n _T	total number of portions used in the bed [dimensionless];	μ _B	fluid viscosity [Pa.s];
Pe	Péclet number [dimensionless];	ρ _B	fluid density [kg.m ⁻³];
q	concentration of solute in adsorbent particles [mmol/g];	ρ _p	dry particle real density [g/L];
		τ	time [dimensionless];

1. Introduction and objective

Adsorption is a unit operation of mass transfer in which compounds present in fluid solutions (mobile phase) adhere to the surface of a solid (adsorptive particles). Using the mass balance

equations for the mobile phase and the adsorptive particles, it is possible to describe the fixed-bed adsorption process through mathematical modeling.

The mathematical modeling of fixed-bed columns has been studied for years [1] [2] [3] [4]. However, even the recent studies consider, in their most, that the particle diameter must be constant along the bed [5] [6].

The proposed model applies to solutions where the solute is in low concentration, allowing the application of Henry's Law. Thus, its main focus is the environmental applications, since studies prove that adsorption is an effective alternative in the removal of emerging contaminants [7] [8], as well as in the final stages of wastewater treatments [9] [10].

The present work is a modification of the mathematical model described by Cremasco; Guirardello and Linda Wang (2003). Its main objective is to allow variations in particle diameter along the bed, allowing the use of different portions in the bed, each one with a specific particle radius. The number of portions of the bed can be set as needed with no limitation and the model is able to predict the results regardless of the column configuration, which may be horizontal or vertical, with downflow or upflow.

2. Methodology

2.1. Hypotheses adopted in the model

The hypotheses and limitations of the proposed model are:

- Constant input flow rate;
- Constant temperature;
- Uniform cross section;
- One-component feed solution;
- Solid phase formed by small spherical particles;
- There are no dead zones and no preferential paths in the bed;
- Diffusion occurs within the pores of the particle;
- Dilute feed solution (Henry's Law is valid);
- There are no chemical reactions;
- Velocity profile in the liquid phase varies very little with the radial position in the bed;
- The external resistance to mass transfer from liquid to solid phase is considered to be very small (Biot number tends to infinity).

2.2. Dimensionless Proposed Mathematical Model

The mass balance for the solute in the mobile phase can be described by:

$$\frac{-1}{Pe} \cdot \frac{\partial^2 C}{\partial x^2} + \left[\frac{\partial C}{\partial x} + \frac{\alpha}{(1+\gamma)} \cdot \frac{\partial C}{\partial \tau} \right] + \frac{1-\alpha}{(1+\gamma)} \cdot \frac{\partial C}{\partial \tau} + \frac{\gamma}{(1+\gamma)} \cdot \frac{\partial B}{\partial \tau} = 0 \quad (1)$$

where

$$x = \frac{z}{L} \quad (2)$$

$$\tau = \frac{t}{t_s} \quad (3)$$

$$Pe = \frac{L \cdot v_i}{E_b} \quad (4)$$

$$v_i = \frac{Q}{A \cdot \varepsilon_b} \quad (5)$$

$$t_s = \frac{L}{v_i} (1 + \gamma) \quad (6)$$

$$\gamma = \frac{(1 - \varepsilon_b)[\varepsilon_p + (1 - \varepsilon_p)k_p]}{\varepsilon_b} \quad (7)$$

$$A = \pi \cdot R_c^2 \quad (8)$$

with initial and boundary conditions [11]:

$$C = 0, \text{ for } \tau = 0 \text{ and } 0 \leq x \leq 1 \quad (9)$$

$$1 = C - \frac{1}{Pe} \frac{\partial C}{\partial x}, \text{ for } x = 0 \text{ and } \tau > 0 \quad (10)$$

$$-\frac{1}{Pe} \frac{\partial C}{\partial x} = 0, \text{ for } x = 1 \text{ and } \tau > 0 \quad (11)$$

Although the proposed model allows variation of the feed solution concentration over time, $C_0=1$ was adopted to obtain the dimensionless concentration of the solute in the mobile phase.

The mass balance for the solute in the particles can be described by [11]:

$$D_p \cdot \varepsilon_p \cdot \frac{1}{r^2} \cdot \frac{\partial}{\partial r} \left(r^2 \frac{\partial c}{\partial r} \right) = \varepsilon_p \cdot \frac{\partial c}{\partial t} + (1 - \varepsilon_p) \cdot \frac{\partial q}{\partial t} \quad (12)$$

with the following initial and boundary conditions [11]:

$$c = 0, \text{ for } \tau = 0 \text{ and } 0 \leq r \leq R \quad (13)$$

$$\frac{\partial c}{\partial r} = 0, \text{ for } r = 0, \tau > 0 \text{ and } 0 \leq x \leq 1 \quad (14)$$

$$c = C, \text{ for } r = R, \tau > 0 \text{ and } 0 \leq x \leq 1 \quad (15)$$

This model considered that the feed solution is in Henry's linear range, obeying the relation:

$$q = k_p \cdot c \quad (16)$$

The correlation between mobile phase and particle concentrations is made by Duhamel's theorem and given by [11]:

$$B(x, \tau) = \int_0^\tau -\frac{d\bar{u}(\tau-\zeta)}{d\zeta} C(x, \zeta) d\zeta \quad (17)$$

where u is the analytical solution obtained for the system formed by the equations (12), after applying the relation (16), together with the equations (13), (14) and (15) with $C=1$ in $r=R$, given by [11]:

$$\bar{u} = 1 - \frac{6}{\pi^2} \sum_{n=1}^{\infty} \frac{1}{n^2} \cdot \exp(-n^2 \pi^2 \theta) \quad (18)$$

where:

$$\theta = \frac{\varepsilon_p}{[\varepsilon_p + (1 - \varepsilon_p) \cdot k_p]} \cdot \frac{D_p \cdot t_s \cdot \tau}{R^2} \quad (19)$$

For small time values ($0 \leq \theta \leq 0.05$), the following asymptote is used:

$$\bar{u} = 6 \sqrt{\frac{\theta}{\pi}} - 3 \cdot \theta \quad (20)$$

To avoid numerical diffusion, the method of characteristics was used in part of the mass balance for the solute in the mobile phase, only in the term in brackets of the equation (1), establishing a relationship between these two intervals, linking x and τ through parametric equations. Therefore, to calculate $\Delta\tau$, the possible values of α were studied considering two extreme particular cases for diffusion within the particle: when there is no diffusion within the particle ($\alpha = 1$) and when diffusion within the particle is infinite ($\alpha = 1+\gamma$). When diffusion within the particle is intermediate, the time interval starts to depend on the particle radius, which is not interesting for this study, because the method must consider the variation of the particle radius along the bed. The two particular cases, $\alpha = 1$ and $\alpha = 1+\gamma$, were evaluated, resulting that $\alpha = 1+\gamma$ presented better results, so this case was adopted in this work. It is important to point out that the model is still applied to finite non-zero values of diffusion coefficients inside the particle, this analysis is just to find the most suitable value of α to avoid numeric diffusion with constant intervals.

As in the model described by Cremasco; Guirardello and Linda Wang (2003), the mass balance for the solute in the particles is analytically solved by the method of separation of variables (linear model) and the concentration in the

particles is related to the concentration in the mobile phase through Duhamel's theorem.

The partial differential equation of the mass balance for the solute in the mobile phase was numerically solved by the trapezoidal rule.

Finally, the Thomas algorithm was used to solve the equation system formed between the partial differential equation solution for calculating the concentration in the mobile phase and the initial and boundary conditions. The equations were solved individually by filling a matrix of concentration values in the mobile phase for each position and time, and were interrupted when reaching the defined number of time and position steps. These values, in turn, were adjusted to use the shortest computational time, but allowing the time interval to be short enough to allow comparisons between simulations, and allowing the concentration at the bed output to equal the input concentration (or approaching it).

3. Results and discussions

3.1. Comparison with an experimental study

The proposed model was simulated in Fortran 77[®], using the same conditions of the adsorption process of copper with the fixed-bed calcined clay "verde-lodo", studied by Almeida Neto (2011) at a flow rate of 3 mL/min, which was the flow that presented the best results according to the author. The number of position steps was set to 350 and the number of time steps was set to 700.

Although the experiment performed by Almeida Neto (2011) is not in the linear region of the isotherm, his study was considered only to evaluate the performance and coherence of breakthrough curve obtained by the proposed model in an experimental study. As the proposed model is restricted to the linear region of the isotherm, the linear adsorption equilibrium constant, k_p , was calculated using Langmuir isotherm data, according to the equation $k_p = \rho_p \cdot q_m \cdot K_L$. The conditions adopted in the experiment used as reference for this evaluation are presented in Table 1.

The parameters not mentioned in the work of Almeida Neto (2011) were estimated by relevant literature correlations. The values obtained and the references of correlations used are presented in Table 2. The Biot number was calculated by the equation $Bi = (k_f \cdot R) / (D_p \cdot \varepsilon_p)$.



Table 1. Conditions adopted in the experiment used as a reference for the performance evaluation of proposed model

Parameter/variable	unit	value
Column radius, R_c	cm	0.7
Temperature, T	K	297
Particle diameter, d_p	cm	0.0855
Particle porosity, ε_p	dim	0.1117
Bed porosity, ε_b	dim	0.4876
Flow rate, Q	cm ³ /min	3.0
Bed length, L	cm	14.0
Langmuir constant, K_L	L/g	3.0089
Maximum adsorption capacity, q_m	mmol/g	0.22
Real density of dry particle, ρ_p	g/L	2716.8

dim: dimensionless.

Source: Almeida Neto (2011).

For unit conversion of the Langmuir constant, the molar mass of copper was used: 63.546 g/mol or 0.063546 g/mmol. Reaching the conversion factor of 15.7366 which corresponds to $K_L = 47.35$ L/mmol.

As shown in Figure 1, although results cannot be compared, since Almeida Neto (2011) study does not work in the linear region of the isotherm, the simulation presented a larger breakpoint time than the one obtained by the author (approximately 6 h).

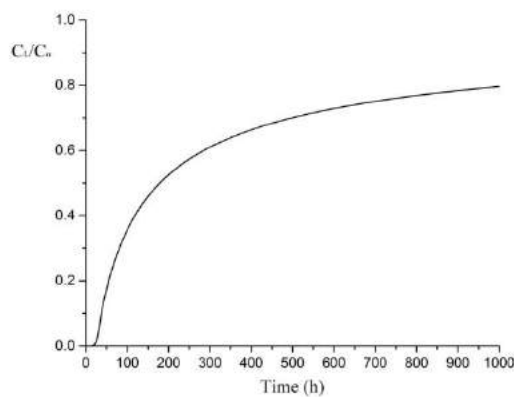


Figure 1 – Breakthrough curve obtained by the Fortran 77® simulation of the proposed model.

This larger breakpoint time is consistent because the concentration range adopted in the proposed model is smaller, since the model only applies to solutions that respect Henry's linear range.

Table 2. Estimated parameters through pertinent correlations for use in the simulation of the proposed model

Estimated parameter	unit	value
Area of the cross section, A	cm ²	1.539
Superficial velocity, v_s [13]	cm/min	1.949
Interstitial velocity, v_i , eq. (5)	cm/min	3.997
Linear adsorption equilibrium constant, k_p	dim	28,300.91
Free diffusion coefficient, D_{AB} [14]	cm ² /min	7.31×10^{-4}
Effective diffusion coefficient, D_p [15]	cm ² /min	5.66×10^{-5}
Coefficient of axial dispersion along the bed, E_b [16]	cm ² /min	0.201
Reynolds number, Re [13]	dim	0.303
Schmidt number, Sc [13]	dim	752.41
Sherwood number, Sh [16]	dim	13.410
External fluid film mass transfer coefficient, k_f [16]	cm/min	0.115
Biot number, Bi	dim	776.052

dim: dimensionless; eq: equation.

The value obtained for the Biot number, 776.052, guarantees the validity of the proposed model, since this value is high enough to be worth considering the Biot number tending to infinity. In practice, values for the Biot number above 10 already allow this consideration.

3.2. Comparative study between variable and uniform d_p along the bed

By adopting the same parameters used for the adsorption process of copper with the fixed-bed calcined clay “verde-lodo”, studied by Almeida Neto (2011) at a flow rate of 3 mL/min, three studies were performed:

- considering a constant particle diameter along the bed, equals 128.25 μm ;

- considering a variable particle diameter along the bed, one portion with bed fraction, $F_{b,n}$, equals 0.9 and particle diameter equals 1282.50 μm and the other portion with bed fraction, $F_{b,n}$, equals 0.1 and particle diameter equals 42.75 μm (one study in ascending and the other in descending particle diameter profile).

These studies respected the recommendation of $D_c/d_p > 10$ [17] and were chosen because the pressure drop of the column by the three studies are similar, 859.50 N/m^2 for constant particle diameter and 780.83 N/m^2 for the variable particle diameter along the bed. D_c is the column diameter [cm].

The change in particle diameter influences calculations of the axial dispersion coefficient along the bed, E_b , of the external fluid film mass transfer coefficient, k_f , and of the Biot number, Bi . These parameters were recalculated for each particle diameter adopted in the studies and are presented in the Table 3.

Table 3. Parameters estimated through the literature correlations for each particle diameter adopted in the study

d_p [μm]	E_b [cm^2/min]	k_f [cm/min]	Biot no. [dim]
42.75	0.039	0.853	288.769
128.25	0.056	0.409	414.955
1282.50	0.286	0.087	887.158

dim: dimensionless.

All other parameters and variables had their values maintained, as previously presented in Tables 1 and This larger breakpoint time is consistent because the concentration range adopted in the proposed model is smaller, since the model only applies to solutions that respect Henry's linear range.

For the studies using a variable particle diameter along the bed it was used the weighted average of the axial dispersion coefficient along the bed, E_b , of each portion, resulting in 0.261 cm^2/min .

The studies were simulated in Fortran 77[®] using the proposed model with number of position steps equals to 300 and the number of time steps equals to 600.

The partial pressure drop, $\Delta P_{n,p}$, for each n^{th} portion of the bed was calculated according to the Ergun equation, and the length of the bed, L ,

multiplied by the bed fraction, $F_{b,n}$, corresponding to the portion in question, as follows:

$$\Delta P_{n,p} = L \cdot F_{b,n} \left[\frac{150 \cdot v_s \cdot \mu_B \cdot (1 - \varepsilon_b)^2}{d p_n^2 \cdot \varepsilon_b^3} + \left(1.75 \cdot \rho_B \cdot v_s^2 \cdot \frac{(1 - \varepsilon_b)}{d p_n \cdot \varepsilon_b^3} \right) \right] \quad (21)$$

The total pressure drop of the column ΔP_T was calculated according to the equation below:

$$\Delta P_T = \sum_{n=1}^{n_T} \Delta P_{n,p} \quad (22)$$

The obtained ΔP_T value is given in N/m^2 , adopting L in [m], v_s in [$\text{m} \cdot \text{s}^{-1}$], μ_B in [$\text{Pa} \cdot \text{s}$] and ρ_B in [$\text{kg} \cdot \text{m}^{-3}$].

The comparative graph between the breakthrough curve adopting a single particle diameter, 128.25 μm , and the breakthrough curve with ascending and descending particle diameter profile along the bed is shown in Figure 2.

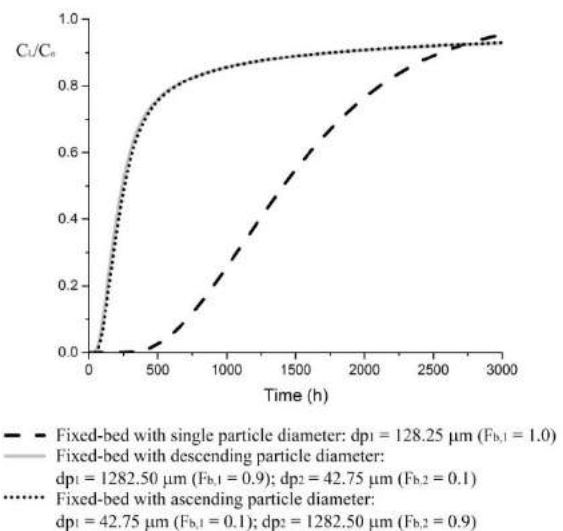


Figure 2. Comparative graph between the breakthrough curve adopting a single particle diameter along the bed, $d_p = 128.25 \mu\text{m}$, the breakthrough curve adopting a descending particle diameter profile along the bed, $d_{p1} = 1282.50 \mu\text{m}$ ($F_{b,1} = 0.9$); $d_{p2} = 42.75 \mu\text{m}$ ($F_{b,2} = 0.1$) and the breakthrough curve adopting a ascending particle diameter profile along the bed, $d_{p1} = 42.75 \mu\text{m}$ ($F_{b,1} = 0.1$); $d_{p2} = 1282.50 \mu\text{m}$ ($F_{b,2} = 0.9$)

As shown in Figure 2, the breakpoint time with variable d_p profile along the bed was about 400 hours less than the breakpoint time with a single d_p along the bed, even though the two studies have a

pressure drop around 800 N/m^2 . Thus the particle diameter profile was not efficient to increase the breakpoint time in relation to a single and intermediate particle diameter along the bed.

The Figure 2 also shows that the difference between the breakthrough curves of an ascending and descending particle diameter profiles are not significant.

4. Conclusions

The proposed model presented a consistent breakthrough curve compared to Almeida Neto (2011) study, since it showed a larger breakpoint time than the one obtained by the author. This behavior was expected, since the proposed model applies to more dilute solutions found in the linear region of the isotherm.

By adopting a variable particle diameter profile along the bed, this study showed that the ascending and descending profiles along the bed presented equivalent breakthrough curves. It was also possible to conclude that studies adopting a variable diameter profile along the bed presented a breakpoint time lower than the bed with a single and intermediate particle diameter, as well as a breakthrough curve shape farther from the ideal profile of a step, that is, the variable particle diameter profile along the bed was not efficient for the optimization of the fixed bed adsorption by reducing the mass transfer zone nether to increase the breakpoint time.

The method proposed in this study, due to the ability to vary the particle diameter along the bed, is a tool of great interest in process optimization cases, being able to predict the behavior of a real process in the use of a bed with different particle diameter portions.

References

- [1] J. B. Rosen, (1952). Kinetics of a Fixed Bed System for Solid Diffusion into Spherical Particles. *The Journal of Chemical Physics*, 20(3), 387–394. <https://doi.org/10.1063/1.1700431>
- [2] T. W. Weber, & R. K. Chakravorti (1974). Pore and solid diffusion models for fixed-bed adsorbers. *AIChE Journal*, 20(2), 228–238. <https://doi.org/10.1002/aic.690200204>
- [3] J. C. Crittenden et al. (1980). Mathematical Model of Sequential Loading in Fixed-Bed Adsorbers. *Water Pollution Control Federation Journal*, 52(11), 2780-2795
- [4] D. W. Hand, J. C. Crittenden, & W. E. Thacker (1984). Simplified Models for Design of Fixed-Bed Adsorption Systems. *Journal of Environmental Engineering*, 110(2), 440–456. [https://doi.org/10.1061/\(asce\)0733-9372\(1984\)110:2\(440\)](https://doi.org/10.1061/(asce)0733-9372(1984)110:2(440))
- [5] Z. Xu, J. Cai, & B. Pan (2013). Mathematically modeling fixed-bed adsorption in aqueous systems. *Journal of Zhejiang University SCIENCE A*, 14(3), 155–176. <https://doi.org/10.1631/jzus.a1300029>
- [6] M. E. Maria, & M. B. Mansur (2017). Mathematical modeling of manganese adsorption onto bone char in a continuous fixed bed column incorporating backmixing and shriking core approaches. *Brazilian Journal of Chemical Engineering*, 34(3), 901–909. <https://doi.org/10.1590/0104-6632.20170343s20150625>
- [7] Z. Jeirani, C. H. Niu, & J. Soltan (2017). Adsorption of emerging pollutants on activated carbon. *Reviews in Chemical Engineering*, 33(5). <https://doi.org/10.1515/revce-2016-0027>
- [8] A. C. Sophia, & E. C. Lima (2018). Removal of emerging contaminants from the environment by adsorption. *Ecotoxicology and Environmental Safety*, 150, 1–17. <https://doi.org/10.1016/j.ecoenv.2017.12.026>
- [9] N. W. Jern, *Industrial Wastewater Treatment*. Singapore: Imperial College Press, 2006. p.153
- [10] R. F. Weiner; R. Matthews, *Environmental Engineering*, Fourth Edition. Burlington: Butterworth Heinemann - Elsevier Science, 2003. 484p.
- [11] M.A. Cremasco; R. Guirardello; N.-H.Linda Wang. Adsorption of aromatic amino acids in a fixed bed column, *Brazilian Journal of Chemical Engineering*, vol.20 no.3 São Paulo July/Sept. 2003. doi: 10.1590/S0104-66322003000300012
- [12] A. F. Almeida Neto. Caracterização e avaliação de argilas como adsorventes na Remoção e eluição de íons cobre e mercúrio em diferentes sistemas. 2011. 145 f. Tese (Doutorado em Engenharia Química) – Faculdade de Engenharia Química, UNIVERSIDADE ESTADUAL DE CAMPINAS, Campinas-SP.
- [13] E. J. Wilson, & C. J. Geankoplis (1966). Liquid Mass Transfer at Very Low Reynolds Numbers in Packed Beds. *Industrial & Engineering Chemistry Fundamentals*, 5(1), 9–14. <https://doi.org/10.1021/i160017a002>
- [14] M. A. Cremasco. *Fundamentos de transferência de massa*. 2. ed. São Paulo: Blucher, 2002.
- [15] A. Ghorbani, R. Karimzadeh, M. Mofarahi (2018). Mathematical Modeling of Fixed Bed Adsorption: Influence of Main Parameters on Breakthrough Curve. *Journal of Chemical and Petroleum Engineering*, 52(2), 135–143. <https://doi.org/10.22059/JCHPE.2018.255078.1226>
- [16] Douglas M. Ruthven, *Principles of adsorption and adsorption processes*. 1st. ed. New York: John Wiley & Sons, Inc, reprinted 1984.
- [17] M. Winterberg, & E. Tsotsas (2000). Impact of tube-to-particle-diameter ratio on pressure drop in packed beds. *AIChE Journal*, 46(5), 1084–1088. <https://doi.org/10.1002/aic.690460519>

Analytical solution for pore volume and surface diffusion model in batch adsorption systems

Gabriel Miglioranza^a, Marcio Schwaab^a

^a Departamento de Engenharia Química, Escola de Engenharia, Universidade Federal Do Rio Grande Do Sul. Rua Ramiro Barcelos, 2777 - Prédio 22202, Porto Alegre, RS, 90035-007, Brazil

Abstract

In this paper, we present a detailed description of a porous particle adsorption / diffusion model within a batch system. A mechanism that combines diffusion, convection and adsorption processes is used as a basis for modeling phenomenological equations. The porous particle is modeled from three spatial geometries, slab, cylinder and sphere, represented by the variable $S = 0$, $S = 1$, $S = 2$ respectively. Thus, a mass balance was obtained inside the particle, involving diffusion and adsorption processes, generalized for the three geometries. This balance is combined with a material balance in the bulk phase. The result of these balances is two differential equations to be solved simultaneously, a partial differential equation for the particle and an ordinary differential equation for the finite bath. These equations are finally solved by applying the Laplace transform method. The main steps for obtaining and solving this model are presented, as well as the closed analytical expression that solves the system of differential equations.

Keywords: adsorption kinetics; analytical solution; phenomenological models;

1. Introduction

Between the 70's and 90's the study of adsorbents gained popularity due to the development of porous adsorbents such as zeolites and activated charcoal[1]. The study of adsorbent materials remains relevant due to the variety of applications: gas separation processes, molecular sieves, drug removal and other emerging pollutants from aqueous solutions, etc.

Laboratory evaluation of adsorbents usually involves the use of batch assay. Briefly, the adsorbent material is contacted with a solution containing the solute of interest; the process ends when the system goes into equilibrium. These assays seek information about the adsorption equilibrium behavior, isotherms and their parameters, and the adsorption kinetic characteristics.

In order to understand the phenomenon, several models were created to represent the experimental data. These Models are separated into two large groups: the empirical models like pseudo first order and pseudo second order models and the phenomenological models like Crank's Model [2]. The first group, are mathematical expressions with

the sole purpose of approximating the experimental points obtained, without the need to present a previous theoretical knowledge about the model parameters. Meanwhile, the second group, phenomenological models, is based on well-established physical principles such as mass conservation; however, the expressions obtained are generally in the form of differential equations, making it difficult to mathematically manipulate this group of models.

Despite complexity, phenomenological models should be preferred when physical consistency and parameters with well-defined physical interpretations are desired [3], [4]. In the group of phenomenological models, only a small portion has an analytical solution, usually numerical methods are needed to approximate the solution.

This paper addresses one of the special cases where an analytical solution is likely to be found. The model adopted will be described in detail, as well as its solution by applying the Laplace transform.

2. Mathematical Modeling

Adsorption is a complex phenomenon, so in the development of mathematical models some

hypotheses and simplifications are necessary for a satisfactory model to be obtained. In this work, the first hypothesis adopted is the continuum hypothesis, so it is not necessary to describe microscopically velocities and position of the molecules involved in the process, as in molecular simulations, microscopic variables are replaced by macroscopic mean variables such as concentrations and mass flows.

However, in this scenario, a descriptive mechanism of the phenomenon must be adopted: the solute initially lies within the homogeneous fluid phase, which migrates to the surface of the porous solid passing through the mass boundary layer (external resistance to mass transfer). Within the particle, two diffusive processes occur concurrently; the first is the diffusion of the solute through the fluid phase found inside the pores; the second is the diffusion of the solute across the solid surface of the particle. Note that the solute that diffuses on the particle surface is considered as adsorbed solute. However, the adsorption dynamics are neglected because they are generally faster than diffusive processes.

Admitting the described mechanism it was possible to write the equations that model the phenomenon of adsorption / diffusion. Initially, the material balance was taken for bulk phase and porous particle.

First, since the bulk phase is homogeneous, the solute concentration in the bulk phase, C_b , was described using an integral phase balance. At each time point dt , the solute concentration varies in proportion to the mass rate, R_b , which enters a porous adsorbent particle. The mass of solid M_s , V_b the bulk phase volume, V_R and ρ_p volume and apparent specific mass of the particle were then used to relate the derivative of bulk concentration over time and the solute removal rate of a particle, Equation (1).

$$\frac{dC_b}{dt} = -\frac{1}{V_b} \frac{M_s}{V_R \rho_p} R_b \quad (1)$$

Then, within the particle a differential mass balance was performed. The main variables of interest are the concentration of the fluid phase, C_p , and the amount of adsorbed mass, q . The amount of solute accumulated within the particle should be equal to the mass flow gradient, $\nabla \cdot \mathbf{J}$, as presented in Equation (2).

$$\varepsilon_p \frac{\partial C_p}{\partial t} + \rho_s (1 - \varepsilon_p) \frac{\partial q}{\partial t} = \nabla \cdot \mathbf{J} \quad (2)$$

The diffusion within the particle is represented by two parallel Fick diffusion laws, one of which depends on the gradient of the fluid phase concentration and the other on the gradient of the adsorbed quantity. The proportionality relationship between concentration and quantity gradient and mass flow also depends on media diffusivities; it is assumed that the diffusivity in the fluid medium must be different from the diffusivity on the particle surface so these are represented by the constants D_p , diffusivity in the fluid phase, and D_s , superficial diffusivity. Using these constants and performing a volumetric mass balance with the particle porosity ε_p , Equation (3).

$$\mathbf{J} = \varepsilon_p D_p \nabla C_p + D_s (1 - \varepsilon_p) \nabla q \quad (3)$$

Since adsorption dynamics are generally faster than diffusion dynamics, the hypothesis of instantaneous adsorption equilibrium is a good approximation [1]. Therefore, we can relate the variables C_p and q through an algebraic relationship, that is, an adsorption isotherm. In order to obtain an analytical expression for the differential model, we must choose Henry's isotherm, with K as the Henry adsorption constant, a linear relationship between the variables, $q = KC_p$. Thus, we can simplify Equation (1) as

$$\varepsilon_p + K \rho_s (1 - \varepsilon_p) \frac{\partial C_p}{\partial t} = \nabla \cdot \mathbf{J} \quad (4)$$

and the Equation (3) as

$$\mathbf{J} = [\varepsilon_p D_s + K (1 - \varepsilon_p) D_p] \nabla C_p \quad (5)$$

By inserting Equation (5) into Equation (4), the expression of differential material balance was finally obtained as showed in Equation (6).

$$\frac{\partial C_p}{\partial t} = D \nabla^2 C_p \quad (6)$$

In Equation (6) D represents the apparent diffusivity, which depends on the effective surface and particle diffusivity as well as the porosity and the Henry's isotherm constant K .

$$D = \frac{\varepsilon_p D_s + K (1 - \varepsilon_p) D_p}{\varepsilon_p + K \rho_s (1 - \varepsilon_p)} \quad (7)$$

In Equation (6), ∇^2 represents the Laplacian operator that depends on the adopted geometry. For this work three special geometries were adopted, the $2R$ thickness slab, the R radius cylinder and the R radius sphere. For the slab and cylindrical case the other dimensions are

considered of sufficient size for the diffusion to be negligible. Thus the problem becomes one-dimensional diffusion. It was also observed that we can write the surface area to volume ratio of each of the geometries, resulting in the following expression:

$$\frac{A_R}{V_R} = \frac{S+1}{R} \quad (8)$$

In Equation (8) A_R is the surface area of the particle, and S is the geometry parameter, $S = 0$ for the flat plate, $S = 1$ for the cylinder and $S = 2$ for the sphere. Using this symbology we can write a single expression of the partial differential equation that represents the three geometries. Using r as the spatial variable the generalized one-dimensional diffusion equation for the three geometries is given by

$$\frac{\partial C_p}{\partial t} = D \left[\frac{S}{r} \frac{\partial C_p}{\partial r} + \frac{\partial^2 C_p}{\partial r^2} \right] \quad (9)$$

a partial differential equation of second order with respect to variable r and first order with respect to time. Thus, two boundary conditions and an initial value condition are required.

The first boundary condition, is the symmetry condition within the particle represented by Equation (10).

$$\left. \frac{\partial C_p}{\partial r} \right|_{r=0} = 0 \quad (10)$$

The second boundary condition is defined on the particle surface, considering the external resistance to mass transfer, where k_m is the convective mass transfer coefficient.

$$\left. \frac{\partial C_p}{\partial r} \right|_{r=R} = \frac{k_m}{\varepsilon_p D_p + K \rho_s D_s (1 - \varepsilon_p)} (C_b - C_p|_{r=R}) \quad (11)$$

For the initial condition is defined that the concentration in the particle is uniform and equal to $C_{p,0}$. Because C_b appears in Equation (11) the partial differential equation must be solved simultaneously with ordinary differential equation, Equation (1), so the mass transfer rate R_b is defined as the mass transfer rate on the particle surface.

$$R_b = A_R \left[\varepsilon_p D_p + K \rho_s D_s (1 - \varepsilon_p) \right] \left. \frac{\partial C_p}{\partial r} \right|_{r=R} \quad (12)$$

Since Equation (1) requires an initial value condition, it is assumed that the bulk phase concentration is $C_{b,0}$ at the initial time of the process. To facilitate the treatment of these equations some dimensionless groupings were

adopted, firstly the variable η represents the dimensionless spatial variable,

$$\eta = \frac{r}{R} \quad (13)$$

τ is the dimensionless time or the Fourier's number,

$$\tau = \frac{Dt}{R^2} \quad (14)$$

Bi_m is the Biot's dimensionless number,

$$Bi_m = \frac{k_m R}{D [\varepsilon_p + \rho_s (1 - \varepsilon_p) K]} \quad (15)$$

α is the mass capacity factor,

$$\alpha = \frac{M_s}{V_b \rho_p} [\varepsilon_p + \rho_s (1 - \varepsilon_p) K] \quad (16)$$

u is the dimensionless particle concentration,

$$u = \frac{C_p - C_{p,0}}{C_{b,0} - C_{p,0}} \quad (17)$$

and, finally, v is the dimensionless bulk concentration.

$$v = \frac{C_b - C_{p,0}}{C_{b,0} - C_{p,0}} \quad (18)$$

with these definitions it was possible to rewrite Equations (1), (9), (10) and (11) as

$$\begin{aligned} \frac{\partial u}{\partial \tau} &= \frac{S}{\eta} \frac{\partial u}{\partial \eta} + \frac{\partial^2 u}{\partial \eta^2} \\ \left. \frac{\partial u}{\partial \eta} \right|_{\eta=0} &= 0 \\ \left. \frac{\partial u}{\partial \eta} \right|_{\eta=1} &= Bi_m (v - u|_{\eta=1}) \\ u(\tau = 0, \eta) &= 0 \\ \frac{dv}{d\tau} &= -(S+1) \alpha \left. \frac{\partial u}{\partial \eta} \right|_{\eta=1} \\ v(0) &= 1 \end{aligned} \quad (19)$$

3. Analytical Solution

Equation (19) is a set of two differential equations, a partial differential equation and an ordinary differential equation. To solve such equations the Laplace transform was applied to the system, this is only possible because the system of

equations is linear. The definition of the Laplace transform is given by Equation (20).

$$U(p, \eta) = \mathcal{L}\{u(\tau, \eta)\} = \int_0^{\infty} u(\tau, \eta) e^{-p\tau} d\tau \quad (20)$$

$$V(p) = \mathcal{L}\{v(\tau)\} = \int_0^{\infty} v(\tau) e^{-p\tau} d\tau$$

the result of this procedure is represented in Equation (20).

$$\frac{d^2U}{d\eta^2} + \frac{S}{\eta} \frac{dU}{d\eta} - pU = 0 \quad (21)$$

For ordinary differential equation the result is Equation (21).

$$pV - 1 = -(S+1)\alpha \left. \frac{dU}{d\eta} \right|_{\eta=1} \quad (22)$$

Since the ordinary differential equation becomes just an algebraic relationship between the U and V functions, we can use it to rewrite the boundary conditions of the problem as

$$\left. \frac{dU}{d\eta} \right|_{\eta=0} = 0 \quad (23)$$

$$\left. \frac{dU}{d\eta} \right|_{\eta=1} = \frac{Bi_m - pBi_m U|_{\eta=1}}{(S+1)\alpha Bi_m + p}$$

In order to obtain the solution of Equation (20) the following change of variables was necessary: $v = (S-1)/2$; $w = \eta^v U$; $z = \eta\sqrt{p}$. The result of the variable change is the following ordinary differential equation.

$$z^2 \frac{d^2w}{dz^2} + z \frac{dw}{dz} - (z^2 + v^2)w = 0 \quad (24)$$

Equation (23) was then identified as the modified Bessel equation and its solution is given by Equation (25) [5].

$$w = C_1 I_\nu(z) + C_2 K_\nu(z) \quad (25)$$

The two special functions that make up the solution of the differential equation are called and hyperbolic Bessel functions, I_ν being the modified first order Bessel function and K_ν the modified second order Bessel function. Returning to the original variables U and η , Equation (26).

$$U(p, \eta) = \eta^{-v} \left[C_1 I_\nu(\sqrt{p\eta}) + C_2 K_\nu(\sqrt{p\eta}) \right] \quad (26)$$

In Equation (26) C_1 and C_2 represent constants to be determined from the boundary conditions of the

problem, Equation (22). First, the boundary condition in the center of the particle is applied. Using the derivative properties of the Bessel equations[6], the boundary condition in the center of the particle reduces to Equation (27).

$$\left. \frac{dU}{d\eta} \right|_{\eta=0} = \lim_{\eta \rightarrow 0} \sqrt{p\eta}^{-v} \left[C_1 I_\nu(\sqrt{p\eta}) - C_2 K_\nu(\sqrt{p\eta}) \right] \quad (27)$$

Using the Bessel function properties it is possible to compute the first term of the limit as

$$\lim_{\eta \rightarrow 0} \sqrt{p\eta}^{-v} C_1 I_\nu(\sqrt{p\eta}) = 0 \quad (28)$$

so the Equation(27) comes down to

$$\left. \frac{dU}{d\eta} \right|_{\eta=0} = \lim_{\eta \rightarrow 0} -\sqrt{p\eta}^{-v} C_2 K_\nu(\sqrt{p\eta}) = 0 \quad (29)$$

In order for Equation (29) to be satisfied C_2 must be zero, otherwise, the first derivative of the U function will not be zero in the center of the particle. Then, the second boundary condition is applied to determine the constant C_1 . After appropriate algebraic treatment the C_1 is isolated as

$$C_1 = \frac{Bi_m}{[2(v+1)\alpha Bi_m + p]\sqrt{p} I_{\nu+1}(\sqrt{p}) + p Bi_m I_\nu(\sqrt{p})} \quad (30)$$

Then, the U function is reduced to

$$U(p, \eta) = C_1 \frac{I_\nu(\sqrt{p\eta})}{\eta^v} \quad (31)$$

Starting from Equation (31) the inverse transform defined by Equation (32) must be applied in order to return to the original variable τ , and thus obtain the final solution of the partial differential equation.

$$u(\tau, \eta) = \mathcal{L}^{-1}\{U(\tau, \eta)\} = \frac{1}{2i\pi} \int_{\sigma-i\infty}^{\sigma+i\infty} U(p, \eta) e^{p\tau} dp \quad (32)$$

Since $U(p, \eta)$ is a meromorphic function, that is, a differentiable function on every complex plane except for a set of isolated points p_n (function poles or singularities), the residue theorem[7] can be applied to compute the integral of Equation (32). The inverse Laplace transformation is reduced to

$$\frac{1}{2i\pi} \int_{\sigma-i\infty}^{\sigma+i\infty} U(p, \eta) e^{p\tau} dp = \sum_{\Re(p_n) < \sigma} \text{Res}(U(p, \eta) e^{p\tau}, p_n) \quad (33)$$

where Res is the residue defined by

$$\text{Res}(U(p, \eta) e^{p\tau}, p_n) = \lim_{p \rightarrow p_n} (p - p_n) U(p, \eta) e^{p\tau} \quad (34)$$

To compute the residue limit the function $U(p, \eta)$ was rewritten as the ratio of two functions,

$U(p, \eta) = F(p, \eta) / G(p)$ F and G being defined in Equation(35).

$$F(p, \eta) = Bi_m \eta^{-\nu} I_\nu(\sqrt{p} \eta) \quad (35)$$

$$G(p) = [2(\nu+1)\alpha Bi_m + p] \sqrt{p} I_{\nu+1}(\sqrt{p}) + p Bi_m I_\nu(\sqrt{p})$$

$G(p)$ represents the function of the poles of U . Analyzing the characteristic of the zeros of the G function we can conclude that all poles are on the real line, and zero is a root of G . Hence, the residuals were calculated using Equation(34). The residue for the non-zero poles is

$$\text{Res}(U(p, \eta) e^{p\tau}, p_n) = \lim_{p \rightarrow p_n} (p - p_n) \frac{F(p, \eta)}{G(p)} e^{p\tau} \quad (36)$$

Applying the l'Hôpital rule on the right side of Equation (35), the residue is then obtained as

$$\text{Res}(U(p, \eta) e^{p\tau}, p_n) = \frac{F(p_n, \eta)}{G'(p_n)} e^{p_n \tau} \quad (37)$$

Thus, it was possible to write the solution of the partial differential equation as

$$u = \lim_{p \rightarrow 0} p U(p, \eta) e^{p\tau} + \sum_{n=1}^{\infty} \frac{F(p_n, \eta)}{G'(p_n)} e^{p_n \tau} \quad (38)$$

where the first term to the right of the equal sign represents the residue at the zero pole.

After calculating at pole zero and performing the first derivative of function G the following expression was obtained

$$u(\tau, \eta) = \frac{1}{1 + \alpha} + \sum_{n=1}^{\infty} b_n \eta^{-\nu} \frac{I_\nu(\sqrt{p_n} \eta)}{I_\nu(\sqrt{p_n})} e^{p_n \tau} \quad (39)$$

being b_n

$$b_n = \frac{2Bi_m[2(\nu+1)\alpha Bi_m + p_n]}{p_n^2 + p_n Bi_m[4\alpha(\nu+1) + 2\nu - Bi_m] + 4\alpha(1 + \alpha)Bi_m^2(\nu+1)^2} \quad (40)$$

Analyzing the poles of the G function, it is concluded that all roots are negative, so the following variable $p_n = -\gamma_n^2$ is introduced in the Equations (39) and (40). Bessel functions J_ν , and their hyperbolic counterparts I_ν , have identities that relate each other[6]. By replacing the roots p_n by γ_n , the switch to Bessel J_ν functions was done so that we didn't have to work with the imaginary i . The Equations (41) and (42) are the result of these operations;

$$u(\tau, \eta) = \frac{1}{1 + \alpha} + \sum_{n=1}^{\infty} b_n \eta^{-\nu} \frac{J_\nu(\gamma_n \eta)}{J_\nu(\gamma_n)} e^{-\gamma_n^2 \tau} \quad (41)$$

$$b_n = \frac{2Bi_m[(2\nu+1)\alpha Bi_m - \gamma_n^2]}{\gamma_n^4 + \gamma_n^2 Bi_m[Bi_m - 4\alpha(\nu+1) - 2\nu] + 4\alpha(1 + \alpha)Bi_m^2(\nu+1)^2} \quad (42)$$

The characteristic equation to compute the γ_n is given by

$$[2(\nu+1)\alpha Bi_m - \gamma_n^2] J_{\nu+1}(\gamma_n) + \gamma_n Bi_m J_\nu(\gamma_n) = 0 \quad (43)$$

The solution presented in the Equation (41) was previously obtained for specific cases, cylindrical geometry by Crank[2] and spherical by Amundson[8]. Crank and Amundson solutions can be recovered by substituting the variable ν and using identities between ν fractional order Bessel functions and sines and cosines[6], as presented in Table 1.

Table 1. Separated solutions for each geometry

Geometry	Solution (u)
Slab ($\nu = -1/2$)	$\frac{1}{1 + \alpha} + \sum_{n=1}^{\infty} b_n \frac{\cos(\gamma_n \eta)}{\cos \gamma_n} e^{-\gamma_n^2 \tau}$
Cylinder ($\nu = 0$)	$\frac{1}{1 + \alpha} + \sum_{n=1}^{\infty} b_n \frac{J_0(\gamma_n \eta)}{J_0(\gamma_n)} e^{-\gamma_n^2 \tau}$
Sphere ($\nu = 1/2$)	$\frac{1}{1 + \alpha} + \sum_{n=1}^{\infty} b_n \frac{\sin(\gamma_n \eta)}{\eta \sin \gamma_n} e^{-\gamma_n^2 \tau}$

Having the expression for u , Equation(39), the bulk phase solution v , is easily obtained from the boundary condition on the particle surface, Equation(19), resulting in

$$v(\tau) = \frac{1}{1 + \alpha} + \sum_{n=1}^{\infty} c_n e^{-\gamma_n^2 \tau} \quad (44)$$

c_n being defined by

$$c_n = \frac{4(\nu+1)\alpha Bi_m^2}{\gamma_n^4 + \gamma_n^2 Bi_m[Bi_m - 2\nu - 4\alpha(\nu+1)] + 4\alpha(1 + \alpha)Bi_m^2(\nu+1)^2} \quad (45)$$

4. Conclusion

In this work we present the detailed description to obtain the phenomenological model of intraparticle adsorption / diffusion in batch systems. In addition, the analytical solution of the differential equation system was obtained from the Laplace transform method. Although the solution of this system has already appeared in the work of other authors, it is noteworthy the generalized presentation for the three geometries, slab, cylinder and sphere. The closed solution presented in this work can be used to represent experimentally



obtained data as long as the adopted hypotheses are respected by the experiments.

Acknowledgements

Special thanks to CAPES (Cooerdenação de Aperfeiçoamento de Pessoal de Nível Superior), UFRGS (Universidade Federal do Rio Grande do Sul) and Graduate Program in Chemical Engineering (PPGEQ-UFRGS).

References

- [1] D. D. Do, *Adsorption Analysis: Equilibria and Kinetics*. Imperial College Press, 1998.
- [2] J. Crank, *The mathematics of diffusion*. Clarendon Press, 1975.
- [3] M. Schwaab, E. Steffani, E. Barbosa-Coutinho, and J. B. Severo Júnior, “Critical analysis of adsorption/diffusion modelling as a function of time square root,” *Chem. Eng. Sci.*, vol. 173, pp. 179–186, Dec. 2017.
- [4] A. E. Rodrigues and C. M. Silva, “What’s wrong with Lagergreen pseudo first order model for adsorption kinetics?,” *Chem. Eng. J.*, vol. 306, pp. 1138–1142, 2016.
- [5] P. J. Davis, *Handbook of Mathematical Functions With Formulas, Graphs and Mathematical Tables - Tenth Printing*. 1972.
- [6] K. B. Oldham, J. Myland, and J. Spanier, *An atlas of functions: with equator, the atlas function calculator*. Springer Science & Business Media, 2010.
- [7] L. V. Ahlfors, *Complex Analysis*, 3rd ed. McGraw-Hill, Inc., 1979.
- [8] F. J. Edeskuty and N. R. Amundson, “Effect of Intraparticle Diffusion: Agitated Nonflow Adsorption Systems,” *Ind. Eng. Chem.*, vol. 44, no. 7, pp. 1698–1703, 1952.

Application of artificial neural network modeling to fit the isotherm parameters of aqueous-phase adsorption systems

J. L. S. Fagundez*, N. P. G. Salau

Universidade Federal de Santa Maria, Roraima Avenue, 1000, Santa Maria, 97105-900, Brazil

** To whom all correspondence should be addressed. E-mail: jeanlucasf@gmail.com*

Abstract

An artificial neural network (ANN) structure was proposed in this research that, unlike conventional optimization methods, allows the fit of several adsorption curves simultaneously by indirectly minimizing the real output error – the equilibrium adsorption capacity. To model a case study of 3-aminophenol adsorption phenomena onto avocado seed activated carbon, the ANN was applied to fit the parameters of the Sips isotherm. Network weights and biases were optimized using the particle swarm optimization (PSO) method, due to its good convergence in large scale problems. Results showed that the ANN modeling was able to accurately fit the model to the experimental equilibrium adsorption capacity data, obtaining Pearson's correlation coefficient of 0.99996 and mean squared error of 0.5135. In addition, the Sips isotherm curves generated by the ANN model were able to precisely fit the experimental data, with estimated parameters similar to those presented in the literature. Thus, the proposed ANN structure was successfully applied to estimate the parameter s of adsorption isotherms, reducing the computational demand and the exhausting task of estimating the parameters of each adsorption isotherm curve.

Keywords: Artificial Neural Network; Particle Swarm Optimization; Adsorption Isotherms; Parameter Estimation.

1. Introduction

To keep up with the rapid development of adsorption technologies, robust computational models such as artificial neural networks (ANNs) have been used for simulation [1,2]. Artificial neural networks can be trained to recognize patterns, classify data and forecast future events by estimating non-linear relationships between the input variables and the selected outputs for the model [3]. In order to optimize the weights and bias of the network modeling, the particle swarm optimization [4] was used, due to its optimal performance on large scale problems [5].

There is a great interest today in finding and successfully purifying adsorbents from waste biomass [6]. Of the various alternatives, the preparation of activated carbon (AC) from avocado seed has been successfully tested in the adsorption of organic compounds [7,8], and hence, it was chosen as case study of this work. AC was prepared using pyrolysis of the avocado seed biomass, with

hold temperature and time optimized through a 2² full-factorial design of experiment, since these are factors that can affect porosity, surface chemistry and the overall performance of the adsorption [9,10].

Along with the ANN modeling, the Sips isotherm [11] was used to represent the 3-aminophenol adsorption onto AC from avocado seed, since it was the most appropriate correlation for the equilibrium curves. [8]. Conventionally, the parameters of each adsorption isotherm curve are separately estimated, which lead to an exhausting parameter estimation procedure, increasing the computational demand.

This work aimed to estimate and validate the Sips isotherm parameters using the ANN modelling of the MatLab® software with simultaneous parameter estimation of the six 3-aminophenol isotherms, i.e. at six different temperatures. The results were compared to those available in the literature, with discussion regarding the potential of the proposed ANN structure.

2. Materials and methods

This section is divided into the experimental procedure for the adsorption of 3-aminophenol onto avocado seeds activate carbon, the ANN equations to estimate the Sips isotherm parameters, the proposed ANN structure and ANN performance analysis.

2.1 Experimental procedure

As a way to rapidly turn carbon biomass in activated carbon, with tunable pore structure and surface area, and reduce activation time and energy consumption [12], microwave energy has been successfully used in both organic and inorganic syntheses [13].

The avocado seeds activate carbon were synthesized using a microwave heating process, where $ZnCl_2$ was the activating agent. In addition, the produced adsorbent was characterized using three analytical techniques: N_2 isotherms; Fourier transform infrared spectroscopy; and scanning electron microscopy. More details on the synthesis and characterization procedure can be found on [7].

Figure 1 shows the adsorption isotherms obtained for the 3-aminophenol at six different temperatures: 25°C, 30°C, 35°C, 40°C, 45°C and 50°C. All data used in Figure 1 is available on [8].

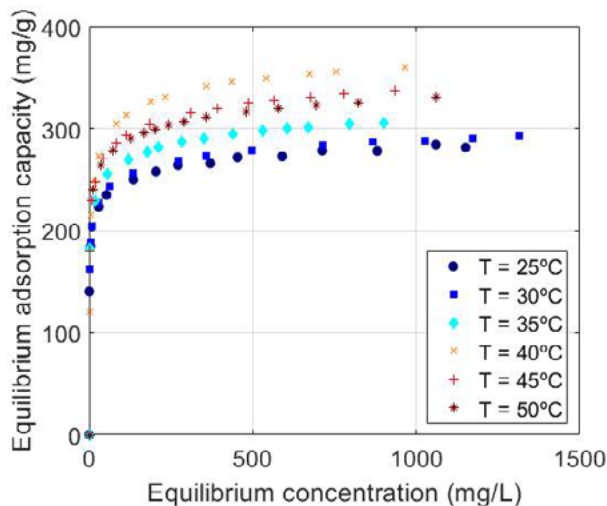


Fig. 1. Adsorption isotherms of 3-aminophenol onto Avocado seed at six different temperatures.

The experiments were made with absorbent mass 30.0 mg, initial pH of adsorbate solution 7.0 and

time of contact between the adsorbent and adsorbate 60 min.

2.2 ANN equations to estimate the Sips isotherm parameters

In order to adjust the measured data for equilibrium adsorption capacity ($q_{e,t}$) of the activated carbon and equilibrium concentration (C_e), the Sips isotherm was selected based on the isotherms tested on [8], to calculate the equilibrium adsorption capacity ($q_{e,o}$), as shown in Equation 1.

$$q_{e,o} = \frac{q_s(K_s C_e)^{N_s}}{1 + (K_s C_e)^{N_s}} \quad (1)$$

where q_s is the theoretical monolayer saturation capacity, K_s (L/mg) is the affinity constant and N_s describes the surface heterogeneity. When N_s equals unity, the Sips isotherm returns to the Langmuir isotherm and predicts homogeneous adsorption. On the other hand, deviation of N_s value from the unity indicates heterogeneous surface [14].

A hybrid approach of ANNs and isotherms in order to model an adsorption process was tested by [15]. In that study, the authors used the ANNs to estimate the Langmuir isotherm parameters related to the adsorption process. Thus, a nonlinear least squares objective function for optimization, through the simulated annealing method [16], was solved using the measured $q_{e,t}$ and the $q_{e,o}$ predicted by the model. The proposed ANN model solves similarly the objective function, then with a more generalized structure to predict the isotherm parameters.

The MatLab® ANN equations are solved in the order presented from Equation 2 to 4.

$$U = W_{Inp} \cdot X + B_H \quad (2)$$

where U is a matrix $n \times q$ with normalized input values, n is the number of neurons in the hidden layer, q is the number of input data points, W_{Inp} is a matrix $n \times m$ of the input weights, m is the number of inputs, X is a matrix $m \times q$ of the input data and B_H is a matrix $n \times q$ of the neurons bias in the hidden layer.

$$Z = \frac{2}{(1 + e^{-2U})} - 1 \quad (3)$$

representing the built-in Matlab® hyperbolic tangent sigmoid transfer function *tansig*, where Z is a matrix $n \times q$ of transformed output values.

$$Y = W_H \cdot z + B_{Out} \quad (4)$$

where Y is a $p \times q$ matrix of normalized output values, p is the number of outputs, W_H is a matrix $p \times n$ of the weights from the hidden layer neurons and B_{Out} is a matrix $p \times q$ of the neurons bias in the output layers.

To normalize input values and denormalize output values, MatLab® uses a built-in function called *mapminmax*.

To solve the values of weights and biases in the ANN layers, a particle swarm optimization (PSO) method was used through the MatLab® built-in function *particleswarm*. The only option altered was the hybrid function which, at the end of PSO evaluations of the objective function, starts a secondary algorithm selected as *fmincon* to further improve the error minimization.

The objective function to be minimized was a nonlinear least-square function of the equilibrium adsorption capacity error, given by Equation 5.

$$F_{obj} = \sum_{i=1}^N (q_{e,t} - q_{e,o})^2 \quad (5)$$

where N is the total number of measured data points.

2.3 Proposed ANN structure

The proposed ANN structure uses the a method of constructing the artificial neural network model with a change in the calculation of the real output, the equilibrium adsorption capacity. Three input variables were selected:

- Initial adsorbate concentration (C_0) [mg/L]
- Adsorbate equilibrium concentration (C_e) [mg/L]
- Adsorption temperature (T) [°C]

Thus, the network structure for determining the value of q_e would be three inputs and one output. This type of structure, however, does not allow the determination of the parameters of an equation such as the Sips isotherm, as it directly adjusts the output variable without calculating values as the process equilibrium constant (K_S).

To work around this issue, the ANN structure for the adsorption process modeling of this case study used the isotherm parameters as proposed to fit the adsorption curves to the experimental data, with a structure of three inputs and three outputs, as shown in Figure 2.

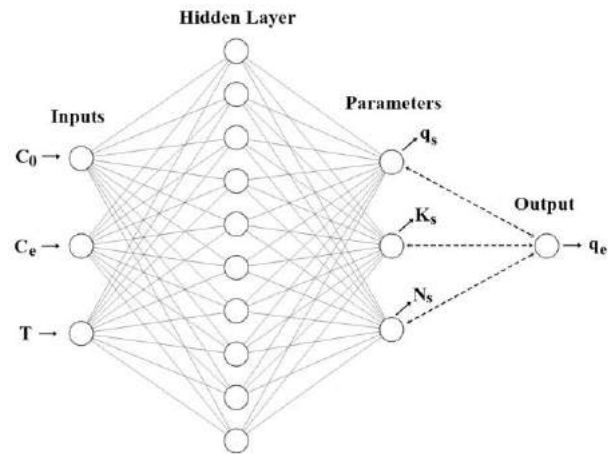


Fig. 2. Proposed ANN structure for parameter estimation.

Another difference between the proposed and the conventional ANN structure was the way that the parameters were estimated through the network calculations. In a standard ANN, the predicted values for the outputs are calculated based on a specific combination of inputs. Thus, if 100 input combinations are tested, 100 output predictions must be generated. For parameter estimation, however, this methodology is not adequate, since the parameters must be generated for the adjustment of curves with several points, not for individual points. Therefore, for the proposed ANN structure, it was necessary to provide two initial information: the number of measurements obtained for each sample curve; and initial guesses for the isotherm parameters that will form a vector for network training. Initial guesses in no way limit the values estimated for each isotherm parameter, then were important for the training speed of the ANN.

The final step of the proposed ANN structure was the provision of the real output values ($q_{e,t}$), which were used in the objective function to be minimized by the PSO method, although they were not used for the network training. Thus, during the minimization of the objective function, the vector q_e was resized in a matrix whose columns contain the number of points of each experimental curve, and the parameter estimation by the ANN modeling was done for each column, not for each point, minimizing the error in the predicted q_e values.

2.4 ANN performance analysis

The analysis to evaluate the performance of the proposed ANN modeling was made graphically, through the Pearson coefficient of correlation (R), and numerically through the coefficient of determination (R^2), the mean squared error (MSE) and the root mean squared error ($RMSE$) between $q_{e,t}$ and $q_{e,o}$, given by Equations 6 to 9.

$$R = \frac{\sum_{i=1}^q (q_{e,t_i} - \bar{q}_{e,t})(q_{e,o_i} - \bar{q}_{e,o})}{\left\{ \sum_{i=1}^q (q_{e,t_i} - \bar{q}_{e,t})^2 \sum_{i=1}^q (q_{e,o_i} - \bar{q}_{e,o})^2 \right\}^{1/2}} \quad (6)$$

$$R^2 = 1 - \left(\frac{\sum_{i=1}^q (q_{e,t_i} - q_{e,o_i})^2}{\sum_{i=1}^q (q_{e,t_i} - \bar{q}_{e,t})^2} \right) \quad (7)$$

$$MSE = \frac{1}{q} \sum_{i=1}^q (q_{e,t_i} - q_{e,o_i})^2 \quad (8)$$

$$RMSE = \sqrt{\frac{1}{q} \sum_{i=1}^q (q_{e,t_i} - q_{e,o_i})^2} \quad (9)$$

where $\bar{q}_{e,t}$ is the average value of the measured output and $\bar{q}_{e,o}$ is the average value of the predicted output.

3. Results and Discussion

The results section is divided into the analysis of the training performance of the proposed ANN structure and the parameter estimation results, with comparison to the parameters obtained by [8].

3.1 ANN performance analysis

Figure 3 shows the R result for the proposed ANN.

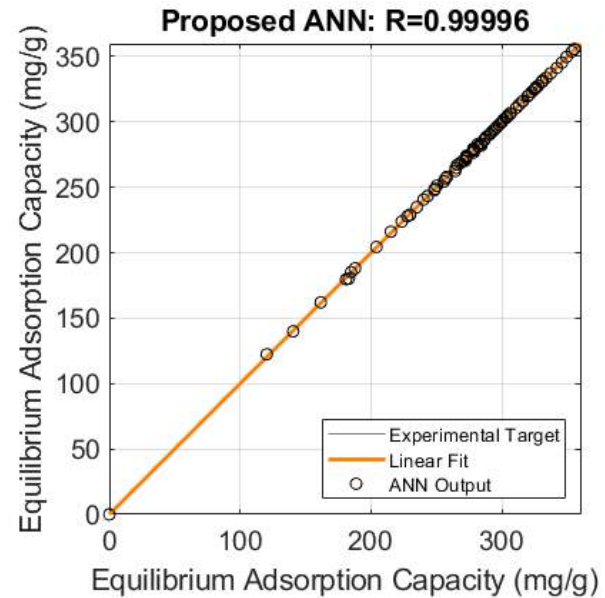


Fig. 3. Proposed ANN correlation between measured and predicted equilibrium adsorption capacity.

As it can be seen, the predicted $q_{e,o}$ results presented almost total correlation to the measured $q_{e,t}$ values. This indicates that the network was able to model, using the Sips isotherm, with excellent precision, the adsorption process of 3-aminophenol in avocado seed activated carbon. A more detailed analysis of the network performance is presented in Table 1.

Table 1. R^2 , MSE and $RMSE$ results for the proposed ANN training.

ANN performance	
R^2	0.99992
MSE	0.51350
$RMSE$	0.71659

The results of Table 1 confirm the good fitting of the predicted data to the measured points. The coefficient of determination (R^2) reinforces the result already seen in Figure 3 for R . The MSE and $RMSE$ results were low, showing that the difference between the predicted and experimental points was small. These results showed that the network generated by the proposed technique had good generalization and precision.

3.2 Parameter estimation and comparison

Figure 4 shows the Sips isotherm curves fitted to the experimental data shown on Figure 1.

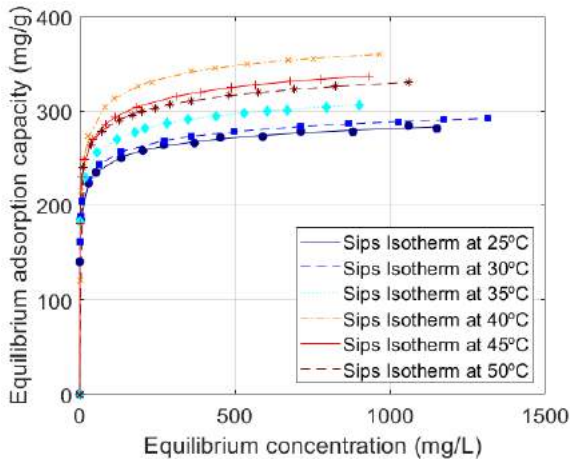


Fig. 4. Sips isotherm fits to the measured $q_{e,t}$ data.

It is possible to see in Figure 4 a very accurate fit to the measured data, which is in accordance to the network performance analysis presented in the previous subsection. Thus, it is evident the capability of the proposed methodology to simultaneously adjust several adsorption curves with parameter estimation of the isotherm equation.

Table 2 shows the estimated parameters for the Sips isotherms in comparison to the parameters available in the literature for the case study [8].

Table 2. Comparison of the estimate parameters for the Sips isotherms.

Temperature	Parameter	Present Work	Lima <i>et al.</i> [8]
25°C	q_S	349.46	352.4
	K_S	0.3846	0.3576
	N_S	0.2381	0.2344
30°C	q_S	371.79	-
	K_S	0.2995	0.2903
	N_S	0.2175	-
35°C	q_S	388.61	-
	K_S	0.2449	0.2593
	N_S	0.2444	-
40°C	q_S	413.97	-
	K_S	0.2137	0.2186
	N_S	0.3565	-

45°C	q_S	429.62	-
	K_S	0.1873	0.1842
	N_S	0.2506	-
50°C	q_S	468.22	-
	K_S	0.1171	0.1549
	N_S	0.1816	-

The three-parameter comparison is only possible at 25°C, since in the other tested temperatures, only the estimated equilibrium constant (K_S) was shown in [8]. The Sips isotherm parameters estimated by the proposed ANN structure obtained very similar results at 25°C, and similar K_S values on the other temperatures. In addition, q_S values increase and K_S values decrease as the temperature increases, which is in accordance to the physical characteristics of the adsorption phenomena.

Thus, it is possible to verify that the proposed ANN structure was able to model the adsorption phenomena and estimate the parameters of several adsorption curves simultaneously, with high accuracy. Since the proposed methodology has no limitation on the number of isotherm curves that it can simultaneously fit, the computational demand for parameter estimation becomes even lower in comparison to the conventional parameter estimation procedure as more experimental data curves require more parameters to be estimated.

4. Conclusion

In order to model the adsorption process, a series of mathematical models and adsorption isotherm equations can be used, with physical meaning parameters being estimated to adjust the simulated curves to the measured experimental points.

In this work, a different ANN structure was proposed to fit the Sips isotherm curve to the experimental data of 3-aminophenol adsorption onto avocado seed activated carbon, with simultaneous parameter estimation for all the curves, i. e. at six different temperatures.

The results showed that the proposed ANN structure was successful in the simultaneous adjustment of six 3-aminophenol adsorption curves, with small error values in the predicted data and estimated parameters with physical meaning. In addition, the proposed methodology has no limitation on the number of simultaneous isotherm curves that it can fit through parameter estimation.

Acknowledgements

The authors would like to thank the Coordination for the Improvement of Higher Education Personnel (CAPES) and the Research Support Foundation of Rio Grande do Sul (FAPERGS) for the financial support for this project.

References

- [1] Souza PR, Dotto GL, Salau NPG. Artificial neural network (ANN) and adaptive neuro-fuzzy interference system (ANFIS) modelling for nickel adsorption onto agro-wastes and comercial activated carbon. *J Environ Chem Eng*, vol 6, pp.7152 – 7160, 2018.
- [2] Sadeghizadeh A, Ebrahimi F, Heydari M, Tahmasebikohyani M. Adsorptive removal of Pb(II) by means of hydroxyapatite/chitosan nanocomposite hybrid nanoadsorbent: ANFIS modeling and experimental tudy. *J Environ Manage*, vol. 232, pp. 342 – 353, 2019.
- [3] Graupe D. Principles of Artificial Neural Networks – 2nd Edition. Advanced Series on Circuits and Systems, vol. 6, World Scientific Publishing, 2007.
- [4] Kennedy J, Eberhart R. Particle swarm optimization. Proceedings of ICNN'95 – International Conference on Neural Networks, Perth, WA – Australia, 1995.
- [5] Clerc M. Particle Swarm Optimization. ISTE Ltd., London, UK, 2006.
- [6] Puchana-Rosero MJ, Lima EC, Ortiz-Monsalve S, Mella B, da Costa D, Poll E, Guterres M. Fungal biomass as biosorbent for the removal of Acid Blue 161 dye in aqueous solution. *Environ Sci Pollut Res*, vol. 24, pp. 4200 – 4209, 2017.
- [7] Leite AJB, Sophia AC, Thue PS, dos Reis GS, Dias SLP, Lima EC, Vaghetti JCP, Pavan FA, de Alencar WS. Activated carbon from avocado seeds for the removal of phenolic compounds from aqueous solutions. *Desalin Water Treat*, vol. 71, pp. 168 -181, 2017.
- [8] Lima EC, Hosseini-Bandegharaei A, Moreno-Piraján JC, Anastopoulos I. A critical review of the estimation of the thermodynamic parameters on adsorption equilibria. Wrong use of equilibrium constant in the Van't Hoof equation for the calculation of thermodynamic parameters of adsorption. *Journal of Molecular Liquids*, vol 273, pp. 425 – 434, 2019.
- [9] Calvete T, Lima EC, Cardoso NF, Dias SLP, Ribeiro ES. Removal of brilliant green dye from aqueous solutions using home made activated carbons. *CLEAN – Soil, Air, Water*, vol 38, pp. 521 – 532, 2010.
- [10] Ribas MC, Adebayo MA, Prola LDT, Lima EC, Cataluna R, Feris LA, Machado FM, Pavan FA, Calvete T. Comparison of a homemade cocoa Shell activated carbon with comercial activated carbon for the removal of reactive violet 5 dye from aqueous solutions. *Chem Eng J*, vol 248, pp. 315- 326, 2014.
- [11] Repo E, Malinen L, Koivula R, Harjula R, Sillanpaa MET. Capture of Co(II) from its aqueous EDTA chelate by DTPA-modified silica gel and chitosan. *J Hazard Mater*, vol. 187, pp. 122 – 132, 2011.
- [12] Wang T, Tan S, Liang G. Preparation and characterization of activated carbón from Wood via microwave-induced ZnCl₂ activation. *Carbon*, vol. 47, pp. 1880 – 1883, 2009.
- [13] Yang RT. Adsorbents: fundamentals and applications. New Jersey, John Wiley & Sons, pp. 78 – 130, 2003.
- [14] Nethaji S, Sivasamy A, Mandal AB. Adsorption isotherms, kinetics and mechanism for the adsorption of cationic and anionic dyes onto carbonaceous particles prepared from *Juglans regia* Shell biomass. *Int. J. Environ. Sci. Technol.*, vol. 10, pp. 231 – 242, 2013.
- [15] Saucedo-Delgado BG, De Haro-DeJ Rio DA, González-Rodríguez LM, Reynel-Ávila HE, Mendoza-Castillo DI, Bonilla-Petriciolet A, Rivera de la Rosa J. Fluoride adsorption from aqueous solution using a protonated clinoptilolite and its modeling with artificial neural network-based equations. *Journal of Fluorine Chemistry*, vol. 204, pp. 98 – 106, 2017.
- [16] Kirkpatrick S, Gellat CD, Vecchi MP. Optimization by Simulated Annealing. *Science*, vol. 220, pp. 671 – 680, 1983.

Insensitivity in the characterization of ultra-microporous carbon materials by CO₂ adsorption

V. Cornette*, J. Villarroel Rocha, K. Sapag, R. Delagdo Mons, J. P. Toso, R. H. López

Dpto. de Física, INFAP "Giorgio Zgrablich", FCMFyN - UNSL-CONICET, Ejercito de los Andes 950, 5700 San Luis, Argentina

Abstract

The determination of pore size distribution (PSD) is one of the most important properties for the characterization and design of materials for applications such as gas storage or separation. In this study, different microporous carbon materials were synthesized and texturally characterized by adsorption of carbon dioxide (CO₂) at 273 K. The PSDs of these materials were obtained from the CO₂ adsorption isotherms, using theory-based models of the functional density (NLDFT) and Monte Carlo simulation in the Grand Canonical Assembly (GCMC).

The PSDs obtained (considering a pseudo-spherical potential for CO₂ interaction) have the same qualitative behavior, reporting three peaks in the ultramicroporous region, as opposed to the hypothesis that in highly disordered microporous carbon materials have a widely distributed PSD without sharp spikes, i.e. the presence of gaps or dominant peaks is not justified. We investigated the origin of the artificial gaps that arise in models with pseudo-spherical potential (NLDFT and GCMC) and additionally, we studied the characterization of these materials using Monte Carlo simulations, which incorporate multi-site model potential that accounts for the correct molecular shape of the CO₂ molecule.

The results obtained show that NLDFT and GCMCC models with pseudo-spherical potential, commonly used in the scientific community, do not necessarily represent the dominant pore size within these materials and should be used with great caution and preferably with complementary information obtained through of other techniques.

We strongly recommend using the multi-site potential to model the interaction of CO₂ in microporous, as these produce a more reliable characterization of these types of materials.

Keywords: Adsorption; Molecular simulation; PSD; Activated Carbons.

1. Introduction

Activated carbons and molecular sieve carbons are used in several industrial processes such as gas separation (e.g., membranes or adsorbents), gas storage, purification and reaction processes. Their properties in such applications depend largely on the geometry, volume and size of the pores present in the material, that is, they depend in particular on the pore size distribution function (PSD). The PSDs are an important characteristic of microporous materials with pore sizes of less than 2 nm because it is related to the transport of molecules. Thus, having an optimal pore size is one of the key aspects to obtain both the maximum deliverable storage capacity and selectivity.

The pore size distribution is traditionally evaluated from the analysis of nitrogen or argon adsorption isotherms measured at cryogenic temperatures. However, to improve the analysis of

carbon molecular sieves and microporous carbons, adsorption of CO₂ at 273 K is often applied.[1,2].

From analyzes performed on different microporous samples, developed with different synthesis processes, we found that all of them have similar PSDs (CO₂ at 273 K) presenting three characteristic peaks. In contrast to the hypothesis that highly disordered microporous carbon materials have broad PSDs, that is, the presence of gaps or dominant peaks is not justified.

The experimental adsorption isotherm N_{exp} can be expressed as a superposition of isotherms corresponding to each pore size, pressure P and temperature T , called local isotherms, with a weight corresponding to the pore-size distribution, PSD(H). The PSD result can be obtained by solving an adsorption integral equation (eq 1, adsorption integral contribution, first term), which is an ill-posed problem, using regularization techniques (eq 1, regularization contribution, second term) such as the discrete Tikhonov regularization with non-negative least squares, etc

[3,4]. Thus, the PSD solution will be dependent upon the chosen regularization parameter, λ (also known as the smoothing parameter).

$$N_{\text{exp}}(P, T) \cong \int_{H_{\text{min}}}^{H_{\text{max}}} N_{\text{NLDFT/GCMC}}(H, P, T) \text{PSD}(H) dH + \lambda \int_{H_{\text{min}}}^{H_{\text{max}}} [\text{PSD}'(H)]^2 dH \quad (1)$$

In the above equation, $N_{\text{exp}}(P, T)$ is the experimentally determined adsorption isotherm for the material at pressure P . Here, $N_{\text{NLDFT/GCMC}}(H, P, T)$ is the local isotherm for a regular model pore of size H , and, H_{min} and H_{max} refer to the minimum and maximum model pore size used in the analysis.

The PSD result may also be different depending on the chosen adsorption kernel using different adsorbate models and assumed pore geometries[5,6].

In light of understanding the results obtained through classical methods such as NLDFT and GCMC. Our purposes in this work are the following:

- Apply the characterization methods (NLDFT and GCMC) to a series of 8 microporous activated carbons synthesized in our Laboratories.
- Design a virtual solid as a test method to explore the influence of the λ factor in the prediction of PSD.
- Apply the GCMC characterization method considering a multi-site potential for the adsorbate interaction.

2. Molecular Model and Simulation Details

Like in most of the PSD calculation methods, we assume the independent pore model which by itself does not account for connectivity. For a given pore model and a potential model for the adsorptive, we use Grand Canonical Monte Carlo simulation, to obtain the theoretical adsorption isotherms. The algorithms implemented in simulations to sample the molecular configurations are both well established and well documented[7,8]. A central part of these algorithms is the calculation of the potential energy of any given molecular configuration. This quantity is determined using suitable interaction

potentials which represent the attraction and repulsion between fluid molecules and between a fluid molecule and the pore wall.

For the interaction between a fluid and pore wall, we considering the superposition of two Steele potentials to slit geometry [9], one per each infinite plate:

$$U_{\text{fs_steele}}(z) = 2\pi\rho_s \varepsilon_{fs} \sigma_{fs}^2 \Delta \times \left\{ \frac{2}{5} \left(\frac{\sigma_{fs}}{z} \right)^{10} + \left(\frac{\sigma_{fs}}{z} \right)^4 - \frac{\sigma_{fs}^4}{3\Delta(z + 0.61\Delta)^3} \right\} \quad (2)$$

where Δ is the separation between layers in graphite (0.335 nm), ρ_s is the number density of carbon atoms per unit volume of graphite (114nm^{-3}), and ε_{fs} and σ_{fs} are the fluid-solid Lennard-Jones parameters.

The fluid-fluid CO_2 interaction was considered by means of two different models. The pseudo-spherical potential via Lennard-Jones:

$$U_{ff}(r_{ij}) = -4\varepsilon_{ff} \left[\left(\frac{\sigma_{ff}}{r_{ij}} \right)^{12} - \left(\frac{\sigma_{ff}}{r_{ij}} \right)^6 \right] \quad (3)$$

and a model based on two sites per molecule interacting via Lennard-Jones potential and electrostatic quadrupolar energies that accounts for the correct molecular shape[10]:

$$U_{ff}(r_{ij}) = -4\varepsilon_{ff} \left[\left(\frac{\sigma_{ff}}{r_{ij}} \right)^{12} - \left(\frac{\sigma_{ff}}{r_{ij}} \right)^6 \right] + \left(\frac{q_i q_j}{4\pi\varepsilon_0 r_{ij}} \right) \quad (4)$$

where the first term is the Lennard-Jones (LJ) 12-6 potential and the second term is the Coulomb interaction potential between point charges q_i and q_j of sites i and j separated by distance r_{ij} . The parameters of the potential models are summarized in Table 1. The parameters for unlike-pair interactions are calculated using the Lorentz-Berthelot combining rules commonly used in molecular simulations[8].



Table 1. Parameters used in the potentials for the GCMC simulations.[5]

Molecule	Potential Model	$\sigma(\text{\AA})$	ϵ/kB (K)	$q(e)$	Distance atom-c.o.m. (\AA)
CO ₂	Pseudo-spherical LJ (1C)	3.648	246.15		
C	Multi-sites (3C)	2.8	27	0.7	1.16
O		3.05	148	-0.35	
Carbon		3.4	28		

2.1 Grand canonical Monte Carlo simulation

Using Monte Carlo simulation it is possible to obtain a collection of adsorption isotherms (the local isotherms, N_{GCMC}) considering different pore sizes both for the slit geometry and two adsorbate models, which we term the independent pore model. The general procedure is as follows: Transition probabilities for each Monte Carlo attempt, adsorption, desorption, translations, and rotations rigid molecules are given by the usual Metropolis rules. In general, the box length is 10 times the collision diameter for the slit geometry; periodic boundary conditions were used in those directions, and the cut-off radius was considered half of the box length. Equilibrium was generally achieved after 10^8 MC attempts, after which mean values were taken over the following 10^7 MC attempts for configurations spaced by 10^3 MC attempts, to ensure statistical independence.

A minimization method for the mean square error, with a regularization term, as described in Ref. [11–13] was proposed to fit an experimental isotherm with the theoretical isotherm given by eq. (1).

3. Results and Discussions

Fig 1 shows the experimental CO₂ adsorption isotherms for a series of different porous activated carbons. All isotherms are of type I but are easy to see the shape changes for different materials. This change is usually associated with a widening of microporosity.

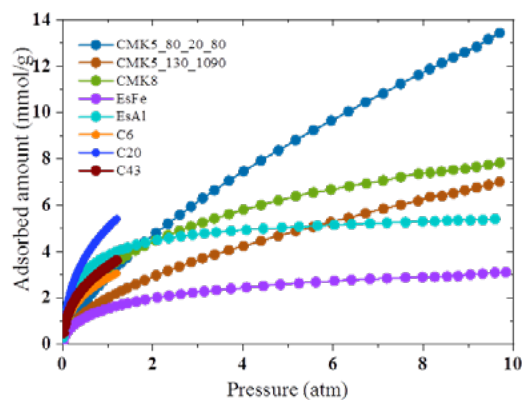


Fig. 1. Experimental CO₂ adsorption isotherms at 273K of carbons: CMK5 series, CMK8, sponges (EsFe, EsAl) and activated carbons series (C6, C20, and C43).

3.1 Predictions of the NLDFT method and GCMC (pseudo-spherical model).

Fig 2 shows the distribution functions obtained by the NLDFT and GCMC (1C) methods. The regularization parameters, λ , are selected using the L-curve method[11,18] in the GCMC case, while the NLDFT fits were obtained from software in micromeritics ASAP 2000.

Artificial peaks and gaps from the NLDFT and GCMC (1C) methods were found throughout the different porous materials. The presence of the artifacts is confirmed, and as has been discussed before[19–21]. Most importantly, the dominant peaks from NLDFT typically reported in the literature do not necessarily represent the truly dominant pore size within a system.[3]

3.2 Influence of the regularization parameter, λ on the PSDs. (Virtual Solid)

Theoretical tests using virtual solids are a useful tool to check models and to explore some properties of porous solids [22–24]. The idea of the test is to generate a virtual solid from a unique (and arbitrary) PSD source and its corresponding pseudo-experimental isotherm. Then, this pseudo-experimental isotherm is fitted by using any given kernel, thus obtaining the resulting PSD.

In this study, using the GCMC (1C) kernel, we calculate the PSD of the pseudo-experimental isotherm obtained through GCMC (3C) simulation from a virtual solid composed by a gaussian distribution centered in 5 Å. The derived PSD is

then compared with the originally specified PSD to check the suitability of using the simple kernels of pseudo-sphere to characterize porous structure.

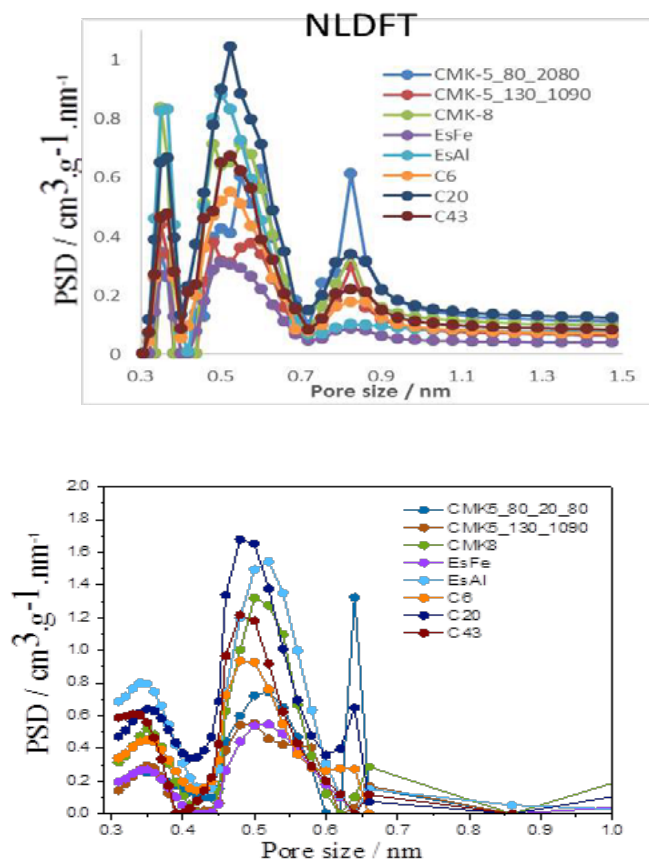


Fig. 2. Pore size distributions of different activated carbons: NLDFT and GCMC (1C) methods.

The choice of the smoothing parameter (λ) in eq. (1) is not at all straightforward and there are several methods reported in the literature, some authors highlight that this is a subjective choice and that different methods may result in quite different PSDs[25,26].

In this study, we use the method call L-curve, (this is also available in SAIEUS software Micromeritics, GA to NLDFT).

L-curves are a plot of some measure of the error of the fit to the data versus the smoothing parameter (λ). In the L-curve method, the roughness of the solution and the goodness of the fit are balanced, which implies that below a threshold value of λ the increase in the error is

often negligible, while above the threshold the error increases rapidly. These curves are used to identify this threshold value which is considered the optimal degree of smoothing. However, recent studies show that varying this λ value can lead to better adsorbent characterization[3].

Fig 3 shows L-curve plot indicating two different λ value. The first is the one chosen using the criteria proposed in the method, the second is a higher value.

In the next section we will discuss the influence of the choice of λ in the prediction of the PSD of the virtual solid.

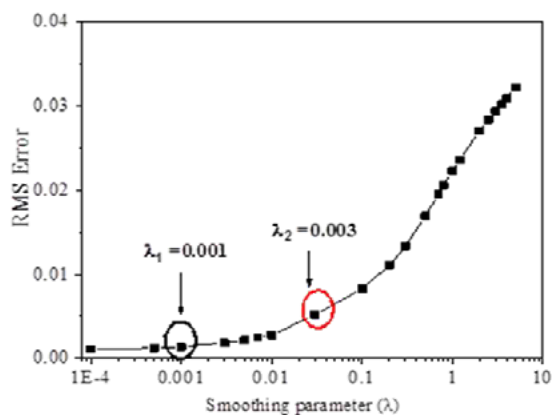


Fig. 3. RMS error vs λ (L-curve method)

The solutions obtained using different smoothing parameter values are shown in Fig 4. It can be clearly observed (Fig 4A) the presence of gaps and three artificial peaks, resulting in a very different distribution of the proposal (virtual solid) when the first smoothing parameter is used. On the other hand a higher value of λ gives a more comparable representation of the original PSD (Fig 4B).

The analysis of the regularization parameter shows that GCMC (1C) PSD is highly sensitive to the choice of λ . If the expected distribution is known a priori, users can adjust λ to obtain the desirable distribution. Unfortunately, this information is usually unknown.

The PSDs of the samples presented in Fig. 1 were obtained for two different smoothing parameters. Artificial peaks and gaps appear with the lowest value of λ (obtained with the L-curve method), while broader and smoother distributions (no gaps or dominant spikes) are obtained with a higher λ , as expected in highly disordered microporous materials (Fig 5).

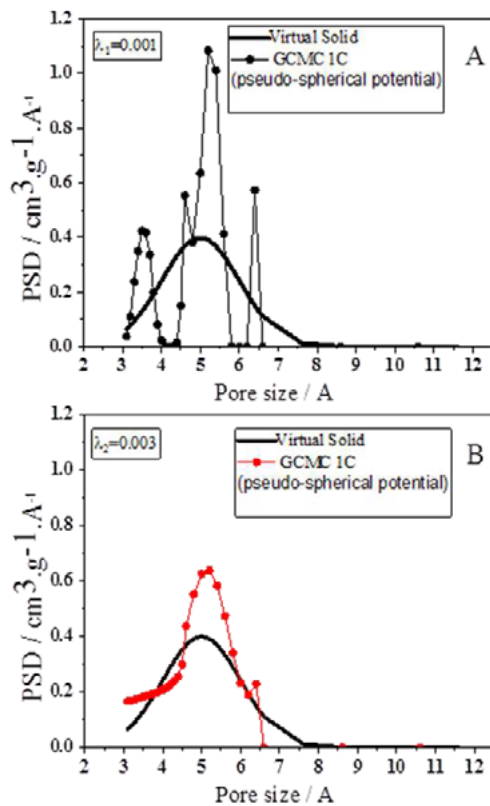


Fig. 4. The derived PSDs from the use of local isotherms obtained with the pseudo-spherical model as the kernel using two different smoothing parameter: A) $\lambda=0.001$; B) $\lambda=0.003$. The virtual solid PSD is in solid line.

Note that the gaps and the dominant spikes reported by the virtual PSD (1C) are in correspondence with those of the PSDs of the experimental samples (1C, $\lambda=0.001$).

3.3 Predictions of the GCMC (multi-site potential model).

In confined space or in pore the molecular shape is very important in the structure of the adsorbed phase and the packing density. Due to the elongated shape of CO_2 molecule and his strong quadrupole moment, is important consider it as a particle composing of three interaction sites with the electrostatic contribution to properly model the adsorbate which is significant in the correct description of the adsorption isotherm and later obtaining the PSD [5,6,27].

In Fig. 6 is shown the PSDs of samples of different activated carbons, derived from the use of local isotherms obtained using the multi-site

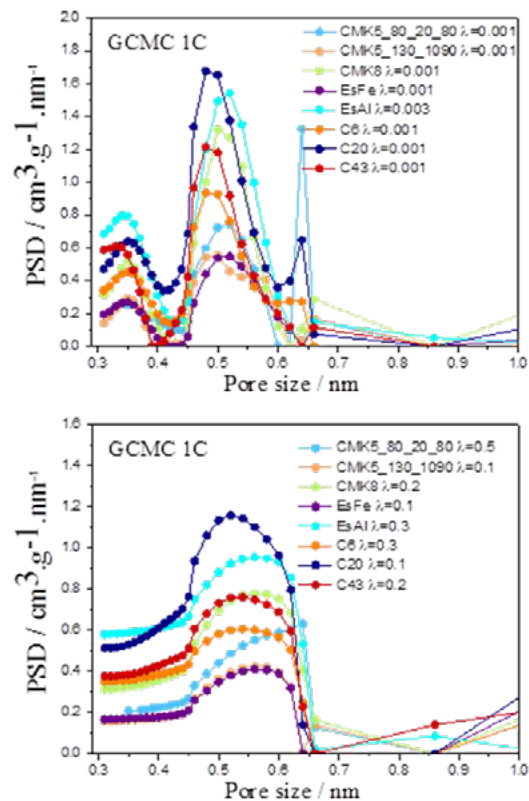


Fig. 5. The PSDs of different activated carbons derived from the use of local isotherms obtained with the pseudo-spherical model as the kernel using two different smoothing parameter λ .

model as the kernel for two different smoothing parameter λ .

The GCMC multi-site potential (3C) model is able to provide a much better representation of pore size distributions and a lower sensitivity to the smoothing parameter, λ , resulting in more reliable solutions.

Finally, in Table 2 the fitting errors are analyzed, it is observed that the GCMC (3C) model using a lower value of λ (L-curve method) present smaller fit errors, suggesting that it produce a more reliable representation of the carbon materials.

4. Conclusions

The results obtained from the study in a virtual solid and the experimental samples show that the NLDFT and GCMC models with pseudo-spherical potential, commonly used in the scientific community, do not necessarily represent the dominant pore size within these materials, and they should be used with great caution and preferably

with complementary information obtained through other techniques.

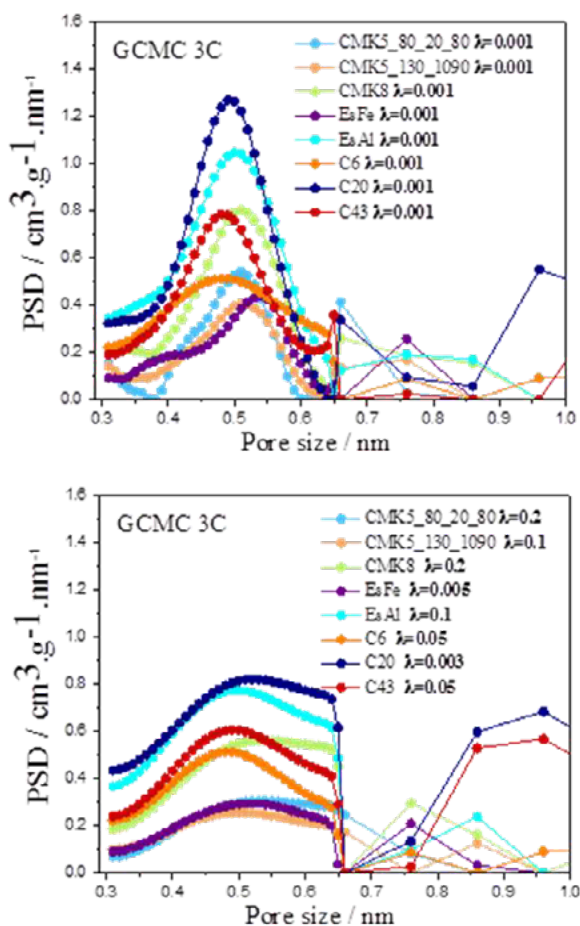


Fig. 6. The PSDs of different activated carbons derived from the use of local isotherms obtained with the multi-site model as the kernel using two different smoothing parameter λ .

The model GCMC (3C) that considers the multisite potential for adsorbate interaction presents less sensitivity to the λ value setting, and produce a better representation of pore size distribution

We strongly recommend using the multisite potential to model the interaction of CO₂ in microporous carbons, since these produce a more reliable characterization of this kind of materials.

Table 2. Fit errors of the experimental isotherms obtained by the different models.

$$Error = \sqrt{\sum_i^n (N_i^{exp} - N_i^{theo})^2}$$

Model/samples	CMK5-80	CMK5-130	CMK8	EsFe
GCMC 1C λ_1	0.3769	0.1901	0.1724	0.0385
GCMC 1C λ_2	0.3857	0.1944	0.1966	0.0501
GCMC 3C λ_1	0.3719	0.1895	0.1534	0.1504
GCMC 3C λ_2	0.3824	0.2021	0.1690	0.1532
Model/samples	EsAl	C6	C20	C43
GCMC 1C λ_1	0.3769	0.1901	0.1724	0.0385
GCMC 1C λ_2	0.3857	0.1944	0.1966	0.0501
GCMC 3C λ_1	0.3719	0.1895	0.1534	0.1504
GCMC 3C λ_2	0.3824	0.2021	0.1690	0.1532

Acknowledgements

The authors acknowledge financial support from CONICET (Argentina). The numerical works were conducted using the BACO parallel cluster and LABSOP porous media laboratory located at Dpto. de Física - INFAP, UNSL.

References

- [1] J. Garrido, R. Torregrosa, Use of N₂ C₀₂ in the Characterization of Activated Carbons, 9 (1987) 76–81. doi:10.1021/la00073a013.
- [2] D. Cazorla-amor, D. Lozano-castell, Usefulness of CO₂ adsorption at 273 K for the characterization of porous carbons, 42 (2004) 1233–1242. doi:10.1016/j.carbon.2004.01.037.
- [3] G. Kupgan, T.P. Liyana-arachchi, C.M. Colina, NLDFT Pore Size Distribution in Amorphous Microporous Materials, (2017) 11138–11145. doi:10.1021/acs.langmuir.7b01961.

- [4] G.M. Davies, N. a. Seaton, Development and validation of pore structure models for adsorption in activated carbons, *Langmuir*. 15 (1999) 6263–6276. doi:10.1021/la990160s.
- [5] D.D. Do, S. Junpirom, D. Nicholson, H.D. Do, Importance of molecular shape in the adsorption of nitrogen, carbon dioxide and methane on surfaces and in confined spaces, *Colloids Surfaces A Physicochem. Eng. Asp.* 353 (2010) 10–29. doi:10.1016/j.colsurfa.2009.10.021.
- [6] R. Delgado, V. Cornette, J. Pablo, D. Soares, R.H. Lopez, Applied Surface Science Effects of potential models on nitrogen adsorption on triangular pore: An improved mixed model for energetic characterization of activated carbon, *Appl. Surf. Sci.* 481 (2019) 1035–1043. doi:10.1016/j.apsusc.2019.02.201.
- [7] D. Frenkel, D. Smit, *Understanding Molecular Simulation*, Academic Press, Sidney, 1991.
- [8] M.P. Allen, D.J. Tildesley, *Computer Simulation of Liquids*, Oxford University Press, Oxford, 1987.
- [9] J. Stecki, Steele (10-4-3) Potential due to a Solid Wall, *Langmuir*. 13 (1997) 597–598. doi:10.1021/la960739f.
- [10] J.J. Potoff, J.I. Siepmann, Vapor-liquid equilibria of mixtures containing alkanes, carbon dioxide, and nitrogen, *AIChE J.* 47 (2001) 1676–1682. doi:10.1002/aic.690470719.
- [11] G.M. Davies, N.A. Seaton, V.S. Vassiliadis, Calculation of Pore Size Distributions of Activated Carbons from Adsorption Isotherms, 36 (1999) 8235–8245.
- [12] G.M. Davies, N.A. Seaton, The effect of the choice of pore model on the characterization of the internal structure of microporous carbons using pore size distributions, *Carbon N. Y.* 36 (1998) 1473–1490.
- [13] M.B. Sweatman, N. Quirke, Modelling gas mixture adsorption in active carbons, *Mol. Simul.* 31 (2005) 667–681. doi:10.1080/08927020500108296.
- [14] G.M. Davies, N.A. Seaton, V.S. Vassiliadis, Calculation of pore size distributions of activated carbons from adsorption isotherms, *Langmuir*. 15 (1999) 8235–8245. doi:10.1021/la9902643.
- [15] G.M. Davies, N. a. Seaton, The effect of the choice of pore model on the characterization of the internal structure of microporous carbons using pore size distributions, *Carbon N. Y.* 36 (1998) 1473–1490. doi:10.1016/S0008-6223(98)00140-7.
- [16] S. Day, R. Fry, R. Sakurovs, S. Weir, Swelling of Coals by Supercritical Gases and Its Relationship to Sorption, *Energy & Fuels*. 24 (2010) 2777–2783. doi:10.1021/ef901588h.
- [17] M.B. Sweatman, N. Quirke, Modelling Gas Adsorption in Slit-Pores Using Monte Carlo Simulation, *Mol. Simul.* 27 (2001) 295–321. doi:10.1080/08927020108031355.
- [18] J. Jagiellot, Stable Numerical Solution of the Adsorption Integral Equation Using Splines, (1994) 2778–2785.
- [19] J.P. Olivier, IMPROVING THE MODELS USED FOR CALCULATING THE SIZEDISTRIBUTION OFMICROPORE VOLUME OF ACTIVATED CARBONS FROM ADSORPTION DATA, 36 (1998) 1469–1472.
- [20] P.I. Ravikovitch, A. Vishnyakov, R. Russo, A. V Neimark, P.I. Ravikovitch, A. Vishnyakov, R. Russo, A. V Neimark, Unified Approach to Pore Size Characterization of Microporous Carbonaceous Materials from N₂, Ar, and CO Adsorption Isotherms Unified Approach to Pore Size Characterization of Microporous Carbonaceous Materials from N₂, Ar, and CO₂ Adsorption



- Isother, (2000). doi:10.1021/la991011c.
- [21] A.D. Lueking, H.-Y. Kim, J. Jagiello, K. Bancroft, J.K. Johnson, M.W. Cole, Tests of Pore-Size Distributions Deduced from Inversion of Simulated and Real Adsorption Data, *J. Low Temp. Phys.* 157 (2009) 410–428. doi:10.1007/s10909-009-9911-1.
- [22] A.D. Lueking, H.Y. Kim, J. Jagiello, K. Bancroft, J.K. Johnson, M.W. Cole, Tests of pore-size distributions deduced from inversion of simulated and real adsorption data, *J. Low Temp. Phys.* 157 (2009) 410–428. doi:10.1007/s10909-009-9911-1.
- [23] J.P. Toso, J.C.A. Oliveira, D.A. Soares Maia, V. Cornette, R.H. López, D.C.S. Azevedo, G. Zgrablich, Effect of the pore geometry in the characterization of the pore size distribution of activated carbons, *Adsorption*. 19 (2013) 601–609. doi:10.1007/s10450-013-9483-x.
- [24] V. Yelpo, V. Cornette, J.P. Toso, H.L. Raúl, Characterization of nanostructured carbon CMK-3 by means of Monte Carlo simulations, 121 (2017) 106–113. doi:10.1016/j.carbon.2017.05.085.
- [25] J.D. Wilson, Statistical approach to the solution of first-kind integral equations arising in the study of materials and their properties, *J. Mater. Sci.* 27 (1992) 3911–3924.
- [26] M. V Szombathely, P. Brauer, M. Jaroniec, The solution of adsorption integral equations by means of the regularization method, *J. Comput. Chem.* 13 (1992) 17–32.
- [27] D.D. Do, H.D. Do, Effects of potential models on the adsorption of carbon dioxide on graphitized thermal carbon black: GCMC computer simulations, *Colloids Surfaces A Physicochem. Eng. Asp.* 277 (2006) 239–248. doi:10.1016/j.colsurfa.2005.11.094.

Evaluation of estimation procedures of mass transfer coefficients from batch adsorption kinetic data

Daniel Souza de Almeida^a, Vânia Queiroz da Silva^a, Evandro Steffani^a, Elisa Barbosa-Coutinho^b, Marcio Schwaab^{a*}

^a Departamento de Engenharia Química, Escola de Engenharia, Universidade Federal do Rio Grande do Sul, R. Ramiro Barcelos, 2777. Sala 253, Prédio 22202, Porto Alegre, RS 90040-040, Brasil

^b Departamento de Físico-Química, Instituto de Química, Universidade Federal do Rio Grande do Sul, Av. Bento Gonçalves, 9500, Porto Alegre, RS, 91501-970, Brasil

Abstract

In this paper it was analyzed the methods proposed by Yao-Chen, Furusawa-Smith and the phenomenological model for estimation of mass transfer parameters, focusing on external mass transfer coefficient, as its applicability and limitations. Two kinetic adsorption experiments were performed using Fast Green dye as adsorbate and Pural SB (Sasol) as adsorbent. Using the data collected in these experiments, the film mass transfer coefficient was estimated using different methodologies. The film mass transfer coefficient presented finite values in the order of 10^{-2} cm/min for both experiments using the simplified methods proposed by Yao-Chen and Furusawa-Smith, while using the phenomenological model the value of this constant tends to infinity. Analyzing the results, it was found that the simultaneous estimation of mass transfer parameters from a theoretical model based on mass balances is more appropriate and that the methods that seek to simplify the determination of the film mass transfer coefficient are extremely limited.

Keywords: Adsorption kinetics; Mass transfer coefficients; Film mass transfer coefficient; Diffusion coefficient;

1. Introdução

Adsorption is a very efficient and used technique. It consists basically of three stages: external diffusion in the film that surrounds the adsorbent particle, diffusion in the internal pores (intraparticle diffusion) and adsorption on the surface of these pores [1, 2, 3,10,15].

Models describing adsorption generally consider that the third step is instantaneous, and that mass transfer is based on intraparticle diffusive and/or convective mass transport [4, 13,15].

In both cases, there are coefficients that are associated with the mass transfer, namely, the convective coefficient, related to the external mass transfer, and the diffusion coefficient, or diffusivity in the particle, associated with the internal mass transfer. The film mass transfer coefficient is directly related to the agitation of the fluid and the diffusivity in the particle to the easiness with which the adsorbate molecules can move in the internal pores of the adsorbent [5].

Considering that the mass transference is fundamental in the adsorption, it must be determined how the coefficients related to the mass transference affect this phenomenon, and allowing that it is possible to understand the present mechanisms and describe the process kinetics [5].

The purpose of this study is evaluating the methods proposed by Yao-Chen, Furusawa-Smith and the phenomenological model to estimate the mass transfer coefficients, mainly for the external mass transfer coefficient, checking the applicability and limitations of each method.

2. Theory

2.1. Phenomenological model of mass transfer

The phenomenological model has a strong theoretical foundation and is obtained from the laws of mass conservation by means of balances in the particle and in the fluid phase (bulk). The model describes how the concentration in the particle C_P varies over time and space, under some assumptions can be represented by the Eq. (1).

$$\frac{\partial C_p}{\partial t} = \frac{D_{ap}}{R^2} \left[\frac{\partial^2 C_p}{\partial \eta^2} + \frac{2}{\eta} \frac{\partial C_p}{\partial \eta} \right] \quad (1)$$

The dimensionless spatial variable is defined in Eq. (2). In addition, it is assumed that the adsorbent particles are spherical and R is the radius. The apparent diffusivity (D_{ap}) is given by Eq. (3), and includes one of the parameters to be estimated, the diffusivity in the particle (D_p).

$$\eta = \frac{r}{R} \quad (2)$$

$$D_{ap} = \frac{\varepsilon D_p}{\varepsilon + \rho_p (\partial q_t / \partial C_p)} \quad (3)$$

In Eq. (3), ε represents the porosity and ρ_p the specific mass of the particle, while the derivative present in the denominator is determined from the adsorption isotherm, considered Freundlich isotherm in this work.

For the partial differential equation of the phenomenological model to be solved, an initial condition and two boundary conditions are necessary. As an initial condition, it is assumed that the adsorbent is free of adsorbate initially, thus it is assumed that the initial solute concentration is zero, according to Eq. (4).

$$C_p|_{\tau=0} = 0 \quad (4)$$

As boundary conditions, in the particle center the condition of symmetry can be applied, according to Eq. (5).

$$\left. \frac{\partial C_p}{\partial \eta} \right|_{\eta=0} = 0 \quad (5)$$

On the surface the convective flow is equal to the diffusive flow, since all the adsorbate mass that leaves the solution goes to the adsorbent. Thus, the first option neglects external resistance to mass transfer and the concentration on surface is equal to solution concentration, C_B , as defined in Eq. (6).

$$C_p(\eta=1, t) = C_B(t) \quad (6)$$

The second, considers the resistance to external mass transfer. as presented in Eq. (7), where k_f is the external mass transfer coefficient.

$$\left. \frac{\partial C_p}{\partial \eta} \right|_{\eta=1} = \frac{k_f R}{\varepsilon D_p} [C_B(t) - C_p(\eta=1, t)] \quad (7)$$

The concentration in the particle is related to the bulk concentration, whose variation over time is given by Eq. (8) or Eq. (9), where M_p represents the adsorbent mass and V_B the solution volume.

$$\frac{dC_B}{dt} = -\frac{M_p}{V_B \rho_p} \frac{3}{R} k_f [C_B(t) - C_p(\eta=1, t)] \quad (8)$$

$$\frac{\partial C_B}{\partial t} = -\frac{M_p}{V_B \rho_p} \frac{3}{R^2} \varepsilon D_p \left. \frac{\partial C_p}{\partial \eta} \right|_{\eta=1} \quad (9)$$

At the instant of time zero the concentration in the bulk phase is the same as the initial concentration as Eq. (10).

$$C_B(t=0) = C_{B_0} \quad (10)$$

The solution of the phenomenological model requires the knowledge of adsorbent particle properties, as well as the estimation of external (k_f) and internal (D_p) mass transfer parameters.

2.2. Furusawa-Smith method

In 1973, Furusawa and Smith [6] developed a method to estimate the film mass transfer coefficient from the initial inclination of the adsorption kinetic curve [6]. Applying Eq. (9) in t equal to zero, it is demonstrated that the variation of the bulk concentration is determined by Eq. (11).

$$\left. \frac{d}{dt} \left(\frac{C_B}{C_{B_0}} \right) \right|_{t=0} = -\frac{M_p}{V_B \rho_p} \frac{3}{R} k_f \quad (11)$$

The mass balance for batch adsorption provides Eq. (12), where q_t represents the amount adsorbed over time.

$$q_t = \frac{V_B}{M_p} [C_{B_0} - C_B(t)] \quad (12)$$

Combining the Eqs. (11) and (12), one may obtain Eq. (13).

$$\left. \frac{dq_t}{dt} \right|_{t=0} = \frac{3C_{B_0} k_f}{R\rho_P} \quad (13)$$

The film mass transfer coefficient can be determined from the derivative in t approaches zero, which is obtained by the inclination of the straight line from origin (t_0 and q_{t_0} equal to zero) and the first experimental point, according to Eq. (14).

$$\left. \frac{dq_t}{dt} \right|_{t=0} \approx \frac{q_{t_1} - q_{t_0}}{t_1 - t_0} = \frac{q_{t_1}}{t_1} \quad (14)$$

Although this method is widely used [10-15], it assumes that the film mass transfer coefficient is finite, which is not true when the external resistance to mass transfer is negligible. It is extremely difficult to determine experimentally the derivative in t equal to zero when there is no external resistance. Moreover, this method depends on experimental measurements with good accuracy at the beginning of the adsorption, which is not easy to obtain in practice, since the measurements in very short time are more sensitive to experimental error.

2.3. Yao-Chen method

Yao and Chen [7] developed, in 2015, a method that tries to solve some of the difficulties of the previous method to obtain the values of the adsorbed quantities in the initial moments of adsorption. The authors propose an adjustment equation, Eq. (15), which is valid for what they call the "first stage of adsorption", when the adsorption quantity is less than or equal to half of that in equilibrium [7].

$$q_t = \frac{r_0 t}{1 + at} \quad (15)$$

The parameter r_0 is equal to the derivative in t equal to zero, according to Eq. (16). So, the value used for the calculation of k_f in Eq. (11) is no longer determined by the inclination of the straight line in the first two points, as proposed by Furusawa and Smith [6], but by the adjustment of the proposed model to the experimental points in the first stage of adsorption [7].

$$\left. \frac{dq_t}{dt} \right|_{t=0} = r_0 \quad (16)$$

The Yao-Chen method still presents the disadvantages of the one proposed by Furusawa-Smith, because the adjustment is strongly dependent on experimental points in short times, which tend to present greater uncertainty. Moreover, if the external resistance to mass transfer is negligible, which means that the film mass transfer coefficient approaches infinity, the adjustment will still provide a finite value if the measurements are not made in sufficiently short times, what is extremely difficult in practice.

3. Materials and methods

Kinetic studies were performed by removing samples from the orbital Dubnoff bath at 40°C along times under stirring of 156 rpm. The adsorbent mass used was 50 mg (Exp. 1) and 20 mg (Exp. 2) in 50 mL Erlenmeyer flasks. Pural SB (SASOL) were used as adsorbent and Fast Green as adsorbate.

Water was initially added to the system and left in a water bath for 30 minutes for all the pores of the adsorbent to be filled with water. After this time, the dye solution was added to the Erlenmeyer flask leading to an initial concentration of 100 mg/L.

After remaining in agitation for the established period, an aliquot was removed and centrifuged at 3000 rpm for 10 minutes in centrifuge. This process was repeated until no more solids were observed at the bottom of the flask containing the aliquot. The experiments were performed in quadruplicate and sample concentrations were determined from spectrophotometric measurements.

With the experimental data, the film mass transfer coefficient was estimated using the simplified methods proposed by Furusawa-Smith and Yao-Chen, according to Eqs. (13-16), and the phenomenological model, according to Eqs. (8-9). For the Yao-Chen method, the parameter r_0 was estimated by a nonlinear adjustment in the STATISTICA software.

The solution of the phenomenological model was made numerically by discretization of the spatial variable by central finite differences. The resulting EDO system was integrated using the DASSL routine [8]. The estimation of mass transfer parameters was done simultaneously minimizing the objective function of weighted least squares,

expressed by Eq. (17), by the Particle Swarm method (PSO) associated with the Newton method. The variable used in the minimization is the bulk concentration, since this is the variable of the model experimentally determined.

$$F_{obj} = \sum_{j=1}^N \frac{(C_{B_j}^{exp} - C_{B_j}^{mod})^2}{\sigma_j^2} \quad (17)$$

The adsorbent properties like particle radius, R , particle (or apparent) density, ρ_p , and porosity, ε , are presented in Table 1.

Table 1. Adsorbent properties

Variable	Value
R (cm)	0.00345
ρ_p (mg/cm ³)	1.264
ε	0.544

The results obtained from the different methodologies analyzed were compared and presented in the sequence with the discussion about the quality of the estimated parameters.

4. Results and Discussion

The results in Table 2 as an estimate for the film mass transfer coefficient were obtained by applying the simplified methods for the first experiment.

Table 2. Film mass transfer coefficient obtained from the Furusawa-Smith and Yao-Chen methods for experiment 1.

Method	r_0 (mg/(g.min))	k_f (cm/min)
Furusawa/Smith	1.39	0.0203
Yao/Chen	1.80	0.0262

It can be verified in Table 2 that both methods provided finite values in the order of 10^{-2} cm/min for the film mass transfer coefficient. Finite values of k_f were also found in the studies of Tao et al. [11] and Červeňanský et al. [12] when they used the methodology proposed by Furusawa [6]. The use of the methods is shown graphically in Figure 1 for the data from the first experiment.

The results obtained from the phenomenological model are presented below. In the estimation of diffusivity, it was established the base power exponent ten as parameter, since the value of diffusivity is close to zero, which could cause

problems of convergence in minimizing the objective function. The estimates of the film mass transfer coefficient and the diffusivity are presented in Table 3 with their respective confidence intervals.

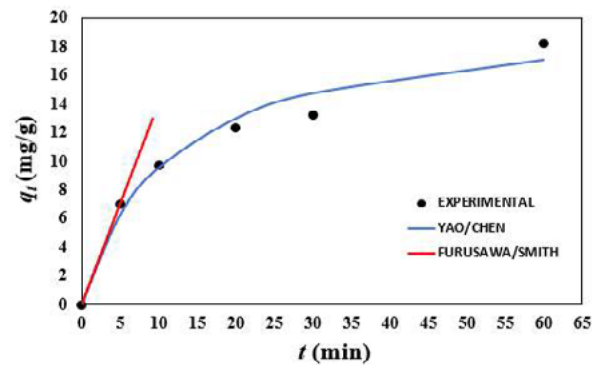


Fig. 1. Graphical representation of the simplified methods applied to Experiment 1.

Table 3. Parameter estimation results from first experiment: model with external and internal resistance.

Obj. Func.: 9.63	Parameter	Lower limit	Upper limit
	k_f (cm/min)	-2.3×10^{12}	4.0×10^{12}
	D_p (cm ² /min)	2.09×10^{-6}	4.31×10^{-6}

Through the analysis of the values found it is verified that the film mass transfer coefficient estimated from the phenomenological model is in the order of 10^{10} cm/min, that is, it tends to infinity. This fact implies that for the experiment in question, there is no external resistance to mass transfer, since the resistance is the inverse of the external mass transfer coefficient. In addition, it should be noted that the uncertainty of this parameter is large (around 10^{12}), which means that it is not estimable, because the model is not sensible to it.

To confirm this observation, the parameters were estimated with the model containing only the diffusivity. In this case, the boundary condition on the surface becomes that the concentration in the particle is the same as the bulk concentration and the adsorption is expressed in terms of the diffusion rate. Eqs. (7) and (8) are replaced by Eqs. (6) and (9), respectively. The result obtained for this estimation is presented in Table 4.

Table 4: Parameter estimation results from first experiment: the model without external resistance.

Obj.Func.:9.67	Parameter	Lower limit	Upper limit
D_p (cm ² /min)	2.99×10^{-6}	2.31×10^{-6}	3.87×10^{-6}

The estimates of diffusivity in the two situations are statistically equivalent, since the confidence intervals are overlapping, confirming that the film mass transfer coefficient approaches infinity and is not relevant in this case. This result is more evident in Figure 2, which shows that the adjustments of the model with one (D_p) and two parameters (k_f and D_p) are practically equivalent.

In the figure 2 are presented the adjustments of the phenomenological model of estimation using the two mass transfer coefficients and using only diffusivity.

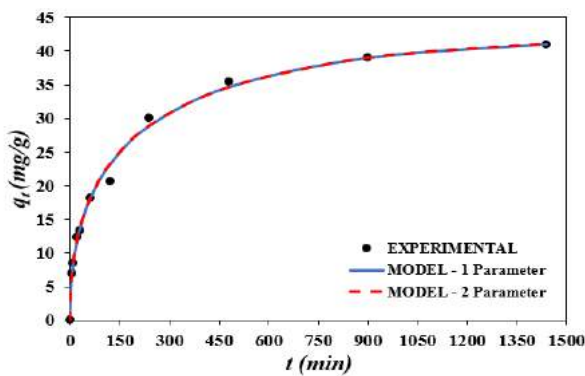


Fig. 2 Adjustments of the phenomenological model with one and two parameters for Experiment 1.

The same estimation procedure, using the simplified models and the phenomenological model, was performed for experiment 2. In the Table 5 are found the values for the parameters estimated by the two simplified models.

Table 5. Film mass transfer coefficient obtained from the Furusawa-Smith and Yao-Chen methods for experiment 2.

Method	r_0 (mg/(g.min))	k_f (cm/min)
Furusawa-Smith	4.87	0.071
Yao-Chen	6.18	0.090

As observed for experiment 1, the values obtained for the film mass transfer coefficient in both simplified methods provide finite values in the order of 10^{-2} cm/min. The decrease in the adsorbent

mass caused an increase of about four times in the constant value. The graphical representation of the models is presented in Figure 3.

The results of the estimation from the phenomenological model applied to the second experiment are presented in Table 6.

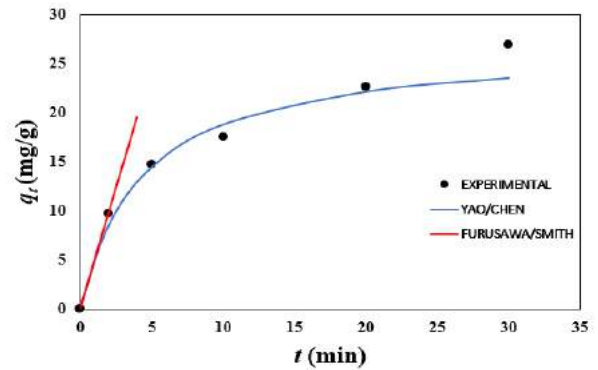


Fig. 3. Graphical representation of the simplified methods applied to Experiment 2.

Table 6. Parameter estimation results from second experiment: model with external and internal resistance.

Obj.Func.:8.40	Parameter	Lower limit	Upper limit
k_f (cm/min)	0.24×10^{10}	-1.4×10^{11}	1.9×10^{11}
D_p (cm ² /min)	1.49×10^{-5}	0.985×10^{-6}	2.26×10^{-5}

Similar to what happened in Experiment 1, it is noticed that the film mass transfer coefficient tends to infinity, besides presenting great uncertainty, which leads to the same conclusion of the first experiment, that there is no external resistance to mass transfer, so that only the internal resistance, manifested by finite diffusivity, is sufficient to mathematically model this adsorption experiment.

This analysis is, once again, confirmed by the estimation using the model that considers only diffusivity, the results are expressed in Table 7.

Table 7. Parameter estimation results from second experiment: the model without external resistance.

Obj.Func.:8.88	Parameter	Lower limit	Upper limit
D_p (cm ² /min)	1.39×10^{-5}	0.592×10^{-6}	3.25×10^{-5}

The values obtained for one parameter are statistically equivalent to that obtained for the model that considers both mass transfer coefficients, as can be inferred from the values in

Table 7 and from the great similarity between the models (figure comparing model prediction with experimental data was not presented since it was similar to Figure 2).

It is important to observe that confidence intervals of parameter D_p are different between Tables 3 and 4 and between Tables 6 and 7 since objective function and degrees of freedom are changed when parameter k_f is omitted. Besides, values of parameter D_p from Tables 4 and 7 are different, but only adsorbent mass was changed. This result is not expected and a better procedure would be the estimation of a single parameter D_p for both (or even more) experiments. However, since the objective of this work is the evaluation of the simplified method of estimation of parameter k_f , this further evaluation was not presented here.

The simplified methods were developed in order to estimate the film mass transfer coefficient from kinetic data without the need to solve partial differential equations. However, such simplification could be justifiable for Furusawa and Smith [6] in 1973 due to the technological limitations of that time. But for Yao and Chen [5] in 2015, such simplification is no longer necessary, and the use of the phenomenological model is the most appropriate and possible due to the use of computers capable of performing calculations in a fast and efficient way [9].

5. Conclusion

The methods proposed by Furusawa-Smith and Yao-Chen have significant limitations, especially because both depend on experimental measurements in very short time. This is more difficult to obtain in practice and tends to present greater uncertainty.

In addition, these methods provide finite values for the film mass transfer coefficient in any circumstances, excluding the possibility of inexistence of external resistance to mass transfer.

The phenomenological model has no restrictions related to the existence of resistance to mass transfer, both external and internal, allowing the simultaneous estimation of the film mass transfer coefficient and the diffusivity in the particle, as well as the statistical evaluation of these parameters, making it possible to obtain more reliable values.

Acknowledgements

This work was financed in part by CNPq-Brasil and by CAPES-Brasil.

References

- [1] Yang RT. Gas separation by adsorption processes. 1st ed, Butterworth-Heinemann, 2013.
- [2] Yao C, Chen T. A film-diffusion-based adsorption kinetic equation and its application. *Chem. Eng. Res. Des.* 2017;119:87–92.
- [3] Schwaab M, Steffani E, Barbosa-Coutinho E, Severo, JB. Critical analysis of adsorption/diffusion modelling as a function of time square root. *Chem. Eng. Sci.* 2017;173:179–186.
- [4] Qiu H, Pan BC, Zhang QJ, Zhang WM, Zhang QX. Critical review in adsorption kinetic models. *J. Zhejiang Univ.-Sci. A* 2009;10:716-724.
- [5] Cremasco MA, Fundamentos de transferência de massa. 3rd ed. Campinas: Blucher 2016.
- [6] Furusawa T, Smith JM. Fluid-Particle and Intraparticle Mass Transport Rates in Slurries. *Ind. Eng. Chem. Fundam.* 1973, 12:197–203.
- [7] Yao C, Chen T. A new simplified method for estimating film mass transfer and surface diffusion coefficients from batch adsorption kinetic data. *Chem. Eng. J.* 2015;265:93-99.
- [8] Pétzold LR. A description of DASSL: a differential/algebraic system solver. Sandia Report, 1982.
- [9] Cassol GO, Gallon R, Schwaab, M, Barbosa-Coutinho E, Júnior JBS, Pinto JC. Statistical evaluation of non-linear parameter estimation procedures for adsorption equilibrium models. *Adsorpt. Sci. Technol.* 2014;32:257-273.
- [10] Torrik E, Mansooreh S, Maryam TR. Application of Kinetic Models for Heavy Metal Adsorption in the Single and Multicomponent Adsorption System. *J. Environ. Sci.* 2019;13:813-828.
- [11] Tao Y, Wu Y, Han Y, Chemat F, Li D, Show PL. Insight into mass transfer during ultrasound-enhanced adsorption/desorption of blueberry anthocyanins on macroporous resins by numerical simulation considering ultrasonic influence on resin properties. *Chem. Eng. J.* 2020; 380:122530.
- [12] Červeňanský I, Mihal' M, Markoš J. Modeling of 2-phenylethanol adsorption onto polymeric resin from aqueous solution: Intraparticle diffusion evaluation and dynamic fixed bed adsorption. *Chem. Eng. Res. Des.* 2019; 147: 292-304.
- [13] Inglezakis VJ, Fyrillas MM. Experimental study of zeolitic diffusion by use of a concentration-dependent surface diffusion model. *Heliyon* 2019;5:e02143.
- [14] Leyva-Ramos R, Ocampo-Perez R, Mendoza-Barron J. External mass transfer and hindered diffusion of organic compounds in the adsorption on activated carbon cloth. *Chem. Eng. J.* 2012;183:141-151.
- [15] Leyva-Ramos R, Geankoplis CJ. Diffusion in liquid-filled pores of activated carbon. I. Pore volume diffusion. *Can. J. Chem. Eng.* 1994;72:262-271.

Analysis of Phenol Removal Capacity from Water by Adsorption on Activated Carbon

Ana Luisa M. Galdino^a, José C. A. Oliveira^a, Madson L. Magalhães^a, Sebastião M. P. Lucena^a

^a Dept. Eng. Química, Grupo de Pesquisa em Separações por Adsorção – GPSA, Universidade Federal do Ceará, Campus do Pici, Bl. 709, 60455-760, Fortaleza, CE, Brazil

Abstract

Phenolic compounds, which exhibit low cost and high efficiency of production, are used in a wide variety of industrial fields. The toxicity of this planar aromatic compound leads to problems of contamination in hydric reservoirs. Alternatives are required to remove these substances from water sources and thus adsorption on activated carbon (AC) has shown to be a successful way. Here, we apply molecular simulation to suggest models in order to better understand the structure of AC and to comprehend the adsorption phenomenon of phenol on carbon surface. A set of simulated isotherms for different pore sizes in addition to the experimental isotherm of the studied system enable us to observe which pores are more significant in the determination of AC properties. This work also evaluates the removal capacity of several activated carbons to purify phenol from water. Moreover it emphasizes how important molecular simulation is to save time and costs by predicting similar results to the experimental models.

Keywords: Phenol; Activated Carbon; Molecular Simulation; Adsorption.

1. Introduction

The presence of organic compounds as contaminants in water is frequent. Among them, there is phenol, which is characterized as a planar aromatic compound with high toxicity. The existence of phenolic compounds in water derive from human activities, like residues of industrial, agricultural and domestic use, or natural phenomenon, like degradation of organic material or synthesis of these substances by microorganisms and plants.

The United States Environmental Protection Agency (USEPA) listed the phenolic compounds as priority concerns, because they are toxic and cause considerable effects of short and long-term on living beings [1]. The World Health Organization (WHO) determined 0,001 mg/L as a limit concentration of phenol in potable water [2].

Whereas contaminants distribution is ubiquitous in plants, and humans ingest daily appreciable quantities of natural and artificial phenolic mixtures [3], our study is related to the clearance of these water pollutants using activated carbon (AC).

Photocatalytic degradation, adsorption, ozonation, extraction, biological remediation, membrane separation and ion exchange are the techniques that can be utilized to remove phenol from water. However, adsorption highlights for

being easier to project and to operate. Furthermore, it does not produce toxic residues.

An appropriate adsorbent must have pores with an extensive superficial area, be highly hydrophobic and accumulate selectively the pollutant on its surface. The efficiency of different adsorbents was tested and revealed that the activated carbon rendered a removal efficiency of 98% against 90% from charcoal and 90% from ash bagasse [4].

The activated carbon is largely utilized in the most diverse industrial and technologic application, it has a favorable porous structure and a high adsorption capacity. Its engineering properties are defined mostly by its capacity of adsorb [5]–[7].

In order to analyze the effect of phenol adsorption by activated carbon and to estimate its adsorptive capacity, simulation of adsorption isotherms for different types of activated carbons was performed. Thus, it was possible to establish a relationship between pore size distribution and phenol removal capacity of activated carbons.

2. Simulation Details

The simulations of adsorption isotherms of N₂ and phenol in microporous were performed using the Monte Carlo algorithm in Grand Canonical Ensemble (GCMC) [8, 9]. This method allows a direct calculation of phase equilibrium [10]. The

interactions among the molecules were computed using the Lennard-Jones (LJ) potential:

$$U_{gg}(r) = -4\epsilon_{gg} \left[\left(\frac{\sigma_{gg}}{r} \right)^6 - \left(\frac{\sigma_{gg}}{r} \right)^{12} \right] \quad (1)$$

where ϵ_{gg} and σ_{gg} are the energetic and geometric parameters of LJ potential, respectively, and r is the distance between the particles. The electrostatic interactions were also computed. The used parameters are shown in Table 1.

Table 1. The parameters used in simulations [5,11].

	$\epsilon(\text{kcal/mol})$	$R_0(\text{\AA})$	Charge(e)
C1	0.0703	3.9845	+0.54
C2, C6	0.0703	3.9845	-0.4125
C3, C5	0.0703	3.9845	-0.03
C4	0.0703	3.9845	-0.3
O	0.1554	3.4458	-0.64
H	-	-	+0.44
H2, H6	0.0301	2.7162	+ 0.2
H3, H5	0.0301	2.7162	+0.143
H4	0.0301	2.7162	+0.159
N ₂ -N ₂	0.2017	4.0575	-
N ₂ -C	0.1059	3.9217	-

The local adsorption isotherms were calculated (N₂ at 77 K) in a set of 24 pores distributed in a logarithm function between 7 and 53 Å. This set of isotherms is called kernel. To phenol, isotherms were calculated at 301 K to only 4 pores (7.0, 8.9, 18.5 and 27.9 Å). The Pore Size Distribution (PSD) were determined using an entire set of isotherms and the representative PSD's were obtained with the 4 representative pores. This methodology of approximation was used and validated in previous study reported in literature [12]. The integral equation of adsorption isotherm for PSD can be written:

$$Q(P) = \int q(P, H) f(H) dH \quad (2)$$

where $Q(P)$ is the total adsorbed amount per gram of adsorbent at pressure P (experimental isotherm), $q(P, H)$ is a function that represents the adsorption isotherm for a material characterized by pores with size H , $f(H)$ is a PSD. The PSD is obtained through deconvolution of Eq. 2 using the experimental isotherm and the kernel of simulated isotherms [13]. The value of cutoff (r_{cutoff}) was $5\sigma_{gg}$. The Monte Carlo steps used were $2 \cdot 10^6$ for equilibrium and $1 \cdot 10^6$ for production.

2.1 Models

The assumed model for the molecular representation of activated carbon is defined as slits of graphene layers. The simulation box is built with $40 \times 40 \text{ \AA}$ and can be observed in Figure 1a. It was used the atom-atom model for the phenol molecule (Figure 1b).

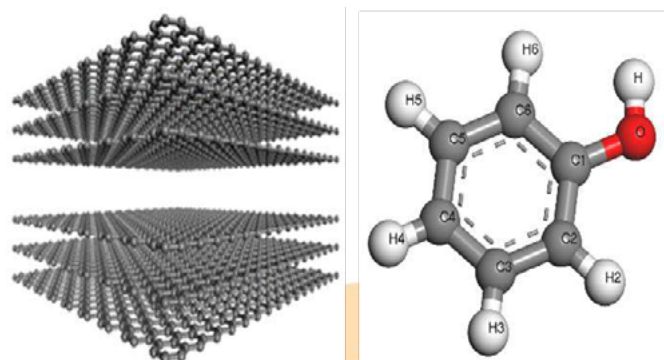


Figure 1. Molecular representation of a pore of activated carbon with size of a) 7.0 Å and b) Phenol molecule.

3. Results

3.1 Validation

The first step was to certify the phenol model. The results obtained presented a good agreement with the authors Kowalczyk et al. [5]. We got a series of pores (7.0, 7.6, 8.9, 12.5 and 18.5 Å). The dependence between Adsorptive Capacity and Pore Size was proven by observing phenol saturation capacity by surface area. This property grows linearly with the increase of pore size as predicted in the literature [5].

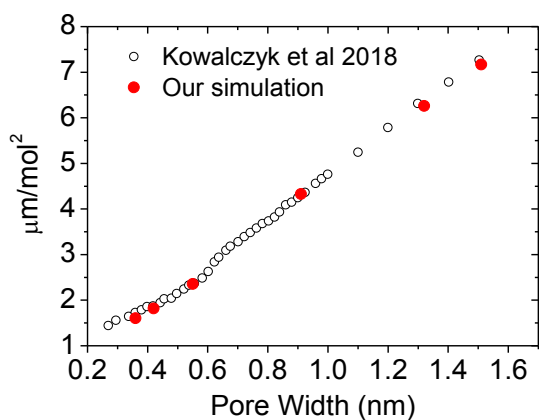


Figure 2. Adsorptive Capacity per Pore Size.

3.2 Phenol adsorption isotherms

Phenol adsorption curves are shown in Figure 3. The two pore sizes have unique adsorption regimes. In the pore of 18.5 Å, we can see the formation of disordered multilayers being the filling of the pore slower. The pore filling of 8.9 Å, because it has a stronger energy potential due to the proximity of the surfaces of the AC plates, occurs quickly at low pressures. This analysis allows us to evaluate that a carbon with a more microporous distribution will have a better trend of Phenol separation.

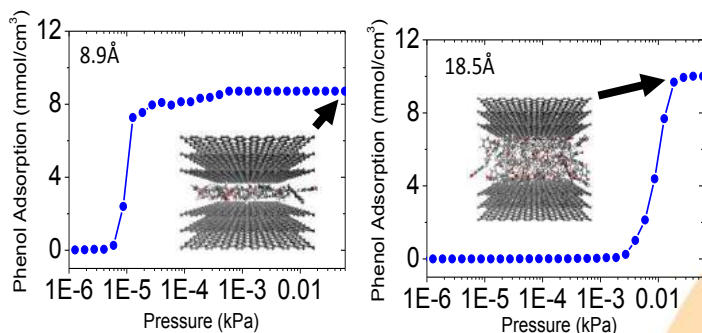


Figure 3. Phenol adsorption isotherms in the pores of 8.9 and 18.5 Å.

The simulation of phenol adsorptive capacity in saturation resulted in a value compatible with the amount obtained experimentally by Kowalczyk et al.[5]. The experimental sample of NCB-8h, in aqueous solution of phenol at atmospheric pressure and at 298 K, obtained 322 mg/g as the maximum capacity of adsorption. In the simulation using the PSD of the commercial activated carbon Norit, the maximum amount adsorbed reached the value of 336 mg/g in saturation (Figure 4). The textural

characteristics of the ACs are very similar: AC-NCB-8h, $V_{NCB-8h} = 0.41 \text{ cm}^3/\text{g}$ and AC-Norit, $V_{Norit} = 0.53 \text{ cm}^3/\text{g}$. The experimental isotherm of the NCB-8h sample is not available, because of that limitation we used a Similar AC (Norit) to evaluate the methodology.

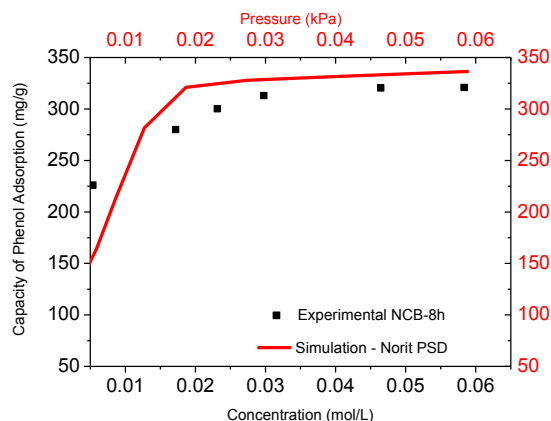


Figure 4. Adsorptive Phenol Capacity for NCB-8h Activated Carbons (symbols) and Norit (line).

Considering pure phenol at 301 K and saturation pressure (59 Pa), it is observed that hydrophobic interactions between activated carbon and phenol come to strongly overcome interactions between phenol and water, thus neglecting the representation of water in the simulation does not significantly affect the result.

The different temperature and pressure conditions, activated carbon model and force field, are some adversities of the empirical and simulation that can make it difficult to obtain an accurate value for adsorptive capacity. Nevertheless, the values were approximate and quite compatible.

3.3 Representative PSD

PSDs are extremely important when choosing the most suitable application for AC, since only volumes and areas are not able to predict adsorption behavior in different pressure, temperature and concentration conditions. Applying the PSD obtained from an analysis of N_2 at 77 K, we can detail the structure of the AC using a slit pore model. Based on this complete PSD, we determine the pore sizes most representative of AC. We characterized the AC using the representative PSD with only 4 pore sizes (Figure 5), reproducing with good agreement the textural properties (Table 2).

Table 2. Total area, total volume and microporous volume obtained from molecular simulation.

Sample	Area (m ² /g)	V _{total} (cm ³ /g)	Area (m ² /g)	V _{total} (cm ³ /g)
	Full PSD	Full PSD	Rep. PSD	Rep. PSD
PC12	553	0.2901	579	0.2890
PC35	1076	0.6316	1066	0.6160
PC58	1366	0.9657	1309	0.9190
PC76	1636	1.4030	1524	1.3030
Norit	755	0.5237	761	0.5330
WV1050	1087	1.1086	1079	1.0810
Maxsorb	1937	1.6660	1915	1.6900

The PSDs shown correspond to a series of ACs [14], in which the effect of different degrees of burn off was analyzed, producing more microporous samples. Thus, it is interesting to evaluate the adsorptive capacity of phenol for these samples with different grades of microporosity. In addition to the PC-AC series, we also evaluated three commercial ACs for comparison purposes.

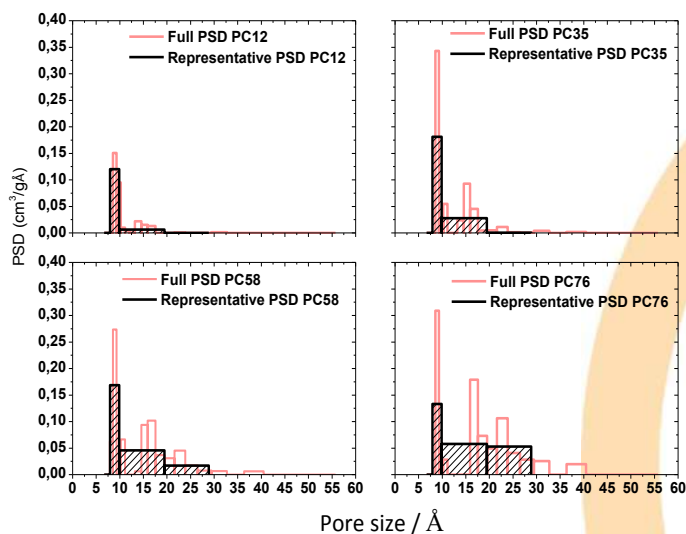


Figure 5. Full and representatives PSDs of ACs series.

3.4 Phenol removal

In Figure 6, we can see the phenol isotherms for the different ACs. In the PC series, the PC76 sample exhibits a higher phenol adsorption capacity, since it has higher total volume in the series, however, this sample has a lower microporous volume, which promotes a lower phenol adsorption at lower pressures. The AC with minor microporosity may not be able to separate phenol at low pressures or concentrations.

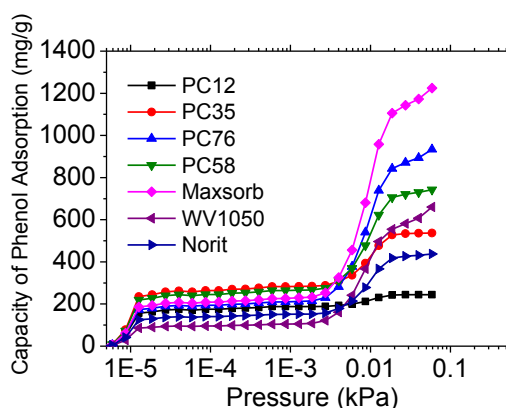


Figure 6. Forecast of phenol isotherms in ACs commercial and in a synthesized series.

The relationship of the adsorption capacity of each AC with their respective volumes is shown in Table 3. The AC Maxsorb had a major highlight among the ACs commercials, that has a higher total volume among all, but in the micropore region, the highlight is the PC35 and PC58 samples, which have a more developed micropore network.

Table 3. Adsorbed capacity data followed by total and microporous volume obtained from molecular simulation.

Sample	Adsorptive Capacity (mg/g)	V _{micropore} (cm ³ /g)	V _{total} (cm ³ /g)
PC12	244	0.2287	0.2890
PC35	536	0.3442	0.6160
PC58	743	0.3202	0.919
PC76	934	0.2533	1.3030
Norit	438	0.1830	0.5330
WV1050	661	0.1253	1.0810
Maxsorb	1224	0.2725	1.6900

4. Conclusions

The simulation can predict adsorptive capacity in the saturation region and can be useful for estimating phenol behavior in adsorption at low concentrations. In addition to the advantage of diminution of costs with experiments.

The characterization of a carbon through representative pores proved to be very efficient and of great value, because it reduces computational cost, since it is unnecessary to obtain isotherms for all pore sizes and does not compromise the result.

We observed that, at low pressures, smaller pores fill faster than the larger ones. Thus, microporous carbon samples are more effective at low pressures.

Finally, the comparison between different carbon samples highlights the Maxsorb with the highest adsorptive capacity in saturation and with volume of micropores comparable to those of PC35 and PC58, which have the highest microporous volumes of the analyzed samples.

Acknowledgements

This research has been supported by CNPq and FINEP/CTPETRO.

References

- [1] "Toxicological profile for phenol. U.S. Department of Health and Human Services. Agency for Toxic Substances and Disease Registry," *ASTDR*, 2008.
- [2] "International Standards for Drinking Water," *WHO*, pp. 40–42, 1963.
- [3] H. F. Stich, "The beneficial and hazardous effects of simple phenolic compounds," *Mutat. Res. Toxicol.*, vol. 259, no. 3–4, pp. 307–324, 1991.
- [4] M. A. K. and F. M. Mukherjee S., Kumar S., "Removal of phenols from water environment by activated carbon, bagasse ash and wood charcoal," *Chem. Eng. J.*, vol. 129, pp. 133–142, 2007.
- [5] P. Kowalczyk *et al.*, "Super-sieving effect in phenol adsorption from aqueous solutions on nanoporous carbon beads," *Carbon N. Y.*, vol. 135, pp. 12–20, 2018.
- [6] D. Zhang, P. Huo, and W. Liu, "Behavior of phenol adsorption on thermal modified activated carbon," *Chinese J. Chem. Eng.*, vol. 24, no. 4, pp. 446–452, 2016.
- [7] J. C. A. de Oliveira *et al.*, "On the influence of heterogeneity of graphene sheets in the determination of the pore size distribution of activated carbons," *Adsorption*, Feb. 2011.
- [8] M. P. ALLEN and D. J. TILDESLEY, *Computer Simulation of Liquids*. New York: Clarendon Press Oxford, 1987.
- [9] D. Frenkel, B. Smit, and Smith B., *Understanding Molecular Simulation From Algorithms to Applications*. 1996.
- [10] D. Nicholson and N. G. Parsonage, *Computer simulation and the statistical mechanics of adsorption*. London: Academic Press, 1982.
- [11] P. Ravikovitch, A. Vishnyakov, and A. Neimark, "Density functional theories and molecular simulations of adsorption and phase transitions in nanopores," *Phys. Rev. E*, vol. 64, no. 1, pp. 1–20, Jun. 2001.
- [12] S. M. P. Lucena, V. a. Gomes, D. V. Gonçalves, P. G. M. Mileo, and P. F. G. Silvino, "Molecular simulation of the accumulation of alkanes from natural gas in carbonaceous materials," *Carbon N. Y.*, vol. 61, pp. 624–632, Sep. 2013.
- [13] S. M. P. Lucena *et al.*, "Molecular simulation of collection of methane isotherms in carbon material using all-atom and united atom models," *Colloids Surfaces A Physicochem. Eng. Asp.*, vol. 357, no. 1–3, pp. 53–60, Mar. 2010.
- [14] J. B. Parra, C. O. Ania, A. Arenillas, and J. J. Pis, *Textural characterisation of activated carbons obtained from poly(ethylene terephthalate) by carbon dioxide activation*, vol. 144. Elsevier Masson SAS, 2002.

Performance of CO₂ AA and UA models in γ -alumina adsorption isotherms

Andréa S. Pereira^a, Rafael V. Gonçalves^a, Lucas Philipovsky^a, Daniel V. Gonçalves^a,
Sebastião M. P. Lucena^{a*}

^a Departamento de Engenharia Química, Universidade Federal do Ceará, Campus do Pici, Bl. 709, 60455-760, Fortaleza, Brazil

Abstract

γ -alumina is most studied metastable phase of the alumina. It is recognized as a very important material to many industrial processes, acting as adsorbent, catalyst or support due to its high surface area, thermal stability and crystallinity. Its characterization is a challenge for studying the chemistry of surfaces. In this context, molecular simulation is becoming the standard technique to characterize by adsorption instead of the phenomenological approach. To apply the molecular simulation, it is necessary to evaluate the impact of the atomic models used to describe the kernel of adsorption isotherms for different pore sizes. This work aims to evaluate the performance of the atom-atom (AA) and united atom model (UA) for the CO₂ molecule (probe gas) in adsorption isotherms of γ -alumina, making possible the structure characterization. A collection of isotherms was calculated applying Monte Carlo method in the grand canonical ensemble for both models. Lennard-Jones parameters to the interaction solid-fluid of the UA model were previously calibrated over the γ -alumina surface. To build the isotherms, different slit-pore sizes were used, which allowed the performance analysis between the kernel of simulated isotherms of the AA and UA models.

Keywords: γ -alumina, CO₂ adsorption, Monte Carlo simulations;

1. Introduction

Aluminum oxide (Al₂O₃), also known as alumina, is obtained from the bauxite and has a large variety of transition structures. Among the metastable phase of the alumina, one can highlight the phase γ due to its high surface area and thermal stability, very important features for the heterogeneous catalysis [1].

The γ -alumina has many application such as automotive and industrial catalyst support, adsorbent for the separation processes and for membrane fabrications, what makes it a very attractive material [2].

However, there are few reports about the γ -alumina structure, which would make possible a better understanding of the system where it is applied.

In the characterization by adsorption, different probe gases may be used, leading to slightly different results. The use of CO₂ has the access of smaller pores as advantage, that in other situations would not be identified by N₂ isotherms at 77 K [3].

Since poor literature production with regards to molecular simulation of a CO₂/ γ -alumina adsorption system, this paper focuses on applying Grand

Canonical Monte Carlo (GCMC) approach to simulate the adsorption isotherms as a function of the pore size and to collect enough data to come up with a kernel to be used in γ -alumina characterization.

Under this motivation, two molecular building models were considered: Atom-Atom (AA) and United Atom (UA). AA model considers all possible atoms in the designed molecule, thus making it a more realistic option, since every single intermolecular interaction will be calculated. UA model simplifies the final structure by agglutinating some atoms in a reduced number of centers. When applied to the CO₂, AA model considers all three atoms in the molecule, hence a three-center model. UA model, on the other hand, simplifies the structure to a single site, therefore a one-center model.

A comparison was made between AA and UA models (which had its fluid-solid Lennard-Jones parameters calculated) so that the UA model was capable of represent the model AA behavior for the CO₂ adsorption isotherms in γ -alumina. The motivation for this analysis was that, when compared to AA model, UA can prove rather attractive, since its greater simplicity implies less

molecular interactions and, therefore, faster simulation times [4].

2. Models and methods

2.1 Alumina model

We used a slit-pore model to represent the structure of γ -alumina ($H = 7.0, 7.6, 8.2, 8.9, 18.5, 27.9$ e 70.0 Å). Each wall of the pore is composed by a γ -alumina surface measuring 33.5 Å x 33.5 Å. This surface was obtained through cleavage on the plane (1 0 0) of the unit cell reported by Verwey [5] (Figure 1). Lennard-Jones parameters for the oxygen atoms composing the pores are shown in Table 1 [6]. It is important to point out that these parameters comprehend the aluminum atoms presence in the structure.

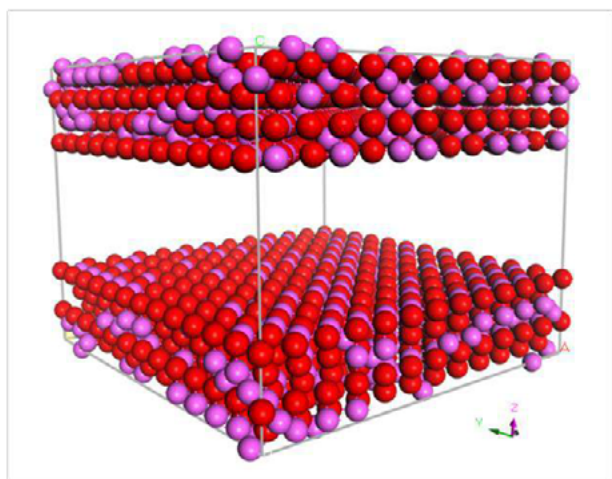


Fig. 1. Slit-pore of γ -alumina (● oxygen and ● aluminum). Pore size of 18.5 Å.

Table 1. Potential parameters for the O^{2-} (Al_2O_3).

atom	O^{2-} (Al_2O_3)	
	$\sigma_{s-s}, \text{Å}$	$\epsilon_{s-s} / k_B, \text{K}$
C(CO_2)	2.95	76.99
O(CO_2)	3.03	108.46

2.2 Carbon dioxide models

Two models were used for the CO_2 molecule, the united atom (UA) proposed by Vishnyakov *et al.* [7] and the atom-atom from TraPPE forcefield [8].

Lennard-Jones parameters and charges are present for both CO_2 models in Table 2.

Table 2. LJ parameters and charges for CO_2 molecule (UA and AA model).

Atom/Pseudoatom	$\sigma, \text{Å}$	$\epsilon/k_B, \text{K}$	q, e^-
C_AA	2.80	27.0	0.70
O_AA	3.050	79.0	-0.35
CO_2 _UA	3.648	246.15	-

2.3 Computational details

CO_2 adsorption isotherms were simulated using Monte Carlo method applied to the grand canonical ensemble. A truncated LJ potential without tail correction and a cutoff of 16 Å were used. Lorentz-Berthelot mixing rules were employed to obtain solid-fluid forcefield parameters. For each pressure, 2×10^6 steps were used for equilibration and 2×10^6 production steps for the calculation of the desired properties. All simulations included random insertion, deletion, rotation and translation moves of guest molecules with equal probabilities.

3. Results and discussion

3.1 Surface

Initially, the adsorption isotherm of CO_2 at 195.5 K using the AA model was simulated in a γ -alumina surface (Figure 2). The surface was built using a 70 Å spacing in a way that interactions between the superior and inferior layers would not simultaneously intervene over adsorbate molecules.

Following this procedure, the UA model simulations were focused. Its performance was evaluated at 195.5 K and low pressure, as an attempt to capture solid-fluid interactions present on the system and minimizing the interference of the fluid-fluid interactions.

The interaction between the γ -alumina and the UA CO_2 was proposed in order to represent the behavior presented by the AA model (Table 3). This way, the geometric parameter was attained through the arithmetic mean between site-site values and the proposed energetic parameter through investigation and comparison between the models.

Table 3. LJ parameters for the O^{2-} (Al_2O_3) when interacting with UA CO_2 .

Pseudo atom	O^{2-} (Al_2O_3)	
	$\sigma, \text{Å}$	$\epsilon/k_B, K$
CO_2_UA	2.99	97.63

Through Figure 2, one can realize that the proposed UA model could reproduce very well the AA model isotherm behavior over the evaluated pressure zone. In other words, UA returned satisfactory results, with advantages of being a simpler model, which requires less computational effort and hence smaller simulation times.

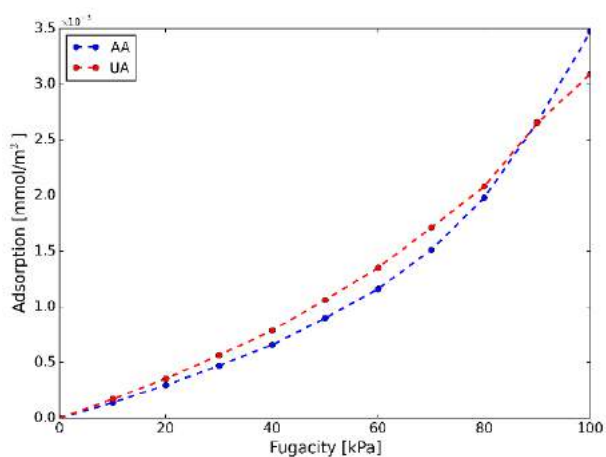


Fig. 2. Adsorption isotherms of CO_2 at 195.5 K in γ -alumina surface: comparison between UA and AA model.

3.2 Slit-pores kernel

A collection of adsorption isotherms was built using six pore sizes. These isotherms were calculated at 298 K and pressures up to 6440 kPa, vapor pressure of CO_2 at room temperature. This way, one could evaluate both AA and UA models performances over a confined space (different pore sizes).

Figure 3 presents the adsorption isotherms of CO_2 at 298 K in slit-pores of γ -alumina both AA and UA models, which allowed a comparative analysis between them. Furthermore, this study generates a slit-pores kernel which allows for the material characterization from pore size distribution (PSD).

Even though we had performed an adsorption isotherms systematic study with regards to their behavior over every pore size, only the most representative and relevant results will be discussed next.

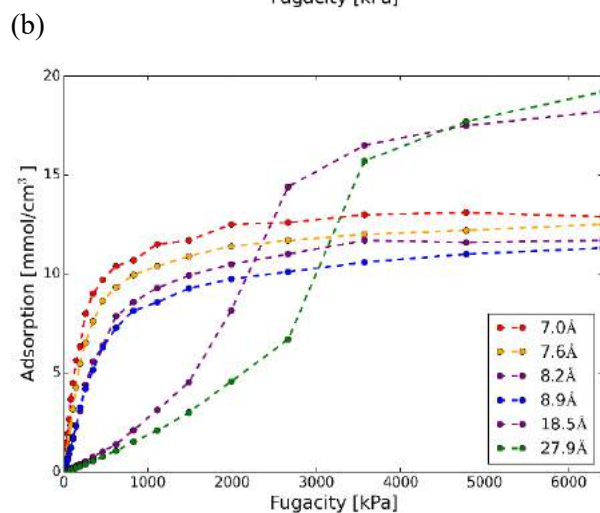
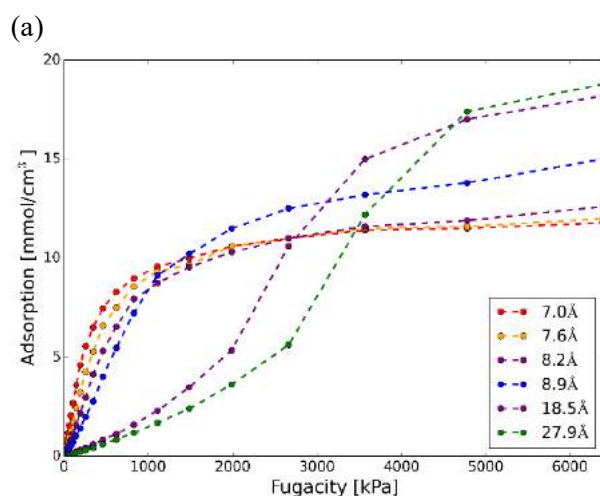


Fig. 3. Kernel of CO_2 isotherms in slit-pores of γ -alumina at 298K: (a) AA model e (b) UA model.

This is the case of the simulated isotherms in slit-pores smaller than 8.9 Å, which exhibit a single layer of CO_2 molecules. In this group, the pore filling happens at a very low pressure. After this point, an increment in the pressure does not change the adsorbed amount due to the strong molecule confinement inside the pores.

The main difference between the obtained results using both CO_2 models in this group (a single adsorbed layer) is the maximum adsorbed quantity. In the UA isotherms, there is a gradual decrease on the adsorption per volume as the pore size increases, which is not perceived in the AA isotherms.

As a comparative example between the CO_2 models from this group, Figure 4 shows the adsorption isotherms in the 7.6 Å slit-pore for both models. One can notice that the adsorbed amount of the UA model is higher than the presented by the AA model, due to its smaller size, allowing a better

packing of the spherical particles inside the pore. This behavior can also be seen in the 7.0, 7.6 and 8.2 Å slit-pore sizes.

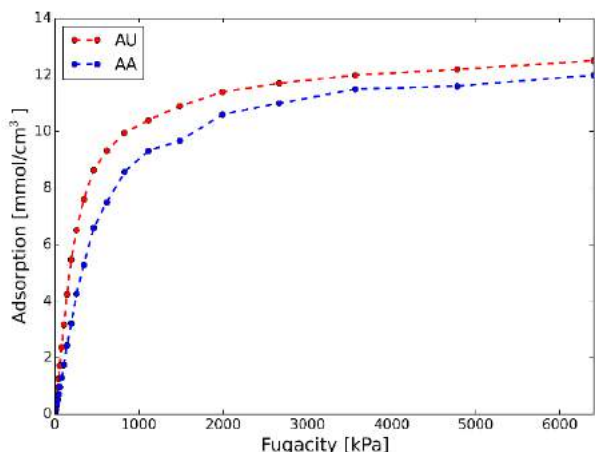


Fig. 4. Adsorption isotherms of CO₂ at 298 K in 7.6 Å slit-pore of γ -alumina: comparison between UA and AA model.

The 8.9 Å pore deserves a spotlight for showing a different behavior from the others, reinforced by a density map analysis (Figure 5). This way, it is possible to observe the possible CO₂ molecule positions inside the pore, showing a two-layer formation for AA and a transition from single to double CO₂ adsorbed layers for UA.

Through Figure 6, one notices a significant increment with regards to adsorption for AA, which can be explained for its better CO₂ packing, promoting the second layer filling before UA, like it is shown in Figure 5(a). For UA, however, one verifies a single adsorbed layer presence, with a smaller amount of adsorbed CO₂ per pore volume.

The second group includes isotherms in slit-pores bigger than 8.9 Å. The capacity to accommodate two CO₂ layers is the main characteristic of this group.

Generally speaking, the adsorbed amount per pore volume decreases as the pore size increases, however this behavior is reversed when two molecules layers are adsorbed. A sudden increase in the adsorbed amount takes place at the high pressure region. This behavior is illustrated by the adsorption isotherms in the slit-pores of 18.5 and 27.9 Å.

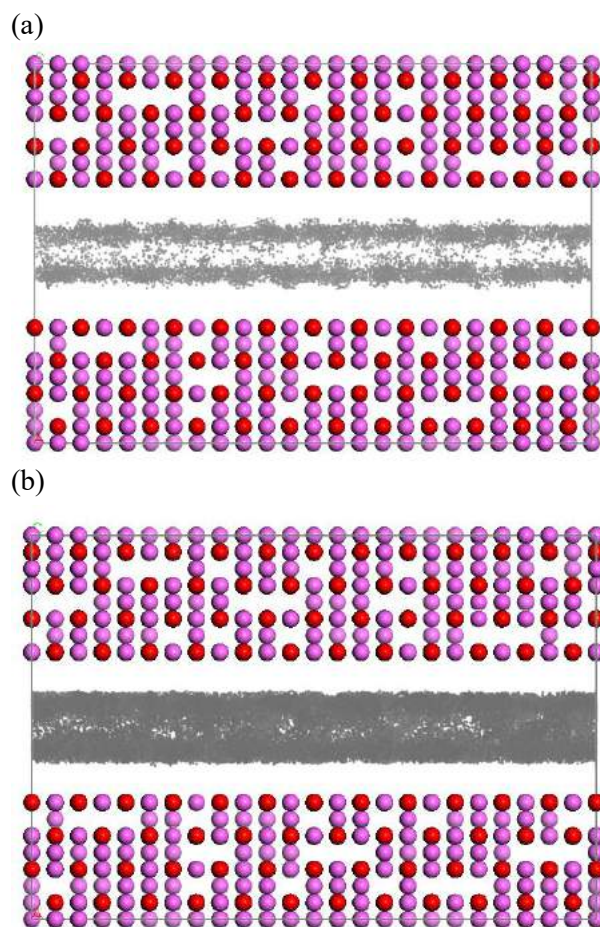


Fig. 5. Density map of adsorbed CO₂ in a 8.9 Å slit-pore of γ -alumina at 298 K and 6440 kPa (a) AA model and (b) UA model.

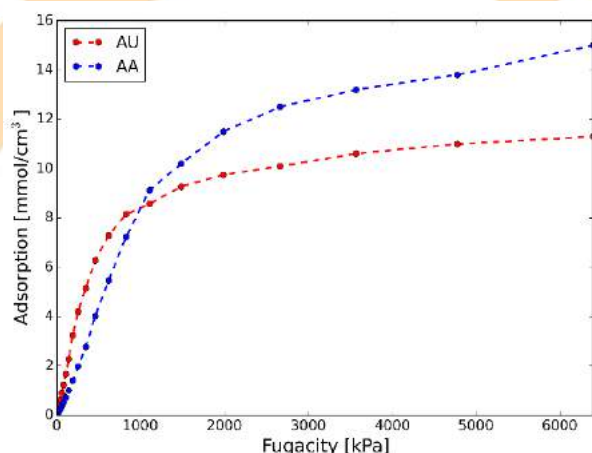


Fig. 6. Adsorption isotherms of CO₂ at 298 K in 8.9 Å slit-pore of γ -alumina: comparison between UA and AA model.

Figure 7 shows the comparative result between AA and UA model for an 18.5 Å pore. In this second group (two adsorbed molecule layers), UA also presents a larger adsorbed amount due to the better packing of the spherical particles inside the pore, following the desired behavior.

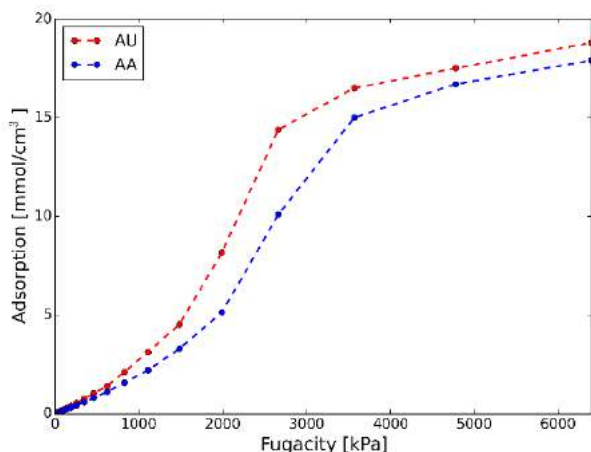


Fig. 7. Adsorption isotherms of CO₂ at 298 K in 18.5 Å slit-pore of γ -alumina: comparison between UA and AA model.

In a similar way that was observed in the pores with a single adsorbed layer, UA presents a stronger fluid-solid interaction, leading to a bigger adsorbed amount of CO₂ inside the pore.

This way, one realizes through AA and UA performances, that both are suitable for capturing the interactions between CO₂ and γ -alumina structure for a pore size distribution, once the simulated isotherms are quite similar.

4 Conclusion

The performances of CO₂ models were evaluated through Monte Carlo method in a grand canonical ensemble. This analysis was based on the calculation of a collection of adsorption isotherms of CO₂ in different slit-pores of γ -alumina.

A simulation in a γ -alumina surface using a AA model allowed a definition of the interaction between the structure and the UA model of CO₂ through investigation and comparison between the models.

This way, it was possible to evaluate the performances of AA and UA model with regards to different pore sizes and to establish typical behaviors according to the number of filled layers.

The models presented quantitatively similar results, being both suitable for capturing the interactions between CO₂ and γ -alumina structure. However, there is a choice for the UA model, for its simplicity, which results in a smaller computational effort and shorter simulation times.

A more broad isotherm collection in different pores can be used for γ -alumina characterization.

Acknowledgements

The authors would like to thank the PETROBRÁS, CAPES E CNPq for the financial support.

References

- [1] L. D. Hart, "Alumina chemicals," *Sci. Technol. tec. hand. Westerv.*, vol. OH, p. 617, 1990.
- [2] F. J. Blas and K. E. Gubbins, "Molecular model of gamma-alumina. Nitrogen adsorption and pore size distribution," *AIChE Symp. Ser.*, vol. 97, no. 325, pp. 317–320, 2001.
- [3] D. Maia *et al.*, "CO₂ gas-adsorption calorimetry applied to the study of chemically activated carbons," *Chem. Eng. Res. Des.*, vol. 136, pp. 753–760, 2018.
- [4] C. Chen *et al.*, "A comparison of united atom, explicit atom, and coarse-grained simulation models for poly(ethylene oxide)," *J. Chem. Phys.*, vol. 124, no. 23, 2006.
- [5] E. J. W. Verwey, "The Structure of the electrolytical oxide Layer on Aluminium," *Zeitschrift für Krist. - Cryst. Mater.*, vol. 91, no. 1–6, pp. 317–320, 2014.
- [6] L. E. Cascarini de Torre, E. S. Flores, J. L. Llanos, and E. J. Bottani, "Gas-Solid Potentials for N₂, O₂, and CO₂ Adsorbed on Graphite, Amorphous Carbons, Al₂O₃, and TiO₂," *Langmuir*, vol. 11, no. 12, pp. 4742–4747, 1995.
- [7] A. Vishnyakov, P. I. Ravikovitch, and A. V. Neimark, "Molecular Level Models for CO₂ Sorption in Nanopores," vol. 0625, no. 18, pp. 8736–8742, 1999.
- [8] J. J. Potoff and J. I. Siepmann, "Vapor-liquid equilibria of mixtures containing alkanes, carbon dioxide, and nitrogen," *AIChE J.*, vol. 47, pp. 1676–1682, 2001.

PSA scheduling and modeling for CH₄/CO₂ separation

Rafael M. Siqueira^{a,b}, Klaus F. R. Soares^a, A. Eurico B. Torres^a, Alexandre F. P. Ferreira^b,
Alírio E. Rodrigues^b, Diana C. S. Azevedo^a, Moises Bastos-Neto^{a,*}

^a Grupo de Pesquisa em Separações por Adsorção – GPSA, Departamento de Engenharia Química, Campus do Pici, Universidade Federal do Ceará, Fortaleza - CE, 60455-760, Brasil.

^b Laboratory of Separation and Reaction Engineering, Associate Laboratory LSRE-LCM, Faculdade de Engenharia, Universidade do Porto, Rua Dr. Roberto Frias, 4200-465, Porto-Portugal.

Abstract

Pressure Swing Adsorption is an attractive technology for gas separation, and it consists of a cyclic operation process involving two or more columns packed with adsorbents. To work appropriately and continuously, the columns should operate in a synchronized way, by varying the cycle steps. Literature about PSA is mostly dedicated to the development of materials and comparisons between the most suitable adsorbents for a given operation. However, the assessment of the most appropriate configuration, such as the number of columns, the number and type of steps, and schedule is also relevant for the process. This work presents a simple PSA setup method using a schematic approach to compare the most appropriate synchronized configuration for CO₂/CH₄ separation. The elementary steps used in this study were pressurization, adsorption (feed), desorption, purge, and pressure equalization (PE). Those steps were evaluated according to the process performance in a multi-bed PSA process operation with different sequences. Simulations provided information regarding the influence of the configuration on product recovery. The presented method has shown that a 2-bed (1 PE) PSA unit with those steps was not able to synchronize properly (*i.e.* discontinuous production). 4-bed (2 PE) PSA process can be synchronized with and without idle. Simulation results have shown, in this particular sequence and configuration that processes with no idle presented higher product recovery.

Keywords: PSA scheduling; Activated carbon; CO₂ adsorption; Simulation.

1. Introduction

The research and development of renewable energy have attracted attention to the use of natural gas and biogas as an energy source. Raw natural gas and biogas mainly consist of methane and carbon dioxide. They can be used directly to generate energy; however, the low fuel value due to the high CO₂ content in them limits the economic feasibility of their use [1]. Adsorption processes are frequently applied for gas separation, but the removal CO₂ from natural gas or biogas is still in the development phase [2].

Pressure Swing Adsorption (PSA) has been reported in the last decades as an alternative technology for natural gas and biogas upgrading. PSA can present economic feasibility for methane production with high productivity and recovery.

PSA most basic cycle is perhaps not sufficient satisfactorily to perform natural gas or biogas upgrading due to the complexity of the requirement of the unit. Therefore, inventive designs of PSA process can be numerous depending on the objective; they may involve as example, bed coupling, counter-current or co-current flow rates and light product or feed pressurization [3].

The design of cyclic adsorption processes is a very complex task. In case of PSA unit, to achieve the desired performance, it usually may consist of several steps, columns, different cycle time, choice of the adsorbents, bed length and composition of the gas mixture at the feed of the column. PSA designs are affected by many variables. Improper determination of any cycle schedule can lead to increase in separation costs due to the decreasing of product recovery, product purity, or productivity [4]. Regarding CH₄ production, a continuous

process is perhaps the most important aspect of a PSA cycle schedule. In some processes, depending on the number of columns and steps, it is impossible to obtain a feasible schedule, and an idle step must be added to synchronize the sequence. However, the addition of an idle step in a PSA cycle sequence may affect the process performance, mainly when its performance is based on kinetic separation [5].

In this work, the synchronizing of cycle schedule was chosen a priori, and the remaining design was evaluated by simulation. The protocol aims to determine an applicable cycle schedule for a CH₄/CO₂ separation process using activated carbon, introducing a procedure to start a design for a PSA process when the number of columns and sequence of the chosen steps are known. Simulated results are presented with respect to each configuration used in the cycle schedule.

2. Scheduling methodology

Skarstrom cycle is the most basic PSA process and was the first to be introduced for cyclic operation, in air separation [6]. The schedule described in this procedure consists of four steps as followed: Adsorption (Feed), Blowdown, Purge, and Pressurization. This basic PSA process operates with two synchronized columns.

In order to set up those steps in a PSA cycle, it was used the schematic graphic block approach, as presented in Figure 1.

	Sub-cycle 1		Sub-cycle 2	
	t_{ads}	t_{bld}	t_{ads}	t_{bld}
Bed 1	ADS	BLD	PU	PR
Bed 2	PU	PR	ADS	BLD
	<i>Act 1</i>	<i>Act 2</i>	<i>Act 3</i>	<i>Act 4</i>

Figure 1. PSA schedule of a basic Skarstrom cycle

Where ADS denotes adsorption, BLD blowdown, PU purge, and PR pressurization. A sub-cycle is defined as the operation where occurs all the steps of the entire cycle, in different columns synchronized with each other. PSA processes, in which the columns involved are synchronized, the number of sub-cycle must be the same as the number of columns. An act is defined

as the actions taken by the steps during all cycle. Taking Skarstrom cycle as an example, it can be noted that the number of acts is equal to the number of steps. One of the restrictions of the presented method is that the number of acts must be at least the same as the number of steps; they can be higher but never lower than the number of steps. The number of acts in each sub-cycle can be various and they are not limited by the number of steps. However, the number of acts in each sub-cycle must also be the same. In Figure 1, each sub-cycle has two acts; therefore a total of four acts in the cycle. These definitions aim to simplify the schedule synchronization when a large number of columns and steps are used.

In most cases, it is interesting that the PSA process allows the continuous production of the target product. The example shown in Figure 1 does not ensure continuous production, due to its second act. The Skarstrom cycle synchronization, by the present methodology, is illustrated in Figure 2. First, it is necessary to evaluate the possibility of increasing the number of acts in each sub-cycle. Since the sub-cycles have all the steps of the process, it is easier to assess only one sub-cycle for a synchronizing procedure (Sub-cycle 1 box in Figure 2).

	Sub-cycle 1		Sub-cycle 2	
	$t_{sub-cycle}$		$t_{sub-cycle}$	
Bed 1	*	*	*	*
Bed 2	*	*	*	*
	<i>Act 1</i>	<i>Act 2</i>	<i>Act 3</i>	<i>Act 4</i>

Figure 2. Scheme of a 2-bed 4-steps PSA scheduling using steps and acts concept.

For a continuous production process, the adsorption step must fill all the sub-cycle operation. When four acts in two beds are used to synchronize those steps, it does not make it possible to synchronize a continuous production for this particular sequence, due to the few acts used in this scheduling. Indeed, more acts should be added in a way that the number of acts must be higher than the number of steps. If one more act is added in sub-cycle 1, another act must be also added in sub-cycle 2. Therefore, this singular sequence, to achieve continuous operation, must have at least six acts, three in each sub-cycle. The duration of

each sub-cycle must be the same. However, it is worth mentioning that the time of each act must not necessarily be equal. The duration of an act is independent of each other and only the sub-cycles duration must be the same.

A synchronized PSA process with continuous production is presented in Figure 3. Both sub-cycles present the same duration. Purge, blowdown, and pressurization time in this sequence, are not necessarily the same. However, the sum of their duration must be equal to the other sub-cycle duration, in this case, must be equal to the adsorption step time.

	Sub-cycle 1			Sub-cycle 2		
	$t_{ads} = t_{PU} + t_{BLD} + t_{PR}$			t_{pu}	t_{bld}	t_{pr}
Bed 1	ADS			PU	BLD	PR
Bed 2		PU	BLD	PR	ADS	
	Act 1	Act 2	Act 3	Act 4	Act 5	Act 6

Figure 3. Scheme of a 2-bed 4-steps synchronized PSA process using six acts for continuous production.

The sequence presented in Figure 3 showed that it is not possible to synchronize a PSA with continuous light product production process with an equalization step using only two columns. According to the methodology, for a continuous production, adsorption step must complete all sub-cycle duration time which makes the equalization unfeasible to be added in such schedule. Although this sequence is not achievable using only two columns, a solution can be developed to solve this problem. Ebneret. al. [7] have studied the numerous possibilities of equalization steps with the aid of tanks in different strains using a minimal number of columns. However, it is not the scope of this work, and we will not evaluate this hypothesis.

Following the presented method, one more column should be added to the PSA unit so that it can perform a continuous production with equalization step. The addition of a new column means one more sub-cycle in the complete sequence of the PSA cycle. Figure 4 shows the method to synchronize the chosen sequence of a PSA with the continuous production, even with an equalization step, with the simple inclusion of one more act per sub-cycle.

	Sub-cycle 1			Sub-cycle 2			Sub-cycle 3		
	1	2	3	4	5	6	7	8	9
Bed 1	1	2	3	•	•	•	•	•	•
Bed 2	4	5	6						
Bed 3	7	8	9						
	Act 1	Act 2	Act 3	Act 4	Act 5	Act 6	Act 7	Act 8	Act 9

$(1) = (7) = (4)$
$(2) = (8) = (5)$
$(3) = (9) = (6)$

Act	Steps
1	ADS
2	ADS
3	ADS
4	EQ ^d
5	BLD
6	PU
7	EQ ^p
8	PR
9	PR

Figure 4. Synchronizing PSA unit with 3 beds and 7 steps.

By doing that, each sub-cycle consists now of three acts. For a continuous production process, the adsorption step must fill all sub-cycle of one column. Therefore, the three first acts in bed 1 represent the feed. According to Figure 4, the restriction is satisfied since act 4 can synchronize with act 7. In Figure 5, it is presented the synchronized sequence.

	Sub-cycle 1			Sub-cycle 2			Sub-cycle 3		
	t_{eq}	t_{bld}	t_{pu}	t_{eq}	t_{bld}	t_{pu}	t_{eq}	t_{bld}	t_{pu}
Bed 1	ADS			EQ ^d	BLD	PU	EQ ^p	PR	PR
Bed 2	EQ ^p	PR	PR	ADS			EQ ^d	BLD	PU
Bed 3	EQ ^d	BLD	PU	EQ ^p	PR	PR			ADS
	Act 1	Act 2	Act 3	Act 4	Act 5	Act 6	Act 7	Act 8	Act 9

Figure 5. 3-bed 7-step PSA continuous process

It is worth pointing out that the time of steps 4 and 7 must be the same, which consequently makes the time of act 1 also be equal to them. It is noted that they are the first act of each sub-cycle. The same sequence was then evaluated in a PSA unit which consists of four beds. The addition of a new column can be considered to increase the productivity and recovery, by the introduction of one more equalization step. Following the methodology, for one more bed, another sub-cycle should be implemented. By doing that, the number of acts inevitably increases, changing in this case from nine to twelve acts, at least. According to Figure 6, to add one more act involving adsorption is not recommended since the sub-cycle is already filled with this step. Two more acts are needed to complete the cycle. It is noteworthy that the addition of one or more steps in the middle of the column in Figure 6 will result in a shift downwards of the following steps. Hence, the first objective intends to complete the number of acts and assess

if the restriction of the equalization steps is satisfied.

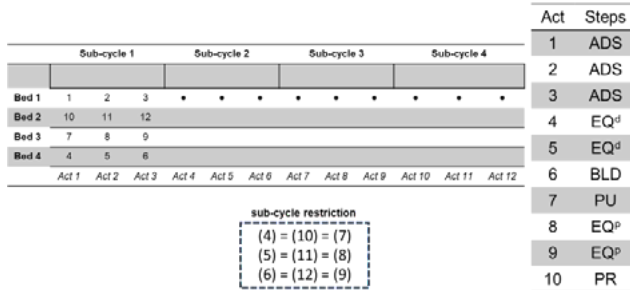


Figure 6. 4-bed 8-step PSA continuous process with sub-cycle restriction not satisfied.

Since there is a new column in the PSA unit, it is interesting to put another equalization step to increase the product recovery of the system. In this case, two equalization steps can be performed. It makes the synchronizing more complex due to the number of restriction of the acts. The restriction block in Figure 7 indicates how the acts should coincide between them. As shown in Figure 7, act 4 must be at the same time that acts 10 or 7. Interact act 4 with 7 is not feasible. Then, act 10 is the only act able to synchronize with act 4.

It is necessary to put another step in the middle of the sequence so that one of the equalization pressurization steps moves to act 10. To avoid breaking the sequence the only step available to put in the middle of the sequence is the idle step. The idle step can introduced from act 5 up to act 7. From that evaluation, the second restriction should be considered. By doing that, act 5 should contain the idle step. It is noted that the restrictions in the block are satisfied and the synchronizing is complete.

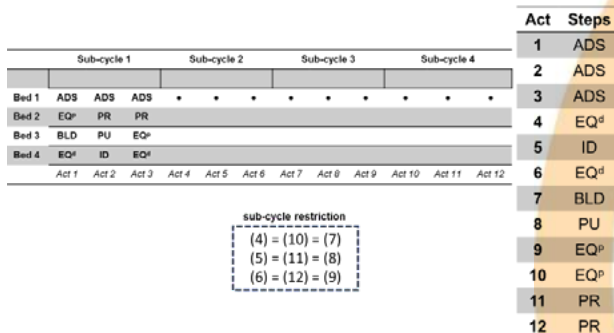


Figure 7. 4-bed 8-step PSA continuous process with sub-cycle restriction satisfied.

Another synchronizing possibility can be the addition of more acts in the sub-cycles. A sequence with no idle, even keeping the same sequence of PSA unit presented in Figure 7, is achievable. In Figure 8, it is presented the sequence of a PSA process with 4 beds and 8 steps with no idle. The sub-cycle restriction is not satisfied since the total act sequence is not complete.

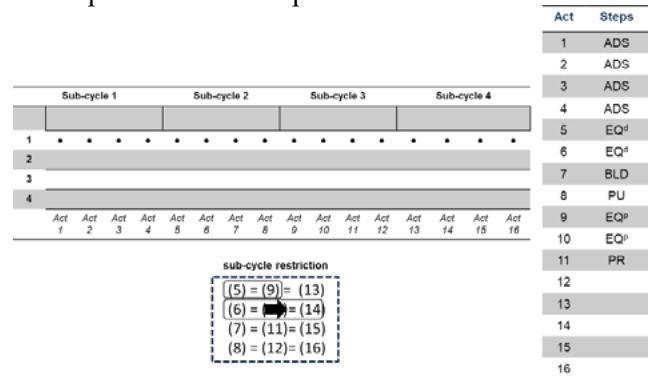


Figure 8. 4-bed and 8 steps PSA unit with the addition of more acts for synchronizing continuous process with no idle.

According to Figure 8, five more acts should introduced in the sequence to maintain the sub-cycle restriction satisfied. This PSA performance was analyzed, keeping the same steps, and sequence with no idle. By evaluating the sub-cycle restrictions, one can conclude that it is feasible to implement more acts as equalization steps. Two more acts with pressure equalization depressurization were put following the sequence. Consequently, two more acts with pressure equalization pressurization were added after the purge step. One more act was missing and pressurization act was chosen to be added at the end of the sequence (Figure 9).

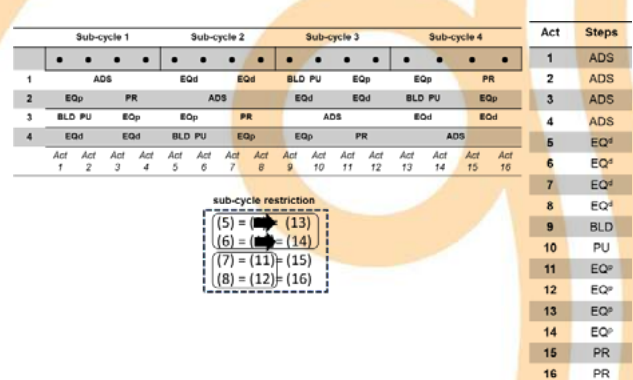


Figure 9. 4-bed and 8 steps PSA unit synchronized with the continuous production process and no idle.

It can be seen in Figure 9 that the sequence first proposed here is kept. According to it, the new eight pressure equalization acts can be linked and be considered only four acts. In fact, this sequence has only four pressure equalization; two for depressurization and two for pressurization. Sub-cycle restrictions were satisfied, in which, the first equalization depressurization step (acts 5 and 6) in the sequence occur in parallel to the equalization pressurization in acts 13 and 14. The second equalization depressurization step (acts 7 and 8) are simultaneous to acts 11 and 12.

In Figure 9, it is noteworthy that an entire sub-cycle was filled only by pressure equalization steps, which means that the time of each pressure equalization step is excessively long for such procedure although it is acceptable. Ribeiro et. al. [8] have shown PSA process for hydrogen separation from a gas mixture in which they have used a 4-bed unit, and a similar sequence to the one presented Figure 9, where they have reached hydrogen purity higher than 99.99% and recovery around 50%.

3. PSA recovery performance

Simulated results presented different values of product recovery when the two sequences with idle and no idle (Figure 8 and Figure 10) were compared to each other. To have a fair comparison between the sequences used, the same volumetric flow rate and time were considered for the adsorption step. In the sequence using idle, the time of pressure equalization steps can be more flexible to set since there is an idle step during the sub-cycle; in this case, the idle step duration does not have to obey to any restriction. Then, the time of pressurization in the sequence of Figure 7 is longer than the time of pressurization when the sequence has no idle (Figure 9). In Figure 9, to reach the target high pressure of the adsorption step in shorter time, to ensure schedule synchronization, the pressurization volumetric flow rate must be increased.

To evaluate the sequence used in the 4-bed 8-step PSA unit, product recovery were compared when idle was and was not used in the schedule. As main consequence the pressurization of the column will be faster if the molar flow rate is kept the same. Hence, the previous steps can have influence on time of pressurization.

In Figure 10, product recovery presents a significant discrepancy. As it was previously explained, the regeneration process in a PSA plays an important key in the separation process performance, and it is worth to be evaluated.

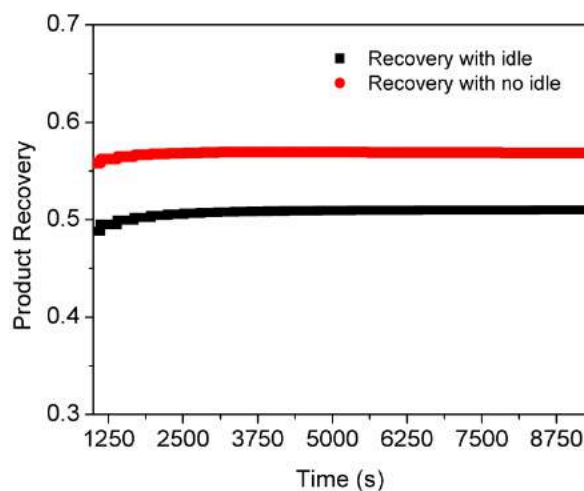


Figure 10. CH₄ Recovery simulation results as function of experiment running time, for a 4-bed 8-step PSA process, with idle and without idle step.

Product recovery is the ratio between the real CH₄ production, *i.e.*, minus the CH₄ fraction used for purge and pressurization steps, and the CH₄ fed in the column. The shorter purge step time in the sequence with idle, maintaining the same volumetric flow rate, requires less CH₄ amount to perform this step, which increases the value on the numerator of the equation. The gas amount of CH₄ required to reach the adsorption pressure in pressurization step is also lower due to the quick blowdown step, which will increase the value on the numerator of the equation. Although the CH₄ production with no idle sequence is lower, the feed of CH₄ amount required to the entire cycle process is much lower that explains the CH₄ recovery result be much higher.

4. Conclusion

A graphical procedure was developed to enable an easy PSA process synchronization, using as example the CO₂/CH₄ separation process, at high pressures. The definition and addition of acts on the scheduling can be useful for PSA steps synchronization; and it has been shown to be a



good start to design a synchronized multi-column process. Taking into account only one sub-cycle of the entire PSA cyclic operation, it enables the synchronization of the global process regardless the number of columns. Additionally, simulation based studies were undertaken to evaluate the influence of different PSA configurations on the product recovery. The possibilities to design a PSA process have shown to be numerous, which is difficult to define an optimum sequence and ideal steps for a general separation processes. This particular separation (CH_4/CO_2) process was easier to set up with the steps and sequence required and to evaluate their performance. Simulation results have shown that more columns in a PSA unit allow the inclusion of more equalization steps, which increases product recovery. In a 4-bed PSA unit, the influence of idle in the sequence was evaluated. The steps sequence presented in this work has shown that it is possible to synchronize the PSA process without idle. However, it is essential to assess the configuration of the process, since depending on the time of each act, the molar flow rate during an adsorption or pressurization step should be changed.

Acknowledgments

The authors acknowledge financial support from CNPq (*Conselho Nacional de Desenvolvimento Científico e Tecnológico*) and CAPES (*Coordenação de Aperfeiçoamento de Pessoal de Nível Superior*). This work is a result of: a) An international PhD internship supported and financed by CAPES (*Coordenação de Aperfeiçoamento de Pessoal de Nível Superior*) with the reference; Rafael Magalhães Siqueira / Programa de Doutorado Sanduíche no Exterior (PDSE) / [88881.188346/2018-01], and b) Project “AIProcMat@N2020 - Advanced Industrial Processes and Materials for a Sustainable Northern Region of Portugal 2020”, with the reference NORTE-01-0145-FEDER-000006, supported by Norte Portugal Regional Operational Programme (NORTE 2020), under the Portugal 2020 Partnership Agreement, through the European Regional Development Fund (ERDF); Associate Laboratory LSRE-LCM - UID/EQU/50020/2019 - funded by national funds through FCT/MCTES (PIDDAC).

References

- [1] Shen Y ,Shi W ,Zhang D ,Na P, and Fu B, The removal and capture of CO_2 from biogas by vacuum pressure swing process using silica gel. 2018.27: 259-271.
- [2] Tao L ,Xiao P ,Qader A, and Webley PA, CO_2 capture from high concentration CO_2 natural gas by pressure swing adsorption at the CO_2 CRC Otway site, Australia. 2019.83: 1-10.
- [3] Yang RT, Gas Separation by Adsorption Processes. 1997: Imperial College Press, Boston.
- [4] Smith OJ and Westerberg AW, The optimal design of Pressure Swing Adsorption systems. 1991.4612: 2967-2976.
- [5] Mohammadi N ,Hossain MI ,Ebner AD, and Ritter JA, New Pressure Swing Adsorption Cycle Schedules for Producing High-Purity Oxygen Using Carbon Molecular Sieve. 2016.5540: 10758-10770.
- [6] Skarstrom CW, *Method and apparatus for fractionating gaseous mixtures by adsorption*. 1960, Esso Research and Engineering Company: US.
- [7] Ebner AD ,Ho JGS, and Ritter JA, Graphical approach for formulating pressure swing adsorption cycle schedules with unlimited equalization steps. 2018.242: 221-232.
- [8] Ribeiro AM ,Grande CA ,Lopes FVS ,Loureiro JM, and Rodrigues AE, A parametric study of layered bed PSA for hydrogen purification. 2008.6321: 5258-5273.

Evaluation of single and binary adsorption equilibrium of cobalt ions and methylene blue in aqueous systems onto ultrasonic modified chitin

P.S. Pauletto*, G.L. Dotto, N.P.G. Salau

Universidade Federal de Santa Maria, 1000, Roraima Avenue, Santa Maria, 97105–900, Brazil

Abstract

Single and binary adsorption isotherms of cobalt ions (Co^{2+}) and methylene blue (MB) onto ultrasonic modified chitin were investigated at different temperatures. Experimental results revealed competitive adsorption since the adsorption capacity was reduced in binary system for each adsorbate. The nonlinear least squares technique was used to estimate the parameters of both Langmuir and Freundlich isotherms. For single systems, the adsorption equilibrium data was well interpreted by Langmuir isotherm, and the maximum adsorption capacity was found as 68.76 mg/g for Co^{2+} at 328 K and 21.79 mg/g for MB at 298 K. The extended Langmuir isotherm was able to predict the binary systems, and the estimated parameters indicated that the MB had no influence on the adsorption of Co^{2+} . On the other hand, Co^{2+} influenced the adsorption of MB mainly at low temperatures, where MB presented the highest adsorption capacity. The symmetrical confidence intervals of 95% had demonstrated that all estimated parameters were significant. Further, the isotherm models could well predict the adsorption equilibrium of both single and binary systems.

Keywords: Extended Langmuir; Binary system; chitin; parameter estimation; confidence interval.

1. Introduction

In the last decades, one of the main environmental problems is the contamination of water resources caused by the improper discharge of industrial effluents. It is estimated that more than 700 chemical contaminants are found in water [1], among them, heavy metals and dyes are considered the priority pollutants due to their toxicity, mutagenic and recalcitrant properties, with adverse effects on human health and the environment [2]. Several techniques have been applied to remove these contaminants; however, adsorption is the most used due to its economic viability, high efficiency, simplicity of operation and high adaptability [3].

The adsorption process involves the mass transfer of molecules from a fluid to the surface of a solid matrix. In particular, the adsorption equilibrium establishes a fundamental relationship between the amount of molecules retained on the surface of the solid with the remaining concentration in the fluid phase [4]. This relationship is usually represented by adsorption isotherms, which are nonlinear empirical models based on experimental data. In this sense, the estimation of isotherm parameters is the first step in the adsorption process evaluation. Since the adsorption isotherms are nonlinear equations, the

parameter estimation may be performed using nonlinear regression in order to preserve the statistical significance of experimental error distributions [5]. Nevertheless, many studies in the literature are made using linear regression [6–11].

In addition, the majority of adsorption researches are performed to study the adsorption equilibrium of a single heavy metal [6–8] or a single dye [9–11]. However, industrial effluents are known to have several contaminants in their composition. Particularly, the coexistence of heavy metals and dyes is very common in the effluents of the textile, paper, leather and cosmetics industries [12]. The modeling of multi-compound adsorption is a complex task, since the adsorption equilibrium is affected by the interactions and competitions among adsorbent and adsorbates [13]. Therefore, the study of a multi-compound adsorption becomes very relevant for industrial applications.

In the present work, the adsorption equilibrium of cobalt ions (Co^{2+}) and methylene blue (MB) onto ultrasonic modified chitin (UM-chitin) was evaluated in single and simultaneous binary systems. The nonlinear least squares method was used to estimate the adsorption equilibrium parameters of different isotherms. In addition,

confidence intervals were determined to assess the significance of the adsorption parameter values.

2. Experimental

2.1. Adsorbates

Cobalt ions (Co^{2+}) and Methylene Blue (MB) were used as adsorbates. Co^{2+} ($\text{CoSO}_4 \cdot 7\text{H}_2\text{O}$) and MB ($\text{C}_{16}\text{H}_{18}\text{ClN}_3\text{S}$) were purchased by Vetec (Brazil) and used without any further purification. For each adsorbate, stock solutions of 1.00 g/L were prepared using deionized water and stored in amber flasks. Working solutions were obtained by diluting the stock solutions until the required concentrations. All other reagents were analytical grade.

2.2. Adsorbent

Ultrasonic modified chitin (UM-chitin) was used as adsorbent. Chitin powder was obtained from shrimp residues and a surface modification using ultrasound was performed to improve its adsorption characteristics [14]. Briefly, UM-chitin presented particle size of 72 μm , porosity of 0.13, BET surface area of 51.3 m^2/g , average pore radius of 40 \AA , pore volume of $8.5 \times 10^{-6} \text{ m}^3/\text{kg}$, crystallinity index of 63 %, and point of zero charge of 5.5. More details regarding the UM-chitin characterization are found in [15].

2.3. Equilibrium experiments

Single and binary batch adsorption experiments were performed with adsorbent dosage of 5 g/L in contact with 50 mL of solution at different initial concentrations of each adsorbent (0 to 650 mg/L) at pH 6. The samples were agitated in a thermostatic agitator (Solab, SL 222, Brazil) at 150 rpm and different temperatures (298, 308, 318 and 328 K). After reaching the equilibrium, the solutions were centrifuged at 4000 rpm for 5 min and the liquid phase was quantified: MB concentration was determined by spectrophotometry at 664 nm (Biospectro, SP-22, Brazil) and Co^{2+} concentration was determined by atomic absorption spectrometry (Agilent, 240 FSAA, USA). Finally, the equilibrium adsorption capacities (q_e) were obtained by Eq. (1) for each adsorbent.

$$q_e = \frac{C_0 - C_e}{m} V \quad (1)$$

where, C_0 (mg/L) is the initial adsorbent concentration, C_e (mg/L) is the adsorbent concentration at equilibrium, m (g) is the adsorbent mass and V (L) is the volume of solution.

3. Mathematical methodology

3.1. Equilibrium models

The adsorption equilibrium is usually interpreted by nonlinear isotherms that relate the amount of adsorbate retained on the surface of an adsorbent (q_e) with the concentration of adsorbate remaining in liquid phase (C_e) at constant temperature [4]. Traditional adsorption equilibrium models, including Langmuir and Freundlich, were used to interpret Co^{2+} and MB experimental data in single and binary systems.

The Langmuir model for mono-compound is based on the monolayer adsorption on the adsorbent homogeneous surface, assuming that each adsorbed molecule occupies one adsorption site and without adsorbate transmigration in the adsorbent surface [16]. Eq. (2) reports the Langmuir model for mono-compound system:

$$q_e = \frac{q_{mL} K_L C_e}{1 + K_L C_e} \quad (2)$$

where, q_{mL} (mg/g) is the maximum adsorption capacity of Langmuir and K_L (L/mg) is the constant of Langmuir.

An extension of Langmuir isotherm for binary system was developed considering the existing competition between adsorbates and active sites of adsorbent material. The extended Langmuir model assumes that all active sites present on surface of the adsorbent are the same and that the adsorbates present in solution compete equally for the same active sites [17]. For binary system, the extended Langmuir model are represented by the following equations:

$$q_{e,1} = \frac{q_{mL,1} K_{L,1} C_{e,1}}{1 + K_{L,1} C_{e,1} + K_{L,2} C_{e,2}} \quad (3)$$

$$q_{e,2} = \frac{q_{mL,2} K_{L,2} C_{e,2}}{1 + K_{L,1} C_{e,1} + K_{L,2} C_{e,2}} \quad (4)$$

where the indexes 1 and 2 refer to components 1 (Co^{2+}) and 2 (MB) of the binary system.

The Freundlich isotherm for mono-compound can predict the behavior of multilayer adsorption and heterogeneous surfaces, based on the hypothesis that the adsorption energy decreases exponentially as the available adsorption sites are occupied [18]. Eq. (5) reports the Freundlich model for mono-compound system:

$$q_e = K_F C_e^{\frac{1}{n_F}} \quad (5)$$

where, K_F ($(\text{mg/g})(\text{L/mg})^{1/n_F}$) and n_F are the constants of Freundlich.

3.2. Parameter estimation procedure

The isotherm parameters were estimated by minimization of the nonlinear least square function, as presented in Eq. (6); which evaluates the difference between the experimental data (q_j) and the predicted model data (\hat{q}_j), for all N_Y experiments.

$$\min |f(p)| = (q_{ej} - \hat{q}_{ej}) \quad (6)$$

The minimization function was solved by the Matlab function *lsqnonlin* along with the Trust-Region-Reflective algorithm [19]. The 95% confidence intervals for each estimated parameter were determined using the Matlab function *nlparci*, while the confidence interval for the predicted values at each point was determined using the Matlab function *nlpredci*. These two functions are based on the t -distribution and provide a symmetrical confidence interval at all points using the covariance matrix (*COVB*) (Eq. (7)) [20].

$$COVB = MSE(J^T J)^{-1} \quad (7)$$

where, *MSE* is the mean squared error determined by Eq. (10) and *J* is the Jacobian computed by Matlab function *lsqnonlin*.

The performance of the adsorption isotherms was evaluated by the mean squared error (*MSE*) and the coefficient of determination (R^2), according to the following equations:

$$MSE = \frac{1}{N_Y - N_P} \sum_{j=1}^{N_Y} (q_{ej} - \hat{q}_{ej})^2 \quad (8)$$

$$R^2 = 1 - \frac{\sum_{j=1}^{N_Y} (q_{ej} - \hat{q}_{ej})^2}{\sum_{j=1}^{N_Y} (q_{ej} - \bar{q}_{ej})^2} \quad (9)$$

4. Results and discussion

4.1. Equilibrium data

The adsorption equilibrium results are fundamental for comparing and evaluating the efficiency of the adsorbent in removing different adsorbates. The experimental equilibrium curves for Co^{2+} and MB in single and binary system are exhibited in Fig. 1 and Fig. 2, respectively. The adsorption isotherm curves can be classified as type L2 [21], where the inclined portion characterizes the affinity among the solutes and the UM-chitin, and the plateau represents the maximum adsorption capacity.

According to these figures, the adsorption capacity for Co^{2+} was higher than MB in both simple and binary systems; this occurs because metal ions are easier to interact with the active sites, since the dye has a larger molecule. Furthermore, adsorption capacity for Co^{2+} decreased with increasing temperature (exothermic process), while the adsorption capacity for MB increased with increasing temperature (endothermic process), and the same thermodynamic tendency remained in the binary system. In addition, it is noted that the adsorption capacity of both adsorbates decreased in the binary system, indicating a competitive adsorption.

4.2. Adsorption isotherm modeling

The Langmuir and Freundlich isotherms were used to interpret the adsorption equilibrium of each adsorbate in single system; the results of the estimated parameters are presented in Table 1 and the graphical representations were added in Fig. 1. Sips isotherm [22] was also tested, but the estimated parameters were the same as Langmuir isotherm, and therefore, the results were not presented.

The results from Table 1 indicate that Langmuir isotherm presented the best fit for both adsorbates, as it presented the lowest mean squared error ($MSE < 3.55$) and the highest coefficient of determination ($R^2 > 0.99$) for all temperatures. In addition, the confidence intervals of estimated parameters of Langmuir isotherm are smaller than those of

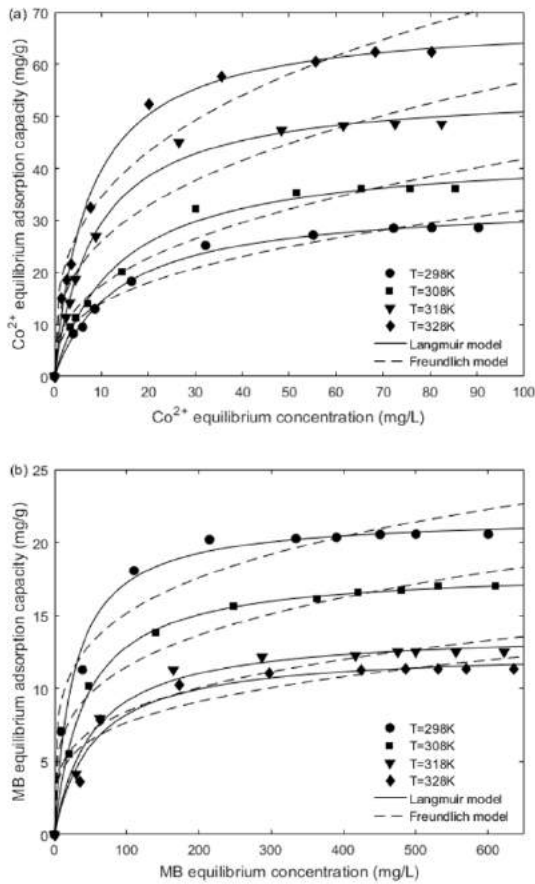


Fig. 1. Equilibrium isotherms of (a) Co^{2+} and (b) MB onto UM-chitin in single system.

Table 1. Isotherm parameters for single adsorption

Model	T (K)	Parameters					
Langmuir	Co^{2+}	q_{mL}	K_L	R^2	MSE		
		298	33.62±1.45	0.075±0.012	0.998	0.473	
	308	43.26±2.91	0.074±0.018	0.996	1.697		
	318	55.28±2.58	0.114±0.021	0.997	2.117		
	328	68.76±3.30	0.136±0.027	0.997	3.533		
	MB	298	21.79±1.08	0.038±0.012	0.994	0.718	
		308	18.16±0.41	0.024±0.003	0.999	0.081	
		318	13.93±0.74	0.019±0.005	0.995	0.227	
		328	12.64±1.02	0.019±0.008	0.988	0.436	
	Freundlich	Co^{2+}	K_F	n_F	R^2	MSE	
			298	6.21±2.17	0.356±0.088	0.983	4.205
		308	7.33±2.79	0.378±0.096	0.982	7.701	
		318	11.92±4.62	0.338±0.010	0.976	19.307	
		328	16.39±5.03	0.323±0.081	0.982	22.810	
		MB	298	5.63±2.53	0.215±0.078	0.977	2.716
			308	3.64±1.60	0.249±0.075	0.984	1.255
318			2.62±1.63	0.254±0.105	0.972	1.227	
328			2.44±1.74	0.248±0.120	0.963	1.309	

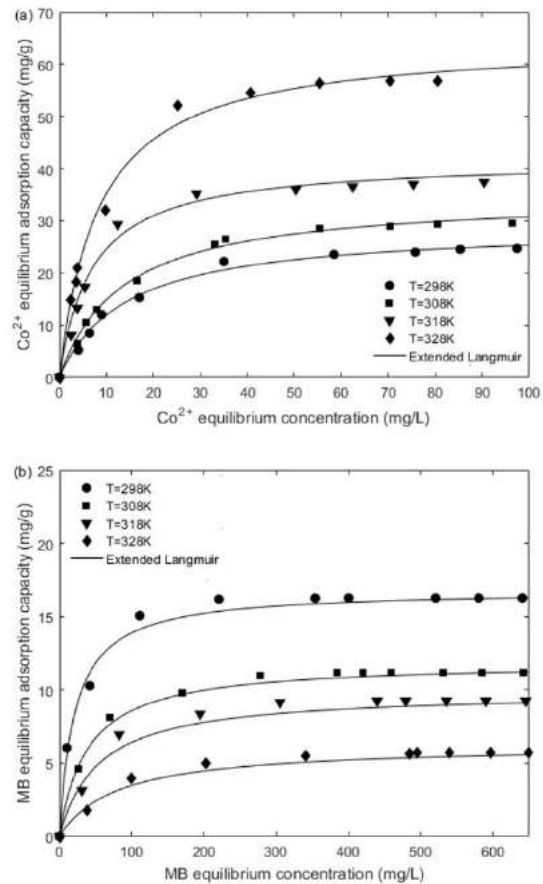


Fig. 2. Equilibrium isotherms of (a) Co^{2+} and (b) MB onto UM-chitin in binary system.

Table 2. Extended Langmuir isotherm parameters for binary adsorption.

	T (K)	q_{mL}	K_1	K_2	R^2	MSE
Co^{2+}	298	28.93±4.60	0.071±0.012	0	0.996	0.326
	308	34.87±3.27	0.075±0.009	0	0.997	0.326
	318	41.76±4.12	0.144±0.034	0	0.994	1.465
	328	64.57±4.36	0.122±0.021	0	0.997	1.562
MB	298	18.71±2.31	0.043±0.012	0.031±0.042	0.997	0.096
	308	12.79±0.654	0.024±0.003	0.012±0.010	0.999	0.010
	318	11.37±1.51	0.016±0.006	0.016±0.016	0.996	0.042
	328	7.21±0.846	0.011±0.003	0.011±0.010	0.997	0.011

Freundlich isotherm, confirming the lower standard deviation between the experimental and model data.

The binary systems were investigated by Extended Langmuir isotherm since the adsorption behavior of the investigated adsorbates in single system followed the Langmuir isotherm model [23]. Thus, the results of the estimated parameters are presented in Table 2.

The results from Table 2 show that the Extended Langmuir isotherm satisfactorily fitted the

adsorption data of both adsorbates ($MSE < 1.60$ and $R^2 > 0.99$). It is also observed that there is significance in the estimated parameters since the confidence intervals are narrow. The graphical representation of Extended Langmuir isotherm was also added in Fig. 2.

As shown in Table 2, the values of maximum adsorption capacity (q_{mL}) follow the same tendency of the single system, in which the maximum adsorption capacity of Co^{2+} was 68.76 mg/g at 328 K and the maximum adsorption capacity of MB was 21.79 mg/g at 298 K. In addition, it is found that the dye does not affect the adsorption of Co^{2+} as the parameter K_2 was null. However, the adsorption of MB is affected by competition with Co^{2+} at all temperatures; wherein the greatest influence of K_2 occurs at lower temperatures.

4.3. Confidence intervals

The 95% confidence interval of the estimated model parameters indicates the region of the parameter space that contains the parameter values that preserve the statistical significance of the model fit to the experimental data [5]. As previously shown by Table 1 and Table 2, the estimated parameters for the Langmuir (single) and Extended Langmuir (binary) isotherms are statistically significant, hence the confidence intervals of the models prediction at 298 K are presented in Fig 3. The narrow confidence region indicates that the covariance matrix contains low deviations values; and most experimental data is contained in the confidence region of the model.

5. Conclusion

In this work, the adsorption equilibrium of cobalt ions (Co^{2+}) and methylene blue (MB) onto ultrasonic modified chitin was investigated in single and binary systems. The experimental results revealed competitive adsorption since the adsorption capacity for each adsorbate was reduced in binary system. Higher adsorption capacities were found for Co^{2+} , which is probably due to the metal ions having a superior mobility in solution and therefore more facility to interact with the active sites.

Traditional nonlinear isotherms were compared to fit the single experimental data at different temperatures; and the nonlinear least squares technique was used to estimate the parameters. The adsorption equilibrium data was well represented by Langmuir model ($MSE < 3.55$ and $R^2 > 0.99$), and

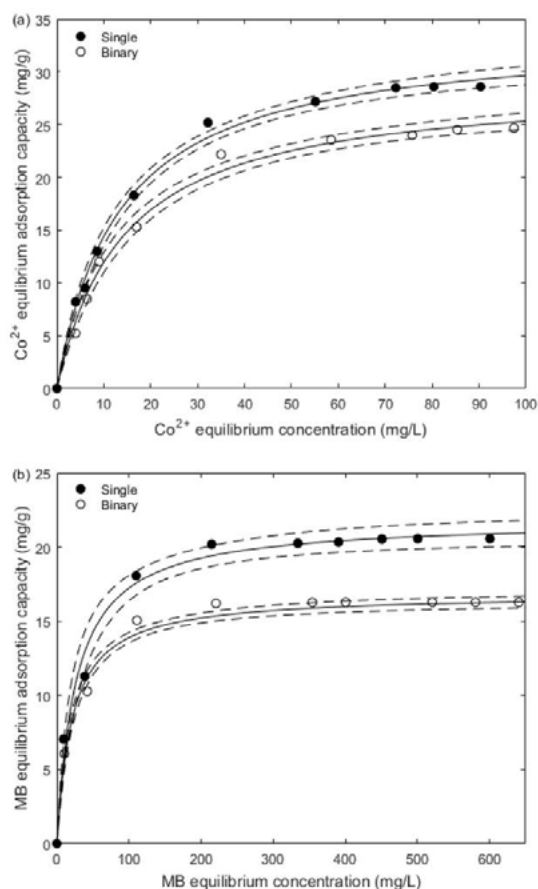


Fig. 3. 95% confidence interval for (a) Co^{2+} and (b) MB prediction at 298 K.

the maximum adsorption capacity was found as 68.76 mg/g for Co^{2+} at 328 K, indicating an exothermic adsorption, whereas the maximum adsorption capacity for MB was 21.79 mg/g at 298 K, indicating an endothermic process. In binary systems, the Extended Langmuir model was able to predict the experimental data, and the estimated constants indicated that the dye did not influence the Co^{2+} adsorption; however, metallic ions influenced the MB adsorption.

The confidence intervals of the estimated parameters were computed by the covariance matrix and 95% confidence. The narrow confidence region indicates low deviations between the predicted and experimental data and, therefore, the estimated parameter values contain statistical significance.

Acknowledgements

The authors are grateful to Coordination for the Improvement of Higher Education Personnel (CAPES) for granting the scholarship to the first author.

References

- [1] Ali I. The quest for active carbon adsorbent substitutes: inexpensive adsorbents for toxic metal ions removal from wastewater. *Sep Purif Rev* 2010; 39:95–171.
- [2] Flores López SL, Moreno Virgen MR, Hernández Montoya V, Montes Morán MA, Tovar Gómez R, Vázquez NA, Pérez Cruz MA, Esparza González MS. Effect of an external magnetic field applied in batch adsorption systems: Removal of dyes and heavy metals in binary solutions. *J Mol Liq* 2018; 269:450–460.
- [3] Lai KC, Lee LY, Hiew BYZ, Thangalazhy-Gopakumar S, Gan S. Environmental application of three-dimensional graphene materials as adsorbents for dyes and heavy metals: Review on ice-templating method and adsorption mechanisms. *J Environ Sci* 2019; 79:174–199.
- [4] Raganati F, Alfè M, Gargiulo V, Chirone R, Ammendola P. Isotherms and thermodynamics of CO₂ adsorption on a novel carbon-magnetite composite sorbent. *Chem Eng Res Des* 2018; 134:540–552.
- [5] Tolazzi N, Steffani E, Barbosa-Coutinho E, Severo Jr JB, Pinto JC, Schwaab M. Adsorption equilibrium models: Computation of confidence regions of parameter estimates. *Chem Eng Res Des* 2018; 138:144–157.
- [6] Liu C, Zhao D, Zhang K, Xuan H, Alsaedi A, Hayat T, Chen C. Fabrication of Si/Ti-based amino-functionalized hybrids and their adsorption towards cobalt(II). *J Mol Liq* 2019; 289:111051.
- [7] Dehghani MH, Yetilmezsoy K, Salari M, Heidarnejad Z, Yousefi M, Sillanpää M. Adsorptive removal of cobalt(II) from aqueous solutions using multi-walled carbon nanotubes and γ -alumina as novel adsorbents: Modelling and optimization based on response surface methodology and artificial neural network. *J Mol Liq* 2019; In Press:112154.
- [8] Awua MR, Alharthi NH, Hasan MM, Karim MR, Islam A, Znad H, Hossain MA, Halim ME, Rahman MM, Khaleque MA. Inorganic-organic based novel nano-conjugate material for effective cobalt(II) ions capturing from wastewater. *Chem Eng J* 201; 324:130–139.
- [9] Egbosiuba TC, Abdulkareem AS, Kovo AS, Afolabi EA, Tijani JO, Auta M, Roos WD. Ultrasonic enhanced adsorption of methylene blue onto the optimized surface area of activated carbon: Adsorption isotherm, kinetics and thermodynamics. *Chem Eng J* 2020; 153:315–336.
- [10] Rezakazemi M, Shirazian S. Lignin-chitosan blend for methylene blue removal: Adsorption modeling. *J Mol Liq* 2019; 274:778–791.
- [11] Youcef LD, Belaroui LS, López-Galindo A. Adsorption of a cationic methylene blue dye on an Algerian palygorskite. *Appl Clay Sci* 2019; 179:10515.
- [12] Qin X, Bai L, Tan Y, Li L, Song F, Wang Y. β -Cyclodextrin-crosslinked polymeric adsorbent for simultaneous removal and stepwise recovery of organic dyes and heavy metal ions: Fabrication, performance and mechanisms. *Chem Eng J* 2019; 372:1007–1018.
- [13] Asfaram A, Ghaedi M, Azqhandi MHA, Goudarzi A, Hajati S. Ultrasound-assisted binary adsorption of dyes onto Mn@CuS/ZnS-NC-AC as a novel adsorbent: Application of chemometrics for optimization and modeling. *J Ind Eng Chem* 2017; 54:377–388.
- [14] Dotto GL, Santos JMN, Rodrigues IL, Rosa R, Pavan FA, Lima EC. Adsorption of Methylene Blue by ultrasonic surface modified chitin. *J Colloid Interface Sci* 2015; 446:133–140.
- [15] Sellaoui L, Franco DSP, Dotto GL, Lima EC, Lamine AB. Single and binary adsorption of cobalt and methylene blue on modified chitin: Application of the Hill and exclusive extended Hill models. *J Mol Liq* 2017; 233:543–550.
- [16] Langmuir I. The adsorption of gases on plane surfaces of glass, mica and platinum. *J Am Chem Soc* 1918; 40:1361–1403.
- [17] Butler JAV, Ockrent C. Studies in Electrocapillarity, III. *J Phys Chem* 1930; 34:2841–2859.
- [18] Freundlich H. Over the adsorption in solution. *Z Phys Chem A* 1906; 57:358–471.
- [19] Coleman TF, LI Y. Trust region approach for nonlinear minimization subject to bounds. *SIAM J Optim* 1996; 6:418–445.
- [20] Seber GAF, Wild CJ. *Nonlinear Regression*. Hoboken: Wiley-Interscience; 2003.
- [21] Giles CH, Smith D, Huitson A. A general treatment and classification of the solute adsorption isotherm. I. Theoretical. *J Colloid Interface Sci* 1974; 47:755–765.
- [22] Sips R. On the structure of a catalyst surface. *J Chem Phys* 1948; 16:490–495.
- [23] Li L, Liu F, Jing X, Ling P, Li A. Displacement mechanism of binary competitive adsorption for aqueous divalent metal ions onto a novel IDA-chelating resin: Isotherm and kinetic modeling. *Water Res* 2011; 45:1177–1188.

Mathematical modeling of low-pressure biogas H₂S removal by granular activated carbon in fixed bed column

Fabiano Bisinella Scheufele^{a,*}, Helton José Alves^b, Rodrigo Sequinel^b, Bárbara Bulhões Cazula^b, Eliane Soares da Silva^b, Laressa Caciano^b, Carlos Eduardo Borba^b, Thiago Fernando Magrini Lopez^c, Alessandra Freddo^c, Giovani Silvero Patuzzo^c

^a *Biotechnology and Bioprocess Engineering - COEBB, Federal Technological University of Paraná, Toledo, 85902-490, Brazil*

^b *Materials and Renewable Energy Laboratory - LABMATER, Federal University of Paraná, Palotina 85950-000, Brazil*

^c *Centro Internacional de Energias Renováveis - Biogás (CIBiogás-ER), Foz do Iguaçu 85867-900, Brazil*

Abstract

This work focused to obtain kinetic and equilibrium experimental data for the H₂S adsorption by using a babassu derived granular activated carbon (GAC) in fixed bed column and to investigate the mechanism involved in the process by applying mathematical modeling aiming to support the design and scale up of fixed bed adsorption systems. For this, a lab-scale fixed bed column was assembled, and breakthrough curves were experimentally obtained for feed H₂S concentrations of 0.152, 1.327, 2.577 mg L⁻¹ (i.e. 50, 500 and 1000 ppm_{mol}) under low pressure conditions (2 bar). The developed mathematical model based on the linear driving model and Langmuir isotherm was able to adequately describe the experimental data, and to determine the equilibrium ($q_{max} = 20.61 \text{ mg g}^{-1}$ and $b = 16.84 \text{ L mg}^{-1}$) and kinetic parameters ($k_G = 3.3 \times 10^{-2} \text{ min}^{-1}$ and $D_{ax} = 6.226 \text{ cm}^2 \text{ s}^{-1}$) of the adsorption process. The proposed mathematical modeling also showed predictivity capacity, hence it is expected to support the design of real scale adsorption systems. Overall, the GAC showed desirable features, especially considering the low-pressure condition, such as favorable kinetics, long bed operation times, high adsorbent-adsorbate affinity and adsorption capacity, as well as practical advantages such as low pressure drop in the fluid flow. Hence, the H₂S adsorption by the GAC in fixed bed column shows remarkable potential for application, even in small-scale biogas plants, since it requires straightforward infrastructure facilities for the treatment systems.

Keywords: mass transfer; LDF model; equilibrium; kinetics; Ergun equation.

1. Introduction

Biogas stands out as one of the most promising renewable sources for energy production. Several residual sources may be used for the anaerobic biodegradation. The swine manure presents several advantages and desirable characteristics as a residual feedstock to the biogas production; however, it is associated to high levels of hydrogen sulfide (H₂S) in the biogas. The H₂S is a toxic and odorous compound and can lead to pipelines and combustion engines corrosion, also the H₂S is potentially harmful for the environment wherein SO_x and can be converted to sulfuric acid and cause acid rain [1,2]. Hence, the sulfur compounds removal from biogas is a major drawback for the biogas chain supply and strongly impacts in the feasibility of this fuel [3].

Amongst the desulfurization techniques, the adsorption using activated carbon is one of the most used [2], wherein the overall process' costs are

mainly related to the adsorbent. Therefore, the development of a suitable adsorbent material as well as the optimization of the operational conditions are a key factor to the process.

Given its complexity, the design and optimization of an appropriate fixed bed adsorption system generally requires a deep understanding on the mechanisms and relevant transport phenomena involved in the adsorption dynamics for a selected adsorbent. For this purpose, a predictive model using independently established equilibrium and kinetic parameters may provide a method of estimating the column dynamic performance without extensive experimentation and further support the design of large-scale equipment [4,5].

In this context, the aim of this work was to obtain kinetic and equilibrium experimental data for the H₂S adsorption by a granular activated carbon in fixed bed column and to assess the data through mathematical modeling aiming to support the design and scale up of fixed bed adsorption systems.

2. Materials and Methods

The activated carbon assessed was a granular activated carbon (GAC) specified as 8×30 with a particle diameter ranging from 3 to 5 mm from Brascarbo Agroindustrial Ltda., produced from babassu peels, an organic waste from the babassu processing industry. The gases used in the experiments were primary standard mixtures (White Martins) of nominal concentrations of 50, 500 and 1000 ppm_{mol} H₂S (0.152, 1.327, 2.577 mg L⁻¹) in N₂ (balance).

Aiming to survey experimental data to support the design of real-scale adsorptions systems for hydrogen sulfide removal from biogas a pilot-scale column was assembled to study the kinetic and equilibrium behavior and the operational conditions influence over the fixed bed performance. Further, based on the experimental data a mathematical model was developed in order to describe the kinetic and equilibrium behavior of the fixed bed column and to simulate other operational conditions aiming the scale up of the system to real scale systems.

Fixed bed column H₂S adsorption onto the commercial activated carbon assays were performed in a temperature-controlled stainless-steel column lined with Teflon of 2.5 cm internal diameter and 48.5 cm of total height, which was packed with a defined mass of activated carbon reaching a bed height of 8.1 cm.

In all adsorption assays, a volumetric flow rate of 1.8 L min⁻¹ (30 mL s⁻¹) was used in upstream flow. Analyzes of the standard gas samples (before starting the adsorption experiments) and the samples collected at bed exit were performed on a gas chromatograph Micro GC model C2V-200, Thermo Scientific, with a nano thermal conductivity detector (TCD) and Plot type columns - MS5A (Molecular Sieve 5A) and Bond-U type (divinylbenzene type U). Helium (99.99%) was used as carrier gas.

The pressure (2 bar) and temperature (45°C) operational conditions were defined in previous experiments by a complete factorial experimental design 2³ (data not shown), with a H₂S feed concentration of 500 ppm_{mol} in N₂ up to the breakthrough time (t_b) (which was defined based on the maximum concentration for H₂S in biomethane (*i.e.* $C = 10$ ppm) preconized by the National Agency of Petroleum, Natural Gas and Biofuels - ANP (ANP Resolution n° 8/2015).

The breakthrough curves were obtained, in which the concentration of H₂S at the bed exit was quantified until reaching t_t (q_{sat}) adsorption capacity were determined, by applying Eq. (1) and (2), respectively.

$$q_b = \frac{C_0 Q}{m_{ads}} \int_0^{t_b} \left(1 - \frac{C|_{z=L}}{C_0}\right) dt \quad (1)$$

$$q_e = \frac{C_0 Q}{m_{ads}} \int_0^{t_t} \left(1 - \frac{C|_{z=L}}{C_0}\right) dt \quad (2)$$

Where, q_b and q_e are the concentration in the solid phase at the breakthrough time and at the saturation condition (mg g⁻¹), respectively; C_0 is the H₂S feed concentration in the gas phase (mg L⁻¹), Q is the volumetric flowrate in the gas stream feed in the bed (L min⁻¹), m_{ads} is the adsorbent mass (d.b.) (g), $C|_{z=L}$ is the H₂S concentration in the bed exit (mg L⁻¹), t_b and t_t are the breakthrough and saturation time of the bed (min). The bed efficiency was also calculated given by the ratio of the solid phase concentration at the breakthrough time and at the saturation (*i.e.* $\eta = q_b/q_{sat}$).

3. Mathematical modeling

In order to evaluate the dynamic and equilibrium behavior of H₂S adsorption by the activated carbon, as well as to investigate and understand the mass transfer mechanisms associated to the adsorption process in fixed bed column a representative mathematical model was elaborated considering the following hypotheses were considered in kinetic model: (i) Isothermal process; (ii) Physical properties constant in both phases; (iii) Constant porosity of the bed; (iv) Constant interstitial velocity; (v) Gas phase behavior as ideal gas; (vi) Thermodynamic equilibrium at the liquid-solid interface (described by the isotherm model); (vii) Negligible radial and angular dispersion in the fixed bed column.

The mass balance for the gas phase was described by Eq. (3) which describes the term of gas phase accumulation, solid phase accumulation (mass transfer rate term), mass transport due to convective and diffusive effects, respectively.

$$\frac{\partial C}{\partial t} + \frac{\rho_L}{\varepsilon_L} \frac{\partial q}{\partial t} + v_0 \frac{\partial C}{\partial z} - D_{ax} \frac{\partial^2 C}{\partial z^2} = 0 \quad (3)$$

Where, C is the H₂S concentration in the gas phase (mg L⁻¹), q the H₂S concentration in the solid phase (mg g⁻¹), ρ_L is the bed density (g L⁻¹); ε_L is the bed porosity (dimensionless); v_0 is the interstitial velocity of the gas in the bed (cm min⁻¹); and D_{ax} is the axial dispersion (cm² min⁻¹).

For the description of the mass transfer term between the gas and solid phase (rate term), it was considered in this work that the overall mass

transfer rate is controlled by diffusive effects. The approach that considers the mass transfer rate is proportional to the concentration difference in the solid phase in relation to the equilibrium condition, called Linear Driving Force (LDF). The LDF model is a concentrated parameter model, which is an approximation that assumes that a global resistance, associated with diffusive effects (internal and external), describes the mass transfer process [6,7]. The LDF model is given by Eq. (4), and considers the following hypotheses: (i) particles of the adsorbent solid are considered as a homogeneous phase (*i.e.* constant effective diffusivity); (ii) reaction kinetics (adsorption at the active site) is much faster than the mass transfer steps.

$$\frac{dq}{dt} = k_G(q_e - q) \quad (4)$$

Where, k_G is the overall mass transfer coefficient (min^{-1}), and q_e is the H_2S concentration in the solid phase in the equilibrium (mg g^{-1}).

To complete the mathematical model, it is necessary to represent the thermodynamic equilibrium relationship at the solid and gas interface (*i.e.* $q_e = f(C)$). For this, the Langmuir equilibrium isotherm model (see Eq. (5)) was used, which is a theoretical model that considers the following hypotheses [8]: (i) Active sites have the same activity (energetically equivalent); (ii) There are no interactions between the adsorbed species; (iii) Adsorption occurs in monolayer onto homogeneous surface.

$$q_e = \frac{q_{max} b C_e}{1 + b C_e} \quad (5)$$

Where, q_{max} is the maximum adsorption (mg g^{-1}), b is the affinity constant, associated to the dynamic equilibrium between the adsorption and desorption (L g^{-1}), q_e and C_e are the H_2S concentrations in the solid phase (mg g^{-1}) and in the gas phase (mg L^{-1}) in the equilibrium, respectively.

For the mathematical model solution, composed by mass balances in the gas (Eq. 3) and in the solid phase (Eq. 4), as well as the equilibrium relation Eq. (5), the initial conditions were used:

$$C(z, 0) = C_0 \quad (6)$$

$$q(z, 0) = 0 \quad (7)$$

Also, two boundary conditions were necessary, given by Eq. (8) and (9) [9].

$$D_{ax} \frac{\partial C}{\partial z} \Big|_{z=0} = v_0(C(t, 0) - C_0) \quad (8)$$

$$\frac{\partial C}{\partial z} \Big|_{z=L} = 0 \quad (9)$$

The mathematical model elaborated to describe the dynamics of H_2S adsorption breakthrough curves in the fixed bed column distinguishes in three groups of variables: (i) directly measured and/or experimentally obtained parameters (H_L, Q, ρ_L and v_0) or indirectly determined from experimental determinations and calculated through fundamental equations (ρ_f, μ_f, D_m); (ii) parameters calculated through existing correlations in the literature (ε_L e D_{ax}); and (iii) fitted parameters from equilibrium and kinetic experimental data (k_G, q_{max}, b), which were estimated by the mathematical model.

The bed porosity (ε_L) was determined by the correlation proposed by Ribeiro et al., [10], based on the experimental determination of the mean particle diameter (\bar{d}_p) by the results of granulometry analysis.

The Reynolds number (Re) for flow in porous beds, was determined by Eq. (10).

$$Re = \frac{\bar{d}_p v_s \rho_f}{\mu_f (1 - \varepsilon_L)} \quad (10)$$

The Schmidt number, which describes the ratio of momentum diffusivity to mass diffusivity, was calculated by Eq. (11).

$$Sc = \frac{\mu_f}{\rho_f D_{m,i}} \quad (11)$$

The molecular diffusivity for each component ($D_{m,i}$) in the gas mixture is a function of the binary diffusivities ($D_{i,j}$) and the molar fraction of the remaining component (y_i), given by Eq. (12).

$$D_{m,i} = \frac{1 - y_i}{\sum_{j=1}^{n_c} \frac{y_j}{D_{i,j}}} \quad (12)$$

The determination of the binary diffusivities ($D_{i,j}$) as well as the fluid viscosity (μ_f) the Chapman-Enskog theory was used, which considers the determination of Lennard-Jones Potential (6-12) parameters to predict the transport properties for low density gases [11,12].

The binary diffusion coefficient of each component i in another component j , was determined by Eq. (13) [12].

$$D_{i,j} = \frac{0,00266 T^{3/2}}{P M_{i,j}^{1/2} \sigma_{i,j}^2 \Omega_D} \quad (13)$$

Where, T is the absolute temperature (K), P is the pressure (bar), $M_{i,j}^{1/2} = 2[(1/M_i) + (1/M_j)]^{-1}$, $\sigma_{i,j}$ is the Lennard-Jones characteristic length for binary mixture (\AA) and Ω_D the integral collision for

diffusion (dimensionless), which were respectively determined by Eq. (14) and (15).

$$\sigma_{i,j} = \frac{\sigma_i + \sigma_j}{2} \quad (14)$$

$$\Omega_D = \frac{C_1}{\omega^{D_1}} + \frac{C_2}{\exp(\omega D_2)} + \frac{C_3}{\exp(\omega D_3)} + \frac{C_4}{\exp(\omega D_4)} \quad (15)$$

Where, $C_1, C_2, C_3, C_4, D_1, D_2, D_3$ e D_4 are the parameters of the collision integral function for diffusivity, found elsewhere Neufeld et al., [13] and ω is the dimensionless temperature ($\omega = \kappa T / \epsilon_{i,j}$), where κ is the Boltzmann constant ($\kappa = 1.38064852 \times 10^{-23} \text{ m}^2 \text{ kg s}^{-2} \text{ K}^{-1}$), and $\epsilon_{i,j} = \sqrt{\epsilon_i \epsilon_j}$ is the Lennard-Jones characteristic energy (J).

Finally, the axial dispersion in the bed ($D_{ax,i}$), for each component i was calculated by the mathematical correlation of Wakao & Funazkri [14], which is valid for $3 < Re < 10000$, given by Eq. (16).

$$\frac{\epsilon_L D_{ax,i}}{D_{m,i}} = 20 + 0.5 S c_i Re \quad (16)$$

It must be highlighted that the effect of axial dispersion is commonly neglected in the analysis of fixed bed column adsorption processes, aiming to facilitate the mathematical resolution of the model. However, especially in the case of gaseous fluid systems, such consideration may lead to significant errors [14,15].

The pressure drop in the bed was calculated using the Ergun equation, according to Eq. (17).

$$\frac{\Delta P}{H_L} = -150 \frac{\mu_f (1 - \epsilon_L)^2}{d_p^2 \epsilon_L^3} v_s - 1.75 \frac{\rho_f (1 - \epsilon_L)}{d_p \epsilon_L^3} v_s^2 \quad (17)$$

Where, ΔP is the pressure drop in the bed (Pa).

Also, the determination of fluid viscosity (μ_f) based on the composition of the gas mixture was also determined on the Chapman-Enskog theory, similarly for the binary diffusivities.

The solution of the mathematical model was performed by using the “line method”, in which the partial differential equations (PDEs) were discretized in relation to the axial spatial coordinate (z coordinate), resulting in a system of ordinary differential equations (ODEs) in relation to the time variable (t) [5]. The resulting ODE system was solved by using the Rosenbrock method [16]. The model was coded in Maple software. The estimation of the adjustable parameters was performed by the Simplex Downhill optimization method proposed by Nelder & Mead [17], which consisted in the objective function minimization search (OF).

4. Results and Discussion

After the definition of the operational conditions from the experimental design (data not shown), the breakthrough curves were performed to obtain the H₂S adsorption equilibrium and kinetic data at the nominal concentrations of 50, 500 and 1000 ppm_{mol} (0.152, 1.327 and 2.577 mg L⁻¹). Table 1 presents the operational conditions in the experiments, as well as parameters employed in the modeling and simulation of the experiments.

Table 1. Operational conditions and parameters used in the modeling of H₂S adsorption experiments by GAC in fixed bed column.

Operational Conditions			
C_0 (mg L ⁻¹)	0.152	1.327	2.577
m (g)	18.0373	18.4052	18.3893
P (bar)	2		
T (°C)	45		
Q (L min ⁻¹)	1.8		
Particle properties		Bed properties	
ρ_p (g cm ⁻³)	2.704	H_L (cm)	8.08
d_p (cm)	0.150	d_L (cm)	2.5
		ρ_L (g cm ⁻³)	0.4691
		ϵ_L (-)	0.373
Fluid properties			
ρ_f (g L ⁻¹)	2.1178		
μ_f (g cm ⁻¹ s ⁻¹)	1.8450×10^{-4}	1.8448×10^{-4}	1.8444×10^{-4}
Flow properties			
Re (-)	16.74 (Laminar flow regime)		
D_{ax} (cm ² s ⁻¹)	6.226		

From the breakthrough curves obtained for different concentrations of H₂S in the feed 0.152, 1.327 and 2.577 mg L⁻¹, as presented in Figure 1, the equilibrium data were determined. By observing the breakthrough curves profiles, the characteristic sigmoidal profile of the fixed bed experiments is verified, which is related to the mass transfer resistances in the bed.

Table 2 shows the performance parameters of the breakthrough curves obtained at the different concentrations of H₂S, wherein higher values for used bed height (H_U) for the lower H₂S feed concentrations (0.152 mg L⁻¹) were observed, consequently lower mass transfer zones (MTZ), what leads to higher bed efficiencies. Thus, the H₂S feed concentration significantly influences the bed efficiency, reaching high efficiencies for low concentrations (*i.e.* 0.152 mg L⁻¹ – $\eta = 92.41\%$).

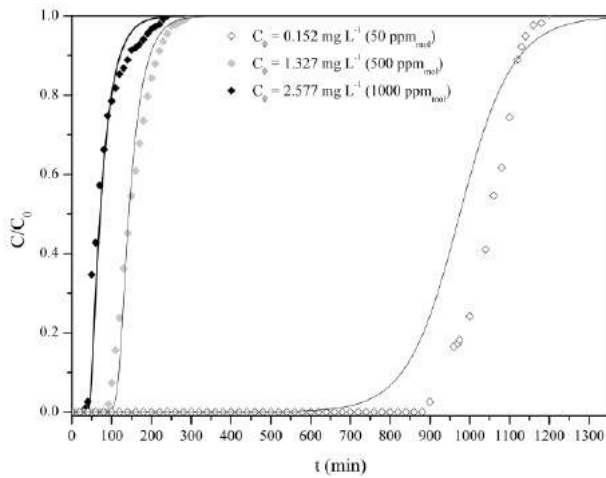


Figure 1. Experimental breakthrough curves for H₂S adsorption by GAC as a function of concentration and the LDF model (Experimental conditions: $P = 2$ bar, $T = 45^\circ\text{C}$, $Q = 1.8$ L min^{-1} , $H_L = 8.08$ cm).

Table 2. Performance parameters of the breakthrough curves for H₂S adsorption by GAC in fixed bed column.

C_0 (mg L^{-1})	Parameter							
	t_b (min)	t_t (min)	H_U (cm)	MTZ (cm)	q_b (mg g^{-1})	q_e (mg g^{-1})	$-\Delta P$ (Pa)	η (%)
0.152	973.9	1044.9	7.47	0.61	13.73	14.86	55.1	92.4
1.327	92.7	154.1	4.85	3.23	12.03	19.86	55.1	60.5
2.577	33.9	79.4	3.45	4.63	8.54	20.02	55.1	42.7

By applying Ergun equation, it was estimated the gas pressure drop in the bed, which was 55.13 Pa. It was also observed that the term of the laminar pressure drop contribution was more expressive (46.1 Pa), in agreement with the observed flow regime, which is in the transition region, but very close to a laminar condition ($Re = 16.74$ - see Table 1). This value indicates that for these conditions of volumetric flowrate and bed height, a small pressure drop associated with energy dissipation in fluid flow through the bed was observed. This has an advantage for large-scale systems in view of the energy demand for fluid flow through the bed [6].

The experimental equilibrium data of H₂S between the solid and gas phases, along with the Langmuir isotherm model fitting, are presented in Figure 2, which shows a typical behavior of a favorable isotherm, evidencing a high affinity between the GAC for the H₂S even at low solute concentrations in the gas phase.

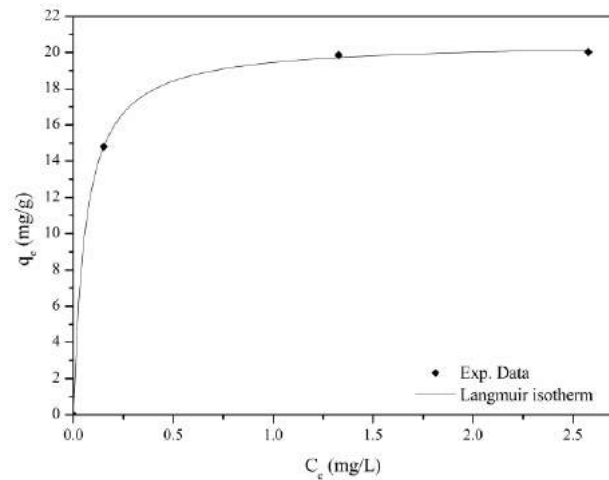


Figure 2. Experimental H₂S adsorption equilibrium data by GAC and Langmuir model fitting.

The estimated parameters for the Langmuir isotherm model were $q_{max} = 20.607 \pm 0.107$ mg g^{-1} and $b = 16.842 \pm 0.652$ L mg^{-1} with a $r^2 = 0.99982$. Figure 2 shows that the highest H₂S adsorption capacity experimentally obtained was 20.02 mg g^{-1} , at the H₂S concentration of 2.577 mg L^{-1} in the gas stream (1000 ppm_{mol}). Therefore, based on the equilibrium parameters as well as by graphical interpretation, a favorable asymptotic behavior for equilibrium data was observed, what evidences the high affinity to the GAC-H₂S system.

After the estimation of the equilibrium parameters, the mathematical modeling of the breakthrough curves was performed. By analyzing Fig. 2, one may notice an adequate prediction of both the breakthrough time (t_b) and the saturation condition (t_t) for all evaluated concentrations. The results of the estimated kinetic parameters for the H₂S adsorption data in fixed bed column by the GAC are presented in Table 3.

Table 3. Estimated kinetic parameters for the H₂S adsorption by the GAC in fixed bed column by the LDF model.

Parameters	C_0 (mg L^{-1})		
	0.152	1.327	2.577
k_G (min^{-1})	3.3×10^{-2}		
D_{ax} ($\text{cm}^2 \text{min}^{-1}$)	373.57		
OF	0.7467	0.0861	0.1124
r^2	0.9534	0.9945	0.9891

By analyzing Table 3, one may notice the same a kinetic constant ($k_G = 3.3 \times 10^{-2}$ min^{-1}) for all concentration values, as well as the axial dispersion

(D_{ax}). Such behavior is expected, considering that in theory the kinetic constants are independent of the gas phase concentration of the species. In fact, the kinetic constant may be dependent on other parameters such as the temperature as commonly described by Arrhenius's Law. However, considering that, except for the concentration, the other operational conditions were kept constant, hence the non-dependence on the kinetic constant is quite plausible.

Overall, it can be observed by the fitting quality parameters (r^2 e OF) that the LDF model adequately described the experimental data for all evaluated feed concentrations. Therefore, the proposed model, based on mass balances in the liquid and gas phase, as well as on the equilibrium isotherm behavior, was able to adequately describe the kinetic behavior of the breakthrough curves

Thus, based on the pilot-scale experimental data obtained, along with the proposed phenomenological model, it is expected to simulate and predict other operating conditions aiming the scale up of adsorption systems for the H_2S removal from biogas. In fact, the proposed model showed predictivity capacity for other independent experiments (data not shown).

5. Conclusions

The results obtained in this work evidenced that GAC showed a high adsorption potential of H_2S activated carbon under low pressures (2 bar). Equilibrium data indicated a high affinity and adsorption capacity of H_2S by the GAC. Also, the breakthrough curves indicated a favorable kinetics and long bed operation times. Small pressure drops in the bed were observed by applying Ergun equation, indicating that the flow through the bed does not lead to significant pressure drop, what is also a practical advantage reducing or even eliminating the fluid flow costs. Given the favorable features presented by the GAC for H_2S removal under low-pressure conditions, the fixed bed adsorption process has a potential for application, since it requires simple infrastructure facilities for H_2S treatment systems.

Acknowledgements

This research was partially supported by CIBiogas/ITAIPU-Brazil (Project RD&I UFPR 80-2018).

References

- [1] X. Liu, R. Wang, Effective removal of hydrogen sulfide using 4A molecular sieve zeolite synthesized from attapulgite, *J. Hazard. Mater.* 326 (2017) 157–164.
- [2] F.J. Gutiérrez Ortiz, P.G. Aguilera, P. Ollero, Biogas desulfurization by adsorption on thermally treated sewage-sludge, *Sep. Purif. Technol.* 123 (2014) 200–213.
- [3] M. Balsamo, S. Cimino, G. de Falco, A. Erto, L. Lisi, ZnO-CuO supported on activated carbon for H_2S removal at room temperature, *Chem. Eng. J.* 304 (2016) 399–407.
- [4] M.S. Shafeeyan, W.M.A. Wan Daud, A. Shamiri, A review of mathematical modeling of fixed-bed columns for carbon dioxide adsorption, *Chem. Eng. Res. Des.* 92 (2014) 961–988.
- [5] M.G. Sausen, F.B. Scheufele, H.J. Alves, M.G.A. Vieira, M.G.C. da Silva, F.H. Borba, C.E. Borba, Efficiency maximization of fixed-bed adsorption by applying hybrid statistical-phenomenological modeling, *Sep. Purif. Technol.* 207 (2018) 477–488.
- [6] F.J. Gutiérrez Ortiz, P.G. Aguilera, P. Ollero, Modeling and simulation of the adsorption of biogas hydrogen sulfide on treated sewage-sludge, *Chem. Eng. J.* 253 (2014) 305–315.
- [7] P. Cruz, F.D. Magalhães, a. Mendes, Generalized linear driving force approximation for adsorption of multicomponent mixtures, *Chem. Eng. Sci.* 61 (2006) 3519–3531.
- [8] I. Langmuir, The Adsorption of Gases on Plane Surfaces of Glass, Mica and Platinum, *J. Am. Chem. Soc.* 40 (1918) 1361–1403.
- [9] P.V. Danckwerts, Continuous flow systems, *Chem. Eng. Sci.* 2 (1953) 1–13.
- [10] A.M. Ribeiro, P. Neto, C. Pinho, Mean Proximity and Pressure Drop Measurements in Packed Beds of Monosized Spheres: Side Wall Effects, *Int. Rev. Chem. Eng.* 2 (2010) 40–46.
- [11] R.B. Bird, W.E. Stewart, E.N. Lightfoot, *Transport phenomena*, 2nd ed., John Wiley and Sons, Inc., New York, 2007.
- [12] B.E. Poling, J.M. Prausnitz, J.P. O'Connell, *The properties of gases & liquids*, McGraw-Hill Educ. (2001).
- [13] P.D. Neufeld, A.R. Janzen, R.A. Aziz, Empirical Equations to Calculate 16 of the Transport Collision Integrals $\Omega(1,s)^*$ for the Lennard-Jones (12–6) Potential, *J. Chem. Phys.* 57 (1972) 1100–1102.
- [14] N. Wakao, T. Funazkri, Effect of fluid dispersion coefficients on particle-to-fluid mass transfer coefficients in packed beds, *Chem. Eng. Sci.* 33 (1978) 1375–1384.
- [15] P.G. Aguilera, F.J. Gutiérrez Ortiz, Prediction of fixed-bed breakthrough curves for H_2S adsorption from biogas: Importance of axial dispersion for design, *Chem. Eng. J.* 289 (2016) 93–98.
- [16] H.H. Rosenbrock, Some general implicit processes for the numerical solution of differential equations, *Comput. J.* 5 (1963) 329–330.
- [17] J.A. Nelder, R. Mead, A simplex method for function minimization, *Comput. J.* 7 (1964) 308–313.

Neural network modeling of successive Ni²⁺-Zn²⁺ adsorption cycles by *Sargassum filipendula* in fixed bed column

Paulo H. N. Ferreira^{a*}, Araceli A. Seolatto^{c,d}, Eneida S. Cossich^d, Célia R. G. Tavares^d,
Edson A. da Silva^b, Tiago D. Martins^{a**}

^a Unifesp, R. São Nicolau 210, Diadema, 09920-000, Brasil

^b Unioeste, Rua da Faculdade 645, Toledo, 85903-000, Brasil

^c UFG, Avenida Esperança s/n, Goiânia, 74690-900, Brasil

^d UEM, Avenida Colombo, 5790, Maringá, 87020-900, Brasil
* phnf17@gmail.com; ** tdmartins@unifesp.br

Abstract

The reuse of adsorbents in wastewater treatment is important because it generates monetary economy and improves natural resources management. In successive adsorption cycles, the phenomenological modeling applicability is limited due the natural variability of the process that changes the kinetics in each cycle. In multicomponent systems this is even more difficult due the complex interactions that take place. The main objective of this work was to obtain a single artificial neural network (ANN) to predict the breakthrough curves of ten Ni²⁺-Zn²⁺ successive adsorption cycles, as an alternative to the phenomenological models. The brown algae *Sargassum filipendula* was used (and reused after desorption) as adsorbent. All collected data were used to train several ANN structures. The best result was obtained when considering the concentrations of both ions at times $t-1$ and t as inputs and the concentrations at time $t+1$ as outputs. The best structure was the ANN 4-18-21-2, which was capable to simulate all the ten curves using only the experimental data at 0 and 10.85 min. The ANN was capable to predict the time of equilibrium, and the extracted mass calculated using the ANN predicted curve was very near to the real one. This work showed that the ANNs can be a powerful tool to predict the kinetic of binary adsorption processes with high accuracy.

Keywords: Water treatment; Artificial intelligence; Mathematical modeling; Brown algae

1. Introduction

Adsorption is one of the most common methods for wastewater treatment. In this process, a solid (the adsorbent) is used to capture soluble molecules in water. Different inorganic and organic materials can be used and the evaluation of its efficiency is necessary for industrial use.

One strategy to efficiently use an adsorbent is to perform several adsorption-desorption cycles. In this case, after the adsorption stage the species are desorbed using an eluent solution, so the solid can be used again in another adsorption cycle.

Maeda et al. [1] showed that reactive blue BF-5G can be desorbed from bone char using ethyl alcohol solution and can be used for at least 6 cycles of adsorption. Tran and Chao [2] observed that cantaloupe peel can be used in 5 cycles to

remove heavy metal from wastewater without loss of efficiency.

In an industrial process, it is important to have an equation to predict the process time, the mass extracted, and also the kinetic profile of the removal. However, the phenomenological models present limitations, since the kinetic changes as the cycles are performed and, thus, the parameters of the model.

In this case, Artificial Neural Networks (ANN) could be a tool of great interest. ANNs are an equation based on artificial intelligence that learns by examples. Their fundamental unit is the artificial neuron, which can be displaced in layers and connected with each other, forming a complex structure. The artificial neuron weights each input, that plus a bias parameter, forms the activation coefficient. Then, an activation function is applied

over the activation coefficient to form the exit of the neuron[3]. The basic equation of the artificial neuron, j , is given by Eq. (1):

$$o_j = f\left(\sum_{i=1}^n w_{ij}x_i + b_j\right) \quad (1)$$

where b is the bias, and x_i and w_{ij} are the value and weight of the input, i , respectively. The activation function can be any continuous function. The most commonly used are the sigmoidal, hyperbolic tangent and linear functions[3].

Recently, Carvalho et al. [4] used ANNs to predict ten cycles of Ni^{2+} adsorption in *Sargassum filipendula* seaweed. The authors trained several ANN structures and showed that the ANN 3-10-10-1 can efficiently predict the breakthrough curve of ten cycles using only the first three experimental data.

The main objective of this work was to evaluate the adsorption efficiency of the mixture Ni^{2+} - Zn^{2+} using the algae *Sargassum filipendula* as adsorbent after ten adsorption-desorption cycles. Also, to model the breakthrough curves using the phenomenological, and obtain one ANN to predict those curves.

2. Materials and Methods

2.1. Experimental

The *Sargassum filipendula* brown seaweed was the adsorbent used in this work. To remove the biomass impurities, the biomass was washed using deionized water, then it was dried during 24 hours at 60 °C. Finally, it was triturated to obtain particles with an average diameter of 2.2 mm.

The binary solution was prepared using NiCl_2 and ZnCl_2 . The concentration of each metal was 25 $\text{mg}\cdot\text{L}^{-1}$. A sulfuric acid solution at 0.1 M was used as eluent for desorption cycles.

All experiments were done using a column with a length of 50 cm and internal diameter of 2.8 cm. The column was filled with 4 g of the brown algae. Then, deionized water added to hydrate the biomass during 6 h. After this, the bed length was fixed in 15 cm. The solution was fed in the column using a peristaltic bomb at 30 °C and pH 3.5. The flow was fixed at 8 $\text{mL}\cdot\text{min}^{-1}$. In pre-defined time intervals, samples of the exit solution were collected to obtain the breakthrough curve. The concentration of each metal was determined by atomic absorption spectroscopy. The adsorbed mass of Ni^{2+} and Zn^{2+} in each cycle was calculated by the equation:

$$q_i = \frac{C_{0,i}Q}{M} \int_0^{t_{final}} \left(1 - \frac{C_i}{C_0}\right) dt \quad (2)$$

where: C_0 is the initial concentration, Q is the volumetric flow, M is the dry mass of the adsorbent, C is the exit concentration, t is time, and the subscript i indicates an individual metal.

Finally, a desorption step was performed to remove the metals from the algae. Overall, 10 adsorption-desorption cycles were done. The total time of adsorption was 36 hours.

2.2. Phenomenological Modeling

All the breakthrough curves obtained were modeled using the Bohart-Adams model [5], which the analytical solution is:

$$\frac{C}{C_0} = \begin{cases} 0 & t < t_r \\ \frac{1}{(e^A + e^{-B} - 1)e^B} & t > t_r \end{cases} \quad (3)$$

$$A = \frac{z\beta}{u_0} \quad (4)$$

$$B = \frac{(-tu_0 + z)\beta}{\alpha u_0} \quad (5)$$

$$\alpha = \frac{\rho_{bed}q_{eq}}{C_0\varepsilon} \quad (6)$$

$$\beta = k_a C_0 \alpha \quad (7)$$

$$t_r = \frac{z}{u_0} \quad (8)$$

Where: ρ_{bed} is the bed density, u_0 is the interstitial velocity, z is the bed length, q_{eq} is the equilibrium capacity of the solute per gram of adsorbent, and k_a is the adsorption kinetic parameter.

The parameter k_a was determined by minimizing the mean square error (F_{Obj}) using the Powell's method[6] written in Fortran 95.

2.3. ANN Modeling

To use Eqs. (3)-(8) it was considered that the adsorption of each metal was independent. Thus, that Ni^{2+} and Zn^{2+} do not interact during the removal process. This may be a drawback, since it is expected that the removal of one ion affects the other [7]. However, to consider this interaction, the knowledge about the binary equilibrium relation and a binary kinetic mechanism is needed – which is difficult. To overcome these issues, in this work was proposed to obtain an ANN to model all the

breakthrough curves, considering the interaction between the ions.

Since the collected data was not in the same time interval, all experimental breakthrough curves were adjusted to a spline using Table Curve 2D®. For each cycle it was generated 200 data points (a total of 2000) in an uniform time interval of 10.85 min.

To train the ANNs, a set of input and output variables are needed. The original development of ANNs considers that the data is static, thus it is needed a viable strategy to model kinetic data. Based on previous works [4, 8, 9], two set of input/output data were proposed, as shows Table 1. Figure 1 shows the general configuration of an ANN with two hidden layers for strategy 1.

Table 1. ANN input/output strategies.

Strategy	Inputs	Outputs
1	$C_{Ni^{2+}}(t-1); C_{Ni^{2+}}(t);$	$C_{Ni^{2+}}(t+1);$
	$C_{Zn^{2+}}(t-1); C_{Zn^{2+}}(t)$	$C_{Zn^{2+}}(t+1)$
2	$C_{Ni^{2+}}(t-2); C_{Ni^{2+}}(t-1);$	
	$C_{Ni^{2+}}(t);$	$C_{Ni^{2+}}(t+1);$
	$C_{Zn^{2+}}(t-2); C_{Zn^{2+}}(t-1);$	$C_{Zn^{2+}}(t+1)$
	$C_{Zn^{2+}}(t)$	

The generated data was randomly divided in training (70 %), test (15 %) and validation (15 %) sets. For each strategy, different ANN structures with one and two hidden layers were tested. The activation function was sigmoidal and linear for the neurons in hidden and output layers, respectively. The mean square error was the objective function (F_{Obj}) minimized by the Levenberg-Marquardt method [10]. Data from all ten cycles were used to train the ANNs.

After obtaining the best structure, the ANN was submitted to a simulation step to confirm its accuracy. All ten cycles were considered again. In this step, the same experiments can be used to check ANN efficiency because it was performed using only the experimental data at times 0 min and 10.85 min. Then, the ANN answers at time k are placed as input to calculate the value at $k+1$. If the ANN is not well trained, it will not predict the full kinetic profile correctly. The best ANN was then chosen based on the simulation step performance.

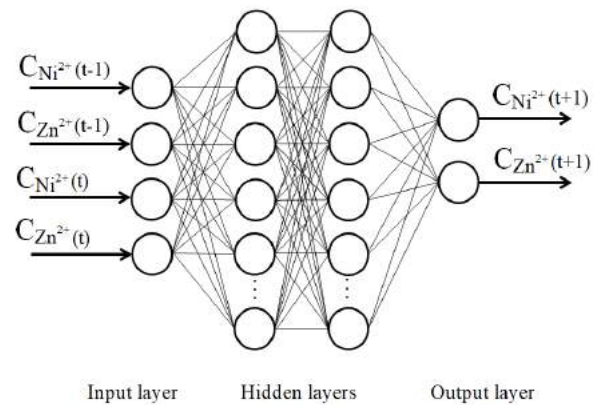


Fig. 1. General ANN used in this work.

3. Results and Discussion

3.1. Experimental

Figure 2 shows the main results obtained. One can see that the adsorbed mass decreased 50 % as long as the biomass was reused. The amount adsorbed per gram of biomass decreased significantly in the first three cycles, but it was almost constant after that. This probably occurred due the mass loss caused in the desorption process. In the first desorption process the sulfuric acid is more aggressive to the biomass in the first contact with the algae.

The total mass adsorbed was 810.9 g and 975.3 for Ni^{2+} and Zn^{2+} , respectively. This result shows that the brown seaweed has more affinity with Zn^{2+} . Ahmady-Asbchin and Jafari [11] showed similar results when removing Ni^{2+} and Zn^{2+} by the algae *Sargassum angustifolium*.

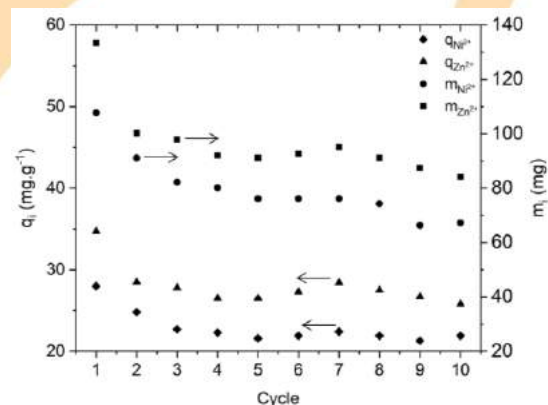


Fig. 2. Summary of experimental results.

Fig. 3 shows the all the breakthrough curves obtained for Ni^{2+} . One can see that the behavior for

cycles 2-10 is similar and apart from the cycle 1, which corroborates with the previous result. In the first cycle the adsorbent is new and has more capacity to adsorb. After the first desorption, the contact with the eluent can change the structure of the adsorbent surface, the charge distribution, and the flow distribution inside the column. Thus, it changes kinetic of the mass transfer [1, 12].

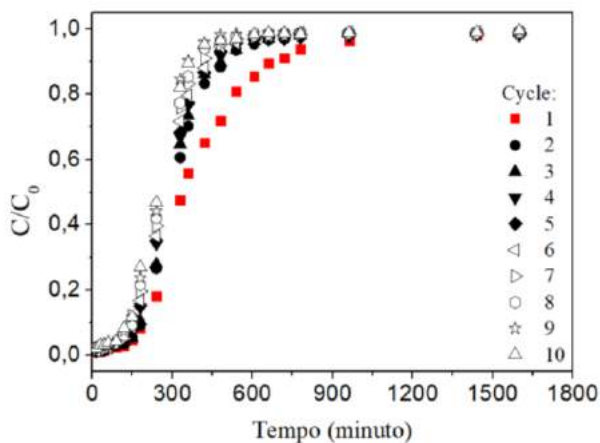


Fig. 3. Breakthrough curves obtained for Ni²⁺.

3.2. Phenomenological Modeling

The Bohart-Adams model was used to describe all breakthrough curves. Table 2 shows the results obtained for cycles 1, 2, 9, and 10. One can see that all F_{obj} values are low, but, as will be discussed in Section 3.3, it is not sufficient to accurately describe the breakthrough curves.

When analyzing the values of k_a , it can be seen that they are different for each metal. Which is a expected result, since it depends on the adsorption mechanism. In general, Ni²⁺ presented higher values of k_a than Zn²⁺, indicating that its adsorption occurs faster.

Table 2. Summary of the phenomenological modeling results.

Ciclo	Ni ²⁺		Zn ²⁺	
	k_a	F_{Obj}	k_a	F_{Obj}
1	$5.8 \cdot 10^{-1}$	0.17	$5.3 \cdot 10^{-1}$	0.06
2	$7.3 \cdot 10^{-1}$	0.19	$7.5 \cdot 10^{-1}$	0.16
9	$7.6 \cdot 10^{-1}$	0.25	$7.5 \cdot 10^{-1}$	0.09
10	$9.5 \cdot 10^{-1}$	0.14	$8.5 \cdot 10^{-1}$	0.09

Another observation is that k_a changed for each cycle. This result is interesting and indicates that the column dynamic varies as the adsorbent is being reused. As showed in Fig. 2, when the

adsorbent is new it removes a higher amount of the metals. This also can be seen in Fig. 3, in which each curve are apart from each other.

3.3. ANN Modeling

The phenomenological modeling performed in this study showed that the model's parameter is specific for a determined cycle. Thus, the utilization of the Bohart-Adams model for practical purposes is limited, because it depends on the cycle run. Thus, it is of great interest to develop only one equation that predicts all breakthrough curves regardless of the cycle.

In this work, several ANN structures were trained to perform this task. Using data from the several cycles, we aimed to obtain one equation that could be used in real time operation of an adsorption process. In Table 3, are shown the results obtained for different ANN structures.

Table 3. Summary of the ANN modeling results. ANNs are presented in increasing order of number of parameters.

Structure	F_{Obj} Training	F_{Obj} Validation	r^2 Simulation
Strategy 1			
4-13-5-2	$2.00 \cdot 10^{-3}$	$2.26 \cdot 10^{-3}$	0.987
4-4-25-2	$2.67 \cdot 10^{-3}$	$2.96 \cdot 10^{-3}$	0.988
4-6-19-2	$2.20 \cdot 10^{-3}$	$2.04 \cdot 10^{-3}$	0.988
4-14-15-2	$1.39 \cdot 10^{-3}$	$1.18 \cdot 10^{-3}$	0.987
4-15-17-2	$1.17 \cdot 10^{-3}$	$1.69 \cdot 10^{-3}$	0.990
4-15-18-2	$2.76 \cdot 10^{-3}$	$2.74 \cdot 10^{-3}$	0.989
4-17-18-2	$7.13 \cdot 10^{-4}$	$9.54 \cdot 10^{-4}$	0.989
4-23-15-2	$7.93 \cdot 10^{-4}$	$9.15 \cdot 10^{-4}$	0.989
4-18-21-2	$1.16 \cdot 10^{-3}$	$4.33 \cdot 10^{-3}$	0.992
Strategy 2			
6-5-5-2	$1.70 \cdot 10^{-3}$	$5.45 \cdot 10^{-4}$	0.952
6-6-6-2	$1.90 \cdot 10^{-3}$	$2.00 \cdot 10^{-3}$	0.939
6-7-7-2	$2.20 \cdot 10^{-3}$	$1.60 \cdot 10^{-3}$	0.944
6-8-8-2	$1.00 \cdot 10^{-3}$	$4.62 \cdot 10^{-4}$	0.949
6-10-10-2	$1.20 \cdot 10^{-3}$	$1.30 \cdot 10^{-3}$	0.954
6-18-18-2	$1.60 \cdot 10^{-3}$	$1.30 \cdot 10^{-3}$	0.954

The results showed that training F_{obj} were similar (in average) for both strategies. Also, validation F_{obj} are slightly lower for Strategy 2. In general, for both strategies, the ANN complexity (number of parameters) has directly relation with the ANN performance: the F_{obj} in training step is lower as the number of parameters increases. This

means that the problem is complex and ANNs with complex structures are needed to describe it.

In this work, the best result was chosen using a simulation step after the ANNs training/validation/test steps. This was done to guarantee that the ANN is capable to provide the kinetic profile using only the initial condition of each cycle.

When analyzing the simulation results, the best result was obtained with the ANN 4-18-21-2, since the r^2 was the highest obtained (Table 3). The correlation coefficient was 0.999 for both outputs in training, test and validation steps.

This ANN structure was not the one with the lowest F_{OBJ} in the training and validation steps. However, it was the best ANN to simulate all 10 adsorption cycles given that only the concentrations at 0 min and 10.85 min are experimental values. This result corroborates the idea that the ANN with the lowest F_{OBJ} could not have the best power of generalization.

It is important to mention that all the ANNs presented excellent agreement between the predicted and experimental data at training/validation/test steps. However, several of them failed to predict the curves in simulation step. The equation to calculate $C(t+1)$ of the ion l using ANN 4-18-21-2 can be written as:

$$C(t+1)_l = g \left(\sum_{k=1}^{21} w_{k,l} f \left(\sum_{j=1}^{18} w_{j,k} f \left(\sum_{i=1}^4 w_{i,j} x_i + b_j \right) + b_k \right) + b_l \right) \quad (9)$$

where: x_i is the input variable i and, f and g are the sigmoidal and linear functions, respectively.

Figs. 4 and 5 show the experimental and simulated breakthrough curves (using Bohart-Adams and ANN 4-18-21-2) for cycles 1 and 2. One can see that the Bohart-Adams model is not accurate for both ions in these two cycles. This is expected since the F_{obj} for this model was at least 100 times higher than those obtained with the ANN 4-18-21-2. The ANN predictions, on the other hand, present excellent agreement between the generated and predicted data, especially for cycle 2.

At Table 4 is shown the extracted mass and the time to reach $0.98C_{final}$ calculated from the experimental breakthrough curve and from the ANN predicted curve for cycles 1 and 2. One can see that the ANN can predict efficiently both parameters. For cycle 1 there were good and poor predictions. The extracted mass of Ni^{2+} in cycle 1 and the time of zinc removal were underestimated.

However for cycle 2 the values predicted are very near the experimental one.

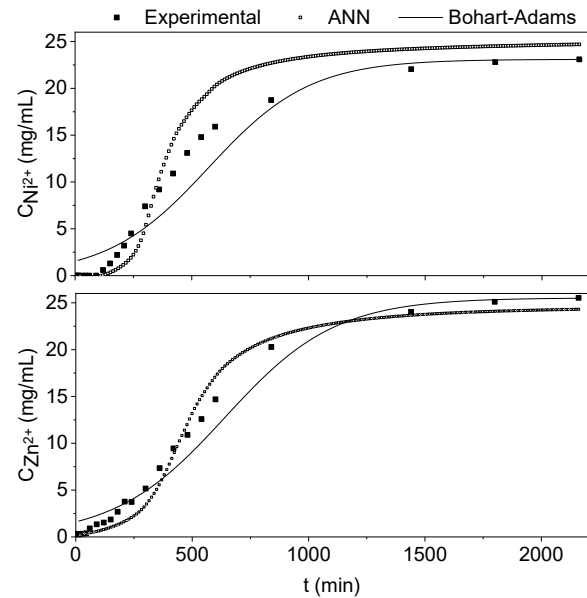


Fig. 4. Experimental and simulated breakthrough curves for cycle 1.

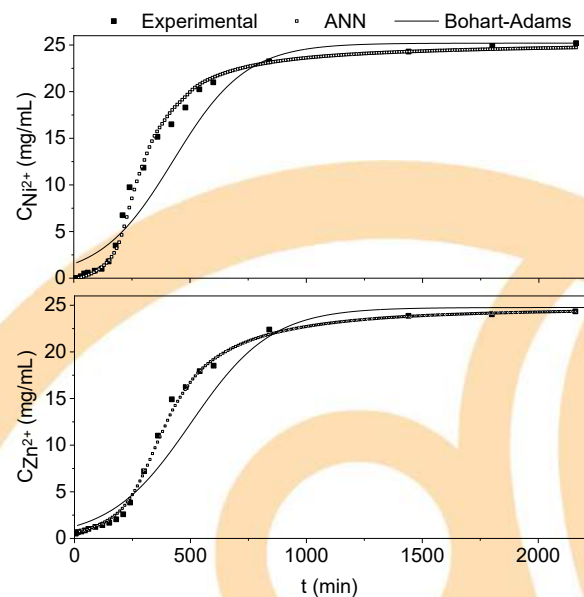


Fig. 5. Experimental and simulated breakthrough curves for cycle 2.

The ANN prediction for the cycles 3-10 was similar to the cycle 2 (data not shown). This result also confirms that the kinetics is very different among the first and the other cycles, as shown at Fig. 3.

Table 4. Summary of main results calculated from the experimental and ANN predicted curves.

Cycle	Ni		Zn	
	Exp.	ANN	Exp.	ANN
Extracted mass				
1	27.80	17.90	35.25	34.51
2	23.51	23.68	26.38	26.51
Time to 0.98C _{final} (min)				
1	1440	1421	1800	1530
2	1440	1400	1440	1443

4. Conclusion

In this work, the reuse of the *Sargassum filipendula* seaweed as adsorbent for the mixture Ni²⁺-Zn²⁺ was evaluated. Ten adsorption-desorption cycles were performed to analyze the removal efficiency, and also to obtain a mathematical model capable to describe all the breakthrough curves. The results showed that after ten cycles, the algae lost 50 % of its capacity, especially from cycle 1 to cycle 2. After the cycle 2, the algae capacity is almost the same. The phenomenological modeling was not capable to predict the kinetic profiles. However, the ANNs showed high accuracy. The best structure was 4-18-21-2. This ANN was able to predict efficiently all the curves, the time of equilibrium, and calculate the extracted mass with low error. In summary, this work showed that the ANNs can be a technique of high accuracy for practical purposes.

References

- [1] Maeda CH, Araki CA, Moretti AL, de Barros MASD, Arroyo PA. Adsorption and desorption cycles of reactive blue BF-5G dye in a bone char fixed-bed column. *Environ Sci Pollut Res* 2019;26:28500-9.
- [2] Tran HN, Chao H-P. Adsorption and desorption of potentially toxic metals on modified biosorbents through new green grafting process. *Environ Sci Pollut Res* 2018;25:12808-20.
- [3] Haykin S, *Neural Networks – A Comprehensive Foundation*, Prentice Hall, Delhi, 2005.
- [4] Carvalho LP, Seolatto AA, Silva EA, Martins TD, Kinetic modeling of Ni²⁺ adsorption cycles in fixed bed column using artificial neural networks, in: I Congresso Brasileiro em Engenharia de Sistemas em Processos - PSE 2019, Rio de Janeiro, 2019.
- [5] Bohart GS, Adams EQ. Some aspects of the behavior of charcoal with respect to chlorine. *J Am Chem Soc* 1920;42:523-44.
- [6] Powell MJD. An efficient method for finding the minimum of a function of several variables without calculating derivatives. *Comput J* 1964;7:155-62.
- [7] Seolatto AA, Martins TD, Bergamasco R, Tavares CRG, Cossich ES, da Silva E. Biosorption study of Ni²⁺ and Cr³⁺ by *Sargassum filipendula*: kinetics and equilibrium. *Braz J Chem Eng* 2014;31:211-27.
- [8] Choji TT, Ottaiano GY, Seolatto AA, Silva EA, Martins TD, Kinetics of Ni²⁺-Cr³⁺ mixture adsorption using artificial neural networks, in: I Congresso Brasileiro em Engenharia de Sistemas em Processos - PSE 2019, Rio de Janeiro, 2019.
- [9] Soares LAP, Andrade RR, Martins TD, Kinetics of second generation ethanol fermentation with cell recycle using artificial neural networks, in: I Congresso Brasileiro em Engenharia de Sistemas em Processos - PSE 2019, Rio de Janeiro, 2019.
- [10] Marquardt DW. An algorithm for least-squares estimation of nonlinear parameters. *J Soc Ind Appl Math* 1963;11:431-41.
- [11] Ahmady-Asbchin S, Jafari N. Removal of nickel and zinc from single and binary metal solutions by *Sargassum angustifolium*. *Water Sci Technol* 2013;68:1384-90.
- [12] Lodeiro P, Herrero R, Sastre de Vicente ME. Batch desorption studies and multiple sorption-regeneration cycles in a fixed-bed column for Cd(II) elimination by protonated *Sargassum muticum*. *J Hazard Mater* 2006;137:1649-55.

Experimental design for adsorption isotherms discrimination

Diego Del Fabro Kunzler^a, Roger Kober^a, Marcio Schwaab^{a,*}, Evandro Staffani^a, Elisa Barbosa-Coutinho^b

^a Departamento de Engenharia Química, Escola de Engenharia, Universidade Federal do Rio Grande do Sul, Rua Ramiro Barcelos, 2777 - Prédio 22202, Porto Alegre, RS, 90035-007, Brasil

^b Departamento de Físico-Química, Instituto de Química, Universidade Federal do Rio Grande do Sul, Av. Bento Gonçalves, 9500, Porto Alegre, RS, 91501-970, Brasil

Abstract

An adsorption process, that is, a pair adsorbate/adsorbent, is initially evaluated by parameter estimation of equilibrium models (adsorption isotherm). Initially, several equilibrium models might fit well to the experimental data set. This way, it is interesting to use a criterion that allow a design of an additional experiment to achieve the discrimination among them, while having to make the least number of experiments possible. This work has the objective of evaluating a method of sequential experimental design for model discrimination for liquid-solid adsorption. Utilizing a hybrid method of Particle Swarm Optimization and Gauss-Newton, the model parameters were estimated and evaluated for the quality of their model fit to the experimental data set by a χ^2 test. Then, additional conditions were calculated using a discrimination criterion, with C_0 as the optimization variable, and V and M as constants, until only one model remained or the discrimination could not be possible. As adsorbate, methyl orange was used and as adsorbent, activated carbon. Each condition had quadruplicates and the experimental error was approximated by the mean experimental variance of C_e , between those repetitions. The discrimination was successful, with the BET model being the only one with a good fit to the experimental data at the end of the sequential experimental design for model discrimination procedure.

Keywords: Experimental design; Model discrimination; Parameter Estimation; Adsorption equilibrium;

1. Introduction

The adsorption equilibrium is described, at a specific temperature, by mathematical relations between the equilibrium concentration, C_e , and the solid equilibrium concentration, Q_e , known as adsorption isotherms [1]. These isotherms can be obtained by thermodynamics, kinetics or empirical rationale, resulting in a vast quantity of different models [1,2,3]

Frequently in adsorption equilibrium analysis, a number of adsorption isotherms are fitted to a set of available experimental data, with the objective of identifying which model fits better to the data. In order to achieve, a certain measurement of the model's goodness of fit is computed, allowing the comparison between the models evaluated. With the best model identified, conclusions are drawn about the adsorption mechanism and thermodynamic of the system studied. One of the most used measurements of the goodness of fit of a model is the determination coefficient, R^2 , which represents the correlation between the experimental

measurements and the model predictions. In this case, the model with the highest R^2 is the one that fits better to the data, thus being used to draw conclusions about the system [4]. However, this coefficient must be used with care, since it tends to increase with the increase in the number of model parameters, leading to erroneous conclusions [5].

Sometimes, however, the amount of data available, or even the experimental conditions used in the preliminary experimental, do not allow the discrimination between all models tested. In these cases, a good alternative is the use of experimental design techniques for model discrimination [6]. These experimental designs are computed through the optimization of certain design criteria. Ideally, the use of such criteria should result in the selection of experimental conditions that lead to the maximum deviation between the model responses, making model discrimination possible without an excessive amount of experiments.

Rodríguez-Aragón and López-Fidalgo [7] considered the T-optimal design methodology, proposed originally by Atkinson and Federov [8], for the discrimination of the BET and GAB

isotherms applied to the adsorption of water vapor onto solid food materials. In both cases, it was shown that the T-optimal designs were independent of the monolayer capacity parameter in the GAB model and that a number of experiments equal to the number of model parameters in this model composed the experimental design.

Even though the works of Rodríguez-Aragón and López-Fidalgo [7] provide interesting insights on optimal designs for model discrimination, these designs do not address sequential experimental designs for the discrimination of adsorption isotherms. This type of experimental design consists in using information from previous experiments to design the next experiment based on the optimization of a certain design criterion [6]. The first researchers to propose a design criterion for model discrimination were Hunter and Reiner [9], where the optimal experimental condition is the one that maximizes the difference between model predictions. An issue with this approach is the fact that the model predictions and experimental uncertainties are not taken into account, which may not make model discrimination possible. Due to this fact, different criteria have been proposed over the last decades, incorporating the variances of model predictions and of the experimental measurements [10-13].

Based on these observations, the objective of this work is to evaluate a sequential design for the discrimination of adsorption isotherms applied to the adsorption of dye into activated carbon. The experiments were design using the design criterion proposed by Schwaab *et al.* [13], which makes use of the posterior variances of model predictions and of the parameter estimates. The sequential design was obtained for the adsorption of methyl orange onto activated carbon and the models evaluated are the Langmuir, Freundlich, Sips, Redlich-Peterson, Toth, Khan, Jovanovich, Temkin and BET isotherms.

2. Methodology

The evaluation of a system of adsorption in equilibrium is given by the determination of isotherm models that describe this phenomenon satisfactorily and the estimation and interpretation of their parameters, in the experimental range considered. Table 1 shows the models of adsorption isotherms used in this work:

Table 1. Isotherm Models.

Code	Name	Model
L	Langmuir	$Q_e = \frac{Q_m K_L C_e}{1 + K_L C_e}$
F	Freundlich	$Q_e = K_F C_e^n$
S	Sips	$Q_e = \frac{Q_m (K_S C_e)^n}{1 + (K_S C_e)^n}$
RP	Redlich-Peterson	$Q_e = \frac{Q_{RP} K_{RP} C_e}{1 + (K_{RP} C_e)^n}$
To	Toth	$Q_e = \frac{Q_m K_{Th} C_e}{[1 + (K_{Th} C_e)^n]^{\frac{1}{n}}}$
J	Jovanovich	$Q_e = Q_m [1 - \exp(-K_J C_e)]$
Tm	Temkin	$Q_e = K_{Tm} \ln(A_{Tm} C_e)$
Kh	Khan	$Q_e = \frac{Q_m K_{Kh} C_e}{(1 + K_{Kh} C_e)^n}$
BET	BET	$Q_e = \frac{Q_m K_{BET1} C_e}{\{(1 - K_{BET2} C_e) \times [(K_{BET1} - K_{BET2}) C_e + 1]\}}$

With those parameters, it's possible to make the equivalency of sorption capacity, given by the adsorption mass balance, with the models, with the objective of predicting the equilibrium concentration of the model. In this way, the response variable of the system is C_e and the independent variable are the volume, V , the mass, M and the sorbate initial concentration, C_0 . This is shown by Equation 1:

$$\frac{V}{M}(C_0 - C_e) = f(C_e) = Q_e \quad (1)$$

2.1. Experimental

Activated charcoal 100-200 mesh was used as adsorbent and methyl orange as adsorbate. The adsorbent was previously dried in a heater for 24 h at 120 °C and the adsorbate at 60 °C. The stock solutions of methyl orange were prepared by the weight of adequate mass on a beaker, dissolution with deionized water, transfer of the solution to a

volumetric flask with addition of more deionized water until the mark is reached. All the experimental conditions were made in quadruplicates. As vessels, 50 mL Erlenmeyer were used. The amount of adsorbent mass and solution volume were set as 0.05 g and 0.05 L respectively. The samples were placed on a Dubnoff bath at 30 °C and 270 rpm for 48 h to reach equilibrium. Then, they were centrifuged on Falcon tubes until no solid remained. Afterwards, they were diluted as necessary and read on a UV-VIS to measure C_e .

2.2. Parameter estimation and experimental design for model discrimination

In several cases it is possible to obtain parameters by direct measure or calculation, if a model is linear in regards to its parameters, but that's not the case for most adsorption isotherms. While it is possible to linearize the models to make direct calculations possible, previous works found on literature showed that in adsorption isotherms, by using the non-linear form of the model and inferring the parameters from experimental data generally yields parameters with better quality [14-19]. This process is known as parameter estimation, that uses an objective function that need to be minimized as the optimization criteria. Equation 2 shows the objective function used on this work:

$$S(\theta) = \sum_{i=1}^{NE} \frac{[C_{e,i}^e - C_{e,i}^m(C_{0,i}, V_i, M_i, \theta)]^2}{\sigma^2} \quad (2)$$

Its deduction can be found on previous works [20,21]. The variance used was calculated as the mean of variance of C_e for each quadruplicate of the experimental conditions, as shown by Equation 3. A previous F-test with 95% certainty level was used beforehand to determine that the variances are statistically equivalent.

$$\bar{\sigma}^2 = \frac{\sum_{i=1}^{NE} \sigma_i^2}{NC} \quad (3)$$

The parameter estimation was done using a hybrid algorithm that is divided in two parts: first, the preliminary values of the parameters are given by Particle Swarm Optimization (PSO), that scans all the search range of each parameters with the objective of reaching the lowest objective function possible. Second, the Gauss-Newton method uses those values as a first-guess to polish the result of the PSO, giving parameters that results in a better fit for its models [22].

After parameters estimation, it is necessary to evaluate the quality of their fit in regards to the experimental data. Since the objective function approximately follows a χ^2 distribution, a probability test can be made, as shown by Equation 4. If the model has a probability below 2.5%, it is considered a bad fit, and temporarily discarded.

$$\phi_m = 1 - p[\chi_v^2 \leq S_m(\hat{\theta})] \quad (4)$$

It is also possible the determine the relative probability in regards to all models, according to Equation 5 below:

$$P_m = \frac{\phi_m}{\sum_{m=1}^M \phi_m} \quad (5)$$

If more than one model has a good enough fit, it's necessary to establish which of those models is the correct one for this data set. This can be made using a standard that differentiate between each model, so the correct one can be chosen as the real model of the specific phenomenon studied. This criterion is called discriminator, that needs to be maximized, so as to give the condition with maximum deviation between models. The model used at his work is given by Equation 6, shown below:

$$\hat{D}_{m,n} = (P_m P_n)^z \frac{[C_e^m - C_e^n]_{NE+1}^2}{2\bar{\sigma}^2 + \hat{\sigma}_{m,NE+1}^2 + \hat{\sigma}_{n,NE+1}^2} \quad (6)$$

Details on how the posterior variances of model predictions are computed are found elsewhere [Schwaab et al., 2008]

This discriminator evaluates models pairwise and the variance used is an approximation considering the experimental condition that has yet to be made. Previous works showed that this way it's possible to obtain parameters with more precision and, consequently, facilitating the discrimination between models. The prediction variance of the models written on this way is known as posterior prediction variance.

The algorithm used for optimization of the discrimination criterion was PSO with only C_0 . As an optimizable variable. As previously discussed, V and M were set as constants with the values of 0.05 L and 0.05 g, and C_0 was optimized in the range of values varying between 1 to 1000 mg/L. Three initial C_0 conditions on this range were prepared before the discrimination process. The values of C_e after equilibrium were measured and each model parameters were estimated. The models were tested to see their fit to the experimental data set and if more than one model was deemed approved, the new experimental condition will be

the one that maximized the current value of the discriminator. Then, the parameter estimation, fit evaluation, and discriminator maximization is made until either:

- One model remains
- No model remains
- The discrimination between the remaining models is considered impossible ($\hat{D}_{m,n} < 1$)

It needs to be explained that the third option is not an absolute truth, since the posterior prediction variance of the models is an approximation in an experimental condition that has yet to be done. Because of this, it's possible that, in the experimental condition that has a discriminator value less than one, the pair of models be successfully discriminated. The opposite can also be said to $\hat{D}_{m,n} > 1$.

3. Results and Discussion

In Table 2 are shown the initial and the experimental design conditions for C_0 , as well as the discriminator value and the pair of models considered. It can be noticed that the experimental design conditions are well distributed in the C_0 range (1 to 1000 mg/L).

Table 2. Initial and Experimental Design Conditions

Experimental Condition	C_0 (mg/L)	$\hat{D}_{m,n}$	m,n
1	50.00		
2	250.0		
3	750.0		
4	178.6	$8.40 \cdot 10^7$	RP and J
5	307.7	5.88	F and J
6	137.8	1.57	L and F
7	1000	2.48	L and BET

This proves the utility of using a discriminator that considers the parametric and experimental variances in its calculation. It can also be noticed that all the values of it were superior to 1 but, as will be shown on Table 3, not in all conditions the discrimination occurred. The reason for this was already explained in Section 2.2.

Table 3 shows the absolute and relative model probabilities, used as the test for the quality of the fit to the experimental data, on each step of the experimental design for model discrimination.

Table 3. Absolute and Relative Probabilities for Isotherm Models During Experimental Design

Model	Experiments				
	1-3	4	5	6	7
L	45.2	46.7	23.9	12.8	0.00
F	47.3	13.5	17.9	12.4	1.34
S	38.1	47.3	44.1	47.8	1.27
RP	38.1	47.3	47.5	50.9	2.38
To	38.1	47.3	44.5	48.2	1.36
J	31.2	5.49	0.01	0.00	0.00
Tm	47.3	20.7	26.0	23.2	1.95
Kh	38.2	47.3	47.6	51.0	2.46
BET	39.1	47.5	50.4	53.2	38.1

It can be noticed that on the last additional condition, only the BET model fitted the experimental data properly. The Jovanovich model was inadequate after the second additional condition, and on the first and third no discrimination was made between models. Also, it can be noticed that the Sips, Redlich-Peterson, Toth and Khan model had probabilities either similar to the Langmuir or Freundlich model, during some parts of the experimental design. This can happen because those models, if they have certain specific parameters, behave exactly like Langmuir or Freundlich models, which makes discrimination between those models difficult.

Another reason that discrimination was not successful on all experimental conditions was because of the use of a mean variance of C_e as the estimation for the experimental error. Since this value does not represent the deviation of error in function of the values of C_e , the discrimination can be hindered. It needs to be said that even in theory it would be possible to determine the experimental error of the experiments, it would be necessary to realize several more experiments, which goes against the principle of experimental design, that is economy of resources and time.

Table 4 shows the final parameters of the BET model for adsorption of methyl orange on activated carbon. It can be seen that BET parameters could be estimated with a relatively good precision. If it was necessary a better precision, experimental sequential design for precise parameter estimation could be employed [6].

Table 4. Final Parameters of the BET Model

Parameter	Value	Std. Dev.	Inf. Lim.	Sup. Lim.
Q_m (mg/g)	2160	36.6	2090	2240
K_{BET1} (L/mg)	4.29	1.32	1.58	7.00
K_{BET2} (L/mg)	2.25×10^{-3}	2.39×10^{-4}	1.76×10^{-3}	2.74×10^{-3}

Figures 1 and 2 shows the initial and final model prediction plots of each isotherm, respectively. It can be clearly observed that when the last experimental designed condition at the higher C_0 value, only BET model was able to provide a suitable fit to all experimental data.

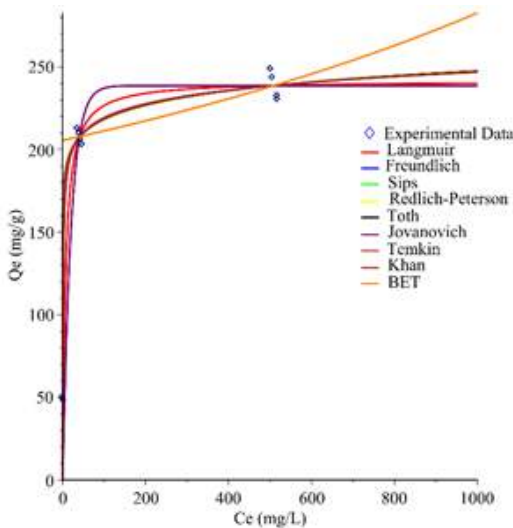


Fig. 1. Models predictions with initial data set

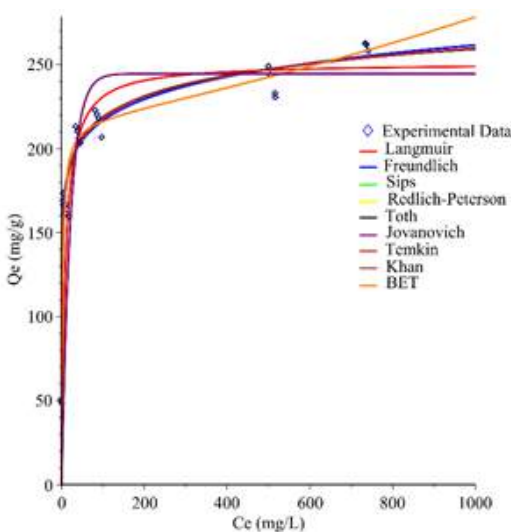


Fig. 2. Models predictions with final data set

It is also interesting to observe that some experimental designed condition presented a relatively high experimental uncertainty, a fact that difficulties model discrimination.

4. Conclusion

With this research, it was possible to show the experimental design for model discrimination, starting with a set number of arbitrary initial C_0 conditions and calculating additional optimal conditions for model discrimination, while keeping V and M constant, for methyl orange adsorption on activated carbon. With the experimental data set obtained, it can be stated with 95 % certainty that, between the evaluated models, only the BET model has a good enough fit to represent the data set. This suggest that the adsorption of methyl orange occurs with the formation of multilayers of adsorbate on the adsorbent surface. Since only one model remained after the discrimination process, it can be concluded that it was successful.

This research also showed that while the discriminator value gives a good idea whether or not the discrimination is possible, it is necessary to actually realize the experiment to draw conclusions.

Lastly it is emphasized the importance of the objective of experimental design. Whether is it for discriminating between models to find out which one is the correct one for the phenomenon at hand or for obtaining the chosen model parameters with the most accuracy possible, the researcher needs to make those consideration to fulfill the objective desired. **Acknowledgements**

The authors are grateful for CNPq/Brazil and CAPES/Brazil for providing scholarships to make this research possible.

References

- [1] Do D. Adsorption analysis: equilibria and kinetics. 1st ed. London: Imperial College Press; 1998.
- [2] Dabrowski A. Adsorption: from theory to practice. Adv Colloid Interface Sci 2007;147:401-411.
- [3] Foo KY, Hameed BH. Insights into the modelling of adsorption isotherm systems. Chem Eng J 2010;156:2-10.
- [4] El-Khaiary MI, Malash GF. Common data analysis errors in batch adsorption studies. Hydrometallurgy 2011;105:314-320.
- [5] Montgomery DC; Runger, GC. Applied Statistics and Probability for Engineers. 3rd. ed. New York: John Wiley & Sons; 2003.



- [6] Schwaab M, Pinto JC. Análise de Dados Experimentais II. Planejamento de Experimentos. Rio de Janeiro: E-Papers; 2011.
- [7] Rodriguez-Aragón LJ, López-Fidalgo J. T-, d- and c-optimum designs for BET and GAB adsorption isotherms. *Chemom Intell Lab Syst* 2007;89:36-44.
- [8] Atkinson AC, Fedorov VV. The design of experiments for discriminating between two rival models. *Biometrika* 1975;62:57-70.
- [9] Hunter WG, Reiner, AM. Design for discriminating between two rival models. *Technometrics* 1965;7:307-323.
- [10] Box GEP, Hill WJ. Discrimination Among Mechanistic Models. *Technometrics* 1967;9:57-71.
- [11] Buzzi-Ferraris G, Forzatti P. A new sequential experimental design procedure for discriminating among rival models. *Chem Eng Sci* 1983;38:225-232.
- [12] Schwaab M, Silva FM, Queipo CA, Barreto Jr. AG, Nele M, Pinto JC. A new approach for sequential experimental design for model discrimination. *Chem Eng Sci* 2006;61:5791-5806.
- [13] Schwaab M, Monteiro JL, Pinto JC. Sequential experimental design for model discrimination. Taking into account the posterior covariance matrix of differences between model predictions. *Chem Eng Sci* 2008;63:2408-2419.
- [14] Osmari TA, Gallon R, Schwaab M, Barbosa-Coutinho E, Severo Jr. JB, Pinto JC. Statistical analysis of linear and non-linear regression for the estimation of adsorption isotherm parameters. *Adsorp Sci Technol* 2013;31:433-458.
- [15] Kumar KV, Sivanesan S. Equilibrium data, isotherm parameters and process design for partial and complete isotherm of Methylene blue onto activated carbon. *J Hazard Mater* 2006;B134:237-244.
- [16] Kumar KV, Sivanesan S. Isotherm parameters for basic dyes onto activated carbon: Comparison of linear and non-linear method. *J Hazard Mater* 2006;B129:147-150.
- [17] Kumar KV. Comparative analysis of linear and non-linear method of estimating the sorption isotherm parameters for Malachite green onto activated carbon. *J Hazard Mater* 2006;B136:197-202.
- [18] Kumar KV, Sivanesan S. Comparison of linear and non-linear method in estimating the sorption isotherm parameters for safranin onto activated carbon. *J Hazard Mater* 2005;B123:2005.
- [19] Kumar KV, Sivanesan S. Prediction of optimum sorption isotherm: Comparison of linear and non-linear method. *J Hazard Mater* 2005;B126:198-201.
- [20] Englezos P, Kalogerakis N. *Applied Parameter Estimation for Chemical Engineers*. 1st. ed. New York; Marcel Dekker Inc.; 2001.
- [21] Schwaab M, Pinto JC. Análise de Dados Experimentais I. Fundamentos de Estatística e Estimação de Parâmetros. Rio de Janeiro: E-Papers; 2007.
- [22] Schwaab M, Biscaia EC, Monteiro JC, Pinto JC. Nonlinear parameter estimation through Particle Swarm Optimization. *Chem Eng Sci* 2008;63:1542-1552.

A framework to estimate the thermodynamic parameters on adsorption equilibria using particle swarm optimization

M. Maraschin, P.L. Limberger, N.P.G. Salau*

Universidade Federal de Santa Maria, Roraima Avenue, 1000, Santa Maria, 97105-900, Brazil

Abstract

In this paper a system composed of 3-aminophenol and activated carbon, obtained from Avocado seed, was studied to determine the thermodynamic parameters: Gibbs free energy, enthalpy and entropy. For this purpose, a new methodology was used to transform the isotherm constants into the dimensionless thermodynamic equilibrium constants. The equilibrium data was interpreted by Langmuir and Sips isotherms at six different temperatures (298.15 K to 323.15K). The parameter estimation was performed by particle swarm optimization and nonlinear least squares as objective function. According to high values of coefficient of determination (R^2) and low Akkaike Information Criterion (AIC), Sips isotherm was the most appropriated to describe the system equilibrium. The thermodynamic parameters were obtained by the nonlinear fit of Van't Hoff equation. The negative values of Gibbs free energy at all temperatures indicated a spontaneous process, while the negative values of enthalpy revealed exothermic process with an absolute value of 24.80 kJ/mol.

Keywords: Keywords: Adsorption, Equilibrium constant; Van't Hoff equation; Thermodynamic parameters; Particle swarm optimization.

1. Introduction

The adsorption phenomena occur by the mass transfer from an adsorbate in a fluid phase, which can be in liquid or gas state, to a surface of an adsorbent solid [1]. The isotherm condition expresses the adsorption capacity as a function of the adsorbate concentration at constant temperature. The most used isotherm is the Langmuir model, which was originally developed by Irving Langmuir for adsorption in gas-solid system with an assumption of homogeneous monolayer adsorption [2]. However, this model can be applied to describe the liquid-solid system [3], according to Equation 1:

$$q_e = \frac{q_m K_L C_e}{1 + K_L C_e} \quad (1)$$

where K_L is the Langmuir equilibrium constant of adsorption (L/mg) and q_m is the maximum adsorption capacity (mg/g).

Sips isotherm (Equation 2) is a combination of Freundlich and Langmuir isotherms, and is able to describe the adsorption capacity for heterogeneous adsorption system [4]:

$$q_e = \frac{q_m (K_s C_e)^n}{1 + (K_s C_e)^n} \quad (2)$$

where K_s is the Sips equilibrium constant of adsorption (L/mg), q_m is the maximum adsorption capacity (mg/g) and n_s is the Sips exponent. For low concentrations, this equation is reduced to the Freundlich equation, while for high concentrations it predicts a monolayer adsorption, equal to the Langmuir model (Equation 1).

Usually, the estimation of Gibbs free energy (Equation 3), enthalpy and entropy of adsorption is obedient to the curve fit of Van't Hoff equation [6-7], from a set of equilibrium constants and temperature (Equation 4):

$$\Delta G = \Delta H - T\Delta S \quad (3)$$

$$\ln(K_{eq}) = -\frac{\Delta H}{RT} + \frac{\Delta S}{R} \quad (4)$$

where R is the universal gas constant (8.314 J/mol K) and K_{eq} is the dimensionless thermodynamic equilibrium constant.

Several methods have been proposed to obtain the dimensionless thermodynamic equilibrium constant from the best isotherm constant equilibrium: (i)

multiplying K_{best} by the factor 55.5 mols of water per liter [6-8], (ii) multiplying K_{best} for the maximum adsorption capacity [9] or (iii) multiplying K_{best} by the factor 1000 [8]. However, Lima et al [10] considered these methods inadequate and proposed Equation 5 as an adequate method:

$$K_{eq} = \frac{1000K_{best}C_rMW_{adsorbate}}{\gamma_{adsorbate}} \quad (5)$$

where K_{best} is the equilibrium isotherm constant (Sips or Langmuir), C_r is the standard concentration (1 mol/L), MW is the molecular weight of adsorbate (g/mol) and γ is activity coefficient of adsorbate in solution.

This paper has the goal to utilizing an appropriated method to convert the equilibrium constant of adsorption, which has units of volume per mass, to the thermodynamic equilibrium constant, which is dimensionless. In order to estimate the correct Gibbs free energy, enthalpy and entropy.

2. Adsorption equilibrium constant

The thermodynamic equilibrium constant is defined by Equation 6 where a_i is the activity of the respective components i :

$$K_{eq} = \frac{a_{adsorbate-adsorbent}}{a_{adsorbate}a_{adsorbent}} \quad (6)$$

From this starting point, with the assumption that the concentration of the solid phase is constant [10], the ratio of adsorbent-adsorbed activity to adsorbent activity is also a constant, which can be incorporated into the numerical value of leading to a new constant. For ideal solution, the thermodynamic equilibrium constant and the adsorbent activity can be defined by Equation 7 and 8, respectively:

$$K_{ideal} = \frac{C_r}{C_e} \quad (7)$$

$$a_{adsorbate} = \frac{C_e}{\gamma_{adsorbate}C_r} \quad (8)$$

where C_e is the concentration of adsorbate (mol/L).

Lima et al. [10] assumed Equation 9, where the factor 1000 is to convert g to mg and the molecular weight is to convert L/mg to L/mol.

$$\frac{K_{ideal}}{\gamma_{adsorbate}} = \frac{1000K_L C_r MW_{adsorbate}}{\gamma_{adsorbate}} \quad (9)$$

An equivalent equation was derived from Ghosal and Gupta [8] for Langmuir isotherm, the fraction of surface coverage, Θ , is defined as:

$$\Theta = \frac{q_e}{q_m} \quad (10)$$

In addition, the thermodynamic equilibrium was obtained by Equation 10:

$$K_{eq} = \frac{\Theta}{(1-\Theta)a_{adsorbate}} \quad (11)$$

Consequently, the Langmuir isotherm can be rewritten according to Equation 11:

$$\Theta = \frac{K_L C_e}{1 + K_L C_e} \quad (12)$$

Using a simple algebraic manipulation, the relation of Equation 4 is obtained.

3. Materials and methods

3.1. Experimental

Experimental data were obtained from the prior literature; Lima et al. [10] adsorbed 3-aminophenol onto activated carbon from Avocado seeds at six different temperatures.

Based on this data, Langmuir and Sips isotherms are modeled using Equations 1 and 2, respectively. For each isotherm, the statistical and model parameters were calculated. The values obtained for the thermodynamic equilibrium constants were dimensionless and used to calculate the free energy of Gibbs, enthalpy and entropy for the system, using Equations 3 and 4, respectively.

3.2. Parameter estimation

The particle swarm method was used together with the trust region method based on interior point techniques in order to improve the parameter estimation. The MathLab® function *particleswarm* optimization is a hybrid method between an evolutionary algorithm method and a genetic algorithm method [11], while the MathLab® function *fmincon* is non-linear constrained

minimization algorithm that uses the trust region method [12].

4. Results and discussion

The numerical results of the parameter estimation of the Langmuir and Sips models, together with their respective statistical metrics, are shown in Table 1.

Table 1. Isotherm parameters of 3-aminophenol adsorption onto Avocado seed activated carbon.

Isotherm	Temperature (K)					
	298.15	303.15	308.15	313.15	318.15	323.15
Langmuir						
q_m (mg/g)	262.2	271.44	289.05	338.79	311.77	314.15
K_L (L/mg)	1.686	0.8509	0.62	0.2932	0.6148	0.21
ARE (%)	7.269	7.4093	4.6399	8.7289	7.2631	3.13
SSE	6132.6	6091.1	3428.7	10792	7595.2	1725
R^2	0.961	0.963	0.9801	0.9702	0.9645	0.99
R^2_{adj}	0.958	0.9602	0.9786	0.9679	0.9618	0.99
AIC	61.50	95.098	86.478	103.67	98.408	76.1
Sips						
q_S (mg/g)	352.7	372.10	390.53	410.56	432.03	452
K_S (L/mg)	0.354	0.2909	0.2583	0.2188	0.1841	0.16
n_S	0.233	0.2182	0.2369	0.3653	0.2464	0.19
ARE (%)	0.313	0.0771	0.0932	0.0982	0.0098	0.01
SSE	15.385	1.2931	1.3963	2.6273	0.0267	0.11
R^2	0.999	1	1	1	1	1
R^2_{adj}	0.999	1	1	1	1	1
AIC	8.562	-28.58	-27.43	-17.94	-86.78	-64.5

Langmuir model reasonably describes the experimental data, since for high values of concentration the model reaches the value of the maximum adsorption capacity while the experimental adsorption capacity keeps increasing, this behavior is visible in Figures 1 to 6. This error predicted by Langmuir equation is also visible by lowers values of coefficient of determination (R^2). In contrast, Sips isotherm was able to predict the values of adsorption capacity at higher

concentration, this explains the value of coefficient of determination closest to the unit, also the AIC values for Sips isotherm results in lower values than Langmuir although the inclusion of a new parameter. Therefore, Sips isotherm was chosen as the best to interpret the adsorption of 3-aminophenol onto Avocado seeds activated carbon.

Table 2 presents the values of thermodynamics parameters:

Table 2. Thermodynamic parameters of 3-aminophenol adsorption onto Avocado seed activated carbon.

Isotherm	T (K)	K°	ΔG° (kJ/mol)	ΔH° (kJ/mol)	ΔS° (kJ/mol)	R^2
Langmuir	298.15	184088.0	-30.05			
	303.15	92857.01	-28.83			
	308.15	67659.36	-28.49			
	313.15	31996.32	-27.01	-54.99	-0.0853	0.93
	318.15	67091.89	-29.40			
	323.15	23691.68	-27.06			
Sips	298.15	38653.13	-26.18			
	303.15	31745.33	-26.12			
	308.15	28187.76	-26.25			
	313.15	23877.20	-26.24	-24.80	0.0046	0.99
	318.15	20090.46	-26.21			
	323.15	17776.95	-26.29			

The negative values of Gibbs free energy demonstrate a spontaneous process. According to Liu [6] the heat involved, received or emitted, in physisorption is between 2.1 to 21.0 kJ/mol. In this study, the values of enthalpy, adjusted with the Sips isotherm, was -24.801 kJ/mol, which is in the same magnitude of the superior limit.

Figures 7 and 8 present the nonlinear fit of dimensionless adsorption equilibrium constant as function of temperature using, respectively Langmuir and Sips equilibrium constants. As was expected the curve fit using Sips values is better described by the Van't Hoff equation than Langmuir, since Sips presents higher values of coefficient of determination.

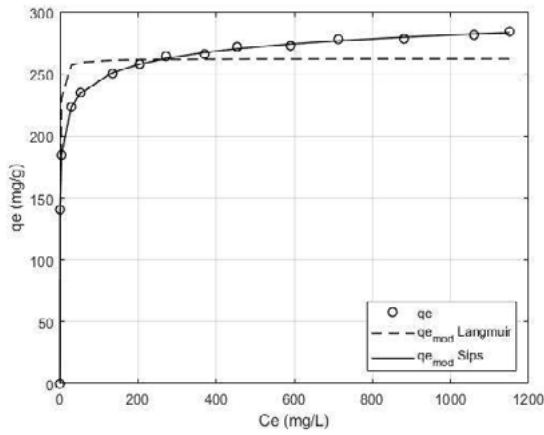


Figure 1: Langmuir and Sips isotherms at 298.15 K.

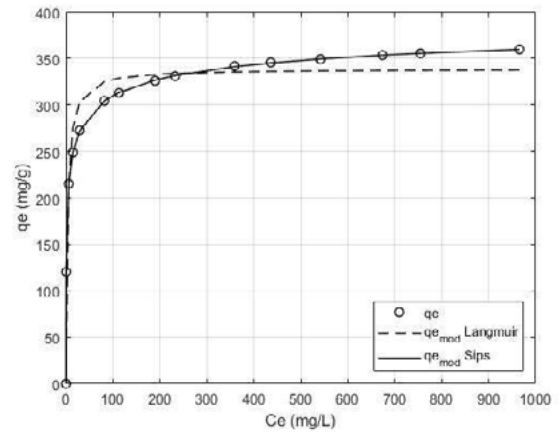


Figure 4: Langmuir and Sips isotherms at 313.15 K.

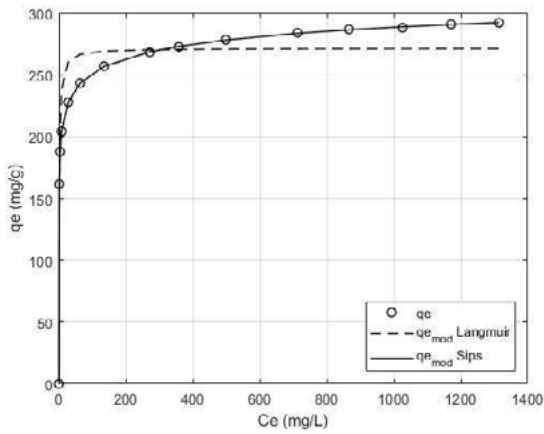


Figure 2: Langmuir and Sips isotherms at 303.15 K.

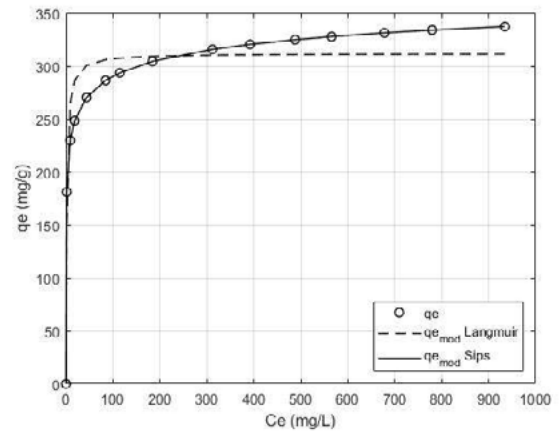


Figure 5: Langmuir and Sips isotherms at 318.15 K.

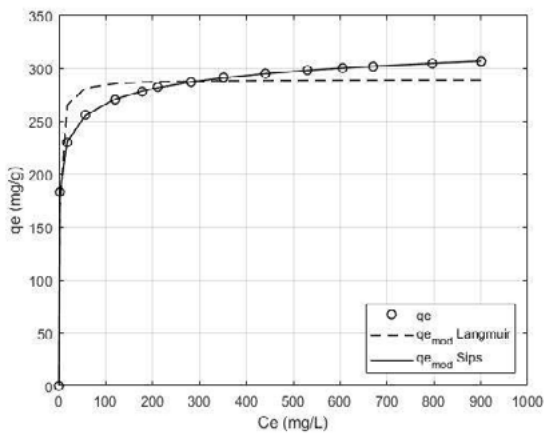


Figure 3: Langmuir and Sips isotherms at 308.15 K.

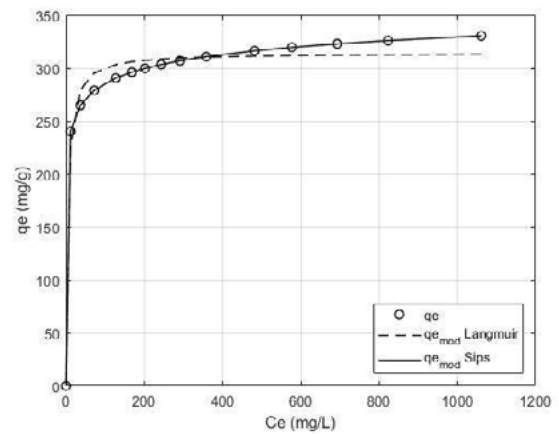


Figure 6: Langmuir and Sips isotherms at 323.15 K.

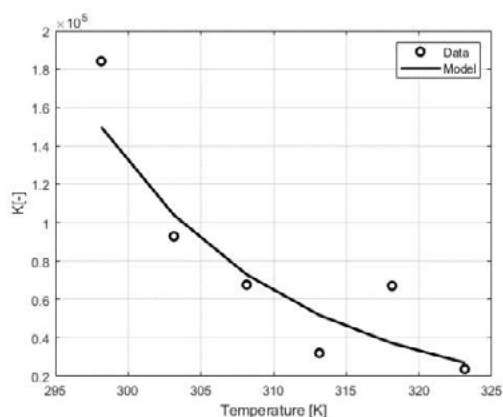


Figure 7: Van't Hoff with dimensionless Langmuir constant.

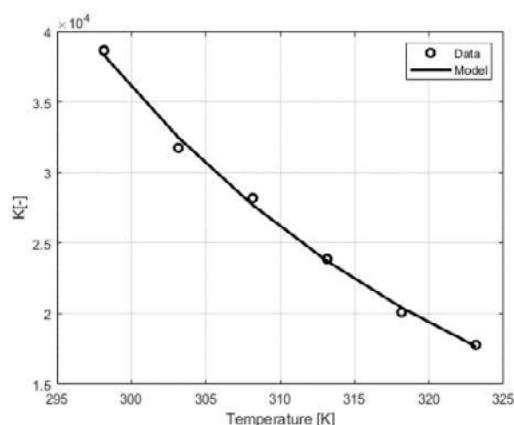


Figure 8: Van't Hoff with dimensionless Sips constant.

5. Conclusion

It is concluded that the enthalpy and entropy values found are consistent with the obtained Gibbs free energy values, which presented an exponentially decay tendency with temperature. The negative sign of Gibbs free energy was in agreement with a spontaneous process. The enthalpy obtained with the Sips equilibrium adsorption constant was similar to the values found in the literature. The achievement of these results provides a validating tool to the methodology to obtain a dimensionless equilibrium constant from equilibrium adsorption constant, thus, it is possible to extend the use of this tool to evaluate other adsorptive systems.

Acknowledgements

The authors thank the Research Support Foundation of the State of Rio Grande do Sul (FAPERGS) and the Coordination for the

Improvement of Higher Education Personnel (CAPES) for the financial support.

References

- [1] Dąbrowski A. Adsorption — from Theory to Practice. *Adv Colloid Interface Sci* 2001;93:135-224.
- [2] Langmuir, I. The adsorption of gases on plane surfaces of glass, mica and platinum. *J Am Chem Soc* 1918;40:1361-1403.
- [3] Ayawei N, Ebelegi AN, Wankasi D. Modelling and Interpretation of Adsorption Isotherms. *J Chem* 2017;2017:1-11.
- [4] Saruchi, Kumar V. Adsorption Kinetics and Isotherms for the Removal of Rhodamine B Dye and Pb+2 Ions from Aqueous Solutions by a Hybrid Ion-Exchanger. *Arab J Chem* 2019;12: 316-329.
- [5] Foo KY, Hameed BH. Insights into the Modeling of Adsorption Isotherm Systems. *Chem Eng J* 2010;156:2–10.
- [6] Liu Y. Is the Free Energy Change of Adsorption Correctly Calculated? *J Chem Eng Data* 2009;54:1981–1985.
- [7] Leite AJB, Sophia AC, Thue PS, dos Reis GS, Dias SLP, Lima EC, Vagheti JCP, Pavan FA, de Alencar WS. Activated carbon from avocado seeds for the removal of phenolic compounds from aqueous solutions. *Desalin Water Treat*, vol. 71, pp. 168 -181, 2017.
- [8] Tran HN, You S J, Hosseini-Bandegharaei A, Chao HP. Mistakes and Inconsistencies Regarding Adsorption of Contaminants from Aqueous Solutions: A Critical Review. *Water Research* 2017;120:88–116.
- [9] Ghosal PS, Gupta AK. Determination of Thermodynamic Parameters from Langmuir Isotherm Constant-Revisited. *J Mol Liq* 2017;225:137–146.
- [10] Lima EC, Hosseini-Bandegharaei A, Moreno-Piraján JC, Anastopoulos I. A critical review of the estimation of the thermodynamic parameters on adsorption equilibria. Wrong use of equilibrium constant in the Van't Hoff equation for the calculation of thermodynamic parameters of adsorption. *J Mol Liq* 2019;273:425-434.
- [11] Kennedy J, Eberhart R. Particle Swarm Optimization. *Proceedings of ICNN'95 - International Conference on Neural Networks*, 1995.
- [12] Byrd RH, Gilbert JC, Nocedal J. A trust region method based on interior point techniques for nonlinear programming. *Math Program* 2000;89:149-185.

Experimental and Computational Analysis of CO₂, N₂, and CO Adsorption on Hydroxyapatite.

Gabriel D. Barbosa^a, Carla L. M. Camargo^b, Frederico W. Tavares^{a,b,*}, Neuman S. Resende^a, Vera M. M. Salim^a

^a Programa de Engenharia Química, PEQ/COPPE, Universidade Federal do Rio de Janeiro, Centro de Tecnologia, Cidade Universitária, Rio de Janeiro, 21941-914, RJ, Brazil

^b Escola de Química, Universidade Federal do Rio de Janeiro, Centro de Tecnologia, Cidade Universitária, Rio de Janeiro, 21941-909, RJ, Brazil

Abstract

Hydroxyapatite is a crystalline material widely used as a catalyst, an adsorbent, and a biomaterial to biomedical applications. In this work, we use a combined experimental-computational approach to investigate the possible mechanisms of CO₂ adsorption on mesoporous hydroxyapatite. First, total and reversible adsorption isotherms were experimentally obtained at different temperatures. In addition to CO₂, we have also obtained equilibrium data to CO and N₂. Second, we have carried out molecular simulations using molecular dynamics (MD) and Monte Carlo (MC) methods. In our simulations, we use the pore size consistent with the sample characterization data used in our experimental assays. Experimental results show greater selectivity for CO₂ especially at low temperatures. At these conditions, we suppose the occurrence of a strong chemical bonding in addition to the formation of a liquid CO₂ film near the pore walls during CO₂ adsorption. This hypothesis is in agreement with the pronounced adsorbent-pore wall interaction observed in MD simulations as well as the similarity between simulated (MC) and reversible CO₂ isotherms.

Keywords: CO₂; hydroxyapatite; molecular simulation; adsorption

1. Introduction

Hydroxyapatite (HAp) is a crystalline material extensively studied due to unique characteristics as biocompatibility and chemical stability, which enables its use as a biomaterial with biomedical applications [1]. HAp is a phosphate with a chemical formula of Ca_{10-x}(HPO₄)_x(PO₄)_{6-x}(OH)_{2-x} [0 ≤ x ≤ 1], in whose x = 0 refers to a stoichiometric structure [2]. With a flexible structure for cationic/anionic substitutions, HAp is also widely used as a catalyst and adsorbent of heavy metals from aqueous phases [3].

In the last decades, the concentration of CO₂ in the atmosphere increased rapidly and new technologies had been developed for its removal. It is known that HAp prepared in air can be easily contaminated with CO₃²⁻ ions coming from

atmospheric CO₂ [4]. Therefore, another potential use for HAp is the CO₂ capture using the low-temperature adsorption process, that is the prevailing technique for this type of gas separation [4,5].

In this context, important questions are a) Is the hydroxyapatite an efficient adsorbent for CO₂ removal at low-temperature? b) Which mechanisms are associated with this process?

In order to ask the first question, we have carried out equilibrium experiments at different temperatures using CO₂. The second question is discussed comparing the obtained CO₂ adsorption isotherms with analogous results for CO and N₂ as well as comparing reversible and total adsorption isotherms. We have also carried out molecular dynamic and Monte Carlo simulations in order to

explain the anomalous behavior of CO₂ adsorption on hydroxyapatite at very low temperatures.

2. Methodology

2.1 Experimental

The hydroxyapatite (HAp) sample was prepared by addition of a 0.3 M solution of dibasic ammonium phosphate (NH₄)₂HPO₄ in a 0.5 M solution of calcium nitrate Ca(NO₃)₂, using the precipitation method, followed by drying and calcination [6]. To obtain a stoichiometric hydroxyapatite, we used a ratio $[Ca^{2+}]/[PO_4^{3-}] = 1.67$. The solid sample was initially analyzed by the X-ray diffraction and thermogravimetric analysis and the characterization of specific surface area, pore volume and diameter were performed by nitrogen adsorption in an ASAP 2000 Micrometrics.

CO, CO₂, and N₂ adsorption measurements were performed on a Micrometrics ASAP 2000 Chemi System device. Solid samples were initially treated under a vacuum of 1.10^{-4} Pa at 473 K for 1 h. The total adsorption isotherms were made at two temperatures (273 and 190 K) for CO, N₂, and CO₂. Additionally, we measured the adsorption isotherm for CO₂ at 353 K. Then a vacuum of 0.0001 Pa was made on the solid sample at the adsorption temperature and new adsorption isotherms were obtained, the reversible isotherm. The difference between the total and reversible isotherm will be called irreversible isotherm, which corresponds to the adsorbed amount that remained in the porous media after the vacuum treatment.

2.2 Molecular Simulation.

In order to analyze the microscopic mechanisms of adsorption of CO, N₂ and CO₂ in hydroxyapatite, molecular simulations of dynamics and Monte Carlo were performed. The molecular dynamics of the hydroxyapatite structure and adsorbates (CO, CO₂, N₂) were carried out at different temperatures using the LAMMPS molecular dynamics simulator [7]. The slit-like pore was built based on the crystallographic structure of apatites refined by Rietveld method reported [8]. We used the software Playmol to build the simulation box [9]. The force field of Lin and Heinz [10] was used to model the

hydroxyapatite interaction. Otherwise, the adsorbate was modeled using the TraPPE force field [11]. The cross parameters were calculated using Lorentz-Berthelot combining rules [12].

Additionally, all simulations were performed for the same number of adsorbate molecules (N = 700 molecules) at 190 K and 273 K. The slit-shaped pore, as well as the initial configuration of CO₂ is shown in Fig. 1.

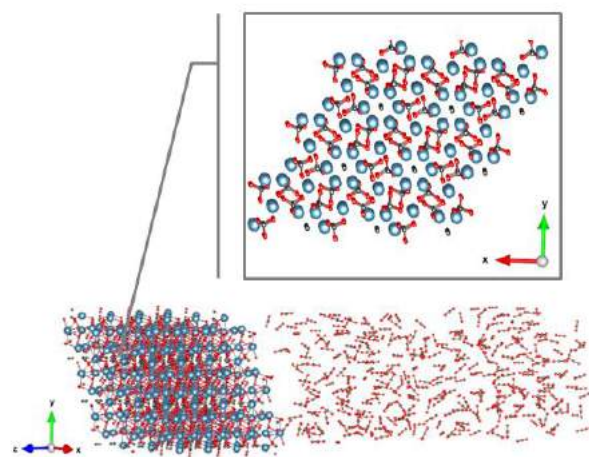


Fig. 1. Hydroxyapatite slit-shaped pore and initial configuration for CO₂.

Initially, we performed the equilibration of the systems for 9 nanoseconds. Then, we started the sampling of the adsorbate coordinates of the system. These samples were then used to obtain the density distributions and xy-plane self-diffusion coefficients of the adsorbates inside the porous media. In particular, the self-diffusion coefficients were obtained through the Einstein relation [12].

To study CO₂ adsorption in 190 K hydroxyapatite, we performed simulations of Monte Carlo in the grand canonical ensemble, in which the chemical potential, volume, and temperature are specified. Particularly, these simulations were carried out in the Software Cassandra [13], using the same force fields used in molecular dynamics simulations. The Peng-Robinson equation of state was used to compute the chemical potential of the gas reservoir at a given bulk pressure. Starting from an initial configuration with no CO₂ molecule within the pore, 2×10^6 of Monte Carlo steps were used for system balancing. Then 1×10^6 Monte Carlo steps were performed for system sampling.

3. Results and Discussion

The hydroxyapatite was characterized as a mesoporous material with a specific area of $41 \text{ m}^2/\text{g}$, pore volume $0.2 \times 10^{-6} \text{ m}^3/\text{g}$ and pore size $167 \times 10^{-10} \text{ m}$.

As observed in Fig. 2 and Fig. 3, CO and N₂ adsorption data are type I. Additionally, total and reversible isotherms of CO and N₂ do not differ significantly at both temperatures. In the pressure and temperature range studied, CO adsorption was slightly higher than N₂. Nonetheless, the CO₂ adsorption data show more complex behavior (Fig. 4). Particularly, the CO₂ adsorption data at 190 K presents type IV behavior differing significantly from the reversible adsorption data at the same temperature. At other temperatures, the total and reversible CO₂ adsorption data are markedly type I and do not show significant differences between them.

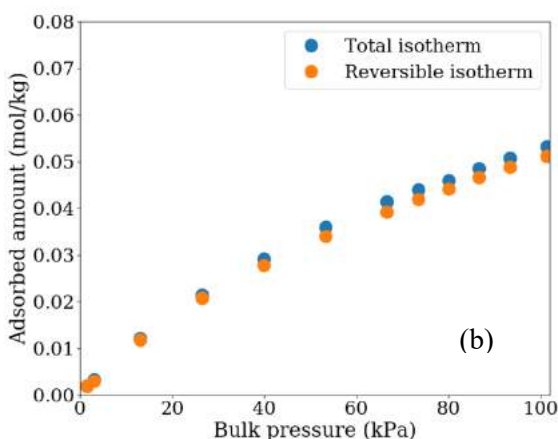
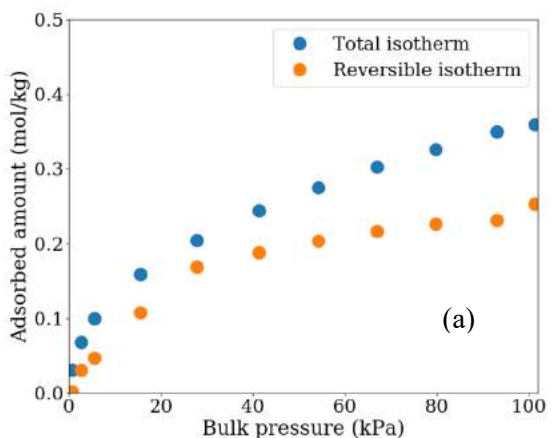


Fig. 2. Experimental adsorbed amount of carbon monoxide at 190 K (a) and 273 K (b).

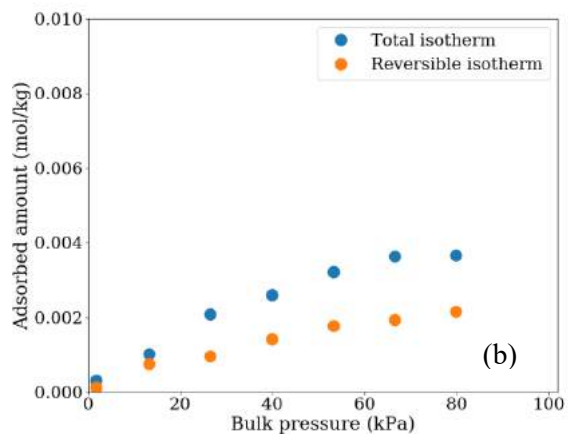
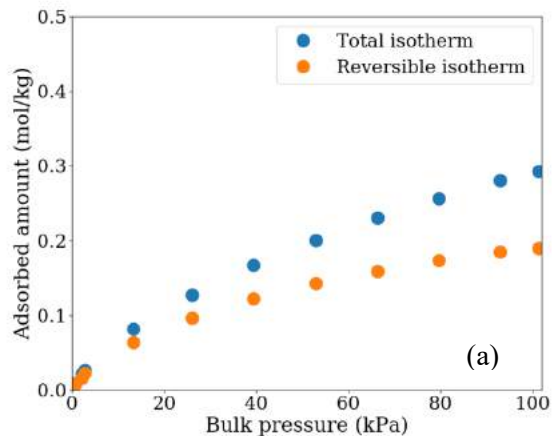


Fig. 3. Experimental adsorbed amount of nitrogen at 190 K (a) and 273 K (b).

Fluid density distributions within the pore obtained in MD simulations are shown in Fig. 5 to 7. In these figures, the center of the pore was chosen as the abscissa reference point. The CO and N₂ distributions, Fig. 5 and 6 respectively, show only a peak near the pore wall. Comparing the CO and N₂ distributions, a slightly higher coordination is observed to N₂ molecules once the N₂ peak is higher than of CO peak.

The pronounced adsorption observed in the total CO₂ adsorption isotherm may initially also be attributed to a pronounced adsorbent-pore wall interaction. However, the appreciable difference between the total and reversible adsorption isotherms at 190 K (Fig 4a) indicate the occurrence of another phenomena at low temperatures.

Herein, we suppose that the CO₂ amount irreversibly fixed on HAp is probably due to the conversion of adsorbed CO₂ to CO₂³⁻, as pointed

out by [14]. The exothermicity of this reaction [15] explains its occurrence only at low temperatures.

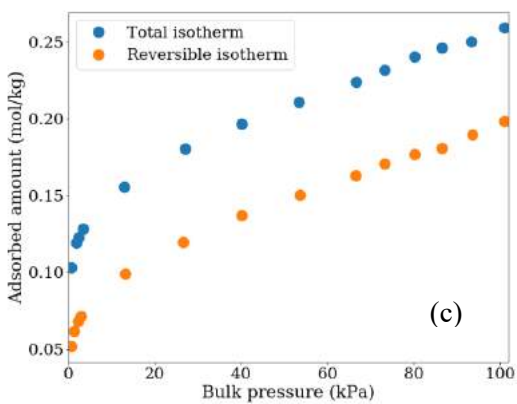
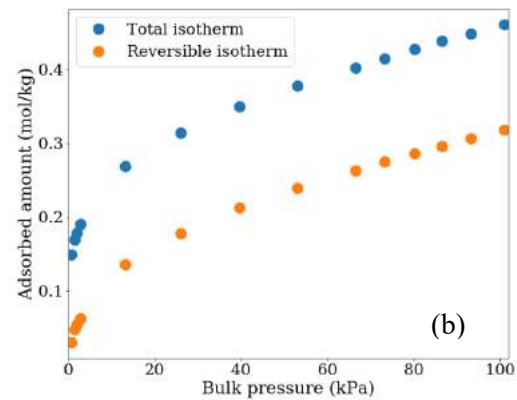
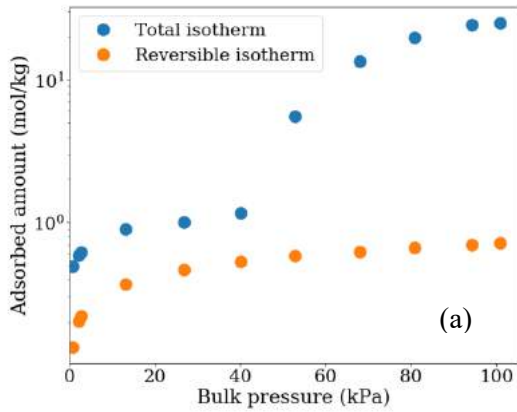


Fig. 4. Experimental adsorbed amount of carbon dioxide at 190 K (a), 273 K (b), and 353 K (c).

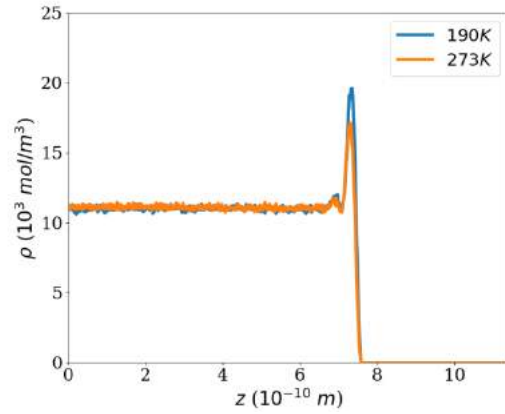


Fig. 5. Density distribution of carbon monoxide within the pore at 190 K and 273 K.

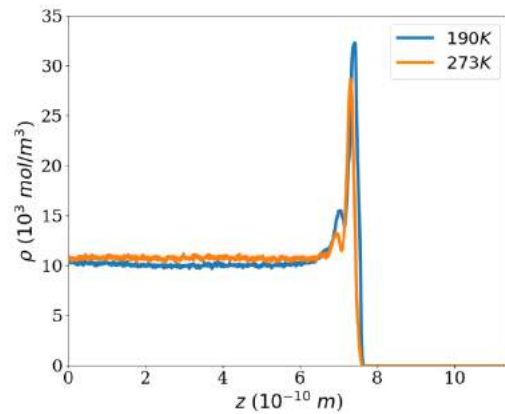


Fig. 6. Density distribution of nitrogen within the pore at 190 K and 273 K.

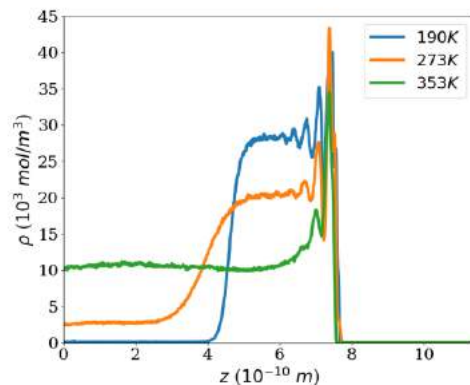


Fig. 7. Density distribution of carbon dioxide within the pore at 190 K and 273 K.

Monte Carlo simulation results can provide insights about the mechanisms involved in the anomalous behavior of CO₂ adsorption on hydroxyapatite at very low temperatures. Fig. 8 shows the comparison of experimental CO₂ adsorption isotherms, in particular, the reversible isotherm, and that obtained by molecular simulation.

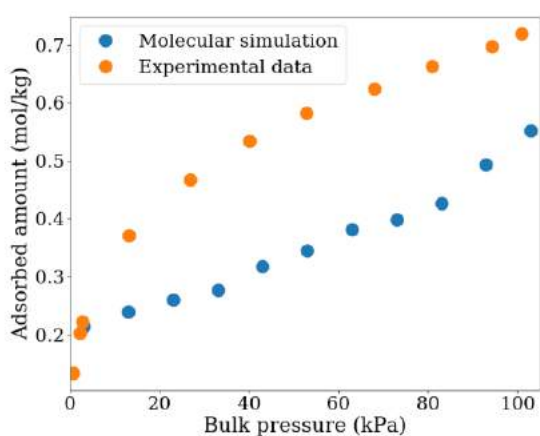


Fig 8. Reversible adsorbed and molecular simulation isotherm of carbon dioxide at 190 K

As can be seen, the simulated isotherm in the same order of magnitude of experimental reversible adsorption isotherm. Once molecular simulations not take into account the occurrence of chemical reactions, the similarity between simulated and reversible experimental data also indicates the occurrence of a chemical bonding beyond the reversible adsorption, which corroborates our hypothesis of chemical reaction occurrence.

Actually, although the simulation shows reasonable agreement with the experimental data, some deviations can be observed in Fig. 8. The difference between these simulated and experimental results can be attributed to the probable structural change of the solid induced by CO₂ reaction, which was not taken into account in the simulation box topology.

The obtained self-diffusion coefficients for the three components are presented in Table 1. For the evaluated temperatures, the value of the CO₂ self-diffusion coefficient is noticeably lower than the other evaluated adsorbates. In particular, for 190 K, the CO and N₂ self-diffusion coefficients are approximately 8 times greater than the CO₂

coefficient value. These results are in agreement with those observed in Fig. 5-7, which show the formation of a CO₂ liquid-like film near to the pore wall.

Table 1. Self-diffusion coefficients for pure adsorbates at different temperatures.

Temperature	Adsorbate A (t)	Self-diffusion coefficient (10 ⁸ m ² /s)
190 K	N ₂	5.175
	CO	5.125
	CO ₂	0.675
273 K	N ₂	6.448
	CO	6.296
	CO ₂	3.070

4. Conclusions

In this work, mesoporous hydroxyapatite samples were used to analyze the adsorption of CO, N₂, and CO₂. Experimental results show a greater selectivity for CO₂ and a significant difference between the irreversible and reversible isotherms for this component at low temperatures. In this particular case, we suppose the occurrence of a chemical bonding with conversion of adsorbed CO₂ to CO₂³⁻. The similarity between the reversible adsorption isotherms at 190 K with analogous results obtained by Monte Carlo molecular simulation also indicates an irreversible chemical mechanism during CO₂ adsorption. Radial density distributions show the formation of a CO₂ liquid-like film near the pore walls, which is also verified by the lower diffusion coefficient for CO₂ in relation to the studied another components.

Acknowledgements

We acknowledge CAPES, CNPq, and ANP-Petrobras for the financial support.

References

- [1] Bhat SS, Waghmare UV, Ramamurty U. First-Principles study of structure, vibrational, and elastic properties of stoichiometric and calcium-deficient



- hydroxyapatite, *Cryst. Growth Des.* 2014, 14:3131-41.
- [2] Faria RMB, César DV, Salim VMM. Surface reactivity of zinc modified hydroxyapatite. *Catal. Today* 2008; 133–135: 168-73.
- [3] Resende NS, Camargo CLM, Reis PC, Salim VMM. Mechanisms of mercury removal from aqueous solution by high-fixation hydroxyapatite sorbents, *Int. J. Environ. Sci. Technol.* 2019, 16:7221–8.
- [4] Cheng, ZH, Yasukawa A, Kandori K, Ishikawa T. FTIR study of adsorption of CO₂ on nonstoichiometric calcium hydroxyapatite. *Langmuir*; 14: 6681-6.
- [5] Younas M, Sohail M, Leong LK, Bashir MJK, Sumath S. Feasibility of CO₂ adsorption by solid adsorbents: a review on low-temperature systems. *Int. J. Environ. Sci. Technol.* 2016; 13: 1839-60.
- [6] Camargo CLM, Salim VMM, Tavares FW, Resende, NS. Phenomenological modeling for elemental mercury capture on hydroxyapatite-based adsorbents: An experimental validation. *Fuel* 2018, 225:509-18.
- [7] Plimpton S, Fast Parallel Algorithms for Short-Range Molecular Dynamics, *J. Comput. Phys.* 1995; 117: 1–19
- [8] Wilson RM, Elliott JC, Dowke, SEP. Rietveld refinement of the crystallographic structure of human dental enamel apatites, *Am. Mineral* 1999; 84: 1406–1414.
- [9] PLAYMOL, Software for building molecular models, (n.d.). <https://github.com/atoms-ufjf/playmol>.
- [10] Lin TJ, Heinz H. Accurate Force Field Parameters and pH Resolved Surface Models for Hydroxyapatite to Understand Structure, Mechanics, Hydration, and Biological Interfaces, *J. Phys. Chem. C.* 2016; 120: 4975–4992.
- [11] Potoff JJ, Siepmann JJ. Vapor–liquid equilibria of mixtures containing alkanes, carbon dioxide, and nitrogen. *AIChE Journal* 2001; 47: 1676-1682.
- [12] Frenkel D, Smit B. Understanding molecular simulation: from algorithms to applications. Vol. 1. Elsevier, 2001.
- [13] Shah, JK, Marin-Rimoldi E, Mullen RG, Keene BP, Khan S, Paluch AS, Rai N, Romaniello LL, Rosch TW, Yoo B, Maginn EJ. Cassandra: An open source Monte Carlo package for molecular simulation. *Journal of computational chemistry* 2017; 38: 1727-1739.
- [14] Cheng ZH, Yasukawa A, Kandori K, Ishikawa T. FTIR Study of Adsorption of CO₂ on Nonstoichiometric Calcium Hydroxyapatite. *Langmuir* 1998; 14: 6681-6686.
- [15] Deitz VR, Carpenter FG, Arnold RG. Interaction of carbon dioxide with carbon adsorbents below 400°C. *Carbon* 1964; 1:245–54.

Estimation of the transfer free energy of POE tails and application for a spherocylindrical structure prediction for a mixture of P123 and F127 surfactants

Marlon S. Gama ^a, Gabriel D. Barbosa ^a, Carla L. M. Camargo ^{b,*}, Frederico W. Tavares^{a,b}

^a Programa de Engenharia Química - PEQ/COPPE, Universidade Federal do Rio de Janeiro, Rio de Janeiro, RJ, Brasil

^b Escola de Química, Universidade Federal do Rio de Janeiro, Rio de Janeiro, RJ, Brasil

* Corresponding author: carlamanske@eq.ufrj.br

Abstract

We develop an algorithm to study micelle formation of non-ionic surfactants based on a well-known molecular thermodynamic model, which relates Gibbs energy and the stability of the microemulsions. The thermodynamic description is obtained by minimizing the Gibbs energy, based on the surfactant molecular information and the conditions of the solution. As a numerical strategy, we use a stochastic optimization method (PSO - Particle Swarm Method), implemented in Fortran. The model results for the CMC at different temperatures and the micelle geometry were compared with literature data of CMC and pore diameter of SBA-15 silica, synthesized using the model surfactant. With the developed algorithm, we study the dependency of silica textural properties with the structure of nonionic surfactants. A successful prediction of the micelle structure using the thermodynamic modeling can be useful to reduce experimental effort, since the silica synthesis shows a high-cost production and exceeding time-consuming.

Keywords: Surfactants; microemulsion; Gibbs energy; optimization

1. Introduction

Polymer surfactants are a class of polymers characterized by presents both hydrophilic and hydrophobic moieties. In the presence of water as a solvent, it is worldwide the ability of surfactants to self-assemble and aggregates into micelles in order to minimize the contact of the solvent with the hydrophobic moiety [1].

The literature reports, for 40 years, the use of micelles as templates for the synthesis of mesoporous silica nanoparticles. The structure of the micelle determines the porous size and the final silica channel geometry, e.g. spherical or cylindrical.

The synthesis consists in entrap the micelles with a silica source (alkoxysilane, e.g. TEOS) with a posterior chemical or thermic treatment to remove the template. Pluronic P123 is the most frequent surfactant used for the synthesis of silica, classified

as a pluronic triblock copolymer containing poly(ethylene oxide) - PEO - and poly(propylene oxide) - POE [2]. Thus, we have considered the Pluronic P123 as a model surfactant, which also present values of CMC in water and quick response to temperature variation.

In this work, we use a molecular thermodynamics approach to describe aggregation of Pluronic P123 in water.

2. Methodology and modeling approach

2.1. Thermodynamic model for the micelle formation: spherocylindrical structure.

Gibbs energy of a system is calculated as Eq. 1.

$$\frac{G'}{kT} = N_g g \frac{\Delta\mu_g}{kT} + \sum_j N_j \ln(X_j) + N_g [\ln(X_g)] \quad (1)$$

The first term in the right is the free energy of micellization (Eq. 2).

$$\left(\frac{\Delta\mu_g^o}{kT}\right) = \left(\frac{\Delta\mu_g^o}{kT}\right)_{transfer} + \left(\frac{\Delta\mu_g^o}{kT}\right)_{Def} + \left(\frac{\Delta\mu_g^o}{kT}\right)_{Mix} + \left(\frac{\Delta\mu_g^o}{kT}\right)_{Def-h} + \left(\frac{\Delta\mu_g^o}{kT}\right)_{Steric} + \left(\frac{\Delta\mu_g^o}{kT}\right)_{interf} \quad (2)$$

where G' is the Gibbs energy, N_g is the number of micelles with g molecules of surfactant, N_j is the number of free surfactant j ; X_j and X_g are the molar fraction in water for the free component j and the micelles with size g . The parameters k and T are, respectively, the Boltzmann constant and the system temperature.

The free energy of micellization is defined as a sum of different contribution. We applied the contributions reported by [3] with the consideration of a spherocylindrical structure (Fig. 01).

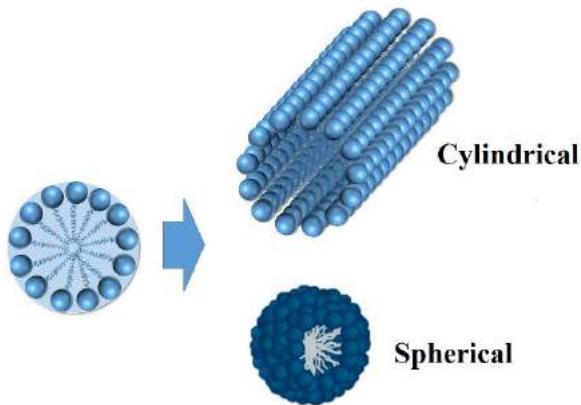


Fig.01 – The aggregation of micelles can lead to a formation of a spherical, cylindrical or a spherocylindrical model. The last structure arise where the spheric structure is formed at the extremities of the cylinder.

The contributions used here are detailed elsewhere [3], [4] and taken in consideration the following energies:

1.2. Deformation-free energies and packaging of the surfactant tail.

For a cylindrical geometry, the deformation energy is giving by:

$$\left(\frac{\Delta\mu_g^o}{kT}\right)_{def} = \left(\frac{10P_f\pi^2}{80}\right) \left(\alpha_{gA} \frac{R_s^2}{N_A L^2} + \alpha_{gB} \frac{Q_g^2}{N_B L^2}\right) \quad (3)$$

where P_f is the packing parameter ($1/3$ for this geometry), α_{gA} and α_{gB} are the molar fractions of surfactants A and B inside the micelle, L is the lattice parameter, R_s is the diameter of the cylinder and $Q_g = N_b L$ if $l_A > Q_g > l_B$, for l_A and l_B being the extended length for the surfactants.

For a spherical geometry:

$$\left(\frac{\Delta\mu_g^o}{kT}\right)_{def} = \left(\frac{9P_f\pi^2}{80}\right) \left(\alpha_{gA} \frac{R_s^2}{N_A L^2} + \alpha_{gB} \frac{Q_g^2}{N_B L^2}\right) \quad (4)$$

and P_f is the packing set as $1/2$.

1.3. Headgroup Mixing and deformation in the Hydrophilic Region of the Micelle

As suggested by Firoozabadi [5], for a nonionic surfactant the mixing and the deformation energies for POE headgroups have different contribution in contrast with an ionic surfactant. A more precise form to consider these contributions are given by:

For a spherical geometry:

$$\left(\frac{\Delta\mu_g^o}{k_B T}\right)_{mix} = \frac{\phi E_x v_E}{L^3} \left(\frac{0.5 - \chi_{WE}}{1 + D/R_s}\right)$$

For a cylindrical geometry:

$$\left(\frac{\Delta\mu_g^o}{k_B T}\right)_{mix} = \frac{\phi E_x v_E}{L^3} \left[\frac{(0.5 - \chi_{WE})D}{R_s}\right] \ln\left(1 + D/R_s\right)$$

For $E_x v_E$ the volume related with the number of oxyethylene units, ϕ is the concentration of heads in the hydrophilic region, χ_{WE} is the water-POE interaction parameter and D is the thickness of the hydrophilic region.

For the headgroup deformation, the energy follow as:

$$\left(\frac{\Delta\mu_g^o}{k_B T}\right)_{def-h} = \frac{1}{2} \left[\frac{D^2 L}{E_x v_E} + \frac{2(E_x v_E)^{1/2}}{DL^{1/2}} - 3 \right]$$

1.4. Energy free from steric interactions between the heads

Reclosing the surfactant head with one end of the tail that the heads become in a region of greater approximation between the same as compared to the infinite dilution condition. This causes them to occur repulsive interactions between the heads:

$$\left(\frac{\Delta\mu_g^o}{kT}\right)_{steric} = -\ln\left(1 - \frac{a_{pA} + a_{pB}}{a}\right)$$

The parameter a_{pA} represents the transversal surfactant head area and a is the area per molecule inside the aggregate.

1.5. Energy of formation of the water-core interface of the aggregate

The formation of a micellar aggregate generates an interface between the domain hydrophobic and the surrounding aqueous medium. This contribution is obtained by:

$$\left(\frac{\Delta\mu_g^o}{kT}\right)_{interf} = \left(\frac{\sigma_{agg}}{kT}\right)(a - \alpha_{gA}a_o - \alpha_{gB}a_o)$$

where σ_{agg} is the interfacial tension for the water-aggregate and a_o is the area per surfactant molecule.

1.6. Numerical Procedure

For this work, we aim to estimate the free energy for the transfer of the surfactant POE tail. We will compare the CMC value for different POE surfactant and applied the energy founded to construct an empirical model to predict this energy as a function of temperature and POE number.

For each simulation the number of surfactant inside the spherocylindrical, the number of aggregates and the diameter of the hydrophilic region are estimated.

The search of the minimum value of Gibbs energy (maximum stability condition) is a optimization problem, whose optimized parameters are properties of the system such as number of micelles and number of surfactant molecules per micelle. We used the stochastic Particle Swarm

Method as a optimization method, which was implemented in the Fortran language.

3. Discussion and Results

We show in this work a preliminary result for the estimation of CMC using the temperature of 25 °C. In Table 01 is demonstrated the values found for the parameter estimation of two different surfactants: P123 and F127.

Table 01 – Comparison between the experimental and estimated values for the Critical micelle concentration.

CMC (mM, T = 25 °C)		
	Estimated	Alexandridis et al. (1994) [1]
P123	$5.62 \cdot 10^{-5}$	$5.22 \cdot 10^{-5}$
F127	$5.94 \cdot 10^{-4}$	$5.55 \cdot 10^{-4}$

The estimation shows a good agreement with the experimental data, showing that the hypotheses applied in the methodology can be valid for POE surfactants.

Aiming a better understanding of the system, Figure 02 shown the result for a mixing of both surfactant at the temperature of 25 °C.

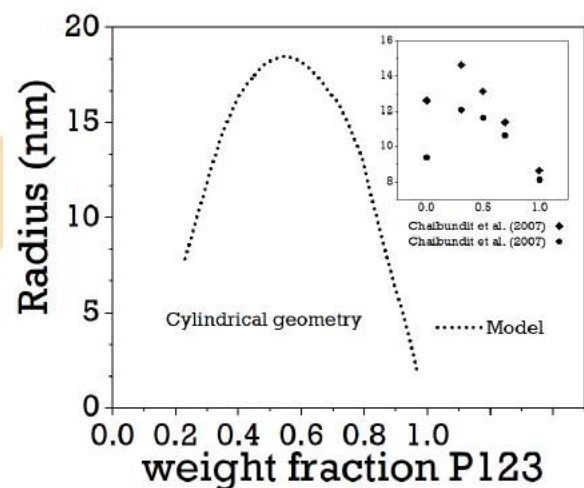


Fig.02 - Effect of the weight fraction of P123 for micelles formation of F127 and the P123 mixtures. $T = 25$ °C. Data points are experimental data from the literature [6] at $T = 40$ °C.

The maximum diameter for the mixing of both surfactant is about 18 nm. A similar behavior is reported by Chaibundit [6] at 40 °C. This result



show a potential prediction for the maximum diameter that a mesoporous material like SBA can reach, only modifying or adding a surfactant in solution.

4. Conclusion

The CMC estimated is close to the values reported by the literature at 25 °C. This result suggests that a spherocylindrical geometry can be used for this purpose. A successful prediction of the micelle radius was obtained for the mixture of P123 and F127 using spherocylindrical micelle structure. The thermodynamic modeling can be useful to reduce experimental effort, since the silica synthesis shows a high-cost production and exceeding time-consuming. We intend to verify the prediction potential for the model using different types of surfactant and hydrocarbons.

Acknowledgements

The authors would like to thank Petrobras, CNPq, CAPES, and FAPERJ foundations by the financial support of this work.

References

- [1] P. Alexandridis, J. F. Holzwarth, and T. A. Hatton, "Micellization of Poly(ethylene oxide)-Poly(propylene oxide)-Poly(ethylene oxide) Triblock Copolymers in Aqueous Solutions: Thermodynamics of Copolymer Association," *Macromolecules*, vol. 27, no. 9, pp. 2414–2425, Apr. 1994.
- [2] S. M. L. Dos Santos, K. A. B. Nogueira, M. De Souza Gama, J. D. F. Lima, I. J. Da Silva Júnior, and D. C. S. De Azevedo, "Synthesis and characterization of ordered mesoporous silica (SBA-15 and SBA-16) for adsorption of biomolecules," *Microporous Mesoporous Mater.*, vol. 180, 2013.
- [3] R. Nagarajan and E. Ruckenstein, "Theory of surfactant self-assembly: a predictive molecular thermodynamic approach," *Langmuir*, vol. 7, no. 12, pp. 2934–2969, Dec. 1991.
- [4] L. A. Moreira and A. Firoozabadi, "Molecular Thermodynamic Modeling of Droplet-Type Microemulsions," *Langmuir*, vol. 28, no. 3, pp. 1738–1752, Jan. 2012.
- [5] A. Khoshnood, B. Lukanov, and A. Firoozabadi, "Temperature Effect on Micelle Formation: Molecular Thermodynamic Model Revisited," *Langmuir*, vol. 32, no. 9, pp. 2175–2183, Mar. 2016.
- [6] C. Chaibundit, N. M. P. S. Ricardo, F. de M. L. L. Costa, S. G. Yeates, and C. Booth, "Micellization and Gelation of Mixed Copolymers P123 and F127 in Aqueous Solution," *Langmuir*, vol. 23, no. 18, pp. 9229–9236, Aug. 2007.

Molecular dynamics of LTA zeolite: checking force fields using X-ray diffraction patterns

Jéssica C. da S. L. Maciel^{a,*}, Carla L. M. Camargo^a, Amaro G. Barreto Jr^a, Frederico W. Tavares^{a,b}

^a Escola de Química, Universidade Federal do Rio de Janeiro, Centro de Tecnologia, Cidade Universitária, Rio de Janeiro, 21941-909, RJ, Brazil

^b Programa de Engenharia Química, PEQ/COPPE, Universidade Federal do Rio de Janeiro, Centro de Tecnologia, Cidade Universitária, Rio de Janeiro, 21941-914, RJ, Brazil

Abstract

Molecular dynamics (MD) is a powerful tool for the screening of adsorbent materials providing insights into adsorption mechanisms. However, an accurate description of the crystalline structure is required. In this work, we investigate force fields for Linde Type A (LTA) zeolites and their ability to maintain a physically consistent structure during MD simulations. We emphasize the challenges to simulate crystalline structures such as the attention with the initial configuration to avoid problems with atoms overlapping. The comparison of simulated results with experimental X-ray diffraction (XRD) data from the literature showed that the crystallinity of the simulated materials could be significantly affected during the MD simulations, depending on the used force field. It is crucial to noteworthy that these structural modifications on zeolites affect their performance in an adsorption-separation process. For the choice of a reliable force field, we strongly recommend the comparison between simulated and experimental XRD patterns showing an acceptable representation of the crystalline framework.

Keywords: zeolite; XRD; molecular simulations; force fields

1. Introduction

Linde Type A (LTA) zeolite is widely used in the separation processes of small molecules such as CO₂, N₂, NH₃, and H₂O [1,2]. This ability is related to their physicochemical properties as the small pore openings and the natural polar sites [2,3]. The Si/Al ratio, the nature, number, and distribution of cations in the structure affect the physicochemical properties and, consequently, the performance of the zeolites [4].

In general, physicochemical characterization techniques have been used to relate the performance of adsorbent to its structural properties [1,5]. However, experimental effort in the adsorbent screening is sometimes time- and cost-consuming, such that molecular simulation appears as a powerful tool to investigate the adsorbent materials [6,7].

Molecular simulation (MD) is a useful tool that allows a quick assessment of different materials. Besides, molecular simulation results can provide insights on the anomalous adsorption behavior as well as help to understand the effect of structural modifications on the adsorbent performance [4]. In this sense, the accuracy of force fields employed in the simulations must be verified to ensure an appropriate description of the systems.

Validation of the force field has been usually done by using experimental infrared spectroscopy (IR) data [8]. This characterization technique provides vibrational properties of species which are indirectly related to the crystal structures. Here, we have tested a force field for zeolites using a validation methodology for force fields by calculation of X-ray diffraction (XRD) patterns. With this methodology, it is possible to verify if the crystalline structure is maintained during the simulations.

2. Methodology

2.1 Molecular dynamics simulations

The simulations were performed using the large-scale atomic/molecular massively parallel simulator (LAMMPS) [9,10] and RASPA [11]. We tested the force fields developed by Gabrieli et al. [12] (Gabrieli FF), Nicholas et al. [13] with modifications of García-Sánchez et al. [14] (Nicholas FF), and Jeffroy et al. [15] (Jeffroy FF). After equilibration, we carried out simulations in the NPT ensemble at 298.15 K and pressure of 1.0 atm. During the production time, the zeolite configurations were sampled, storing the relative coordinates.

2.2 Simulated X-Ray diffraction (XRD) patterns

Simulated XRD patterns were calculated using the methodology previously proposed [16], which enables the comparison between simulated and experimental XRD intensities. Essential information to construct the XRD patterns is the scattering factors for each atom type [17], the X-ray wavelength (1.54 Å for copper), and the configuration samples with the respective unit cell parameters.

3. Results and Discussion

A unit cell of the basic crystalline structure of an Al-free zeolite (LTA-Si) is shown in Fig. 1, which is obtained by optimization of the atom coordinates and the cell parameters assuming a pure SiO_2 composition [18,19]. In this case, the cubic cell presents the symmetry of the $\text{Pm}\bar{3}\text{m}$ space group and an edge length of 11.919 Å. In a general case, TO_4 tetrahedra (T can be either Si or Al) that are connected to each other, generating a framework with different topologies. The presence of aluminum generates a charge imbalance compensated by extra framework cations (Fig. 2).

With a chemical formula of $[\text{Na}_{91.78}][\text{Si}_{96}\text{Al}_{96}\text{O}_{384}]$, a cubic unit cell presents the symmetry according to the $\text{Fm}\bar{3}\text{c}$ space group and an edge cell 24.555 Å [19]. Fig. 3 shows the Zeolite LTA4A supercell (96 Na^+ ions) used as the initial configuration in the simulation box of our MD simulations.

As can be observed, this supercell has a size of 2x2x2 times larger than the unit cell of the original zeolite (Fig. 1 and Fig. 2), due to a reduction in symmetry associated with the presence of extra framework cations. At this step, the atoms must be removed from cell edges. This procedure avoids the overlapping of atoms when the cell is replicated and when periodic boundary conditions are applied.

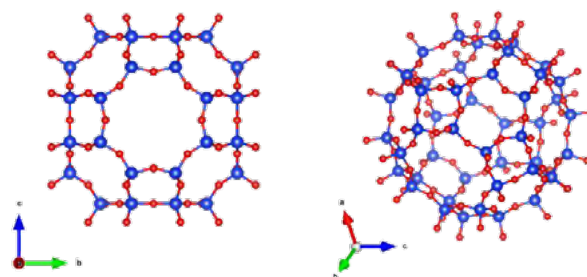


Fig. 1. The unit cell of the Al-free LTA zeolite. Blue: silicon (Si), red: oxygen (O).

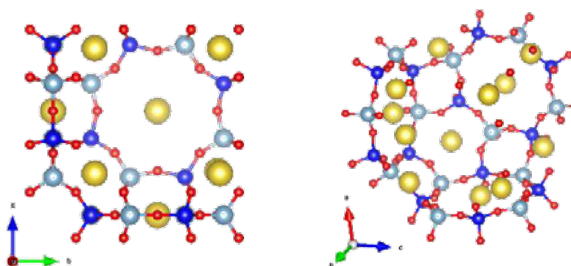


Fig. 2. Representation of an LTA4A zeolite unit cell containing aluminum and a type of extra framework cation. Blue: silicon (Si), red: oxygen (O), gray: aluminum (Al), yellow: sodium (Na^+).

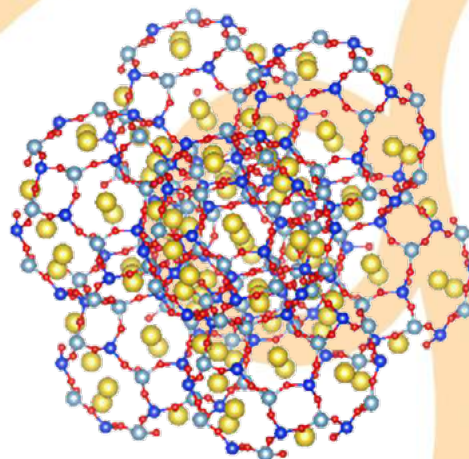


Fig. 3. Supercell of the LTA4A zeolite. Blue: silicon (Si), red: oxygen (O).

Table 1 shows the average supercell parameters obtained by MD simulations (672 atoms) using the force field of Gabrieli et al. [12] (Gabrieli FF). However, despite the acceptable values of average parameters calculated during the simulation, the integrity of the crystal structure seems to have been affected, as can be seen in Fig. 4 (comparison with experimental XRD data).

Table 1. Supercell parameters calculated using the Gabrieli FF [12].

Cell parameter	Mean	Standard Deviation
a (Å)	25.4564	0.0708
b (Å)	25.2846	0.0679
c (Å)	25.2937	0.0715
α (°)	89.6119	0.3007
β (°)	88.0100	0.2598
γ (°)	90.3004	0.2678

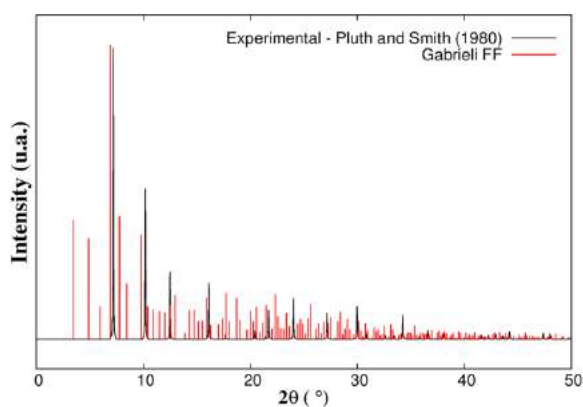


Fig. 4. Simulated XRD pattern for LTA4A zeolite using the Gabrieli FF compared with the experimental data of Pluth and Smith [19].

Then, other force fields were investigated in order to obtain a more realistic representation of the LTA-zeolite crystal structures. Here, we point out the difficulties in the use of flexible force fields for aluminum-substitute zeolites, which is sometimes unclear in the literature [15, 20, 21].

Preliminary results obtained using Nicholas FF and Jeffroy FF in a large simulation box (4608 atoms) are shown in Figs. 5 and 6. As can be seen in Fig. 5, the absence of aluminum and sodium in the Al-free LTA zeolite (LTA-Si) leads to displacement on XRD peaks compared with LTA4A using the same force field (Nicholas FF).

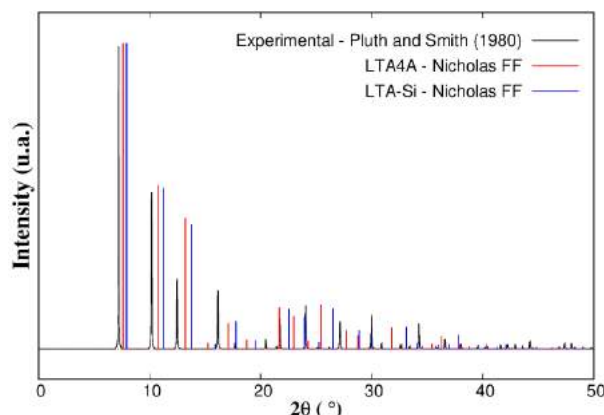


Fig. 5. Simulated XRD pattern for LTA-Si and LTA4A zeolites using Nicholas FF compared with the experimental results of Pluth and Smith [19].

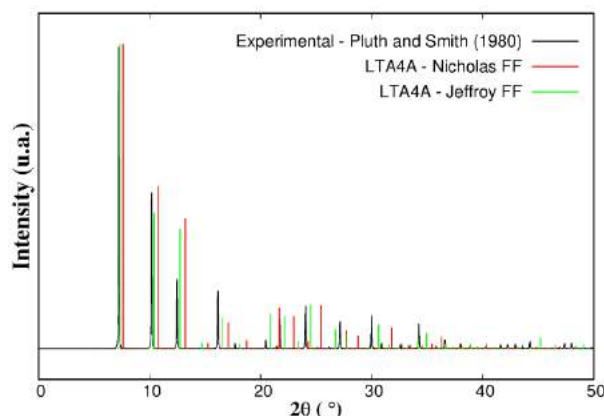


Fig. 6. Comparison between simulated XRD pattern for LTA4A zeolite using Nicholas FF and Jeffroy compared with the experimental results of Pluth and Smith [19].

Our results show a higher similarity between experimental peak positions and simulated ones using Jeffroy FF compared to Nicholas FF (Fig. 6). Then, the force field of Jeffroy et al. [15] seems more able to describe the zeolite LTA4A crystalline structure. To reinforce these preliminary results, we intend to carefully investigate simulation conditions such as the production time as well as explore other force fields.

3. Conclusions

In this study, the quality of LTA4A zeolite force fields of the literature was tested in NPT molecular dynamics simulations. Despite the acceptable

values of average thermodynamic properties calculated, we demonstrate that the crystal structure can be affected during the simulations. Therefore, the choice of an adequate force field should be carried out by obtaining XRD patterns from simulated structures and comparing them with experimental results. Next step, the study is the comparison between rigid and flexible force fields for zeolites through adsorption isotherms. Additionally, the methodology proposed here can be used to compare force fields and to obtain insights about structural modifications during the adsorption process. Using a reliable force field, we can explore the influence of aluminum and extra framework cation positions as well as the adsorption capacity of different adsorbents.

Acknowledgments

The authors thank CENPES/PETROBRAS for the financial support of this work.

References

- [1] Montanari T, Busca G, On the mechanism of adsorption and separation of CO₂ on LTA zeolites: An IR investigation. *Vib Spectrosc* 2008; 46:45-51.
- [2] Jaramillo E, Chandross M. Adsorption of small molecules in LTA zeolites. 1. NH₃, CO₂, and H₂O in zeolite 4A. *J Phys Chem B* 2004; 108:20155-9.
- [3] Speybroeck VV, Hemelsoet K, Joors L, Waroquier M, Bell RG, Catlow RA. Advances in theory and their application within the field of zeolite chemistry. *Chem Soc Rev* 2015; 44: 7044-111.
- [4] Martin-Carlvo A, Parra JB, Ania CA, Calero S. Insights on the anomalous adsorption of carbon dioxide in LTA zeolites. *J Phys Chem C* 2014; 118:25460-7.
- [5] Hu S, Song G, Xue D, Li F, Influence of alkalinity on the synthesis of hierarchical LTA zeolite by using bridged polysilsesquioxane. *RSC Adv* 2019; 9:2551-8.
- [6] Chen S, Zhu M, Tang Y, Li W, Xiao B, Molecular simulation and experimental investigation of CO₂ capture in a polymetallic cation-exchanged 13X zeolite. *J Mater Chem A* 2018; 6:19570-83.
- [7] Abdelrasoul A, Zhang H, Cheng C-H, Doan H. Applications of molecular simulations for separation and adsorption in zeolites. *Micropor Mesopor Mat* 2017; 242:294-348.
- [8] Guo J, Hammond KD. Comparison of siliceous zeolite potentials from the perspective of infrared spectroscopy. *J Phys Chem C* 2018; 122:6093-102.
- [9] Plimpton S. Fast Parallel Algorithms for Short-range Molecular Dynamics. *J Comput Phys* 1995; 117:1-19.
- [10] LAMMPS, Lammmps molecular dynamics simulator. <http://lammmps.sandia.gov>.
- [11] Dubbeldam D, Calero S, Ellis DE, Snurr RQ. RASPA: molecular simulation software for adsorption and diffusion in flexible nanoporous materials. *Mol Simulat* 2015;42(2):81-101.
- [12] Gabrieli A, Sant M, Demontis P, Suffritti GB. Development and Optimization of a New Force Field for Flexible Aluminosilicates, Enabling Fast Molecular Dynamics Simulations on Parallel Architectures. *H Phys Chem C* 2013; 117: 503-9.
- [13] Nicholas JB, Hopfinger, Trow FR, Iton LE. Molecular modeling of zeolite structure. 2. Structure and dynamics of silica sodalite and silicate force field. *J Am Chem Soc* 1991; 113(13) 4792-800.
- [14] García-Sánchez A, Dubbeldam D, Calero S. Modeling adsorption and self-diffusion of methane in LTA zeolites: the influence of framework flexibility. *The Journal of Physical Chemistry C* 2010; 114(35) 15068-74.
- [15] Jeffroy M, Carlos N-D, Anne B. Molecular simulation of zeolite flexibility. *Mol Simulat* 2014; 40(1-3) 6-15.
- [16] Camargo CLM, Resende NS, Perez CAC, Abreu CRA, Salim VMM, Tavares FW. Molecular dynamics simulation and experimental validation by X-ray data of hydroxyapatite crystalline structures. *J Fluid Phase Equilib* 2018;470:60-7.
- [17] Doyle PA, and Turner PS. Relativistic Hartree-Fock X-ray and electron scattering factors. *Acta Cryst A*. 1968;24(3):390-7.
- [18] Baerlocher C, McCusker LB, Database of Zeolite Structures: <http://www.iza-structure.org/databases/>
- [19] Pluth JJ, Smith JV. Accurate redetermination of crystal structure of dehydrated zeolite A. Absence of near zero coordination of sodium. Refinement of silicon,aluminum-ordered superstructure. *J Am Chem Soc*. 1980;102:4704-8.
- [20] Jeffroy M, Borissenko E, Bountin A, Lella AD, Porcher F, Souhassou M, Lecomte C, Fuchs AH. Evidence of a framework induced cation redistribution upon water adsorption in cobalt exchanged X faujasite zeolite: A joint experimental and simulation study. *Micropor Mesopor Mat* 2011; 138:45-50.
- [21] Salazar JM, Badawi M, Radola B, Macaud M, Simon JM. Quantum Effects on the Diffusivity of Hydrogen Isotopes in Zeolites. *J Phys Chem C* 2019;123(38) 23455-63.

ASSESSING INTERACTIONS IN DIESEL FUEL ADSORPTIVE DESULFURIZATION OVER Ag/MCM-41 BY COMPUTATIONAL AND EXPERIMENTAL STUDIES

Rafael V. Sales^a, Enrique Rodríguez-Castellón^c, Anne B. F. Câmara^a, Heloise O. M. A. Moura^a, Sergio R. B. Silva^a, Miguel A. F. de Souza^a, Leila M. A. Campos^b, Luciene S. de Carvalho^{a*}

a Energetic Technologies Laboratory (LTEN), Institute of Chemistry, Federal University of Rio Grande do Norte, Energetic Technologies Research Group, 59078-900, Natal, Brazil.

b School of Engineering, Architecture and Information Technology, Salvador University (UNIFACS), Salvador, BA 40140-110, Brazil

c Dpto. de Química Inorgánica, Cristalografía y Mineralogía, Facultad de Ciencias, Universidad de Málaga, 29071, Málaga, Spain

*E-mail: luciene_car@hotmail.com

Abstract

Molecular dynamics simulation performed by the DFT/ONIOM method and X-ray photoemission spectroscopy (XPS) data were employed for studying the adsorbate-adsorbent interaction system in diesel desulfurization over Ag/MCM-41 produced from beach sand silica (MPI). The morphology and structure of the materials were characterized via powder X-ray diffraction (XRD), scanning transmission electron microscopy (STEM) and field emission scanning electron microscopy (FESEM) together with energy dispersive spectrometry (EDS) analysis. The results proved a high dispersion of different Ag nanodomains onto MCM-41 and their chemical interaction with support and sulfur compounds by π -complexation. The best fit of kinetic and equilibrium data to pseudo-second order ($R^2 > 0.99$) and Langmuir models ($R^2 > 0.98$), respectively, demonstrate the occurrence of chemisorptive/catalytic interactions with organosulfur compounds, as seen in the XPS results. Its adsorption capacity ($q_m = 31.25$ mgS/g) was 10 times higher than that obtained for pure MCM-41 and double the q_m for Ag/MCM-41(C) adsorbent from commercial silica. The computational modeling approach provided valuable insight towards molecular level understanding of the mechanism in aromatic S-compounds adsorption over functionalized MCM-41 and the role of Ag species in this process.

Keywords: Adsorptive Desulfurization; MPI silica; Ag/MCM-41 adsorbent; π -Complexation; DFT/ONIOM.

1. Introduction

Organosulfur compounds removal from diesel fuel is a recurrent issue discussed in the petroleum industry and the focus of many studies. The hydrodesulfurization (HDS) method currently used in refineries is very expensive; in addition, some aromatic organosulfurs are not removed by this technique. Researchers have observed that adsorbents functionalized with transition metals are capable of capturing aromatic sulfur compounds refractory to HDS processes via π -complexation [1].

It is reported in literature that Ag nanodomains over MCM-41 silanol groups present high efficiency in desulfurization. The Ag(0) sites present high reactivity both by adsorbing and activating atmospheric O₂ at ambient conditions (300 K, 1 atm) [2] and by increasing the mobility of lattice oxygens from the adsorbent structure. This increase in mobility can occur by bridging bonds between Ag(0) and the metal oxide molecules [3], but it is

also reported by covalent bonding in the case of a more oxidized state of silver as Ag(I), and in a cation exchange of hydrolyzed silica silanol groups (Si-O-H) [4].

The molecular level comprehension about the activity of Ag/MCM-41 material and the mechanisms involved in sulfur adsorption is lacking. X-ray photoemission spectroscopy (XPS) data and computational modeling can be efficient tools to identify the Ag species on MCM-41 and to indicate what kind of interactions could be involved in impregnation and chemisorption processes [4].

XPS is able to identify chemical changes in the material by displacements in binding energies of each element [5], while computational simulations, especially using density functional theory (DFT) optimization and ONIOM (our own n-layered integrated molecular orbital and molecular mechanics) method, produce accurate results in investigating confinement effects and non-local interactions in the adsorbent-adsorbate system with minimal computational requirements and less expensive models [6].

This work performed the investigation of chemical species, interactions and mechanisms involved in diesel fuel deep desulfurization over a highly efficient Ag/MCM-41 adsorbent produced from beach sand amorphous silica (MPI). The DFT/ONIOM method was applied for modeling the adsorption of different recalcitrant organosulfur over Ag/MCM-41 and the results were evaluated in comparison to X-ray photoelectron spectra (XPS) data.

2. Experimental

2.1 Synthesis of the supports

The synthesis methods for the MPI silica (96.0%) obtained from beach sand and the MCM-41 molecular sieve are described in Carvalho et al. (2015) [7]. MPI and commercial silica gel 60 (Macherey-Nagel) were used for synthesizing MCM-41 and MCM-41(C), respectively. The final gel had a molar composition of 1.0 CTAB : 4.0 SiO₂ : 2.0 NaOH : 200.0 H₂O. The materials were functionalized with Ag(I) cations via wet impregnation with ethanol solutions of AgNO₃ for producing Ag/MCM-41 and Ag/MCM-41(C) adsorbents with 2% Ag (w/w), at 120 rpm for 1 h at room temperature and subsequently underwent progressive heating (10 °C/30 min) in a water bath for 3.5 h.

2.2 Instrumental analysis

The X-ray diffraction (XRD) patterns were obtained with a Bruker D2 Phaser with CuK α radiation ($\lambda=1.5406$ Å), 30 kV filament, 10 mA current, Ni filter and a LYNXEYE detector. Textural parameters were determined by N₂ adsorption-desorption isotherms at 77 K using a Micrometrics ASAP 2420 apparatus. The samples were previously degassed at 200 °C and 10⁻⁴ mbar. The pore size distribution was calculated by the Barrett-Joyner-Halenda (BJH) method.

The morphology and composition of the samples were investigated using a field emission scanning electron microscope (FESEM, Auriga, Carl Zeiss) and energy dispersive X-ray spectroscopy (EDS, XFlash Detector 410-M), respectively. The structure of the adsorbents was evaluated by high-resolution transmission electron microscopy (HRTEM, Philips CCCM 200 Supertwin-DX4 microscope).

A high-angle annular dark field (HAADF)

detector (TALOS F200x) was used for recording scanning transmission electron microscopy (STEM) images at 200 kV and 200 nA. X-ray photoelectron spectra (XPS) was performed by a Physical Electronics PHI 5700 spectrometer with non-monochromatic Al K α radiation (95.2 W, 15 kV, and 1486.6 eV) and a multi-channel detector. Binding energy (BE) was calibrated to the C1s line (284.8 eV). Multipack software version 9.6.0.15 was used for data analysis.

2.3 Adsorption tests

A set of adsorption tests in fixed bed columns were performed with model diesel solutions prepared with DBT (Sigma Aldrich, 98.0%) and n-decane (Sigma Aldrich, 99.0%) in a concentration of about 2000 ppm sulfur. This procedure was used exclusively for analyzing the adsorbents after desulfurization via XPS analysis, since real diesel has many interferences and would hinder the collection of spectroscopic data.

The adsorption experiments were performed by the finite bath method at ambient temperature and pressure. 0.3 g of adsorbent and 8.0 mL of diluted real diesel prepared by a solution of the high (1234.9 ppm) and low-sulfur (5.1 ppm) samples donated by Clara Camarão Potiguar Refinery (RPCC), were placed in erlenmeyer flasks under constant stirring (100 rpm) in a stirring table (Solab, SL 180/DT). A solution of real diesel with 500 ppm sulfur was used for kinetic tests. The supernatant fluid was collected at predetermined times between 5 and 180 minutes of stirring.

Real diesel solutions containing different sulfur contents (25-1000 ppm) were kept under constant agitation for 24 h for evaluating the sulfur adsorption equilibrium over MCM-41, Ag/MCM-41, MCM-41(C) and Ag/MCM-41(C) materials. The solids were separated by centrifugation and the residual sulfur contents in the liquid phase were collected for quantification by a total sulfur analyzer via ultraviolet fluorescence (UVF) spectrometry (Antek Multitek, PAC, L.P) in triplicate, following ASTM D5453 methodology. Sulfur adsorption capacity per gram of adsorbent at equilibrium (q_e) was calculated using the following equation:

$$q_e = \frac{V(C_i - C_e)}{M_{\text{adsorbent}}} \quad (1)$$

where V is the diesel solution volume (L), $M_{\text{adsorbent}}$ is

the adsorbent mass (g) and C_i and C_e are the initial sulfur content in the fuel (mg/L) and at equilibrium, respectively.

2.4 Molecular dynamics simulations

The MCM-41 was simulated by DFT-ONIOM as the $H_{36}O_{66}Si_{24}$ cluster (the oxygen dangling bonds are saturated with hydrogen) shown in Fig. 1. This cluster is large enough to account for the interactions of Ag(I) and organosulfur molecules with the MCM-41 framework. Thiophene (T), benzothiophene (BT) and dibenzothiophene (DBT) were used for calculations. The cluster was partitioned in a two-level ONIOM-2 (high:low) method.

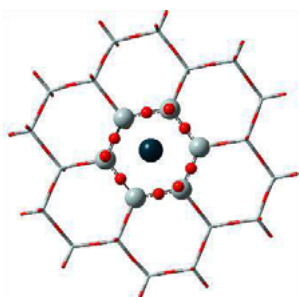


Fig. 1. Structure optimized by the B3LYP/LanL2DZ:HF/3-21G (high:low) method for the $H_{36}O_{66}Si_{24}$ cluster. The high-level part of ONIOM is displayed in “balls-and-sticks” form and the low-level part is only displayed as “tubes.” All saturating H atoms were not included. Oxygen atoms are red and silicon atoms are grey.

The high-level part of ONIOM calculations were performed using the B3LYP method with the LanL2DZ basis set, while the HF/3-21G was used in the low-level part. Optimization calculations were performed by scanning conformations and possible types of binding in order to indicate the more favorable interaction structures for this system. In these cases, the Ag(I) ion and thiophenic sulfur compound were included in the high-level part of ONIOM. All optimizations were performed by the Gaussian-09 program.

3. Results and Discussion

3.1 Characterizations

The X-ray diffraction patterns of MCM-41 and Ag/MCM-41 are presented in Fig. 2. The presence of diffraction peaks indexed by (100), (110) and

(200), Figure 2a, confirms a well-ordered structure with hexagonal $p6mm$ symmetry, typical of MCM-41 mesoporous material [8]. Wide-angle XRD patterns of the Ag/MCM-41 sample (Fig. 2b) did not show any reflection referent to deposited transition-metal atoms, except for the peak centered at 22.8° from amorphous MPI silica. This may indicate that Ag species are highly dispersed and have high interaction with the mesoporous support, or that the size of these species (<3 nm) is below the detection limit of X-ray radiation.

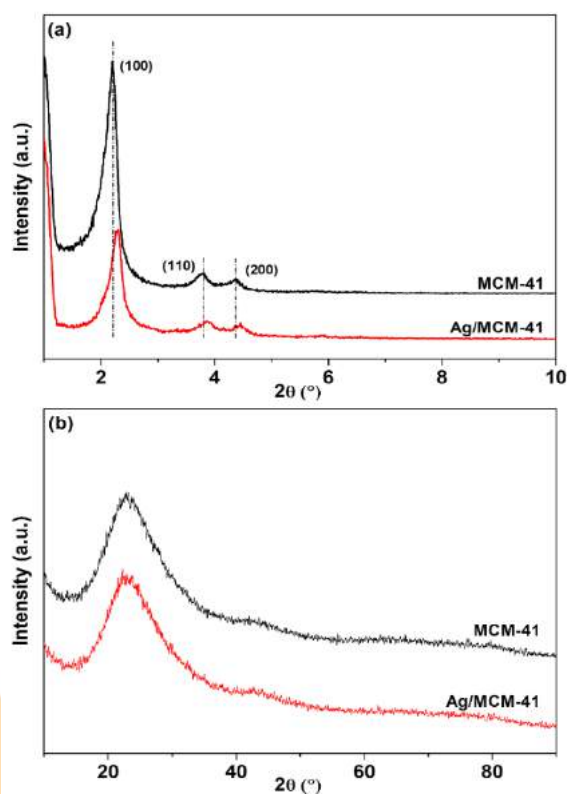


Fig. 2. (a) Low-angle and (b) wide-angle X-ray diffractograms of the adsorbents.

HRTEM images of pure MCM-41 confirm the presence of well-ordered hexagonal arrangements and mesoporous channels with high uniformity (Fig. 3a and b).

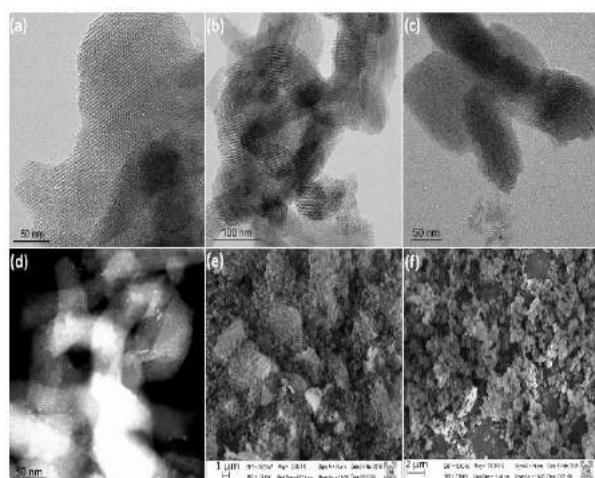


Fig. 3. (a), (b) HRTEM micrograph for pure MCM-41; (c) HRTEM, (d) STEM and (e), (f) FESEM images.

Mapping the elemental distribution of Ag (Fig. 4) reveals that these particles were homogeneously distributed on the surface of MCM-41.

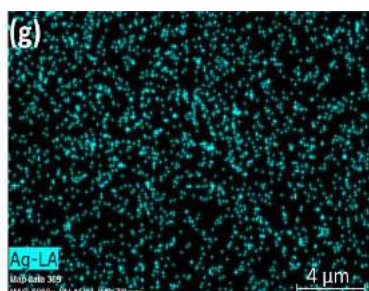


Fig. 4. EDS elemental mapping.

The N_2 adsorption-desorption isotherms of the sorbents corresponded to type IV according to the IUPAC classification, which is associated for mesoporous materials with an apparent H3-type hysteresis loop due to capillary condensation. According to Appaturi and Adam (2019) [10], this type of hysteresis is typical for slit pore solids originating from non-rigid aggregates of plate-like particles.

The incorporation of Ag to the mesoporous support did not cause changes in the nature of the isotherm or in the hysteresis loop shape, thus indicating preservation of its structure as observed for XRD patterns and HRTEM images. The pore size distribution estimated by the BJH method suggests uniform mesoporosity with a maximum distribution in the range of 23.48-24.82 Å for the materials. The results presented in Table 1 show a reduction in specific area (S_{BET}) and pore volume

(V_P) after impregnation, which occurs due to pore occlusion by Ag species.

Table 1. Textural properties of the adsorbents.

Sample	S_{BET} (m ² /g) ^a	V_P (cm ³ /g) ^b	Maximum pore diameter (Å)
MCM-41	722	0.79	23.48
Ag/MCM-41	656	0.74	24.82

3.2 Adsorption kinetics

The results for the adsorption of recalcitrant sulfur in real diesel over Ag/MCM-41 were better fitted to the pseudo-second order model, with higher determination coefficient ($R^2 > 0.99$) and similar calculated and experimental q_e values, followed by the Elovich model ($R^2 > 0.97$). Both models suggest that the chemisorption process is the rate determining step of adsorption [11]. The pseudo-second order model was the most adequate to describe the experimental data of the adsorption performed by pure MCM-41, with determination coefficient higher than 0.89. Moreover, the q_e result obtained by the pseudo-second order model (1.60 mg/g) was close to the value obtained experimentally (1.64 mg/g).

3.3 Adsorption equilibrium

Experimental adsorption results for MCM-41 and MCM-41(C) were better adjusted to the Freundlich model with $R^2 > 0.99$, indicating that the process preferably occurs by physisorption [12]. However, the Langmuir isotherm model was more efficient in describing the desulfurization of real diesel performed by the Ag impregnated support, suggesting that the physisorption mechanism was preferably substituted by chemisorption, and the process became governed by the Langmuir adsorption principles: monolayer and homogeneous adsorption [1].

The values for n remained within the 1-10 range for all adsorbents and indicated favorable adsorption. Ag/MCM-41 and Ag/MCM-41(C) obtained higher maximum adsorptive capacities (q_m) in relation to the pure materials. Ag/MCM-41 from sustainable MPI silica reached a higher q_m (31.25 mg/g) among all the studied materials.

3.4 Evaluation of interactions via the DFT/ONIOM and XPS techniques

Theoretical calculations suggested a strong association between Ag(I) and the MCM-41 cluster. The Ag(I) cation is quasi-symmetrically localized in the center of the ring (Fig. 5). This cooperative

association is very favorable energetically, with $\Delta E = -69.3 \text{ kcal mol}^{-1}$ (where $\Delta E = E_{\text{MCM-41/Ag}^+} - E_{\text{MCM-41}} + E_{\text{Ag(I)}}$). The interaction between the adsorbents and organosulfurs is driven by the sulfur atom in all cases. However, the sulfur molecule for the system with Ag(I) is almost horizontally located on top of the cation.

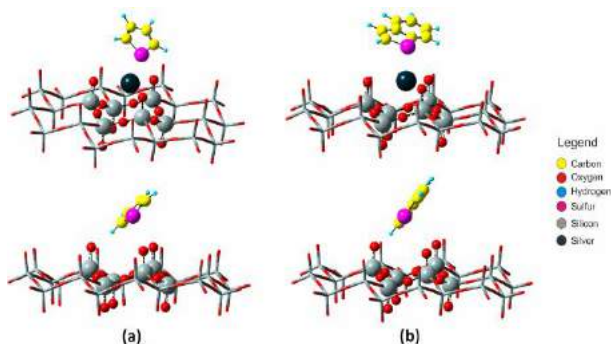


Fig. 5. Structure optimized by the B3LYP/LanL2DZ:HF/3-21G (high:low) method for (a) MCM-41/BT and Ag/MCM-41/BT, and (b) MCM-41/DBT and Ag/MCM-41/DBT.

The optimized structures were then used for interaction energy calculations according to the following expression: $\Delta E_{\text{ads}} = E_{\text{adsorbent-adsorbate}} - (E_{\text{adsorbate}} + E_{\text{adsorbent}})$, where $E_{\text{adsorbate}}$ is free adsorbate energy, $E_{\text{adsorbent}}$ the free adsorbent energy, and $E_{\text{adsorbent-adsorbate}}$ the adsorbate/adsorbent system energy. A lower ΔE_{ads} corresponds to stronger adsorption. ΔE_{ads} calculated values are reported in Table 2. The values calculated in this work are compatible with the calculated values of desulfurization of fuels by transition metal/zeolite reported in a previous work [14]. As can be observed in Table 2, ΔE_{ads} values suggested that both Ag/MCM-41 and MCM-41 adsorbents are able to efficiently remove organosulfur molecules. However, ΔE_{ads} values for the Ag/MCM-41 adsorbent are almost twice more favorable when compared to pure MCM-41 adsorbent, with increasing interaction strength for higher insaturation in the molecule ($T < BT < DBT$).

Table 2. Adsorption energy (ΔE_{ads}) in kcal/mol.

Adsorbents	Adsorbates		
	T	BT	DBT
MCM-41	-5.8	-8.7	-9.0
Ag/MCM-41	-15.0	-18.5	-21.5

The XPS spectra for the Ag/MCM-41 material (Fig. 6a) presented broad peaks in between the

characteristic BE for the Ag $3d_{5/2}$ and $3d_{3/2}$ orbitals of Ag(I) species (367.5 and 373.8 eV) and Ag(0) nanoparticles (369.7 and 375.9 eV) [2] at 368.1 and 374.1 eV, respectively. This may indicate stabilization of Ag(I) ions by interactions with other atoms such as silanol groups (Ag-O-Si) of MCM-41, adsorbed atmospheric oxygen (Ag-O_{ads}) and lattice oxygen (Ag-O_{lat}), generating species with BE state in between the ionic and metallic forms ($\text{Ag}^{\delta+}$, $0 < \delta < 1$) [4].

The peaks at 369.0 and 375.0 eV are assigned to the rare occurrence of highly dispersed Ag (0) nanoparticles [2], unlike the typical BE region for this species (368.1 and 373.2 eV), which may be generated due to the photolysis of the AgNO₃ molecule in the presence of light or to autoreduction processes. Cao et al. (1997) [14] concluded that the peak at ~368 eV is attributed to an aggregated state of silver metal (large particles) because of its small charge effect, while the peak at ~370 eV is referent to a highly dispersed metallic state with a great charge effect.

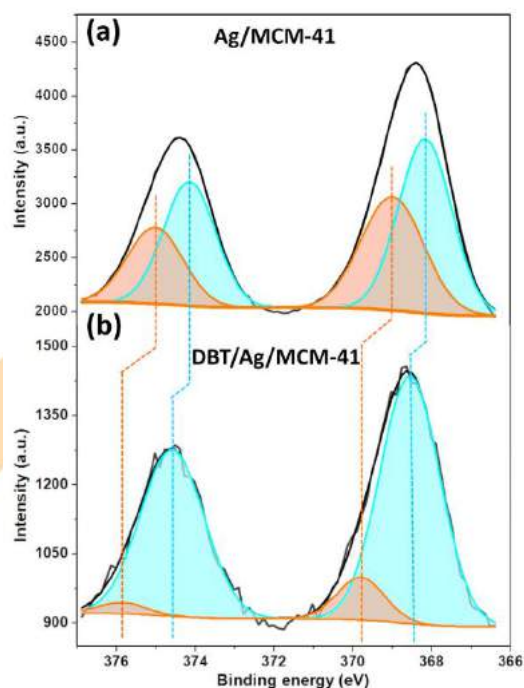


Fig. 6. XPS spectra for Ag/MCM-41 (a) before and (b) after desulfurization.

After DBT adsorption (Fig. 6b), the increase in BEs of oxygenated Ag(I) species (368.4 and 374.5 eV) can be assigned to oxygen loss and the broad peaks which emerged at 369.4 and 375.6 eV are ascribed to Ag-S-R bridging configuration formed

via π -complexation (S-R = DBT) [15]. Ag(0) ($[\text{Kr}]4d^{10}5s^1$) and Ag(I) ($[\text{Kr}]4d^{10}5s^0$) species are able to form bonds in this mechanism with their empty or semi-filled s orbitals, and their d orbitals can retrograde electronic density to the π anti-ligands (π^*) of aromatic organosulfur rings [13]. Then, the MCM-41 modification with Ag(I) species from AgNO_3 can offer a high quantity of interaction sites between the adsorbent and the sulfur compounds, as observed in experimental results and theoretical calculations.

4. Conclusions

The optimized adsorption structures calculated by the DFT/ONIOM modeling for aromatic organosulfur enabled proving that the adsorption is controlled by the interaction between the sulfur atom and Ag sites, considerably promoting more effective removal than the pure MCM-41 support. XPS data showed the formation of Ag-S-R bridging bonds via π -complexation and confirmed these interactions by displacements in the BE of Ag(0) and $\text{Ag}\delta^+$ ($0 < \delta < 1$) $3d$ orbitals. The experimental and computational approach used in this work proved the high efficiency of adsorptive desulfurization of diesel over a sustainable Ag/MCM-41 material and brings further investigation into the adsorption structures, mechanisms, energy and species involved in this process at a molecular level.

Acknowledgements

The authors thank the Coordination for the Improvement of Higher Education Personnel (CAPES - Brazil) - Finance Code 001.

References

- [1] Saleh TA, Sulaiman KO, AL-Hammadi SA, Dafalla H, Danmaliki GI. Adsorptive desulfurization of thiophene, benzothiophene and dibenzothiophene over activated carbon manganese oxide nanocomposite: with column system evaluation. *J Clean Prod* 2017;154:401-12.
- [2] Losurdo M, Bergmair I, Dastmalchi B, Kim TH, Giangregorio MM, Jiao W, Bianco GV, Brown AS, Hingerl K, Bruno G. Graphene as an Electron Shuttle for Silver Deoxidation: Removing a Key Barrier to Plasmonics and Metamaterials for SERS in the Visible. *Adv Funct Mater* 2014;24:1864-78.
- [3] Chen Y, Huang Z, Zhou M, Ma Z, Chen J, Tang X. Single Silver Adatoms on Nanostructured Manganese Oxide Surfaces: Boosting Oxygen Activation for Benzene Abatement. *Environ Sci Technol* 2017;51:2304-11.
- [4] Dutov V, Mamontov GV, Zaikovskii VI, Vodyankina OV. The effect of support pretreatment on activity of Ag/SiO₂ catalysts in low-temperature CO oxidation. *Catal Today* 2016;278:150-6.
- [5] Padin J, Yang RT. New sorbents for olefin/paraffin separations by adsorption via π -complexation: synthesis and effects of substrates. *Chem Eng Sci* 2000;55:2607-16.
- [6] Farrokhpour H, Ghandehari M, Eskandari K. ONIOM DFT study of the adsorption of cytosine on the Au/Ag and Ag/Au bimetallic nanosurfaces: The effect of sublayer. *Appl Surf Sci* 2018;457:712-25.
- [7] Carvalho LS, Silva E, Andrade JC, Silva JA, Urbina M, Nascimento PF, Carvalho F, Ruiz JA. Low-cost mesoporous adsorbents amines-impregnated for CO₂ capture. *Adsorption* 2015;21:597-609.
- [8] Beck JS, Vartulli JC, Roth WJ, Leonowicz ME, Kresge CT, Schmitt KD, Chu CTW, Olson DH, Sheppard EW, McCullen SB, Higgins JB, Schlenker JL. A new family of mesoporous molecular sieves prepared with liquid crystal templates. *J Am Chem Soc* 1992;114:10834-43.
- [9] Kowalczyk A, Borcuch A, Michalik M, Rutkowska M, Gil B, Sojka Z, Indyka P, Chmielarz L. MCM-41 modified with transition metals by template ion-exchange method as catalysts for selective catalytic oxidation of ammonia to dinitrogen. *Microporous Mesoporous Mater* 2017;240:9-21.
- [10] Appaturi JN, Adam F. ImX-MCM-41 (X = Cl, Br and I): Active catalysts for the solvent free synthesis of phenyl glycidyl carbonate. *Surfaces Interfaces* 2019;14:305-13.
- [11] Habibi A, Belaroui LS, Bengueddach A, Galindo AL, Diaz CIS, Peña A. Adsorption of metronidazole and spiramycin by an Algerian palygorskite. Effect of modification with tin. *Microporous Mesoporous Mater* 2018;268:293-302.
- [12] Muzic M, Sertic-Bionda K, Gomzi Z, Podolski S, Telen S. Study of diesel fuel desulfurization by adsorption. *Chem Eng Res Des* 2010;88:487-95.
- [13] Hernández-Maldonado AJ, Yang FH, Qi G, Yang RT. Desulfurization of transportation fuels by π -complexation sorbents: Cu(I)-, Ni(II)-, and Zn(II)-zeolites. *Appl Catal B-Environ* 2005;56:111-26.
- [14] Cao Y, Dai WL, Deng JF. The oxidative dehydrogenation of methanol over a novel Ag/SiO₂ catalyst. *Appl Catal A: General* 1997;158:127-34.
- [15] Battocchio C, Meneghini C, Fratoddi I, Venditti I, Russo MV, Aquilanti G, Maurizio C, Bondino F, Matassa R, Rossi M, Mobilio S, Polzonetti G. Silver Nanoparticles Stabilized with Thiols: A Close Look at the Local Chemistry and Chemical Structure. *J Phys Chem C*, 2012;116:19571-78.

Phenomenological and neural network modeling of successive Ni²⁺ desorption cycles with eluent recycle

Lucas P. de Carvalho^{a*}, Araceli A. Seolatto^{c,d}, Edson A. da Silva^b, Eneida S. Cossich^d, Célia R. G. Tavares^d, Tiago D. Martins^{a**}

^a Unifesp, R. São Nicolau 210, Diadema, 09920-000, Brasil

^b Unioeste, Rua da Faculdade 645, Toledo, 85903-000, Brasil

^c UFG, Avenida Esperança s/n, Goiânia, 74690-900, Brasil

^d UEM, Avenida Colombo, 5790, Maringá, 87020-900, Brasil
* lucas.paliotta@gmail.com; ** tdmartins@unifesp.br

Abstract

Desorption processes are important to reuse the adsorbent in wastewater treatment by adsorption process. This is crucial to promote monetary economy and a rational utilization of natural resources. The development of mathematical models to predict the time of desorption is important to efficient equipment design, process control, and to define optimum operational conditions. Thus, the main objective of this work was to propose two models to predict the kinetics of successive Ni²⁺ desorption cycles: one dispersion model, which considered the effect of axial dispersion, first order kinetics, and the influence of the flow of the eluent solution (H₂SO₄ 0.1 M) and one artificial neural network (ANN) model. The case study considered in this work was ten adsorption-desorption cycles of Ni²⁺ using (and reusing) *Sargassum filipendula* as adsorbent. From the ten cycles available, data from seven cycles were used to train, validate, and test the ANNs. Three cycles were used exclusively to simulate the ANNs and define the best model. The dispersion model was capable to predict all curves, but with different set of parameters for each cycle. On the other hand, it was possible to obtain only one ANN to predict all ten curves. The best result was obtained when considering the Ni²⁺ concentrations at times $t-2$, $t-1$ and t as inputs and the concentration at time $t+1$ as output. The best structure was the ANN 3-15-15-1, which was able to simulate all the ten curves using only the first three experimental data. Also, it predicted the desorbed mass within an error of 3%. This work showed that the one ANN is a viable alternative to predict the kinetic of multiple desorption cycles with high accuracy.

Keywords: Water treatment; Artificial intelligence; Mathematical modeling; Brown algae

1. Introduction

Adsorption is widely used to treat wastewater in the industry environment. The process consists in use a solid to remove undesirable molecules, the adsorbate (such as: heavy metals, antibiotics, organic dyes, etc.), from the water before it can be released on the rivers [1].

After the adsorption cycle is performed, the adsorbent containing the adsorbate can become a solid-waste problem, since it usually contains toxic molecules in its pores. One way to overcome this problem is to desorb the adsorbate from the solid and reuse the adsorbent in as many adsorption cycles as possible.

The desorption process is the inverse of the adsorption and consists in resetting the adsorbent

using an eluent solution that remove the adsorbate. It is widely used and several studies concerning its efficiency can be found in the recent literature [2,3].

In an industrial process, it is important to have an equation to predict the process time, the mass extracted, and also the kinetic profile of the desorption process. This can be done by using either conventional phenomenological models or more recent techniques, such as Artificial Neural Networks (ANN).

The phenomenological models provide information about the process phenomenology and they are very important for the development of new materials, equipment dimensioning, cost estimation, etc. However, they present some

limitations, since the kinetic changes, and thus, the models' parameters, as the cycles are performed.

This dependence of the parameters on the cycle run jeopardizes the industrial application of such models, especially in process control. One way to overcome this difficulty is the use of intelligent algorithms. Artificial Neural Networks (ANNs) are equations that emulate the human brain. By collecting precise data, they can learn about the relation among the dependent and independent variables. The primary unit of an ANN is the artificial neuron. They are distributed in layers that connect with each other and create this artificial brain. The equation of the artificial neuron includes a weight that is assigned to each input and a bias parameter. The Eq. (1) shows the how the neuron output (o_j) is calculated:

$$o_j = f\left(\sum_{i=1}^n w_{ij}x_i + b_j\right) \quad (1)$$

where b is the bias, and x_i and w_{ij} are the value and weight of the input, i , respectively. The function f , is called activation function and can be any continuous function. The most commonly used are the sigmoidal, hyperbolic tangent and linear functions.

Recently, Carvalho et al. [4] used ANNs to predict ten cycles of Ni^{2+} adsorption in *Sargassum filipendula* seaweed. They showed that an ANN with the structure 3-10-10-1 (each number refers to the size (number of neurons) of each ANN layer) can predict the all the kinetic profile of ten cycles using only the first three experimental data.

Although the adsorption cycles were successfully predicted by the ANNs, the modeling of the desorption cycles is still lacking. Thus, the main objective of this work was to model the desorption of Ni^{2+} from the algae *Sargassum filipendula* in ten adsorption-desorption cycles using H_2SO_4 as eluent solution, by proposing one phenomenological model and one ANN. Finally, to compare the efficiency of both models and define which are the best one to perform this task.

2. Materials and Methods

2.1. Experimental

All experimental data used in this work was published by Seolatto et al. [5]. On that paper, the authors used the 3.84 g of *Sargassum filipendula* brown seaweed as adsorbent. The adsorption was carried out using a Nickel solution prepared with NiCl_2 at $50 \text{ mg}\cdot\text{L}^{-1}$.

All adsorption experiments were done using a column with a length of 50 cm and internal diameter of 2.8 cm, at 30°C , pH 3.5, and the flow was $8 \text{ mL}\cdot\text{min}^{-1}$. In pre-defined time intervals, samples were collected at the column exit and the adsorbed mass (m_{Ads}) was calculated using the equation:

$$m_{\text{Ads}} = C_0 Q \int_0^{t_{\text{final}}} \left(1 - \frac{C(t)}{C_0}\right) dt \quad (2)$$

where: C_0 is the initial concentration, Q is the volumetric flow, C is the exit concentration, and t is time.

To desorb the ions from the algae, a sulfuric acid solution at 0.1 M was used as eluent. The desorption cycles were performed by flowing the eluent solution through the column at $5 \text{ mL}\cdot\text{min}^{-1}$. It was done by recirculating a fixed amount of the eluent solution (330 mL), as shown at Figure 1, aiming to maximize the amount of Ni^{2+} per mL of eluent. This was done until the concentration of Ni^{2+} at the feed tank was constant.

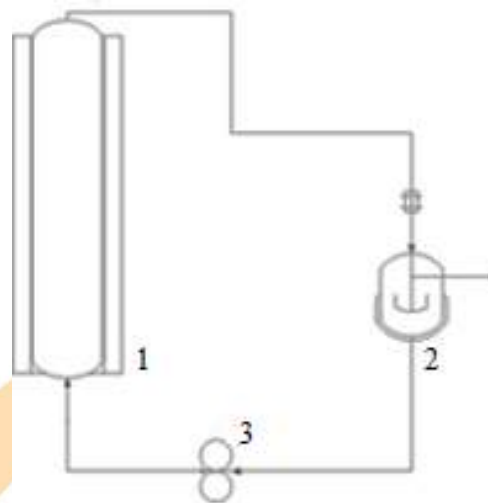


Fig. 1. Desorption experimental apparatus: 1: Desorption column; 2: feed tank; 3: peristaltic pump.

In pre-defined time intervals, samples were collected from the tank containing the eluent solution to obtain the desorption curve. The concentration of Ni^{2+} was determined by atomic absorption spectroscopy. The desorbed mass (m_{des}) of Ni^{2+} in each cycle was calculated by the equation:

$$m_{\text{des}}(t) = V_T C(t) \quad (3)$$

where: V is the volume of eluent solution used and the subscript T means tank. Overall, 10 adsorption-desorption cycles were performed.

2.2. Phenomenological Modeling

In this work, all the desorption curves were modeled by using the dispersion model:

$$\frac{\partial C}{\partial t} + \rho_{bed} \frac{1}{\varepsilon} \frac{\partial q}{\partial t} = -u \frac{\partial C}{\partial z} + D_L \frac{\partial^2 C}{\partial z^2} \quad (4)$$

$$C(z, 0) = 0 \quad (5)$$

$$D_L \left. \frac{\partial C}{\partial z} \right|_{z=0} = u(C(0, t) - C^{F0}) \quad (6)$$

$$\left. \frac{\partial C}{\partial z} \right|_{z=L} = 0 \quad (7)$$

where: ρ_{bed} is the bed density, u is the interstitial velocity, z is the bed length coordinate, L is the bed length, q is the adsorbed amount of the solute per gram of adsorbent, C^{F0} is the Ni^{2+} concentration entering the column, and D_L is the axial dispersion. To improve the mathematical model, it was considered that the desorption only occurred after the eluent solution was in contact with the adsorbent (Eqs. (8)-(11)). This is necessary since at $t = 0$ there is no eluent molecules inside the column, and thus, there is no desorption.

$$\frac{\partial C_{el}}{\partial t} = -u \frac{\partial C_{el}}{\partial z} + D_L \frac{\partial^2 C_{el}}{\partial z^2} \quad (8)$$

$$C_{el}(z, 0) = 0 \quad (9)$$

$$\left. \frac{\partial C_{el}}{\partial z} \right|_{z=0} = 0 \quad (10)$$

$$C_{el}(0, t) = C_{el}^{F0} \quad (11)$$

where: C_{el} is the eluent concentration. Finally, it was considered that the rate of Ni^{2+} desorption from the solid phase was proportional to its concentration on the solid, and to the eluent concentration at the fluid phase:

$$\frac{\partial q}{\partial t} = -\frac{K_s \varepsilon}{\rho_{bed} C_{el}^{F0}} C_{el} q \quad (12)$$

$$q(z, 0) = q_0 \quad (13)$$

where, q_0 is the amount of Ni^{2+} per gram of adsorbent at $t = 0$. In this system, the samples were collected from the tank. Thus, it was necessary to include equations for volume variation and Ni^{2+} mass balance in this equipment:

$$\frac{dV_T}{dt} = -(Q_{T,in} - Q_{T,out}) \quad (14)$$

$$\frac{dC^{F0} V_T}{dt} = -(Q_{T,in} C^{out} - Q_{T,out} C^{F0}) \quad (15)$$

$$V_T(0) = 0 \quad (16)$$

$$C^{F0} V_T(0) = 0 \quad (17)$$

where: V is the liquid volume, C^{out} is the Ni^{2+} concentration at the column exit.

To solve the Eqs. (4)-(17), the finite volume method and the DASSL routine [6] were used. The parameters K_S and D_L were determined by using the Downhill Simplex method to minimize the following objective function:

$$F_{Obj} = \sum_{i=1}^N (C_i^{out,EXP} - C_i^{out,MOD})^2 \quad (18)$$

All routines were written in Fortran language. After the parameters were obtained, the Pearson correlation coefficient, and m_{des} were calculated.

2.3. ANN Modeling

Since the collected data was not in a constant time interval, all experimental desorption curves were adjusted to a spline using Table Curve 2D®. For each cycle it was generated 60 data points (a total of 600) in a uniform time interval of 2 min.

To train the ANNs, two set of input/output data were proposed, as showed at Table 1. These strategy was already used with success in the studies of Carvalho et al. [4] and Choji et al. [7]. Figure 2 shows the general configuration of an ANN with two hidden layers for strategy 2.

Table 1. ANN input/output strategies.

Strategy	Inputs	Outputs
1	$C(t-1); C(t);$	$C(t+1)$
2	$C(t-2); C(t-1); C(t);$	$C(t+1)$

The difference between the two strategies is the amount of information about the desorption curve behavior that the ANN is being exposed. In strategy 1, the inputs are related to the slope of the curve in one time interval (between $t-1$ and t). In strategy 2, the networks receives information about the slope of the desorption curve of two time intervals. The best strategy is determined by using a trial and error method.

This step was divided into two parts: (i) ANN obtaining, in which the ANNs were trained, validated and tested; (ii) ANN simulation, which were performed to check the ANN efficiency using only data at times 0 and 2 min for strategy 1, and data at times 0, 2, and 4 min for strategy 2. The rest of the profile was calculated by retrofeeding the answer for time $k+1$ as input. If the ANN is not

well trained, it will not predict the full kinetic profile correctly.

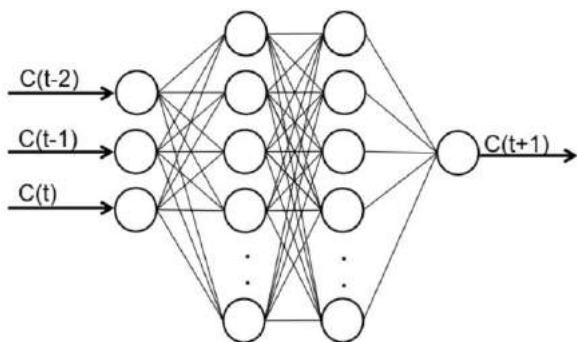


Fig. 2. General ANN used in this work.

In part (i) seven cycles were presented to the ANN. The generated data (420) was randomly divided in training (70 %), test (15 %) and validation (15 %) sets. For each strategy, different ANN structures with one and two hidden layers were tested. The activation function was sigmoidal and linear for the neurons in hidden and output layers, respectively. The mean square error was the objective function (F_{Obj}) minimized by the Levenberg-Marquardt method [8]. In part (ii), all the ten cycles were used (three of them were used exclusively in this step). Then, the Pearson correlation coefficient, and m_{des} were calculated. The best ANN was then chosen based on the simulation step performance.

3. Results and Discussion

3.1. Experimental

Fig. 2 shows the all the desorption curves obtained for Ni^{2+} by Seolatto et al. [5]. One can see that the behavior for cycles 2-10 is similar and apart from the cycle 1. According to the authors, this is expected since the eluent causes mass loss after each desorption cycle. However, they are not superposed, which indicated that each cycle presents different kinetics mechanism.

3.2. Phenomenological Modeling

A dispersion model was used to describe all desorption curves. Table 2 shows the results obtained for cycles 1, 2, 9, and 10. It was considered that the value of D_L does not change and it was equal to $1.40 \cdot 10^{-2}$ for all cycles (this value was adjusted only for the first cycle). One can see that all F_{obj} values are low and it describes

very well each curve. It is also shown that the values of K_S is not the same for all the cycles, i.e. the desorption kinetics is different for each cycle.

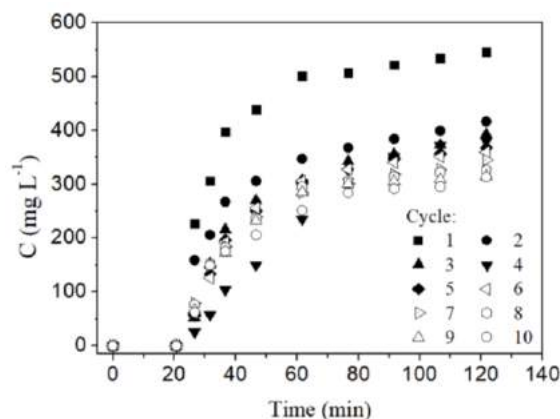


Fig. 2. Desorption curves obtained for Ni^{2+} .

Table 2. Summary of the phenomenological modeling results.

Cycle	k_a	F_{Obj}	r^2
1	$3.29 \cdot 10^{-2}$	$8.05 \cdot 10^{-2}$	0.989
2	$3.75 \cdot 10^{-2}$	$3.82 \cdot 10^{-2}$	0.988
9	$3.52 \cdot 10^{-2}$	$6.43 \cdot 10^{-2}$	0.988
10	$3.13 \cdot 10^{-2}$	$4.52 \cdot 10^{-2}$	0.989

In fact, when we used the parameter of a cycle i , to simulate the curve of another cycle, the result was not accurate. This indicates that the column dynamic varies as the adsorbent is being reused and can be seen in Fig. 2, in which the curves are not superposed.

3.3. ANN Modeling

The phenomenological modeling performed in this study showed that the model's parameter depends on the desorption cycle. Thus, the utilization of this model for process control is limited since it is necessary to determine which running is on. Thus, the use of ANNs could be an interesting approach, since they can learn about the process, deal with noise data, and predict the desorption curve using only one set of parameters, regardless the desorption cycle.

In this work, several ANN structures were trained. By using data from the seven out of ten cycles, we aimed to obtain one equation that could be used in real time operation of a desorption process. At Table 3, are shown the best results obtained for different ANN structures.

Table 3. Summary of the ANN modeling results. ANNs are presented in increasing order of number of parameters.

Structure	F_{OBJ}	F_{OBJ}	r^2
	Training	Validation	Simulation
Strategy 1			
2-5-5-1	$1.80 \cdot 10^{-5}$	$7.45 \cdot 10^{-5}$	0.959
2-15-15-1	$1.16 \cdot 10^{-6}$	$2.70 \cdot 10^{-6}$	0.985
2-20-15-1	$1.64 \cdot 10^{-6}$	$3.15 \cdot 10^{-6}$	0.979
2-20-25-1	$1.57 \cdot 10^{-6}$	$3.21 \cdot 10^{-6}$	0.975
Strategy 2			
3-5-5-1	$1.09 \cdot 10^{-6}$	$4.90 \cdot 10^{-7}$	0.970
3-5-10-1	$1.17 \cdot 10^{-6}$	$1.75 \cdot 10^{-6}$	0.979
3-5-10-1	$9.67 \cdot 10^{-7}$	$8.74 \cdot 10^{-7}$	0.964
3-15-10-1	$9.70 \cdot 10^{-7}$	$3.75 \cdot 10^{-7}$	0.978
3-15-15-1	$3.21 \cdot 10^{-7}$	$6.72 \cdot 10^{-7}$	0.985

The best results were obtained using ANNs with four layers, i.e. an input layer, two hidden layers and the output layer. The number of neurons in the input layer is equal to the number of inputs (2 for strategy 1 and 3 for strategy 2). The number of output neurons is equal to the number of outputs (only $C(t+1)$). The number of neurons in the hidden layers, which represents the ANN size, is what was modified until the optimal result was found.

The results showed that the F_{obj} were slightly lower in training and validation steps for strategy 2 (in average). Also there was no directly relation between the ANN complexity (number of hidden neurons) and the ANN performance. However, more inputs were needed to obtain a result more accurate. This means that more information about the rate of removal was needed to the ANN learn about the process dynamics.

The best result was defined using the results of the simulation step after the ANNs obtaining. This was done to guarantee that the ANN is capable to predict the desorption curve given only the initial condition of each cycle. When analyzing the simulation results, the best result was obtained with the ANN 3-15-15-1, since the r^2 was the highest obtained (Table 3).

It is important to mention that all the ANNs presented excellent agreement between the predicted and experimental data in the obtaining steps. The correlation coefficient was up to 0.999. However, in the simulation step the behavior was not so accurate. This happened because at the obtaining steps the ANN uses experimental data to

predict $C(t+1)$ and at the simulation step the ANN exit at a determined time $t+1$ becomes an input (as time t) to calculate the next point ($t+2$). Thus, if the ANN did not learn about the phenomenon, the cumulative error of the wrong predictions will generate poor results, even if the ANN presents good results in the obtaining step.

Fig. 3 shows the experimental and simulated desorption curves using the dispersion model and the ANN 3-15-15-1 for cycle 1 (which presented the lower accuracy) and cycle 9 (which was used exclusively in the ANN simulation step). These plots were generated providing only the initial condition to the ANN.

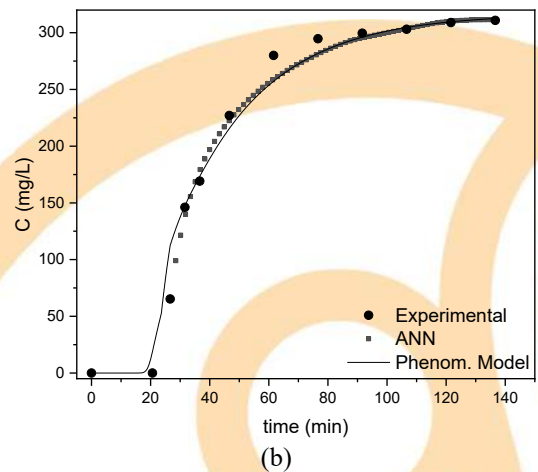
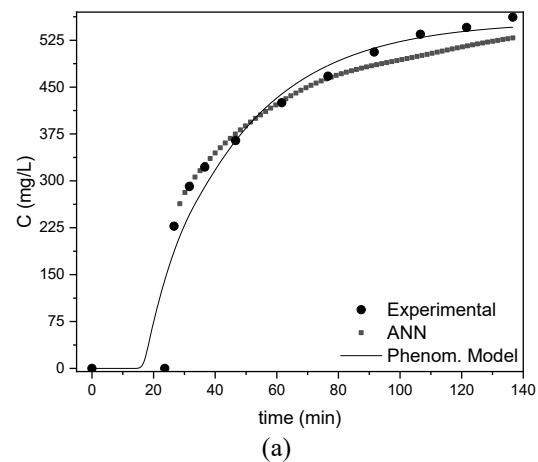


Fig. 3. Experimental and simulated desorption curves for: (a) cycle 1 (b) cycle 9.

One can see that both models were very accurate and presented similar behavior. The r^2 for the ANN was higher than for the dispersion model for all cycles, except for cycle 1. For cycle 9 it was

equal to 0.994, (slightly superior when comparing with the dispersion model).

One information that can be extracted from the model's desorption curve is the desorbed mass, which can be calculated using Eq. (3). At Table 4 is shown the experimental and the predicted desorbed mass using the dispersion model and the ANN 3-15-15-1 for cycles 1, 2, 9, and 10. One can see that both models underestimated the desorption mass, within an error of 3 %. Also, except for cycle 1, the ANN predicted the desorbed mass with higher precision than the dispersion model. This result confirms that the ANN can be useful for practical applications.

Table 4. Desorbed mass calculated from the experimental and ANN predicted curves.

Cycle	Exp.	ANN	Dispersion Model
1	185.39	174.45	180.01
2	138.60	137.99	137.07
9	104.61	103.72	103.14
10	104.77	103.67	102.98

At the end, an ANN is an equation that is simple to use and can be programmed in any language. To calculate $C(t+1)$ using ANN 3-15-15-1 one can use the following equation:

$$C(t+1) = f \left(\sum_{k=1}^{15} w_{k,l} f \left(\sum_{j=1}^{15} w_{j,k} f \left(\sum_{i=1}^3 w_{i,j} x_i + b_j \right) + b_k \right) + b_l \right) \quad (19)$$

where: x_i is the input variable i and, f is the hyperbolic tangent function. Eq. (19) is capable to predict any desorption curve in these experimental conditions.

4. Conclusion

In this work, the successive desorption cycles of Ni^{2+} from the *Sargassum filipendula* seaweed using a H_2SO_4 0.1M solution was evaluated. Data from ten adsorption-desorption cycles were used to obtain one phenomenological and one ANN mathematical model capable to describe all the desorption curves. The results showed that both models were capable to predict the kinetic profiles. However, the ANNs showed high accuracy. The best structure found was 3-15-15-1. This ANN was

able to predict efficiently all the curves and calculated the extracted mass with low error.

In summary, this work showed that desorption curves with eluent recycle can be modeled with success using phenomenological and ANN equations. However, the ANN presented the advantage of predicting the curves of the ten cycles performed with the same set of parameters. Future work will focus in the study of different operational conditions to improve the ANN model.

References

- [1] Ruthven DM. Principles of adsorption and desorption processes. New York: John Wiley & Sons; 1984
- [2] Maeda CH, Araki CA, Moretti AL, de Barros MASD, Arroyo PA. Adsorption and desorption cycles of reactive blue BF-5G dye in a bone char fixed-bed column. Environ Sci Pollut Res 2019; 26:28500-28509.
- [3] Tran HN, Chao H-P. Adsorption and desorption of potentially toxic metals on modified biosorbents through new green grafting process. Environ Sci Pollut Res 2018; 25:12808-12820.
- [4] Carvalho LP, Seolatto AA, Silva EA, Martins TD Kinetic modeling of Ni^{2+} adsorption cycles in fixed bed column using artificial neural networks. In: I Congresso Brasileiro em Engenharia de Sistemas em Processos - PSE 2019, Rio de Janeiro, 2019.
- [5] Seolatto AA, Câmara MM, Tavares CR, Cossich ES, Silva EA. Removal of nickel (II) from aqueous solutions by *Sargassum filipendula* biomass in multiple cycles of sorption-desorption. Acta Scientiarum Technology 2009; 31:57-64.
- [6] Petzold LR. A description of DASL: A differential/algebraic system solver in scientific computing In: IMACS World Congress, Motreal, 1982.
- [7] Choji TT, Ottaiano GY, Seolatto AA, Silva EA, Martins TD Kinetics of Ni^{2+} - Cr^{3+} mixture adsorption using artificial neural networks. In: I Congresso Brasileiro em Engenharia de Sistemas em Processos - PSE 2019, Rio de Janeiro, 2019.
- [8] Marquardt DW. An algorithm for least-squares estimation of nonlinear parameters. Journal of the society for Industrial and Applied Mathematics 1963; 11:431-441.

Effect of Ultrasound on Sulfur Adsorption in Activated Carbon Using Synthetic and Commercial Diesel

Thaís Becker, Cassio G. Dal Molin, Fernanda S. Maia, João L. Uller, Carlos I. Yamamoto, Myriam Lorena M. N. Cerutti

Universidade Federal do Paraná, Departamento de Engenharia Química, Av. Cel. Francisco H. dos Santos, 100 - Jardim das Américas, Curitiba - PR, 81530-000, Brasil

Abstract

Global environmental legislation requires low sulfur in fossil fuels to reduce toxic sulfur dioxide emissions during fuel combustion. This study evaluated the effect of ultrasonic agitation on sulfur adsorption process in granulated activated carbon of plant origin using synthetic diesel and commercial diesel. Sulfur adsorption capacity and efficiency within 30 minutes of contact and adsorption kinetic curves were experimentally obtained in a finite bath at 60 °C with 135 W ultrasonic agitation and with 120 rpm conventional agitation. Synthetic diesel consisted of four binary solutions of n-decane/benzothiophene, n-decane/4-methylbenzothiophene, n-hexadecane/benzothiophene, n-hexadecane/4-methylbenzothiophene containing 500 ppm (w/w) sulfur and diesel commercial was Brazilian Diesel S500. On all diesel samples, sulfur adsorption capacity and adsorption efficiency decreased with ultrasonic agitation compared to conventional agitation which was attributed to the power level and ultrasonic frequency employed. The highest adsorption capacities of 2.89 mg/g (ultrasound) and 3.03 mg/g (shaker) were obtained with n-decane/4-methylbenzothiophene and the lowest adsorption efficiencies of 3 % (ultrasound) and 6 % (shaker) were obtained with commercial diesel. The n-hexadecane/benzothiophene sulfur adsorption process with conventional agitation followed the pseudo-second order kinetics and with ultrasonic agitation followed the intra-particle diffusion model.

Keywords: Ultrasound; Adsorption; Diesel; Activated carbon; Kinetics.

1. Introduction

Desulfurization of transportation fuels such as diesel has increasingly gained importance since most of the countries, particularly the developed ones, have implemented more stringent legislation to regulate sulfur content of transportation fuels. Currently, the common sulfur specification is 500 ppm in several countries; however, some countries have tighter specification. Due to the additional desulfurization process required for fuel refining, there has been a growing concern to the long term economics of petroleum refineries.

Many researches have attempted to develop alternate or complementary processes to conventional hydrodesulfurization (HDS), such as adsorptive desulfurization [1,2,3]. Adsorptive desulfurization is based on the ability of a solid material to physically adsorb organo-sulfur compounds like thiophene (T), benzothiophene (BT) and dibenzothiophene (DBT) [3]. The efficiency of the desulfurization is determined

mainly by the adsorbent properties, such as adsorption capacity, selectivity for organo-sulfur compounds, durability, and regenerability [4]. Activated carbons have been recognized and widely used as adsorbents in gas-phase and liquid-phase adsorptions for removal of organic sulfur compounds [5,6]. This is due to their very high surface areas, large pore volumes, and tunable surface properties by introducing functional groups.

Ultrasound is a green technology because it requires no additional chemicals and only involves sound energy [7]. Previous study had proven that it can increase the rate of reaction and adsorption capacity [8]. Ultrasound produces the sound wave within the liquid medium, generating mechanical vibration and acoustic streaming [9]. Ultrasound wave causes cavitation in liquid, involving formation of small bubbles, grow, and collapse due to pressure fluctuation [10].

The objective of this work is to evaluate the effect of ultrasonic agitation on sulfur adsorption capacity, efficiency and kinetics in granular activated carbon using synthetic and commercial diesel. The

adsorption study was performed in a finite bath at a constant temperature of 60 °C with ultrasonic agitation and with conventional agitation.

2. Materials and methods

2.1. Materials

The granulated activated carbon used in this study (designated as CAC7) was kindly provided by Industria Química Carbomafra S.A. and has as precursor the bark of babassu coconut. Synthetic diesel was prepared from binary solutions of a solvent with a sulfur compound. The solvents used were n-decane (Sigma Aldrich, 99 %) and n-hexadecane (Sigma Aldrich, 99 %). The sulfur compounds were benzothiophene, BT, (Sigma Aldrich, ≥ 95 %) and 4-methyl dibenzothiophene, MDBT, (Sigma Aldrich, 96 %). Commercial diesel (designated as S500) was Brazilian Diesel S500 purchased from a local gas station containing approximately 500 ppm sulfur.

2.2. Sulfur analysis

The total sulfur content of all samples was determined on a Sindie 7039 G3 M-SERIES XOS X-ray fluorescence device in accordance with ASTM D7039.

2.3. Adsorption experiment

Adsorption experiments were conducted in batch and triplicate. The system consisted of a ground-glass Erlenmeyer flask containing approximately 2.0 g of CAC7 activated carbon, previously oven-dried at 120 °C, and 20 mL of synthetic diesel solution or commercial diesel with 500 ppm (w/w) sulfur at a temperature of 60 °C. Ultrasonic agitation was carried out using a Unique MaxiClean USC-1400A ultrasonic bath with 135 W ultrasonic power, 40 kHz ultrasonic frequency, 30-minute timer and fixed heating at 60 °C (± 5 °C). Conventional agitation was performed in a Marconi model MA 410 orbital shaker incubator with agitation speed of 120 rpm and heating of 60 °C (± 0.1 °C). After the specified adsorption time, samples were collected with a glass syringe containing a disposable Millipore filter membrane and deposited in 2 mL vials for sulfur analysis. The amount adsorbed was calculated from the Equation 1.

$$q_t = \frac{(C_i - C_t)V}{m} \quad (1)$$

where q_t is the amount adsorbed, V is the volume of the solution, C_i is the concentration of the solution at initial, C_t is the concentration of the solution at any given time, and m is the amount of adsorbent.

2.3.1. Adsorption capacity in 30 minutes

Synthetic diesel (binary solutions) and commercial diesel (S500) were placed in contact (according to item 2.3) with the adsorbent (CAC7) for a stipulated time of 30 min., under ultrasonic agitation and under conventional agitation to determine adsorption capacity q_t (mg S/g CAC7). The binary solutions studied were:

- n-decane/benzothiophene (BT),
- n-decane/4-methyldibenzothiophene (MDBT),
- n-hexadecane/benzothiophene (BT),
- n-hexadecane/4-methyldibenzothiophene (MDBT).

The sulfur removal efficiency (%R) of the CAC7 samples was calculated using the Equation 2:

$$\%R = \frac{(C_i - C_t)}{C_i} \times 100 \quad (2)$$

2.3.2. Adsorption kinetics

The kinetic study of sulfur adsorption in activated carbon CAC7 was performed with synthetic diesel and commercial diesel (according to the procedure detailed in item 2.3) under ultrasonic agitation and under conventional agitation. For synthetic diesel was obtained the kinetic curve of the n-hexadecane/benzothiophene (BT) binary solution. Sampling in the ultrasonic bath was performed at 1, 3, 5, 10, 15, 30, 40, 50, 60, 90, 120 and 150 min and in the orbital shaker incubator at 5, 10, 15, 30 min. and 1, 2, 3, 5, 7 and 24 h. The kinetic curve of the commercial diesel was performed under ultrasonic agitation for times 1, 3, 5, 10, 15, 30, 40, 50, 60, 90 and 120 min.

Three widely used kinetics models, the pseudo-first-order model (PFOM), pseudo-second-order model (PSOM) and intra-particle diffusion model (IPDM) were employed to fit the kinetics data by using their linear forms.

The PFOM equation can be expressed correctly in nonlinear (Equation 3) and linear form (Equation 4).

$$q_t = q_e(1 - e^{-k_1 t}) \quad (3)$$

$$\ln(q_e - q_t) = \ln(q_e) - k_1 t \quad (4)$$

where q_e is the amount of adsorbate uptake per mass of adsorbent at equilibrium time, t is the time, and the k_1 is the rate constant of the pseudo-first order sorption [11]. The values of q_e and k_1 are obtained from the intercept and the slope of the linear plot of $\ln(q_e - q_t)$ versus t , respectively.

The nonlinear form of the PSOM equation (Equation 5) and the linear form (Equation 6) are:

$$q_t = \frac{q_e^2 k_2 t}{1 + q_e k_2 t} \quad (5)$$

$$\frac{t}{q_t} = \frac{1}{q_e^2 k_2} + \left(\frac{1}{q_e}\right) t \quad (6)$$

where k_2 is the rate constant of the pseudo-second order sorption [11]. The values of q_e and k_2 are the slope and intercept of the linear plot of t/q_t versus t , respectively.

The linearized transformation of the intra-particle diffusion model (IPDM) [12] is presented as follows:

$$q_t = k_p \sqrt{t} + C \quad (7)$$

where C is the intercept of the linear portion of the plot. The k_p is the intra-particle diffusion rate constant, which can be evaluated from the slope of the linear plot of q_t versus $t^{1/2}$.

3. Results and discussion

The results presented refer to the adsorption study in a finite bath containing 2 g of CAC7 activated carbon and 20 mL of solution (synthetic or commercial diesel) at 60 °C. The binary solutions were prepared with 500 ppm sulfur and the analyzed sulfur content of commercial diesel was 168 ppm (w/w). In the calculations, the specific mass of S500 diesel was 0.815 g/mL and binary solutions was 0.730 g/mL for decane and 0.773 g/mL for hexadecane. To evaluate the effect of ultrasound on the adsorption process by comparison, the samples were agitated in an ultrasonic bath and orbital shaker (conventional agitation).

3.1. Adsorption capacity in 30 minutes

Due to limitation of the continuous agitation ultrasonic bath up to 30 min., in a first step sulfur adsorption capacity was investigated in binary solutions and commercial diesel with 30 min of contact. The same procedure was followed with conventional agitation. The results obtained are

presented in Tables 1 and 2. Fig. 1 illustrates the adsorption capacities obtained in 30 min. for both agitation types. Overall, there is a slight reduction in adsorption capacity (q_t) and the amount of sulfur removed (%R) in ultrasonic agitation compared to conventional agitation. This reduction was also observed in another study using low ultrasonic power [13]. However, by increasing the ultrasonic power and frequency, the adsorption capacity and efficiency increased, surpassing the conventional agitation [13]. Higher adsorption performances were obtained when ultrasonic agitation was compared to a system without agitation [14,15]. This indicates that the ultrasonic agitation interferes with the adsorption process and that its performance is a function of the ultrasonic power employed.

Table 1. Ultrasound adsorption results.

Diesel	C_t (ppm)	q_t (mg/g)	% R
decane/BT	157 ± 5.3	2.34 ± 0.026	67
decane/MDBT	118 ± 2.1	2.89 ± 0.015	77
hexadecane/BT	310 ± 5.4	1.43 ± 0.027	38
hexadecane/MDBT	342 ± 3.5	1.92 ± 0.106	41
S500	164 ± 3.1	0.04 ± 0.025	3

Table 2. Shaker adsorption results.

Diesel	C_t (ppm)	q_t (mg/g)	% R
decane/BT	151 ± 4.4	2.40 ± 0.035	69
decane/MDBT	98 ± 2.7	3.03 ± 0.019	81
hexadecane/BT	248 ± 2.8	1.85 ± 0.069	50
hexadecane/MDBT	253 ± 2.1	2.54 ± 0.016	57
S500	158 ± 2.3	0.08 ± 0.018	6

Regardless of the type of agitation, the comparative study of synthetic diesel with commercial diesel makes evident the competition of sulfur adsorption with other diesel compounds when they are present, since for commercial diesel the lowest adsorption efficiencies were obtained of 3 % (ultrasound; Table 1) and 6 % (shaker; Table 2). According to Fig.1 the highest adsorption capacities of 2.89 mg/g (ultrasound) and 3.03 mg/g (shaker) were obtained with the n-decane/MDBT binary solution.

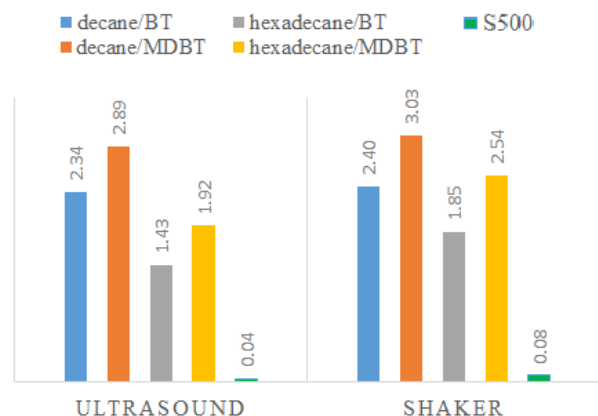


Fig. 1. Comparison of adsorption capacities.

In the study with synthetic diesel it was also possible to evaluate the effect of solvents, n-decane and n-hexadecane, on the adsorption of benzothiophene (BT) and 4-methylbenzothiophene (MDBT). Fig. 1 shows, in both agitations types, a higher selectivity of MDBT in relation to BT in both n-decane and n-hexadecane. The n-decane solvent interfered less with the adsorption process.

3.2. Adsorption kinetics

The kinetic adsorption behavior of sulfur with ultrasonic agitation was studied for n-hexadecane/benzothiophene binary solution and S500 diesel. For comparative purposes, the kinetic curve of S500 diesel with conventional agitation (shaker) was also obtained. Adsorption time in the ultrasonic bath was limited to 2 h and in the shaker to 24 h. The results are presented in Table 3.

Fig. 2 and 3 show the variation in the amount of sulfur adsorbed on CAC7 activated carbon with adsorption progress at 60 °C for synthetic and commercial diesel, respectively. In the beginning of the adsorption process, the sulfur was rapidly adsorbed, then the adsorption rate was slowed down and finally the equilibrium was gradually reached. The highest rates of sulfur removal at the beginning was probably due to the larger surface area of CAC7 available for adsorption and probably the strong interaction between the sulfur and the surface of adsorbent. In the later periods, the surface adsorption sites become exhausted and the removal rate was controlled by the rate of sulfur transportation from the exterior to the interior sites of the adsorbent particles [15]. Fig. 2 shows a comparison of n-hexadecane/BT sulfur adsorption kinetic curves up to 7 h contact for shaker agitation and up to 1.5 h for ultrasonic agitation. In agreement

with other research [13], there is a higher rate of sulfur removal with conventional agitation compared to ultrasonic agitation at the studied power. Fig. 3 shows the sulfur adsorption kinetic curve in commercial diesel up to 2 h operating timeout. Looking at the kinetic curves of Fig. 2 and 3, it can be stated that the curve obtained for n-hexadecane/BT with conventional agitation reached equilibrium with a maximum adsorption capacity around 3 mg/g. To confirm if equilibrium was reached in the kinetic curves under ultrasonic agitation, the data were adjusted to the adsorption kinetic models.

Table 3. Adsorption kinetics results.

<i>t</i> (h)	hexadec/BT ultrasound <i>q_t</i> (mg/g)	hexadec/BT shaker <i>q_t</i> (mg/g)	S500 shaker <i>q_t</i> (mg/g)
0.00	0.000	0.000	0.000
0.02	0.637	-	-
0.05	0.838	-	0.012
0.08	0.721	0.815	-
0.17	0.895	1.255	0.031
0.25	1.143	1.463	-
0.50	1.432	1.847	0.057
0.67	1.637	-	0.078
0.83	1.808	-	-
1.00	1.866	2.327	0.092
1.50	2.212	-	0.128
2.00	-	2.649	0.174
3.00	-	2.817	-
5.00	-	2.937	-
7.00	-	3.017	-
24.00	-	3.273	-

Each liquid–solid sorption process involves several steps such as:

- diffusion of the solute from the solution to the film surrounding the sorbent particles (bulk diffusion),
- diffusion of the solute through the film to the particle surface (external diffusion),
- diffusion of the solute from the particle surface through pores to the internal active sites (internal or pore diffusion), and
- uptake of the solute on active sites by different mechanisms (physico-chemical sorption, ion exchange, etc.) [16].

The rate of each step can generally control the overall sorption rate. To examine the controlling

mechanism of adsorption process studied, three kinetic models, namely pseudo first-order (PFOM), pseudo second-order (PSOM) and intra-particle diffusion (IPDM) were used to test the experimental data. The experimental data of the commercial diesel kinetic curve (Fig. 3) was not adjusted to any of the kinetic models indicating that the adsorption equilibrium was not reached. For n-hexadecane/BT, values of the parameters of the kinetic models applied and the linear correlation coefficient of their linear forms are shown in Table 4 and 5.

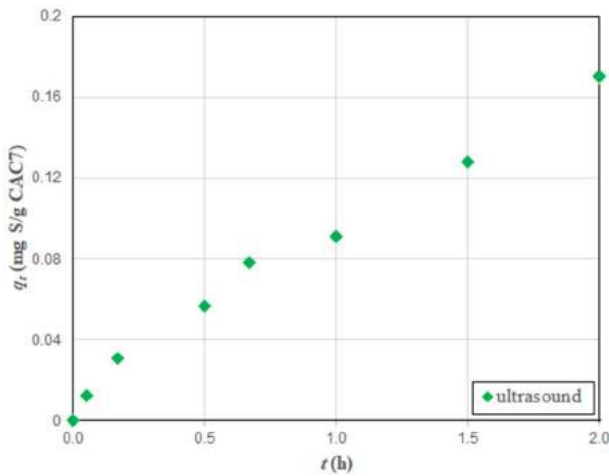


Fig. 3. Sulfur adsorption kinetics in commercial diesel.

Table 4. Parameters of n-hexadecane/BT adsorption kinetic models with ultrasound.

pseudo-first order model (PFOM)		
q_e (mg/g)	k_1 (min^{-1})	R^2
2.250	0.042	0.862
pseudo-second order model (PSOM)		
q_e (mg/g)	k_2 ($\text{g}/\text{mg}\cdot\text{min}^{-1}$)	R^2
2.555	0.023	0.909
intra-particle diffusion model (IPDM)		
C (g/mg)	k_p ($\text{mg}/\text{g}\cdot\text{min}^{1/2}$)	R^2
0.344	0.190	0.965

Table 5. Parameters of n-hexadecane/BT adsorption kinetic models with shaker.

pseudo-first order model (PFOM)		
q_e (mg/g)	k_1 (min^{-1})	R^2
2.889	2.522	0.951
pseudo-second order model (PSOM)		
q_e (mg/g)	k_2 ($\text{g}/\text{mg}\cdot\text{min}^{-1}$)	R^2
3.131	1.085	0.991
intra-particle diffusion model (IPDM)		
C (g/mg)	k_p ($\text{mg}/\text{g}\cdot\text{min}^{1/2}$)	R^2
1.176	0.598	0.658

The kinetic curves obtained in the kinetic models are presented in Fig. 4 and 5. Considering the linear correlation coefficients, the best fit for experimental ultrasound data ($R^2 = 0.965$; Tabela 4) was obtained with the IPDM model. The intra-particle diffusion model can be useful for identifying the reaction pathways and adsorption mechanisms and predicting the rate-controlling step. If the intra-particle diffusion plot gives multiple linear regions, then the adsorption process is controlled by a multistep mechanism [17]. The best linear correlation coefficient for the shaker ($R^2 = 0.991$; Table 5) was obtained with the PSOM model. This model is based on the assumption that the rate-limiting step might be a chemical reaction between the adsorbent and the adsorbate [16]. Thus, the pseudo second-order model is potentially a generalized kinetic model for the adsorption system studied.

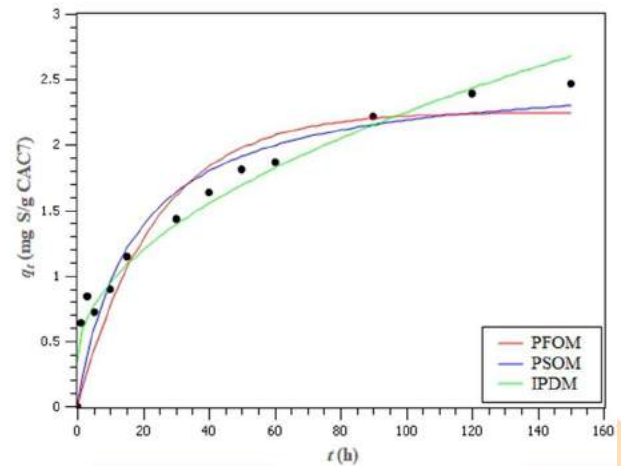


Fig. 4. Kinetic curves of n-hexadecane/BT adsorption kinetic models with ultrasound.

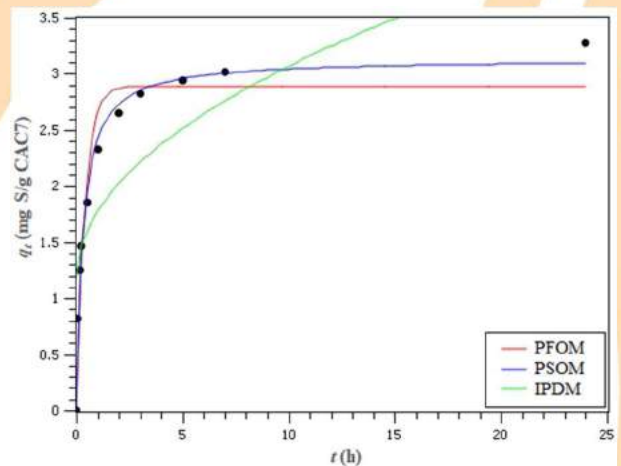


Fig. 5. Kinetic curves of n-hexadecane/BT adsorption models with shaker.

4. Conclusions

The influence of ultrasonic agitation on sulfur adsorption capacity, efficiency and kinetics of granular activated carbon was evaluated compared to conventional agitation for synthetic and commercial diesel solutions. Experimental results showed that in both synthetic and commercial diesel sulfur adsorption capacity and efficiency were higher in conventional agitation compared to ultrasonic agitation. The lowest performance was attributed to the ultrasonic power and frequency used in the ultrasound equipment.

The kinetics of sulfur removal on activated carbon from n-hexadecane/benzothiophene with shaker follows the pseudo second order model, which is a generalized kinetic model for the adsorption system studied. As the intra-particle diffusion model fits well the kinetic data for n-hexadecane/benzothiophene with ultrasound, adsorption of sulfur on the activated carbons is also diffusion controlled.

Acknowledgements

We thank to the Laboratório de Análises de Combustíveis Automotivos – LACAUT of the Universidade Federal do Paraná – UFPR for providing the infrastructure for the development of this work.

References

- [1] Chen, T.C. Shen, Y.H. Lee, W.J. Lin, C.C. Wan, M.W. The study of ultrasound-assisted oxidative desulfurization process applied to the utilization of pyrolysis oil from waste tires. *J. Clean. Prod.* 2010; 18; 1850-1858.
- [2] Cerutti, M.L.M.N. · Hackbarth, F.V. Maass, D. Chiaro, S.S.X. · Pinto, R.R.C. Cardoso, M.J.B. Arroyo, P.A. · U. de Souza, A.A. · U. de Souza, S.M.A.G. Copper-exchanged Y zeolites for gasoline deep-desulfurization. *Adsorption* 2019; 25 (8); 1595-1609.
- [3] Saleh, T.A. Sulaiman, K.O. AL-Hammadi, S.A. Dafalla, H. Danmaliki, G.I. Adsorptive desulfurization of thiophene, benzothiophene and dibenzothiophene over activated carbon manganese oxide nanocomposite: with column system evaluation. *J. Clean. Prod.* 2017; 154; 401-412.
- [4] Babich, I.V. Moulijn, J.A. Science and technology of novel processes for deep desulfurization of oil refinery streams: a review. *Fuel* 2003; 82; 607-631.
- [5] Yang, Y.X. Liu, H.Y. Ying, P.L. Jiang, Z.X. Li, C. Selective dibenzothiophene adsorption on modified activated carbons. *Carbon* 2007; 45; 3042-3044.
- [6] Ania, C.O. Bandosz, T.J. Importance of structural and chemical heterogeneity of activated carbon surfaces for adsorption of dibenzothiophene. *Langmuir* 2005; 21; 7752-7759.
- [7] Wang, X. Wang, A. Ma, J. Fu, M. Facile green synthesis of functional nanoscale zero valent iron and studies of its activity toward ultrasound-enhanced decolorization of cationic dyes. *Chemosphere* 2017; 166; 80-88.
- [8] Jing, G. Zhou, Z. Song, L. Dong, M. Ultrasound enhanced adsorption and desorption of chromium (VI) on activated carbon and polymeric resin. *Desalination* 2011; 279; 423-427.
- [9] São José, J.F.B.d. Andrade, N.J.d. Ramos, A.M. Vanetti, M.C.D. Stringheta, P.C. Chaves, J.B.P. Decontamination by ultrasound application in fresh fruits and vegetables. *Food Control* 2014; 45; 36-50.
- [10] Hamdaoui, O. Chiha, M. Naffrechoux, E. Ultrasound-assisted removal of malachite green from aqueous solution by dead pine needles. *Ultrason. Sonochem* 2008; 15; 799-807.
- [11] Lagergren, S. About the theory of so-called adsorption of soluble substances. *K. Sven. Vetensk. Handl.* 24 (4); 1898, p. 1-39.
- [12] Weber, W.J. Morris, J.C. Kinetics of adsorption on carbon from solution. *J. Sanit. Eng. Div.* 1963; 89 (2); 31-60.
- [13] Low, S.K. Tan, M.C. Chin, N.L. Effect of ultrasound pre-treatment on adsorbent in dye adsorption compared with ultrasound simultaneous adsorption. *Ultrasonics Sonochemistry* 2018; 48; 64-70.
- [14] Bono, A. Sarbatly, R. Krishnaiah, D. San, P.M. Yan, F.Y. Effect of ultrasound on liquid phase adsorption of azeotropic and non-azeotropic mixture. *Catalysis Today* 2008; 131; 472-476.
- [15] Milenkovic, D.D. Dasic, P.V. Veljkovi, V.B. Ultrasound-assisted adsorption of copper(II) ions on hazelnut shell activated carbon. *Ultrasonics Sonochemistry* 2009; 16; 557-563.
- [16] Milenkovic, D.D. Bojic, A.L. Veljkovic, V.B. Ultrasound-assisted adsorption of 4-dodecylbenzene sulfonate from aqueous solutions by corn cob activated carbon. *Ultrasonics Sonochemistry* 2013; 20; 955-962.
- [17] Tran, H.N. You, S-J. Hosseini-Bandegharaci, A. Chao, H-P. Mistakes and inconsistencies regarding adsorption of contaminants from aqueous solutions: A critical review. *Water Research* 2017; 120; 88-116.

Adsorbents based on metal-organic porous structures for small-scale energy-saturated adsorption systems

M.K.Knyazeva^{a*}, O.V. Solovtsova^a, A.A. Fomkin^a, A.V. Shkolin^a, I.E. Men'shchikov^a,
E.V. Khozina^a, and A.L. Pulin^a

^a *Frumkin Institute of Physical Chemistry and Electrochemistry, Russian Academy of Sciences, Moscow, 119071 Russia*

**e-mail: batrakovamk@mail.ru*

Abstract

In the present study, the adsorbents based on metal-organic porous structures (M_1 -BTC, M_1 =Cu, Al, Fe, BTC³ 1,3,5-benzenetricarboxylate; M_2 -BDC, M_2 =Al, Fe, BDC² 1,4-benzenedicarboxylate) were synthesized for accumulation of energy gases as methane and hydrogen. As follows from the standard nitrogen vapor adsorption measurements at 77 K, the porous structure of the synthesized powder adsorbents was characterized by the BET surface area varied within a range from 1250 to 2250 m²/g and the micropore volume varied from 0.46 to 0.83 cm³/g. The hydrogen adsorption on the adsorbents was measured at 77 K and the pressures up to 140 kPa. Al-BDC powder demonstrated the highest hydrogen storage of 2.6 wt.%. The synthesized powder adsorbents were shaped at different pressures and with the use of various binders or carbon containing compounds. The specific methane adsorption capacity was calculated for the shaped adsorbents. Al-BTC demonstrated the highest volumetric storage capacity of methane 270 m³(NTP)/m³ at 273 K and the pressure of about 10 MPa. Under the same conditions, the methane adsorption capacities of the shaped Cu-BTC and Fe-BDC adsorbents reached the values of 200 and 120 m³(NTP)/m³, respectively.

Keywords: adsorption; metal organic compounds; porous structure; adsorption of methane; adsorption of hydrogen.

1. Introduction

In modern energy industry, the energy gases such as methane and hydrogen are promising environmentally friendly fuels used in motor vehicles, pilotless aircraft, and robotics machines. However, the secure storage and transportation of these gases are difficult to carry out because of their explosive properties, restricting the wide use of these fuels. Metal organic porous structures (MPOS) possess a number of properties needed to address the problems of safe storage, transportation, and separation of energy gases including hydrogen: a high characteristic energy of adsorption, developed regular nanoporous structure with a considerable specific surface and pore volume [1]. MOPS are the coordination compounds, which consist of metal ions or clusters coordinated and linked by organic ligands [2]. A great variety of ligands and metal ions makes it possible to synthesize numerous coordination porous structures with specified surface chemical properties, which can be used in the energy saturated adsorption systems (ESAS) as the high-performance adsorbents. The main disadvantages of these adsorbents are a certain degree of thermal and mechanical instability,

insufficient durability and low packing density. Therefore, the preparation of adsorbents from metal organic porous structures, which possess an appropriate degree of thermal and mechanical stability and a high adsorption activity toward the energy gases is currently the relevant and very timely task. A synergetic combination of MOPS and functional materials implemented in MOPS-based composites resolve this matter.

2. Experimental

2.1 Synthesis of materials

Metal organic porous structures synthesized by solvothermal method [3–5] and the shaped composites prepared from MOPS and carbon-containing materials [6] were studied.

In the work, the reagents used to synthesize MOPS were:

- 1,3,5-benzenetricarboxylic acid (H₃BTC) with a degree of purity of 98% (Acros Organics);
- 1,4-benzenedicarboxylic acid (H₂BDC) with a degree of purity of 98% (Acros Organics);
- copper(II) nitrate, hemipentahydrate (Cu(NO₃)₂·2.5H₂O) with a degree of purity of 99% (Acros Organics);
- aluminum nitrate, nanohydrate (Al(NO₃)₃·9H₂O)

with a degree of purity of 99% (Acros Organics); e) iron nitrate, nanohydrate ($\text{Fe}(\text{NO}_3)_3 \cdot 9\text{H}_2\text{O}$) with a degree of purity of 99% (Acros Organics); f) N,N' dimethylformamide (DMF) with a degree of purity of 99% (Scharlau).

A metal cation source, namely inorganic salt – metal nitrate was dissolved in N,N-dimethylformamide (DMF) used as an organic solvent. An organic aromatic acid was dissolved in the same solvent, and then it was mixed with the solution of the salt and heated while stirring. A Teflon glass with the resultant solution was placed into an oven, where the synthesis was realized in the oven at the temperature varied from 100 to 130 °C. Samples suitable for studies were prepared by exposing in the oven for several days, and multiple washing with DMF before drying at room temperature for several hours and the temperature of synthesis for 24h. The compositions of the synthesized samples were as follows: Cu-BTC, Al-BDC, Al-BTC, Fe-BDC, and Fe-BTC.



Fig.1. Photographs of synthesized MOPS powders: Cu BTC, Al BTC, Al BDC, Fe BTC, and Fe BDC, in the order of pictures.

2.2 Measurements of adsorption.

The structural and energy characteristics of the obtained samples were determined from the isotherms of standard nitrogen vapors at 77 K with the use of a Quantachrome Autosorb iQ multifunctional surface area analyzer.

The hydrogen adsorption measurements were carried out on a adsorption set up described in [7] at the temperature of 77 K and pre up to 140 MPa.

2.3 Calculations of adsorption.

The methane adsorption activity of the samples was estimated based on the Dubinin theory of volume filling of micropores [8] within the temperature range from 243 to 333 K and at a pressures up to 30 MPa following the procedure reported in the works [9-10]. The specific characteristics of the methane accumulation systems based on the obtained materials were calculated using the procedure described in [11-12].

The efficiency of the adsorption gas storage system is determined by the parameter of the total specific volumetric capacity of the storage system VF, which is determined by the equation:

$$V_f(P, T) = a(P, T)\mu \frac{d}{\rho} + \varepsilon \frac{\rho_g(P, T)}{\rho}, \quad (1)$$

where μ is the molar mass of methane (hydrogen), [g/mmol]; d is the packing density of an adsorbent, [kg/m³]; ρ is the density of the free gas phase at NTP, [kg/m³]; ε is the porosity (void content) of an adsorbent layer.

The first term of equation (1) is responsible for the adsorbed phase of the gas, the second for the bulk. As follows from (1), in order to increase VF due to the adsorbed phase, it is necessary to increase the fraction of the system space occupied by the adsorbent, and therefore it is necessary to increase its bulk density d , which used for the objects of study [12].

2.4 Materials of increased bulk density

To increase the bulk density, the synthesized MOPS powders mechanically molded under pressure. To increase the mechanical characteristics and preserve the porous MOPS from collapse, adsorbents, molding was carried out using of a 5% polyvinyl alcohol solution (PVA) as a binder on a 1:1 ratio upon pressing, and carbon containing materials, the content of which varied from 30 to 70 wt.%. A pure MOPS powder or its mixture with the polyvinyl alcohol solution was mixed in a blender, which was used to thoroughly homogenize the mixture. The obtained mixture was loaded into a cylindrical press die and pressed under the action of a hydraulic press. The sample was exposed under the pressure of 160 MPa for 1 min. The shaped samples were dried in a ventilated heat chamber at the temperature of 110 120°C for 6–12 h. Various active carbons prepared from peat (AC 1T and AC 6T), plant (AC RW), and polymer raw materials (AC P) were used as carbon containing components in order to produce the shaped composite adsorbents.



Fig.2. Photographs of shaped MOPS samples: Cu-BTC, Fe-BDC, Al-BTC, and the Cu-BTC/AC-6T composite, in the order of pictures.

3. Results and discussion

3.1 Porous structure of materials

Table 1 summarizes the structural and energy characteristics of the synthesized MOPS samples, which were determined according to the Dubinin theory of volume fillings of micropores (TVFM) [8].

Table 1. Structural and energy characteristics of MOPS adsorbents.

Parameter	Cu BTC	Al BDC	Al BTC	Fe BDC	Fe BTC
$W_0, \text{cm}^3/\text{g}$	0.30	0.52	0.55	0.83	0.46
$S_{\text{BET}}, \text{m}^2/\text{g}$	750	1250	1600	2250	1300
X_0, nm	0.35	0.48	0.77	0.90	0.77
$E_0, \text{kJ/mol}$	34.6	25.0	15.6	13.4	15.5
$d, \text{g/cm}^3$	0.375	0.365	0.231	0.297	0.276

Here, W_0 is the micropore volume; S_{BET} is the BET surface area; X_0 is an effective width of micropores; E_0 is the standard characteristic energy of benzene adsorption, d is the packing density of an adsorbent.

As follows from Table 1, the MOPS adsorbents possess a developed microporous structure, which is characterized by a high values of BET surface, which is essential for their adsorption capacity in respect to energy gases as methane and hydrogen.

3.2 Properties of shaped materials

The MOPS samples with the most appropriate characteristics S_{BET} and W_0 were selected for shaping, namely Cu-BTC, Al-BTC, and Fe BDC. After compacting these MOPS, the adsorption measurements were carried out and the structural and energy characteristics were determined. The results are provided in Table 2.

Table 2. Structural and energy characteristics of the shaped MOPS adsorbents.

Parameter	Cu BTC	Al BTC	Fe BDC
$W_0, \text{cm}^3/\text{g}$	0.30	0.13	0.14
$S_{\text{BET}}, \text{m}^2/\text{g}$	710	340	350
X_0, nm	0.35	0.62	0.59
$E_0, \text{kJ/mol}$	34.6	19.3	20.5
$d, \text{g/cm}^3$	1.29	1.16	0.95

As follows from Table 2, the structural and energy characteristics of the shaped samples are less than that of initial MOPS. However, the bulk density of the samples increased by about 3.5 times in comparison with the initial MOPS.

Figure 3 demonstrates the degradation of the BET specific surface with an increase in the compacting pressure for Cu-BTC and Al-BTC compared with and without PVA used as a binder.

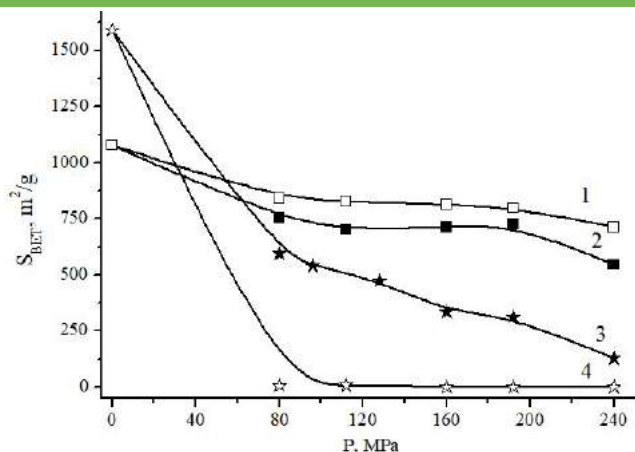


Fig.3. Dependence of S_{BET} of the MOPS compacted adsorbents on the compacting pressure: 1 – Cu-BTC/PVA; 2 – Cu-BTC; 3 – Al-BTC; 4 – Al-BTC/PVA.

As can be seen from fig. 3, molding at high pressures leads to degradation of the structure, which confirmed by a decrease in the specific surface area. In addition, molding with a PVA binder led to a decrease in the specific surface area of the Al-BTC sample, and the S_{BET} values for the Cu-BTC sample without a binder changed slightly.

Table 3 gives the structural and energy characteristics of the MOPS-based composites depending on the percentage of carbon-containing material AC-6T added to Cu-BTC.

Table 3. Structural and energy characteristics of the MOPS/AC-6T composites.

Parameter	Cu-BTC/AC-6T (30%)	Cu-BTC/AC-6T (50%)	Cu-BTC/AC-6T (70%)
$W_0, \text{cm}^3/\text{g}$	0.32	0.36	0.38
$S_{\text{BET}}, \text{m}^2/\text{g}$	800	870	940
X_0, nm	0.61	0.52	0.66
$E_0, \text{kJ/mol}$	19.8	23.3	18.1

The data from Table 3 indicate that the MOPS/AC-6T composites containing the largest amount of active carbon possess the most developed porous system because AC-6T stabilizes the MOPS structure retaining the values of structural and energy characteristics of the adsorbent.

3.3 Methane adsorption

Methane adsorption was studied for the MOPS with the highest adsorption activity toward methane. The values of methane adsorption capacity were calculated for the compacted adsorbents prepared from Cu-BTC, Al-BTC, and Fe-BDC (see Figs. 4–6).

It is evident, that at the temperature of 243 K, the largest amount of accumulated methane is achieved in the storage system with the Al-BTC adsorbent ($270\text{--}280 \text{ m}^3(\text{NTP})/\text{m}^3$), the values of accumulated methane $200\text{--}210 \text{ m}^3(\text{NTP})/\text{m}^3$ were obtained in the storage systems with the Cu-BTC

adsorbent. Fe BDC seemed to be the least effective adsorbent for methane accumulation since the value of V_F attained only 130 140 $\text{m}^3(\text{NTP})/\text{m}^3$.

The absolute effectiveness of methane accumulation grows with a decrease in temperature. Indeed, as follows from Fig. 6, the specific volumetric capacity of methane accumulation in the system with Al BTC attains the values less than 250 $\text{m}^3(\text{NTP})/\text{m}^3$ at the pressure of 30 MPa when the temperatures are higher than 300 K.

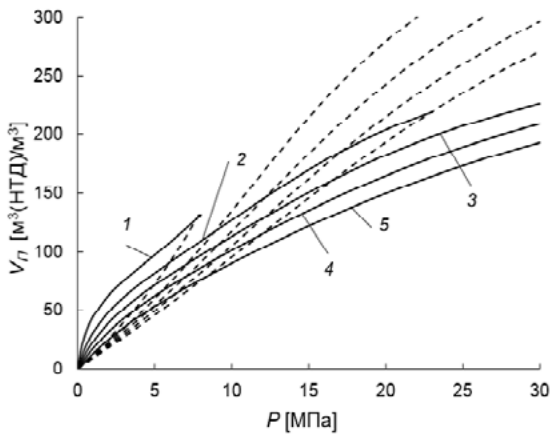


Fig. 4. Full specific methane volumetric capacity of the adsorption storage system with the adsorbent Fe-BDC (solid lines) and a compressed methane system (dashed lines) vs. pressure at temperatures, K: 1 243; 2 273; 3 293; 4 313; 5 333.

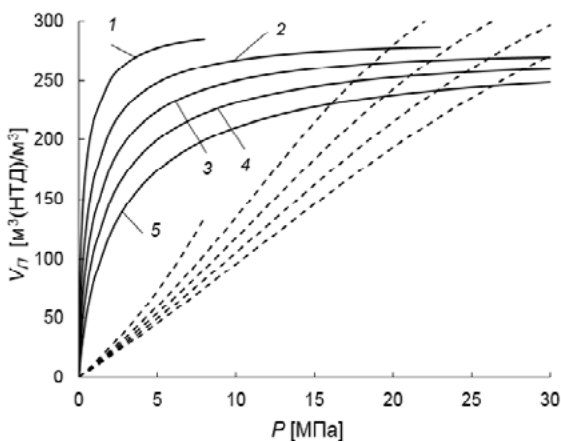


Fig. 5. Full specific methane volume capacity of the adsorption storage system with the adsorbent Cu BTC (solid lines) and a compressed methane system (dashed lines) vs. pressure at temperatures, K: 1 243; 2 273; 3 293; 4 313; 5 333.

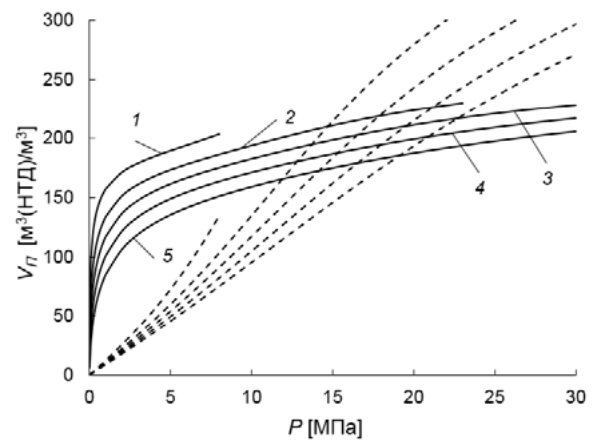


Fig. 6. Full specific methane volumetric capacity of the adsorption storage system with the adsorbent Al-BTC (solid lines) and a compressed methane system (dashed lines) vs. pressure at temperatures, K: 1 243; 2 273; 3 293; 4 313; 5 333.

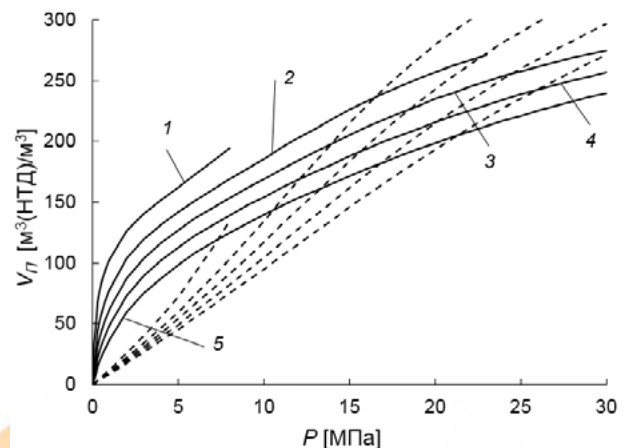


Fig. 7. Full specific methane volumetric capacity of the adsorption storage system with the adsorbent Cu-BTC/AC-6T (70%) shown by solid lines and a compressed methane system (dashed lines) vs. pressure at temperatures, K: 1 243; 2 273; 3 293; 4 313; 5 333.

The calculations of methane adsorption capacity of the storage system with the composite adsorbent Cu BTC/AC 6T(70%) indicated that the methane adsorption capacity of the system becomes higher with the growing pressure and decreasing temperature (see Fig. 7). Moreover, the system of methane adsorption storage with Cu-BTC/AC-6T(70%) occurred to be more efficient compared to the compressed methane system at relatively low pressures below 7 MPa and temperatures below 333 K. The compressed methane system is more efficient at higher pressures.

3.4. Hydrogen adsorption

MOPS adsorbent Al-BDC has a high characteristic adsorption energy, which positively affects the adsorption of non-polar molecules, which means that it can be a promising material for the accumulation of hydrogen. Hydrogen adsorption onto the synthesized MOPS materials was measured in order to assess their effectiveness in the adsorption storage systems for energy gas. Figure 8 demonstrates the results of hydrogen adsorption measurements.

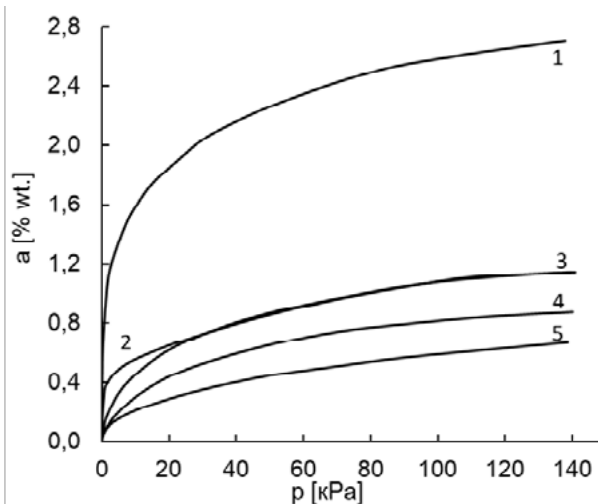


Fig. 8. Isotherms of total content of hydrogen adsorption on the MOPS samples: 1 – Al-BDC; 2 – Fe-BDC; 3 – Fe-BTC; 4 – Cu-BTC; 5 – Al-BTC.

As is clear from Fig. 8, at the pressure of 0.1 MPa, Al-BDC adsorbs the largest amount of hydrogen: $a = 2.6$ wt.%. The absorption of hydrogen at the closest analogue of the Al-BDC adsorbent is $= 2.1$ wt.%. at a pressure of 0.1 MPa [13].

4. Conclusion

MOPS adsorbents of high density are the promising materials for implementation in adsorption storage systems. The highest hydrogen adsorption were observed for the system with the Al-BDC adsorbent $a = 2.6$ wt.%. It was found that the Al-BTC demonstrated the highest volumetric methane storage: $270 \text{ m}^3(\text{NTP})/\text{m}^3$ at 273 K and the pressure of about 10 MPa. The MOPS prepared from Cu-BTC and Fe-BDC demonstrated the methane adsorption capacities of about 200 and $120 \text{ m}^3(\text{NTP})/\text{m}^3$ at the same conditions. Al-BDC adsorbs the largest amount of hydrogen: $a = 2.6$ wt.%.

Acknowledgements

The work was implemented in the frames of State Scientific Program of the Russian Federation N 0067-2019-0011, state registration number AAAA-A19-119111590053-4.

References

- [1] I. D. Zhao, D. Yuan, H.-C. Zhou // *Energy Environ. Sci.* 2008.V.1.P.222 235.
- [2] Hoskins B. F., Robson R. // *Journal of the American Chemical Society.* 1989. T. 111, № 15. C. 5962 5964.
- [3] Batrakova M.K., Solovtsova O.V., Fomkin, Tsivadze, A.Y., Shkolin, A.V. et al. *Prot. Met. Phys. Chem. Surfaces* (2017) V.53, №6, P.961 966.
- [4] Knyazeva M.K., Shkolin, A.V., Fomkin, A.A., Tsivadze, A.Y., Solovtsova O.V., et al. *Prot. Met. Phys. Chem. Surfaces* (2018) V.54, №6, P.1004-1009.
- [5] Knyazeva M.K., Tsivadze, A.Y., Solovtsova O.V., Fomkin, A.A., Shkolin, A.V., Men'shchikov et al. *Prot. Met. Phys. Chem. Surfaces* (2019) V.55, №1, P.9 14.
- [6] Solovtsova O.V., Shkolin A.V., Men'shchikov I.E., Knyazeva M.K., Pulin A.L., Fomkin A.A., Tsivadze A.Yu., Aksyutin O.E., Ishkov A.G. // *Prot. Met. Phys. Chem. Surfaces* (2019) V.55, №5, P.826-832
- [7] Shkolin, A.V. and Fomkin, A.A. // *Measurement Techniques*, 2018, V. 61, P. 395 401.
- [8] Dubinin, M.M., *Adsorbtsiya i poristost'* (Adsorption and Porosity), Moscow: Military Academy of Chemical Defense Named after Marshal of the USSR S.K. Timoshenko, 1972.
- [9] Men'shchikov, I.E., Fomkin, A.A., Tsivadze, A.Yu., Shkolin, A.V., Strizhenov, E.M., and Pulin, A.L., *Prot. Met. Phys. Chem. Surf.*, 2015, vol. 51, no. 4, pp. 493 498.
- [10] Men'shchikov, I.E., Fomkin, A.A., Arabei, A.B., Shkolin, A.V., and Strizhenov, E.M., *Prot. Met. Phys. Chem. Surf.*, 2016, vol. 52, no. 4, pp. 575–580.
- [11] Men'shchikov, I.E., Fomkin, A.A., Tsivadze, A.Yu., Shkolin, A.V., Strizhenov, E.M., and Khozina, E.V., *Adsorption*, 2017, vol. 23, nos. 2 3, pp. 327 339.
- [12] Tsivadze, A.Yu., Aksyutin, O.E., Ishkov, A.G., Men'shchikov, I.E., Fomkin, A.A., Shkolin, A.V., Khozina, E.V., and Grachev, V.A., *Russ. Chem. Rev.*, 2018, vol. 87, no. 4, pp. 950 983.
- [13] Ferey G., Latroche M., Serre C. et al. // *Chem. Commun.* 2003. V.24. P. 2976 2977.

OPTIMIZATION OF ADSORPTION PROCESS IN THE REMOVAL OF BASIC NITROGENOUS COMPOUNDS FROM PETROLEUM USING ACTIVATED CARBON

M. A. F. Carvalho^a, L. A. de Andrade^a, B. G. Vaz^a, I. C. Ostroski^a

^a Instituto de Química, Universidade Federal de Goiás, CEP 74690-900, Goiânia – GO, Brasil.

Abstract

This work was studied the removal basic nitrogenous compounds from real crude oil samples by batch adsorption process using chemically treated palm oil coconut shell activated carbon. The technique central composites design was used combined with the response surface methodology, in order to evaluate the operating variables temperature, adsorbent mass and stirring speed. The analysis of the effects showed that the adsorbent mass is the most significant variable in adsorption and that the upper limits each process variable were the most suitable to optimize the removal percentage, resulting in effective removal of 30.77%.

Keywords: crude oil, activated carbon, chemical treatment, central composites design.

1. Introduction

Sweeter and lighter oil reserves have decreased and as this occurs, more attention been paid to the heavier oil reserves and their fractions. Heavier oils require more severe and complex refinery treatments compared to light oils to produce high value-added products [1][2]. Pre-salt reserves, discovered by Petrobras S.A., currently have a daily production of 1.5 million barrels/day, an intermediate quality oil, show a large number of impurities such as sulfur, nitrogen, oxygenated and organometallic compounds, causing complications in the refining process [3][4].

Although found in low concentrations, nitrogenous compounds must be removed during oil refining as they cause several problems. The amount nitrogenous compounds ranges from 0.01 to 0.8% in total oil mass and, in Brazilian oil, the basic nitrogenous compounds predominate [5]. One the problems related to the presence nitrogen compounds in petroleum fuels is environmental pollution. During incomplete combustion of fossil fuels, nitrogen converted to nitrogen oxides, NO and

NO₂, which are responsible for ozone layer and acid rain [6].

In refineries, basic nitrogen compounds have a strong inhibitory effect on the process hydrodesulfurization (HDS) by strongly adsorbing on the active sites acid catalysts, reducing the efficiency of sulfur removal [7]. These compounds are still precursors of polymerization reactions in the products, leading to gum formation, color and odor modification and fuel deterioration [8].

Traditionally, the removal nitrogenous compounds in refineries been carried out via hydrodenitrogenation (HDN), a high-cost process and extreme temperature and pressure conditions [9]. As an alternative to HDN, researchers have been studying new nitrogen removal techniques, especially adsorption.

The adsorption process is a promising removal technique in which the adsorbents used are generally less expensive than the catalysts and the process can operate under milder pressure and temperature conditions. In the middle of the adsorbents, activated carbon has been widely used, as it is an effective and economical alternative, presenting high surface area, highly developed porosity, chemical resistance, and low production cost, which is

often used in agricultural and industrial residues as precursor materials [10][11].

In the adsorption process, some parameters strongly influence the removal efficiency. To reduce the number of experimental tests needed to evaluate the effect of each parameter and allow the study of interactions between them, the design of experiments (DOE) method been used. This approach presents an ideal experimental design that reduces waste of chemical reagents and minimizes experimental time. Among the DOE approaches, there is the response surface methodology (RSM), an efficient strategy that allows the identification of the impact of different independent process variables and suggests optimal conditions to achieve the maximum possible result. In order to evaluate this combined effect among process variables, the central compound factorial design is adequate, as it provides a quadratic response surface that can explain the effects [12][13].

In this context, this paper presents the study of the adsorption of basic nitrogenous compounds present in a real oil charge using activated carbon from the palm oil coconut shell chemically treated with sulfuric acid (CDAS) as adsorbent. Through a central composite design (CCD), the effects of temperature, rotation and adsorbent mass on the adsorption process studied and the optimal parameters were determined to obtain the maximum adsorption capacity.

2. Materials and Methods

All materials and chemicals in this research study were of analytical reagent grade and used as received. The reagents, toluene and sulfuric acid were procured from Synth; glacial acetic acid were procured from Neon. The activated carbon from the palm oil coconut shell was produced by Bahiacarbon Agroindustrial. The adsorbent was chemically treated according to the methodology described by Gomes et al., 1960 [14].

1.1. Factorial Planning

The efficiency of removal of basic nitrogen compounds present in oil samples using CDAS as adsorbent studied by performing 24 hours batch system tests. The percentage by weight (% m/m) of total basic nitrogen present in the sample before and after adsorption was

determined by potentiometric titration according to the UOP 269-10 method.

The experimental matrix of the central compound design at two levels, plus four replicates at the central point and six axial points, totaling 18 experiments, presented in Table 1. The control factors chosen for statistical analysis: temperature (X_1), rotation (X_2) and mass adsorbent (X_3); and as response variable the percentage of removal, calculated by equation 1.

$$\text{Rem}(\%) = 100 * \left(1 - \frac{C_{\text{eq}}}{C_0}\right) \quad (1)$$

C_0 (mg L^{-1}) is the initial concentration of adsorbate, C_{eq} (mg L^{-1}) is the concentration of adsorbate after reaching equilibrium.

Table 1. Central Composite Design

Test	X_1 (°C)	X_2 (rpm)	X_3 (g)
1	(-1) 30	(-1) 90	(-1) 0,500
2	(-1) 30	(-1) 90	(1) 1,000
3	(-1) 30	(1) 140	(-1) 0,500
4	(-1) 30	(1) 140	(1) 1,000
5	(1) 50	(-1) 90	(-1) 0,500
6	(1) 50	(-1) 90	(1) 1,000
7	(1) 50	(1) 140	(-1) 0,500
8	(1) 50	(1) 140	(1) 1,000
9	(-1,41) 26	(0) 115	(0) 0,750
10	(1,41) 54	(0) 115	(0) 0,750
11	(0) 40	(-1,41) 80	(0) 0,750
12	(0) 40	(1,41) 150	(0) 0,750
13	(0) 40	(0) 115	(-1,41) 0,396
14	(0) 40	(0) 115	(1,41) 1,104
15	(0) 40	(0) 115	(0) 0,750
16	(0) 40	(0) 115	(0) 0,750
17	(0) 40	(0) 115	(0) 0,750
18	(0) 40	(0) 115	(0) 0,750

The design was performed with the aid of Statistica software and from the values obtained from the response variable, it was possible to generate the response surfaces.

1.2. Optimization

From the values of the response variables that can be used in a factorial design, a process optimization was performed to maximize the percentage of basic nitrogen removal used in the adsorption process. The optimization problem was uni-objective, adopting a maximization of the removal percentage as an objective function. A resolution methodology based on the combined use of the differential evolution algorithm and the regression equation applied in the execution of central composite design tests. The code implemented in the Matlab 15 software and was based on the technique employed by Silva et al., (2012).

3. Results and discussion

3.1. Adsorption Tests

Firstly, the mass percentage of total basic nitrogenous compounds present in the crude oil sample before the adsorption tests were determined by duplicate potentiometric titration and a value of 0.29% reached. After adsorption tests values were obtained between 0.205-0.254 (%w/w) of basic nitrogenous. From these values, we calculated the percentage of removal, the planning response variable, whose values ranged from 12.4 - 29.2%.

The regression model in terms of coded factors obtained through statistical analysis of the data. Equation 2 presents the proposed model, except for the independent variables and interactions that had no significant statistical effect, for a confidence level of 95%. The coefficient of determination was 0.962, which allows considering the proposed regression model if adjusted to the adsorption data.

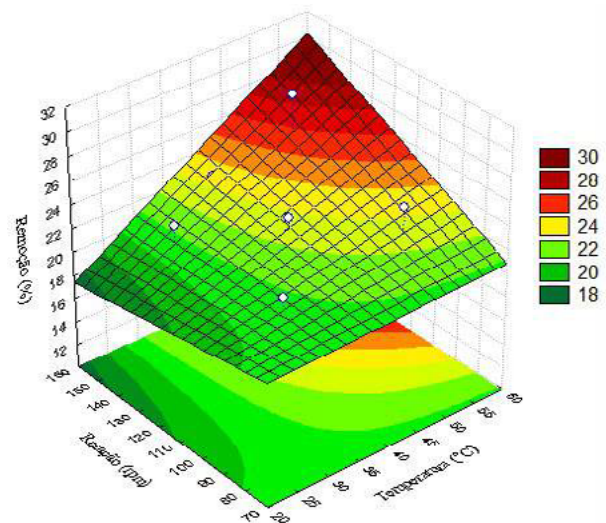
$$Y = 22,234 + 3,337 * X_1 + 1,783 * X_2 + 7,278 * X_3 - 2,889 * X_1^2 + 1,718 * X_1 X_2 + 1,524 X_1 X_3 \quad (2)$$

3.2. Response Surface Methodology (RSM) Analysis

From the response surface shown in Figure 1, obtained with X_3 at the central point, it observed that nitrogen removal was more favorable when the values of temperature and rotation variables reached extreme values. It can also be noted that the temperature has a

more significant positive influence on the process because for the same rotation value the increase in temperature causes a significant increase in response, which is no longer observed with such force with the increase in rotation.

Figure 1. Response surface as a function of temperature and rotation.



Considering the response surface shown in Figure 2, obtained with X_2 at the central point, it is noted that for small values of adsorbent mass the nitrogen removal is minimal, regardless of temperature. For values with larger adsorbent mass, the stabilization of the removal observed when at low temperatures, but at elevated temperatures, any increase in the adsorbent mass results in a greater removal.

Figure 3 represents the effect of the interaction between adsorbent mass and system rotation. It observed that the increase in adsorbent mass reflects a significant increase in the percentage of removal, up to a limit where the response variable varies subtly with the increase in mass. Rotation, on the other hand, has a subtle effect on the nitrogen removal rate, regardless of the mass used.

Figure 2. Response surface as a function of temperature and mass of adsorbent.

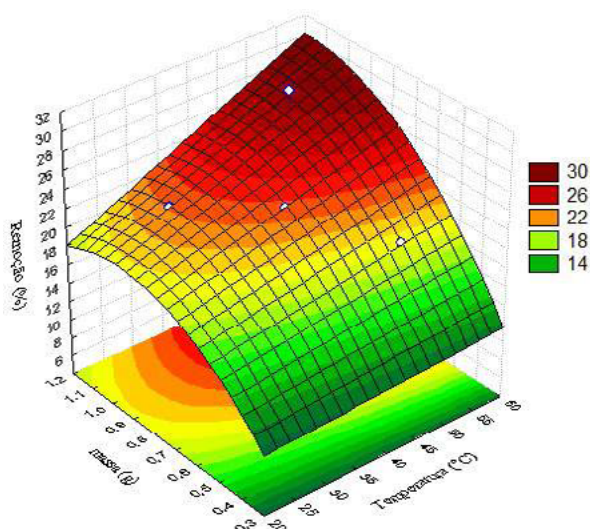
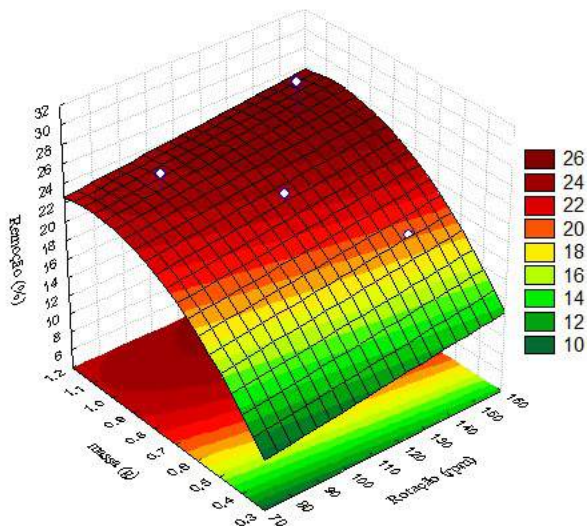


Figure 3. Response surface as a function of mass of adsorbent and rotation.



3.3. Optimization

The optimal values of the parameters studied in the central composite design, in order to maximize the removal of basic nitrogenous compounds, presented in Table 2.

Table 2. Optimization of process variables.

	Optimized Values
(X ₁)	1,41 (54°C)
(X ₂)	1,41 (150 rpm)
(X ₃)	1,41 (1,104 g)

Comparing the optimization and response surfaces, observe whether the results agree. A percentage by mass of basic nitrogen in the petroleum sample after the adsorption test under maximum conditions was 0.2008% and, consequently, the removal rates were 30.77%, above all tests in the factorial study. By Matlab software, an expected response variable of 32.51%, which represents a relative error between experimental and theoretical only 5.3%. From this result, it is possible to determine that the optimization was satisfactory and the adsorption process effective.

4. Conclusion

The Central Compound Design showed satisfactory results of removal of basic nitrogenous compounds in the crude oil sample, the extreme positive points of each independent variable, temperature (54 ° C), rotation (150 rpm) and adsorbent mass (1.104 g) were the optimum points of the adsorption process and the removal of basic nitrogen of 30.77% in the optimization test was consistent with the predicted theory.

5. Acknowledgements

Financial support provided by Capes.

6. References

- [1] KEKÄLÄINEN T.; PAKARINEN J.M.H.; WICKSTRÖM K.; LOBODIN V.V.; MCKENNA A.M.; JÄNIS J. Compositional analysis of oil residues by ultrahigh-resolution fourier transform ion cyclotron resonance mass spectrometry; Energy Fuel, 27, p. 2002-2009, 2013.
- [2] SOUSA JUNIOR, C. S. Tecnologia de óleos pesados e ultrapesados. Dissertação de Mestrado. Escola de Química. Universidade Federal do Rio de Janeiro. Rio de Janeiro, 2008.
- [3] PETROBRAS. Available in:

<<http://www.petrobras.com.br/pt/nossas-atividades/areas-de-atuacao/exploracao-e-producao-de-petroleo-e-gas/pre-sal/>>

[4] AGÊNCIA NACIONAL DE PETRÓLEO, GÁS NATURAL E BIOCOMBUSTÍVEIS (ANP), 2019. Boletim Mensal de Produção – BMP. Available in: <http://www.anp.gov.br/images/publicacoes/boletins-anp/Boletim_Mensal-Producao_Petroleo_Gas_Natural/boletim-agosto-2019.pdf>

[5] VAZ, B. G. Petroleômica por FT-ICR MS: Desvendando a Composição de Polares do Petróleo e Derivados. Tese de Doutorado. Universidade Estadual de Campinas, Campinas, p.191, 2010.

[6] HEEB, N. V.; SAXER, C. J.; FORSS, A. M.; BRUHLMANN, S. Trends of NO, NO₂ and NH₃ emissions from gasoline-fueled Euro-3-to Euro-4-passengers cars. Atmospheric Environment, Oxford, v.42, n.10, p. 2543-2554, 2008.

[7] MACIEL, G. P. S. Extração de compostos nitrogenados do diesel e análise por cromatografia gasosa bidimensional abrangente acoplada à espectrometria de massas (GCxGC/qMS), Tese de Doutorado em Química – Pós-graduação em Química, Universidade Federal do Rio Grande do Sul, Porto Alegre, 2016.

[8] OKUMURA, L. L.; STRADIOTTO, N. R. Simultaneous determination of neutral nitrogen compounds in gasoline and diesel by differential pulse voltammetry, Talanta, v. 72, p. 1106-1113, 2007.

[9] HERNÁNDEZ-MALDONADO, A. J.; YANG, R. T. Denitrogenation of transportation fuels by zeolites at ambient temperature and pressure. Angewandte Chemie - International Edition, v. 43, n. 8, p. 1004–1006, 2004.

[10] SKOUTERIS, G.; SAROJ, D.; MELIDIS, P.; FAISAL, I. H.; OUKI, S. The effect of activated carbon addition on membrane bioreactor processes for wastewater treatment and reclamation – A critical review. Bioresour. Technol. 2015.

[11] FERREIRA, M. E. O; VAZ, B. G.; BORBA, C. E.; ALONSO, C. G.; OSTROSKI, I. C. Modified activated carbon as a promising adsorbente for quinoline removal. Microporous and Mesoporous Materials, v. 277, p. 208-216, 2019.

[12] R.R. KARRI, J.N. SAHU. Modeling and optimization by particle swarm embedded neural network for adsorption of zinc(II) by palm kernel shell based activated carbon from aqueous environment. J. Environ. Manag., p.178-191, 206, 2017.

[13] LINGAMDINNE L. P.; KODURU J. R.; CHANG Y.; KARRI R. R. Process optimization and adsorption modeling of Pb(II) on nickel ferrite-reduced grapheme oxide nano-composite. Journal of Modecular Liquids, v.250, p. 202-211, 2018.

[14] GOMES, H. T.; MIRANDA, S. M.; SAMPAIO, M. J.; SILVA, A. M. T. T.; FARIA, J. L. Activated carbons treated with sulphuric acid: Catalysts for catalytic wet peroxide oxidation. **Catalysis Today**, v. 151, n. 1–2, p. 153–158, 2010.

Adsorption of CO₂ and CH₄ on MIL-101: mixture prediction utilizing Tóth and IAST

Guilherme Magon Martins^a, Marcus Vinicius Pereira^a, Leonardo Hadlich de Oliveira^a,
Jailton Ferreira do Nascimento^b, Gisella Maria Zanin^c, Pedro Augusto Arroyo^a

^a *Laboratory of Adsorption and Ion Exchange (LATI), Department of Chemical Engineering (DEQ), State University of Maringá (UEM), 87020-900, Maringá-PR, Brazil*

^b *PETROBRAS/CENPES/PDDP/TPP, 21941-915, Rio de Janeiro-RJ, Brazil*

^c *Department of Chemical Engineering (DEQ), State University of Maringá (UEM), 87020-900, Maringá-PR, Brazil*

Abstract

Natural gas has some contaminants that need to be removed in order to provide a cleaner energy. Adsorption technology gained attraction due to its low costs in providing deeper treatment, where the choice of the adsorbent material is crucial. Several materials have been studied for this purpose but one of them had a step up over the last years: MOFs. Several works were published utilizing MOFs for gas treatment, however most of them shows only monocomponent adsorption data. Therefore, the objective in this work was to obtain CH₄ and CO₂ experimental adsorption data on MIL-101 at different temperatures and pressures up to 110 kPa and then fit Tóth model parameters in order to predict mixture behavior with IAST. Data indicate that uptake of CO₂ is higher than CH₄ for all temperatures and that physisorption is the main mechanism. Results indicate that MIL-101 can be an alternative material to produce a cleaner natural gas when the contaminant is mainly CO₂.

Keywords: Natural gas; MIL-101; CO₂; CH₄; mixture; Tóth; IAST.

1. Introduction

Facing new concerns over climatic changes has been doing the world think in a transition from total petroleum consumption to cleaner and more energetic fonts, being natural gas one of the main trends in disruptive technologies at the moment.^[1,2]

However natural gas still has some contaminants like CO₂, H₂S, N₂ and others that need to be removed, since they lower the calorific power and cause corrossions to pipeline and equipment.^[3,4]

Among technologies studied, adsorption is getting more and more prominence due to the lower costs compared to absorption, membrane systems and cryogenic distillation^[4]. Besides, adsorption can provide a deeper treatment when low concentrations are required. The main factor when using adsorption is the best choice of the adsorbent that should fit some requirements such as large specific surface,

low regeneration heat and high selectivity towards the target adsorbate.^[5]

MOFs gained attention in the last years as alternative materials for gas separation. MIL-101 (with MIL meaning Matériel Institute Lavoisier) has been excelled among other MOFs mainly due to its high specific area that presents values above 2500 m² g⁻¹, but also by been stable at ambient conditions, not degrading with humidity or water like MOF-177^[6], for instance, which makes easier the handling and application of this structure.

Regarding CO₂ and CH₄ adsorption on these materials, previous works show some experimental data^[1,7], data correlation between experimental data and known models^[8,9], but prediction of mixture behavior is scarce^[10].

Therefore, the objective in this study was to determine adsorption data for CO₂ and CH₄ on MIL-101 at different temperatures, modeling the experimental data with Tóth equation and predict mixture behavior with IAST.

2. Experimental Section

2.1. Materials

Cr(NO₃)₃ (99%), terephthalic acid (98%), N,N-Dimethylformamide (99,8%) and Methanol (>99,9%) were purchased from Sigma-Aldrich Brazil Ltda. and nitrogen (99,995%), methane (99,995%) and carbon dioxide (99,99%), purchased from Linde, were utilized in this work. All materials were used as purchased.

2.2. Synthesis

MIL-101 was synthesized using the same procedure of Bromber et al. (2012)^[11] via solvothermal route. Briefly, 2 g of Cr(NO₃)₃ was dissolved in 20 mL of deionized water. It was stirred until completed salt solubilization. Then 0,839 g of Terephthalic acid was added. The reaction system was transferred to a Teflon-line stainless steel autoclave and then stirred for 10 min in order to disperse the reagents. After that, autoclave was sealed and kept at 220 °C for 18 h in an oven. After cooling down to room temperature, the mixture was centrifuged and solids were washed with 20 mL of N,N-dimethylformamide (DMF) for 12 h at 70 °C, followed by another centrifugation and washed again with 20 mL of methanol, in order to remove trapped non reacted reagents. The final solution was then filtered, and solids dried at 70 °C for 12 h.

2.3. Characterization

XRD analysis was performed in a Shimadzu Labx 6000 X-ray diffractometer. Measurements were performed utilizing CuK α radiation with 40 kV voltage and 30 mA current using a Ni filter Cu tube, with 2 °2 θ min⁻¹ speed, acquisition time of 1 s, in the range of 4 ≤ 2 θ ≤ 14.

Textural properties were determined by nitrogen adsorption/desorption isotherms at -196 °C and pressures from 9 × 10⁻⁴ up to 94.5 kPa using the Micromeritics ASAP 2020. Before analysis, the adsorbent was degassed at 1.3 Pa and held at 150 °C for 24 h. Surface area was determined utilizing BET^[12] equation, total pore volume was determined using Gurvich's rule at P/P₀ at 0.95 and micropore area and volume were determined applying t-plot method using Harkins-Jura^[13] equation. Pore size distribution was obtained by NLDFT method.

FTIR spectrum was determined utilizing a Bruker Vertex 70v spectrometer. The pellet was prepared by grinding together 198 mg of KBr and 1

mg of MIL-101. The sample was analyzed from wavenumber 4000 to 400 cm⁻¹, with 4 cm⁻¹ resolution and 128 scans.

Thermogravimetric analysis experiments were performed in duplicate in a TA instruments SDT 600 analyzer, where TGA and DTG profiles were determined. An aliquot of 100 mg of sample was heated from ambient temperature up to 1000 °C with a 10 °C min⁻¹ ramp rate at nitrogen atmosphere.

2.4. Adsorption Equilibria Data

Equilibrium adsorption experiments were conducted at Micromeritics ASAP 2020 utilizing pure methane and carbon dioxide to obtain isotherm data at 10, 30 and 50 °C, and total pressure from 0.01 up to 110 kPa. Temperatures were controlled by a Julabo F25 thermostatic bath with ME V.2 Controller. Experiments were performed in duplicate on each temperature.

Prior to adsorption experiments, samples were degassed under vacuum at 150 °C for 12 h.

3. Modeling

3.1. Monocomponent Adsorption Model

The experimental measurements for CO₂ and CH₄ were correlated with Tóth equation reported by Sircar^[14]:

$$n_i^0 = \frac{mb_i P}{(1 + (b_i P)^k)^{1/k}} \quad (1)$$

where n_i^0 is the adsorbate loading, P is the equilibrium adsorption pressure for pure gas at temperature T , m is the temperature-independent saturation adsorption capacity, k (≤ 1) is the dimensionless adsorbent heterogeneity parameter, which is a function of T ($dk/dT > 0$) and b_i is the Henry's law constant for component i , given as:

$$b_i = b_i^0 e^{\left(\frac{q_i^*}{RT}\right)} \quad (2)$$

where q_i^* can be considered as the potential energy of adsorption of pure gas i at the limit zero coverage ($\theta_i \rightarrow 0$)^[15]. This also defines the Henry's law constant since $\theta_i^0 = n_i^0/m_i$.

Correlation was evaluated using the Root Mean Square deviation between experimental and calculated amount, given by:

$$RMS = \frac{100}{np} \sqrt{\sum_{i=1}^{np} (n_{exp} - n_{cal})^2} \quad (6)$$

Modeling using Tóth isotherm model was determined using Python® to minimize iterative parameters.

3.2. Heat of adsorption

The isosteric heat of adsorption of a pure gas (q_i^0) at a given specific adsorbate loading (n_i^0) can be calculated from the adsorption isotherms at different temperatures by Clausius-Clapeyron equation:

$$q_i^0 = RT^2 \left[\frac{\partial \ln P}{\partial T} \right] \quad (3)$$

Applying equation (3) in equation (1) to obtain q_i^0 as a function of θ_i^0 for the Tóth model, gives:

$$q_i^0 = q_i^* + \left(\frac{RT^2}{k} \right) \left(\frac{d \ln k}{dT} \right) F_i(\theta_i^0) \quad (4)$$

$$F_i(\theta_i^0) = \frac{[1 - (\theta_i^0)^k] \ln [1 - (\theta_i^0)^k] + (\theta_i^0)^k \ln (\theta_i^0)^k}{1 - (\theta_i^0)^k} \quad (5)$$

3.3. IAST + Tóth

Prediction of binary adsorption data with Tóth isotherm model and IAST was determined using the algorithm suggested by Myers and Valenzuela^[16].

3.4. Selectivity

For multicomponent adsorption processes, a common term must be considered: Selectivity (S_i). This property indicates the adsorbate that is preferable adsorbed compared to others species^[17]. Equilibrium selectivity is defined in terms of phase composition:

$$S_{ij} = \frac{K_i}{K_j} = \left(\frac{x_i}{y_i} \right) / \left(\frac{x_j}{y_j} \right) \quad (16)$$

Where K_i is the partition coefficient for each component.

4. Results and Discussion

4.1. Characterization Results

XDR pattern are shown in figure 1. It shows well defined peaks at $4 \leq 2\theta \leq 6$ and $8 \leq 2\theta \leq 9.5$, which agrees with other results found in literature for this material. These peaks are also characteristic of crystalline materials.

N_2 isotherms are shown in figure 2a. The isotherm is classified as Type 1b according to IUPAC^[18], indicating wide microporous solid and narrow mesoporous distribution. The pore size distribution, obtained by NLDFT method is shown in figure 2b, showing a predominance of micropores with some mesopores (~25 Å).

Based in these results, the surface area obtained by BET equation is $3031 \text{ m}^2 \text{ g}^{-1}$, the total pore volume is $1.53 \text{ cm}^3 \text{ g}^{-1}$, with a micropore area obtained by t-plot of $2961 \text{ m}^2 \text{ g}^{-1}$.

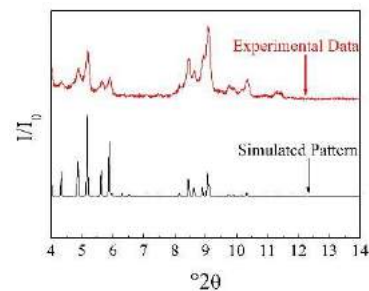


Figure 1. XRD of MIL-101.

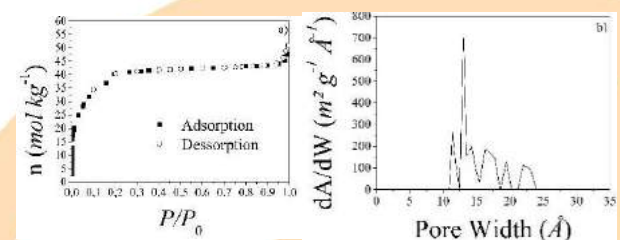


Figure 2. a) Nitrogen adsorption/desorption isotherms. b) Pore size distribution calculated by NLDFT.

FTIR spectrum, in Figure 3 shows a large peak in 3423 cm^{-1} attributed to -OH group, probably due to physisorbed water and hydrogen bonds in the surface. Bands at 1624 and 1670 cm^{-1} are related to presence of asymmetric stretching of CO_2^- in aromatic rings while 1406 cm^{-1} is related to symmetric stretching of this same group provided from deprotonation of terephthalic acid.

Peaks appearing at 1506 and 1548 cm^{-1} indicate C=C related to aromatic rings and peaks from 666

to 886 cm^{-1} are related to a ring “breathing” of a benzene para-disubstituted, in this case for two groups of CO_2^- as indicated before. Finally, the 585 cm^{-1} peak indicates the vibration provided from Cr-O link.^[7,19,20]

TGA results shown in Figure 4, indicate that from 25 °C up to 100 °C 28% of mass is lost due to water physisorbed. From 100 °C up to 330 °C , another 9% of mass is lost, probably due to some trapped non reacted terephthalic acid. From 330 °C up to 400 °C mass remains practically constant, where it starts to decrease until 600 °C , losing more 30% of its initial mass. From 600 °C up to 700 °C , mass remains almost constant, losing only 3% of initial mass. Finally, from 700 °C up to 800 °C mass remains constant, lasting only 30% of the initial mass since all organic elements were previously removed.

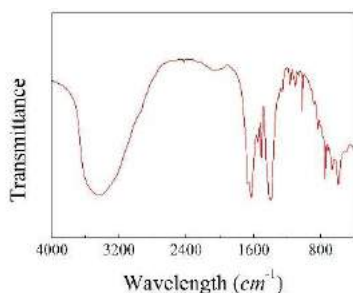


Figure 3. FTIR spectra of MIL-101.

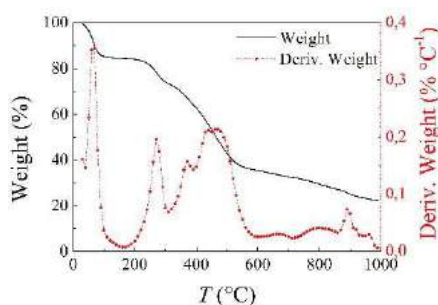


Figure 4. Thermogravimetric analysis of MIL-101.

4.2. Monocomponent Adsorption Isotherms

Experimental adsorption data for CO_2 and CH_4 on MIL-101 at $10, 30$ and 50 °C and pressure up to 110 kPa are shown in Figure 5 with Tóth model fitted in experimental data.

In both cases, isotherms are lightly favorable and almost linear. Uptake decreases with increase on temperature, indicating that physisorption phenomenon is the main mechanism and the process is exothermic. At 30 °C the maximum uptake for CO_2 is 2.014 mol kg^{-1} which represents 8.86% in

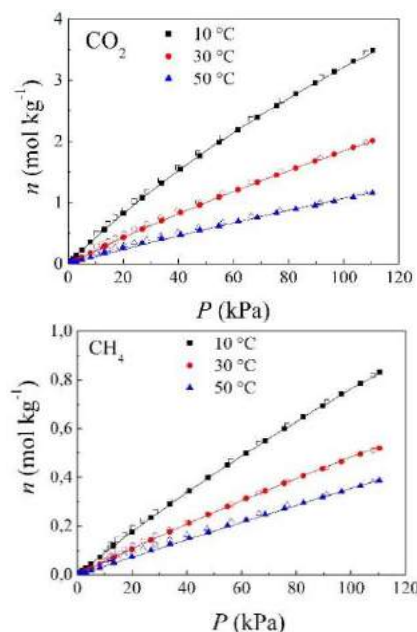


Figure 5. Adsorption isotherms on MIL-101 symbols, experimental data; full symbol, adsorption; empty symbol, desorption; solid lines, Tóth adsorption model.

weight, while for CH_4 the maximum uptake at the same conditions is 0.52 mol kg^{-1} , that represents 0.832% in weight. For all three temperatures, CO_2 uptake is higher than CH_4 . As both components are present in natural gas, this result indicates that this material possibly can be used as a promising adsorbent to separate these gases.

In Table 1 the parameters calculated using equations (1) e (2) for Tóth model for CO_2 and CH_4 are presented.

Table 1. Tóth model parameters obtained through correlation with experimental data for pure gases.

Parameter	CH_4	CO_2
$m\text{ (mol kg}^{-1}\text{)}$	15.08	19.94
$b_0\text{ (kPa}^{-1}\text{)}$	2.38×10^{-7}	5.11×10^{-8}
$q^*\text{ (kJ mol}^{-1}\text{)}$	18.59	25.24
$k_{10^\circ\text{C}}$	0.6523	0.7688
$k_{30^\circ\text{C}}$	0.6523	0.7852
$k_{50^\circ\text{C}}$	0.9996	0.7853
$\Delta n\text{ (%)}$	0.12	0.47

Once k indicates the energetic heterogeneity of the adsorbent, results show that there are different sites of adsorption for both gases in every temperature, except for CH_4 at 50 °C . The result in this temperature indicates that only one kind of site participates on the adsorption process, since k_{50} is practically equal to 1.

In Figure 6, isosteric heat of adsorption is presented. For CO₂, the isosteric heat is practically constant along all coverage range and higher than for CH₄. Also, for CH₄, it decreases almost linearly, except for low coverages.

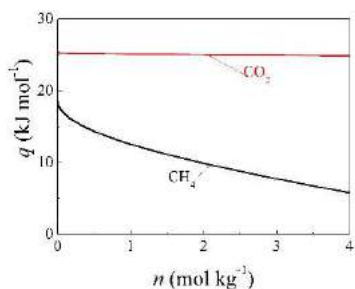


Figure 6. Isosteric heat on MIL-101: red, CO₂; black, CH₄.

4.3. Multicomponent Adsorption

In Figure 7 the prediction of adsorption data for a mixture with an inlet composition of 10% of CO₂ and 90% of CH₄ at 30 °C is presented. This condition was chosen regarding a condition close to operational processes. Despite the CH₄ uptake is higher, the result means that 26% of total adsorbed is CO₂. Thus, the outlet stream will have a composition purer in CH₄ compared with the initial inlet.

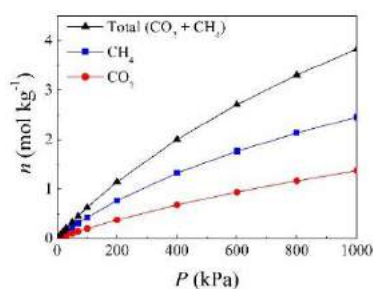


Figure 7. Uptake of mixture with 90% of CH₄ and 10% CO₂ at 30 °C.

In Figure 8, the variation in uptake *versus* variation in inlet composition for a pressure of 100 kPa and 30 °C is shown. Since for pure gases CO₂ presents a higher uptake at same molar fraction in all temperatures, it is expected that higher concentration of CH₄ in the gas phase will increase its content in solid phase compared to CO₂.

In Figure 9 it is shown how selectivity varies with temperature and pressure considering the same feed composition of 10 % of CO₂ and 90% CH₄. In both temperatures of 10 and 30 °C, selectivity increases with pressure, but at 50 °C selectivity diminish with

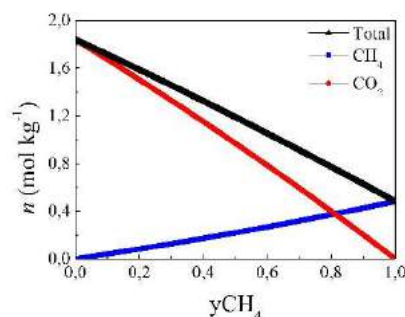


Figure 8. Adsorption capacity at 30 °C and 100 kPa.

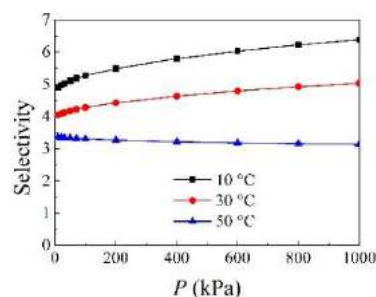


Figure 9. Selectivity of CO₂ over CH₄.

increase in temperature, probably because adsorption of CO₂ is more exothermic than CH₄, as shown in Figure 6 by the isosteric heat, so an increase in temperature, will favor the less exothermic phenomenon.

5. Conclusions

MIL-101 was successfully synthesized and characterized with DRX, FTIR, TGA and N₂ physisorption, showing agreement with other reports in literature. Experimental adsorption data for CH₄ and CO₂ on MIL-101 was well fitted with Tóth model for all temperatures used in this study, presenting a deviation smaller than 0.5% for each point for both gases. This allowed to predict a multicomponent adsorption using IAST + Tóth model. With an uptake of 8.86 %wt for CO₂ and 0.832 %wt for CH₄ at 30 °C, MIL-101 shows a higher affinity for adsorption of CO₂ than CH₄. Moreover, the fact that increasing temperature decreases the adsorption rate for both gases, indicates a physisorption phenomena and this allows a regenerative process only by shifting temperature and/or pressure in a fixed bed. Therefore, results presented herein indicates that MIL-101 is a promising adsorbent to treat natural gas.

Acknowledgements

Authors would like to thank Petrobras for the financial support (Cooperation Number 5850.0102576.16.9) and the personal from PUC-RS for their support in TGA analyses.

References

- [1] Hamon, L., Serre, C., Devic, T., Loiseau, T. & F. Comparative Study of Hydrogen Sulfide Adsorption in the MIL-53 (Al, Cr, Fe), MIL-47 (V), MIL-100 (Cr), and MIL-101 (Cr) Metal– Organic Frameworks at Room. *J Am Chem Soc* **131**, 8775–8777 (2009)
- [2] Lilienthal, P. Natural Gas Improves Economic Feasibility of Hybrid Distributed Energy Systems. *Nat. Gas Electr.* **35**, 1–7 (2019)
- [3] Speight, J. G. *Handbook of Natural Gas Analysis. Handbook of Natural Gas Analysis* (Wiley, 2018). doi:10.1002/9781119240297
- [4] Mokhatab, S., Poe, W. A. & Mak, J. Y. *Handbook of Natural Gas Transmission and Processing*. (Gulf Professional Publishing, 2015).
- [5] Chen, S. J. *et al.* CO₂ separation from offshore natural gas in quiescent and flowing states using 13X zeolite. *Appl. Energy* **205**, 1435–1446 (2017)
- [6] Saha, D. & Deng, S. Structural stability of metal organic framework MOF-177. *J. Phys. Chem. Lett.* **1**, 73–78 (2010)
- [7] Kayal, S. & Chakraborty, A. Activated carbon (type Maxsorb-III) and MIL-101(Cr) metal organic framework based composite adsorbent for higher CH₄ storage and CO₂ capture. *Chem. Eng. J.* **334**, 780–788 (2018)
- [8] Zhou, Z. *et al.* A novel bimetallic MIL-101(Cr, Mg) with high CO₂ adsorption capacity and CO₂/N₂ selectivity. *Chem. Eng. Sci.* **147**, 109–117 (2016)
- [9] Zhang, Z., Huang, S., Xian, S., Xi, H. & Li, Z. Adsorption equilibrium and kinetics of CO₂ on chromium terephthalate MIL-101. *Energy and Fuels* **25**, 835–842 (2011)
- [10] Zhou, X. *et al.* Enhanced separation performance of a novel composite material GrO@MIL-101 for CO₂/CH₄ binary mixture. *Chem. Eng. J.* **266**, 339–344 (2015)
- [11] Bromberg, L., Diao, Y., Wu, H., Speakman, S. A. & Hatton, T. A. Chromium(III) Terephthalate Metal Organic Framework (MIL-101): HF-Free Synthesis, Structure, Polyoxometalate Composites, and Catalytic Properties. *Am. Chem. Soc.* **24**, 1664–1675 (2012)
- [12] Brunauer, S., Emmett, P. H. & Teller, E. Adsorption of Gases in Multimolecular Layers. *J. Am. Chem. Soc.* **60**, 309–319 (1938)
- [13] Harkins, W. D. & Jura, G. Surface of Solids. XIII. A Vapor Adsorption Method for the Determination of the Area of a Solid without the Assumption of a Molecular Area, and the Areas Occupied by Nitrogen and Other Molecules on the Surface of a Solid. *J. Am. Chem. Soc.* **66**, 1366–1373 (1944)
- [14] Sircar, S. Isosteric Heats of Multicomponent Gas Adsorption on Heterogeneous Adsorbents. *Langmuir* **7**, 3065–3069 (1991)
- [15] Toth, J. Uniform interpretation of gas/solid adsorption. *Adv. Colloid Interface Sci.* **55**, 1–239 (1995)
- [16] Myers, A. L. & Valenzuela, D. Computer Algorithm and Graphical Method for Calculating Adsorption Equilibria of Gas Mixtures. *J. Chem. Eng. Jpn.* **19**, 392–396 (1986)
- [17] Oliveira, L. H. De, Meneguim, J. G., Pereira, M. V, Nascimento, J. F. & Arroyo, P. A. Adsorption of hydrogen sulfide, carbon dioxide, methane, and their mixtures on activated carbon. *Chem. Eng. Commun.* **206**, 1544–1564 (2019)
- [18] Thommes, M. *et al.* Physisorption of gases, with special reference to the evaluation of surface area and pore size distribution (IUPAC Technical Report). *Pure Appl. Chem.* **87**, 1051–1069 (2015)
- [19] Lin-Vien, D., Colthup, N. B., Fateley, W. G. & Grasselli, J. G. *The Handbook of Infrared and Raman Characteristic Frequencies of Organic Molecules*. (Academic Press, 1991).
- [20] Anbia, M. & Hoseini, V. Enhancement of CO₂ adsorption on nanoporous chromium terephthalate (MIL-101) by amine modification. *J. Nat. Gas Chem.* **21**, 339–343 (2012)

Pilot plant for H₂S and CO₂ separation from humid mixtures with CH₄ through swing adsorption processes: concept and operation

Leonardo Hadlich de Oliveira^a, Marcus Vinicius Pereira^a, Rafael Luan Sehn Canevesi^b,
Marcelo da Costa Amaral^c, Jailton Ferreira do Nascimento^c, Pedro Augusto Arroyo^a

^a State University of Maringá, Av. Colombo 5790, Maringá – PR, 87020-900, Brazil

^b State University of Western Paraná, R. da Faculdade 645, Maringá – PR, 85093-000, Brazil

^c Petrobras/CENPES/PDDP/TPP, Av. Horácio, Rio de Janeiro – RJ, 21941-915 Brazil

Abstract

H₂S and CO₂ must be removed from Brazilian pre salt layer natural gas humid streams. Adsorption is a promising alternative technology to separate these compounds and help to attend composition regulatory restrictions. In order to turn adsorption processes reality for natural gas purification, researches should step from bench to pilot plant scale. However, there are no reports concerning pilot plants constructed to remove H₂S and CO₂ from natural gas streams. In this work, the concept and operation of a pilot plant for H₂S and CO₂ separation from humid mixtures with CH₄ through swing adsorption processes are presented. Pilot plant concept was based on Skarström cycle, developed after a proper scale up and study of variables that affect production, recovery and purity of CH₄ rich streams. The sectored layout was optimized in order to provide a versatile pilot plant, where it is possible to operate pressure, temperature and concentration swing adsorption processes, parallel and series fixed bed adsorption experiments, recycling the outlet gas streams, which turns the equipment more economic. Adsorption sector, the plant's core, is formed by two columns, each one with three flange modular fixed beds, where it is possible to test combinations of different adsorbents. After installation, the pilot plant will serve as experimental protocol to test new adsorbents developed to purify natural gas streams.

Keywords: pilot plant; swing adsorption process; H₂S; CO₂; natural gas.

1. Introduction

Natural gas commercialized in Brasil should attend restrictions for H₂S (< 10 mg m⁻³) and CO₂ (< 3 mol%) composition accord to ANP Resolution n° 16 [1]. However some fields present H₂S compositions greater than 100 mg m⁻³ and CO₂ compositions from 5 to 80% [2].

Removal these acid gases have been studied with absorption, membrane and cryogenic processes [3].

However the majority of these studies are bench scale and does not report H₂S adsorption.

Therefore, in this work a concept of pilot plant was developed in order to provide a swing adsorption apparatus to remove H₂S and CO₂ from humid natural gas streams

2. Concept and layout optimization

Pilot plant concept was based on Skarström cycle, developed after a proper scale up and study of variables that affect production, recovery and purity of CH₄ rich streams.

The sectored layout was optimized in order to provide a versatile pilot plant, where it is possible to operate pressure, temperature and concentration swing adsorption processes, parallel and series fixed bed adsorption experiments, recycling the outlet gas streams, which turns the equipment more economic.

Flowchart shown in Figure 1 presents all devices that should be present in the pilot plant.

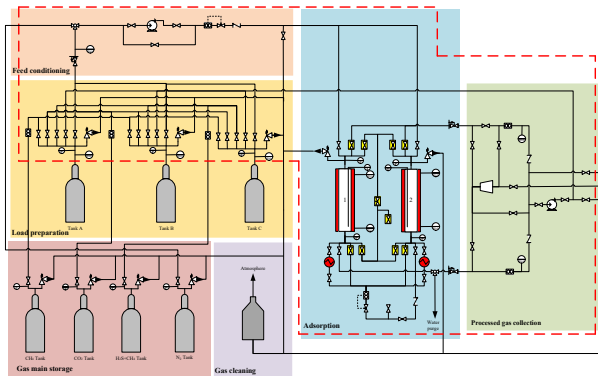


Fig. 1. Simplified, sectorized flowchart of the pilot plant.

All devices shown in Figure 1 are listed in Table 1.

Table 1. Symbols used in the pilot plant flowchart.

Symbol	Description
	Two-way <i>on-off</i> automatic valve.
	Two-way <i>on-off</i> automatic valve that suffers Joule-Thomson effect
	Check valve (retention).
	Automated pressure regulator valve.
	Needle valve.
	Pressure relief valve (PSV).
	Three-way automatic selector valve.
	Flowmeter.
	Flow controller.
	Collection point for residual gas analyzer.
	Electronic pressure transducer.
	Electronic temperature transducer.
	Heat exchangers for heating purge stream.
	Gas compressor.
	Vacuum pump.
	Gas cylinder.
	Gas cleaner
	Adsorption column composed by three modules with external heating / cooling system.

3. Operation

Operation of each sector of the pilot plant are described below.

3.1. Gas main storage

In Figure 2, pilot plant gas main storage is shown. This sector comprises the gas inventory that is used to feed the pilot plant.

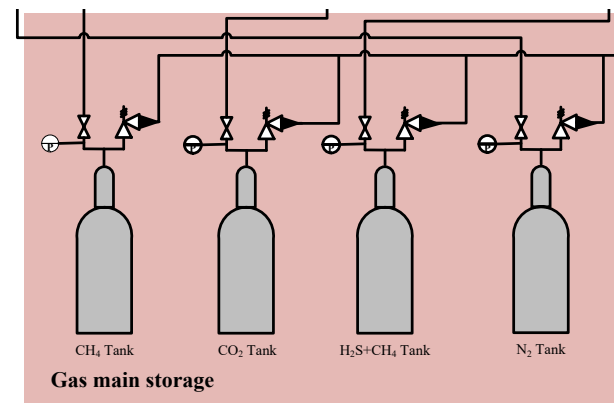


Fig. 2. Gas main storage sector.

Gas main storage comprises pure CH₄ and CO₂ cylinder baskets, a H₂S + CH₄ make up cylinder and pure N₂ cylinder basket that is utilized for activation of adsorbent bed.

3.2. Load preparation

Load preparation sector is used to prepare gas mixture that will be processed and to received the gas stream from processed gas collection sector.

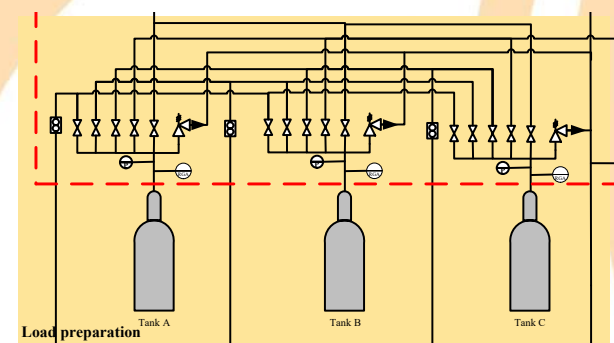


Fig. 3. Load preparation sector.

With a mass flow for each tubing prevented from main storage, it is possible to know exactly the mass

of each gas inside three previously designed tanks that turn possible continuous operation of the plant.

Each valve in these tanks is used for a specific gas stream. From left to right: a) inlet CH₄ stream; b) inlet CO₂ stream; c) inlet H₂S+CH₄ stream; d) processed gas stream; e) feed gas stream; f) safety valve

Gas recycle is applied for economic reasons, since instead send the gas mixture to gas cleaning sector, it can be reused several times if leakage is avoided in the plant.

3.3. Feed conditioning

Feed conditioning sector is made of a composition analyzer, a compressor and a mass flow controller, as shown in Figure 4.

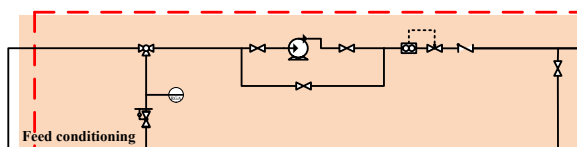


Fig. 4. Feed conditioning sector.

Gas analyzer is used to check feed composition prepared in load preparation sector. Compressor and mass flow controller guarantees the operational pressure and mass flow rate in the adsorption sector.

3.4. Adsorption

Adsorption sector, shown in Figure 5, is the heart of the pilot plant. Here, two columns were design to operate PSA and TSA processes.

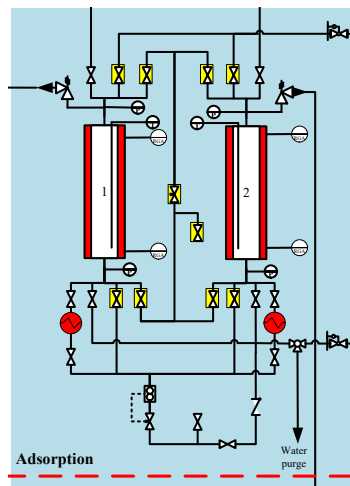


Fig. 5. Adsorption sector.

Both columns can be heated for activation of adsorbent bed or to operate a TSA process, that can also be achieved heating the purge stream. Gas streams can be processed in parallel or series.

Each column is a three flange modular fixed bed, where it is possible to test combinations of different adsorbents.

Valves painted in yellow should be heated to avoid freezing of gas stream due to Joule-Thomson effect.

A water purge is necessary in activation step, since water initially presented on adsorbent pores condensates after its removal and then is collected here.

There are also two valves disconnected, that are used when an equilibration vessel is connected, achieving constant feed flow when operating.

3.5. Processed gas collection

Processed gas collection sector is shown in Figure 6.

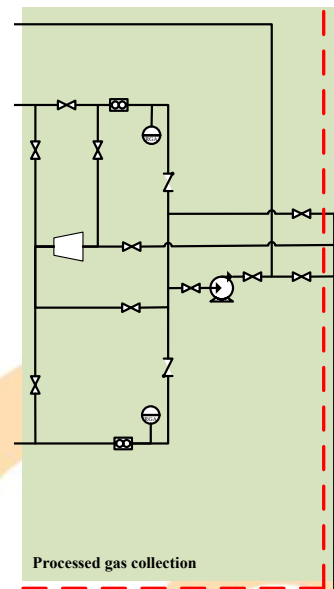


Fig. 6. Processed gas collection sector.

It contains a vacuum pump to operate VSA processes, mass flow controllers for both light and heavy streams that leave the adsorption sector.

Mass flow controllers and gas analyzers are installed for both light and heavy streams.

In this sector, the pressure of the streams are ambient. Then, a second compressor is present to repressurize the processed gas in order to recycle it to load preparation sector.

3.6. Gas cleaning

Gas cleaning sector is responsible for ensuring the safety of the personnel who operates the pilot plant, as well as the equipment to be installed. As can be seen in Figure 1, this sector is connected to all pipelines in the plant and to all safety valves.

In this sector, a gas scrubber is the main equipment (Figure 7), so that in case of an emergency the entire system is evacuated in timely manner, i.e., an emergency depressurization.

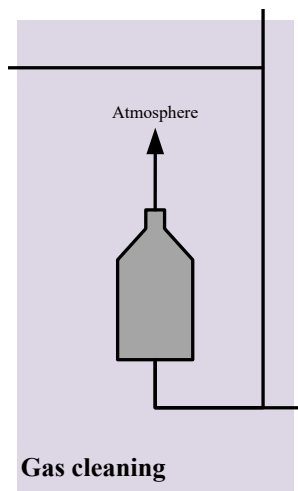


Fig. 7. Processed gas collection sector.

Since gases CO_2 and H_2S are acid gases, basic solutions should be used in the gas scrubber in order to neutralize them through chemical reaction.

Conclusions

A pilot plant concept based on Skarström cycle was developed. It has a sectored layout optimized to provide a versatile equipment, where it is possible to operate pressure, vacuum, temperature and concentration swing adsorption processes, parallel and series fixed bed adsorption experiments, recycling the outlet gas streams, which turns the equipment more economic.

Adsorption sector is formed by two columns with with three flange modular fixed beds, where it is possible to test combinations of different adsorbents.

After installation at State University of Maringá, the pilot plant will serve as experimental protocol to test new adsorbents developed to purify natural gas streams.

Acknowledgements

Authors would like to thank Petrobras for the financial support (Cooperation Terms 0050.0045268.08.4, 0050.0073910.12.9 and 0050.0073910.12.9).

References

- [1] ANP. Resolução nº 16. 2008.
- [2] MME. Informe: Custos de gás natural no pré-sal brasileiro. 2019.
- [3] Shafeeyan MS, Daud WMAW, Houshmand A, Shamiri A. A review on surface modification of activated carbon for carbon dioxide adsorption. *J. Anal. Appl. Pyrolysis* 2010;89:143–151.

Adsorption of a Natural Surfactant obtained from Crude Glycerin in Sandstone Reservoirs

Panazzolo, Guilherme F.T.^a, Prates, Viviane R.^a, Camargo, Carla M.^a, Nicolini, João Victor^b, Nele, Márcio^{a,c}, Ferraz, Helen, C.^c

^a Escola de Química, Universidade Federal do Rio de Janeiro, Rio de Janeiro, Brazil

^b Departamento de Engenharia Química, Universidade Federal Rural do Rio de Janeiro, Seropédica, Brazil

^c Programa de Engenharia Química, COPPE, Universidade Federal do Rio de Janeiro, Rio de Janeiro, Brazil

Abstract

Enhanced Oil Recovery (EOR) is an increasingly widespread practice in the oil industry. This practice has several techniques that help to optimize the oil flow in the reservoirs and increase productivity. One of these techniques is the injection of surfactants, which reduces the oil-water interfacial tension and can also alter the rock/reservoir wettability, promoting greater oil recoveries. In this study, the main objective was to investigate the interaction of the natural surfactant additive salicylic acid salt (SACA) with Berea sandstone in the presence of Low Salinity Water (LSW) and its interaction with a crude oil sample. SACA was extracted from crude glycerin, a byproduct of biodiesel production. Its adsorption was evaluated by surface tension and zeta potential measurements. By measuring surface tension, the critical micellar concentration (c.m.c.) of the SACA was determined at 0.05% (mass/mass). In addition, the adsorption density was determined to be around 2.9 g of SACA per kg of Berea sandstone, much lower than that found for commercial surfactants. The increase of zeta potential as a function of pH and surfactant concentration results in the increase of sandstone load magnitude, showing higher adsorption. At concentrations above c.m.c., it is observed that the magnitude of the zeta potential becomes very negative, due to the high adsorption of the SACA, probably due to hemi micelles formation. Finally, the results of this study are of great importance for future applications of this surfactant in advanced oil recovery.

Keywords: Natural Surfactant, Berea Sandstone, Enhanced Oil Recovery;

1. Introduction

In the EOR methods, surfactants are employed in reducing the interfacial tensions between water and oil, increasing the recovery efficiency. The combination with another methods, like polymer flooding and low salinity injection, will result in good mobility rate and, consequently, increases the oil recovery factor [1].

Adsorption of surfactants at the solid/liquid interface is one of the most useful phenomena involved in surfactant applications. Through adsorption onto a solid surface, a surfactant can transform the surface from a hydrophobic to a hydrophilic one and vice versa. It can also turn the solid to be easily or very difficult to wet by a given liquid [2]. Surfactant adsorption is a transfer process

of surfactant molecules from bulk solution phase to the surface/interface. It consists in the segregation of the adsorbate species between the interface and bulk phases, and it occurs if the interface is energetically favored by the surfactant in comparison to the bulk solution. The adsorption of surfactants on a rock-solid matrix may have an effect of loss and reduction of their concentration, which may result in a less efficient practical treatment [3].

The importance of surfactant mostly comes from its many technological and industrial applications, such as detergency, mineral flotation, corrosion inhibition, dispersion of solids and oil recovery [4]. On the enhanced oil recovery (EOR) of reservoirs, for example, surfactant loss due to adsorption on the reservoir rocks decreases the effectiveness of the chemical solution injected to minimize the oil-water interfacial tension (IFT) and renders the process



economically unfeasible [5]. One possible origin of surfactants is from the main by-product of the biodiesel industry, the crude glycerin. Even with all the impurities originated from the production process, the crude glycerin is a marketable product. However, the market absorbs much more purified glycerin with high added value. Thus, there is a great interest in reusing this product in processes and technologies which will provide sustainability to the process of biodiesel production, contributing to produce biodiesel to become more competitive [6]. One of these alternatives is to extract the natural surfactant. The usage of the natural surfactant from crude glycerin as a mechanism to enhance the oil recovery has not been reported by literature so far.

There are many studies about the adsorption of single surfactants at a pure solid–liquid interface, but the case of adsorption of single surfactants to natural soils is not very common. As the surfactant adsorption by soils depends on the type of surfactant and the soil properties, it is fundamental to understand how they interact with each other.

Thus, the experimental study of the adsorption of a natural surfactant onto Berea sandstone with different concentrations was realized in order to verify its future application on the enhanced oil recovery.

2. Materials and Methods

2.1 Materials

The natural surfactant was previously extracted from crude glycerin according to the following steps: acid hydrolysis, hot washing, centrifugation and route evaporation. The crude glycerin originated from the biodiesel production was acidified at pH range of 4.6 - 5.0 with a strong acid to neutralize the residue and separate it into two phases. Then, the glycerin was deposited in the lower part (heavy phase) and the fatty acids in the upper part (light phase) allowing separating the glycerin and the fatty acids. Subsequently, the light phase with the carboxylic acids are treated with carboxymethylcellulose, giving rise to the additive natural surfactant (SACA).

The Table 1 presents the composition of the low salinity water employed in this study. The composition was based on [7]. For the preparation of the solution, analytical grade reagents were employed.

Table 1. Composition and properties of LSW.

Ion	Composition (mg. L ⁻¹)
Na ⁺	467
K ⁺	23
Mg ²⁺	5.2
Ca ²⁺	1.1
Ba ²⁺	0.4
Cl ⁻	780
Br ⁻	1.0
SO ₄ ²⁻	49
HCO ₃ ⁻	19
pH	6.5
Density (g.cm ⁻³)	0,998

The Berea sandstone rock was finely ground to a grain size of less than 45 µm for the adsorption tests. For the zeta potential tests were used rock powders between 45 e 150 µm.

2.2 Methods

2.2.1 Berea sandstone characterization

The Berea sandstone rock samples were characterized by X-ray diffraction (XRD; Rigaku MiniFlex equipment with Cu-Ka radiation, $\lambda = 15,418 \text{ \AA}$) and X-ray fluorescence (XRF; Rigaku equipment, Rix 3100 with rhodium tube)

2.2.2 Zeta potential measurements

Zeta potential of the Berea sandstone rock was determined by the streaming potential method with an electrokinetic analyser (SurPASS, Anton Paar) according Figure 1. Zeta potential was measured as a function of pH and SACA concentration.

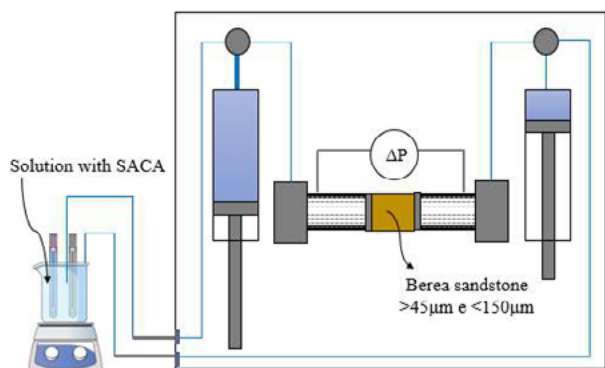


Fig. 1. Scheme of the zeta potential measurement procedure.

2.2.3 Adsorption tests

SACA solutions at concentrations ranging from 0.001 to 1.5 wt.% were prepared in LSW. Before contacting the Berea sandstone, the surface tension of the SACA solutions were measured to determine critical micellar concentration (c.m.c.). Subsequently, 10 mL of each solution was transferred to tubes containing 2 g of Berea sandstone powder. These solutions were shaken in a rotating shaker at 20 rpm for at least 12 hours to achieve equilibrium. Then the solid and liquid phases were separated by placing them in a centrifuge (5910R, Eppendorf) for 40 minutes at approximately 4000 rpm. The supernatant liquid was collected, and surface tension was measured and then the c.m.c. was determined. Aliquots of SACA samples were obtained before and after adsorption and surface tension was measured. The amount of surfactant that was adsorbed was calculated from the difference in c.m.c. values before and after the adsorption experiment, according to equation (1) [3; 8].

$$\frac{SACA\ adsorbed_{(g)}}{Berea\ sandstone_{(g)}} = \frac{\Delta c.m.c. \times 10g_{SACA}}{2g_{sandstone}} \quad (1)$$

2.2.4 Surface tension measurements

The surface tension of SACA solutions was measured for c.m.c determination. For this was employed a goniometer (Dataphysics OCA 15) through the pendant-drop method, as shown in Figure 2.

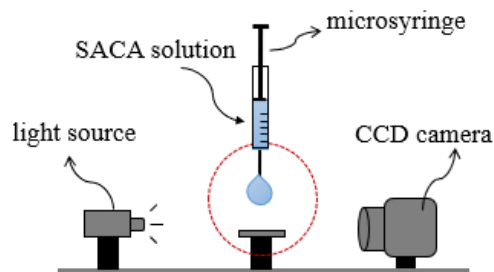


Fig. 2. Schematic diagram of the drop-shape analyzer for surface tension measurement.

3. Results and discussion

Berea sandstone comprise of minerals with majority quartz and kaolinite. XRD analysis is presented in Figure. XRF analysis confirms high percentages of O, Si, K and Al (51.85, 37.07, 1.35 and 7.70 %, respectively) [7].

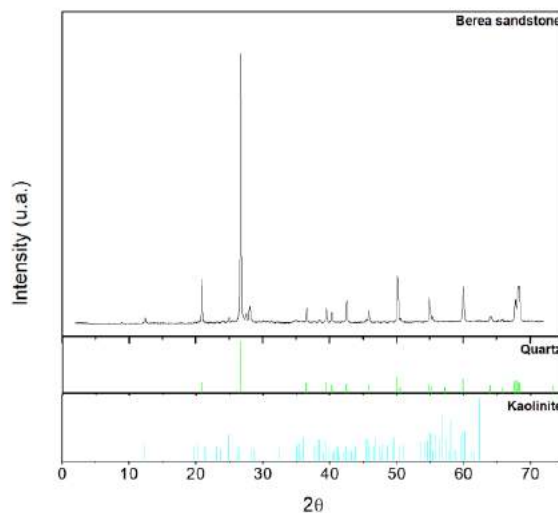


Fig. 3. XRD of Berea sandstone.

The Figure 4 show the zeta potential results as function pH. In the LSW, the zeta potential was negative in the all pH range, due dissociation of the surface silanol groups (-SiOH) of the quartz, producing deprotonated silanol groups (-Si-O⁻). In presence of SACA, the magnitude of the negative zeta potential increased due SACA adsorption. The SACA is a carboxylic acid salt, that is manocarboxylic acids which have the carboxylic group (-COOH). Then, in aqueous solution, this

carboxylic group dissociation and gives negative charge.

Fig. 4. Zeta potential as a function of pH for Berea sandstone.

This tendency towards adsorption is observed as the concentration of natural surfactant increases, possibly due to hemi micelle formation. The Figure 5 shows the change in zeta potential as they increase the SACA concentration.

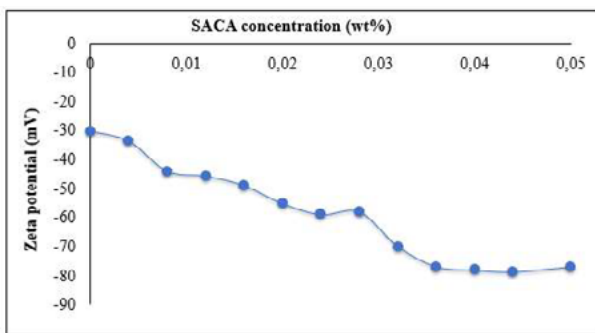


Fig. 5. Zeta potential as a function of SACA concentration for Berea sandstone.

Figure 6 shows the c.m.c measurements of SACA before and after equilibration with sandstone. Comparing the c.m.c. results, it is possible to see that the system with SACA before equilibration with sandstone has a higher potential to decrease the surface tension than do after equilibration with sandstone, which indicates that the c.m.c. value for the case with SACA before equilibration with sandstone is lower. This is confirmed by the CMC values which are 0.05 and 0.10 wt.% for the SACA before and after equilibration with sandstone, respectively.

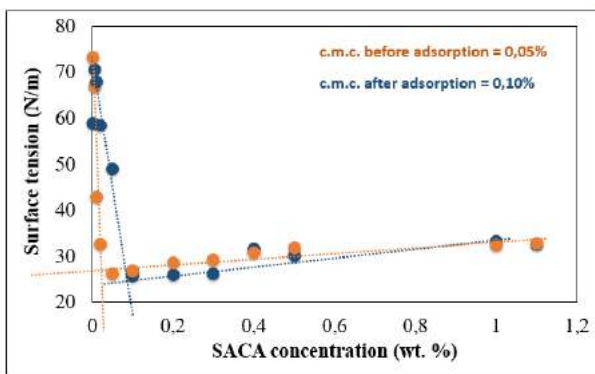
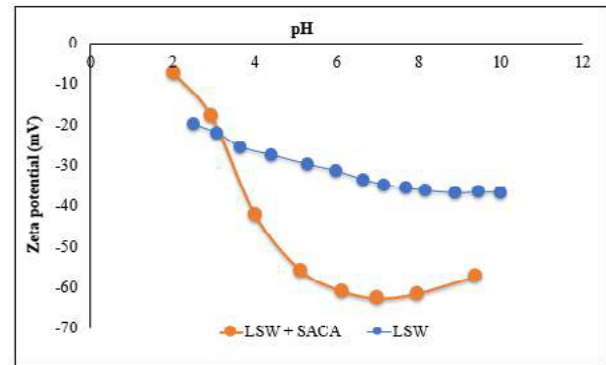


Fig. 6. Critical micellar concentration of SACA before and after adsorption.

Also, in Figure 6, it can be observed that the surface tension of the SACA at certain



concentration before the c.m.c. is higher for the case after equilibration with sandstone. This behavior is explained by the fact that a certain amount of SACA was adsorbed by the sandstone. Then, the difference in the c.m.c. of SACA as determined from the surface tension curves was found to be 0.05 wt.%. Then, by equation 1 was possible to calculate the mass of SACA adsorbed on sandstone: 2.9 g of SACA per kg of sandstone.

According to [3] and [9], at low surfactant concentrations, the adsorption on adsorbents, for example, sandstone, occurs as monomers. As increasing surfactant concentrations, surfactant monomers that were adsorbed on a solid surface start to form structures called ad-micelles or hemi-micelles. The extent to which these structures aggregate and begin to form surfactant mono or double layers on the solid surface. Thus, at high concentration, they form a solid surface and have physical properties like solution micelles. Joshi and contributors studied the adsorption of the commercial surfactant TX100 on shale. It was found amount of TX100 adsorbed to shale of the 7.5 g/kg and for TX100/SDS mixtures it was found amount of TX100/SDS adsorbed to shale of the 4.5 g/kg [9].

4. Conclusions

The increase in zeta potential as a function of pH and surfactant concentration results in the increase of negative charges in the sandstone, evidencing higher SACA adsorption.

At concentrations above c.m.c., it is observed that the magnitude of the zeta potential is very negative, due to the high adsorption of the SACA, probably due to the formation of hemi micelles.

The adsorption density was determined around 2.9 g of SACA per kg of Berea sandstone, much lower than that found for commercial surfactants.



Acknowledgements

To CNPQ for the financial support.

References

- [1] Negin C, Ali S, Xie Q. Most common surfactants employed in chemical enhanced oil recovery. *Petroleum*. 2007; 3: 197-211.
- [2] Zhu, B Y, Gu, T. Surfactant adsorption at solid-liquid interfaces. *Adv Colloid Interf Sc* 1991; 37: 1-32.
- [3] Muherei, MA, Junin, R, Bin Merdhah, AB. Adsorption of sodium dodecyl sulfate, Triton X100 and their mixtures to shale and sandstone: A comparative study. *J Petroleum Sci Eng*. 2009; 67: 149-154.
- [4] Paria, S Khilar, KC. A review on experimental studies of surfactant adsorption at the hydrophilic solid-water interface. *Adv in Colloid Interf Sci*. 2004; 110: 75-95.
- [5] Curbelo, FD, Santanna, VC, Neto, EL, Dutra, TV, Dantas, TN, Neto, AA, Garnica, AI. Adsorption of nonionic surfactants in sandstones. *Colloids and Surfaces A: Physicochemical and Engineering Aspects*. 2007; 293: 1-4.
- [6] Yong, K, Yunus, W, Ooi, T, Dzulkey, K,. Refining of crude glycerine recovered from glycerol residue by simple vacuum distillation. *Journal of Oil Palm Research*. 2001; 13.
- [7] Nicolini, JV, Ferraz, HC, Borges, CP. Effect of seawater ionic composition modified by nanofiltration on enhanced oil recovery in Berea sandstone. *Fuel*. 2017; 203: 222-232.
- [8] Amirianshoja, T, Junin, R, Idris, AK, Rahmani, O. A comparative study of surfactant adsorption by clay minerals. *Journal of Petroleum Science and Engineering*. 2013; 101: 21-27.
- [9] Joshi, T, Mata, J, Bahadur, P. Micellization and interaction of anionic and nonionic mixed surfactant systems in water. *Colloids and Surfaces A: Physicochemical and Engineering Aspects*. 2005; 260: 209-215.

Deoxygenation of oleic acid as a model compound to produce diesel-range hydrocarbons over Ni₂P/H-ZSM-5

Mariana de Oliveira Camargo^a, Celso Hissao Maeda^a, João Lourenço C. W. Pimenta^a, Pedro Augusto Arroyo^{a*}

^a Department of Chemical Engineering, State University of Maringá, 5790 Colombo Avenue, Maringá, ZIP 87020-650, Brazil

* e-mail: paarroyo@uem.br

Abstract

A nickel phosphide (Ni₂P) catalyst supported on H-ZSM-5 zeolite was prepared to evaluate the deoxygenation of oleic acid as a model compound to produce diesel-like hydrocarbons. The catalyst was synthesized by temperature programmed reduction of the oxidic precursors and incipient wetness impregnation and characterized by atomic absorption spectroscopy (AAS), X ray diffraction (XRD), nitrogen adsorption/desorption, temperature programmed desorption of ammonia (TPD) and transmission electron microscopy (TEM). The deoxygenation test was performed on an autoclave batch reactor operated at 300 °C, 50 bar of hydrogen and for 6 h. The catalyst exhibited achieved a total amount of 27.9 wt% of hydrocarbons, and the major hydrocarbon obtained was C17, derived from decarboxylation and decarbonylation pathways, which consume less hydrogen.

Keywords: green diesel; hydrotreating; deoxygenation; nickel phosphides; zeolite.

1. Introduction

Due to exhaustion of oil reserves, economic reasons and more environmental and political concerns, there is an urgent need to develop renewable fuels [1–3]. Triglyceride based biomass is an appealing alternative to produce transportation fuels as they are readily available, renewable [2] and its long chain usually contains carbons between 16 and 18 [4], which is within diesel range [5] and it results in high heating value [4]. However, they cannot be directly used as fuel due to the high amount of oxygen and consequently engine incompatibility [5,6] and therefore, in order to be used as fuels, vegetable oils need to be upgraded [5,6]. Deoxygenation is a process to remove oxygen from feedstocks, producing green diesel, a fuel similar to oil derived diesel and with enhanced properties, such as high cetane number [2,5,7]. Other advantages are absence of sulfur [8], the use of established structure for storage and distribution, and green diesel can be used in diesel engines pure or blended with petrol-diesel at any ratio [9].

Deoxygenation of fatty acids can be achieved by three main pathways: hydrodeoxygenation, decarbonylation and decarboxylation, which the former yields hydrocarbons with the same number of carbons that the corresponding fatty acid, while decarbonylation and decarboxylation result in a hydrocarbon with one carbon shorter than the precursor fatty acid [2,9–11]. Furthermore, decarbonylation and decarboxylation remove the carboxyl group releasing CO and H₂O and CO₂, respectively, while hydrodeoxygenation removes oxygen in the form of H₂O [2,3,9,11].

Lately, many studies have investigated the use of nickel phosphides as hydrotreating catalysts, due to low cost compared to noble metals [12], high activity in hydrotreating reactions (*i.e.* removal of S, N and O) [12], low activities in other reactions than deoxygenation reactions when compared with non-noble metals [11,13], and they present bifunctional sites (*i.e.* acid sites and metallic sites) [10,12,13]. In addition, they present both Lewis and Brønsted acid sites [14].

The aim of this work was to investigate the deoxygenation of oleic acid as a model compound



over nickel phosphide supported on H-ZSM-5 zeolite to produce hydrocarbons, in particular hydrocarbons with 18 and 17 carbons. The catalytic test was carried on a batch reactor operated at 300 °C, 50 bar of H₂ and for 6 h. In addition, the catalyst was thoroughly characterized in order to investigate how surface area, acidity and size of metallic particles play a role in deoxygenation of fatty acids.

2. Experimental

2.1. Materials

The materials used were nickel hexahydrate (Vetec), ammonium phosphate dibasic (Acros organics, 99%) and oleic acid (90 wt%, Synth). The commercial zeolites used was H-ZSM-5 (Si/Al = 50) supplied by Clariant.

2.2. Catalyst synthesis

The catalyst was prepared by temperature programmed reduction and incipient wetness impregnation of the oxidic precursors with 10 wt% Ni₂P. Afterwards, the reduction was performed with hydrogen (50 mL/min) at a rate of 5 °C/min up to 350 °C and then at a rate of 2 °C/min up to 650 °C and held for 3 h. The passivation, needed due to the pyrophoric behavior of this active phase, was performed under 0.5 % O₂/N₂ (50 mL/min) at room temperature for 1 h.

2.3. Characterization

Atomic absorption spectroscopy (AAS) to determine the amount of Si, Al and Ni was conducted on a Spectra AA 50 B (Varian) spectrometer.

X-ray diffraction powder analysis was recorded on a XRD 6000 (Shimadzu) diffractometer in order to evaluate the crystallographic properties.

Nitrogen adsorption/desorption analysis was performed on an ASAP 2020 (Micromeritics) instrument to evaluate textural properties.

Temperature programmed desorption (TPD) of ammonia was conducted on an Autochem II (Micromeritics) instrument to investigate the strength and amount of acid sites.

Transmission electron microscopy (TEM) was performed on a JEM 1400 (JEOL) microscopy to determine the morphology.

2.4. Catalytic test

The deoxygenation test was carried on an autoclave batch reactor (160 mL) equipped with a sampling cylinder. 1.5 g of passivated catalyst was reactivated under hydrogen flow (50 mL/min) at 250 °C for 12 h. Then, the deoxygenation reaction was performed adding 50 g of oleic acid free of oxygen through purge of the sampling device and adding 50 bar of hydrogen after the desired temperature was reached (300 °C). The test was conducted for 6 h, when a sample was taken to measure the amount of remaining fatty acids and hydrocarbons produced.

Afterwards, the liquid product was methylated in order to convert free fatty acids into fatty acid methyl ester, according to a procedure found in the literature [15,16]. The amount of hydrocarbons and fatty acids contained in the sample was measured by gas chromatography (GC) using a GC-10 Plus chromatograph (Shimadzu) equipped with flame ionization detector (FID) coupled with a VA-5 (Varian) capillary column with dimensions 30 m x 0.25 mm x 0.25 µm. In order to determine the respective retention time of each compound, it was a procedure of another research group at the same department [16].

3. Results and discussion

XRD patterns of the support and the reduced catalyst are illustrated on Fig. 1. The support has only peaks ascribed to the ZSM-5 zeolite [17,18]. Besides the peaks ascribed to MFI framework [17,18], the Ni₂P/H-ZSM-5 catalyst exhibits five peaks attributed to the Ni₂P phase [19]. During the synthesis, it was used a surplus of P, necessary due to loss on P in the form of PH₃ during reduction [20]. Therefore, we conclude that this amount was enough to form only the Ni₂P phase, the most active nickel phosphide phase on hydrotreating reactions [21].

Physicochemical and acid properties of the support and the reduced catalysts are summarized on Table 1. The Si/Al mole ratio obtained for the support was 51.82, close to 50, the value given by the supplier. In addition, the impregnation of the catalyst was effective because it was possible to impregnate 10 Ni₂P wt%, which is equal to 7.91 wt% Ni.

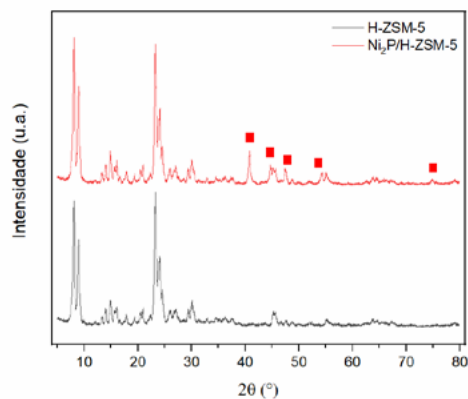


Fig. 1. XRD patterns of the support (—) H-ZSM-5 and the reduced catalysts (—) $\text{Ni}_2\text{P}/\text{H-ZSM-5}$.

Nitrogen adsorption/desorption of the sample are shown on Fig. 2. Both sample exhibit type I isotherm, a characteristic of microporous materials with low specific surface area [22] and they also display a H4 hysteresis, which indicates the presence of mesopores, generated by intercrystal voids [18]. The specific surface area of the catalyst is smaller than the area of the support, due to reduction of pore volume [23] and clogging caused by P and deposition of nickel phosphide [24].

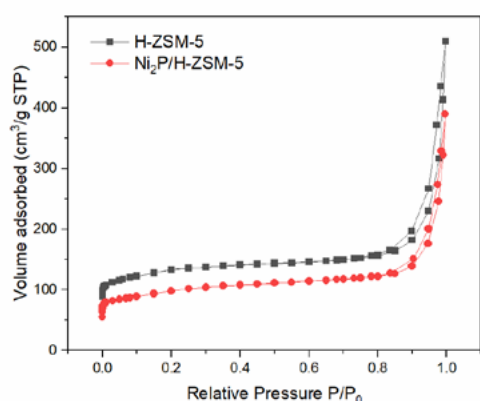


Fig. 2. Nitrogen adsorption/desorption isotherms of the zeolite (■) H-ZSM-5 and the reduced catalysts (●) $\text{Ni}_2\text{P}/\text{H-ZSM-5}$.

TPD profile of the sample are shown on Fig. 3 and the total amount of acid sites are shown on Table 1. There is a decrease on the total amount of acid sites after impregnation of nickel phosphide, which is in accordance with previous studies [23,25]. Moreover, there is a reduction of the amount of weak and strong acid sites, and this is more intense on strong acid sites. According to the literature, the loss of acid sites after impregnation on ZSM-5 zeolite is due to interaction between Ni and acid OH of the zeolite [17].

Table 1. Physicochemical and acid properties of the support and the reduced catalysts.

	H-ZSM-5	$\text{Ni}_2\text{P}/\text{H-ZSM-5}$
Si/Al ^a	51.82	-
Ni (wt %) ^b	-	7.84
A_{total} (m ² /g) ^c	463	350
A_{meso} (m ² /g) ^d	97	111
A_{acid} (mmol/g) ^e	1.55	1.29

^a Si/Al mole ratio determined by AAS

^b Ni (wt %) determined by AAS

^c Specific surface area obtained by BET method

^d Mesoporous area obtained by t-plot method

^e Total amount of acid sites obtained by TPD

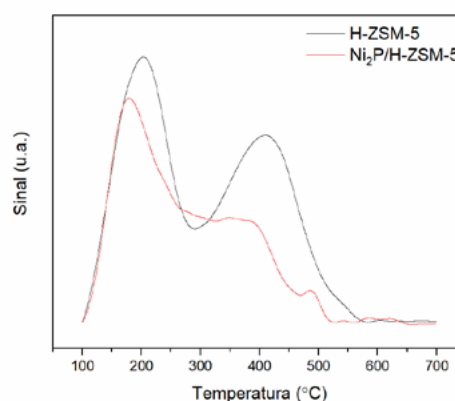


Fig. 3. TPD acid profiles of the bare zeolite (—) H-ZSM-5 and the reduced catalysts (—) $\text{Ni}_2\text{P}/\text{H-ZSM-5}$.

The TEM image of the catalyst is illustrated on Fig. 4. The hexagonal morphology with coffin-shape of ZSM-5 [26,27] is not clear due to agglomeration of crystals. There are globular nanoparticles of nickel phosphides with sizes

varying from 5 nm to 35 nm and an average diameter of 10.25 nm. In addition, the size is close to the value obtained by Koike *et al.* (2016), they obtained nickel phosphide particles of 10 nm supported on silica [20].

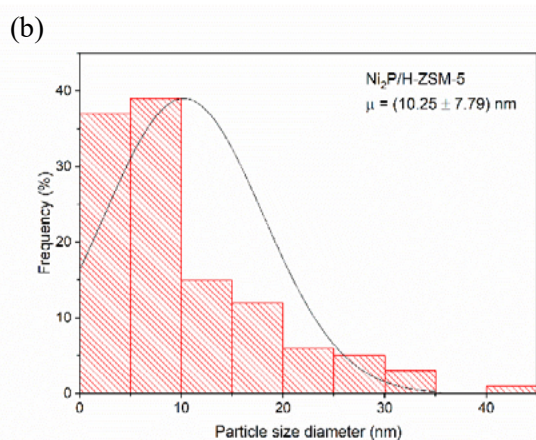
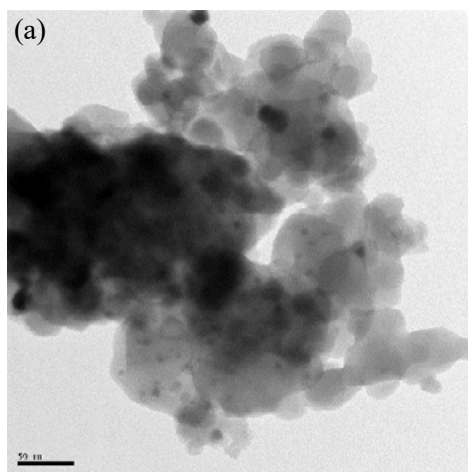


Fig. 4. TEM image of the reduced catalyst $\text{Ni}_2\text{P}/\text{H-ZSM-5}$ (a) and particle size distribution (b).

The range and amount of hydrocarbons yielded by the catalyst is illustrated on Fig. 5. The deoxygenation resulted in 27.9 wt% of hydrocarbons in total. As oleic acid has a straight chain with 18 carbons, hydrocarbons with 18 and 17 carbons are ascribed to deoxygenation and decarbonylation/decarboxylation reactions [2,5,7]. The reactant also contained palmitic acid (5 wt%), which explains the presence of C16 and C15 hydrocarbons, derived from hydrodeoxygenation

and decarbonylation/decarboxylation of this fatty acid, respectively.

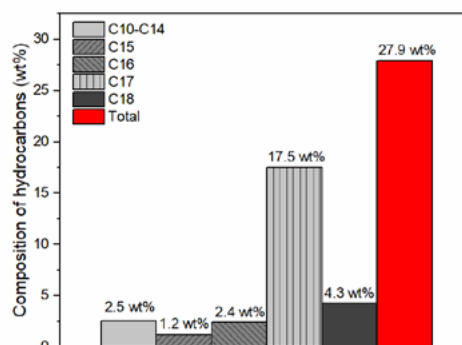


Fig. 5. Composition of hydrocarbons over $\text{Ni}_2\text{P}/\text{H-ZSM-5}$. Reaction conditions: 300 °C, 50 bar of H_2 , 50 g of oleic acid, 1.5 g of catalyst and 6 h.

It is clear that the highest yield is due to C17 hydrocarbons, which is beneficial, because the decarbonylation/decarboxylation pathways consumes less hydrogen than deoxygenation [2]. In addition, there is a small but significant amount of lighter hydrocarbons, ascribed to the cracking activity of this zeolite [28]. Moreover, another factor that can influence the deoxygenation activity is the Ni_2P particle size [17]. It is known that Ni_2P bulk structure has two type of Ni sites: tetrahedral Ni(1) and pyramidal Ni(2) sites and with a reduction of the particle size, the amount of Ni(2) increases and this site is responsible for the hydrodeoxygenation pathway [29]. Therefore, we can speculate that the size on nickel phosphide achieved (average diameter of 10.25 nm) is large enough, which increases the amount of Ni(1) sites on the structure of the metal phosphide, and it is responsible for decarbonylation/decarboxylation reactions [29].

4. Conclusion

The $\text{Ni}_2\text{P}/\text{H-ZSM-5}$ catalysts exhibited only the Ni_2P phases, which is more active on hydrotreating reactions. The impregnation of nickel phosphide can be confirmed by the reduction of the specific surface area and by a decrease of the total amount of acid sites when compared with the bare zeolite. The TEM showed a particle size of an average

diameter of 10.25 nm, a particle size that yielded more C17 hydrocarbons, derived from decarbonylation/decarboxylation reactions. Besides, as these reactions are predominant over hydrodeoxygenation, there is less consumption of hydrogen, resulting in a more efficient process.

Acknowledgements

We would like to acknowledge CAPES for the scholarship and COMCAP/UEM for the analyses conducted on its research facilities.

References

- [1] Kochaputi, Kongmark, Khemthong, Butburee, Kuboon, Worayingyong, et al. Catalytic Behaviors of Supported Cu, Ni, and Co Phosphide Catalysts for Deoxygenation of Oleic Acid. *Catalysts* 2019;9:715.
- [2] Phimsen S, Kiatkittipong W, Yamada H, Tagawa T, Kiatkittipong K, Laosiripojana N, et al. Nickel sulfide, nickel phosphide and nickel carbide catalysts for bio-hydro-treated fuel production. *Energy Convers Manag* 2017;151:324–33.
- [3] Snåre M, Kubičková I, Mäki-Arvela P, Eränen K, Murzin DY. Heterogeneous catalytic deoxygenation of stearic acid for production of biodiesel. *Ind Eng Chem Res* 2006;45:5708–15.
- [4] Snåre M, Kubičková I, Mäki-Arvela P, Chichova D, Eränen K, Murzin DY. Catalytic deoxygenation of unsaturated renewable feedstocks for production of diesel fuel hydrocarbons. *Fuel* 2008;87:933–45.
- [5] Hollak SAW, Gosselink RW, Van Es DS, Bitter JH. Comparison of tungsten and molybdenum carbide catalysts for the hydrodeoxygenation of oleic acid. *ACS Catal* 2013;3:2837–44.
- [6] Gosselink RW, Hollak SAW, Chang SW, Van Haveren J, De Jong KP, Bitter JH, et al. Reaction pathways for the deoxygenation of vegetable oils and related model compounds. *ChemSusChem* 2013;6:1576–94.
- [7] Stepacheva AA, Sapunov VN, Sulman EM, Nikoshvili LZ, Sulman MG, Sidorov AI, et al. Catalytic hydrodeoxygenation of fatty acids for biodiesel production. *Bull Chem React Eng Catal* 2016;11:125–32.
- [8] Shimada I, Kato S, Hirazawa N, Nakamura Y, Ohta H, Suzuki K, et al. Deoxygenation of triglycerides by catalytic cracking with enhanced hydrogen transfer activity. *Ind Eng Chem Res* 2017;56:75–86.
- [9] Silva LN, Fortes ICP, De Sousa FP, Pasa VMD. Biokerosene and green diesel from macauba oils via catalytic deoxygenation over Pd/C. *Fuel* 2016;164:329–38.
- [10] Shi H, Chen J, Yang Y, Tian S. Catalytic deoxygenation of methyl laurate as a model compound to hydrocarbons on nickel phosphide catalysts: Remarkable support effect. *Fuel Process Technol* 2013;116:161–70.
- [11] Shim JO, Jeon KW, Jang WJ, Na HS, Cho JW, Kim HM, et al. Facile production of biofuel via solvent-free deoxygenation of oleic acid using a CoMo catalyst. *Appl Catal B Environ* 2018;239:644–53.
- [12] Pham LKH, Tran TTV, Kongparakul S, Reubroycharoen P, Karnjanakom S, Guan G, et al. Formation and activity of activated carbon supported Ni2P catalysts for atmospheric deoxygenation of waste cooking oil. *Fuel Process Technol* 2019;185:117–25.
- [13] Gonçalves VOO, de Souza PM, da Silva VT, Noronha FB, Richard F. Kinetics of the hydrodeoxygenation of cresol isomers over Ni2P/SiO2: Proposals of nature of deoxygenation active sites based on an experimental study. *Appl Catal B Environ* 2017;205:357–67.
- [14] Alvarez-Galvan M, Campos-Martin J, Fierro J. Transition Metal Phosphides for the Catalytic Hydrodeoxygenation of Waste Oils into Green Diesel. *Catalysts* 2019;9:293–317.
- [15] Hartman L, Lago RC. Rapid preparation of fatty acid methyl esters from lipids. *Lab Pract* 1973;22:475–6 passim.
- [16] Pimenta JLCW. Síntese e avaliação de catalisador não convencional na produção de hidrocarbonetos a partir de óleo de soja. Universidade Estadual de Maringá, 2018.
- [17] Zhang L, Fu W, Yu Q, Tang T, Zhao Y, Li Y. Effect of citric acid addition on the morphology and activity of Ni2P supported on mesoporous zeolite ZSM-5 for the hydrogenation of 4,6-DMDBT and phenanthrene. *J Catal* 2017;345:295–307.
- [18] Luo CW, Huang C, Li A, Yi WJ, Feng XY, Xu ZJ, et al. Influence of Reaction Parameters on the Catalytic Performance of Alkaline-Treated Zeolites in the Novel Synthesis of Pyridine Bases from Glycerol and Ammonia. *Ind Eng Chem Res* 2016;55:893–911.
- [19] Liu Y, Yao L, Xin H, Wang G, Li D, Hu C. The production of diesel-like hydrocarbons from palmitic acid over HZSM-22 supported nickel phosphide catalysts. *Appl Catal B Environ* 2015;174–175:504–14.
- [20] Koike N, Hosokai S, Takagaki A, Nishimura S, Kikuchi R, Ebitani K, et al. Upgrading of pyrolysis bio-oil using nickel phosphide catalysts. *J Catal* 2016;333:115–26.
- [21] Wagner JL, Jones E, Sartbaeva A, Davis SA, Torrente-Murciano L, Chuck CJ, et al. Zeolite Y supported nickel phosphide catalysts for the hydrodenitrogenation of quinoline as a proxy for crude bio-oils from hydrothermal liquefaction of microalgae. *Dalt Trans* 2018;47:1189–201.
- [22] Figueiredo JL, Ribeiro FR. *Catalise heterogênea*. 2a. Lisboa: Fundação Calouste Gulbenkian; 2007.
- [23] Kim YS, Yun GN, Lee YK. Novel Ni2P/zeolite catalysts for naphthalene hydrocracking to BTX. *Catal Commun* 2014;45:133–8.
- [24] Yu Z, Wang A, Liu S, Yao Y, Sun Z, Li X, et al. Hydrodeoxygenation of phenolic compounds to cycloalkanes over supported nickel phosphides. *Catal Today* 2019;319:48–56.
- [25] Zarchin R, Rabaev M, Vidruk-Nehemya R, Landau M V., Herskowitz M. Hydroprocessing of soybean oil on nickel-phosphide supported catalysts. *Fuel* 2015;139:684–91.

- [26] Sang S, Chang F, Liu Z, He C, He Y, Xu L. Difference of ZSM-5 zeolites synthesized with various templates. *Catal Today* 2004;93–95:729–34.
- [27] van der Bij HE, Weckhuysen BM. Phosphorus promotion and poisoning in zeolite-based materials: synthesis, characterisation and catalysis. *Chem Soc Rev* 2015;44:7406–28.
- [28] Pütun E, Uzun BB, Putün AE. Rapid pyrolysis of olive residue. Effect of catalytic upgrading of pyrolysis vapors in a two-stage fixed-bed reactor. *Energy and Fuels* 2009;23:2248–58.
- [29] Ruddy DA, Schaidle JA, Ferrell JR, Wang J, Moens L, Hensley JE. Recent advances in heterogeneous catalysts for bio-oil upgrading via “ex situ catalytic fast pyrolysis”: Catalyst development through the study of model compounds. *Green Chem* 2014;16:454–90.

Adsorption of carbon dioxide on CHA molecular sieve – a model to account for thermal degradation

Geovani Rocha de Freitas, Rafaelle Gomes Santiago, Darley Carrijo de Melo, Diana Cristina Silva de Azevedo, Moisés Bastos-Neto*

Universidade Federal do Ceará, Department of Chemical Engineering, Fortaleza - CE, 60455-760, Brazil

Abstract

In this work, the adsorption of carbon dioxide was investigated in a magnetic suspension balance for a molecular sieve of CHA (chabazite) type at constant temperature (303 K). The hydrothermal stability of the adsorbent was investigated by submitting it to similar conditions as in a typical TSA plant. Samples were collected after 5, 14, 24 and 35 heating/cooling cycles and named as E1, E2, E3 and E4, respectively. CO₂ isotherms were measured for the fresh and “En” samples in the range of 0 to 10 bar. The results revealed that the samples were degraded to a certain extent and the sample collected after 35 cycles (420 h) showed around 25% decrease in CO₂ uptake. Toth model showed a better fit to the equilibrium data of the fresh adsorbent than the Langmuir model. The activity of the adsorbent, i.e. the ratio of the adsorption capacity on a deactivated adsorbent to the adsorption capacity on a fresh adsorbent, was adequately described by the deactivation model. These values of activity in combination with the Toth model were able to describe the experimental isotherm curves properly. Coke is likely to be formed in the deactivated samples given the color change of the adsorbent.

Keywords: Deactivation; molecular sieve; chabazite; modelling; CO₂ adsorption

1. Introduction

Natural gas is a complex mixture of several components, such as carbon dioxide, methane, ethane and higher hydrocarbons. Among these constituents, methane is the main component with a typical composition between 75% and 90% in v/v, followed by ethane, higher hydrocarbons, and undesirable impurities, such as water and carbon dioxide. Depending on the source from which crude natural gas is extracted, these components may vary in different compositions [1].

Due to its high methane content, natural gas has been used as a fuel for various purposes and is considered as one of the cleanest energy sources, especially when compared to other fossil fuels, such as coal and gasoline. However, the heterogeneous composition of natural gas with the presence of impurities represents a complex task in the processing of this gas. For this reason, a prior purification of natural gas is required. This purification procedure usually involves processes,

like absorption, adsorption and condensation, which remove water, mercury, carbon dioxide and other compounds [2].

Adsorption is a surface phenomenon which involves the use of a solid material, also known as adsorbent, to remove a certain contaminant. Among the several adsorbents available in the industry, molecular sieves have drawn attention due to their capacity to remove water in natural gas plants. The water adsorption in molecular sieves occurs mainly via physisorption and the highly polar surface within the pores of molecular sieves enables a high capacity for water and other polar components. With strict specifications being imposed on the moisture content of natural gas, the use of molecular sieves is of utmost importance when processing this gas [3].

In natural gas plants, adsorption units are usually employed to perform the dehydration of natural gas. Water vapor should be significantly removed to prevent undesirable effects, among others, such as: (i) hydrate formation in pipelines; (ii) freezing and condensation of moisture; (iii) occurrence of corrosion and erosion; and (iv) presence of



hydrolysis, i.e. chemical reaction with the fluid itself [4]. The dehydration process by adsorption is typically employed in cyclic systems, where the simplest version operates with two beds, one adsorbing and the other one desorbing (adsorbent regeneration) [5].

The regeneration of molecular sieves in natural gas dehydration is usually performed by increasing the temperature. This cyclic process that regenerates the adsorbent by heating is called thermal swing adsorption (TSA) [1]. In TSA units, one property of the adsorbent that must be taken into account is its deactivation degree, i.e. the reduction in the capacity or life of the adsorbent. Although TSA units are indicated for compounds that are strongly adsorbed, such as water adsorption in molecular sieves, adsorbent regeneration subjected to repeated thermal treatment and in combination with reactive hydrocarbons can result in the degradation of the adsorbent structure and formation of coke [6,7].

CHA-type molecular sieve is one of the adsorbents used in natural gas dehydration. Santiago et al. (2018) addressed the thermal deactivation process of this molecular sieve. They carried out an accelerated aging test in order to verify some effects responsible for adsorbent deactivation, such as presence of hydrocarbons and other gases. They concluded that the presence of n-heptane was a determining factor in adsorbent deactivation [8]. Deactivation models proposed in the literature for gas adsorption are barely found. In general, these models try to predict the influence of the deactivation in the shifting of breakthrough curves [9,10].

The goal of this study is to propose a model for the thermal deactivation of CHA-type molecular sieve that is able to predict the decrease in adsorbent capacity observed in the lab-scale aging protocol. This model is not meant to describe the actual mechanisms responsible for adsorbent deactivation, but rather to predict the loss in adsorbent capacity after a certain number of cycles in TSA units.

2. Materials and Methods

2.1 Experimental deactivation procedure

The molecular sieve was deactivated as described in Santiago et al. (2018). Briefly, the setup comprised a 500-mL stainless steel high-pressure reactor (Parr Instrument Company, EUA), a boiler for steam production and temperature

controllers for the reactor and boiler. 25 g molecular sieve was placed inside the reactor. Then the adsorbent was humidified with a continuous stream of nitrogen bubbled in water for 24 h at 303 K. Then, liquid n-heptane was added to the reactor at a proportion of 0.6 mL.g⁻¹. The system was then closed and pressurized to 30 bar with a 1:4 (mol) CO₂/CH₄ mixture for 1 h. Then the sample was subject to heating (523 K) and cooling (303 K). The total time of a cycle comprised of heating and cooling was 12 hours. Samples of the adsorbent were collected after 5, 14, 24 and 35 cycles and named as E1, E2, E3 and E4, respectively. Further details of this experimental procedure can be found on Santiago et al. (2018) [8].

2.2 Adsorption Isotherms

For adsorbent samples obtained in different degrees of deactivation, equilibrium adsorption isotherms were measured using a magnetic suspension balance (Rubotherm GmbH, Germany). 1.0 g adsorbent was outgassed under vacuum for 12 h at 558 K. After that, the sample was submitted to stepwise increments of pressure, from 0.1 to 10 bar CO₂.

The excess adsorbed amount was calculated based on Equation (1).

$$m_{exc} = \Delta m + \rho(V_b + V_s) \quad (1)$$

Where m_{exc} is the excess adsorbed weight (g), Δm is the weight change detected by the balance (g), ρ is the bulk density (g.cm⁻³), V_b is the volume of the balance (cm³) and V_s is the specific volume of the sample (cm³). Note that, within this pressure range, the excess adsorbed concentration is practically the same as the absolute adsorbed concentration.

The CO₂ adsorption equilibrium for CHA molecular sieve was described using two models: Langmuir and Toth. Both models are given by Equations (2) and (3), respectively.

$$q = \frac{q_{max} bP}{(1 + bP)} \quad (2)$$

Where q is the equilibrium concentration on the adsorbed phase (mmol.g⁻¹), q_{max} is the maximum concentration on the adsorbed phase (mmol.g⁻¹), b is the Langmuir parameter related to adsorption affinity (bar⁻¹) and P is the pressure of the gas in equilibrium with the adsorbed phase (bar).

$$q = \frac{q_{\max} KP}{(1 + (KP)^n)^{1/n}} \quad (3)$$

Where K is the Toth isotherm constant (bar^{-1}) and n is the Toth dimensionless parameter related to the heterogeneity of the adsorbent.

To evaluate the fitting of the model to the experimental data, a squared deviation error (R^2) was calculated, as in Equation (4).

$$R^2 = 1 - \frac{\sum_{i=1}^N (q^{\text{exp}} - q^{\text{calc}})^2}{\sum_{i=1}^N (q^{\text{exp}} - \bar{q})^2} \quad (4)$$

Where N is the number of experimental data, q^{exp} is the experimental value, q^{calc} is the value calculated by the model and \bar{q} is the average of the observed values.

2.3 Deactivation model

As mentioned in the previous section, one important property of the adsorbent is its deactivation degree, which is related to the adsorbent service life. In order to describe the loss in adsorption capacity, we will define the activity of the adsorbent as the ratio of the adsorption capacity of a deactivated adsorbent to the adsorption capacity on the fresh adsorbent:

$$a = \frac{q(\text{deactivated})}{q(\text{fresh})} \quad (5)$$

This activity term usually decreases exponentially with time (in service or in lab tests). For this reason, a deactivation model for the activity term was assumed as an exponential decay. This model can be expressed by Equation (6):

$$\frac{da}{dt} = -K_d a^m \quad (6)$$

Where K_d is the deactivation constant (cycle^{-1}) and m is the dimensionless parameter of adsorbent deactivation, while t is the independent variable. In this work, the activity was dependent on the number of cycles, which means that the independent variable has dimension of number of cycles, instead of seconds or hours. However, it is

worth reminding that one cycle (heating and cooling) lasts 12 h.

This Equation does not take into account the specific mechanism (sintering, coking, binder phase changes) that cause the deactivation process. The purpose of this Equation is to predict the loss of adsorbent capacity based on two adjustable parameters.

The activity term is then added to the Toth model, as shown in Equation (7):

$$q = a \frac{q_{\max} KP}{(1 + (KP)^n)^{1/n}} \quad (7)$$

The values of the Toth parameters are based on the isotherm of the fresh sample. Regarding the parameters related to adsorbent deactivation, they are estimated based on the minimization of the residual sum of squares of the observed values:

$$\sum_{i=1}^N (a_i - \hat{a}_i)^2 \xrightarrow{K_d, m} \text{Min} \quad (8)$$

Where a_i is the activity term based on the experimental data and \hat{a}_i is the activity term based on the deactivation model.

3. Results and Discussion

3.1 Adsorption Isotherms

Figure 1 shows the adsorption isotherms of CO_2 using the molecular sieve AW500 fresh and deactivated after 5, 14, 24 and 35 cycles.

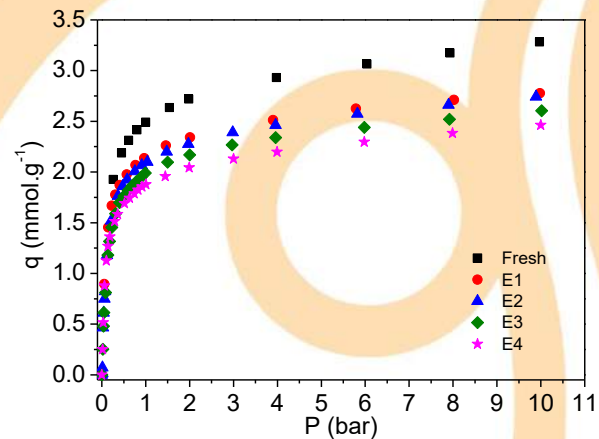


Fig. 1. Adsorption curves of carbon dioxide using AW500 fresh and deactivated at 303 K.

According to Figure 1, the CO₂ adsorption capacity decreased gradually over the cycles as compared to the fresh sample. The adsorbed quantities are similar for samples E1 and E2, and after that, it decreases subtly for the other samples. The loss of adsorption capacity after 35 cycles of heating and cooling (420 h) is around 25%. This result suggests that the laboratory deactivation protocol is able to age adsorbent particles with a relative high deactivation degree.

Langmuir and Toth models were used to fit the equilibrium data regarding the fresh sample. Figure 2 shows the fittings of both models.

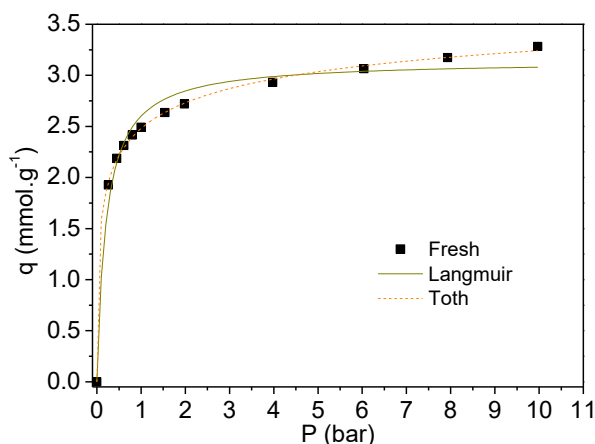


Fig. 2. Adjustment of Langmuir and Toth models to the equilibrium data of CO₂ adsorption.

From Figure 2, it can be observed that both models fit properly the experimental data. However, Toth model presented a better adjustment than the Langmuir model. The best fit of the Toth model is probably due to the heterogeneity of the adsorbent that this model takes into account [11]. The parameters of both models are shown in Table 1.

Table 1. Parameters obtained from Langmuir and Toth models.

Model	Parameters	Values for the fresh sample
Langmuir	q_{\max} (mmol.g ⁻¹)	3.14
	b (bar ⁻¹)	4.79
	R^2	0.98
Toth	q_{\max} (mmol.g ⁻¹)	4.57
	K (bar ⁻¹)	663.38
	n	0.27
	R^2	0.99

According to Table 1, Toth model fits better to the experimental data than Langmuir model does, given the highest value of R^2 . Regarding the parameter related to the heterogeneity of the adsorbent, n , it is observed that this value is lower than 1, indicating that the heterogeneity degree of the adsorbent is not prevailing [12].

After obtained the isotherm parameters for CO₂ adsorption on the fresh molecular sieve, Equations (6) and (8) of the deactivated model were calculated in order to fit the experimental activity curve. This result is shown in Figure 3.

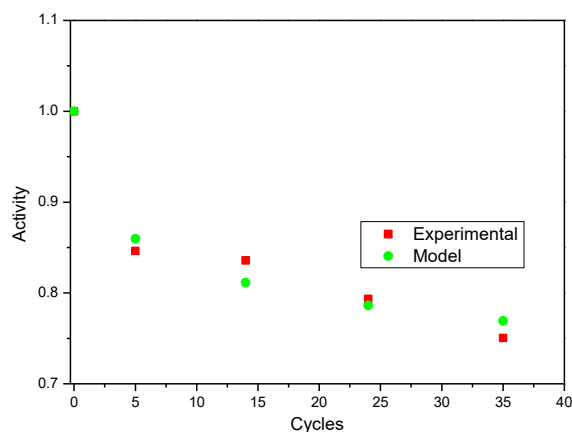


Fig. 3. Adjustment of the deactivation model to the data of activity of the molecular sieve AW500.

From Figure 3, the experimental activity term can be adequately described by the deactivation model, which is corroborated by the highest value of R^2 (0.96). Although this model does not take into account which mechanism is responsible for the deactivation, its Equation is able to predict the values of experimental activity.

The parameters obtained from the fitting of the deactivation model to the experimental data are shown in Table 2.

Table 2. Parameters of deactivation model fits of CO₂ isotherms at 303 K on AW500.

Model	Parameters	Values
Deactivation	K_d (cycle ⁻¹)	0.14
	m	17.85
	R^2	0.96

After obtained the values of activity and the parameters from Toth model, Equation (7) was calculated for the four situations, in which the adsorbent was being deactivated. Figure 4 shows the curves calculated by this Equation.

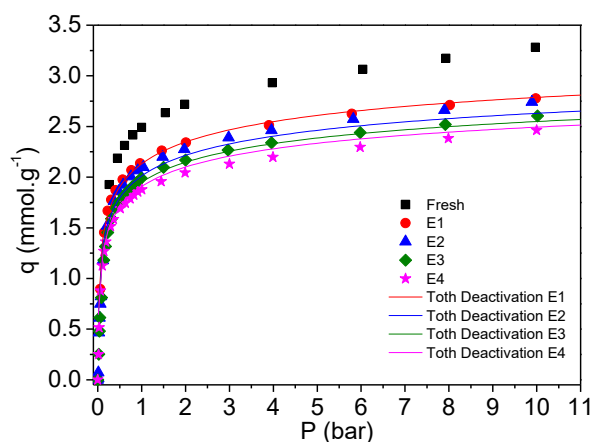


Fig. 4. Adsorption isotherm for CO₂ at 303 K on AW500 fresh and deactivated. Symbols and lines represent experimental data and predictions of the model, respectively.

From Figure 4, it can be observed that the activity term calculated from the deactivation model in combination with Toth model is able to present a reasonable prediction of the adsorption capacity after a certain deactivation degree.

Although the deactivation model can predict the adsorption capacity after several cycles of the described aging protocol, it brings no information about deactivation mechanisms. Among the deactivation types described in the literature, three types are traditionally cited: sintering, coking and poisoning [13, 14]. The occurrence of sintering and poisoning are very often found in catalytic deactivation, however it is difficult to conclude the presence of these types. On the other hand, coking is easily observed by the generation of a carbonaceous material deposited on the surface of the adsorbent [15].

Figure 5 shows the difference in color of the adsorbents after 5, 14, 24 and 35 cycles.



Fig. 5. Visual appearance of the molecular sieve AW500 fresh and deactivated.

According to Figure 5, the color of the fresh adsorbent is between orange and beige. However, after 5 cycles, the color of the adsorbent changed to black, and as the cycles were carried out, the color became even darker. This color change is possibly due to the presence of hydrocarbons in the cycles,

especially the heavier ones. Under specific conditions, like high temperature and presence of water, there may be polymerization and deposition of carbonaceous material, or coke.

4. Conclusions

The results of a simple aging protocol of adsorbents showed that the conditions employed were able to produce samples deactivated to a certain degree. A deactivation model based on an exponential decay was able to reproduce the CO₂ isotherms obtained for increasing degrees of deactivation and therefore, may be used and extended to the prediction of early breakthrough in TSA units.

Acknowledgements

The authors would like to thank FUNCAP and Petrobras for the financial support received for this research.

References

- [1] Berg F, Pasel C, Eckardt T, Bathen D. Temperature Swing Adsorption in Natural Gas Processing: A Concise Overview. *ChemBioEng Rev* 2019; 59–71.
- [2] Kong ZY, Mahmoud A, Liu S, Sunarso J. Revamping existing glycol technologies in natural gas dehydration to improve the purity and absorption efficiency: Available methods and recent developments. *J Nat Gas Sci Eng* 2018; 56:486–503.
- [3] Aleghafouri A, Davoudi M. Modeling and simulation of a pressure–temperature swing adsorption process for dehydration of natural gas. *Adsorption* 2018; 24:121–133.
- [4] Nastaj J, Ambrozek B. Analysis of gas dehydration in TSA system with multi-layered bed of solid adsorbents. *Chem Eng Process Process Intensif* 2015; 96:44–53.
- [5] Ruthven DM. *Principles of Adsorption and Adsorption Processes*, 1st ed. New York: John Wiley & Sons; 1984.
- [6] Sigfried H, Helmut H. Refrigeration Technology. In: *Ulmann's Encycl Ind Chem*. Weinheim: Wiley-VCH Verlag GmbH & Co; 2002. p. 309–337.
- [7] Thomas WJ, Crittenden B. *Adsorption Technology & Design*. Oxford: Elsevier; 1998.
- [8] Santiago RG, Santos BF, Lima IG, Moura KO, Melo DC, Grava WM, Bastos-Neto M, Lucena SMP, Azevedo DCS. Investigation of premature aging of zeolites used in the drying of gas streams. *Chem Eng Commun* 2018; 1–8.
- [9] Rezaei S, Avila AM, Kuznicki SM. Chemisorption of H₂S on Copper-ETS-2: Experiment and Modeling of a Packed Column. *J Nanosci Nanotechnol* 2018; 18:7882–7888.
- [10] Suyadal Y, Erol M, Oğuz H. Deactivation model for the adsorption of trichloroethylene vapor on an

- activated carbon bed. *Ind Eng Chem Res* 2000; 39:724–730.
- [11] Toth J. State equations of the solid gas interface layer. *Acta Chem Acad Hung* 1971; 69:311–317.
- [12] Ayawei N, Ebelegi AN, Wankasi D. Modelling and Interpretation of Adsorption Isotherms. *J Chem* 2017; 1-11.
- [13] Fogler HS. Elements of chemical reaction engineering, 3rd ed. Michigan: LTC; 2002.
- [14] Levenspiel O. Chemical Reaction Engineering, 3rd ed. New York: John Wiley & Sons; 1998.
- [15] Guisnet M, Costa L, Ribeiro FR. Prevention of zeolite deactivation by coking. *J Mol Catal A Chem* 2009; 305:69–83.

Kinetic and equilibrium studies of Ni-OEP adsorption on coconut shell activated carbon

Gabriela Costa Caetano^a, Indianara Conceição Ostroski^{a,*}

^a Federal University of Goiás, Institute of Chemistry, Av. Esperança, s/n, Goiânia, 74690-900, Brazil

Abstract

The recent scenario of exploration of non-conventional oil sources has brought difficulties to its processing, due to the great presence of contaminants and heterocompounds in its constitution, among them petroporphyrins. At the same time that the removal of these compounds from the oil is necessary to avoid damage to the quality of the formed by-products, their recovery is interesting for supplying their application sectors. In this context, adsorption was proposed as an alternative separation process to the commonly used extractive and chromatographic methods. In this work, kinetic and equilibrium data were collected and evaluated for the batch adsorption process of nickel octaethylporphyrin (Ni-OEP) on coconut shell activated carbon (CSAC), in order to obtain information about possible adsorption mechanisms involved. The adsorption equilibrium was reached in a period of time close to 600 min, with an equilibrium adsorption capacity of 6.833 mg.g⁻¹. The best fit model for the kinetic data was the Elovich equation ($R^2 = 0.981$), while the equilibrium data were better adjusted by the Freundlich isothermal model ($R^2 = 0.987$). The fitting results are indicative of the importance of the functionalized surface of CSAC in the establishment of acid-base interactions with porphyrinic molecules, whose physical-chemical properties may have caused the formation of adsorbed multilayers. These less intense interactions may be possible agents which facilitate a later desorption process.

Keywords: Petroporphyrins; Adsorption mechanism; Multiporphyrinic aggregates; Acid-base interactions.

1. Introduction

The processing of heavy oils has been an alternative found by the oil refining sector to deal with the reduced availability of sources of light and medium oils [1]. Heavier oils contain higher concentrations of resins, asphaltenes and metallic compounds, which can alter the physicochemical properties of the oil, causing negative impacts on its processing [2]. Nickel and vanadium stand out among these metallic compounds, being present predominantly in porphyrinic form [3].

Porphyrins belong to a class of organic, aromatic and heterogeneous compounds [4], which have numerous applications in areas related to surface science [5,6] and in mechanisms that involve energy transfer [4,7], in addition to constituting important biomarker components of oil [8].

Despite its numerous applications, the presence of these organometallic compounds in oil is associated with losses both in the processing stages and in the quality of its by-products. Petroporphyrins, as they are known, can cause

changes in the physicochemical properties of the oil [9] and poisoning and deactivating the catalysts used in the catalytic stages of refining [10].

Physical and chemical techniques have been widely used in the separation and isolation of these compounds, especially the extractive [11] and chromatographic methods [12], associated with the high consumption of inputs and limited to the bench scale, respectively.

Thus, adsorption was proposed as an alternative process, mainly due to its operational simplicity [13] and the possibility of recovering the materials used (adsorbent, adsorbate and solvents) [14], among its countless advantages.

Chen *et al.* (2013 and 2017) evaluated the adsorption process of oxovanadium and nickel octaethylporphyrin (VO-OEP and Ni-OEP) on asphaltene [15,16]. While Chen *et al.* (2018) studied the adsorption of the same petroporphyrins on graphene [17].

However, there is a need to evaluate other adsorbent materials, with interesting surface properties, such as activated carbon [18]. New of kinetics and equilibrium studies are essential to

obtain characteristics of the adsorption mechanism, fundamental information for assessing the possibility of a later desorption process [19].

In this work, the process of adsorption of Ni-OEP on coconut shell activated carbon (CSAC) was studied. Adsorption kinetic and equilibrium data were collected in order to obtain information about the characteristics of the possible adsorption mechanism involved in the process.

2. Material and Methods

2.1. Material

Ni-OEP, whose structural formula is shown in Fig. 1, was purchased from Sigma Aldrich. The adsorbent CSAC (*Elaeis guineenses*), used in the form of particles less than 150 µm in diameter, was supplied by the company Bahiacarbon Agro-industrial Ltda (Bahia, Brazil). The solvent used was analytical grade: toluene (99.9%), from Bio-Grade.

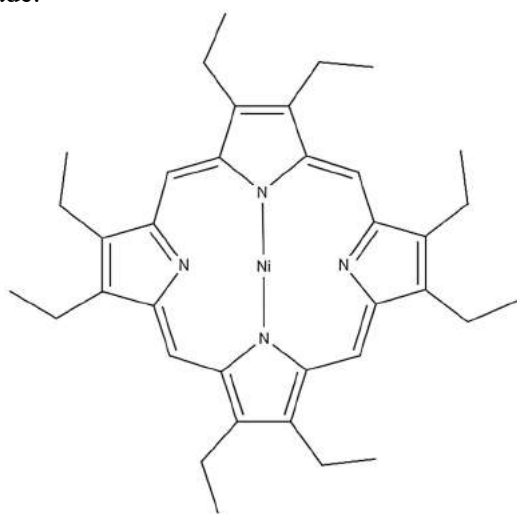


Fig.1. Structure of nickel octaethylporphyrin.

2.2. Methods

Ni-OEP solutions in toluene were subjected to batch adsorption tests to obtain kinetic and equilibrium data. These data were analyzed through fitting to the kinetic and isothermal models present in the literature.

For fitting evaluation, it was necessary to know the adsorption capacities, at time t (q_t) and at equilibrium (q_e), which can be calculated using Equations 1 and 2, respectively.

$$q_t = \frac{(C_0 - C_t)V}{M} \quad (1)$$

where C_0 is the initial concentration of the solution, C_t is the concentration in the time t , V is the solution volume, and M is the adsorbent mass.

$$q_e = \frac{(C_0 - C_e)V}{M} \quad (2)$$

where C_e is the concentration of the solution in equilibrium.

The concentrations of Ni-OEP solutions were analyzed using UV-Vis spectrophotometer (BEL Photonics 1105).

2.3. Adsorption kinetic

For the adsorption kinetics tests, Ni-OEP solutions with an initial concentration of 8 µg.mL⁻¹, volumes of 5 mL and doses of 2.5 mg of adsorbent were used. The systems were subjected to agitation (120 rpm) on rotary shaker, at constant temperature of 293 K, for predefined time intervals between 0 and 1440 min (24 h).

The fittings experimental data to the theoretical kinetic models of pseudo-first order, pseudo-second order, Elovich equation and intraparticle diffusion were evaluated. The integral forms of the models can be represented by Equations 3 to 6, respectively.

$$q_t = q_e(1 - e^{-k_1 t}) \quad (3)$$

where k_1 is a parameter of the equation referring to the adsorption rate (min⁻¹).

$$q_t = \frac{k_2 q_e^2 t}{(1 + k_2 q_e t)} \quad (4)$$

where k_2 is a parameter of the equation referring to the adsorption rate (g.mg⁻¹.min⁻¹).

$$q_t = \frac{\ln(AB)}{B} + \frac{\ln(t)}{B} \quad (5)$$

where A (mg.g⁻¹.min⁻¹) and B (g.mg⁻¹) are the Elovich parameters, referring to the initial adsorption rate and desorption rate, respectively.

$$q_t = k_p t^{0.5} + C \quad (6)$$

where k_p ($\text{mg}\cdot\text{g}^{-1}\cdot\text{min}^{-0.5}$) and C ($\text{mg}\cdot\text{g}^{-1}$) are parameters of the equation, referring to the intraparticle diffusion rate and resistance to diffusion, respectively.

2.4. Adsorption equilibrium

For the adsorption equilibrium tests, Ni-OEP solutions with initial concentration ranging from 1 to 20 $\mu\text{g}\cdot\text{mL}^{-1}$ were used, with the other conditions used similar to those used in the kinetic tests.

The fittings of the equilibrium data to the theoretical isothermal models of Langmuir (Equation 7) and Freundlich (Equation 8) were evaluated.

$$q_e = \frac{q_{\max} K_L C_e}{1 + K_L C_e} \quad (7)$$

where q_{\max} ($\text{mg}\cdot\text{g}^{-1}$) is the maximum adsorption capacity, and K_L ($\text{L}\cdot\text{mg}^{-1}$) is a Langmuir constant.

$$q_e = K_F C_e^n \quad (8)$$

where K_F and n are Freundlich parameters.

3. Results and discussion

3.1. Kinetic study

The experimental kinetic data and the fitting curves to the theoretical models were plotted on the graph shown in Fig. 2.

The kinetics of Ni-OEP adsorption on CSAC is characterized by a region of high initial adsorption rate ($0 < t < 200$ min), due to the greater amount of active sites available on the surface of the adsorbent material. As the sites were occupied by the porphyrin molecules, the kinetics became slower ($200 < t < 600$ min), until the equilibrium was established ($t > 600$ min), with no significant differences in q_t over time t . The value of q_e obtained was close to $6.833 \text{ mg}\cdot\text{g}^{-1}$.

At 293 K, lower q_e values were obtained for the use of asphaltene ($4.836 \text{ mg}\cdot\text{g}^{-1}$) [16] and graphene ($5.725 \text{ mg}\cdot\text{g}^{-1}$) [17], as an adsorbent material for Ni-OEP adsorption.

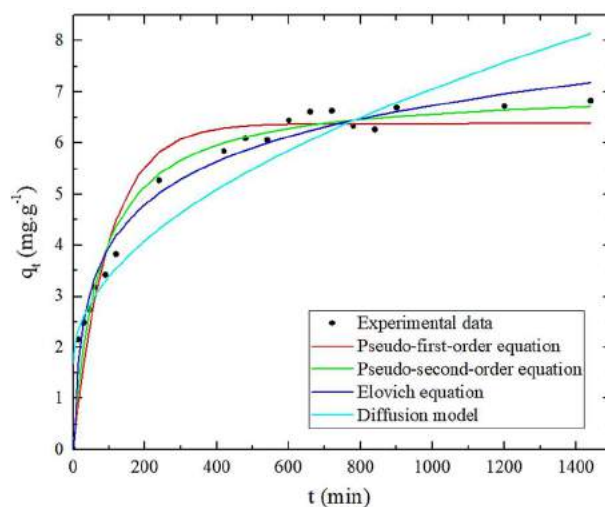


Fig. 2. Fitting of the experimental data to theoretical kinetic models.

The fitting quality of the experimental data to the kinetic models was evaluated through the analysis of the determination coefficients (R^2) calculated, presented in Table 1.

Table 1. Parameters obtained with the fitting experimental data to theoretical kinetic models.

Pseudo-first-order model		
$q_{e, \text{mod}} (\text{mg}\cdot\text{g}^{-1})$	$k_1 (\text{min}^{-1})$	R^2
6.380 ± 0.153	$(1.020 \pm 0.117) \cdot 10^{-2}$	0.939
Pseudo-second-order model		
$q_{e, \text{mod}} (\text{mg}\cdot\text{g}^{-1})$	$k_2 (\text{g}\cdot\text{mg}^{-1}\cdot\text{min}^{-1})$	R^2
7.054 ± 0.153	$(1.930 \pm 0.245) \cdot 10^{-3}$	0.972
Elovich equation		
$A (\text{mg}\cdot\text{g}^{-1}\cdot\text{min}^{-1})$	$B (\text{g}\cdot\text{mg}^{-1})$	R^2
0.325 ± 0.048	0.830 ± 0.034	0.981
Intraparticle diffusion model		
$C (\text{mg}\cdot\text{g}^{-1})$	$k_p (\text{mg}\cdot\text{g}^{-1}\cdot\text{min}^{-0.5})$	R^2
1.687 ± 0.324	0.170 ± 0.015	0.881

The Elovich equation ($R^2 = 0.981$) was the most adequate model in the kinetic data fitting, giving evidence that the heterogeneous surface of the CSAC was relevant in the adsorption process. The diversity of functional groups present on its surface [20] were decisive in the establishment of the adsorption mechanism, characterized by the formation of interactions at different energy levels.

As a parameter of the Elovich equation, it was obtained an adsorption rate value (A) close to

0.325 mg.g⁻¹.min⁻¹, lower than which obtained for the use of graphene (7.263 mg.g⁻¹.min⁻¹) [17], indicating that the equilibrium was established more quickly with the use of graphene. However, as the desorption rate (*B*) obtained for the use of CSAC (0.830 g.mg⁻¹) was also lower than which obtained for graphene (1.426 g.mg⁻¹) [17], a value of *q_e* higher was obtained for the use of the activated carbon.

3.2. Adsorption equilibrium

The experimental equilibrium data and the fitting curves to the theoretical isothermal models were plotted on the graph shown in Fig. 3; while the fitting parameters and determination coefficients are shown in Table 2.

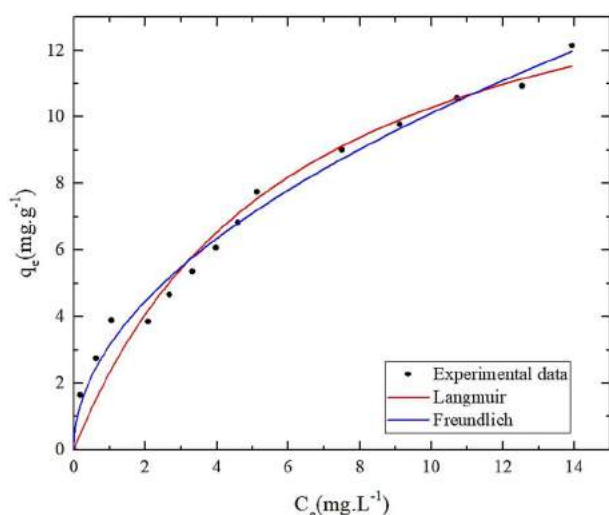


Fig. 3. Fitting of the experimental data to theoretical equilibrium models.

Table 2. Parameters obtained with the fitting of experimental data to theoretical isothermal models.

Langmuir model		
<i>q_{max}</i> (mg.g ⁻¹)	<i>K_L</i> (min ⁻¹)	<i>R</i> ²
16.638 ± 1.429	0.162 ± 0.030	0.964
Freundlich model		
<i>n</i>	<i>K_F</i>	<i>R</i> ²
0.508 ± 0.023	3.142 ± 0.154	0.987

The best fit model was the Freundlich isotherm (*R*² = 0.987), which describes adsorptive processes that occur on non-ideal and heterogeneous adsorbent surfaces [21,22], with the possible

formation of multilayers [23]. The presence of different functional groups on the surface of the CSAC and of basic (presence of basic nitrogen) and acidic (metallic center) regions in the Ni-OEP molecule [6] may have induced the formation of acid-base interactions, with different interaction energies. The tendency of metalloporphyrins to form multiporphyrinic aggregates may have contributed to the formation of adsorbate multilayers, interactions with characteristics of physisorption.

As parameters of the Freundlich model, it was obtained *n*, related to the level of favorability of the adsorption process and intensity of the interactions formed [24], close to 0.508, and *K_F*, related to the affinity of the adsorbate by the adsorbent surface [25], close to 3.142. Since (*1/n*)_{CSAC} is greater than (*1/n*)_{asphaltene} (0.769) [16], it is possible that Ni-OEP molecules have a higher intensity of adsorption on the surface of the activated carbon used, in relation to asphaltene. *K_{F,CSAC}* value is also superior to *K_{F,asphaltene}* value (0.465) [16], being possible that the affinity of Ni-OEP molecules is greater for the CSAC surface, when compared to asphaltene, and, consequently, the adsorption capacity in the equilibrium of the first material higher than the second.

The Langmuir isothermal model was also adequate (*R*² = 0.964) to describe the behavior of the equilibrium data, it is possible to discuss the parameters obtained. The *q_{max,CSAC}* value was lower than which obtained for the use of asphaltene (*q_{max,asphaltene}* = 20.000 mg.g⁻¹) [16], but higher than which obtained for the use of graphene (*q_{max,graphene}* = 10.386 mg.g⁻¹) [17]. This results indicate that the use of more functionalized surfaces can be more efficient in removing the metalloporphyrins present in solution by adsorption.

4. Conclusion

The fittings of the experimental data to the theoretical kinetic and isothermal models were essential for the proposition of an adsorption mechanism compatible with the process. The Elovich model was the best fit model for the kinetic data, while the Freundlich's was the best fit model for the equilibrium data obtained.

The fitting results obtained indicate that the functionalized surface of the CSAC was relevant for

the establishment of the adsorbent-adsorbent interactions, which can be of the acid-base type. Since multilayer formation is possible during the adsorption process, due to the physical-chemical properties of porphyrins, the presence of less intense interactions is probable, making the subsequent desorption process viable. With the recovery of both adsorbent material and adsorbate, adsorption is approaching an economically viable and more environmentally correct process, and the recovered porphyrins can be used as alternatives to their synthetic analogues.

Acknowledgements

This study was financed by the Coordenação de Aperfeiçoamento de Pessoal de Nível Superior – Brasil (CAPES) – Finance Code 001. The authors would like to acknowledge CAPES, for financial support, and Bahiacarbon Agro-industrial (Bahia, Brazil), for the samples of activated carbon that were kindly granted.

References

- [1] Mironov NA *et al.* Methods for Studying Petroleum Porphyrins. *Petroleum Chemistry*, v. 59, n. 10, p. 1077-1091, 2019.
- [2] Munoz G *et al.* Redox activity of nickel and vanadium porphyrins: a possible mechanism behind petroleum genesis and maturation?. *RSC advances*, v. 9, n. 17, p. 9509-9516, 2019.
- [3] Rytting BM *et al.* High-Purity Vanadyl Porphyrins: Their Aggregation and Effect on the Aggregation of Asphaltenes. *Energy & Fuels*, v. 34, n. 1, p. 164-178, 2019.
- [4] Gottfried JM. Surface chemistry of porphyrins and phthalocyanines. *Surface Science Reports*, v. 70, n. 3, p. 259-379, 2015.
- [5] Kuzmin SM, Chulovskaya SA, Parfenyuk VI. Structures and properties of porphyrin-based film materials part I. The films obtained via vapor-assisted methods. *Advances in Colloid and Interface Science*, v. 253, p. 23-34, 2018.
- [6] Lee H, Hong K, Jang W. Design and applications of molecular probes containing porphyrin derivatives. *Coordination Chemistry Reviews*, v. 354, p. 46-73, 2017.
- [7] Jurow M *et al.* Porphyrins as molecular electronic components of functional devices. *Coordination Chemistry Reviews*, v. 254, n. 19-20, p. 2297-2310, 2010.
- [8] Moustafa YM, Morsi RE. Biomarkers. In: *Chromatography and Its Applications*. IntechOpen, 2012.
- [9] Silva HS *et al.* The role of metalloporphyrins on the physical-chemical properties of petroleum fluids. *Fuel*, v. 188, p. 374-381, 2017.
- [10] Etim UJ *et al.* Vanadium and nickel deposition on FCC catalyst: Influence of residual catalyst acidity on catalytic products. *Microporous and Mesoporous Materials*, v. 273, p. 276-285, 2019.
- [11] Kurbanova AN *et al.* Removal of nickel and vanadium from crude oil by using solvent extraction and electrochemical process. *Physical Sciences and Technology*, v. 4, n. 1, p. 74-80, 2018.
- [12] Mironov NA *et al.* Chromatographic isolation of vanadyl porphyrins from heavy oil resins. *Russian Chemical Bulletin*, v. 66, n. 8, p. 1450-1455, 2017.
- [13] Bhatnagar A, Sillanpää M. A review of emerging adsorbents for nitrate removal from water. *Chemical Engineering Journal*, v. 168, n. 2, p. 493-504, 2011.
- [14] Banerjee M, Basu RK, Das SK. Cr (VI) adsorption by a green adsorbent walnut shell: adsorption studies, regeneration studies, scale-up design and economic feasibility. *Process Safety and Environmental Protection*, v. 116, p. 693-702, 2018.
- [15] Chen F *et al.* Adsorption kinetics and thermodynamics of vanadyl etioporphyrin on asphaltene in pentane. *Energy & Fuels*, v. 27, n. 11, p. 6408-6418, 2013.
- [16] Chen F *et al.* Metal porphyrin adsorption onto asphaltene in pentane solution: a comparison between vanadyl and nickel etioporphyrins. *Energy & Fuels*, v. 31, n. 4, p. 3592-3601, 2017.
- [17] Chen F *et al.* The function of poly aromatic nuclei structure for adsorption of vanadyl/nickel etioporphyrin on asphaltene/graphene. *Fuel Processing Technology*, v. 174, p. 132-141, 2018.
- [18] Pallarés J, González-Cencerrado A, Arauzo I. Production and characterization of activated carbon from barley straw by physical activation with carbon dioxide and steam. *Biomass and Bioenergy*, v. 115, p. 64-73, 2018.
- [19] Prado GHC, Rao Y, De Klerk A. Nitrogen removal from oil: a review. *Energy & Fuels*, v. 31, n. 1, p. 14-36, 2016.
- [20] Ferreira MEO *et al.* Modified activated carbon as a promising adsorbent for quinoline removal. *Microporous and Mesoporous Materials*, v. 277, p. 208-216, 2019.
- [21] Freundlich HMF *et al.* Over the adsorption in solution. *J. Phys. Chem*, v. 57, n. 385471, p. 1100-1107, 1906.
- [22] Ho YS, Porter JF, McKay G. Equilibrium isotherm studies for the sorption of divalent metal ions onto peat: copper, nickel and lead single component systems. *Water, Air, and Soil Pollution*, v. 141, n. 1-4, p. 1-33, 2002.
- [23] Wen J *et al.* A critical study on the adsorption of heterocyclic sulfur and nitrogen compounds by activated carbon: equilibrium, kinetics and thermodynamics. *Chemical Engineering Journal*, v. 164, n. 1, p. 29-36, 2010.
- [24] Wu C. Adsorption of reactive dye onto carbon nanotubes: equilibrium, kinetics and thermodynamics. *Journal of Hazardous Materials*, v. 144, n. 1-2, p. 93-100, 2007.
- [25] Kano F *et al.* Fractal model for adsorption on activated carbon surfaces: Langmuir and Freundlich adsorption. *Surface Science*, v. 467, n. 1-3, p. 131-138, 2000.

Experimental design and optimization of Ni-OEP adsorption and desorption processes on coconut shell activated carbon

Gabriela Costa Caetano^a, Laiane Alves de Andrade^a, Indianara Conceição Ostroski^{a,*}

^a Federal University of Goiás, Institute of Chemistry, Av. Esperança, s/n, Goiânia, 74690-900, Brazil

Abstract

The reduction of light and medium oil reserves has led to the search for potentially exploitable regions, whose study and identification can be facilitated by analyzing the distribution of biomarkers. Petroporphyrins are examples of this type of compound, whose oil removal is interesting, due to the damage caused mainly to the catalytic stages of refining. Therefore, adsorption can be studied as an alternative process to the extractive and reactive methods currently employed. For the analysis of adsorption and desorption of nickel octaethylporphyrin (Ni-OEP) on coconut shell activated carbon (CSAC), experimental designs were used, followed by an optimization process, in order to select the variables solvent, temperature, and solid/liquid ratio, of adsorption and desorption, which maximize the response variables adsorption capacity (q_e) and percentage of desorption ($\%_{desorption}$). The solvent and diluent associated with the highest values of the evaluation variables were toluene and chloroform, respectively. The change in adsorption temperature did not cause significant changes in q_e , while all quantitative variables were significant in the results of $\%_{desorption}$. The optimum conditions obtained were compatible with the response surfaces constructed for q_e and $\%_{desorption}$ and they were validated through new adsorption and desorption procedures, with results of adsorption capacity close to 7.12 mg.g⁻¹ and a desorption percentage of 37.7%, and errors below 7%.

Keywords: Petroporphyrins; Biomarkers; Adsorption separation; Multiobjective problem optimization.

1. Introduction

The depletion of traditional sources of oil has made the exploration and processing of heavy oils a challenging reality for the refining sector [1]. Due to the difficulties associated with the processing of unconventional oils, the identification of regions potentially producing high-quality oils can be an interesting alternative. In this evaluative study, the distribution of biomarkers is an important factor to be considered [2].

Among these compounds, which act as “molecular fossils”, stand out the porphyrins, tetrapyrrolic, aromatic, heterogeneous molecules [3], commonly found in the most polar fractions of oil: resins and asphaltenes [4]. Identified as components of oils and shales, by Treibs, in 1934 [5], the most abundant petroporphyrins are distributed in ethioporphyrins (ETIO), deoxophylloerythroetioporphyryns (DPEP) and rhodoporphyrins (RHODO) [6]; being the most common metalloporphyrins the nickel and oxovanadium porphyrins [7].

Despite being in the form of trace elements [8], porphyrins can cause adverse and complicated situations in refineries by causing changes in the physicochemical properties of the oil [9,10], promoting corrosion in pipes [11] and poisoning the catalysts [12], being possible the contamination of derivative products [13].

Currently, it is common to use physical methods, with a predominance of the extractives [14], and chemical methods, with emphasis on demetallization [15] and hydrogenation of the tetrapyrroles [16], in order to reduce the impacts caused by the presence of porphyrins in oil. However, these techniques are associated with high solvent and reagent consumption [17], severe operating conditions, and the possibility of altering the structural information of the porphyrin molecule [18].

Adsorption can be seen as an alternative process to those commonly used [19], due to its advantages such as operational simplicity [20], with the application of milder conditions, and the possibility of regenerating the adsorbent and adsorbate [21], considering that it can be an economically viable method [22] and more environmentally friendly



[23]. This method has already been the subject of study for the removal of petroporphyrins using asphaltene and graphene as adsorbents [24-26]. However, new process conditions and adsorbent materials must be studied, aiming at a continuous improvement of the performance of the separation and recovery processes of these porphyrinic compounds.

In this context, this work aims to contemplate the adsorption and desorption studies of nickel octaethylporphyrin (Ni-OEP) on coconut shell activated carbon (CSAC). The conditions of solvent, diluent, temperature, and solid/liquid ratio, which maximize the performance of these processes, evaluated by the variables: adsorption capacity in equilibrium (q_e) and percentage of desorption ($\%_{desorption}$), were analyzed.

2. Material and Methods

2.1. Material

Ni-OEP was purchase from Sigma Adrich. Granular CSAC (*Elaies guineenses*), supplied by Bahiacarbon Agro-industrial Ltda. (Bahia, Brazil), was used in the form of particles less than 150 μm in diameter. Solvents used were analytical grade: toluene (99.9%) from Bio-Grade, chloroform (99.8%) from Isofar, and dichloromethane (99.9%) from TEDIA High Purity Solvents.

2.2. Methods

The evaluation of the effects of the conditions of solvent, diluent, temperature, and solid/liquid ratio on the performance of the adsorption and desorption batch processes was carried out through qualitative and quantitative experimental designs. The experiments were maintained under agitation (120 rpm) on a rotary shaker for 24 h. Ni-OEP solutions with initial concentration of 8 $\text{mg}\cdot\text{L}^{-1}$ were used in the adsorption procedures. The other conditions were varied according to the objectives of the experimental designs.

The evaluation variables, q_e and $\%_{desorption}$, can be calculated using the Equations 1 and 2, respectively:

$$q_e = \frac{(C_0 - C_e)V}{M} \quad (1)$$

where C_0 is the initial concentration of the solution, C_e is the concentration of the solution in the equilibrium, V is the solution volume, and M is the adsorbent mass.

$$\%_{desorption} = \frac{q_{e,des}}{q_e} \times 100 \quad (2)$$

with

$$q_{e,des} = \frac{C_d V_{dil}}{M_s} \quad (3)$$

where C_d is the concentration of the solution at the end of the desorption, V_{dil} is the diluent volume, and M_s is the mass of saturated adsorbent.

Ni-OEP concentrations in different solvents and temperatures were determined using UV-Vis spectrophotometer (BEL Photonics 1105).

The consistency of the regression equations obtained was verified through the analysis of the statistical parameters and deviations associated. These equations were used in the subsequent optimization process.

2.3. Experimental designs

The evaluation of the effects of qualitative variables, solvent and diluent, on the performance of the adsorption and desorption processes, respectively, was performed using a qualitative experimental design 2². The levels of the selected qualitative variables are shown in Table 1.

Table 1. Levels of the factors used in the study of the effect of the solvent on the adsorption and desorption of Ni-OEP in CSAC using a qualitative experimental design.

Factor	Level	
	1	2
Solvent	Toluene	Chloroform
Diluent	Chloroform	Dichloromethane

The evaluation of the effects of the quantitative variables, temperature and solid/liquid ratio, on the results of the response variables was performed using central composite orthogonal designs (CCOD).

Two quantitative experimental designs were elaborated: one to evaluate the effects of the conditions of temperature (T_{ads}) and solid/liquid

ratio $((S/L)_{ads})$ of adsorption, in the adsorption capacity of CSAC, q_e ; and the second to evaluate the effects of the conditions temperature of adsorption (T_{ads}) and desorption (T_{des}) and solid/liquid ratio of adsorption $((S/L)_{ads})$ and desorption $((S/L)_{des})$ on the desorption percentage, $\%_{desorption}$.

The levels selected for the study variables in both designs are shown in Tables 2 and 3.

Table 2. Levels of the factors used in the study of the effect of the adsorption temperature and solid/liquid ratio on the adsorption of Ni-OEP in CSAC, using a CCOD 2.1.10 ($\alpha = 1.078$).

Factor	Code	Level				
		- α	-1	0	+1	+ α
T_{ads} (K)	x_1	294	295	313	331	332
$(S/L)_{ads}$ ($mg.mL^{-1}$)	x_2	0.50	0.55	1.25	1.95	2.00

Table 3. Levels of the factors used in the study of the effect of the adsorption and desorption temperature and solid/liquid ratio on the desorption of Ni-OEP in CSAC, using a CCOD 4.1.26 ($\alpha = 1.483$).

Factor	Code	Level				
		- α	-1	0	+1	+ α
T_{ads} (K)	x_1	294	300	313	326	332
$(S/L)_{ads}$ ($mg.mL^{-1}$)	x_2	0.50	0.75	1.25	1.75	2.00
T_{des} (K)	x_3	293	298	308	318	323
$(S/L)_{des}$ ($mg.mL^{-1}$)	x_4	0.20	0.25	0.35	0.45	0.50

2.4. Optimization

For the selection of the conditions of $T_{ads/des}$ and $(S/L)_{ads/des}$ which maximize q_e and $\%_{desorption}$ simultaneously, the regression equations, obtained with the quantitative experimental designs, were used in combination with the Evolution Differential algorithm (PRICE; STORN, 1995), in an optimization code available in software Matlab 20. In this, the weighted sum method was used (MARLER; ARORA, 2010), in order to obtain a single solution point for a multiobjective problem. Weights were applied to the response variables in order to obtain results consistent with the behavior of the response surfaces plotted for q_e and $\%_{desorption}$. The resulting conditions were validated through adsorption and desorption procedures.

3. Results and discussion

3.1. Qualitative experimental design

The results of the qualitative experimental design are shown in Table 4.

Table 4. Qualitative design matrix and respective results of q_e , in $mg.g^{-1}$, and $\%_{desorption}$, in %, for each applied condition.

Solvent	Diluent	q_e ($mg.g^{-1}$)	$\%_{desorption}$ (%)
1	1	5.36 ± 0.06	31.5 ± 0.8
2	1	5.07 ± 0.06	15.4 ± 0.7
1	2	5.38 ± 0.05	9.9 ± 0.1
2	2	5.11 ± 0.05	8.6 ± 0.4

By analyzing the data presented in Table 4, it is possible to infer that the higher adsorption capacities are associated with the use of toluene as solvent, probably due to the greater solubility of Ni-OEP in chloroform. This inverse relationship between the adsorbate solubility and the extension of the adsorption capacity was observed in the study of the adsorption of aromatic compounds on activated carbon [27].

Although Ni-OEP has a greater solubility coefficient in dichloromethane, the use of chloroform as a diluent provided the highest desorption percentages.

Thus, toluene and chloroform were used, respectively as solvent and diluent, in subsequent procedures, due to their superior performance.

3.2. Quantitative experimental designs

The results of q_e obtained through CCOD 2.1.10 are shown in Table 5.

Table 5. CCOD 2.1.10 matrix and experimental results of q_e , in $mg.g^{-1}$, for each condition.

x_1	x_2	q_e ($mg.g^{-1}$)
-1	-1	6.99 ± 0.07
+1	-1	6.34 ± 0.07
-1	+1	3.60 ± 0.01
+1	+1	3.47 ± 0.02
-1.078	0	4.68 ± 0.05
+1.078	0	4.67 ± 0.03
0	-1.078	6.31 ± 0.07
0	+1.078	3.56 ± 0.01
0	0	4.99 ± 0.03
0	0	4.88 ± 0.02

The parameters obtained from the analysis of variance (ANOVA) of the linear, quadratic and two-way interaction effects of the independent variables, on the dependent variable q_e , are shown in Table 6.

Table 6. ANOVA for CCOD 2.1.10.

Factor	SS ¹	df ²	MS ³	F ⁴	p ⁵
x_1	0.10	1	0.10	1.32	0.32
x_1^2	0.00	1	0.00	0.01	0.94
x_2	13.45	1	13.45	180.59	0.00*
x_2^2	0.12	1	0.12	1.63	0.27
$x_1.x_2$	0.07	1	0.07	0.91	0.39
Error	0.30	4	0.07		
Total	14.04	9			

¹Sum of Squares; ²degrees of freedom; ³Mean of Squares
⁴F-value; ⁵p-value. *p-value < 0.10

At the 90% significance level, analyzing the F and p-values, it was found that only the variable $(S/L)_{ads}$, represented by x_2 , in linear form, had significant effect on the response variable q_e , within the range of conditions selected. It was observed that the lowest adsorption solid/liquid ratios are associated with the higher adsorption capacities of the material, a result similar to that of analogous works [24-26]. The regression equation of q_e as a function of the significant variables was summarized in Equation 4, with R^2 close to 0.953.

The results of CCOD 4.1.26 are shown in Table 7.

Table 7. CCOD 4.1.26 matrix and experimental results of %_{desorption}, in %, for each condition.

x_1	x_2	x_3	x_4	% _{desorption} (%)
-1	-1	-1	-1	20.6 ± 0.5
+1	-1	-1	-1	22.2 ± 1.6
-1	+1	-1	-1	17.4 ± 1.4
+1	+1	-1	-1	23.0 ± 1.4
-1	-1	+1	-1	27.5 ± 0.6
+1	-1	+1	-1	26.8 ± 0.4
-1	+1	+1	-1	30.3 ± 0.9
+1	+1	+1	-1	36.3 ± 2.5
-1	-1	-1	+1	15.3 ± 0.7
+1	-1	-1	+1	15.7 ± 0.5
-1	+1	-1	+1	14.8 ± 1.5
+1	+1	-1	+1	14.9 ± 0.7
-1	-1	+1	+1	23.9 ± 0.3
+1	-1	+1	+1	24.1 ± 0.3
-1	+1	+1	+1	27.7 ± 0.6
+1	+1	+1	+1	29.6 ± 0.5
-1.483	0	0	0	22.2 ± 0.5
+1.483	0	0	0	22.5 ± 1.7
0	-1.483	0	0	25.3 ± 0.7
0	+1.483	0	0	22.1 ± 0.8
0	0	-1.483	0	10.4 ± 1.1
0	0	+1.483	0	28.5 ± 1.0
0	0	0	-1.483	28.2 ± 1.4
0	0	0	+1.483	15.2 ± 0.7
0	0	0	0	16.1 ± 0.6
0	0	0	0	17.3 ± 0.2

$$q_e = 4.95 - 1.46x_2 \quad (4)$$

The statistical parameters resulting from ANOVA for the effects of interactions between independent variables, on the result of %_{desorption}, are shown in Table 8.

Table 8. ANOVA for CCOD 4.1.26.

Factor	SS ¹	df ²	MS ³	F ⁴	p ⁵
x_1	11.81	1	11.81	2.35	0.15
x_1^2	22.75	1	22.75	4.53	0.06*
x_2	8.36	1	8.360	1.67	0.22
x_2^2	45.73	1	45.73	9.11	0.01*
x_3	583.68	1	583.68	116.31	0.00*
x_3^2	0.54	1	0.54	0.11	0.75
x_4	161.37	1	161.37	32.16	0.00*
x_4^2	14.91	1	14.91	2.97	0.11
$x_1.x_2$	9.17	1	9.17	1.83	0.20
$x_1.x_3$	0.01	1	0.01	0.00	0.97
$x_1.x_4$	5.97	1	5.97	1.19	0.30
$x_2.x_3$	40.15	1	40.15	8.00	0.02*
$x_2.x_4$	0.23	1	0.23	0.05	0.83
$x_3.x_4$	3.10	1	3.10	0.62	0.45
Error	55.20	11	5.02		
Total	962.98	25			

¹Regression coefficient; ²Sum of Squares; ³Degrees of freedom; ⁴F-value; ⁵p-value. *p-value < 0.10

At the 90% significance level, analyzing the F and p-values, it was found that the factors T_{ads} and $(S/L)_{ads}$, in the quadratic form, T_{des} and $(S/L)_{des}$, in the linear form, and the interaction between $(S/L)_{ads}$ and T_{des} had significant effects on the response variable %_{desorption}, within the pre-established conditions.

The statistical parameters allow us to infer that the desorption variables (T_{des} and $(S/L)_{des}$) are more significant in the performance of the desorption process than those related to adsorption (T_{ads} and $(S/L)_{ads}$). It was obtained that the lowest desorption solid/liquid ratios and the highest desorption temperatures favor the highest %_{desorption} values. The regression equation of %_{desorption} as a function of the significant variables was summarized in Equation 5, with R^2 close to 0.871.

$$\begin{aligned} \%_{desorption} = & 18.4 + 1.5x_1^2 + 2.2x_2^2 + \\ & + 5.4x_3 - 2.8x_4 + 1.6x_2x_3 \end{aligned} \quad (5)$$

The values of the determination coefficients (R^2) close to 1 and the low deviations associated with the regression coefficients indicate the quality of the regression equations (4 and 5) in the adjustment of the experimental data of q_e and %_{desorption}.

3.3. Optimization

Considering the pre-selected conditions for the independent T_{ads} study variables, it was obtained that the lowest T_{ads} (293 K), the lowest $(S/L)_{ads}$ (0.5 mg.mL^{-1}), the highest T_{des} (323 K) and the lowest $(S/L)_{des}$ (0.2 mg.mL^{-1}) maximize the values of q_e and $\%_{desorption}$. These optimal values of the dependent variables are shown in Table 9, in which they are compared with the experimental results of the validation processes.

The optimum conditions obtained are compatible with the behavior of the surfaces built for the variables q_e and $\%_{desorption}$, as a function of the independent variables considered, illustrated in Fig. 1 to 3.

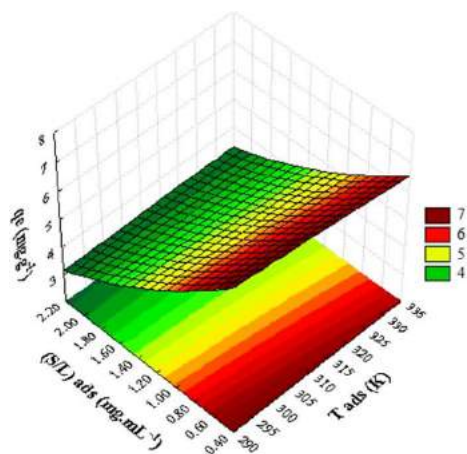


Fig. 1. Response surface obtained for q_e (mg.g^{-1}), as a function of the adsorption variables, T_{ads} (K) and $(S/L)_{ads}$ (mg.mL^{-1}), within the pre-established conditions.

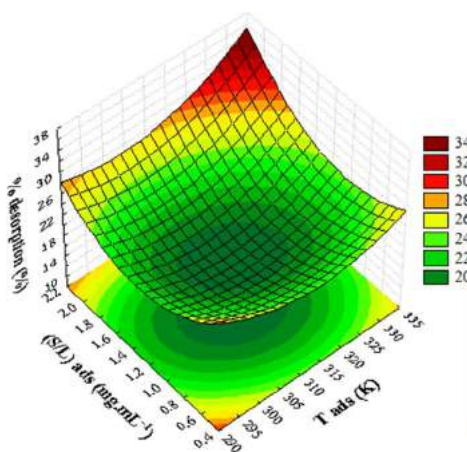


Fig. 2. Response surface obtained for $\%_{desorption}$ (%), as a function of the adsorption variables, T_{ads} (K)

and $(S/L)_{ads}$ (mg.mL^{-1}), within the pre-established conditions.

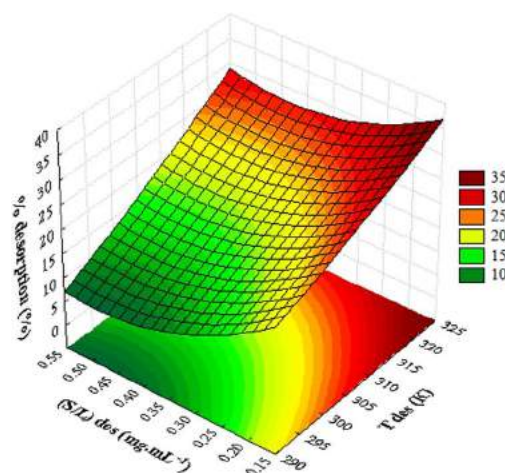


Fig. 3. Response surface obtained for $\%_{desorption}$ (%), as a function of the desorption variables, T_{des} (K) and $(S/L)_{des}$ (mg.mL^{-1}), within the pre-established conditions.

Table 9. Comparison between predicted and experimental values of q_e (mg.g^{-1}) e $\%_{desorption}$ (%), resulting of optimization process validation.

Variable	Predicted	Experimental	Error (%)
q_e (mg.g^{-1})	6.91	7.12 ± 0.07	3.1
$\%_{desorption}$ (%)	35.2	37.7 ± 1.4	6.9

The experimental results are close to the values predicted by the conditions obtained using the optimization process, with a maximum deviation of 7%, approximately. Thus, the adequacy of the regression equations in the optimization process of the evaluation variables is verified.

It was found that the experimental conditions employed in this work provided results of equilibrium adsorption capacity higher than those obtained with the conditions selected by Chen *et al.* (2017 and 2018), which obtained 4.836 mg.g^{-1} for the adsorption of Ni-OEP on asphaltene [25] and 5.725 mg.g^{-1} for the adsorption of the same porphyrin on graphene [26], respectively.

4. Conclusion

The experimental designs and optimization process revealed that the use of toluene as solvent,

chloroform as diluent, lowest T_{ads} , lowest $(S/L)_{ads}$, highest T_{des} , and lowest $(S/L)_{des}$, within the range of pre-established conditions, favor the highest values of q_e and $\%_{desorption}$.

The regression equations obtained and the results of the optimization process are adequate to the behaviors of the experimental data of the adsorption and desorption processes of Ni-OEP in CSAC.

Acknowledgements

This study was financed by the Coordenação de Aperfeiçoamento de Pessoal de Nível Superior – Brasil (CAPES) – Finance Code 001. The authors would like to acknowledge CAPES, for financial support, and Bahiacarbon Agro-industrial (Bahia, Brazil), for the samples of activated carbon that were kindly granted.

References

- [1] Demirbas A, Bafail A, Nizami A. Heavy oil upgrading: Unlocking the future fuel supply. *Petroleum Science and Technology*, v. 34, n. 4, p. 303-308, 2016.
- [2] Affouri H, Sahraoui O. The sedimentary organic matter from a Lake Ichkeul core (far northern Tunisia): Rock-Eval and biomarker approach. *Journal of African Earth Sciences*, v. 129, p. 248-259, 2017.
- [3] Gottfried JM. Surface chemistry of porphyrins and phthalocyanines. *Surface Science Reports*, v. 70, n. 3, p. 259-379, 2015.
- [4] Mousavi M *et al.* Preferential adsorption of nickel porphyrin to resin to increase asphaltene precipitation. *Fuel*, v. 236, p. 468-479, 2019.
- [5] Treibs A. Chlorophyll- und Hämin-derivate in bituminösen Gesteinen, Erdölen, Erdwachsen und Asphalten. Ein Beitrag zur Entstehung des Erdöls. *Justus Liebigs Annalen der Chemie*, v. 510, n. 1, p. 42-62, 1934.
- [6] Dechaine GP, Gray MR. Chemistry and association of vanadium compounds in heavy oil and bitumen, and implications for their selective removal. *Energy & Fuels*, v. 24, n. 5, p. 2795-2808, 2010.
- [7] Rytting BM *et al.* High-Purity Vanadyl Porphyrins: Their Aggregation and Effect on the Aggregation of Asphaltenes. *Energy & Fuels*, v. 34, n. 1, p. 164-178, 2019.
- [8] Sugiyama I, Williams-Jones AE. An approach to determining nickel, vanadium and other metal concentrations in crude oil. *Analytica Chimica Acta*, v. 1002, p. 18-25, 2018.
- [9] Silva HS *et al.* The role of metalloporphyrins on the physical-chemical properties of petroleum fluids. *Fuel*, v. 188, p. 374-381, 2017.
- [10] Munoz G. *et al.* Redox activity of nickel and vanadium porphyrins: a possible mechanism behind petroleum genesis and maturation?. *RSC advances*, v. 9, n. 17, p. 9509-9516, 2019.
- [11] Wang B *et al.* Investigation of corrosion and fouling in syngas cooler tubes. *Fuel Processing Technology*, v. 141, p. 202-209, 2016.
- [12] Etim UJ *et al.* Vanadium and nickel deposition on FCC catalyst: Influence of residual catalyst acidity on catalytic products. *Microporous and Mesoporous Materials*, v. 273, p. 276-285, 2019.
- [13] Sorokina TP *et al.* Conversion of nickel and vanadium porphyrins under catalytic cracking conditions. *Petroleum Chemistry*, v. 50, n. 1, p. 51-55, 2010.
- [14] Kurbanova AN *et al.* Removal of nickel and vanadium from crude oil by using solvent extraction and electrochemical process. *Physical Sciences and Technology*, v. 4, n. 1, p. 74-80, 2018.
- [15] Ramirez S. *et al.* Non-catalytic hydrodesulfurization and hydrodemetallization of residua. *Fuel*, v. 90, n. 12, p. 3571-3576, 2011.
- [16] Shang H *et al.* Microwave-assisted nickel and vanadium removal from crude oil. *Fuel Processing Technology*, v. 142, p. 250-257, 2016.
- [17] Li Y *et al.* Theoretical study of the structure and properties of Ni/V porphyrins under microwave electric field: A DFT study. *Fuel*, v. 278, p. 118305, 2020.
- [18] Castillo J, Vargas V. Metal porphyrin occlusion: Adsorption during asphaltene aggregation. *Petroleum Science and Technology*, v. 34, n. 10, p. 873, 2016.
- [19] Lin X *et al.* Estimation of fixed-bed column parameters and mathematical modeling of breakthrough behaviors for adsorption of levulinic acid from aqueous solution using SY-01 resin. *Separation and Purification Technology*, v. 174, p. 222-231, 2017.
- [20] Bhatnagar A, Sillanpää M. A review of emerging adsorbents for nitrate removal from water. *Chemical Engineering Journal*, v. 168, n. 2, p. 493-504, 2011.
- [21] Banerjee M, Basu RK, Das SK. Cr (VI) adsorption by a green adsorbent walnut shell: adsorption studies, regeneration studies, scale-up design and economic feasibility. *Process Safety and Environmental Protection*, v. 116, p. 693-702, 2018.
- [22] Crini G *et al.* Adsorption-oriented processes using conventional and non-conventional adsorbents for wastewater treatment. In: *Green Adsorbents for Pollutant Removal*. Springer, Cham, p. 23-71, 2018.
- [23] Fan L *et al.* Highly selective adsorption of lead ions by water-dispersible magnetic chitosan/graphene oxide composites. *Colloids and Surfaces B: Biointerfaces*, v. 103, p. 523-529, 2013.
- [24] Chen F *et al.* Adsorption kinetics and thermodynamics of vanadyl etioporphyrin on asphaltene in pentane. *Energy & Fuels*, v. 27, n. 11, p. 6408-6418, 2013.
- [25] Chen F *et al.* Metal porphyrin adsorption onto asphaltene in pentane solution: a comparison between vanadyl and nickel etioporphyrins. *Energy & Fuels*, v. 31, n. 4, p. 3592-3601, 2017.
- [26] Chen F *et al.* The function of poly aromatic nuclei structure for adsorption of vanadyl/nickel etioporphyrin on asphaltene/graphene. *Fuel Processing Technology*, v. 174, p. 132-141, 2018.
- [27] Villacañas F *et al.* Adsorption of simple aromatic compounds on activated carbons. *Journal of Colloid and Interface Science*, v. 293, n. 1, p. 128-136, 2006.

Evaluation of sericin and alginate particles chemically crosslinked by polyvinyl alcohol for rare-earth metals removal from aqueous solutions

Talles Barcelos da Costa^a, Meuris Gurgel Carlos da Silva^a, Melissa Gurgel Adeodato Vieira^{a,*}

^a University of Campinas, School of Chemical Engineering, Albert Einstein Avenue, 500, 13083-852 Campinas, Brazil

Abstract

The use of sericin and alginate particles chemically crosslinked with polyvinyl alcohol (SAPVA) as bioadsorbent of rare-earth metals (REMs) present in industrial effluents is promising. Sericin is a protein, which externally covers the silk yarn (fibroin). Although treated as industrial waste of silk spinning process, the chemical and physical properties of this protein enable their use in various materials. Alginate, a natural polysaccharide mainly extracted from the brown seaweed, presents as peculiar characteristic affinity for several cations. The sericin and alginate particles are economically interesting, being low cost, renewable, and abundant, besides adding value to waste material from silk processing in textile industries. The objective of this work was to evaluate potential for bioadsorption of SAPVA particles by metallic affinity tests with the rare-earth ions lanthanum, cerium, neodymium, dysprosium, ytterbium and yttrium. The results showed that the removal percentage was about 100% in both initial concentrations of REMs studied and rare-earth ions presented the following order of adsorptive metallic affinity: Nd > Ce > Dy > Y > La > Yb.

Keywords: Rare-earth metals; Sericin; Alginate; polyvinyl alcohol.

1. Introduction

Sericin, present in the silkworm cocoon (*Bombyx mori*), is a natural, macromolecular and globular protein with molecular weight distribution ranging from 10 to 300 kDa. This protein represents about 15-35% of the cocoon weight [1] and it surrounds the structural filaments of the fibroin fiber in successive layers [2]. In the textile industry, during processing of silk yarns, much of the sericin separated from fibroin is discarded along with the effluents generated in the process [3,4]. However, improper disposal of this protein in water resources can cause serious environmental damage due to the increased chemical and biochemical oxygen demand required for the degradation of this effluent [3].

The use of sericin as a bioadsorbent of REMs can be an interesting application. However, the high solubility of sericin in water and its poor structural properties make it difficult to use as bioadsorbent. Such limitations can be solved by combining sericin with other macromolecules. Alginate or alginic acid, a branchless linear natural

polysaccharide formed by the β -D-manuronic and α -L-guluronic acid monomers, is abundant in the brown algal cell wall. The way sodium alginate is extracted is not stable, so the use of protonated or calcium-saturated forms stabilizes the alginate hydrogel structures, making it less soluble in water and thus increasing the possibilities of application of this material [5].

The easy copolymerization, crosslinking and blending between sericin and alginate results in protein products having improved structural, physical and chemical properties [4].

REMs are a group of seventeen chemical elements whose constituents are scandium (Sc), yttrium (Y) and the lanthanides serie (La, Ce, Pr, Nd, Pm, Sm, Eu, Gd, Tb, Dy, Ho, Er, Tm, Yb, and Lu) [6]. These elements are becoming increasingly important due to their unique chemical and physical properties and their growing applications in the fields of chemical engineering, metallurgy, nuclear power, optics, magnetic, luminescence and laser materials, high temperature superconductors, batteries, screens computer, cell phones, wind turbines, war industry, catalysts, among other various applications [7,8,9]. The demand for REMs

in high technology industries has been intensified and coupled with the fact that China accounts for about 90% of world production and is actually creating trade restrictions for these elements; the search for new resources has been encouraged in several countries. In addition, China has about 40% of REMs world reserves, followed by Brazil (16%) and the USA (10%) [8,9].

Several methods can be applied for the recovery of these elements, such as precipitation, ion exchange and solvent extraction. However, besides being economically unattractive, these methods require a high concentration of ions in solution. In contrast, the bioadsorption process has been considered an alternative to these processes due to its simplicity, low cost and efficiency for rare-earth ions recovery at low concentrations [7,9]. In recent years, studies have reported the use of selective bioadsorbents for recovery of REMs such as grapefruit peels for Ce and La [10,11], chitosan microparticles and shrimp carapace for Eu [12] and alginate microspheres for Nd [13], among other alternative biomaterials. Effective bioadsorbents for REMs require high selectivity over common metal ions, high adsorption and desorption rates, high adsorptive capacity, durability, low cost and high mechanical strength [7].

In this context, this work aims to investigate the potential use of particles produced from the blend between sericin and alginate in bioadsorption processes in dilute solutions for recovery of rare-earth ions. Sericin was autoclaved and fractionated by freezing/thawing. Particles production was made from the mixture between sericin, alginate, and polyvinyl alcohol (PVA). The Ca^{2+} ion gelation method was employed and the particles produced were thermally crosslinked to be used in bioadsorption tests. This study involved the evaluation of the metallic affinity between SAPVA particles and the REMs: La, Ce, Nd, Dy, Yb, and Y.

2. Materials and methods

2.1. Materials

Silkworm cocoon (*Bombyx mori*) were provided by Bratac Silk Mills Company (Paraná-BR). Sodium alginate, polyvinyl alcohol (87-90% hydrolysed, molecular weight distribution 30,000-70,000 Da) and neodymium ($\text{Nd}(\text{NO}_3)_3 \cdot 6\text{H}_2\text{O}$, 99.9%), dysprosium ($\text{Dy}(\text{NO}_3)_3 \cdot 6\text{H}_2\text{O}$, 99.9%), ytterbium ($\text{Yb}(\text{NO}_3)_3 \cdot 5\text{H}_2\text{O}$, 99.9%), and yttrium nitrates ($\text{Y}(\text{NO}_3)_3 \cdot 6\text{H}_2\text{O}$, 99.9%), were obtained

from Sigma-Aldrich, UK. Cerium nitrate ($\text{Ce}(\text{NO}_3)_3 \cdot 6\text{H}_2\text{O}$, 99.9%) was obtained from Neon, BR. Lanthanum nitrate ($\text{La}(\text{NO}_3)_3 \cdot 6\text{H}_2\text{O}$, 99.9%), calcium nitrate ($\text{Ca}(\text{NO}_3)_2 \cdot 4\text{H}_2\text{O}$, 99%), sodium acetate ($\text{CH}_3\text{COONa} \cdot 3\text{H}_2\text{O}$, 99%), xilenol Orange ($\text{C}_{31}\text{H}_{28}\text{N}_2\text{Na}_4\text{O}_{13}\text{S}$, 99%), and acetic acid ($\text{C}_2\text{H}_4\text{O}_2$, 99.88%), were acquired from Dinamics Contemporary Chemistry, BR. Ethanol ($\text{C}_2\text{H}_6\text{O}$, 99.5%) was obtained from Anidrol, BR. The ultrapure water employed in the experiments was delivered by the system reverse osmosis (Gehaka), and bioadsorption experiment pH was adjusted with nitric acid (HNO_3 , purity of 65%, Synth, BR).

2.2. Preparation of bioadsorbent and samples

2.2.1. Bioadsorbent

The steps described to obtain the bioadsorbent material were developed according to the methodologies proposed by Silva et al. [14] and Santos et al. [15].

The first step of bioadsorbent material preparation was the manually cleaning of *Bombyx mori* silkworm cocoons to guarantee the removal of impurities. The cocoons were cut in small pieces (about 1 cm^2), and washed abundantly with deionized water. Subsequently, the cocoons were dried in a laboratory continuous flow oven at 40 °C until constant weight at this temperature for 12 h.

The extraction of sericin from the cocoons was performed by the degumming process in autoclave at 120 °C (1 kgf/cm^2 for 40 min). The ratio of cocoons and deionized water was 40:1,000 (g of cocoons: mL of deionized water). The sericin solution was filtered to remove the fibers of fibroin, packed in a closed container and kept at room temperature (~25 °C) for 12 h, in order to stabilize the formed hydrogel.

Freezing/thawing method was used to separate high molar weight sericin from low molar weight sericin. In this method, sericin was frozen in a standard freezer at -4 °C for 24 h, thawed at room temperature, and filtered. Then, sericin solution concentration was adjusted to 2.5% (m/V) by dilution with deionized water.

The sericin solution with concentration adjusted to 2.5% (m/v) was added commercial sodium alginate 2.0% (m/v). In the blend between sericin and alginate formed, the PVA crosslinking agent was added in the proportion of 0.5% (m/V). The sericin and alginate particles covalently crosslinked by polyvinyl alcohol were instantly obtained by dripping the blend into calcium nitrate

solution (4.1% m/V) maintained under stirring on a magnetic stirrer.

After dripping, the particles produced were kept in a jar test at 80 rpm rotation for 24 h to ensure complete calcium diffusion into the particles interstices. The particles were washed in deionized water and heated in a continuous flow oven at 40 °C for 24 h and then heated in a continuous flow oven at 100 °C for 24 h for complete thermal crosslinking. The particles were chemically and thermally crosslinked to ensure the best physical and chemical stability.

2.2.2. Rare-earth metals concentration determination

Initial and final REMs concentration were determined with a UV-VIS spectrophotometer (Shimadzu, UVmini-1240, BR) by means of the xylenol orange method at 575 nm [16], adapted by Costa et al. [17]. According to this method, samples of 2 mL of the supernatant were added with 3 mL of xilenol orange solution (4.5×10^{-4} mol/L). The final volume of 10 mL was completed with a buffer solution acetic acid/sodium acetate (0.1 mol/L) of pH = 5.6 and measured in the spectrophotometer.

Previously to REMs quantification after bioadsorption process, samples were collected and centrifuged at 4000 rpm for 10 min (Cence, L600, China) to remove bioadsorbent residues that could interfere in the bioadsorption experiments results.

2.3. Metallic speciation tests

Chemical equilibrium diagrams for REMs La, Ce, Nd, Dy, Yb, and Y were simulated using the Visual MINTEQ 3.0 software [18] with the concentration of 3.0 mmol/L that corresponds to the maximum rare-earth ions concentration. From these diagrams, which show the different chemical species in aqueous medium as a function of pH, the appropriate pH range was determined for the rare-earth ions bioadsorption experiments. Metallic speciation was performed considering the stoichiometric ratios of the rare-earth metals salts used.

2.4. Metallic Affinity tests

Rare-earth metals solutions were prepared by dissolving the metal salts ($\text{La}(\text{NO}_3)_3 \cdot 6\text{H}_2\text{O}$, $\text{Ce}(\text{NO}_3)_3 \cdot 6\text{H}_2\text{O}$, $\text{Nd}(\text{NO}_3)_3 \cdot 6\text{H}_2\text{O}$, $\text{Dy}(\text{NO}_3)_3 \cdot 6\text{H}_2\text{O}$, $\text{Yb}(\text{NO}_3)_3 \cdot 5\text{H}_2\text{O}$, and $\text{Y}(\text{NO}_3)_3 \cdot 6\text{H}_2\text{O}$) in deionized

water at pH 5.0. The affinity of SAPVA particles for lanthanum, cerium, neodymium, dysprosium, ytterbium, and yttrium ions was performed by adding 0.5 g of particles and 50 mL of each rare-earth metal solution (1.0 and 3.0 mmol/L) into erlenmeyer flasks (125 mL). The pH control, defined by the metallic speciation tests for each rare-earth ion, was performed with HNO_3 (0.1 mol/L) and kept below the minimum chemical precipitation point of these metals. The test was conducted in a shaker incubator (Lab Companion Jeio Tech, Korea), under fixed agitation (200 rpm) and at room temperature (25.0 °C). After 24 h, the initial and final concentrations were determined as described in "2.2.2 Rare-earth metals concentration determination". The SAPVA particle bioadsorption capacity at equilibrium, q_e (mmol/g), and the removal percentage (%R) were calculated by Equations (1) and (2), respectively.

$$q_e = (C_0 - C_e) \cdot V / m \quad (1)$$

$$\%R = (C_0 - C_e / C_0) \cdot 100 \quad (2)$$

wherein, C_0 is the initial concentration of rare-earth ions in solution (mmol/L), C_e is the concentration of rare-earth ions at equilibrium (mmol/L), V is the solution volume (L), and m is the mass of SAPVA particles (g).

3. Results and discussion

3.1. Metallic speciation

The REMs bioadsorption is highly affected by solution pH due to chemical speciation and the dissociation of active functional groups of the bio/adsorbent [17]. Formerly, Lima [19] determined the point of zero charge (pH_{ZPC}) of sericin and alginate particles as 3.2, and Silva [20] of sericin and alginate particles crosslinked with poly(ethylene glycol) diglycidyl ether (SAPEG) as 3.19, both using Zeta Potential (Anton Paar/SurPASS Electrokinetic, Austria). Hence, at solution pH lower than about 3.0, the serin and alginate particles surface presents positive net charge, and vice versa. In order to assess the pH ranges that should be avoided due to REMs precipitation, metallic speciation diagrams for rare-earth ions were obtained by Visual MINTEQ 3.0 software, considering the composition of the metallic salts [18].

From Figure 1 (a and b) it can be seen the percentage of rare-earth ions in the solutions of lanthanum, cerium, neodymium, yttrium,

dysprosium, and ytterbium nitrates as a pH function at a concentration of 3.0 mmol/L.

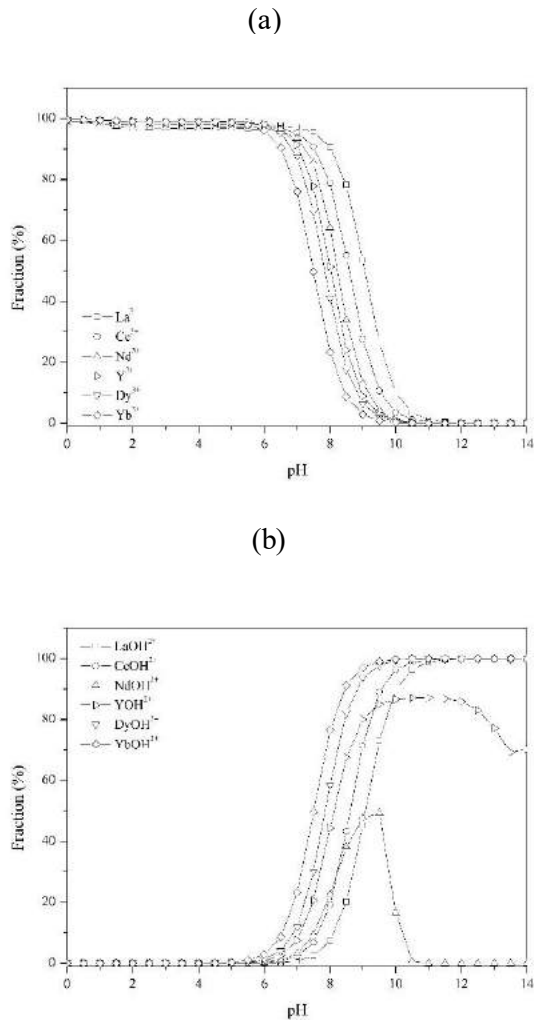


Fig. 1. Rare-earth ions species in aqueous solution (Calculated using Visual MINTEQ 3.0; pH ranging from 1 to 14 at 0.5 intervals; temperature of 25°C).

It can be noted that the La³⁺ remains dominant below pH 7, while LaOH²⁺ is thermodynamically the most stable phase above this pH. On the other hand, Ce³⁺, Nd³⁺, Y³⁺, Dy³⁺, and Yb³⁺ remain as the dominant species below pH 6.0, exhibiting a wider pH range prior to precipitate as hydroxides. Therefore, the pH was adjusted and controlled during the metallic affinity tests to 5.0 ± 0.5. In this range, the soluble ionic fraction of rare-earth ions are dominant, besides to safely avoids that rare-earth hydroxides occurs. Finally, sericin and alginate particles have negative net charge, so in this condition, the bioadsorption is favored.

3.2. Metallic Affinity

The efficiency of bioadsorption process is dictated by the affinity between the adsorbate/bioadsorbent system. In the case of REMs, among many factors, this affinity has been reported in the literature to be strongly dependent on the experimental conditions and the functional groups present on the bioadsorbent surface [21]. The removal percentages and bioadsorption capacity of SAPVA particles by La, Ce, Nd, Dy, Yb, and Y rare-earth ions, are presented in Figure 2.

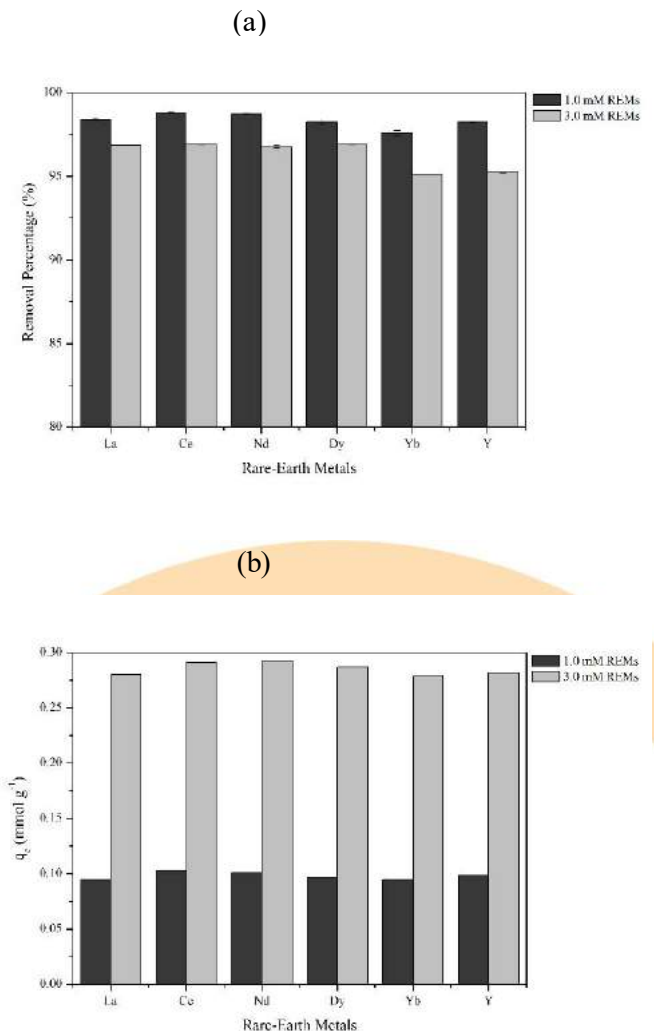


Fig. 2. Metallic affinity of La, Ce, Nd, Dy, Yb, and Y by SAPVA particles at fixed metals initial concentration (1.0 and 3.0 mmol/L), T = 25 °C, and pH = 4.5–5.0: removal percentage (a) and bioadsorption capacity (b).

From Figure 2 (a) and (b) it can be seen that SAPVA particles showed high metallic affinity by rare earth ions in both concentrations studied, with a higher percentage of removal (almost 100%) for the affinity assays conducted at the initial concentration of 1.0 mmol/L REMs. For the assays at the initial concentration of 3.0 mmol/L REMs, SAPVA particles reached removal percentage of 96.90 ± 0.03 , 96.90 ± 0.03 , 96.85 ± 0.02 , 96.77 ± 0.07 , 95.28 ± 0.09 , $95.13 \pm 0.02\%$, and bioadsorption capacity of 0.2908 ± 0.0001 , 0.2874 ± 0.0001 , 0.2800 ± 0.0003 , 0.2934 ± 0.0003 , 0.2822 ± 0.0003 , 0.2791 ± 0.0001 mmol/g, for Ce, Dy, La, Nd, Y, and Yb, respectively. Thus, SAPVA particles presented the following order of metallic affinity by rare-earth ions: Nd > Ce > Dy > Y > La > Yb.

Silva et al. [22] verified that sericin and alginate particles showed satisfactory affinity with precious metals and toxic metals. These particles obtained removal percentages of 99.38, 88.63, 66.35, and 61.31% for gold, palladium, platinum, and silver metals, respectively, and 79.95, 74.41, 74.38, and 72.11% for lead, chrome, copper, and cadmium, respectively. Santos et al. [15], in turn, found that the addition of proanthocyanidins (PAs) and PVA to the sericin and alginate blend did not compromise the adsorption capacity of sericin and alginate particles crosslinked by proanthocyanidins (SAPAs) and SAPVA particles. Both biosorbents exhibited a high removal percentage for gold (99.6% for SAPAs and 96.2% for SAPVA), palladium (88.3% for SAPAs and 95.6% for SAPVA), and platinum (67.9% for SAPAs and 70.6% for SAPVA). On the other hand, Costa et al. [23] evaluated the affinity metallic of SAPEG and SAPAs particles by REMs. The SAPEG particles obtained higher removal percentages of 95.69, 96.89, 96.69, 97.07, 94.62 and 94.91% for La, Ce, Nd, Dy, Yb, and Y metals, respectively, compared the SAPAs particles. These results showed that the addition of crosslinking agents PEG, PAs and PVA the sericin and alginate blend did not compromise the adsorptive capacity of these metals.

The same result was obtained in this study for the addition of PVA to the serine and alginate blend. In fact, the addition of PVA to the sericin and alginate blend, besides promoting a reduction in the solubility of the particles, also did not negatively affect the removal percentage and bioadsorption capacity of rare-earth ions [15]. According to Gimenes et al. [24], incorporation of PVA as crosslinked in polymeric matrices is an interesting alternative because it is a biodegradable

material, easily prepared, has excellent chemical resistance and mechanical properties, and also has characteristic groups such as hydroxyl and amine that allow so that this material can be bonded with silk sericin. Thus, the addition of PVA to the sericin and alginate blend is promising for the removal and recovery of REMs from wastewater.

REMs salts used in this study are predominantly in a cationic form under the acidic condition employed (4.5–5.0). Therefore, these metal complex ionic species should be taken into consideration [25] when evaluating the affinity of REMs for SAPVA. Thus, the Pearson's [26] classification of hard, soft, and borderline ions, frequently used to understand and explain simple metal ion affinity for different types of bio/adsorbents. The lanthanides are considered to be hard acids in the terminology of Pearson and will bond preferentially with hard bases that contain oxygen as donor atoms. This means that these rare-earth ions will bond more weakly with soft bases, such as those with donor sulfur or phosphorus. Therefore, the dominant ligands contain at least one oxygen donor atom like that in the carboxylic group [21].

In the case of sericin, the polar side chain groups, such as amino, hydroxyl, and carboxyl groups [27], are nucleophilic centers for the bonding process, whereas for alginate, the carboxyl group [28] in its structure is the crosslinking agent main target. In fact, given the hydrophilic nature of PVA, it is potentially miscible with sericin due to its ability to form hydrogen bonds with protein hydroxyl and amine groups [24]. The amino, hydroxyl, and carboxyl groups present in the studied blend are classified as hard bases, just as rare-earth ions are classified as hard acid, which explains their high affinity with SAPVA particles.

The results obtained in this study indicate a potential use of SAPVA particles for the recovery of REMs present in aqueous solutions. Subsequent studies will be performed to investigate the kinetics and equilibrium bioadsorption of the rare-earth ions in batch system, as well as to obtain breakthrough curves in continuous fixed-bed bioadsorption system, aiming at later application in industrial scale.

4. Conclusion

Analyzing the results obtained for the metallic affinity tests, it can be concluded that the addition of PVA to the sericin and alginate blend showed promising results for removal and, therefore, good

capacity of bioadsorption for REMs. The removal percentage was greater than 95% in both initial concentrations of REMs studied and SAPVA particles presented the following order of metallic affinity by rare-earth ions: Nd > Ce > Dy > Y > La > Yb. These results indicate a potential use of PVA chemically crosslinked sericin and alginate particles for the removal and recovery of rare-earth ions from aqueous effluents.

Acknowledgements

This work was supported by CAPES, CNPq, and grant 2017/18236-1, FAPESP. The authors thank Bratac Silk Mills Company for *Bombyx mori* silkworm cocoon donation.

References

- [1] Cao TT, Zhang YQ. Processing and characterization of silk sericin from *Bombyx mori* and its application in biomaterials and biomedicines. *Materials Sci and Eng: C* 2016;61: 940-52.
- [2] Matsumoto A, Kim HJ, Tsai IY, Wang X, Cebe P, Kaplan D L. Silk. In: Lewin M, editor. *Handbook of Fiber Chemistry*. New York: CRC Press; 2007. p. 383-404.
- [3] Gulrajani ML, Brahma KP, Kumar PS, Purwar R. Application of silks sericin to polyester fabric. *J App Pol Sci* 2008;109:314-21.
- [4] Aramwit P, Siritientong T, Srichana T. Potential applications of silk sericin, a natural protein from textile industry by-products. *Waste Manag Res* 2012;30:217-24.
- [5] Augst AD, Kong HJ, Mooney DJ. Alginate hydrogels as biomaterials. *Macrom Biosc* 2006;6:623-33.
- [6] Das N, Das D. Recovery of rare earth metals through biosorption: An overview. *J Rare Earths* 2013;31:933-43.
- [7] Ogata T, Narita H, Tanaka M. Adsorption behavior of rare earth elements on silica gel modified with diglycol amic acid. *Hydrometallurgy* 2015;152:178-82.
- [8] Anastopoulos I, Bhatnagar A, Lima EC. Adsorption of rare earth metals: a review of recent literature. *J Mol Liq* 2016;221:954-62.
- [9] Costa TB, Silva MGC, Vieira MGA. Recovery of rare-earth metals from aqueous solutions by bio/adsorption using non-conventional materials: A review with recent studies and promising approaches in column applications. *J Rare Earths*. <https://doi.org/10.1016/j.jre.2019.06.001>
- [10] Torab-Mostaedi M, Asadollahzadeh M, Hemmati A, Khosravi A. Biosorption of lanthanum and cerium from aqueous solutions by grapefruit peel: equilibrium, kinetic and thermodynamic studies. *Res Chem Intermed* 2015;41:559-73.
- [11] Wu DB, Zhao J, Zhang L, Wu QS, Yang YH. Lanthanum adsorption using iron oxide loaded calcium alginate beads. *Hydrometallurgy* 2010;101:76-83.
- [12] Cadogan EI, Lee CH, Popuri SR, Lin HY. Efficiencies of chitosan nanoparticles and crab shell particles in europium uptake from aqueous solutions through biosorption: synthesis and characterization. *Int Biodeterior Biodegrad* 2014;95:232-40.
- [13] Wang FC, Zhao JM, Wei XT, Huo F, Li WS, Hu QY, et al. Adsorption of rare earths (III) by calcium alginate-poly glutamic acid hybrid gels. *J Chem Technol Biotechnol* 2014;89:969-77.
- [14] Silva TL, Junior ACS, Vieira MGA, Gimenes ML, Silva MGC. Biosorption study of copper and zinc by particles produced from silk sericin e alginate blend: evaluation of blend proportion and thermal cross-linking process in particles production. *J Clean Prod* 2016;137:1470-78.
- [15] Santos N, Silva M, Vieira M. Development of novel sericin and alginate-based biosorbents for precious metal removal from wastewater. *Environ Sci Pollut Res* 2018;1-15.
- [16] Mukherji AK. Simultaneous spectrophotometric determination of thorium and the rare earths with Xylenol Orange. *Microchem J* 1966;11:243-54.
- [17] Costa TB, da Silva MGC, Vieira MGA. Evaluation of Metal Affinity of Lanthanum using different alternative bio/adsorbent materials. *Chem Eng Trans* 2019;74:1129-34.
- [18] Gustafsson JP. Visual MINTEQ Version 3.0. KTH Royal Institute of Technology, Stockholm, Sweden 2012. <https://vminteq.lwr.kth.se/download/>.
- [19] Lima JO. Aplicação da blenda de sericina/alginato na produção de partículas para adsorção de íons metálicos. Dissertation, University of Campinas 2015.
- [20] Silva TL. Desenvolvimento e avaliação de partículas à base de blendas entre sericina e alginato para aplicação ambiental. Thesis, University of Campinas 2016.
- [21] Diniz V, Volesky B. Biosorption of La, Eu and Yb using *Sargassum biomass*. *Water Res* 2005;39:239-47.
- [22] Silva TL, Meinerz VH, Vidart JMM, Gimenes ML, Vieira MGA, Silva MGC. Metallic affinity of toxic and noble metals by particles produced from sericin, alginate and poly-(ethylene glycol). *Chem Eng Trans* 2017;56:1903-08.
- [23] Costa TB, Silva MGC, Vieira MGA. Bioadsorção de íons terras-raras em partículas de blenda de sericina e alginato: avaliação da afinidade metálica. In: XXXIX Congresso Brasileiro de Sistemas Particulados - XXXIX ENEMP, 2019.
- [24] Gimenes ML, Liu L, Feng X. Sericin/poly(vinyl alcohol) blend membranes for pervaporation separation of ethanol/water mixtures. *J Membrane Sci* 2007;295:71-9.
- [25] Mack C, Wilhelmi B, Duncan JR, Burgess JE. Biosorption of precious metals. *Biotech Adv* 2007;25:264-71.
- [26] Pearson RG. Hard and soft acids and bases, HSAB. Part 1: fundamental principles. *J Chem Ed* 1968;45:581-87.
- [27] Zhang YQ. Applications of natural silk protein sericin in biomaterials. *Biothch Adv* 2002; 20:91-100.
- [28] Azeredo HMC, Waldron KW. Crosslinking in polysaccharide and protein films and coatings for food contact-a review. *Trends Food Sci Technol* 2016;52:109-22.

Adsorption of the antibiotic ofloxacin in calcined Verde-lodo clay: Experimental design

Raissa Antonelli^a, Geoffroy Roger Pointer Malpass^b, Meuris Gurgel Carlos da Silva^a,
Melissa Gurgel Adeodado Vieira^{a,*}

^a School of Chemical Engineering, University of Campinas – UNICAMP, Albert Einstein Avenue, 500, Campinas, 13083-852, Brazil

^b Department of Chemical Engineering, Federal University of the Triângulo Mineiro – UFTM, Randalfo Borges Júnior Avenue, 1400, Uberaba, 38064-200, Brazil

* melissagav@feq.unicamp.br

Abstract

Due to growing concern about the detection of emerging contaminants such as antibiotics in the environment and the fact that conventional wastewater and water treatment methods are inefficient in removing these compounds, new and more effective treatment processes need to be investigated and improved. The objective of this work was to evaluate the adsorption of the ofloxacin antibiotic in calcined Verde-lodo bentonite clay using statistical techniques of experimental design to determine the best condition to maximize the adsorption capacity of the ofloxacin antibiotic. Assays were performed containing 50 mL of ofloxacin solution (initial concentration 100 $\mu\text{mol L}^{-1}$) in Shaker for 24 hours at 25 ± 1 °C. Agitation speed, adsorbent mass and adsorbent particle size were evaluated by the rotational central composite design (RCCD). The linear term of adsorbent mass was the most significant with negative influence on response, followed by the quadratic terms of agitation speed and adsorbent particle size. The other terms were not significant in the evaluated range, but they were enough to promote effective antibiotic removal. The optimum condition obtained by RCCD was 160 rpm (agitation speed), 0.06 g (adsorbent mass) and 0.85 mm (adsorbent particle size).

Keywords: Emerging contaminant; Clay; Adsorption; Experimental design; Effluent treatment

1. Introduction

Antibiotics belong to the class of emerging contaminants found at low concentrations in the environment (ng L^{-1} – $\mu\text{g L}^{-1}$) [1] that can negatively affect the ecosystem, especially as regards the development of bacterial resistance [2,3].

Ofloxacin represents an antibiotic belonging to the fluoroquinolone carboxylic acid class used in human and veterinary medicine [1]. This antibiotic has great environmental importance due to its wide occurrence, its genotoxic properties and persistence in the environment due to its limited potential for microbial degradation [4]. About 90% of the administered dose of ofloxacin is excreted unchanged in the urine within 48 hours after oral doses and less than 10% of the compound is excreted as metabolites [5]. Therefore, the removal of ofloxacin from water and wastewater is essential.

Conventional treatment methods are inefficient and unable to effectively remove all constituents present in pharmaceutical wastewater [6]. However, the adsorption process has been shown to be

effective in removing effluent contaminants at low concentrations [7]. In addition, the adsorption process has numerous advantages over other conventional treatment methods, for example, it has simple, economical operation and no added by-products [4].

Activated carbon is widely used as an adsorbent in domestic and industrial wastewater management. However, large-scale use of activated carbon is costly. Thus, there is interest in the use of cheap and highly available alternative adsorbents [7]. Clays are considered potential alternative adsorbents due to their high cation exchange capacity, high chemical and mechanical stability, abundance and low cost compared to commercial activated carbon [8].

Based on the above, this study aimed to investigate the adsorption of the antibiotic ofloxacin in calcined Verde-lodo bentonite clay using statistical techniques of experimental design. Agitation speed, adsorbent mass and adsorbent particle size were evaluated by rotational central composite design in order to obtain the optimum process condition.

2. Experimental

1.1. Adsorbent

Calcined Verde-lodo bentonite clay, supplied by Dolomil Industrial Ltda., was used in the evaluation of the adsorption process as an alternative adsorbent. The clay was ground and sorted by sieving to obtain an average particle diameter of 0.855 mm. The clay was then calcined in a muffle furnace at 500 °C for 24 h [9].

1.2. Adsorbate

The emergency contaminant evaluated was the ofloxacin antibiotic, supplied by EMS pharmaceutical company. Contaminant solutions (initial concentration of 100 $\mu\text{mol L}^{-1}$) were prepared using reverse osmosis ultrapure water (model OS20LXE, Gehaka, Brazil).

The collected samples were centrifuged (model L600, Cence[®]) at 4,000 rpm for 10 minutes and filtered through Teflon syringe filters with hydrophilized polytetrafluoroethylene membrane (25 mm 0.45 μm) (Macherey-Nagel). Residual antibiotic concentrations were determined by UV-Vis spectrophotometry (UV-vis) (Mini 1240 model, Shimadzu).

The adsorbed amount (q , $\mu\text{mol g}^{-1}$), being the response of interest of the experimental design, was calculated by Eq. 1:

$$q = \frac{C_0 - C_f}{m} V \quad (1)$$

where C_0 and C_f ($\mu\text{mol L}^{-1}$) are the initial and final concentration of ofloxacin in the solution, respectively. V (L) is the volume of ofloxacin solution contained and m (g) is the clay mass.

1.3. Experimental design

The experimental design and data analysis were performed using the software Statistica[®]. Among the main variables that influence the adsorption process, the following parameters were evaluated the agitation speed (X_1), adsorbent mass (X_2) and adsorbent particle size (X_3), in order to optimize the adsorbed amount of ofloxacin (q). Preliminary tests were performed to characterize the system and choose the studied variables and their respective levels. Table 1 shows the levels of each variable

studied in rotational central composite design (RCCD). Assays were conducted containing 50 mL of ofloxacin solution in Shaker (Lab Companion SI-600R) for 24 h at 25 ± 1 °C.

Table 1. Variables studied with coded and real values for the RCCD.

Factor	Level				
	-1.68	-1	0	+1	+1.68
X_1 (rpm)	76	110	160	210	244
X_2 (g)	0.06	0.4	0.9	1.4	1.74
X_3 (mm)	0.27	0.51	0.85	1.21	1.44

3. Results and discussion

The matrix of the experimental design and results (Table 2) was generated by the software Statistica[®] 7, obtaining 17 tests proposed according to methodology, relating to the experimental conditions of agitation speed (X_1), adsorbent mass (X_2) and adsorbent particle size (X_3), with the response of interest of the process being the adsorbed amount (q). The experiments were performed in randomized order to minimize deviations in the results.

Table 2. RCCD matrix and adsorbed amount of ofloxacin.

X_1	X_2	X_3	q ($\mu\text{mol g}^{-1}$)
-1	-1	-1	12.36
-1	-1	+1	12.36
-1	+1	-1	3.50
-1	+1	+1	3.50
+1	-1	-1	12.41
+1	-1	+1	12.32
+1	+1	-1	3.49
+1	+1	+1	3.36
-1.68	0	0	5.47
+1.68	0	0	5.47
0	-1.68	0	55.43
0	+1.68	0	2.83
0	0	-1.68	5.47
0	0	+1.68	5.47
0	0	0	5.47
0	0	0	5.52
0	0	0	5.52

Statistica[®] 7 software analysis was performed with a 95% confidence interval ($p = 0.05$). Table 3 was obtained to analyze the data regarding the interaction effects between the factors.

Table 3. Regression ratios obtained for each response monitored by RCCD.

Factor	p value	Coefficient	Error
Mean	0.00	5.89	0.01
X_1	0.34	-0.01	0.01
X_1^2	0.00	-1.34	0.01
X_2	0.00	-9.08	0.01
X_2^2	0.00	7.05	0.01
X_3	0.12	-0.02	0.01
X_3^2	0.00	-1.33	0.01
X_1X_2	0.14	-0.02	0.01
X_1X_3	0.08	-0.03	0.01
X_2X_3	0.61	-0.01	0.01

From Table 3 it is possible to verify that the factors X_1 (agitation speed), X_3 (adsorbent particle size), X_1X_2 (interaction between agitation speed and adsorbent mass), X_1X_3 (interaction between agitation speed and adsorbent particle size) and X_2X_3 (interaction between adsorbent mass and adsorbent particle size) are not significant ($p > 0.05$), so it would be necessary to exclude these factors for a more refined analysis of the effects. However, it was preferable to leave these factors, because with their gradual elimination the value of R^2 would decrease considerably, reducing the reliability of the adjustment.

Thus, the statistical model obtained from the process is expressed by Eq. 2 with R^2 of 0.784.

$$q = 5.89 - 0.01X_1 - 1.34X_1^2 - 9.08X_2 + 7.05X_2^2 - 0.02X_3 - 1.33X_3^2 - 0.02X_1X_2 - 0.03X_1X_3 - 0.01X_2X_3 \quad (2)$$

The Pareto graph (Fig. 1) was constructed in order to analyze the intensity of the effects generated by the process variables. As can be seen in Fig. 1, the linear term X_2 (adsorbent mass) had the most significant effect in the 95% confidence interval, with negative influence, i.e. the smaller the mass, the better the adsorption capacity of the process. The quadratic term X_2^2 is the second most significant effect on the confidence interval, with a positive influence on the process. The quadratic terms X_1^2 (agitation speed) and X_3^2 (adsorbent particle size) were significant with negative influence on the process. Other terms and interactions were not significant in the 95% confidence interval. This does not mean that agitation speed, particle size and factor interaction are not important for adsorption to occur, only that in the evaluated ranges the adsorption capacity of

floxacin by calcined Verde-lodo clay does not vary significantly. The agitation speed (X_1) and particle size (X_3) were enough to promote adequate contact between the adsorbent and the solute and to promote effective removal.

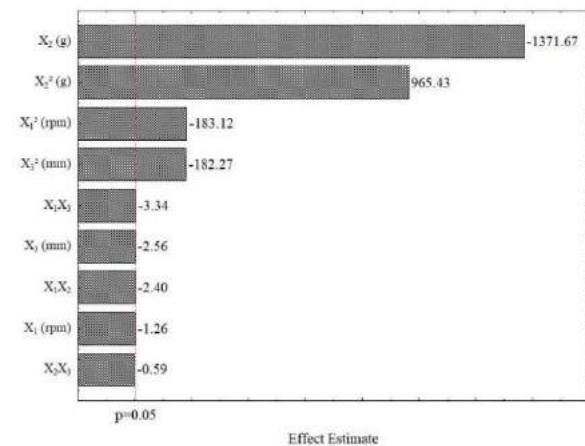
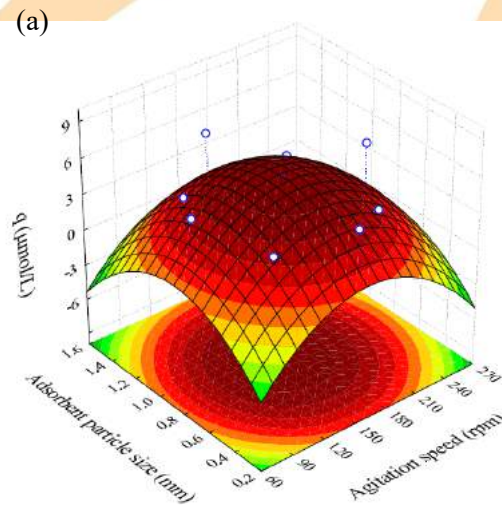


Fig. 1. Pareto graph.

The response surfaces (Fig. 2 (a), (b), and (c)) were constructed in order to evaluate the influence of the variables on the adsorption capacity of the process.

Interpreting the contour surfaces (Fig. 2 (a), (b) and (c)) shows that the best adsorption capacity results are with the lowest adsorbent mass values, which may be an indication that for levels higher than this parameter there is no adsorbent saturation. A study found in the literature of dye adsorption by oyster shell residues [10] also found that adsorbent mass had the greatest significant effect among the other factors evaluated.



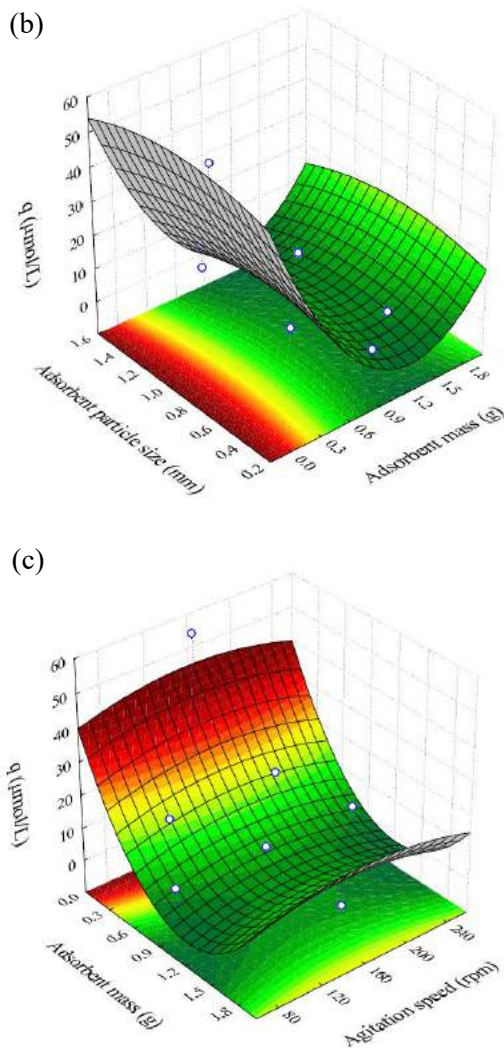


Fig. 2. Response surface between (a) agitation speed (X_1) and adsorbent particle size (X_3), (b) adsorbent mass (X_2) and adsorbent particle size (X_3), and (c) agitation speed (X_1) and adsorbent mass (X_2).

As X_1 (agitation speed) and X_3 (adsorbent particle size) were not significant in the confidence interval analyzed, there is little variation in the data of q presented in Fig. 2 (a). Moreover, as observed in the Pareto graph (Fig. 1) and response surfaces Fig 2 (b) and (c), the interactions between X_2X_3 (interaction between adsorbent mass and adsorbent particle size) and X_1X_2 (interaction between agitation speed and adsorbent mass) were also not significant in the confidence interval (95%), being that factors X_1 and X_3 did not show significant variation in the values of q presented in Fig. 2 (a), (b) and (c).

The fact that the agitation speed (X_1) is not significant in the studied conditions does not mean

that the agitation is not important for the adsorption to occur, but that in the evaluated range the amount of ofloxacin adsorbed by the calcined Verde-lodo clay did not vary significantly. The agitation speeds of the conditions studied were enough to promote adequate contact between the clay and the drug, minimizing the effect of mass transfer resistance that would occur at low agitation values and promoting effective removal. Similar results were observed in the literature in studies that evaluated agitation in the ranges: 150-200 rpm in dibenzothiophene adsorption on activated carbon [11], and 300-500 rpm in reactive gray dye adsorption by green coconut mesocarp [12]. Both studies also found that agitation speed was not a significant parameter.

Regarding the variable X_3 (adsorbent particle size), a similar result was obtained in a study of the literature on dye adsorption by leather residue with particle diameter variation of 0.9-2.9 mm [13], obtaining that factor particle size was not significant. Particle size is a relevant factor in dynamic system tests, and the reduction in particle size favors the adsorption process due to the increase in surface area available for adsorbate/adsorbent contact. However, low particle size values should be avoided due to material compaction and packaging in fixed bed dynamic system studies. Average particle diameter of 0.855 mm of calcined Verde-lodo clay has been previously studied [9] and has shown excellent sieving performance and does not exceed one tenth of the internal diameter of the column used in the dynamic tests.

The optimal point obtained was 160 rpm, 0.06 g and 0.85 mm. The optimal condition was experimentally verified (Table 4) in order to validate the model. The obtained result supports the sufficiency of RCCD optimization of the effects of the independent adsorption variables.

Table 4. Model validation

Optimized condition	Experimental
160 rpm	$q = 62.93 \mu\text{mol g}^{-1}$
0.06 g	
0.85 mm	

4. Conclusion

Tests indicate promising application of calcined Verde-lodo clay in the removal of the ofloxacin antibiotic. Based on the experimental design, it can be concluded that the linear term of the adsorbent



mass presented the greatest influence among the analyzed variables, with negative influence on the response, that is, lower mass values favor the adsorbed amount. The other factors studied and the interaction between them were not significant in the 95% confidence interval; however, the factors were enough to promote effective removal of the ofloxacin antibiotic. The optimum condition obtained by RCCD was 160 rpm (agitation speed), 0.06 g (adsorbent mass) and 0.85 mm (adsorbent particle size) with experimental result of model validation of $62.93 \mu\text{mol g}^{-1}$.

Considering the importance of studies of removal of emerging contaminants in water and wastewater, and taking into account the results obtained so far, it is interesting that in the future the extension of this study in the evaluation of adsorption kinetics and thermodynamics, as well as dynamic system tests (fixed bed) aiming at possible industrial application.

Acknowledgements

The authors thank CAPES, FAPESP (Proc. 2016/05007-1), and CNPq (Proc. 406193/2018-5) for their financial support. Dolomil Industrial Ltda. donation of the clay used as adsorbent in this study. EMS Pharmaceutical for the donation of the antibiotic ofloxacin.

References

- [1] Goynes KW, Chorover J, Kubicki JD, Zimmerman AR, Brantley SL. Sorption of the antibiotic ofloxacin to mesoporous and nonporous alumina and silica. *J Colloid Interface Sci* 2005;283:160-170.
- [2] de Andrade JR, Oliveira MF, da Silva MGC, Vieira MGA. Adsorption of Pharmaceuticals from Water and Wastewater Using Nonconventional Low-Cost Materials: A Review. *Ind Eng Chem Res* 2018;57:3103-3127.
- [3] de Sousa DNR, Insa S, Mozeto AA, Petrovic M, Chaves TF, Fadini PS. Equilibrium and kinetic studies of the adsorption of antibiotics from aqueous solutions onto powdered zeolites. *Chemosphere* 2018;205:137-146.
- [4] Kong Q, He X, Shu L, Miao-sheng M. Ofloxacin adsorption by activated carbon derived from luffa sponge: Kinetic, isotherm, and thermodynamic analyses. *Process Saf Environ Prot* 2017;112:254-264.
- [5] Al-Omar MA. Ofloxacin, Profiles of Drug Substances, Excipients and Related Methodology 2009;34:1075-6280.
- [6] Marcelino RBP, Leão MMD, Lago RM, Amorim CC. Multistage ozone and biological treatment system for real wastewater containing antibiotics. *J Environ Manage* 2017;195:110-116.
- [7] Putra EK, Pranowo R, Sunarso J, Indraswati N, Ismadji S. Performance of activated carbon and bentonite for adsorption of amoxicillin from wastewater: Mechanisms, isotherms and kinetics. *Water Res* 2009;43:2419-2430.
- [8] Chen WJ, Hsiao LC, Chen KKY. Metal desorption from copper (II)/nickel (II)-spiked kaolin as a soil component using plant-derived saponin biosurfactant. *Process Biochemistry* 2008;43:488-498.
- [9] Almeida Neto AF, Vieira MGA, Silva MGC. Cu(II) adsorption on modified bentonitic clays: different isotherm behaviors in static and dynamic systems. *Mater Res* 2011;15:114-124.
- [10] Menezes GA, Sobrinho MAM. Estudo através de planejamento experimental da adsorção de corantes têxteis por resíduos cascas de ostra e por carvão ativado. 2015. XXIII CONIC/VII CONIT/IV ENEC.
- [11] Fontana JF. Modificação superficial de adsorventes para a adsorção de dibenzotiofeno presente em óleo lubrificante. 2016. Florianópolis, SC, 168 p.
- [12] da Rocha ORS, do Nascimento GE, Campos NF, da Silva VL, Duarte MMB. Avaliação do processo adsorptivo utilizando mesocarpo de coco verde para remoção do corante cinza reativo BF-2R. *Quim. Nova* 2012; 35:1369-1374.
- [13] Gomes, CS, Trucolo ACF, Veber W, Piccin JS, Gutterres M. Adsorção aplicada ao tratamento de efluentes de tingimento de curtumes. 2014. XX COBEQ.

2. Materials and Methods

1.1 Adsorbent

Expanded vermiculite was applied as adsorbent on batch adsorption mode. This mineral was donated by Brasil Minérios S/A.

1.2 Adsorbate

Dysprosium solution was prepared from a stock solution. The stock solution was formed by the dissolution of 5.0 g of dysprosium (III) pentahydrate nitrate (Aldrich, 99.9%) in 100 mL of acidified water (pH \cong 5.0) with the addition of few drops of nitric acid (0.1 mol/L)

1.3 Adsorption experiments

Adsorption tests were conducted in a shaker (SI-600R Jeio Tech). The fixed parameters were rotation (200 rpm), time (24 h), temperature (25 °C), volume (50 mL) and concentration of the Dy³⁺ solution (3 mmol/L). Few drops of nitric acid (0.01 mol/L) and ammonium hydroxide (0.01 mol/L) were added to control the pH during the experiment, according to the proposed RCCD (1.32 < pH < 4.68). The solid phase (adsorbent) was separated by centrifugation at 4000 rpm for 10 min (CENCE L600 centrifuge) and the supernatant was filtrated with a syringe filter (Macherey-Nagel, porous of 0.45 μ m).

The adsorption capacity (q) and the removal percentage (%R) were determined by Equations 1 and 2, respectively.

$$q = \frac{(C_0 - C_f)V}{m} \quad (1)$$

$$\%R = \frac{(C_0 - C_f)}{C_0} 100 \quad (2)$$

Where C_0 is the initial concentration (3 mmol/L), C_f is the concentration after 24 h of contact time (mmol/L), V is the metallic solution volume (L) and m is the adsorbent mass (g).

1.4 Determination of Dy concentration

The metal concentration in the aqueous solution was quantified by UV-vis spectroscopy (UVmini-1240, Shimadzu). Xylenol orange (0.00045 mol/L) was used as a complexing agent at a wavelength of 575 nm (maxima absorption) [20, 21].

1.5 RCCD

Particle size (A), adsorbent amount (B) and pH (C) were varied by a rotational central composite design to optimize the %R (response variable). Therefore,

the experiment plan totalizes 17 runs: 3 factors in 2 levels (8 runs), axial points (6 runs) and central point triplicate (3 runs). The RCCD levels are presented in Table 1.

The variance analysis test (ANOVA) with a confidence interval of 95% and the generation of the surface responses were performed on Statistics 8.0 software.

Table 1. Experimental Domain of RCCD for the Dysprosium adsorption on EV.

Factor	Levels				
	$-\alpha$	-1	0	+1	$+\alpha$
A (mm)	0.48	0.65	0.85	1.09	1.30
B (g)	0.163	0.300	0.500	0.700	0.836
C	1.3	2.0	3.0	4.0	4.7

The pH range (1.32 to 4.68) was based on the usual pH of the effluents that can contain Dy (\cong 2.0) [22-24] and on the pH of the Dy(OH)₃ formation in aqueous media (\cong 6.0) [25]. The separation of the expanded vermiculite according to its particle size was performed by a set of sieves (40 to 12 mesh) on a vibratory base (Produtest). The mass of adsorbent range was chosen to guarantee the availability of the process (low adsorbent amounts).

An empiric-squared model was proposed to represent de %R (Equation 3). This model was submitted to a backward elimination to improve the adjustment.

$$\%R = b_0 + b_1A + b_2B + b_3C + b_4A^2 + b_5B^2 + b_6C^2 + b_7AB + b_8AC + b_9BC \quad (3)$$

The best model was validated by an adsorption test (triplicate) under the optimal conditions obtained by RSM analysis.

3. Results and Discussion

3.1 Parameters Optimization

The results of adsorption capacity and Dy removal percentage are displayed in Table 2.

According the Table 2, the %R was from 27.6% (run 13) to 99.1% (run 8) and the q varied from 0.08 mmol/g (run 13) to 0.37 mmol/g (run 6).

The standardized effects of the independent variables and their interactions on the response variable (%R) are presented in Fig. 1 (Pareto Chart). The effects in which t value was higher than ± 2.365 (t -student test for seven freedom degrees (fd)) and had the $p < 0.05$ were considered significant.

Table 2. %R and q as results of Dy adsorption on EV.

Run	Coded Variables			q (mmol/g)	%R
	A	B	C		
1	-1	-1	-1	0.20	42.2
2	+1	-1	-1	0.26	55.8
3	-1	+1	-1	0.16	80.6
4	+1	+1	-1	0.18	89.3
5	-1	-1	+1	0.35	73.9
6	+1	-1	+1	0.37	79.6
7	-1	+1	+1	0.20	98.9
8	+1	+1	+1	0.20	99.1
9	-α	0	0	0.27	94.1
10	+α	0	0	0.27	97.3
11	0	-α	0	0.28	32.1
12	0	+α	0	0.17	98.8
13	0	0	-α	0.08	27.6
14	0	0	+α	0.28	98.9
15	0	0	0	0.27	95.8
16	0	0	0	0.27	95.6
17	0	0	0	0.27	95.8

According to Fig.1, the factors that affected the %R significantly with 95% of confidence were: the amount of adsorbent (g) and the pH, both on linear (B, C) and squared (B², C²) form. Particle size (A, A²), and all the interactions between the factors (AC, BC, AB) were not significant.

The highest effect on the %R was the mass of adsorbent (g) followed by the pH, both positives. Squared effects (B², C²) were smaller than linear and they were negative.

The positive effect of the amount of adsorbent on the %R can be explained by the fact that the increment of the adsorbent amount increases the available sites to adsorb metallic ions. While the positive effect of the pH is due to the increase of the negative surface charge of the vermiculite with the intensification of the pH. The isoelectric point of the expanded vermiculite is about 2.9 [26] which means when the pH < 2.9, the surface of the vermiculite is positively charged what promotes a repulsion of the cations Dy³⁺. The pH effect can be evidenced by comparing the results of Table 2 (runs 13 and 14), where just pH was varied, at pH 1.3 the %R was 27.6% and at pH 4.8 the %R was 98.9%.

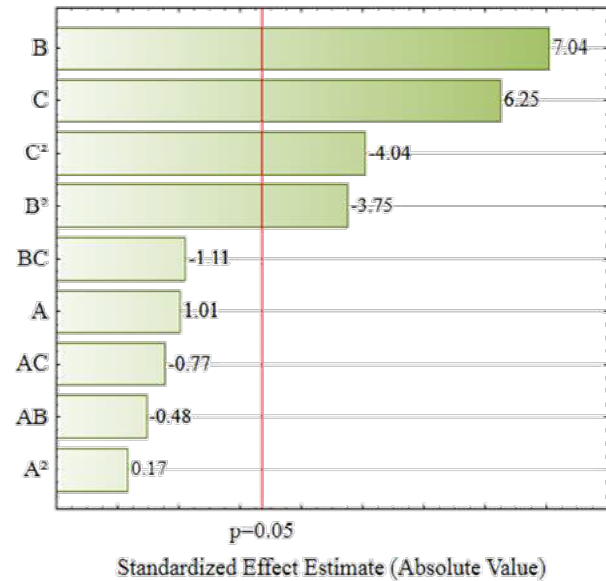


Fig. 1. Pareto chart (standardized effects on Dy removal percentage)

Table 3 presents the variance analysis for the completed model with main and interaction effects, while Table 4 contains the ANOVA for the reduced model that considers just the significant parameters.

Table 3. Variance Analysis (ANOVA) for the completed squared model ($\alpha=0.05$, $F_{tab} = 3.68$)

Source of variation	SS	fd	MS	F _{calc}	F _{calc} /F _{tab}
Regression	9318.7	9	1035.4	13.5	3.7
Error	536.6	7	76.7		
Total	9855.4	16			

The completed model, firstly proposed (Equation 3), was significant with 95% confidence although the model considers the non-significant effects. It could be concluded by $F_{calc}/F_{tab} = 3.7$. The model adjusted the data with a determination coefficient (R^2) equal to 0.9455, and an adjusted determination coefficient (R_{adj}^2) equal to 0.8755. However, the ANOVA of the reduced model (Table 4) after the backward elimination showed $F_{calc}/F_{tab} = 10.8$, a $R^2 = 0.9217$ and a $R_{adj}^2 = 0.8949$. The increase of the F-test value from 3.7 to 10.8, and the R_{adj}^2 from 0.8755 to 0.8949 indicated that the reduced model is more significant than the completed model. The reduced model was chosen to represent the %R because presented $F_{calc}/F_{tab} > 10$, ratio recommended in the literature to consider a regression as useful for forecasting purposes [27].

Table 4. Variance Analysis (ANOVA) for the reduced squared model ($\alpha=0.05$, $F_{tab}= 3.26$)

Source of variation	SS	fd	MS	F _{cal}	F _{cal} /F _{tab}
Regression	9078.4	4	2269.6	35.1	10.8
Error	776.9	12	64.7		
Total	9855.4	16			

Fig. 2 shows the predicted values versus the observed values. The prediction can be considered adequate because, in general, the model values are similar to experimental data. However, predicted values were closer to observed values for %R between 90 and 100%.

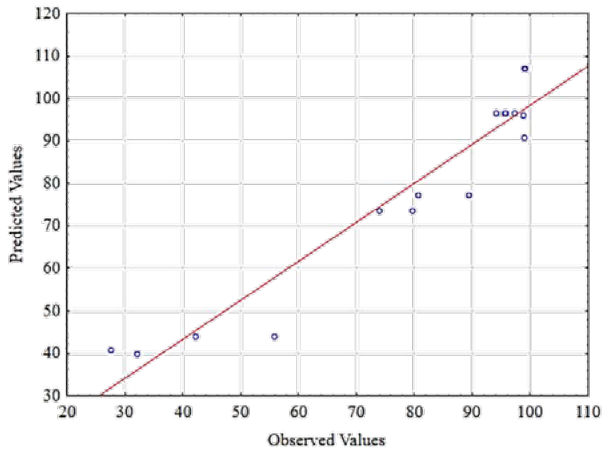


Fig. 2. Correlation between predicted and observed values.

The response surfaces (Fig. 3) elaborated from the %R model of Equation 4 that excluded non-significant effects.

$$\%R = 96.58_{\pm 3.48} + 16.74_{\pm 2.18}B + 14.91_{\pm 2.18}C - 10.09_{\pm 2.28}B^2 - 10.90_{\pm 2.29}C^2 \quad (4)$$

Fig.3A presents the response surface of the %R as a function of the pH and amount of the adsorbent (g). Through the curve can be observed in a region of maximum removal percentage. Fig.3B shows the contour surface where just the positive responses were plotted. The highest %R values were found at pH between 3.0 and 3.5, and with an adsorbent amount between 0.5 to 0.8. The critical values obtained by the Statistics 8.0 Software were pH equal to 3.5 and the amount of adsorbent equal to 0.65 g.

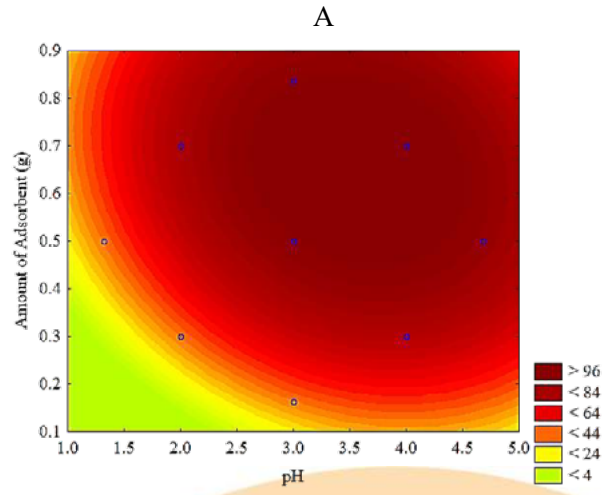
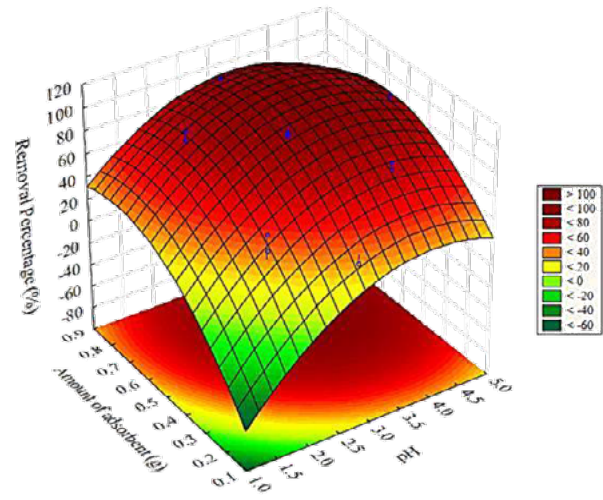


Fig. 3. Dy removal percentage as a function of pH and amount of adsorbent: (A) response surface and (B) contour surface.

3.2 Model Validation

The results of the validation test that occurred at the optimal conditions are showed in Table 5.

Table 5. Model Validation at pH 3.5 and 0.65 g of adsorbent.

q (mmol/g)	%R	
Experimental	Experimental	Model
0.23	99.2±0.10	106.5

In Table 5, the %R experimentally obtained by adsorption test was higher than the %R showed in Table 2, it means that there was an effective optimization of the conditions to maximize the response variable (%R). At the best conditions, the model predicted a removal percentage of 106.5%,

despite the limitations due to the empirical origin, the model could optimize effectively the Dy³⁺ adsorption.

In Table 6, there is a comparison between the present study and other research works about dysprosium adsorption. The data in Table 6 were obtained from the studies of the effect of the adsorbent mass and pH. The mass of adsorbent was recalculated for a volume of 50.0 mL (solution volume of this study).

According to Table 6, it is possible to note that the Dy³⁺ removal percentage on expanded vermiculite was 99.2 %, which was similar to other results, and the adsorption capacity achieved was higher than the majority. However, the initial Dy concentration of this study is much higher than other *C_i*. Consequently, due to the presence of more Dy ions in solution, in this study the highest mass of adsorbent was employed. Comparing expanded

vermiculite (present study) with the functionalized silica (BBH-SBA-15) that used the lowest initial concentration, the expanded vermiculite attained the same removal percentage for a solution 4,838.7 times more concentrated using just 2.56 times more adsorbent mass.

Comparing the optimal conditions of pH, at pH 7.0 [30, 32] insoluble form of dysprosium probably can be formed (Dy(OH)₃) even in few quantities [25], consequently, the precipitation of the Dy maybe be being included as an adsorption result. Dy adsorption at pH 2.0 is unusual [24], but the authors considered this condition as optimal because, in acid media, the adsorption ability of the adsorbent (IMS) towards Dy³⁺ is not only based on the chelating capacity but also on the spatial structure for the coordination of Dy³⁺ conferred by the imprint process.

Table 6. Comparison between different optimal conditions to Dy³⁺ adsorption

Adsorbent	C ₀ (mmol/L)	pH	Mass of adsorbent (g)	%R	q (mmol/g)	Reference
Ion imprinted mesoporous silica (IMS)	0.3	2	0.05	*34	0.10	[28]
Activated carbon (chemical activation)	0.03	4.0	0.075	94	*0.19	[29]
Activated carbon (physical activation)	0.03	4.0	0.075	100	*0.21	[29]
γ-Fe ₂ O ₃ -NH ₄ OH@SiO ₂ nanoparticles	0.002	7.0	0.15	90	*6.0x10 ⁻⁴	[30]
Functionalized silica (BBH-SBA-15)	6.2x10 ⁻⁴	5.0	0.25	100	*2.0x10 ⁻⁵	[31]
Zeolitic imidazolate frameworks NPs	0.074	7.0	0.012	*95.8	0.28	[32]
Polyacrylic acid grafted silica fume	1.2	6.0	0.025	*68.9	1.69	[33]
Expanded Vermiculite	3.0	3.5	0.64	99.2	0.23	Present Work

* Calculated from the informed data (values not presented in the original paper).

4. Conclusions

Dy adsorption on expanded vermiculite was improved by RCCD and RSM analysis to optimize pH, the mass of adsorbent and particle size.

The amount of adsorbent and pH had a significant effect on the removal percentage of dysprosium. The optimal values were pH 3.5 and 0.65 g of adsorbent. The size particle was not significant (confidence interval of 95%).

The results of the validation step indicated that the model is effective to predict the %R as a function of pH and amount of adsorbent in the studied range. Furthermore, the optimization was confirmed due to the highest %R achieved at the optimal conditions.

Acknowledgements

This work was financially supported by the Fundação de Amparo à Pesquisa do Estado de São Paulo (FAPESP) (Proc. 2017/18236-1), Coordenação de Aperfeiçoamento de Pessoal de

Nível Superior (CAPES), Conselho Nacional de Desenvolvimento Científico e Tecnológico (CNPq). The adsorbent material was donated by Brasil Minérios S/A.

References

- [1] IUPAC: Nomenclature of inorganic chemistry – IUPAC recommendations 2005. Cambridge, UK 2005: International Union of Pure and Applied Chemistry (IUPAC).
- [2] Clark A, Zheng S. China's rare earth potential, industry, and policy. Materials Science Forum. International Conference on Rare Earth Minerals and Minerals for Electronic Uses, January 23–25, HatYai, Thailand, 1991. Trans Tech Publications, Switzerland, p. 577-602.
- [3] Charalampides G et al. Rare Earth Elements: Industrial Applications and Economic Dependency of Europe. *Procedia Econ* 2015; 24 (15): 126-135.
- [4] Binnemans K, Jones PT. Rare earths and the balance problem. *J Sustain Metall* 2015; 1:29–38.
- [5] Elshkaki A, Graedel TE. Dysprosium, the balance problem and wind power technology. *Appl Energy* 2014, 136:548-559.

- [6] Constantine S. The Important Role of Dysprosium in Modern Permanent Magnets. New York: Arnold Magnetic Technologies, 2012.
- [7] Eggert R, Wadia C, Anderson C, Bauer D, Fields F, Meinert L, Taylor P. Rare earths: market disruption, innovation, and global supply chains. *Annu Rev Environ Resour* 2016; 41:199-222.
- [8] Jowitt SM et al. Recycling of the rare earth elements. *Green Sust Chem* 2018; 13:1-7.
- [9] Peelman S, Venkatesan P, Abrahamsi S, Yang Y. Recovery of REEs from End-of-Life Permanent Magnet Scrap Generated in WEEE Recycling Plants. In: Davis B et al. *Extraction 2018: The Minerals, Metals & Materials Series*. Springer, Cham, 2018.
- [10] Anastopoulos I, Bhatnagar A, Lima EC. Adsorption of rare earth metals: A review of recent literature. *J Mol Liq* 2016; 221: 954-962.
- [11] Udoudo O et al. Understanding the performance of a pilot vermiculite exfoliation system through process mineralogy. *Min Eng* 2015; 82: 84-91.
- [12] Paula RF, Carvalhães C. Vermiculita. In: *Sumário Mineral 2017*. Brasília: Departamento Nacional de Produção Mineral; 2017. v. 36. p. 110-111.
- [13] Valaskova M, Martynková GS. Vermiculite: Structural Properties and Examples of the Use. In: Valaskova M, Martynková GS, editors. *Clay Minerals in Nature - Their Characterization, Modification and Application*. InTechOpen; 2012. v. 2. p. 64.
- [14] Arruda GM. Vermiculite Utilization on the Treatment of Water Contaminated with Organic Compounds. In: 2 Mercosur Congress on Chemical Engineering and 4 Mercosur Congress on Process Systems Engineering, 2005. Rio de Janeiro: Anais [...] Rio de Janeiro 2005; p. 1-10.
- [15] Box GEP, Wilson K B. On the experimental attainment of optimum conditions. *J R Stat Soc Series B* 1951; 13:1- 45.
- [16] Biswas S et al. Process Optimization Study of Zn²⁺ Adsorption on Biochar-Alginate Composite Adsorbent by Response Surface Methodology (RSM). *Water* 2019; 11(325): 1-15.
- [17] Mondal NK, Basu S, Das B. Decontamination and optimization study of hexavalent chromium on modified chicken feather using response surface methodology. *Appl Water Sci* 2019; 9: 50.
- [18] Javanbakht V, Ghoreishi SM. Application of response surface methodology for optimization of lead removal from an aqueous solution by a novel superparamagnetic nanocomposite. *Adsorpt Sci Technol* 2017; 35 (1-2): 241-260.
- [19] Ümit H K. A modeling and optimization study by response surface methodology (RSM) on UO₂²⁺ ions adsorption using nano-MgO particles prepared with combustion synthesis. *Inorg Nano-Met Chem* 2018; 48 (3):187-195.
- [20] Mukherji AK. Simultaneous spectrophotometric determination of thorium and the rare earths with Xylenol Orange. *Microchem J* 1966;11: 243-254.
- [21] Granados-Correa et al. Adsorption Behaviour of La(III) and Eu(III) Ions from Aqueous Solutions by Hydroxyapatite: Kinetic, Isotherm, and Thermodynamic Studies. *J Chem* 2013; 2013:1-9.
- [22] Riaño S, Binnemans K. Extraction and separation of neodymium and dysprosium from used NdFeB magnets: An application of ionic liquids in solvent extraction towards the recycling of magnets. *Green Chem* 2015; 17(5): 2931-2942.
- [23] Xu J. Recovery of rare-earth elements from NdFeB magnets by zirconium phosphate ion exchangers. Department of Chemistry, Faculty of Science of the University of Helsinki. (dissertação de mestrado); 2018.
- [24] Gergorić M. Hydrometallurgical Treatment of Neodymium Magnet Waste. Department of Chemistry and Chemical Engineering. Chalmers University of Technology, Gothenburg -Sweden (tese de doutorado); 2018.
- [25] Brião GV, Silva MGC, Vieira MGA. Ensaios de afinidade de íons terras raras em concentrado de vermiculita e vermiculita expandida. *Anais do SimAPI 40 Anos, São Carlos - SP*; 2019, p. 497 - 505.
- [26] Padilla-Ortega E, Leyva-Ramos R, Mendoza-Barron J. Role of electrostatic interactions in the adsorption of cadmium (II) from aqueous solution onto vermiculite. *Appl Clay Sci* 2014; 88-89:10-17.
- [27] Neto BB, Scarminio IS, Bruns RE. *Como fazer experimentos*. 4. ed. Porto Alegre: Bookman, 2010.
- [28] Zheng X, Liu E, Zhang F, Yan Y, Pan J. Efficient adsorption and separation of dysprosium from NdFeB magnets in an acidic system by ion imprinted mesoporous silica sealed in a dialysis bag. *Green Chem* 2016; 18(18): 5031-5040.
- [29] Alcaraz L, Escudero M E, Alguacil FJ, Llorente I, Urbieta A, Fernández P, López FA. Dysprosium Removal from Water Using Active Carbons Obtained from Spent Coffee Ground. *Nanomaterials* 2019; 9: 1372.
- [30] Kegla T, Bana I, Lobnik A, Košak A. Synthesis and characterization of novel $\gamma\text{-Fe}_2\text{O}_3\text{-NH}_4\text{OH}@\text{SiO}_2$ (APTMS) nanoparticles for dysprosium adsorption. *J. Hazard. Mater* 2019; 378:120764.
- [31] Berijani S, Ganjali MR, Sereshti H, Norouzi P. A selective modified nanoporous silica as sorbent for separation and preconcentration of dysprosium in water samples prior to ICP-OES determination. *Int J Environ An Ch* 2012; 92(3): 355-365.
- [32] Abdel-Magied AF, Abdelhamid HN, Ashour RM, Zou X, Forsberg K. Hierarchical porous zeolitic imidazolate frameworks nanoparticles for efficient adsorption of rare-earth elements. *Micropor Mesopor Mat* 2019; 278: 175-184.
- [33] Liang T et al. Polyacrylic acid grafted silica fume as an excellent adsorbent for dysprosium (III) removal from industrial wastewater. *Water Sci Technol* 2018; 77(6): 1570-1580.

CO₂ adsorption in 13X zeolites modified by cation exchange with alkaline earth metals

Vanessa R. C. Moura Barbalho^a, Mariana M. V. M. Souza^a

^a Escola de Química- Universidade Federal do Rio de Janeiro - Av. Athos da Silveira Ramos, 149 – Bloco E – Centro de Tecnologia – Cidade Universitária, 21941-909, Rio de Janeiro, Brasil

Abstract

In this study, the effect of ion exchange of Na⁺ cations by Ba²⁺ and Sr²⁺ in Na13X zeolites on the CO₂ adsorption capacity was evaluated. The samples were characterized by X-ray fluorescence, X-ray diffraction, N₂ physisorption and thermogravimetric analysis. CO₂ adsorption isotherms were measured using thermogravimetric analysis instrument. It was found that the crystalline structure was not significantly altered, although there was a decrease in the specific surface area of the modified samples, probably caused by the obstruction of the pores by the metal. CO₂ adsorption was conducted at 30, 50 and 75 °C. The best results of adsorption capacity were obtained at lower temperature. Exchange with Ba and Sr cations did not significantly alter adsorption capacity. For all the samples, the adsorption equilibrium was measured at 30 °C.

Keywords: zeolite 13X; ion exchange; carbon dioxide; adsorption.

1. Introduction

The continuous accumulation of greenhouse gases in the atmosphere has intensified global warming and increased irreversible changes and damage to the environment. High consumption of fossil fuels for energy supply is one of the major contributors to high rates of CO₂ emissions in the earth's atmosphere. In this context, carbon capture and storage (CCS) has been identified as a potential approach for reducing anthropogenic CO₂ emissions into the atmosphere.

Zeolites are aluminosilicate minerals with interconnected channels and cavities of molecular dimensions, which contain compensating ions, water molecules or other adsorbates and salts. Zeolite structure allows the transfer of matter through the intracrystalline spaces. However, this transfer is limited by the pore diameter of zeolites [1]. Compensation cations present in zeolites are known to induce specific interactions with different molecules [2].

These crystalline aluminosilicates have three-dimensional structures formed by TO₄ tetrahedra (T = Si and Al). Tetrahedra are connected by sharing oxygen atoms and negative aluminum-oxygen charges are compensated with cations, usually alkaline or alkaline earth metals. The adsorption capacity of zeolites depends on some

factors that include polarization power, size, distribution and number of cations in their porous structure, Si/Al ratio, pore shape and adsorbed molecule size [3]. In general, the polarization force of cations is inversely proportional to their ionic radius. This cation-quadrupole interaction is the most important mechanism of CO₂ adsorption in zeolites [4].

The objective of this work is to evaluate the effect of ion exchange of Na⁺ cations by Ba²⁺ and Sr²⁺ in Na13X zeolites on CO₂ adsorption capacity by varying the adsorption temperature.

2. Methodology

2.1. Adsorbent Modification

The 13X zeolite, purchased in powder from Sigma-Aldrich, was modified by exchanging sodium (Na⁺) cations for barium (Ba²⁺) and strontium (Sr²⁺) cations to obtain new adsorbents, Ba13X and Sr13X.

The procedure for obtaining modified zeolites was reported by Moraes and Machado [5]. Barium nitrate (Ba(NO₃)₂) and strontium nitrate (Sr(NO₃)₂) solution were used to perform the ion exchange. The amount of barium and strontium ions in the solution was calculated based on the equivalent number in grams of sodium present in zeolite 13X.

The equivalent ratio in grams Ba^{2+}/Na^+ and Sr^{2+}/Na^+ was 2.

Na13X was heated in a muffle furnace at 400 °C with heating rate of 3 °C min⁻¹ for 3 h. After Na13X pretreatment, the 14 h ion exchange procedure was performed in a reflux system at 75 °C. A Na13X water suspension of 15 % (w/w) was prepared. This suspension was acidified with hydrochloric acid (HCl) to maintain the pH between 5 and 6 while stirring for 1 h at 75 °C. Then barium nitrate/strontium nitrate solution was added to the mixture to perform ion exchange.

After this procedure, the suspension was filtered by vacuum and washed three times: the first with the same salt solution added to the suspension, and the last two with deionized water. The washes were conducted at the same temperature as the ion exchange. The samples were oven-dried at 120 °C for 24 h.

2.2. Characterization of adsorbent

X-ray fluorescence analyzes were executed using a Rigaku Primini device with a rhodium tube, for the quantitative analysis of the chemical composition of the samples.

X-ray diffraction measurements were performed on a Rigaku Miniflex II diffractometer with a $CuK\alpha$ radiation source (30 kV and 15 mA) to evaluate structural changes in the ion exchange procedure.

Textural analysis, by means of the physisorption of N_2 at -196 °C, allowed to calculate the specific surface area by the Brunauer-Emmett-Teller (BET) method and the pore volume using the Barret-Joyner-Hallender method (BJH). Analysis were performed on TriStar II model 3020 Micromeritics equipment. The samples were pretreated at 300 °C for 24 h under vacuum to remove adsorbed components on their surface.

Thermogravimetric curves (ATG) were performed on a TA SDT Q600 thermogravimetric analysis instrument. About 5 mg of each sample was placed in a crucible with a heating rate of 20 °C min⁻¹ to 1000 °C under inert atmosphere (N_2) at a 100 mL min⁻¹ flow rate.

2.3. Evaluation of adsorbents in CO_2 capture

The tests were performed at atmosphere pressure on a TA SDT Q600 thermogravimetric analysis instrument. Initially, the adsorbents underwent an in-situ heat treatment up to 200 °C. Then, the system was cooled to the adsorption

temperature (30, 50 and 75 °C). In the heating and cooling steps, nitrogen gas was used at a flow rate of 100 mL min⁻¹. The adsorption step was carried out using high purity carbon dioxide (CO_2) (99.99%) at a flow rate of 50 mL min⁻¹.

2.4. CO_2 adsorption isotherms

The CO_2 adsorption isotherm experiments were also performed on TA SDT Q600 thermogravimetric analysis equipment. The experimental procedure was the same as previously reported. The different CO_2 concentrations were obtained by modification of the furnace inlet flow. The adsorption temperature used was 30 °C at atmosphere pressure.

If the adsorption isotherm exhibits type I behavior, adsorption equilibrium data can be described with Langmuir adsorption isothermal regression [6].

In order to describe the behavior of the adsorption isotherm, equilibrium data were correlated using the Langmuir equation (Eq. 1).

$$q_e = \frac{q_m b C_e}{1 + b C_e} \quad (1)$$

where q_e is the amount adsorbed at equilibrium; q_m is the maximum amount adsorbed to the monolayer; b is the Langmuir constant; and C_e is the CO_2 concentration.

3. Results and discussion

Chemical analysis of the zeolites is shown in Table 1. The analysis confirms the presence of aluminum, silicon and sodium for Na13X zeolite and the occurrence of cation exchange in Ba13X and Sr13X adsorbents.

Table 1. Chemical composition of zeolites.

Element	% weight		
	Na13X	Ba13X	Sr13X
Si	35.9	33.9	38.3
Al	26.3	26	25.5
Na	37.8	-	-
Ba	-	40	-
Sr	-	-	36.2

The XRD patterns of the raw and ion-exchanged materials are shown in Fig. 1. Crystalline phases were identified using the database Joint Committee on Powder Diffraction Standards (JCPDS). Zeolite characteristic peaks were identified (JCPDS 43-0168), confirming the structure of this material,

showing that it was maintained after the ion exchange process.

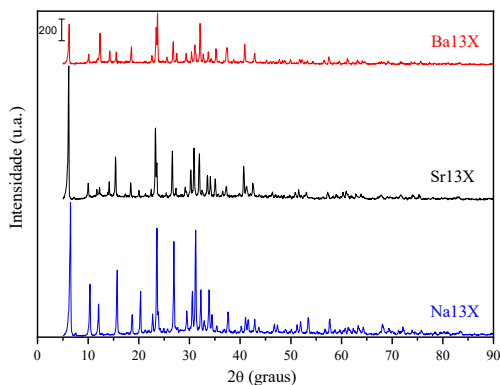


Fig. 1. X-ray diffractograms of the zeolites.

In Figure 1, it can also be observed that in samples modified by ion exchange, there was a decrease in the characteristic intensities of the peaks, indicating a small reduction in the Ba13X and Sr13X crystallinity. These XRD results are in accordance with the literature [7].

Table 2 shows the specific surface area, pore volume and diameter for Na13X zeolite and ion exchanged zeolites. The specific surface area decreased from $657 \text{ m}^2 \text{ g}^{-1}$ to $401 \text{ m}^2 \text{ g}^{-1}$ and $427 \text{ m}^2 \text{ g}^{-1}$ for Ba13X and Sr13X zeolites, respectively. The reduction in area, pore volume and diameter of modified zeolite samples in relation to its precursor, Na13X, may occur due to the clogging of some pores by metal cation.

Table 2. Textural characteristics of the adsorbents.

Adsorbent	S_{BET} ($\text{m}^2 \text{ g}^{-1}$)	V_p ($\text{cm}^3 \text{ g}^{-1}$)	D_p (nm)
Na13X	657	0.32	6.05
Ba13X	401	0.23	4.77
Sr13X	427	0.22	5.03

Moura et al. [2] studied the viability of CH_4 and CO_2 adsorption in 13X zeolite pellets by ionic exchange of Na^+ cations by NH_4^+ , Li^+ , Ba^{2+} and Fe^{3+} . The authors found specific surface area and pore volume of $652 \text{ m}^2 \text{ g}^{-1}$ and $0.43 \text{ cm}^3 \text{ g}^{-1}$ for Na13X zeolite and of $590 \text{ m}^2 \text{ g}^{-1}$ and $0.39 \text{ cm}^3 \text{ g}^{-1}$ for modified Ba13X zeolite.

The adsorption-desorption isotherms of N_2 are shown in Figures 2, 3 and 4 for zeolites Na13X, Ba13X and Sr13X, respectively.

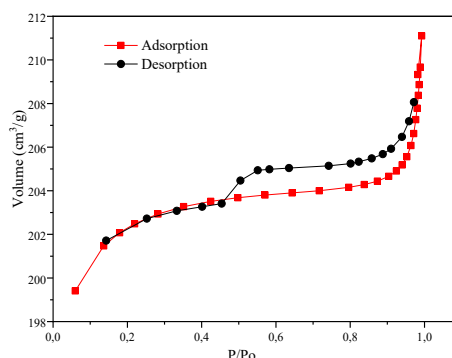


Fig. 2. Nitrogen adsorption isotherm of Na13X zeolite.

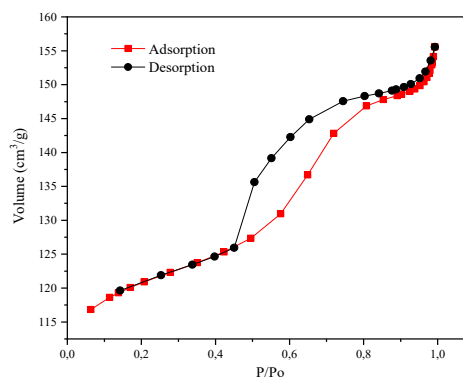


Fig. 3. Nitrogen adsorption isotherm of Ba13X zeolite.

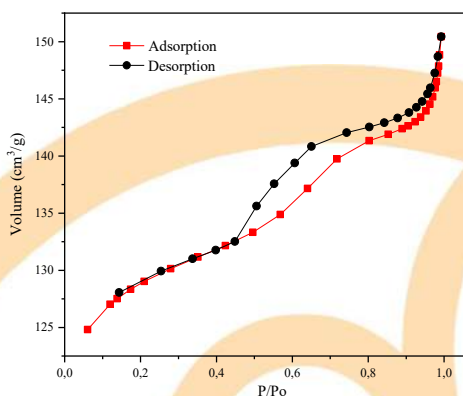


Fig. 4. Nitrogen adsorption isotherm of Sr13X zeolite.

According to the IUPAC classification, the obtained isotherm can be classified as type IV, characteristic of mesoporous adsorbents. In low pressure regions, they are similar to type II, and the amount adsorbed tends to infinity when P/P_0 is equal to 1. Type IV isotherms exhibit hysteresis, which is associated with capillary condensation. This effect is related to pore size and morphology. The type of hysteresis is similar to type H3 [8]. Modified zeolites have lower N_2 adsorption

because sodium cation ion exchange decreases the pore sizes available for N₂ adsorption because barium and strontium ions have larger ionic radius.

The results of thermogravimetric analysis for Na13X, Ba13X and Sr13X samples are presented in Figures 5, 6 and 7. The figures show the percentage of mass loss and its derivative as a function of temperature. It is observed that the zeolite samples had different behaviors of mass loss. Na13X zeolite presented two stages of mass loss due to hydration and zeolitic water losses. The sample had a total mass loss of around 18.6% due to the heating process. On the other hand, Sr13X and Ba13X zeolite showed a higher mass loss due to the increased hydration of zeolite, precisely to the presence of hydrated cation Sr²⁺ and Ba²⁺.

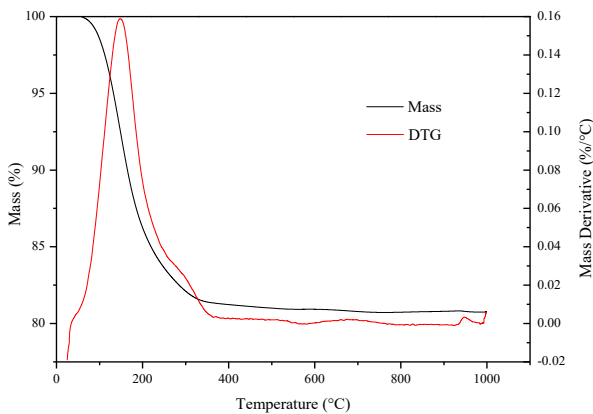


Fig.5. TG and DTG curves for Na13X zeolite.

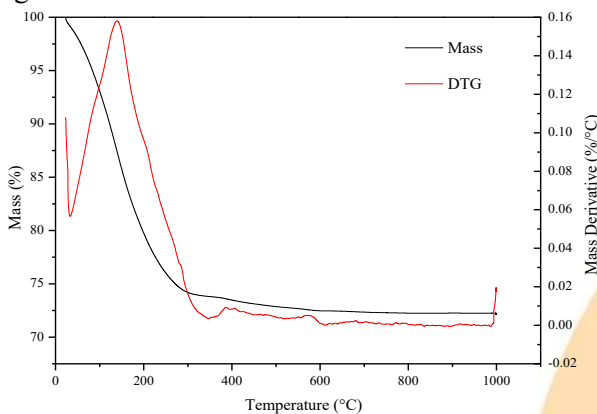


Fig. 6. TG and DTG curves for Ba13X zeolite.

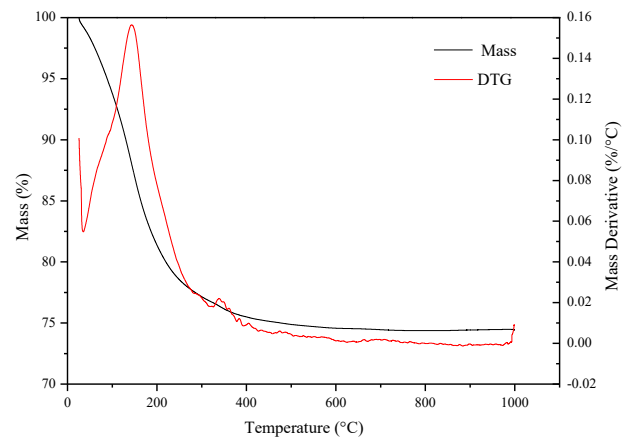


Fig. 7. TG and DTG curves for Sr13X zeolite.

Tables 3 shows the adsorption values for three temperatures. Temperature is an important parameter to determine adsorption capacity. It can be seen from Table 3 that decreasing temperature increases the adsorption capacity. This is probably because rising this parameter provides more internal energy to molecules in the gas phase. It is also important to note that increased energy allows gas molecules to diffuse in a higher rate. At the same time, it could reduce the chance which gas molecules get trapped or restricted at fixed adsorption sites on the adsorbent surface [7].

Table 3. CO₂ adsorption capacity at different temperatures.

Temperature (°C)	Adsorption of CO ₂ (mmol g ⁻¹)		
	Na13X	Ba13X	Sr13X
30	3.36	3.18	3.34
50	2.62	2.67	2.50
75	1.73	2.48	1.45

Salehi and Anbia [7] evaluated the adsorption capacity and selectivity of CO₂ and N₂ in faujasite (FAU) and LTA zeolites at three temperatures (25, 50, 75 °C) using pressures up to 5 bar. An ion exchange was performed with the NaX, NaY and NaA zeolites with Ca²⁺ cations. The authors obtained results for NaX and CaX at 25 °C approximately equal to 2.4 and 1.8 mmol g⁻¹, which are lower than the values of this study.

Kareem et al. [9] studied the critical and supercritical conditions for CO₂ adsorption in 13X and 5A zeolites at 150 bar and two different operating temperatures (50 and 70 °C). 13X zeolite showed higher adsorption under supercritical conditions of 7.5 mmol g⁻¹ at 50 °C and 6.8 mmol g⁻¹ at 70 °C, while 5A zeolite adsorbed 6.4 mmol g⁻¹ and 5.2 mmol g⁻¹, respectively.

Figure 8 shows the equilibrium adsorption isotherms at 30 °C of pure CO₂ in the different cation-exchanged zeolites. In general, adsorption equilibrium data for zeolites can be considered as type I adsorption isotherms. Therefore, Langmuir isothermal models were employed in the experimental data and the corresponding parameters are presented in Table 4.

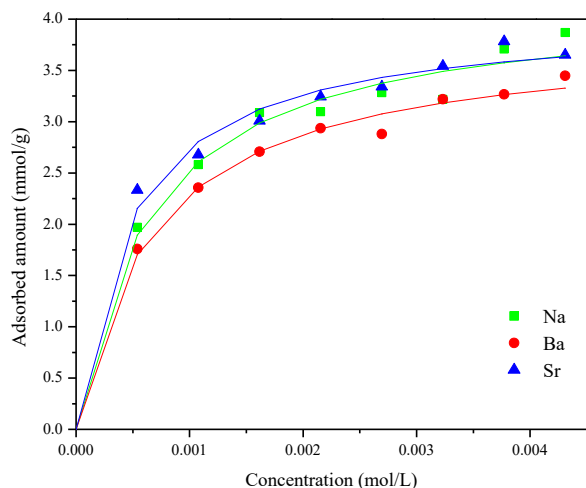


Fig. 8. Adsorption isotherms for CO₂ at 30 °C.

Table 4 presents the parameters q_m and b that are related to the maximum adsorption capacity and magnitude of adsorption affinity, respectively.

Table 4. Parameters of Langmuir adsorption model for 13X zeolites.

Langmuir parameters	Sample		
	Na13X	Ba13X	Sr13X
q_m (mmol g ⁻¹)	4.19	3.85	4.03
b (L mol ⁻¹)	1529.6	1474	2135.3

Zeolite Na13X has the highest adsorption capacity, therefore the q_m parameter is in accordance with the adsorbed quantities in Table 3.

Kennedy and Tezel [6] studied the modification of natural clinoptilolite by cation exchange using alkaline earth metal cations (Be²⁺, Mg²⁺, Ca²⁺, Sr²⁺, Ba²⁺). Adsorption isotherms for CO₂, N₂ and CH₄ were measured at 30 °C using microgravimetric adsorption analyser at a pressure range of 0 to 8 atm and classified as type I isotherms. Langmuir and Toth isotherms were adjusted to the experimental adsorption equilibrium data and the resulting parameters of these isotherms were determined. They found values for q_m of 1.861 and 1.825 mmol g⁻¹ and for b 6.868 and 6.462 atm⁻¹ for Ba and Sr cations, respectively.

4. Conclusion

The effect of temperature on the adsorption of CO₂ was studied on Na13X zeolite and cation exchanged with Ba²⁺ and Sr²⁺, in order to quantify the efficiency in CO₂ capture. A decrease in adsorption capacity was observed with increasing temperature, probably due to the exothermic adsorption process. The higher adsorption capacity was 3.36 mmol g⁻¹ at 30 °C for NaX and the ion exchange did not have great influence on adsorption values. Langmuir isotherms were fitted to the experimental adsorption equilibrium data and the resultant parameters of these isotherms were determined.

Acknowledgments

The authors thank CAPES, CNPq, and FAPERJ for financial support granted to carry out this work and the Greentec laboratory for conducting the textural analysis.

References

- [1] Luz AB da. Zeólitas: Propriedades e Usos Industriais. Rio de Janeiro: CETEM/CNPq, 1995.
- [2] Moura PAS, Bezerra DP, Vilarrasa-Garcia E, Bastos-Neto M, Azevedo DCS. Adsorption equilibria of CO₂ and CH₄ in cation-exchanged zeolites 13X. *Adsorption*. 2016;22:71-80.
- [3] Olajire AA. CO₂ capture and separation technologies for end-of-pipe applications – A review. *Energy*. 2010;35:2610-2628.
- [4] Bonenfant D, Kharoune M, Niquetti P, Mimeault M, Hausler R. Advances in principal factors influencing carbon dioxide adsorption on zeolites. *Science and Technology*. 2008;10:29-33.
- [5] Moraes EP, Machado NRCF. Clarification of Stevia rebaudiana (Bert.) Bertoni extract by adsorption in modified zeolites. *Acta Scientiarum*. 2001;23:1375-1380.
- [6] Kennedy DA, Tezel FH. Cation exchange modification of clinoptilolite – Screening analysis for potential equilibrium and kinetic adsorption separations involving methane, nitrogen, and carbon dioxide. *Microporous and Mesoporous Materials*. 2018;262: 235-250.
- [7] Salehi S, Anbia M. Characterization of CPs/Ca-exchanged FAU- and LTA-type zeolite nanocomposites and their selectivity for CO₂ and N₂ adsorption. *Journal of Physics and Chemistry of Solids*. 2017;110:116-128.
- [8] Metz B, Davidson O, Coninck HD, Loos M. Meyer L. IPCC Special Report on Carbon Dioxide Capture and Storage, Cambridge, 2005.
- [9] Kareem FAA, Shariff AM, Ullah S, Dreisbach F, Mellon N, L. K. Keong, Garg S. Experimental measurements and modeling of supercritical CO₂ adsorption on 13X and 5A zeolites. *Journal of Gas Science and Engineering*. 2018;50:115-127.

Ionic Flocculation obtained from sunflower oil for the removal Methylene Blue

Teixeira, Y.N.^a, Melo, R.P.F.^b, Carmo, S.K.S.^c, Evangelista, M.N.D.^d

^aUFERSA, Av. Francisco Mota N°572, Mossoró 59625900, Brazil

^bUFERSA, BR-226 s/n, Pau dos Ferros 59900000, Brazil

^cUFERSA, BR-226 s/n, Pau dos Ferros 59900000, Brazil

^dUFERSA, Av. Francisco Mota N°572, Mossoró 59625900, Brazil

Abstract

Contamination of water by organic compounds is characterized by great diversity and low degradability. In view of this, this research proposes the use of ionic flocculation to remove a model pollutant (methylene blue, MB) from the water. This process consists in the mixture of surfactants, obtained from industrialized sunflower oil, with the solution containing the pollutant and, later, the addition of the calcium to the system. The reaction of the surfactant and calcium forms a precipitate, which aggregates to form flocs when the system is agitated. The flocs form an adsorbent surface, attracting MB molecules present in the water, and can be removed by a centrifugation process. The ionic flocculation was evaluated by varying the parameters: surfactant concentration, MB concentration, presence of electrolytes, effect pH and temperature. A maximum MB removal efficiency of 67.12% was obtained adjusting the pH of the solution to pH 12, demonstrating that the process has potential for removal of pollutant.

Keywords: Ionic Flocculation; Methylene Blue; Surfactants; Adsorption.

1. Introduction

Treatment of dye-containing effluents is a growing concern in the industry due to the visible aesthetic negative impact of releasing these effluents on a receiving water body, as well as potential toxicity problems. This leads to the search of an adequate scheme of operation of feasible cost and complexity, which is a function of the legal requirements of treated water, the degree of contamination and of the amount of water to be processed to develop a viable cost-benefit efficient project [1].

MB is a dye widely used not only in textile industries but also in other processes, such as pharmaceutical, medicinal, biological and chemical [2].

Ionic flocculation is a separation process in which the main agent is the anionic surfactant molecule. The process is carried out from the mixture of the surfactant with the sample containing the organic pollutant to be removed. Right after, a divalent or trivalent metal is added to promote the

precipitation of the surfactant, which under stirring will form flocs capable of removing organic compounds from system. The entire blending process up to the centrifugation step to collect the flocs is carried out in ten minutes, demonstrating a rapid operation when compared to other treatment processes.

This work was carried out to evaluate the efficiency of the ionic flocculation in the removal of MB in aqueous medium. To perform the ionic flocculation a surfactant obtained from industrialized sunflower oil was chosen, using calcium as the metal to promote precipitation. Parameters such as MB concentration, surfactant concentration, electrolytes, pH and temperature were evaluated for the influence on MB removal efficiency.

2. Material and Methods

In this work a laboratory-produced surfactant from industrialized sunflower oil (Liza) was selected to perform the ionic flocculation and MB (molecular mass = 0.31985 g/mol, C₁₆H₁₈N₃Cl)



was used as the pollutant model. Calcium chloride (CaCl_2 , Synth) is used to obtain the calcium ions necessary to precipitate the surfactant. In the experiments that evaluated the effect of pH, the adjustment is performed with hydrochloric acid (36.46 kg/mol) and sodium hydroxide (40 kg/mol). NaCl (Synth) is used in the experiments to evaluate the effect of electrolytes in the dye removal process. All reagents are of analytical grade.

2.1. Experimental process

Initially, the MB solution (0.01 kg/m^3) is prepared from a stock solution of 0.1 kg/m^3 . Soon after the masses of surfactant and calcium chloride are weighed to obtain the desired concentrations of the surfactant and calcium in solution respectively. The mass of calcium chloride is weighed so that the concentration of calcium ions in solution is half the concentration of surfactant, providing the complete reaction of the surfactant with the calcium ion, resulting in precipitation.

Then, the surfactant is mixed with the MB solution, dissolving it with the aid of a stirrer. Calcium is always added after complete dissolution of the surfactant, causing it to precipitate and form the flocs. This system is subjected to light agitation for 5 minutes to avoid breaking the flocs, obtaining aggregates of appropriate size to perform the separation of the flocs by a centrifugation process. After separation, the samples are analyzed in a spectrophotometer in order to determine the final concentration of MB.

2.2. Efficiency calculation

The removal efficiency of MB was calculated using equation 1.

$$\%E = \left(\frac{C_{iMB} - C_{fMB}}{C_{iMB}} \right) * 100\% \quad (1)$$

Where %E is MB removal efficiency, C_{iMB} and C_{fMB} are initial and final MB concentration, respectively.

2.3. Surfactant concentration

For the analysis of the effect of the surfactant concentration, a concentration range of 0.5 to 1.7 kg/m^3 , ranging from 0.1 to 0.1 kg/m^3 , was used, and the MB concentration in the solution was fixed at 0.01 kg/m^3 . The experimental procedure was

performed as explained in section 2.1.

In this step, it was also analyzed if only flocculation, only CaCl_2 in the solution, would be able to remove part of MB.

2.4. MB concentration

In the study of the variation of the MB concentration, a concentration range between 0.01 kg/m^3 and 0.1 kg/m^3 was used, maintaining the surfactant concentration fixed at 1 kg/m^3 . This value was used as a model concentration based on the result presented in the surfactant concentration study.

2.5. Electrolytes effect

The flocs that promote the removal of MB from the solution are produced in the system from anionic surfactants. These are recognized for their instability to presence of electrolytes in solution [3,4]. It is also common to find industrial effluents containing organic compounds and present electrolytes simultaneously, for example, textile effluent [5]. Considering these factors, NaCl in different concentrations (1.16 , 2.34 , 3.51 and 4.67 kg/m^3) was used in this study as the source of electrolytes.

2.6. pH effect

In the ionic flocculation, the pH becomes an important factor to be studied due to the instability of the anionic surfactant, which returns to fatty acid when present in an acid medium.

In experiments to evaluate the pH effect, the effluent solution was restricted to the MB concentration of 0.01 kg/m^3 and the surfactant concentration of 1 kg/m^3 . The process was evaluated at a pH range of 7-12. The pH adjustment step was performed after the addition of the surfactant to the effluent and prior to the addition of the calcium chloride. In the pH of 7 and 8, the solutions become turbid, which makes spectrophotometric analysis difficult.

2.7. Temperature effect

The temperature is essential to evaluate because it affects the equilibrium of any separation process. In the study of the influence of temperature, a temperature range of 313-343 K was used, aiming

for the solubilization of the surfactant that does not occur at room temperature. Temperature control was performed with the sample in a Becker on a magnetic stirrer with temperature control, constantly measuring the temperature with a precision mercury thermometer of 1.0 °C.

3. Results and discussion

3.1. Effect of surfactant concentration

Figure 1 shows the results of MB removal efficiency as a function of the surfactant concentration.

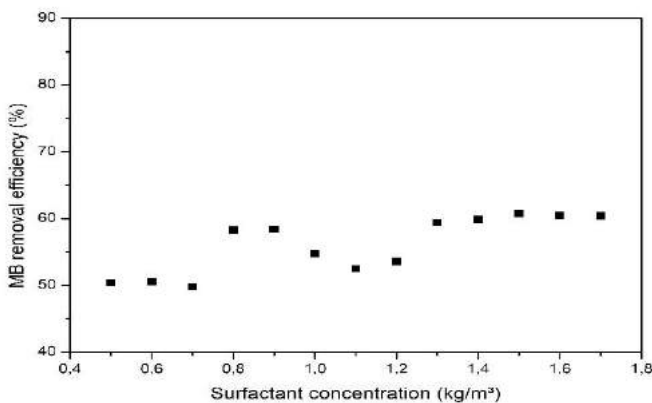


Figure 1. MB removal efficiency vs. Surfactant Concentration. Temperature = 303 K, without pH adjustment.

The variation in surfactant concentration does not significantly alter the removal efficiency. This characterizes that the process is independent of the concentration of surfactant in the range studied. For this reason, the surfactant concentration of 1 kg/m³ was adopted as standard in the other stages. However, the use of surfactant concentrations below this range is impracticable, since the amount of surfactant employed is not enough to produce flocs capable of being separated by centrifugation or filtration due to small size of the floc.

Only the addition of CaCl₂ promotes a small MB removal, approximately 25%, proving that the addition of surfactant makes the process more efficient.

For a removal of 60.72%, surfactant concentration at 1.5 kg/m³, the final concentration of MB was 0.0032 kg/m³. Figure 2 illustrates the ionic flocculation.



Figure 2. Effluent contaminated by MB (left) and after the ionic flocculation (right).

3.2. Effect of MB concentration

Figure 3 shows the effect of MB concentration versus MB removal efficiency.

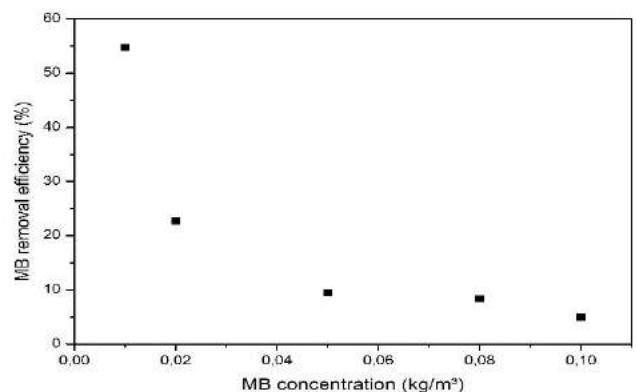


Figure 3. MB removal efficiency vs. MB Concentration. Temperature = 303 K.

According to Figure 3, it is concluded that by keeping the surfactant concentration fixed at 1 kg/m³ and varying the concentration of MB, the results differ considerably from each MB concentration. This occurs because the surfactant has an adsorption limit, consequently increasing its efficiency at lower pollutant concentrations and decreasing its efficiency at higher concentrations of MB.

3.3. Effect of electrolytes

Figure 4 shows the results of the dye removal efficiency for different concentrations of NaCl.

These concentrations were used to avoid the precipitation of the surfactant by NaCl, because above 4.67 kg/m³ of NaCl the precipitation of the surfactant was observed even without adding calcium.

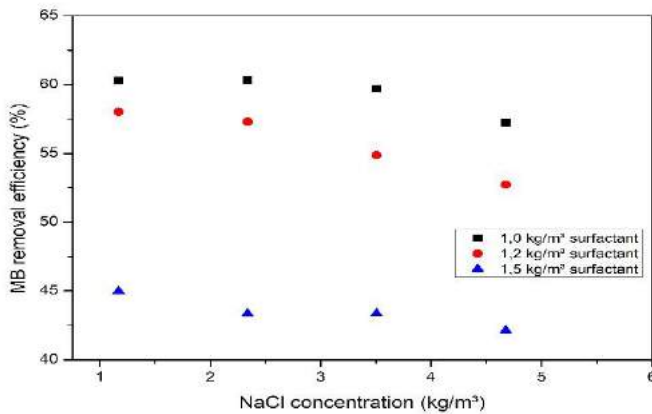


Figure 4. Effect of the presence of electrolytes at different concentrations of NaCl.

The addition of NaCl decreases the removal efficiency as seen in Figure 4. The effect of electrolytes reduces the removal efficiency as the amount of NaCl added to the system increases. The results show that the maximum removal efficiency (69.31%) is obtained at 1.17 kg/m³ NaCl for the concentration of 1 kg/m³ and the lowest removal efficiency (42.14%) at 4.67 kg/m³ NaCl for concentration of 1.5 kg/m³. With the high concentration of electrolytes in solution, the dissociation of the surfactant is disadvantageous, reducing the amount of surfactant that would react with calcium to form the floc [6, 7].

Mouni et al. [8] affirms that, using Caulim as an adsorbent, as the amount of electrolytes in the solution increases, the removal efficiency decreases as already observed by Rida et al. [9].

3.4. Effect of pH

Figure 5 shows the effect of pH variation on the removal efficiency of MB. The pH was evaluated between 7 and 12, since the visual observations show that the medium is cloudy at pH 7, indicating the formation of an oil-in-water emulsion. This occurs because the surfactant returns to its respective fatty acids as a result of the lower pH, preventing the formation of flocs due to the absence

of carboxylate anions, making the process unfeasible [10].

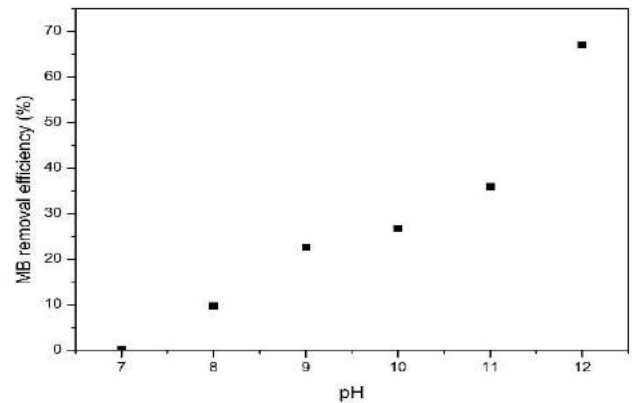


Figure 5. Effect of the variation of pH of the solution.

During the analyzes it was verified that, without adjusting the pH, the samples with only the effluent have pH between 7-8 and the samples with surfactant have pH between 9-10, which corresponds to the pH resulting from the reactions between fatty acids with strong bases. Figure 5 shows that a pH between 11-12 yields the best results. At pH 12, at 1 kg/m³ surfactant, the dye removal reached 67.12%, an increase of 13.17% over the experiments under the same conditions without adjusting the pH (pH \cong 9.2). For the removal of 62.12%, the final MB concentration is 0.0026 kg/m³.

Shu et al. [11] states that with increasing pH the MB removal efficiency from the solution using modified electrolytic manganese residue (MEMR), also increases. The increase in pH also brings about the change of SiOH groups to SiO present in the MEMR, the SiO groups present a relatively strong chemical or electrostatic association with the MB, facilitating its adsorption [12].

3.5. Effect of temperature

Figure 6 presents the results for the MB removal efficiency as a function of temperature for different surfactant concentrations.

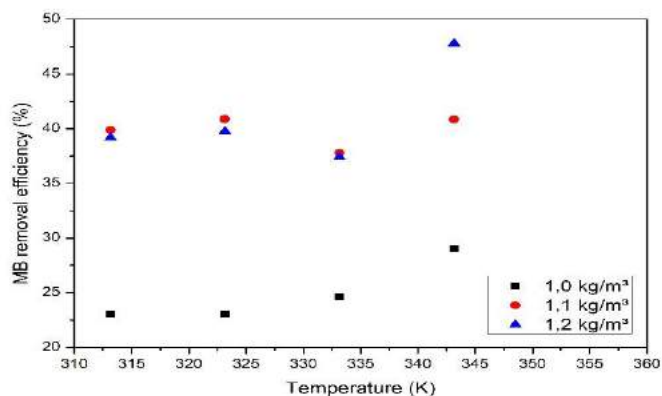


Figure 6. Effect of temperature variation on the solution, without pH adjustment, [MB] = 0.01 kg/m³.

The removal efficiency increased as the temperature increased. However, the variation was very low in the three concentrations studied in relation to the temperature variation. With the surfactant concentration at 1 kg/m³, the variation in efficiency between temperatures of 313-343 K was only about 6%.

Therefore, for this study, the temperature factor has little influence on the removal variation of the MB. This is because the fatty acid salt, which makes up the floc, formed in the reaction between surfactant and the calcium ion has a high Krafft point and therefore very low solubility [13], being able to withstand temperature variations without considerably altering its adsorption capacity.

4. Conclusions

Ionic flocculation proved to be an efficient method of effluent treatment, and it can be used not only for MB but also for others organic compounds. From the results, it is concluded that only flocculation already promotes a dye removal, but with the addition of surfactant the efficiency increases, there is a minimum surfactant concentration (0.5 kg/m³) to perform MB removal, the surfactant has a limit of adsorption of pollutant particles, proving to be more effective at low dye concentrations. Presence of electrolytes in the solution decreases the removal efficiency, raising the pH improves the process removal efficiency, reaching removals up to 67.12% and increasing the temperature has little influence on the separation.

Acknowledgements

The authors thank the Universidade Federal Rural do Semi-Árido (UFERSA) for the support provided for the research.

References

- [1] Cheremisinoff, N. P. (2002) Handbook of Water and Wastewater Treatment Technologies, 1st ed., Butterworth-Heinemann, Massachusetts.
- [2] Honorato, H. A., Machado, J. M., Celante, G., Borges, W. G. P., Dragunski, D. C., Caetano, J. (2015) 'Biossorção de azul de metileno utilizando resíduos agroindustriais', Revista Brasileira de Engenharia Agrícola e Ambiental, Vol. 19 No. 7, pp. 1807 – 1929. <http://dx.doi.org/10.1590/18071929/agriambi.v19n7.p705-710>.
- [3] Soontravanich, S. and Scamehorn J. F. (2010) 'Use of a nonionic surfactant to inhibit precipitation of anionic surfactants by calcium', Journal of Surfactants and Detergents, Vol. 13 No. 1, pp. 13 - 18. <https://doi.org/10.1007/s11743-009-1149-z>.
- [4] Talens F. I., Páton P., Gaya S. (1998) 'Micelar flocculation of anionic surfactants', Langmuir, Vol. 14 No. 18, pp. 5046 – 5050. <http://dx.doi.org/10.1021/la971130x>.
- [5] Mirbolooki, H., Amirnezhad, R., Pendashteh, A. R. (2017) 'Treatment of high saline textile wastewater by activated sludge microorganisms', Journal of Applied Research and Technology, Vol. 15 No. 2, pp. 167 – 172. <http://dx.doi.org/10.1016/j.jart.2017.01.012>.
- [6] Baviere, M., Bazin, B., Aude, R. (1983) 'Calcium effect on the solubility of sodium dodecyl sulfate in sodium chloride solutions', Journal of Colloid and Interface Science, Vol. 92 No. 2, pp.580 - 583. [https://doi.org/10.1016/0021-9797\(83\)90179-0](https://doi.org/10.1016/0021-9797(83)90179-0).
- [7] Stellner, K. L. and Scamehorn J. F. (1989) 'Hardness tolerance of anionic surfactant solution. 1. Anionic surfactant with added monovalent electrolyte', Langmuir, Vol. 5 No. 1, pp. 70 – 77. <http://dx.doi.org/10.1021/la00085a014>.
- [8] Mouni, L., Belkhiri, L., Bollinger, J., Bouzaza, A., Assadi, A., Tirri, A., Dahmoune, F., Madani, K., Remini, H. 'Removal of methylene blue from aqueous solutions by adsorption on kaolin: kinetic and equilibrium studies', Applied Clay Science, Vol. 153 No. 1, pp. 38-45. <https://doi.org/10.1016/j.clay.2017.11.034>.
- [9] Rida, K., Bouraoui, S., Hadnine, S. (2013) 'Adsorption of methylene blue from aqueous solution by kaolin and zeolite', Applied Clay Science, Vol. 83-84, pp. 99 – 105. <https://doi.org/10.1016/j.clay.2013.08.015>.
- [10] Melo, R. P. F., Barros Neto, E. L., Moura, M. C. P. A., Castro Dantas, T. N., Dantas Neto, A. A.,



- Oliveira, H. N. M. (2015) 'Removal of direct Yellow 27 dye using animal fat and vegetable oil-based surfactant', *Journal Water Process Engineering*, Vol. 7, pp. 196 – 202. <http://dx.doi.org/10.1016/j.jwpe.2015.06.009>.
- [11] Shu, J., Renlong, L., Haiping, W., Zuohua, L., Xiaolong, S., Changyuan, T. (2018) 'Adsorption of methylene blue on modified electrolytic manganese residue: kinetics, isotherm, thermodynamics and mechanism analysis', *Journal of the Taiwan Institute of Chemical Engineers*, Vol. 82, 351 - 359. <https://doi.org/10.1016/j.jtice.2017.11.020>
- [12] Wang P., Cao, M., Wang, C., Ao, Y., Hou, J., Qian, J. (2014) 'Kinetics and thermodynamics of adsorption of methylene blue by a magnetic graphene-carbon nanotube composite', *Applied Surface Science*, Vol. 290, pp. 116 – 124. <https://doi.org/10.1016/j.apsusc.2013.11.010>.
- [13] Zapf, A., Beck, R., Hoffmann, H. (2003) 'Calcium surfactants: a review', *Advances in Colloid and Interface Science*, Vol. 100-102, pp. 349 – 380. [https://doi.org/10.1016/S0001-8686\(02\)00065-9](https://doi.org/10.1016/S0001-8686(02)00065-9) (Accessed 27 September 2019).

Effluent treatment contaminated by Malachite Green through ionic flocculation

Teixeira, Y.N.^a, Melo, R.P.F.^b, Fernandes, M.R.^c, Carmo, S.K.S.^d

^aUFERSA, Av. Francisco Mota N°572, Mossoró 59625900, Brazil

^bUFERSA, BR-226 s/n, Pau dos Ferros 59900000, Brazil

^cUFERSA, Av. Francisco Mota N°572, Mossoró 59625900, Brazil

^dUFERSA, BR-226 s/n, Pau dos Ferros 59900000, Brazil

Abstract

One of the main forms of pollution in industries is the discharge of effluents into water bodies. Therefore, this work proposes the use of ionic flocculation to remove a model pollutant (Malachite Green, MG) from water. This process consists of mixing surfactant obtained from industrialized sunflower oil with the solution containing the pollutant, adjusting the pH of the solution and then adding calcium to the system. The reaction of surfactant with calcium forms a precipitate, which aggregates into flocs when the system is agitated. The flocs form an adsorbent surface, attracting the MG molecules present in the water, and can be removed by a centrifugation process. Ionic flocculation was evaluated by varying the parameters: surfactant concentration, MG concentration and contact time. It was evaluated that the isotherm model and adsorption kinetics that best fit this process are the Langmuir and Pseudo-Second Order models, respectively. A maximum MG removal efficiency of 96% was obtained only by adjusting the pH to 10, with a surfactant concentration of 1.4 kg/m³ and a MG concentration of 0.01 kg/m³, demonstrating that the process has potential for pollutant removal.

Keywords: Ionic Flocculation; Malachite Green; Adsorption; Effluent treatment.

1. Introduction

One of the main forms of pollution in industries is the discharge of effluents into water bodies. As is well known, water is an indispensable resource for the survival of life on the planet and only 0.02% of existing water is suitable for consumption [1].

Given this, the industries began to give greater importance to the consequences of their production processes, ensuring that their liquid effluent, solid waste and atmospheric emissions do not harm the environment [2].

Among the various residues present in textile effluents, dyes are easily detected, being visible even at low concentrations such as 0.001 kg/m³. When released into the receiving aquatic bodies, even small amounts can alter the natural coloration of rivers, causing serious aesthetic problems as well as reducing some photosynthetic processes. They have varied chemical composition, low biological degradability, high COD, besides the presence of recalcitrant compounds that may be associated with chronic and acute toxicity [3, 4].

Malachite green dye (MG) is a triphenylmethane class dye, very effective in the treatment of parasites, fungal and bacterial infections in fish and fish eggs, and is also widely used as a bacteriological and analytical dye [5].

The MG is water soluble and has different colors with varying pH, being yellow at pH below 2, green at pH 2, bluish green at pH 11 and colorless at pH 14. It has a cationic form in its molecule, with three benzene rings, and its chemical formula is as follows: C₂₃H₂₅N₂ [6].

Although there are several wastewater treatment processes and techniques, they have disadvantages such as processes involving the application of oxidizing agents such as ozone, Fenton reagents, and photochemical sonolysis, which are expensive and difficult to handle, produce large amounts of byproducts and large amounts of dissolved oxygen. Biological processes are not harmful to the environment, but they are slow, require adequate nutrient levels and have a limited working temperature range [7].

Therefore, the use of surfactant is a viable alternative as it can be obtained from low cost raw



material such as vegetable oil and animal fat. The addition of calcium (Ca^{2+}) to the most anionic surfactant solution causes the formation of insoluble surfactant salts, a process known as ionic flocculation.

These salts are in the form of surfactant flocs and may be separated from the mixture by filtration or centrifugation. Surfactant flocs have a significant decontamination potential for organic compounds due to their amphiphilic characteristic.

Clearly, ionic flocculation is a new type of treatment process, so it requires studies to evaluate what steps can be taken to maximize the efficiency of this technique and minimize costs. The parameters evaluated in this work were: surfactant concentration, dye concentration and contact time. Adsorption isotherm and adsorption kinetics were also evaluated.

2. Material and Methods

The surfactant used is synthesized in the laboratory from industrialized sunflower oil (Liza) and Synth sodium hidroxide (NaOH) PA by a saponification reaction with a mass percentage of 55.55% and 44.45%, respectively.

Initially, the masses of sunflower oil and NaOH (0.01 kg of oil and 0.008 kg of NaOH) are weighed. Then dilute the oil in $9 \times 10^{-5} \text{ m}^3$ of ethyl alcohol and NaOH in $4 \times 10^{-5} \text{ m}^3$ of distilled water. Immediately afterwards, the solutions are mixed in a reaction flask and it is heated in a heating blanket, an Allihn condenser (ball condenser) is used to reflux the alcohol and keep it in the system during the whole saponification process.

2.1. Adsorption Process

Initially, the effluent (MG-contaminated solution) is prepared from a stock solution of dye concentration equal to 0.12 kg/m^3 . Soon after, the surfactant and CaCl_2 masses are weighed to obtain the desired surfactant and calcium concentrations in solution. The CaCl_2 mass is weighed so that the concentration of calcium ions in solution is half the surfactant concentration, providing the reaction of surfactant with calcium ion, resulting in precipitation of the surfactant. This proportionality of 0.5 calcium/surfactant will not considerably affect the process efficiency. Therefore, it was decided to use it in order to avoid the high consumption of CaCl_2 [8].

The surfactant is then added to the effluent solution, being dissolved with the aid of a stirrer. Calcium is always added after the complete dissolution of the surfactant, causing it to precipitate and form the surfactant flocs. This system is agitated again for 300 seconds to promote adsorption of the pollutant onto the surface formed by the surfactant flocs, removing it from water.

Afterwards, the solutions are centrifuged at 120000 rps for 300 seconds in an *OEM / Unbrand Model 80-2B Tabletop* centrifuge to separate the pollutant-impregnated flocs from the solution. After the separation, the solution samples are analyzed in a spectrophotometer, *Gehaka model UV-340G*, to determine the final concentration of pollutant in the effluent.

2.2. Efficiency calculation

The removal efficiency of MG was calculated using Equation 1.

$$\%E = \left(\frac{C_{iMG} - C_{fMG}}{C_{iMG}} \right) * 100\% \quad (1)$$

Where $\%E$ is MG removal efficiency, C_{iMG} and C_{fMG} are initial and final MG concentrations, respectively.

2.3. Surfactant concentration

For the analysis of the effect of the surfactant concentration, a concentration range of 0.5 to 2 kg/m^3 , varying from 0.1 to 0.1 kg/m^3 , was used, and the MG concentration in the solution was fixed at 0.01 kg/m^3 , this concentration was adopted as standard for the following reasons: dye concentration is already sufficient to change the characteristics of the solution. The experimental procedure was performed as explained in section 2.1.

2.4. Concentration of MG

In the study of the variation of MG concentration in solution, a concentration range between 0.01 kg/m^3 and 0.12 kg/m^3 is used, keeping the surfactant concentration fixed at 1.4 kg/m^3 . The effluent samples were studied at the following concentrations (0.01, 0.02, 0.04, 0.06, 0.08 and 0.12 kg/m^3). The concentration of 0.12 kg/m^3 was the highest MG concentration because this

concentration is already much higher than the concentration of dyes presents in a textile effluent [9].

2.5. Contact Time

To analyze the contact time, effluents with the following concentrations were used: 0.01; 0.02; 0.04; 0.06; 0.08 and 0.12 kg/m³. The surfactant concentration was fixed at 1.4 kg/m³ and the contact periods were: 600, 1800, 3600, 5400, 7200, 9000 and 10800 seconds. Initially, the surfactant is dissolved in the effluent and then CaCl₂ is added to promote ionic flocculation. The time at which the process was started is observed and in the estimated time the sample is taken from each solution and the spectrophotometric analysis is performed.

2.6. Adsorption isotherm

For this step, the Langmuir model was evaluated, with MG concentrations ranging from 0.01 to 0.12 kg/m³, keeping the surfactant concentration fixed at 1.4 kg/m³ and the temperature of 298 K. Rated contact time was 600 seconds.

The Langmuir model is capable of providing the maximum surfactant adsorption capacity, the MG/Surfactant interaction constant and the separation factor, which is related to the degree of adsorption development.

2.7. Adsorption kinetics

At this stage, the pseudo-second order model was evaluated, with a fixed MG concentration of 0.01 kg/m³, a surfactant concentration of 1.4 kg/m³, a temperature of 298 K and a time varying from 600, 1800, 3600, 5400, 7200, 9000, 10800 and 12600 s. A solution was made for each time interval analyzed.

3. Results and discussion

3.1. Effect of surfactant concentration

Figure 1 presents the results of MG removal efficiency as a function of surfactant concentration. At this stage, only the pH was adjusted to 10, because the MG undergoes color changes at pH above 10.

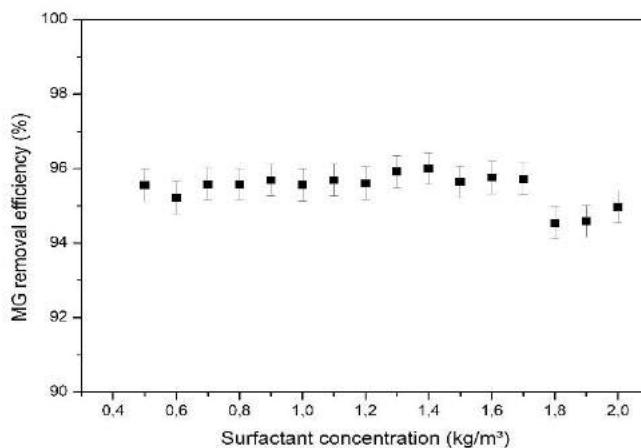


Figure 1. MG removal efficiency vs. Surfactant concentration. Temperature = 298 K, pH 10.

It is concluded that the variation in surfactant concentration does not considerably change the removal efficiency. This characterizes, for this case, an ionic flocculation independent of the surfactant concentration in the studied range. Surfactant concentrations below 0.5 kg/m³ make the process unfeasible, because the amount of surfactant is not sufficient to produce flocs that provide MG adsorption.

The highest efficiency obtained in this step was 96% for a surfactant concentration of 1.4 kg/m³, the final concentration of MG in the solution was only 0.00041 kg/m³.

The ionic flocculation is independent of the surfactant concentration for methylene blue treatment, having an average efficiency of 58.31% using only surfactant flocs without any adjustment [10].

The ionic flocculation is independent of surfactant concentration for the treatment of black solophenyl, having an average efficiency of 95.48% using only surfactant flocs without any adjustment [11]. Figure 2 illustrates the effluent before and after treatment, respectively.

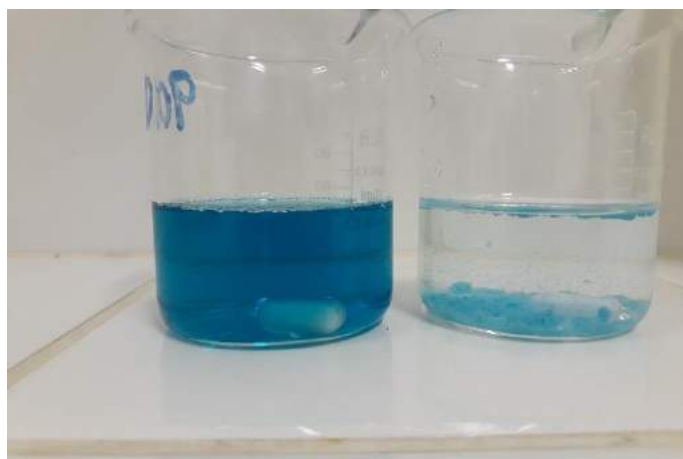


Figure 2. MG contaminated effluent before and after the ionic flocculation process.

3.2. Effect of MG concentration

Figure 3 shows the effect of varying MG concentration on MG removal efficiency. The maximum concentration of MG in solution was 0.12 kg/m^3 because this concentration is already well above dye concentrations in textile effluents [9].

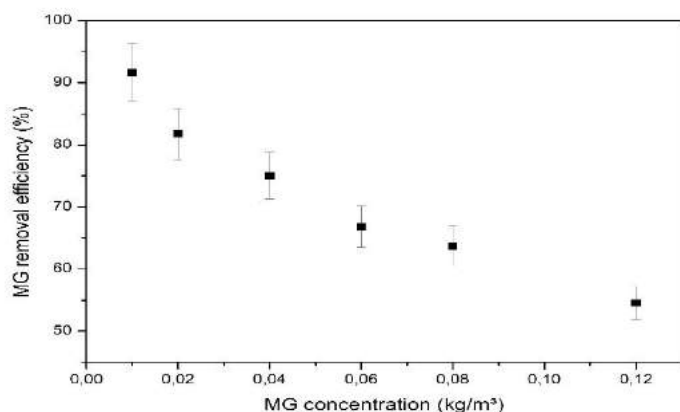


Figure 3. MG removal efficiency vs. MG concentration. Temperature = 298 K.

According to Figure 3, it is concluded that keeping the surfactant concentration fixed at 1.4 kg/m^3 and varying the MG concentration, the results differ considerably from each MG concentration. This occurs because the surfactant has an adsorption limit, consequently increasing its efficiency at lower pollutant concentrations and decreasing its efficiency at higher MG concentrations. This surfactant adsorption limit will be calculated later in the adsorption isotherm step.

3.3. Contact Time

Figure 4 presents the results of the removal efficiency of a MG concentration range as a function of the contact time of the effluent with the surfactant. Contact times are shown in the Figure 4 as follows: A (600s), B (1800s), C (3600s), D (5400s), E (7200s), F (9000s) and G (10800s).

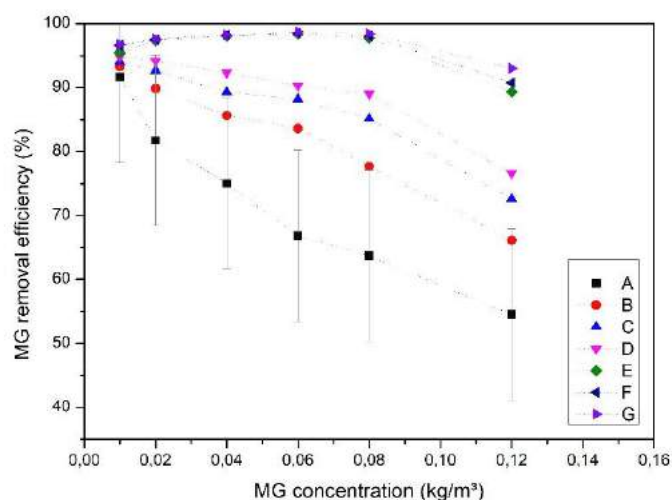


Figure 4. Effect of the contact time at different concentrations of MG.

From Figure 4, it can be concluded that the surfactant presents optimal results in the 600 seconds for MG concentration equal to 0.01 kg/m^3 , removing up to 91.69% of the dye. At concentrations above this value, the surfactant takes longer to adsorb until it reaches equilibrium.

While for the MG concentration of 0.01 kg/m^3 can adsorb approximately 91.69% in the first 600 seconds, for the MG concentration of 0.12 kg/m^3 can adsorb a maximum of 93% after 10800 seconds in contact with the solution.

Therefore, it is concluded that the relation between equilibrium time and the MG concentration is directly proportional. This is because there is a higher amount of dye in the effluent, consequently, the active sites of surfactant flocs will take longer to adsorb a higher amount of dye.

3.4. Adsorption Isotherm

Langmuir isotherm can be obtained by plotting the equilibrium adsorption capacity, represented by q_e on the y axis, as a function of the final MG concentration in the effluent. The isotherm is represented by Figure 5.

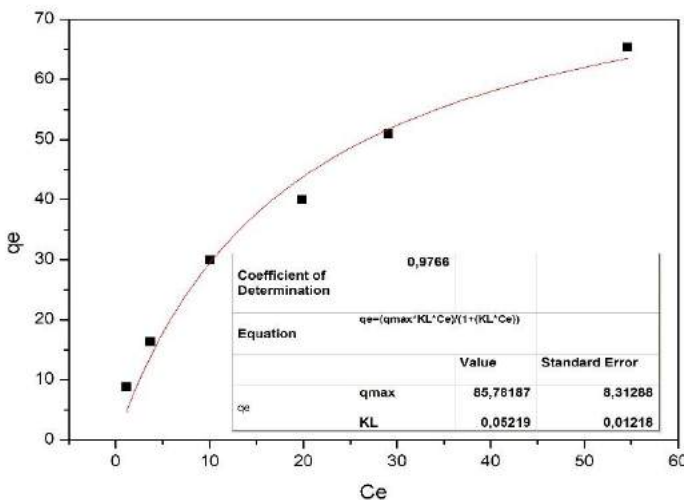


Figure 5. Langmuir isotherm. Temperature = 298 K, pH 10.

It is possible to calculate kL , interaction constant, and q_{max} , maximum adsorption capacity, from a non-linear model. The values of these parameters, such as the adjusted coefficient of determination value and the RL (Separation Factor) parameter, which indicates whether the adsorption process is favorable or not for each initial MG concentration value, are shown in Table 1 and Table 2 explains how to interpret the separation factor value.

Table 1. Values for Langmuir isotherm

Parameter	Value
q_{max}	0.08 kg (MG)/kg (Surfactant)
kL	0.05
RL	0.67
R^2	0.98

Table 2. Separation factor behavior

Separation factor	Behavior
$0 < RL < 1$	Favorable adsorption
$RL > 1$	Unfavorable adsorption
$RL = 1$	Linear isotherm

The results indicate that the Langmuir model is suitable for this adsorption process, since the coefficient of determination is approximately 0.98 and the error estimate value is low. Maximum adsorption capacity is approximately 0.08 kg MG/kg surfactant, the interaction constant MG/Surfactant is approximately 0.05 and the separation factor is approximately 0.67, indicating that the adsorption process between MG dye and surfactant is favorable [12].

3.5. Adsorption Kinetics

For the adsorption kinetics, the pseudo-second order model were evaluated.

The results for the pseudo-second order kinetic model (Figure 6) can be obtained from a non-linear model, plotting qt (amount of MG adsorbed in a given time) versus te (adsorption time).

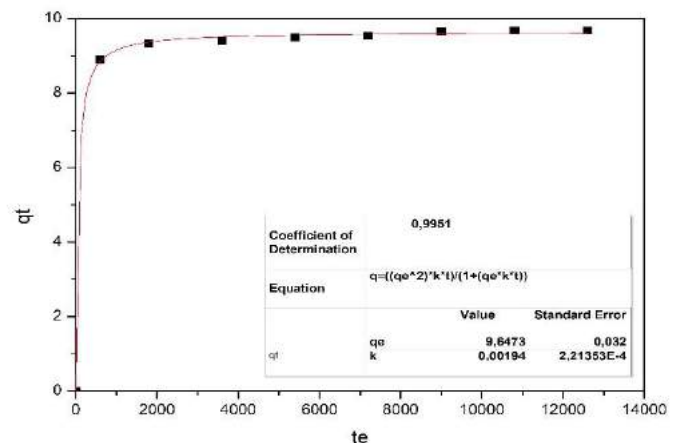


Figure 6. Pseudo-second order kinetic model. Temperature = 298.15 K, pH 10.

Analyzing the value of the coefficient of determination and the error estimates of Figure 6, it can be seen that the experimental data present an adequate fit to this kinetic model. Therefore, the most suitable kinetic model for this process is the pseudo-second order model.

For adsorption of MG in aqueous medium using a ferromagnetic composite, the kinetic model that best suits the process is the pseudo-second order model [13].

For adsorption of MG using Caulinite or Bentonite (N₃) or Bentonite (N₆), the kinetic model that best suits the process is the pseudo-second order model [14].

In the adsorption process of MG using sawdust, the most suitable kinetic model is the pseudo-second order model [15].

4. Conclusions

In this work, the efficiency of anionic surfactant in removing Malachite Green (MG) dye from water was evaluated. The results show that the surfactant has a MG removal efficiency of approximately 96% at a temperature of 298 K at pH 10; As dye concentration increases, MG removal efficiency tends to decrease due to saturation of active sites; The contact time is directly proportional to the MG concentration, i.e., the higher the MG concentration the longer it will take for the equilibrium to be reached; Langmuir Isotherm model fits this adsorption process, with a separation factor value of 0.67; The process fits the pseudo-second order kinetic model. Therefore, ionic flocculation is a suitable process for the treatment of MG contaminated effluent, as the results are considerably satisfactory.

Acknowledgements

The authors thank the Universidade Federal Rural do Semi-Árido (UFERSA) by support provided for the research.

References

- [1] Costa, A. P. J.; Silva, A. L.; Martins, R. D. S. Um estudo sobre estações de tratamento de efluentes industriais e sanitários da empresa Dori Alimentos Ltda. **Regrad**, Marília-sp, v. 1, p. 6-22, jan./dez. 2009. Disponível em: <file:///c:/users/cliente/downloads/165-1-584-2-10-20100301.pdf>. Accessed on: 29 oct. 2019.
- [2] Silveira, G. E. *Sistema de tratamento de efluentes industriais*. TCC. Universidade Federal do Rio Grande do Sul – UFRS, Porto Alegre – RS, 2010.
- [3] Guaratini, C. C. I.; Zanoni, M. V. B. Corantes Têxteis. **Quim. Nova**, Araraquara, v. 23, p. 71-78, jan/mar. 1999.
- [4] Kunz, A.; Peralta-Zamora, P.; Moraes, S. G.; Durán, N. Novas tendências no tratamento de efluentes têxteis. **Quim. Nova**, Curitiba, v. 25, n. 1, p. 78-82, jan/jun. 2001.
- [5] Apolônio, L. F. *Desenvolvimento de método para pré-concentração e determinação de leuco verde malaquita e verde malaquita em águas por análise de imagem digital em superfície adsorvente*. Dissertação de Mestrado. Universidade Federal de Viçosa – UFV, Viçosa – MG, 2015.
- [6] Peruzzo, L. C. *Influência de agentes auxiliares na adsorção de corantes de efluentes da indústria têxtil em colunas de leito fixo*. Dissertação de Mestrado. Universidade Federal de Santa Catarina - UFSC, Florianópolis – SC, 2003.
- [7] Melo, R. P. F. *Remoção de corantes utilizando tensoativos: extração por ponto de nuvem e floculação iônica*. Tese de Doutorado. Universidade Federal do Rio Grande do Norte – UFRN, Natal – RN, 2015.
- [8] Cavalcante, P. R. M. et al. Removal of phenol from aqueous medium using micellar solubilization followed by ionic flocculation. **Journal of Environmental Chemical Engineering**, Natal, v. 6, n. 2, p. 2778-2784, mar/abr. 2018.
- [9] Sirianuntapiboom, S.; Sadahiro, O.; Salee, P. Some properties of a granular activated carbon-sequencing batch reactor (GAC-SBR) system for treatment of textile wastewater containing direct dyes. **Journal of Environmental Management**, Bangkok, v. 85, n. 1, p. 162-170, 2006.
- [10] Teixeira, Y. N. *Educação Ambiental: Ecopedagogia e sustentabilidade dos recursos naturais*. 1ª Ed. Ituiutaba: Barlavento, 2017.
- [11] Lima, L. N. *Remoção do corante solophenyl preto utilizando floculação iônica*. TCC. Universidade Federal Rural do Semi-Árido – UFERSA, Pau dos Ferros – RN, 2018.
- [12] Nascimento, R. F. et al. *Adsorção: Aspectos teóricos e aplicações ambientais*. 1ª Ed. Fortaleza: Imprensa Universitária, 2014.
- [13] Marco, C. et al. *Adsorção do corante verde de malaquita em meio aquoso utilizando um composto ferromagnético*. Disponível em: <https://www.researchgate.net/publication/319244220_Adsorcao_do_corante_verde_de_malaquita_em_meio_aquoso_utilizando_um_composito_ferromagnético>. Accessed on: 28 oct. 2019.
- [14] Alves, F. C. *Estudos dos processos de adsorção utilizando argilas como adsorventes para remoção do corante verde malaquita*. Dissertação de Mestrado. Universidade Federal de Lavras – UFLA, Lavras – MG, 2013.
- [15] Silva, L. F. *Utilização do pó de serragem como adsorvente alternativo na remoção de verde de malaquita*. TCC. Universidade Tecnológica Federal do Paraná – UTFPR, Campo Mourão – PR, 2014.

Kinetic study of adsorption and ionic-exchange of Cd²⁺ ions in expanded vermiculite and sodium-treated vermiculite

Henrique S. de C. Neves, Meuris G. C da Silva, Reginaldo Guirardello, Melissa G. A. Vieira*

*Department of Processes and Products Design, School of Chemical Engineering–University of Campinas, Albert Einstein Avenue, 500, 13083-852 Campinas, São Paulo, Brazil.

Abstract

Vermiculite is a clay mineral that has characteristics such as high surface area, low density, and high cation exchange capacity. It can be applied as an alternative adsorbent due to its abundance and low-cost. This study evaluated the kinetic behavior during removal of Cd²⁺ ions by expanded (Ver) and sodium-treated vermiculite (VNa). Analysis of atomic composition by EDX revealed that all K⁺ is exchanged after adsorptive process and there are no exchangeable Ca²⁺ and Na⁺ ions in Ver samples. Evaluating the ion exchange kinetics, it is observed that after treatment with sodium there is a significant reduction of exchangeable ions in the adsorbent, generating empty sites for adsorption. The fit of the kinetic models indicated that the adsorptive process is controlled by three resistances. The pseudo-second-order kinetic model obtained the best fit, where the adsorption capacity of Ver was 0.1057 mmol.g⁻¹ (R² = 0.9858) and VNa was 0.1304 mmol.g⁻¹ (R² = 0.9994), under the same condition, indicating that sodium treatment improves the adsorbent characteristics of cadmium removal. Therefore, VNa has shown promise for future applications in wastewater treatment.

Keywords: Vermiculite; Cadmium; Adsorption; Ionic-exchange, Sodium treatment.

1. Introduction

Contamination of water bodies can occur through the disposal of urban, pesticide and industrial waste, where one way is related to the dumping of toxic metals that are generated in various industrial processes and that can cause health problems for humans and affect irreversibly the ecosystems [1].

Cadmium is one of the most toxic metals with the lowest release patterns in Brazil [2]. Electroplating, pigment, and paint industries are among the main generators of effluents contaminated with this metal [3]. This micro-pollutant can be bioaccumulated along the food chain causing several risks to the environment and human health, due to the long time it takes organisms to eliminate it [4]. Therefore, the study of low-cost techniques that achieve a high level of efficiency in the treatment of effluents is of great environmental relevance.

Adsorption has attracted interest from the industrial and academic sectors due to its low cost and its operational simplicity. In addition, various materials have the potential to be applied,

depending on their affinity with the pollutant to be removed. The literature highlights the study with clay minerals, as they exist in abundance and have a high potential for the removal of metal ions, oils, dyes, among other pollutants [5].

In the LEPA/LEA laboratory of the Unicamp Faculty of Chemical Engineering, several studies have evaluated the application of clay minerals as emerging adsorbents. Cu²⁺ and Hg²⁺ adsorption studies were performed by Bofe and Verde-lodo bentonite clays [6]; monovalent ionic silver adsorption [7] and competitive with copper in bentonite sludge-type clay [8]. A significant improvement in Cu²⁺ removal was also observed after Na⁺ treatment of a Bofe clay [9].

Vermiculite is a clay mineral of the mica family that has low density, laminated particles. It is considered a promising adsorbent because it has low cost, is chemically inert and has high cation exchange capacity [10]. This material has been satisfactorily applied as adsorbent for removal of Zn²⁺ and Cu²⁺ ions [11, 12]. The aim of this work is to evaluate the kinetic adsorption and ion-exchange

behavior of Cd²⁺ ions removal by expanded vermiculite and sodium-treated expanded vermiculite.

2. Materials and methods

2.1. Adsorbent preparation

The expanded vermiculite (Ver) applied as adsorbent was produced by Brasil Minérios. In order to favor ion exchange, expanded vermiculite was treated with sodium in acid medium, which was renamed Na-vermiculite (VNa). The procedure consisted of subjecting the vermiculite to a 1% NaCl solution and pH 3 and stirring for 3 hours in the shaker (magnetic stirrer TE-0851 Tecnal) [13]. After treatment, the clay was washed with 4 liters of deionized water on a paper filter, dried at 105 °C for 24 hours (continuous flow oven TE-394/1 Tecnal) and sieved to an average diameter of 0.885 mm (sieve system model T Produtest).

2.2. Metallic speciation

With the help of Hydra and Medusa softwares, the profile of the metallic species formed by Cd²⁺ at a concentration of 1 mmol/L was estimated as a function of pH. Up to pH 8.2, all metal species were found to be water-soluble. Therefore, the pH control was set to 6 to perform the adsorption experiments to avoid minimal precipitation.

2.3. Chemical composition by SEM-EDX

Ver and VNa samples before and after the adsorption process had their atomic composition evaluated semi-quantitatively by scanning electron microscopy coupled with energy dispersive X-ray (SEM-EDX) technique (LEO Electron Microscopy, LEO 440i/6070 - England) was used to perform semi-quantitative analysis. The samples were metalized with a thin layer of gold and an acceleration voltage of 15 kV was employed.

2.4. Kinetic assays

A synthetic Cd²⁺ solution was prepared by dissolving the appropriate amount of cadmium nitrate tetrahydrate (Cd(NO₃)₂·4H₂O, Vetec). The two kinetic assays were performed using 1600 mL of 1 mmol.L⁻¹ Cd²⁺ solution and 16 g of adsorbent (Ver and VNa). The experiments were conducted in a Becker at room temperature (25 ± 0.5 °C), kept under constant agitation, on a magnetic stirrer

(Tecnal, TE-0851), and the pH was carefully controlled at 6.

Aliquots of 4 mL were collected at pre-set times. The concentrations of the metals in liquid phase, Cd²⁺ and exchangeable ions (Na⁺, Mg²⁺ and K⁺) were determined by Atomic Absorption Spectrophotometry (AAS AA-7000 Shimadzu). From a mass balance, it is possible to determine the amount of adsorbed Cd²⁺ according to Eq. 1.

$$q(t) = \frac{V}{m}(C_0 - C(t)) \quad (1)$$

where q (t) (mmol/g) and C (t) (mmol/L) are the concentrations of adsorbents in the solid and liquid phase, respectively, at time t (min); V (L) is the solution volume and m (g) is the adsorbent mass.

To evaluate the dissolution effect of light metals (Mg²⁺ and K⁺) from expanded vermiculite, control experiments were performed, where adsorbents are kept in contact with deionized water and aliquots are collected under the same conditions as kinetic experiments. No control experiment was required for Na-vermiculite as it is already washed with deionized water. The experiment was carried out in triplicate

2.5. Kinetic modeling

Kinetic models can represent cadmium removal behavior over time. In order to evaluate this behavior the pseudo-first-order (PFO, Eq. (2)) [14], pseudo-second-order (PSO, Eq. 3) [15], Boyd (Eq. 4) [16], intraparticle diffusion (ID, Eq. 5) [17] and external film mass transfer (EFMT, Eq. 6) [18] were adjusted to the experimental data.

$$q(t) = q_e(1 - e^{-K_1 t}) \quad (2)$$

$$q(t) = \frac{K_2 q_e^2 t}{1 + K_2 q_e t} \quad (3)$$

$$B(t) = -\ln\left(\frac{\pi^2}{6}\left(1 - \frac{q(t)}{q_e}\right)\right) \quad (4)$$

$$q(t) = K_I t^{1/2} + C \quad (5)$$

$$\frac{dC_s(t)}{dt} = \frac{K_{TM} aV}{mq_{max} K_L} [1 + K_L C_s(t)]^2 \cdot [C(t) - C_s(t)] \quad (6)$$

where q(t) (mmol/g) is the adsorbed amount of cadmium at the arbitrary time t (min), q_e (mmol / g) is the amount adsorbed at equilibrium in each experiment; K₁ (min⁻¹), K₂ (g.mmol⁻¹.min⁻¹) and K_I

($\text{mmol.g}^{-1}.\text{min}^{-1/2}$) are the kinetic constants of PFO, PSO and ID models, respectively; $B(t)$ is a mathematical function of the ratio between the amount adsorbed at time t and the equilibrium used to construct the Boyd plot; and C (mmol.g^{-1}) is a resistance-related intraparticle diffusion model constant in the external film; $C(t)$ (mmol/L) and $C_s(t)$ (mmol/L) are the concentrations in the liquid phase and particle surface, respectively, at a time (t); K_{MT} (min^{-1}) is the mass transfer coefficient; a (m^2/m^3) is the specific surface area of the particle; q_{max} (mmol/g) and K_L (L/mmol) are the maximum adsorption capacity and equilibrium constant, respectively, of the Langmuir model.

Boyd's model provides the effective diffusion coefficient, D_{eff} ($\text{cm}^2.\text{s}^{-1}$), calculated from the angular coefficient (B) of the linear fit of the graph $B(t)$ versus t and Eq. 7.

$$B = \frac{D_{\text{eff}}\pi^2}{r^2} \quad (7)$$

The above models were adjusted with the aid of Origin 8.1 and Maple 17 software.

3. Result and Discussion

3.1. Chemical composition by SEM-EDX

Table 1 presents the atomic percentages obtained from EDX of Ver and VNa.

Table 1. Element mass percentage composition for Ver and VNa before and after the adsorption process.

El.	Ver	VNa	Ver+Cd	VNa+Cd
O	55.9±3.2	54.3±1.1	54.1±2.1	52.6±1.0
Mg	13.2±1.0	13.7±1.5	13.5±0.4	12.2±4.1
Al	6.1±0.2	6.1±0.8	4.6±1.4	5.8±1.8
Si	17.5±1.3	18.8±0.9	16.2±1.5	18.8±1.2
K	1.5±0.5	0	0	0
Ti	0.7±0.1	0.4±0.3	0.7±0.3	0.4±0.3
Cr	0.4±0.1	0.2±0.1	0.3±0.2	0.3±0.2
Fe	4.7±1.0	4.3±1.1	6.9±2.5	4.8±2.4
Na	0	2.2±0.6	0	0.5±0.3
Cd	0	0	4.0±0.3	4.3±1.1

Due to the semiquantitative character of this analysis, the analyzed values represent an average

of 4 readings. This analysis was used to aid in the determination of exchangeable ions and the analysis of the effectiveness of ion exchange. It can be observed that the ion exchange occurred effectively, where the samples after sodium treatment and after adsorption presented a considerable percentage of Na^+ and Cd^{2+} ions, respectively. Based on the total K^+ ion exchange, as observed in Table 1, and the high presence of exchangeable Mg^{2+} according to the literature [19], these light metals were selected for the Ver ion ion-exchange kinetic study, as well as the Na^+ ion for VNa. Chromium and titanium are probably contaminations that occur in the processing of vermiculite. The variation of these metals after treatments is not significant when considering the deviation, indicating that they do not influence the ion exchange.

3.2. Ionic-exchanged

Fig. 1 and 2 show the kinetic behavior of Cd^{2+} adsorption and light metals involved in ion-exchange, for Ver and VNa, respectively. Ver's kinetics required a control experiment in deionized water to determine the dissolution of light metals, a value excluded from the stoichiometric ion-exchange balance.

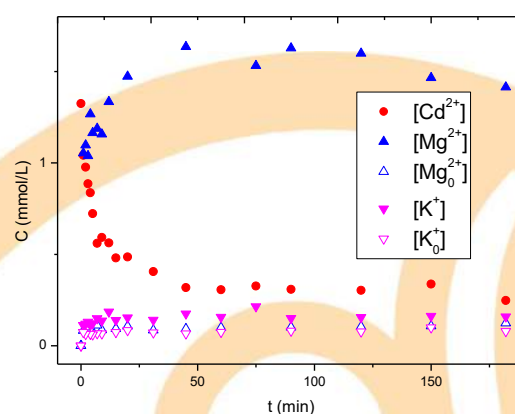


Fig. 1. Kinetic profiles of ionic exchanged during assays with expanded Ver. Equilibrium time = 45 minutes. Subtitle: $[\text{Mg}_0^{2+}]$ and $[\text{K}_0^+]$ = concentration of light metals in the control experiment.

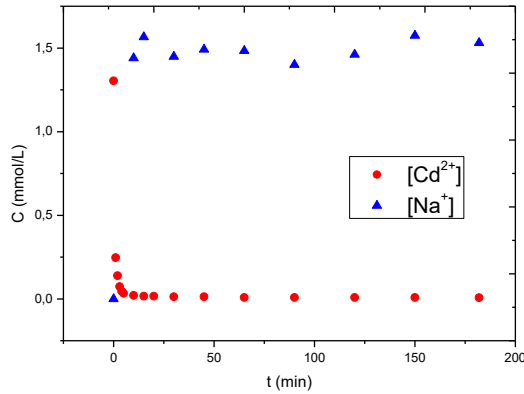
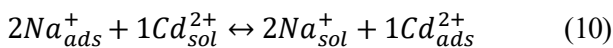
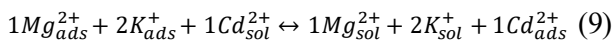


Fig. 2. Kinetic profiles of ionic exchanged during assays with VNa. Equilibrium time = 10 minutes.

By analyzing the kinetic profiles, it is possible to verify that the light metals reach equilibrium in a time very close to the Cd^{2+} equilibrium. This fact indicates that the main removal mechanism is possibly ion-exchange. The stoichiometric balance is an aspect of fundamental importance in ion exchange. It is represented by Eqs. 9 and 10, for the kinetics with Ver and VNa, respectively:



where the subscript *ads* and *sol* refer to ions present in the solid and liquid phases, respectively. Fig. 3 presents the theoretical kinetic behavior of ions involved in ion exchange, where it is considered that for each adsorbed Cd^{2+} , the amount of ions with the same charge is desorbed.

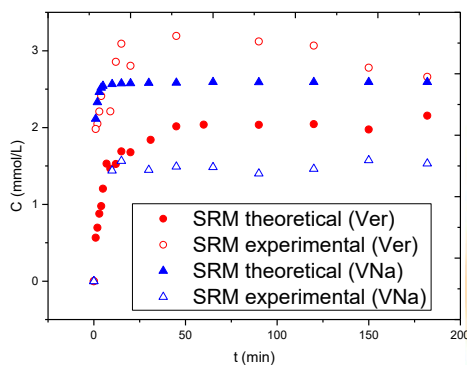


Fig 3. Theoretical and experimental kinetic profiles for SRM (Sum of the loads of the released metals) Ver and VNa.

The Ver assay desorbed 37.75% more than the theoretical. This may be due to the occurrence of other simultaneous phenomena of ion exchange and adsorption. In the experiment with VNa, the desorbed exchangeable ion experimental value is 58.73% of the theoretical value. This reduction is due to the treatment of vermiculite with sodium in an acid medium that promotes the formation of ion exchange sites with Na^{+} and other free ions for adsorption.

3.3. Kinetic assays

Fig. 4 illustrates the fit of the PFO, PSO and EMTR models to the kinetic data. Initial measured Cd^{2+} concentrations were 1.325 mmol/L and 1.304 mmol/L for the Ver and VNa assays, respectively. The experimental curves obtained an average deviation below 2.2%

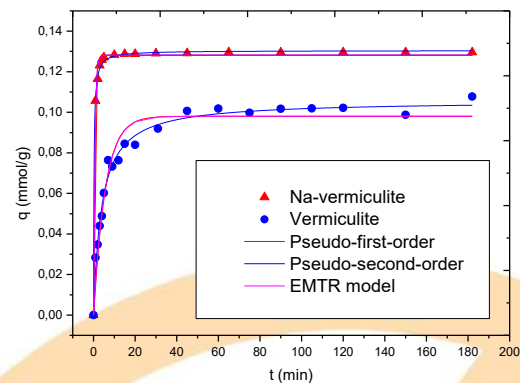


Fig. 4. Cd^{2+} adsorption kinetics adjusted to PFO, PSO, and EMTR models for Ver and VNa.

It can be seen that there was a significant reduction in the adsorption time after Ver was treated with sodium acid treatment. As observed experimentally, the Ver kinetics reached equilibrium in about 45 min and the VNa system in about 10 min. This reduction can be explained by the formation of new active sites during the acid treatment of the adsorbent and that sodium is the most easily exchangeable metal in several systems.

The percentage of Cd^{2+} ion removal increased from 82.6% in Ver to 99.4% removal in VNa. Experiments in similar conditions, for removal of Cu^{2+} with Ver, obtained 89.13% removal suggesting

expanded vermiculite as a promising material for the treatment of heavy metals [20].

Fig. 5 and 6 show the adjustments of the Boyd and ID models to the kinetic data, respectively, and in Table 2 the parameters obtained from the adjustments. For the Boyd model, only the region before equilibrium should be considered.

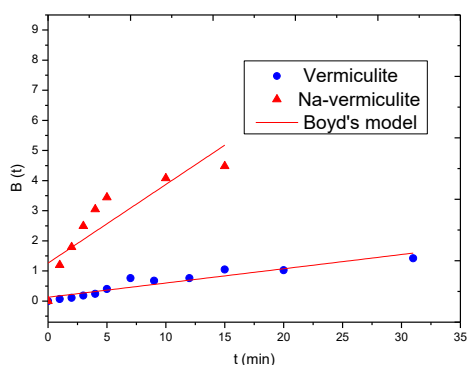


Fig. 5. Boyd model for cadmium adsorption kinetics for Ver and VNa.

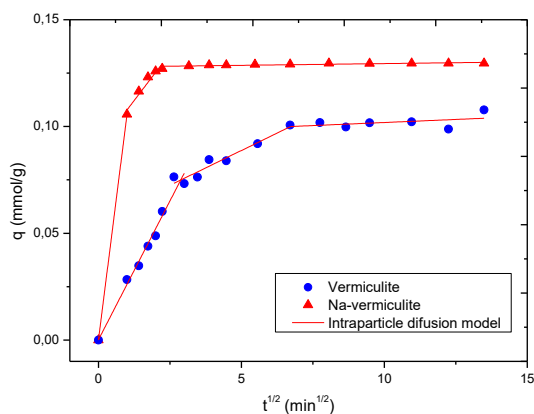


Fig. 6. Intraparticle diffusion model for cadmium adsorption kinetics for vermiculite expanded and sodium treated vermiculite.

The PFO and PSO models satisfactorily describe the experimental data, where the pseudo-second-order model obtained a higher calculated R^2 (> 0.98) for both systems. In the last stage, adsorption occurs slowly possibly due to micropore diffusion [14, 21]. The kinetic constants (K_1 and K_2) increased considerably after sodium treatment, in agreement with the experimentally reduced equilibrium time.

Boyd's model assesses whether intraparticle diffusion is the limiting step in the process. For this

to occur, the linear fitting of the Boyd's graph (Fig. 5) must go through the origin. It is observed that the Ver kinetic presents a certain linearity and the angular coefficient closest to zero. This indicates that the adsorptive process of this clay has a greater intraparticle diffusion than VNa kinetics.

Table 2. Parameters of kinetic models.

Model	Parameter	Ver	Na-Ver
Pseudo-first-order	q_e (mmol.g^{-1})	0.0980	0.1281
	K_1 (min^{-1})	0.1789	1.6109
	R^2	0.9568	0.9967
Pseudo-second-order	q_e (mmol.g^{-1})	0.1057	0.1304
	K_2 (min^{-1})	2.4371	35.026
	R^2	0.9858	0.9994
Boyd	B	0.0473	0.2611
	D_i ($\text{cm}^2.\text{s}^{-1}$)	$8.76 \cdot 10^{-6}$	$4.83 \cdot 10^{-5}$
	R^2	0.8848	0.7268
Intraparticle diffusion	K_d ($\text{mmol.g}^{-1}.\text{min}^{-1/2}$)	0.0065	0.0176
	C (mmol.g^{-1})	0.0562	0.0902
	R^2	0.9296	0.9214
EFMT	K_{MT} (min^{-1})	0.1324	1.5827
	R^2	0.9805	0.9972

Due to the satisfactory fit of the EFMT model and the presence of three ID model linear regions, adsorption should be controlled by three steps: external film mass resistance, intraparticle diffusion and intraparticle diffusion. Parameters such as D_i and K_d have higher values for VNa, therefore, the treatment of Ver with sodium made the material more efficient in removing toxic metal such as Cd^{2+} ions.

4. Conclusions

According to EDX and the literature, the main exchangeable ions in vermiculite are Mg^{2+} and K^+ for Ver and Na^+ for VNa. After sodium treatment of

Ver, there was a significant decrease in the sum of exchangeable ions and the formation of empty active sites. Consequently, there was a reduction in equilibration time and removal of Cd^{2+} by the treated adsorbent. The PFO and PSO models were well adjusted ($R^2 > 0.95$) to the kinetic data, where the latter more predictively represents the experimental data, indicating micropore diffusion at the end of the process. The adsorptive process must be controlled by three steps as indicated in the ID model. Equilibrium removal capacity and kinetic constants were higher for VNa corroborating the improvement generated by sodification treatment. Therefore, sodium treatment of vermiculite was successfully applied, producing a material with enhanced Cd^{2+} removal properties.

Acknowledgments

The authors would like to thank CNPq and CAPES for financial support.

Reference

- [1] Ahmaruzzaman, M. Industrial wastes as low-cost potential adsorbents for the treatment of wastewater laden with heavy metals. *Advances in Colloid and Interface Science*, v. 166, p. 36–59, 2011.
- [2] Brasil, Resolução CONAMA nº430, de 13 de maio de 2011. Dispõe sobre as condições e padrões de lançamento de efluentes, complementa e altera a Resolução no 357, de 17 de março de 2005, do Conselho Nacional do Meio Ambiente-CONAMA. Publicado no D.O.U.
- [3] Lesmana, SO; Febriana, N; Soetaredjo, FE; Sunarso, J; Ismajli, S. Studies on potential applications of biomass for the separation of heavy metals from water and wastewater. *Biochemical Engineering Journal*. v. 44, issue 1, p. 19-41, 2009.
- [4] Da'na, E. Adsorption of heavy metals on functionalized-mesoporous sílica: A review. *Microporous and Mesoporous Materials*, v. 247, p. 145-157, 2017.
- [5] Uddin, MK. A review on the adsorption of heavy metals by clay minerals, with special focus on the past decade. *Chemical Engineering Journal*, 308, 438 – 462, 2017.
- [6] Vieira, MGA; Almeida Neto, AF ; Silva, MGC ;Carneiro, CN ; Melo Filho, AA. Influence of the system on adsorption of Pb(II) and Cu(II) by calcined rice husks: kinetic study. *Chemical Engineering Transactions*, v. 24, p. 1213-1218. 2011.
- [7] Cantuaria, ML; Nascimento, ES; Almeida Neto, AF; Santos, OAA; Vieira, MGA. Removal and Recovery of Silver by Dynamic Adsorption on Bentonite Clay Using a Fixed-Bed Column System. *Adsorption Science & Technology*. v. 33. p. 91-104. 2015.
- [8] Freitas, ED; de Almeida, HJ; Almeida Neto, AF; Vieira, MGA. Continuous adsorption of Silver and Copper by Verde-lodo bentonite in a fixed bed flow-through column. *Journal of Cleaner Production*, v. 171, p. 613-621, 2018.
- [9] Soeiro TN; Freitas ED; Maia GS; Santos AB; Vieira MGA; Guirardello R. Evaluation of Cu^{2+} Ions Adsorption Equilibrium in Calcined Bentonite Clay and after Treatment with Sodium. *Chemical Engineering Transaction*. 57, 619-624.
- [10] Machado, LCR; Torchia, CB, Lago, RM. Floating photocatalysts based on TiO_2 supported on high surface area exfoliated vermiculite for water decontamination. *Catalysis Communications*, 7, 538–541, 2006.
- [11] Nishikawa, E; Almeida Neto AF; Vieira, MGA. Equilibrium and Thermodynamic Studies of Zinc Adsorption on Expanded Vermiculite. *Adsorption Science & Technology*, Vol. 30, No. 8/9, 2012.
- [12] Freitas, ED; de Almeida, HJ; Vieira, MGA. Binary adsorption of zinc and copper on expanded vermiculite using a fixed bed column. *Applied Clay Science*, v. 146, p. 503-509, 2017.
- [13] Almeida Neto, AF de; Vieira, MGA; Silva, MGC da. Insight of the removal of nickel and copper ions in fixed bed through acid activation and treatment with sodium of clay. *Brazilian Journal of Chemical Engineering*, v. 31, Nº. 04, p. 1047 - 1056, 2014.
- [14] Lagergren, S. Zur theorie der sogenannten adsorption gelöster stoffe, *Kungliga Svenska Vetenskapsakademiens. Handlingar*, v. 24, p. 1-39, 1898.
- [15] Ho, YS; Mckay, G. A kinetic study of dye sorption by biosorbent waste product pith. *Resources, Conservation and Recycling*, v. 25, p. 171-193, 1999.
- [16] Boyd, GE; Adamson, AE; Meyers, LS. The exchange of adsorption ions from aqueous solutions by organic zeolites II. Kinetics. *Journal of American Chemical Society*. v. 69, p. 2836-2848, 1947.
- [17] Weber, WJ; Morris, JC. Kinetics of adsorption on carbon from solution. *Journal of Sanitary Engineering Division ASCE*, v. 89, n. 2, p. 31-60, 1963.
- [18] Puranik, PR, Modak, JM, Paknikar, KM. A comparative study of the mass transfer kinetics of metal biosorption by microbial biomass. *Hydrometallurgy*, v. 52, p. 189-197, 1999.
- [19] Mathieson, AMcl.; Walker, GF. Crystal structure of magnesium-vermiculite. *Amer. Min.* 39, 231-55, 1954.
- [20] Nishikawa, E; Almeida Neto, AF; Vieira, MGA. Adsorption of copper in expanded vermiculite: kinetics and equilibrium. *XX Congresso Brasileiro de Engenharia Química*, Florianópolis, SC, 2014.
- [21] Simonin, J. On the comparison of pseudo-first order and pseudo-second order rate laws in the modeling of adsorption kinetics. *Chem. Eng. J.* 300, 254-263, 2016.

characteristics of the biomass through scanning electron microscopy (SEM) analysis. Additionally, the behavior of biosorption was verified by the thermodynamic analysis, which defined the thermodynamic parameters of the system, such as enthalpy, entropy and Gibbs free energy, aiming at assessing the viability of application as an alternative for the treatment of textile industrial wastewater.

2. Methodology

2.1. Scanning electron microscopy

Scanning electron microscopy (SEM) was the technique used to characterize the malt bagasse. Analysis was performed before and after the batch system biosorption process.

Based on the study of malt bagasse morphology, existing structures in the biosorbent and their influence on the removal of the ARB8G dye were identified.

2.2. Thermodynamic study

0.15 g of malt bagasse was added to 25 mL of 25 mg L⁻¹ ARB8G solution at pH 2, according to previous studies [7].

Experimental tests were performed under constant agitation in a metabolic bath at 130 rpm and 30, 40, 50, and 60 °C. Samples were taken at predetermined time intervals from 0 to 10,080 minutes (1 week), and they were subsequently centrifuged and analyzed using a UV-Vis spectrophotometer to determine the final concentration.

The parameters that define biosorption from a thermodynamic point of view are Gibbs free energy (ΔG°), enthalpy (ΔH°) and entropy (ΔS°), which can be calculated from equations (1), (2) and (3).

Equation (1) found the adsorption equilibrium constant, kd (L g⁻¹), which reflects the endothermic nature of the process from the temperature rise [9]. With the experimental data of concentration in equilibrium and capacity of biomass in equilibrium, the constant kd is multiplied by the relationship between mass and volume, making it dimensionless.

$$kd = \frac{q_{eq}}{C_{eq}} \times \frac{ms}{V} \quad (1)$$

In which q_{eq} stands for the maximum amount of adsorbed adsorbate per unit mass of biosorbent at equilibrium (mg g⁻¹), C_{eq} for the dye concentration at equilibrium at any given time (mg L⁻¹), m_s for the biosorbent mass (g), and V for the dye solution volume (L).

Thus, the calculation of the adsorption equilibrium constant is necessary to determine Gibbs free energy, enthalpy and entropy, as well as the relationship between the nature of the process and temperature.

Gibbs free energy is determined by equation (2):

$$\Delta G^\circ = -RT \ln kd \quad (2)$$

Where kd is the dimensionless constant of adsorption equilibrium, R is the universal gas constant (8.314 J mol⁻¹ K⁻¹), and T is the operational temperature (K).

Enthalpy and entropy were found by the Van't Hoff equation, as follows:

$$\ln kd = \frac{-\Delta H^\circ}{RT} + \frac{-\Delta S^\circ}{R} \quad (3)$$

From Van't Hoff's linearized equation, experimental data can be validated from the plot of ($\ln kd$) versus ($1/T$), in which the angular coefficient of curve gives the enthalpy, while the linear coefficient gives the entropy.

Finally, it was possible to verify the minimum kinetic energy involved for the reaction to occur and the energy barrier that the adsorbate needs to overcome before biosorption, at temperatures of 30, 40, 50 and 60 °C. This can be done from the graph of $\ln k$ versus $1/T$, using the kinetic parameters taken from the linearized Arrhenius equation (equation (4)):

$$\ln k = \ln A - \frac{Ea}{RT} \quad (4)$$

Where Ea is the activation energy (J mol⁻¹), A is the Arrhenius constant (g mg⁻¹ min⁻¹), R is the universal gas constant (8.314 J mol⁻¹ K⁻¹), and T is the solution temperature (K)

3. Results and Discussion

3.1. Scanning electron microscopy

Using the scanning electron microscopy (SEM) technique, it was possible to analyze how morphological features presented by the malt bagasse, before and after biosorption.

The sample, before biosorption, has irregular and rough cavities that favor the removal of the ARB8G dye by the malt bagasse, as shown in Fig. 1.

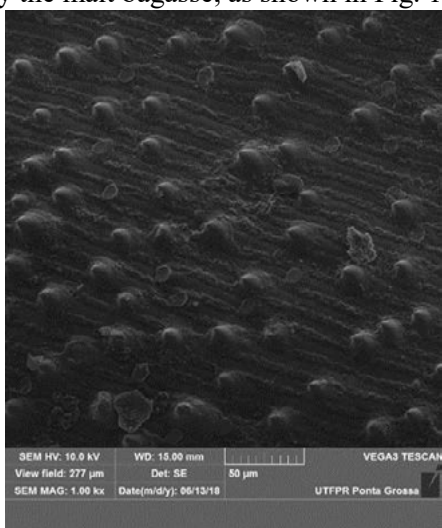


Fig. 1. SEM image of malt bagasse before biosorption at zoom of 500 times.

Recent work shows that radioactive waste, metal ions and textiles dyes are easily removed when the structure of the biosorbent material has irregularities and gaps, due to the increase in the surface area for absorption [10,11,12,13,14,15].

The existing cavities in the malt bagasse were filled by the mass transfer process as seen in Fig. 2.

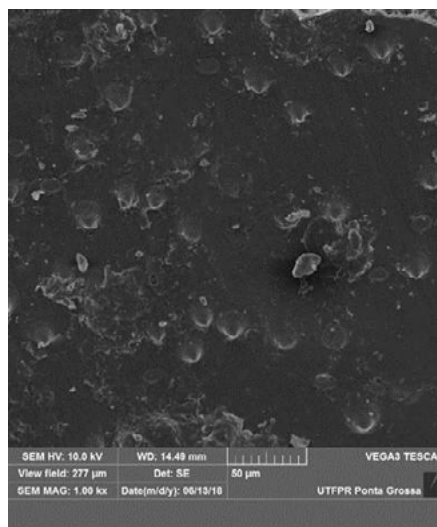


Fig. 2. SEM image of malt bagasse after biosorption at zoom of 500 times.

Therefore, there are changes in the structure / surface of the biosorbent, which showed a reduction in its rough appearance, due to the filling of the ARB8G dye between the fibers of the material after biosorption.

3.2. Thermodynamic study

Equations (1), (2) and (3) were applied to the experimental data obtained at the temperatures of 30, 40, 50, and 60 °C and 6 hours (removal stability). The thermodynamic parameters calculated are presented in Table 1

Table 1. Thermodynamic parameters for the biosorption of ARB8G dye onto malt bagasse at 30, 40, 50, and 60 °C.

T (°C)	ΔG° (J/mol)	ΔH° (J/mol)	ΔS° (J/mol K)
30	-7381.2	-28018.18	-67.8763
40	-6832.1		
50	-6140.6		
60	-5338.6		

The value of enthalpy (ΔH°) indicated that the biosorption process is exothermic for the temperatures under study, and therefore, the process could be occurring under physical adsorption, characterized mainly by the Van der Waals interactions [16].

The negative values of Gibbs free energy (ΔG°) indicated that the process occurs spontaneously,

while the negative values of entropy (ΔS°) suggest reduction of randomness at the solid-solution interface [17].

The dimensionless constant of equilibrium (kd) were determined as 18.70, 13.79, 9.83, and 6.87 at the temperatures of 30, 40, 50, and 60 °C, respectively.

Using this data, the Arrhenius equation (equation 4) was applied and the Arrhenius constant (A) and the activation energy (E_a) could be obtained based on the linear and angular coefficients of the linear curve of the plot of $\ln(kd)$ versus $1/T$, presented in Fig. 3.

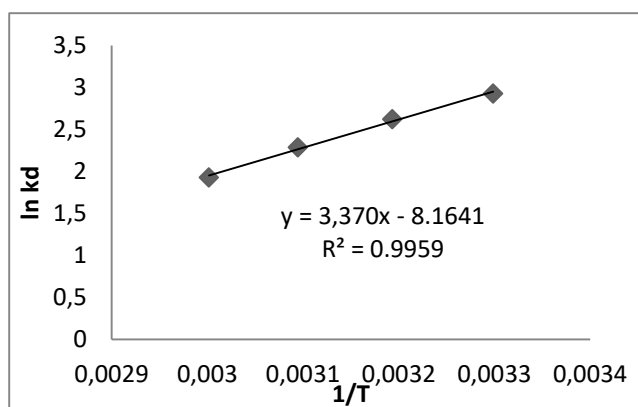


Fig. 3. Linear adjustment of the parameters derived from the Arrhenius equation.

According to Fig. 3, the correlation coefficient (R^2) is close to 1, indicating that the experimental data were significantly represented by the linear equation presented. Therefore, the activation energy was determined as 28.0182 kJ mol⁻¹, which again indicated the physical adsorption mechanism. This process has the advantage of easy recovery of the adsorbate without the requirement for high amounts of energy [18].

In another study, it was observed an optimum temperature for biosorption of ARB8G dye by malt bagasse was 30 °C, an activation energy of the system presented was 24.10 kJ mol⁻¹ and the k values increased in a similar behavior with the increase of the temperature [8].

4. Conclusion

In this study, the morphological characteristics and thermodynamic parameters were evaluated in the removal of Reafix Yellow B8G dye using malt bagasse as biosorbent.

The morphology was assessed by scanning electron microscopy (SEM) of the malt bagasse before biosorption showed an irregular surface filled by the dye after biosorption.

The kinetic constant calculated based on different temperatures allowed to determine activation energy of A 28.0182 kJ mol⁻¹, which classifies the removal through physical adsorption.

From the thermodynamic data, associated with the activation energy, it was possible to describe the process as exothermic and spontaneous due to negative values for enthalpy and free Gibbs energy, respectively.

In conclusion, based on the experimental data assessed in this study, the malt bagasse may be a feasible option as a biosorbent of dyes when subjected to favorable conditions. The mitigation of environmental impacts associated with the textile and brewing industries could be achieved aiming at the context of the circular economy.

References

- [1] BRAZILIAN ASSOCIATION OF THE TEXTILE AND CLOTHING INDUSTRY (ABIT). Sector Profile. [S. l.], october 2018. Available in: <<http://www.abit.org.br/cont/perfil-do-setor>>.
- [2] DELGOBO, Emanuele Sansana. CORRÊA Joelma. Utilization of Brewer Byproduct in Reafix B8G Yellow Textile Dye Biosorption: Kinetic, Balance and Thermodynamic Study. 2019. 92 p. Graduation Work Bachelor Degree in Chemical Engineering – Federal University of Technology - Paraná. Ponta Grossa, 2019.
- [3] HONORIO, Jacqueline Ferandin. Use of soybean husk as an adsorbent in the removal of reactive textile dyes. 2013. 114 p. Dissertation (Master) - Chemical Engineering Course, Western Paraná State University, Toledo, 2013.
- [4] ROSA, M. F.; SOUZA FILHO, M S. M.; FIGUEIREDO, M. C. B.; MORAIS, J. P. S.; SANTAELLA, S. T. LEITÃO, R. C. Valorization of agro-industrial waste. II International Symposium on Management of Agricultural and Agro-Industrial Residues - II SIGERA March 15-17, 2011 - Foz do Iguaçu, PR Volume I - Lectures.
- [5] FERRARI, Leila Denise Fiorentin. Removal of Effluent Dye from Indústria Textile Using Membrane Processes and Adsorption in Orange Bagasse. 2009. 166 p. Dissertation (Master's) - Chemical Engineering Course, State University of Maringá, Maringá, 2009.

- [6] LIM, L. B. L.; et al. Breadnut peel as a highly effective low-cost biosorbent for methylene blue: Equilibrium, thermodynamic and kinetic studies. *Arabian Journal of Chemistry*, v. 10, p. S3216-S3228, 2017.
- [7] DELGOBO, E. S.; SILVA, B. C.; PIETROBELLI, J. M. T. A. Biosorption of Reafix B8G Yellow dye using brewing by-product: study of operational and kinetic parameters. In: BRAZILIAN MEETING ON ADSORPTION. 12., 2018, Gramado. Annals ... Gramado: 2018.
- [8] SILVA, Bruna Cassia da. Biosorption Yellow Reafix B8G dye by malt bagasse in batch and continuous system: experimental evaluation and computational fluid dynamics simulation. 2019. 175 p. Dissertation (Master Degree in Chemical Engineering) - Federal University of Technology - Paraná. Ponta Grossa, 2019.
- [9] ALVES, Fernanda Cristina. Study of the adsorption processes using clays as an adsorbent to remove the malachite green dye. 2013. 107 p. Dissertation (Master's Degree) - Agrochemical Course, Federal University of Lavras, 2013.
- [10] FERREIRA, Rafael Vicente de Padua. Application of biosorbents in the treatment of liquid radioactive waste. 2014. 105 p. Thesis (PhD) - Nuclear Technology - Applications Course, Energy and Nuclear Research Institute, São Paulo, 2014.
- [11] FONTANA, Klaiani B. et al. BIOSORPTION OF PB (II) BY URUCUM SHELL (*Bixa orellana*) IN WATER SOLUTIONS: KINETIC, BALANCE AND THERMODYNAMIC STUDY. *New Chemistry*, v. 00, n. XY, p.1-7, Jun 17 2016.
- [12] BÓAS, Naiza Vilas et al. Copper biosorption using chemically treated mesocarp and endocarp from natural macadamia. *Brazilian Evista of Agricultural and Environmental Engineering*, Campina Grande, v. 12, n. 16, p.1359-1366, 21 sep. 2012.
- [13] CARDOSO, Natali Farias. Removal of Methylene Blue Dye from Aqueous Effluents Using Natural and Carbonized Pine Nut Bark as an Adsorber. 2010. 54 p. Dissertation (Master) - Chemistry Course, Federal University of Rio Grande do Sul, Porto Alegre, 2010.
- [14] LIM, Linda B. L. et al. Breadnut peel as a highly effective low-cost biosorbent for methylene blue: Equilibrium, thermodynamic and kinetic studies. *Arabian Journal Of Chemistry*. [s. L.], p. S3216-S3228. 02 jan. 2014.
- [15] ORSOLETTA, Gabriel Dall. TECHNOLOGICAL USE OF PEANUT SHELL IN A TEXTILE DYE BIOSORPTION PROCESS. 2017. 91 f. Dissertation (Master) - Chemical and Biochemical Process Technology Course, Federal Technological University of Paraná, Pato Branco, 2017.
- [16] BANERJEE, S.; CHATTOPADHYAYA, M. C. Adsorption Characteristics for the Removal of a Toxic Dye, Tartrazine from Aqueous Solutions by a Low Cost Agricultural by-product. *Arabian Journal of Chemistry*, [s.l.], v. 10, p. 1629-1638, maio 2017. Elsevier BV.
<http://dx.doi.org/10.1016/j.arabjc.2013.06.005>.
- [17] AL-DEGS, Y.; KHRAISHEH, M. A. M.; ALLEN, S. J.; AHMAD, M. N. 2000. Effect of carbon surface chemistry on the removal of reactive dyes from textile effluent. *Water Research*, v.34, n.3, p.927-935.
- [18] BARKA, N.; ABDENNOURI, M.; EL MAKHFOUK, M. 2011. Removal of Methylene Blue and Eriochrome Black T from aqueous solutions by biosorption on *Scolymus hispanicus* L. Kinetics, equilibrium and thermodynamics. *Journal of the Taiwan Institute of Chemical Engineers*, v.42, n.2, p.320-326.

Concentration of betalains from beetroot in alginate beads through the adsorption operation

Cláudio P. Pinheiro^a, João O. Castro^a, Loreane M. K. Moreira^a, Stephany S. Alves^a, Tito R. S. C. Junior^a, Luiz A. A. Pinto^a

^a Escola de Química e Alimentos, Universidade Federal do Rio Grande (FURG), Rio Grande and 96203-900, Brazil

Abstract

Adsorption of the betalains from an aqueous solution allows the concentration of betalains in sodium alginate beads for application in food products. Thus, the aim of this work was to prepare sodium alginate beads for discontinuous adsorption of betalains from beetroot. Betalains were extracted from beetroots with distilled water as solvent at 328 K and the ratio of beetroot mass and solvent volume was of 1:15. Sodium alginate beads were performed for betalain adsorption. The equilibrium adsorption was determined for different pH (3, 4, 5, 6, 7 and 8), and adsorption isotherms were performed at pH 4 in temperatures of 298 K, 308 K and 318 K, with different betalains concentrations. The adsorption isotherms experimental data were adjusted to Henry, Langmuir and Freundlich models. Adsorption equilibrium was reached in 24 h, with maximum adsorption capacities of 62 mg g⁻¹ and the removal percentage around 41.0% at pH values of 3 and 4. The increase in temperature favored adsorption, and the Freundlich and Langmuir isotherm models presented good fitting. Thermogravimetric analysis (TGA) showed a difference between beads before and after adsorption. It was possible to concentrate betalains on sodium alginate beads.

Keywords: Equilibrium isotherms; Extraction; TGA; Betaxanthins; Betacyanins

1. Introduction

Betalains are water-soluble nitrogen pigments that replace anthocyanins in a small number of taxonomically related plants, being that anthocyanins do not contain nitrogen, and they have never been found in the same plant together. Betalains are divided into two groups betaxanthins, and betacyanins. The first group is the product of the condensation of betalamic acid with amino acids or amines; the second group is the product of the condensation of betalamic acid with glycosides [1]. The intense color of beetroots derives from high concentrations of betalains, and these are used as natural dyes in food processing, but they arouse great interest due to the health benefits, especially their antioxidant and anti-inflammatory activities [2].

For the drug delivery systems, the biodegradable polymeric carriers (alginate) has gained a wide interest, mainly due to your biocompatibility. The usual preparation consists of dissolving the drug in an aqueous solution containing the soluble polymer. In the case of carboxylate polymers (alginate), the beads formation is reached by the addition of Ca²⁺ or Al³⁺, where the alginate interact with metal ions to form crosslinked insoluble complexes, the precipitation offers a drug entrapping ability [3]. The adsorption operation is an alternative method for the formation of this complex, having the advantage to achieve high concentrations of drug in the complex, since adsorption proceeds until reached equilibrium.

Betainin (the main pigment of the betalains) in acid medium has two protonated structures in resonance, because the presence of two nitrogen atoms, one in the glycoside group and the other in the betalamic acid. However, due to the presence of

three carboxylic groups and hydroxyl groups, betanin may be electrically neutral [4]; therefore, it is necessary to use an adsorbent, such as sodium alginate, which is insoluble and may interact with betalains in acidic medium. Thus, the aim of this work was to preparation sodium alginate beads for discontinuous adsorption of betalains from beetroot.

2. Methods

2.1. Extraction of betalains from beetroot

The beetroots were obtained from local commerce in Rio Grande City-RS-Brazil. The beetroots were washed, and the stem and root were removed. The bulb was fractionated into particles (5 cm long, 0.5 cm thick and 0.08 cm high), and the moisture content was determined. The extraction conditions for betalains were with distilled water as the solvent at 328.15 K and the solvent:solid ratio of 15:1. The betalain pigments concentration was calculated as the sum of the betacyanins and betaxanthins concentrations obtained by the spectrophotometer. The light absorptions for betacyanins and betaxanthins were measured at 536 nm and 485 nm, respectively, and the concentrations were calculated by Eq. 1 [2]; where $[y]$ is the betacyanins or betaxanthins concentration (mg L^{-1}), A is the absorbance difference between the wavelengths 536 nm and 650 nm for betacyanins and 485 nm and 650 nm for betaxanthins, DF is the dilution factor, MW is the molecular weight (550 g mol^{-1} for betacyanins and 339 g mol^{-1} for betaxanthins), ϵ is the molar extinction coefficient ($\text{L mol}^{-1} \text{ cm}^{-1}$), 60000 for betacyanins and 48000 for betaxanthins, and i is cuvette the length (cm).

$$[y] = \frac{A \times DF \times MW \times 1000}{e \times i} \quad (1)$$

2.2. Adsorbent beads

The sodium alginate beads were prepared by a solution with 2 g of sodium alginate in 50 mL of distilled water, under stirring (600 rpm) for 2 h, at room temperature ($25 \pm 2 \text{ }^\circ\text{C}$). Then, the solution was dripped on a coagulant solution of CaCl_2 (10%, m v^{-1}), by a burette (50 ml) positioned 1.5 cm from the solution surface and remained in for 4 h. Then, the solution was filtered, and the beads were washed with 0.85% NaCl solution (m v^{-1}). The moisture

content and the mean diameter (D_m) were determined.

2.3. Equilibrium adsorption experiments

The equilibrium assays were carried out at pH 3, 4, 5, 6, 7 and 8, with McIlvaine buffer (10% v v^{-1}) totaling 200 mL, under stirring (50 rpm) at 298 K. 150 mg of beads (dry basis) were used and 200 mg L^{-1} betalains. The betalains solution was concentrated by vacuum evaporation, $40 \text{ }^\circ\text{C}$. Betalains concentration were determined before and after adsorption, 24 h and 48 h, where the adsorption capacity at equilibrium, q_e (mg g^{-1}), was calculated by Eq. 2, and removal percentage, $R(\%)$ was calculated by Eq. 3. In which, C_0 and C_e are the initial and equilibrium concentrations in the liquid phase (mg L^{-1}), respectively. m is the adsorbent mass (g) and V is the volume of the solution (L).

$$q_e = \frac{(c_0 - c_e)V}{m} \quad (2)$$

$$R(\%) = \frac{C_e}{C_0} 100 \quad (3)$$

2.4. Equilibrium isotherms

The equilibrium isotherms curves were obtained experimentally at different temperatures (298, 308 and 318 K) in pH 4, using McIlvaine buffer (10% v v^{-1}) totaling 200 mL of solution, under the stirring of 50 rpm. The betalain concentrations were determined before and after (24 h) adsorption, the betalains concentrations varied from 50 to 300 mg L^{-1} . In each assay, 150 mg (d. b.) of beads were used. Results were evaluated by fitting the isotherms models of Henry, Langmuir, Freundlich, according to Eqs. 4, 5 and 6 respectively; where k_H is the Henry equilibrium constant, q_m is the maximum adsorption capacity in the monolayer (mg g^{-1}), k_L is the Langmuir constant (L mg^{-1}), k_F Freundlich's constant ($(\text{mg g}^{-1}) (\text{L mg}^{-1})^{1/n}$) and n^{-1} the heterogeneity factor.

$$q_e = k_H C_e \quad (4)$$

$$q_e = \frac{q_m k_L C_e}{1 + k_L C_e} \quad (5)$$

$$q_e = k_F C_e^{1/n} \quad (6)$$

Thermogravimetric analyses (TGA) of the beads before and after adsorption were performed on a thermal balance (PG Instruments, SDT Q600, ING), with a heating rate of 10 °C min⁻¹ in N₂ modified atmosphere (100 mL min⁻¹).

3. Results

The extracted betalains concentration was of 118.14 ± 2.6 mg L⁻¹, the moisture content of beetroots was of 86.7 ± 0.5%, and the betalains concentration in beetroots was of 9.18 g kg⁻¹ (d.b.). The betacyanins: betaxanthines ratio was 1.81 ± 0.08, and in the literature there is a ratio of 1.75 [2]. This indicates that the ratio between betacyanins and betaxanthines was similar to literature, despite the variety. The adsorption capacities for 24h e 48h showed no significant difference (p>0.05). The best adsorption capacities were obtained at pH 3 and 4 (Table 1), but there was not statistically significant difference between pH 3 and 4. At pH 7 and 8, the beads dissolved in the solution. This can be attributed to a chain expansion from the ionic carboxylate groups of alginate to a higher pH value [4] that may have caused the Ca²⁺ cross-linker rupture.

Table 1. Effect of pH on the percentage of removal and adsorption capacity.

pH	*q _c (mg g ⁻¹)	*R(%)
3	98.64±1.32 ^a	41.1±0.2 ^a
4	97.92±1.12 ^a	40.8±0.4 ^a
5	81.60±1.13 ^b	34.0±0.3 ^b
6	62.88±1.23 ^c	26.2±0.4 ^c
7	-	-
8	-	-

*Mean ± standard deviation (n = 3). Different letters in same column indicate significant differences (p < 0.05).

Thus, pH 4 was chosen for the studies of adsorption isotherms. Betanin (the main betalain pigment) in aqueous acid medium has two protonated structures in resonance, due to the presence of two nitrogen atoms, one in the glycoside group and the other in betalamic acid [5]. While, the alginate may interact with various divalent cations (Ca²⁺, Mg²⁺) due to the carboxylate groups. In addition, under acidic conditions, the carbonyl group becomes protonated, and thus activated

toward nucleophilic acyl substitution. The Henry, Langmuir and Freundlich models were adjusted to the experimental data of the isotherms to describe the betalains adsorption behavior in alginate beads. The coefficient of determination and the mean relative error were evaluated to choose the most appropriate model, and they are presented in Table 2. The model of Henry was used to demonstrate that the data does not present a linear behavior. Freundlich and Langmuir isotherm model showed good fit to the experimental data (Fig. 1). Langmuir isotherm showed a maximum adsorption capacity (q_m) of 119.9 mg g⁻¹, q_m was of 12.3% higher than the experimental value for the betalains concentration of 300 mg L⁻¹.

Table 2. Parameters of adsorption isotherm models

T (K)	Henry			
	*k _H (L g ⁻¹)	R ²	MRE(%)	
298	0.454±0.004	0.484	6.5	
308	0.474±0.005	0.429	3.7	
318	0.498±0.005	0.384	1.7	
T (K)	Langmuir			
	*k _L (L mg ⁻¹)	*q _m (mg g ⁻¹)	R ²	MRE(%)
298	0.0414±0.0005	110.8±0.6	0.994	2.4
308	0.0443±0.0003	114.9±0.4	0.995	2.0
318	0.0476±0.0006	119.9±0.6	0.995	1.4
T (K)	Freundlich			
	*k _F (mg g ⁻¹) (L mg ⁻¹) ^{1/n}	*n	R ²	MRE(%)
298	38.6±0.2	5.7±0.06	0.999	2.4
308	42.6±0.4	6.0±0.03	0.999	2.4
318	46.2±0.5	6.3±0.05	0.999	2.6

*Mean ± standard deviation (n = 3). R²: coefficient of determination; MRE: mean relative error.

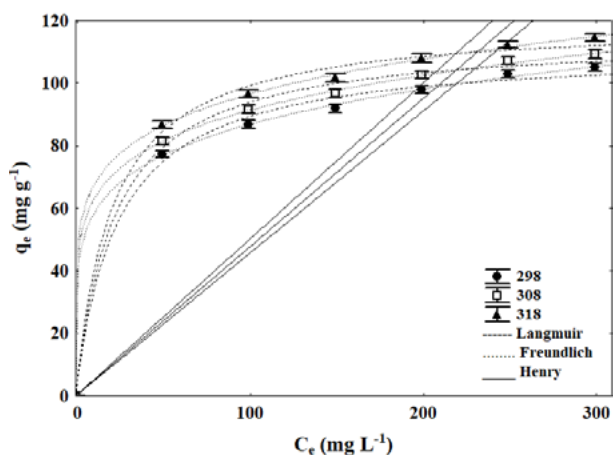


Fig. 1. Fitting to experimental data by Henry, Langmuir and Freundlich models.

Fig.2 shows the thermogravimetric analyses (TGA) of the beads before and after the betalains adsorption from beetroot. The thermal decomposition polymers, in general, includes the desorption of physically absorbed water, the dehydration, follows the rupture of C-O and C-C bonds generating CO, CO₂ and H₂O, and the formation of polynuclear aromatic and graphitic carbon structures [6].

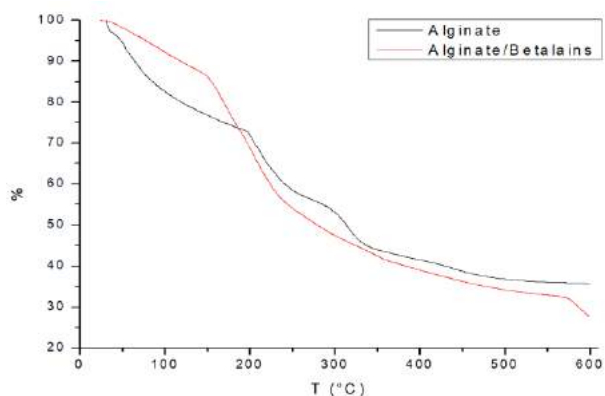


Fig. 2. TGA of alginate beads before and after adsorption.

In Fig. 2, the loss of water molecules for alginate beads occurred at temperature range between 40 °C and 200 °C. However, the mass loss of beads with betalains was constant until to 160 °C, subsequently, there was an abrupt weight loss, probably due to the presence of betalains, as they are more sensitive to thermal degradation. The residue left was 35.8% and 27.6% for alginate and alginate plus betalains, respectively. However, an

improvement in thermal stability was observed for beads with betalains, as weight loss was lower up to 150 °C. This result is promising as it broadens product range that beads with betalains can be applied without degradation.

4. Conclusion

The adsorption capacities of betalains from beetroot, in batch adsorption, onto sodium alginate beads in 24 h and 48 h showed no significant difference ($p > 0.05$). The best adsorption capacities were obtained in pH 3 and 4. Freundlich and Langmuir adsorption isotherm models showed good fitting to experimental data. Thermogravimetric analysis showed that beads after adsorption presented a greater degradation.

Acknowledgements

The authors would like to thank CAPES (Coordination for the Improvement of Higher Education Personnel), Finance Code: 001, and CNPq (National Council for Scientific and Technological Development).

References

- [1] Herbach KM, Stintzing FC, R. Carle R. Betalain stability and degradation—structural and chromatic aspects. *J. Food Sci.* 2006;71:R41-R50.
- [2] Wruss J, Waldenberger G, Huemer S, Uygun P, Lanzerstorfer P, Müller U, Höglinger O, Weghuber J. Compositional characteristics of commercial beetroot products and beetroot juice prepared from seven beetroot varieties grown in Upper Austria. *J Food Comp Anal.* 2015;42:46–55.
- [3] González-Rodríguez ML, Holgado MA, Sánchez-Lafuente C, Rabasco AM, Fini A. Alginate/chitosan particulate systems for sodium diclofenac release. *Int J Pharm* 2002;232:225-234
- [4] Chuang JJ, Huang YY, Lo SH, Hsu TF, Huang WY, Huang SL, Lin YS. Effects of pH on the shape of alginate particles and its release behavior. *Int. J Polym Sci.* 2017;1:1-9
- [5] Świągło AG, Szymusiak H, Malinowska P. Betanin, the main pigment of red beet - molecular origin of its exceptionally high free radical scavenging activity. *Food Addit Contam* 2006;23:1079-1087.
- [6] Adzmi F, Meon S, Musa MH, Yusuf NA. Preparation, characterisation and viability of encapsulated *Trichoderma harzianum* UPM40 in alginate-montmorillonite clay. *J Microencapsul* 2012;29:205-10

Calcined sludge from a water treatment plant as adsorbent for fluoride removal

Renata Segatto Pigatto^a, Nátalie De Paula^a, Manoel Maraschin^a, Ezequiel Andrei Somavilla^a, Sérgio Luiz Jahn^a, Elvis Carissimi^a, Guilherme Luiz Dotto^a

^a Universidade Federal de Santa Maria, Avenida Roraima, 1000, Santa Maria, 97105-900, Brazil

Abstract

Sludge from a water treatment plant was modified by calcination at two different temperatures (200 °C and 600 °C) and compared to the raw one as adsorbents for fluoride removal, once it has aluminum in its composition. The materials characterization was evaluated by Fourier transform infrared spectroscopy, thermogravimetric analysis, Brunauer-Emmett-Teller surface analysis and point of zero charge. The sludge calcined at 200 °C presented best performance, with 98.13% of fluoride removal and 1.05 mg g⁻¹ of adsorption capacity. Raw sludge got 88.58% and 0.946 mg g⁻¹, while the material treated at 600 °C got 59.36% and 0.634 mg g⁻¹, respectively. These results indicated calcination as an alternative modification to water treatment sludge in order to reuse this residue as low-cost adsorbent for fluoride removal.

Keywords: water treatment sludge; fluoride adsorption; calcination

1. Introduction

Water treatment plant sludge is a by-product from the conventional treatment plants, specifically from the coagulation-flocculation step. First, colloidal particles in raw water are destabilized and then agglomerated into larger aggregates, which sediment or are filtered. The commonly used inorganic coagulants are alum-based salts, which are ionized when added to water and form trivalent ions, Al(III) [1]. So, sludge containing a wide range of organic and inorganic substances [2], and can be a low cost and effective adsorbent for inorganic contaminants as fluoride ions.

Fluoride is an inorganic ion present naturally in groundwater and has an important role in human health. Its ideal and recommended concentration is 1 mg L⁻¹ [3] which is supposed to be enough to avoid dental caries. However, people continuously exposed to higher concentrations can develop dental fluorosis in first stage and skeletal fluorosis in advanced one caused by its deposition. Considering that groundwater is the major source of domestic water for people living in rural and semi-urban areas in most parts of the world [4], it is necessary a technology able to remove this excess and make it potable with a low cost, simplicity and effectiveness.

In this study, sludge from a local water treatment plant was evaluated in three distinct forms, being two of them modified by calcination at temperatures of 200 and 600 °C. The removal in percentage and the adsorption capacity (mg g⁻¹) of fluoride ions from a synthetic solution under the same operational conditions were the studied parameters. All the materials were characterized to identify changes performed by calcination.

2. Materials and methods

2.1. Water treatment plant sludge calcination

The raw water treatment plant sludge was obtained from decanter of the local water treatment plant in Santa Maria, Rio Grande do Sul, Brazil. The sample was dried at 80 °C for 12 h in air oven and then calcinated at two different temperatures (200 and 600 °C) in oxidizing atmosphere furnace for 2 h and 10 °C min⁻¹ heating rate. The samples were named as In_natura, 200C and 600C.

2.2. Sludge characterization

Functional groups were identified by Fourier transform infrared (FT-IR) spectroscopy (Shimadzu, IR Prestige model) using KBr in wavelength range of 400-4500 cm⁻¹. Brunauer-

Emmett-Teller (BET) surface area, pore volume and average pore size were measured by BET surface analyzer (Micromeritics, ASAP 2020 model) with N₂ adsorption isotherm. Weight loss was measured by thermogravimetric analysis (TGA) with 50 mL min⁻¹ flow air, temperature from 25 to 1000 °C and 20 °C min⁻¹ heating rate (Shimadzu, TGA-50/50H model). Point of zero charge values (PZC) were determined by the 11 points experiment. 0.2 g of each material were added into 250 mL erlenmeyer containing 80 mL 0.1 mol L⁻¹ NaCl solution. The initial pH was adjusted with HCl 1.0 mol L⁻¹ and NaOH 1.0 mol L⁻¹ to 2, 3, 4, 5, 6, 7, 8, 9, 10, 11 and 12 values and the final pH was measured after 24 h at 120 rpm rotation at room temperature.

2.3. Adsorption experiments

A synthetic solution was prepared with 0.221 g of NaF in 1 L of distilled water and then diluted to a 5.34 mg L⁻¹ of fluoride. The experiments were carried out using 0.5 g of sludge samples with 100 mL of F⁻ solution in a 250 mL polypropylene erlenmeyers. The solutions initial pH was adjusted to 6.0. Solutions were stirred in a dubnoff shaker (Marconi, MA095 model) at 25 °C and 150 rpm for 2 h. The fluoride concentration was measured by ion chromatography (Metrohm, 930 Compact IC Flex model) after filtering using a syringe filter with 0.22 µm. All the experiments were carried out in triplicate.

The results were expressed in terms of removal percentage *R* (%) according to equation (1) and adsorption capacity *q* (mg g⁻¹) according to equation (2).

$$R = \frac{(C_0 - C)}{C_0} 100 \quad (1)$$

$$q = \frac{(C_0 - C)}{m} V \quad (2)$$

where *C*₀ and *C* are the initial and final concentrations of fluoride ions (mg L⁻¹), respectively, *m* is the mass of adsorbent (g) and *V* is the volume of solution (L).

3. Results and discussion

3.1. Sludge characterization

Fig. 1 shows the Fourier transform infrared (FT-IR) spectra for the different sludge's. Most of

bands are kept through de calcination as 3000-3500 cm⁻¹ OH stretching band [5]; 1600 cm⁻¹ complexed carbonyl double bonded carbon with oxygen (C=O) band; 1100 cm⁻¹ Si-O stretching band [6]; 500 cm⁻¹ Al-O-Al or Al-O-Si bending vibrations band [6]. With the temperature increase, temperature, the band 1400 cm⁻¹ disappeared, which is characteristic of carboxyl groups from natural organic matter [1]. Besides, other bands in 900-500 cm⁻¹ are related to Al-O bonds and its changes [7]. The results indicated that the calcination reduced, or even eliminated all the organic matter from the raw sample. Bands relative to Al and Si were maintained.

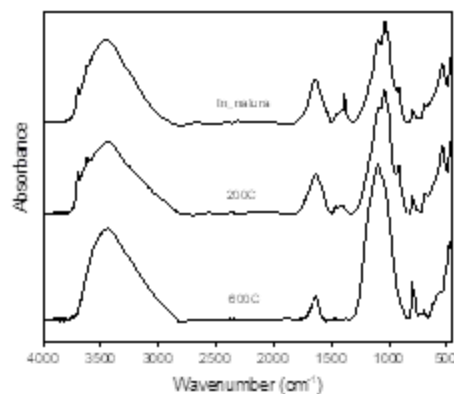


Fig. 1. FT-IR spectra of the sludge's.

The BET analysis results (Table 1) shows a surface area reduction from 70.1 to 55.1 m² g⁻¹ with the temperature increase. Probably the In_natura sludge would have a surface area smaller than the 200C one, although its area could not be measured since the analysis equipment uses temperatures above 80 °C and, being above the drying temperature, it could cause some other characteristic to the material.

This is also probably to be the explanation for difference in removal and adsorption capacity. The average pore size was 11.31 and 19.22 nm which means decomposition of organic matter by calcination process reveals the mesopores blocked by organic matter [1].

Besides, it is possible that surface area decrease and average pore size increase occur because of crystallization of aluminum oxides/hydroxides during thermal treatment [1].

Table 1. Brunauer-Emmett-Teller analysis results.

Analysis	200C	600C
Surface area ($\text{m}^2 \text{g}^{-1}$)	70.07	55.14
Pore volume ($\text{cm}^3 \text{g}^{-1}$)	0.115	0.155
Average pore size (nm)	11.31	19.22

Fig. 2 shows the sludge weight loss with temperature increasing due to especially organic matter and carbon degradation. Losses until 110 °C may be attributed to strong physical bond between water and sludge and water contiguous to aluminum hydroxide was driven out between 200 and 400 °C [8]. The exothermic peak between 470 and 510 °C is probably attributed to dehydroxylation of clay materials [9].

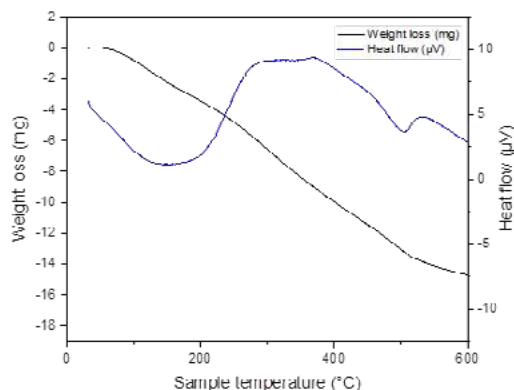


Fig. 2. Thermogravimetric analysis profile.

Fig. 3 shows the point of zero charge. As calcination temperature increases surface charges changes to higher values. The In_natura material presented a PZC of 5.5, which is very close to the 200C value. However, 600C presents close to 6.0. Because of this, adsorption experiments were carried out in a solution pH of 6.0 which in general is acceptable limit in drinking water legislation.

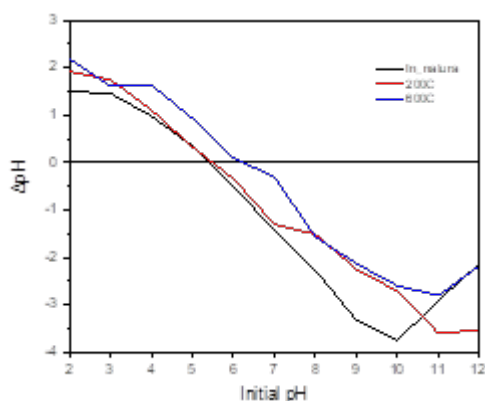


Fig. 3. Point of zero charge of adsorbents.

3.2. Adsorption results

After 2-h experiment in fluoride synthetic solution, Table 2 shows final solution pH and final fluoride concentration (mg L^{-1}). As the best removal percentage and adsorption capacity, 200C sludge reduced the fluoride concentration from 5.34 mg L^{-1} to 0.10 mg L^{-1} and decreased the pH from 6.0 to 5.66. In a drinking water treatment real situation, it would be probably necessary to adjust final pH value to 6.0.

Table 2. Adsorption experiments results.

Material	Final solution pH	C (mg L^{-1})
In_natura	6.07	0.61
200C	5.66	0.10
600C	6.74	2.17

As it is possible visualize in Fig. 4, 600C sludge had the worst performance as fluoride adsorbent, probably because the crystallization of aluminum oxides/hydroxides during thermal treatment and its reduced surface area.

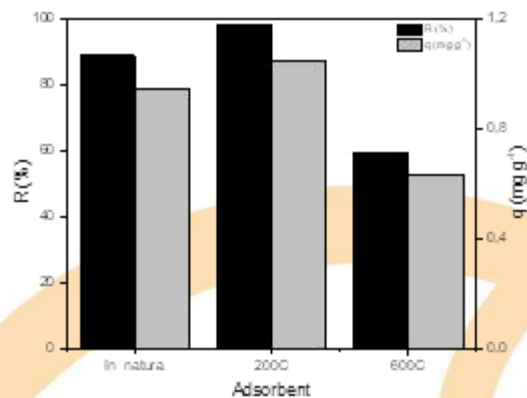


Fig. 4. Fluoride removal percentage and adsorption capacity

Highest adsorption capacity was found to be 1.05 mg g^{-1} for 200C sludge resulting in 98.13% removal compared to 0.946 mg g^{-1} for In_Natura (88.58% removal) and 0.634 mg g^{-1} for 600C one (59.36% removal). About the removal values close to 100%, it can be considered that acid solution initial pH favors fluoride adsorption, being possible not only adjust value lower than legal one, but also removing it completely. This situation would be interesting in a large-scale water treatment once two streams can be mixture – one concentrated and another fluoride free to be diluted to the ideal value concentration.

Besides these results, the use of a low calcination temperature is an advantage considering that there is less energy consumption to raise the temperature and keep it at 200 °C during 2-hour calcination compared to the others.

In a comparison to other studies, granular red mud in the same adsorbent concentration (5 g L⁻¹), obtained 0.851 mg g⁻¹ adsorption capacity [10]. Other residues like banana peel in 16 g L⁻¹ adsorbent concentration obtained 1.34 mg g⁻¹ [11], and bone char in 50 mg L⁻¹ adsorbent concentration obtained 5.889 mg g⁻¹ [12]. These results show that materials considered as waste or by-products need high concentrations in order to guarantee great adsorption capacities.

Therefore, in present study, the 200C sludge presented a reasonable value and can be considered high given the process conditions. Thus, it is possible produce an accessible, cheap and available material through a simple process to avoid a health human problem.

4. Conclusions

Water treatment sludge were submitted to different temperatures of calcination and evaluated as adsorbent for fluoride removal. The best performance was verified for the material calcined at 200 °C (200C), with 98.13% of removal and 1.05 mg g⁻¹ of adsorption capacity. The In_natura got 88.58% and 0.946 mg g⁻¹, and 600C got 59.36% and 0.634 mg g⁻¹, respectively. The process at 600 °C removed organic matter totally but reduced surface area of material, resulting in lower adsorption potential. These results indicated calcination as an alternative modification to water treatment sludge in order to reuse this residue as low-cost adsorbent for fluoride removal.

References

- [1] Jeon EK, Ryu S, Park SW, Wang L, Tsang DCW, Baek K. Enhanced adsorption of arsenic onto alum sludge modified by calcination. *J Cleaner Production* 2018;176:54-62.
- [2] The CY, Budiman PM, Shak KPY, Wu TY. Recent advancement of coagulation–flocculation and its application in wastewater treatment. *Industrial & Engineering Chemistry Research* 2016;55:4363-4389.
- [3] World Health Organization. *Guidelines for Drinking Water Quality, 2nd. Health Criteria and Supporting Information Recommendations*. Geneva: 1993.
- [4] Ahamad KU, Singh R, Baruah I, Choudhury H, Sharma MR. Equilibrium and kinetics modeling of fluoride adsorption onto activated alumina, alum and brick powder. *Groundwater for sustainable development* 2018;7:452-458.
- [5] Sifontes AB, Gutierrez B, Mónaco A, Yanez A, Díaz Y, Méndez FJ, Llovera L, Cañizales E, Brito JL. Preparation of functionalized porous nano-g-Al₂O₃ powder employing colophony extract. *Biotechnology reports* 2014;4:21-29.
- [6] Huang C, Behrman EC. Structure and properties of calcium aluminosilicate glasses. *Journal of Non-Crystalline Solid* 1991;128:310-321.
- [7] Sebdani MM, Mauro JC, Jensen LR, Smedskjaer MM. Structure-property relations in calcium aluminate glasses containing different divalent cations and SiO₂. *Journal of Non-Crystalline Solids* 2015;427:160-165.
- [8] Shahin SA, Mossad M, Fouad M. Evaluation of copper removal efficiency using water treatment sludge. *Water science and engineering* 2019;12:37-44.
- [9] Ling YP, Tham RH, Lim SM, Fahim M, Ooi CH, Krishnan P, Matsumoto A, Yeoh FY. Evaluation and reutilization of water sludge from fresh water processing plant as a green clay substituent. *Applied Clay Science* 2017;143:300-306.
- [10] Tor A, Danaoglu N, Arslan G, Cengeloglu Y. Removal of fluoride from water by using granular red mud: Batch and column studies. *Journal of Hazardous Materials* 2009;164:271–278.
- [11] Mohammad A, Majumder CB. Removal of Fluoride From Synthetic Waste Water By Using “Bio-Adsorbents”. *International Journal of Research in Engineering and Technology* 2014;03:776–785.
- [12] Leyva-Ramos R, Rivera-Utrilla J, Medellín-Castillo NA, Sanchez-Polo M. Kinetic modeling of fluoride adsorption from aqueous solution onto bone char. *Chemical Engineering Journal* 2010;158:458–467.

Lecithin removal of vegetable oils by sucrose adsorption

Ana Amélia de Lurdes Coelho Rodrigues^a, Valter Luís Zuliani Stroppa^b, Sandra Bizarria Lopes Villanueva^c, Igor Tadeu Lazzarotto Bresolin^a

^a Universidade Federal de São Paulo, São Nicolau, Diadema 09913-030, Brazil

^b Universidade Metodista de Piracicaba, Rodovia SP-306 km 1, Santa Bárbara d'Oeste 13450-001, Brazil

^c Faculdade de Engenharia de Sorocaba, Rodovia Senador José Ermirio de Moraes, Sorocaba 18087-712, Brazil

Abstract

The aim of this paper is to investigate a possible alternative and innovative method for the removal of lecithin from oils of vegetable origin, a process known as degumming. Degumming is the first stage on vegetable oil refining process, usually conducted by extraction to remove the gum present in the crude lipid system. This is an important step that avoids sludge formation, rancidity and oil oxidation, among other negative effects throughout the refining process. By contrast, lecithin is a by-product of great commercial interest. The innovative study is based on the use of sucrose as lecithin adsorbent material, a theme not evidenced in previous works. The current methods employed are wet degumming and acid degumming, which consist of the addition of water or a mixture of water and acid to the crude oil, respectively, and which may deteriorate the oil and extracted lecithin. Thence, it is interesting to develop an alternative degumming method, which has a satisfactory yield, which does not use water and acids and is energy efficient. To this end, sugar characteristics such as porosity, particle size and surface area were determined, and kinetic and equilibrium data were collected. The results indicate that it was possible to extract about 60% of lecithin with sugar adsorption. The contact time between sugar and oil to achieve adsorption equilibrium is in the range of 45 to 60 minutes. In addition, the by-product, lecithin adsorbed on sugar, has market-share for commercialization.

Keywords: Degumming; Adsorption; Lecithin

1. Introduction

Degumming is the first step in refining oils and fats. It is an extraction unit operation process that aims to remove the gum present in the crude oil. Gum, is a majority mixture of phospholipids (also called lecithin), along with other compounds that are dragged during their extraction. It is an important step that prevents sludge formation, rancidity and oil oxidation, among other negative effects throughout the refining process [1].

Lecithin is a by-product of commercial interest in the oil industry as it has several applications such as emulsifier, stabilizer, dispersant and homogenizer [1]. The main sectors of the industry where it is used involve margarine, chocolate and ice cream, paint, cosmetics and pharmaceutical industry [2].

The methods currently employed are wet degumming and acid degumming. Wet degumming consists of adding 1 to 3% of water to the oil heated at 60 to 70 ° C, with gentle stirring for about 30

minutes followed by centrifugation. Acid degumming uses from 0.1 to 0.4% phosphoric acid 85% (m/m), which is mixed with crude oil at a temperature of approximately 60°C [3].

Wet degumming removes 70 to 80% of phosphatides from crude oil, however it uses considerable amount of water in a large-scale process, about 1 to 3%. The acid treatment removes 90% of the gums, but makes the extracted lecithin impure and of less commercial value [3]. Thence, it is interesting to develop an alternative and innovative method of degumming, which presents satisfactory yield, which does not use water and acids and is energy efficient.

The subject of this paper is the development of an alternative and innovative method for the removal of lecithin from oils of vegetable origin. It is based on the hypothesis of lecithin adsorption phenomenon in sugar, a mechanism reported in the literature that justifies the application of phospholipids as emulsifiers in the production of chocolates. This phenomenon causes a better

interaction of sugar particles (polar) in the fat phase (nonpolar) [4].

Thus, it is the general objective of this work to establish the parameters of a possible alternative method of lecithin removal from oils of plant origin by means of sugar adsorption. For this, sugar characteristics such as porosity, particle size and surface area were determined, as well as kinetic and equilibrium data, aiming to obtain an oil with lower lecithin content (removal of about 60%).

2. Materials and methods

2.1 Materials

2.1.1 Sample

Crude oil donated by Granol company (Brazil);
Crystal sugar, Guarani brand (Brazil);
Commercial lecithin, Adicel brand, (Brazil).

2.1.2 Equipment

The equipment used was a scanning electron microscopy TM3000 (Hitachi, Japan), an analytical balance Q-500L210C (Quimis, Brazil), a water bath MOD555 (Fisatom, Brazil), an oven Q317M (Quimis, Brazil) and a centrifuge MOD17250-10, (Cole Parmer, Unites States).

2.2 Adsorbent characterization test

To characterize the adsorbent, scanning electron microscopy was performed. It was possible to produce high-resolution images of the crystal sugar surface with 25 to 600 times magnification.

2.3 Test for determination of lecithin adsorption kinetics in sugar

The reaction kinetics determination test was performed at the Sorocaba School of Engineering (Sorocaba, Brazil) laboratory with crude oil.

For the test, approximately equal amounts of crystal sugar were added in different oil samples (Table 1).

Each sample remained for a predetermined time, from 15 to 90 minutes in agitation, ensuring contact between the sugar particles and 50 mL of the crude oil. Subsequently, the oil was separated from the sugar particles decantation from the bottom of the beaker.

The initial lecithin contents and the remaining content in each sample after the time of contact with

sugar were determined according to the method described in Item 3.3.

Table 1. Sample for kinetics test

Sample	1	2	3	4	5
Sugar (g)	1,0034	1,0056	1,0068	1,0050	1,0009
Contact time (min)	15	30	45	60	90

2.4 Method of determining lecithin in oils by insoluble in acetone

The method is based on the partial solubility of lecithin in acetone and the total solubility of the other components of the lipid phase (AOCS JA 4-46) [5]. When a saturated solution of lecithin in acetone is mixed with the crude oil, the excess amount of lecithin (which reaches the solubility limit) contained in the oil precipitates. The following procedures discuss in more detail solution preparation and the analysis method.

2.4.1 Preparation of purified lecithin

Using the analytical balance, 6 g of commercial lecithin was weighed into a clean beaker and about 10 mL of cold acetone was added with a graduated pipette. Stir with a drumstick in a water bath at 30 °C. The yellowish acetone was discarded and more acetone was added. This process was repeated until the color of acetone changes from yellow to transparent (approximately 3 times).

2.4.2 Preparation of saturated acetone solution

6 g of purified lecithin prepared as described in Item 3.3.1 was dissolved in 1 L of acetone. The mixture was kept at room temperature for 2 hours and stirred every 20 minutes. The solution was cooled for 2 hours in a refrigerator and then the insoluble part was collected on filter paper before use.

2.4.3 Determination of lecithin content in oil with acetone insoluble method

The oil samples were conditioned at 60 °C using a water bath and homogenized manually with the aid of a drumstick. Approximately 2 g of the sample was weighed into a test tube (M₁) and 15 mL of cold saturated acetone was added.

The sample tube was heated in a water bath to 45 °C and the sample was stirred with a stick. After this time, the test tube was kept in an ice bath for 5 minutes, and then, at room temperature, 35 mL of cold saturated acetone was slowly added. Place in the ice bath again for 15 minutes and stirred.

The mixture contained in the test tube was equally distributed into 6 smaller glass test tubes of predetermined mass (M_0). These filled tubes were placed in a centrifuge at 3400 rpm for 5 minutes. Subsequently, the supernatant liquid was discarded and the tubes were placed in oven at 110 °C for one hour. After this period, this sample was placed in a desiccator for 30 minutes. Finally, on an analytical balance, the new mass of the 6 tubes together (M_2) with the precipitates was determined.

The evaluation of the insoluble lecithin fraction can be done with Equation 1.

$$\text{Lecithin (\%)} = \frac{M_2 - M_0}{M_1} \times 100 \quad (1)$$

which M_0 is the initial mass of tubes, M_1 is the mass of sample, and M_2 is the mass of tubes after test.

3. Results and discussion

The images produced in the scanning electron microscopy assay are presented in Item 4.1 and the results obtained in the determination of adsorption kinetics are presented in Item 4.2.

3.1 Electronic scan microscopy

Figure 1 show different angles and magnifications SEM analysis.

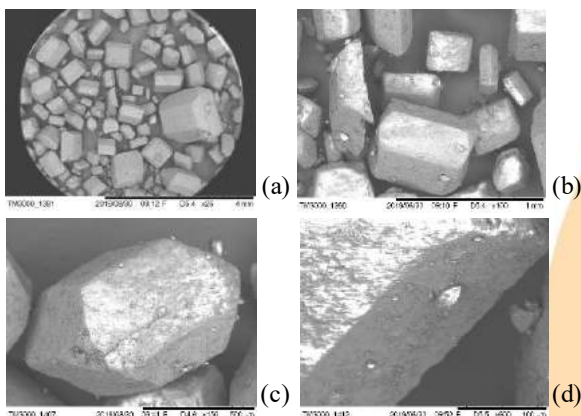


Fig. 1. SEM of sucrose in different magnifications: (a) 25x; (b) 100x; (c) 150x; (d) 600x

Crystal sugar, for the most part, has particles of regular polygon shape with sharp angles. Straight corners, rough surface and a large number of

microparticles adhered to the surface are observed. Apparently, the surface is not microporous.

There is a wide variation in particle size, in an approximate ratio of 10 times. The average grain size, calculated from the images produced, approximately 30 particles.

The representation of the shape and average size of crystal sugar grains can be seen in Figure 2.

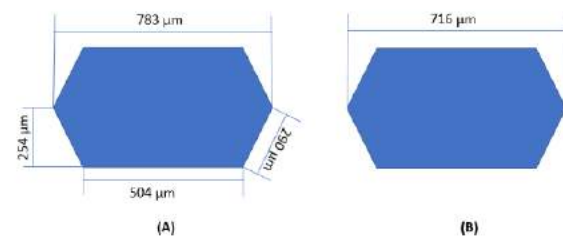


Fig. 2. (A) Front view (B) Middle side view of crystal sugar grains

With the average size, the specific area is 393,337 $\mu\text{m}^2.\text{mg}^{-1}$ and specific volume of 281,629,394 $\mu\text{m}^3.\text{mg}^{-1}$.

3.2 Results for the Adsorption Kinetics Test

The results obtained for the adsorption test can be seen in Table 2, considering that the lecithin content found in the crude oil was 0.77 g in 50 g of crude oil.

Table 2. Results regarding the adsorption tests

Sample	1	2	3	4	5
Contact time (min)	15	30	45	60	90
Lecithin content (g/ 50 g oil)	0.415	0.400	0.315	0.305	0.330
Lecithin removal (%)	46.10	48.05	59.09	60.39	57.14

The results show that extraction can reach approximately 60%, therefore satisfactory. The contact time between sugar and oil to achieve adsorption equilibrium is in the range of 45 to 60 minutes.

4. Conclusion

The obtained results indicate that sugar has potential to be used as an innovative method of lecithin removal from oils of vegetal origin, which makes the continuation of this study relevant.

The contact time between sugar and oil to achieve adsorption equilibrium is in the range of 45 to 60 minutes.

It was possible to extract significant amount of lecithin, about 60%, without the use of water and acids, and without heating, which tends to preserve oil quality parameters. In addition, the by-product, lecithin adsorbed on sugar, has market-share for commercialization.

Acknowledgements

Acknowledgment to the Sorocaba School of Engineering, the Federal University of São Paulo and the Federal University of São Carlos for the resources and laboratories available.

Thanks to the company Granol for the donated crude oil.

References

- [1] Vanaclocha, A. C. et al. Technology of plant-based foods: Oils, fresh vegetables, vegetables preserved by heat or freezing, fruit juices, fruits preserved by reduction of their water activity, dehydrated vegetables. Volume 1. Spain: Synthesis, 2014.
- [2] Soares, M. S. Processing soybean oil using ultrafiltration at various stages of lecithin removal and recovery. Doctoral dissertation, Unicamp 2004.
- [3] Mandarino, J. M. G; Roessing, A. C. Embrapa Documents 171-Soybean Oil Production Technology: Description of Steps, Equipment, Products and By-Products. 1st ed. Londrina, Brazil: Embrapa, 2001.
- [4] Beckett, S. T. Industrial chocolate manufacture and Use. 4th ed. York, United Kingdom: Blackwell, 2009.
- [5] America Oil Chemists' Society. Official methods and recommended practices of the American Oil Chemists' Society. 5ªed. Champaign, United States, AOCS, 2004.

Bovine immunoglobulin G adsorption onto monolithic cryogel of polyacrylamide/alginate derivatized with IDA

Igor F. Fioravante^a, Camila Marcuz^a, and Sônia M. A. Bueno^a

^a State University of Campinas, School of Chemical Engineering, Av. Albert Einstein, 500, Barão Geraldo, 13083-852, Campinas - SP, Brazil

Abstract

A monolithic cryogel was prepared using acrylamide (AAm), bis-acrylamide (MBAm), alginate (Alg), and allyl glycidyl ether (AGE) (PAAm-Alg-AGE). The ligand iminodiacetic acid (IDA) was immobilized onto this material, in order to be used as a stationary phase in affinity chromatography. The monolith PAAm-Alg-AGE-IDA showed macroporous sponge like and opaque structure, a degree of swelling of 4.68 g H₂O/g dry cryogel, and a porosity of 70,8%. The chromatographic procedures were performed to evaluate the potential of this adsorbent to adsorb bovine immunoglobulin G (bIgG) in three different buffer systems and pH: Tris (hydroxymethyl) aminomethane (Tris-HCl), (3-(N-morpholino) propanesulfonic acid (MOPS), and MOPS-acetate (MA). The cryogel was able to adsorb bIgG in all the conditions, but the best result was observed when MOPS buffer was used in pH 6.0, reaching an adsorption of 82% of the protein fed in the column. The synthesized cryogel showed potential for use as stationary phase for bIgG adsorption.

Keywords: Cryogel; bovine immunoglobulin G; adsorption, polyacrylamide, alginate, monolith

1. Introduction

Immunoglobulin G (IgG) is an antibody synthesized by the immune system of vertebrates in response to a specific antigen. The bovine IgG (bIgG) has a growing interest for the industry, specially food and pharmaceutical, since antibodies can be used for therapeutic, nutritional, and diagnosis proposes^[1].

Research has shown that IgG from bovine serum is helpful in treatment of recurrent respiratory tract infections and diarrhea in children^[2] and adults, in blood pressure control^[3], and in patients with complications from HIV^[4].

However, for these purposes are required IgG molecules with high degree of purity. To achieve this, different purification methods are used such as precipitation^[5], filtration^[6], and affinity chromatography^[7].

For chromatographic procedures, the choice of the stationary phase plays an important role in the process. Some different matrices were introduced to be used in affinity chromatography, such as the gels^[8], membranes^[9], and monolithic columns^[10].

The polymeric monolithic columns can be prepared by cryogelation technique. Cryogels are materials prepared from different monomers in presence of a crosslinking agent. The polymerization takes place in temperatures under 0°C. The resulting materials present a macroporous structures, able to purify large molecules^[10].

According to Mourão and collaborators^[11], when cryogels are synthesized with acrylamide and natural polysaccharides, such as alginate, the resulting structure (PAAm-Alg cryogel) has good mechanical strength and low pressure drop, which makes this monolith interesting for use as a stationary phase in chromatography.

For protein purification, it is suitable a cryogel selective for the target protein. The immobilization of an affinity ligand at the stationary phase provides the adsorbent greater selectivity. It was shown previously that chelating agent iminodiacetic acid (IDA) can be immobilized onto hollow fiber membranes to obtain a chromatographic support for purification of monoclonal antibodies^[12].

The aim of this work was to combine the specificity of the IDA ligand with PAAm-Alg-



AGE cryogel technology to create a powerful device for the adsorption of bIgG.

2. Material and methods

2.1. Material

Acrylamide, N, N'-methylene bisacrylamide (bisacrylamide), sodium alginate, ammonium persulfate (APS), trizma base, allyl glycidyl ether (AGE), MOPS (3-(N-morpholino) propanesulfonic acid), and bIgG were obtained from Sigma-Aldrich (USA). Calcium chloride (CaCl₂), sodium carbonate, and sodium acetate were obtained from Merck (USA). N, N, N-tetramethylethylenediamine (TEMED) was obtained from Bio-Rad (USA); iminodiacetic acid (IDA) was obtained from ACROS (USA); sodium acetate was obtained from Scientific Exodus (Brazil). Millipore's ultra-pure Milli-Q water (USA) was used. All other chemicals were of analytical grade.

2.2. Methods

Synthesis of the cryogel PAAm-Alg-AGE-IDA:

The synthesis of the cryogel was performed according method described by Mourão and collaborators^[11], however, the epoxy groups were introduced by addition of AGE. First, solutions of acrylamide and bis-acrylamide (6% w/v) were mixed with a sodium alginate solution (1% w/v) and then it was degassed for 20 min. CaCl₂ (0.04%), TEMED (20 µL), APS (2%), and AGE (200 µL) were added in the cooled solution under magnetic stirring and the mixture (3 mL) was poured in a column (20.0 cm x 1.0 cm I.D., GE Healthcare, USA). The column was placed in the freezer at -20 °C for 16 h. The cryogels were thawed and washed with water. IDA immobilization was performed based on the method purpose by Porath and Olin^[14]. In briefly, the monolithic column was equilibrated with sodium carbonate solution (4.24 g in 20 mL) and 20 mL of a 2 mol/L NaOH solution containing 4 g of IDA and 4.42 g of sodium carbonate was recirculated at a flow rate of 0.5 mL/min for 4 h keeping the temperature constant of 60 °C.

Chromatographic procedures: The chromatographic experiments were carried out on in a low-pressure chromatography system (Biologic

LP System - Biorad, USA) in C10/10 column (GE Healthcare, USA) containing 3.0 mL of PAAm-Alg-AGE-IDA cryogel at flow rate of 1.0 ml/min and 25 °C.. First the column was washed with water and fed with 1.0 mL of bIgG solution prepared with the adsorption buffer (2 mg of total protein/mL). After, the column was washed with the adsorption buffer. The adsorption conditions employed were at 25 mmol/L: MOPS and MA (MOPS and sodium acetate) at pH 6.0, 6.5, and 7.0, and Tris-HCl at pH 7.0, 7.5, and 8.0. The elution conditions were the same buffer used in adsorption step containing 0.5 mol/L of NaCl. The fraction volumes of 2.0 mL were collected and the total protein quantification was performed by the Bradford^[16] method.

Scanning Electron Microscopy (SEM): For the SEM images, the cryogel was lyophilized after frozen in liquid nitrogen. Then, after to cover the material with gold, all sections were examined using LEO Electron Microscopy (England) at Laboratório de Caracterização de Biomassa Recursos Analíticos e Calibração (LRAC), UNICAMP, Brazil.

Swelling capacity: The swelling capacity of cryogel was determined as described by Arvidsson and collaborators^[16]. The cryogel was sucked dry and weighed (m_w) and the dry mass (m_d) was measured after drying in the oven at the temperature of 60°C until it reaches constant mass. The degree of swelling ($S_{w/w}$) was calculated as Equation 1:

$$S_{w/w} = \frac{(m_w - m_d)}{m_d} \quad (1)$$

Porosity of the cryogel: The porosity (ϕ) of the cryogel was determined as described by Sun and collaborators^[17]. Samples of the PAAm-Alg-AGE-IDA cryogel were saturated with Milli Q water and placed in a cylindrical container in which the volume of water is known (V_r). The volume was measured (V_f), thus the volume occupied by the cryogel was estimated. After, the water saturated cryogel was weighed (m_s) and the water was removed by compression and a new weighing was obtained. To obtain the porosity based on water expelled, the Equation 2 was used:

$$\varphi = \frac{m_s - m_u}{\rho_{water} * V_o} \quad (2)$$

3. Results and discussions

The monolithic cryogel PAAm-Alg-AGE-IDA consist in an uniform and homogenous macroporous structure, confirmed by the SEM images of the longitudinal (Figure 1a) and cross section (Figure 1b) of the cryogels . The synthetized cryogels were white, elastic, and spongy. The macroporous structure of the cryogel minimize the resistance to mass transfer, which is an important characteristic for chromatographic beds.

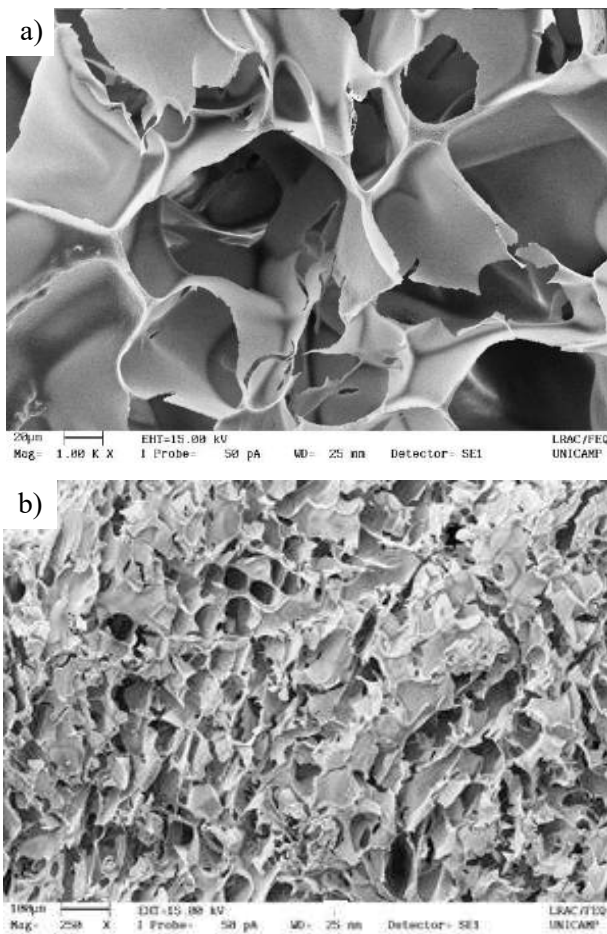


Figure 1 – SEM images of PAAm-Alg-AGE cryogel a) longitudinal (1000x) and b) cross section, respectively. Magnification: 250x.

The swelling capacity of the cryogel and the porosity degree are other ways to confirmed the structure proposed for this material as described by Arvidsson and collaborators^[16]. The swelling capacity 4.61 g of H₂O /g dry cryogel, was lower than that reported for Mourão and collaborators^[11], 5.46 g of H₂O/g dry cryogel. This difference may be related with the introduction of the epoxy groups by AGE in the synthesis of the material, which probably decreased the superficial area of the monolith, but according to Plieva and collaborators^[18] this value is among the required for cryogels.

The porosity of the monolith derivatized with IDA was 71%, lower than reported for Marcuz^[19] 82% (without IDA), which may be related with the presence of this amino acid in the material synthesis, leading to a smaller pore size and a larger pore wall.

The chromatographic procedures of bIgG using the PAAm-Alg-AGE-IDA cryogel were performed with three buffer systems, MOPS (zwitterionic), Tris-HCl (positive charged), and MA (negative charged) in three different pH between 6.0 to 8.0 and the results are showed in the Figure 2.

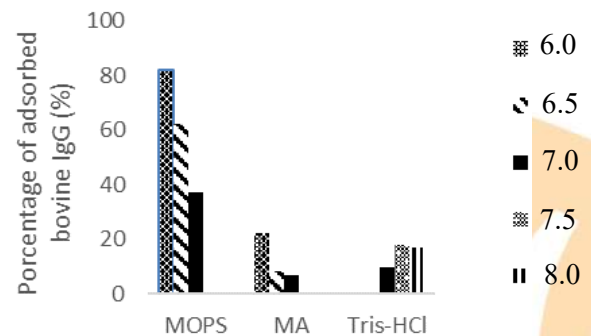


Figure 2 - Percentage of bIgG adsorbed on PAAm-Alg-AGE-IDA as a function of the pH values of each buffer system.

The PAAm-Alg-AGE-IDA cryogel was able to adsorb bIgG in all buffer systems employed. MOPS was the best buffer for bIgG adsorption, reaching 81.9% in its best condition, pH 6.0. However, the positive charged Tris-HCl and the negative charged MA adsorbed lower amount bIgG. The bIgG adsorption decreases when the pH is increased, except for Tris-HCl. Similar results were found by

Pavan and collaborators^[20] for human IgG adsorption in agarose gels with the amino acid P-Tyr immobilized (phosphorylated-tyrosine). These results demonstrated that the monolith has potential for bIgG adsorption as well as the agarose gels.

4. Conclusion

The monolith of polyacrylamide, alginate and AGE with IDA immobilized (PAAm-Alg-AGE-IDA) showed good characteristics to be used as a stationary phase in chromatography for bovine IgG adsorption. The cryogel showed a heterogenous and macroporous structure with the porous size ranging from 38 to 68 μm and porosity of 71%. These results indicated that the PAAm-Alg-AGE-IDA is a potential stationary phase for adsorption bIgG when MOPS was used, adsorbing 82% of the bIgG fed.

References

- [1]Janeway CA, Travers P, Walport M, Shlomchik M. Immunobiology: The immune system in health and disease. Garland Publishing 2001; 5: 884
- [2]Saad K, Abo-Elela MGM, El-Baseer KAA, Ahmed AE, Ahmad FA, Tawfeek MSK, El-Houfey AA, Aboulkhair MD, Abdel-Salam AM, Abo-Elgheit A, Qubaisey H, Ali AM, Abdel-Mawgoud E. Effects of bovine colostrum on recurrent respiratory tract infections and diarrhea in children. *Medicine* 2016; 95: 37.
- [3]Sharpe SJ, Gamble GD, Sharpe DN. Cholesterol-lowering and blood pressure effects of immune milk. *American Journal of Clinical Nutrition* 1994; 59: 929-934.
- [4]Asmuth DM, Ma ZM, Albanese A, Sandler NG, Devaraj S, Knight TH, Flynn NM, Yotter T, Garcia JC, Tsuchida E, Wu TT, Douek DC, Miller CJ. Oral serum-derived bovine immunoglobulin improves duodenal immune reconstitution and absorption function in patients with HIV enteropathy. *Aids* 2013; 27: 2207-2217.
- [5]Outinen M, Tossavainen O, Tupasela T, Koskela P, Koskinen H, Rantamäki P. *et al.*, Fractionation of proteins from whey with different pilot scale processes. *Lebensm-Wiss u-Technol* 1996; 29: 411-417.
- [6]Zydney AL, Protein separation using membrane filtration: new opportunities for whey fractionation. *International Dairy Journal* 1998; 8: 243-250.
- [7]Fukumoto LR, Li-Chan E, Kwan L, Nakail S. Isolation of immunoglobulins from cheese whey using ultrafiltration and immobilized metal affinity chromatography. *Food Research International* 1994; 27: 335-348.
- [8]Vançan,S, Bueno SMA, Miranda EA. IMAC of human IgG: studies with IDA-immobilized copper,nickel, zinc, and cobalt ions and different buffer systems. *Process Biochemistry* 2002; 37: 573-579.
- [9]Ribeiro MB, Vijayalakshmi M., Todorova-Balvay D, Bueno SMA. Effect of IDA and TREN chelating agents and buffer systems on the purification of human IgG with immobilized nickel affinity membranes. *Journal of Chromatography B* 2008; 861: 64-73.
- [10] Erturk G, Mattiasson B. Cryogels versatile tools in bioseparation. *Journal of chromatography A* 2014; 1357: 24-35.
- [11]Mourão CA, Marcuz C, Haupt K, Bueno SA. Polyacrylamide-alginate(PAAm-Alg) and phospho-L-tyrosine-linked PAAm-Algmonolithic cryogels: Purification of IgG from human serum. *Journal of Chromatography B* 2019; 1129.
- [12]Borsoi-Ribeiro M, Bresolin ITL, Vijayalakshmi MA, Bueno SMA. Behavior of human immunoglobulin G adsorption onto immobilized Cu(II) affinity hollow-fiber membranes. *Journal of Molecular Recognition* 2013; 26: 514-520.
- [13]Bresolin ITL, Miranda EA, Bueno SMA. Cromatografia de afinidade por íons metálicos imobilizados (IMAC) de biomoléculas: aspectos fundamentais e aplicações tecnológicas. *Química Nova* 2009;32:1288-1296.
- [14]Porath J, Olin B. Immobilized metal ion affinity adsorption and immobilized metal ion affinity chromatography of biomaterials. Serum protein affinities for gel-immobilized iron and nickel ions. *Biochem* 1983; 1621-1630.
- [15]Bradford MM.; A rapid and sensitive method for the quantitation of microgram quantities of protein utilizing the principle of protein-dye binding. *Anal. Biochem* 1976; 72: 1-2.
- [16]Arvidsson P, Plieva F, Lozinsky VI, Galaev IY, Mattiasson, B. Direct chromatographic capture of enzyme from crude homogenate using immobilized metal affinity chromatography on a continuous supermacroporous adsorbent. *Journal of chromatography A* 2003; 986: 275-290.
- [17]Sun S, Tang Y, Fu Q, Liu X, Guo L, Zhao Y. Preparation of agarose/chitosan composite. *Journal Separation Science* 2012; 35: 893-900.
- [18]Plieva FM, Karlsson M, Aguilar MR, Gomez D, Mikhalovsky S, Galaev IY. Pore structure in supermacroporous polyacrylamide based cryogels. *Soft Matter* 2005; 1: 303-309.
- [19]Marcuz, C. Adsorção de IgG humana no criogel monolítico de acrilamida-alginato-alil-o-fosfo-l-tirosins Dissertação (Mestrado em Engenharia Química) – Faculdade de Engenharia Química, Universidade Estadual de Campinas, Campinas 2019; 98.
- [20]Pavan GL, Bresolin ITL, Grespan A, Bueno SMA. Phosphorylated-tyrosine based pseudobioaffinity adsorbent for the purification of immunoglobulin G. *Journal of Chromatography B* 2017; 1052: 10-18.

Adsorption of 2-nitrophenol by calcium and nickel hidrotalcites

Keterli Dalmagro, Bianca S. Marques, Matias S. Netto, Sérgio L. Jahn, Guilherme L. Dotto

Chemical Engineering Department, Federal University of Santa Maria, Av. Roraima - 100, Santa Maria, 97105-900, Brazil

Abstract

The research was led with the objective of measuring the adsorption of composite 2-nitrophenol in aqueous solutions using two different types of adsorbents: calcium hydrotalcite and nickel hydrotalcite. The kinetic analysis, equilibrium and the influence of pH in adsorption were performed, as well as the characterization of both adsorbents by XRD, FTIR and PZC. For the kinetic, the experimental data was adjusted to pseudo-first, pseudo-second and N orders models, being the better adjustment for the N-order model with R^2 0,988, for the calcium hydrotalcite, and 0,995, for the nickel one. For the equilibrium tests, the experiment data were adjusted by the Langmuir, Freundlich and Sips model, being better adjustment for the Sips model with R^2 0,994, for the calcium hydrotalcite, and 0,996, for the nickel one. There were obtained maximum removal percentage and adsorption capacity values for pH 5, for both adsorbents. It's fair to highlight that were reached a higher removal percentage for pH 5 utilizing nickel hydrotalcite (88.5%) than calcium (78.7%). Therefore, both hydrotalcites present themselves as potential adsorbents in the contaminant 2-nitrophenol removal for aqueous solutions.

Keywords: adsorption; hydrotalcite; 2-nitrophenol.

1. Introduction

Phenolithic compounds and its derivatives present a large use at industry and agriculture, mainly when speaking about fungicides and herbicides. However, these compounds are a potential contamination source of the hydric system, because their high level of toxicity and bioaccumulation in food chain, beyond the significantly affect to the organoleptics water properties [1].

As a result of it, different physicist and chemical methods are being studied aiming the removal of these contaminants. Between them, the adsorption must be highlighted, for its great efficiency, low cost and operational facility. This method grounds in its transference of compound from the fluid phase to solid phase [2]. The most used adsorbents are the activated charcoal, which present high superficial area and developed porosity. Although, due to its high cost, there are still difficulties in using at industry scale. Thereby, the study of new materials with adsorptive properties and that has low operational cost is growing, so that could be used in

large scale [3]. There is a new material being studied recently: the hydrotalcite. The hydrotalcites are composites obtained through the co-precipitation of bivalent cations (like Zn^{2+} and Ca^{2+}) and trivalent (like Al^{3+} e Fe^{3+}), intercalated with interlayered anions like carbonates and nitrates [4].

Therefore, the present study purpose the adsorption analysis of 2-nitrophenol composite in aqueous solutions, using as adsorbents two different hydrotalcites in its carbonated forms: the calcium-aluminum ($Ca-Al-CO_3$) and the nickel-aluminum ($Ni-Al-CO_3$). In the present study therefore, so were realized the characterization of hydrotalcites, their analysis of pH influence in adsorption, besides the study of kinetic and equilibrium models.

2. Materials e methods

2.1 Adsorbate

The 2-nitrophenol (chemical formula $2-(NO_2)C_6H_4OH$; molar mass $139.11 \text{ g mol}^{-1}$; $\lambda_{\max} = 279 \text{ nm}$; CAS number 88-75-5) was provided by

Hiedel-de Haen Research Chemicals. Its molecular structure is represented in Figure 1.

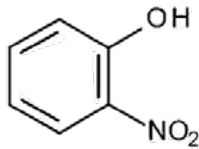


Fig. 1. Molecular structure of 2-nitrofenol. Source: Merck Millipore, 2019.

2.2 Adsorbent

The Ca-Al hydrotalcite synthesis was based on Cao *et al* (2018) [5], with some adaptations. For the synthesis, the aqueous solution prepared contained $\text{Ca}(\text{NO}_3)_2 \cdot 4\text{H}_2\text{O}$ (8 M) with $\text{Al}(\text{NO}_3)_3 \cdot 9\text{H}_2\text{O}$ (0.4 M). Then, an aqueous solution of NaOH (1.6 M) e Na_2CO_3 (0.1 M) was added. The new solution was heated for 24 hours, at a temperature of 353 K with magnetic agitation.

The Ni-Al hydrotalcite synthesis was based on Li *et al* (2006) [6], with some adaptations. The solution prepared was composed of $\text{Ni}(\text{NO}_3)_2 \cdot 6\text{H}_2\text{O}$ (0.618 M), $\text{Al}(\text{NO}_3)_3 \cdot 9\text{H}_2\text{O}$ (0.249 M), urea (9.9 M) and 0.5 L deionized H_2O . The solution was heated for 10 minutes at room temperature and aged at 100 °C for 24 hours.

Both adsorbents were characterized by point of zero charge (pH_{pzc}), the Fourier Transform Infrared Spectroscopy (FTIR) analysis and X-Ray Difraction (XRD).

2.3 Adsorption Testing

There were prepared solutions containing 2-nitrophenol with 50 mg L^{-1} concentration and volume equal to 50 mL, for the verification of pH influence over adsorption, the pH values were adjusted with NaOH (0.1 M) and HCL (0.1 M), varying its range from 2 to 10. Afterwards, for each solution, 0.05 g of adsorbent was added, proceeding the batch adsorption (Shaker SL 222 Incubator – SOLAB), under an agitation of 150 rpm, temperature of 298 K for 180 minutes. The collected samples were filtered through conventional way and quantified at the spectrometer (IL 593 – KASUAKI). Through the interpretation of the wave-length obtained by the equipment, the removal percentage (R,%) could be determined its adsorption capacity at time t (q , mg g^{-1}), according to the Equations 1 and 2, respectively.

$$R = \frac{C_0 - C_t}{C_0} \cdot 100 \quad (1)$$

$$q_t = \frac{C_0 - C_t}{m} \cdot V \quad (2)$$

C_0 and C_t (mg L^{-1}) represent the 2-nitrophenol concentration at the beginning and at the collect time t , respectively, V (L) corresponds to the solution volume and m (g) to the adsorbent mass used on the experiment.

2.4 Kinetic Model

The experimental data were adjusted from the kinetic study to pseudo-first order model [7], pseudo-second order [8] and N-order [9], indicated, respectively, for Equations 3, 4 and 5.

$$q_t = q_1(1 - \exp(-k_1 t)) \quad (3)$$

$$q_t = \frac{t}{\frac{1}{k_2 q_2^2} + \frac{t}{q_2}} \quad (4)$$

$$q_t = q_n - \frac{q_n}{[k_n (q_n)^{n-1} t(n-1) + 1]^{1/(n-1)}} \quad (5)$$

q_1 , q_2 and q_n (mg g^{-1}) represent the adsorption capacity for the respective models. k_1 (min^{-1}), k_2 ($\text{g mg}^{-1} \text{min}^{-1}$) and k_n ($\text{min}^{-1}(\text{g mg}^{-1})^{n-1}$) represent the kinetic constants.

2.5 Equilibrium Models

The experimental data from the equilibrium study to Langmuir [10], Freundlich [11] and Sips [12] models were adjusted, according to the Equations 6, 7 and 8, respectively.

$$q_e = \frac{q_m k_L C_e}{1 + (k_L C_e)} \quad (6)$$

$$q_e = k_F C_e^{1/n_F} \quad (7)$$

$$q_e = \frac{q_{mS} (k_S C_e)^{mS}}{1 + (k_S C_e)^{mS}} \quad (8)$$

k_L (L mg^{-1}), k_F ($(\text{mg g}^{-1})(\text{mg L}^{-1})^{-1/n_F}$) and k_S (L mg^{-1}) are the constants of Langmuir, Freundlich and Sips, respectively, q_m e q_{mS} (mg g^{-1}) are the adsorption maximum capacities of Langmuir and

Sips, mS is the exponent of Sips model e $1/nF$ is heterogeneity factor.

2.6 Models statistic analysis

With the assistance of Statistica 8.0 software (Statsoft, EUA), the parameters could be determined for the suggested kinetic and equilibrium models, through non-linear regression. The quality of adjustments were verified by the coefficient determination (R^2) and average relative error (ARE), which was obtained from Microsoft Excel 15.0 software (Microsoft, EUA).

3. Results and Discussion

3.1 Structural Characterization

3.1.1 X-ray diffraction (XRD)

The XRD is used to determine the crystallinity level of materials and their layered structure types, being them interleaved or exfoliated [13]. The Figures 2 and 3 show the X-ray diffraction of calcium and nickel hydroxalcsites, respectively.

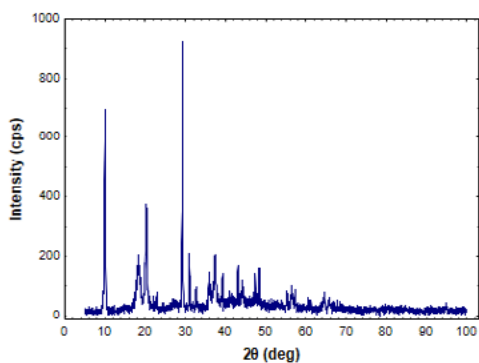


Fig. 2. XRD of calcium hydroxalcsite.

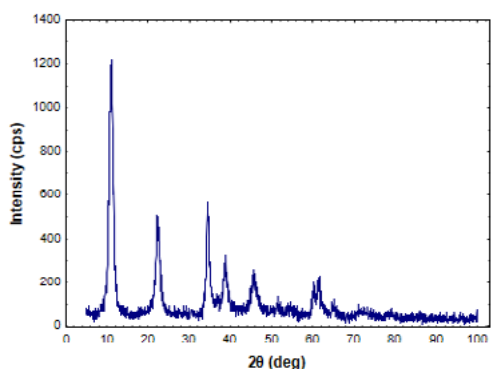


Fig. 3. XRD of nickel hydroxalcsite.

The XRD analysis from Fig. 2 points the main diffraction peaks in $2\theta = 11^\circ, 22^\circ$ e 34° approximately, which shows concordance with peaks obtained for nickel hydroxalcsite in study of Wu *et al* (2010) [14], characterizing it by the formation of rhombohedral symmetrical crystalline structure, while the smaller peaks represent the simultaneous formation of CaCO_3 little phases.

The Fig. 3 shows diffraction peaks at $2\theta = 11^\circ, 22^\circ$ e 34° approximately, which indicate, from literature (Chakraborty *et al* (2014)), that it is a crystalline and layered structure characteristic of nickel hydroxalcsites.

3.1.2 Fourier-transform infrared spectroscopy (FTIR)

The Figures 4 and 5 show the FTIR of calcium and nickel hydroxalcsites, respectively.

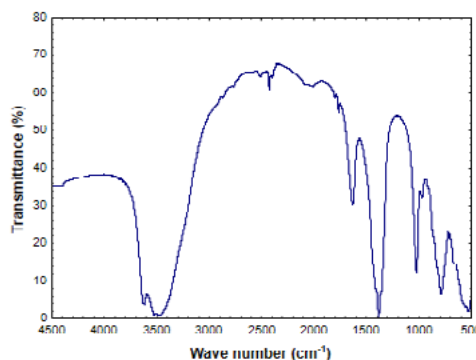


Fig. 4. FTIR of calcium hydroxalcsite.

According to literature (Wu *et al* (2010)) and by the Fig. 4 analysis, the peak at 3500 cm^{-1} occurs in function of the hydroxil group vibration in the hydroxalcsite layers. Besides that, there were also detected bands in $1385, 1025$ and 785 cm^{-1} , which are due to carbonate vibrations in the hydroxalcsite layers structure.

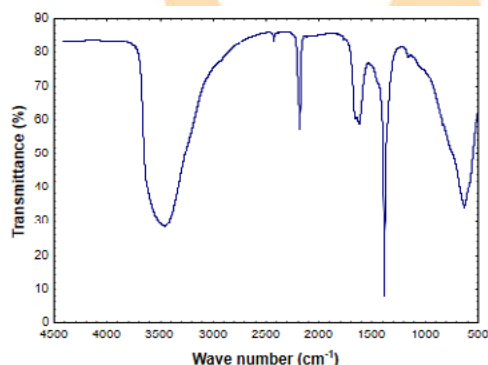


Fig. 5. FTIR of nickel hydrotalcite.

For the Fig. 5, the 3500 cm^{-1} peak occurs, according to literature (Chakraborty *et al* (2014)), suggesting the O-H stretching vibration of hydrogen bonded metal hydroxile layer and interlayer water molecules. Furthermore, there is bands in 1625 cm^{-1} due to bending of interlayer water molecule. Moreover, there is also a band on low frequency region (630 cm^{-1}) in function of the vibration of metal linked to oxygen.

3.1.3 Point of zero charge (PZC)

The point of zero charge was determined either for the calcium hydrotalcite as the nickel one. In Figure 6 the determination results were presented.

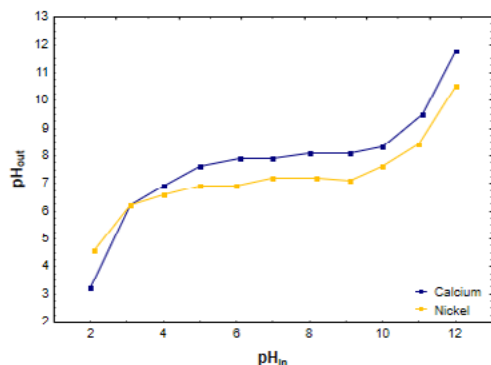


Fig. 6. Point of zero charge to calcium and nickel Hydrotalcites.

Through Fig. 6 analysis, the point of zero charge of both hydrotalcites is approximate to 7.0. Thus, it's known that in aqueous solution, with pH lesser than 7, the hydrotalcite's surface is positively charged. For pH higher than 7, the negative charges are predominant on surface of the adsorbent.

3.2 pH effect

The Figures 7 and 8 show the graph which relate the removal percentage of composite 2-nitrophenol and its adsorption capacity in function of solution's pH, being the first when the calcium hydrotalcite is used as a adsorbent and the second for the nickel one. By graphical analysis, it is fair to evaluate that for both there is a growing behavior of removal percentage and adsorption capacity values for pH higher than 2, reaching maximum values at pH 5, which correspond to 78.7% and 39,3 mg g⁻¹ to Fig.

7 and 88.5% and 44.3 mg g⁻¹ for Fig. 8, respectively. Above pH 5, the removal percentage and adsorption capacity values begin to present descending behavior.

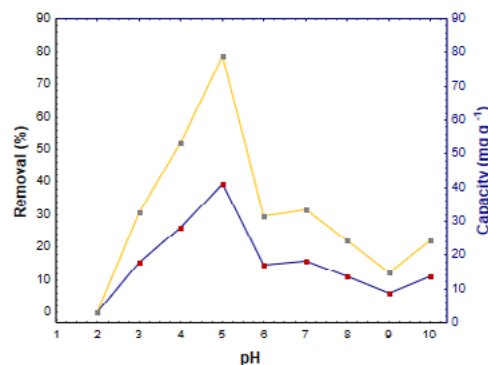


Fig. 7. pH effect in 2-nitrophenol adsorption using calcium hydrotalcite.

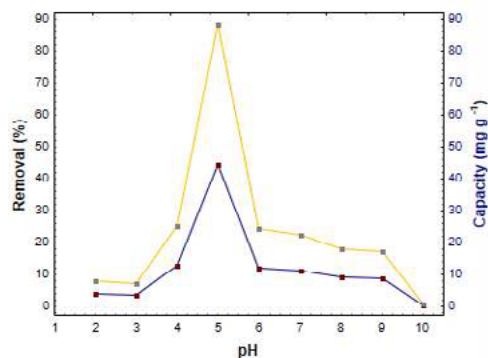


Fig. 8. pH effect in 2-nitrophenol using nickel hydrotalcite.

3.3 Kinetic behavior

The Figures 9 and 10 show the adsorption kinetic curve of 2-nitrophenol composite with calcium and nickel hydrotalcites, respectively. Based on that, it can be verified the increasing of adsorption capacity over time, reaching a maximum value of 42.5 mg g⁻¹ at 300 minutes, for the calcium hydrotalcite, and 45.8 mg g⁻¹ at 180 minutes for the nickel one. Comparatively, the studies developed by Aratesh *et al* (2010) [15] and Kupeta *et al* (2018) [16], about the 2-nitrophenol adsorption with adsorbents which carbon nanotubes or modified pinion seed residue, demonstrate adsorption maximum capacity of approximately 35 and 29 mg g⁻¹.

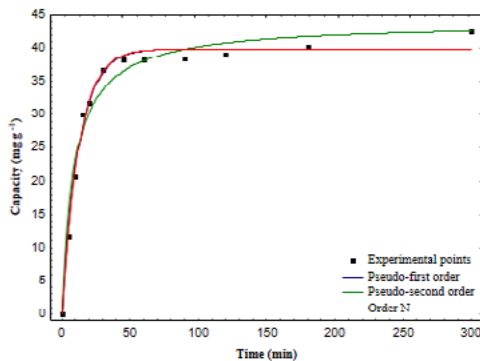


Fig. 9. Kinetic curves of 2-nitrophenol adsorption using calcium hydrotalcite.

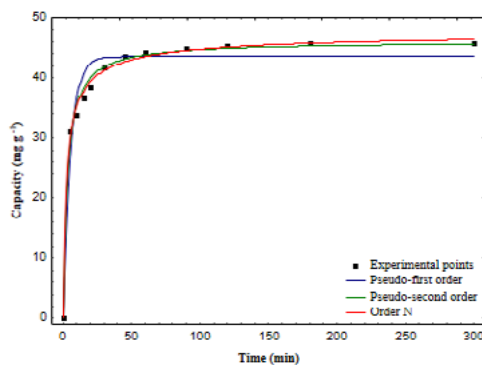


Fig. 10. Kinetic curves of 2-nitrophenol adsorption using nickel hydrotalcite.

At Table 1, the parameters referent to suggested kinetic models can be verified, besides the values of determination coefficient (R^2) and average relative error (ARE).

Table 1. Parameters referent to kinetic models, R^2 and ARE.

	Calcium	Nickel
Pseudo-first order		
q_1 (mg g ⁻¹)	38,00	43,55
k_1 (min ⁻¹)	0,0800	0,1810
R^2	0,989	0,950
ARE (%)	3,91	6,10
Pseudo-second order		
q_2 (mg g ⁻¹)	43,83	46,03
k_2 (min ⁻¹)	0,0030	0,0070
R^2	0,972	0,992
ARE (%)	7,56	2,33
N order		
q_n (mg g ⁻¹)	39,85	48,03

k_n (min ⁻¹)	0,0909	0,0009
n	0,957	2,601
R^2	0,988	0,995
ARE (%)	3,71	1,89

Through the R^2 and MRE values contained in Table 1, it is realized the N-order model provides the best adjustment to experimental points, either for calcium hydrotalcite ($R^2 > 0.98$ and ARE < 4%), as well as for the nickel one ($R^2 > 0.99$ and ARE < 2%).

3.4 Equilibrium study

The Figures 11 and 12 show the isotherms obtained in 2-nitrophenol adsorption at 298 K, with calcium and nickel hydrotalcites, respectively, for the Sips model, adjusted to experimental points.

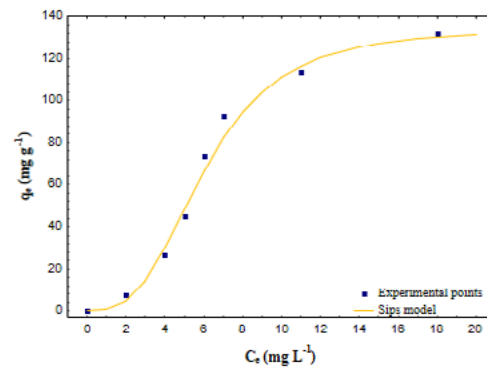


Fig 11. Equilibrium isotherm with calcium hydrotalcite.

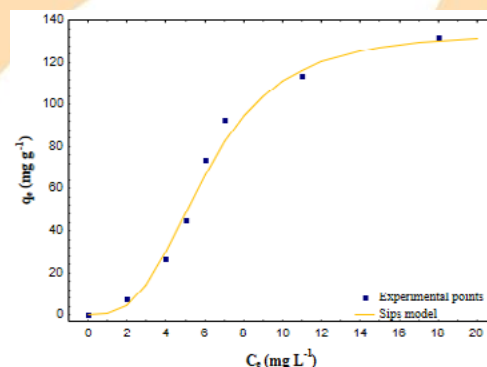


Fig 12. Equilibrium isotherm with nickel hydrotalcite.

Based in isotherm, it can be observed an adsorption capacity increase with the equilibrium concentration increase for both adsorptions. The

maximum adsorption capacity values obtained were 132.3 mg g⁻¹ and 123.97 mg g⁻¹ for calcium and nickel hydrotalcites, respectively.

The Table 2 shows the parameters for proposed models, besides the values of R² and ARE.

Table 2. Equilibrium model parameters, R² and ARE.

	Calcium	Nickel
Langmuir Model		
q _m	388,36	202,99
k _L (L mg ⁻¹)	0,0321	0,0755
R ²	0,920	0,881
ARE (%)	44,09	53,66
Freundlich Model		
k _F ((mg g ⁻¹)(mg L ⁻¹))	14,0428	21,4366
n _F	1,231	1,741
R ²	0,900	0,814
ARE (%)	46,54	63,85
Sips Model		
q _{ms}	135,08	122,07
k _s (L mg ⁻¹)	0,1650	0,1864
m _s	3,046	3,280
R ²	0,994	0,996
ARE (%)	6,48	4,26

It's checked through Table 2 that, for the Sips model, is the highest determination coefficient (R² > 0.99) and the lower average relative error (ARE < 6.5%), proving the validity of the model proposed.

4. Final considerations

There were developed calcium and nickel hydrotalcites which fit as adsorbents for 2-nitrophenol composite. For the adsorption performance, promising results were obtained. Through the characterization, the material has shown to have a crystalline and layered structure. By the analyzing of adsorption better results were obtained using nickel hydrotalcite, at pH 5, resulting in a 88.5% removal percentage. Lastly, from the kinetic and equilibrium studies, the N-order and Sips models has shown as the most suitable for them, respectively.

References

- [1] Britto JM, Rangel MC. Processos avançados de oxidação de compostos fenólicos em efluentes industriais. *Quím. Nova* 2008; 31:114-122.
- [2] Marques BS, Dotto GL. Adsorção do corante azul de metileno utilizando fibra de piaçara. EBA. Gramado:2018.
- [3] Franco DSP *et al.* Estudo do processo contínuo da adsorção do corante fucsina básica utilizando o cactus mandacaru (*Cereus Jamacaru*). ENEMP. Pará: 2019.
- [4] Mishra G, Dash B, Pandey S. Layered double hydroxides: A brief review from fundamentals to application as evolving biomaterials. *Appl Clay Sci* 2018; 153:172-186.
- [5] Cao L, Guo J, Tian J, Xu Y, Hu M, Wang M, Fan J. Preparation of Ca/Al-layered Double Hydroxide and the influence of their structure on early strength of cement. *Constr Build Mater* 2018;184:203-214.
- [6] Li B, He J, Evans DG, Duan X. Morphology and size control of Ni-Al layered double hydroxides using chitosan as template 2006; 67:1067-1070.
- [7] Lagergren S. *Kung. Svenska Vetenskap*; 1898:1-39.
- [8] Ho YS, McKay G. Process safety environmental protection 1998;76:183-191.
- [9] Alencar WS, Lima EC, Royer B, dos Santos BD, Calvete T, da Silva EA, Alves CN 2012. Application of açaí stalks as biosorbents for the removal of the dye Procion BlueMX-R from aqueous solution. *Sep Sci Technol* 2012; 47:513-526.
- [10] Langmuir IJ. *Amer. Chem Soc* 1918;40:1361-1403.
- [11] Freundlich HZ. *Phys Chem* 1906; 57:358-471.
- [12] Sips RJ. *Chem Phys* 1948; 16:490-495.
- [13] Chakraborty S, Kumar M, Suresh K, Pugazhenth G. Influence of organically modified Ni-Al layered double hydroxide (LDH) loading on the rheological properties of poly (methyl methacrylate) (PMMA)/LDH blend solution. *Powder Technol* 2014; 256:196-203.
- [14] Wu CH, Chang YP, Chen SY, Liu DM, Yu CT, Pen BL. Characterization and structure Evolution of Ca-Al-CO₃ hydrotalcite film for high temperature CO₂ adsorption. *J Nanosci Nanotechnol* 2010; 10:4716-4720.
- [15] Arasteh R, Masoumi M, Rashidi AM, Moradi L, Samimi V, Mostafavi ST. Adsorption of 2-nitrophenol by multi-wall carbon nanotubes from aqueous solutions. *Appl Surf Sci* 2010; 256:4447-4455.
- [16] Kupeta AJK, Naidoo EB, Ofomaja AE. Kinetics and equilibrium study of 2-nitrophenol adsorption onto polyurethane crosslinked pine cone biomass. *J Clean Prod* 2018.

Liquid phase adsorption of siloxane D4 on white and blue silica gel

E.N. Silva^a, D.A.S. Maia^a, K.O. Moura^b, M.C. Castrillon^c, W. M. Barcellos^c,
M. Bastos-Neto^a, D.C.S. Azevedo^a

^a Federal University of Ceará, Department of Chemical Engineering, Pici Campus, Fortaleza-Ceará, Brazil

^b Federal Institute of Piauí, Paulistana Campus, Paulistana-Piauí, Brazil

^c Federal University of Ceará, Department of Mechanical Engineering, Pici Campus, Fortaleza-Ceará, Brazil

Abstract

Biogas is a source of heat and energy, produced from anaerobic digestion of various feedstocks, including sewage. When biogas is used as a fuel in combustion engines, problems commonly arise due to the presence of siloxanes, mainly Octamethylcyclotetrasiloxane (D4) and Decamethylcyclopentasiloxane (D5). Upon combustion, siloxane convert into silicon dioxide, which builds up inside the engine, causing corrosion by abrasion and consequently increasing maintenance costs and service interruptions. In this context, the objective of this work is to study the liquid phase adsorption of D4 using blue and white silica gel as adsorbents. Textural and chemical characterizations of the samples were performed. Regular (white) silica gel has a larger surface area (BET) and pore volume than blue silica gel, due to the Cobalt salt used as a moisture indicator. For adsorption equilibrium isotherms of D4 at 20 ° C, the maximum adsorption capacity achieved was 66 mg/g for white silica and 21 mg/g for blue silica.

Keywords: adsorption, biogas, siloxane, equilibrium.

1. Introduction

Biogas stands out as a very interesting energy source from a commercial and environmental point of view. This is a gas mixture produced by anaerobic digestion of organic waste from several origin [1].

Brazil still has inefficient sewage collection and treatment service, accounting for only 52.4% of the generated waste and 73.7% of what is collected [2]. In this scenario, biogas production from municipal waste becomes an attractive option to the problem. Due to the variety of nutrients in these wastes, gas composition varies from region to region. All the same, the standard biogas composition is mainly methane (40-65%), followed by carbon dioxide (25-30%) and lower concentrations of other compounds such as hydrogen sulfide (H₂S), halides, and siloxanes. Siloxanes are used in the manufacture of various products: glues, paints, cosmetics, cleaning products, pharmaceuticals, among others [3]–[5]. Wastewater comes mostly from toilets, bathing and washing [6]. Worldwide siloxane production is estimated at over 1 million tonnes [7], and about 10% of this production goes to the sewers because they are present in most cosmetics [8].

Siloxanes are compounds that contain S-O bonds, and a silicon-bound organic radical. They are

commonly used in beauty and cleaning products and ultimately end up in sewage [9]. Among the hundreds of existing siloxanes, those commonly found in biogas are: L2-L5 and D3-D5 [3]. Of these, the ones found in highest concentrations are: octamethylcyclotetrasiloxane (D4) and decamethylcyclopentasiloxane (D5), which may represent 90% of the total biogas siloxanes [7]. In Figure 1 it is possible to observe the molecular structure of these compounds.

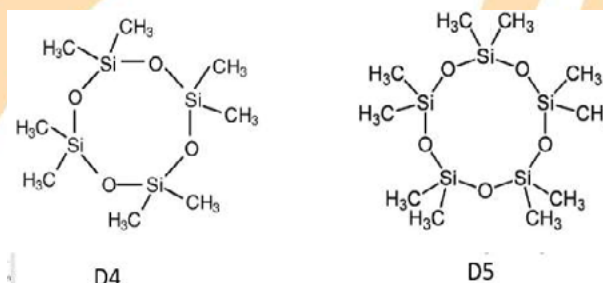


Fig. 1. Siloxane D4 and D5 molecular structure

Siloxanes are very harmful to engines used for power generation [10]. During combustion of biogas within the engines, siloxanes are oxidized to microcrystalline silica, with glass-like properties, which acts as thermal insulator on equipment surfaces and causes abrasion damage [7]. In Figure

2 we can observe some parts of an engine affected by silica deposition.



Fig. 2. Engine components damaged by siloxanes

The main technologies used in siloxane removal are adsorption, absorption, condensation, and membrane separation [3][11]. Non-regenerative activated carbon adsorption has been the most widely used method in industrial units. In this case, the adsorbent is one of the determining factors for this technology to be feasible, but few materials with high selectivity and adsorption capacity have been reported in the literature [12]. Thus the screening of new siloxane adsorbents becomes an opportunity to improve this technology.

Due to the difficulty of conducting studies directly with biogas (gas phase and very low siloxane concentrations), this exploratory work aimed to study the adsorption of D4 in liquid phase using commercial silica gel (blue and white), and to discuss how their textural characteristics and composition influence the adsorption process.

2. Materials and Methods

2.1 . Solvents and adsorbents

The adsorbents used in this work were 1-4mm White Silica gel (Scientific Exodus) and 1-4mm Blue silica gel (VETEC). The reagents used were: Octamethylcyclotetrasiloxane 98% (TCI), n-Octane 99.0% (VETEC).

2.2 . Textural characterization

Silica gel textural characterization data were assessed by N₂ adsorption / desorption isotherms at 77K using Autosorb iQ3 (Quantachrome Instruments). The sample was previously degassed at 453K under vacuum for 10 hours. The specific surface area was calculated by the BET (Brunauer-

Emmett-Teller) method. The total pore volume was determined by the Gurvich rule and the micropore volume by the DR (Dubinin-Radushkevich) equation. The pore size distribution was obtained using the Density Functional Theory (DFT).

2.3 . Chemical composition

The chemical composition of the solids was made from the X-Ray Fluorescence (FRX) analysis. The method was performed using Rigaku X-ray fluorescence equipment, model ZSX-Mini. The present oxides in the sample were quantified by semi-quantitative analysis.

2.4 . GC-MS Analysis

The concentration of D4 in the solutions was determined using a gas chromatograph model 7820A coupled to a mass spectrometer model 5977B (Agilent Technologies). An HP5-MS 5% phenyl 95% dimethylsiloxane capillary column (25 m x 0.25 inner diameter x 0.25 film) was used. The temperatures employed were: injector - 280°C, transfer line - 250°C, ion source - 230°C, quadrupole - 150°C. The oven was programmed as follows: 50°C for 4 min, heating ramp up to 180°C (15°C/min) keeping for 2 min. The carrier gas used was Helium with a constant flow of 1 mL/min. 1µL aliquots were manually injected with 1:100 split.

2.5 Adsorption kinetics

For the kinetic tests, a D4 solution (200 mg/L in octane) was prepared and distributed in ten 4.5 ml vials containing 100 mg silica each. The volume of solution transferred to each vial was 4mL. The system was shaken at 30 RPM (TE-165 (TECMAL) tube shaker), liquid phase was withdrawn at different contact times and analyzed on the GC-MS.

2.6 . Adsorption equilibrium

Equilibrium adsorption isotherms were performed at room temperature (20 ± 2°C), adding known amounts of silica to 4.5 mL glass vials. The silicas were kept in a greenhouse at 100 ° C to eliminate moisture. The vials were filled with 4 mL solutions at the following concentrations: 5, 50, 100, 200, 250, 300, 400, 600, 800, 1000 mg/L D4 in octane. The vials were sealed and shaken for 7 days until equilibrium was reached. After this time the measurement of the fluid phase concentration was carried out using the GC-MS.

3. Results and discussion

3.1. Textural and chemical characterization

The surface area (S_{BET}) total pore volume, and micropore volume are important parameters to understand characteristics and mechanisms of the adsorption process. The characterization of the two silicas are summarized in Tab.1.

Table 1. White and blue silica textural characteristics

Materials	BET (m^2/g)	Pore Volume (cm^3/g)	Micropore volume (cm^3/g)
White silica	795	0,466	0,293
Blue Silica	472	0,301	0,165

The results found in the characterization are in agreement with those normally found in the literature for comercial silicas [13]. In Fig.3. It is possible to observe the pore size distribution (PSD) calculated by the NLDFT method.

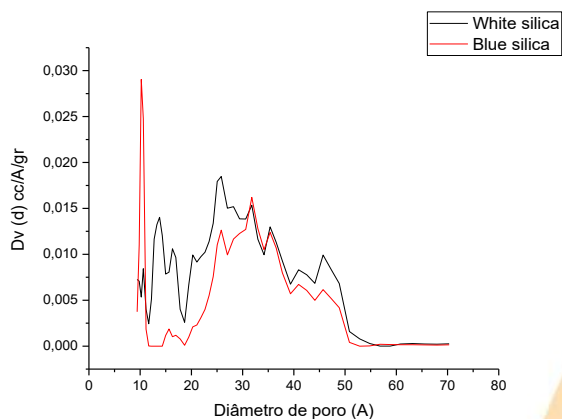


Fig.3. Pore size distribution of white and blue silica calculated by the NLDFT method

The results found in the characterization are in agreement with those normally found in the commercial silica literature [13]. From the pore size distribution data it is possible to observe one pore networks, at 10 Å to 50 Å for both silicas. As the approximate kinetic diameter of D4 is 10 Å, the existence of these pores makes adsorption of D4 is physically possible [14]. The literature [15] states

that the most interesting pore size for the adsorption of these siloxanes are in the range of 17 to 30 Å. From Fig. 3 It can be seen that white silica has more pores in this pore size range than blue silica, so it is expected that its performance will be better.

Chemical composition data can be seen in Table 2. For the composition of both silicas, a high content oin SiO2 is to be expected, but it was significantly lower for blue silica with a considerable amount of cobalt.

Table 2. White and blue silica chemical composition

Compounds (m/m %)	White silica	Blue silica
SiO2	99.252	85.494
CaO	0.5627	-
Fe2O3	0.1858	2.004
Co2O3	-	11.259
CuO	-	0.587
TiO2	-	0,656

3.2. Adsorption kinetics

The kinetic data were treated using the intraparticle diffusion model (Eq. 1) based on the theory proposed by Weber and Morris (1963), which considers that resistance to intraparticle diffusion is the only influenced by kinetics.

$$q_t = K_{dif} t^{1/2} + C \quad (1)$$

Where q_t (mg / g) is the amount of adsorbed D5, t (h) the contact time, K_{dif} is the intraparticle diffusion constant, and C is a diffusion resistance constant of the species involved.

The graph q_t versus $t^{1/2}$ should be a straight line starting from the origin point if the adsorption mechanism is only the intraparticle diffusion mechanism and will have more than one linear region if the surface adsorption is considerable [16]. We can see in Fig. 4 the kinetic data and intraparticle model.

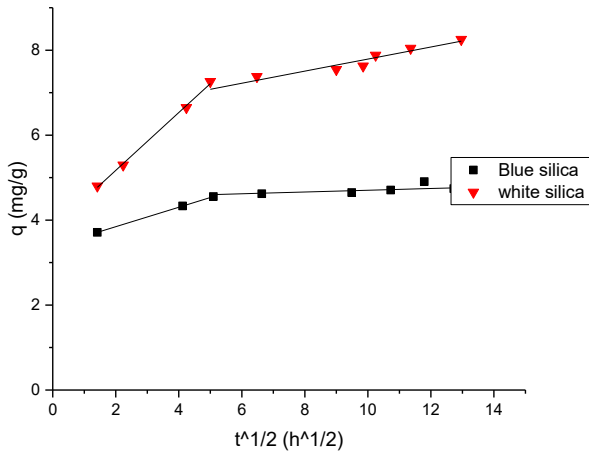


Fig.4. kinetic data intraparticle model

We can observe that for both materials there are two linear regions. For blue silica it was only possible to observe a linear region with variations in adsorption capacity over time, in the second region the equilibrium has already been reached, suggesting that the kinetics is only governed by the resistance to intraparticle diffusion. For white silica, the first linear region indicates that the adsorption at readily available sites on the surface of the material is not negligible and it is characterized by being faster, occurring within the first 24 hours. The second linear region occurs when D4 adsorption is controlled by intra-particle transport and it is slower because over time the adsorption sites become increasingly more difficult to access [17].

We can see from Fig. 4 that the line intercept does not pass at the origin, as in Weber and Morris (1963) model theory. According to Wu(2009) [18], this model deviation occurs in many cases due to rapid adsorption in a short time.

3.3. Equilibrium isotherms

Equilibrium isotherms provide various information such as: adsorbed amount, adsorbent/adsorbate interactions, and many others. These parameters are important in the study of the viability of a material for a given application [19].

In this work each point in equilibrium with the fluid phase was obtained according to Equation 2.

$$q_{eq} = \frac{(c_i - c_f)V}{m} \quad (2)$$

Where q_{eq} is the amount adsorbed in mg of D4/g adsorbent at equilibrium, V is the volume of

solution, in L, m is the mass of adsorbent, in g, and c_i and c_f are the initial and final concentration of D4 in the phase fluid, both in mg/L.

To describe the equilibrium relationship between the concentration of adsorbed D4 and solution, we used the Langmuir and Sips model, which are described in equations 3 and 4, respectively. To evaluate the error between the adjustments, the statistical test was used. χ^2 as defined in Equation 5:

$$q_{eq} = q_{max} \frac{K_L C_{eq}}{1 + K_L C_{eq}} \quad (3)$$

$$q_{eq} = q_{max} \frac{K_s C_{eq}^{n_s}}{1 + K_s C_{eq}^{n_s}} \quad (4)$$

$$\chi^2 = \sum \frac{(q_{eq\ exp} - q_{eq\ mod})^2}{q_{eq\ mod}} \quad (5)$$

Where q_q is the amount adsorbed at equilibrium, q_{max} is the maximum measure of adsorbate required to form the monolayer, K_L is an affinity parameter that includes the equilibrium constant, C_{eq} (mg/g), is the concentration of D4 in the phase fluid at equilibrium, K_s is the Sips constant, n_s is a characterization parameter of heterogeneity (the closer to a greater homogeneity) [20]. In equation (5), $q_{eq\ exp}$ and $q_{eq\ mod}$ are the adsorption capacities corresponding to the experimental data and calculated by the model. The adsorption equilibrium isotherm and the adjustments of the two models can be observed in Figure 6.

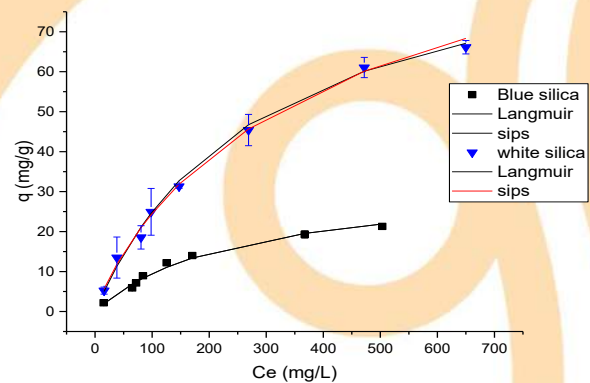


Fig.6. White and blue silica equilibrium isotherms

We can observe that both isotherms of Fig. 6 are of L type, according to the classification of Giles [21]. This type of isotherm may not have a clearly

defined saturation point due to the low solubility of the adsorbate with the solvent used [19].

The data obtained with Langmuir and sips models can be seen in Table 3.

Table 3. Langmuir and Sips model parameters.

Langmuir	Blue silica	White silica	Sips	Blue silica	White silica
K_L (L/mg)	0.004	0.0034	K_s (L/mg)	0.004	0.0043
Q_{max} (mg/g)	32.51	97.00	Q_{max} (mg/g)	32.51	116.66
X^2	0.393	0.871	X^2	0.393	0.677
R^2	0.989	0.996	R^2	0.989	0.995
			n_s	1.000	0.893

It is evident that white silica has a much higher adsorption capacity (66 mg / g) than that found for blue silica (21 mg / g). This occurs probably due to the dye used in blue silica, that can be occluding some pores, since its surface area and pore volume is smaller than that of white silica.

Although a saturation plateau is not reached in the adsorption isotherm of Fig.6, it is possible to observe that for white silica the highest measured uptake is around 66 mg/g and the saturation limit is 97 mg/g, as predicted by the Langmuir isotherm. These values are in agreement with D4 uptakes in gas systems reported for silica in the literature, which range between 56 to 182 mg/g [21][22]. In this case, the liquid phase isotherms (in linear apolar hydrocarbon, as well as methane, which is the compound found in the largest amount in biogas) shown in this work are a reliable approximation of the behavior of D4 in silica gel adsorption under real gas phase conditions. Once it is an easy-to-implement (liquid phase) test, it can be used for the screening of new adsorbents for later application under real gas phase conditions.

3. Conclusions

The siloxane equilibrium data in liquid phase using an apolar hydrocarbon as solvent can be an exploratory step for the screening of adsorbents to be employed in biogas purification. Silica-based mesoporous adsorbents may be an interesting candidate for the retention of this biogas contaminant, which may have open possibilities to treat silicon-rich wastes produced at the biogas plant itself.

References

- [1] V. P. Garcilasso, A. D. jr Ferraz, M. M. Santos, and C. L. Joppert, *Tecnologias de produção e uso e Biogás e Biometano*, vol. 3. 2018.
- [2] S. N. de I. sobre S. SNIS, "Diagnóstico dos Serviços de Água e Esgotos," Fevereiro de 2017, 2017. [Online]. Available: <http://www.snis.gov.br/diagnostico-agua-e-esgotos/diagnostico-ae-2017>.
- [3] M. Ajhar, M. Travesset, S. Yüce, and T. Melin, "Siloxane removal from landfill and digester gas – A technology overview," *Bioresour. Technol.*, vol. 101, no. 9, pp. 2913–2923, 2010.
- [4] L. Appels, J. Baeyens, J. Degre, and R. Dewil, "Principles and potential of the anaerobic digestion of waste-activated sludge," vol. 34, pp. 755–781, 2008.
- [5] M. Schweigkofler and R. Niessner, "Removal of siloxanes in biogases," *J. Hazard. Mater.*, vol. 83, no. 3, pp. 183–196, 2001.
- [6] M. Arnold, *Reduction and monitoring of biogas trace compounds*. VTT Research Notes 2496, 2009.
- [7] S. Rasi, J. Lehtinen, and J. Rintala, "Determination of organic silicon compounds in biogas from wastewater treatments plants, landfills, and co-digestion plants," *Renew. Energy*, vol. 35, no. 12, pp. 2666–2673, 2010.
- [8] D. Brooke, M. Crookes, D. Gray, and S. Robertson, *Environmental Risk Assessment Report: Dodecamethylcyclohexasiloxane*. 2009.
- [9] R. Dewil, L. Appels, and J. Baeyens, "Energy use of biogas hampered by the presence of siloxanes," *Energy Convers. Manag.*, vol. 47, no. 13–14, pp. 1711–1722, 2006.
- [10] T. Matsui and S. Imamura, "Removal of siloxane from digestion gas of sewage sludge," *Bioresour. Technol.*, vol. 101, no. 1 SUPPL., pp. S29–S32, 2010.
- [11] N. De Arespachoga, C. Valderrama, J. Raich-Montiu, M. Crest, S. Mehta, and J. L. Cortina, "Understanding the effects of the origin, occurrence, monitoring, control, fate and removal of siloxanes on the energetic valorization of sewage biogas-A review," *Renew. Sustain. Energy Rev.*, vol. 52, pp. 366–381, 2015.
- [12] N. de Arespachoga, C. Valderrama, C. Mesa, L. Bouchy, and J. L. Cortina, "Biogas deep clean-up based on adsorption technologies for Solid Oxide Fuel Cell applications," *Chem. Eng. J.*, vol. 255, pp. 593–603, 2014.
- [13] H. Jung, D. Y. Lee, and J. Jurng, "Low-temperature regeneration of novel polymeric adsorbent on dodecamethylcyclopentasiloxane (D5) removal for cost-effective purification of biogases from siloxane," *Renew. Energy*, vol. 111, pp. 718–723, 2017.

- [14] J. L. Hamelink, P. B. Simon, and E. M. Silberhorn, "Henry's law constant volatilization rate, and aquatic half-life of octamethylcyclotetrasiloxane," *Environ. Sci. Technol.*, vol. 30, no. 6, pp. 1946–1952, 1996.
- [15] M. Yu, H. Gong, Z. Chen, and M. Zhang, "Adsorption characteristics of activated carbon for siloxanes," *J. Environ. Chem. Eng.*, vol. 1, no. 4, pp. 1182–1187, 2013.
- [16] A. M. G. Tavares, M. A. S. A. Jr., A. R. Cestari, and E. F. S. Vieira, "Síntese e caracterização de pastas de cimento aditivadas com resinas epóxi – análises cinéticas, termodinâmicas e calorimétricas," 19o Congr. Bras. Eng. e Ciência dos Mater. – CBECiMat, no. 1, pp. 1748–1755, 2010.
- [17] A. Bhatnagar, A. K. Minocha, and M. Sillanpää, "Adsorptive removal of cobalt from aqueous solution by utilizing lemon peel as biosorbent," *Biochem. Eng. J.*, vol. 48, no. 2, pp. 181–186, 2010.
- [18] F. C. Wu, R. L. Tseng, and R. S. Juang, "Initial behavior of intraparticle diffusion model used in the description of adsorption kinetics," *Chem. Eng. J.*, vol. 153, no. 1–3, pp. 1–8, 2009.
- [19] G. Limousin, J. P. Gaudet, L. Charlet, S. Szenknect, V. Barthès, and M. Krimissa, "Sorption isotherms: A review on physical bases, modeling and measurement," *Appl. Geochemistry*, vol. 22, no. 2, pp. 249–275, 2007.
- [20] K. Y. Foo and B. H. Hameed, "Insights into the modeling of adsorption isotherm systems," *Chem. Eng. J.*, vol. 156, no. 1, pp. 2–10, 2010.
- [21] C. H. Giles, D. Smith, and A. Huitson, "A General Treatment and Classification of the Solute Adsorption Isotherm Part I. Theoretical," *J. Colloid Interface Sci.*, vol. 47, no. 3, 1974.
- [22] S. Nam, W. Namkoong, J. H. Kang, J. K. Park, and N. Lee, "Adsorption characteristics of siloxanes in landfill gas by the adsorption equilibrium test," *Waste Manag.*, vol. 33, no. 10, pp. 2091–2098, 2013.
- [23] L. Sigot, G. Ducom, and P. Germain, "Adsorption of octamethylcyclotetrasiloxane (D4) on silica gel (SG): Retention mechanism," *Microporous Mesoporous Mater.*, vol. 213, pp. 118–124, 2015. V. P. Garcilasso, A. D. jr Ferraz, M. M. Santos, and C. L. Joppert, *Tecnologias de produção e uso e Biogás e Biometano*, vol. 3. 2018.

Evaluation of binary adsorption of bright blue and tartrazine dyes under dynamic conditions using rice husk

Kevin Jhon Fernández-Andrade^{a,b}, María Cristina González-Vargas^{a,b}, Ricardo José Baquerizo-Crespo^{b,c}, Enrique Ruiz-Reyes^d, Luis Santiago Quiroz-Fernández^e, Joan Manuel Rodríguez-Díaz^{a,f*}

^aLaboratorio de Análisis Químicos y Biotecnológicos, Universidad Técnica de Manabí. Av. Urbina y Che Guevara, Portoviejo, Manabí - Ecuador.

^bDepartamento de procesos químicos, Universidad Técnica de Manabí. Av. Urbina y Che Guevara, Portoviejo, Manabí - Ecuador. E-mail address: rbaquerizo@utm.edu.ec

^cPrograma de Doctorado Ingeniería Química, Facultad de Ingeniería Química, Universidad Tecnológica de La Habana "José Antonio Echeverría", Cujae, La Habana Cuba.

^dDepartamento de Química, Instituto de Ciencias Básicas, Universidad Técnica de Manabí. Av. Urbina y Che Guevara, Portoviejo, Manabí - Ecuador.

^eInstituto de Postgrado. Universidad Técnica de Manabí, Ecuador. Av. Urbina y Che Guevara, Portoviejo, Manabí - Ecuador

^fPrograma de Pós-graduação em Engenharia Química. Universidade Federal da Paraíba. João Pessoa 58051-900, Brasil

Abstract

Industrial growth has increased the amount and complexity of contaminant mixtures in industrial aqueous effluents. The objective of the research is to evaluate the adsorption process of bicomponent mixtures of Tartrazine and Brilliant Blue FCF dyes in a dynamic regime (fixed bed column), with the use of rice husk as adsorbent material. Through a 3-level surface response experimental design, the adsorption process of each of the mixed dyes at different initial concentrations were evaluated (0.0216, 0.0739, 0.1261, 0.1477 mmol l⁻¹). The operating conditions of the fixed bed column (16.5 cm high) considered a flow of 0.5 ml min⁻¹ and pH 2. Through the analysis of the optimized responses and values of the experimental design, it was possible to identify that the adsorption process occurs competitively, with a higher affinity of the adsorbent for the dye that was at a higher concentration at the entrance of the column. It was observed that the rice husk had a higher affinity for the FCF Bright Blue dye, with higher adsorption capability values (15 mg g⁻¹). One of the possible adsorption mechanisms was proposed through the formation of hydrogen bonds between the sulfonic groups of the dyes and the OH-groups present on the surface of the adsorbent. It was demonstrated that the rice husk waste material can be used as adsorbent material for the removal of mixtures of Brilliant Blue FCF and Tartrazine dyes present in industrial waste.

Keywords: Food dyes; Binary mixture; Dynamic state; Agroindustrial waste.

1. Introduction

The improper use of water and the unscrupulous discharge of industrial effluents without treatment have caused it to be increasingly scarce [1]. The impact of the pollution generated varies and can be caused by a number of pollutants, including agrotoxics [2], drugs [3], heavy metals [4], dyes [5], among others. The accumulation of dyes causes serious genetic damage in human lymphocytes [6].

About 2% of dyes produced worldwide are discharged directly to water bodies [7]. One of the main industries responsible for this source of contamination is the food industry, whose effluents have a high organic load as well as dyes that are used in the production chain as additives. Among

the main dyes used in the food industry are: FD&C Blue # 1, FD&C Yellow # 5 (Tartrazine), FD&C Yellow # 6 and FD&C Red # 40 [8].

These dyes can be detected in industrial effluents in concentrations between 10 mg l⁻¹ and 200 mg l⁻¹ [7]. Due to the mixtures of food dyes and their varying concentrations represent a challenge for science due to the complexity of the studies. For this reason, technologies have been developed for the treatment of these effluents prior to their discharges to the receiving water bodies. Advanced oxidation processes [9], membrane filtrations [10], microbiological biotechnological processes [11] and adsorption [12] are among the main treatments, with favorable results, mostly in monocomponent studies and in static regime.

The use of residual biomass in adsorption processes has been shown as one of the viable and economical alternatives for effluent treatment. Previous studies have shown that residual biomass from rice cultivation has been used for the removal of metals, dyes, drugs and other contaminants [12]. However, the literature consulted does not report studies that allow the evaluation of this adsorbent in contaminant mixtures. Given this scenario, the objective of the present work is to evaluate the interactions of the mixtures of Brilliant Blue FCF and Tartrazine dyes in the fixed bed column adsorption process using rice husk as adsorbent.

2. Methodology

2.1. Adsorbent material

Rice husk was used as waste from the “Loor” rice dehusker located at km 1 via Correagua, in Manabí-Ecuador, at coordinates S 0° 50' 40.147" W 80° 30' 2.133". The pre-treatment of the rice husk consisted in a size reduction stage and subsequently a screening to select particles of sizes between 0.595 mm and 0.841 mm. Then the material was washed with distilled water until impurities and starches were removed. The material was dried in a Memmert oven, model VO200cool at 80 ° C for a period of 24 h.

2.2. Solution preparation

The FCF Bright Blue food dyes, also known as Blue 1 or Erioglucine [B1] (CAS: 3844-45-9) and Tartrazine or Yellow 5 [Y5] (CAS: 1934-21-0). Solutions of the dyes were prepared according to the design of experiments from a stock solution of 4000 ppm (5.04 mmol l⁻¹ of blue dye and 7.48 mmol l⁻¹ of yellow dye), which were adjusted to pH 2 with dilution of 5% hydrochloric acid.

2.3. Experimental procedure

The adsorbent material was placed inside the column whose dimensions were 16.5 cm high and a diameter of 1.7 cm. The flow used was 0.5 ml min⁻¹ upstream, dosed by a multi-channel peristaltic pump model Masterflex L/S 7535-04. At the exit of the column, samples were taken with a Gilson brand FC203B fraction collector, every 5 min until bed saturation.

2.4. Analytical method

To perform the dye calibration curves, the wavelengths were determined from an aqueous solution of the two dyes with a concentration of 0.12 mmol l⁻¹. A Thermo Scientific Evolution 60s UV-Visible scanning spectrophotometer was used, with wavelengths between 300 nm and 800 nm (Fig. 1). The calibration curve for the blue dye was performed at a wavelength of 629 nm and for the yellow at 427 nm.

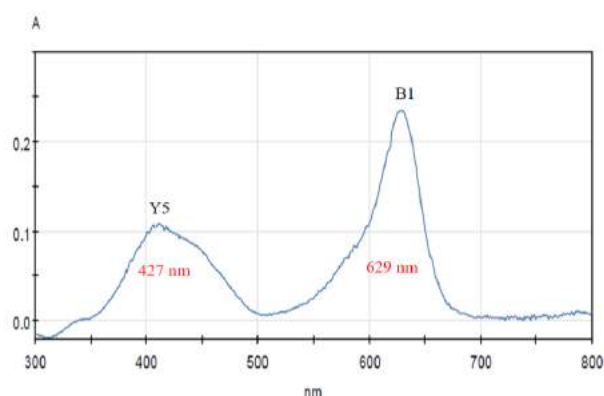


Fig. 1 Spectrum UV-Vis of tartrazine and blue bright.

2.5. Composite central response surface design

A central response surface experiment design composed of axial points was used to replicate possible real conditions in industrial discards. For the design of experiments, responses were evaluated below the minimum and above the maximum of operation 0.0216 mmol l⁻¹ and 0.1261 mmol l⁻¹, respectively. The experimental runs were randomized, in order to reduce systematic errors. The design used was orthogonal and rotatable, which allowed adjustment using quadratic models with variable response of constant variance. For the design of experiments, the minimum and maximum levels mentioned above were established, from which the axial and central points were estimated. The coding corresponding to the proposed experiment design Table 1, was performed with the Statgraphic program.

The study variables were the mass transfer zone (MTZ), the useful adsorption capability (q_u), the total adsorption capability (q_t), stoichiometric advance velocity of the mass transfer zone (V_a MTZ), these were calculated using the Geankoplis method [13].

Table 1. Codification of the experimental design.

Experiment	Codification		Concentration (mmol l ⁻¹)	
	X1	X2	Blue	Yellow
1	-1	-1	0.0216	0.0216
2	0	0	0.0739	0.0739
3	0	1.41421	0.0739	0.1477
4	1	1	0.1261	0.1261
5	-1	1	0.0216	0.1261
6	1.41421	0	0.1477	0.0739
7	-1.41421	0	0	0.0739
8	1	-1	0.1261	0.0216
9	0	-1.41421	0.0739	0

3. Results and Discussion

3.1. Bicomponent study of column adsorption of B1 and Y5

3.1.1. Influence in the Mass Transfer Zone

The low concentrations of both dyes (less than 0.0216 mmol l⁻¹), allowed to obtain low values for both MTZ–B1 and MTZ–Y5, 6.7 cm and 6.3 cm, respectively (Fig. 2). Similarly, with higher concentrations of both dyes (equal to or greater than 0.1261 mmol l⁻¹) higher MTZ values were obtained, 11.7 cm for B1 and 11.9 cm for Y5 (Fig. 2). The higher the concentration of dyes in the feed, the greater the amount of adsorbate molecules that travel along the column. Although a positive effect occurs as the adsorption rate increases, the MTZ is distributed throughout the column bed, which causes it to not fully saturate. According to Fig. 2A, the values of MTZ–B1 are negatively affected when Y5 concentrations increase, this is due to the formation of interference caused by another dye, even if the concentration of B1 is low. A similar effect occurs for Y5 in the presence of B1 (Fig. 2B), but only when Y5 is in low concentrations. By increasing the concentration of B1 when that of Y5 is high, a positive effect on MTZ–Y5 is observed, since its values decrease. [14] In multicomponent adsorption processes, there are interferences caused by interactions between components. However, the interactions between B1 and Y5 are not sufficient to affect their adsorption at the active sites present in the adsorbent, depending only on the initial concentration of the feed in the column.

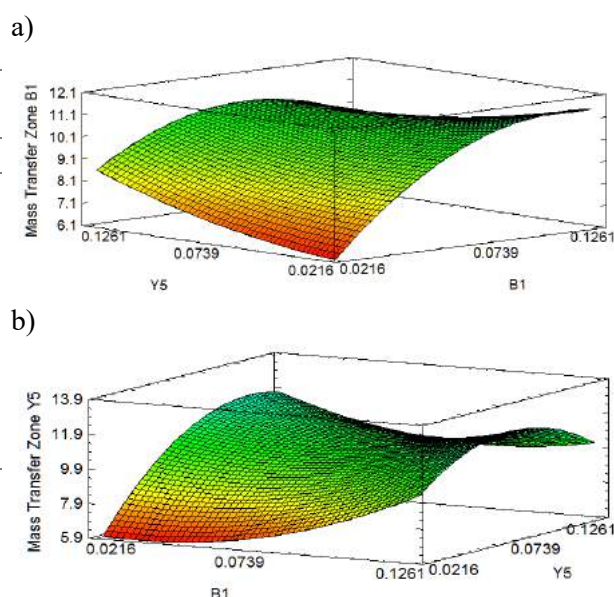


Fig. 2. Response surface for the MTZ (cm): a) MTZ–B1, b) MTZ–Y5

3.1.2. Influence on useful capability

The useful adsorption capability showed a different behavior, when the concentration of B1 is increased to 0.1261 mmol l⁻¹ in the absence of Y5 (Fig. 3A), q_u –B1 (1.2 mg g⁻¹) is maximized. However, in the presence of Y5, q_u –B1 is limited. A similar phenomenon occurs for q_u –Y5 (Fig. 3B), since in the absence of B1 at a high concentration of Y5 (0.1261 mmol l⁻¹), the value q_u –Y5 reaches the maximum (0.5 mg g⁻¹).

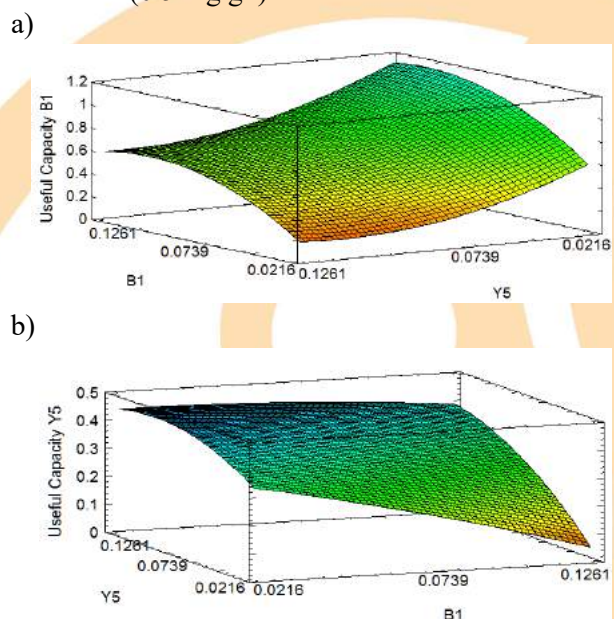
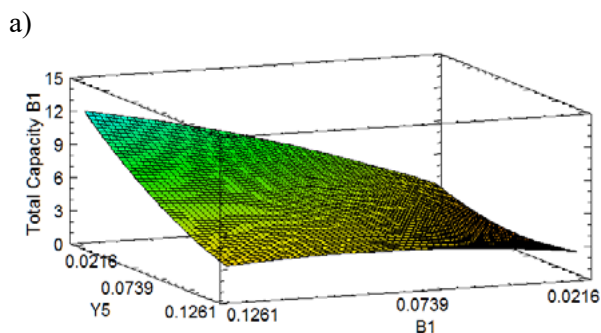


Fig. 3. Response surface for q_u (mg g⁻¹): a) q_u –B1, b) q_u –Y5.

The presence of one component affects the adsorption process of another component because the active sites of the adsorbent are shared for both dyes. It is observed that the quadratic interactions for the yellow dye (Y5: Y5), affect the interactions with the adsorbent, so that the adsorption of B1 is favored. In multicomponent solutions, processes of desorption of components with higher concentrations and lower bonding forces occur, resulting in the release of active sites for the B1 dye.

3.1.3. Influence on total adsorption capability

An effect similar to that of the useful adsorption capability was observed in the total adsorption capability (q_t), higher concentrations of adsorbate in feed solution favored the adsorption process. However, in Fig. 4A, is observed that the concentration of B1 has a slight effect on q_t -B1, whereby in the concentration variations the q_t -B1 is maintained at values close to 3 mg g^{-1} . The q_t -B1 is maximized (15 mg g^{-1}) when the interference caused by Y5 is eliminated. Since Y5 is not present, all active sites of the adsorbent will be available for adsorption of B1. On the other hand, q_t -Y5 is affected by the initial concentrations of Y5 (Fig. 4B), so when the concentration is lower (0.0216 mmol l^{-1}) the q_t decreased (1.4 mg g^{-1}). Likewise, when the concentration is higher (0.1261 mmol l^{-1}), the q_t increased (2.7 mg g^{-1}). As in the case of B1, q_t -Y5 is maximized (4.2 mg g^{-1}) by eliminating the interference caused by B1. However, it can be seen in Fig. 4B, that Y5 concentrations greater than the central point (0.0739 mmol l^{-1}), affect q_t due to the increase in adsorbate-adsorbate interactions [15].



b)

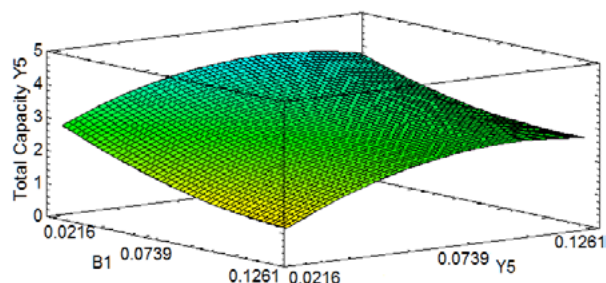


Fig. 4. Response surface for q_t (mg g^{-1}): a) q_t -B1, b) q_t -Y5

The total adsorption capability of the rice husk in B1 is higher than that presented by Y5, according to Villar da Gama, Elisandra do Nascimento [16], in a multicomponent adsorption process, organic adsorbate molecules tend to form complexes on the surface of the adsorbent that prevent the passage of other molecules, thus preventing the adsorption of Y5. On the other hand, the adsorption force of said complexes depends on the bond strength generated between adsorbate-adsorbent. From this point of view, B1 presents greater bond strength and, therefore, greater affinity with the adsorbent, with higher values of q_t compared to Y5.

3.1.4. Influence on the mass of stoichiometric velocity advance

The speed of stoichiometric advance of the MTZ for both B1 and Y5 has a linear behavior (Fig. 5). Such behavior indicates that there was no interference in the interactions between the dyes or that these are negligible. Therefore, V_{aMTZ} -B1 will not be affected by the initial concentrations of Y5. The same behavior is presented in V_{aMTZ} -Y5. Therefore, by increasing the concentrations of B1 and Y5, V_{aMTZ} -B1 and V_{aMTZ} -Y5 will also increase. It can be concluded that the stoichiometric feed rate of the ZMT will only depend on the concentration of the dyes in the feed solution. This is due to the fact that, as there is a greater amount of molecule in the adsorbent bed, the higher the adsorption rate and therefore the MTZ will advance faster.

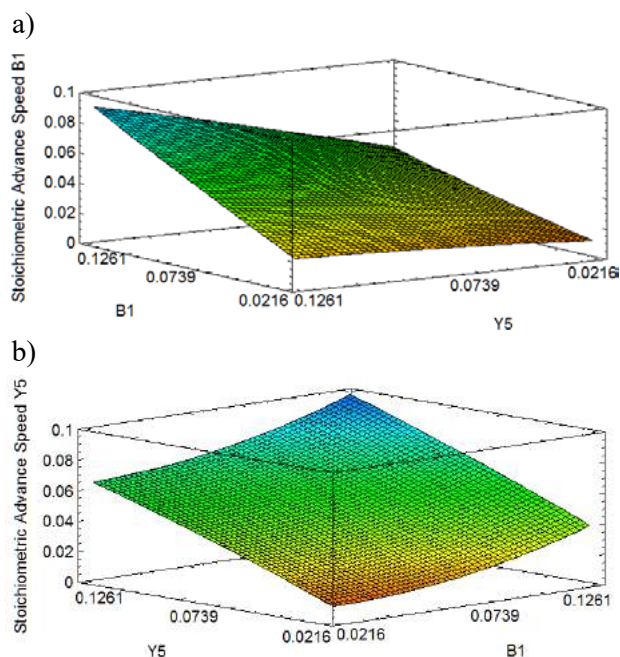


Fig. 5. Response surface for V_a MTZ (cm min^{-1}): a) V_a MTZ-B1, b) V_a MTZ-Y5.

3.2. Mechanism Adsorption

The raw rice husk usually contains 32.24% cellulose, 21.44% lignin, 21.34% hemicellulose, 8.11% water, 1.82% extracts and 15.05% minerals (of which contain 96.34% silica), assembled in the form of cable, where lignin covers cellulose and hemicellulose [17, 18]. Therefore, at pH 2, the dye molecules that contain sulfonate and carboxylate groups in their saline form with delocalized negative charge decrease delocalization with the formation of the acids corresponding to the S–O and C–O groups (Fig. 6).

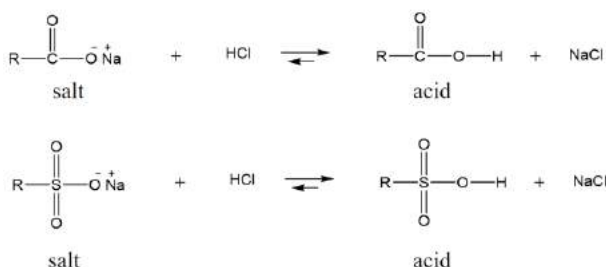


Fig. 6. General reactions for the formation of the corresponding acid.

The acidic pH leads to the partial hydrolysis of the lignin, hemicellulose and cellulose of the rice husk, whereby –OH groups are formed. This enables molecular interaction by forming hydrogen bonds between the sulfonate and carboxylate groups of the dyes and the molecules containing –OH groups in the rice husk (Fig. 7).

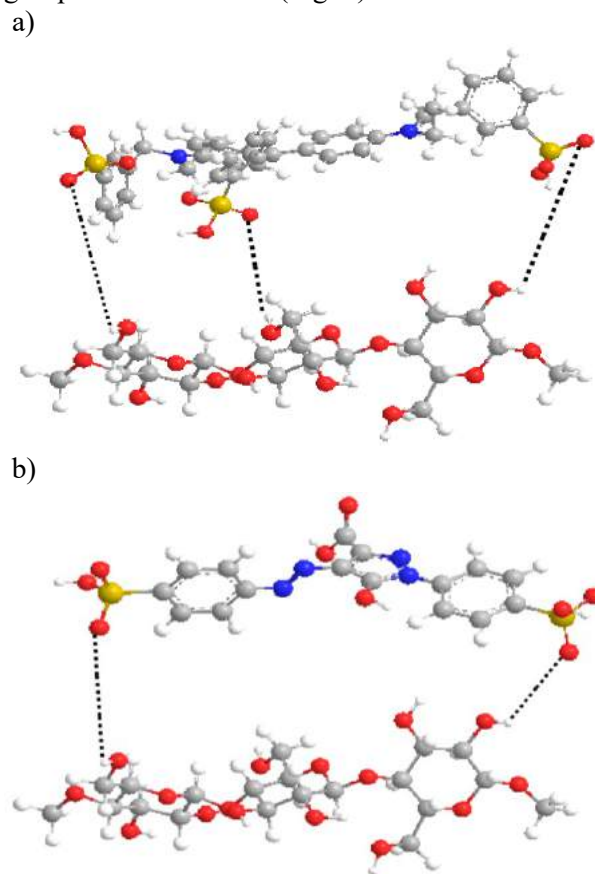


Fig. 7. Hydrogen bond interaction of the molecule of, a) B1 and b) Y5; with the rice husk.

4. Conclusion

The bicomponent study showed that the rice husk showed affinity for both dyes, with an inclination towards the component with the highest initial concentration. However, it did not show significant selectivity in the distribution of active sites when the dyes were found in equal concentrations. Through the adsorption mechanism, it was possible to verify that the greatest adsorption capacity obtained for the B1 dye was due to the greater presence of sulfonate groups that facilitated the greatest interaction by forming hydrogen bonds with the –OH groups present in the surface of the rice husk.

Acknowledgement

The authors wish to thank the Technical University of Manabí and its Research Institute for providing the opportunity to carry out this work.

References

- [1] Stefanakis, A. and B. J.A, A review of emerging contaminants in water: Classification, sources and potential risks. 2015. p. 57-82.
- [2] Chen, M., et al., Bioremediation of soils contaminated with polycyclic aromatic hydrocarbons, petroleum, pesticides, chlorophenols and heavy metals by composting: Applications, microbes and future research needs. *Biotechnology Advances*, 2015. 33(6, Part 1): p. 745-755.
- [3] Fick, J., et al., Contamination of surface, ground, and drinking water from pharmaceutical production. *Environmental Toxicology and Chemistry*, 2009. 28(12): p. 2522-2527.
- [4] Wang, Q. and Z. Yang, Industrial water pollution, water environment treatment, and health risks in China. *Environmental Pollution*, 2016. 218: p. 358-365.
- [5] Gil, M.J., et al., Contaminantes emergentes en aguas, efectos y posibles tratamientos. *Producción + Limpia*, 2012. 7: p. 52-73.
- [6] Atlı Şekeroğlu, Z., et al., Effects of tartrazine on proliferation and genetic damage in human lymphocytes. *Toxicology Mechanisms and Methods*, 2017. 27(5): p. 370-375.
- [7] Robinson, T., et al., Remediation of dyes in textile effluent: a critical review on current treatment technologies with a proposed alternative. *Bioresource Technology*. 2001. 77(3): p. 247-255.
- [8] FDA, U.S., Food and Drug Administration, HHS in 21 C.F.R. § 70 (2015), 21 C.F.R. § 80 (2015). 2015, U.S., FDA: Virginia, USA.
- [9] Deng, Y. and R. Zhao, Advanced Oxidation Processes (AOPs) in Wastewater Treatment. *Current Pollution Reports*, 2015. 1(3): p. 167-176.
- [10] Jepsen, K., et al. Challenges of membrane filtration for produced water treatment in offshore oil & gas production. in *OCEANS 2016 MTS/IEEE Monterey*. 2016.
- [11] Turkayeva, A., et al., Chemical and Microbiological Nature of Produced Water Treatment Biotechnology. *Energy Procedia*, 2017. 113: p. 116-120.
- [12] Shamsollahi, Z. and A. Partovinia, Recent advances on pollutants removal by rice husk as a bio-based adsorbent: A critical review. *Journal of Environmental Management*, 2019. 246: p. 314-323.
- [13] Geankoplis, C.J., *Procesos De Transporte Y Operaciones Unitarias*. 1998.
- [14] Lima, L., et al., Fixed Bed Adsorption of BTX Contaminants from Monocomponent and Multicomponent Solutions using a Commercial Organoclay. *Industrial & Engineering Chemistry Research*, 2017. 56.
- [15] Solenov, D., et al., Tunable Adsorbate-Adsorbate Interactions on Graphene. *Physical Review Letters*, 2013. 111(11): p. 115502.
- [16] Villar da Gama, B.M., et al., Mono and binary component adsorption of phenol and cadmium using adsorbent derived from peanut shells. *Journal of Cleaner Production*, 2018. 201: p. 219-228.
- [17] Chuah, T.G., et al., Rice husk as a potentially low-cost biosorbent for heavy metal and dye removal: an overview. *Desalination*, 2005. 175(3): p. 305-316.
- [18] Wan Ngah, W.S. and M.A.K.M. Hanafiah, Removal of heavy metal ions from wastewater by chemically modified plant wastes as adsorbents: A review. *Bioresource Technology*, 2008. 99(10): p. 3935-3948.

A comparison of Numerical Methods for the Dynamic Simulation of Temperature Swing Adsorption

Caio Curitiba Marcellos^a, Felipe Rocha Pinto^a, Yuri Paiva^a, Carla Manske Camargo^a,
Amaro Gomes Barreto^{a*}

^a Programa em Engenharia de Processos Químicos e Bioquímicos, Escola de Química, Universidade Federal do Rio de Janeiro

Abstract

In this study, we compare the finite difference method (FDM) and a range of finite volume method (FVM) schemes in a dynamic simulation of a temperature swing adsorption (TSA) process for dehydration of natural gas. The work also presents discretized equations for flux limiters in high-resolution (HR) schemes and the weighted essentially non-oscillatory (WENO) technique. Both classes are well recognized as attractive solutions for engineering problems due to the conservation of physical properties and the total variation diminishing (TVD) characteristic. The numerical solutions were compared with a reference solved with the WENO scheme with 500 grids. In the chosen set of operational conditions, the simulation showed that the high-resolution schemes presented a reduced error in comparison to FDM with 50 or 100 grids, while requiring more computational time. Namely, the van Albada1, minmod, Osher, HQUICK, WENO and HCUS schemes were faster and had smaller errors than FDM with 100 grids. Lastly, it is graphically shown the effects of numerical diffusion in the construction of breakthrough curves for adsorption as well as in the concentration profile at regeneration.

Keywords: Temperature swing adsorption; Finite difference method; Finite volume method; CH₄/H₂O separation

1. Introduction

Adsorption separation processes are based on the selective adsorption of one or more components in a gas mixture, with adsorbent regeneration by partial pressure decrease (Pressure Swing Adsorption - PSA) or by temperature increase (Temperature Swing Adsorption - TSA) [1]. These processes are widely used to remove contaminants in natural gas (carbon dioxide, sulfur compounds, water, nitrogen), that are largely responsible for pipeline corrosion problems.

TSA processes offer a great efficiency in the removal of adsorbed contaminants. These processes have become the state-of-the-art unit operation for the removal of trace impurities from a gas stream [2]. Compared to PSA and Vacuum Swing Adsorption, TSA processes have already shown a higher degree of purification in CO₂/CH₄ separation, but still do not achieve the same values of efficiency in the recovery, productivity and economic cost. The main drawback of TSA based processes is the elevated supply heat required to the regeneration gas and that is why we observe

efforts to integrate TSA with waste heat from other applications[3].

During the operational interval for the adsorption phase, wet natural gas enters the vessels in downward flow and leaves already dehydrated by the lower opening. After the end of this step, a part of the dehydrated gas is heated and then used to regenerate the adsorption bed. In this sort of processes even a simple increase of temperature could cause a decrease in the quantity adsorbed. A two-bed system is usually utilized for most vapor phase applications such as gas driers, solvent recovery systems and other unit processes for natural gas.

In order to predict the performance of these processes it is necessary to apply balances of mass, energy and momentum, as well as equations of adsorption equilibrium and kinetics. In most cases, there is a need to use numerical methods for evaluating the partial differential equations and then simulate the process. [11] Fortunately, numerical solutions have moved from the field of scientific research to the field of applied engineering through a variety of existing process

simulators, as a consequence of the constant evolution of computers. Therefore, several schemes for simulating adsorption processes have been observed in recent works, such as finite difference [4]–[7], orthogonal collocation [7], finite element and finite volume [1], [8]–[12].

In this context, the present work compares two methods widely used and commented on in literature: FDM and FVM. Both methods are commonly confused due to the similarity of discretized equations in certain cases. However, the FDM originates from mathematical deduction based on the Taylor series derivative approximation, while the FVM has a physical basis aiming to decrease the calculation domain in a number of subdomains, in which the physical conservation law is valid [13]. FVM has been successfully employed for heat transfer and mass flow transfer, due to its suitability for modeling hyperbolic conservation laws and given its inherent conservative properties [8].

2. Bibliography Review

There has been a usage of such numerical methods in recent engineering research: Kaczmarzski and Antos (1996) [7] presented a FDM for solving adsorption process model and compared the results obtained with an orthogonal collocation (OC). They concluded that FDM has relatively small computation time, from tens to several hundred times shorter in comparison with the OC. More recently, Kim et al. (2015) [5] simulated the separation process of methane from natural gas using a PSA model where FDM is applied. Also in PSA simulation, Sun et al. (1996) [6] applied FDM with a third order discretization (QUICK) for the convective terms for a diffusion-limited process and Makarem et al. (2019) [4] combined differential quadrature method (DQM) and FDM for discretizing modeling equations. According to the authors, this combination has been performed in order to apply the DQM for solving the model equations and FDM for time integration, since the latter shows numerical diffusion phenomenon.

Most of recent literature indicates that FVM offers the stability for an extensive range of systems. It solves the integral rather than the differential forms of the conservation equations, providing better closure of mass, energy, and momentum balances [10]. In this context, some works in the adsorption area have implemented FVM in recent years: Webley and He (2000) [8]

presented an oscillation-free quadratic upwind finite volume technique with second-order accuracy to simulate any type of step that may occur in cyclic adsorption systems. Wang et al. (2018) [9] combined FVM and grand canonical Monte Carlo (GCMC) to investigate and design the capture of CO₂ in an adsorption bed with no available experimental data. Rossi et al. (2019) [12] went further and simulated a dual reflux PSA adsorption process via FVM and FDM, leading to conclude that the former was the most effective approach for this specific case.

Despite widespread use to solve mass and heat transfer problems, conventional high-order finite volume methods are often not adequate for accurate resolution of steep gradient phenomena due to the introduction of non-physical effects and oscillations [1]. In order to overcome these difficulties, a number of techniques have been developed and schemes, such as High-Resolution (HR), that exhibit a Total Variation Diminishing (TVD) characteristic started to get more attention.

Nowadays, the HR schemes are commonly employed in the numerical solution of partial differential equations (PDE) where high accuracy is required. In summary, high-resolution schemes for FVM achieve better results by employing flux limiters and associating the stability of lower-order methods with the accuracy of higher-order methods [10]. Cruz et al. (2015) compared different HR schemes for the solution of PDE in cyclic adsorption separation processes and they concluded that the use of these techniques conduces always to stable solutions with a high convergence to the reference solution.

In this sense, the present work compares a number of high-resolution upwind schemes with flux limiters: HCUS, HQUICK, Koren, MC, minmod, Osher, ospre, smart, superbee, Sweby, UMIST, vanAlbada1, vanAlbada2 and vanLeer. Another class of HR scheme, an accurate weighted essentially non-oscillatory (WENO) technique, that was first introduced in 1994, is also used. These WENO schemes are known for their capability to achieve arbitrarily high order accuracy in smooth regions while maintaining stable, non-oscillatory solutions in the vicinity of sharp discontinuities. [10]

3. Methodology

The model used in this work is based on the contribution of Nikolic et. al (2008) and, for brevity, the equations are not shown here. The

main assumptions are: linear driving force for pore diffusion, mono-component *langmuir* isotherm type for water, nonisothermal operation, negligible pressure drop, Peng-Robinson equation of state for pure methane and negligible axial diffusion.

The simulation of temperature swing adsorption processes requires numerical methods capable of handling both adsorption and desorption modes, which are operated in opposite flow direction. This introduces a difficulty for the numerical solution, since the concentration moving front changes its direction.

The change in flow direction can be handled numerically by different approaches. A possible procedure is by reversing the discretized grid, such that the fluid flow always enters at the first cell and leaves at the last cell. For that, the initial condition has to be modified from the previous mode to the new mode by reversing the spatial domain. The advantage is that the same numerical method can be applied to both modes and the downside is the additional computation for adjusting the state vector. Another approach is to maintain the same grid configuration for both operation modes and change the flow direction. For that, the boundary conditions have to be adjusted and also the numerical method, since the moving front direction is modified. The advantage of this approach is that the dynamic profiles of the states can be directly obtained from the numerical solution. The disadvantage is the necessity of changing the numerical method. Hence, the latter approach is expected to be more efficient for iterative procedures, such as optimization and parameter estimation, but the model development is more challenging.

The TSA model is a partial differential algebraic equation (PDAE). A common strategy for the numerical solution is the method of lines, in which the spatial domain is discretized resulting in a set of differential algebraic equations and the temporal domain is solved by numerical integration methods. Efficient differential algebraic equation integration solvers are available in the literature (SUNDIALS[14], etc). These solvers are more efficient if the *Jacobian* of the system is provided. As the model equations get more complicated, the analytical *Jacobian* calculation can become cumbersome. Automatic differentiation techniques are attractive for such cases and there are open-source packages for it, such as ADOLC[15]. As is known, considerable time is spent in a linear solver, hence an efficient solver with sparsity and parallel

capabilities are of crucial importance. One can find state-of-the-art open-source libraries for each of these tasks, but their integration can become quite complex.

Because of the high importance of PDAE simulations, there are softwares available that incorporate all the discussed features, such as EMSO, APMonitor, Jmodelica, gPROMS. However, they can be proprietary or based on special-purpose programming languages, denoted as Domain Specific Languages. These languages, although very readable and intuitive for the modeling task, have limited capabilities when compared to conventional languages, as Python, C++, Matlab.

The software called DAETOOLS [16] incorporates all the required features for an efficient solution of PDAE systems, while allowing the model development to be performed in general purpose languages: Python and C. Because of these capabilities, this software was employed in this study. The Python language was used for model definition, which allowed on-the-fly model customization based on configuration file, such as the choice of adsorption isotherm, equation of state, pressure drop equation, etc.

Because of the consideration of negligible axial dispersion, for the finite difference methods the adsorption mode can be solved using the backward finite difference method (BFDM). For the reversed direction, desorption, the backward numerical scheme becomes unstable. In this case, the proper method is the forward finite difference method (FFDM). The first order approximation is used and the formulation can be obtained elsewhere [17]. For simulation cases in which the axial dispersion is relevant, central finite difference methods are usually more adequate.

Finite volume methods solve the integral formulation rather than the differential form. There are variants, but for cases with propagating discontinuities, the high-resolution total variation diminishing (TVD) method is widely used. The TVD class employs flux limiters to prevent gradients that exceed certain defined limits. Applying an upwind FVM scheme with flux limiter for a discretized cell boundary results in Equation 1.

$$y_{i+1/2} = y_i + \frac{1}{2} \phi(r_{i+1/2})(y_{i+1} - y_i) \quad (1)$$

where ϕ is the flux limiter and r is the ratio of consecutive solution gradients and also a measure of the solution's smoothness (δ is a small number to avoid zero division):

$$r_{i+1/2} = \frac{y_i - y_{i-1} + \delta}{y_{i+1} - y_i + \delta} \quad (2)$$

There are several definitions for flux limiters in literature [18]. This work has implemented all listed in Table 1.

Table 1. Literature values of various flux limiters

Flux limiter	Function $\phi(r)$
Minmod	$\max[0, \min(r, 1)]$
MC	$\max[\min(2r, 0.5(r+1)), 2]$
Superbee	$\max[0, \min(2r, 1), \min(r, 2)]$
Koren	$\max[0, \min(2r, (2r+1)/3, 2)]$
Smart	$\max[0, \min(2r, 0.75r+0.25, 4)]$
Osher	$\max[0, \min(r, \beta)]$
Sweby	$\max[0, \min(\beta r, 1), \min(r, \beta)]$
UMIST	$\max[0, \min(2r, (0.75+0.25r), 2)]$
Van Leer	$(r+ r)/(r+1)$
HQUICK	$[2(r +r)]/(r+3)$
OSPRE	$[1.5(r^2+r)]/(r^2+r+1)$
HCUS	$[1.5(r +r)]/(r+2)$
Van Albada 1	$(r^2+r)/(r^2+1)$
Van Albada 2	$(2r)/(r^2+1)$

Similarly, the WENO variant is presented by Equation 3:

$$y_{i+1/2} = \frac{\alpha_{0,i}}{\alpha_{0,i} + \alpha_{1,i}} \left[\frac{1}{2}(y_i + y_{i+1}) \right] + \frac{\alpha_{1,i}}{\alpha_{0,i} + \alpha_{1,i}} \left[\frac{3}{2}y_i - \frac{1}{2}y_{i-1} \right] \quad (3)$$

$$\alpha_{0,i} = \frac{2/3}{(c_{i+1} - c_i + \delta)^4}; \alpha_{1,i} = \frac{1/3}{(c_i - c_{i-1} + \delta)^4} \quad (4)$$

The FVM methods can be adjusted to both adsorption and desorption modes by proper adjustment of the indexes: $i+1$ to $i-1$ in the previous equations; and by adjusting the boundary conditions.

4. Results and Discussions

Figure 1 presents a comparison of numerical errors for the bulk and adsorbed concentration profiles along the bed (denoted as axial error)

compared to a reference solution, WENO method with 500 grid points. Also, the computational time is presented in the x-coordinate. The FDM with 50 points had higher axial profile error, but at the smallest computational time. With 100 points the FDM method error is higher than the FVMs and the computational cost is smaller, except to the minmod flux demiliter. For the FVM variants, the errors are relatively similar and the vanAlbada1, minmod, Osher, HQUICK, WENO and HCUS were faster while the superbee and vanAlbada2 schema are slower

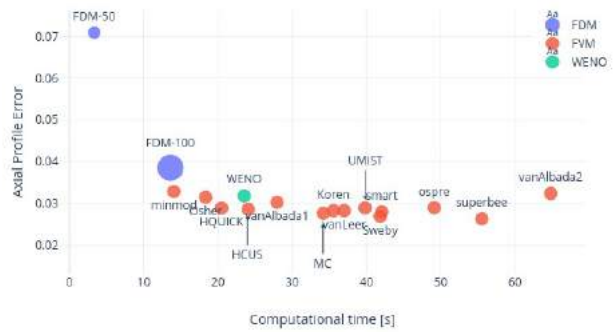


Fig 1: Comparison of numerical methods for TSA operation with Adsorption followed by Desorption.

Breakthrough curves are often used for inspecting numerical methods performance, such as numerical dispersion [11]. Figure 2 shows the breakthrough profiles considering only adsorption mode for the minmod, superbee and WENO finite volume methods, FDM with 50 and 100 points and the reference solution. FDM with 50 points, represented by circles, shows considerable numerical dispersion, which leads to error in the breakthrough time definition. It is also observed that all FVMs presented overlapping curves, resulting in similar profiles with attenuated numerical dispersion than the FDM with 50 points. The FDM with 100 points, represented by squares, showed greater proximity to the reference curve.

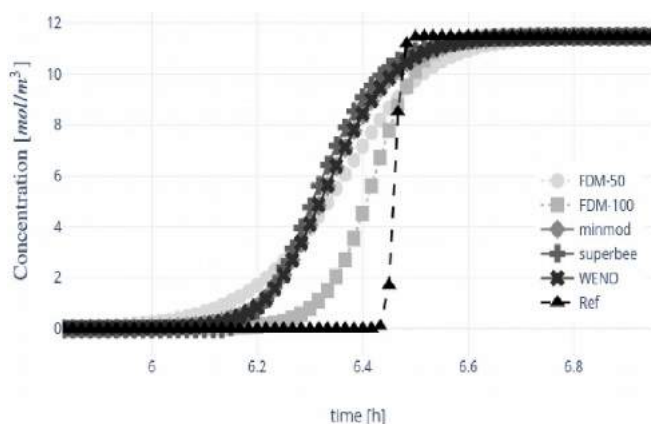


Fig 2: Breakthrough curves for adsorption mode comparing numerical methods

The temporal concentration profile is also compared for the evaluated numerical methods after adsorption operation mode is completed and the regeneration mode is initiated. Figure 3 presents the concentration profile at bed upper boundary, where the gas stream exits the bed during regeneration, which starts at 4 hour of operation. One can note that the FDM-50 profile is the less accurate compared with the reference. Also, the FDM with 100 points presented an intermediate curve between FDM-50 and the reference. In general, all of the volume finite based schemes had good accuracy, with emphasis on superbee that slightly overlaps the reference profile.

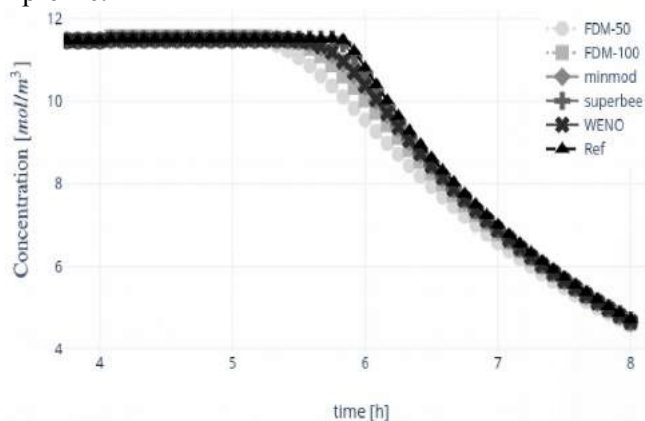


Fig 3: Concentration profile at regeneration exit boundary for different numerical methods.

5. Conclusions

This work considered the simulation of Temperature Swing Adsorption and a comparison of finite difference methods with finite volume methods was evaluated. Several flux delimiters of

high resolution upwind FVM were tested and also the WENO variant. The axial diffusion was considered, i.e. infinity Peclet, hence the backward and forward finite difference methods could be used.

The results showed that for the studied case all the FVM had comparable axial profile error compared to the reference solution. However, the computational time can be very distinct. The superbee and vanAlbada2 schemes were the slowest, while minmod, Osher, WENO, HCUS and HQUICK presented reduced computational time. Furthermore, finite difference method had high numerical dispersion with 50 points, but increasing to 100 points the error was slightly higher than the FVM variants.

Lastly, the concentration profiles in adsorption and regeneration modes display that FDM-50 had inferior results. The minmod, superbee and WENO schemes had similar curves on both cases, but presented more accurate profiles at regeneration exit. An interesting result was FDM-100 which showed the best approximation to the reference in adsorption mode, but did not repeat that performance in regeneration mode.

References

- [1] P. Cruz, J. C. Santos, F. D. Magalhaes, and A. Mendes, "Simulation of separation processes using finite volume method," *Comput. Chem. Eng.*, vol. 30, no. 1, pp. 83–98, 2005.
- [2] S. Sircar, "Applications of Gas Separation by Adsorption for the Future," *Adsorpt. Sci. Technol.*, vol. 19, no. 5, pp. 347–366, Jun. 2001.
- [3] D. G. Pahinkar, S. Garimella, and T. R. Robbins, "Feasibility of Temperature Swing Adsorption in Adsorbent-Coated Microchannels for Natural Gas Purification," *Ind. Eng. Chem. Res.*, vol. 56, no. 18, pp. 5403–5416, May 2017.
- [4] M. A. Makarem, M. Mofarahi, B. Jafarian, and C.-H. Lee, "Simulation and analysis of vacuum pressure swing adsorption using the differential quadrature method," *Comput. Chem. Eng.*, vol. 121, pp. 483–496, 2019.
- [5] S. Kim, D. Ko, and I. Moon, "Dynamic Optimisation of CH₄/CO₂ Separating Operation using Pressure Swing Adsorption Process with Feed Composition Varies,"



- Chem. Eng. Trans.*, vol. 45, pp. 853–858, 2015.
- [6] L. M. Sun, P. Le Quere, and M. D. Levan, “Numerical simulation of diffusion-limited PSA process models by finite difference methods,” *Chem. Eng. Sci.*, vol. 51, no. 24, pp. 5341–5352, 1996.
- [7] K. Kaczmarski and D. Antos, “Fast finite difference method for solving multicomponent adsorption-chromatography models,” *Comput. Chem. Eng.*, vol. 20, no. 11, pp. 1271–1276, 1996.
- [8] P. A. Webley and J. He, “Fast solution-adaptive finite volume method for PSA/VSA cycle simulation; 1 single step simulation,” *Comput. Chem. Eng.*, vol. 23, no. 11–12, pp. 1701–1712, 2000.
- [9] H. Wang, Z. G. Qu, J. Q. Bai, and Y. S. Qiu, “Combined grand canonical Monte Carlo and finite volume method simulation method for investigation of direct air capture of low concentration CO₂ by 5A zeolite adsorbent bed,” *Int. J. Heat Mass Transf.*, vol. 126, pp. 1219–1235, 2018.
- [10] R. Haghpanah *et al.*, “Multiobjective Optimization of a Four-Step Adsorption Process for Postcombustion CO₂ sub(2) Capture Via Finite Volume Simulation,” *Ind. Eng. Chem. Res.*, vol. 52, no. 11, pp. 4249–4265, 2013.
- [11] H. R. S. Anna, A. G. Barreto Jr, F. W. Tavares, and J. F. do Nascimento, “Methane/nitrogen separation through pressure swing adsorption process from nitrogen-rich streams,” *Chem. Eng. Process. Process Intensif.*, vol. 103, pp. 70–79, 2016.
- [12] E. Rossi, M. Paloni, G. Storti, and R. Rota, “Modeling dual reflux-pressure swing adsorption processes: Numerical solution based on the finite volume method,” *Chem. Eng. Sci.*, vol. 203, pp. 173–185, 2019.
- [13] M. Schäfer, *Computational engineering: Introduction to numerical methods*, vol. 321. Springer, 2006.
- [14] A. C. Hindmarsh *et al.*, “SUNDIALS: Suite of nonlinear and differential/algebraic equation solvers,” *ACM Trans. Math. Softw. TOMS*, vol. 31, no. 3, pp. 363–396, 2005.
- [15] A. Walther and A. Griewank, “Getting started with adol-c,” *Comb. Sci. Comput.*, no. 09061, pp. 181–202, 2009.
- [16] D. D. Nikolic, “DAE Tools: equation-based object-oriented modelling, simulation and optimisation software,” *PeerJ Comput. Sci.*, vol. 2, p. e54, 2016.
- [17] R. G. Rice and D. D. Do, *Applied mathematics and modeling for chemical engineers*. New York: Wiley, 1995.
- [18] H. Hassanzadeh, J. Abedi, and M. Pooladi-Darvish, “A comparative study of flux-limiting methods for numerical simulation of gas–solid reactions with Arrhenius type reaction kinetics,” *Comput. Chem. Eng.*, vol. 33, no. 1, pp. 133–143, 2009.

Application of an important Brazilian agricultural residue to water decontamination: using modified sugarcane bagasse to remove Cd(II) and Pb(II) from monometal spiked aqueous solution

Megg Madonyk Cota Elias Carvalho^a, Mariana Viviane Lima Dias^a, Luisa Cardoso Maia^a, Liliane Catone Soares^a, Leandro Vinícius Alves Gurgel^{a,*}

^aGrupo de Físico-Química Orgânica, Departamento de Química, Universidade Federal de Ouro Preto, Campus Universitário Morro do Cruzeiro, s/n°, Bauxita, 35400-000 Ouro Preto, Minas Gerais, Brazil. *legurgel@ufop.edu.br

Abstract

Currently, various anthropogenic activities produce industrial effluents containing a high concentration of toxic metals causing pollution of recipient water bodies. These inorganic contaminants are persistent and non-biodegradable pollutants that must be eliminated from water. A promising alternative to water decontamination is biosorption using widely available, low-cost lignocellulosic residues and by-products. In this work, the biosorption of two toxic metal ions, Cd(II) and Pb(II), was investigated using an important Brazilian agricultural residue: the sugarcane bagasse. Both metals are listed by the World Health Organization (WHO) among the ten major contaminants of major public health concern. Sugarcane bagasse, constituted mainly of cellulose and lignin, was chemically modified with 1,2,3,4-butanetetracarboxylic acid dianhydride and it is used in batch adsorption studies. Adsorptive process parameters such as pH, contact time and initial concentration were investigated. The maximum amounts of adsorbed Cd(II) and Pb(II) were 0.54 and 1.16 mmol.g⁻¹, respectively. Desorption studies were performed to evaluate the reuse of adsorbent material. Desorption efficiencies of approximately 90% and 88% were found for Cd(II) and Pb(II), respectively.

Keywords: biosorption; toxic metals; lignocellulosic biosorbent; agricultural waste.

1. Introduction

Metal contamination has been growing in recent years creating environmental and human health problems with economic consequences [1]. Conventional methods for removal of inorganic contaminants are mainly biological treatment, flocculation, membrane separation processes, chemical precipitation and ion exchange[2]. An alternative method that has been widely investigated is adsorption because it is efficient to remove low concentrations of a huge range of pollutants. Furthermore, it can be an inexpensive method, especially when using widely available bioadsorbents such as lignocellulosic matrix agricultural residues [3]. Brazil is the largest producer of sugarcane, therefore, bagasse constitutes a waste that is widely available in the national territory [4]. Several studies investigate the bagasse in its natural state as bioadsorbent, but many others have shown that the chemical modification of its surface increases its properties as adsorbent [5-8]. Several studies report the use of sugarcane bagasse

to remove inorganic contaminants such as Co, Ni, Cr, Cu, Zn, Pb, Cd, Hg and others[8, 9]. Some metals are considered toxic and some of them are considered to be carcinogenic resulting in serious health problems [10, 11]. Among the toxic metals of great emerging concern, Pb and Cd stand out for causing various diseases and disorders [12]. In adults, it causes bone marrow, liver, kidney and central nervous system toxicity [13]. When introduced into the body, Pb²⁺ can replace other metal ions, such as Ca²⁺, Fe²⁺ or Zn²⁺, compromising metabolic activity and cell life[14]. Cd and its compounds are classified by the International Cancer Research Agency (IARC) as carcinogenic to humans. It also causes pulmonary fibrosis, dyspnea, weight loss, and *itai-itai* disease[2]. Various adsorbents are reported in the literature to remove Cd and Pb as sugarcane bagasse, chitosan, olive cake, bark powder, bagasse fly ash, rice and banana peels as starting material, among others [15-18]. Production cost, production viability, availability, granulometry, among others characteristics are also important to choose an adsorbent. In this context, the present work aims to use sugarcane bagasse

modified with 1,2,3,4-butanetetracarboxylic acid dianhydride to remove Cd(II) and Pb(II) from monometal spiked aqueous solution in batch adsorption studies as a function of pH, contact time and initial concentration. Furthermore, to evaluate its environmental applicability considering its adsorptive capacity and its reuse.

2. Material and methods

2.1. Material

The sugarcane bagasse (SB) is provided by Jatiboca mill, Urucânia, Minas Gerais, Brazil. Acetone, pyridine, hexane, ethanol, acetic anhydride, sodium acetate trihydrate, HCl and HNO₃ were acquired by Synth (Brazil). Pb(NO₃)₂ PA, NaCl PA and NaOH PA were purchased from Vetec (Brazil). N,N-dimethylacetamide (DMAc) was purchased from Neon. 1,2,3,4-butanetetracarboxylic acid (BTCA) (98%) was purchased from Alfa Aesar. Cd(NO₃)₂·4H₂O PA was purchased from Dynamics. Glacial acetic acid PA was purchased from Alphatec Black Belt Quantitative Filter Paper (JP-41) was purchased from Jprolab, Brazil. Deionized water was produced by a Millipore ultrapurifier Milli-Q Simplicity® model.

2.2. Methods

2.2.1. Synthesis of modified sugarcane bagasse (MSB)

SB was pretreated as described by Elias et al (2019) [8]. The methodology for preparing butane-1,2,3,4-tetracarboxylic acid dianhydride (BTCAD) was adapted from Blackwell (1993)[19]. In a 50 mL round bottom flask, pyridine (7.5 mL) and DMAc (7.5 mL) were added to SB (1.0 g) and BTCAD (4.0 g). The flask was connected to a ball condenser and immersed in a previously stabilized 70°C canola oil bath plate (Corning®, model PC 420 D) for 1h, under stirring (300 rpm). Adsorption and desorption studies were performed in duplicate. Thermostatization was performed at 25°C in an incubator (Tecnal, model TE-424, Piracicaba, São Paulo) with orbital shaking at 130 rpm. Filtrations were performed using black ribbon quantitative filter paper (JP-41). Metal quantifications were performed using a flame absorption spectrophotometer (Varian, model SpectrAA 50B).

2.2.2. Batch adsorption studies

An amount of 0.0200±0.0001g of MSB was weighed into cylindrical glasses (1.8 mm height × 2.2 mm diameter). In 250 mL Erlenmeyer flasks, 100 mL of buffered metal solution (buffer solution of 0.05 M CH₃COOH/ CH₃COONa) was added and thermostated for 1h. After, the cylindrical glasses containing the adsorbent were carefully added to the Erlenmeyer flasks and they were stirred at 130 rpm (25°C) for a determined contact time (Table 1). Then, the samples were filtered to polyethylene plastic and the metal content was quantified. The adsorption studies of Cd(II) and Pb(II) were performed as a function of the solution pH, the time of contact and the initial concentration of metal. The adsorption capacity (q_e) is calculated by Eq. (1).

$$q_e = \frac{(C_i - C_f) \cdot V}{m_{MSB}} \quad (1)$$

Where C_i and C_f are, respectively, the initial and after contact time concentrations (mmol.L⁻¹), V is the volume (L) of the metal solution and m_{MSB} is the mass (g) of the MSB biosorbent.

Table 1. Experimental conditions of Cd(II) and Pb(II) adsorption studies onto MSB in batch mode and monometal system.

Adsorption process variables	Adsorption studies in function of		
	pH	Contact time	Initial concentration
pH	2.00-5.25 for Pb and 2.00-5.75 for Cd	5.25 for Pb and 5.75 for Cd	5.25 for Pb and 5.75 for Cd
Metal concentration (mmol.L ⁻¹)	0.559 for Pb and 0.300 for Cd	0.624 for Pb and 0.283 for Cd	0.017-1.700 for Pb and 0.012-1.243 for Cd
Contact time (min)	240	2-540	240

2.2.3. Desorption studies

In a 125 mL Erlenmeyer flask were added 0.0200 ± 0.001g of the metal-loaded MSB (MSB-Cd or MSB-Pb) and 20.0 mL of HNO₃ solution at specific concentration and they were thermostated for a determined time (Table 2). Then, samples were filtered and metal contents were quantified. Doehlert multivariate design was used to evaluate the desorption time (min) and the HNO₃

concentration (mol.L^{-1}) in a percentage of desorption (E_{des}) for the two metals which were the response variables ($E_{des,Cd}$ and $E_{des,Pb}$). This planning was built using the Statistica 12.0 program (StatSoft Inc. 2010, USA) and the model was validated using the statistical analysis of variance (ANOVA), evaluating the regression and lack of fit model at level of significance of 0.05 (95% confidence). A matrix with seven different desorption conditions was generated, one of them corresponding to the central point condition which was done in triplicate, totaling nine experiments. Desorption efficiency was calculated according to Eq. (2).

$$E_{des}/(\%) = \left(\frac{C_{e,X^{n+}} V_{HNO_3}}{Q_{T,max} m'_{MSB}} \right) \times 100 \quad (2)$$

where E_{des} (%) is the desorption efficiency, $C_{e,X^{n+}}$ (mg.L^{-1}) is the equilibrium concentration of adsorbate ($X^{n+} = \text{Cd}^{2+}$ or Pb^{2+}), V_{HNO_3} (L) is the volume of HNO_3 solution, $Q_{T,max}$ (mg.g^{-1}) is the maximum metal adsorption capacity, m'_{MSB} (g) is the mass of MSB adsorbent contained in the adsorbent-loaded ($m_{MSB-X^{n+}}$). The mass only of the adsorbent present in the adsorbent loaded can be calculated using Eq. (3).

$$m'_{BCBTCA}/(g) = \frac{m_{BCBTCA-X^{n+}}}{\left(\frac{Q_{T,max}}{1000}\right)+1} \quad (3)$$

Table 2. Doehlert planning variables and levels for optimizing the Cd(II) and Pb(II) desorption condition of MSB.

Variables	Levels				
HNO ₃ concentration (mol.L^{-1})	-1	-0.5	0	+0.5	+1
	0.01	0.2575	0.505	0.7525	1.0
Contact time (min)	-0.866	0	+0.866		
	5	25	45		

3. Results and Discussion

3.1. Batch adsorption studies

The adsorbent was successfully synthesized as indicated by the characterization results (data not presented here). The adsorption capacity increases from pH 3.5 for Pb(II) and from 4.0 for Cd(II) (Fig 1.). Within the pH range studied, the maximum adsorption pH values were 5.25 for Pb(II) and 5.75 for Cd(II). These pH values were fixed for the kinetics and equilibrium studies (isotherms).

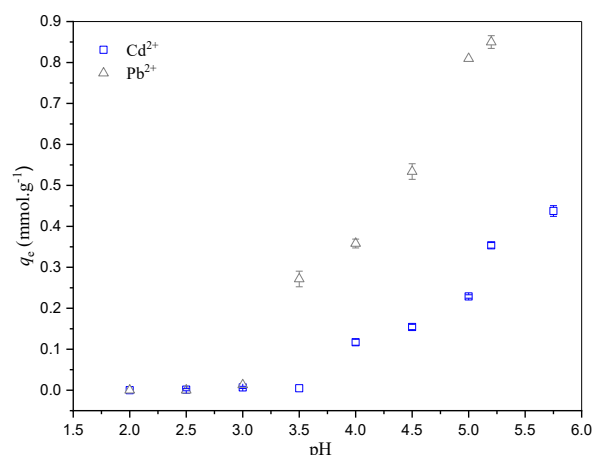


Fig. 1. Cation adsorption on MSB in function of pH solution (0.2 mg.L^{-1} MSB, $0.559 \text{ mmol}_{Pb} \cdot \text{L}^{-1}$, $0.300 \text{ mmol}_{Cd} \cdot \text{L}^{-1}$, 130 rpm, 240 min, 25°C).

For both cations, adsorption capacity has increased over time and equilibrium times were 240 min. Experimental data were modeled using the pseudo first order (PFO)[20] and pseudo second order [21] (PSO) models (Table 3). Microcal OriginPro 2015™ software was used to perform nonlinear regression analysis using the Levenberg-Marquardt interaction algorithm and a weighting method for the statistical treatment that was used to minimize the χ^2 value. The PSO model best described the adsorption of Pb(II) and Cd(II) because it presented the best fit and the smallest error. In addition, the model well predicted the adsorption capacity values for both cations. Adsorption kinetics of both cations have the same equilibrium time but, at this time, $q_{e,Pb}$ is almost double than $q_{e,Cd}$. This result may indicate that MSB shows greater affinity for Pb(II) than Cd(II). Experimental data of equilibrium were modeled using the Langmuir [22], Redlich-Peterson [23] and Dubinin-Radushkevich [24] models using Microcal OriginPro 2015™ software (Table 4). For Pb(II) adsorption data, RP presented the best fit while for Cd(II), all models fit well. According to the Langmuir model, adsorption occurs at uniform adsorption sites and coating occurs only in monolayer on the adsorbent surface, i.e. adsorption is homogeneous, and the number of adsorbed species does not exceed the total number of adsorptive sites. So there is a finite number and equal energies of adsorption sites, at each of which an adsorption molecule can be adsorbed[25]. However, SB matrix is complex and studies has shown that it does not have equivalent adsorption sites of the same energy[7, 8].

Table 3. Nonlinear regression results for monometal adsorption kinetics of Cd(II) and Pb(II) on MSB (0.2 mg.L⁻¹ MSB, 0.624 mmol_{Pb}.L⁻¹, 0.283 mmol_{Cd}.L⁻¹, 130 rpm, 25°C, pH 5.25 for Pb(II) and pH 5.75 for Cd(II)).

Parameters	Pb(II)	Cd(II)
$q_{e,exp}$ (mmol.g ⁻¹)	0.84 ± 0.01	0.44 ± 0.01
t_e (min)	240	240
PFO		
$q_{e,est}$ (mmol.g ⁻¹)	0.73 ± 0.05	0.41 ± 0.02
k_1 (min ⁻¹)	0.05 ± 0.01	0.06 ± 0.01
R^2	0.71	0.91
χ^2_{red}	0.02	0.01
PSO		
$q_{e,est}$ (mmol.g ⁻¹)	0.80 ± 0.04	0.44 ± 0.01
k_2 (min ⁻¹)	0.09 ± 0.02	0.17 ± 0.02
R^2	0.86	0.97
χ^2_{red}	0.01	0.00

The RP model best predicted the $q_{e,max}$ for Pb(II). The system can be described by Langmuir model when β is closer to unity. Thus, RP model suggests that MSB-Cd system has more Langmuirian characteristics than the MSB-Pb system. The constant k from D-R model is associated to the average adsorption energy ($E = 1/\sqrt{k}$). E values are similar for both cations ($E_{Cd} = 5.87$ kJ mmol⁻¹ and $E_{Pb} = 5.77$ kJ mmol⁻¹) and their magnitude are characteristics of physisorption [26]. MSB adsorbs more Pb(II) than Cd(II) in a single metal system. It may be related to the cation hydration energy (ΔH_{hid}) ($\Delta H_{hid,Pb} = -1481$ kJ.mol⁻¹ and $\Delta H_{hid,Cd} = -1807$ kJ.mol⁻¹[27]). The lower the ΔH_{hid} , the greater the possibility of displacement of H₂O molecules that solvate the cations. In addition, the hydrated ionic radius (\bar{H}) of the cation ($\bar{H}_{Pb} = 4.01$ Å and $\bar{H}_{Cd} = 4.26$ Å [27]) also influences the affinity of Pb(II). On the other hand, since some cations have an \bar{H} greater than the radius of the adsorbent pores, a partial dehydration of these ions may occur. So that they have access to the inner surface of the adsorbent. Therefore, the lower the \bar{H} , the more favorable the adsorption, which was observed for Pb(II). Table 5 shows some adsorbents reported in the literature to remove Cd(II) and Pb(II). MSB has relevance to remove Pb(II), but in relation to Cd(II), the adsorption is modest. For a more complete analysis should be performed an economic analysis of the production of the adsorbent, in addition to the

feasibility of its synthesis. Since SB is widely available in our country, MSB synthesis occurs in a single step and its elaboration is relatively simple, MSB is a promising adsorbent.

Table 4. Nonlinear regression results for monometal adsorption isotherms of Cd(II) and Pb(II) on MSB (0.2 mg.L⁻¹ MSB, 130 rpm, 25°C, 240 min, pH 5.25 for Pb(II) and pH 5.75 for Cd(II)).

Parameters	Pb	Cd
$q_{e,exp}$ (mmol.g ⁻¹)	1.16 ± 0.00	0.54 ± 0.01
Langmuir		
$q_{e,max}$ (mmol.g ⁻¹)	1.05 ± 0.06	0.59 ± 0.01
b (L/mmol)	10 ± 2	15.9 ± 0.7
R^2	0.94	0.99
χ^2_{red}	0.02	0.01
Redlich-Petersom (RP)		
K_R (L/g)	83 ± 23	9.7 ± 0.6
a_R (L/mmol)	75 ± 21	16 ± 1
$q_{e,max}$ (mmol.g ⁻¹)	1.1 ± 0.6	0.6 ± 0.1
β	0.66 ± 0.01	0.92 ± 0.03
R^2	0.99	0.99
χ^2_{red}	0.00	0.00
Dubinin-Radushkevich (DR)		
$q_{e,max}$ (mmol.g ⁻¹)	0.95 ± 0.04	0.59 ± 0.01
k (mmol ² /kJ ²)	0.015 ± 0.001	0.014 ± 0.000
R^2	0.94	0.99
χ^2_{red}	0.02	0.00

Table 5. Different bioadsorbents used to remove Cd(II) and Pb(II) from aqueous solutions.

Adsorbent material	q_e (mmol.g ⁻¹)		Ref.
	Pb(II)	Cd(II)	
Chitosan modified with ECH-TPP	0.81	0.74	[28]
SB modified with ethylene diamine	0.91	1.46	[29]
SB modified with SA	2.41	2.28	[15]
<i>Acacia leucocephala</i> bark powder	0.89	1.49	[30]
Peels of banana	0.01	0.05	[18]
Bagasse fly ash	0.01	-	[17]
Rice husk	-	0.08	[31]
Olive cake	0.09	0.08	
Charred xanthated SB	1.58	1.95	[32]
Biochar derived from SB	0.42	-	[33]
MSB	1.16	0.54	This work

SB = sugarcane bagasse, ECH-TPP= epichlorohydrin-triphosphate, SA=succinic anhydride, MSB = SB modified with DBTCA, Ref. = reference.

Table 6. Doehlert planning matrix for optimizing Cd(II) and Pb(II) desorption conditions.

Experiment	Independent variables		Dependent variables	
	C_{HNO_3} (mol L ⁻¹)	Time (min)	$E_{\text{des,Cd}}$ (%)	$E_{\text{des,Pb}}$ (%)
1	1.0000	25	89.14	81.85
2	0.7525	45	91.32	85.77
3	0.0100	25	79.37	70.74
4	0.2575	5	78.01	73.16
5	0.7525	5	76.16	79.78
6	0.2575	45	87.25	79.67
7 (C)	0.5050	25	88.51	83.42
8 (C)	0.5050	25	87.42	81.93
9 (C)	0.5050	25	90.60	84.84

Experimental data were tested by the Shapiro-Wilk test and proved to be data that follow a normal distribution, ie parametric, indicating that this statistical analysis can be performed [34]. For the $E_{\text{des,Cd}}$ response, the time at its linear term was significant with positive effect (7.545) (Pareto's charts not shown here). For the $E_{\text{des,Pb}}$ response, the terms HNO₃ concentration at both linear (10.068) and quadratic (-7.399) and linear time (6.242) were significant. These results indicate that time at its maximum level produces a better desorption efficiency for both cations. The desirability profile indicated an optimal desorption condition when using a 0.703 mol.L⁻¹ HNO₃ solution and a desorption time of 42 min with a prediction of 99.4%. This condition was validated and E_{des} values were 90.05% for Cd(II) and 87.54% for Pb(II).

4. Conclusions

The biosorbent MSB is able to remove Cd(II) and Pb(II) from aqueous solutions synthetically contaminated with optimal adsorptive capacities. Desorption studies indicate that almost all adsorbed metal can be removed with acid solution treatment.

Acknowledgements

The authors are grateful to the Federal University of Ouro Preto (UFOP), Rede Mineira de Química (RQ-MG) and the funding agencies Conselho Nacional de Desenvolvimento Científico e Tecnológico

(CNPQ) and Fundação de Amparo à Pesquisa do Estado de Minas Gerais (FAPEMIG). This study was financed in part by Coordenação de Aperfeiçoamento de Pessoal de Nível Superior – Brasil (CAPES) Finance Code 001.

References

- [1] Barakat M. New trends in removing heavy metals from industrial wastewater. *Arabian Journal of Chemistry* 2011;4:361.
- [2] Rosales E, Mejjide J, Pazos M, Sanromán MA. Challenges and recent advances in biochar as low-cost biosorbent: from batch assays to continuous-flow systems. *Bioresource technology* 2017;246:176.
- [3] Sud D, Mahajan G, Kaur M. Agricultural waste material as potential adsorbent for sequestering heavy metal ions from aqueous solutions—A review. *Bioresource technology* 2008;99:6017.
- [4] Mendes F. Efeito da umidade nas propriedades físicas e estruturais do bagaço de cana. *Blucher Chemical Engineering Proceedings* 2015;1:6401.
- [5] Dos Santos VC, De Souza JV, Tarley CR, Caetano J, Dragunski DC. Copper ions adsorption from aqueous medium using the biosorbent sugarcane bagasse in natura and chemically modified. *Water, Air, & Soil Pollution* 2011;216:351.
- [6] GERON LJV, MIGUEL GZ, AGOSTINHO A. Composição química, valor de ph e temperatura do bagaço de cana-de-açúcar in natura e hidrolisado com cal (CaO) conservados em mini silos. *Revista de Ciências Agro-Ambientais, Alta Floresta* 2010;8:57.
- [7] de Almeida FTR, Elias MMC, Xavier ALP, Ferreira GMD, Silva IA, Filgueiras JG, et al. Synthesis and application of sugarcane bagasse cellulose mixed esters. Part II: Removal of Co²⁺ and Ni²⁺ from single spiked aqueous solutions in batch and continuous mode. *Journal of colloid and interface science* 2019;552:337.
- [8] Elias MMC, Ferreira GMD, de Almeida FTR, Rosa NCM, Silva IA, Filgueiras JG, et al. Synthesis and application of sugarcane bagasse cellulose mixed esters. Part I: Removal of Co²⁺ and Ni²⁺ from single spiked aqueous solutions in batch mode using sugarcane bagasse cellulose succinate phthalate. *Journal of colloid and interface science* 2019;533:678.
- [9] de Almeida FTR, Ferreira BCS, Moreira ALdSL, de Freitas RP, Gil LF, Gurgel LVA.

Application of a new bifunctionalized chitosan derivative with zwitterionic characteristics for the adsorption of Cu 2+, Co 2+, Ni 2+, and oxyanions of Cr 6+ from aqueous solutions: Kinetic and equilibrium aspects. *Journal of colloid and interface science* 2016;466:297.

[10] Valko M, Morris H, Cronin M. Metals, toxicity and oxidative stress. *Current medicinal chemistry* 2005;12:1161.

[11] Tchounwou PB, Yedjou CG, Patlolla AK, Sutton DJ. Heavy metal toxicity and the environment. *Molecular, clinical and environmental toxicology*: Springer; 2012, p. 133.

[12] Flora G, Gupta D, Tiwari A. Toxicity of lead: a review with recent updates. *Interdisciplinary toxicology* 2012;5:47.

[13] Wang J, Yang Z, Lin L, Zhao Z, Liu Z, Liu X. Protective effect of naringenin against lead-induced oxidative stress in rats. *Biological trace element research* 2012;146:354.

[14] Ho Y, McKay G. Kinetic model for lead (II) sorption on to peat. *Adsorption science & technology* 1998;16:243.

[15] Gurgel LVA, de Freitas RP, Gil LF. Adsorption of Cu (II), Cd (II), and Pb (II) from aqueous single metal solutions by sugarcane bagasse and mercerized sugarcane bagasse chemically modified with succinic anhydride. *Carbohydrate Polymers* 2008;74:922.

[16] Doyurum S, Celik A. Pb (II) and Cd (II) removal from aqueous solutions by olive cake. *Journal of Hazardous Materials* 2006;138:22.

[17] Gupta VK, Ali I. Removal of lead and chromium from wastewater using bagasse fly ash—a sugar industry waste. *Journal of colloid and interface science* 2004;271:321.

[18] Anwar J, Shafique U, Salman M, Dar A, Anwar S. Removal of Pb (II) and Cd (II) from water by adsorption on peels of banana. *Bioresource technology* 2010;101:1752.

[19] Blackwell GB. Dental/medical composition and use. Google Patents; 1993.

[20] Lagergren S. Zur theorie der sogenannten absorption gelöster stoffe: PA Norstedt & söner; 1898.

[21] Ho Y, McKay G. A kinetic study of dye sorption by biosorbent waste product pith. *Resources, conservation and recycling* 1999;25:171.

[22] Langmuir I. THE DISSOCIATION OF HYDROGEN INTO ATOMS. III. THE

MECHANISM OF THE REACTION. *Journal of the American Chemical Society* 1916;38:1145.

[23] Redlich O, Peterson DL. A useful adsorption isotherm. *Journal of Physical Chemistry* 1959;63:1024.

[24] Dubinin M. The potential theory of adsorption of gases and vapors for adsorbents with energetically nonuniform surfaces. *Chem Rev* 1960;60:235.

[25] Langmuir I. The adsorption of gases on plane surfaces of glass, mica and platinum. *Journal of the American Chemical society* 1918;40:1361.

[26] Smith JM. *Chemical engineering kinetics*: McGraw-Hill; 1981.

[27] Shinzato MC. Remoção de metais pesados em solução por zeólitas naturais: revisão crítica. *Revista do Instituto Geológico* 2007;27:65.

[28] Laus R, Costa TG, Szpoganicz B, Fávère VT. Adsorption and desorption of Cu (II), Cd (II) and Pb (II) ions using chitosan crosslinked with epichlorohydrin-triphosphate as the adsorbent. *Journal of hazardous materials* 2010;183:233.

[29] Karnitz O, Gurgel LVA, De Melo JCP, Botaro VR, Melo TMS, de Freitas Gil RP, et al. Adsorption of heavy metal ion from aqueous single metal solution by chemically modified sugarcane bagasse. *Bioresource Technology* 2007;98:1291.

[30] Munagapati VS, Yarramuthi V, Nadavala SK, Alla SR, Abburi K. Biosorption of Cu (II), Cd (II) and Pb (II) by *Acacia leucocephala* bark powder: Kinetics, equilibrium and thermodynamics. *Chemical Engineering Journal* 2010;157:357.

[31] Kumar U, Bandyopadhyay M. Sorption of cadmium from aqueous solution using pretreated rice husk. *Bioresource technology* 2006;97:104.

[32] Homagai PL, Ghimire KN, Inoue K. Adsorption behavior of heavy metals onto chemically modified sugarcane bagasse. *Bioresource Technology* 2010;101:2067.

[33] Abdelhafez AA, Li J. Removal of Pb (II) from aqueous solution by using biochars derived from sugar cane bagasse and orange peel. *Journal of the Taiwan Institute of Chemical Engineers* 2016;61:367.

[34] Razali NM, Wah YB. Power comparisons of shapiro-wilk, kolmogorov-smirnov, lilliefors and anderson-darling tests. *Journal of statistical modeling and analytics* 2011;2:21.

ADSORPTIVE PROCESSES FOR DYE REMOVAL USING ADSORBENTS OBTAINED FROM ALGINATE AND CHITOSAN DOPED WITH Cu^{2+} IONS

Francisco Mateus Gomes do Nascimento^a, Francisco Renan Lima Amorim^a,
Guilherme Augusto Magalhães Júnior^a, Mayara de Sousa Oliveira^{a*}

^a IFCE campus Quixadá, Av. José de Freitas Queiroz, Quixadá, 63902-580, Brazil

Abstract

Today many industrial effluents are expelled to nature without proper treatment such as colored effluents or dye solutions. These effluents are toxic and have a high resistance to the treatments used. In addition, it causes an environmental imbalance by preventing aquatic plants from performing photosynthesis by blocking sunlight and causing fish to die when they ingest the solution. In order to reduce this pollution, research is underway on the production of biomaterials with adsorptive capacity for application as adsorbents of various pollutant compounds, such as the microsphere synthesized from biopolymers, alginate (AL) and chitosan (CH), incorporated with metals. Thus, this project aims to evaluate the batch adsorption of Indigo Carmine (I.C.) dye present in synthetic effluents from microspheres produced by electrolytic complexation of Cu^{2+} doped AL and CH natural polymers. The characterization of the microspheres was performed by analyzing the swelling kinetics, particles analysis and Fourier Transform Infrared Spectroscopy (FTIR). For the adsorption kinetics studies a 150 rpm rotating shaker, 120 min reaction time, room temperature, 50 mg adsorbent mass and three dye solution concentrations (5, 10 and 25mg/L) were used. Indigo carmine in aqueous medium. The results obtained were modeled according to the pseudo 1st and 2nd order Lagergren models, the latter having the best correlations with the experimental data. It was observed that the adsorbents studied were efficient in the removal of indigo carmine dye, reaching about 91% of removal.

Keywords: Effluent. Dye. Biomaterial. Adsorption. Removal.

1. Main text

Environmental pollution and environmental degradation have been increasing over the years, and with this the concern regarding the conservation of natural resources has gained a lot of importance today (FERNANDES, 2005).

According to Freire et al. 2000, industrial processes that use large volumes of water end up contributing to the pollution of water bodies, often due to the lack of appropriate treatments for these effluents. Over time these industrial

processes release unwanted resources into the environment from oil refinery activities, mainly chemical and textile industries, and sewage systems that positively contribute to increased pollution (FREIRE et al., 2000).

It is reported that there are over 10,000 different dyes and commercial pigments, and each year more than seven hundred thousand tons of dyes are produced. About 10% to 20% of total world dye production is lost during the dyeing step, and as a result, a large amount of dyes appear as waste in wastewater (WANG et al., 2010; SHARMA and KAUR, 2011; ANBIA and SALEHI, 2012).

The main contributor to the disposal of various types of dyes are the textile and food industries, which has been facing several difficulties for the treatment of these effluents, since in their release they have visible dye concentrations and in their structures they present aromatic rings that make their use difficult degradation, and also by the fact that these compounds do not belong to the same group of compounds, but differ in solubility, volatility, reactivity and stability, making degradation difficult. What can lead to the death of aquatic life, are carcinogenic and toxic and cause major problems for riparian populations (SAHA et al., 2011). There are several processes used for wastewater treatment, chemical, biological, and physical processes, adsorption being the main one. This process is based on the principle of using a solution and a material which has the ability to remove unwanted particles present in solution.

Adsorption processes by pi-complexation have been widely used, because the bond formed between the analyte and the adsorbent is stronger than intermolecular interactions characteristic of physical adsorption (HUANG et al, 1999).

Thus, this research aimed to synthesize alginate and chitosan based adsorbent materials to analyze the adsorption potential of indigo carmine dye in synthetic colored effluents.

2. Methodology

2.1 Synthesis and characterization of the adsorbents

The synthesis of adsorbents was performed using Soluc chitosan, sodium alginate and calcium chloride from Vetec. Initially an aqueous 1% AL solution and a 1% CH solution in 2% acetic acid were prepared and the two systems were stirred for 24h. After the stirring time, a 1% solution of calcium chloride and 0,01g of the copper (II) nitrate salt was added to the chitosan solution. After this time, simple filtration was performed to separate the microspheres from the solution.

Finally, the obtained microspheres were oven dried for a period of 2h at a temperature of 60°C, to avoid possible breakdown of the polymeric structure. The obtained microspheres were characterized by the swelling kinetics, which analyzes the amount of water absorbed in relation to the microsphere mass over the contact time of the complexes with the solvent. In the swelling tests, 0.1g of adsorbent material was used and the water absorption kinetics was analyzed over a period of 60min in order to analyze the swelling balance. The microspheres were also characterized by Fourier Transform Infrared Spectroscopy (FTIR), in the region from 500 cm⁻¹ to 4000 cm⁻¹ to determine the main groups present in the structure of the synthesized complex.

2.2 Adsorptive process

Experimentally three adsorbent masses were evaluated in order to verify an optimal performance and lower cost for application in future experiments. In a 150 rpm orbital rotation shaker at room temperature (27 ° C) and 2 hours stirring period, 125 mL erlenmeyer containing 25, 50, 75 mg of adsorbent and 25 mL of Indigo Carmine dye solution (IC) (5, 10 and 25 mg / L), corresponding to dosages of 1, 2 and 3 g / L at natural pH (6.9±0.1). The solutions used in the adsorptive tests were obtained from dilution of a dye stock solution of 100mg / L concentration. During the contact time between the solution and the adsorbents, aliquots of the system were collected at predetermined times and compared with the initial concentration of the tests in order to quantify the percentage of dye removal. Aliquots were analyzed by UV-Vis Spectrophotometer over a wavelength range of 610 to 640nm. The obtained data were treated with mathematical models of Lagergren Pseudo 1st and 2nd Orders, in order to verify the best correlation of the experimental data obtained.

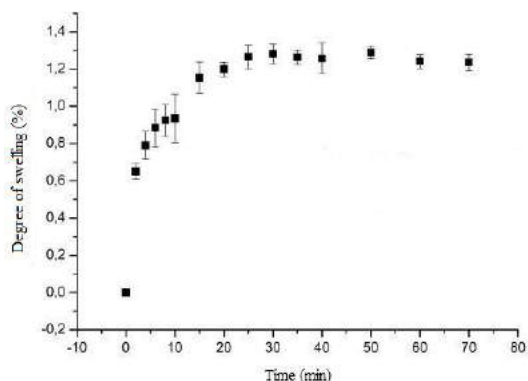
3. Results and discussion

3.1 Synthesis and characterization of the adsorbents

The following graph shows the swelling kinetics of the microspheres over time:



Image 1: Swelling kinetics of microspheres in water.



Analyzing the graph, it is observed that around 30 minutes the mass of water absorbed becomes constant at macroscopic level, as the system has reached equilibrium. The graph shows that the mass of water absorbed was over 120%, showing that the mass of the microspheres increased significantly.

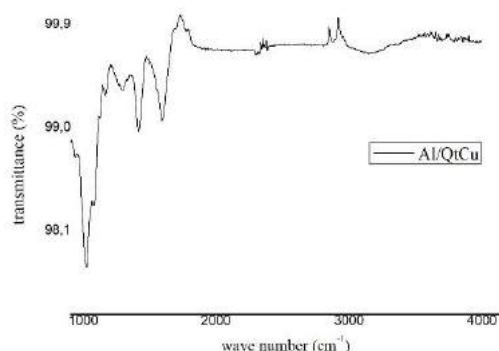
Micrographs of the synthesized material were also performed with the aid of a microscope as shown in Figure 2 below:

Image 2 – Micrograph of microspheres



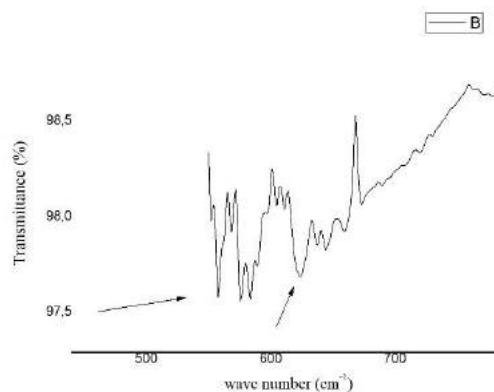
The images 3 and 4 represent the FTIR spectrum of the microspheres:

Image 3 - FTIR of microspheres in the region of 4000 to 1000 cm^{-1}



It is possible to observe a characteristic band of the O-H and N-H connections in the region from 2960 to 3500 cm^{-1} , however it is observed that it is a weak band that is not common for the stretching of these connections (PAVIA, 2012). A possible explanation for this may be the complexation of copper ions by the microspheres, by the pairs of non-binding electrons in the structure of the hydroxide and amino groups, with the possible deprotonation of these groups, and with this, the number of O-H and N-H bonds is reduced. It is also observed in the spectrum peaks in the region of 2945 cm^{-1} referring to the stretching of C-H bonds of carbon sp^3 . The bands in 1700 cm^{-1} and 1550 to 1600 cm^{-1} refer of vibration of asymmetric and symmetrical stretching, respectively, of the C=O bond of the carboxylate group present in the structure of the sodium alginate that makes up the microsphere (LIMA, 2007).

Image 4 - FTIR of microspheres in the region of 800 to 500 cm^{-1}



In the spectrum, stretches are also observed in wave numbers approximately equal to 624 cm^{-1} for Cu-O bond and 558 cm^{-1} for Cu-N bond, where values were similar to those found by Hottes in a synthesized complex. Although the complex worked on presents a different structure from the alginate and chitosan microsphere, these peaks may be possible indicative of the possibility of metal complexation in the microsphere.

3. 2 Adsorptive studies

In the adsorptive tests studies were carried out varying the concentration of the dye solution and the material dosage used (ratio between the mass of

adsorbent used and the volume of dye solution). It was observed in the tests performed after 2 hours of contact time the removals and adsorptive capacities presented in Table 1, below.

Table 1 - Effect of adsorbent dosage on adsorptive capacity and removal efficiency of I.C. for synthesized microspheres. $C_0 = 5, 10$ and 25 mg / L , $T = 27^\circ \text{ C}$, $\text{pH} = 6.9$ (natural), rotation = 150 rpm .

Concentration	Adsorbent dosage (g/L)	q_e (mg/g)	Removal (%)
5	1	0,59	45
	2	0,42	57
	3	1,84	91
10	1	0,62	32,5
	2	0,65	59,5
	3	0,92	79
25	1	1,84	26
	2	0,86	27,5
	3	1,68	60

Adsorbent dosage is an important parameter in determining adsorption capacity and percentage of adsorption (removal efficiency). The results indicated that adsorption removals were maximal at 3 g / L . Table 1 allowed us to observe that with the increase of adsorbent mass the adsorption potential was enhanced due to the larger number of adsorptive sites available for the process and besides, with the increase of adsorbent particles, the total surface area of the material increases. It can also be observed the increase of adsorptive capacity with the decrease of the removal percentage, and this can be explained due to an excess of adsorbent material that does not interact with the adsorbate molecules, evidencing the saturation process of the microspheres (OLIVEIRA, 2013).

The experimental data for the adsorption kinetics of the dye I.C. in aqueous solution were modeled according to the pseudo first and second order Lagergren equations. Figures 3, 4 and 5 and Table 2 show the models and

parameters of adsorption kinetics according to these models.

Image 5 – Adsorption kinetics of I.C under microspheres with 1g / L dosage.

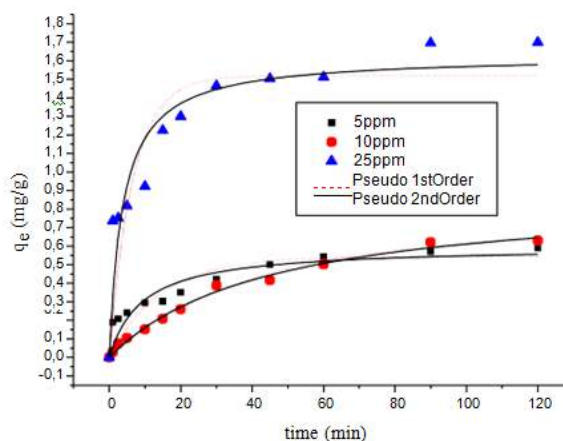


Image 6 – Adsorption kinetics of I.C under microspheres with 2g / L dosage.

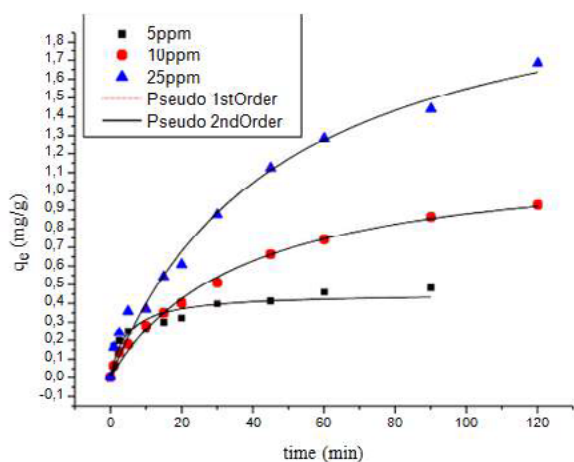


Image 7 – Adsorption kinetics of I.C under microspheres with 3g / L dosage.

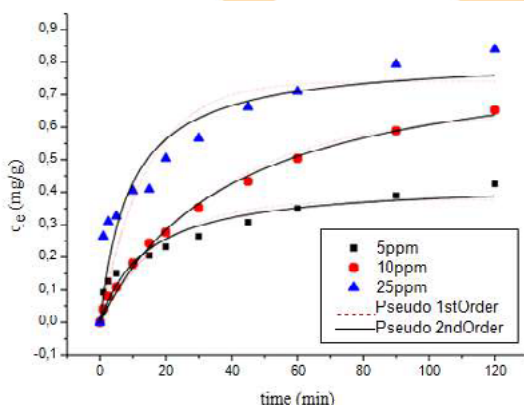




Table 2 - Kinetic parameters obtained for the adsorption of I.C. in aqueous medium on the investigated adsorbent. T = 27 ° C.

Concentration	Adsorbent dosage (g/L)	q_{exp} (mg/g)	Pseudo 1 ^a order			Pseudo 2 ^a order		
			q_{e1}	k_1	R ²	q_{e2}	k_2	R ²
5	1	0,5900	0,5437	0,0163	0,8234	0,5989	0,1805	0,8867
	2	0,4255	0,3782	0,0120	0,8656	0,4323	0,1684	0,9178
	3	0,5600	0,4101	0,0320	0,7874	0,4487	0,4935	0,8870
10	1	0,6200	0,6625	0,0060	0,9893	0,8879	0,0245	0,9908
	2	0,6500	0,6490	0,0064	0,9875	0,8489	0,0296	0,9947
	3	0,9200	0,9220	0,0068	0,9863	1,1947	0,0227	0,9924
25	1	1,8400	1,5187	0,0354	0,7935	1,6278	0,1626	0,8851
	2	0,8600	0,7417	0,0165	0,7915	0,8161	0,1361	0,8673
	3	1,68	1,6959	0,0056	0,9761	2,2789	0,0091	0,9807

Thus, it was observed in the data obtained in the adsorption kinetic tests better correlation coefficients with the Pseudo 2nd Order model, because the values approached more than 1. Although the adsorptive tests obey the second order kinetics, for some Tests carried out the Pseudo 1st Order adsorptive capacity values were closer to the experimental values, showing that in some cases the Pseudo 1st Order Lagergren model better represented the process. Analyzing the velocity constant values of the adsorptive processes under study, we observed higher k values according to the Pseudo 2nd Order model, showing faster kinetic processes according to this model.

4 Conclusion

It was observed that the adsorbent synthesized from AL and CH by the drip method had characteristics that allowed to absorb a good amount of water in the swelling test which could contribute to the promising character in the removal of the dye under study. with percentages ranging from 60 to 91% using the 3 g / L (most efficient) dosage. Thus it can be considered that application of these biomaterials as economically and environmentally viable and desirable for the removal of the dye I.C., constituting a promising alternative to the use of commercial adsorbents in treatment of colored effluents.

5 References

- ANBIA, M.; SALEHI, S. Removal of acid dyes from aqueous media by adsorption onto amino-functionalized nanoporous silica SBA-3. *Dyes and Pigm*, v. 94, p. 1-9, 2012.
- BEDABRATA, S.; SOURAV, D.; JIBAN, S.; GOPAL, D. Preferential and enhanced adsorption of diferente dyes on iron oxide nanoparticles: a comparative study. *Journal of Physical Chemistry C.*, v. 115, p. 8024-8033, 2011.
- CRONJE, K, J. et al. Optimization o chromium(VI) sorption potencial using developed active carbon from sugarcane bagasse with chemical activation by zinc chloride. *Desalination*, 2011, v. 275, n. 1-3, p. 276-284.
- FERNANDES, R. Adsorventes alternativos para remoção de fenol em solução aquosa. Programa de Pós-Graduação em Engenharia Química. Universidade Federal de Santa Catarina. Mestre em Engenharia Química. p. 78, 2005;
- FREIRE, R. S.; PELEGRINI, R.; KUBOTA, L. T.; DURAN, N.; PERALTA-ZAMORA, P. Novas tendências para o tratamento de resíduos industriais contendo espécies organocloradas. *Química Nova*, v. 23, n. 4, p. 504-511, 2000.

HOTTES, S. **Novos complexos de platina (II) e cobre (II) derivados de oximas 1,2,3-triazólicas como potenciais agentes antitumorais e protótipos de pró-drogas biorredutíveis.** 2013. (número de páginas). Dissertação (Mestrado em Química) – Pontifícia Universidade Católica, Rio de Janeiro, 2013.

HUANG, H. Y.; PADIN, J.; YANG, R. T. Anion and Cation Effects on Olefin Adsorption on Silver and Copper Halides: Ab Initio Effective Core Potential Study of π -Complexation. **J. Phys. Chem. B**, v. 103, p. 3206-3212, 1999.

LIMA, A. M. F.; ANDREAN, L.; SOLDI, V.; BORSALI, R. Influência da adição de plastificante e do processo de reticulação na morfologia, absorção de água e propriedades mecânicas de filmes de alginato de sódio. **Quím. Nova**, vol.30 no.4 São Paulo, July/Aug. 2007

OLIVEIRA, M. S. **Remoção de azo corantes acid red em meio aquoso usando processo de adsorção.** 2013. 114f. Dissertação (Mestrado em Tecnologia e Gestão Ambiental) – Instituto Federal de Educação, Ciência e Tecnologia do Ceará, Fortaleza, 2013.

PAVIA, D. L. et al. **Introdução à espectroscopia.** Trad. Pedro Barros. – São Paulo: Cengage Learning, 2012.

SANTOS, J. E.; SOARES, J. P.; DOCKAL, E. R.; CAMPANA FILHO, S. P.; CAVALHEIRO, É. T. G. Caracterização de quitosanas comerciais de diferentes origens. **Polímeros**, vol.13, no. 4, São Carlos, Oct./Dec. 2003.

SHARMA, P.; KAUR, H. Sugarcane bagasse for the removal of erythrosine Band methylene blue from aqueous waste. **Applied Water Science**, v. 1, p. 135-145, 2011.

SOTELO, J. L. et al. Removal of caffeine and diclofenac on activated carbon in fixed bed column. **Chemical Engineering Research and Design**, 2012, v. 90, n. 7, p. 967-974.

WANG, Y.; ZHANG, H.; TANG, B. The interaction of C.I. acid red 27 with human hemoglobin in solution. **J. Photochem. Photobio. B: Biology**, v. 100, p. 76-83, 2010.

CO₂ capture by biochars produced from “açai” stones

Júnior Staudt^{a,*}, Rafael Luan Sehn Canevesi^a, Helton José Alves^{a,b}, Lázaro José Gasparini^b,
Fabiano Bisinella Schefe^c and Carlos Eduardo Borba^a

^a West Parana State University, Faculdade St., 645, Toledo, 85903-000, Brazil

^b Federal University of Parana, Pioneiro St., 2153, Palotina, 8595000, Brazil

^c Federal University of Technology – Paraná, Cristo Rei St., 19, Toledo, 85902-490, Brazil

Abstract

The use of biogas as energy source has been treated as a promising alternative to the fossil fuels. However, for the generation of biomethane, for instance, a previous capture of the CO₂ is required, in order to provide a biogas with enriched fraction of methane (biogas upgrading). The capture of CO₂ from the mixture gases instead of CH₄, strongly depends on the characteristics of the adsorbent, such as affinity and selectivity. The present work aimed to assess the CO₂ capture by biochars produced from residual “açai” stones for the future application of the most promising ones on the separation of CO₂/CH₄ mixtures in a pressure swing adsorption (PSA) system. To this end, two materials were produced (BC_{KOH} and BC_{NaOH}) following different activation methods and then compared according to their characterizations and their performances on capturing CO₂ with zeolite ZSM5 (commercial reference material). The main results showed that the biochars as well as the ZSM5 were microporous, showing physisorption isotherms of Type I and mean pore diameter of 0.6 nm. Furthermore, all materials showed an homogeneous pore size distribution. In relation to the CO₂ capture itself, which were performed in a thermogravimetric analyzer, the following adsorption capacities were observed: $q_{ZSM5}=36 \text{ mg g}^{-1}$, $q_{BC_{KOH}}=95 \text{ mg g}^{-1}$, and $q_{BC_{NaOH}}=49 \text{ mg g}^{-1}$, with regenerations of 77%, 89.0%, and 90.8%, respectively. Although further tests must be conducted for CH₄/CO₂, the biochars made from residual biomass presented a great potential for capturing CO₂ and textural characteristics that may favor their selectiveness to this molecule.

Keywords: Biogas upgrading; gas adsorption; activated carbon; residual biomass.

1. Introduction

The global energy matrix has been facing changes over the past years, which are related to the urge of reduction in the emissions of greenhouse gases to the atmosphere, which are mainly originated from the burning of fossil fuels [1]. The expansion of the use of renewable energy sources such as biogas to the generation of electricity or biomethane thus could represent an effective way to contribute with the sustainability [2–6]. However, a previous removal of hydrogen sulfide (H₂S) and carbon dioxide (CO₂) is needed for the generation of electricity and biomethane, respectively, because these components lead to high toxicity and oxidative potential of the biogas. The so-called biogas upgrading, which provides a gas with enriched fraction of methane (CH₄), is thus essential to the feasibility of application of the gas, either for

electrical energy production or as a biofuel for the supply of vehicles [7–9].

To perform the purification, it is essential to work with a technique that could promote a selective capture of the undesirable compounds. The pressure swing adsorption (PSA), which provides adsorption/desorption cycles by pressure variation, could be highlighted as a suitable process for that purpose, since it presents high purification of methane, low energy consumption, high automation capacity, and absence of chemical agents, fast installation and easy operation. On other hand, the choice of the adsorbent plays a crucial role, since it must present high selectivity, easy regeneration, high adsorption capacity for the species of interest, and, especially, low cost [8,10,11]. It is worth mentioning that the capture of H₂S does not commonly occur by PSA but as a preliminary step, since the adsorbent used for this purpose are not easily regenerated. Therefore, PSA plants are mostly



built to the capture of CO₂ from mixtures containing predominantly CO₂ and CH₄ [12,13]. There are several reports on the use of commercial adsorbents such as the zeolite ZSM5 to this end [14–18].

However, besides the fact that commercial adsorbents could represent high costs to the final project of a PSA system, it is important to test the capacity of a new adsorbent in a smaller scale prior to the application in PSA cycles [19]. The present study thus aims to assess the CO₂ capture by biochars produced from residual biomasses for the future application of the most promising ones on the separation of CO₂/CH₄ mixtures in a PSA system.

2. Materials and methods

The precursor material used to produce the biochars was stones of “açai”, which is a Brazilian palm fruit). Moreover, both helium (He) and carbon dioxide (CO₂) were pure gases (99.999%).

2.1. Synthesis of the biochars

The synthesis of the biochars (BCs) took place as follows: i) impregnation: a mass of 5 g of precursor material was impregnated for 6 h at the ratio of 1:4 ($m_{\text{precursor}}/V_{\text{activatingagent}}$). Potassium hydroxide (KOH) and sodium hydroxide (NaOH) at concentrations of 1.5 mol L⁻¹ were used as activating agents for the biochars BS_{KOH} and BC_{NaOH}, respectively. Thereafter, the material was dried in oven at 105 °C until constant mass was achieved. ii) Pyrolysis and activation: The material was activated in a pyrolysis furnace (FIVE PQ 10P–EDG) at controlled atmosphere with N₂ flow of 100 mL min⁻¹ for 1 h at 900 °C (10 °C min⁻¹ of heating rate). The material was then washed into a hydrochloric acid solution (HCl – 1.0 mol L⁻¹) for 6 h, which was constantly agitated at room temperature. To remove the excess of solution, the material was washed with distilled water 90 °C to achieve neutral pH and finally dried in oven at 110 °C.

2.2. Characterization of the biochars

In order to support the analysis of the kinetic behavior and the capacity of the tested adsorbents, their textural properties were assessed by CO₂ physisorption isotherms, which were measured in the relative pressure range from 10⁻⁶ to 1, at 0 °C (NOVA 200e, Quantachrome). The samples were outgassed at 150 °C for 12 h prior to the tests. Surface area and pore size distribution were

determined and by the non-local density functional theory (NLDFT), whereas the total pore volume was found from the amount of CO₂ adsorbed at P/P₀ = 0.99.

2.3. Tests of CO₂ capture

The kinetic behavior of the CO₂ capture was evaluated in a thermogravimetric analyzer (Perkin Elmer STA 600), in which by the mass of the samples was recorded and monitored according to the following procedure: first of all, samples of around 11 mg were heated from 30 to 120 °C under gas helium (He) flow of 40 mL/min (step i). This temperature was kept constant 60 min to the outgassing of the samples (step ii). After that, the temperature was reduced to 30 °C and the inlet gas was replaced by a CO₂ flow of 40 mL/min (step iii). The temperature was then kept constant at 30 °C for 60 min (step iv). Thus, the procedures taken in steps i and ii can be considered as a pre-treatment, while steps iii and iv represent the CO₂ capture by the adsorbent. On other hand, the regeneration was assessed by switching the gas flow again to He, keeping the temperature at 30 °C and the flow at 40 mL/min (step v).

Besides the kinetic behavior, it was possible to evaluate the adsorption capacity of each tested material. Since after the outgassing there was only pure CO₂ entering the system, the amount of CO₂ captured at equilibrium per mass of adsorbent can be obtained by the Eq. 1.

$$q_{\text{sat}} = \frac{m_c}{m_i} \quad (1)$$

where q_{sat} is the total adsorption capacity of each tested material at the equilibrium (mg CO₂ g adsorbent⁻¹); m_c the amount of CO₂ captured at equilibrium (mg); and m_i the mass of the adsorbent at the time at which the CO₂ flow begins to be fed into the system.

Moreover, the regeneration of the adsorbent (CO₂ desorption) was calculated by the Eq. 2.

$$R (\%) = 1 - \left(\frac{q_r}{q_{\text{sat}}} \right) \quad (2)$$

where R is the percentage regeneration of the adsorbent (%); and q_r represents the amount of CO₂ on the adsorbent at the equilibrium (mg CO₂ g adsorbent⁻¹).

3. Results and discussion

3.1. Characterization of the adsorbents

In Figure 1, the CO₂ adsorption/desorption isotherms for the ZSM5 (commercial reference material) are showed, wherein one may notice that both capture and release of CO₂ show very similar profiles (i.e., there is almost no hysteresis). This profile may be ascribed to type I isotherms, which are common for microporous solids such as zeolite, carbon molecular sieves and some activated carbons. The reversibility may also indicate a small surface, leading to the fact that the limiting uptake of the adsorbate is governed by the accessible micropore volume rather than by the internal surface area [20].

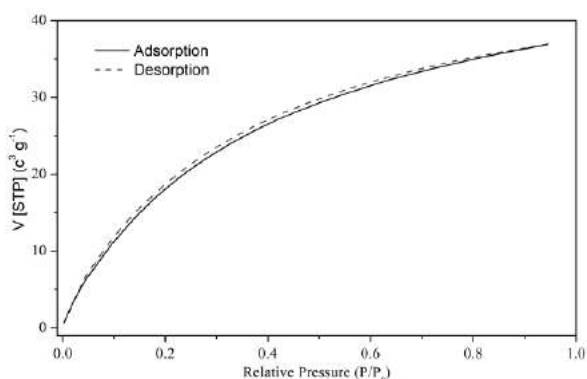


Figure 1. CO₂ physisorption for the zeolite ZSM5, at relative pressure range from 10⁻⁶ to 1 and 0 °C.

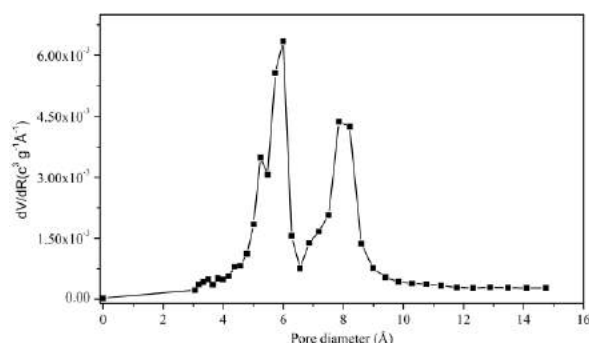


Figure 2. Pore size distribution of zeolite ZSM5.

In fact, the values obtained for surface area and mean pore diameter (see Table 1) along with the pore size distribution presented in Fig. 2 corroborate the hypothesis of microporous material. This characteristics are thus the references for the production of BCs from residual biomass, since they are essential for the selective separation of CO₂

from the CH₄/CO₂ mixture (i.e., biogas upgrading) due to the fact that carbon dioxide presents a smaller kinetic diameter than the methane [21].

The curve profiles presented by BC_{KOH} and BC_{NaOH} were also close to the type I Isotherm [20], as presented in Fig. 3. Similarly, the values of surface area and mean pore diameter indicate that the produced materials show similar textural properties to the commercial one (see Table 1), fitting into the microporous range, which embraces materials that have pore diameters of less than 2 nm [20].

Table 1. Textural properties of the tested adsorbents.

Material	Mean pore diameter (nm)	Surface area (m ² g ⁻¹)
Zeolite ZSM5	0.60	43.21
BC _{KOH}	0.63	90.40
BC _{NaOH}	0.60	67.50

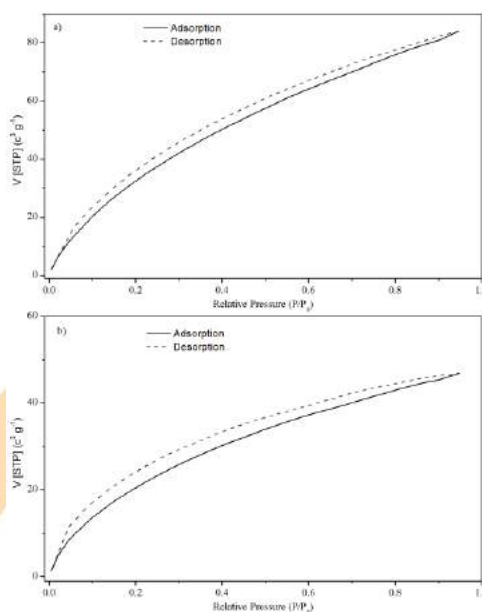


Figure 3. CO₂ adsorption/desorption isotherms for the biochars produced from “açai” stones. Relative pressure range from 10⁻⁶ to 1, at 0 °C. a) BC_{KOH} and b) BC_{NaOH}.

On other hand, although the characteristics are very similar both BCs could adsorb higher amounts of CO₂ in comparison with the zeolite ZSM5 (e.g., CO₂ capture at $p/p_0=0.9$ was 81 cm³ g⁻¹ and 45 cm³ g⁻¹ for V_{BC_{KOH}} and V_{BC_{NaOH}}, respectively (Fig. 3), whereas V_{ZSM5} was 36 cm³ g⁻¹ (Fig. 1)).

Furthermore, it can be said that the BCs are relatively homogeneous, since most pores are concentrated in a small region between 4 and 10 nm (i.e., 0.4 to 1 nm), which is inside the micropore size, as showed in Fig. 4).

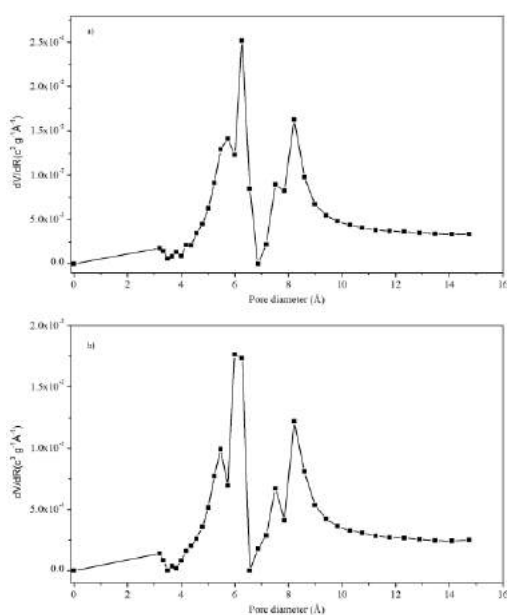


Figure 4. Pore size distribution. a) BC_{KOH} and b) BC_{NaOH}.

3.2. CO₂ capture

Kinetic behavior as well as the CO₂ adsorption capacity of two biochars made from stones of “açai” (BC_{KOH} and BC_{NaOH}) were tested at 30 °C and atmospheric pressure and then compared with a widely used commercial adsorbent (Zeolite ZSM5).

In Fig. 5, the behavior of the mass loss/gain of the Zeolite ZSM5, which was the commercial adsorbent taken as reference, is presented, wherein all steps of the methodology described in section 2.3 can be observed (temperature variation, gas switching, and mass variation).

It can be noticed that in step (i), in which the sample was heated to 120 °C under constant He flow, there is an important mass loss that is probably related to the the dehydration of the zeolite’s surface. Thereafter, the mass remains constant up to step iii, when the feed gas is switched to CO₂, wherein one may notice that even before the

temperature approaches 30 °C, there is an expressive mass increase, caused by the adsorption of CO₂. Since high temperatures favor the adsorption kinetic behavior, the curve is more inclined at the beginning of step iii. On other hand, as the temperature approaches 30 °C, the equilibrium is favored, which is why a slight variation on the CO₂-capture curve profile can be observed for all tested samples.

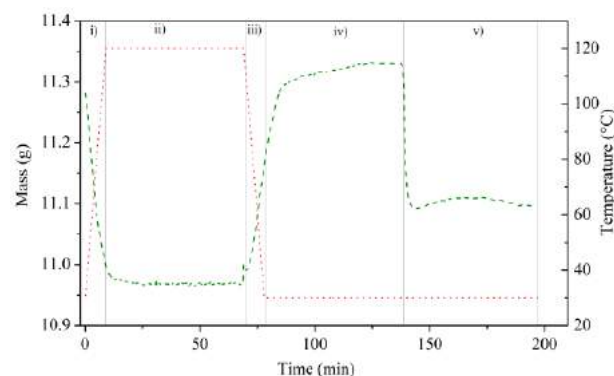


Fig. 5. Methodology used in the thermogravimetric analyzer with the reference adsorbent (zeolite ZSM5); — — — Mass variation; ····· Temperature variation; i) and ii) outgassing with gas helium; iii) and iv) gas switching to CO₂ and measurement of the CO₂-capture; v) CO₂ desorption by switching the gas flow to He.

Since this procedure was repeated for all samples, the further results will be presented only from step iii to step v (i.e., CO₂-adsorption and adsorbents’ regeneration). By analyzing the Fig. 6a, one may notice that the total adsorption capacity was reached after 20 and 30 min, which indicates a favorable kinetic behavior. Furthermore, it could be noted that all samples presented a high adsorption capacities (see Table 2).

On other hand, the activation process may have influenced the adsorption capacity, since the textural properties of the materials were very similar (see section 3.1), and thus they would not explain the expressive difference in the capacities of capturing CO₂. The capture of CO₂ may be generally favored on materials with basic surface, in contrast with the acidic characteristic of this gas molecule [22].

Therefore, we suggest that the CO₂ was not only kinetic (i.e., related to the pore characteristics of the materials) but also might be influenced by affinity between adsorbent’s surface and the gas molecule, since the only difference on the synthesis of the materials was the activating agent, although both were hydroxides, namely KOH (BC_{KOH}) and NaOH

(BC_{NaOH}). As reported elsewhere [23], Scanning Electron Micrographs showed that the activation with KOH may have produced more pores on the surface of the material than the one performed with NaOH. Moreover, the adsorption of compounds from liquid phase was also higher for the adsorbents activated with KOH.

The regeneration of the adsorbents is presented in Fig. 6b, wherein one may notice that not all CO₂ captured was released. Future studies will allow the understanding of more adsorption cycles, in order to evaluate if potential of CO₂ is reduced or stays constant, considering the purpose of applying the adsorbents in PSA system (adsorption cycles by pressure variation).

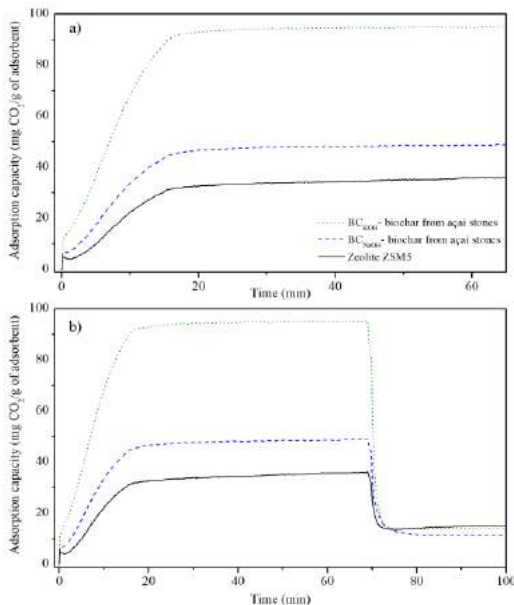


Fig. 6. CO₂ capture by commercial zeolite and by biochars produces from residual biomass. a) CO₂ uptake; b) adsorption cycle (adsorption/regeneration).

Table 2. Adsorption capacity and regeneration of each tested adsorbent.

Adsorbent	CO ₂ adsorption capacity (mg g ⁻¹)	Regeneration (%)
Zeolite ZSM5	36	77.3
BC _{KOH}	95	89.0
BC _{NaOH}	49	90.8

In summary, the potential of residual biomasses such as “açai” stones for the capture of carbon

dioxide was evidenced in the present study. Further studies will evaluate the selectiveness of the produced biochars in CH₄/CO₂ mixtures for future application in PSA system.

Acknowledgements

The authors thank the National Council for Scientific and Technological Development (CNPq) and BRF S.A. for the financial support.

References

- [1] G.A. Florides, P. Christodoulides, Global warming and carbon dioxide through sciences, *Environment International*. 35 (2009) 390–401. doi:10.1016/j.envint.2008.07.007.
- [2] J. Xuan, M.K.H. Leung, D.Y.C. Leung, M. Ni, A review of biomass-derived fuel processors for fuel cell systems, *Renewable and Sustainable Energy Reviews*. 13 (2009) 1301–1313. doi:10.1016/j.rser.2008.09.027.
- [3] M. Poeschl, S. Ward, P. Owende, Environmental impacts of biogas deployment - Part II: Life Cycle Assessment of multiple production and utilization pathways, *Journal of Cleaner Production*. 24 (2012) 184–201. doi:10.1016/j.jclepro.2011.10.030.
- [4] IPCC, *Climate Change 2013: The Physical Science Basis. Contribution of Working Group I to the Fifth Assessment Report of the Intergovernmental Panel on Climate Change*, Intergovernmental Panel on Climate Change, Working Group I Contribution to the IPCC Fifth Assessment Report (AR5)(Cambridge Univ Press, New York). (2013) 1535. doi:10.1029/2000JD000115.
- [5] P.A. Webley, A. Qader, A. Ntiamoah, J. Ling, P. Xiao, Y. Zhai, A New Multi-bed Vacuum Swing Adsorption Cycle for CO₂ Capture from Flue Gas Streams, *Energy Procedia*. 114 (2017) 2467–2480. doi:10.1016/j.egypro.2017.03.1398.
- [6] J. Krischan, A. Makaruk, M. Harasek, Design and scale-up of an oxidative scrubbing process for the selective removal of hydrogen sulfide from biogas, *Journal of Hazardous Materials*. 215–216 (2012) 49–56. doi:10.1016/j.jhazmat.2012.02.028.
- [7] M. Pöschl, S. Ward, P. Owende, Evaluation of energy efficiency of various biogas production and utilization pathways, *Applied Energy*. 87 (2010) 3305–3321. doi:10.1016/j.apenergy.2010.05.011.
- [8] D. Andriani, A. Wresta, T.D. Atmaja, A.



- Saepudin, A Review on Optimization Production and Upgrading Biogas Through CO₂ Removal Using Various Techniques, *Applied Biochemistry and Biotechnology*. 172 (2014) 1909–1928. doi:10.1007/s12010-013-0652-x.
- [9] M.A.E. de Franco, C.B. de Carvalho, M.M. Bonetto, R. de P. Soares, L.A. Féris, Removal of amoxicillin from water by adsorption onto activated carbon in batch process and fixed bed column: Kinetics, isotherms, experimental design and breakthrough curves modelling, *Journal of Cleaner Production*. (2017). doi:10.1016/j.jclepro.2017.05.197.
- [10] C.A. Grande, R. Blom, Dual Pressure Swing Adsorption Units for Gas Separation and Purification, *Industrial & Engineering Chemistry Research*. 51 (2012) 8695–8699. doi:10.1021/ie300341v.
- [11] S. Singhal, S. Agarwal, S. Arora, P. Sharma, N. Singhal, Upgrading techniques for transformation of biogas to bio-CNG: a review, *International Journal of Energy Research*. 41 (2017) 1657–1669. doi:10.1002/er.3719.
- [12] C.A. Grande, R. Blom, Utilization of Dual-PSA Technology for Natural Gas Upgrading and Integrated CO₂ Capture, *Energy Procedia*. 26 (2012) 2–14. doi:10.1016/j.egypro.2012.06.004.
- [13] C.A. Grande, R. Blom, K.A. Andreassen, R.E. Stensrød, Experimental Results of Pressure Swing Adsorption (PSA) for Pre-combustion CO₂ Capture with Metal Organic Frameworks, *Energy Procedia*. 114 (2017) 2265–2270. doi:10.1016/j.egypro.2017.03.1364.
- [14] T.S. Frantz, W.A. Ruiz, C. Augusto, V.B. Mortola, Microporous and Mesoporous Materials Synthesis of ZSM-5 with high sodium content for CO₂ adsorption, *Microporous and Mesoporous Materials*. 222 (2016) 209–217. doi:10.1016/j.micromeso.2015.10.022.
- [15] Q. Zhao, F. Wu, Y. Men, X. Fang, J. Zhao, P. Xiao, P.A. Webley, C.A. Grande, CO₂ capture using a novel hybrid monolith (H-ZSM5 / activated carbon) as adsorbent by combined vacuum and electric swing adsorption (VESA), *Chemical Engineering Journal*. 358 (2019) 707–717. doi:10.1016/j.cej.2018.09.196.
- [16] H.G.T.N.L. Espinal, R.D.V.Z.M. Thommes, B.T.M.S.L.H.E. Mangano, A reference high-pressure - CO₂ adsorption isotherm for ammonium ZSM-5 zeolite: results of an interlaboratory study, *Adsorption*. 24 (2018) 531–539. doi:10.1007/s10450-018-9958-x.
- [17] Y. Wang, T. Du, Z. Qiu, Y. Song, S. Che, X. Fang, CO₂ adsorption on polyethylenimine-modified ZSM-5 zeolite synthesized from rice husk ash, *Materials Chemistry and Physics*. 207 (2018) 105–113. doi:10.1016/j.matchemphys.2017.12.040.
- [18] L. Ohlin, P. Bazin, J. Hedlund, M. Grahn, Adsorption of CO₂, CH₄, and H₂O in Zeolite ZSM-5 Studied Using In Situ ATR-FTIR Spectroscopy, (2013). doi:10.1021/jp4037183.
- [19] M.L. Botomé, P. Poletto, J. Junges, D. Perondi, A. Dettmer, M. Godinho, Preparation and characterization of a metal-rich activated carbon from CCA-treated wood for CO₂ capture, *Journal of Cleaner Production*. (2017) 614–621. doi:10.1016/j.jclepro.2017.04.004.
- [20] M. Thommes, K. Kaneko, A. V. Neimark, J.P. Olivier, F. Rodriguez-Reinoso, J. Rouquerol, K.S.W. Sing, Physisorption of gases, with special reference to the evaluation of surface area and pore size distribution (IUPAC Technical Report), *Pure and Applied Chemistry*. (2015). doi:10.1515/pac-2014-1117.
- [21] C.A. CANEVESI, R. L.S., ANDREASSEN, DA SILVA E. A., E. A., BORBA, C. E., GRANDE, Pressure swing adsorption for biogas upgrading with carbon molecular sieve, *Industrial & Engineering Chemistry Research*. (2018). doi:10.1021/acs.iecr.8b00996.
- [22] R.L.S. Canevesi, K.A. Andreassen, E.A. Da Silva, C.E. Borba, C.A. Grande, Pressure Swing Adsorption for Biogas Upgrading with Carbon Molecular Sieve, *Industrial and Engineering Chemistry Research*. 57 (2018). doi:10.1021/acs.iecr.8b00996.
- [23] J.P.V.D.E. Berni, J. V., Cesaro, F.B. Rossato, I. G., Módenes, A. N., Scheufele, ESTUDO DE DIFERENTES AGENTES ATIVANTES NA PRODUÇÃO DE CARVÕES ATIVADOS DE CAROÇO DE AÇAÍ PARA REMOÇÃO DE AMOXICILINA DE SOLUÇÕES AQUOSAS, (2019). <https://proceedings.science/p/114608>.

Evaluation of the fruit *Terminalia catappa* Linn as adsorbent of dyes present in aqueous effluents

Lizeth Vanessa Amado Jurado, Gabriela Machado Chemp, Marisa Fernandes Mendes

Department of Chemical Engineering, University Federal Rural of Rio de Janeiro, Rod BR 465 Km 7, Seropédica, CEP 23897-000, Brazil

Abstract

Health and environmental problems associated with the presence of toxic dye compounds in water from textil industries have motivated a lot of researches to develop effective and economically viable technologies to remove these pollutants. Adsorption has been an attractive technique for dye removal due to its advantages such as reuse of biomaterials, low operating cost, among others. The application of alternative adsorbents of residues from biomasses has been increasingly studied. *Terminalia catappa* Linn (TCL), for example, generates organic wastes such as fruits, which fall to the ground, and tend to cause manhole clogging in the cities of Rio de Janeiro. Therefore, this work evaluated the efficiency of the almond fruit endocarp in the adsorption process of an organic methyl orange (MO) dye. Adsorption studies were performed by analyzing equilibrium and kinetics. The experiments were performed in triplicate, fixing the adsorbent mass (0.10 g), temperature (298 K), stirring speed (180 rpm), particle size (80 to 150 mesh), and varying the dye concentration of 200 ppm and 400 ppm. The maximum removal potential was 99% and the pseudo-second order model was the one that best described the adsorption process.

Keywords: biomass; adsorption; methyl orange; kinetic models.

1. Introduction

Water pollution has been a persistent problem due to the variety of industries that causes the uncontrolled growth of the presence of different toxic substances in water, altering the properties and making it inappropriate for consumption [1].

Among the different toxic substances, dyes are the most harmful substances due to their high toxicity, and low degradability along the years. They are abundant in wastewater, generated by textile, paint, food, plastic, cosmetic, graphic, photographic plants, as additives in petroleum derivatives, among others [2,3].

Conventional treatments, physicochemical and biological, that present high costs as electrochemistry, precipitation, filtration, ozonation, are not efficient in the treatment and, consequently, in the removal of dyes. This occurred because the dyes have, in their chemical structure, aromatic rings, amine groups, sulfonic groups and metal ions which, as a result, are difficult to degrade [4].

One of the most efficient methods to remove the dyes is the physical-chemical adsorption method. The main advantages are the possibility to reuse biomaterials [5], low operating cost, improved

selectivity for specific materials of interest, removal of heavy effluent compounds regardless of toxicity, and the absence of byproducts that could be toxic [6].

In this way, this work has the motivation to use the seeds from *Terminalia catappa* Linn, commonly known as “Indian almond”. It comprises of kernel (10.32%), fibrous covering (8.97%), husk (34.08%), and hard endocarp (46.63%) [7]. Apart from the natural biological cycle, significant amount of fruit has been discarded as a waste agricultural biomass. In the present study, the endocarp was chosen as the raw material for the preparation of an activated carbon, that will be applied for the removal of dyes from aqueous solutions, evaluating the process kinetics and thermodynamic behavior.

2. Materials and methods

2.1. Preparation and synthesis of the adsorbent

Indian almond (TCL) fruit samples were collected from Universidade Rural do Rio de Janeiro, Seropédica, Brazil. The fruit was peeled for endocarp separation, washed with distilled water and dried in an oven at 373.15 K for 24 h. The dried almond endocarp biomass was grounded, and the

sample of diameter between 80 and 150 mesh sieves were used.

Chemical activation of the biomass was performed using $m_{\text{endocarp}}/m_{\text{H}_3\text{PO}_4}$ ratio of 1:1, followed by the addition of distilled water (250 mL). The biomass/ H_3PO_4 mixture was allowed to heat stand within 4 hours under light agitation; after that washed and dried at 100 °C, over 36 h. After this time, in a muffle furnace, the material was heated at the rate of 10 °C.min⁻¹ from room temperature to 350 °C, and remained at this temperature for 2 h. The material was then washed with distilled water until pH characteristic of water.

2.2. Batch adsorption procedure

The potential of activated carbon to adsorb MO dye was evaluated by adsorption tests, which were carried out in a batch mode. Erlenmeyer flasks were used adding 25 mL of dye solutions and 0.1 g of adsorbent. The solution was stirred at 180 rpm until the equilibrium time. The kinetic curves were constructed with dye solutions with initial concentrations of 200 and 400 mg.L⁻¹. All experiments were performed at natural pH of solutions and 298 K.

The measurements of MO concentration in liquid phase were carried out in a spectrophotometer at 645 nm (UV-M51 - BEL). The adsorption of MO on activated carbon was evaluated in terms of dye removal percentage, calculated by Eq. (1) (%R), equilibrium adsorption capacity (q_e , mg g⁻¹) and adsorption capacity at time (q_t , mg g⁻¹). These values were obtained by global mass balance, calculated by Eq. (2):

$$\%R = (C_0 - C_t) \left(\frac{100}{C_0} \right) \quad (1)$$

$$q_e = q_t = \frac{(C_0 - C_{e,t})V}{W} \quad (2)$$

with C_0 as the initial concentration of MO, C_e as MO concentration at equilibrium, C_t as MO concentration at t time, V (L) as the volume of the solution, and W (g) as the weight of adsorbent used.

2.3. Kinetic and equilibrium evaluation

The behavior of the adsorption process dynamics of MO-endocarp system was evaluated according to the kinetic, and equilibrium aspects. For this purpose, some conventional models present in the

literature were employed, as presented in Table 1. The best theoretical models that described the experimental data were chosen from correlation coefficients (R^2) and the normalized standard deviation Δq (%) calculated by Eq. (3):

$$\Delta q(\%) = 100 \sqrt{\frac{\sum [|q_{\text{exp}} - q_{\text{cal}}| / q_{\text{exp}}]^2}{N - 1}} \quad (3)$$

with N as the number of data points, q_{exp} and q_{cal} (mg.g⁻¹) as the experimental and calculated adsorption capacity value, respectively.

Table 1. Kinetic equations that represent the adsorption process.

kinetic Models	Equations
Pseudo-first order [8]	$q_t = q_1(1 - e^{(-k_1 t)})$
Pseudo-second order [9]	$q_t = \frac{1}{\left(\frac{1}{k_2 q_2^2}\right) + \left(\frac{t}{q_2}\right)}$
Intraparticle diffusion [10]	$q_t = k_{id} t^{1/2} + C_i$

* q_1, q_2 = theoretical adsorption capacities. k_1, k_2, k_{id} = as rate constants. A = speed of initial chemisorption; B = number of suitable sites for adsorption; C_i = suggests the thickness of the boundary layer effect.

3. Results and discussion

Adsorption kinetics studies were performed in order to evaluate the equilibrium time for the process (Fig. 1). The adsorption using a 200 ppm solution was faster probably dye to the fact that the active sites were regularly occupied. As it is shown, the time necessary to reach equilibrium was approximately 60 and 90 min for 200 and 400 ppm, respectively. The higher removal percentage was 99% for 200 ppm, and the minimum was 92% for 400 ppm.

The kinetic mechanism that controls the adsorption process, was evaluated using the pseudo-first-order, pseudo-second order and intraparticle diffusion models. A good correlation of the kinetic data can explain the adsorption mechanism of the dye at the solid/liquid interface [11]. The estimated

parameters through linear and non-linear regressions are listed in Table 2.

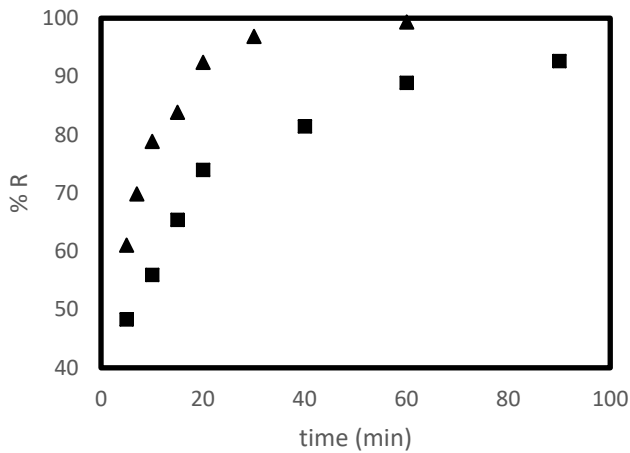


Fig. 1. Kinetic for endocarp adsorption at 200 ppm (▲) and 400 ppm (■).

Table 2. Parameters of pseudo-first order, pseudo-second order and intraparticle diffusion mathematical models for the endocarp.

Models		Parameters			
Pseudo-first order	ppm	q_e (mg.g ⁻¹)	k_1 (min ⁻¹)	r^2	
	200	50.921	0.169	0.954	
	400	95.156	0.094	0.900	
Pseudo-second order		q_e (mg.g ⁻¹)	k_2 (g.(mg.min) ⁻¹)	r^2	
	200	54.644	5.36E ⁻⁰³	0.999	
	400	102.040	1.37E ⁻⁰³	0.998	
Intraparticle diffusion		C (mg.g ⁻¹)	k_{di} (g.(mg.min) ^{0.5}) ⁻¹	r^2	
	200	14.491	6.268	0.756	
	400	22.241	9.139	0.841	

It should be noted that the r^2 values obtained from the pseudo-order model and pseudo second order were the highest. On the other hand, the intraparticle diffusion model demonstrated a poor fit, with low values of r^2 and besides the non-zero parameter C. Therefore, the intraparticle diffusion mechanism could indicate that was not the velocity-determining step in the mass transfer process, and other mechanisms must act simultaneously in the control of the adsorption process.

The normalized standard deviation Δq (%) was calculated for the models that obtained the highest

correlation coefficients, and the values obtained are presented in Table 3. The behavior of the models can be seen in Figure 2, showing that the pseudo-second order model was the best one.

Table 3. Normalized standard deviation Δq (%) of pseudo-first order and pseudo-second order models for the endocarp.

Models			Δq (%)
Pseudo-first order	200 ppm		5.17
	400 ppm		12.88
Pseudo-second order	200 ppm		1.92
	400 ppm		6.74

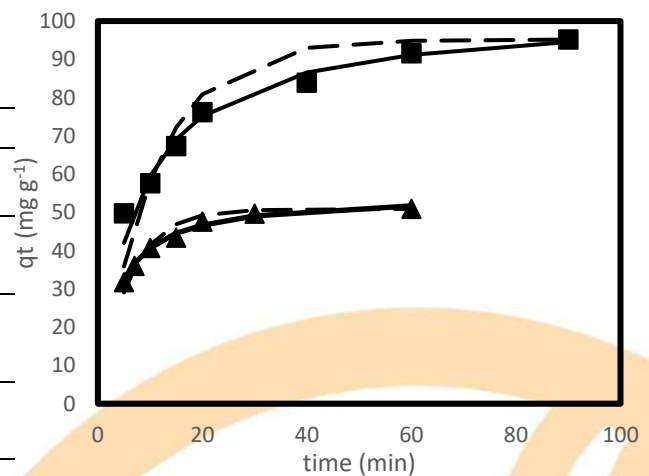


Fig. 2. Kinetic for endocarp adsorption at 200 ppm (▲), 400 ppm (■) and fit the pseudo-first order (---) and pseudo-second order (—) models.

The pseudo-first-order kinetic model is based on the assumption that the rate of adsorption is proportional to the number of adsorption active sites of the adsorbent [12]. The calculated q_t values were not in agreement with the experimental q_t values for the adsorbent at each concentration. This behavior indicated that the adsorption kinetics data cannot be well predicted by this model.

The best fit was pseudo-second order model, which presented good regression coefficients. It can be concluded that the limiting step in the adsorption process is caused by a chemical interaction [13]. Similar results could be observed by Wu *et al.* (2019) when they studied the adsorption of methyl

orange onto microspheres, and by Hasan *et al.* (2019) when studied the adsorption of methyl orange onto polyaniline/activated carbon composite.

4. Conclusion

The byproducts originated from the fruit of *Terminalia catappa* Lin tree, demonstrated to be effective adsorbent for dye removal from aqueous solutions. The dye removal potential was 99% for the 200 ppm solution in 60 min, and 92% for 400 ppm in 90 min. Adsorption kinetics followed the pseudo second-order equation, indicating that the rate-limiting step was the chemisorption. Finally, this biomass seemed to have a huge potential as adsorbent, due to the abundance of biomass, and its low cost.

Acknowledgements

The authors would like to thank FAPERJ and CNPq / PIBIC for their financial support. This work was carried out with the support of the Higher Education Personnel Improvement Coordination - Brazil (CAPES) - Financing Code 001”.

References

- [1] Alves MF, Brito MJP, Borges MV, Batista AS, De Jesus FWA, De Albuquerque FSA. Produção de carvão ativado obtido a partir do endocarpo da Amêndoa-da-Praia (*Terminalia catappa* Linn) para adsorção de corantes orgânicos em meio aquoso. Caderno de Ciências Agrárias 2015; 7:50-55.
- [2] Guaratini CCI, Zanoni MVB. Corantes têxteis. Química nova 2000; 23:71-78.
- [3] Kunz A, Peralta-zamora P, Moraes SGD, Durán N. Novas tendências no tratamento de efluentes têxteis. Química nova 2002; 25:78-82.
- [4] Rutz EG, Carvalho CF, Pires CS, Curiel GL. Adsorção do corante têxtil amarelo remazol usando um dos rejeitos da fabricação da alumina como adsorvente. Revista Escola de Minas 2008; 61:443-448.
- [5] Chen S, Yue Q, Gao B, Li Q, Xu X, Fu K. Adsorption of hexavalent chromium from aqueous solution by modified corn stalk: a fixed-bed column study. Bioresource Technology 2012; 113:114-120.
- [6] Ramakul P, Yachanawakul Y, Leepipatpiboon N, Sunsandee N. Biosorption of palladium (II) and platinum (IV) from aqueous solution using tannin from Indian almond (*Terminalia catappa* L.) leaf biomass: Kinetic and equilibrium studies. Chemical Engineering Journal 2012; 193:102-111.
- [7] Inbaraj BS, Sulochana N. Mercury adsorption on a carbon sorbent derived from fruit shell of *Terminalia catappa*. Journal of Hazardous Materials 2006; 133: 283-290.
- [8] Ho YS, McKay G. Sorption of copper (II) from aqueous solution by peat. Water Air and Soil Pollution 2004; 158:77-97.
- [9] Ho YS, McKay G. Pseudo-second-order model for sorption process. Process Biochemistry 1999; 34:451-465.
- [10] Ho YS, McKay G. Sorption of copper (II) from aqueous solution by peat. Water Air and Soil Pollution 2004; 158:77-97.
- [11] Wu FC, Tseng RL, Juang RS. Kinetic modeling of liquid-phase adsorption of reactive dyes and metal ions on chitosan. Water Res 2001; 35:613- 618.
- [12] Shooto ND, Naidoo EB, Maubane, M. Sorption studies of toxic cations on ginger root adsorbent. Journal of Industrial and Engineering Chemistry 2019; 76:133-140.
- [13] Martini BK, Daniel TG, Corazza MZ. Methyl orange and tartrazine yellow adsorption on activated carbon prepared from boiler residue: Kinetics, isotherms, thermodynamics studies and material characterization. Journal of Environmental Chemical Engineering 2018; 6:6660-6679.
- [14] Wu Y, Su M, Chen J, Xu Z, Tang J, Chang X, Chen D. Superior adsorption of methyl orange by h-MoS₂ microspheres: Isotherm, kinetics, and thermodynamic studies. Dyes and Pigments 2019; 170:107-591.
- [15] Hassan M, Rashid MM, Hossain MM, Al Mesfer MK, Arshad M, Danish M, Lee M, Jerry AE, Kumar N. Fabrication of polyaniline/activated carbon composite and its testing for methyl orange removal: Optimization, equilibrium, isotherm and kinetic study. Polymer Testing 2019; 77:105-909.

STUDY OF ADDITION OF ZEOLITES A, X AND Y IN POLYASPARTIC COATING TO REMOVE MOISTURE

Machado, M. P. M.^{a,b}, Gomes, E. L.^b, Bresolin, I. T. L.^b

^a Covestro, Rua Domingos Jorge, 1100, São Paulo, 05713-510, Brazil

^b Universidade Federal de São Paulo, Rua Artur Riedel, 275, Diadema, 09972-270, Brazil

Abstract

In this study the commercial LTA zeolite was modified by ion exchange, producing the zeolites K-LTA (3A), Na-LTA (4A) and Ca-LTA (5A). It was synthesized a NaY zeolite using consolidated methods. These zeolites plus a NaX provided by IPT-SP were characterized by traditional methods in order to determinate their chemical composition, crystalline structure and morphology. Finally, the selected zeolites were used as adsorbents in formulations of polyaspartic paints to evaluate the efficiency in the removal of water molecules. The aluminum content (hydrophilicity), channel structure and micropores openings has shown that a balance between these two parameters play an important role in water adsorption by the zeolites. The best adsorbent was NaX zeolite and the less efficient was zeolite 3A.

Keywords: Corrosion Protect Coating; Polyaspartic; Molecular Sieves; Zeolites.

1. Introduction

One of the resins that emerged as a sustainable alternative to conventional solvent-based paints is polyaspartic resin, developed and marketed by Covestro. Polyaspartic chemistry is based on the reaction of an aliphatic polyisocyanate with an aspartic ester, resulting in an aliphatic polyurea. However, polyaspartics differ greatly in the application properties and performance of conventional polyureas. The main characteristics of polyaspartic resin are: high reactivity, which results in short drying times, enabling high productivity in the workplace, excellent weather resistance, it is possible to apply a thicker layer, it has low content of volatile organic components (VOC) and can be used in conventional equipment because it has low viscosity, despite the non-volatile content [1].

1.1. Moisture and the coating polyaspartic

In addition to the reaction with the aspartic ester, polyisocyanates are also reactive with water, resulting in the formation of polyurea and carbon dioxide. The water in the system comes from the other raw materials involved in the paint preparation, such as solvents and pigments. According to Zwiener et al. [2], the reactions involved are as follows:



Besides interfering with reaction kinetics, another problem that may occur in the coating is related to the formation of CO₂. The gas generated results in the formation of “microbubbles”, which give the film low or no paint layers applied. These points interfere significantly in properties such as corrosion resistance and paint visual appearance and must be avoided [3].

1.2. Moisture Removal

The traditional alternative to reduce this residual moisture is by adding 3A zeolites, which trap the water molecules present in the system, making it impossible to react with polyisocyanate. These molecular sieves showed excellent performance, resulting in a significant improvement in pot life (time to apply the paint, which is related to reaction kinetics), which makes the application easier, increasing yield and improving the physical properties of the applied coating such as corrosion resistance and hardness [4].

There is no papers in the literature that compares the performance of exchanged LTA with Na⁺, K⁺ an Ca²⁺ or other zeolites, such as X and Y.

2. OBJECTIVES

The objective of this study was to compare the performance of the zeolites 3A (or K-LTA), 4A (or Na-LTA) and 5A (or Ca-LTA), zeolites NaX and NaY as moisture adsorbents in the process of polyaspartic preparation. For the zeolites X and Y (FAU) it was verified the effect of the structural aluminum content in the adsorption process (same structure, steric effect of the sodium content) and for the LTA zeolites, the effect of the variation in the opening of the micropores by changing of the compensating cation.

3. MATERIALS AND METHODS

The experimental studies were performed at the Laboratório de Catálise e Química Verde (UNIFESP, Diadema, SP) and at the Covestro Laboratories (São Paulo, SP).

3.1. Zeolites

A commercial LTA zeolite starting material was provide by UOP® (Universal Oil Products) containing K⁺ and Na⁺ cations compensating the structural charges in the molecular sieve. A NaX zeolite was provided by IPT-SP (Instituto de Pesquisas Tecnológicas do Estado de São Paulo - Brazil) and was synthesized by the method described in the Verified Synthesis of Zeolites [11]. The NaY zeolite was synthesized using the method developed by Padilha [6].

3.2. Preparation of the K-LTA (3A), Na-LTA (4A) and Ca-LTA (5A) zeolites from the commercial LTA

An ion exchange procedure was used to obtain LTA zeolites with only one type of compensating cation (Na⁺, K⁺ or Ca²⁺). The experimental procedure was adapted from the method of Watanabe et al. [5], using sodium, potassium or calcium chloride in a 0.5 mol.L⁻¹ exchanging solution. A 2 L glass flask of the desired cation chloride solution was prepared. After that, 5.0 g of commercial zeolite LTA were added to the solution and the mixture stirred during 24 h at room temperature. Then, the solids were separated from the solution by filtration in a Büchner funnel and washed with 2 L distilled water. Finally, the solids were dried for 24 h at 120 °C [5], thus obtaining the exchanged zeolite (Na-, K- or Ca-LTA).

3.3. Synthesis of Zeolite NaY

This molecular sieve was prepared with molar composition of Na₂O:Al₂O₃:9,5 SiO₂:136 H₂O. The reagents used were: sodium aluminate (NaAlO₂, Sigma-

Aldrich, > 99% m/m), sodium hydroxide, and Ludox® HS-30 (colloidal silica, solution 30% w/w). After mixing the reagents, producing a reactional mixture of a white colour, it was aged for 24 h at room temperature. After that, the system was crystallized at 100 °C at atmospheric pressure for 16 h. The formed solids were filtered, washed with distilled water and dried at 120 °C for 24 h.

3.4. Characterization Techniques

X-Ray diffraction. The diffractograms were obtained using a diffractometer Bruker, D8 Advanced model, employing CuK α radiation and nickel filter, operating at 40 kV and 40 mA with goniometer speed of 2°/min. The samples were scanned in the range of 2 θ from 5 to 45°.

Scanning electron microscopy (SEM) and Energy Dispersive X-Ray Spectroscopy (EDS). The analyses were performed in SEM FEI - Company SEM, Quanta 3D FEG model, operating at 30 kV. For the EDS analysis the equipment used was an EDAX AMETEK coupled to the SEM FEI.

3.5. Evaluation of Polyaspartic Reaction Kinetics (Pot Life)

To evaluate the performance of addition of molecular sieves in polyaspartic coating formulations, zeolites are first incorporated into the aspartic ester (1 % m zeolite/m ester) and, after that, the reaction with polyisocyanate was carried out. The formulations were subjected to Karl Fischer tests to assess the remaining water, pot life test to evaluate reaction kinetics and corrosion resistance testing [4].

The experiments were performed in accordance with ABNT NBR 15742 for the evaluation of the pot-life of paints and varnishes consisting of two or more components. The shelf life of the mixture is the period of time when the flow properties (such as viscosity) of the paint will not change within an acceptable range for its application [8, 9]. The method is based on measuring the viscosity immediately after mixing the two components of the paint and evaluate the increase of this property over a period until the viscosity found reaches twice the initial value. In this study, the viscosity monitoring for the determination of the shelf life of the mixture was performed with the Ford Cup 4.

4. RESULTS AND DISCUSSION

4.1. X-ray Diffraction

This technique was used to check the formation of the desired zeolite structure and if there was other parallel solid phases. Figure 1 presents the diffractogram obtained for the zeolite NaX provided. Comparing to the

known diffractogram pattern [12], it can be observed that the sample provided refers to a well-formed NaX zeolite with good crystallinity and defined planes.

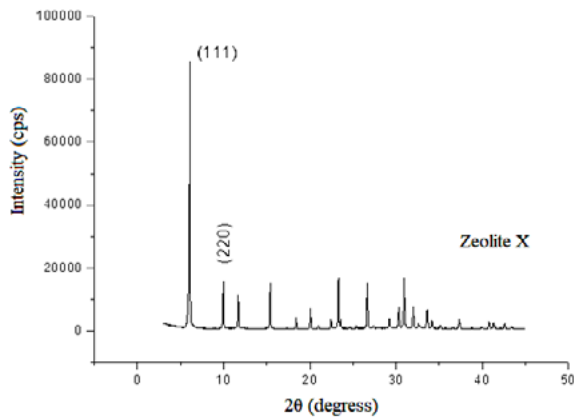


Figure 1. Diffractogram of zeolite NaX with the main crystallographic planes.

Similarly, the XRD analysis for the synthesized zeolite NaY was performed to check the structure (Figure 2). Comparing the obtained diffractogram to the known pattern [12], it is verified that the zeolite was well formed, with good crystallinity, defined plans and no formation of parallel solid phases.

Finally, the XRD analysis for the commercial zeolite A was performed (Figure 3) and comparing the diffractogram obtained with the reference [12], it is showed that the zeolite is well formed, with good crystallinity and defined planes. Only the diffractogram of the commercial zeolite LTA was presented, since the diffractograms of the K-, Na- and Ca-LTA zeolites are similar, since the ion exchange process does not affect the stable structure of the zeolite LTA, but only its chemical composition.

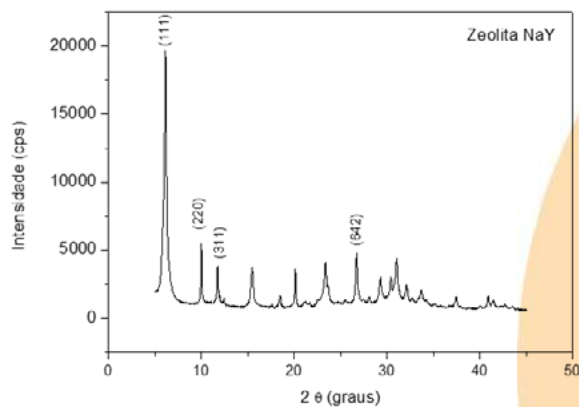


Figure 2. Diffractogram of synthesized zeolite NaY with the main crystallographic planes.

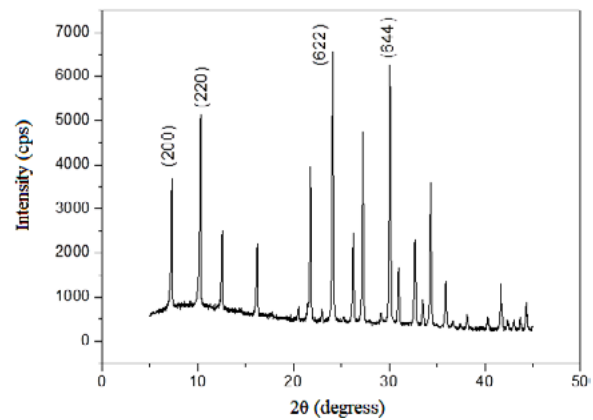


Figure 3. Diffractogram of commercial zeolite A, with the main crystallographic planes.

4.2. Scanning electron microscopy (SEM)

SEM results are presented in the Figure 4 (a to f) of the zeolites used in this work. Figure 4a shows the micrograph of NaX zeolite. It is observed that the particles are globular, formed by smaller granules that agglomerate forming the larger ones, which was also observed in the literature [6], since in the crystallization of this material, individual crystallites are rarely observed due to the composition of the reaction medium. The high aluminum content induces a large amount of nuclei during crystallization, preventing the growth of large single crystallites. Here the agglomerates have dimensions between 0.5 and 2.2 μm .

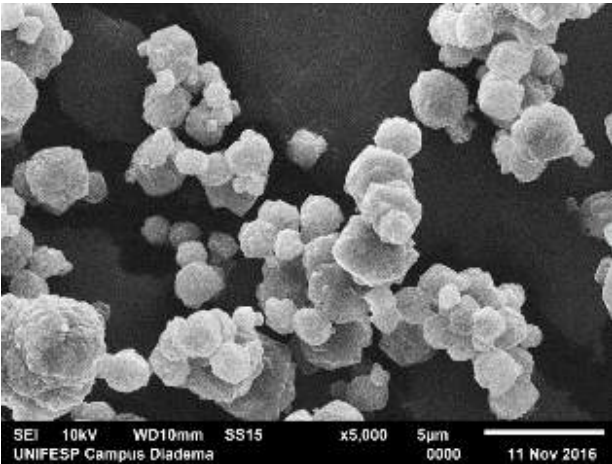


Figure 4a. Micrograph of NaX zeolite (5,000 X).

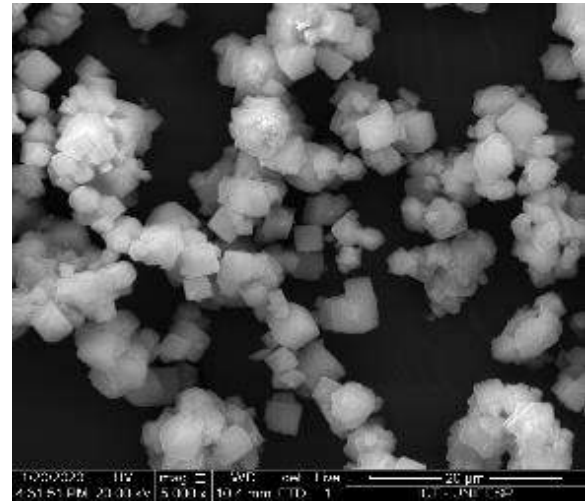


Figure 4d. Micrograph of K-LTA (or 3A) zeolite (5,000 X).

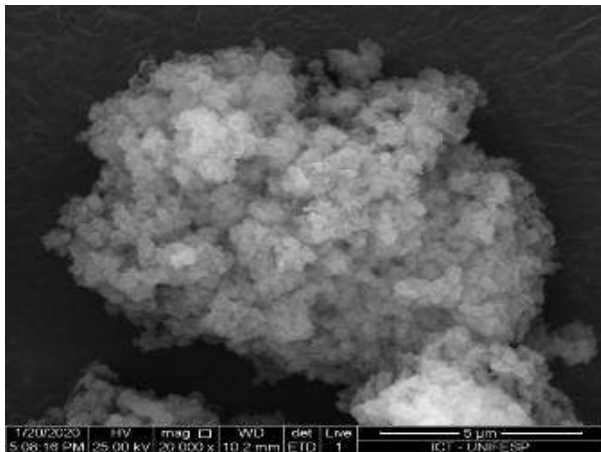


Figure 4b. Micrograph of NaY Zeolite (20,000 X).

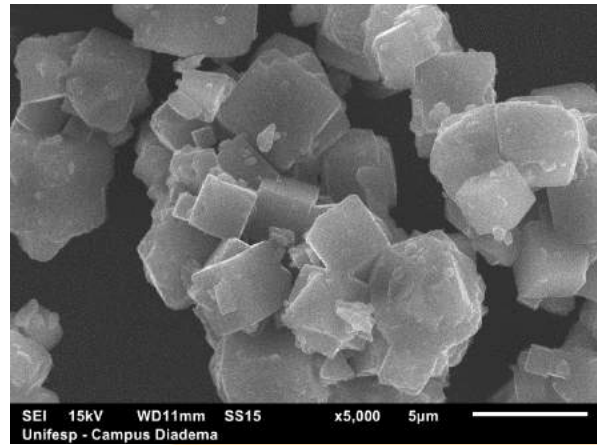


Figure 4e. Micrograph of Na-LTA (or 4A) zeolite (10,000 X).

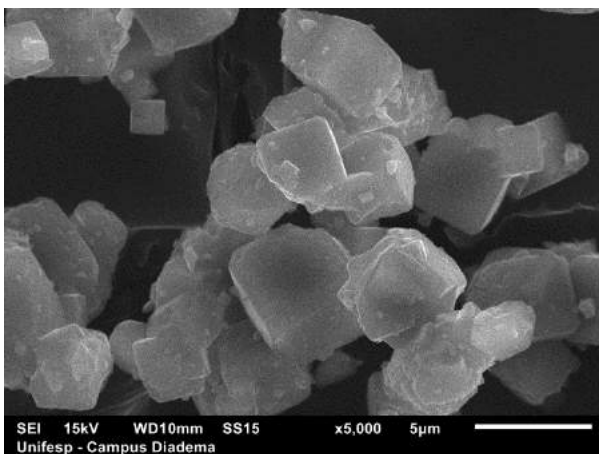


Figure 4c. Micrograph of commercial A zeolite. (20,000 X).

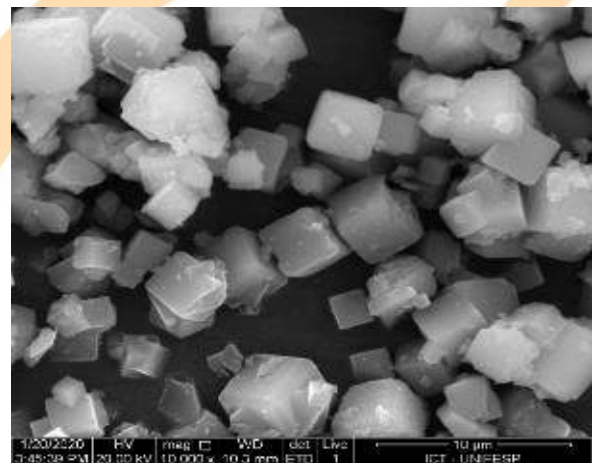


Figure 4f. Micrograph of Ca-LTA (or 5A) zeolite (5,000 X).

Figure 4b shows the micrograph of the synthesized NaY zeolite. Similarly to the NaX zeolite, it is possible to observe that the particles are agglomerated of small granules. This kind of morphology is also related to the aluminum content as discussed earlier, although their content is lower in NaY synthesis, FAU-type zeolites tend to form clusters of this type. The difference in the size of the granules formed will depend on the rate of nucleation and its agglomeration.

Figures 4c to f present the micrographs of LTA zeolites. We can observe the typical cubic habit of these zeolite crystals. As we can see, comparing the morphology of the original source, the commercial zeolite A, with the exchanged zeolites, there is no change in morphology or agglomeration. The crystallites are homogeneous in size, between 1.0 and 5.0 μm , which is expected according to the literature [5].

4.3. Energy Dispersive X-Ray Spectroscopy

Table 1 presents the chemical compositions obtained by EDS (molar ratios) and the ion exchange degree. It was observed that the Si/Al ratio = 1.26 for zeolite NaX (similar to the nominal ratio of 1.20 provided by IPT-SP) and Si/Al = 2,56 for Zeolite NaY.

For LTA zeolites, the Si/Al ratio between 1.00 and 1.03 is in line with the expected. The composition of the commercial LTA showed that the material has both exchangeable cations K^+ (59,6% mol/mol) and Na^+ (40,5% mol/mol). The zeolite K-LTA was obtained a high content of K (96,4%) and Na-LTA also presented a high Na content (95.6%). The same can be said for the Ca-LTA zeolite, which achieved a good ion-exchange degree (94.3%). This value can be raised to close to 100% by employing later exchange steps, but the obtained result was enough for the proposed application.

Table 1. Chemical compositions by EDS (molar ratios) and the ion exchange rate

Zeolite	Si/Al	Ion-Exchange rate
NaX	1,26	-
NaY	2,56	-
Commercial LTA	1,00	59,6% K 40,5% Na
K-LTA	1,00	96,4% K 3,6% Na
Na-LTA	1,03	95,9% Na 4,1% K
Ca-LTA	1,03	94,3% Ca 2,6% Na 3,1% K

4.4. Evaluation of Polyaspartic Reaction Kinetics (Pot Life)

As previously described, the water content present in the aspartic ester greatly impairs the application time of the coating (modifies the polymerization kinetics, pot life) and the quality of this coating due to the formation of CO_2 "microbubbles".

In order to evaluate the time limit to apply each formulation, first the formulated aspartic ester (pure or with 1% of zeolite) was mixed with the polyisocyanate, initiating the reaction. Next, the viscosity of each formulation was determined with a Ford Cup 4. The viscosity was measured every 3 minutes.

Figure 5 shows the pot life for the formulations used in this study. The test was performed on the formulation without addition of zeolites, called "PAS", and in zeolite-added formulations called "PAS + K-LTA", "PAS + Na-LTA", "PAS + Ca-LTA", "PAS + Na-X" and "PAS + Na-Y". The formulation "PAS" showed a pot life of 9 min and the formulation with longest pot life, PAS + Na-X, 21 min. The others formulations had a similar performance, with a pot life of 17 – 18 min.

As expected, the non-addition of an adsorbent to eliminate moisture (formulation "PAS") yielded the shortest pot life, as there was no impediment to unwanted effects. In all cases where there was the addition of adsorbent, the pot life time was at least twice that of the formulation without adsorbent.

Water molecules adsorb on zeolite surface through dipole-field interaction as well as hydrogen bonds with residual hydroxyl groups. The number of the latter also depends on the population of Al atoms in the framework. Therefore, the affinity of zeolites with water molecules is dependent on their Si/Al ratio [13].

Comparing LTA zeolites, which have Si/Al \cong 1 and the same high hydrophilicity, the pot life time was practically the same, with a small decrease for K-LTA (3A), with a smaller micropore diameter and greater restriction on the diffusion of water into the interior of its channels. That is, for the adsorption of water in the LTA structure, the steric hindrance related to the exchanged cation was not very relevant, since for Na-LTA (4A) and Ca-LTA (5A) it was not possible to observe an advantage in increasing the micropore diameter. We could say that for this case, the hydrophilicity is more important than the micropore diameter.

It is interesting to note that the NaY zeolite, with a 7.2 Å micropore diameter, much larger than for the LTA zeolites, did not perform better than the latter. Zeolite NaY, with Si/Al ratio = 2.56, is less hydrophilic than zeolite A, but with a larger micropore diameter. This allowed its performance to be similar to the first one. It can be seen that there is a related balance between hydrophilicity and accessibility to micropores. The lower

the hydrophilicity, the larger the micropores must be in order to allow the adsorption of water molecules.

Now comparing the NaX and NaY zeolites, the zeolite with the highest aluminum content was the one with the highest water adsorption capacity. This may be also related to the known greater hydrophilicity of NaX in relation to NaY, allowing greater adsorption of water in its micropores.

Comparing the zeolites with almost same structural aluminum content (same hydrophilicity), but different structures (LTA and NaX zeolites), clearly we can observe the better performance of NaX because of the lower hindrance to diffusion of water molecules.

In these processes, the aluminum content, which is associated to hydrophilicity, is therefore an extremely important property, affecting the distribution of the negative charge density in the network and thus, the ion exchange capacity, the density and strength of the Brønsted acid sites (when present), as well as the hydrophilicity / hydrophobicity of the internal and external surfaces.

Thus, it can be concluded that the most efficient molecular sieve is Na-X zeolite, which had the greatest impact on the pot life of the material.

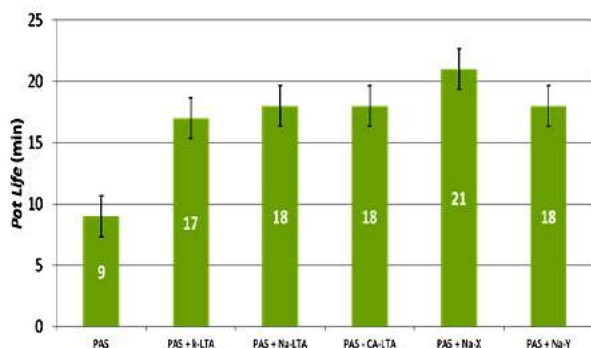


Figure 5. Evaluation reaction kinetics (pot life) of the aspartic ester (pure and with zeolites) and polyisocyanate.

5. CONCLUSIONS

The zeolites were characterized by several techniques. The cation exchange in the commercial zeolite for preparation of K-LTA, Na-LTA and Ca-LTA zeolite was satisfactory. It can be noted that zeolite NaX is suitable for the proposed tests, since it has the joined properties of hydrophilicity and micropore opening that allows a better water adsorption into the channels. In the pot life test, it was observed that all zeolites had a positive impact on polyaspartic coating, but the best is the zeolite Na-X. It can be concluded that the addition of NaX zeolite is beneficial to the polyaspartic process of coating

and it is better than the traditional LTA zeolite (3A) used for this purpose. The NaX zeolite will contribute to increase the application time, increasing the productivity of the painting process.

6. REFERENCES

- [1] COVESTRO. Coatings with reduced VOC emissions and increased productivity. Available in: <<https://www.coatings.covestro.com/en/Technologies/High-Solids-Solventfree/Polyaspartics>>, Accessed: May 10th of 2018.
- [2] Zwiener, C., Schmalstieg, L., Sonntag, M., Nachtkamp, K., Pedain, J., Buechel, K. H. New Concepts for Two-Pack Polyurethane Coatings. Farbe & Lack. (1991) Nr. 12, p. 1052
- [3] Fazenda, J. MR. Tintas & Vernizes—Ciência e Tecnologia—Editora Edgard Blücher. São Paulo. 3rd Edition, 2005.
- [4] Machado, M. P. M. Estudo da influência de adsorvedores e absorvedores de umidade em revestimentos de poliaspártico. Diadema: 64 p. 2015.
- [5] Watanabe, Y. et al. Ammonium ion exchange of synthetic zeolites: The effect of their open window sizes, pore structures, and cation exchange capacities. Separation science and technology, v. 39, n. 9, p. 2091-2104, 2005b. ISSN 0149-6395.
- [6] Padilha, J. F. Preparação e caracterização de zeólitas HY modificadas. 1987. Masters dissertation. Universidade Federal de São Carlos.
- [8] Koleske, J. V. Paint and coating testing manual: of the Gardner-Sward handbook; Paint testing manual, 1995.
- [9] Associação Brasileira de Normas Técnicas. ABNT NBR 15742. Tintas e vernizes — Avaliação do tempo de vida útil da mistura (pot life)
- [10] Thomes, M. et al. Physisorption of gases, with special reference to the evaluation of surface area and pore size distribution (IUPAC Technical Report). Pure and Applied Chemistry, v. 87, n. 9-10, p. 1051-1069, 2015.
- [11] ROBSON, Harry (Ed.); LILLERUD, Karl Petter (Padrões de DRX). Verified synthesis of zeolitic materials. 2 ed., Elsevier, 2001.
- [12] TREACY, M.M.J. and HIGGINS, J.B. Collection of simulated XRD powder patterns for zeolites. Elsevier, 4th ed., 2001.
- [13] KAWAY, T. and TSUTSUMI, K. Evaluation of hydrophilic-hydrophobic character of zeolites by measurements of their immersions heats in water. Colloid Polym Sci 270:711-715 (1992).

Technical evaluation of activated carbon from ginger (*Zingiber officinale* Roscoe) residues as adsorbent of methyl orange dye

Ana Carolina da Silva¹, Marisa Fernandes Mendes¹

Chemical Engineering Department, BR 465 km 7, Seropédica, 23897-000, Brazil

Abstract

Among different sectors of industry, textile is considered the greater source of water pollution due to the high amount and variety of dyes and pigments used in its processes. The presence of these compounds is associated to several damages to human health, aquatic systems and environment. As consequence, there is a trend in the development of water purification techniques and adsorption has gained interest due to its simplicity, low cost and great performance. So, the adsorption of methyl orange dye onto activated carbon from ginger residues (*Zingiber officinale* Roscoe) was investigated in a batch mode analyzing the kinetics. Experiments were conducted using 0.15 g of adsorbent in contact with 25 mL of dye solution with concentration of 100 mg/L. Different contact times were used ranging from 0 to 360 min. Among the kinetic models tested, the pseudo second order kinetic model well fitted the experimental results.

Keywords: biosorption; ginger residues; methyl orange; kinetic modeling.

1. Introduction

A current challenging task faced by different sectors in industries is the removal of toxic elements and compounds such as heavy metals, dyes and microorganisms [1].

The presence of these contaminants in water bodies, specially dyes and pigments, has being of great concern because they are commonly discharged by many industries such as food, textile, paper, rubber, plastics, cosmetics, pharmaceutical and others [1,2].

Among these sectors, textile industries are known as the main generators of colored effluents due to the considerable amount of water used in dyeing and washing processes [3].

It is estimated that fifteen percent of the total world dye production e dyeing process and is released in textile effluent. Even in low concentrations, these substances causes changes in natural color of hydric resources and affects light penetration [2,3].

In addition to environmental damages, they presents adverse effects for human health due to its its carcinogenic, genotoxic, mutagenic and teratogenic properties [1,3,4].

By this reason, several studies have been realized in order to propose an adequate treatment of theses effluents before they are released into water bodies [2,3,4].

As the majority of them do not show significant effectiveness or economic advantage, adsorption stands out as an alternative technique [4], being considered a promising and suitable technology for wastewater treatment due to its simplicity and cost effectiveness [1].

The current trend in the development of adsorbents from natural and easily available materials such as agricultural wastes and residues, industrial byproducts and biomass materials has drawing attention for this technique [1].

In this context, the development of adsorbents from ginger residues would be an interesting alternative for the use of rhizomes declassified for commercialization in nature, or even the ginger processing industries, which focus on extraction of essential oils and oleoresins, as raw materials [5]. Therefore, in addition to increasing the production chain of ginger, the adsorption allows a suitable destination for this industrial waste.

Although there are recent studies proving its adsorbent capacity in the removal of dyes and metals from aqueous solutions [1,3,4], there is a

lack of information about the adsorbent capacity of activated carbon from ginger (*Zingiber officinale* Roscoe) residues and its kinetic behavior in adsorption process.

Kinetic analysis plays an important role on the design and scale-up of an adsorption process because provides information which are required to select the optimal conditions for a future application of the process on an industrial scale [6]. By this reason, kinetic models are usually employed to analyze experimental data because it makes possible to investigate the adsorption mechanism and the potential rate-controlling steps involved in the process [6,3].

Adsorption kinetics describes the speed in which molecules of a fluid phase are adsorbed onto an adsorbent. This speed is dependent of several variables, such as physic-chemical characteristics of adsorbate (nature of adsorbate, molecular weight, solubility and others), of adsorbent (nature and pore structure) and from initial concentration of solution [7]

By this reason, the aim of this work is to evaluate the kinetic behavior of activated carbon from ginger residues (*Zingiber officinale* Roscoe) in the removal of methyl orange dye in aqueous solution.

2. Material and Methods

2.1. Material

Ginger rhizomes were bought in a local market in Seropédica-RJ. Methyl orange dye was purchased from VETEC Química Fina.

2.2. Experimental Procedure

Activated carbon preparation: In order to remove all the impurities, ginger rhizomes were washed with distilled water and dried at ambient temperature. After that, the material was pressed in a manual hydraulic press to obtain ginger residues. Ginger residues were dried at 60 °C for 12 h and was converted in two desired particle size: A1 (42-80 mesh) and A2 (80-150 mesh). The powder material passed through calcination process at 350 °C for 180 min in a muffle furnace. The calcinated material was washed with distilled water for the removal of ash and other impurities and then was dried at 60 °C for 12 h.

2.2.1. Batch adsorption studies

Adsorption kinetics studies were carried out by keeping in contact 0.15 g of activated carbon with 25 mL of dye solution of 100 mg/L in erlenmeyers. Different contact times were considered varying from 0 to 360 min. The flasks were stirred for 6 h on a mechanical shaker at 180 rpm and 25 °C. The concentration of dye in the samples during the experiments was determined by using UV-Visible spectrophotometer (Bel UV-M51) at maximum wavelength absorption at 465 nm. The amount of dye adsorbed at a determined time (q_t) and equilibrium (q_e), both in mg/g, were calculated from the following Equations 1 and 2, respectively:

$$q_t = (C_0 - C_t) \frac{V}{m} \quad (1)$$

$$q_e = (C_0 - C_e) \frac{V}{m} \quad (2)$$

with C_0 and C_e (mg/L) as the liquid phase concentrations of dye at initial and equilibrium states, respectively, C_t (mg/L) as the liquid phase concentration of dye at a time, V as the volume of the dye solution (L) and m as the mass of biosorbent (g).

2.2.2. Kinetic Modeling

In order to investigate the mechanism of the adsorption process, models of intraparticle diffusion, pseudo-first-order adsorption and pseudo-second-order adsorption were used to evaluate adsorption rate data. In addition, kinetic modeling provides information about the potential rate-controlling steps involved in the process of adsorption [3]

Intraparticle diffusion model [8] is shown in Equation 3:

$$q_t = k_{di} t^{0.5} + C \quad (3)$$

with q_t as the amount of dye adsorbed on the adsorbent (mg.g^{-1}) at time t , and k_{di} as the intraparticle diffusion rate constant ($\text{mg.g}^{-1}.\text{min}^{-0.5}$) which is obtained when we plot q_t versus $t^{0.5}$.

The pseudo first order model [9] is described by Equation 4:

$$q_t = q_e (1 - \exp^{-k_t t}) \quad (4)$$

with q_e and q_t as the amounts of dye adsorbed on the adsorbent (mg.g^{-1}) at equilibrium and at

time t , respectively, and K_1 as the rate constant (min^{-1}).

The pseudo second order kinetic rate equation [10] is expressed as:

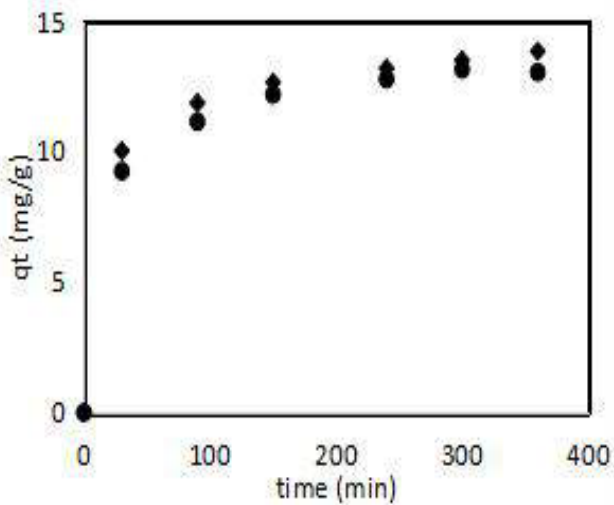
$$\frac{t}{q_t} = \frac{1}{K_2 q_e^2} + \frac{1}{q_e} t \quad (5)$$

with K_2 as the constant of the pseudo-second-order rate ($\text{g.mg}^{-1}.\text{min}^{-1}$), which is obtained by plotting $t.q_t^{-1}$ versus t .

3. Results and Discussion

Figure 1 shows the kinetic adsorption of methyl orange dye onto activated carbon from ginger residues, considering both particle size.

Fig. 1. Kinetic adsorption of methyl orange using different particle size (●: A1, ◆: A2).



The dye was rapidly adsorbed in the first 45–60 min, and then the adsorption rate decreased gradually and reached equilibrium in 200 min. The behavior of adsorption process was similar to the one find out by Kumar & Ahmad (2011).

At the beginning, the dye ions were firstly adsorbed in the exterior surface of activated carbon. However, when the saturation is reached, the dye ions entered into the pores of adsorbent particles, and were adsorbed by their interior surface. This process takes a long time and due to it the adsorption rate is slow.

Figures 2 and 3 shows the kinetic models for both particle sizes.

Fig 2. Kinetic models for adsorption of methyl orange dye onto activated carbon with 42-80 mesh particle size: (a) Pseudo-first order; (b) Pseudo-second order; (c) Intraparticle diffusion.

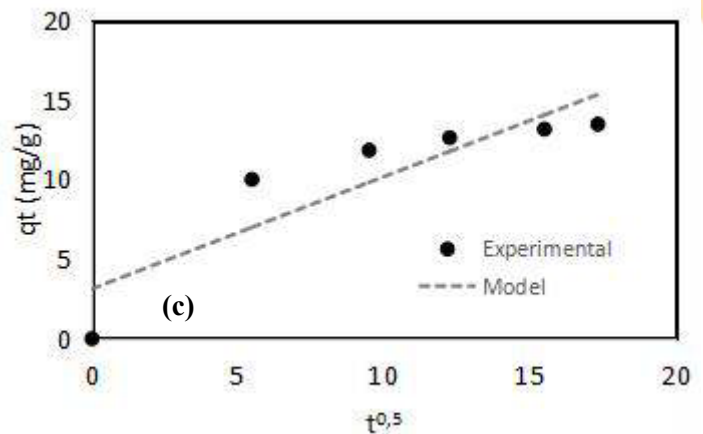
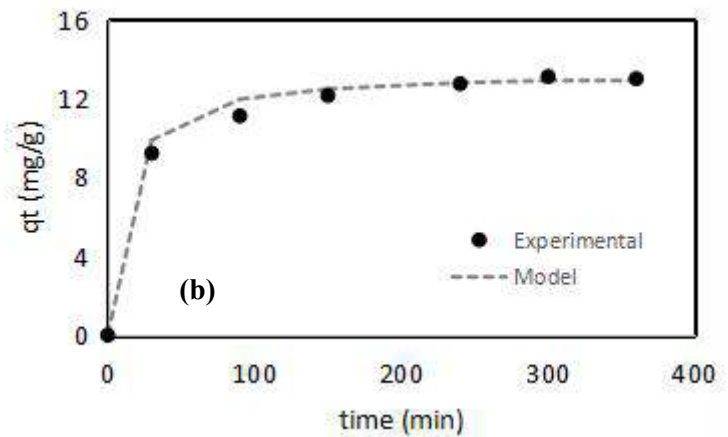
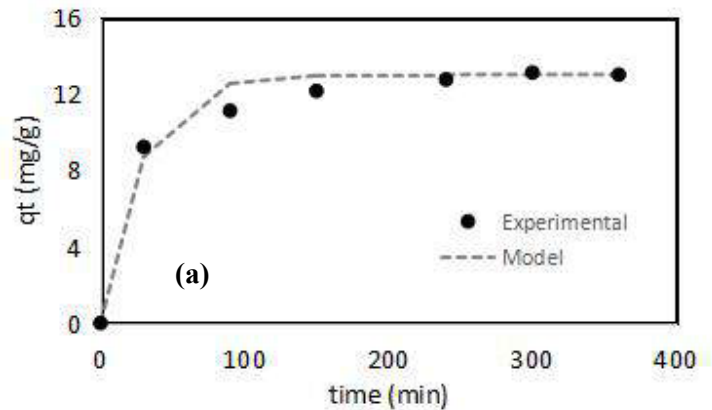


Fig 3. Kinetic models for adsorption of methyl orange dye onto activated carbon with 80-150 mesh particle size: (a) Pseudo-first order; (b) Pseudo-second order; (c) Intraparticle diffusion.

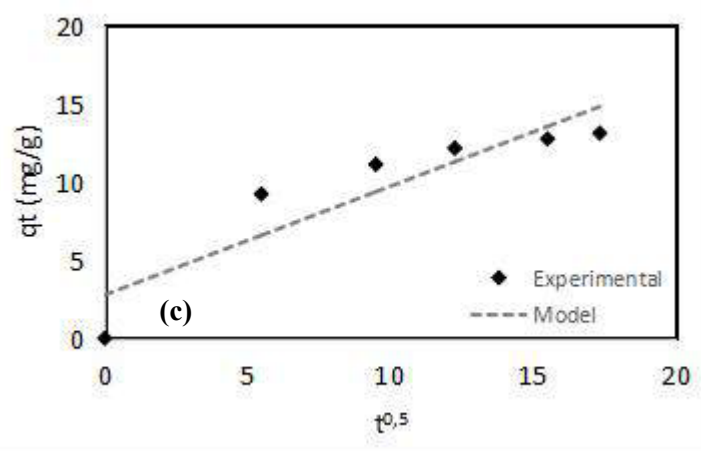
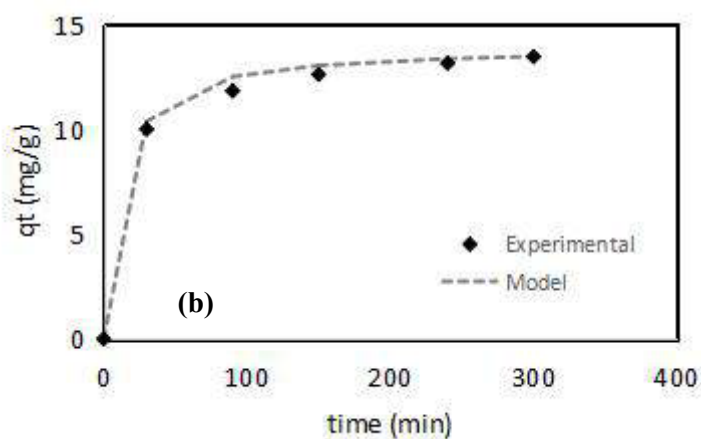
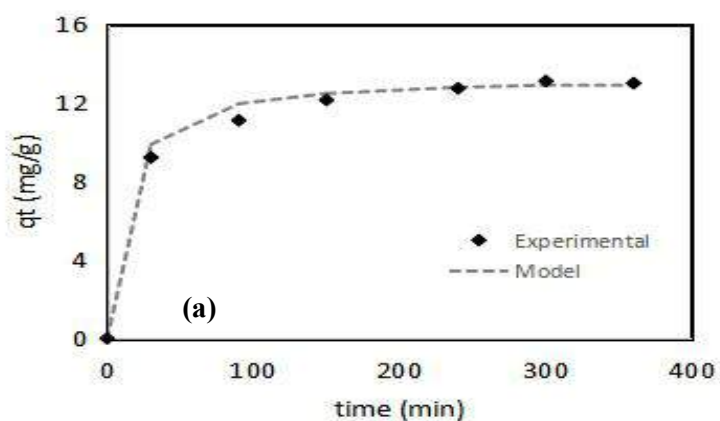


Table 1 shows the results of kinetic modeling for all particle sizes studied which comprises the model parameters, rate constants k_1 and k_2 , adsorption capacity (q_e), and correlation coefficient.

The experimental amount adsorbed at equilibrium (q_{exp}) was 13,124 mg/g and 13,473 mg/g for A₁ (42-80 mesh) and A₂ (80-150 mesh), respectively.

Table 1. Kinetic parameters of adsorption process

Pseudo-First Order Model			
Sample	K_1 (min^{-1})	q_e (calc.)	R^2
A1	0.037	13.014	0.989
A2	0.042	13.473	0.990
Pseudo-Second Order Model			
Sample	K_2 ($\text{g}/\text{mg}\cdot\text{min}$)	q_e (calc.)	R^2
A1	0.007	13.369	0.998
A2	0.007	13.947	0.998
Intraparticle Diffusion Model			
Sample	K_{di} ($\text{g}/(\text{mg}\cdot\text{min}^{0.5})^{-1}$)	C (mg/g)	R^2
A1	0.696	2.772	0.906
A2	0.705	3.131	0.888

Through a comparison between the results obtained, it is possible to notice that the values calculated (q_{calc}) by pseudo-second order model well matched the experimental ones, suggesting that this model described the adsorption process more effectively. It can be confirmed by the good agreement with experimental data due to the higher correlation coefficients ($R^2 > 0.99$).

Weber & Morri's model suggests that if linear coefficient is nonzero, the controlling step of process can be intraparticle diffusion. By this reason, it can be concluded that the constant $C > 0$ encountered for both particle sizes indicated that the intraparticle diffusion is not the controlling step of the adsorption process.

4. Conclusion

The aim of this work was to evaluate kinetic analysis of adsorption process of methyl orange dye onto activated carbon from ginger residues. From kinetic modeling, was possible to determine that this process was best fitted by pseudo second order model.

Acknowledgements

The authors would like to thank FAPERJ for the financial support, and CNPq/PIBIC for the scientific initiation scholarship. Furthermore, this work was carried out with the support of the

Higher Education Personnel Improvement
Coordination - Brazil (CAPES) - Financing Code
001.

References

- [1] Singh N B, Nagpal G, Agrawal S, Rachna. Water purification by using Adsorbents: A Review. *Environmental Technology & Innovation*, 2018 p. 187–240.
- [2] Kumar R, Ahmad R. Biosorption of hazardous crystal violet dye from aqueous solution onto treated ginger waste (TGW). *Desalination*, 2011 p. 112–118.
- [3] Ahmad R, Kumar R. Adsorption studies of hazardous malachite green onto treated ginger waste. *Journal of Environmental Management*, 2010 p. 1032–1038.
- [4] Gupta VK, Pathania D, Sharma S, Agarwal S, Singh P. Remediation and recovery of methyl orange from aqueous solution onto acrylic acid grafted *Ficus carica* fiber: Isotherms, kinetics and thermodynamics.
- [5] Magalhães MT, Koketsu M, Gonçalves SM, Duarte, FR, Godoy, RLO, Lopes D. Gengibre (*Zingiber officinale* Roscoe) brasileiro: aspectos gerais, óleo essencial e oleoresina: Parte 1 – Aspectos gerais, óleo essencial. *Ciência e Tecnologia dos Alimentos*, 1997 p. 64-69.
- [6] Febrianto J, Kosasih AN, Sunarso J, Ju YH, Indraswati N, Ismadji S. Equilibrium and kinetic studies in adsorption of heavy metals using biosorbent: a summary of recent studies. *Journal of hazardous materials*, 2009 p. 616-64.
- [7] Claudino A. Preparação de carvão ativado a partir de turfa e sua utilização na remoção de poluentes. *Dissertação (Mestrado em Engenharia Química) - Universidade Federal de Santa Catarina, Florianópolis*, 2003 101.
- [8] Weber WJ, Morris JC. Kinetics of Adsorption on Carbon from Solution. *Journal of the Sanitary Engineering Division*, 1963 p. 31-60.
- [9] Ho YS, McKay G. Sorption of copper (II) from aqueous solution by peat. *Water Air and Soil Pollution* 2004; 158:77–97.
- [10] Ho YS, McKay G. Pseudo-second-order model for sorption process. *Process Biochemistry* 1999; 34:451–465.

Application of Southwell Plot Method for Determining Equilibrium Time in Adsorption Processes

Maíra Luane S. de Almeida^a, Tamille A. Souza^b, Daniel S. Costa Neto^a, Koji de J. Nagahama^a, Alexilda O. Souza^c, Tereza S. M. Santos^a

^aUniversidade Estadual de Feira de Santana (UEFS), Programa de Pós-graduação Engenharia Civil e Ambiental (PPGCEA). Av. Transnordestina, s/n, Novo Horizonte, 44036-900 Feira de Santana, Bahia, Brazil

^bInstituto de Química – Universidade Federal da Bahia – Rua Barão de Jeremoabo – CEP:40170-115- Salvador –BA –Brasil

^cLaboratório de Pesquisa em Catálise e Química de Materiais (LCQM) – Programa de Pós-Graduação em Química – Universidade Estadual do Sudoeste da Bahia – Campus Juvino Oliveira – CEP:45700-000–Itapetinga-BA–Brasil.

Abstract

Among the different factors that influence the solid-liquid adsorption technique, equilibrium time is one of the most relevant and it requires long-term experiments. In an attempt to optimize the amount of experiments and resources, this work applies the Southwell Plot Method to determine the equilibrium time in phosphate removal in adsorbents produced from domestic sewage sludge and shell residue. The dry sludge and clam shell, 10% w/w clam, were ground and sieved (80 mesh) and sintered in a muffle at 700°C for 1 h. The material was characterized by chemical analysis (EDX), X-ray diffraction (XRD) and adsorption kinetics. The effect of the initial phosphate solution concentration on adsorption kinetics was evaluated using three different concentrations: 30 mgP L⁻¹, 50 mgP L⁻¹ and 100 mgP L⁻¹. The main oxides present in the material are CaO and SiO₂. The kinetic data were better fitted to the pseudo-second order model for all initial concentration conditions, according to their R² values. The Southwell Plot method was applied to the experimental data and demonstrated that it can be used during the test to determine the equilibrium time. In this case, considering the results of the adaptation of experimental data to the Southwell Plot method and the error variations, the 240 min time is sufficient to estimate the q_e stabilization point, i.e. the adsorption equilibrium time.

Keywords: Southwell Plot Method, Sewage Sludge; Phosphorous Adsorption .

1. Introduction

Adsorption is a separation process that results from the accumulation of the solute on the surface of an adsorbent [1]. This process is widely used in the removal of pollutants in liquid effluents due to its high efficiency and low cost. Due to its versatility, adsorption is widely applied in the process of removing heavy metals, dyes, drugs, and other types of contaminants found in effluents. This is an economically viable technique because it can be performed with materials available in the environment, for example biomass, minerals, sawdust, sewage sludge, coconut fiber, rice husks, husk, fruit cake and seeds [2-4]. Although easy to apply, the adsorption process requires the analysis

of many variables at the same time, such as the amount of adsorbent dosage, initial adsorption concentrations, pH of the solution, equilibration periods, among others, in order to determine the parameters of the operation [1].

The method called Southwell Plot has been widely used to estimate the critical buckling load of columns [5]. Column buckling is a typical structural engineering problem and obtaining experimental results is a major challenge because instrumentation equipment cannot record large displacements, such as displacement transducers. These displacements are necessary to follow the equilibrium trajectory of the phenomenon characterized by load versus displacement [6-9].

The equilibrium trajectories of the column buckling phenomenon are very similar to those of



adsorption kinetics. It is therefore possible to apply the Southwell Plot method to accurately estimate the value of q_e without the need for long-term observations. In this case, time is analogous to displacement. The same way in which the critical buckling load on columns is estimated, by analogy, the stabilization q_e can also be estimated

The Southwell Plot method consists of maintaining the magnitude of the abscissa and the axis of the ordinates to replace the quantity q_e with the ratio t/q_e . From this, the inverse of the slope of the line adjusted between these points will indicate the value of q_e which determines the asymptotic point, that is, the value to which it stabilizes.

The objective of this work is to evaluate the application of the Southwell Plot Method to determine the equilibrium time in phosphate removal in adsorbents produced from domestic sewage sludge and shell residue.

In addition to its high carbon content, domestic sewage sludge also presents mineral compounds containing Si, Al, Fe, Ca and others which enable different types of active sites that would favor the phosphate removal from the aqueous medium [10-12]. The use of calcium oxide-containing residues such as shell residues in the preparation of the adsorbent to improve phosphate removal is a more sustainable strategy [13]

2 Material and methods

2.1 Materials

The sewage sludge (LED) was provided by a sewage treatment plant located in Feira de Santana, state of Bahia, Brazil (ETE-Subaé). Waste clam shells (RCM) were used as a source of calcium and were collected from artisanal fishing units located in Maragogipe, state of Bahia, Brazil. The residues were obtained from the bivalve clams shells *Anomalocardia brasiliana* and *Tagelus plebeius*.

The solutions were prepared using monobasic sodium phosphate ($\text{NaH}_2\text{PO}_4 \cdot \text{H}_2\text{O}$) and stored in dark flasks to prevent any photodecomposition. Initial concentrations for the kinetic studies were 30 mgP L^{-1} , 50 mgP L^{-1} and 100 mgP L^{-1} .

2.2 Preparations

The method used to produce the adsorbent was adapted from Souza (2018) [13]. The dry sludge and clam shells, 10% w/w clam, were ground and sieved (80 mesh) and sintered in a muffle at 700°

C for 1 h. The prepared sample was named MAD10.

2.3 Characterization

The chemical composition of the adsorbent sample MAD10 sample was determined on a Shimadzu EDX720 energy dispersive X-ray fluorescence spectrometer, operating with a rhodium source, using a semi-quantitative method. The X-ray diffraction patterns of the samples were collected on a Shimadzu XRD-6000, operating with $\text{CuK}\alpha$ radiation at a voltage of 40 kV, current of 30 mA, and graphite monochromator, in the region of $1.4\text{--}50^\circ 2\theta$ at scan rate of 2° min^{-1} .

2.4 Kinetic Studies

The adsorption kinetics was performed in duplicate, and the suspensions were separated by vacuum filtration on $0.45 \mu\text{m}$ cellulose acetate membrane. The determination of the phosphate concentration was performed using a TU-1880 double-beam UV-VIS spectrophotometer at a wavelength (λ) of 880 nm, according to the molybdenum blue method [14]. The effect of the initial phosphate solution concentration on the adsorption kinetics was evaluated using three different concentrations: $30 \text{ mgP}\cdot\text{L}^{-1}$, $50 \text{ mgP}\cdot\text{L}^{-1}$ e $100 \text{ mgP}\cdot\text{L}^{-1}$.

The value of q_e was determined by Equation 1, where C_o and C_e are the initial concentration and equilibrium concentration of the adsorbate in mg L^{-1} , respectively; V the volume of the solution in L, and m the mass of the adsorbent in mg:

$$q_e = \frac{(C_o - C_e)V}{m} \quad \text{Equation 1}$$

The adsorption kinetics were studied using the pseudo-first order; pseudo-second order and the Elovich kinetic models. The pseudo first order rate is generally described by the Lagergren equation (15, 16)

$$q_t = q_e(1 - e^{-k_1 t})$$

while the pseudo second order model is described by the Ho-Mackay equation [15]:

$$q_t = \frac{tk_2 q_e^2}{1 + q_e tk_2}$$

where q_t and q_e represent the amount of phosphorous (mg g^{-1}) adsorbed at time t (min) and equilibrium, respectively. k_1 is the rate constant of the pseudo first order (min^{-1}) and k_2 is the pseudo

second order rate constant ($\text{g mg}^{-1} \text{min}^{-1}$). For comparative effect, the models were considered the best fit according to the analysis of different types of errors: the correlation coefficient (R^2).

3. Result and Discussion

The chemical composition of MAD10 was determined as oxides by EDX and are presented in Table 1:

Table 1: Chemical composition of MAD10 on a dry basis (wt%).

Constituents	MAD10(%)
CaO	29.75 ± 0.02
SiO ₂	18.68 ± 0.08
Fe ₂ O ₃	15.61 ± 0.02
Al ₂ O ₃	10.20 ± 0.12
P ₂ O ₅	9.47 ± 0.05
SO ₃	5.75 ± 0.02
MgO	3.60 ± 0.22
ZnO	2.28 ± 0.01
Others	4.59

The compound with the highest concentration is calcium oxide, CaO. The calcium added to the sewage sludge by sintering with the shell residue is in the form of CaO. Then silicon oxide appears in a larger amount, SiO₂, due to the presence of common minerals (sand, silt and clay) in the sewage sludge. Iron oxide (Fe₂O₃) and aluminum oxide (Al₂O₃) form the basis of the chemical composition of the MAD10.

The XRD patterns of the sample are shown in Figure 1, where the observed phases are those formed during the sintering step of the adsorbent preparation.

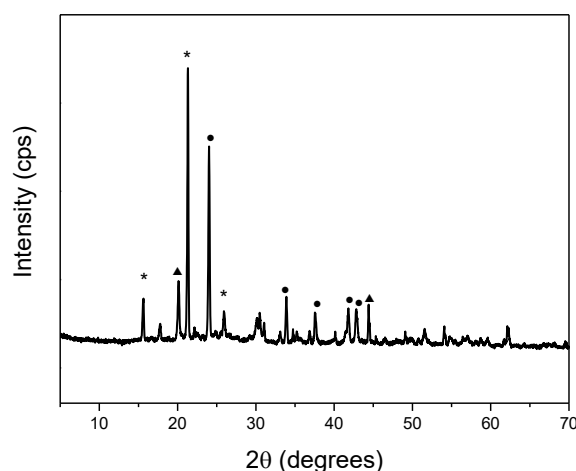


Fig. 1: Powder X-ray diffraction patterns of sample: α -quartzo(*), calcite(▲) and hematite(●).

Sample MAD10 has heterogeneity in terms of its crystalline structure, due to the variety of inorganic oxides present in its composition, as shown by the EDX results. The phases identified by X-ray diffraction patterns as a function of oxide concentration and detection limit of the equipment were α -quartz (SiO₂), calcite (CaCO₃) and hematite (α -Fe₂O₃).

The kinetics of phosphate adsorption on the sewage sludge-clam shell combined adsorbent was investigated considering the initial phosphate concentration. The results are shown in Fig. 2.

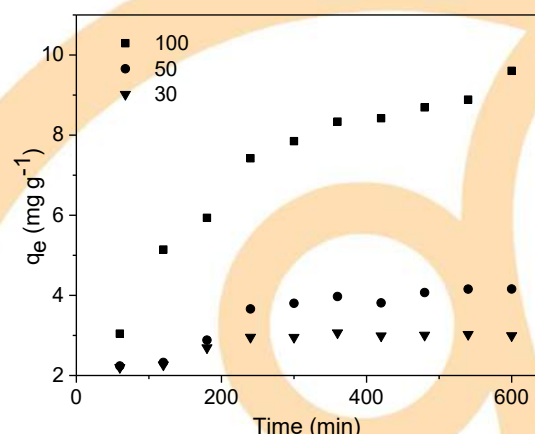


Fig.2: Effect of initial phosphate concentration on adsorption kinetics on MAD10.

Regardless of the initial solute concentration, the increase in adsorption rate with increasing solute concentration is predicted due to the higher amount of solute in the aqueous medium [17]. This

behavior can be effective in the system using MAD10 as an adsorbent in phosphate removal. At the beginning of the process, the adsorption rate is high, and gradually decreases over time by saturation of available sites.

The kinetics of the phosphate adsorption on the MAD10 adsorbent was investigated and the data were fitted to the pseudo-first order and pseudo-second order model. The results are presented in Table 2:

Table 2: Kinetic parameters for the phosphate adsorption on MAD10 adsorbent using different models.

Concentration	Parameters pseudo-first order	Parameters pseudo-second order
30	$q_e = 2.973 \text{ mg g}^{-1}$ $k_1 = 0.02 \text{ h}^{-1}$ $R^2 = 0.7261$	$q_e = 3.23 \text{ mg g}^{-1}$ $k_2 = 0.01 \text{ g mg}^{-1} \cdot \text{h}^{-1}$ $R^2 = 0.8578$
50	$q_e = 4.106 \text{ mg g}^{-1}$ $k_1 = 0.01 \text{ h}^{-1}$ $R^2 = 0.8605$	$q_e = 4.861 \text{ mg g}^{-1}$ $k_2 = 10^{-3} \text{ g mg}^{-1} \cdot \text{h}^{-1}$ $R^2 = 0.8984$
100	$q_e = 9.348 \text{ mg g}^{-1}$ $k_1 = 0.01 \text{ h}^{-1}$ $R^2 = 0.9826$	$q_e = 11.911 \text{ mg g}^{-1}$ $k_2 = 10^{-4} \text{ g mg}^{-1} \cdot \text{h}^{-1}$ $R^2 = 0.9858$

Based on the data presented in Table 2, pseudo-second order kinetics clearly fitted better with the experimental data for all initial concentration conditions, according to their R^2 values.

The Southwell Plot method was applied to phosphate adsorption kinetic data on MAD10. The data were graphically analyzed. For this on the abscissa axis the magnitude t and on the ordinate axis replace the quantity q_e by the ratio t/q_e . The inverse of the slope of the each line adjusted between these points will indicate the value of q_e which determines the asymptotic point, that is, the value to which it stabilizes. The mean values of q_e were obtained from the mean of two observations, in their respective observation times, for each initial concentration value. Note also the ratio t/q_e . The results are shown in Figures 3 to 5.

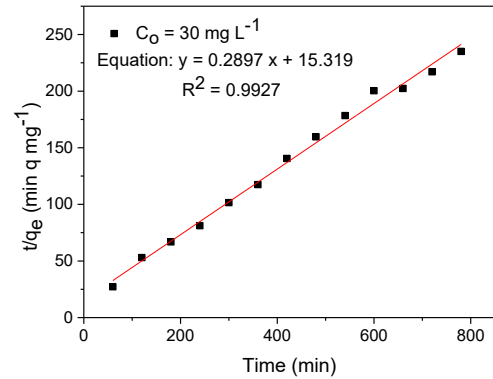


Fig. 3: The Southwell Plot method applied to phosphate adsorption on MAD10, initial concentration 30 mg L^{-1} .

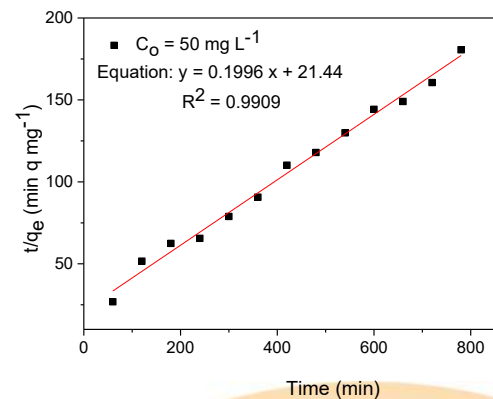


Fig. 4: The Southwell Plot method applied to phosphate adsorption on MAD10, initial concentration 50 mg L^{-1} .

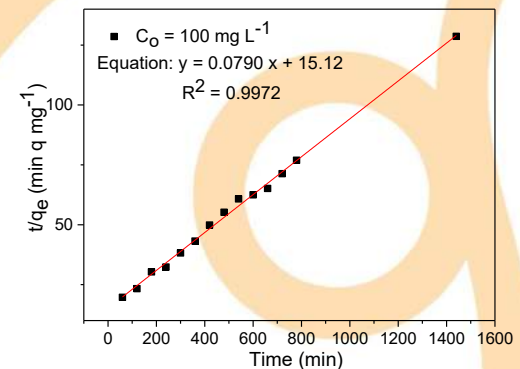


Fig. 5: The Southwell Plot method applied to phosphate adsorption on MAD10, initial concentration 100 mg L^{-1} .

After constructing graphs (Fig. 3, 4 and 5) with their respective adjusted trend lines, the slope values are obtained and their inverse values determine the stabilization value of q_e . This procedure was performed with all the observations made.

In order to minimize the required observation time, the same procedure was performed considering shorter observation times and comparing the results obtained with those initially determined with the maximum observed time. The results are shown in Table 3 and from these it can be seen that observations over 240 min present approximately the same error variation. From this it can be inferred that observations up to 240 min are sufficient to estimate the stabilization point of q_e , applying the Southwell Plot method.

Table 3: Results of application Southwell Plot Method.

Concentration (mg L ⁻¹)	30		50		100	
Time (min)	q_e est	error	q_e est	error	q_e est	error
120	2.334	-32.386	2.421	-51.686	16.527	30.706
180	3.032	-12.170	3.366	-32.818	11.296	-10.661
240	3.416	-1.068	4.721	-5.779	13.370	5.743
300	3.392	-1.735	5.078	1.338	13.037	3.106
360	3.436	-0.471	5.195	3.685	12.802	1.250
420	3.337	-3.349	4.875	-2.700	12.169	-3.760
480	3.280	-4.997	4.901	-2.184	11.838	-6.376
540	3.249	-5.902	4.919	-1.825	11.617	-8.121
600	3.200	-7.319	4.882	-2.562	11.942	-5.555
660	3.307	-4.213	5.000	-0.220	12.394	-1.980
720	3.397	-1.598	5.078	1.337	12.535	-0.862
780	3.452	0.000	5.011	0.000	12.550	-0.744
1440	*	*	*	*	12.644	0.000

The adsorption studies with the initial concentration of 100 mg L⁻¹ showed a greater range of error variation. In order to confirm the tendency to stabilize the q_e value, the tests were carried out over a 24 hour period, which corroborated the stabilization trend predicted by the Southwell Plot Method. The results observed experimentally remained within the range of variation of the errors considering the predicted value as average.

4. Conclusion

The Southwell Plot Method can be used to determine the equilibrium time of adsorption in order to contribute to the reduction of experiments and resources in processes of adsorption. The kinetic adsorption data for the different concentrations were better adjusted to the pseudo-second order model, according to R^2 . Kinetic adsorption data were also applied to the Southwell

Plot model and it was observed that equilibrium time was reached in 240 min, not requiring a higher number of observations over a longer time. The adsorbents used were prepared from two residual materials (sewage sludge and clam shells) and the process proved efficient for the removal of phosphate. From an environmental point of view, the use of this adsorbent represents an advance in the reuse of materials.

References

- [1] Ruthven. Principles of adsorption and adsorption process. [S.l.]: John Wiley & Sons, 1984.
- [2] Fu F, Wang Q. Removal of heavy metal ions from wastewaters: A review. J. Environ. Manage. 2011, 92:407-418.
- [3] Huang W, Zhang Y, Li D. Adsorptive removal of phosphate from water using mesoporous materials: A review. J. Environ. Manage. 2017, 193:470-482.
- [4] Li, R. et al., Science of the Total Environment Recovery of phosphate and dissolved organic matter from aqueous solution using a novel CaO-MgO hybrid carbon composite and its feasibility in phosphorus recycling. Science of the Total Environment, v. 642, p.526-536, 2018.
- [5] Blum HB, Rasmussen KJR. Elastic buckling of columns with a discrete elastic torsional restraint. Thin-Walled Structures 2018, 129:502-511.
- [6] Ko LW. Accuracies of Southwell and ForcelStiffness Methods in the Prediction of Buckling Strength of Hypersonic Aircraft Wing, Tubular Panels. Ames Research Center, Dryden Flight Research Facility, Edwards, California. NASA Technical Memorandum 88295, 1987, p. 28.
- [7] Kalkan I. Application of Southwell Method on the Analysis of Lateral Torsional Buckling Tests on Reinforced Concrete Beams. Int. J. Eng. Research & Development 2010, 2:58-66.
- [8] Singer J. On the Applicability of the Southwell Plot to Plastic Buckling. Experimental Mechanics 1989, 205-208.
- [9] Mandal P, Calladine CR. Lateral-torsional buckling of beams and the Southwell plot. International Journal of Mechanical Sciences 2002, 44:2557-2571.
- [10] Nguyen TAH, Ngo HH, Guo WS, Zhang J, Liang S, Lee DJ, Nguyen PD, Bui XT. Modification of agricultural waste/byproducts for enhanced phosphate removal and recovery: potential obstacles. Bioresour Technol. 2014, 169:750-762.
- [11] Smith, K. M., Fowler, G. D., Pullket, S., Graham, N. J. D. Sewage sludge-based adsorbents: A review of their production, properties and use in water treatment applications. Water Res. 2009, 43: 2569-2594.
- [12] Xu G, Yang X, Spinosa L. Development of sludge-based adsorbents: Preparation, characterization,



utilization and its feasibility assessment. *J. Environ Manage* 2015, 151:221-232.

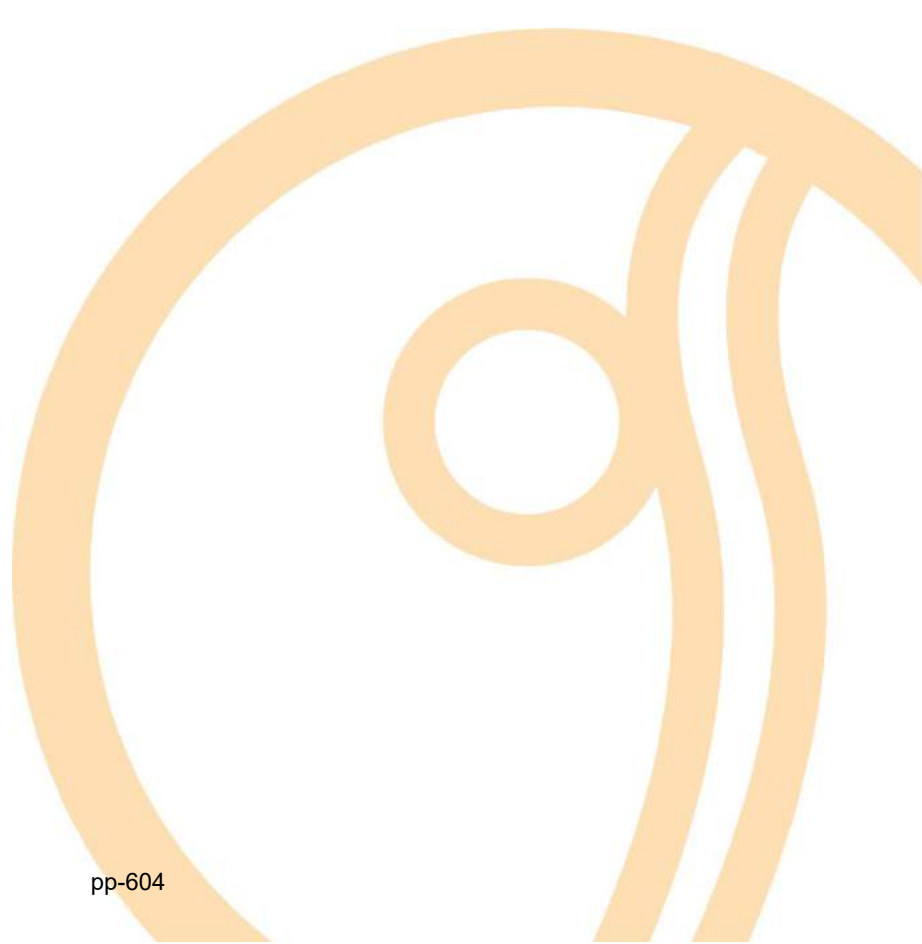
[13] Souza TA; Mascarenhas AJS. Andrade H, Santos TSM. Combining Sewage Sludge and Clam Shell Waste to Prepare Adsorbents for Efficient Phosphorous Removal. *Water Air Soil Pollut*, p. 1–13, 2018.

[14] Eaton AD, Clesceri LS, Rice E W, Greenberg, A. E. (Eds), 2005. APHA, AWWA, WPCF: Standard Methods for the Examination of Water and Wastewater, 21th edn.

[15]Ho YS, McKay G,. Pseudo-second order model for sorption processes. *Process Biochem*1999; 34:451 – 465.

[16]Ho Y S. Review of second-order models for adsorption systems. *J. Hazard. Mater.* 2006; 136:681 – 689.

[17] Mezenner NY, Bensmaili A. Kinetics and thermodynamic study of phosphate adsorption on iron hydroxide-eggshell waste. *Chemical Engineering Journal* 2009; 147:87–96.



Adsorption of estradiol hormone in bone activated carbon

Mara Heloisa Neves Scalianta^a, Ramiro Picoli Nippes^a, Fernando Henrique da Silva^a,
Gabriela Nascimento da Silva^a, Thaisa Frossard Coslop^a.

^a Maringa state university, Av. Colombo, 5790 - Zona 7, Maringá - PR, 87020-900, Brazil

Abstract

The adsorption process is a very promising alternative for removing compounds called emerging micro-pollutants, such as estradiol hormone. However, for its efficiency it is necessary to apply an adsorbent that has affinity with the compound to be removed. Among the available adsorbents activated charcoals have wide application and a wide range of activated charcoal types from the most varied raw materials. In this context, the objective of this study is to evaluate the adsorption of estradiol hormone in bone activated charcoal. Activated bone charcoal presented characteristics with predominance of macropores, completely amorphous character, an irregular surface with presence of well defined pores, with high levels of calcium and phosphorus and bands that characterize the presence of hydroxyapatite structure. The adsorption of estradiol in activated bone charcoal obeyed a pseudo first order kinetics with constant kinetic $k = 0.3199 \text{ min}^{-1}$ and the Langmuir model was better adjusted to the experimental data and $q_{\text{máx}} = 0.004009 \text{ mg mg}^{-1}$. The adsorption process of estradiol in activated bone charcoal was extremely efficient achieving 100% removal.

Keywords: adsorption; bone activated carbon ; estradiol.

1. Introduction

The quality of water for human consumption has always been a latent concern in society, given its fundamental importance in maintaining human life and all living beings. Concern grew from the discovery that a range of substances were present in water and that the effect of theirs on the environment could have dangerous consequences for living things. These substances were called emerging micro pollutants.

Among the micro-pollutants found in the environment, sex hormones, such as estradiol, are the most concerned because of their ability to interfere with the endocrine system of humans and other animals, affecting health, growth and reproduction. Be known as endocrine disruptors [1].

The major concern is that the conventional treatment used in wastewater treatment plants is not efficient in eliminating endocrine disruptors such as estradiol. Hence the need to complement the conventional process with efficient and environmentally friendly treatments. In this context the adsorption process has emerged as a very promising alternative, due to some advantages of its application, such as low cost, ease of operation, efficiency and non-formation of byproducts [2].

However for the removal of a pollutant it is necessary to apply an adsorbent that has affinity with the compound. As there is a range of adsorbents available from a variety of raw material sources such as clays, zeolites, polymers, and activated carbon from plant, mineral and even animal sources produced from bones, it is of utmost importance to evaluate performance of an adsorbent in the removal of emerging micro pollutants. Thus, the objective of this study is to evaluate estradiol hormone adsorption in commercial activated bovine bone carbon.

2. Materials and methods

2.1. Materials

The adsorbent used in this work is bovine bone activated carbon produced by the company Bonechar Activated Carbon (Maringá-PR). The hormone used was 17 β -estradiol from Sigma company with purity $\geq 98\%$ and all experiments were performed with distilled water. Hormone concentration readings were taken in a quartz cuvette on the Shimadzu UV-vis spectrophotometer.

2.2. Characterizations

Activated bone carbon was characterized by textural analysis with N₂ adsorption/desorption isotherms at 77K. Scanning electron microscopy (SEM) with dispersive energy spectroscopy (EDS). Ion source x-ray diffraction covers 40 kV and 30 mA. Fourier transform infrared spectroscopy (FTIR) in the 400 to 4000 cm⁻¹ spectral range, with 100 scans and 4 cm⁻¹ resolution.

2.3. Adsorption tests

Adsorption tests were performed in a thermostatic bath with agitation. Adsorption kinetics were performed using a fixed contaminant concentration (25 mg L⁻¹) and carbon mass (1.5 g) with regular sampling. For the adsorption isotherms, the hormone concentration varied from 0 to 25 mg L⁻¹ and the mass of 1.5 g of activated bone of carbon. All tests were performed at 28 ° C.

3. Results and discussion

3.1. Characterization

From the N₂ adsorption/desorption isotherm shown in Figure 1, it is possible to observe that bone activated carbon presented a heterogeneous pore distribution, with predominance of macropores and multilayer adsorption. The specific area calculated by the BET method was 113 m².g⁻¹ and average pore size 17.73 Å as shown in table 1. The value of the specific area obtained in this work is in accordance with the specifications of the manufacturer. of bone activated carbon, according to the company, the total area of bone activated carbon is 120 m².g⁻¹ calculated using the BET/N₂ method.

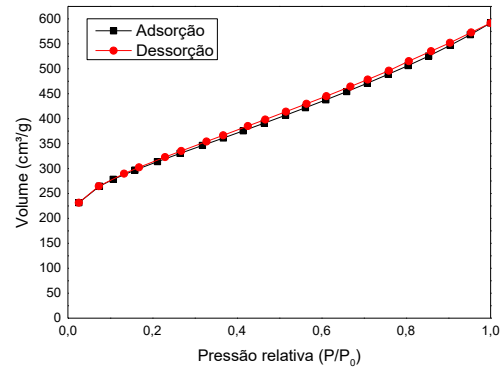


Fig. 1. N₂ adsorption/desorption isotherm at 77 K for the morphological characterization of bone activated carbon.

Table 1. Values of specific area, volume and average pore size for bone activated carbon.

Adsorbent	Area (m ² .g ⁻¹)		Volume (cm ³ .g ⁻¹)		Average size (Å)	
	BET	Micro	Meso	Micro		Meso
Bone activated carbon	113	29.48	24.00	0.047	0.0139	17.73

From the diffractogram of activated bone carbon it is possible to identify a completely amorphous character as shown in Figure 2. This characteristic indicates that the heat treatment applied to the material to obtain activated carbon may not have caused the formation of an ordering of the planes, characteristic of crystalline materials. This also interfered in the absence of diffraction peaks for compounds such as calcium and phosphorus oxides, characteristic of the raw material employed, which other authors have identified in commercial bone coal samples [3, 4].

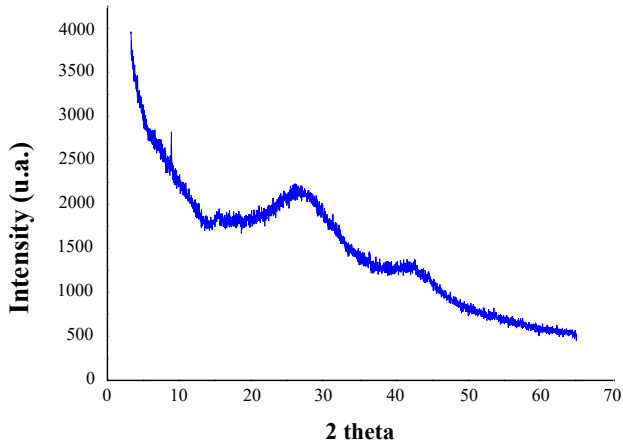


Fig. 2. Diffractogram of bone activated carbon.

From the micrographs for bone activated carbon it was possible to observe an irregular surface with the presence of well defined pores as can be seen in Figure 3. Regarding the identification of chemical species on the surface of the coal by EDS, high levels were found. calcium and phosphorus, which is in agreement with the raw material (bone) of coal as can be seen in Figure 4.

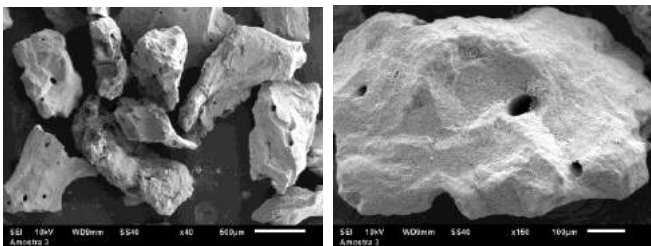


Fig. 3. Micrographs for of bone activated carbon.

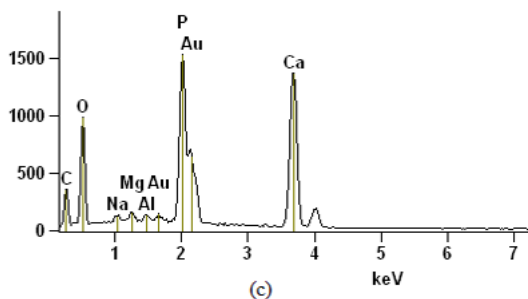


Fig. 4 Dispersive energy spectrum of bone activated carbon.

Figure 5 shows the infrared spectrum of bone activated carbon. The main bands that characterize the presence of hydroxyapatite structure in bone activated carbon are located at 1030 cm^{-1} ($-\text{PO}_4^{3-}$) and 600 cm^{-1} (Ca^{2+}) [5, 6].

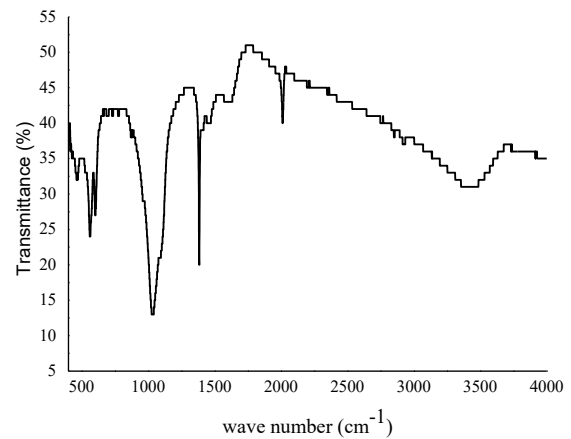


Fig. 5. Infrared spectrum for bone activated carbon.

3.2. Adsorption kinetics

From the data obtained from estradiol adsorption on bone activated carbon it was possible to draw important conclusions about the process. Regarding the adsorption kinetics, the model that best fit the experimental data was the pseudo first order model, which obtained the highest value of the R^2 parameter, however it is possible to state that both models are capable of describing the process as shown in Figure 6. The kinetic constant value for the pseudo first order model was $K = 0.3199\text{ min}^{-1}$, as can be seen in Table 1. Equilibrium was reached after 40 minutes adsorption. These results achieved are in accordance with the literature, according to Fuerhack et al., 2001 the adsorption of 17 β -estradiol in three types of activated carbon reaches conditions close to equilibrium after 50-180 min and the process approached more than one kinetic mechanism of pseudo-first order [7].

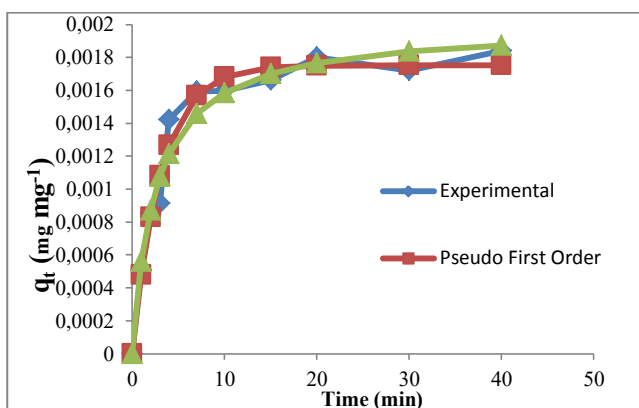


Fig. 6. Estradiol adsorption kinetics in the adsorbent bone activated carbon. Experimental conditions: Estradiol concentration 25 mg.L⁻¹. Adsorbent dosage: 3.75 g. Adsorption temperature: 28 °C.

Table 2. Pseudo-first order, pseudo-second order parameters of estradiol adsorption in bone activated carbon.

Models	kinetic constant	R ²
Pseudo First Order	0,3199 min ⁻¹	0,9785
Pseudo Second Order	195,3818 g mg ⁻¹ min ⁻¹	0,9707

3.3. Adsorption isotherm

Regarding the adsorption isotherm, the model that best fit the experimental data was the Langmuir model with the highest R² value, however the Freundlich model also fitted the data well, as can be seen in Figure 7. The maximum amount adsorbed was max = 0.004009 mg mg⁻¹. Regarding Freundlich isotherm parameter n, the value obtained was greater than 1, according to the literature, indicating a favorable adsorption with affinity between estradiol and the surface of activated bone carbon. The shape of the isotherm also indicates favorable adsorption [8]. As for the performance of activated carbon for removing estradiol, it may be extremely efficient, reaching 100% removal in approximately 40 minutes of adsorption. This result is superior to that achieved by Fuerhack et al., 2001, who uses another type of activated carbon, different from the one employed in this present work [7]. It was possible to observe from the FTIR technique the presence of the hydroxyapatite mineral matrix. This characteristic is the differential of bone activated carbon used in

this work. A hydroxyapatite mineral matrix is a crystalline network that acts on adsorption and ion exchange, in several compounds, both inorganic and organic. It is important to emphasize that in this work the pore size distribution was not calculated, which has a great influence on the adsorption capacity and kinetics.

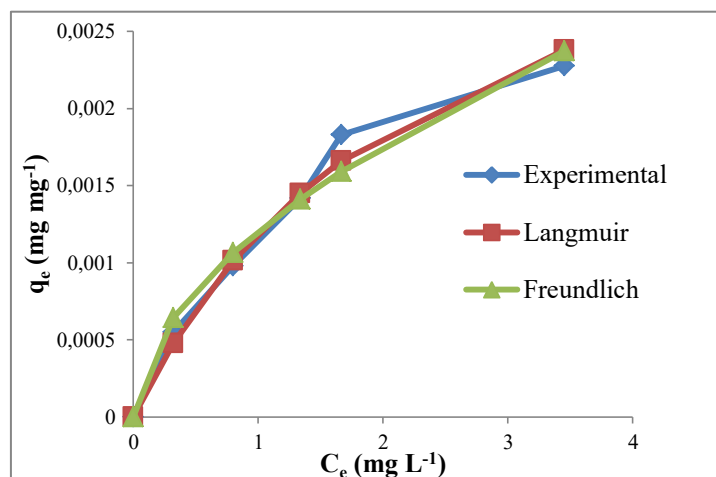


Fig. 7. Estradiol adsorption isotherm in bone activated carbon.

Table 3. Parameters of Langmuir and Freundlich nonlinear models for estradiol adsorption in the adsorbent bone activated carbon.

Models	Parameters	
Langmuir	q _{máx} (mg mg ⁻¹)	0,004009
	K _L (mg L ⁻¹)	0,423642
	R ²	0,986577
Freundlich	n	1,825140
	K _F ((mg.mg ⁻¹)(L.mg ⁻¹) ^{1/n})	0,001203
	R ²	0,976676



Conclusion

From the results obtained in this work it was possible to conclude that bone activated carbon was a great adsorbent in the removal of the estradiol hormone reaching a removal percentage of 100% in 40 minutes of adsorption. The adsorption process approached the pseudo-first order kinetic model and the Langmuir model was the one that best fitted the experimental data.

Acknowledgements

Thanks to PEQ-UEM and CAPES.

References

- [1] Daniele Maia Bila, Márcia Dezotti. Endocrine disrupters in the environment: part 1 - effects and consequences. *Quimica Nova* 2007;30:651-666.
- [2] Park HJ, Yong SO, Kim CH, Cho JC, Heo SJ, Ronald DD, Seo CD. Competitive adsorption of heavy metals onto sesame straw biochar in aqueous solutions. *Chemosphere* 2016;142:77-83.
- [3] Wilson JA, Pulford ID, Thomas S. Sorption of Cu and Zn by bone carbon. *Environment Geochemistry and Health*;25:51-56.
- [4] San Miguel G, Lambert SD, Graham NJD. A practical review of the performance of organic and inorganic adsorbents for the treatment of contaminated waters. *Journal of Chemical Technology and Biotechnology* 2006;8:1685-1696.
- [5] Bennett MC, Abram JC. Adsorption from Solution on the carbon and hydroxyapatite components of bone char. *J Colloid Interface Sci* 1957;23: 513-521.
- [6] Lurtwitayapont S, Thares ST. Comparison of Lead Removal by Various Types of Swine Bone Adsorbents. *Environment Asia* 2010;3:32-38.
- [7] Fuerhacker M, Dürauer A, Jungbauer A. Adsorption isotherms of 17 β -estradiol on granular activated carbon (GAC). *Chemosphere* 2001;44:1573-1579.
- [8] da Silva J E, Rodrigues FIL, Pacífico SN, Santiago LF, Muniz CR, Saraiva GD, Nascimento RF, Sousa Neto VO. Estudo de Cinética e Equilíbrio de Adsorção Empregando a Casca do Coco Modificada Quimicamente para a Remoção de Pb(II) de Banho Sintético. *Rev. Virtual Quim.* 2018;10.

pH effect and kinetics of diclofenac sodium (DCF) adsorption in solution using activated carbon from the tucuma (*Astrocaryum aculeatum*) endocarp

W.J.P. Costa^a, R.L.T. Costa^a, R.C.S. Araújo^a, R.A. Nascimento^a, R.L. Santos^a, E.M.P. Sousa^b, L.J.G. Faria^a

^a Universidade Federal do Pará, Augusto Corrêa 01, Belém 66075-110, Brazil

^b Universidade Federal Rural da Amazônia, Capanema, Brazil

Abstract

Drugs are substances of high human consumption, causing these compounds to present high concentrations in aqueous matrices, which serve as receptive bodies for domestic and industrial effluents. These contaminants affect the aquatic ecosystem and become bioaccumulative. In this work, there were studies of the adsorption mechanisms: kinetic, mass transfer and sodium diclofenac pH (DCF) on activated carbon produced from tucuma fruit residues (endocarp), using ZnCl₂ as activating agent, with carbonization temperature of 500 °C. The models used for kinetic adjustment were pseudo first-order and pseudo second-order, being the last one, which presented the best fit to the experimental data (R² = 0.98). The mass transfer mechanisms were studied from the intraparticle diffusion model, which determined that the external diffusion governs the adsorptive process, corroborating the interpretation of the Boyd model that defines the limiting step. Natural pH (6.06) was the condition that presented the highest adsorbent capacity (4.98 mg/g). Tests such as pH PCZ and the determination of functional groups were performed to characterize the charcoal, indicating it as a potential adsorbent used in the treatment of DCF contaminated effluents.

Keywords: diclofenac; activated carbon; *Astrocaryum aculeatum*

1. Introduction

It's growing the increased pollution of aqueous matrices by emerging contaminants (ECs), by pharmaceutical waste, personal hygiene and some industrial subproducts [1]. These ECs are harmful to aquatic life, from the reproduction of living beings, therein, until its bioaccumulation [2] and although a significant amount of these compounds are being discharged into the environment, studies are needed on how to control, monitor and decrease the incidence of these contaminants in the environment [3].

As examples of ECs, drugs belonging to the class of nonsteroidal anti-inflammatory agents (NSAIDs) are not registered for medical prescription, facilitating their consumption [4,5].

Among these compounds, diclofenac sodium (DCF) is among the most consumed in the world, obtaining the European Commission classification as a priority hazardous substance [6]. Thus, due to population demand for drugs, domestic effluents are polluting sources, requiring that appropriate treatments are investigated and implemented prior disposal into recipient bodies [7].

Separation processes are widely used in wastewater treatment plants, emphasizing the adsorption process for the removal of pollutants in wastewater. Activated carbon, besides being a precursor, is shown as one of the most efficient adsorbents in this process and can be obtained by organic solid waste, generally agroindustrial waste, which has a high content of lignin and cellulose in its composition, making production costs low and promoting sustainability and environmental



promotion [8,9]. The tucuma (*Astrocaryum aculeatum*) is one of the well-known fruits in the Amazon region, its occurrence occurs in almost the entire Amazon. In Brazil, states of Acre, Mato Grosso, Pará, Rondônia, Roraima and Amazonas are the places where tucuma is most found, especially in the last result until the other name for the fruit: tucuma-do-amazonas. The planting of tucuma is relatively easy, due to its ease of adaptation to poor soils, deforested areas and even after exposure to burning. Its palms can reach 30 m in height, its leaves (with thorns) 5 m in length. The fruit consists of peel, pulp and seed/core. In this work, the adsorption process of the removal of DCF (aqueous solution) in activated carbon produced by chemical activation, from the endocarp of the Amazonian fruit tucuma was investigated. The adsorption mechanism was analyzed in batch, with emphasis on the kinetics study, mass transfer, pH influence and characterization of the produced activated carbon.

2. Materials and Methods

2.1. Materials

Tucuma lumps (endocarp) were washed, dried (105 °C), separated from almonds and ground. NaOH solution (0.1 N) was used to wash the biomass for 24 h, followed by washing with distilled water of this material to pH 7, followed by activation of the biomass with ZnCl₂ solution (1:2 w/w) under immersion for 4 h. The activated biomass was dried at 105 °C and baked in the muffle furnace at an initial temperature of 200 °C and rising every 1 h at 100 °C to a final temperature of 500 °C. After carbonization, the material was washed with HCl (1 N) solution to remove excess ZnCl₂, dried at 105 °C and sieved to obtain a particle size (1.00-1.18 mm).

In order to prevent the moisture of the activated carbon of the tucuma endocarp (CATC) from interfering negatively in the adsorption tests, before the beginning of the experiments the adsorbent material was dried (105 °C) for 12 h. Diclofenac sodium (DCF) was obtained from Sigma-Aldrich MERCK (CAS number 15307-79-6).

2.2. Characterization

Physicochemical characterizations were performed in activated carbon in order to obtain greater interpretations about the DCF adsorption mechanism.

2.2.1. Functional Groups

Boehm's method was used to identify and quantify the functional groups present on the surface of solid material (CATC). In these tests, 2 g of activated carbon were used for 25 mL of solutions (HCl, NaOH, NaHCO₃ and Na₂CO₃).

2.2.1. Point Zero Charge (pH_{PZC})

The determination of pH at point zero charge (pH_{PZC}) was performed using the 11 point method.

Solutions (50 mL) at different pH in the range of 1-12 (initial pH) were placed in conical flasks (125 mL) and in contact with 50 mg of activated carbon from the tucuma endocarp (CATC). After 24 h under stirring, the CATC was separated from the solutions and pH readings for each (final pH) were taken.

2.3. Mass test

For the CATC mass test, several predetermined coal masses (0.025 - 0.5 g) were used and placed in contact with the DCF solution (25 mL) at natural pH. After 24 h, under stirring, a SHIMADZU UV-1800 spectrophotometer reading at 276 nm was taken and the corresponding concentrations after adsorption were calculated.

2.4. pH test

In order to evaluate the effect of pH of diclofenac sodium solution on the adsorption process of this drug in activated carbon of the tucuma endocarp, assays were performed for 24 h (time beyond equilibration time) with DCF (25 mL) and CATC. (0.2 g) in 125 mL conical flasks and room temperature (27 °C). DCF solutions with pH ranging from 2 - 10 were used.

2.5. Adsorption kinetics

In the adsorption kinetics study 25 mL of DCF solution at 10 mg.L⁻¹ and contact time

with CATC ranging from 1 to 480 min were used, all at room temperature (27 ° C).

The determination of the DCF concentration present in the solutions was performed by reading on UV-Vis spectrophotometer, wavelength 276 nm. From Eq. 1, the adsorption capacity (amount of diclofenac adsorbed by CATC) was obtained.

$$q = \frac{(C_0 - C) \cdot V}{m} \quad (1)$$

Where q is the adsorption capacity ($\text{mg}\cdot\text{g}^{-1}$); C_0 is the initial DCF concentration ($\text{mg}\cdot\text{L}^{-1}$); C is the concentration of DCF at time t ; V is the volume of solution used (L) and m is the activated carbon mass (g).

Statistica 7.0 software was used to adjust the mathematical models (pseudo-first-order, pseudo-second-order, intra-particle diffusion and Boyd) to the experimental data using the Quasi-Newton method.

2.6.1. Pseudo First-Order model (PFO)

This is one of the models capable of explaining data that suffers the process of external diffusion (mostly) [10]. The PFO model is given by Eq. 2, where $t = 0$, $q_t = 0$.

$$q(t) = q_e \cdot (1 - e^{-k_1 \cdot t}) \quad (2)$$

Where, q_e is the amount of DCF adsorbed to the equilibrium CATC ($\text{mg}\cdot\text{g}^{-1}$); k_1 is the adsorption constant of the PFO model and t is the time (min).

2.6.2. Pseudo Second-Order model (PSO)

It is also a model capable of predicting external diffusion data and described by Eq. 3 [11].

$$q(t) = \frac{t}{\left(\frac{1}{k_2 \cdot q_e^2}\right) + \left(\frac{t}{q_e}\right)} \quad (3)$$

Where k_2 is the adsorption constant of the PSO model.

2.6.3. Intraparticle Diffusion Model

This is an important model to describe adsorption processes governed mainly by intraparticle diffusion and having velocity as a determining factor of this process [12,13]. From this model, Eq. 4, we obtain intraparticle diffusion coefficient ($K_i - \text{mg}\cdot\text{g}^{-1}\cdot\text{min}^{-0.5}$) and C ($\text{mg}\cdot\text{g}^{-1}$) which is able to measure the boundary layer thickness:

$$q = K_i t^{0.5} + C \quad (4)$$

2.6.4. Boyd Model

Kinetic model widely applied to the adsorption process, as well as equilibrium study. It is capable of determining diffusion within the pores of the adsorbent and predicting the limiting step of the process (Eq. 5) [14] and the fraction of adsorbed solute at time t , given by Eq. 6:

$$F = 1 - (6\pi^2) \cdot e^{-Bt} \quad (5)$$

$$F = \frac{q_t}{q_e} \quad (6)$$

3. Results and Discussion

Data of functional groups present on the surface of CATC are described in Table 1, obtained from Boehm's methodology. The activation process by impregnation with ZnCl_2 results in an acid adsorbent [55].

Table 1. Functional groups of activated carbon y tucuma endocarp.

Sample	Acid Groups total ($\text{mEq}\cdot\text{g}^{-1}$)	Basic Groups Total ($\text{mEq}\cdot\text{g}^{-1}$)
CATC	2.20	1.59

The pH value at the zero charge point of the activated carbon of the tucuma endocarp was determined by graph and shown in Fig. 1.

The pH_{PZC} the CATC was 5.54, which features its surface with acid characteristics, confirming the analysis made of the same material surface groups.

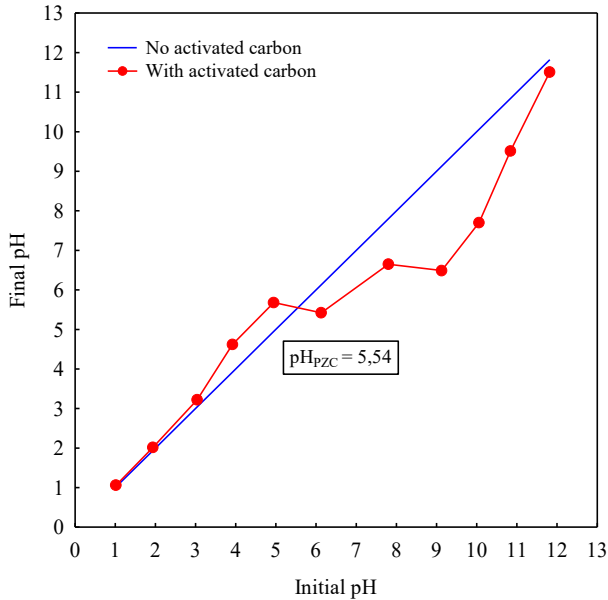


Fig. 1 Determination of point zero charge pH (pH_{PZC}).

Fig. 2 shows the tests performed on CATC mass evaluation in adsorption of sodium diclofenac in solution. It was noted that when using 5 g.L^{-1} CATC the adsorbed amount at equilibrium was 1.98 mg g^{-1} but removal was at 78.15%.

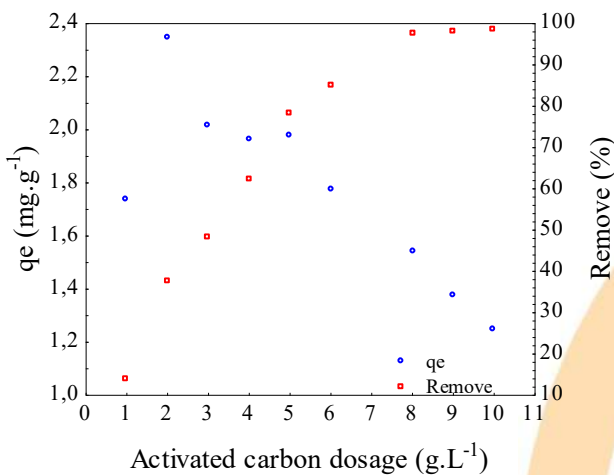


Fig. 2. Effect of CATC mass on DCF adsorption.

In order to reconcile optimal removal to a not so distant q_e from the aforementioned, the mass of 0.2 g (8 g.L^{-1}) of CATC was chosen for DCF adsorption in a 25 mL solution, as a q_e of 1.54 mg.g^{-1} and removal greater than 97% was presented. This percentage of removal is similar to DCF adsorption in activated carbon of the olive

stones [9], also performing pH effect and adsorption kinetics in his study.

Using the mass defined in the mass test (0.2 g), Fig. 3 shows the effect of DCF pH on the adsorption capacity of this tucuma endocarp activated carbon solute. The q_e had a $4.02 - 4.98$ variation under the tested pH, being this maximum value found for pH 6 (very close to the natural pH of the DCF solution). Thereby, the natural pH was chosen for the DCF adsorption kinetic study, aiming to minimize possible treatments to the adsorbate.

In the study of DCF adsorption kinetics in CATC, adjustments were made to the external diffusion mathematical models (pseudo-first-order and pseudo-second-order). It were used the coefficient of determination (R^2) and mean percentage error (ϵ), described by Eq. 7. The adjustment data are shown in Table 2.

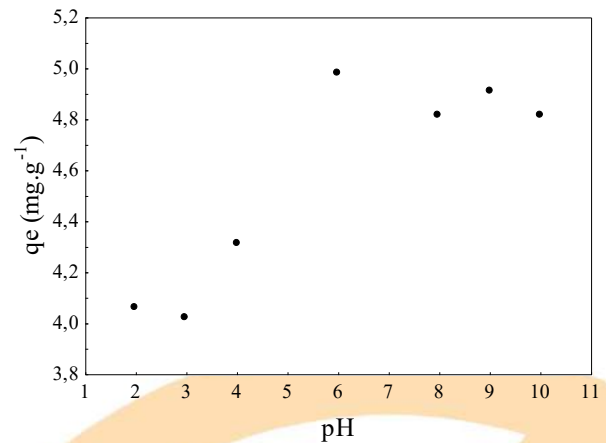


Fig. 3. Effect DCF pH adsorption solution on CATC.

$$\epsilon = \frac{100}{N} \cdot \sum_{i=1}^N \frac{|q_{exp} - q_{pred}|}{q_{exp}} \quad (7)$$

Where: N is the number of experiments; q_{exp} is the experimental adsorption capacity at time t ; q_{pred} is the adsorption capacity predicted by the model.

The pseudo-second-order model presented higher termination coefficient value (0.9820) than that of the pseudo-first-order and lower mean percentage error (0.4428%), although both models were satisfactory in predicting the DCF adsorption kinetics in CATC.

Table 2. Parameters of external diffusion kinetic models and statistics values.

Parameters				
Model	q (mg.g-1)	k (min ⁻¹)	R ²	ε (%)
PFO	1.5116	0.0129	0.9660	0.6155
Model	q (mg.g-1)	k (g.mg ⁻¹ .min ⁻¹)	R ²	ε (%)
PSO	1.7569	0.0092	0.9820	0.4428

Larous [9] studied the adsorption of DCF on activated carbon of *Moringa oleifera*, which presented a pseudo second order model as the best fit to the experimental data. Fig. 4 shows the comparison of mathematical models to experimental data.

From the intraparticle diffusion model, the graph (Fig. 5) was constructed with the experimental adsorption kinetics data, showing multilinearity and allowing the visualization of the adsorption steps: external diffusion, intraparticle diffusion and equilibrium.

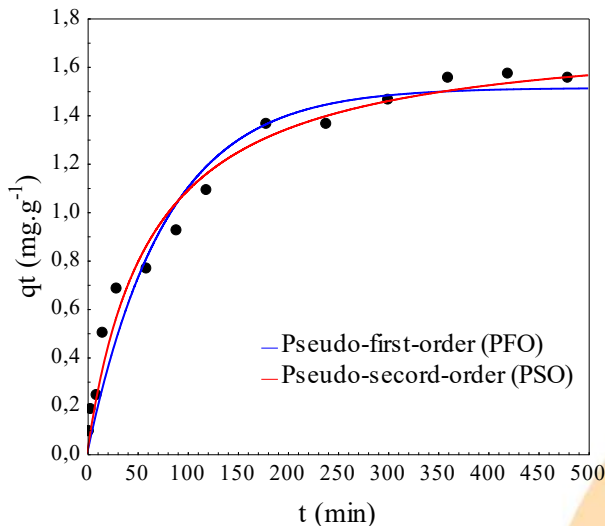


Fig. 4. Adsorption kinetics and adjustment of the PFO and PSO models.

The adsorption process of diclofenac sodium by activated carbon of the tucuma endocarp was by intraparticle diffusion and external diffusion, the latter being much superior.

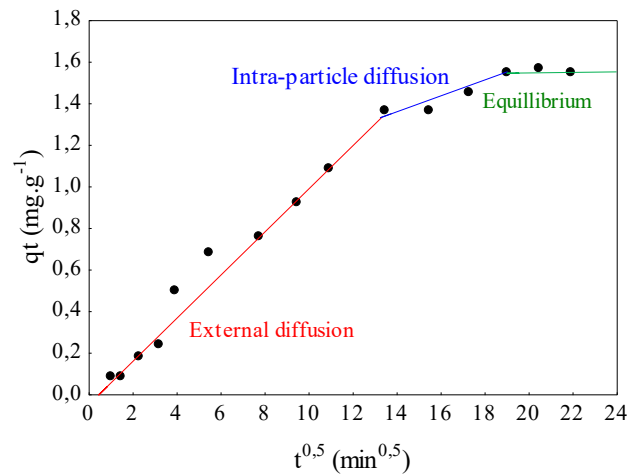


Fig. 5 Adjustment of the intraparticle diffusion model.

The process of external diffusion was noted as a limiting step of adsorption, a fact confirmed by the graphic method from the Boyd model (Fig. 6). When the constructed line passes through the origin (0,0) is said that the intraparticle diffusion dictate the adsorption process, otherwise any other conformation of this line indicates that the external diffusion is the limiting step of the process.

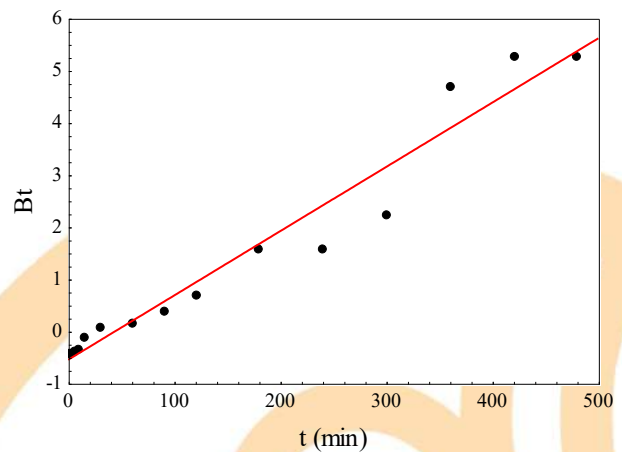


Fig. 6. Adjustment of Boyd's kinetic model to the experimental data

4. Conclusion

The activated carbon of the endocarp tucumã presented mostly acidic character of the surface area and pH PZC equal to 5.54, due to its activation with zinc chloride.



The DCF solution (10 mg.L^{-1}) at pH 6 (natural pH) was used for kinetic studies, and the pseudo-second order model was able to satisfactorily explain the experimental data and presented equilibrium time (solid saturation) of 350 minutes. The graph constructed from Boyd's model was able to determine the external diffusion step as limiting the adsorption process.

The activated carbon produced from the residues of the tucumã fruit (endocarp) proved an effective and promising adsorbent material in the removal of diclofenac at natural pH without the need for pre-treatment in the effluent.

[9] Larous S, Meniai AH. Adsorption of Diclofenac from aqueous solution using activated carbon prepared from olive stones. *International journal of hydrogen energy* 2016; 41; 10380 – 10390.

[10] Lagergren S. *Handlingar*, v.24, p. 1 – 39, 1898.

[11] Ho YS, McKay G. *Process Biochem.*, v.34, p. 451-465, 1999.

[12] Weber Jr WJ, Morris JC. *Advances in Water Pollution Research*, New York: Pergamon Press, 1962.

[13] Nascimento RF, Lima ACA, Vidal CB, Melo DQ, Raulino GSC. *Adsorção – aspectos teóricos e aplicações ambientais*. Ed. UFC: Fortaleza; 2014.

[14] Boyd GE, Adamson AE, Meyers LS. *J. Am. Chem. Soc.*, v. 69, p. 2836-2848, 1947.

References

[1] Klaper R, Welch LC. *Emerging Contaminant Threats and the Great Lakes: Existing science, estimating relative risk and determining policies*. Alliance for the Great Lakes; 2011.

[2] Kwak K, Ji K, Kho Y, Kim P, Lee J, Ryu J, Choi K. Chronic toxicity and endocrine disruption of naproxen in freshwater waterfleas and fish, and steroidogenic alteration using H295R cell assay. *Chemosphere* 2018; 204; 156 – 162.

[3] Petrie B, Barden R, Kasprzyk-Hordern B. A review on emerging contaminants in wastewaters and the environment: Current knowledge, understudied areas and recommendations for future monitoring. *Water Research* 2015, 72; p. 3 - 27.

[4] Vitor RS, Lopes CP, Menezes HS, Kerkhoff CE. Padrão de consumo de medicamentos sem prescrição médica na cidade de Porto Alegre, RS. *Ciência e Saúde Coletiva* 2008, vol.13.

[5] Monteiro ECA, Trindade JMF, Duarte ALBP, WH Chahade. Os antiinflamatórios não esteroidais (AINEs). *Temas de Reumatologia Clínica* 2008; vol. 9; nº 2.

[6] European Commission, 2012. Proposal for a Directive of the European Parliament and of the Council Amending Directives 2000/60/EC and 2008/105/EC as Regards Priority Substances in the Field of Water Policy.

[7] Nishi I, Kawakami T, Onodera S. Monitoring the concentrations of nonsteroidal anti-inflammatory drugs and cyclooxygenase-inhibiting activities in the surface waters of the Tone Canal and Edo River Basin. *Journal of Environmental Science and Health* 2015, Part A, 50:11, 1108-1115.

[8] Moura FCC, Rios RDF, Galvão BRL. Emerging contaminants removal by granular activated carbon obtained from residual Macauba biomass. *Environmental Science and Pollution Research* 2018; 25; 26482–26492

Adsorption of Remazol Black B dye using biochar produced from gasification residues

Bruna F. do Nascimento^a, Adjane D. de Oliveira^b, Rafaella de Moura Medeiros^b, Alisson C. do Nascimento^a, Caroline Maria B. de Araujo^a, Maryne Patrícia da Silva^a, Ronald K. da Silva Santos^a, Maurício A. da Motta Sobrinho^a

^a Departamento de Engenharia Química, Universidade Federal de Pernambuco, Av. Prof. Moraes Rego 1235, Recife-PE, 50670-910, Brazil

^b Universidade Federal de Pernambuco, Av. da Arquitetura s/n, Cidade Universitária, Recife-PE, 50740-550, Brazil

Abstract

The presence of dyes in textile wastewater is one of the main problems faced by textile industry. Adsorption processes are widely used in the removal of these dyes, however, seeking to minimize costs, the need for developing adsorbents with low production cost and reused from other processes has arisen. Thus, the aim of this work was to evaluate the removal capacity of Remazol Black B dye using as adsorbent a biochar produced from wood waste used during gasification for energy production. The adsorbent was characterized using X-ray diffraction (XRD), surface area (BET), thermogravimetric analysis (TGA), scanning electron microscopy (SEM) and pH at the point of zero charge (pH_{PZC}). In the adsorption assays kinetic and equilibrium studies were performed. The microporosimetric analysis showed that the biochar is majorly composed of mesoporous, which is evidenced when the SEM micrograph is evaluated. XRD showed characteristics of predominantly amorphous structures. The biochar surface presented basic characteristics with pH_{PZC} = 8.02. The adsorbent-adsorbate equilibrium was reached in 90 min, and the data followed pseudo-second order kinetic model. It was found that the Sips isotherm model best fit to the equilibrium data. The maximum adsorption capacity was 34.41mg.g⁻¹. Thus, the results exhibited the potential of the adsorbent produced by the gasification of vegetal biomass for water treatment.

Keywords: Dyes; Gasification; Adsorption; Biomass Residues, Biochar.

1. Introduction

Due to the rapid growth and use of large quantities of water, as well as the chemical inputs during the processing, textile industries have become a serious threat to water resources [1]. Among the various complex substances present in these effluents, dyes are considered the main contaminants that threaten ecosystems, because of their high toxicity, low biodegradability, carcinogenicity and bioaccumulation [2,3].

Therefore, several approaches have been successfully developed and applied for textile wastewater treatment. Among these, adsorption stands out for its low cost, simple operation, high efficiency in the removal of dyes from textile

wastewater and most importantly, there is a wide variety and availability of adsorbents [3].

However, adsorption using commercial activated carbon is normally a high cost process, being also unjustifiable from an environmental point of view, as it uses chemicals for activation and vegetation as raw material. Thus, it motivates the search for new alternatives for producing activated carbon in a more economical and sustainable way [4].

Thermochemical processing of biomass in a gasifier produces, in addition to energy and synthesis gas, a solid residue containing coal (mainly carbon) and ashes. This coal can be burned for heat and energy, carbonated, activated for adsorption, or even applied to the soil as a soil altering agent and carbon sequestering [5,6]. The use of agricultural waste in coal production for process use is a proposal that seeks to reduce

process costs while providing a solution for waste management [6].

This study aims to evaluate the removal of the textile dye Remazol Black B, using a biochar produced from the gasification of wood residues as adsorbent.

2. Methodology

2.1 Biosorbent production and characterization

Wood chips were used, as well as wood waste from Campus I of the Federal University of Paraíba (UFPB), located in the city of João Pessoa – PB (Brazil). The gasifier was purchased from the Indian Institute of Science/Combustion Gas Propulsion Laboratory IISc/CGPL (India). It is a fixed bed type with open top gas lighter and downflow air inlet with 4kW thermal capacity. The equipment is located at the Activated Charcoal Laboratory, on campus I, UFPB (see Fig. 1).



Fig. 1. Photograph of the gasifier

The methodology for the biochar production starts with the introduction of the biomass at the top of the gasifier. As the material descends, due to gravity force, the wood pyrolysis process takes place, with an initial temperature of 40.5 °C reaching 1079 °C. After gasification, the biochar was macerated and classified in a 100 mesh screen.

The adsorbent was characterized using scanning electron microscopy (SEM), X-ray diffraction (XRD), thermogravimetric analysis (TGA/DTG), microporosimetric analysis and determination of pH at the point of zero charge (pH_{PZC}).

2.2 Adsorption batch tests

For the adsorption of Remazol Black B using as adsorbent the biochar produced by the gasification

of wood waste, the experiments were performed in replicate and conducted in a shaker at room temperature, using properly closed 125 mL erlenmeyers.

The synthetic solution of Remazol Black B, 100 mg.L⁻¹, was prepared using distilled water. No pH adjustment was proceeded.

By the end of each experiment, the samples were filtered and the final concentrations were determined by a UV-Visible spectrophotometer at 319 nm wavelength.

2.3 Adsorption kinetics

To perform the kinetic experiments at room temperature, 125 mL enlenmeyer flasks were used, in which 0.03 g of adsorbent and 25 ml of Remazol Black B solution (100 mg.L⁻¹) were placed. The flasks were then transferred to a shaker table at 300 rpm and after the time intervals - 1, 5, 10, 15, 30, 15, 60, 90, 120, 150 and 180 min, each sample was removed. The solution was filtered and the final concentration value obtained.

Experimental data were adjusted to non-linear pseudo-first order (Eq. 1), pseudo-second order (Eq. 2) and Elovich (Eq. 3) kinetic models.

$$\frac{\partial q}{\partial t} = k_1(q_e - q_t) \quad (1)$$

$$\frac{\partial q}{\partial t} = k_2(q_e - q_t)^2 \quad (2)$$

$$\frac{\partial q}{\partial t} = \alpha e^{(-\beta q_t)} \quad (3)$$

In which, q_e and q_t are the adsorptive capacities (mg.g⁻¹) at the equilibrium and at time t (min), respectively; k_1 and k_2 correspond to the pseudo-first order (min⁻¹) and pseudo-second order (g.mg⁻¹.min⁻¹) adsorption rate constants. Elovich constants are given by α and β , where α is related to the initial rate, since (d_q/d_t) tends to α when $q_t \rightarrow 0$.

2.4 Adsorption isotherm

For the isotherm experiments, different concentrations of the dye were used (5, 15, 25, 50, 75 e 100 mg.L⁻¹). Thus, 25 mL aliquots were taken from each solution and transferred into elernmeyers containing 0.03 g of the adsorbent. The flasks were placed on a shaker at 25 °C until the equilibrium was reached. After that, samples

were filtered and the final concentration was determined.

Experimental data were adjusted to Langmuir (Eq. 3), Freundlich (Eq. 4) and Sips /Langmuir-Freundlich (Eq. 5) models.

$$q_e = \frac{q_{max}K_L C_e}{1 + K_L C_e} \quad (3)$$

$$q_e = K_F C_e^{1/n} \quad (4)$$

$$q_e = \frac{K_{LF} q_{max} C_e^m}{1 + K_{LF} C_e^m} \quad (5)$$

In which C_e represents the concentration of the dye in the equilibrium (g.L^{-1}); q_{max} is the maximum adsorptive capacity (mg.g^{-1}); n is the heterogeneity factor; K_L Langmuir Constant (L.mg^{-1}), K_F Freundlich Constant (L.mg^{-1}), K_{LF} Langmuir-Freundlich Constant (L.mg^{-1}) and m is the heterogeneity parameter.

3. Results

3.1. Characterization of the biochar

The parameters obtained from the microporosimetric analysis, such as surface area, pore volume and pore diameter were $403.7670 \text{ m}^2.\text{g}^{-1}$, $0.1338 \text{ cm}^3.\text{g}^{-1}$ and 26.8230 \AA , respectively. By analyzing the results, it is possible to conclude that the biochar is essentially mesoporous, as it can be observed in the result obtained from the pore distribution, which is evidenced when the scanning electron microscopy is evaluated.

Fig. 2 exhibits the SEM images of the biochar. It is observed that both samples are composed of particles of approximate size and shape, presenting a regular surface with homogeneous structure. At the 3000-fold magnification of the sample (Fig. 2b), it is possible to observe both meso and macroporous structures; as well as the formation of visible pores on the surface of the adsorbent with homogeneous cavities.

XRD pattern in Fig. 3 presents a predominantly amorphous structure due to the total absence of sharp peaks, characteristic of crystalline compounds [6]. However, it can also be observed that the crystalline phase of cellulose is determined by the presence of the most intense characteristic peak, which is found in $2\theta = 26^\circ$.

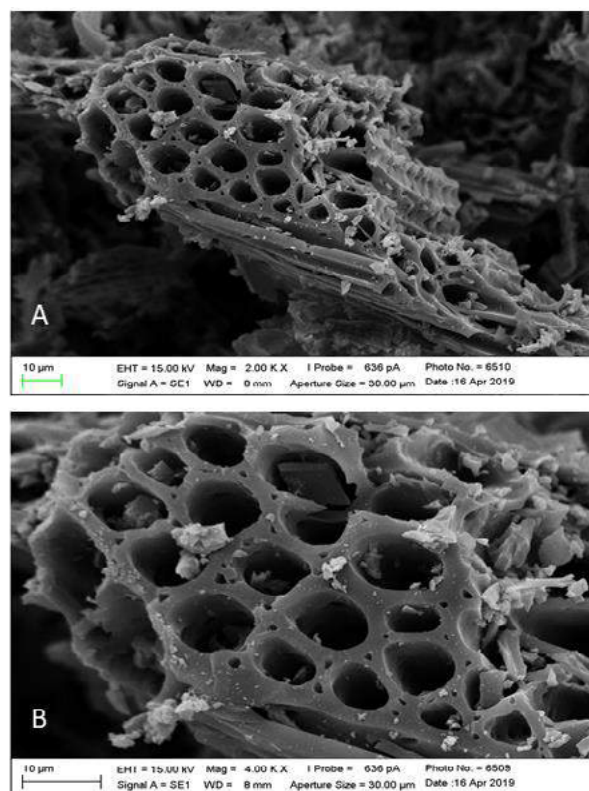


Fig. 2. SEM images of the biochar with magnifications of: A) 2000 and B) 3000 X.

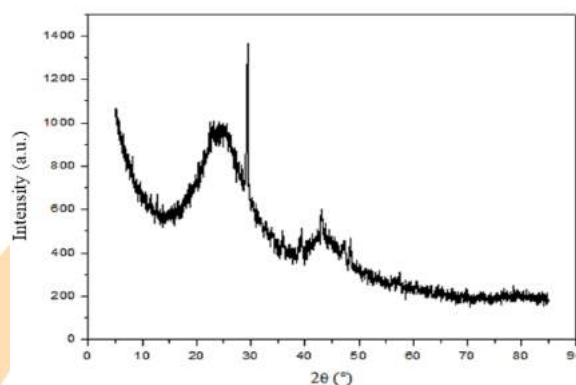


Fig. 3. XRD pattern of the biochar.

Results regarding the thermogravimetric analysis of the biochar produced are exhibited in Fig. 4. As it can be seen, the first mass loss occurs between 30 and 100 °C, being attributed to the adsorbed water. The second weight loss is observed between 200 and 600 °C, being related to the decomposition of all functional groups on the surface of the biochar, followed by the production of volatile compounds, such as CO_2 , CO , CH_4 , H_2O and H_2 [7,8]. The peak near 650 °C is attributed to the decomposition of phenolic groups, as the peak from 800 °C may be due to the

decomposition of structural carbon, with CH bond breakage [6].

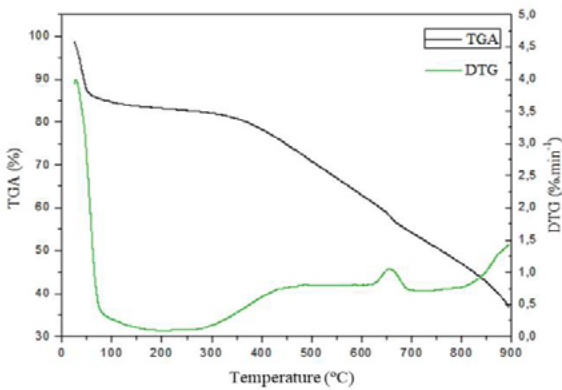


Fig.4. TGA /DTG curves of the adsorbent

Based on the TGA/ DTG results, it is observed the formation of three main stages, including the initial evaporation of free water (which is linked by physical forces to macromolecules) and combined water (water that is free to be used by microorganisms and can then participate in chemical reactions or act as a solvent). This evaporation occurs at 25–120 °C. The second stage occurs due to the decomposition of hemicellulose, this decomposition occurs between 200–400 °C. Regarding the third stage (400 -750 °C), there is a great weight loss, which probably corresponds to the decomposition of most thermally resistant components, such as lignin [6].

pH_{PCZ} (Fig. 5) is a parameter that indicates the pH value in which the adsorbent surface charge is null, which means that the number of positive and negative charges are equivalent [7]. From this analysis it is possible to predict how the adsorbent will behave in solution. The pH_{PCZ} for the biochar obtained was 8.02.

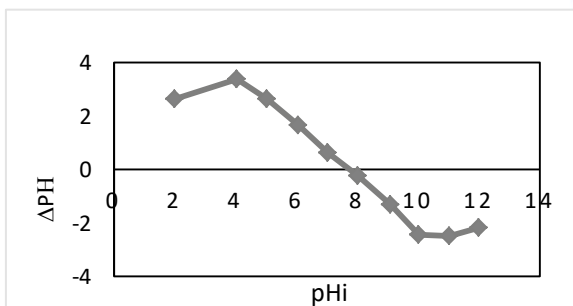


Fig. 5. pH_{PCZ} of the biochar.

3.2. Adsorption kinetics

Fig. 6 exhibits the effect of contact time on dye adsorption. There is an initial steep rise, which is

followed by a slower approach to a plateau, where the amount of adsorbed dye remains virtually constant.

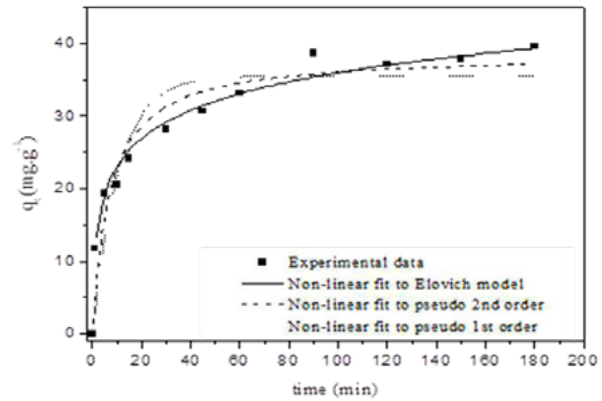


Fig. 6. Contact time and nonlinear adjustments of kinetic models (Experimental conditions: $C_0 = 100 \text{ mg.L}^{-1}$, $T = 25 \text{ }^\circ\text{C}$, $m_{ads} = 0.03 \text{ g}$ and 300 rpm).

By analyzing the curve, it can be noticed that most of the dye was adsorbed in the first 40 min of experiment. This result may be related to the fact that adsorption sites are available on the material surface at the beginning of the experiment [7].

In general, the increase in adsorption capacity occurs initially at a rapid rate, and stabilization takes about 90 min. After that, the data only slightly changes, indicating that the system has reached equilibrium, which may be due to the surface saturation of the adsorbent.

Contact time is of significant importance for the application of adsorption in wastewater treatment. The rapid removal rates of adsorbate and the attainment of equilibrium in a short period of time is a characteristics that indicates the adsorbent effectiveness [7,8]. Kinetic parameters are listed in Table 1.

Table 1. Parameters of kinetic models determined by nonlinear regression fit of experimental data.

Model	Parameter	Values
Pseudo-first order	$q \text{ (mg.g}^{-1}\text{)}$	35.53 ± 1.83
	$k_1 \text{ (min}^{-1}\text{)}$	0.094 ± 0.022
	R^2	0.86
	SSE	203.37
Pseudo-second order	$q \text{ (mg.g}^{-1}\text{)}$	38.56 ± 1.76
	$k_2 \text{ (g.mg}^{-1}\text{.min}^{-1}\text{)}$	0.004 ± 0.001
	R^2	0.93
	SSE	102.49
Elovich	α	32.84 ± 7.73
	β	0.177 ± 0.009

R^2	0.98
SSE	23.31

According to the data in Table 1, the Elovich model best described the adsorption kinetics of Remazol Black B with R^2 equal to 0.98. This model also presented the lowest value for SSE (23.31), when compared to both pseudo-first and pseudo-second order models.

This kinetic model is widely used to describe chemical adsorption, being normally suitable for systems in which the solid presents heterogeneous surface. However, sometimes the kinetic behavior of some mildly rising adsorption systems can also be satisfactorily described by the Elovich equation [9].

3.3. Adsorption isotherm

Regarding the equilibrium study, data converged neither to Langmuir nor Freundlich isotherms, only Sips isotherm fitted to experimental data, as it can be seen in Fig. 7. In Fig.7, it is observed that the adsorption isotherm presented a growing profile, with increasing equilibrium concentration until reaching a constant value. The following parameters were obtained for the Sips model: $q_{max} = 34.41 \pm 4.73 \text{ mg.g}^{-1}$; $K_{LF} = 0.734 \pm 0.37 \text{ (L. mg}^{-1}\text{)}$ and $n = 1.16 \pm 0.48$.

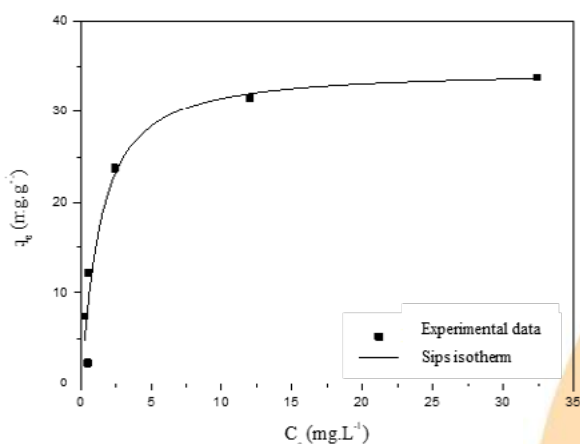


Fig. 7. Adsorption isotherm on biochar (Experimental conditions: $T = 25 \text{ }^\circ\text{C}$, $m_{ads} = 0.03 \text{ g}$, $t = 90 \text{ min}$ and 300 rpm stirring).

This model indicates that at lower concentrations of Remazol Black B, experimental data follow Freundlich model, considering the multilayer adsorption; while for higher concentrations, the adsorption capacity follows the

Langmuir model, considering the existence of a saturation point [10, 11].

In the Sips model the coefficient n can indicate surface heterogeneity, being more heterogeneous when its value is close to zero. Therefore, it is noted that for the equilibrium isotherm obtained, the n value is ~ 1 , which indicates the surface homogeneity [12].

Table 3 exhibits a comparison with previous works regarding the maximum adsorption capacity (q_{max}) using different adsorbents to remove Remazol Black B dye from aqueous solution.

Table 3. Maximum adsorption capacity values of Remazol Black B using different adsorbents according to previous works.

Adsorbent	q_{max} (mg.g^{-1})	Reference
Green coconut mesocarp	2.93	[13]
Mixed biomass of <i>Aspergillus niger</i> and elephant grass	9.645	[14]
Activated carbon from <i>Araucaria angustifolia</i> bark	446.2	[15]
Sugarcane bagasse	1.098	[16]
Fresh pinion bark	74.6	[17]
Biochar produced from gasification residues	34.41	This study

4. Conclusions

The results showed the feasibility of using the biochar produced during the gasification of biomass, as well as data regarding the adsorption process, which encourages the advance of more detailed research with this material, investigating different operating conditions, such as the temperature effect, and also using different types of textile dyes.

Acknowledgements

The authors thank the financial support provided by the Conselho Nacional de Desenvolvimento Científico e Tecnológico (CNPq), the Coordenação de Aperfeiçoamento de Pessoal de Nível Superior (CAPES), as well as the Fundação de Apoio à Ciência e Tecnologia do Estado de Pernambuco (FACEPE).

References

- [1] CINPERI, N. C.; OZTURK, E.; YIGIT, N. O.; KITIS, M. Treatment of woolen textile wastewater using membrane bioreactor, nanofiltration and

- reverse osmosis for reuse in production processes. *Journal of Cleaner Production*, 2019; 223:837-848.
- [2] LAFI, R.; GZARA, L.; LAJIMI, R. H.; HAFIANE, A. Treatment of textile wastewater by a hybrid ultrafiltration/electrodialysis process. *Chemical Engineering and Processing- Process Intensification*, 2018; 132:105-113.
- [3] PESSOA, T. S.; FERREIRA, L. E. L.; SILVA, M. P.; NETO, L. M. P.; NASCIMENTO, B. F.; FRAGA, T. J. M.; JÁGUARIBE, E. F.; CAVALCANTI, J. V.; SOBRINHO, M. A. M. Açai waste benefiting by gasification process and its employment in the treatment of synthetic and raw textile wastewater. *Journal Cleaner Production*, 2019;240.
- [4] EL-SAYED, G. O.; YEHIA, M. M.; ASAAD, A. A. Assessment of activated carbon prepared from cornob by chemical activation with phosphoric acid. *Water Resources and Industry*, 2014; 8: 66-75.
- [5] BREWER, Catherine E. et al. Characterization of biochar from fast pyrolysis and gasification systems. *Environmental Progress & Sustainable Energy*, 2009; 28(3):386-396.
- [6] KELM, M. A. P.; Jr. SILVA, M. J.; HOLANDA, S. H. B.; ARAUJO, C. M. B.; ASSIS, R. B. F.; FREITAS, E. J.; DOS SANTOS, D. R.; SOBRINHO, M. A. M. Removal of azo dye from via adsorption on biochar produced by the gasification of wood wastes. *Environmental Science and Pollution Research*, 2019; 1-16.
- [7] NASCIMENTO, Bruna Figueiredo do. Adsorção de furfural em carvão ativado do endocarpo de açai. 2019. Dissertação de Mestrado. Universidade Federal de Pernambuco. Disponível em <<https://repositorio.ufpe.br/handle/123456789/33819>>.
- [8] DANISH, M., AHMAD, T., HASHIM, R., SAID, N., AKHTAR, M. N., MOHAMAD-SALEH, J., & SULAIMAN. Comparison of surface properties of wood biomass activated carbons and their application against rhodamine B and methylene blue dye. *Surfaces and Interfaces*, 2018; 11:1-13.
- [9] WU, F. C.; TSENG, R. L.; JUANG, R. S. Characteristics of Elovich equation used for the analysis of adsorption kinetics in dye-chitosan systems. *Chemical Engineering Journal*, 2009; 150 (2-3): 366-373.
- [10] MALL, I.D., SRIVASTAVA, V.C.; AGARWAL, N.K. (2006). Removal of Orange-G and Methyl Violet Dyes by Adsorption onto Bagasse Fly Ash— Kinetic Study and Equilibrium Isotherm Analyses. *Dyes & Pigments*, 69, 210-223.
- [11] CRUZ, Í. J.; MARQUES, L. M.; SOUZA, K. C.; LIMA, V. F. MARQUES, O. M.; NASCIMENTO JÚNIOR, A. J. Removal of Remazol Black B by use of mixed biomass of *Aspergillus niger* and elephant grass (*Pennisetum purpureum* Schum). *ENGEVISTA*, 2016; 18 (2):265-279.
- [12] FERREIRA, R. C.; LIMA, H. H. C.; COUTO JÚNIOR, O. M.; ARROYO, P. A.; CARVALHO K. Q.; BARROS, M. A. S. D. Utilização de carvão ativado de dendê in natura e funcionalizado em meio ácido na adsorção de paracetamol. *Revista Matéria*, 2018;23(1).
- [13] LEAL, C. C. A. Avaliação da remoção do corante remazol black b de efluentes têxteis utilizando como adsorvente o mesocarpo do coco. Dissertação apresentada ao Curso de Mestrado do Departamento de Engenharia Química da Universidade Federal de Pernambuco, como requisito parcial à obtenção do título de Mestre em Engenharia Química. Recife, 2003.
- [14] CRUZ, I. J.; MARQUES, L. M.; SOUZA, K. C.; LIMA, V. F. MARQUES, O. M.; NASCIMENTO JÚNIOR, A. J. Removal of Remazol Black B by use of mixed biomass of *Aspergillus niger* and elephant grass (*Pennisetum purpureum* Schum). *ENGEVISTA*, V. 18, n. 2, p. 265-279, Novembro 2016.
- [15] CARDOSO, N. F.; PINTO, R. B. LIMA, E. C.; CALVETE, T.; AMAVISCA, C.; ROYER, B.; CUNHA, M. L.; FERNANDES, T. H. M. PINTO, I. S. Removal of remazol black B textile dye from aqueous solution by adsorption. *Desalination*. Volume 269, Issues 1–3, 15 March 2011, Pages 92-103.
- [15] REIS, G. S.; LIMA, E. C.; SAMPAIO, C. H. Produção de carvão ativado a partir de lodo de esgoto doméstico e sua aplicação na adsorção do corante preto remazol 5 em solução aquosa. *Exacta*, Belo Horizonte, v. 8, n.2, p. 15-23. (2015). Editora UniBH.
- [16] OLIVEIRA, C. C. N. Estudo de equilíbrio e modelagem cinética da adsorção de corante têxtil “Remazol Black B” sobre bagaço de cana in natura e carvão ativado. Dissertação apresentada ao Curso de Mestrado do Departamento de Engenharia Química da Universidade Federal de Pernambuco, como requisito parcial à obtenção do título de Mestre em Engenharia Química. Recife, 2003.
- [17] PINTO, R. B. Remoção do corante têxtil preto de remazol b de soluções aquosas usando adsorventes a base de casca de pinhão. Dissertação apresentada como requisito parcial para a obtenção do grau de Mestre em Química no Programa de Pós-Graduação em Química da Universidade Federal do Rio Grande do Sul. Porto Alegre, 2012.

Furfural adsorption using a biochar obtained from the gasification of acai endocarp

Bruna F. do Nascimento^a, Alisson C. do Nascimento^a, Caroline Maria B. de Araujo^a, Riann de Queiroz Nóbrega^b, Francisco Everton T. de Luna^c, Flávio Luiz H. da Silva^b, Jorge Vinícius F. Lima Cavalcanti^a, Maurício A. da Motta Sobrinho^a

^a Departamento de Engenharia Química, Universidade Federal de Pernambuco, Av. Prof. Moraes Rego 1235, Recife-PE, 50670-910, Brazil

^b Departamento de Engenharia Química, Universidade Federal de Paraíba, Campos I, Cidade Universitária, João Pessoa-PB, 58051-900, Brazil

^c Departamento de Engenharia Mecânica, Universidade Federal de Paraíba, Campos I, Cidade Universitária, João Pessoa-PB, 58051-900, Brazil

Abstract

Furfural is an organic compound formed as a product of pentose degradation which in high concentrations, can negatively affect the fermentation process, inhibiting the growth and metabolic activity of microorganisms. One way to reduce the effects of this inhibitor is to apply hydrolysate detoxification processes prior to fermentation, such as adsorption. Thus, this work aims to evaluate the adsorptive removal of furfural using a biochar obtained from the gasification process of the acai endocarp, and activated with NaOH. The influence of important parameters on the adsorption process such as stirring speed and adsorbent dosage were evaluated. Adsorption kinetics and isotherms were performed in batch mode. The studies exhibited maximum furfural removal capacity with agitation speed of 200 rpm and adsorbent dosage of 7 g.L⁻¹. The adsorbent-adsorbate equilibrium time was 90 min, and kinetic data followed pseudo-second order model. In the equilibrium studies, the model that best fitted the data was the Sips, presenting a maximum adsorption capacity of 48.016 mg.g⁻¹.

Keywords: Furfural; Adsorption; Gasification; Biochar; Acai waste.

1. Introduction

Furfural production occurs under high pressure and temperature conditions as a product of pentose degradation [1]. The hemicellulose present in the biomass undergoes hydrolysis in acid medium to form xylose, which dehydrates forming furfural [2]. Various inorganic acids, such as HCl and H₂SO₄, can be employed as catalysts in the acid hydrolysis process [3]. Arabinose can also be converted into furfural, although, unlike xylose, it is less present in the lignocelluloses' liquor [4].

At high concentrations, furfural may negatively affect the microbial fermentation process of the treated materials, inhibiting their growth and metabolic activity [5]. Thus, a strategy to reduce the harmful effects of this inhibitor is to use hydrolysate detoxification processes prior to fermentation [3,6]. Among detoxification techniques, adsorption stands

out for its ability to remove /reduce inhibitors without affecting the concentration of valuable compounds such as soluble monosaccharides and polysaccharides, which are the sources converted into ethanol during fermentation [6].

On the other hand, the acai berry (*Euterpe oleracea Mart.*), a native fruit to South America, is of great importance in Brazil, not only for its potential health benefits, but also for the economy, especially in the Northern and Northeast regions of the country. The main residue of acai is an oleaginous seed rich in cellulose, hemicellulose and lignin. Normally, there is no proper disposal of these wastes, so they are often disposed in the streets, posing risk to the environment [7].

Therefore, the aim of this work was to evaluate the adsorptive removal of furfural using activated biochar obtained from residues of the gasification process of the acai endocarp (acai seeds).

2. Methodology

2.1 Adsorbent

The adsorbent used was a biochar produced by the gasification process of the acai seeds. Then, the residue was activated with NaOH and was characterized according to Pessoa et al. (2019) [7].

2.2 Synthetic furfural solution

Adsorption tests were proceeded using the furfural solution (1000 mg.L⁻¹) acquired from Sigma-Aldrich. Synthetic solution and furfural quantifications were performed according to the methodology described by the Adolfo Lutz Institute [8], which consists of diluting 10 g of furfural in 100 mL of pure ethanol (Modern Chemistry) in a 100 mL flask. From that, the synthetic solutions were obtained using 10 mL of freshly prepared solution for each 1000 mL of ethanol 50%.

The quantification was performed based on Hewitt's method, which consists in producing an imine, which is the condensation product of a primary amine (Aniline-NEON) with an aldehyde in acid medium (Acetic Acid-Modern Chemistry), and later analysis of that compound using a spectrophotometer at the characteristic wavelength of 520 nm.

2.3 Stirring speed effect

To optimize the stirring speed, samples containing 0.5 g of adsorbent were placed in contact with 25 mL of furfural synthetic solution. Then the vials were stirred at 0, 50, 100, 150 and 200 rpm for 3 h. The stirring speed was defined based on the adsorptive capacity obtained according to Eq. 1.

$$q = \frac{(C_i - C_f)V_L}{m_{ads}} \quad (1)$$

In which q is the adsorbed amount of furfural in mg adsorbate per g adsorbent; C_i and C_f are the initial and final furfural concentrations in the solution, mg.L⁻¹; V_L is the volume of the solution in L, and m_{ads} is the mass of adsorbent in g.

2.4 Effect of the adsorbent dosage

In order to find the best adsorbate /adsorbent mass ratio, different quantities of biochar (0.1, 0.2, 0.5, 1.0, 1.5 g) were used. The quantities were added into flasks containing 50 mL of the furfural solution,

which was equivalent to 2, 4, 10, 20 and 30 g. L⁻¹. The system was placed under constant stirring for 3 h. The amount of furfural adsorbed per mass of adsorbent at the equilibrium was determined for each case, also applying Eq. 1.

2.5 Adsorption kinetics and isotherms

Kinetic study was performed to determine the equilibrium time. In this case, the contact times were 1, 5, 10, 15, 30, 45, 60, 90, 120, 150, 180 and 240 min. The experimental data were adjusted to non-linear pseudo-first order and pseudo-second order models.

To obtain the isotherms, the adsorbent was placed into erlenmeyers containing 50 mL of the furfural synthetic solution, with the following concentrations: 0.05; 0.1; 0.25; 0.5; 0.6; 0.75; 0.8 and 1.0 g L⁻¹, which are the furfural concentrations mostly found in acid hydrolysates [9]. The flasks were kept under stirring at 30 °C until equilibrium was reached. To adjust the experimental data, Langmuir, Freundlich and Sips isotherms were applied.

3. Results

3.1. Stirring speed effect

Figure 1 shows the influence of changing the stirring speed on furfural adsorption. As it can be observed, as higher the stirring speed as higher the adsorptive capacity is when speed increases from 0 to 100 rpm. However, from 100 to 200 rpm, the adsorptive capacities exhibited no significant differences remaining virtually constant. Therefore, the 200 rpm stirring speed was selected as the ideal velocity for the following tests.

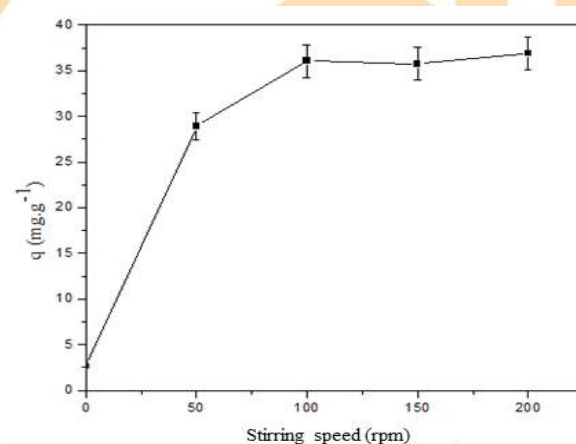


Fig. 1. Effect of varying the stirring speed on furfural adsorption (Experimental conditions: $C_0 = 1000 \text{ mg.L}^{-1}$ and $T = 30^\circ \text{C}$).

3.2. Effect of the adsorbent dosage

Figure 2 shows the variations in percentage removal and adsorptive capacities as a function of the adsorbents dosage. It can be seen that furfural adsorption capacity decreases with the increasing of activated carbon dosage; while the percentage removal of furfural increases as the adsorbent dosage increases. Therefore, the dosage of activated carbon used in the subsequent adsorption studies was defined by the intersection between the percentage removal and adsorption capacity curves, which is estimated to be approximately 7 g.L^{-1} [10].

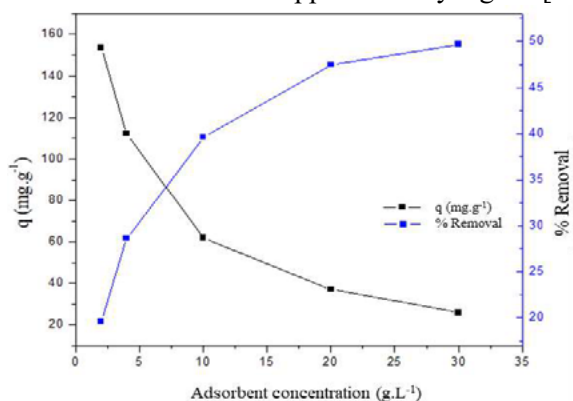


Fig. 2. Effect of the biochar dosage on the adsorption process (Experimental conditions: $C_0 = 1000 \text{ mg.L}^{-1}$ $T = 30^\circ \text{C}$, $\text{pH} = 5$, 200 rpm and $t = 180 \text{ min}$).

3.3. Adsorption kinetics

In order to evaluate the furfural adsorption kinetics in activated charcoal /biochar, the pseudo-first order and pseudo-second order models were adjusted to the experimental data, being exhibited in Figure 4. Kinetic parameters are listed in Table 1.

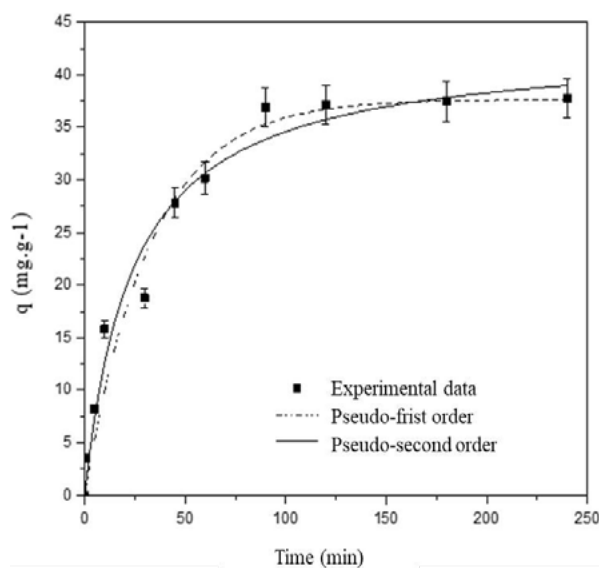


Fig. 3. Furfural adsorption kinetics and nonlinear adjustments to kinetic models (Experimental conditions: $C_0 = 1000 \text{ mg.L}^{-1}$, $T = 30^\circ \text{C}$, $C_{m/v} = 7 \text{ g.L}^{-1}$ and 200 rpm).

Table 1. Parameters for the nonlinear adjustments of experimental data to kinetic models

Models	Parameters	Values
Pseudo-first order	$q \text{ (mg.g}^{-1}\text{)}$	37.657 ± 1.615
	$k_1 \text{ (min}^{-1}\text{)}$	0.031 ± 0.005
	$S_R^2 \text{ (mg}^2\text{.g}^{-2}\text{)}$	68.761
	R^2	0.963
Pseudo-second order	$q \text{ (mg.g}^{-1}\text{)}$	42.869 ± 2.192
	$k_2 \text{ (g.mg}^{-1}\text{.min}^{-1}\text{)}$	0.001 ± 4.760
	$S_R^2 \text{ (mg}^2\text{.g}^{-2}\text{)}$	53.160
	R^2	0.972
F Test	F_{cal}	1.293
	F_{tab}	3.982

Adsorption kinetics occur rapidly to equilibrium, with approximately 40% furfural removed within 90 min. After the equilibrium was reached, adsorption occurred more slowly. Based on Table 1, as the pseudo-second order model presented a R^2 value slightly higher than the pseudo-first order one, it is proposed that it might better describe the kinetic behavior of this experiment.

3.4. Adsorption isotherms

Three models of adsorption isotherms in their nonlinear forms were applied to the equilibrium data and are presented in Figure 4.

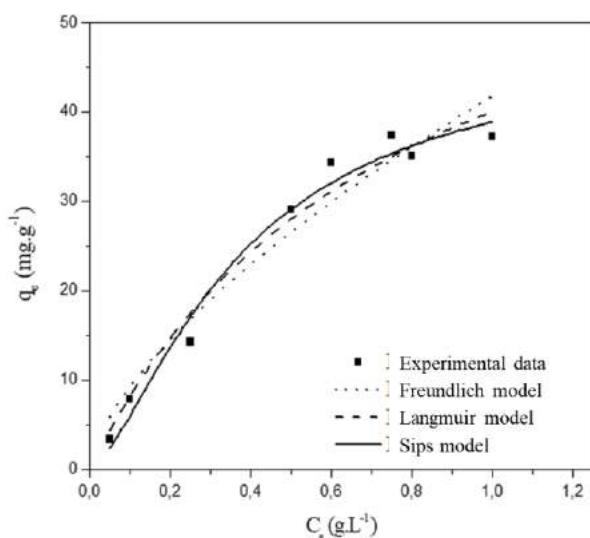


Fig. 4. Activated carbon furfural adsorption isotherms (Experimental conditions: $T = 30\text{ }^{\circ}\text{C}$, $C_m/v = 7\text{ g.L}^{-1}$, 200 rpm and $t = 90\text{ min}$).

In Figure 4, it is observed that the adsorption isotherms presented a growing profile with increasing equilibrium concentration until reaching a constant value. The maximum adsorption capacities, correlation coefficients and other constants obtained for the experimental data models are shown in Table 2.

Table 2. Data regarding the nonlinear fit of experimental data to different adsorption isotherms

Models	Parameters	Values
Freundlich	$K_F\text{ (mg.g}^{-1}\text{).(g.L}^{-1}\text{)}^{-1/n_F}$	41.774 ± 2.350
	n_F	1.527 ± 0.098
	$S_{R^2}\text{ (mg}^2\text{.g}^{-2}\text{)}$	70.611
	R^2	0.940
Langmuir	$q_{\text{máx}}\text{ (mg.g}^{-1}\text{)}$	70.193 ± 13.090
	$K_L\text{ (L.g}^{-1}\text{)}$	1.327 ± 0.267
	$S_{R^2}\text{ (mg}^2\text{.g}^{-2}\text{)}$	37.777
	R^2	0.968
Sips	$q_{\text{máx}}\text{ (mg.g}^{-1}\text{)}$	48.016 ± 8.650
	$K_{LF}\text{ (L.g}^{-1}\text{)}$	4.274 ± 3.297
	n	1.473 ± 0.349
	$S_{R^2}\text{ (mg}^2\text{.g}^{-2}\text{)}$	25.906
	R^2	0.974

From Table 2, it can be noted that the model that best fit the experimental data was the Sips model, presenting the highest correlation coefficient with a maximum adsorption capacity of 48.016 ± 8.650

mg.g^{-1} and n value > 1 , indicating that there is a favorable adsorption of furfural into the biochar.

4. Conclusions

In general, the conditions that showed maximum furfural adsorption were: adsorbent dosage of 7 g.L^{-1} and 200 rpm stirring speed. Furfural removal using activated biochar can be considered a rapid adsorption, since most of the furfural was removed within the first 90 min of experiment. The kinetic model that better fit the experimental data was the pseudo-second order model. For the equilibrium study, it was observed that the Sips model better represented the experimental data, exhibiting a maximum adsorption capacity of 42.016 mg.g^{-1} .

Acknowledgements

The authors thank the financial support provided by the Conselho Nacional de Desenvolvimento Científico e Tecnológico (CNPq), the Coordenação de Aperfeiçoamento de Pessoal de Nível Superior (CAPES), as well as the Fundação de Apoio à Ciência e Tecnologia do Estado de Pernambuco (FACEPE).

References

- [1] DESHAVATH, N. N.; MOHAN, M.; VEERANKI, V. D.; GOUD, V. V.; PINNAMANENI, S. R.; BENARJEE, T. Dilute acid pretreatment of sorghum biomass to maximize the hemicellulose hydrolysis with minimized levels of fermentative inhibitors for bioethanol production. *3 Biotec*, v. 7, p. 1-12, 2017.
- [2] MAZAR, A.; JEMAA, N.; AL DAJANI, W. W.; MARINOVA, M.; PERRIER, M. Comparative study: Furfural Production from two types of pre-hydrolysate produced using aspen and maple chips. *Biomass and Bioenergy*, v. 111, p. 103-113, 2018.
- [3] KASSAYE, S.; PANT, K. K.; JAIN, S. Hydrolysis of cellulosic bamboo biomass into reducing sugars via a combined alkaline solution and ionic liquid pretreatment steps. *Renewable Energy*, v. 104, p. 177-184, 2017.
- [4] PELETEIRO, S.; RIVAS, S.; ALONSO, J. L.; SANTOS, V.; PARAJÓ, J. C. Furfural Production using ionic liquids: A review. *Bioresource Technology*, v. 202, p. 181-191, 2016.
- [5] HASUNUMA, T.; ISMAIL, K. S. K.; NAMBU, Y.; KONDO, A. Co-expression of TAL 1 and ADH1 in recombinant xylose-fermenting *Saccharomyces cerevisiae* improves ethanol Production from lignocellulosic hydrolysis in the presence of furfural. *Journal of Bioscience and Bioengineering*, v. 117, p. 165-169, 2014.

- [6] DENG, F.; AITA, G. M. Detoxification of dilute ammonia pretreated energy cane bagasse enzymatic hydrolysate by soluble polyelectrolyte flocculants. *Industrial Crops & Products*, v. 112, p. 681-690, 2018.
- [7] PESSOA, T. S.; LIMA FERREIRA, L. E.; SILVA, M. P.; NETO, L. M. P.; NASCIMENTO, B. F.; FRAGA, T. J. M.; JAGUARIBE, E. F.; CAVALCANTI, J. V.; MOTTA SOBRINHO, M. A. Açai waste benefiting by gasification process and its employment in the treatment of synthetic and raw textile wastewater. *Journal of Cleaner Production*, v. 240, p. 118047, 2019.
- [8] INSTITUTO ADOLFO LUTZ. Normas Analíticas: Métodos físico-químicos para análise de alimentos. 4 ed. São Paulo: IMESP, 2008. 427-428 p.
- [9] CUEVAS, M.; QUERO, S. M.; HIDAIFA, G.; LÓPEZ, A. J. M.; SÁNCHEZ, S. Furfural removal from liquid effluents by adsorption onto comercial actived carbono in a batch heterogeneous reactor. *Ecological Engineering*, v. 68, p. 241-250, 2014.
- [10] WU, Z.; ZHONG, H.; YUAN, X.; WANG, H.; WANG, L.; CHEN, X.; ZANG, G.; WU, Y. Adsorptive removal of methylene blue by rhamnolipid-functionalized graphene oxide from wastewater. *Water Research*, v. 67, p. 330-344, 2014.

Phosphorus adsorption in aqueous medium using biocarbon from cassava agricultural residue (*Manihot esculenta*)

Carlos Augusto de Sousa Araújo Neto^a, Walber José Pereira Costa^b, Yan Nunes Dias^c, Marcelo Costa Santos^a, Erika Milene Pinto de Sousa^a, Edna Santos de Souza^d

^a Universidade Federal Rural da Amazônia, Av. Barão de Capanema- Areia Branca, Capanema-PA, 5514-6434, Brasil

^b Universidade Federal do Pará, R. Igarapé Tucunduba, Universitário, Belém PA, 66075 110, Brasil

^c Universidade Federal Rural da Amazônia, Estr. Principal da Ufra, Curió Utinga, Belém PA, 2150 2476, Brasil

^d Universidade Federal do Sul e Sudeste do Pará, R. Constantino Viana - Centro, São Félix do Xingu - PA, 68380-000, Brasil

Abstract

The pollution of water bodies caused by the discharge of effluents generates numerous environmental impacts, highlighting the increase in nutrients, such as phosphorus, which helps in eutrophication. Thus, the search for methods of removal of these organic compounds from effluents is extremely important and, in this context, the adsorption by means of biocarbon from agricultural residues stands out. The use of biocarbon for remediation is a promising technology due to its sorption potential, as well as the reuse of residues. Thus, the objective of this study is to evaluate the adsorption potential of cassava peel biocarbon in the removal of phosphorus in aqueous medium. The adsorption process was evaluated by kinetics and isotherm adsorption, modeling this behavior according to equations described in the literature. The biocarbon produced from cassava peel obtained adsorption similar to other studies, with maximum adsorption capacity of 61 % and adsorption equilibrium after 20 h. Elovich and Freundlich models were the most suitable for predicting the experimental behavior of kinetics and isotherm, respectively.

Keywords: Biosorption; Effluent treatment; Eutrophication.

1. Introduccion

Water pollution is currently one of the biggest problems for society, especially with constant effluent discharges. The release of effluents in water bodies causes numerous environmental impacts, which highlights the increase in nutrients that help in the eutrophication process.

Eutrophication is a process of enrichment of water bodies by nutrients, especially phosphorus and nitrogen, which increase the biomass of primary producers [1,2].

The search for methods of removal of these organic compounds from effluents is extremely important, both from an environmental and social perspective and, in this context, adsorption stands out. This is the most widely used method for advanced effluent treatment [3], being used for separation and purification purposes, having an important application in the removal of color and organic pollutants from industrial effluents [4].

Studies have been directed to the production of alternative adsorbents known as biocarbon. Biocarbon is a carbon-rich aromatic compound produced by pyrolysis of biomass under limited oxygen conditions [5]. It is a porous material with various properties that can increase plant growth and pollutant adsorption and can be produced from raw materials including crop residues, wood residues, fertilizers and sewage sludge [6].

The production of cheaper and effective alternative adsorbents requires materials that are abundant in nature and easily obtainable. As a result, natural products or certain residues from industrial or agricultural operation are some low cost sources of adsorbents [7].

In Brazil, agriculture and agro industry are responsible for moving much of the economy and cause major environmental damage due to little concern with the generation, treatment and disposal of solid waste [8].

The production of cassava flour (*Manihot esculenta*) has a prominent role in the agricultural

industry, being among the ten most important crops in the world as a source of food [9]. One of the byproducts of this activity is the peel originated in the beneficiation process, generating large amounts of solid waste [10].

With the problem related to the disposal of phosphorus-containing effluents and the possibility of treating this problem using natural products, the objective of this study was to evaluate the adsorption potential of cassava peel biocarbon in the removal of phosphorus in aqueous medium.

2. Material and Methods

For the production of biocarbon, cassava peels (*Manihot esculenta*) were collected in a flour factory in the municipality of Ourém, northeast of Pará, Eastern Amazon, located 185 Km far from the capital Belém, at 01°33'07" south latitude and 47°06'52" west longitude. The obtained shells were washed with distilled water to remove impurities, dried at room temperature for 48 h and then placed in model a LUCADEMA oven for 5 h at a temperature of 105 °C.

To obtain the biocarbon, the peels after drying were weighed, on average, 100 g, placed in porcelain crucibles under limited oxygen conditions and pyrolysed in muffle furnace, Quimis brand, model Q318M24, from room temperature to the desired temperature (700 °C) at a heating rate of 3.3 °C/min and kept for 1 h at maximum temperature. After warming up at the maximum temperature the muffle was turned off and cooled to room temperature. After pyrolysis the biocarbon was broken into a porcelain pistil grit and passed through a 100 mesh sieve.

For the adsorption tests, a stock solution of 1000 mg.L⁻¹ of phosphorus was prepared by dissolving potassium dihydrogen phosphate (KH₂PO₄) in distilled water.

The evaluation of phosphorus adsorption capacity of biochar was carried out using triplicate batch experiments. In this work, adsorption was characterized by testing the effect of contact time on adsorption (adsorption kinetics) and the maximum adsorption capacity or pollutant removal equilibrium (adsorption isotherm).

The kinetics was evaluated using 0.1 g of biocarbon in portions of 20 mL of phosphate solution (10 mg P.L⁻¹) in centrifuge tubes of 50 mL. The tubes were then shaken horizontally at 130 rpm

(Lucadema horizontal shaking table) at room temperature and natural pH (without any adjustment) as well as [11]. The monitoring was conducted by removing one tube every 1 h at a 24 h interval.

The adsorption isotherm was determined by placing 0.1 g of the adsorbent in 20 mL portions of the phosphate solution in 50 mL centrifuge tubes [11]. The concentration of P in the solutions were 10, 50, 100, 200 and 300 mg P.L⁻¹. The tubes were then shaken on a horizontal shaker at 130 rpm (LUCADEMA horizontal shaking table) for a time of 20 h at room temperature and natural pH (without any adjustment). The time of 20 h was the one in the kinetics test that presented the highest adsorption.

In the phase of determination of the amount of phosphorus, the samples were filtered through quantitative filter paper for separation of solid and liquid. The filtrate was then analyzed by the blue molybdenum spectrophotometric method in UV - VIS Spectrophotometer (BEL supplier) to determine the amount of phosphate in the solution. Adsorbed phosphate concentrations and removal rate were calculated based on the difference between the initial and final aqueous concentrations according to Equations (1) and (2).

$$q_e = \frac{(C_0 - C_e) \cdot V}{m} \quad (1)$$

$$R = \left(\frac{C_0 - C_e}{C_0} \right) \cdot 100 \quad (2)$$

Where: q_e is the amount of adsorbed P (mg.g⁻¹), R is the phosphate removal rate (%), C_0 is the initial concentration (mg.L⁻¹), C_e is the equilibrium concentration (mg.L⁻¹), V is the volume of the solvent (L), in the mass of the adsorbent sample (g).

For the adjustment of experimental kinetics and isotherms adsorption data we used the pseudo first order, pseudo second order and Elovich mathematical models for kinetics and the Freundlich and Langmuir models for the isotherms [12].

Pseudo First Order:

$$qt = q_e (1 - e^{-k_1 t}) \quad (3)$$

Pseudo Second Order:

$$qt = \frac{k_2 q_e^2 t}{1 + k_2 q_e^2 t} \quad (4)$$

Elovich:

$$qt = \frac{1}{\beta} (1 + \beta \alpha t) \quad (5)$$

Freundlich:

$$q_e = k_f C_e^n \quad (6)$$

Langmuir:

$$q_e = \frac{q_m K C_e}{1 + K C_e} \quad (7)$$

Where qt and q_e represent the amount of sorbate removed at time t and steady state, respectively (mg.g^{-1}), k_1 is the first order absorption rate constant (min^{-1}) and k_2 the second order absorption rate constant ($\text{g.mg}^{-1}.\text{min}^{-1}$), α is the initial sorption rate (mg.g^{-1}) and β is the desorption constant; C_e is the concentration of the equilibrium solution (mg.L^{-1}), q_m is the maximum adsorption capacity (mg.g^{-1}) and K is the Langmuir equilibrium constant; n and K_f are the Freundlich equilibrium constants [13].

The graphs and tables were generated from the Excel 2016 program. The kinetic and isotherm models and the quality parameters of the models were calculated using the Statistica 7.0® program. To measure the quality of adjustment, the criterion used was the correlation coefficient (R^2), % percent error (ε) and graph adjustment. The average percentage error between the predicted and experimental acquisitions was determined from the Equation 8.

$$\varepsilon (\%) = 100 \cdot \frac{\sum_{i=1}^n (q_{exp,i} - q_{pred,i}) / q_{exp,i}}{n} \quad (8)$$

Where q_{pred} e q_{exp} indicate the predicted and experimental biocarbon adsorption capacity, respectively, and n is the number of samples.

3. Results and Discussion

The biocarbon adsorbed phosphorus in the first hour of contact, with 5 % retention (Figure 1). The adsorption continued to increase over time and reached equilibrium after 20 h, when hit 59 % of retention. The time required to reach steady state was equivalent to that of other phosphorus recovery studies, such as those produced from oak chips with lanthanum and beet tailings, where it was estimated to be around 24 h [14,15].

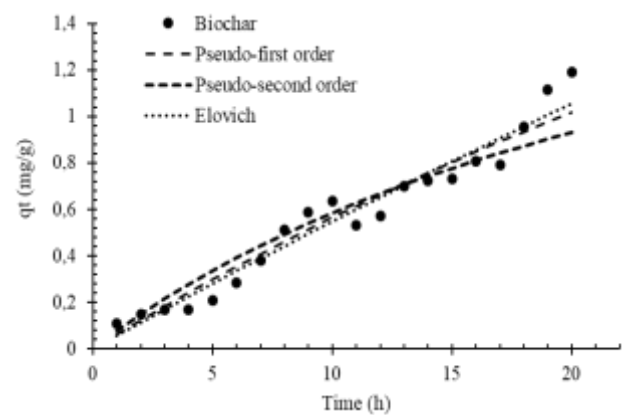


Fig. 1. Cassava peels biocarbon adsorption kinetics

The Elovich model fit better in the adsorption kinetics, with R^2 values higher than the other models and lower mean percentage error, thus being the most appropriate for the experimental data restitution (Table 1). This behavior compares when using mallee (*Eucalyptus polybractea*) for phosphorus adsorption [11]. The validation of the Elovich model shown in both studies suggests that the adsorption of P of these biosorbents is a chemical process and that the chemisorption mechanism is probably the main determinant step in adsorption rate [16].

Table 1. Statistical parameters of adsorption kinetics

Model	K	q_e	β	α	R^2	ε (%)
P.First order	3.63×10^{-04}	2.88	-	-	0.94	15.64
P.Second order	2.54×10^{-04}	2.27	-	-	0.90	17.88
Elovich	-	-	0.14	9.49×10^{-04}	0.95	14.29

k = absorption rate constant (min^{-1}), q_e = amount of sorbate at steady state, β = desorption constant, α = initial sorption ratio (mg.g^{-1}), R^2 = correlation coefficient, ε (%) = % of mean percentage error.

In phosphorus recovery capacity there was a reduction in phosphate adsorption on the early stage (10 to 50 mg.L⁻¹), and an increase when the initial concentrations of aqueous phosphorus increased (Figure 2). Raising initial phosphorus concentrations from 50 to 300 mg.L⁻¹ allowed biocarbon to increase adsorption from 0.71 to 1.22 mg.g⁻¹, with a maximum adsorption capacity of 61 %.

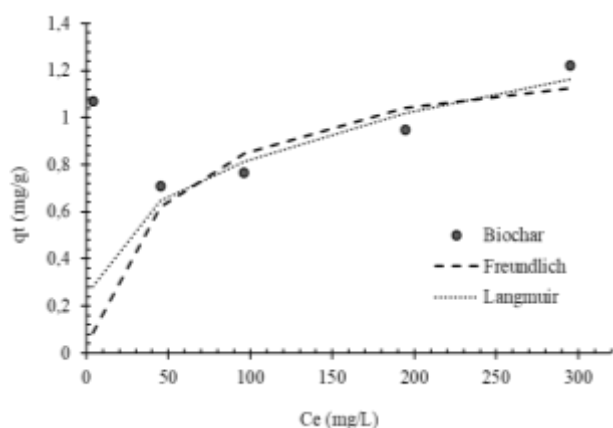


Fig. 2. Cassava peel biocarbon isotherm adsorption

The amount adsorbed was similar to studies with eucalyptus (*Eucalyptus polybractea*) and sawdust of Korean pine (*Pinus koraiensis*)^[11,17]. However, the amount was low when compared to studies that activated the carbonaceous material chemically with magnesium to adsorb phosphorus, such as cypress sawdust, sugarcane straw and bird manure^[12,18]. This behavior may have occurred due to the change of electrostatic carbonaceous material to introduce magnesium, making the adsorption of anionic pollutants easier, as well as increase of contact.

Freundlich's model represented the experimental behavior data better than Langmuir's, having higher regression coefficient and lower mean percentage error (Table 2). Thus, the Freundlich model is the best that it fits the data experimental study. These results indicate that cassava peel adsorption occurs on heterogeneous and multilayer surfaces^[19].

Table 2. Statistical parameters of adsorption isotherm

Modelo	K	qmax	kf	n	R ²	ε (%)
Langmuir	1.7E-02	1.34	-	-	0.80	10.32

Freundlich	-	-	1.81E-01	0.33	0.91	6.84
------------	---	---	----------	------	------	------

K and qm = Langmuir equilibrium constant, kf e n = Freundlich equilibrium constants, R² = regression coefficient, ε(%) = average percentage error.

4. Conclusion

The biocarbon produced from cassava peel was able to retain phosphorus in the first contacts and maintained the adsorption capacity until it reached a steady state in 20 h, with a maximum adsorption capacity of 61 %. The Elovich and Freundlich models are the most suitable for predicting the experimental performance in kinetics and isotherm, respectively.

The results allow for good expectations in the introduction of new research aimed at the reuse of cassava peel as chemically activated biocarbon to adsorb phosphorus.

References

- [1] Jarvie HP., Neal C., Withers PJA. Sewage-effluent phosphorus: A greater risk to river eutrophication than agricultural phosphorus? Science of the Total Environment, v. 360, p. 246-253, 2006.
- [2] Vidal TF., Capelo Nt J. Dinâmica de nitrogênio e fósforo em reservatório na região semiárida utilizando balanço de massa. Revista Brasileira de Engenharia Agrícola e Ambiental-Agriambi, v. 18, n. 4, 2014.
- [3] Valle BO. Cinética de adsorção de azul de metileno com resíduo de torta de babaçu (*orbignya phalerata*) como bioadsorvente. 2017. 68 f. TCC (Graduação) - Curso de Engenharia Química, Universidade Federal do Pará, Belém, 2017.
- [4] Ince Nilsun H, Apikyan IG. Combination of activated carbon adsorption with light-enhanced chemical oxidation via hydrogen peroxide. Water Research, v. 34, n. 17, p. 4169-4176, 2000
- [5] Coelho MA, Fusconi R, Pinheiro L, Ramos IC, Ferreira AS. The combination of compost or biochar with urea and NBPT can improve nitrogen-use efficiency in maize. Anais da Academia Brasileira de Ciências, v. 90, n. 2, p.1695-1703, abr. 2018. FapUNIFESP (SciELO). <http://dx.doi.org/10.1590/0001-3765201820170416>.
- [6] Gwenzi W, Muzava M, Mapanda F, Tauro TP. Comparative short-term effects of sewage sludge and its biochar on soil properties, maize growth and uptake of nutrients on a tropical clay soil in



- Zimbabwe. *Journal of Integrative Agriculture*, v. 15, n. 6, p.1395-1406, jun. 2016. Elsevier BV. [http://dx.doi.org/10.1016/s2095-3119\(15\)61154-6](http://dx.doi.org/10.1016/s2095-3119(15)61154-6).
- [7] Feitosa EDA. Estudo da utilização da biomassa casca de palma forrageira seca em estufa para remoção de gasolina contida em água de descarte, utilizando o processo de adsorção. 2018. 38 f. Monografia (Especialização) - Curso de Engenharia de Biotecnologia e Bioprocessos, Universidade Federal de Campina Grande, Campina Grande, 2018.
- [8] Silva RVTO. Resíduos de coco, acerola e caju para produção de carvão ativado. 2015. 62 f. Dissertação (Mestrado) - Curso de Desenvolvimento de Processos Ambientais, Universidade Católica de Pernambuco, Recife, 2015.
- [9] Woiciechowski AL., Carvalho JC., Habu S., Caroline TY, Ghiggi, V.; Soccol CR. Emprego de Resíduos Agroindustriais em Bioprocessos Alimentares. In: Glaucia Maria Pastore; Juliano Lemos Bicas; Mario Roberto Marostica Junior. (Org.). *Biotecnologia de Alimentos*. 1ed. São Paulo: Atheneu, 2013, v. 12, p. 143-172.
- [10] Peixoto TS, Resch S. Resíduos de mandioca: um estudo sobre a destinação da massa de mandioca pelas feculárias brasileiras. In: II Encontro Internacional de Gestão, Desenvolvimento e Inovação (EIGEDIN), 2018, Naviraí/MS. *Anais do II Encontro Internacional de Gestão, Desenvolvimento e Inovação (EIGEDIN)*. Naviraí/MS: Campo Grande, 2018. v. 2. p. 1-20.
- [11] Zhang H, Chen C, Gray EM, Boyd SE, Yang H, Zhang D. Roles of biochar in improving phosphorus availability in soils: A phosphate adsorbent and a source of available phosphorus. *Geoderma*, v. 276, p.1-6, ago. 2016. Elsevier BV. <http://dx.doi.org/10.1016/j.geoderma.2016.04.020>.
- [12] Haddad K., Jellali S., Jeguirim M., Ben HTA., Limousy L. Investigations on phosphorus recovery from aqueous solutions by biochars derived from magnesium-pretreated cypress sawdust. *Journal of Environmental Management*, 216, 305–314, 2018. doi: 10.1016/j.jenvman.2017.06.020
- [13] Yu P., Xue Y., Gao F., Liu Z., Cheng X., Yang K. Phosphorus Removal from Aqueous Solution by Pre- or Post-Modified Biochars Derived from Agricultural Residues. *Water, Air, & Soil Pollution*, v. 227, n. 10, p.1-12, 6 set. 2016. Springer Nature. <http://dx.doi.org/10.1007/s11270-016-3066-x>.
- [14] Yao Y., Gao B., Inyang M., Zimmerman AR., Cao, XD., Pullammanappallil P, Yang LY. Removal of phosphate from aqueous solution by biochar derived from anaerobically digested sugar beet tailings. *Journal of Hazardous Materials* 190 (1–3), 501–507, 2011.
- [15] Wang Z., Shen D., Shen F., Li T. Phosphate adsorption on lanthanum loaded biochar. *Chemosphere*, v. 150, p.1-7, maio 2016. Elsevier BV. <http://dx.doi.org/10.1016/j.chemosphere.2016.02.004>.
- [16] Silva J., Silva FLH., Santos SFM., Ribeiro JES., Medeiros LL., Ferreira ALO. Produção de biomassa e lipídios pela levedura *Rhodotorula mucilaginosa* utilizando a manipueira como substrato. *Brazilian Journal of Food Technology*, v. 21, p.1-6, 11 out. 2018. FapUNIFESP (SciELO). <http://dx.doi.org/10.1590/1981-6723.14517>.
- [17] Lou K., Rajapaksha AU, Ok YS, Chang SX. Pyrolysis temperature and steam activation effects on sorption of phosphate on pine sawdust biochars in aqueous solutions. *Chemical Speciation & Bioavailability*, v. 28, n. 1-4, p.42-50, 24 mar. 2016. Informa UK Limited. <http://dx.doi.org/10.1080/09542299.2016.1165080>.
- [18] Novais SV, Zenero MDO, Tronto J., Conz RF, Cerri CEP. Poultry manure and sugarcane straw biochars modified with MgCl₂ for phosphorus adsorption. *Journal of Environmental Management*, v. 214, p.36-44, maio 2018. Elsevier BV. <http://dx.doi.org/10.1016/j.jenvman.2018.02.088>.
- [19] Ye Z.-L., Deng Y., Lou Y., Ye X., Zhang J., Chen S. Adsorption behavior of tetracyclines by struvite particles in the process of phosphorus recovery from synthetic swine wastewater. *Chemical Engineering Journal*, v. 313, p.1633-1638, abr. 2017. Elsevier BV. <http://dx.doi.org/10.1016/j.cej.2016.11.062>.

Relations between Ni²⁺, Cu²⁺, and Cr³⁺ during adsorption in multielementary solutions using activated carbon from passion fruit peel

Bianca de Paula Ramos^a, Isadora Dias Perez^{a*}, Rosane Freire Boina^b

^aCampinas University, Chemical Engineering School, 13083-852 Campinas, São Paulo, Brazil

^bSão Paulo State University, School of Technology and Sciences, 19060-900, Presidente Prudente, São Paulo, Brazil

Abstract

Adsorption is a process widely used to recovery metallic ion in wastewater. However, the multielementary nature of the wastewaters is rarely considered. Thus, this work aims to analyze the interference caused by three metallic ions into the adsorption process. For this, it was analyzed the adsorption of Ni²⁺, Cu²⁺, and Cr³⁺ in mono and multielementary solutions and applied a Tukey test to verify if have a significant difference in the efficiencies obtained. Three carbons activated from passion fruit peel were synthesized as adsorbents. They were activated with sodium acetate, phosphoric acid, and potassium hydroxide. The competition for activated sites made the efficiency of Cu²⁺ adsorption decrease in all the multimetallic conditions. While the Cr³⁺ and Ni²⁺ were benefited by the presence of other ions during the adsorption with the activated carbon with potassium hydroxide. This study presents an innovate approach of the adsorption in multielementary solutions, revealing that the interferences between metallic ions is not limited to competition for active sites, but is related to a series of intermolecular interactions.

Keywords: Activated carbons; *Passiflora Edulis F. Flavicarpa*; Passion fruit shells; Metals.

1. Introduction

Pollution by metal ions is one of the most serious environmental problems since these compounds are toxic and have a high capacity of bioaccumulation - causing damage to nature and human health [1]. The removal of metallic ions is not compatible with most of the conventional treatment processes, and usually has a high cost of implementation and execution, besides the possibility of generates toxic waste [2].

In the adsorption process, the substances in the fluid spontaneously concentrate on the solid surface [3]. The attraction between the surface and the adsorbate occurs due to the polarity, which is related to the presence of heteroatoms [4]. It involves materials with ion-exchange properties, which may have different selectivity, according to morphology and functional group [5].

Copper, chromium, and nickel are metals commonly used in industrial processes, such as electroplating, metal alloy manufacturing, electrical wires, pesticides, construction and steel [6, 7]. These activities generate wastewater composed by a

mixture of metals [8]. However, most of the adsorption studies are carried out in monoelementary solution, which is necessary to verify the kinetic and isotherms [9]. In this work, we propose the analyzes in multimetallic solutions, to be similar to industrial systems, and verify the interferences that adsorption may present when applied in real wastewater.

To identify the relation between the ions, the process was analyzed in three adsorbents. Both of them were made from passion fruit shells and modified by burning and chemical activating, using as a chemical precursor: sodium acetate (C₂H₃NaO₂), phosphoric acid (H₂PO₄) or potassium hydroxide (KOH).

This work aims to analyze the adsorption of Cu²⁺, Ni²⁺, and Cr³⁺ in mono and multielementary solution and to verify the interferences that the presence of these ions may cause in the adsorption of the other metals. The process was analyzed in three different activated carbons to differentiate the interferences caused by the ions and by the selectivity of the adsorbate.

2. Methodology

2.1. Manufactured of the activated carbons

The passion fruit shells were burned in muffle (Fornitec HW1.000) for 40 minutes at 200°C. In order to clear the pores of the carbon and to remove carbonization residues, the product was washed in Jar Test (Milan 303m) at 240 rpm for 30 minutes, with a ratio of 100 mL of water per gram of carbon.

Chemical activation was performed with a ratio of 1:1 mass of adsorbent and activator in 100 mL solution. The mixture was stirred in the Jar Test for 30 minutes at 240 rpm. Three chemical activators were used: phosphoric acid (H₂PO₄), potassium hydroxide (KOH) and sodium acetate (C₂H₃NaO₂), generating the three activated carbons used.

The material was filtered and washed with distilled water and hydrochloric acid (0.5 mol/L - HCl) until the resulting solution had a neutral pH, then, the solid was oven dried (SOLAB SL 100/80) at 100 °C.

2.2. Batch Adsorption Experiments

The experiments were carried out with synthetic solutions of Cu²⁺, Cr³⁺, and Ni²⁺ in all the possible combinations of them: monoelementary, in pairs or threes. The solution was made with 5.0 ppm of each metallic ion and pH 3.5.

The metallic solution (100 mL) mixed with 1.0 g of each activated carbon and stirred for 360 minutes at 120 rpm at 25°C. The mixtures were filtered, subjected nitroperchloric digestion, and have the final metal concentration determined by atomic absorption spectroscopy (Perkin-Elmer AAnalyst200). Then, the adsorption efficiency was calculated according to Equation 1.

$$E = \frac{(C_0 - C_f) * 100}{C_0} \quad (1)$$

Where: E is removal efficiency (%), C₀ is the initial concentration of metal ion (mg/L) and C_f is the final concentration of metal ion (mg/L).

The efficiencies obtained for each component of the metallic solution (mono or multielementary) were analyzed by the Tukey test, verifying if they have significant differences at 95% confidence.

3. Results and discussion

Table 1 present the average adsorption efficiency with the standard deviations under parentheses and the result of the Tukey test for each metallic ion in all the kinds of solutions studied. Each capital letter represents that a specific ion is under analyze: “A” for Cu²⁺, “B” for Cr³⁺ and “C” for Ni²⁺. Each lower-case letter represents a significantly different treatment. Thus, equal lower-case letters in different solutions compositions mean that the efficiency obtained was equal to both of them, at 95% confidence. Different lower-case letters mean that the efficiency was significantly different, i.e. there was interference from the composition.

The three synthesized adsorbents showed high performance in removing the metallic ions in mono or multielementary solutions. The highest removal percentage was obtained using the activated carbon whit sodium hydroxide: 98.83 % for Ni²⁺, 92.91 % for Cu²⁺ and 80.55 % for Cr³⁺.

With the three activated carbons, Cu²⁺ has a high adsorption efficiency in monoelementary solution. Although the efficiency of Cu²⁺ decrease in the presence of the other two metallic ions, due to the competition of the activated sites. The adsorption of Cr³⁺, in the activated carbon with sodium acetate, is significative highest in monoelementary solution. However, in the other two activated carbons, the highest efficiency was obtained when the three metallic ions were in the solution. In these conditions, a multi-layer phenomenon may have occurred. Our previous studies indicate that the isotherm adsorption of Cr³⁺ in these activated carbons fit the Freundlich model, which previous this behavior.

Regarding the Ni²⁺, in the carbons activated with sodium bicarbonate and phosphoric acid, the efficiency was significantly equal in the monoelementary solution and in the presence of Cu²⁺ but decreased in the presence of Cr³⁺. This indicates a competition between Ni²⁺ and Cr³⁺. Worth to mention that in the carbon activated with potassium hydroxide, the efficiency increased in multimetallic solutions, indicating the possibility of multilayers adsorption.

Table 1. Average adsorption efficiencies with their respective standard deviations and Tukey test results.

Ion	Synthetic solution	Activated carbons		
		<i>C₂H₃NaO₂</i>	<i>H₂PO₄</i>	<i>KOH</i>
Cu ²⁺	Cu ²⁺	92.91(±4.25)Aa	81.81(±2.75)Aa	86.95(±1.56)Aa
	Cu ²⁺ + Ni ²⁺	87.77(±4.25)Ab	79.70(±2.75)Aab	83.71(±1.56)Ab
	Cu ²⁺ + Cr ³⁺	79.93(±4.25)Ac	78.50(±2.75)Abc	82.32(±1.56)Ab
	Cu ²⁺ + Ni ²⁺ + Cr ³⁺	77.64(±4.25)Ac	76.17(±2.75)Ac	80.17(±1.56)Ac
Cr ³⁺	Cr ³⁺	80.55(±3.73)Ba	70.52(±1.56)Ba	75.22(±2.71)Bab
	Cr ³⁺ + Cu ²⁺	72.71(±3.73)Bb	70.69(±1.56)Ba	76.85(±2.71)Bb
	Cr ³⁺ + Ni ²⁺	69.86(±3.73)Bb	71.29(±1.56)Ba	73.92(±2.71)Ba
	Cr ³⁺ + Cu ²⁺ + Ni ²⁺	70.65(±3.73)Bb	75.52(±1.56)Bb	73.13(±2.71)Ba
Ni ²⁺	Ni ²⁺	98.83(±6.28)Ca	92.43(±1.20)Ca	93.74(±3.97)Ca
	Ni ²⁺ + Cu ²⁺	93.96(±6.28)Cab	91.86(±1.20)Ca	98.47(±3.97)Cb
	Ni ²⁺ + Cr ³⁺	91.55(±6.28)Cb	90.19(±1.20)Cb	97.02(±3.97)Cab
	Ni ²⁺ + Cu ²⁺ + Cr ³⁺	92.81(±6.28)Cab	87.68(±1.20)Cc	96.28(±3.97)Cab

Footnotes: A: efficiency in function of Cu²⁺; B: efficiency in function of Cr³⁺; C: efficiency in function of Ni²⁺; different lower-case letters indicate significantly different efficiencies, and equal lower-case letters indicate that the response was equal within the confidence interval.

4. Conclusion

The methodology applied was effective to verify the relation between the metallic ion during the adsorption processes. It was verified that the adsorption of Cu²⁺ decreased in the presence of Ni²⁺ or Cr³⁺ but promote an increase of Ni²⁺ adsorption. It was identified competition between Cr³⁺ and Ni²⁺, once the presence of these ions in the same solution made the efficiency decrease to both of them. In multimetallic solutions, the phenomenons of multilayer adsorption, the competition by active sites and the tamponade of pores occur simultaneously and must be considered for adsorption analyzes.

Acknowledgements

This work was supported by FAPESP Research Foundation - Project N° 2015/09170-1.

References

- [1] Cheng SY, Show P L, Lau BF, Chang J S, Ling TC. New Prospects for Modified Algae in Heavy Metal Adsorption. *Trends in Biotechnology* 2019;37:1255-68.
- [2] Wang Y, Feng Y, Zhang X-F, Zhang X, Jiang J, Yao J. Alginate based attapulgitic foams as efficient and recyclable adsorbents for the removal of heavy metals. *Journal of Colloid and Interface Science* 2018;514:190-8.
- [3] Bergna D, Hu T, Prokkola H, Romar H, Lassi U. Effect of Some Process Parameters on the Main Properties of Activated Carbon Produced from Peat in a Lab-Scale Process. *Waste and Biomass Valorization* 2019; 1-12.
- [4] El Sheikh AH, Newman AP, Al Daffae HK, Phull S, Cresswell N. Characterization of activated carbon prepared from a single cultivar of Jordanian olive stones by chemical and physicochemical techniques. *Journal of Analytical and Applied Pyrolysis* 2004;71:151-164.
- [5] Mohammad L. *Ion Exchange Technology I: Theory and Materials*. New York: Springer, 2012.
- [6] Perez ID, Botelho Jr. AB, Aliprandini P, Espinosa DCR. Copper recovery from nickel laterite with high iron content: A continuous process from mining waste. *The Canadian journal of chemical engineering* 2019:1-12.
- [7] Scarazzato T, Panossian Z, Tenório JAS, Pérez-Herranz V, Espinosa DCR. A review of cleaner production in electroplating industries using electrodialysis. *Journal of Cleaner Production* 2017;168:1590-1602.
- [8] Du H, Chen W, Cai P, Rong X, Feng X, Huang Q. Competitive adsorption of Pb and Cd on bacteria montmorillonite composite. *Environmental Pollution* 2016;218:168-175.
- [9] Kentish SE, Stevens GW. Innovations in separations technology for the recycling and re-use of liquid waste streams. *Chemical Engineering Journal* 2001;84:149-59.

Furfural's adsorption using activated carbon from sisal (*Agave sisalana*)

Ysrael Simões Lins de Oliveira^a, Flávio Luiz Honorato da Silva^a, Ellen Alves dos Santos^a, Josevan da Silva^b, Leanderson Marques Túlio Lemos^b, Odelsia Leonor Sánchez de Alsina^c, Acácia Lima Silva^c, Joan Manuel Rodríguez Díaz^a

^a Chemical Engineering Department, Universidade Federal da Paraíba, Cidade Universitária, João Pessoa-PB, 58051-900, Brazil

^b Graduate Program in Food Science and Technology, Universidade Federal da Paraíba, Cidade Universitária, João Pessoa-PB, 58051 900, Brazil

^c Graduate Program in Process Engineering, Universidade Tiradentes, Av Murilo Dantas, Aracaju-SE, 49032-490, Brazil.

Abstract

The adsorption of microbial growing inhibitors obtained in fermentative processes' hydrolysis constitutes an optimization method of bioprocesses. In this way, this worked aimed the production of activated carbon from sisal (*Agave sisalana*), plant in which Brazil is one of the major producers, and the evaluation of its potential in the furfural's adsorption, one of the main inhibitors formed in acid hydrolysis. The carbon was obtained by physic activation with a water vapor flux and by chemical activation through impregnation with phosphoric acid. It was characterized with isotherms of nitrogen's adsorption/desorption, being identified isotherms of type IV and with hysteresis. From BET and BJH methods, the activated carbon presented a superficial area of 390.481 m²/g and a specific area of 74.696 m²/g. It was also done the infrared spectroscopy, whose peaks indicated the sisal's lignocellulosic character and P-O ligations from phosphoric acid use. The furfural's adsorption experiments proved its potential (brought through characterization) for the adsorption of mesoporous components, e.g., the furfural.

Keywords: Bioprocesses' optimization; Inhibitors; Agroindustrial wastes.

1. Introduction

The agroindustry wastes' use for the obtention of bioproducts of industrial's interest has developed in last years. The lack of fossil sources and Ambiental pollution triggered by their use have awakened the attention for the use of renewable resources in industrial processes. Agroindustry wastes solve that problem and, at the same time, are a low-cost feedstock. From them, there are the lignocellulosic materials, the renewable sources more abundant found in nature [1].

The lignocellulosic material is constituted by a complex of cellulose, hemicellulose and lignin, resistant to microbial attacks [2]. In the context of the biorefinery, a lot of products can be obtained from them. By the hemicellulose, of

heteropolysaccharidic content, they are a potential source of sugars through fermentative processes [3].

For sugars' obtention from hemicellulose, it is necessary, though, a pre-treatment step. The lignin constitutes an aromatic polymer that acts in the structure resistance, not allowing the microbial attack [1]. In this way, the fermentative process has to be preceded by a hydrolysis step, in which the lignin protection is broken and the fermentable sugars of the hemicellulose are released.

The pre-treatment could be by acid, basic or enzymatic hydrolysis. The acid hydrolysis, though is the most used, degrades some of the liberated sugars, forming inhibitors of microbial growth [4]. The main inhibitors formed in lignocellulosic biomass hydrolysis are furfural, 5-hydroximetilfurfural and acetic acid.



Thus, a good way to improve the fermentable potential of lignocellulosic hydrolysates is low the concentration or eliminate completely the toxic compounds liberated in hydrolysis [5]. One mechanism that is shown very efficient for the detoxification of hydrolysate is the adsorption with activated carbon [6].

The activated carbon is one of the main adsorbents used in liquid phase adsorption currently, mostly by being easily obtained: any biomass with a high carbonaceous content and low ash content could be a source of it [8]. Its productive process occurs in two steps: the carbonization, the heat treatment for the carbon production, and the activation, which could be physical (through a water vapor flux in high temperatures for the development of its porosity) and/or chemical (impregnation of carbon with some activate agent, for the development of its pores too).

In this way, the has been done a lot of scientific research that investigates different biomasses for activated carbon obtention through physical or chemical activation. Coconut husk [7], coffee shell [8] and rice husk [9] are some of the biomasses still used for activated carbon production.

However, a biomass very important for Brazil low researched as activated carbon source is sisal (*Agave sisalana*). This plant has been highlighted for its high productivity and low cost, being Brazil the biggest global exporter [11].

An important current fact is that the sisal's improper disposal is generating environmental problems. Only about 4% of sisal's leaves are used for the fiber obtention, in a way the rest of the biomass is not utilized, being a waste (called bagasse) [12]. So, its use for activated carbon production could low the environmental impact caused by its improper disposal in nature and, at the same time, high the value of this important Brazilian feedstock.

Thus, the aim of this study was the activated carbon obtention from sisal bagasse (*Agave sisalana*), and the study of its utilization in furfural's adsorption, as a strategy of bioprocesses optimization.

2. Materials and Methods

2.1. *Sisal pulp activated carbon production*

The sisal pulp was obtained in Nova Floresta, Paraíba (6 ° 27 '18' 'S, 36 ° 12' 10 " W). Initially, was performed with *in natura* washing, from repeated cycles with boiling water, followed by kiln drying at 100 ° C. Then, chemical activation of the sisal pulp was performed, using as activating agent phosphoric acid (H₃PO₄) in a 1: 1 ratio, with the closed container, heated in a temperature range of 70 - 90 ° C and periodically shaken for a total time interval of 1h 30 min to 3 h [26]. The container was opened and kept heated for evaporation of the liquid.

Then, activated carbon was produced in a rotary electric oven (CHINO brand) under temperature conditions between 400-600 ° C, for a interval time between 0.5 and 3h, with a heating ramp. 10°C / min. The temperature was keeping and proceeded with the physical activation, which occurred from the introduction of a water vapor flow at 0.4-1.0 kg / h during a time interval of 0.5-3 h [26].

Afterwards, the activated carbon obtained was washed to neutralize the pH, carried out by successive washes with boiling water. The carbon was placed in a kiln to drying, and after 24 hours was milled.

2.2 *Sisal pulp activated carbon characterization*

The first characterization step was to obtain curves of nitrogen adsorption / desorption isotherms. The samples of activated carbon of sisal pulp and commercial activated carbon were submitted to heat and vacuum pretreatment. 0.2g of each sample were weighed in analytical balance (Mettler Toledo - AL 204, precision ± 10⁻⁴) in a specific glass bulb for the analysis. Then, the samples were submitted to a heat treatment at 120 ° C and a vacuum of 100 mmHg in the NOVA 1200e equipment for a period of 4h [13,14].

Thus, with the aid of NOVA 1200e Standard Model V.11.02 equipment (Quantachome Instruments / Florida / USA) and NOVA WIN® software, adsorption and desorption isotherms were obtained using nitrogen as adsorbate under cryogenic conditions (77 K). Data were obtained by the BET method [15].

From the adsorption and desorption isotherms, with the aid of NOVA WIN® software, it was possible to obtain the surface area and pore volume by the BET method [15].

According to the iterative method of Barret, Joyner and Hallendy (BJH) it was possible to determine the pore distribution and size from the values obtained of the NOVA WIN® software [16].

Finally, for the observation of the chemical elements and chemical bonds constituting the material, the infrared region spectroscopy (FT-IR) analysis was performed using the Shimadzu Corporation spectrometer, using the infrared region of 4000 cm⁻¹ to 400 cm⁻¹, with a resolution of 1 cm⁻¹.

2.3 Furfural adsorption with sisal pulp activated carbon

Adsorption essays were performed in synthetic furfural solutions, with activated carbon obtained from sisal pulp. Furfural solutions were prepared according to the methodology of the Adolf Lutz Institute [16]. From a solution of furfural 5g / L in ethyl alcohol, volumes of 5 mL were removed; 8 mL; 15 mL; 25 mL and 30 mL, with 50 mL volumes completed with 50% ethyl alcohol solution. Then, the pH of each solution was controlled to be between 4 and 5 and 1g of activated carbon was added.

Adsorption occurred in an orbital shaker rotating at 200 rpm at a temperature of 30 ° C, during an interval of 1h. After this step and equilibrium to be reached, the solutions were centrifuged at 3600 rpm in Excelsa ® Centrifuge for 5 min for adsorbent separation.

The supernatant was collected and utilized to determine final furfural concentrations by the spectrophotometric method. Readings were taken on a U2M spectrophotometer (QUIMIS®) using a 520 nm wavelength

2. Results

3.1. Characterization of sisal activated charcoal

The adsorption and desorption isotherms of nitrogen using physically and chemically activated charcoal from sisal and commercial activated charcoal are shown in Figures 1 and 2. They provide qualitative aspects about the adsorption process and the surface area availability for adsorbate [17]. A superficial analysis allows the observation that both charcoals presented a similar porosity.

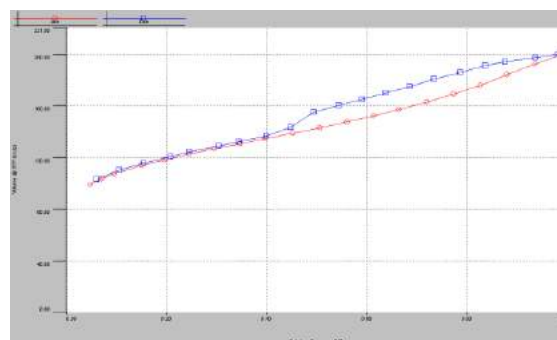


Fig. 1. Nitrogen adsorption / desorption isotherms based on the BET method for sisal activated charcoal.

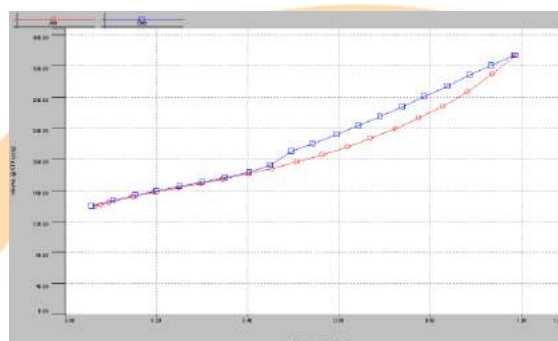


Fig. 2. Nitrogen adsorption / desorption isotherms based on the BET method for commercial activated charcoal.

The isotherms found presented hysteresis, an indicative the types IV or V. By its configuration, are characterized as type IV, typical of mesoporous materials and solids with relatively large pores [18]. This condition is more interesting than microporosity (ideal for adsorption of gases, which has generally small molecules) for liquid phase

applications such as furfural [19]. The type IV isotherm is quite common for activated carbon, such as for activated charcoal obtained from peanut shell and rice shell [20, 21].

Table 1 shows the charcoal characterization data analyzed, allowing to observe the surface area (BET method) and specific area (BJH method), as well as the mean radius.

Table 01. Charcoal characterization data.

Condition	Surface area (m ² /g)	Specific area (m ² /g)	Pores mean radius (Å)
Sisal activated charcoal	390.481	74.696	17.077
Commercial activated charcoal	514.403	150.177	19.939

Activated charcoal from sisal presented a considerable surface area (390,481 m²/g), relatively close to that present in commercial activated charcoal (514,403 m²/g). Yakout produced activated charcoal from olives using chemical treatment also with phosphoric acid, obtaining a surface area of 257 m²/g [17]. Alves et al. observed a surface area of 1172 m²/g for a chemically activated charcoal with H₃PO₄ from the bay coconut endocarp, using, however, more intense carbonization and activation conditions (temperature and longer time intervals) [22].

The other verified factor that affects the adsorption and the type of molecule to be adsorbed, pores radius of the adsorbent, were fundamental in the classification of the pores of the charcoal. The average pore radius shown in Table 1 allowed the conclusion based on the IUPAC classification that both are mesoporous: according to this institute, diameters within a range of 20 and 500 Å presents a mesoporous structure and the sisal's activated carbon presented a diameter of 34.154, confirming the condition previously indicated by the isotherm's configuration [23].

In infrared spectroscopy range, on the other hand, Figure 3, relates the transmittances for the wave numbers from 4000 to 400 cm⁻¹ for sisal activated carbon.

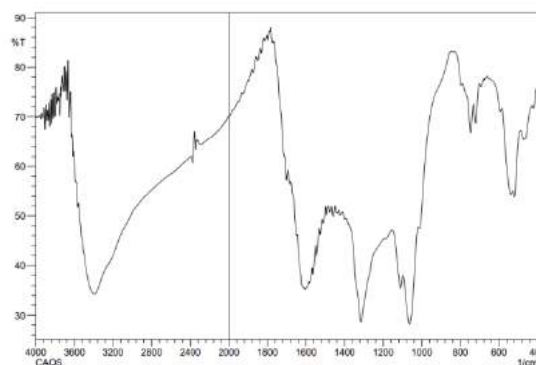


Fig 3. Infrared spectroscopy for sisal activated charcoal.

From Figure 3, the functional groups present in the charcoal were analyzed. The wavelength range 4000 to 400 cm⁻¹ peaked at the 3400 cm⁻¹ range, related to the possible OH vibrational elongation due to the decomposition of lignocellulosic and cellulosic material [7]. Zhong, in his work on peanut shell activated charcoal, reports that bands located at 2362, 1570, and 1215 cm⁻¹ suggest a high content of lignocellulosic material, as lignin is another carbon-carbon rich compound and in alkaline groups, typical of these wave numbers [20]. The bands of the present work showed wave numbers at 1600 and 1290 cm⁻¹, near of the values found by Zhong, also suggesting the same [20]. Part of the characteristic lignocellulosic content of sisal was maintained, and part was degraded resulting in OH bonds.

The peak located at 1080 cm⁻¹ indicates P-O-type bonds, while those at 725 cm⁻¹ and 525 cm⁻¹ also indicate phosphorus bonding, which is a result from the chemical activation performed with H₃PO₄ [24, 25].

3.2. Adsorption of furfural with sisal activated charcoal

For furfural adsorption using physically and chemically activated charcoal from sisal at 30 °C, the final concentration and adsorption equilibrium constant data detailed in Table 2 and the adsorption isotherm shown in Figure 4 were obtained.

Table 2. Initial (I_c) and final (F_c) concentrations and adsorption capacity (c) of furfural with sisal activated charcoal at 30 ° C.

I_c (g/L)	c (mg/g)	F_c (g/L)
0.5	3.22	0.436
0.8	11.42	0.572
1.5	35.94	0.781
2.5	40.27	1.695
3.0	31.83	2.363

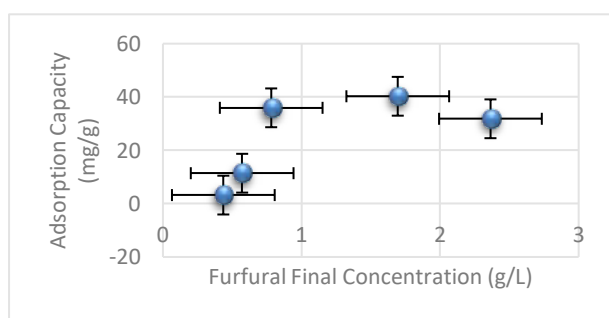


Fig. 4. Furfural adsorption isotherm using activated charcoal at 30 ° C.

According to Figure 4, furfural adsorption with the activated carbon produced was favorable at 30 ° C, since the adsorbate mass retained in an adsorbent mass is high for a low equilibrium concentration [18]. There was a high furfural removal capacity mainly at 1.5 g/L and 2.5 g/L concentrations, which resulted in final equilibrium concentrations of 0.781 and 1.695 g/L, respectively, with the adsorption capacity being stabilized as shown in the graph. Duarte observed in this concentration range up to 100% inhibition of cell growth, which, according to the sisal's activated carbon adsorption capacity, could be reversed by this adsorptive process [27].

4. Conclusion

The chemical and physical treatment of sisal bagasse made it a competitive precursor for the obtention of an effective mesoporous activated carbon, which can be used in a lot of application, such as effluent treatment and bioprocesses optimization through hydrolysate detoxification.

For furfural's synthetic solutions adsorption, the carbon showed favorable itself, in a way that next studies can evaluate the adsorption of the inhibitor in the own hydrolysate and can fit the data into adsorption models, also studying its kinetic.

References

- [1] Castro AM, Pereira JR N. Produção, propriedades e aplicação de celulases na hidrólise de resíduos agroindustriais. *Química Nova* (Impresso) 2010;33:181-8.
- [2] Santos, FA. et al. Potencial da palha de cana-de-açúcar para produção de etanol. *Química Nova* 2012;35:1004-10.
- [3] Tamanini C, Haully MCO. Resíduos agroindustriais para produção biotecnológica de xilitol. *Semina: Ciências Agrárias* 2004; 25:315-30.
- [4] Moon J, Liu ZL. Engineered NADH-dependent GRE2 from *Saccharomyces cerevisiae* by directed enzyme evolution enhances HMF reduction using additional cofactor NADPH. *Enz. and Microbial Technol.* 2012;50:115-20.
- [5] Monlau F, Sambusiti C, Antoniou N, Zabaniotou A, Solhy A, Barakat A. Pyrochars from bioenergy residue as novel bio-adsorbents for lignocellulosic hydrolysate detoxification. *Bioresource Technology* 2015;187:379-86.
- [6] Miyafuji H et al. Detoxification of wood hydrolysates with wood charcoal for increasing the fermentability of hydrolysates. *Enzyme and Microbial Technology* 2003;32(3-4):396-400.
- [7] Talat M, Mohan S, Dixit V, Singh DK, Hasan SH, Srivastasa ON. Effective removal of fluoride from water by coconut husk activated carbon in fixed bed column: Experimental and breakthrough curves analysis. *Groundwater for Sustainable Development* 2018;7:48-55.
- [8] Ioannidou, O, Zabaniotou A. Agricultural residues as precursors for activated carbon production—a review. *Renewable and sustainable energy reviews* 2007;11(9):1966-2005.
- [9] Shengan S, Qiongfeng Y, Ming L, Hong Z, Chunxiang W. Preparation of coffee-shell activated carbon and its application for water vapor adsorption. *Renewable Energy* 2019;142:11-9.
- [10] Yaumi AL, Bakar MZA, Hameed BH. Melamine-nitrogenated mesoporous activated carbon derived from rice husk for carbon dioxide adsorption. *Energy* 2018;155:46-55.
- [11] Benítez-Guerrero M, López-Beceiro J, Sánchez-Jiménez PE, Pascual-Cosp J. Comparison on termal behaviour of natural and hot-washed sisal fibers based on their main components: Cellulose, xylan and lignin. TG-FTIR analysis of volatatile products. *Thermochimica Acta* 2014;581:70-86.
- [12] Maran JP, Priya B. Ultrasound-assisted extraction of pectin from sisal waste. *Carbohydrate Polymers* 2015;115:732-8.
- [13] Juszczak L, Fortuna T, Wodnicka K. Characteristics of cereal starch granules surface using



nitrogen adsorption. *Journal of Food Engineering* 2002;54:103-10.

[14] Santana MFS, Katekawa ME, Tannous K, Lima AKVO, Gasparetto CA. Área superficial e porosidade da fibra alimentar do albedo de laranja. *Revista Brasileira de Produtos Agroindustriais* 2012;14:261-73.

[15] Branauer S, Emmett PH, Teller E. Adsorption of gases in multimolecular layers. *Journal of the American Chemical Society* 1938;60(2):309-19.

[15] Barrett EP, Joyner LG, Halenda PP. The determination of pore volume and area distributions in porous substances. Computations from nitrogen isotherms. *Journal of the American Chemical Society* 1951;73:373-80.

[16] Instituto Adolfo Lutz. Métodos físico-químicos para análise de alimentos. 4th ed. São Paulo: Instituto Adolfo Lutz; 2008.

[17] Yakout SM, Sharaf El-Deen G. Characterization of activated carbon prepared by phosphoric acid activation of olive stones. *Arabian Journal of Chemistry* 2016;9:S1155-62.

[18] Nascimento R, Lima ACA, Vidal CB, Melo DQ, Raulino GSC. Adsorção: Aspectos teóricos e aplicações ambientais. Fortaleza: Imprensa Universitária; 2014.

[19] Nobre JRC, Castro JP, Motta JP, Bianchi ML, Trugilho PF, Borges WSM, Moulin JC. Produção de carvão ativado de resíduo madeireiro da Região Amazônica. *Scientia Forestalis/Forest Sciences* 2015;43:895-906.

[20] Zhong Z, Yang Q, Li X, Luo K, Liu Y, Zeng G. Preparation of peanut hull-based activated carbon by microwave-induced phosphoric acid activation and its application in Remazol Brilliant Blue R adsorption. *Industrial Crops and Products* 2012;37:178–85.

[21] Ding L, Zou B, Shen L, Zhao C, Wang Z, Guo Y, Wang X, Liu Y. A simple route for consecutive production of activated carbon and liquid compound fertilizer from rice husk. *Colloids and Surfaces A: Physicochemical and Engineering Aspects* 2014;446:90-96.

[22] Alves RF, Alves JFA, Manguiera ESV, Gomes SF, Sena RF. Produção de carvão ativado a partir de endocarpo de coco da baía visando o armazenamento de gás natural. *Proceedings of Congresso Nacional de Engenharia de Petróleo, Gás Natural e Biocombustíveis; 2015, Campina Grande. Campina Grande: Editora Realize; 2015.*

[23] Angin D, Köse TE, Selengil U. Production and characterization of activated carbon prepared from safflower seed cake Biochar and its ability to absorb reactive dyestuff. *Applied Surface Science* 2013;280:705–10.

[24] Guo Y, Rockstraw DA. Physical and chemical properties of carbons synthesized from xylan, cellulose, and Kraft lignin by H₃PO₄ activation. *Carbon* 2006;44:1464-75.

[25] Gupta VK, Pathania D, Sharma S. Adsorptive remediation of Cu(II) and Ni(II) by microwave assisted H₃PO₄ activated carbon. *Arabian Journal of Chemistry* 2017;10(2):S2836-S2844.

[26] Oliveira YSL, Santos EA, Silva J, Lemos LTM, Silva FLH, Queiroz ALM, Jaguaribe EF, inventors; Universidade Federal da Paraíba, assignee. Processo de produção de carvão ativado a partir do bagaço do sisal. Brazil patent BR 10 2018 015530 0. 2018 Jul 30.

[27] Duarte LC, Carvalho F, Neves I, Girio FM. Effects of aliphatic acids, furfural and phenolic compounds on *Debaryomyces hansenii* CCMI 941. *Applied Biochemistry and Biotechnology* 2005;121:413-25.

CO₂ capture using high surface area activated carbon

Simone F. Santos^{a,b}, José L.C. Cordeiro^{a,b}, Raildo A. Fiuza-Jr^{a,b,c*}

^aLaboratório de Catálise e Materiais – LABCAT, Dept. de Química Geral e Inorgânica, Campus Ondina, Universidade Federal da Bahia, Salvador-BA, 40170-280, Brazil.

^bGrupo de Pesquisa em Eletroquímica Energia e Materiais – GPEEM, Dept. de Química Geral e Inorgânica, Campus Ondina, Universidade Federal da Bahia, Salvador-BA, 40170-280, Brazil.

^cLaboratório Multianálises – LABMULTI, Centro Interdisciplinar de Energia e Ambiente, Campus Ondina, Universidade Federal da Bahia, Salvador-BA, 40170-280, Brazil

Abstract

This work researched the capacity of CO₂ capture in activated carbons derived from biomass from yellow mombin stones. Biomass was characterized by thermogravimetric analysis, presenting volatile, fixed carbon and ash contents of 76.46%, 21.29% and 2.25%, respectively. The high value obtained from fixed carbon indicates that biomass has potential for activated carbons production. The activated carbons were prepared and chemically activated from different times. The pyrolysis was performed at a temperature of 600 °C in an inert atmosphere and a level of 2 hours, at a rate of 10°C/min. Subsequently, the material was impregnated with potassium hydroxide solution (KOH) in a proportion of 1:5 (biochar/KOH) and heated for 1 hour at a temperature of approximately 60°C. The resulting material was dried in an oven and activated in an inert atmosphere at 800° C at a rate of 10°C/min at different levels: 30 min, 60 min and 120 min. The textural analysis of the activated carbon by adsorption and nitrogen desorption showed that the activated carbon in 120 minutes presented the largest surface area BET, 3333 m²/g, followed by the activated carbon in 60 minutes, which presented 3232 m²/g, and the activated carbon in 30 minutes, 2083 m²/g, indicating that the increase in heat treatment time maximizes the activation process. The adsorption study showed that the activated sample in 30 minutes presented the highest CO₂ adsorption capacity, which was 2.76 mmol/g.

Keywords: activated carbon; yellow mombin stones; CO₂ capture.

1. Introduction

Increasing the level of atmospheric carbon dioxide (CO₂) is a major contributor to global warming and consequently climate change [1]. According to World Bank statistics, 4.9 metric tons of CO₂ per person were added to the atmosphere each year [2]. Different technologies have been developed to reduce the concentration of CO₂ [3]. CO₂ capture has been extensively studied, mainly by temperature oscillation adsorption (TSA) using equipment for thermogravimetric analysis [4]. Among the main solid adsorbents we can mention the molecular sieves and activated carbons [4]. Molecular sieves have the disadvantage of absorbing moisture, on the other hand activated coals are resistant to moisture and have shown good capture results. Activated carbons can be prepared using biomass waste,

benefiting the environment by reducing the cost of production. This study evaluates CO₂ capture in activated carbons prepared using yellow mombin stones residues.

2. Materials and Methods

2.1 Samples

The fruit pits used in this study were obtained in a fruit pulp industry in the Bahia Recôncavo (Feira de Santana). For this work, yellow mombin stones (*Spondias lutea* L.) was chosen. The samples were dried in an oven at 115 ± 5 °C and ground to particle size between 0.15 and 0.5 mm.



Figure 1- Yellow mombin stones.

2.2 Carbon preparation

The yellow mombin stones were crushed in a Willye TE-680 mill and sieved. The biomass was pyrolyzed in a vertical tubular oven (EDG10PS) at 600 °C, heating rate of 10 °C min⁻¹ and nitrogen atmosphere for 2 hours. The material obtained without chemical treatment was called precursor coal (CCJ600). Part of this sample was impregnated with a 1:5 potassium hydroxide KOH solution (biochar: KOH solution) under stirring at 60 °C, then oven dried in Teflon cups. The dried material was divided into three parts and pyrolyzed at 800 °C at a rate of 10 °C min⁻¹ for 30, 60 and 120 minutes to obtain the following materials CAK30, CAK60 and CAK120, respectively. The activated carbon was washed with 0.1 M hydrochloric acid (HCl) solution to pH 7.0 to remove potassium hydroxide residues.

2.3 Characterization

2.3.1 Characterization of biomass and activated carbons

Biomass was characterized by thermogravimetry analysis (Shimadzu DTG-60H) for determination of volatile, fixed carbon and ash content, biomass was characterized by TG based on ASTM E1131-08 method. Elemental analysis of biomass and coal was performed by X-ray fluorescence spectrometry (Shimadzu EDX-720). Material morphology was assessed by scanning electron microscopy (SEM) using a scanning electron microscope (S-3400N, Hitachi) without prior metallization.

The characterization of pore volume distribution and surface area of the produced materials was performed by N₂ adsorption and desorption using the ASAP 2020 equipment, Micromeritics, in the range of 10⁻⁵ <P / P_o <0.3, the micropore area. were calculated using the Dubinin-Astakhov (DA) equation. The pore size distribution (PSD) was calculated based on the functional density theory (DFT) for the slit pore model.

2.3.2 CO₂ adsorption

Adsorption studies were performed using Shimadzu DTG-60H thermogravimetric analysis (TG), with an accuracy of ± 2 °C and 0.001 mg.

The experimental conditions used were similar to those performed by Fiuza-Jr. R.A et al [1] as shown below: I - The sample heated to 200°C for 60 minutes in a current of N₂ (100 mL min⁻¹) to remove moisture and adsorbed gases; II - cooled to 40°C in a current of N₂; III - then a mixture of 50%-50% CO₂:N₂ was introduced, maintaining a total flow of 100 mL min⁻¹ for 60 min; IV - The gas was modified back to N₂, 100 mL min⁻¹, and the sample was heated to 150°C for 60 min for desorption.

3. Results and discussion

3.1 Characterization

3.1.1 Thermogravimetry of biomass

Figure 2 and table 1 present the results of the thermal analysis.

The curve profile in the range 105-500 °C, under dinitrogen atmosphere, shows a high mass loss related to the decomposition of biomass macrocomponents, this mass loss is represented as volatile (76.46%), at the end of this thermal event is Given the fixed carbon amount (21.29%). These thermal events occur with heat absorption as observed by the DTA. When switching gas to synthetic air, the fixed carbon is burned, forming the ash with a content of 2.25%, this event is accompanied by heat release as shown in the DTA. This biomass contains an important fixed carbon content for the production of activated carbon and a low ash content that favors a smaller clogging of the pores produced.

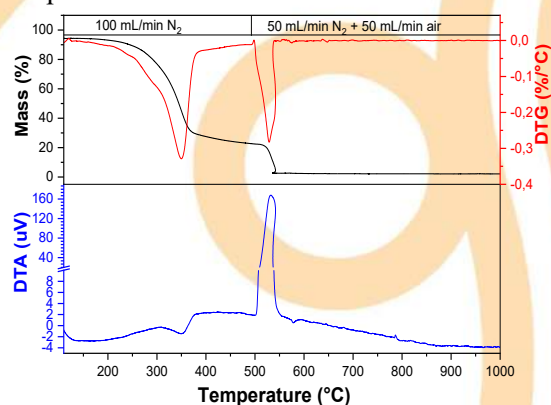


Figure 2. TG analysis of in natura biomass using the ASTM (E1131-08) method.

Table 1. Result of the thermogravimetric analysis.

Material	Content (%)	Temperature(°C)
Volatile	76.46	105-500
Fixed carbon	21.29	500
Ash	2.25	600

3.1.2 Elemental analysis of biomass and activated carbons

The elemental composition in the form of oxides, biomass and activated carbon is presented in Table 2. The predominant composition in biomass was calcium and potassium, elements normally found in biomass. The heat treatment used in the production of coal favors the increase of the concentration of the elements present in the biomass, but the washing of the carbon with HCl after the preparation favors the reduction of the concentration of these species according to its degree of solubility and opening of the pores of the activated carbon.

Table 2. Elementary analysis by EDX.

Oxide	Biomass	CAK30	CAK60	CAK120
CaO	36.85%	45.86%	13.11%	14.24%
ZnO	4.22%	0.69%	0.82%	0.92%
CuO	2.12%	0.44%	--	0.37%
K ₂ O	28,12%	1,02%	0,76%	0,62%
MgO	--	13.57%	7.00%	9.32%
MnO	--	0.39%	1.02%	0.99%
NiO	--	--	2.64%	3.35%

3.1.3 Scanning electron microscopy

The micrographs show that the coals have a rough and porous structure. No significant change could be observed with the increase of the activation time, only a certain reduction in the pore size of the CAK120 sample.

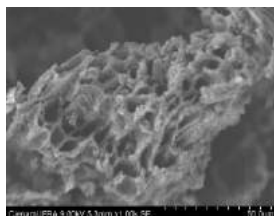


Figure 3 - SEM micrograph of the CAK60 sample

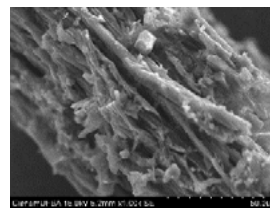


Figure 4- SEM micrograph of the CAK30 sample

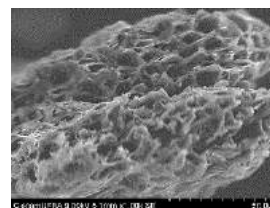


Figure 5- SEM micrograph of the CAK120 sample

3.1.4 Textural analysis by adsorption and nitrogen desorption

The nitrogen adsorption isotherms of activated carbon are shown in Figure 6. All materials exhibited type I isotherms, characteristic of microporous materials, according to the IUPAC classification. The activated carbon precursor material (CCJ600P) presented type Ia isotherm, when the low pressure inflection is close to the y axis, indicating that most of the pores are of similar size. Activation favors the enlargement of the pores, causing the y-axis to move away from the inflection at low pressures, naming these isotherms as type I b. Activation of KOH pyrolyzed biomass promoted the development of the microporous structure and a large development in the surface area. Increasing activation time improved microporous structure, increasing the BET area of the CAK sample from 2083 to 3333 m²/g and total pore volume from 0.95 to 1.60 cm³/g, Table 3.

This fact is promoted by the oxidation process caused by potassium [5]. The pore size distribution was calculated using the NLDFT method for the slit pore model, allowing to evaluate the micropore distribution in the range (<2 nm) and mesoporous (2 nm <x <50 nm) shown in Figure 6.

The precursor carbon showed pore concentration in the micropore range (<1 nm). Activated charcoal presented pore concentration in the range from 1 to 5 nm, indicating the presence of micro and even pores. The heterogeneity of the porous structure decreases with increasing activation time.

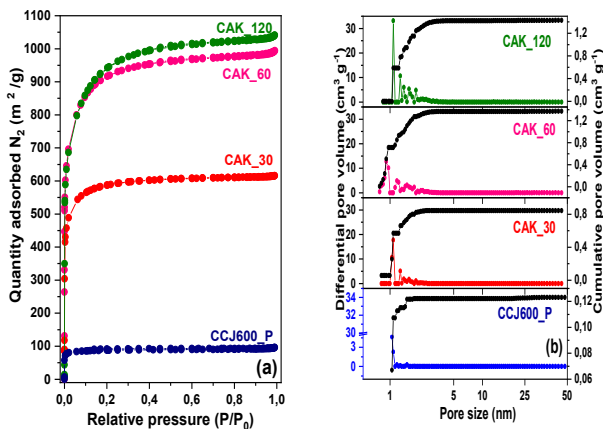


Figure 6 - (a) Adsorption-desorption isotherms of nitrogen. (b) Pore size distribution by NLDFT and accumulated pore volume.

Table 3. Textural properties of precursor carbon and activated carbon

Samples	^a S _{BET} (m ² /g)	^b S _{mic} (m ² /g)	^c S _{meso} (m ² /g)	^d V _t (cm ³ /g)
CCJ600	310	350	2.38	0.15
CAK30	2083	2263	26.48	0.95
CAK60	3232	3378	71.45	1.53
CAK120	3333	3805	93.93	1.60

a. S_{BET}, surface area calculated by BET equation at P/P₀ = 0.05-0.2.

b. S_{mic}, surface area calculated by DA method.

c. BJH desorption cumulative surface area of pores between 2.0 nm and 300nm diameter.

d. V_{total}, total pore volume estimated from the adsorption amount at P/P₀ = 0.98.

Table 3.1 Textural properties of precursor carbon and activated carbon [Cont.]

Samples	V ¹ _{mic} (0,7- 0,8nm)	V ² _{mic} (0,8- 1,0nm)	V ³ _{mic} (1,0- 2,0nm)	V ⁴ _{mic} (2,0- 50nm)
CCJ600	-	0,0670 (54,4%)	0,1222 (44,8%)	0,1231 (0,7%)
CAK30	-	0,2559 (30,3%)	0,8243 (67,4%)	0,8432 (2,2%)
CAK60	0,0631 (1,1%)	0,7118 (50,7%)	1,2853 (41,8%)	1,3717 (6,2%)
CAK120	-	-	1,2603 (88,3%)	1,4264 (11,6%)

3.2 Adsorption studies

Adsorption CO₂ experiments were performed by thermal analysis at a concentration of 50% N₂ diluted CO₂ and are shown in figure 7.

The CAK30 sample showed the highest adsorption capacity, 12.15%, CAK60 and CAK120 showed 9.88% and 7.56%, respectively.

The table 4 shows the adsorption capacity of activated coals from different types of biomass. Compared to the literature data, considering similar conditions in activated carbon production, the samples of this study presented higher CO₂ capture capacity.

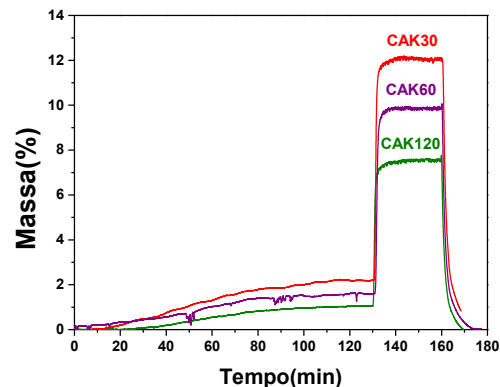


Figure 7 - Adsorption of CO₂ on activated carbon, determined by thermogravimetry, using nitrogen as a diluent gas at a temperature of 40°C. (Mass of activated carbon 12 mg)

Table 4 - Adsorption of CO₂ by activated carbons prepared from different starting materials

Material	Temp. (°C)	Adsorption Capacity(mmol/g)	Ref.
Bamboo	25	0.54	[3]
Coconut shell	25	0.44	[3]
Carbon spheres	0	6.6	[6]
d-glucose	0	6.62	[6]
Rapeseed/Wal nut shell	25	1.51	[5]
Yellow Mombin	25	2.76	This work

The CO₂ adsorption capacity shown by activated carbon is mainly influenced by the surface area, porosity and functional groups [5]. In this research, it was not possible to establish a clear relationship between the surface area and the volume of pore micropores with the CO₂ adsorption capacity, a fact also observed in other studies in the literature [5] [7]. Indicating that some other effect must be influencing CO₂ adsorption, possibly the basicity of the activated carbon surface.

4. Conclusions

The biomass used showed to be promising for the production of activated carbon, presenting low ash content and high fixed carbon value.

Activation with KOH resulted in the obtaining of surface area values between 2083 and 3333 m² / g.

CO₂ capture results observed for these materials were superior to those reported in the literature.

The adsorption capacity was influenced by the high surface area and porosity, however a direct relationship was not observed.

Acknowledgements

The authors gratefully acknowledges the financial support provided by Fundação de Amparo à Pesquisa do Estado da Bahia –FAPESB.

References

- [1] Yu-Chun, C. et al. Carbon Dioxide Adsorption on Porous and Functionalized Activated Carbon Fibers.2019
- [2] Younas, M., et al. Feasibility of CO₂ adsorption by solid adsorbents: a review on low-temperature systems. 2016
- [3] Tiwari, D.,et al.Adsorption of CO₂ on KOH activated, N-enriched carbon derived from urea formaldehyde resin: kinetics, isotherm and thermodynamic studies. In: Applied Surface Science.2018
- [4] Fiuza-Junior, R.A.Valorização de caroços de frutas regionais e captura de CO₂.2016. Tese (Doutorado em Química)- Instituto de Química, Universidade Federal da Bahia.
- [5]David, E; Kopac. J. Activatad carbons derived from residual biomass pyrolysis and their CO₂ adsorption capacity. In: Journalof Analytical and Applied Pyrolysis.2014
- [6] Singh, G., et al. A facile synthesis of activated porous carbon spheres from D-glucose using a non-corrosive activating agent for efficient carbon dioxide capture. In: Applied Energy.2019
- [7] Serafin, J., et al. Direct conversion of biomass to nanoporous activated biocarbons for high CO₂ adsorption and supercapacitor applications. In: Applied Surface Science

Rhodamine 6G adsorption from aqueous solution using as a biosorbent the NaOH-activated aqai stalk

R.C.S. Araújo^a, C.A. Azevedo^a, R.L.T. Costa^a, W.J.P. Costa^a, R.L. Santos^a,
C.A. Azevedo^b, L.J.G. Faria^{a,*}

^a Federal University of Pará, Postgraduate Program in Chemical Engineering, Augusto Corrêa Street 01, Belém, 66075-110, Brazil.

^b Federal University of Pará, Postgraduate Program in Mechanical Engineering, Augusto Corrêa Street 01, Belém, 66075-110, Brazil.

Abstract

The adsorption process has high efficiency in the removal of textile dyes from aqueous solutions using low cost materials as adsorbents. The biosorbents produced from the acai palm stalk fibers (AB) were used to remove Rhodamine 6G textile dye from 200 mg.L⁻¹ aqueous solution and natural pH of 4.51 in batch system. The biosorbent was characterized by PZC and SEM/EDS analysis. The affinity of the adsorbate to the solid surface was chemically improved by modifying AB in NaOH (AAB) solution. In the adsorption tests, the amount of biosorbent, kinetics, equilibrium and thermodynamics were evaluated. The results obtained in the biosorption studies indicated a favorable performance in the 5 g.L⁻¹ adsorbent dosage. Experimental data showed that the minimum equilibrium time was at 210 min and a good fit with the pseudo second order kinetic model. The Sips model provided the best fit to the experimental equilibrium points, with the raise of temperature implying the increase of adsorption capacity (38.88 mg.g⁻¹), leading to a 97% dye removal. The thermodynamic study of enthalpy (ΔH°), Gibbs energy (ΔG°) and entropy (ΔS°) variations showed that the adsorption between dye and AAB is spontaneous, favorable and endothermic. This work demonstrated that the aqai stalk is a potential biosorbent, due to its low cost and efficiency in pollutant removal.

Keywords: Biosorption; Aqai Palm Stalk; Textile dye

1. Introduction

The discharge of effluents into the environment has become a major concern of the industrial sector, not only to comply with Conama Resolution No. 430/2011, which deals with the conditions and standards for waste disposal, but also to contribute to sustainability in the industrial environment, with less waste and greater efficiency in the production process [1].

In the textile industry, the environmental impact is significant due to the large amount of high chemical wastewater generated by incomplete fixation of dyes, pigments and other additive compounds [2]. This contributes to variations in oxygen, temperature, turbidity and toxicity in the water beds to occur and in addition, some substances cause risks to population [3], requiring

an effective removal method that meets the environmental legislation.

The adsorption process is considered a versatile alternative because it is economically viable, has simple applicability, efficient removal rates of dissolved organic substances and ability to use various materials and tailings as adsorbents [4-6].

In this context, there is the açazeiro (*Euterpe oleracea* Mart.), a tropical palm from northern Brazil, which supplies the aqai juice, whose consumption is on the rise worldwide. A large amount of tailing is produced, one of them being the aqai cluster, also known as the aqai stalk, normally discarded at harvest sites, with no prospect of recycling [7, 8]. In short, studies with the aqai stalk, a fibrous and porous biodegradable waste, claim that this is a material with high potential as biosorbent, that considerably decreases the concentration of textile dyes in industrial effluents [9-12].

The present work aimed to study the biosorption process in a batch system to remove the basic Rhodamine 6G textile dye (Basic Red 1) in aqueous solution, using the NaOH modified aqai palm stalk as biosorbent. The biosorbent was characterized and the effect of dosage, the kinetic and equilibrium studies were investigated in the adsorptive process.

2. Materials and methods

2.1. Adsorbate solution preparation

The adsorbate solutions were prepared by dissolving Rhodamine 6G dye (CI: 45160, Basic Red 1) in distilled water, at the initial concentration of 200 mg.L⁻¹ and natural pH of 4.51. The concentrations were determined by using a SHIMADZU UV-1800 spectrophotometer at wavelength of 526 nm.

2.2. Biosorbent (AB) preparation and characterization

The aqai stalk (*Euterpe oleracea* Mart.) was supplied by farmers from Ilha das Onças, in the state of Pará. The biosorbent was washed with tap water and then with distilled water to remove impurities. Posteriorly, it was dried in an air supplied oven with ventilation at 323 K for 24 hours. The dried samples were ground in a knife mill and Metvisa® industrial blender and sieved in a Produtest® shaker, with standardized sieves, with the fiber grading in the 1.180-0.850 mm particle size range.

Point of zero charge (PZC): Using the 11-point methodology [13], eleven samples were prepared with 50 mg of biosorbent and 50 mL of standardized HCl or NaOH solution, with pH values adjusted to: 1.0; 2.0; 3.0; 4.0; 5.0; 6.0; 8.0; 9.0; 10.0; 11.0 and 12.0. These samples were kept under stirring at 303 K for 24 hours in a Dubnoff-157 bath. Posteriorly, the solutions were filtered and had their final pH measured with a pH meter (benchtop W3B model).

Chemical modification: The chemical impregnation methodologies [14, 15] were adapted for this work. Approximately 15 g of fibers was added to 300 mL of NaOH solution (3.0 M), and then kept with constant homogenization on a shaker table for 1 hour. The solution was filtered, washed with distilled water, dried in an air supplied oven at 378 K for 24 hours and stored in a desiccator.

Scanning Electron Microscopy (SEM) with Dispersive Energy X-ray Spectrometry (EDS): The morphology of the in natural and chemically modified aqai stalk surfaces were evaluated by the Hitachi TM/TM 3000 Scanning Electron Microscope (SEM) coupled to Energy Dispersive X-Ray Spectroscopy (EDS) detector, Swift ED 3000 X-Ray model, performing semi-quantitative analysis and mapping the elements on the surfaces of the in natural and NaOH activated biosorbent.

2.3. Chemically modified AB (AAB) adsorption tests

Adsorbent dosage: In order to investigate the influence of biosorbent dosage on Rhodamine 6G dye removal from aqueous solution, this study was carried out using biosorbent dosages ranging from 2.5 to 20 g.L⁻¹ in 50 mL adsorbate (200 mg.L⁻¹). The solutions were stirred in a Dubnoff -157 bath for 6 hours and 303 K. The percentage of dye removal (%Removal) from solutions, the amount of dye adsorbed per unit mass of the adsorbent in relation to contact time (q_t) and equilibrium (q_e) were calculated by using Equations 1, 2 and 3, respectively. Where the initial concentration, at a time t and at equilibrium are represented by C_o , C_t and C_e (mg.L⁻¹), V is the volume of the solution (L) and m is the mass of the biosorbent (g).

$$\%removal = \left(\frac{C_o - C_e}{C_o} \right) \cdot 100 \quad (1)$$

$$q_t = \frac{(C_o - C_t) \cdot V}{m} \quad (2)$$

$$q_e = \frac{(C_o - C_e) \cdot V}{m} \quad (3)$$

Adsorption kinetics: The kinetic tests were performed with 0.250 g AAB in 50 mL of dye solution (200 mg.L⁻¹). The solutions were kept in a Dubnoff-157 bath at a temperature of 303 K, at established contact times between 1 and 840 minutes. Experimental data were adjusted in the pseudo first order [16], pseudo second order [17] and intraparticle diffusion [18] models, respectively, Equations 4, 5 and 6.

$$\frac{dq_t}{dt} = k_1(q_e - q_t) \quad (4)$$

$$\frac{dq_t}{dt} = k_2(q_e - q_t)^2 \quad (5)$$

$$q_t = k_{di}\sqrt{t} + C \quad (6)$$

Where q_t and q_e represent the amount of adsorbed dye per gram of adsorbent (mg.g^{-1}) at any time and equilibrium, respectively, k_1 is the pseudo first order rate constant (min^{-1}), k_2 indicates the pseudo second order rate constant ($\text{g.mg}^{-1}.\text{min}^{-1}$), k_{di} is the intraparticle diffusion constant ($\text{mg.g}^{-1}.\text{min}^{-0.5}$) and C is a constant related to diffusion resistance (mg.g^{-1}).

Adsorption equilibrium: The tests were carried out at 303, 313 and 323 K. The samples were prepared using 0.250 g of AAB and 50 mL of the dye solution ($1\text{-}200 \text{ mg.L}^{-1}$) under stirring for 6 hours in Dubnoff-157 bath at 303 K. The data obtained from experimental tests were fitted to the adsorption models of Langmuir [19], Freundlich [20], Sips [21] and Redlich-Peterson [22], according to Equations 7, 8, 9 and 10, respectively:

$$q_e = \frac{q_{\max}k_L C_e}{1 + k_L C_e} \quad (7)$$

$$q_e = k_f C_e^{1/n_F} \quad (8)$$

$$q_e = \frac{q_{\max}k_S C_e^{1/n_S}}{1 + k_S C_e^{1/n_S}} \quad (9)$$

$$q_e = \frac{k_{RP}C_e}{1 + (a_{RP}C_e)^\beta} \quad (10)$$

Where q_e is the amount of the dye sorbed per unit mass of sorbent at equilibrium (mg.g^{-1}), q_{\max} the maximum adsorption capacity, C_e is the equilibrium dye concentration in the solution (mg.L^{-1}); k_L (L.mg^{-1}), k_F ($(\text{mg.g}^{-1})(\text{mg.L}^{-1})^{-1/n_F}$), k_S (L.mg^{-1}) and k_{RP} (L.g^{-1}) represent the respective constants of Langmuir, Freundlich, Sips and Redlich-Peterson model equilibrium, while $1/n_F$ and n_S is the surface heterogeneity factor of Freundlich and Sips (dimensionless), respectively; a_{RP} (mg.L^{-1}) and β are the Redlich-Peterson constants.

Thermodynamic parameters: For analysis of thermodynamic behavior, the graph $\ln K^\circ$ versus T^{-1} was constructed, where the value of the angular coefficient represents the parameter $(-\frac{\Delta H^\circ}{R})$ and linear coefficient represents the parameter $(\frac{\Delta S^\circ}{R})$, being possible to calculate the respective values of the enthalpy (ΔH° , KJ.mol^{-1}) and entropy (ΔS° , $\text{J.mol}^{-1}.\text{K}^{-1}$) variations. The Equation 11 calculates the changes in Gibbs standard free energy (ΔG° , KJ.mol^{-1}).

$$\Delta G^\circ = -RT \ln K^\circ \quad (11)$$

Where R is the ideal gas constant ($8.314 \text{ J.mol}^{-1}.\text{K}^{-1}$), T is the absolute work temperature (K), K° is the equilibrium constant (dimensionless), calculated by the expression [22]: $K^\circ = k_S \times \text{MM}_{\text{adsorbate}} \times 10^3 \times 55.5$, where k_S is the Sips constant (L.mg^{-1}), $\text{MM}_{\text{adsorbate}}$ is the molecular weight of the dye (442.5 g.mol^{-1}); the factor 55.5 represents the number of moles of pure water per liter (mol.L^{-1}) calculated as ($1000 \text{ g.L}^{-1}/18 \text{ g.mol}^{-1}$).

3. Results and discussion

3.1. Biosorbent characterization

Point of zero charge (PZC): The pH values of the aqai stalk (AB) showed that the adsorbent surface has a zero charge point of 6.69, characterizing the sample surface as acidic. Therefore, for the natural pH of the adsorbate, the sample will have its electrically charged positive surface. However, bioadsorbent is more effective for removing cationic dyes when placed in contact with a pH solution higher than the PZC found in this study [6, 15]. In this case, chemical modifications are required on the surface of the solid.

After chemical impregnation with NaOH, the AAB showed a removal efficiency around 97%, in preliminary test. This result confirms the cationic behavior of the aqai stalk in the solution, occurring interaction with greater affinity between the basic adsorbent surface and the Rhodamine 6G dye solution.

Scanning Electron Microscopy (SEM) with Dispersive Energy X-ray Spectrometry (EDS): The Fig. 1 presents the SEM analysis of AB and AAB, showing samples of fibrous nature and a larger porous structure, implying a larger surface area available for the adsorption process.

In the EDS analysis, it was found that the samples have in its composition: oxygen, carbon, sodium, potassium, calcium and magnesium; corroborating with [7], who mentions Mg, K, Ca and C as chemical elements of organic fibers *Euterpe oleracea* Mart. However, the percentage increase in oxygen and a significant rise in the amount of sodium in the AAB sample is attributed to the chemical treatment of the surface.

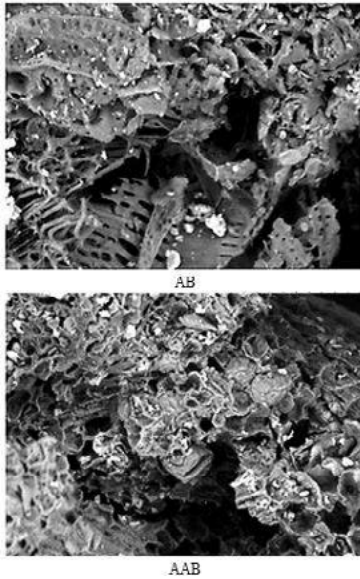


Fig. 1. SEM of AB and AAB (1200x).

3.2. Biosorption experiments

Adsorbent dosage: As apparent in Fig. 2, the maximum amount of removal occurred for biosorbent doses of at least 7 g.L⁻¹. However, the values of the adsorptive amount per mass of adsorbent from this dosage become significantly low. The dosage of 5 g.L⁻¹ corresponds to the minimum amount of adsorbent required for constant percentage dye removal and best defines this adsorptive process.

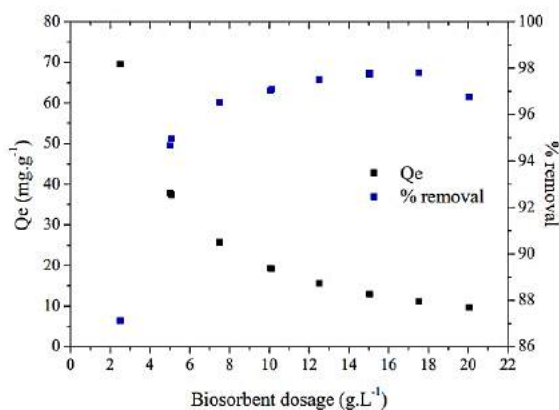


Fig. 2. Effect of adsorbent dosage.

Adsorption kinetics: The values showed in Table 1 confirm that the process satisfactorily fitted the pseudo second order model ($R^2_{adj} = 0.970$), where the equilibrium adsorption capacity was approximately 36.54 mg.g⁻¹, close to q_{exp} as shown in Fig. 3.

Table 1. Parameter values of kinetic models for Rhodamine 6G/AAB adsorption.

Model	Parameter
Pseudo first order	
q_e (mg.g ⁻¹)	36.538
K_1 (min ⁻¹)	0.119
R^2_{adj}	0.750
Pseudo second order	
q_e (mg.g ⁻¹)	38.060
K_2 (mg.g ⁻¹ .min ⁻¹)	0.006
R^2_{adj}	0.970
Intraparticle diffusion	
C (mg.g ⁻¹)	28.50
k_{dt} (mg.(g.min ^{-1/2}) ⁻¹)	0.511
R^2_{adj}	0.610

Furthermore, it is demonstrated that the overall rate of the adsorption process can be controlled in its totality by chemisorption [24].

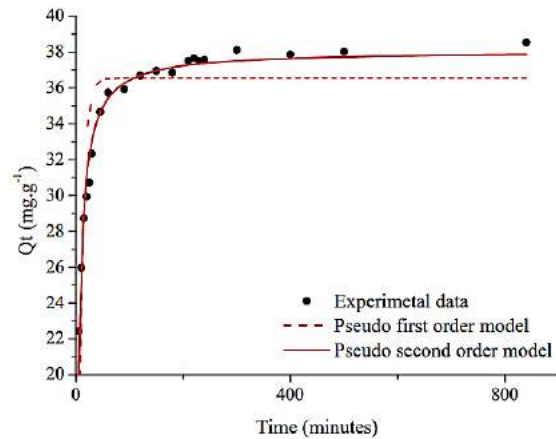


Fig. 3. Kinetic adjustment for Rhodamine 6G/AAB adsorption.

However, in intraparticle diffusion the C value differed from zero, suggesting that intraparticle diffusion is not the determinant step of the adsorption process presented, i.e., other transfer mechanisms must act in the process control [18].

Adsorption equilibrium: The parameter values of the adsorption equilibrium models and the adjusted determination coefficient (R^2_{adj}) values at

temperatures 303 K, 313 K and 323 K are shown in Table 2.

Table 2. Parameter values of isothermal models of Rhodamine 6G adsorption by AAB.

T (K)	303 K	313 K	323 K
Langmuir			
q_{max} (mg.g ⁻¹)	42489.5	1059.1	367449.0
k_L (L.mg ⁻¹)	1.04e-4	0.005	2.07e-5
R^2_{adj}	0.977	0.965	0.971
Freundlich			
k_F (L.mg ⁻¹)	4.424	5.647	7,614
n_F	0.999	0.999	0.999
R^2_{adj}	0.977	0.964	0.971
Sips			
q_{max} (mg.g ⁻¹)	72.087	50.221	57.434
k_S (L.mg ⁻¹)	0.040	0.063	0.113
n_S	0.651	0.495	0.574
R^2_{adj}	0.985	0.993	0.986
Redlich-Peterson			
k_{RP} (L.g ⁻¹)	36.393	14.899	58.104
a_{RP} (mg.L ⁻¹)	7.224	1.637	6.628
β	2.47e-17	7.88e-16	1e-16
R^2_{adj}	0.974	0.960	0.967

The experimental data of the adsorptive systems presents coefficients of determination close to linearity in all isothermal models investigated. However, Sips model showed the best fit with the experimental data, with values of R^2_{adj} higher and closer to the unit value, as shown in Table 2. In Fig. 4, comparisons between adsorption isotherms at temperatures 303, 313 and 323 K for the Sips model are presented.

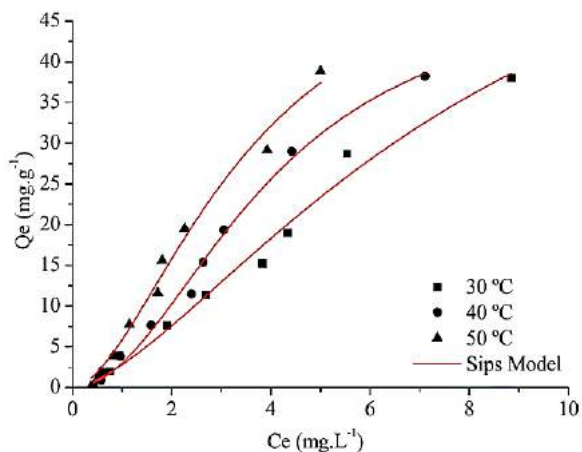


Fig. 4. Sips model adsorption isotherms for Rhodamine 6G/AAB adsorption at 303, 313 and 323 K.

The Sips model is the mathematical combination between the Langmuir and Freundlich models, when at low concentrations the behavior is of a Freundlich isotherm, while at high concentrations the adsorption process takes place in monolayers, assuming an isotherm of Langmuir [21].

As evident from Fig. 4, in which the system is directly influenced by the concentration of the adsorbate solution and demonstrates favorable isotherm behavior considering the attraction effects between the adsorbent and adsorbate, with higher correlation coefficient ($R^2_{adj} > 0.98$) when compared to other models. Besides that, the n_S values lower than 1.0 indicate that the adsorbent surface is heterogeneous, and it can be concluded that there is formation of more than one adsorption layer or multilayer in the treatment of aqueous solution.

The q_{max} values found were 72.087 (mg.g⁻¹) (303 K), 50.221 (mg.g⁻¹) (313 K) and 57.434 (mg.g⁻¹) (323 K) indicating that AAB is an efficient biosorbent for the removal of Rhodamine 6G from aqueous solutions and the activation promotes faster diffusion of the dye through the pores and also allows high amounts to be adsorbed. It is highlighted that the Sips model showed the best experimental conditions research using this same adsorbent material to remove different types of textile dyes [9, 10, 12].

Thermodynamic parameters: For the established work temperatures, the negative values of ΔG° (KJ.mol⁻¹) suggests a spontaneous and favorable thermodynamic process, especially with temperature increase, as shown in Table 3. The enthalpy variation ΔH° (KJ.mol⁻¹) indicates positive values, confirming the endothermic nature of the 6G Rhodamine biosorption by AAB.

Table 3. Thermodynamic parameters of Rhodamine 6G/AAB adsorption.

T (K)	ΔG° (KJ.mol ⁻¹)	ΔH° (KJ.mol ⁻¹)	ΔS° (J.mol ⁻¹ .K)
303 K	-34.765		
313 K	-35.884	41.860	252.654
323 K	-37.362		

The entropy variation ΔS° (J.mol⁻¹.K) implies increased interaction and randomness between AAB active sites and dye molecules at higher temperatures. This is classified as a chemical process because the ΔH° values are greater than 21 KJ.mol⁻¹ [25, 26].

4. Conclusion

The adsorption of Rhodamine 6G by AAB showed that the best fit kinetic model was the pseudo second order. The equilibrium model showed that the Sips model describes the adsorption process well, considering the system is directly influenced by the concentration of the adsorption solution. The thermodynamic parameters found evidence that Rhodamine 6G adsorption process is spontaneous, favorable and endothermic. These results demonstrate that the açaí stalk is an efficient adsorbent for removal of Rhodamine 6G dye from aqueous solutions.

References

- [1] BRASIL. Ministério do Meio Ambiente, Conselho Nacional do Meio Ambiente, CONAMA. Resolução CONAMA Nº430, de 13 de maio de 2011. Condições e padrões de lançamento de efluentes. Publicado no DOU n. 92, p.92
- [2] Faria FP, Pacheco EBAV. Experiência de Produção Mais Limpa no Setor Têxtil. Revista de Design, Inovação e Gestão Estratégica-REDIGE. Rio de Janeiro; 2011. v. 2, n. 1, p.63-82.
- [3] Noorimotlagha Z, Soltanib RDC, Khataee AR, Shahriyara S, Nourmoradia H. Adsorption of a textile dye in aqueous phase using mesoporous activated carbon prepared from Iranian milk vetch. Journal of the Taiwan Institute of Chemical Engineers, v. 45, p. 1783–1791, 2014.
- [4] Gupta VK, Saleh TA. Sorption of pollutants by porous carbon, carbon nanotubes and fullerene - An overview. Environ Sci Pollut Res, v.20, p.2828–2843, 2013.
- [5] Peixoto F. et.al. Corantes Têxteis: uma revisão. Holos, 20, v. 5, p. 98-106, 2013.
- [6] Nascimento RF. et al. Adsorção: aspectos teóricos e aplicações ambientais. 256 f. Fortaleza: Imprensa Universitária, 2014.
- [7] Rogez H. Açaí: Preparo, Composição e Melhoramento da Conservação; EDUFPA: Belém, Brasil, 313p, 2000.
- [8] EMBRAPA. Empresa Brasileira de Pesquisa e Agropecuária. Sistemas de Produção 4 – Açaí. Belém, 2005.
- [9] Alencar WS, Lima EC, Royer B, Dos Santos BD, Calvete T, Da Silva EA, Alves CN. Application of açaí stalks as biosorbent for the removal of the dye Procion Blue MX-R from aqueous solution. Separation Science Technology, 2011, v. 47, p. 513-526.
- [10] Cardoso NF, Lima, EC, Calvete T, Pinto IS, Amavisca CV, Fernandes THM, Pinto RB, Alencar WS. Application of açaí stalks as biosorbent for the removal of the dyes Reactive Black 5 and Reactive Orange 16 from aqueous solution. Journal of Chemical and Engineering; 2011. v. 56, p. 1857-1868.
- [11] Cardoso NF. Adsorção de corantes têxteis utilizando biossorventes alternativos. Departamento de Pós-Graduação em Química, Universidade Federal do Rio Grande do Sul. Porto Alegre, 2012.
- [12] Prola LDT, Acayanka E, Lima EC, Bestetti IC, Santos WO, Pavan FA, Dias SLP, Tarley CRT. Application of açaí stalks as biosorbent for the removal of Evans Blue and Vilmafix Red RR-2B dyes from aqueous solution. Desalination and Water Treatment. 2013. v. 51, p. 4582-4592.
- [13] Regalbuto JR, Robles J. The engineering of Pt/carbon catalyst preparation for application on Proton Exchange Fuel Cell Membrane (PEFCM). University of Illinois: Chicago; 2004.
- [14] Dos Santos VCG, Souza JVTM, Taley CRT, Caetano J, Dragunski DC. Copper ions adsorption from aqueous medium using the biosorbent sugarcane bagasse in natura and chemically modified. Water, Air and Soil Pollution; 2011. v. 216, p.351-359.
- [15] Araújo NC, Scarponi GHG, Carvalho DC. Utilização de coco in natura e modificado quimicamente como adsorvente alternativo para tratamento de efluente têxtil. Revista Perquirere. Patos de Minas; 2017. v. 2, p. 178-179.
- [16] Lagergren, S. About the theory of so-called adsorption of soluble substance, K Sven Vetenskapsakademiens Handl. 1898. v. 24, p.1–39.
- [17] Ho Y, Mckay G. Kinetic models for the sorption of dye from aqueous solution by wood. Process Saf. Environ Prot. 1998. v.76, p.183–19.
- [18] Weber WJ, Morris JC. Kinetics of adsorption on carbon from solution. Sanit Eng Div; 1963. v.89, p.31–60.
- [19] Langmuir I. The adsorption of gases on plane surfaces of glass, mica and platinum. J Am Chem Soc, 1918. v.40, p.361–1403.
- [20] Freundlich HMF. Over the adsorption in solution, J Phys Chem A. 1906. v. 57, p.385–470.
- [21] Sips R. On the structure of a catalyst surface. J. Chem. Phys. 1948, 16, 490–495.
- [22] Redlich O, Peterson DL. A useful adsorption isotherm, J. Chem. Phys; 1959. V. 63; p. 1024-1027.
- [23] Zhou X, Zhou X. The Unit Problem in the Thermodynamic Calculation of Adsorption Using the Langmuir Equation, Chem. Eng. Commun.2014. v. 11, p. 1459–467.
- [24] Ho YS, Mckay G. Pseudo-second order model for sorption processes. Process Biochem, 1999. v.34, p.451–465.
- [25] Khormaei M, Nasernejad B, Edrisi M, Eslamzadeh T. Copper biosorption from aqueous solutions by sour orange residue, J. Hazard. Mater, 2007, p. 269–274.
- [26] Senturk, HB, Ozdes D, Duran C. Biosorption of Rhodamine 6G from aqueous solutions onto almond shell (Prunus dulcis) as a low cost biosorbent. Desalination, 2010, p. 81–87.

Multivariate optimization of textile wastewater treatment by adsorption using blast furnace dust

Larissa Granjeiro Lucena^{a,b}, Antonia Mayza de Moraes França^{a,*}, Nayara Oliveira Lima^a,
Ronaldo Ferreira do Nascimento^a

^a Federal University of Ceara, Av. Mister Hull, s/n – Pici, Fortaleza (CE), CEP 60455-760, Brazil

^b Federal University of Ceara, Rodovia BR-226, Km 03, s/n, Crateús (CE), CEP 63700-000, Brazil

Abstract

In this study, central composite design (CCD) and response surface methodology (RSM) were applied to optimize the adsorption process using blast furnace dust (BFD) as low cost adsorbent to treat textile wastewater. Two variables were investigated: adsorbent concentration and initial pH of the reaction. The objectives were to maximize the removal of total organic carbon (TOC) and color. According to the analysis of variance (ANOVA), all the response models using the selected variables were statistically significant, with determination coefficient (R^2) equal to 0.945 (TOC removal model) and 0.875 (color removal model). The optimal operational ranges were represented in contour plots, leading to 92.5% TOC and 87% color removals. Finally, steel waste proved to be an effective adsorbent for textile wastewater treatment.

Keywords: experimental design; adsorption; textile wastewater; biorefractory wastewater; steel waste.

1. Introduction

One of the major environmental problems nowadays is water pollution, aggravated by the inadequate treatment of industrial effluents, especially the effluents generated in the textile industry.

In this sense, adsorption is an efficient method for removing recalcitrant pollutants in effluents, being one of the most simple, effective, economical and viable methodologies for physical-chemical treatment [1].

Low cost waste from the agricultural, domestic and industrial sectors has been recognized as a sustainable solution that allows the removal of pollutants from wastewater and at the same time contributes to the minimization, recovery and reuse of such waste [2]. Emphasis should be given to iron-rich solid waste, which can be used for effluent treatment and remediation of contaminated environments, with applicability in adsorption processes [3]. In this work, the applicability of blast furnace dust (BFD) in the adsorption of textile wastewater will be investigated.

BFD is a waste released from the cast house dust system of the blast furnace in the steel industry. Due to the large quantities generated, many efforts have been directed to the development of environmentally and economically suitable destinations for BFD. Previous works used the BFD in environmental application such as for oxidation of azo dyes by heterogeneous Fenton reaction [4], foto-fenton reaction [5], demulsification to separate oil/water in metalworking fluid [6], and with tar pitch as binding and reductant of BFD in order to produce reactive materials for reduction of Cr(VI) species and elimination of textile dyes [7].

2. Materials and methods

2.1. Characterization of textile wastewater

The studied wastewater comes from a textile industry, whose physicochemical characteristics give it a high polluting potential, which requires a more efficient treatment. The samples were collected in the equalization tank, before the treatment employed by the industry, being in its raw form.

A 5 L sample volume was collected in a plastic container and immediately transported to the Advanced Oxidative Processes laboratory of the Federal University of Ceará, where it was stored at 4 °C to preserve its characteristics [8]. The characterization of the raw sample corresponded to the determination of physicochemical parameters according to the methodologies described in the Standard Methods for Examination of Water and Wastewater 22th [8], according to Table 1.

Table 1. Characterization of the textile wastewater.

Parameter	Method or Equipment	Method Number
pH	Potentiometric	4500-H ⁺ B
Conductivity	Potentiometric	2510 B
Alkalinity	Potentiometric Titration	2320 B
Total hardness	Titrimetric	2340 C
Biochemical Oxygen Demand (BOD ₅)	Respirometric	5210 D
Chemical Oxygen Demand (COD)	Closed reflux colorimetric	5220 D
Total Organic Carbon (TOC)	Total Organic Carbon Analyzer (Shimadzu TOC-L)	
Iron	Flame Atomic Absorption	3111 B-Fe
Nickel	Absorption Ion	3111 B-Ni
Chrome		3111 B-Cr
Bromide		4500-BrO E
Chloride	Chromatography - Dionex	4500-Cl ⁻ B
Fluoride	Chromatograph (ICS-3000)	4500-FI ⁻ E
Phosphate		4500-PO ₄ ³⁻
Nitrate		4500-NO ₃ ⁻
Sulphate		4500-SO ₄ ²⁻ E
Absorbance	SHIMADZU UV 18000 Spectrophotometer	

2.2. Experimental design and statistical model

Central composite design (CCD) and response surface methodology (RSM) were applied to analyse the data and optimize the interfering variables of the adsorption process: adsorbent concentration and initial pH of the reaction. The responses were defined based on the treatment goals: organic matter

degradation in terms of TOC (total organic carbon) and removal of dissolved solids in terms of color. Table 2 summarises the coded levels, the minimum (-1) and maximum (+1) factorial points, the minimum (-1.41) and maximum (+1.41) axial points, and the central point (0), as well as the respective decoded values of the two variables in the factorial design. A total of 11 tests were performed, 4 in the full factorial design, 4 at the axial points, and 3 at the central point. The variables were in the following ranges: adsorbent concentration between 35.15 and 204.85 g·L⁻¹, and initial pH between 8.09 and 10.91.

Table 2. Variation levels of adsorption process variables in the 2² central composite design.

Experimental variable	Coded and decoded variables				
	-1.41	-1	0	1	1.41
Adsorbent concentration (X ₁)	35.15	60	120	180	204.85
pH (X ₂)	8.09	8.5	9.5	10.5	10.91

The experimental data were statistically analysed through the RSM procedure in the Statistica software (version 5.0, StatSoft) and fitted to an empirical second order polynomial model, as shown in Eq. (1) [9]:

$$Y = \beta_0 + \sum_{i=1}^k \beta_i X_i + \sum_{i=1}^k \beta_{ii} X_i^2 + \sum_{i < j=2}^k \beta_{ij} X_i X_j + \varepsilon \quad (1)$$

where Y is the response; β_0 is the intercept constant, β_i is the coefficient of the first order term of factor i , β_{ii} is the coefficient of the quadratic term of factor i , and β_{ij} is the interaction coefficient between factors i and j . X_i and X_j are the decoded values of the factors, k is the number of variables, and ε is the residue.

The terms of the model were selected or rejected based on a P-value of a 95% confidence level. The results were statistically analysed by analysis of variance (ANOVA). The quality of the fit of the model to the experimental responses was expressed by the determination coefficient R^2 , and its statistical significance was checked by the Fisher's F-test.

The optimal operational region of the variables that interfere with the adsorption process using BFD was obtained from the contour plots generated by the Statistica software, post-edited in the Adobe Illustrator CS6 software, by overlaying the contour plots considering the optimization criteria of the selected responses (Table 3).

Table 3. Optimization criteria of the selected responses.

Response	Symbol	Limit
COT removal	Y1	>80%
Color removal	Y2	>80%

2.3. Experimental Procedures

All the reagents used in the experiments were of analytical quality. First, the designated amount of adsorbent was added to 125 mL Erlenmeyers (according to Table 2). Then 50 ml of textile wastewater was added to the Erlenmeyer. The pH was previously adjusted with sulfuric acid (H₂SO₄, 98%, Modern Chemistry) and 0.1M sodium hydroxide solution. Immediately, all tests were conducted for rapid mixing on a shaker table (Orbital MA 140 CFT) at room temperature and rotation of 200 rpm for 24h of reaction.

After the reaction, the samples were centrifuged at 7000 rpm for 5 min (Centrifuge 5430 eppendorf) and filtered with 14 µm filter paper, to stop the reaction and to reduce the interference of suspended particles in the TOC and color analyses. TOC was performed as previously stated on section 1.1.1.

The color number (CN) defined in Eq. (2) was used to characterize the color, based on the determination of the spectral absorption coefficient (SAC in cm⁻¹) in the visible range, at wavelengths of 436 nm, 525 nm and 620 nm. The SAC was calculated for the absorbance value of a cell of thickness *l* (cm) with Eq. (3) [10]. The absorbance value was determined using a Shimadzu (UV- 1800) spectrophotometer.

$$CN = \frac{SAC_{436}^2 + SAC_{525}^2 + SAC_{620}^2}{SAC_{436} + SAC_{525} + SAC_{620}} \quad (2)$$

$$SAC = \frac{Abs}{l} \quad (3)$$

3. Results and Discussion

3.1. Characterization of textile wastewater

The results of the physical-chemical characterization of the raw textile effluent are shown in Table 4.

Table 4. Characterization of the textile effluent.

Parameter	Unit	Value
pH (26.3 ° C)	-	9.52
Conductivity	µS·cm ⁻¹	8266.67
Alkalinity	mg·L ⁻¹	5633.33
Total hardness	mg·L ⁻¹	62.00
DBO ₅	mg·L ⁻¹	1620.00
COD	mg·L ⁻¹	2927.30
DBO ₅ / COD	-	0.55
Total Organic Carbon (TOC)	mg·L ⁻¹	733.88
Iron	mg·L ⁻¹	0.13
Nickel	mg·L ⁻¹	1.69
Chrome	mg·L ⁻¹	<D.L.
Bromide (Br ⁻)	mg·L ⁻¹	<D.L.
Chloride (Cl ⁻)	mg·L ⁻¹	192.4
Fluoride (F ⁻)	mg·L ⁻¹	<D.L.
Phosphate (PO ₄ ³⁻)	mg·L ⁻¹	<D.L.
Nitrate (NO ₃ ⁻)	mg·L ⁻¹	113.75
Sulfate (SO ₄ ²⁻)	mg·L ⁻¹	524.17

The textile effluent samples have the following characteristics: basic pH, low biodegradability ratio (BOD₅ / COD), high alkalinity and conductivity. The presence of the metals iron and nickel was detected, as well as the chloride, nitrate and sulfate anions. The presence of these elements and the high organic load is related to the numerous compounds that are added in the fabric manufacturing process, including: indigo dye (main dye), sulfurous black dye (large carbon chains), caustic soda, surfactants, sequestrants, dyes, pigments, fixatives.

3.2. Formulation of the quadratic regression models

The coded variables, their experimental values (X1-X2) and the observed responses (Y1-Y2) are shown in Table 5.

Table 5. Planning matrix and responses observed in the central composite design.

Test No.	Variables				Responses	
	X ₁		X ₂		Y ₁	Y ₂
	Coded	Decoded	Coded	Decoded	(%)	(%)
1	-1	60.0	-1	8.5	83.5	61.9
2	-1	60.0	1	10.5	71.5	31.2
3	1	180.0	-1	8.5	89.1	87.0
4	1	180.0	1	10.5	74.1	18.2
5	-1.41	35.2	0	9.5	75.5	53.2
6	1.41	204.9	0	9.5	84.3	79.4
7	0	120.0	-1.41	8.1	90.3	74.8
8	0	120.0	1.41	10.9	65.2	40.3
9	0	120.0	0	9.5	71.2	81.8
10	0	120.0	0	9.5	75.6	81.5
11	0	120.0	0	9.5	68.7	81.0

Where, X_1 = Adsorbent concentration; X_2 = pH; Y_1 = TOC removal; Y_2 = color removal.

The results obtained were analysed by ANOVA. Equations from the first ANOVA analysis were modified by eliminating the terms found statistically insignificant. Then, only the statistically significant terms (P -value < 0.05) were considered in the reduced quadratic model (Table 6). The coefficients of the reduced models in the polynomial expression were calculated by multiple regression analysis.

Table 6. Regression models in terms of decoded variables.

Response	Proposed quadratic model	R ²
Y_1	$Y(X) = 438.77 - 0.24X_1 - 66.97X_2 + 0.001X_1^2 + 3.11X_2^2$	0.945
Y_2	$Y(X) = -1,333.62 + 2.32X_1 + 285.87X_2 - 0.00X_1^2 - 15.02X_2^2 - 0.16X_1X_2$	0.875

Where, X_1 = Adsorbent concentration; X_2 = pH; Y_1 = TOC removal; Y_2 = color removal.

The interactions between the variables were significant for the removal of color (Table 6). It would not be possible to consider the interactions between the variables in the one-factor-at-a-time method, where the behaviour of each variable affecting the process is studied individually. All models were satisfactorily fitted to the experimental responses ($R^2 > 0.75$)

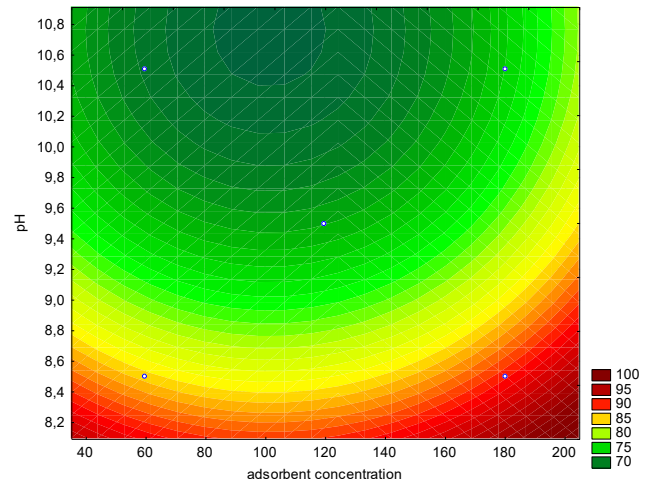
The reduced quadratic models were statistically analysed through ANOVA (Table 7). The TOC and color models can be considered statistically significant ($F_{\text{value}}/F_{\text{table}} = 1.39$ and 15.28 , respectively).

Table 7. ANOVA chart of the response models.

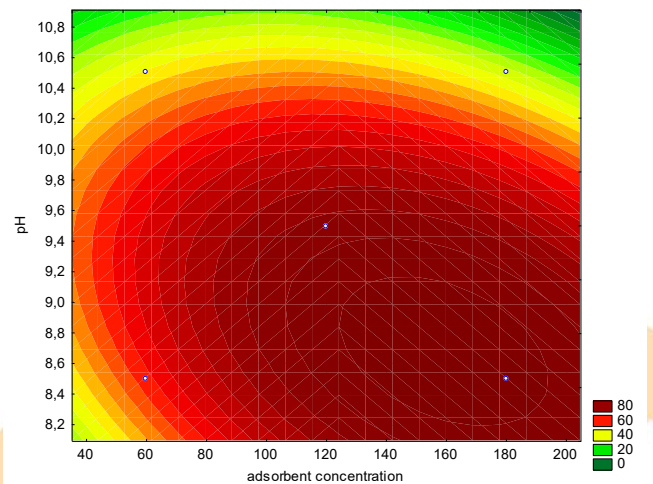
Response	Source of variation	Sum of squares	Degrees of freedom	Mean square	F _{value}	F _{table}
Y_1	Regression	664.01	2	332.00	69.23	4.95
	Residual	38.37	8	4.80		
	Total	702.37				
Y_2	Regression	4934.24	5	986.85	7.02	5.05
	Residual	702.69	5	140.54		
	Total	5636.94				

3.3. Optimization of the responses and optimal conditions

The contour plots of the interaction between the adsorbent concentration and pH are shown in Fig. 1.



(a)



(b)

Fig. 1. Contour plot as a function of pH and adsorbent concentration for the responses: (a) COD removal (Y_1) and (b) color removal (Y_2).

The intersection between the contour plots according to the pre-defined limits (Table 3) was obtained to determine the optimal region (in grey, Fig. 2).

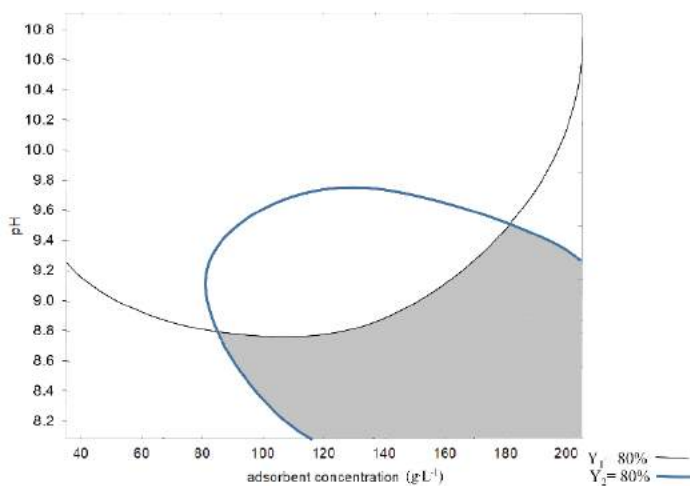


Fig. 2. Optimal region of the variables adsorbent concentration and pH. Y_1 : COT removal >80%, Y_2 : color removal >80%.

It can be seen in Figure 2 that removals of organic matter and color from textile effluents using BFD as adsorbent are dependent on the variables pH, concentration of adsorbent and the relationship between these variables. Such importance was also reported by Kanel (2006) [11]. The ideal pH ratio ranged from 8.1 to 9.5, that is, the process can be conducted at the natural pH of the effluent, differently from what was found in the literature for oily effluents [12] and synthetic textile effluents [13], in which the ideal pH was approximately 3. The ideal adsorbent concentration ranged from 85 to 205 g·L⁻¹, similar results have been found in the literature using BFD as an adsorbent for removal of synthetic dyes [13].

3. Conclusion

An investigation on a real textile effluent was conducted to analyse the effectiveness of the BFD as a low cost adsorbent, applying CCD and RSM in order to develop a predictive model and to determine the optimal conditions. The ideal pH ratio and adsorbent concentration ranged from 8.1 to 9.5 and 85 to 205 g·L⁻¹, respectively, reaching high removals of color and organic matter (above 80%). Such results stimulate new experiments to optimize other parameters, as well as to understand the degradation mechanisms, reaction kinetics and regeneration of the adsorbent.

Acknowledgements

The authors thank the National Council for Scientific and Technological Development (CNPq) for financial support. Special thanks to the Federal University of Ceará for the opportunity to develop the research.

References

- [1] Zhou Y, Lu J, Zhou Y, Liu Y. Recent advances for dyes removal using novel adsorbents: A review. *Environ Pollut* [Internet]. 2019 Sep;252:352–65. Available from: <https://linkinghub.elsevier.com/retrieve/pii/S0269749119305949>
- [2] De Gisi S, Lofrano G, Grassi M, Notarnicola M. Characteristics and adsorption capacities of low-cost sorbents for wastewater treatment: A review. *Sustain Mater Technol* [Internet]. 2016 Sep;9:10–40. Available from: <http://linkinghub.elsevier.com/retrieve/pii/S2214993715300221>
- [3] Bhatnagar A, Sillanpää M. Utilization of agro-industrial and municipal waste materials as potential adsorbents for water treatment—A review. *Chem Eng J* [Internet]. 2010 Mar 1;157(2–3):277–96. Available from: <http://linkinghub.elsevier.com/retrieve/pii/S1385894710000288>
- [4] Amorim CC, Dutra PR, Leão MMD, Pereira MC, Henriques AB, Fabris JD, et al. Controlled reduction of steel waste to produce active iron phases for environmental applications. *Chem Eng J* [Internet]. 2012 Oct;209:645–51. Available from: <https://linkinghub.elsevier.com/retrieve/pii/S1385894712010777>
- [5] Amorim CC, Leão MMD, Moreira RFPM, Fabris JD, Henriques AB. Performance of blast furnace waste for azo dye degradation through photo-Fenton-like processes. *Chem Eng J* [Internet]. 2013 May;224:59–66. Available from: <http://linkinghub.elsevier.com/retrieve/pii/S1385894713000934>
- [6] Andrade LN, Amorim CC, Santos S V., Teixeira IF, Leão MMD, Lago RM. Efficient demulsification of wastewater by steel furnace dust with amphiphilic and surface charge properties. *Chem Eng J* [Internet]. 2015 Jul;271:281–6. Available from: <http://linkinghub.elsevier.com/retrieve/pii/S1385894715002922>
- [7] Amorim CC, Leão MMD, Dutra PR, Tristão JC, Magalhães F, Lago RM. Use of tar pitch as a binding and reductant of BFD waste to produce reactive materials for environmental applications. *Chemosphere* [Internet]. 2014 Aug;109:143–9. Available from: <https://linkinghub.elsevier.com/retrieve/pii/S0045653514001337>
- [8] APHA; AWWA; WEF. *Standard Methods For The Examination of Water and Wastewater*. 22nd ed. Washington, DC: APHA; AWWA; WEF; 2012. 1360 p.

Diffusion Model on Solid Applied to Kinetics of Dye Adsorption on Different Activated Carbons

Celso Hissao Maeda^a, Artur Lemes Moretti^a, Mariana de Oliveira Camargo^a, Dayane Samara de Carvalho Coltre^b, Caroline Apoloni Cionek^b, Pedro Augusto Arroyo^{a*}

^a Chemical Engineering Department, State University of Maringá, 5790 Colombo Avenue, Maringá, ZIP 87020-620, Brazil

^b Textile Engineering Department, Federal University of Technology - Paraná, 635 Marcílio Dias Street, Apucarana, ZIP 86812-460, Brazil

Abstract

The main characteristic of the textile industry is the contamination of a high amount of water during the dyeing process. Overall, approximately 10-15% of all dyes used on this industry are disposed with wastewaters. For this reason, this work evaluated the adsorption kinetic data on different activated carbons by a phenomenological diffusion on solid model. The obtained results showed that even though the bone char exhibited the highest amount of dye adsorbed on its external surface, it also exhibited a higher resistance to mass transfer, which was demonstrated by the smaller diffusivity coefficient ($\frac{D_s}{R_c^2}=0.33 \cdot 10^{-8}$). This occurred probably due to factors such as average particles diameter, technical equilibrium and aggregates formation. On the other hand, the dende char obtained the best diffusivity coefficient ($\frac{D_s}{R_c^2}=3.19 \cdot 10^{-8}$), which provided the adsorbate a faster diffusion into the pores.

Keywords: bone char, babassu, coconut shell, dende, azo dye.

1. Introduction

Dyes represent an important type of pollutants, which the main source is the textile industry and its function is to modify the color characteristics of different substrates [1]. The reactive blue BF-5G dye is an example of an organic dye responsible for fabric color and texture, however, due to its non-total attachment on cellulosic fibers, it contaminates a large amount of water and it result in a volume of wastewater that needs to be treated [2]. Therefore, the wastewater treatment generally occurs by means of three consecutive steps: the primary, the secondary and the tertiary. The former one comprehends techniques such as reverse osmosis, electrodialysis, oxidative processes, ion exchange and adsorption [3]. Within the techniques mentioned, the adsorption process stands out as an advantageous alternative to removal of dyes present on textile wastewaters, mainly, when conducted

with the use of different adsorptive materials that are affordable and can be reused [1].

Dyes represent the solid phase on the adsorption process, which function is to retain the contaminant material present on the fluid phase [4]. Therefore, the adsorbent performance on the process depends on the success of the solid adsorbent on the equilibrium and on the adsorption kinetics. Between the adsorbents, stands out the use of zeolites, clays, alumina and active carbons. The former is widely used to remove undesirable smells, flavors, dyes, heavy metals and organic material. Moreover, this term is broadly used to denominate carbon-based material such as wood, coconut shell, dende, babassu and bone char [5], in other words, activated carbons are complex solids, however, they are versatile due to their high specific surface and high pore volume. Consequently, there are many studies about adsorption processes using activated carbons from agricultural and industrial wastes, in order to determine its possibility to being used on removal of different contaminants.



Within the adsorption process, the kinetics investigation is considered indispensable to obtain relevant information about the mechanisms involved during the process steps, the residence time and the design of adsorption equipment [6]. Therefore, the mathematical modelling of experimental data is a crucial tool to obtain these information. Several mathematical models have been used to describe an adsorption process, mainly the empirical models of pseudo first order and pseudo second order [7]. Nevertheless, due to limitation of their hypotheses, another class of models, called diffusion by mass transfer, describes the adsorption phenomena as a more detailed diffusion, in other words, the adsorbate diffuses on the film around the adsorbent particles and afterward, it diffuses to pore inward until it reaches the equilibrium phase between the adsorbate and its active sites [8]. In view of that, this work used a phenomenological kinetics model based on a mass transfer mechanism to diffuse dye molecules to the bulk pores of different activated carbons.

2. Experimental

2.1. Materials

The solids used as adsorbents were the activated carbons bone char (Bone char Carvão do Brasil Ltda), coconut shell (Indústrias Químicas Carbomafra S.A.), dende (Carvão Ativado Carbonmar) and babassu (Tobasa Bioindustrial de Babassu S.A.). The solids were crushed and sieved to obtain particles with average diameter of 0.725 mm. The adsorbate used was the reactive blue BF-5G dye (C.I. Reactive Blue 203) supplied by Texpal Indústria Química S/A.

2.2. Characterization

The textural properties of the adsorbent materials were determined by nitrogen physisorption, which the specific area was obtained by the Brunauer-Emmet-Teller (BET) and the Dubinin-Radushkevich (DR) methods, and the average pore diameter was calculated by the Barret-Joyler-Halenda (BJH) method.

The point of zero charge (pH_{ZPC}) was used to determine the superficial chemical nature of the materials by means of a procedure performed by Regalbuto and Robles (2004), also known as “11 points method”.

2.3. Kinetics and adsorption equilibrium

The kinetics of adsorption runs were performed in a closed system operated in batch. The tests were conducted with an initial concentration of 60 mg L⁻¹ in Erlenmeyers containing 20 mL of a solution of dye and 0.2 g of adsorbent, which were put in a thermostatic bath under agitation at 80 rpm and at a temperature of 30 °C.

2.4. Technical equilibrium

According to Keller and Staudt (2005) the technical equilibrium can be defined by means of the Deborah number (D_e)

$$D_e = \frac{\Delta m}{\Delta t} \left(\frac{t_c}{m} \right) \quad (1)$$

where $\left(\frac{\Delta m}{m} \right)$ is the adsorption of mass relative to the total mass (m) within a time span (Δt) and t_c is the time of the last experimental data. The Deborah (D_e) portrays the distance of real state of an adsorption process from its thermodynamic equilibrium state. There, if $D_e \rightarrow 0$ the process is close to the technical equilibrium and if $D_e \gg 100$ the process is in a non-equilibrium state.

2.5. Mathematical modelling

The mathematical modelling, which was fitted to the experimental data, was performed using a phenomenological approach, that considers the limiting step of mass transfer the diffusion into bulk pore. This model is derived from a mass balance performed on the adsorbent particles, considering some assumptions related to the phenomena that occur through the adsorption process. On this work, some assumptions were made:

- (i) The solution is homogeneous, that means, the solute concentration decreases with time evenly on the entire solution;
- (ii) The adsorbate diffusion through pore interior on the solid phase is the limiting step;
- (iii) The diffusivity coefficient on the solid is constant through the particle;
- (iv) There is symmetry on adsorbate concentration through the particle radius;
- (v) The mass transfer external resistance is negligible when compared to the internal resistance;
- (vi) There is instantaneous equilibrium between the solution and the particle external surface;
- (vii) The particles are spherical;
- (viii) The system is isothermal;

The assumption (i) ensures that the adsorbate concentration on the solution (C) varies with time (t) according to Equation 2:

$$\frac{dC}{dt} = -\frac{M_s}{V} \frac{d\bar{q}}{dt} \quad (2)$$

where M_s is the adsorbent mass, V is the solution volume and \bar{q} is the average amount adsorbed on the particles, which is the average of distributed concentration through the particle.

$$\bar{q} = \frac{3}{R_p} \int_0^{R_p} r^2 q \, dr \quad (3)$$

where X (m) is the particle radius and r (m) is the distance from the bulk to the surface edge of the particle.

The assumptions (ii) and (iii) imply that the mass balance into the adsorbate bulk can be simplified by Equation 7 [10], giving the amount distributed through the particle.

$$\frac{\partial q}{\partial t} = \frac{D_s}{r^2} \frac{\partial}{\partial r} \left(r^2 \frac{\partial q}{\partial r} \right) \quad (4)$$

Where X (xx) is the diffusivity coefficient on the solid.

On time $t = 0$ the particle is adsorbate free ($q = 0$). Moreover, the symmetry hypothesis defines the boundary condition given by Equation 5, while the hypotheses (v) and (vi) imply on boundary condition defined on Equation 6.

$$r = 0, t > 0 \rightarrow \frac{\partial q}{\partial r} = 0 \quad (5)$$

$$r = 0, t > 0 \rightarrow q = q_{eq}(C) \quad (6)$$

The adsorption isotherm chosen $q_{eq}(C)$ was the one that best fitted the equilibrium experimental data.

The model was numerically solved by means of the lines method (MOL). On this method, the spatial derivatives of a partial differential equation are approximated by the finite difference method [12]. The differential equations system (ODE) with respect with time obtained were solved by numerical integration. The diffusivity coefficient on the solid (D_s) was determined by parameters optimization by means of comparison with experimental data. The objective function used was the sum of squared residuals (SQR), using the data of concentration and amount adsorbed.

$$F_{OBJ} = \sum_{i=1}^{N_{exp}} \left[(C(t_i) - C_{exp,i})^2 + (\bar{q}(t_i) - q_{exp,i})^2 \right] \quad (7)$$

The software used was MATLAB® 2019a. The function ode 15s solved the ODEs system using 1001 elements of discretization, while the *fminsearch* function was used to minimize the objective function, with relative and absolute threshold tolerance of the function equal to 1×10^{-10} .

3. Results and discussion

3.1. N_2 physisorption

Between the chars studied, the babassu char exhibited the highest specific surface area, followed by the coconut shell carbon, dende carbon and bone char as can be shown on Table 1.

Table 1 – Textural properties of the adsorbents

Properties	Specific area ($m^2 g^{-1}$)	Average pore diameter (Å)
Babassu	^a 1096	31
Coconut shell	^a 986	30
Dende	^a 751	32
Bone char	^b 103	98

^aDR method, ^bBET method, ^cBJH method

Comparing the bone char with the other types of char, it has a specific area relatively smaller than the others and this can be attributed to the average diameter of its pores, due to the fact that a bigger pore diameter can be related with a smaller specific area.

3.2. Zero charge point (pH_{ZPC})

The babassu, dende and bone chars exhibited similar pH_{ZPC} values and slightly alkaline, which the values obtained were 7.5, 7.6 and 7.5, respectively. In addition, only the coconut shell char exhibited a higher pH_{ZPC} of approximately 9.2, emphasizing that the surface of all chars is alkaline, as can be seen on Figure 1. The dye solution used on all tests has a pH of 6.0~7.0, which was close of the pH_{ZPC} of the activated carbons. Therefore, the surface electrostatic charge balance of the activated carbons exhibited close values.

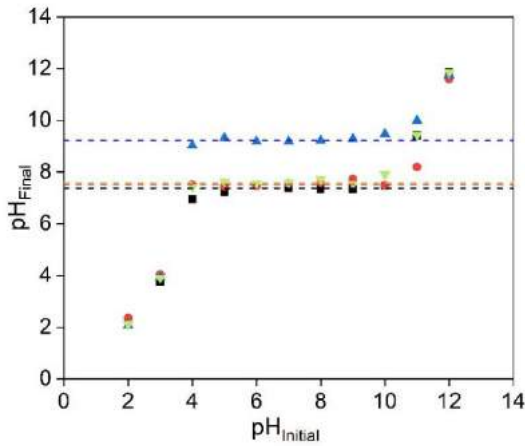
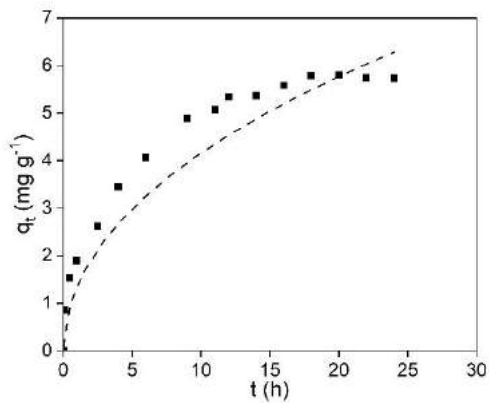


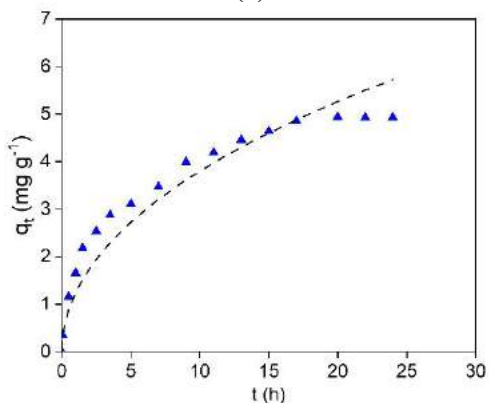
Figure 1 – Zero charge point of the activated carbons (■) babassu, (▲) coconut shell, (▼) dende and (●) bone char.

3.3. Mathematical modelling

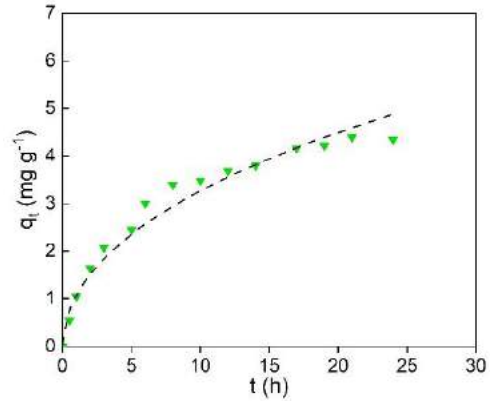
The experimental data were fitted by the diffusion on solid method, which the outcome suggests that the resistance to mass transfer prevailing on adsorption on batch system is the mass transfer of the surface of the particle's pores [11], which can be seen on Figure 2.



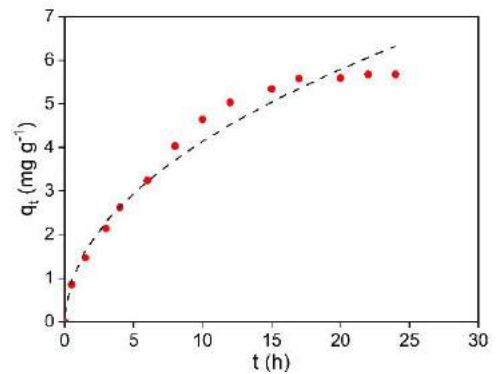
(a)



(b)



(c)



(d)

Figure 2 – Experimental adsorbed and adsorbate concentration on the solution (---) as function of time on the (a) babassu, (b) coconut shell, (c) dende and (d) bone char.

The results referring to the relation of diffusion on solid per squared particle radius ($\frac{D_s}{R_p^2}$) are shown on Table 2, where can be seen that this relation increases with the following order: bone char < babassu < coconut shell < dende.

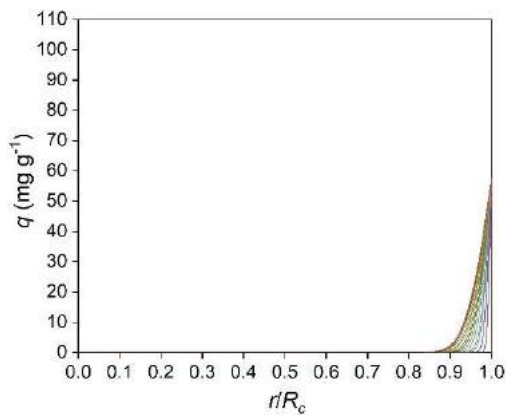
Table 2 – Relation of diffusion on solid per squared particle radius

Activated carbons	$\frac{D_s}{R_p^2}$
babassu	$1.39 \cdot 10^{-8}$
coconut shell	$1.53 \cdot 10^{-8}$
dende	$3.19 \cdot 10^{-8}$
bone char	$0.33 \cdot 10^{-8}$

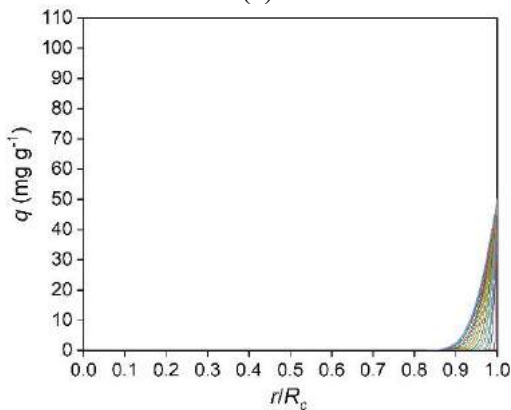
This increasing order of diffusion indicates that the adsorbate diffuses more rapidly on the solid activated carbon of dende and more slowly on the bone char activated carbon.

The Figure 3 shows the bone char amount adsorbed as function of particle radius. On the

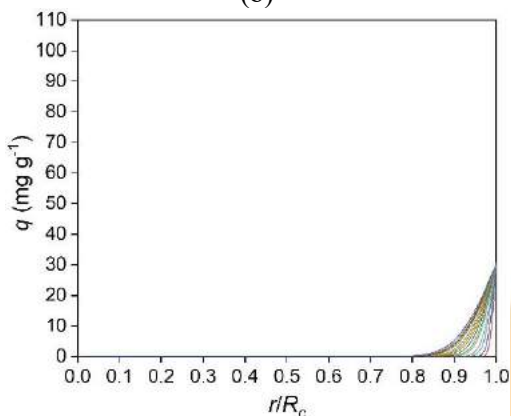
external surface $\frac{r}{R_c} = 1$ the amount adsorbed, on equilibrium with the solution, decreases with time due to the fact that the solution concentration decreases as the adsorbates is being transferred to the particles.



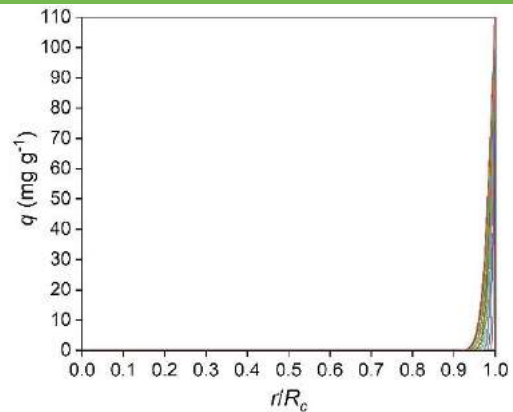
(a)



(b)



(c)



(d)

Figure 3 – Amount adsorbed as function of particle radius for the activated carbons (a) babassu, (b) coconut shell, (c) dende and (d) bone char.

With time, the adsorbate close to the external surface of the particle diffuses to the bulk solid. Therefore, the solid concentration is maintained uniformly and the equilibrium plateau is achieved, in other words, there is not driving force to transfer mass to the bulk particle. According to Figure 3, it can be seen that the curve referring to dye adsorption on dende activated carbon is more advanced than the others, suggesting that the dye diffusion over these particles was faster than over the particles of the other types of chars. Therefore, the dye adsorbed on the external surface of the dende char was less than the other types of char. This can be related to factors such as particle average diameter, technical equilibrium and formation of aggregated molecules.

The size of the average particle diameter can influence on the saturation of adsorbate. This can be ascribed with the particle external and internal diffusional resistance, that occurs because the adsorbate molecule finds a resistance to diffuse into the interior of the particle pore even though this having mesoporous [13]. A smaller average particle diameter can decrease the way covered by the molecule dye to get to the pore interior and increase the adsorption capacity of the dye due to a higher contact area [14].

The diffusion of adsorbate molecules to the interior of pores can take several hours, days and even weeks. That way, the thermodynamic equilibrium can take the same time to be reached and that means that the state of “technical equilibrium” prevails on the assumptions of a time span. Indeed, the Deborah number $De \rightarrow 0$ proves the state of technical equilibrium of all activated carbons [15], as can be seen on Table 3.

Table 3 –Deborah number (D_e) of the activated carbons

Activated carbons	D_e
babassu	0.034
coconut shell	0.024
dende	0.406
bone char	0.155

According to Coates (1969) the dyes ions can auto aggregate into aqueous solutions, mainly on high concentrations forming dimers, trimers even micelles. A study of Giles (1958) showed that formed micelles aggregate on a plane way during adsorption, in order that the area of the adsorbed micelle is equal to the area of only one dye molecule. Dyes can be adsorbed on the solid phase on available sites as an aggregate complex (micelles) instead of only one molecule, which the aggregation state is function of factors such as pH, temperature and concentration. For this reason, this hypothesis suggests that bone char adsorbed more dye molecules on its external surface than the others activated carbons, however, this occurred on the form of aggregate molecules that consequently had a hindered diffusion into pore interior even though the bone char is the only material of this study with prevalence of mesopores.

4. Conclusion

The results of kinetics modelling by model of diffusion on solid suggest that the resistance to mass transfer occurs on the surface of the pores of the particle. Moreover, it was possible to determine that the diffusion on pores was more effective on the babassu, coconut shell and dende chars, even though they are present micropores. On the other hand, the bone char was the only adsorbent mesoporous, however, its intraparticule diffusion found impediments that were significative on the final outcome. Even with a higher amount of dye adsorbed on its external surface when compared with the other chars, factors as average particle diameter, technical equilibrium and molecule dye aggregation on the surface hinders the intraparticle diffusion.

Acknowledgements

We would like to acknowledge CAPES for the financial support and COMCAP/UEM for the analyses conducted on its research facilities.

References

- [1] Anastopoulos L, Kyzas GZ. Agricultural peels for dye adsorption: a review of recent literature. *Journal of Molecular Liquids*, v. 200, p. 381-389, 2014.
- [2] Maeda CH et al. Adsorption and desorption cycles of reactive blue BF-5G dye in a bone char fixed-bed column. *Environmental Science and Pollution Research*, v. 26, n. 28, p. 28500-28509, 2019.
- [3] Ghaly AE et al. Production, characterization and treatment of textile effluents: a critical review. *J Chem Eng Process Technol*, v. 5, n. 1, p. 1-19, 2014.
- [4] McCabe WL, Smith JC, Harriott P. *Unit operations of chemical engineering*. New York: McGraw-Hill, 1993.
- [5] Hassler JW, Cheremisinoff EF. *Carbon Adsorption Handbook*, Ann Arbor Science, 1980.
- [6] Ruthven DM. *principles of adsorption and desorption process*. New York. John Wiley & Sons, 1984.
- [7] Vadivelan V, Kumar KV. Equilibrium, kinetics, mechanism, and process design for the sorption of methylene blue onto rice husk. *Journal of Colloid and Interface Science*, v. 286, p. 90-100, 2005.
- [8] Fröhlich AC et al. Three-dimensional mass transfer modelling of ibuprofen adsorption on activated carbon prepared by sonication. *Chemical Engineering Journal*, v. 341, p. 65-74, 2018.
- [9] Regalbutto J, Robles J. *The engineering of Pt/Carbon catalyst preparation*. University of Illinois, Chicago, 2004.
- [10] Walker GM, Weatherley LR. Adsorption of dyes from aqueous solution – the effect of adsorbent pore size distribution and dye aggregation. *Chemical Engineering Journal*, v. 83, n. 3, p. 201-206, 2001.
- [11] Do DD. *Adsorption analysis: equilibria and kinetics*. 1 st ed. Imperial College Press, Londres, 1998.
- [12] Schiesser WE, Griffiths GW. *A compendium of partial differential equation models: method of lines analysis with matlab*. Cambridge University Press, 2009.
- [13] Youssef AM et al. Sorption properties of chemically activated carbons: 1. sorption of cadmium (II) ions. *Colloids and Surfaces A: Physicochemical and Engineering Aspects*, v. 235, n. 1-3, p. 153-163, 2004.
- [14] Fiorentin LD et al. Biosorption of reactive blue 5G dye onto drying orange bagasse in batch system: kinetic and equilibrium modelling. *Chemical Engineering Journal*, v. 163, p. 68-77, 2010.
- [15] Keller JU, staudt R. *Gas adsorption equilibria: Experimental methods and adsorptive isotherms*. 1 st ed. Springer, 2005.
- [16] Coates E. Aggregation of dyes in aqueous solutions. *Journal society Dye Colour*, v. 85, n. 8, p. 335-368, 1969.
- [17] Giles CH et al. *Studies in adsorption. Part XI. A system of classification of solution adsorption isotherms and its use in diagnosis of adsorption mechanisms and in measurement of specific surface areas of solids*. *Journal of the Chemical Society*, v. 846, p. 3963, 1958.

Effect of pH on cephalixin adsorption using mesoporous silica

Kiara Montiel-Centeno^a, Deicy Barrera^{*a}, Leslie Aragón^b, Elbio Saidman^b Karim Sapag^{a*}

^a Porous Solid laboratory, Institute of Applied Physics, Faculty of Mathematical and Natural Physical Sciences, National University of San Luis, Ave. Ejército de los Andes 950, D5700, Argentina

^b Drug Quality Control Laboratory, Faculty of Biochemical Chemistry and Pharmacy, National University of San Luis, Ave. Ejército de los Andes 950, D5700, Argentina

Abstract

The effect of pH on the aqueous adsorption of cephalixin (CFX) was studied using as an adsorbent an ordered mesoporous silica materials of the SBA-15 type. This materials was synthesized and subsequently characterized by different techniques such as adsorption-desorption from N₂ at 77 K, FTIR, SEM and point zero charge. Different interesting textural and chemical properties were found to carry out drugs adsorption process. CFX adsorption assays were performed at different pH values (1.3-10.3), adsorbed amount were quantified by UV-Vis. The SBA-15 material was again characterized after adsorption of CFX. It was found that pH has a strong influence on adsorption capacity of this drug, which is closely related to the charge density of the adsorbent material as well the distribution of the species of the CFX molecule and the textural properties of the adsorbent.

Keywords: Adsorption, cephalixin, pH, SBA-15

1. Introduction

Cephalixin is a broad-spectrum antibiotic which has a good therapeutic effect on Gram-negative and Gram positive bacteria [1]. It is effective in the treatment of infection of genitourinary system, bacteremia, bacterial endocarditis and meningitis. However, the main disadvantage of cephalixin is that the half-life is short, ca. 0.9 h [2]. Nowadays, ordinary tablets and capsules are used in clinical use, but patients need to take many times a day to ensure the therapeutic effect. Moreover, patients with poor kidney function need to be taken with caution because too much medicine often imposes a heavy burden on kidney organs [3].

On the other hand, antibiotics such as cephalixin are considered as emerging pollutants and it has been the core of different research, mainly for their massive use. According to a study conducted by The Global Point Prevalence Survey (Global PPS) in Latin America, the highest frequency of treatment of infections associated with health care is recorded

[4]. As a consequence, a high rate of antibiotic consumption is recorded, and around 80% is excreted without metabolizing or partially metabolized, which has been widely demonstrated by its presence in water and soil. This leads to serious problems in the ecosystem, in addition to promoting the development of resistance by different bacteria [5].

Considering the different problems caused by the current delivery cephalixin doses, it is necessary to find alternatives for improvement. One of these alternatives is the design of nanostructured materials that allow adsorbing the drug molecules in their structure and subsequently deliver it in a controlled way by the different routes of administration. Likewise, these materials could be used to adsorb antibiotics from contaminated effluents.

Among the promising nanostructured materials in this type of applications are the ordered mesoporous silica materials, due to their interesting properties such as high specific surface area, uniform pore size distribution, high total pore volume, presence of micropores and mesopores. In addition, mesoporous silica materials have silanol group in their structure

that allow a chemical interaction with the drug molecules and improve their adsorptive capacity.

SBA-15 is well-known ordered mesoporous silica materials with 2D hexagonal structure and silanol groups present on the surface. The adsorption molecules onto the external and pore surface of SBA-15 does not modify the hexagonal planar ordering [6]. This fact, along with its relatively large pore size, suggests that this particular mesoporous structure could be an appropriate matrix for loading and further release drugs as cephalexin.

In order to maximize the loading capacity cephalexin in the mesoporous silica, it is necessary to know factors favouring matrix-drug interactions [7]. Therefore, the main objective of this work was to analyse one of these factors: the effect of change in the pH solution of cephalexin adsorption, and also the changes in the textural properties of SBA-15 after the cephalexin adsorption process.

2. Materials and methods

2.1. Synthesis of mesoporous materials

The synthesis of the SBA-15 material was performed based on previous work reported by [6]. The following reagents were used in this synthesis: Pluronic P123 (EO20–PO70–EO20) (Sigma-Aldrich) as pore structure driver agent; tetraethyl orthosilicate (TEOS 98%) (Merck) as silica source; hydrochloric acid (Merck) as catalyst; and deionized water as solvent. The reagents molar ratio used was: 0.017P123: 1TEOS: 6HCl: 140H₂O. The quantity of Pluronic P123 was completely dissolved in an aqueous solution of 2 M HCl under vigorous stirring at 40 °C. After obtaining a transparent color, TEOS was added dropwise to the solution. The mixture was permanently stirred at the same temperature for 4 h. The resulting mixture was aged at 40 °C for 20 h without stirring. Afterwards, the temperature was raised to 80 °C and kept for 48 h. The resultant precipitated solid was washed with deionized water to remove the residual HCl. Then, the material was dried at 60 °C overnight and calcined at 350 °C for 6 h with a heating rate of 1 °C/min.

2.2 Cephalexin adsorption

Cephalexin (CFX) adsorption at different pH values (from 1.3 to 10.3) was carried out by soaking 10 mg of SBA-15 in 20 mL of CFX solution in water (concentration 1 mg/mL). The suspensions were left

at room temperature with stirring (200 rpm) for 24 h. Then, the solid phases were separated from the liquids by filtration and dried at room temperature; the sample was denoted as *SBA-15/CFX*. The residual concentration of liquid phases was determined using UV-Vis spectrophotometry at 262 nm. The amount of CFX adsorbed was calculated by:

$$q_t = \frac{(C_i - C_f) \cdot V}{m} \quad (1)$$

Where; q_t is the adsorbed amount of CFX per gram of SBA-15 (mg/g); C_i is the initial concentration of CFX before being in contact with adsorbent material (mg/mL); C_f is the final aqueous phase concentration after removing the adsorbent material (mg/mL); V is the volume of CFX solution used in the experiment (mL); m is the mass of SBA-15 used (mg).

2.3 Characterization techniques

Nitrogen adsorption-desorption isotherms were measured at 77 K using a manometric equipment Micromeritics, ASAP 2000. The samples SBA-15 and SBA-15/CFX were previously degassed in vacuum at 200 °C and 60 °C for 12 h, respectively. The specific surface areas (S_{BET}) were obtained by the Brunauer Emmet and Teller method in the relative pressure range of 0.05–0.15. The total pore volumes (V_{TP}) were calculated at a relative pressure of 0.98. Micropore volumes ($V_{\mu P}$) were estimated by the macroscopic α_s plot method. The pore size distributions, PSD, were evaluated with the NLDFT (non-local DFT) method using the desorption branch kernel for N₂ on silica for cylindrical pores at 77 K. The IR spectra were measured in a Nicolet Protégé 460 spectrometer, with a He Ne laser. The spectra were taken in the spectral range from 4000 to 400 cm⁻¹. SEM micrographs were taken using an FEI Quanta 200 microscope; the samples were coated with a gold film (~10 nm). The point zero charge (PZC) was determined by salt addition method [8]. The samples were characterized before and after loading with CFX. We select the sample loaded at pH 10 to perform the different characterizations.

3. Result and discussion

3.1 Characterization of SBA-15 before and after cephalixin adsorption

Nitrogen adsorption-desorption isotherms at 77 K are displayed in Fig. 1, the SBA-15 and SBA-15/CFX samples presented type IV(a) isotherms according to the IUPAC classification [9], these isotherms are characteristics of these mesoporous materials. The isotherms also present a hysteresis loop type H1, characteristics of porous materials with well-defined mesoporous. The SBA-15 loading with CFX exhibited a decrease in adsorption capacity and textural properties as can be seen in Table 1. The BET surface area values in the SBA-15 samples decreases considerably after loading CFX, indicating that the drug molecules were retained mostly on the surface of the silica materials. On the other hand, the micropore volume value also decreases, probably due to some CFX molecules were located at the micropores entrance and not inside since the molecule has a larger size (1.8 nm) than the micropores (1.4 nm).

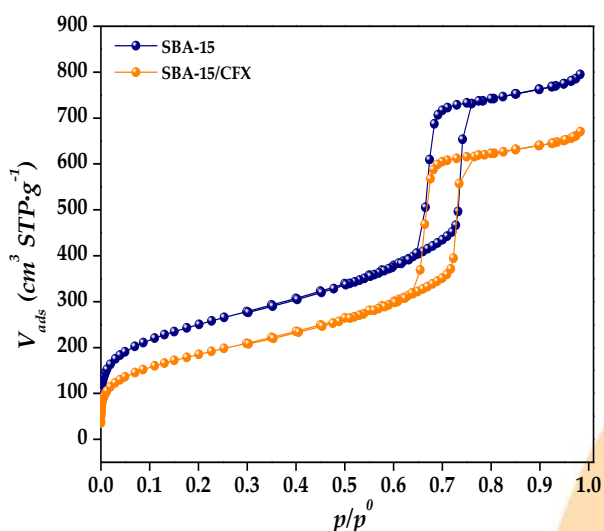


Fig. 1. Nitrogen adsorption-desorption isotherms at 77 K of SBA-15 and SBA-15/CFX samples

Table 1. Textural properties of SBA-15 and SBA-15/CFX samples

Sample	S_{BET} m ² /g	$V_{\mu P}$ cm ³ /g	V_{TP} cm ³ /g
SBA-15	910	0.05	1.23
SBA-15/CFX	670	0.01	1.03

The pore size distribution, PSD, presented in Fig. 2 correspond to the SBA-15 pure and loaded with CFX. In both samples, it is observed that the most amount of pores lies within the mesopores region around 8 nm and it is observed a little contribution in the micropore region. Likewise, in this figure it is possible to observe that there are no significant changes in the PSD of the SBA-15 after the incorporation of CFX, suggesting that the CFX molecules were adsorbed on the SBA-15 surface and not within mesopores.

Fig. 3 shows the FTIR spectrum of SBA-15 (a) and SBA-15 loading with CFX (b). The typical signature of SBA-15 were observed with absorption bands at 2800-3700, 1639, 1080, 960, 800 and 460 cm⁻¹. The broadband observed at 2800-3700 cm⁻¹ was associated with -OH groups caused by the physisorbed water on the surface. The bands at 1080 and 800 cm⁻¹ correspond to the asymmetric and symmetric stretching from Si-O-Si bonds and the band at 960 cm⁻¹ was due to the stretching of silanol groups (Si-OH). The absorption band at 460 cm⁻¹ corresponds to the stretching of Si-O-Si. The small broadening and slight shifting of Si-OH (2800-3700 cm⁻¹) band in SBA-15/CFX as compared with SBA-15 hinted that it was due to adsorption of CFX. Besides, in SBA-15/CFX samples appearing other bands at 1758 cm⁻¹ and 1656 cm⁻¹ due to four-membered lactam carbonyl and secondary amine carbonyl groups, respectively. Finally, the band at 1388 cm⁻¹ was due to C-H bending vibrations [10].

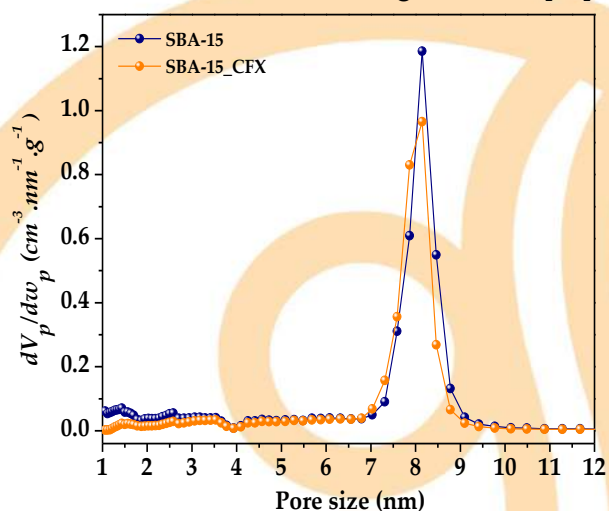


Fig. 2. Pore size distribution of SBA-15 and SBA-15/CFX samples

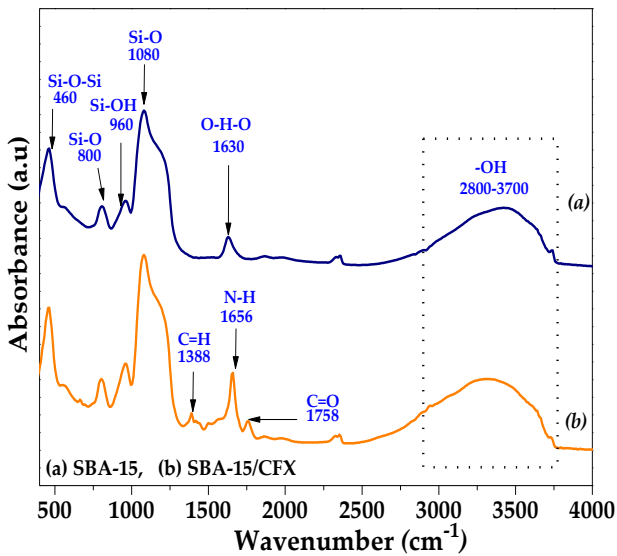


Fig. 3. FTIR of SBA-15 and SBA-15/CFX samples

The Scanning Electron Micrographs (SEM) for both samples are shown in Fig. 4. In the case of SBA-15 is observed a rod-like morphology with homogeneous particle size characteristic of this type materials. Nevertheless, when the SBA-15 silica is loaded with CFX the particles do not have their rod-like shape, because they are wrapped by the drug. This technique also confirms the presence of CFX on the surface of silica.

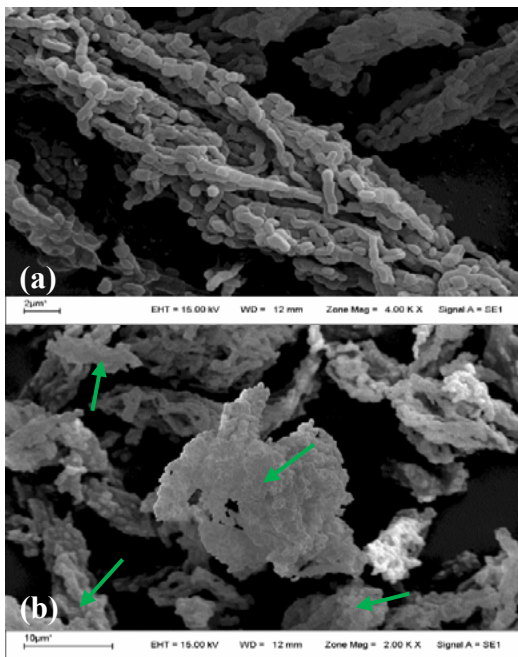


Fig. 4. SEM images of SBA-15 and SBA-15/CFX samples

PZC value was determined in SBA-15 material to know the behavior of the charges in the surface of this material against different pH values, as is shown in Fig. 5. The changes in pH values (ΔpH) against the initial pHs yields PZC at pH where ΔpH is zero. In this sample the ΔpH values in the range 2-4 are negative and at pH 4.7 the PZC is observed. Then, when the pH increases in a range of 5-10 the charges in the surface are positive.

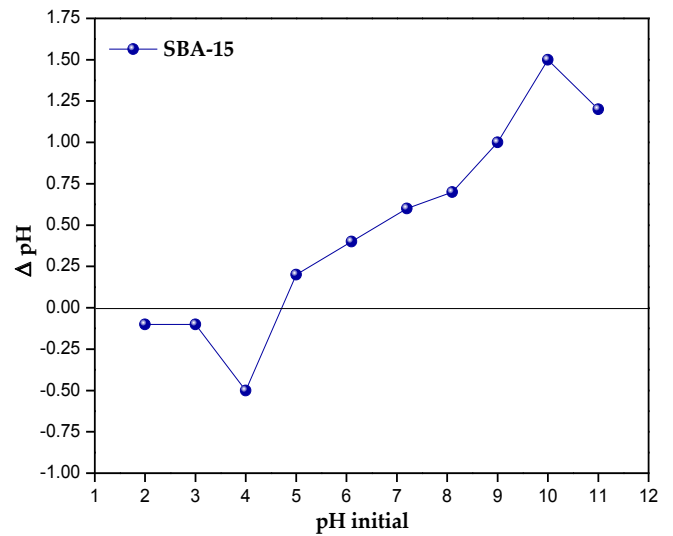


Fig. 5. Point zero charge of SBA-15

3.2 Effect of pH on CFX adsorption

The presence of the different protonated groups in the structure of the CFX resulting in two pK_a values, one at 2.56 (pK_{a1}) related to the carboxyl group ($-\text{COOH}$) and another at 6.88 (pK_{a2}) related to the amino group ($-\text{NH}$). The different species in the pH dependent solution of the medium can be represented by the corresponding speciation diagram as shown in Fig. 6 and was obtained with the method reported by [11].

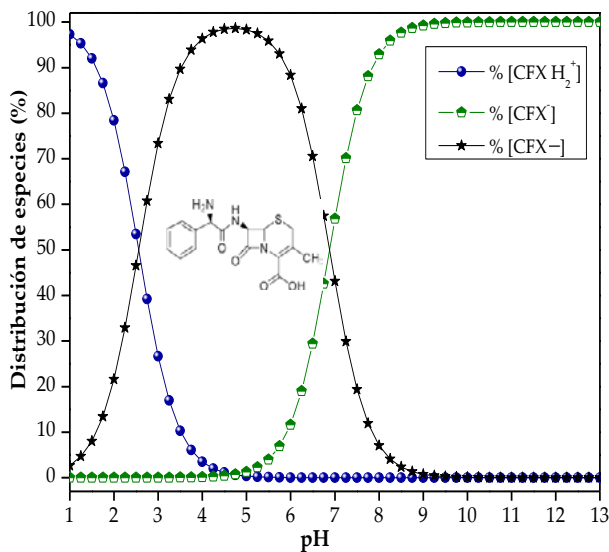


Fig. 6. Speciation diagram of CFX

As can be seen in Fig.6 at pH values below pK_{a1} the carboxyl group has not been deprotonated and CFX molecule is mostly as cation ($CFXH_2^+$) due to protonation of the amino group. When the pH reaches the value of pK_{a1} , the solution consists of 50 % cationic species and 50 % zwitterionic species (CFX^\pm) generated by the deprotonation of the carboxyl group. Between pK_{a1} and pK_{a2} the predominant species is CFX^\pm reaching the highest concentration at pH 4.8. When the pH is equal to pK_{a2} the solution is again constituted by 50 % CFX^\pm and 50 % of the corresponding anion (CFX^-) generated by the loss of the proton associated with the amino group. Finally, when this pH value is exceeded, only the anionic species prevails in solution.

The pH effect on CFX loading is shown in Fig. 7, it can be seen that pH has an important effect on the CFX adsorption process, using SBA-15 as adsorbent material. When pH values are between 1.3-4.3 the higher adsorption capacity is observed at pH 1.3, this is because at this pH values, the SBA-15 has a negative charge density and also the CFX molecule is mostly found as a cation (100 %) due to the protonation of the amino group, therefore there is a strong electrostatic interaction between amino group (NH_3^+) and silanol (Si-OH) groups of the SBA-15. On the other hand, it can be observed that a pH 5.3, the material has the lowest adsorption capacity and this is possibly due to this pH value is near to the PZC where the surface of the material does not exert electrostatic interaction with CFX ions. Despite the low chemical interaction at this pH, the material adsorbed CFX although in a

smaller amount compared to the other pH values, this result is interesting because it indicates that not only surface chemistry has an influence on the adsorption process, but also porosity. In addition, as the pH values increase (6.3-10.3) the amount adsorbed also increase, this is due to the surface of the SBA-15 at these pH values, it has a positive charge density that allows a strong interaction with the anions (COO^-) that are found as a majority species.

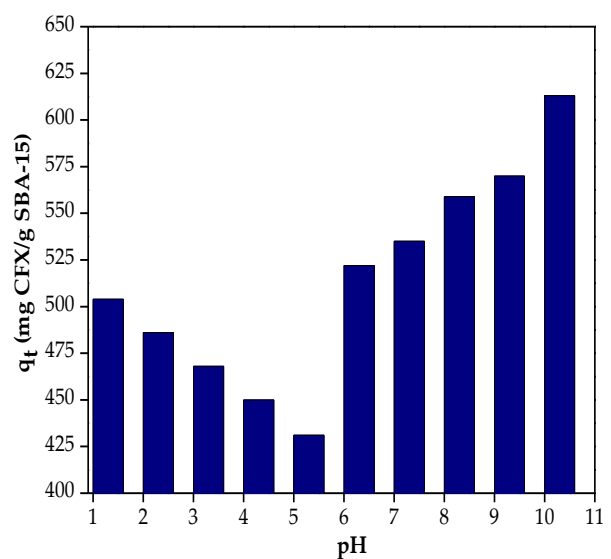


Fig. 7. CFX loading on SBA-15

4. Conclusion

The effect of pH on the adsorption of CFX was studied using an ordered mesoporous silica material (SBA-15 type). SBA-15 was previously characterized by different techniques and it was found interesting properties such as high specific surface area, high total pore volume, ordered pore size distribution and presence of silanol groups that favor molecule adsorption. Besides, it was found the PZC of SBA-15 at pH 4.8. On the other hand, it was found that the adsorption capacity of CFX is greater at pH 10.3 since this pH value CFX molecule is mostly protonated (100 %) as anionic specie. Finally, in the adsorption process not only chemical interactions influence, but also the porosity, since even at pH 5, near the PZC, the porous materials also adsorbs small amount of CFX.



Acknowledgements

This work was financially supported by UNSL and CONICET (Argentina). Authors are also grateful with Puntanos laboratory for donation of Cephalexin. K.M.C. is grateful to UNAN-Managua, Nicaragua, would like to scholarship awarded.

References

- [1] Zhai Q, Li X. Immobilization and sustained release of cefalexin on MCF nano-mesoporous material. *J Disper Sci Technol* 2019;40:1675-1685.
- [2] Legnoverde M, Basaldella E. Influence of particle size on the adsorption and release of cephalexin encapsulated in mesoporous silica SBA-15. *Mat Letters* 2016;181:331-334.
- [3] Ghafelehbashi R, Akbarzadeh I, Tavakkoli M, Yaraki T, Lajevardi A, Fatemized M, Saremi L. Preparation Physicochemical properties, in vitro evaluation and release behavior of cephalexin-loaded niosomes. *Int J Pharm* 2019;569:118580.
- [4] Versporten A, Zarb P, Caniaux I, Gros M, Drapier N, Miller M, Jarlier V. Antimicrobial consumption and resistance in adult hospital inpatients in 53 countries: results of an internet-based global point prevalence survey. *The Global PPS network* 2018:619-629.
- [5] Bottoni P, Caroli S. Presence of residues and metabolites of pharmaceuticals in environmental compartments, food commodities and workplaces: environmental compartments, food commodities and workplaces: A review spanning the three-year period 2014–2016. *Microchem J* 2017;136:2-24.
- [6] Barrera D, Villarroel-Rocha J, Marengo L, Oliva M, Sapag K. Non-hydrothermal synthesis of cylindrical mesoporous materials: Influence of the surfactant/silica molar ratio. *Ads Sci & Tech* 2011;29:957-988.
- [7] Legnoverde M, Simonetti S, Basaldella E. Influence of pH on cephalexin adsorption onto SBA-15 mesoporous silica: Theoretical and experimental study. *App Surf Sci* 2014;300:37-42.
- [8] Mustafa S, Dilara B, Nargis K, Naeem A, Shahida P. Surface properties of the mixed oxides of iron and silica. *Col and Surf A* 2002;205:273-282.
- [9] Thommes M, Kaneko K, Neimark A, Olivier J, Rodriguez-Reinoso F, Rouquerol J, Sing K. Physisorption of gases, with special reference to the evaluation of surface area and pore size distribution (IUPAC Technical Report). *Pure. Appl. Chem.* 2015;87:1051-1069.
- [10] Rao B, Mukherji R, Shitre G, Alam F, Prabhune A, Kale S. Controlled release of antimicrobial cephalexin drug from silica microparticles. *Mat Sci and Eng C* 2014;34:9-14.
- [11] Del Piero S, Melchior A, Polese P, Portanova R, Tolazzi M. A novel multipurpose Excel tool for equilibrium speciation based on netwon-raphson method and on a hybrid genetic algorithm. *Annali di Chim* 2006;96:29-49.

Temperature Influence in the Deactivation of LTA Commercial Zeolites

Beatriz O. Nascimento^a, Bianca F. dos Santos, Débora A. S. Maia^a, Darley C. Melo^b,
Enrique Vilarrasa-García^a, Moisés Bastos-Neto^a, Diana C. S. de Azevedo^{a*}

^a GPSA, Departamento de Engenharia Química – Universidade Federal do Ceará, Campus do Pici, bl. 731 – 60760-400, Fortaleza Ceará, Brasil

^b PETROBRAS/CENPES, Rio de Janeiro, Brazil *email: diana@gpsa.ufc.br

Abstract

In an industrial process it is common the utilization of adsorption fixed bed with zeolitic material for gas drying and the adsorbent regeneration may be conducted using a TSA process, which in its turn, can cause the loss of activity, like an aging process. So, the goal of this study is promoting the premature aging of a commercial zeolite, LTA type, by cycles of heating and cooling at two different temperatures, 523 and 573 K. It was made the crystallinity study, textural characterization, FTIR spectroscopy, TGA and carbon dioxide isotherms at 298 K as the probe molecule, to evaluate the adsorption capacity. The crystallinity study does not show any changes in the crystal structure of the zeolite. So, the reduction in the adsorption capacity could be associated to an organic compound deposit in the porous of the material, which might cause the block effect. The temperature study presents a slight variation in the results, but this is not the only factor in the aging process. The number or the duration of the cycles might be key variables in the optimization of this study.

Keywords: Deactivation; LTA Zeolite; TSA Process.

1. Introduction

The high capacity water adsorption on microporous zeolites of low Si/Al ratio make them the best adsorbent for gas drying. This process occurs because of the highly polar surface of this material, which promote the physisorption of polar substances, like water, even at very low concentrations. This process is industrially conducted in a fixed bed with pelletized material [1]. The Temperature Swing Adsorption (TSA) is a common way to regenerate the adsorbent manly for the strongly adsorbed species, but with the repetition this may cause a reduction in the adsorption capacity due the loss of crystallinity or coke formation when the regeneration step is carried out in presence heavy of hydrocarbons [2].

The use of the TSA process goes back to the 50's, where that was employed in the natural gas purification. After this the TSA had a rapid growth

and, today, can be found in systems with two or three fixed beds. In a plant's operation one of the fixed beds was maintained in the adsorption temperature and the interest compound are accumulated in the porous material. In the same time another fixed bed, which was previously saturated by the adsorptive, is regenerated by a hot purge [3].

At last, the goal of this work is promoting the accelerate aging in a commercial zeolite, using TSA cycles at two different temperatures. Then investigate the mechanism of this deactivation and its impact in CO₂ adsorption capacity.

2. Experimental

2.1. Material

The adsorbent used in this work is a zeolite LTA type with sodium as the exchange cation in pellets shape of 1.6 mm of diameter. The crystal form of

the same zeolite, was used in the crystallinity study. Both materials were supplied by Sigma Aldrich.

2.2. Aging Test

The aging test was conducted following the methodology showed by Santiago *et al.* in 2018 [4]. That consists in placing 25 g of the zeolite in a stainless steel reactor (Parr Instrument Company, USA) with volume of 500 mL. The sample had passed by a pre-stage, where it was humidified by a stream of nitrogen bubbled in water for 24 h, at 303 K and 1 bar of pressure. After this stage it was added 0.6 mL of n-heptane per gram of zeolite and the reactor was pressurized at 30 bar with a mix of carbon dioxide and methane in the proportion of 1:4 for an hour. At last, the heating/cooling cycles were initiated. The Sample was heated until 523 K and kept for 3 hours and it was cooled to 303 K by natural convection. This process was repeated and aliquots was collected in 14, 24 and 35 cycles, that samples being called A1, A2 and A3, respectively. The same process was made changing the temperature to 573 K in the heating/cooling process. In this case the samples were called by B1, B2 and B3, in the same order, that is, samples collected after 14, 24 and 35 cycles, respectively.

2.3. X-Ray Diffraction (XRD)

The X-ray diffraction analysis for the fresh samples, A3 and B3 were carried out with X'PERT PRO Powder diffractometer (PANalytical, UK) equipped with a Co-K α anode. The samples were analyzed in the range of 2 θ between 5 and 70° and with steps of 0,013°.

The diffraction patterns were used to determine the crystallinity based on in a standard sample, in this case the commercial LTA in crystal form. The equation 1 was used to calculate this parameter:

$$\text{Crystallinity}(\%) = \frac{S_x}{S_s} \cdot 100 \quad (1)$$

Where S_x is the average of the area of the selected peaks of the sample and S_s is the average of the area of the selected peaks of the standard sample. The peaks correspond to the crystalline planes 222, 420, 442, 620, 642 and 644 [5].

2.4. Textural Characterization

The BET area and total pore volume was determined by the adsorption/desorption nitrogen isotherms at 77 K and this was conducted in an Autosorb-iQ3 (Quantachrome, EUA). The samples were degassed before the measurements by application of 10⁻⁶ bar of vacuum and temperature of 573 K by 8 h.

2.5. Fourier-Transform Infrared Spectroscopy (FTIR)

The FTIR analyses were conducted in a spectrometer VERTES 70 (Bruker, UK), with sensibility of 2 cm⁻¹. The samples were conformed in KBr pellets.

2.6. Thermogravimetric Analysis (TGA)

The thermal stability and the release of volatile compounds were analyzed in STA 409 CD/403/5/G SKIMMER (Netzsch, Germany). The samples were submitted to a final temperature of 1072 K through a 10 K min⁻¹ heating hate. The inert atmosphere was obtained by constant flux of nitrogen at 20 ml min⁻¹.

2.7. CO₂ Adsorption Isotherm

The CO₂ isotherms at 298 K were obtained in a volumetric system, the Autosorb-iQ3 (Quantachrome, EUA). The samples were degassed before the analysis under vacuum and 573 K for 8 h.

3. Results and discussion

3.1. X-Ray Diffraction (XRD)

This technique was used to determinate the crystallinity and purity of the zeolite type LTA. Figure 1 shows the diffractogram of the standard material, the fresh samples, A3 and B3. The diffraction pattern results agree with the literature patterns [6]. These results show that there were no changes in the zeolite main structure with the aging cycles.

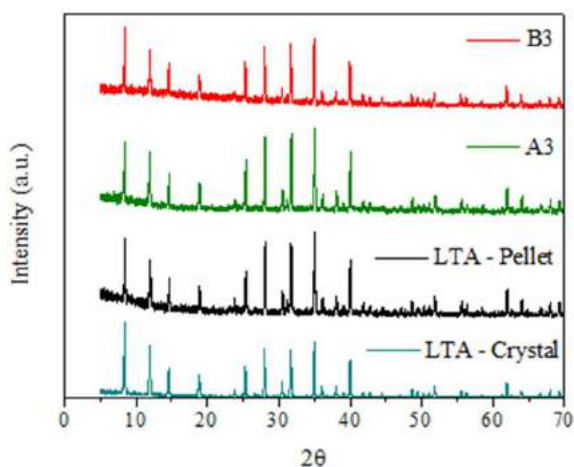


Fig. 1. The diffraction patterns to the fresh sample in crystal and pellet form, A3 and B3.

This is confirmed by the crystallinity data presented in the Table 1, the results show any significantly change with the cycles. The values are in the error range of the method.

Table 1. Crystallinity data of the samples.

Sample	Crystallinity (%)
LTA	58.6
A3	61.1
B3	66.9

3.2. Textural Characterization

Figure 2 shows the adsorption and desorption isotherms of nitrogen at 77 K. The isotherms are the Type II according the IUPAC classification, which are characteristic of macroporous and non-porous materials [7]. These indicate that nitrogen adsorption occurred in the macroporous of the binder. Zavareh, Farrokhzad and Darvishi have tried in 2018 measure the BET area of the zeolite 4A, but they had no success because the “window” size of the crystal cage was smaller than the diameter of the nitrogen molecules [8].

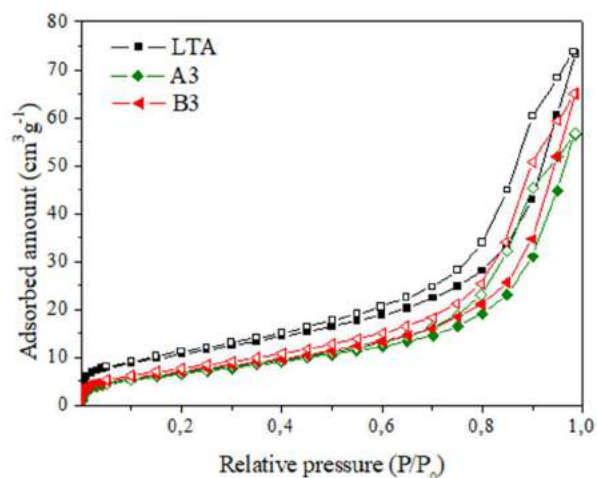


Fig. 2. Nitrogen adsorption and desorption isotherm at 77 K to the fresh sample, A3 and B3.

Table 2 resumes the textural characterization. We can observe a reduction in the textural properties of the zeolite, which can suggest a block effect by the coke formation in the macroporous during heating/cooling cycles.

Table 2. Textural characterization.

Sample	BET area (m ² g ⁻¹)	Pore volume (cm ³ g ⁻¹)	DR volume (cm ³ g ⁻¹)
LTA	39	0.094	0.010
A1	29	0.079	0.007
A2	26	0.088	0.006
A3	25	0.087	0.006
B1	35	0.093	0.007
B2	33	0.090	0.007
B3	26	0.080	0.006

This technique is not recommended to characterize polar surfaces due to the quadrupolar moment. The nature of nitrogen has influenced the molecule orientation on the adsorption and in the micropore filling pressure. The equilibrium of the isotherm was difficulted by the specific interactions of the nitrogen with the material surface [7].

3.3. Fourier-Transform Infrared Spectroscopy (FTIR)

The FTIR spectroscopy was used to determine if any functional groups were present in the sample before and after the aging tests. The Figure 3 show the spectra for the fresh LTA.

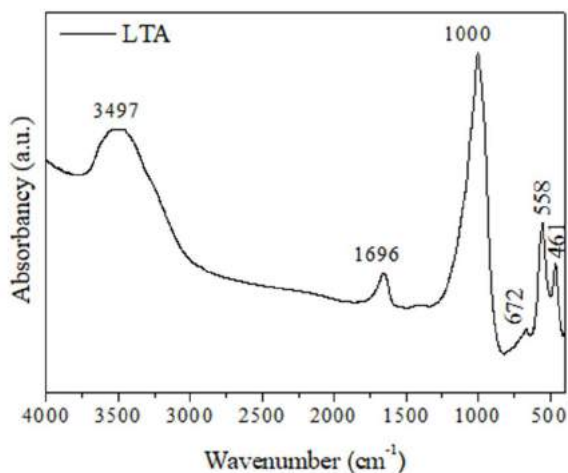


Fig. 3. The FTIR spectrum for fresh sample.

The fresh sample presents bands at 3500 and 1650 cm^{-1} that indicate the presence of water. In the first, we had the stretch vibrations of the groups OH and in the second the adsorbed water. The bands around of 1000, 660 and 460 cm^{-1} demonstrate the aluminosilicate structure that indicates, respectively, the asymmetric and symmetric stretch and deformation of the TO_4 where T is a silicon or aluminum atom. The band at 557 cm^{-1} was associated with the external vibration of a secondary structure of the zeolite A, the DR4 (the rings of four members in the secondary structure of the LTA) [9].

Figure 4 (A) presents the FTIR results of the aged samples. One can notice in the aging material the presence of the bands around 2962-2936 and 2877-2449 cm^{-1} , which is characteristic of the CH_3 and CH_2 , respectively, asymmetric stretching vibration in aliphatic compounds. In the Figure 4 (B) were showed the deformation vibrations which usually appear. The asymmetric deformation of the group methyl is presented in the region of 1466 cm^{-1} . The deformation of the methylene group might occur between 1347 and 1189 cm^{-1} , but close to carbonyl groups that can appears at 1380 cm^{-1} [10].

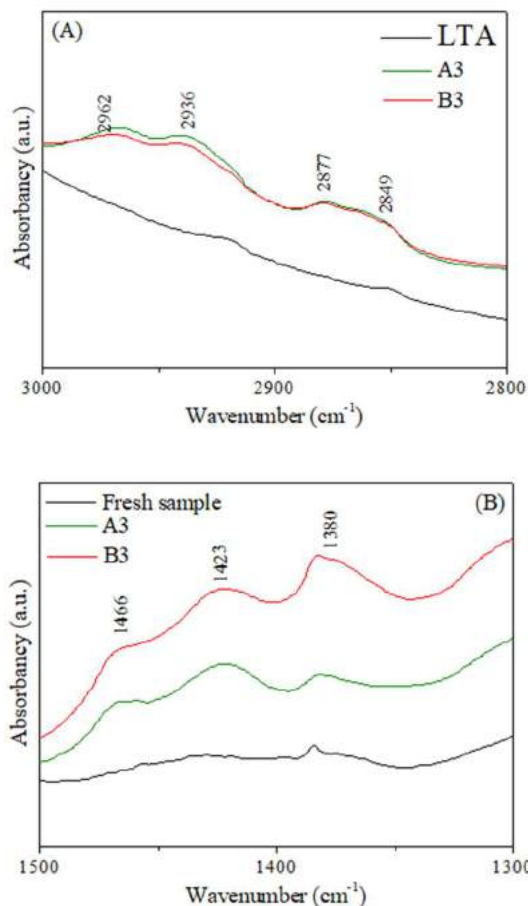


Fig. 4. The FTIR spectra of fresh sample, A3 and B3 samples.

The bands around 1435 were associated to the stretching of the CO_3 ions, which might be presented in both samples [11]. These results suggest that the presence of carbon dioxide in the aging method can change the positions of the bands in the same way to the carbonyl groups. The rock vibrations appear at 724 cm^{-1} in the spectrum. These bands are typical of long noncyclic CH_2 chains [10]. The absence of these bands can infer the n-heptane might be cracking in smaller compounds.

3.4. Thermogravimetric Analysis (TGA)

The thermogravimetric analysis of the fresh sample and of the most aged samples are exhibited in Figure 5. The patterns of mass losses were different from each other that indicate different kind of compound. The fresh sample presented the mass loss until 200°C. This might be associated to the free water losses [12]. In the aged materials, it was observed another mass loss that was stabilized at

823 K. This might indicate the presence of organic compounds more thermic stable in the zeolite cages after the aging tests.

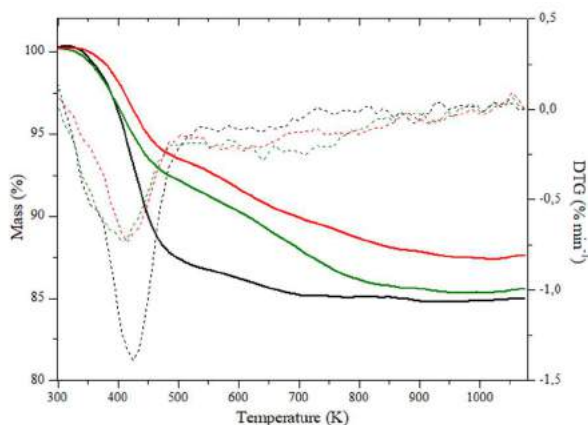


Fig. 5. TGA (continuous line) and DTG (dotted line) of LTA (black), A3 (green) and B3 (red) samples.

3.5. CO₂ Adsorption Isotherm

The Figure 6 shows the carbon dioxide isotherms at 298 K of the aged samples at 523 K. These samples presented a decrease of adsorption CO₂ capacity, where the difference between the samples were equal to 22, 43 and 49%, respectively, to 14, 24 and 35 cycles of heating/cooling. That result was in agreement with the textural characterization, FTIR spectra and thermogravimetric analyses, where it was indicated the loss of the zeolite textural properties by formation of organic compounds inside the material pores.

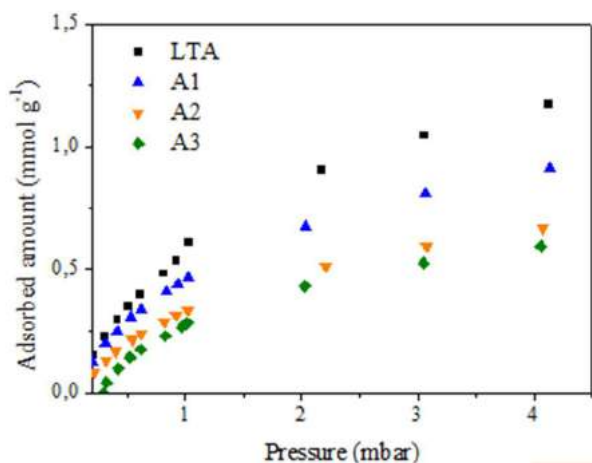


Fig. 6. CO₂ adsorption isotherms at 298 K of the aging samples at 523 K.

Santiago and coworkers studied the deactivation on microporous zeolites by TSA process in 2018 [4]. They found a reduction of the 25% in the CO₂ adsorption capacity at 303 K in the samples aged by 35 heating and cooling cycles. These results indicate the commercial LTA was more susceptible to the deactivation than that another sample in the same conditions.

The samples aged at 573 K are presented in Figure 7. In this temperature, the reduction in the adsorption capacity is the 29% for B1, 37% for B2 and 51% for B3. That is comparable with the values of the experiment at 523 K. These results indicate the change in the temperature is not enough to promote a premature aging test in the zeolite type LTA.

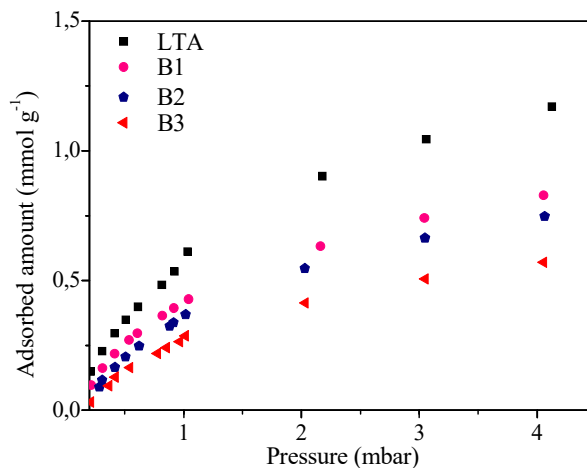


Fig. 7. CO₂ adsorption isotherm at 298 K to the samples B1, B2 and B3.

4. Conclusions

The aging methodology tested is efficient in the deactivation of zeolites type LTA pointed by the reduction in the adsorption capacity of a probe molecule, as the carbon dioxide at 298 K. The crystallinity showed no changes in the zeolite main structure. FTIR has showed that deactivation mechanism could be the accumulation of organic material in the porous. The study presented the temperature as important variable, but not the only one that should be considered in the understanding of the aging process.

Acknowledgements

The authors acknowledge the PETROBRAS for the financial support. And to the Conselho Nacional



de Desenvolvimento Científico e Tecnológico – CNPq by the process 402561/2007-4, Notice MCT/CNPq n°10/2007 by the DRX analyses. At last, to the Laboratório de Microscopia Vibracional (LEVM) by the FTIR analyses.

pure phase zeolite 4A from coal fly ash. **Journal of Cleaner Production**, v. 219, p. 258–267, 2019.

References

- [1] ALEGHAFOURI, A.; DAVOUDI, M. Modeling and simulation of a pressure–temperature swing adsorption process for dehydration of natural gas. **Adsorption**, v. 24, n. 1, p. 121–133, 2018
- [2] RUTHVEN, D. M. **Principles of Adsorption and Adsorption Processes**. New York: John Wiley & Sons, 1984.
- [3] BERG, F. *et al.* Temperature Swing Adsorption in Natural Gas Processing: A Concise Overview. **ChemBioEng Reviews**, n. 3, p. 59–71, 2019.
- [4] SANTIAGO, R. G. *et al.* Investigation of premature aging of zeolites used in the drying of gas streams. **Chemical Engineering Communications**, v. 0, n. 0, p. 1–8, 2018.
- [5] GARCÍA-SOTO, A. R.; RODRÍGUEZ-NIÑO, G.; TRUJILLO, C. A. Zeolite LTA synthesis: Optimising synthesis conditions by using the modified sequential simplex method. **Ingeniería e Investigación**, v. 33, n. 3, p. 22–27, 2013.
- [6] BAERLOCHER, C.; MCCUSKER, L. B.; OLSON, D. H. **Atlas of Zeolite Framework Types**. 6. ed. Amsterdam: Elsevier B.V., 2007.
- [7] THOMMES, M. *et al.* Physisorption of gases, with special reference to the evaluation of surface area and pore size distribution (IUPAC Technical Report). **Pure and Applied Chemistry**, v. 87, n. 9–10, p. 1051–1069, 2015.
- [8] ZAVAREH, S.; FARROKHZAD, Z.; DARVISHI, F. Modification of zeolite 4A for use as an adsorbent for glyphosate and as an antibacterial agent for water. **Ecotoxicology and Environmental Safety**, v. 155, n. December 2017, p. 1–8, 2018.
- [9] MOREIRA, J. C. *et al.* Evaluation of different reaction systems to obtain zeolite 4A via reverse microemulsion. **Microporous and Mesoporous Materials**, v. 279, n. December 2018, p. 262–270, 2019
- [10] COLTHUP, N. B.; DALY, L. H.; WIBERLEY, S. E. **Introduction to Infrared and Raman Spectroscopy**. 3rd. ed. San Diego: Academic Press, 1990.
- [11] MONTANARI, T.; BUSCA, G. On the mechanism of adsorption and separation of CO₂ on LTA zeolites: An IR investigation. **Vibrational Spectroscopy**, v. 46, n. 1, p. 45–51, 2008.
- [12] IQBAL, A. *et al.* Synthesis and characterization of

Biobased phenolic resin: an alternative material for micropollutant removal

Wardleison Martins Moreira^{a,b}, Paula Valéria Viotti^{a,*}, Mara Heloisa Neves Olsen Scaliante^a, Cristina Maria Gaudencio Baptista^b, Marcelino Luiz. Gimenes^a

^aPEQ, Department of Chemical Engineering, State University of Maringá, Avenida Colombo, 5790, Maringá, Paraná, 87020-900, Brazil;

^bCIEPQPF, Department of Chemical Engineering, University of Coimbra, Rua Silvío Lima, Coimbra, 3030-790, Portugal.

Abstract

Alternative use of a byproduct from the pulping process proved to be a promising route to reduce dependence on fine chemicals and produce new materials. A biobased phenolic resin was synthesized from a blend of Kraft black liquor and tannin, used as alternative phenolic precursors. The material properties and carbon content were improved by pyrolyzing the produced resin. Once micropollutants are an emerging problem as they affect the health and quality of life of humans and aquatic environment, the adsorption process emerges as a promising alternative for water decontamination. As a result, the present work evaluated the use of the hydrothermal and the pyrolyzed phenolic resin as a potential adsorbent for indomethacin removal from wastewater. Even though the pyrolyzed resin appears with a greater specific surface area, indomethacin removal is not greater than the one obtained for the hydrothermal only phenolic resin. That suggests that the chemical functional groups presented on the hydrothermal favor the adsorption by chemical linkages with the adsorbent.

Keywords: Adsorption; biobased resin; Indomethacin; Kraft black liquor; tannin

1. Introduction

The growing global industrialization and the inherent generation of waste have had a major environmental impact. Black liquor is a main byproduct of the pulp industry, which is intended for burning in the boiler for power supply and inorganic chemicals recovery [1–3]. As a source of phenolic compounds, black liquor could be used as an alternative source of phenol, in order to add value to this by-product while promoting sustainability.

In front of the need of technologies for emerging micropollutants removal, such as drugs and pesticides, the interest onto the adsorption process has increased in environmental chemistry. That is due to the fact that those contaminants are resistant to biological treatment and not completely eliminated with the conventional wastewater treatment process [4].

Even though drugs are nowadays found in trace-level concentrations in aquatic systems, they may cause chronic effects and ecotoxicological impacts on ecosystems [4]. Among all the drugs,

indomethacin is a widely used nonsteroid anti-inflammatory drug.

This work aimed at synthesizing an innovative hydrothermal phenolic resin obtained from a blend of crude Kraft black liquor and tannin. In order to increase the carbon content and improve the materials properties, a fraction of the the resin was pyrolyzed. In addition to the new materials characterization, the potential of its use as a low-cost adsorbent was assessed for the indomethacin removal, a contaminant of emerging concern, in aqueous environments.

2. Methodology

The biobased resin reaction was carried out in a reflux system, by following four steps: (i) 108 g of the raw Kraft black liquor was hydroxymethylated with 32 g of formaldehyde 37% (wt.) aqueous solution, at 343 K, for 1 hour; (ii) 12 g of tannin were mixed with 12 g of a sodium hydroxide 5% (wt.) aqueous solution and blended with the hydroxymethylated black liquor; (iii) 16 g of formaldehyde 37% (wt.) aqueous solution were added to the blend and stirred for 2 hours, at 343 K; (iv) the hydroxymethylated blend was

introduced in a PTFE vessel, sealed, and placed in a convective oven and hydrothermally cured. Then, the resin was solvent exchanged with an acetone:ethanol 1:1 solution for 48 hours and dried overnight at 293 K. Afterwards, the obtained resin was thermally activated at 473 K for 2 hours, with a 5 K.min⁻¹ rate. The obtained resin was washed with distilled water until constant pH, dried overnight at 293 K, and labeled as RFA.

A fraction of the obtained resin was pyrolyzed with a nitrogen flow of 20 ml.min⁻¹, 5 K.min⁻¹ rate and a ramp at 623 K for 1 hours and other at 1123 K for 2 hours. The obtained resin was also washed with distilled water until constant pH, dried overnight at 293 K, and labeled as RFC.

The adsorption was performed batchwise, by adding 20 mL of a 10 mg.L⁻¹ indomethacin aqueous solution (with 1% methanol addition) to 20 mg of the adsorbent, at 298 K and 150 rpm. Then, the samples were filtered, and the indomethacin concentration measured in a UV-VIS spectrophotometer at a wavelength of 270 and 320 nm. The adsorption capacity, q_t (mg g⁻¹) was calculated using Equation 1.

$$q_t = \frac{(C_0 - C_t)}{m} V \quad (\text{Equation 1})$$

Where C_0 and C_t are the initial and time t indomethacin aqueous solution concentrations (mg.L⁻¹), respectively, V is the indomethacin solution volume (L) and m the adsorbent weight (g).

3. Results and discussion

3.1 Indomethacin solution stability

Firstly, the indomethacin stability was investigated on its natural (initial) pH and for 5 different pH's: 2, 5, 7, 9 and 12. Peaks in the wavenumber within the range 190 – 230 nm were neglected once the NaOH and HCl used to change the solution pH absorbs the UV light in the mentioned range. As a result, only the peak at 270 (*) and 320 (+) nm were considered in the present study, as shown for the initial solution peaks.

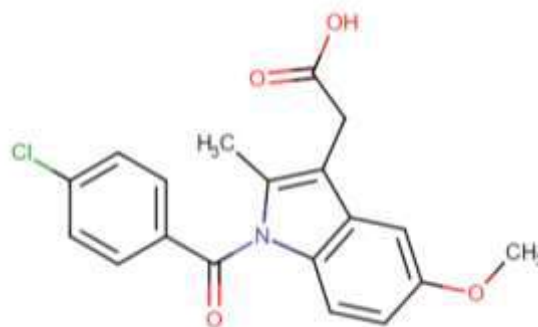


Fig. 1. Indomethacin chemical structure.

The solution absorbance was accompanied over the time, during 2 weeks, to assure that the indomethacin concentration will not have significantly changes by its own. Fig. 2 reveals that the absorbance kept constant after approximately 9 days. As a result, the indomethacin solution was prepared 10 days prior to conduct the experiments.

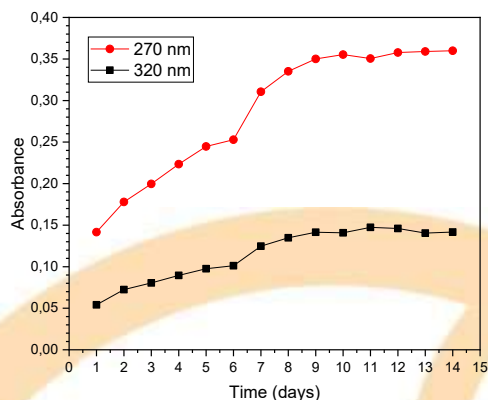


Fig.2. Indomethacin solution absorbance evolution over time.

Since the indomethacin pKa is 4.13, above the pH 4 it is on its neutral state and as the pH increase it starts to ionize and for a pH greater than 5 it assumes the negatively charged ionized state. As a result, in Fig. 3, at a pH of 2 the peaks at 270 and 320 nm diminish in intensity and are barely perceived. However, sharp peaks were observed for the solutions at pH 5 and 7. Once indomethacin undergoes through a base catalyzed hydrolysis, it decomposes as the pH increase, as mentioned by [5].

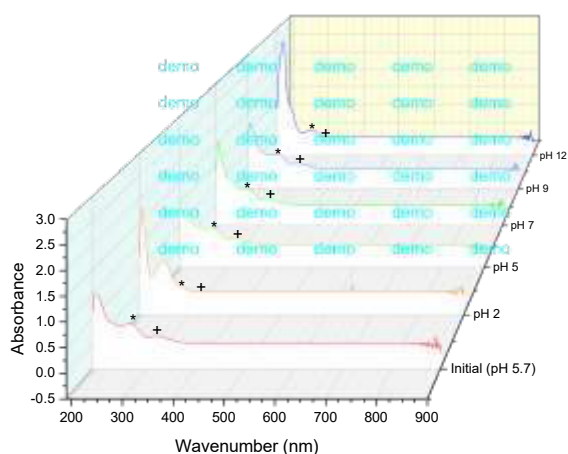


Fig.3. Indomethacin absorbance changes with the solution pH.

As a result, the adsorption was investigated only for the pH 2, 5, 7 and 9. Moreover, confirming the previously mentioned result, the indomethacin adsorption and, consequently its removal, was favored as the pH increases and the drug becomes completely ionized.

3.2 Adsorbents characterization

The adsorbents characterizations are summarized in Table 1. Textural characterization reveals the RFA lower specific surface area, when compared with RFC. The pyrolysis counterparts acquired a specific surface area 3 times higher.

The pH point of zero charge (pH_{PZC}) for the RFA and RFC were 4 and 8, respectively. On the other hand, both materials present an isoelectric point (IP) between the pH 1.5 and 2. According to [6] the pH_{PZC} corresponds to the solution pH in which the net total surface charge (external and internal) density equals zero. On the other hand, the IP stands for the solution pH in which the material external surface charge electro kinetic potential equals zero. Moreover, a difference between the pH_{PZC} and the IP greater than zero indicates that the material is more negatively charged on its external surface than on its interior (but the net total surface charge is positive when $IP < pH < pH_{PZC}$). On the other hand, when the pH_{PZC} equal the IP, there is a homogeneous charge distribution on the material surface. As a result, the RFA has a more homogeneous charge distribution than the RFC.

Table 1. Characterization summary.

	RFA	RFC
BET ($m^2 g^{-1}$)	31	100
pH_{PZC}	4	8
Isoelectric point	1.5 - 2	1.5 - 2

3.3 pH influence

In front of the above mentioned, for the pH greater than 4, the RFA becomes more negatively charged. Once the RFA was not thermally degraded by pyrolysis, it has more functional groups, favoring the chemical linkages between the drug and the RFA. On the contrary, the RFC is more positively charged for pH values below 8, favoring the indomethacin-RFC attractive electrostatic interactions. After that, it also becomes more negatively charged, and charge repulsion takes place. Once the pH 7 showed a better adsorption capacity for the RFA and RFC, it was chosen to conduct further tests.

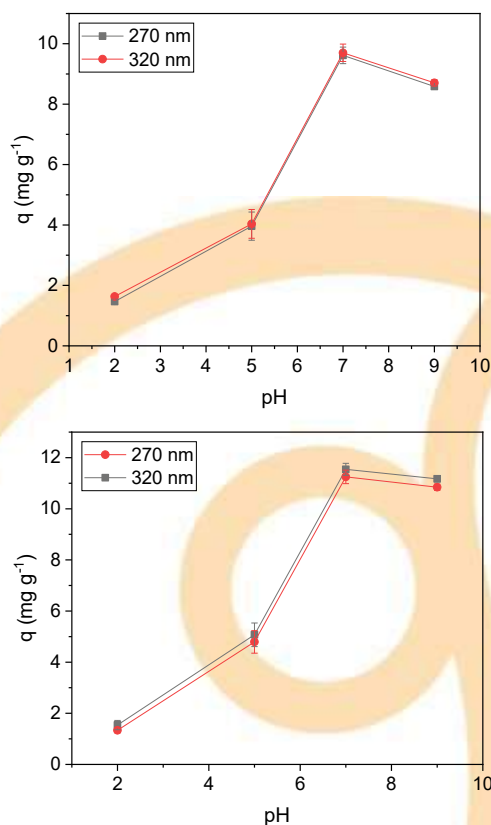


Fig. 4. pH influence of indomethacin adsorption onto (a) RFA and (b) RFC.

3.4 Adsorbent weight influence

Even though the lower weight showed a greater adsorption capacity, it is near the balance accuracy limit. Moreover, aiming not only to increase de adsorption capacity, but also the indomethacin removal, the adsorbent weight needs to be balanced in order to optimize the process. For the RFA, as the adsorbent weight increase to values higher 0.02 g, the removal also increase and the adsorption capacity go below 10 mg g^{-1} , with a removal greater than 70 %. Contrarily, onto the RFC, the indomethacin removal achieved 85 % for an adsorbent weight of 0.02 g and achieved a plateau of 92 % for higher weight.

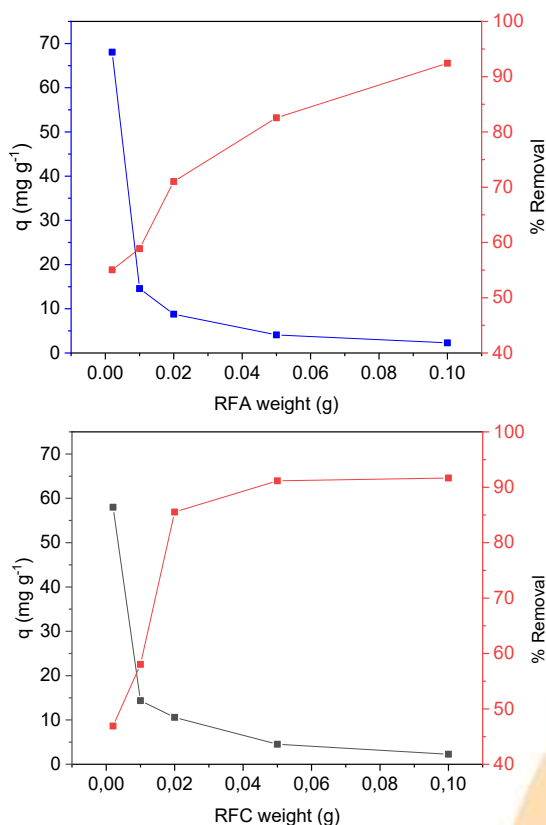


Fig. 5. Adsorbent weight influence onto indomethacin adsorption.

4. Conclusion

The potential of using a new biobased phenolic resin for indomethacin removal by adsorption was investigated. Due to the materials point of zero charge and isoelectric points, the adsorption at a pH of 7 returns a better adsorption capacity and a

more stable indomethacin solution. The adsorption capacity of RFA increased with increasing the materials loading with an indomethacin removal greater than to 90%. Therefore, for the RFC, a plateau was achieved for the adsorbent weight greater than 0.02 g, with and indomethacin removal of 92 %.

Moreover, indomethacin adsorption is rarely reported in literature, since most researches concern in the study of the drug controlled release. As a result, a more in-depth research is needed in order to develop new materials and remove this drug from contaminated water.

Acknowledgements

The authors gratefully acknowledge the Higher Education Personnel Improvement Coordination (CAPES) financial support.

References

- [1] Azhar Zakir MJ, Ramalingam S, Balasubramanian P, Rathinam A, Sreeram KJ, Rao JR, Nair BU. Innovative material from paper and pulp industry for leather processing. *J Clean Prod* 2015;104:436–444.
- [2] Al-Kaabi Z, Pradhan R, Thevathasan N, Gordon A, Chiang YW, Dutta A. Bio-carbon production by oxidation and hydrothermal carbonization of paper recycling black liquor. *J Clean Prod* 2019;213:332–341.
- [3] Oliveira RCP, Mateus M, Santos DMF. Chronoamperometric and chronopotentiometric investigation of Kraft black liquor. *Int J Hydrogen Energy* 2018;43:16817–16823.
- [4] Zhang D, Gersberg RM, Ng WJ, Tan SK. Removal of pharmaceuticals and personal care products in aquatic plant-based systems: A review. *Environ Pollut* 2014;184:620–639.
- [5] Comer J, Judge S, Matthews D, Tows L, Falcone B, Goodman J, Dearden J. The intrinsic aqueous solubility of indomethacin. *Admet Dmpk* 2014;2:18–32.
- [6] Tran HN, You S, Hosseini-Bandegharai A, Chao H. Mistakes and inconsistencies regarding adsorption of contaminants from aqueous solutions: A critical review. *Water Res* 2017;120:88–116.

Investigation of Natural Clinoptilolite Over the Adsorption Process of Psychotropic Drug

Tháísa Frossard Coslop^a, Ramiro Picoli Nippes^a, Gabriela Nascimento da Silva^a, Rosângela Bergamasco^a, Mara Heloisa Neves Olsen Scaliante^a, Marcelino Luiz Gimenes^a

^a Maringá state university, Av. Colombo, 5790 - Zona 7, Maringá - PR, 87020-900, Brazil

Abstract

Diazepam has been detected in water sources around the world affecting the quality of drinking water. Even in small quantities, recent studies have proven the negatives effects of the drug in human body. Since traditional water and sewage treatment do not remove this type of contaminant, it became interesting to evaluate forms to remove them from water sources. A cheap and eco-friendly alternative to remove this drug from the water is through adsorption using the natural clinoptilolite zeolite as an adsorbent. This work goal was to study the characterizations of clinoptilolite, such as Scanning electron microscopy (SEM), energy-dispersive X-ray spectroscopy (EDS), X-ray diffractometer (XRD) and Fourier transform infrared spectroscopy (FTIR), and analyze the potential of this material as an adsorbent. The adsorption tests were made using diazepam as adsorbate. Kinetic studies and isotherm analysis were performed and the material was able to remove the pollutant in an aqueous medium. The adsorption process followed a pseudo-second order kinetics and the Freundlich model fit the experimental data better.

Keywords: Natural zeolite; Clinoptilolite; Characterization; Adsorption; Diazepam.

1. Introduction

According to the UN World Water Development Report published in 2019, less than 3% of the world's water is appropriate for human consumption. Population growth, socioeconomic development and changes in consumption are the main responsible of the increasing contamination in water sources [1]. In the last decades a new class of contaminants, present in environmental matrices, called emergent pollutants has been discovered. More than 1000 substances, divided into 16 classes, have already been detected and although found in very low concentrations, these contaminants are known to have an adverse effect on human and animal health. Currently, most of wasted water treatment plants (WWTP) are not able to remove these pollutants [2].

Pharmaceuticals products are among these emerging pollutants. Most of the drugs found in nature come from therapeutic use in humans and animals by its excretion, as metabolites or original form, in sewage as metabolites or even in their natural form. Another route of exposure is during

the drug production process. Once inside the organism, these drugs are partially or completely absorbed, distributed, metabolized and subsequently excreted as metabolites or in their original form [3].

Diazepam, known commercially as Valium, is a drug used to treat anxiety disorder, alcohol withdrawal syndrome, muscle spasm, seizures, insomnia and restless leg syndrome [4]. Studies have detected the presence of diazepam in surface water (0.5 ng L^{-1}) and drinking water (0.16 ng L^{-1}) [5, 6].

There are already advanced techniques used for its removal in literature, i.e., ozonation, photodegradation and adsorption. Among the alternatives mentioned, adsorption stands out for allowing the use of various types of materials as sorbents, including low cost ones, besides having a good efficiency [7].

Environmental remediation using natural zeolites became an interesting alternative because of its low cost, ease of access in large quantities, broad thermal and mechanical properties and high capacity of sorption. In addition, its use does not add new pollutants to the environment [8]. The

main types found are clinoptilolite, mordenite, phillipsite, chabazite, stilbite, analcima and laumontite, among which clinoptilolite is the most abundant, consequently, cheaper and most used. Clinoptilolite has been used as sorbent for removal of heavy metals and dyes [9-11].

Once understood the importance of detecting these new pollutants and proposing low-cost and efficient ways to remove them from water, this study presents the characterizations of clinoptilolite, as its potential to be used as adsorbent and finally run experimental tests in the adsorption of diazepam in aqueous solution and applying models to calculate the kinetics and isotherm of the process.

2. Materials and methods

2.1. Materials

The natural zeolite used as adsorbent was kindly provided by Celta Brasil, which is located on Vila Jovina – Cotia/SP, 06705150. It was a clinoptilolite type mainly composed of SiO₂ and Al₂O₃. Before the experimental tests the zeolite was washed with deionized water, oven dried and sieved (0.4 -1.0 mm). The adsorption tests were run with distilled water. The drug Diazepam used as adsorbate was obtained commercially.

2.2. Adsorbent characterization

The morphology and chemical composition of the clinoptilolite were determined using the Scanning electron microscopy (SEM) and energy-dispersive X-ray spectroscopy (EDS) both realized by a FEI – QUANTA 250. To identify the crystal species, an X-ray Analysis was performed by a diffractometer with 40 kV and 30 mA copper ion sources. A Fourier transform infrared spectroscopy (FTIR) was used to identify the functional groups present on the surface of the zeolite, spectral range 400 to 4000 cm⁻¹, 100 scans and 4 cm⁻¹ resolution.

2.3. Adsorption experiments

The adsorption tests were conducted to study the performance capabilities of the clinoptilolite regarding its removal efficiencies. It was realized in batch condition and parameters like concentration of adsorbate (initial and final) and time were examined. To determine the adsorption isotherms, solutions containing 100 mL of

different concentrations of Diazepam (ranging from 1 to 5 mg L⁻¹) were carried in 125 mL Erlenmeyer flasks with 2 g of Clinoptilolite until the equilibrium of the reaction was reached. The transfer of the particles of adsorbed material in time and determine the speed of the reaction, also known as adsorption kinetics, were determined using a 250 mL solution of Diazepam 5 mg L⁻¹, 5 g of adsorbent. All the runs were made in a shaker machine 150 rpm, at 27 °C and the samples were filtered using a 0.22 mm membrane before the quantification of the drug performed by reading the absorbance in the UV-VIS spectrophotometer and the results were used to calculate the efficiency of the process and adsorption capacity. The Eq. (1) was used to calculate the adsorption capacity in mg/g.

$$q_e = \frac{v(C_o - C_e)}{m} \quad (1)$$

where q_e is the mass of the adsorbed drug per unit of adsorbent mass (mg g⁻¹), C_o and C_e are the initial and final concentrations of Diazepam (mg L⁻¹), v is the volume of the aqueous phase (L) and m the mass of adsorbent used (g).

2.3.1. Isotherms of adsorption

Isotherm models of Langmuir and Freundlich were used for mathematical modeling of adsorption [12]. both are reported as Eqs. (2) and (3) Langmuir model assumes that adsorption occurs on the monolayer coverage, where substances are adsorbed onto energy-equivalent active holes and there are no interactions between the adsorbed compounds. Differently, Freundlich model proposes that an equilibrium on heterogeneous surfaces exists, having a high number of adsorption sites with different affinities.

$$q_e = \frac{q_{max} K_L C_e}{(1 + K_L C_e)} \quad (2)$$

$$q_e = K_F + C_e n^{-1} \quad (3)$$

where q_e is the amount of Diazepam adsorbed (mg g⁻¹); C_e is the Diazepam concentration at equilibrium (mg L⁻¹); q_{max} the maximum clinoptilolite adsorption capacity (mg g⁻¹); K and n

are constants related to adsorption capacity and adsorption intensity.

2.3.2. Kinetics of adsorption

The kinetics models of pseudo first order and pseudo second order were examined. Both models have been shown in (4) and (5):

$$qt = qe (1 - e^{-k_1 t}) \quad (4)$$

$$qt = \frac{k_2 qe^2 t}{1 + k_2 qe t} \quad (5)$$

where qt and qe (mg g^{-1}) are the uptake at time t and at equilibrium; k_1 (min^{-1}) and k_2 ($\text{g mg}^{-1} \text{min}^{-1}$) are the equilibrium rate constant of pseudo-first-order and pseudo-second-order equation, respectively [13].

3. Results and discussion

3.1. Adsorbent characterization

Raw clinoptilolite was carried out to explore the surface morphology by SEM analysis. It was possible to see, in Figure 1, some light spots with small size, which correspond to cavities and voids in natural clinoptilolite. Another characteristic that can be noticed in SEM analysis it is not organized crystal shape of the zeolite. The EDS analysis found in Figure 2 has shown the presence of expressive peaks of Si, O and Al, known as the main compounds of zeolite, but once this material was found in nature the presence of others elements is also expected.

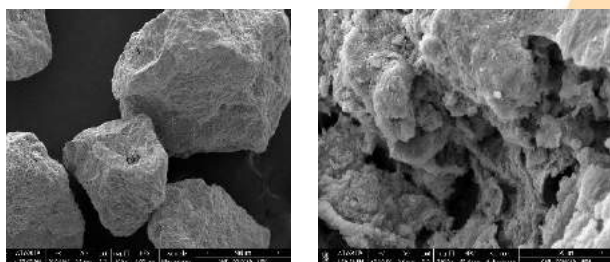


Fig. 1. SEM images of natural clinoptilolite.

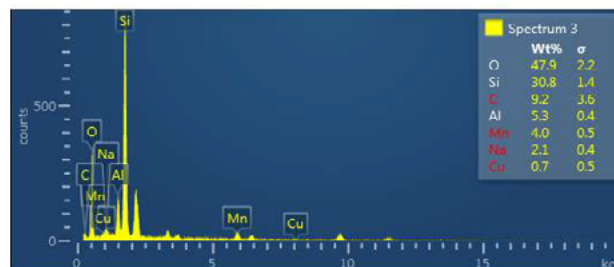


Fig. 2. EDS of clinoptilolite.

The XRD pattern of the clinoptilolite sample are presented in Figure 3. First, was necessary to visually compare the result to the characteristic patterns of the zeolite found in literature [14, 15]. The peak intensity patterns were used to quantify the structural purity. It was possible to identify Clinoptilolite and mordenite as the main phases in the diffractogram, with 71,04% of clinoptilolite and 11,57% of mordenite.

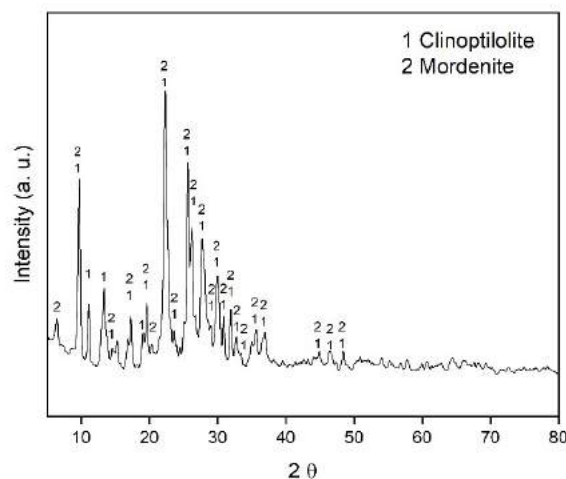


Fig. 3. XDR of the natural zeolite with characteristics clinoptilolite and mordenites peaks.

The infrared spectrum of the zeolite is presented in Figure 4. It is possible to affirm that occurring band in the range of $3640\text{-}3620 \text{ cm}^{-1}$ is result from vibration of free OH-groups represented by water. In the range of $1750\text{-}1600 \text{ cm}^{-1}$ is notice the presence of vibration due to the presence of water adsorbed. The most intensive vibration frequency is between $1060\text{-}1040 \text{ cm}^{-1}$ is a result from the structural units of the alumina-silicate lattice Si (Al)-O of the zeolite, which confirms the main

composition of the material used in this study. In the range of 470-460 cm^{-1} was observed a characteristic vibration of Metal-Oxygen (Me-O) [16].

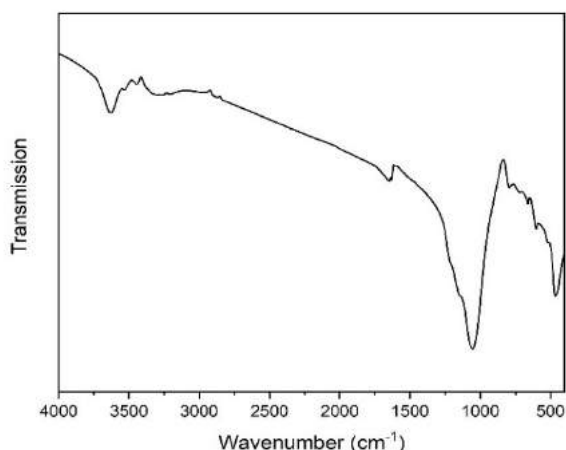


Fig. 4. FT-IR spectra of natural clinoptilolite.

3.2. Isotherms of adsorption

Regarding removal efficiencies of the process calculated, 2 g of clinoptilolite reached 52 % for 1 mg g^{-1} of Diazepam and 28 % for 6 mg g^{-1} .

The Diazepam adsorption isotherm onto natural zeolite was obtained under the experimental conditions described in item 2.3 is present in Figure 5. The nonlinear adjustment of Langmuir and Freundlich models were calculated and the main parameters calculated were extracted to Table 1.

Table 1. Isotherm parameters for diazepam adsorption onto natural clinoptilolite.

Models	Parameters	Values
Langmuir	q_{max} (mg g^{-1})	0,000171943
	K_L (mg L^{-1})	0,23162
	R^2	0,96609
Freundlich	n	1,62068
	K_F ($(\text{mg g}^{-1}) (\text{L mg}^{-1})^{-n}$)	0,000035172
	R^2	0,97939

Although both models have shown able to adjust to the process, the model that best fits the experimental data was Freundlich, presenting the highest R^2 , which means that equilibrium on heterogeneous surfaces exists, having a high number of adsorption sites with different affinities. It is possible to observe the n^{-1} value indicates the heterogeneity of the adsorbent [17].

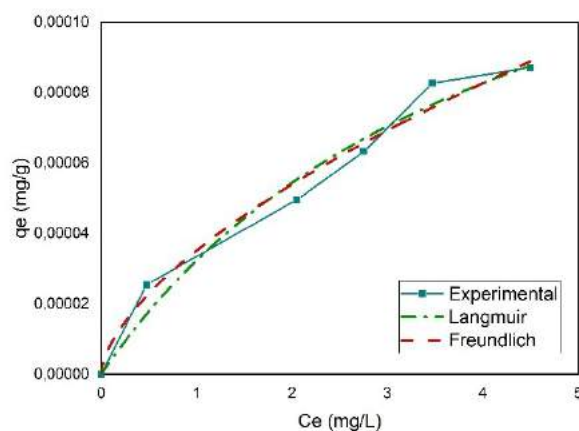


Fig. 5. Diazepam adsorption isotherm onto natural clinoptilolite and nonlinear models Langmuir and Freundlich adjustment.

3.3. Kinetics of adsorption

The experimental data of the Diazepam uptake is present in Figure 6. The adsorption was possible and more intense in the first hour approximately. After that, there were no significant vacant surface sites for adsorption, which means the equilibrium of the process was reached. The pseudo-first order and pseudo-second order kinetic models were adjusted to the experimental data and the main parameters are summarized in Table 2. Due the values of r , is possible to affirm that both models fitted well to the experimental data. However, the lower value of chi-square (χ^2) at the pseudo-second order indicates that this model brings better approximation between theoretical and experimental data [18].

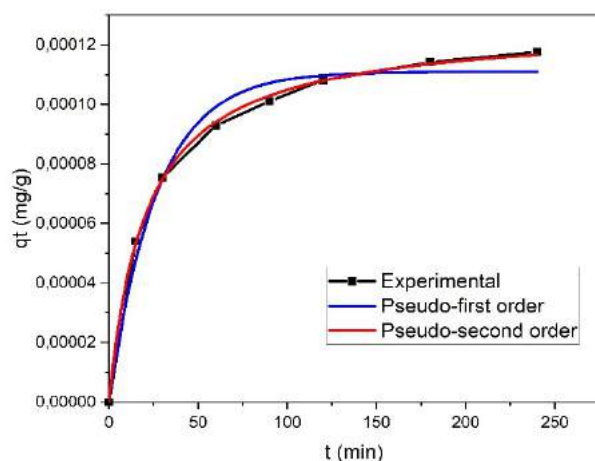


Fig. 6. Experimental adsorption data through time and the adjustment of pseudo-first order and pseudo-second order kinetics models.

Table 2. Kinetics parameters for diazepam adsorption onto natural clinoptilolite.

Models	Parameters	Values
Pseudo-first order	k (min ⁻¹)	0,03735
	R ²	0,98144
	χ ²	2,92E-11
Pseudo-second order	k (g mg ⁻¹ min ⁻¹)	380,02126
	R ²	0,99922
	χ ²	1,22E-12

4. Conclusion

The natural zeolite clinoptilolite proved to be a good option in the removal of emergent pollutant diazepam from aqueous solution through adsorption. The kinetics study using non-linear models had shown that pseudo-second order better fitted the experimental data, given the approximation of theoretical calculation. Regarding the equilibrium analysis Langmuir and Freundlich models described the process well. Overall, the results indicated the possibility of using this natural zeolite in filters to remove the drug diazepam. It is also worth mentioning the low cost of this material and the fact that it is eco-friendly.

Acknowledgements

The authors would like to thank PEQ-UEM, Celta Brasil and CAPES.

References

- [1] WHO, WHO drinking water guideline. 2017.
- [2] C. Teodosiu, A. F. Gilca, G. Barjoveanu, and S. Fiore, "Emerging pollutants removal through advanced drinking water treatment: A review on processes and environmental performances assessment," *J. Clean. Prod.*, vol. 197, pp. 1210–1221, 2018.
- [3] K. Van Der Ven, W. Van Dongen, B. U. W. Maes, E. L. Esmans, R. Blust, and W. M. De Coen, "Determination of diazepam in aquatic samples by capillary liquid chromatography-electrospray tandem mass spectrometry," *Chemosphere*, vol. 57, no. 8, pp. 967–973, 2004.
- [4] L. P. Lingamdinne, J. R. Koduru, H. Roh, Y. L. Choi, Y. Y. Chang, and J. K. Yang, "Adsorption removal of Co(II) from waste-water using graphene oxide," *Hydrometallurgy*, vol. 165, pp. 90–96, 2016.
- [5] B. V. Laws, E. R. V. Dickenson, T. A. Johnson, S. A. Snyder, and J. E. Drewes, "Attenuation of contaminants of emerging concern during surface-spreading aquifer recharge," *Sci. Total Environ.*, vol. 409, no. 6, pp. 1087–1094, 2011.
- [6] X. Zhang et al., "Determination of emerging chlorinated byproducts of diazepam in drinking water," *Chemosphere*, vol. 218, pp. 223–231, 2019.
- [7] S. I. Siddiqui, M. Naushad, and S. A. Chaudhry, "Promising prospects of nanomaterials for arsenic water remediation: A comprehensive review," *Process Saf. Environ. Prot.*, vol. 126, pp. 60–97, 2019.
- [8] P. Misaelides, "Application of natural zeolites in environmental remediation: A short review," *Microporous Mesoporous Mater.*, vol. 144, no. 1–3, pp. 15–18, 2011.
- [9] S. Wang and Y. Peng, "Natural zeolites as effective adsorbents in water and wastewater treatment," *Chem. Eng. J.*, vol. 156, no. 1, pp. 11–24, 2010.
- [10] L. Joseph, B. M. Jun, J. R. V. Flora, C. M. Park, and Y. Yoon, "Removal of heavy metals from water sources in the developing world using low-cost materials: A review," *Chemosphere*, vol. 229, pp. 142–159, 2019.
- [11] C. Perego, R. Bagatin, M. Tagliabue, and R. Vignola, "Zeolites and related mesoporous materials for multi-talented environmental solutions," *Microporous Mesoporous Mater.*, vol. 166, pp. 37–49, 2013.
- [12] M. Hong et al., "Heavy metal adsorption with zeolites: The role of hierarchical pore architecture," *Chem. Eng. J.*, vol. 359, no. November 2018, pp. 363–372, 2019.
- [13] Y. Huang, X. Zeng, L. Guo, J. Lan, L. Zhang, and D. Cao, "Heavy metal ion removal of wastewater by zeolite-imidazolate frameworks," *Sep. Purif. Technol.*, vol. 194, no. November 2017, pp. 462–469, 2018.
- [14] D. A. Kennedy, M. Mujčin, C. Abou-Zeid, and F. H. Tezel, "Cation exchange modification of clinoptilolite –thermodynamic effects on adsorption separations of carbon dioxide, methane, and nitrogen," *Microporous Mesoporous Mater.*, vol. 274, no. September 2018, pp. 327–341, 2019.
- [15] Y. Li, P. Bai, Y. Yan, W. Yan, W. Shi, and R. Xu, "Microporous and Mesoporous Materials clinoptilolite," *Microporous Mesoporous Mater.*, vol. 273, no. July 2018, pp. 203–211, 2019.
- [16] M. Z. Kussainova, R. M. Chernyakova, U. Z. Jussipbekov, and S. Paşa, "Structural investigation of raw clinoptilolite over the Pb 2+ adsorption process from phosphoric acid," *J. Mol. Struct.*, vol. 1184, pp. 49–58, 2019.
- [17] A. Zendelska, M. Golomeova, K. Lisichkov, and S. Kuvendziev, "Characterization and Application of Clinoptilolite for Removal of," *Geol. Maced.*, vol. Vol. 32, no. June, pp. 20–32, 2018.
- [18] D. A. Kennedy and F. H. Tezel, "Cation exchange modification of clinoptilolite – Screening analysis for potential equilibrium and kinetic adsorption separations involving methane, nitrogen, and carbon dioxide," *Microporous Mesoporous Mater.*, vol. 262, pp. 235–250, 2018.

Development of a biosorbent from coconut fiber biorefinery for removing Rhodamine B from textile wastewater

Rogério José Melo Nascimento^{a*}, Kilton R. A. Pereira^a, Francisco Avelino^a

^aFederal Institute of Education, Science and Technology of Ceará, 63503-790, Iguatu, CE, Brazil

Abstract

The prospection of alternative adsorbents has attracted the attention of scientific community. The aim of this work was evaluate the potential of a biorefinery process as a chemical modification process for improving the adsorption properties of coconut fiber for removing Rhodamine B (Rh-B) from a simulated textile wastewater. The formosolv process was carried out under mild conditions (atmospheric pressure) using 85 % wt. formic acid at 100 °C during 1,2 and 3 hours in a fiber mass/solution volume ratio of 1:10 (g/mL). The physicochemical and structural features of crude and modified coconut fibers (CCF and MCF) were evaluated by their lignocellulosic composition, water contact angle (WCA) and scanning electron microscopy (SEM). The main adsorption parameters involved in Rh-B removal were evaluated by batch adsorption assays. The reaction time did not influence significantly the fiber yield during the organosolv process. It was observed an increase in the amount of α -cellulose in MCF, which influenced on its structural, superficial and morphological properties. The adsorption assays showed that the removal efficiency of Rh-B was about 80 % for MCF and 35 % for CCF. In addition, the maximum adsorptive capacity (q_{max}) values were 17.48 mg g⁻¹ for MCF and 5.16 mg g⁻¹ for CCF. It can be concluded that the coconut fiber represents a potential alternative to replace the traditional adsorbents, in which the use of a mild biorefinery process can significantly increases its adsorptive performance.

Keywords: agrowastes; coconut wastes; biomass valorization; eco-friendly process.

1. Introduction

Water has always been the most important resource for the development of the human race. However, aquatic pollution has become a serious problem to be faced over the centuries [1]. Contamination of effluents by dyes, even in small quantities, can cause aquatic imbalance and diseases in living beings [2,3]. Rhodamine B (Rh-B) is one of those dyes that cause imbalance in the environment, widely used in the textile and food industries, Rh-B is a toxic cationic compound, causing irritation to the skin and eyes, besides its carcinogenic effect in situations of prolonged exposure [4]. For this reason, several researches are done annually in order to solve the problem of water pollution [5]. Among the main used decontamination methods, the chemical, biological and physical ones stand out [6]. Adsorption, a physicochemical process, stands out among the others, due to its advantages, which are that it does not cause secondary pollution, unlike chemical processes, and does not have environmental restrictions unlike biological methods [6,7]. Therefore, numerous researches are being carried out for developing new types of adsorbents worldwide [1].

Among these new adsorbents, agroindustrial wastes are frequently sought, as it is found on a large scale worldwide, a factor that also raises concern as many of these end up becoming passive pollutants [8]. In addition, agroindustrial wastes are extremely rich in several functional groups, such as carbonyls and hydroxyls, which can serve as active sites [6]. Coconut is one of the most produced crop in the world that generates an annual production of approximately 60.3 million fruits on approximately 12.3 million hectares around the world, with Brazil being one of the five most producers [9].

The presence of several functional groups on the surface of the coconut fiber, such as hydroxyls, phenolic and aliphatic, make it possible to carry out chemical modifications, in order to increase its adsorption capacity. [6]. The application of biorefinery processes would be a way of adding value to all components of the fiber, since this biomass is rich in cellulose, hemicellulose and lignin [10].

Kraft process is one of the most used pulping processes in the pulp and paper industry, which is responsible for 90% of the cellulose pulp production on the market [11]. However, this type of pulping generates a sulfur-rich and impure lignin, in contrast

to the organosolv process that generates a high-quality lignin for applications in other technological purposes [12], thus respecting the principles of biorefinery, in which all parts of biomass can be used [10].

Based on the background, the aim of this work was to evaluate the potential of modified green coconut fiber by the organosolv process as a biosorbent for removing Rh-B from a simulated textile wastewater, comparing its performance to that of crude green coconut fiber.

2. Materials and methods

2.1. Raw material pre-treatment

The green coconut fibers were gently donated by Embrapa Agroindústria Tropical (Fortaleza, Ceará, Brazil), which were processed using a pilot knife mill (Fritsch pulverisette 19) equipped with sieves of 0.5 mm diameter pores, yielding the crude coconut fibers (CCF).

2.2. Chemical modification of fiber

The organosolv process was carried out using 10 g of green coconut fiber and 100 mL of 85 % wt. formic acid and 2.0 % v/v HCl as catalyst at 100 °C during 1, 2 and 3 hours and atmospheric pressure, yielding the modified coconut fiber (MCF).

2.3. Characterization of the biosorbents

The lignocellulosic composition of coconut fibers was determined as described in the literature [13]. The hydrophilicity of the samples were evaluated by water contact angle (WCA) measurements that were carried out using a GBX Instrumentation Scientifique equipment. The morphology of the biosorbents were analysed by scanning electron microscopy (SEM), in which an electronic microscope Inspect 50 operating at an accelerating voltage of 20 kV was used.

2.4. Batch adsorption tests

The Rh-B concentrations were calculated according to the calibration curve constructed using standard concentration (5 to 100 ppm), obtaining the following equation: $Abs = 0.01976_{RhB} - 0.00414$. The adsorption tests were carried out in a batch system an incubator/shaker (Marconi MA-420) at λ

= 479 nm under the following conditions: shaking speed (150 rpm), 25 mL of Rh-B solution (50 ppm) at 25 °C, different biosorbent dosage (2, 3 and 4 g L⁻¹) and contact times (5 at 60 minutes). The adsorption parameters such as removal efficiency (RE, %) and quantity of Rh-B adsorbed per mass of biosorbent at time t (q_t , mg g⁻¹) were calculated using Equations 1 and 2, respectively [14]:

$$RE (\%) = \frac{C_0 - C_t}{C_0} \times 100 \quad (1)$$

$$q_t = \frac{V}{m} (C_0 - C_t) \quad (2)$$

where C_0 and C_t are the initial concentration and the concentration at time t of Rh-B (mg L⁻¹), respectively; m is the mass of biosorbent (CCF or MCF) (g) and V (L) is the volume of Rh-B solution. The experiments were performed in triplicate.

3. Results and discussion

3.1. Biorefinery process

It can be seen that the reaction time did not affect considerably the pulp yield during the organosolv process (Figure 1). This fact was proved by performing an One Way ANOVA statistical test with 95% confidence, which showed that the pulp yields obtained in 1, 2 and 3 hours were statistically equal. According to this result, the lowest reaction time (1 h) was chosen for the next steps of this work.

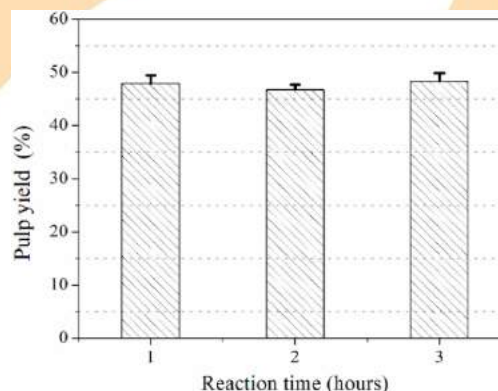


Figure 1 – Variation of pulp yield with the reaction time during the organosolv process.

3.2. Physicochemical and structural characterization of the biosorbents

3.2.1. Lignocellulosic composition

Table 1 shows the chemical composition of the CCF and MCF in a dry basis.

Table 1. Lignocellulosic composition of the coconut fiber-based biosorbents.

Component	CCF (%)	MCF (%)
Holocellulose	54.9 ± 2.2	55.1 ± 1.4
α-cellulose	23.3 ± 0.5	31.7 ± 0.2
hemicellulose	22.7 ± 0.8	14.3 ± 1.6
Insoluble lignin	27.41 ± 0.25	33.6 ± 0.9
Soluble lignin	0.03 ± 0.005	0.006 ± 0.002
Extractives	15.2 ± 0.48	1.04 ± 0.1
Ash	4.5 ± 0.1	1.2 ± 0.2

Table 1 shows that there was an increase in the cellulose content, as expected, after the formosolv process, with a considerable increase in the α-cellulose content from 23.3% to 31.7%, which represents the crystalline part of the cellulose. This chemical modification can cause an improvement in the material as an adsorbent, due to the greater exposure of hydroxyls, which can act as active sites, resulting from the removal of amorphous components present in the fiber, such as lignin, hemicellulose and extracts (Table 1).

However, insoluble lignin showed an unusual increase, which may be possibly related to the recondensation reactions occurred during the pulping process or even due to an error during gravimetric analysis, which may have accounted for other constituents that were on the surface of the fiber. Nevertheless, the other characterizations will show that lignin was removed due to significant changes in the thermal, morphological, structural and surface properties of the MCF [15].

3.2.2. WCA analysis

Figures 2 (A) and 2 (B) show the contact angle formed between water and CCF and modified MCF, in which a change in the fiber surface is notorious, given the difference in the drop shape of water. This difference is best evidenced in Figure 2 (C), which shows that the angles obtained were 71.3 ° for CCF from 63.2 ° for the MCF.

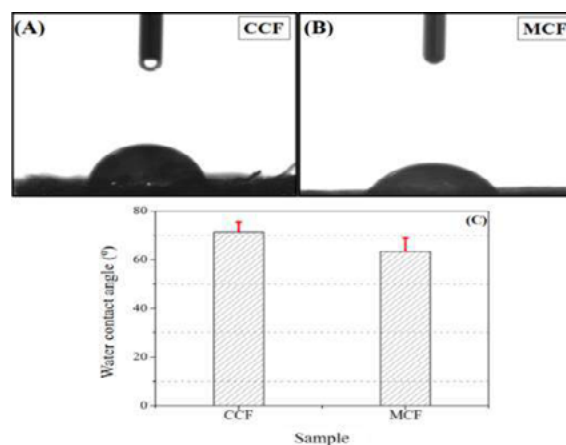


Figure 2 – Water droplet shapes for (A) CCF; (B) MCF and (C) WCA values for CCF and MCF.

The analysis of Figures 2 (A), (B) and (C), show that there was a change in the WCA of the samples. The MCF had a smaller contact angle than that of CCF, indicating greater hydrophilicity, which can be attributed to the removal of hemicellulose and lignin from its surface, causing a greater exposure of cellulose and, consequently, of its hydroxyl groups, which interacted with water, reducing the contact angle in relation to that of CCF.

The WCA is another indication that corroborates with the chemical modification of the fiber, suggesting that there was a removal of lignin from the MCF, since lignin confers a certain hydrophobicity to the fiber, due to its aromatic structure [15]. This change in the chemical composition of the fiber directly influences the properties of the material surface, as seen in Figures 2 (A), (B) and (C).

3.2.3. Scanning electron microscopy (SEM)

The morphology of CCF (Figures 3(A), (B) and (C)) and MCF (Figures 3(D), (E) and (F)) are shown in the SEM micrographs under different magnifications (350, 2000 and 7000 x, respectively).

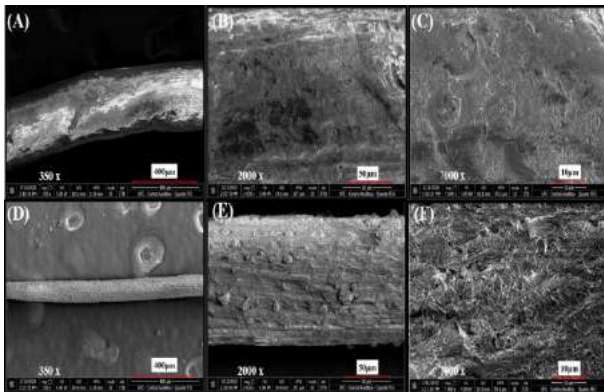


Figure 3 - SEM micrographs for CCF (A, B and C) and MCF (D, E and F) under different magnifications (350, 2000 and 7000 x, respectively).

From the SEM micrographs, it is possible to observe that the CCF had a porous and homogeneous surface, which has changed significantly after formosolv process, yielding a rough and heterogeneous surface, suggesting that a chemical modification occurred in the material. Therefore, these differences can be explained as result of removing lignin, hemicellulose and extractives from the crude material by the formosolv process, resulting in a modification in the material's morphology.

3.3. Batch adsorption tests

3.3.1. Removal efficiency and adsorption capacity

The influence of the biosorbents dosage on Rh-B removal and on their adsorptive capacity can be seen in Figures 4(A), (B), (C) and (D). Moreover, Figure 4(E) shows a picture of the effluents at the final time for each biosorbent (CCF and MCF) under different dosages.

It is possible to observe that RE increased as the both biosorbent dosage increased. This behavior is directly attributed to the fact to the increase in the quantity of active sites available to interact with the adsorbate [18,19]. However, it is clearly that MCF showed a considerable increase in the RE values than those of CCF.

It is worth mentioning that despite the fact that q_t reached a minimum at 4 g L^{-1} for both biosorbents, the maximum RE values were reached at this concentration for both biosorbents (Figure 4(D)).

In addition, Figure 4(D) also shows a remarkable behavior for q_t values, in which they were almost

two times higher for MCF than those for CCF. This suggests that the applied biorefinery process promoted significant structural modifications on MCF structure that positively influenced on its adsorption properties, showing the potential of the method and the final material for wastewater treatment purposes.

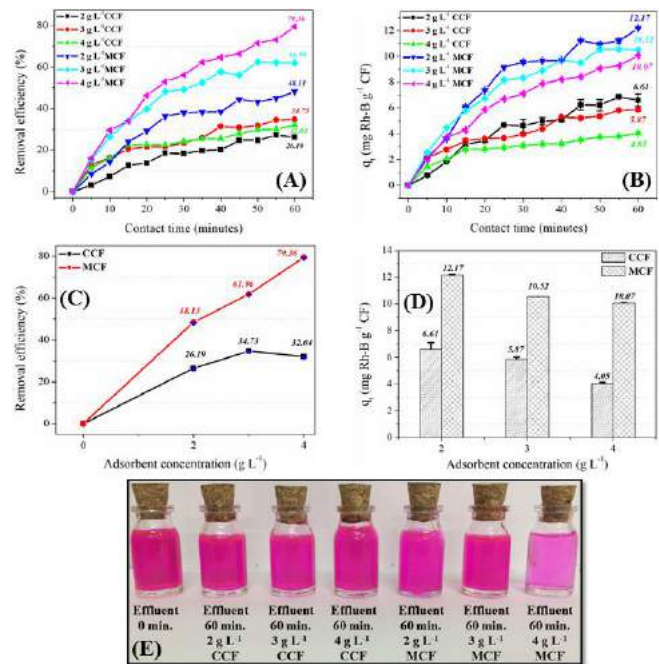


Figure 4 – Variation of (A) RE vs contact time; (B) q_t vs contact time; (C) RE vs adsorbent dosage; (D) q_t vs adsorbent dosage and (E) picture of the effluents at the end of the assays for each biosorbent under different dosages.

Conclusions

The results obtained in the present study showed the potential of using an agro-industrial residue (coconut fiber) as a biosorbent for removing Rh-B from a simulated effluent, which was modified through a biorefinery process under mild conditions. MCF showed a high removal efficiency of Rh-B ($\approx 80\%$) in a period of only 1 hour, while CCF presented less than half of MCF efficiency ($\approx 34.7\%$). Furthermore, MCF also presented higher adsorption capacity value ($q_{\max} = 17.48 \text{ mg g}^{-1}$) than CCF ($q_{\max} = 5.16 \text{ mg g}^{-1}$), showing its potential to be used as an alternative adsorbent for wastewater treatment in detriment to the traditional ones.

Acknowledgments

The authors acknowledge Brazilian agencies CNPq, CAPES and FUNCAP (DEP – 0164-00174.01.00/19) for the financial support, Laboratório de Raios X at UFC for XRD analyses, Central Analítica-UFC/CT-INFRA/MCTI-SISNANO/Pró Equipamentos for SEM analyses, Dr. Niédja Fittipaldi for the assistance with XRD data and BSc. Luiz Carlos for the technical assistance in the adsorption assays.

References

- [1] A. Azari, R. Nabizadeh, S. Nasser, A. H. Mahvi, and A. R. Mesdaghinia, "Comprehensive systematic review and meta-analysis of dyes adsorption by carbon-based adsorbent materials: Classification and analysis of last decade studies," *Chemosphere*, vol. 250, p. 126238, 2020, doi: 10.1016/j.chemosphere.2020.126238.
- [2] A. Kausar *et al.*, "Dyes adsorption using clay and modified clay: A review," *J. Mol. Liq.*, vol. 256, pp. 395–407, 2018, doi: 10.1016/j.molliq.2018.02.034.
- [3] K. G. Pavithra, S. K. P., V. Jaikumar, and S. R. P., "Removal of colorants from wastewater: A review on sources and treatment strategies," *J. Ind. Eng. Chem.*, vol. 75, pp. 1–19, 2019, doi: 10.1016/j.jiec.2019.02.011.
- [4] C. Lops *et al.*, "Sonophotocatalytic degradation mechanisms of Rhodamine B dye via radicals generation by micro- and nano-particles of ZnO," *Appl. Catal. B Environ.*, vol. 243, pp. 629–640, 2019, doi: 10.1016/j.apcatb.2018.10.078.
- [5] O. Guselnikova *et al.*, "Magnetic polyurethane sponge for efficient oil adsorption and separation of oil from oil-in-water emulsions," *Sep. Purif. Technol.*, vol. 240, p. 116627, 2020, doi: 10.1016/j.seppur.2020.116627.
- [6] Y. Zhou, J. Lu, Y. Zhou, and Y. Liu, "Recent advances for dyes removal using novel adsorbents: A review," *Environ. Pollut.*, vol. 252, pp. 352–365, 2019, doi: 10.1016/j.envpol.2019.05.072.
- [7] M. A. Al-Ghouti, M. A. Al-Kaabi, M. Y. Ashfaq, and D. A. Da'na, "Produced water characteristics, treatment and reuse: A review," *J. Water Process Eng.*, vol. 28, no. September 2018, pp. 222–239, 2019, doi: 10.1016/j.jwpe.2019.02.001.
- [8] Y. Dai *et al.*, "Utilizations of agricultural waste as adsorbent for the removal of contaminants: A review," *Chemosphere*, vol. 211, pp. 235–253, 2018, doi: 10.1016/j.chemosphere.2018.06.179.
- [9] M. Mayara *et al.*, "Ecophysiology of the tall coconut growing under different coastal areas of northeastern Brazil," *Agric. Water Manag.*, vol. 232, no. January, p. 106047, 2020, doi: 10.1016/j.agwat.2020.106047.
- [10] R. C. Rajak, S. Jacob, and B. S. Kim, "A holistic zero waste biorefinery approach for macroalgal biomass utilization: A review," *Sci. Total Environ.*, p. 137067, 2020, doi: 10.1016/j.scitotenv.2020.137067.
- [11] D. S. Bajwa, G. Pourhashem, A. H. Ullah, and S. G. Bajwa, "Industrial Crops & Products A concise review of current lignin production, applications, products and their environment impact," *Ind. Crop. Prod.*, vol. 139, no. June, p. 111526, 2019, doi: 10.1016/j.indcrop.2019.111526.
- [12] P. P. Thoresen, L. Matsakas, and U. Rova, "Recent advances in organosolv fractionation: Towards biomass fractionation technology of the future," *Bioresour. Technol.*, p. 123189, 2020, doi: 10.1016/j.biortech.2020.123189.
- [13] T. Y. Yokoyama, J. F. Kadla, and H.-M. Chang, "Microanalytical Method for the Characterization of Fiber Components and Morphology of Woody Plants," *J. Agric. Food Chem.*, vol. 50, pp. 1040–1044, 2002, doi: 10.1021/jf011173q.
- [14] M. T. Yagub, T. K. Sen, and M. Ang, "Removal of cationic dye methylene blue (MB) from aqueous solution by ground raw and base modified pine cone powder," *Environ. Earth Sci.*, vol. 71, no. 4, pp. 1507–1519, 2014, doi: 10.1007/s12665-013-2555-0.
- [15] N. F. Souza, J. A. Pinheiro, A. I. S. Brígida, J. P. S. Morais, M. de Sá M. de Souza Filho, and M. de Freitas Rosa, "Fibrous residues of palm oil as a source of green chemical building blocks," *Ind. Crops Prod.*, vol. 94, pp. 480–489, 2016, doi: 10.1016/j.indcrop.2016.09.012.
- [16] F. P. Marques, L. M. A. Silva, D. Lomonaco, M. de F. Rosa, and R. C. Leitão, "Steam explosion pretreatment to

- obtain eco-friendly building blocks from oil palm mesocarp fiber.” *Ind. Crops Prod.*, vol. 143, no. August 2019, p. 111907, 2020, doi: 10.1016/j.indcrop.2019.111907.
- [17] D. M. Nascimento *et al.*, “A novel green approach for the preparation of cellulose nanowhiskers from white coir,” *Carbohydr. Polym.*, vol. 110, pp. 456–463, 2014, doi: 10.1016/j.carbpol.2014.04.053.
- [18] J. Bortoluz, A. Cemin, L. R. Bonetto, F. Ferrarini, V. I. Esteves, and M. Giovanela, “Isolation , characterization and valorization of lignin from *Pinus elliottii* sawdust as a low-cost biosorbent for zinc removal,” *Cellulose*, vol. 26, pp. 4895–4908, 2019, doi: 10.1007/s10570-019-02399-9.
- [19] R. F. Nascimento, D. Q. Melo, A. C. A. Lima, A. L. Barros, C. B. Vidal, and G. S. C. Raulino, *Equilíbrio de adsorção*. 2014.

Kinetic Modeling of the Adsorption Process Using Different Biomass

Ana Carolina da Silva, Lizeth Vanessa Amado Jurado, Eliana Zaroni Megale, Gabriela Machado Chemp, Bruno Almeida de Carvalho e Silva, Matheus Santos Parente Carneiro, Francisco Eduardo Aragão Catunda Júnior^a, Marisa Fernandes Mendes

^aCenter for Exact, Natural and Technological Sciences, Universidade Estadual da Região Tocantina do Maranhão, Imperatriz, Maranhão, CEP 65900-000, Brazil.

Department of Chemical Engineering, Universidade Federal Rural do Rio de Janeiro, Rod BR 465 Km 7, Seropédica, CEP 23897-000, Brazil

Abstract

Among different separation processes, adsorption has been extensively studied due to its simplicity, low cost, and high efficiency. The behavior of the adsorption mechanisms and its controlling steps can be predicted and calculated by kinetic models. The kinetic parameters also offer necessary information to select the best conditions for different applications, and for the processes project. In this work, it was evaluated six kinetic models: pseudo-first, pseudo-second, pseudo-nth order, Elovich and Boyd's external model, each one having its own characteristics to predict the behavior of the process. Therefore, the present paper aims the evaluation of contaminants adsorption through three different organic residues as the rubber seed shell, the endocarp of the almond fruit, and the resulting residue obtained from ginger's mechanical pressing process. Adsorption studies were based on the analysis of the kinetic and equilibrium terms. The experiments were conducted in triplicate, fixing the adsorbent mass (0.05 g for ginger, 0.15 g for rubber seed shell and 0.1 g for almond fruit), the agitation speed (180 rpm), and the temperature (45 °C), analyzing different contact times. The kinetic study indicated that depending on the raw material, the process kinetics was influenced by different mechanisms. For ginger adsorbent and rubber seed shell, the model that best fitted the experimental data was Elovich, whereas for almond it was the PNO. For the all adsorbents, the Boyd's external model indicated that the diffusion of the contaminants transferred through the boundary liquid layer surrounding the carbon particles was the main step limiting the rate of adsorption.

Keywords: batch process; mass transfer; Boyd model; activated carbon

1. Introduction

Water pollution has been a persistent problem due to the variety of industries that causes the uncontrolled growth of the presence of different toxic substances in their effluents [1]. Among the different toxic substances, dyes are the most harmful substances due to their high toxicity, and low biodegradability along the years [2]. One of the most efficient methods for the removal of dyes is the physical-chemical adsorption method. The adsorption process is a mass transfer process through which the solid substance can selectively remove dissolved constituents from an aqueous solution by attracting the dissolved solute toward its surface [3].

The design and scale-up of an adsorption process depends on kinetic analysis of the operation, as it provides the information that is required to select the optimal conditions for a future application of the process on an industrial scale. In order to investigate the adsorption mechanism and the potential rate-controlling steps involved in the process, kinetic models can be used to analyze experimental data [4,5].

Adsorption kinetics describes the speed in which molecules of a fluid phase are adsorbed onto an adsorbent. This speed is dependent of several variables, such as physic-chemical characteristics of adsorbate (nature of adsorbate, molecular weight, solubility, and others), of adsorbent (nature and pore structure) and from initial concentration of solution [6].

A satisfactory rate equation does not often provide all the information necessary to elucidate the mechanism. However, the calculated kinetic parameters can be of great practical and technological value regarding the times and amount of material consumed in the experiments. It is necessary to know the adsorption rate to evaluate the capacity of an adsorbent. In this way, the present study used three organic residues, fruit endocarp of almond (*Terminalia catappa* Linn), rubber seed shell (*Hevea brasiliensis*) and ginger (*Zingiber officinale* Roscoe) for the preparation of three different adsorbents, that will be applied for the removal of contaminants from aqueous solutions, evaluating the kinetics behavior.

2. Materials and methods

2.1. Biomass preparation

Ginger: Ginger rhizomes were bought in a local market in Seropédica-RJ. They were washed to remove all impurities and dried at ambient temperature. After that, the material was pressed in a manual and hydraulic press to obtain ginger residues, which were dried at 60 °C for 12 h in a muffle furnace. Then, they were milled, and it was done a granulometric analysis. The sample retained between the 20-80 mesh particle size was passed through a calcination process at 350 °C for 180 min. The calcined material was washed with distilled water for the removal of ash and other impurities, and then was dried again at 60 °C for 12 h. After that, activated carbon from ginger was obtained (G).

Rubber tree: The seed samples were collected in Maranhão, a state of the northeast region of Brazil. The rubber seed shells were washed and dried in an oven at 80 °C for 12 h. Then, the rubber seed shells were milled, and the samples were separated using the mesh sieves of the Tyler series. The particles retained between 24 and 80 mesh were selected for the analyses. The material was calcinated in a muffle at 400 °C for 90 min. After the calcination, the material was washed with distilled water and dried in an oven at 100 °C for 12 h. Then, the chemical activation was performed adding nitric acid 25% in a ratio of 1:2, and putting it in a muffle furnace at 500 °C for 20 min. After this process, the material was washed to remove the residue of nitric acid and dried again in an oven at 105 °C for 12 h. After this process, the chemically

activated adsorbent from rubber seed shells was obtained (RSS).

Almond: Chemical activation of the biomass was performed using $m_{\text{endocarp}}/m_{\text{H}_3\text{PO}_4}$ ratio of 1:1, followed by the addition of distilled water (250 mL). The biomass/ H_3PO_4 mixture was allowed to heat stand within 4 h under light agitation; after that washed and dried at 100 °C, over 36 h. After this time, in a muffle furnace, the material was heated at the rate of 10 °C.min⁻¹ from room temperature to 350 °C and remained at this temperature for 2 h. The material was then washed with distilled water until pH characteristic of water.

2.2. Batch biosorption procedure

The potential of the adsorbents to remove the two different contaminants was evaluated, with glycerol being tested for the rhizomes of ginger and methyl orange dye (MO) for the endocarp of almond tree and rubber seed shell.

The adsorption experiments were conducted in a batch mode, using Erlenmeyer flasks with 25 mL of solutions, at 318 K, maintaining the agitation at 180 rpm until the equilibrium time and fixed mass of 0.05 g for ginger, 0.1 g for almond fruit and 0.15 g for rubber seed shell.

The concentration of dye in the samples was determined during adsorption experiments using a UV-Visible spectrophotometer (Bel UV-M51) at maximum wavelength absorption at 465 nm. The studied dye concentration was 25 and 100 mg.L⁻¹ for RSS, and 200 to 800 mg.L⁻¹ for endocarp of almond.

The concentration of glycerol in the samples was determined by using UV-Visible spectrophotometer (Bel UV-M51) at maximum wavelength absorption at 410 nm. In this case, due to the colorless nature of the samples, it was necessary to employ a methodology to better analyse [7]. The studied glycerol concentration was 30 to 90 mg.L⁻¹ for 0.05 g of adsorbent.

After the completion of the reaction period, the flasks were taken out and the contaminant concentration were determined from the mass balance equation:

$$q_e = \frac{(C_0 - C_e)V}{W} \quad (1)$$

where C_0 and C_t are the initial and at time contaminant concentrations (mg/L), respectively, V the solution volume (L) and W is the mass of the adsorbent (g). When t is equal to the equilibrium time, $C_t = C_e$, $q_t = q_e$, then the amount of contaminant adsorbed at equilibrium, q_e .

2.3. Kinetic modeling

In order to investigate the mechanism and the controlling step of adsorption process, models of pseudo-first order (PFO), pseudo-second order (PSO) and Elovich were employed. In addition to traditional models, the Pseudo-Nth-Order (PNO) and Boyd's model were also evaluated.

The pseudo-first order model was firstly proposed by Lagergren (1898) to describe the rate of adsorption in liquid-solid phase systems [8,9].

$$q_t = q_e(1 - \exp^{-k_1 t}) \quad (2)$$

The pseudo-second model was proposed for modelling the chemisorption of divalent metals ions onto peat [10,11].

$$q_t = \frac{k_2 q_e^2 t}{1 + k_2 q_e t} \quad (3)$$

where k_2 is the pseudo-second-order rate constant (min^{-1}).

Elovich model was proposed to describe the kinetics of the chemisorption of gases onto heterogeneous solid surfaces. However, it has been successfully employed in the adsorption of chemical species in liquid phases [12, 13].

$$q_t = \frac{1}{\beta_E} \ln(1 + \alpha_E \beta_E t) \quad (4)$$

with α_E ($\text{g} \cdot \text{g}^{-1} \cdot \text{min}^{-1}$) as the initial sorption rate and β_E as the desorption constant ($\text{g} \cdot \text{g}^{-1}$).

The pseudo-nth-order (PNO) model was deduced to describe the adsorption kinetics of Pb(II) onto wheat bran treated with sulfuric acid [14].

$$\frac{dq_t}{dt} = k_n (q_e - q_t)^n \quad (5)$$

where k_n ($\text{g}^{n-1} \cdot \text{mg}^{-1n} \cdot \text{min}^{-1}$) is nth order rate constant and n is the number of active sites occupied by and adsorbate or ion molecule.

The Boyd's Model plays an important role in the distinguishment between the pore and film diffusion because provides information about which one is the controlling step in the adsorption process [15].

$$q_t = q_\infty (1 - e^{-Rt}) \quad (6)$$

where q_∞ is the equilibrium adsorption capacity at infinite time ($\text{mg} \cdot \text{g}^{-1}$) and R is the rate coefficient (h^{-1}).

2.4. Model validity evaluation

In order to evaluate the performance of the models used in this study, the following statistical parameters were employed:

$$R^2 = \frac{\sum (q_{\text{mean}} - q_{\text{cal}})^2}{\sum (q_{\text{mean}} - q_{\text{cal}})^2 + \sum (q_{\text{cal}} - q_{\text{exp}})^2} \quad (8)$$

$$\chi^2 = \sum \frac{(q_{\text{exp}} - q_{\text{cal}})^2}{q_{\text{cal}}^2} \quad (9)$$

$$MSE = \frac{1}{N_{\text{exp}}} \sum (q_{\text{exp}} - q_{\text{cal}})^2 \quad (10)$$

where q_{exp} is adsorption capacity at equilibrium ($\text{mg} \cdot \text{L}^{-1}$), q_{cal} is calculated adsorption capacity ($\text{mg} \cdot \text{L}^{-1}$), q_{mean} is the average value of experimental adsorption capacity ($\text{mg} \cdot \text{L}^{-1}$), N_{exp} is the number of data points and N_{para} is the number of the model parameters.

3. Results and Discussion

The kinetic parameters estimated for all models are shown in Tables 1 and 2. For ginger, the results showed that the correlation coefficients were higher than 0.98 for PSO, PSO and Elovich models, which were higher than the other kinetic models.

Table 1. Parameters of PFO, PSO and PNO models

PFO Model		
Conc.	Parameters	Statistical parameters
Ginger		
30	$k_1 = 0.764$	$R^2=0.998; \chi^2=0.045$
	$q_{cal} = 14.854$	MSE=0.16
90	$k_1 = 1.1$	$R^2=0.993; \chi^2=0.124$
	$q_{cal} = 13.169$	MSE=0.408
Rubber		
25	$k_1 = 0.013$	$R^2=0.969; \chi^2=0.944$
	$q_{cal} = 2.867$	MSE=0.030
100	$k_1 = 0.013$	$R^2=0.986; \chi^2=1.00$
	$q_e = 4.768$	MSE=0.037
Almond		
200	$k_1 = 0.305$	$R^2=0.959; \chi^2=0.094$
	$q_{cal} = 50.056$	MSE=0.629
800	$k_1 = 0.125$	$R^2=0.798; \chi^2=3.100$
	$q_{cal} = 166.81$	MSE=69.202
PSO Model		
Conc.	Parameters	Statistical parameters
Ginger		
30	$k_2 = 0.119$	$R^2=0.989; \chi^2=0.068$
	$q_{cal} = 14.299$	MSE=0.242
90	$k_2 = 0.452$	$R^2=0.999; \chi^2=0.114$
	$q_{cal} = 12.844$	MSE=0.373
Rubber		
25	$k_2 = 0.004$	$R^2=0.986; \chi^2=0.547$
	$q_{cal} = 3.4536$	MSE=0.013
100	$k_2 = 0.003$	$R^2=0.994; \chi^2=0.618$
	$q_{cal} = 5.801$	MSE=0.014
Almond		
200	$k_2 = 0.012$	$R^2=0.975; \chi^2=0.052$
	$q_{cal} = 53.219$	MSE=0.354
800	$k_2 = 0.001$	$R^2=0.957; \chi^2=0.579$
	$q_{cal} = 177.927$	MSE=12.778
PNO Model		
Conc.	Parameters	Statistical parameters
Ginger		
30	$k_n = 10.256$	$R^2=0.946; \chi^2=0.047$
	$n=914.8262$	MSE=1.608
90	$k_n = 1.662$	$R^2=0.989; \chi^2=0.115$
	$n=73.019$	MSE=0.242
Rubber		
25	$k_n = 0.008$	$R^2=0.970; \chi^2=0.380$
	$n=1.730$	MSE=0.021
100	$k_n = 0.235$	$R^2=0.994; \chi^2=7.244$
	$n=1.103$	MSE=0.014
Almond		
200	$k_n = 0.098$	$R^2=0.993; \chi^2=0.015$
	$n=1.362$	MSE=0.099
800	$k_n = 4.42E^{-03}$	$R^2=0.981; \chi^2=0.004$
	$n=1.5286$	MSE=0.001

Table 2. Parameters of Elovich, Boyd's and W&M models

Elovich Model		
Conc.	Parameters	Statistical parameters
Ginger		
30	$\alpha_E = 182.451$	$R^2=0.999; \chi^2=0.001$
	$\beta_E = 0.424$	MSE=0.003
90	$\alpha_E = 3.56E+09$	$R^2=0.993; \chi^2=0.143$
	$\beta_E = 2.1014$	MSE=0.4571
Rubber		
25	$\alpha_E = 0.094$	$R^2=0.996; \chi^2=0.181$
	$\beta_E = 1.259$	MSE=0.003
100	$\alpha_E = 0.139$	$R^2=0.994; \chi^2=0.257$
	$\beta_E = 0.721$	MSE=0.015
Almond		
200	$\alpha_E = 15793.14$	$R^2=0.950; \chi^2=0.008$
	$\beta_E = 0.231$	MSE=0.001
800	$\alpha_E = 1756.19$	$R^2=0.998; \chi^2=0.0004$
	$\beta_E = 0.054$	MSE=5.79E-05
Boyd's Model		
Conc.	Parameters	Statistical parameters
Ginger		
30	$R = 0.731$	$R^2=0.976; \chi^2=0.307$
	$q_e = 15.637$	MSE=0.79
90	$R = 49.162$	$R^2=0.979; \chi^2=0.017$
	$q_e = 13.169$	MSE=0.503
Rubber		
25	$R = 0.011$	$R^2=0.967; \chi^2=1.145$
	$q_e = 2.98$	MSE=0.036
100	$R = 0.0126$	$R^2=0.986; \chi^2=1.086$
	$q_e = 4.827$	MSE=0.04
Almond		
200	$R = 0.305$	$R^2=0.988; \chi^2=0.002$
	$q_e = 50.057$	MSE=2.93E-04
800	$R = 0.1249$	$R^2=0.125; \chi^2=0.020$
	$q_e = 176.903$	MSE=0.003

This indicated a good correlation of the experimental data and demonstrated that the process could be controlled by physisorption, with the contribution of the chemisorption mechanism.

As observed experimentally, adsorption process occurred fastly suggesting that is controlled by the PFO kinetics, which is governed by the mass transfer in the liquid film with the occurrence of electrostatic interactions between adsorbate and adsorbent [16, 17]. Similar result was obtained with the study of the adsorption of glycerol pigments by activated carbon that was better described by the PFO model despite PSO and Elovich models [18].

For rubber seed shell, the correlation coefficients of the PFO, PSO, PNO and Elovich were higher than 0.95, indicating a good



correlation to experimental data. However, analyzing the statistical parameters, it is possible to infer that the PSO and Elovich models were better than the others, as observed by ginger. Moreover, the correlation with PSO and Elovich models confirms the contribution of chemisorption in adsorption process, and the Elovich model also indicated that the surface of the biochars is heterogeneous in energy [18]. This suggested the multilinearity of the process, once in a real adsorption process the occupation of the active sites by the adsorbate is more complex and may involve both the PFO and the PSO mechanisms [19].

For the almond fruit, the correlation coefficients of the PSO and PNO model were higher than 0.95, showing a good correlation. On the other hand, the PFO model presented the lowest correlation coefficient value indicating a low adjustment of the experimental data for the concentration of 800 ppm, being 0.79. The orders of adsorbent were between 1 and 2, indicating their PNO-derived curves lay between PFO- and PSO-derived curves. Similar behaviors were observed for microporous activated carbons prepared from betel trunk via KOH activation when used to adsorb acid blue 74, 2,4-dichlorophenol, 4-chlorophenol, 4-cresol, and phenol in aqueous solutions [20].

The same behavior shown by the correlation coefficient was also observed when analyzing the statistical validation parameters of the models. It can be seen that they presented the lowest value for the PNO model, followed by the PSO and PFO model.

The Elovich model had a good adjustment of the experimental data for the almond. It is interesting to indicate that the values of a , in this model, correspond to the initial adsorption rate [21]. The high velocity of adsorption can be associated to the high value of this parameter. According to the values presented in Table 2, the initial adsorption rate of MO onto Almond fruit was higher than that observed for Rubber/MO system. Therefore, it seems that the higher SBET ($698.75 \text{ m}^2 \cdot \text{g}^{-1}$) of almond fruit probably provided more vacant sites, compared to rubber ($381.30 \text{ m}^2 \cdot \text{g}^{-1}$), for MO adsorption at the beginning of adsorption process [22, 23].

The body's external model assumed that the diffusion of adsorbate in a bounding liquid film around the adsorbent is the slowest step [24]. For

the almond fruits, rubber seed shell and ginger, the high R^2 values and low statistical parameters for the body's external model, indicated that diffusion of contaminants transferred through the boundary liquid layer surrounding the carbon particles was the main step limiting the rate of adsorption under the selected conditions. A similar behavior was observed for the adsorption kinetics of metronidazole onto microporous activated carbon using Boyd's equation [24].

4. Conclusion

According to the kinetic studies, it was concluded that, depending on the raw material, the process kinetics was influenced by different mechanisms. For ginger adsorbent and rubber seed shell, the model that best fitted the experimental data was Elovich, whereas for almond it was the PNO. For all the adsorbents, the Boyd's external model, indicated that diffusion of contaminants transferred through the boundary liquid layer surrounding the carbon particles was the main step limiting the rate of adsorption.

Acknowledgements

The authors would like to thank FAPERJ and CNPq/PIBIC for their financial support. This work was carried out with the support of the Higher Education Personnel Improvement Coordination - Brazil (CAPES) - Financing Code 001”.

References

- [1] Alves MF, Brito MJ, Borges MJP, Batista MV, de Jesus AS, de Albuquerque FWA. Produção de carvão ativado obtido a partir do endocarpo da Amêndoa-da-Praia (*Terminalia catappa* Linn) para adsorção de corantes orgânicos em meio aquoso. *Cad. Cienc. Agrar.* 2015;7:50-55.
- [2] Kunz A, Peralta-Zamora P, Moraes SGD, Durán N. Novas tendências no tratamento de efluentes têxteis. *Quím Nova* 2002;25:78-82.
- [3] Kausar A, Iqbal M, Javed A, Aftab K, Bhatti HN, Nouren S. Dyes adsorption using clay and modified clay: a review. *J Mol Liq* 2018;256:395-407.
- [4] Febrianto J, Kosasih AN, Sunarso J, Ju YH, Indraswati N, Ismadji S. Equilibrium and kinetic studies in adsorption of heavy metals using biosorbent: a summary of recent studies. *J Hazard Mater* 2019;162:616-64.



- [5] Ahmad R, Kumar R. Adsorption studies of hazardous malachite green onto treated ginger waste. *J Environ Manage* 2010;91:1032–1038.
- [6] Claudino A. Preparação de carvão ativado a partir de turfa e sua utilização na remoção de poluentes. Dissertação (Mestrado em Engenharia Química) - Universidade Federal de Santa Catarina, Florianópolis 2003, 101p.
- [7] Bondioli P, Bella D. An alternative spectrophotometric method for the determination of free glycerol in biodiesel. *Eur J Lipid Sci Technol*. 2005;107:153–157.
- [8] Lagergren SS. About the Theory of so Called Adsorption of Soluble Substances. *Kungl Svenska Vetenskapsakademiens Handlingar* 1898;24:1-39.
- [9] Plazinski W, Rudzinski W, Plazinska A. Theoretical models of sorption kinetics including a surface reaction mechanism: A review. *Adv Colloid Interface Sci* 2009;152: 2–13.
- [10] Ho S, McKay G. The sorption of lead (II) ions on peat. *Water Res* 1999;33:578-584.
- [11] McLintock I. The Elovich equation in chemisorption kinetics. *Nature* 1967; 216:1204-1205.
- [12] Inyang HI, Onwawoma A, Bae S. The Elovich equation as a predictor of lead and cadmium sorption rates on contaminant barrier minerals. *Soil Till Res* 2016;155:124–132.
- [13] Khaled A, Nemr AE, El-Sikaily A, Abdelwahab O. Removal of Direct N Blue-106 from artificial textile dye effluent using activated carbon from orange peel: Adsorption isotherm and kinetic studies. *J Hazard Mater* 2009;165: 100–110.
- [14] Wang J, Guo X. Adsorption kinetic models: Physical meanings, applications, and solving methods: *J Hazard Mater* 2020;390:122156.
- [15] Magdy YH, Altaher H. Kinetic analysis of the adsorption of dyes from high strength wastewater on cement kiln dust, *J Environ Chem Eng* 2018;6:834-841.
- [16] Silva RTS, Dervanoski A, Hauptenthal LD, Souza SMA, Souza AAU, Luz C. Simulação numérica e ensaios experimentais da remoção de Fe (III) da água para utilização nas indústrias alimentícias. *Eng Sanit Ambient* 2015;20:653-663.
- [17] Shooto ND, Naidoo EB, Maubane M. Sorption studies of toxic cations on ginger root adsorbent. *J Ind Eng Chem* 2019;76:133-140.
- [18] Silveira Jr N, Frantz TS, Lukte SF, Arabidiano VC, Cadaval Jr TRS. Treatment of industrial glycerol from biodiesel production by adsorption operation: kinetics and thermodynamics analyses. *Chem Eng Commun* 2019;206:1399-1409.
- [18] Zhang P, Li Y, Cao Y, Han L. Characteristics of tetracycline adsorption by cow manure biochar prepared at different pyrolysis temperatures. *Bioresour Technol* 2019;285-121348.
- [19] Guo X, Wang J. A general kinetic model for adsorption: Theoretical analysis and modeling. *J Mol Liq* 2019;288:e111100.
- [20] Tseng RL, Wu PH, Wu FC, Juang RS. A convenient method to determine kinetic parameters of adsorption processes by nonlinear regression of pseudo nth-order equation. *Chem. Eng. J.* 2014; 237:153–161.
- [21] Heidarinejad Z, Rahmanian O, Fazlzadeh M, Heidari M. Enhancement of methylene blue adsorption onto activated carbon prepared from Date Press Cake by low frequency ultrasound. *J. Mol. Liq.* 2018;264:591–599.
- [22] Megale EZ. Avaliação da casca da semente da seringueira como adsorvente no tratamento de efluentes aquosos: Estudo cinético e termodinâmico. Dissertação (Mestrado em Engenharia) – Departamento de Engenharia Química, UFRRJ. Rio de Janeiro, p. 85. 2019.
- [23] Jurado LVA. Avaliação da biomassa da *Terminalia catappa Linn* (amendoeira) como adsorvente: estudo cinético e termodinâmico. Dissertação (Mestrado em Engenharia) – Departamento de Engenharia Química, UFRRJ. Rio de Janeiro, p. 104. 2020.
- [24] Sartape SA, Mandhare AM, Jadhav VV, Raut PD, Anuse MA, Kolekar SS. Removal of malachite green dye from aqueous solution with adsorption technique using *Limonia acidissima* (wood apple) shell as low cost adsorbent. *Arab J Chem* 2017;10:S3229-S3238.
- [25] Ahmed MJ, Theydan SK. Microwave assisted preparation of microporous activated carbon from sins seed pods for adsorption of metronidazole antibiotic. *Chem Eng J* 2013;214:310–318.

Synthesis of molecularly imprinted polymer for recovery of 5-hydroxymethyl-2-furfuraldehyde in hemicellulosic hydrolysate

N.R.M. Tanure^{a*}, B.E.L. Baeta^a, L.C. Soares^a, L.V.A. Gurgel^a

^aGrupo de Físico-Química Orgânica, Instituto de Ciências Exatas e Biológicas, Campus Universitário Morro do Cruzeiro, s/nº, Universidade Federal de Ouro Preto, Ouro Preto 35400-000, MG, Brazil.

*Corresponding author. Tel.: +55 37 99122-0888; E-mail address: natalia@ufop.edu.br (N. R. M., Tanure)

Abstract

5-hydroxymethyl-2-furfuraldehyde (HMF) is a toxic compound for microorganisms produced in the pretreatment step of lignocellulosic biomass for production of bioenergy. In counterpoint to its negative bias, HMF is a high added-value compound, and one of the renewable building blocks with greatest potential and versatility. In order to selectively recover the HMF, an alternative is the use of molecularly imprinted polymer (MIP) due to their intrinsic features such as high selectivity, affinity for the molecule of interest, great stability, durability, and reuse. In this study, a novel type of organic-inorganic hybrid molecularly imprinted polymer (MIP) based on silica and the corresponding non imprinted polymer (NIP) were synthesized. It was used HMF as template, itaconic acid (IA), and 4-vinylpyridine (4VP) as organic monomers and tetraethoxysilane (TEOS) as inorganic monomer. The polymers were crushed, ground, and sieved to obtain regularly sized particles of 250, 150 and 106 μm . Adsorption experiments were carried out to determine the performance of the adsorbents. The MIP1 synthesized with IA presented the best results, with respectively bonding percentage (B) of 15%, 22%, and 19% and adsorption capacity (q_e) of 34, 50, and 43 mg g^{-1} , and imprinting factor (IF) of 0.9, 2.5, and 2.9, the MIP2 synthesized with 4-VP showed respectively the results of 13%, 17%, and 16% and 30, 39, and 37 mg g^{-1} , and IF of 0.7, 1.5, and 0.7.

Keywords: 5-Hydroxymethyl-2-furfuraldehyde; pretreatment; inhibitor; MIP; lignocellulosic biomass

1. Introduction

There is a worldwide trend of reducing consumption of products derived from fossil resources, due to their finitude, high cost, and cause several environmental impacts.

Biorefineries offer the possibility to develop the same products made from petroleum, using renewable raw materials, replacing oil for biomass, which have the advantage of being inexpensive, abundant, and sustainable. [1]

In order to convert lignocellulosic biomass into bioenergy, a pretreatment step is required, whose process, instead of only making sugars available, produces secondary by-products, such as 5-hydroxymethyl-2-furfuraldehyde (HMF), which has a potential inhibitory action on microbial metabolism interfering in the efficiency and

productivity of ethanol and biogas, for example. [2,3]

HMF is one of the renewable building blocks with the greatest potential and versatility. It is a good starting material for the synthesis of precursors of various compounds such as polymers, solvents, and biofuels, providing the basis for various industries. [4,5,6]

In order to selectively recover the HMF, a high-added-value compound, and at the same time to improve the efficiency of the bioenergy production process, an alternative is the use of molecularly imprinted polymer (MIP) due to their intrinsic features such as high selectivity, affinity for the molecule of interest, great stability, durability, and reuse. [7]

Based on the reasons outlined above, this research aims to develop a novel type of organic-inorganic hybrid molecularly imprinted polymer

based on silica for adsorption and recovery of HMF generated during the pretreatment process of lignocellulosic biomass for the production of various fermentation products such as biogas, bioethanol, xylitol, organic acids, liquid fuels, among others.

2. Experimental

2.1. Synthesis of Molecularly Imprinted Polymers (MIPs)

The synthesis of the hybrid molecularly imprinted polymers (MIPs) was based on the literature data [8-9], with adaptation.

In order to analyze the best conditions for the production of a specific MIP for HMF, two different MIPs and NIPs were synthesized varying the organic monomer. For this purpose, it was employed one organic monomer with acidic characteristics, itaconic acid (IA), and other with basic characteristics, 4-vinylpyridine (4-VP).

In summary, 0.5 mmol of HMF as template and 2.0 mmol of IA (MIP1) or 4-VP (MIP2) as functional monomer, were dissolved in the solvent into a round-bottomed flask and the mixture was stirred at room temperature. For MIP 1, was employed a mixture of dimethyl sulfoxide (DMSO):acetonitrile (ACN) (1:4, v v⁻¹, 2.0 mL) and, for MIP 2, the porogenic solvent ACN. After 30 min, the following reagents were added under continuous flow of nitrogen gas for 5 min: 0.75 mmol of trimethylolpropane trimethacrylate (TRIM) as the cross-link agent, 1 mmol of 3-propyl trimethoxysilane methacrylate (KH 570) as a coupling agent, 761 µL of 2,20-azoisobutyronitrile (AIBN) (in toluene) as the radical initiator and 0.5 mmol of tetraethoxysilane (TEOS) (in ethanol) as the inorganic monomer and, lastly, 0.19 mL of 1 mol L⁻¹ HCl. The flask was sealed and the polymerization was carried out at 60.0 °C, for 24 h in glycerin bath, under stirring. The obtained material was removed from the flask, dried at 60.0 °C for 24 h, crushed in an agate mortar, ground and sieved to obtain regularly sized particles of 250, 150 and 106 µm. For both syntheses, to ensure the complete removal of the excess of reagents and template, the materials were firstly washed with acetic acid 10% (v v⁻¹) and distilled water. After, the polymers were Soxhlet extracted with a ternary mixture of acetone: ethanol: petroleum ether (4:4:1) for 48 h and, finally, they were dried at 60.0 °C for 24 h. The non-imprinted (NIP) or control polymer

was prepared using the same synthesis conditions but in the absence of template.

2.2 Quantitative Analysis

HMF concentration was measured by high-performance liquid chromatograph (HPLC) (model 20A Shimadzu®) adjusted with a diode array detector (DAD) SPD-20A set at 283 nm and an ion exchange column Fermentation 150 × 7.8 mm (Bio-Rad®) kept at 65 °C. The mobile phase (5.0 mmol L⁻¹ H₂SO₄) was pumped through the column at an isocratic flow of 0.8 mL min⁻¹, and the injection volume was 10 µL.

2.3. Performance study

The adsorption experiments provide the basic information to determine the performance of the polymers for HMF removal, obtaining the recognition capacity of the synthesized adsorbents. 10.0 mg of polymers (MIP or NIP) and 2.50 mL of 1000 mg L⁻¹ HMF solution at pH 4.0 (acetic acid/sodium acetate buffer) were added in a cylindrical amber glass flask and stirred in a shaker at 170 rpm for 24 h, at 25 °C. This pH was selected because it is the pH value observed in hemicellulosic hydrolysate, the environment in which the material will be used. After 24 h, the samples were filtered through 0.22 µm cellulose acetate to remove adsorbent particles, and analyzed by HPLC. The experiments were carried out in triplicate.

MIP efficiency was evaluated by the adsorption capacity (q_e), bonding percentage (B), distribution coefficient (K_d), and imprinting factor (IF), according to Eqs. Eq (1), (2), (3), and (4), respectively:

$$q_e / (\text{mg g}^{-1}) = (C_i - C_e) \times \frac{V}{w} \quad (1)$$

$$B / (\%) = \frac{C_i - C_e}{C_i} \times 100 \quad (2)$$

$$K_d / (\text{L g}^{-1}) = \frac{q_e}{C_e} \quad (3)$$

$$IF = \frac{K_d \text{ MIP}}{K_d \text{ NIP}} \quad (4)$$

where C_i and C_e are the initial and the equilibrium concentrations of HMF, respectively, V is the solution volume, and w is the polymer mass.

3. Results and discussion

3.1 Synthesis of Molecularly Imprinted Polymers

Considering the complex nature of hemicellulosic hydrolysate, the hybrid synthesis based on silica was chosen for the several advantages that these polymers present, such as better texture and morphological properties, low swelling effect in organic solvents, and better chemical stability over a wide pH range.

Several attempts have been made before achieving the protocol described in the Section 2.1. The synthesized MIPs and NIPs presented good physical characteristics, with an adequate morphology.

The Fig. 1 and Fig. 2 illustrate the molecular interactions in the prepolymerization process between the template and the functional monomer, itaconic acid (MIP 1) and 4 vinylpyridine (MIP 2), respectively.

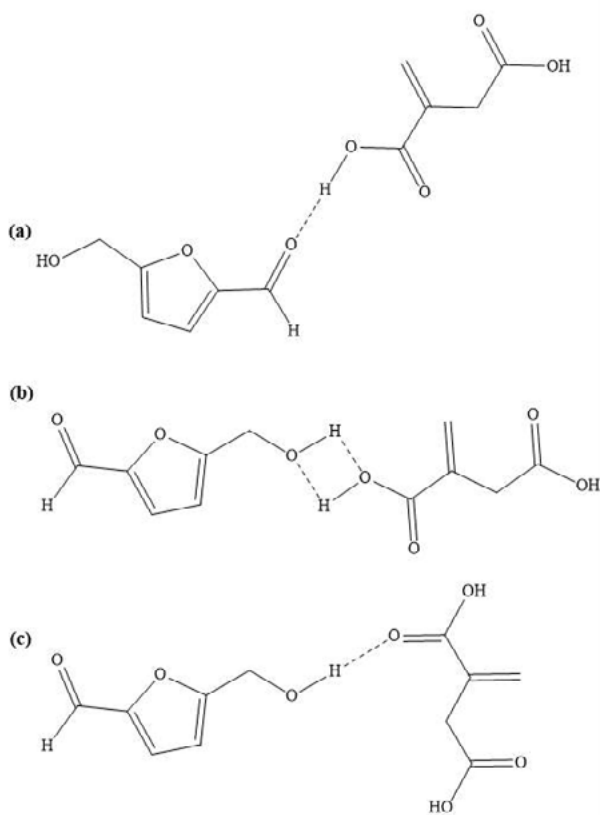


Fig. 1. Molecular interactions between HMF and IA.

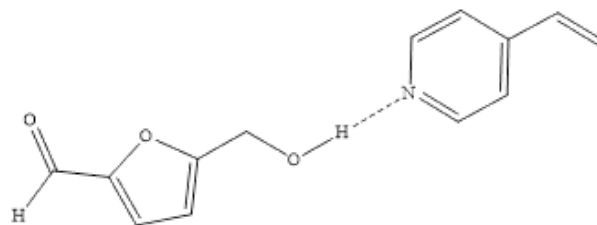


Fig. 2. Molecular interaction between HMF and 4-VP.

3.2. Performance study

Results from the adsorption experiments of MIP 1, NIP 1, MIP 2, and NIP 2 synthesized with the functional monomer IA and 4-VP respectively, classified into three different particle sizes, are shown in Table 1 and Table 2.

Table 1. Performance parameters of MIP 1 and NIP 1

Polymer	<i>B</i> (%)	* <i>q_e</i> (mg g ⁻¹)	<i>K_d</i> (L g ⁻¹)	<i>IF</i>
NIP 1-250	16	37	0.05	0.9
MIP 1-250	15	34	0.04	
NIP 1-150	10	24	0.03	2.5
MIP 1-150	22	50	0.07	
NIP 1-106	7	17	0.02	2.9
MIP 1-106	19	43	0.06	

Table 2. Performance parameters of MIP 2 and NIP 2

Polymer	<i>B</i> (%)	* <i>q_e</i> (mg g ⁻¹)	<i>K_d</i> (L g ⁻¹)	<i>IF</i>
NIP 2-250	18	41	0.05	0.7
MIP 2-250	13	30	0.037	
NIP 2-150	13	29	0.036	1.5
MIP 2-150	17	39	0.05	
NIP 2-106	21	48	0.07	0.7
MIP 2-106	16	37	0.048	

*The Grubbs test was used to verify the consistency of the experimental data of adsorption capacity at equilibrium, *q_e*, which is a statistical test used to decide which value to discard from a data set [10]



It was possible to verify that the polymers presented great results, with adsorption capacity values up to 50 mg g^{-1} and imprinting factor (IF) of 2.9. It is known that materials with IF values greater than 1.5 are considered adsorbents with high selectivity for the target molecule. The higher the IF values, the better the molecular impression and, consequently, the better the specificity of the selective adsorbent. Comparing the particle size of each material, the MIP 1 of $106 \mu\text{m}$ is the one with the highest specificity with IF equal to 2.9.

Although MIP 2 does not present the appropriate IF value to be considered selective, this adsorbent showed moderate results in terms of adsorption capacity, with values close to 40 mg g^{-1} . The low IF value is due to MIP 2 having a greater adsorption capacity of HMF than its respective MIP, with values close to 50 mg g^{-1} as in the case of size $106 \mu\text{m}$, showing the lack of selectivity of this polymer.

The values of B and q_e indicate that the MIP $150 \mu\text{m}$ is the one that presented the best adsorption capacity. An interesting fact is that the polymers 1 and 2, synthesized without the presence of the template with a particle size of $250 \mu\text{m}$, presented greater adsorption capacity when compared to the respective MIP, which may indicate that the adsorption did not occur due to the formation of selective adsorption sites in these cases.

The influence of functional monomers used in the polymers synthesis is of great importance, when comparing MIP 1 with MIP 2, whose main difference is the functional monomer used. It is clear that the polymer synthesized with itaconic acid performed better than the one synthesized with 4-vinylpyridine, showing greater specificity ($IF = 2.9$). Thus, it may be concluded that the specific adsorption sites for HMF have been formed with greater efficiency in these polymers. This result is interesting, considering that, usually, proton acceptor monomers such as 4-VP interact more easily with acid templates, which did not happen, probably because HMF does not have a hydrogen with high acidity constant. Nonetheless, when analyzing the possible interactions between HMF and IA, the hydrogen bond with the oxygen atom is stronger than with the nitrogen atom in the case of 4-VP. Furthermore, if ionized, the itaconic acid can interact by ion-dipole with the HMF, this interaction is stronger than the hydrogen bond. Comparing all the adsorbents, it is possible to conclude that the MIP $150 \mu\text{m}$ synthesized with itaconic acid and DMSO/ACN (1:4) is the one with the best adsorption capacity (50 mg g^{-1}) and the greater

bonding percentage (22%). The MIP 1-106 is the one that presented the greater specificity with the compound of interest, with $IF = 2.9$.

4. Conclusions

The synthesis of a hybrid molecularly imprinted polymer based on silica for adsorption and recovery of HMF was accomplished after optimizing the parameters: solvent proportion, amount of coupling agent and cross-link agent.

The MIP 1 synthesized with IA presented the best results, with respectively bonding percentage (B) of 15%, 22%, 19%, adsorption capacity (q_e) of 34 mg g^{-1} , 50 mg g^{-1} , and 43.1 mg g^{-1} , and imprinting factor (IF) of 0.9, 2.5, and 2.9. The MIP 2 synthesized with 4-VP showed respectively the results of 13%, 17%, and 16%, and 30 mg g^{-1} , 39 mg g^{-1} , and 37 mg g^{-1} , and IF of 0.7, 1.5, and 0.7. As stated above, MIP 1-150 and MIP1-106 presented $IF > 1.5$, showing that the adsorbents have high selectivity for the target molecule, HMF.

The polymers presented promising results, with adequate morphology and moderate performance in terms of adsorption.

Acknowledgements

The authors would like to thank the Universidade Federal de Ouro Preto for the financial support.

References

- [1] YANASE, H. et al. Ethanol production from wood hydrolysate using genetically engineered *Zymomonas mobilis*. **Applied Microbiology and Biotechnology**, v. 94, n. 6, p. 1667–1678, 2012.
- [2] ALMEIDA, J. R. M. et al. Screening of *Saccharomyces cerevisiae* strains with respect to anaerobic growth in non-detoxified lignocellulose hydrolysate. **Bioresource Technology**, v. 100, n. 14, p. 3674–3677, 2009.
- [3] HEREDIA-OLEA, E.; PÉREZ-CARRILLO, E.; SERNA-SALDÍVAR, S. O. Effects of different acid hydrolyses on the conversion of sweet sorghum bagasse into C5 and C6 sugars and yeast inhibitors using response surface methodology. **Bioresource Technology**, v. 119, p. 216–223, 2012
- [4] LEWKOWSKI, J., Synthesis, Chemistry and Applications of 5-Hydroxymethyl-furfural and Its Derivatives. *Arkivoc*, v. 1, p. 17-54, 2001
- [5] ROMÁN-LESHKOV, Y. et al. Production of dimethylfuran for liquid fuels from biomass-derived

- carbohydrates. **Nature**, v. 447, n. 7147, p. 982–985, 2007.
- [6] VAN PUTTEN, R. et al. Hydroxymethylfurfural, A Versatile Platform Chemical Made from Renewable Resources. **Chemical Reviews**, v. 113, p. 1499–1597, 2013.
- [7] VASAPOLLO, G. et al. Molecularly imprinted polymers: Present and future prospective. **International Journal of Molecular Sciences**, v. 12, n. 9, p. 5908–5945, 2011
- [8] DE OLIVEIRA, F. M.; SEGATELLI, M. G.; TARLEY, C. R. T. Hybrid molecularly imprinted poly(methacrylic acid-TRIM)-silica chemically modified with (3-glycidyloxypropyl)trimethoxysilane for the extraction of folic acid in aqueous medium. **Materials Science and Engineering C**, v. 59, p. 643–651, 2016.
- [9] CLAUSEN, D. N.; VISENTAINER, J. V.; TARLEY, C. R. T. Development of molecularly imprinted poly(methacrylic acid)/silica for clean-up and selective extraction of cholesterol in milk prior to analysis by HPLC-UV. **Analyst**, v. 139, n. 19, p. 5021–5027, 2014.
- [10] GRUBBS, F. E. Procedures for Detecting Outlying Observations in Samples. **Technometrics**, v. 11, n. 1, p. 1–21, 1969

Adsorption of Ethidium Bromide from Aqueous and Whey Solutions by Activated Carbon and Natural Pumice Stone

Paola Giambiaggi^a, Silvia Bentancur^a, Andres Cuña^b, Mirian Casco^a

^a Departamento de Ingeniería, Universidad Católica del Uruguay, Av. 8 de Octubre 2738, CP 11600 Montevideo, Uruguay

^b Área Físicoquímica, DETEMA, Facultad de Química, Universidad de la República, Av. General Flores 2124, CP 11800 Montevideo, Uruguay

Abstract

The removal of ethidium bromide (EtBr) from aqueous and whey solutions, in both batch and continuous systems, by activated carbon (AC) and natural pumice stone (PS) was investigated. The purpose of this study is to develop an efficient treatment for the effluent generated after the somatic cell count (SCC) in agroindustry dairy laboratories in Uruguay, which is raw milk contaminated with EtBr. Batch experiments were carried out to determine the maximum adsorption capacity and the most adequate adsorbent for this application. The AC maximum capacity is superior to the PS, being 35.78 and 3.71 mg g⁻¹ respectively. The equilibrium data of both adsorbents fits better the Freundlich isotherm model, indicating that both have a heterogenous surface. The adsorption rate was well described by the pseudo-second-order kinetics model for both adsorbents. Since the AC shown a superiority in the adsorption capacity, the adsorption experiments in whey solution were performed using AC. Both batch and continuous adsorption experiments, present satisfactory results, the removal capacity is 18mL g⁻¹ and 15mL g⁻¹, respectively.

Keywords: Adsorption; ethidium bromide; whey; activated carbon; pumice stone.

1. Introduction

Ethidium bromide (EtBr) is a dark red, crystalline and fluorescent dye used as a cell marker in different techniques. In particular, agroindustry dairy laboratories in Uruguay use it in flow cytometry to perform the somatic cell count (SCC) in raw milk [1]. The SCC is a quality milk indicator and, as indicated in Uruguayan legislation, it is mandatory to perform this analysis prior to milk industrialization [2]. After the SCC is done the milk samples containing EtBr have no more use and need to be discarded.

Scientific evidence supports that EtBr is a highly mutagenic and toxic compound [3]. As it is an acid nucleic intercalating agent, it causes frameshift mutations [3, 4]. Therefore, proper treatment before its disposal is required.

There have been studied several methods to remove EtBr from aqueous solutions. Some of them are chemical degradation [5], electrochemical degradation [6] and photocatalytic degradation [7].

Adsorption operations have demonstrated to be efficient in the removal of pollutants from water and wastewater [8]. There are several studies which

support that adsorption can be an efficient method to remove EtBr from aqueous solution. A wide range of materials have been tested for this purpose, such as single walled carbon nanotubes [9], CuO nanoparticles [10], pumice stone [11] and polymeric resins [12, 13].

Although it has been proved the EtBr removal efficiency in aqueous solution by different materials, no scientific studies were found on the removal of this pollutant present in any solution other than water.

Given this and in view of the environmental problem that agroindustry dairy laboratories in Uruguay face with the effluent generated after the SCC, the aim of this study is to investigate the technical feasibility of removing EtBr from whey solutions obtained from the raw milk after the SCC is done.

For this purpose, it has been studied two adsorbent solids: a commercial activated carbon and natural pumice stone, to evaluate which is more adequate for this specific application. Firstly, it was studied the adsorption of EtBr in aqueous solution because is a simpler system than in whey solution due to the presence of other components such as lactose, calcium, phosphorus, and others [14]. Then, with the solid which have superior



capacities, it has been evaluated its performance in whey solution for both batch and continuous systems to determinate which one is the most adequate for a future industrial application.

2. Materials and methods

2.1 Reagents

The EtBr was purchased to Bentley Instruments under the commercial name of SomaGlo and used as received. The molecular weight of EtBr is 394.294 g mol⁻¹ and has a maximum adsorption wavelength in the visible spectrum at 480 nm.

2.2 Adsorbent solids

The AC was acquired locally to the company FILSA. It was washed with distilled water several times to take away the dust. Later, it was sieved between 18 and 10 mesh. Previously to its use, it was dried in the oven at 105°C for at least 24h.

The natural pumice stone was purchased in a local pharmacy. It was crushed and sieved between 18 and 35 mesh. It was kept in HCl 1 M for 24h to remove any acid impurities [11, 15]. After that, it was washed several times with distilled water until a neutral pH was reached. Then it was dried in the oven at 105°C for at least 24h.

The AC and PS surface morphology was characterised by Scanning Electron Microscopy (Joel, JSM-5900LV). The specific surface of the solids was determined using the Brunauer, Emmet and Teller (BET) method (Beckman, Coulter SA3100).

2.3 Whey

The whey was obtained from raw milk which was collected in a milking parlour located in Colonia, Uruguay. The samples collected were added 1.25 mL L⁻¹ of the preservative Lactopol. The steps taken to obtain the whey were: centrifugate to separate the milk fat, manually add HCl 1M until the skimmed milk pH lowers to 4.5 when the casein precipitates [16], finally centrifugate to separate the phases and obtain the whey.

2.4 Adsorption experiments

Batch experiments in aqueous solution were conducted in 100 mL Erlenmeyer flasks containing 25 mL of different EtBr concentration (30 -160 mg

L⁻¹) for both adsorbents. For the kinetics studies, it was used a beaker containing 500 mL of stock solution of initial concentration 30 mg L⁻¹. The flasks were kept in an orbital shaker at 100 rpm. After reaching the equilibrium time, the EtBr concentration was determined at 480 nm using an UV-Vis spectrophotometer (Merk, Spectroquant Prove 300). It was considered that the system reaches the equilibrium when the EtBr concentration of two consecutives samples varied less than 10%.

Batch experiments in whey solution were conducted in a beaker containing 250 mL of contaminated whey obtain from the real effluent (raw milk contaminated with EtBr) with different AC doses (4, 8, 28 and 60 g L⁻¹). As the whey have many components apart from the EtBr, the initial and final absorbance it is measured using water as a blank. All measures were performed at room temperature.

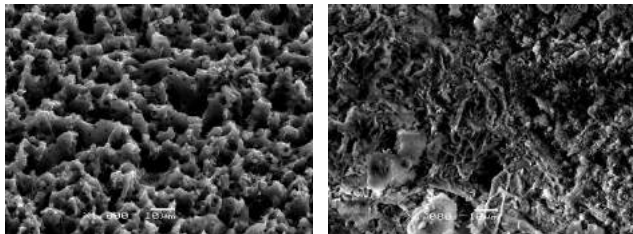
Column experiments were using a storage beaker containing EtBr in aqueous or whey solution which fed a 1 cm diameter glass column packed with AC using a peristaltic pump. For aqueous solutions, the process parameters were as follows: column height 1.3 cm, volumetric flow 2 mL min⁻¹, initial concentration 10 and 35 mg L⁻¹, AC mass 0.8994 g and 0.8915g respectively to each initial concentration. For whey solutions, the process parameters are the following: initial absorbance 0.727, height 2.5 cm, volumetric flow 2 mL min⁻¹, AC mass 2.0217g.

It is considered that the column is saturated when the outlet concentration corresponds to a 10% of the initial concentration. In regular intervals of time a sample was taken at the end of the column and it was determined the concentration or final absorbance, for aqueous or whey solution respectively, using the UV-Vis spectrophotometer

3. Results and discussion

3.1 Adsorbent characteristics

The AC and PS external surface morphology obtain by SEM are shown in Fig. 1. As it can be observed, AC shows a more uniform morphology, while that the pumice stone presents certain heterogeneities on the surface (grains and needles). The surface area determined by BET method is 1148 and 19 m² g⁻¹ for AC and PS, respectively.



(a) (b)

Fig. 1. SEM images of (a) activated carbon and (b) pumice natural stone.

3.2 Adsorption isotherms for EtBr in aqueous solution

It is important to understand the adsorption equilibrium characteristics that occurs between the adsorbent medium and the adsorbate, which is characterized by the adsorption isotherms.

For this purpose, adsorption equilibrium experimental data was adjusted to the Langmuir and Freundlich isotherm models. The constants values (K for Langmuir, K_f and n for Freundlich), maximum adsorption capacity (q_m) and the determination coefficient (R^2) for Langmuir and Freundlich are shown in Table 1.

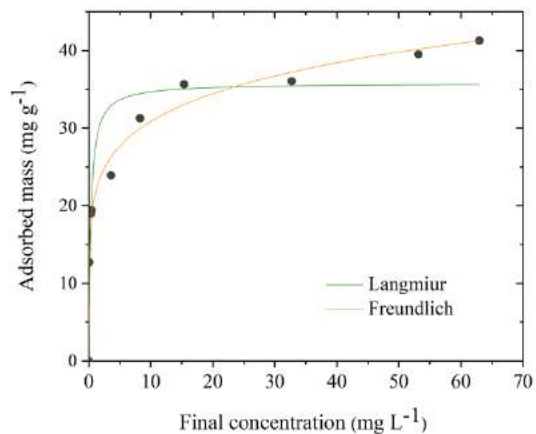
The Freundlich isotherm fits better the experimental equilibrium data than Langmuir, since the determination coefficient R^2 was higher for both adsorbents. The Freundlich isotherm model assumes that the adsorbent surface is energetically heterogeneous [17]. This means that the active sites are different along the surface. Most AC present a heterogenous surface with different acid and basic porous [18]. On the other hand, as other studies reported for PS and EtBr in aqueous solution adsorption experiments, the experimental data also fitted Freundlich [11]. The maximum adsorption capacity for AC and PS is 35.78 and 3.71 mg g^{-1} respectively, indicating that AC had a greater capacity to adsorb EtBr than the PS for the studied conditions.

3.3 Adsorption kinetics studies for EtBr in aqueous solution

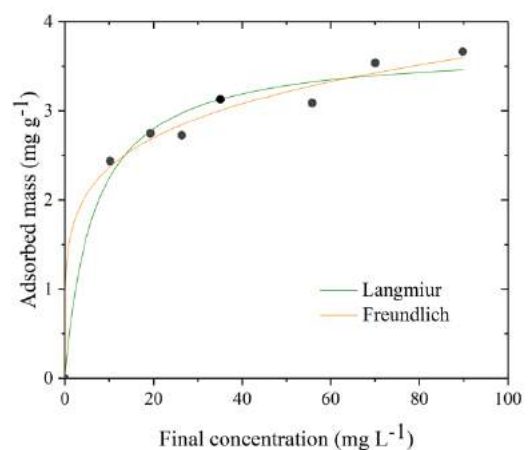
The adsorption kinetics describes the rate at which the adsorbate is adsorbed on the adsorbent material surface. This rate determines the time in which the adsorption equilibrium is reached [19-21]. The pseudo-first order equation and pseudo-second order equation were used to adjust the experimental

Table 1. Langmuir and Freundlich constants and the determination coefficient for AC and PS.

Langmuir			
Adsorbent	q_m (mg g^{-1})	K (L mg^{-1})	R^2
AC	35.78	3.16	0.87
PS	3.71	0.15	0.97
Freundlich			
Adsorbent	n	K_f (mg g^{-1})	R^2
AC	6.33	21.45	0.99
PS	5.25	1.52	0.99



(a)



(b)

Fig. 2. Adjustment to Langmuir and Freundlich. (a) Isotherm for AC. Process parameters: initial concentration 30 - 160 mg L^{-1} , contact time 5 days, pH 7, adsorbent dose 2.4 mg L^{-1} ; (b) Isotherm for PS. Process parameters: initial concentration 30 - 130 mg L^{-1} , contact time 5 days, pH 12 y adsorbent dose 8 g L^{-1} .

Table 2. Constants and equilibrium masses for the pseudo first and second order model for both adsorbents.

Adsorbent	C_0 (mg L ⁻¹)	Pseudo first order				Pseudo second order			
		$q_{e,exp}$ (mg g ⁻¹)	$q_{e,cal}$ (mg g ⁻¹)	k_1	R^2	$q_{e,cal}$ (mg g ⁻¹)	K^2	R^2	
AC	30	16.96	10.84	5.14	0.97	13.22	1.24	0.98	
PS	30	2.21	1.76	0.89	0.88	2.08	0.01	0.94	

data in this study. The constant values (K_1 and K_2 , for pseudo first order and pseudo second order respectively), experimental and the calculated mass adsorbed ($q_{e,exp}$ and $q_{e,cal}$, respectively) and the determination coefficient (R^2) obtained are shown in Table 2.

For both solids, the experimental data fits better the pseudo second model order. These results are in accordance with the results reported in other studies which also showed that the pseudo-second order model described adequately the kinetics of EtBr in pumice stone and other adsorbents [10, 11, 22].

In addition, the equilibrium is reached after six and seven days for AC and PS respectively, indicating the slow adsorption kinetics presented by the EtBr molecule in both adsorbent solids.

3.4 Column studies for EtBr in aqueous solution

The fix-bed column treatment is preferred for industrial application rather than batch treatment [23]. The performance of the fixed-bed column is studied by the breakthrough curves. These curves show the evolution of the ratio output-input concentration over time [24]. The breakthrough curve obtained is shown in figure 3.

The system with the highest initial concentration reached the breakthrough point after 20 minutes while the lowest initial concentration at 29 minutes. By increasing the initial concentration and keeping the other parameters constant, it is reduced the volume that can be treated before the column is saturated. A higher EtBr initial concentration saturates the column faster decreasing the breakthrough time [25].

Adsorption, in continuous systems, occurs due to the pollutant concentration difference in the adsorbent and in the solution. If the concentration gradient is low, it causes a slow transport and therefore it takes a longer time to saturate the AC. As a consequence, by increasing the initial concentration, the adsorption rate is modified, and adsorption capacity is increased [26].

Due to the slow kinetics between EtBr and the AC, the column does not get completely saturated although it was leave in contact with the solution for 31 hours.

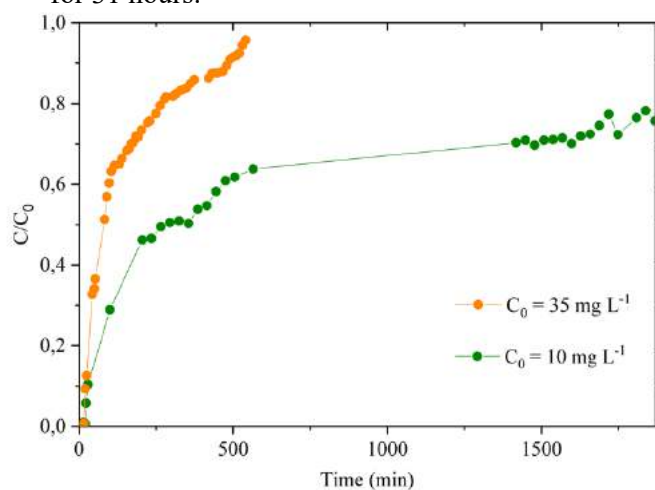


Fig. 3. Breakthrough curve for EtBr in aqueous solution. Higher concentration curve: Initial concentration 35 mg L⁻¹, height 1.3 cm, flow 2 mL min⁻¹, AC mass 0.8995 g. Lower concentration curve: initial concentration 10 mg L⁻¹, height 1.3 cm, flow 2 mL min⁻¹, AC mass 0.8915 g.

3.5 Batch adsorption experiments for EtBr in whey solution

As can be observed in figure 4, for lower adsorbent mass, the carbon is saturated before it can finish adsorbing all the components in the whey. For the case of 4 g L⁻¹, the AC is saturated when the initial and the final absorbance have a difference of 10% only.

As the AC mass is increased, there is more porous volume where the EtBr molecules can be adsorbed. In this way, for 8 g L⁻¹ the AC is saturated at 40%. Furthermore, for a mass 28 and 60 g L⁻¹, after 25 hours of contact time, the AC adsorbed nearly to a 55%. The final absorbance it was measured after 75 hours but the whey was already discomposed so the measure was discarded. There was no significant difference between the adsorption capacity for 28 and 60 g L⁻¹

¹, indicating that the 28 g L⁻¹ is the most efficient option. Therefore, it can be said that 7 g of AC it is possible to treat 125 mL of contaminated whey after 25 hours of contact time. In conclusion, in batch system, the AC can treat 18 mL of contaminated whey per AC gram.

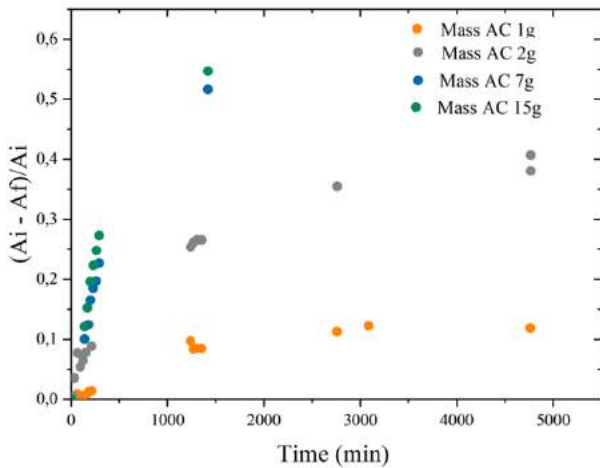


Fig. 4. Comparison of the whey adsorption kinetics in activated carbon for different adsorbent masses.

3.6 Column studies for EtBr in whey solution

The breakthrough curve for EtBr in whey solution differs from the one in aqueous solution. The reason for this is that the whey has other components apart from EtBr (e.g. Lactopol preservative). At the outlet of the column, the whey is transparent, this means that all the components that colors the whey are co-adsorbed in the AC. The breakthrough time is between 15 and 20 minutes. Although this system, is a multi-component one, for the data analysis it is treated as a single component system. The breakthrough curve can be seen in the Figure 5. The indicator bed volumen (BV) [24] shows that the column can be feed with contaminated whey 3.82 times its own volume. In other words, the column can treat 15mL of contaminated whey per AC gram.

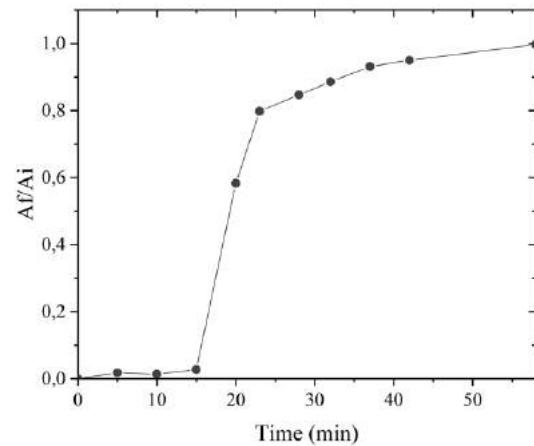


Fig. 5. Breakthrough curve for EtBr and whey Parameters: initial absorbance, 0.727, height 5 cm, flow 2 mL min⁻¹, AC mass 2.0217g.

Table 3. Column parameters determinate by the breakthrough curve considering the breakthrough when Af/Ai=0.1.

Parameter	Value
Column density (g mL ⁻¹)	0.26
Adsorbent mass (g)	2.02
Column volume (mL)	7.85
Height (cm)	2.50
Radio (cm)	1.00
Surface (cm ²)	3.14
Column porosity	0.66
Adsorbent volume (mL)	2.67
Particle density (g mL ⁻¹)	0.76
Lineal velocity (cm min ⁻¹)	0.64
Flow (mL min ⁻¹)	2.00
Effective flow velocity (cm mL ⁻¹)	0.96
Empty bed contact time, EBCT (min)	3.93
Effective residence time (min)	2.59
t (min)	15
Bed volumes, BV	3.82
Specific throughput, Vsp (mL g ⁻¹)	14.87

4. Conclusion

As a conclusion, the EtBr removal efficiency from aqueous solution by pumice stone depends strongly on the solution pH while for activated carbon it is independent. Based on the isotherm analysis, the experimental data of both adsorbents can be explained by the Freundlich isotherm. The adsorption kinetics fitted the pseudo-second order kinetics model for both adsorbents. The maximum adsorption capacity is 35.78 and 3.71 mg g⁻¹ for AC and PS, respectively. The AC has a superior

capacity than PS, being this adsorbent better for this specific application.

In regard to the EtBr removal from whey solution, it has been proven that is technically viable having satisfactory results. In batch experiments, the efficiency removal of the AC is of 18mL g^{-1} while in column its 15mL g^{-1} . Although, the efficiency its slightly better in batch, it is recommended the column application since the whey can be treated in less time avoiding the decomposition of it.

Acknowledgements

PG acknowledges the Centro de Innovación en Ingeniería for the financial support (FFI UCU2). MEC acknowledges the Alexander von Humboldt foundation and Agencia Nacional de Investigación e Innovación (PD_NAC_2018_1_150145) for financial support.

References

- [1] J. Fariña Gonzalez, "Técnicas de Citometría." [Online]. Available: <http://www.conganat.org/icongreso/conferencias/020/tecnicas.htm>. [Accessed: 01-Mar-2018].
- [2] "Decreto N° 90/995 Aprobación del Sistema Nacional de Calidad de Leche," 1995. [Online]. Available: <https://www.impo.com.uy/bases/decretos/90-1995>. [Accessed: 30-Oct-2019].
- [3] Technical Resources International Inc., "Summary of Data for Chemical Selection."
- [4] J. T. Macgregor and I. J. Johnson, "In Vitro Metabolic Activation of Ethidium Bromide and Other Phenanthridinium Compounds: Mutagenic Activity in Salmonella Typhimurium," 1977.
- [5] E. B. Sansone and G. Lunn, "Ethidium Bromide: Destruction and Decontamination of Solutions," vol. 458, pp. 453–458, 1987.
- [6] C. Zhang, L. Liu, J. Wang, F. Rong, and D. Fu, "Electrochemical degradation of ethidium bromide using boron-doped diamond electrode," *Sep. Purif. Technol.*, vol. 107, pp. 91–101, 2013.
- [7] C. Adán, A. Martínez-Arias, M. Fernández-García, and A. Bahamonde, "Photocatalytic degradation of ethidium bromide over titania in aqueous solutions," *Appl. Catal. B Environ.*, vol. 76, no. 3–4, pp. 395–402, 2007.
- [8] V. Gupta, "Application of low-cost adsorbents for dye removal - A review," *J. Environ. Manage.*, vol. 90, pp. 2313–2342, 2009.
- [9] F. Najafi, M. Norouzi, K. Zare, and A. Fakhri, "Removal of ethidium bromide by carbon nanotube in aqueous solution: isotherms, equilibrium mechanism studies, and its comparison with nanoscale of zero valent iron as adsorbent."
- [10] A. Fakhri, "Assessment of Ethidium bromide and Ethidium monoazide bromide removal from aqueous matrices by adsorption on cupric oxide nanoparticles," *Ecotoxicol. Environ. Saf.*, 2014.
- [11] B. Heibati et al., "Adsorption of ethidium bromide (EtBr) from aqueous solutions by natural pumice and aluminium-coated pumice," *J. Mol. Liq.*, vol. 213, pp. 41–47, 2016.
- [12] G. Lunn and E. B. Sansone, "Ethidium bromide: Destruction and decontamination of solutions," *Anal. Biochem.*, 1987.
- [13] M. W. De Oliveira, A. W. S. Hilsdorf, A. F. De Souza Silva, and A. F. Oliveira, "Estudo da adsorção de brometo de etídeo em resina XAD-7," *Quim. Nova*, 2009.
- [14] H. Reyes, J. M. Médico, and V. Zootecnista, "Importancia del conteo de células somáticas en la calidad de la leche (Importance of the somatic cells count in the quality of milk)," *Agosto*, vol. IX, no. 9, 2008.
- [15] M. N. Sepehr, A. Amrane, K. A. Karimaian, M. Zarrabi, and H. R. Ghaffari, "Potential of waste pumice and surface modified pumice for hexavalent chromium removal: Characterization, equilibrium, thermodynamic and kinetic study," *J. Taiwan Inst. Chem. Eng.*, vol. 45, no. 2, pp. 635–647, 2014.
- [16] M. Hernández Rojas and J. F. Vélez Ruíz, "Suero de leche y su aplicación en la elaboración de alimentos funcionales," *Temas Sel. Ing. Aliment.*, 2014.
- [17] L. R. Ramos, "Importancia y Aplicaciones de la Adsorción en Fase Líquida," *Sólidos porosos*, *Prep. Caracter. y Apl.*, no. 1, pp. 160–170, 2007.
- [18] R. Leyva, J. V. Flores, P. E. Díaz, and M. S. Berber, "Adsorción de cromo (VI) en solución acuosa sobre fibra de carbón activado," *Inf. Tecnol.*, vol. 19, no. 5, pp. 27–36, 2008.
- [19] M. Drahanisky et al., "Modelling of Adsorption Kinetic Processes—Errors, Theory and Application," *Intech*, vol. i, no. tourism, p. 13, 2016.
- [20] S. Azizian, "Kinetic models of sorption: A theoretical analysis," *J. Colloid Interface Sci.*, vol. 276, no. 1, pp. 47–52, 2004.
- [21] Y. Ho and G. McKay, "Pseudo-second order model for sorption processes," *Org. Process Res. Dev.*, vol. 21, no. 6, pp. 866–870, 2017.
- [22] O. Moradi, M. Norouzi, A. Fakhri, and K. Naddafi, "Interaction of removal Ethidium Bromide with Carbon Nanotube: Equilibrium and Isotherm studies," 2014.
- [23] H. Patel, "Fixed-bed column adsorption study: a comprehensive review," *Appl. Water Sci.*, vol. 9, no. 3, pp. 1–17, 2019.
- [24] E. Worch, *Adsorption Technology in Water Treatment*. 2012.
- [25] V. C. Taty-Costodes, H. Fauduet, C. Porte, and Y. S. Ho, "Removal of lead (II) ions from synthetic and real effluents using immobilized *Pinus sylvestris* sawdust: Adsorption on a fixed-bed column," *J. Hazard. Mater.*, vol. 123, no. 1–3, pp. 135–144, 2005.
- [26] J. S. Valencia Ríos and G. C. Castellar Ortega, "Prediction of breakthrough curves for the removal of lead (II) in aqueous solution onto activated carbon in a packed column," *Rev. Fac. Ing.*, vol. 66, no. Ii, pp. 141–158, 2013.

Ammonium removal from aqueous solution by activated orange peel biochar: kinetic, isotherm and thermodynamic analysis

Larissa Firmino de Lima^{a,*}, Carlos Eduardo Rodrigues Barquilha^a, Maria Cristina Borba Braga^a

^a Department of Hydraulic and Sanitation, Federal University of Parana, 100 Cel. F. H. dos Santos Ave., Curitiba 81531-990, Brazil

Abstract

The use of biochar as an eco-friendly and low-cost adsorbent for ammonium (N-NH_4^+) adsorption from water and wastewater has received increasing attention. Therefore, kinetic, isotherm and thermodynamic studies can provide substantial information about the adsorption behavior of N-NH_4^+ onto biochar, such as uptake capacity and adsorption mechanisms. In this study, biochar was produced from orange peel at 400 °C and chemically activated with KOH 3M. Batch adsorption experiments were conducted to evaluate the ammonium adsorption capacity of biochar. Pseudo-first-order (PFO), pseudo-second-order (PSO), and Vermeulen models were adjusted to the kinetic experimental data, while Freundlich, Langmuir, and Sips adsorption isotherm models were fitted to the equilibrium data. Gibbs free energy change (ΔG°), enthalpy change (ΔH°), entropy change (ΔS°) and thermodynamics constant (K_c) were also determined from equilibrium experiments at temperatures of 15°C, 25°C and 35°C. The equilibrium was reached after 360 min. Both PSO and Vermeulen models may be used to predict the N-NH_4^+ adsorption kinetic, with high R^2 values (0.988 and 0.995, respectively). The Langmuir isotherm can be defined as the best model to describe the experimental data ($R^2 > 0.99$). The theoretical maximum adsorption capacity of N-NH_4^+ was 9.19 mg g⁻¹. The thermodynamic parameters suggest an endothermic and spontaneous process, with N-NH_4^+ adsorption more favorable at higher temperatures. The results from kinetics and thermodynamic analysis may indicate the occurrence of physisorption and chemisorption. Additionally, this study suggests that the activated orange peel biochar may be used as an efficient adsorbent for N-NH_4^+ removal from water and wastewater.

Keywords: Adsorption; kinetic models; isotherm models; ammonia nitrogen; chemical activation

1. Introduction

The use of biochar as an eco-friendly and low-cost adsorbent for the removal of ammonia nitrogen (N-NH_4^+) from aqueous solutions has received increasing attention. In order to investigate the feasibility of using biochar in practical applications, such as water and wastewater treatment, it is necessary to understand how N-NH_4^+ interacts with this particular adsorbent material. Kinetics, isotherms, and thermodynamic studies can provide substantial information about uptake capacity and adsorption mechanisms (chemical or physical interactions) [1].

The adsorption kinetics allows to estimate the N-NH_4^+ uptake rate and to predict the required time for the adsorption process to reach equilibrium, which

are important data for the scale-up of an adsorption system [2]. Several kinetic models have been used to fit the experimental results. These include models based on reaction order, such as pseudo-first-order (PFO) and pseudo-second-order (PSO), and models based on mass transport process, as Vermeulen model.

The PFO model originated from the Lagergren's equation and it is based on the assumption that the adsorption capacity of the biochar follows a first-order rate. While the PSO model assumed a second-order rate for the N-NH_4^+ uptake due to the availability of the active sites. However, for mass transfer based models, the adsorption process can be divided into four steps: (i) transport of N-NH_4^+ in the bulk solution; (ii) diffusion of N-NH_4^+ through the film; (iii) intraparticle diffusion of N-NH_4^+ through the pores of the biochar; and (iv) attachment of N-NH_4^+



NH_4^+ to the active sites of biochar [3]. The Vermeulen model considers the intraparticle diffusion as the sole rate-controlling step [4].

Adsorption isotherms can describe the equilibrium relationship between the remaining N-NH_4^+ concentration in solution and the amount of N-NH_4^+ adsorbed on biochar at a constant temperature. This equilibrium analysis is useful to estimate the maximum adsorption capacity of the biochar and the adsorbent-adsorbate interaction affinity [5]. Various isotherm models are available to analyze the adsorption data. The two parameters models, such as Langmuir and Freundlich, are the most commonly used. In case of three parameters, one of the most common adsorption isotherms is the Sips equation [6].

The Freundlich isotherm is one of the earliest empirical equations. It assumes the occurrence of multilayer adsorption on heterogeneous surfaces and that there is no saturation limit. While, the Langmuir theoretical equation implies that the adsorbent has a homogeneous surface, where finite and monolayer adsorption occurs. On the other hand, the Sips isotherm combines the Freundlich and the Langmuir equations. This model predicts adsorption on heterogeneous surfaces, however, avoids the infinity increase in the adsorbed amount associated with the Freundlich isotherm [7].

The thermodynamics parameters, which are the Gibbs free energy change (ΔG°), the enthalpy change (ΔH°), and the entropy change (ΔS°), can be calculated from the adsorption isotherms at different temperatures. This analysis indicates the degree of spontaneity, the feasibility, and the nature of the adsorption process [8]. They are essentials to understand the adsorption mechanisms. However, to determine the exact adsorption mechanism, it is necessary to carry out several analytical techniques together with the analyzes mentioned above [7].

Thus, this study aimed to explore the adsorption behavior of N-NH_4^+ on orange peel derived biochar and to investigate potential adsorption mechanisms involved in the process through kinetics, isotherms, and thermodynamics studies.

2. Materials and methods

2.1. Biochar preparation

The biochar used in this study was produced from orange peel waste. This feedstock was particularly selected due to its low cost and wide availability in Brazil. The biomass was cut into 8 mm particle size,

washed three times with deionized water, and dried in an oven at 105 °C for 24 h. The dried orange peels were pyrolyzed in a muffle furnace at 400 °C for 1 h, with a heating rate of 10 °C min^{-1} . The resulting biochar was washed with deionized water and oven dried at 105 °C for 24 h. The orange peel biochar was then modified with alkali treatment. It was soaked in a 3 M KOH solution for 16 h at a 1:5 impregnation ratio (weight/volume). The activated biochar was washed several times with deionized water, rinsed with 0.1 M HCl to reach neutral pH, and dried in an oven at 105 °C for 24 h. All reagents used in this study were from analytical grade.

2.2. Batch ammonium adsorption experiments

The ammonia nitrogen stock solution (N-NH_4^+ , 1000 mg L^{-1}) was prepared by dissolving 3.819 g of NH_4Cl in 1 L of deionized water. From this stock solution, diluted solutions were made by adding deionized water. All batch adsorption experiments were conducted in duplicate, using Erlenmeyer flasks (125 mL) and an orbital shaking incubator (Tecnal, TE-420) at 100 rpm. The remaining N-NH_4^+ content was measured with an ammonia gas sensing electrode (OAKTON, 35802-00).

2.2.1. Adsorption kinetics

For the adsorption kinetics study, 2 g of biochar and 50 mL of solution (500 mg L^{-1}) were added to a series of flasks. The flasks were shaken at 25 °C and collected after 10, 20, 30, 45, 60, 120, 240, 360, 480 and 1440 min. The samples were filtered and the residual N-NH_4^+ concentrations were analyzed. The amount of N-NH_4^+ adsorbed on orange peel biochar were calculated using the following equation:

$$q_t = [(C_0 - C_t)V]/m_d \quad (1)$$

where q_t is the amount of adsorbed N-NH_4^+ at time 't' (mg g^{-1}), C_0 is the initial N-NH_4^+ concentration in solution (mg L^{-1}), C_t is the N-NH_4^+ concentration in solution at time t (mg L^{-1}), V is the volume of solution (L), and m_d is the dry mass of biochar (g).

In this study, pseudo-first order, pseudo-second order and Vermeulen models were adjusted to the experimental data to investigate the N-NH_4^+ adsorption rate onto orange peel biochar.

The pseudo-first-order model equation can be expressed as [9]:

$$q_t = q_e(1 - e^{-k_1 t}) \quad (2)$$

The pseudo-second-order model equation can be written as follows [10]:

$$q_t = \frac{q_e^2 k_2 t}{1 + q_e k_2 t} \quad (3)$$

where q_e is the amount of N-NH₄⁺ adsorbed at equilibrium (mg g⁻¹), k_1 and k_2 are the rate constants of the equations (min⁻¹), and t is the time (min).

The Vermeulen model equation can be described as [11]:

$$\frac{q_t}{q_e} = \sqrt{1 - \exp[(-D\pi^2 t)/R^2]} \quad (4)$$

where D is the diffusion coefficient (cm² min⁻¹) and R is the particle radius (cm).

2.2.2. Adsorption isotherms

Adsorption isotherms experiments were carried out using 2 g of biochar and a series of solutions (50 mL) with different concentrations. The N-NH₄⁺ concentrations were 50, 100, 150, 200, 300, 400, 500, 600, 800 and 1000 mg L⁻¹. The flasks with the mixtures were shaken for 15 h at 15, 25 and 30 °C (288, 298 and 308 K). The samples were filtered and the concentrations of N-NH₄⁺ were determined. The amount of N-NH₄⁺ adsorbed on biochar at equilibrium were calculated by the following equation:

$$q_e = [(C_0 - C_e)V]/m_d \quad (5)$$

where C_e is the N-NH₄⁺ concentration in solution at equilibrium (mg L⁻¹).

The equilibrium data obtained in this study were fitted to Freundlich, Langmuir and Sips adsorption isotherm models.

The Freundlich isotherm model can be described by the following equation [12]:

$$q_e = K_F C_e^{1/n} \quad (6)$$

where K_F is the Freundlich equilibrium constant [(L mg⁻¹)^{1/n} (mg g⁻¹)] and $1/n$ is the Freundlich intensity parameter (dimensionless), which also indicates the surface heterogeneity. The values of $1/n$ from 0 to 1 indicate favorable adsorption.

The Langmuir isotherm model can be written as [13]:

$$q_e = \frac{q_{max} K_L C_e}{1 + K_L C_e} \quad (7)$$

where q_{max} is the maximum adsorption capacity of N-NH₄⁺ (mg g⁻¹) and K_L is the Langmuir constant (L mg⁻¹).

The Sips isotherm model can be expressed as follows [14]:

$$q_e = \frac{q_s K_s C_e^{n_s}}{1 + K_s C_e^{n_s}} \quad (8)$$

where q_s is the Sips maximum adsorption capacity of N-NH₄⁺ (mg g⁻¹), K_s is the Sips equilibrium constant (mg g⁻¹), and n_s is the Sips exponent (dimensionless, limited from 0 to 1).

2.2.3. Adsorption thermodynamics

The thermodynamics study was carried out using the data from the adsorption isotherms (288, 298 and 308 K). Thus, four parameters were calculated: thermodynamics constant (K_C), Gibbs free energy change (ΔG°), enthalpy change (ΔH°) and entropy change (ΔS°).

The K_C can be calculated based on the Langmuir constant as follows [15]:

$$K_C = 55.5 \times 1000 \times 14.01 K_L \quad (9)$$

where the factor 55.5 is the number of moles of pure water per liter, the term 1000 is applied to convert g to mg, 14.01 is the molecular weight of nitrogen and then K_C can be obtained as a dimensionless parameter.

The ΔG° is related to the K_C as shown below:

$$\Delta G^\circ = -RT \ln(K_C) \quad (10)$$

where R is the universal gas constant (8.314 J mol⁻¹ K⁻¹) and T is the temperature (K).

The ΔH° and ΔS° parameters are related to ΔG° by the following equation:

$$\Delta G^\circ = \Delta H^\circ - T\Delta S^\circ \quad (11)$$

The replacement of Eq. 10 into Eq. 11 results in the van't Hoff's thermodynamics equation:

$$\ln(K_C) = \frac{-\Delta H^\circ}{R} \frac{1}{T} + \frac{\Delta S^\circ}{R} \quad (12)$$

Thus, the values of ΔH° and ΔS° can be obtained from the slope and intercept, respectively, by plotting $\ln(K_C)$ versus $1/T$.

Origin Pro 9.0 was used to fit and analyze the data from kinetic, isotherm, and thermodynamic studies.

3. Results and discussion

3.1. Adsorption kinetic

The adsorption kinetic of orange peel biochar is shown in Fig. 1. According to the experimental data, the N-NH_4^+ uptake takes place in two different steps. The first step occurs rapidly at the initial minutes (0-120 min), where more than 85% of the adsorption capacity was reached by adsorbent. On the other hand, the second step occurs slowly from the first step until the adsorption equilibrium is reached. This behavior can be attributed to the larger availability of active sites at the beginning. In addition, the amount of N-NH_4^+ adsorbed on biochar was slightly changed after 360 min. Thus, the equilibrium time was reached at approximately 360 min.

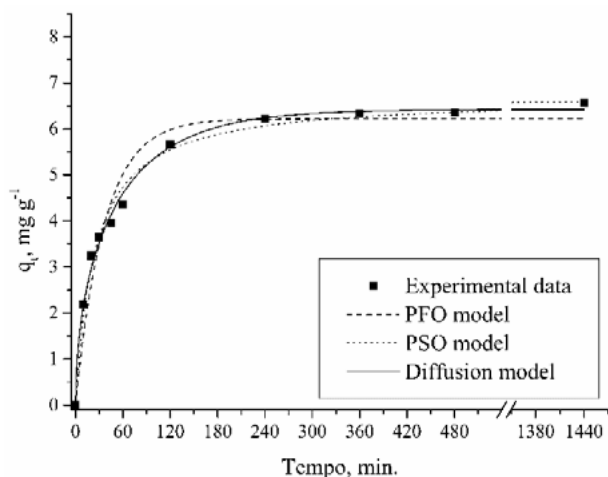


Fig. 1. Kinetic of N-NH_4^+ adsorption onto orange peel biochar.

Table 1. Kinetic parameters for N-NH_4^+ adsorption by orange peel biochar.

Model	Parameters	Value
PFO	q_e (mg g^{-1})	6.216
	k_1 (min^{-1})	0.027
	R^2	0.954
PSO	q_e (mg g^{-1})	6.695
	$k_2 \times 10^{-2}$ ($\text{g mg}^{-1} \text{min}^{-1}$)	0.599
	R^2	0.988
Diffusion	q_e (mg g^{-1})	6.425
	$D_{\text{eff}} \times 10^{-2}$ ($\text{cm}^2 \text{min}^{-1}$)	0.761
	R^2	0.995

The fitting parameters of the kinetic models and their determination coefficients (R^2) are presented

in Table 1. As can be seen, the PFO equation did not adequately fit the kinetic data, with the lowest R^2 (0,954) among the three models. The PSO equation had a relatively high value of R^2 (0,988). It suggests that the N-NH_4^+ adsorption can follow the PSO kinetic and may suggest the occurrence of chemical interaction [2]. In addition, the experimental data fitted closely with the Vermeulen (diffusion) equation ($R^2 = 0.995$), indicating that intraparticle diffusion can be considered as the rate-controlling step [4]. Based on the high R^2 values achieved by PSO and Vermeulen equations, both models may be used to predict the N-NH_4^+ adsorption kinetic. Thus, it indicates that the adsorption of N-NH_4^+ onto orange peel biochar may include chemisorption involving complexation and ion exchange, and it would be controlled by intraparticle diffusion.

3.2. Adsorption isotherms

The calculated parameters of the Langmuir, Freundlich and Sips models are shown in Table 2. The obtained results suggested that both Langmuir and Sips isotherm models can describe the N-NH_4^+ adsorption onto orange peel biochar due to their high R^2 values. The determination coefficients of the Sips model were slightly higher than those of the Langmuir model. However, the maximum theoretical adsorption capacities and the K_S , equilibrium constant associated with the adsorbent-adsorbate affinity, are not agreeing with the effect of the temperature. This can be attributed to the greater freedom of adjustment due to the larger number of parameters. Consequently, the Langmuir model can be defined as the best model to describe the experimental data. Thus, it indicates that the N-NH_4^+ adsorption onto orange peel biochar may occur in monolayer [16]. It is worth to mention that all values of $1/n$ obtained from the Freundlich equation are from 0 to 1 (0,38, 0,38, and 0,36), suggesting favorable adsorption [17].

The Langmuir adsorption isotherms of N-NH_4^+ on orange peel biochar are illustrated in Fig. 2. It shows that the adsorption capacity of the biochar enhanced with an increase in reaction temperature. The rise in temperature favored the N-NH_4^+ uptake and it probably means that the adsorption sites are more active at higher temperatures [18]. Overall, the maximum theoretical adsorption capacity of N-NH_4^+ on orange peel biochar was 9.19 mg g^{-1} at 35°C . This uptake capacity is superior to the found by other authors that worked with non-activated orange peel biochar and N-NH_4^+ [2,19]. It suggests that the chemical treatment with 3 M KOH solution may

have improved the N-NH₄⁺ adsorption capacity by biochar.

Table 2. Isotherm parameters for N-NH₄⁺ adsorption by orange peel biochar.

Model	Parameters	15 °C	25 °C	35 °C
Langmuir	q _{max}	8.676	8.885	9.190
	K _L	0.0098	0.0102	0.011
	R ²	0.998	0.998	0.998
Freundlich	K _F	0.685	0.713	0.847
	n	2.634	2.633	2.787
	R ²	0.969	0.974	0.956
Sips	q _S	9.155	9.950	9.396
	K _S	0.013	0.016	0.012
	ns	0.910	0.851	0.974
	R ²	0.999	0.999	0.998

Note: q_{max}, q_S (mg/g); K_F, K_S (L/mg); K_F (L/mg)^{1/n} (mg/g)

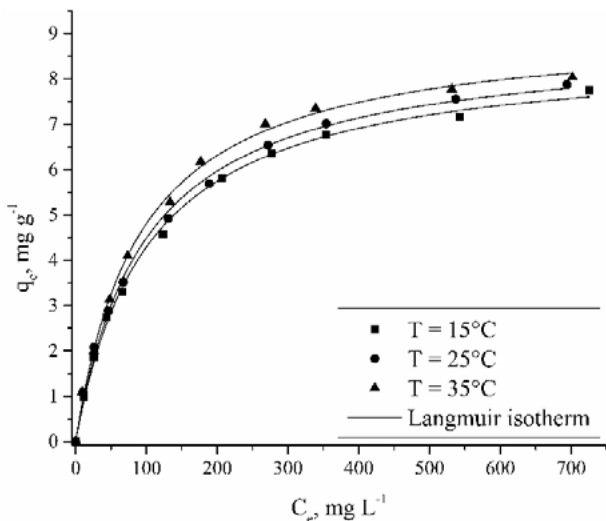


Fig. 2. Langmuir isotherms of N-NH₄⁺ adsorption onto orange peel biochar.

3.3. Adsorption thermodynamics

The results of the thermodynamic parameters are shown in Table 3 and Fig.3. The increase of K_c values with the rise in temperature and the positive value of enthalpy change (ΔH°) suggest that the N-NH₄⁺ adsorption is an endothermic process [19]. The positive value of entropy change (ΔS°) reflects a more random interaction at the solution/solid interface, with an increase in the degree of freedom [20]. The negative values of the Gibbs free energy change (ΔG°) indicate the spontaneous of the adsorption process. The higher absolute value of ΔG° at 308 K suggests that the N-NH₄⁺ adsorption

is more favorable at higher temperatures [1]. In addition, the magnitude of the negative ΔG° values is close to the range of 20 to 0 kJ mol⁻¹, suggesting physical adsorption. Although the kinetic data points out to chemical interaction, the thermodynamic data indicates physisorption. It can be concluded that both mechanisms may occur in the N-NH₄⁺ adsorption on orange peel biochar [18].

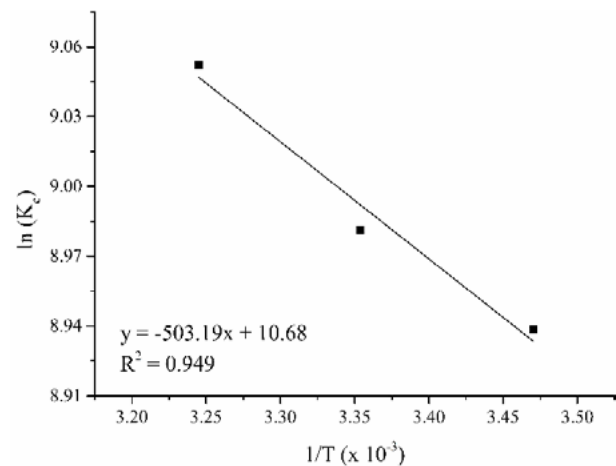


Fig. 1. Thermodynamic parameters of N-NH₄⁺ adsorption onto orange peel biochar.

Table 3. Thermodynamic parameters for N-NH₄⁺ adsorption by orange peel biochar.

T (K)	K _c	ΔH° (kJ/mol)	ΔS° (J/mol)	ΔG° (kJ/mol)
288.15	7620.0			-21.847
298.15	7954.4	+ 4.184	88.798	-22.735
308.15	8537.6			-23.623

4. Conclusion

The ammonia nitrogen adsorption onto activated orange peel biochar was evaluated through kinetic, isotherm, and thermodynamic analysis. The maximum theoretical adsorption capacity of N-NH₄⁺ was 9.19 mg g⁻¹. The experimental data fitted both PSO and Vermeulen kinetic models, suggesting chemical interactions governed by intraparticle diffusion. However, the results from the thermodynamic data suggested physisorption. Therefore, both mechanisms may be involved in the adsorbent-adsorbate interaction. This study shows that kinetic, isotherm and thermodynamic studies can provide important information regarding N-NH₄⁺ uptake and potential adsorption mechanisms. Additionally, the results suggest that the activated



orange peel biochar may be used as an efficient adsorbent for N-NH_4^+ removal from water and wastewater rich in nitrogen.

Acknowledgements

This study was supported by the Brazilian research funding agency CAPES and the Postgraduate Program in Water Resources and Environmental Engineering – PPGERHA/UFPR.

References

- [1] Tan X, Liu Y, Zeng G, Wang X, Hu X, Gu Y, Yang Z. Application of biochar for the removal of pollutants from aqueous solutions. *Chemosphere*. 2015;125:70-85.
- [2] Hu X, Zhang X, Ngo HH, Guo W, Wen H, Li C, Zhang Y, Ma C. Comparison study on the ammonium adsorption of the biochars derived from different kinds of fruit peel. *Science of the Total Environment*. 2020;707:135544.
- [3] Ho YS, Ng JC, McKay G. Kinetics of pollutant sorption by biosorbents. *Separation and purification methods*. 2000;29(2):189-232.
- [4] Tan KL, Hameed BH. Insight into the adsorption kinetics models for the removal of contaminants from aqueous solutions. *Journal of the Taiwan Institute of Chemical Engineers*. 2017;74:25-48.
- [5] Tran HN, You SJ, Chao HP. Effect of pyrolysis temperatures and times on the adsorption of cadmium onto orange peel derived biochar. *Waste Management & Research*. 2016;34(2):129-38.
- [6] Saadi R, Saadi Z, Fazaeli R, Fard NE. Monolayer and multilayer adsorption isotherm models for sorption from aqueous media. *Korean Journal of Chemical Engineering*. 2015;32(5):787-99.
- [7] Lima EC, Adebayo MA, Machado FM. Kinetic and equilibrium models of adsorption. In: Bergmann CP, Machado FM, editors. *Carbon nanomaterials as adsorbents for environmental and biological applications*. Springer; 2015. p. 33-69.
- [8] Vithanage M, Mayakaduwa SS, Herath I, Ok YS, Mohan D. Kinetics, thermodynamics and mechanistic studies of carbofuran removal using biochars from tea waste and rice husks. *Chemosphere*. 2016;150:781-9.
- [9] Lagergren SK. About the theory of so-called adsorption of soluble substances. *Sven. Vetenskapsakad. Handlingar*. 1898;24:1-39.
- [10] Blanchard G, Maunaye M, Martin G. Removal of heavy metals from waters by means of natural zeolites. *Water research*. 1984;18(12):1501-7.
- [11] Vermeulen T. Theory for irreversible and constant-pattern solid diffusion. *Industrial & Engineering Chemistry*. 1953;45(8):1664-70.
- [12] Freundlich H. Über die adsorption in lösungen. *Zeitschrift für physikalische Chemie*. 1907;57(1):385-470.
- [13] Langmuir I. The adsorption of gases on plane surfaces of glass, mica and platinum. *Journal of the American Chemical society*. 1918;40(9):1361-403.
- [14] Sips R. On the structure of a catalyst surface. *The Journal of Chemical Physics*. 1948;16(5):490-5.
- [15] Tran HN, You SJ, Hosseini-Bandegharai A, Chao HP. Mistakes and inconsistencies regarding adsorption of contaminants from aqueous solutions: a critical review. *Water research*. 2017;120:88-116.
- [16] Vu TM, Doan DP, Van HT, Nguyen TV, Vigneswaran S, Ngo HH. Removing ammonium from water using modified corncob-biochar. *Science of the Total Environment*. 2017;579:612-9.
- [17] Alshameri A, He H, Zhu J, Xi Y, Zhu R, Ma L, Tao Q. Adsorption of ammonium by different natural clay minerals: characterization, kinetics and adsorption isotherms. *Applied Clay Science*. 2018;159:83-93.
- [18] Kizito S, Wu S, Kirui WK, Lei M, Lu Q, Bah H, Dong R. Evaluation of slow pyrolyzed wood and rice husks biochar for adsorption of ammonium nitrogen from piggery manure anaerobic digestate slurry. *Science of the Total Environment*. 2015;505:102-12.
- [19] Xue S, Zhang X, Ngo HH, Guo W, Wen H, Li C, Zhang Y, Ma C. Food waste based biochars for ammonia nitrogen removal from aqueous solutions. *Bioresource technology*. 2019;292:121927.
- [20] Tran HN, You SJ, Chao HP. Thermodynamic parameters of cadmium adsorption onto orange peel calculated from various methods: a comparison study. *Journal of Environmental Chemical Engineering*. 2016;4(3):2671-82.

Uranium biosorption by hydroxyapatite and bone meal

Tamires Watanabe, Sabine Neusatz Guilhen, Júlio Takehiro Marumo, Leandro Goulart de Araujo*

Instituto de Pesquisas Energéticas e Nucleares, Av. Prof. Lineu Prestes 2242, São Paulo 05508-000, Brazil

Corresponding author: Dr. Leandro Goulart de Araujo

*E-mail address: lgoulart@alumni.usp.br

Abstract

Biosorption has been widely examined for the treatment of aqueous solutions containing uranium, a radiotoxic pollutant. The use of hydroxyapatite and bone meal as potential biosorbents in the removal of uranium (U) from aqueous solutions has not yet been previously addressed. In this work, the efficiency of these biosorbents in the removal of U was investigated according to their adsorption removal capacities. Surface transformations in both materials were observed after U adsorption by scanning electron microscopy combined with energy-dispersive X-ray spectroscopy (SEM/EDS). The biomass/U solution ratio was kept at 0.1 g/5 mL. Contact times for the batch experiments were 15, 30, 60, 120, and 180 min, and the concentration of U tested was 680 mg L⁻¹. The equilibrium was achieved in less than 15 min for both materials. The morphological characteristics of each biomass, before and after biosorption experiments were analyzed. Bone meal highlighted slightly superior adsorption results in terms of maximum capacity ($q_{max} = 33.83 \text{ mg g}^{-1}$), compared to hydroxyapatite ($q_{max} = 33.36 \text{ mg g}^{-1}$), with the removal percentages being also similar, 99.97 and 98.57 %, respectively. The results so far indicate that these materials are potential biosorbents for the treatment of uranium-contaminated solutions, especially liquid radioactive waste.

Keywords: uranium; adsorption; bone meal; hydroxyapatite.

1. Introduction

The presence of uranium (U) in aqueous streams is harmful, mainly because this radionuclide may persist in the natural environment for a long time. Sources of possible U contamination are numerous, including mineral mining, smelting, nuclear fuel manufacturing, and nuclear research. Furthermore, given the growing demands for electric energy generation in the last decades, U-containing nuclear wastes have significantly increased with the ascension of the nuclear power industry [1]. Several methods have been developed specifically for U extraction such as covalent binding [2], ion-exchange [3,4], electrostatic attraction [5], surface complexation [6–8], and Van der Waal's forces [9].

New and alternative processes are constantly being developed, aiming at removing radionuclides

from aqueous solutions, which also helps to overcome known issues of the conventional methods. To name a few, the high costs and the generation of higher volumes of liquid waste as a result of some varieties of treatment.

Biosorption can be defined as the use of biomass to uptake metal(loid) ions from aqueous environments. Examples of such biomaterials are algae, bacteria, yeast, fungi, plant leaves, and root tissues. Biosorption has many advantages, e.g. low capital and operating costs, selective removal of metals, the possibility of biosorbent regeneration and metal recovery, rapid kinetics of adsorption and desorption, and no sludge generation [10]. In this context, many biomaterials have been extensively studied for the removal of U from aqueous solutions, including biomass such as rice stem [11], *Solanum incanum* leaves [12], *Eichhornia crassipes* [13], macrophytes [14], coconut fiber [15], coffee and



rice husks [16]; microorganisms such as *Saccharomyces cerevisiae* [17,18], *Penicillium piscarium* [19], *Penicillium citrinum* [20], *Aspergillus fumigatus* [21], and biochars such as the ones derived from macauba [22], eucalyptus wood [23], *Opuntia ficus indica* [24], rice straw [25,26]; bone [27], and rice husk [28].

However, the use of bone meal for the removal of U from radioactive aqueous solutions has not yet been investigated as an alternative for the conventional adsorption processes. Therefore, as regards radioactive waste treatment, good mechanical properties are a very important feature of the biosorbent, especially if the final goal is the solidification of biomass waste. This will further impact the conditioning of the waste into a stable solid form which will allow immobilization and containment of the radioactive content for the necessary period. The application of bone meal is attractive and advantageous because it is economically feasible in comparison with commercial adsorbents. It consists of a natural, abundant substance that contains a large amount of calcium phosphate in the form of hydroxyapatite.

Phosphate-derived materials have been studied extensively to efficiently extract uranium from the aqueous phase owing to their adsorption capability, which has been ascribed to the surface complexation and mineralization of phosphate with U [29]. It can also be used to remove radionuclides from liquid aqueous solutions, such as liquid radioactive waste generated in many industrial or research activities. This biomaterial may be able to remove significantly hazardous radionuclides, heavy metals, and organic substances from radioactive liquid waste. Previous research has indicated that hydroxyapatite alone is capable to efficiently remove thorium from aqueous solutions [30]. Furthermore, studies indicate that radionuclides such as $^{90}\text{Sr}^{2+}$ [31], $^{208}\text{Tl}^+$, $^{226}\text{Ra}^{2+}$, $^{212}\text{Bi}^{3+}$ and $^{228}\text{Ac}^{3+}$ [32] were also adsorbed by hydroxyapatite.

The objective of this work was to evaluate the adsorption capacity of hydroxyapatite and bone meal for uranium removal from aqueous solutions. Moreover, the morphological characteristics of both materials were evaluated by Scanning Electron Microscopy/Energy Dispersive X-Ray Spectroscopy (SEM/EDS).

2. Materials and methods

2.1. Biosorbents

Bone meal (Super Verde, Fênix Indústria e Comércio de Fertilizantes LDA-ME) and hydroxyapatite (produced in CCTM/IPEN) were ground and sieved to obtain particle sizes between 0.297 mm and 0.125 mm. Subsequently, they were stored in sealed polyethylene flasks in the laboratory for later use.

2.2. Synthetic solution

A synthetic solution of U was prepared by adding 0.165 g of uranyl nitrate ($\text{UO}_2(\text{NO}_3)_2 \cdot 6\text{H}_2\text{O}$) in 100 mL distilled water (2.91 mmol L^{-1}). pH was adjusted to 4 by adding nitric acid (Merck, Brazil) or sodium hydroxide (Merck, Brazil). Initial pH was adjusted at 4 because it is the measured pH of the radioactive liquid waste stored at the Radioactive Waste Management Laboratory of the Nuclear and Energy Research Institute (IPEN-CNEN/SP). Our concern is to investigate how bone meal and hydroxyapatite behave under real radwaste conditions. Moreover, according to [33] and software projection, pH 4 favors the biosorption of a great number of species because of its speciation. At this pH, most of the U ions in solution is in the form of non-complexed free uranyl ions (UO_2^{2+} or U(VI)). pH behavior was evaluated during the experiments.

2.3. Biosorption experiments

2.3.1 Adsorption study

Batch biosorption experiments were performed to determine the metal uptake capacity under different contact times. The vials containing the solution and the biosorbent were stirred (130 rpm) at controlled temperature ($25 \text{ }^\circ\text{C}$). The mass of 0.1 g of the bone meal was suspended in 5 mL of U aqueous solutions and kept in contact during different time intervals: 0, 15, 30, 60, 120, and 180 min. The bone meal was removed by filtration in a vacuum system. The experiments were carried out in duplicate. Inductively coupled plasma optical emission spectrometry (ICP-OES) was used to determine the concentration of U. The uptake amount of U onto the biomaterial was calculated using equation Eq. (1) [34].

$$q = \frac{(C_0 - C)V}{m} \quad (1)$$

where q is the uptake of uranium (mmol g^{-1}), C_0 is the initial uranium concentration in solution (mmol L^{-1}), C is the equilibrium concentration in solution (mmol L^{-1}), V is the volume of solution (L), and m is the mass of the biosorbent (g).

2.4. Equipment and analytical methods

Scanning electron microscopy (SEM) images of the biosorbents were collected by a Hitachi TM3000 (Tokyo, Japan) tabletop microscope. EDS data were collected by this microscope coupled with a tungsten source and acceleration voltages of 5 and 15 kV with an electron beam resolution of 30 nm. Images were obtained with magnification from 500 to 1500 times. The determination of U in the adsorbate solutions was made by ICP-OES from Perkin Elmer (EUA), model Optima 7000 DV.

3. Results and discussion

3.1. Morphological analysis

Morphological analysis by SEM was conducted to investigate surface transformations during U adsorption. Fig. 1 shows the micrographs and X-ray spectrometry (EDS) for hydroxyapatite and bone meal before biosorption and Fig. 2 after the treatment.

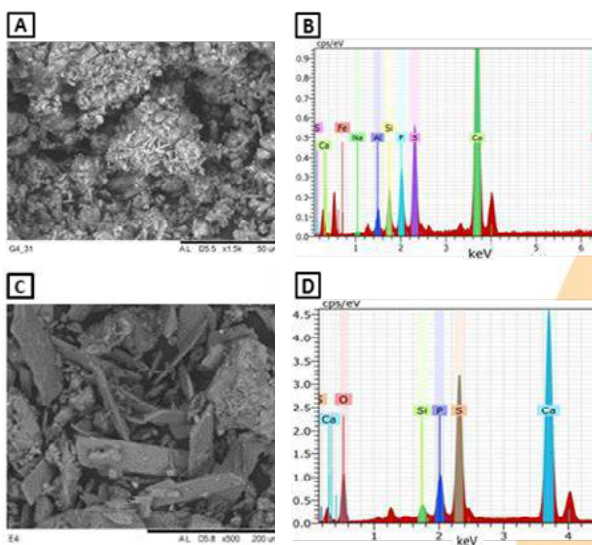


Fig. 1. Morphological analysis of raw material: (A) Micrograph of the bone meal; (B) X-ray spectrometry (EDS) of bone meal; (C) Micrograph

of hydroxyapatite; (D) X-ray spectrometry (EDS) of hydroxyapatite.

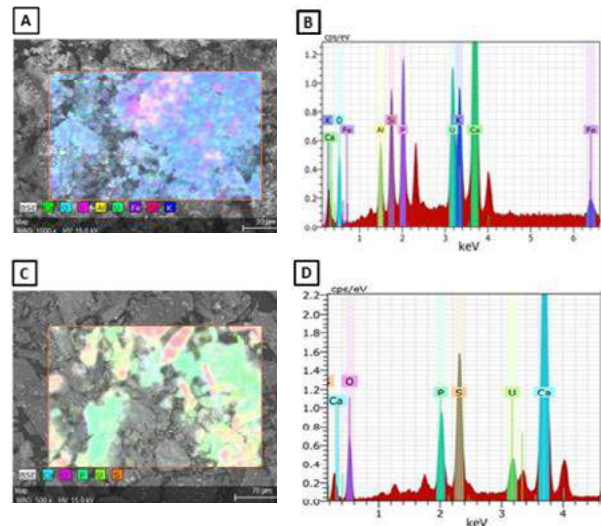


Fig. 2. Morphological analysis after 30 min in contact with the solution: (A) Micrograph of the bone meal; (B) X-ray spectrometry (EDS) of bone meal; (C) Micrograph of hydroxyapatite; (D) X-ray spectrometry (EDS) of hydroxyapatite.

The predominance of Ca and P was observed in the EDS, which is consistent with the composition of both hydroxyapatite and bone meal. After treatment, it was possible to observe a peak of U in both materials, evidencing its adsorption.

3.2. Experimental data obtained through the biosorption technique

The efficiency and the equilibrium adsorption capacity of each adsorbent were evaluated by adsorption over 180 min. The effect of the contact time on the removal of uranium by bone meal and hydroxyapatite is shown in Fig. 3. Although most of the uranyl ions had been removed after approximately 15 min, a minimum of 30 min was necessary to reach pH and adsorption equilibrium, at which the adsorption capacities were of 34 mg g^{-1} for both biosorbents ($> 98\%$ removal efficiency).

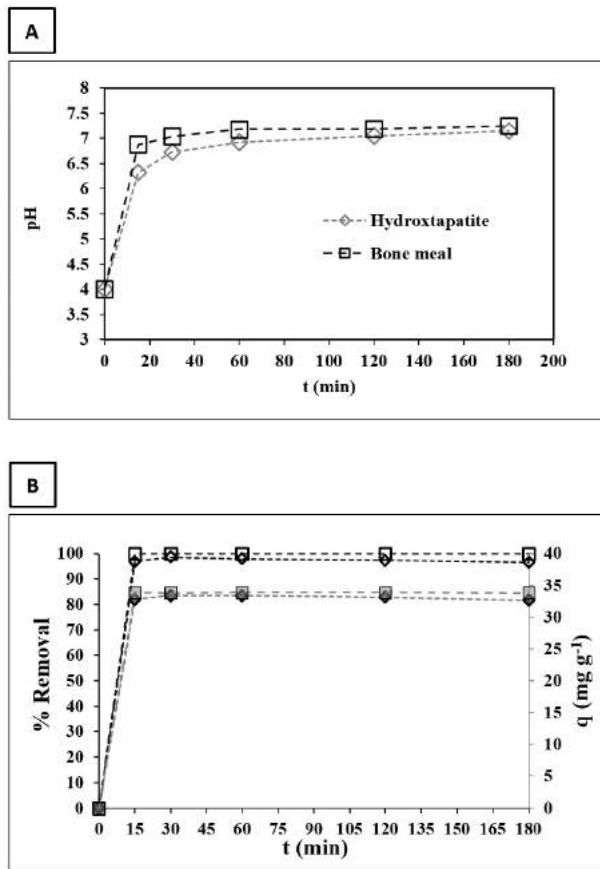


Fig. 3. Effects of experimental condition on uranium adsorption ability: (A) pH value, (B) contact time. In (B), q (mg g^{-1}) values are given by (filled square) – hydroxyapatite and (filled diamond) – bone meal; % Removal is given by (empty square) – hydroxyapatite and (empty diamond) – bone meal.

4. Conclusions

The adsorption capacity to remove U from aqueous solution by bone meal and hydroxyapatite was evaluated in this work. The application of these biomaterials for this purpose is attractive and advantageous because of their efficiency in removing this hazardous radionuclide and for being low cost materials. The uptake of U was fast and achieved in approximately 15 min. The biosorption assays were carried out in a batch system and indicated a viable treatment procedure for extracting U. Further investigations might be necessary to ascertain the biosorption performance by these materials by analyzing changes in variables such as concentration and pH.

Acknowledgements

We gratefully acknowledge the financial support provided by CNPq (T. Watanabe) and CNEN (L.G. de Araujo).

References

- [1] S. Kahouli, Re-examining uranium supply and demand: New insights, *Energy Policy*. 39 (2011) 358–376. <https://doi.org/10.1016/j.enpol.2010.10.007>.
- [2] S. Chen, J. Hong, H. Yang, J. Yang, Adsorption of uranium (VI) from aqueous solution using a novel graphene oxide-activated carbon felt composite, *J. Environ. Radioact.* 126 (2013) 253–258. <https://doi.org/10.1016/j.jenvrad.2013.09.002>.
- [3] A.C.Q. Ladeira, C.A. Morais, Uranium recovery from industrial effluent by ion exchange-column experiments, *Miner. Eng.* 18 (2005) 1337–1340. <https://doi.org/10.1016/j.mineng.2005.06.012>.
- [4] E. Rosenberg, G. Pinson, R. Tsosie, H. Tutu, E. Cukrowska, Uranium remediation by ion exchange and sorption methods: A critical review, *Johnson Matthey Technol. Rev.* 60 (2016) 59–77. <https://doi.org/10.1595/205651316X690178>.
- [5] C. Zhao, J. Liu, G. Yuan, J. Liu, H. Zhang, J. Yang, Y. Yang, N. Liu, Q. Sun, J. Liao, A novel activated sludge-graphene oxide composites for the removal of uranium(VI) from aqueous solutions, *Elsevier B.V.*, 2018. <https://doi.org/10.1016/j.molliq.2018.09.069>.
- [6] A. Waychunas, Uranium (VI) adsorption to ferrihydrite: application of a surface complexation model, *Int. J. Rock Mech. Min. Sci. Geomech. Abstr.* 32 (1995) A261. [https://doi.org/10.1016/0148-9062\(95\)99083-a](https://doi.org/10.1016/0148-9062(95)99083-a).
- [7] J.A. Davis, D.E. Meece, M. Kohler, G.P. Curtis, Approaches to surface complexation modeling of Uranium(VI) adsorption on aquifer sediments, *Geochim. Cosmochim. Acta.* 68 (2004) 3621–3641. <https://doi.org/10.1016/j.gca.2004.03.003>.
- [8] F.M. Coutelot, J.C. Seaman, M. Baker, Uranium(VI) adsorption and surface complexation modeling onto vadose sediments from the Savannah River Site, *Environ. Earth Sci.* 77 (2018). <https://doi.org/10.1007/s12665-018-7316-7>.
- [9] M. Sprynskyy, T. Kowalkowski, H. Tutu, E.M. Cukrowska, B. Buszewski, Adsorption performance of talc for uranium removal from aqueous solution, *Chem. Eng. J.* 171 (2011) 1185–1193. <https://doi.org/10.1016/j.cej.2011.05.022>.
- [10] I. Ismail, T. Moustafa, Biosorption of heavy metals, *Heavy Met. Sources, Toxic. Remediat. Tech.* (2016) 131–174.
- [11] Z. Xiao-Teng, J. Dong-Mei, X. Yi-Qun, C. Jun-Chang, H. Shuai, X. Liang-Shu, Adsorption of Uranium(VI) from Aqueous Solution by Modified Rice Stem, *J. Chem.* 2019 (2019). <https://doi.org/10.1155/2019/6409504>.
- [12] O.Y. Bakather, N. Zouli, A. Abutaleb, M.A. Mahmoud, A. Daher, M. Hassan, M.A. Eldoma, S.O. Alasweda, A.A. Fowad, Uranium (VI) ions uptake from liquid wastes by *Solanum incanum* leaves: Biosorption, desorption and recovery, *Alexandria*

- Eng. J. (2020). <https://doi.org/10.1016/j.cej.2020.03.013>.
- [13] Z. J. Yi, J. Yao, H. L. Chen, F. Wang, Z. M. Yuan, X. Liu, Uranium biosorption from aqueous solution onto *Eichhornia crassipes*, *J. Environ. Radioact.* 154 (2016) 43–51. <https://doi.org/10.1016/j.jenvrad.2016.01.012>.
- [14] L.C. Vieira, L.G. de Araujo, R.V. de Padua Ferreira, E.A. da Silva, R.L.S. Canevesi, J.T. Marumo, Uranium biosorption by *Lemna* sp. and *Pistia stratiotes*, *J. Environ. Radioact.* 203 (2019) 179–186. <https://doi.org/10.1016/j.jenvrad.2019.03.019>.
- [15] R.V.P. Ferreira, E.A. Silva, R.L.S. Canevesi, E.G.A. Ferreira, M.H.T. Taddei, M.C. Palmieri, F.R.O. Silva, J.T. Marumo, Application of the coconut fiber in radioactive liquid waste treatment, *Int. J. Environ. Sci. Technol.* 15 (2018) 1629–1640. <https://doi.org/10.1007/s13762-017-1541-6>.
- [16] R.V. de P. Ferreira, L.G. de Araujo, R.L.S. Canevesi, E.A. da Silva, E.G.A. Ferreira, M.C. Palmieri, J.T. Marumo, The use of rice and coffee husks for biosorption of U (total), ^{241}Am , and ^{137}Cs in radioactive liquid organic waste, *Environ. Sci. Pollut. Res. Int.* (2020). <https://doi.org/10.1007/s11356-020-09727-8>.
- [17] M. Liu, F. Dong, X. Yan, W. Zeng, L. Hou, X. Pang, Biosorption of uranium by *Saccharomyces cerevisiae* and surface interactions under culture conditions, *Bioresour. Technol.* 101 (2010) 8573–8580. <https://doi.org/10.1016/j.biortech.2010.06.063>.
- [18] J. Zhang, X. Chen, J. Zhou, X. Luo, Uranium biosorption mechanism model of protonated *Saccharomyces cerevisiae*, *J. Hazard. Mater.* 385 (2020) 121588. <https://doi.org/10.1016/j.jhazmat.2019.121588>.
- [19] E. Coelho, T.A. Reis, M. Cotrim, M. Rizzutto, B. Corrêa, Bioremediation of water contaminated with uranium using *Penicillium piscarium*, *Biotechnol. Prog.* (2020). <https://doi.org/10.1002/btpr.3032>.
- [20] C. Pang, Y.H. Liu, X.H. Cao, M. Li, G.L. Huang, R. Hua, C.X. Wang, Y.T. Liu, X.F. An, Biosorption of uranium(VI) from aqueous solution by dead fungal biomass of *Penicillium citrinum*, *Chem. Eng. J.* 170 (2011) 1–6. <https://doi.org/10.1016/j.cej.2010.10.068>.
- [21] J.S. Wang, X.J. Hu, Y.G. Liu, S.B. Xie, Z.L. Bao, Biosorption of uranium (VI) by immobilized *Aspergillus fumigatus* beads, *J. Environ. Radioact.* 101 (2010) 504–508. <https://doi.org/10.1016/j.jenvrad.2010.03.002>.
- [22] S.N. Guillhen, O. Mašek, N. Ortiz, J.C. Izidoro, D.A. Fungaro, Pyrolytic temperature evaluation of macauba biochar for uranium adsorption from aqueous solutions, *Biomass and Bioenergy.* 122 (2019) 381–390. <https://doi.org/10.1016/j.biombioe.2019.01.008>.
- [23] V. Mishra, M.K. Sureshkumar, N. Gupta, C.P. Kaushik, Study on sorption characteristics of uranium onto biochar derived from Eucalyptus Wood, *Water. Air. Soil Pollut.* 228 (2017). <https://doi.org/10.1007/s11270-017-3480-8>.
- [24] L. Hadjittofi, I. Pashalidis, Uranium sorption from aqueous solutions by activated biochar fibres investigated by FTIR spectroscopy and batch experiments, *J. Radioanal. Nucl. Chem.* 304 (2014) 897–904. <https://doi.org/10.1007/s10967-014-3868-5>.
- [25] L. Dong, J. Yang, Y. Mou, G. Sheng, L. Wang, W. Linghu, A.M. Asiri, K.A. Alamry, Effect of various environmental factors on the adsorption of U(VI) onto biochar derived from rice straw, *J. Radioanal. Nucl. Chem.* 314 (2017) 377–386. <https://doi.org/10.1007/s10967-017-5414-8>.
- [26] S.M.E. Yakout, A.A. Abdeltawab, K. Elhindi, A. Askalany, Uranium dynamic adsorption breakthrough curve onto rice straw based activated carbon using bed depth service time model, *BioResources.* 13 (2018) 9143–9157. <https://doi.org/10.15376/biores.13.4.9143-9157>.
- [27] A. Ashry, E.H. Bailey, S.R.N. Chenery, S.D. Young, Kinetic study of time-dependent fixation of UVI on biochar, *J. Hazard. Mater.* 320 (2016) 55–66. <https://doi.org/10.1016/j.jhazmat.2016.08.002>.
- [28] S. Wang, W. Guo, F. Gao, Y. Wang, Y. Gao, Lead and uranium sorptive removal from aqueous solution using magnetic and nonmagnetic fast pyrolysis rice husk biochars, *RSC Adv.* 8 (2018) 13205–13217. <https://doi.org/10.1039/c7ra13540h>.
- [29] L. Kong, Y. Ruan, Q. Zheng, M. Su, Z. Diao, D. Chen, L. Hou, X. Chang, K. Shih, Uranium extraction using hydroxyapatite recovered from phosphorus containing wastewater, *J. Hazard. Mater.* 382 (2020) 120784. <https://doi.org/10.1016/j.jhazmat.2019.120784>.
- [30] E.G.A. Ferreira, E. Alves, R.V.P. Ferreira, V.L.K. Isiki, E.A. Silva, R.L. Canevesi, J.T. Marumo, Biosorption of Thorium by Bone Meal. WM2015 Conference, March 15–19, 2015, Phoenix, Arizona, USA
- [31] J. Kim, N.S. Sambudi, K. Cho, Removal of Sr^{2+} using high-surface-area hydroxyapatite synthesized by non-additive in-situ precipitation, *J. Environ. Manage.* 231 (2019) 788–794. <https://doi.org/10.1016/j.jenvman.2018.10.100>.
- [32] R. Akkaya, Thermodynamic parameters of Ti^{+} , Ra^{2+} , Bi^{3+} and Ac^{3+} adsorption onto polyhydroxyethylmethacrylate-hydroxyapatite composite, *J. Radioanal. Nucl. Chem.* 292 (2012) 771–775. <https://doi.org/10.1007/s10967-011-1513-0>.
- [33] J. Yang, B. Volesky, Biosorption of uranium on *Sargassum* biomass, *Water Res.* 33 (1999) 3357–3363.
- [34] H.N. Tran, S.J. You, A. Hosseini-Bandegharai, H.P. Chao, Mistakes and inconsistencies regarding adsorption of contaminants from aqueous solutions: A critical review, *Water Res.* 120 (2017) 88–116. <https://doi.org/10.1016/j.watres.2017.04.014>.

H₂ storage in modified natural clinoptilolite

V. C. de Souza^{a,b}, J. Villarroel-Rocha^b, M. K. Sapag^b, S. B. C. Pergher^{a*}

^a Laboratório de Peneiras Moleculares (LABPEMOL) – Universidade Federal do Rio Grande do Norte, Campus de Lagoa Nova, Natal, CEP: 59078-900, Brasil

^b Laboratório de Sólidos Porosos (LabSoP) – Universidad Nacional de San Luis, Campus de San Luis, San Luis, CEP: 59078-900, Argentina

Abstract

Acid (HNO₃), basic (NaOH) and combined treatments on clinoptilolite natural zeolite (ZN) and treated zeolites were performed. The treated and natural materials were characterized by X-ray diffraction, X-ray fluorescence, N₂ adsorption and desorption at 77K, and CO₂ adsorption at 273K. Was possible to observe that the acid and basic treatments generate silicates and aluminosilicates. The basic treatment applied after the acid treatment favors the removal of silicates and aluminosilicates, generating an increase of the clinoptilolite proportion (from 19% to 38%). The basic treatment allowed the removal of silicon from the material, which generate a decrease of the Si/Al ratio in the material, where as the acid treatment allowed the removal of aluminum, improving the specific surface area and micropore volume of the material. The samples were evaluated in H₂ storage H₂ 77K, where the sample with acid treatment presented the best performance (1.98 mmol·g⁻¹).

Keywords: Clinoptilolite; Acid treatment; Basic treatment; Combined treatment; H₂ storage.

1. Introduction

Zeolites are materials constituted by the connection of tetrahedrons of silico-oxygen and aluminum-oxygen arranged in a crystalline structure with channels and cavities that generate voids of various shapes and sizes [1,2,3,4]. The channels make it possible for zeolite to adsorb molecules smaller than the diameter of these spaces, so zeolites are known as molecular sieves [5].

Natural zeolites occur in large quantities [2,6] and are inexpensive but are not pure (in relation to synthetic zeolites). Based on this behavior, post-synthesis treatments are used to obtain natural zeolites with better physicochemical properties and thus to extend their range of applications by joining good properties with low cost. Alternatively, acid, basic and acid-basic treatments can be used to remove impurities and amorphous material (low concentrations) from zeolitic materials and/or Si-O-Al (high concentrations) rupture because they result in efficient hydrolysis. The extraction of aluminum or silicon promotes defects in the structure, modifies the porosity of

the material and promotes ionic exchange of the cations present in the pores of the material [6, 7]. The association of acid and basic treatment is favorable to mesoporous formation in zeolitic materials [8, 9].

Alkaline treatment is very effective for zeolites with low aluminum (Si/Al between 25 - 50), which facilitates the removal of silicon, leading to the formation of mesopores (5 to 20nm) [10, 11]. For materials with Si/Al <15 ratio, aluminum prevents silicon removal, limiting the improvement of textural properties [10]. However, acid treatment may remove some of the acidity of the material that is supplied by the aluminum from the structure.

On the other hand, energy storage systems are one of the possible alternatives to respond to emerging problems related to the environmental impact caused by the use and extraction of fossil fuels. One of the proposed models of alternative energy is based on the use of hydrogen as an energy vector, i.e., as a carrier and storage of energy. The advantages of Hydrogen as fuel is that this presents as a product of its oxidation heat and water vapor, in addition, it also has a higher energy efficiency than combustion, due to these factors it is a clean fuel [12]. One of the alternatives that

have attracted considerable attention from the scientific community for hydrogen storage is based on the physisorption of hydrogen, using porous materials.

Thus, the present work aims is improve the physicochemical properties of natural zeolites by different treatments, and then evaluate the performance in H₂ storage of these materials.

2. Materials and methods

2.1. Raw Material

Natural clinoptilolite from Cuba was used, supplied by Celta Brasil, and this zeolite presented the following elemental composition: 13.13% Al₂O₃, 73% SiO₂, 4.38% CaO, 2.45% Fe₂O₃, 4.6% K₂O, 1.3% MgO, 0.4% Na₂O, 0.03% MnO, 0.32% TiO₂, 0.05% SrO, 0.03% ZrO₂, and 0.06% SO₃.

2.2. Modification of Materials

For the acid treatment was used 2g of natural zeolite (ZN) and 40mL of HNO₃ (4mol/L) under stirring at 363K and 4h obtaining the ZNac sample. For the acid-basic was used 2g of natural zeolite (ZN) and 40mL HNO₃ (4mol/L) under stirring at 363K and 4h obtaining the ZNac sample after was used 2g of ZNac 40mL of NaOH (0.1mol/L) under stirring at 323K and 0.5h obtaining the ZNacbs. For the basic treatment was used 2g of natural zeolite (ZN) and 40mL of NaOH (3mol/L) under stirring at 363K and 4h obtaining the ZNbs sample. After the treatments, the material was separated by filtration and washed with distilled water until the pH of the wash water reached approximately 7. Subsequently, the material was dried at 373K for 16h.

2.3. Characterization of Materials

X-ray diffraction analyses (XRD) were performed on a Bruker D2 Phaser diffractometer (Billerica, MA, USA). Analysis conditions: slit = 0.6nm; ACS = 1; detector = 5.82keV; time = 0.1s; step size = 0.02.

For the chemical analysis by X-ray fluorescence (XRF), a Bruker S2 Ranger (Billerica, MA, USA).

N₂ (99.999%) adsorption/desorption analyses at 77K were performed on an Autosorb-1MP manometric adsorption instrument (Quantachrome Instruments, Boynton Beach, FL, USA), using 0.3g

of the zeolites. Degassing was performed at a temperature of 353K for 48h up to 0.5Pa of final pressure. The Brunauer–Emmett–Teller (BET) method [13] was used to calculate the specific surface area (S_{BET}) of the samples from the N₂ adsorption data, taking into account the criteria proposed by Rouquerol [14]. The α_S -plot method using LiChrospher Si-1000 as reference material [15] was used to calculate the micropore volume ($V_{\mu P}$). The Gurvich rule was used to measure the total pore volume (V_{TP}) from the N₂ adsorption data obtained at a relative pressure of 0.98. From the CO₂ adsorption data obtained at 273K, the micropore volume was obtained using the Dubinin–Radushkevich (DR) method [16], and the micropore size distribution was obtained using the Horvath and Kawazoe (HK) method [17].

H₂ adsorption analyses at 77K was carried out up to 800kPa of pressure using an ASAP 2050, from Micromeritics, with zeolite mass of 0.3g and degassing at 353K for 4h.

3. Results and discussion

3.1. XRD

In Figure 1, the main reflections of the clinoptilolite phases ($2\theta = 9.9^\circ, 22.5^\circ$ and 30°). It is possible to observe that the acid treatment generate removal of aluminum that is accompanied with the appearance of other phases such as quartz, calcium and magnesium silicate and orthoclase due to the destruction of clinoptilolite (ZNac). When we apply the basic treatment after acid treatment, generate a leaching of the secondary phases of aluminosilicates and silicates resulting in an increase of clinoptilolite percentage (ZNacbs). The basic treatment remove Si and decrease %clinoptilolite in the sample (ZNbs).

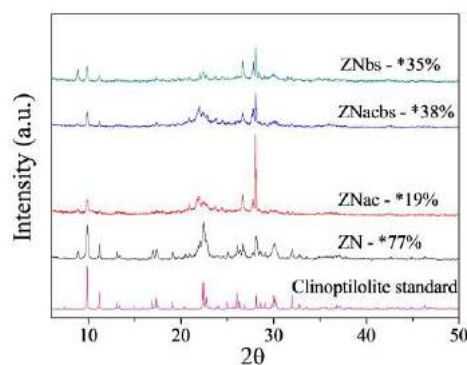


Fig. 1. XRD clinoptilolite standard, natural and treated samples. (* %Clinoptilolite)

3.2. Si/Al ratio molar

The molar ratio Si/Al can be obtained from the values of silicon and aluminum obtained from the chemical analysis. In Table 1 we can see that acid treatment generate the aluminum removal achieve an increase in molar ratio Si/Al while basic treatment generate demetallization with the preferential removal of silicon, obtain an decrease in molar ratio Si/Al

Table 1. Si/Al ratio molar for natural and treated samples.

Samples	Si/Al
ZN	4.70
ZNac	10.06
ZNacbs	9.13
ZNbs	2.60

3.3. Textural Analysis

Fig. 2 shows the N₂ adsorption/desorption isotherms for zeolites before and after treatments, where the amount adsorbed increases with the treatment, exhibiting low adsorption at low relative pressure and a hysteresis characteristic of interparticle mesopores of the aggregates present in the zeolites.. In Table 2 we can see that basic treatment increase the volume mesopore therefore the samples treated with NaOH show accessibility to larger molecules.

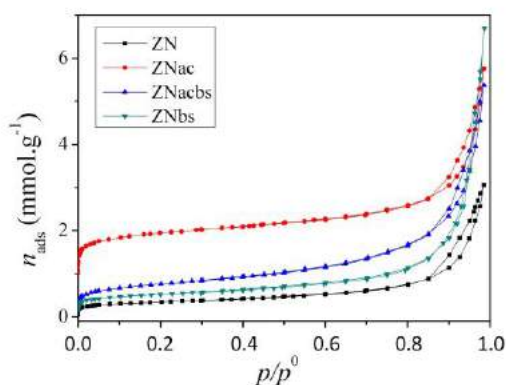


Fig. 2. N₂ adsorption and desorption isotherms at 77K for the zeolites before and after treatments.

Table 2. Textural properties for natural and treated samples.

Samples	Textural Properties				
	S_{BET} (m ² /g)	$V_{\mu P-N_2}$ (cm ³ /g)	$V_{\mu P-CO_2}$ (cm ³ /g)	V_{meso}^* (cm ³ /g)	w_p^{**} (nm)
ZN	27	0	0.05	0.10	0.40
ZNac	165	0.04	0.09	0.15	0.50
ZNacbs	62	0	0.06	0.18	0.45
ZNbs	42	0	0.04	0.22	0.40

* mesopore volume ($V_{TP} - V_{\mu P-N_2}$)

** modal micropore size

When we observe the CO₂ adsorption isotherms (which permits analyze the narrow micropores) of natural and treated materials in Fig. 3, where it can be seen that the sample treated with acid show the largest CO₂ amount adsorbed. In Table 2 we can see that the samples treated present the higher narrow micropore volume ($V_{\mu P-CO_2}$) and the sample ZNac has the largest S_{BET} value and micropore size. The sample treated with base show the micropore volume less than natural zeolite and the treatment basic applied after acid treatment also decreases the micropore volume obtained with acid treatment.

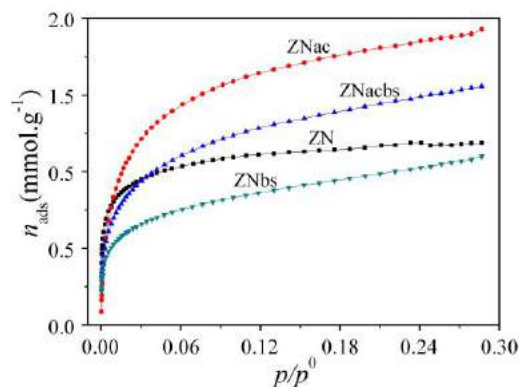


Fig. 3. CO₂ adsorption at 273K for the zeolites before and after treatments.

3.4. H₂ storage

In Fig. 4 we can see that the zeolites with basic and combined treatments exhibit a slightly improve in their H₂ adsorption capacities, whereas the zeolite with acid treatment has the highest H₂ adsorption capacity, which was to be expected since the acid-treated sample had the highest textural properties (165 m²·g⁻¹ and 0.09 cm³·g⁻¹ of specific surface area and micropore volume,

respectively). After acid treatment the sample increased H₂ adsorption capacity (at 800 kPa) from 0.17 mmol·g⁻¹ to 1.98mmol·g⁻¹, whereas that the other treated samples exhibit capacities around 0.5mmol·g⁻¹.

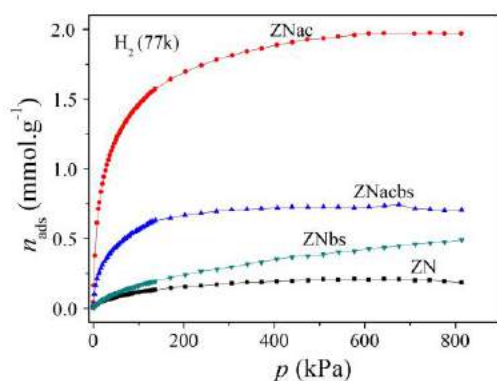


Fig. 4. H₂ adsorption at 77K before and after treatments.

3. Conclusions

Although the basic treatment improved the mesoporosity of the material, the acid treatment was the one that increased the microporosity of the material and, consequently, presented the highest H₂ storage capacity. The natural zeolite treated with HNO₃ showed promise for H₂ storage.

Acknowledgements

This study was financed in part by the Coordenação de Aperfeiçoamento de Pessoal de Nível Superior—Brasil (CAPES)—Finance Code 001; Universidad Nacional de San Luis (UNSL), Consejo Nacional de Investigaciones Científicas y Técnicas (CONICET) and Secretaría de Políticas Universitarias (SPU) from Argentina.

References

[1] Van der Geer J, Hanraads JAJ, Lupton RA. The art of writing a scientific article. *J SciComm*2000;163:51-9.
 [2] Strunk Jr W, White EB. The elements of style. 3rd ed. New York: Macmillan; 1979.
 [3] Mettam GR, Adams LB. How to prepare an electronic version of your article. In: Jones BS, Smith RZ, editors. Introduction to the electronic age. New York: E-Publishing Inc; 1999. p. 281-304.
 [1] Mascarenhas A, Oliveira E, Pastore H. Peneiras moleculares: Selecionando as moléculas por seu tamanho. *Cad.Tem.de Quím. Nov. Edição especial*, 2001; 25-34.

[2] Calvo B, *et al.* Continuous elimination of Pb²⁺, Cu²⁺, Zn²⁺, H⁺ and NH₄⁺ from acidic waters by ionic exchange on natural zeolites. *Journal of Hazardous Materials*2009; 166: 619–627.
 [3] Firas N, Yang P, Webley A. Adsorption characteristics of a fully exchanged potassium chabazite zeolite prepared from decomposition of zeolite Y. *MicMesMat*2009; 117:497–507.
 [4] Leyva-Ramos R, *et al.* Removal of ammonium from aqueous solution by ion exchange on natural and modified chabazite. *Journal of Environmental Management*2010; 91: 2662-2668.
 [5] Yeliz Y. Characterization of two natural zeolites for geotechnical and geoenvironmental applications. *Applied Clay Science*2010; 50: 130–136.
 [6] Dziejdzicka A, Sulikowski B, Ruggiero-Mikołajczyk M. Catalytic and physicochemical properties of modified natural clinoptilolite. *CatTod*2015; 259: 50–58.
 [7] Chal R, Gérardin C, Bulut M, Van Donk S. Overview and Industrial Assessment of Synthesis Strategies towards Zeolites with Mesopores. *ChemCatChem*2011; 3: 67–81.
 [8] Valtchev V, Majano G, Mintova S; Pérez-Ramírez J. Tailored crystalline microporous materials by post-synthesis modification. *ChemSocRev*2013; 42: 263.
 [9] Verboekend D, Chabaneix AM, Thomas K, Gilson JP, Javier PR. Mesoporous ZSM-22 zeolite obtained by desilication: peculiarities associated with crystal morphology and aluminium distribution. *CrystEngComm*2011; 13: 3408-3416.
 [10] Groen JC, Jansen JC, Moulijn JA, Pérez-Ramírez J. Optimal Aluminum-Assisted Mesoporosity Development in MFI Zeolites by Desilication. *J. PhysChemB*2004; 108: 13062-13065.
 [11] Pérez-Ramírez J, Christensen CH, Egeblad K, Groen JC. Hierarchical zeolites: enhanced utilisation of microporous crystals in catalysis by advances in materials design. *ChemSocRev*2008; 37: 2530–2542.
 [12] Laborde MA, Lombardo EA, Noronha FB, Boaventura Filho JA, Fierro JLG, González Marcos MP. Potencialidades del hidrógeno como vector de energía en Iberoamérica. 2010
 [13] Brunauer, S.; Emmett, P.H.; Teller, E. Adsorption of Gases in Multimolecular Layers. *JAmChemSoc*1938; 60: 309.
 [14] Rouquerol, F.; Rouquerol, J.; Sing, K. Adsorption by Powder sand Porous Solids; Academic Press: San Diego, CA, USA, 1999.
 [15] Jaroniec M, Kruk M, Olivier J. Standard nitrogen adsorption data for characterization of nanoporous silicas. *Langmuir*1999; 15; 5410–5413.
 [16] Dubinin, M.M. The Potential Theory of Adsorption of Gases and Vapors for Adsorbents with Energetically Nonuniform Surfaces. *ChemRev*1960; 60: 235.
 [17] Horváth, G.; Kawazoe, K. Method for the calculation of effective pore size distribution in molecular sieve carbon. *JChemEngJpn*1983; 16: 470–475.

Equilibrium studies of europium biosorption by dead fungal biomass

Ana Carolina Sales Pereira de Souza, Nice Vasconcelos Coimbra, Ellen Cristine Giese*

Centro de Tecnologia Mineral, Avenida Pedro Calmon 900, Rio de Janeiro, RJ, 21941-908, Brazil

Abstract

Europium is the most reactive rare-earth element. Due to their chemical and physical properties, Europium plays an essential role in the manufacture of technological products, in the development of clean technologies, in color television tubes, phosphors, and fluorescent lamps. In this way, the industrial sector has been looking for goodness processes for separation and purification of Europium. The present work aims to evaluate the biosorption process as an alternative methodology to separation of Europium from diluted solution. Four equilibrium isotherm models were used to fit the experimental data. Both Langmuir ($R^2 = 0.925$) and Freundlich ($R^2 = 0.984$) models were found able to describe the biosorption mechanism of Europium onto dead fungal biomass. Dubinin-Radushkevich model showed that this process occurs as physical adsorption ($E = 7$ kJ/mol). Temkin model ($R^2 = 0.935$) assumed that the mechanism studied was characterized by a uniform distribution of the binding energies.

Keywords: biosorption; Europium; Equilibrium studies

1. Introduction

Rare-earth elements (REEs) have received considerable attention with their increasing demands due to its technological importance [1]. Europium belongs to the REEs and only their trivalent oxidation states are stable in aqueous solutions. The trivalent europium ion is well known for its strong luminescence in the red spectral region [2].

Europium (Eu) is used mainly in the manufacture of cathode ray tubes, fluorescent lamps, and screen for X-rays; in the nuclear industry europium is used as absorbent of neutrons for the extinction and control rods of the reactors [2]. Europium presents bio-applications due to its optical properties as nanoprobe with an emphasis on their bio-detection as well as in vitro and in vivo bio-imaging [3].

The application and costs of Europium and other REEs (including the fifteen lanthanides, scandium, and yttrium) depends on their purity. Biosorption is a green technology that has been considered to recovery and separation of Europium once this bioprocess is similar to an ion-exchange mechanism [4,5]. Europium can bind to oxygen donor atom from carboxylic or phosphoric groups present in the biosorbent material [4].

Fungal biomass has been successfully employed as biosorbents for treating metals and dyes from aqueous/oil effluents. Recent studies have been developed aiming to apply the process of biosorption in the separation and recuperation of metals [6] and rare-earth elements [7].

In this paper, we examined the use of dead fungal biomass as a biosorbent of europium from a synthetic solution.

2. Methodology

2.1. Biosorption experiments

Pulverized autoclaved fungal mycelium [7] was used as a biosorbent. The biosorbent was added to 50 mL of EuNO_3 (1.0 g dry wt. cell L^{-1}) in 125 ml Erlenmeyer flasks at pH 3 in following initial concentrations: 5, 10, 25, 50, 75, 100 and 125 mg L^{-1} . The assays were conducted in a rotary shaker at 100 rpm at 30 °C for 60 min. The samples were centrifuged (15 min, 6000 rpm) and the clear supernatant was analyzed for Eu^{3+} ions by inductively coupled plasma atomic emission spectrometry (ICP-OES).

The amount of Eu sorbed by the biosorbent was calculated using the following equation:

$$Q = V(C_0 - C_f) / M \quad (1)$$

where Q is the Eu uptake (mg/g), C_0 and C_f are the initial and equilibrium Eu concentration in the solution (mg/L), respectively, V is the solution volume (L), and M is the mass of the biosorbent (g).

2.2. Isotherm modeling

Four equilibrium isotherm models were used to fit the Eu isotherm experimental data, as follows:

- 1) Langmuir equation [8] described by:

$$q_e = \frac{q_{max} K_L C_e}{1 + K_L C_e} \quad (2)$$

where q_{max} (mg/g) is the maximum amount of Eu per fungal biomass and K_L is a constant related to the affinity of the binding sites. q_e is the amount adsorbed at equilibrium (mg/g). q_{max} and K_L can be determined from the linear plot of C_e/q_e vs C_e .

- 2) Freundlich equation [9] described by:

$$q_e = K_f C_e^{\frac{1}{n}} \quad (3)$$

where q_e is the Eu uptake coefficient (mg/g), K_f is the Freundlich constant, C_e is the equilibrium concentration (mg/L) and n is a constant indicating the adsorption intensity.

- 3) Dubinin-Radushkevich (DRK) equation [10] described by:

$$q_e = q_s \exp \left[-\beta \left(RT \ln \left(1 + \frac{1}{C_e} \right) \right)^2 \right] \quad (5)$$

where q_s is the Dubinin-Radushkevich constant representing the theoretical monolayer saturation capacity, β is the constant of the adsorption energy (kJ²/mol).

- 4) Temkin equation [11] described by:

$$q_e = \frac{RT}{b} \ln (AC_e) \quad (4)$$

where R is the gas constant, T the absolute temperature (K), b is the constant related to the heat of adsorption and A is the Temkin isotherm constant

3. Results and Discussion

A biosorption isotherm, the plot of uptake (Q) versus the equilibrium sorbate concentration in the solution (C_f), is often used to evaluate the sorption performance of the biosorbent [12].

In this study, isotherm curves were evaluated by varying the initial Eu concentrations (5-125 mg/L), while fixing the equilibrium solution pH at 3.0. Fig. 1 illustrates the biosorption isotherms observed during Eu removal by fungal biomass. It can be observed that the Eu concentration in the solution and this element sorbed onto fungal biomass ratio decreases with an increase in the Eu concentration, providing a concave curve with a strict plateau.

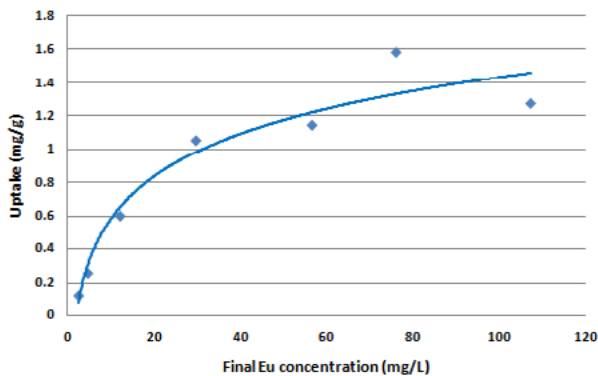


Fig. 1. Isotherm during Eu biosorption onto fungal biomass at pH 3.0.

The rare-earth elements biosorption appears generally increases with an increase in the metal concentration and reaches saturation at higher concentrations [12]. Similar behavior was observed to the rare-earth elements lanthanum (La) and samarium (Sm) biosorption by *Botryosphaeria rhodina* dead fungal biomass [7] as well to *Bacillus subtilis* free [13] and immobilized [14] bacterial cells.

Four equilibrium isotherm models were used to elucidate the equilibrium of Eu biosorption by dead fungal biomass as shown in Table 1.

Table 1. Isotherm model constants and correlation coefficients for Eu biosorption by fungal biomass.

Isotherm models		Value
Langmuir	Q_0 (mg/g)	3.39
	K_L (L/g)	20.73
	R^2	0.925
	R_L	0.954
Freundlich	K_F (mg/g)	0.085
	n	1.527
	R^2	0.984
DRK	Q_s	0.143
	K (mol/kJ) ²	2,00E-08
	E (kJ/mol)	7,07
	R^2	0.864
Temkin	B	0.372
	b_T (L/mg)	6660.14
	R^2	0.935

It was found that the experimental data fit well with both Langmuir and Freundlich models. In detail, coefficients of determination (R^2) for the Langmuir and Freundlich model are 0.925 and 0.984, respectively.

The maximum monolayer adsorption capacities of Eu on dead fungal biomass were found to be 3.39 mg/g. Corresponding n_F values, usually attributed to the adsorption intensity, was 1.527. The magnitudes of K_F and n show the easy separation of Eu^{3+} ions from diluted solution and indicate favorable adsorption onto dead fungal biomass.

The Langmuir and Freundlich isotherms are presented in Fig. 2.

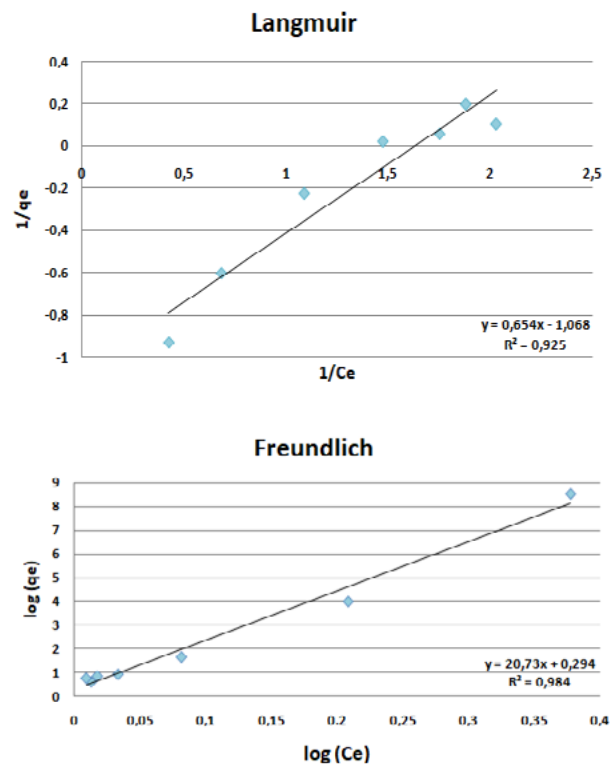


Fig. 2. Linear presentation of Langmuir and Freundlich sorption models for Eu biosorption onto dead fungal biomass.

The magnitude of E is used to estimate the reaction mechanism of the adsorption process. The E value of Eu adsorption obtained as 7 kJ/mol. This value indicates that the magnitudes of E value are in the energy range of physical adsorption. Physical adsorption of the metal ions onto the adsorbent surface implies more feasibility of the regeneration of the adsorbent [15].

The high R^2 value, given in Table 1, indicated that the experimental data fitted satisfactorily to Temkin isotherm, assuming that the Eu biosorption by dead fungal biomass is characterized by a uniform distribution of the binding energies.



4. Conclusion

Batch sorption experiments were carried out to study the effects of the initial concentration of Eu in the biosorption process on dead fungal biomass. Both Langmuir and Freundlich models were found able to describe the biosorption mechanism. Further inspection of the sorption data based on the DKR model leads to the conclusion that the physical interactions are most important in the process studied. As the physical adsorption of the metal ions onto the adsorbent surface implies more feasibility of the regeneration of the adsorbent, in turn, is a useful feature for employment of a biosorption process on a larger scale.

Acknowledgments

The authors gratefully acknowledge the National Council for Scientific and Technological Development (CNPq-Brazil) (303377/2016-0 and 403048/2018-4) - Brazil for financial support. A.C. S. P. Souza is grateful for the scientific initiation scholarship granted by CNPq/PIBITI/CETEM.

References

- [1] Balaram V. Rare earth elements: A review of applications, occurrence, exploration, analysis, recycling, and environmental impact. *Geoscience Frontiers* 2019;10(4):1285-1303.
- [2] Binnemans K. Interpretation of europium(III) spectra. *Coordination Chemistry Reviews* 2015;295:1-45.
- [3] Giese EC. Rare earth elements: Therapeutic and diagnostic applications in modern medicine. *Clinical and Medical Reports* 2018;2(1):1-2.
- [4] Giese EC, Magalhães DP, Egler SC. *Biossorção de Elementos terras-raras. Série Tecnologia Ambiental*. 1st ed. Rio de Janeiro: CETEM; 2016.
- [5] Giese EC. Prospecção de tecnologias relacionadas ao processo de biossorção de metais. *Revista Geintec: Gestão, Inovação e Tecnologias* 2019;9:5046-5057.
- [6] Muñoz AJ, Espínola F, Ruiz E, Barbosa-Dekker AM, Dekker RFH, Castro E. Assessment of by-product from *Botryosphaeria rhodina* MAMB-05 as an effective biosorbent of Pb(II). *Molecules* 2019;24:3306.
- [7] Giese EC, Dekker RFH, Barbosa-Dekker AM. Biosorption of lanthanum and samarium by viable and autoclaved mycelium of *Botryosphaeria rhodina* MAMB-05. *Biotechnology Progress* 2019;36:e2783.
- [8] Langmuir I. Adsorption of gases on plane surfaces of glass, mica, and platinum. *Journal of the American Chemical Society* 1918;40:1361-1403.
- [9] Freundlich H. Adsorption in solution. *Zeitschrift für Physikalische Chemie* 1906;57:384-470.
- [10] Dubinin LV, Zaverina MM, Radushkevich ED. Sorption and structure of active carbons I. Adsorption of organic vapors. *Zhurnal Fizicheskoi Khimii* 1947;21:1351-1362.
- [11] Temkin MJ, Pyzhev V. Recent Modifications to Langmuir Isotherms. *Acta Physiochim URSS* 1940;12:217-225.
- [12] Vijayaraghavan K, Sathishkumar M, Balasubramanian R. Biosorption of lanthanum, cerium, europium, and ytterbium by a brown marine alga, *Turbinaria Conoides*. *Industrial and Engineering Chemistry Research* 2010;49:4405-4411.
- [13] Giese EC, Jordão CS. Biosorption of lanthanum and samarium by chemically modified free *Bacillus subtilis* cells. *Applied Water Science* 2019;9:182-190.
- [14] Coimbra NV, Gonçalves FS, Nascimento M, Giese EC. Study of adsorption isotherm models on rare earth elements biosorption for separation purposes. *International Journal of Materials and Metallurgical Engineering* 2019;13:86.
- [15] Khan TA, Nazir M, Ali I, Kumar A. Removal of Chromium (VI) from aqueous solution using guar gum-nano zinc oxide biocomposite adsorbent. *Arabian Journal of Chemistry* 2017;10:S2388-S2398.

Evaluation of different adsorbents for the purification of anthocyanins from *Syzygium cumini* L.

Luiz Bruno de Sousa Sabino^a, Edy Sousa de Brito^b, Ivanildo José da Silva Júnior^a

^a Universidade Federal do Ceará (Campus universitário do Pici, Bloco 709, Fortaleza – CE, CEP 60455-760, Brazil)

^b Embrapa Agroindústria Tropical

Abstract

The aim of this work was to evaluate different adsorbents for the purification of the anthocyanins extracted from jambolan. The resins XAD-4, DOWEX, FPX-66 and the natural clays sepiolite, attapulgite and montmorillonite were tested for the adsorption and desorption capacities and for sugar removal. For the adsorption 0.05 g of each adsorbent was added to 10 mL of anthocyanins extract in 25 mL Falcon tube while agitating on an orbital vibratory shaker at 25 °C for 12 h to reach the adsorption equilibrium. For desorption, acidified ethanol (80% v/v and 0.01% HCl) were employed as eluent and the desorption capacity was evaluated in 30, 60 and 90 min. Sugar removal was evaluated considering the initial concentration of the crude extract. Among the resins Dowex presented the highest adsorption capacity ($Q_e = 45.0$ mg/g) followed by FPX-66 (37.4 mg/g). Between the clays, attapulgite presented the highest Q_e (32.61 mg/g). FPX-66 presented the highest desorption capacity ($Q_d = 46.56$ mg/g) and this result was obtained in the lower time of desorption evaluated (30 min). For the sugar removal, the decrescent order was: FPX-66 (99.0%) > Dowex (86.0%) > XAD-4 (85.0%) > montmorillonite (42.83%) > attapulgite (41.5%) > sepiolite (22.8%). The mass spectra showed no difference in anthocyanins the quality of both crude and purified extract. However, it was possible to notice a spectrum free of interferents after the purification of the crude extract with FPX-66. This work suggests the use of FPX-66 to obtain a purified anthocyanin extract due its higher adsorption and desorption capacities and, mainly, due its excellent capacity of sugar removal. This is a prelaminary study and a first step for the scale up purification process of anthocyanins extracted from jambolan.

Keywords: anthocyanins; adsorbents; resin; clays.

1. Introduction

Jambolan is the fruit of the *Syzygium cumini* L. (Syn. *Eugenia jambolana* Lam.; *Eugenia cumini* Druce) trees, widely distributed in Asia and Latina America. The fruit is recognized by its medicinal properties (e.g. diuretic, antidiabetic, antioxidant and antiproliferative actions), which is related to phenolic composition, including phenolic acids, flavones, flavonoids, and anthocyanins [1].

Anthocyanins play an important role in physical and sensorial properties of jambolan. They are responsible for its intense purple color and remarkable exotic flavor [1]. Chemically, anthocyanins are glycosylated polyhydroxy and polymethoxyderivatives of 2-phenylbenzopyrylium (flavylium) salts. In nature, anthocyanins are responsible for the red, orange, blue or purple colors in several fruits, vegetables and. Previous reports showed that the anthocyanin profile in jambolan is marked by the presence of different diglucosides aglycones deriving from cyanidin-3,5-diglucosides, delphinidin-3,5-diglucosides, malvidin-3,5-

diglucosides, peonidine-3,5-diglucosides and petunidine-3,5-diglucosides [2].

Anthocyanins are water-soluble and non-toxic pigments, becoming promising candidates for industrial application as food colorants or in the pharmaceutical industry for tablet/capsule coatings, syrups, health concentrates and as supplements [2].

Extraction methods of anthocyanins from plant material are non-selective and yield pigment solutions with large amounts of other compounds such as sugars, sugar alcohols, organic acids, amino acids and proteins which are detrimental to stability of pigments.

Stability of colorants is strongly influenced by sugars, light, oxygen, pH, temperature and UV-light [1]. The free sugars and their degradation products in the anthocyanins extract lead to the milliard reaction and form brown compounds. Hence, removal of sugars from anthocyanins extract is very such desirable for the stability of these pigments and also to facilitate their application in food processing.

The separation of anthocyanins from plants has been studied using high-speed counter-current chromatography (HSCCC), preparative high-

performance liquid chromatography (HPLC) solid-phase extraction (SPF) and so on [3]. However, these methods are fraught with several disadvantages, in that they are time-consuming, laborious, expensive with poor recovery, and unsuitable for large-scale industrial production. stability of these pigments and also to facilitate their application in food processing. Adsorption is an effective method for purification of bioactive components in a single step. Different adsorbents were reported for the separation of anthocyanins from crude vegetable extracts [4].

Resin adsorption technology is being explored to concentrate polyphenols and to remove sugars (Synthetic resins allow adsorption of polyphenols from aqueous solution via hydrophobic binding and aromatic stacking. They desorb phytochemicals in organic solvents, such as methanol or ethanol. Because sugars do not interact with resins, they can be easily removed by water elution. Clay is a natural, low cost material that plays an important role as an alternative adsorbent medium. It has been used to remove contaminants, such as dyes, from industrial effluents. When dispersed in water, clays are prone to form a colloidal dispersion mainly due to their small particle sizes [5].

Considering the large number of research reports being available in the literature on enormous medicinal and food applications, there is a paucity of information regarding the purification of jambolan anthocyanins by any method especially by adsorption. Thus, the aim of this work was evaluating the use of different adsorbents for a partial purification of the crude extract obtained from jambolan fruit, bringing valuable information for the scale-up process and application of natural pigments in different industrial fields.

2. Materials and Methods

2.1. Materials

2.1.1 Chemicals

Ethanol (99%), acetone, methanol and trifluoroacetic acid were obtained from Sigma Aldrich (Saint Louis, USA), HPLC grade acetonitrile and methanol from J.T. Baker (Pennsylvania, USA), and Milli-Q grade water was obtained from Millipore Lab. (Bedford, Massachusetts, USA). The resin XAD-4, was obtained from Sigma Aldrich (Saint Louis, USA Sepiolite), DOWEX and FPX-66 from Lenntech (Miami, USA). Sepiolite, montmorillonite and

attapulgitite clays were obtained from the La Serrata de Nijar deposits and the Madrid Basin. The characteristics of the adsorbents evaluated in this work are present in Table 1. All the other chemicals were analytical grade.

Table 1- Polarity and average pore diameter of the adsorbents

Adsorbent	Polarity	Average pore diameter (nm)
XAD-4	Moderate polarity	5.80
DOWEX	Strong polarity	9.00
FPX-66	Non-polar	25.0
Sepiolite	Polar	4.18
Attapulgitite	Strong polarity	8.30
Montmorillonite	Polar	3.00

2.2 Plant material

The jambolan fruits were obtained from a domestic organic cultivar in Cascavel city (Ceará state, Brazil). The selection of the fruits was based on the intense violet color of the epicarp, which is an indicative of their complete maturity. The seeds were manually removed and edible portions (peel and pulp) were freeze dried using a Labconco Freeze Dry-5 dryer (Missouri, USA) at -50 °C under pressure of 0.6 Pa and vacuum for 48 h. After drying, the sample was crushed in a porcelain mortar and sieved on a 700 µm screen to obtain a powder. Jambolan powder was stored under refrigeration (-5 °C) in polyethylene bowls until the analysis.

2.2. Methods

2.2.1 Anthocyanins extraction

A QR500 probe ultrasound extractor (Ultronique, Brazil, 20 kHz) coupled with a 13 mm titanium tip was used to extract the ACNs. Aqueous ethanol solution (80% v/v) acidified with TFA acid (0.1% v/v) was used as solvent. Vegetal material and solvent were mixed in a 250 mL jacketed beaker (proportion fruit:solvent was 1:15 w/v) and subjected to ultrasound. The temperature was controlled with a thermostatic water bath (30 °C ± 0.1) through the beaker jacket. The ultrasound power (300 W) and extraction time (7.5 min) were controlled. After, the extract was filtered and the

solvent removed in a R-215 rotavapor (Bunch, Flawil, SWI) at 40 °C.

The anthocyanins concentration in the extract was estimated using pH differential method, employing the following equation:

$$AntT = \frac{A \times Mw \times DF \times 1000}{\epsilon \times l}$$

where A = [(A530–A700) pH 1.0 – (A530–A700) pH 4.5], Mw the molecular weight of anthocyanins (449.2 g/mol), DF is the dilution factor, ϵ is the extinction coefficient (26,900 L/cm mol) and l is the path length (1 cm). Absorbance at 530 and 700 nm was measured using UV–VIS spectrophotometer Biomate 3 (Thermo Scientific, EUA).

2.2.2 Static adsorption and desorption tests

The adsorbents (0.05 g dry weight) was added to 10 mL of anthocyanins extract in 25 mL Falcon tube while agitating on an orbital vibratory shaker at 25 °C for 12 h to reach the adsorption equilibrium. After adsorption, filtration was completed, and the filtrate was subjected to further analysis. After reaching the adsorption equilibrium, the resins and the clays were washed with deionized water for 2–3 times and then desorbed with 20 mL 80% ethanol (acidified with 0.01% of HCl) in a 25 mL Falcon tube while agitating on an orbital vibratory shaker for 30 min to reach the desorption equilibrium. The content of anthocyanins was then measured using the pH differential method.

The adsorption capacity was quantified as follows:

$$Q_e = \frac{(C_o - C_e) \times V_i}{W}$$

$$Q_{re} = \frac{(C_o - C_e)}{C_o} \times 100\%$$

where C_o and C_e are the initial and equilibrium concentrations of anthocyanins in the solution, respectively (mg/g); Q_e represents the adsorption capacity at adsorption equilibrium (mg/g dry resin); V_i is the volume of the initial sample solution (mL); W is the dry weight of the tested resins (g); Q_{re} (%) is the adsorption ratio.

The desorption capacity was quantified as follows:

$$Q_d = \frac{(C_d \cdot V_d)}{W}$$

where C_d is the concentration of solutes in the desorption equilibrium solution (mg/mL); Q_d is the desorption capacity after desorption equilibrium (mg/g dry resin); V_d is the volume of the desorption solution (mL).

2.2.3 Sugar concentration

The Dubois method was used for the estimation of total sugars present in the extract before and after purification process according to equation; Glucose was used as a standard for the determination of sugars (DUBOIS, GILLES, HAMILTON & REBERS, 1956).

2.2.4 Anthocyanins identification

The identification of the anthocyanins presented was performed using UPLC-ESI-QTOF-MS (Waters, USA) system. For each method, the ethanolic extract with the higher concentration of anthocyanins was evaluated. A C18 column (150 mm × 2.1, 1.7 μ m) Waters (USA) was used at a flow rate of 0.4 mL.min⁻¹ at 40 °C and injection volume of 5 μ L. The eluent was the combination of acidified water (0.1% of formic acid) and acidified acetonitrile (0.1% formic acid). The gradient varied linearly from 5 to 95% acetonitrile (v/v) in 15 min. The mass spectra were acquired using positive electrospray ionization at 80 V fragmentation tension for 100–1000 m/z. Drying gas pressure of 241 kPa, spray gas pressure of 275 kPa, drying gas temperature of 370 °C, capillary tensions of 3500 V and spray shield tension of 600 V were used. The LC system was coupled to the MS detector with a 50% split.

2.3 Statistical analysis

The statistical analysis was performed using software Statistica version 10 (Stat Soft Inc., Oklahoma, USA). The experiments were carried out in triplicate and the data were described as means \pm SD (standard deviation). The analysis of variance (ANOVA) and the effect and regression coefficients of individual linear, quadratic and interaction terms were determined.

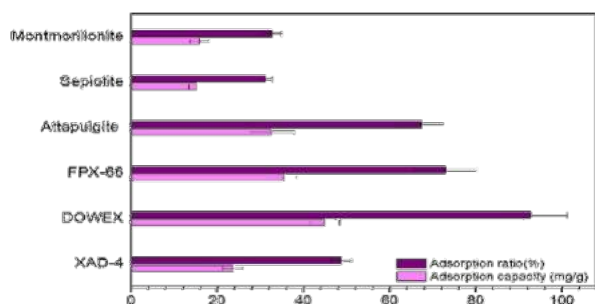
3. Results and Discussion

In our study was used a jambolan crude extract with an initial concentration of anthocyanin and sugar equal to 0.24 mg/g and 2.44 g/L, respectively. These information were considered for the eventual measurements regarding the adsorption and desorption values.

3.1. Static adsorption and desorption capacities

The adsorption capacity (mg/g) and adsorption rate of the different adsorbents evaluated is shown in Figure 1.

Figure 1 - Adsorption capacity and adsorption ration of the adsorbents evaluated for purification of anthocyanins extracted from jambolan



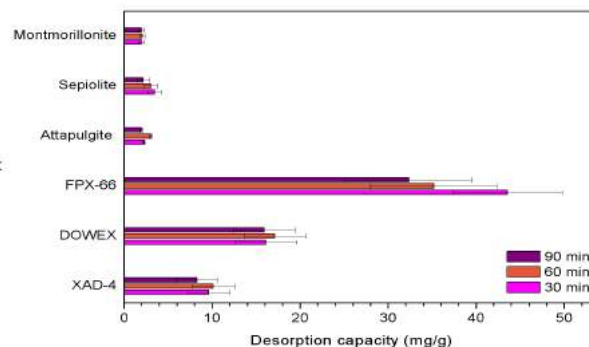
Among the resins Dowex presented the highest adsorption capacity ($Q_e = 45.0$ mg/g) followed by FPX-66 (37.4 mg/g) and XAD-4 ($Q_e = 23.6$ mg/g). The higher Q_e observed for Dowex can be attributed to its strongly acidic cation exchanger adsorption mode. In general, the group of clays exhibited an adsorption capacity lower than resins group, except for attapulgite that presented both Q_e (32.61 mg/g) and Q_{re} (67.4 %) higher than XAD-4. That result can be explained once the polarity and pore size of the attapulgite is higher than XAD-4, which facilitates the adsorption of the anthocyanins. In addition, previous research suggested that the surface area in combination with pore size were the determining factors in predicting the adsorption capacity [4].

The desorption was evaluated in 30, 60 and 90 min. The results are shown in Figure 2.

Between all the adsorbents evaluated FPX-66 presented the higher desorption capacity, reaching its highest value at 30 min of experiment ($Q_d = 46.56$ mg/g). As present in Table 1, FPX-66 are a non-polar adsorbent. Polarity was one of the most significant variables that affected the desorption

capacity of resin. Thus, the higher the polarity of resin, the weaker the desorption capacity, which can explain the higher Q_d from FPX-66 compared to Dowex [6]. In addition, the large particle size of FPX-66 which tends to have higher mass exchange rates and allows more material to be transferred to and from the resin, thereby increasing the desorption ratio and recovery. The extremely low recovery of anthocyanins observed for the clays group may be attributed to an irreversible adsorption of these molecules in clays layers. At 60 min the values of Q_d were 3.05 mg/g for attapulgite and sepiolite and 2.08 for montmorillonite.

Figure 2 - Desorption capacities of the adsorbents evaluated for purification of anthocyanins extracted from jambolan



In general, it was observed that the desorption decreased after 60 min of experiment for all adsorbents evaluated. The result can be attributed to the degradation of the anthocyanins due the longer exposition to the acidified media.

3.2 Sugar removal

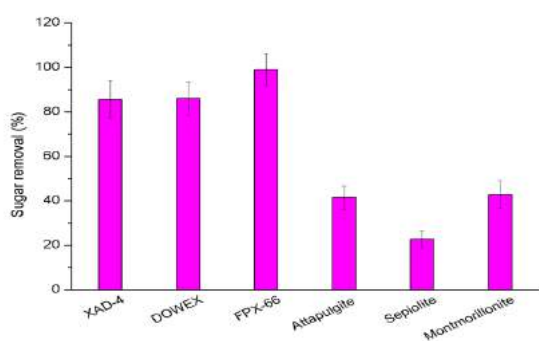
Extraction process is not a selective technique and usually a large content of sugar and organic acids are extracted with the anthocyanins. The sugar concentration in the crude vegetable extracts are the main problem in the maintenance of anthocyanins stability. Thus, the removal of total sugar is required when prospect the use of anthocyanins for industrial applications

Based in the initial concentration (2.44 g/L) the Figure 3 shows the sugar removal capacity of the adsorbents evaluated in this work. The sugar concentration was measured after 30 min of desorption (the minimal time evaluated for desorption capacity).

The capacity of removal the sugar followed the decrescent order: FPX-66 (99.0%) > Dowex

(86.0%) > XAD-4 (85.0%) > montmorillonite (42.83%) > attapulgite (41.5%) > sepiolite (22.8%). FPX-66 demonstrate a good selectivity for anthocyanins, removing almost 100% of the sugar content in the initial extract after the purification process. This result, supported by the adsorption and desorption capacities, point FPX-66 as promising adsorbent for obtaining purified anthocyanins.

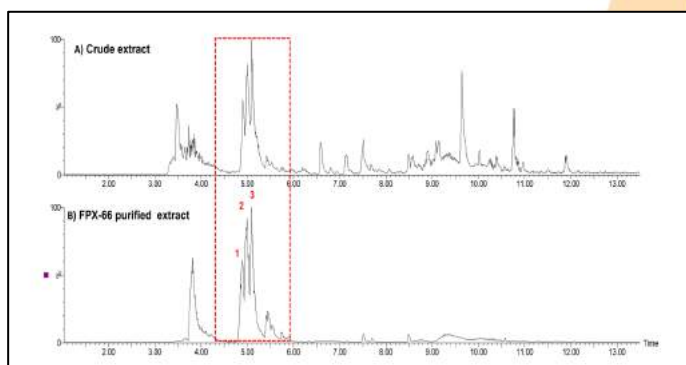
Figura 3 - Sugar removal capacity



3.3 Anthocyanins identification

Three major anthocyanins were identified in the crude and purified extracts. From Figure 3A-B it is possible to check the peak identified as: (1) delphinidin, (2) petunidin, and (3) malvidin (Fig. 5D-F). These results were corroborated by previous works [7]. As is possible to check in the Figure 3, the mass spectrum obtained after the purification of the extract with FPX-66 are cleaner with less interfering compared to crude extract spectrum. Even the anthocyanins profile was not influenced by the purification process, FPX-66 demonstrated be able to reduce the sugar content and other contaminants, resulting in an extract able to be used in sequential process.

Figure 4 - Mass spectra of anthocyanins crude (A) and purified (B) extracts.



4. Conclusion

The bath purification of anthocyanins was studied employing different adsorbents. FPX-66 showed a great adsorption and desorption capacities and removed 99% of the sugars present in the crude extract. This is a preliminary study, that aimed verify the potential of different adsorbents for the purification of anthocyanins and indicates FPX-66 resin for sequential recovery process of these pigments.

Acknowledgements

The authors are grateful to Funcap for providing financial support for this research.

References

- [1] Aqil, F., Gupta, A., Munagala, R., Jeyabalan, J., & Kausar, H. (2012). Antioxidant and Antiproliferative Activities of Anthocyanin / Ellagitannin-Enriched Extracts From *Syzygium cumini* L. (Jamun , the Indian Blackberry). *Nutrition and Cancer*, 64(October), 428–438.
- [2] Faria, A. F., Marques, M. C., & Mercadante, A. Z. (2011). Identification of bioactive compounds from jambolão (*Syzygium cumini*) and antioxidant capacity evaluation in different pH conditions. *Food Chemistry*, 126(4), 1571–1578.
- [3] Castañeda-ovando, A., Pacheco-hernández, M. D. L., Páez-hernández, M. E., Rodríguez, J. A., & Galán-vidal, C. A. (2009). Chemical studies of anthocyanins : A review. *Food Chemistry*, 113(4), 859–871.
- [4] Pu Jinga, Si-Yu Ruan, Ying Dong, Xiao-Guang Zhang, Jin Yuea, Jian-Quan Kanc, Margaret Slavina, Liangli Yua, Optimization of purification conditions of radish (*Raphanus sativus* L.) anthocyanin-rich extracts using chitosan, *LWT – Food Science and Technology* 44 (2011) 2097–2103.
- [5] Baik, M.H., Lee, S.Y., 2010. Colloidal stability of bentonite clay considering surface charge.
- [6] Buran, T.J., Sandhu, A.K., Li, Z., Rock, C.R., Yang, W.W., Gu, L., 2014. Adsorption/desorption characteristics and separation of anthocyanins and polyphenols from blueberries using macroporous adsorbent resins. *J. Food Eng.* 128, 167–173.
- [7] Veigas, J. M., Narayan, M. S., Laxman, P. M., & Neelwarne, B. (2007). Chemical nature, stability and bioefficacies of anthocyanins from fruit peel of *syzygium cumini* Skeels. *Food Chemistry*, 105(2), 619–627.
<https://doi.org/10.1016/j.foodchem.2007.04.022>

Protease immobilization onto graphene oxide via adsorption: a preliminary study

Paula Valéria Viotti^a, Wardleison Martins Moreira^a, Paulo Waldir Tardioli^b, Marcelo Fernandes Vieira^{a*}

^a Department of Chemical Engineering, State University of Maringá, Av. Colombo, 5790, Maringá, CEP 87020-900, Brazil

^b Department of Chemical Engineering, Federal University of São Carlos, Rodovia Washington Luiz, Km 235, São Carlos, CEP 13565-90, Brazil

Abstract

The biocatalysis are extremely important in the industrial scenario and are constantly discussed and emphasized through the need of essential technologies that viabilize the enzyme immobilization. Consequently, their commercialization and industrial usage will be promoted. In front of the stated, the present work aimed to primarily investigate the chymotrypsin immobilization onto graphene oxide by adsorption. Initially, the graphene oxide was synthesized and morphologically characterized by SEM and the pH point of zero charge. Then, the immobilization was performed with a support mass of 0.01 g, at pH 7 and 298 K. The immobilization was tracked for 24 hours by varying the initial protein loading from 0 to ≈ 200 mg of protein/g of support. The adsorption was found to occur rapidly, achieving the equilibrium, for most of the assays, within 4 hours. Moreover, the adsorption kinetics revealed that the highest adsorption rate occurred during the first hour of the process. Analyzing the graphene oxide loading capacity study, the maximum adsorption capacity of chymotrypsin in graphene oxide was 203.3 mg g^{-1} . Thus, almost all the enzyme offered was immobilized, showing the high specific area of the support, as well as its interaction with the enzyme. Finally, the preliminary results showed a great adsorption capacity, revealing the graphene oxide is a potential support for enzymatic immobilization.

Keywords: Chymotrypsin immobilization; Graphene oxide; Protease adsorption

1. Introduction

Thankful to the microbiology technological advances in engineering, the industrial application of enzymes, as well as the protein engineering and the chemistry, environment and economic development, have exploded in recent years.

Enzymes are catalysts with excellent properties, such as high activity, selectivity and specificity. Once they operate under a less severe operating conditions, they offer much more competitive processes when compared to the chemical catalysts [1, 2]. However, their use in their natural free form is limited by the difficulty in their recovery and stability over a long period of time. As a result, enzyme immobilization techniques can be powerful tools to improve, diversify and disseminate the enzyme industrial applications [3].

Among all the immobilization methods, the adsorption process on an insoluble support is the most widely used [4, 5]. The adsorption accounts not only for the physical interactions between the

enzyme and the support, but also include the chemical linkage, including the weak bonding forces, such as van der Waals, the electrostatic interactions and the strong hydrogen bonds. The adsorption process do not alter the enzymes conformation, preservation their structure [6].

In the enzymatic immobilization process onto a solid support, the support choice ends up being a determining factor in the process cost. Among the supports used in the immobilization process, the graphene oxide appears as a potential source, which has not been extensively studied yet.

Graphene oxide (GO) is a nanomaterial that has been the subject of numerous studies and applied in several areas of research. It consists in a two-dimensional structure of sp^2 hybridized carbon atoms [7], which also contains oxygenated groups (hydroxyl, epoxy and carboxyl) within its structure's terminal sites. Its outstanding applications are not only due to its excellent properties, such as high specific surface area, good mechanical resistance and thermal stability [8], but also due to the presence of

oxygenated functional groups, which provides various binding sites with external molecules. All in all, those features increased the GO potential as a support with ideal properties for the enzyme immobilization.

This work aims to primarily investigate the chymotrypsin immobilization onto graphene oxide via adsorption, aiming to evaluate the support protein load capacity.

2. Experimental

2.1 Materials

α -Chymotrypsin from bovine pancreas (EC 3.4.21.4), type II, lyophilized, and N-Benzoyl-L-Tyrosine ethyl ester (BTEE) were purchased from Sigma Aldrich.

2.2 Synthesis and characterization of GO

In this study, graphene oxide (GO) was synthesized through a modified Hummers method [9] and used as a solid support for enzyme immobilization.

GO morphological investigation was performed in by the Scanning Electron Microscopy (SEM), in FEI Quanta 250 (ThermoFisher Scientific) equipment. Prior to analysis, GO was oven dried for 24 hours and covered with a thin layer of gold.

The GO pH point of zero charge (pH_{pzc}) was obtained according to a methodology adapted [10]. The analysis was conducted by adjusting the pH of 25 mL of 0.01 mol L⁻¹ KCl solution from 2 to 12 and adding 25 mg of GO in each obtained solution. The suspensions were agitated at 150 rpm, in a thermostatic bath at 298 K for 24 hours.

2.3 Chymotrypsin immobilization by adsorption

For the chymotrypsin adsorption onto GO, an enzyme solution was initially prepared in a 5 mM phosphate buffer (low ionic strength), at pH 7. Then, the support was added to the flask containing the enzyme solution, and the suspension was maintained at 298 K in an orbital shaker. The immobilization was performed by using 0.01 g of GO ranging from 0 to \approx 203 mg protein/g GO. During the process, the disappearance of the enzyme activity and protein content of the supernatant were measured to monitor the adsorption kinetics. The immobilized enzyme was finally washed, vacuum filtered and stored at 277 K.

2.4 Determination of immobilization parameters

The kinetic immobilization was accompanied by the protein concentration of the supernatant solution measured by Bradford's methodology [11]. To quantify protein content, a calibration curve was made using Bovine Serum Albumin (BSA) as standard.

Adsorption capacity, q_t (mg g⁻¹), was calculated by equation below:

$$q_t = \frac{(C_0 - C_t) V}{m}$$

Where C_0 e C_t (mg mL⁻¹) are initial protein concentration and at time t of supernatant solution), respectively, V (mL) is the volume of enzyme solution and m (g) is the mass of GO used. Enzymatic activity was measured by the increase in absorbance at 258 nm due to hydrolysis of synthetic substrate, BTEE, at pH 7 and 298 K. One unit (U_{BTEE}) will be defined as hydrolysis of 1 μ mol BTEE per minute under the conditions described.

3. Results and discussion

3.1 Characterization of GO

GO was characterized by determining its pH_{pzc} (Fig. 1) and by SEM (Fig. 2).

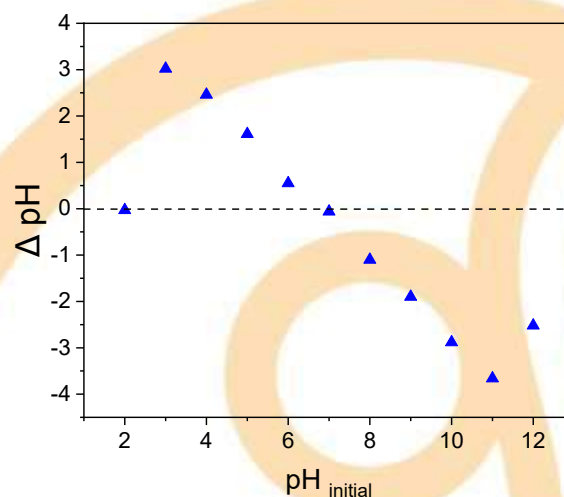


Fig. 1. GO pH_{pzc}.

The pH_{pzc} was determined in order to identify the density electric charges on the surface of the GO. The result of analysis is presented in Fig. 1, which plotted the graph of Δ pH. Fig. 1 shows that at pH 7 the positive and negative charges cancel

each other out so that the surface of the material is neutral. This indicates that at pHs less than 7, the surface of the GO is mostly positive, and at pHs greater than 7, the surface is mostly negative.

The presence of oxygenated functional groups in GO structure can provide various binding sites with external molecules. Immobilization was performed at pH 7, since the surface of the support is neutral, which facilitates the adsorption. At pH 7, the carboxylic groups present in the GO structure are dissociated ($pK_a \approx 4.8$), as well as amino terminal groups present in the enzyme are protonated ($pK_a \approx 9$). Thus, the electrostatic interaction may be one of the mechanisms present in the adsorption.

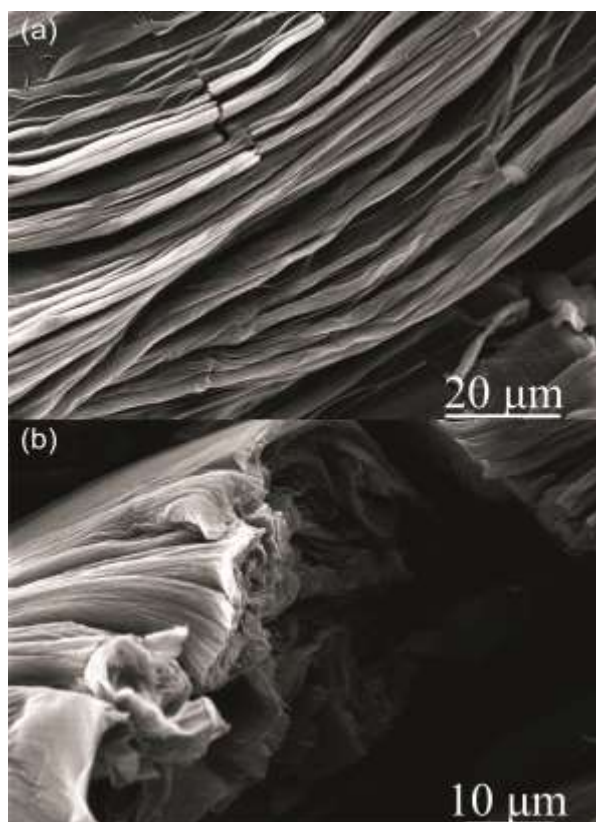


Fig. 2. Scanning Electron Microscopy of GO at 4000 x magnitude (a) and 6000 x magnitude (b).

Graphite oxide (grapheme oxide before exfoliation) is a multilayer material formed by the controlled oxidation of graphite [12]. The Fig.2 clearly shows this characteristic, which confirms the synthesis of graphene oxide.

3.2 Effect of initial protein loading

Enzyme immobilization was performed by varying the initial protein load offered (0 to ≈ 203 mg protein/g support), and the protein content of the supernatant was monitored for 24 hours. The evaluation of chymotrypsin adsorption capacity in GO is presented in Fig. 3.

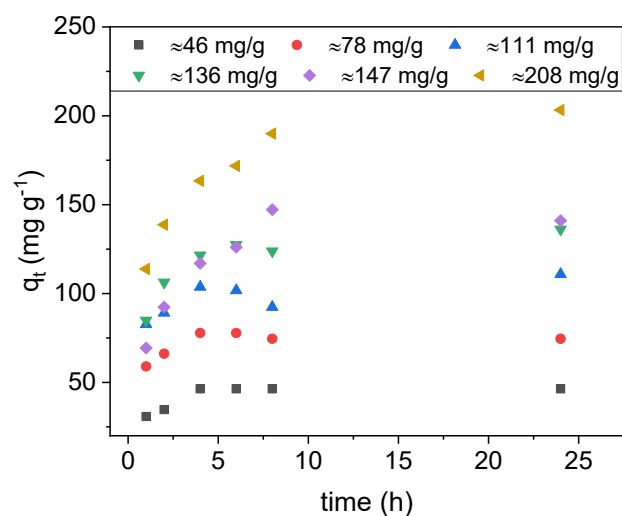


Fig. 3. Evaluation of chymotrypsin adsorption capacity in GO.

As expected, at the beginning of adsorption there are many active sites available for ion exchange. Fig. 3 shows for all initial protein loads offered, adsorption occurs more rapidly in the first hour of processing, slowly decreasing over time. For most cases, adsorption reaches equilibrium until 4 hours.

The adsorption capacity of the enzyme in GO is proportional to the initial protein load offered, once all enzyme available in the medium has been adsorbed. This result suggests that the GO has a great chymotrypsin adsorption capacity, being possible to further increase the enzymatic concentration in the support.

Despite the high protein loading capacity that can be immobilized, the molecular diffusion problems can be a difficulty in the industrial application of the biocatalyst.

There are few studies in the literature that study the immobilization of chymotrypsin, mainly via adsorption. The Table 1 shows some studies about chymotrypsin immobilization, as well as the supports used.

Table 1. Chymotrypsin immobilization studies.

Support	Enzymatic immobilization method	Reference
Magnetic chitin nanofiber composite	Covalent immobilization	[13]
Calcium alginate beads	Encapsulating	[14]
Amine-functionalized magnetic nanogel	Covalent immobilization	[15]
Aldehyde-agarose gels	Covalent immobilization	[16]

4. Conclusion

In this study we evaluated the adsorption capacity of chymotrypsin in graphene oxide. The synthesis of GO was well performed, characterizing the support morphologically and in relation to the density of electric charges of its surface. The immobilization was performed at the zero load point of the support, since at this pH the adsorption is facilitated. Adsorption occurred very quickly in the first hour of the process, and in most cases was in equilibrium within the first 4 hours. The maximum adsorption capacity found was 203.35 mg g⁻¹. However, the results suggest that higher adsorption can be achieved by increasing the initial protein load offered. Therefore, due to its high adsorption capacity and good mechanical and thermal resistance, GO can be considered the great support in chymotrypsin immobilization.

Acknowledgements

The authors would like to thank Higher Education Personnel Improvement Coordination (CAPES) for financial support.

References

[1] Mateo C, Palomo JM, Fernandez-Lorente G, Guisan JM, Fernandez-Lafuente R. Improvement of enzyme activity, stability and selectivity via immobilization techniques. *Enzyme Microb Technol* 2007;40:1451-1463.

[2] Choi JM, Han SS, Kim HS. Industrial applications of enzyme biocatalysis: Current status and future aspects. *Biotechnol Adv* 2015;33:1443-1454.

[3] Sheldon RA., Van Pelt S. Enzyme immobilisation in biocatalysis: why, what and how. *Chem Soc Ver* 2013;42:6223-6235.

[4] Christopher LP, Kumar H, Zambare VP. Enzymatic biodiesel: Challenges and opportunities. *Appl Energy* 2014;119:497-520.

[4] Pourzolfaghar H, Abnisa F, Daud WMAW, Aroua MK. A review of the enzymatic hydroesterification process for biodiesel production. *Renew Sust Energ Ver* 2016;61:245-257.

[6] Johnvesly B, Naik GR. Studies on production of thermostable alkaline protease from thermophilic and alkaliphilic *Bacillus* sp JB-99 in a chemically defined medium. *Process Biochem* 2001;37:139-144.

[7] Geim AK., Novoselov KS. The rise of graphene. *Nat. Mater* 2007 6:183-191.

[8] Xing HT, Chen JH, Sun X, Huang YH, Su ZB, Hu SR, Weng W, Li SX, Guo HX, Wu WB, He YS, Li FM, Huang Y. NH₂-rich polymer/graphene oxide use as a novel adsorbent for removal of Cu(II) from aqueous solution. *Chem Eng J* 2015;263:280-289.

[9] Hummers WS, Offeman RE. Preparation of graphitic oxide. *J Am Chem Soc* 1958;80:1339-1339.

[10] Tran HN, You S, Chao H. Effect of pyrolysis temperatures and times on the adsorption of cadmium onto orange peel derived biochar. *Waste Manag Res* 2016; 34: 129-138.

[11] Bradford MM. A rapid and sensitive method for the quantitation of microgram quantities of protein utilizing the principle of protein-dye binding. *Anal. Biochem* 1976;72:248-254.

[12] Stankovich S, Dikin DA, Dommett GHB, Kohlhaas KM, Zimney EJ, Stach EA, Piner RD, Nguyen ST, Ruoff RS. Graphene-based composite materials. *Nature* 2006;442:282-286.

[13] Huang W, Wang W, Xue C, Mao X. Effective Enzyme Immobilization onto a Magnetic Chitin Nanofiber Composite. *ACS Sustain Chem Eng* 2018;6:8118-8124.

[14] Abd El-Ghaffar MA, Hashen MS. Calcium alginate beads encapsulated PMMA-g-CS nano-particles for α -chymotrypsin immobilization. *Carbohydr Polym* 2013;92:2095-2102.

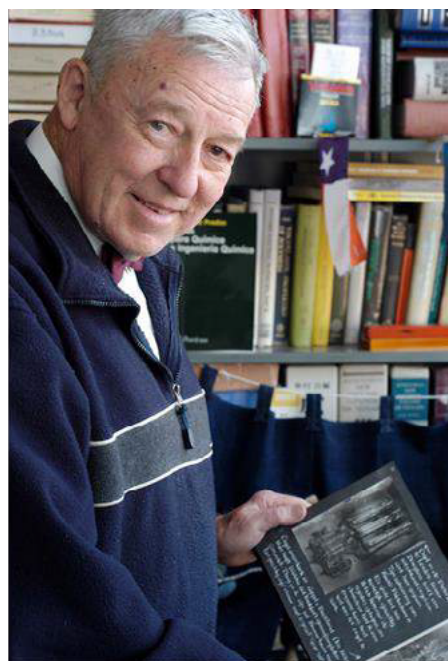
[15] Hong J, Gong P, Xu D, Dong L, Yao S. Stabilization of α -chymotrypsin by covalent immobilization on amine-functionalized superparamagnetic nanogel. *J Biotechnol* 2007;128:597-605.

[16] Guisán JM, Bastida A, Cuesta C, Fernández-Lafuente R, Rosell C M. Immobilization-stabilization of α -chymotrypsin by covalent attachment to aldehyde-agarose gels. *Biotechnol Bioeng* 1991;38:1144-1152.

In memory of two great ones



Francisco Rodríguez Reinoso
Universidade de Alicante - Spain
Aug 25, 2020 (aged 79)



Robert "Bob" Byron Bird
University of Wisconsin-Madison
Nov 13, 2020 (aged 96)